

Appendices provided on accompanying CD

Appendix A: Wall Design Memo	A-1
Appendix B: Site Piezometric Data	A-28
Appendix C: Site Moisture Content Data	A-32
Appendix D: Site and Vicinity Meteorological Data	A-66
Appendix E: Wall Construction and Installation of Field Instrumentation	A-70
Appendix F: Field Inclinator Data	A-113
Appendix G: Strain Gauge Data	A-260
Appendix H: Earth Pressures vs. Displacements	A-292
Appendix I: Finite Element Analysis	A-302
Appendix J: Finite Difference Analysis	A-306
Appendix K: Student Theses and Dissertation	A-434

APPENDIX A: WALL DESIGN MEMO

A.1: Background

The objective of this research project is to provide TxDOT with guidance for the design of drilled shaft retaining walls in expansive clay soils. The research will involve instrumenting a full-scale drilled shaft retaining wall constructed in an expansive clay soil and monitoring its performance over three years. The project site is located at R&L Transfer & Storage, 13806 Old Highway 20, Manor, Texas.

The purpose of this document is to describe the wall and provide the basis for its design.

A.2: Wall Description

The wall consists of 25 drilled shafts with a diameter of 24 inches and spaced 30 inches on center (Figure A.1). The wall will support a 15-foot deep excavation (Figure A.2 and Figure A.3). Each shaft will include 12 No. 7 reinforcing bars (Figure A.4). Three shafts will be instrumented with inclinometers and optical strain gauges (Figure A.5). The total length of shaft is 835 lineal feet, with 735 lineal feet of drilling (Table A-1).

Table A-1: Length of Individual Shafts

Shaft Designations	1-2, 24-25	3-4, 22-23	5-7, 19-21	8-18	Totals
Number of Shafts	4	4	6	11	25
Shaft Length (ft)	22	27	35	39	835
Shaft Penetration (ft)	18	23	31	35	735

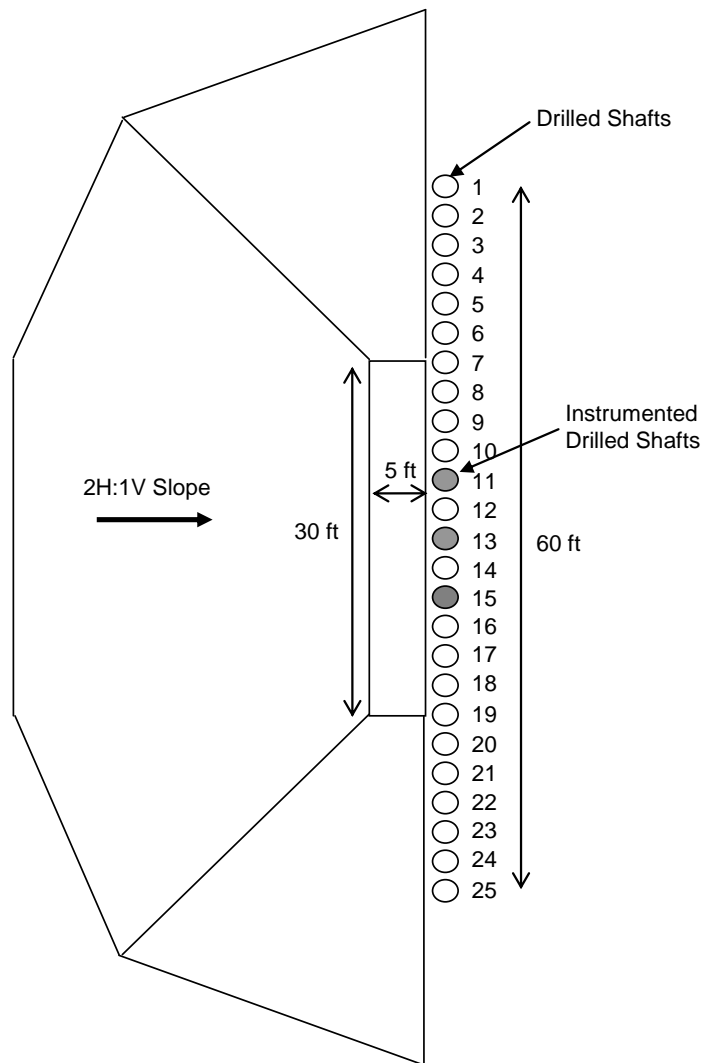


Figure A.1: Plan view of wall and excavation.

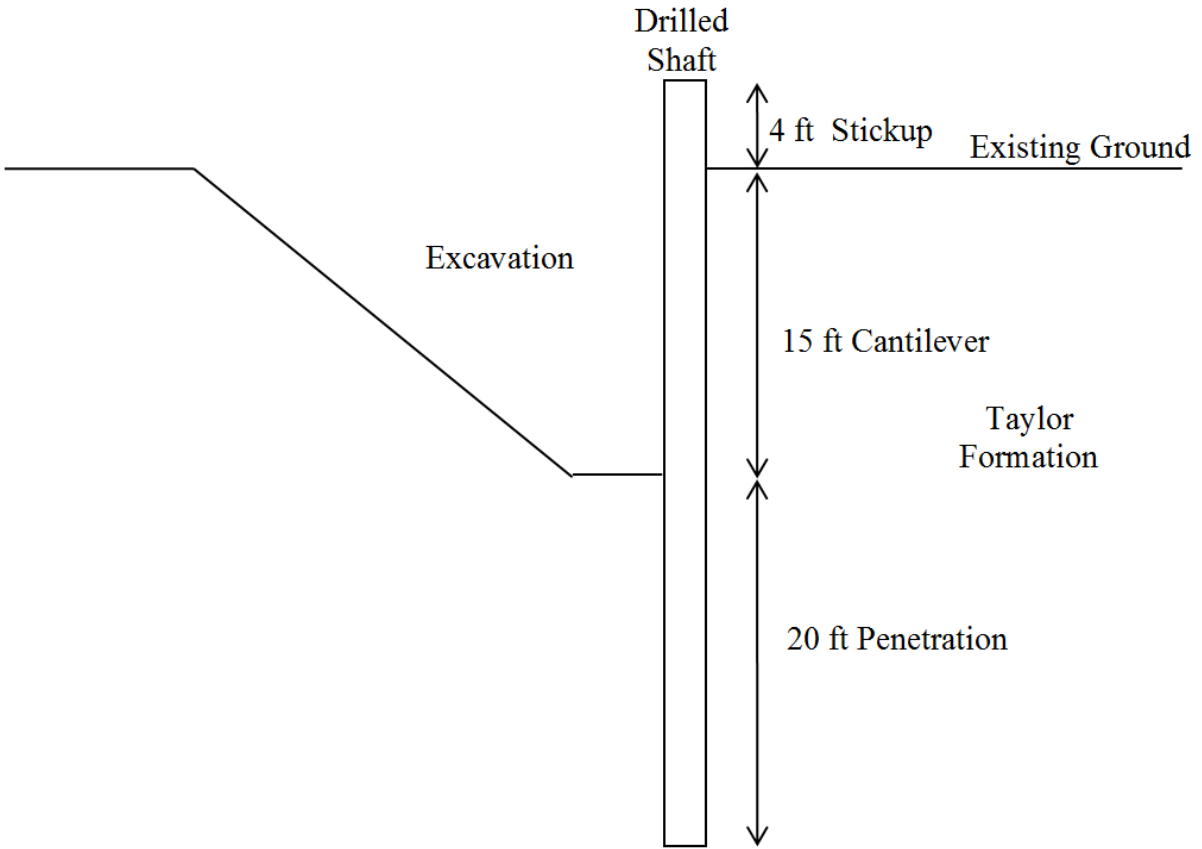


Figure A.2: Cross-section of wall at center of excavation (Shaft No. 13)

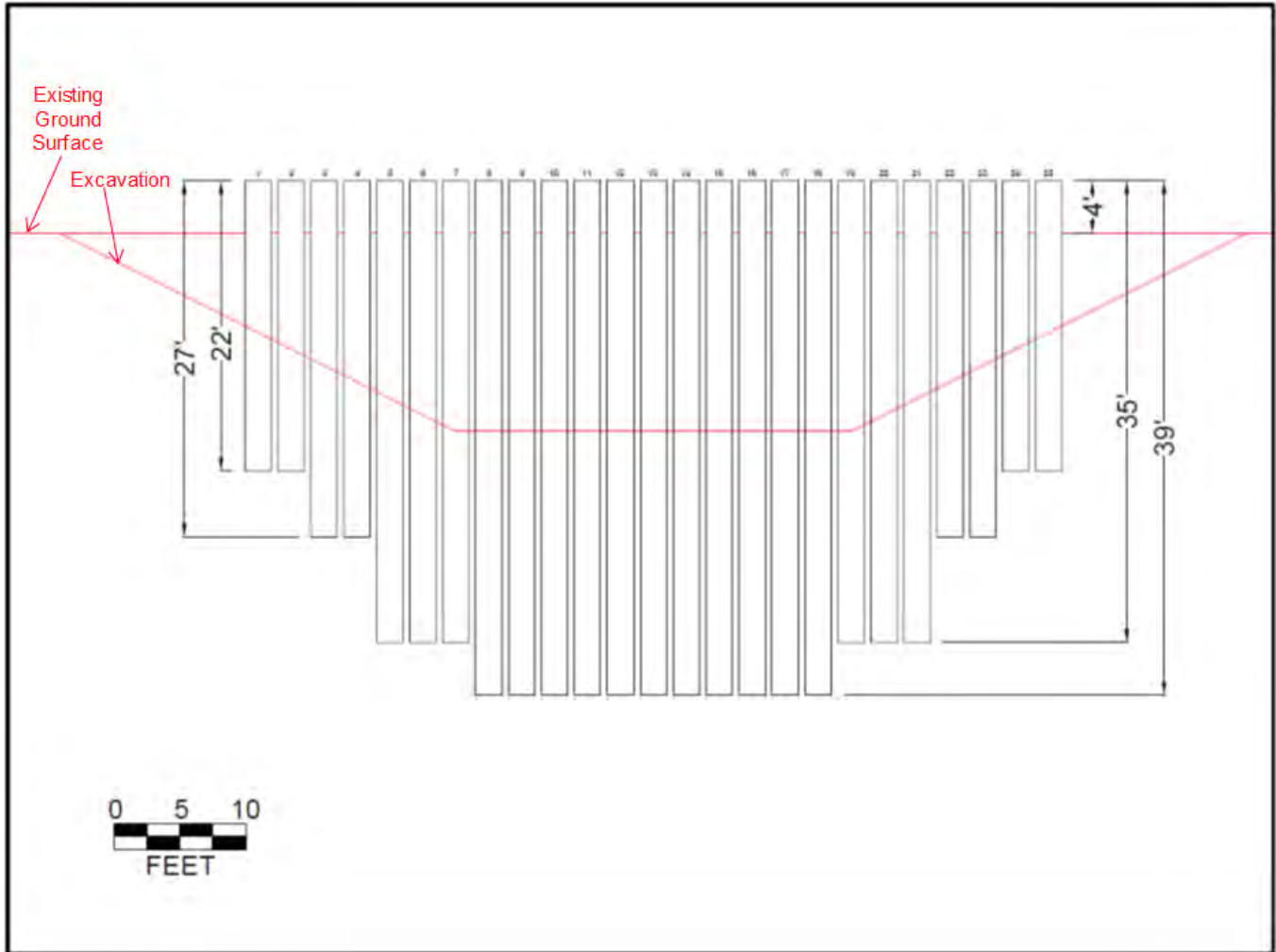


Figure A.3: Profile of wall and excavation.

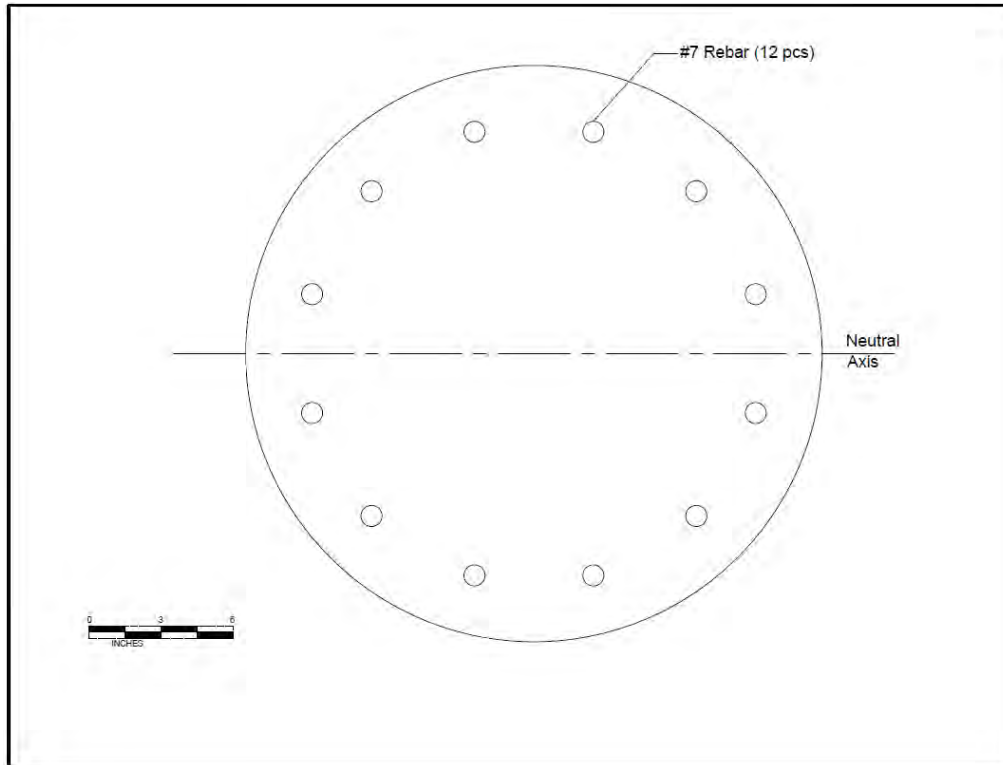


Figure A.4: Drilled shaft cross-section (without instrumentation – 22 shafts).

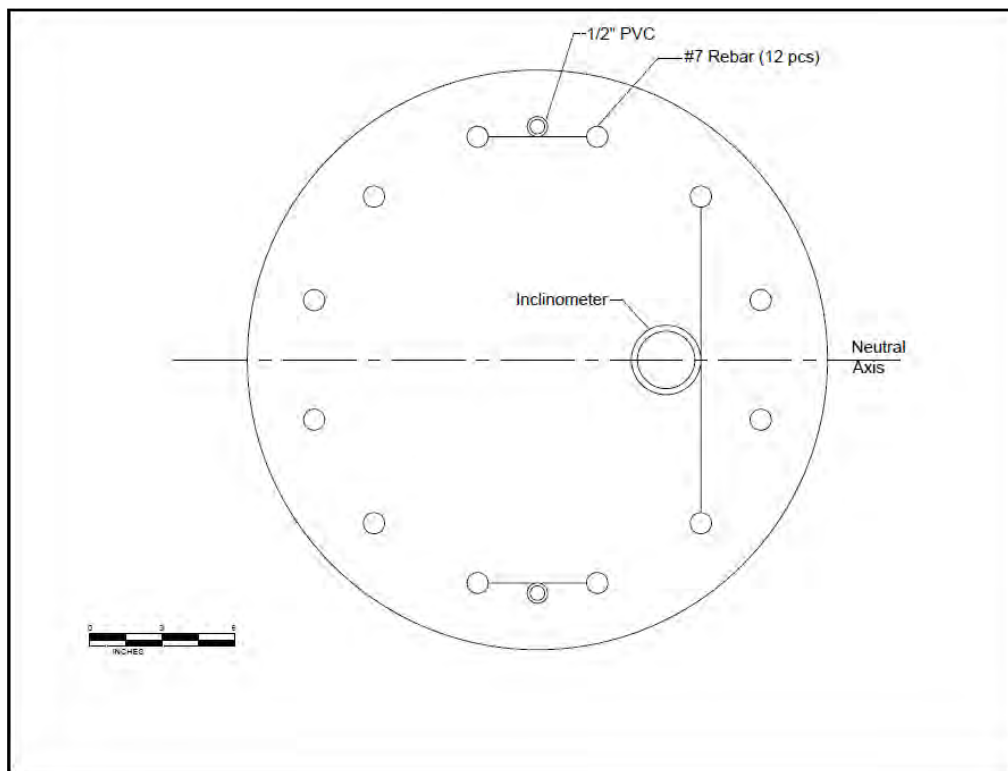


Figure A.5: Drilled shaft cross-section (with instrumentation – 3 shafts, Nos. 11, 13, and 15).

A.3: Site Investigation

A site investigation, consisting of three borings (Figure A.6), was performed at the site on January 12 and 13, 2010. Preliminary boring logs for these borings are presented in a later section. The site conditions were as expected, with stiff to hard clay of the Taylor Formation extending down to 50 feet below the ground surface.

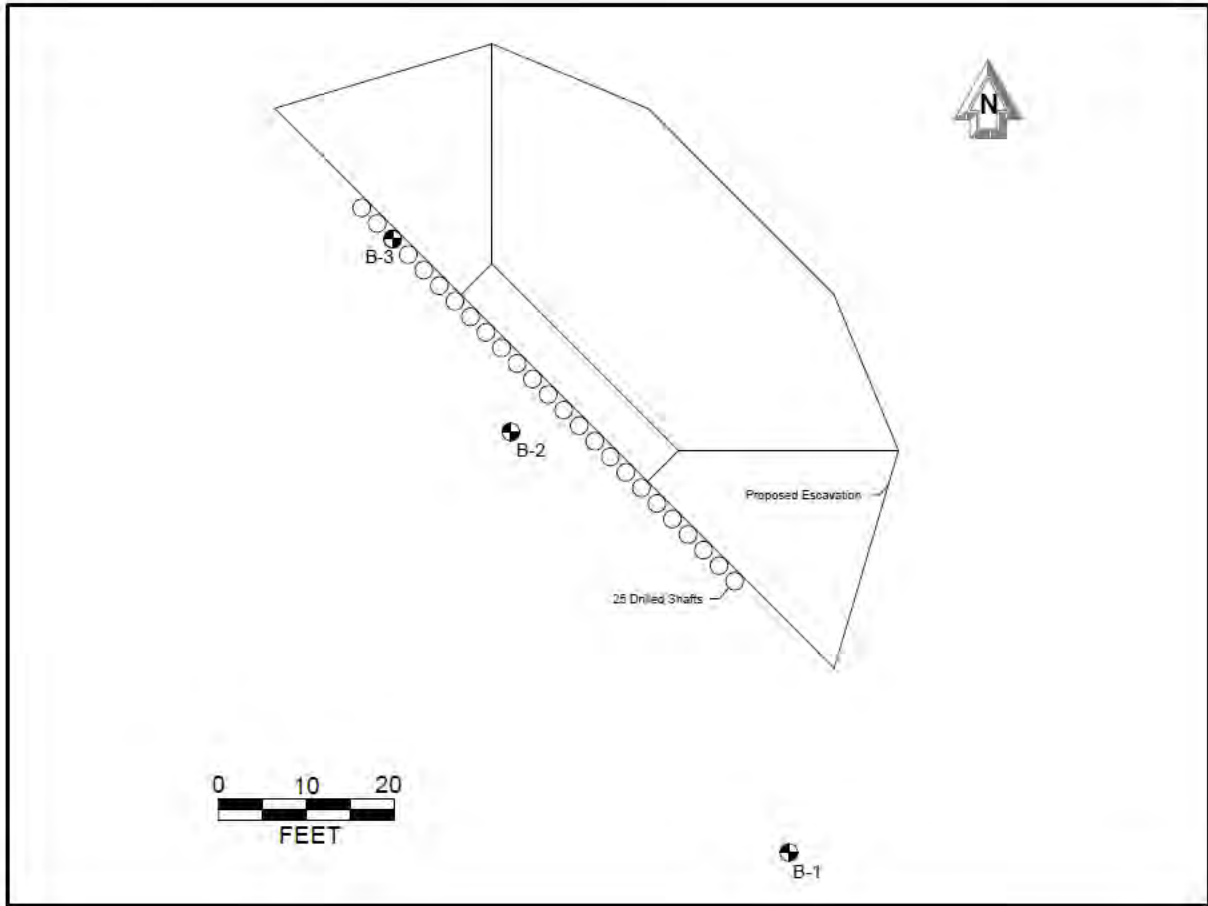


Figure A.6: Boring plan.

A.4: Design Check

The design was developed to provide a structure that would be structurally sound and consistent with other TXDOT walls of this type, while producing enough deformations to infer the pressures behind the wall. The proposed wall design was checked using the TXDOT Procedure for the design of drilled shaft retaining walls. Supplemental analyses were also performed and are proved in a later section.

Table A-2 lists the design parameters. The structural shaft properties are shown in Figure A.7 and Figure A.8.

Table A-2: Baseline assumptions and design parameters for TXDOT procedure.

Parameter	Value
Total Unit Weight of Soil, γ_t	130 pcf
Coefficient of Active Earth Pressure, k_a	0.31
Equivalent Fluid Pressure for Earth Pressures on Wall, γ_{EF}	40 psf/ft
Undrained Shear Strength for Clay below Cantilever, S_U	3,000 psf
Cracking Moment, M_{Cr}	680 k-in.
Yielding Moment, M_y	3,200 k-in.
Uncracked Bending Stiffness, EI_{uc}	67×10^6 k-in ²
Cracked Bending Stiffness, EI_{cr}	18×10^6 k-in ²
c-c Spacing Between Shafts, B	30 in.
Shaft Diameter	24 in.
Height of Retained Soil, H	180 in.
Reinforcement	12 #7 bars (1.6% of gross area)

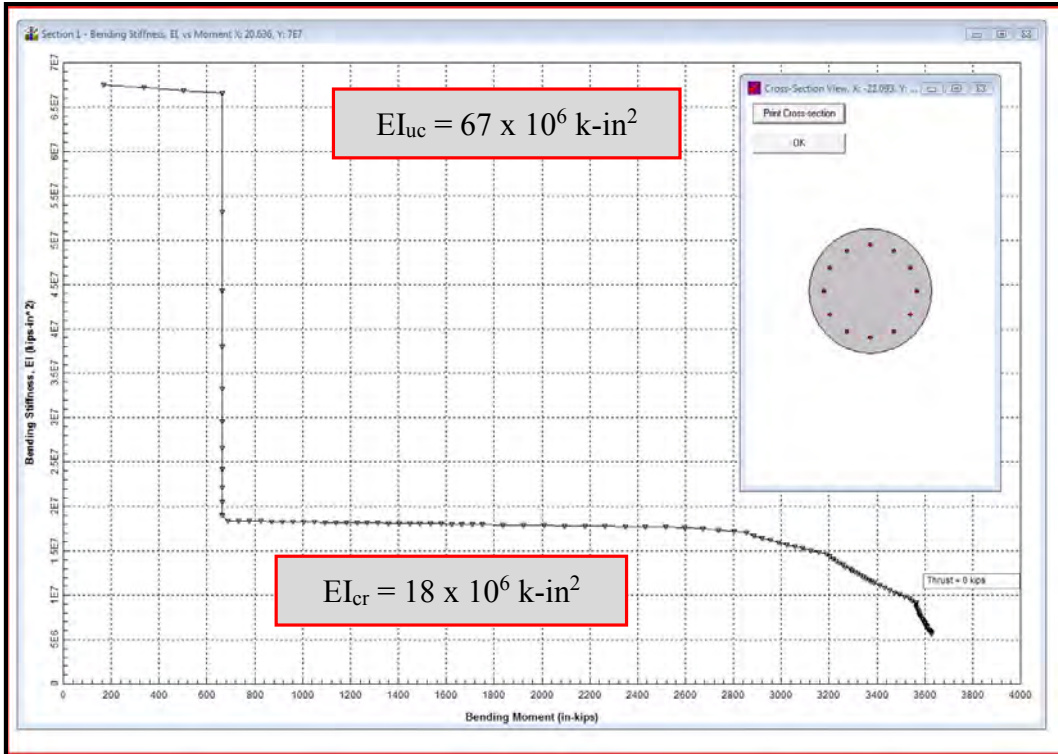


Figure A.7: Bending stiffness vs. bending moment for drilled shaft.

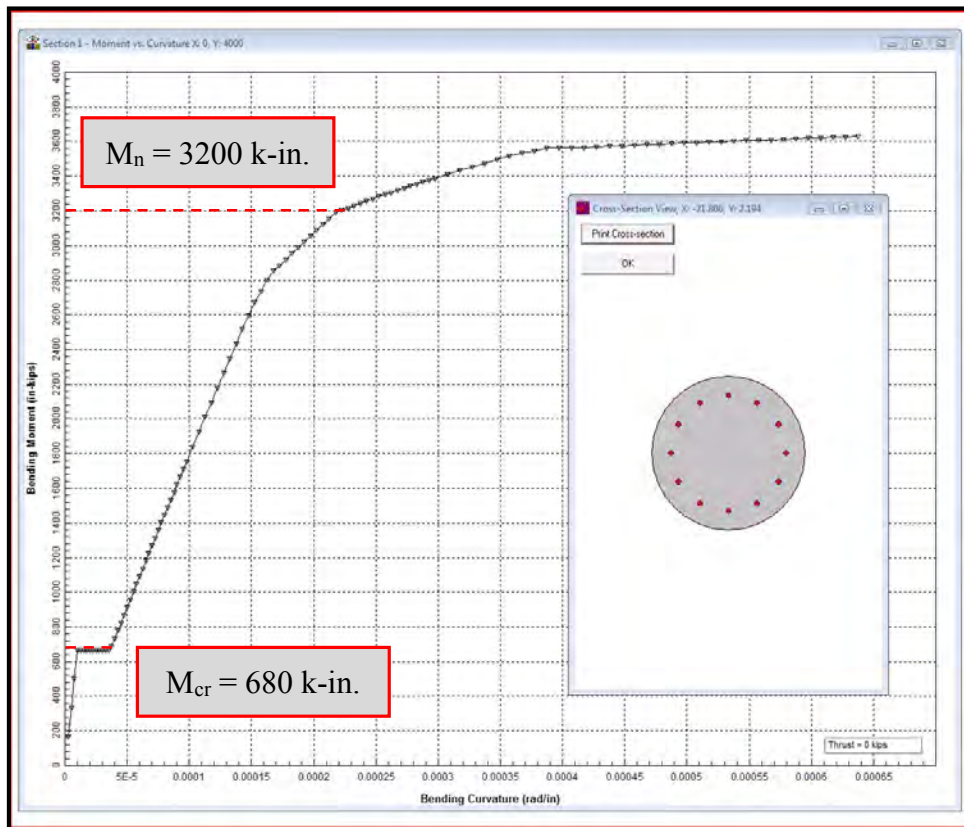


Figure A.8: Bending capacity for drilled shaft.

Preliminary Check from TXDOT Procedure

Calculate the cantilevered load:

$$P_{\text{soil}} = 0.5 \cdot \gamma \cdot k_a \cdot H^2 \cdot B = 0.5 \cdot 130 \text{ lb/ft}^3 \cdot 0.31 \cdot (15 \text{ ft})^2 \cdot 2.5 \text{ ft} = 11.3 \text{ kips}$$

Calculate the groundline moment:

$$M_{\text{GL}} = P_{\text{soil}} \cdot (H / 3) = 11.3 \text{ k} \cdot (15 \text{ ft} / 3) = 680 \text{ in-kip}$$

Estimate maximum moment (use Factor of Safety = 1.5 here):

$$M_{\text{max}} = M_{\text{GL}} \cdot 1.5 = (680 \text{ in-kip}) \cdot 1.5 = 1020 \text{ in-kip}$$

Calculate the ultimate moment (use Load Factor = 1.7 here):

$$M_u = M_{\text{max}} \cdot 1.7 = 1020 \text{ in-kip} \cdot 1.7 = 1500 \text{ in-kip}$$

Determine shaft capacity ($\phi \cdot M_n$) from structural analysis. From Figure 8, M_n is taken to be 3,200 in-kip. Calculate the factored moment capacity with a resistance factor of 0.9:

$$\phi \cdot M_n = 0.9 \cdot 3200 \text{ in-kip} = 2880 \text{ in-kip}$$

Check that $M_u < (\phi \cdot M_n)$:

$$M_u = 1500 \text{ in-kip} < 2880 \text{ in-kip} = (\phi \cdot M_n)$$

Because $M_u < (\phi \cdot M_n)$, the design is deemed to be acceptable based on the preliminary check.

Detailed Design from TXDOT Procedure

After the preliminary check indicated the design was acceptable, the more detailed TXDOT procedure was performed with L-Pile. An undrained shear strength of 3,000 psf was assumed for the clay supporting the drilled shafts below the depth of the excavation. In accordance with Research Report 415-2F, the undrained shear strength of the soil was reduced with a factor of 0.6 to account for the close shaft spacing.

L-Pile runs were performed first using an assumed earth pressure distribution of 40 psf/ft, which is consistent with the TXDOT procedure for determining the cantilevered load and groundline moment in the Preliminary Design Check above. The results are shown in Figure A.9.

Based on this analysis, the depth of fixity is approximately 10 feet below the cantilever. Therefore, a 15-foot deep shaft embedment should satisfy the fixity requirement of 1.33 times this depth.

The estimated deflection at the top of the wall is 0.8 inches, which is less than 1 percent of the wall height (1.8 inches).

The maximum moment is calculated to be 880 in.-kips. For a load factor of 1.7, the factored moment is

$$M_u = M_{\max} \cdot 1.7 = 880 \text{ in-kip} \cdot 1.7 = 1500 \text{ in-kip}$$

and this factored moment satisfies the check with the factored capacity:

$$M_u = 1500 \text{ in-kip} < 2880 \text{ in-kip} = (\phi \cdot M_n)$$

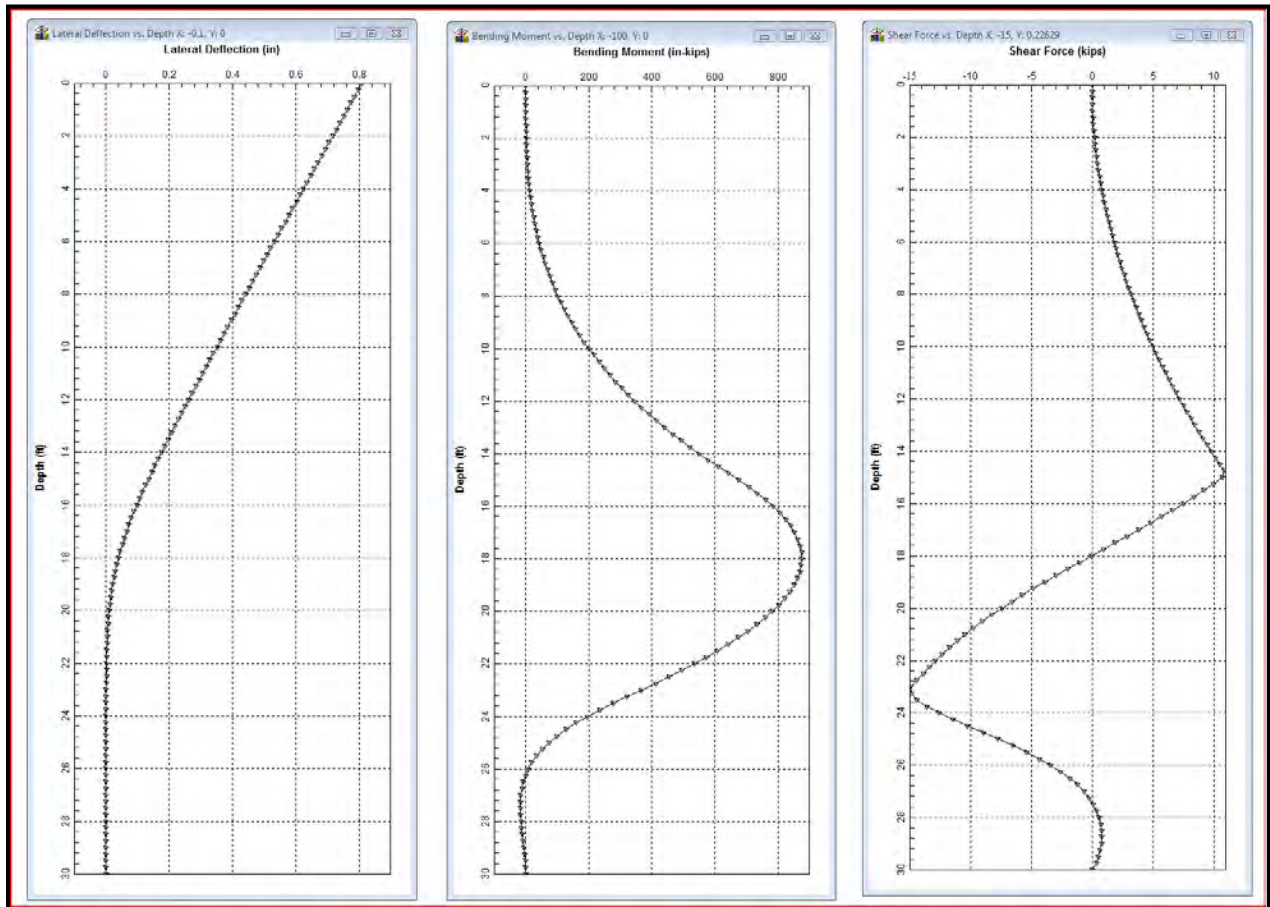


Figure A.9: LPILE output for the proposed design (40 psf/ft earth pressure)

A sensitivity analysis was also performed for the earth pressure and the strength of the clay below the excavation. Figure A.10 shows an L-Pile analysis with an earth pressure distribution of 80 psf/ft. While the top wall deflection exceeds 1 percent of the wall height in this case, the moment capacity of the shaft is not exceeded (2,000 in.-kip maximum versus 3,200 in.-kip capacity, both unfactored) and the depth of fixity is still above the base of the shaft. Therefore, the wall will not fail if the earth pressures are as high as 80 psf/ft.

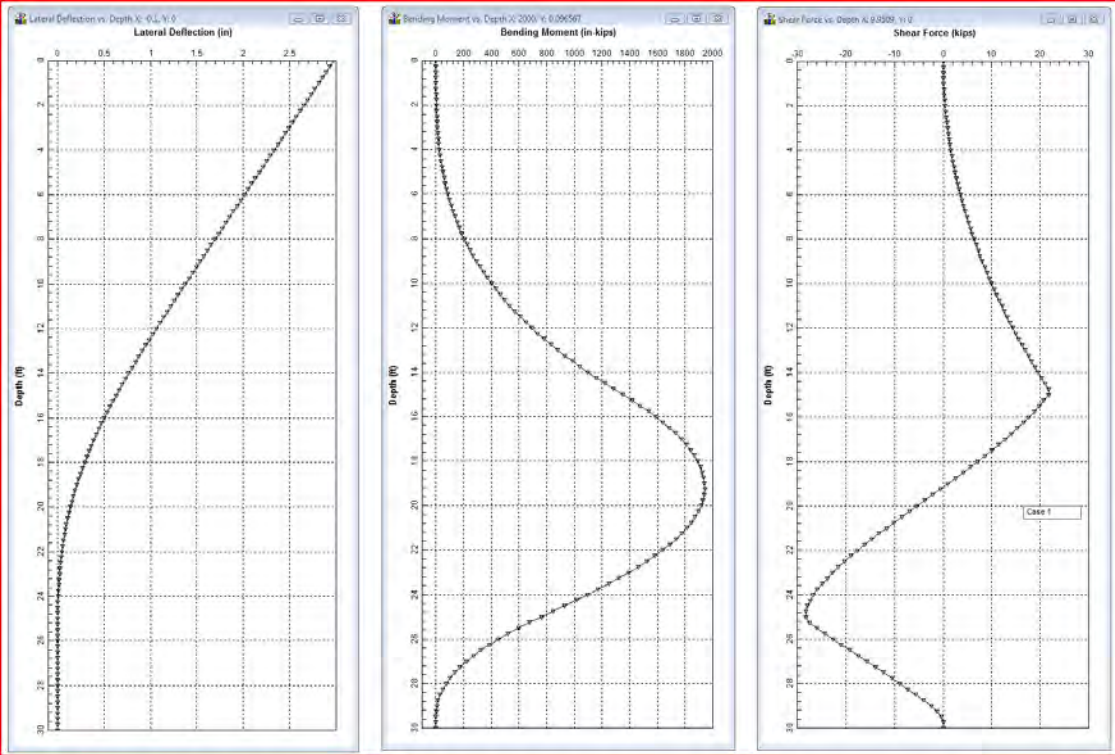


Figure A.10: LPILE output for the proposed design (80 psf/ft earth pressure)

Figure A.11 to Figure A.13 show the top wall deflection versus shaft length for different assumptions about the earth pressure and the undrained shear strength for the clay at the base of the excavation. For the assumed undrained shear strength of 3,000 psf below the excavation base, 30-foot long shafts will be long enough with either 40 psf/ft or 80psf/ft of earth pressure (Figures 11 and 12). However, Figure 13 shows that an undrained shear strength profile that increases from 1,500 to 3,000 psf from the base of the excavation to the tip of the shaft (instead of a constant of 3,000 psf over the entire length) will produced excessive deflection with an 80 psf/ft earth pressure. Since removal of overburden and access to moisture for the clay at the base of the excavation may reduce its undrained shear strength, the shaft lengths in the center of the wall be set at 35 feet below the ground surface to minimize the potential of excessive deflection.

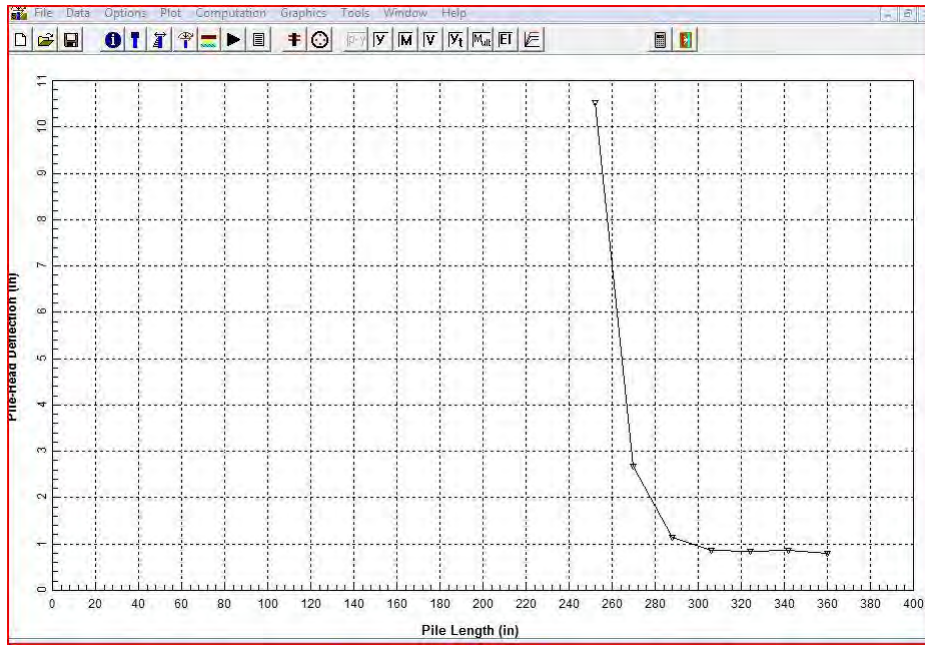


Figure A.11: Pile head deflection versus length with 40 psft/ft earth pressure.

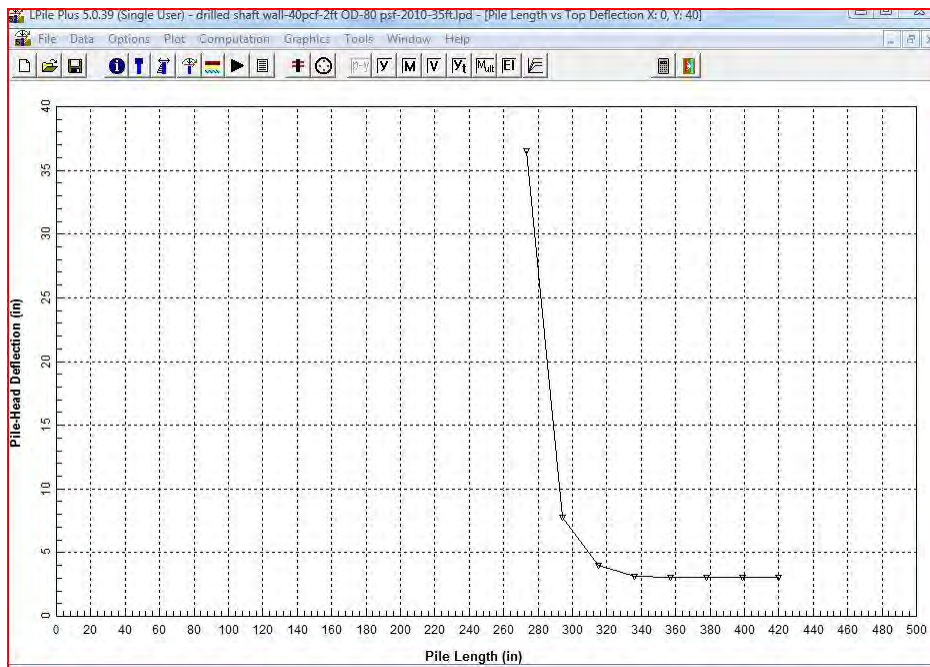


Figure A.12: Pile head deflection versus length with 80 psft/ft earth pressure.

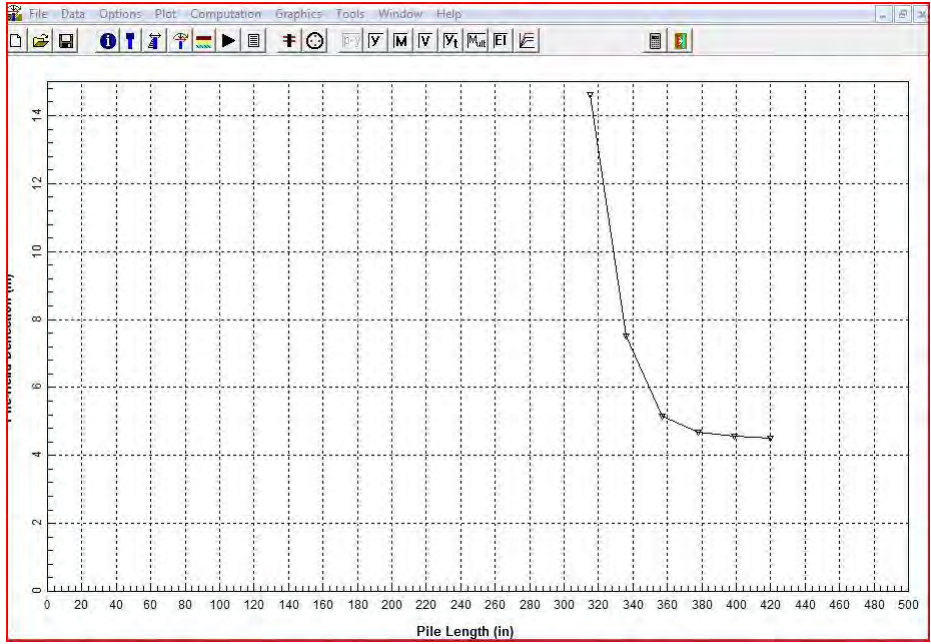


Figure A.13: LPILE output for the proposed design (80 psft/ft earth pressure).

A.5: Recommendations

The proposed wall design will work well for reasonable ranges of conditions based on the available information. In order to minimize the possibility of excessive deflection if the soil strength is lower and the earth pressures are higher than we expect, the shaft lengths in the center of the wall are set at 35 feet below the ground surface (Figure A.2 and Figure A.3). The shaft lengths will be progressively reduced in accordance with the depth of the cantilever away from the center of the wall in order to provide (1) a length of penetration below the cantilever that is at least as great as the height of the cantilever at all locations (Figure A.3) and (2) a total length for all shafts of 835 lineal feet so that the cost of the wall is unchanged from the original proposal price (Table A-1).

A.6: Boring Logs

TERMS AND SYMBOLS USED ON TxDOT BORING LOGS



SOIL TYPES

CH, Fat Clay	Sand
CL, Lean Clay	Gravel
ML, Silt	Fill/Other

ROCK TYPES

Limestone
Shale

SOIL GRAIN SIZE
U.S. STANDARD SIEVE

6"	3"	GRAVEL		SAND			SILT		CLAY
152	76.2	4.76	2.00	0.420	0.074	0.0075	0.002		
		COARSE	FINE	COARSE	MEDIUM	FINE			
		19.1	4.76	2.00	0.420	0.074	0.0075		

SOIL GRAIN SIZE IN MILLIMETERS

STRENGTH OF GRANULAR SOILS ⁽¹⁾	
CONSISTENCY	THD Penetrometer (blows/ft or blows/300mm)
Very Loose	0 to 8
Loose	8 to 20
Slightly Compact	20 to 40
Compact	40 to 80
Dense	80 to 5"/100 (125mm/100)
Very Dense	5"/100 to 0"/100 (125mm/100 to 0mm/100)

STRENGTH OF COHESIVE SOILS ⁽¹⁾	
DENSITY	THD Penetrometer (blows/ft or blows/300mm)
Very Soft	0 to 8
Soft	8 to 20
Stiff	20 to 40
Very Stiff	40 to 80
Hard	80 to 5"/100 (125mm/100)
Very Hard	5"/100 to 0"/100 (125mm/100 to 0mm/100)

BEDROCK HARDNESS ⁽¹⁾	
HARDNESS	THD Penetrometer (blows/ft or blows/300mm)
Very Hard	0" - 2"/100 (0 - 50mm/100)
Hard	1" - 5"/100 (25 - 125mm/100)
Soft	4" - 6"/100 (100 - 150mm/100)

1) TxDOT Geotechnical Manual, Chapter 3 - Soil and Bedrock Classification & Logging (3-15)

ASTM D 2488 TABLE 7 Criteria for Describing Structure

Description	Criteria
Stratified	Alternating layers of varying material or color with layers at least 6 mm thick; note thickness
Laminated	Alternating layers of varying material or color with the layers less than 6mm thick; note thickness
Fissured	Breaks along definite planes of fracture with little resistance to fracturing
Slickensided	Fracture planes appear polished or glossy, sometimes striated
Blocky	Cohesive soil that can be broken down into small angular lumps which resist further breakdown
Lensed	Inclusion of small pockets of different soils, such as small lenses of sand scattered through a mass of clay; note thickness
Homogeneous	Same color and appearance throughout

Criteria for Describing Inclusions

Description	Criteria
Parting	Inclusion <1/8" thick extending through sample
Seam	Inclusion 1/8" to 3" thick extending through sample
Layer	Inclusion >3" thick extending through sample

Terms used in Additional Remarks on Wincore Logs

Description	Criteria
PP	Pocket Penetration Test (tsf)
SPT	Modified Standard Penetration Test (bpf)
REC	Rock Core Recovery (%)
RQD	Rock Quality Designation, ASTM (D 6032)
Q	Unconsolidated Undrained Triaxial Test (tsf)
U	Unconfined Compression Test (tsf)



WinCore
Version 3.1

DRILLING LOG

1 of 1

County	Travis	Hole	B-1	District	
Highway		Structure	Retaining Wall	Date	1/12/10
CSJ	UT Manor Wall Project	Station		Grnd. Elev.	0.00 ft
		Offset		GW Elev.	-45.70 ft

Elev. (ft)	LOG	Texas Cone Penetrometer	Strata Description	Triaxial Test		Properties				Additional Remarks
				Lateral Press. (psi)	Deviator Stress (psi)	MC	LL	PI	Wet Den. (pcf)	
-5.5		4 (6) 4 (6)	CLAY, soft, dark brown, w/scattered sand and fine gravel. (Residual Soil) (CH)							SPT = 12
		9 (6) 8 (6)	CLAY, soft to hard, tan and light gray, blocky, calcareous, w/ferrous staining and selenite seams. (Taylor) (CH)							SPT = 12
10		8 (6) 8 (6)								SPT = 16 w/increasing selenite seams
15		10 (6) 12 (6)								SPT = 20
20		19 (6) 22 (6)								SPT = 19
25		24 (6) 24 (6)								SPT = 22
30		37 (6) 50 (6)								SPT = 30
35		50 (6) 50 (6)	CLAY SHALE, low to moderate hardness, dark gray, slightly fissile, w/occasional pyritic seams and nodules. (Taylor)							w/occasional tan seams SPT = 35
-39										
40										
45										
-47										
50										
55										
60										

Remarks: Boring was drilled to the 47.0-ft depth using dry drilling techniques. Upon completion of the borehole, groundwater recorded at 45.7 ft after a 1.5 hour waiting period. A 2-inch diameter piezometer was set in the borehole with a screened interval of 5.0 to 20.0 ft below ground surface. Standard Penetration Test (SPT) blowcounts were performed using a 170-lb hammer with a 24-inch hammer drop.

Any ground water elevation information provided on this boring log is representative of conditions existing on the day and for the specific location where this information was collected. The actual groundwater elevation may fluctuate due to time, climatic conditions, and/or construction activity.

Driller: Fugro Consultants, Inc. Logger: Fugro Consultants, Inc. Organization: Fugro Consultants, Inc.

M:\GEO\REPORTS\2009\04.30091079 UT Manor Wall Project\UT Manor Wall logs 1-28-10.clg



WinCore
Version 3.1

DRILLING LOG

1 of 1

County	Travis	Hole	B-2	District	
Highway		Structure	Retaining Wall	Date	1/12/10
CSJ	UT Manor Wall Project	Station		Grnd. Elev.	0.00 ft
		Offset		GW Elev.	-29.10 ft

Elev. (ft)	LOG	Texas Cone Penetrometer	Strata Description	Triaxial Test		Properties				Additional Remarks
				Lateral Press. (psi)	Deviator Stress (psi)	MC	LL	PI	Wet Den. (pcf)	
5			CLAY, very stiff to hard, dark gray, w/scattered shell fragments, roots, and fine rounded gravel. (Residual Soil) (CH)							PP = 2.25
6										PP = 4.5+
10			CLAY, very stiff to hard, tan and light gray, blocky, calcareous, w/ferrous staining and selenite seams. (Taylor) (CH)							PP = 3.5
15										PP = 3.75
20										PP = 4.5+
25										PP = 4.5+
30										PP = 4.0
35										PP = 2.5 w/increasing selenite seams
39.5										PP = 4.5+
40			CLAYSHALE, low to moderate hardness, dark gray, slightly fissile, w/occasional pyritic seams and nodules. (Taylor)							PP = 4.5+ w/selenite-coated joints at 38 ft
45										PP = 4.5+ w/occasional tan seams
50										PP = 4.5+

Remarks: Boring was drilled to the 50.0-ft depth using dry drilling techniques and groundwater was recorded at 29.1 ft after a 15 minute waiting period. Upon completion of the borehole, groundwater was recorded at 41.0 ft. A slope inclinometer casing was set in the borehole.

Any ground water elevation information provided on this boring log is representative of conditions existing on the day and for the specific location where this information was collected. The actual groundwater elevation may fluctuate due to time, climatic conditions, and/or construction activity.

Driller: Fugro Consultants, Inc.

Logger: Fugro Consultants, Inc.

Organization: Fugro Consultants, Inc.

M:\GEOREPORTS\2009\04\30091079 UT Manor Wall Project\UT Manor Wall logs 1-28-10.clg



DRILLING LOG

1 of 1

WinCore
 Version 3.1
 County Travis
 Highway
 CSJ
 UT Manor Wall Project
 Hole B-3
 Structure Retaining Wall
 Station
 Offset
 District
 Date 1/13/10
 Grnd. Elev. 0.00 ft
 GW Elev. -42.50 ft

Elev. (ft)	LOG	Texas Cone Penetrometer	Strata Description	Triaxial Test		Properties				Additional Remarks
				Lateral Press. (psi)	Deviator Stress (psi)	MC	LL	PI	Wet Den. (pcf)	
5			CLAY, stiff to very stiff, dark gray, w/scattered shell fragments, roots, and fine rounded gravel. (Residual Soil) (CH)							PP = 1.75
-6										PP = 1.75 PP = 2.0 PP = 2.0
10		7 (6) 8 (6)	CLAY, very stiff to hard, tan and light gray, blocky, calcareous, w/ferrous staining and selenite seams. (Taylor) (CH)							PP = 3.25
15		9 (6) 11 (6)								PP = 2.5
20		13 (6) 15 (6)								PP = 3.5
25		14 (6) 20 (6)								PP = 3.25 w/increasing selenite seams
30		34 (6) 33 (6)								PP = 4.5+
35		50 (6) 50 (4)								PP = 4.5+
40		30 (6) 50 (4.25)								PP = 4.5+
-43.3		50 (2.25) 50 (1.25)	CLAYSHALE, low to moderate hardness, dark gray, slightly fissile, w/occasional pyritic seams and nodules. (Taylor)							PP = 4.5+ w/occasional tan seams
50		50 (0.75) 50 (3)								PP = 4.5+
55										
60										

Remarks: Boring was drilled to the 50.3-ft depth using dry drilling techniques and groundwater was recorded at 42.5 ft after a 15 minute waiting period. Upon completion of the borehole, the boring was backfilled with soil cuttings.

Any ground water elevation information provided on this boring log is representative of conditions existing on the day and for the specific location where this information was collected. The actual groundwater elevation may fluctuate due to time, climatic conditions, and/or construction activity.

Driller: Fugro Consultants, Inc.

Logger: Fugro Consultants, Inc.

Organization: Fugro Consultants, Inc.

M:\GEO\REPORTS\2009\04-30091079 UT Manor Wall Project\UT Manor Wall logs 1-28-10.clg

A.7: Supplemental Design Analyses

In addition to the TXDOT procedure, other scenarios were analyzed using Broms method and a non-dimensional procedure for a variety of earth pressures. More detailed calculations and charts can be found at the end of this report. For all of these earth pressure and analysis combinations, the wall performance was found to be adequate. A summary of our results is presented below in Table A-3.

Table A-3: Summary of additional wall analysis procedures.

Design Method	Broms Method				Non-Dimensional Procedure (Soil-Structure Interaction)			
	40	60	80	90	40	60	80	90
Equivalent Fluid Density, pcf	40	60	80	90	40	60	80	90
Source of γ_{ef}	TXDOT Proc.	Coulomb Drained	Design Guide	"Swell"	TXDOT Proc.	Coulomb Drained	Design Guide	"Swell"
Depth to Fixity, feet	N/A	N/A	N/A	N/A	4	4	8	8
Max Moment in Shaft, kip-in	1070	1500	2030	2280	720	1100	1490	1680
Stress Level (Moment)	0.33	0.47	0.63	0.71	0.23	0.34	0.47	0.53
Factor of Safety (Moment)	3.0	2.1	1.6	1.4	4.4	2.9	2.1	1.9

Selection of Equivalent Fluid Pressures

The decision to use a variety of equivalent fluid pressures was based on the uncertainty associated with earth pressures in expansive clays. A value of 40 pcf was based on the TXDOT design procedure. The value of 80 pcf was based on the common rule of thumb that equivalent fluid pressures may be as high as twice their typical values in expansive soils, and the value of 90 pcf was selected to represent an extreme case for sensitivity analysis. The intermediate value of 60 pcf was based on an active Coulomb analysis using drained parameters, as described in the following section.

Coulomb Active Earth Pressure Approximation

For this analysis, cohesion was assumed to be zero, and friction angle was taken to be 18 degrees (consistent with drained data from the Taylor formation). The active earth pressure was calculated using Coulomb theory for cohesionless material, with a vertical wall and level backfill. A summary of this analysis is presented below in Table A-4.

Table A-4: Summary of long-term drained analysis.

Parameter	Value
Total Unit Weight of Soil, γ_t	130 pcf
Angle of Internal Friction (ϕ , degrees)	18
Cohesion	0
Angle of Wall Friction (ϕ_w , degrees)	12
Coefficient of Active Earth Pressure, k_a	0.47
Active Earth Pressure (per unit width)	6.8 kips / ft
Active Earth Pressure (per shaft)	17 kips / shaft
Groundline Moment (per shaft)	1015 kip-inch / shaft
Equivalent Fluid Pressure, γ_{EF}	60 psf / ft

The coefficient of active earth pressure was calculated using the following equation:

$$K_a = \frac{\cos^2(\phi - \alpha)}{\cos^2(\alpha) \times \cos(\phi_w + \alpha) \times \left[1 + \sqrt{\frac{\sin(\phi + \phi_w) \times \sin(\phi - \beta)}{\cos(\phi_w + \alpha) \times \cos(\alpha - \beta)}} \right]^2}$$

Because of the vertical wall and level backfill, $\alpha = \beta = 0$ and this equation simplifies to:

$$K_a = \frac{\cos^2(\phi)}{\cos(\phi_w) \times \left[1 + \sqrt{\frac{\sin(\phi + \phi_w) \times \sin(\phi)}{\cos(\phi_w)}} \right]^2} = 0.4735$$

The active earth pressures were calculated as follows (with shafts spaced 2.5 feet on center):

$$\frac{P_a}{b} = \frac{\gamma \times H^2 \times K_a \times \cos(\phi_w)}{2} = 6770 \frac{lb}{ft} \times \frac{2.5 ft}{shaft} = 17,000 \frac{lb}{shaft}$$

This force is located five feet above the base of the excavation (at one-third of the wall height). The equivalent groundline moment for use in subsequent calculations was estimated to be:

$$M_{GL} = \left(\frac{\text{Wall Height}}{3} \right) \times P_a = 5 \text{ ft} \times 17 \frac{\text{kips}}{\text{shaft}} = 84.6 \frac{\text{kip} \cdot \text{ft}}{\text{shaft}} = 1015 \frac{\text{kip} \cdot \text{in}}{\text{shaft}}$$

For reference, this analysis is comparable to an equivalent fluid pressure of 60 psf / ft:

$$\frac{P_a}{b} = 6770 \frac{\text{lb}}{\text{ft}} = \frac{\gamma_{ef} \times H^2}{2} \Rightarrow \gamma_{ef} = 60 \frac{\text{lb}}{\text{ft}^3} = 60 \frac{\text{psf}}{\text{ft}}$$

Wall Analysis using Broms Method

Broms method predicts the load and groundline moment (at a specified eccentricity) that will cause the shaft to exceed its yielding moment during undrained loading. It is important to note that this method negates any soil resistance that occurs within a distance of 1.5 shaft diameters (3 ft) below the groundline. Broms Method was used via spreadsheet to analyze the wall. The spreadsheet computations assume that failure will occur in the shaft, and not in the soil. If there is any concern of the latter, a “short shaft” analysis can be used. However, the Taylor formation is quite stiff at the construction site.

Table A-4 summarizes the parameters from Broms method. The L-parameter was altered until the maximum moment in the shaft reached the estimated M_{Max} from the preliminary TxDOT method. Brom’s method was used for equivalent fluid pressures of 40, 60, 80, and 90 pcf. Figure A.14 to Figure A.17 show the predicted shear and bending moment diagrams, respectively, for the drilled shafts at failure.

Table A-5: Broms method parameters.

b (in)	b (ft)	t (in)	fy (ksi)	I (in4)	M_y (in-k)	M_y (ft-k)	S_u (ksf)	e (ft)
24	2	N/A	36	16286	48858	265	4	5
L (ft)	L* (ft)	a	b	c	P (k)	f (ft)	g (ft)	M_{max} (ft-k)
7.285	4.285	0.00347	10.1425	-330.5	32.2	0.45	3.8	265

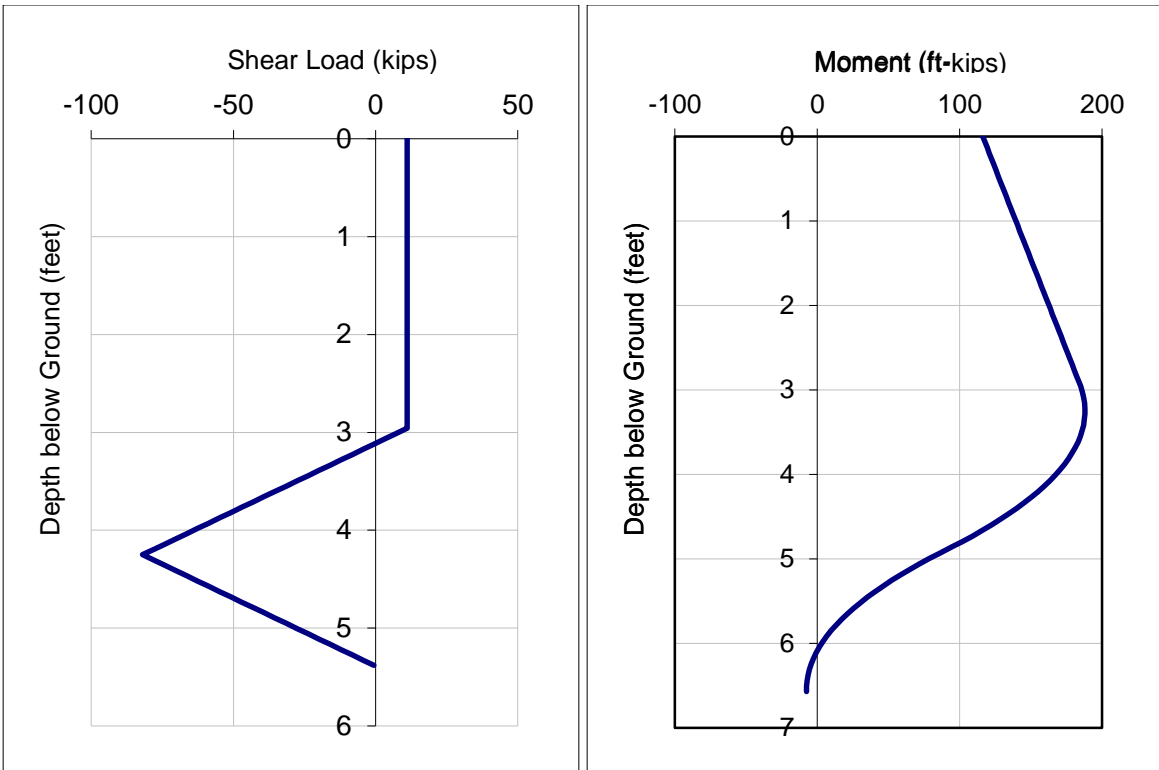


Figure A.14: Shear and bending moment on shaft predicted by Broms Method ($\gamma_{ef}=40$ pcf)

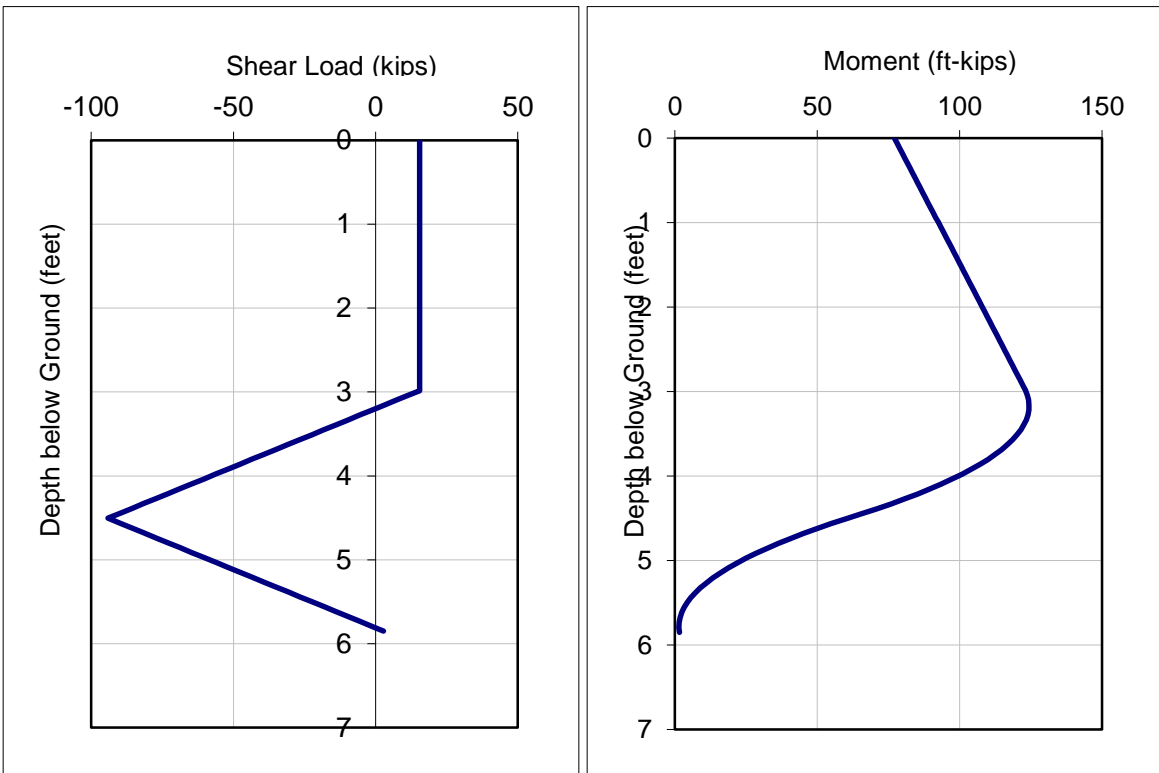


Figure A.15: Shear and bending moment on shaft predicted by Broms Method ($\gamma_{ef}=60$ pcf)

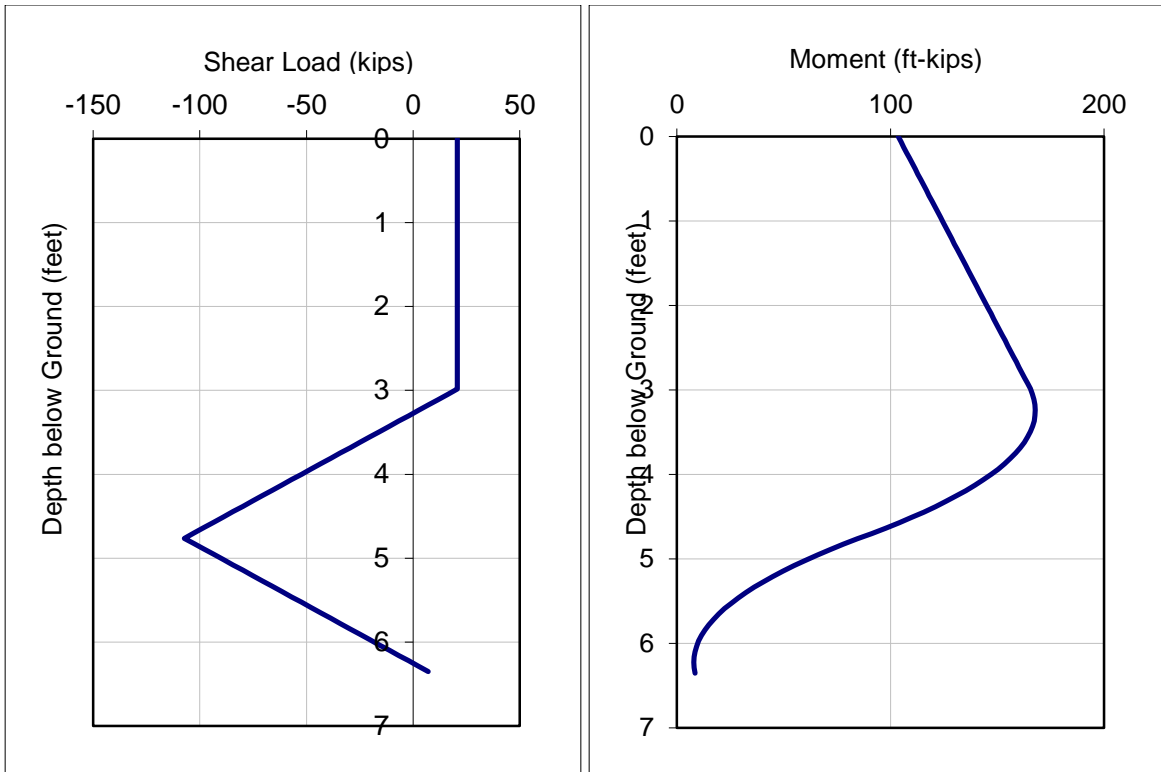


Figure A.16: Shear and bending moment on shaft predicted by Broms Method ($\gamma_{ef}=80$ pcf)

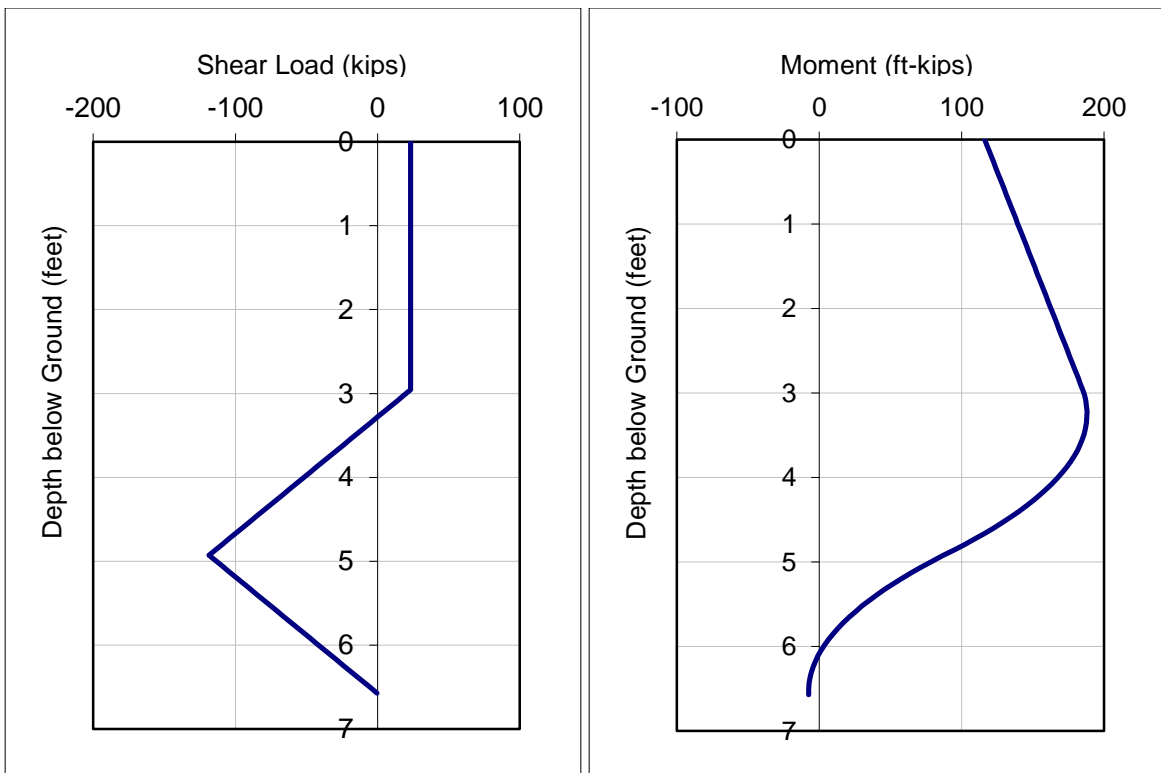


Figure A.17: Shear and bending moment on shaft predicted by Broms Method ($\gamma_{ef}=90$ pcf)

Non-Dimensional Procedure (Soil-Structure Interaction)

A spreadsheet was developed to analyze the wall in terms of limit equilibrium. This method uses P-y curves and a series of non-dimensional curves to model the soil-structure interaction. Values of $\epsilon_{50} = 0.004$ and $J = 0.5$ were assumed based on recommendations in the literature for stiff clays. The analysis was conducted at depths of 0, 0.5, 1, 1.5, 2, 3, 4, 5, 8, 10 and 15 ft below the excavation groundline. The iterative procedure was conducted with both cracked and uncracked shaft properties so that appropriate properties can be shown at moments both above and below M_{cr} . If the bending moment in the drilled shaft exceeds the cracking moment (M_{cr}), cracked shaft properties are only applicable over the depths above the location where this occurs. Figure A.18 through Figure A.21 illustrate the results of these analyses for equivalent fluid pressures of 40, 60, 80, and 90 psf / ft.

The results of this analysis provide some useful insights. First, the results are comparable to the values calculated using L-Pile. This provides a good check, and serves to further validate the results of both methods. Second, the maximum moment in the shaft stays within its capacity, even up to the extreme earth pressure of 90 psf / ft. This indicates that the proposed design should be adequate for the likely range of earth pressures encountered.

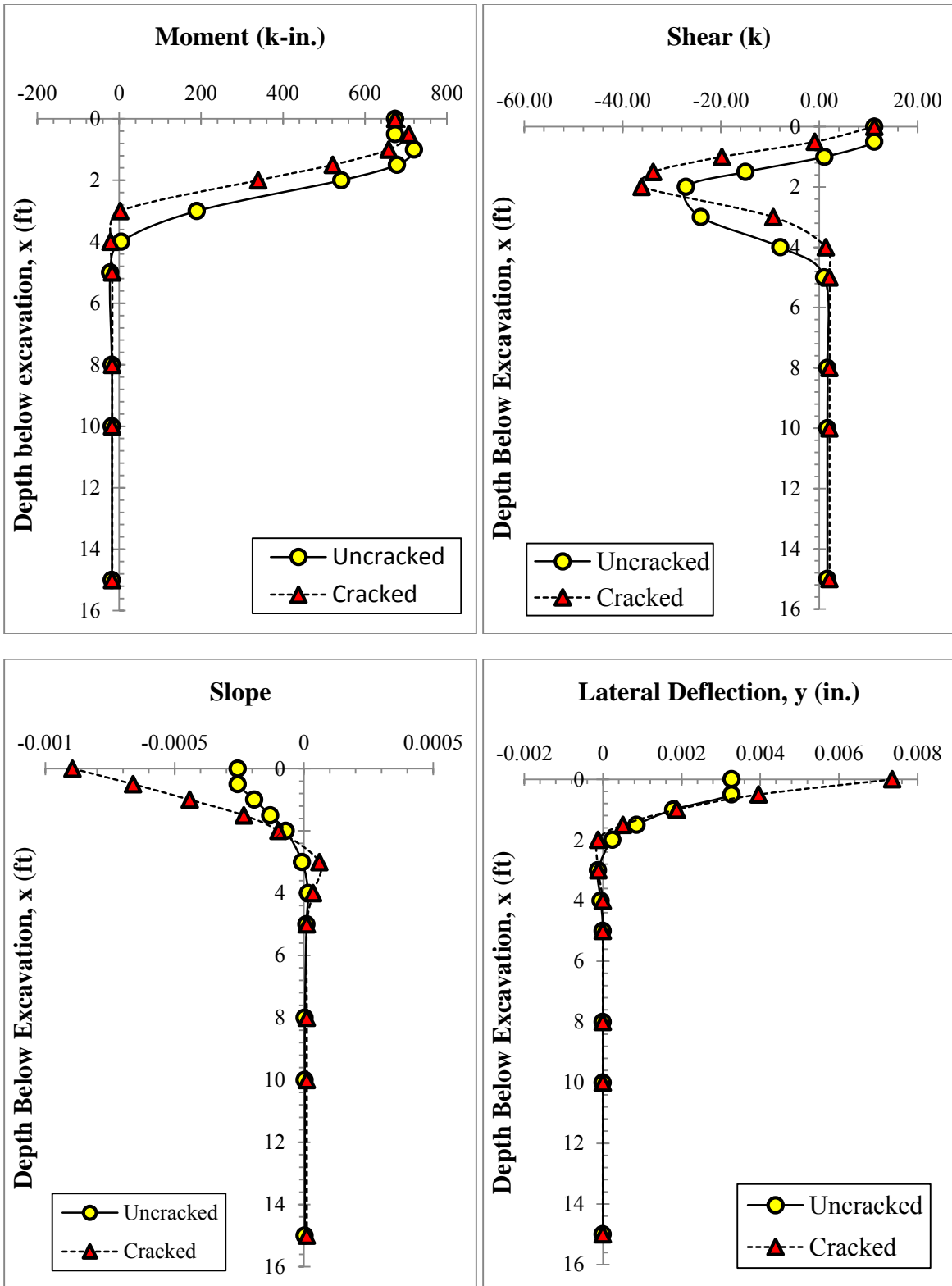


Figure A.18: Moment, shear, slope, and deflection for non-dimensional method ($\gamma_{ef}=40$ pcf)

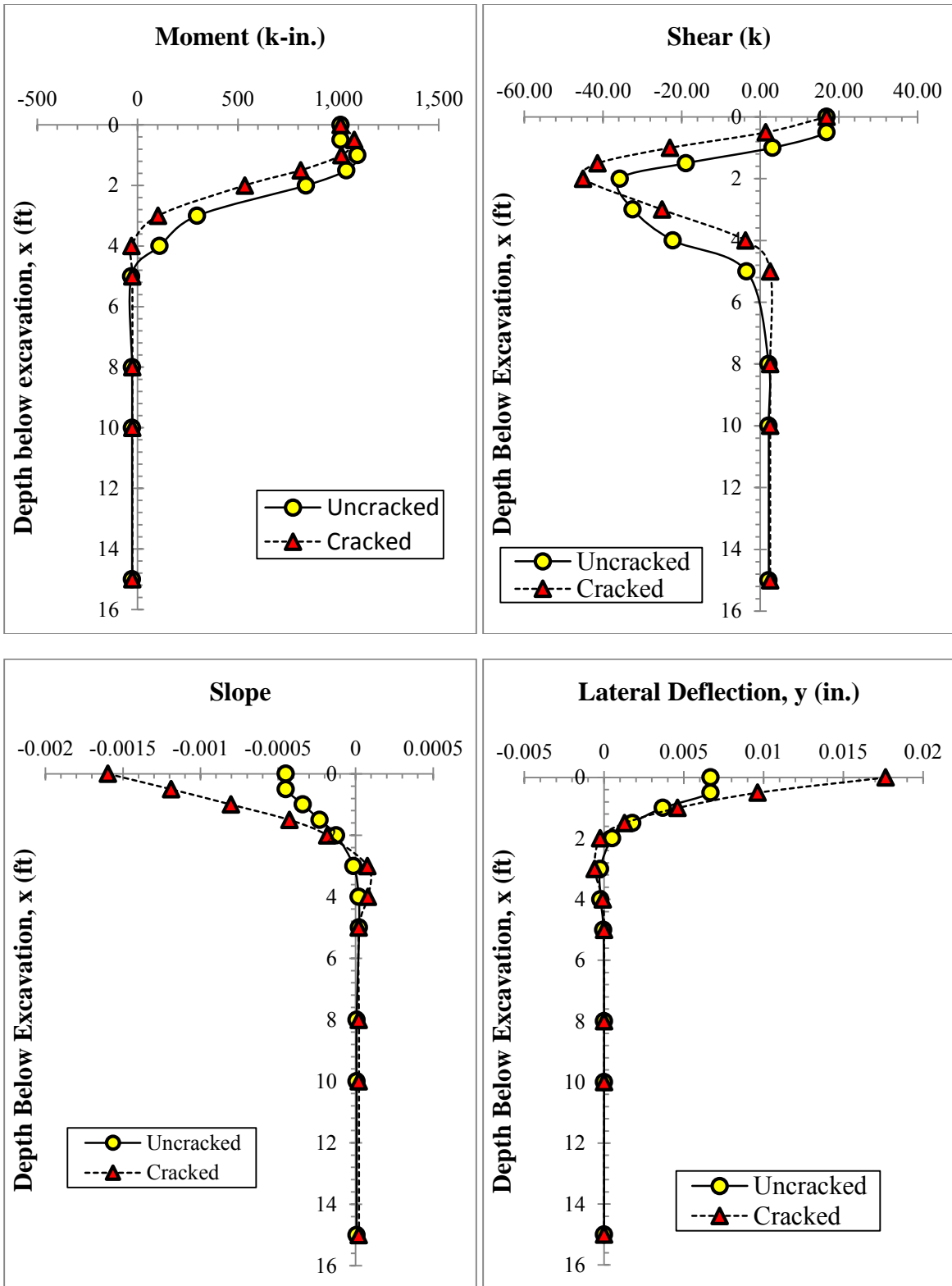


Figure A.19: Moment, shear, slope, and deflection for non-dimensional method ($\gamma_{ef}=60$ pcf)

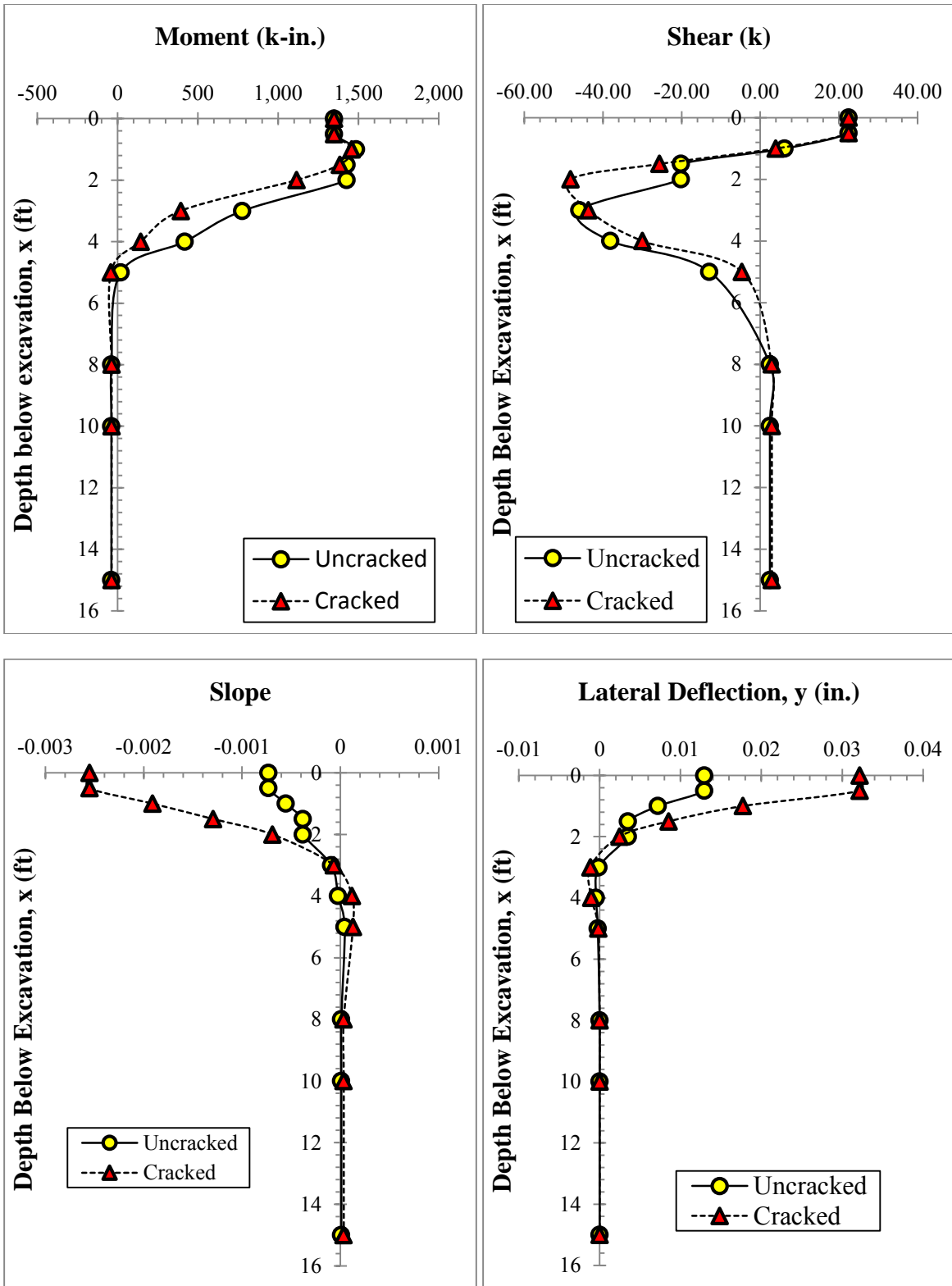


Figure A.20: Moment, shear, slope, and deflection for non-dimensional method ($\gamma_{ef}=80$ pcf)

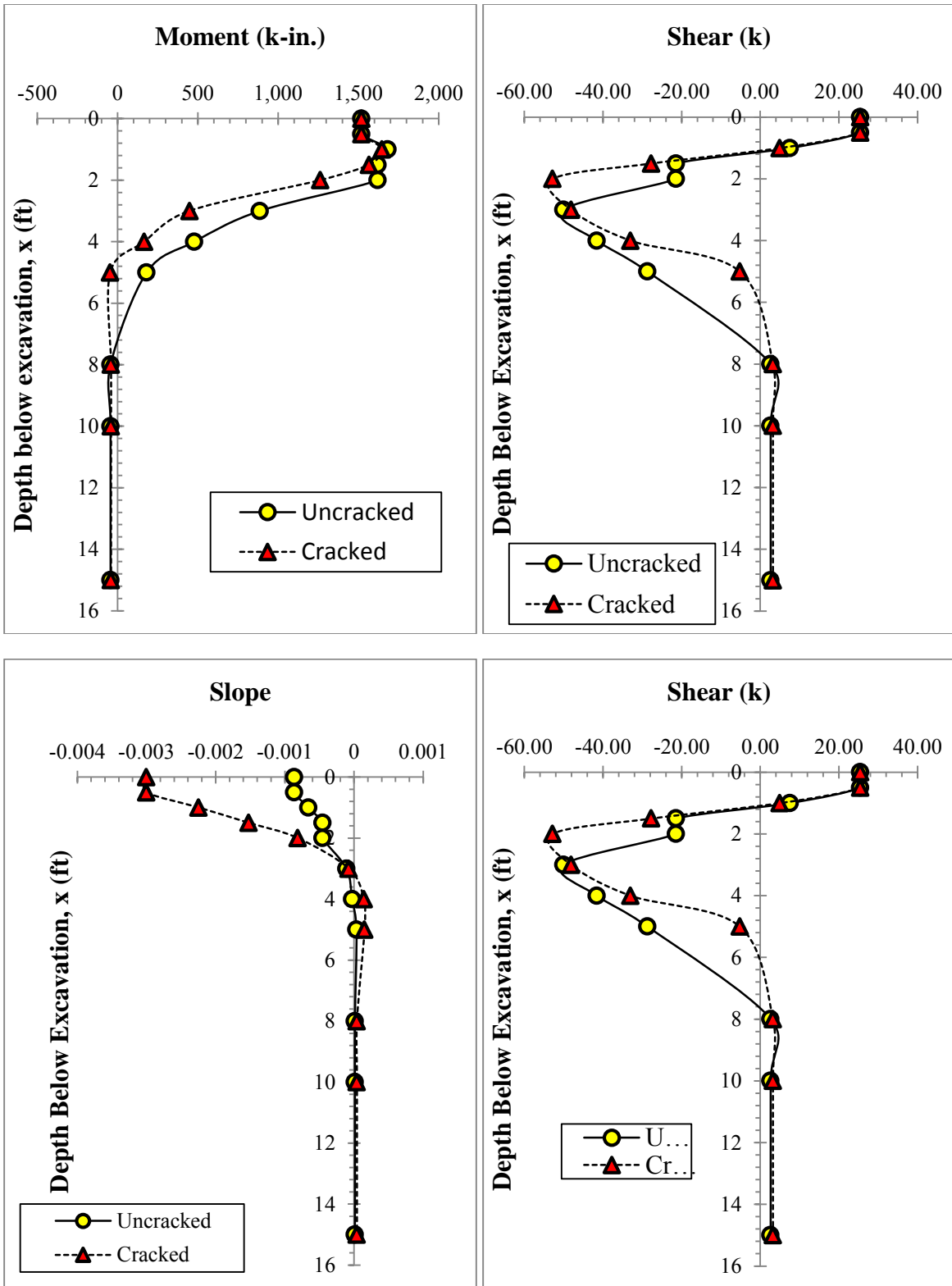


Figure A.21: Moment, shear, slope, and deflection for non-dimensional method ($\gamma_{ef}=90$ pcf)

APPENDIX B: SITE PIEZOMETRIC DATA

This section presents the data from the piezometers. A total of five borings were installed on site. On January 12, 2010, a piezometer screened 5 to 15 feet was installed in a boring from the site investigation by Fugro, Inc. (Table B-1 and Figure B.1). This piezometer was used to monitor the local water level conditions. On February 23, 2012, four more piezometers were installed in boring holes for a site investigation by Fugro, Inc. (Table B-1 and Figure B.1). These piezometers were used to monitor the water levels in the inundation test area. The piezometers were surrounded with a permeable sand and gravel interface between the piezometer and the walls of the borehole. Readings were taken using a buzzing water level indicator and a tape measure.

Table B-1: Location, installation date, and screen location for the piezometers

Piezometer	Installation date	Diameter	Screen location	Location	
				Distance perpendicular from the wall	Distance from wall center-line
B-3	12-Jan-10	2 inches	5 to 15 feet	16 feet	54 feet east
A	23-Feb-12	2 inches	5 to 15 feet	9 feet	9 feet west
B	23-Feb-12	1 inch	3.4 to 4.6 feet	15.1 feet	5.5 feet west
C	23-Feb-12	2 inches	5 to 15 feet	15.5 feet	3 feet east
D	23-Feb-12	1 inch	3.6 to 4.8 feet	7.3 feet	7.5 feet east

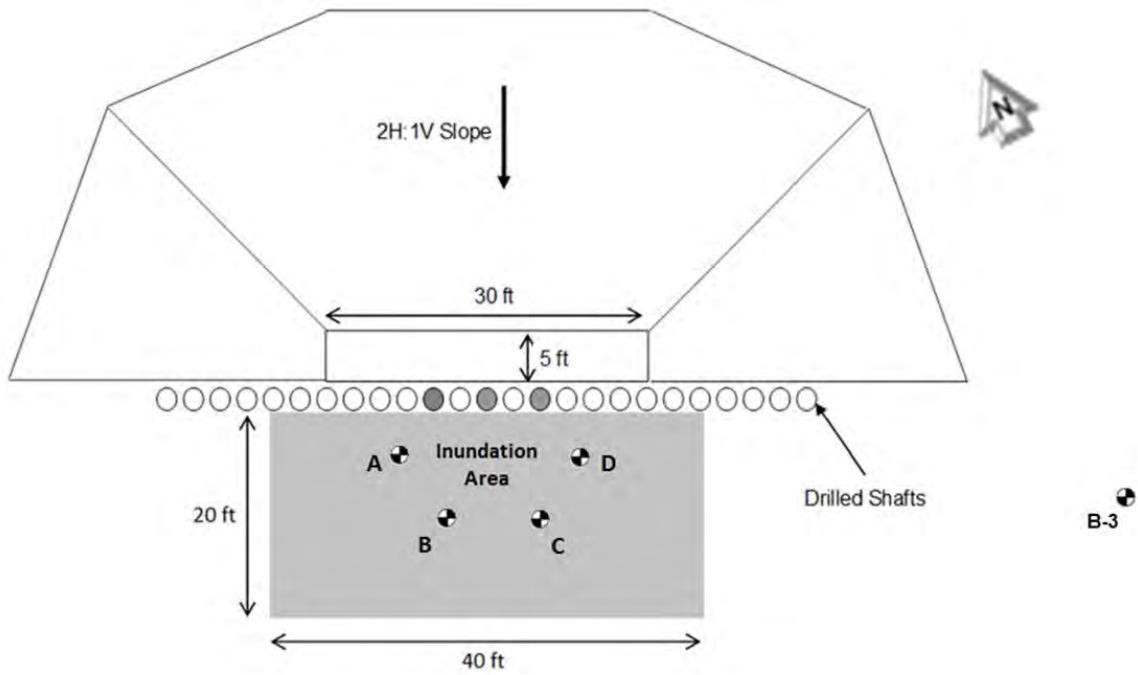


Figure B.1: Plan view of piezometer locations.

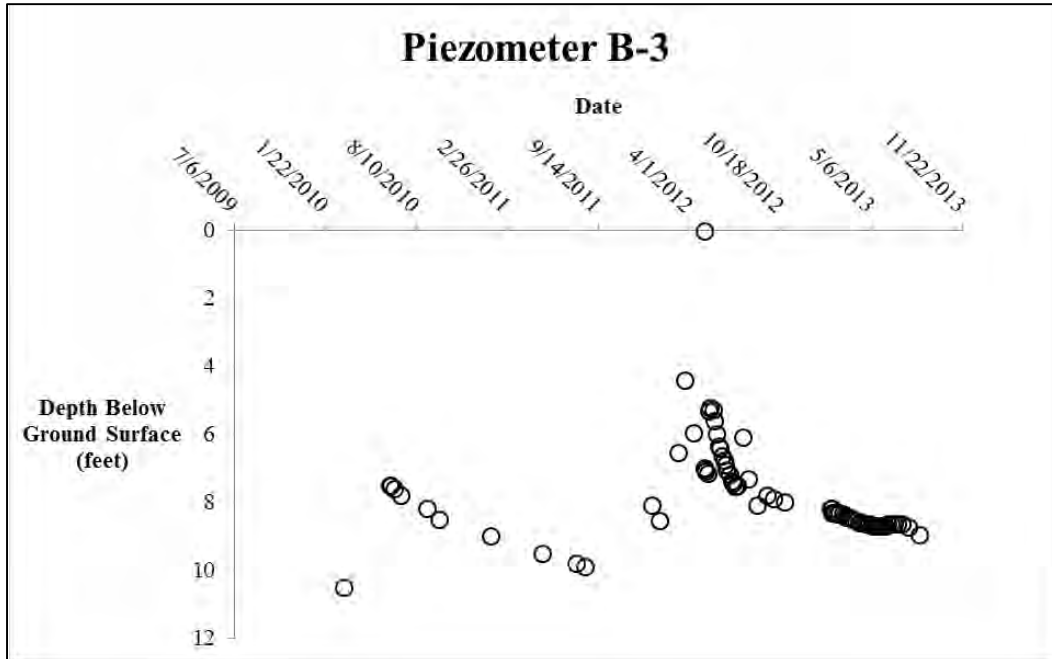


Figure B.2: Piezometer readings for Piezometer B-3

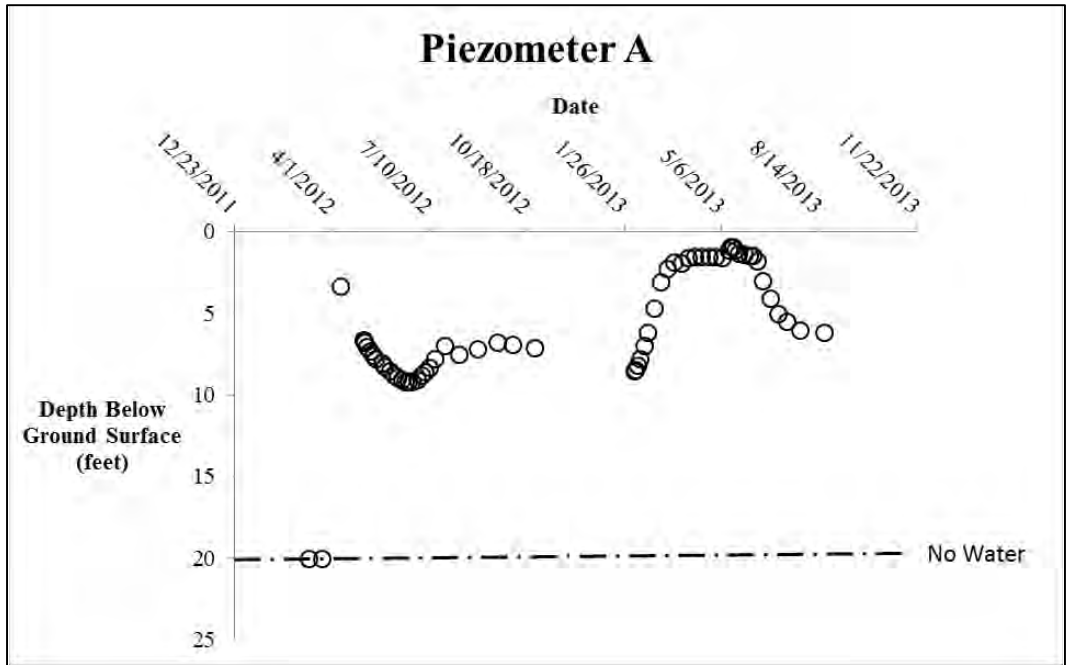


Figure B.3: Piezometer readings for Piezometer A

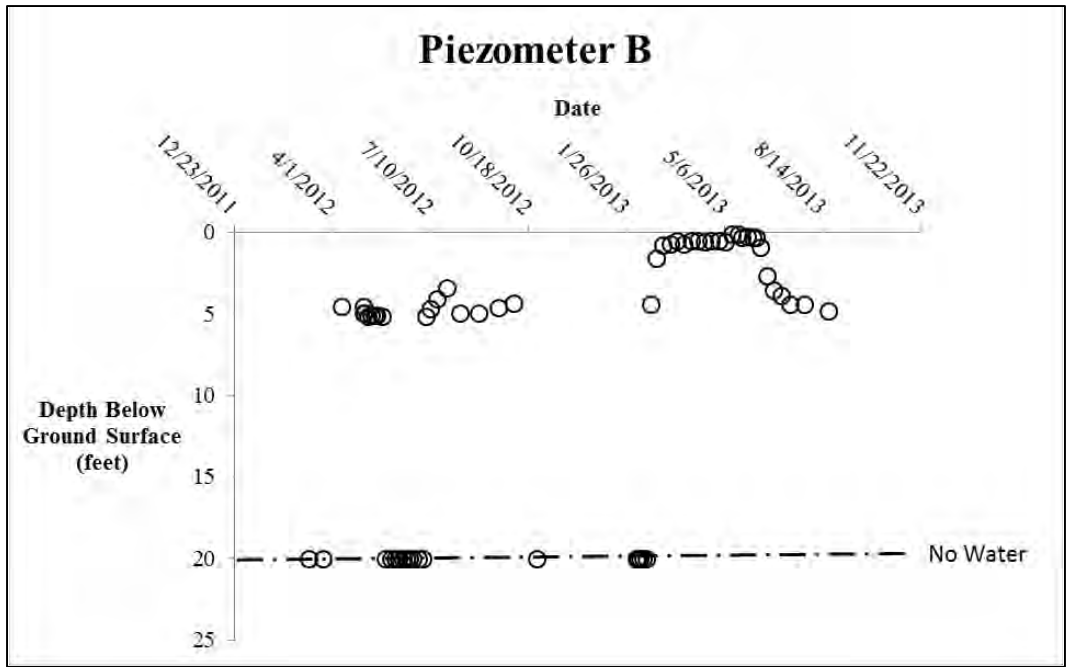


Figure B.4: Piezometer readings for Piezometer B

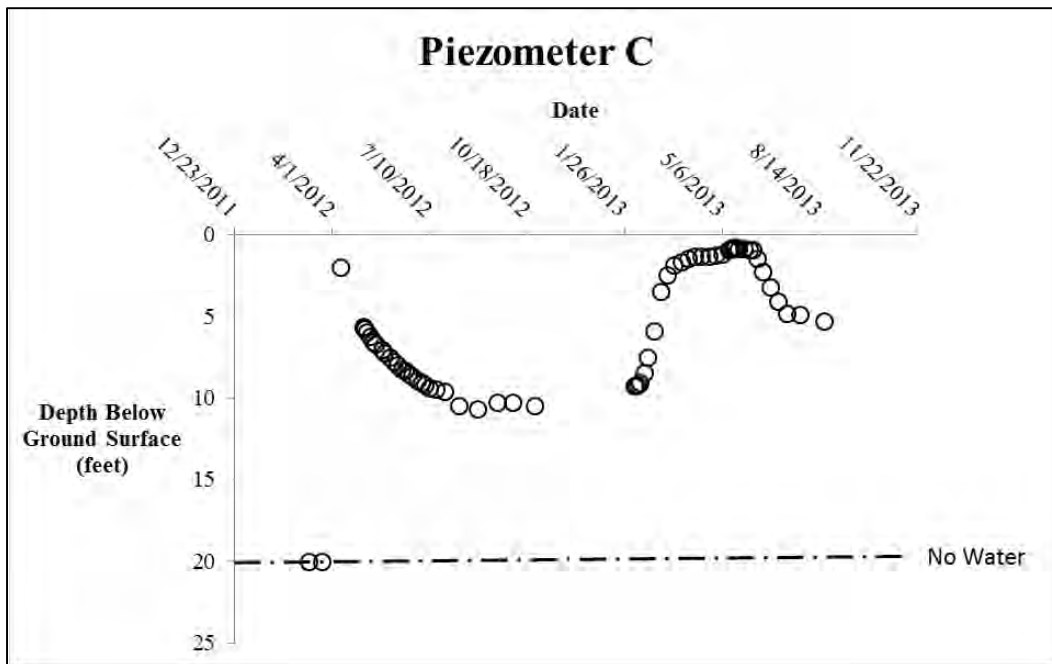


Figure B.5: Piezometer readings for Piezometer C

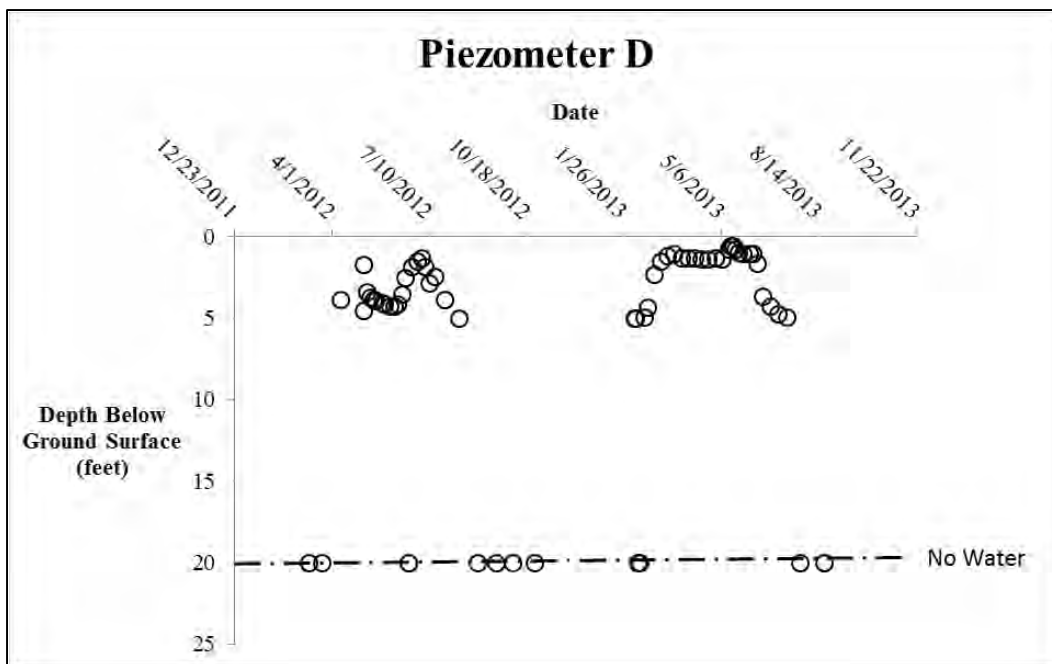


Figure B.6: Piezometer readings for Piezometer D

APPENDIX C: SITE MOISTURE CONTENT DATA

This section presents the moisture content data taken from physical samples and the data obtain from the Time Domain Reflectometry (TDR) probes.

C.1: Moisture Contents

Physical moisture contents were taken using a hand auger and using a drilling rig to take split spoon samples. Table C.1 provides the dates and descriptions of the moisture content measurements. The results of the measurements are shown in Figure C.1 through Figure C.17.

Table C.1: Dates of moisture content measurements and description.

Date	Description
January 12, 2010	Initial site investigation before construction of the wall by Fugro, Inc. Moisture contents were taken from two borings.
August 3, 2010	Grab samples taken during excavation.
October 6 & 14, 2010	Grab samples taken during installation of TDR probes.
March 25, 2011	Samples taken with a hand auger. M-1 consisted of gravel and dust. M-2 consisted of good samples of the dark clay.
May 13, 2011	Samples taken with a hand auger after two inches of rain fell that morning and previous day. M-5 and M-6 had a small amount of standing water at the time of
May 23, 2011	An infiltration test was performed away from the wall. Samples from a hand auger were taken before and after.
December 15, 2011	Samples taken using a hand auger.
January 26, 2012	Samples taken using a hand auger.
February 23, 2012	A site investigation was performed by Fugro, Inc. Moisture measurements were taken from trimmings and from samples used for UU testing. Four borings were performed.
May 3, 2012	Samples were taken using a hand auger prior to the first inundation cycle.
July 5, 2012	Samples were taken using a hand auger at the end of the first inundation cycle.
July 18, 2012	A site investigation was performed by Fugro, Inc. Three borings were performed.
January 31, 2013	A site investigation was performed by Fugro, Inc. Three borings were performed.
February 4, 2013	Samples were taken using a hand auger prior to the second inundation cycle.
June 12, 2013	Samples were taken using a hand auger at the end of the second inundation cycle.
June 26, 2013	A site investigation was performed by Fugro, Inc. Two borings were performed in the inundation area.
June 26, 2013	A site investigation was performed by Fugro, Inc. One boring was performed away from area affected by the inundation area.

January 12, 2010

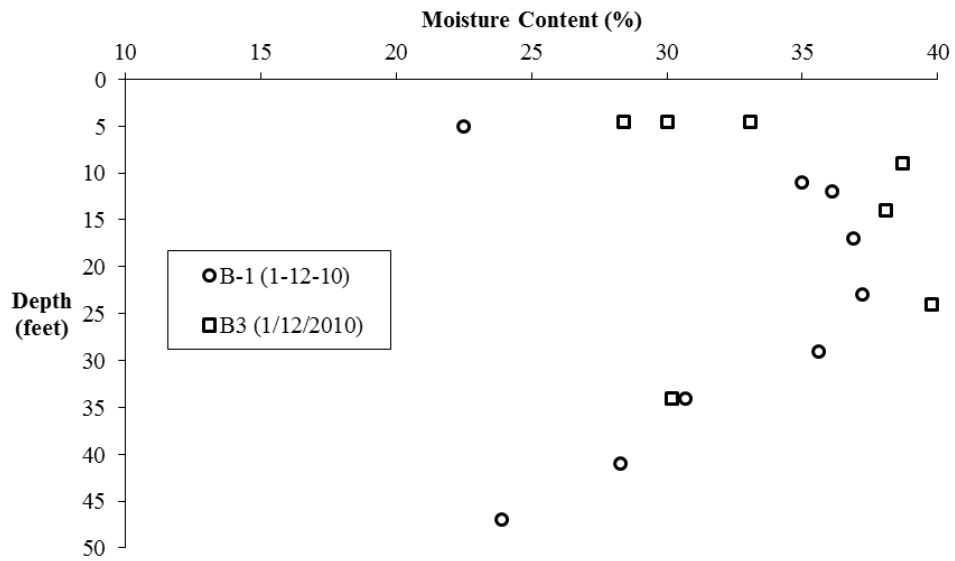


Figure C.1: Initial site investigation before construction of the wall by Fugro, Inc. Moisture contents were taken from two borings.

August 3, 2010

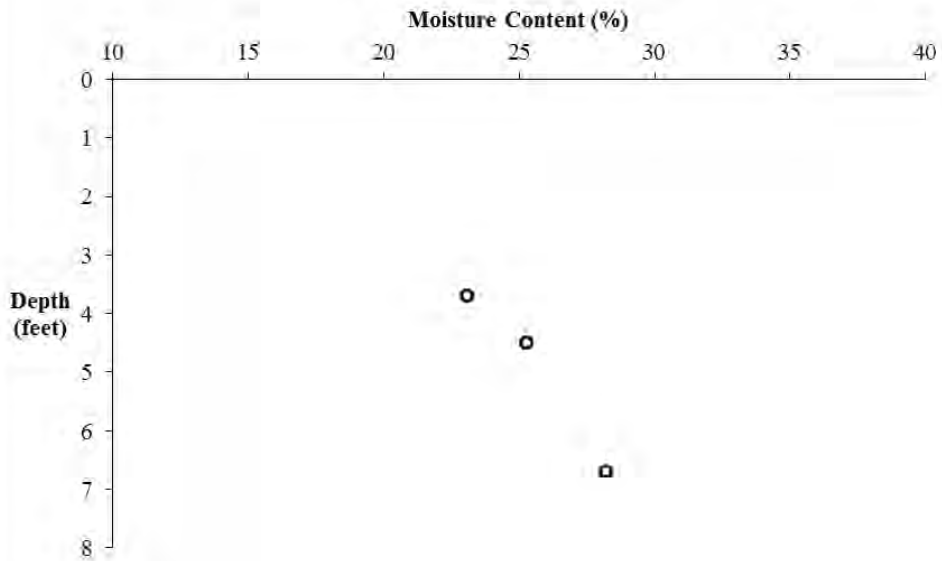


Figure C.2: Grab samples taken during excavation.

October 6 & 14, 2010

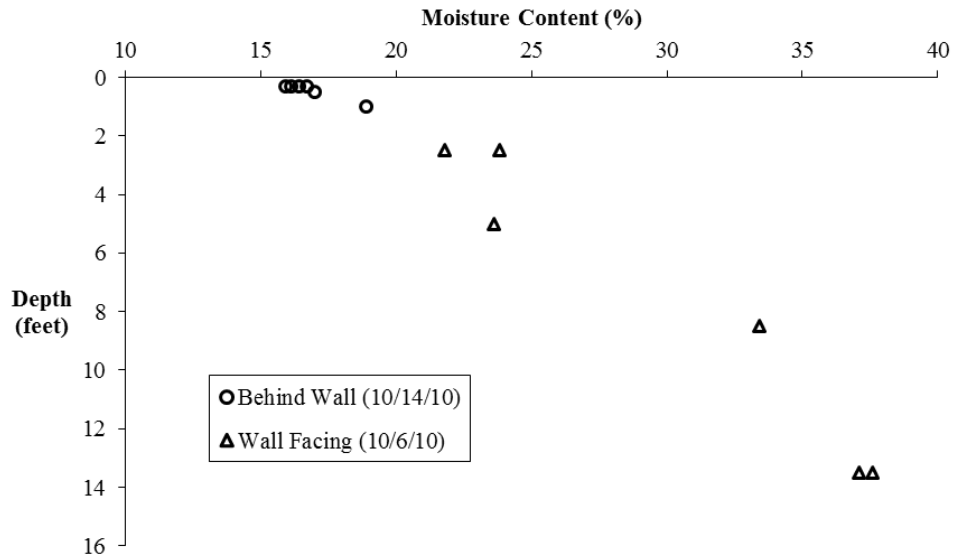


Figure C.3: Grab samples taken during installation of TDR probes.

March 25, 2011

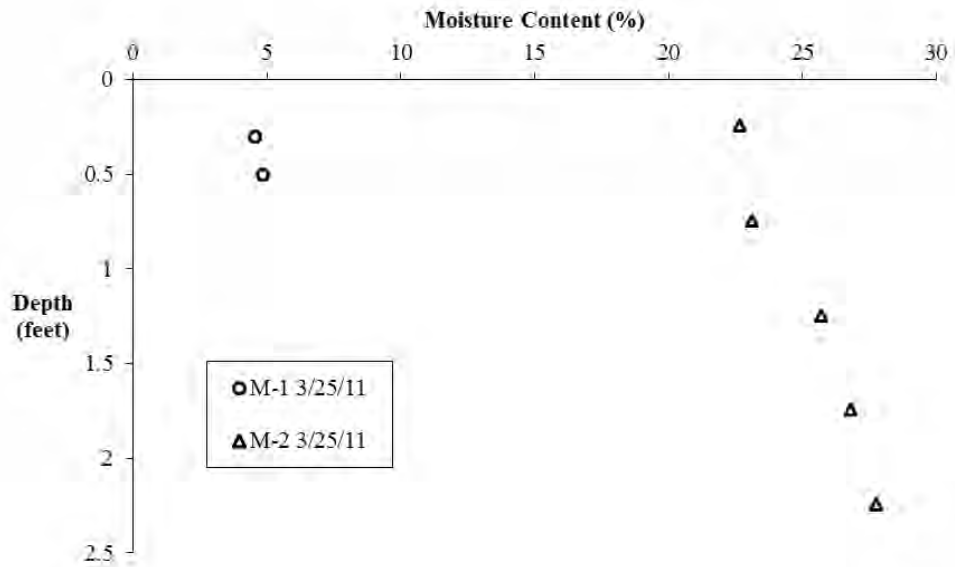


Figure C.4: Samples taken with a hand auger. M-1 consisted of gravel and dust. M-2 consisted of good samples of the dark clay.

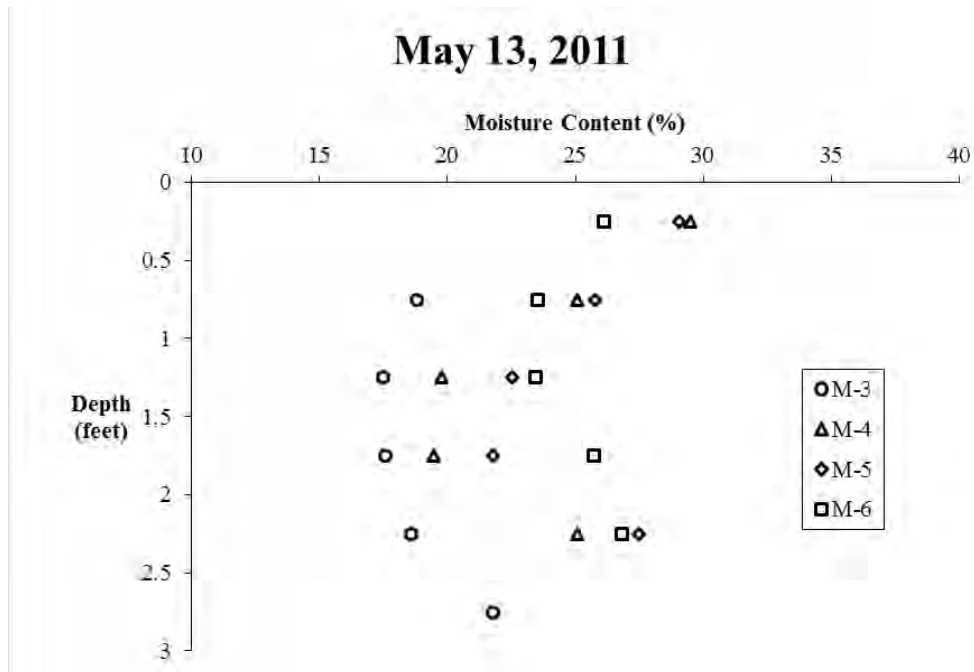


Figure C.5: Samples taken with a hand auger after two inches of rain fell that morning and previous day. M-5 and M-6 had a small amount of standing water at the time of sampling.

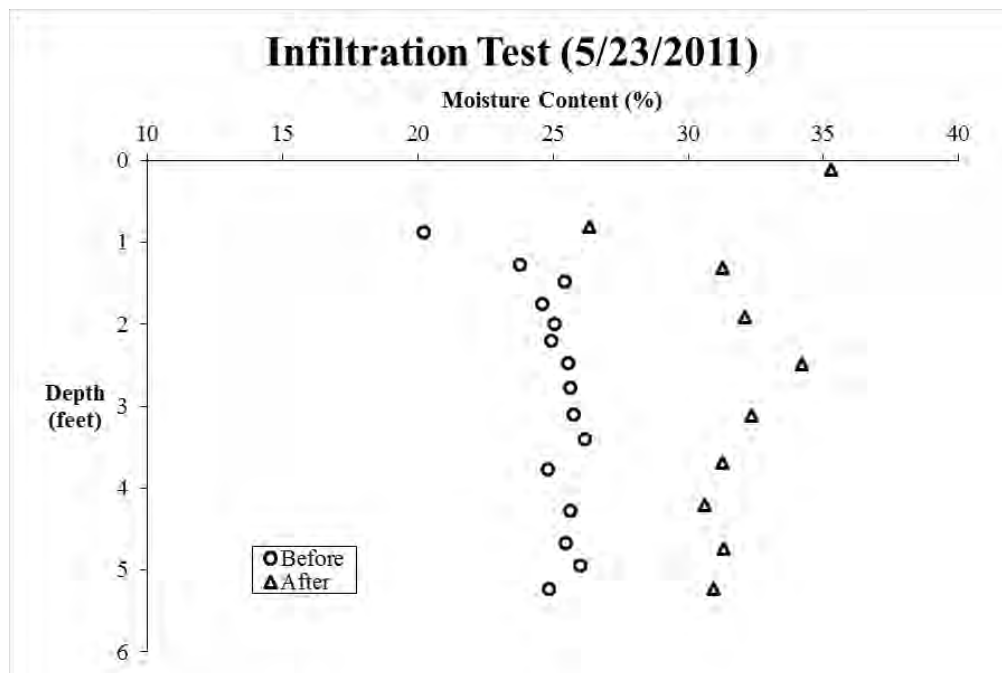


Figure C.6: An infiltration test was performed away from the wall. Samples from a hand auger were taken before and after.

December 15, 2011

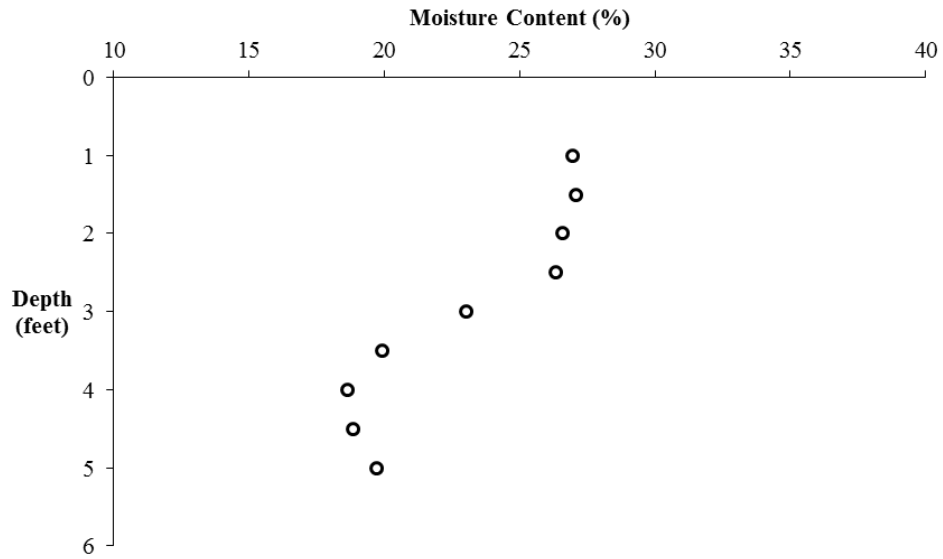


Figure C.7: Samples taken using a hand auger.

January 26, 2012

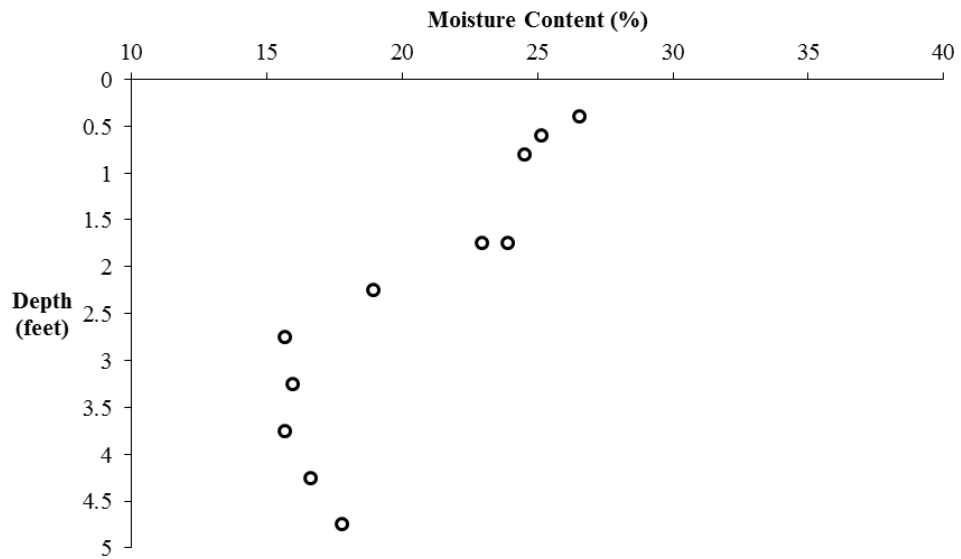


Figure C.8: Samples taken using a hand auger.

February 23, 2012

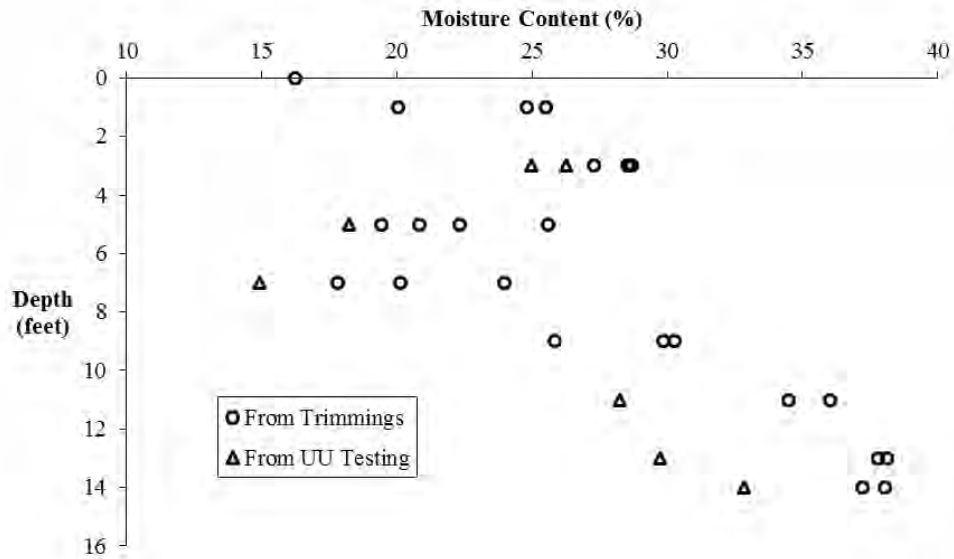


Figure C.9: A site investigation was performed by Fugro, Inc. Moisture measurements were taken from trimmings and from samples used for UU testing. Four borings were performed.

May 3, 2012

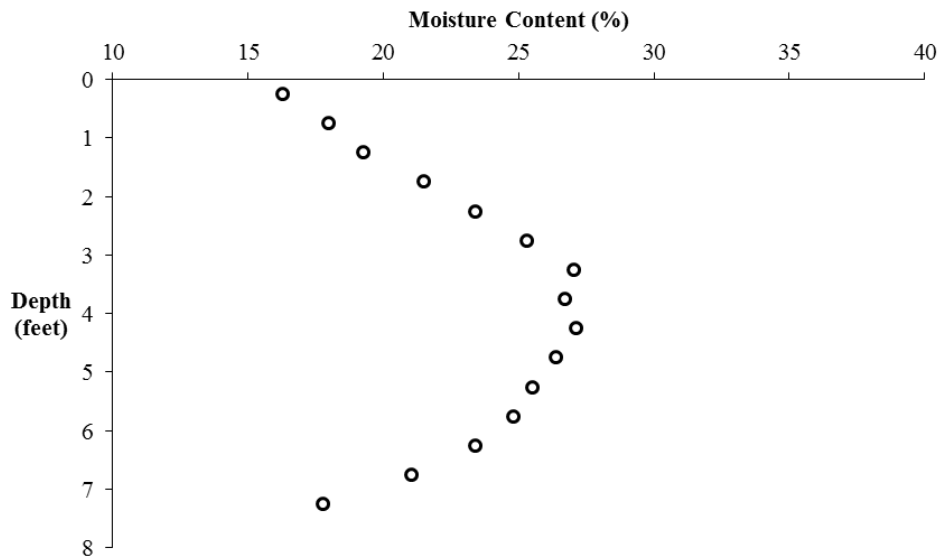


Figure C.10: Samples were taken using a hand auger prior to the first inundation cycle.

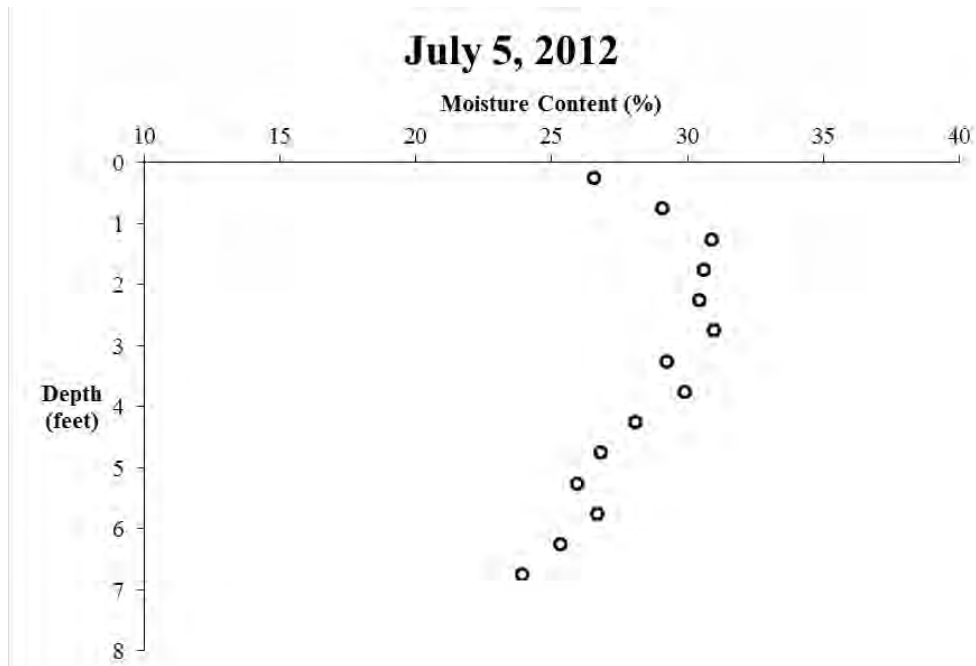


Figure C.11: Samples were taken using a hand auger at the end of the first inundation cycle.

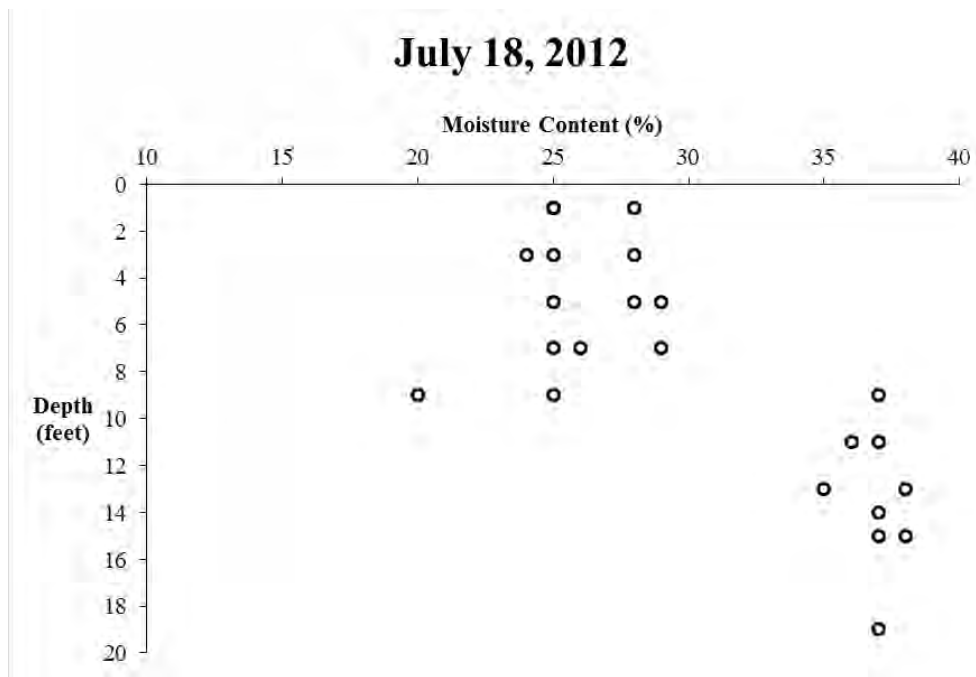


Figure C.12: A site investigation was performed by Fugro, Inc. Three borings were performed.

January 31, 2013

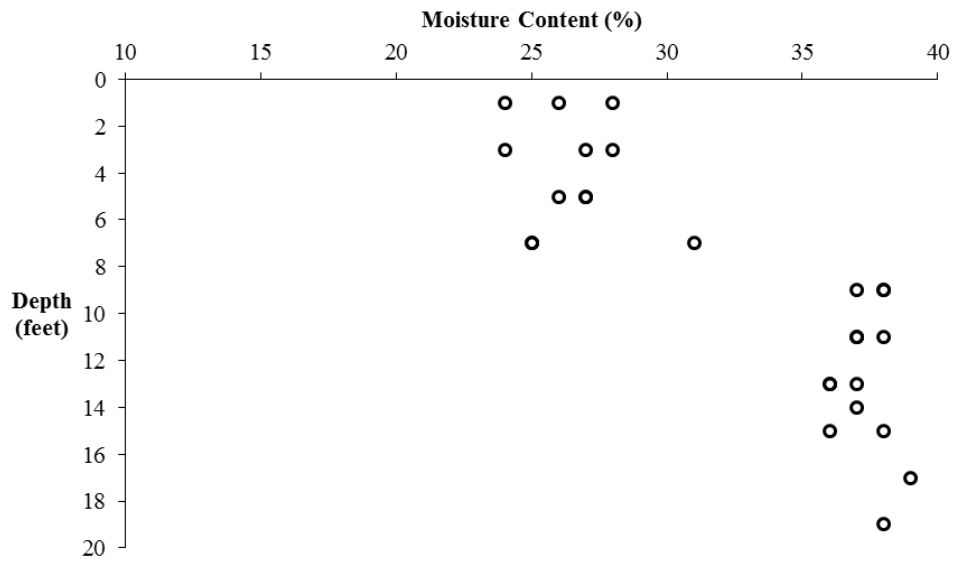


Figure C.13: A site investigation was performed by Fugro, Inc. Three borings were performed.

February 4, 2013

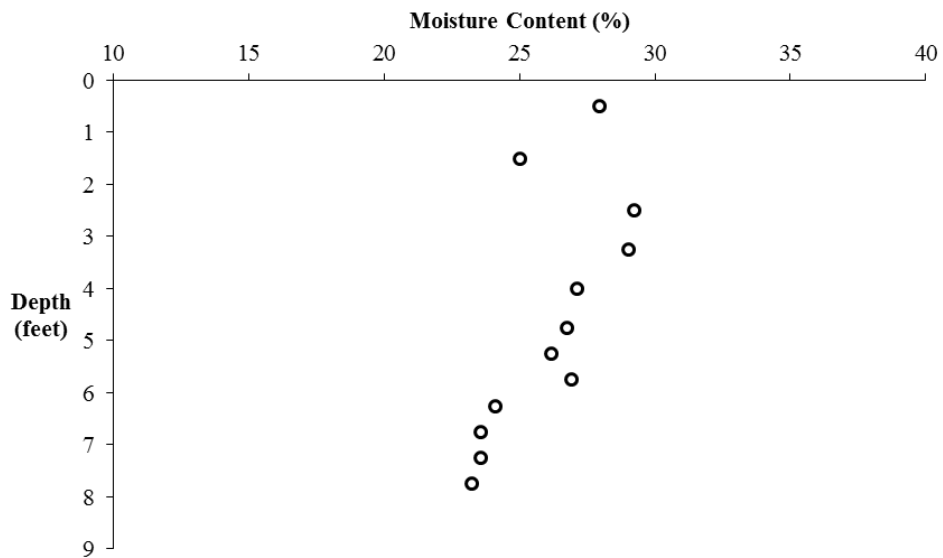


Figure C.14: Samples were taken using a hand auger prior to the second inundation cycle.

June 12, 2013

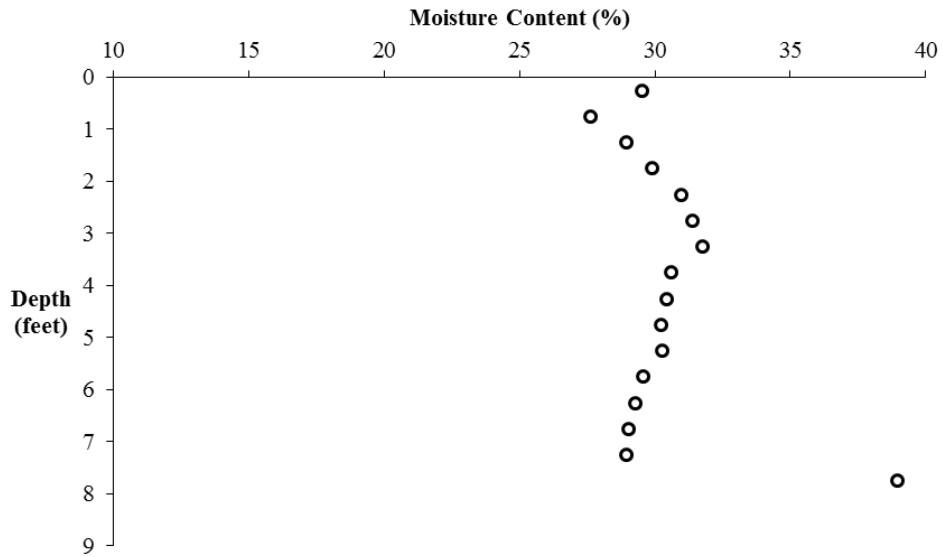


Figure C.15: Samples were taken using a hand auger at the end of the second inundation cycle.

June 26, 2013

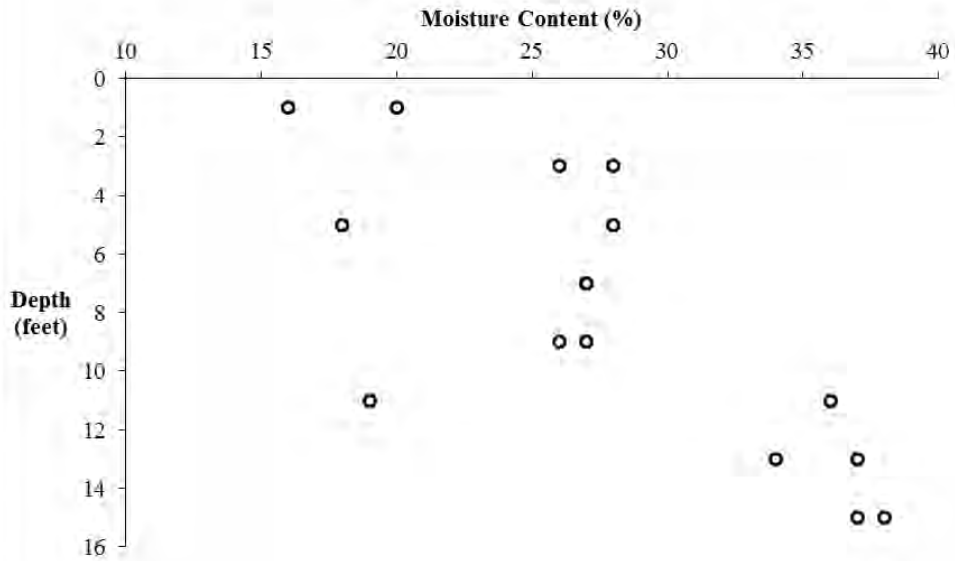


Figure C.16: A site investigation was performed by Fugro, Inc. Two borings were performed in the inundation area.

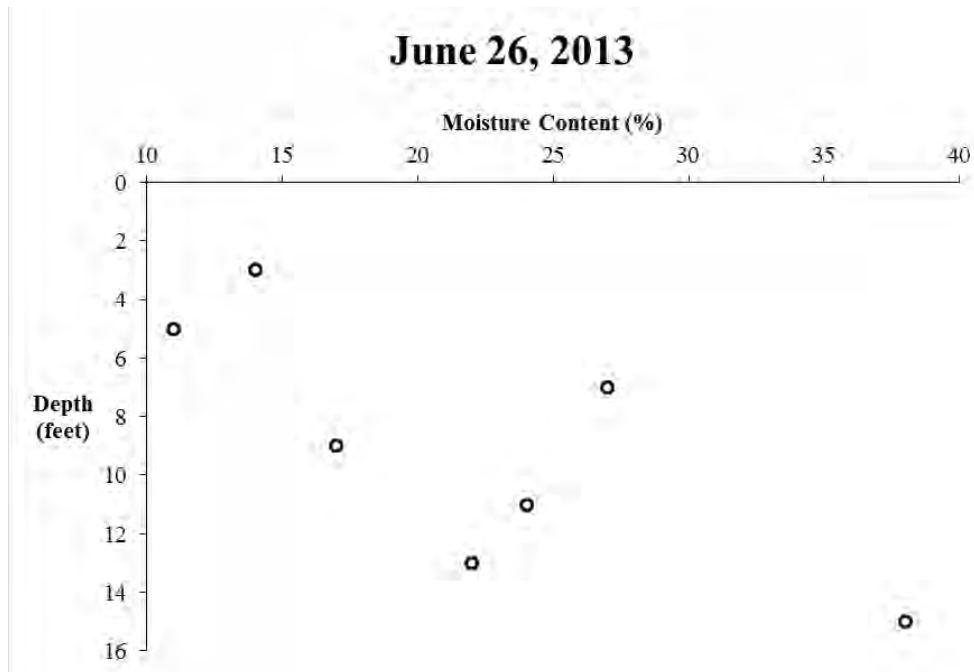


Figure C.17: A site investigation was performed by Fugro, Inc. One boring was performed away from area affected by the inundation area.

C.2: Time Domain Reflectometry Probes

The TDR probes were used in an attempt to monitor the volumetric water content of the soil on site. The system consists of 20 Campbell Scientific, Inc. CS645-L probes with 70 feet of LMR-200 low loss cable length, a Campbell Scientific, Inc. TDR100, three Campbell Scientific, Inc. SDX50 multiplexers, and a Campbell Scientific, Inc. CR1000. The TDR100 generates the signals that are sent to the probes and the CR1000 logs the data. CS645-L probes are manufactured with rod lengths of 7.5 centimeters (2.95 inches) and rod diameters of 0.159 centimeters (0.06 inches).

The TDR probes were to be installed at various depths behind the wall along the 15 feet cantilevered height of the wall. Table C.1 and Figure C.18 show the location of the 20 TDR probes in the ground.

Table C. 1: Location of the TDR probes installed in the soil

Probe #	Depth below Ground Surface (feet)	Distance Behind the Wall (feet)
1	1	20
2	1.75	1
3	13.5	1.6
4	1.5	1
5	0.9	1
6	0.5	10
7	3.7	5.2
8	13.6	1.7
9	6	3.5
10	2.5	1.7
11	9.2	1.8
12	1.8	1.9
13	1.5	4.9
14	5.8	5.3
15	5.1	0.9
16	0.9	10
17	1.75	1
18	0.5	1
19	0.5	1
20	0.5	20

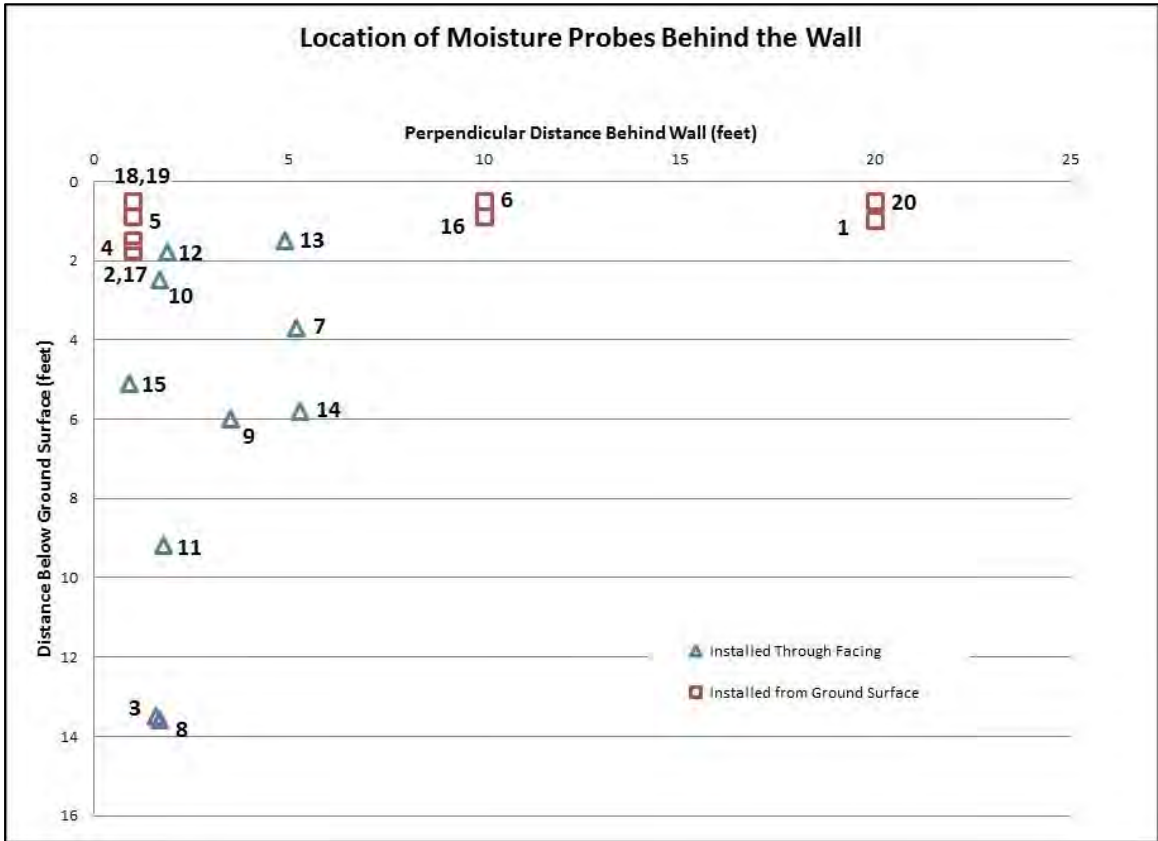


Figure C.18: Location of the 20 TDR probes installed behind the wall.

C.2.1: LA/L MEASUREMENTS

The following figures are the La/L measurements taken since installation of the TDR probes.

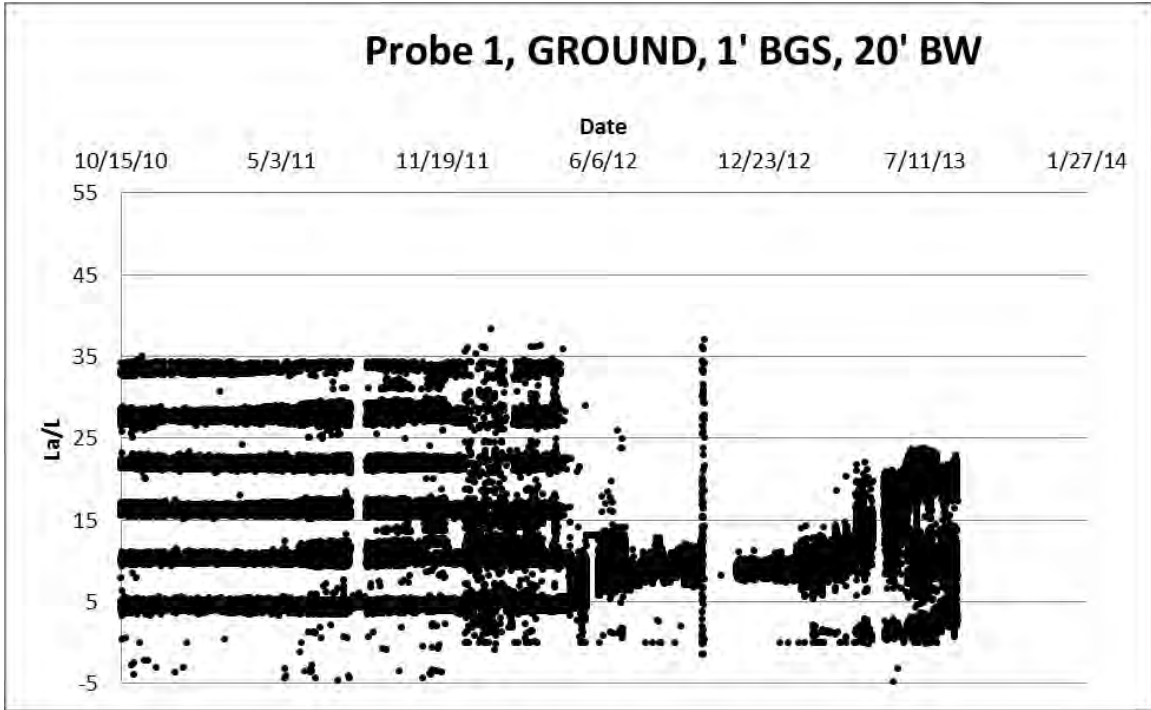


Figure C.19: Probe 1 installed from the ground surface located 1 foot below ground surface and 20 feet behind the wall.

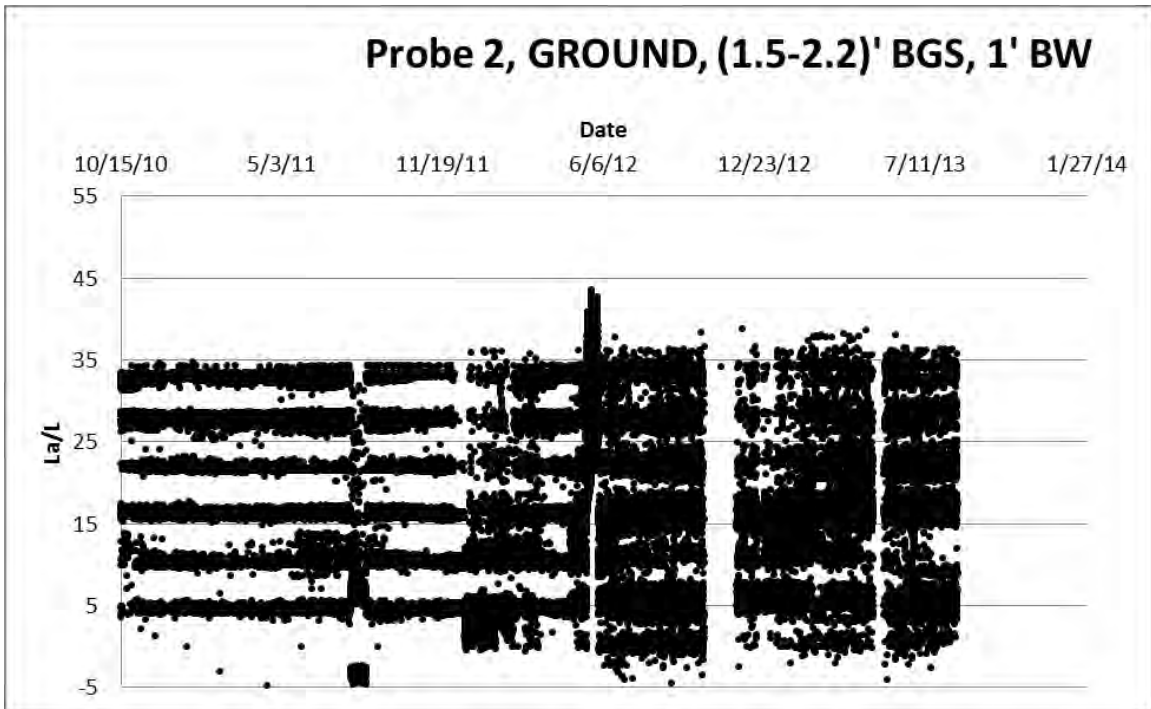


Figure C.20: Probe 2 installed from the ground surface located 1.5 to 2.2 feet below ground surface and 1 foot behind the wall.

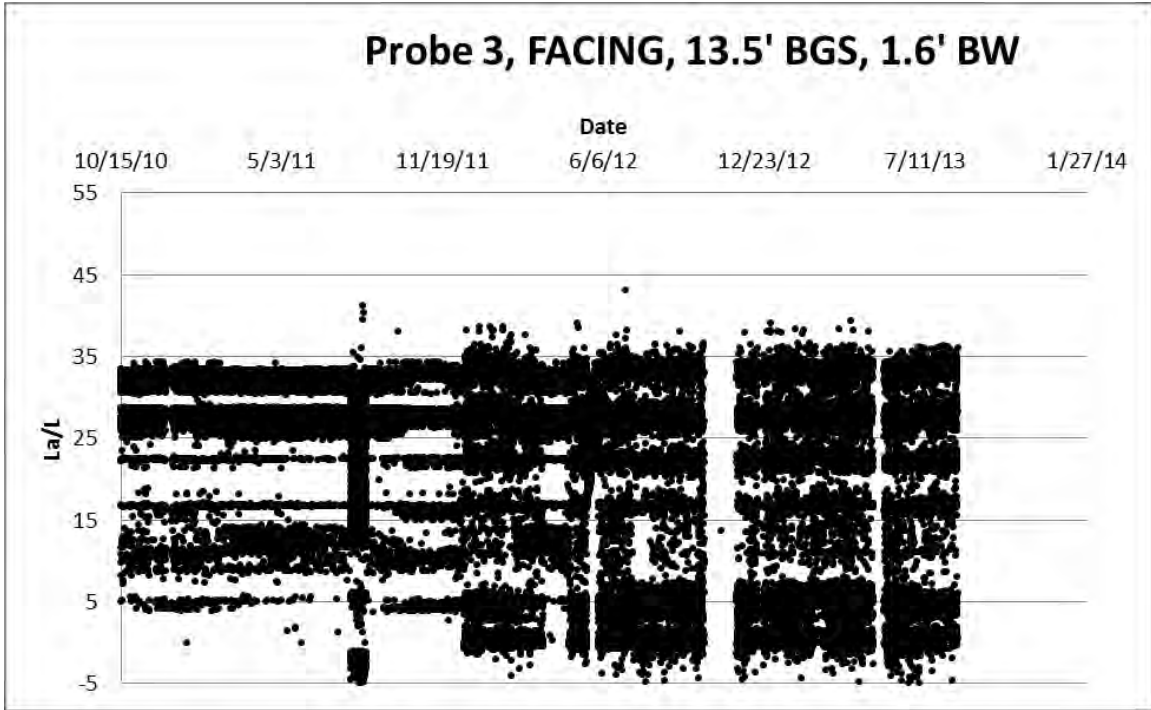


Figure C.21: Probe 3 installed through the facing located 13.5 feet below ground surface and 1.6 feet behind the wall.

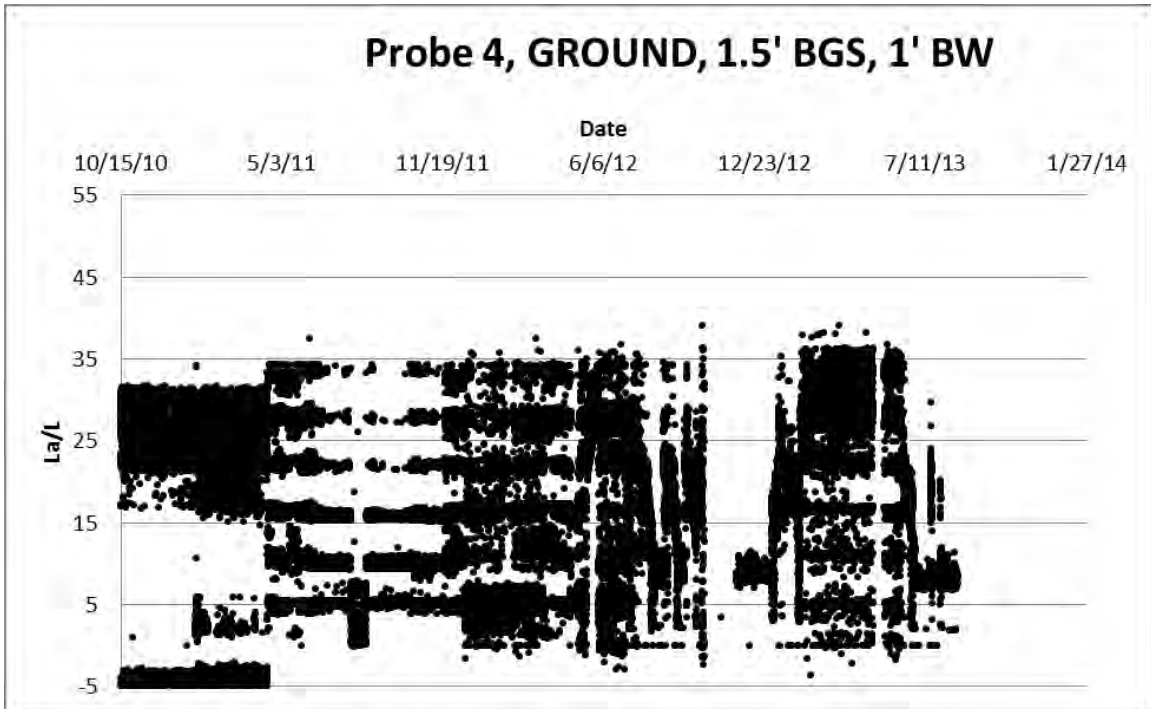


Figure C.22: Probe 4 installed from the ground surface located 1.5 feet below ground surface and 1 foot behind the wall.

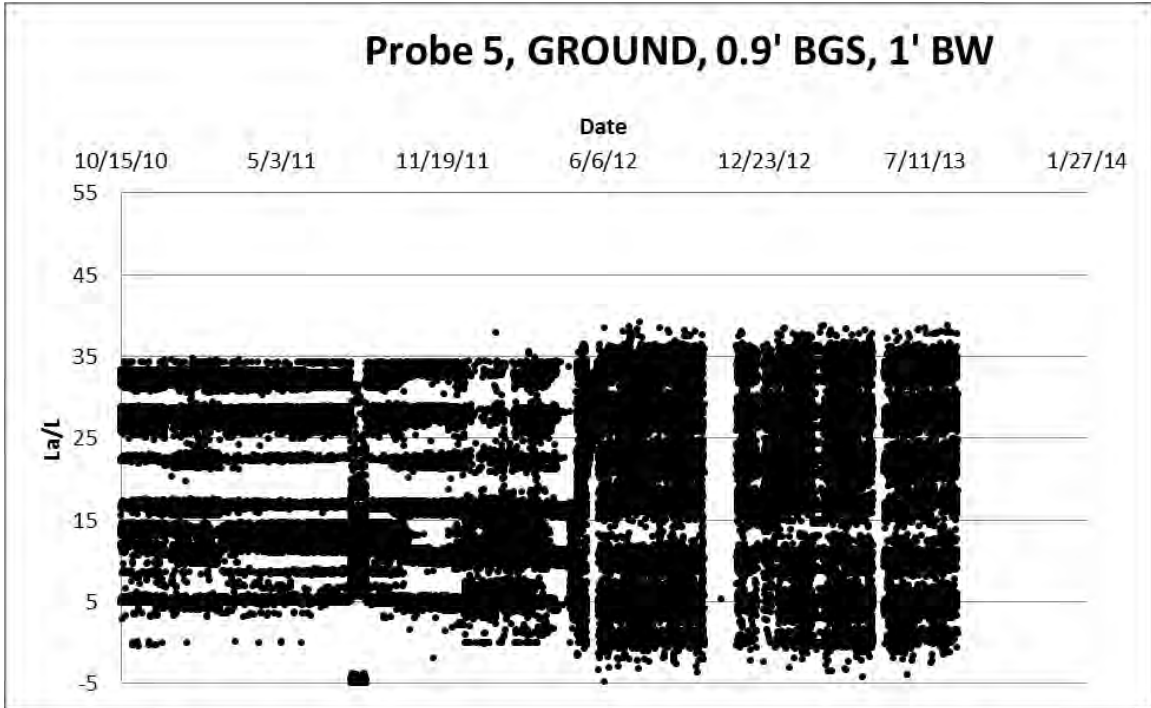


Figure C.23: Probe 5 installed from the ground surface located 0.9 feet below ground surface and 1 foot behind the wall.

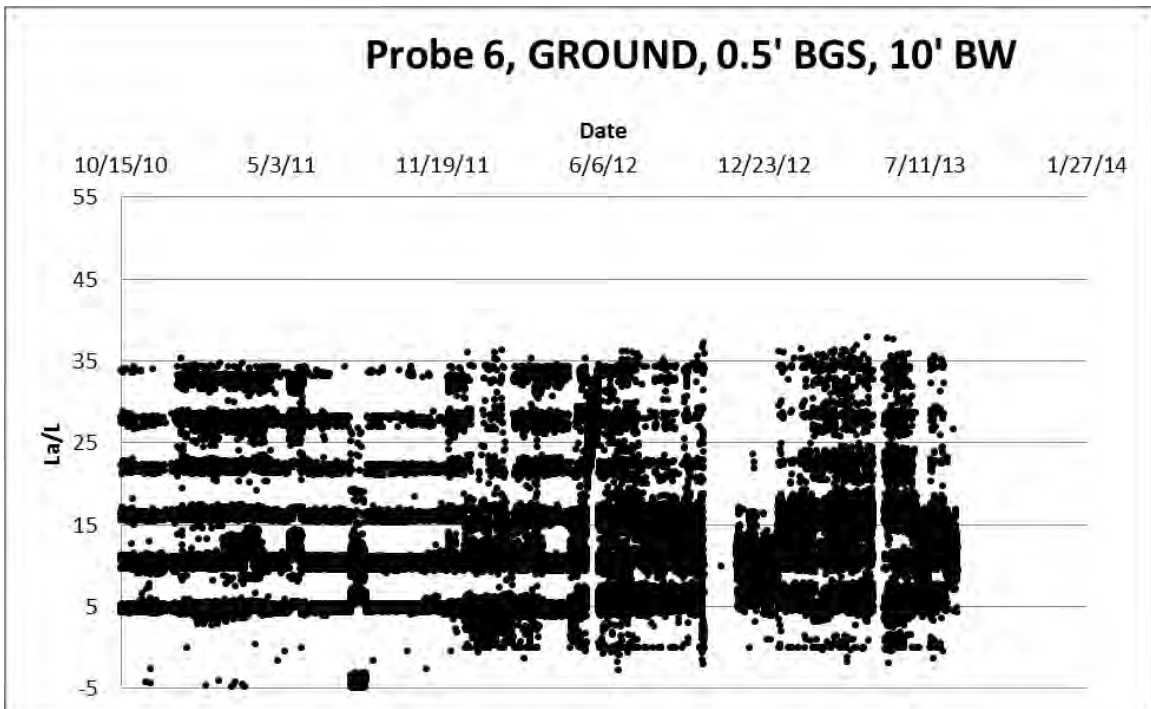


Figure C.24: Probe 6 installed from the ground surface located 0.5 feet below ground surface and 10 feet behind the wall.

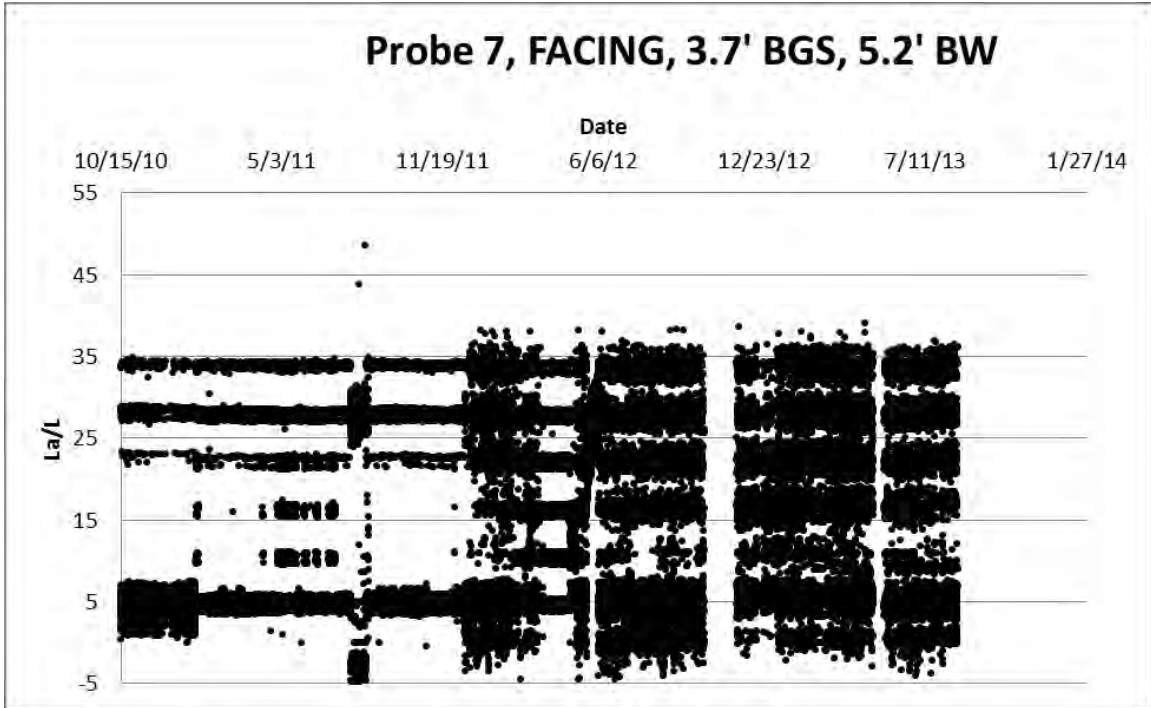


Figure C.25: Probe 7 installed from through the facing located 3.7 feet below ground surface and 5.2 feet behind the wall.

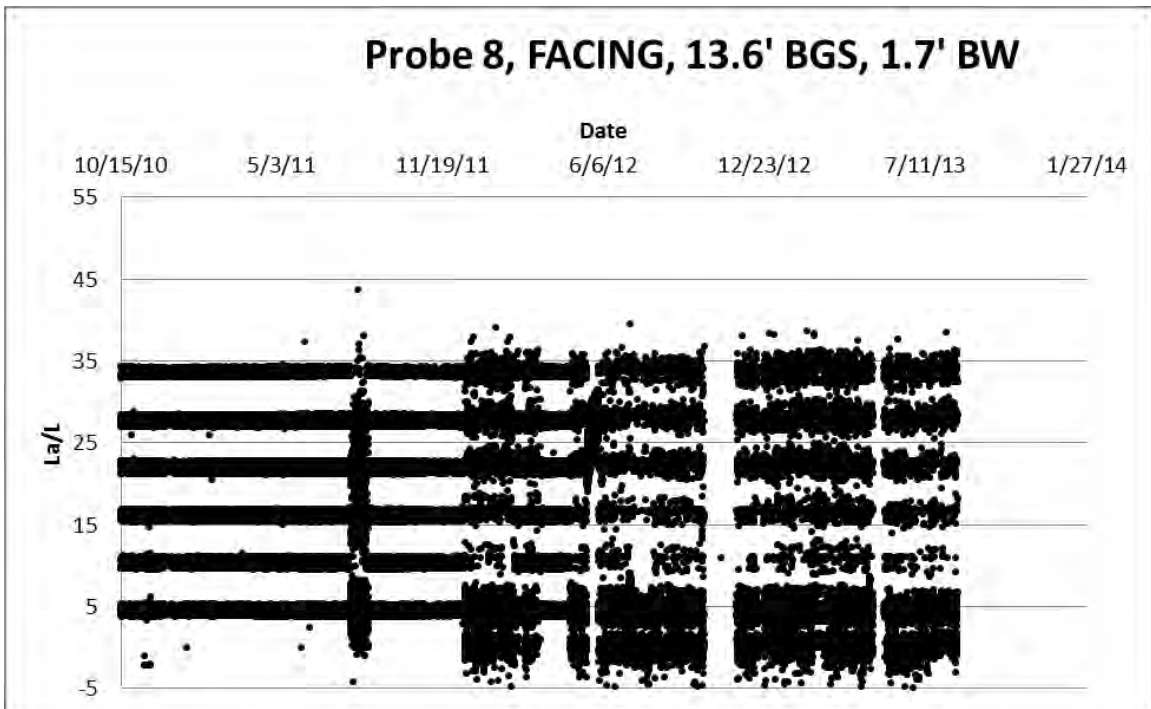


Figure C.26: Probe 8 installed from through the facing located 13.6 feet below ground surface and 1.7 feet behind the wall.

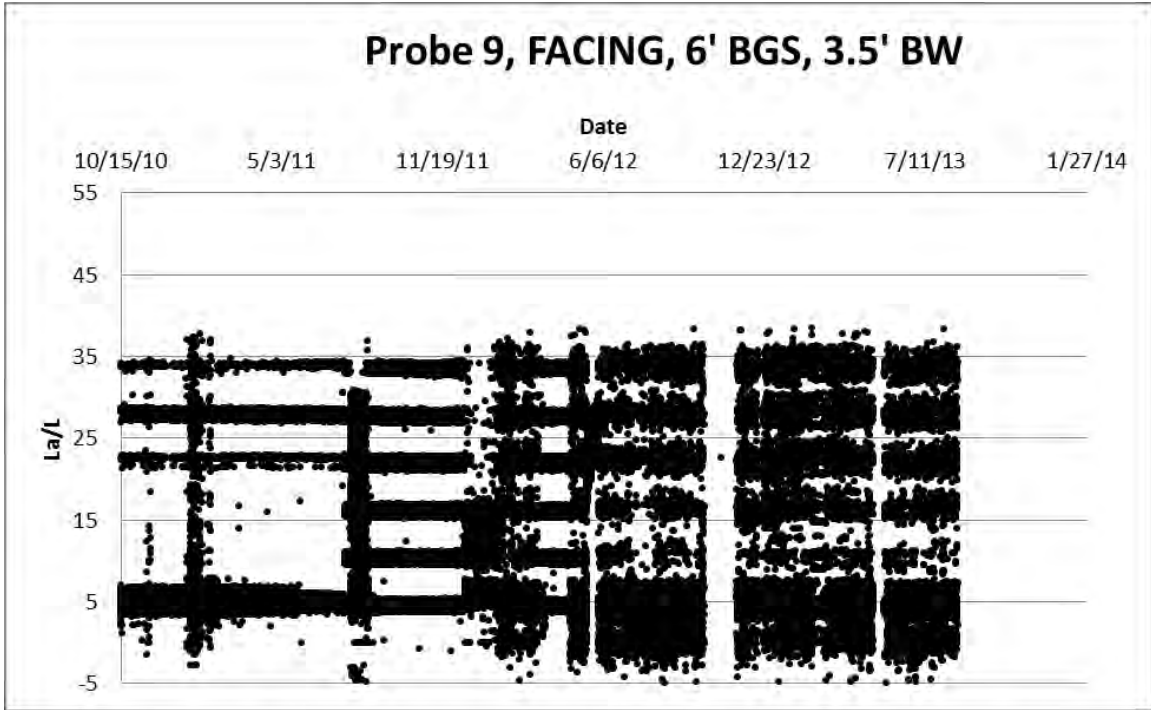


Figure C.27: Probe 9 installed from through the facing located 6 feet below ground surface and 3.5 feet behind the wall.

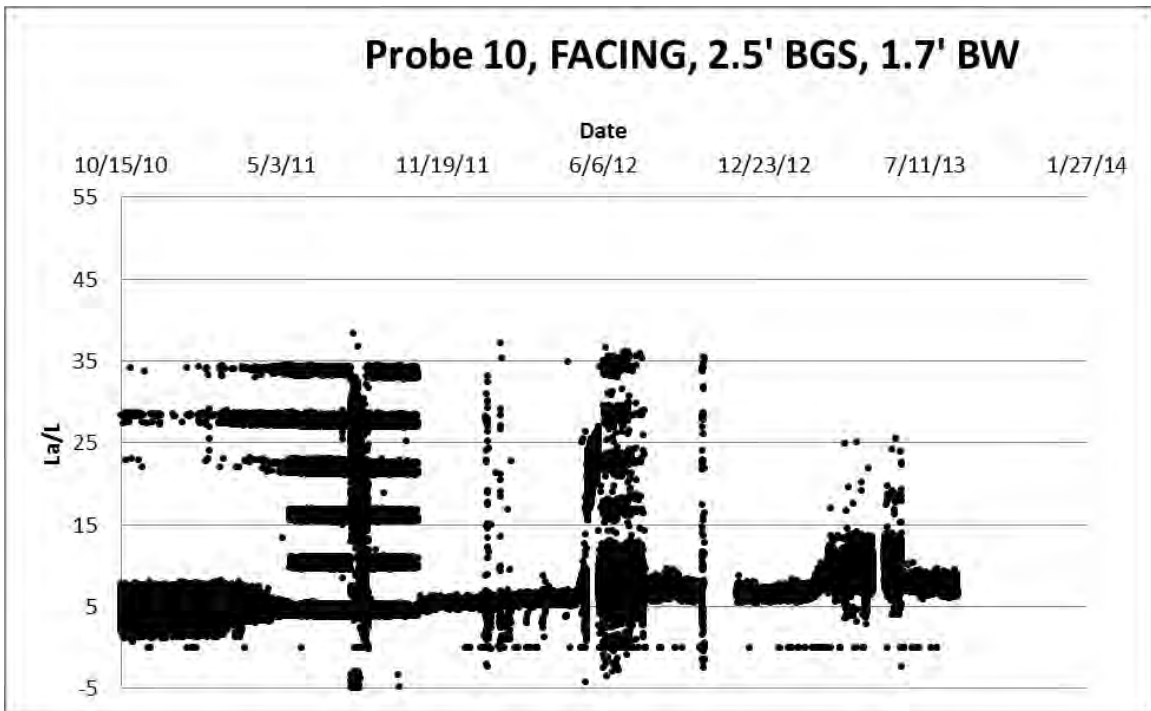


Figure C.28: Probe 10 installed from through the facing located 2.5 feet below ground surface and 1.7 feet behind the wall.

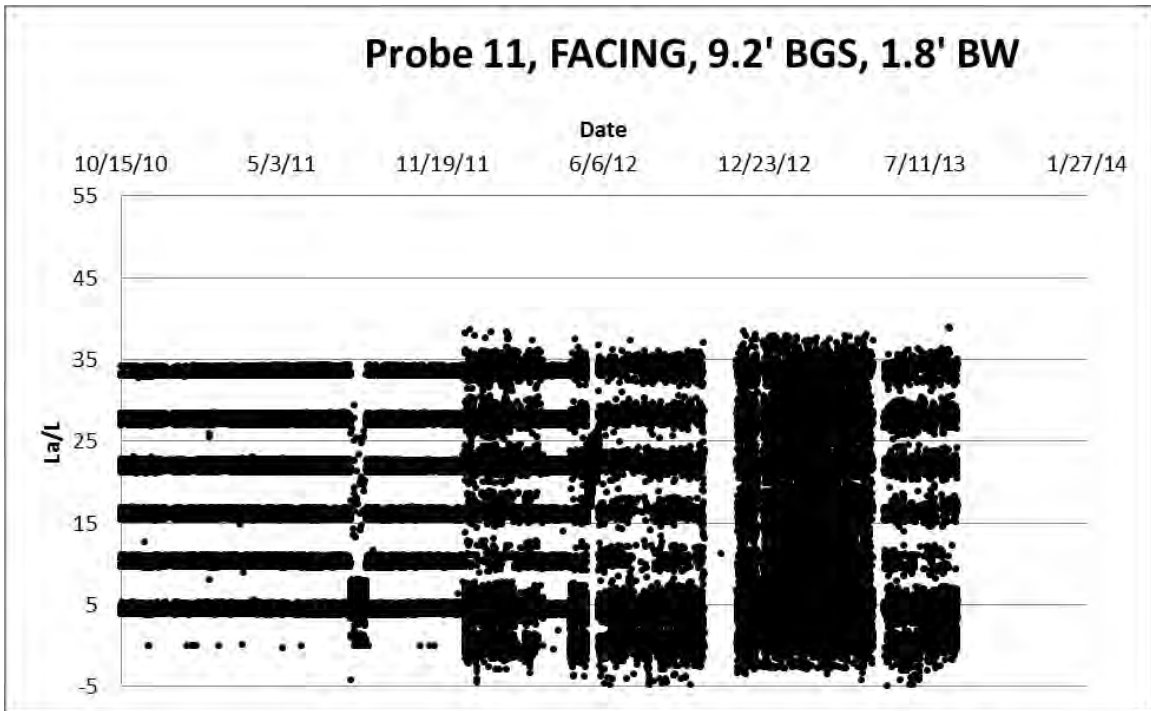


Figure C.29: Probe 11 installed from through the facing located 9.2 feet below ground surface and 1.8 feet behind the wall.

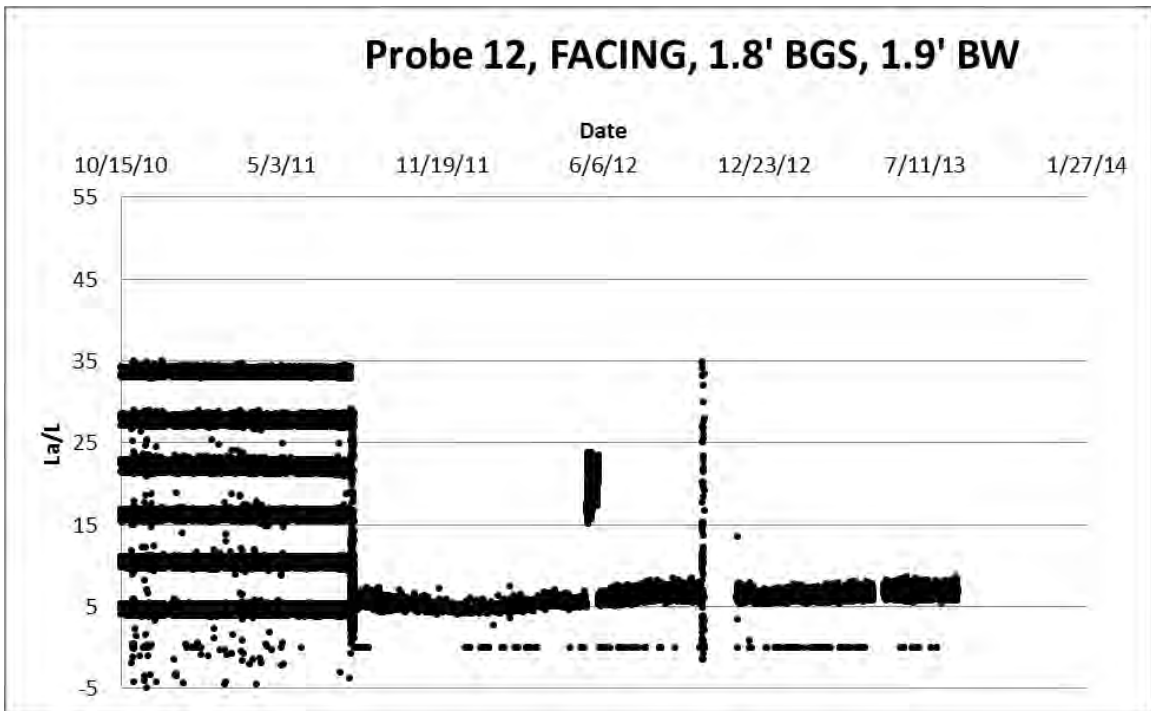


Figure C.30: Probe 12 installed from through the facing located 1.8 feet below ground surface and 1.9 feet behind the wall.

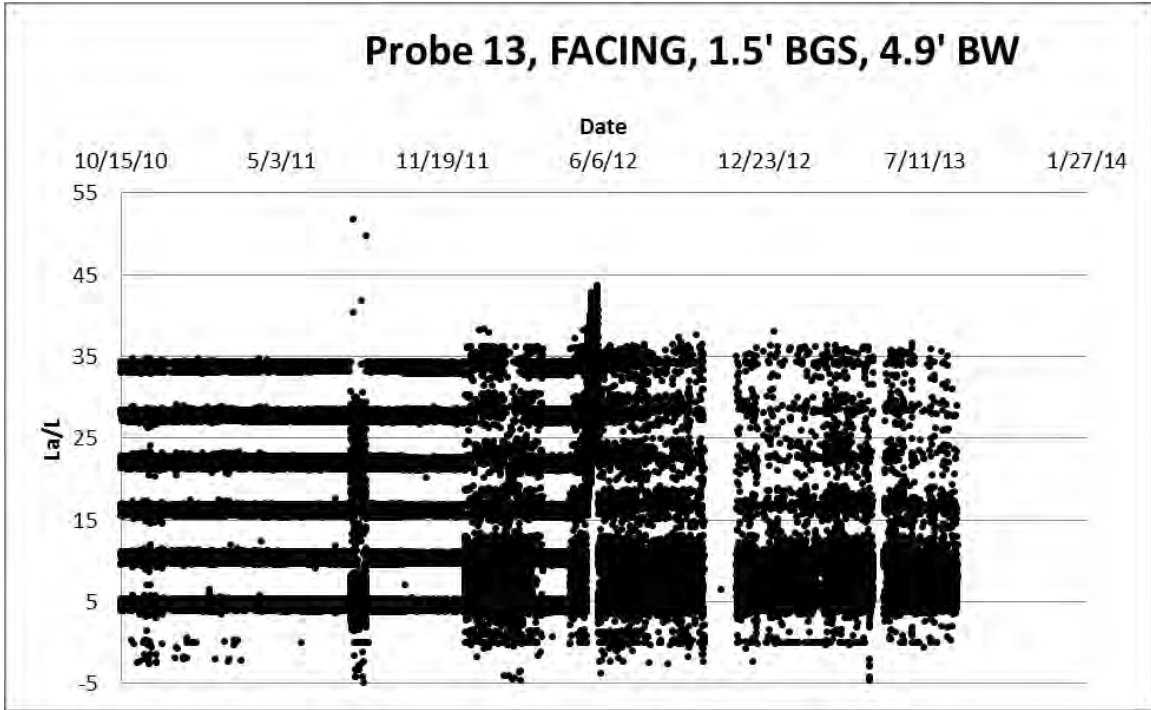


Figure C.31: Probe 13 installed from through the facing located 1.5 feet below ground surface and 4.9 feet behind the wall.

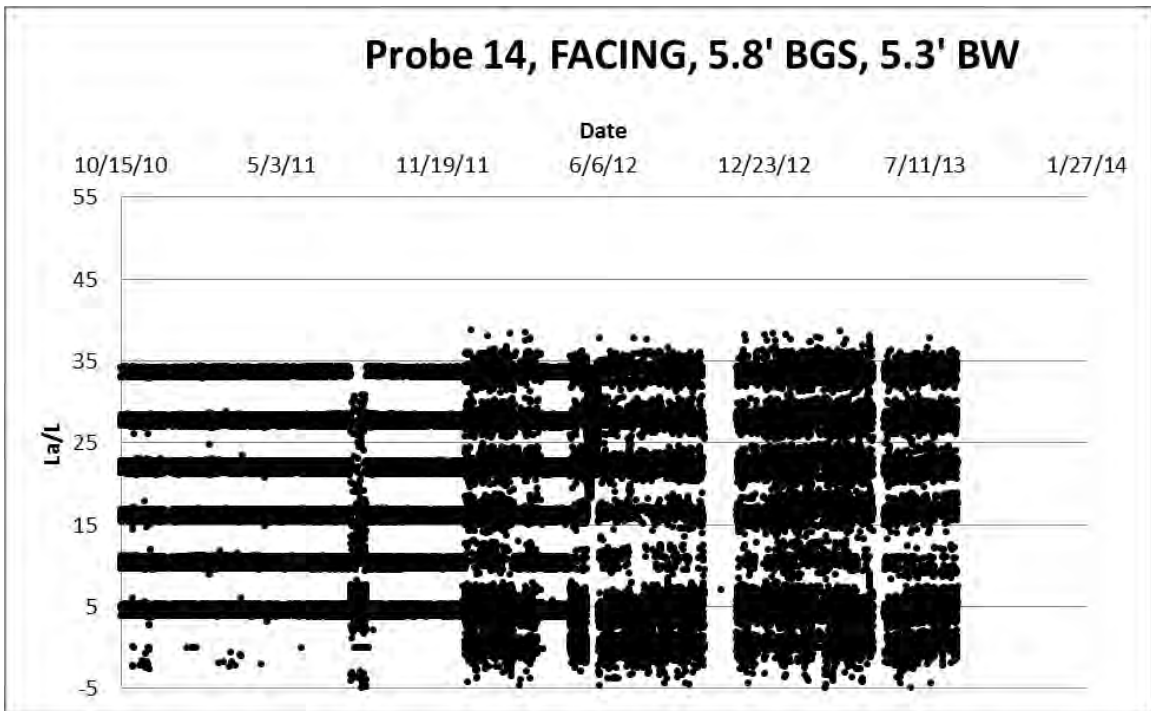


Figure C.32: Probe 14 installed from through the facing located 5.8 feet below ground surface and 5.3 feet behind the wall.

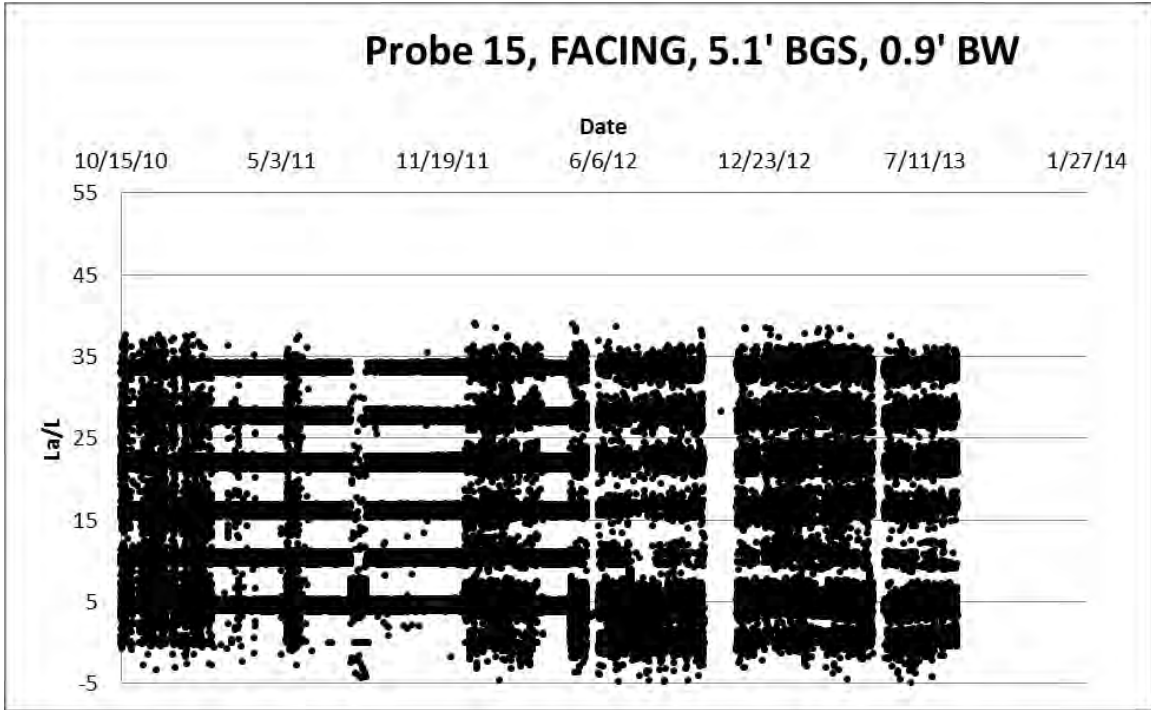


Figure C.33: Probe 15 installed from through the facing located 5.1 feet below ground surface and 0.9 feet behind the wall.

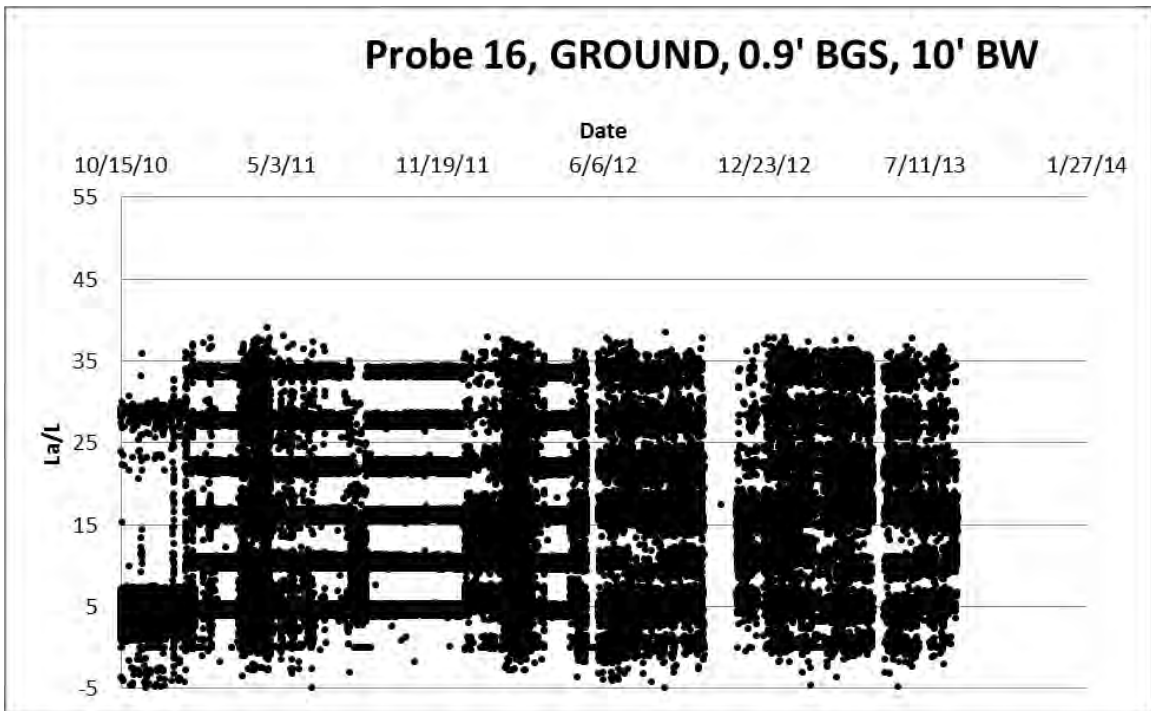


Figure C.34: Probe 16 installed from the ground surface located 0.9 feet below ground surface and 10 feet behind the wall.

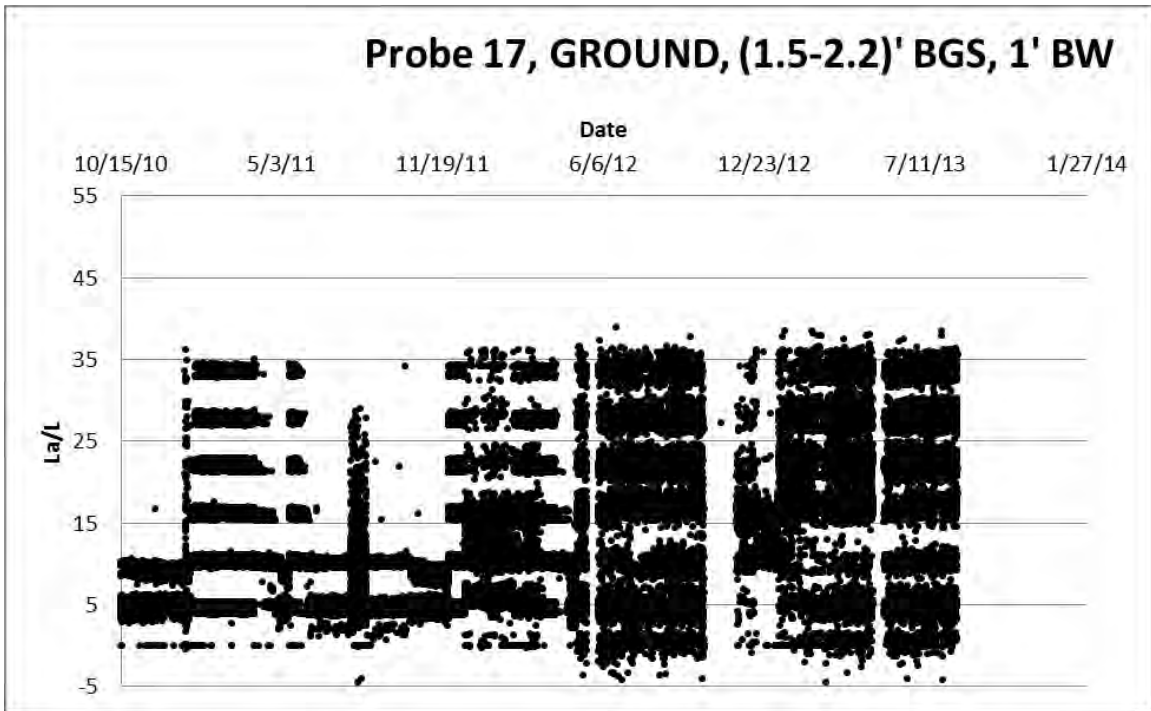


Figure C.35: Probe 17 installed from the ground surface located 1.5 to 2.2 feet below ground surface and 1 foot behind the wall.

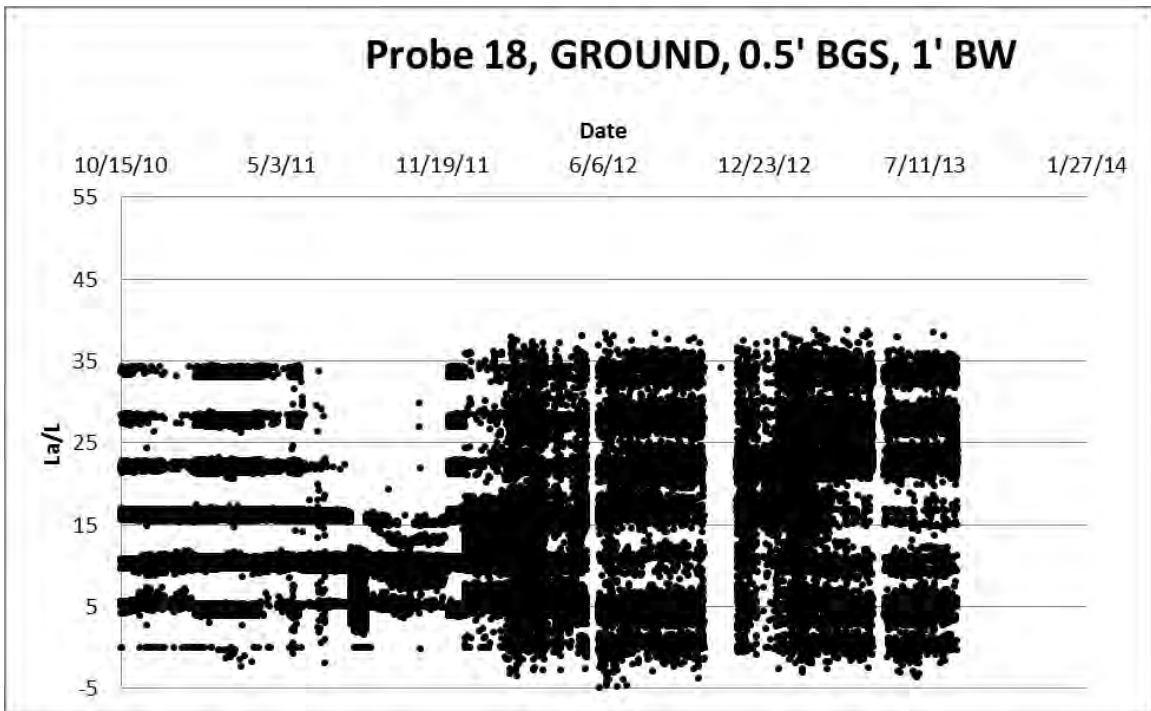


Figure C.36: Probe 18 installed from the ground surface located 0.5 feet below ground surface and 1 foot behind the wall.

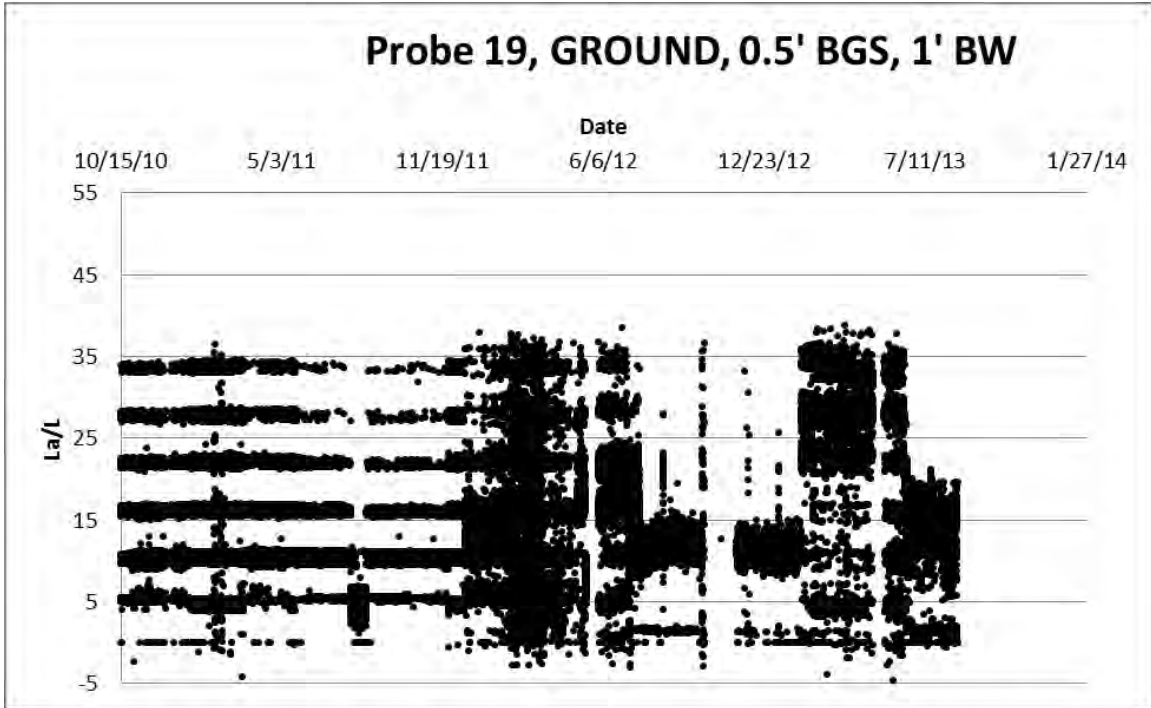


Figure C.37: Probe 19 installed from the ground surface located 0.5 feet below ground surface and 1 foot behind the wall.

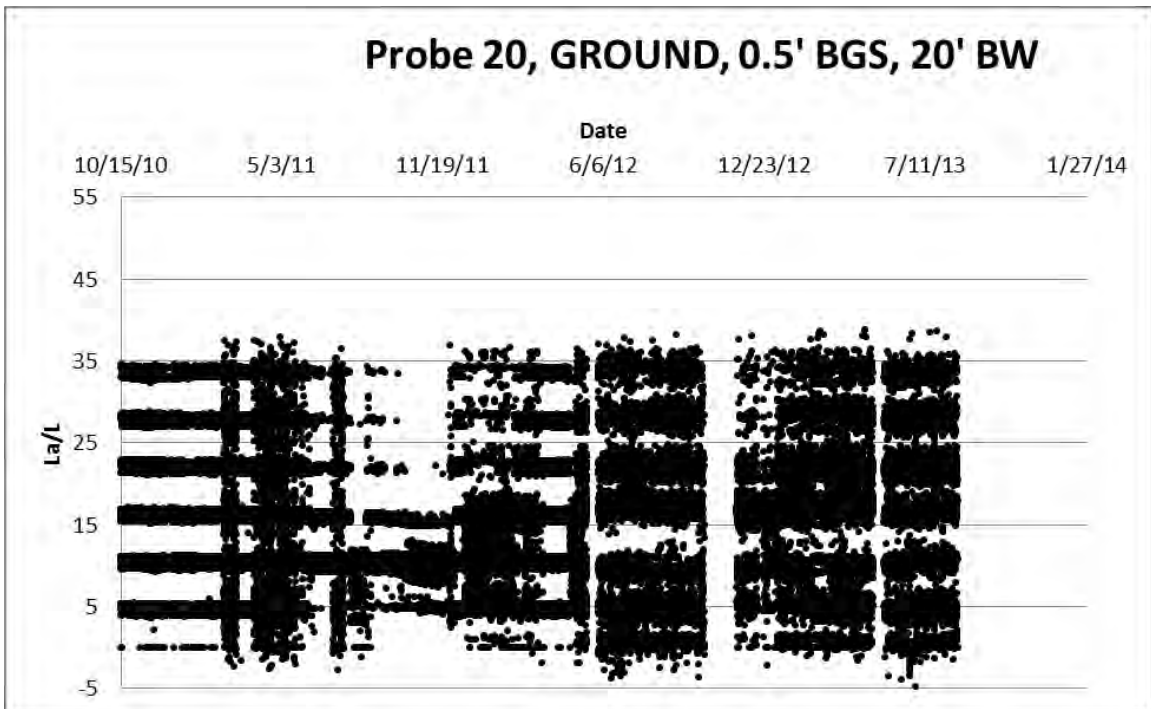


Figure C.38: Probe 20 installed from the ground surface located 0.5 feet below ground surface and 20 feet behind the wall.

C.2.2: ELECTRICAL CONDUCTIVITY MEASUREMENTS

The following figures are the electrical conductivity measurements taken since installation of the TDR probes.

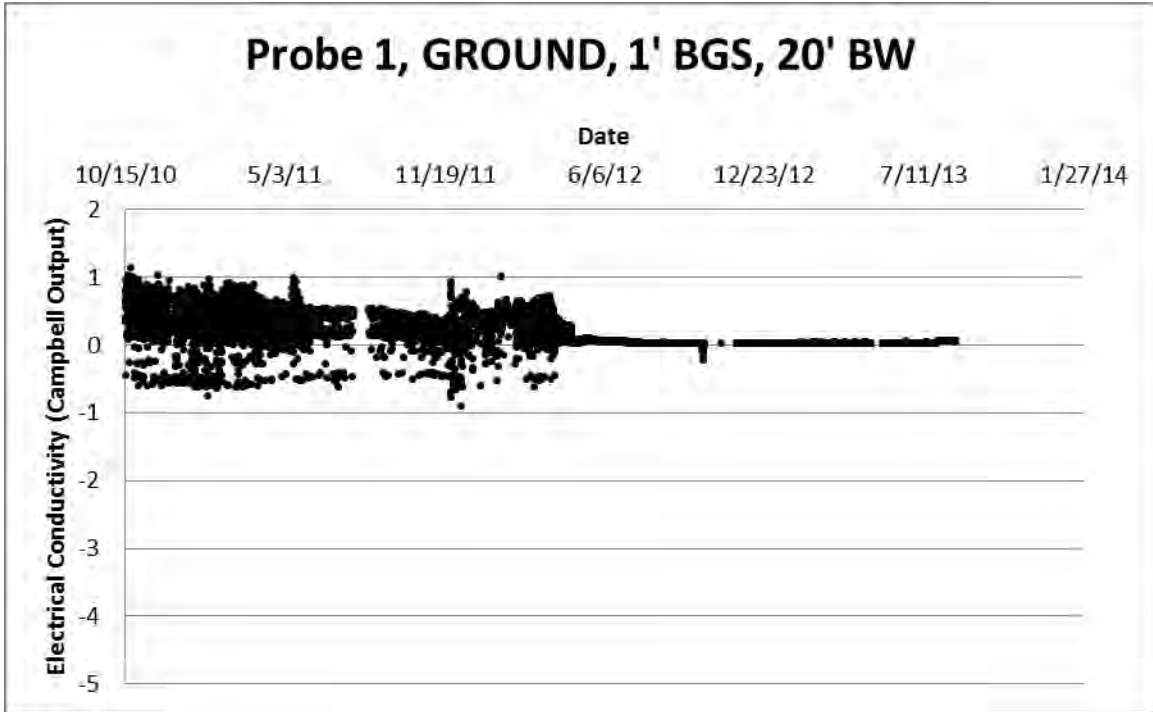


Figure C.39: Probe 1 installed from the ground surface located 1 foot below ground surface and 20 feet behind the wall.

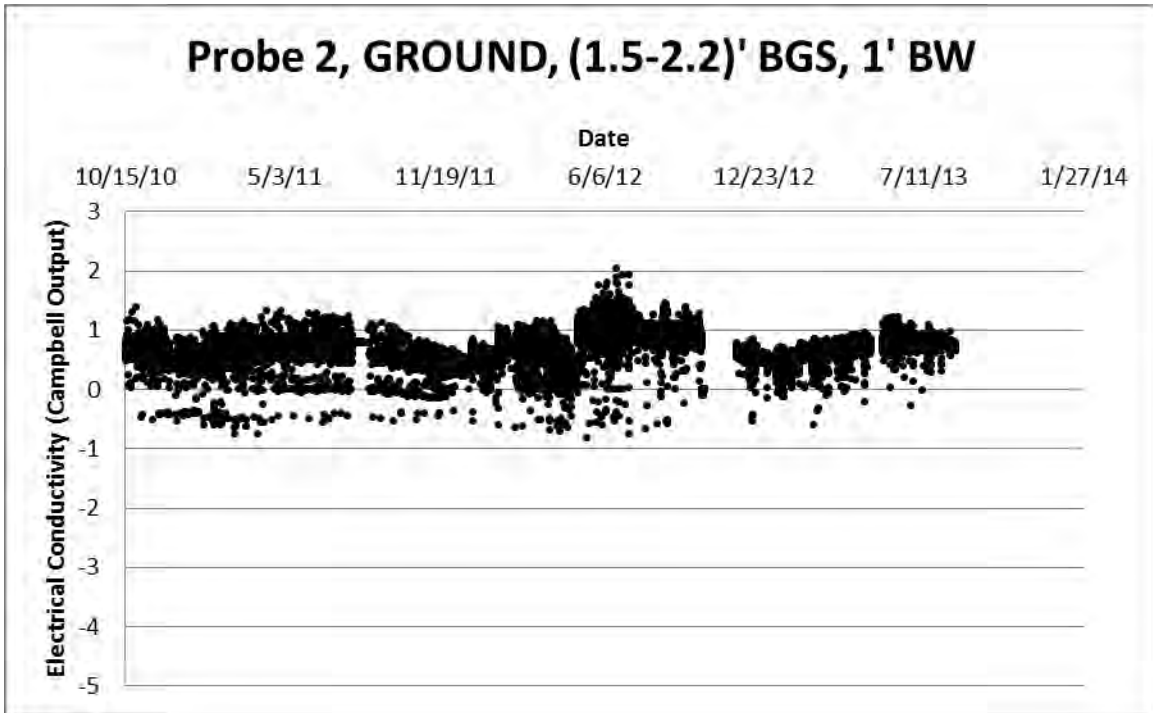


Figure C.40: Probe 2 installed from the ground surface located 1.5 to 2.2 feet below ground surface and 1 foot behind the wall.

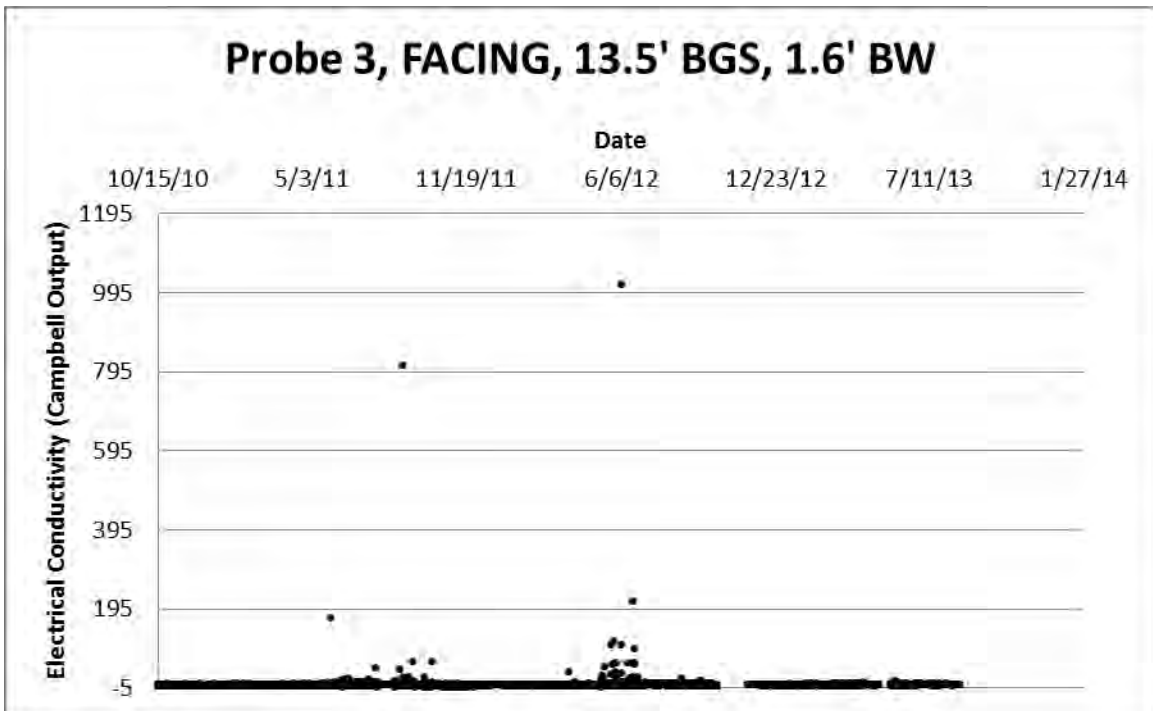


Figure C.41: Probe 3 installed through the facing located 13.5 feet below ground surface and 1.6 feet behind the wall.

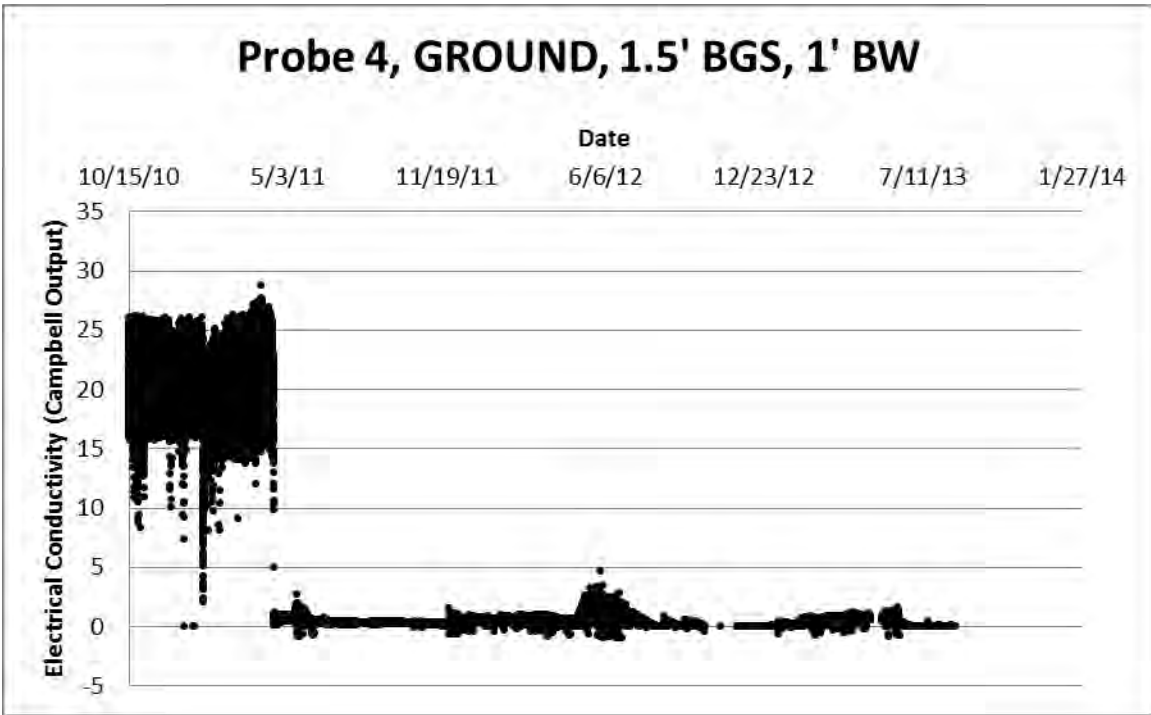


Figure C.42: Probe 4 installed from the ground surface located 1.5 feet below ground surface and 1 foot behind the wall.

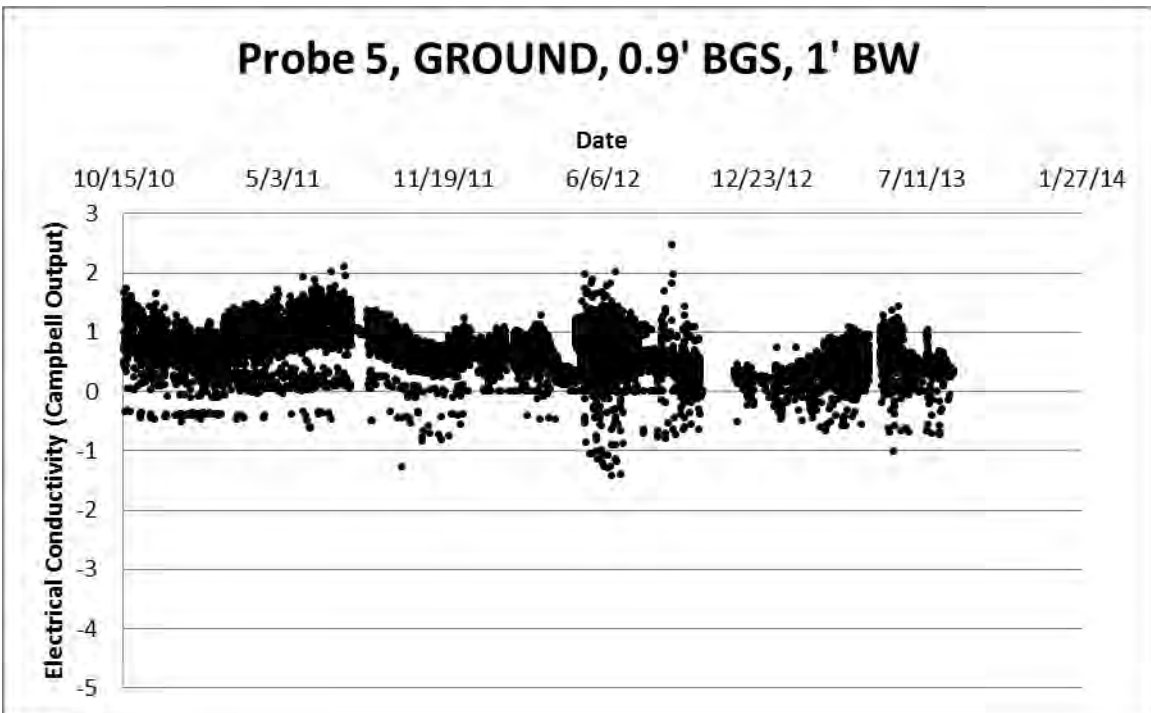


Figure C.43: Probe 5 installed from the ground surface located 0.9 feet below ground surface and 1 foot behind the wall.

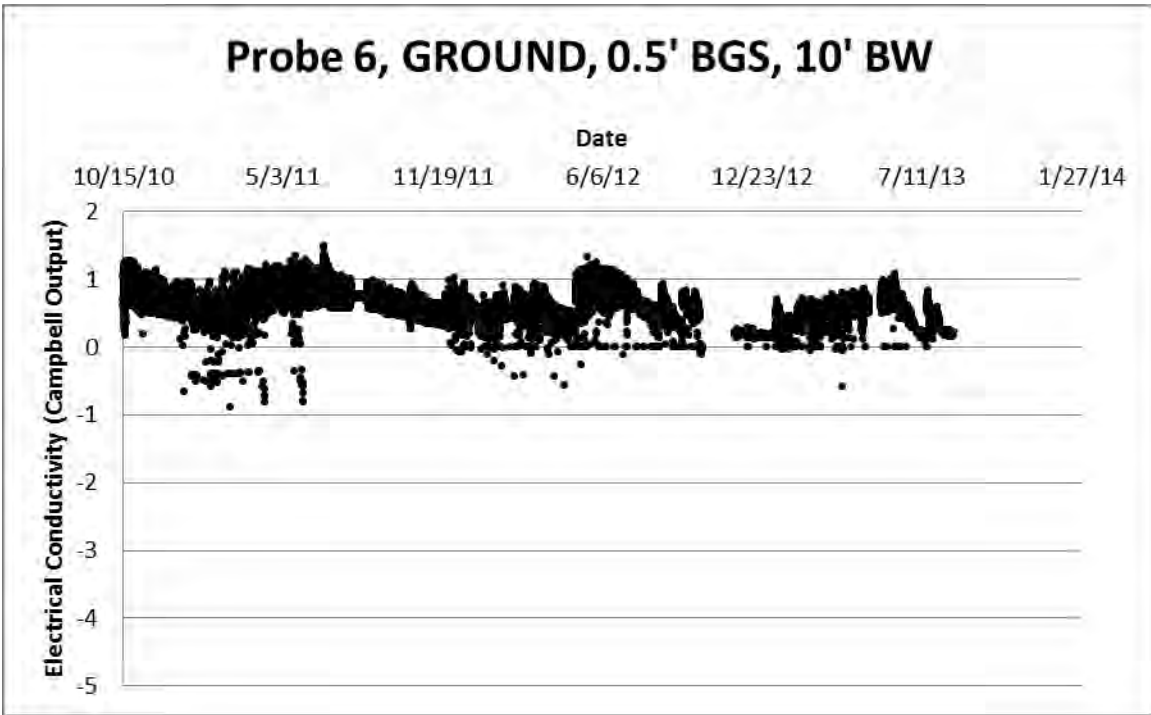


Figure C.44: Probe 6 installed from the ground surface located 0.5 feet below ground surface and 10 feet behind the wall.

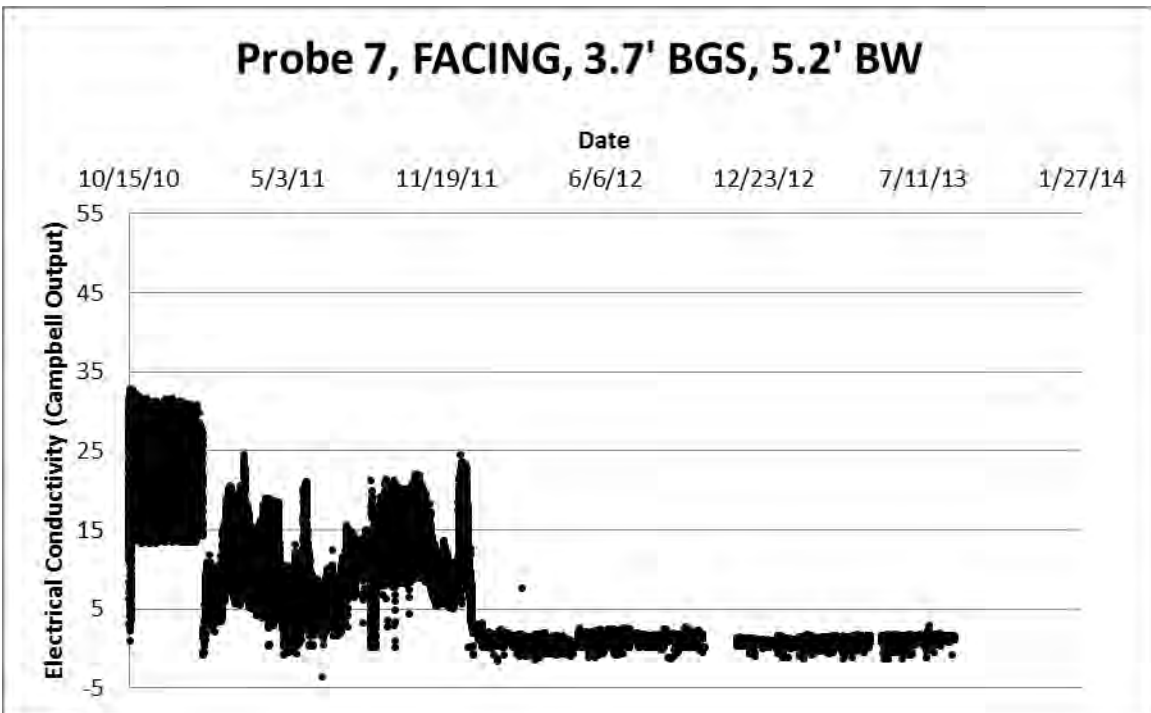


Figure C.45: Probe 7 installed from through the facing located 3.7 feet below ground surface and 5.2 feet behind the wall.

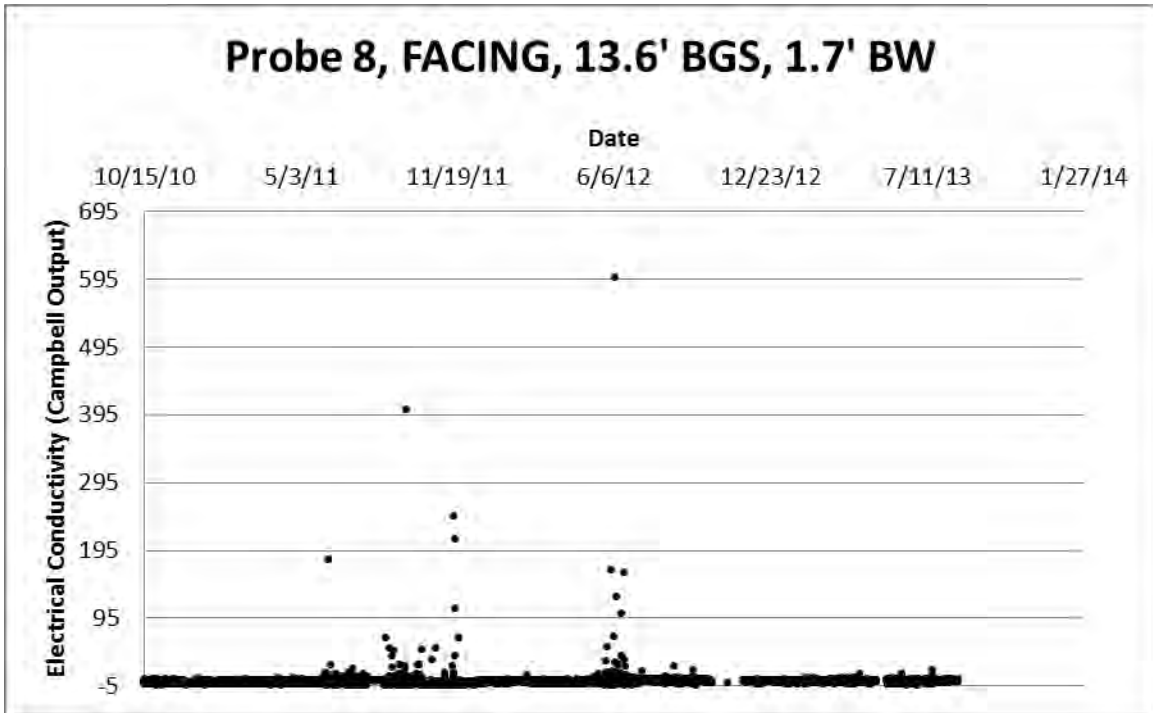


Figure C.46: Probe 8 installed from through the facing located 13.6 feet below ground surface and 1.7 feet behind the wall.

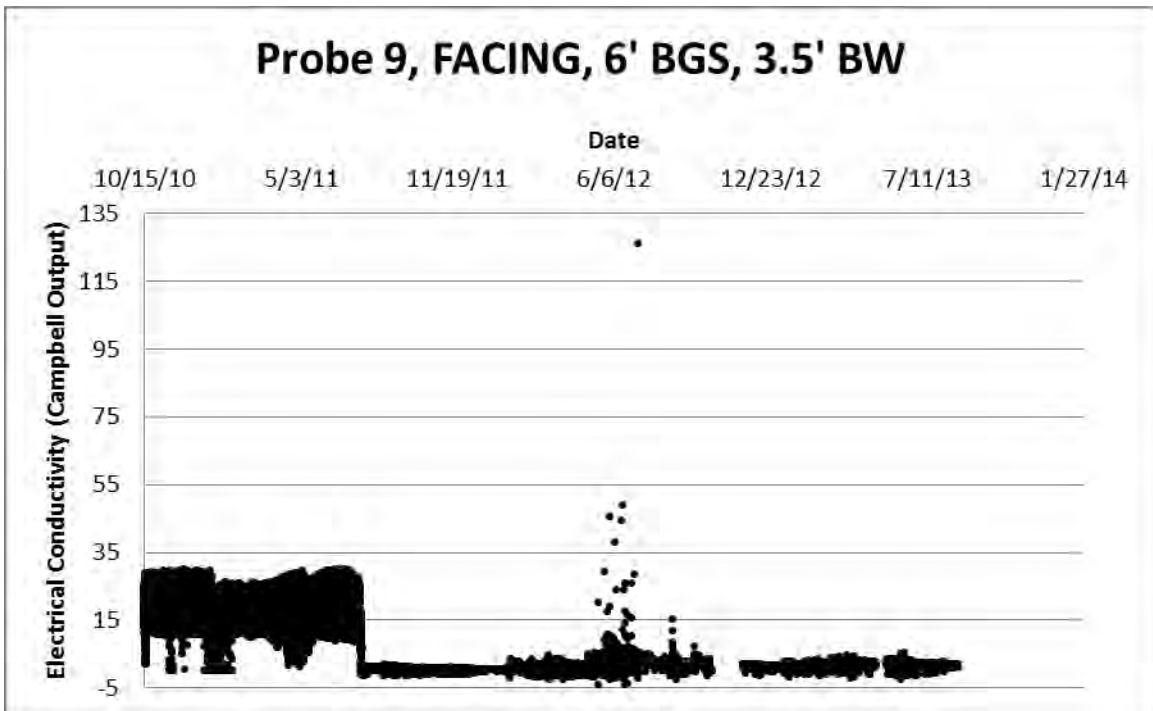


Figure C.47: Probe 9 installed from through the facing located 6 feet below ground surface and 3.5 feet behind the wall.

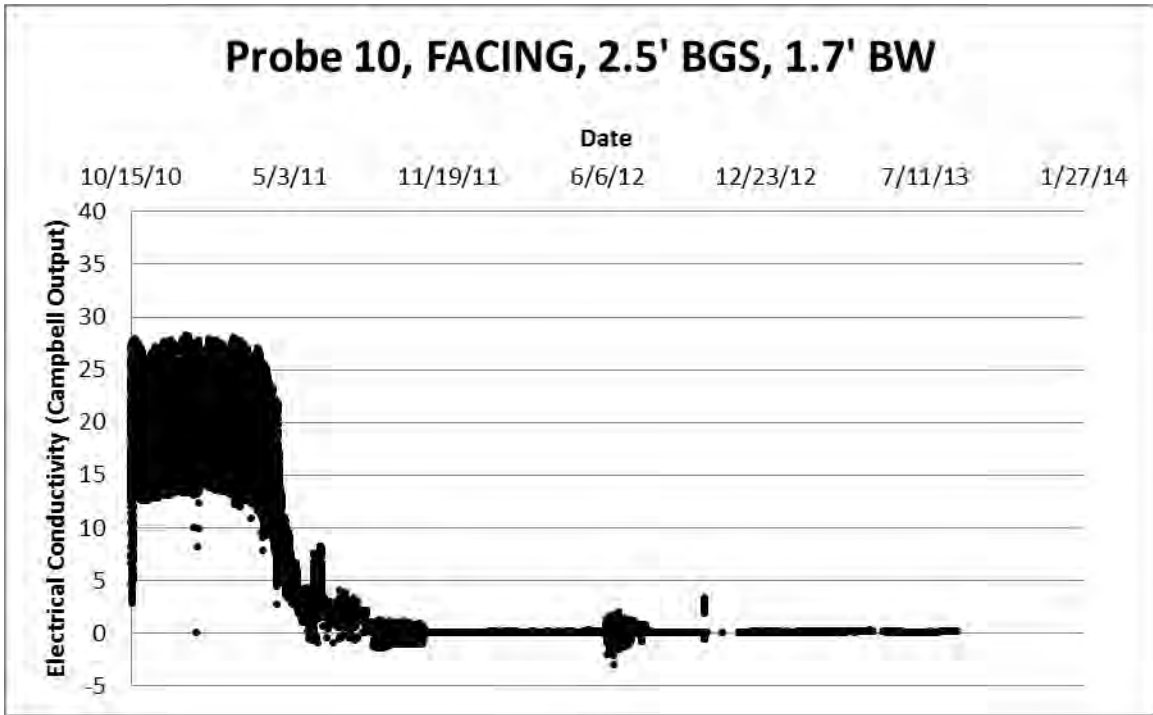


Figure C.48: Probe 10 installed from through the facing located 2.5 feet below ground surface and 1.7 feet behind the wall.

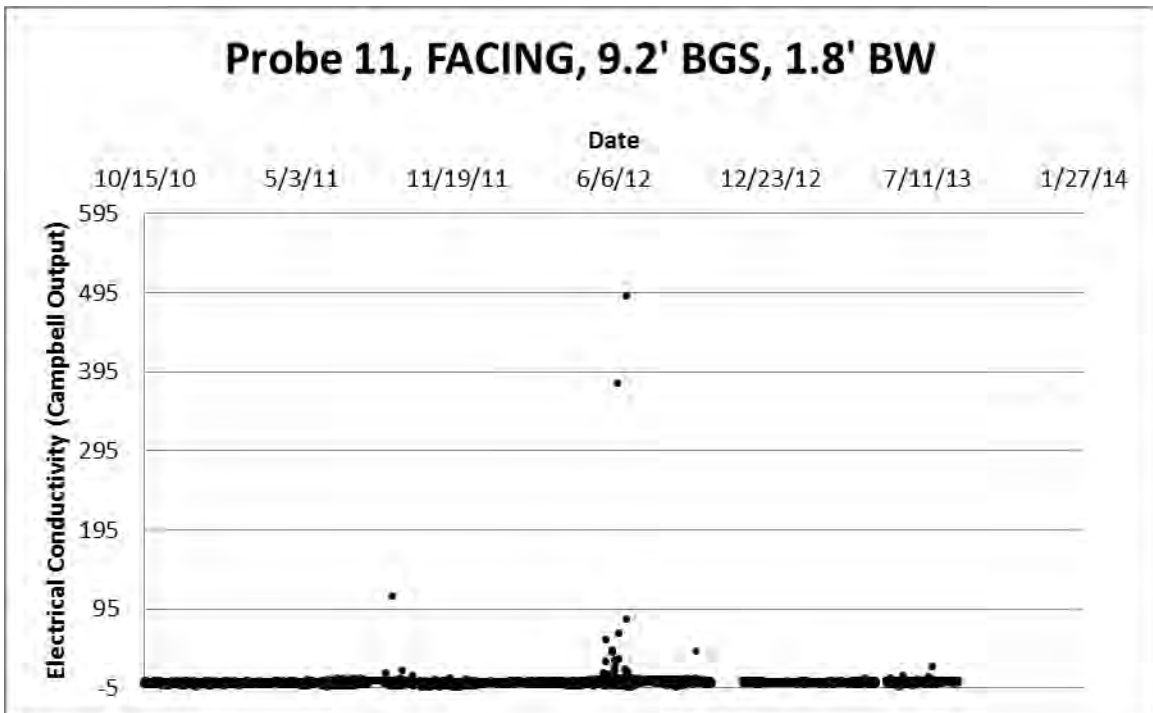


Figure C.49: Probe 11 installed from through the facing located 9.2 feet below ground surface and 1.8 feet behind the wall.

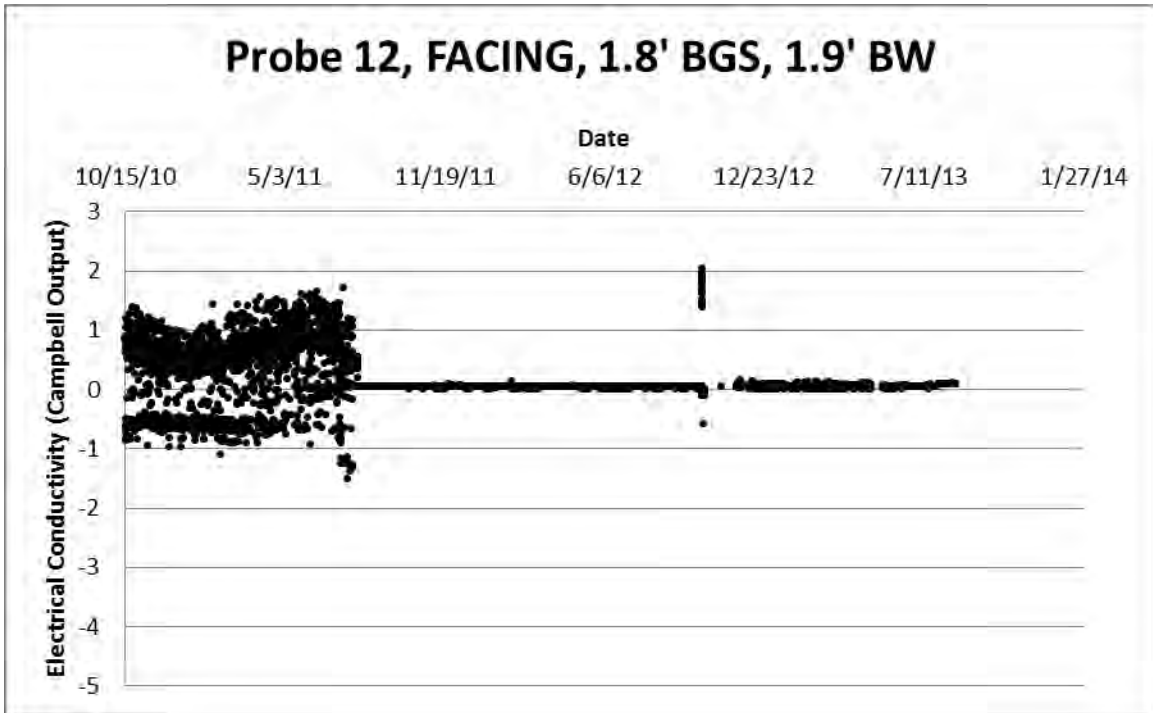


Figure C.50: Probe 12 installed from through the facing located 1.8 feet below ground surface and 1.9 feet behind the wall.

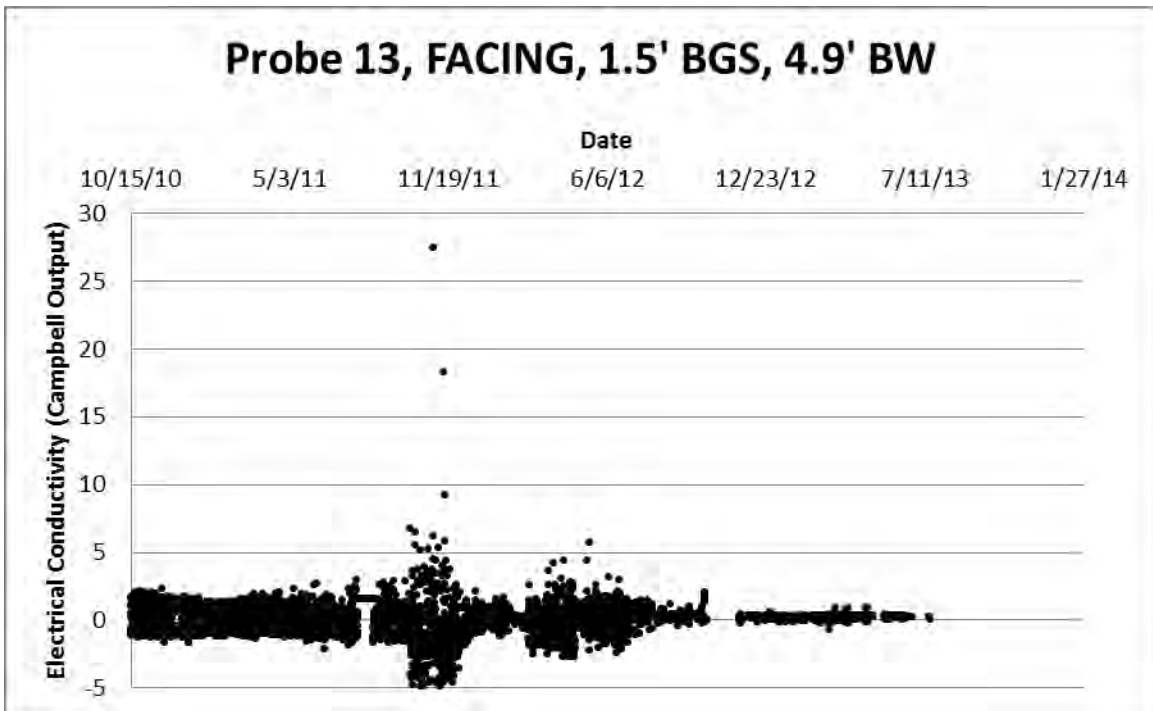


Figure C.51: Probe 13 installed from through the facing located 1.5 feet below ground surface and 4.9 feet behind the wall.

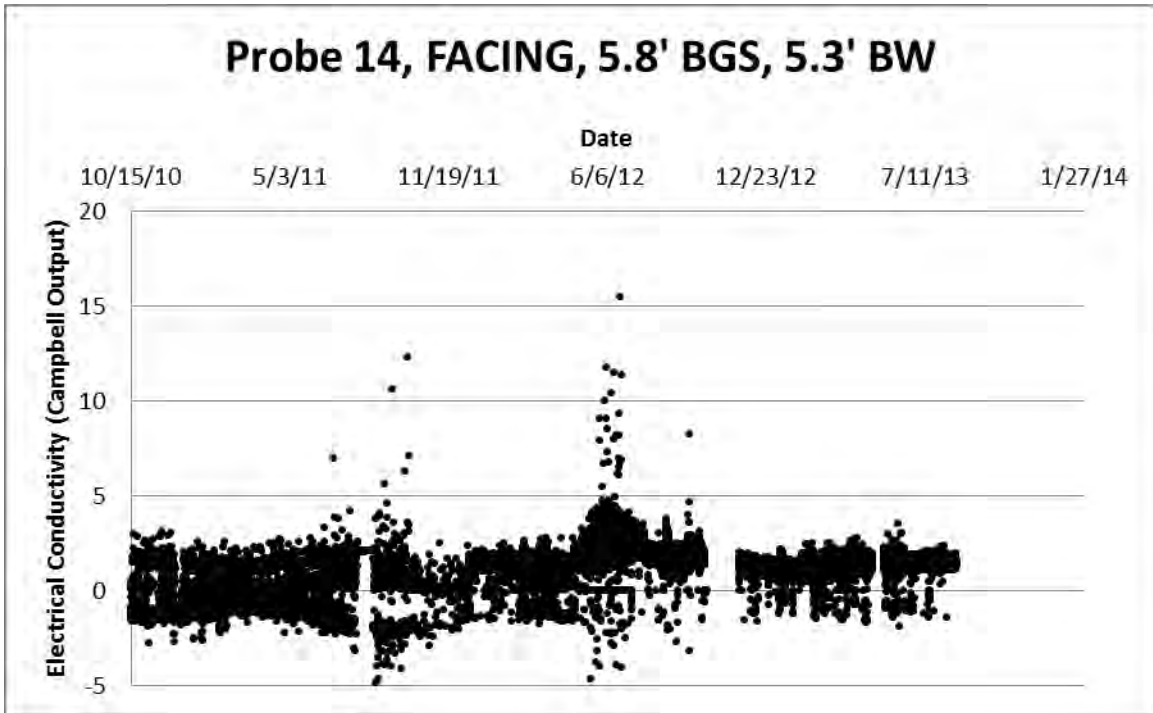


Figure C.52: Probe 14 installed from through the facing located 5.8 feet below ground surface and 5.3 feet behind the wall.

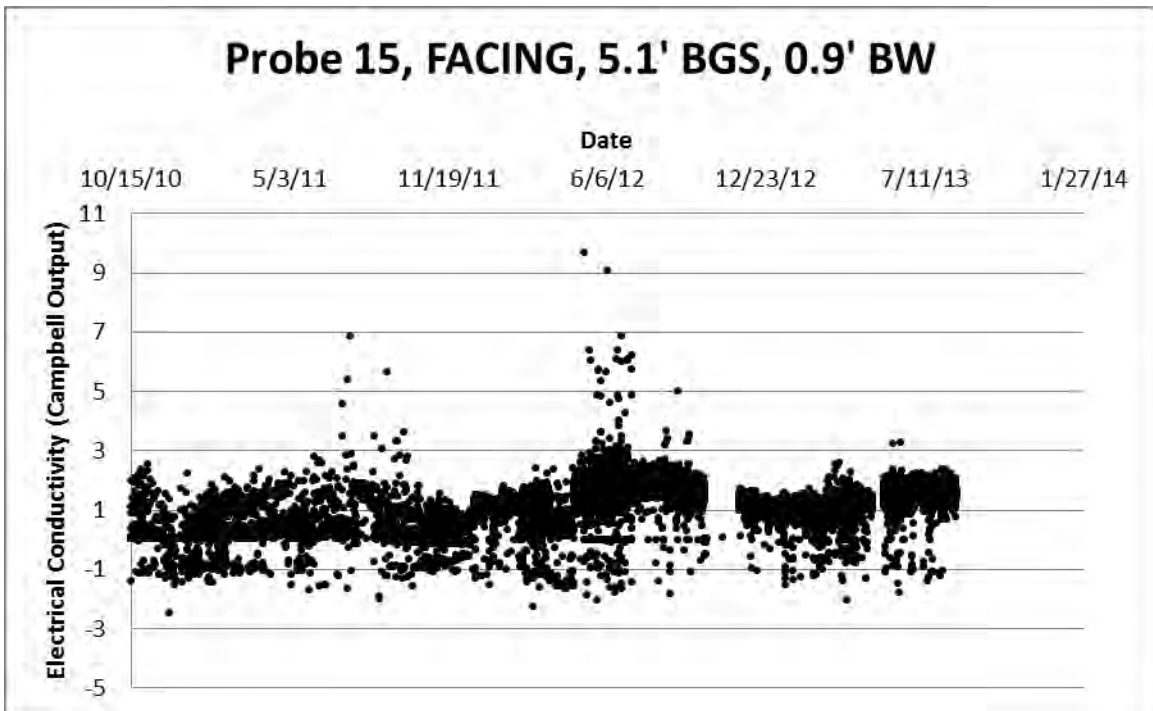


Figure C.53: Probe 15 installed from through the facing located 5.1 feet below ground surface and 0.9 feet behind the wall.

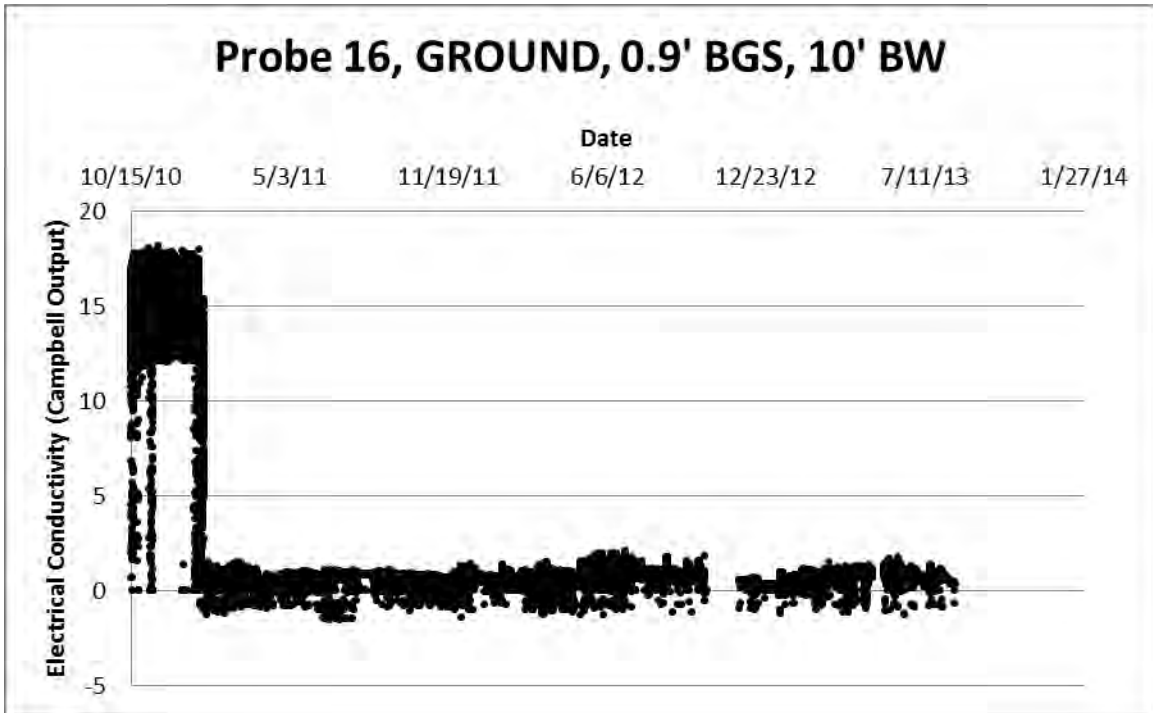


Figure C.54: Probe 16 installed from the ground surface located 0.9 feet below ground surface and 10 feet behind the wall.

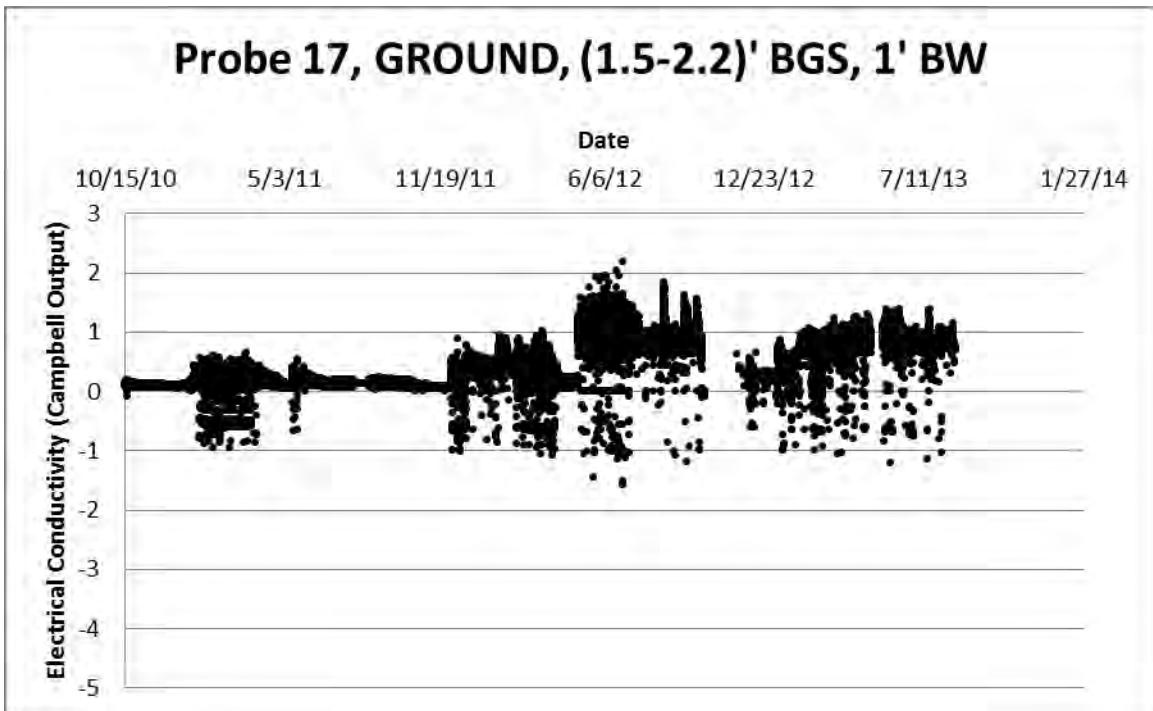


Figure C.55: Probe 17 installed from the ground surface located 1.5 to 2.2 feet below ground surface and 1 foot behind the wall.

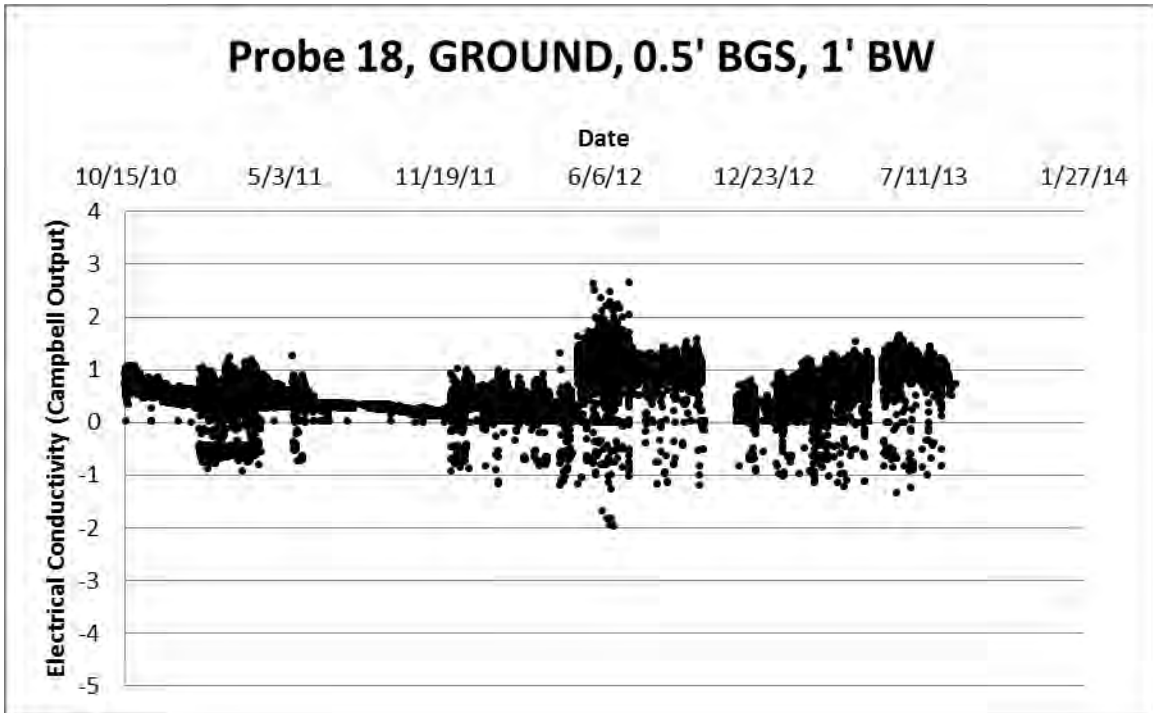


Figure C.56: Probe 18 installed from the ground surface located 0.5 feet below ground surface and 1 foot behind the wall.

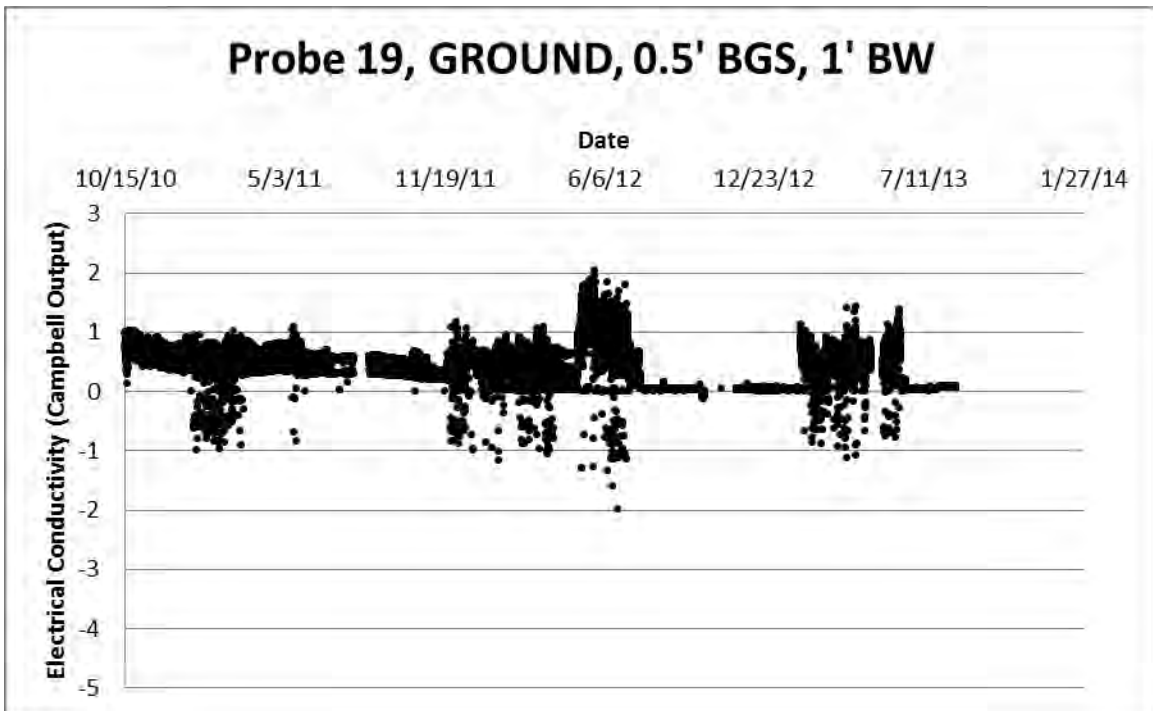


Figure C.57: Probe 19 installed from the ground surface located 0.5 feet below ground surface and 1 foot behind the wall.

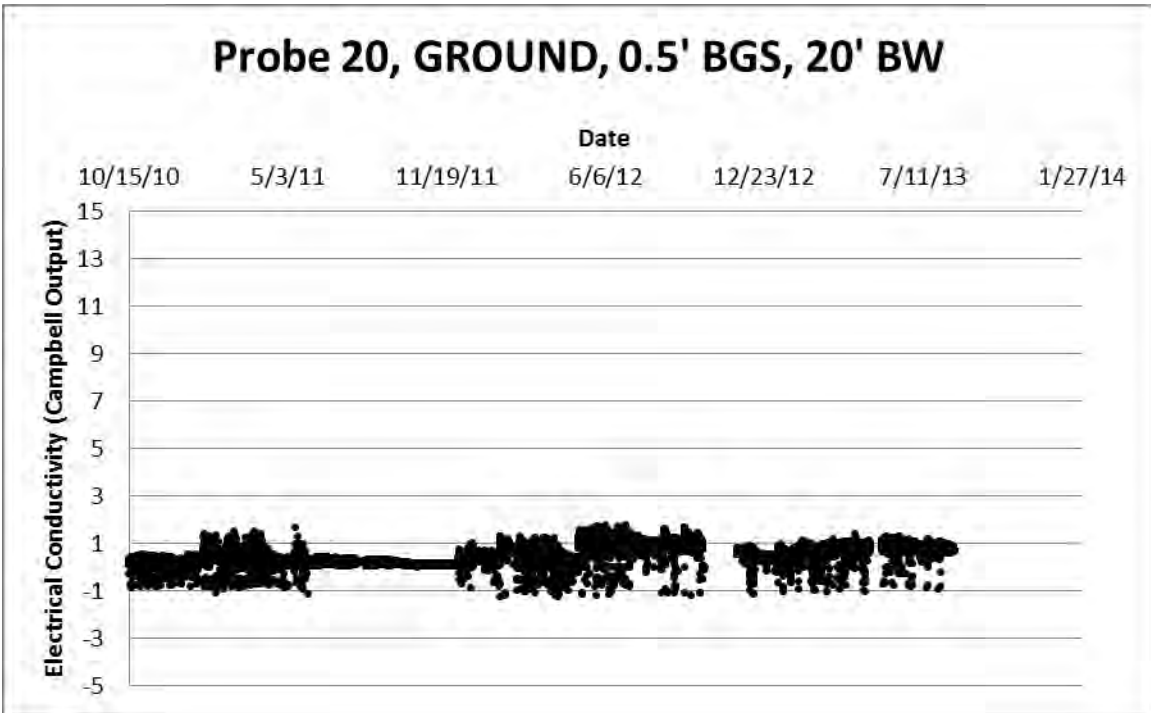


Figure C.58: Probe 20 installed from the ground surface located 0.5 feet below ground surface and 20 feet behind the wall.

APPENDIX D: SITE AND VICINITY METEOROLOGICAL DATA

This section presents the meteorological data for the site over the duration of the project. Specifically, the average temperature, monthly rainfall, and the cumulative rainfall since October 8, 2010 are presented. The meteorological data since August 2009 was collected from a weather station located approximately 35 miles northwest using Weather Underground (2013).

The average daily temperature ranged from 96 to 20 degrees Fahrenheit. The daily maximum temperature ranged from 107 to 24 degrees while the daily minimum temperature ranged from 95 to 17 degrees Fahrenheit.

Figure D.4 and Figure D.5 compare the monthly rainfall with the historic average. This project occurred during a historic drought. Most months recorded rainfall less than the historic average for that month.

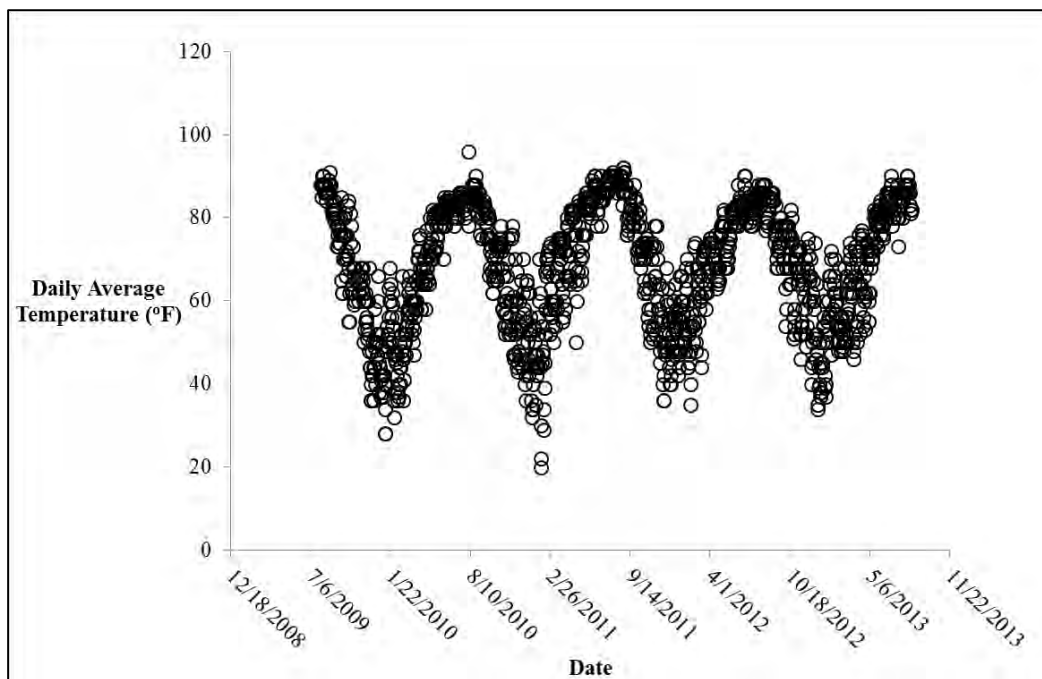


Figure D.1: The daily average temperature in degrees Fahrenheit. Data from Weather Underground (2013)

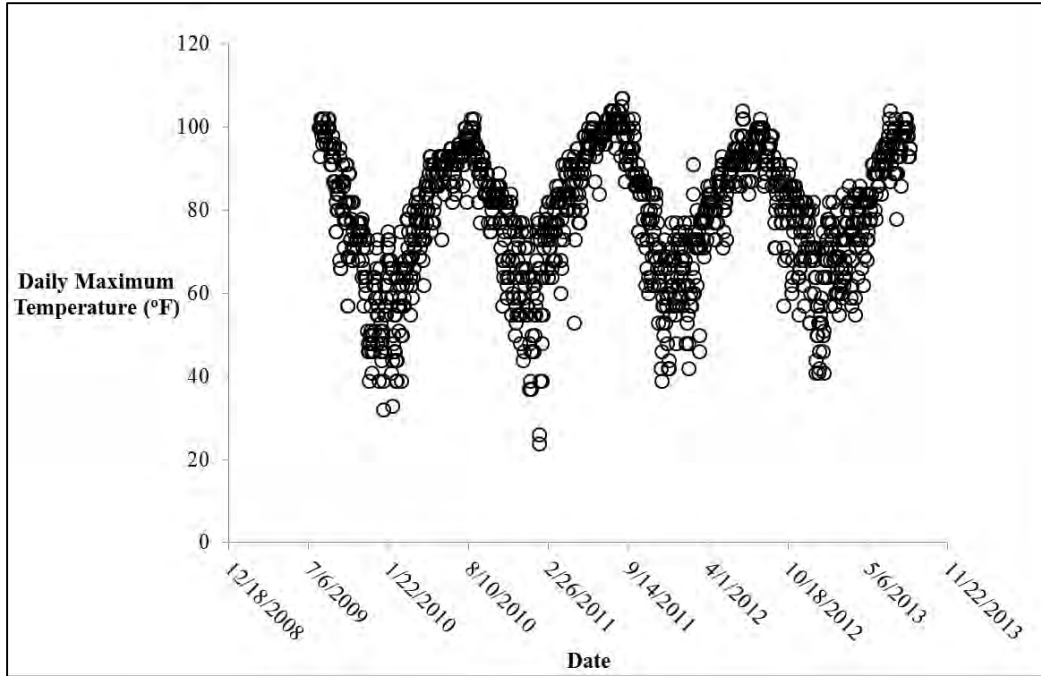


Figure D.2: The daily maximum temperature in degrees Fahrenheit. Data from Weather Underground (2013)

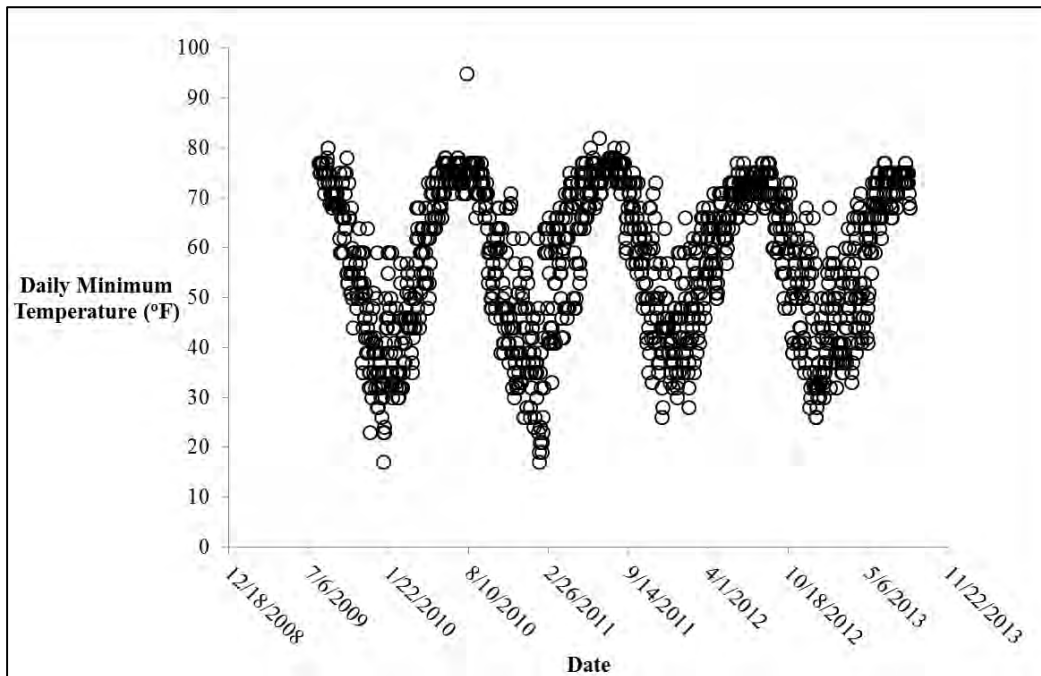


Figure D.3: The daily minimum temperature in degrees Fahrenheit. Data from Weather Underground (2013)

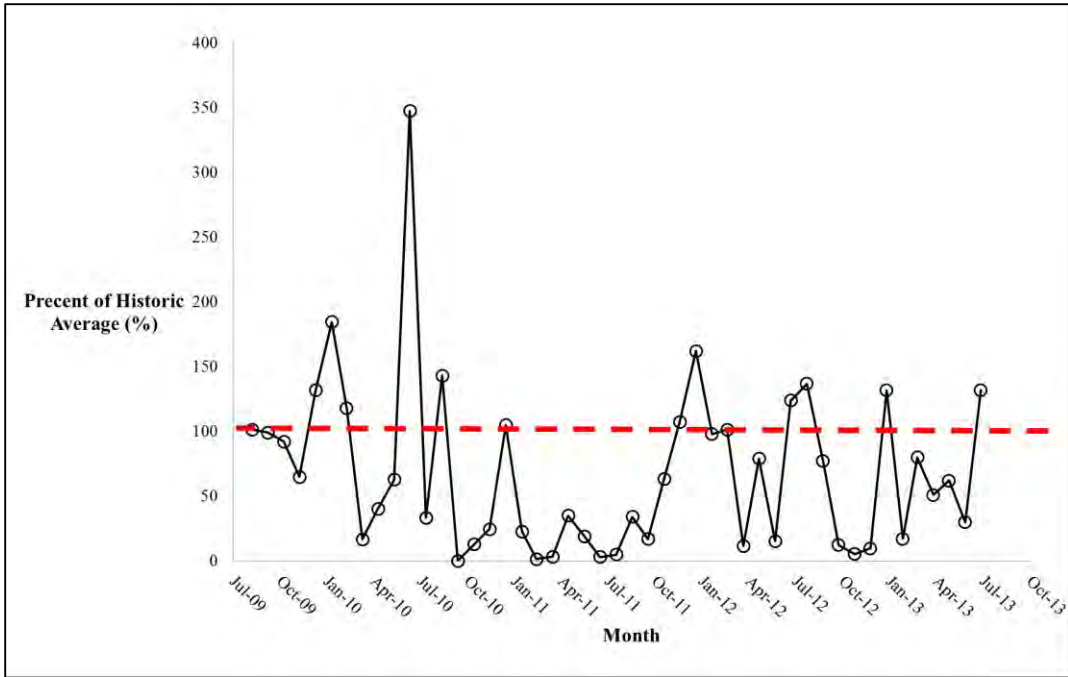


Figure D.4: The percent of actual rainfall compared to the history average. The dashed lined indicates the threshold where the actual rainfall was equal to the historic average rainfall for that month (100% of the historic average). Data from Weather Underground (2013)

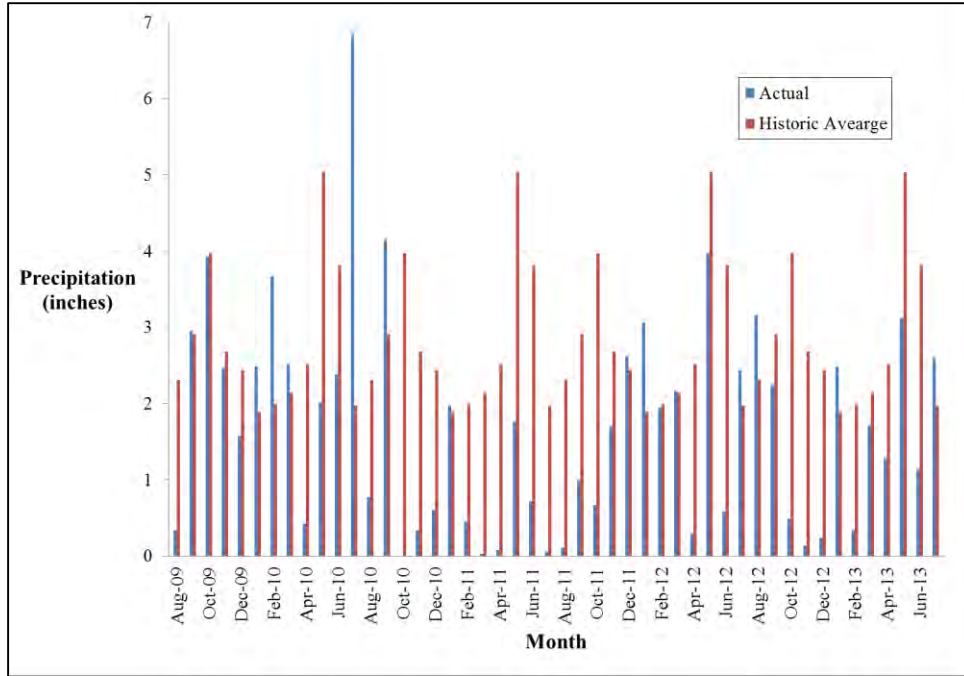


Figure D.5: Comparison of the monthly precipitation to the historic average for that month. Data from Weather Underground (2013)

APPENDIX E: WALL CONSTRUCTION AND INSTALLATION OF FIELD INSTRUMENTATION

The construction of the wall and installation of the instrumentation are discussed in this section. Specifically, the construction of the shafts, the excavation process, the installation of the shotcrete facing, the construction of the inundation berm, and the installation of the strain gauges, inclinometers, piezometers, and moisture sensors are discussed.

E.1: Shaft Installation

McKinney Drilling Company began installation of the drilled shafts on March 30, 2010. Installation of all shafts took about one week, during which temperatures stayed between about 50 and 80°F and there was no appreciable rainfall.



Figure E.1: Tensile reinforcements for transport.

The rebar cages were assembled on site and fitted with tensile reinforcements to provide stability in during transport, Figure E.1. Additional transverse bars were also tied onto the ends of each cage to provide a strong point for attaching lifting cables, Figure E.2.



Figure E.2: Additional transverse reinforcement for picking up rebar cages.

Most of the shafts were drilled with the rig shown in Figure E.3. Control points at each end of the retaining wall were marked and connected by a string line, Figure E.4. The auger was lined up at the appropriate location for each shaft and centered above the string line. A plumb-bob was used to verify the verticality of the holes whenever the auger was raised to remove cuttings, Figure E.5.



Figure E.3: Rig mobilized to drill the shafts.



Figure E.4: String line used to mark wall location.



Figure E.5: Plumb-bob for verifying verticality of drilled shaft.

Most of the drilled shafts remained dry between drilling and placement of the rebar cage, but a small amount of water was observed in the bottom of some shafts on the western end of the

wall. No major sand seams were encountered in any of the shafts, and minor caving was observed at the bottom of isolated shafts. These issues did not inhibit construction.

Once the shafts were drilled, a crane was used to pick up the appropriate rebar cage and lower it into the hole. The non-instrumented shafts were lifted from a single point as shown in Figure E.6. The bending during transport was minimized for the instrumented shafts by using two pickup points, Figure E.7.



Figure E.6: One-point pickup for non-instrumented shafts.



Figure E.7: Two-point pickup for instrumented shafts.

Once the rebar cages were lifted above the hole, spacers were clamped onto each side of the cage at multiple locations to center the rebar in the hole. Three-inch concrete blocks were attached to the bottom edges of the longitudinal rebar to provide the required three inches of concrete cover for the rebar, Figure E.8. The rebar cage was lowered as soon as the spacers were attached, being careful to avoid any twisting of the cage, Figure E.9.



Figure E.8: Installing spacers to the rebar cage.



Figure E.9: Rebar cage placed into drilled shaft.

Concrete trucks usually arrived within an hour or two of placing the cage in the drilled shaft. The concrete was directed down the center of the shafts with hand shovels, Figure E.10. Vibratory compactors were used to consolidate the top several feet of the shaft, Figure E.11.

The shell surrounding the top of the rebar cage is sonotube that was used to provide four feet of stickup above the natural ground surface, as requested by the land owner. Most of the sonotube casings were removed after the concrete had cured for a day or two. Moist blankets were kept on top of the shafts during the first day of curing.



Figure E.10: Free fall method for pouring concrete.



Figure E.11: Vibratory compaction of top of shaft.

E.2: Construction Sequence and Concrete Strengths

The sequence of shaft installation was designed to minimize disturbance to green concrete. The construction sequence is presented in Table E-1, along with break data from each day's concrete.

Table E-1: Date shafts were installed and the concrete strength from that day.

Date	Notes (* = Instrumented Shaft)	Concrete 7-Day Strength (psi)	Concrete 28-Day Strength (psi)
March 30, 2010	Mobilized Equipment, Assembled Instrument Cages, Constructed Shafts 1 and 4	6055	7955
March 31, 2010	Constructed Shafts 7, 10, 13*, 22, and 25	4970	7000
April 1, 2010	Constructed Shafts 2, 5, 8, 11*, 15*, and 17	4480	6065
April 2, 2010	Constructed Shafts 3, 6, 9, 16, 19, and 23	4410	5875
Apr. 3 - 4, 2010	Weekend	N/A	N/A
April 5, 2010	Constructed Shafts 18, 21, and 24	4000	5950

April 6, 2010	Constructed Shafts 12, 16, and 14	4400	6800
April 7, 2010	Demobilize Equipment	N/A	N/A

E.3: Installation of Instrumentation

Each of three shafts was instrumented with optical strain gauges and inclinometer casing. The strain gauges were attached to threaded sister bars and arranged along the tension and compression ends of the shafts. An inclinometer casing was installed along the neutral axis of each instrumented shaft to a depth of about 35 feet below ground level.

The same type of inclinometer casing was installed in borehole B-1, a few feet back from the center of the retaining wall and to a depth of 50 feet below ground level. A piezometer was installed in borehole B-3, approximately 30 feet south of the east edge of the wall. Moisture sensors utilizing time domain reflectometry were installed behind the wall.

E.3.1: INSTALLATION OF STRAIN GAUGES

The optical strain gauges were attached to sister bars and calibrated at Ensoft, Inc. in Austin, TX. The thread-like sensor elements were attached to the sister bars using an epoxy. The sister bars were finely sanded and thoroughly cleaned before the gauges were epoxied to the bars. The sensor was aligned as closely as possible to an orientation parallel to the longitudinal axis of the bar. After the epoxy had dried, the connection was covered with wax. The wax layer was then covered with electrical tape, and a tough piece of protective rubber was secured around the entire assembly with cable ties.

Gauge factors were provided by the manufacturer and verified in the lab. Verification involved using a load frame to apply specific loads to the sister bars. The gauge factor was then used to convert the physical reading from the gauge (nanometers) to microstrains. The known load and elastic modulus of the sister bar allowed a quick calculation to verify the optical strain

reading. R-squared values were generally higher than 0.999. Each sensor was labeled in a way that identified the shaft, axis and depth for installation.

The sensors were brought out to the field on the first day of construction to be assembled in the correct orientation and installed in rebar cages. The first step of assembly was to lay out all the gauges (attached to the center of 24-inch sister bars) on the ground in the correct order and orientation so that cables fed out toward the eventual top of the shaft, Figure E.12. Once placed in the correct orientation, the sister bars were connected with couplers with the same threading as the sister bars, Figure E.13. The unrolled cables were then threaded into a slotted PVC pipe and held in place by securing zip ties around the pipe, Figure E.14. Securing the cables inside a PVC pipe reduced the chance of damage during the concrete pour. Finally, the slotted PVC pipe was secured to the sister bar with zip ties, Figure E.15.

Once prepared, the assembly of sister bars and PVC pipe was carried to the appropriate rebar cage and carefully slid into place. At least five people were involved in this process to provide multiple support points and avoid bending the assembly and loosening the connections at the couplers. Once in the cage, the line of sister bars was tied to the rebar cage between two longitudinal reinforcements. The PVC pipe was then detached from the sister bars and re-attached to the rebar cage between two adjacent longitudinal rebar, Figure E.16. All connections to the rebar cage were made using cable ties.



Figure E.12: Laying out the sensors in the correct orientation.



Figure E.13: Couplers for connecting sister bars.



Figure E.14: Securing cables inside slotted PVC pipe.



Figure E.15: Attaching slotted PVC pipe to sister bars with zip ties.



Figure E.16: Sister bars and PVC pipes being tied to rebar cage.

As noted earlier, each drilled shaft contained four feet of stickup above ground level, and the stickup region was not instrumented with strain gauges. The strain gauge cables were fed through the stickup portion within a PVC pipe connected to a PVC elbow joint that would stick out of the side of the shaft. The elbow joints were fed outside of the cage so that the cable assemblies could hang over the top rebar and into the cage during transport to the drilled hole, Figure E.17. Once placed in the hole, holes were drilled in the sonotube, through which the elbows could lead the cable ends out of the side of the shaft and away from the concrete pour. The elbows were pulled back into the inside of the shaft and oriented outward to fit through the holes, Figure E.18.



Figure E.17: Placement of cable assemblies during transport of rebar cage.



Figure E.18: Orientation of elbow and Cable assemblies after placement and prior to pour.

The cable ends were wrapped in plastic sheeting during the concrete pour to protect them from concrete spray. As soon as practical after the pour, the cable ends were fed into a NEMA-4 electrical enclosure. The cables ends were connected to the back end of a patch panel, the patch panel was secured in the enclosure and the enclosure was mounted in front of the instrumented

shaft. Once all shafts had been installed, a wooden platform was installed to house loose cable ends and support all three enclosures, as shown in Figure E.19.



Figure E.19: Construction of platform to house loose cables and hold electrical enclosures.

The strain gauges were all checked for connectivity, and initial measurements indicated that 88 out of the 90 sensors survived the installation. In the time between wall construction and excavation, concrete curing and stress redistribution may have damaged some sensors. Currently, 86 of 90 sensors are operational.

E.3.2: INCLINOMETER INSTALLATION

Inclinometer casings were installed into borehole B-2 during the subsurface investigation (Figure E.20). The casing was lowered into the borehole, surrounded by a bentonite slurry and capped with a concrete pad and locking cover plate (Figure E.20). The concrete pad was later damaged during construction, but a new one was cast with leftover concrete.

The inclinometers in the instrumented shafts were installed along the neutral axis, half-way between the tension and compression ends of each shaft. This was accomplished by securing a

piece of bent rebar to the longitudinal members of the cage and using zip ties to connect the PVC casing to the bent rebar, Figure E.22. The inclinometer casings were extended to a depth of approximately 30 feet below ground level, beyond which no appreciable movement is expected.



Figure E.20: Installation of the inclinometer casing in borehole B-2.



Figure E.21: The inclinometer casing installed behind the wall.



Figure E.22: Connections for inclinometer casings in instrumented shafts.

E.3.3: PIEZOMETER INSTALLATION

Five piezometers were installed on site. The locations can be seen in Table B-1 and Figure B.1. On January 12, 2010, a piezometer screened 5 to 15 feet was installed in a boring from the site investigation by Fugro, Inc. (Figure

E.24 and Figure E.25). This piezometer was used to monitor the local water level conditions. On February 23, 2012, four more piezometers were installed in boring holes for a site investigation by Fugro, Inc. (Figure E.27). These piezometers were used to monitor the water levels in the inundation test area. The piezometers were surrounded with a permeable sand and gravel interface between the piezometer and the walls of the borehole. Readings were taken using a buzzing water level indicator and a tape measure.

Table E-2: Location, installation date, and screen location for the piezometers.

Piezometer	Installation date	Diameter	Screen location	Location	
				Distance perpendicular from the wall	Distance from wall center-line
B-3	12-Jan-10	2 inches	5 to 15 feet	16 feet	54 feet east
A	23-Feb-12	2 inches	5 to 15 feet	9 feet	9 feet west
B	23-Feb-12	1 inch	3.4 to 4.6 feet	15.1 feet	5.5 feet west
C	23-Feb-12	2 inches	5 to 15 feet	15.5 feet	3 feet east
D	23-Feb-12	1 inch	3.6 to 4.8 feet	7.3 feet	7.5 feet east

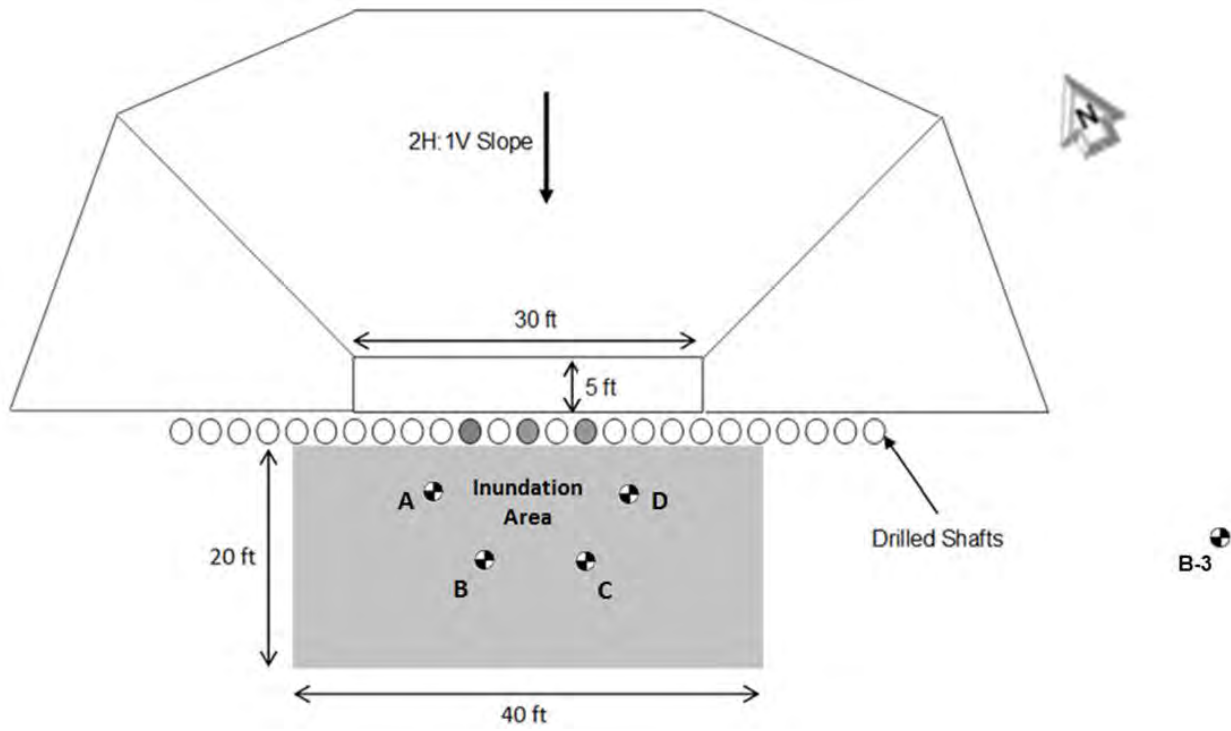


Figure E.23: Plan view of piezometer locations.



Figure E.24: The piezometer installed in borehole B-3 being lowered into position.



Figure E.25: The piezometer installed and covered in borehole B-3.



Figure E.26: Piezometer being installed in borehole A.



Figure E.27: The four standpipe piezometers installed behind the wall in the inundation berm.

E.3.4: MOISTURE SENSOR INSTALLATION

A total of 20 Time Domain Reflectometry (TDR) probes were installed in order to measure the moisture content of the soil behind the wall. The sensors were installed through the

facing of the wall prior to the shotcrete facing being installed and through the ground surface behind the wall.

The sensors installed through the facing of the wall were placed on September 30 and October 1, 2010. The sensors that were installed through the ground surface behind the wall were placed on October 14, 2010. The layout of the probes can be seen in Table E-3 and Figure E.28.

Table E-3: Location of the TDR probes installed in the soil

Probe #	Depth below Ground Surface (feet)	Distance Behind the Wall (feet)	Installation Method
1	1	20	ground surface
2	1.75	1	ground surface
3	13.5	1.6	facing
4	1.5	1	ground surface
5	0.9	1	ground surface
6	0.5	10	ground surface
7	3.7	5.2	facing
8	13.6	1.7	facing
9	6	3.5	facing
10	2.5	1.7	facing
11	9.2	1.8	facing
12	1.8	1.9	facing
13	1.5	4.9	facing
14	5.8	5.3	facing
15	5.1	0.9	facing
16	0.9	10	ground surface
17	1.75	1	ground surface
18	0.5	1	ground surface
19	0.5	1	ground surface
20	0.5	20	ground surface

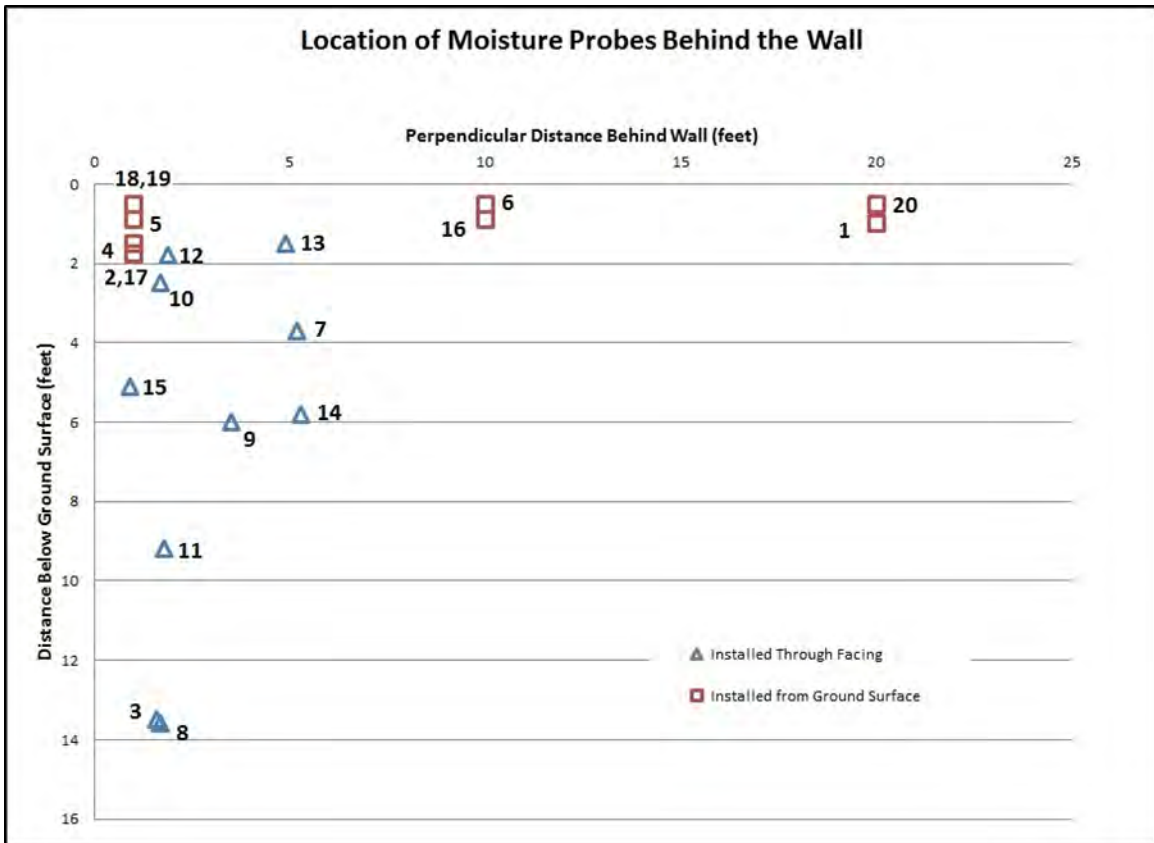


Figure E.28: Location of the 20 TDR probes installed behind the wall.

The ten holes to place the probes in the soil through the wall facing were drilled by Craig Olden, Inc. using a soil nail rig. Each hole was drilled with an angle of approximately 15 degrees from horizontal. Figure E.29 shows Craig Olden, Inc. drilling one of the holes for the probes. Figure E.30 shows an example of the placing of the moisture probe through the facing of the wall.

In the locations the probes could not be installed by hand, the probes were pushed into the soil using a slotted PVC pipe. Once the probe was in place, the hole was backfilled with dry native clay from the site. The holes were backfilled with native dry clay so the soil would swell and fill the voids when the water reached the dry soil. The dry clay fill was tamped into place and sealed with a wet clay to hold the fill until the shotcrete was placed.

The cables from the TDR probes were protected from damage from the shotcrete impact by placing the cables in slotted PVC pipes. Tape and cable ties were used to keep the cables within the PVC pipe and the slotted side was faced towards the inside of the wall to prevent the shotcrete from directly hitting the cables. Figure E.31 shows the cables being protected by the PVC pipe.



Figure E.29: A hole being drilled by Craig Olden, Inc.



Figure E.30: A sample installation of a probe installed through the facing of the wall.



Figure E.31: The PVC pipe protection for the TDR probe cables to minimize damage from the shotcrete.

The ten sensors that were installed through the ground surface were installed by digging holes using a pick axe and shovels for shallow depths. For the probes that were deeper than one foot, a drill with a custom drill bit, made by owner of site, was used to reach the desired depths. Once the probes were placed in the soil, the holes were backfilled with the dried native clay soil so the fill would swell and fill the voids when wetted. Figure E.32 shows one of the probes installed in the ground before the dried native clay fill was placed.



Figure E.32: A sample probe installation from the ground surface.

E.4: Shotcrete Facing Installation

The shotcrete facing was installed by Olden, Inc. on October 1, 2010. Olden, Inc. also installed drains between the shafts to move allow the water to flow to the base of the excavation. A picture of the drains placed between the shafts can be seen in Figure E.33. Figure E.34 shows Olden, Inc. placing the shotcrete facing on the wall.



Figure E.33: Installation of the drains on facing of the wall.



Figure E.34: Placement of shotcrete.

E.5: Wall Excavation

After a period of pre-excavation monitoring, excavation began on July 29, 2010 and took place over a period of approximately four weeks (Figure E.35 - Figure E.41). The full cantilever depth of 14-15' was reached on August 13, and the preliminary slopes were completed on August 19. The slopes were improved on September 30 by Olden, Inc. On August 17, 2011, Ranger Excavating reshaped the slopes to remove the bench and apply erosion control (Figure E.42).



Figure E.35: Excavation process as of 7/29/2010.



Figure E.36: Excavation process as of 8/1/2010.



Figure E.37: Excavation process as of 8/1/2010.



Figure E.38L: Excavation process as of 8/1/2010.



Figure E.39: Excavation process as of 8/23/2010.



Figure E.40: Excavation process as of 9/10/2010.



Figure E.41: Excavation process as of 10/1/2010.



Figure E.42: Excavation after Ranger Excavating reshaped the slopes and applied erosion control.

E.6: Inundation Berm Construction

The inundation berm encloses an area approximately 40 feet wide and 20 feet behind the test wall (Figure E.43). A cross-section of the berm design is shown in Figure E.44. The berm is keyed into the native soil with a 2-foot deep trench and is lined with a geomembrane to minimize the lateral loss of water (Figure E.45).

The inundation berm was constructed by Ranger Excavating on April 26, 2012. A backhoe was used to excavate the trench (Figure E.46). After excavation of the trench, the geomembrane was installed (Figure E.47). The soil was replaced and compacted, along with stockpiled soil from the project site, using the backhoe bucket (Figure E.48). After the installation of the geomembrane and compacted soil (Figure E.49), the seams were joined together with duct tape (Figure E.49). The completed inundation berm is shown in Figure E.50. Initial filling of the berm occurred on May 2, 2012 (Figure E.51). While some leakage of the

seams occurred, the leakage rate was slow enough that the water level could be maintained with water from the on-site supply (Figure E.52 - Figure E.53).

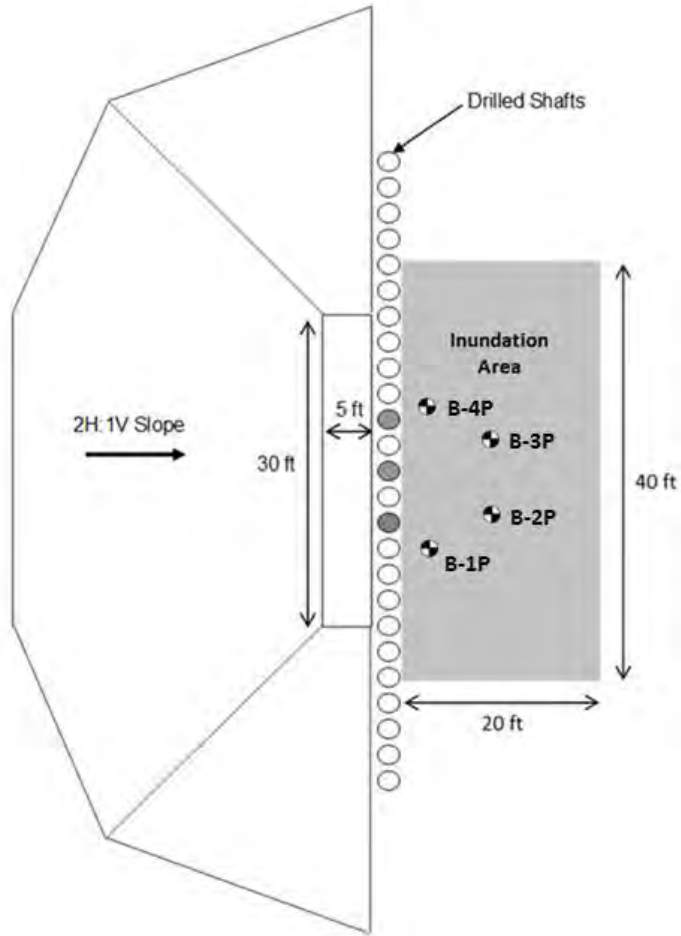


Figure E.43: Plan view of inundation zone.

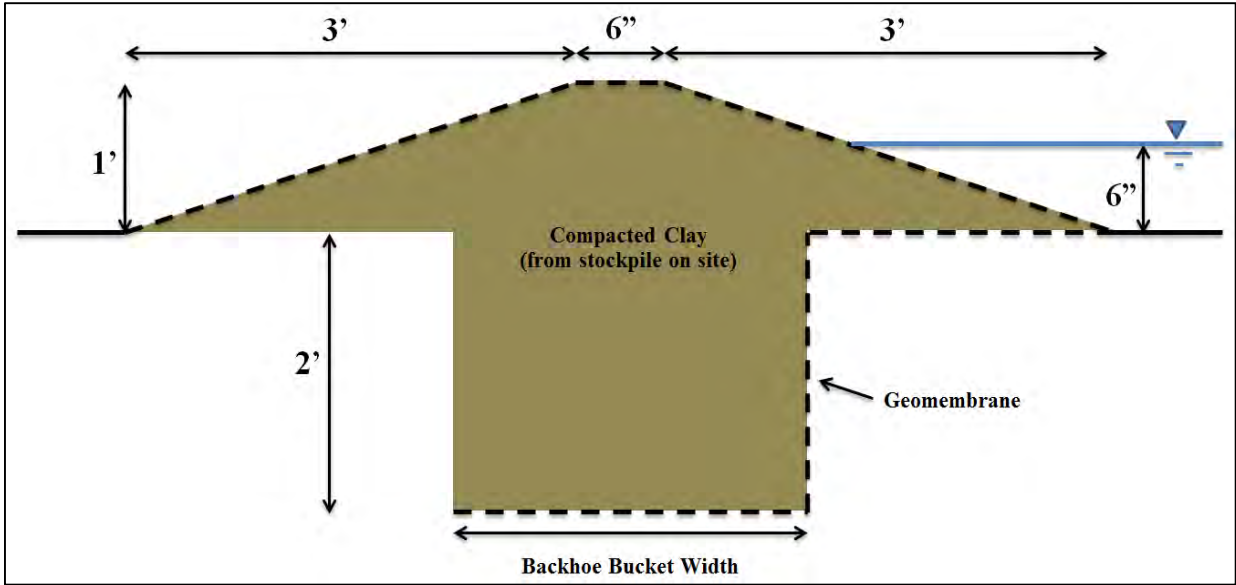


Figure E.44: Cross-section of inundation berm design.



Figure E.45: Excavation of trench for inundation berm.



Figure E.46: Installation of geomembrane in trench.



Figure E.47: Compacting soil with backhoe bucket.



Figure E.48: Compacting soil with backhoe bucket.



Figure E.49: Detail of geomembrane seam.



Figure E.50: Completed inundation berm.



Figure E.51: Filling the inundation zone.



Figure E.52: Leakage from southeast corner of inundation zone.



Figure E.53: Leakage from west side of inundation zone.

E.7: Final Wall Geometry

The wall, as constructed, matched the final dimensions which consisted of 25 drilled shafts with a 24 inch diameter spaced six inches edge to edge (Figure E.54). The shafts are embedded to depths from 18 to 35 feet below the ground surface with the deepest shafts being in the center (Figure E.55). At the center of the wall, the cantilever height is 15 feet, the penetration depth is 20 feet, and top of the shafts is four feet above the ground surface (Figure E.56).

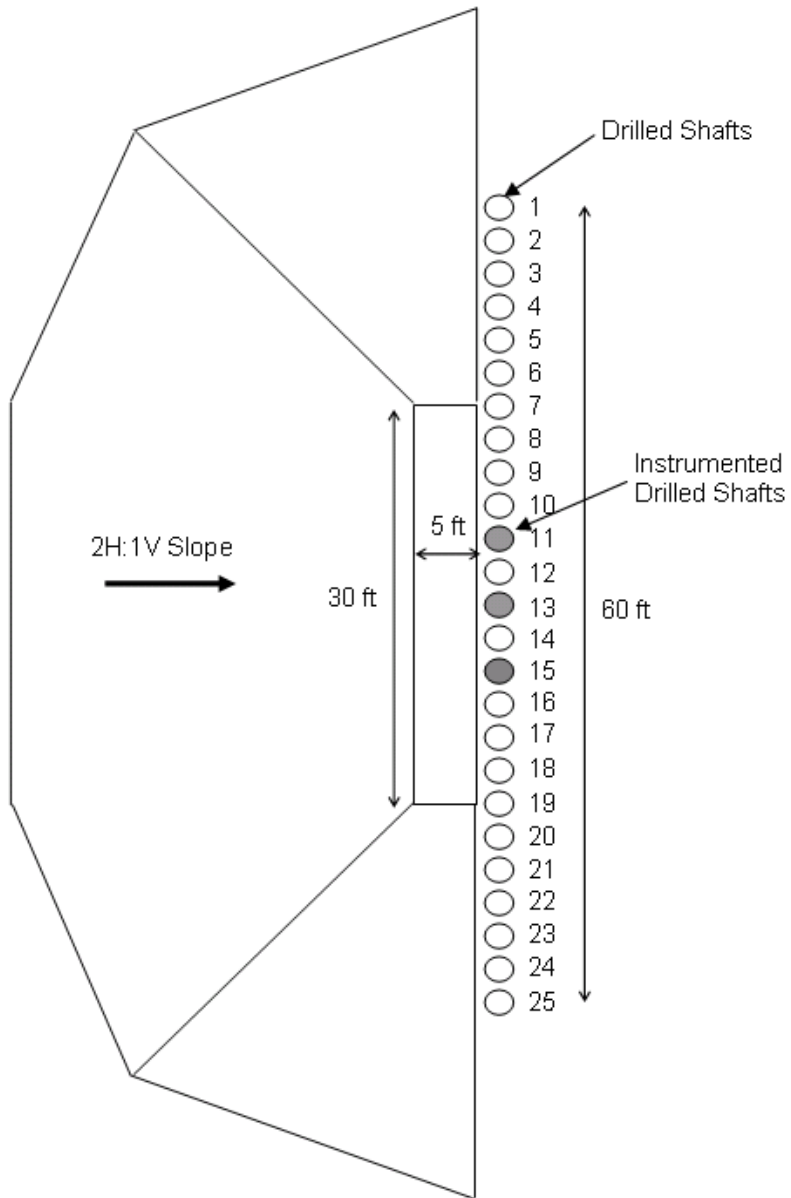


Figure E.54: Plan view of wall and excavation.

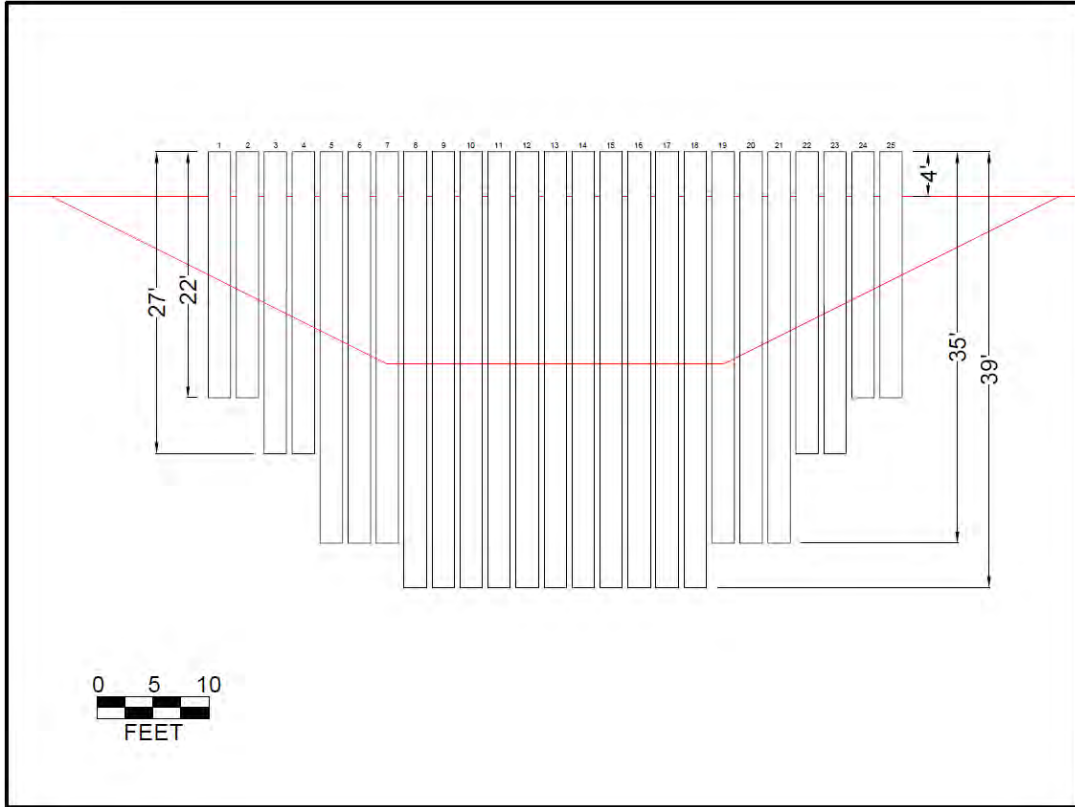


Figure E.55: Profile of wall and excavation.

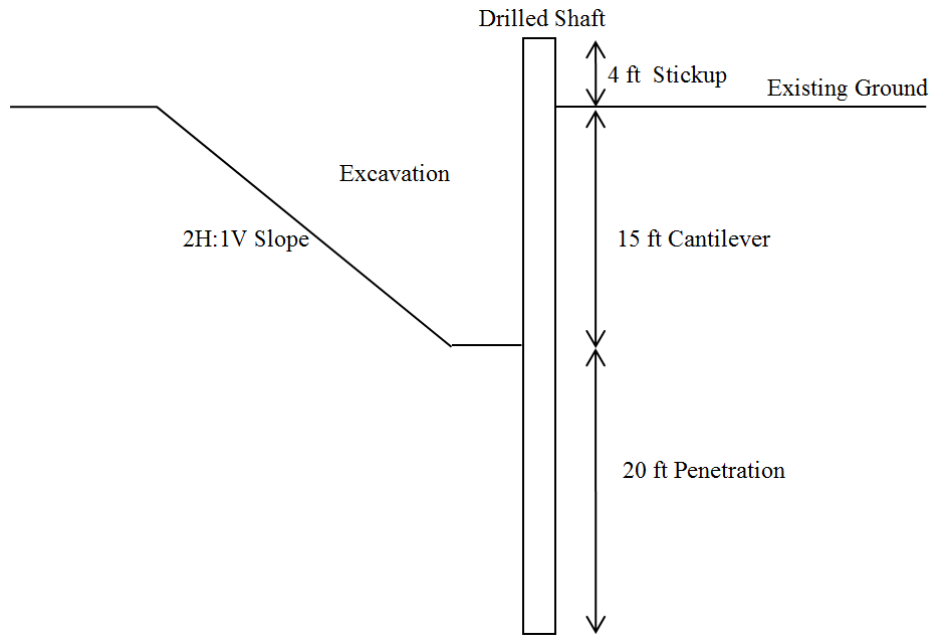


Figure E.56: Cross-section of wall at center of excavation, facing east (Shaft No. 13).

APPENDIX F: FIELD INCLINOMETER DATA

This section presents the data obtained from the inclinometer and linear potentiometer.

F.1: Overview of Instrument

Three shafts were instrumented with one inclinometer casing (Figure F.1 and Figure F.2) with a casing installed 5.5 feet behind the wall.

By running an inclinometer probe up the inclinometer casing, a lateral deflection profile is able to be calculated. The inclinometer probe works by measuring the angle of tilt over a two foot measuring interval. The deviation at the top of the measurement interval relative to the bottom of the interval is calculated by multiplying the measurement interval by the sine of the tilt angle. Taking measurements every two feet allows for a lateral deflection profile to be developed by summing the deviations (Figure F.4).

The inclinometer probe measures the inclination in two directions; the A-axis (in the direction of the wheels) and the B-axis (in the direction perpendicular to the wheels). This allows for the lateral deflection to be determined in any direction.

The inclinometer casing was installed so the grooves for the A-axis were not perpendicular to the wall. Therefore, both the A-axis and B-axis are needed to calculate the deflection of the wall. The standard two-pass survey method was used when taking readings. This provided two readings per axis at each interval where the probe is oriented 180 degrees the second pass. The tilt angles from the two measurements are averaged when calculating the deflection. This method is done in order to eliminate sensor bias, smooth the effect of random errors, and to allow for a means to detect errors.

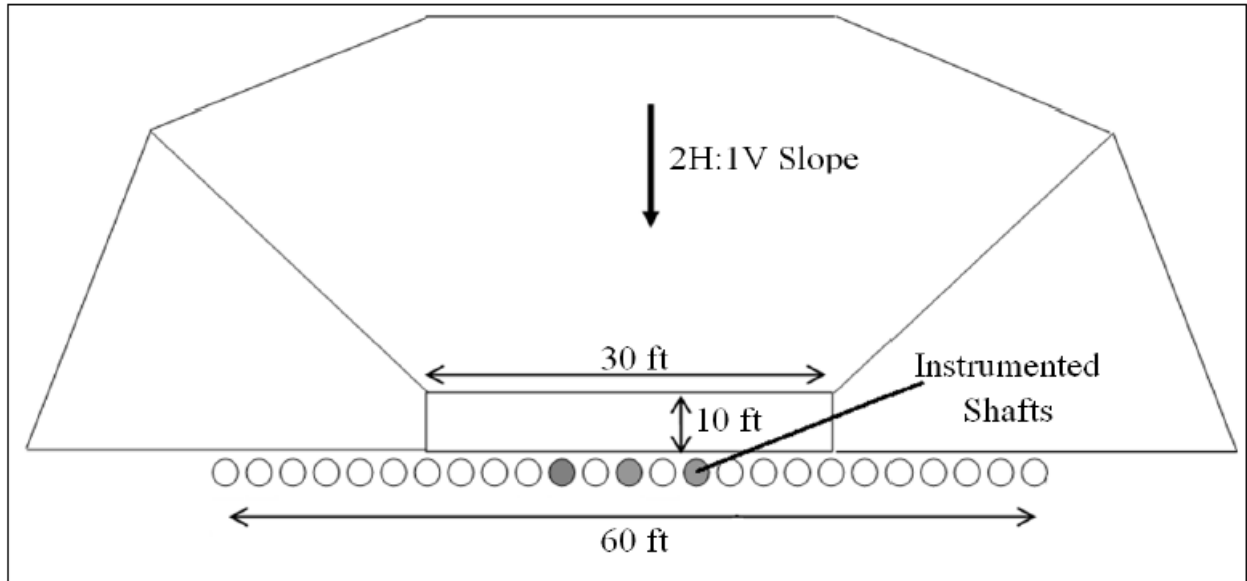


Figure F.1: Plan view of wall and excavation.

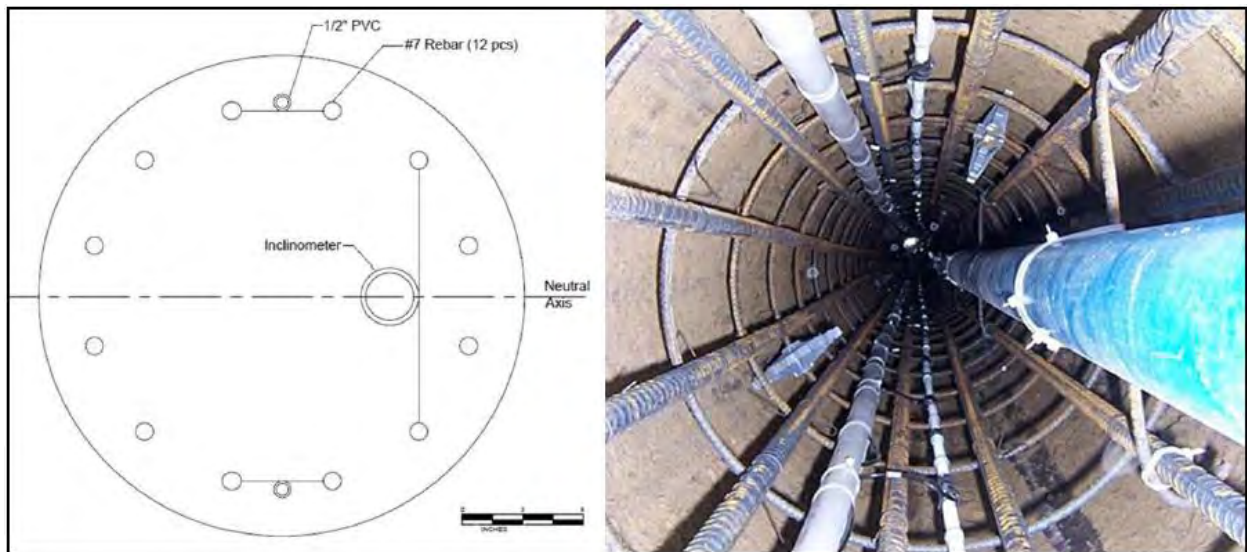


Figure F.2: Plan view of instrumented rebar cage before concrete placement.

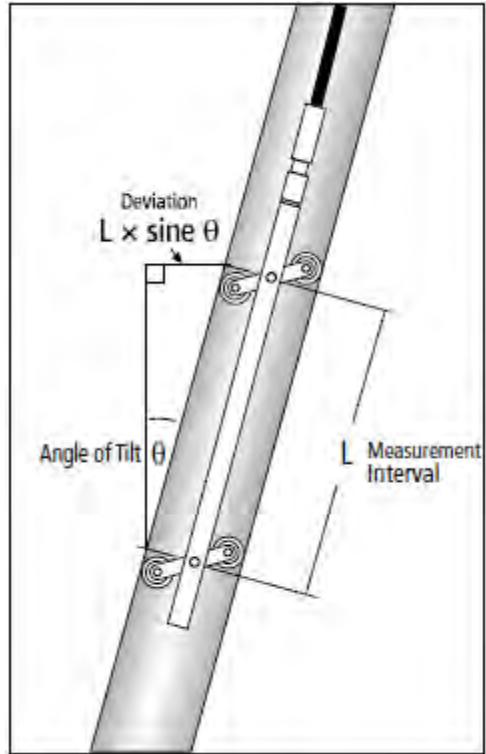


Figure F.3: Inclinometer probe within an inclinometer casing (Durham Geo-Enterprises Inc. 2011).

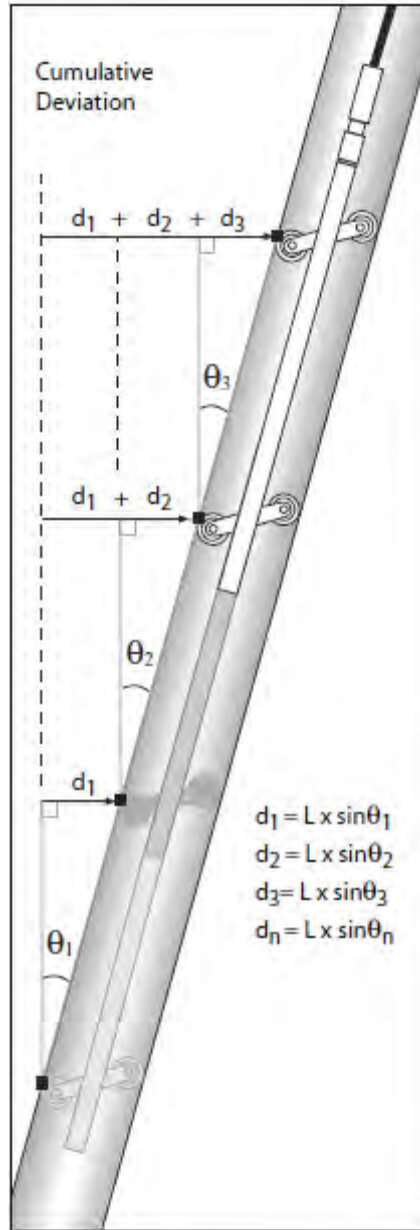


Figure F.4: Calculation of lateral deviations within the inclinometer casing (Durham Geo-Enterprises Inc. 2011).

F.2: Data from Instrumented Shafts

The inclinometer data from the inclinometers installed in the three instrumented shafts are presented in the following figures.

Summary of Inclinometer Data From 7/29/2010

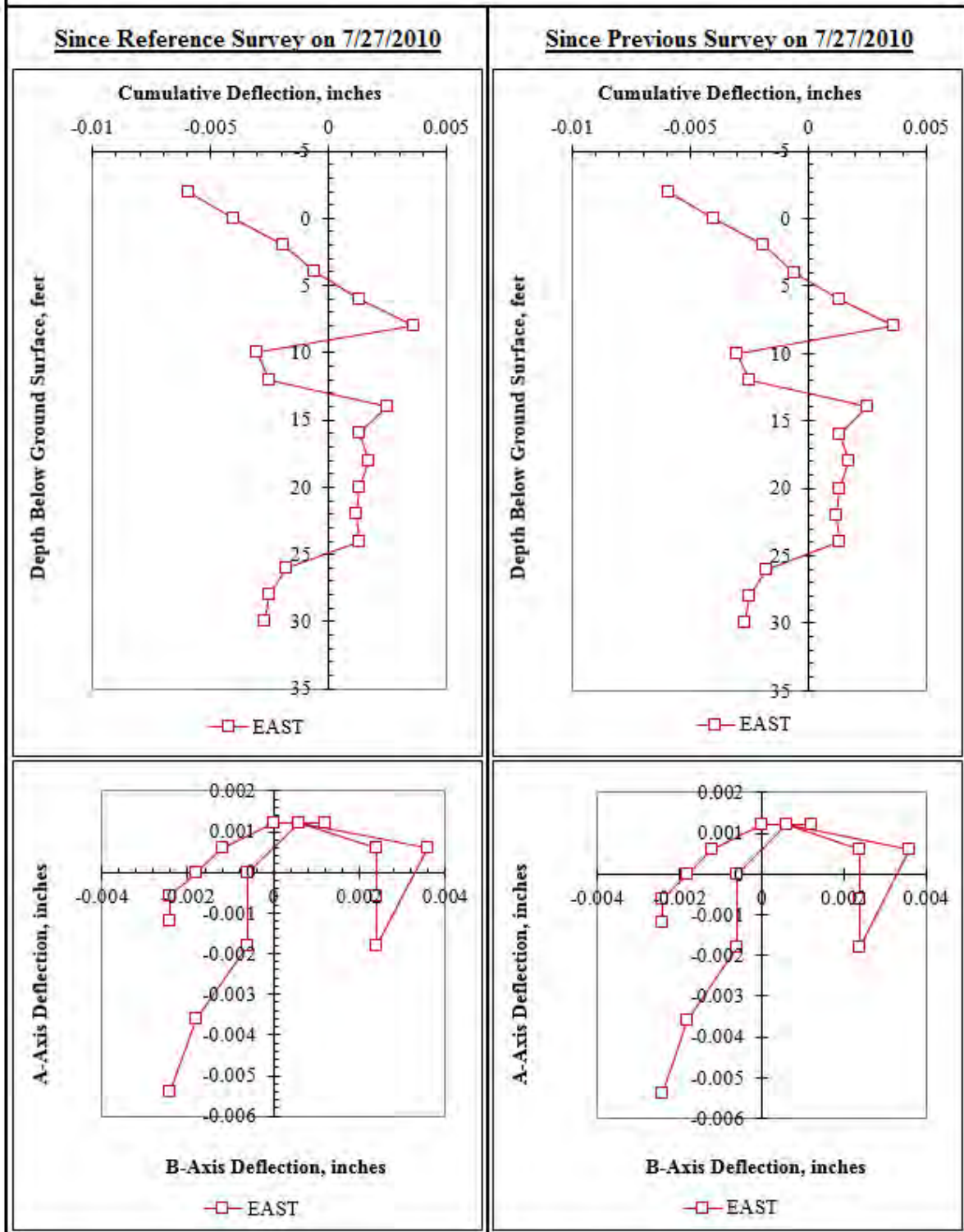


Figure F.5: Summary of inclinometer data from 7/29/2010.

Summary of Inclinometer Data From 7/29/2010

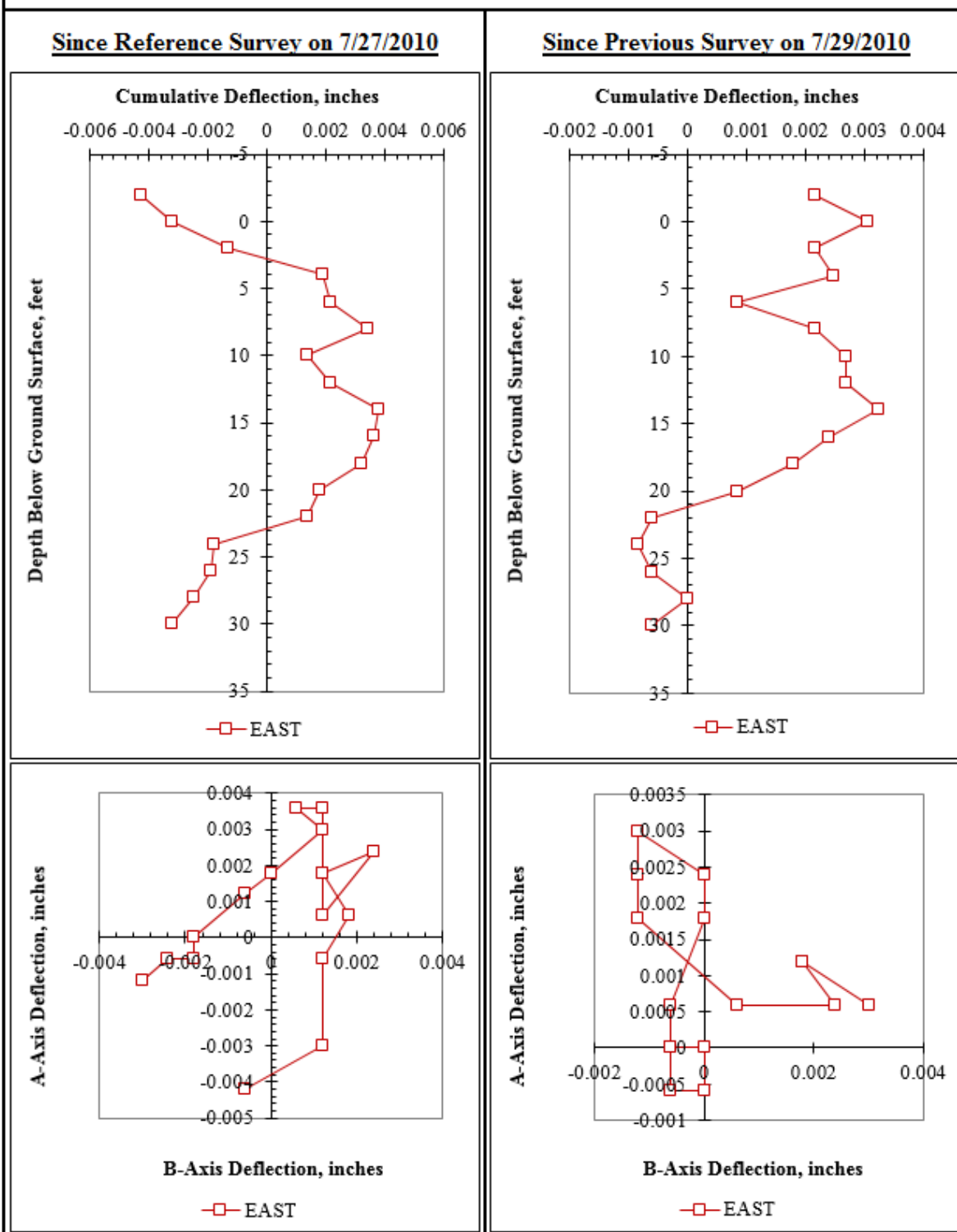


Figure F.6: Summary of inclinometer data from 7/29/2010.

Summary of Inclinometer Data From 7/29/2010

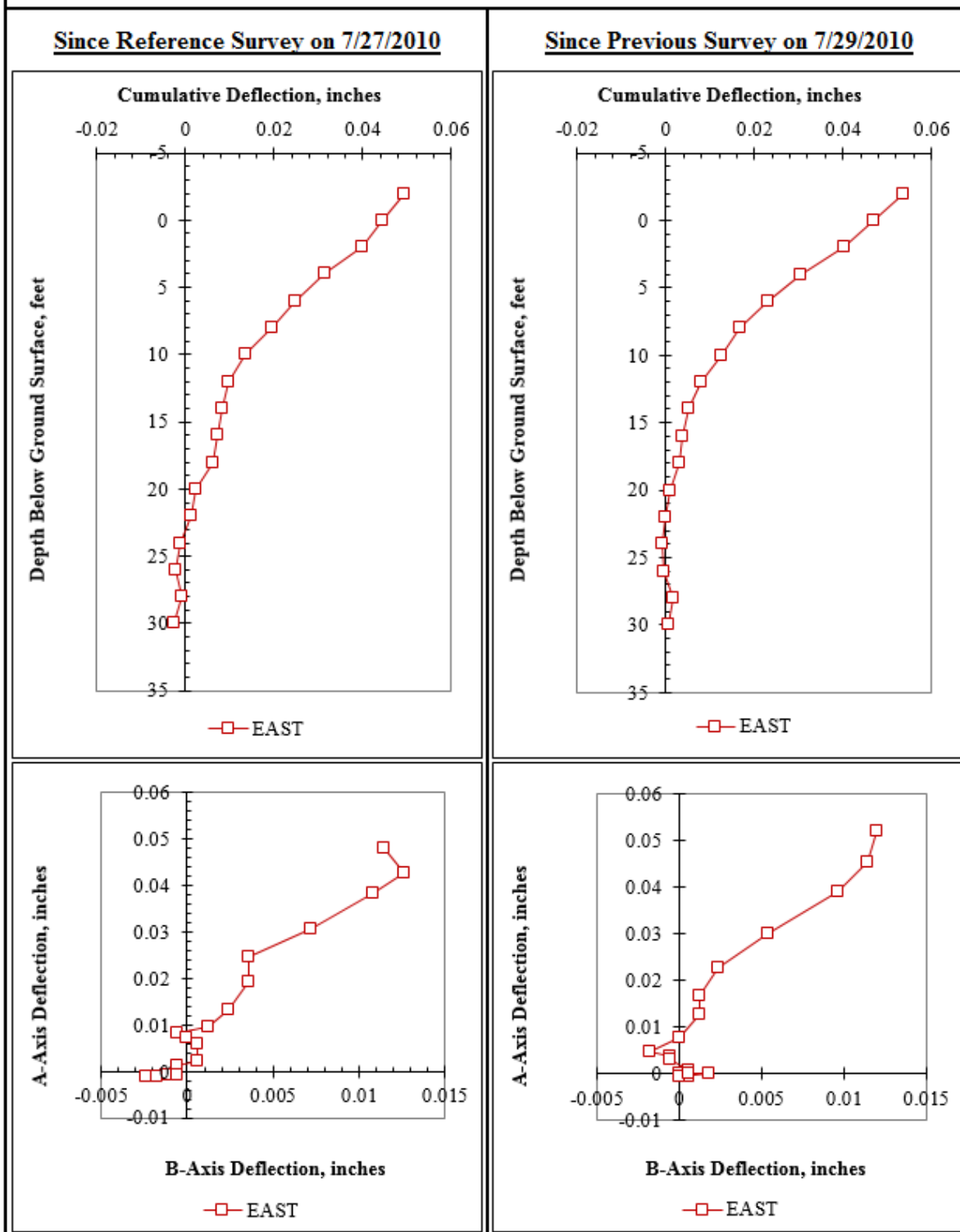


Figure F.7: Summary of inclinometer data from 7/29/2010.

Summary of Inclinometer Data From 7/30/2010

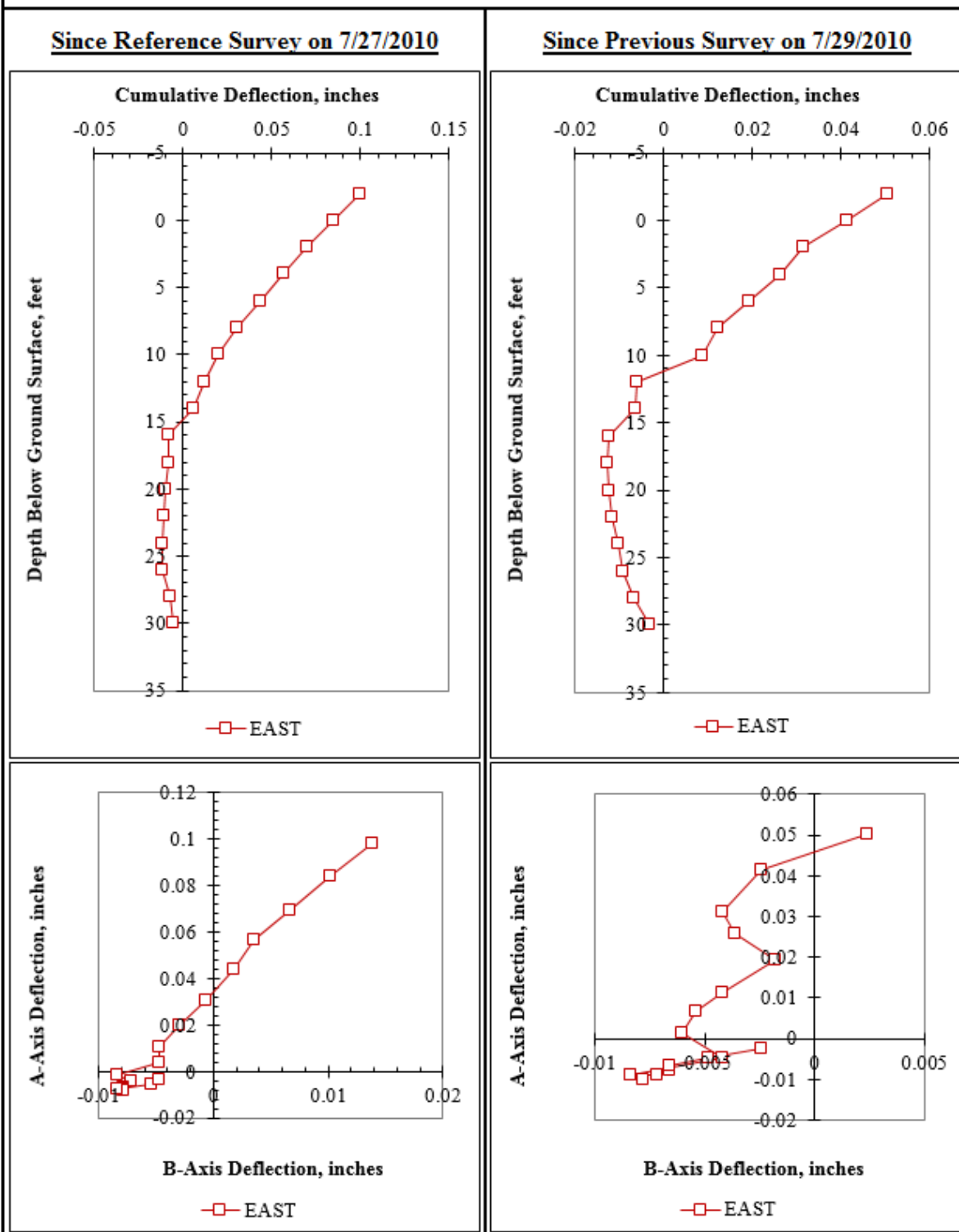


Figure F.8: Summary of inclinometer data from 7/30/2010.

Summary of Inclinometer Data From 7/30/2010

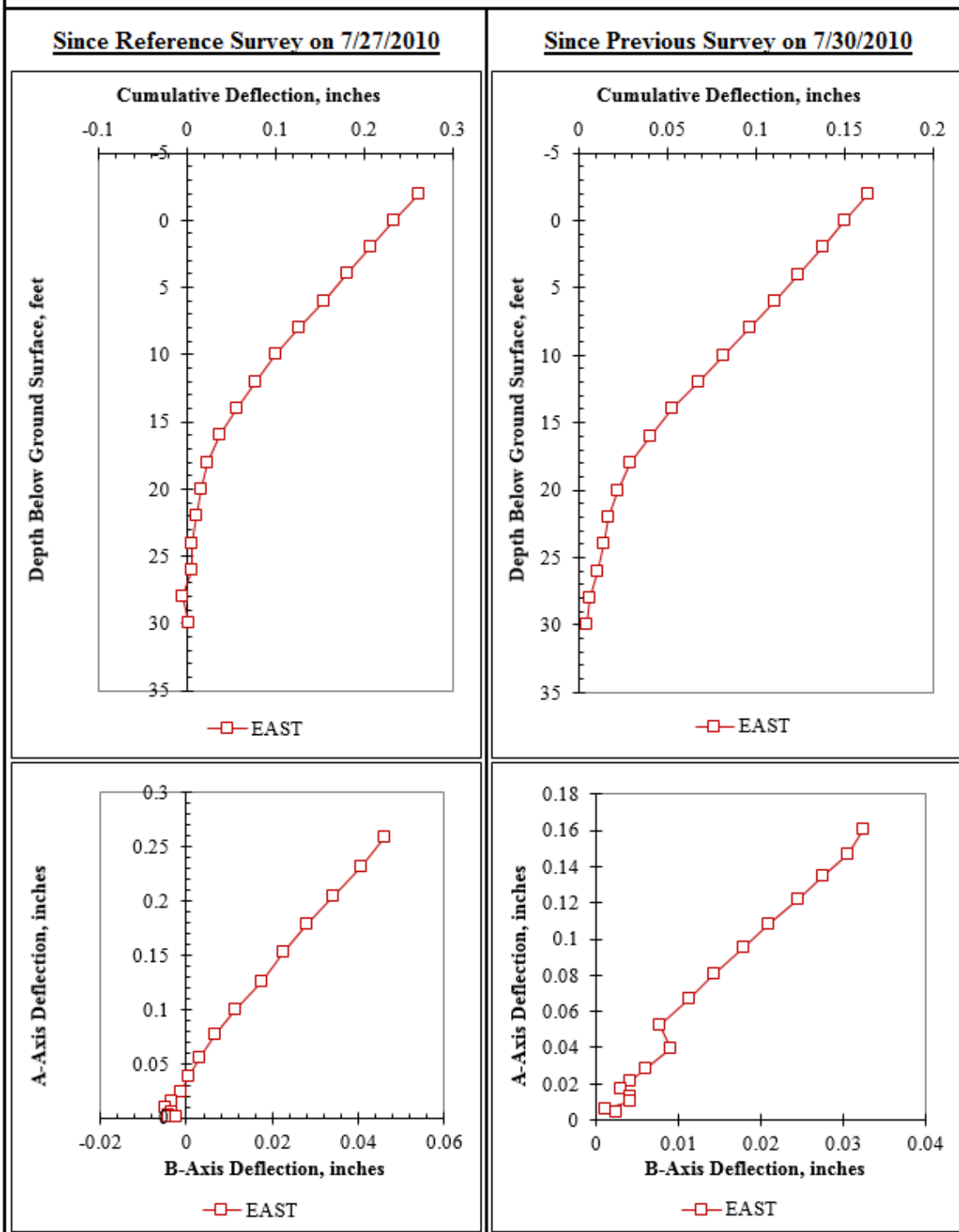


Figure F.9: Summary of inclinometer data from 7/30/2010.

Summary of Inclinometer Data From 7/31/2010

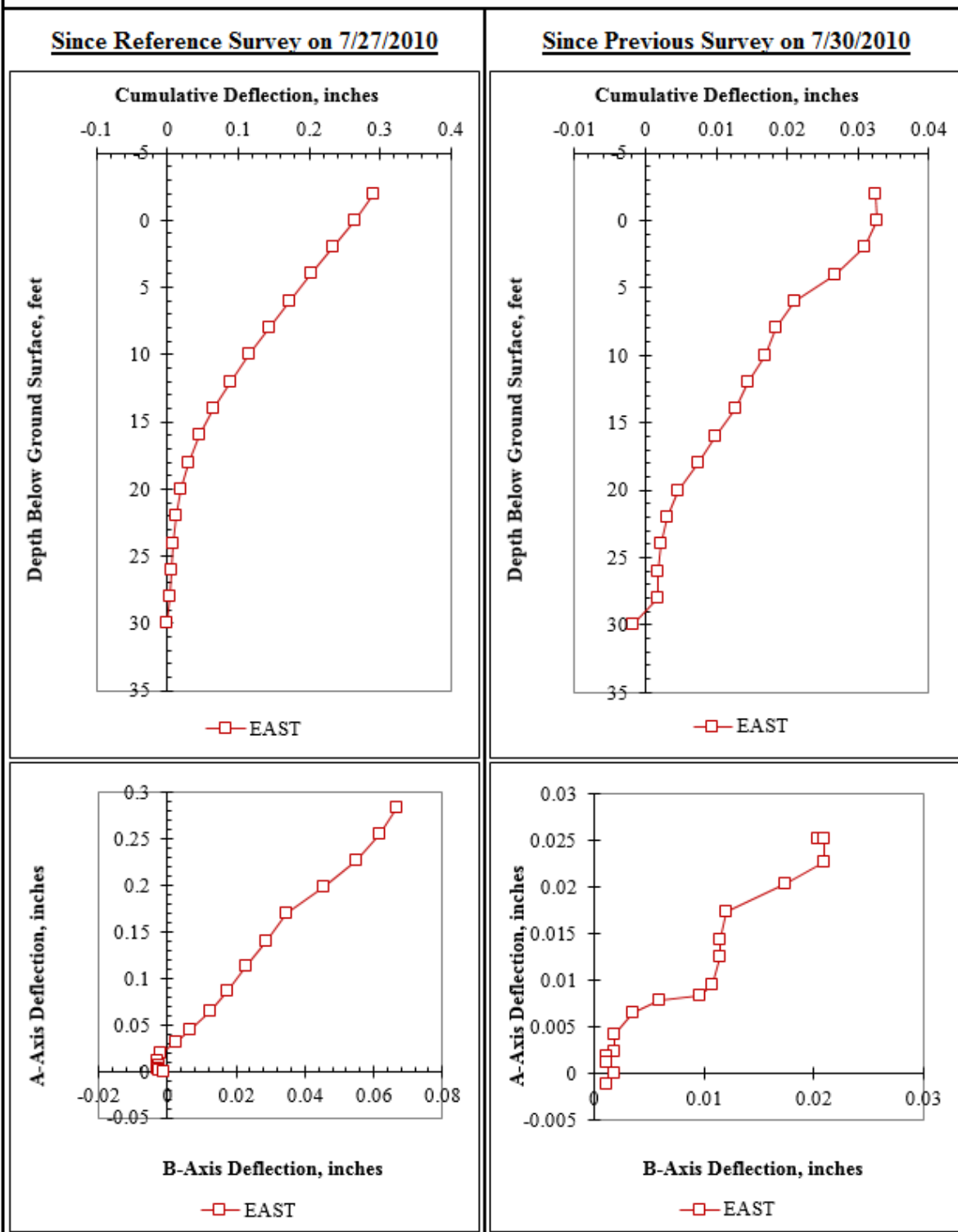


Figure F.10: Summary of inclinometer data from 7/31/2010.

Summary of Inclinometer Data From 7/31/2010

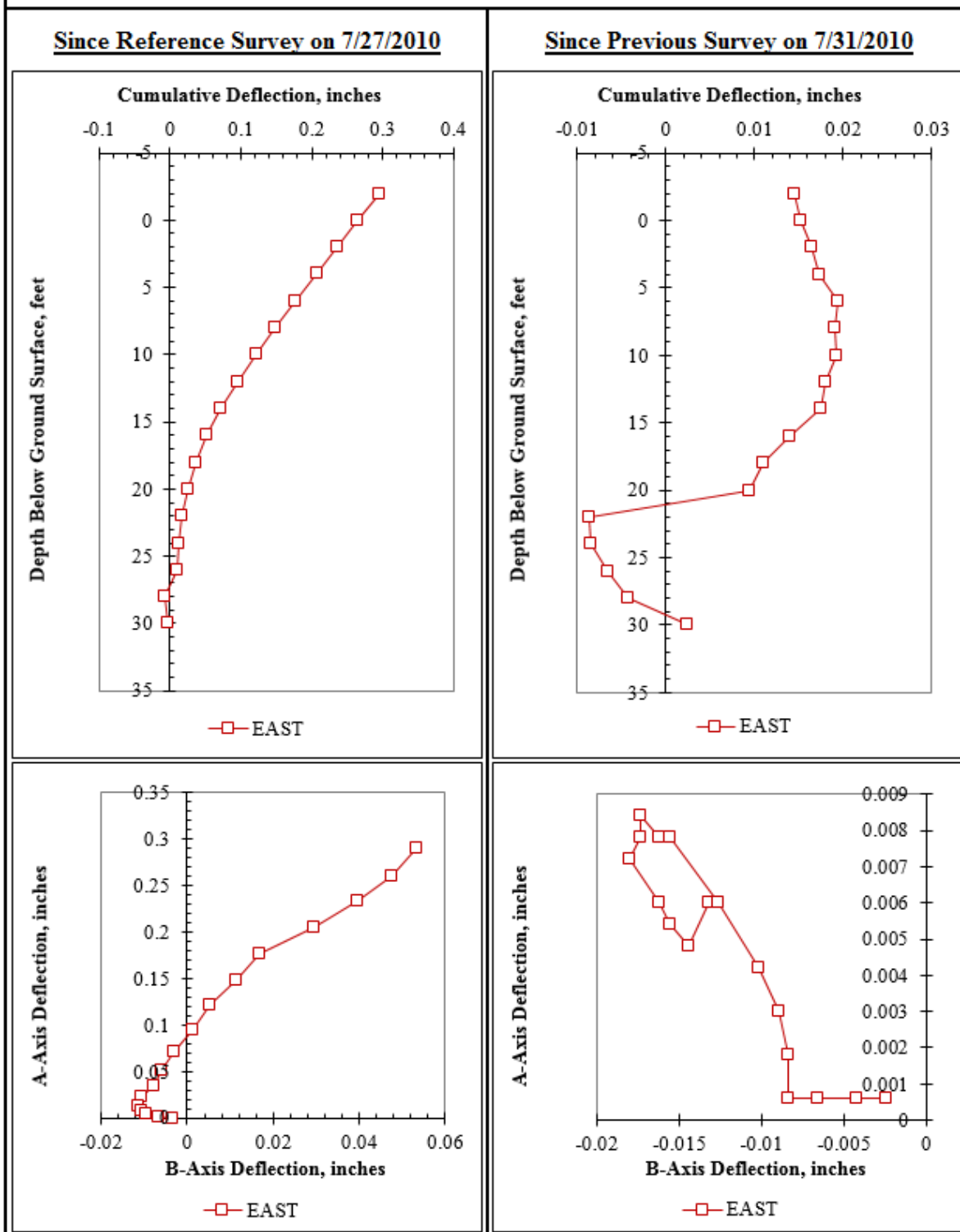


Figure F.11: Summary of inclinometer data from 7/31/2010.

Summary of Inclinometer Data From 8/1/2010

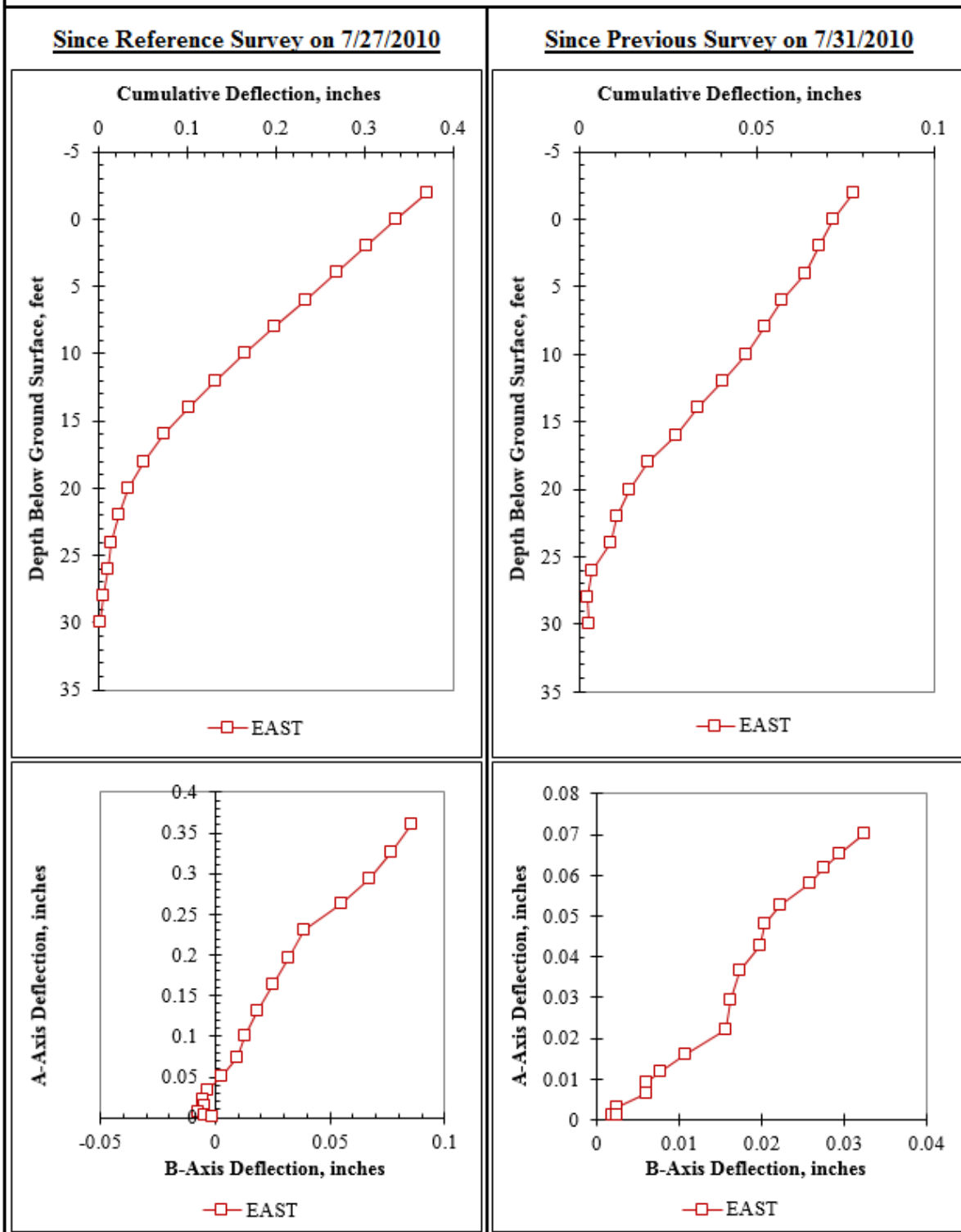


Figure F.12: Summary of inclinometer data from 8/1/2010.

Summary of Inclinometer Data From 8/4/2010

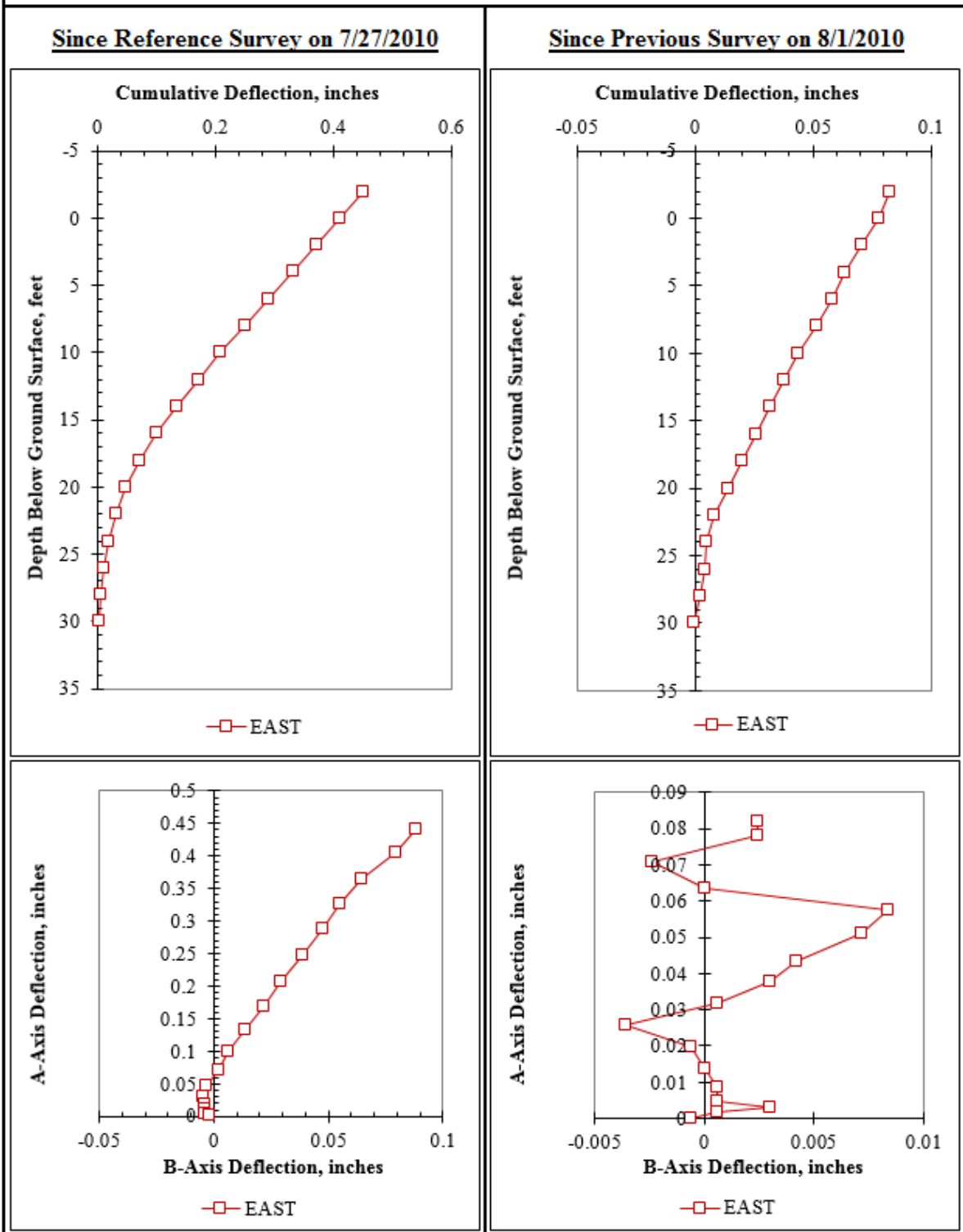


Figure F.13: Summary of inclinometer data from 8/4/2010.

Summary of Inclinometer Data From 8/5/2010

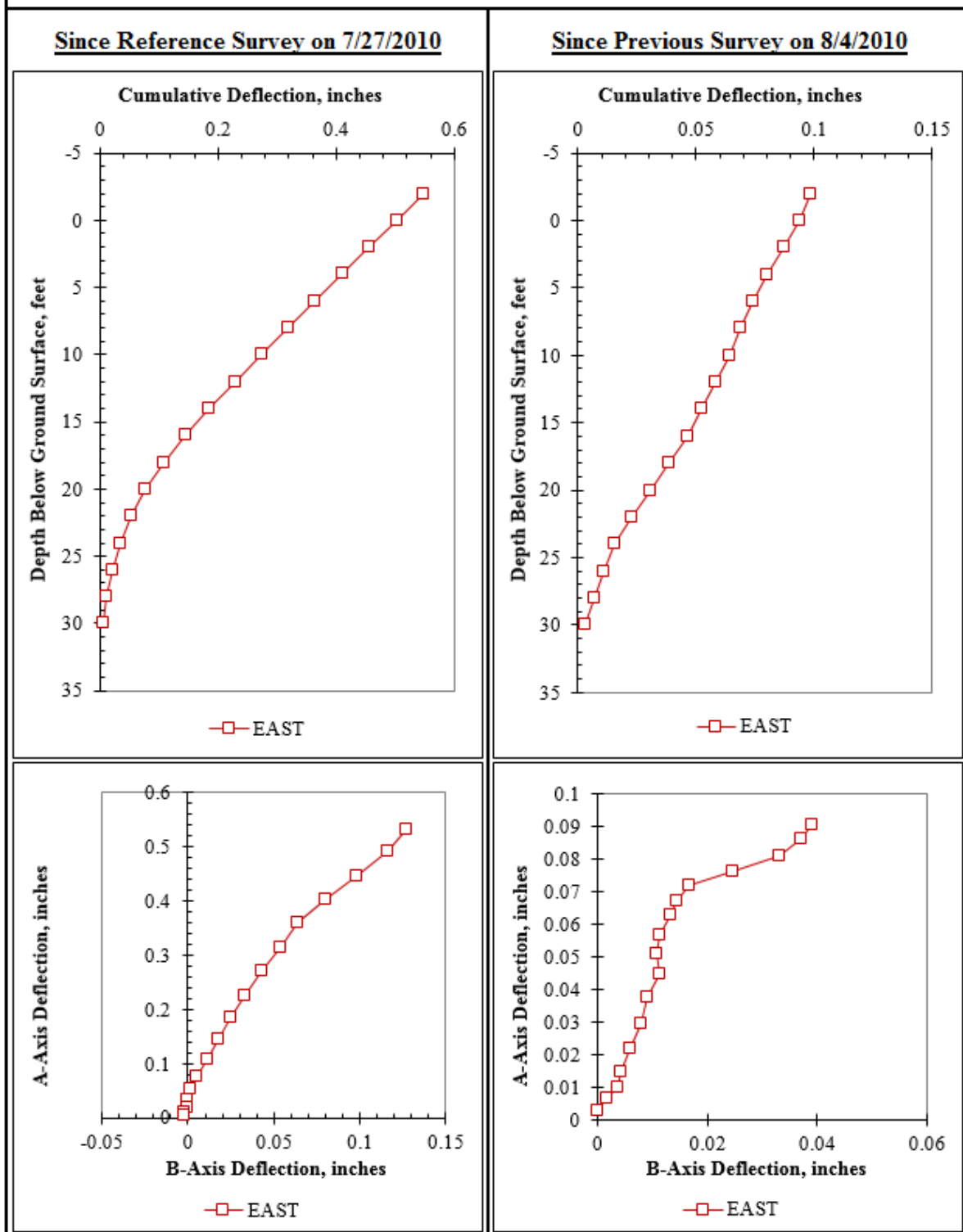


Figure F.14: Summary of inclinometer data from 8/5/2010.

Summary of Inclinometer Data From 8/6/2010

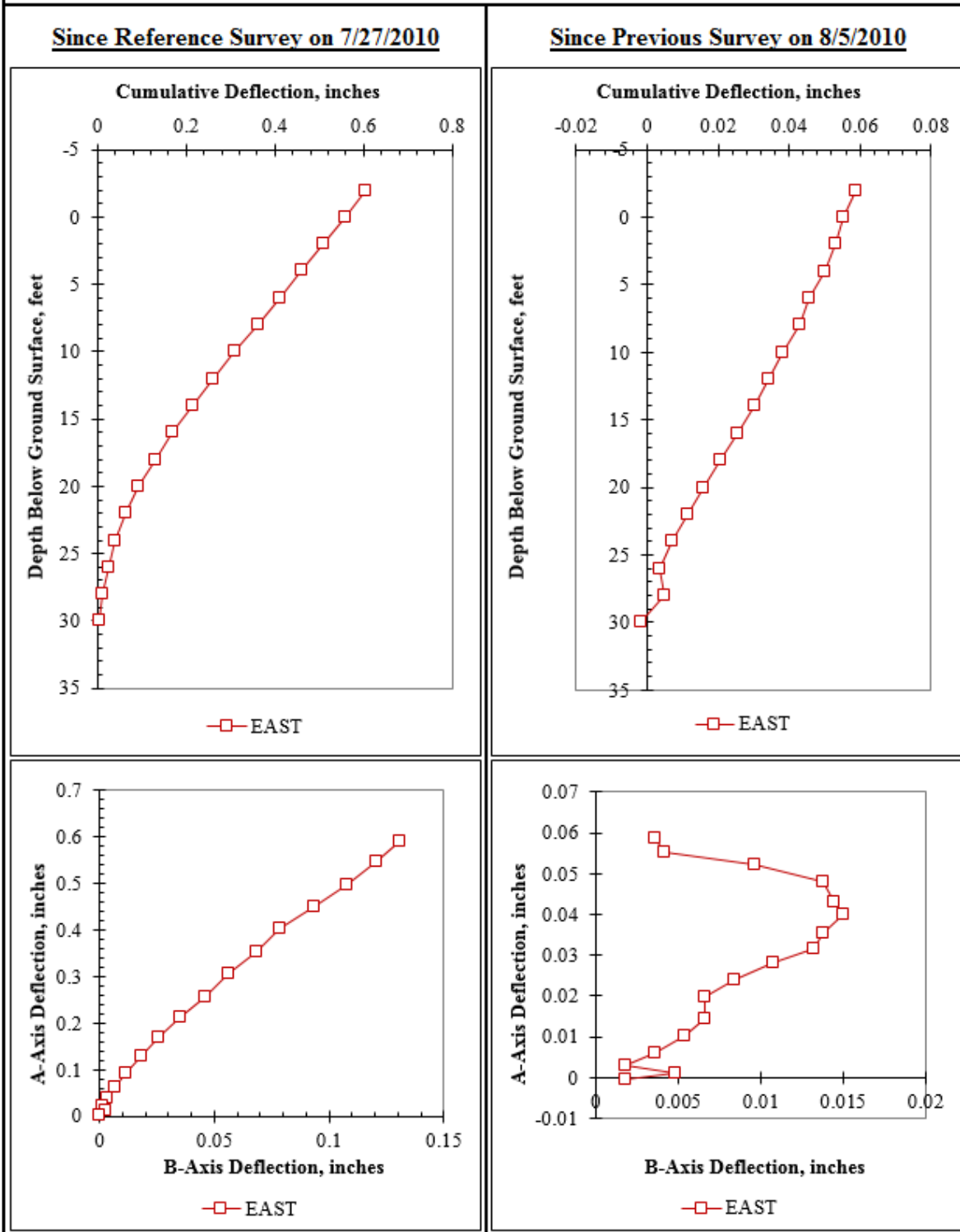


Figure F.15: Summary of inclinometer data from 8/6/2010.

Summary of Inclinometer Data From 8/9/2010

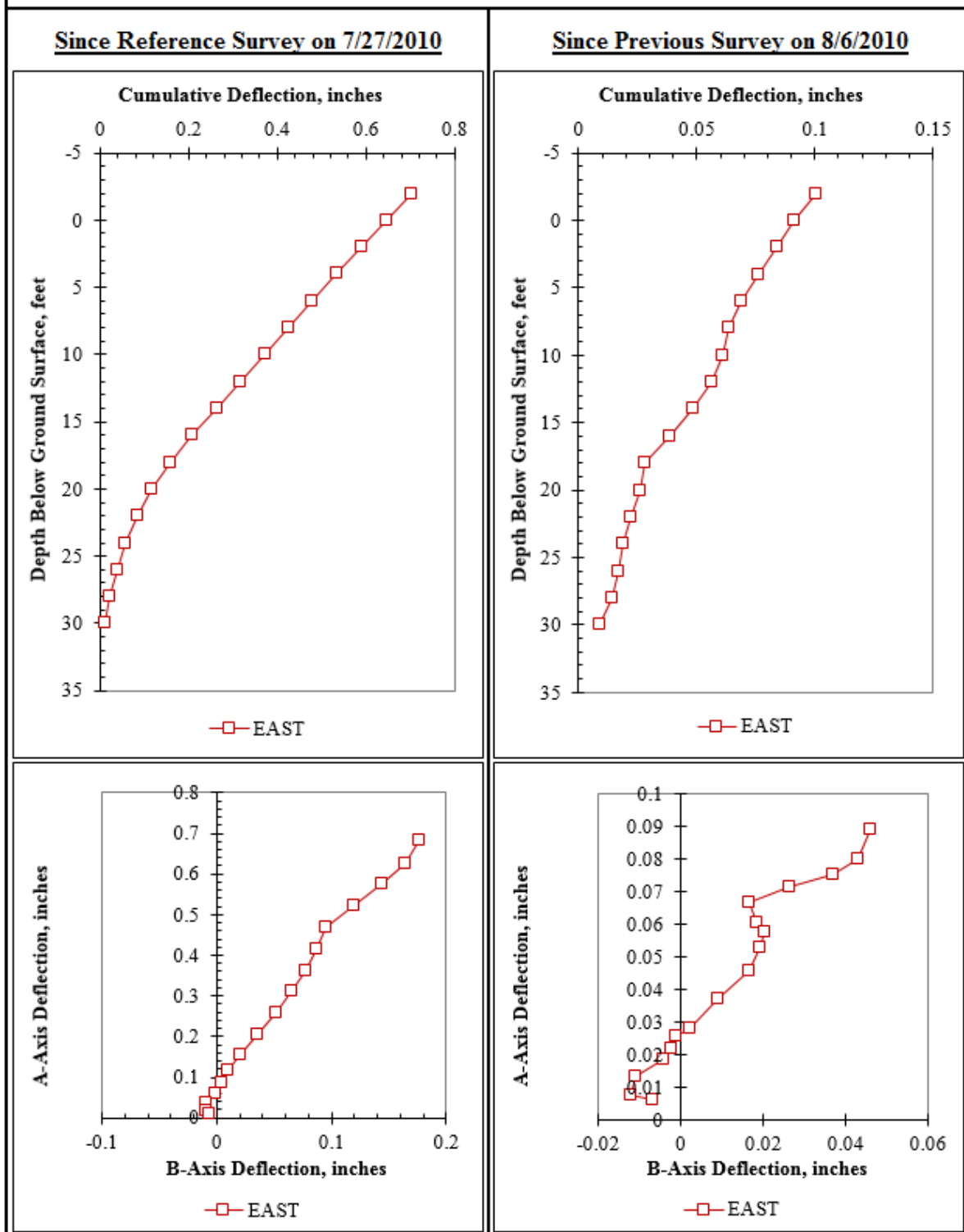


Figure F.16: Summary of inclinometer data from 8/9/2010.

Summary of Inclinator Data From 8/10/2010

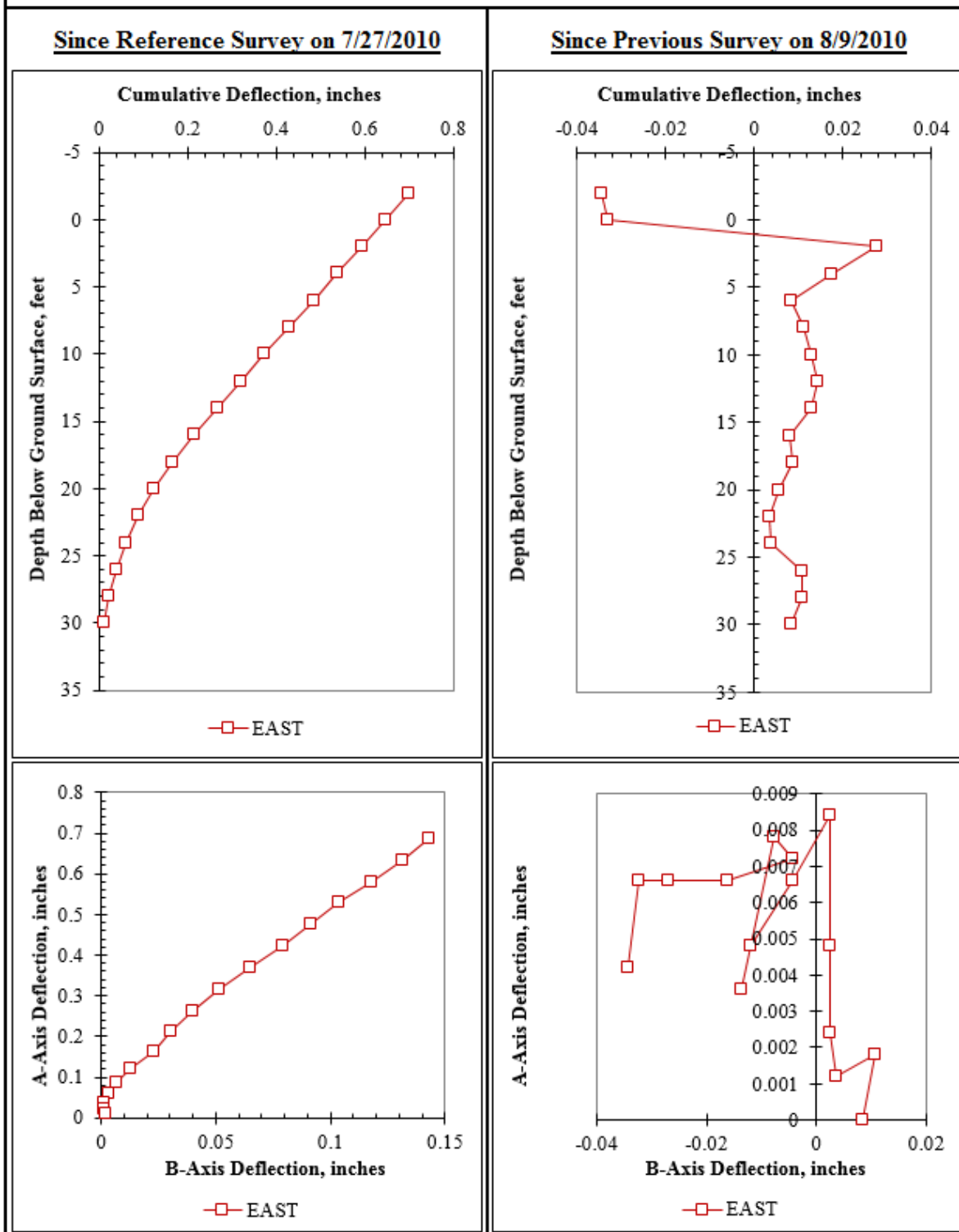


Figure F.17: Summary of inclinometer data from 8/10/2010.

Summary of Inclinator Data From 8/13/2010

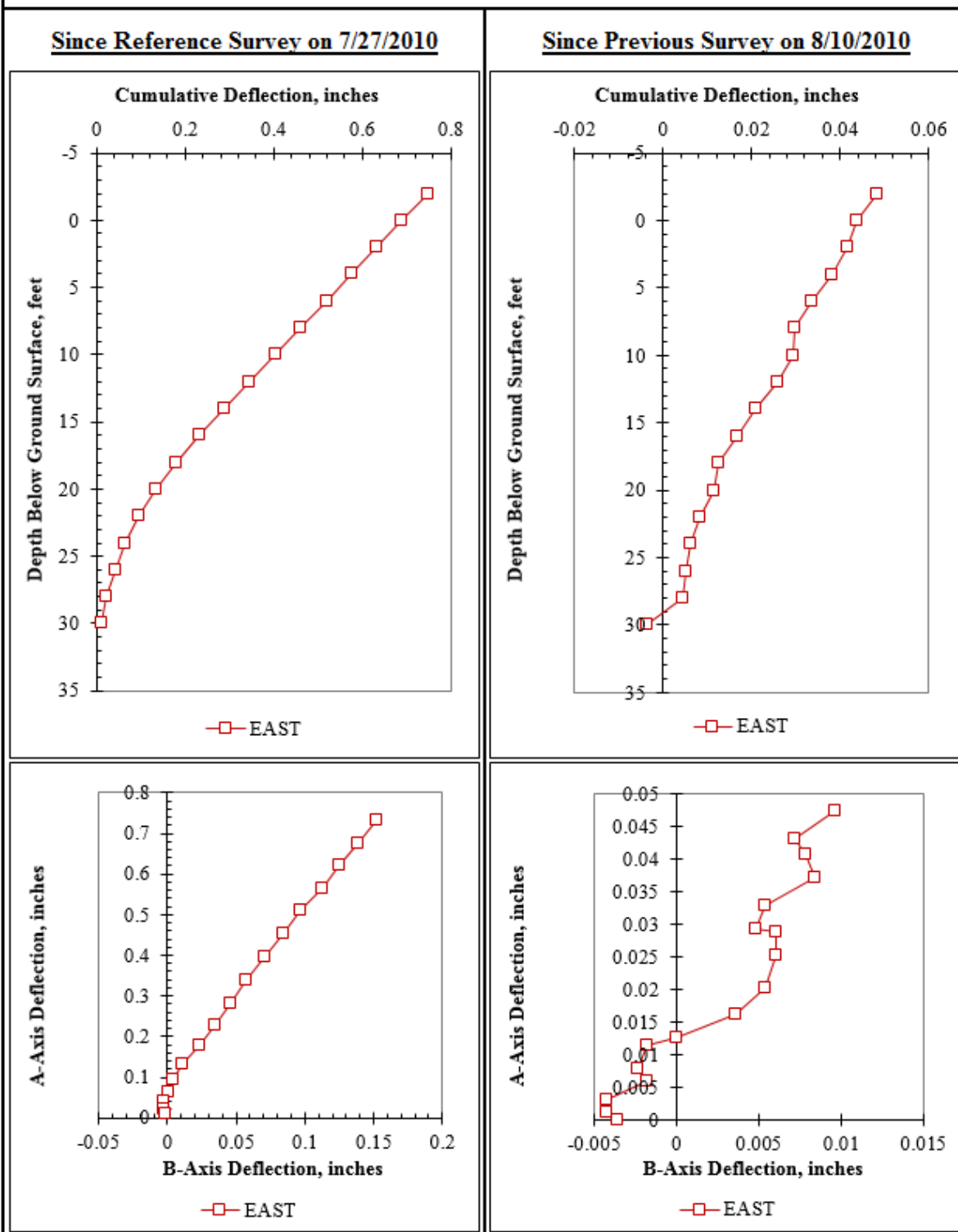


Figure F.18: Summary of inclinometer data from 8/13/2010.

Summary of Inclinometer Data From 8/16/2010

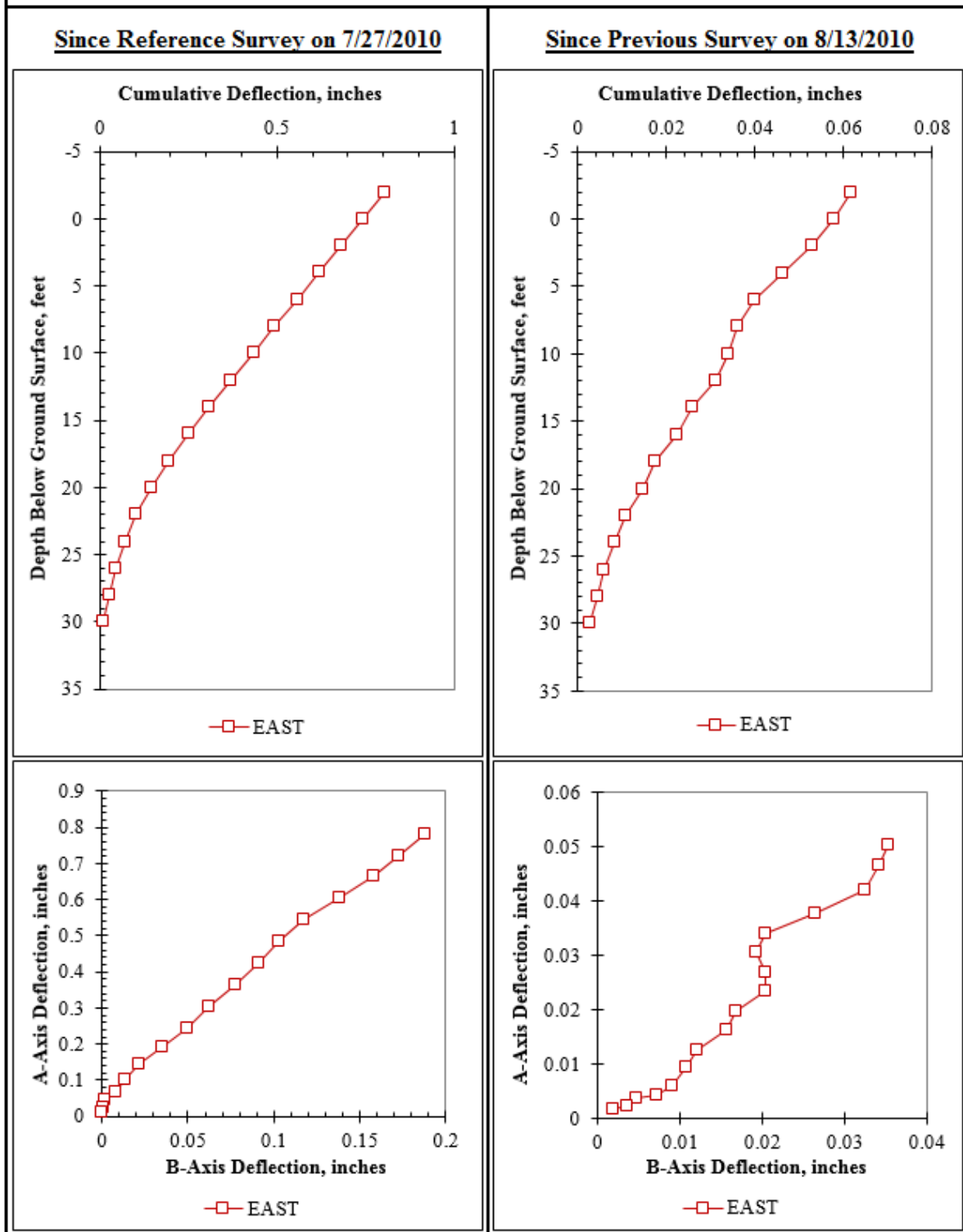


Figure F.19: Summary of inclinometer data from 8/16/2010.

Summary of Inclinator Data From 8/19/2010 (1 of 2)

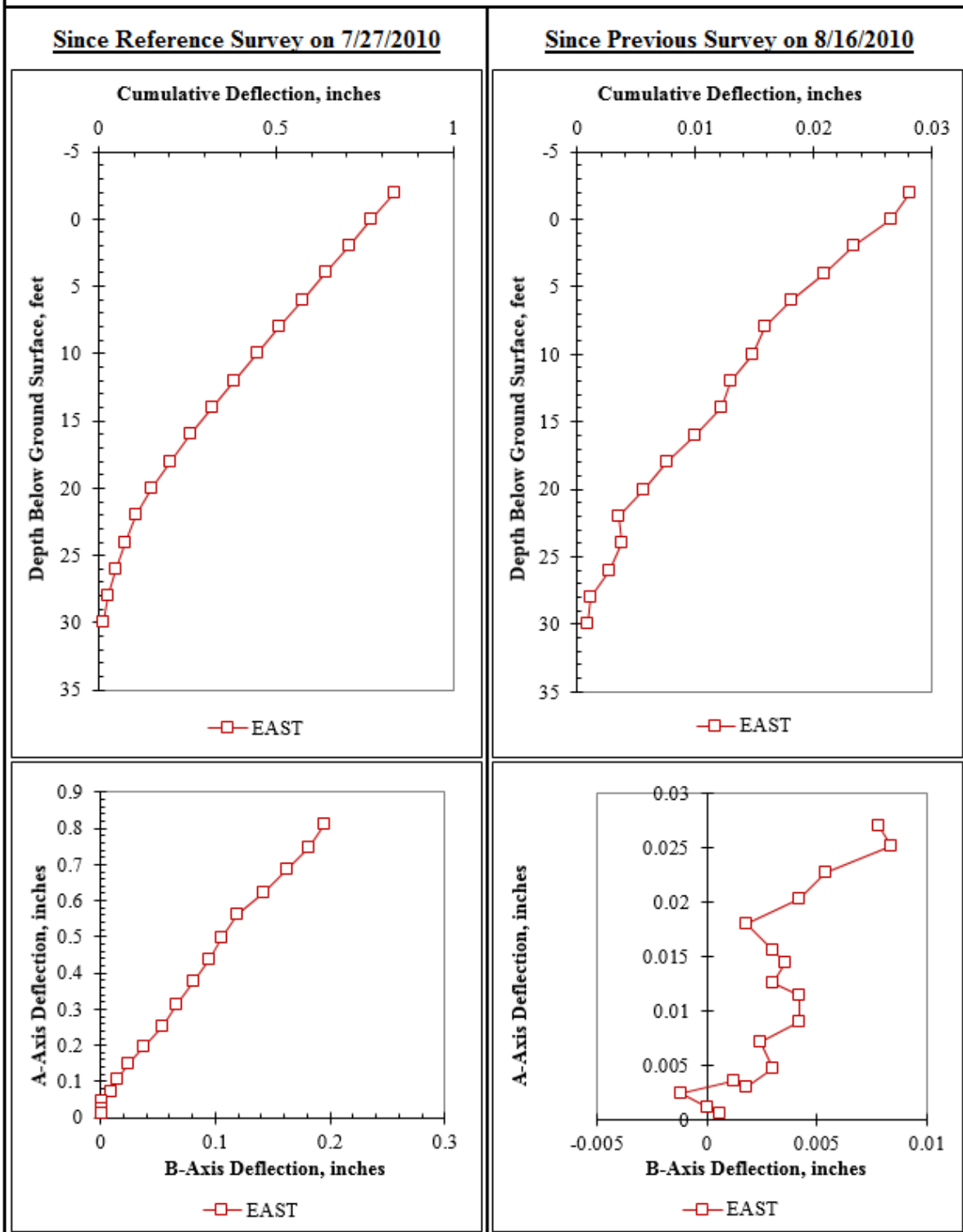


Figure F.20: Summary of inclinometer data from 8/19/2010.

Summary of Inclinometer Data From 8/19/2010 (2 of 2)

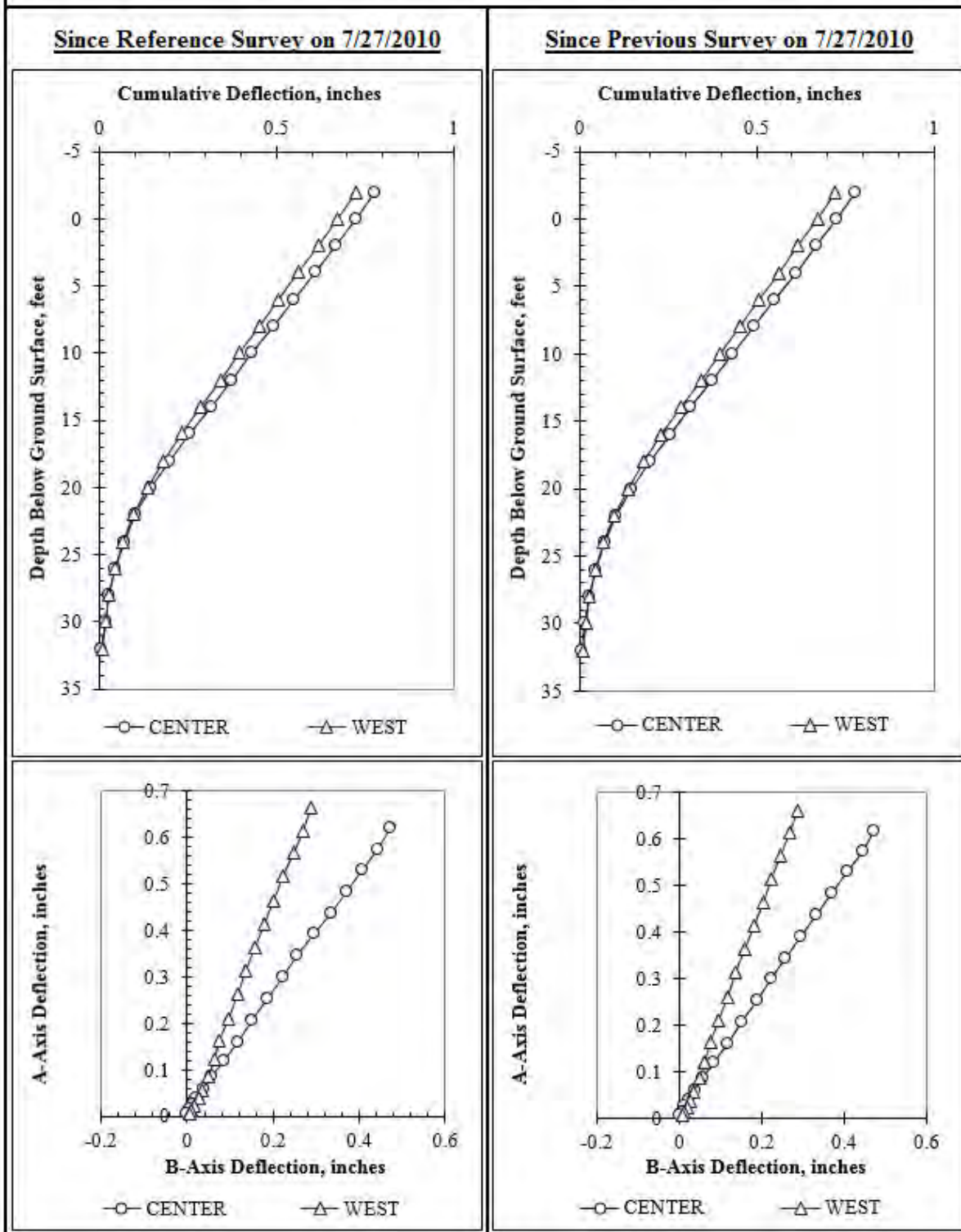


Figure F.21: Summary of inclinometer data from 8/19/2010.

Summary of Inclinometer Data From 8/23/2010

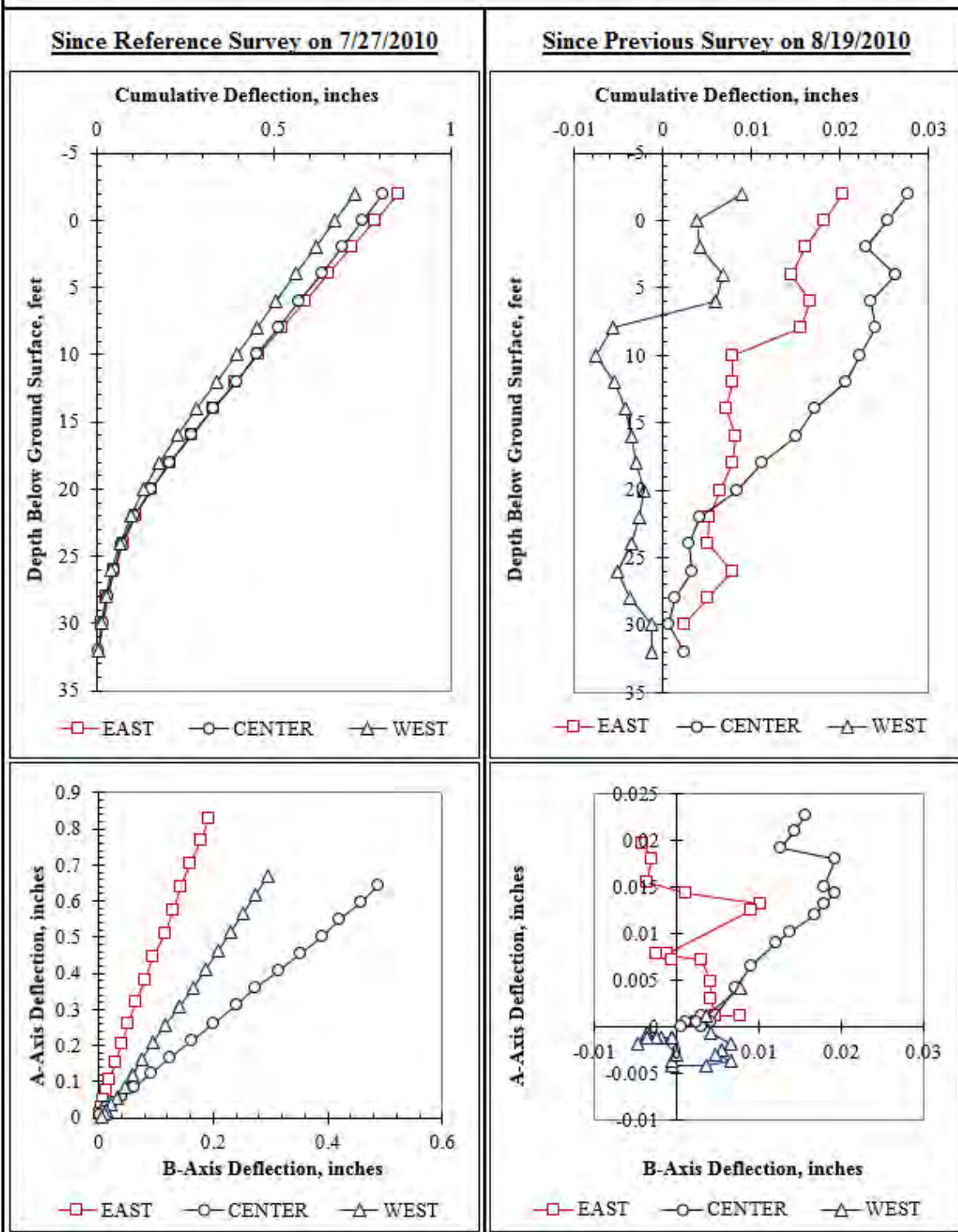


Figure F.22: Summary of inclinometer data from 8/23/2010.

Summary of Inclinometer Data From 9/1/2010

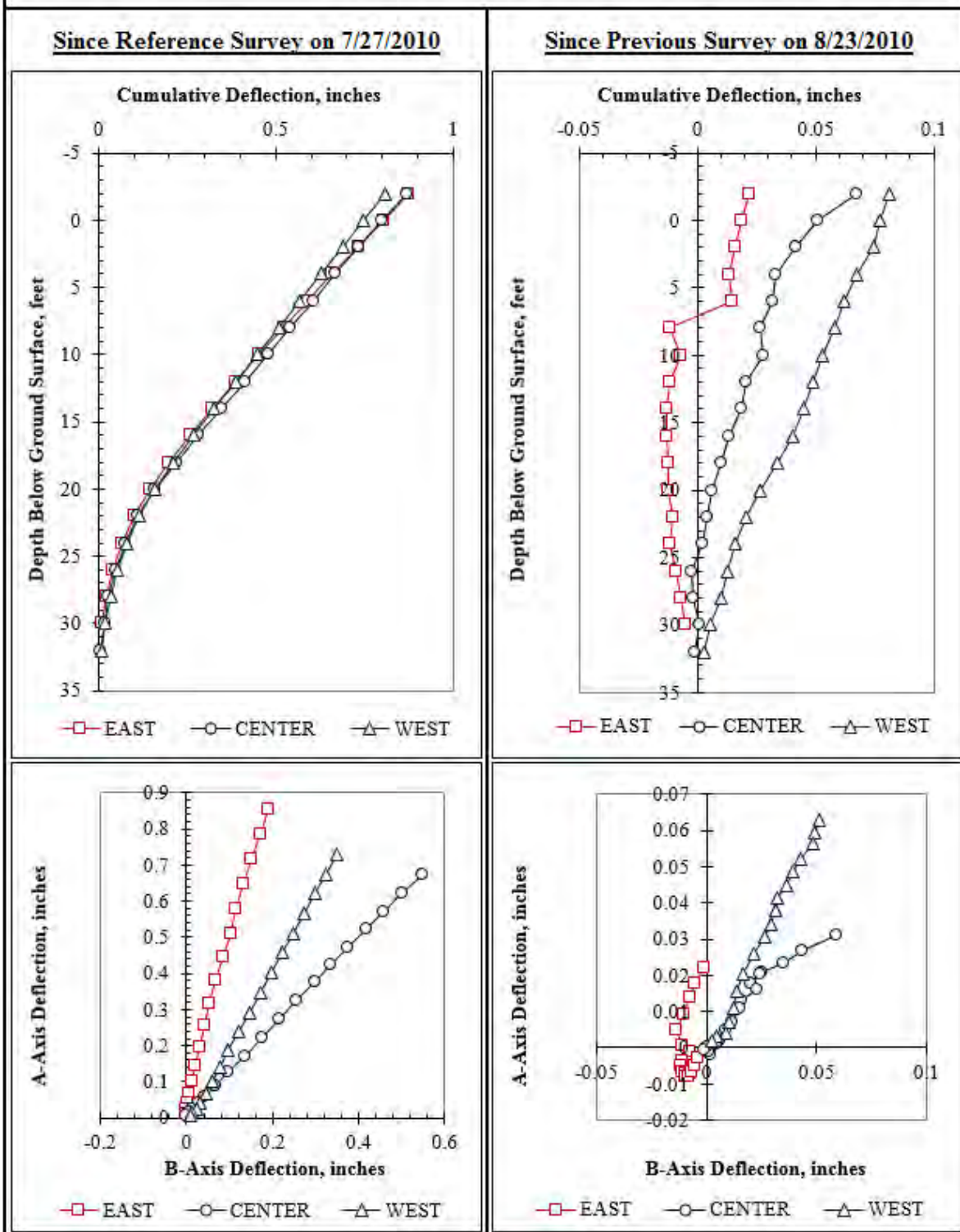


Figure F.23: Summary of inclinometer data from 9/1/2010.

Summary of Inclinometer Data From 9/10/2010

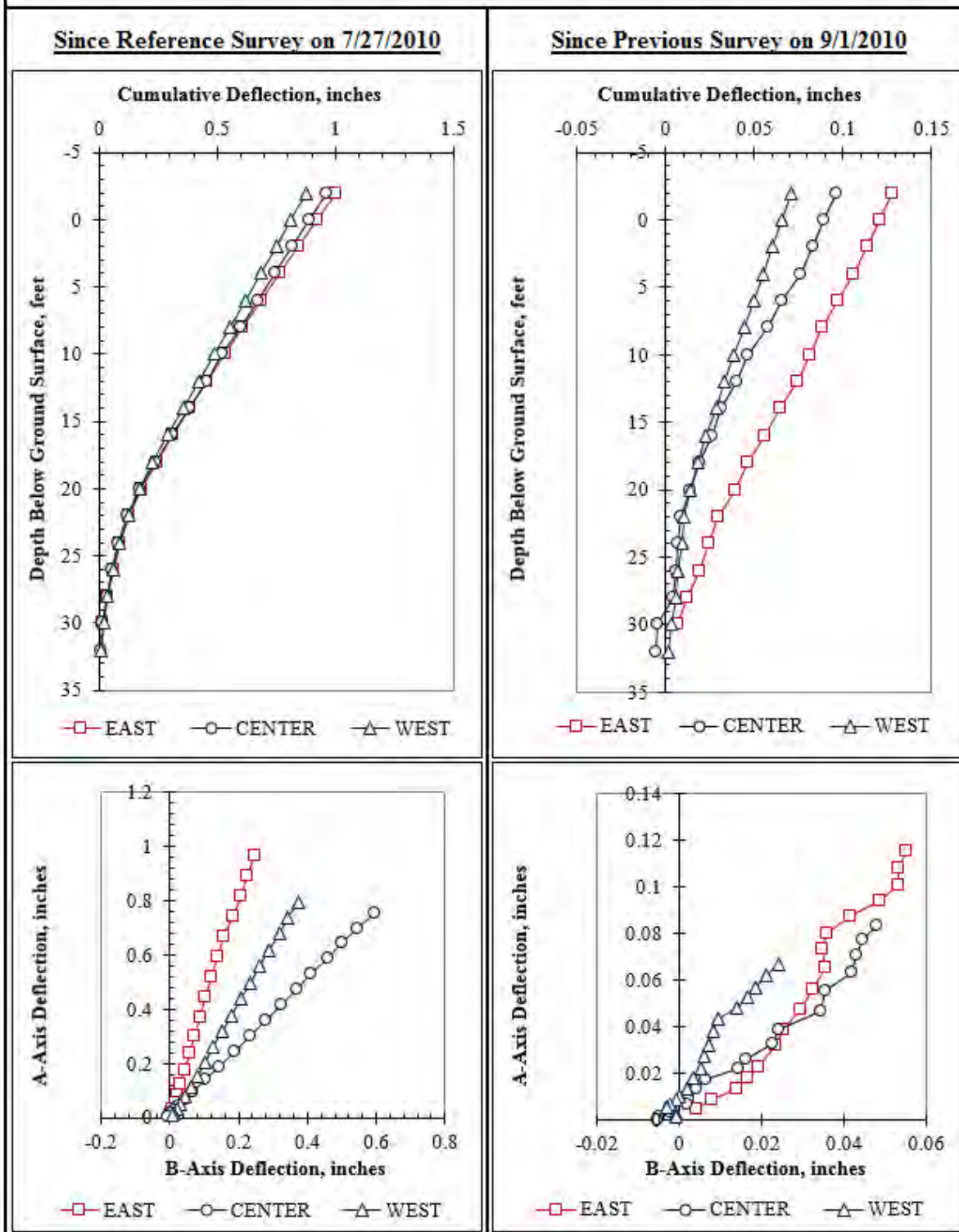


Figure F.24: Summary of inclinometer data from 9/10/2010.

Summary of Inclinometer Data From 9/21/2010

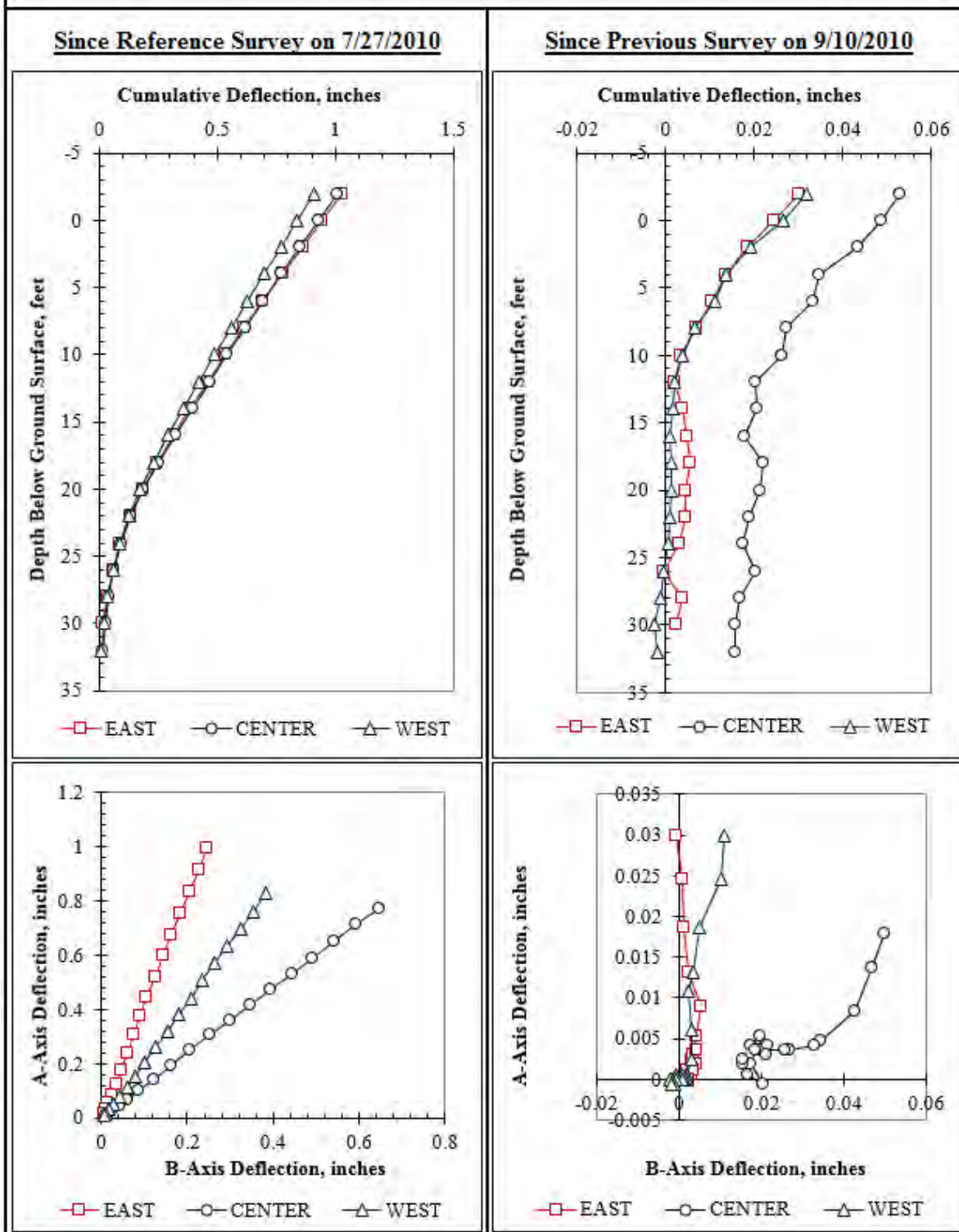


Figure F.25: Summary of inclinometer data from 9/21/2010.

Summary of Inclinometer Data From 9/29/2010

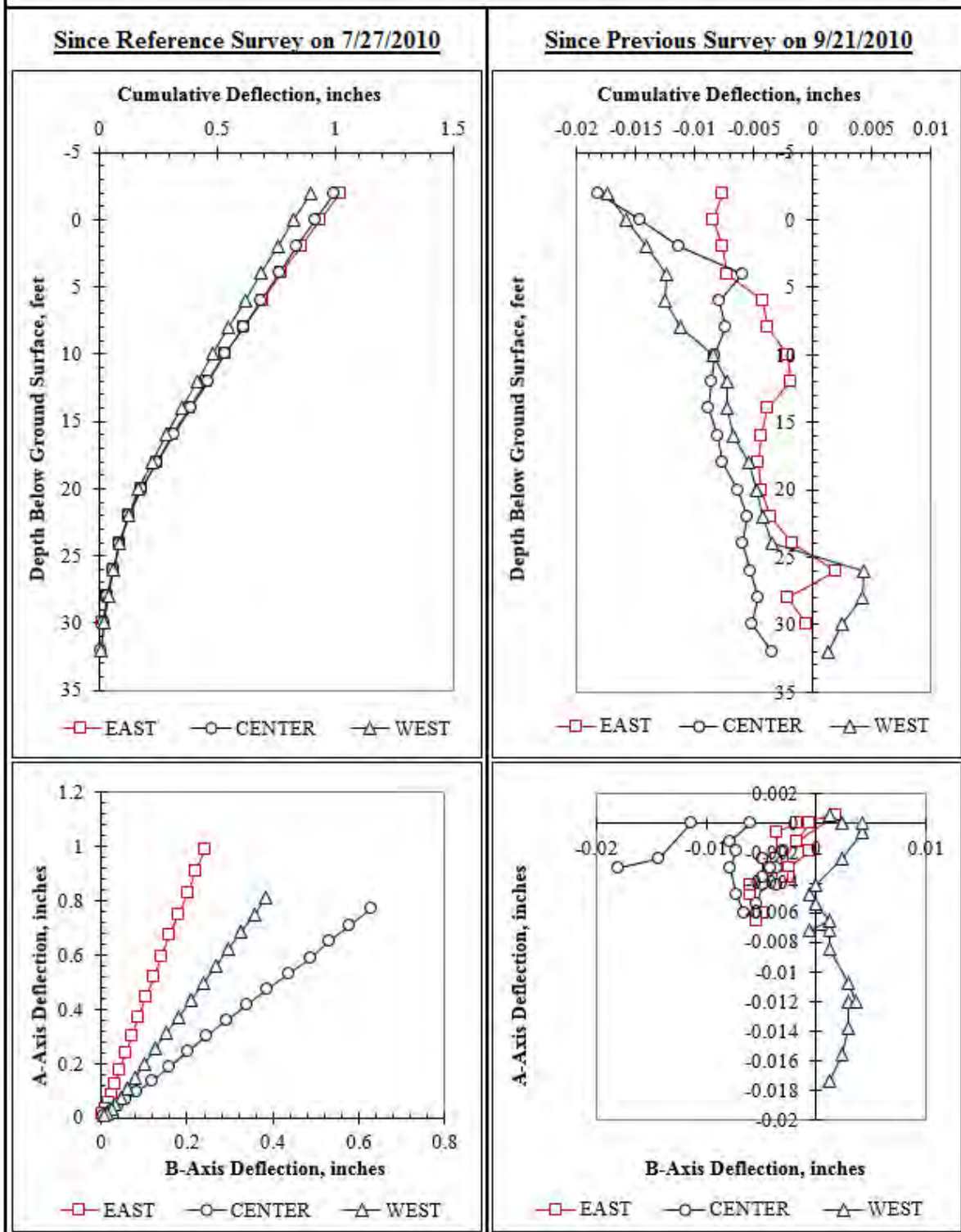


Figure F.26: Summary of inclinometer data from 9/29/2010.

Summary of Inclinometer Data From 10/8/2010

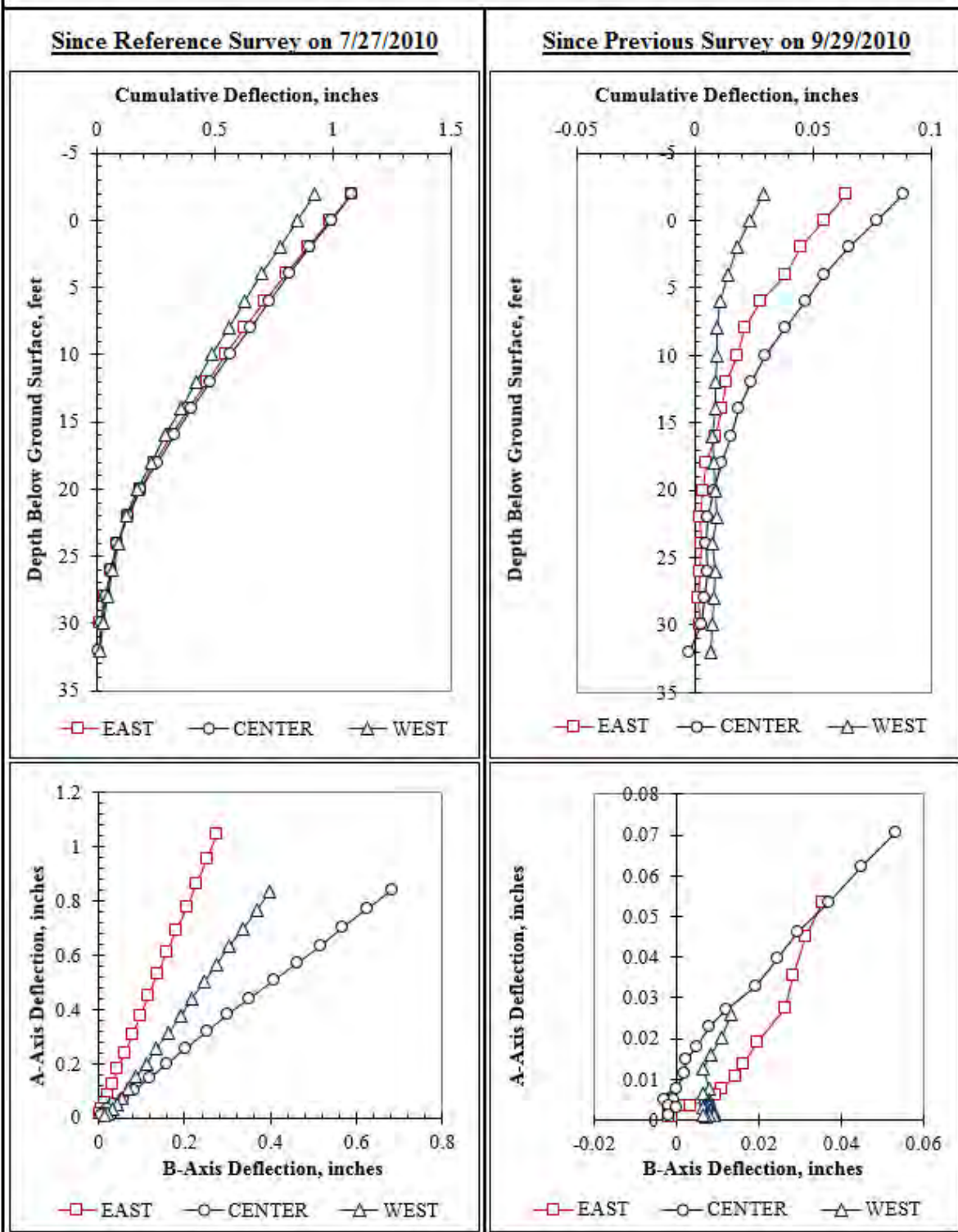


Figure F.27: Summary of inclinometer data from 10/8/2010.

Summary of Inclinometer Data From 10/15/2010

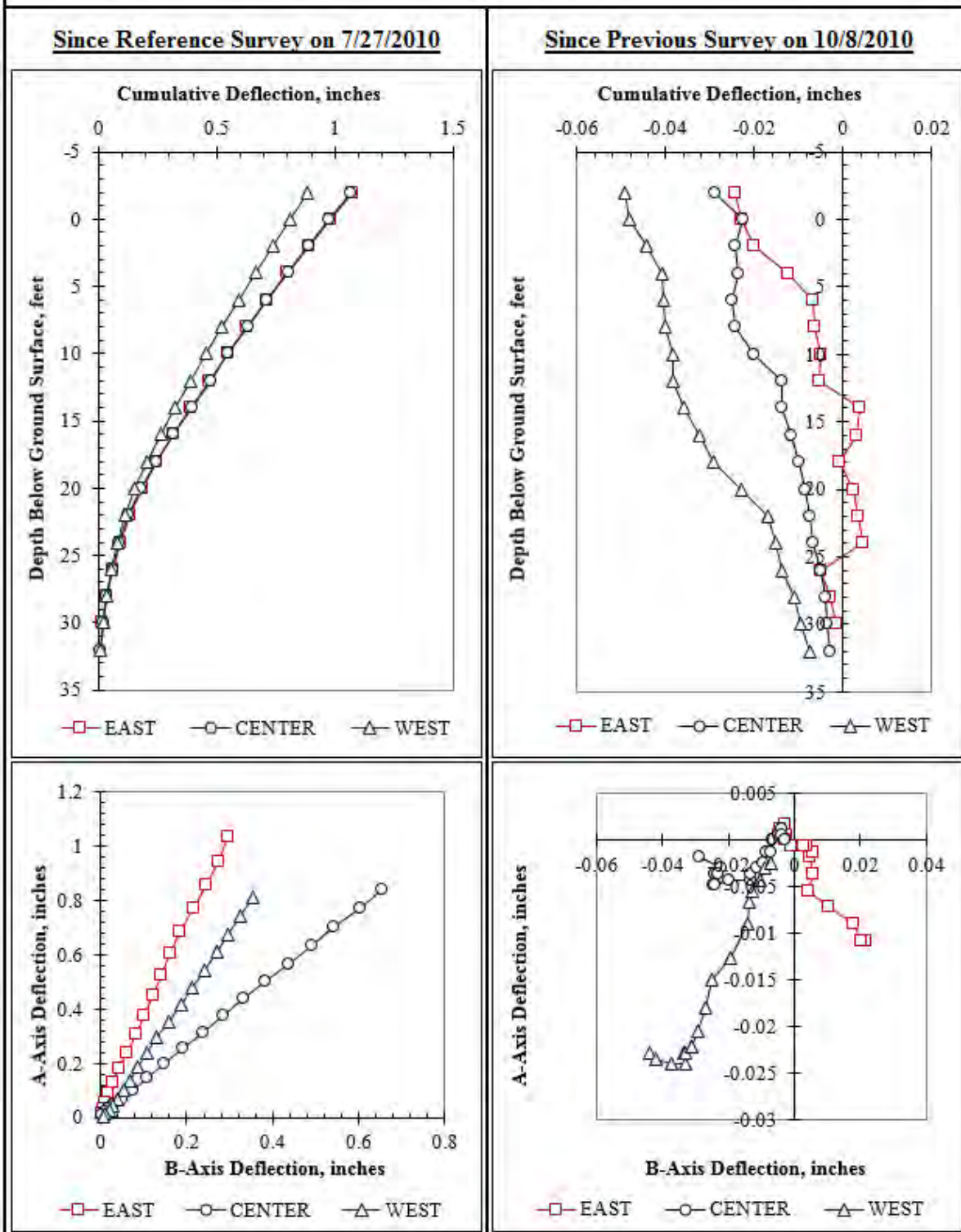


Figure F.28: Summary of inclinometer data from 10/15/2010.

Summary of Inclinometer Data From 10/25/2010

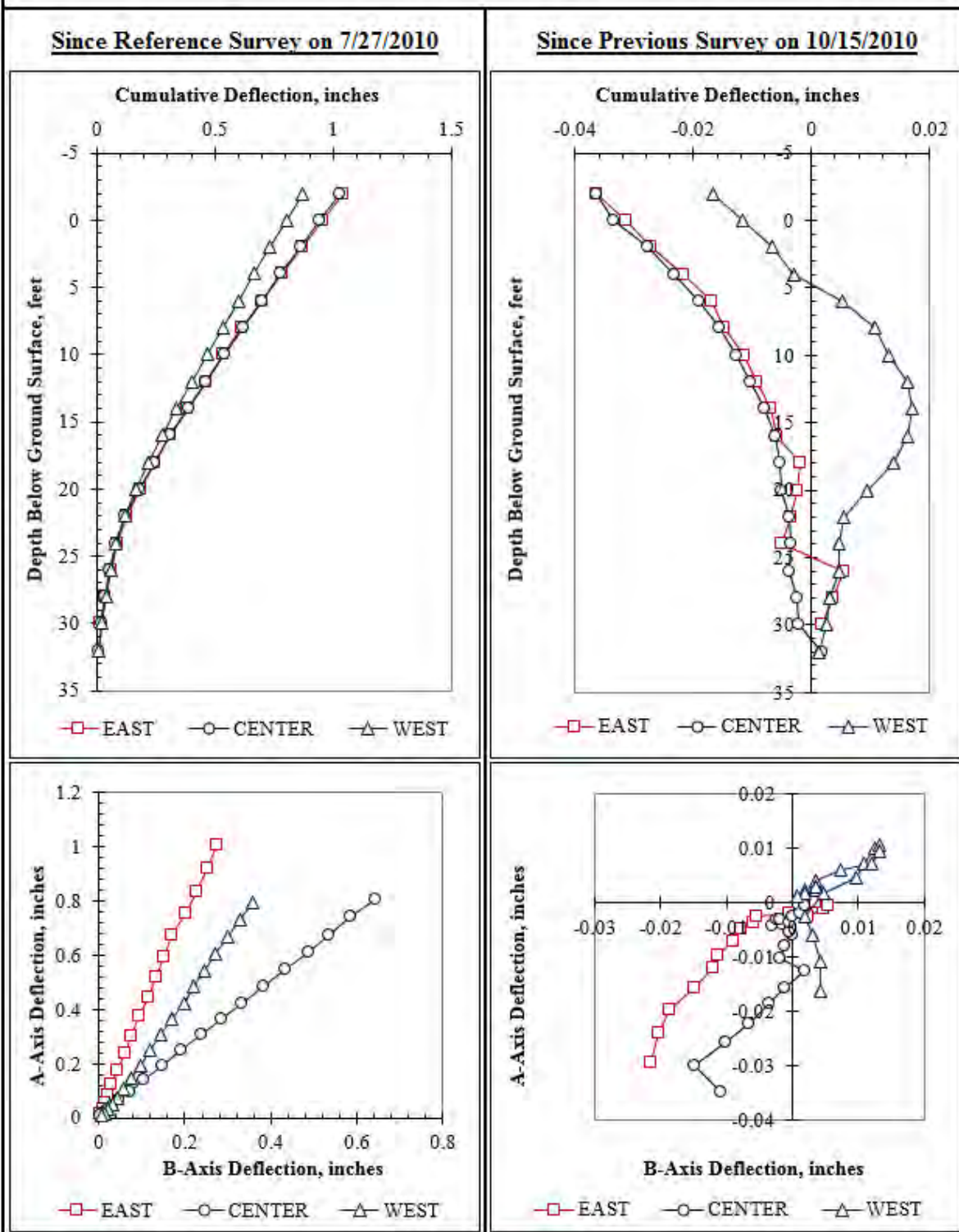


Figure F.29: Summary of inclinometer data from 10/25/2010.

Summary of Inclinometer Data From 11/8/2010

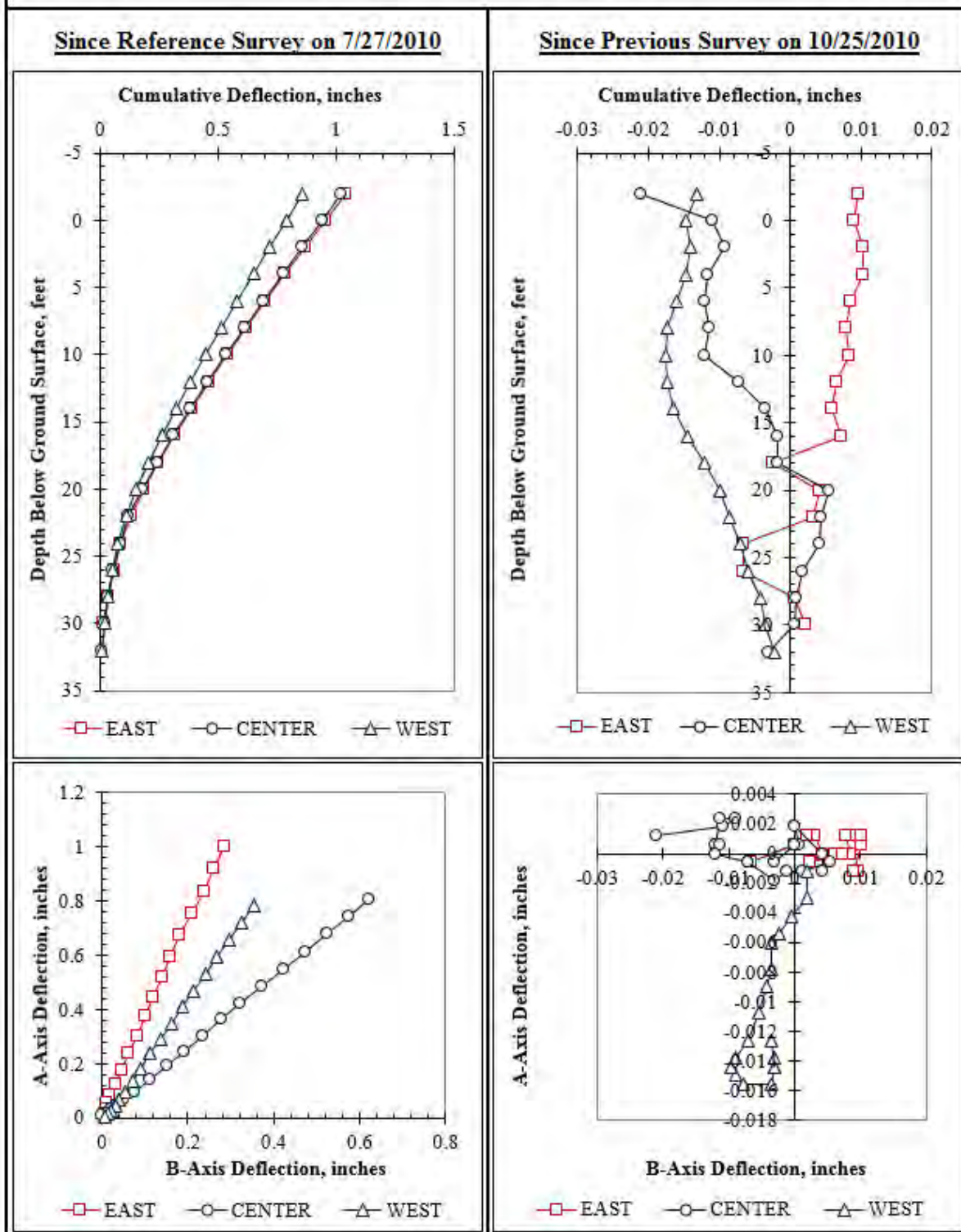


Figure F.30: Summary of inclinometer data from 11/8/2010.

Summary of Inclinometer Data From 11/23/2010

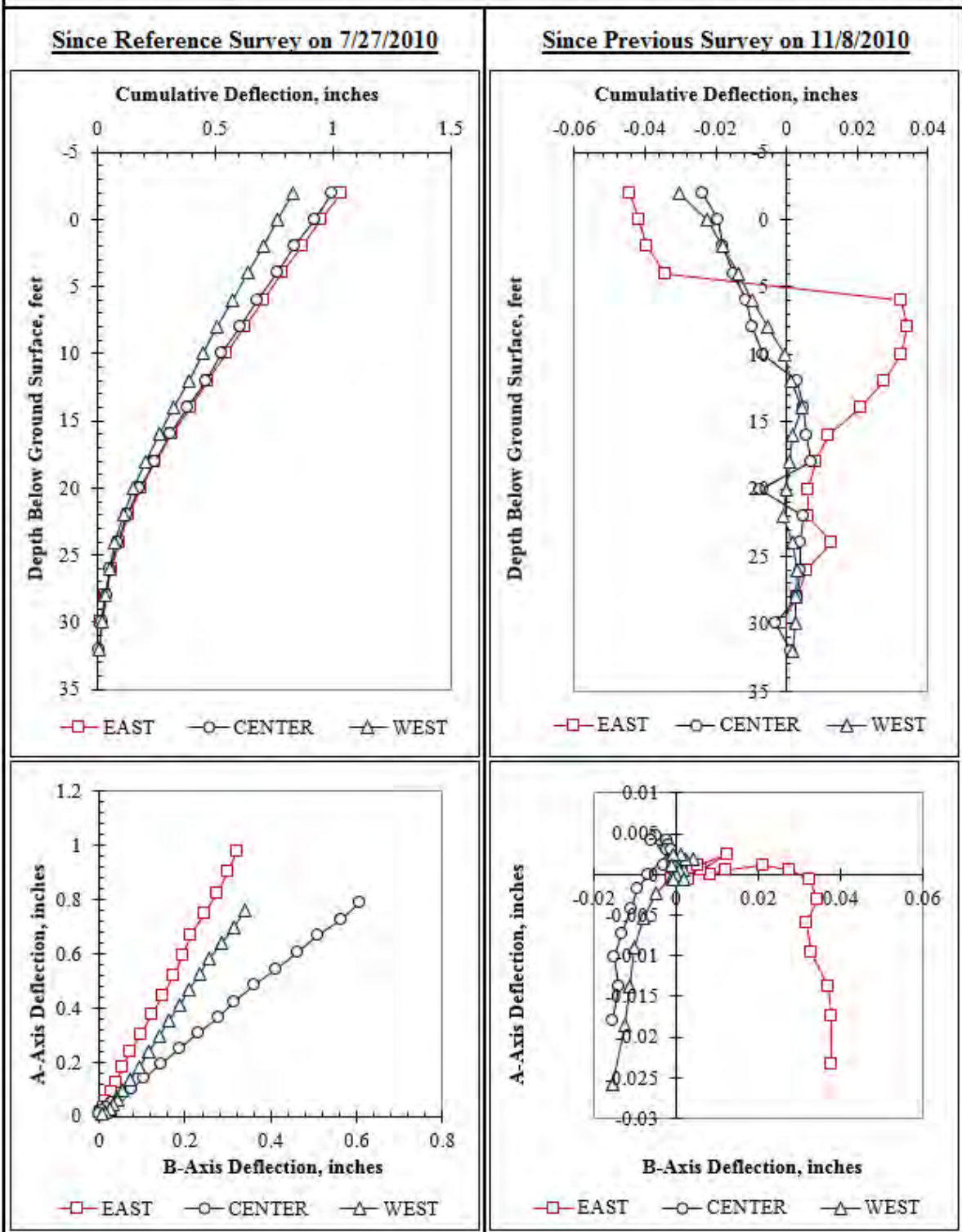


Figure F.31: Summary of inclinometer data from 11/23/2010.

Summary of Inclinometer Data From 12/10/2010

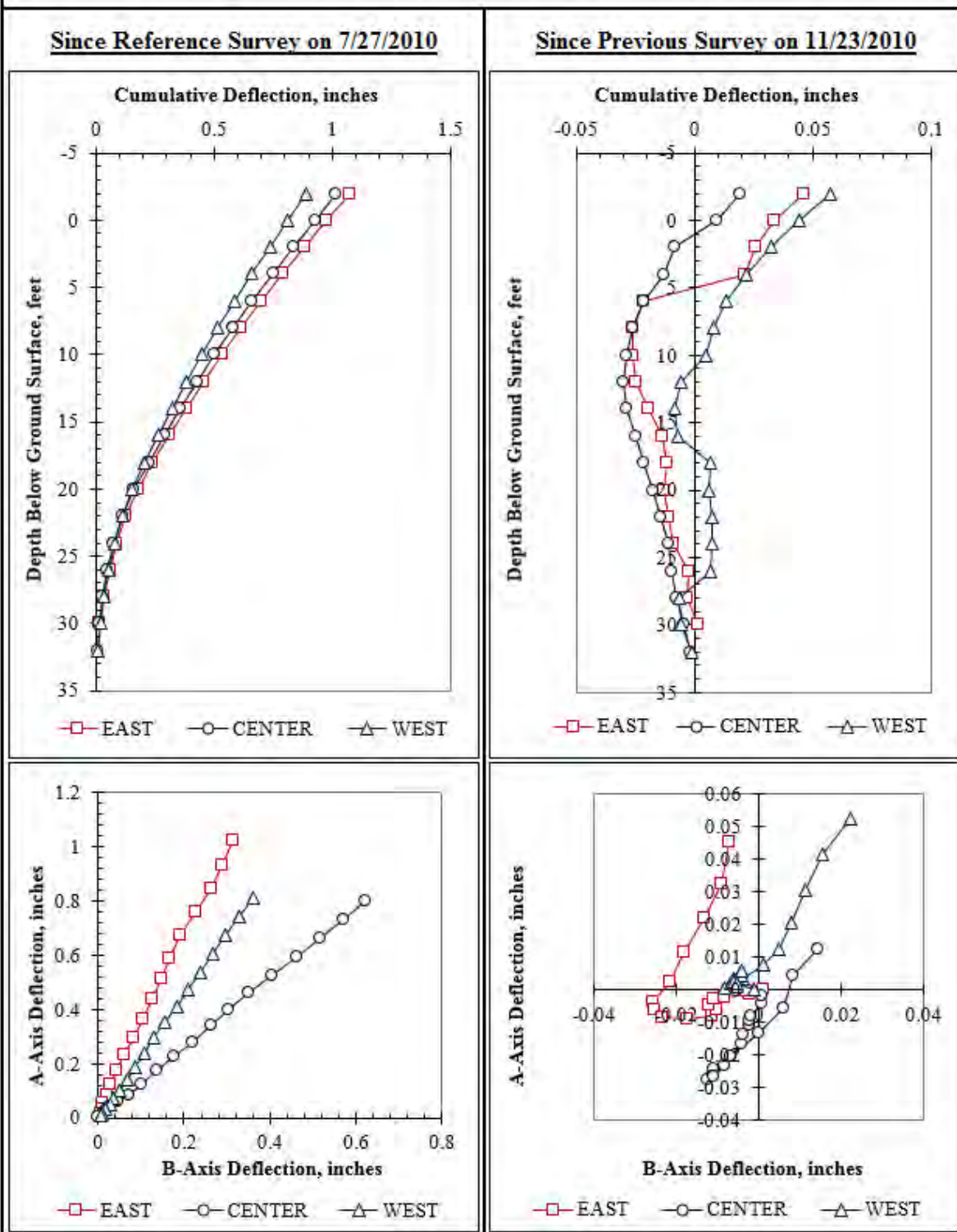


Figure F.32: Summary of inclinometer data from 12/10/2010.

Summary of Inclinometer Data From 12/28/2010

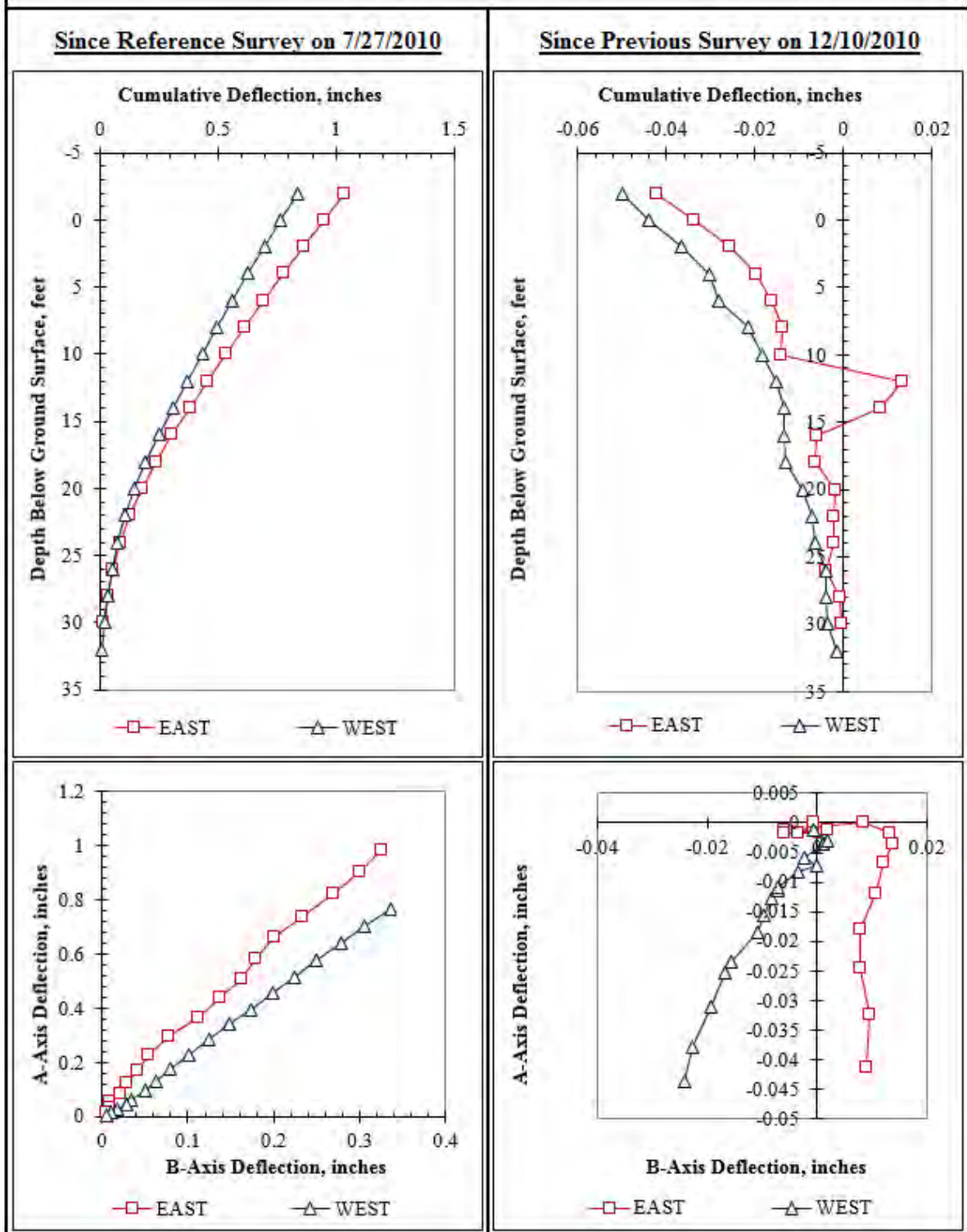


Figure F.33: Summary of inclinometer data from 12/28/2010.

Summary of Inclinometer Data From 1/6/2011 (1 of 2)

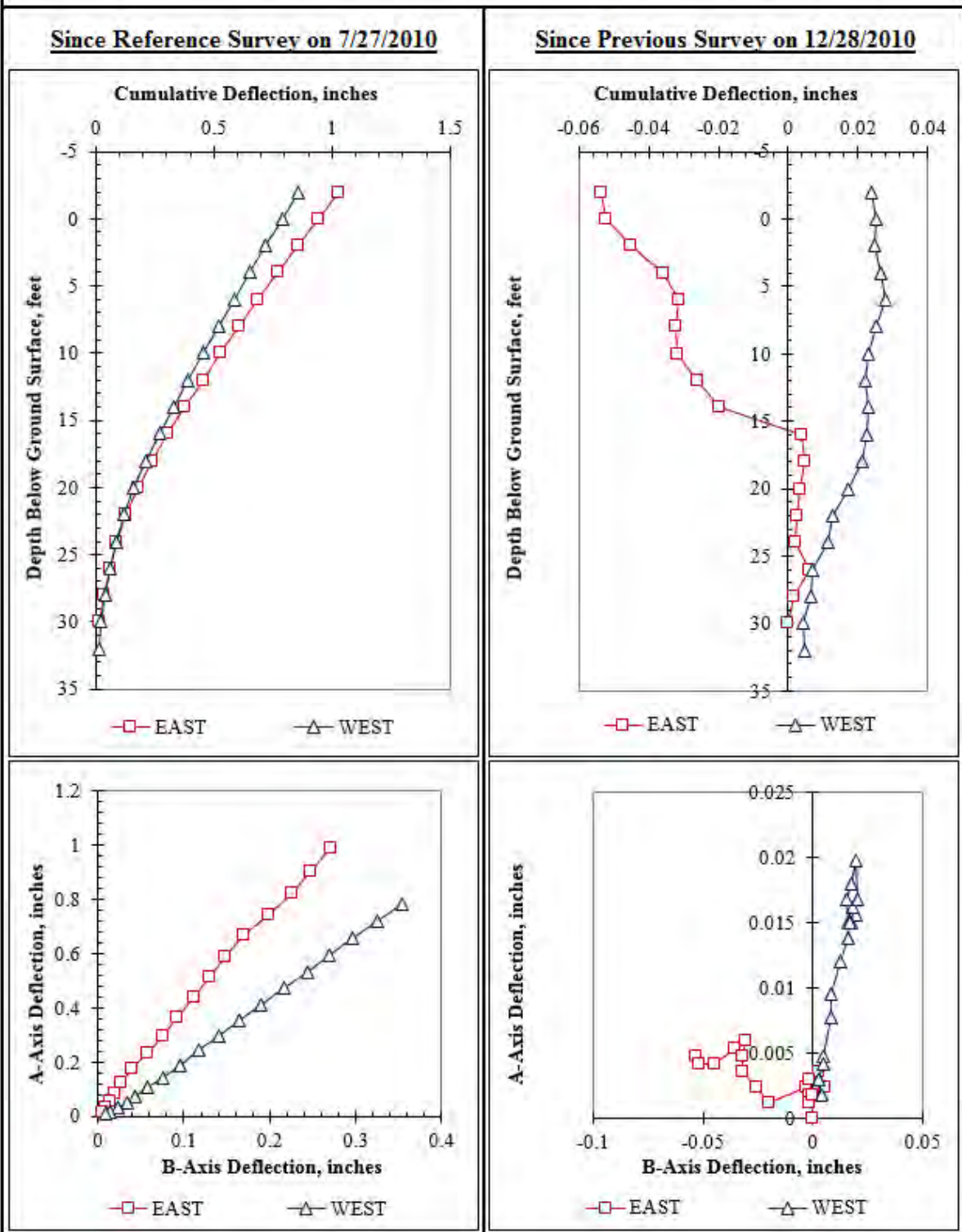


Figure F.34: Summary of inclinometer data from 1/6/2011.

Summary of Inclinometer Data From 1/6/2011 (2 of 2)

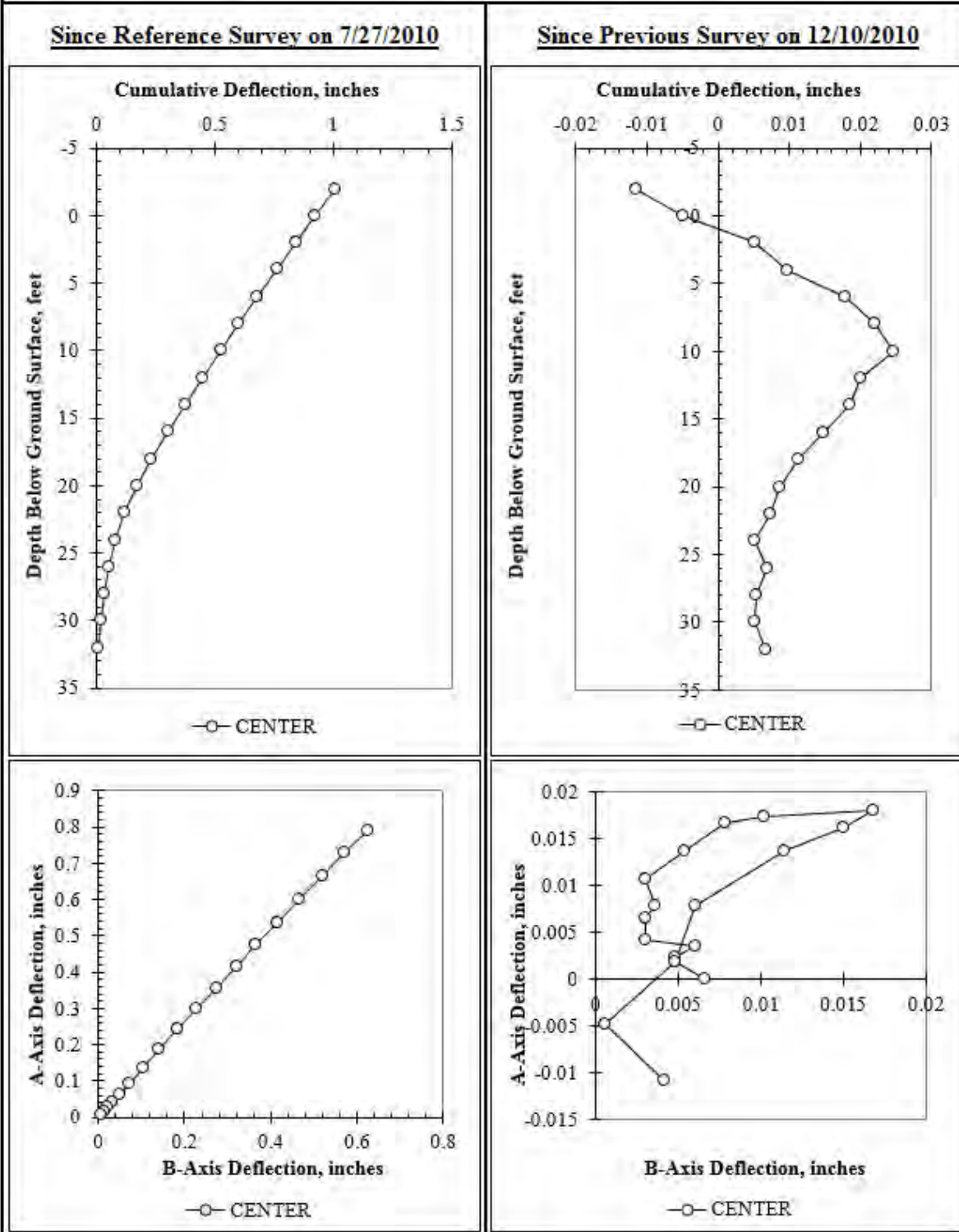


Figure F.35: Summary of inclinometer data from 1/6/2011.

Summary of Inclinometer Data From 1/19/2011 (1 of 2)

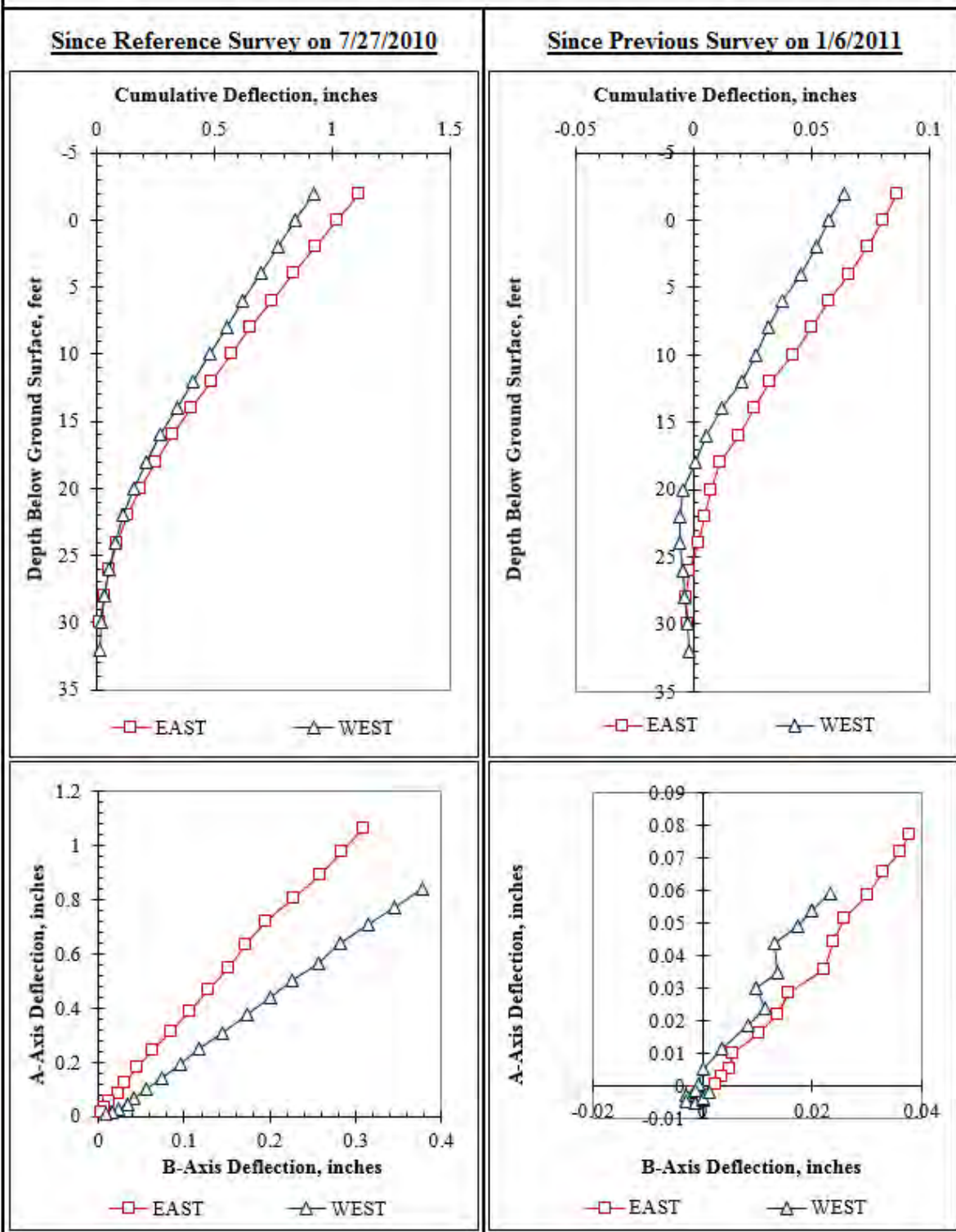


Figure F.36: Summary of inclinometer data from 1/19/2011.

Summary of Inclinometer Data From 1/19/2011

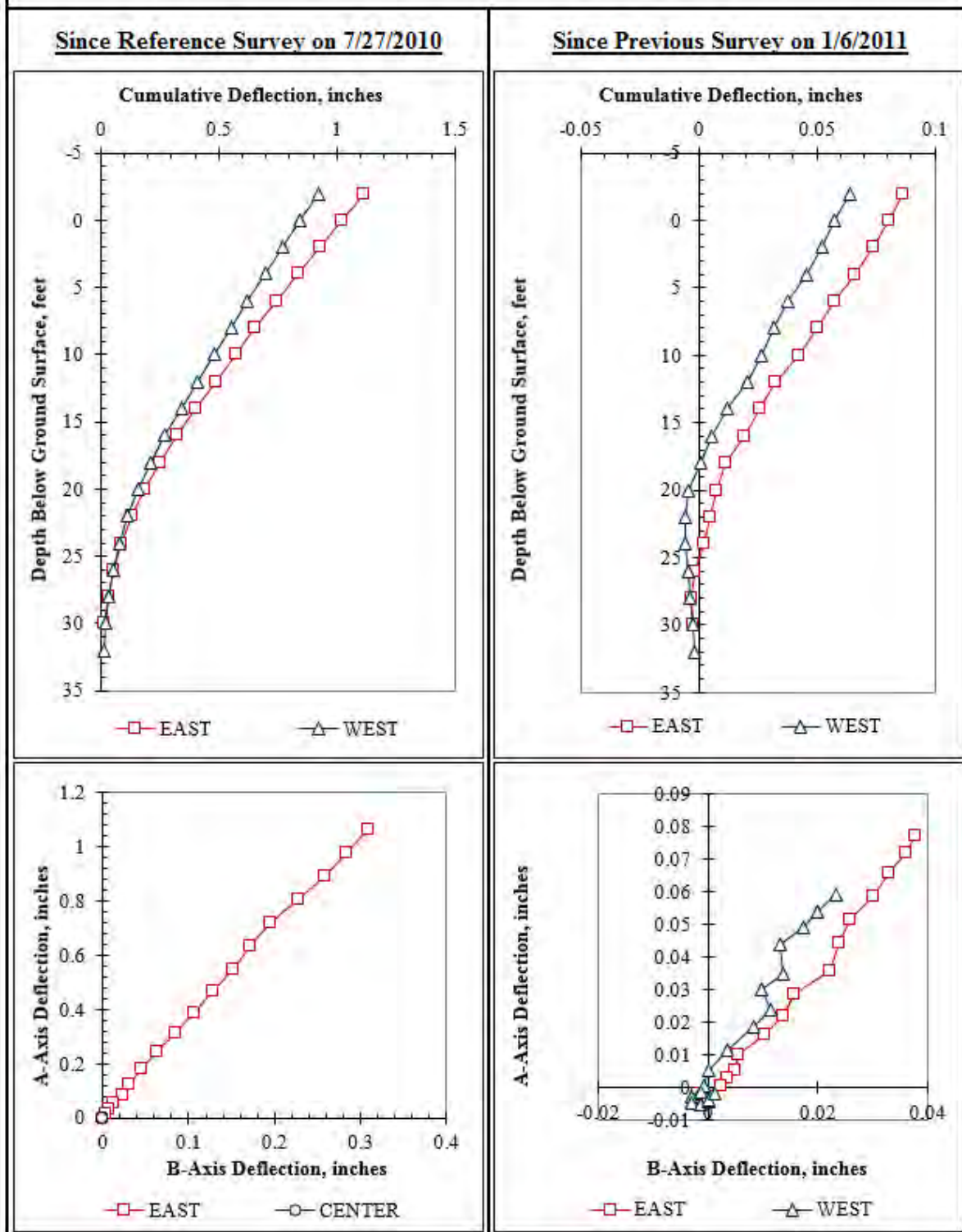


Figure F.37: Summary of inclinometer data from 1/19/2011.

Summary of Inclinometer Data From 1/20/2011 (1 of 2)

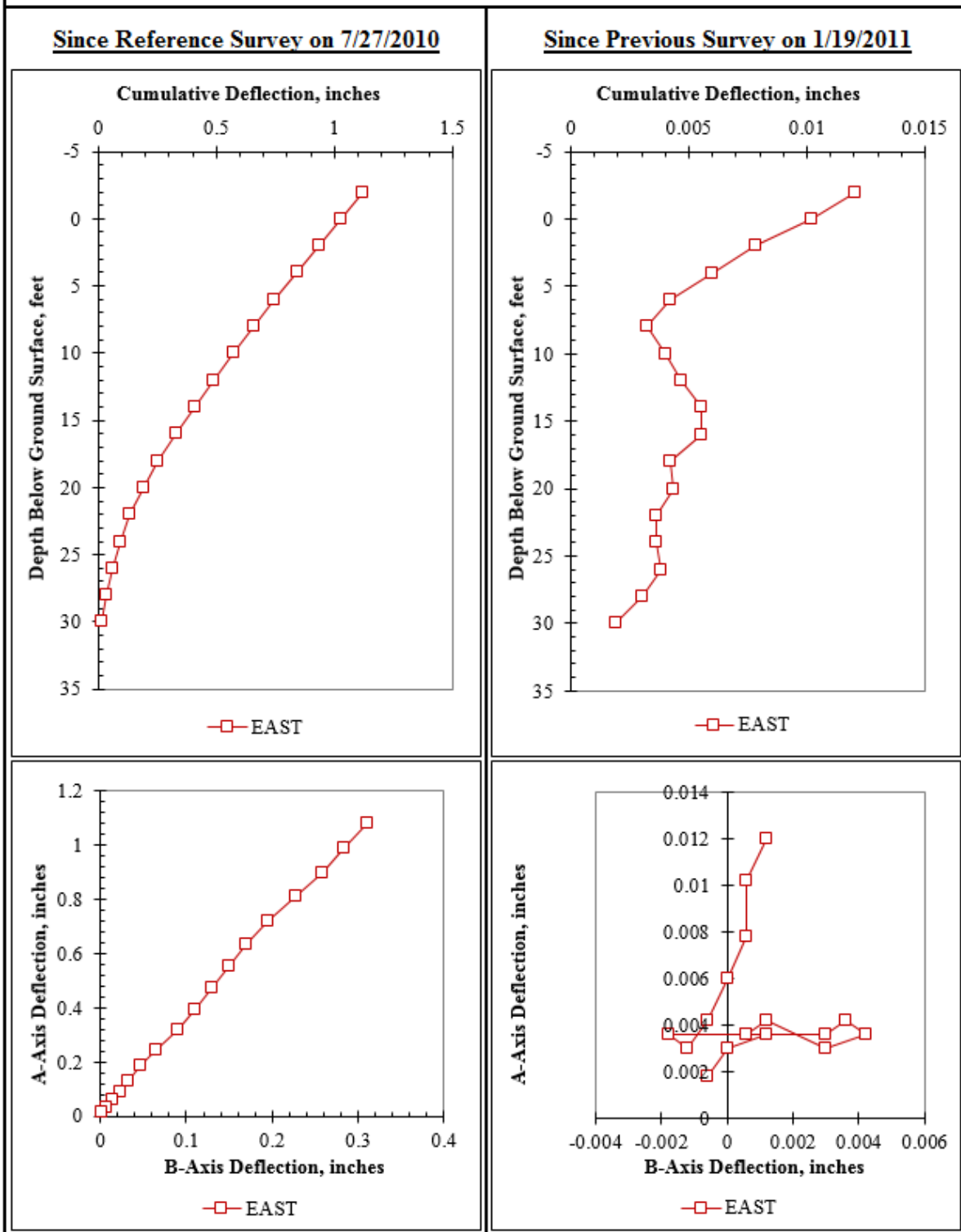


Figure F.38: Summary of inclinometer data from 1/20/2011.

Summary of Inclinometer Data From 1/20/2011 (2 of 2)

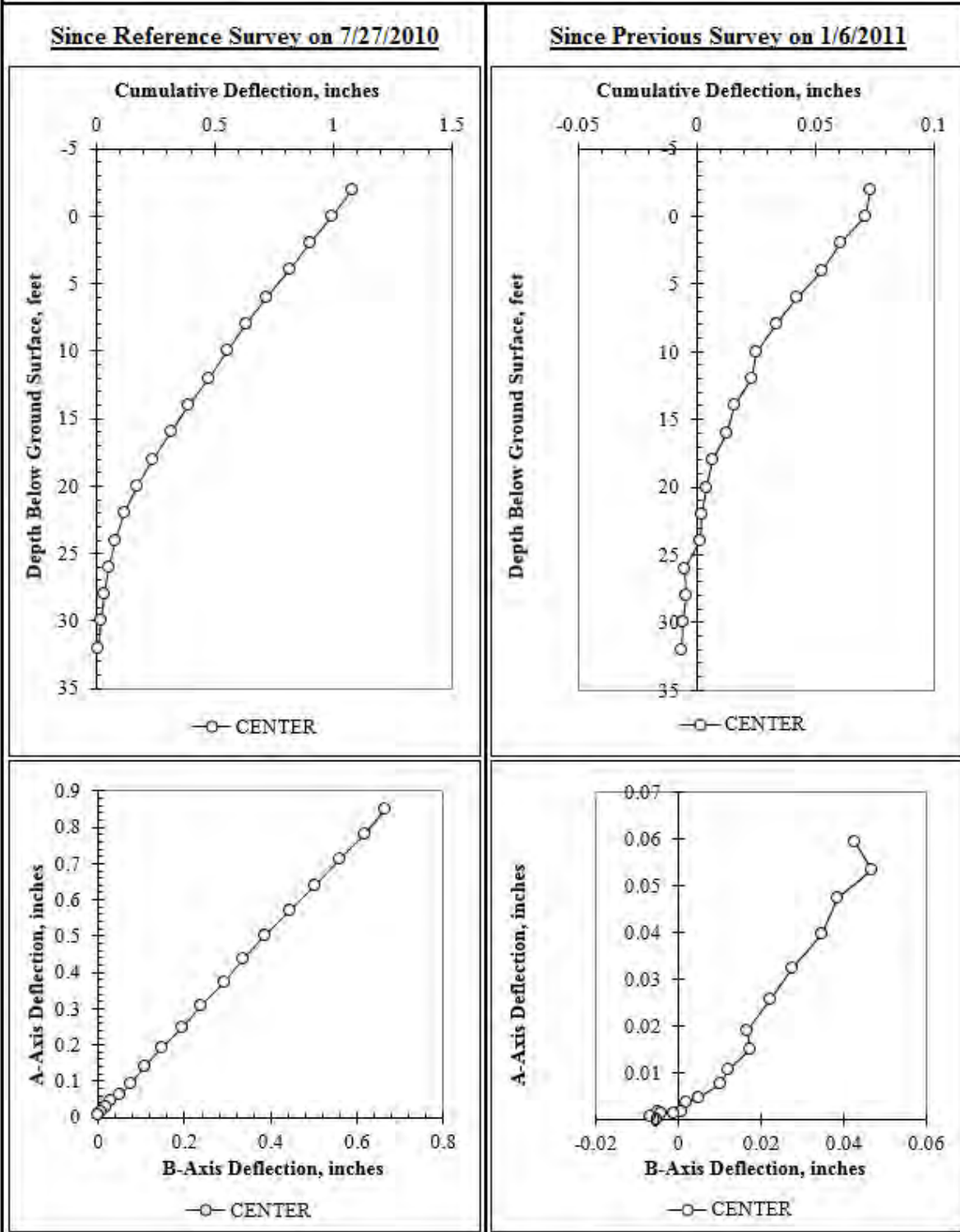


Figure F.39: Summary of inclinometer data from 1/20/2011.

Summary of Inclinometer Data From 2/8/2011 (1 of 2)

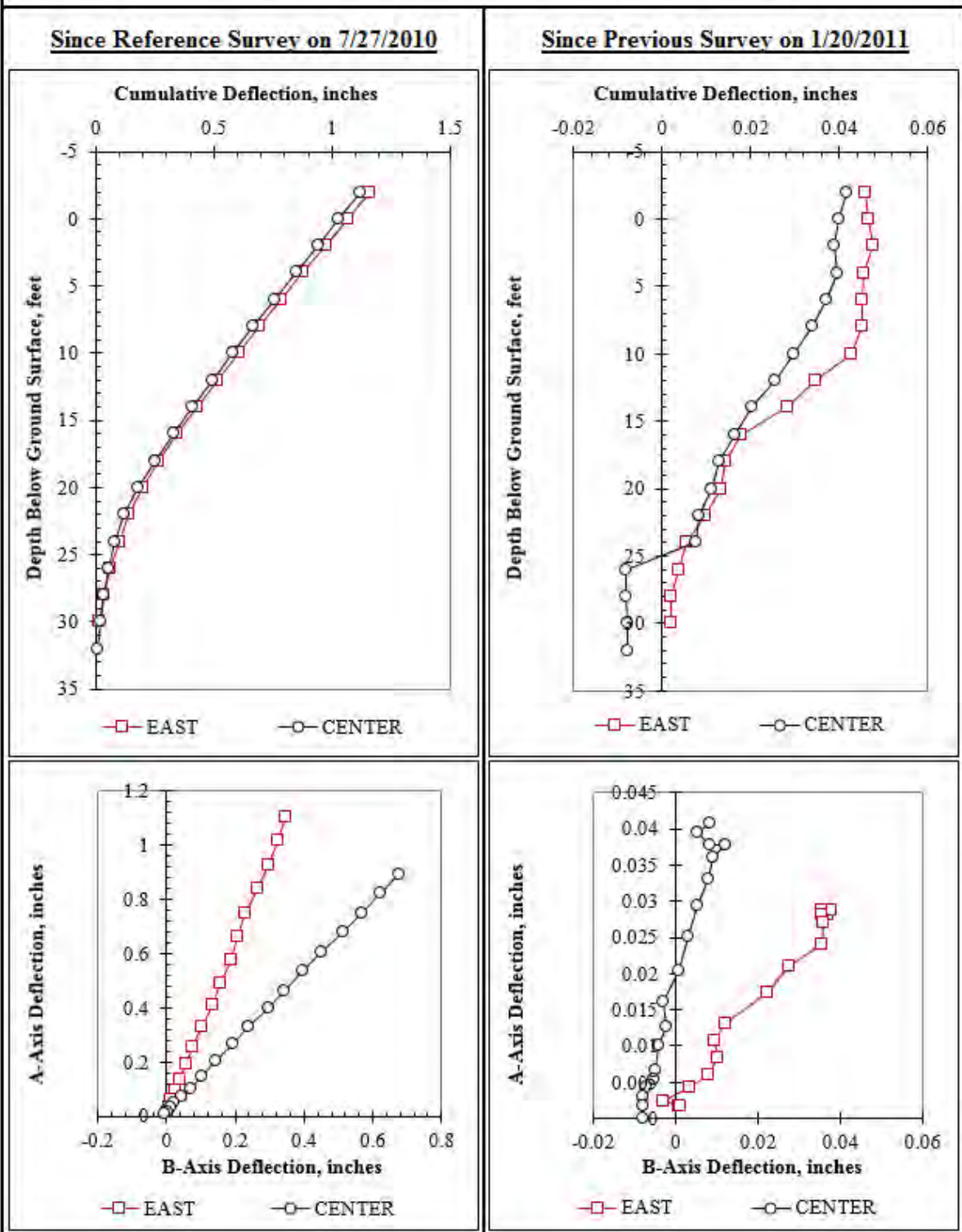


Figure F.40: Summary of inclinometer data from 2/8/2011.

Summary of Inclinometer Data From 2/8/2011 (2 of 2)

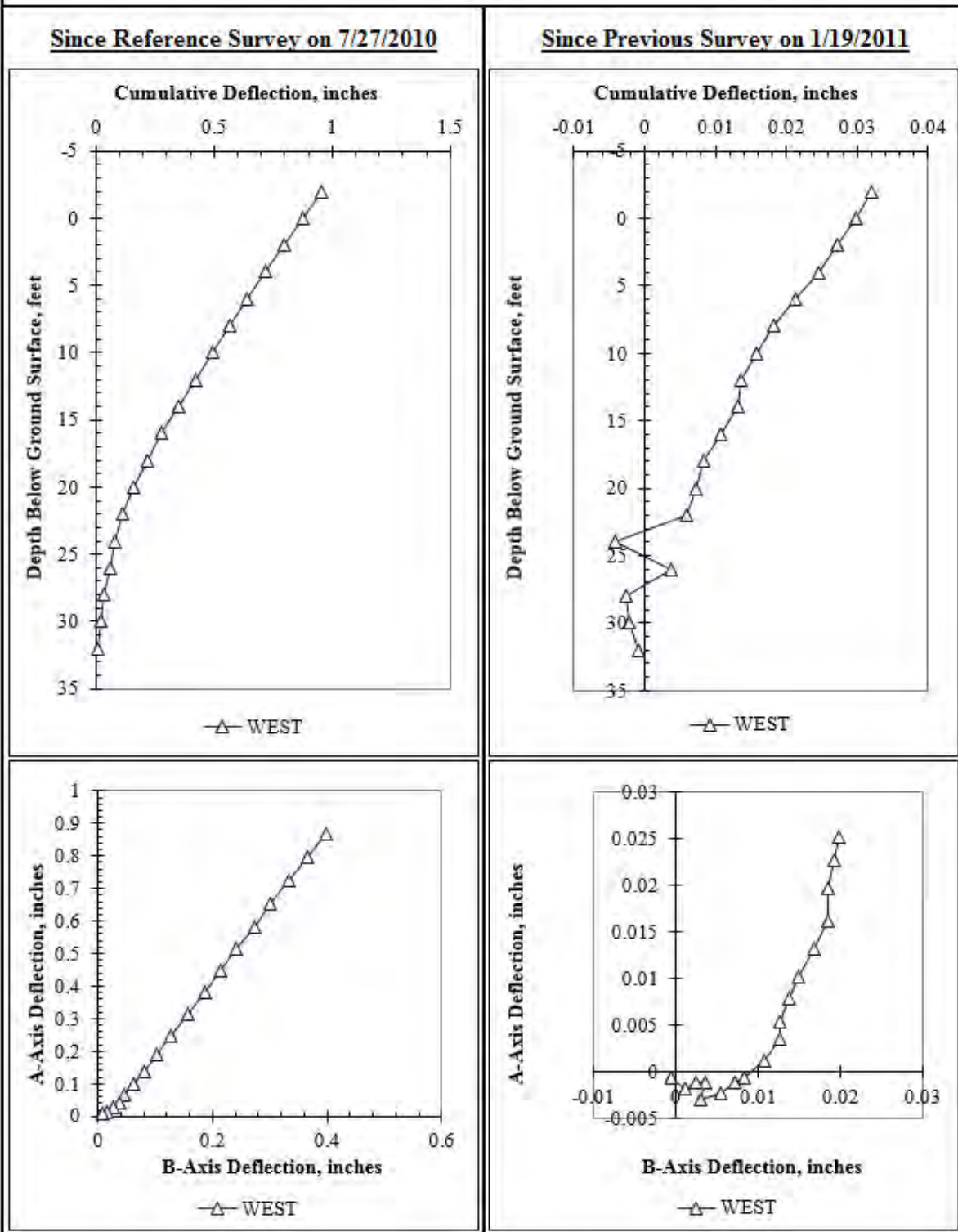


Figure F.41: Summary of inclinometer data from 2/8/2011.

Summary of Inclinometer Data From 2/23/2011

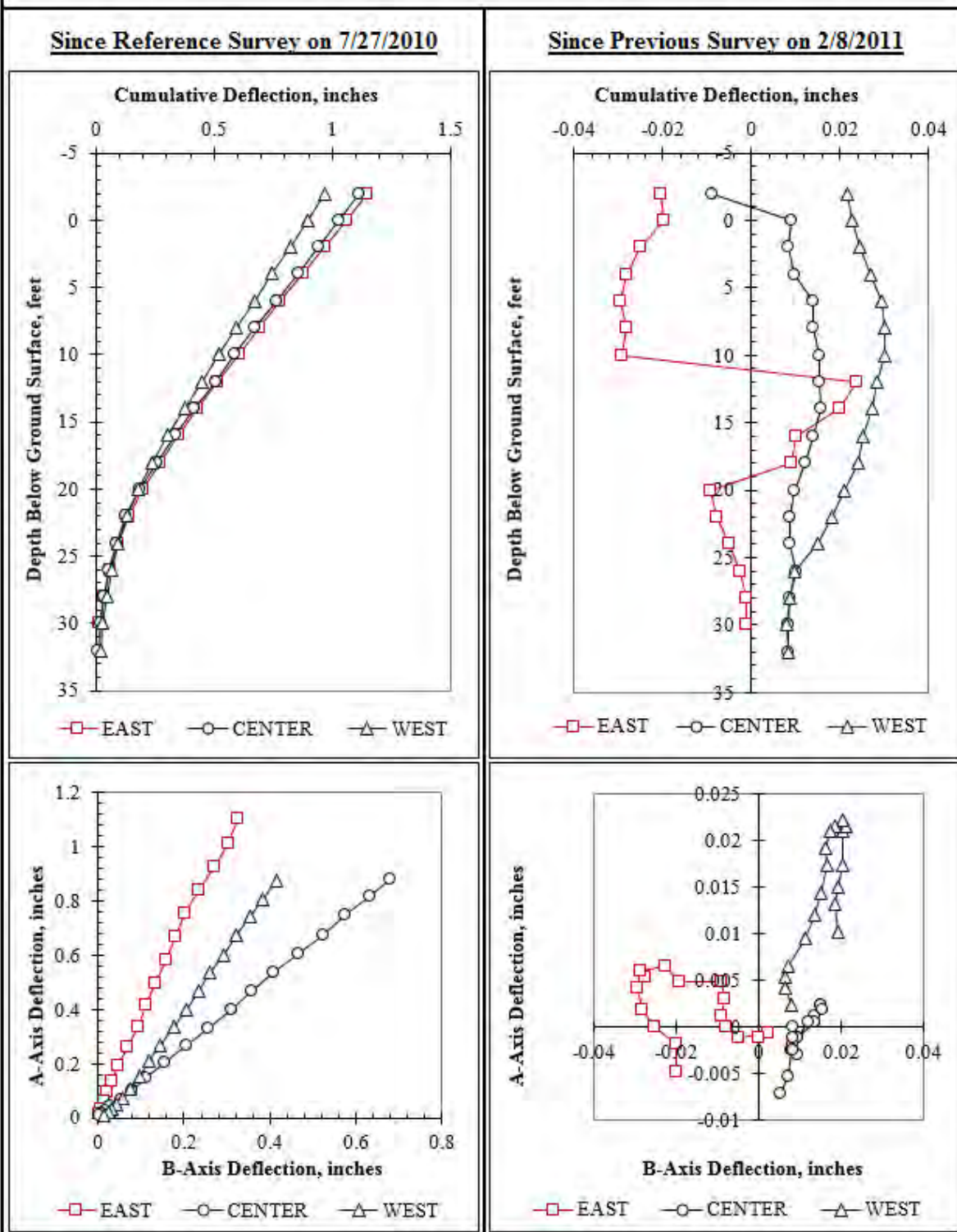


Figure F.42: Summary of inclinometer data from 2/23/2011.

Summary of Inclinator Data From 3/11/2011

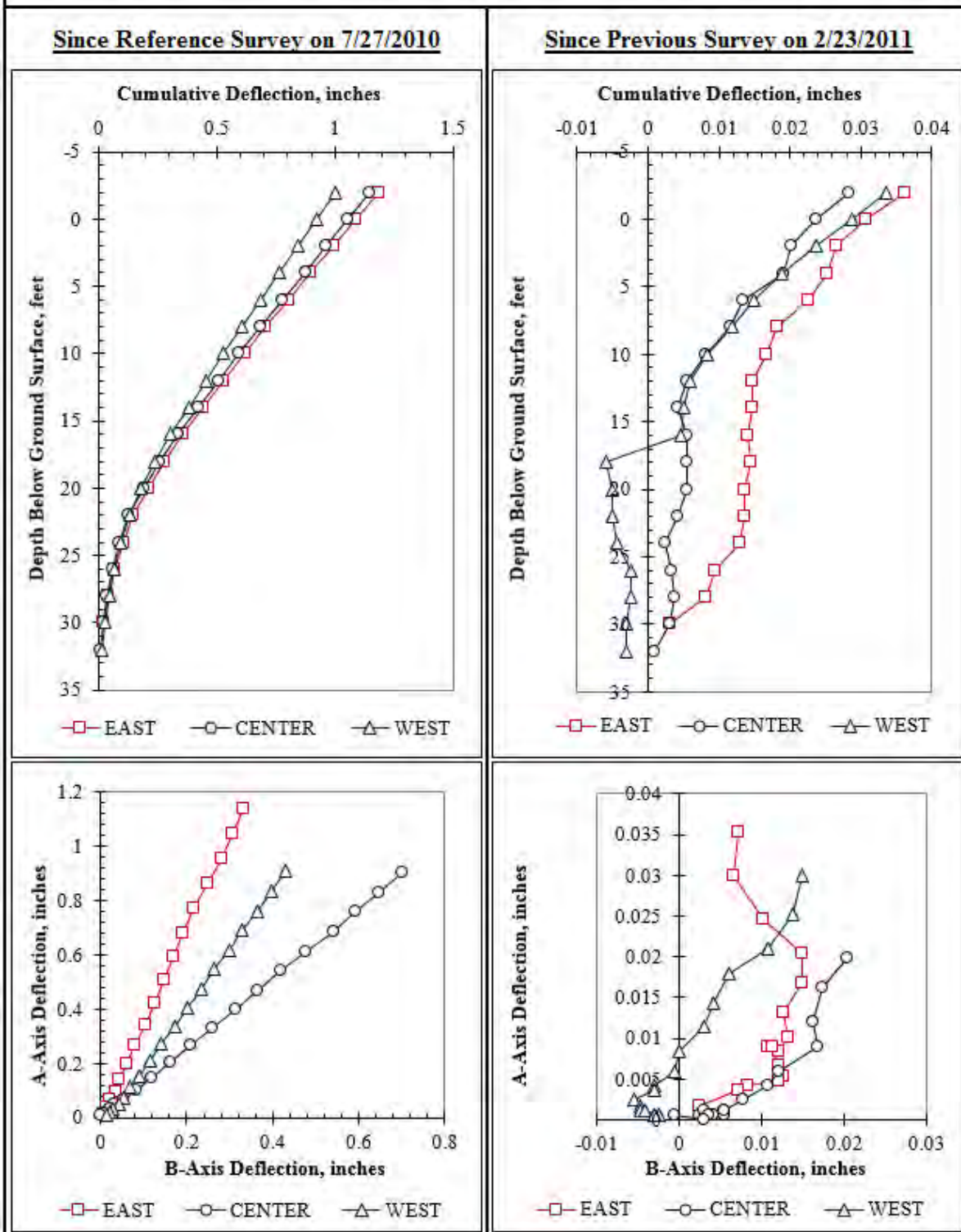


Figure F.43: Summary of inclinometer data from 3/11/2011.

Summary of Inclinometer Data From 3/31/2011

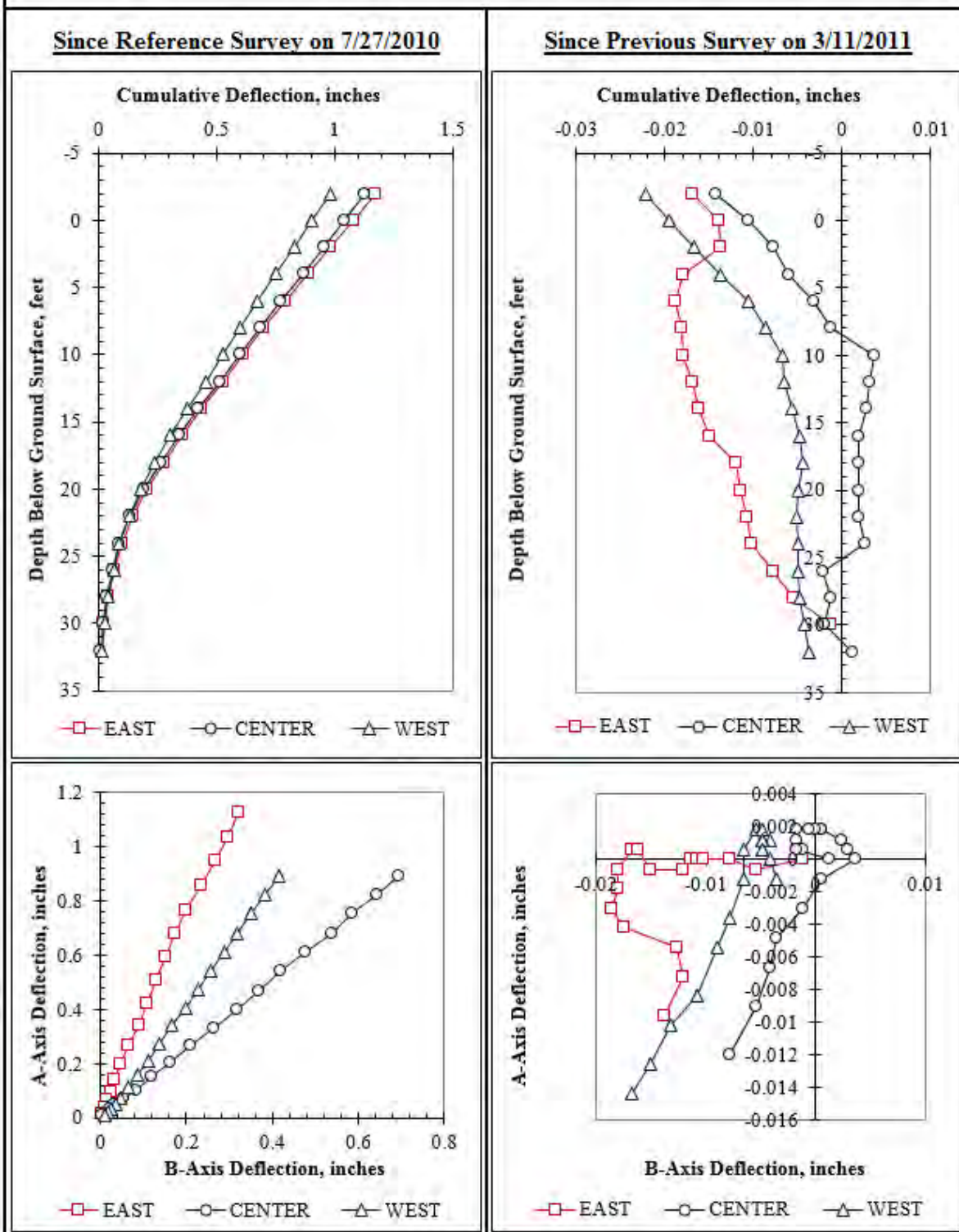


Figure F.44: Summary of inclinometer data from 3/31/2011.

Summary of Inclinometer Data From 4/19/2011

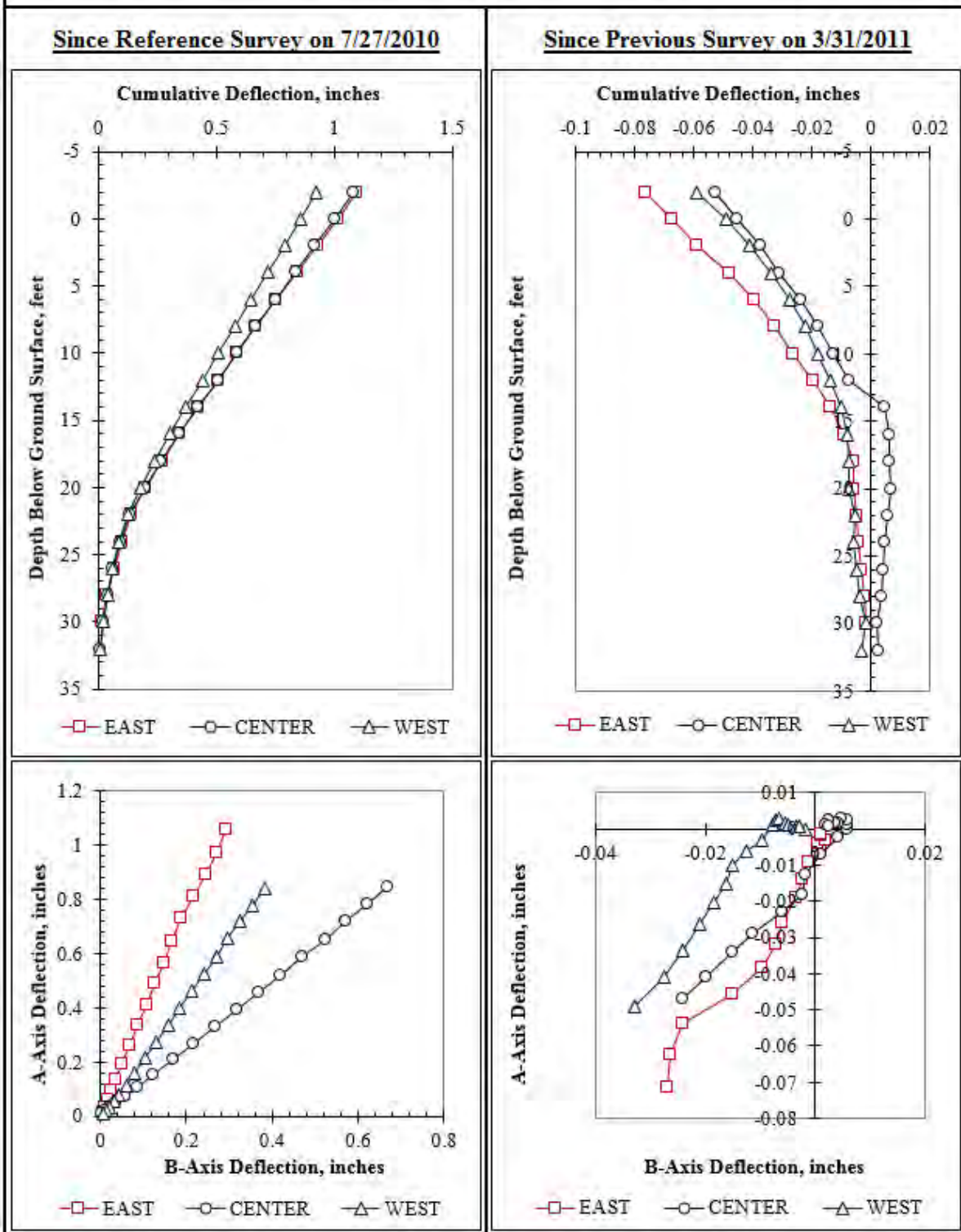


Figure F.45: Summary of inclinometer data from 4/19/2011.

Summary of Inclinometer Data From 5/13/2011

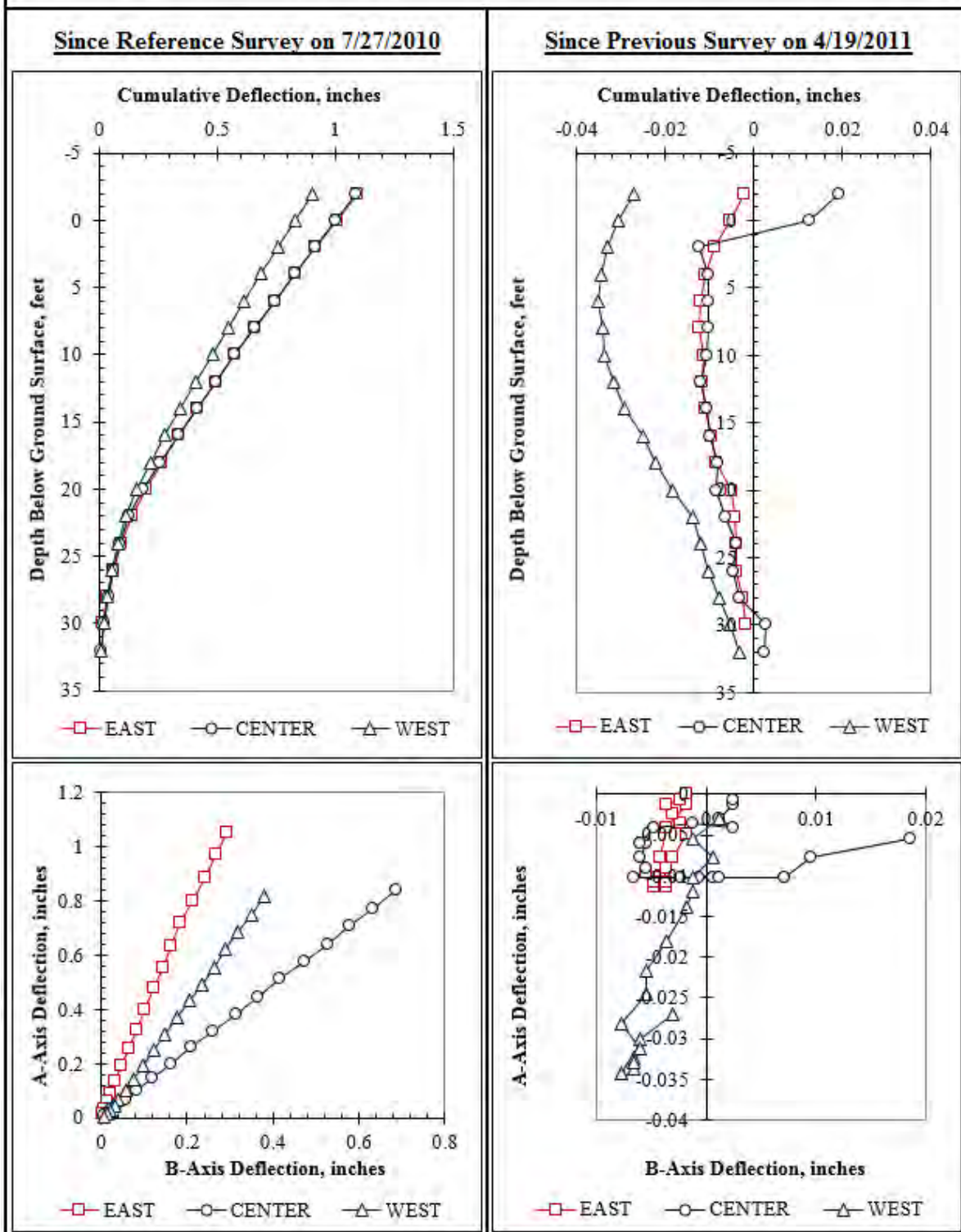


Figure F.46: Summary of inclinometer data from 5/13/2011.

Summary of Inclinometer Data From 6/2/2011

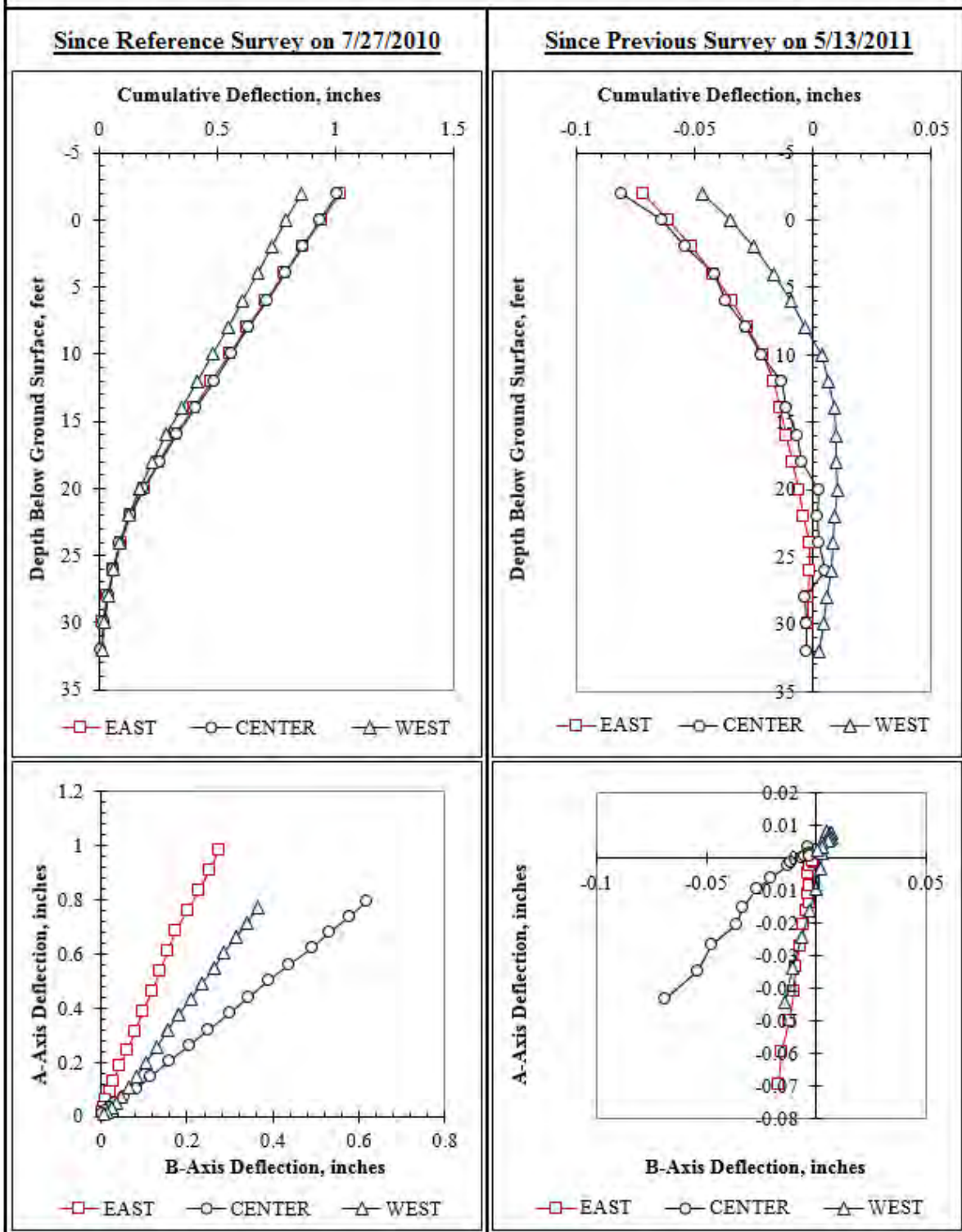


Figure F.47: Summary of inclinometer data from 6/2/2011.

Summary of Inclinator Data From 6/22/2011

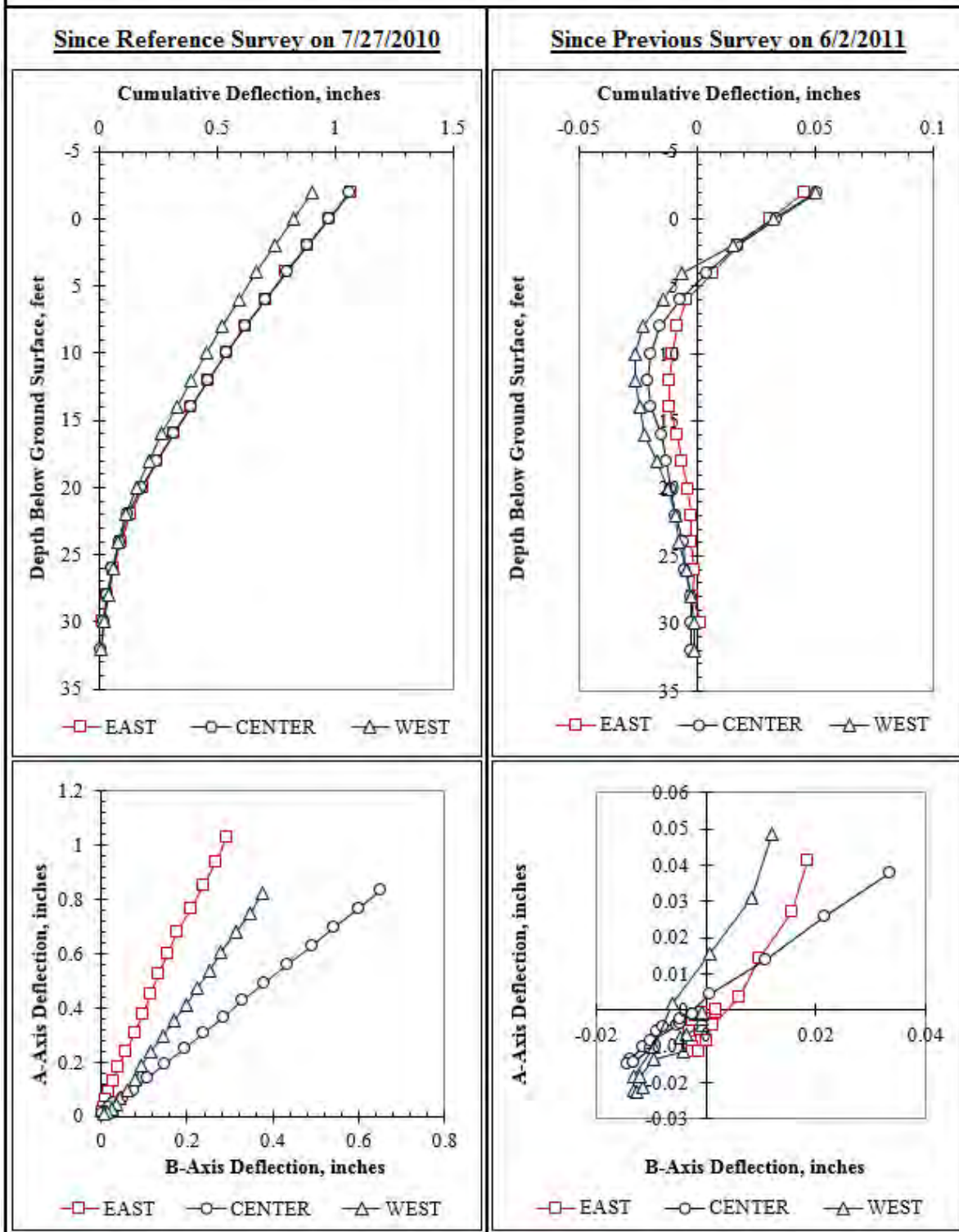


Figure F.48: Summary of inclinometer data from 6/22/2011.

Summary of Inclinometer Data From 7/28/2011

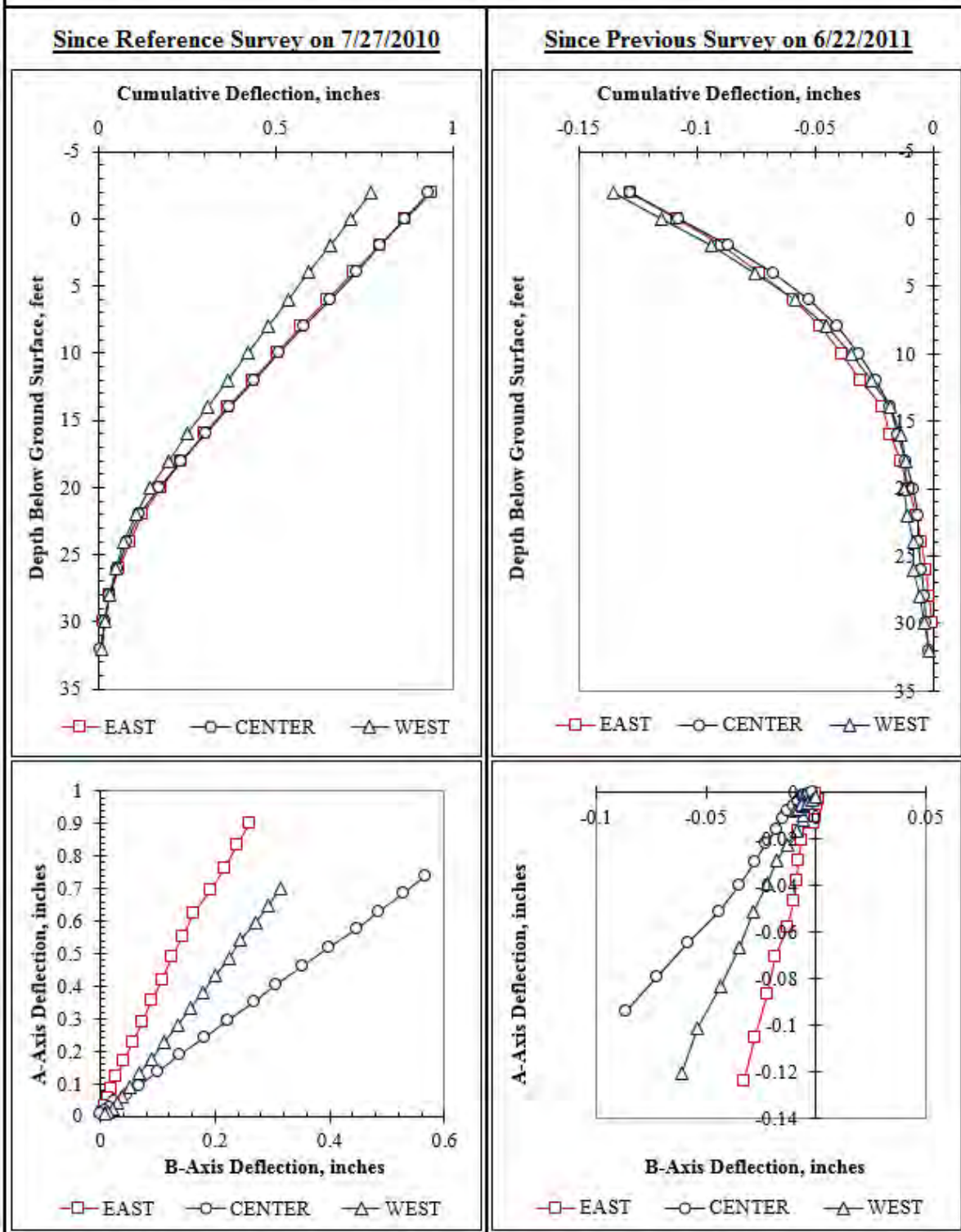


Figure F.49: Summary of inclinometer data from 7/28/2011.

Summary of Inclinometer Data From 8/16/2011

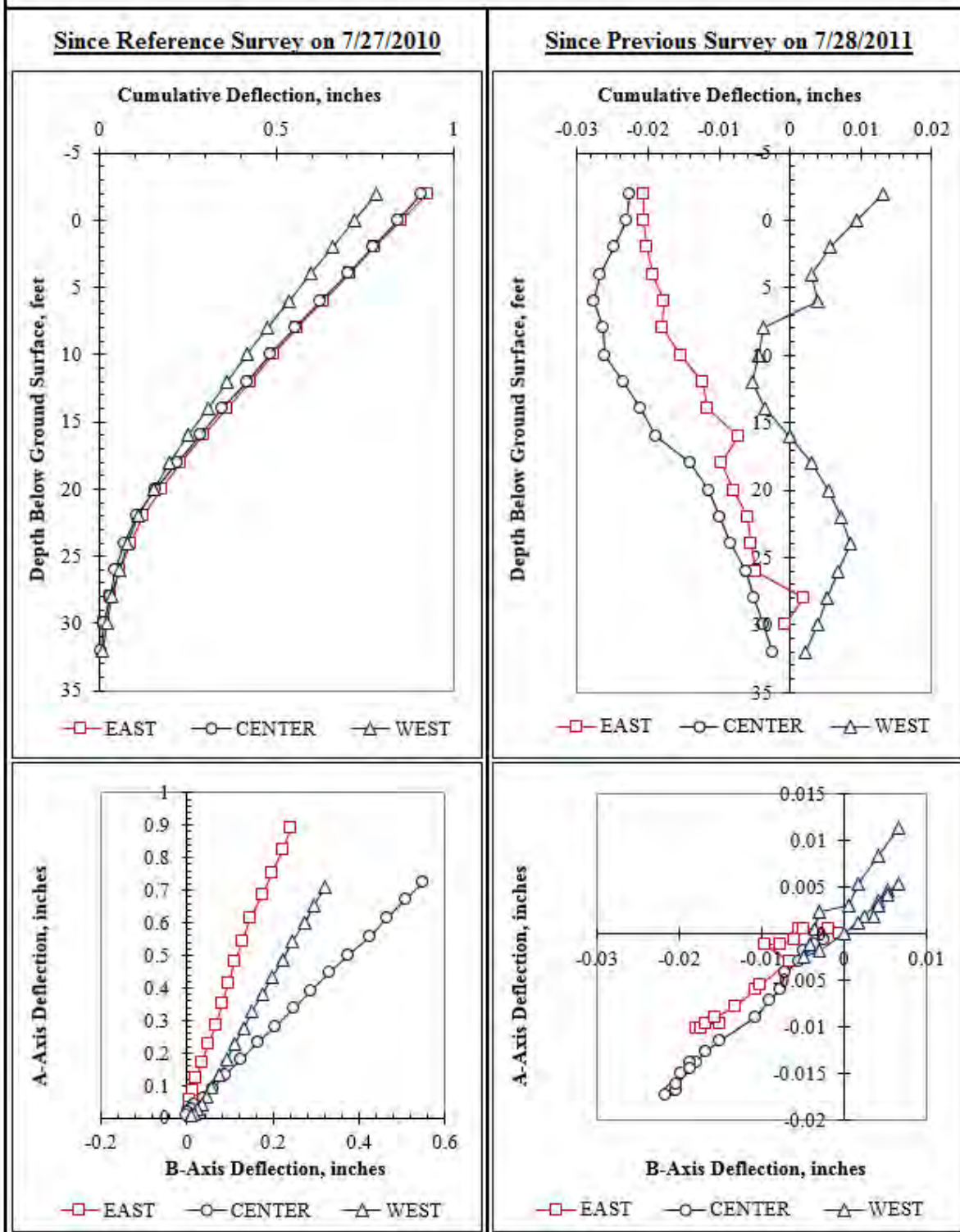


Figure F.50: Summary of inclinometer data from 8/16/2011.

Summary of Inclinator Data From 8/17/2011

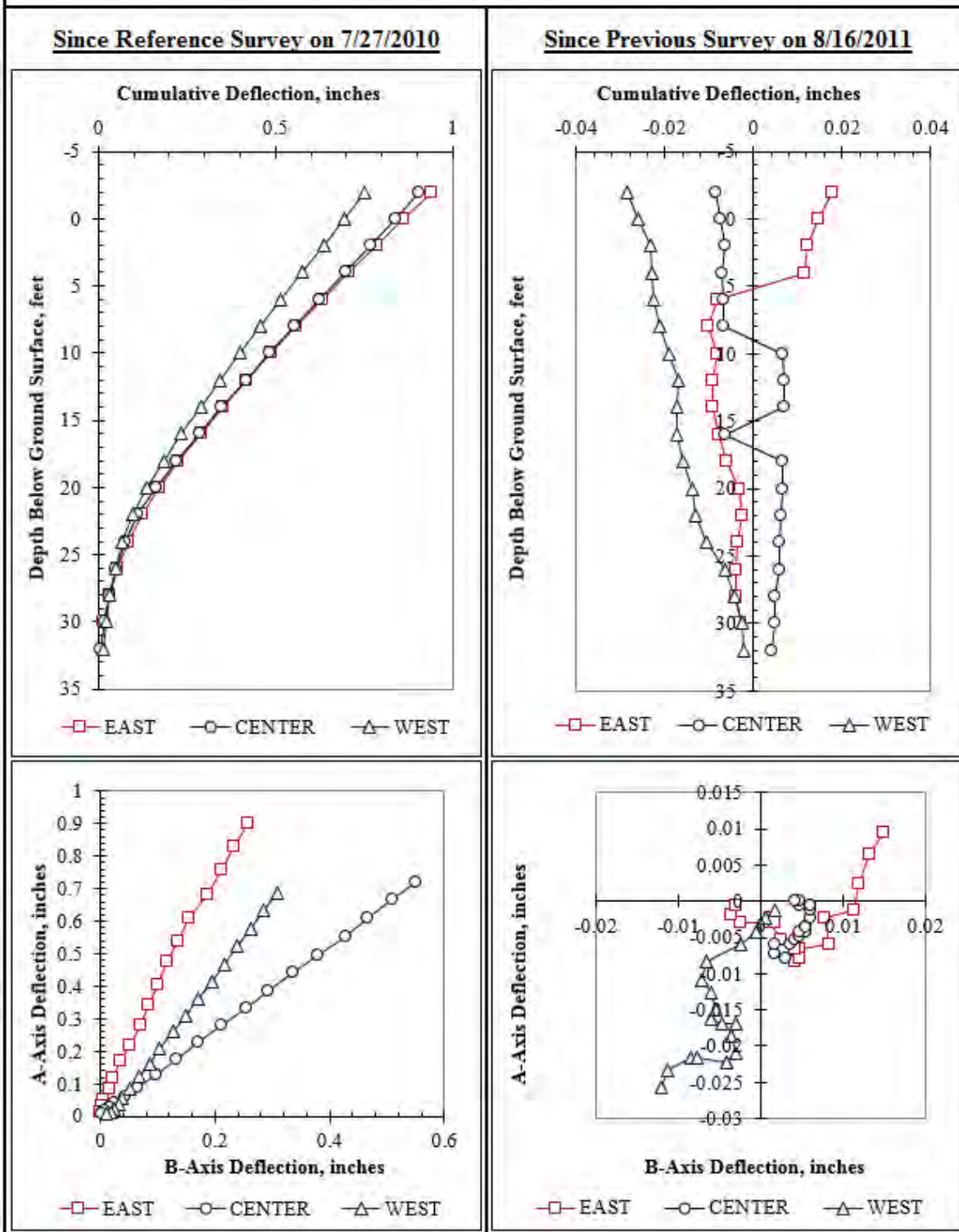


Figure F.51: Summary of inclinometer data from 8/17/2011.

Summary of Inclinometer Data From 9/1/2011

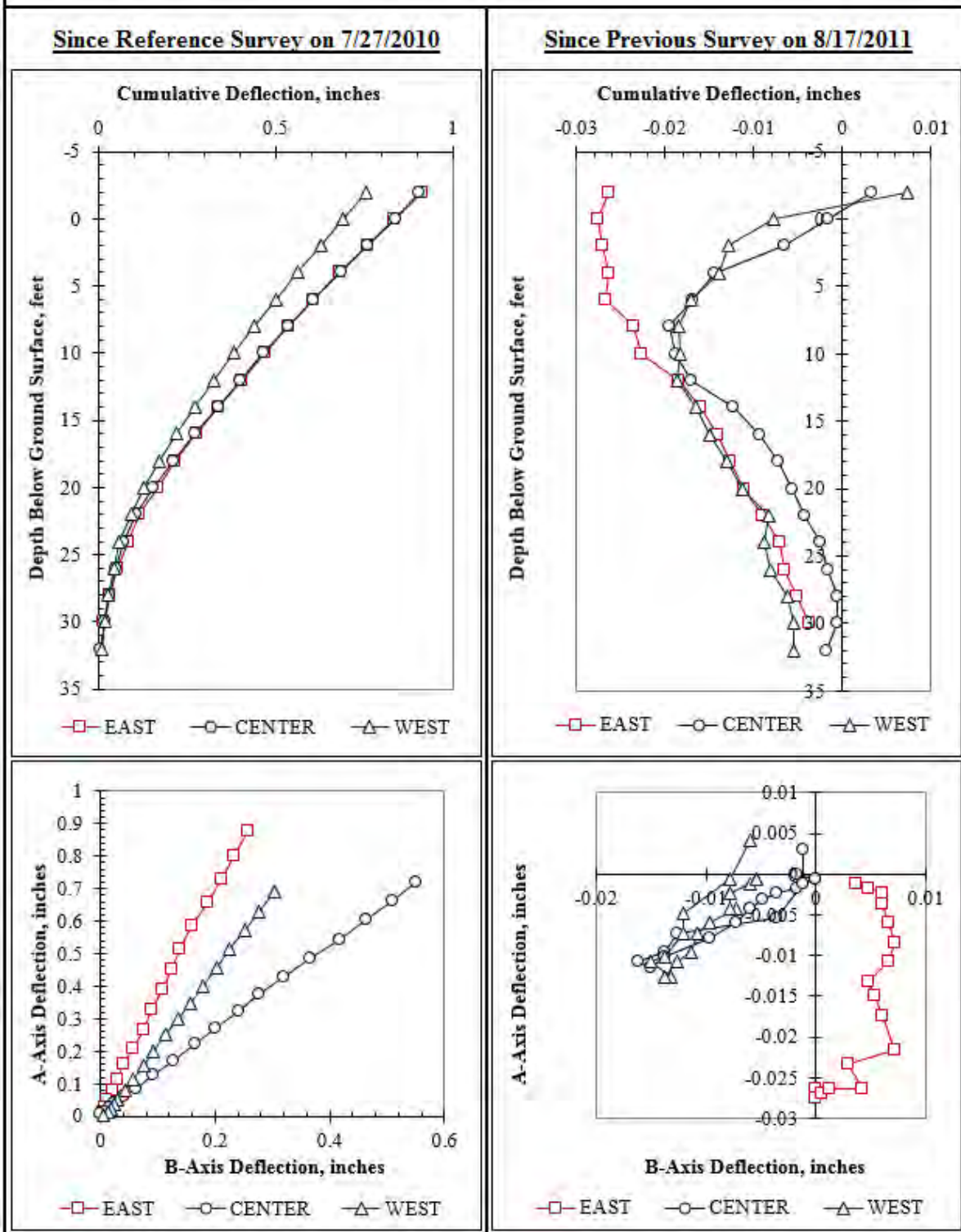


Figure F.52: Summary of inclinometer data from 9/1/2011.

Summary of Inclinometer Data From 9/15/2011

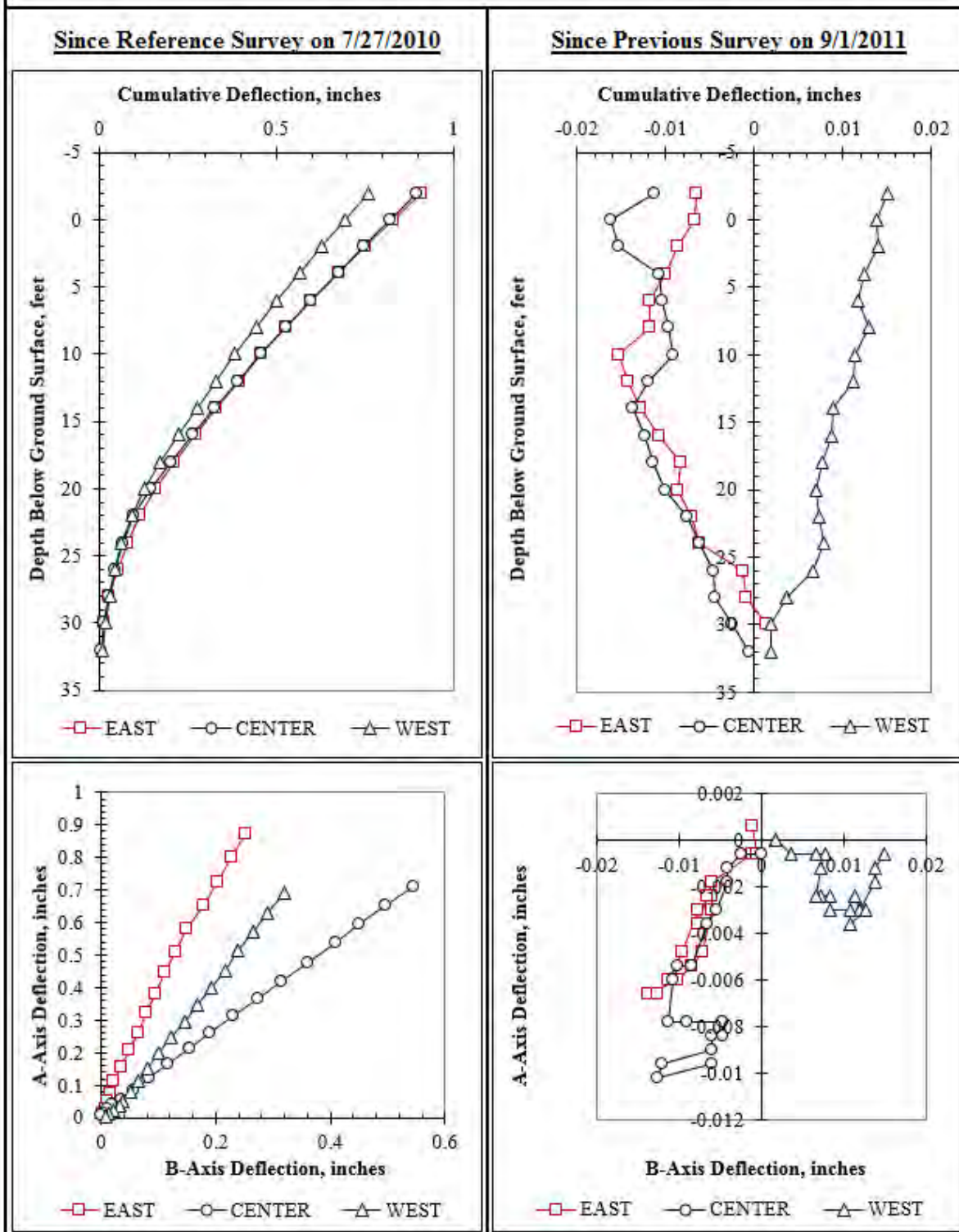


Figure F.53: Summary of inclinometer data from 9/15/2011.

Summary of Inclinometer Data From 9/29/2011

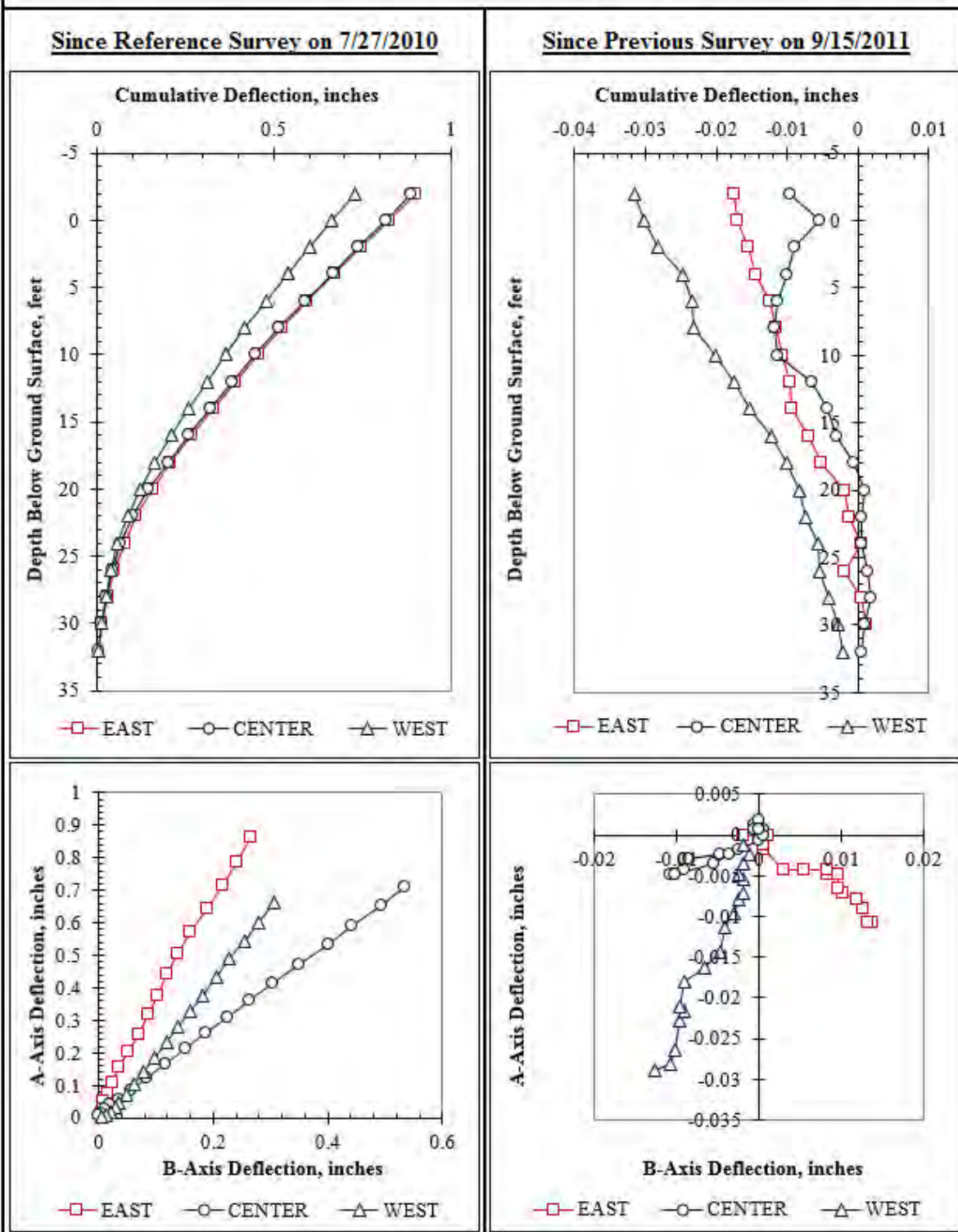


Figure F.54: Summary of inclinometer data from 9/29/2011.

Summary of Inclinometer Data From 10/10/2011

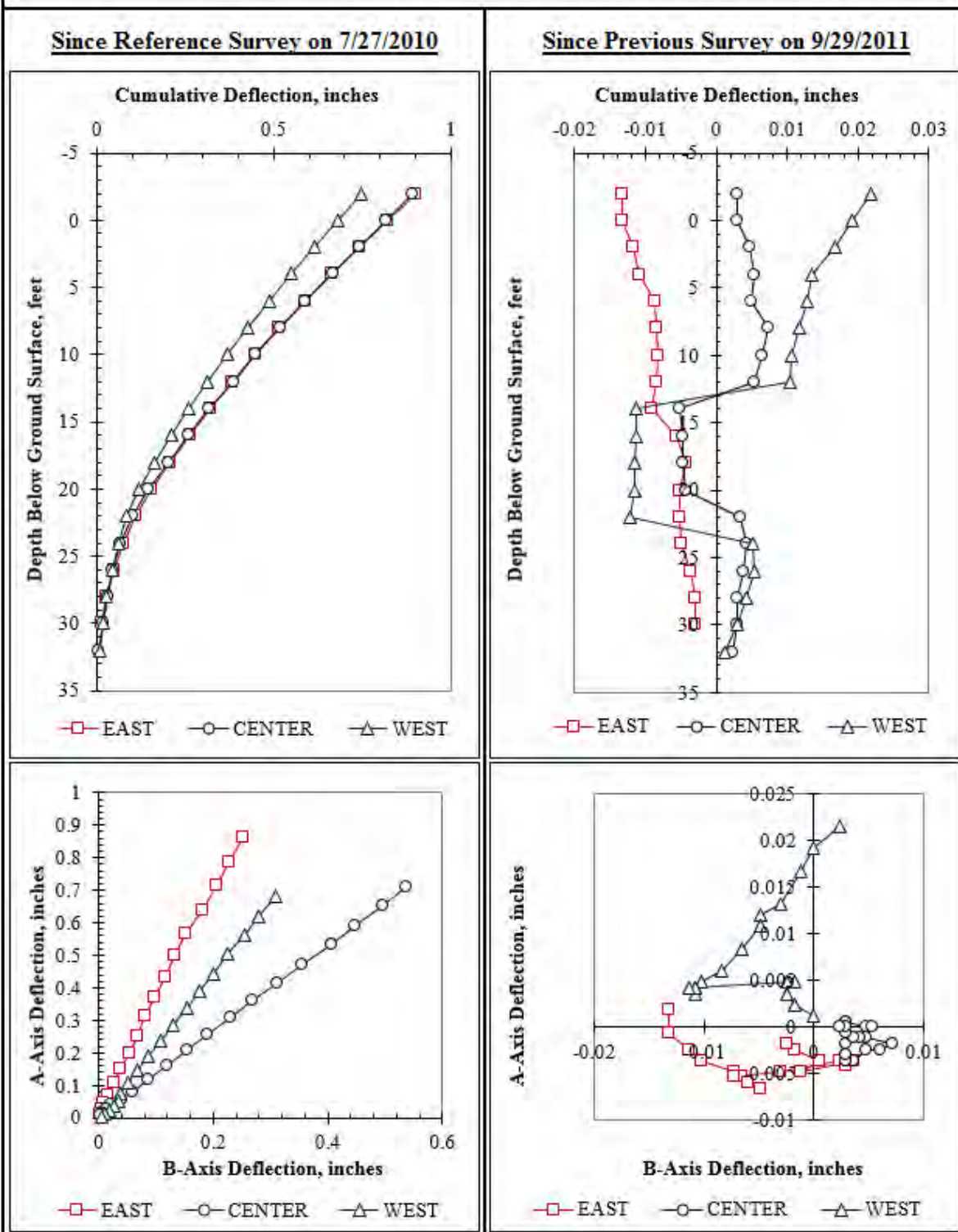


Figure F.55: Summary of inclinometer data from 10/10/2011.

Summary of Inclinometer Data From 10/27/2011

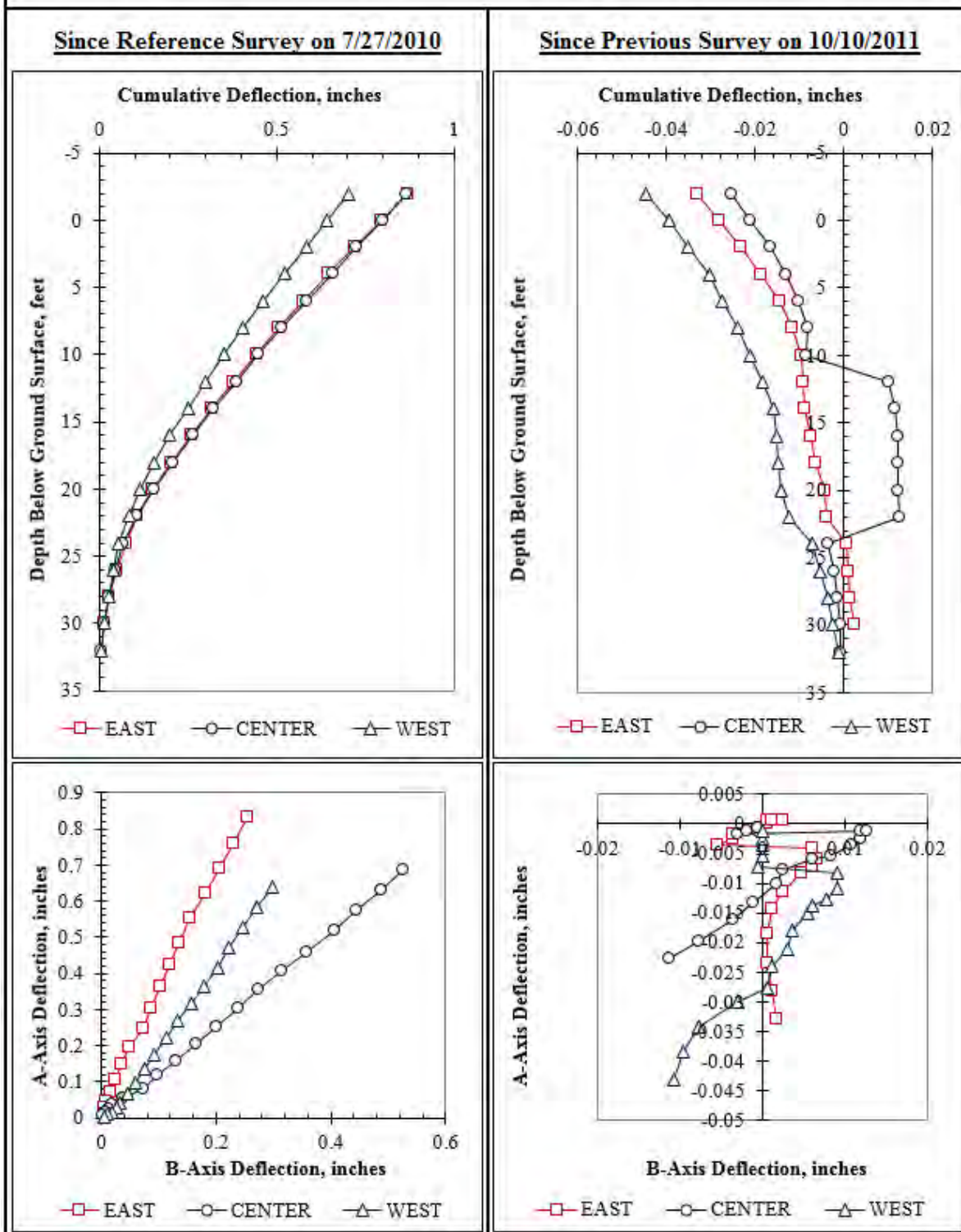


Figure F.56: Summary of inclinometer data from 10/27/2011.

Summary of Inclinometer Data From 11/16/2011

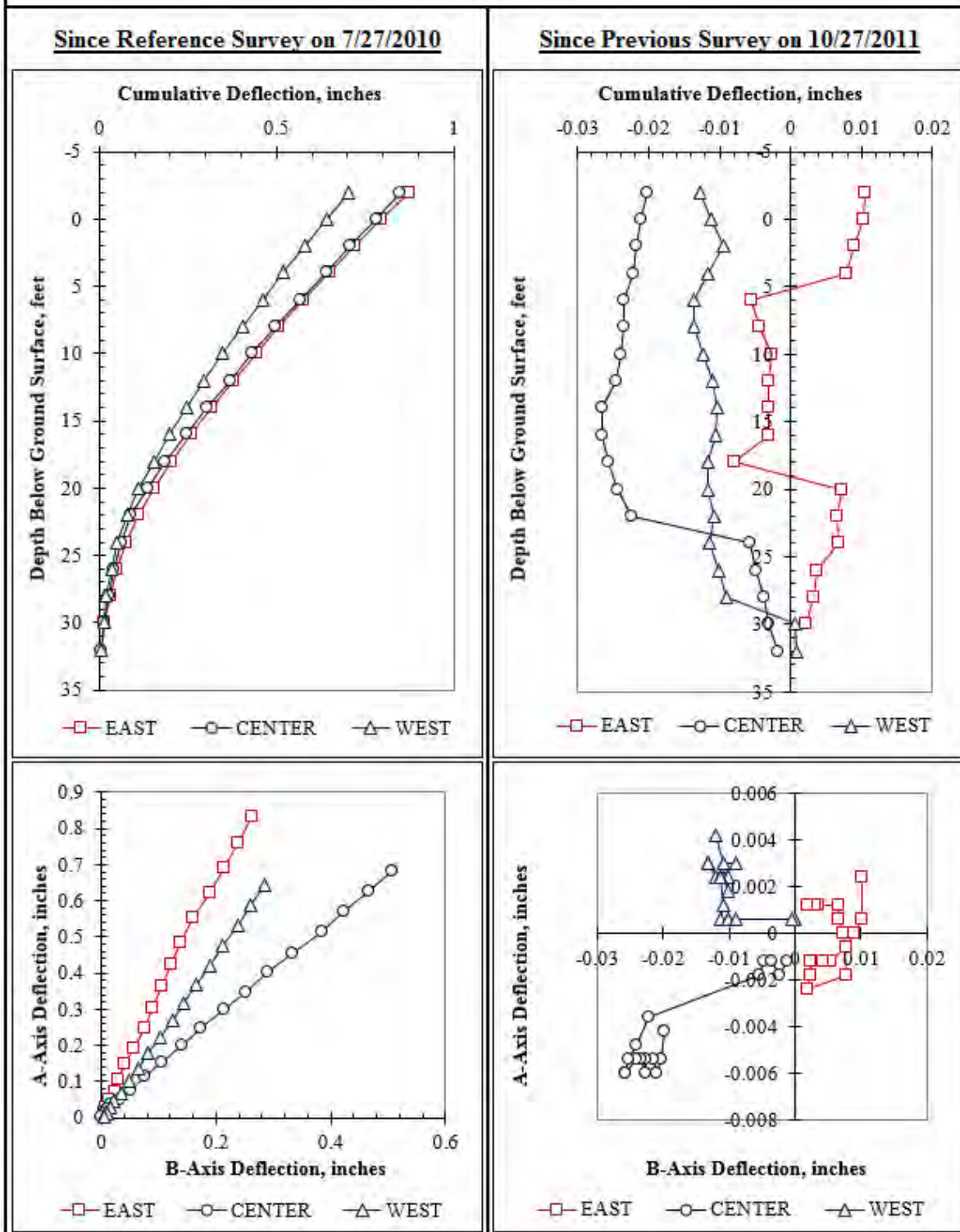


Figure F.57: Summary of inclinometer data from 11/16/2011.

Summary of Inclinometer Data From 11/28/2011

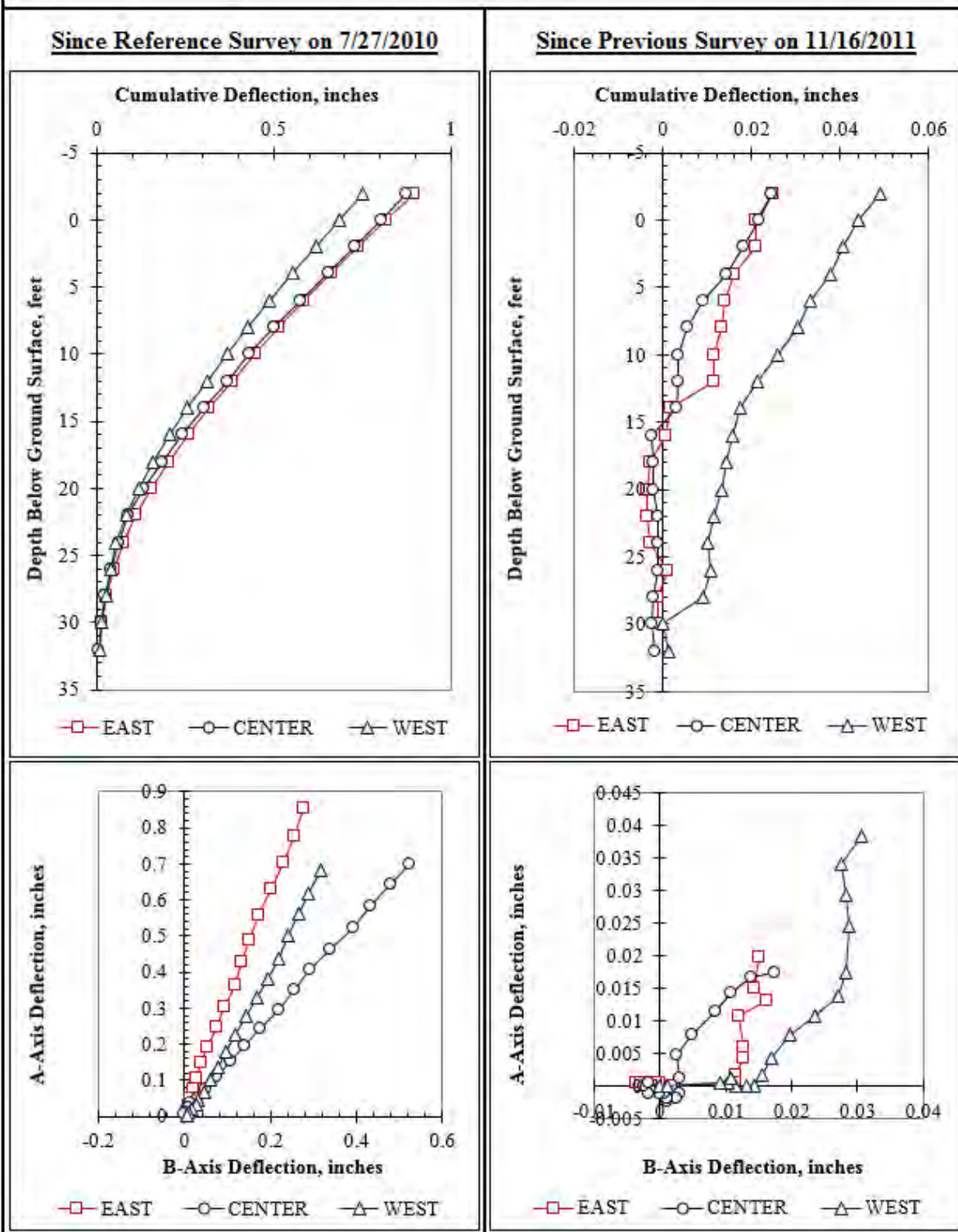


Figure F.58: Summary of inclinometer data from 11/28/2011.

Summary of Inclinometer Data From 12/6/2011

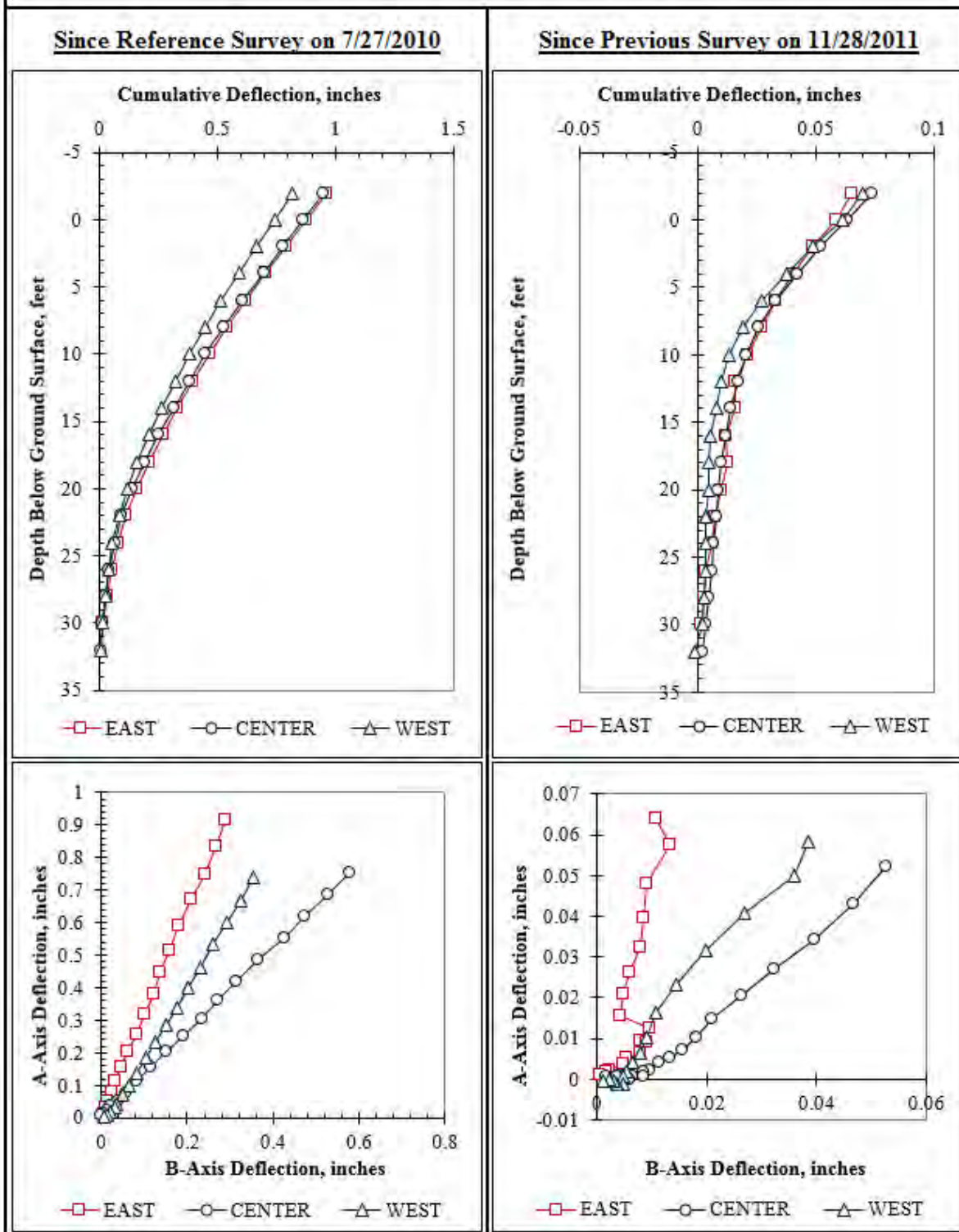


Figure F.59: Summary of inclinometer data from 12/6/2011.

Summary of Inclinometer Data From 12/16/2011

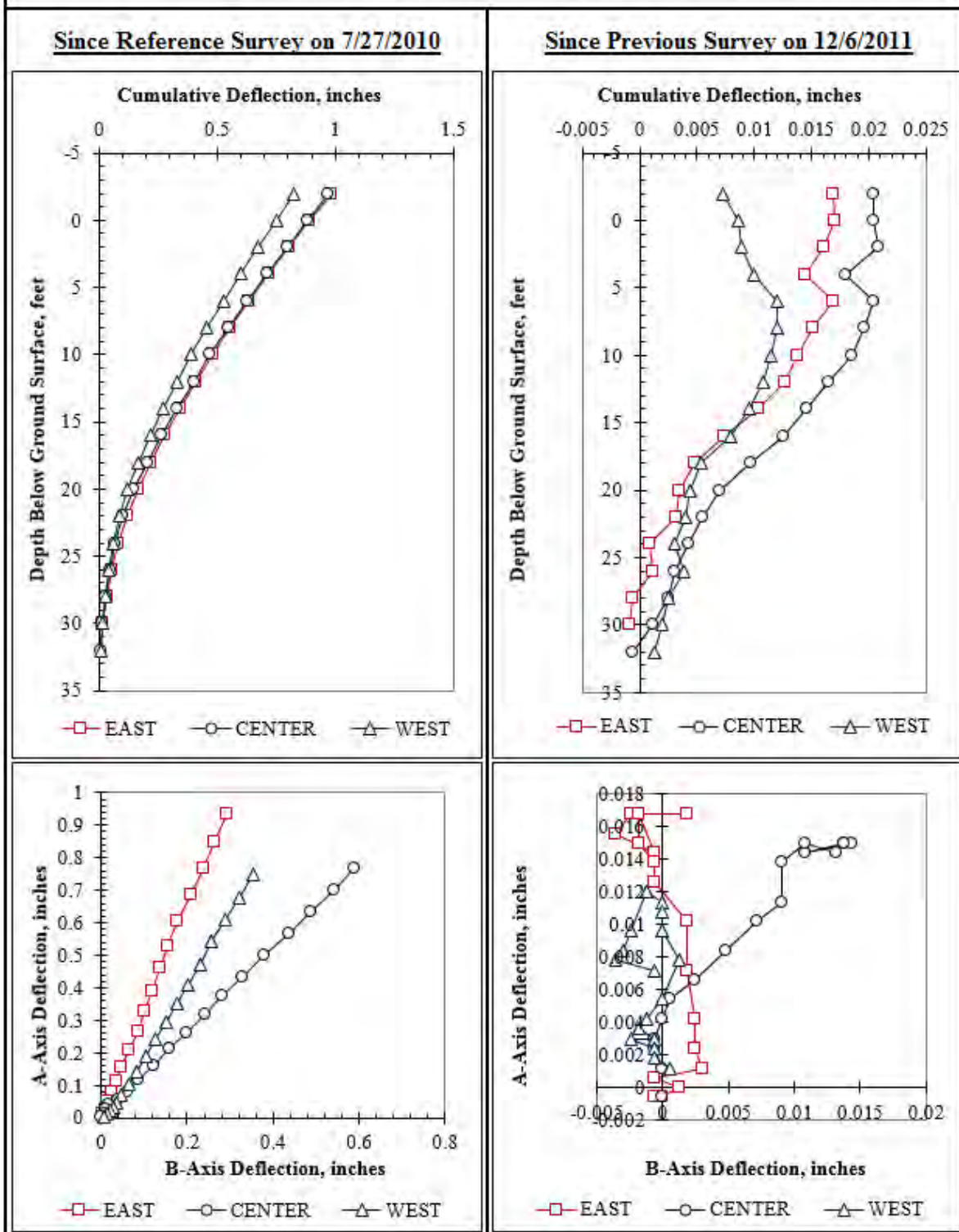


Figure F.60: Summary of inclinometer data from 12/16/2011.

Summary of Inclinometer Data From 12/23/2011

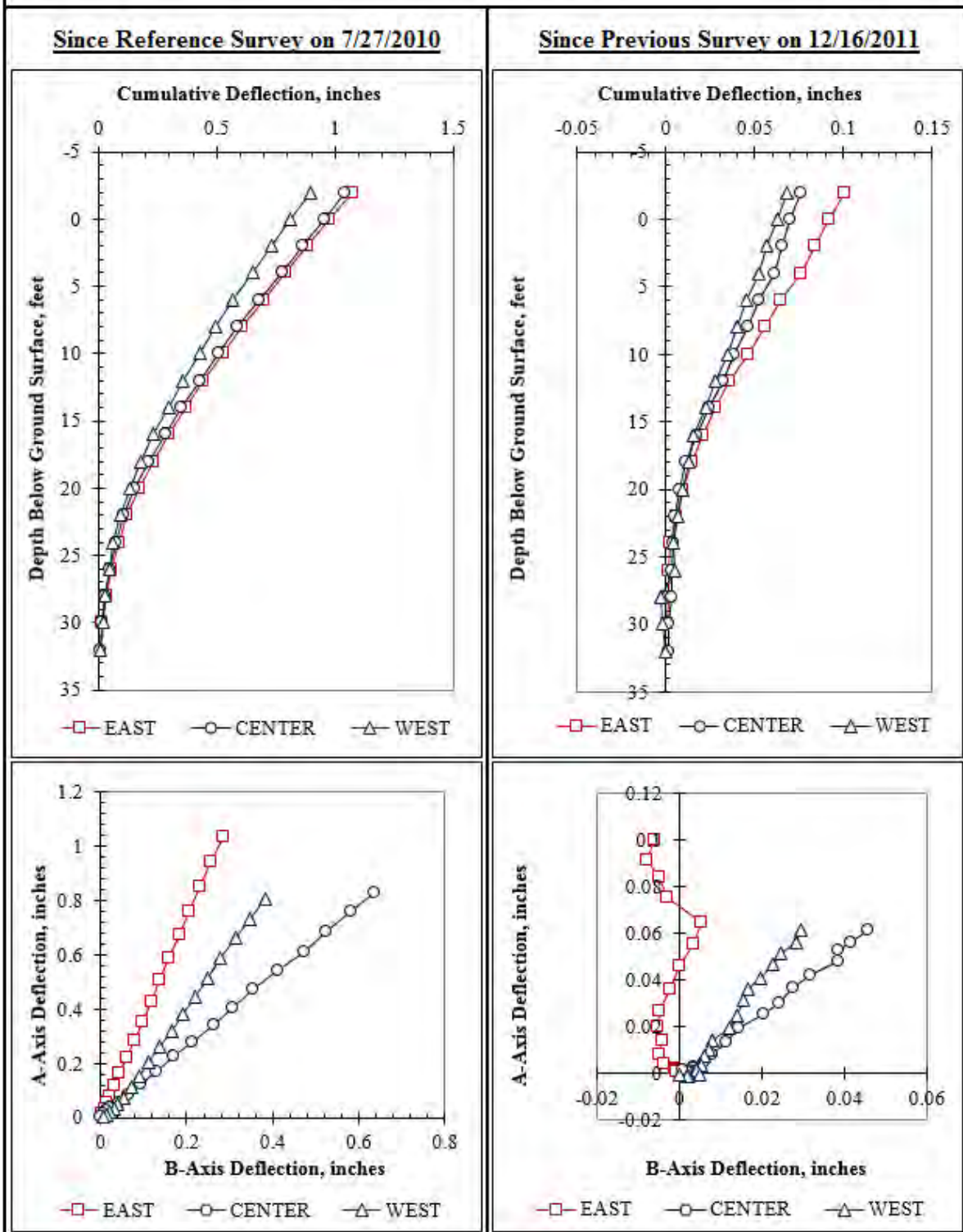


Figure F.61: Summary of inclinometer data from 12/23/2011.

Summary of Inclinometer Data From 1/10/2012

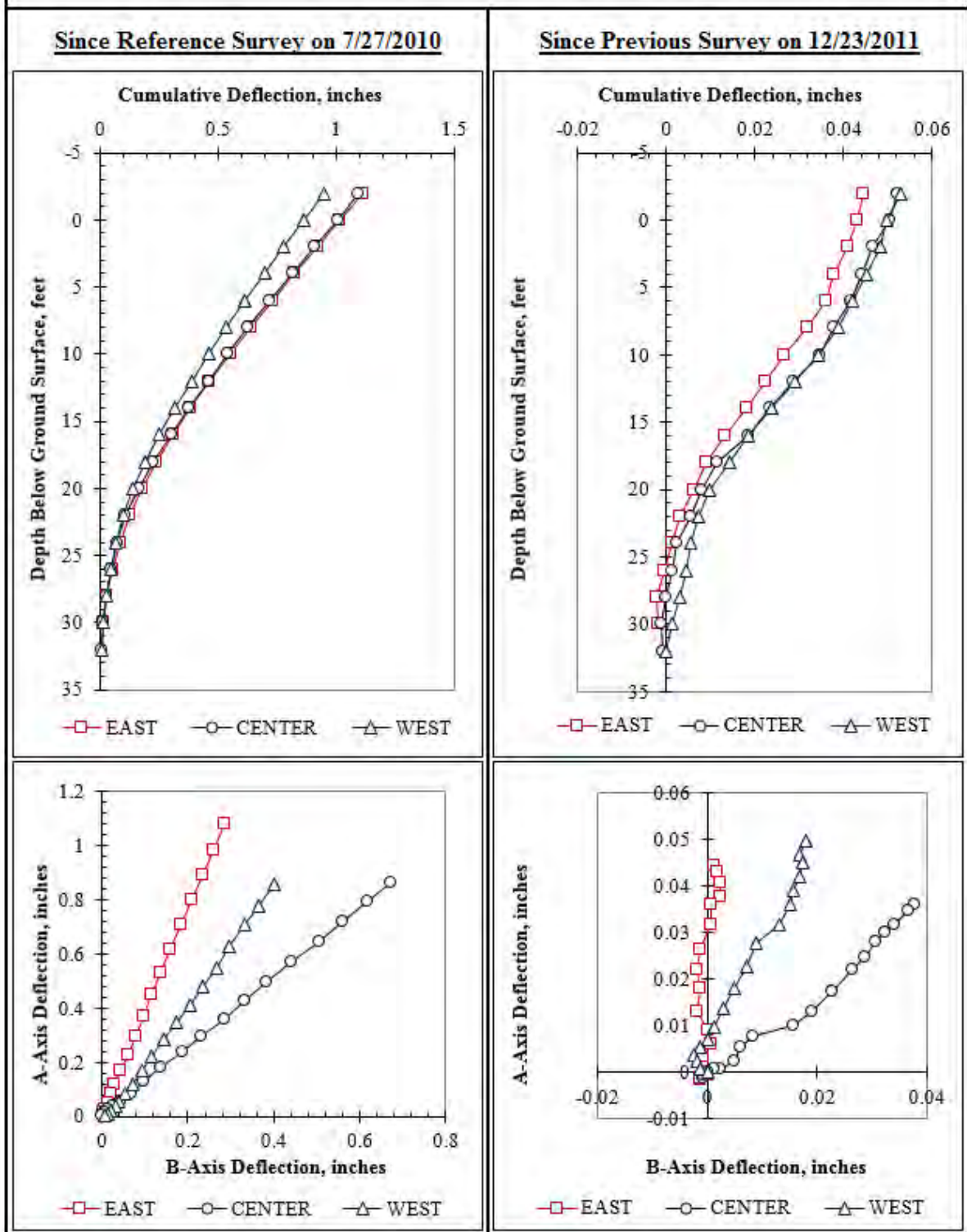


Figure F.62: Summary of inclinometer data from 1/10/2012.

Summary of Inclinometer Data From 1/25/2012

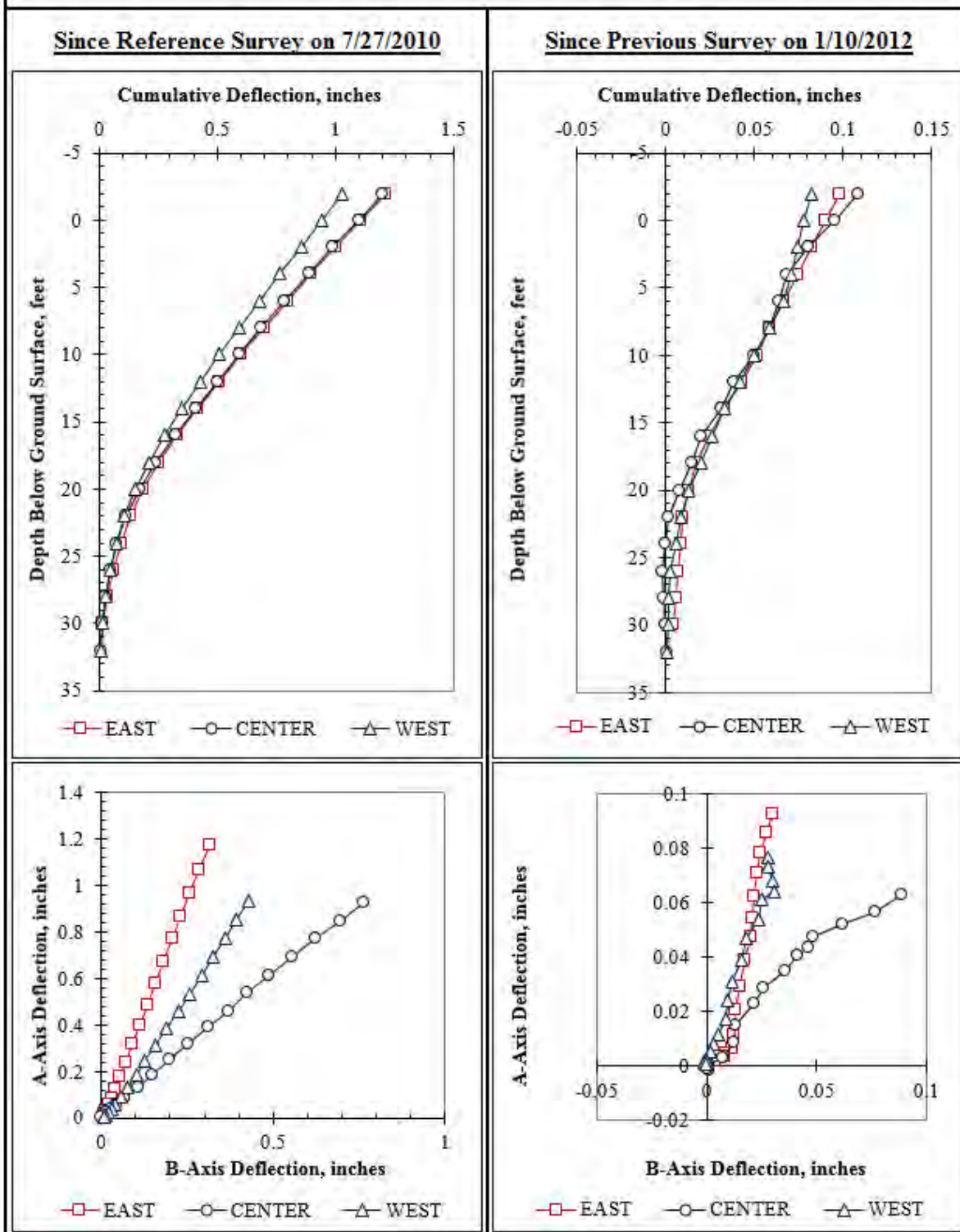


Figure F.63: Summary of inclinometer data from 1/25/2012.

Summary of Inclinometer Data From 1/26/2012

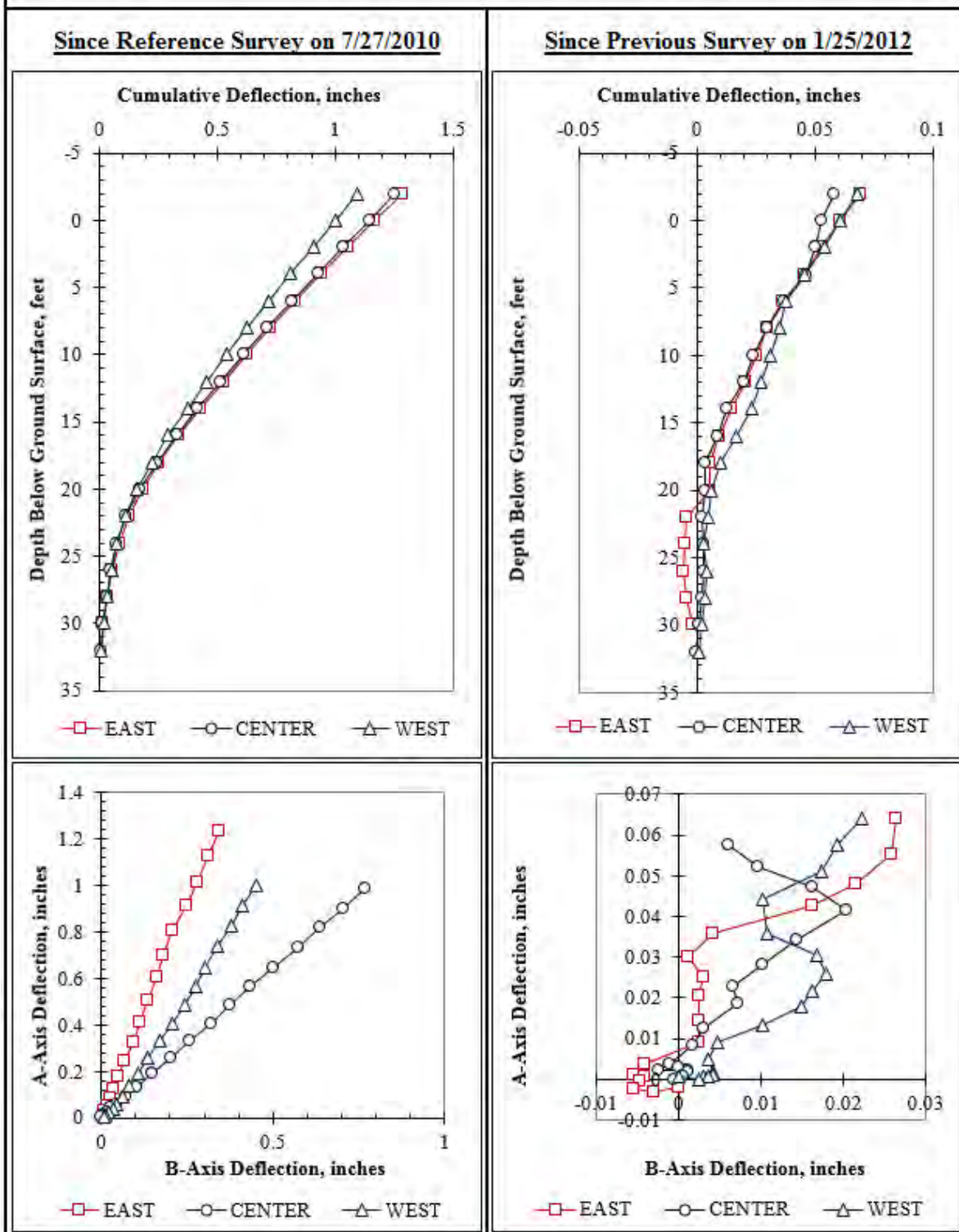


Figure F.64: Summary of inclinometer data from 1/26/2012.

Summary of Inclinometer Data From 1/27/2012

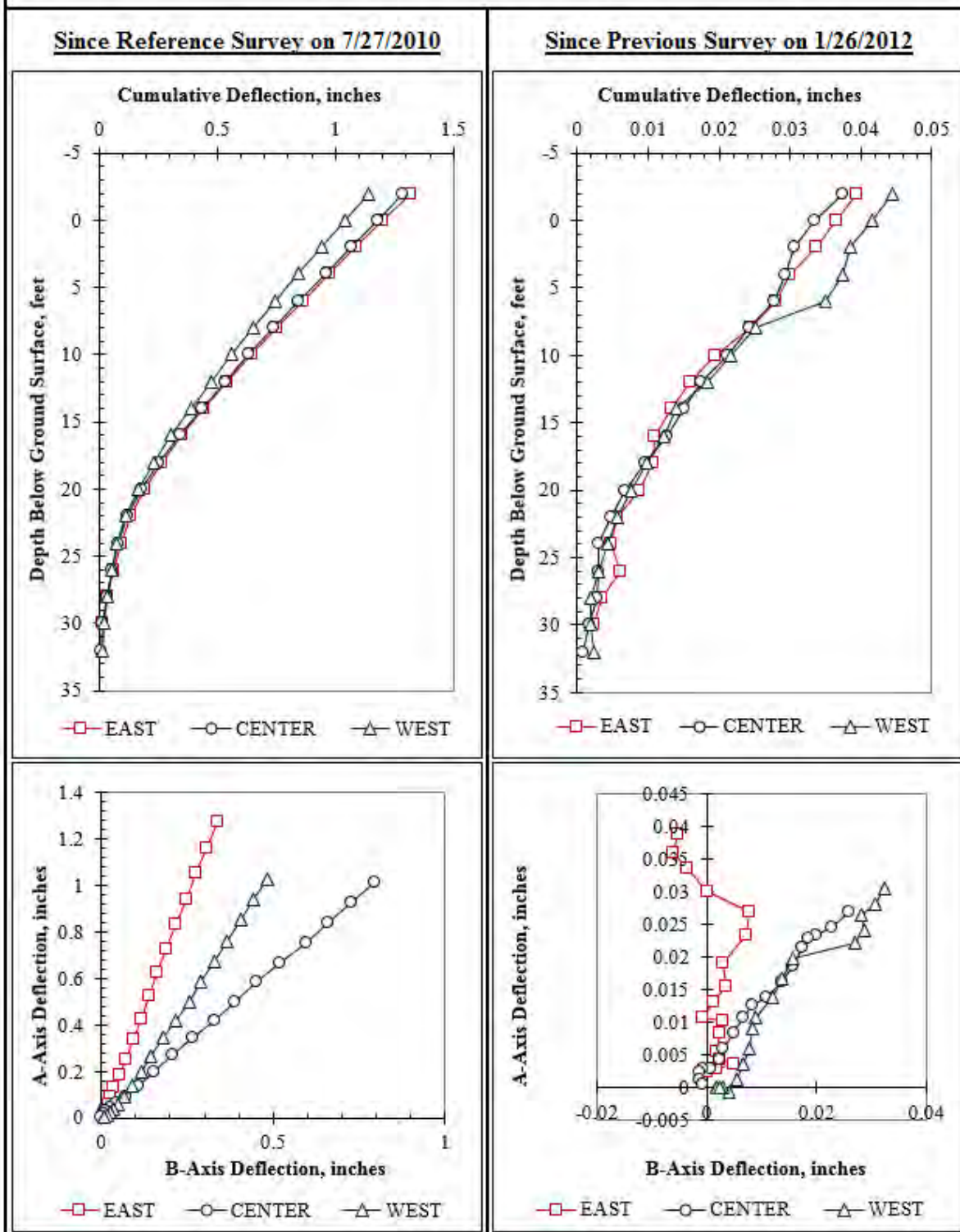


Figure F.65: Summary of inclinometer data from 1/27/2012.

Summary of Inclinometer Data From 1/30/2012

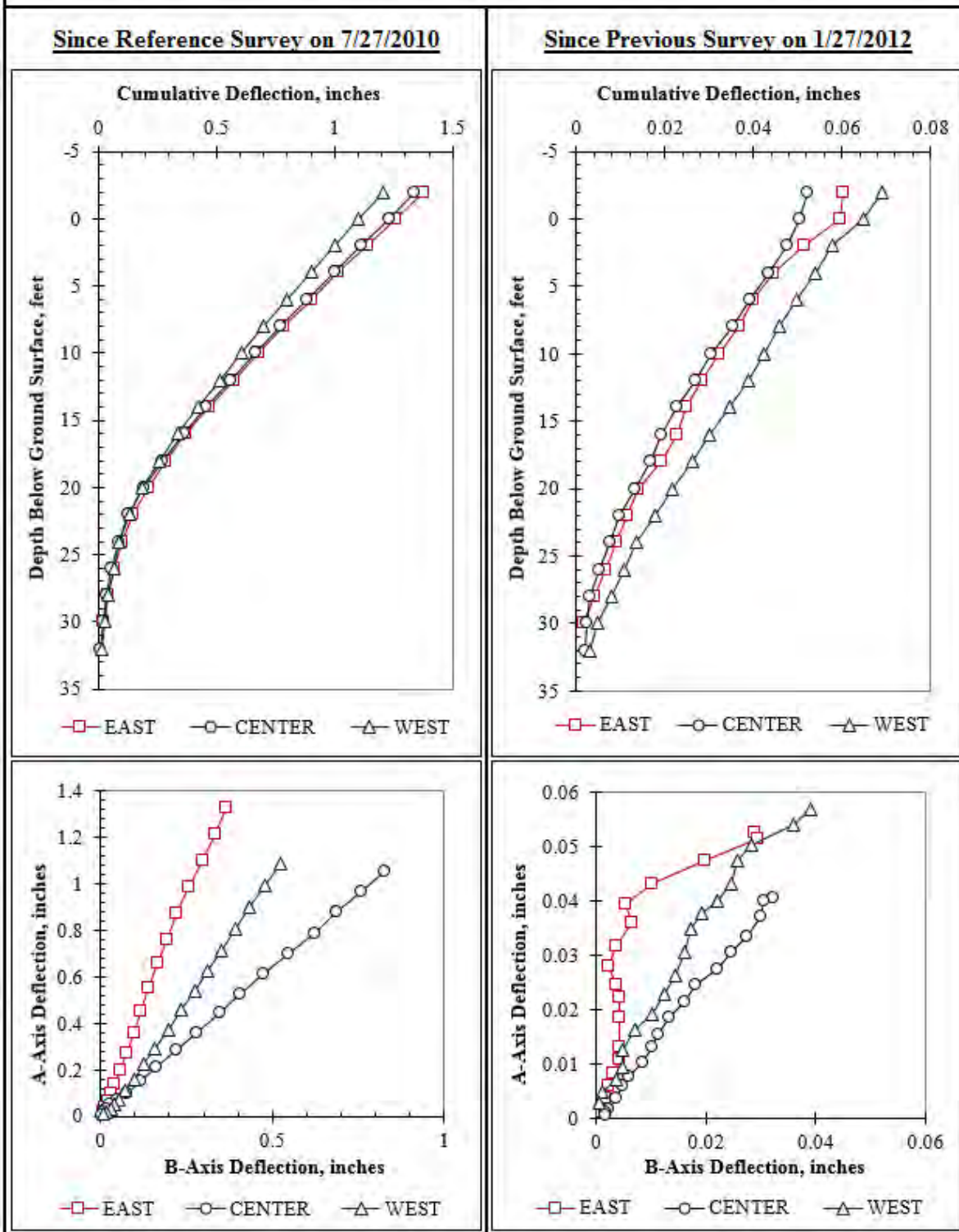


Figure F.66: Summary of inclinometer data from 1/30/2012.

Summary of Inclinometer Data From 2/16/2012

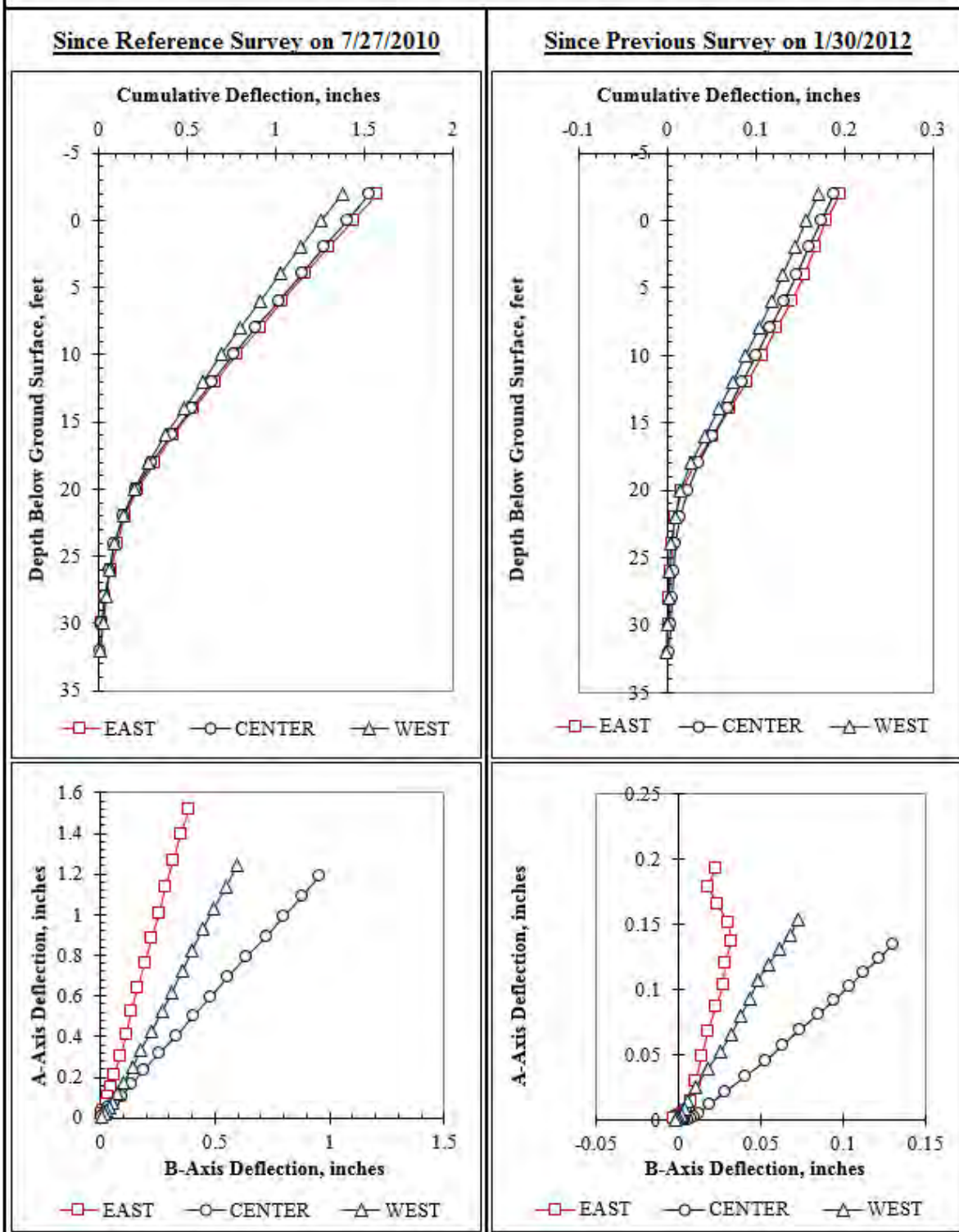


Figure F.67: Summary of inclinometer data from 2/16/2012.

Summary of Inclinometer Data From 3/8/2012

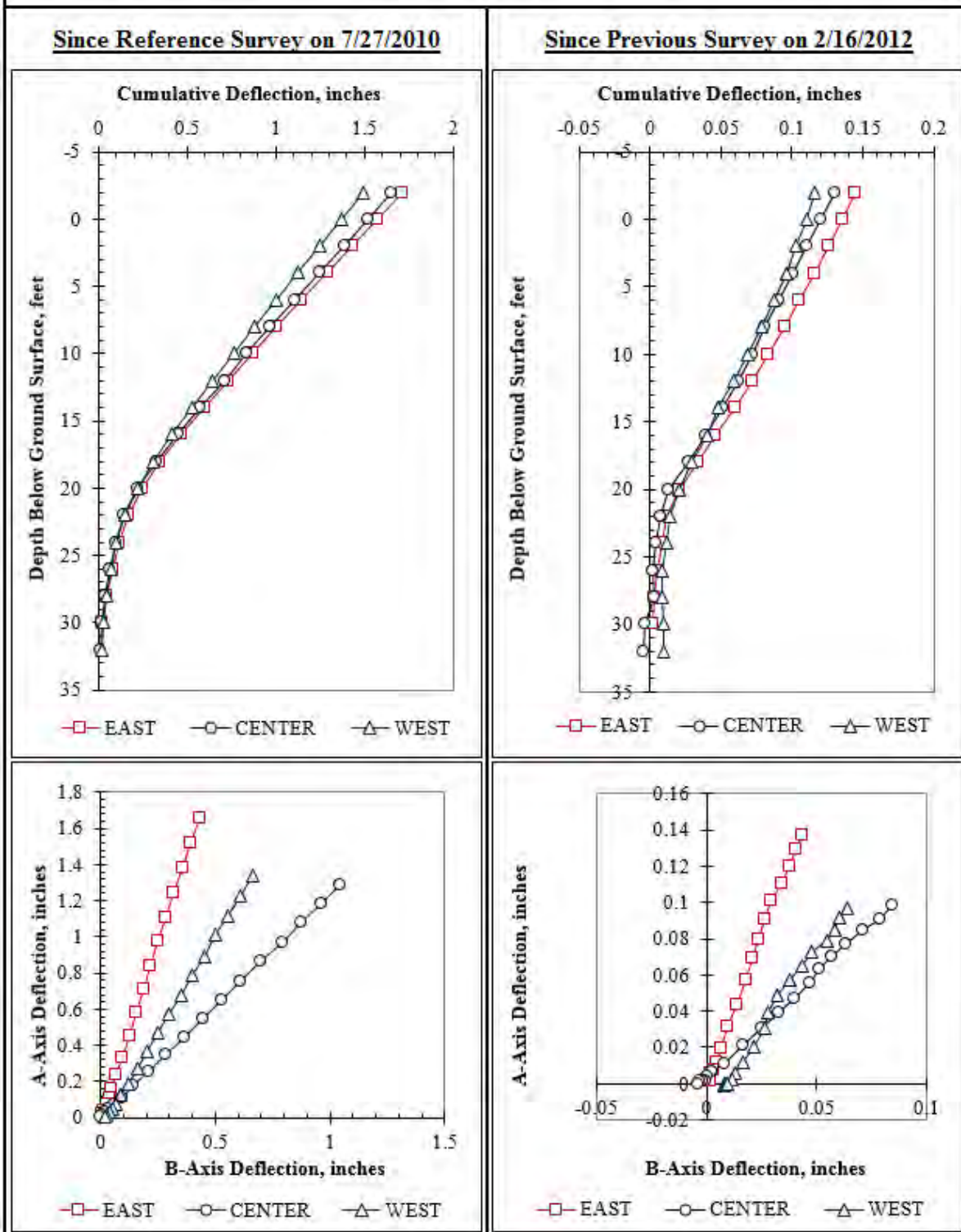


Figure F.68: Summary of inclinometer data from 3/8/2012.

Summary of Inclinometer Data From 3/22/2012

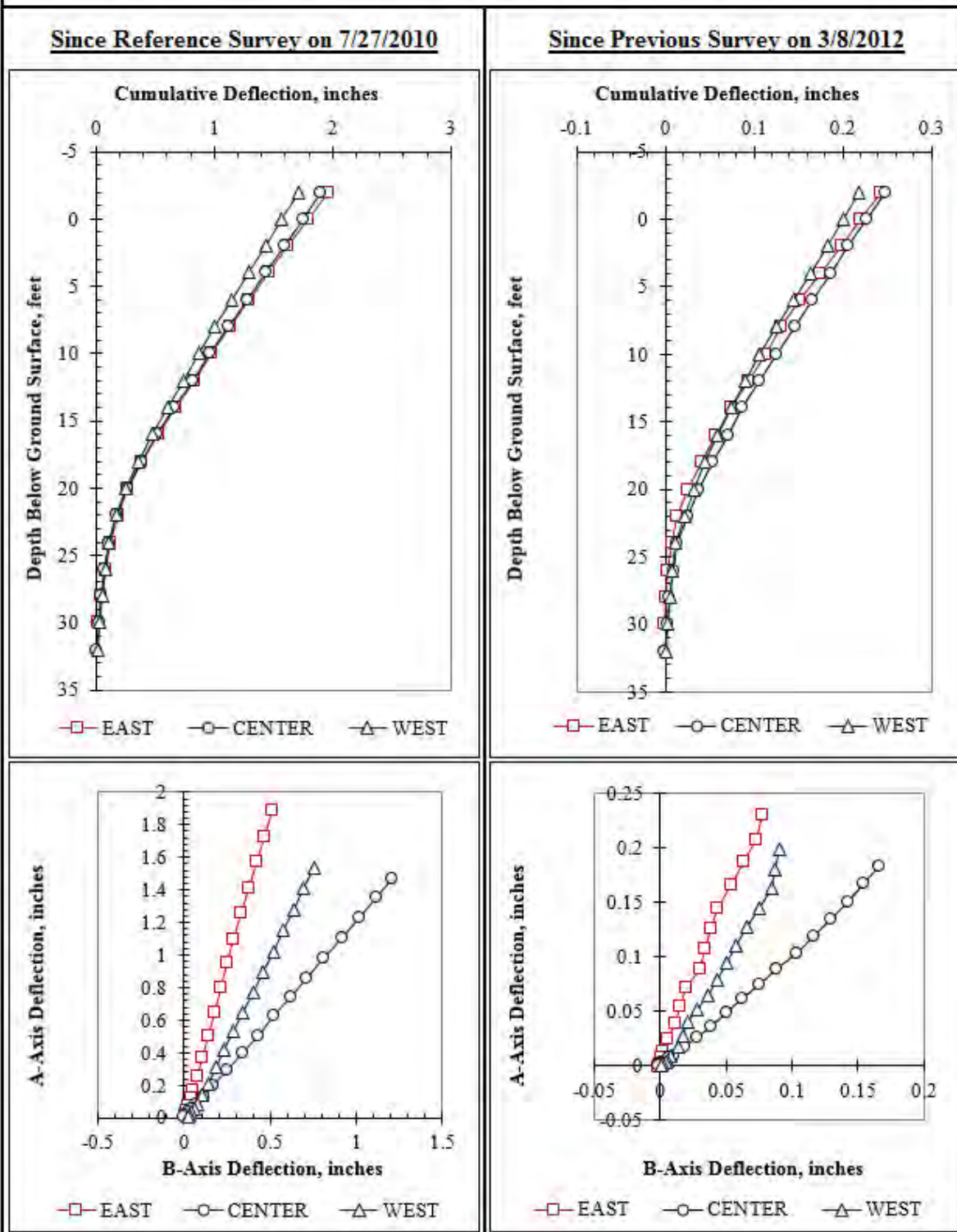


Figure F.69: Summary of inclinometer data from 3/22/2012.

Summary of Inclinometer Data From 4/10/2012

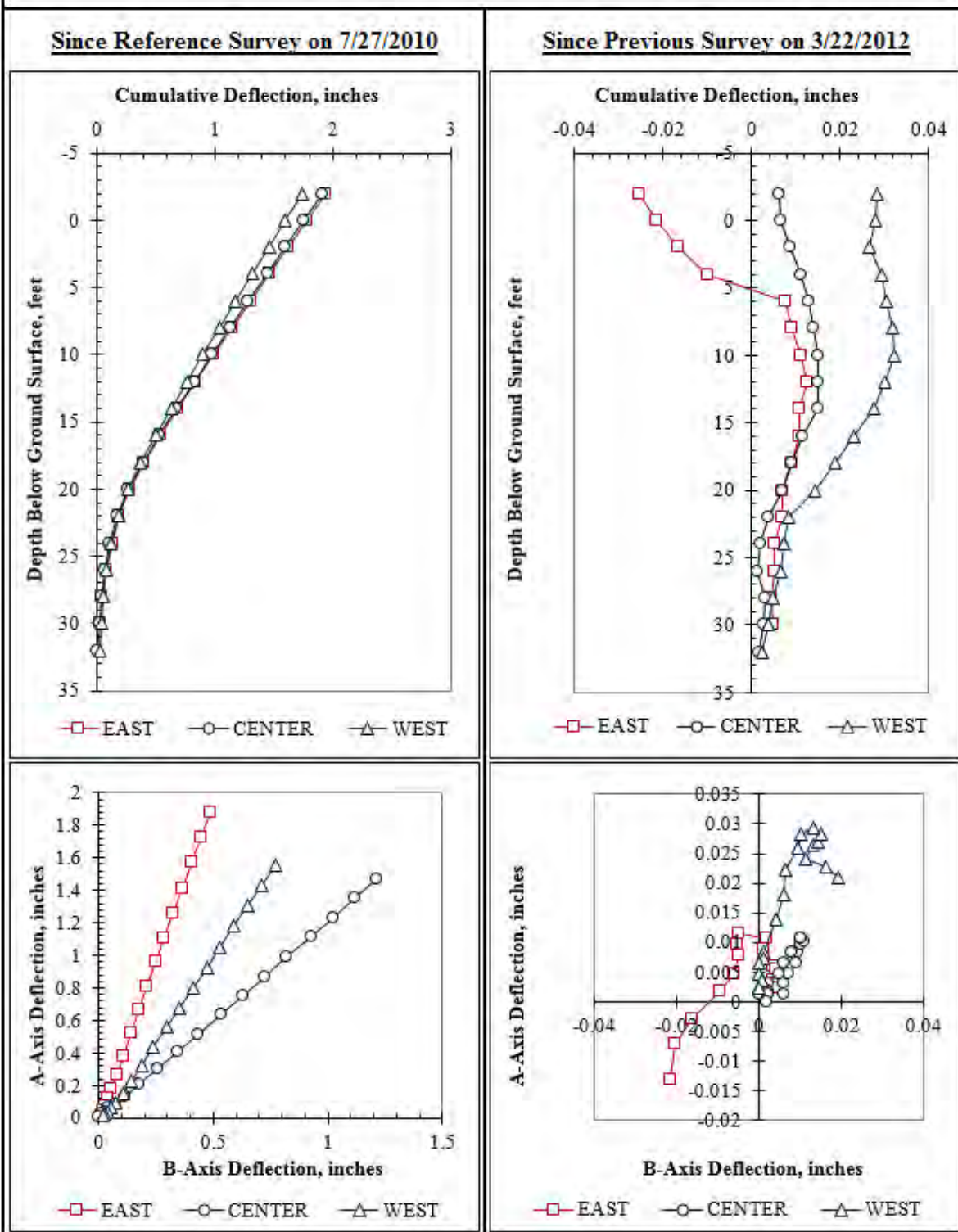


Figure F.70: Summary of inclinometer data from 4/10/2012.

Summary of Inclinometer Data From 5/2/2012

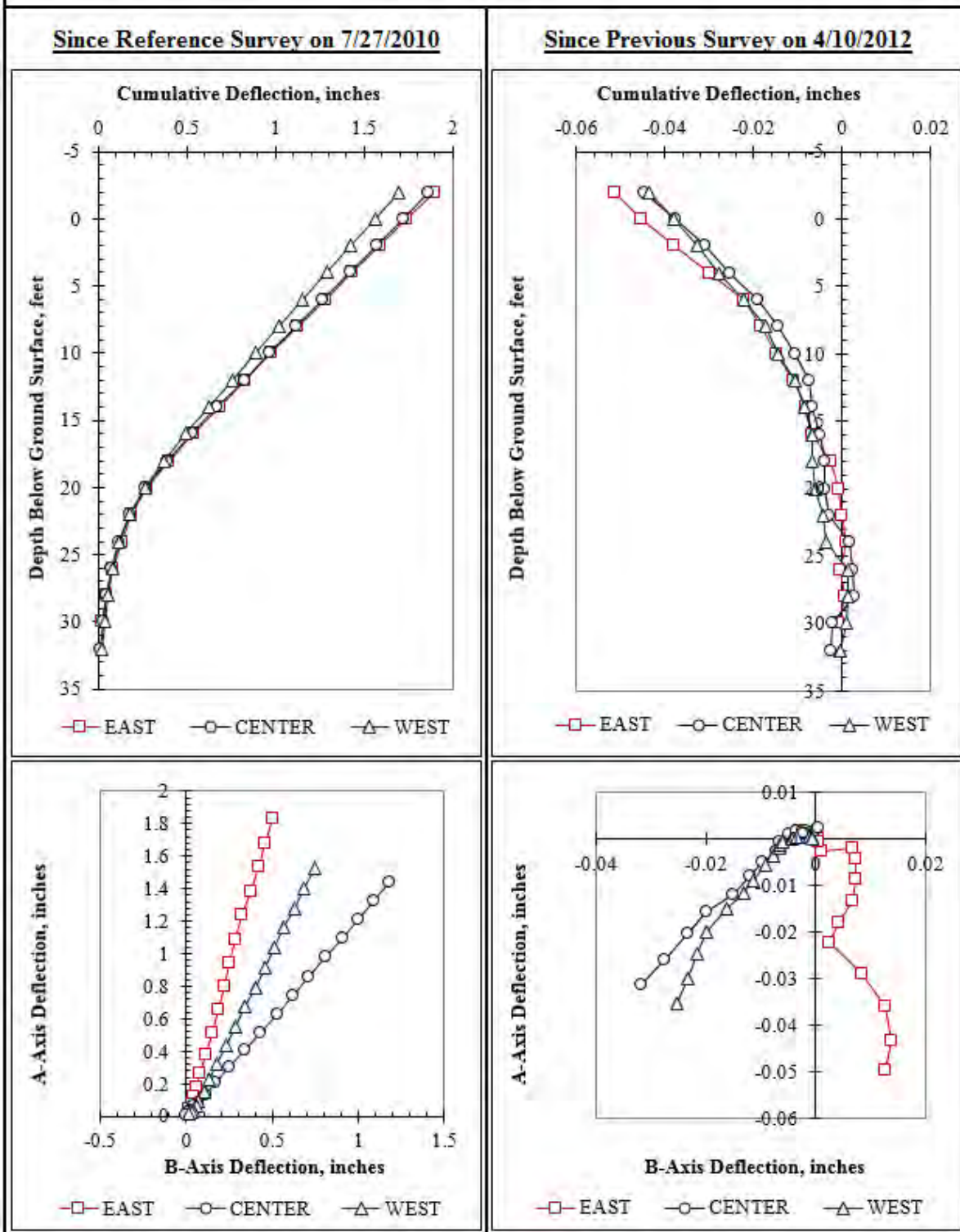


Figure F.71: Summary of inclinometer data from 5/2/2012.

Summary of Inclinometer Data From 5/3/2012

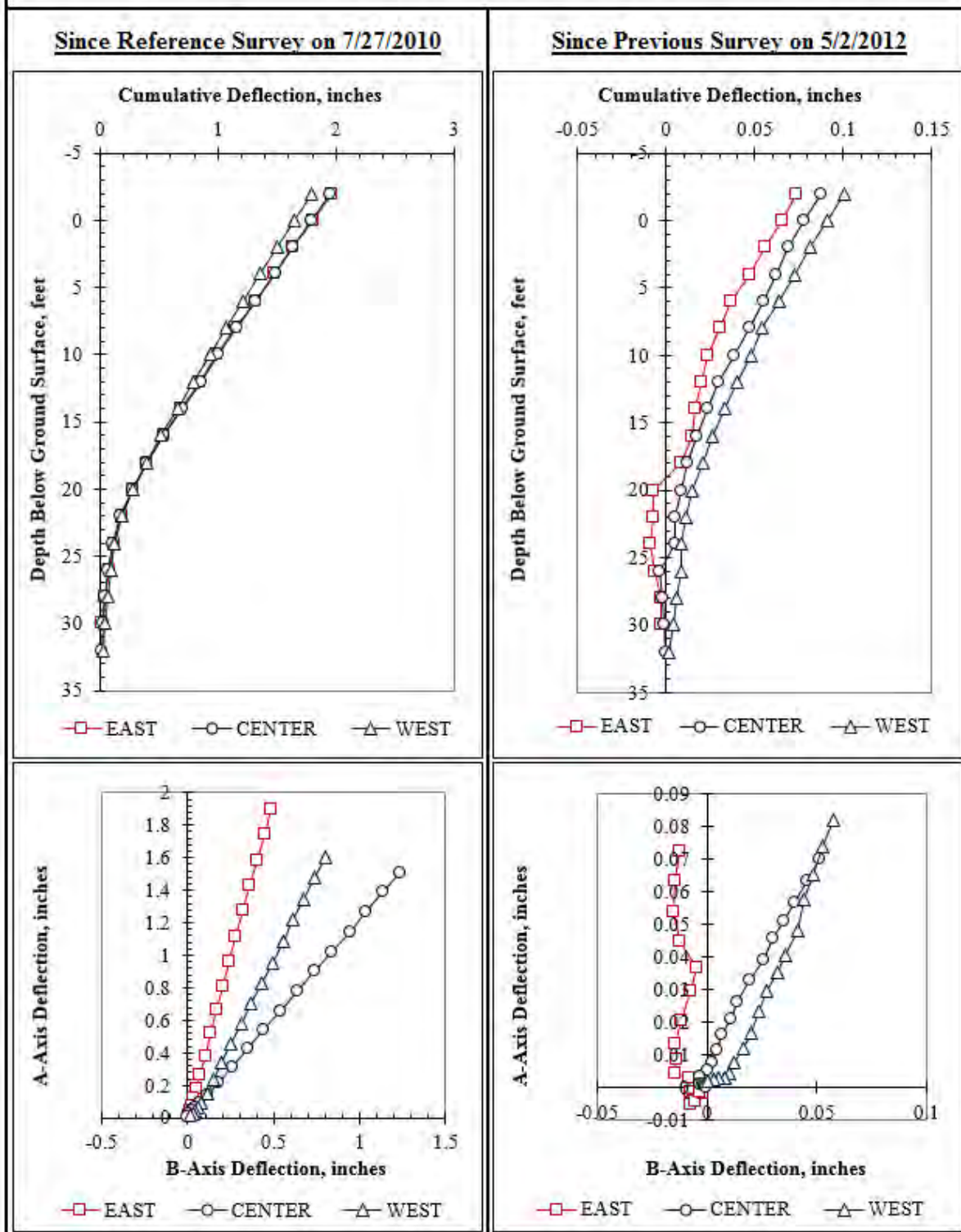


Figure F.72: Summary of inclinometer data from 5/3/2012.

Summary of Incliner Data From 5/4/2012

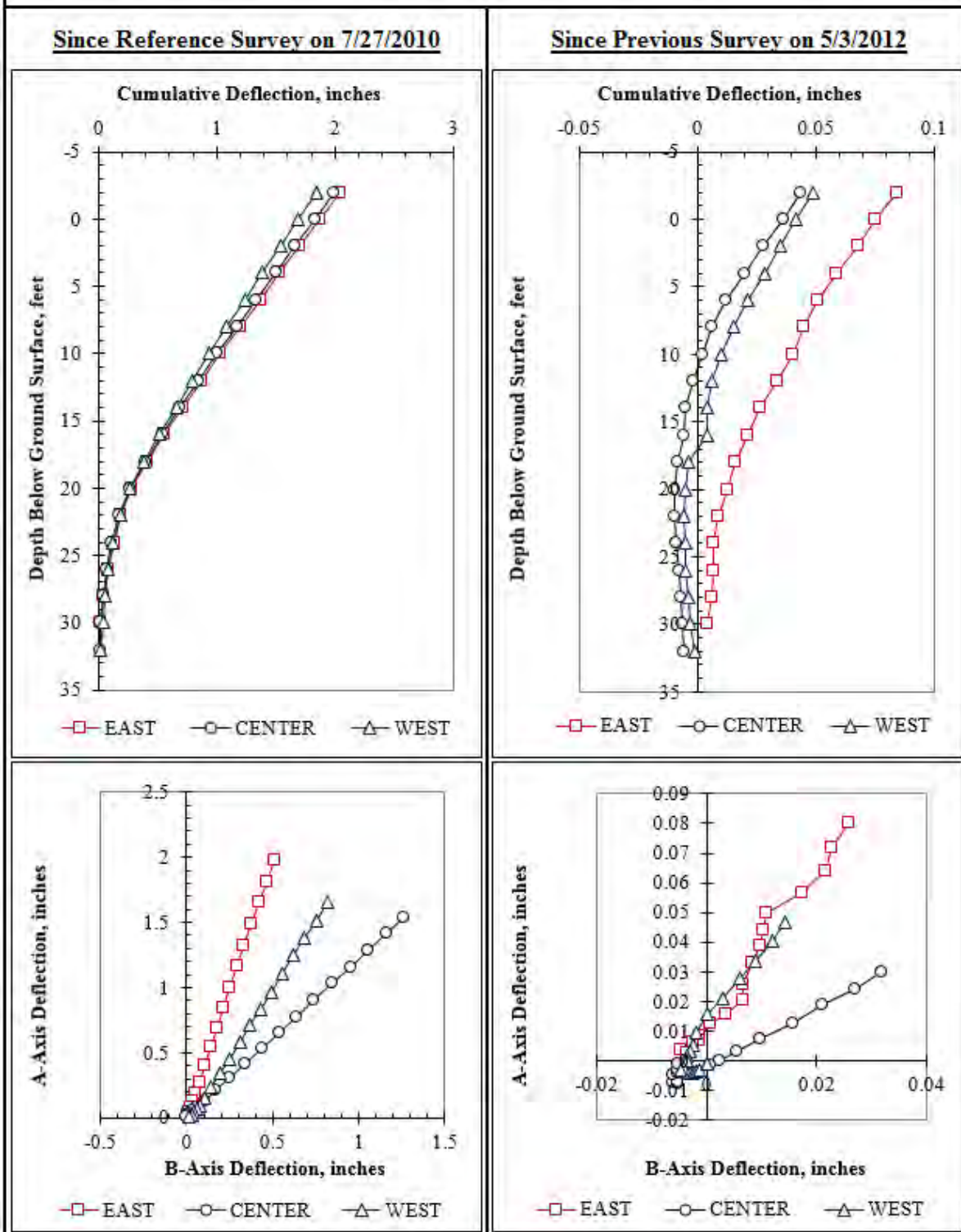


Figure F.73: Summary of inclinometer data from 5/4/2012.

Summary of Inclinometer Data From 5/5/2012

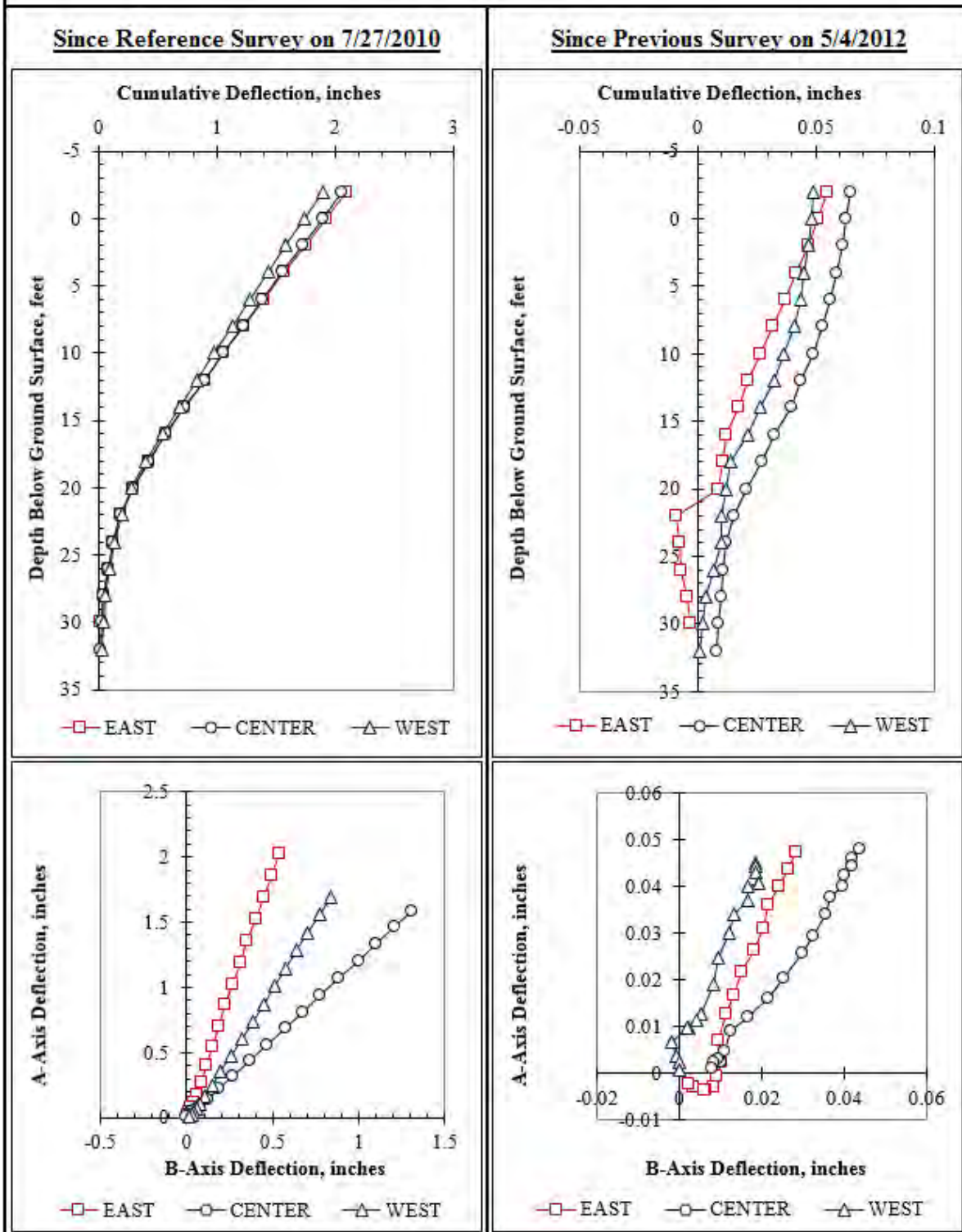


Figure F.74: Summary of inclinometer data from 5/5/2012.

Summary of Inclinometer Data From 5/7/2012

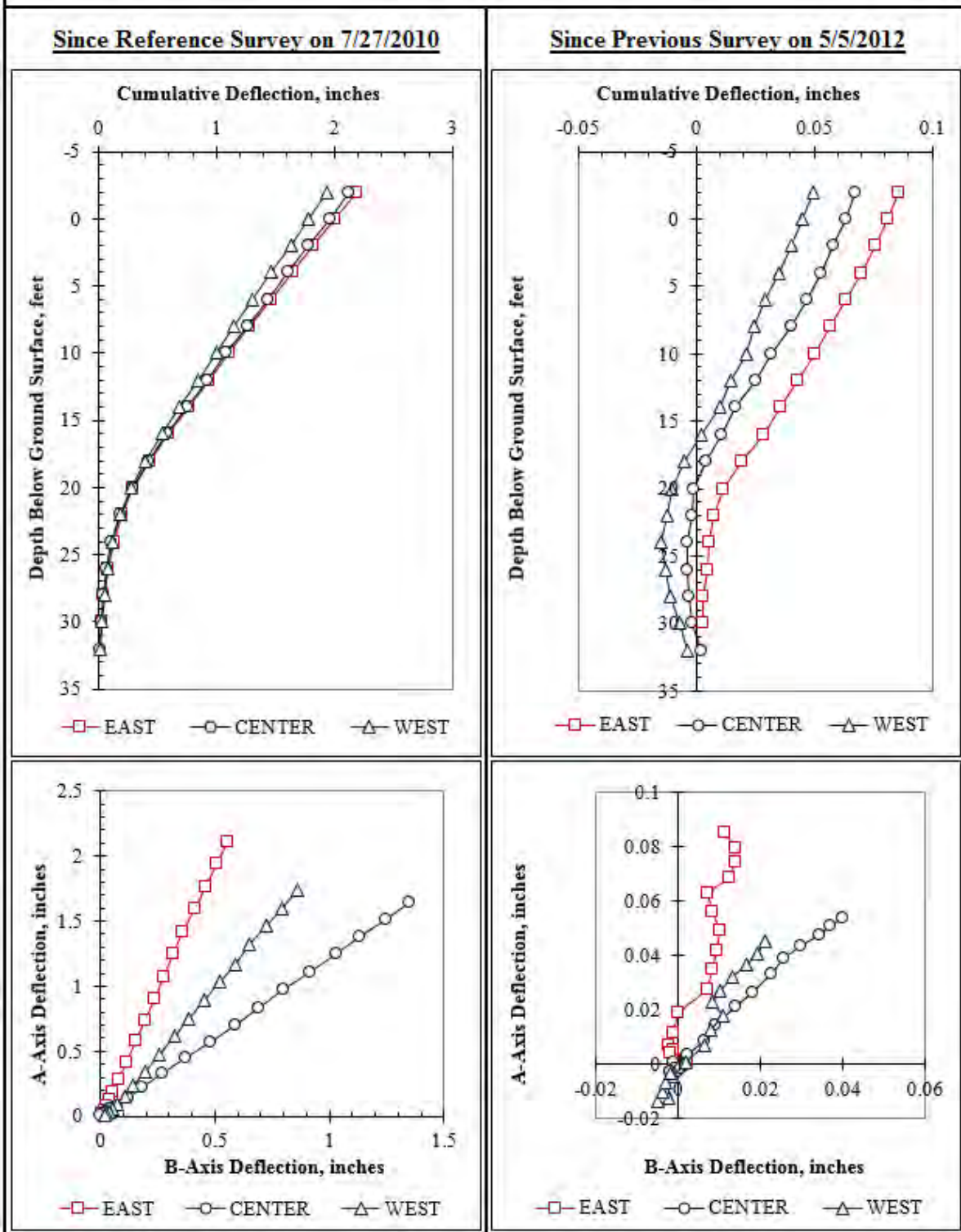


Figure F.75: Summary of inclinometer data from 5/7/2012.

Summary of Inclinator Data From 5/10/2012

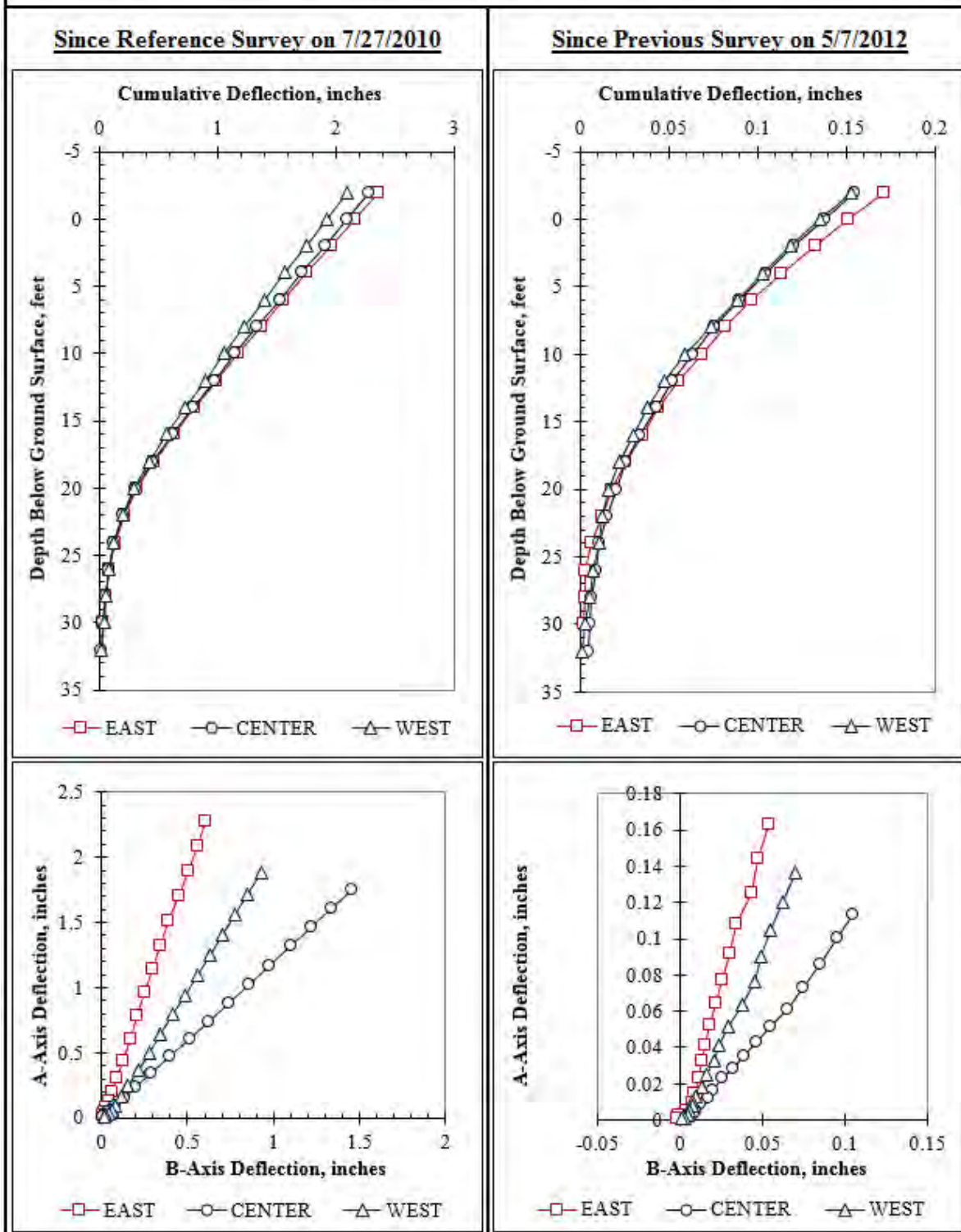


Figure F.76: Summary of inclinometer data from 5/10/2012.

Summary of Inclinometer Data From 5/14/2012

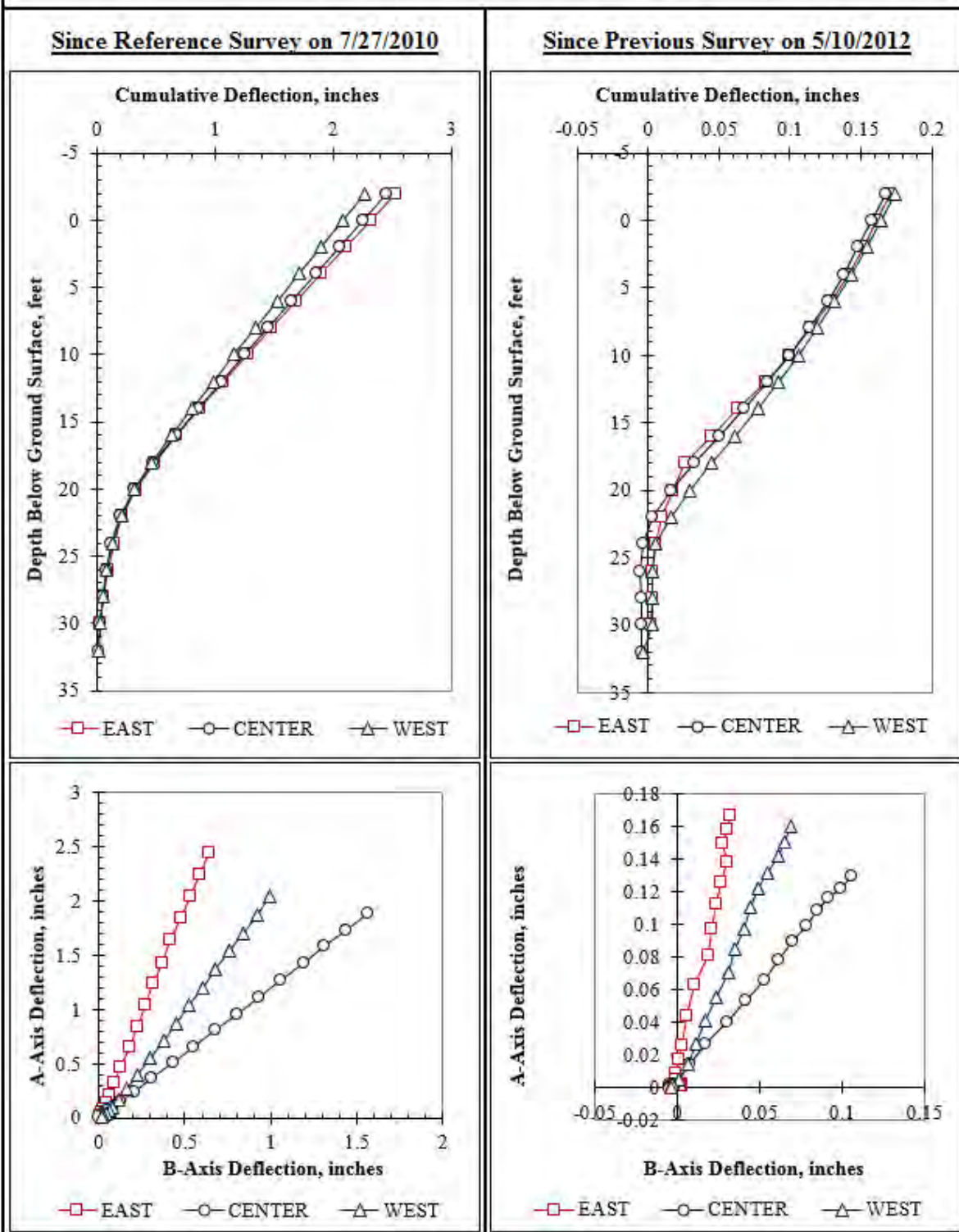


Figure F.77: Summary of inclinometer data from 5/14/2012.

Summary of Inclinometer Data From 5/16/2012

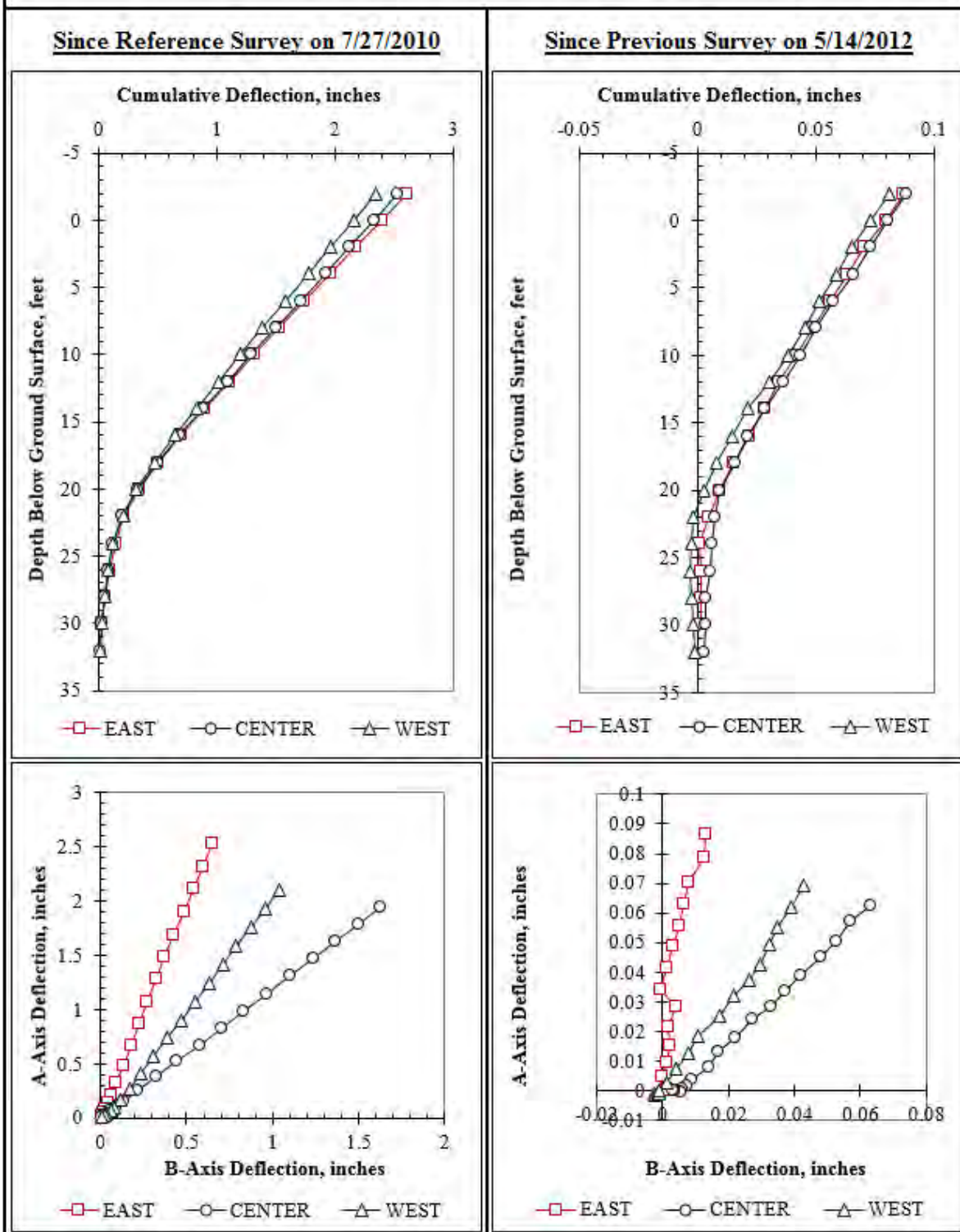


Figure F.78: Summary of inclinometer data from 5/16/2012.

Summary of Inclinometer Data From 5/18/2012

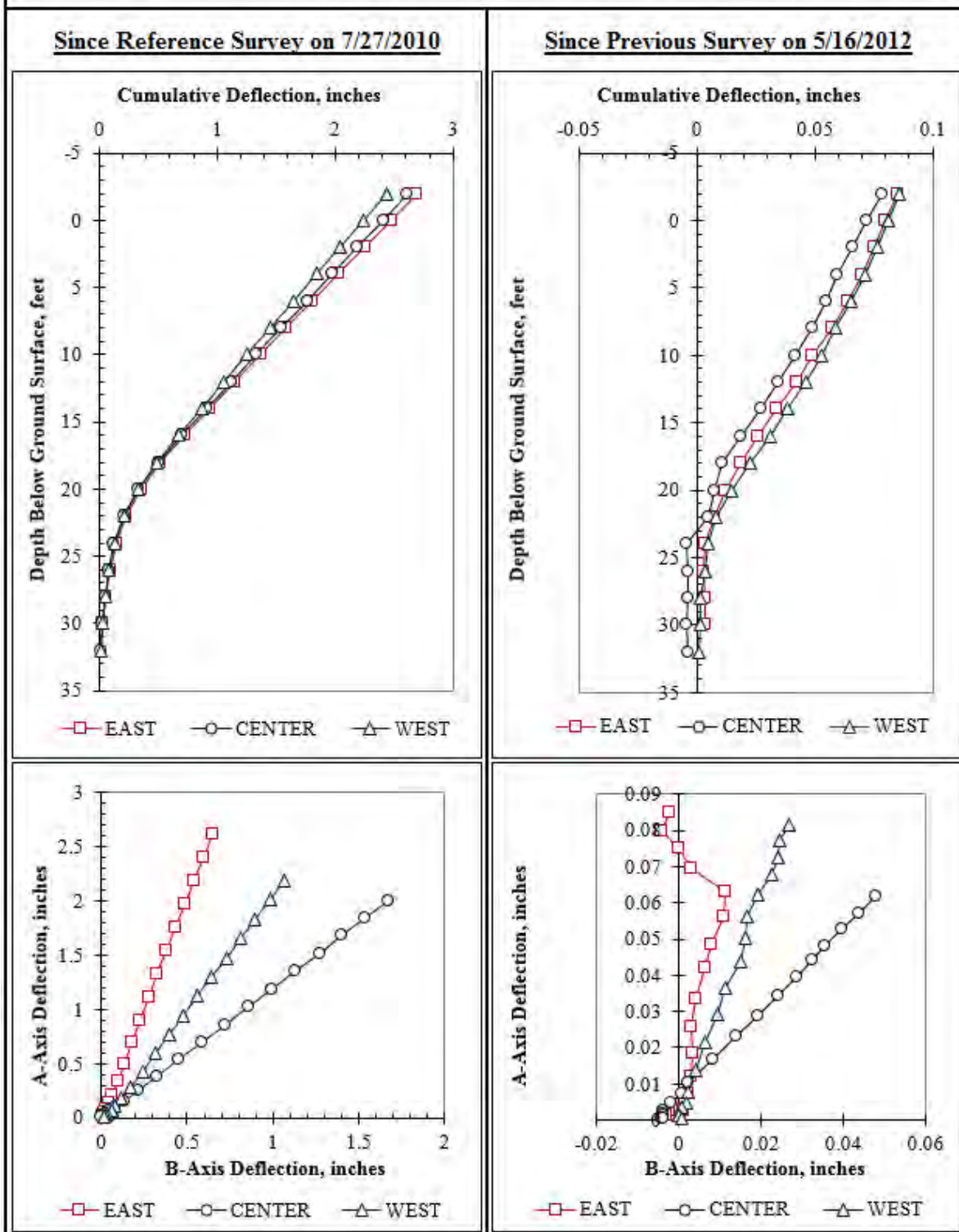


Figure F.79: Summary of inclinometer data from 5/18/2012.

Summary of Inclinometer Data From 5/22/2012

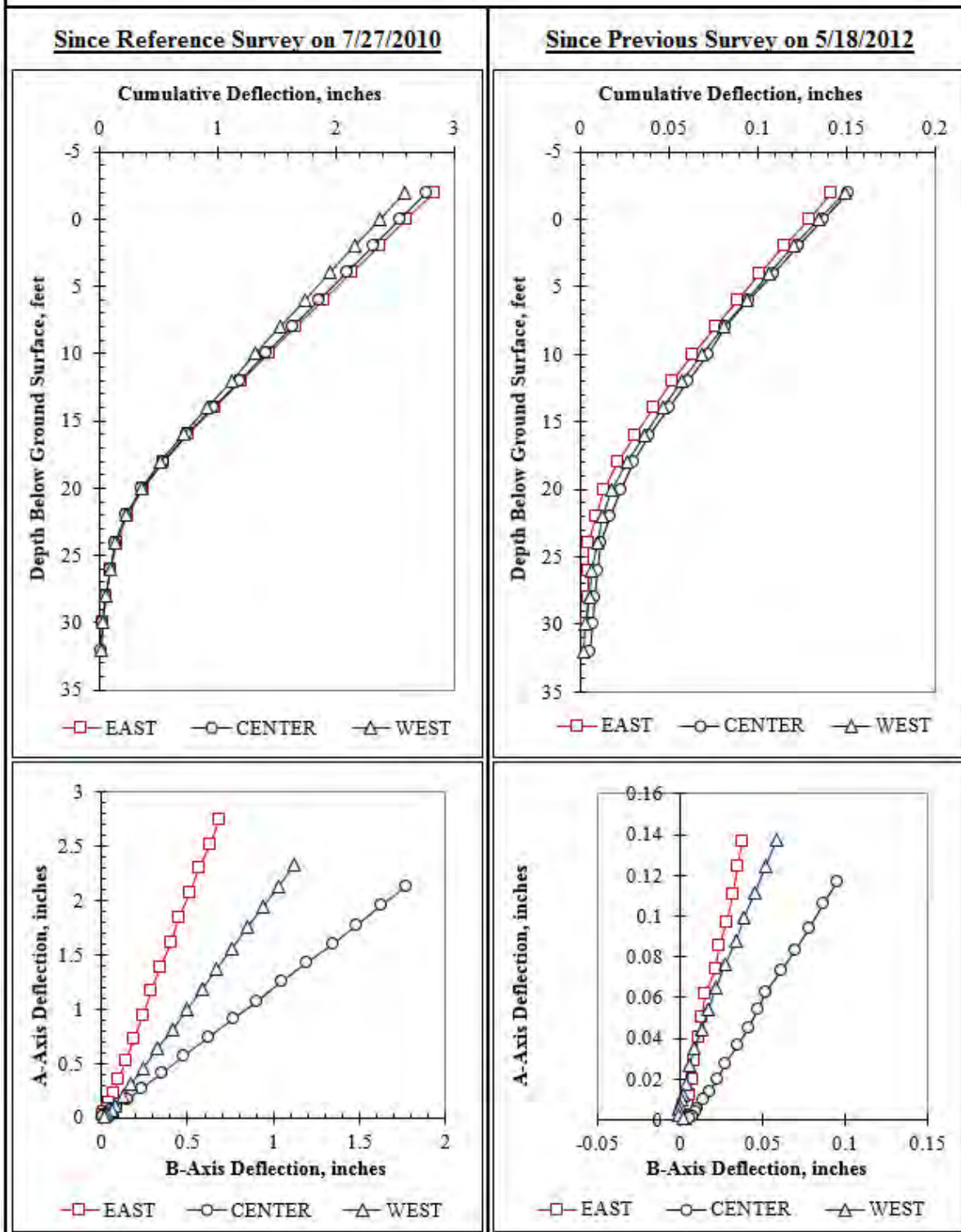


Figure F.80: Summary of inclinometer data from 5/22/2012.

Summary of Inclinometer Data From 5/25/2012

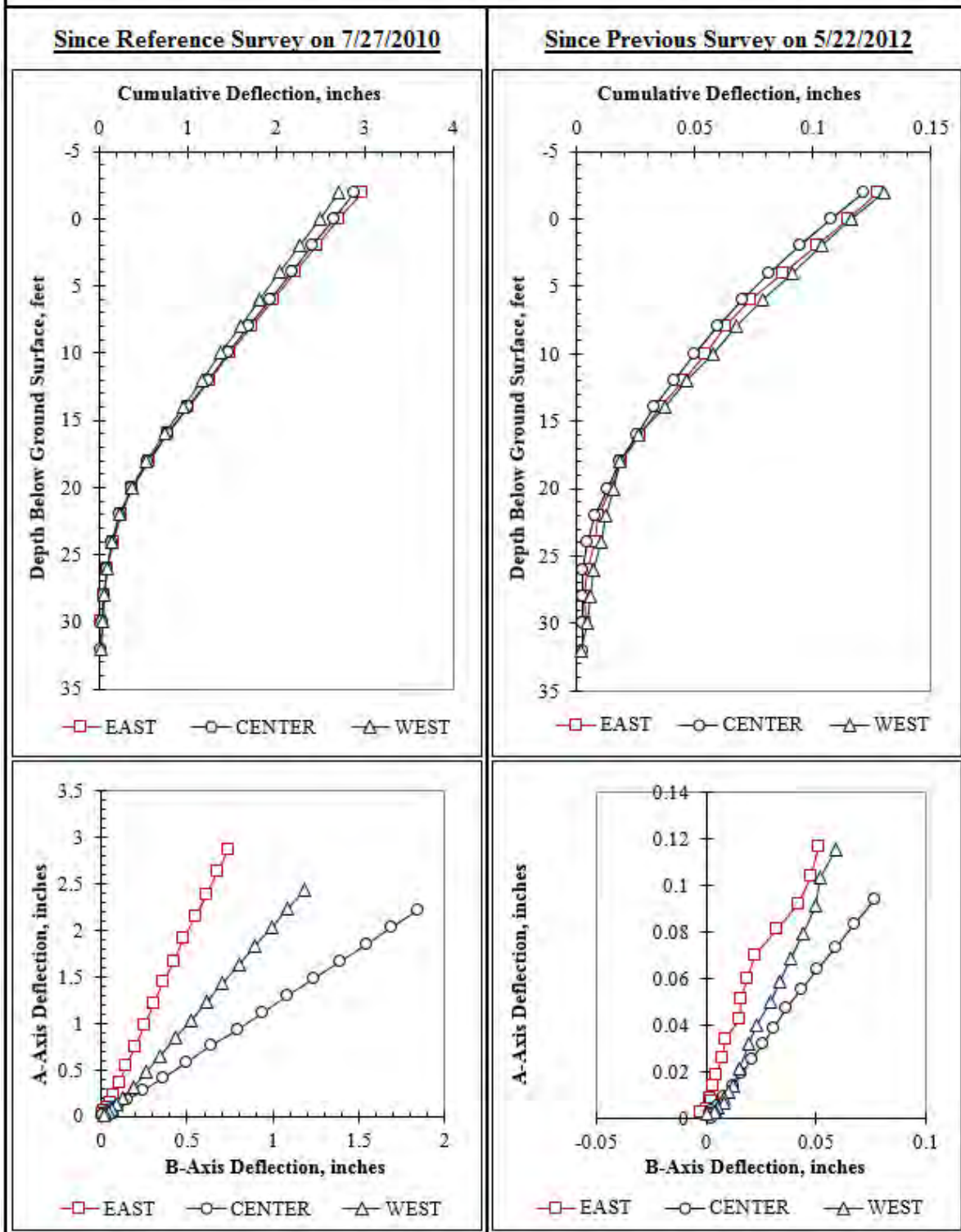


Figure F.81: Summary of inclinometer data from 5/25/2012.

Summary of Inclinometer Data From 5/30/2012

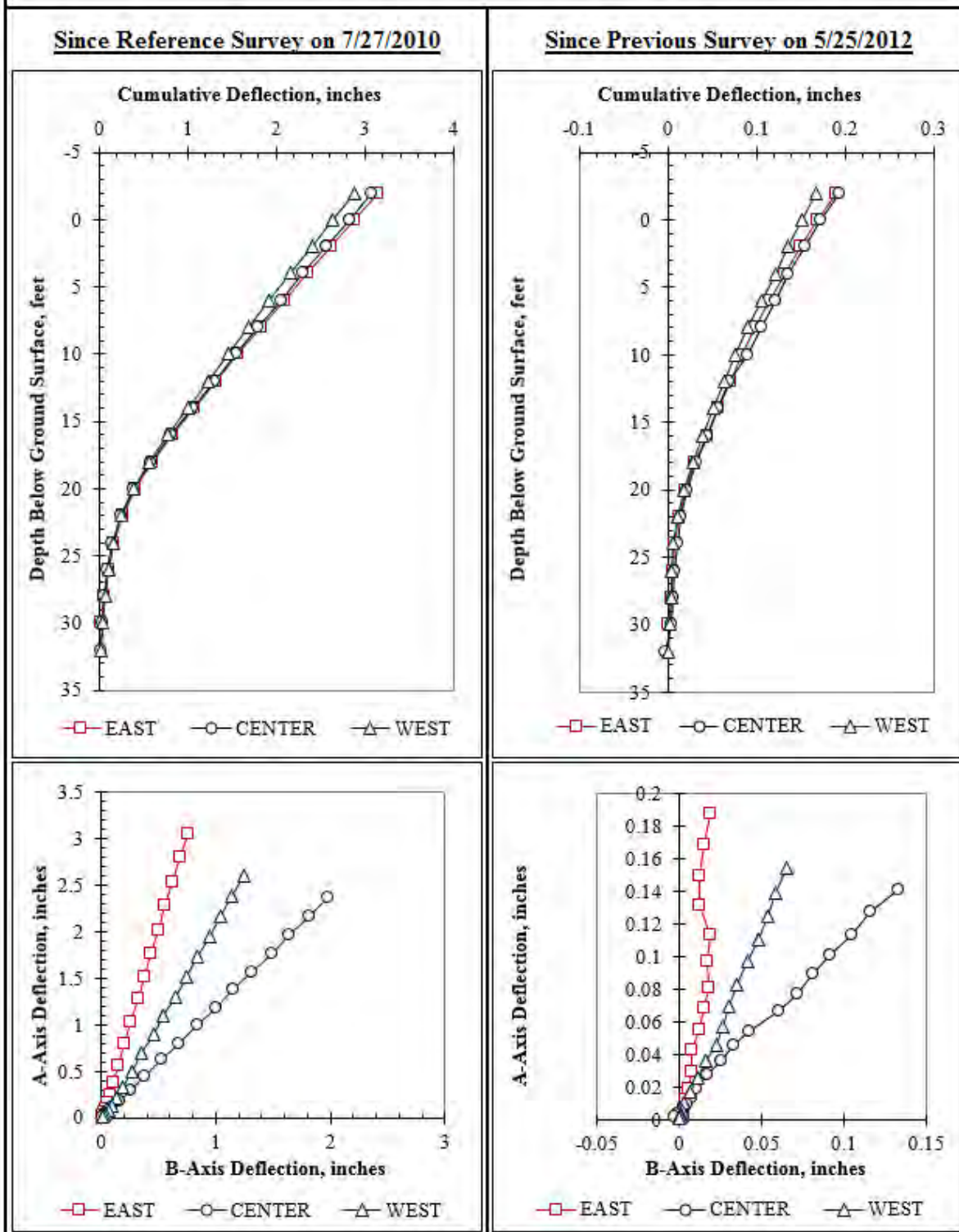


Figure F.82: Summary of inclinometer data from 5/30/2012.

Summary of Inclinometer Data From 6/4/2012

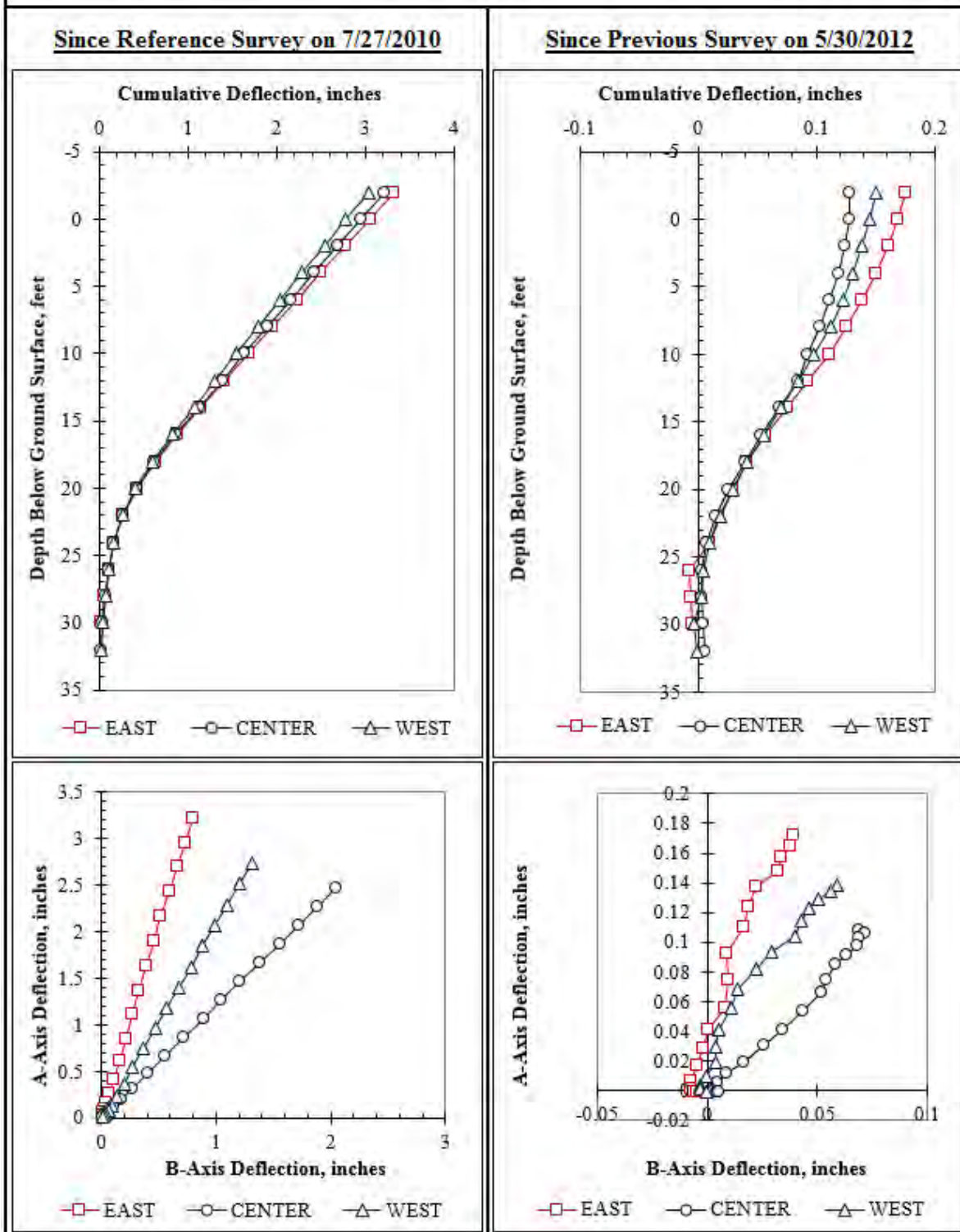


Figure F.83: Summary of inclinometer data from 6/4/2012.

Summary of Inclinometer Data From 6/7/2012

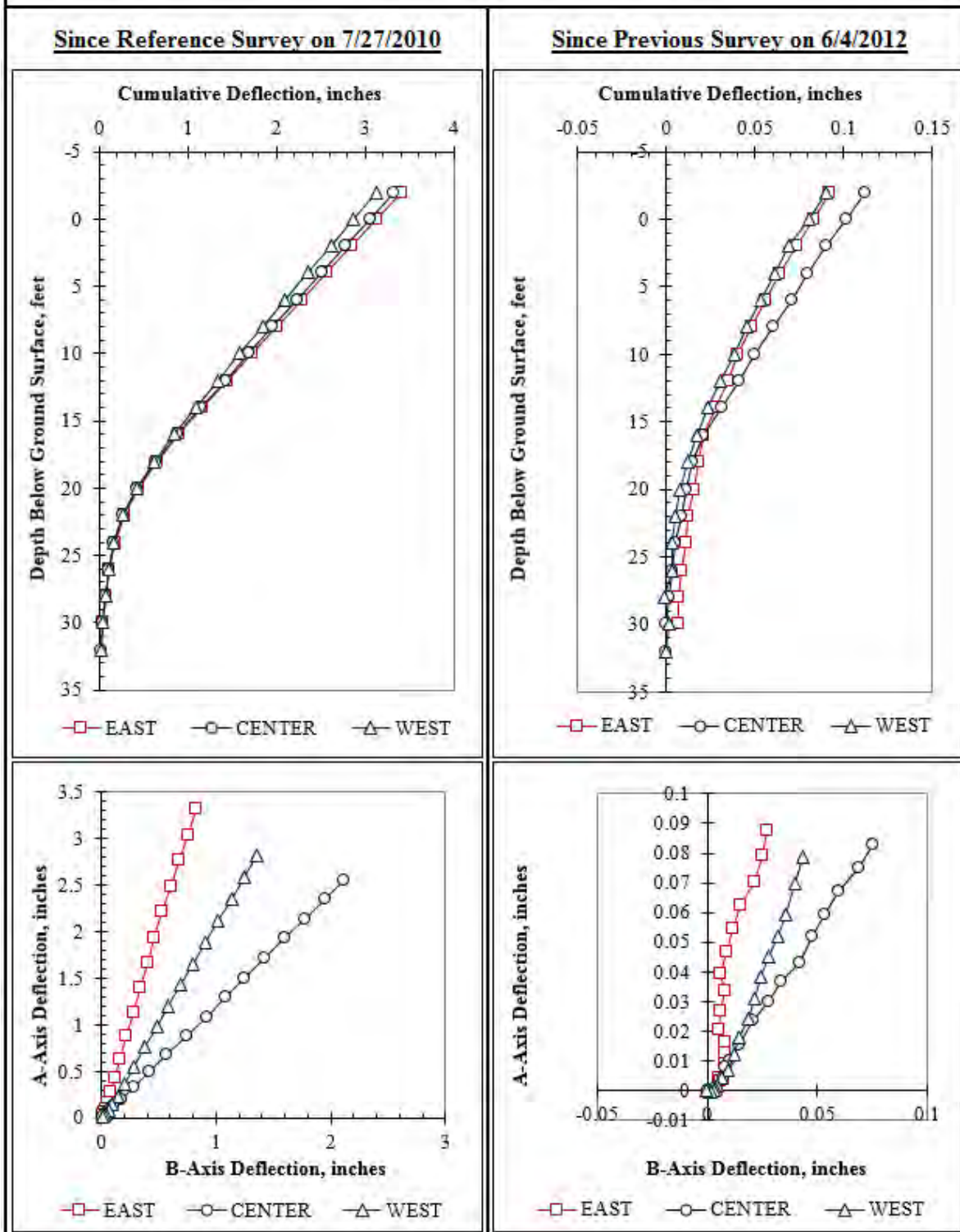


Figure F.84: Summary of inclinometer data from 6/7/2012.

Summary of Inclinometer Data From 6/12/2012

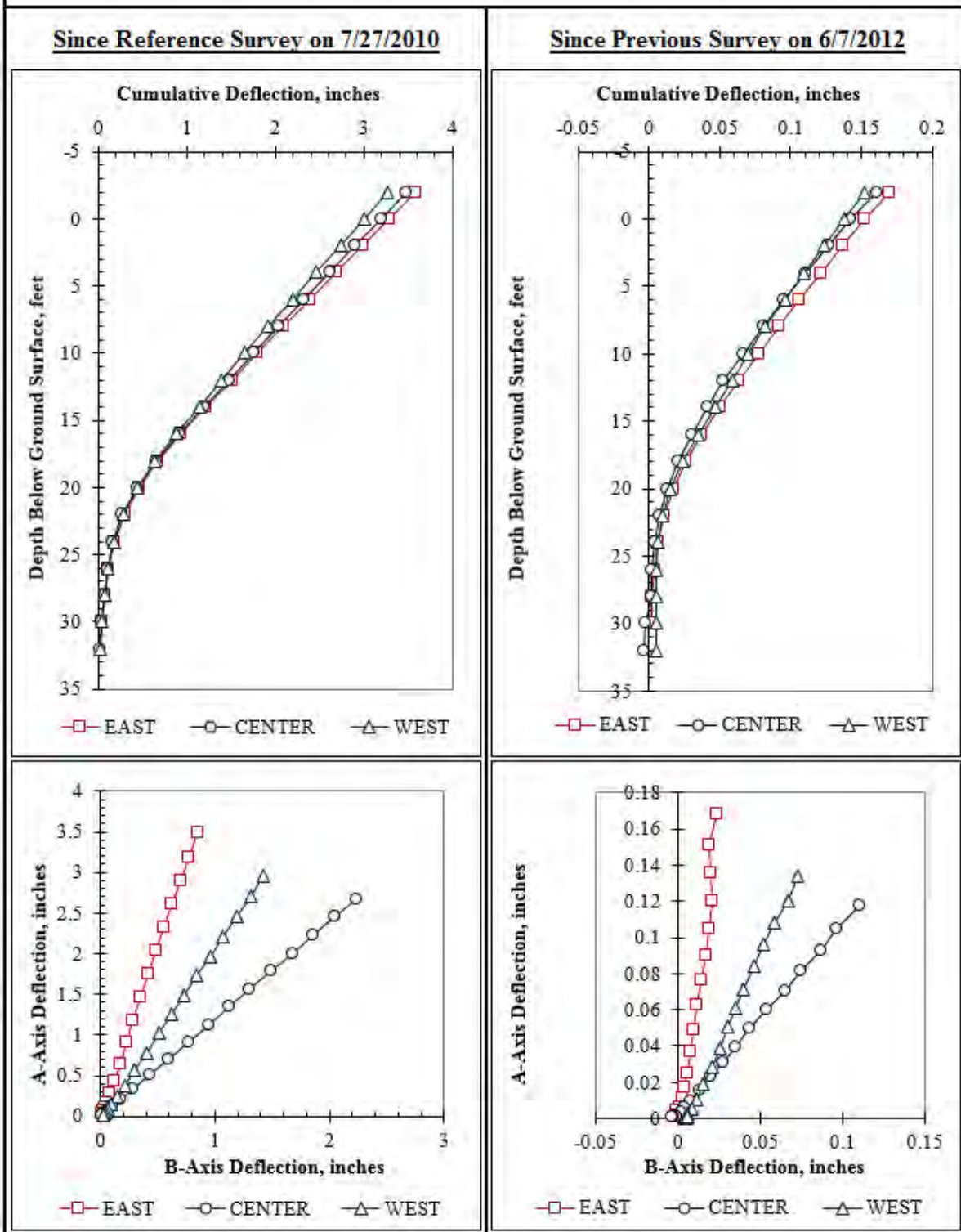


Figure F.85: Summary of inclinometer data from 6/12/2012.

Summary of Inclinometer Data From 6/15/2012

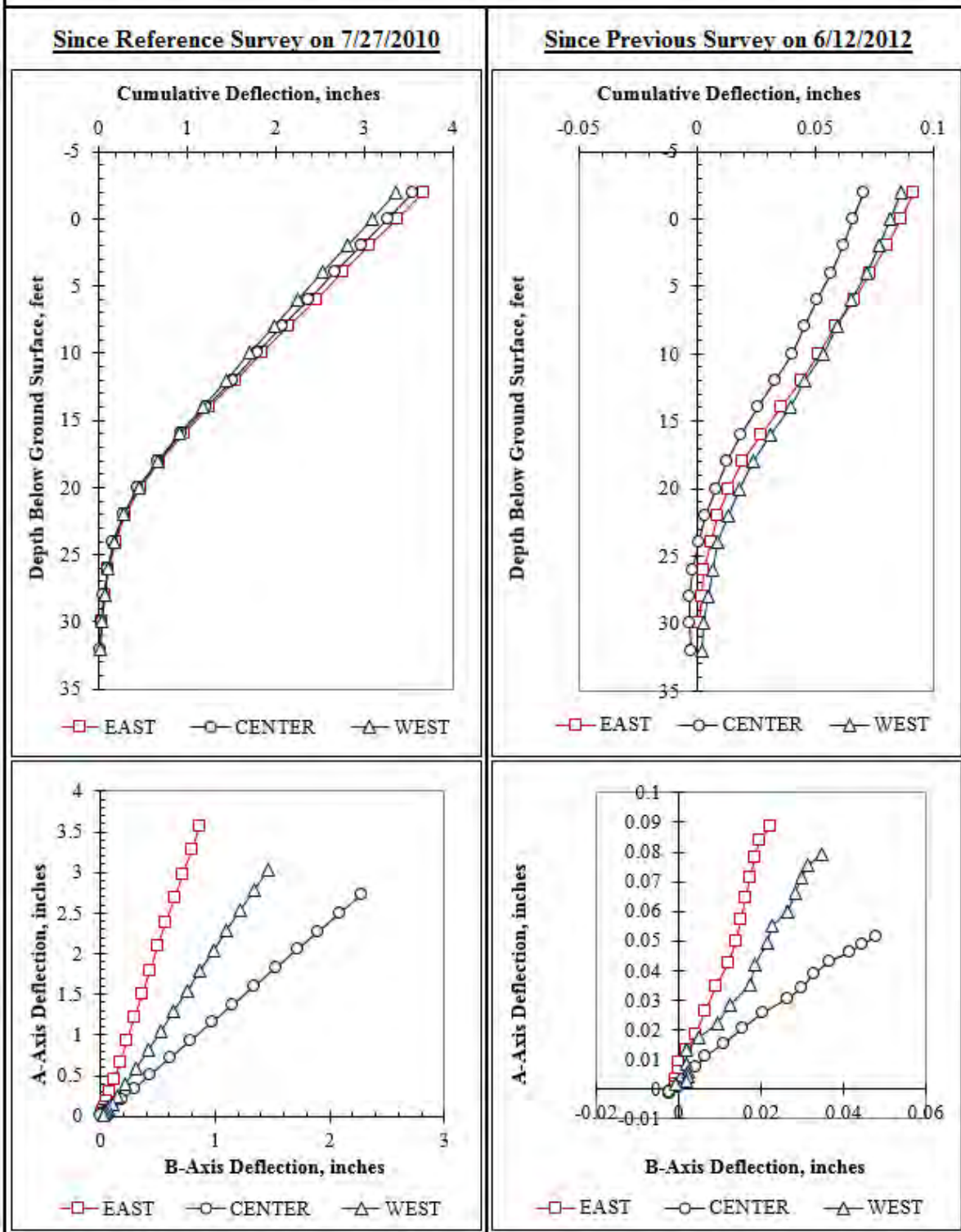


Figure F.86: Summary of inclinometer data from 6/15/2012.

Summary of Inclinometer Data From 6/18/2012

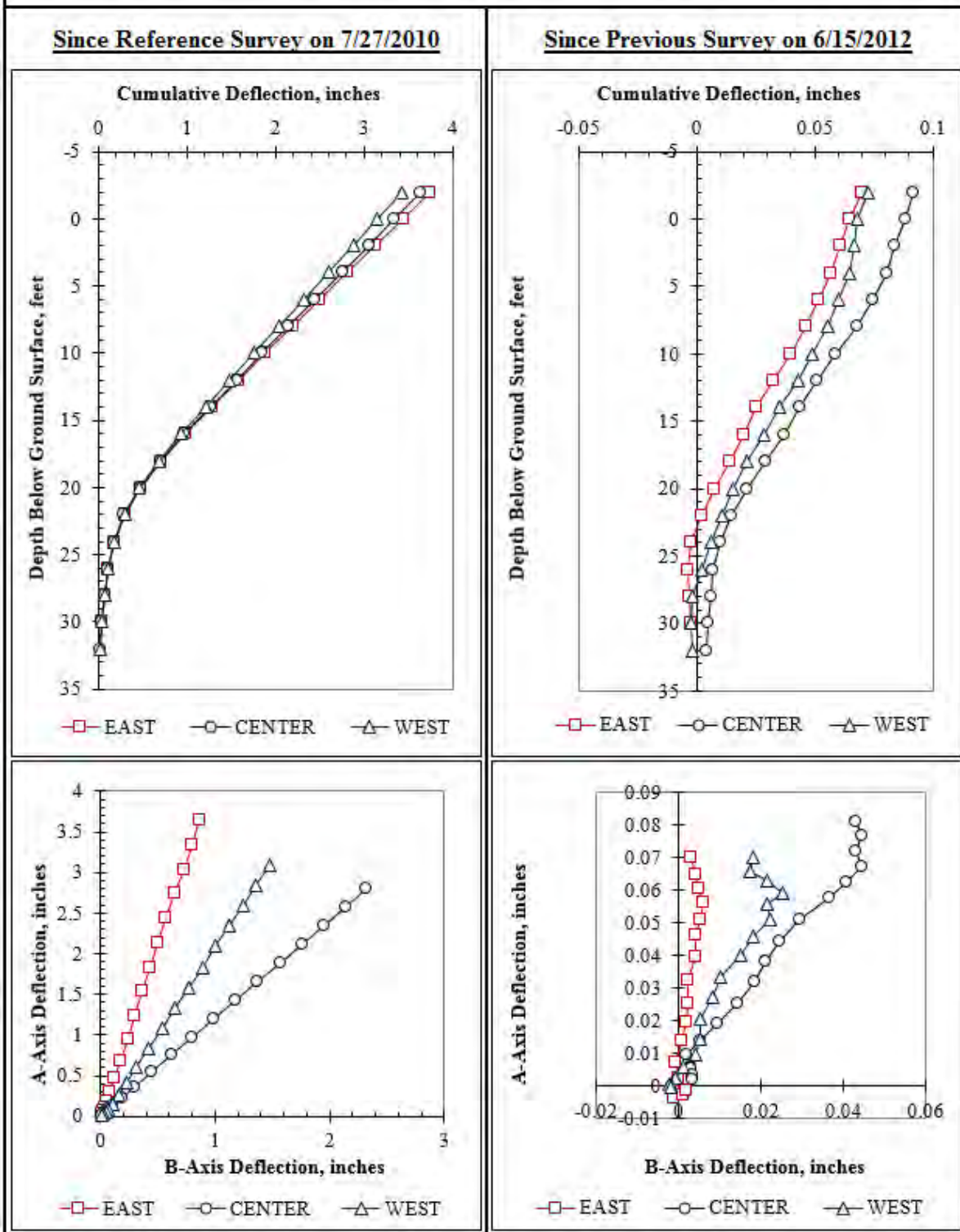


Figure F.87: Summary of inclinometer data from 6/18/2012.

Summary of Inclinometer Data From 6/22/2012

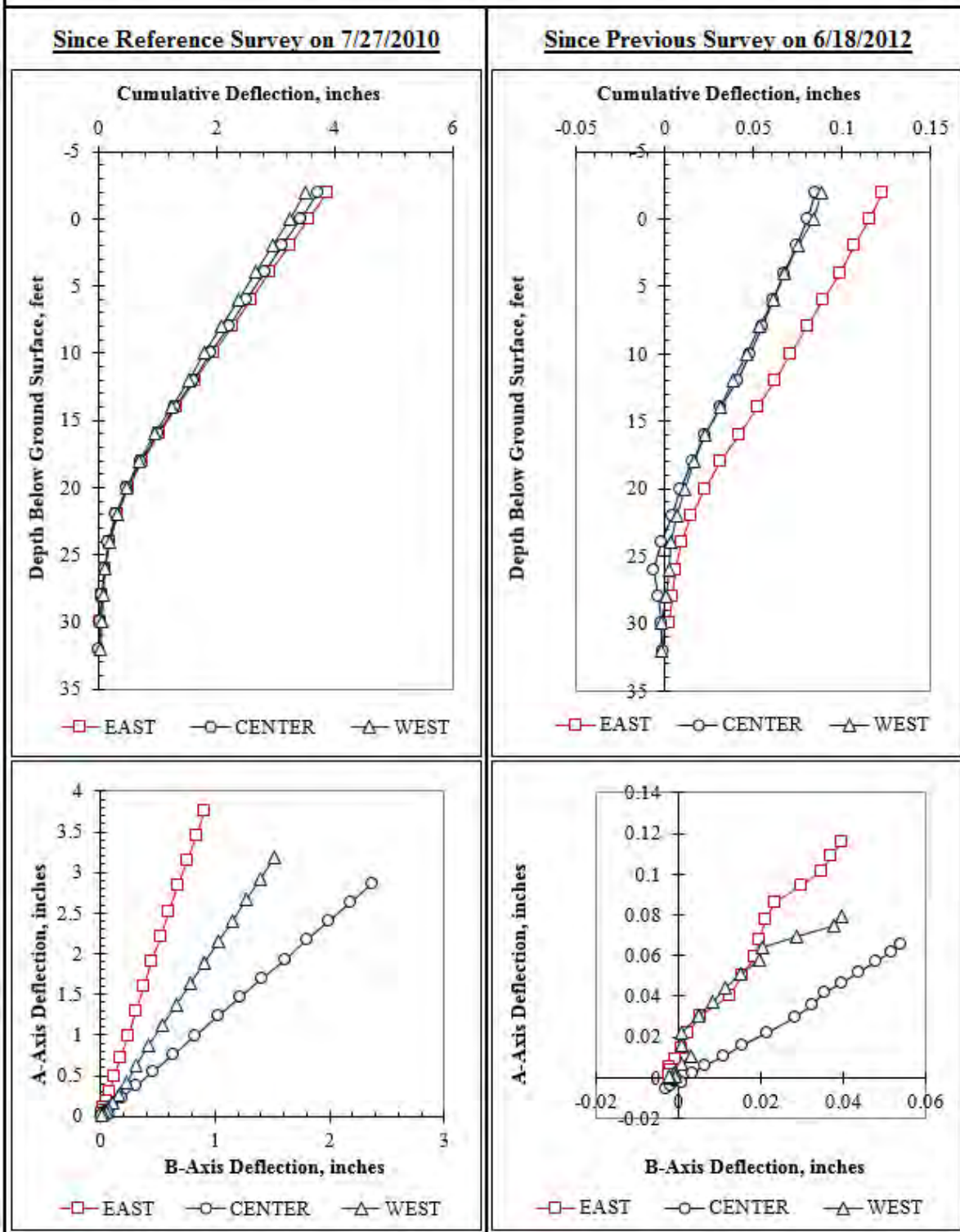


Figure F.88: Summary of inclinometer data from 6/22/2012.

Summary of Inclinometer Data From 6/27/2012

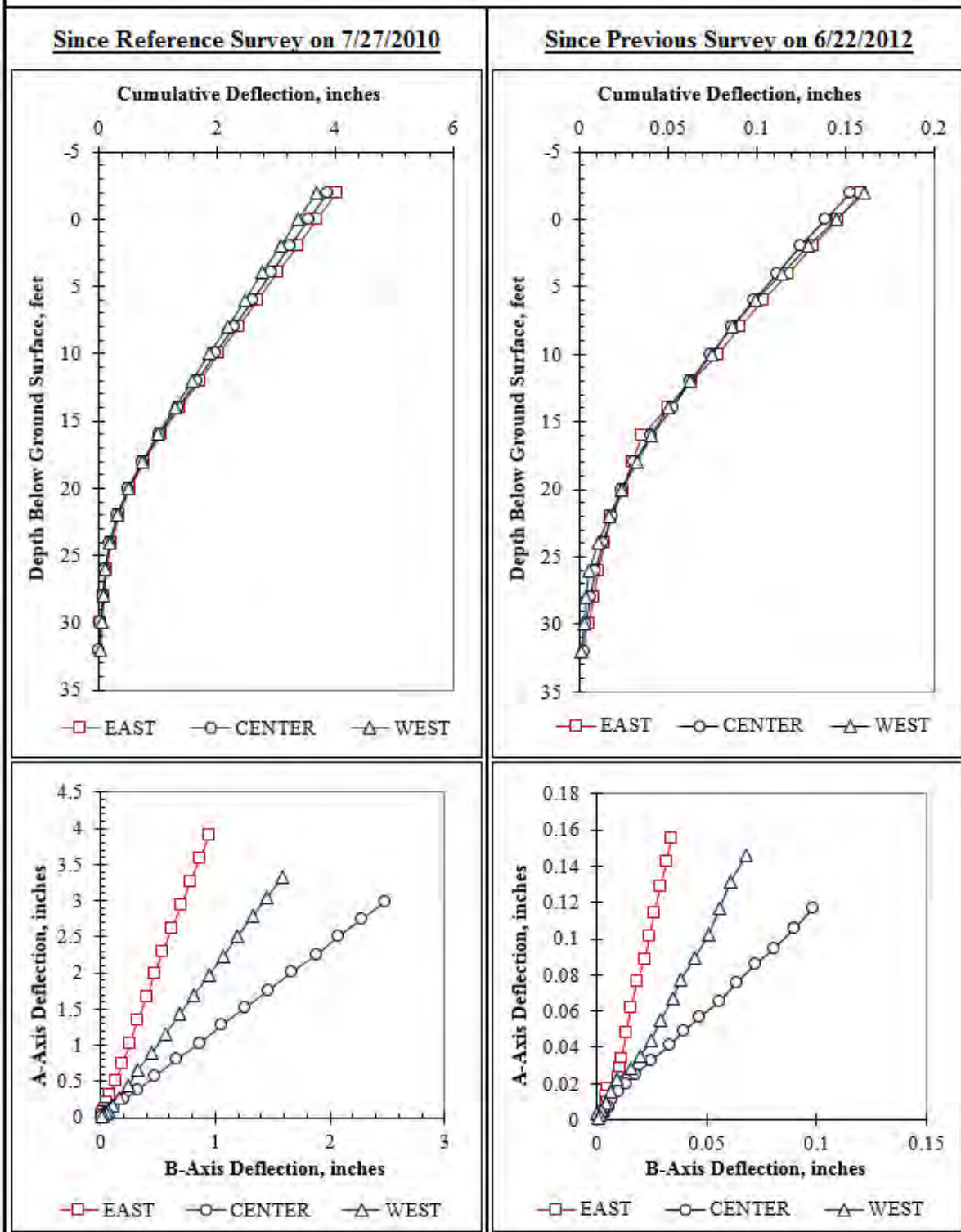


Figure F.89: Summary of inclinometer data from 6/27/2012.

Summary of Inclinometer Data From 7/2/2012

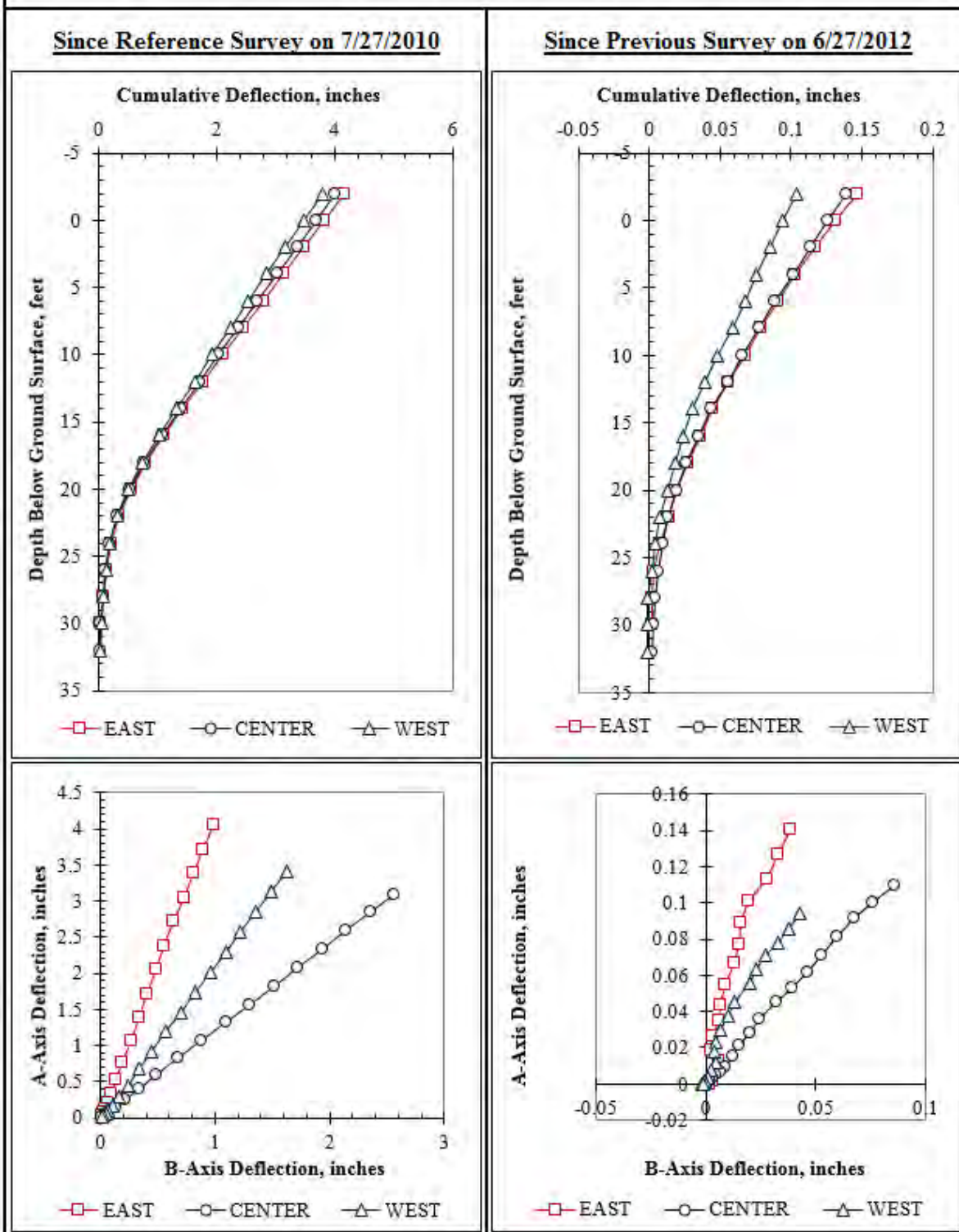


Figure F.90: Summary of inclinometer data from 7/2/2012.

Summary of Inclinometer Data From 7/3/2012

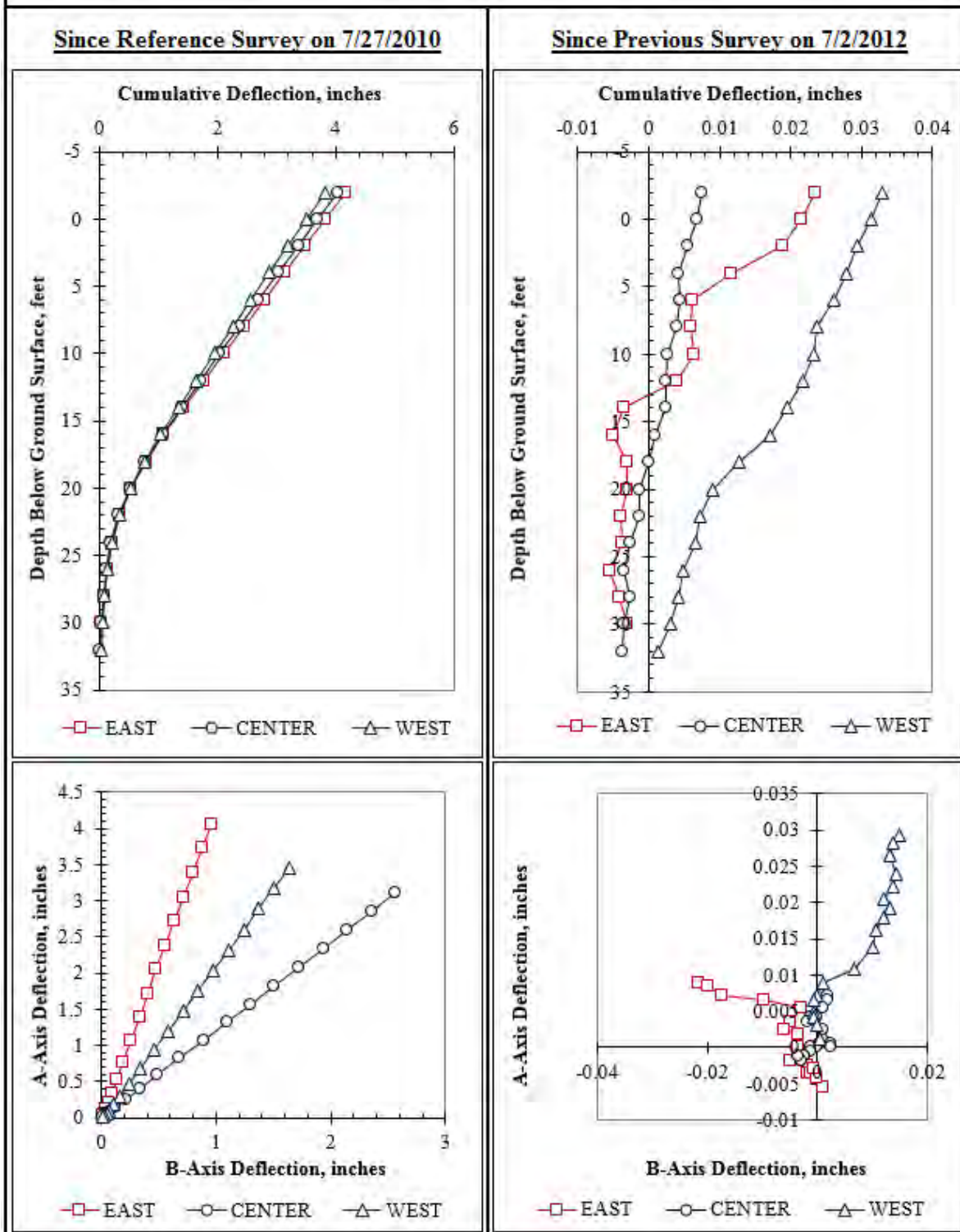


Figure F.91: Summary of inclinometer data from 7/3/2012.

Summary of Inclinometer Data From 7/5/2012

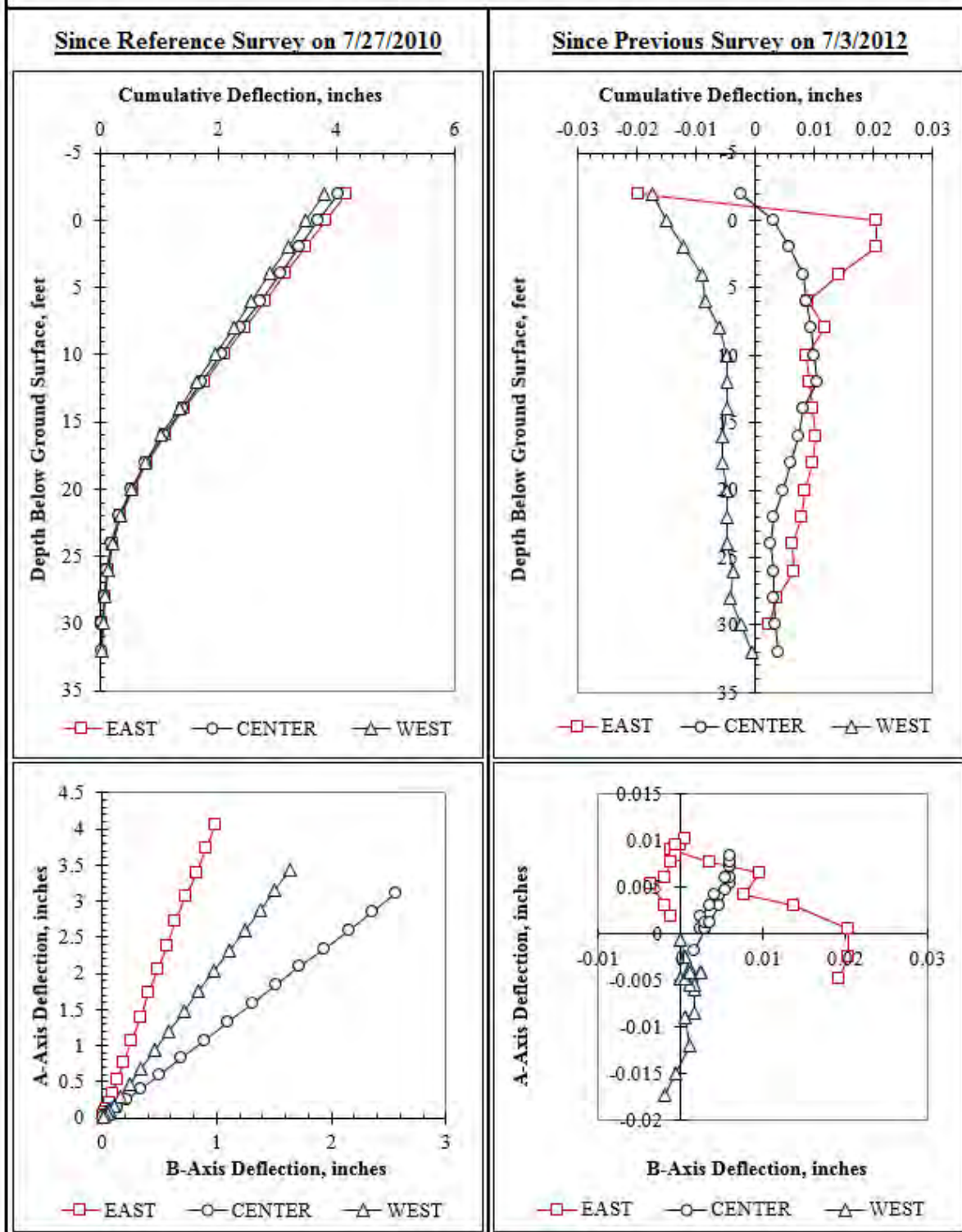


Figure F.92: Summary of inclinometer data from 7/5/2012.

Summary of Inclinometer Data From 7/10/2012

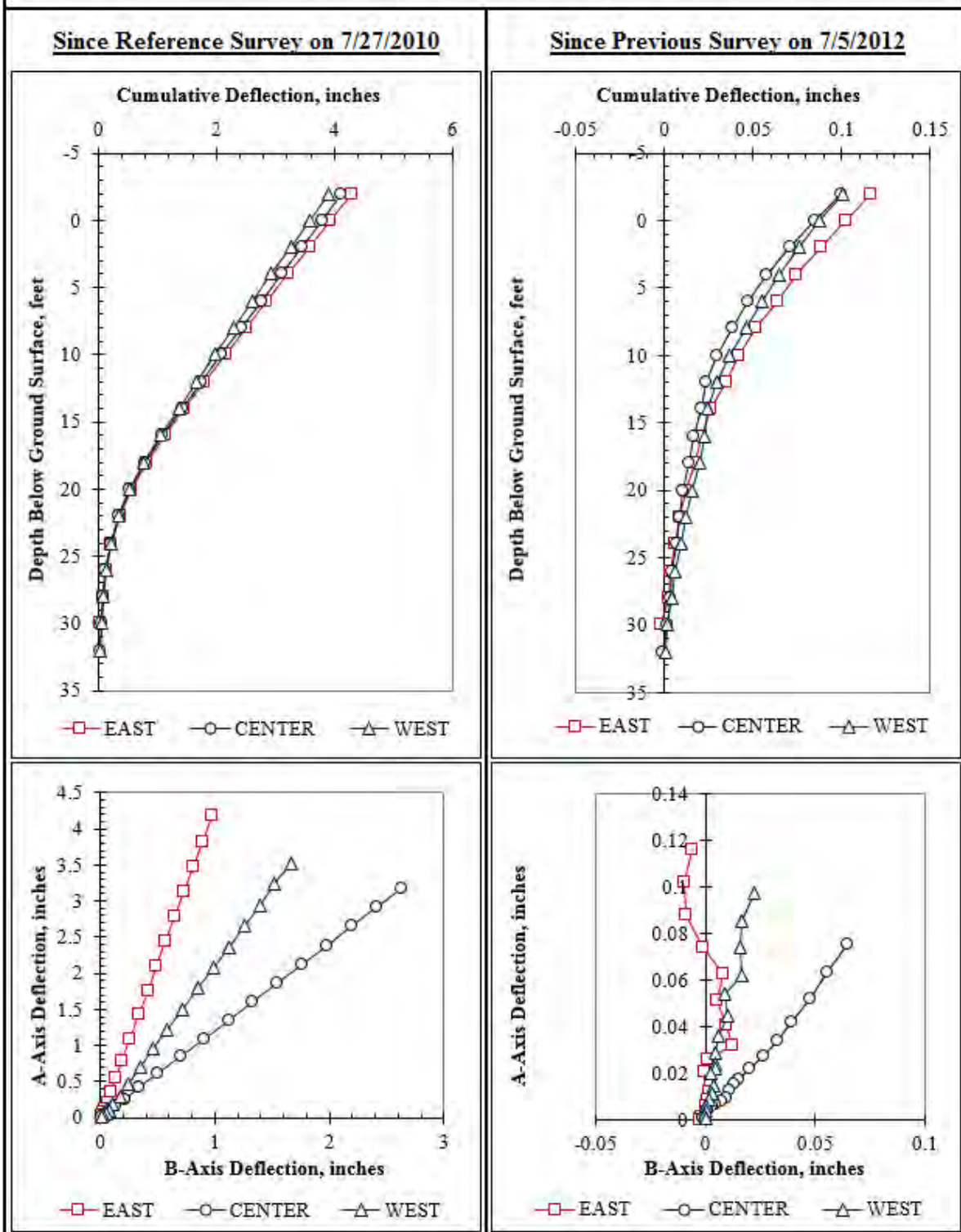


Figure F.93: Summary of inclinometer data from 7/10/2012.

Summary of Inclinometer Data From 7/16/2012

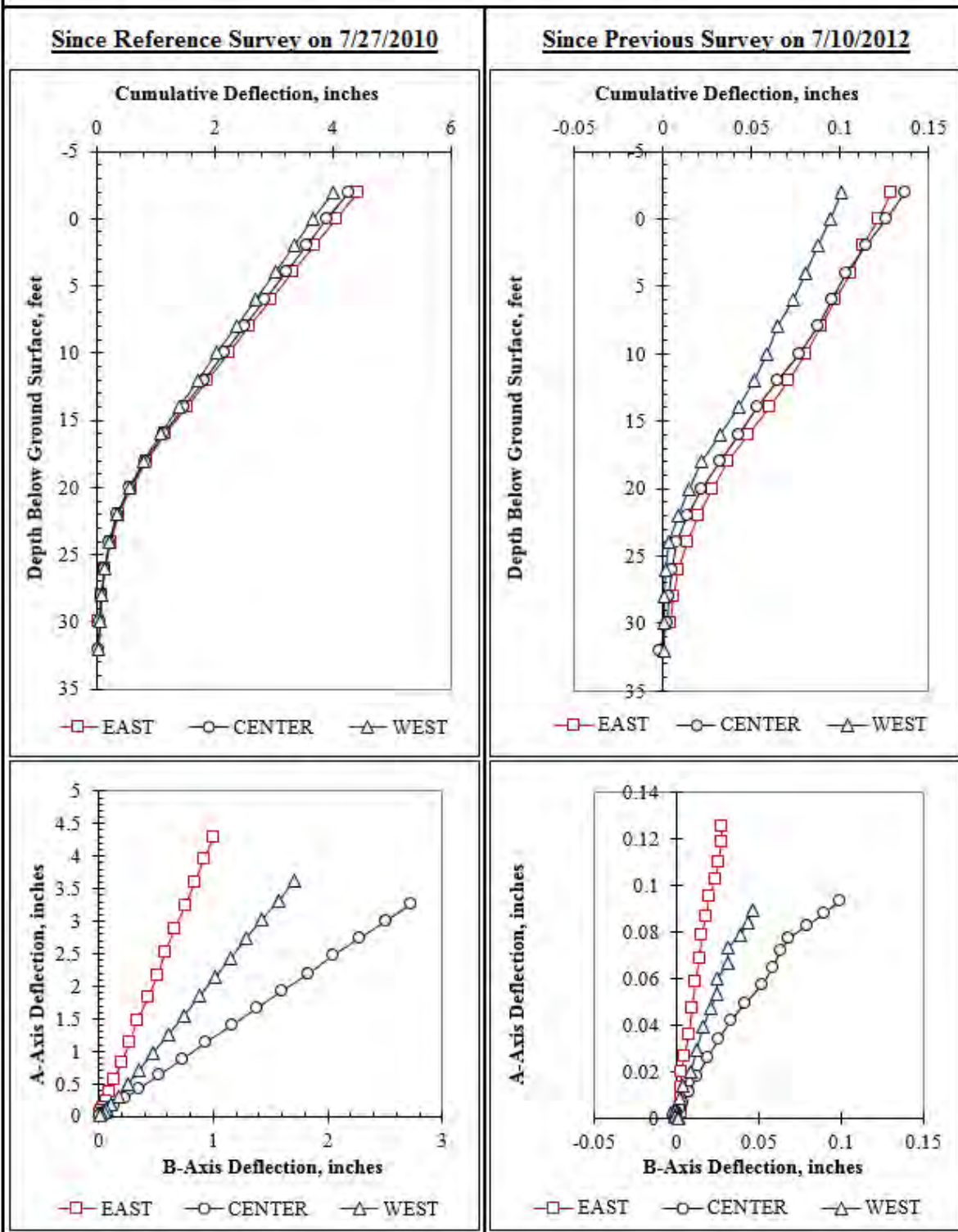


Figure F.94: Summary of inclinometer data from 7/16/2012.

Summary of Inclinometer Data From 7/26/2012

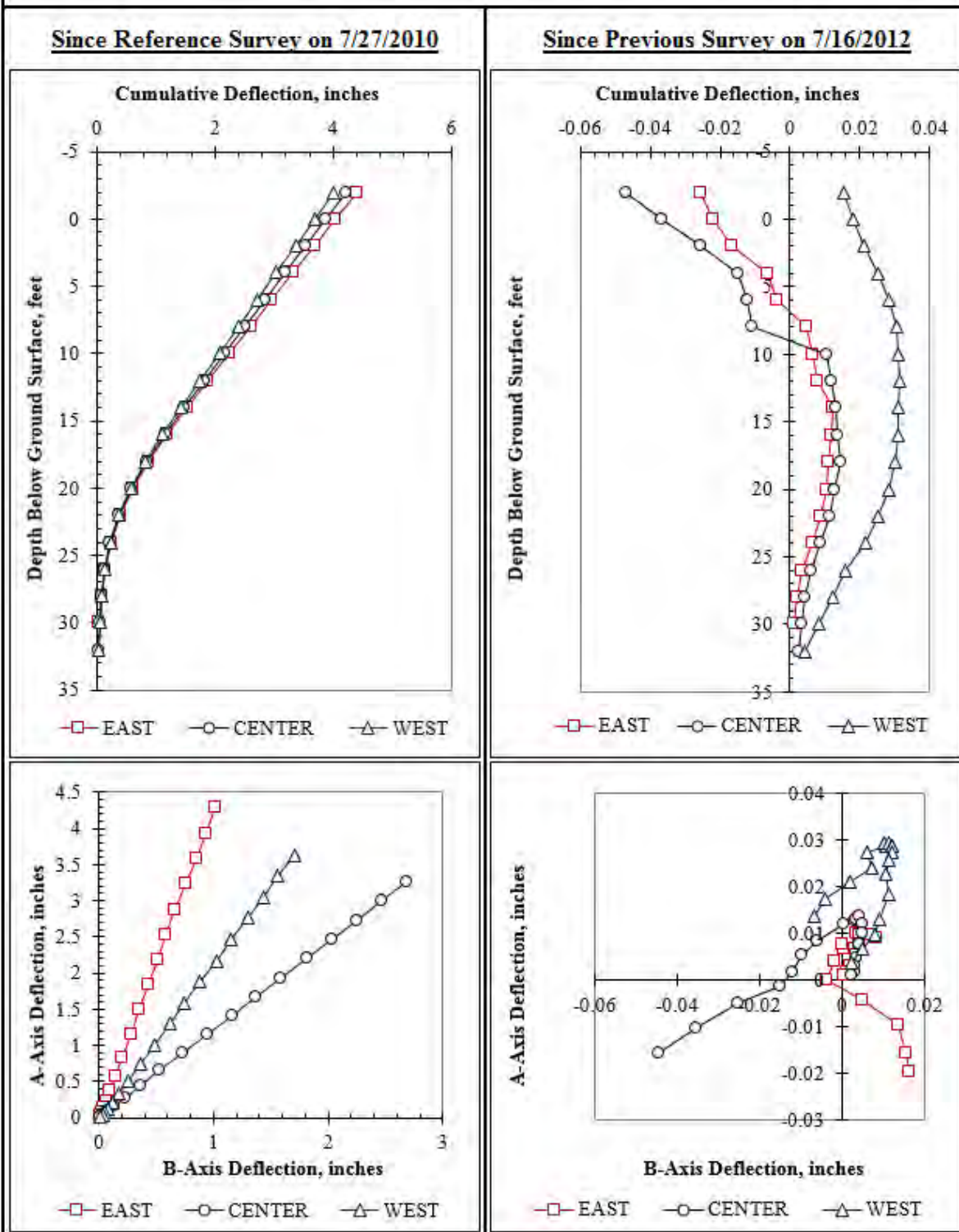


Figure F.95: Summary of inclinometer data from 7/26/2012.

Summary of Inclinometer Data From 8/9/2012

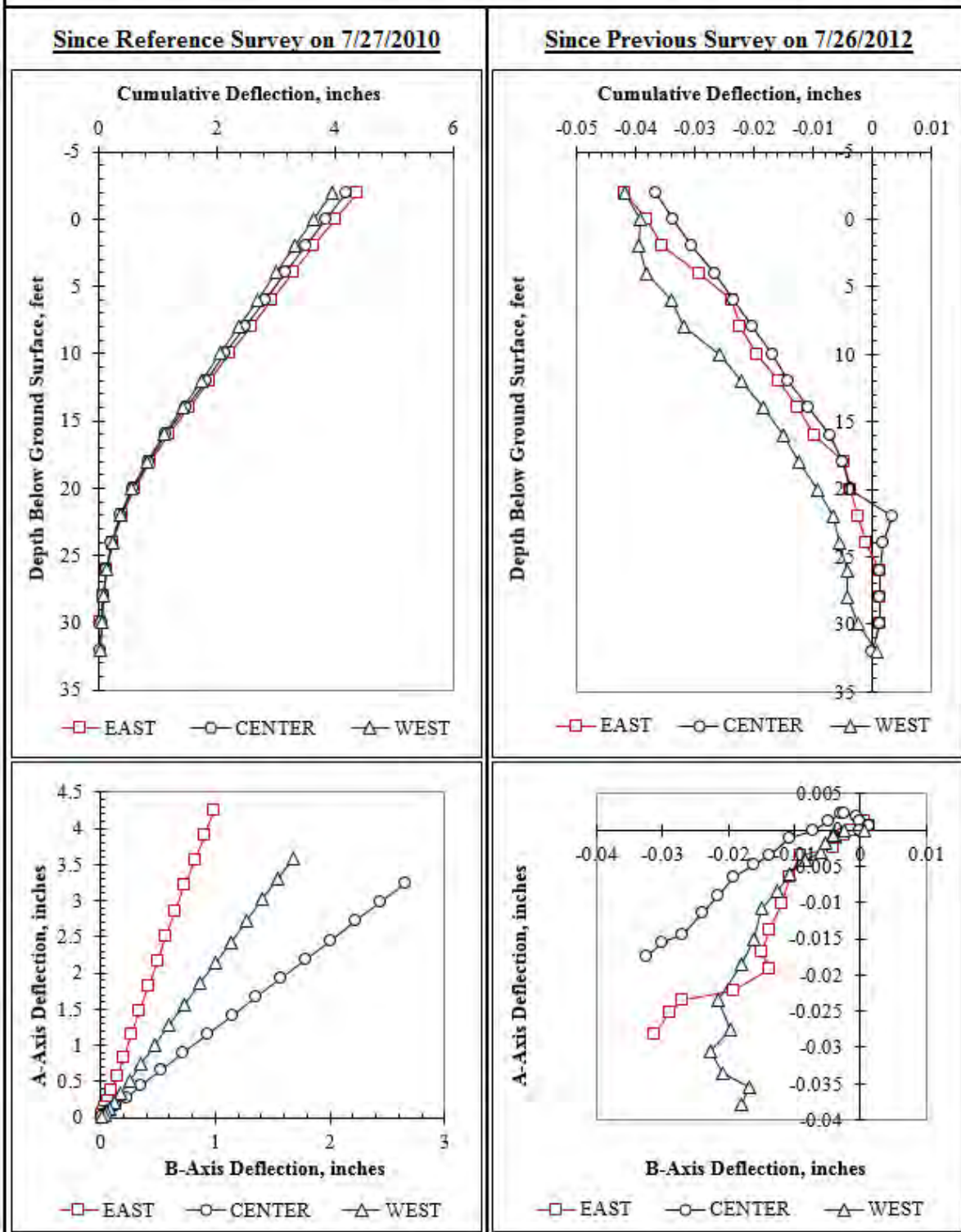


Figure F.96: Summary of inclinometer data from 8/9/2012.

Summary of Inclinometer Data From 8/28/2012

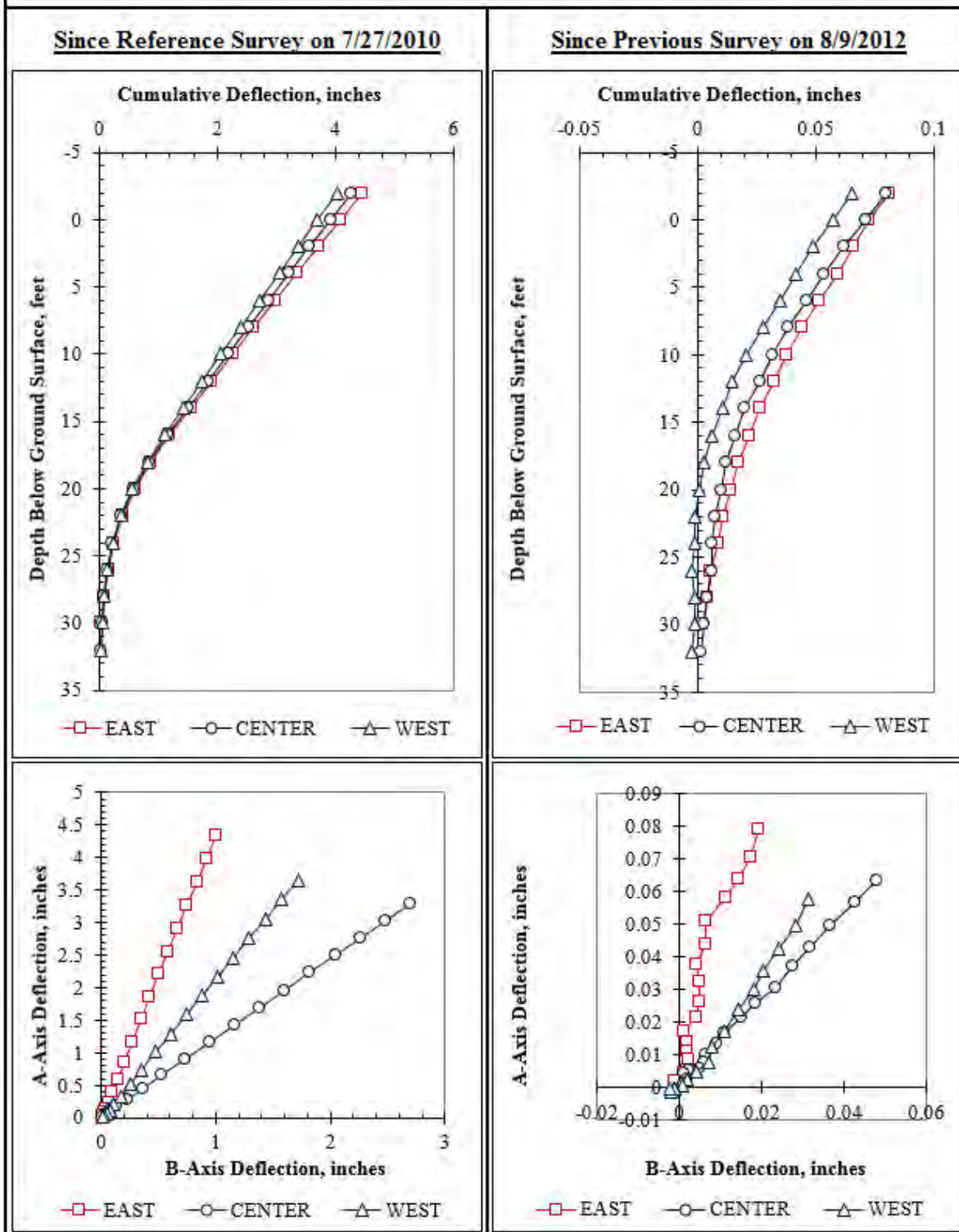


Figure F.97: Summary of inclinometer data from 8/28/2012.

Summary of Inclinometer Data From 9/17/2012

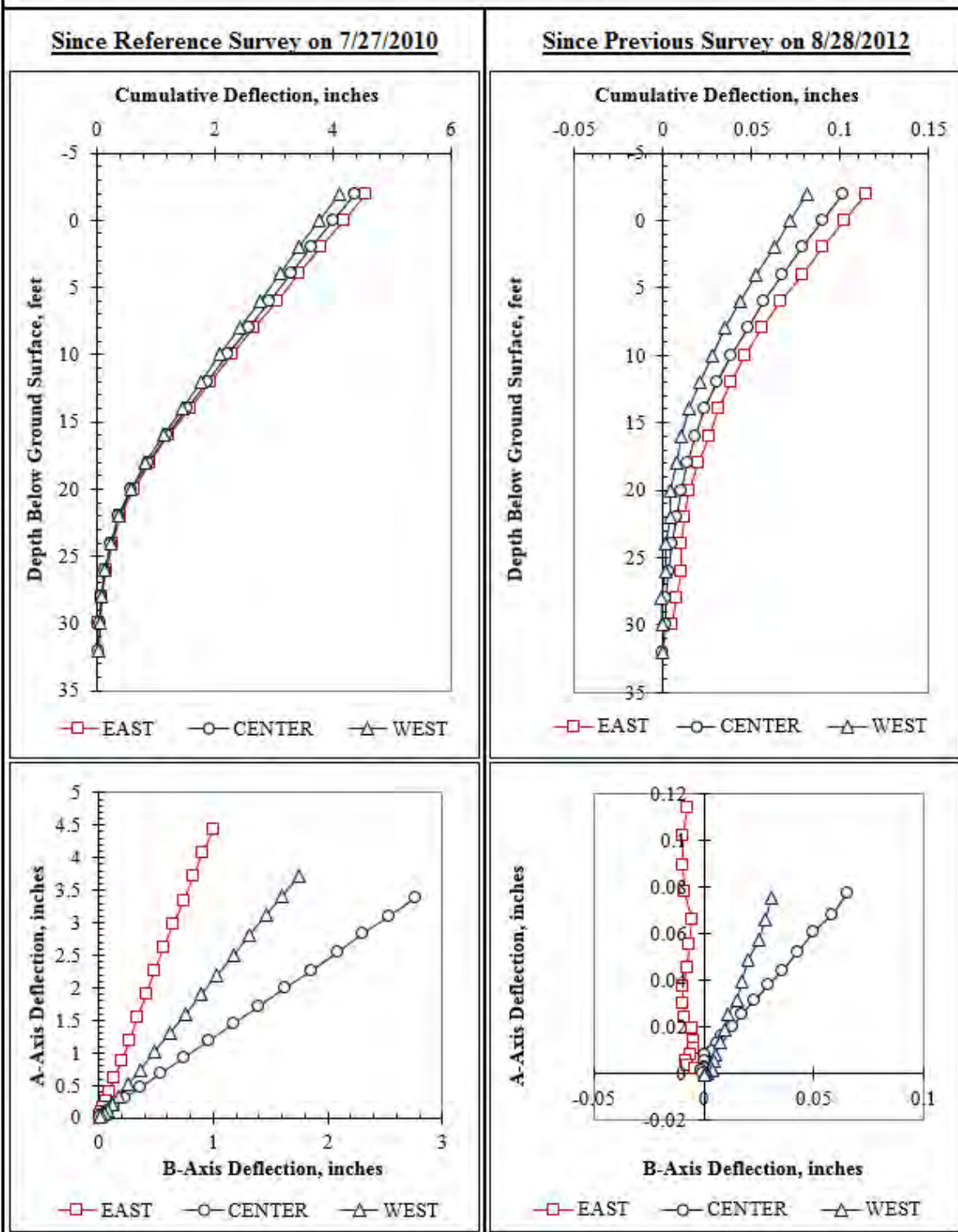


Figure F.98: Summary of inclinometer data from 9/17/2012.

Summary of Inclinometer Data From 10/3/2012

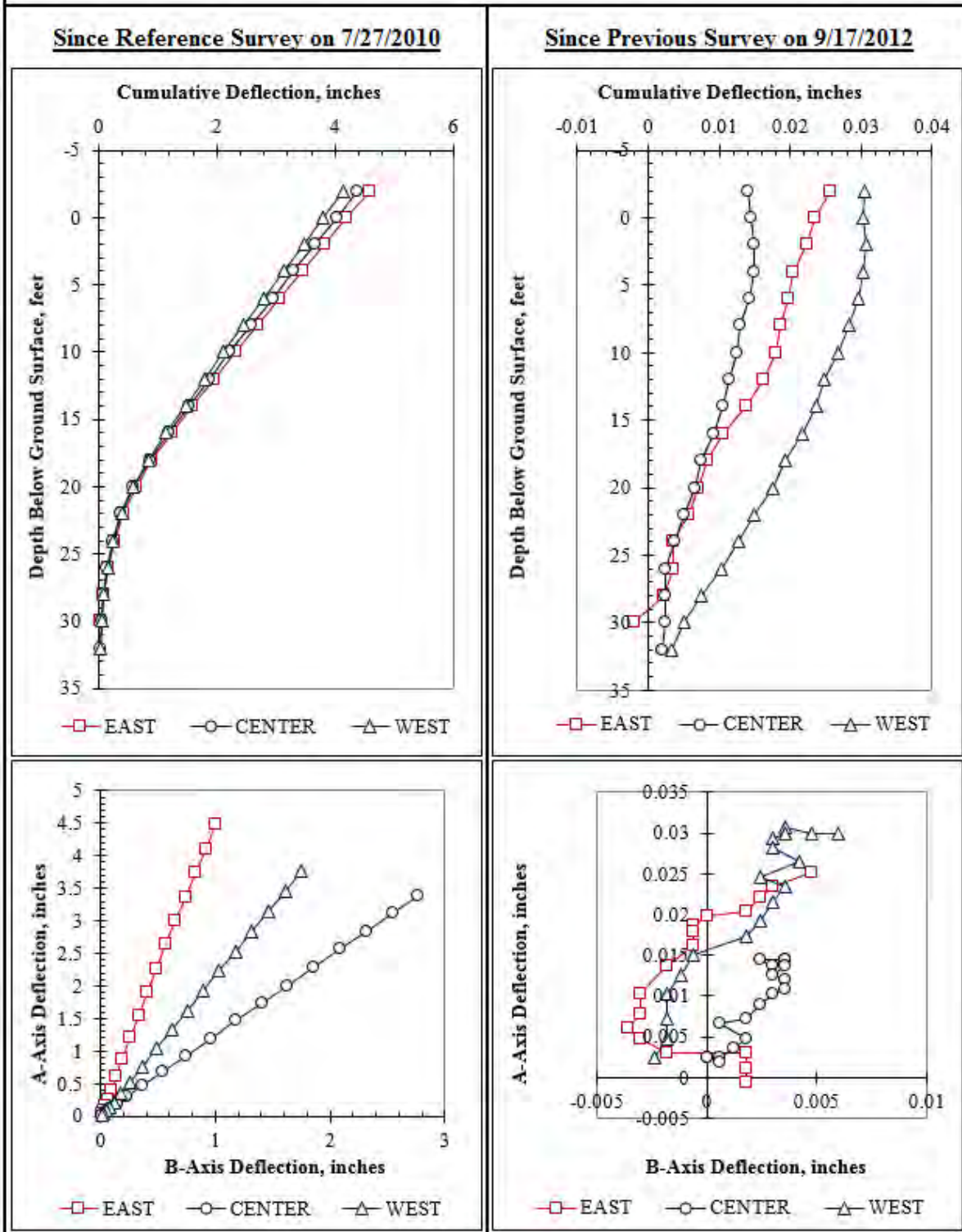


Figure F.99: Summary of inclinometer data from 10/3/2012.

Summary of Inclinometer Data From 10/26/2012

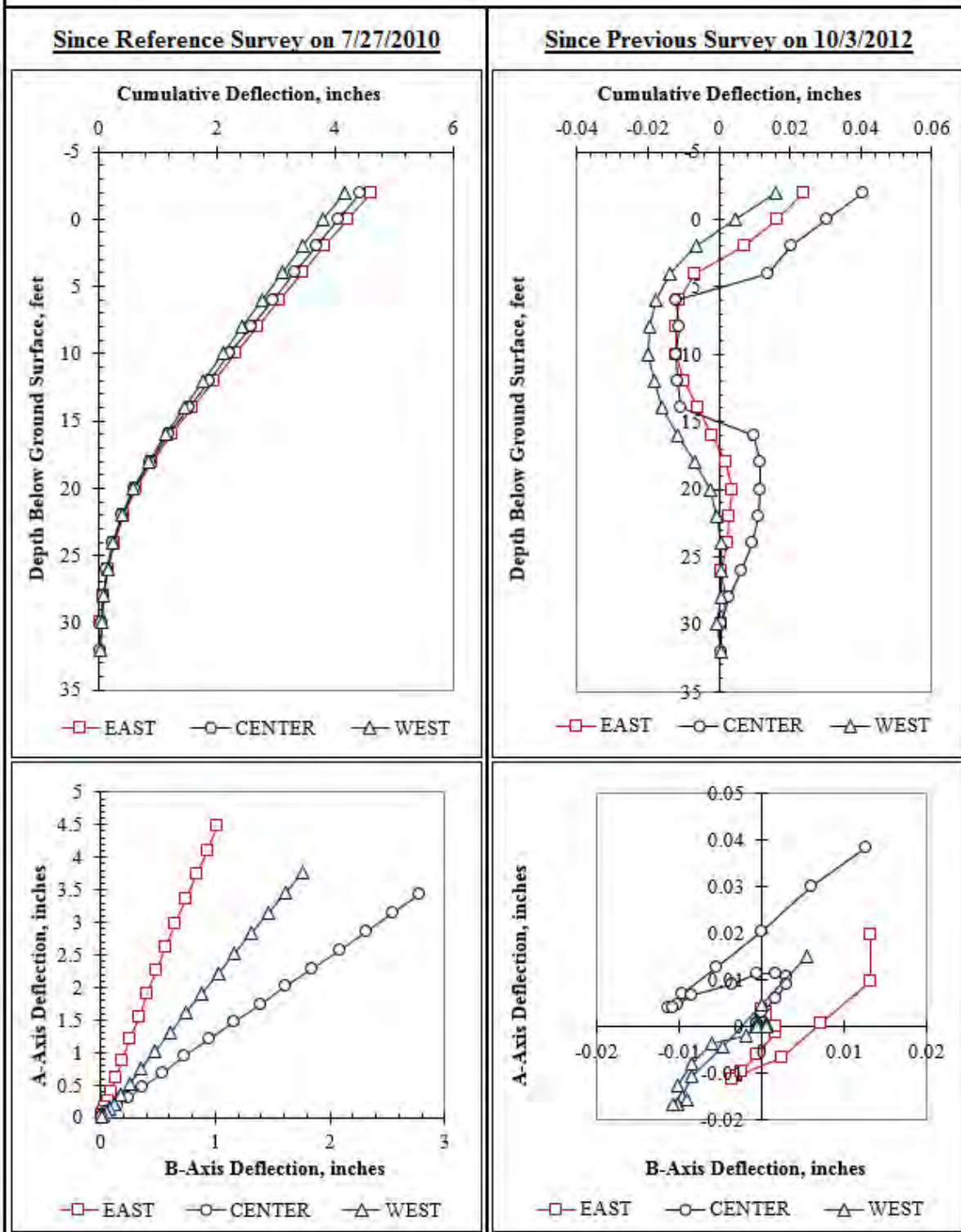


Figure F.100: Summary of inclinometer data from 10/26/2012.

Summary of Inclinometer Data From 11/16/2012

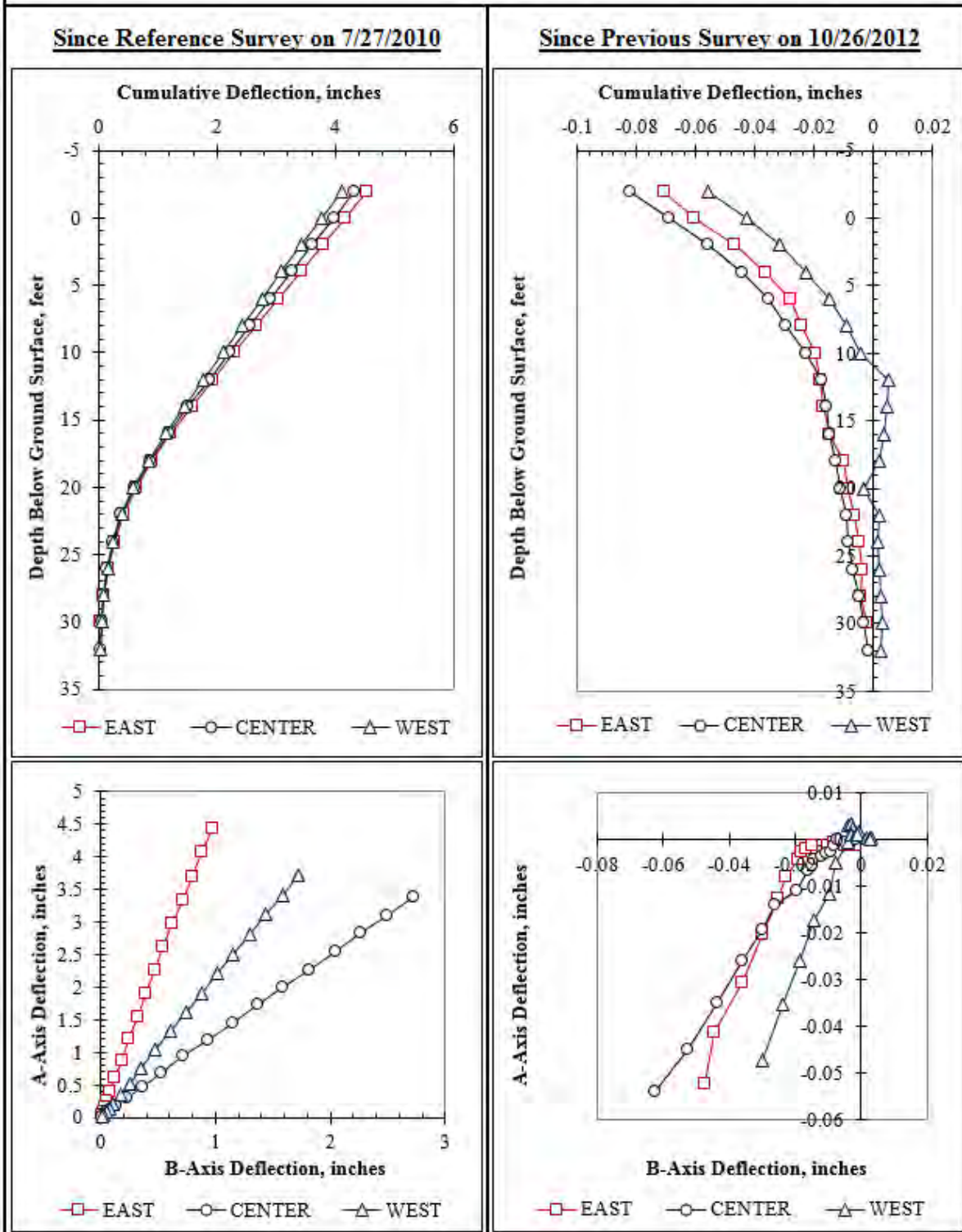


Figure F.101: Summary of inclinometer data from 11/16/2012.

Summary of Inclinometer Data From 12/7/2012

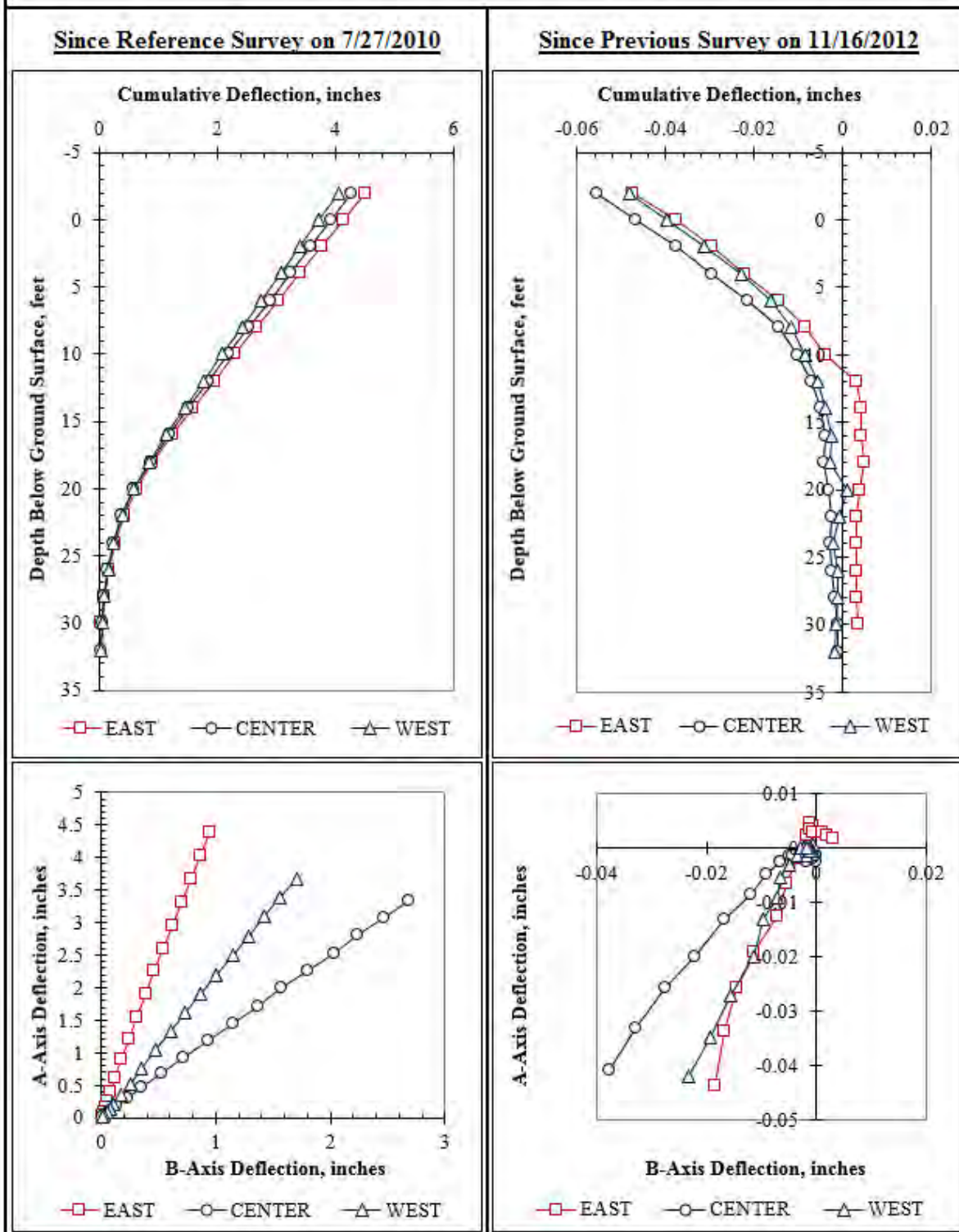


Figure F.102: Summary of inclinometer data from 12/7/2012.

Summary of Inclinometer Data From 1/10/2013

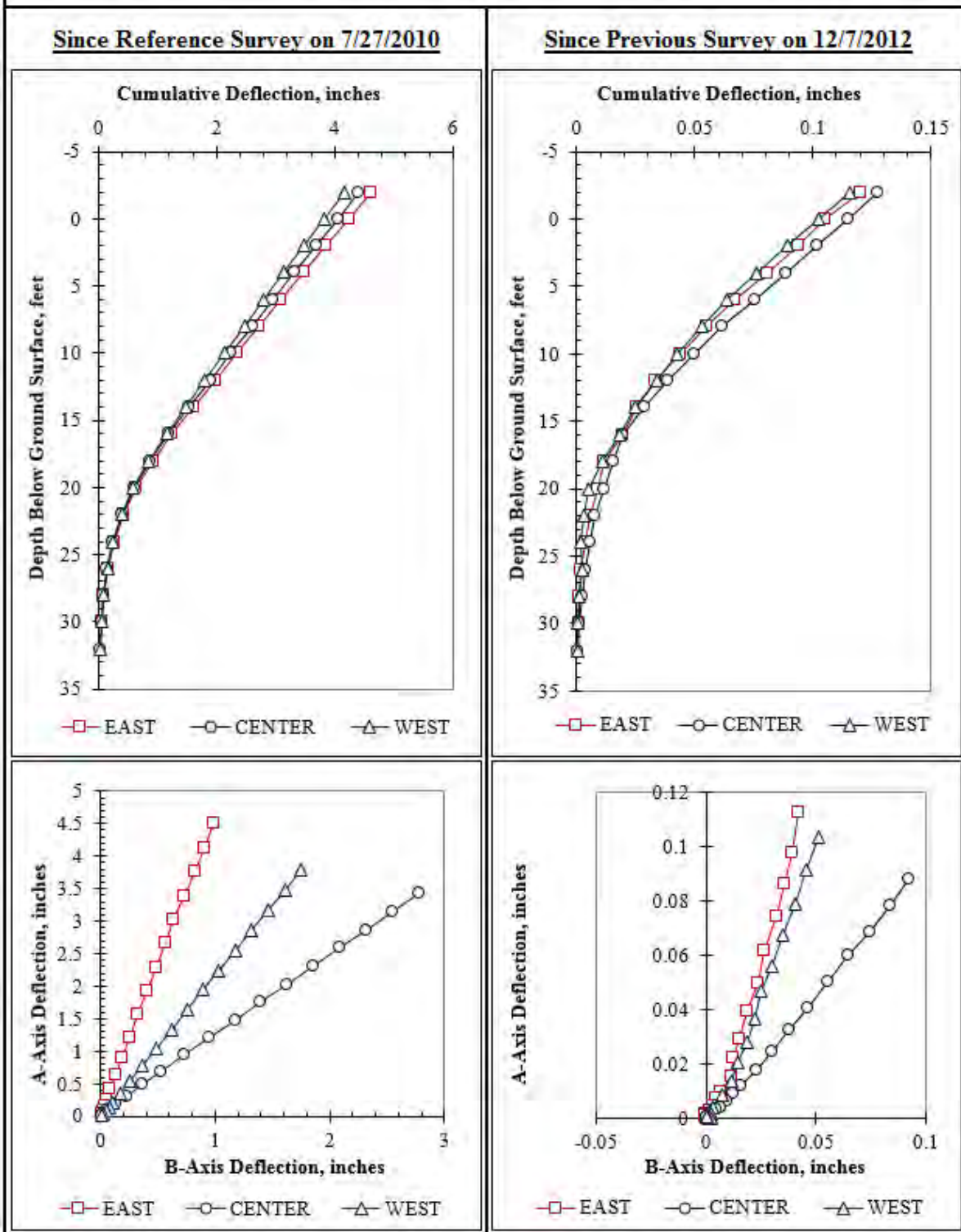


Figure F.103: Summary of inclinometer data from 1/10/2013.

Summary of Inclinometer Data From 2/4/2013

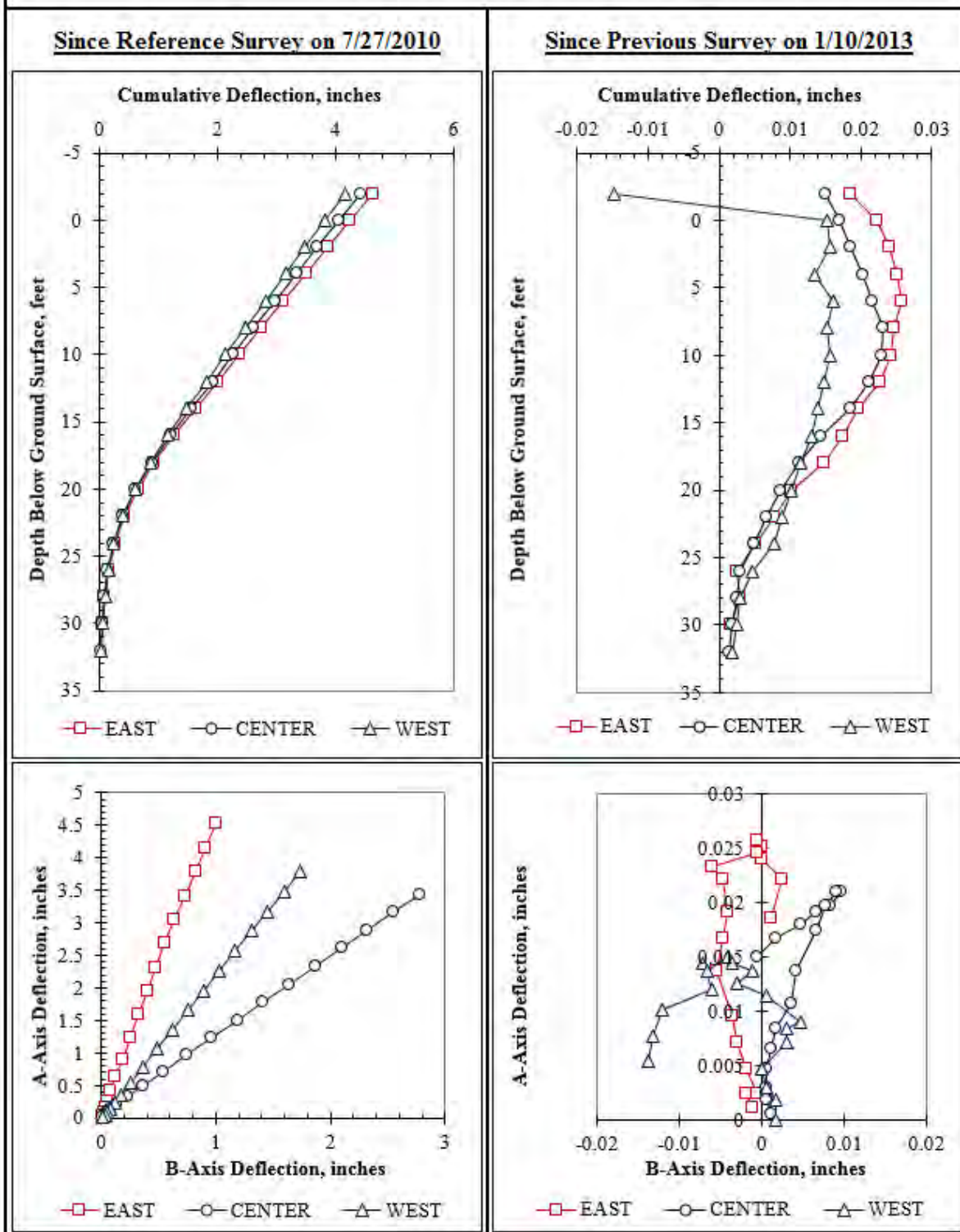


Figure F.104: Summary of inclinometer data from 2/4/2013.

Summary of Inclinometer Data From 2/6/2013

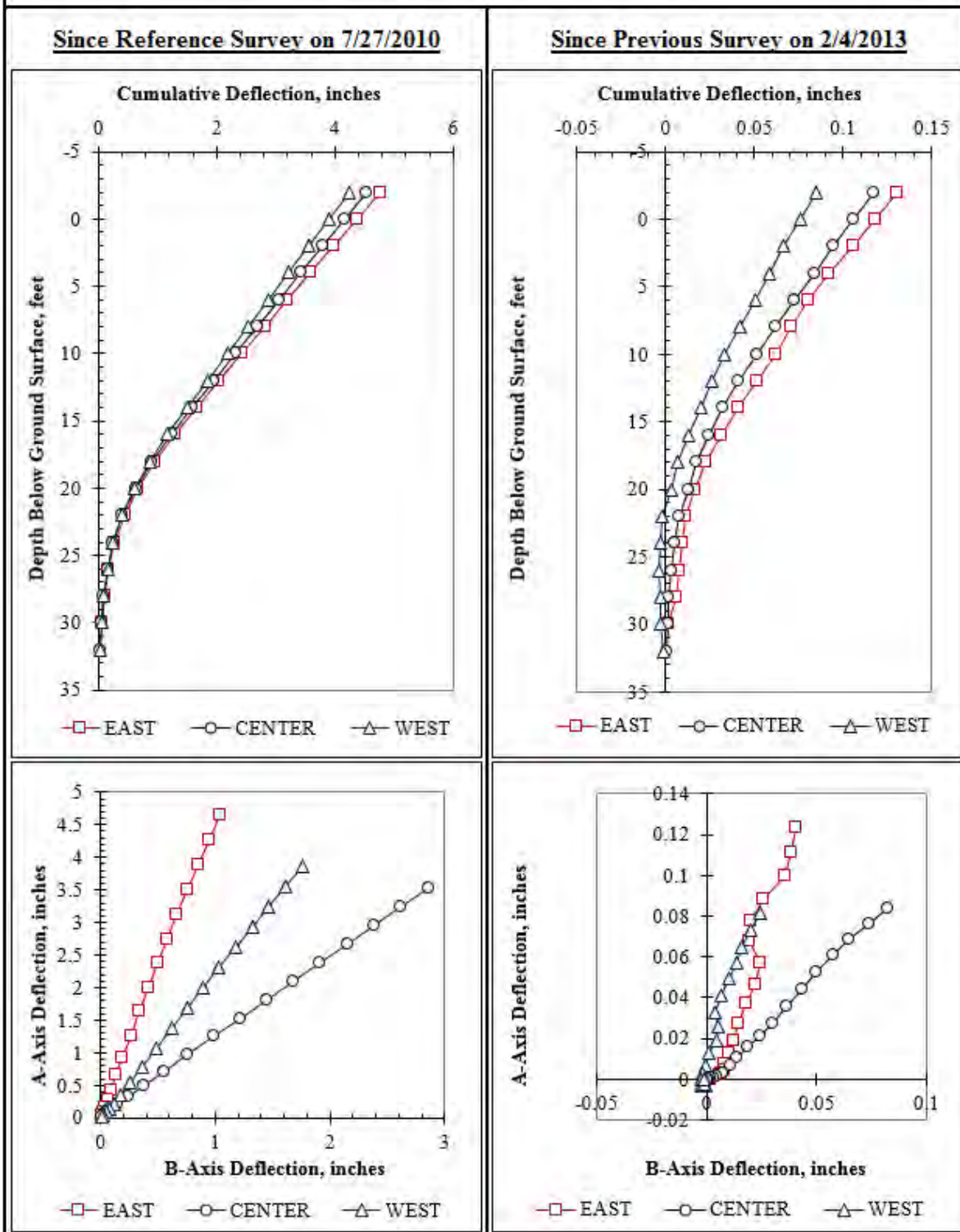


Figure F.105: Summary of inclinometer data from 2/6/2013.

Summary of Inclinometer Data From 2/8/2013

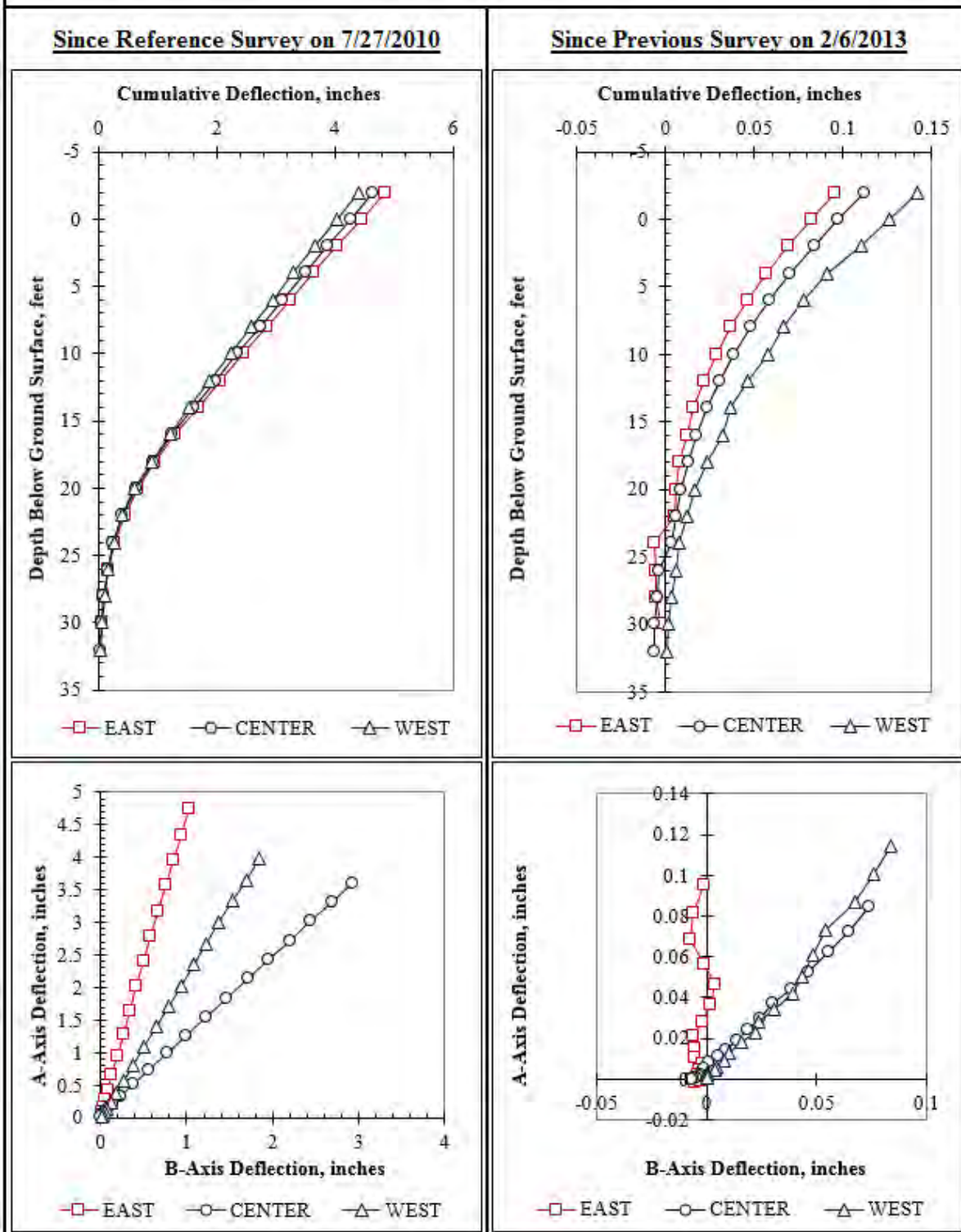


Figure F.106: Summary of inclinometer data from 2/8/2013.

Summary of Inclinometer Data From 2/11/2013

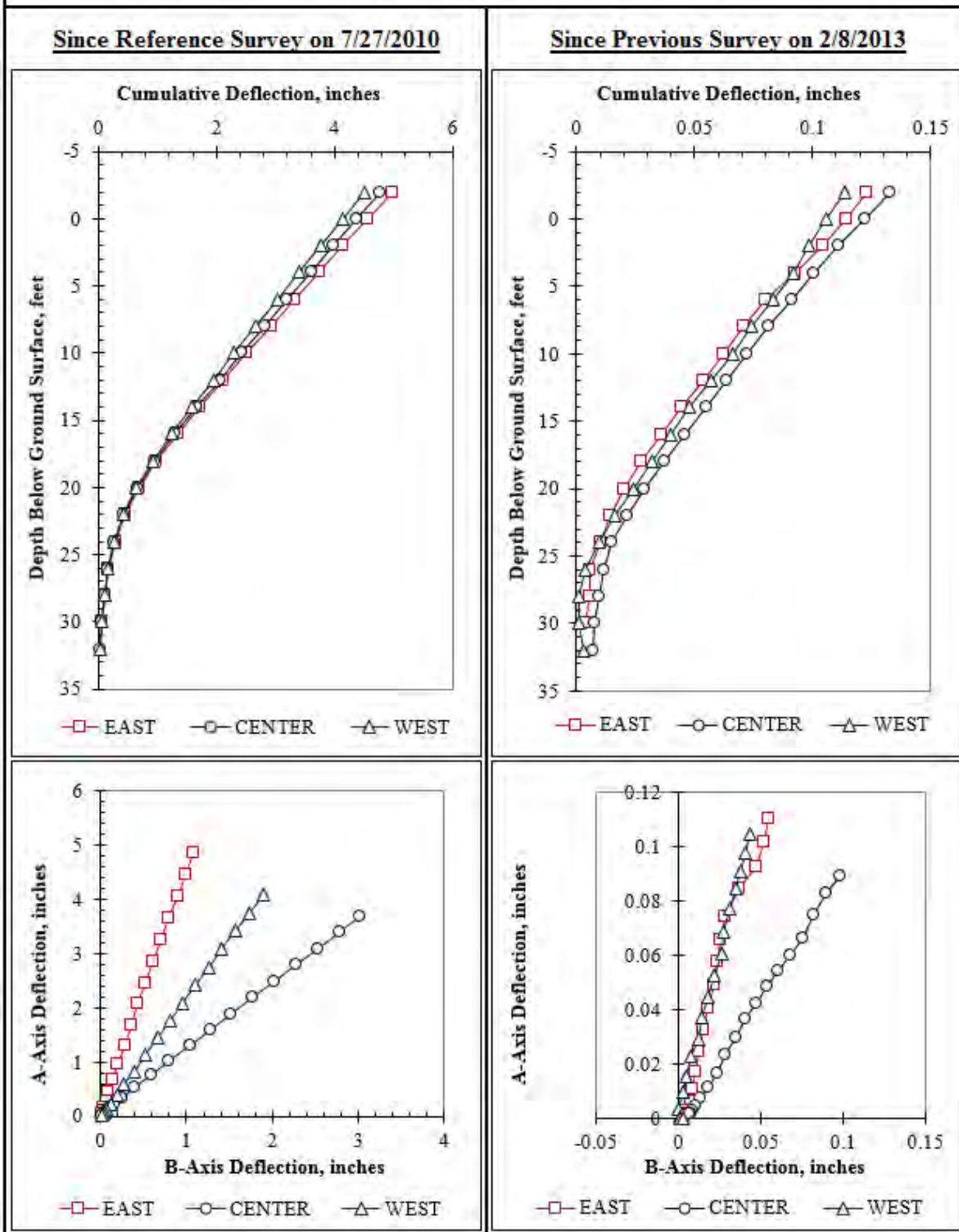


Figure F.107: Summary of inclinometer data from 2/11/2013.

Summary of Inclinometer Data From 2/15/2013

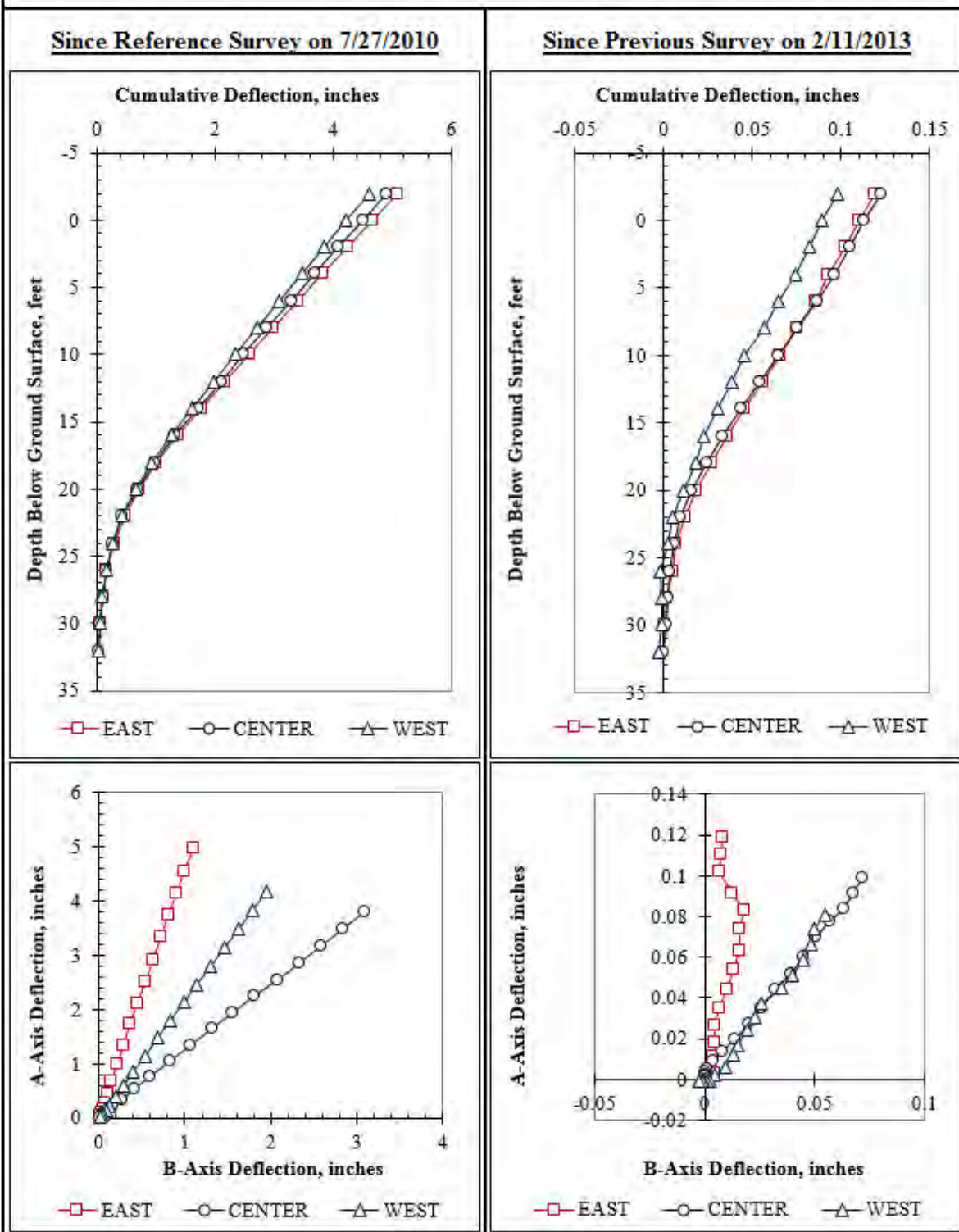


Figure F.108: Summary of inclinometer data from 2/15/2013.

Summary of Inclinometer Data From 2/19/2013

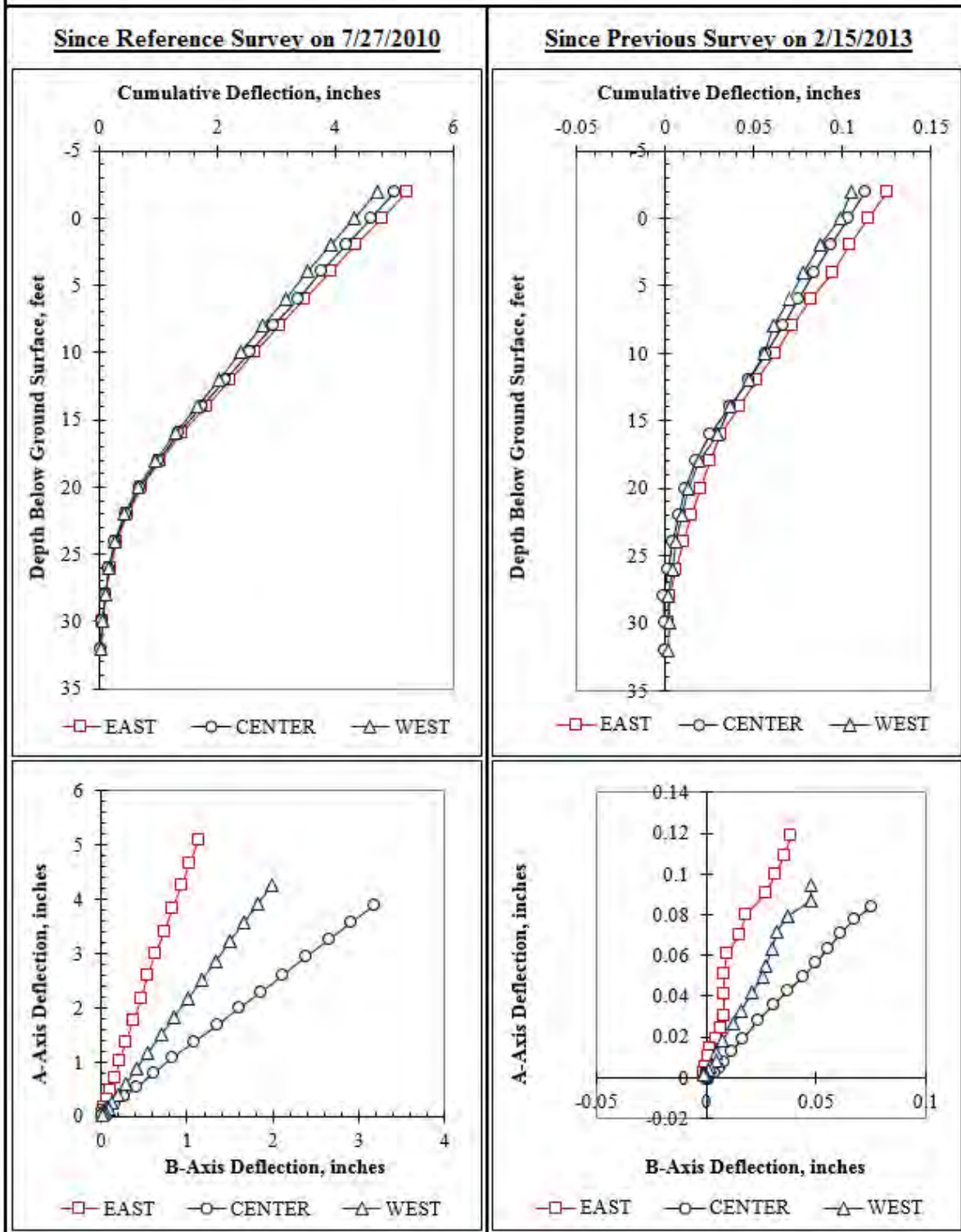


Figure F.109: Summary of inclinometer data from 2/19/2013.

Summary of Inclinometer Data From 2/25/2013

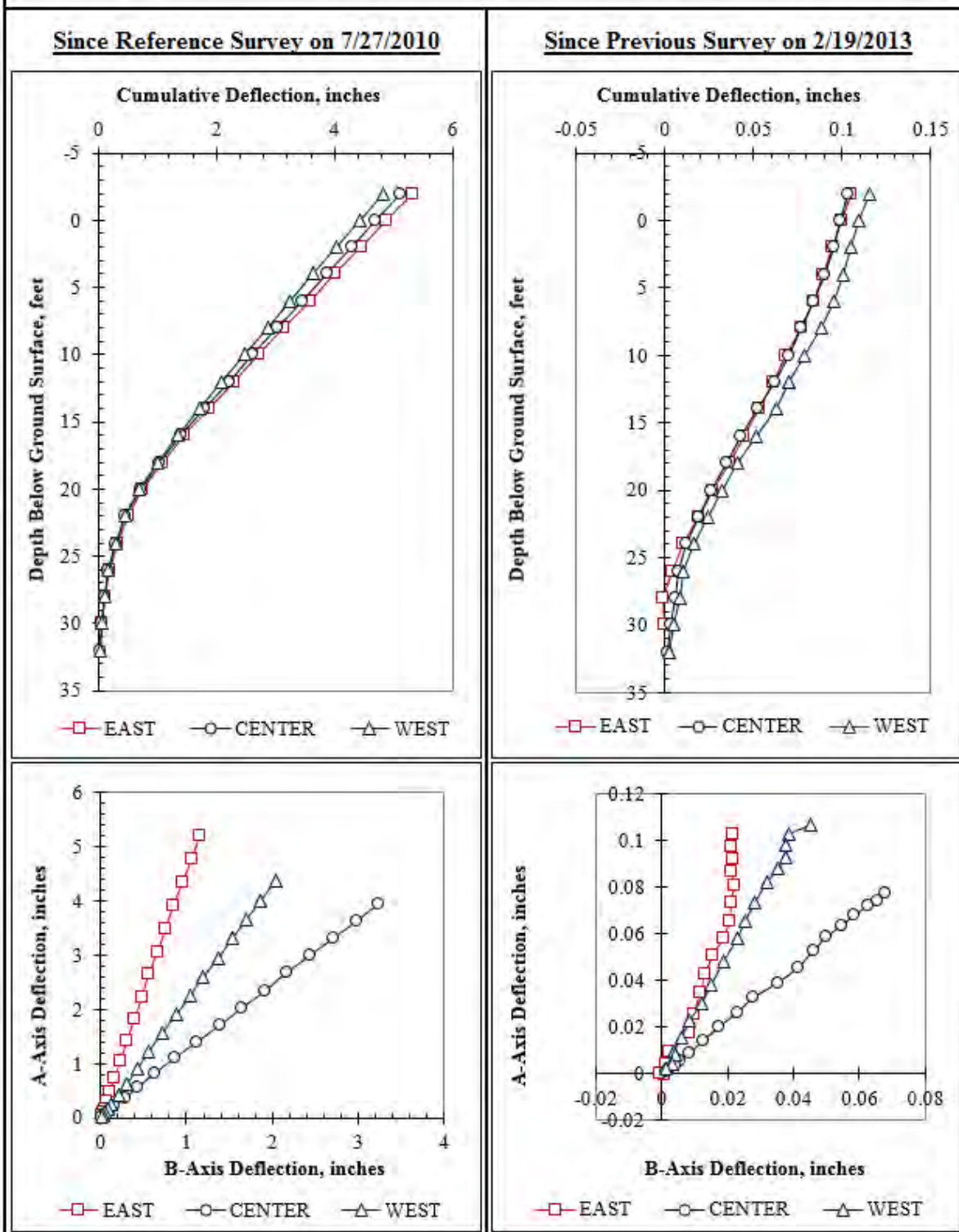


Figure F.110: Summary of inclinometer data from 2/25/2013.

Summary of Inclinometer Data From 3/4/2013

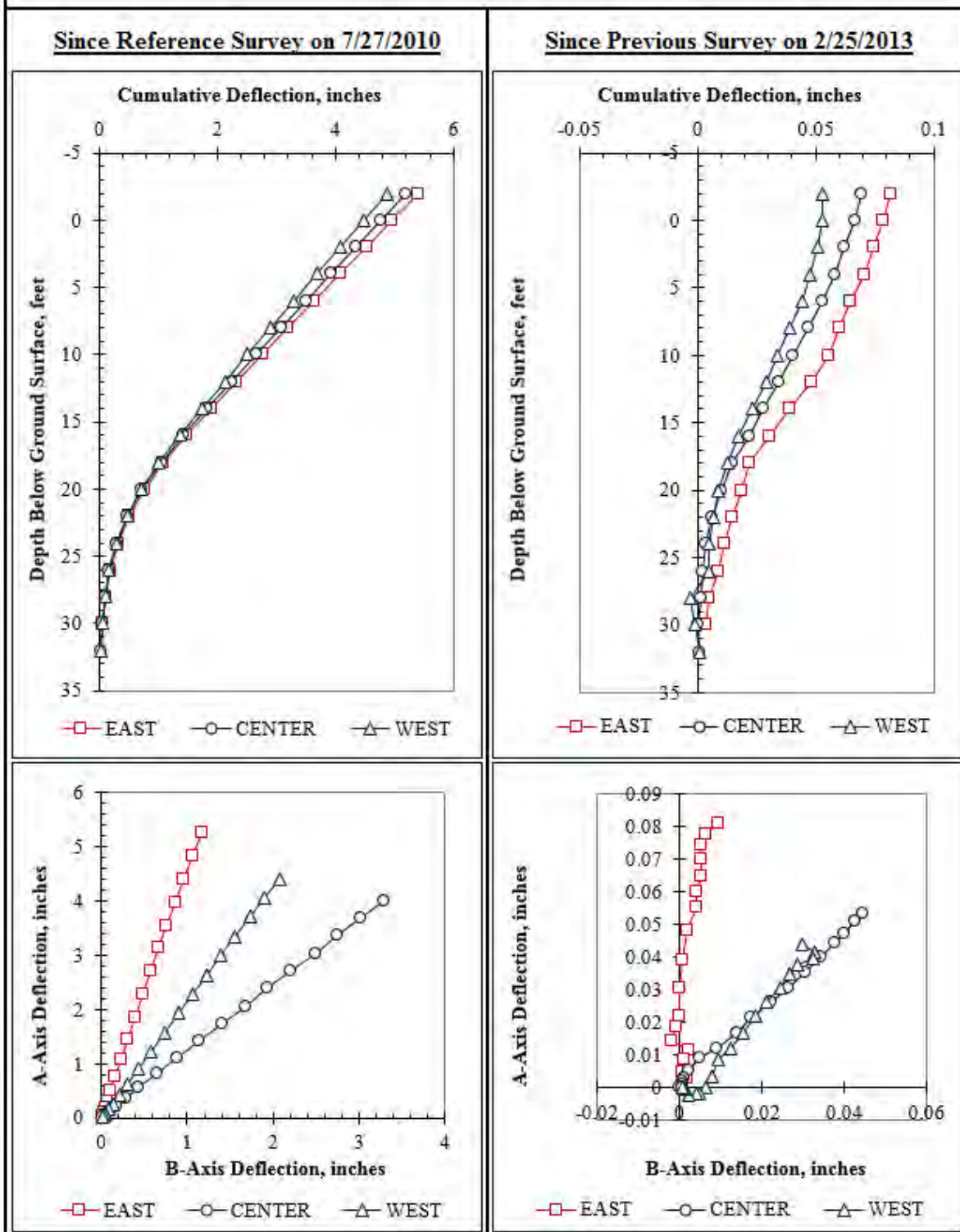


Figure F.111: Summary of inclinometer data from 3/4/2013.

Summary of Inclinometer Data From 3/11/2013

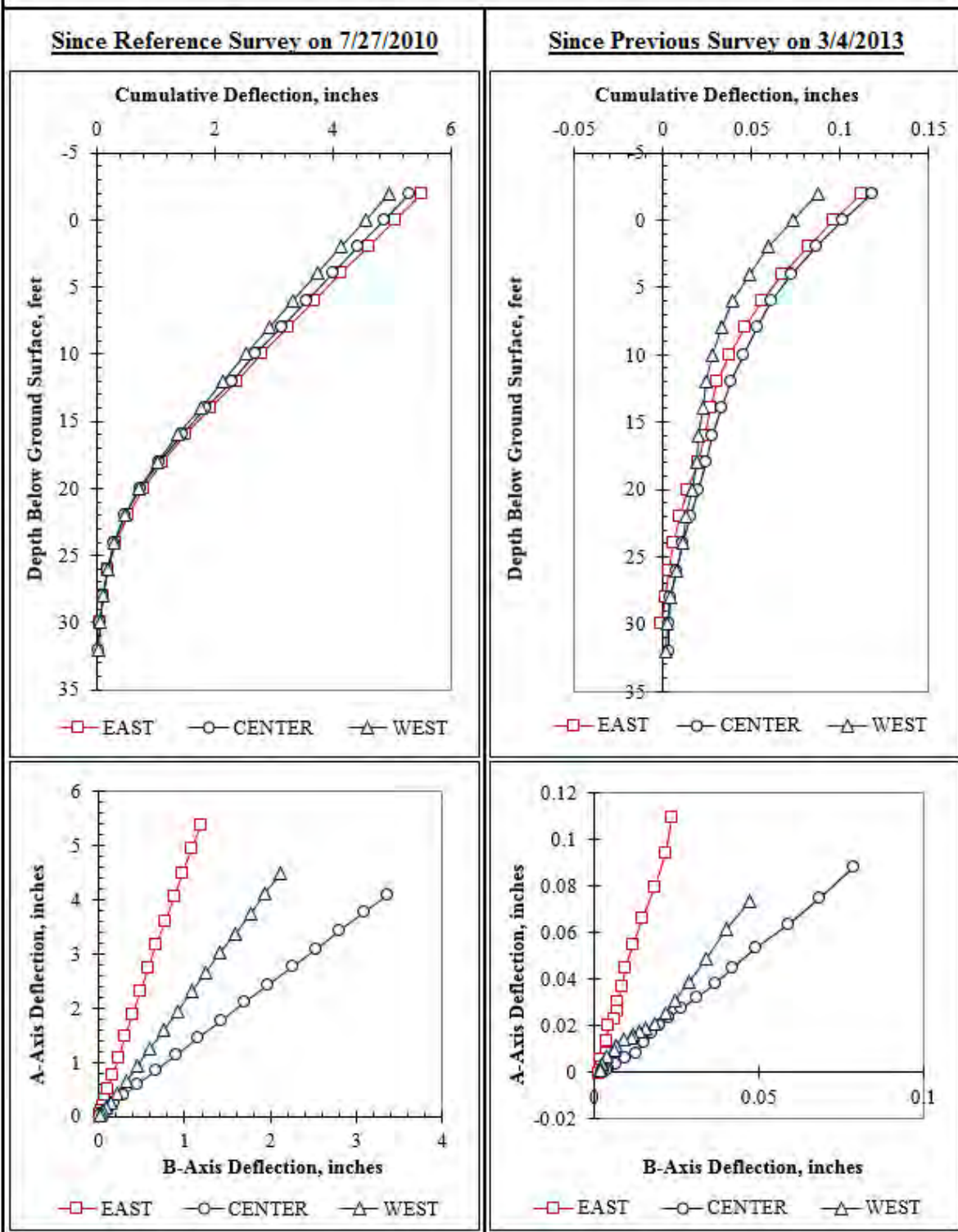


Figure F.112: Summary of inclinometer data from 3/11/2013.

Summary of Inclinator Data From 3/18/2013

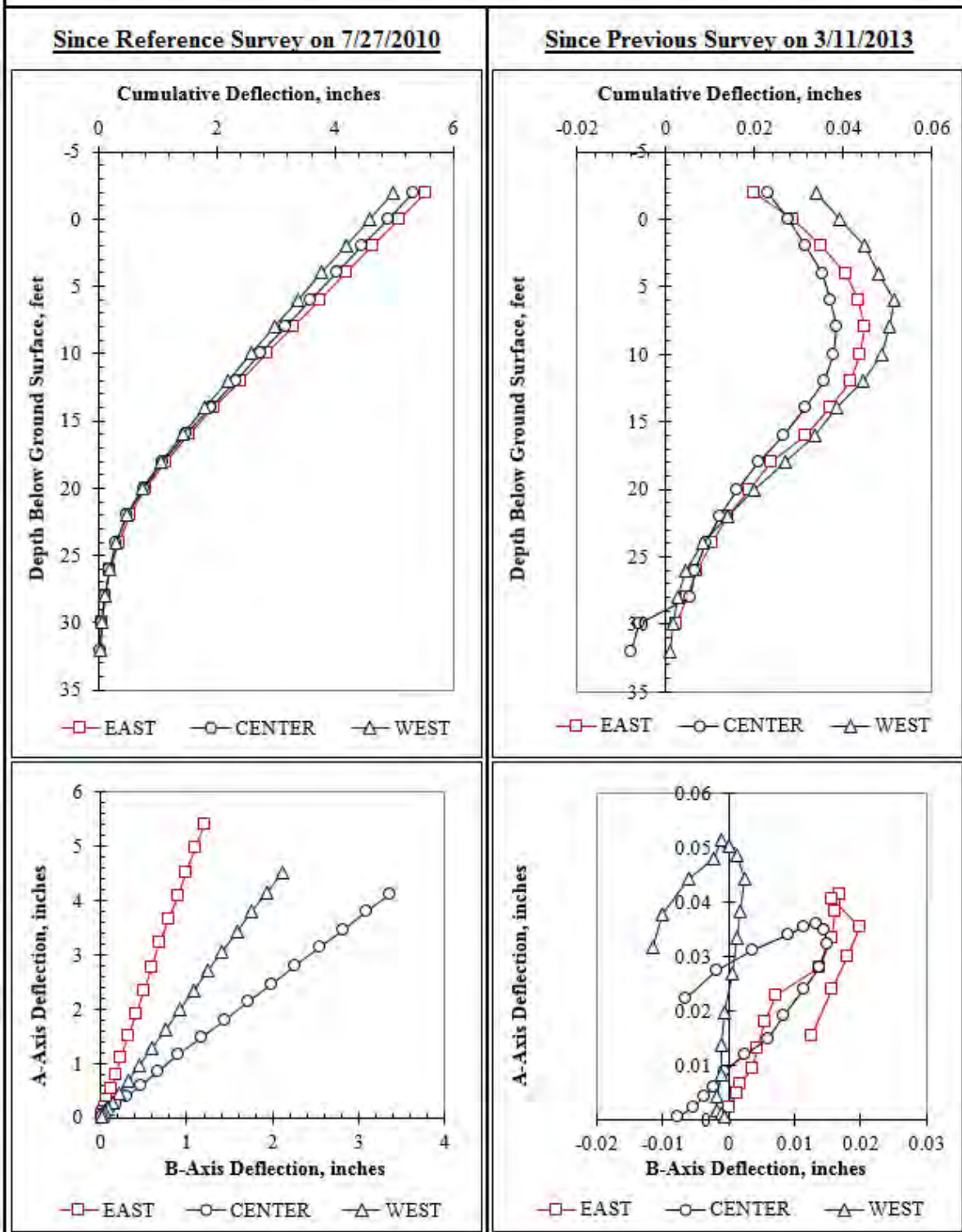


Figure F.113: Summary of inclinometer data from 3/18/2013.

Summary of Inclinometer Data From 3/25/2013

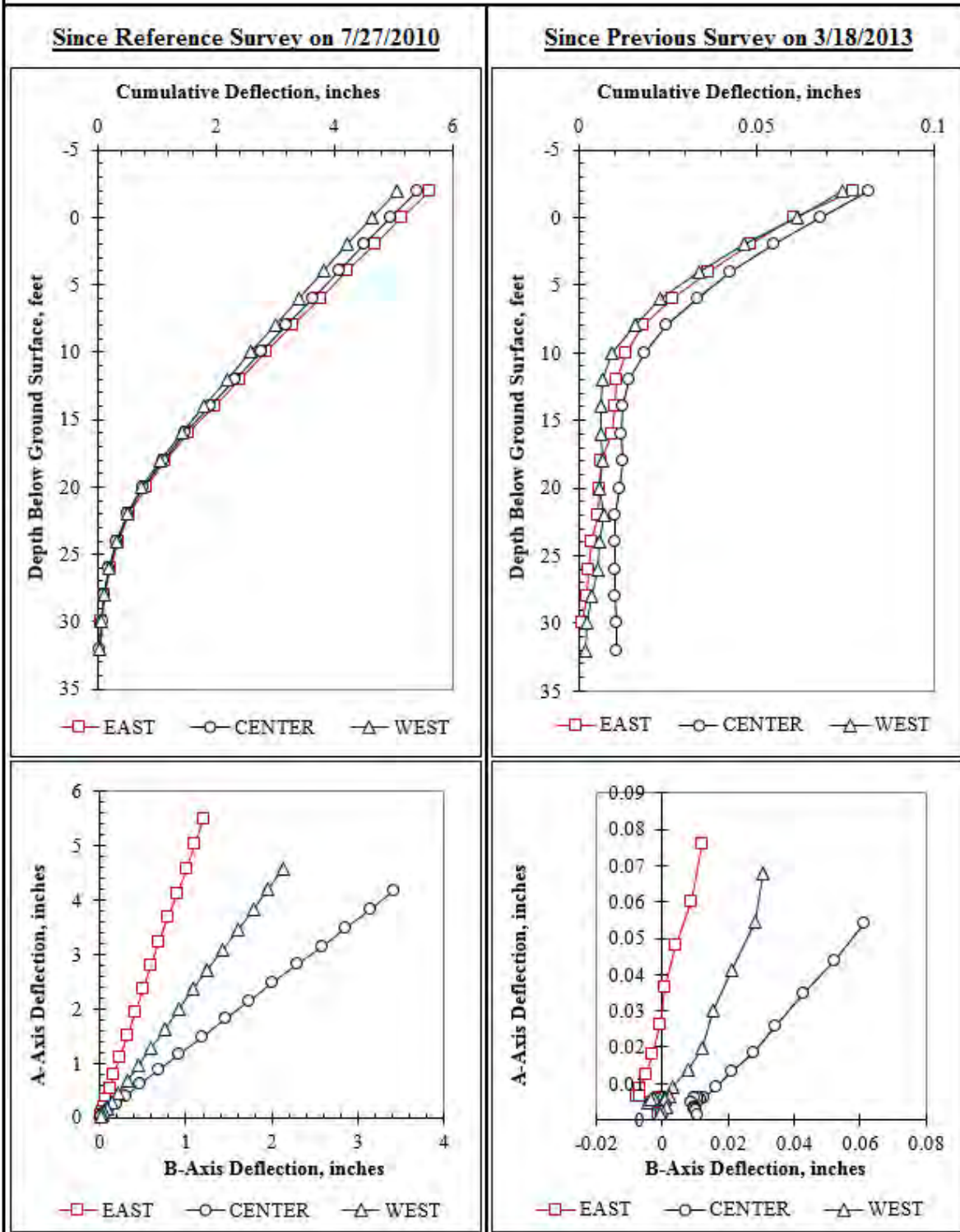


Figure F.114: Summary of inclinometer data from 3/25/2013.

Summary of Inclinometer Data From 4/1/2013

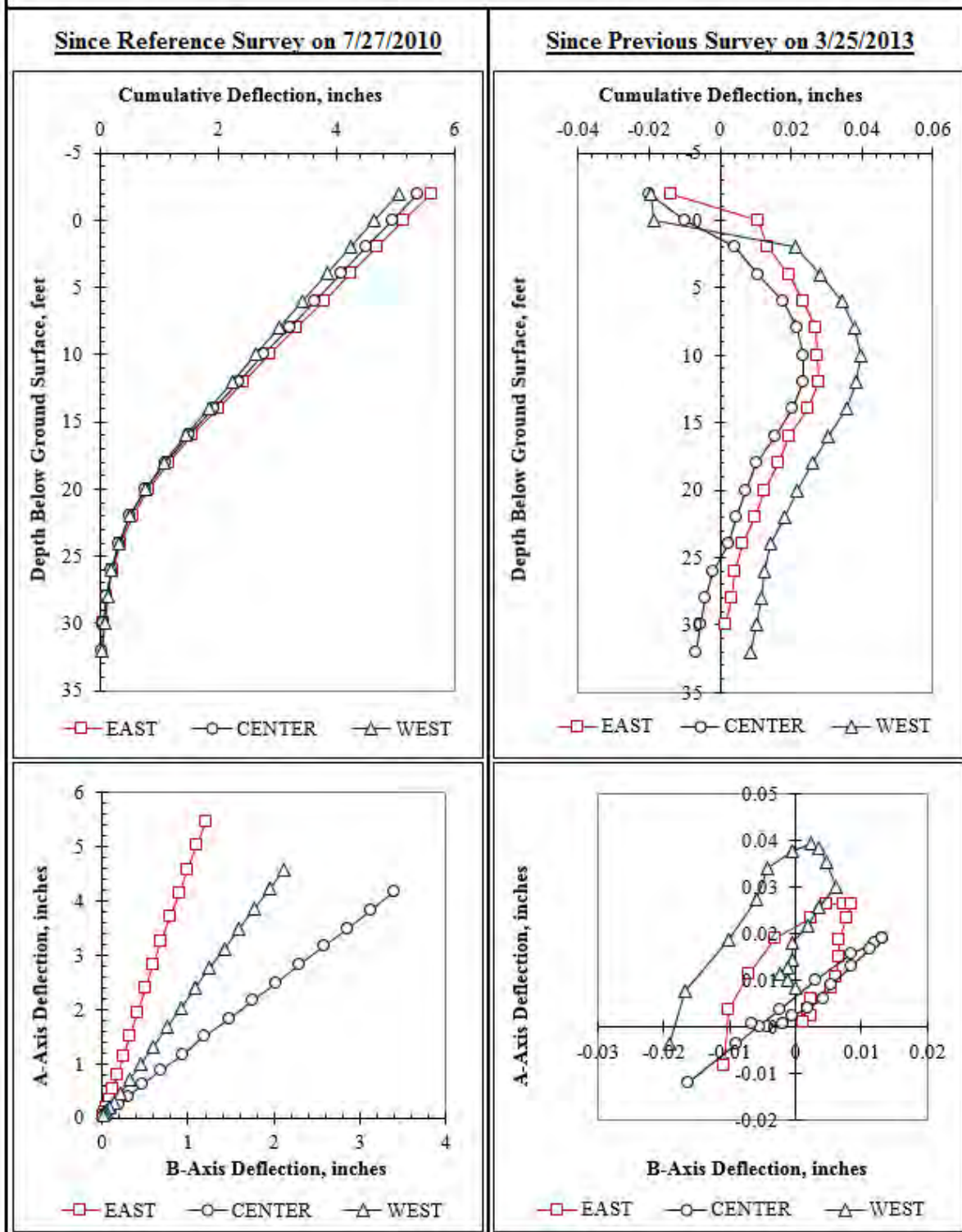


Figure F.115: Summary of inclinometer data from 4/1/2013.

Summary of Inclinometer Data From 4/8/2013

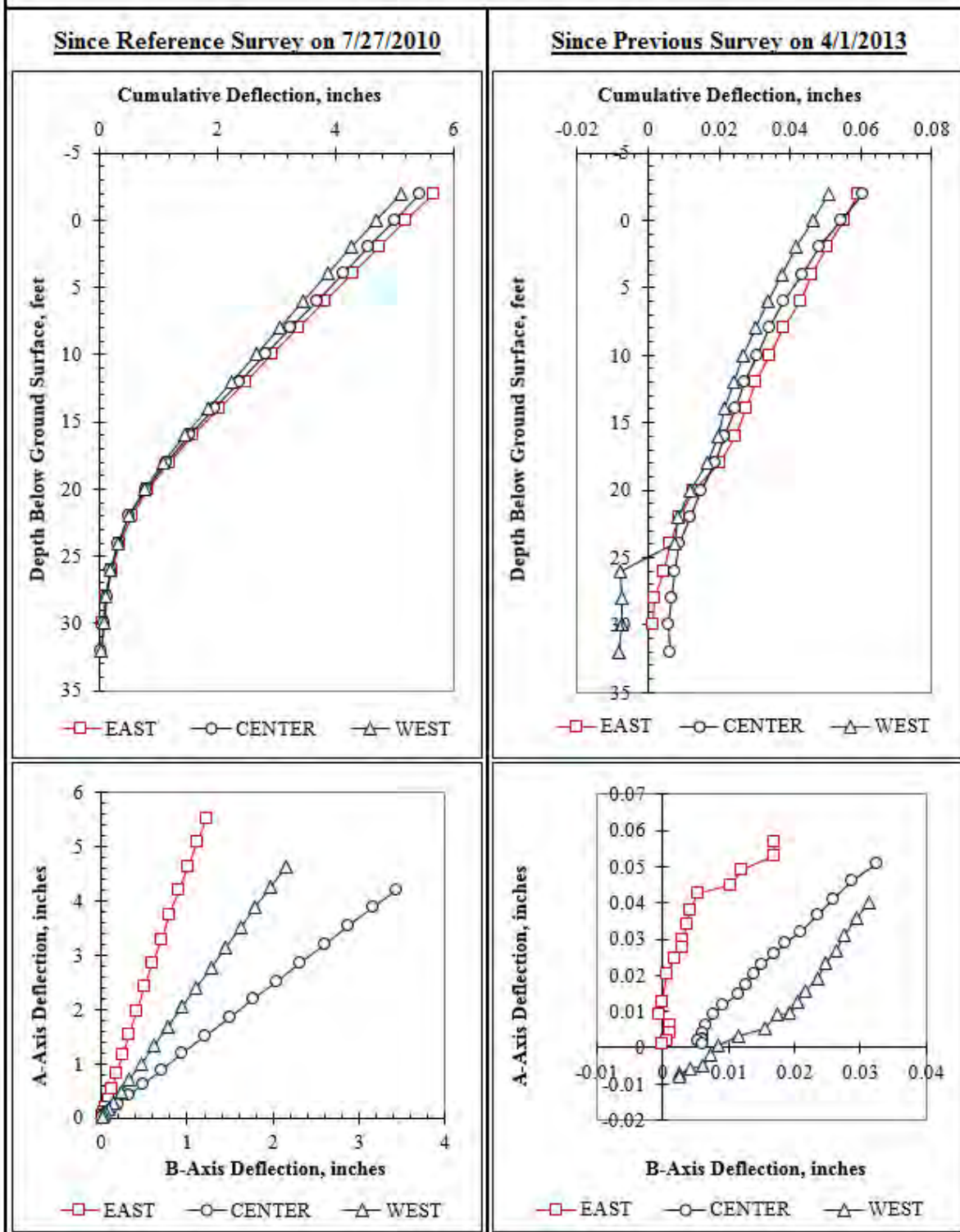


Figure F.116: Summary of inclinometer data from 4/8/2013.

Summary of Inclinometer Data From 4/15/2013

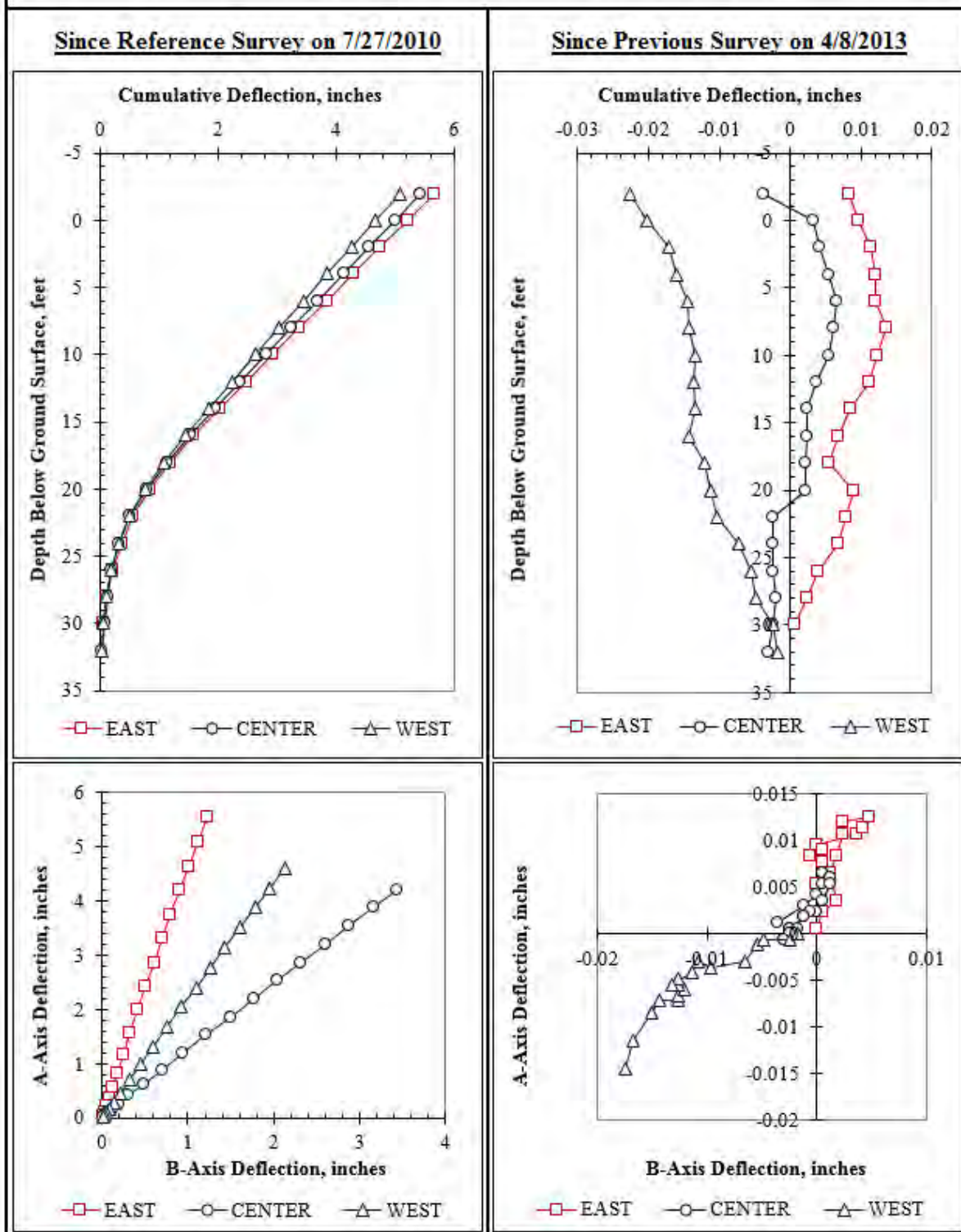


Figure F.117: Summary of inclinometer data from 4/15/2013.

Summary of Inclinometer Data From 4/22/2013

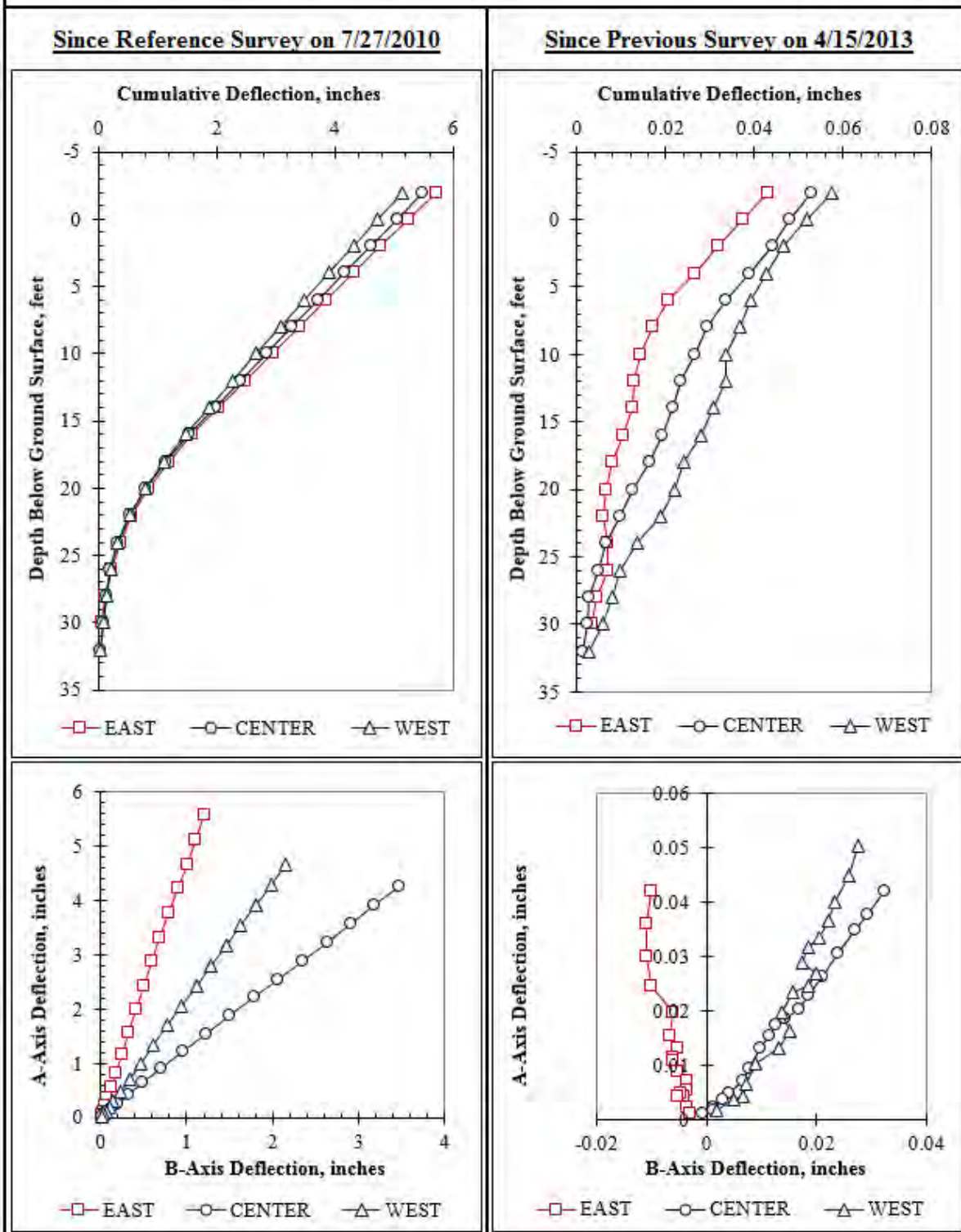


Figure F.118: Summary of inclinometer data from 4/22/2013.

Summary of Inclinometer Data From 4/29/2013

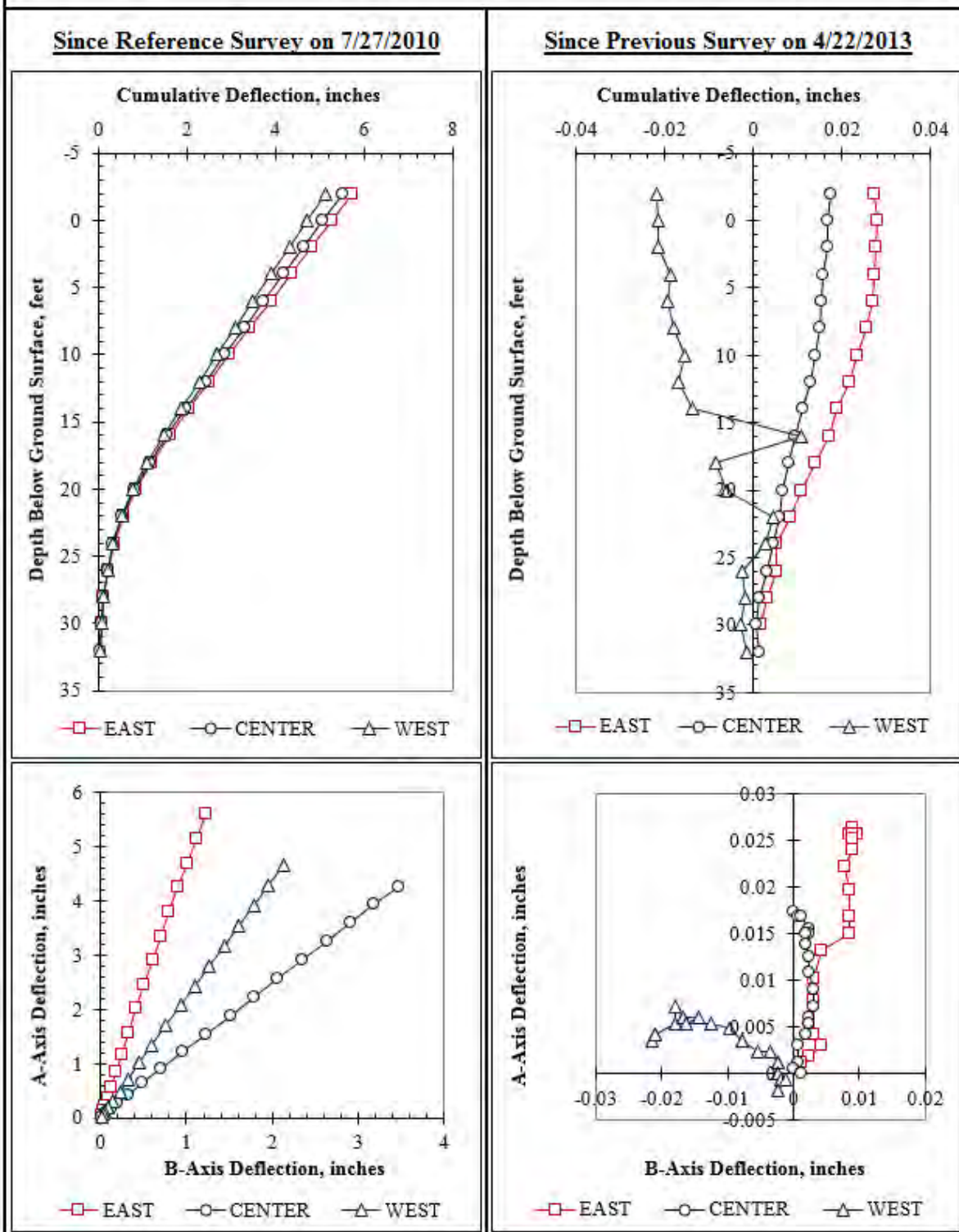


Figure F.119: Summary of inclinometer data from 4/29/2013.

Summary of Inclinometer Data From 5/6/2013

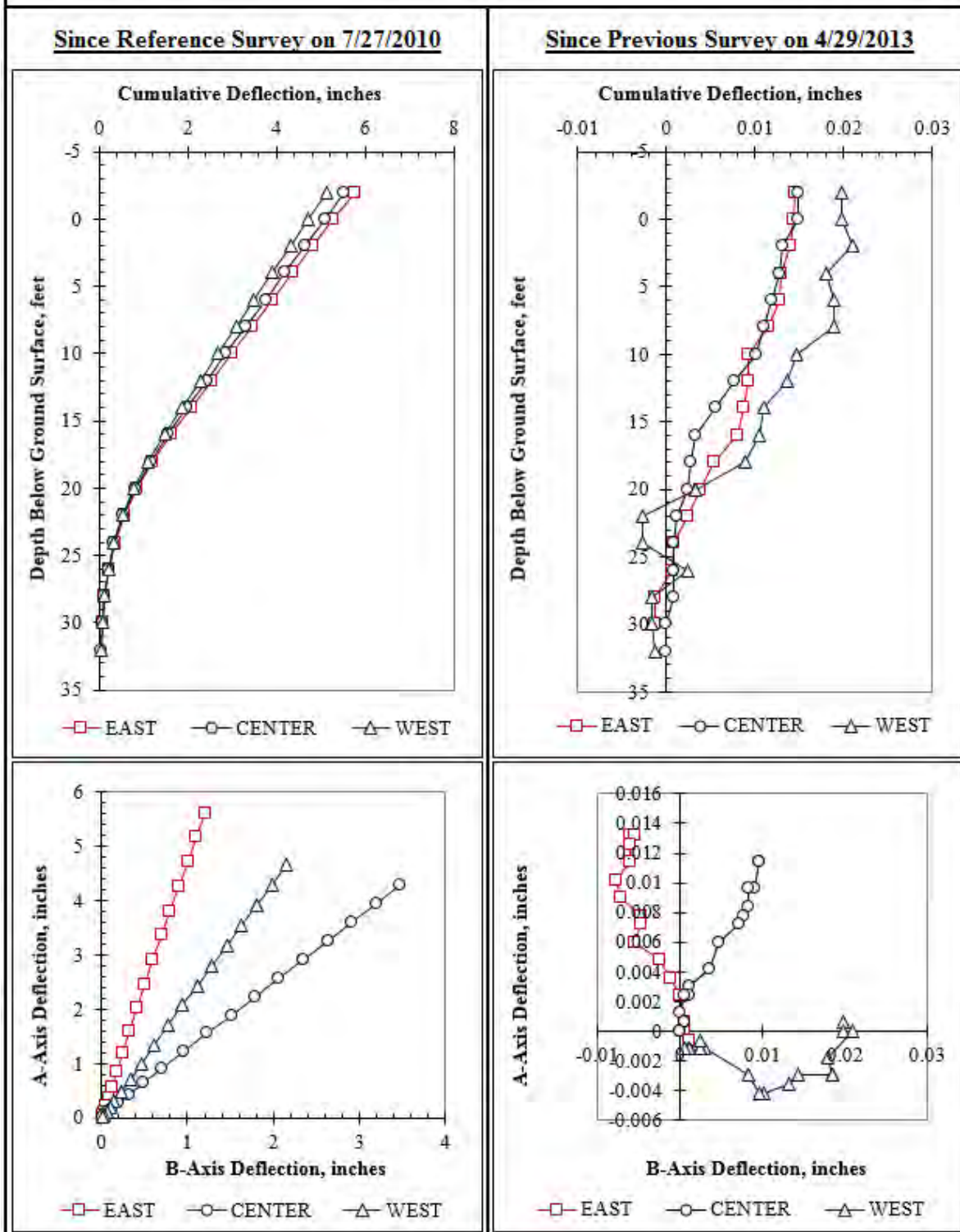


Figure F.120: Summary of inclinometer data from 5/6/2013.

Summary of Inclinometer Data From 5/13/2013

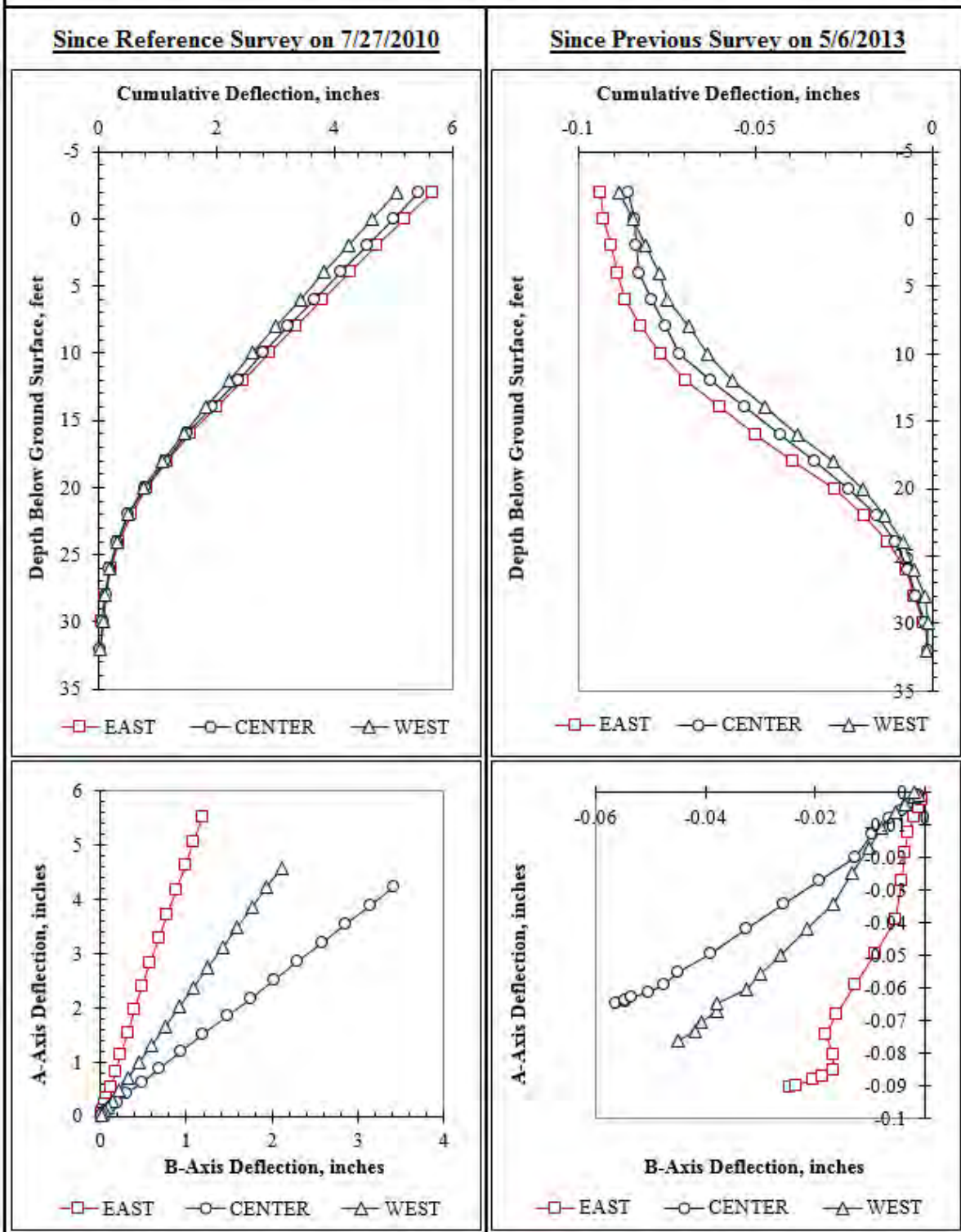


Figure F.121: Summary of inclinometer data from 5/13/2013.

Summary of Inclinometer Data From 5/15/2013

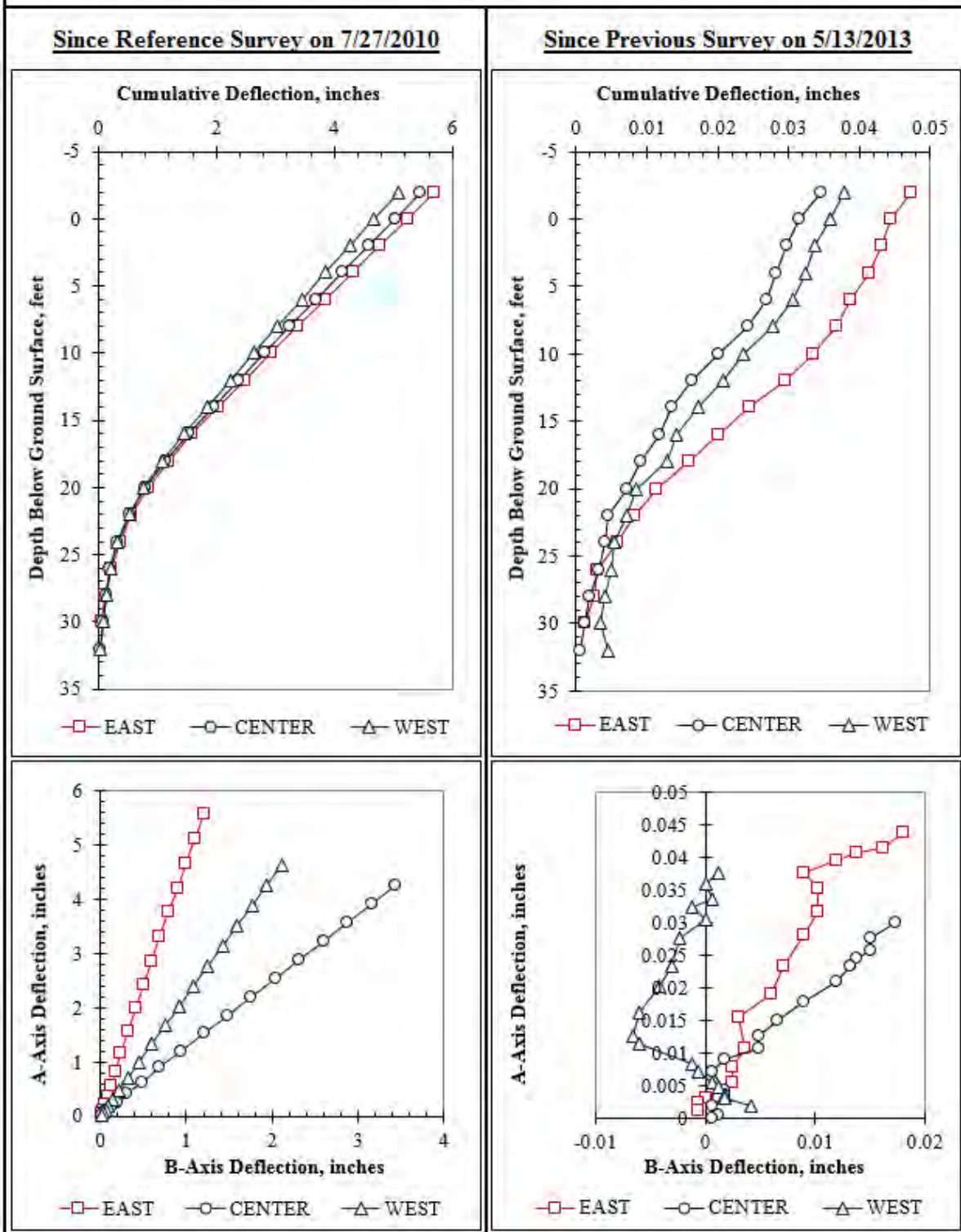


Figure F.122: Summary of inclinometer data from 5/15/2013.

Summary of Inclinometer Data From 5/17/2013

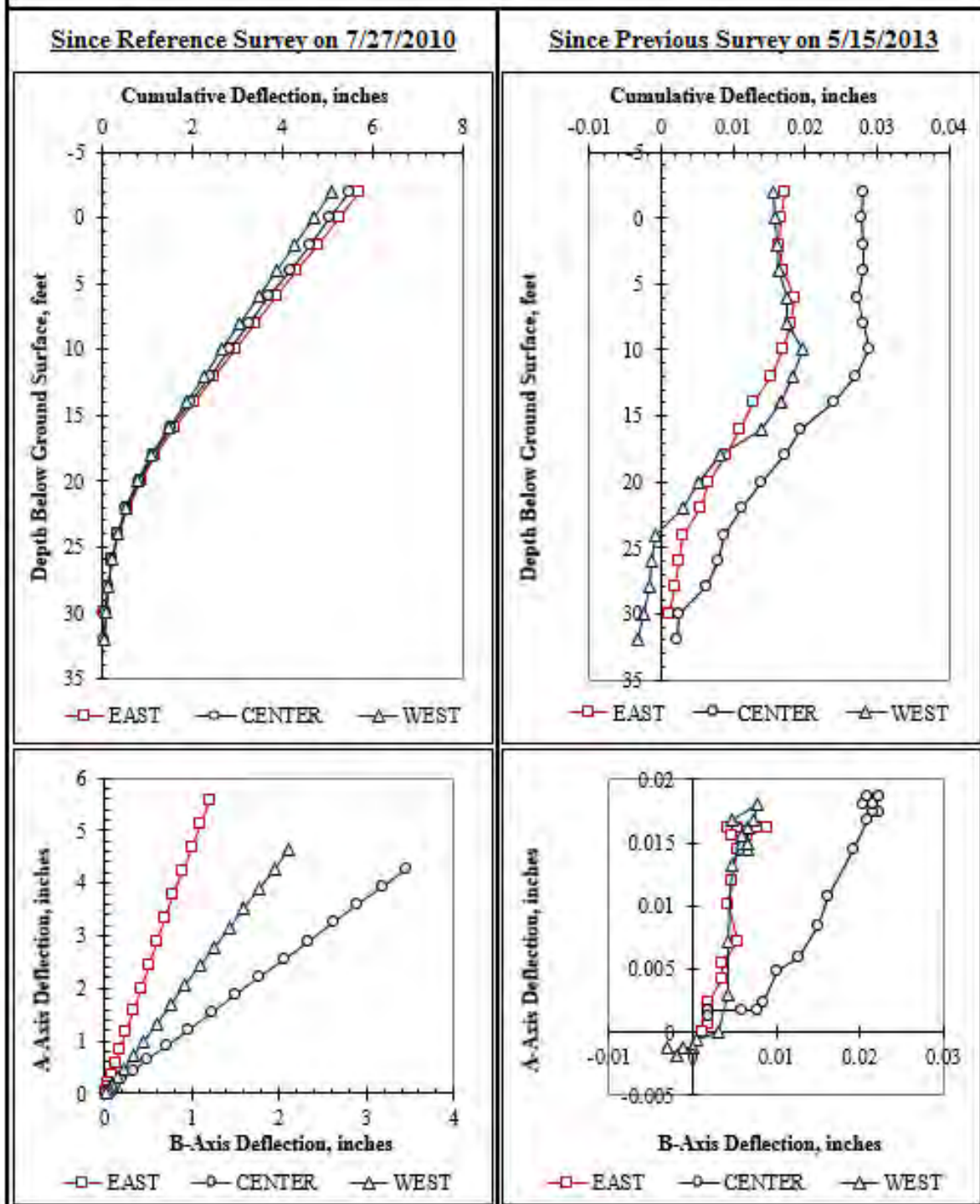


Figure F.123: Summary of inclinometer data from 5/17/2013.

Summary of Inclinometer Data From 5/20/2013

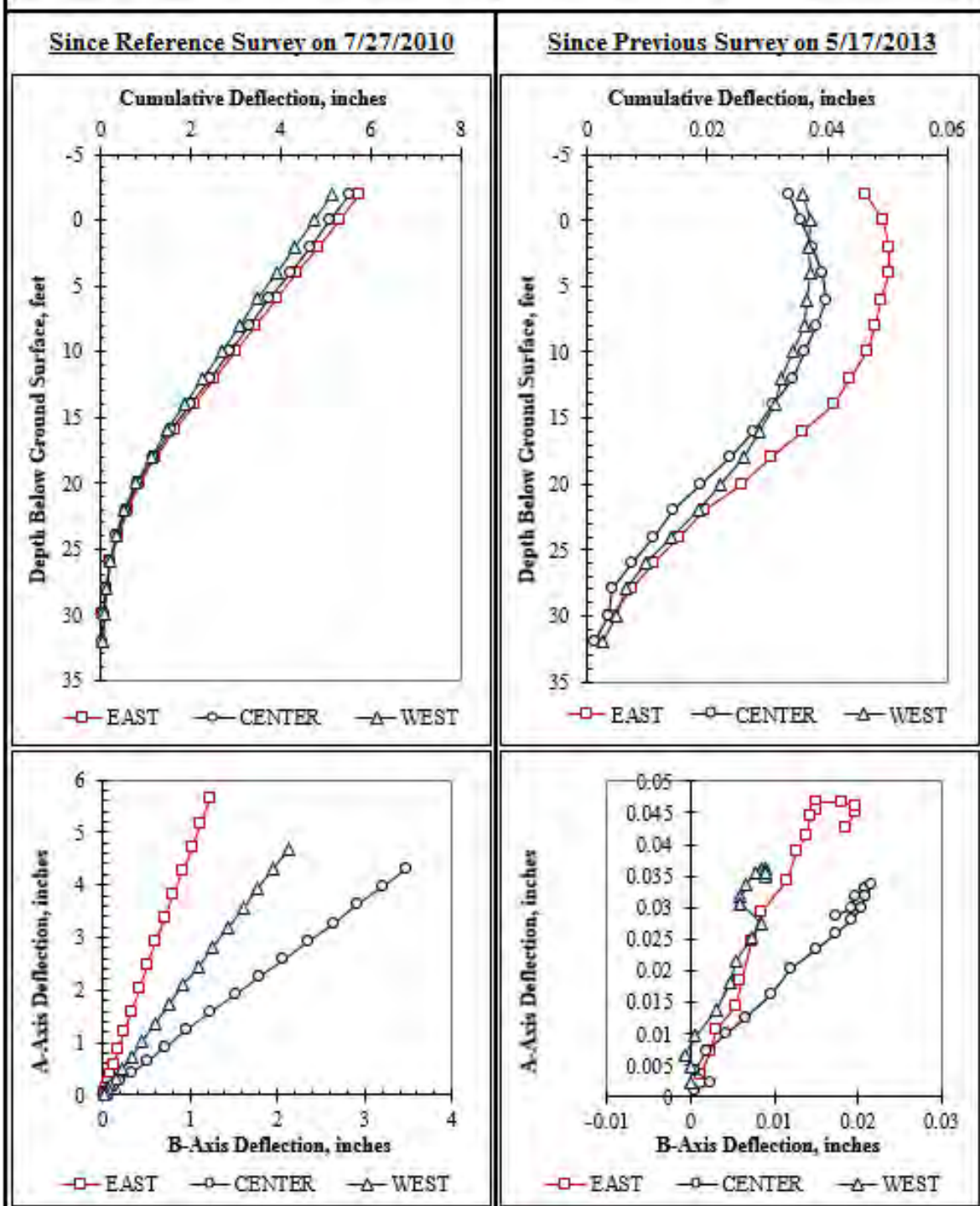


Figure F.124: Summary of inclinometer data from 5/20/2013.

Summary of Inclinometer Data From 5/23/2013

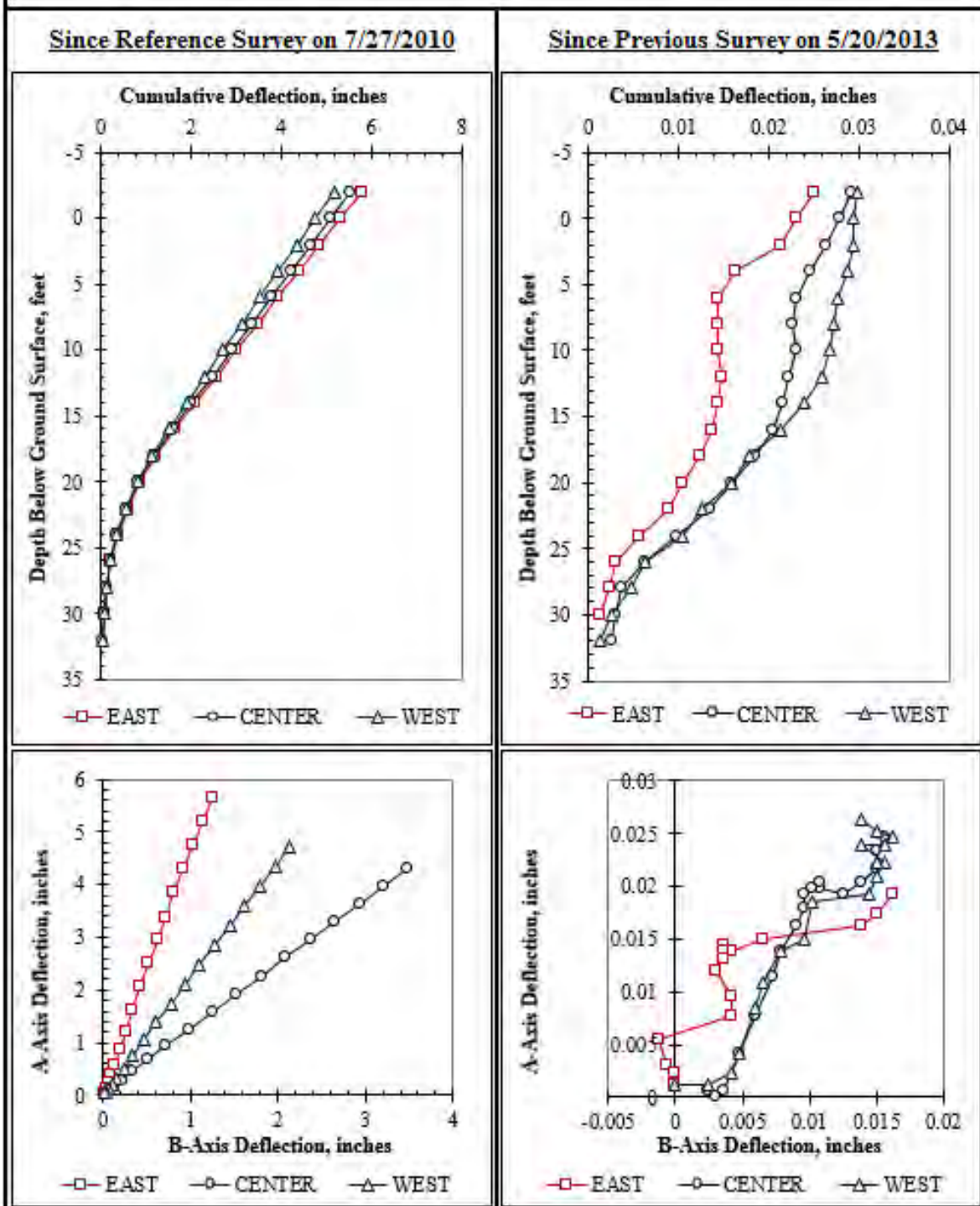


Figure F.125: Summary of inclinometer data from 5/23/2013.

Summary of Inclinometer Data From 5/28/2013

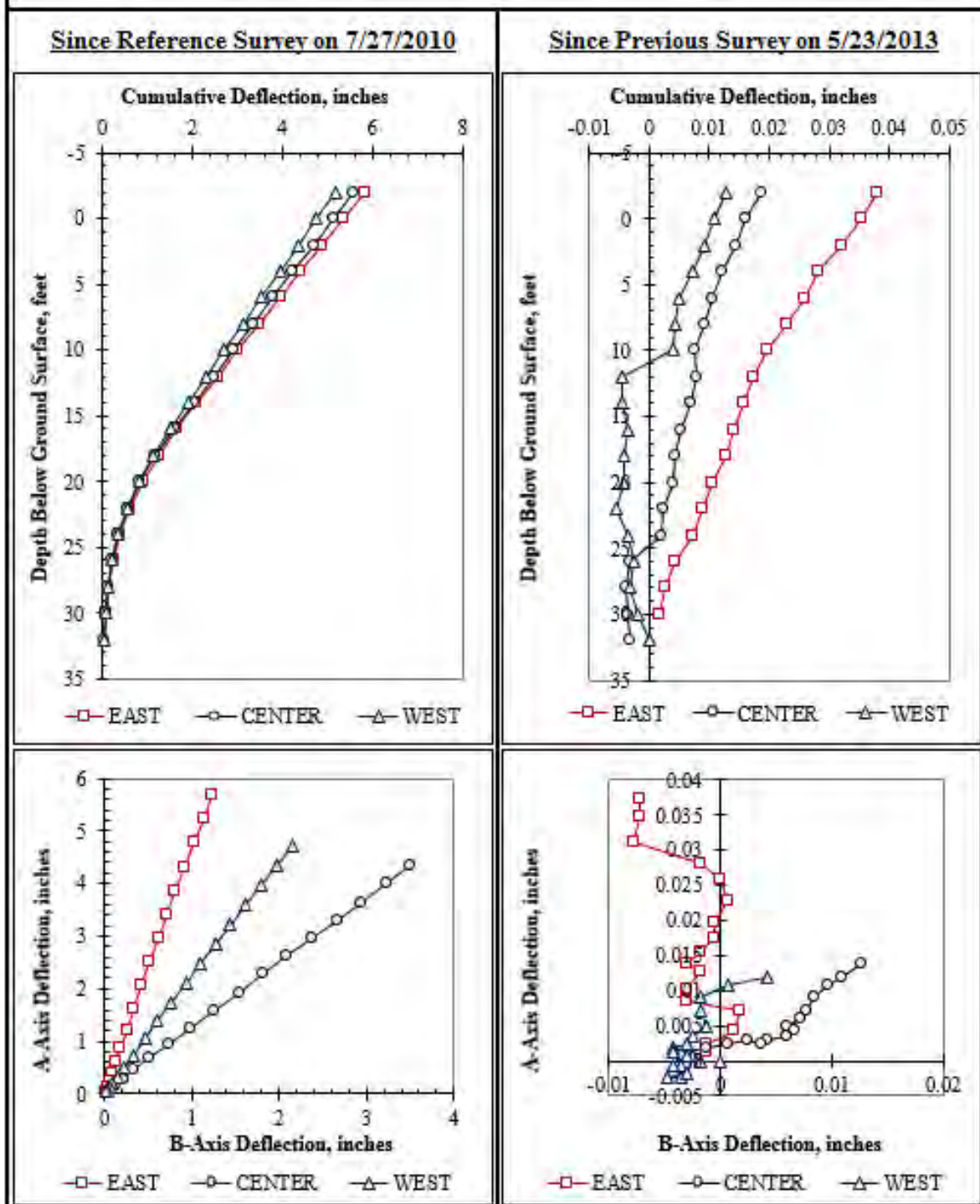


Figure F.126: Summary of inclinometer data from 5/28/2013.

Summary of Inclinometer Data From 6/3/2013

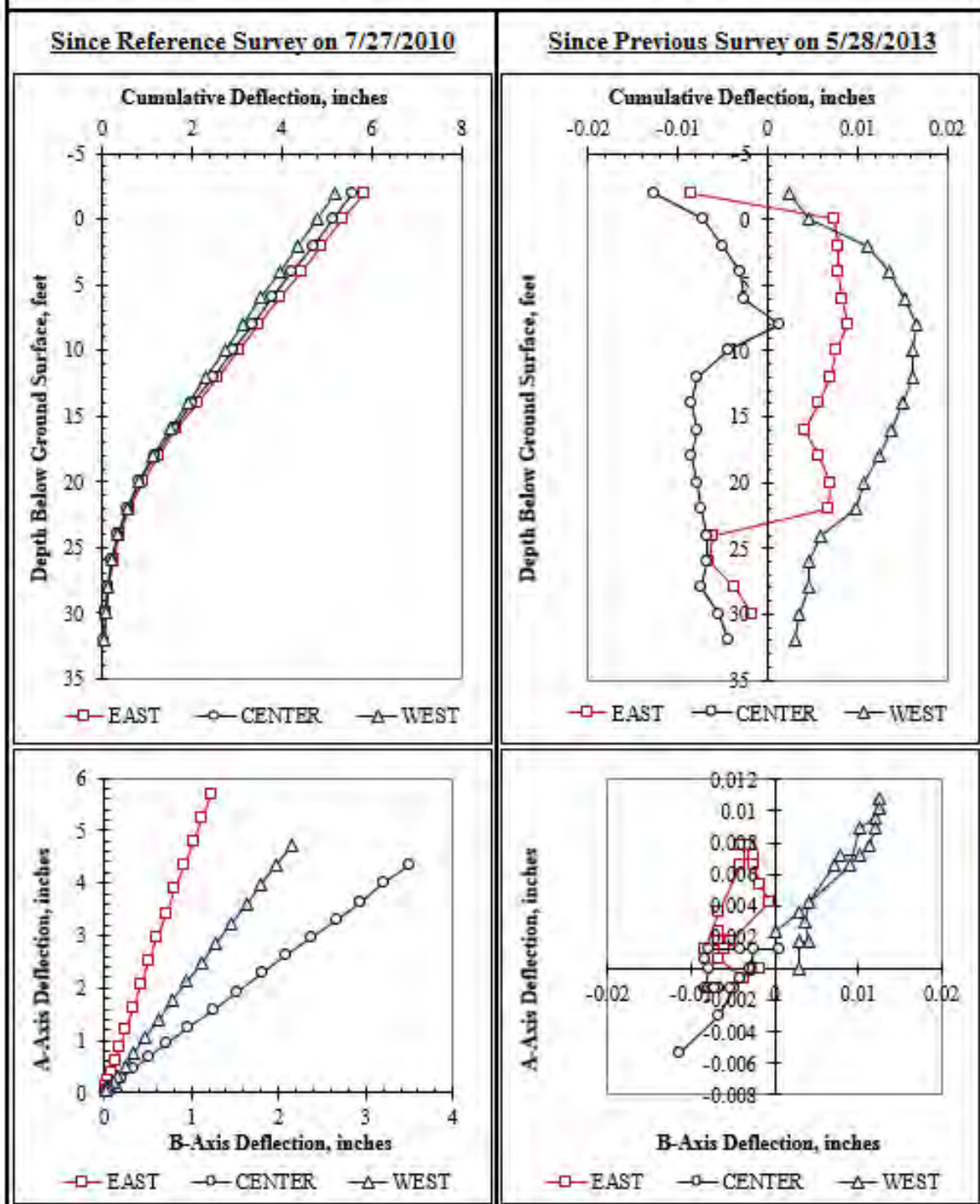


Figure F.127: Summary of inclinometer data from 6/3/2013.

Summary of Inclinometer Data From 6/6/2013

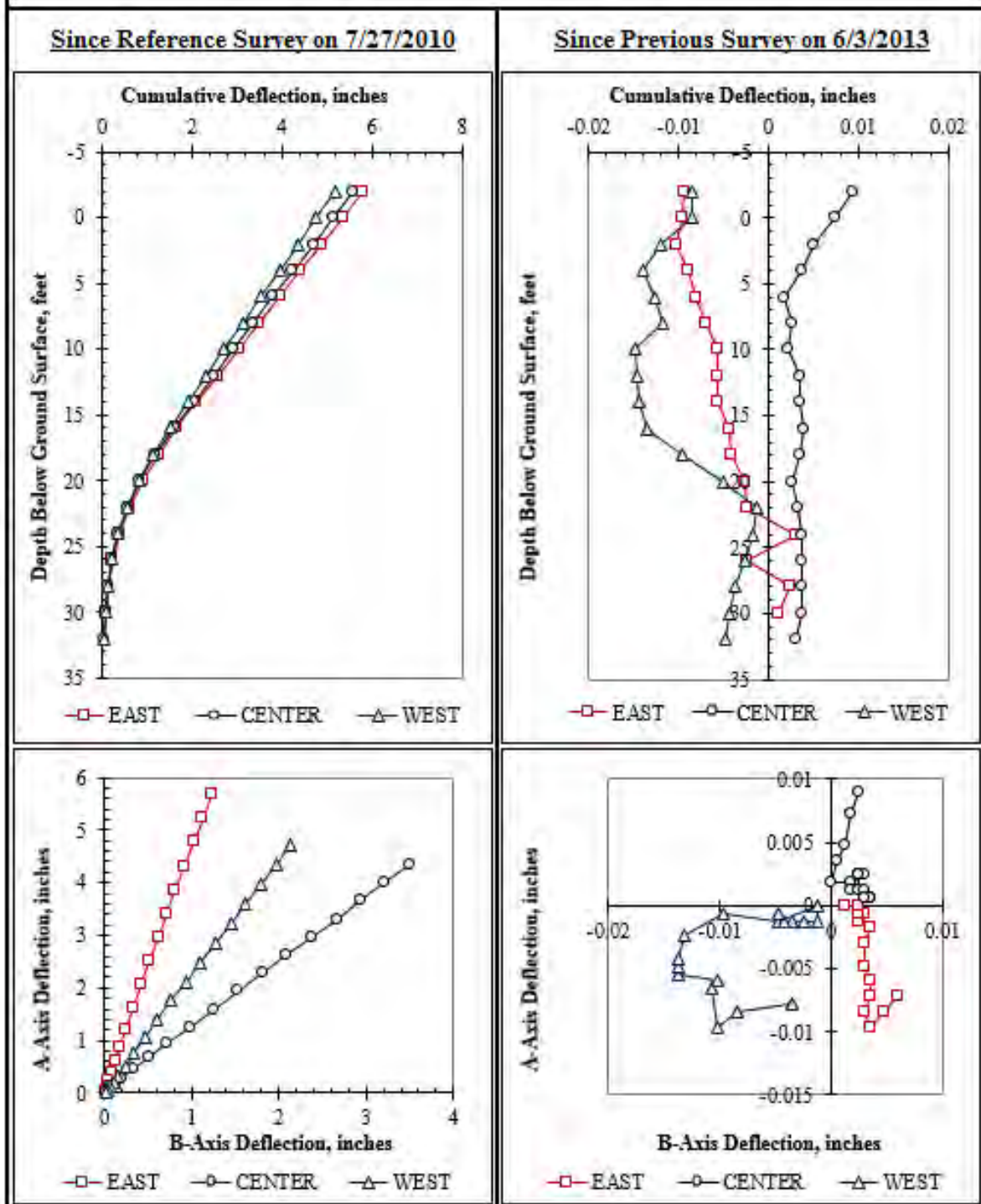


Figure F.128: Summary of inclinometer data from 6/6/2013.

Summary of Inclinator Data From 6/11/2013

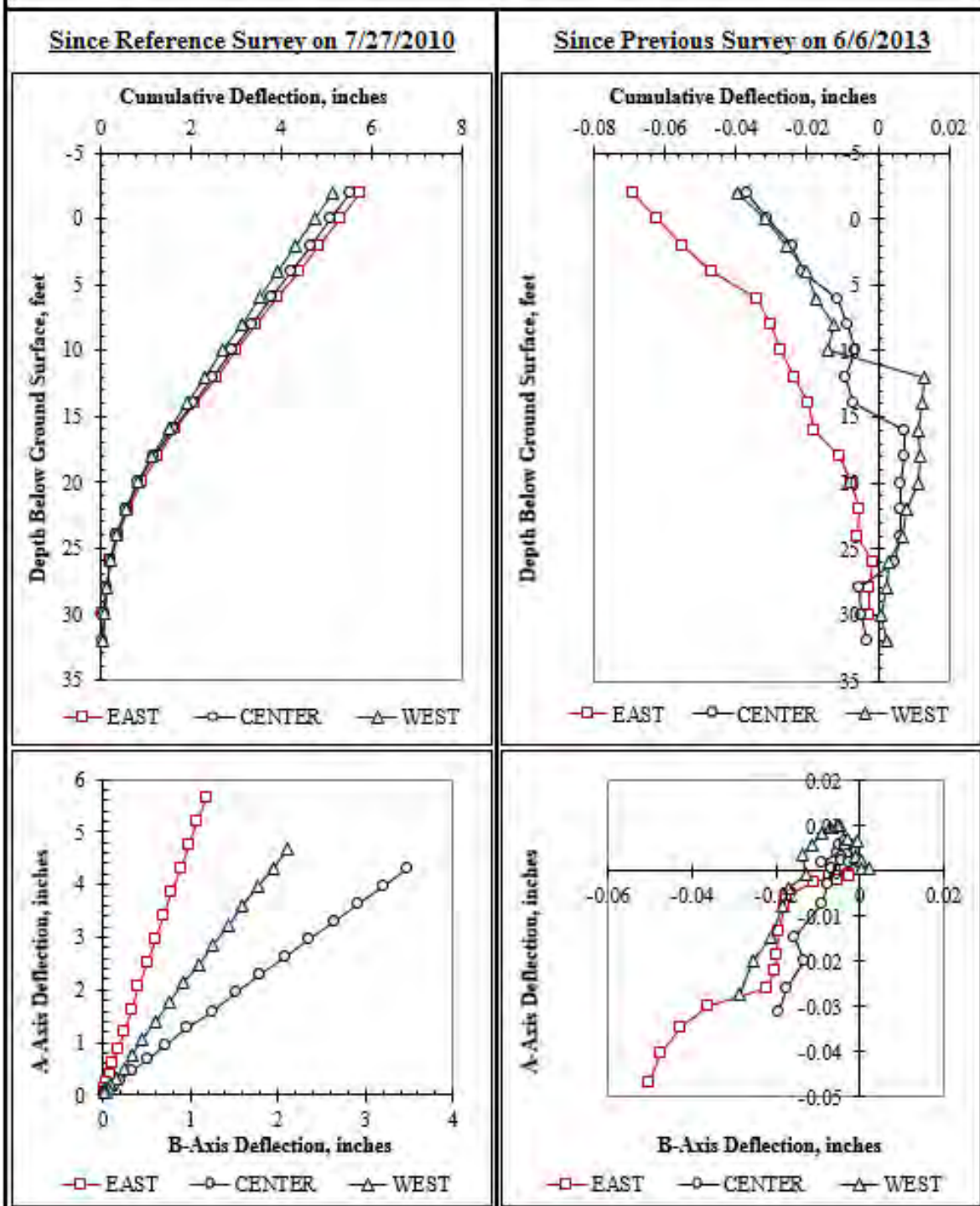


Figure F.129: Summary of inclinometer data from 6/11/2013.

Summary of Inclinometer Data From 6/17/2013

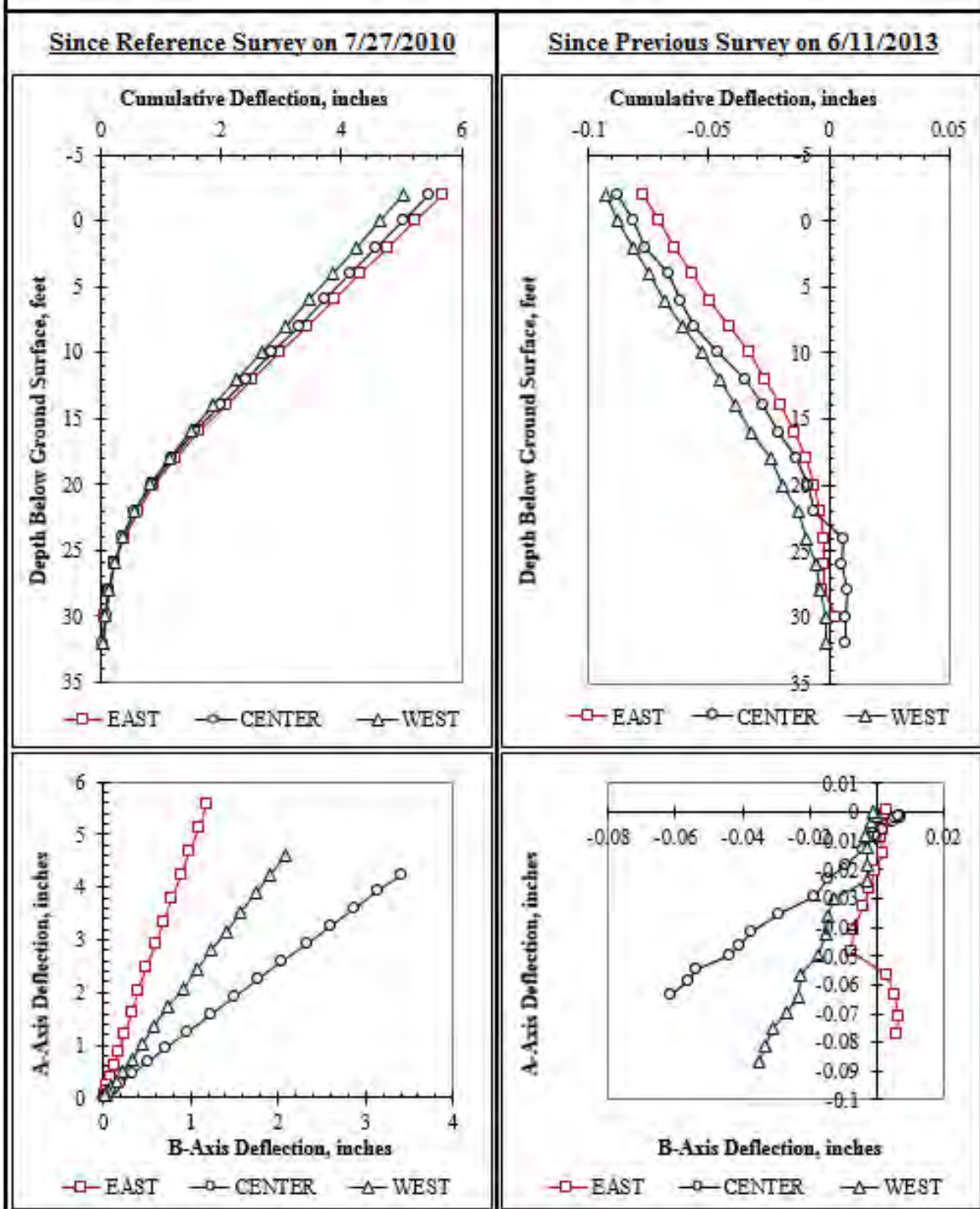


Figure F.130: Summary of inclinometer data from 6/17/2013.

Summary of Inclinometer Data From 6/24/2013

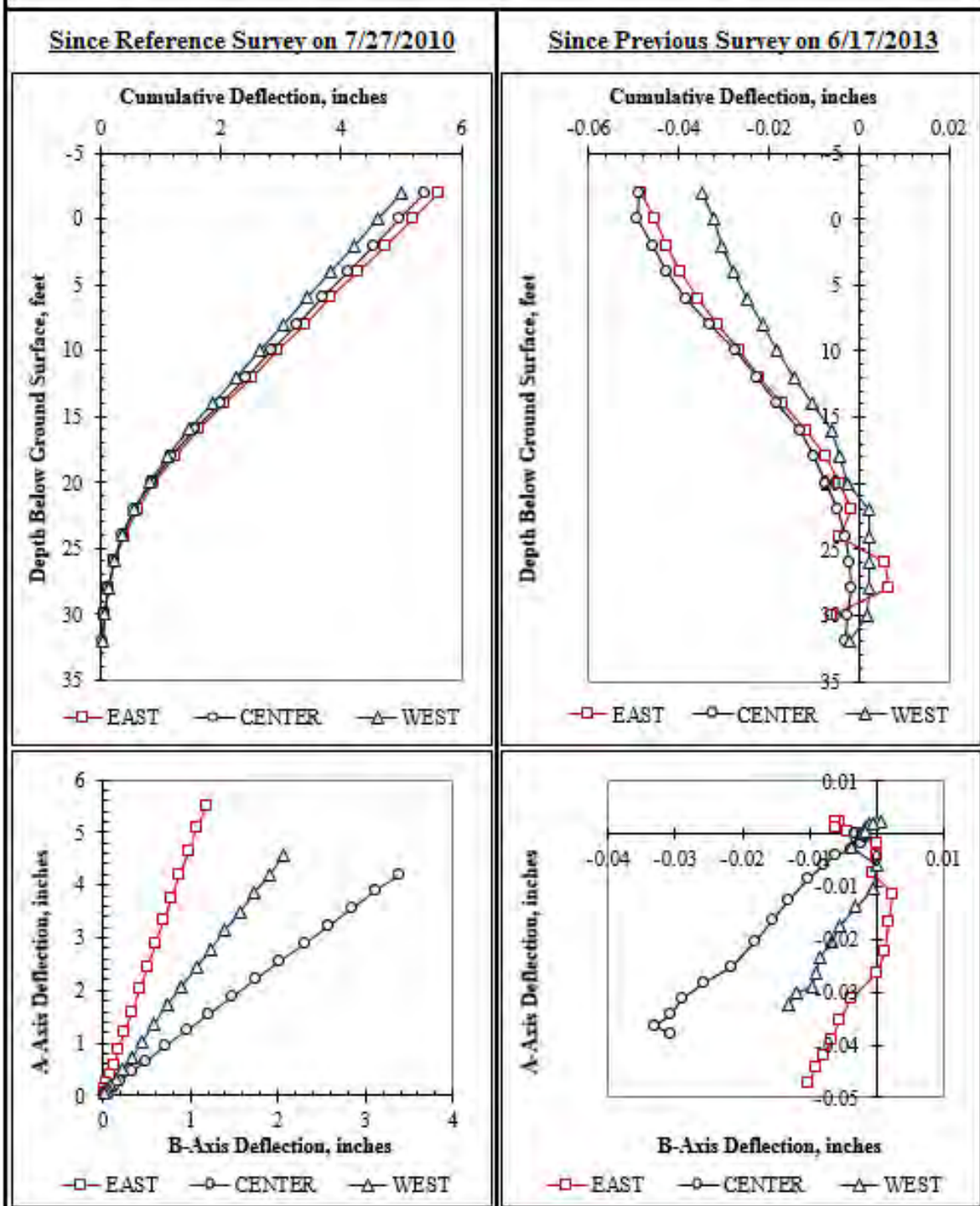


Figure F.131: Summary of inclinometer data from 6/24/2013.

Summary of Inclinometer Data From 7/2/2013

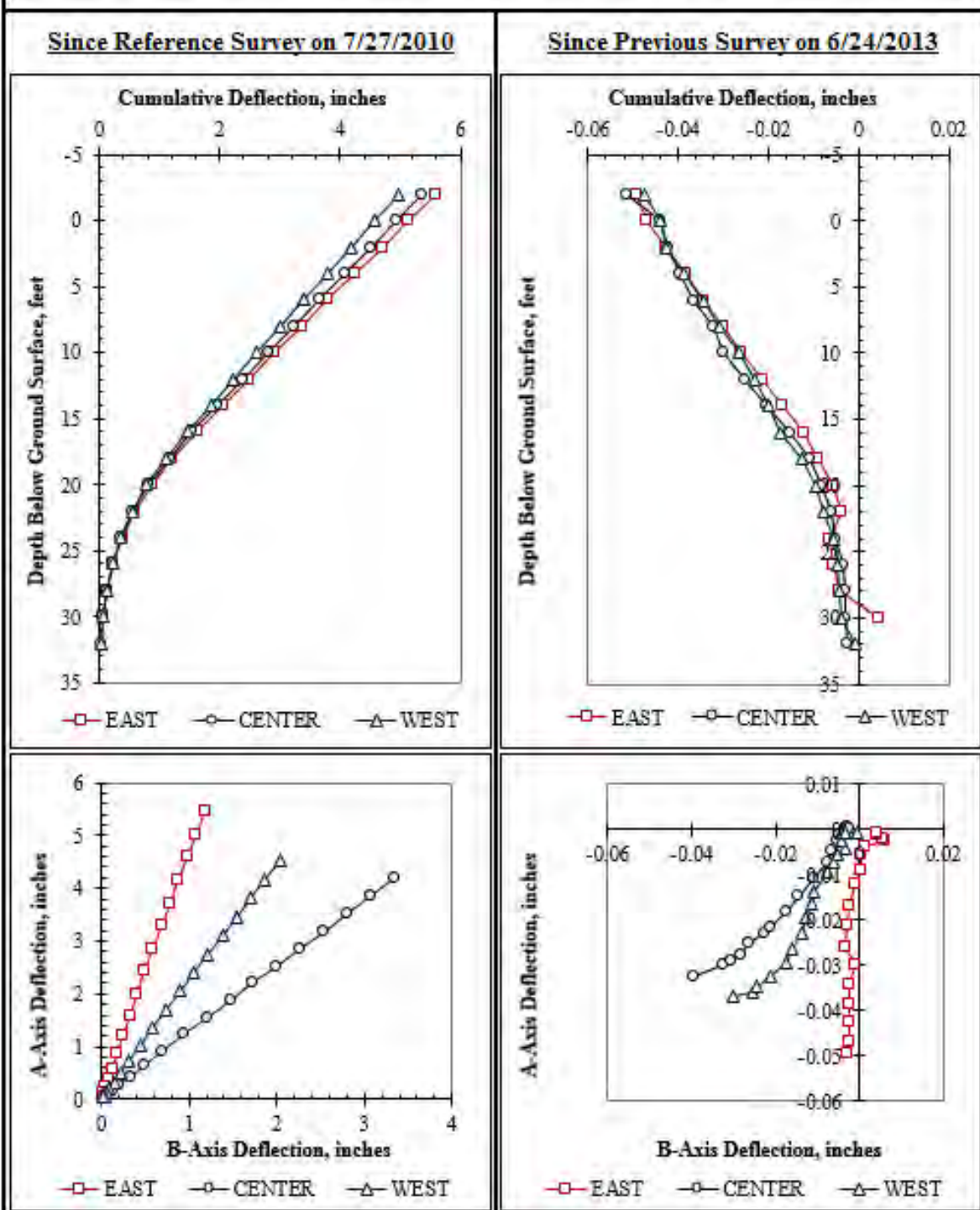


Figure F.132: Summary of inclinometer data from 7/2/2013.

Summary of Inclinometer Data From 7/11/2013

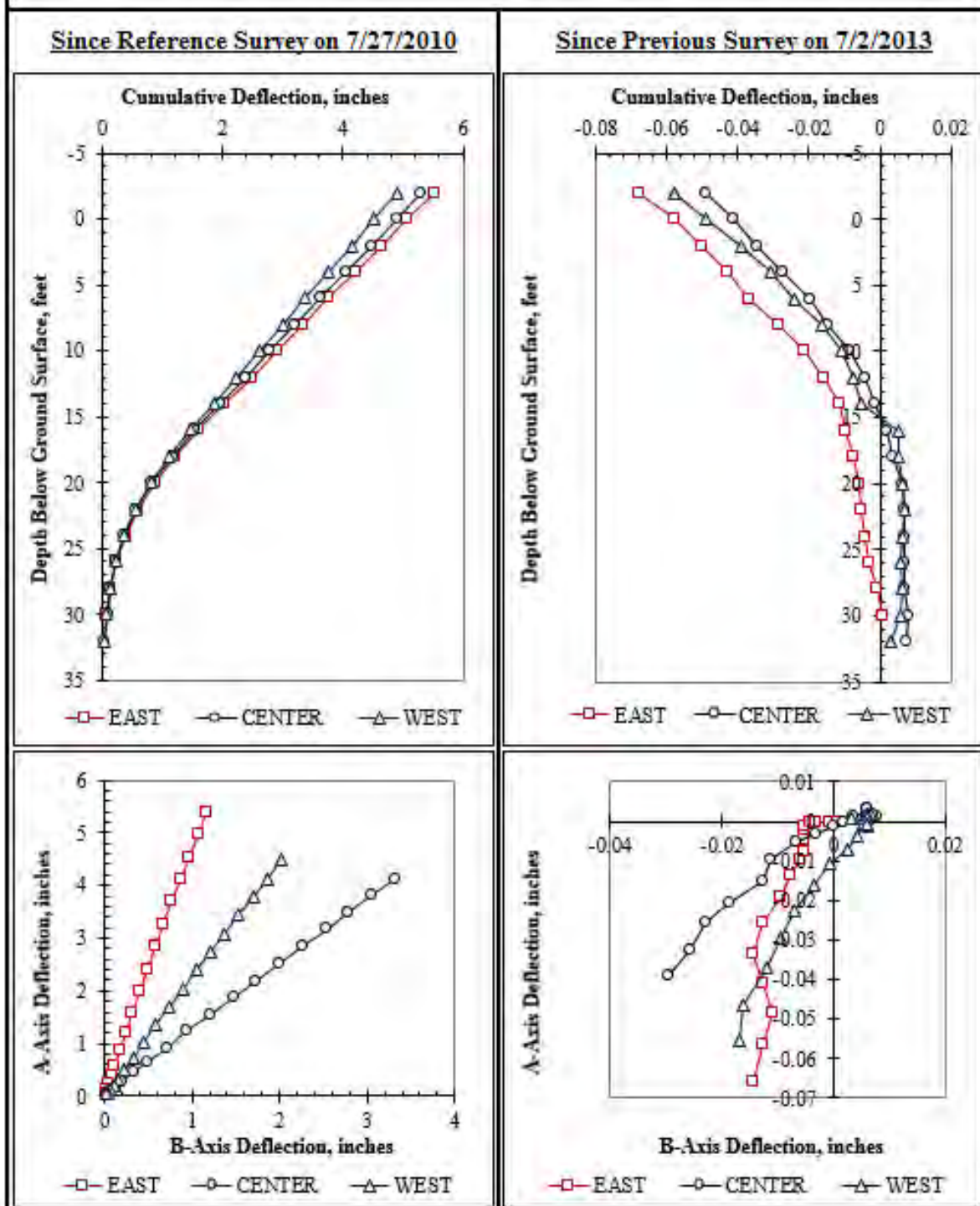


Figure F.133: Summary of inclinometer data from 7/11/2013.

Summary of Inclinometer Data From 7/25/2013

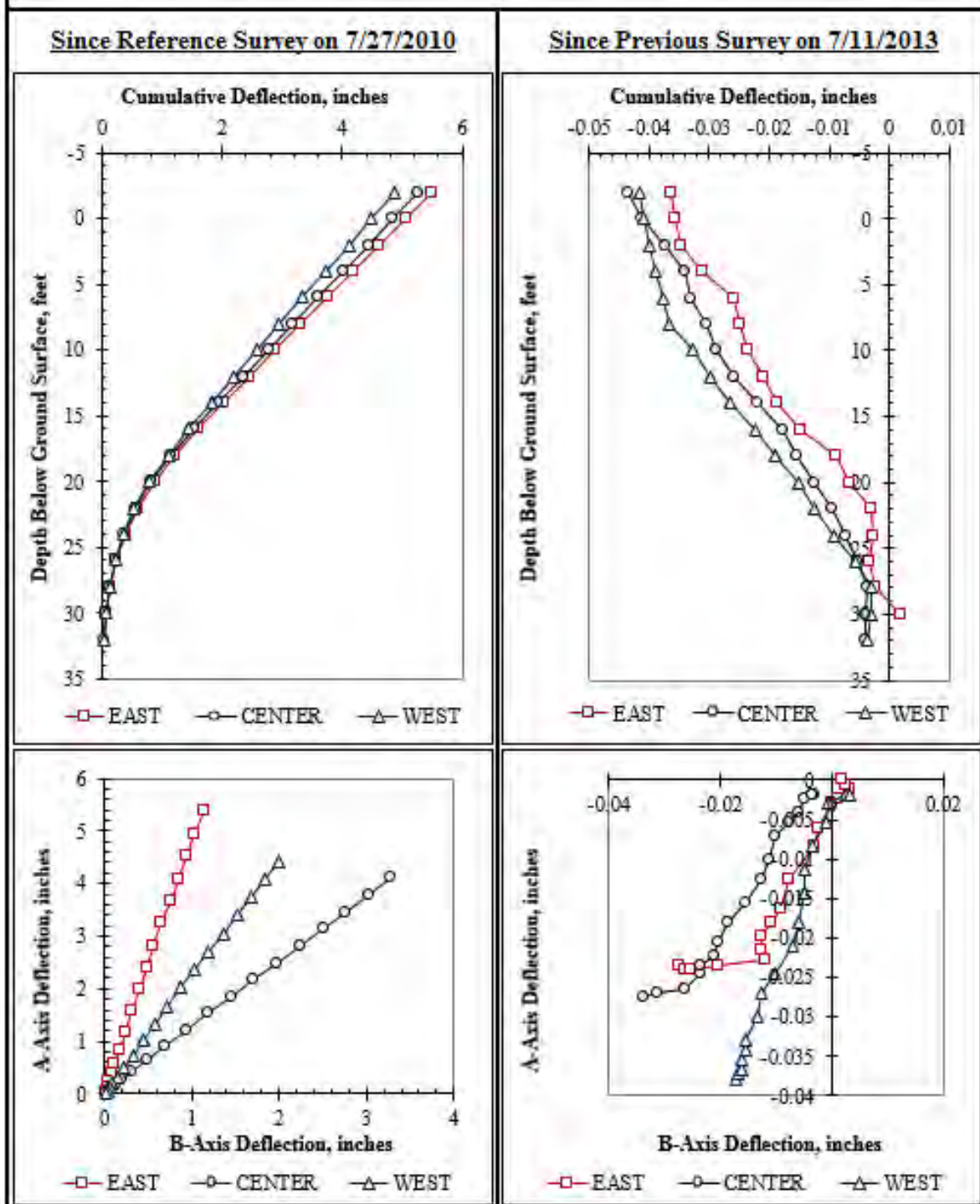


Figure F.134: Summary of inclinometer data from 7/25/2013.

Summary of Inclinometer Data From 8/19/2013

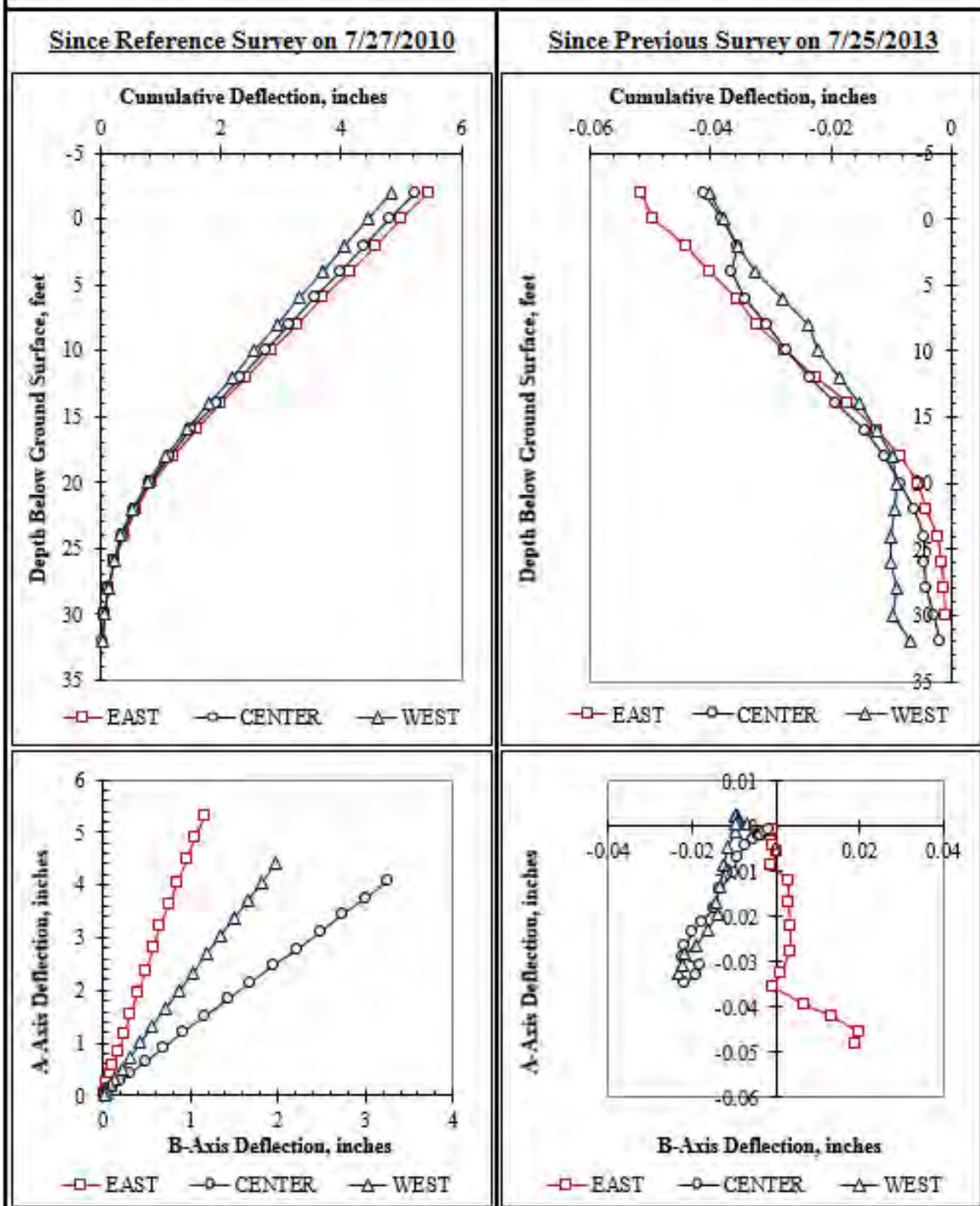


Figure F.135: Summary of inclinometer data from 8/19/2013.

F.3: Data from Inclinerometer Casing Behind the Wall

The inclinometer data from the inclinometer installed approximately 5.5 feet behind the wall to a depth of 50 feet below ground surface are presented in the following figures.

Summary of Inclinometer Data From 7/27/2010 to 9/29/2010

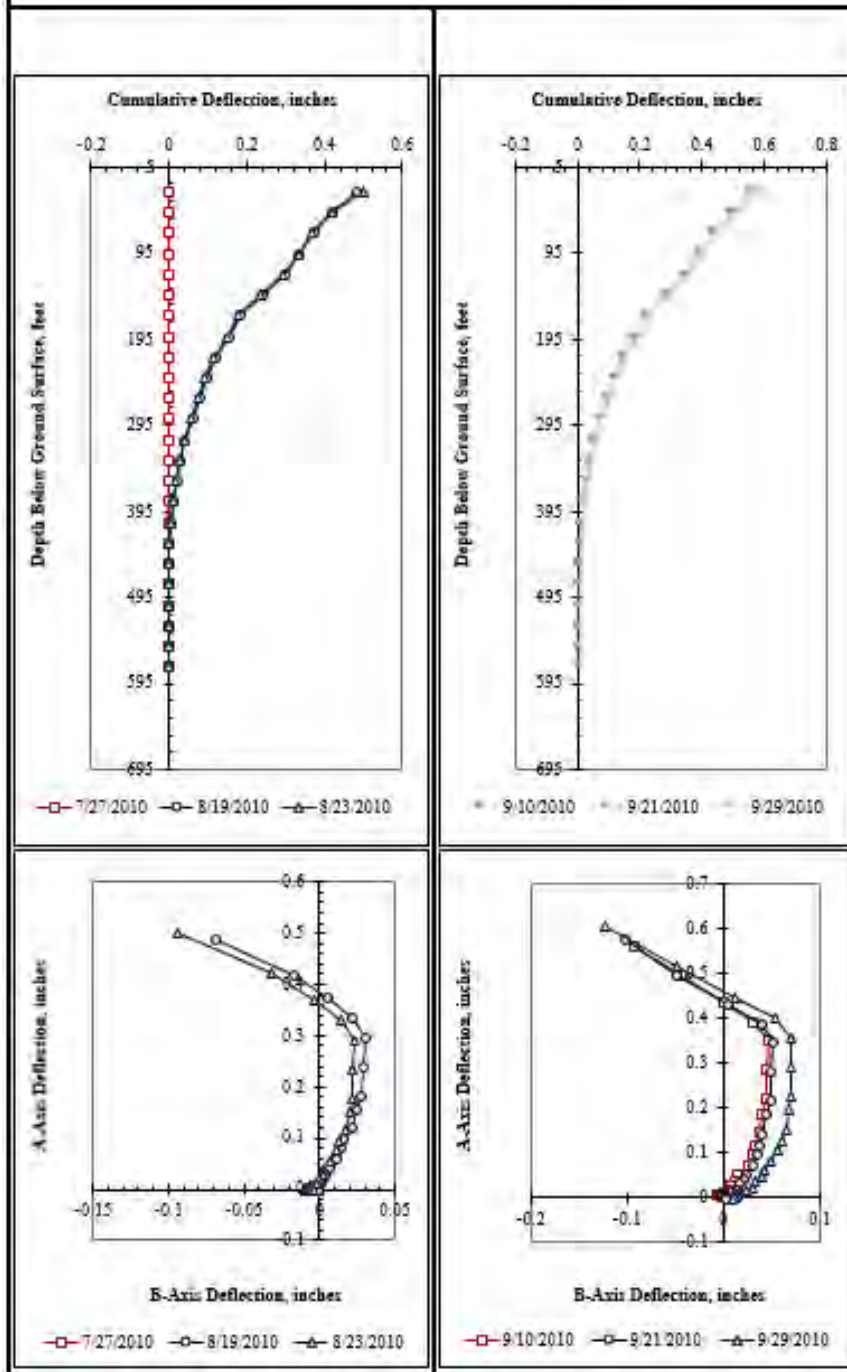


Figure F.136: Summary of behind the wall inclinometer data from 7/27/2010 to 9/29/2010.

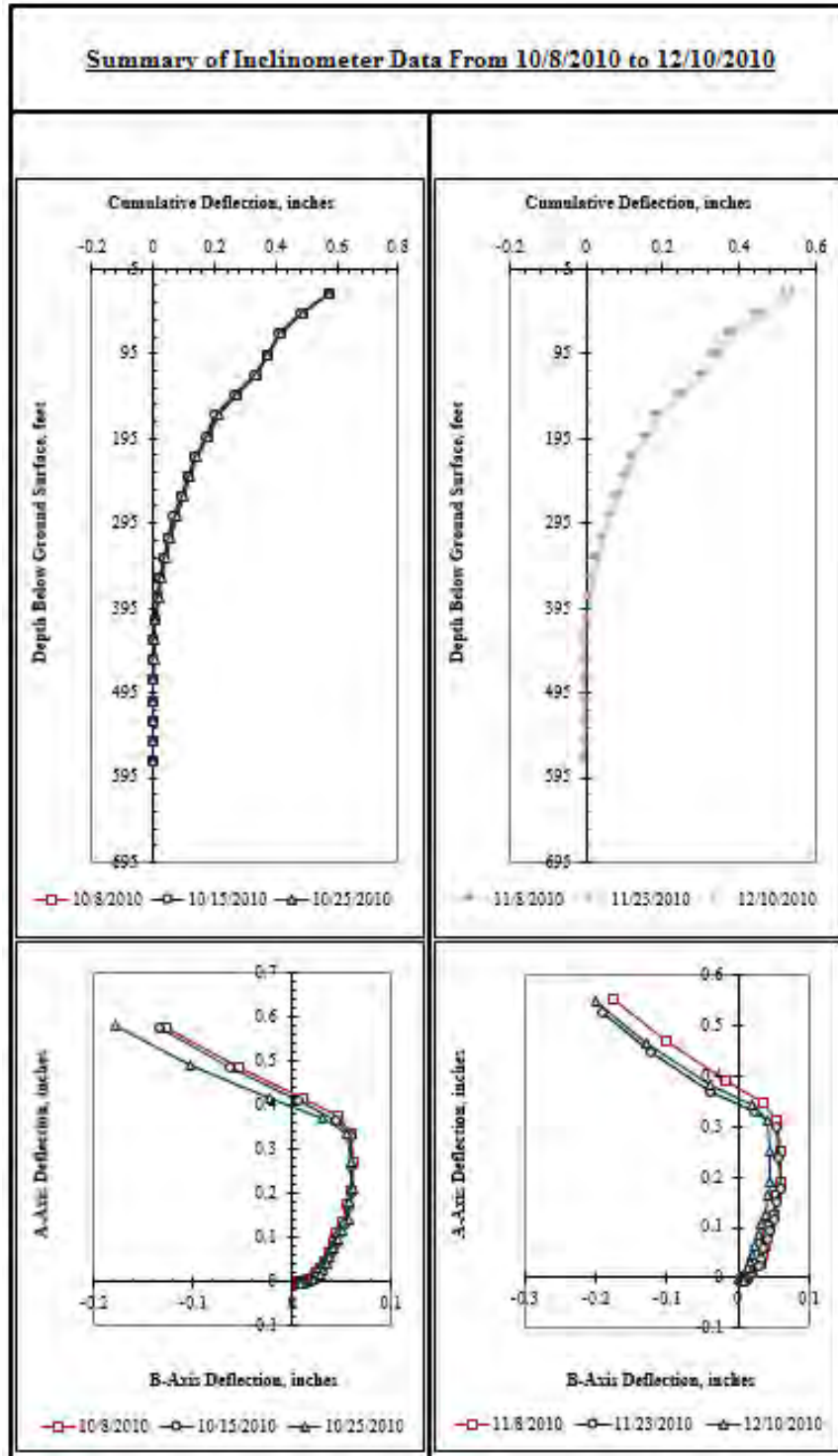


Figure F.137: Summary of behind the wall inclinometer data from 10/8/2010 to 12/10/2010.

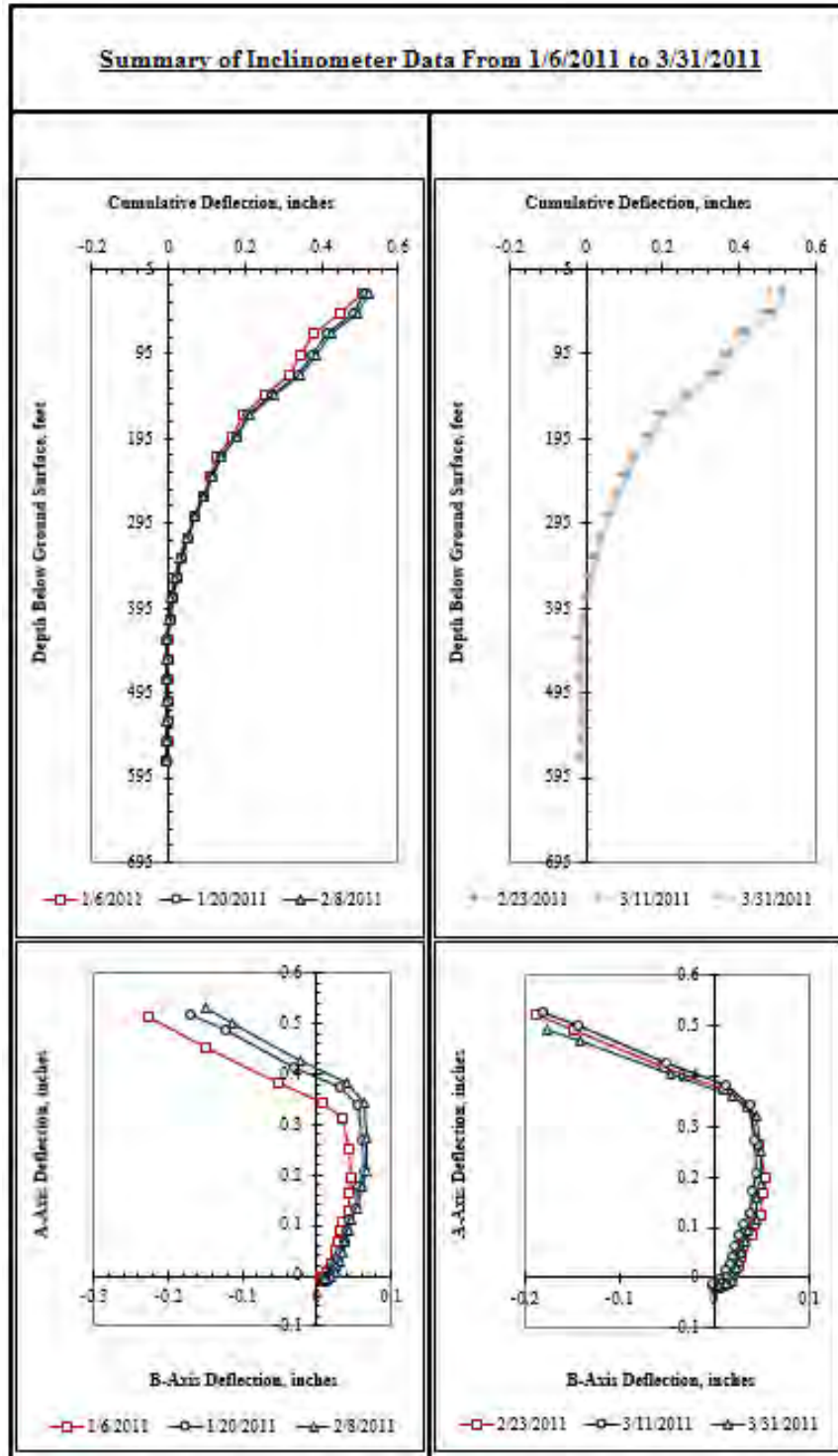


Figure F.138: Summary of behind the wall inclinometer data from 1/6/2011 to 3/31/2011.

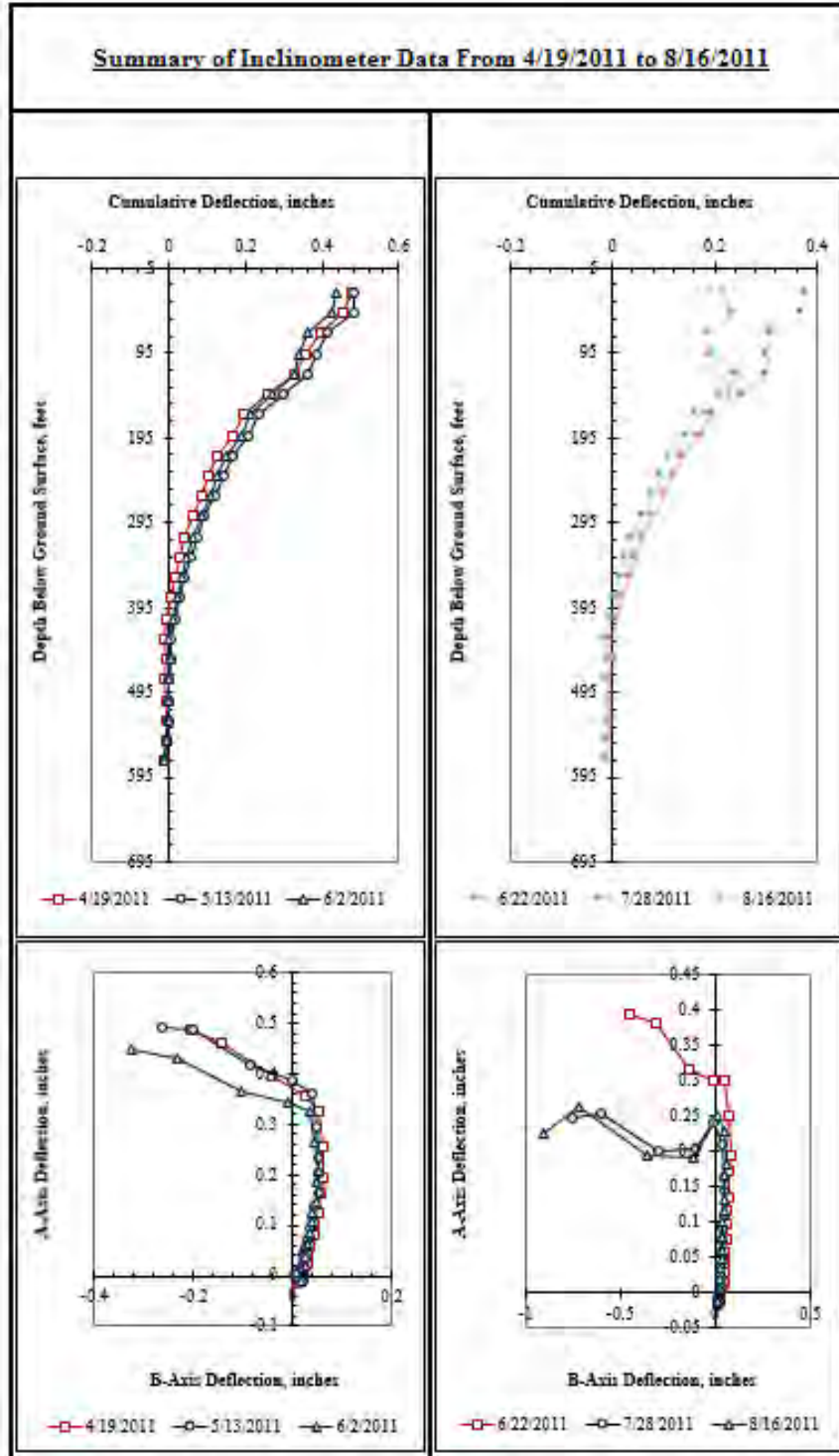


Figure F.139: Summary of behind the wall inclinometer data from 4/19/2011 to 8/16/2011.

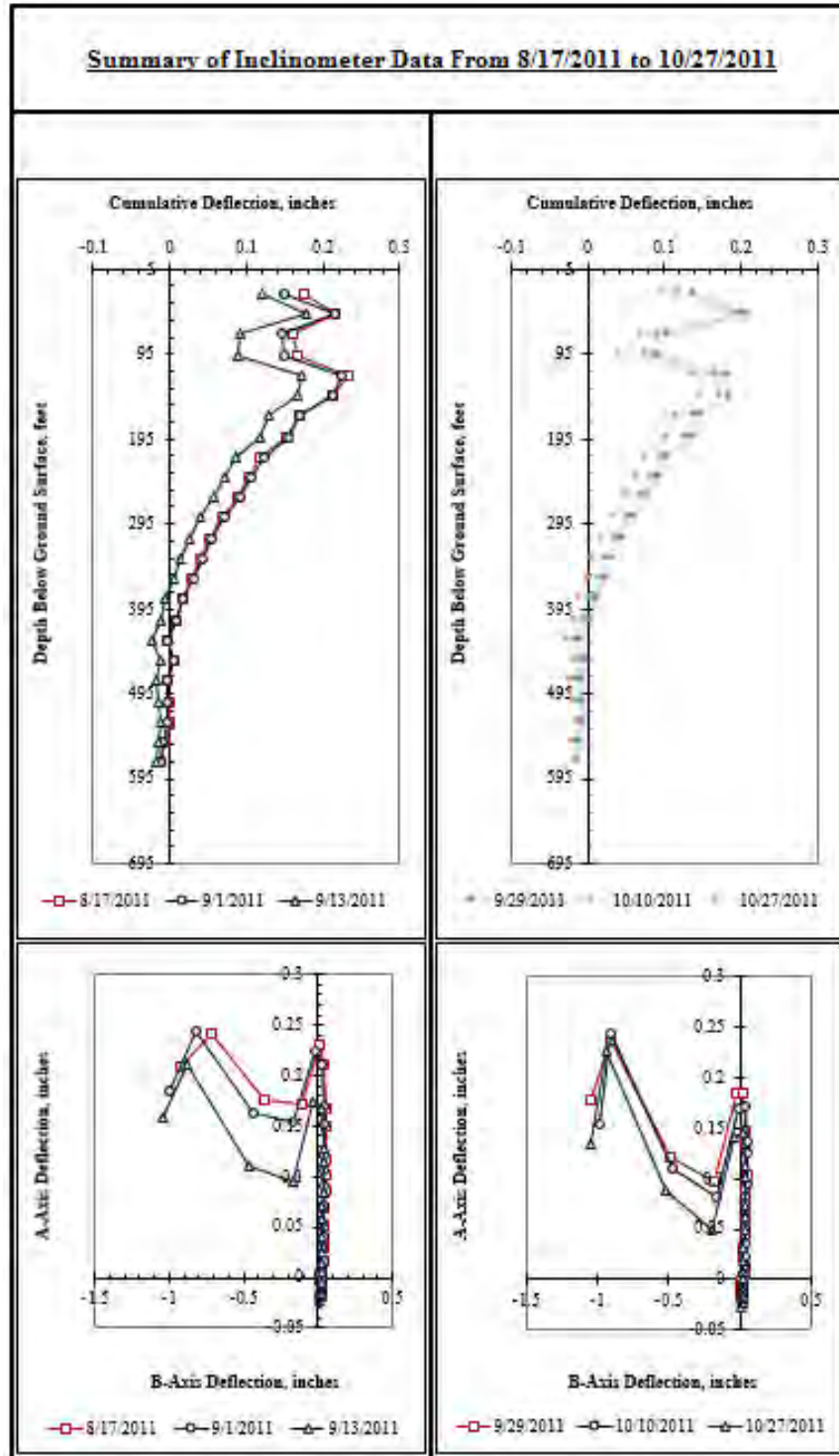


Figure F.140: Summary of behind the wall inclinometer data from 8/17/2011 to 10/27/2011.

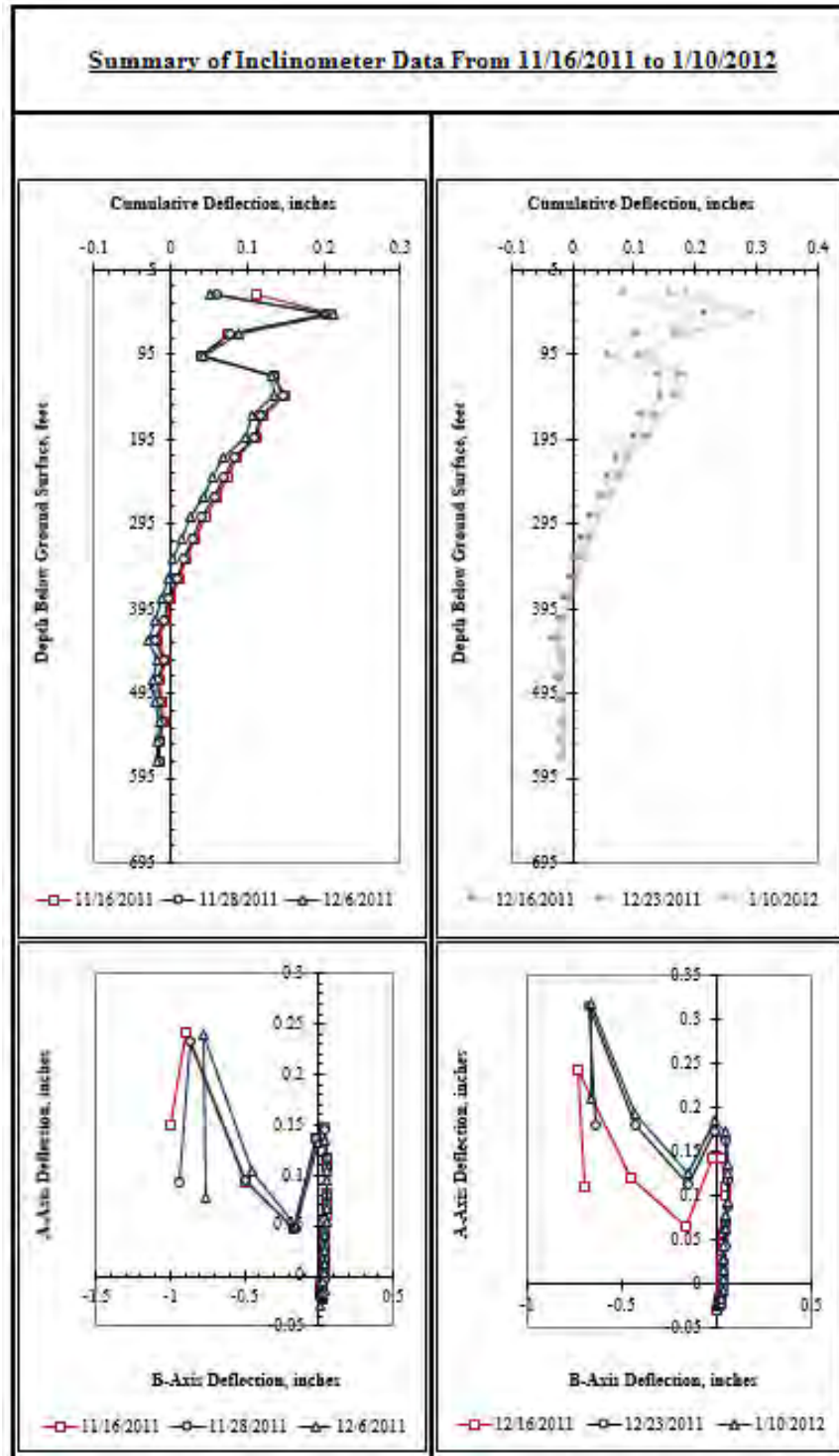


Figure F.141: Summary of behind the wall inclinometer data from 11/16/2011 to 1/10/2012.

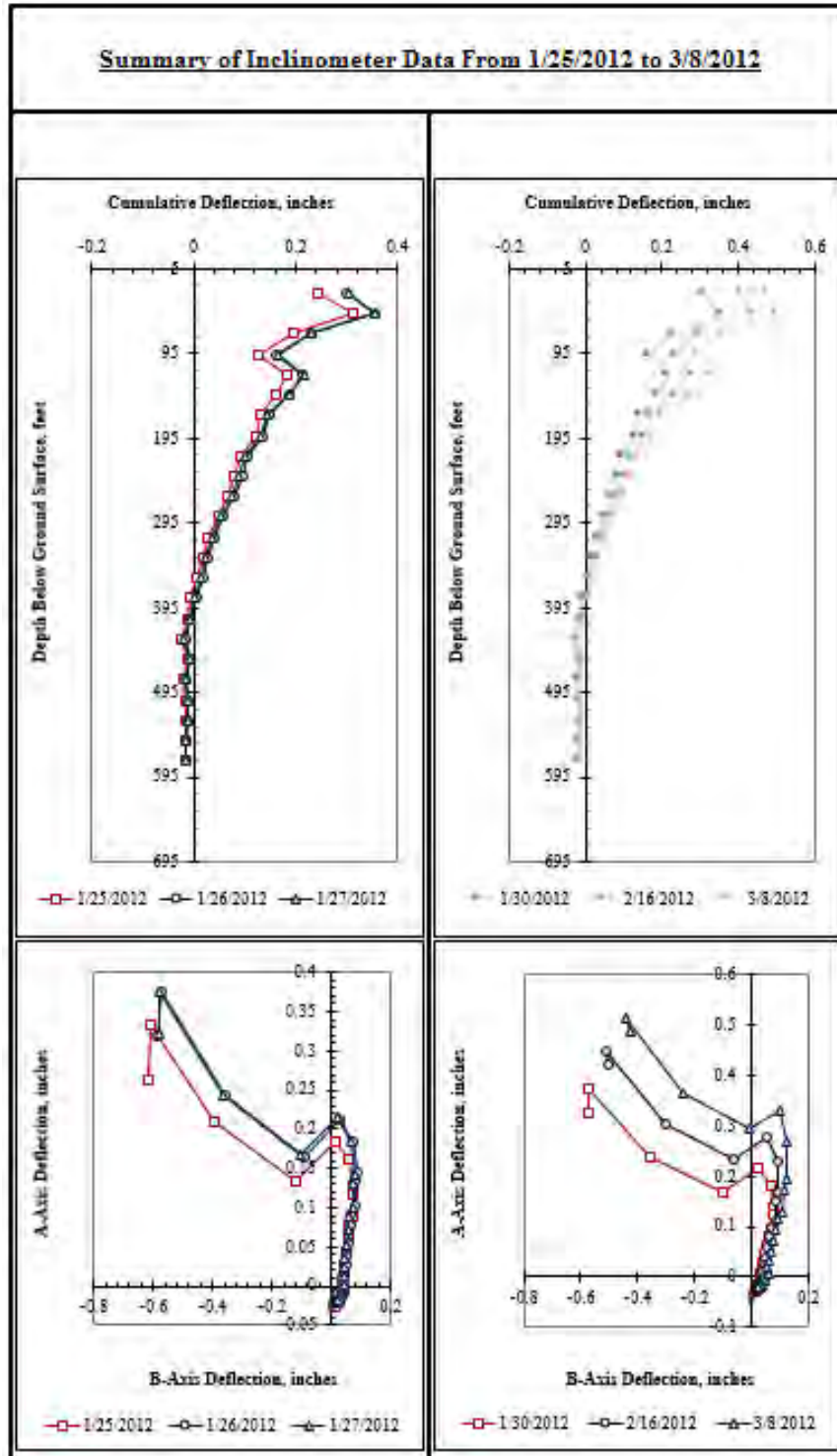


Figure F.142: Summary of behind the wall inclinometer data from 1/25/2012 to 3/8/2012.

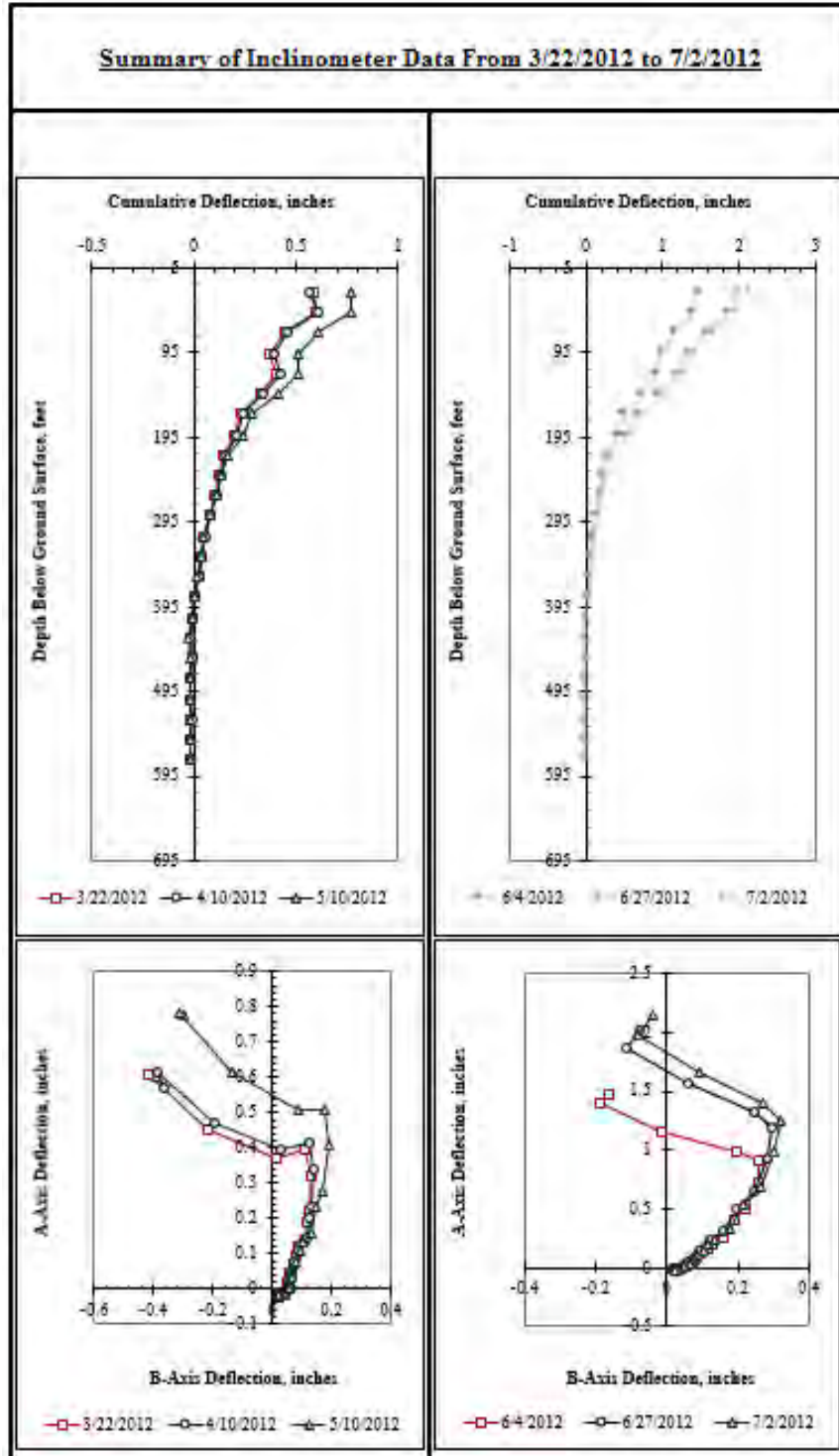


Figure F.143: Summary of behind the wall inclinometer data from 3/22/2012 to 7/2/2012.

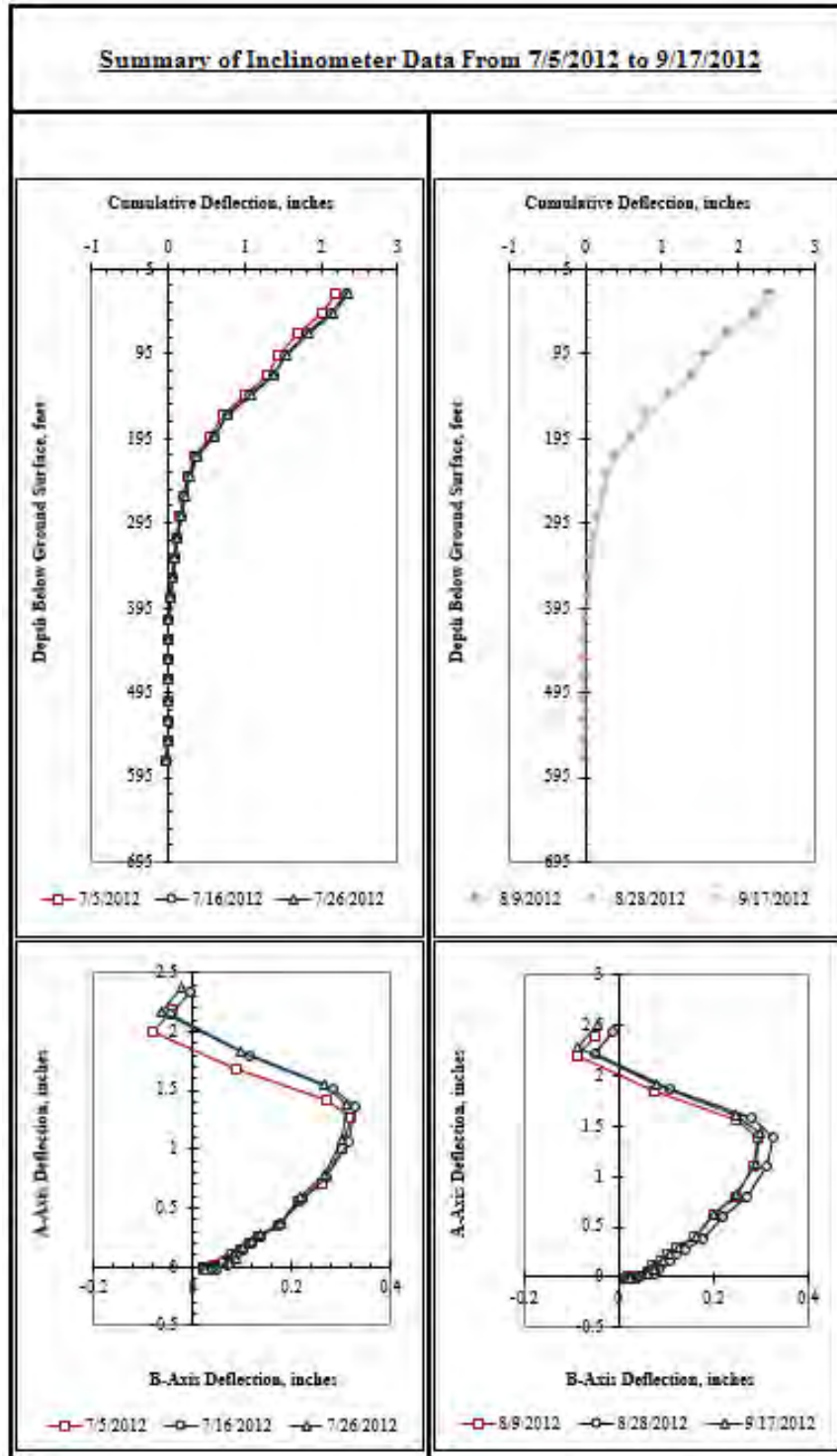


Figure F.144: Summary of behind the wall inclinometer data from 7/5/2012 to 9/17/2012.

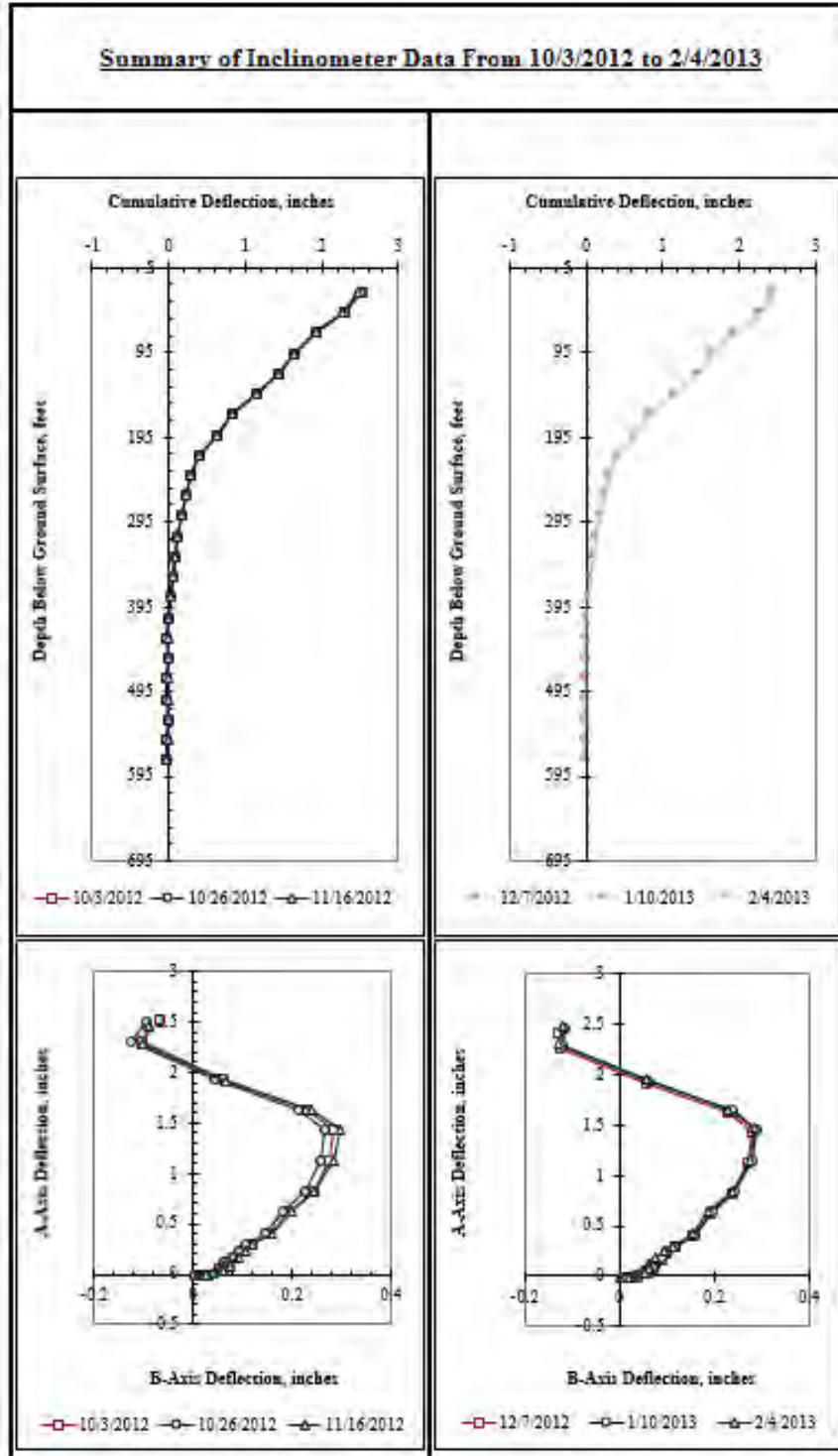


Figure F.145: Summary of behind the wall inclinometer data from 10/3/2012 to 2/4/2013.

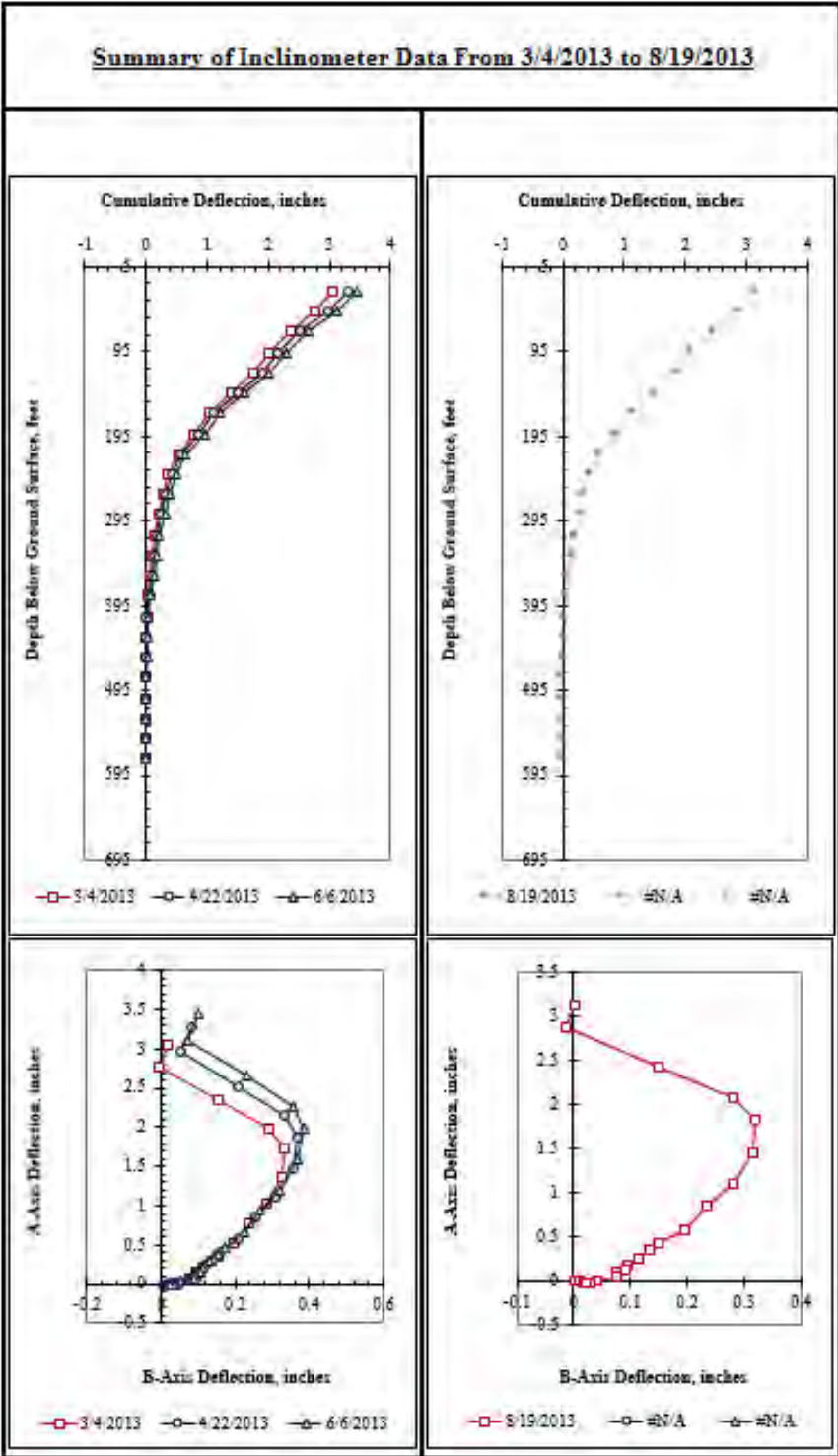


Figure F.146: Summary of behind the wall inclinometer data from 3/4/2013 to 8/19/2013.

APPENDIX G: STRAIN GAUGE DATA

G.1: Overview

This section summarizes the raw strain data recorded during the test wall monitoring period. The optical strain gauges were purchased from OPSENS in Canada, and the sister bars were fabricated by Lymon C. Reese and Associates of Austin, Texas. Prior to installation, each sister bar was calibrated to ensure linearity in the readings within the operating strain range of 1,000 microstrains and to establish a response curve. There are a total of 90 optical strain gauges installed in the test wall; in each instrumented shaft, there are 15 gauges on either side of the neutral axis.

The strain gauges placed on either side of the shaft's neutral axis measure axial strains in the tensile and compressive direction (ϵ_t and ϵ_c , respectively). The difference in tensile and compressive strains on either side of the neutral axis is divided by the horizontal distance between the gauges to obtain a value of bending curvature at a given depth. The calculated value of bending curvature is converted to a value of bending moment according to the moment-curvature relationship defined by the structural properties of the shaft. Following this procedure at each depth where strain gauges are installed yields a profile of bending moment in the shaft versus depth, which can be differentiated once to obtain a profile of shear force versus depth, or differentiated twice to obtain a profile of soil resistance versus depth. This process is summarized in Figure G.1. A more detailed explanation of strain gauge data reduction for the Lymon C. Reese research wall can be found in Koutrouvelis (2012).

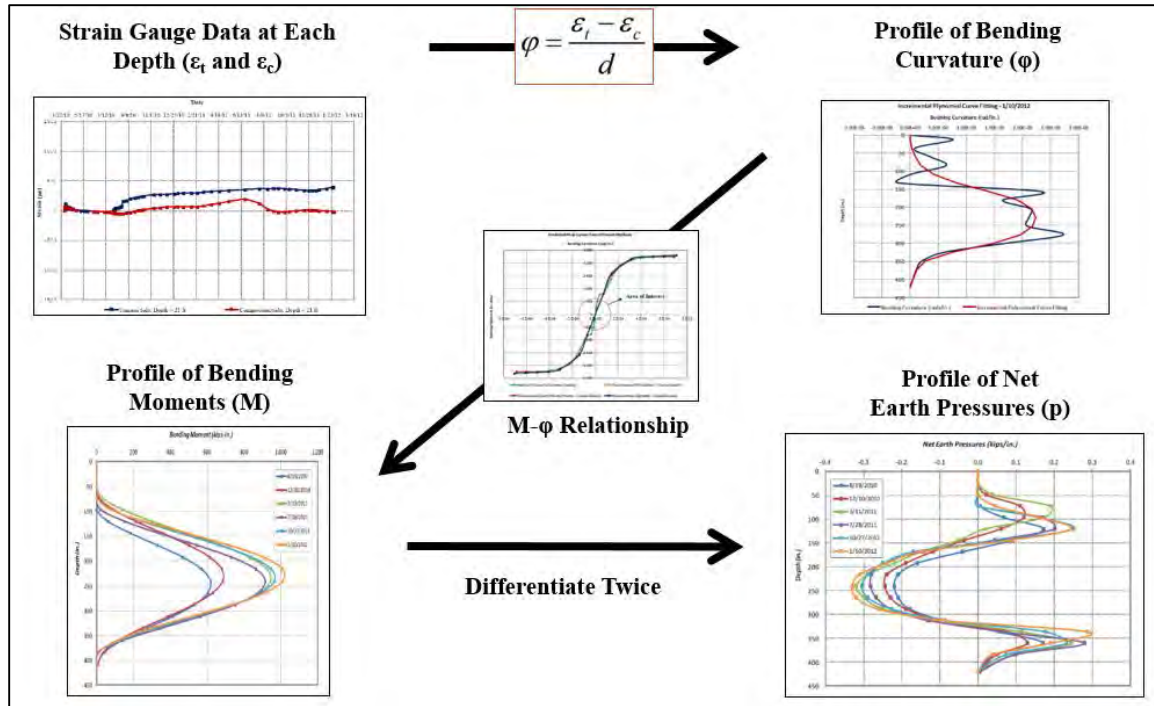


Figure G.1: Strain gauge data reduction (after Koutrouvelis 2012).

For this research study, strain gauge nomenclature indicates which instrumented shaft the gauge is installed in (East, Center, or West), the depth of the strain gauge below original ground surface (1 – 29 feet), and which side of the neutral axis the gauge is installed on (Tension or Compression; tensile strains are positive). Using this nomenclature, gauge E.17.T is located in the east instrumented shaft, 17 feet below ground surface, on the tensile side of the neutral axis.

G.2: Strain Data Before Excavation

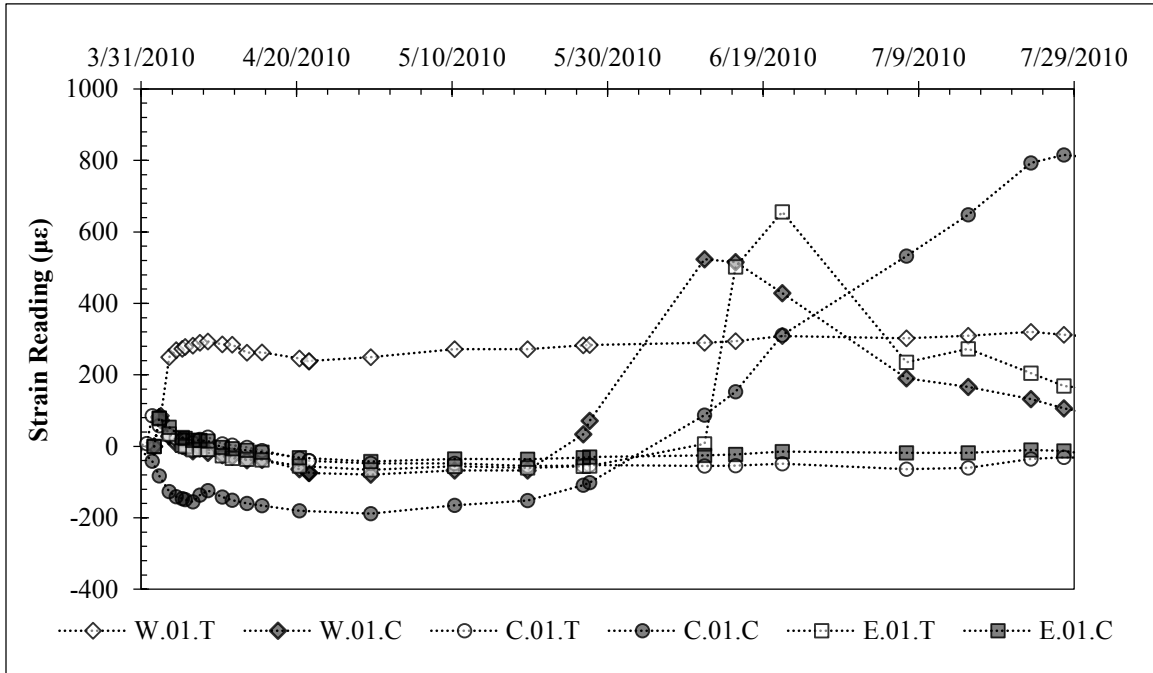


Figure G.2: Pre-Excavation Strain Data for Gauges 1 Foot Below Ground Surface.

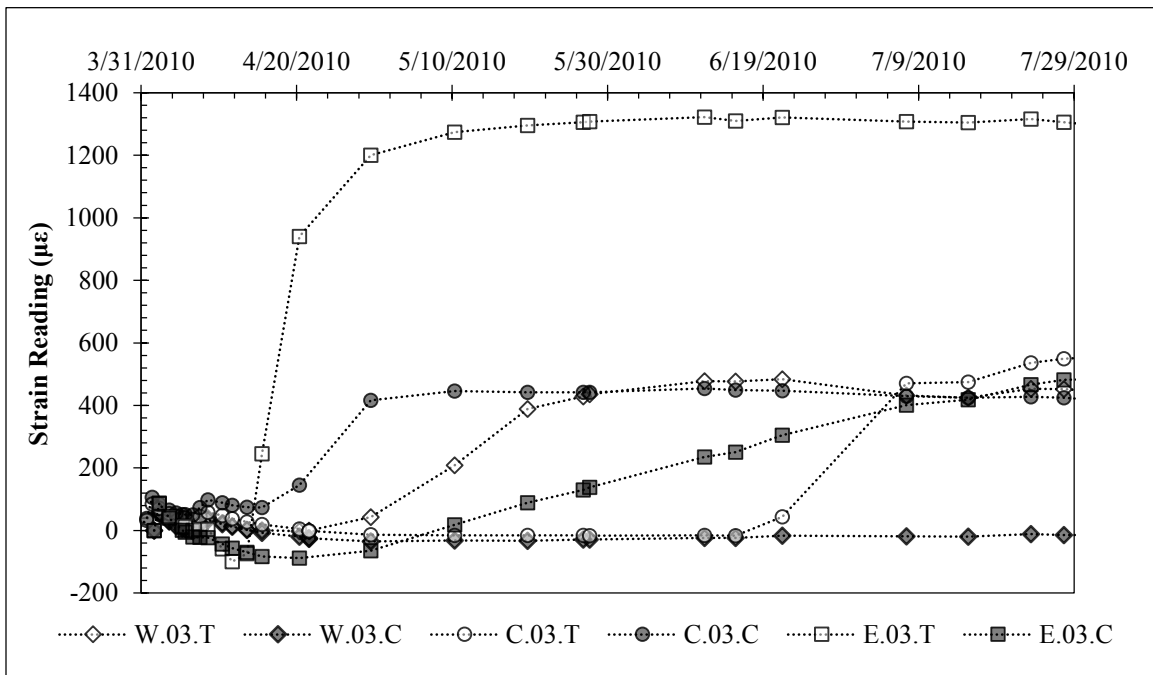


Figure G.3: Pre-Excavation Strain Data for Gauges 3 Feet Below Ground Surface.

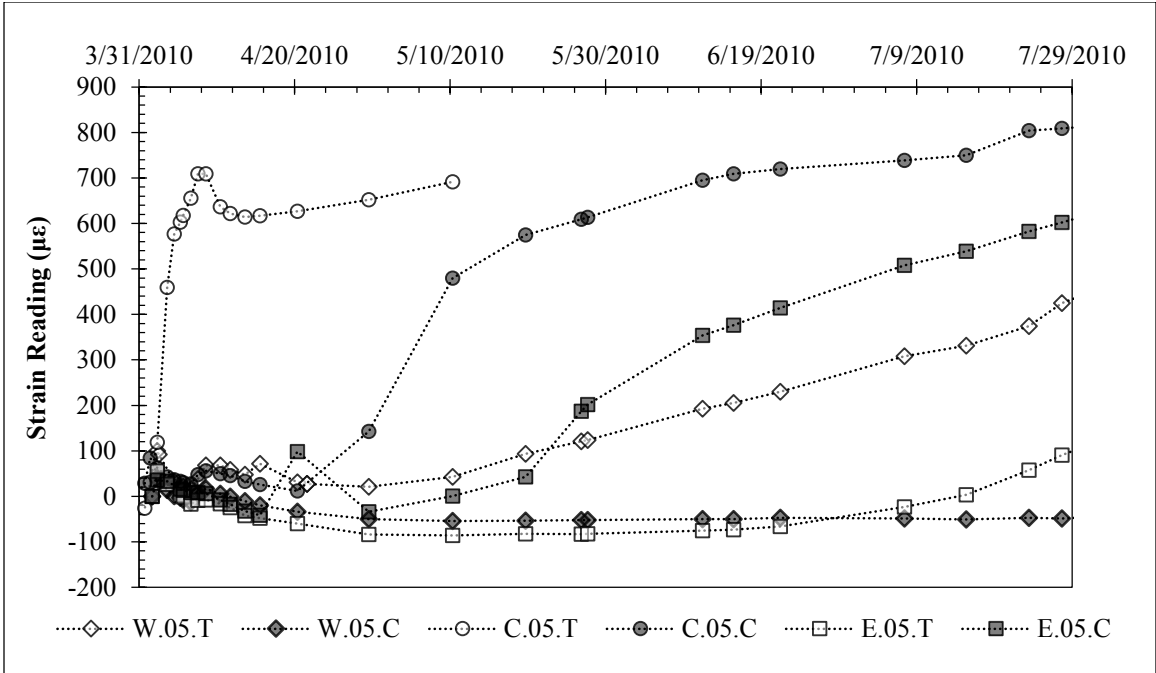


Figure G.4: Pre-Excavation Strain Data for Gauges 5 Feet Below Ground Surface.

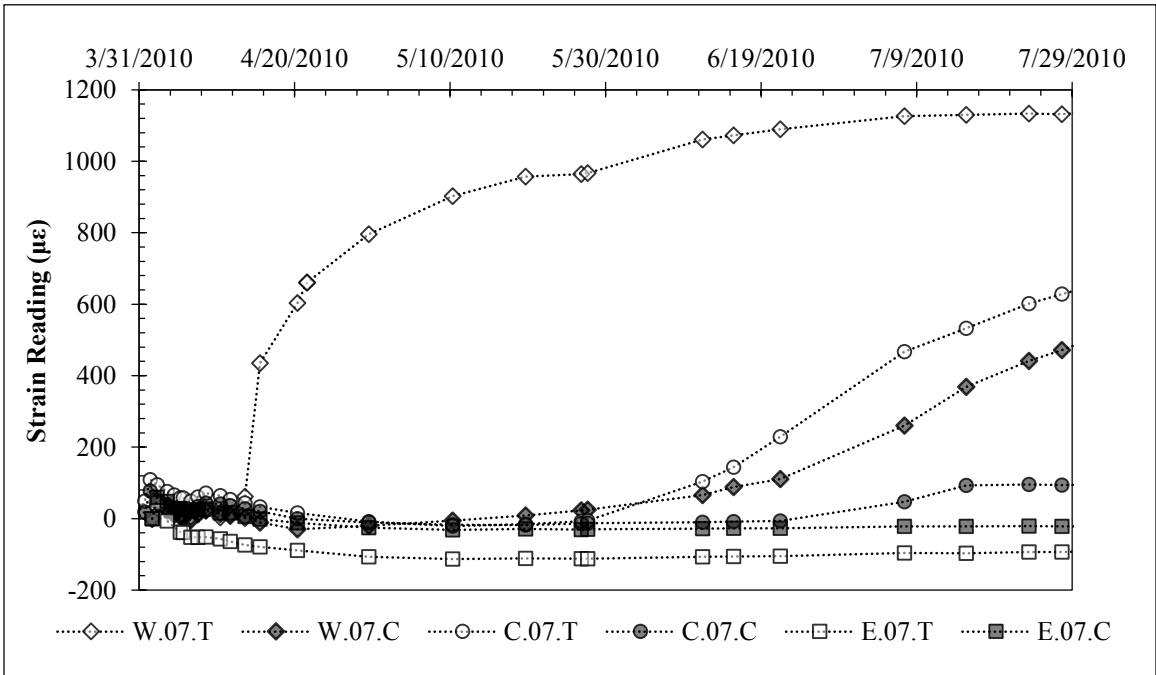


Figure G.5: Pre-Excavation Strain Data for Gauges 7 Feet Below Ground Surface.

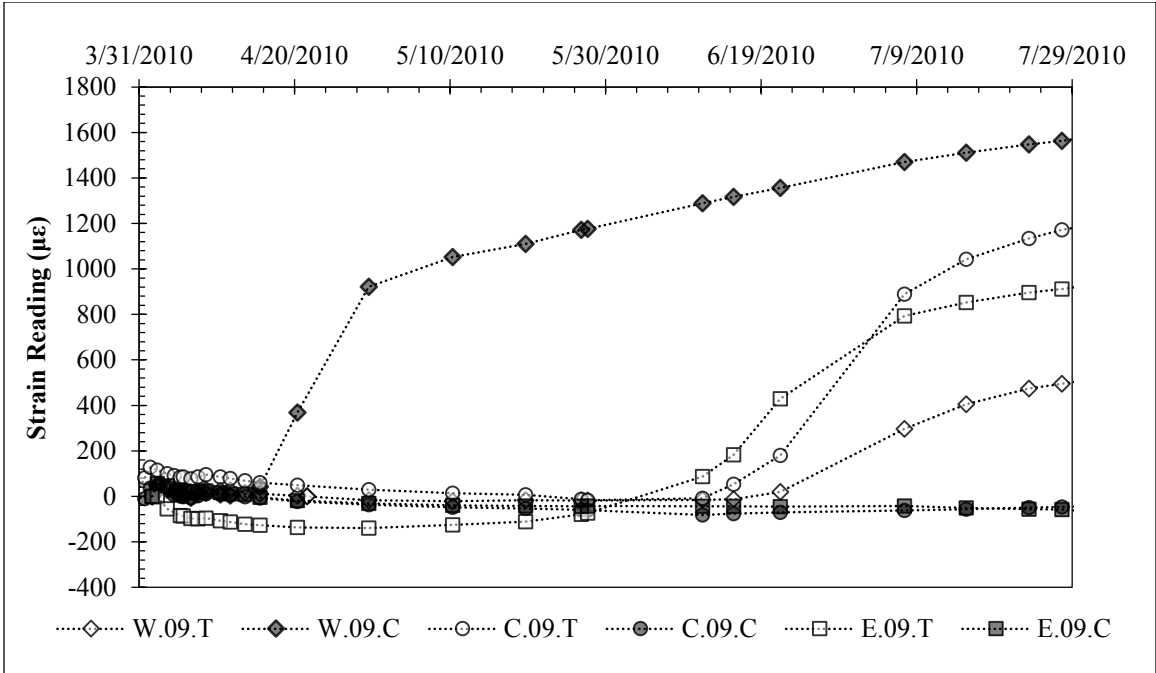


Figure G.6: Pre-Excavation Strain Data for Gauges 9 Feet Below Ground Surface.

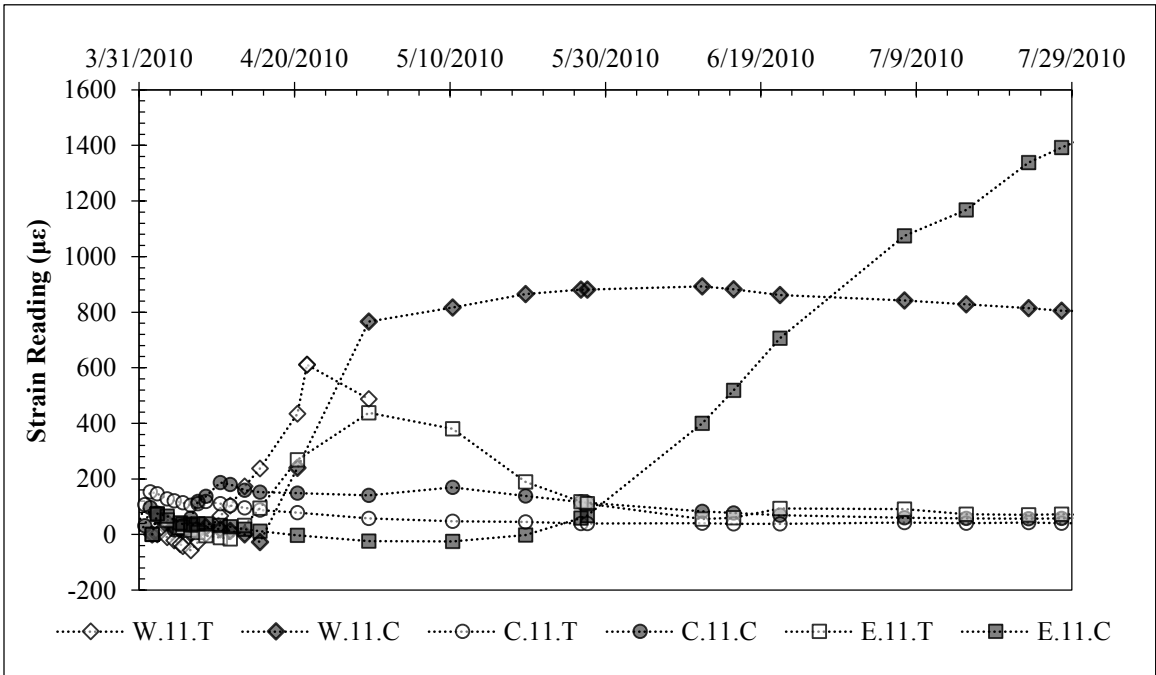


Figure G.7: Pre-Excavation Strain Data for Gauges 11 Feet Below Ground Surface.

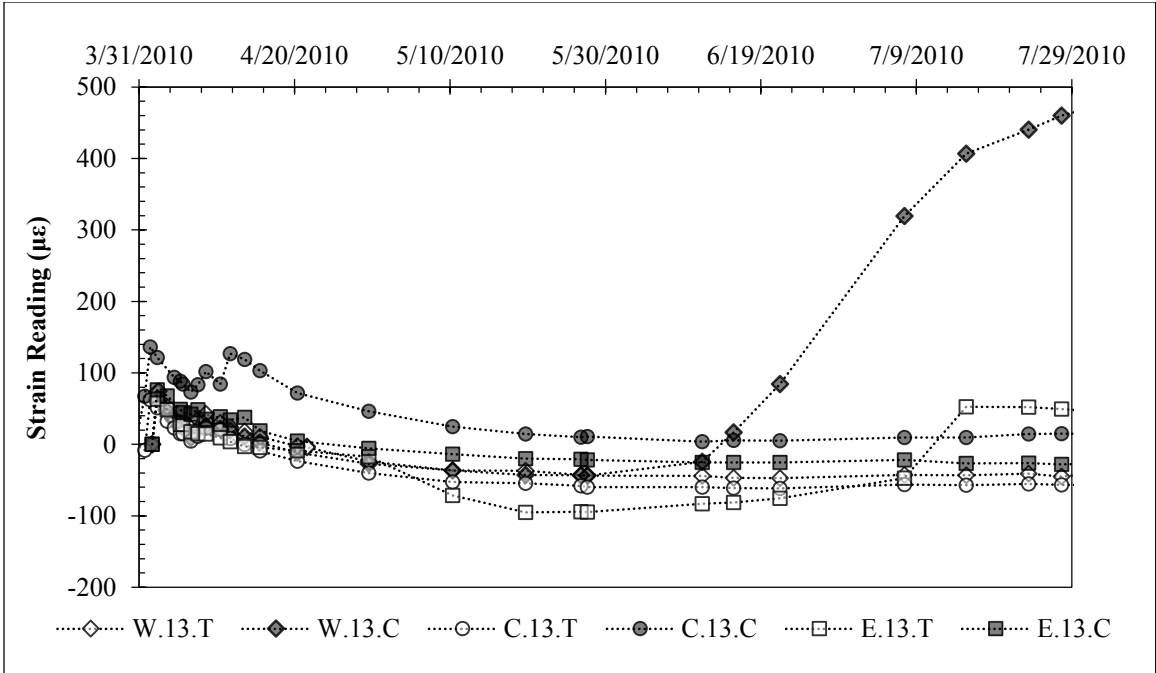


Figure G.8: Pre-Excavation Strain Data for Gauges 13 Feet Below Ground Surface.

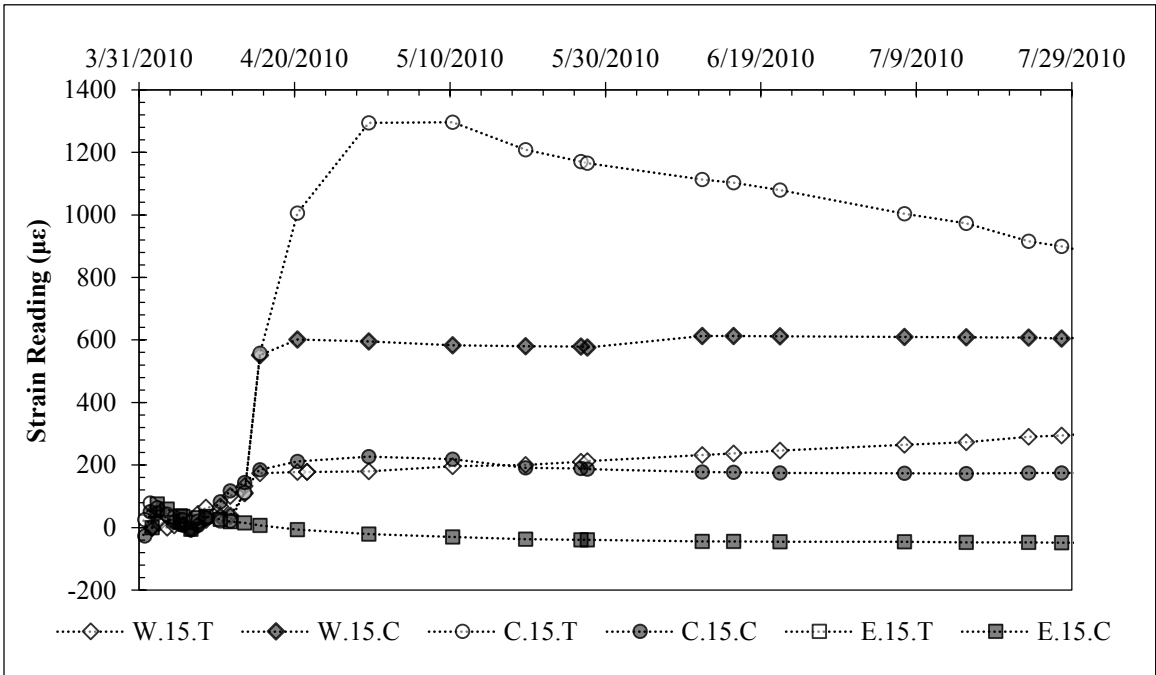


Figure G.9: Pre-Excavation Strain Data for Gauges 15 Feet Below Ground Surface.

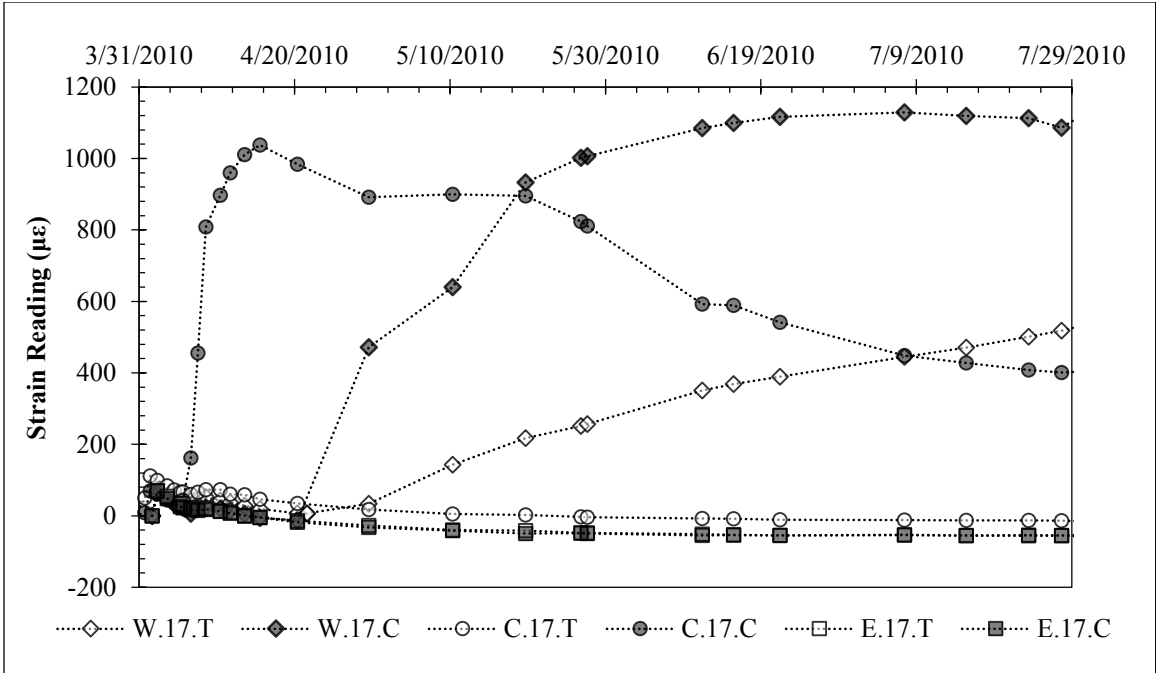


Figure G.10: Pre-Excavation Strain Data for Gauges 17 Feet Below Ground Surface.

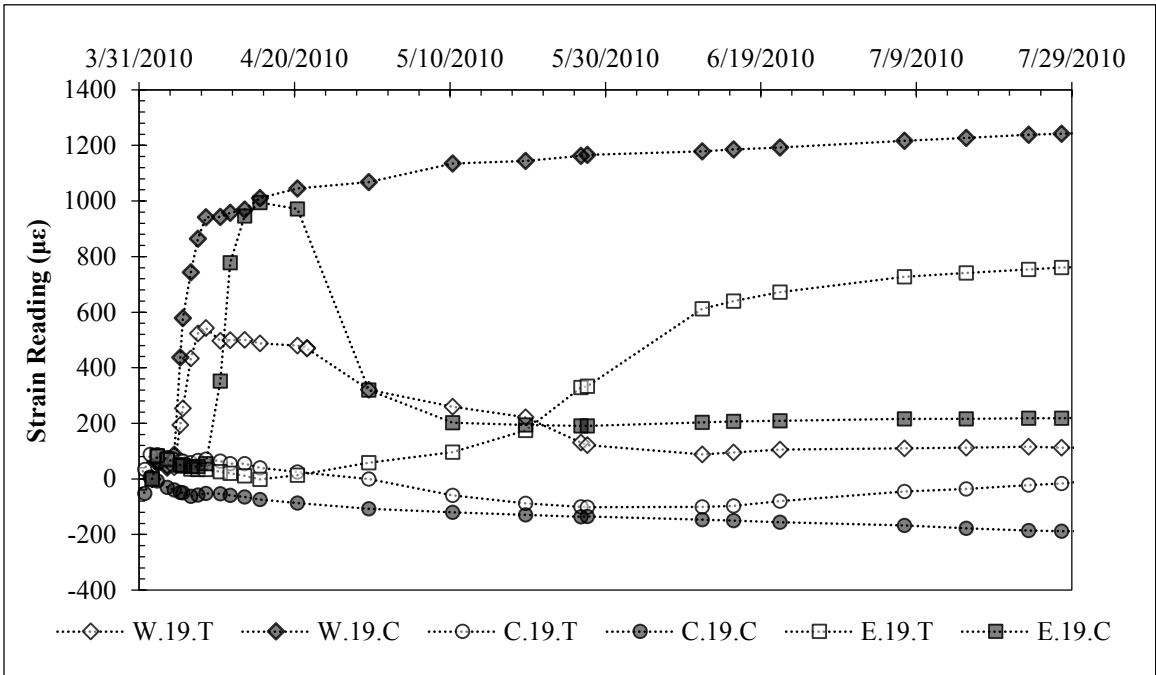


Figure G.11: Pre-Excavation Strain Data for Gauges 19 Feet Below Ground Surface.

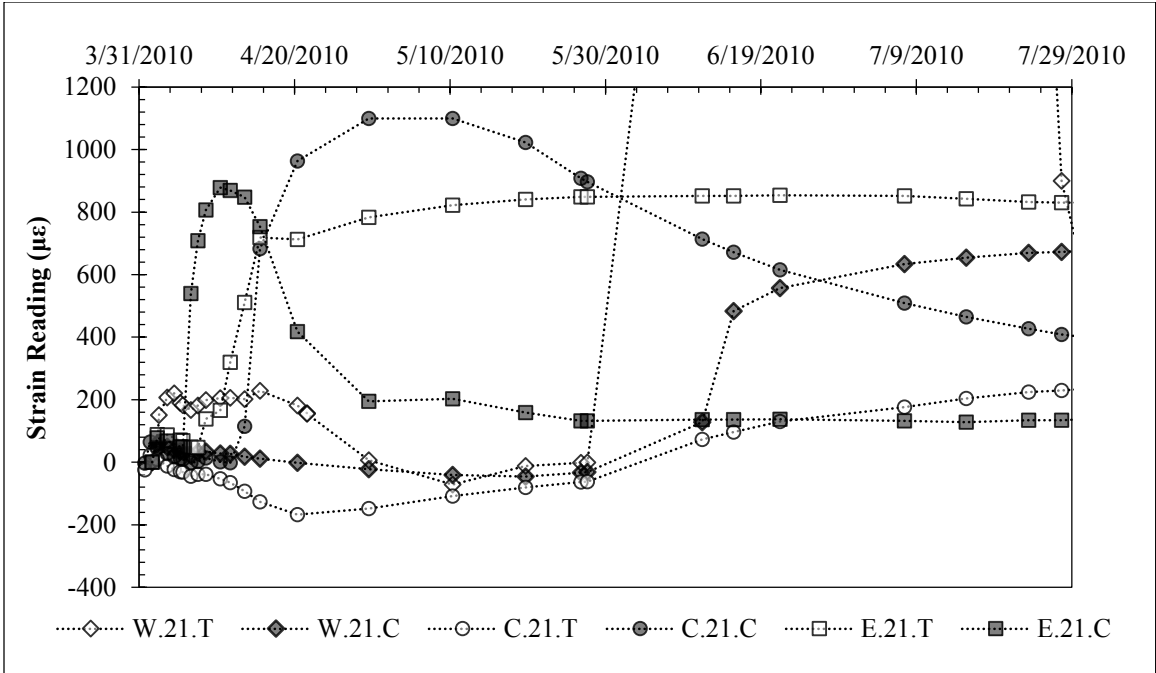


Figure G.12: Pre-Excavation Strain Data for Gauges 21 Feet Below Ground Surface.

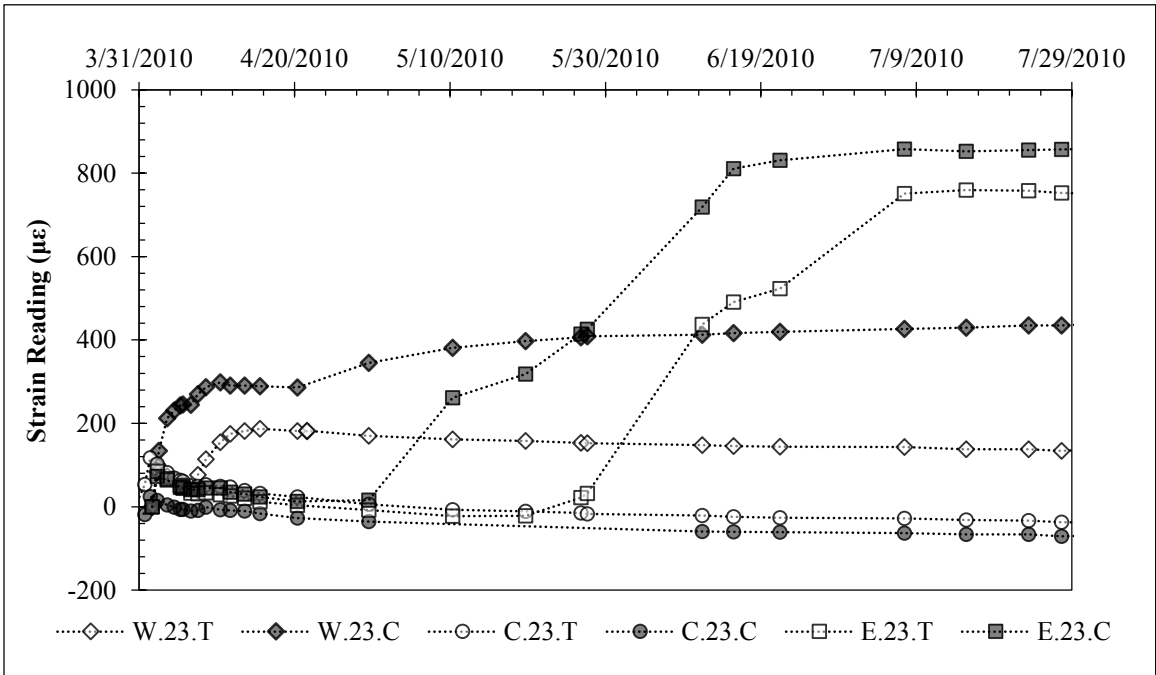


Figure G.13: Pre-Excavation Strain Data for Gauges 23 Feet Below Ground Surface.

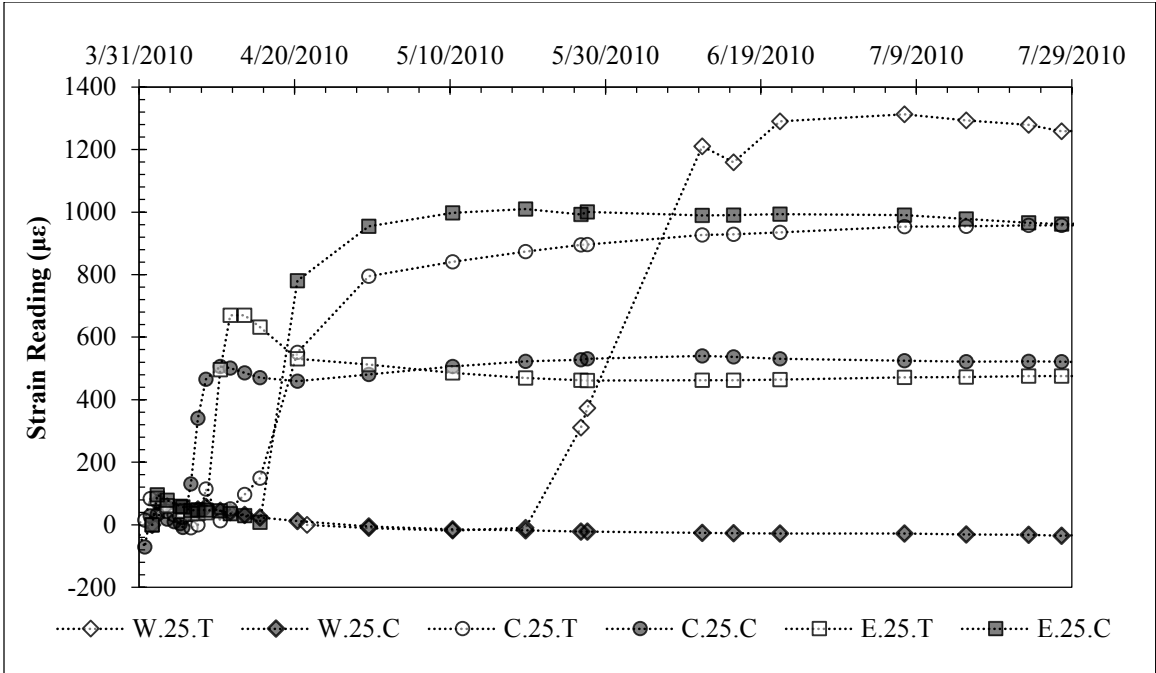


Figure G.14: Pre-Excavation Strain Data for Gauges 25 Feet Below Ground Surface.

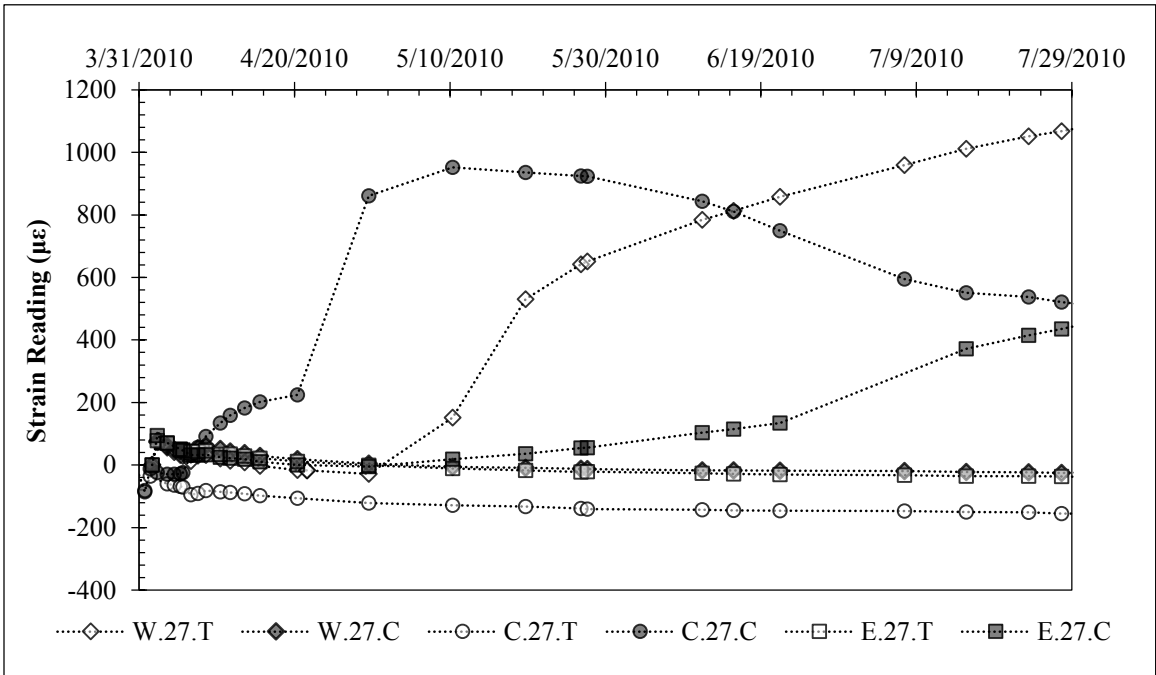


Figure G.15: Pre-Excavation Strain Data for Gauges 27 Feet Below Ground Surface.

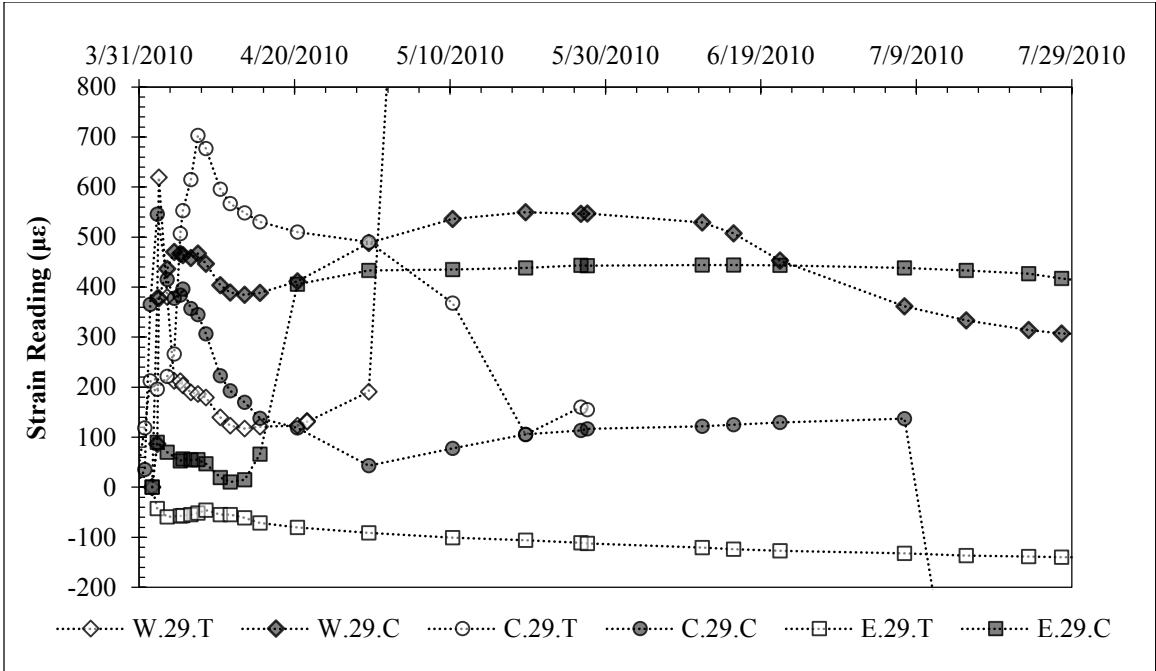


Figure G.16: Pre-Excavation Strain Data for Gauges 29 Feet Below Ground Surface.

G.3: Strain Data During Excavation

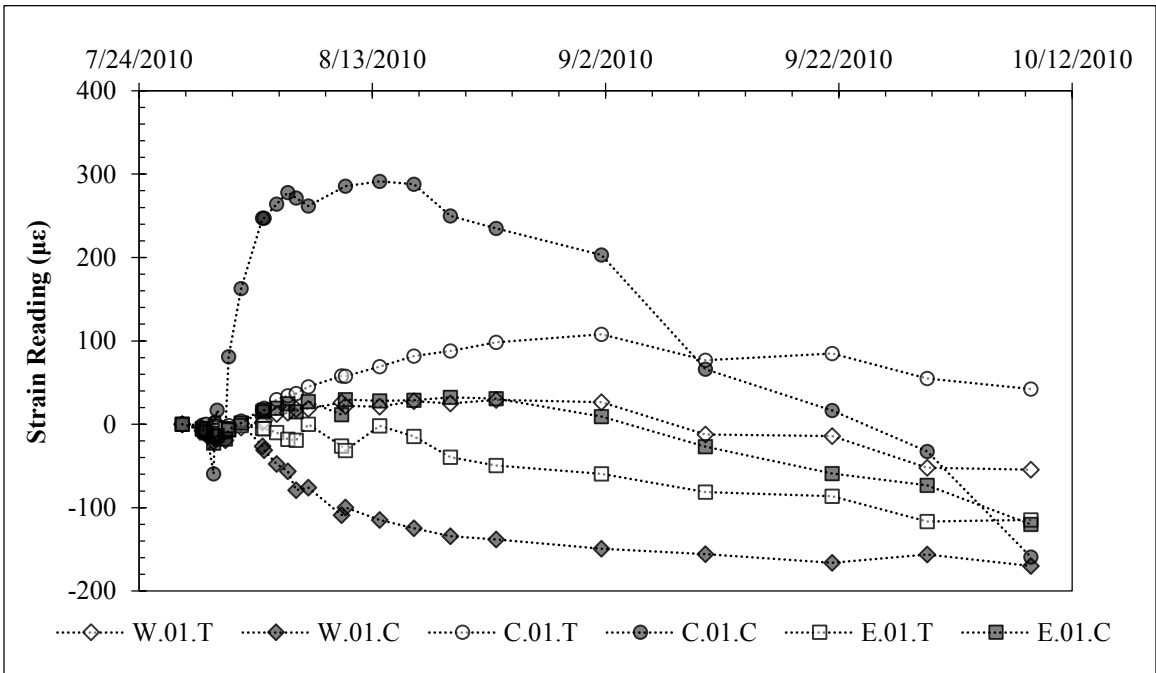


Figure G.17: Strain Data 1 Foot Below Ground Surface During Excavation.

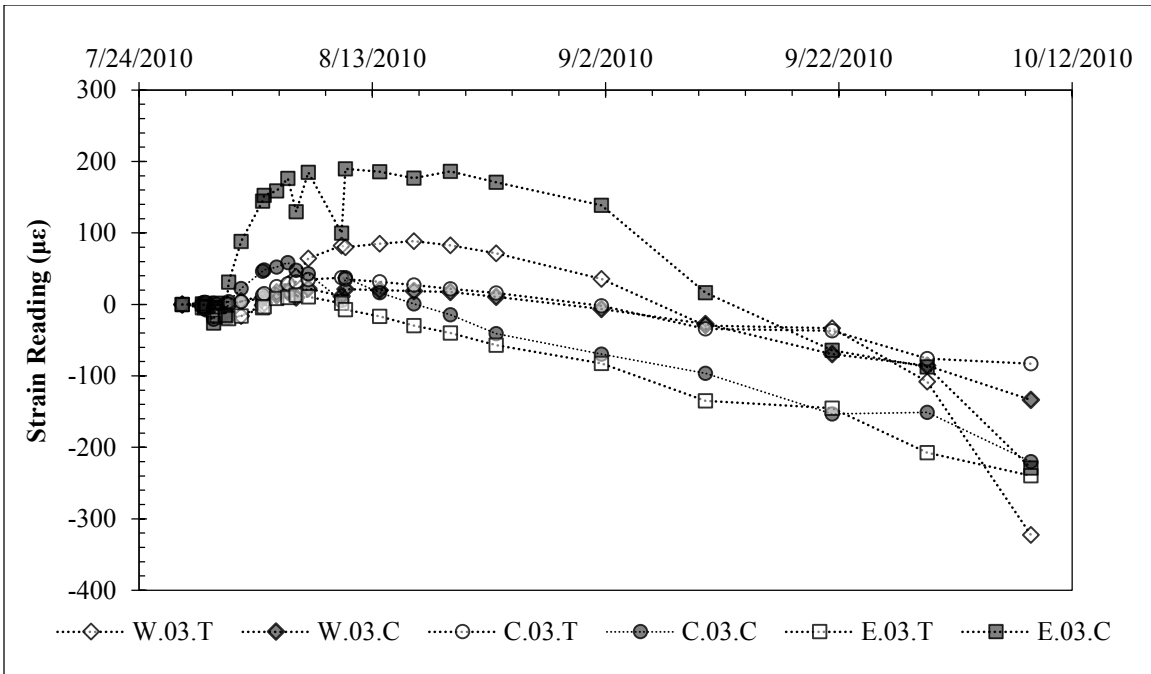


Figure G.18: Strain Data 3 Feet Below Ground Surface During Excavation.

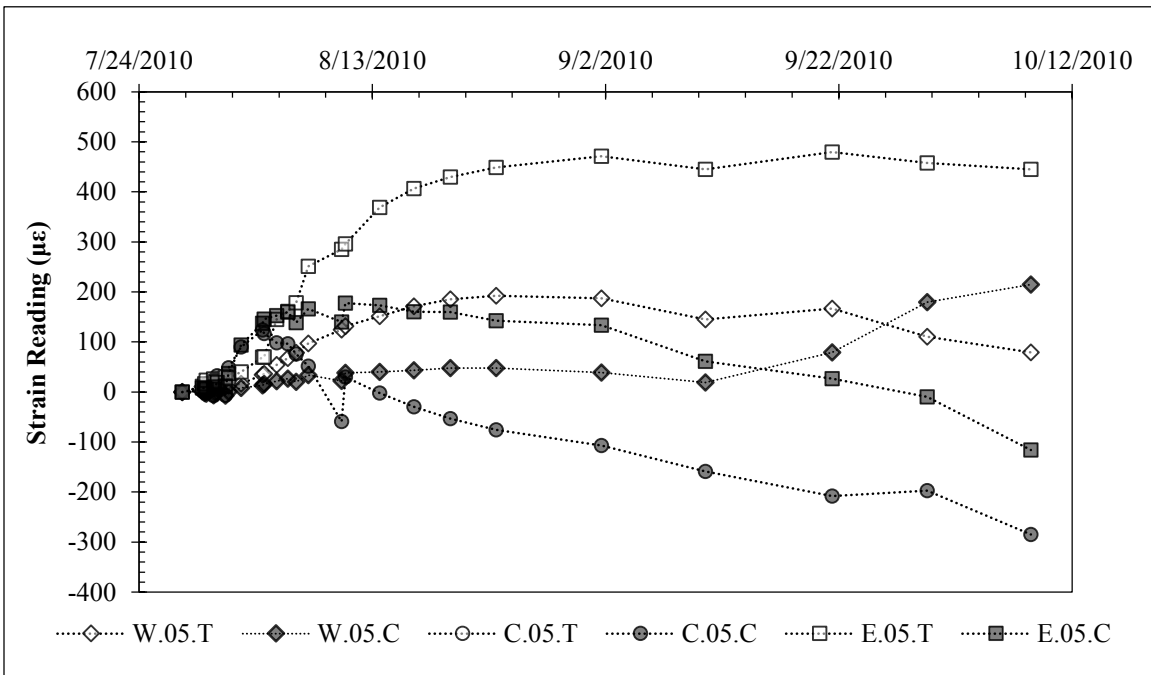


Figure G.19: Strain Data 5 Feet Below Ground Surface During Excavation.

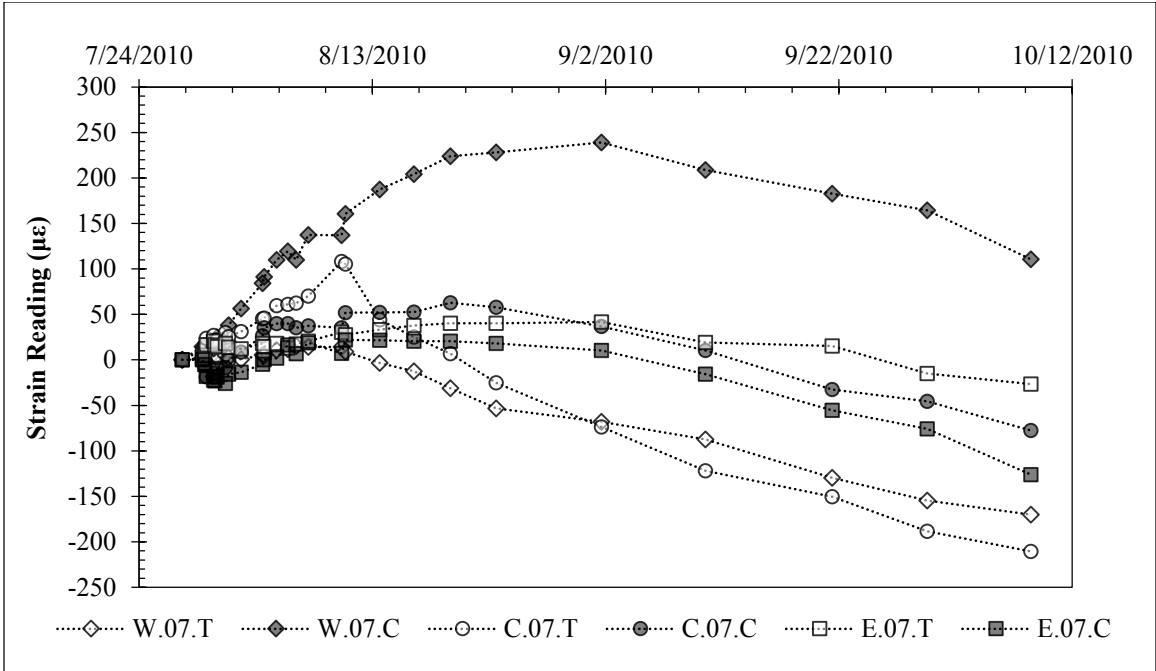


Figure G.20: Strain Data 7 Feet Below Ground Surface During Excavation.

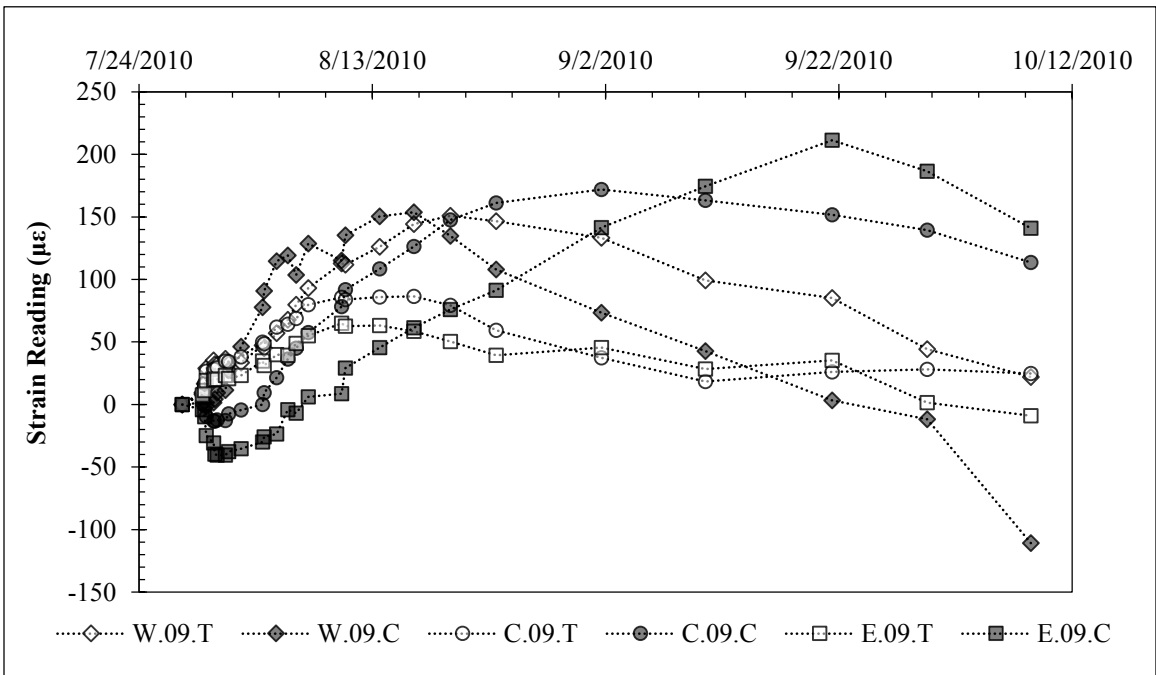


Figure G.21: Strain Data 9 Feet Below Ground Surface During Excavation.

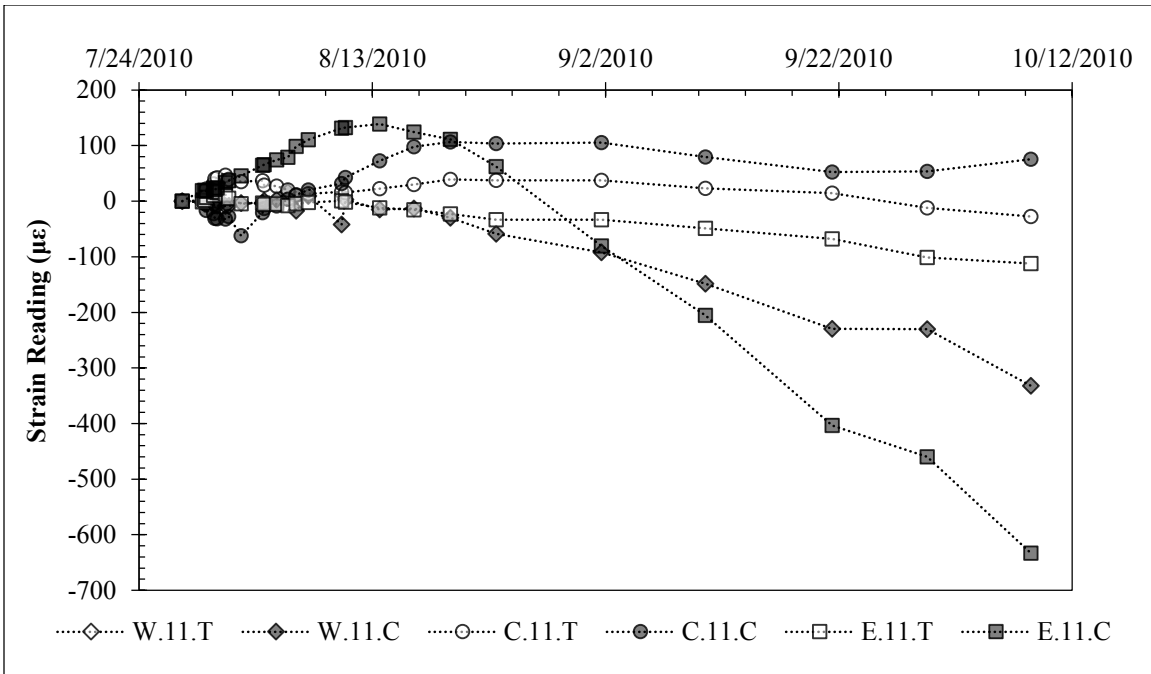


Figure G.22: Strain Data 11 Feet Below Ground Surface During Excavation.

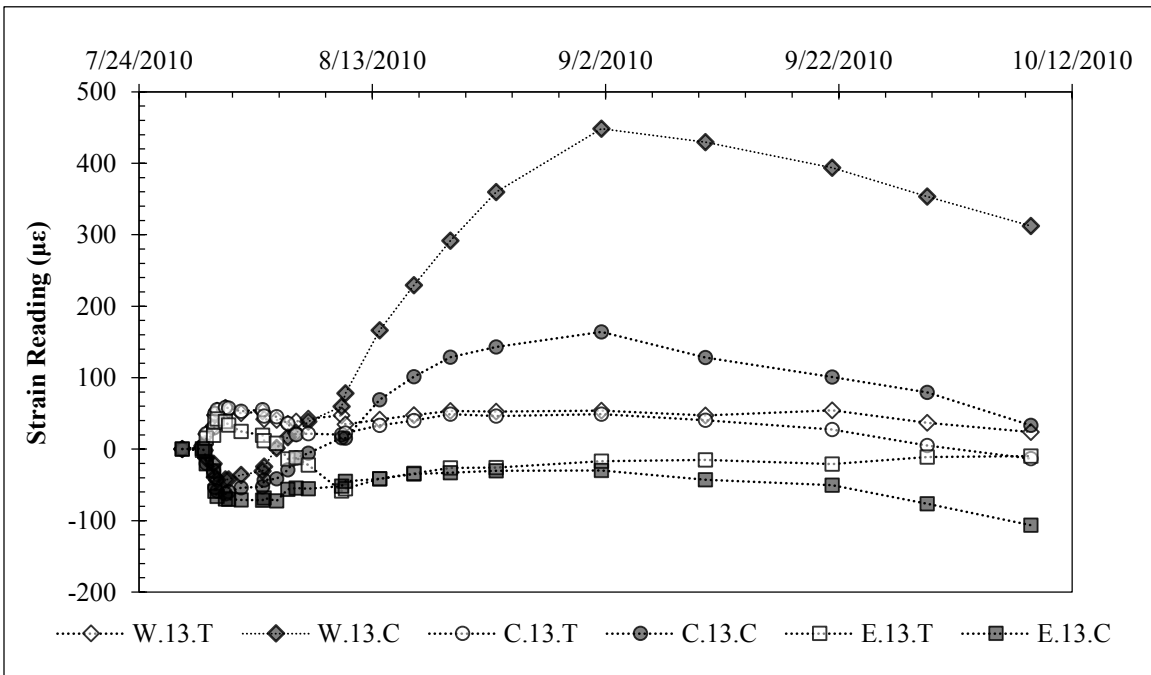


Figure G.23: Strain Data 13 Feet Below Ground Surface During Excavation.

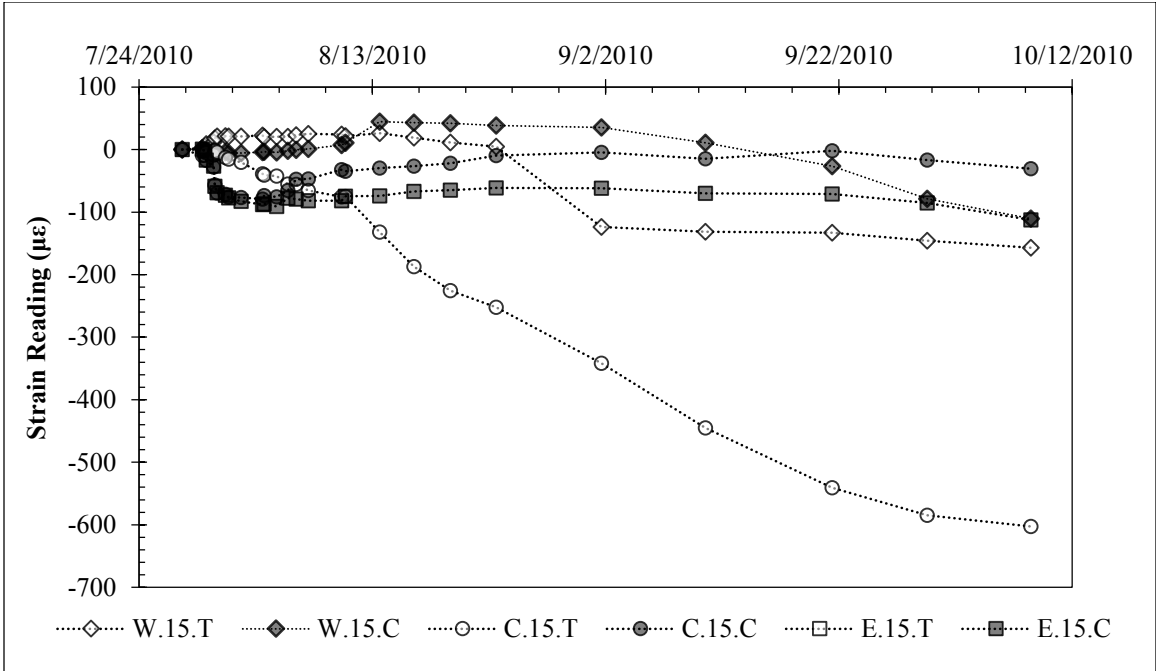


Figure G.24: Strain Data 15 Feet Below Ground Surface During Excavation.

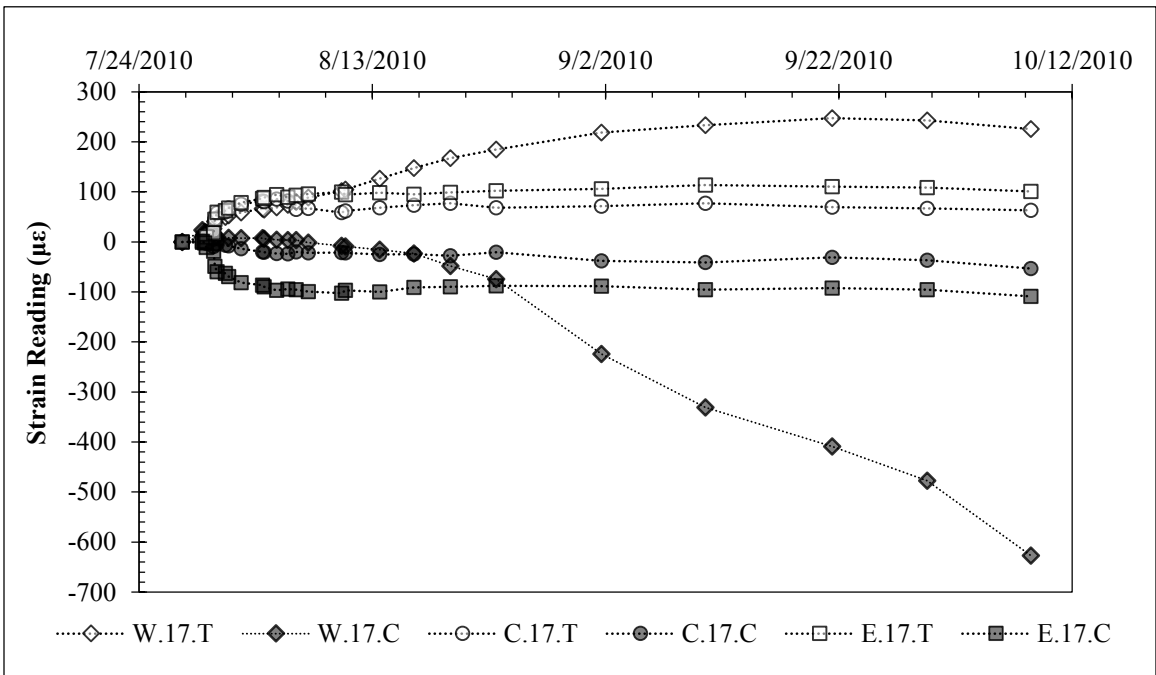


Figure G.25: Strain Data 17 Feet Below Ground Surface During Excavation.

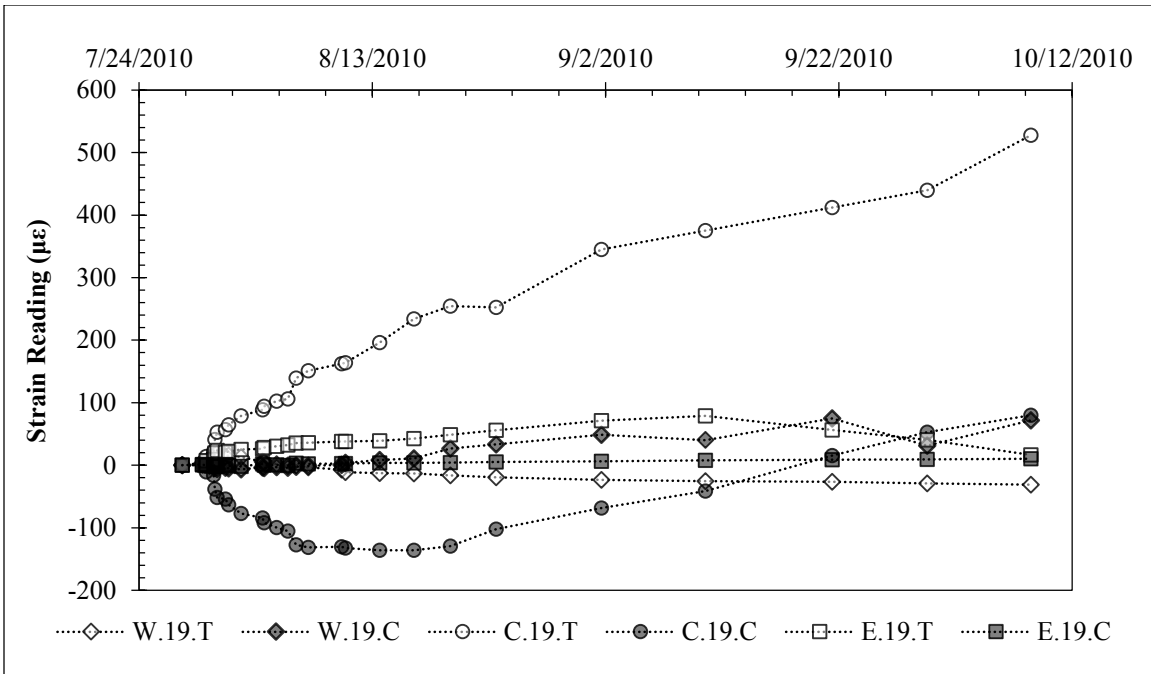


Figure G.26: Strain Data 19 Feet Below Ground Surface During Excavation.

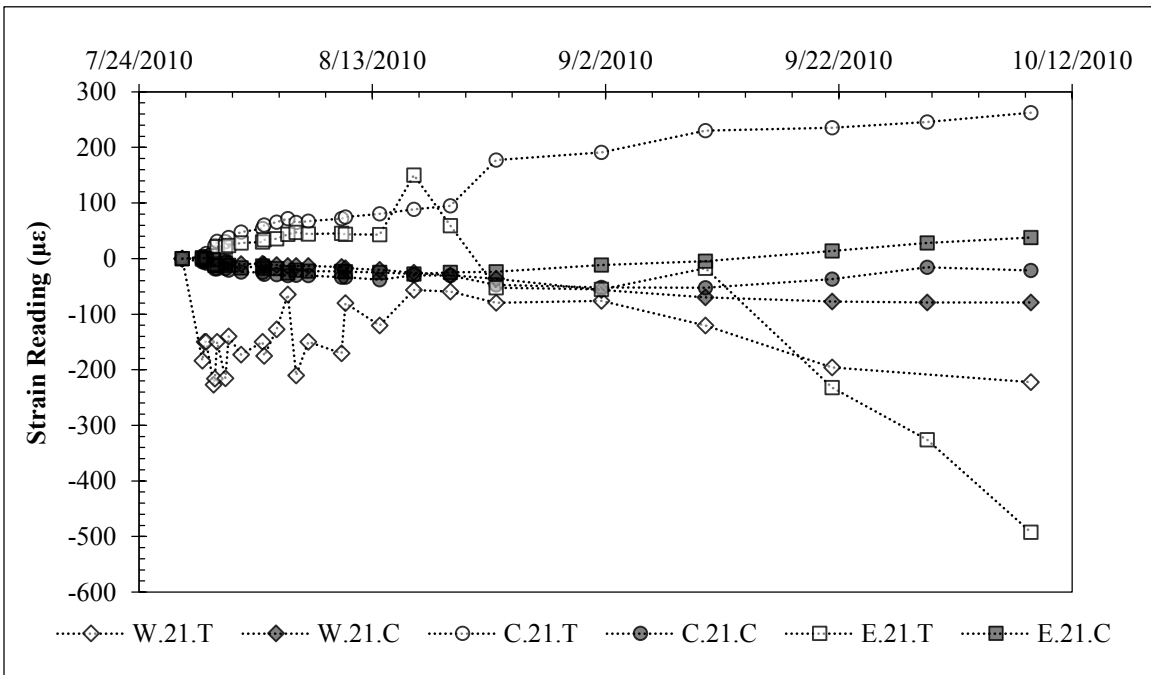


Figure G.27: Strain Data 21 Feet Below Ground Surface During Excavation.

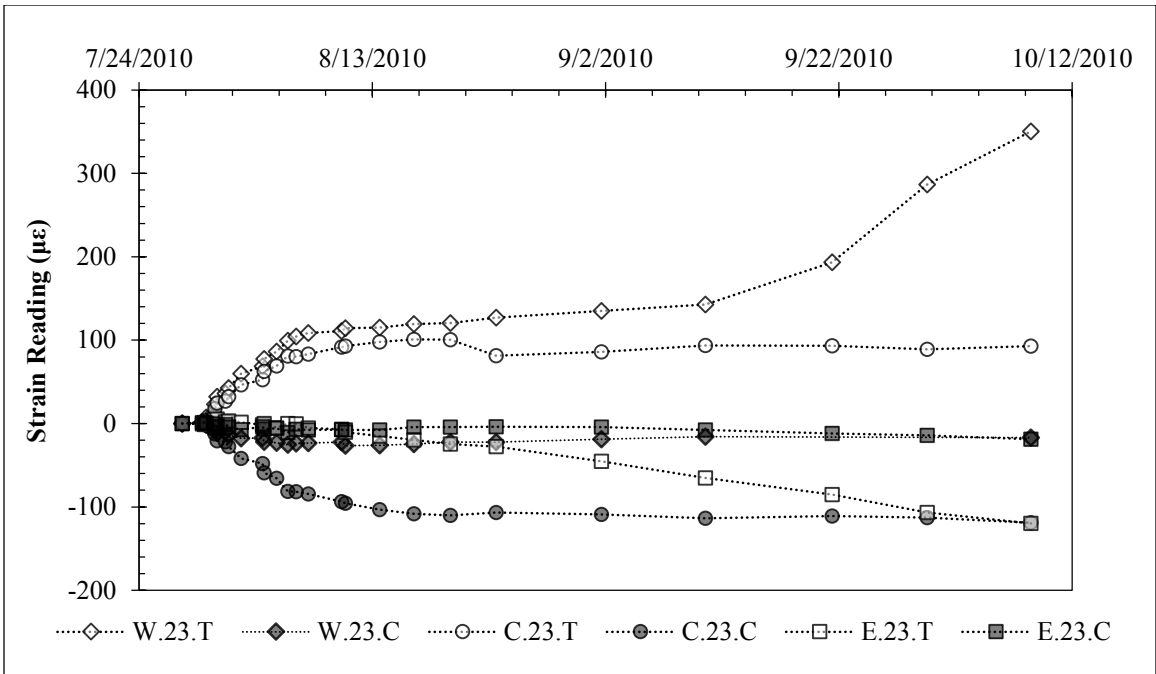


Figure G.28: Strain Data 23 Feet Below Ground Surface During Excavation.

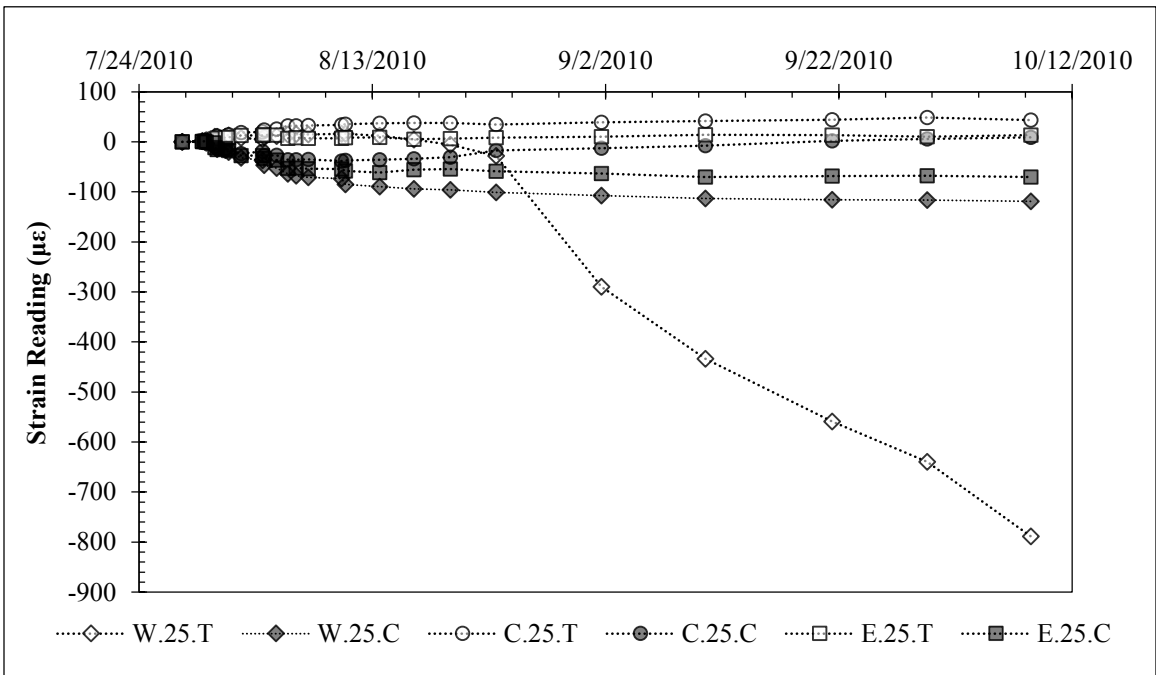


Figure G.29: Strain Data 25 Feet Below Ground Surface During Excavation.

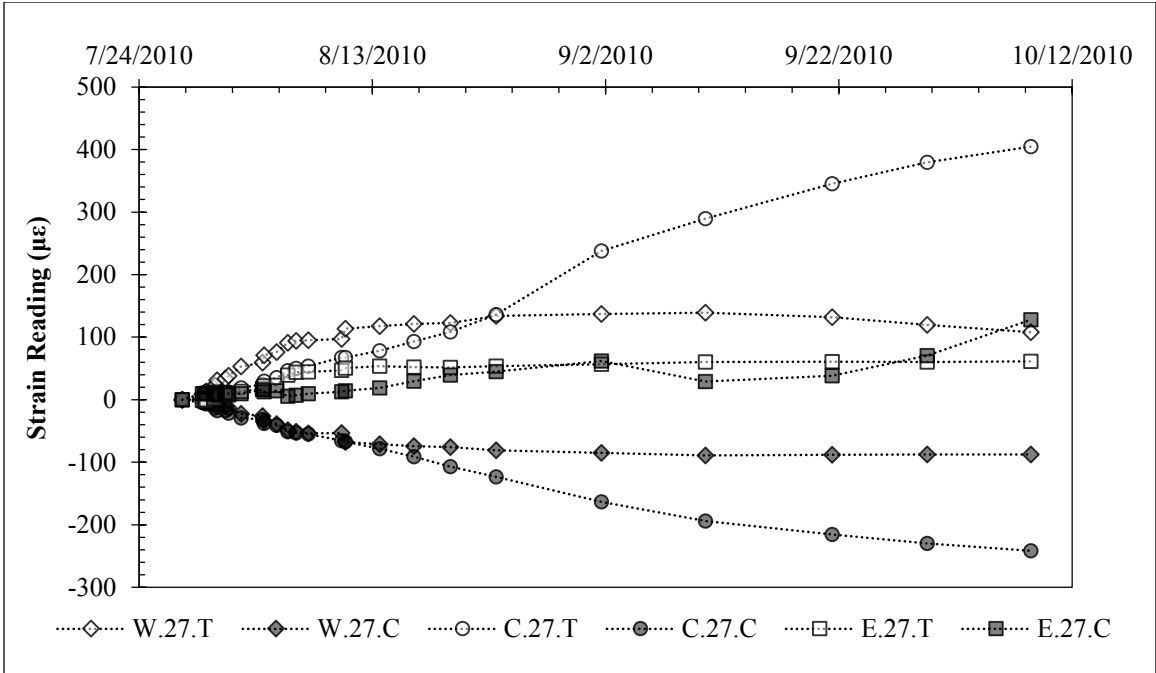


Figure G.30: Strain Data 27 Feet Below Ground Surface During Excavation.

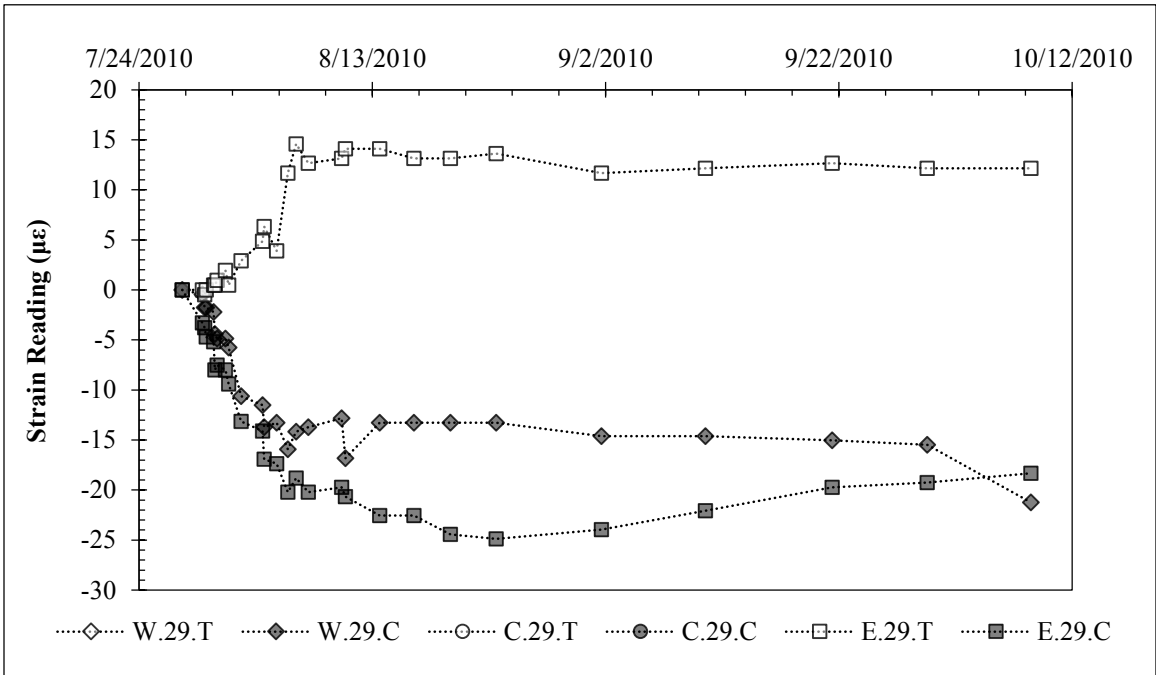


Figure G.31: Strain Data 29 Feet Below Ground Surface During Excavation.

G.4: Strain Data During Natural Moisture Cycles

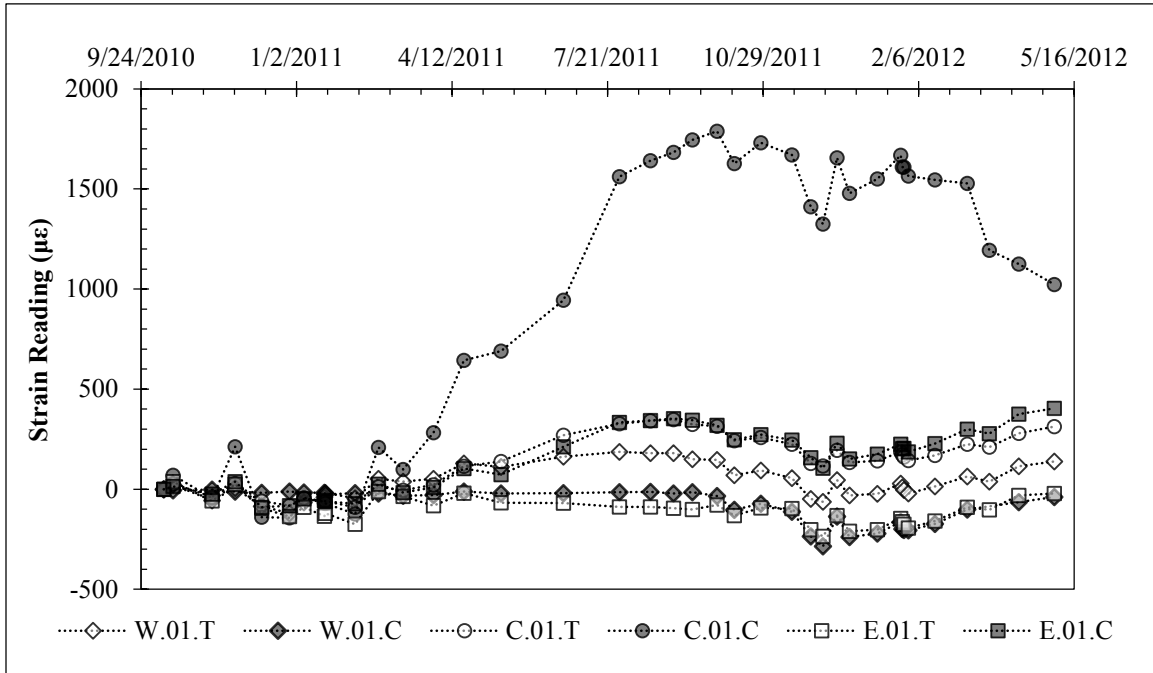


Figure G.32: Strain Data 1 Foot Below Ground Surface (Oct. 2010 – Apr. 2012).

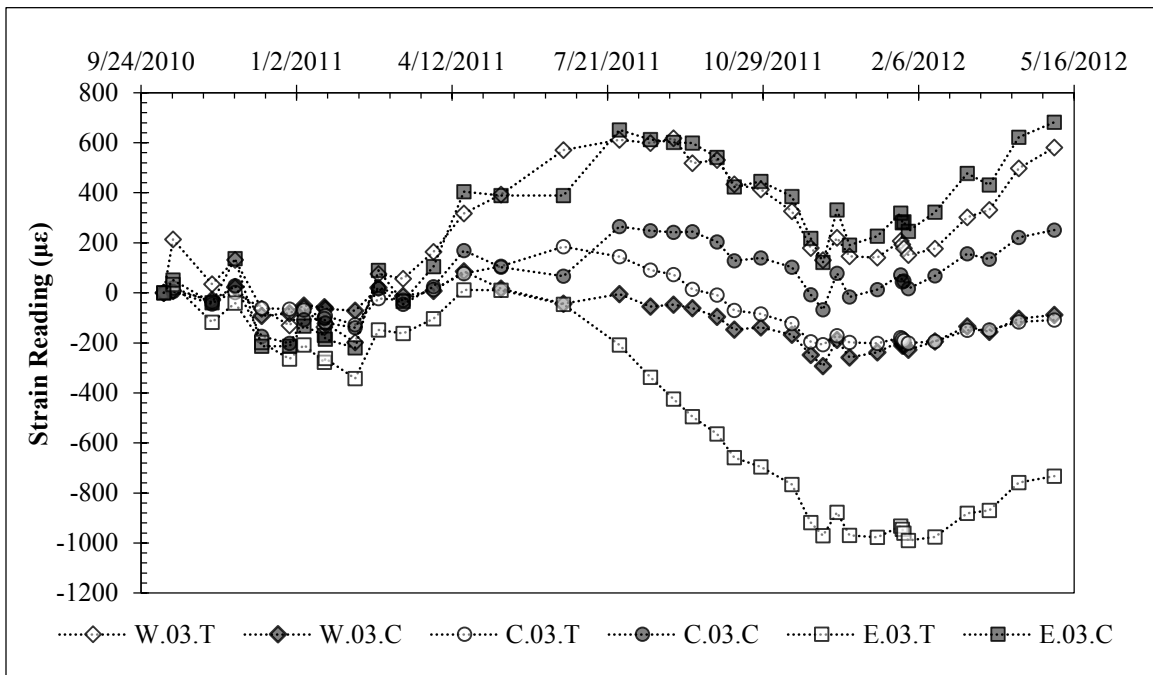


Figure G.33: Strain Data 3 Feet Below Ground Surface (Oct. 2010 – Apr. 2012).

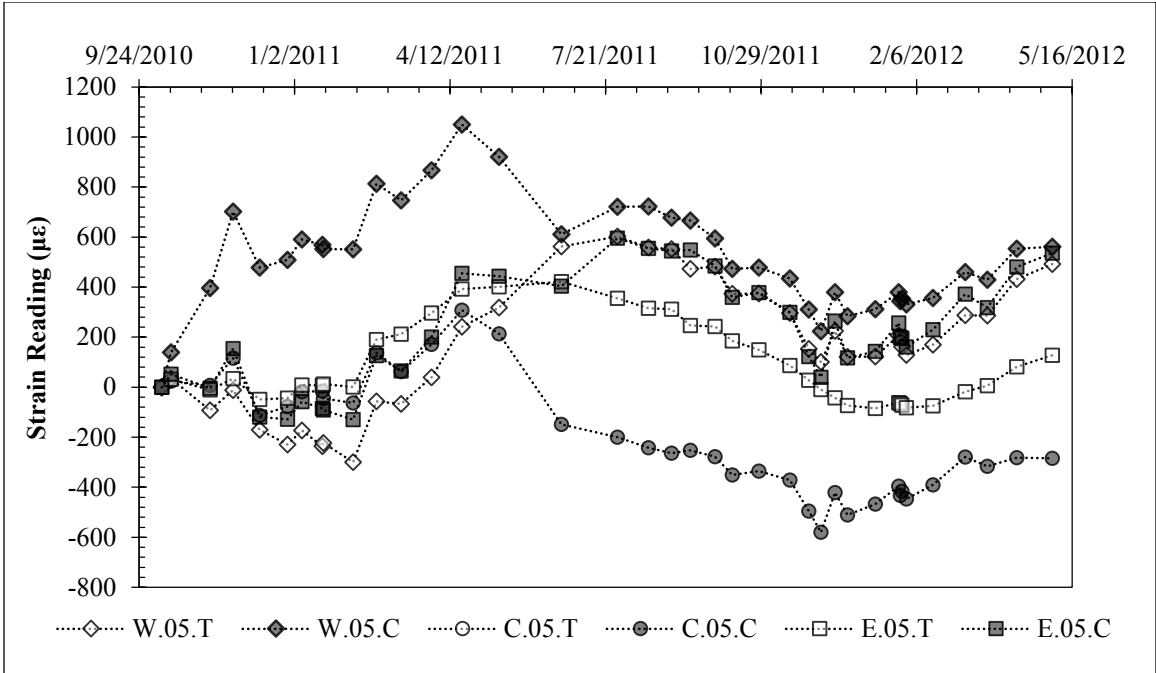


Figure G.34: Strain Data 5 Feet Below Ground Surface (Oct. 2010 – Apr. 2012).

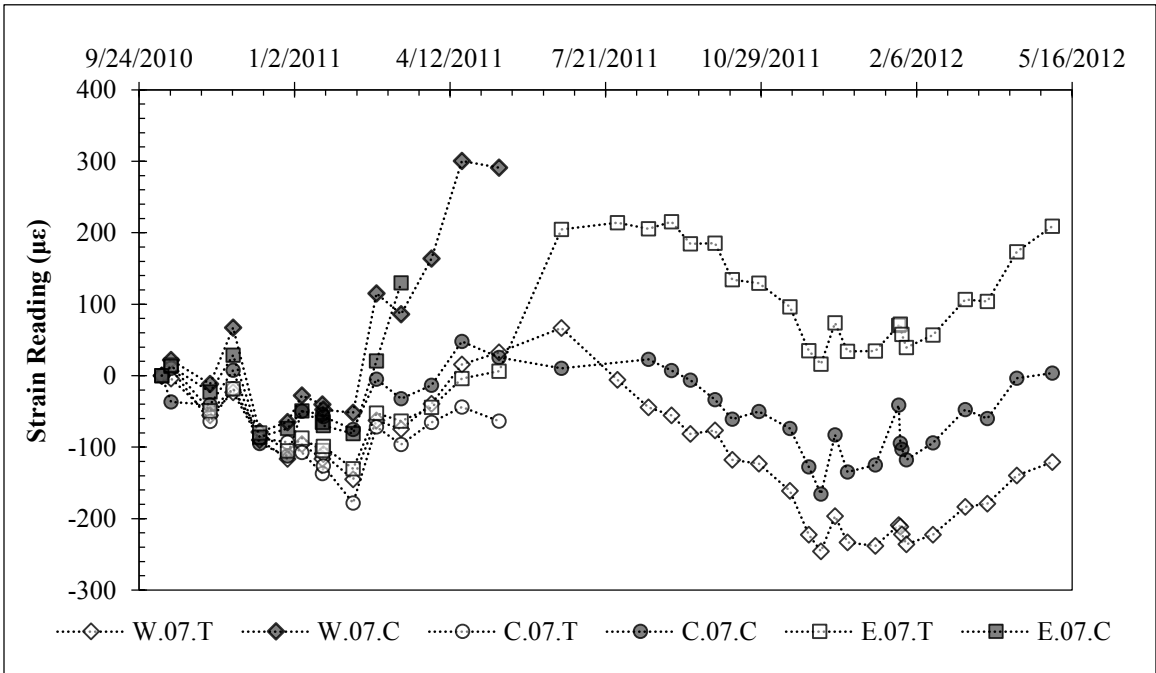


Figure G.35: Strain Data 7 Feet Below Ground Surface (Oct. 2010 – Apr. 2012).

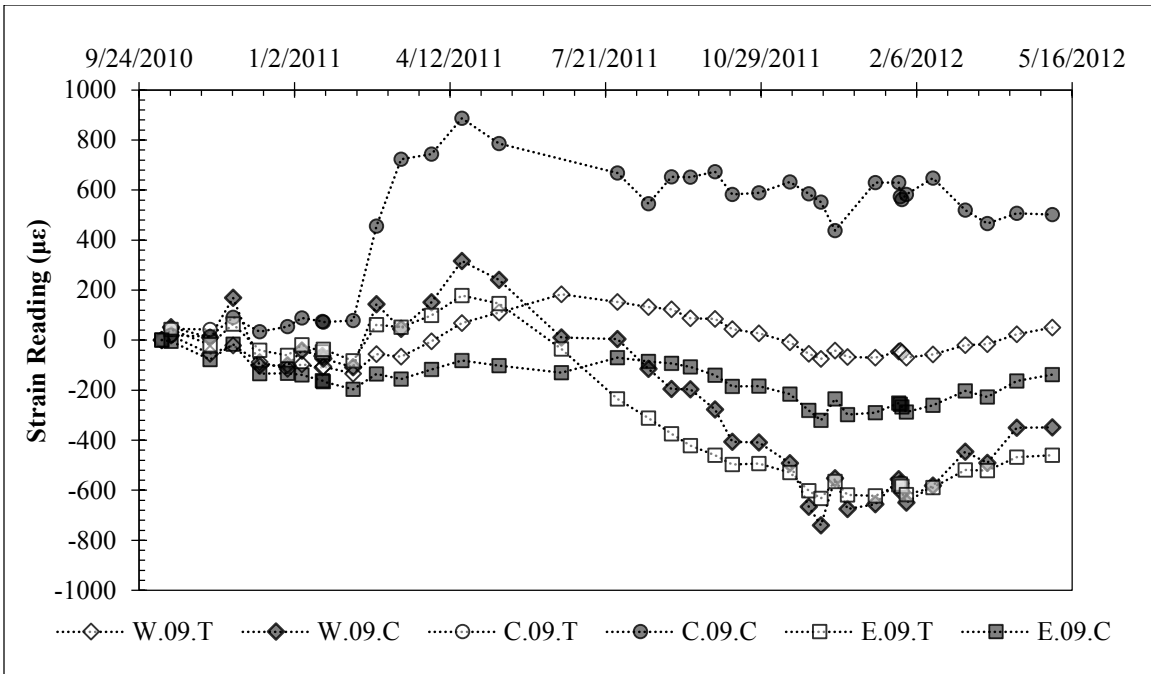


Figure G.36: Strain Data 9 Feet Below Ground Surface (Oct. 2010 – Apr. 2012).

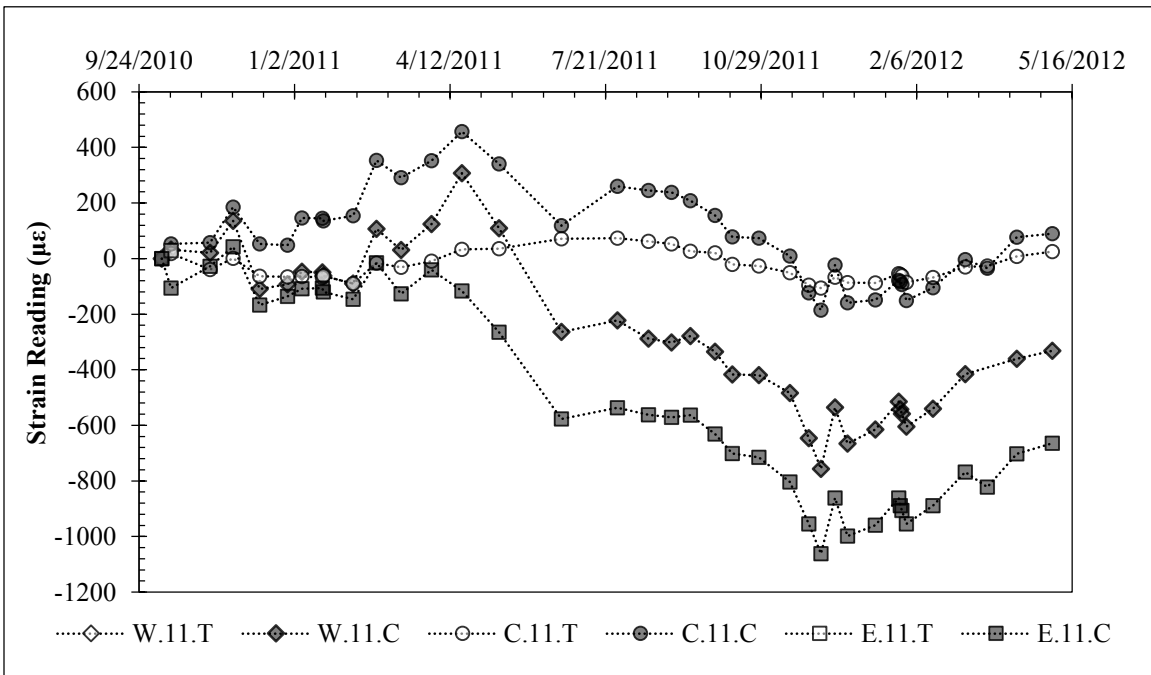


Figure G.37: Strain Data 11 Feet Below Ground Surface (Oct. 2010 – Apr. 2012).

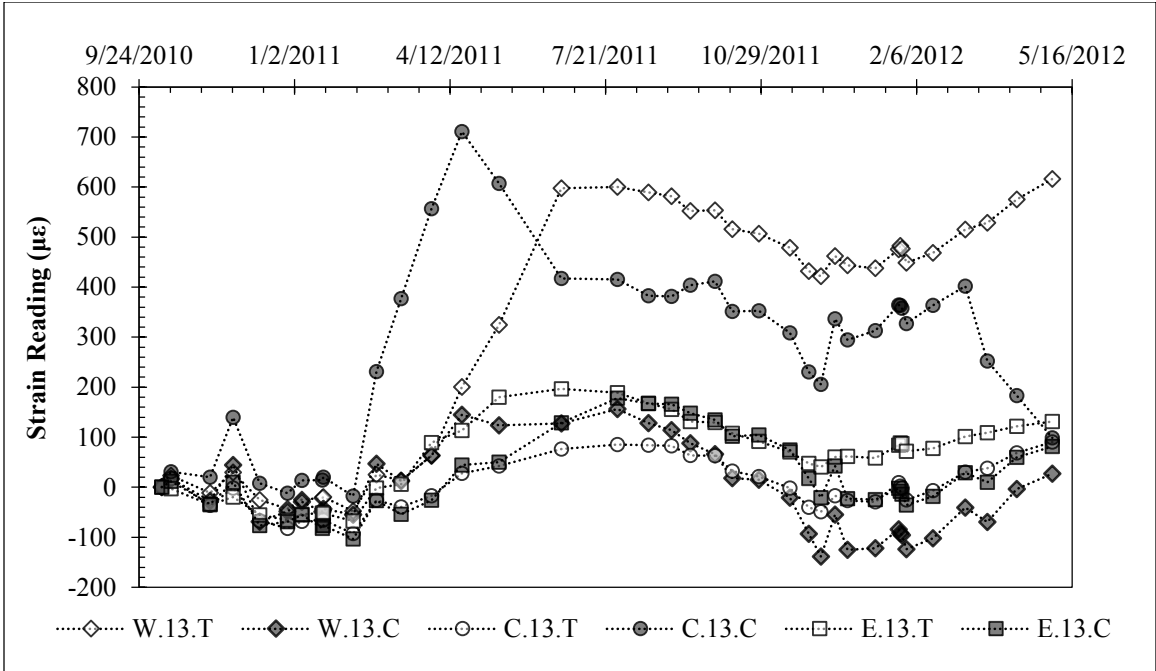


Figure G.38: Strain Data 13 Feet Below Ground Surface (Oct. 2010 – Apr. 2012).

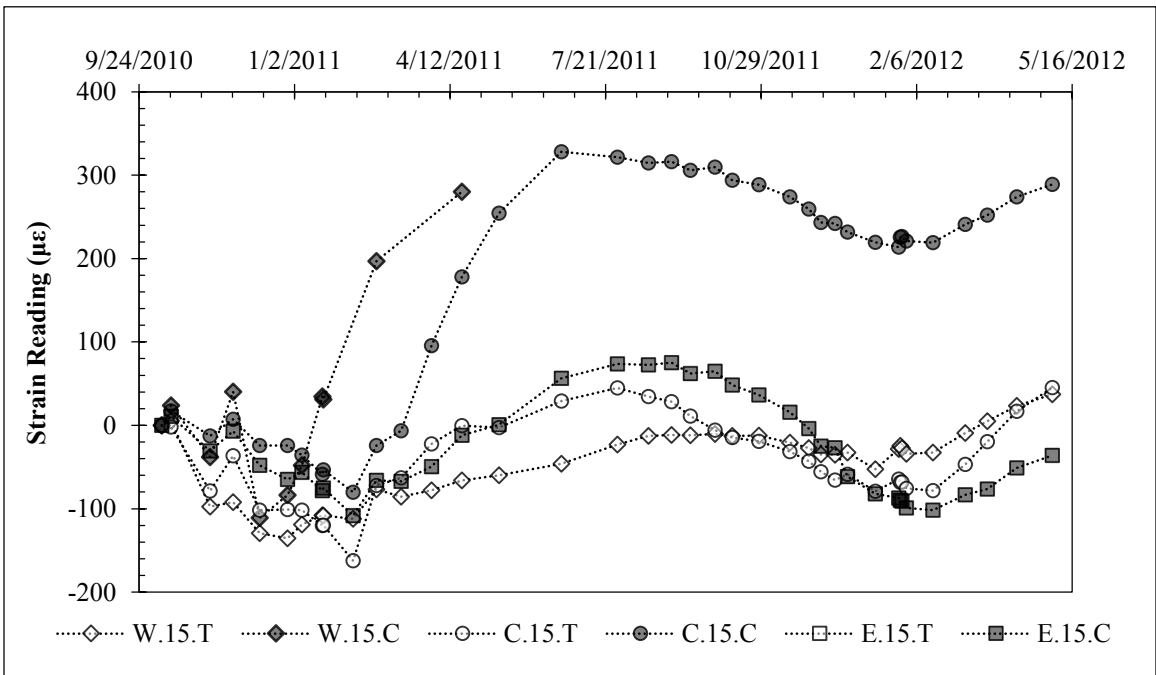


Figure G.39: Strain Data 15 Feet Below Ground Surface (Oct. 2010 – Apr. 2012).

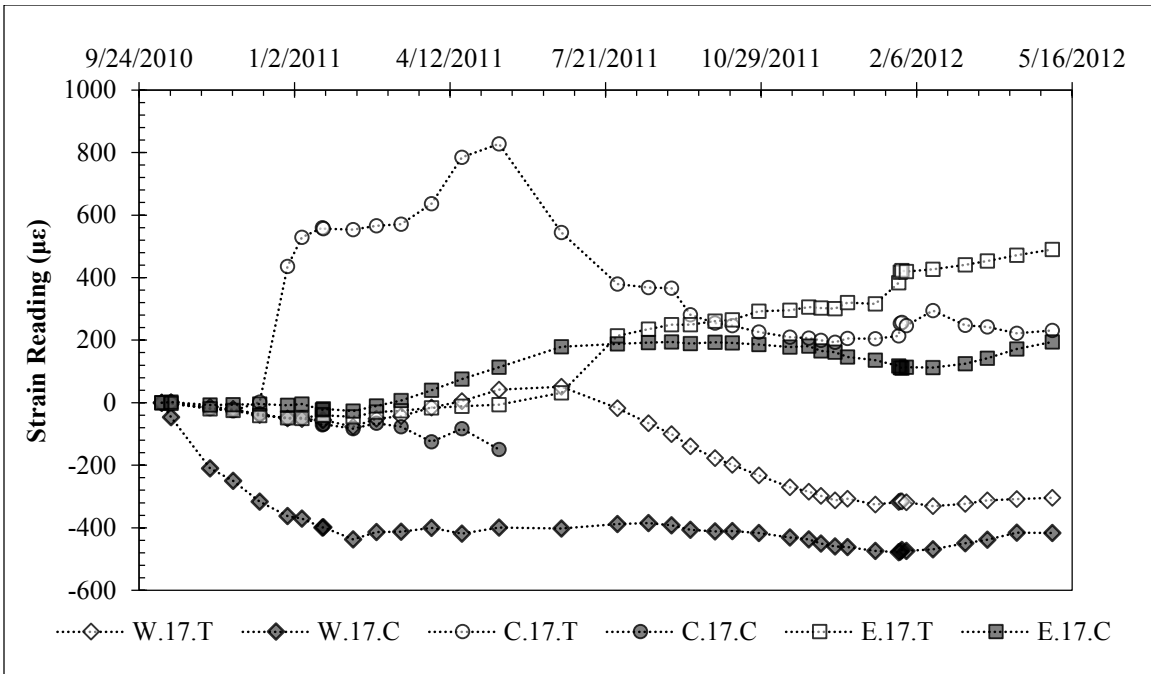


Figure G.40: Strain Data 17 Feet Below Ground Surface (Oct. 2010 – Apr. 2012).

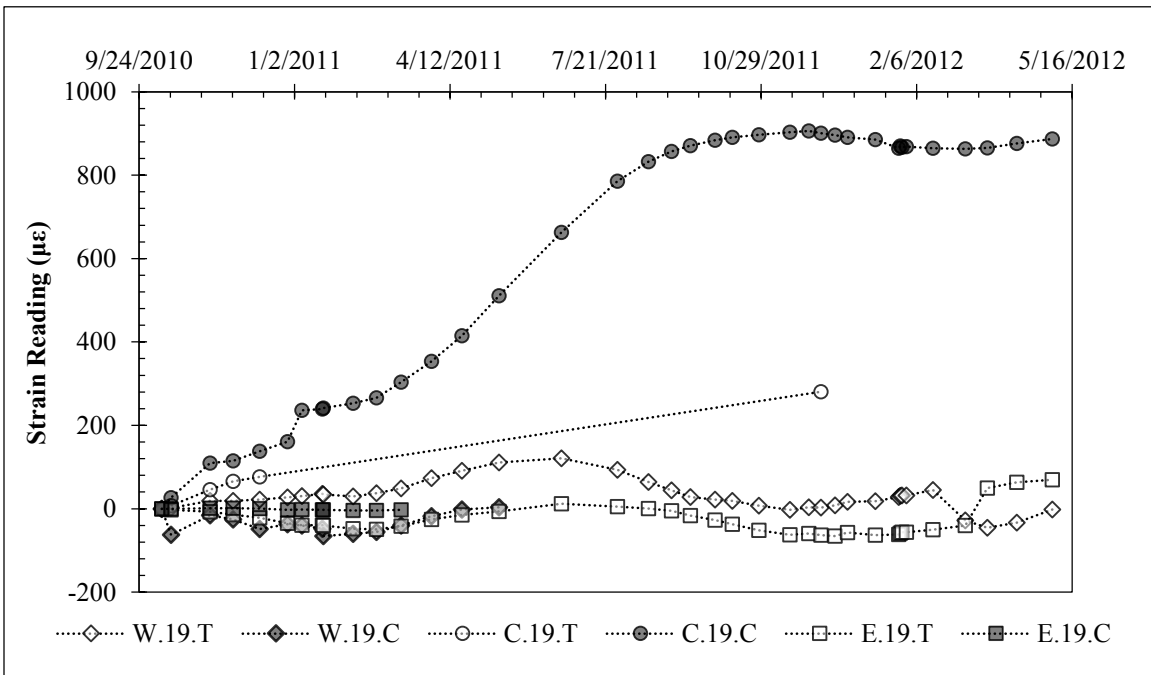


Figure G.41: Strain Data 19 Feet Below Ground Surface (Oct. 2010 – Apr. 2012).

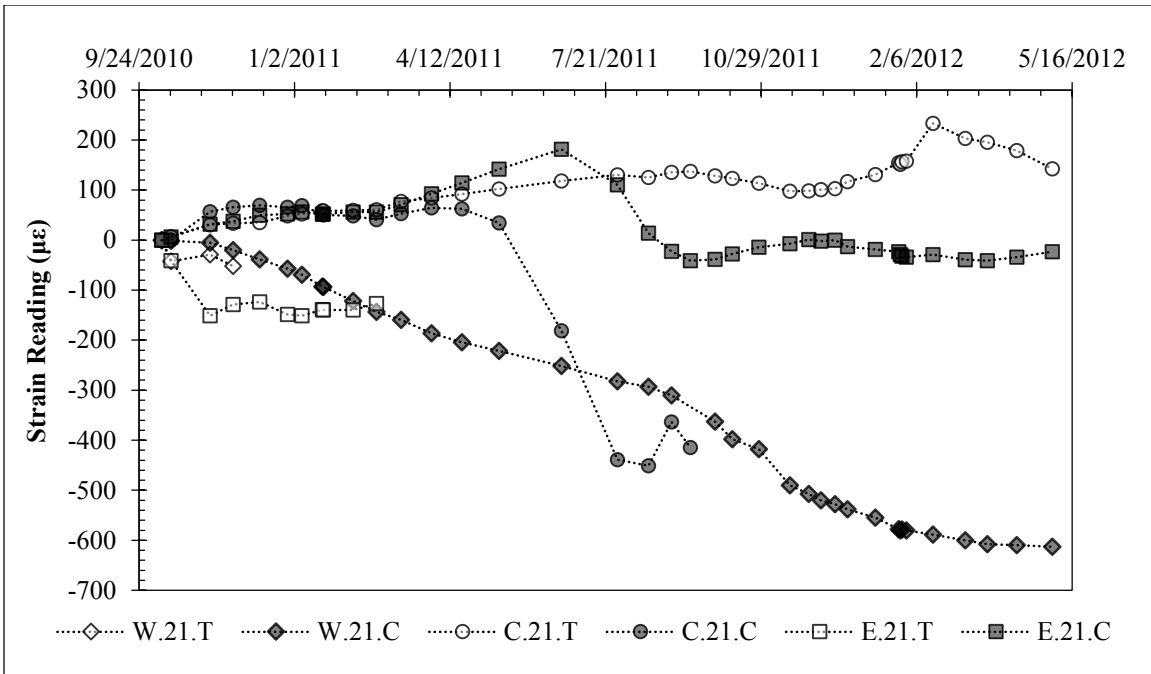


Figure G.42: Strain Data 21 Feet Below Ground Surface (Oct. 2010 – Apr. 2012).

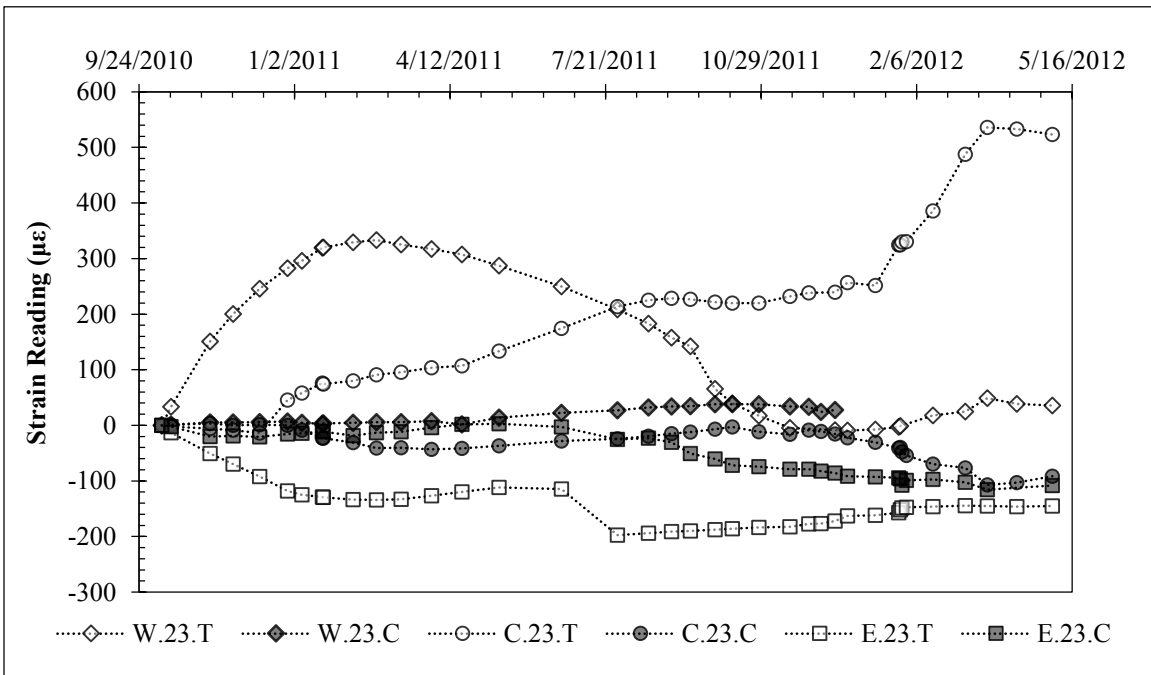


Figure G.43: Strain Data 23 Feet Below Ground Surface (Oct. 2010 – Apr. 2012).

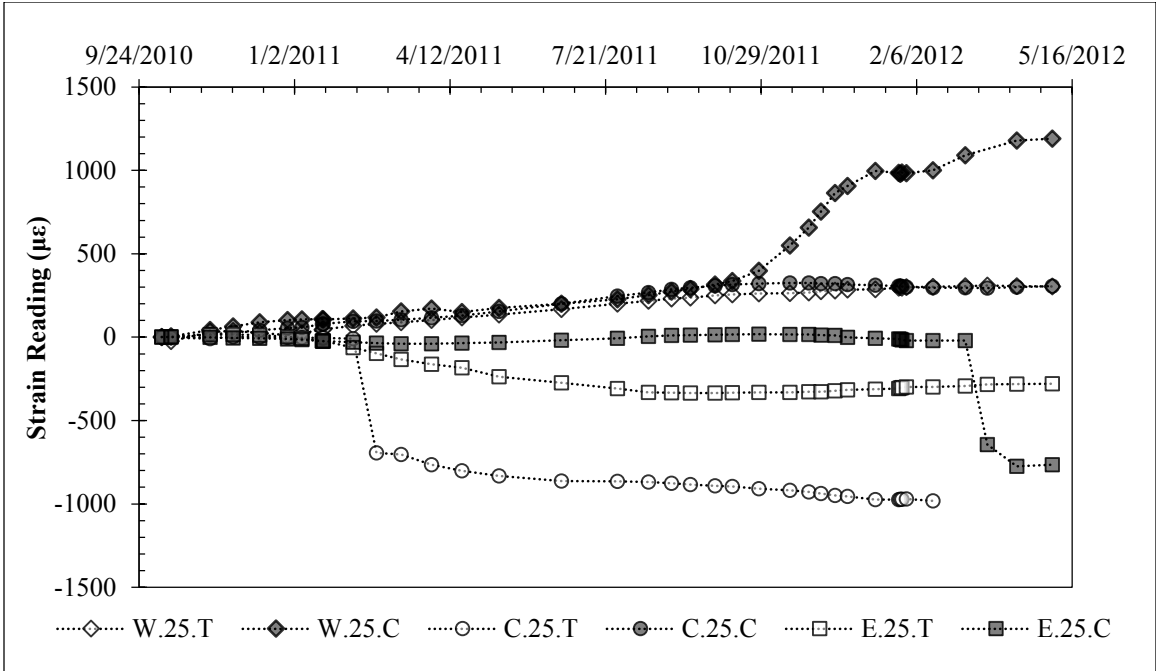


Figure G.44: Strain Data 25 Feet Below Ground Surface (Oct. 2010 – Apr. 2012).

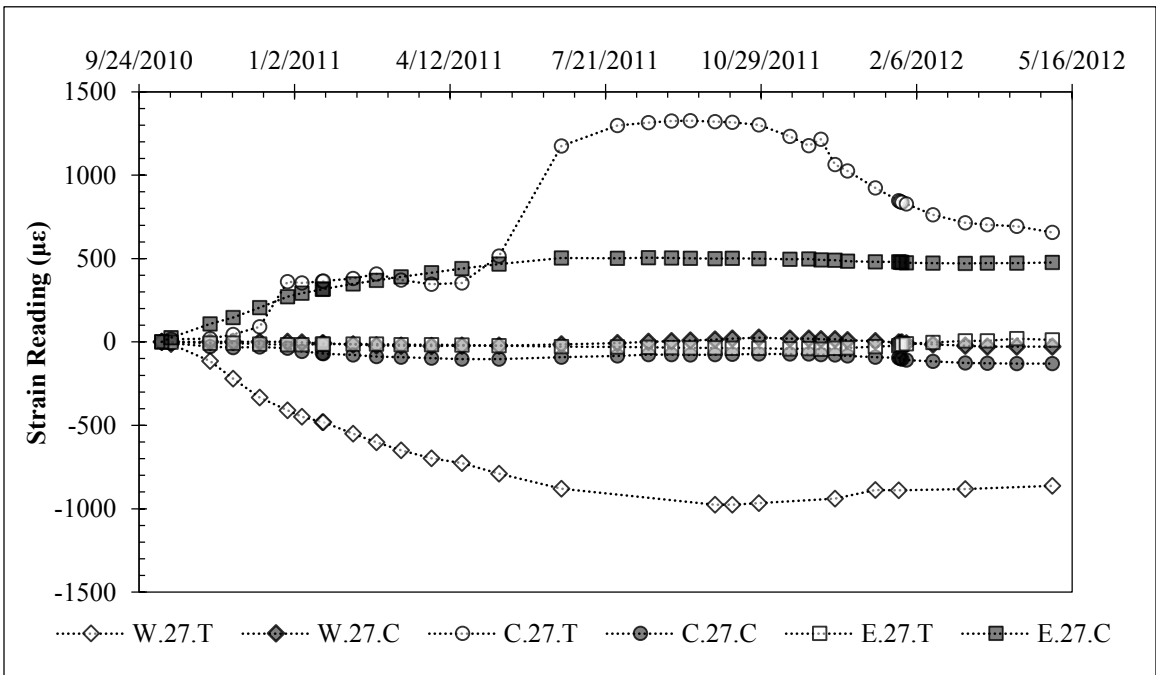


Figure G.45: Strain Data 27 Feet Below Ground Surface (Oct. 2010 – Apr. 2012).

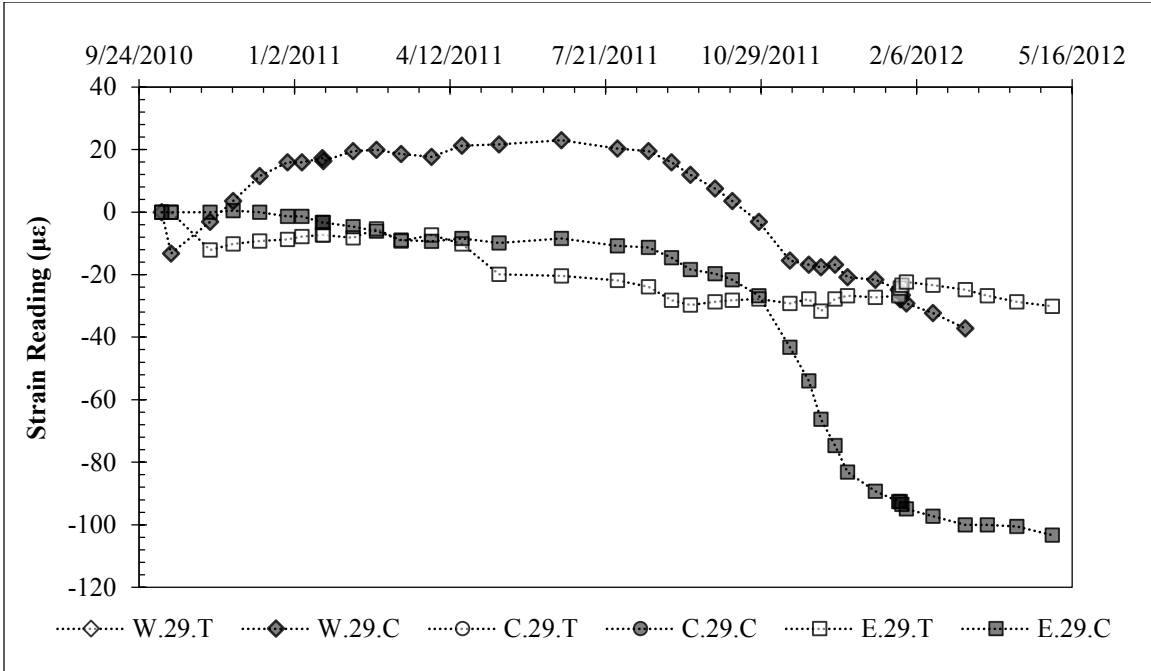


Figure G.46: Strain Data 29 Feet Below Ground Surface (Oct. 2010 – Apr. 2012).

G.5: Strain Data During Controlled Inundation Testing

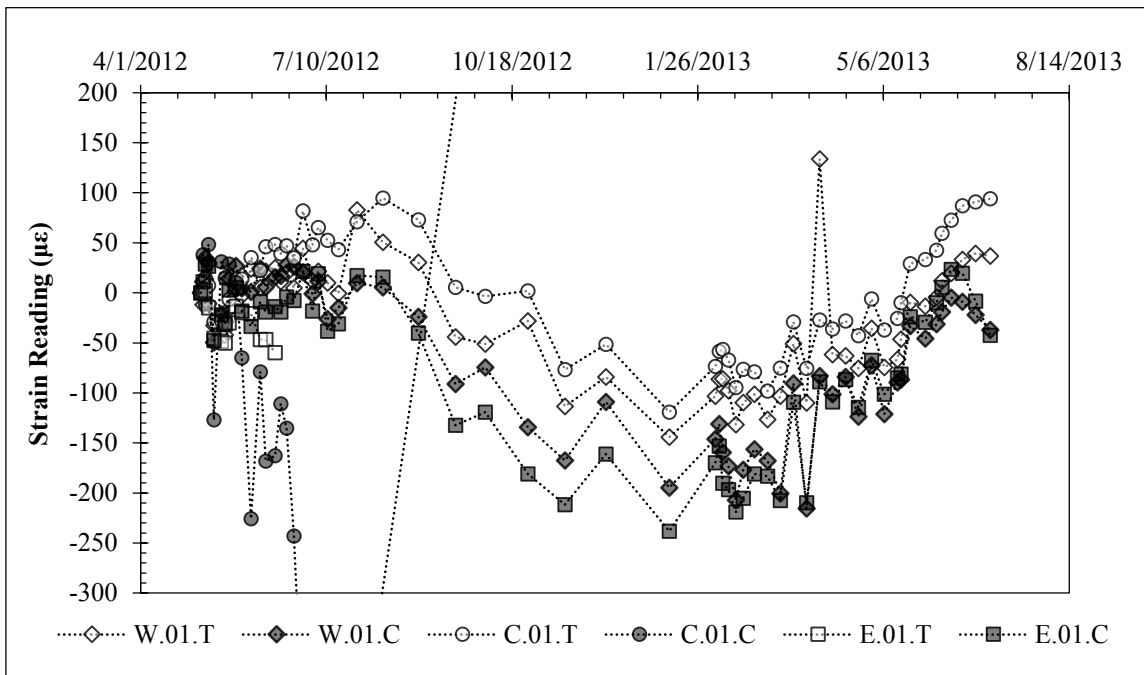


Figure G.47: Strain Data 1 Foot Below Ground Surface (May 2012 – July 2013).

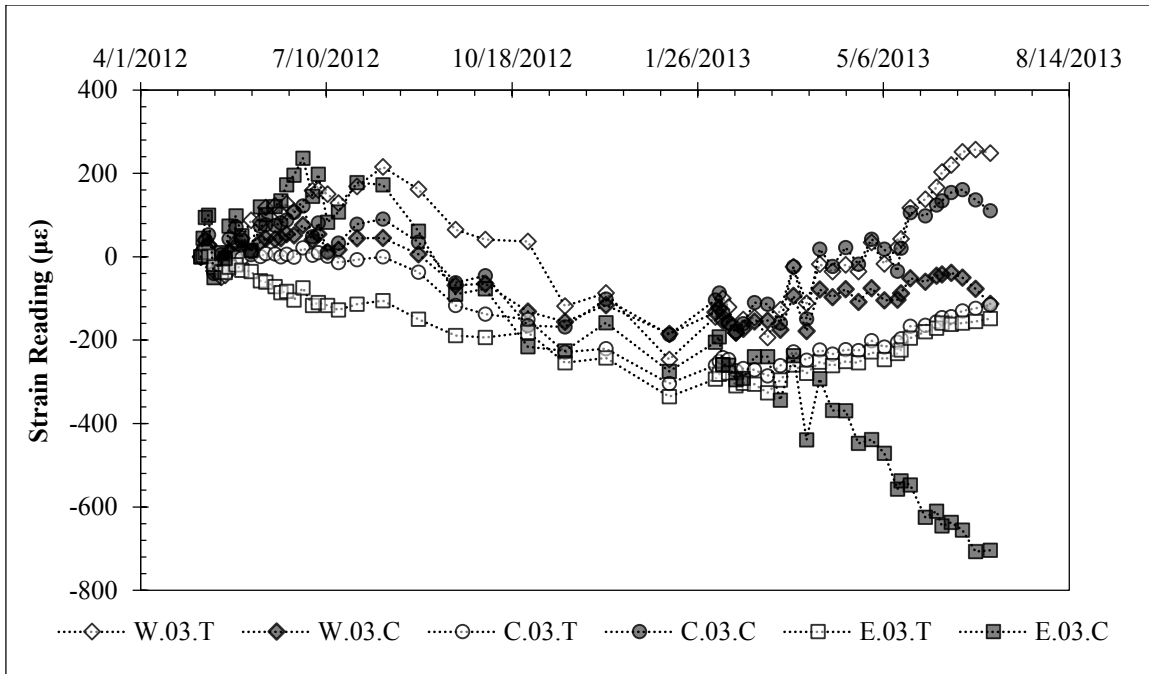


Figure G.48: Strain Data 3 Feet Below Ground Surface (May 2012 – July 2013).

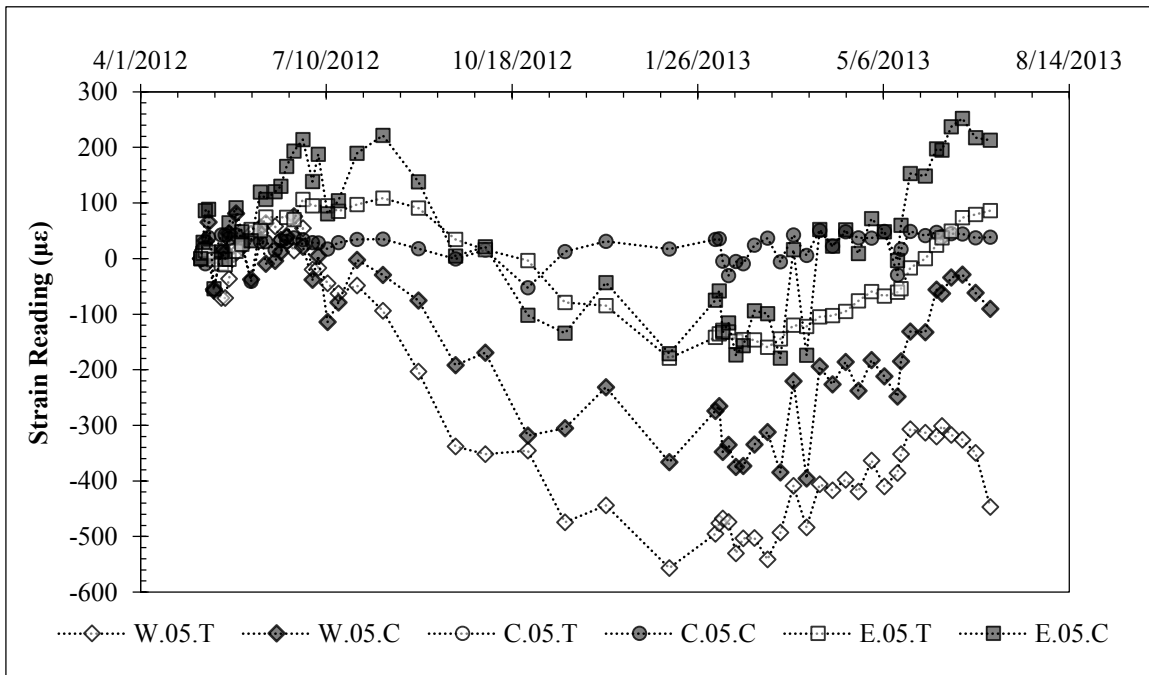


Figure G.49: Strain Data 5 Feet Below Ground Surface (May 2012 – July 2013).

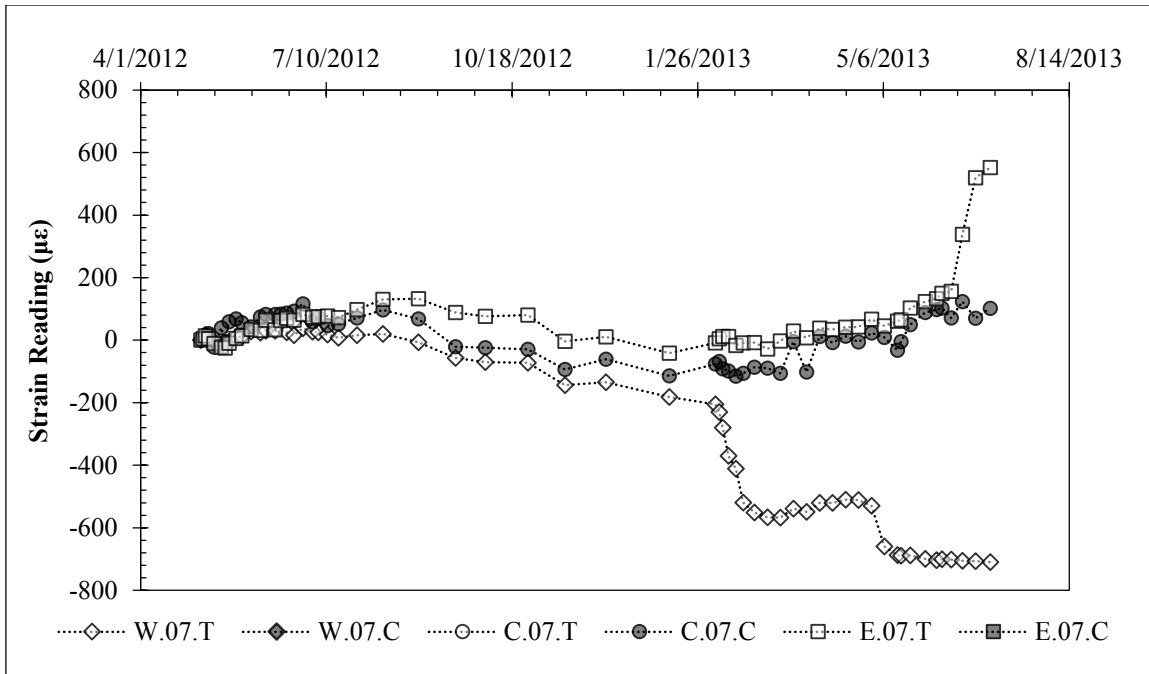


Figure G.50: Strain Data 7 Feet Below Ground Surface (May 2012 – July 2013).

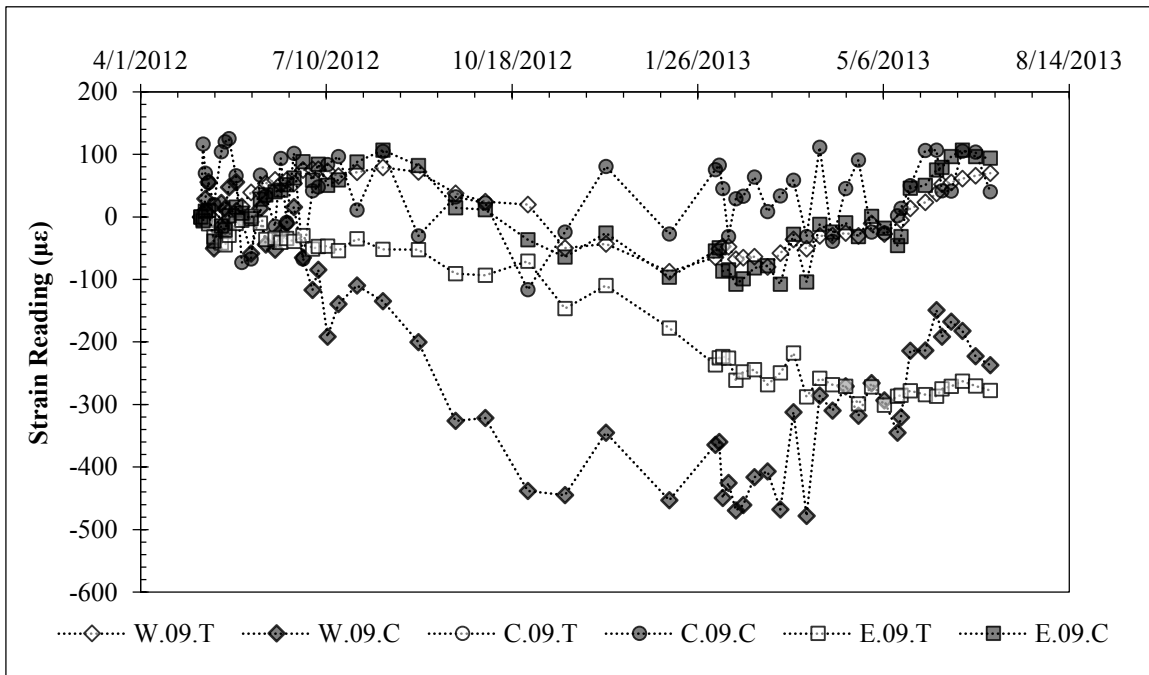


Figure G.51: Strain Data 9 Feet Below Ground Surface (May 2012 – July 2013).

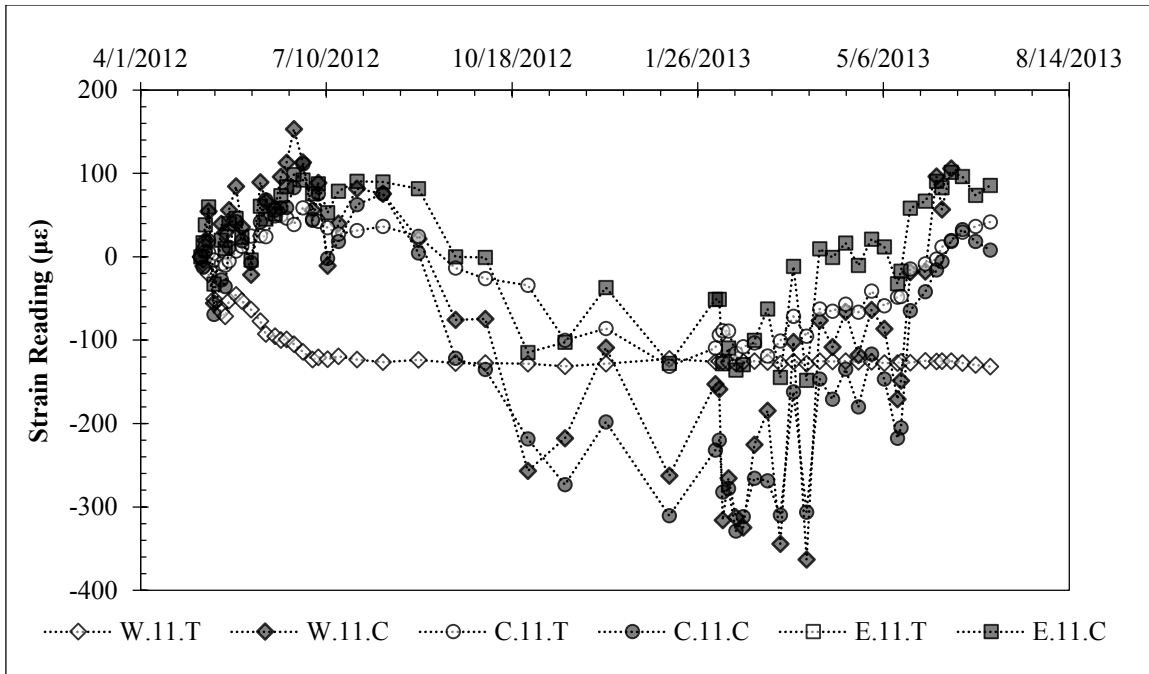


Figure G.52: Strain Data 11 Feet Below Ground Surface (May 2012 – July 2013).

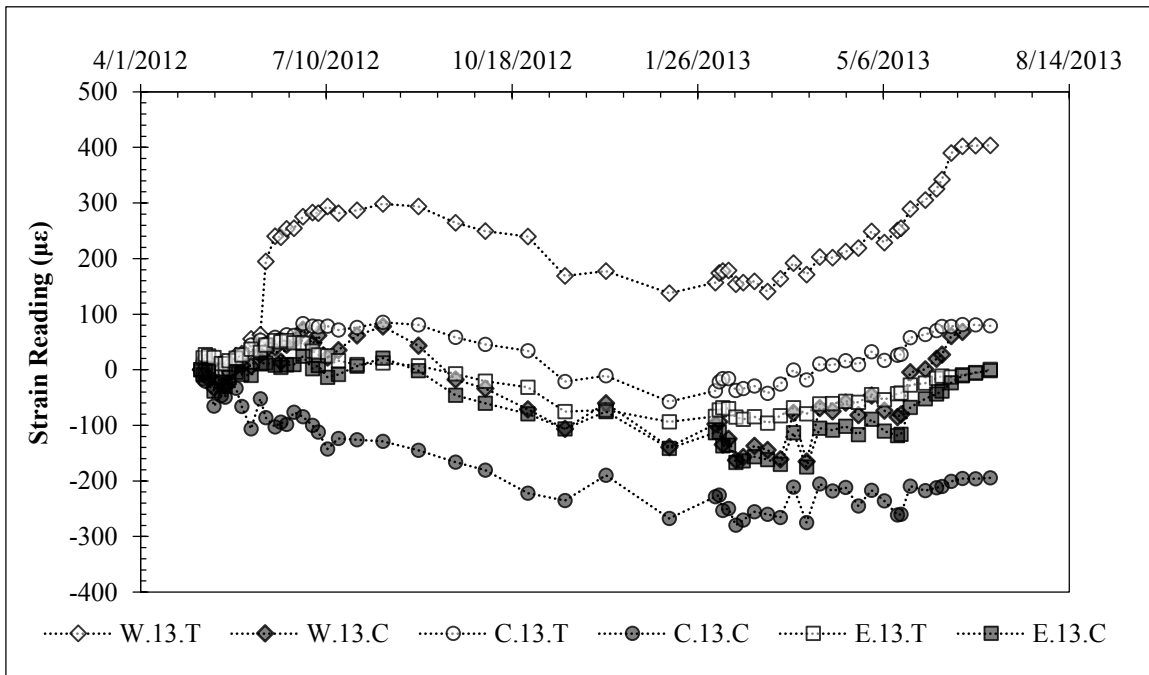


Figure G.53: Strain Data 13 Feet Below Ground Surface (May 2012 – July 2013).

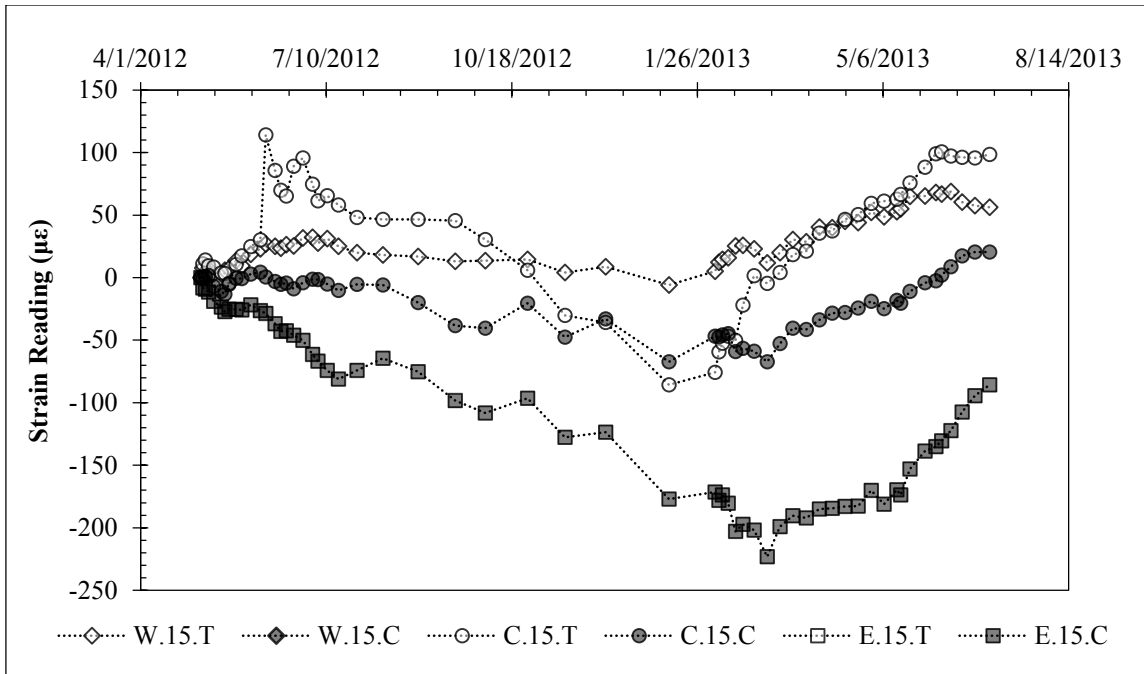


Figure G.54: Strain Data 15 Feet Below Ground Surface (May 2012 – July 2013).

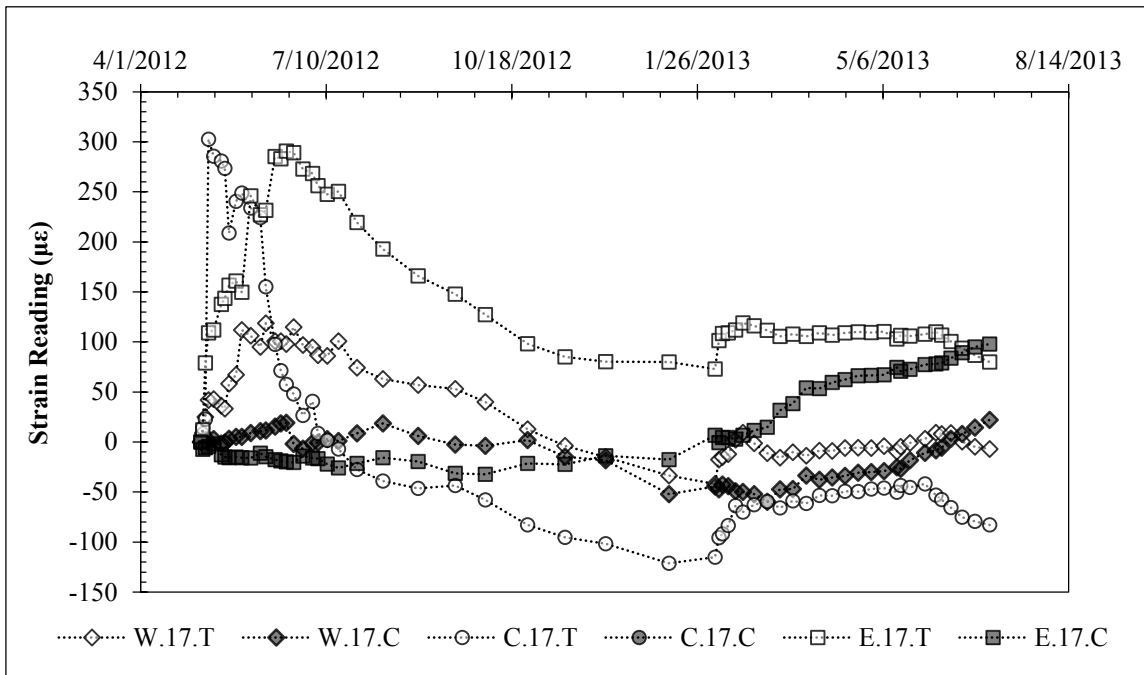


Figure G.55: Strain Data 17 Feet Below Ground Surface (May 2012 – July 2013).

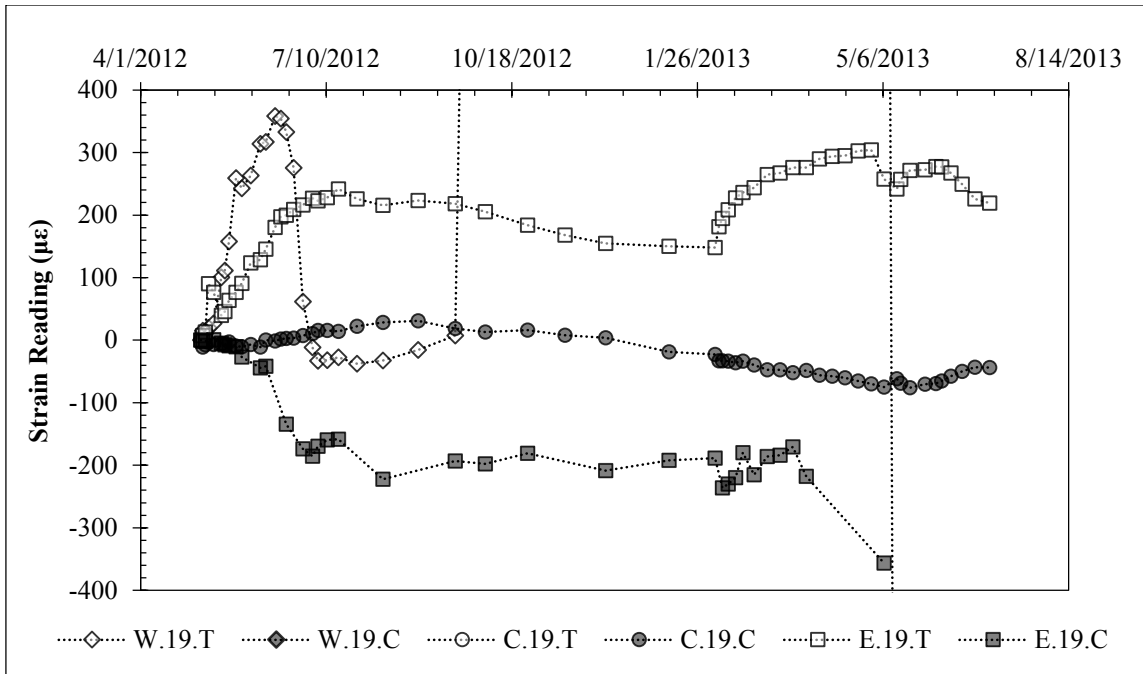


Figure G.56: Strain Data 19 Feet Below Ground Surface (May 2012 – July 2013).

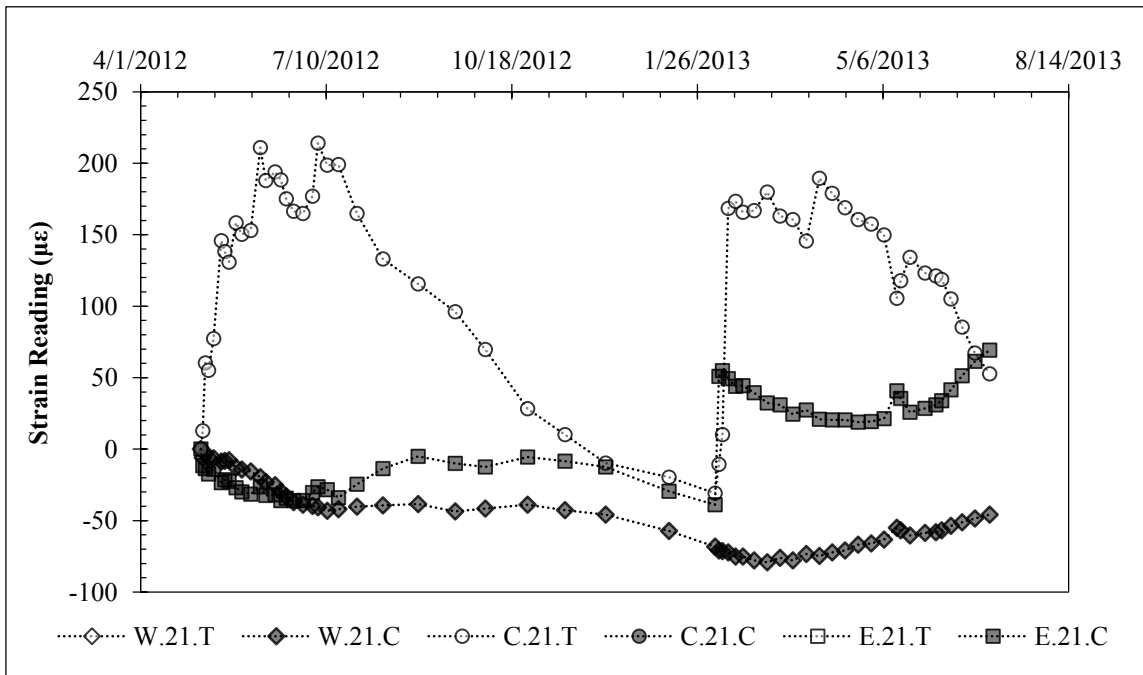


Figure G.57: Strain Data 21 Feet Below Ground Surface (May 2012 – July 2013).

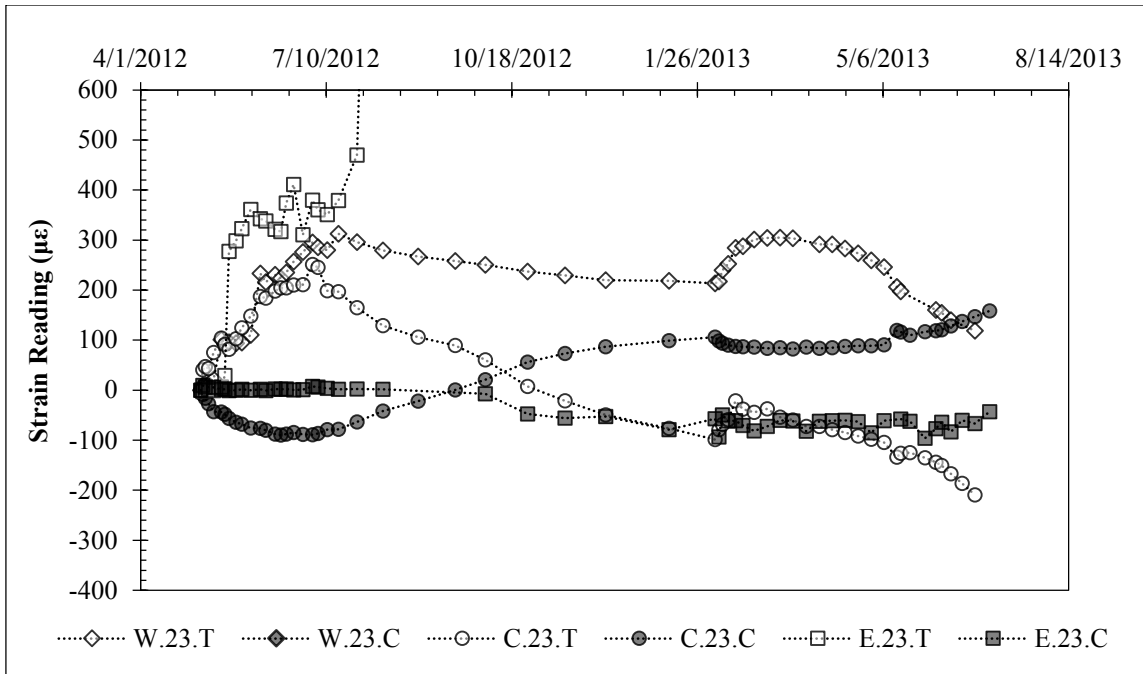


Figure G.58: Strain Data 23 Feet Below Ground Surface (May 2012 – July 2013).

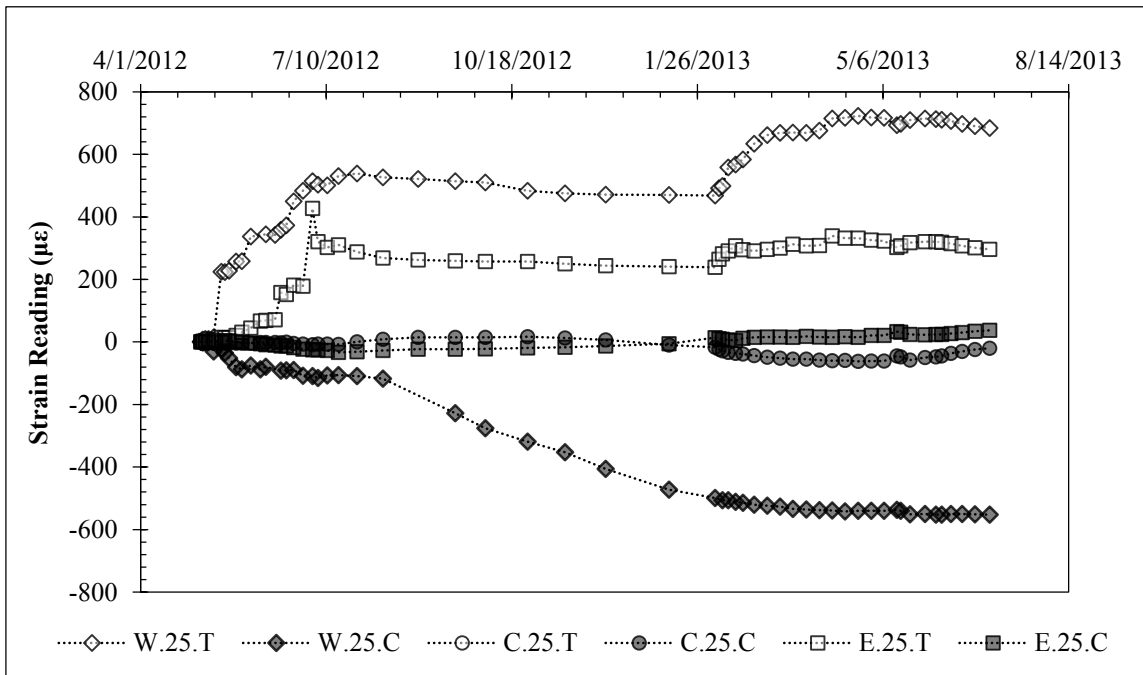


Figure G.59: Strain Data 25 Feet Below Ground Surface (May 2012 – July 2013).

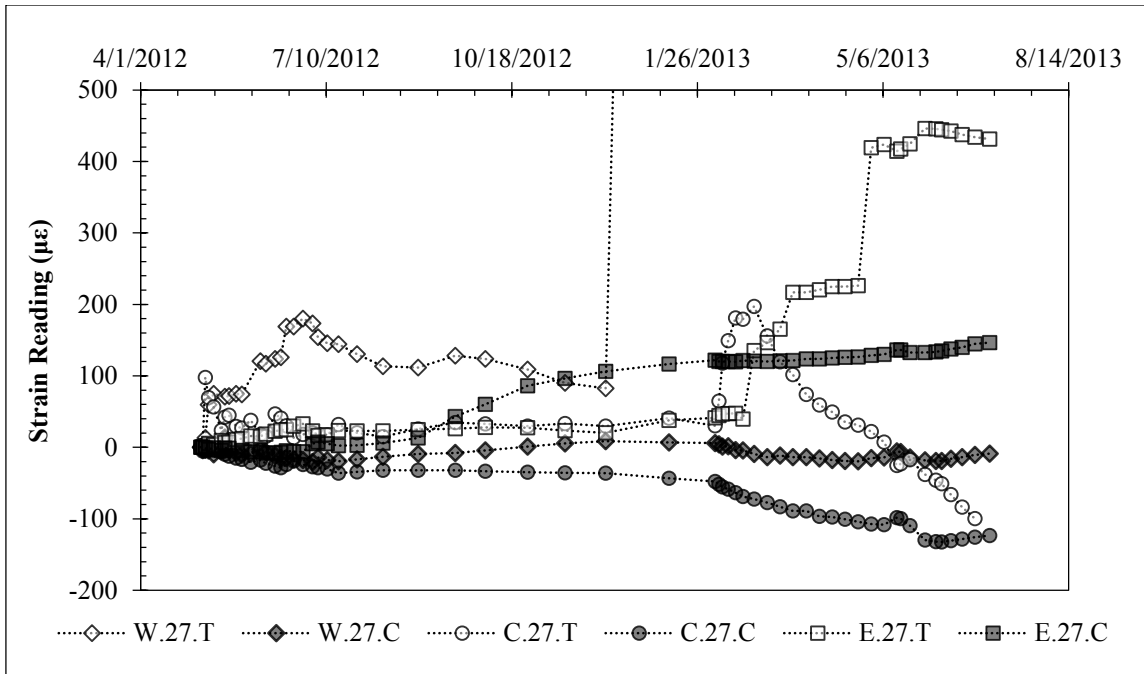


Figure G.60: Strain Data 27 Feet Below Ground Surface (May 2012 – July 2013).

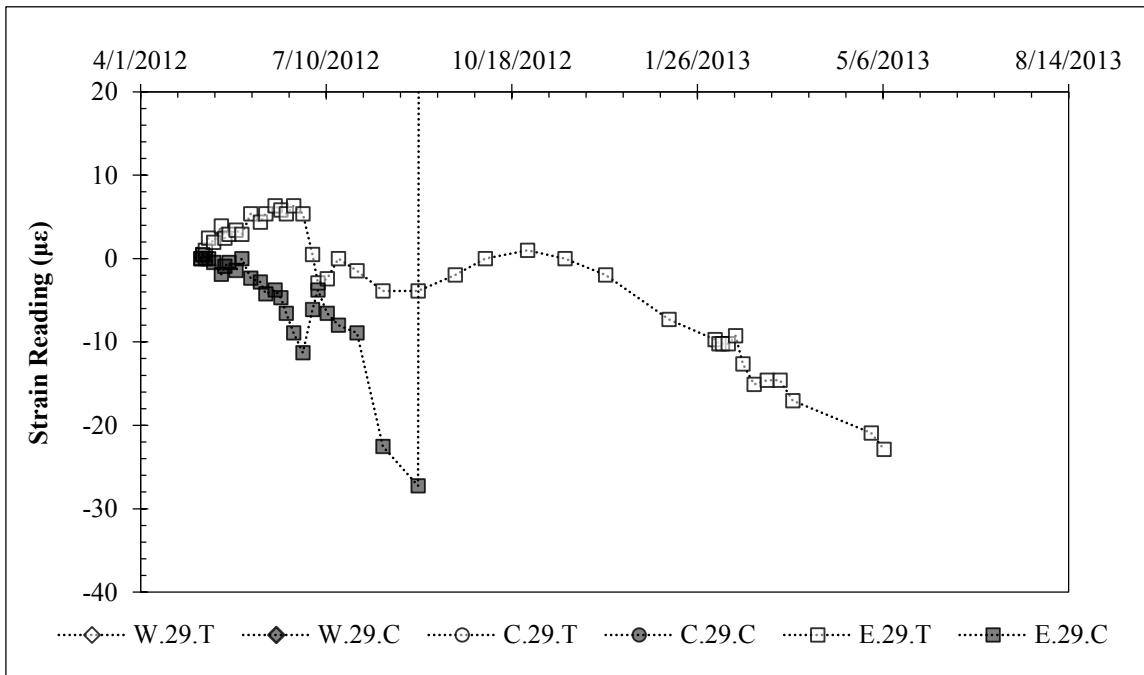


Figure G.61: Strain Data 29 Feet Below Ground Surface (May 2012 – July 2013).

APPENDIX H: EARTH PRESSURES VS. DISPLACEMENTS

H.1: Overview

This section presents p-y curves calculated from inclinometer rotation profiles. The data reduction process is described in detail in Chapter 3. Calculated p-y curves for short-term (during excavation) and long-term (during natural moisture cycles and inundation testing) loading conditions are presented.

H.2: Measured p-y Curves During Excavation (7/27/2010 – 10/08/2010)

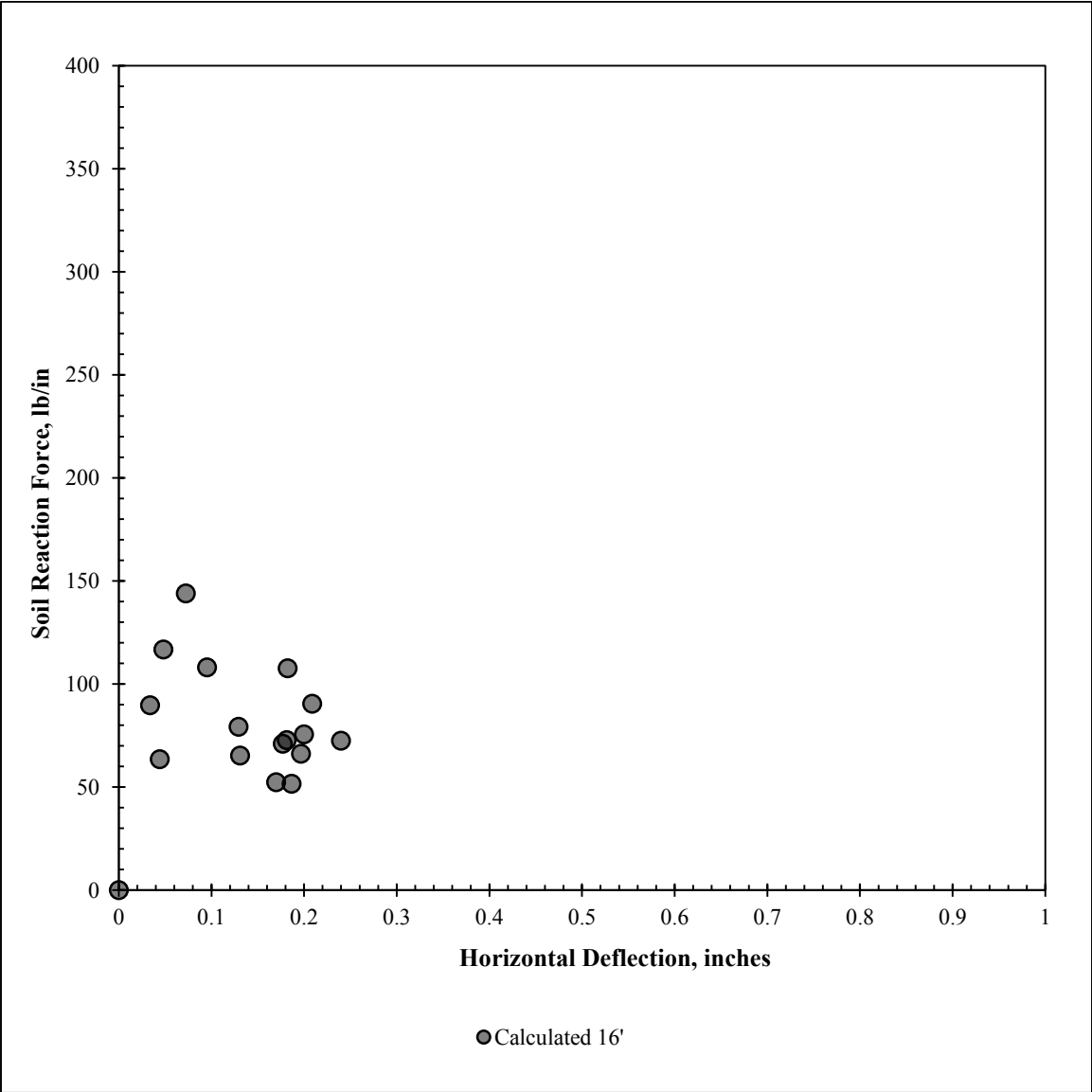


Figure H.1: Calculated p-y curves during excavation at a depth of 16 feet below original ground surface.

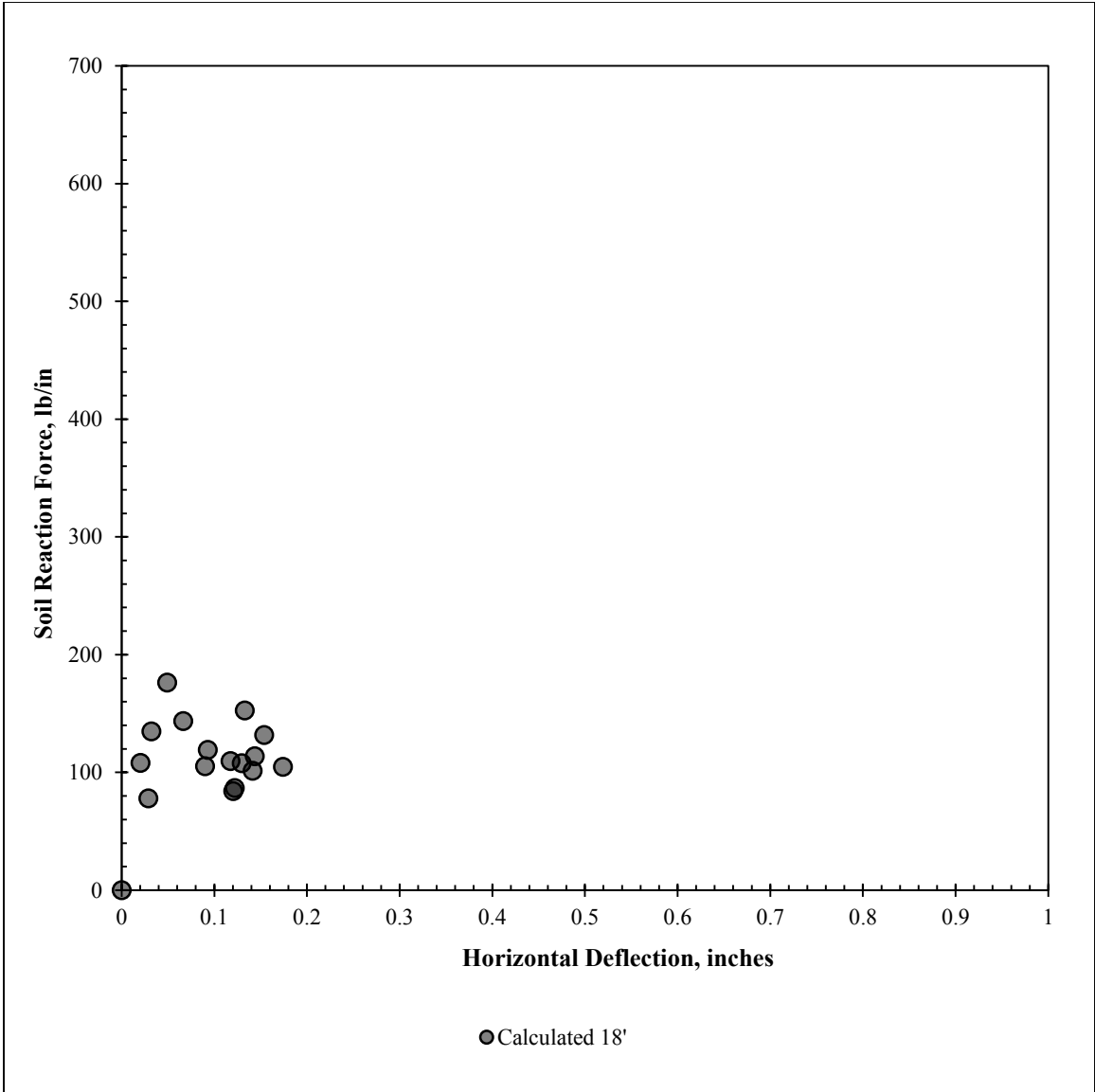


Figure H.2: Calculated p-y curves during excavation at a depth of 18 feet below original ground surface.

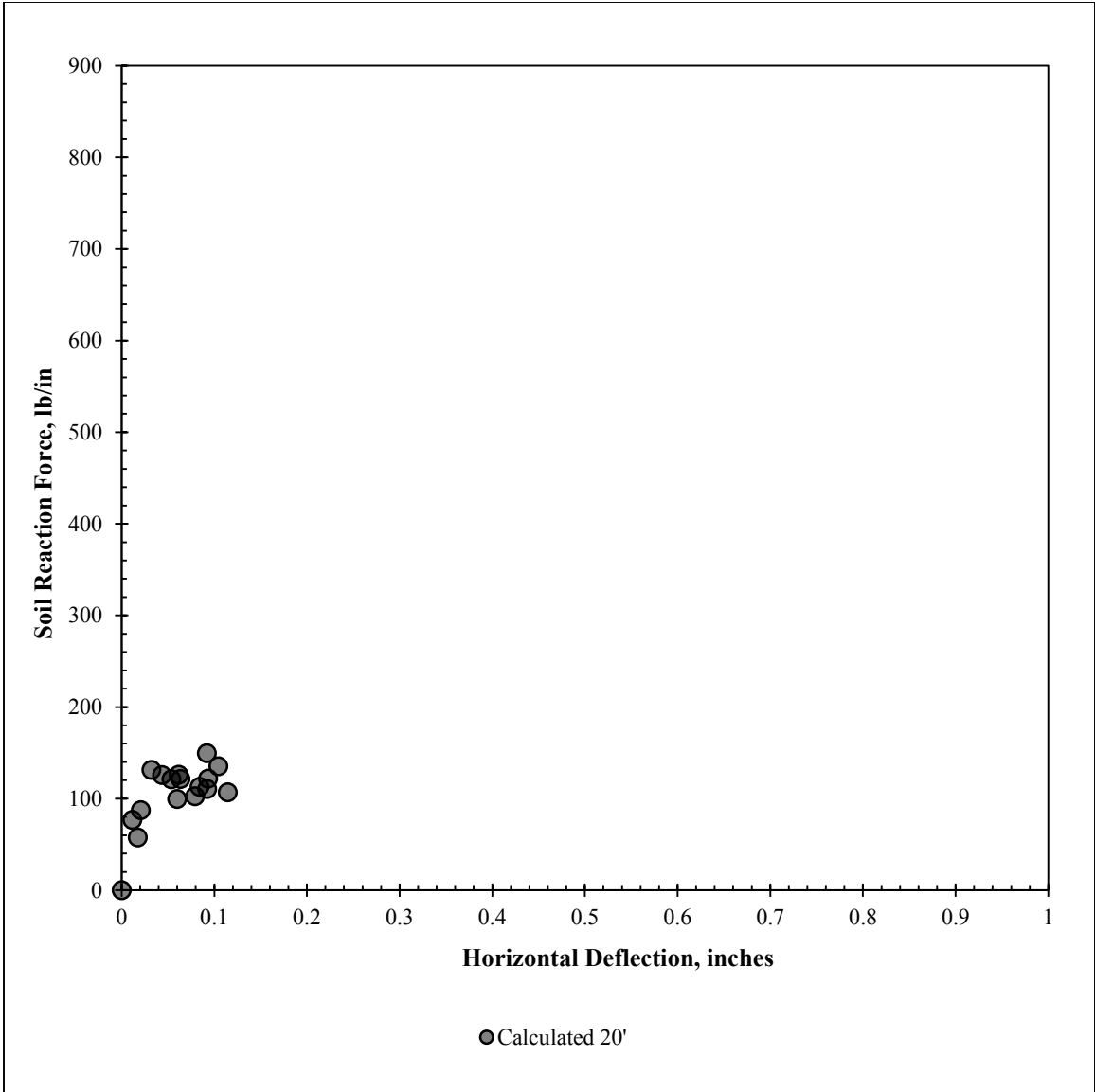


Figure H.3: Calculated p-y curves during excavation at a depth of 20 feet below original ground surface.

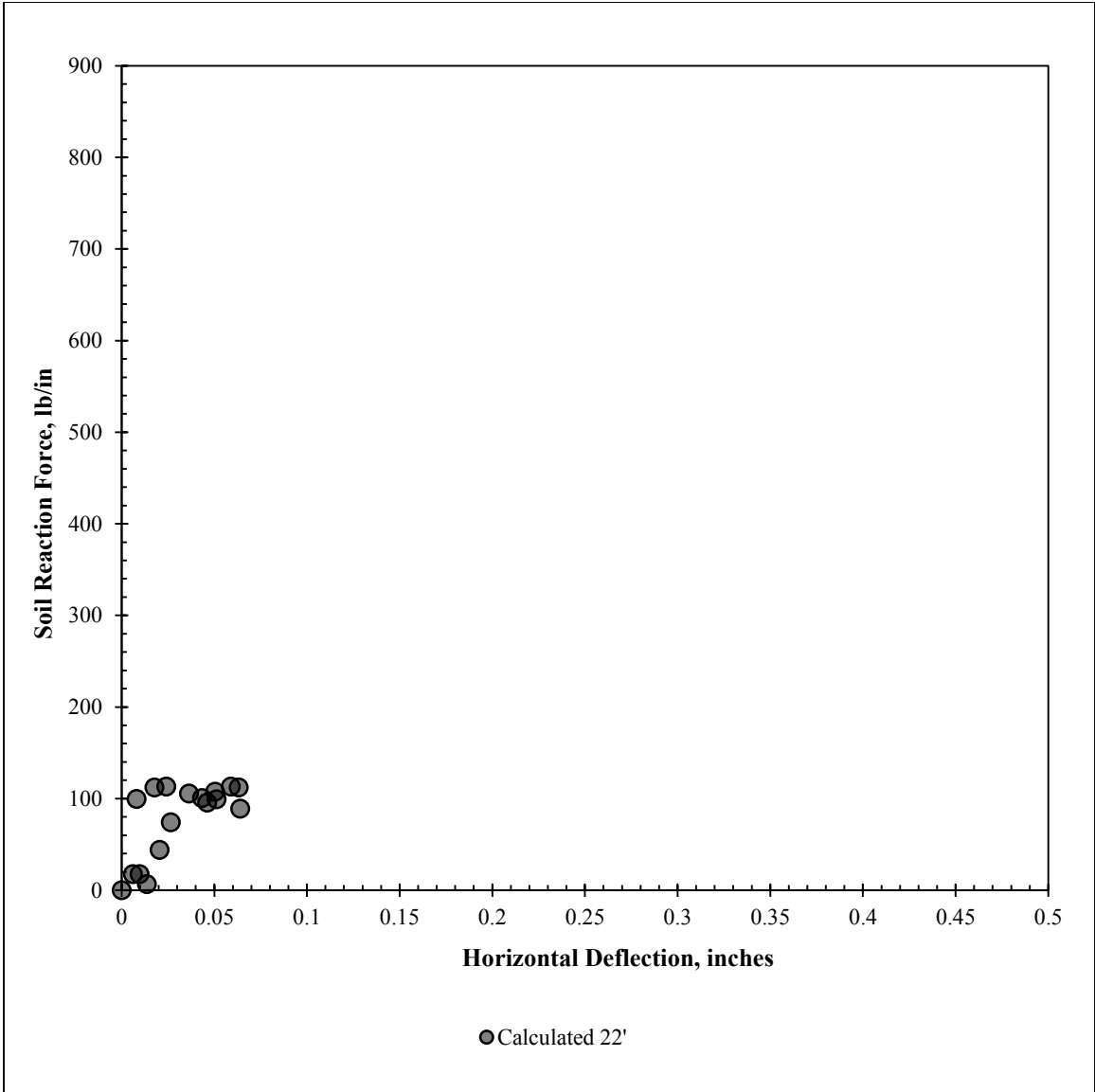


Figure H.4: Calculated p-y curves during excavation at a depth of 22 feet below original ground surface.

H.3: Long-Term p-y Curves (10/08/2010 – 5/28/2013)

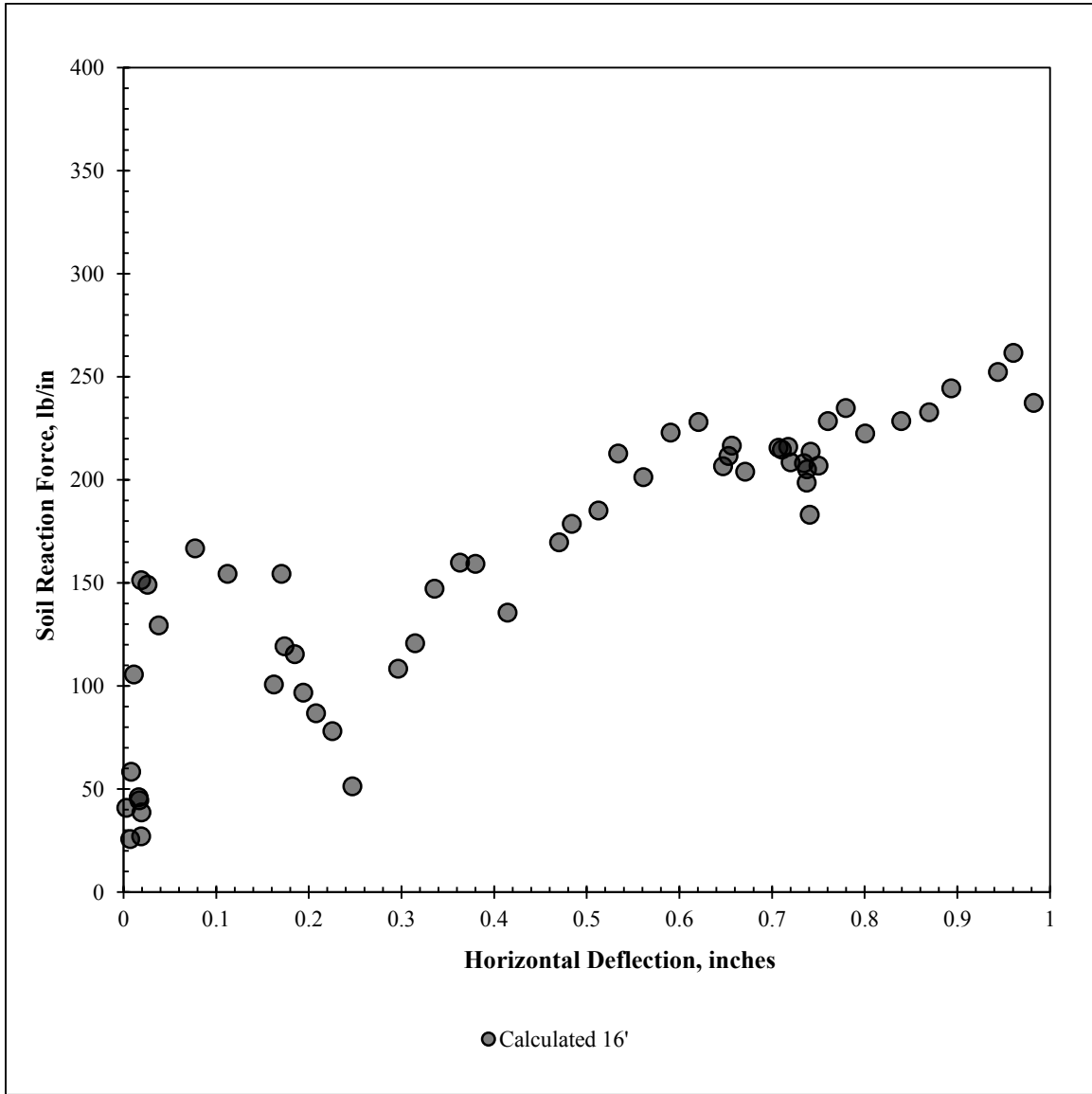


Figure H.5: Calculated long-term p-y curves during inundation testing at a depth of 16 feet below original ground surface (reference survey is installation of facing on 10/08/2010).

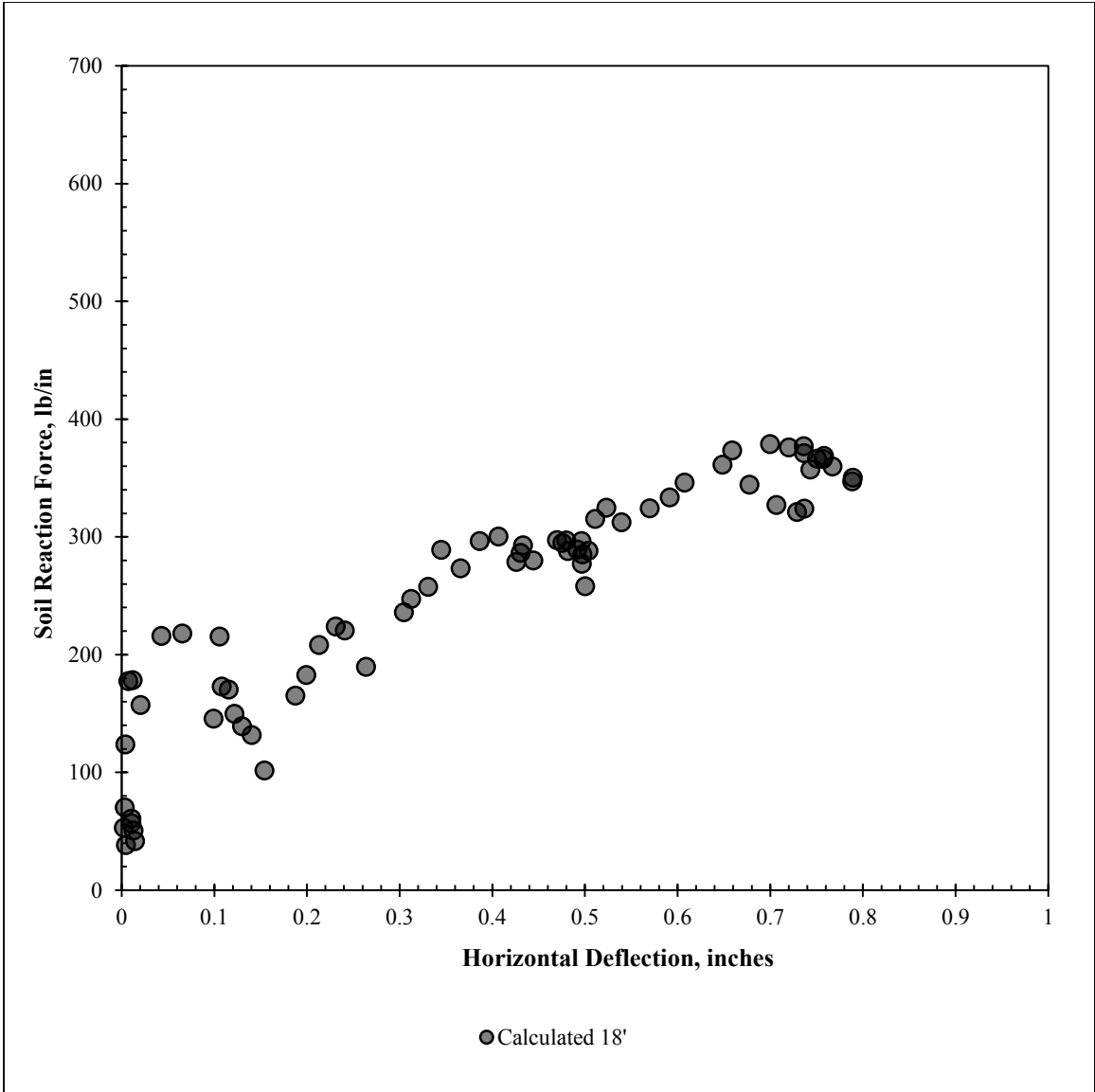


Figure H.6: Calculated long-term p-y curves during inundation testing at a depth of 18 feet below original ground surface (reference survey is installation of facing on 10/08/2010).

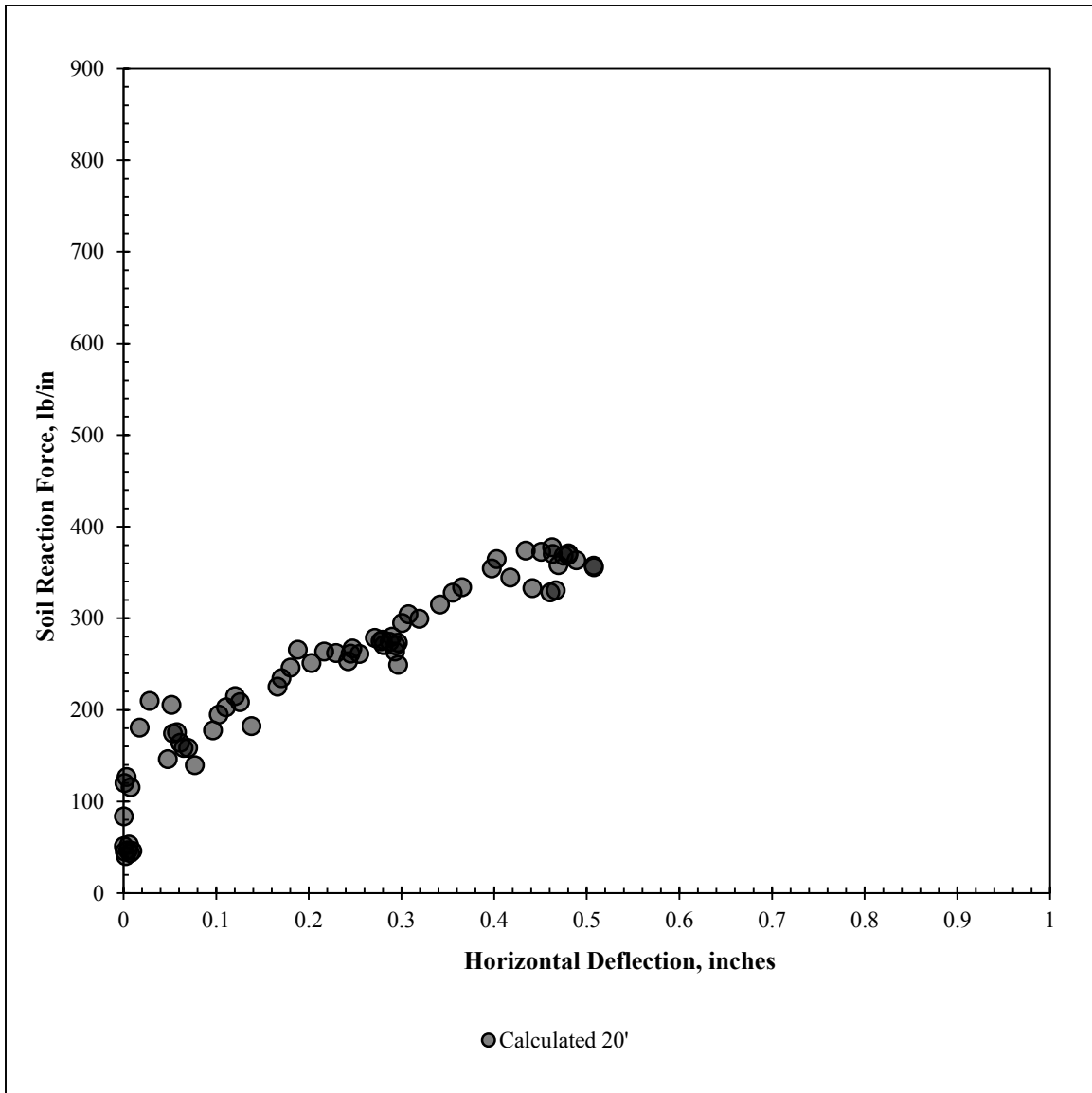


Figure H.7: Calculated long-term p-y curves during inundation testing at a depth of 20 feet below original ground surface (reference survey is installation of facing on 10/08/2010).

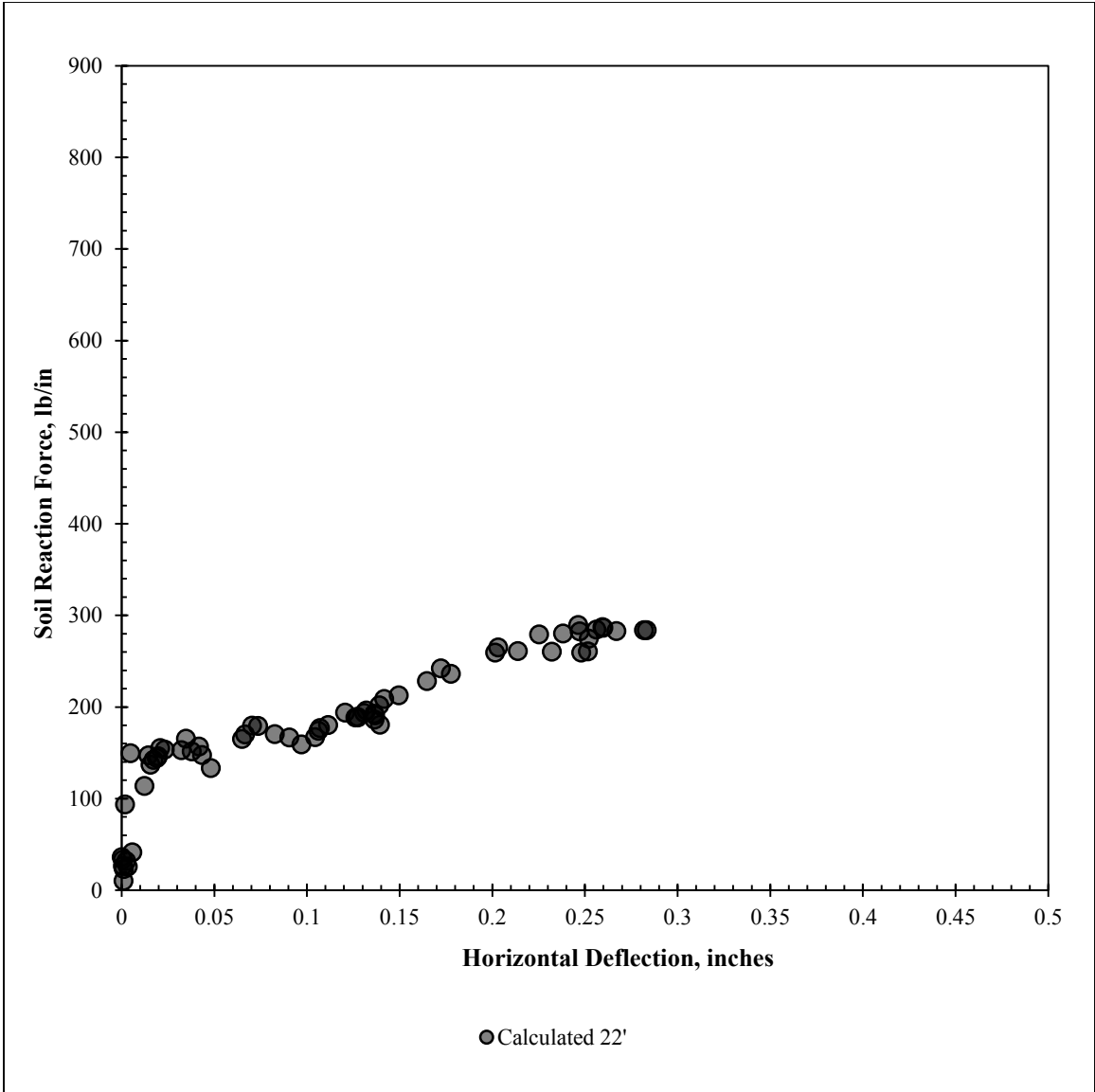


Figure H.8: Calculated long-term p-y curves during inundation testing at a depth of 22 feet below original ground surface (reference survey is installation of facing on 10/08/2010).

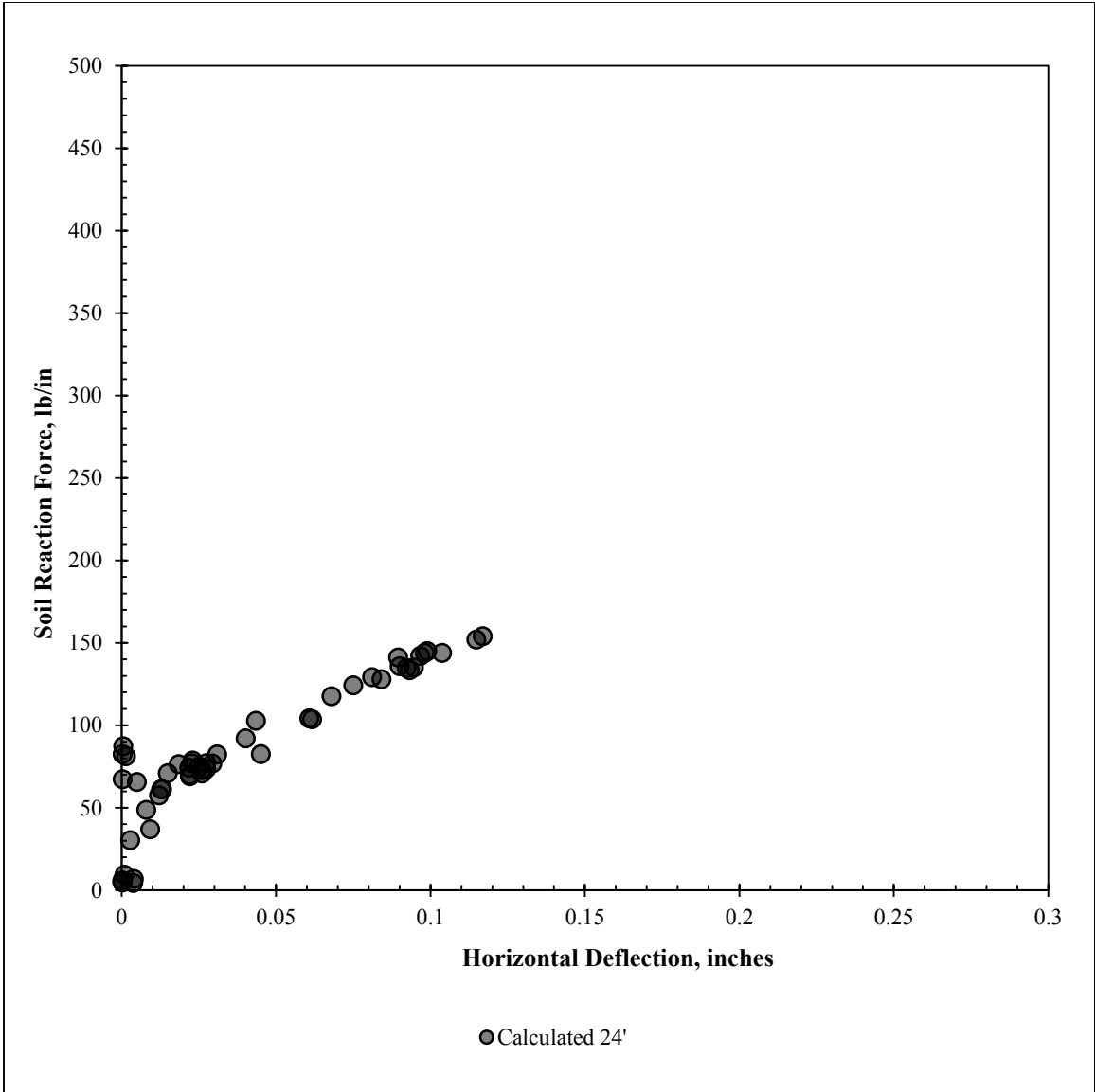


Figure H.9: Calculated long-term p-y curves during inundation testing at a depth of 24 feet below original ground surface (reference survey is installation of facing on 10/08/2010).

APPENDIX I: FINITE ELEMENT ANALYSIS

I.1: Overview

This appendix presents the input soil parameters and results of the finite element model conducted using the program ABAQUS. Two field conditions were considered in the analysis: 1) short term (un-drained conditions), and 2) long term (drained conditions) with steady state ground water conditions. Short term conditions were modeled adopting two different soil models: a) linear elastic model, and, b) Cam- Clay model.

Short term conditions are captured in field data by inclinometer readings dated 10/8/2010. Ground water table is considered to be hydrostatic, with phreatic surface at a depth of 15ft below ground surface. The following sections present input data adopted in both linear elastic model and Cam- Clay model, and the output results.

Short term conditions were modeled using a simplified linear elastic model. The model is based on total stress analysis (all parameters are given in terms of total stress). This model is an attempt to capture the wall behavior monitored on 10/8/2010.

Table I-1: Model input parameters for Linear Elastic FEM.

	Top Layer	Bottom Layer
Model	Linear elastic	Linear elastic
E (psf)	324,000	1,600,000
ν	0.45	0.45
Unit weight (pcf)	125	125
K0	3	3

I.2: Parameters Considered in Linear Elastic Model

I.2.1: YOUNG'S MODULUS (E)

Values of Young's Modulus (E) were varied in order to match the deflections measured in field with the computed deflection values. The ratio of E/S_u for the linear elastic model is summarized in Figure I.1 and Table I-2. Figure I.3 presents computed deflections versus depth, based on a range of E/S_u ratios.

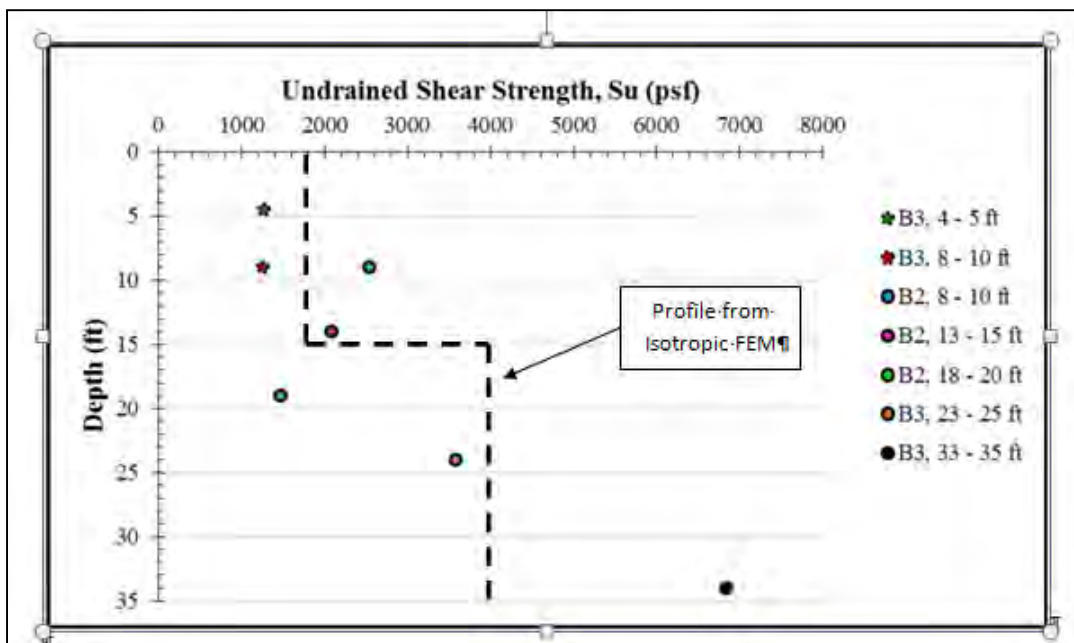


Figure I.1: Undrained shear strength vs depth from UU testing after Ellis, 2011

Table I-2: Modulus of elasticity based on best match E/S_u ratio

	Top Layer	Bottom Layer
S_u (psf) (UU test)	1,800	4,000
E/S_u	180	400

I.2.2: AT-REST EARTH PRESSURE COEFFICIENT (K_0)

Figure I.2 presents values of horizontal stress versus depth obtained from dilatometer tests in Eagle Ford Shale soil. Results show that a K_0 value of approximately 3.0 could be assigned to Taylor clay soil.

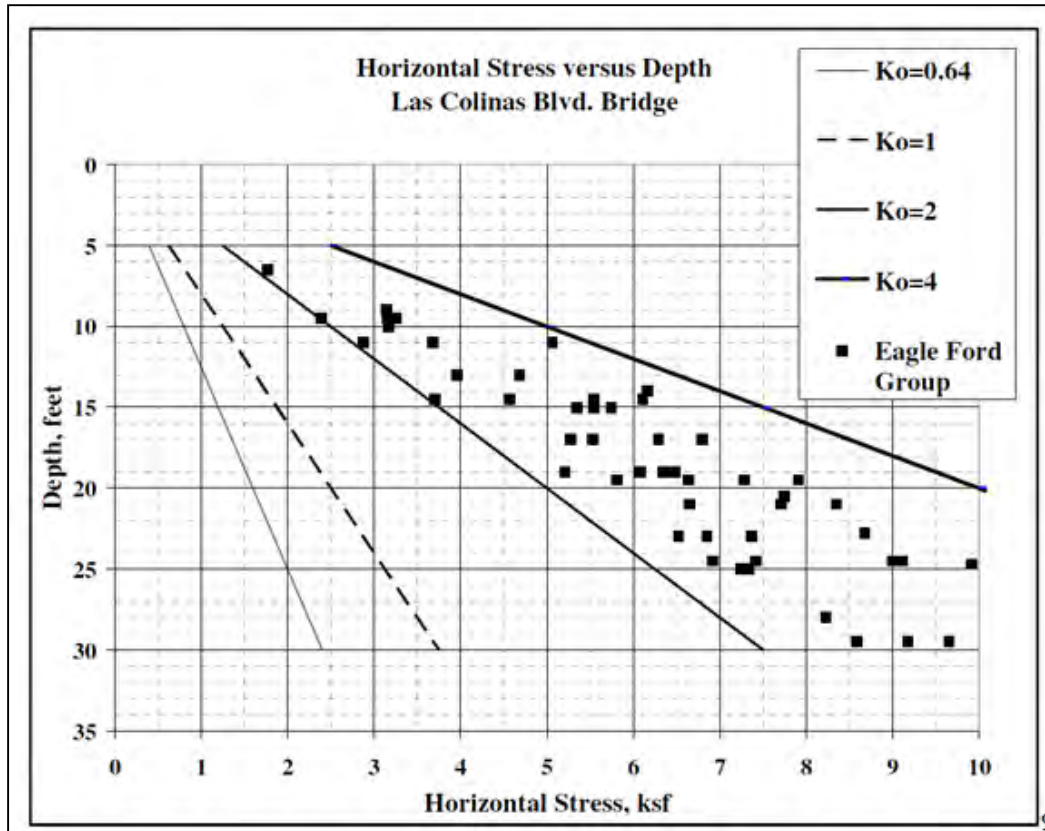


Figure I.2: DMT test field data adopted in the estimation of K_0 (after Smith et al. 2009).

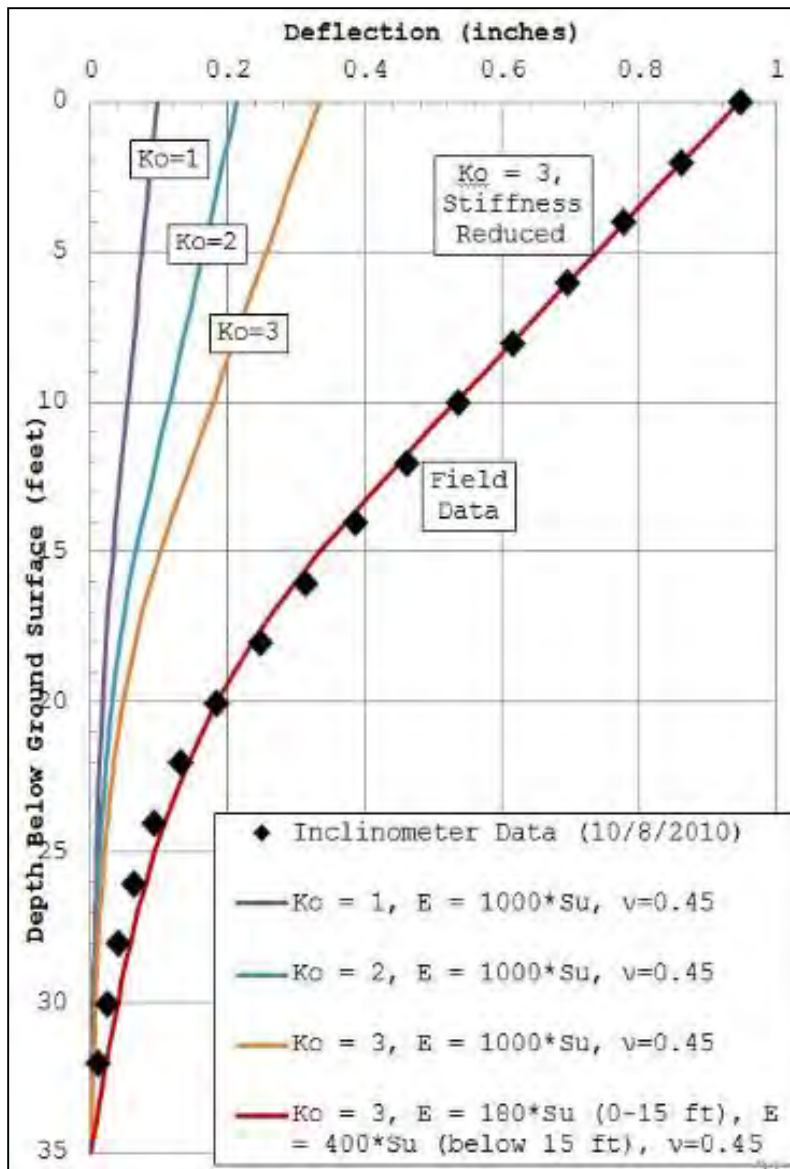


Figure I.3: Computed deflections vs. depth based on different E/S_u ratios

APPENDIX J: FINITE DIFFERENCE ANALYSIS

J.1: Overview

This section presents the output files for the LPILE analyses discussed in this research report.

J.2: Initial Design of Test Wall

```
=====
LPILE Plus for Windows, Version 2012-06.037
Analysis of Individual Piles and Drilled Shafts
Subjected to Lateral Loading Using the p-y Method

© 1985-2012 by Ensoft, Inc.
All Rights Reserved

=====

This copy of LPILE is licensed to:

Andy Brown
University of Texas - Austin

Serial Number of Security Device:      226662924
Company Name Stored in Security Device: UT Austin - Prof. Gilbert

-----
Files Used for Analysis
-----

-----
Date and Time of Analysis
-----

Date: August 29, 2013   Time: 18:20:11

-----
Problem Title
-----

Project Name:
Job Number:
Client:
Engineer:
Description:

-----
Program Options
-----

Engineering units are US Customary Units: pounds, inches, feet

Basic Program Options:

This analysis computes pile response to lateral loading and will compute nonlinear
moment-curvature and nominal moment capacity for section types with nonlinear properties.

Computation Options:
- Analysis does not use p-y multipliers (individual pile or shaft only)
- Analysis assumes no shear resistance at pile tip
- Analysis for fixed-length pile or shaft only
- No computation of foundation stiffness matrix values
- Report summary table of pile-top values for deflection, maximum bending
  moment, and shear force only
- Analysis assumes no loading by soil movements acting on pile
- p-y curves computed and reported at user-specified depths

Solution Control Parameters:
- Number of pile increments           =          100
- Maximum number of iterations allowed =          250
- Deflection tolerance for convergence = 1.0000E-05 in
- Maximum allowable deflection        =    100.0000 in
```

Pile Response Output Options:
 - Only summary tables of pile-head deflection, maximum bending moment,
 and maximum shear force are to be written to output report file.

 Pile Structural Properties and Geometry

Total number of pile sections = 1
 Total length of pile = 35.00 ft
 Depth of ground surface below top of pile = 15.00 ft
 Pile diameter values used for p-y curve computations are defined using 2 points.

p-y curves are computed using pile diameter values interpolated with depth over
 the length of the pile.

Point	Depth X ft	Pile Diameter in
1	0.00000	24.0000000
2	35.000000	24.0000000

 Input Structural Properties:

Pile Section No. 1:

Section Type = Drilled Shaft (Bored Pile)
 Section Length = 35.00000000 ft
 Section Diameter = 24.00000000 in

 Ground Slope and Pile Batter Angles

Ground Slope Angle = 0.000 degrees
 = 0.000 radians
 Pile Batter Angle = 0.000 degrees
 = 0.000 radians

 Soil and Rock Layering Information

The soil profile is modelled using 2 layers

Layer 1 is stiff clay without free water

Distance from top of pile to top of layer = 15.00000 ft
 Distance from top of pile to bottom of layer = 20.00000 ft
 Effective unit weight at top of layer = 130.00000 pcf
 Effective unit weight at bottom of layer = 130.00000 pcf
 Undrained cohesion at top of layer = 1120.00000 psf
 Undrained cohesion at bottom of layer = 1120.00000 psf
 Epsilon-50 at top of layer = 0.0000
 Epsilon-50 at bottom of layer = 0.0000

NOTE: Internal default values for Epsilon-50 will be computed for the above soil layer.

Layer 2 is stiff clay without free water

Distance from top of pile to top of layer = 20.00000 ft
 Distance from top of pile to bottom of layer = 50.00000 ft
 Effective unit weight at top of layer = 130.00000 pcf
 Effective unit weight at bottom of layer = 130.00000 pcf
 Undrained cohesion at top of layer = 2240.00000 psf
 Undrained cohesion at bottom of layer = 2240.00000 psf
 Epsilon-50 at top of layer = 0.0000
 Epsilon-50 at bottom of layer = 0.0000

NOTE: Internal default values for Epsilon-50 will be computed for the above soil layer.

(Depth of lowest soil layer extends 15.00 ft below pile tip)

 Summary of Soil Properties

Layer Num.	Layer Soil Type (p-y Curve Criteria)	Layer Depth ft	Effective Unit Wt. pcf	Undrained Cohesion psf	Strain Factor Epsilon 50
1	Stiff Clay w/o Free Water	15.000	130.000	1120.000	default
		20.000	130.000	1120.000	default
2	Stiff Clay w/o Free Water	20.000	130.000	2240.000	default
		50.000	130.000	2240.000	default

 Loading Type

Static loading criteria were used when computing p-y curves for all analyses.

 Distributed Lateral Loading

Distributed lateral load intensity defined using 2 points

Point No.	Depth X in	Dist. Load lbs/in
1	0.000	0.000
2	180.000	125.000

 Pile-head Loading and Pile-head Fixity Conditions

Number of loads specified = 1

Load No.	Load Type	Condition 1	Condition 2	Axial Thrust Force, lbs	Compute Top y vs. Pile Length
1	1	V = 0.0000 lbs	M = 0.0000 in-lbs	0.0000000	No

V = perpendicular shear force applied to pile head
 M = bending moment applied to pile head
 y = lateral deflection relative to pile axis
 S = pile slope relative to original pile batter angle
 R = rotational stiffness applied to pile head
 Axial thrust is assumed to be acting axially for all pile batter angles.

 Specified Depths for Output of p-y Curves

Lateral load-transfer (p-y) curves are computed and output at 6 depths.
 (Note that these curves are independent from the curves used at nodal point depths)

Depth No.	Depth Below Pile Head ft	Depth Below Ground Surface ft
1	15.000	0.000
2	19.000	4.000
3	21.000	6.000
4	25.000	10.000
5	30.000	15.000
6	35.000	20.000

Depth of ground surface below top of pile = 15.00 ft

 Computations of Nominal Moment Capacity and Nonlinear Bending Stiffness

Axial thrust force values were determined from pile-head loading conditions

Number of Pile Sections Analyzed = 1

Pile Section No. 1:

Dimensions and Properties of Drilled Shaft (Bored Pile):

Length of Section = 35.00000000 ft
 Shaft Diameter = 24.00000000 in

Concrete Cover Thickness = 3.0000000 in
 Number of Reinforcing Bars = 12 bars
 Yield Stress of Reinforcing Bars = 60.0000000 ksi
 Modulus of Elasticity of Reinforcing Bars = 29000. ksi
 Gross Area of Shaft = 452.38934212 sq. in.
 Total Area of Reinforcing Steel = 7.20000000 sq. in.
 Area Ratio of Steel Reinforcement = 1.59 percent
 Edge-to-Edge Bar Spacing = 3.55727615 in
 Maximum Concrete Aggregate Size = 0.75000000 in
 Ratio of Bar Spacing to Aggregate Size = 4.74
 Offset of Rebar Cage Center from Center of Pile = 0.0000000 in

Axial Structural Capacities:

Nom. Axial Structural Capacity = $0.85 F_c A_c + F_y A_s$ = 1945.644 kips
 Tensile Load for Cracking of Concrete = -209.248 kips
 Nominal Axial Tensile Capacity = -432.000 kips

Reinforcing Bar Dimensions and Positions Used in Computations:

Bar Number	Bar Diam. inches	Bar Area sq. in.	X inches	Y inches
1	0.87500	0.60000	8.56250	0.00000
2	0.87500	0.60000	7.41534	4.28125
3	0.87500	0.60000	4.28125	7.41534
4	0.87500	0.60000	0.00000	8.56250
5	0.87500	0.60000	-4.28125	7.41534
6	0.87500	0.60000	-7.41534	4.28125
7	0.87500	0.60000	-8.56250	0.00000
8	0.87500	0.60000	-7.41534	-4.28125
9	0.87500	0.60000	-4.28125	-7.41534
10	0.87500	0.60000	0.00000	-8.56250
11	0.87500	0.60000	4.28125	-7.41534
12	0.87500	0.60000	7.41534	-4.28125

NOTE: The positions of the above rebars were computed by LPile

Minimum spacing between any two bars not equal to zero = 3.55728 inches between Bars 7 and 8

Spacing to aggregate size ratio = 4.74303

Concrete Properties:

Compressive Strength of Concrete = 4.0000000 ksi
 Modulus of Elasticity of Concrete = 3604.99653259 ksi
 Modulus of Rupture of Concrete = -0.47434164 ksi
 Compression Strain at Peak Stress = 0.00188627
 Tensile Strain at Fracture of Concrete = -0.00011537
 Maximum Coarse Aggregate Size = 0.75000000 in

Number of Axial Thrust Force Values Determined from Pile-head Loadings = 1

Number	Axial Thrust Force kips
1	0.000

Definitions of Run Messages and Notes:

C = concrete in section has cracked in tension.
 Y = stress in reinforcing steel has reached yield stress.
 T = ACI 318-08 criteria for tension-controlled section met, tensile strain in reinforcement exceeds 0.005 while simultaneously compressive strain in concrete more than than 0.003. See ACI 318-08, Section 10.3.4.
 Z = depth of tensile zone in concrete section is less than 10 percent of section depth.

Bending Stiffness (EI) = Computed Bending Moment / Curvature.
 Position of neutral axis is measured from edge of compression side of pile.
 Compressive stresses and strains are positive in sign.
 Tensile stresses and strains are negative in sign.

Axial Thrust Force = 0.000 kips

Bending Curvature rad/in.	Bending Moment in-kip	Bending Stiffness kip-in ²	Depth to N Axis in	Max Comp Strain in/in	Max Tens Strain in/in	Max Concrete Stress ksi	Max Steel Stress ksi	Run Msg
0.000001250	94.3056923	75444554.	11.9999611	0.0000150	-0.0000150	0.0627333	-0.4306514	
0.000002500	188.1518190	75260728.	11.9999609	0.0000300	-0.0000300	0.1249707	-0.8613028	
0.000003750	281.5383800	75076901.	11.9999608	0.0000450	-0.0000450	0.1867124	-1.2919542	
0.000005000	374.4653753	74893075.	11.9999606	0.0000600	-0.0000600	0.2479582	-1.7226057	
0.000006250	466.9328050	74709249.	11.9999605	0.0000750	-0.0000750	0.3087081	-2.1532571	
0.000007500	558.9406690	74525423.	11.9999603	0.0000900	-0.0000900	0.3689623	-2.5839086	

0.0003588	3485.7362924	9716338.	6.2059959	0.0022264	-0.0063836	3.9974827	60.0000000	CY
0.0003688	3496.6767150	9482513.	6.1796364	0.0022787	-0.0065713	3.9999624	60.0000000	CY
0.0003788	3504.3297058	9252356.	6.1515330	0.0023299	-0.0067601	3.9964331	60.0000000	CY
0.0003888	3509.6407015	9028015.	6.1224910	0.0023801	-0.0069499	3.9995811	60.0000000	CY
0.0003988	3514.5071712	8813811.	6.0935253	0.0024298	-0.0071402	3.9946161	60.0000000	CY
0.0004088	3519.1714741	8609594.	6.0663968	0.0024796	-0.0073304	3.9977956	60.0000000	CY
0.0004188	3523.7155934	8414843.	6.0410171	0.0025297	-0.0075203	3.9998910	60.0000000	CY
0.0004288	3528.0670760	8228728.	6.0174609	0.0025800	-0.0077100	3.9931542	60.0000000	CY
0.0004388	3532.2870223	8050797.	5.9954470	0.0026305	-0.0078995	3.9976707	60.0000000	CY
0.0004488	3536.4046900	7880568.	5.9747997	0.0026812	-0.0080888	3.9998150	60.0000000	CY
0.0004588	3540.3593233	7717405.	5.9555957	0.0027321	-0.0082779	3.9936955	60.0000000	CY
0.0004688	3544.1882331	7560935.	5.9376465	0.0027833	-0.0084667	3.9960535	60.0000000	CY
0.0004788	3547.9317058	7410823.	5.9207714	0.0028346	-0.0086554	3.9990963	60.0000000	CY
0.0004888	3551.5795261	7266659.	5.9049340	0.0028860	-0.0088440	3.9991486	60.0000000	CY
0.0004988	3555.0609250	7127942.	5.8902642	0.0029378	-0.0090322	3.9917525	60.0000000	CY
0.0005088	3558.4438120	6994484.	5.8760912	0.0029895	-0.0092205	3.9963782	60.0000000	CY
0.0005188	3561.6790741	6865887.	5.8617779	0.0030408	-0.0094092	3.9991045	60.0000000	CYT
0.0005288	3564.8464332	6742026.	5.8482830	0.0030923	-0.0095977	3.9998562	60.0000000	CYT
0.0005388	3567.8682029	6622493.	5.8358002	0.0031440	-0.0097860	3.9907772	60.0000000	CYT
0.0005488	3570.8381723	6507222.	5.8239950	0.0031959	-0.0099741	3.9939756	60.0000000	CYT
0.0006088	3587.3288166	5892943.	5.7663073	0.0035102	-0.0110998	3.9964516	60.0000000	CYT
0.0006688	3601.8049954	5385877.	5.7263001	0.0038295	-0.0122205	3.9955298	60.0000000	CYT

 Summary of Results for Nominal (Unfactored) Moment Capacity for Section 1

Moment values interpolated at maximum compressive strain = 0.003
 or maximum developed moment if pile fails at smaller strains.

Load No.	Axial Thrust kips	Nominal Mom. Cap. in-kip	Max. Comp. Strain
1	0.000	3559.108	0.00300000

Note note that the values of moment capacity in the table above are not factored by a strength reduction factor (phi-factor).

In ACI 318-08, the value of the strength reduction factor depends on whether the transverse reinforcing steel bars are tied hoops (0.65) or spirals (0.70).

The above values should be multiplied by the appropriate strength reduction factor to compute ultimate moment capacity according to ACI 318-08, Section 9.3.2.2 or the value required by the design standard being followed.

The following table presents factored moment capacities and corresponding bending stiffnesses computed for common resistance factor values used for reinforced concrete sections.

Axial Load No.	Resistance Factor for Moment	Nominal Moment Capacity in-kip	Ultimate (Factored) Axial Thrust kips	Ultimate (Factored) Moment Capacity in-kip	Bending Stiffness at Ult. Mom. Cap. kip-in ²
1	0.65	3559.108	0.000	2313.420	17399923.290
1	0.70	3559.108	0.000	2491.376	17328316.949
1	0.75	3559.108	0.000	2669.331	17140950.140

 p-y Curves Reported for Specified Depths

p-y Curve Computed Using Static Criteria for Stiff Clay without Free Water

Soil Layer Number	=	1
Depth below pile head	=	15.000 ft
Depth below ground surface	=	0.000 ft
Equivalent Depth	=	0.000 ft
Ground Slope Angle	=	0.000 degrees
Pile Batter Angle	=	0.000 degrees
Effective Slope	=	0.000 degrees
Diameter	=	24.000 in
Undrained cohesion, c	=	7.77778 psi
Undrained cohesion, c	=	1120.00000 psf
Average Eff. Unit Weight	=	0.07523 pci
Average Eff. Unit Weight	=	130.00000 pcf
Epsilon-50	=	0.00700
Pct	=	560.000 lbs/in
Pcd	=	1680.000 lbs/in
Pu	=	560.000 lbs/in
y50	=	0.420 in
p-multiplier	=	1.00000
y-multiplier	=	1.00000

y, in	p, lbs/in
0.0000	0.0000
0.0000672	31.49111
0.0003360	47.09020

0.0006720	56.00000
0.00336	83.73953
0.00672	99.58365
0.03360	148.91228
0.06720	177.08755
0.16800	222.67580
0.33600	264.80765
0.50400	293.05784
0.67200	314.91114
1.68000	395.97980
3.36000	470.90199
6.72000	560.00000
6.88800	560.00000
7.05600	560.00000

p-y Curve Computed Using Static Criteria for Stiff Clay without Free Water

Soil Layer Number	=	1
Depth below pile head	=	19.000 ft
Depth below ground surface	=	4.000 ft
Equivalent Depth	=	4.000 ft
Ground Slope Angle	=	0.000 degrees
Pile Batter Angle	=	0.000 degrees
Effective Slope	=	0.000 degrees
Diameter	=	24.000 in
Undrained cohesion, c	=	7.77778 psi
Undrained cohesion, c	=	1120.00000 psf
Average Eff. Unit Weight	=	0.07523 pci
Average Eff. Unit Weight	=	130.00000 pcf
Epsilon-50	=	0.00700
Pct	=	833.333 lbs/in
Pcd	=	1680.000 lbs/in
Pu	=	833.333 lbs/in
y50	=	0.420 in
p-multiplier	=	1.00000
y-multiplier	=	1.00000

y, in	p, lbs/in
0.0000	0.0000
0.0000672	46.86178
0.0003360	70.07470
0.0006720	83.33333
0.00336	124.61240
0.00672	148.18995
0.03360	221.59566
0.06720	263.52314
0.16800	331.36280
0.33600	394.05901
0.50400	436.09798
0.67200	468.61777
1.68000	589.25565
3.36000	700.74701
6.72000	833.33333
6.88800	833.33333
7.05600	833.33333

p-y Curve Computed Using Static Criteria for Stiff Clay without Free Water

Soil Layer Number	=	2
Depth below pile head	=	21.000 ft
Depth below ground surface	=	6.000 ft
Equivalent Depth	=	3.827 ft
Ground Slope Angle	=	0.000 degrees
Pile Batter Angle	=	0.000 degrees
Effective Slope	=	0.000 degrees
Diameter	=	24.000 in
Undrained cohesion, c	=	15.55556 psi
Undrained cohesion, c	=	2240.00000 psf
Average Eff. Unit Weight	=	0.07523 pci
Average Eff. Unit Weight	=	130.00000 pcf
Epsilon-50	=	0.00500
Pct	=	1560.123 lbs/in
Pcd	=	3360.000 lbs/in
Pu	=	1560.123 lbs/in
y50	=	0.300 in
p-multiplier	=	1.00000
y-multiplier	=	1.00000

y, in	p, lbs/in
0.0000	0.0000
0.0000480	87.73213
0.0002400	131.19014
0.0004800	156.01225
0.00240	233.29273
0.00480	277.43338
0.02400	414.85965

0.04800	493.35405
0.12000	620.35988
0.24000	737.73638
0.36000	816.43952
0.48000	877.32136
1.20000	1103.17320
2.40000	1311.90142
4.80000	1560.12250
4.92000	1560.12250
5.04000	1560.12250

p-y Curve Computed Using Static Criteria for Stiff Clay without Free Water

```

Soil Layer Number      =          2
Depth below pile head  =        25.000 ft
Depth below ground surface =      10.000 ft
Equivalent Depth       =         7.827 ft
Ground Slope Angle     =         0.000 degrees
Pile Batter Angle      =         0.000 degrees
Effective Slope        =         0.000 degrees
Diameter               =        24.000 in
Undrained cohesion, c =       15.55556 psi
Undrained cohesion, c =    2240.00000 psf
Average Eff. Unit Weight =       0.07523 pci
Average Eff. Unit Weight =    130.00000 pcf
Epsilon-50            =         0.00500
Pct                   =       2020.123 lbs/in
Pcd                   =       3360.000 lbs/in
Pu                    =       2020.123 lbs/in
y50                   =         0.300 in
p-multiplier          =         1.00000
y-multiplier          =         1.00000

```

y, in	p, lbs/in
0.0000	0.0000
0.0000480	113.59984
0.0002400	169.87138
0.0004800	202.01225
0.00240	302.07878
0.00480	359.23423
0.02400	537.18046
0.04800	638.81882
0.12000	803.27215
0.24000	955.25696
0.36000	1057.16561
0.48000	1135.99837
1.20000	1428.44232
2.40000	1698.71377
4.80000	2020.12250
4.92000	2020.12250
5.04000	2020.12250

p-y Curve Computed Using Static Criteria for Stiff Clay without Free Water

```

Soil Layer Number      =          2
Depth below pile head  =        30.000 ft
Depth below ground surface =      15.000 ft
Equivalent Depth       =       12.827 ft
Ground Slope Angle     =         0.000 degrees
Pile Batter Angle      =         0.000 degrees
Effective Slope        =         0.000 degrees
Diameter               =        24.000 in
Undrained cohesion, c =       15.55556 psi
Undrained cohesion, c =    2240.00000 psf
Average Eff. Unit Weight =       0.07523 pci
Average Eff. Unit Weight =    130.00000 pcf
Epsilon-50            =         0.00500
Pct                   =       2595.123 lbs/in
Pcd                   =       3360.000 lbs/in
Pu                    =       2595.123 lbs/in
y50                   =         0.300 in
p-multiplier          =         1.00000
y-multiplier          =         1.00000

```

y, in	p, lbs/in
0.0000	0.0000
0.0000480	145.93446
0.0002400	218.22292
0.0004800	259.51225
0.00240	388.06133
0.00480	461.48530
0.02400	690.08146
0.04800	820.64979
0.12000	1031.91248
0.24000	1227.15767
0.36000	1358.07321
0.48000	1459.34463
1.20000	1835.02872
2.40000	2182.22921

4.80000 2595.12250
 4.92000 2595.12250
 5.04000 2595.12250

p-y Curve Computed Using Static Criteria for Stiff Clay without Free Water

Soil Layer Number = 2
 Depth below pile head = 35.000 ft
 Depth below ground surface = 20.000 ft
 Equivalent Depth = 17.827 ft
 Ground Slope Angle = 0.000 degrees
 Pile Batter Angle = 0.000 degrees
 Effective Slope = 0.000 degrees
 Diameter = 24.000 in
 Undrained cohesion, c = 15.55556 psi
 Undrained cohesion, c = 2240.00000 psf
 Average Eff. Unit Weight = 0.07523 pci
 Average Eff. Unit Weight = 130.00000 pcf
 Epsilon-50 = 0.00500
 Pct = 3170.123 lbs/in
 Pcd = 3360.000 lbs/in
 Pu = 3170.123 lbs/in
 y50 = 0.300 in
 p-multiplier = 1.00000
 y-multiplier = 1.00000

y, in	p, lbs/in
0.0000	0.0000
0.0000480	178.26909
0.0002400	266.57446
0.0004800	317.01225
0.00240	474.04389
0.00480	563.73636
0.02400	842.98247
0.04800	1002.48075
0.12000	1260.55282
0.24000	1499.05838
0.36000	1658.98082
0.48000	1782.69089
1.20000	2241.61512
2.40000	2665.74465
4.80000	3170.12250
4.92000	3170.12250
5.04000	3170.12250

Summary of Pile Response(s)

Definitions of Pile-head Loading Conditions:

Load Type 1: Load 1 = Shear, lbs, and Load 2 = Moment, in-lbs
 Load Type 2: Load 1 = Shear, lbs, and Load 2 = Slope, radians
 Load Type 3: Load 1 = Shear, lbs, and Load 2 = Rotational Stiffness, in-lbs/radian
 Load Type 4: Load 1 = Top Deflection, inches, and Load 2 = Moment, in-lbs
 Load Type 5: Load 1 = Top Deflection, inches, and Load 2 = Slope, radians

Load Case No.	Load Type No.	Pile-head Condition 1 V(lbs) or y(inches)	Pile-head Condition 2 in-lb, rad., or in-lb/rad.	Axial Loading lbs	Pile-head Deflection inches	Maximum Moment in Pile in-lbs	Maximum Shear in Pile lbs	Pile-head Rotation radians
1	1	V = 0.000	M = 0.000	0.0000000	1.04545703	918983.	-14735.	-0.00477046

The analysis ended normally.

J.3: Long-Term Design with Hydrostatic Pressures at Ground Surface

=====
LPIle Plus for Windows, Version 2012-06.037
Analysis of Individual Piles and Drilled Shafts
Subjected to Lateral Loading Using the p-y Method
© 1985-2012 by Ensoft, Inc.
All Rights Reserved
=====

This copy of LPIle is licensed to:

Andy Brown
University of Texas - Austin

Serial Number of Security Device: 226662924
Company Name Stored in Security Device: UT Austin - Prof. Gilbert

Files Used for Analysis

Date and Time of Analysis

Date: August 29, 2013 Time: 18:27:14

Problem Title

Project Name:
Job Number:
Client:
Engineer:
Description:

Program Options

Engineering units are US Customary Units: pounds, inches, feet

Basic Program Options:

This analysis computes pile response to lateral loading and will compute nonlinear moment-curvature and nominal moment capacity for section types with nonlinear properties.

Computation Options:

- Analysis does not use p-y multipliers (individual pile or shaft only)
- Analysis assumes no shear resistance at pile tip
- Analysis for fixed-length pile or shaft only
- No computation of foundation stiffness matrix values
- Report summary table of pile-top values for deflection, maximum bending moment, and shear force only
- Analysis assumes no loading by soil movements acting on pile
- p-y curves computed and reported at user-specified depths

Solution Control Parameters:

- Number of pile increments	=	100
- Maximum number of iterations allowed	=	750
- Deflection tolerance for convergence	=	1.0000E-05 in
- Maximum allowable deflection	=	100.0000 in

Pile Response Output Options:

- Only summary tables of pile-head deflection, maximum bending moment, and maximum shear force are to be written to output report file.

Pile Structural Properties and Geometry

Total number of pile sections	=	1
Total length of pile	=	35.00 ft
Depth of ground surface below top of pile	=	13.50 ft

Pile diameter values used for p-y curve computations are defined using 2 points.

p-y curves are computed using pile diameter values interpolated with depth over

the length of the pile.

Point	Depth X ft	Pile Diameter in
1	0.00000	24.0000000
2	35.000000	24.0000000

Input Structural Properties:

Pile Section No. 1:

Section Type = Drilled Shaft (Bored Pile)
Section Length = 35.0000000 ft
Section Diameter = 24.0000000 in

Ground Slope and Pile Batter Angles

Ground Slope Angle = 0.000 degrees
= 0.000 radians
Pile Batter Angle = 0.000 degrees
= 0.000 radians

Soil and Rock Layering Information

The soil profile is modelled using 1 layers

Layer 1 is sand, p-y criteria by Reese et al., 1974

Distance from top of pile to top of layer = 13.50000 ft
Distance from top of pile to bottom of layer = 50.00000 ft
Effective unit weight at top of layer = 62.60000 pcf
Effective unit weight at bottom of layer = 62.60000 pcf
Friction angle at top of layer = 24.00000 deg.
Friction angle at bottom of layer = 24.00000 deg.
Subgrade k at top of layer = 375.00000 pci
Subgrade k at bottom of layer = 375.00000 pci

(Depth of lowest soil layer extends 15.00 ft below pile tip)

Summary of Soil Properties

Layer Num.	Layer Soil Type (p-y Curve Criteria)	Layer Depth ft	Effective Unit Wt. pcf	Angle of Friction deg.	kpy pci
1	Sand (Reese, et al.)	13.500 50.000	62.600 62.600	24.000 24.000	375.000 375.000

Loading Type

Static loading criteria were used when computing p-y curves for all analyses.

Distributed Lateral Loading

Distributed lateral load intensity defined using 2 points

Point No.	Depth X in	Dist. Load lbs/in
1	0.000	0.000
2	162.000	241.200

Pile-head Loading and Pile-head Fixity Conditions

Number of loads specified = 1

Load No.	Load Type	Condition 1	Condition 2	Axial Thrust Force, lbs	Compute Top y vs. File Length
1	1	V = 0.0000 lbs	M = 0.0000 in-lbs	0.0000000	No

V = perpendicular shear force applied to pile head
M = bending moment applied to pile head
y = lateral deflection relative to pile axis
S = pile slope relative to original pile batter angle
R = rotational stiffness applied to pile head
Axial thrust is assumed to be acting axially for all pile batter angles.

Specified Depths for Output of p-y Curves

Lateral load-transfer (p-y) curves are computed and output at 5 depths.
(Note that these curves are independent from the curves used at nodal point depths)

Depth No.	Depth Below Pile Head ft	Depth Below Ground Surface ft
1	16.000	2.500
2	18.000	4.500
3	20.000	6.500
4	22.000	8.500
5	24.000	10.500

Depth of ground surface below top of pile = 13.50 ft

Computations of Nominal Moment Capacity and Nonlinear Bending Stiffness

Axial thrust force values were determined from pile-head loading conditions

Number of Pile Sections Analyzed = 1

Pile Section No. 1:

Dimensions and Properties of Drilled Shaft (Bored Pile):

Length of Section	=	35.00000000 ft
Shaft Diameter	=	24.00000000 in
Concrete Cover Thickness	=	3.00000000 in
Number of Reinforcing Bars	=	12 bars
Yield Stress of Reinforcing Bars	=	60.00000000 ksi
Modulus of Elasticity of Reinforcing Bars	=	29000. ksi
Gross Area of Shaft	=	452.38934212 sq. in.
Total Area of Reinforcing Steel	=	7.20000000 sq. in.
Area Ratio of Steel Reinforcement	=	1.59 percent
Edge-to-Edge Bar Spacing	=	3.55727615 in
Maximum Concrete Aggregate Size	=	0.75000000 in
Ratio of Bar Spacing to Aggregate Size	=	4.74
Offset of Rebar Cage Center from Center of Pile	=	0.00000000 in

Axial Structural Capacities:

Nom. Axial Structural Capacity = $0.85 F_c A_c + F_y A_s$	=	1945.644 kips
Tensile Load for Cracking of Concrete	=	-209.248 kips
Nominal Axial Tensile Capacity	=	-432.000 kips

Reinforcing Bar Dimensions and Positions Used in Computations:

Bar Number	Bar Diam. inches	Bar Area sq. in.	X inches	Y inches
1	0.87500	0.60000	8.56250	0.00000
2	0.87500	0.60000	7.41534	4.28125
3	0.87500	0.60000	4.28125	7.41534
4	0.87500	0.60000	0.00000	8.56250
5	0.87500	0.60000	-4.28125	7.41534
6	0.87500	0.60000	-7.41534	4.28125
7	0.87500	0.60000	-8.56250	0.00000
8	0.87500	0.60000	-7.41534	-4.28125
9	0.87500	0.60000	-4.28125	-7.41534
10	0.87500	0.60000	0.00000	-8.56250
11	0.87500	0.60000	4.28125	-7.41534
12	0.87500	0.60000	7.41534	-4.28125

NOTE: The positions of the above rebars were computed by LFile

Minimum spacing between any two bars not equal to zero = 3.55728 inches between Bars 7 and 8

Spacing to aggregate size ratio = 4.74303

Concrete Properties:

 Compressive Strength of Concrete = 4.00000000 ksi
 Modulus of Elasticity of Concrete = 3604.99653259 ksi
 Modulus of Rupture of Concrete = -0.47434164 ksi
 Compression Strain at Peak Stress = 0.00188627
 Tensile Strain at Fracture of Concrete = -0.00011537
 Maximum Coarse Aggregate Size = 0.75000000 in

Number of Axial Thrust Force Values Determined from Pile-head Loadings = 1

Number	Axial Thrust Force kips
1	0.000

Definitions of Run Messages and Notes:

 C = concrete in section has cracked in tension.
 Y = stress in reinforcing steel has reached yield stress.
 T = ACI 318-08 criteria for tension-controlled section met, tensile strain in reinforcement exceeds 0.005 while simultaneously compressive strain in concrete more than 0.003. See ACI 318-08, Section 10.3.4.
 Z = depth of tensile zone in concrete section is less than 10 percent of section depth.

Bending Stiffness (EI) = Computed Bending Moment / Curvature.
 Position of neutral axis is measured from edge of compression side of pile.
 Compressive stresses and strains are positive in sign.
 Tensile stresses and strains are negative in sign.

Axial Thrust Force = 0.000 kips

Bending Curvature rad/in.	Bending Moment in-kip	Bending Stiffness kip-in ²	Depth to N Axis in	Max Comp Strain in/in	Max Tens Strain in/in	Max Concrete Stress ksi	Max Steel Stress ksi	Run Msg
0.000001250	94.3056923	75444554.	11.9999611	0.0000150	-0.0000150	0.0627333	-0.4306514	
0.000002500	188.1518190	75260728.	11.9999608	0.0000300	-0.0000300	0.1249707	-0.8613028	
0.000003750	281.5383800	75076901.	11.9999608	0.0000450	-0.0000450	0.1867124	-1.2919542	
0.000005000	374.4653753	74893075.	11.9999606	0.0000600	-0.0000600	0.2479582	-1.7226057	
0.000006250	466.9328050	74709249.	11.9999605	0.0000750	-0.0000750	0.3087081	-2.1532571	
0.000007500	558.9406690	74525423.	11.9999603	0.0000900	-0.0000900	0.3689623	-2.5839086	
0.000008750	650.4889673	74341596.	11.9999602	0.0001050	-0.0001050	0.4287206	-3.0145600	
0.000010000	650.4889673	65048897.	6.5897908	0.0000659	-0.0001741	0.2696892	-5.0141606	C
0.000011300	650.4889673	57821242.	6.5921648	0.0000742	-0.0001958	0.3028475	-5.6401562	C
0.000012500	650.4889673	52039117.	6.5945447	0.0000824	-0.0002176	0.3358821	-6.2659775	C
0.000013800	650.4889673	47308289.	6.5969305	0.0000907	-0.0002393	0.3687929	-6.8916239	C
0.000015000	650.4889673	43365931.	6.5993223	0.0000990	-0.0002610	0.4015796	-7.5170948	C
0.000016300	650.4889673	40030090.	6.6016606	0.0001073	-0.0002827	0.4342380	-8.1424174	C
0.000017500	650.4889673	37170798.	6.6039811	0.0001156	-0.0003044	0.4667697	-8.7675795	C
0.000018800	650.4889673	34692745.	6.6063073	0.0001239	-0.0003261	0.4991756	-9.3925704	C
0.000020000	650.4889673	32524448.	6.6086391	0.0001322	-0.0003478	0.5314557	-10.0173893	C
0.000021300	650.4889673	30611246.	6.6109766	0.0001405	-0.0003695	0.5636097	-10.6420356	C
0.000022500	650.4889673	28910621.	6.6133198	0.0001488	-0.0003912	0.5956373	-11.2665088	C
0.000023800	650.4889673	27389009.	6.6156688	0.0001571	-0.0004129	0.6275384	-11.8908080	C
0.000025000	650.4889673	26019559.	6.6180236	0.0001655	-0.0004345	0.6593125	-12.5149328	C
0.000026300	650.4889673	24780532.	6.6203842	0.0001738	-0.0004562	0.6909596	-13.1388825	C
0.000027500	650.4889673	23654144.	6.6227506	0.0001821	-0.0004779	0.7224793	-13.7626563	C
0.000028800	650.4889673	22625703.	6.6251229	0.0001905	-0.0004995	0.7538715	-14.3862537	C
0.000030000	650.4889673	21682966.	6.6275011	0.0001988	-0.0005212	0.7851358	-15.0096740	C
0.000031300	650.4889673	20815647.	6.6298852	0.0002072	-0.0005428	0.8162720	-15.6329165	C
0.000032500	650.4889673	20015045.	6.6322753	0.0002155	-0.0005645	0.8472798	-16.2559805	C
0.000033800	650.4889673	19273747.	6.6346714	0.0002239	-0.0005861	0.8781591	-16.8788653	C
0.000035000	650.4889673	18585399.	6.6370735	0.0002323	-0.0006077	0.9089095	-17.5015704	C
0.000036300	651.6439619	17976385.	6.6394816	0.0002407	-0.0006293	0.9395309	-18.1240949	C
0.000037500	673.8592485	17969580.	6.6418958	0.0002491	-0.0006509	0.9700228	-18.7464382	C
0.000038800	696.0569468	17962760.	6.6443162	0.0002575	-0.0006725	1.0003852	-19.3685996	C
0.000040000	718.2369981	17955925.	6.6467426	0.0002659	-0.0006941	1.0306176	-19.9905785	C
0.000041300	740.3993436	17949075.	6.6491753	0.0002743	-0.0007157	1.0607199	-20.6123740	C
0.000042500	762.5439241	17942210.	6.6516142	0.0002827	-0.0007373	1.0906918	-21.2339854	C
0.000043800	784.6706797	17935330.	6.6540593	0.0002911	-0.0007589	1.1205330	-21.8554122	C
0.000045000	806.7795505	17928434.	6.6565107	0.0002995	-0.0007805	1.1502433	-22.4766535	C
0.000046300	828.8704760	17921524.	6.6589684	0.0003080	-0.0008020	1.1798224	-23.0977086	C
0.000047500	850.9433954	17914598.	6.6614325	0.0003164	-0.0008236	1.2092700	-23.7185767	C
0.000048800	872.9982475	17907656.	6.6639029	0.0003249	-0.0008451	1.2385859	-24.3392572	C
0.000051300	917.0534735	17893726.	6.6688630	0.0003418	-0.0008882	1.2968212	-25.5800526	C
0.000053800	961.0357107	17879734.	6.6738490	0.0003587	-0.0009313	1.3545263	-26.8200881	C
0.000056300	1004.9444284	17865679.	6.6788612	0.0003757	-0.0009743	1.4116989	-28.0593579	C
0.000058800	1048.7791151	17851559.	6.6838999	0.0003927	-0.0010173	1.4683367	-29.2978558	C
0.000061300	1092.5392522	17837376.	6.6889654	0.0004097	-0.0010603	1.5244375	-30.5355756	C
0.000063800	1136.2243142	17823126.	6.6940579	0.0004267	-0.0011033	1.5799990	-31.7725109	C

0.0000663	1179.8337685	17808812.	6.6991777	0.0004438	-0.0011462	1.6350189	-33.0086552	C
0.0000688	1223.3670749	17794430.	6.7043252	0.0004609	-0.0011891	1.6894947	-34.2440021	C
0.0000713	1266.8236858	17779982.	6.7095007	0.0004781	-0.0012319	1.7434241	-35.4785447	C
0.0000738	1310.2030461	17765465.	6.7147044	0.0004952	-0.0012748	1.7968046	-36.7122765	C
0.0000763	1353.5045926	17750880.	6.7199368	0.0005124	-0.0013176	1.8496339	-37.9451905	C
0.0000788	1396.7277544	17736225.	6.7251980	0.0005296	-0.0013604	1.9019095	-39.1772798	C
0.0000813	1439.8719523	17721501.	6.7304885	0.0005469	-0.0014031	1.9536288	-40.4085373	C
0.0000838	1482.9365987	17706706.	6.7358085	0.0005641	-0.0014459	2.0047894	-41.6389559	C
0.0000863	1525.9210978	17691839.	6.7411585	0.0005814	-0.0014886	2.0553886	-42.8685282	C
0.0000888	1568.8248448	17676900.	6.7465387	0.0005988	-0.0015312	2.1054238	-44.0972470	C
0.0000913	1611.6472263	17661887.	6.7519496	0.0006161	-0.0015739	2.1548924	-45.3251046	C
0.0000938	1654.3876196	17646801.	6.7573914	0.0006335	-0.0016165	2.2037918	-46.5520934	C
0.0000963	1697.0453929	17631640.	6.7628645	0.0006509	-0.0016591	2.2521192	-47.7782057	C
0.0000988	1739.6199049	17616404.	6.7683694	0.0006684	-0.0017016	2.2998720	-49.0034337	C
0.0001013	1782.1105047	17601091.	6.7739063	0.0006859	-0.0017441	2.3470472	-50.2277692	C
0.0001038	1824.5165314	17585702.	6.7794757	0.0007034	-0.0017866	2.3936421	-51.4512042	C
0.0001063	1866.8373141	17570234.	6.7850779	0.0007209	-0.0018291	2.4396540	-52.6737304	C
0.0001088	1909.0721714	17554687.	6.7907134	0.0007385	-0.0018715	2.4850797	-53.8953394	C
0.0001113	1951.2204116	17539060.	6.7963826	0.0007561	-0.0019139	2.5299165	-55.1160227	C
0.0001138	1993.2813320	17523352.	6.8020858	0.0007737	-0.0019563	2.5741614	-56.3357715	C
0.0001163	2035.2542188	17507563.	6.8078236	0.0007914	-0.0019986	2.6178114	-57.5545771	C
0.0001188	2077.1383470	17491691.	6.8135962	0.0008091	-0.0020409	2.6608634	-58.7724305	C
0.0001213	2118.9329799	17475736.	6.8194042	0.0008269	-0.0020831	2.7033142	-59.9893225	CY
0.0001238	2160.6373692	17459696.	6.8252481	0.0008446	-0.0021254	2.7451609	-60.0000000	CY
0.0001263	2202.2507541	17443570.	6.8311281	0.0008624	-0.0021676	2.7864002	-60.0000000	CY
0.0001288	2243.7723616	17427358.	6.8370449	0.0008803	-0.0022097	2.8270288	-60.0000000	CY
0.0001313	2285.2043886	17411081.	6.8428841	0.0008981	-0.0022519	2.8670098	-60.0000000	CY
0.0001338	2326.5455257	17394733.	6.8486454	0.0009160	-0.0022940	2.9063386	-60.0000000	CY
0.0001363	2367.7935566	17378301.	6.8544419	0.0009339	-0.0023361	2.9450462	-60.0000000	CY
0.0001388	2408.9473664	17361783.	6.8602742	0.0009519	-0.0023781	2.9831290	-60.0000000	CY
0.0001413	2450.0065543	17345179.	6.8661427	0.0009698	-0.0024202	3.0205840	-60.0000000	CY
0.0001438	2490.9695337	17328484.	6.8720479	0.0009879	-0.0024621	3.0574071	-60.0000000	CY
0.0001463	2531.8358595	17311698.	6.8779903	0.0010059	-0.0025041	3.0935953	-60.0000000	CY
0.0001488	2572.0000921	17290757.	6.8834458	0.0010239	-0.0025461	3.1289904	-60.0000000	CY
0.0001588	2710.9553394	17076884.	6.8881218	0.0010935	-0.0027165	3.2590586	-60.0000000	CY
0.0001688	2817.9750843	16699112.	6.8688865	0.0011591	-0.0028909	3.3720085	-60.0000000	CY
0.0001788	2888.6656697	16160367.	6.8233294	0.0012197	-0.0030703	3.4677780	-60.0000000	CY
0.0001888	2957.8043783	15670487.	6.7827012	0.0012802	-0.0032498	3.5565558	-60.0000000	CY
0.0001988	3026.2212779	15226271.	6.7480653	0.0013412	-0.0034288	3.6360939	-60.0000000	CY
0.0002088	3093.4197170	14818777.	6.7181443	0.0014024	-0.0036076	3.7088405	-60.0000000	CY
0.0002188	3146.3244275	14383197.	6.6794857	0.0014611	-0.0037889	3.7709433	-60.0000000	CY
0.0002288	3177.3979568	13890264.	6.6250528	0.0015155	-0.0039745	3.8217039	-60.0000000	CY
0.0002388	3204.7505816	13423039.	6.5719340	0.0015690	-0.0041610	3.8655125	-60.0000000	CY
0.0002488	3231.5375808	12991106.	6.5229988	0.0016226	-0.0043474	3.9031406	-60.0000000	CY
0.0002588	3257.9092454	12590954.	6.4790232	0.0016764	-0.0045336	3.9347725	-60.0000000	CY
0.0002688	3283.8546785	12218994.	6.4394845	0.0017306	-0.0047194	3.9603038	-60.0000000	CY
0.0002788	3309.3624045	11872152.	6.4039366	0.0017851	-0.0049049	3.9796252	-60.0000000	CY
0.0002888	3334.4203989	11547776.	6.3719970	0.0018399	-0.0050901	3.9926227	-60.0000000	CY
0.0002988	3358.9215355	11243252.	6.3422958	0.0018948	-0.0052752	3.9991584	-60.0000000	CY
0.0003088	3382.8669819	10956654.	6.3150458	0.0019498	-0.0054602	3.9974474	-60.0000000	CY
0.0003188	3406.3200295	10686494.	6.2907097	0.0020052	-0.0056448	3.9987011	-60.0000000	CY
0.0003288	3429.2309060	10431121.	6.2691256	0.0020610	-0.0058290	3.9994285	-60.0000000	CY
0.0003388	3451.6105377	10189256.	6.2499561	0.0021172	-0.0060128	3.9967643	60.0000000	CY
0.0003488	3470.8904462	9952374.	6.2295126	0.0021725	-0.0061975	3.9999499	60.0000000	CY
0.0003588	3485.7362924	9716338.	6.2059959	0.0022264	-0.0063836	3.9974827	60.0000000	CY
0.0003688	3496.6767150	9482513.	6.1796364	0.0022787	-0.0065713	3.9999624	60.0000000	CY
0.0003788	3504.3297058	9252356.	6.1515330	0.0023299	-0.0067601	3.9964331	60.0000000	CY
0.0003888	3509.6407015	9028015.	6.1224910	0.0023801	-0.0069499	3.9995811	60.0000000	CY
0.0003988	3514.5071712	8813811.	6.0935253	0.0024298	-0.0071402	3.9946161	60.0000000	CY
0.0004088	3519.1714741	8609594.	6.0663968	0.0024796	-0.0073304	3.9977956	60.0000000	CY
0.0004188	3523.7155934	8414843.	6.0410171	0.0025297	-0.0075203	3.9998910	60.0000000	CY
0.0004288	3528.0670760	8228728.	6.0174609	0.0025800	-0.0077100	3.9931542	60.0000000	CY
0.0004388	3532.2870223	8050797.	5.9954470	0.0026305	-0.0078995	3.9976707	60.0000000	CY
0.0004488	3536.4046900	7880568.	5.9747997	0.0026812	-0.0080888	3.9998150	60.0000000	CY
0.0004588	3540.3593233	7717405.	5.9555957	0.0027321	-0.0082779	3.9936955	60.0000000	CY
0.0004688	3544.1882331	7560935.	5.9376465	0.0027833	-0.0084667	3.9960535	60.0000000	CY
0.0004788	3547.9317058	7410823.	5.9207714	0.0028346	-0.0086554	3.9990963	60.0000000	CY
0.0004888	3551.5795261	7266659.	5.9049340	0.0028860	-0.0088440	3.9991486	60.0000000	CY
0.0004988	3555.0609250	7127942.	5.8902642	0.0029378	-0.0090322	3.9917525	60.0000000	CY
0.0005088	3558.4438120	6994484.	5.8760912	0.0029895	-0.0092205	3.9963782	60.0000000	CY
0.0005188	3561.6790741	6865887.	5.8617779	0.0030408	-0.0094092	3.9991045	60.0000000	CYT
0.0005288	3564.8464332	6742026.	5.8482830	0.0030923	-0.0095977	3.9998562	60.0000000	CYT
0.0005388	3567.8682029	6622493.	5.8358002	0.0031440	-0.0097860	3.9907772	60.0000000	CYT
0.0005488	3570.8381723	6507222.	5.8239950	0.0031959	-0.0099741	3.9939756	60.0000000	CYT
0.0006088	3587.3288166	5892943.	5.7663073	0.0035102	-0.0110998	3.9964516	60.0000000	CYT
0.0006688	3601.8049954	5385877.	5.7263001	0.0038295	-0.0122205	3.9955298	60.0000000	CYT

Summary of Results for Nominal (Unfactored) Moment Capacity for Section 1

Moment values interpolated at maximum compressive strain = 0.003
or maximum developed moment if pile fails at smaller strains.

Load No.	Axial Thrust kips	Nominal Mom. Cap. in-kip	Max. Comp. Strain
1	0.000	3559.108	0.00300000

Note note that the values of moment capacity in the table above are not factored by a strength reduction factor (ϕ -factor).

In ACI 318-08, the value of the strength reduction factor depends on whether the transverse reinforcing steel bars are tied hoops (0.65) or spirals (0.70).

The above values should be multiplied by the appropriate strength reduction factor to compute ultimate moment capacity according to ACI 318-08, Section 9.3.2.2 or the value required by the design standard being followed.

The following table presents factored moment capacities and corresponding bending stiffnesses computed for common resistance factor values used for reinforced concrete sections.

Axial Load No.	Resistance Factor for Moment	Nominal Moment Capacity in-kip	Ultimate (Factored) Axial Thrust kips	Ultimate (Factored) Moment Capacity in-kip	Bending Stiffness at Ult. Mom. Cap. kip-in ²
1	0.65	3559.108	0.000	2313.420	17399923.290
1	0.70	3559.108	0.000	2491.376	17328316.949
1	0.75	3559.108	0.000	2669.331	17140950.140

 p-y Curves Reported for Specified Depths

p-y Curve in Sand Computed Using Reese Criteria for Static Loading Conditions

```

Soil Layer Number          =          1
Depth below pile head      =         16.000 ft
Depth below ground surface =          2.500 ft
Equivalent Depth (see note) =          2.500 ft
Ground Slope Angle         =          0.000 degrees
Pile Batter                 =          0.000 degrees
Effective Slope             =          0.000 degrees
Pile Diameter, b           =          24.000 in
Angle of Friction           =          24.000 degrees
Avg. Eff. Unit Weight      =        62.60000 pcf
kpy                          =        375.000 pci
K active                    =          0.422
K passive                   =          2.371
KO                           =          0.400
Pst                          =          87.049 lbs/in
Psd                          =        362.861 lbs/in
Ps = Pst (shallow controls) =          87.049 lbs/in
A (static)                  =          1.9350
B (static)                  =          1.4050
C = Pm/(Ym^(1/n))          =        161.2614
n = Pm/(m Ym)              =          3.3137
m = (Pu-Pm)/(Yu-Ym)        =        92.2720
Yk = [c/(kx)]^(n/(n-1))    =          0.0023 in
Pk                           =          25.745 lbs/in
Ym = b/60                  =          0.4000 in
Pm = B ps                   =        122.304 lbs/in
Yu = 3b/80                  =          0.9000 in
Pu = A Ps                   =        168.440 lbs/in
Es,lim                       =       11250.000 lbs/in/in
p-multiplier                =          1.00000
y-multiplier                =          1.00000
  
```

This p-y curve is computed using the equivalent depth.

This curve has the normal shape for a Reese sand p-y curve where $Y_k < Y_m < Y_u$.

y, in	p, lbs/in
0.0000	0.0000
0.00229	25.74512 *
0.03844	60.31997
0.07460	73.67933
0.11076	83.01170
0.14691	90.39918
0.18307	96.60531
0.21922	102.00534
0.25538	106.81456
0.29153	111.16917
0.32769	115.16136
0.36384	118.85676
0.40000	122.30392
0.65000	145.37192
0.90000	168.43991
0.92250	168.43991
0.94500	168.43991

* p value(s) computed using $p = k * \text{Eff} * y$

p-y Curve in Sand Computed Using Reese Criteria for Static Loading Conditions

Soil Layer Number = 1

```

Depth below pile head = 18.000 ft
Depth below ground surface = 4.500 ft
Equivalent Depth (see note) = 4.500 ft
Ground Slope Angle = 0.000 degrees
Pile Batter = 0.000 degrees
Effective Slope = 0.000 degrees
Pile Diameter, b = 24.000 in
Angle of Friction = 24.000 degrees
Avg. Eff. Unit Weight = 62.60000 pcf
kpy = 375.000 pci
K active = 0.422
K passive = 2.371
K0 = 0.400
Pst = 208.817 lbs/in
Psd = 653.150 lbs/in
Ps = Pst (shallow controls) = 208.817 lbs/in
A (static) = 1.3550
B (static) = 0.9550
C = Pm/(Ym^(1/n)) = 271.0886
n = Pm/(m Ym) = 2.9844
m = (Pu-Pm)/(Yu-Ym) = 167.0540
Yk = [c/(kx)]^(n/(n-1)) = 0.0015 in
Pk = 30.837 lbs/in
Ym = b/60 = 0.4000 in
Pm = B ps = 199.421 lbs/in
Yu = 3b/80 = 0.9000 in
Pu = A Ps = 282.948 lbs/in
Es,lim = 20250.000 lbs/in/in
p-multiplier = 1.00000
y-multiplier = 1.00000

```

This p-y curve is computed using the equivalent depth.

This curve has the normal shape for a Reese sand p-y curve where $Y_k < Y_m < Y_u$.

y, in	p, lbs/in
0.0000	0.0000
0.00152	30.83749 *
0.03775	90.41888
0.07397	113.28240
0.11020	129.46871
0.14642	142.40508
0.18265	153.35395
0.21887	162.93881
0.25510	171.51901
0.29132	179.32279
0.32755	186.50525
0.36377	193.17714
0.40000	199.42066
0.65000	241.18415
0.90000	282.94764
0.92250	282.94764
0.94500	282.94764

* p value(s) computed using $p = k * \text{Eff} * y$

p-y Curve in Sand Computed Using Reese Criteria for Static Loading Conditions

```

Soil Layer Number = 1
Depth below pile head = 20.000 ft
Depth below ground surface = 6.500 ft
Equivalent Depth (see note) = 6.500 ft
Ground Slope Angle = 0.000 degrees
Pile Batter = 0.000 degrees
Effective Slope = 0.000 degrees
Pile Diameter, b = 24.000 in
Angle of Friction = 24.000 degrees
Avg. Eff. Unit Weight = 62.60000 pcf
kpy = 375.000 pci
K active = 0.422
K passive = 2.371
K0 = 0.400
Pst = 376.923 lbs/in
Psd = 943.439 lbs/in
Ps = Pst (shallow controls) = 376.923 lbs/in
A (static) = 1.0200
B (static) = 0.6650
C = Pm/(Ym^(1/n)) = 370.6990
n = Pm/(m Ym) = 2.3415
m = (Pu-Pm)/(Yu-Ym) = 267.6152
Yk = [c/(kx)]^(n/(n-1)) = 0.0005 in
Pk = 14.286 lbs/in
Ym = b/60 = 0.4000 in
Pm = B ps = 250.654 lbs/in
Yu = 3b/80 = 0.9000 in
Pu = A Ps = 384.461 lbs/in
Es,lim = 29250.000 lbs/in/in
p-multiplier = 1.00000
y-multiplier = 1.00000

```


This p-y curve is computed using the equivalent depth.

This curve has the normal shape for a Reese sand p-y curve where $Y_k < Y_m < Y_u$.

y, in	p, lbs/in
0.0000	0.0000
0.0004884	14.28588 *
0.03681	90.48569
0.07313	121.31247
0.10945	144.11028
0.14577	162.87155
0.18208	179.10513
0.21840	193.57124
0.25472	206.71519
0.29104	218.82373
0.32736	230.09406
0.36368	240.66852
0.40000	250.65369
0.65000	317.55750
0.90000	384.46130
0.92250	384.46130
0.94500	384.46130

* p value(s) computed using $p = k * \text{Eff} x * y$

p-y Curve in Sand Computed Using Reese Criteria for Static Loading Conditions

Soil Layer Number	=	1
Depth below pile head	=	22.000 ft
Depth below ground surface	=	8.500 ft
Equivalent Depth (see note)	=	8.500 ft
Ground Slope Angle	=	0.000 degrees
Pile Batter	=	0.000 degrees
Effective Slope	=	0.000 degrees
Pile Diameter, b	=	24.000 in
Angle of Friction	=	24.000 degrees
Avg. Eff. Unit Weight	=	62.60000 pcf
kpy	=	375.000 pci
K active	=	0.422
K passive	=	2.371
K0	=	0.400
Pst	=	591.365 lbs/in
Psd	=	1233.728 lbs/in
Ps = Pst (shallow controls)	=	591.365 lbs/in
A (static)	=	0.8950
B (static)	=	0.5225
C = $Pm / (Ym^{1/n})$	=	521.0762
n = $Pm / (m Ym)$	=	1.7534
m = $(Pu - Pm) / (Yu - Ym)$	=	440.5672
$Yk = [c / (kx)]^{n / (n-1)}$	=	0.0000 in
Pk	=	1.739 lbs/in
Ym = b/60	=	0.4000 in
Pm = B ps	=	308.988 lbs/in
Yu = 3b/80	=	0.9000 in
Pu = A Ps	=	529.272 lbs/in
Es,lim	=	38250.000 lbs/in/in
p-multiplier	=	1.00000
y-multiplier	=	1.00000

This p-y curve is computed using the equivalent depth.

This curve has the normal shape for a Reese sand p-y curve where $Y_k < Y_m < Y_u$.

y, in	p, lbs/in
0.0000	0.0000
0.0000455	1.73917 *
0.03640	78.75549
0.07276	116.89988
0.10912	147.29685
0.14548	173.54999
0.18184	197.09712
0.21820	218.69043
0.25456	238.78361
0.29092	257.67590
0.32728	275.57739
0.36364	292.64239
0.40000	308.98836
0.65000	419.13014
0.90000	529.27193
0.92250	529.27193
0.94500	529.27193

* p value(s) computed using $p = k * \text{Eff} x * y$

p-y Curve in Sand Computed Using Reese Criteria for Static Loading Conditions

```

Soil Layer Number           =          1
Depth below pile head       =        24.000 ft
Depth below ground surface  =        10.500 ft
Equivalent Depth (see note) =        10.500 ft
Ground Slope Angle          =          0.000 degrees
Pile Batter                  =          0.000 degrees
Effective Slope              =          0.000 degrees
Pile Diameter, b            =        24.000 in
Angle of Friction           =        24.000 degrees
Avg. Eff. Unit Weight       =       62.60000 pcf
kpy                           =       375.000 pci
K active                     =          0.422
K passive                    =          2.371
K0                            =          0.400
Pst                           =        852.145 lbs/in
Psd                           =       1524.017 lbs/in
Ps = Pst (shallow controls)  =        852.145 lbs/in
A (static)                   =          0.8800
B (static)                   =          0.5000
C = Pm/(Ym^(1/n))            =        743.7567
n = Pm/(m Ym)                =          1.6447
m = (Pu-Pm)/(Yu-Ym)          =        647.6300
Yk = [c/(kx)]^(n/(n-1))      =          0.0000 in
Pk                            =          1.188 lbs/in
Ym = b/60                    =          0.4000 in
Pm = B ps                     =        426.072 lbs/in
Yu = 3b/80                   =          0.9000 in
Pu = A Ps                     =        749.887 lbs/in
Es,lim                       =       47250.000 lbs/in/in
p-multiplier                 =          1.00000
y-multiplier                 =          1.00000
    
```

This p-y curve is computed using the equivalent depth.

This curve has the normal shape for a Reese sand p-y curve where $Y_k < Y_m < Y_u$.

y, in	p, lbs/in
0.0000	0.0000
0.0000252	1.18846 *
0.03639	99.19337
0.07275	151.15328
0.10911	193.39740
0.14547	230.35528
0.18183	263.82158
0.21819	294.74499
0.25455	323.70226
0.29092	351.07635
0.32728	377.13754
0.36364	402.08539
0.40000	426.07238
0.65000	587.97988
0.90000	749.88738
0.92250	749.88738
0.94500	749.88738

* p value(s) computed using $p = k * \text{Eff} x * y$

 Summary of Pile Response(s)

Definitions of Pile-head Loading Conditions:

```

Load Type 1: Load 1 = Shear, lbs, and Load 2 = Moment, in-lbs
Load Type 2: Load 1 = Shear, lbs, and Load 2 = Slope, radians
Load Type 3: Load 1 = Shear, lbs, and Load 2 = Rotational Stiffness, in-lbs/radian
Load Type 4: Load 1 = Top Deflection, inches, and Load 2 = Moment, in-lbs
Load Type 5: Load 1 = Top Deflection, inches, and Load 2 = Slope, radians
    
```

Load Case No.	Load Type No.	Pile-head Condition 1 V(lbs) or y(inches)	Pile-head Condition 2 in-lb, rad., or in-lb/rad.	Axial Loading lbs	File-head Deflection inches	Maximum Moment in Pile in-lbs	Maximum Shear in Pile lbs	File-head Rotation radians
1	1	V = 0.000	M = 0.000	0.0000000	5.42056208	2182696.	-21374.	-0.02149364

The analysis ended normally.

J.4: As-Built Test Wall with Natural Water Table Conditions

=====
LPIle Plus for Windows, Version 2012-06.037
Analysis of Individual Piles and Drilled Shafts
Subjected to Lateral Loading Using the p-y Method

© 1985-2012 by Ensoft, Inc.
All Rights Reserved

=====
This copy of LPIle is licensed to:

Andy Brown
University of Texas - Austin

Serial Number of Security Device: 226662924
Company Name Stored in Security Device: UT Austin - Prof. Gilbert

Files Used for Analysis

Date and Time of Analysis

Date: August 29, 2013 Time: 18:30:38

Problem Title

Project Name:
Job Number:
Client:
Engineer:
Description:

Program Options

Engineering units are US Customary Units: pounds, inches, feet

Basic Program Options:

This analysis computes pile response to lateral loading and will compute nonlinear moment-curvature and nominal moment capacity for section types with nonlinear properties.

Computation Options:

- Analysis does not use p-y multipliers (individual pile or shaft only)
- Analysis assumes no shear resistance at pile tip
- Analysis for fixed-length pile or shaft only
- No computation of foundation stiffness matrix values
- Report summary table of pile-top values for deflection, maximum bending moment, and shear force only
- Analysis assumes no loading by soil movements acting on pile
- p-y curves computed and reported at user-specified depths

Solution Control Parameters:

- Number of pile increments = 100
- Maximum number of iterations allowed = 750
- Deflection tolerance for convergence = 1.0000E-05 in
- Maximum allowable deflection = 100.0000 in

Pile Response Output Options:

- Only summary tables of pile-head deflection, maximum bending moment, and maximum shear force are to be written to output report file.

Pile Structural Properties and Geometry

Total number of pile sections = 1
Total length of pile = 35.00 ft
Depth of ground surface below top of pile = 15.00 ft

Pile diameter values used for p-y curve computations are defined using 2 points.

p-y curves are computed using pile diameter values interpolated with depth over

the length of the pile.

Point	Depth X ft	Pile Diameter in
1	0.00000	24.0000000
2	35.000000	24.0000000

Input Structural Properties:

File Section No. 1:

Section Type = Drilled Shaft (Bored Pile)
Section Length = 35.00000000 ft
Section Diameter = 24.00000000 in

Ground Slope and Pile Batter Angles

Ground Slope Angle = 0.000 degrees
= 0.000 radians
Pile Batter Angle = 0.000 degrees
= 0.000 radians

Soil and Rock Layering Information

The soil profile is modelled using 1 layers

Layer 1 is sand, p-y criteria by Reese et al., 1974

Distance from top of pile to top of layer = 15.00000 ft
Distance from top of pile to bottom of layer = 50.00000 ft
Effective unit weight at top of layer = 62.60000 pcf
Effective unit weight at bottom of layer = 62.60000 pcf
Friction angle at top of layer = 24.00000 deg.
Friction angle at bottom of layer = 24.00000 deg.
Subgrade k at top of layer = 375.00000 pci
Subgrade k at bottom of layer = 375.00000 pci

(Depth of lowest soil layer extends 15.00 ft below pile tip)

Summary of Soil Properties

Layer Num.	Layer Soil Type (p-y Curve Criteria)	Layer Depth ft	Effective Unit Wt. pcf	Angle of Friction deg.	kpy pci
1	Sand (Reese, et al.)	15.000 50.000	62.600 62.600	24.000 24.000	375.000 375.000

Loading Type

Static loading criteria were used when computing p-y curves for all analyses.

Distributed Lateral Loading

Distributed lateral load intensity defined using 3 points

Point No.	Depth X in	Dist. Load lbs/in
1	0.000	0.000
2	96.000	78.100
3	180.000	203.400

Pile-head Loading and Pile-head Fixity Conditions

 Number of loads specified = 1

Load No.	Load Type	Condition 1	Condition 2	Axial Thrust Force, lbs	Compute Top y vs. File Length
1	1	V = 0.0000 lbs	M = 0.0000 in-lbs	0.0000000	No

V = perpendicular shear force applied to pile head
 M = bending moment applied to pile head
 y = lateral deflection relative to pile axis
 S = pile slope relative to original pile batter angle
 R = rotational stiffness applied to pile head
 Axial thrust is assumed to be acting axially for all pile batter angles.

 Specified Depths for Output of p-y Curves

Lateral load-transfer (p-y) curves are computed and output at 5 depths.
 (Note that these curves are independent from the curves used at nodal point depths)

Depth No.	Depth Below Pile Head ft	Depth Below Ground Surface ft
1	16.000	1.000
2	18.000	3.000
3	20.000	5.000
4	22.000	7.000
5	24.000	9.000

Depth of ground surface below top of pile = 15.00 ft

 Computations of Nominal Moment Capacity and Nonlinear Bending Stiffness

Axial thrust force values were determined from pile-head loading conditions

Number of Pile Sections Analyzed = 1

Pile Section No. 1:

Dimensions and Properties of Drilled Shaft (Bored Pile):

Length of Section	=	35.00000000 ft
Shaft Diameter	=	24.00000000 in
Concrete Cover Thickness	=	3.00000000 in
Number of Reinforcing Bars	=	12 bars
Yield Stress of Reinforcing Bars	=	60.00000000 ksi
Modulus of Elasticity of Reinforcing Bars	=	29000. ksi
Gross Area of Shaft	=	452.38934212 sq. in.
Total Area of Reinforcing Steel	=	7.20000000 sq. in.
Area Ratio of Steel Reinforcement	=	1.59 percent
Edge-to-Edge Bar Spacing	=	3.55727615 in
Maximum Concrete Aggregate Size	=	0.75000000 in
Ratio of Bar Spacing to Aggregate Size	=	4.74
Offset of Rebar Cage Center from Center of Pile	=	0.00000000 in

Axial Structural Capacities:

Nom. Axial Structural Capacity = $0.85 F_c A_c + F_y A_s$	=	1945.644 kips
Tensile Load for Cracking of Concrete	=	-209.248 kips
Nominal Axial Tensile Capacity	=	-432.000 kips

Reinforcing Bar Dimensions and Positions Used in Computations:

Bar Number	Bar Diam. inches	Bar Area sq. in.	X inches	Y inches
1	0.87500	0.60000	8.56250	0.00000
2	0.87500	0.60000	7.41534	4.28125
3	0.87500	0.60000	4.28125	7.41534
4	0.87500	0.60000	0.00000	8.56250
5	0.87500	0.60000	-4.28125	7.41534
6	0.87500	0.60000	-7.41534	4.28125
7	0.87500	0.60000	-8.56250	0.00000
8	0.87500	0.60000	-7.41534	-4.28125
9	0.87500	0.60000	-4.28125	-7.41534
10	0.87500	0.60000	0.00000	-8.56250
11	0.87500	0.60000	4.28125	-7.41534
12	0.87500	0.60000	7.41534	-4.28125

NOTE: The positions of the above rebars were computed by LFile

Minimum spacing between any two bars not equal to zero = 3.55728 inches between Bars 7 and 8

Spacing to aggregate size ratio = 4.74303

Concrete Properties:

 Compressive Strength of Concrete = 4.00000000 ksi
 Modulus of Elasticity of Concrete = 3604.99653259 ksi
 Modulus of Rupture of Concrete = -0.47434164 ksi
 Compression Strain at Peak Stress = 0.00188627
 Tensile Strain at Fracture of Concrete = -0.00011537
 Maximum Coarse Aggregate Size = 0.75000000 in

Number of Axial Thrust Force Values Determined from Pile-head Loadings = 1

Number	Axial Thrust Force kips
-----	-----
1	0.000

Definitions of Run Messages and Notes:

 C = concrete in section has cracked in tension.
 Y = stress in reinforcing steel has reached yield stress.
 T = ACI 318-08 criteria for tension-controlled section met, tensile strain in reinforcement exceeds 0.005 while simultaneously compressive strain in concrete more than 0.003. See ACI 318-08, Section 10.3.4.
 Z = depth of tensile zone in concrete section is less than 10 percent of section depth.

Bending Stiffness (EI) = Computed Bending Moment / Curvature.
 Position of neutral axis is measured from edge of compression side of pile.
 Compressive stresses and strains are positive in sign.
 Tensile stresses and strains are negative in sign.

Axial Thrust Force = 0.000 kips

Bending Curvature rad/in.	Bending Moment in-kip	Bending Stiffness kip-in ²	Depth to N Axis in	Max Comp Strain in/in	Max Tens Strain in/in	Max Concrete Stress ksi	Max Steel Stress ksi	Run Msg
0.000001250	94.3056923	75444554.	11.9999611	0.0000150	-0.0000150	0.0627333	-0.4306514	
0.000002500	188.1518190	75260728.	11.9999609	0.0000300	-0.0000300	0.1249707	-0.8613028	
0.000003750	281.5383800	75076901.	11.9999608	0.0000450	-0.0000450	0.1867124	-1.2919542	
0.000005000	374.4653753	74893075.	11.9999606	0.0000600	-0.0000600	0.2479582	-1.7226057	
0.000006250	466.9328050	74709249.	11.9999605	0.0000750	-0.0000750	0.3087081	-2.1532571	
0.000007500	558.9406690	74525423.	11.9999603	0.0000900	-0.0000900	0.3689623	-2.5839086	
0.000008750	650.4889673	74341596.	11.9999602	0.0001050	-0.0001050	0.4287206	-3.0145600	
0.000010000	650.4889673	65048897.	6.5897908	0.0000659	-0.0001741	0.2696892	-5.0141606	C
0.000011300	650.4889673	57821242.	6.5921648	0.0000742	-0.0001958	0.3028475	-5.6401562	C
0.000012500	650.4889673	52039117.	6.5945447	0.0000824	-0.0002176	0.3358821	-6.2659775	C
0.000013800	650.4889673	47308289.	6.5969305	0.0000907	-0.0002393	0.3687929	-6.8916239	C
0.000015000	650.4889673	43365931.	6.5993223	0.0000990	-0.0002610	0.4015796	-7.5170948	C
0.000016300	650.4889673	40030090.	6.6016606	0.0001073	-0.0002827	0.4342380	-8.1424174	C
0.000017500	650.4889673	37170798.	6.6039811	0.0001156	-0.0003044	0.4667697	-8.7675795	C
0.000018800	650.4889673	34692745.	6.6063073	0.0001239	-0.0003261	0.4991756	-9.3925704	C
0.000020000	650.4889673	32524448.	6.6086391	0.0001322	-0.0003478	0.5314557	-10.0173893	C
0.000021300	650.4889673	30611246.	6.6109766	0.0001405	-0.0003695	0.5636097	-10.6420356	C
0.000022500	650.4889673	28910621.	6.6133198	0.0001488	-0.0003912	0.5956373	-11.2665088	C
0.000023800	650.4889673	27389009.	6.6156688	0.0001571	-0.0004129	0.6275384	-11.8908080	C
0.000025000	650.4889673	26019559.	6.6180236	0.0001655	-0.0004345	0.6593125	-12.5149328	C
0.000026300	650.4889673	24780532.	6.6203842	0.0001738	-0.0004562	0.6909596	-13.1388825	C
0.000027500	650.4889673	23654144.	6.6227506	0.0001821	-0.0004779	0.7224793	-13.7626563	C
0.000028800	650.4889673	22625703.	6.6251229	0.0001905	-0.0004995	0.7538715	-14.3862537	C
0.000030000	650.4889673	21682966.	6.6275011	0.0001988	-0.0005212	0.7851358	-15.0096740	C
0.000031300	650.4889673	20815647.	6.6298852	0.0002072	-0.0005428	0.8162720	-15.6329165	C
0.000032500	650.4889673	20015045.	6.6322753	0.0002155	-0.0005645	0.8472798	-16.2559805	C
0.000033800	650.4889673	19273747.	6.6346714	0.0002239	-0.0005861	0.8781591	-16.8788653	C
0.000035000	650.4889673	18585399.	6.6370735	0.0002323	-0.0006077	0.9089095	-17.5015704	C
0.000036300	651.6439619	17976385.	6.6394816	0.0002407	-0.0006293	0.9395309	-18.1240949	C
0.000037500	673.8592485	17969580.	6.6418958	0.0002491	-0.0006509	0.9700228	-18.7464382	C
0.000038800	696.0569468	17962760.	6.6443162	0.0002575	-0.0006725	1.0003852	-19.3685996	C
0.000040000	718.2369981	17955925.	6.6467426	0.0002659	-0.0006941	1.0306176	-19.9905785	C
0.000041300	740.3993436	17949075.	6.6491753	0.0002743	-0.0007157	1.0607199	-20.6123740	C
0.000042500	762.5439241	17942210.	6.6516142	0.0002827	-0.0007373	1.0906918	-21.2339854	C
0.000043800	784.6706797	17935330.	6.6540593	0.0002911	-0.0007589	1.1205330	-21.8554122	C
0.000045000	806.7795505	17928434.	6.6565107	0.0002995	-0.0007805	1.1502433	-22.4766535	C
0.000046300	828.8704760	17921524.	6.6589684	0.0003080	-0.0008020	1.1798224	-23.0977086	C
0.000047500	850.9433954	17914598.	6.6614325	0.0003164	-0.0008236	1.2092700	-23.7185767	C
0.000048800	872.9982475	17907656.	6.6639029	0.0003249	-0.0008451	1.2385859	-24.3392572	C
0.000050100	917.0534735	17893726.	6.6688630	0.0003348	-0.0008882	1.2968212	-25.5800526	C
0.000051300	961.0357107	17879734.	6.6738490	0.0003587	-0.0009313	1.3545263	-26.8200881	C
0.000052600	1004.9444284	17865679.	6.6788612	0.0003757	-0.0009743	1.4116989	-28.0593579	C
0.000053800	1048.7791151	17851559.	6.6838999	0.0003927	-0.0010173	1.4683367	-29.2978558	C
0.000055100	1092.5392522	17837376.	6.6889654	0.0004097	-0.0010603	1.5244375	-30.5355756	C

0.0000638	1136.2243142	17823126.	6.6940579	0.0004267	-0.0011033	1.5799990	-31.7725109	C
0.0000663	1179.8337685	17808812.	6.6991777	0.0004438	-0.0011462	1.6350189	-33.0086552	C
0.0000688	1223.3670749	17794430.	6.7043252	0.0004609	-0.0011891	1.6894947	-34.2440021	C
0.0000713	1266.8236858	17779982.	6.7095007	0.0004781	-0.0012319	1.7434241	-35.4785447	C
0.0000738	1310.2030461	17765465.	6.7147044	0.0004952	-0.0012748	1.7968046	-36.7122765	C
0.0000763	1353.5045926	17750880.	6.7199368	0.0005124	-0.0013176	1.8496339	-37.9451905	C
0.0000788	1396.7277544	17736225.	6.7251980	0.0005296	-0.0013604	1.9019095	-39.1772798	C
0.0000813	1439.8719523	17721501.	6.7304885	0.0005469	-0.0014031	1.9536288	-40.4085373	C
0.0000838	1482.9365987	17706706.	6.7358085	0.0005641	-0.0014459	2.0047894	-41.6389559	C
0.0000863	1525.9210978	17691839.	6.7411585	0.0005814	-0.0014886	2.0553886	-42.8685282	C
0.0000888	1568.8248448	17676900.	6.7465387	0.0005988	-0.0015312	2.1054238	-44.0972470	C
0.0000913	1611.6472263	17661887.	6.7519496	0.0006161	-0.0015739	2.1548924	-45.3251046	C
0.0000938	1654.3876196	17646801.	6.7573914	0.0006335	-0.0016165	2.2037918	-46.5520934	C
0.0000963	1697.0453929	17631640.	6.7628645	0.0006509	-0.0016591	2.2521192	-47.7782057	C
0.0000988	1739.6199049	17616404.	6.7683694	0.0006684	-0.0017016	2.2998720	-49.0034337	C
0.0001013	1782.1105047	17601091.	6.7739063	0.0006859	-0.0017441	2.3470472	-50.2277692	C
0.0001038	1824.5165314	17585702.	6.7794757	0.0007034	-0.0017866	2.3936421	-51.4512042	C
0.0001063	1866.8373141	17570234.	6.7850779	0.0007209	-0.0018291	2.4396540	-52.6737304	C
0.0001088	1909.0721714	17554687.	6.7907134	0.0007385	-0.0018715	2.4850797	-53.8953394	C
0.0001113	1951.2204116	17539060.	6.7963826	0.0007561	-0.0019139	2.5299165	-55.1160227	C
0.0001138	1993.2813320	17523352.	6.8020858	0.0007737	-0.0019563	2.5741614	-56.3357715	C
0.0001163	2035.2542188	17507563.	6.8078262	0.0007914	-0.0019986	2.6178114	-57.5545771	C
0.0001188	2077.1383470	17491691.	6.8135936	0.0008091	-0.0020409	2.6608634	-58.7724305	C
0.0001213	2118.9329799	17475736.	6.8194042	0.0008269	-0.0020831	2.7033142	-59.9893225	CY
0.0001238	2160.6373692	17459696.	6.8252481	0.0008446	-0.0021254	2.7451609	-60.0000000	CY
0.0001263	2202.2507541	17443570.	6.8311281	0.0008624	-0.0021676	2.7864002	-60.0000000	CY
0.0001288	2243.7723616	17427358.	6.8370449	0.0008803	-0.0022097	2.8270288	-60.0000000	CY
0.0001313	2285.2043886	17411081.	6.8428841	0.0008981	-0.0022519	2.8670098	-60.0000000	CY
0.0001338	2326.5455257	17394733.	6.8486454	0.0009160	-0.0022940	2.9063386	-60.0000000	CY
0.0001363	2367.7935566	17378301.	6.8544419	0.0009339	-0.0023361	2.9450462	-60.0000000	CY
0.0001388	2408.9473664	17361783.	6.8602742	0.0009519	-0.0023781	2.9831290	-60.0000000	CY
0.0001413	2450.0065543	17345179.	6.8661427	0.0009698	-0.0024202	3.0205840	-60.0000000	CY
0.0001438	2490.9695337	17328484.	6.8720479	0.0009879	-0.0024621	3.0574071	-60.0000000	CY
0.0001463	2531.8358595	17311698.	6.8779903	0.0010059	-0.0025041	3.0935953	-60.0000000	CY
0.0001488	2572.0000921	17290757.	6.8834458	0.0010239	-0.0025461	3.1289904	-60.0000000	CY
0.0001588	2710.9553394	17076884.	6.8881218	0.0010935	-0.0027165	3.2590586	-60.0000000	CY
0.0001688	2817.9750843	16699112.	6.8868865	0.0011591	-0.0028909	3.3720085	-60.0000000	CY
0.0001788	2888.6656697	16160367.	6.8233294	0.0012197	-0.0030703	3.4677780	-60.0000000	CY
0.0001888	2957.8043783	15670487.	6.7827012	0.0012802	-0.0032498	3.5565658	-60.0000000	CY
0.0001988	3026.2212779	15226271.	6.7480653	0.0013412	-0.0034288	3.6360939	-60.0000000	CY
0.0002088	3093.4197710	14818777.	6.7181443	0.0014024	-0.0036076	3.7088405	-60.0000000	CY
0.0002188	3146.3244275	14383197.	6.6794857	0.0014611	-0.0037889	3.7709433	-60.0000000	CY
0.0002288	3177.3979568	13890264.	6.6250528	0.0015155	-0.0039745	3.8217039	-60.0000000	CY
0.0002388	3204.7505816	13423039.	6.5719340	0.0015690	-0.0041610	3.8655125	-60.0000000	CY
0.0002488	3231.5375808	12991106.	6.5229988	0.0016226	-0.0043474	3.9031406	-60.0000000	CY
0.0002588	3257.9092454	12590954.	6.4790232	0.0016764	-0.0045336	3.9347725	-60.0000000	CY
0.0002688	3283.8546785	12218994.	6.4394845	0.0017306	-0.0047194	3.9603038	-60.0000000	CY
0.0002788	3309.3624045	11872152.	6.4039366	0.0017851	-0.0049049	3.9796252	-60.0000000	CY
0.0002888	3334.4203989	11547776.	6.3719970	0.0018399	-0.0050901	3.9926227	-60.0000000	CY
0.0002988	3358.9215355	11243252.	6.3422958	0.0018948	-0.0052752	3.9991584	-60.0000000	CY
0.0003088	3382.8669819	10956654.	6.3150458	0.0019498	-0.0054602	3.9974474	-60.0000000	CY
0.0003188	3406.3200295	10686494.	6.2907097	0.0020052	-0.0056448	3.9987011	-60.0000000	CY
0.0003288	3429.2309060	10431121.	6.2691256	0.0020610	-0.0058290	3.9994285	-60.0000000	CY
0.0003388	3451.6105377	10189256.	6.2499561	0.0021172	-0.0060128	3.9967643	-60.0000000	CY
0.0003488	3470.8904462	9952374.	6.2295126	0.0021725	-0.0061975	3.9999499	-60.0000000	CY
0.0003588	3485.7362924	9716338.	6.2059959	0.0022264	-0.0063836	3.9974827	-60.0000000	CY
0.0003688	3496.6767150	9482513.	6.1796364	0.0022787	-0.0065713	3.9999624	-60.0000000	CY
0.0003788	3504.3297058	9252356.	6.1515330	0.0023299	-0.0067601	3.9964331	-60.0000000	CY
0.0003888	3509.6407015	9028015.	6.1224910	0.0023801	-0.0069499	3.9995811	-60.0000000	CY
0.0003988	3514.5071712	8813811.	6.0935253	0.0024298	-0.0071402	3.9946161	-60.0000000	CY
0.0004088	3519.1747471	8609594.	6.0663968	0.0024796	-0.0073304	3.9977956	-60.0000000	CY
0.0004188	3523.7155934	8414843.	6.0410171	0.0025297	-0.0075203	3.9998910	-60.0000000	CY
0.0004288	3528.0670760	8228728.	6.0174609	0.0025800	-0.0077100	3.9931542	-60.0000000	CY
0.0004388	3532.2870223	8050797.	5.9954470	0.0026305	-0.0078995	3.9976707	-60.0000000	CY
0.0004488	3536.4046900	7880568.	5.9747997	0.0026812	-0.0080888	3.9998150	-60.0000000	CY
0.0004588	3540.3593233	7717405.	5.9555957	0.0027321	-0.0082779	3.9936955	-60.0000000	CY
0.0004688	3544.1882331	7560935.	5.9376465	0.0027833	-0.0084667	3.9960535	-60.0000000	CY
0.0004788	3547.9317058	7410823.	5.9207714	0.0028346	-0.0086554	3.9990963	-60.0000000	CY
0.0004888	3551.5795261	7266659.	5.9049340	0.0028860	-0.0088440	3.9991486	-60.0000000	CY
0.0004988	3555.0609250	7127942.	5.8902642	0.0029378	-0.0090322	3.9917525	-60.0000000	CY
0.0005088	3558.4438120	6994484.	5.87660912	0.0029895	-0.0092205	3.9963782	-60.0000000	CY
0.0005188	3561.6790741	6865887.	5.8617779	0.0030408	-0.0094092	3.9991045	-60.0000000	CYT
0.0005288	3564.8464332	6742026.	5.8482830	0.0030923	-0.0095977	3.9998562	-60.0000000	CYT
0.0005388	3567.8682029	6622493.	5.8358002	0.0031440	-0.0097860	3.9907772	-60.0000000	CYT
0.0005488	3570.8381723	6507222.	5.8239950	0.0031959	-0.0099741	3.9939756	-60.0000000	CYT
0.0006088	3587.3288166	5892943.	5.7663073	0.0035102	-0.0110998	3.9964516	-60.0000000	CYT
0.0006688	3601.8049954	5385877.	5.7263001	0.0038295	-0.0122205	3.9955298	-60.0000000	CYT

 Summary of Results for Nominal (Unfactored) Moment Capacity for Section 1

Moment values interpolated at maximum compressive strain = 0.003
 or maximum developed moment if pile fails at smaller strains.

Load No.	Axial Thrust kips	Nominal Mom. Cap. in-kip	Max. Comp. Strain
1	0.000	3559.108	0.00300000

Note note that the values of moment capacity in the table above are not factored by a strength reduction factor (phi-factor).

In ACI 318-08, the value of the strength reduction factor depends on whether the transverse reinforcing steel bars are tied hoops (0.65) or spirals (0.70).

The above values should be multiplied by the appropriate strength reduction factor to compute ultimate moment capacity according to ACI 318-08, Section 9.3.2.2 or the value required by the design standard being followed.

The following table presents factored moment capacities and corresponding bending stiffnesses computed for common resistance factor values used for reinforced concrete sections.

Axial Load No.	Resistance Factor for Moment	Nominal Moment Capacity in-kip	Ultimate (Factored) Axial Thrust kips	Ultimate (Factored) Moment Capacity in-kip	Bending Stiffness at Ult. Mom. Cap. kip-in ²
1	0.65	3559.108	0.000	2313.420	17399923.290
1	0.70	3559.108	0.000	2491.376	17328316.949
1	0.75	3559.108	0.000	2669.331	17140950.140

p-y Curves Reported for Specified Depths

p-y Curve in Sand Computed Using Reese Criteria for Static Loading Conditions

```

Soil Layer Number          =          1
Depth below pile head      =         16.000 ft
Depth below ground surface =          1.000 ft
Equivalent Depth (see note) =          1.000 ft
Ground Slope Angle         =          0.000 degrees
Pile Batter                 =          0.000 degrees
Effective Slope             =          0.000 degrees
Pile Diameter, b           =          24.000 in
Angle of Friction           =          24.000 degrees
Avg. Eff. Unit Weight      =        62.60000 pcf
kpy                         =        375.000 pci
K active                    =          0.422
K passive                   =          2.371
K0                           =          0.400
Pst                          =          26.131 lbs/in
Psd                          =          145.144 lbs/in
Ps = Pst (shallow controls) =          26.131 lbs/in
A (static)                  =          2.4800
B (static)                  =          1.8300
C = Pm/(Ym^(1/n))          =          62.0426
n = Pm/(m Ym)              =          3.5192
m = (Pu-Pm)/(Yu-Ym)        =          33.9709
Yk = [c/(kx)]^(n/(n-1))    =          0.0025 in
Pk                           =          11.328 lbs/in
Ym = b/60                   =          0.4000 in
Pm = B ps                   =          47.821 lbs/in
Yu = 3b/80                  =          0.9000 in
Pu = A Ps                   =          64.806 lbs/in
Es,lim                       =          4500.000 lbs/in/in
p-multiplier                =          1.00000
y-multiplier                =          1.00000

```

This p-y curve is computed using the equivalent depth.

This curve has the normal shape for a Reese sand p-y curve where $Y_k < Y_m < Y_u$.

y, in	p, lbs/in
0.0000	0.0000
0.00252	11.32823 *
0.03865	24.61679
0.07479	29.69507
0.11092	33.21458
0.14706	35.98556
0.18319	38.30384
0.21933	40.31428
0.25546	42.09976
0.29160	43.71254
0.32773	45.18796
0.36387	46.55111
0.40000	47.82052
0.65000	56.31323
0.90000	64.80595
0.92250	64.80595
0.94500	64.80595

* p value(s) computed using $p = k * \text{Eff} * x * y$

p-y Curve in Sand Computed Using Reese Criteria for Static Loading Conditions

```

Soil Layer Number          =          1
Depth below pile head      =        18.000 ft
Depth below ground surface =         3.000 ft
Equivalent Depth (see note) =         3.000 ft
Ground Slope Angle        =         0.000 degrees
Pile Batter               =         0.000 degrees
Effective Slope           =         0.000 degrees
Pile Diameter, b         =        24.000 in
Angle of Friction         =        24.000 degrees
Avg. Eff. Unit Weight     =       62.60000 pcf
kpy                      =       375.000 pci
K active                  =         0.422
K passive                 =         2.371
K0                       =         0.400
Pst                      =        113.147 lbs/in
Psd                      =        435.433 lbs/in
Ps = Pst (shallow controls) =        113.147 lbs/in
A (static)               =         1.7600
B (static)               =         1.2700
C = Pm/(Ym^(1/n))       =        190.6671
n = Pm/(m Ym)           =         3.2398
m = (Pu-Pm)/(Yu-Ym)     =        110.8841
Yk = [c/(kx)]^(n/(n-1)) =         0.0021 in
Pk                      =        28.463 lbs/in
Ym = b/60                =         0.4000 in
Pm = B ps               =        143.697 lbs/in
Yu = 3b/80              =         0.9000 in
Pu = A Ps               =        199.139 lbs/in
Es,lim                  =       13500.000 lbs/in/in
p-multiplier            =         1.00000
y-multiplier            =         1.00000

```

This p-y curve is computed using the equivalent depth.

This curve has the normal shape for a Reese sand p-y curve where $Y_k < Y_m < Y_u$.

y, in	p, lbs/in
0.0000	0.0000
0.00211	28.46306 *
0.03828	69.64581
0.07445	85.52006
0.11062	96.63828
0.14680	105.45635
0.18297	112.87545
0.21914	119.33890
0.25531	125.10122
0.29148	130.32357
0.32766	135.11514
0.36383	139.55368
0.40000	143.69676
0.65000	171.41779
0.90000	199.13882
0.92250	199.13882
0.94500	199.13882

* p value(s) computed using $p = k * \text{Eff} \times y$

p-y Curve in Sand Computed Using Reese Criteria for Static Loading Conditions

```

Soil Layer Number          =          1
Depth below pile head      =        20.000 ft
Depth below ground surface =         5.000 ft
Equivalent Depth (see note) =         5.000 ft
Ground Slope Angle        =         0.000 degrees
Pile Batter               =         0.000 degrees
Effective Slope           =         0.000 degrees
Pile Diameter, b         =        24.000 in
Angle of Friction         =        24.000 degrees
Avg. Eff. Unit Weight     =       62.60000 pcf
kpy                      =       375.000 pci
K active                  =         0.422
K passive                 =         2.371
K0                       =         0.400
Pst                      =        246.500 lbs/in
Psd                      =        725.722 lbs/in
Ps = Pst (shallow controls) =        246.500 lbs/in
A (static)               =         1.2300
B (static)               =         0.8600
C = Pm/(Ym^(1/n))       =        290.5897
n = Pm/(m Ym)           =         2.9054
m = (Pu-Pm)/(Yu-Ym)     =        182.4098
Yk = [c/(kx)]^(n/(n-1)) =         0.0013 in
Pk                      =        29.644 lbs/in
Ym = b/60                =         0.4000 in
Pm = B ps               =        211.990 lbs/in
Yu = 3b/80              =         0.9000 in
Pu = A Ps               =        303.195 lbs/in
Es,lim                  =       22500.000 lbs/in/in
p-multiplier            =         1.00000

```

y-multiplier = 1.00000

This p-y curve is computed using the equivalent depth.

This curve has the normal shape for a Reese sand p-y curve where $Y_k < Y_m < Y_u$.

y, in	p, lbs/in
0.0000	0.0000
0.00132	29.64432 *
0.03756	93.91311
0.07381	118.49272
0.11005	135.95892
0.14629	149.95530
0.18254	161.82567
0.21878	172.23467
0.25502	181.56581
0.29127	190.06297
0.32751	197.89206
0.36376	205.17163
0.40000	211.98975
0.65000	257.59220
0.90000	303.19464
0.92250	303.19464
0.94500	303.19464

* p value(s) computed using $p = k * \text{Eff} \times y$

p-y Curve in Sand Computed Using Reese Criteria for Static Loading Conditions

Soil Layer Number	=	1
Depth below pile head	=	22.000 ft
Depth below ground surface	=	7.000 ft
Equivalent Depth (see note)	=	7.000 ft
Ground Slope Angle	=	0.000 degrees
Pile Batter	=	0.000 degrees
Effective Slope	=	0.000 degrees
Pile Diameter, b	=	24.000 in
Angle of Friction	=	24.000 degrees
Avg. Eff. Unit Weight	=	62.60000 pcf
kpy	=	375.000 pci
K active	=	0.422
K passive	=	2.371
K0	=	0.400
Pst	=	426.189 lbs/in
Psd	=	1016.011 lbs/in
Ps = Pst (shallow controls)	=	426.189 lbs/in
A (static)	=	0.9800
B (static)	=	0.6200
C = $P_m / (Y_m^{1/n})$	=	404.4304
n = $P_m / (m \cdot Y_m)$	=	2.1528
m = $(P_u - P_m) / (Y_u - Y_m)$	=	306.8563
$Y_k = [c / (kx)]^{n / (n-1)}$	=	0.0003 in
Pk	=	9.248 lbs/in
$Y_m = b / 60$	=	0.4000 in
$P_m = B \cdot p_s$	=	264.237 lbs/in
$Y_u = 3b / 80$	=	0.9000 in
$P_u = A \cdot P_s$	=	417.666 lbs/in
Es,lim	=	31500.000 lbs/in/in
p-multiplier	=	1.00000
y-multiplier	=	1.00000

This p-y curve is computed using the equivalent depth.

This curve has the normal shape for a Reese sand p-y curve where $Y_k < Y_m < Y_u$.

y, in	p, lbs/in
0.0000	0.0000
0.0002936	9.24812 *
0.03663	87.04140
0.07297	119.88065
0.10930	144.63573
0.14564	165.26319
0.18198	183.27830
0.21832	199.45171
0.25465	214.23817
0.29099	227.93235
0.32733	240.73794
0.36366	252.80260
0.40000	264.23740
0.65000	340.95149
0.90000	417.66557
0.92250	417.66557
0.94500	417.66557

* p value(s) computed using $p = k * \text{Eff} \times y$

p-y Curve in Sand Computed Using Reese Criteria for Static Loading Conditions

```

Soil Layer Number          =          1
Depth below pile head      =         24.000 ft
Depth below ground surface =          9.000 ft
Equivalent Depth (see note) =          9.000 ft
Ground Slope Angle        =          0.000 degrees
Pile Batter                =          0.000 degrees
Effective Slope            =          0.000 degrees
Pile Diameter, b          =         24.000 in
Angle of Friction          =         24.000 degrees
Avg. Eff. Unit Weight      =        62.60000 pcf
kpy                        =        375.000 pci
K active                   =          0.422
K passive                  =          2.371
K0                         =          0.400
Pst                        =         652.216 lbs/in
Psd                        =        1306.300 lbs/in
Ps = Pst (shallow controls) =         652.216 lbs/in
A (static)                 =          0.8900
B (static)                 =          0.5150
C = Pm/(Ym^(1/n))          =         572.8072
n = Pm/(m Ym)              =          1.7167
m = (Pu-Pm)/(Yu-Ym)        =         489.1621
Yk = [c/(kx)]^(n/(n-1))    =          0.0000 in
Pk                         =          1.504 lbs/in
Ym = b/60                  =          0.4000 in
Pm = B ps                  =         335.891 lbs/in
Yu = 3b/80                 =          0.9000 in
Pu = A Ps                  =         580.472 lbs/in
Es,lim                     =       40500.000 lbs/in/in
p-multiplier               =          1.00000
y-multiplier               =          1.00000
    
```

This p-y curve is computed using the equivalent depth.

This curve has the normal shape for a Reese sand p-y curve where $Y_k < Y_m < Y_u$.

y, in	p, lbs/in
0.0000	0.0000
0.0000371	1.50448 *
0.03640	83.13751
0.07276	124.45867
0.10912	157.60121
0.14548	186.34505
0.18184	212.20586
0.21820	235.97922
0.25456	258.14620
0.29092	279.02482
0.32728	298.83870
0.36364	317.75238
0.40000	335.89127
0.65000	458.18178
0.90000	580.47229
0.92250	580.47229
0.94500	580.47229

* p value(s) computed using $p = k * \text{Eff} * y$

 Summary of Pile Response(s)

Definitions of Pile-head Loading Conditions:

```

Load Type 1: Load 1 = Shear, lbs, and Load 2 = Moment, in-lbs
Load Type 2: Load 1 = Shear, lbs, and Load 2 = Slope, radians
Load Type 3: Load 1 = Shear, lbs, and Load 2 = Rotational Stiffness, in-lbs/radian
Load Type 4: Load 1 = Top Deflection, inches, and Load 2 = Moment, in-lbs
Load Type 5: Load 1 = Top Deflection, inches, and Load 2 = Slope, radians
    
```

Load Case No.	Load Type No.	File-head Condition 1 V(lbs) or y(inches)	File-head Condition 2 in-lb, rad., or in-lb/rad.	Axial Loading lbs	File-head Deflection inches	Maximum Moment in Pile in-lbs	Maximum Shear in Pile lbs	File-head Rotation radians
1	1	V = 0.000	M = 0.000	0.0000000	4.25388915	1675578.	-17498.	-0.01587832

The analysis ended normally.

J.5: Test Wall (Increased Dimensions) with Natural Water Table Conditions

```
=====
LPIle Plus for Windows, Version 2012-06.037
Analysis of Individual Piles and Drilled Shafts
Subjected to Lateral Loading Using the p-y Method
© 1985-2012 by Ensoft, Inc.
All Rights Reserved
=====

This copy of LPIle is licensed to:

Andy Brown
University of Texas - Austin

Serial Number of Security Device: 226662924
Company Name Stored in Security Device: UT Austin - Prof. Gilbert

-----
Files Used for Analysis
-----

-----
Date and Time of Analysis
-----

Date: August 29, 2013 Time: 18:31:42

-----
Problem Title
-----

Project Name:
Job Number:
Client:
Engineer:
Description:

-----
Program Options
-----

Engineering units are US Customary Units: pounds, inches, feet

Basic Program Options:

This analysis computes pile response to lateral loading and will compute nonlinear
moment-curvature and nominal moment capacity for section types with nonlinear properties.

Computation Options:
- Analysis does not use p-y multipliers (individual pile or shaft only)
- Analysis assumes no shear resistance at pile tip
- Analysis for fixed-length pile or shaft only
- No computation of foundation stiffness matrix values
- Report summary table of pile-top values for deflection, maximum bending
moment, and shear force only
- Analysis assumes no loading by soil movements acting on pile
- p-y curves computed and reported at user-specified depths

Solution Control Parameters:
- Number of pile increments = 100
- Maximum number of iterations allowed = 750
- Deflection tolerance for convergence = 1.0000E-05 in
- Maximum allowable deflection = 100.0000 in

Pile Response Output Options:
- Only summary tables of pile-head deflection, maximum bending moment,
and maximum shear force are to be written to output report file.

-----
Pile Structural Properties and Geometry
-----

Total number of pile sections = 1
Total length of pile = 45.00 ft
Depth of ground surface below top of pile = 15.00 ft

Pile diameter values used for p-y curve computations are defined using 2 points.
```


p-y curves are computed using pile diameter values interpolated with depth over the length of the pile.

Point	Depth X ft	Pile Diameter in
1	0.00000	30.0000000
2	45.000000	30.0000000

Input Structural Properties:

Pile Section No. 1:

Section Type = Drilled Shaft (Bored Pile)
 Section Length = 45.00000000 ft
 Section Diameter = 30.00000000 in

Ground Slope and Pile Batter Angles

Ground Slope Angle = 0.000 degrees
 = 0.000 radians
 Pile Batter Angle = 0.000 degrees
 = 0.000 radians

Soil and Rock Layering Information

The soil profile is modelled using 1 layers

Layer 1 is sand, p-y criteria by Reese et al., 1974

Distance from top of pile to top of layer = 15.00000 ft
 Distance from top of pile to bottom of layer = 50.00000 ft
 Effective unit weight at top of layer = 62.60000 pcf
 Effective unit weight at bottom of layer = 62.60000 pcf
 Friction angle at top of layer = 24.00000 deg.
 Friction angle at bottom of layer = 24.00000 deg.
 Subgrade k at top of layer = 375.00000 pci
 Subgrade k at bottom of layer = 375.00000 pci

(Depth of lowest soil layer extends 5.00 ft below pile tip)

Summary of Soil Properties

Layer Num.	Layer Soil Type (p-y Curve Criteria)	Layer Depth ft	Effective Unit Wt. pcf	Angle of Friction deg.	kpy pci
1	Sand (Reese, et al.)	15.000 50.000	62.600 62.600	24.000 24.000	375.000 375.000

Loading Type

Static loading criteria were used when computing p-y curves for all analyses.

Distributed Lateral Loading

Distributed lateral load intensity defined using 3 points

Point No.	Depth X in	Dist. Load lbs/in
1	0.000	0.000
2	96.000	78.100
3	180.000	203.400

 Pile-head Loading and Pile-head Fixity Conditions

Number of loads specified = 1

Load No.	Load Type	Condition 1	Condition 2	Axial Thrust Force, lbs	Compute Top y vs. File Length
1	1	V = 0.0000 lbs	M = 0.0000 in-lbs	0.0000000	No

V = perpendicular shear force applied to pile head
 M = bending moment applied to pile head
 y = lateral deflection relative to pile axis
 S = pile slope relative to original pile batter angle
 R = rotational stiffness applied to pile head
 Axial thrust is assumed to be acting axially for all pile batter angles.

 Specified Depths for Output of p-y Curves

Lateral load-transfer (p-y) curves are computed and output at 5 depths.
 (Note that these curves are independent from the curves used at nodal point depths)

Depth No.	Depth Below Pile Head ft	Depth Below Ground Surface ft
1	16.000	1.000
2	18.000	3.000
3	20.000	5.000
4	22.000	7.000
5	24.000	9.000

Depth of ground surface below top of pile = 15.00 ft

 Computations of Nominal Moment Capacity and Nonlinear Bending Stiffness

Axial thrust force values were determined from pile-head loading conditions

Number of Pile Sections Analyzed = 1

Pile Section No. 1:

Dimensions and Properties of Drilled Shaft (Bored Pile):

Length of Section	=	45.00000000 ft
Shaft Diameter	=	30.00000000 in
Concrete Cover Thickness	=	3.00000000 in
Number of Reinforcing Bars	=	12 bars
Yield Stress of Reinforcing Bars	=	60.00000000 ksi
Modulus of Elasticity of Reinforcing Bars	=	29000. ksi
Gross Area of Shaft	=	706.85834706 sq. in.
Total Area of Reinforcing Steel	=	9.48000000 sq. in.
Area Ratio of Steel Reinforcement	=	1.34 percent
Edge-to-Edge Bar Spacing	=	4.95283804 in
Maximum Concrete Aggregate Size	=	0.75000000 in
Ratio of Bar Spacing to Aggregate Size	=	6.60
Offset of Rebar Cage Center from Center of Pile	=	0.00000000 in

Axial Structural Capacities:

Nom. Axial Structural Capacity = $0.85 F_c A_c + F_y A_s$	=	2939.886 kips
Tensile Load for Cracking of Concrete	=	-321.764 kips
Nominal Axial Tensile Capacity	=	-568.800 kips

Reinforcing Bar Dimensions and Positions Used in Computations:

Bar Number	Bar Diam. inches	Bar Area sq. in.	X inches	Y inches
1	1.00000	0.79000	11.50000	0.00000
2	1.00000	0.79000	9.95929	5.75000
3	1.00000	0.79000	5.75000	9.95929
4	1.00000	0.79000	0.00000	11.50000
5	1.00000	0.79000	-5.75000	9.95929
6	1.00000	0.79000	-9.95929	5.75000
7	1.00000	0.79000	-11.50000	0.00000
8	1.00000	0.79000	-9.95929	-5.75000
9	1.00000	0.79000	-5.75000	-9.95929
10	1.00000	0.79000	0.00000	-11.50000
11	1.00000	0.79000	5.75000	-9.95929
12	1.00000	0.79000	9.95929	-5.75000

NOTE: The positions of the above rebars were computed by L-Pile

Minimum spacing between any two bars not equal to zero = 4.95284 inches between Bars 7 and 8

Spacing to aggregate size ratio = 6.60378

Concrete Properties:

 Compressive Strength of Concrete = 4.0000000 ksi
 Modulus of Elasticity of Concrete = 3604.99653259 ksi
 Modulus of Rupture of Concrete = -0.47434164 ksi
 Compression Strain at Peak Stress = 0.00188627
 Tensile Strain at Fracture of Concrete = -0.00011537
 Maximum Coarse Aggregate Size = 0.75000000 in

Number of Axial Thrust Force Values Determined from Pile-head Loadings = 1

Number	Axial Thrust Force kips
1	0.000

Definitions of Run Messages and Notes:

 C = concrete in section has cracked in tension.
 Y = stress in reinforcing steel has reached yield stress.
 T = ACI 318-08 criteria for tension-controlled section met, tensile strain in reinforcement exceeds 0.005 while simultaneously compressive strain in concrete more than than 0.003. See ACI 318-08, Section 10.3.4.
 Z = depth of tensile zone in concrete section is less than 10 percent of section depth.

Bending Stiffness (EI) = Computed Bending Moment / Curvature.
 Position of neutral axis is measured from edge of compression side of pile.
 Compressive stresses and strains are positive in sign.
 Tensile stresses and strains are negative in sign.

Axial Thrust Force = 0.000 kips

Bending Curvature rad/in.	Bending Moment in-kip	Bending Stiffness kip-in ²	Depth to N Axis in	Max Comp Strain in/in	Max Tens Strain in/in	Max Concrete Stress ksi	Max Steel Stress ksi	Run Msg
0.000001250	229.5318331	183625467.	15.0001048	0.0000188	-0.0000187	0.0783399	0.5383163	
0.000002500	457.6620743	183064830.	15.0001052	0.0000375	-0.0000375	0.1559051	1.0766326	
0.000003750	684.3907235	182504193.	15.0001057	0.0000563	-0.0000562	0.2326956	1.6149490	
0.000005000	909.7177808	181943556.	15.0001062	0.0000750	-0.0000750	0.3087113	2.1532653	
0.000006250	1133.6432461	181382919.	15.0001067	0.0000938	-0.0000937	0.3839523	2.6915818	
0.000007500	1356.1671194	180822283.	15.0001072	0.0001125	-0.0001125	0.4584185	3.2298982	
0.000008750	1356.1671194	154990528.	7.8562230	0.0000687	-0.0001938	0.2808684	-5.5809209	C
0.0000100	1356.1671194	135616712.	7.8596647	0.0000786	-0.0002214	0.3202979	-6.3771972	C
0.0000113	1356.1671194	120548188.	7.8631168	0.0000885	-0.0002490	0.3595526	-7.1732206	C
0.0000125	1356.1671194	108493370.	7.8665794	0.0000983	-0.0002767	0.3986320	-7.9689899	C
0.0000138	1356.1671194	98630336.	7.8700526	0.0001082	-0.0003043	0.4375358	-8.7645040	C
0.0000150	1356.1671194	90411141.	7.8735364	0.0001181	-0.0003319	0.4762635	-9.5597616	C
0.0000163	1356.1671194	83456438.	7.8770309	0.0001280	-0.0003595	0.5148147	-10.3547617	C
0.0000175	1356.1671194	77495264.	7.8805362	0.0001379	-0.0003871	0.5531890	-11.1495029	C
0.0000188	1356.1671194	72328913.	7.8840523	0.0001478	-0.0004147	0.5913860	-11.9439840	C
0.0000200	1356.1671194	67808356.	7.8875793	0.0001578	-0.0004422	0.6294052	-12.7382040	C
0.0000213	1356.1671194	63819629.	7.8911172	0.0001677	-0.0004698	0.6672463	-13.5321615	C
0.0000225	1356.1671194	60274094.	7.8946663	0.0001776	-0.0004974	0.7049087	-14.3258552	C
0.0000238	1356.1671194	57101773.	7.8982264	0.0001876	-0.0005249	0.7423921	-15.1192841	C
0.0000250	1356.1671194	54246685.	7.9017977	0.0001975	-0.0005525	0.7796959	-15.9124467	C
0.0000263	1356.1671194	51663509.	7.9053802	0.0002075	-0.0005800	0.8168199	-16.7053418	C
0.0000275	1356.1671194	49315168.	7.9089741	0.0002175	-0.0006075	0.8537635	-17.4979682	C
0.0000288	1356.1671194	47171030.	7.9125793	0.0002275	-0.0006350	0.8905263	-18.2903245	C
0.0000300	1356.1671194	45205571.	7.9161960	0.0002375	-0.0006625	0.9271078	-19.0824094	C
0.0000313	1356.1671194	43397348.	7.9198243	0.0002475	-0.0006900	0.9635076	-19.8742217	C
0.0000325	1356.1671194	41728219.	7.9234642	0.0002575	-0.0007175	0.9997253	-20.6657600	C
0.0000338	1379.1834683	40864695.	7.9271158	0.0002675	-0.0007450	1.0357603	-21.4570229	C
0.0000350	1429.6716529	40847762.	7.9307791	0.0002776	-0.0007724	1.0716122	-22.2480092	C
0.0000363	1480.1157946	40830781.	7.9344543	0.0002876	-0.0007999	1.1072806	-23.0387174	C
0.0000375	1530.5157056	40813752.	7.9381414	0.0002977	-0.0008273	1.1427649	-23.8291462	C
0.0000388	1580.8711970	40796676.	7.9418405	0.0003077	-0.0008548	1.1780648	-24.6192942	C
0.0000400	1631.1820782	40779552.	7.9455517	0.0003178	-0.0008822	1.2131797	-25.4091600	C
0.0000413	1681.4481568	40762380.	7.9492751	0.0003279	-0.0009096	1.2481091	-26.1987422	C
0.0000425	1731.6698079	40745172.	7.9528944	0.0003380	-0.0009370	1.2828354	-26.9881826	C
0.0000438	1781.8464540	40727919.	7.9564971	0.0003481	-0.0009644	1.3173701	-27.7773819	C
0.0000450	1831.9778721	40710619.	7.9601112	0.0003582	-0.0009918	1.3517167	-28.5663049	C
0.0000463	1882.0638444	40693272.	7.9637369	0.0003683	-0.0010192	1.3858749	-29.3549503	C
0.0000475	1932.1041791	40675877.	7.9673743	0.0003785	-0.0010465	1.4198441	-30.1433170	C
0.0000488	1982.0986829	40658435.	7.9710233	0.0003886	-0.0010739	1.4536238	-30.9314034	C
0.0000513	2081.9492926	40623401.	7.9783567	0.0004089	-0.0011286	1.5206129	-32.5067304	C
0.0000538	2181.6143285	40588174.	7.9857379	0.0004292	-0.0011833	1.5868384	-34.0809193	C
0.0000563	2281.0920743	40552748.	7.9931675	0.0004496	-0.0012379	1.6522961	-35.6539589	C
0.0000588	2380.3808976	40517122.	8.0006460	0.0004700	-0.0012925	1.7169821	-37.2258378	C

0.0000613	2479.4791381	40481292.	8.0081743	0.0004905	-0.0013470	1.7808922	-38.7965440	C
0.0000638	2578.3851071	40445257.	8.0157529	0.0005110	-0.0014015	1.8440222	-40.3660655	C
0.0000663	2677.0970869	40409013.	8.0233826	0.0005315	-0.0014560	1.9063679	-41.9343900	C
0.0000688	2775.6133296	40372558.	8.0310641	0.0005521	-0.0015104	1.9679249	-43.5015049	C
0.0000713	2873.9320568	40335889.	8.0387981	0.0005728	-0.0015647	2.0286889	-45.0673976	C
0.0000738	2972.0514583	40299003.	8.0465853	0.0005934	-0.0016191	2.0886555	-46.6320549	C
0.0000763	3069.9696919	40261898.	8.0544265	0.0006142	-0.0016733	2.1478201	-48.1954637	C
0.0000788	3167.6853225	40224576.	8.0623226	0.0006349	-0.0017276	2.2061784	-49.7576081	C
0.0000813	3265.1955930	40187023.	8.0702742	0.0006557	-0.0017818	2.2637253	-51.3184788	C
0.0000838	3362.4989671	40149241.	8.0782821	0.0006766	-0.0018359	2.3204562	-52.8780595	C
0.0000863	3459.5934642	40111229.	8.0863473	0.0006974	-0.0018901	2.3763664	-54.4363360	C
0.0000888	3556.4770666	40072981.	8.0944705	0.0007184	-0.0019441	2.4314509	-55.9932937	C
0.0000913	3653.1477187	40034496.	8.1026527	0.0007394	-0.0019981	2.4857049	-57.5489176	C
0.0000938	3749.6033259	39995769.	8.1108946	0.0007604	-0.0020521	2.5391232	-59.1031924	C
0.0000963	3845.8417533	39956797.	8.1191973	0.0007815	-0.0021060	2.5917008	-60.0000000	CY
0.0000988	3941.8608247	39917578.	8.1275615	0.0008026	-0.0021599	2.6434323	-60.0000000	CY
0.0001013	4037.6583216	39878107.	8.1359884	0.0008238	-0.0022137	2.6943125	-60.0000000	CY
0.0001038	4133.2319816	39838381.	8.1444788	0.0008450	-0.0022675	2.7443361	-60.0000000	CY
0.0001063	4228.5794973	39798395.	8.1530337	0.0008663	-0.0023212	2.7934974	-60.0000000	CY
0.0001088	4323.6985153	39758147.	8.1616541	0.0008876	-0.0023749	2.8417909	-60.0000000	CY
0.0001113	4417.5992610	39708757.	8.1697263	0.0009089	-0.0024286	2.8890581	-60.0000000	CY
0.0001138	4504.0367010	39659527.	8.1734277	0.0009297	-0.0024828	2.9343407	-60.0000000	CY
0.0001163	4582.1936791	39416720.	8.1723985	0.0009500	-0.0025375	2.9775421	-60.0000000	CY
0.0001188	4657.5694019	39221637.	8.1701899	0.0009702	-0.0025923	3.0195446	-60.0000000	CY
0.0001213	4730.3303514	39013034.	8.1668920	0.0009902	-0.0026473	3.0603720	-60.0000000	CY
0.0001238	4791.8705927	38722187.	8.1571228	0.0010094	-0.0027031	3.0986866	-60.0000000	CY
0.0001263	4839.2699976	38330851.	8.1392298	0.0010276	-0.0027599	3.1340847	-60.0000000	CY
0.0001288	4880.0234016	37903094.	8.1181776	0.0010452	-0.0028173	3.1678140	-60.0000000	CY
0.0001313	4920.0159034	37485835.	8.0977409	0.0010628	-0.0028747	3.2008269	-60.0000000	CY
0.0001338	4959.9098246	37083438.	8.0782910	0.0010805	-0.0029320	3.2332270	-60.0000000	CY
0.0001363	4999.7044132	36695078.	8.0597755	0.0010981	-0.0029894	3.2650113	-60.0000000	CY
0.0001388	5039.3989068	36319992.	8.0421456	0.0011158	-0.0030467	3.2961767	-60.0000000	CY
0.0001413	5078.9925321	35957469.	8.0253563	0.0011336	-0.0031039	3.3267202	-60.0000000	CY
0.0001438	5118.4845047	35606849.	8.0093653	0.0011513	-0.0031612	3.3566387	-60.0000000	CY
0.0001463	5157.8740290	35267515.	7.9941337	0.0011691	-0.0032184	3.3859288	-60.0000000	CY
0.0001488	5197.1602978	34938893.	7.9796249	0.0011870	-0.0032755	3.4145875	-60.0000000	CY
0.0001513	5239.2756736	34696225.	7.9243173	0.0012580	-0.0033504	3.5219452	-60.0000000	CY
0.0001538	5281.1812655	342226259.	7.8354749	0.0013222	-0.0034703	3.6095243	-60.0000000	CY
0.0001563	5300.6167175	30772681.	7.7419860	0.0013839	-0.0035978	3.6851548	-60.0000000	CY
0.0001588	5322.1817967	29468513.	7.6603790	0.0014459	-0.0042166	3.7530452	-60.0000000	CY
0.0001613	5346.2523722	28288062.	7.5851644	0.0015076	-0.0044549	3.8123691	-60.0000000	CY
0.0001638	5373.3557610	27216076.	7.5184758	0.0015695	-0.0046930	3.8637728	-60.0000000	CY
0.0001663	5401.5628129	26238001.	7.4597404	0.0016318	-0.0049307	3.9072278	-60.0000000	CY
0.0001688	5430.8468086	25341407.	7.4079712	0.0016946	-0.0051679	3.9425742	-60.0000000	CY
0.0001713	5461.1789221	24515933.	7.3623498	0.0017578	-0.0054047	3.9696439	-60.0000000	CY
0.0001738	5492.2941967	23751936.	7.3203004	0.0018209	-0.0056416	3.9881520	-60.0000000	CY
0.0001763	5524.6263086	23032372.	7.2801528	0.0018837	-0.0058788	3.9980783	-60.0000000	CY
0.0001788	5558.6866547	22320695.	7.2347352	0.0019463	-0.0061182	3.9955559	-60.0000000	CY
0.0001813	5602.0861437	21603896.	7.1808718	0.0020017	-0.0063608	3.9998867	-60.0000000	CY
0.0001838	5637.1430678	20907855.	7.1252930	0.0020574	-0.0066051	3.9976823	-60.0000000	CY
0.0001863	5672.8487746	20253887.	7.0738278	0.0021133	-0.0068492	3.9990680	-60.0000000	CY
0.0001888	5709.5983817	19639185.	7.0250475	0.0021690	-0.0070935	3.9980661	60.0000000	CY
0.0001913	5747.6217626	19060774.	6.9784043	0.0022244	-0.0073381	3.9989315	60.0000000	CY
0.0001938	5787.1239753	18515966.	6.9358195	0.0022802	-0.0075823	3.9971970	60.0000000	CY
0.0001963	5828.3185825	18002416.	6.8965664	0.0023362	-0.0078263	3.9999389	60.0000000	CY
0.0001988	5870.0408865	17516963.	6.8606647	0.0023927	-0.0080698	3.9946396	60.0000000	CY
0.0002013	5912.4636834	17057738.	6.8275324	0.0024494	-0.0083131	3.9990655	60.0000000	CY
0.0002038	5955.5593806	16622534.	6.7970047	0.0025064	-0.0085561	3.9963358	60.0000000	CY
0.0002063	6000.2719177	16209299.	6.7689820	0.0025638	-0.0087987	3.9958056	60.0000000	CY
0.0002088	6046.6678405	15816509.	6.7422894	0.0026211	-0.0090414	3.9993913	60.0000000	CY
0.0002113	6094.5348599	15442094.	6.7158906	0.0026780	-0.0092845	3.9955705	60.0000000	CY
0.0002138	6143.1077089	15085279.	6.6915448	0.0027352	-0.0095273	3.9943664	60.0000000	CY
0.0002163	6192.5137310	14745107.	6.6688526	0.0027926	-0.0097699	3.9985530	60.0000000	CY
0.0002188	6243.7488907	14420406.	6.6477099	0.0028502	-0.0100123	3.9999994	60.0000000	CY
0.0002213	6296.6487844	14109741.	6.6283609	0.0029082	-0.0102543	3.9894462	60.0000000	CY
0.0002238	6351.4105950	13812614.	6.6102836	0.0029664	-0.0104961	3.9953637	60.0000000	CY
0.0002263	6407.0352870	13528142.	6.5933958	0.0030247	-0.0107378	3.9988942	60.0000000	CYT
0.0002288	6464.5109775	13255490.	6.5776496	0.0030833	-0.0109792	3.9994702	60.0000000	CYT
0.0002313	6523.6998185	12993629.	6.5632699	0.0031422	-0.0112203	3.9890009	60.0000000	CYT
0.0002338	6584.7817328	12742264.	6.5498011	0.0032012	-0.0114613	3.9931614	60.0000000	CYT
0.0002363	6647.7544979	12500761.	6.5371953	0.0032604	-0.0117021	3.9974867	60.0000000	CYT
0.0002388	6713.6158097	12268532.	6.5254086	0.0033198	-0.0119427	3.9996974	60.0000000	CYT
0.0002413	6781.2914740	12044899.	6.5145571	0.0033794	-0.0121831	3.9953855	60.0000000	CYT
0.0002438	6851.7951987	11829400.	6.5045614	0.0034393	-0.0124232	3.9857598	60.0000000	CYT
0.0002463	6924.2149803	11621745.	6.4951914	0.0034993	-0.0126632	3.9920582	60.0000000	CYT
0.0002488	6998.5492044	11421502.	6.4864181	0.0035594	-0.0129031	3.9965482	60.0000000	CYT
0.0002513	6979.1508460	10314827.	6.4708570	0.0036191	-0.0131432	3.9974822	60.0000000	CYT

 Summary of Results for Nominal (Unfactored) Moment Capacity for Section 1

Moment values interpolated at maximum compressive strain = 0.003
 or maximum developed moment if pile fails at smaller strains.

Load No.	Axial Thrust kips	Nominal Mom. Cap. in-kip	Max. Comp. Strain
1	0.000	6202.805	0.00300000

Note note that the values of moment capacity in the table above are not factored by a strength reduction factor (phi-factor).

In ACI 318-08, the value of the strength reduction factor depends on whether the transverse reinforcing steel bars are tied hoops (0.65) or spirals (0.70).

The above values should be multiplied by the appropriate strength reduction factor to compute ultimate moment capacity according to ACI 318-08, Section 9.3.2.2 or the value required by the design standard being followed.

The following table presents factored moment capacities and corresponding bending stiffnesses computed for common resistance factor values used for reinforced concrete sections.

Axial Load No.	Resistance Factor for Moment	Nominal Moment Capacity in-kip	Ultimate (Factored) Axial Thrust kips	Ultimate (Factored) Moment Capacity in-kip	Bending Stiffness at Ult. Mom. Cap. kip-in ²
1	0.65	6202.805	0.000	4031.823	39880511.049
1	0.70	6202.805	0.000	4341.964	39748540.169
1	0.75	6202.805	0.000	4652.104	39235782.244

 p-y Curves Reported for Specified Depths

p-y Curve in Sand Computed Using Reese Criteria for Static Loading Conditions

```

Soil Layer Number           =          1
Depth below pile head       =        16.000 ft
Depth below ground surface  =         1.000 ft
Equivalent Depth (see note) =         1.000 ft
Ground Slope Angle         =         0.000 degrees
Pile Batter                 =         0.000 degrees
Effective Slope             =         0.000 degrees
Pile Diameter, b           =        30.000 in
Angle of Friction           =        24.000 degrees
Avg. Eff. Unit Weight      =       62.60000 pcf
kpy                         =       375.000 pci
K active                    =         0.422
K passive                   =         2.371
K0                          =         0.400
Pst                         =        31.216 lbs/in
Psd                         =       181.431 lbs/in
Ps = Pst (shallow controls) =        31.216 lbs/in
A (static)                  =         2.5500
B (static)                  =         1.8920
C = Pm/(Ym^(1/n))          =        71.6235
n = Pm/(m Ym)              =         3.5942
m = (Pu-Pm)/(Yu-Ym)        =        32.8645
Yk = [c/(kx)]^(n/(n-1))    =         0.0032 in
Pk                          =       14.518 lbs/in
Ym = b/60                  =         0.5000 in
Pm = B ps                  =        59.061 lbs/in
Yu = 3b/80                 =         1.1250 in
Pu = A Ps                  =       79.601 lbs/in
Es,lim                     =      4500.000 lbs/in/in
p-multiplier               =         1.00000
y-multiplier               =         1.00000
  
```

This p-y curve is computed using the equivalent depth.

This curve has the normal shape for a Reese sand p-y curve where $Y_k < Y_m < Y_u$.

y, in	p, lbs/in
0.0000	0.0000
0.00323	14.51836 *
0.04839	30.84018
0.09355	37.04877
0.13871	41.33991
0.18387	44.71218
0.22903	47.52955
0.27419	49.97006
0.31936	52.13541
0.36452	54.08973
0.40968	55.87632
0.45484	57.52590
0.50000	59.06116
0.81250	69.33130
1.12500	79.60145
1.15313	79.60145
1.18125	79.60145

* p value(s) computed using $p = k * \text{Eff} * x * y$

p-y Curve in Sand Computed Using Reese Criteria for Static Loading Conditions

```

Soil Layer Number          =          1
Depth below pile head      =         18.000 ft
Depth below ground surface =          3.000 ft
Equivalent Depth (see note) =          3.000 ft
Ground Slope Angle        =          0.000 degrees
Pile Batter               =          0.000 degrees
Effective Slope           =          0.000 degrees
Pile Diameter, b         =         30.000 in
Angle of Friction         =         24.000 degrees
Avg. Eff. Unit Weight     =        62.60000 pcf
kpy                      =        375.000 pci
K active                  =          0.422
K passive                 =          2.371
K0                       =          0.400
Pst                      =        128.402 lbs/in
Psd                      =        544.292 lbs/in
Ps = Pst (shallow controls) =        128.402 lbs/in
A (static)               =          1.9700
B (static)               =          1.4320
C = Pm/(Ym^(1/n))       =        226.4594
n = Pm/(m Ym)           =          3.3271
m = (Pu-Pm)/(Yu-Ym)     =        110.5280
Yk = [c/(kx)]^(n/(n-1)) =          0.0029 in
Pk                      =         39.093 lbs/in
Ym = b/60                =          0.5000 in
Pm = B ps                =        183.871 lbs/in
Yu = 3b/80              =          1.1250 in
Pu = A Ps                =        252.951 lbs/in
Es,lim                  =       13500.000 lbs/in/in
p-multiplier            =          1.00000
y-multiplier            =          1.00000

```

This p-y curve is computed using the equivalent depth.

This curve has the normal shape for a Reese sand p-y curve where $Y_k < Y_m < Y_u$.

y, in	p, lbs/in
0.0000	0.0000
0.00290	39.09338 *
0.04809	90.96256
0.09328	111.00669
0.13847	125.00204
0.18366	136.07686
0.22885	145.37816
0.27404	153.46954
0.31923	160.67431
0.36443	167.19694
0.40962	173.17587
0.45481	178.70959
0.50000	183.87099
0.81250	218.41100
1.12500	252.95101
1.15313	252.95101
1.18125	252.95101

* p value(s) computed using $p = k * \text{Eff} * x * y$

p-y Curve in Sand Computed Using Reese Criteria for Static Loading Conditions

```

Soil Layer Number          =          1
Depth below pile head      =         20.000 ft
Depth below ground surface =          5.000 ft
Equivalent Depth (see note) =          5.000 ft
Ground Slope Angle        =          0.000 degrees
Pile Batter               =          0.000 degrees
Effective Slope           =          0.000 degrees
Pile Diameter, b         =         30.000 in
Angle of Friction         =         24.000 degrees
Avg. Eff. Unit Weight     =        62.60000 pcf
kpy                      =        375.000 pci
K active                  =          0.422
K passive                 =          2.371
K0                       =          0.400
Pst                      =        271.924 lbs/in
Psd                      =        907.153 lbs/in
Ps = Pst (shallow controls) =        271.924 lbs/in
A (static)               =          1.4800
B (static)               =          1.0500
C = Pm/(Ym^(1/n))       =        358.3107
n = Pm/(m Ym)           =          3.0523
m = (Pu-Pm)/(Yu-Ym)     =        187.0836
Yk = [c/(kx)]^(n/(n-1)) =          0.0021 in
Pk                      =         47.667 lbs/in
Ym = b/60                =          0.5000 in
Pm = B ps                =        285.520 lbs/in
Yu = 3b/80              =          1.1250 in
Pu = A Ps                =        402.447 lbs/in
Es,lim                  =       22500.000 lbs/in/in
p-multiplier            =          1.00000

```


y-multiplier = 1.00000

This p-y curve is computed using the equivalent depth.

This curve has the normal shape for a Reese sand p-y curve where $Y_k < Y_m < Y_u$.

y, in	p, lbs/in
0.0000	0.0000
0.00212	47.66700 *
0.04738	131.93524
0.09264	164.34895
0.13790	187.22725
0.18317	205.47258
0.22843	220.88892
0.27369	234.36628
0.31895	246.41705
0.36421	257.36640
0.40948	267.43509
0.45474	276.78069
0.50000	285.52001
0.81250	343.98364
1.12500	402.44728
1.15313	402.44728
1.18125	402.44728

* p value(s) computed using $p = k * \text{Eff} x * y$

p-y Curve in Sand Computed Using Reese Criteria for Static Loading Conditions

Soil Layer Number	=	1
Depth below pile head	=	22.000 ft
Depth below ground surface	=	7.000 ft
Equivalent Depth (see note)	=	7.000 ft
Ground Slope Angle	=	0.000 degrees
Pile Batter	=	0.000 degrees
Effective Slope	=	0.000 degrees
Pile Diameter, b	=	30.000 in
Angle of Friction	=	24.000 degrees
Avg. Eff. Unit Weight	=	62.60000 pcf
kpy	=	375.000 pci
K active	=	0.422
K passive	=	2.371
K0	=	0.400
Pst	=	461.783 lbs/in
Psd	=	1270.014 lbs/in
Ps = Pst (shallow controls)	=	461.783 lbs/in
A (static)	=	1.1280
B (static)	=	0.7700
C = $P_m / (Y_m^{1/n})$	=	460.1467
n = $P_m / (m Y_m)$	=	2.6885
m = $(P_u - P_m) / (Y_u - Y_m)$	=	264.5094
$Y_k = [c / (kx)]^{n / (n-1)}$	=	0.0012 in
Pk	=	37.663 lbs/in
$Y_m = b / 60$	=	0.5000 in
$P_m = B ps$	=	355.573 lbs/in
$Y_u = 3b / 80$	=	1.1250 in
$P_u = A Ps$	=	520.891 lbs/in
Es,lim	=	31500.000 lbs/in/in
p-multiplier	=	1.00000
y-multiplier	=	1.00000

This p-y curve is computed using the equivalent depth.

This curve has the normal shape for a Reese sand p-y curve where $Y_k < Y_m < Y_u$.

y, in	p, lbs/in
0.0000	0.0000
0.00120	37.66329 *
0.04654	147.02873
0.09189	189.35699
0.13723	219.82444
0.18258	244.45249
0.22792	265.47782
0.27327	284.01302
0.31862	300.70315
0.36396	315.96006
0.40931	330.06486
0.45465	343.21914
0.50000	355.57303
0.81250	438.23221
1.12500	520.89139
1.15313	520.89139
1.18125	520.89139

* p value(s) computed using $p = k * \text{Eff} x * y$

p-y Curve in Sand Computed Using Reese Criteria for Static Loading Conditions

```

Soil Layer Number           =          1
Depth below pile head       =        24.000 ft
Depth below ground surface  =          9.000 ft
Equivalent Depth (see note) =          9.000 ft
Ground Slope Angle         =          0.000 degrees
Pile Batter                 =          0.000 degrees
Effective Slope             =          0.000 degrees
Pile Diameter, b           =        30.000 in
Angle of Friction           =        24.000 degrees
Avg. Eff. Unit Weight      =       62.60000 pcf
kpy                         =       375.000 pci
K active                    =          0.422
K passive                   =          2.371
K0                          =          0.400
Pst                         =       697.979 lbs/in
Psd                         =       1632.875 lbs/in
Ps = Pst (shallow controls) =       697.979 lbs/in
A (static)                  =          0.9640
B (static)                  =          0.6020
C = Pm/(Ym^(1/n))          =       586.4805
n = Pm/(m Ym)              =          2.0787
m = (Pu-Pm)/(Yu-Ym)        =       404.2697
Yk = [c/(kx)]^(n/(n-1))    =          0.0003 in
Pk                          =       11.569 lbs/in
Ym = b/60                   =          0.5000 in
Pm = B ps                   =       420.184 lbs/in
Yu = 3b/80                  =          1.1250 in
Pu = A Ps                   =       672.852 lbs/in
Es,lim                      =      40500.000 lbs/in/in
p-multiplier                =          1.00000
y-multiplier                =          1.00000
    
```

This p-y curve is computed using the equivalent depth.

This curve has the normal shape for a Reese sand p-y curve where $Y_k < Y_m < Y_u$.

y, in	p, lbs/in
0.0000	0.0000
0.0002856	11.56866 *
0.04571	132.93939
0.09114	185.27395
0.13657	225.06450
0.18200	258.40514
0.22743	287.64405
0.27286	313.98061
0.31829	338.12495
0.36371	360.53843
0.40914	381.54075
0.45457	401.36415
0.50000	420.18364
0.81250	546.51793
1.12500	672.85221
1.15313	672.85221
1.18125	672.85221

* p value(s) computed using $p = k * \text{Eff} * y$

 Summary of Pile Response(s)

Definitions of Pile-head Loading Conditions:

```

Load Type 1: Load 1 = Shear, lbs, and Load 2 = Moment, in-lbs
Load Type 2: Load 1 = Shear, lbs, and Load 2 = Slope, radians
Load Type 3: Load 1 = Shear, lbs, and Load 2 = Rotational Stiffness, in-lbs/radian
Load Type 4: Load 1 = Top Deflection, inches, and Load 2 = Moment, in-lbs
Load Type 5: Load 1 = Top Deflection, inches, and Load 2 = Slope, radians
    
```

Load Case No.	Load Type No.	Pile-head Condition 1 V(lbs) or y(inches)	Pile-head Condition 2 in-lb, rad., or in-lb/rad.	Axial Loading lbs	Pile-head Deflection inches	Maximum Moment in Pile in-lbs	Maximum Shear in Pile lbs	Pile-head Rotation radians
1	1	V = 0.000	M = 0.000	0.0000000	1.63765338	1740773.	15525.	-0.00591258

The analysis ended normally.

J.6: Test Wall Active Loading Hydrostatic with $\phi=24^0$ and Passive with $\phi=37^0$ with group reduction factor

LPILE Plus for Windows, Version 2013-07.001

Analysis of Individual Piles and Drilled Shafts
Subjected to Lateral Loading Using the p-y Method

© 1985-2013 by Ensoft, Inc.
All Rights Reserved

This copy of LPILE is licensed to:

The University of Texas at Austin
Geotech

Serial Number of Security Device: 226662924
Company Name Stored in Security Device: UT Austin - Prof. Gilbert

Files Used for Analysis

Path to file locations: C:\Users\Geotex\Desktop\LPILE Sensitivity Analysis\Excavation at 13.5feet\Final\
Name of input data file: Inundation Avg phi 37 - reduced strength.lp7d
Name of output report file: Inundation Avg phi 37 - reduced strength.lp7o
Name of plot output file: Inundation Avg phi 37 - reduced strength.lp7p
Name of runtime message file: Inundation Avg phi 37 - reduced strength.lp7r

Date and Time of Analysis

Date: October 21, 2013 Time: 11:07:57

Problem Title

Project Name:
Job Number:
Client:
Engineer:
Description:

Program Options

Engineering Units of Input Data and Computations:
- Engineering units are US Customary Units: pounds, inches, feet

Analysis Control Options:
- Maximum number of iterations allowed = 750
- Deflection tolerance for convergence = 1.0000E-05 in
- Maximum allowable deflection = 100.0000 in
- Number of pile increments = 100

Loading Type and Number of Cycles of Loading:

- Static loading specified

Computational Options:

- Use unfactored loads in computations
- No computation of pile-head foundation stiffness matrix
- Compute pile response under loading and nonlinear bending properties of pile (if nonlinear properties are specified)
- Push-over analysis of pile not selected
- Buckling analysis of pile not selected

Input Data Options:

- Analysis does not use p-y modification factors (individual pile or shaft only)
- Analysis assumes zero shear resistance at the pile tip
- Analysis includes loading by soil movements acting on pile

Output Options:

- p-y curves computed and reported at user-specified depths
- Only summary tables of pile-head deflection, maximum bending moment, and maximum shear force are to be written to output report file.

Pile Structural Properties and Geometry

Total number of pile sections = 1

Total length of pile = 35.00 ft

Depth of ground surface below top of pile = 13.50 ft

Pile diameter values used for p-y curve computations are defined using 2 points.

p-y curves are computed using pile diameter values interpolated with depth over the length of the pile.

Point	Depth X ft	Pile Diameter in
1	0.00000	24.0000000
2	35.000000	24.0000000

Input Structural Properties:

Pile Section No. 1:

Section Type = Drilled Shaft (Bored Pile)
Section Length = 35.00000 ft
Section Diameter = 24.00000 in

Ground Slope and Pile Batter Angles

Ground Slope Angle = 0.000 degrees
= 0.000 radians

Pile Batter Angle = 0.000 degrees
= 0.000 radians

Soil and Rock Layering Information

The soil profile is modelled using 12 layers

Layer 1 is modelled using user-specified p-y curves

Distance from top of pile to top of layer = 13.50000 ft
Distance from top of pile to bottom of layer = 15.00000 ft
Effective unit weight at top of layer = 62.60000 pcf
Effective unit weight at bottom of layer = 62.60000 pcf

User-input p-y curve at top of layer 1, Depth = 13.500 ft

Point No.	y in	p lbs/in
1	0.0000	0.0000
2	0.00813	0.0000
3	0.04375	0.0000
4	0.07938	0.0000
5	0.11500	0.0000
6	0.15063	0.0000
7	0.18625	0.0000
8	0.22188	0.0000
9	0.25750	0.0000
10	0.29313	0.0000
11	0.32875	0.0000
12	0.36438	0.0000
13	0.40000	0.0000
14	0.65000	0.0000
15	0.90000	0.0000
16	0.92250	0.0000
17	0.94500	0.0000

User-input p-y curve at bottom of layer 1, Depth = 15.000 ft

Point No.	y in	p lbs/in
1	0.0000	0.0000
2	0.00813	34.02412
3	0.04375	55.39559
4	0.07938	65.82539
5	0.11500	73.28632
6	0.15063	79.24359
7	0.18625	84.26855
8	0.22188	88.65008
9	0.25750	92.55668
10	0.29313	96.09608
11	0.32875	99.34179
12	0.36438	102.34639
13	0.40000	105.14898
14	0.65000	124.18188
15	0.90000	143.21479
16	0.92250	143.21479
17	0.94500	143.21479

Layer 2 is modelled using user-specified p-y curves

Distance from top of pile to top of layer = 15.00000 ft
Distance from top of pile to bottom of layer = 17.00000 ft
Effective unit weight at top of layer = 62.60000 pcf
Effective unit weight at bottom of layer = 62.60000 pcf

User-input p-y curve at top of layer 2, Depth = 15.000 ft

Point No.	y in	p lbs/in
1	0.0000	0.0000
2	0.00813	34.02412
3	0.04375	55.39559
4	0.07938	65.82539
5	0.11500	73.28632
6	0.15063	79.24359
7	0.18625	84.26855
8	0.22188	88.65008
9	0.25750	92.55668
10	0.29313	96.09608
11	0.32875	99.34179
12	0.36438	102.34639
13	0.40000	105.14898
14	0.65000	124.18188
15	0.90000	143.21479
16	0.92250	143.21479
17	0.94500	143.21479

User-input p-y curve at bottom of layer 2, Depth = 17.000 ft

Point No.	y in	p lbs/in
1	0.0000	0.0000
2	0.00764	74.63520
3	0.04331	129.39967
4	0.07898	156.56899
5	0.11465	176.21856
6	0.15032	192.03120
7	0.18599	205.45061
8	0.22166	217.21014
9	0.25732	227.73933
10	0.29299	237.31380
11	0.32866	246.12219
12	0.36433	254.29989
13	0.40000	261.94772
14	0.65000	313.88565
15	0.90000	365.82356
16	0.92250	365.82356
17	0.94500	365.82356

Layer 3 is modelled using user-specified p-y curves

Distance from top of pile to top of layer = 17.00000 ft
 Distance from top of pile to bottom of layer = 19.00000 ft
 Effective unit weight at top of layer = 62.60000 pcf
 Effective unit weight at bottom of layer = 62.60000 pcf

User-input p-y curve at top of layer 3, Depth = 17.000 ft

Point No.	y in	p lbs/in
1	0.0000	0.0000
2	0.00764	74.63520
3	0.04331	129.39967
4	0.07898	156.56899
5	0.11465	176.21856
6	0.15032	192.03120

7	0.18599	205.45061
8	0.22166	217.21014
9	0.25732	227.73933
10	0.29299	237.31380
11	0.32866	246.12219
12	0.36433	254.29989
13	0.40000	261.94772
14	0.65000	313.88565
15	0.90000	365.82356
16	0.92250	365.82356
17	0.94500	365.82356

User-input p-y curve at bottom of layer 3, Depth = 19.000 ft

Point No.	y in	p lbs/in
1	0.0000	0.0000
2	0.00489	75.00985
3	0.04081	163.39158
4	0.07673	205.98255
5	0.11265	237.14528
6	0.14857	262.49067
7	0.18448	284.19481
8	0.22040	303.36180
9	0.25632	320.63921
10	0.29224	336.44368
11	0.32816	351.06114
12	0.36408	364.69744
13	0.40000	377.50631
14	0.65000	464.06826
15	0.90000	550.63022
16	0.92250	550.63022
17	0.94500	550.63022

Layer 4 is modelled using user-specified p-y curves

Distance from top of pile to top of layer = 19.00000 ft
Distance from top of pile to bottom of layer = 21.00000 ft
Effective unit weight at top of layer = 62.60000 pcf
Effective unit weight at bottom of layer = 62.60000 pcf

User-input p-y curve at top of layer 4, Depth = 19.000 ft

Point No.	y in	p lbs/in
1	0.0000	0.0000
2	0.00489	75.00985
3	0.04081	163.39158
4	0.07673	205.98255
5	0.11265	237.14528
6	0.14857	262.49067
7	0.18448	284.19481
8	0.22040	303.36180
9	0.25632	320.63921
10	0.29224	336.44368
11	0.32816	351.06114
12	0.36408	364.69744
13	0.40000	377.50631
14	0.65000	464.06826
15	0.90000	550.63022
16	0.92250	550.63022
17	0.94500	550.63022

User-input p-y curve at bottom of layer 4, Depth = 21.000 ft

Point No.	y in	p lbs/in
1	0.0000	0.0000
2	0.00118	24.70043
3	0.03744	142.91673
4	0.07369	201.58082
5	0.10995	246.99731
6	0.14621	285.46090
7	0.18246	319.45055
8	0.21872	350.24829
9	0.25497	378.61972
10	0.29123	405.06563
11	0.32749	429.93483
12	0.36374	453.48191
13	0.40000	475.89943
14	0.65000	626.94580
15	0.90000	777.99212
16	0.92250	777.99212
17	0.94500	777.99212

Layer 5 is modelled using user-specified p-y curves

Distance from top of pile to top of layer = 21.00000 ft
 Distance from top of pile to bottom of layer = 23.00000 ft
 Effective unit weight at top of layer = 62.60000 pcf
 Effective unit weight at bottom of layer = 62.60000 pcf

User-input p-y curve at top of layer 5, Depth = 21.000 ft

Point No.	y in	p lbs/in
1	0.0000	0.0000
2	0.00118	24.70043
3	0.03744	142.91673
4	0.07369	201.58082
5	0.10995	246.99731
6	0.14621	285.46090
7	0.18246	319.45055
8	0.21872	350.24829
9	0.25497	378.61972
10	0.29123	405.06563
11	0.32749	429.93483
12	0.36374	453.48191
13	0.40000	475.89943
14	0.65000	626.94580
15	0.90000	777.99212
16	0.92250	777.99212
17	0.94500	777.99212

User-input p-y curve at bottom of layer 5, Depth = 23.000 ft

Point No.	y in	p lbs/in
1	0.0000	0.0000
2	0.0003939	10.43956
3	0.03672	155.13899
4	0.07305	233.59650
5	0.10938	297.02209
6	0.14571	352.29279
7	0.18203	402.19125

8	0.21836	448.18580
9	0.25469	491.16768
10	0.29102	531.72773
11	0.32734	570.28241
12	0.36367	607.13877
13	0.40000	642.53123
14	0.65000	881.50217
15	0.90000	1120.47311
16	0.92250	1120.47311
17	0.94500	1120.47311

Layer 6 is modelled using user-specified p-y curves

Distance from top of pile to top of layer = 23.00000 ft
Distance from top of pile to bottom of layer = 25.00000 ft
Effective unit weight at top of layer = 62.60000 pcf
Effective unit weight at bottom of layer = 62.60000 pcf

User-input p-y curve at top of layer 6, Depth = 23.000 ft

Point No.	y in	p lbs/in
1	0.0000	0.0000
2	0.0003939	10.43956
3	0.03672	155.13899
4	0.07305	233.59650
5	0.10938	297.02209
6	0.14571	352.29279
7	0.18203	402.19125
8	0.21836	448.18580
9	0.25469	491.16768
10	0.29102	531.72773
11	0.32734	570.28241
12	0.36367	607.13877
13	0.40000	642.53123
14	0.65000	881.50217
15	0.90000	1120.47311
16	0.92250	1120.47311
17	0.94500	1120.47311

User-input p-y curve at bottom of layer 6, Depth = 25.000 ft

Point No.	y in	p lbs/in
1	0.0000	0.0000
2	0.0004524	14.51489
3	0.03677	210.43497
4	0.07310	319.53248
5	0.10942	408.35061
6	0.14574	486.09694
7	0.18206	556.51927
8	0.21839	621.60289
9	0.25471	682.55639
10	0.29103	740.18285
11	0.32735	795.04944
12	0.36368	847.57509
13	0.40000	898.08011
14	0.65000	1239.35055
15	0.90000	1580.62099
16	0.92250	1580.62099
17	0.94500	1580.62099

Layer 7 is modelled using user-specified p-y curves

Distance from top of pile to top of layer = 25.00000 ft
 Distance from top of pile to bottom of layer = 27.00000 ft
 Effective unit weight at top of layer = 62.60000 pcf
 Effective unit weight at bottom of layer = 62.60000 pcf

User-input p-y curve at top of layer 7, Depth = 25.000 ft

Point No.	y in	p lbs/in
1	0.0000	0.0000
2	0.0004524	14.51489
3	0.03677	210.43497
4	0.07310	319.53248
5	0.10942	408.35061
6	0.14574	486.09694
7	0.18206	556.51927
8	0.21839	621.60289
9	0.25471	682.55639
10	0.29103	740.18285
11	0.32735	795.04944
12	0.36368	847.57509
13	0.40000	898.08011
14	0.65000	1239.35055
15	0.90000	1580.62099
16	0.92250	1580.62099
17	0.94500	1580.62099

User-input p-y curve at bottom of layer 7, Depth = 27.000 ft

Point No.	y in	p lbs/in
1	0.0000	0.0000
2	0.0006415	24.16210
3	0.03695	284.08343
4	0.07325	430.69497
5	0.10956	550.12496
6	0.14586	654.69241
7	0.18217	749.42165
8	0.21847	836.97675
9	0.25478	918.98043
10	0.29108	996.51131
11	0.32739	1070.33148
12	0.36369	1141.00386
13	0.40000	1208.95889
14	0.65000	1668.36327
15	0.90000	2127.76758
16	0.92250	2127.76758
17	0.94500	2127.76758

Layer 8 is modelled using user-specified p-y curves

Distance from top of pile to top of layer = 27.00000 ft
 Distance from top of pile to bottom of layer = 29.00000 ft
 Effective unit weight at top of layer = 62.60000 pcf
 Effective unit weight at bottom of layer = 62.60000 pcf

User-input p-y curve at top of layer 8, Depth = 27.000 ft

Point	y	p
-------	---	---

No.	in	lbs/in
1	0.0000	0.0000
2	0.0006415	24.16210
3	0.03695	284.08343
4	0.07325	430.69497
5	0.10956	550.12496
6	0.14586	654.69241
7	0.18217	749.42165
8	0.21847	836.97675
9	0.25478	918.98043
10	0.29108	996.51131
11	0.32739	1070.33148
12	0.36369	1141.00386
13	0.40000	1208.95889
14	0.65000	1668.36327
15	0.90000	2127.76758
16	0.92250	2127.76758
17	0.94500	2127.76758

User-input p-y curve at bottom of layer 8, Depth = 29.000 ft

Point No.	y in	p lbs/in
1	0.0000	0.0000
2	0.0008722	37.71628
3	0.03716	369.17263
4	0.07344	558.64825
5	0.10973	713.10683
6	0.14601	848.38332
7	0.18229	970.95205
8	0.21858	1084.24974
9	0.25486	1190.37123
10	0.29115	1290.70968
11	0.32743	1386.24944
12	0.36372	1477.71811
13	0.40000	1565.67199
14	0.65000	2160.62734
15	0.90000	2755.58268
16	0.92250	2755.58268
17	0.94500	2755.58268

Layer 9 is modelled using user-specified p-y curves

Distance from top of pile to top of layer = 29.00000 ft
Distance from top of pile to bottom of layer = 31.00000 ft
Effective unit weight at top of layer = 62.60000 pcf
Effective unit weight at bottom of layer = 62.60000 pcf

User-input p-y curve at top of layer 9, Depth = 29.000 ft

Point No.	y in	p lbs/in
1	0.0000	0.0000
2	0.0008722	37.71628
3	0.03716	369.17263
4	0.07344	558.64825
5	0.10973	713.10683
6	0.14601	848.38332
7	0.18229	970.95205
8	0.21858	1084.24974
9	0.25486	1190.37123
10	0.29115	1290.70968

11	0.32743	1386.24944
12	0.36372	1477.71811
13	0.40000	1565.67199
14	0.65000	2160.62734
15	0.90000	2755.58268
16	0.92250	2755.58268
17	0.94500	2755.58268

User-input p-y curve at bottom of layer 9, Depth = 31.000 ft

Point No.	y in	p lbs/in
1	0.0000	0.0000
2	0.00115	56.01213
3	0.03741	465.98636
4	0.07367	703.58902
5	0.10993	897.44591
6	0.14618	1067.28697
7	0.18244	1221.20265
8	0.21870	1363.49346
9	0.25496	1496.78273
10	0.29122	1622.81615
11	0.32748	1742.82769
12	0.36374	1857.72956
13	0.40000	1968.21945
14	0.65000	2716.14287
15	0.90000	3464.06623
16	0.92250	3464.06623
17	0.94500	3464.06623

Layer 10 is modelled using user-specified p-y curves

Distance from top of pile to top of layer = 31.00000 ft
Distance from top of pile to bottom of layer = 33.00000 ft
Effective unit weight at top of layer = 62.60000 pcf
Effective unit weight at bottom of layer = 62.60000 pcf

User-input p-y curve at top of layer 10, Depth = 31.000 ft

Point No.	y in	p lbs/in
1	0.0000	0.0000
2	0.00115	56.01213
3	0.03741	465.98636
4	0.07367	703.58902
5	0.10993	897.44591
6	0.14618	1067.28697
7	0.18244	1221.20265
8	0.21870	1363.49346
9	0.25496	1496.78273
10	0.29122	1622.81615
11	0.32748	1742.82769
12	0.36374	1857.72956
13	0.40000	1968.21945
14	0.65000	2716.14287
15	0.90000	3464.06623
16	0.92250	3464.06623
17	0.94500	3464.06623

User-input p-y curve at bottom of layer 10, Depth = 33.000 ft

Point No.	y in	p lbs/in
-----------	------	----------

-----	-----	-----
1	0.0000	0.0000
2	0.00147	79.94028
3	0.03770	574.86249
4	0.07393	865.75225
5	0.11016	1103.32119
6	0.14639	1311.54360
7	0.18262	1500.28375
8	0.21885	1674.79354
9	0.25508	1838.27948
10	0.29131	1992.87679
11	0.32754	2140.09548
12	0.36377	2281.05223
13	0.40000	2416.60128
14	0.65000	3334.90975
15	0.90000	4253.21823
16	0.92250	4253.21823
17	0.94500	4253.21823

Layer 11 is modelled using user-specified p-y curves

Distance from top of pile to top of layer = 33.00000 ft
Distance from top of pile to bottom of layer = 35.00000 ft
Effective unit weight at top of layer = 62.60000 pcf
Effective unit weight at bottom of layer = 62.60000 pcf

User-input p-y curve at top of layer 11, Depth = 33.000 ft

Point No.	y in	p lbs/in
-----	-----	-----
1	0.0000	0.0000
2	0.00147	79.94028
3	0.03770	574.86249
4	0.07393	865.75225
5	0.11016	1103.32119
6	0.14639	1311.54360
7	0.18262	1500.28375
8	0.21885	1674.79354
9	0.25508	1838.27948
10	0.29131	1992.87679
11	0.32754	2140.09548
12	0.36377	2281.05223
13	0.40000	2416.60128
14	0.65000	3334.90975
15	0.90000	4253.21823
16	0.92250	4253.21823
17	0.94500	4253.21823

User-input p-y curve at bottom of layer 11, Depth = 35.000 ft

Point No.	y in	p lbs/in
-----	-----	-----
1	0.0000	0.0000
2	0.00184	110.44456
3	0.03804	696.19527
4	0.07423	1045.41331
5	0.11043	1330.94272
6	0.14663	1581.31787
7	0.18282	1808.32498
8	0.21902	2018.25066
9	0.25521	2214.93735
10	0.29141	2400.94560
11	0.32761	2578.08729

12	0.36380	2747.70267
13	0.40000	2910.81748
14	0.65000	4016.92804
15	0.90000	5123.03867
16	0.92250	5123.03867
17	0.94500	5123.03867

Layer 12 is modelled using user-specified p-y curves

Distance from top of pile to top of layer = 35.00000 ft
Distance from top of pile to bottom of layer = 50.00000 ft
Effective unit weight at top of layer = 62.60000 pcf
Effective unit weight at bottom of layer = 62.60000 pcf

User-input p-y curve at top of layer 12, Depth = 35.000 ft

Point No.	y in	p lbs/in
1	0.0000	0.0000
2	0.00184	110.44456
3	0.03804	696.19527
4	0.07423	1045.41331
5	0.11043	1330.94272
6	0.14663	1581.31787
7	0.18282	1808.32498
8	0.21902	2018.25066
9	0.25521	2214.93735
10	0.29141	2400.94560
11	0.32761	2578.08729
12	0.36380	2747.70267
13	0.40000	2910.81748
14	0.65000	4016.92804
15	0.90000	5123.03867
16	0.92250	5123.03867
17	0.94500	5123.03867

User-input p-y curve at bottom of layer 12, Depth = 50.000 ft

Point No.	y in	p lbs/in
1	0.0000	0.0000
2	0.00184	110.44456
3	0.03804	696.19527
4	0.07423	1045.41331
5	0.11043	1330.94272
6	0.14663	1581.31787
7	0.18282	1808.32498
8	0.21902	2018.25066
9	0.25521	2214.93735
10	0.29141	2400.94560
11	0.32761	2578.08729
12	0.36380	2747.70267
13	0.40000	2910.81748
14	0.65000	4016.92804
15	0.90000	5123.03867
16	0.92250	5123.03867
17	0.94500	5123.03867

(Depth of lowest soil layer extends 15.00 ft below pile tip)

 Summary of Soil Properties

Layer Num.	Layer Soil Type (p-y Curve Criteria)	Layer Depth ft	Effective Unit Wt. pcf
1	User Input p-y Curves	13.500	62.600
		15.000	62.600
2	User Input p-y Curves	15.000	62.600
		17.000	62.600
3	User Input p-y Curves	17.000	62.600
		19.000	62.600
4	User Input p-y Curves	19.000	62.600
		21.000	62.600
5	User Input p-y Curves	21.000	62.600
		23.000	62.600
6	User Input p-y Curves	23.000	62.600
		25.000	62.600
7	User Input p-y Curves	25.000	62.600
		27.000	62.600
8	User Input p-y Curves	27.000	62.600
		29.000	62.600
9	User Input p-y Curves	29.000	62.600
		31.000	62.600
10	User Input p-y Curves	31.000	62.600
		33.000	62.600
11	User Input p-y Curves	33.000	62.600
		35.000	62.600
12	User Input p-y Curves	35.000	62.600
		50.000	62.600

 Lateral Soil Movements

Profile of soil movement with depth defined using 2 points

Point No.	Depth X ft	Soil Movement in
1	0.00000	0.00000
2	0.00000	0.00000

 Loading Type

Static loading criteria were used when computing p-y curves for all analyses.

 Distributed Lateral Loading

Distributed lateral load intensity defined using 2 points

Point No.	Depth X in	Dist. Load lbs/in
1	0.000	0.000
2	162.000	242.000

Pile-head Loading and Pile-head Fixity Conditions

Number of loads specified = 1

Load No.	Load Type	Condition 1	Condition 2	Axial Thrust Force, lbs	Compute Top y vs. Pile Length
1	1 V =	0.0000 lbs	M =	0.0000 in-lbs	0.0000000 No

V = perpendicular shear force applied to pile head
M = bending moment applied to pile head
y = lateral deflection relative to pile axis
S = pile slope relative to original pile batter angle
R = rotational stiffness applied to pile head
Axial thrust is assumed to be acting axially for all pile batter angles.

Specified Depths for Output of p-y Curves

Lateral load-transfer (p-y) curves are computed and output at 12 depths.
(Note that these curves are independent from the curves used at nodal point depths)

Depth No.	Depth Below Pile Head ft	Depth Below Ground Surface ft	Number of Specified y-Values
1	13.500	0.000	0
2	15.000	1.500	0
3	17.000	3.500	0
4	19.000	5.500	0
5	21.000	7.500	0
6	23.000	9.500	0
7	25.000	11.500	0
8	27.000	13.500	0
9	29.000	15.500	0
10	31.000	17.500	0
11	33.000	19.500	0
12	35.000	21.500	0

Depth of ground surface below top of pile = 13.50 ft
If number of specified y-values is 0 then 17 default y-values are used for output

Computations of Nominal Moment Capacity and Nonlinear Bending Stiffness

Axial thrust force values were determined from pile-head loading conditions

Number of Pile Sections Analyzed = 1

Pile Section No. 1:

Dimensions and Properties of Drilled Shaft (Bored Pile):

Length of Section = 35.00000 ft
Shaft Diameter = 24.00000 in

Concrete Cover Thickness = 2.00000 in
 Number of Reinforcing Bars = 12 bars
 Yield Stress of Reinforcing Bars = 60.00000 ksi
 Modulus of Elasticity of Reinforcing Bars = 29000. ksi
 Gross Area of Shaft = 452.38934 sq. in.
 Total Area of Reinforcing Steel = 7.20000 sq. in.
 Area Ratio of Steel Reinforcement = 1.59 percent
 Edge-to-Edge Bar Spacing = 4.07491 in
 Maximum Concrete Aggregate Size = 0.75000 in
 Ratio of Bar Spacing to Aggregate Size = 5.43
 Offset of Center of Rebar Cage from Center of Pile = 0.0000 in

Axial Structural Capacities:

Nom. Axial Structural Capacity = $0.85 F_c A_c + F_y A_s$ = 1945.644 kips
 Tensile Load for Cracking of Concrete = -209.248 kips
 Nominal Axial Tensile Capacity = -432.000 kips

Reinforcing Bar Dimensions and Positions Used in Computations:

Bar Number	Bar Diam. inches	Bar Area sq. in.	X inches	Y inches
1	0.87500	0.60000	9.56250	0.00000
2	0.87500	0.60000	8.28137	4.78125
3	0.87500	0.60000	4.78125	8.28137
4	0.87500	0.60000	0.00000	9.56250
5	0.87500	0.60000	-4.78125	8.28137
6	0.87500	0.60000	-8.28137	4.78125
7	0.87500	0.60000	-9.56250	0.00000
8	0.87500	0.60000	-8.28137	-4.78125
9	0.87500	0.60000	-4.78125	-8.28137
10	0.87500	0.60000	0.00000	-9.56250
11	0.87500	0.60000	4.78125	-8.28137
12	0.87500	0.60000	8.28137	-4.78125

NOTE: The positions of the above rebars were computed by LPile

Minimum spacing between any two bars not equal to zero = 4.07491 inches between Bars 7 and 8

Spacing to aggregate size ratio = 5.43322

Concrete Properties:

Compressive Strength of Concrete = 4.00000 ksi
 Modulus of Elasticity of Concrete = 3604.99653 ksi
 Modulus of Rupture of Concrete = -0.47434 ksi
 Compression Strain at Peak Stress = 0.00189
 Tensile Strain at Fracture of Concrete = -0.0001154
 Maximum Coarse Aggregate Size = 0.75000 in

Number of Axial Thrust Force Values Determined from Pile-head Loadings = 1

Number	Axial Thrust Force kips
1	0.000

Definitions of Run Messages and Notes:

C = concrete in section has cracked in tension.
 Y = stress in reinforcing steel has reached yield stress.
 T = ACI 318-08 criteria for tension-controlled section met, tensile strain in reinforcement exceeds 0.005 while simultaneously compressive strain in concrete more than than 0.003. See ACI 318-08, Section 10.3.4.
 Z = depth of tensile zone in concrete section is less than 10 percent of section depth.

Bending Stiffness (EI) = Computed Bending Moment / Curvature.
 Position of neutral axis is measured from edge of compression side of pile.
 Compressive stresses and strains are positive in sign.
 Tensile stresses and strains are negative in sign.

Axial Thrust Force = 0.000 kips

Bending Curvature rad/in.	Bending Moment in-kip	Bending Stiffness kip-in2	Depth to N Axis in	Max Comp Strain in/in	Max Tens Strain ksi	Max Concrete Stress ksi	Max Steel Stress ksi	Run
0.00001250	96.3241126	77059290.	11.9999599	0.0000150	-0.0000150	0.0627333	-0.4306514	
0.00002500	192.1913103	76876524.	11.9999598	0.0000300	-0.0000300	0.1249707	-0.8613029	
0.00003750	287.6015933	76693758.	11.9999596	0.0000450	-0.0000450	0.1867124	-1.2919544	
0.00005000	382.5549614	76510992.	11.9999595	0.0000600	-0.0000600	0.2479581	-1.7226058	
0.00006250	477.0514147	76328226.	11.9999593	0.0000750	-0.0000750	0.3087081	-2.1532573	
0.00007500	571.0909532	76145460.	11.9999592	0.0000900	-0.0000900	0.3689622	-2.5839088	
0.00008750	664.6735769	75962695.	11.9999590	0.0001050	-0.0001050	0.4287205	-3.0145603	
0.0000100	664.6735769	66467358.	6.6009075	0.0000660	-0.0001740	0.2701445	-5.0109368	C
0.0000113	664.6735769	59082096.	6.6031920	0.0000743	-0.0001957	0.3033533	-5.6365586	C
0.0000125	664.6735769	53173886.	6.6054820	0.0000826	-0.0002174	0.3364371	-6.2620127	C
0.0000138	664.6735769	48339897.	6.6077775	0.0000909	-0.0002391	0.3693956	-6.8872987	C
0.0000150	664.6735769	44311572.	6.6100786	0.0000992	-0.0002608	0.4022286	-7.5124158	C
0.0000163	664.6735769	40902989.	6.6123851	0.0001075	-0.0002825	0.4349359	-8.1373635	C
0.0000175	664.6735769	37981347.	6.6146973	0.0001158	-0.0003042	0.4675171	-8.7621411	C
0.0000188	664.6735769	35449257.	6.6170151	0.0001241	-0.0003259	0.4999722	-9.3867480	C
0.0000200	664.6735769	33233679.	6.6193385	0.0001324	-0.0003476	0.5323008	-10.0111836	C
0.0000213	664.6735769	31278757.	6.6216675	0.0001407	-0.0003693	0.5645027	-10.6354473	C
0.0000225	664.6735769	29541048.	6.6240023	0.0001490	-0.0003910	0.5965777	-11.2595385	C
0.0000238	664.6735769	27986256.	6.6263428	0.0001574	-0.0004126	0.6285255	-11.8834564	C
0.0000250	664.6735769	26586943.	6.6286890	0.0001657	-0.0004343	0.6603459	-12.5072004	C
0.0000263	664.6735769	25320898.	6.6310410	0.0001741	-0.0004559	0.6920386	-13.1307700	C
0.0000275	664.6735769	24169948.	6.6333988	0.0001824	-0.0004776	0.7236034	-13.7541644	C
0.0000288	664.6735769	23119081.	6.6357624	0.0001908	-0.0004992	0.7550400	-14.3773830	C
0.0000300	664.6735769	22155786.	6.6381319	0.0001991	-0.0005209	0.7863483	-15.0004252	C
0.0000313	664.6735769	21269554.	6.6405073	0.0002075	-0.0005425	0.8175278	-15.6232902	C
0.0000325	664.6735769	20451495.	6.6428886	0.0002159	-0.0005641	0.8485785	-16.2459774	C
0.0000338	669.6175849	19840521.	6.6452759	0.0002243	-0.0005857	0.8795000	-16.8684861	C
0.0000350	694.1816530	19833762.	6.6476692	0.0002327	-0.0006073	0.9102920	-17.4908157	C
0.0000363	718.7282930	19826987.	6.6500685	0.0002411	-0.0006289	0.9409544	-18.1129655	C
0.0000375	743.2574475	19820199.	6.6524738	0.0002495	-0.0006505	0.9714869	-18.7349347	C
0.0000388	767.7690589	19813395.	6.6548852	0.0002579	-0.0006721	1.0018891	-19.3567227	C
0.0000400	792.2630691	19806577.	6.6573027	0.0002663	-0.0006937	1.0321609	-19.9783288	C
0.0000413	816.7394195	19799744.	6.6597264	0.0002747	-0.0007153	1.0623020	-20.5997522	C
0.0000425	841.1980514	19792895.	6.6621562	0.0002831	-0.0007369	1.0923121	-21.2209924	C
0.0000438	865.6389055	19786032.	6.6645923	0.0002916	-0.0007584	1.1221910	-21.8420485	C
0.0000450	890.0619222	19779154.	6.6670346	0.0003000	-0.0007800	1.1519384	-22.4629198	C
0.0000463	914.4670416	19772260.	6.6694831	0.0003085	-0.0008015	1.1815540	-23.0836057	C
0.0000475	938.8542032	19765352.	6.6719380	0.0003169	-0.0008231	1.2110375	-23.7041054	C
0.0000488	963.2233462	19758428.	6.6743992	0.0003254	-0.0008446	1.2403887	-24.3244181	C
0.0000513	1011.9073029	19744533.	6.6793407	0.0003423	-0.0008877	1.2986931	-25.5644801	C
0.0000538	1060.5184714	19730576.	6.6843080	0.0003593	-0.0009307	1.3564649	-26.8037851	C
0.0000563	1109.0563252	19716557.	6.6893014	0.0003763	-0.0009737	1.4137020	-28.0423274	C
0.0000588	1157.5203567	19702474.	6.6943210	0.0003933	-0.0010167	1.4704021	-29.2801009	C
0.0000613	1205.9100513	19688327.	6.6993673	0.0004103	-0.0010597	1.5265628	-30.5170992	C
0.0000638	1254.2248875	19674116.	6.7044404	0.0004274	-0.0011026	1.5821820	-31.7533161	C
0.0000663	1302.4643368	19659839.	6.7095408	0.0004445	-0.0011455	1.6372573	-32.9887452	C
0.0000688	1350.6278632	19645496.	6.7146686	0.0004616	-0.0011884	1.6917862	-34.2233800	C
0.0000713	1398.7149235	19631087.	6.7198242	0.0004788	-0.0012312	1.7457666	-35.4572138	C
0.0000738	1446.7249668	19616610.	6.7250079	0.0004960	-0.0012740	1.7991958	-36.6902400	C

0.0005388	3738.0859759	6938443.	5.5479061	0.0029889	-0.0099411	3.9988671	60.0000000	CY
0.0005488	3741.6957192	6818580.	5.5326768	0.0030361	-0.0101339	3.9904891	60.0000000	CYT
0.0006088	3762.4651203	6180641.	5.4554862	0.0033210	-0.0112890	3.9889160	60.0000000	CYT
0.0006688	3780.6321105	5653282.	5.4009538	0.0036119	-0.0124381	3.9873440	60.0000000	CYT
0.0007288	3782.5161914	5190417.	5.3841027	0.0039237	-0.0135663	3.9918348	60.0000000	CYT

Summary of Results for Nominal (Unfactored) Moment Capacity for Section 1

Moment values interpolated at maximum compressive strain = 0.003
or maximum developed moment if pile fails at smaller strains.

Load No.	Axial Thrust kips	Nominal Mom. Cap. in-kip	Max. Comp. Strain
1	0.000	3738.934	0.00300000

Note note that the values of moment capacity in the table above are not factored by a strength reduction factor (phi-factor).

In ACI 318-08, the value of the strength reduction factor depends on whether the transverse reinforcing steel bars are tied hoops (0.65) or spirals (0.70).

The above values should be multiplied by the appropriate strength reduction factor to compute ultimate moment capacity according to ACI 318-08, Section 9.3.2.2 or the value required by the design standard being followed.

The following table presents factored moment capacities and corresponding bending stiffnesses computed for common resistance factor values used for reinforced concrete sections.

Axial Load No.	Resistance Factor for Moment	Nominal Moment Capacity in-kip	Ultimate (Factored) Axial Thrust kips	Ultimate (Factored) Moment Capacity in-kip	Bending Stiffness at Ult. Mom. Cap. kip-in ²
1	0.65	3738.934	0.000	2430.307	19297694.007
1	0.70	3738.934	0.000	2617.254	19231742.433
1	0.75	3738.934	0.000	2804.200	18981601.532

p-y Curves Reported for Specified Depths

p-y Curve Computed by Interpolation Between User-input Curves

Soil Layer Number	=	1
Depth below pile head	=	13.500 ft
Depth below ground surface	=	0.000 ft
Pile diameter	=	24.000 in
p-multiplier	=	1.000
y-multiplier	=	1.000

y, in	p, lbs/in
0.0000	0.0000
0.0048	0.0000
0.0300	0.0000
0.0600	0.0000
0.0900	0.0000
0.1200	0.0000
0.1500	0.0000
0.1800	0.0000

0.2100	0.0000
0.2400	0.0000
0.2700	0.0000
0.3000	0.0000
0.3300	0.0000
0.3600	0.0000
0.9600	0.0000
1.8000	0.0000
2.4000	0.0000

p-y Curve Computed by Interpolation Between User-input Curves

Soil Layer Number = 2
 Depth below pile head = 15.000 ft
 Depth below ground surface = 1.500 ft
 Pile diameter = 24.000 in
 p-multiplier = 1.000
 y-multiplier = 1.000

y, in	p, lbs/in
0.0000	0.0000
0.0048	20.0880
0.0300	47.1441
0.0600	60.1518
0.0900	68.0497
0.1200	74.1218
0.1500	79.1385
0.1800	83.3866
0.2100	87.1893
0.2400	90.6374
0.2700	93.7984
0.3000	96.7223
0.3300	99.4471
0.3600	101.9774
0.9600	143.2148
1.8000	143.2148
2.4000	143.2148

p-y Curve Computed by Interpolation Between User-input Curves

Soil Layer Number = 3
 Depth below pile head = 17.000 ft
 Depth below ground surface = 3.500 ft
 Pile diameter = 24.000 in
 p-multiplier = 1.000
 y-multiplier = 1.000

y, in	p, lbs/in
0.0000	0.0000
0.0048	46.8720
0.0300	108.9610
0.0600	142.1111
0.0900	162.6394
0.1200	178.5905
0.1500	191.8901
0.1800	203.1981
0.2100	213.3673
0.2400	222.6252

0.2700	231.1417
0.3000	239.0440
0.3300	246.4289
0.3600	253.3069
0.9600	365.8236
1.8000	365.8236
2.4000	365.8236

p-y Curve Computed by Interpolation Between User-input Curves

Soil Layer Number = 4
 Depth below pile head = 19.000 ft
 Depth below ground surface = 5.500 ft
 Pile diameter = 24.000 in
 p-multiplier = 1.000
 y-multiplier = 1.000

y, in	p, lbs/in
0.0000	0.0000
0.0048	73.6560
0.0300	136.7991
0.0600	186.1490
0.0900	217.4981
0.1200	242.3344
0.1500	263.3576
0.1800	281.4851
0.2100	297.8102
0.2400	312.7877
0.2700	326.6571
0.3000	339.6007
0.3300	351.7591
0.3600	363.1482
0.9600	550.6302
1.8000	550.6302
2.4000	550.6302

p-y Curve Computed by Interpolation Between User-input Curves

Soil Layer Number = 5
 Depth below pile head = 21.000 ft
 Depth below ground surface = 7.500 ft
 Pile diameter = 24.000 in
 p-multiplier = 1.000
 y-multiplier = 1.000

y, in	p, lbs/in
0.0000	0.0000
0.0048	36.5023
0.0300	118.6687
0.0600	179.4249
0.0900	222.0077
0.1200	257.6598
0.1500	289.0180
0.1800	317.1424
0.2100	342.8425
0.2400	366.9017
0.2700	389.5794
0.3000	411.0805

0.3300	431.5667
0.3600	451.0505
0.9600	777.9921
1.8000	777.9921
2.4000	777.9921

p-y Curve Computed by Interpolation Between User-input Curves

Soil Layer Number = 6
 Depth below pile head = 23.000 ft
 Depth below ground surface = 9.500 ft
 Pile diameter = 24.000 in
 p-multiplier = 1.000
 y-multiplier = 1.000

y, in	p, lbs/in
0.0000	0.0000
0.0048	27.9899
0.0300	128.3654
0.0600	205.4133
0.0900	263.1907
0.1200	313.1838
0.1500	358.1920
0.1800	399.3988
0.2100	437.6002
0.2400	473.7885
0.2700	508.2628
0.3000	541.2619
0.3300	572.9767
0.3600	603.4132
0.9600	1120.4731
1.8000	1120.4731
2.4000	1120.4731

p-y Curve Computed by Interpolation Between User-input Curves

Soil Layer Number = 7
 Depth below pile head = 25.000 ft
 Depth below ground surface = 11.500 ft
 Pile diameter = 24.000 in
 p-multiplier = 1.000
 y-multiplier = 1.000

y, in	p, lbs/in
0.0000	0.0000
0.0048	37.9655
0.0300	173.8918
0.0600	280.1934
0.0900	360.8638
0.1200	430.9967
0.1500	494.3516
0.1800	552.5157
0.2100	606.5740
0.2400	657.8713
0.2700	706.8144
0.3000	753.7287
0.3300	798.8744
0.3600	842.2571

0.9600	1580.6210
1.8000	1580.6210
2.4000	1580.6210

p-y Curve Computed by Interpolation Between User-input Curves

Soil Layer Number	=	8
Depth below pile head	=	27.000 ft
Depth below ground surface	=	13.500 ft
Pile diameter	=	24.000 in
p-multiplier	=	1.000
y-multiplier	=	1.000

y, in	p, lbs/in
0.0000	0.0000
0.0048	53.9341
0.0300	234.3489
0.0600	377.1789
0.0900	485.7888
0.1200	580.2018
0.1500	665.4874
0.1800	743.7646
0.2100	816.5420
0.2400	885.5994
0.2700	951.4858
0.3000	1014.6403
0.3300	1075.4134
0.3600	1133.8117
0.9600	2127.7676
1.8000	2127.7676
2.4000	2127.7676

p-y Curve Computed by Interpolation Between User-input Curves

Soil Layer Number	=	9
Depth below pile head	=	29.000 ft
Depth below ground surface	=	15.500 ft
Pile diameter	=	24.000 in
p-multiplier	=	1.000
y-multiplier	=	1.000

y, in	p, lbs/in
0.0000	0.0000
0.0048	73.5970
0.0300	303.7982
0.0600	488.4606
0.0900	629.1388
0.1200	751.4137
0.1500	861.8631
0.1800	963.2032
0.2100	1057.4642
0.2400	1146.9023
0.2700	1232.2313
0.3000	1314.0205
0.3300	1392.7248
0.3600	1468.3514
0.9600	2755.5827
1.8000	2755.5827

2.4000 2755.5827

p-y Curve Computed by Interpolation Between User-input Curves

Soil Layer Number = 10
Depth below pile head = 31.000 ft
Depth below ground surface = 17.500 ft
Pile diameter = 24.000 in
p-multiplier = 1.000
y-multiplier = 1.000

y, in	p, lbs/in
0.0000	0.0000
0.0048	97.3133
0.0300	382.2426
0.0600	614.0382
0.0900	790.9176
0.1200	944.6367
0.1500	1083.4829
0.1800	1210.8285
0.2100	1329.3396
0.2400	1441.7802
0.2700	1549.0510
0.3000	1651.8698
0.3300	1750.8091
0.3600	1845.8758
0.9600	3464.0662
1.8000	3464.0662
2.4000	3464.0662

p-y Curve Computed by Interpolation Between User-input Curves

Soil Layer Number = 11
Depth below pile head = 33.000 ft
Depth below ground surface = 19.500 ft
Pile diameter = 24.000 in
p-multiplier = 1.000
y-multiplier = 1.000

y, in	p, lbs/in
0.0000	0.0000
0.0048	125.4387
0.0300	469.6843
0.0600	753.9130
0.0900	971.1304
0.1200	1159.8766
0.1500	1330.3520
0.1800	1486.6367
0.2100	1632.1670
0.2400	1770.2329
0.2700	1901.9457
0.3000	2028.1888
0.3300	2149.6668
0.3600	2266.3849
0.9600	4253.2182
1.8000	4253.2182
2.4000	4253.2182

p-y Curve Computed by Interpolation Between User-input Curves

Soil Layer Number = 11
 Depth below pile head = 35.000 ft
 Depth below ground surface = 21.500 ft
 Pile diameter = 24.000 in
 p-multiplier = 1.000
 y-multiplier = 1.000

y, in	p, lbs/in
0.0000	0.0000
0.0048	158.3257
0.0300	566.1280
0.0600	908.0878
0.0900	1169.7836
0.1200	1397.1401
0.1500	1602.4768
0.1800	1790.6237
0.2100	1965.9452
0.2400	2132.2607
0.2700	2290.9159
0.3000	2442.9784
0.3300	2589.2986
0.3600	2729.8783
0.9600	5123.0387
1.8000	5123.0387
2.4000	5123.0387

 Summary of Pile Response(s)

Definitions of Pile-head Loading Conditions:

Load Type 1: Load 1 = Shear, lbs, and Load 2 = Moment, in-lbs
 Load Type 2: Load 1 = Shear, lbs, and Load 2 = Slope, radians
 Load Type 3: Load 1 = Shear, lbs, and Load 2 = Rotational Stiffness, in-lbs/radian
 Load Type 4: Load 1 = Top Deflection, inches, and Load 2 = Moment, in-lbs
 Load Type 5: Load 1 = Top Deflection, inches, and Load 2 = Slope, radians

Case No.	Load No.	Pile-head Condition 1 V(lbs) or y(inches)	Pile-head Condition 2 in-lb, rad., or in-lb/rad.	Axial Loading lbs	Maximum Pile-head Deflection in inches	Maximum Moment in Pile lbs	Shear in Pile lbs	Pile-head Rotation radians
1	1	V = 0.000	M = 0.000	0.0000000	3.84089091	2073167.	20385.	-0.01613249

The analysis ended normally.

J.7: Test Wall Active Loading Hydrostatic with $\phi=24^0$ and Passive with $\phi=30^0$ with group reduction factor

LPIle Plus for Windows, Version 2013-07.001

Analysis of Individual Piles and Drilled Shafts
Subjected to Lateral Loading Using the p-y Method

© 1985-2013 by Ensoft, Inc.
All Rights Reserved

This copy of LPIle is licensed to:

The University of Texas at Austin
Geotech

Serial Number of Security Device: 226662924
Company Name Stored in Security Device: UT Austin - Prof. Gilbert

Files Used for Analysis

Path to file locations: C:\Users\Geotex\Desktop\LPILE Sensitivity Analysis\Excavation at 13.5feet\Final\
Name of input data file: Inundation Avg phi 30 - reduced strength.lp7d
Name of output report file: Inundation Avg phi 30 - reduced strength.lp7o
Name of plot output file: Inundation Avg phi 30 - reduced strength.lp7p
Name of runtime messeage file: Inundation Avg phi 30 - reduced strength.lp7r

Date and Time of Analysis

Date: October 21, 2013 Time: 11:08:47

Problem Title

Project Name:
Job Number:
Client:
Engineer:
Description:

Program Options

Engineering Units of Input Data and Computations:
- Engineering units are US Customary Units: pounds, inches, feet

Analysis Control Options:
- Maximum number of iterations allowed = 750
- Deflection tolerance for convergence = 1.0000E-05 in
- Maximum allowable deflection = 100.0000 in
- Number of pile increments = 100

Loading Type and Number of Cycles of Loading:
- Static loading specified

Computational Options:
- Use unfactored loads in computations
- No computation of pile-head foundation stiffness matrix
- Compute pile response under loading and nonlinear bending properties of pile

- (if nonlinear properties are specified)
- Push-over analysis of pile not selected
 - Buckling analysis of pile not selected

Input Data Options:

- Analysis does not use p-y modification factors (individual pile or shaft only)
- Analysis assumes zero shear resistance at the pile tip
- Analysis includes loading by soil movements acting on pile

Output Options:

- p-y curves computed and reported at user-specified depths
- Only summary tables of pile-head deflection, maximum bending moment, and maximum shear force are to be written to output report file.

 Pile Structural Properties and Geometry

Total number of pile sections = 1

Total length of pile = 35.00 ft

Depth of ground surface below top of pile = 13.50 ft

Pile diameter values used for p-y curve computations are defined using 2 points.

p-y curves are computed using pile diameter values interpolated with depth over the length of the pile.

Point	Depth X ft	Pile Diameter in
1	0.00000	24.0000000
2	35.000000	24.0000000

Input Structural Properties:

Pile Section No. 1:

Section Type = Drilled Shaft (Bored Pile)
 Section Length = 35.00000 ft
 Section Diameter = 24.00000 in

 Ground Slope and Pile Batter Angles

Ground Slope Angle = 0.000 degrees
 = 0.000 radians

Pile Batter Angle = 0.000 degrees
 = 0.000 radians

 Soil and Rock Layering Information

The soil profile is modelled using 12 layers

Layer 1 is modelled using user-specified p-y curves

Distance from top of pile to top of layer = 13.50000 ft

Distance from top of pile to bottom of layer = 15.00000 ft
 Effective unit weight at top of layer = 62.60000 pcf
 Effective unit weight at bottom of layer = 62.60000 pcf

User-input p-y curve at top of layer 1, Depth = 13.500 ft

Point No.	y in	p lbs/in
1	0.0000	0.0000
2	0.00431	0.0000
3	0.04029	0.0000
4	0.07626	0.0000
5	0.11223	0.0000
6	0.14820	0.0000
7	0.18417	0.0000
8	0.22014	0.0000
9	0.25611	0.0000
10	0.29209	0.0000
11	0.32806	0.0000
12	0.36403	0.0000
13	0.40000	0.0000
14	0.65000	0.0000
15	0.90000	0.0000
16	0.92250	0.0000
17	0.94500	0.0000

User-input p-y curve at bottom of layer 1, Depth = 15.000 ft

Point No.	y in	p lbs/in
1	0.0000	0.0000
2	0.00431	18.05632
3	0.04029	34.48408
4	0.07626	41.48384
5	0.11223	46.39623
6	0.14820	50.28657
7	0.18417	53.55303
8	0.22014	56.39284
9	0.25611	58.91964
10	0.29209	61.20547
11	0.32806	63.29919
12	0.36403	65.23559
13	0.40000	67.04045
14	0.65000	79.17537
15	0.90000	91.31029
16	0.92250	91.31029
17	0.94500	91.31029

Layer 2 is modelled using user-specified p-y curves

Distance from top of pile to top of layer = 15.00000 ft
 Distance from top of pile to bottom of layer = 17.00000 ft
 Effective unit weight at top of layer = 62.60000 pcf
 Effective unit weight at bottom of layer = 62.60000 pcf

User-input p-y curve at top of layer 2, Depth = 15.000 ft

Point No.	y in	p lbs/in
1	0.0000	0.0000

2	0.00431	18.05632
3	0.04029	34.48408
4	0.07626	41.48384
5	0.11223	46.39623
6	0.14820	50.28657
7	0.18417	53.55303
8	0.22014	56.39284
9	0.25611	58.91964
10	0.29209	61.20547
11	0.32806	63.29919
12	0.36403	65.23559
13	0.40000	67.04045
14	0.65000	79.17537
15	0.90000	91.31029
16	0.92250	91.31029
17	0.94500	91.31029

User-input p-y curve at bottom of layer 2, Depth = 17.000 ft

Point No.	y in	p lbs/in
1	0.0000	0.0000
2	0.00364	35.55903
3	0.03967	75.85809
4	0.07571	93.11691
5	0.11174	105.35741
6	0.14777	115.12608
7	0.18380	123.37776
8	0.21984	130.58725
9	0.25587	137.02905
10	0.29190	142.87781
11	0.32793	148.25228
12	0.36397	153.23729
13	0.40000	157.89580
14	0.65000	189.20273
15	0.90000	220.50966
16	0.92250	220.50966
17	0.94500	220.50966

Layer 3 is modelled using user-specified p-y curves

Distance from top of pile to top of layer = 17.00000 ft
Distance from top of pile to bottom of layer = 19.00000 ft
Effective unit weight at top of layer = 62.60000 pcf
Effective unit weight at bottom of layer = 62.60000 pcf

User-input p-y curve at top of layer 3, Depth = 17.000 ft

Point No.	y in	p lbs/in
1	0.0000	0.0000
2	0.00364	35.55903
3	0.03967	75.85809
4	0.07571	93.11691
5	0.11174	105.35741
6	0.14777	115.12608
7	0.18380	123.37776
8	0.21984	130.58725
9	0.25587	137.02905
10	0.29190	142.87781
11	0.32793	148.25228
12	0.36397	153.23729
13	0.40000	157.89580

14	0.65000	189.20273
15	0.90000	220.50966
16	0.92250	220.50966
17	0.94500	220.50966

User-input p-y curve at bottom of layer 3, Depth = 19.000 ft

Point No.	y in	p lbs/in
1	0.0000	0.0000
2	0.00210	32.26810
3	0.03828	93.55825
4	0.07445	119.42233
5	0.11062	138.09643
6	0.14679	153.20072
7	0.18297	166.09552
8	0.21914	177.46076
9	0.25531	187.69173
10	0.29148	197.04120
11	0.32766	205.68189
12	0.36383	213.73775
13	0.40000	221.30111
14	0.65000	272.04531
15	0.90000	322.78951
16	0.92250	322.78951
17	0.94500	322.78951

Layer 4 is modelled using user-specified p-y curves

Distance from top of pile to top of layer = 19.00000 ft
Distance from top of pile to bottom of layer = 21.00000 ft
Effective unit weight at top of layer = 62.60000 pcf
Effective unit weight at bottom of layer = 62.60000 pcf

User-input p-y curve at top of layer 4, Depth = 19.000 ft

Point No.	y in	p lbs/in
1	0.0000	0.0000
2	0.00210	32.26810
3	0.03828	93.55825
4	0.07445	119.42233
5	0.11062	138.09643
6	0.14679	153.20072
7	0.18297	166.09552
8	0.21914	177.46076
9	0.25531	187.69173
10	0.29148	197.04120
11	0.32766	205.68189
12	0.36383	213.73775
13	0.40000	221.30111
14	0.65000	272.04531
15	0.90000	322.78951
16	0.92250	322.78951
17	0.94500	322.78951

User-input p-y curve at bottom of layer 4, Depth = 21.000 ft

Point No.	y in	p lbs/in
1	0.0000	0.0000
2	0.0003856	8.06777

3	0.03671	81.58535
4	0.07304	115.69696
5	0.10937	142.02254
6	0.14570	164.28957
7	0.18203	183.95291
8	0.21836	201.76188
9	0.25469	218.16285
10	0.29101	233.44731
11	0.32734	247.81809
12	0.36367	261.42304
13	0.40000	274.37396
14	0.65000	361.45787
15	0.90000	448.54179
16	0.92250	448.54179
17	0.94500	448.54179

Layer 5 is modelled using user-specified p-y curves

Distance from top of pile to top of layer = 21.00000 ft
Distance from top of pile to bottom of layer = 23.00000 ft
Effective unit weight at top of layer = 62.60000 pcf
Effective unit weight at bottom of layer = 62.60000 pcf

User-input p-y curve at top of layer 5, Depth = 21.000 ft

Point No.	y in	p lbs/in
1	0.0000	0.0000
2	0.0003856	8.06777
3	0.03671	81.58535
4	0.07304	115.69696
5	0.10937	142.02254
6	0.14570	164.28957
7	0.18203	183.95291
8	0.21836	201.76188
9	0.25469	218.16285
10	0.29101	233.44731
11	0.32734	247.81809
12	0.36367	261.42304
13	0.40000	274.37396
14	0.65000	361.45787
15	0.90000	448.54179
16	0.92250	448.54179
17	0.94500	448.54179

User-input p-y curve at bottom of layer 5, Depth = 23.000 ft

Point No.	y in	p lbs/in
1	0.0000	0.0000
2	0.0000984	2.60702
3	0.03645	88.07248
4	0.07281	132.93104
5	0.10916	169.15986
6	0.14552	200.71826
7	0.18187	229.20314
8	0.21823	255.45592
9	0.25458	279.98684
10	0.29094	303.13398
11	0.32729	325.13555
12	0.36365	346.16709
13	0.40000	366.36259
14	0.65000	502.62060

15	0.90000	638.87863
16	0.92250	638.87863
17	0.94500	638.87863

Layer 6 is modelled using user-specified p-y curves

Distance from top of pile to top of layer = 23.00000 ft
 Distance from top of pile to bottom of layer = 25.00000 ft
 Effective unit weight at top of layer = 62.60000 pcf
 Effective unit weight at bottom of layer = 62.60000 pcf

User-input p-y curve at top of layer 6, Depth = 23.000 ft

Point No.	y in	p lbs/in
1	0.0000	0.0000
2	0.0000984	2.60702
3	0.03645	88.07248
4	0.07281	132.93104
5	0.10916	169.15986
6	0.14552	200.71826
7	0.18187	229.20314
8	0.21823	255.45592
9	0.25458	279.98684
10	0.29094	303.13398
11	0.32729	325.13555
12	0.36365	346.16709
13	0.40000	366.36259
14	0.65000	502.62060
15	0.90000	638.87863
16	0.92250	638.87863
17	0.94500	638.87863

User-input p-y curve at bottom of layer 6, Depth = 25.000 ft

Point No.	y in	p lbs/in
1	0.0000	0.0000
2	0.0001058	3.39355
3	0.03646	118.42163
4	0.07281	180.33249
5	0.10917	230.67982
6	0.14552	274.73145
7	0.18188	314.62359
8	0.21823	351.48588
9	0.25458	386.00529
10	0.29094	418.63799
11	0.32729	449.70603
12	0.36365	479.44713
13	0.40000	508.04303
14	0.65000	701.09941
15	0.90000	894.15575
16	0.92250	894.15575
17	0.94500	894.15575

Layer 7 is modelled using user-specified p-y curves

Distance from top of pile to top of layer = 25.00000 ft
 Distance from top of pile to bottom of layer = 27.00000 ft
 Effective unit weight at top of layer = 62.60000 pcf
 Effective unit weight at bottom of layer = 62.60000 pcf

User-input p-y curve at top of layer 7, Depth = 25.000 ft

Point No.	y in	p lbs/in
1	0.0000	0.0000
2	0.0001058	3.39355
3	0.03646	118.42163
4	0.07281	180.33249
5	0.10917	230.67982
6	0.14552	274.73145
7	0.18188	314.62359
8	0.21823	351.48588
9	0.25458	386.00529
10	0.29094	418.63799
11	0.32729	449.70603
12	0.36365	479.44713
13	0.40000	508.04303
14	0.65000	701.09941
15	0.90000	894.15575
16	0.92250	894.15575
17	0.94500	894.15575

User-input p-y curve at bottom of layer 7, Depth = 27.000 ft

Point No.	y in	p lbs/in
1	0.0000	0.0000
2	0.0001477	5.56437
3	0.03650	158.57423
4	0.07285	241.39257
5	0.10920	308.75132
6	0.14555	367.69036
7	0.18190	421.06576
8	0.21825	470.38815
9	0.25460	516.57632
10	0.29095	560.24043
11	0.32730	601.81121
12	0.36365	641.60675
13	0.40000	679.87005
14	0.65000	938.22064
15	0.90000	1196.57129
16	0.92250	1196.57129
17	0.94500	1196.57129

Layer 8 is modelled using user-specified p-y curves

Distance from top of pile to top of layer = 27.00000 ft
 Distance from top of pile to bottom of layer = 29.00000 ft
 Effective unit weight at top of layer = 62.60000 pcf
 Effective unit weight at bottom of layer = 62.60000 pcf

User-input p-y curve at top of layer 8, Depth = 27.000 ft

Point No.	y in	p lbs/in
1	0.0000	0.0000
2	0.0001477	5.56437
3	0.03650	158.57423
4	0.07285	241.39257
5	0.10920	308.75132

6	0.14555	367.69036
7	0.18190	421.06576
8	0.21825	470.38815
9	0.25460	516.57632
10	0.29095	560.24043
11	0.32730	601.81121
12	0.36365	641.60675
13	0.40000	679.87005
14	0.65000	938.22064
15	0.90000	1196.57129
16	0.92250	1196.57129
17	0.94500	1196.57129

User-input p-y curve at bottom of layer 8, Depth = 29.000 ft

Point No.	y in	p lbs/in
1	0.0000	0.0000
2	0.0001985	8.58446
3	0.03654	204.57726
4	0.07289	311.29021
5	0.10924	398.09721
6	0.14558	474.05846
7	0.18193	542.85166
8	0.21827	606.42255
9	0.25462	665.95471
10	0.29096	722.23422
11	0.32731	775.81604
12	0.36365	827.11007
13	0.40000	876.42946
14	0.65000	1209.47263
15	0.90000	1542.51579
16	0.92250	1542.51579
17	0.94500	1542.51579

Layer 9 is modelled using user-specified p-y curves

Distance from top of pile to top of layer = 29.00000 ft
Distance from top of pile to bottom of layer = 31.00000 ft
Effective unit weight at top of layer = 62.60000 pcf
Effective unit weight at bottom of layer = 62.60000 pcf

User-input p-y curve at top of layer 9, Depth = 29.000 ft

Point No.	y in	p lbs/in
1	0.0000	0.0000
2	0.0001985	8.58446
3	0.03654	204.57726
4	0.07289	311.29021
5	0.10924	398.09721
6	0.14558	474.05846
7	0.18193	542.85166
8	0.21827	606.42255
9	0.25462	665.95471
10	0.29096	722.23422
11	0.32731	775.81604
12	0.36365	827.11007
13	0.40000	876.42946
14	0.65000	1209.47263
15	0.90000	1542.51579
16	0.92250	1542.51579
17	0.94500	1542.51579

User-input p-y curve at bottom of layer 9, Depth = 31.000 ft

Point No.	y in	p lbs/in
1	0.0000	0.0000
2	0.0002587	12.62963
3	0.03660	256.46456
4	0.07294	390.04868
5	0.10928	498.73514
6	0.14562	593.84953
7	0.18196	679.99213
8	0.21830	759.59746
9	0.25464	834.14676
10	0.29098	904.62383
11	0.32732	971.72346
12	0.36366	1035.95850
13	0.40000	1097.72116
14	0.65000	1514.85524
15	0.90000	1931.98925
16	0.92250	1931.98925
17	0.94500	1931.98925

Layer 10 is modelled using user-specified p-y curves

Distance from top of pile to top of layer = 31.00000 ft
 Distance from top of pile to bottom of layer = 33.00000 ft
 Effective unit weight at top of layer = 62.60000 pcf
 Effective unit weight at bottom of layer = 62.60000 pcf

User-input p-y curve at top of layer 10, Depth = 31.000 ft

Point No.	y in	p lbs/in
1	0.0000	0.0000
2	0.0002587	12.62963
3	0.03660	256.46456
4	0.07294	390.04868
5	0.10928	498.73514
6	0.14562	593.84953
7	0.18196	679.99213
8	0.21830	759.59746
9	0.25464	834.14676
10	0.29098	904.62383
11	0.32732	971.72346
12	0.36366	1035.95850
13	0.40000	1097.72116
14	0.65000	1514.85524
15	0.90000	1931.98925
16	0.92250	1931.98925
17	0.94500	1931.98925

User-input p-y curve at bottom of layer 10, Depth = 33.000 ft

Point No.	y in	p lbs/in
1	0.0000	0.0000
2	0.0003288	17.88715
3	0.03666	314.27634
4	0.07300	477.69566
5	0.10933	610.68612
6	0.14566	727.08001

7	0.18200	832.50004
8	0.21833	929.92293
9	0.25467	1021.16003
10	0.29100	1107.41467
11	0.32733	1189.53677
12	0.36367	1268.15370
13	0.40000	1343.74528
14	0.65000	1854.36848
15	0.90000	2364.99167
16	0.92250	2364.99167
17	0.94500	2364.99167

Layer 11 is modelled using user-specified p-y curves

Distance from top of pile to top of layer = 33.00000 ft
Distance from top of pile to bottom of layer = 35.00000 ft
Effective unit weight at top of layer = 62.60000 pcf
Effective unit weight at bottom of layer = 62.60000 pcf

User-input p-y curve at top of layer 11, Depth = 33.000 ft

Point No.	y in	p lbs/in
1	0.0000	0.0000
2	0.0003288	17.88715
3	0.03666	314.27634
4	0.07300	477.69566
5	0.10933	610.68612
6	0.14566	727.08001
7	0.18200	832.50004
8	0.21833	929.92293
9	0.25467	1021.16003
10	0.29100	1107.41467
11	0.32733	1189.53677
12	0.36367	1268.15370
13	0.40000	1343.74528
14	0.65000	1854.36848
15	0.90000	2364.99167
16	0.92250	2364.99167
17	0.94500	2364.99167

User-input p-y curve at bottom of layer 11, Depth = 35.000 ft

Point No.	y in	p lbs/in
1	0.0000	0.0000
2	0.0004094	24.55518
3	0.03674	378.05963
4	0.07306	574.26353
5	0.10939	733.97472
6	0.14572	873.76916
7	0.18204	1000.39058
8	0.21837	1117.41069
9	0.25469	1227.00331
10	0.29102	1330.61306
11	0.32735	1429.26002
12	0.36367	1523.69762
13	0.40000	1614.50170
14	0.65000	2228.01241
15	0.90000	2841.52305
16	0.92250	2841.52305
17	0.94500	2841.52305

Layer 12 is modelled using user-specified p-y curves

Distance from top of pile to top of layer = 35.00000 ft
 Distance from top of pile to bottom of layer = 50.00000 ft
 Effective unit weight at top of layer = 62.60000 pcf
 Effective unit weight at bottom of layer = 62.60000 pcf

User-input p-y curve at top of layer 12, Depth = 35.000 ft

Point No.	y in	p lbs/in
1	0.0000	0.0000
2	0.0004094	24.55518
3	0.03674	378.05963
4	0.07306	574.26353
5	0.10939	733.97472
6	0.14572	873.76916
7	0.18204	1000.39058
8	0.21837	1117.41069
9	0.25469	1227.00331
10	0.29102	1330.61306
11	0.32735	1429.26002
12	0.36367	1523.69762
13	0.40000	1614.50170
14	0.65000	2228.01241
15	0.90000	2841.52305
16	0.92250	2841.52305
17	0.94500	2841.52305

User-input p-y curve at bottom of layer 12, Depth = 50.000 ft

Point No.	y in	p lbs/in
1	0.0000	0.0000
2	0.0004094	24.55518
3	0.03674	378.05963
4	0.07306	574.26353
5	0.10939	733.97472
6	0.14572	873.76916
7	0.18204	1000.39058
8	0.21837	1117.41069
9	0.25469	1227.00331
10	0.29102	1330.61306
11	0.32735	1429.26002
12	0.36367	1523.69762
13	0.40000	1614.50170
14	0.65000	2228.01241
15	0.90000	2841.52305
16	0.92250	2841.52305
17	0.94500	2841.52305

(Depth of lowest soil layer extends 15.00 ft below pile tip)

 Summary of Soil Properties

Layer Num.	Layer Soil Type (p-y Curve Criteria)	Layer Depth ft	Effective Unit Wt. pcf
------------	--------------------------------------	----------------	------------------------

1	User Input p-y Curves		13.500	62.600
		15.000	62.600	
2	User Input p-y Curves		15.000	62.600
		17.000	62.600	
3	User Input p-y Curves		17.000	62.600
		19.000	62.600	
4	User Input p-y Curves		19.000	62.600
		21.000	62.600	
5	User Input p-y Curves		21.000	62.600
		23.000	62.600	
6	User Input p-y Curves		23.000	62.600
		25.000	62.600	
7	User Input p-y Curves		25.000	62.600
		27.000	62.600	
8	User Input p-y Curves		27.000	62.600
		29.000	62.600	
9	User Input p-y Curves		29.000	62.600
		31.000	62.600	
10	User Input p-y Curves		31.000	62.600
		33.000	62.600	
11	User Input p-y Curves		33.000	62.600
		35.000	62.600	
12	User Input p-y Curves		35.000	62.600
		50.000	62.600	

Lateral Soil Movements

Profile of soil movement with depth defined using 2 points

Point No.	Depth X ft	Soil Movement in
1	0.00000	0.00000
2	0.00000	0.00000

Loading Type

Static loading criteria were used when computing p-y curves for all analyses.

Distributed Lateral Loading

Distributed lateral load intensity defined using 2 points

Point No.	Depth X in	Dist. Load lbs/in
1	0.000	0.000
2	162.000	242.000

Pile-head Loading and Pile-head Fixity Conditions

Number of loads specified = 1

Load No.	Load Type	Condition 1	Condition 2	Axial Thrust Force, lbs	Compute Top y vs. Pile Length	
1	V =	0.0000 lbs	M =	0.0000 in-lbs	0.0000000	No

V = perpendicular shear force applied to pile head
M = bending moment applied to pile head
y = lateral deflection relative to pile axis
S = pile slope relative to original pile batter angle
R = rotational stiffness applied to pile head
Axial thrust is assumed to be acting axially for all pile batter angles.

Specified Depths for Output of p-y Curves

Lateral load-transfer (p-y) curves are computed and output at 12 depths.
(Note that these curves are independent from the curves used at nodal point depths)

Depth No.	Depth Below Pile Head ft	Depth Below Ground Surface ft	Number of Specified y-Values
1	13.500	0.000	0
2	15.000	1.500	0
3	17.000	3.500	0
4	19.000	5.500	0
5	21.000	7.500	0
6	23.000	9.500	0
7	25.000	11.500	0
8	27.000	13.500	0
9	29.000	15.500	0
10	31.000	17.500	0
11	33.000	19.500	0
12	35.000	21.500	0

Depth of ground surface below top of pile = 13.50 ft
If number of specified y-values is 0 then 17 default y-values are used for output

Computations of Nominal Moment Capacity and Nonlinear Bending Stiffness

Axial thrust force values were determined from pile-head loading conditions

Number of Pile Sections Analyzed = 1

Pile Section No. 1:

Dimensions and Properties of Drilled Shaft (Bored Pile):

Length of Section	=	35.00000 ft
Shaft Diameter	=	24.00000 in
Concrete Cover Thickness	=	2.00000 in
Number of Reinforcing Bars	=	12 bars
Yield Stress of Reinforcing Bars	=	60.00000 ksi
Modulus of Elasticity of Reinforcing Bars	=	29000. ksi
Gross Area of Shaft	=	452.38934 sq. in.
Total Area of Reinforcing Steel	=	7.20000 sq. in.
Area Ratio of Steel Reinforcement	=	1.59 percent

Edge-to-Edge Bar Spacing = 4.07491 in
 Maximum Concrete Aggregate Size = 0.75000 in
 Ratio of Bar Spacing to Aggregate Size = 5.43
 Offset of Center of Rebar Cage from Center of Pile = 0.0000 in

Axial Structural Capacities:

Nom. Axial Structural Capacity = $0.85 F_c A_c + F_y A_s$ = 1945.644 kips
 Tensile Load for Cracking of Concrete = -209.248 kips
 Nominal Axial Tensile Capacity = -432.000 kips

Reinforcing Bar Dimensions and Positions Used in Computations:

Bar Number	Bar Diam. inches	Bar Area sq. in.	X inches	Y inches
1	0.87500	0.60000	9.56250	0.00000
2	0.87500	0.60000	8.28137	4.78125
3	0.87500	0.60000	4.78125	8.28137
4	0.87500	0.60000	0.00000	9.56250
5	0.87500	0.60000	-4.78125	8.28137
6	0.87500	0.60000	-8.28137	4.78125
7	0.87500	0.60000	-9.56250	0.00000
8	0.87500	0.60000	-8.28137	-4.78125
9	0.87500	0.60000	-4.78125	-8.28137
10	0.87500	0.60000	0.00000	-9.56250
11	0.87500	0.60000	4.78125	-8.28137
12	0.87500	0.60000	8.28137	-4.78125

NOTE: The positions of the above rebars were computed by LPile

Minimum spacing between any two bars not equal to zero = 4.07491 inches between Bars 7 and 8

Spacing to aggregate size ratio = 5.43322

Concrete Properties:

Compressive Strength of Concrete = 4.00000 ksi
 Modulus of Elasticity of Concrete = 3604.99653 ksi
 Modulus of Rupture of Concrete = -0.47434 ksi
 Compression Strain at Peak Stress = 0.00189
 Tensile Strain at Fracture of Concrete = -0.0001154
 Maximum Coarse Aggregate Size = 0.75000 in

Number of Axial Thrust Force Values Determined from Pile-head Loadings = 1

Number	Axial Thrust Force kips
1	0.000

Definitions of Run Messages and Notes:

C = concrete in section has cracked in tension.
 Y = stress in reinforcing steel has reached yield stress.
 T = ACI 318-08 criteria for tension-controlled section met, tensile strain in reinforcement exceeds 0.005 while simultaneously compressive strain in concrete more than than 0.003. See ACI 318-08, Section 10.3.4.
 Z = depth of tensile zone in concrete section is less than 10 percent of section depth.

Bending Stiffness (EI) = Computed Bending Moment / Curvature.
 Position of neutral axis is measured from edge of compression side of pile.
 Compressive stresses and strains are positive in sign.
 Tensile stresses and strains are negative in sign.

Axial Thrust Force = 0.000 kips

Bending Curvature rad/in.	Bending Moment in-kip	Bending Stiffness kip-in2	Depth to N Axis in	Max Comp Strain in/in	Max Tens Strain ksi	Max Concrete Stress ksi	Max Steel Stress ksi	Run Msg
0.00001250	96.3241126	77059290.	11.9999599	0.0000150	-0.0000150	0.0627333	-0.4306514	
0.00002500	192.1913103	76876524.	11.9999598	0.0000300	-0.0000300	0.1249707	-0.8613029	
0.00003750	287.6015933	76693758.	11.9999596	0.0000450	-0.0000450	0.1867124	-1.2919544	
0.00005000	382.5549614	76510992.	11.9999595	0.0000600	-0.0000600	0.2479581	-1.7226058	
0.00006250	477.0514147	76328226.	11.9999593	0.0000750	-0.0000750	0.3087081	-2.1532573	
0.00007500	571.0909532	76145460.	11.9999592	0.0000900	-0.0000900	0.3689622	-2.5839088	
0.00008750	664.6735769	75962695.	11.9999590	0.0001050	-0.0001050	0.4287205	-3.0145603	
0.0000100	664.6735769	66467358.	6.6009075	0.0000660	-0.0001740	0.2701445	-5.0109368	C
0.0000113	664.6735769	59082096.	6.6031920	0.0000743	-0.0001957	0.3033533	-5.6365586	C
0.0000125	664.6735769	53173886.	6.6054820	0.0000826	-0.0002174	0.3364371	-6.2620127	C
0.0000138	664.6735769	48339897.	6.6077775	0.0000909	-0.0002391	0.3693956	-6.8872987	C
0.0000150	664.6735769	44311572.	6.6100786	0.0000992	-0.0002608	0.4022286	-7.5124158	C
0.0000163	664.6735769	40902989.	6.6123851	0.0001075	-0.0002825	0.4349359	-8.1373635	C
0.0000175	664.6735769	37981347.	6.6146973	0.0001158	-0.0003042	0.4675171	-8.7621411	C
0.0000188	664.6735769	35449257.	6.6170151	0.0001241	-0.0003259	0.4999722	-9.3867480	C
0.0000200	664.6735769	33233679.	6.6193385	0.0001324	-0.0003476	0.5323008	-10.0111836	C
0.0000213	664.6735769	31278757.	6.6216675	0.0001407	-0.0003693	0.5645027	-10.6354473	C
0.0000225	664.6735769	29541048.	6.6240023	0.0001490	-0.0003910	0.5965777	-11.2595385	C
0.0000238	664.6735769	27986256.	6.6263428	0.0001574	-0.0004126	0.6285255	-11.8834564	C
0.0000250	664.6735769	26586943.	6.6286890	0.0001657	-0.0004343	0.6603459	-12.5072004	C
0.0000263	664.6735769	25320898.	6.6310410	0.0001741	-0.0004559	0.6920386	-13.1307700	C
0.0000275	664.6735769	24169948.	6.6333988	0.0001824	-0.0004776	0.7236034	-13.7541644	C
0.0000288	664.6735769	23119081.	6.6357624	0.0001908	-0.0004992	0.7550400	-14.3773830	C
0.0000300	664.6735769	22155786.	6.6381319	0.0001991	-0.0005209	0.7863483	-15.0004252	C
0.0000313	664.6735769	21269554.	6.6405073	0.0002075	-0.0005425	0.8175278	-15.6232902	C
0.0000325	664.6735769	20451495.	6.6428886	0.0002159	-0.0005641	0.8485785	-16.2459774	C
0.0000338	669.6175849	19840521.	6.6452759	0.0002243	-0.0005857	0.8795000	-16.8684861	C
0.0000350	694.1816530	19833762.	6.6476692	0.0002327	-0.0006073	0.9102920	-17.4908157	C
0.0000363	718.7282930	19826987.	6.6500685	0.0002411	-0.0006289	0.9409544	-18.1129655	C
0.0000375	743.2574475	19820199.	6.6524738	0.0002495	-0.0006505	0.9714869	-18.7349347	C
0.0000388	767.7690589	19813395.	6.6548852	0.0002579	-0.0006721	1.0018891	-19.3567227	C
0.0000400	792.2630691	19806577.	6.6573027	0.0002663	-0.0006937	1.0321609	-19.9783288	C
0.0000413	816.7394195	19799744.	6.6597264	0.0002747	-0.0007153	1.0623020	-20.5997522	C
0.0000425	841.1980514	19792895.	6.6621562	0.0002831	-0.0007369	1.0923121	-21.2209924	C
0.0000438	865.6389055	19786032.	6.6645923	0.0002916	-0.0007584	1.1221910	-21.8420485	C
0.0000450	890.0619222	19779154.	6.6670346	0.0003000	-0.0007800	1.1519384	-22.4629198	C
0.0000463	914.4670416	19772260.	6.6694831	0.0003085	-0.0008015	1.1815540	-23.0836057	C
0.0000475	938.8542032	19765352.	6.6719380	0.0003169	-0.0008231	1.2110375	-23.7041054	C
0.0000488	963.2233462	19758428.	6.6743992	0.0003254	-0.0008446	1.2403887	-24.3244181	C
0.0000513	1011.9073029	19744533.	6.6793407	0.0003423	-0.0008877	1.2986931	-25.5644801	C
0.0000538	1060.5184714	19730576.	6.6843080	0.0003593	-0.0009307	1.3564649	-26.8037851	C
0.0000563	1109.0563252	19716557.	6.6893014	0.0003763	-0.0009737	1.4137020	-28.0423274	C
0.0000588	1157.5203567	19702474.	6.6943210	0.0003933	-0.0010167	1.4704021	-29.2801009	C
0.0000613	1205.9100513	19688327.	6.6993673	0.0004103	-0.0010597	1.5265628	-30.5170992	C
0.0000638	1254.2248875	19674116.	6.7044404	0.0004274	-0.0011026	1.5821820	-31.7533161	C
0.0000663	1302.4643368	19659839.	6.7095408	0.0004445	-0.0011455	1.6372573	-32.9887452	C
0.0000688	1350.6278632	19645496.	6.7146686	0.0004616	-0.0011884	1.6917862	-34.2233800	C
0.0000713	1398.7149235	19631087.	6.7198242	0.0004788	-0.0012312	1.7457666	-35.4572138	C
0.0000738	1446.7249668	19616610.	6.7250079	0.0004960	-0.0012740	1.7991958	-36.6902400	C
0.0000763	1494.6574344	19602065.	6.7302200	0.0005132	-0.0013168	1.8520715	-37.9224516	C
0.0000788	1542.5117598	19587451.	6.7354609	0.0005304	-0.0013596	1.9043913	-39.1538420	C
0.0000813	1590.2873684	19572768.	6.7407308	0.0005477	-0.0014023	1.9561525	-40.3844039	C
0.0000838	1637.9836775	19558014.	6.7460301	0.0005650	-0.0014450	2.0073528	-41.6141303	C
0.0000863	1685.6000958	19543190.	6.7513591	0.0005823	-0.0014877	2.0579894	-42.8430140	C
0.0000888	1733.1360235	19528293.	6.7567182	0.0005997	-0.0015303	2.1080599	-44.0710475	C
0.0000913	1780.5908520	19513324.	6.7621077	0.0006170	-0.0015730	2.1575615	-45.2982235	C

0.0000938	1827.9639638	19498282.	6.7675280	0.0006345	-0.0016155	2.2064917	-46.5245344	C
0.0000963	1875.2547322	19483166.	6.7729795	0.0006519	-0.0016581	2.2548476	-47.7499724	C
0.0000988	1922.4625211	19467975.	6.7784624	0.0006694	-0.0017006	2.3026267	-48.9745298	C
0.0001013	1969.5866849	19452708.	6.7839772	0.0006869	-0.0017431	2.3498261	-50.1981985	C
0.0001038	2016.6265683	19437365.	6.7895242	0.0007044	-0.0017856	2.3964429	-51.4209706	C
0.0001063	2063.5815058	19421944.	6.7951039	0.0007220	-0.0018280	2.4424745	-52.6428377	C
0.0001088	2110.4508218	19406444.	6.8007167	0.0007396	-0.0018704	2.4879178	-53.8637916	C
0.0001113	2157.2338302	19390866.	6.8063629	0.0007572	-0.0019128	2.5327699	-55.0838238	C
0.0001138	2203.9298343	19375207.	6.8120429	0.0007749	-0.0019551	2.5770280	-56.3029256	C
0.0001163	2250.5381264	19359468.	6.8177572	0.0007926	-0.0019974	2.6206889	-57.5210882	C
0.0001188	2297.0579876	19343646.	6.8235062	0.0008103	-0.0020397	2.6637497	-58.7383029	C
0.0001213	2343.4886874	19327742.	6.8292903	0.0008281	-0.0020819	2.7062072	-59.9545604	C
0.0001238	2389.8294839	19311753.	6.8351100	0.0008458	-0.0021242	2.7480583	-60.0000000	CY
0.0001263	2436.0806733	19295689.	6.8409302	0.0008637	-0.0021663	2.7892897	-60.0000000	CY
0.0001288	2482.2439853	19279565.	6.8466049	0.0008815	-0.0022085	2.8298539	-60.0000000	CY
0.0001313	2528.3160473	19263360.	6.8523138	0.0008994	-0.0022506	2.8698014	-60.0000000	CY
0.0001338	2574.2958079	19247071.	6.8580574	0.0009173	-0.0022927	2.9091286	-60.0000000	CY
0.0001363	2620.1825005	19230697.	6.8638362	0.0009352	-0.0023348	2.9478322	-60.0000000	CY
0.0001388	2665.1795524	19208501.	6.8689690	0.0009531	-0.0023769	2.9857072	-60.0000000	CY
0.0001413	2707.3949012	19167398.	6.8718545	0.0009706	-0.0024194	3.0222763	-60.0000000	CY
0.0001438	2746.2010562	19104007.	6.8720120	0.0009879	-0.0024621	3.0573965	-60.0000000	CY
0.0001463	2782.6868543	19026919.	6.8704415	0.0010048	-0.0025052	3.0913650	-60.0000000	CY
0.0001488	2818.9055263	18950625.	6.8689540	0.0010218	-0.0025482	3.1247191	-60.0000000	CY
0.0001513	2854.8294839	18874331.	6.8674635	0.0010387	-0.0025912	3.1580732	-60.0000000	CY
0.0001538	2890.7534419	18798037.	6.8659730	0.0010557	-0.0026342	3.1914273	-60.0000000	CY
0.0001563	2926.6773999	18721743.	6.8644825	0.0010726	-0.0026772	3.2247814	-60.0000000	CY
0.0001588	2962.6013579	18645449.	6.8630000	0.0010896	-0.0027202	3.2581355	-60.0000000	CY
0.0001613	2998.5253159	18569155.	6.8615195	0.0011065	-0.0027632	3.2914896	-60.0000000	CY
0.0001638	3034.4492739	18492861.	6.8600390	0.0011235	-0.0028062	3.3248437	-60.0000000	CY
0.0001663	3070.3732319	18416567.	6.8585585	0.0011404	-0.0028492	3.3581978	-60.0000000	CY
0.0001688	3106.2971899	18340273.	6.8570780	0.0011574	-0.0028922	3.3915519	-60.0000000	CY
0.0001713	3142.2211479	18263979.	6.8555975	0.0011743	-0.0029352	3.4249060	-60.0000000	CY
0.0001738	3178.1451059	18187685.	6.8541170	0.0011913	-0.0029782	3.4582601	-60.0000000	CY
0.0001763	3214.0690639	18111391.	6.8526365	0.0012082	-0.0030212	3.4916142	-60.0000000	CY
0.0001788	3250.0000000	18035097.	6.8511560	0.0012252	-0.0030642	3.5249683	-60.0000000	CY
0.0001813	3285.9249620	17958803.	6.8496755	0.0012421	-0.0031072	3.5583224	-60.0000000	CY
0.0001838	3321.8489240	17882509.	6.8481950	0.0012591	-0.0031502	3.5916765	-60.0000000	CY
0.0001863	3357.7728860	17806215.	6.8467145	0.0012760	-0.0031932	3.6250306	-60.0000000	CY
0.0001888	3393.6968480	17729921.	6.8452340	0.0012930	-0.0032362	3.6583847	-60.0000000	CY
0.0001913	3429.6208100	17653627.	6.8437535	0.0013100	-0.0032792	3.6917388	-60.0000000	CY
0.0001938	3465.5447720	17577333.	6.8422730	0.0013269	-0.0033222	3.7250929	-60.0000000	CY
0.0001963	3501.4687340	17501039.	6.8407925	0.0013439	-0.0033652	3.7584470	-60.0000000	CY
0.0001988	3537.3926960	17424745.	6.8393120	0.0013608	-0.0034082	3.7918011	-60.0000000	CY
0.0002013	3573.3166580	17348451.	6.8378315	0.0013778	-0.0034512	3.8251552	-60.0000000	CY
0.0002038	3609.2406200	17272157.	6.8363510	0.0013947	-0.0034942	3.8585093	-60.0000000	CY
0.0002063	3645.1645820	17195863.	6.8348705	0.0014117	-0.0035372	3.8918634	-60.0000000	CY
0.0002088	3681.0885440	17119569.	6.8333900	0.0014286	-0.0035802	3.9252175	-60.0000000	CY
0.0002113	3717.0125060	17043275.	6.8319095	0.0014456	-0.0036232	3.9585716	-60.0000000	CY
0.0002138	3752.9364680	16966981.	6.8304290	0.0014625	-0.0036662	3.9919257	-60.0000000	CY
0.0002163	3788.8604300	16890687.	6.8289485	0.0014795	-0.0037092	4.0252798	-60.0000000	CY
0.0002188	3824.7843920	16814393.	6.8274680	0.0014964	-0.0037522	4.0586339	-60.0000000	CY
0.0002213	3860.7083540	16738099.	6.8259875	0.0015134	-0.0037952	4.0919880	-60.0000000	CY
0.0002238	3896.6323160	16661805.	6.8245070	0.0015303	-0.0038382	4.1253421	-60.0000000	CY
0.0002263	3932.5562780	16585511.	6.8230265	0.0015473	-0.0038812	4.1586962	-60.0000000	CY
0.0002288	3968.4802400	16509217.	6.8215460	0.0015642	-0.0039242	4.1920503	-60.0000000	CY
0.0002313	4004.4042020	16432923.	6.8200655	0.0015812	-0.0039672	4.2254044	-60.0000000	CY
0.0002338	4040.3281640	16356629.	6.8185850	0.0015981	-0.0040102	4.2587585	-60.0000000	CY
0.0002363	4076.2521260	16280335.	6.8171045	0.0016151	-0.0040532	4.2921126	-60.0000000	CY
0.0002388	4112.1760880	16204041.	6.8156240	0.0016320	-0.0040962	4.3254667	-60.0000000	CY
0.0002413	4148.1000500	16127747.	6.8141435	0.0016490	-0.0041392	4.3588208	-60.0000000	CY
0.0002438	4184.0240120	16051453.	6.8126630	0.0016659	-0.0041822	4.3921749	-60.0000000	CY
0.0002463	4219.9479740	15975159.	6.8111825	0.0016829	-0.0042252	4.4255290	-60.0000000	CY
0.0002488	4255.8719360	15898865.	6.8097020	0.0016998	-0.0042682	4.4588831	-60.0000000	CY
0.0002513	4291.7958980	15822571.	6.8082215	0.0017168	-0.0043112	4.4922372	-60.0000000	CY
0.0002538	4327.7198600	15746277.	6.8067410	0.0017337	-0.0043542	4.5255913	-60.0000000	CY
0.0002563	4363.6438220	15669983.	6.8052605	0.0017507	-0.0043972	4.5589454	-60.0000000	CY
0.0002588	4399.5677840	15593689.	6.8037800	0.0017676	-0.0044402	4.5922995	-60.0000000	CY
0.0002613	4435.4917460	15517395.	6.8023000	0.0017846	-0.0044832	4.6256536	-60.0000000	CY
0.0002638	4471.4157080	15441101.	6.8008195	0.0018015	-0.0045262	4.6590077	-60.0000000	CY
0.0002663	4507.3396700	15364807.	6.7993390	0.0018185	-0.0045692	4.6923618	-60.0000000	CY
0.0002688	4543.2636320	15288513.	6.7978585	0.0018354	-0.0046122	4.7257159	-60.0000000	CY
0.0002713	4579.1875940	15212219.	6.7963780	0.0018524	-0.0046552	4.7590700	-60.0000000	CY
0.0002738	4615.1115560	15135925.	6.7948975	0.0018693	-0.0046982	4.7924241	-60.0000000	CY
0.0002763	4651.0355180	15059631.	6.7934170	0.0018863	-0.0047412	4.8257782	-60.0000000	CY
0.0002788	4686.9594800	14983337.	6.7919365	0.0019032	-0.0047842	4.8591323	-60.0000000	CY
0.0002813	4722.8834420	14907043.	6.7904560	0.0019202	-0.0048272	4.8924864	-60.0000000	CY
0.0002838	4758.8074040	14830749.	6.7889755	0.0019371	-0.0048702	4.9258405	-60.0000000	CY
0.0002863	4794.7313660	14754455.	6.7874950	0.0019541	-0.0049132	4.9591946	-60.0000000	CY
0.0002888	4830.6553280	14678161.	6.7860145	0.0019710	-0.0049562	4.9925487	-60.0000000	CY
0.0002913	4866.5792900	14601867.	6.7845340	0.0019880	-0.0050000	5.0259028	-60.0000000	CY
0.0002938	4902.5032520	14525573.	6.7830535	0.0020049	-0.0050430	5.0592569	-60.0000000	CY
0.0002963	4938.4272140	14449279.	6.7815730	0.0020219	-0.0050860	5.0926110	-60.0000000	CY
0.0002988	4974.3511760	14372985.	6.7800925	0.0020388	-0.0051290	5.1259651	-60.0000000	CY
0.0003013	5010.2751380	14296691.	6.7786120	0.0020558	-0.0051720	5.1593192	-60.0000000	CY
0.0003038	5046.1991000	14220397.	6.7771315	0.0020727	-0.0052150	5.1926733	-60.0000000	CY
0.0003063	5082.1230620	14144103.	6.7756510	0.0020897	-0.0052580	5.2260274	-60.0000000	CY
0.0003088	5118.0470240	14067809.	6.7741705	0.0021066	-0.0053010	5.2593815	-60.0000000	CY
0.0003113	5153.9709860	13991515.	6.7726900	0.0021236	-0.0053440	5.2927356	-60.0000000	CY
0.0003138	5189.8949480	13915221.	6.7712095	0.0021405	-0.0053870	5.3260897	-60.0000000	CY
0.0003163	5225.8189100	13838927.	6.7697290	0.0021575	-0.0054300	5.3594438	-60.0000000	CY
0.0003188	5261.7428720	13762633.	6.7682485	0.0021744	-0.0054730	5.3927979	-60.0000000	CY
0.0003213	5297.6668340	13686339.	6.7667680	0.0021914	-0.0055160	5.4261520	-60.0000000	CY
0.0003238	5333.5907960	13610045.	6.7652875	0.0022083	-0.0055590	5.4595061	-60.0000000	CY
0.0003263	5369.5147580	13533751.	6.7638070	0.0022253	-0.0056020	5.4928602	-60.0000000	CY
0.0003288	5405.4387200	13457457.	6.7623265	0.0022422	-0.0056450	5.5262143	-60.0000000	CY
0.0003313	5441.3626820	13381163.	6.7608460	0.0022592	-0.0056880	5.5595684	-60.0000000	CY
0.0003338	5477.2866440	13304869.	6.7593655	0.0022761	-0.0057310	5.5929225	-60.0000000	CY
0.0003363	5513.2106060	13228575.	6.7578850	0.0022931	-0.0057740	5.6262766	-60.0000000	CY
0.000								

 Summary of Results for Nominal (Unfactored) Moment Capacity for Section 1

Moment values interpolated at maximum compressive strain = 0.003
 or maximum developed moment if pile fails at smaller strains.

Load No.	Axial Thrust kips	Nominal Mom. Cap. in-kip	Max. Comp. Strain
1	0.000	3738.934	0.00300000

Note note that the values of moment capacity in the table above are not factored by a strength reduction factor (phi-factor).

In ACI 318-08, the value of the strength reduction factor depends on whether the transverse reinforcing steel bars are tied hoops (0.65) or spirals (0.70).

The above values should be multiplied by the appropriate strength reduction factor to compute ultimate moment capacity according to ACI 318-08, Section 9.3.2.2 or the value required by the design standard being followed.

The following table presents factored moment capacities and corresponding bending stiffnesses computed for common resistance factor values used for reinforced concrete sections.

Axial Load No.	Resistance Factor for Moment	Nominal Moment Capacity in-kip	Ultimate (Factored) Axial Thrust kips	Ultimate (Factored) Moment Capacity in-kip	Bending Stiffness at Ult. Mom. Cap. kip-in ²
1	0.65	3738.934	0.000	2430.307	19297694.007
1	0.70	3738.934	0.000	2617.254	19231742.433
1	0.75	3738.934	0.000	2804.200	18981601.532

 p-y Curves Reported for Specified Depths

p-y Curve Computed by Interpolation Between User-input Curves

Soil Layer Number = 1
 Depth below pile head = 13.500 ft
 Depth below ground surface = 0.000 ft
 Pile diameter = 24.000 in
 p-multiplier = 1.000
 y-multiplier = 1.000

y, in	p, lbs/in
0.0000	0.0000
0.0048	0.0000
0.0300	0.0000
0.0600	0.0000
0.0900	0.0000
0.1200	0.0000
0.1500	0.0000
0.1800	0.0000
0.2100	0.0000
0.2400	0.0000
0.2700	0.0000
0.3000	0.0000
0.3300	0.0000
0.3600	0.0000
0.9600	0.0000

1.8000 0.0000
 2.4000 0.0000

p-y Curve Computed by Interpolation Between User-input Curves

Soil Layer Number = 2
 Depth below pile head = 15.000 ft
 Depth below ground surface = 1.500 ft
 Pile diameter = 24.000 in
 p-multiplier = 1.000
 y-multiplier = 1.000

y, in	p, lbs/in
0.0000	0.0000
0.0048	18.2780
0.0300	29.7866
0.0600	38.3203
0.0900	43.3606
0.1200	47.2367
0.1500	50.4500
0.1800	53.1742
0.2100	55.5921
0.2400	57.7877
0.2700	59.8020
0.3000	61.6661
0.3300	63.4038
0.3600	65.0187
0.9600	91.3103
1.8000	91.3103
2.4000	91.3103

p-y Curve Computed by Interpolation Between User-input Curves

Soil Layer Number = 3
 Depth below pile head = 17.000 ft
 Depth below ground surface = 3.500 ft
 Pile diameter = 24.000 in
 p-multiplier = 1.000
 y-multiplier = 1.000

y, in	p, lbs/in
0.0000	0.0000
0.0048	36.8547
0.0300	65.0386
0.0600	85.5938
0.0900	97.9724
0.1200	107.5969
0.1500	115.6363
0.1800	122.5065
0.2100	128.6190
0.2400	134.1919
0.2700	139.3227
0.3000	144.0856
0.3300	148.5380
0.3600	152.6884
0.9600	220.5097
1.8000	220.5097
2.4000	220.5097

p-y Curve Computed by Interpolation Between User-input Curves

Soil Layer Number = 4
 Depth below pile head = 19.000 ft
 Depth below ground surface = 5.500 ft
 Pile diameter = 24.000 in
 p-multiplier = 1.000
 y-multiplier = 1.000

y, in	p, lbs/in
0.0000	0.0000
0.0048	36.8381
0.0300	79.5367
0.0600	109.0919
0.0900	127.4512
0.1200	142.0131
0.1500	154.3441
0.1800	165.0385
0.2100	174.5897
0.2400	183.3614
0.2700	191.4886
0.3000	199.0758
0.3300	206.2041
0.3600	212.8853
0.9600	322.7895
1.8000	322.7895
2.4000	322.7895

p-y Curve Computed by Interpolation Between User-input Curves

Soil Layer Number = 5
 Depth below pile head = 21.000 ft
 Depth below ground surface = 7.500 ft
 Pile diameter = 24.000 in
 p-multiplier = 1.000
 y-multiplier = 1.000

y, in	p, lbs/in
0.0000	0.0000
0.0048	17.0012
0.0300	67.9980
0.0600	103.4502
0.0900	127.9851
0.1200	148.5372
0.1500	166.6171
0.1800	182.8550
0.2100	197.6651
0.2400	211.5328
0.2700	224.6060
0.3000	237.0019
0.3300	248.8132
0.3600	260.0481
0.9600	448.5418
1.8000	448.5418
2.4000	448.5418

p-y Curve Computed by Interpolation Between User-input Curves

Soil Layer Number = 6
 Depth below pile head = 23.000 ft
 Depth below ground surface = 9.500 ft
 Pile diameter = 24.000 in
 p-multiplier = 1.000
 y-multiplier = 1.000

y, in	p, lbs/in
0.0000	0.0000
0.0048	13.6600
0.0300	72.9021
0.0600	117.1274
0.0900	150.0638
0.1200	178.5676
0.1500	204.2307
0.1800	227.7365
0.2100	249.5153
0.2400	270.1479
0.2700	289.8040
0.3000	308.6195
0.3300	326.7030
0.3600	344.0582
0.9600	638.8786
1.8000	638.8786
2.4000	638.8786

p-y Curve Computed by Interpolation Between User-input Curves

Soil Layer Number = 7
 Depth below pile head = 25.000 ft
 Depth below ground surface = 11.500 ft
 Pile diameter = 24.000 in
 p-multiplier = 1.000
 y-multiplier = 1.000

y, in	p, lbs/in
0.0000	0.0000
0.0048	18.2466
0.0300	97.9822
0.0600	158.5106
0.0900	204.1339
0.1200	243.8056
0.1500	279.6454
0.1800	312.5651
0.2100	343.1409
0.2400	372.1573
0.2700	399.8433
0.3000	426.3824
0.3300	451.9215
0.3600	476.4644
0.9600	894.1558
1.8000	894.1558
2.4000	894.1558

p-y Curve Computed by Interpolation Between User-input Curves

Soil Layer Number = 8
 Depth below pile head = 27.000 ft
 Depth below ground surface = 13.500 ft
 Pile diameter = 24.000 in
 p-multiplier = 1.000
 y-multiplier = 1.000

y, in	p, lbs/in
0.0000	0.0000
0.0048	25.1473
0.0300	131.2223
0.0600	212.1200
0.0900	273.1758
0.1200	326.2654
0.1500	374.2267
0.1800	418.2777
0.2100	459.1954
0.2400	498.0260
0.2700	535.0759
0.3000	570.5909
0.3300	604.7676
0.3600	637.6110
0.9600	1196.5713
1.8000	1196.5713
2.4000	1196.5713

p-y Curve Computed by Interpolation Between User-input Curves

Soil Layer Number = 9
 Depth below pile head = 29.000 ft
 Depth below ground surface = 15.500 ft
 Pile diameter = 24.000 in
 p-multiplier = 1.000
 y-multiplier = 1.000

y, in	p, lbs/in
0.0000	0.0000
0.0048	33.3979
0.0300	169.2884
0.0600	273.4453
0.0900	352.1561
0.1200	420.5952
0.1500	482.4228
0.1800	539.2053
0.2100	591.9542
0.2400	642.0118
0.2700	689.7736
0.3000	735.5565
0.3300	779.6141
0.3600	821.9526
0.9600	1542.5158
1.8000	1542.5158
2.4000	1542.5158

p-y Curve Computed by Interpolation Between User-input Curves

Soil Layer Number = 10
 Depth below pile head = 31.000 ft
 Depth below ground surface = 17.500 ft
 Pile diameter = 24.000 in
 p-multiplier = 1.000
 y-multiplier = 1.000

y, in	p, lbs/in
0.0000	0.0000
0.0048	43.1010
0.0300	212.1880
0.0600	342.4860
0.0900	441.0752
0.1200	526.7955
0.1500	604.2341
0.1800	675.3477
0.2100	741.4171
0.2400	804.1148
0.2700	863.9365
0.3000	921.2793
0.3300	976.4611
0.3600	1029.4893
0.9600	1931.9893
1.8000	1931.9893
2.4000	1931.9893

p-y Curve Computed by Interpolation Between User-input Curves

Soil Layer Number = 11
 Depth below pile head = 33.000 ft
 Depth below ground surface = 19.500 ft
 Pile diameter = 24.000 in
 p-multiplier = 1.000
 y-multiplier = 1.000

y, in	p, lbs/in
0.0000	0.0000
0.0048	54.3607
0.0300	259.9274
0.0600	419.2420
0.0900	539.9335
0.1200	644.8670
0.1500	739.6613
0.1800	826.7044
0.2100	907.5840
0.2400	984.3349
0.2700	1057.5646
0.3000	1127.7594
0.3300	1195.3085
0.3600	1260.2209
0.9600	2364.9917
1.8000	2364.9917
2.4000	2364.9917

p-y Curve Computed by Interpolation Between User-input Curves

Soil Layer Number = 11
 Depth below pile head = 35.000 ft
 Depth below ground surface = 21.500 ft
 Pile diameter = 24.000 in

p-multiplier = 1.000
y-multiplier = 1.000

y, in	p, lbs/in
0.0000	0.0000
0.0048	67.2820
0.0300	312.5115
0.0600	503.7128
0.0900	648.7315
0.1200	774.8103
0.1500	888.7051
0.1800	993.2747
0.2100	1090.4548
0.2400	1182.6723
0.2700	1270.6580
0.3000	1354.9969
0.3300	1436.1566
0.3600	1514.1474
0.9600	2841.5231
1.8000	2841.5231
2.4000	2841.5231

Summary of Pile Response(s)

Definitions of Pile-head Loading Conditions:

Load Type 1: Load 1 = Shear, lbs, and Load 2 = Moment, in-lbs
Load Type 2: Load 1 = Shear, lbs, and Load 2 = Slope, radians
Load Type 3: Load 1 = Shear, lbs, and Load 2 = Rotational Stiffness, in-lbs/radian
Load Type 4: Load 1 = Top Deflection, inches, and Load 2 = Moment, in-lbs
Load Type 5: Load 1 = Top Deflection, inches, and Load 2 = Slope, radians

Case No.	Load Type	Pile-head V(lbs) or y(inches)	Pile-head Condition 1 in-lb, rad., or in-lb/rad.	Condition 2	Axial Loading lbs	Maximum Pile-head Deflection inches	Maximum Moment in Pile lbs	Shear in Pile lbs	Pile-head Rotation radians
1	1	V = 0.000	M = 0.000	0.0000000	5.33020905	2304168.	-22786.	-0.02079245	

The analysis ended normally.

J.8: Test Wall Active Loading Hydrostatic with $\phi=24^0$ and Passive with $\phi=24^0$ with group reduction factor

=====

LPile Plus for Windows, Version 2013-07.001

Analysis of Individual Piles and Drilled Shafts
Subjected to Lateral Loading Using the p-y Method

© 1985-2013 by Ensoft, Inc.
All Rights Reserved

=====
=====
This copy of LPILE is licensed to:

The University of Texas at Austin
Geotech

Serial Number of Security Device: 226662924
Company Name Stored in Security Device: UT Austin - Prof. Gilbert

Files Used for Analysis

Path to file locations: C:\Users\Geotex\Desktop\LPILE Sensitivity Analysis\Excavation at 13.5feet\Final\
Name of input data file: Inundation Avg phi E,C - reduced strength - updated.lp7d
Name of output report file: Inundation Avg phi E,C - reduced strength - updated.lp7o
Name of plot output file: Inundation Avg phi E,C - reduced strength - updated.lp7p
Name of runtime message file: Inundation Avg phi E,C - reduced strength - updated.lp7r

Date and Time of Analysis

Date: October 21, 2013 Time: 11:04:28

Problem Title

Project Name:
Job Number:
Client:
Engineer:
Description:

Program Options

Engineering Units of Input Data and Computations:
- Engineering units are US Customary Units: pounds, inches, feet

Analysis Control Options:
- Maximum number of iterations allowed = 750
- Deflection tolerance for convergence = 1.0000E-05 in
- Maximum allowable deflection = 100.0000 in
- Number of pile increments = 100

Loading Type and Number of Cycles of Loading:
- Static loading specified

Computational Options:
- Use unfactored loads in computations
- No computation of pile-head foundation stiffness matrix
- Compute pile response under loading and nonlinear bending properties of pile (if nonlinear properties are specified)
- Push-over analysis of pile not selected
- Buckling analysis of pile not selected

Input Data Options:
- Analysis does not use p-y modification factors (individual pile or shaft only)
- Analysis assumes zero shear resistance at the pile tip

- Analysis includes loading by soil movements acting on pile

Output Options:

- p-y curves computed and reported at user-specified depths
- Only summary tables of pile-head deflection, maximum bending moment, and maximum shear force are to be written to output report file.

Pile Structural Properties and Geometry

Total number of pile sections = 1

Total length of pile = 35.00 ft

Depth of ground surface below top of pile = 13.50 ft

Pile diameter values used for p-y curve computations are defined using 2 points.

p-y curves are computed using pile diameter values interpolated with depth over the length of the pile.

Point	Depth X ft	Pile Diameter in
1	0.00000	24.0000000
2	35.000000	24.0000000

Input Structural Properties:

Pile Section No. 1:

Section Type = Drilled Shaft (Bored Pile)
Section Length = 35.00000 ft
Section Diameter = 24.00000 in

Ground Slope and Pile Batter Angles

Ground Slope Angle = 0.000 degrees
= 0.000 radians

Pile Batter Angle = 0.000 degrees
= 0.000 radians

Soil and Rock Layering Information

The soil profile is modelled using 12 layers

Layer 1 is modelled using user-specified p-y curves

Distance from top of pile to top of layer = 13.50000 ft
Distance from top of pile to bottom of layer = 15.00000 ft
Effective unit weight at top of layer = 62.60000 pcf
Effective unit weight at bottom of layer = 62.60000 pcf

User-input p-y curve at top of layer 1, Depth = 13.500 ft

Point No.	y in	p lbs/in
1	0.0000	0.0000
2	0.00222	0.0000
3	0.03838	0.0000
4	0.07455	0.0000
5	0.11071	0.0000
6	0.14687	0.0000
7	0.18303	0.0000
8	0.21919	0.0000
9	0.25535	0.0000
10	0.29152	0.0000
11	0.32768	0.0000
12	0.36384	0.0000
13	0.40000	0.0000
14	0.65000	0.0000
15	0.90000	0.0000
16	0.92250	0.0000
17	0.94500	0.0000

User-input p-y curve at bottom of layer 1, Depth = 15.000 ft

Point No.	y in	p lbs/in
1	0.0000	0.0000
2	0.00250	10.45953
3	0.03864	23.11604
4	0.07477	27.98727
5	0.11091	31.37255
6	0.14705	34.04264
7	0.18318	36.27951
8	0.21932	38.22145
9	0.25545	39.94762
10	0.29159	41.50805
11	0.32773	42.93653
12	0.36386	44.25711
13	0.40000	45.48753
14	0.65000	53.72118
15	0.90000	61.95483
16	0.92250	61.95483
17	0.94500	61.95483

Layer 2 is modelled using user-specified p-y curves

Distance from top of pile to top of layer = 15.00000 ft
Distance from top of pile to bottom of layer = 17.00000 ft
Effective unit weight at top of layer = 62.60000 pcf
Effective unit weight at bottom of layer = 62.60000 pcf

User-input p-y curve at top of layer 2, Depth = 15.000 ft

Point No.	y in	p lbs/in
1	0.0000	0.0000
2	0.00250	10.45953
3	0.03864	23.11604
4	0.07477	27.98727
5	0.11091	31.37255
6	0.14705	34.04264
7	0.18318	36.27951
8	0.21932	38.22145

9	0.25545	39.94762
10	0.29159	41.50805
11	0.32773	42.93653
12	0.36386	44.25711
13	0.40000	45.48753
14	0.65000	53.72118
15	0.90000	61.95483
16	0.92250	61.95483
17	0.94500	61.95483

User-input p-y curve at bottom of layer 2, Depth = 17.000 ft

Point No.	y in	p lbs/in
1	0.0000	0.0000
2	0.00193	18.81148
3	0.03811	48.49278
4	0.07430	59.93075
5	0.11049	67.97000
6	0.14668	74.36203
7	0.18287	79.75037
8	0.21906	84.45204
9	0.25525	88.64929
10	0.29143	92.45761
11	0.32762	95.95534
12	0.36381	99.19831
13	0.40000	102.22789
14	0.65000	122.49722
15	0.90000	142.76654
16	0.92250	142.76654
17	0.94500	142.76654

Layer 3 is modelled using user-specified p-y curves

Distance from top of pile to top of layer = 17.00000 ft
Distance from top of pile to bottom of layer = 19.00000 ft
Effective unit weight at top of layer = 62.60000 pcf
Effective unit weight at bottom of layer = 62.60000 pcf

User-input p-y curve at top of layer 3, Depth = 17.000 ft

Point No.	y in	p lbs/in
1	0.0000	0.0000
2	0.00193	18.81148
3	0.03811	48.49278
4	0.07430	59.93075
5	0.11049	67.97000
6	0.14668	74.36203
7	0.18287	79.75037
8	0.21906	84.45204
9	0.25525	88.64929
10	0.29143	92.45761
11	0.32762	95.95534
12	0.36381	99.19831
13	0.40000	102.22789
14	0.65000	122.49722
15	0.90000	142.76654
16	0.92250	142.76654
17	0.94500	142.76654

User-input p-y curve at bottom of layer 3, Depth = 19.000 ft

Point No.	y in	p lbs/in
1	0.0000	0.0000
2	0.00102	15.60690
3	0.03729	58.50553
4	0.07356	75.06726
5	0.10983	86.95983
6	0.14610	96.55767
7	0.18237	104.74156
8	0.21864	111.94915
9	0.25492	118.43396
10	0.29119	124.35773
11	0.32746	129.83080
12	0.36373	134.93223
13	0.40000	139.72088
14	0.65000	171.75878
15	0.90000	203.79669
16	0.92250	203.79669
17	0.94500	203.79669

Layer 4 is modelled using user-specified p-y curves

Distance from top of pile to top of layer = 19.00000 ft
Distance from top of pile to bottom of layer = 21.00000 ft
Effective unit weight at top of layer = 62.60000 pcf
Effective unit weight at bottom of layer = 62.60000 pcf

User-input p-y curve at top of layer 4, Depth = 19.000 ft

Point No.	y in	p lbs/in
1	0.0000	0.0000
2	0.00102	15.60690
3	0.03729	58.50553
4	0.07356	75.06726
5	0.10983	86.95983
6	0.14610	96.55767
7	0.18237	104.74156
8	0.21864	111.94915
9	0.25492	118.43396
10	0.29119	124.35773
11	0.32746	129.83080
12	0.36373	134.93223
13	0.40000	139.72088
14	0.65000	171.75878
15	0.90000	203.79669
16	0.92250	203.79669
17	0.94500	203.79669

User-input p-y curve at bottom of layer 4, Depth = 21.000 ft

Point No.	y in	p lbs/in
1	0.0000	0.0000
2	0.0001467	3.06983
3	0.03650	50.55546
4	0.07285	71.81171
5	0.10920	88.20047
6	0.14555	102.05728
7	0.18190	114.29124
8	0.21825	125.36999
9	0.25460	135.57192

10	0.29095	145.07870
11	0.32730	154.01674
12	0.36365	162.47811
13	0.40000	170.53246
14	0.65000	224.65799
15	0.90000	278.78351
16	0.92250	278.78351
17	0.94500	278.78351

Layer 5 is modelled using user-specified p-y curves

Distance from top of pile to top of layer = 21.00000 ft
 Distance from top of pile to bottom of layer = 23.00000 ft
 Effective unit weight at top of layer = 62.60000 pcf
 Effective unit weight at bottom of layer = 62.60000 pcf

User-input p-y curve at top of layer 5, Depth = 21.000 ft

Point No.	y in	p lbs/in
1	0.0000	0.0000
2	0.0001467	3.06983
3	0.03650	50.55546
4	0.07285	71.81171
5	0.10920	88.20047
6	0.14555	102.05728
7	0.18190	114.29124
8	0.21825	125.36999
9	0.25460	135.57192
10	0.29095	145.07870
11	0.32730	154.01674
12	0.36365	162.47811
13	0.40000	170.53246
14	0.65000	224.65799
15	0.90000	278.78351
16	0.92250	278.78351
17	0.94500	278.78351

User-input p-y curve at bottom of layer 5, Depth = 23.000 ft

Point No.	y in	p lbs/in
1	0.0000	0.0000
2	0.0000296	0.78449
3	0.03639	54.10081
4	0.07275	81.70221
5	0.10911	103.98868
6	0.14547	123.40032
7	0.18183	140.92058
8	0.21820	157.06741
9	0.25456	172.15489
10	0.29092	186.39106
11	0.32728	199.92252
12	0.36364	212.85725
13	0.40000	225.27773
14	0.65000	309.06328
15	0.90000	392.84884
16	0.92250	392.84884
17	0.94500	392.84884

Layer 6 is modelled using user-specified p-y curves

Distance from top of pile to top of layer = 23.00000 ft
 Distance from top of pile to bottom of layer = 25.00000 ft
 Effective unit weight at top of layer = 62.60000 pcf
 Effective unit weight at bottom of layer = 62.60000 pcf

User-input p-y curve at top of layer 6, Depth = 23.000 ft

Point No.	y in	p lbs/in
1	0.0000	0.0000
2	0.0000296	0.78449
3	0.03639	54.10081
4	0.07275	81.70221
5	0.10911	103.98868
6	0.14547	123.40032
7	0.18183	140.92058
8	0.21820	157.06741
9	0.25456	172.15489
10	0.29092	186.39106
11	0.32728	199.92252
12	0.36364	212.85725
13	0.40000	225.27773
14	0.65000	309.06328
15	0.90000	392.84884
16	0.92250	392.84884
17	0.94500	392.84884

User-input p-y curve at bottom of layer 6, Depth = 25.000 ft

Point No.	y in	p lbs/in
1	0.0000	0.0000
2	0.0000300	0.96219
3	0.03639	72.16957
4	0.07275	109.96932
5	0.10911	140.70150
6	0.14547	167.58817
7	0.18183	191.93481
8	0.21820	214.43155
9	0.25456	235.49796
10	0.29092	255.41263
11	0.32728	274.37218
12	0.36364	292.52178
13	0.40000	309.97237
14	0.65000	427.76187
15	0.90000	545.55137
16	0.92250	545.55137
17	0.94500	545.55137

Layer 7 is modelled using user-specified p-y curves

Distance from top of pile to top of layer = 25.00000 ft
 Distance from top of pile to bottom of layer = 27.00000 ft
 Effective unit weight at top of layer = 62.60000 pcf
 Effective unit weight at bottom of layer = 62.60000 pcf

User-input p-y curve at top of layer 7, Depth = 25.000 ft

Point No.	y in	p lbs/in
-----------	------	----------

1	0.0000	0.0000
2	0.0000300	0.96219
3	0.03639	72.16957
4	0.07275	109.96932
5	0.10911	140.70150
6	0.14547	167.58817
7	0.18183	191.93481
8	0.21820	214.43155
9	0.25456	235.49796
10	0.29092	255.41263
11	0.32728	274.37218
12	0.36364	292.52178
13	0.40000	309.97237
14	0.65000	427.76187
15	0.90000	545.55137
16	0.92250	545.55137
17	0.94500	545.55137

User-input p-y curve at bottom of layer 7, Depth = 27.000 ft

Point No.	y in	p lbs/in
1	0.0000	0.0000
2	0.0000413	1.55405
3	0.03640	96.02466
4	0.07276	146.30505
5	0.10912	187.18579
6	0.14548	222.95164
7	0.18184	255.33890
8	0.21820	285.26546
9	0.25456	313.28940
10	0.29092	339.78129
11	0.32728	365.00266
12	0.36364	389.14661
13	0.40000	412.36072
14	0.65000	569.05779
15	0.90000	725.75489
16	0.92250	725.75489
17	0.94500	725.75489

Layer 8 is modelled using user-specified p-y curves

Distance from top of pile to top of layer = 27.00000 ft
Distance from top of pile to bottom of layer = 29.00000 ft
Effective unit weight at top of layer = 62.60000 pcf
Effective unit weight at bottom of layer = 62.60000 pcf

User-input p-y curve at top of layer 8, Depth = 27.000 ft

Point No.	y in	p lbs/in
1	0.0000	0.0000
2	0.0000413	1.55405
3	0.03640	96.02466
4	0.07276	146.30505
5	0.10912	187.18579
6	0.14548	222.95164
7	0.18184	255.33890
8	0.21820	285.26546
9	0.25456	313.28940
10	0.29092	339.78129
11	0.32728	365.00266
12	0.36364	389.14661

13	0.40000	412.36072
14	0.65000	569.05779
15	0.90000	725.75489
16	0.92250	725.75489
17	0.94500	725.75489

User-input p-y curve at bottom of layer 8, Depth = 29.000 ft

Point No.	y in	p lbs/in
1	0.0000	0.0000
2	0.0000548	2.36925
3	0.03641	123.23769
4	0.07277	187.74616
5	0.10913	240.19739
6	0.14549	286.08684
7	0.18185	327.64179
8	0.21821	366.03973
9	0.25457	401.99662
10	0.29092	435.98786
11	0.32728	468.34901
12	0.36364	499.32779
13	0.40000	529.11354
14	0.65000	730.17667
15	0.90000	931.23981
16	0.92250	931.23981
17	0.94500	931.23981

Layer 9 is modelled using user-specified p-y curves

Distance from top of pile to top of layer = 29.00000 ft
Distance from top of pile to bottom of layer = 31.00000 ft
Effective unit weight at top of layer = 62.60000 pcf
Effective unit weight at bottom of layer = 62.60000 pcf

User-input p-y curve at top of layer 9, Depth = 29.000 ft

Point No.	y in	p lbs/in
1	0.0000	0.0000
2	0.0000548	2.36925
3	0.03641	123.23769
4	0.07277	187.74616
5	0.10913	240.19739
6	0.14549	286.08684
7	0.18185	327.64179
8	0.21821	366.03973
9	0.25457	401.99662
10	0.29092	435.98786
11	0.32728	468.34901
12	0.36364	499.32779
13	0.40000	529.11354
14	0.65000	730.17667
15	0.90000	931.23981
16	0.92250	931.23981
17	0.94500	931.23981

User-input p-y curve at bottom of layer 9, Depth = 31.000 ft

Point No.	y in	p lbs/in
1	0.0000	0.0000

2	0.0000707	3.45251
3	0.03643	153.81385
4	0.07279	234.29621
5	0.10914	299.73899
6	0.14550	356.99589
7	0.18186	408.84513
8	0.21821	456.75564
9	0.25457	501.62057
10	0.29093	544.03304
11	0.32729	584.41167
12	0.36364	623.06553
13	0.40000	660.23087
14	0.65000	911.11858
15	0.90000	1162.00629
16	0.92250	1162.00629
17	0.94500	1162.00629

Layer 10 is modelled using user-specified p-y curves

Distance from top of pile to top of layer = 31.00000 ft
Distance from top of pile to bottom of layer = 33.00000 ft
Effective unit weight at top of layer = 62.60000 pcf
Effective unit weight at bottom of layer = 62.60000 pcf

User-input p-y curve at top of layer 10, Depth = 31.000 ft

Point No.	y in	p lbs/in
1	0.0000	0.0000
2	0.0000707	3.45251
3	0.03643	153.81385
4	0.07279	234.29621
5	0.10914	299.73899
6	0.14550	356.99589
7	0.18186	408.84513
8	0.21821	456.75564
9	0.25457	501.62057
10	0.29093	544.03304
11	0.32729	584.41167
12	0.36364	623.06553
13	0.40000	660.23087
14	0.65000	911.11858
15	0.90000	1162.00629
16	0.92250	1162.00629
17	0.94500	1162.00629

User-input p-y curve at bottom of layer 10, Depth = 33.000 ft

Point No.	y in	p lbs/in
1	0.0000	0.0000
2	0.0000892	4.85138
3	0.03644	187.75928
4	0.07280	285.95943
5	0.10916	365.81379
6	0.14551	435.68127
7	0.18187	498.95090
8	0.21822	557.41471
9	0.25458	612.16241
10	0.29093	663.91764
11	0.32729	713.19115
12	0.36364	760.36006
13	0.40000	805.71263

14	0.65000	1111.88339
15	0.90000	1418.05420
16	0.92250	1418.05420
17	0.94500	1418.05420

Layer 11 is modelled using user-specified p-y curves

Distance from top of pile to top of layer = 33.00000 ft
 Distance from top of pile to bottom of layer = 35.00000 ft
 Effective unit weight at top of layer = 62.60000 pcf
 Effective unit weight at bottom of layer = 62.60000 pcf

User-input p-y curve at top of layer 11, Depth = 33.000 ft

Point No.	y in	p lbs/in
1	0.0000	0.0000
2	0.0000892	4.85138
3	0.03644	187.75928
4	0.07280	285.95943
5	0.10916	365.81379
6	0.14551	435.68127
7	0.18187	498.95090
8	0.21822	557.41471
9	0.25458	612.16241
10	0.29093	663.91764
11	0.32729	713.19115
12	0.36364	760.36006
13	0.40000	805.71263
14	0.65000	1111.88339
15	0.90000	1418.05420
16	0.92250	1418.05420
17	0.94500	1418.05420

User-input p-y curve at bottom of layer 11, Depth = 35.000 ft

Point No.	y in	p lbs/in
1	0.0000	0.0000
2	0.0001103	6.61611
3	0.03646	225.08114
4	0.07282	342.74071
5	0.10917	438.42552
6	0.14552	522.14590
7	0.18188	597.96137
8	0.21823	668.01875
9	0.25459	733.62349
10	0.29094	795.64259
11	0.32729	854.68804
12	0.36365	911.21171
13	0.40000	965.55886
14	0.65000	1332.47126
15	0.90000	1699.38361
16	0.92250	1699.38361
17	0.94500	1699.38361

Layer 12 is modelled using user-specified p-y curves

Distance from top of pile to top of layer = 35.00000 ft
 Distance from top of pile to bottom of layer = 50.00000 ft
 Effective unit weight at top of layer = 62.60000 pcf
 Effective unit weight at bottom of layer = 62.60000 pcf

User-input p-y curve at top of layer 12, Depth = 35.000 ft

Point No.	y in	p lbs/in
1	0.0000	0.0000
2	0.0001103	6.61611
3	0.03646	225.08114
4	0.07282	342.74071
5	0.10917	438.42552
6	0.14552	522.14590
7	0.18188	597.96137
8	0.21823	668.01875
9	0.25459	733.62349
10	0.29094	795.64259
11	0.32729	854.68804
12	0.36365	911.21171
13	0.40000	965.55886
14	0.65000	1332.47126
15	0.90000	1699.38361
16	0.92250	1699.38361
17	0.94500	1699.38361

User-input p-y curve at bottom of layer 12, Depth = 50.000 ft

Point No.	y in	p lbs/in
1	0.0000	0.0000
2	0.0001103	6.61611
3	0.03646	225.08114
4	0.07282	342.74071
5	0.10917	438.42552
6	0.14552	522.14590
7	0.18188	597.96137
8	0.21823	668.01875
9	0.25459	733.62349
10	0.29094	795.64259
11	0.32729	854.68804
12	0.36365	911.21171
13	0.40000	965.55886
14	0.65000	1332.47126
15	0.90000	1699.38361
16	0.92250	1699.38361
17	0.94500	1699.38361

(Depth of lowest soil layer extends 15.00 ft below pile tip)

 Summary of Soil Properties

Layer Num.	Layer Soil Type (p-y Curve Criteria)	Layer Depth ft	Effective Unit Wt. pcf
1	User Input p-y Curves	13.500	62.600
2	User Input p-y Curves	15.000	62.600
3	User Input p-y Curves	17.000	62.600
		19.000	62.600

4	User Input p-y Curves	19.000	62.600
		21.000	62.600
5	User Input p-y Curves	21.000	62.600
		23.000	62.600
6	User Input p-y Curves	23.000	62.600
		25.000	62.600
7	User Input p-y Curves	25.000	62.600
		27.000	62.600
8	User Input p-y Curves	27.000	62.600
		29.000	62.600
9	User Input p-y Curves	29.000	62.600
		31.000	62.600
10	User Input p-y Curves	31.000	62.600
		33.000	62.600
11	User Input p-y Curves	33.000	62.600
		35.000	62.600
12	User Input p-y Curves	35.000	62.600
		50.000	62.600

Lateral Soil Movements

Profile of soil movement with depth defined using 2 points

Point No.	Depth X ft	Soil Movement in
1	0.00000	0.00000
2	0.00000	0.00000

Loading Type

Static loading criteria were used when computing p-y curves for all analyses.

Distributed Lateral Loading

Distributed lateral load intensity defined using 2 points

Point No.	Depth X in	Dist. Load lbs/in
1	0.000	0.000
2	162.000	242.000

Pile-head Loading and Pile-head Fixity Conditions

Number of loads specified = 1

Load No.	Load Type	Condition 1	Condition 2	Axial Thrust Force, lbs	Compute Top y vs. Pile Length
1	1 V =	0.0000 lbs	M = 0.0000 in-lbs	0.0000000	No

V = perpendicular shear force applied to pile head
M = bending moment applied to pile head
y = lateral deflection relative to pile axis
S = pile slope relative to original pile batter angle
R = rotational stiffness applied to pile head
Axial thrust is assumed to be acting axially for all pile batter angles.

Specified Depths for Output of p-y Curves

Lateral load-transfer (p-y) curves are computed and output at 12 depths.
(Note that these curves are independent from the curves used at nodal point depths)

Depth No.	Depth Below Pile Head ft	Depth Below Ground Surface ft	Number of Specified y-Values
1	13.500	0.000	0
2	15.000	1.500	0
3	17.000	3.500	0
4	19.000	5.500	0
5	21.000	7.500	0
6	23.000	9.500	0
7	25.000	11.500	0
8	27.000	13.500	0
9	29.000	15.500	0
10	31.000	17.500	0
11	33.000	19.500	0
12	35.000	21.500	0

Depth of ground surface below top of pile = 13.50 ft
If number of specified y-values is 0 then 17 default y-values are used for output

Computations of Nominal Moment Capacity and Nonlinear Bending Stiffness

Axial thrust force values were determined from pile-head loading conditions

Number of Pile Sections Analyzed = 1

Pile Section No. 1:

Dimensions and Properties of Drilled Shaft (Bored Pile):

Length of Section = 35.00000 ft
Shaft Diameter = 24.00000 in
Concrete Cover Thickness = 2.00000 in
Number of Reinforcing Bars = 12 bars
Yield Stress of Reinforcing Bars = 60.00000 ksi
Modulus of Elasticity of Reinforcing Bars = 29000. ksi
Gross Area of Shaft = 452.38934 sq. in.
Total Area of Reinforcing Steel = 7.20000 sq. in.
Area Ratio of Steel Reinforcement = 1.59 percent
Edge-to-Edge Bar Spacing = 4.07491 in
Maximum Concrete Aggregate Size = 0.75000 in
Ratio of Bar Spacing to Aggregate Size = 5.43
Offset of Center of Rebar Cage from Center of Pile = 0.0000 in

Axial Structural Capacities:

Nom. Axial Structural Capacity = $0.85 F_c A_c + F_y A_s = 1945.644$ kips
 Tensile Load for Cracking of Concrete = -209.248 kips
 Nominal Axial Tensile Capacity = -432.000 kips

Reinforcing Bar Dimensions and Positions Used in Computations:

Bar Number	Bar Diam. inches	Bar Area sq. in.	X inches	Y inches
1	0.87500	0.60000	9.56250	0.00000
2	0.87500	0.60000	8.28137	4.78125
3	0.87500	0.60000	4.78125	8.28137
4	0.87500	0.60000	0.00000	9.56250
5	0.87500	0.60000	-4.78125	8.28137
6	0.87500	0.60000	-8.28137	4.78125
7	0.87500	0.60000	-9.56250	0.00000
8	0.87500	0.60000	-8.28137	-4.78125
9	0.87500	0.60000	-4.78125	-8.28137
10	0.87500	0.60000	0.00000	-9.56250
11	0.87500	0.60000	4.78125	-8.28137
12	0.87500	0.60000	8.28137	-4.78125

NOTE: The positions of the above rebars were computed by LPILE

Minimum spacing between any two bars not equal to zero = 4.07491 inches between Bars 7 and 8

Spacing to aggregate size ratio = 5.43322

Concrete Properties:

Compressive Strength of Concrete = 4.00000 ksi
 Modulus of Elasticity of Concrete = 3604.99653 ksi
 Modulus of Rupture of Concrete = -0.47434 ksi
 Compression Strain at Peak Stress = 0.00189
 Tensile Strain at Fracture of Concrete = -0.0001154
 Maximum Coarse Aggregate Size = 0.75000 in

Number of Axial Thrust Force Values Determined from Pile-head Loadings = 1

Number	Axial Thrust Force kips
1	0.000

Definitions of Run Messages and Notes:

C = concrete in section has cracked in tension.
 Y = stress in reinforcing steel has reached yield stress.
 T = ACI 318-08 criteria for tension-controlled section met, tensile strain in reinforcement exceeds 0.005 while simultaneously compressive strain in concrete more than than 0.003. See ACI 318-08, Section 10.3.4.
 Z = depth of tensile zone in concrete section is less than 10 percent of section depth.

Bending Stiffness (EI) = Computed Bending Moment / Curvature.
 Position of neutral axis is measured from edge of compression side of pile.
 Compressive stresses and strains are positive in sign.
 Tensile stresses and strains are negative in sign.

Axial Thrust Force = 0.000 kips

Bending Curvature rad/in.	Bending Moment in-kip	Bending Stiffness kip-in2	Depth to N Axis in	Max Comp Strain in/in	Max Tens Strain ksi	Max Concrete Stress ksi	Max Steel Stress ksi	Run
0.000001250	96.3241126	77059290.	11.9999599	0.0000150	-0.0000150	0.0627333	-0.4306514	
0.000002500	192.1913103	76876524.	11.9999598	0.0000300	-0.0000300	0.1249707	-0.8613029	
0.000003750	287.6015933	76693758.	11.9999596	0.0000450	-0.0000450	0.1867124	-1.2919544	
0.000005000	382.5549614	76510992.	11.9999595	0.0000600	-0.0000600	0.2479581	-1.7226058	
0.000006250	477.0514147	76328226.	11.9999593	0.0000750	-0.0000750	0.3087081	-2.1532573	
0.000007500	571.0909532	76145460.	11.9999592	0.0000900	-0.0000900	0.3689622	-2.5839088	
0.000008750	664.6735769	75962695.	11.9999590	0.0001050	-0.0001050	0.4287205	-3.0145603	
0.0000100	664.6735769	66467358.	6.6009075	0.0000660	-0.0001740	0.2701445	-5.0109368	C
0.0000113	664.6735769	59082096.	6.6031920	0.0000743	-0.0001957	0.3033533	-5.6365586	C
0.0000125	664.6735769	53173886.	6.6054820	0.0000826	-0.0002174	0.3364371	-6.2620127	C
0.0000138	664.6735769	48339897.	6.6077775	0.0000909	-0.0002391	0.3693956	-6.8872987	C
0.0000150	664.6735769	44311572.	6.6100786	0.0000992	-0.0002608	0.4022286	-7.5124158	C
0.0000163	664.6735769	40902989.	6.6123851	0.0001075	-0.0002825	0.4349359	-8.1373635	C
0.0000175	664.6735769	37981347.	6.6146973	0.0001158	-0.0003042	0.4675171	-8.7621411	C
0.0000188	664.6735769	35449257.	6.6170151	0.0001241	-0.0003259	0.4999722	-9.3867480	C
0.0000200	664.6735769	33233679.	6.6193385	0.0001324	-0.0003476	0.5323008	-10.0111836	C
0.0000213	664.6735769	31278757.	6.6216675	0.0001407	-0.0003693	0.5645027	-10.6354473	C
0.0000225	664.6735769	29541048.	6.6240023	0.0001490	-0.0003910	0.5965777	-11.2595385	C
0.0000238	664.6735769	27986256.	6.6263428	0.0001574	-0.0004126	0.6285255	-11.8834564	C
0.0000250	664.6735769	26586943.	6.6286890	0.0001657	-0.0004343	0.6603459	-12.5072004	C
0.0000263	664.6735769	25320898.	6.6310410	0.0001741	-0.0004559	0.6920386	-13.1307700	C
0.0000275	664.6735769	24169948.	6.6333988	0.0001824	-0.0004776	0.7236034	-13.7541644	C
0.0000288	664.6735769	23119081.	6.6357624	0.0001908	-0.0004992	0.7550400	-14.3773830	C
0.0000300	664.6735769	22155786.	6.6381319	0.0001991	-0.0005209	0.7863483	-15.0004252	C
0.0000313	664.6735769	21269554.	6.6405073	0.0002075	-0.0005425	0.8175278	-15.6232902	C
0.0000325	664.6735769	20451495.	6.6428886	0.0002159	-0.0005641	0.8485785	-16.2459774	C
0.0000338	669.6175849	19840521.	6.6452759	0.0002243	-0.0005857	0.8795000	-16.8684861	C
0.0000350	694.1816530	19833762.	6.6476692	0.0002327	-0.0006073	0.9102920	-17.4908157	C
0.0000363	718.7282930	19826987.	6.6500685	0.0002411	-0.0006289	0.9409544	-18.1129655	C
0.0000375	743.2574475	19820199.	6.6524738	0.0002495	-0.0006505	0.9714869	-18.7349347	C
0.0000388	767.7690589	19813395.	6.6548852	0.0002579	-0.0006721	1.0018891	-19.3567227	C
0.0000400	792.2630691	19806577.	6.6573027	0.0002663	-0.0006937	1.0321609	-19.9783288	C
0.0000413	816.7394195	19799744.	6.6597264	0.0002747	-0.0007153	1.0623020	-20.5997522	C
0.0000425	841.1980514	19792895.	6.6621562	0.0002831	-0.0007369	1.0923121	-21.2209924	C
0.0000438	865.6389055	19786032.	6.6645923	0.0002916	-0.0007584	1.1221910	-21.8420485	C
0.0000450	890.0619222	19779154.	6.6670346	0.0003000	-0.0007800	1.1519384	-22.4629198	C
0.0000463	914.4670416	19772260.	6.6694831	0.0003085	-0.0008015	1.1815540	-23.0836057	C
0.0000475	938.8542032	19765352.	6.6719380	0.0003169	-0.0008231	1.2110375	-23.7041054	C
0.0000488	963.2233462	19758428.	6.6743992	0.0003254	-0.0008446	1.2403887	-24.3244181	C
0.0000513	1011.9073029	19744533.	6.6793407	0.0003423	-0.0008877	1.2986931	-25.5644801	C
0.0000538	1060.5184714	19730576.	6.6843080	0.0003593	-0.0009307	1.3564649	-26.8037851	C
0.0000563	1109.0563252	19716557.	6.6893014	0.0003763	-0.0009737	1.4137020	-28.0423274	C
0.0000588	1157.5203567	19702474.	6.6943210	0.0003933	-0.0010167	1.4704021	-29.2801009	C
0.0000613	1205.9100513	19688327.	6.6993673	0.0004103	-0.0010597	1.5265628	-30.5170992	C
0.0000638	1254.2248875	19674116.	6.7044404	0.0004274	-0.0011026	1.5821820	-31.7533161	C
0.0000663	1302.4643368	19659839.	6.7095408	0.0004445	-0.0011455	1.6372573	-32.9887452	C
0.0000688	1350.6278632	19645496.	6.7146686	0.0004616	-0.0011884	1.6917862	-34.2233800	C
0.0000713	1398.7149235	19631087.	6.7198242	0.0004788	-0.0012312	1.7457666	-35.4572138	C
0.0000738	1446.7249668	19616610.	6.7250079	0.0004960	-0.0012740	1.7991958	-36.6902400	C
0.0000763	1494.6574344	19602065.	6.7302200	0.0005132	-0.0013168	1.8520715	-37.9224516	C
0.0000788	1542.5117598	19587451.	6.7354609	0.0005304	-0.0013596	1.9043913	-39.1538420	C
0.0000813	1590.2873684	19572768.	6.7407308	0.0005477	-0.0014023	1.9561525	-40.3844039	C
0.0000838	1637.9836775	19558014.	6.7460301	0.0005650	-0.0014450	2.0073528	-41.6141303	C
0.0000863	1685.6000958	19543190.	6.7513591	0.0005823	-0.0014877	2.0579894	-42.8430140	C
0.0000888	1733.1360235	19528293.	6.7567182	0.0005997	-0.0015303	2.1080599	-44.0710475	C
0.0000913	1780.5908520	19513324.	6.7621077	0.0006170	-0.0015730	2.1575615	-45.2982235	C
0.0000938	1827.9639638	19498282.	6.7675280	0.0006345	-0.0016155	2.2064917	-46.5245344	C
0.0000963	1875.2547322	19483166.	6.7729795	0.0006519	-0.0016581	2.2548476	-47.7499724	C
0.0000988	1922.4625211	19467975.	6.7784624	0.0006694	-0.0017006	2.3026267	-48.9745298	C
0.0001013	1969.5866849	19452708.	6.7839772	0.0006869	-0.0017431	2.3498261	-50.1981985	C
0.0001038	2016.6265683	19437365.	6.7895242	0.0007044	-0.0017856	2.3964429	-51.4209706	C
0.0001063	2063.5815058	19421944.	6.7951039	0.0007220	-0.0018280	2.4424745	-52.6428377	C
0.0001088	2110.4508218	19406444.	6.8007167	0.0007396	-0.0018704	2.4879178	-53.8637916	C

0.0001113	2157.2338302	19390866.	6.8063629	0.0007572	-0.0019128	2.5327699	-55.0838238	C
0.0001138	2203.9298343	19375207.	6.8120429	0.0007749	-0.0019551	2.5770280	-56.3029256	C
0.0001163	2250.5381264	19359468.	6.8177572	0.0007926	-0.0019974	2.6206889	-57.5210882	C
0.0001188	2297.0579876	19343646.	6.8235062	0.0008103	-0.0020397	2.6637497	-58.7383029	C
0.0001213	2343.4886874	19327742.	6.8292903	0.0008281	-0.0020819	2.7062072	-59.9545604	C
0.0001238	2389.8294839	19311753.	6.8351100	0.0008458	-0.0021242	2.7480583	-60.0000000	CY
0.0001263	2436.0806733	19295689.	6.8409302	0.0008637	-0.0021663	2.7892897	-60.0000000	CY
0.0001288	2482.2439853	19279565.	6.8466049	0.0008815	-0.0022085	2.8298539	-60.0000000	CY
0.0001313	2528.3160473	19263360.	6.8523138	0.0008994	-0.0022506	2.8698014	-60.0000000	CY
0.0001338	2574.2958079	19247071.	6.8580574	0.0009173	-0.0022927	2.9091286	-60.0000000	CY
0.0001363	2620.1825005	19230697.	6.8638362	0.0009352	-0.0023348	2.9478322	-60.0000000	CY
0.0001388	2665.1795524	19208501.	6.8689690	0.0009531	-0.0023769	2.9857072	-60.0000000	CY
0.0001413	2707.3949012	19167398.	6.8718545	0.0009706	-0.0024194	3.0222763	-60.0000000	CY
0.0001438	2746.2010562	19104007.	6.8720120	0.0009879	-0.0024621	3.0573965	-60.0000000	CY
0.0001463	2782.6868543	19026919.	6.8704415	0.0010048	-0.0025052	3.0913650	-60.0000000	CY
0.0001488	2818.9055263	18950625.	6.8689540	0.0010218	-0.0025482	3.1247191	-60.0000000	CY
0.0001588	2932.1180462	18470035.	6.8386903	0.0010856	-0.0027244	3.2446656	-60.0000000	CY
0.0001688	3008.1865249	17826291.	6.7820460	0.0011445	-0.0029055	3.3471408	-60.0000000	CY
0.0001788	3083.3954567	17249765.	6.7333881	0.0012036	-0.0030864	3.4426156	-60.0000000	CY
0.0001888	3157.9628715	16730929.	6.6916806	0.0012631	-0.0032669	3.5310388	-60.0000000	CY
0.0001988	3230.7997728	16255596.	6.6548876	0.0013227	-0.0034473	3.6120181	-60.0000000	CY
0.0002088	3282.7963225	15725970.	6.6041332	0.0013786	-0.0036314	3.6809708	-60.0000000	CY
0.0002188	3312.8281738	15144357.	6.5363558	0.0014298	-0.0038202	3.7380646	-60.0000000	CY
0.0002288	3341.3084442	14606813.	6.4742476	0.0014810	-0.0040090	3.7894771	-60.0000000	CY
0.0002388	3369.4552936	14112902.	6.4184007	0.0015324	-0.0041976	3.8354955	-60.0000000	CY
0.0002488	3397.2612418	13657332.	6.3680819	0.0015841	-0.0043859	3.8760386	-60.0000000	CY
0.0002588	3424.4629991	13234640.	6.3204915	0.0016354	-0.0045746	3.9106647	-60.0000000	CY
0.0002688	3451.2727507	12841945.	6.2770165	0.0016869	-0.0047631	3.9397126	-60.0000000	CY
0.0002788	3477.7357100	12476182.	6.2376550	0.0017387	-0.0049513	3.9631797	-60.0000000	CY
0.0002888	3503.8434366	12134523.	6.2020040	0.0017908	-0.0051392	3.9809737	-60.0000000	CY
0.0002988	3529.5869190	11814517.	6.1697161	0.0018432	-0.0053268	3.9929983	-60.0000000	CY
0.0003088	3554.9567407	11514030.	6.1404901	0.0018959	-0.0055141	3.9991532	-60.0000000	CY
0.0003188	3579.8811284	11231000.	6.1137310	0.0019488	-0.0057012	3.9969286	-60.0000000	CY
0.0003288	3604.2943994	10963633.	6.0883832	0.0020016	-0.0058884	3.9999894	-60.0000000	CY
0.0003388	3625.6079105	10702902.	6.0621824	0.0020536	-0.0060764	3.9985465	-60.0000000	CY
0.0003488	3641.9963415	10443000.	6.0322941	0.0021038	-0.0062662	3.9974160	-60.0000000	CY
0.0003588	3653.4357590	10183793.	5.9987710	0.0021521	-0.0064579	3.9985783	60.0000000	CY
0.0003688	3661.2688353	9928865.	5.9631052	0.0021989	-0.0066511	3.9990989	60.0000000	CY
0.0003788	3667.0100950	9681875.	5.9275385	0.0022451	-0.0068449	3.9971595	60.0000000	CY
0.0003888	3672.6346517	9447292.	5.8942597	0.0022914	-0.0070386	3.9997562	60.0000000	CY
0.0003988	3677.9030045	9223581.	5.8618466	0.0023374	-0.0072326	3.9936409	60.0000000	CY
0.0004088	3682.8888405	9010126.	5.8303965	0.0023832	-0.0074268	3.9979554	60.0000000	CY
0.0004188	3687.7844668	8806649.	5.8008263	0.0024291	-0.0076209	3.9998893	60.0000000	CY
0.0004288	3692.5308021	8612317.	5.7731734	0.0024752	-0.0078148	3.9928278	60.0000000	CY
0.0004388	3697.1755281	8426611.	5.7471761	0.0025216	-0.0080084	3.9972845	60.0000000	CY
0.0004488	3701.7450236	8249014.	5.7226532	0.0025680	-0.0082020	3.9996243	60.0000000	CY
0.0004588	3706.2040478	8078919.	5.6996101	0.0026147	-0.0083953	3.9959947	60.0000000	CY
0.0004688	3710.5491636	7915838.	5.6779628	0.0026615	-0.0085885	3.9947286	60.0000000	CY
0.0004788	3714.8331197	7759443.	5.6574798	0.0027085	-0.0087815	3.9982457	60.0000000	CY
0.0004888	3719.0352508	7609279.	5.6379138	0.0027555	-0.0089745	3.9998763	60.0000000	CY
0.0004988	3722.9581654	7464578.	5.6179612	0.0028020	-0.0091680	3.9943762	60.0000000	CY
0.0005088	3726.8086986	7325423.	5.5990911	0.0028485	-0.0093615	3.9935775	60.0000000	CY
0.0005188	3730.6155589	7191548.	5.5811528	0.0028952	-0.0095548	3.9972678	60.0000000	CY
0.0005288	3734.3780089	7062653.	5.5640962	0.0029420	-0.0097480	3.9994102	60.0000000	CY
0.0005388	3738.0859759	6938443.	5.5479061	0.0029889	-0.0099411	3.9988671	60.0000000	CY
0.0005488	3741.6957192	6818580.	5.5326768	0.0030361	-0.0101339	3.9904891	60.0000000	CYT
0.0006088	3762.4651203	6180641.	5.4554862	0.0033210	-0.0112890	3.9889160	60.0000000	CYT
0.0006688	3780.6321105	5653282.	5.4009538	0.0036119	-0.0124381	3.9873440	60.0000000	CYT
0.0007288	3782.5161914	5190417.	5.3841027	0.0039237	-0.0135663	3.9918348	60.0000000	CYT

Summary of Results for Nominal (Unfactored) Moment Capacity for Section 1

Moment values interpolated at maximum compressive strain = 0.003
or maximum developed moment if pile fails at smaller strains.

Load No.	Axial Thrust kips	Nominal Mom. Cap. in-kip	Max. Comp. Strain
1	0.000	3738.934	0.00300000

Note note that the values of moment capacity in the table above are not factored by a strength reduction factor (phi-factor).

In ACI 318-08, the value of the strength reduction factor depends on whether the transverse reinforcing steel bars are tied hoops (0.65) or spirals (0.70).

The above values should be multiplied by the appropriate strength reduction factor to compute ultimate moment capacity according to ACI 318-08, Section 9.3.2.2 or the value required by the design standard being followed.

The following table presents factored moment capacities and corresponding bending stiffnesses computed for common resistance factor values used for reinforced concrete sections.

Axial Load No.	Resistance Factor for Moment	Nominal Moment Capacity in-kip	Ultimate (Factored) Axial Thrust kips	Ultimate (Factored) Moment Capacity in-kip	Bending Stiffness at Ult. Mom. Cap. kip-in ²
1	0.65	3738.934	0.000	2430.307	19297694.007
1	0.70	3738.934	0.000	2617.254	19231742.433
1	0.75	3738.934	0.000	2804.200	18981601.532

p-y Curves Reported for Specified Depths

p-y Curve Computed by Interpolation Between User-input Curves

Soil Layer Number = 1
Depth below pile head = 13.500 ft
Depth below ground surface = 0.000 ft
Pile diameter = 24.000 in
p-multiplier = 1.000
y-multiplier = 1.000

y, in	p, lbs/in
0.0000	0.0000
0.0048	0.0000
0.0300	0.0000
0.0600	0.0000
0.0900	0.0000
0.1200	0.0000
0.1500	0.0000
0.1800	0.0000
0.2100	0.0000
0.2400	0.0000
0.2700	0.0000
0.3000	0.0000
0.3300	0.0000
0.3600	0.0000
0.9600	0.0000
1.8000	0.0000
2.4000	0.0000

p-y Curve Computed by Interpolation Between User-input Curves

Soil Layer Number = 2
 Depth below pile head = 15.000 ft
 Depth below ground surface = 1.500 ft
 Pile diameter = 24.000 in
 p-multiplier = 1.000
 y-multiplier = 1.000

y, in	p, lbs/in
0.0000	0.0000
0.0048	11.2653
0.0300	20.0914
0.0600	25.9960
0.0900	29.4138
0.1200	32.0443
0.1500	34.2256
0.1800	36.0826
0.2100	37.7207
0.2400	39.2094
0.2700	40.5757
0.3000	41.8405
0.3300	43.0196
0.3600	44.1159
0.9600	61.9548
1.8000	61.9548
2.4000	61.9548

p-y Curve Computed by Interpolation Between User-input Curves

Soil Layer Number = 3
 Depth below pile head = 17.000 ft
 Depth below ground surface = 3.500 ft
 Pile diameter = 24.000 in
 p-multiplier = 1.000
 y-multiplier = 1.000

y, in	p, lbs/in
0.0000	0.0000
0.0048	21.1683
0.0300	41.8370
0.0600	55.4099
0.0900	63.4177
0.1200	69.6494
0.1500	74.8563
0.1800	79.3232
0.2100	83.2753
0.2400	86.8810
0.2700	90.2019
0.3000	93.2855
0.3300	96.1683
0.3600	98.8567
0.9600	142.7665
1.8000	142.7665
2.4000	142.7665

p-y Curve Computed by Interpolation Between User-input Curves

Soil Layer Number = 4
 Depth below pile head = 19.000 ft
 Depth below ground surface = 5.500 ft
 Pile diameter = 24.000 in
 p-multiplier = 1.000
 y-multiplier = 1.000

y, in	p, lbs/in
0.0000	0.0000
0.0048	20.0810
0.0300	49.8856
0.0600	68.8759
0.0900	80.4578
0.1200	89.6508
0.1500	97.4372
0.1800	104.2061
0.2100	110.2314
0.2400	115.7673
0.2700	120.8976
0.3000	125.6876
0.3300	130.1884
0.3600	134.4078
0.9600	203.7967
1.8000	203.7967
2.4000	203.7967

p-y Curve Computed by Interpolation Between User-input Curves

Soil Layer Number = 5
 Depth below pile head = 21.000 ft
 Depth below ground surface = 7.500 ft
 Pile diameter = 24.000 in
 p-multiplier = 1.000
 y-multiplier = 1.000

y, in	p, lbs/in
0.0000	0.0000
0.0048	9.1486
0.0300	42.0682
0.0600	64.2991
0.0900	79.5451
0.1200	92.3184
0.1500	103.5557
0.1800	113.6524
0.2100	122.8560
0.2400	131.4747
0.2700	139.5998
0.3000	147.3042
0.3300	154.6454
0.3600	161.6286
0.9600	278.7835
1.8000	278.7835
2.4000	278.7835

p-y Curve Computed by Interpolation Between User-input Curves

Soil Layer Number = 6
 Depth below pile head = 23.000 ft

Depth below ground surface = 9.500 ft
 Pile diameter = 24.000 in
 p-multiplier = 1.000
 y-multiplier = 1.000

y, in	p, lbs/in
0.0000	0.0000
0.0048	7.7794
0.0300	44.7303
0.0600	72.0226
0.0900	92.2742
0.1200	109.8011
0.1500	125.5814
0.1800	140.0367
0.2100	153.4281
0.2400	166.1150
0.2700	178.2015
0.3000	189.7712
0.3300	200.8908
0.3600	211.5627
0.9600	392.8488
1.8000	392.8488
2.4000	392.8488

p-y Curve Computed by Interpolation Between User-input Curves

Soil Layer Number = 7
 Depth below pile head = 25.000 ft
 Depth below ground surface = 11.500 ft
 Pile diameter = 24.000 in
 p-multiplier = 1.000
 y-multiplier = 1.000

y, in	p, lbs/in
0.0000	0.0000
0.0048	10.3035
0.0300	59.6540
0.0600	96.7129
0.0900	124.5475
0.1200	148.7520
0.1500	170.6190
0.1800	190.7064
0.2100	209.3610
0.2400	227.0644
0.2700	243.9564
0.3000	260.1486
0.3300	275.7308
0.3600	290.7053
0.9600	545.5514
1.8000	545.5514
2.4000	545.5514

p-y Curve Computed by Interpolation Between User-input Curves

Soil Layer Number = 8
 Depth below pile head = 27.000 ft
 Depth below ground surface = 13.500 ft
 Pile diameter = 24.000 in

p-multiplier = 1.000
 y-multiplier = 1.000

y, in	p, lbs/in
0.0000	0.0000
0.0048	13.9183
0.0300	79.3931
0.0600	128.6584
0.0900	165.6874
0.1200	197.8871
0.1500	226.9771
0.1800	253.6993
0.2100	278.5159
0.2400	302.0671
0.2700	324.5387
0.3000	346.0795
0.3300	366.8087
0.3600	386.7295
0.9600	725.7549
1.8000	725.7549
2.4000	725.7549

p-y Curve Computed by Interpolation Between User-input Curves

Soil Layer Number = 9
 Depth below pile head = 29.000 ft
 Depth below ground surface = 15.500 ft
 Pile diameter = 24.000 in
 p-multiplier = 1.000
 y-multiplier = 1.000

y, in	p, lbs/in
0.0000	0.0000
0.0048	18.1439
0.0300	101.9172
0.0600	165.0856
0.0900	212.5992
0.1200	253.9158
0.1500	291.2421
0.1800	325.5296
0.2100	357.3727
0.2400	387.5922
0.2700	416.4263
0.3000	444.0660
0.3300	470.6642
0.3600	496.2252
0.9600	931.2398
1.8000	931.2398
2.4000	931.2398

p-y Curve Computed by Interpolation Between User-input Curves

Soil Layer Number = 10
 Depth below pile head = 31.000 ft
 Depth below ground surface = 17.500 ft
 Pile diameter = 24.000 in
 p-multiplier = 1.000
 y-multiplier = 1.000

y, in	p, lbs/in
0.0000	0.0000
0.0048	23.0113
0.0300	127.2301
0.0600	205.9943
0.0900	265.2829
0.1200	316.8381
0.1500	363.4140
0.1800	406.1972
0.2100	445.9315
0.2400	483.6397
0.2700	519.6191
0.3000	554.1081
0.3300	587.2976
0.3600	619.1926
0.9600	1162.0063
1.8000	1162.0063
2.4000	1162.0063

p-y Curve Computed by Interpolation Between User-input Curves

Soil Layer Number = 11
 Depth below pile head = 33.000 ft
 Depth below ground surface = 19.500 ft
 Pile diameter = 24.000 in
 p-multiplier = 1.000
 y-multiplier = 1.000

y, in	p, lbs/in
0.0000	0.0000
0.0048	28.5520
0.0300	155.3354
0.0600	251.3846
0.0900	323.7385
0.1200	386.6541
0.1500	443.4930
0.1800	495.7021
0.2100	544.1922
0.2400	590.2096
0.2700	634.1171
0.3000	676.2058
0.3300	716.7086
0.3600	755.6316
0.9600	1418.0542
1.8000	1418.0542
2.4000	1418.0542

p-y Curve Computed by Interpolation Between User-input Curves

Soil Layer Number = 11
 Depth below pile head = 35.000 ft
 Depth below ground surface = 21.500 ft
 Pile diameter = 24.000 in
 p-multiplier = 1.000
 y-multiplier = 1.000

y, in	p, lbs/in
0.0000	0.0000
0.0048	34.7986

0.0300	186.2366
0.0600	301.2564
0.0900	387.9660
0.1200	463.3638
0.1500	531.4791
0.1800	594.0441
0.2100	652.1549
0.2400	707.3020
0.2700	759.9205
0.3000	810.3592
0.3300	858.8973
0.3600	905.5422
0.9600	1699.3836
1.8000	1699.3836
2.4000	1699.3836

Summary of Pile Response(s)

Definitions of Pile-head Loading Conditions:

- Load Type 1: Load 1 = Shear, lbs, and Load 2 = Moment, in-lbs
- Load Type 2: Load 1 = Shear, lbs, and Load 2 = Slope, radians
- Load Type 3: Load 1 = Shear, lbs, and Load 2 = Rotational Stiffness, in-lbs/radian
- Load Type 4: Load 1 = Top Deflection, inches, and Load 2 = Moment, in-lbs
- Load Type 5: Load 1 = Top Deflection, inches, and Load 2 = Slope, radians

Load Case No.	Load Type	Pile-head Condition 1 V(lbs) or y(inches)	Pile-head Condition 2 in-lb, rad., or in-lb/rad.	Axial Loading lbs	Maximum Pile-head Deflection inches	Maximum Moment in Pile in-lbs	Shear in Pile lbs	Pile-head Rotation radians
1	1	V = 0.000	M = 0.000	0.0000000	8.45016541	2597139.	-29648.	-0.02978819

The analysis ended normally.

J.9: Test Wall Active Loading from data and Passive with $\phi=24^0$ with group reduction factor

LPile Plus for Windows, Version 2013-07.001

Analysis of Individual Piles and Drilled Shafts
Subjected to Lateral Loading Using the p-y Method

© 1985-2013 by Ensoft, Inc.
All Rights Reserved

This copy of LPile is licensed to:

The University of Texas at Austin
Geotech

Serial Number of Security Device: 226662924
Company Name Stored in Security Device: UT Austin - Prof. Gilbert

Files Used for Analysis

Path to file locations: C:\Users\Geotex\Desktop\LPILE PLAY\
Name of input data file: Inundation active from field and phi 23.lp7d
Name of output report file: Inundation active from field and phi 23.lp7o
Name of plot output file: Inundation active from field and phi 23.lp7p
Name of runtime message file: Inundation active from field and phi 23.lp7r

Date and Time of Analysis

Date: October 21, 2013 Time: 11:10:55

Problem Title

Project Name:
Job Number:
Client:
Engineer:
Description:

Program Options

Engineering Units of Input Data and Computations:
- Engineering units are US Customary Units: pounds, inches, feet

Analysis Control Options:
- Maximum number of iterations allowed = 750
- Deflection tolerance for convergence = 1.0000E-05 in
- Maximum allowable deflection = 100.0000 in
- Number of pile increments = 100

Loading Type and Number of Cycles of Loading:
- Static loading specified

Computational Options:
- Use unfactored loads in computations
- No computation of pile-head foundation stiffness matrix
- Compute pile response under loading and nonlinear bending properties of pile
(if nonlinear properties are specified)
- Push-over analysis of pile not selected
- Buckling analysis of pile not selected

Input Data Options:
- Analysis does not use p-y modification factors (individual pile or shaft only)
- Analysis assumes zero shear resistance at the pile tip
- Analysis includes loading by soil movements acting on pile

Output Options:
- p-y curves computed and reported at user-specified depths
- Only summary tables of pile-head deflection, maximum bending moment,
and maximum shear force are to be written to output report file.

Pile Structural Properties and Geometry

Total number of pile sections = 1

Total length of pile = 35.00 ft

Depth of ground surface below top of pile = 13.50 ft

Pile diameter values used for p-y curve computations are defined using 2 points.

p-y curves are computed using pile diameter values interpolated with depth over the length of the pile.

Point	Depth X ft	Pile Diameter in
1	0.00000	24.0000000
2	35.000000	24.0000000

Input Structural Properties:

Pile Section No. 1:

Section Type = Drilled Shaft (Bored Pile)
Section Length = 35.00000 ft
Section Diameter = 24.00000 in

Ground Slope and Pile Batter Angles

Ground Slope Angle = 0.000 degrees
= 0.000 radians

Pile Batter Angle = 0.000 degrees
= 0.000 radians

Soil and Rock Layering Information

The soil profile is modelled using 2 layers

Layer 1 is sand, p-y criteria by Reese et al., 1974

Distance from top of pile to top of layer = 13.50000 ft
Distance from top of pile to bottom of layer = 16.00000 ft
Effective unit weight at top of layer = 62.60000 pcf
Effective unit weight at bottom of layer = 62.60000 pcf
Friction angle at top of layer = 18.00000 deg.
Friction angle at bottom of layer = 18.00000 deg.
Subgrade k at top of layer = 375.00000 pci
Subgrade k at bottom of layer = 375.00000 pci

Layer 2 is sand, p-y criteria by Reese et al., 1974

Distance from top of pile to top of layer = 16.00000 ft
Distance from top of pile to bottom of layer = 50.00000 ft
Effective unit weight at top of layer = 62.60000 pcf

Effective unit weight at bottom of layer = 62.60000 pcf
 Friction angle at top of layer = 18.00000 deg.
 Friction angle at bottom of layer = 18.00000 deg.
 Subgrade k at top of layer = 375.00000 pci
 Subgrade k at bottom of layer = 375.00000 pci

(Depth of lowest soil layer extends 15.00 ft below pile tip)

 Summary of Soil Properties

Layer Num.	Layer Soil Type (p-y Curve Criteria)	Layer Depth ft	Effective Unit Wt. pcf	Angle of Friction deg.	kpy pci
1	Sand (Reese, et al.)	13.500	62.600	18.000	375.000
		16.000	62.600	18.000	375.000
2	Sand (Reese, et al.)	16.000	62.600	18.000	375.000
		50.000	62.600	18.000	375.000

 Lateral Soil Movements

Profile of soil movement with depth defined using 2 points

Point No.	Depth X ft	Soil Movement in
1	0.00000	0.00000
2	0.00000	0.00000

 Loading Type

Static loading criteria were used when computing p-y curves for all analyses.

 Distributed Lateral Loading

Distributed lateral load intensity defined using 7 points

Point No.	Depth X in	Dist. Load lbs/in
1	0.000	0.000
2	48.000	3.500
3	72.000	60.000
4	96.000	148.000
5	120.000	184.000
6	144.000	155.000
7	162.000	98.000

Pile-head Loading and Pile-head Fixity Conditions

Number of loads specified = 1

Load No.	Load Type	Condition 1	Condition 2	Axial Thrust Force, lbs	Compute Top y vs. Pile Length
1	V =	0.0000 lbs	M =	0.0000 in-lbs	0.0000000 No

V = perpendicular shear force applied to pile head
M = bending moment applied to pile head
y = lateral deflection relative to pile axis
S = pile slope relative to original pile batter angle
R = rotational stiffness applied to pile head
Axial thrust is assumed to be acting axially for all pile batter angles.

Specified Depths for Output of p-y Curves

Lateral load-transfer (p-y) curves are computed and output at 12 depths.
(Note that these curves are independent from the curves used at nodal point depths)

Depth No.	Depth Below Pile Head ft	Depth Below Ground Surface ft	Number of Specified y-Values
1	13.500	0.000	0
2	15.000	1.500	0
3	17.000	3.500	0
4	19.000	5.500	0
5	21.000	7.500	0
6	23.000	9.500	0
7	25.000	11.500	0
8	27.000	13.500	0
9	29.000	15.500	0
10	31.000	17.500	0
11	33.000	19.500	0
12	35.000	21.500	0

Depth of ground surface below top of pile = 13.50 ft
If number of specified y-values is 0 then 17 default y-values are used for output

Computations of Nominal Moment Capacity and Nonlinear Bending Stiffness

Axial thrust force values were determined from pile-head loading conditions

Number of Pile Sections Analyzed = 1

Pile Section No. 1:

Dimensions and Properties of Drilled Shaft (Bored Pile):

Length of Section	=	35.00000 ft
Shaft Diameter	=	24.00000 in
Concrete Cover Thickness	=	2.00000 in
Number of Reinforcing Bars	=	12 bars
Yield Stress of Reinforcing Bars	=	60.00000 ksi
Modulus of Elasticity of Reinforcing Bars	=	29000. ksi

Gross Area of Shaft = 452.38934 sq. in.
 Total Area of Reinforcing Steel = 7.20000 sq. in.
 Area Ratio of Steel Reinforcement = 1.59 percent
 Edge-to-Edge Bar Spacing = 4.07491 in
 Maximum Concrete Aggregate Size = 0.75000 in
 Ratio of Bar Spacing to Aggregate Size = 5.43
 Offset of Center of Rebar Cage from Center of Pile = 0.0000 in

Axial Structural Capacities:

Nom. Axial Structural Capacity = $0.85 F_c A_c + F_y A_s$ = 1945.644 kips
 Tensile Load for Cracking of Concrete = -209.248 kips
 Nominal Axial Tensile Capacity = -432.000 kips

Reinforcing Bar Dimensions and Positions Used in Computations:

Bar Number	Bar Diam. inches	Bar Area sq. in.	X inches	Y inches
1	0.87500	0.60000	9.56250	0.00000
2	0.87500	0.60000	8.28137	4.78125
3	0.87500	0.60000	4.78125	8.28137
4	0.87500	0.60000	0.00000	9.56250
5	0.87500	0.60000	-4.78125	8.28137
6	0.87500	0.60000	-8.28137	4.78125
7	0.87500	0.60000	-9.56250	0.00000
8	0.87500	0.60000	-8.28137	-4.78125
9	0.87500	0.60000	-4.78125	-8.28137
10	0.87500	0.60000	0.00000	-9.56250
11	0.87500	0.60000	4.78125	-8.28137
12	0.87500	0.60000	8.28137	-4.78125

NOTE: The positions of the above rebars were computed by LPile

Minimum spacing between any two bars not equal to zero = 4.07491 inches between Bars 7 and 8

Spacing to aggregate size ratio = 5.43322

Concrete Properties:

Compressive Strength of Concrete = 4.00000 ksi
 Modulus of Elasticity of Concrete = 3604.99653 ksi
 Modulus of Rupture of Concrete = -0.47434 ksi
 Compression Strain at Peak Stress = 0.00189
 Tensile Strain at Fracture of Concrete = -0.0001154
 Maximum Coarse Aggregate Size = 0.75000 in

Number of Axial Thrust Force Values Determined from Pile-head Loadings = 1

Number	Axial Thrust Force kips
1	0.000

Definitions of Run Messages and Notes:

C = concrete in section has cracked in tension.
 Y = stress in reinforcing steel has reached yield stress.
 T = ACI 318-08 criteria for tension-controlled section met, tensile strain in reinforcement exceeds 0.005 while simultaneously compressive strain in

concrete more than than 0.003. See ACI 318-08, Section 10.3.4.
 Z = depth of tensile zone in concrete section is less than 10 percent of section depth.

Bending Stiffness (EI) = Computed Bending Moment / Curvature.
 Position of neutral axis is measured from edge of compression side of pile.
 Compressive stresses and strains are positive in sign.
 Tensile stresses and strains are negative in sign.

Axial Thrust Force = 0.000 kips

Bending Curvature rad/in.	Bending Moment in-kip	Bending Stiffness kip-in ²	Depth to N Axis in	Max Comp Strain in/in	Max Tens Strain ksi	Max Concrete Stress ksi	Max Steel Run
0.00001250	96.3241126	77059290.	11.9999599	0.0000150	-0.0000150	0.0627333	-0.4306514
0.00002500	192.1913103	76876524.	11.9999598	0.0000300	-0.0000300	0.1249707	-0.8613029
0.00003750	287.6015933	76693758.	11.9999596	0.0000450	-0.0000450	0.1867124	-1.2919544
0.00005000	382.5549614	76510992.	11.9999595	0.0000600	-0.0000600	0.2479581	-1.7226058
0.00006250	477.0514147	76328226.	11.9999593	0.0000750	-0.0000750	0.3087081	-2.1532573
0.00007500	571.0909532	76145460.	11.9999592	0.0000900	-0.0000900	0.3689622	-2.5839088
0.00008750	664.6735769	75962695.	11.9999590	0.0001050	-0.0001050	0.4287205	-3.0145603
0.00010000	664.6735769	66467358.	6.6009075	0.0000660	-0.0001740	0.2701445	-5.0109368 C
0.00011300	664.6735769	59082096.	6.6031920	0.0000743	-0.0001957	0.3033533	-5.6365586 C
0.00012500	664.6735769	53173886.	6.6054820	0.0000826	-0.0002174	0.3364371	-6.2620127 C
0.00013800	664.6735769	48339897.	6.6077775	0.0000909	-0.0002391	0.3693956	-6.8872987 C
0.00015000	664.6735769	44311572.	6.6100786	0.0000992	-0.0002608	0.4022286	-7.5124158 C
0.00016300	664.6735769	40902989.	6.6123851	0.0001075	-0.0002825	0.4349359	-8.1373635 C
0.00017500	664.6735769	37981347.	6.6146973	0.0001158	-0.0003042	0.4675171	-8.7621411 C
0.00018800	664.6735769	35449257.	6.6170151	0.0001241	-0.0003259	0.4999722	-9.3867480 C
0.00020000	664.6735769	33233679.	6.6193385	0.0001324	-0.0003476	0.5323008	-10.0111836 C
0.00021300	664.6735769	31278757.	6.6216675	0.0001407	-0.0003693	0.5645027	-10.6354473 C
0.00022500	664.6735769	29541048.	6.6240023	0.0001490	-0.0003910	0.5965777	-11.2595385 C
0.00023800	664.6735769	27986256.	6.6263428	0.0001574	-0.0004126	0.6285255	-11.8834564 C
0.00025000	664.6735769	26586943.	6.6286890	0.0001657	-0.0004343	0.6603459	-12.5072004 C
0.00026300	664.6735769	25320898.	6.6310410	0.0001741	-0.0004559	0.6920386	-13.1307700 C
0.00027500	664.6735769	24169948.	6.6333988	0.0001824	-0.0004776	0.7236034	-13.7541644 C
0.00028800	664.6735769	23119081.	6.6357624	0.0001908	-0.0004992	0.7550400	-14.3773830 C
0.00030000	664.6735769	22155786.	6.6381319	0.0001991	-0.0005209	0.7863483	-15.0004252 C
0.00031300	664.6735769	21269554.	6.6405073	0.0002075	-0.0005425	0.8175278	-15.6232902 C
0.00032500	664.6735769	20451495.	6.6428886	0.0002159	-0.0005641	0.8485785	-16.2459774 C
0.00033800	669.6175849	19840521.	6.6452759	0.0002243	-0.0005857	0.8795000	-16.8684861 C
0.00035000	694.1816530	19833762.	6.6476692	0.0002327	-0.0006073	0.9102920	-17.4908157 C
0.00036300	718.7282930	19826987.	6.6500685	0.0002411	-0.0006289	0.9409544	-18.1129655 C
0.00037500	743.2574475	19820199.	6.6524738	0.0002495	-0.0006505	0.9714869	-18.7349347 C
0.00038800	767.7690589	19813395.	6.6548852	0.0002579	-0.0006721	1.0018891	-19.3567227 C
0.00040000	792.2630691	19806577.	6.6573027	0.0002663	-0.0006937	1.0321609	-19.9783288 C
0.00041300	816.7394195	19799744.	6.6597264	0.0002747	-0.0007153	1.0623020	-20.5997522 C
0.00042500	841.1980514	19792895.	6.6621562	0.0002831	-0.0007369	1.0923121	-21.2209924 C
0.00043800	865.6389055	19786032.	6.6645923	0.0002916	-0.0007584	1.1221910	-21.8420485 C
0.00045000	890.0619222	19779154.	6.6670346	0.0003000	-0.0007800	1.1519384	-22.4629198 C
0.00046300	914.4670416	19772260.	6.6694831	0.0003085	-0.0008015	1.1815540	-23.0836057 C
0.00047500	938.8542032	19765352.	6.6719380	0.0003169	-0.0008231	1.2110375	-23.7041054 C
0.00048800	963.2233462	19758428.	6.6743992	0.0003254	-0.0008446	1.2403887	-24.3244181 C
0.00050100	1011.9073029	19744533.	6.6793407	0.0003423	-0.0008877	1.2986931	-25.5644801 C
0.00051300	1060.5184714	19730576.	6.6843080	0.0003593	-0.0009307	1.3564649	-26.8037851 C
0.00052500	1109.0563252	19716557.	6.6893014	0.0003763	-0.0009737	1.4137020	-28.0423274 C
0.00053800	1157.5203567	19702474.	6.6943210	0.0003933	-0.0010167	1.4704021	-29.2801009 C
0.00055000	1205.9100513	19688327.	6.6993673	0.0004103	-0.0010597	1.5265628	-30.5170992 C
0.00056300	1254.2248875	19674116.	6.7044404	0.0004274	-0.0011026	1.5821820	-31.7533161 C
0.00057500	1302.4643368	19659839.	6.7095408	0.0004445	-0.0011455	1.6372573	-32.9887452 C
0.00058800	1350.6278632	19645496.	6.7146686	0.0004616	-0.0011884	1.6917862	-34.2233800 C
0.00060100	1398.7149235	19631087.	6.7198242	0.0004788	-0.0012312	1.7457666	-35.4572138 C
0.00061300	1446.7249668	19616610.	6.7250079	0.0004960	-0.0012740	1.7991958	-36.6902400 C
0.00062500	1494.6574344	19602065.	6.7302200	0.0005132	-0.0013168	1.8520715	-37.9224516 C
0.00063800	1542.5117598	19587451.	6.7354609	0.0005304	-0.0013596	1.9043913	-39.1538420 C
0.00065000	1590.2873684	19572768.	6.7407308	0.0005477	-0.0014023	1.9561525	-40.3844039 C
0.00066300	1637.9836775	19558014.	6.7460301	0.0005650	-0.0014450	2.0073528	-41.6141303 C

0.0000863	1685.6000958	19543190.	6.7513591	0.0005823	-0.0014877	2.0579894	-42.8430140	C
0.0000888	1733.1360235	19528293.	6.7567182	0.0005997	-0.0015303	2.1080599	-44.0710475	C
0.0000913	1780.5908520	19513324.	6.7621077	0.0006170	-0.0015730	2.1575615	-45.2982235	C
0.0000938	1827.9639638	19498282.	6.7675280	0.0006345	-0.0016155	2.2064917	-46.5245344	C
0.0000963	1875.2547322	19483166.	6.7729795	0.0006519	-0.0016581	2.2548476	-47.7499724	C
0.0000988	1922.4625211	19467975.	6.7784624	0.0006694	-0.0017006	2.3026267	-48.9745298	C
0.0001013	1969.5866849	19452708.	6.7839772	0.0006869	-0.0017431	2.3498261	-50.1981985	C
0.0001038	2016.6265683	19437365.	6.7895242	0.0007044	-0.0017856	2.3964429	-51.4209706	C
0.0001063	2063.5815058	19421944.	6.7951039	0.0007220	-0.0018280	2.4424745	-52.6428377	C
0.0001088	2110.4508218	19406444.	6.8007167	0.0007396	-0.0018704	2.4879178	-53.8637916	C
0.0001113	2157.2338302	19390866.	6.8063629	0.0007572	-0.0019128	2.5327699	-55.0838238	C
0.0001138	2203.9298343	19375207.	6.8120429	0.0007749	-0.0019551	2.5770280	-56.3029256	C
0.0001163	2250.5381264	19359468.	6.8177572	0.0007926	-0.0019974	2.6206889	-57.5210882	C
0.0001188	2297.0579876	19343646.	6.8235062	0.0008103	-0.0020397	2.6637497	-58.7383029	C
0.0001213	2343.4886874	19327742.	6.8292903	0.0008281	-0.0020819	2.7062072	-59.9545604	C
0.0001238	2389.8294839	19311753.	6.8351100	0.0008458	-0.0021242	2.7480583	-60.0000000	CY
0.0001263	2436.0806733	19295689.	6.8409302	0.0008637	-0.0021663	2.7892897	-60.0000000	CY
0.0001288	2482.2439853	19279565.	6.8466049	0.0008815	-0.0022085	2.8298539	-60.0000000	CY
0.0001313	2528.3160473	19263360.	6.8523138	0.0008994	-0.0022506	2.8698014	-60.0000000	CY
0.0001338	2574.2958079	19247071.	6.8580574	0.0009173	-0.0022927	2.9091286	-60.0000000	CY
0.0001363	2620.1825005	19230697.	6.8638362	0.0009352	-0.0023348	2.9478322	-60.0000000	CY
0.0001388	2665.1795524	19208501.	6.8689690	0.0009531	-0.0023769	2.9857072	-60.0000000	CY
0.0001413	2707.3949012	19167398.	6.8718545	0.0009706	-0.0024194	3.0222763	-60.0000000	CY
0.0001438	2746.2010562	19104007.	6.8720120	0.0009879	-0.0024621	3.0573965	-60.0000000	CY
0.0001463	2782.6868543	19026919.	6.8704415	0.0010048	-0.0025052	3.0913650	-60.0000000	CY
0.0001488	2818.9055263	18950625.	6.8689540	0.0010218	-0.0025482	3.1247191	-60.0000000	CY
0.0001588	2932.1180462	18470035.	6.8386903	0.0010856	-0.0027244	3.2446656	-60.0000000	CY
0.0001688	3008.1865249	17826291.	6.7820460	0.0011445	-0.0029055	3.3471408	-60.0000000	CY
0.0001788	3083.3954567	17249765.	6.7333881	0.0012036	-0.0030864	3.4426156	-60.0000000	CY
0.0001888	3157.9628715	16730929.	6.6916806	0.0012631	-0.0032669	3.5310388	-60.0000000	CY
0.0001988	3230.7997728	16255596.	6.6548876	0.0013227	-0.0034473	3.6120181	-60.0000000	CY
0.0002088	3282.7963225	15725970.	6.6041332	0.0013786	-0.0036314	3.6809708	-60.0000000	CY
0.0002188	3312.8281738	15144357.	6.5363558	0.0014298	-0.0038202	3.7380646	-60.0000000	CY
0.0002288	3341.3084442	14606813.	6.4742476	0.0014810	-0.0040090	3.7894771	-60.0000000	CY
0.0002388	3369.4552936	14112902.	6.4184007	0.0015324	-0.0041976	3.8354955	-60.0000000	CY
0.0002488	3397.2612418	13657332.	6.3680819	0.0015841	-0.0043859	3.8760386	-60.0000000	CY
0.0002588	3424.4629991	13234640.	6.3204915	0.0016354	-0.0045746	3.9106647	-60.0000000	CY
0.0002688	3451.2727507	12841945.	6.2770165	0.0016869	-0.0047631	3.9397126	-60.0000000	CY
0.0002788	3477.7357100	12476182.	6.2376550	0.0017387	-0.0049513	3.9631797	-60.0000000	CY
0.0002888	3503.8434366	12134523.	6.2020040	0.0017908	-0.0051392	3.9809737	-60.0000000	CY
0.0002988	3529.5869190	11814517.	6.1697161	0.0018432	-0.0053268	3.9929983	-60.0000000	CY
0.0003088	3554.9567407	11514030.	6.1404901	0.0018959	-0.0055141	3.9991532	-60.0000000	CY
0.0003188	3579.8811284	11231000.	6.1137310	0.0019488	-0.0057012	3.9969286	-60.0000000	CY
0.0003288	3604.2943994	10963633.	6.0883832	0.0020016	-0.0058884	3.9999894	-60.0000000	CY
0.0003388	3625.6079105	10702902.	6.0621824	0.0020536	-0.0060764	3.9985465	-60.0000000	CY
0.0003488	3641.9963415	10443000.	6.0322941	0.0021038	-0.0062662	3.9974160	-60.0000000	CY
0.0003588	3653.4357590	10183793.	5.9987710	0.0021521	-0.0064579	3.9985783	60.0000000	CY
0.0003688	3661.2688353	9928865.	5.9631052	0.0021989	-0.0066511	3.9990989	60.0000000	CY
0.0003788	3667.0100950	9681875.	5.9275385	0.0022451	-0.0068449	3.9971595	60.0000000	CY
0.0003888	3672.6346517	9447292.	5.8942597	0.0022914	-0.0070386	3.9997562	60.0000000	CY
0.0003988	3677.9030045	9223581.	5.8618466	0.0023374	-0.0072326	3.9936409	60.0000000	CY
0.0004088	3682.8888405	9010126.	5.8303965	0.0023832	-0.0074268	3.9979554	60.0000000	CY
0.0004188	3687.7844668	8806649.	5.8008263	0.0024291	-0.0076209	3.9998893	60.0000000	CY
0.0004288	3692.5308021	8612317.	5.7731734	0.0024752	-0.0078148	3.9928278	60.0000000	CY
0.0004388	3697.1755281	8426611.	5.7471761	0.0025216	-0.0080084	3.9972845	60.0000000	CY
0.0004488	3701.7450236	8249014.	5.7226532	0.0025680	-0.0082020	3.9996243	60.0000000	CY
0.0004588	3706.2040478	8078919.	5.6996101	0.0026147	-0.0083953	3.9959947	60.0000000	CY
0.0004688	3710.5491636	7915838.	5.6779628	0.0026615	-0.0085885	3.9947286	60.0000000	CY
0.0004788	3714.8331197	7759443.	5.6574798	0.0027085	-0.0087815	3.9982457	60.0000000	CY
0.0004888	3719.0352508	7609279.	5.6379138	0.0027555	-0.0089745	3.9998763	60.0000000	CY
0.0004988	3722.9581654	7464578.	5.6179612	0.0028020	-0.0091680	3.9943762	60.0000000	CY
0.0005088	3726.8086986	7325423.	5.5990911	0.0028485	-0.0093615	3.9935775	60.0000000	CY
0.0005188	3730.6155589	7191548.	5.5811528	0.0028952	-0.0095548	3.9972678	60.0000000	CY
0.0005288	3734.3780089	7062653.	5.5640962	0.0029420	-0.0097480	3.9994102	60.0000000	CY
0.0005388	3738.0859759	6938443.	5.5479061	0.0029889	-0.0099411	3.9988671	60.0000000	CY
0.0005488	3741.6957192	6818580.	5.5326768	0.0030361	-0.0101339	3.9904891	60.0000000	CYT
0.0006088	3762.4651203	6180641.	5.4554862	0.0033210	-0.0112890	3.9889160	60.0000000	CYT
0.0006688	3780.6321105	5653282.	5.4009538	0.0036119	-0.0124381	3.9873440	60.0000000	CYT

0.0007288 3782.5161914 5190417. 5.3841027 0.0039237 -0.0135663 3.9918348 60.0000000 CYT

 Summary of Results for Nominal (Unfactored) Moment Capacity for Section 1

Moment values interpolated at maximum compressive strain = 0.003
 or maximum developed moment if pile fails at smaller strains.

Load No.	Axial Thrust kips	Nominal Mom. Cap. in-kip	Max. Comp. Strain
1	0.000	3738.934	0.00300000

Note note that the values of moment capacity in the table above are not factored by a strength reduction factor (phi-factor).

In ACI 318-08, the value of the strength reduction factor depends on whether the transverse reinforcing steel bars are tied hoops (0.65) or spirals (0.70).

The above values should be multiplied by the appropriate strength reduction factor to compute ultimate moment capacity according to ACI 318-08, Section 9.3.2.2 or the value required by the design standard being followed.

The following table presents factored moment capacities and corresponding bending stiffnesses computed for common resistance factor values used for reinforced concrete sections.

Axial Load No.	Resistance Factor for Moment	Nominal Moment Capacity in-kip	Ultimate (Factored) Axial Thrust kips	Ultimate (Factored) Moment Capacity in-kip	Bending Stiffness at Ult. Mom. Cap. kip-in ²
1	0.65	3738.934	0.000	2430.307	19297694.007
1	0.70	3738.934	0.000	2617.254	19231742.433
1	0.75	3738.934	0.000	2804.200	18981601.532

 p-y Curves Reported for Specified Depths

p-y Curve in Sand Computed Using Reese Criteria for Static Loading Conditions

Soil Layer Number	=	1
Depth below pile head	=	13.500 ft
Depth below ground surface	=	0.000 ft
Equivalent Depth (see note)	=	0.000 ft
Ground Slope Angle	=	0.000 degrees
Pile Batter	=	0.000 degrees
Effective Slope	=	0.000 degrees
Pile Diameter, b	=	24.000 in
Angle of Friction	=	18.000 degrees
Avg. Eff. Unit Weight	=	62.60000 pcf
kpy	=	375.000
K active	=	0.528
K passive	=	1.894
K0	=	0.400
Pst	=	0.000 lbs/in
Psd	=	0.000 lbs/in
Ps = Psd (deep controls)	=	0.000 lbs/in
A (static)	=	2.8300
B (static)	=	2.1400
C = Pm/(Ym ^{1/n})	=	0.0000
n = Pm/(m Ym)	=	0.0000

$$\begin{aligned}
m &= (P_u - P_m) / (Y_u - Y_m) &= & 0.0000 \\
Y_k &= [c / (kx)]^{n / (n-1)} &= & 0.0000 \text{ in} \\
P_k & &= & 0.000 \text{ lbs/in} \\
Y_m &= b / 60 &= & 0.4000 \text{ in} \\
P_m &= B \text{ ps} &= & 0.000 \text{ lbs/in} \\
Y_u &= 3b / 80 &= & 0.9000 \text{ in} \\
P_u &= A \text{ Ps} &= & 0.000 \text{ lbs/in} \\
E_{s,lim} & &= & 0.000 \text{ lbs/in/in} \\
p\text{-multiplier} & &= & 1.00000 \\
y\text{-multiplier} & &= & 1.00000
\end{aligned}$$

This p-y curve is computed using the equivalent depth.

This curve has the normal shape for a Reese sand p-y curve where $Y_k < Y_m < Y_u$.

y, in	p, lbs/in
0.0000	0.0000
0.0000	0.0000 *
0.03636	0.0000
0.07273	0.0000
0.10909	0.0000
0.14545	0.0000
0.18182	0.0000
0.21818	0.0000
0.25455	0.0000
0.29091	0.0000
0.32727	0.0000
0.36364	0.0000
0.40000	0.0000
0.65000	0.0000
0.90000	0.0000
0.92250	0.0000
0.94500	0.0000

* p value(s) computed using $p = k * \text{Eff } x * y$

p-y Curve in Sand Computed Using Reese Criteria for Static Loading Conditions

$$\begin{aligned}
\text{Soil Layer Number} &= 1 \\
\text{Depth below pile head} &= 15.000 \text{ ft} \\
\text{Depth below ground surface} &= 1.500 \text{ ft} \\
\text{Equivalent Depth (see note)} &= 1.500 \text{ ft} \\
\text{Ground Slope Angle} &= 0.000 \text{ degrees} \\
\text{Pile Batter} &= 0.000 \text{ degrees} \\
\text{Effective Slope} &= 0.000 \text{ degrees} \\
\text{Pile Diameter, b} &= 24.000 \text{ in} \\
\text{Angle of Friction} &= 18.000 \text{ degrees} \\
\text{Avg. Eff. Unit Weight} &= 62.60000 \text{ pcf} \\
k_{py} &= 375.000 \text{ pci} \\
K_{\text{active}} &= 0.528 \\
K_{\text{passive}} &= 1.894 \\
K_0 &= 0.400 \\
P_{st} &= 28.629 \text{ lbs/in} \\
P_{sd} &= 105.440 \text{ lbs/in} \\
P_s = P_{st} \text{ (shallow controls)} &= 28.629 \text{ lbs/in} \\
A \text{ (static)} &= 2.2950 \\
B \text{ (static)} &= 1.6850 \\
C = P_m / (Y_m^{1/n}) &= 62.9008 \\
n = P_m / (m Y_m) &= 3.4529 \\
m = (P_u - P_m) / (Y_u - Y_m) &= 34.9275 \\
Y_k = [c / (kx)]^{n / (n-1)} &= 0.0014 \text{ in} \\
P_k &= 9.350 \text{ lbs/in} \\
Y_m = b / 60 &= 0.4000 \text{ in} \\
P_m = B \text{ ps} &= 48.240 \text{ lbs/in}
\end{aligned}$$

$Y_u = 3b/80 = 0.9000 \text{ in}$
 $P_u = A P_s = 65.704 \text{ lbs/in}$
 $E_{s,lim} = 6750.000 \text{ lbs/in/in}$
 $p\text{-multiplier} = 1.00000$
 $y\text{-multiplier} = 1.00000$

This p-y curve is computed using the equivalent depth.

This curve has the normal shape for a Reese sand p-y curve where $Y_k < Y_m < Y_u$.

y, in	p, lbs/in
0.0000	0.0000
0.00139	9.34954 *
0.03762	24.32691
0.07386	29.57553
0.11010	33.20033
0.14634	36.05207
0.18257	38.43779
0.21881	40.50711
0.25505	42.34540
0.29129	44.00643
0.32752	45.52648
0.36376	46.93134
0.40000	48.24000
0.65000	56.97187
0.90000	65.70374
0.92250	65.70374
0.94500	65.70374

* p value(s) computed using $p = k * \text{Eff} x * y$

p-y Curve in Sand Computed Using Reese Criteria for Static Loading Conditions

Soil Layer Number = 2
Depth below pile head = 17.000 ft
Depth below ground surface = 3.500 ft
Equivalent Depth (see note) = 3.484 ft
Ground Slope Angle = 0.000 degrees
Pile Batter = 0.000 degrees
Effective Slope = 0.000 degrees
Pile Diameter, b = 24.000 in
Angle of Friction = 18.000 degrees
Avg. Eff. Unit Weight = 62.60000 pcf
 $k_{py} = 375.000 \text{ pci}$
 $K_{active} = 0.528$
 $K_{passive} = 1.894$
 $K_0 = 0.400$
 $P_{st} = 88.741 \text{ lbs/in}$
 $P_{sd} = 246.027 \text{ lbs/in}$
 $P_s = P_{st} \text{ (shallow controls)} = 88.741 \text{ lbs/in}$
 $A \text{ (static)} = 1.6245$
 $B \text{ (static)} = 1.1635$
 $C = P_m / (Y_m^{1/n}) = 138.0479$
 $n = P_m / (m Y_m) = 3.1552$
 $m = (P_u - P_m) / (Y_u - Y_m) = 81.8132$
 $Y_k = [c / (kx)]^{n / (n-1)} = 0.0010 \text{ in}$
 $P_k = 15.360 \text{ lbs/in}$
 $Y_m = b / 60 = 0.4000 \text{ in}$
 $P_m = B p_s = 103.254 \text{ lbs/in}$
 $Y_u = 3b / 80 = 0.9000 \text{ in}$
 $P_u = A P_s = 144.161 \text{ lbs/in}$

Es,lim = 15677.457 lbs/in/in
 p-multiplier = 1.00000
 y-multiplier = 1.00000

This p-y curve is computed using the equivalent depth.

This curve has the normal shape for a Reese sand p-y curve where $Y_k < Y_m < Y_u$.

y, in	p, lbs/in
0.0000	0.0000
0.0009798	15.36022 *
0.03725	48.66081
0.07353	60.36227
0.10980	68.54300
0.14608	75.03325
0.18235	80.49772
0.21863	85.26208
0.25490	89.51295
0.29118	93.36835
0.32745	96.90818
0.36373	100.18936
0.40000	103.25400
0.65000	123.70729
0.90000	144.16058
0.92250	144.16058
0.94500	144.16058

* p value(s) computed using $p = k * \text{Eff} * y$

p-y Curve in Sand Computed Using Reese Criteria for Static Loading Conditions

Soil Layer Number = 2
 Depth below pile head = 19.000 ft
 Depth below ground surface = 5.500 ft
 Equivalent Depth (see note) = 5.484 ft
 Ground Slope Angle = 0.000 degrees
 Pile Batter = 0.000 degrees
 Effective Slope = 0.000 degrees
 Pile Diameter, b = 24.000 in
 Angle of Friction = 18.000 degrees
 Avg. Eff. Unit Weight = 62.60000 pcf
 kpy = 375.000 pci
 K active = 0.528
 K passive = 1.894
 K0 = 0.400
 Pst = 174.988 lbs/in
 Psd = 386.614 lbs/in
 Ps = Pst (shallow controls) = 174.988 lbs/in
 A (static) = 1.1477
 B (static) = 0.7874
 C = $P_m / (Y_m^{1/n})$ = 192.7041
 n = $P_m / (m Y_m)$ = 2.7316
 m = $(P_u - P_m) / (Y_u - Y_m)$ = 126.1040
 $Y_k = [c / (kx)]^{n / (n-1)}$ = 0.0005 in
 Pk = 11.692 lbs/in
 $Y_m = b / 60$ = 0.4000 in
 $P_m = B ps$ = 137.789 lbs/in
 $Y_u = 3b / 80$ = 0.9000 in
 $P_u = A Ps$ = 200.841 lbs/in
 Es,lim = 24677.457 lbs/in/in
 p-multiplier = 1.00000
 y-multiplier = 1.00000

This p-y curve is computed using the equivalent depth.

This curve has the normal shape for a Reese sand p-y curve where $Y_k < Y_m < Y_u$.

y, in	p, lbs/in
0.0000	0.0000
0.0004738	11.69208 *
0.03679	57.52442
0.07311	73.96501
0.10944	85.73260
0.14576	95.21632
0.18208	103.29631
0.21840	110.40850
0.25472	116.80491
0.29104	122.64612
0.32736	128.04156
0.36368	133.06960
0.40000	137.78852
0.65000	169.31452
0.90000	200.84053
0.92250	200.84053
0.94500	200.84053

* p value(s) computed using $p = k * \text{Eff} \times y$

p-y Curve in Sand Computed Using Reese Criteria for Static Loading Conditions

Soil Layer Number	=	2
Depth below pile head	=	21.000 ft
Depth below ground surface	=	7.500 ft
Equivalent Depth (see note)	=	7.484 ft
Ground Slope Angle	=	0.000 degrees
Pile Batter	=	0.000 degrees
Effective Slope	=	0.000 degrees
Pile Diameter, b	=	24.000 in
Angle of Friction	=	18.000 degrees
Avg. Eff. Unit Weight	=	62.60000 pcf
kpy	=	375.000 pci
K active	=	0.528
K passive	=	1.894
K0	=	0.400
Pst	=	286.985 lbs/in
Psd	=	527.201 lbs/in
Ps = Pst (shallow controls)	=	286.985 lbs/in
A (static)	=	0.9413
B (static)	=	0.5765
$C = P_m / (Y_m^{1/n})$	=	263.0926
$n = P_m / (m Y_m)$	=	1.9750
$m = (P_u - P_m) / (Y_u - Y_m)$	=	209.4068
$Y_k = [c / (kx)]^{n / (n-1)}$	=	0.0001 in
Pk	=	1.815 lbs/in
$Y_m = b / 60$	=	0.4000 in
$P_m = B p_s$	=	165.433 lbs/in
$Y_u = 3b / 80$	=	0.9000 in
$P_u = A P_s$	=	270.136 lbs/in
Es,lim	=	33677.457 lbs/in/in
p-multiplier	=	1.00000
y-multiplier	=	1.00000

This p-y curve is computed using the equivalent depth.

This curve has the normal shape for a Reese sand p-y curve where $Y_k < Y_m < Y_u$.

y, in	p, lbs/in
-----	-----

0.0000	0.0000
0.0000539	1.81505 *
0.03641	49.16270
0.07277	69.80584
0.10913	85.70314
0.14549	99.13548
0.18185	110.98919
0.21821	121.71980
0.25457	131.59829
0.29092	140.80146
0.32728	149.45222
0.36364	157.64017
0.40000	165.43296
0.65000	217.78466
0.90000	270.13636
0.92250	270.13636
0.94500	270.13636

* p value(s) computed using $p = k * \text{Eff } x * y$

p-y Curve in Sand Computed Using Reese Criteria for Static Loading Conditions

Soil Layer Number	=	2
Depth below pile head	=	23.000 ft
Depth below ground surface	=	9.500 ft
Equivalent Depth (see note)	=	9.484 ft
Ground Slope Angle	=	0.000 degrees
Pile Batter	=	0.000 degrees
Effective Slope	=	0.000 degrees
Pile Diameter, b	=	24.000 in
Angle of Friction	=	18.000 degrees
Avg. Eff. Unit Weight	=	62.60000 pcf
kpy	=	375.000 pci
K active	=	0.528
K passive	=	1.894
K0	=	0.400
Pst	=	424.734 lbs/in
Psd	=	667.788 lbs/in
Ps = Pst (shallow controls)	=	424.734 lbs/in
A (static)	=	0.8852
B (static)	=	0.5077
$C = Pm/(Ym^{(1/n)})$	=	371.8776
$n = Pm/(m Ym)$	=	1.6816
$m = (Pu - Pm)/(Yu - Ym)$	=	320.6054
$Yk = [c/(kx)]^{(n/(n-1))}$	=	0.0000 in
Pk	=	0.354 lbs/in
$Ym = b/60$	=	0.4000 in
$Pm = B ps$	=	215.655 lbs/in
$Yu = 3b/80$	=	0.9000 in
$Pu = A Ps$	=	375.958 lbs/in
Es,lim	=	42677.457 lbs/in/in
p-multiplier	=	1.00000
y-multiplier	=	1.00000

This p-y curve is computed using the equivalent depth.

This curve has the normal shape for a Reese sand p-y curve where $Yk < Ym < Yu$.

y, in	p, lbs/in
0.0000	0.0000
8.2851E-06	0.35359 *
0.03637	51.82447
0.07273	78.25588
0.10910	99.59149

0.14546	118.17179
0.18182	134.93970
0.21819	150.39174
0.25455	164.82891
0.29091	178.45061
0.32727	191.39727
0.36364	203.77242
0.40000	215.65503
0.65000	295.80638
0.90000	375.95774
0.92250	375.95774
0.94500	375.95774

* p value(s) computed using $p = k * \text{Eff } x * y$

p-y Curve in Sand Computed Using Reese Criteria for Static Loading Conditions

Soil Layer Number	=	2
Depth below pile head	=	25.000 ft
Depth below ground surface	=	11.500 ft
Equivalent Depth (see note)	=	11.484 ft
Ground Slope Angle	=	0.000 degrees
Pile Batter	=	0.000 degrees
Effective Slope	=	0.000 degrees
Pile Diameter, b	=	24.000 in
Angle of Friction	=	18.000 degrees
Avg. Eff. Unit Weight	=	62.60000 pcf
kpy	=	375.000 pci
K active	=	0.528
K passive	=	1.894
K0	=	0.400
Pst	=	588.233 lbs/in
Psd	=	808.375 lbs/in
Ps = Pst (shallow controls)	=	588.233 lbs/in
A (static)	=	0.8800
B (static)	=	0.5000
$C = Pm/(Ym^{(1/n)})$	=	513.4127
$n = Pm/(m Ym)$	=	1.6447
$m = (Pu - Pm)/(Yu - Ym)$	=	447.0567
$Yk = [c/(kx)]^{(n/(n-1))}$	=	0.0000 in
Pk	=	0.402 lbs/in
$Ym = b/60$	=	0.4000 in
$Pm = B ps$	=	294.116 lbs/in
$Yu = 3b/80$	=	0.9000 in
$Pu = A Ps$	=	517.645 lbs/in
Es_lim	=	51677.457 lbs/in/in
p-multiplier	=	1.00000
y-multiplier	=	1.00000

This p-y curve is computed using the equivalent depth.

This curve has the normal shape for a Reese sand p-y curve where $Yk < Ym < Yu$.

y, in	p, lbs/in
0.0000	0.0000
7.7755E-06	0.40182 *
0.03637	68.45476
0.07273	104.32818
0.10910	133.49215
0.14546	159.00609
0.18182	182.10934
0.21819	203.45696
0.25455	223.44716
0.29091	242.34437

0.32727	260.33520
0.36364	277.55740
0.40000	294.11627
0.65000	405.88046
0.90000	517.64464
0.92250	517.64464
0.94500	517.64464

* p value(s) computed using $p = k * \text{Eff } x * y$

p-y Curve in Sand Computed Using Reese Criteria for Static Loading Conditions

Soil Layer Number	=	2
Depth below pile head	=	27.000 ft
Depth below ground surface	=	13.500 ft
Equivalent Depth (see note)	=	13.484 ft
Ground Slope Angle	=	0.000 degrees
Pile Batter	=	0.000 degrees
Effective Slope	=	0.000 degrees
Pile Diameter, b	=	24.000 in
Angle of Friction	=	18.000 degrees
Avg. Eff. Unit Weight	=	62.60000 pcf
kpy	=	375.000 pci
K active	=	0.528
K passive	=	1.894
K0	=	0.400
Pst	=	777.482 lbs/in
Psd	=	948.962 lbs/in
Ps = Pst (shallow controls)	=	777.482 lbs/in
A (static)	=	0.8800
B (static)	=	0.5000
$C = Pm/(Ym^{1/n})$	=	678.5907
$n = Pm/(m Ym)$	=	1.6447
$m = (Pu - Pm)/(Yu - Ym)$	=	590.8864
$Yk = [c/(kx)]^{n/(n-1)}$	=	0.0000 in
Pk	=	0.638 lbs/in
$Ym = b/60$	=	0.4000 in
$Pm = B ps$	=	388.741 lbs/in
$Yu = 3b/80$	=	0.9000 in
$Pu = A Ps$	=	684.184 lbs/in
Es,lim	=	60677.457 lbs/in/in
p-multiplier	=	1.00000
y-multiplier	=	1.00000

This p-y curve is computed using the equivalent depth.

This curve has the normal shape for a Reese sand p-y curve where $Yk < Ym < Yu$.

y, in	p, lbs/in
0.0000	0.0000
0.0000105	0.63814 *
0.03637	90.48218
0.07274	137.89583
0.10910	176.44196
0.14546	210.16397
0.18182	240.69981
0.21819	268.91523
0.25455	295.33657
0.29091	320.31329
0.32727	344.09205
0.36364	366.85491
0.40000	388.74105
0.65000	536.46264
0.90000	684.18424

0.92250 684.18424
 0.94500 684.18424

* p value(s) computed using $p = k * \text{Eff } x * y$

p-y Curve in Sand Computed Using Reese Criteria for Static Loading Conditions

Soil Layer Number = 2
 Depth below pile head = 29.000 ft
 Depth below ground surface = 15.500 ft
 Equivalent Depth (see note) = 15.484 ft
 Ground Slope Angle = 0.000 degrees
 Pile Batter = 0.000 degrees
 Effective Slope = 0.000 degrees
 Pile Diameter, b = 24.000 in
 Angle of Friction = 18.000 degrees
 Avg. Eff. Unit Weight = 62.60000 pcf
 kpy = 375.000 pci
 K active = 0.528
 K passive = 1.894
 K0 = 0.400
 Pst = 992.482 lbs/in
 Psd = 1089.549 lbs/in
 Ps = Pst (shallow controls) = 992.482 lbs/in
 A (static) = 0.8800
 B (static) = 0.5000
 C = Pm/(Ym^(1/n)) = 866.2441
 n = Pm/(m Ym) = 1.6447
 m = (Pu-Pm)/(Yu-Ym) = 754.2865
 Yk = [c/(kx)]^(n/(n-1)) = 0.0000 in
 Pk = 0.960 lbs/in
 Ym = b/60 = 0.4000 in
 Pm = B ps = 496.241 lbs/in
 Yu = 3b/80 = 0.9000 in
 Pu = A Ps = 873.384 lbs/in
 Es,lim = 69677.457 lbs/in/in
 p-multiplier = 1.00000
 y-multiplier = 1.00000

This p-y curve is computed using the equivalent depth.

This curve has the normal shape for a Reese sand p-y curve where $Yk < Ym < Yu$.

y, in	p, lbs/in
0.0000	0.0000
0.0000138	0.95994 *
0.03638	115.50930
0.07274	176.03263
0.10910	225.23713
0.14546	268.28377
0.18183	307.26330
0.21819	343.28083
0.25455	377.00822
0.29091	408.89155
0.32728	439.24566
0.36364	468.30298
0.40000	496.24114
0.65000	684.81276
0.90000	873.38439
0.92250	873.38439
0.94500	873.38439

* p value(s) computed using $p = k * \text{Eff } x * y$

p-y Curve in Sand Computed Using Reese Criteria for Static Loading Conditions

Soil Layer Number	=	2
Depth below pile head	=	31.000 ft
Depth below ground surface	=	17.500 ft
Equivalent Depth (see note)	=	17.484 ft
Ground Slope Angle	=	0.000 degrees
Pile Batter	=	0.000 degrees
Effective Slope	=	0.000 degrees
Pile Diameter, b	=	24.000 in
Angle of Friction	=	18.000 degrees
Avg. Eff. Unit Weight	=	62.60000 pcf
kpy	=	375.000 pci
K active	=	0.528
K passive	=	1.894
K0	=	0.400
Pst	=	1233.233 lbs/in
Psd	=	1230.136 lbs/in
Ps = Psd (deep controls)	=	1230.136 lbs/in
A (static)	=	0.8800
B (static)	=	0.5000
C = Pm/(Ym^(1/n))	=	1073.6696
n = Pm/(m Ym)	=	1.6447
m = (Pu-Pm)/(Yu-Ym)	=	934.9034
Yk = [c/(kx)]^(n/(n-1))	=	0.0000 in
Pk	=	1.375 lbs/in
Ym = b/60	=	0.4000 in
Pm = B ps	=	615.068 lbs/in
Yu = 3b/80	=	0.9000 in
Pu = A Ps	=	1082.520 lbs/in
Es_lim	=	78677.457 lbs/in/in
p-multiplier	=	1.00000
y-multiplier	=	1.00000

This p-y curve is computed using the equivalent depth.

This curve has the normal shape for a Reese sand p-y curve where $Y_k < Y_m < Y_u$.

y, in	p, lbs/in
0.0000	0.0000
0.0000175	1.37483 *
0.03638	143.17650
0.07274	218.18985
0.10910	279.17523
0.14547	332.52864
0.18183	380.84127
0.21819	425.48276
0.25455	467.28582
0.29091	506.80330
0.32728	544.42544
0.36364	580.44029
0.40000	615.06803
0.65000	848.79387
0.90000	1082.51972
0.92250	1082.51972
0.94500	1082.51972

* p value(s) computed using $p = k * \text{Eff} x * y$

p-y Curve in Sand Computed Using Reese Criteria for Static Loading Conditions

Soil Layer Number = 2
 Depth below pile head = 33.000 ft
 Depth below ground surface = 19.500 ft
 Equivalent Depth (see note) = 19.484 ft
 Ground Slope Angle = 0.000 degrees
 Pile Batter = 0.000 degrees
 Effective Slope = 0.000 degrees
 Pile Diameter, b = 24.000 in
 Angle of Friction = 18.000 degrees
 Avg. Eff. Unit Weight = 62.60000 pcf
 kpy = 375.000 pci
 K active = 0.528
 K passive = 1.894
 K0 = 0.400
 Pst = 1499.735 lbs/in
 Psd = 1370.723 lbs/in
 Ps = Psd (deep controls) = 1370.723 lbs/in
 A (static) = 0.8800
 B (static) = 0.5000
 C = Pm/(Ym^(1/n)) = 1196.3747
 n = Pm/(m Ym) = 1.6447
 m = (Pu-Pm)/(Yu-Ym) = 1041.7495
 Yk = [c/(kx)]^(n/(n-1)) = 0.0000 in
 Pk = 1.532 lbs/in
 Ym = b/60 = 0.4000 in
 Pm = B ps = 685.362 lbs/in
 Yu = 3b/80 = 0.9000 in
 Pu = A Ps = 1206.236 lbs/in
 Es,lim = 87677.457 lbs/in/in
 p-multiplier = 1.00000
 y-multiplier = 1.00000

This p-y curve is computed using the equivalent depth.

This curve has the normal shape for a Reese sand p-y curve where $Y_k < Y_m < Y_u$.

y, in	p, lbs/in
0.0000	0.0000
0.0000175	1.53173 *
0.03638	159.53952
0.07274	243.12583
0.10910	311.08097
0.14547	370.53191
0.18183	424.36598
0.21819	474.10936
0.25455	520.68991
0.29091	564.72368
0.32728	606.64548
0.36364	646.77632
0.40000	685.36151
0.65000	945.79889
0.90000	1206.23626
0.92250	1206.23626
0.94500	1206.23626

* p value(s) computed using $p = k * \text{Eff } x * y$

p-y Curve in Sand Computed Using Reese Criteria for Static Loading Conditions

Soil Layer Number = 2
 Depth below pile head = 35.000 ft
 Depth below ground surface = 21.500 ft
 Equivalent Depth (see note) = 21.484 ft
 Ground Slope Angle = 0.000 degrees

Pile Batter	=	0.000 degrees
Effective Slope	=	0.000 degrees
Pile Diameter, b	=	24.000 in
Angle of Friction	=	18.000 degrees
Avg. Eff. Unit Weight	=	62.60000 pcf
kpy	=	375.000 pci
K active	=	0.528
K passive	=	1.894
K0	=	0.400
Pst	=	1791.987 lbs/in
Psd	=	1511.310 lbs/in
Ps = Psd (deep controls)	=	1511.310 lbs/in
A (static)	=	0.8800
B (static)	=	0.5000
$C = Pm/(Ym^{(1/n)})$	=	1319.0798
$n = Pm/(m Ym)$	=	1.6447
$m = (Pu-Pm)/(Yu-Ym)$	=	1148.5956
$Yk = [c/(kx)]^{(n/(n-1))}$	=	0.0000 in
Pk	=	1.689 lbs/in
$Ym = b/60$	=	0.4000 in
$Pm = B ps$	=	755.655 lbs/in
$Yu = 3b/80$	=	0.9000 in
$Pu = A Ps$	=	1329.953 lbs/in
Es,lim	=	96677.457 lbs/in/in
p-multiplier	=	1.00000
y-multiplier	=	1.00000

This p-y curve is computed using the equivalent depth.

This curve has the normal shape for a Reese sand p-y curve where $Yk < Ym < Yu$.

y, in	p, lbs/in
0.0000	0.0000
0.0000175	1.68863 *
0.03638	175.90253
0.07274	268.06180
0.10910	342.98670
0.14547	408.53518
0.18183	467.89070
0.21819	522.73596
0.25455	574.09400
0.29091	622.64406
0.32728	668.86553
0.36364	713.11236
0.40000	755.65500
0.65000	1042.80390
0.90000	1329.95280
0.92250	1329.95280
0.94500	1329.95280

* p value(s) computed using $p = k * \text{Eff } x * y$

Summary of Pile Response(s)

Definitions of Pile-head Loading Conditions:

Load Type 1: Load 1 = Shear, lbs, and Load 2 = Moment, in-lbs

Load Type 2: Load 1 = Shear, lbs, and Load 2 = Slope, radians
 Load Type 3: Load 1 = Shear, lbs, and Load 2 = Rotational Stiffness, in-lbs/radian
 Load Type 4: Load 1 = Top Deflection, inches, and Load 2 = Moment, in-lbs
 Load Type 5: Load 1 = Top Deflection, inches, and Load 2 = Slope, radians

Case No.	Load Type	Pile-head Condition 1 V(lbs) or y(inches)	Pile-head Condition 2 in-lb, rad., or in-lb/rad.	Axial Loading lbs	Maximum Pile-head Deflection inches	Maximum Moment in Pile in-lbs	Maximum Shear in Pile lbs	Pile-head Rotation radians
1	1	V = 0.000	M = 0.000	0.0000000	4.05726193	1511811.	-16008.	-0.01472004

 Summary of Warning Messages

The following warning was reported 2306 times

**** Warning ****

An unreasonable value was input for friction angle has been specified for a soil layer defined using the sand criteria. The input value is either smaller than 20 degrees or higher than 48 degrees. The input data should be checked for correctness.

The analysis ended normally.

APPENDIX K: STUDENT THESES AND DISSERTATION

This section presents previously published theses and a dissertation by students. The contents include:

- Ellis (2011): A Subsurface Investigation in Taylor Clay
- Dellinger (2011): The Use of Time Domain Reflectometry Probes for the Moisture Monitoring of a Drilled Shaft Retaining Wall in Expansive Clay
- Koutrouvelis (2012): Earth Pressures Applied on Drilled Shaft Retaining Walls in Expansive Clay during Natural Cycles of Moisture Fluctuation
- Brown (2013): The Behavior of Drilled Shaft Retaining Walls in Expansive Clay Soils

Copyright
by
Trenton Blake Ellis
2011

**The Thesis Committee for Trenton Blake Ellis
Certifies that this is the approved version of the following thesis:**

A Subsurface Investigation in Taylor Clay

**APPROVED BY
SUPERVISING COMMITTEE:**

Supervisor:

Chadi S. El Mohtar

Robert B. Gilbert

A Subsurface Investigation in Taylor Clay

by

Trenton Blake Ellis, B.S.C.E.

Thesis

Presented to the Faculty of the Graduate School of

The University of Texas at Austin

in Partial Fulfillment

of the Requirements

for the Degree of

Master of Science in Engineering

The University of Texas at Austin

August 2011

Acknowledgements

The author is indebted to many people for their help and support throughout this research project. Many thanks are in order to Fugro Consultants, Inc. for their help with the subsurface investigation and valuable laboratory guidance. This project would not have been possible without funding from the Texas Department of Transportation. Though not directly related to the research presented herein, it was also a pleasure to work with Lymon C. Reese and Associates, McKinney Drilling Company and HVJ and Associates. Perhaps most importantly, the author wishes to thank Roy Lee for allowing the research team to dig holes in his property over the past two years.

The author's advisors, Dr. Chadi El Mohtar and Dr. Robert Gilbert, have provided meaningful insight throughout the study. The author would also like to thank the other two students involved with this research project, Andrew Brown and Greg Dellinger, for their help in the laboratory and the field. Thanks also extend to the University of Texas soil dynamics research group for braving extreme heat to run seismic tests on site. Finally, the author offers his thanks to friends and family who have kept life interesting and lively in the midst of long hours in the field and the lab.

Abstract

A Subsurface Investigation in Taylor Clay

Trenton Blake Ellis, M.S.E.

The University of Texas at Austin, 2011

Supervisor: Chadi S. El Mohtar

A comprehensive field and laboratory investigation at the location of the Lymon C. Reese Research Wall is presented. Soil at the site is a stiff, fissured and heavily overconsolidated clay from the Taylor Group. Index properties such as Atterberg limits and clay fractions were used with common empirical guidelines to assess the qualitative swell potential. The soil's compressibility and strength characteristics were difficult to measure in the lab, owing to the stiff soil's secondary structure. Measured values were compared to well established correlations and test results from similar soils sampled from locations near the present test site. Cyclic swell tests were to predict the soil's lateral swell potential after multiple cycles of wetting and drying. Empirical guidelines indicated the soil has a "high" to "very high" swell potential. This was validated by the swelling that was observed during consolidation and cyclic swell tests. The soil's drained and undrained strengths were both rather large, often more typical of rock than soil. The stress history was not evident from consolidation results, either due to disturbance, cementation or extreme overconsolidation. The hydraulic conductivity was particularly elusive, again due to the soil's secondary structure.

Table of Contents

1	Introduction	1
1.1	Background	1
1.2	Setting: Lymon C. Reese Research Wall	1
1.3	Scope.....	2
1.4	Objectives.....	2
1.5	Thesis Organization	3
1.6	Sign Convention	3
2	Literature Review	4
2.1	Swell Potential in Expansive Clays.....	4
	<i>2.1.1 Overview</i>	<i>4</i>
	<i>2.1.2 Effects of Mineral Structure and Orientation</i>	<i>6</i>
	<i>2.1.3 Empirical Correlations</i>	<i>7</i>
	<i>2.1.4 Mechanistic Predictions.....</i>	<i>11</i>
2.2	Stiff Fissured Clays	16
	<i>2.2.1 Overview</i>	<i>16</i>
	<i>2.2.2 Hydraulic Conductivity.....</i>	<i>17</i>

	2.2.3	<i>Shear Strength</i>	17
	2.2.4	<i>Crumb Structure and Cyclic Moisture Fluctuations</i>	18
3		Properties of Taylor Clay at the Lymon C. Reese Research Wall	19
	3.1	Geology	19
	3.2	Laboratory and Field Investigations	27
4		Field Investigation at the Lymon C. Reese Research Wall	35
	4.1	Overview	35
		4.1.1 <i>Site Location and Subsurface Investigation</i>	35
		4.1.2 <i>Geologic Setting</i>	36
		4.1.3 <i>Climactic Setting</i>	40
	4.2	In-Situ Tests	41
		4.2.1 <i>Pocket Penetrometer</i>	41
		4.2.2 <i>Standard Penetration Test (SPT)</i>	42
		4.2.3 <i>Texas Cone Penetration Test</i>	43
		4.2.4 <i>Spectral Analysis of Surface Waves (SASW)</i>	44
5		Laboratory Investigation	50
	5.1	Index Properties	50

5.1.1	<i>Moisture Content</i>	50
5.1.2	<i>Atterberg Limits</i>	51
5.1.3	<i>Unit Weight</i>	54
5.1.4	<i>Grain-Size Analysis</i>	59
5.2	Consolidation	60
5.2.1	<i>Test Procedures</i>	60
5.2.2	<i>Summary of Results</i>	64
5.3	Cyclic Lateral Shrink and Swell	72
5.3.1	<i>Overview of Test Method</i>	72
5.3.2	<i>Trimming Procedure</i>	72
5.3.3	<i>Equipment Setup</i>	75
5.3.4	<i>Test Method</i>	76
5.3.5	<i>Summary of Results</i>	82
5.4	Undrained Shear Strength	97
5.5	Drained Shear Strength	99
5.5.1	<i>Testing Procedure</i>	99
5.5.2	<i>Summary of Results</i>	102
6	Comprehensive Analysis of the Taylor Clay	105

6.1	Soil Classification	105
6.2	Identifying the Active Zone.....	106
6.3	Delineation of Strata.....	106
6.4	Compressibility	107
6.5	Shear Strength.....	109
6.6	Hydraulic Conductivity	114
6.7	Swell Potential	115
7	Conclusions and Recommendations	119
Appendix A:	Boring Logs	121
Appendix B:	Consolidation Test 1	126
Appendix C:	Consolidation Test 2	154
Appendix D:	Consolidation Test 3	179
Appendix E:	Consolidation Test 4	203
Appendix F:	Consolidation Test 5	226
Appendix G:	Unconsolidated Undrained Triaxial Test Results...	247
Appendix H:	Direct Shear Test Results.....	255
References.....		271

1 Introduction

1.1 Background

Highly plastic and overconsolidated clay soils can present many challenges for geotechnical engineers. Over geologic time, these soils have experienced stresses that impart a secondary structure of slickensided fissures, mineral-filled bands and micro-cracks. This chaotic matrix of discontinuities significantly affects the soil's strength and permeability. The process of overconsolidation – whether by evapotranspiration or static loading – also locks some amount of stress into the soil structure, which can vary in magnitude depending on direction. For soils rich in montmorillonite, the swell potential associated with a strong affinity for water also influences the soil's behavior.

Researchers have attempted to understand the combined effect of these factors for decades, but the field behavior of this type of soil remains shrouded in uncertainty. By and large, the associated design procedures for any application are limited to empirical guidelines, local experience and engineering judgment. The laboratory methods that are available for measuring expansion potential and permeability must be carefully planned to model site conditions, typically involve several weeks of testing time and require careful interpretation.

1.2 Setting: Lymon C. Reese Research Wall

The Lymon C. Reese Research Wall is a drilled shaft retaining wall that was installed in the Taylor clay of Manor, TX. The drilled shafts were instrumented with optical strain gages and inclinometers to measure the wall's movement as moisture

fluctuations cause the retained soil to shrink and swell. Time domain reflectometry (TDR) sensors were installed in soil around the retaining wall to measure changes in volumetric moisture content, and a piezometer was installed near the retaining wall to monitor the groundwater level (Dellinger, 2011). The purpose of the project as a whole is to gain a better understanding of the magnitude and distribution of lateral pressures that an expansive soil may exert on a retaining structure. This thesis describes the subsurface investigation and soil properties at the test site.

1.3 Scope

The research presented in this thesis applies to clays from the Taylor Group in central Texas. The clays are very stiff, highly overconsolidated, highly plastic and fissured. In a qualitative sense, Taylor clay has properties that could pertain to either a hard blocky soil or a very soft rock. All of the test samples for this project were obtained from the Lymon C. Reese Research Wall test site in Manor, TX.

1.4 Objectives

This research was conducted to study the lateral pressures that can develop in shallow regions of the Taylor clay. This involved several approaches. First, a number of index properties such as Atterberg limits and clay fractions were measured. These values are commonly used to characterize this type of soil on an empirical basis. Standard engineering tests were also conducted to quantify the compressibility and strength properties of the soil at the Lymon C. Reese Research Wall test site. In addition, more

specialized tests were conducted to measure the lateral swell pressure under cyclic wetting and drying. The objective is to combine field and laboratory tests with a thorough review of local experience to gain a better understanding of the soil at the test site.

1.5 Thesis Organization

The thesis is organized into seven chapters. Chapter 2 is a literature review that provides background on expansive soils and stiff-fissured clays. Chapter 3 reviews the geology and engineering properties of Taylor clays near the test site. Chapter 4 summarizes the sampling and testing that occurred during the subsurface investigation. Chapter 5 describes the laboratory tests that were conducted and summarizes the results. Test results from Chapters 2, 3, 4 and 5 were compared in Chapter 6. General conclusions from the study are presented in Chapter 7.

1.6 Sign Convention

Measurements of axial strain are presented throughout the thesis in the discussion of various laboratory tests. In each case, positive strains refer to compression while negative strains refer to swelling. This is consistent with the geotechnical tradition of referring to compressive forces in the positive sense.

2 Literature Review

2.1 Swell Potential in Expansive Clays

2.1.1 Overview

In the presence of water, expansive clays can expand by sucking free water molecules into their mineral structure. This phenomenon causes volumetric strains and/or the exertion of swell pressures, depending on boundary conditions. The boundary conditions – which may include stress history, in-situ confinement, structural boundaries and a seasonally imposed system of dynamic moisture pathways – are difficult, if not impossible to replicate in the lab with small-scale samples.

Expansive soils are also prone to shrinking as water molecules are removed from the mineral structure. This process occurs much slower than swelling under normal field conditions because of the attraction between the clay and the water. During swelling, the clay pulls free water molecules into its structure and locks them into place. The water molecules are no longer “free” during shrinking, and external factors such as heat and air flow are required to overcome the attraction. As the clay minerals are robbed of water molecules, the soil exhibits volumetric shrinkage and cracking. Meanwhile, the surface tension in the water imparts negative pore pressures to the clay’s skeletal structure. The negative pore pressures can be very large in magnitude – corresponding to the large tensile forces required to remove the water molecules – which results in high effective stress and stiffness. The potential for a clay soil to swell is therefore a function of climate as well as clay mineralogy.

Katti (1994) ran large-scale laboratory tests to measure the lateral pressure exerted by a column of expansive Black Cotton soil. The researchers built a 9-ft tall stiffened steel frame, fitted for the measurement of lateral pressure at several depths and lined with a thin sand layer to distribute water. The lateral pressure was around zero near the surface after wetting for 60 to 90 days, but lateral pressures increased rapidly up to a 1.2-meter depth, thereafter remaining constant. The largest lateral stresses exceeded vertical stresses by 18 times, far greater than typical at-rest or passive earth pressures. Katti attributes this deviation from typical Coulomb and Rankine assumptions to physical and physiochemical alterations within the clay that occur during and after saturation. This may or may not be typical for other expansive soils with different mineralogies. It does, however, indicate that expansive soils can exhibit fundamentally different behavior than we expect from typical soils.

It has been also been shown that stress history can also influence the swell potential of expansive clays. Laboratory tests by Joshi and Katti (1980) have shown that, for a given surcharge, overconsolidated clays can exert larger lateral swell pressures than their normally consolidated counterparts. This change in swell potential caused by preloading was shown by measuring the lateral swell pressures that developed upon wetting under various surcharge loads. The higher surcharge loads were gradually reduced, overconsolidating the soil. The authors surmised that overconsolidation can cause a subtle rearrangement of the matrix of clay minerals and water molecules, essentially locking some amount of stress into the soil, Figure 1.

These concepts are not well understood, but designers mostly agree that highly overconsolidated soils are prone to exhibit additional swell potential that cannot be predicted based solely on the clay mineralogy and climate. The same holds true for most aspects of design involving expansive soils.

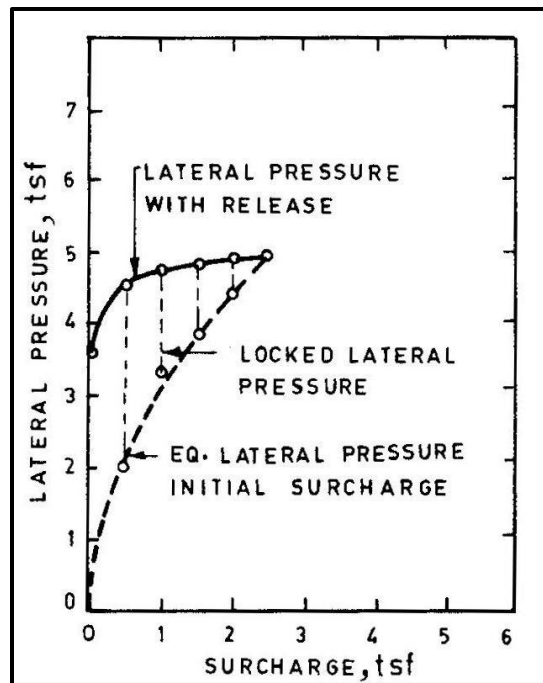


Figure 1. Locked-In Swell Potential from Overconsolidation, Joshi and Katti (1980)

2.1.2 Effects of Mineral Structure and Orientation

Expansive soils owe their swell potential to a unique aluminosilicate mineral structure that has been well documented extensively in the literature (Mitchell 2005). Smectite minerals, including montmorillonite, generally contain the most swell potential. Smectite's mineral sheets are connected to one another by weak van der Waals forces,

allowing cations within the mineral structure to be substituted with ease during formation. Isomorphic substitution, as the process is called, tends to replace silicon and aluminum with other cations. These cations are attracted to the region between mineral plates, whose surfaces are covered with negative charges. The interplate space is mostly populated with dipolar water molecules; the exchangeable cations bond with the negative ends of those water molecules. Owing to the weak van der Waals forces that connect the mineral plates, additional water can infiltrate between a mature soil's mineral plates as boundary conditions such as confinement and climate change. The influx of water into the mineral structure is the genesis for expansive behavior.

Young soils often have a neat arrangement of flatly stacked clay mineral sheets that would be expected to swell essentially perpendicular to the faces of the mineral plates. The particle arrangement of young soils is modified by processes including over-consolidation, weathering, shearing and cycles of wetting and drying. This process – termed ripening – creates a more complicated microstructure. The ripened microstructure first becomes more chaotic, then rearranges to a more stable pattern through multiple wetting and drying cycles. The microstructure of ripened clays becomes more random, consisting of a matrix of various structural arrangements (Kodikara et al., 1999). The resulting swell potential is difficult to predict, but is certainly three-dimensional.

2.1.3 Empirical Correlations

It is usually more practical to predict expansive potential with inexpensive index tests than to invest in a limited number of more robust laboratory methods. Index

properties do not measure any mechanistic aspect of swell potential, but they correlate well enough with swell potential to provide a qualitative indicator of what to expect. Laboratory tests, although complicated and expensive, do not generally replicate field conditions well enough to provide high quality predictions of field behavior.

Atterberg limits are widely used to estimate various aspects of clay behavior. Atterberg limits essentially measure the amount of water a soil can hold under specific – and arbitrary – dynamic loading conditions. The ability to hold more water under these arbitrary conditions is analogous to the weakness of the soil’s interlayer bonds and its ability to add water to its mineral structure. Table 1 (Chen, 1988) and Figure 2 (Daksanamurthy and Raman, 1973) present two guidelines that are used to qualitatively predict swell potential with Atterberg limits.

Table 1. Qualitative Relationship between PI and Swell Potential, Chen (1988)

Swell Potential	Plasticity Index
Low	0 – 15
Medium	10 – 35
High	20 – 55
Very High	35 and above

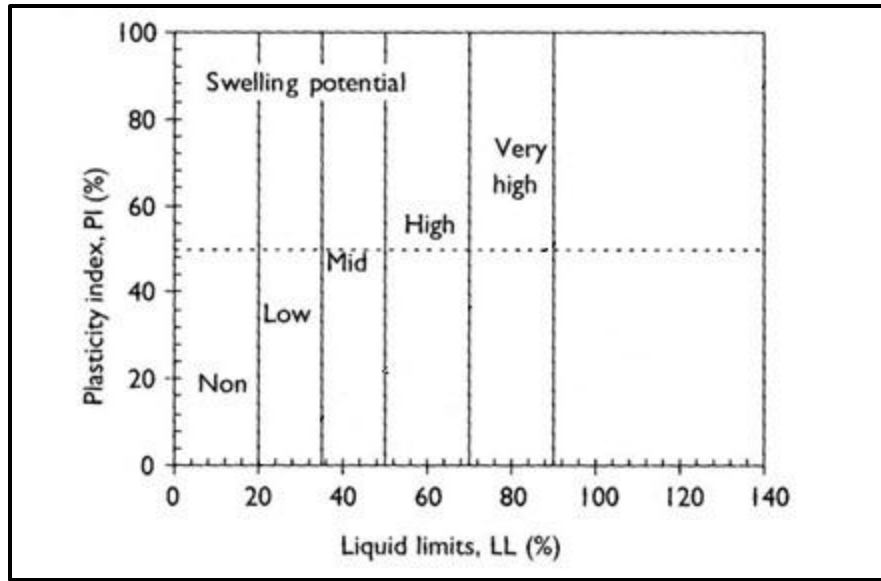


Figure 2. Qualitative Relationship Between PI, LL and Swelling Potential, Daksanamurthy and Raman (1973)

Swell potential is similarly related to the amount of suction that a soil can exert to bring water into its structure. Both measures (water carrying capacity and suction) are essentially functions of the physico-chemical structure of the soil. A soil’s physico-chemical structure can be quantified by a parameter termed colloidal activity (A_c). Skempton (1953) defined colloidal activity as the ratio of plasticity index (PI) to clay fraction (CF), Equation 1. Clay fraction is the percent of particles smaller in diameter than 0.002 mm. Higher A_c values indicate higher swelling potential, and Table 2 provides a simple guideline for classifying A_c values.

$$A_c = \frac{PI}{CF} \dots\dots\dots \text{Eq. 1}$$

The physico-chemical structure is also quantified by its cation exchange capacity (CEC), which is the milliequivalent of exchangeable cations per 100 grams of dry clay. Table 3 lists ranges of CEC and A_c values for the common clay minerals. As the table suggests, montmorillonite – particularly, sodium montmorillonite – possesses much greater swell potential than any other common clay mineral.

Table 2. Guideline for Interpreting Colloidal Activity (A_c) Values

A_c	Activity Class
< 0.75	Inactive
0.75 – 1.25	Normal
> 1.25	Active

Table 3. Cation Exchange Capacities and Activities of Common Clay Minerals, Nelson and Miller (1992)

Clay Mineral	CEC (meq/100 g)	A_c
Kaolinite	3 – 15	0.33 – 0.46
Illite	10 – 40	0.9
Montmorillonite (Ca)	80 - 150	1.5
Montmorillonite (Na)		7.2

2.1.4 Mechanistic Predictions

The swell potential of expansive soils is most commonly measured with the same type of equipment used to conduct one-dimensional consolidation tests. A remolded or undisturbed specimen is prepared in a rigid ring, typically 2.5 inches in diameter and 0.5 – 1.0 inches thick. An appropriate normal stress is applied to the specimen for a short time to allow seating and the closing of fissures and microcracks in the specimen. The specimen is then wetted, and the resulting strains from swelling are measured. ASTM D4546 describes several standard methods for conducting these types of tests.

In other cases the normal load is progressively increased to prevent swelling strains. The load required to achieve and maintain constant volume is a measure of the soil's heave potential. Fredlund (1980) has reported that heave measurements on trimmed specimens may lead to very unconservative results owing to sampling disturbance. Fredlund reports that measured heave values can be as low as half of the heave to be expected in-situ, and he has presented a method for correcting those errors.

According to Fredlund, the effects of disturbance during heave tests may be corrected as follows. The method applies to heave tests that involve swelling under constant volume, then loading up to a very large vertical effective stress and finally unloading back to some token load. First, the machine deflections are subtracted from the analysis and the resulting e -log- P' curve is plotted. The point of maximum curvature – usually just beyond the swell pressure – is then located. From this point, three lines are drawn: (1) horizontal, (2) tangent and (3) bisector of (1) and (2). Next, a line parallel to the rebound curve is drawn where it is tangent to the virgin compression curve. The

intersection of this line with the previously drawn bisector marks the corrected swell pressure corresponding to an undisturbed state of stress.

Another type of test has also been used in which the soil is allowed to swell and shrink while subjected to wetting and drying cycles. As the specimen is subjected to repeated drying and wetting cycles, it experiences volumetric shrinking and swelling. This essentially remolds the sample in a manner consistent with in-situ conditions while measuring the axial strains that occur throughout the successive cycles. In addition, the soil can be removed and weighed between cycles and periodically during drying cycles to track the moisture content throughout the test. After four or five cycles of wetting and drying, the soil ripens to a steady state of swell behavior, Figures 3 and 4.

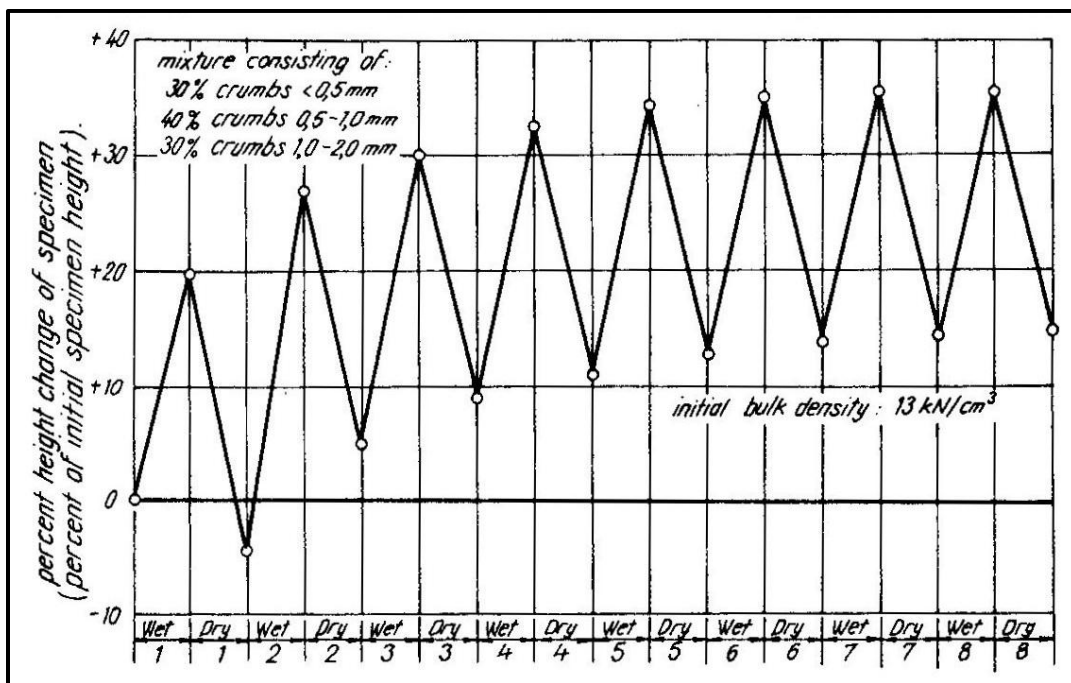


Figure 3. Cyclic Swell and Shrink Results from Popescu (1980)

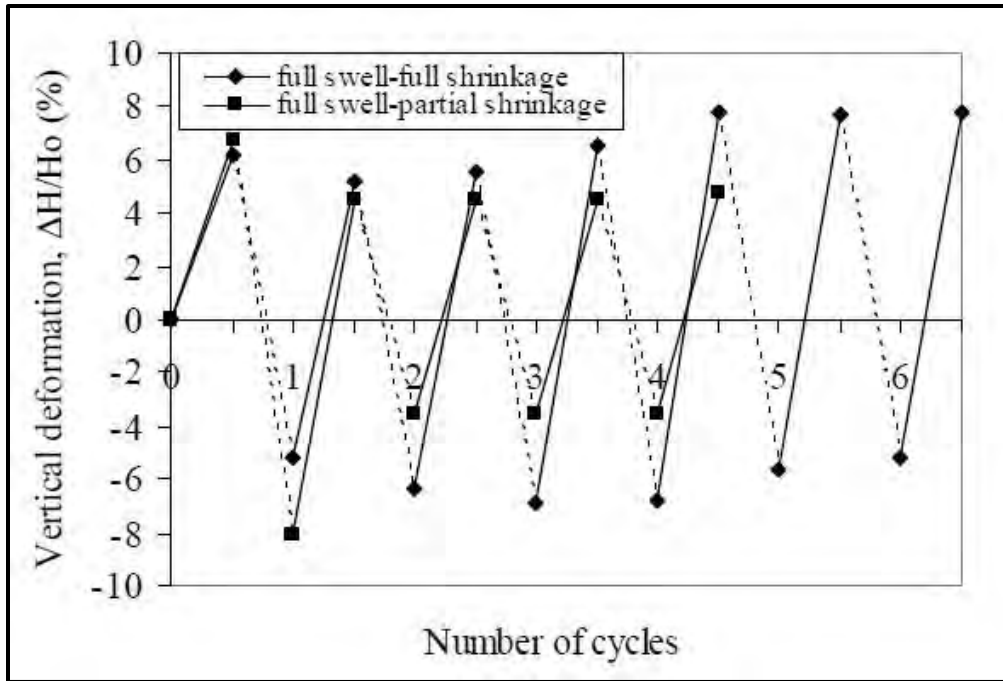


Figure 4. Cyclic Swell and Shrink Results from Tawfiq (2009)

Marr (2003) began developing a cyclic swell test method as a practical way to predict swell potential without resorting to more expensive procedures and complicated constitutive modeling. He used traditional, commonly available one-dimensional consolidation equipment during the study. Specimens were completely inundated in water and subject to a constant total stress during swelling stages. The consolidometer was removed from the frame and disassembled once swelling reached equilibrium. The specimen was then weighed and reassembled into the consolidometer.

During shrinking stages the consolidometer was again loaded into the frame and the same total stress was applied as for the swelling stage. During shrinking, however, water was not added to the cell. The soil was allowed to shrink as it air-dried until the

changes in height became negligible. Periodically, the specimen would be removed, weighed and reloaded to track the moisture content.

Shrinking by air-drying required approximately one month per shrink stage. In a later study, Allen (2005) developed a procedure for forced ventilation to accelerate the shrink stages. Allen modified a standard consolidometer so that air could be forced through the assembly at a pressure sufficiently large to shorten the drying time without damaging the soil specimen. A pressure of 5 psi was found to work well and shorten the drying time to just one or two days.

After each swell and shrink cycle, a plot is developed of height or axial strain versus moisture content. Marr originally tracked the specimen's void ratio, but as the soil shrinks three-dimensionally the total specimen volume becomes an unknown value. The void ratio may or may not be a meaningful description during shrinking stages, but the height or axial strain is certainly more straight-forward.

Additional cycles of swell and shrink stages are then performed until the relationship between height and moisture content reaches a steady state. For preliminary calculations, the initial moisture content of the specimen – prior to the first swell stage – may be assumed equal to the moisture content of high-quality samples obtained during trimming. The additional swell and shrink stages are performed exactly as described for the initial stages. Approximately four to five cycles of swell and shrink stages are typically required to reach the steady state. Figure 5 presents an example of the results from one full test.

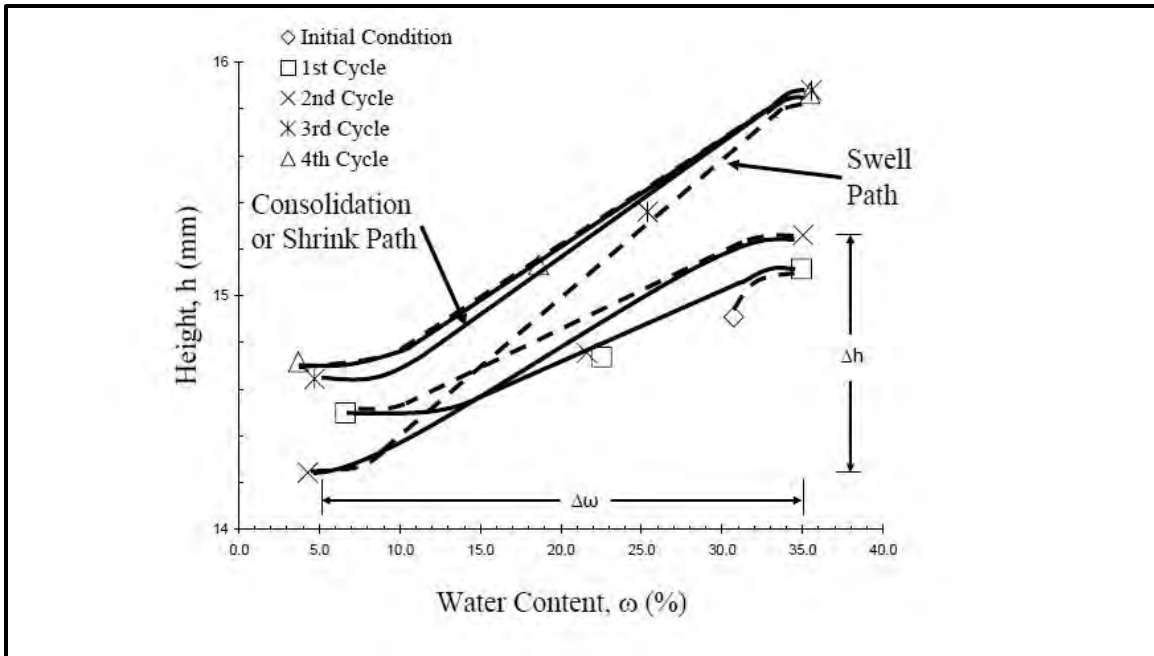


Figure 5. Example of Cyclic Swell-Shrink Behavior, Allen (2005)

The slope of the steady state line is the ultimate parameter gained from a cyclic swell test. It represents the rate at which swelling and shrinking strains may be expected to occur with changes in moisture content. The slope of each steady state line corresponds to a single constant value of total stress. Marr proposed combining multiple test results with different total stresses to define the constitutive surface in Figure 6. The range of moisture contents to be expected in the field is a detail that must be determined separately. One major benefit from this type of test is the remolding by shrinking and swelling that seems to recreate naturally occurring field conditions and results in a highly repeatable measurement.

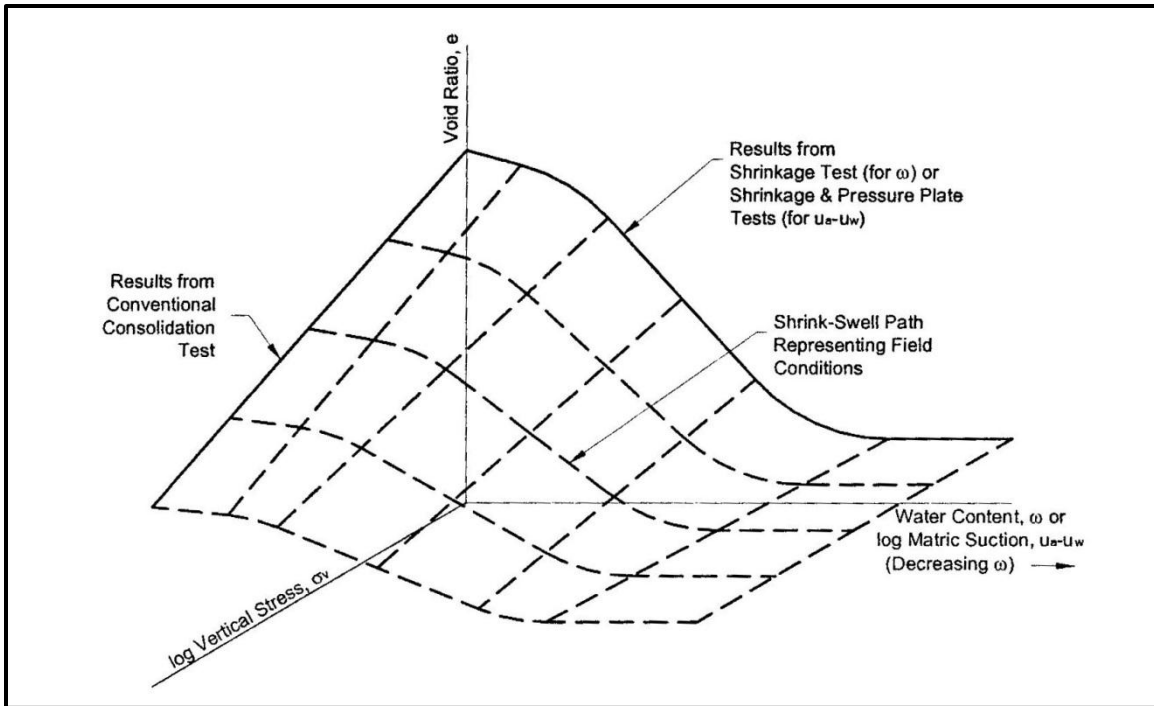


Figure 6. Constitutive Surface Measured with Cyclic Swell Tests, Marr (2003)

2.2 Stiff Fissured Clays

2.2.1 Overview

The stiff fissured variety of expansive soils is particularly problematic in geotechnical design and remediation. The intact soil can be very strong and nearly impermeable. Problems arise because of their secondary structure of cracks and fissures, which form a chaotic network of relatively slick and permeable surfaces throughout the clay structure. The hydraulic conductivity and shear strength of these soils is a function of both the intact soil and the secondary structural boundaries.

2.2.2 Hydraulic Conductivity

It is well known that clays exhibit much lower hydraulic conductivities than sands and silts. Still, the measurement of moisture flow through clay is a well-established practice as long as the soil structure permits Darcian flow. Cracked and fissured clays may not abide this fundamental rule. Within the clay's structure, there may be at least three flow zones with significantly different flow properties. The intact clay is usually very nearly impermeable, but microcracks and fissures provide relatively preferential moisture pathways. Surface desiccation cracks, on the other hand, provide a zone of completely uninhibited flow while they are open. Owing to the variability and incalculable spatial arrangement of flow zones, the overall hydraulic conductivity of fissured clays is quite difficult to predict or measure.

2.2.3 Shear Strength

Stiff fissured clays have several unique shear strength characteristics. Skempton and Larochelle (1965) summarized a number of important implications. First, laboratory and field tests that only utilize a small volume of soil are likely to be measuring strength of the intact soil alone. There may be very little if any shear resistance along open fissures, and this lowers the overall in-situ shear resistance. When loaded, pore water tends to migrate toward these fissures which lowers the effective stress and further reduces the shear resistance. As a consequence, laboratory tests are likely to overestimate shear strength if the specimens are too small and if the rate of loading is too fast to allow pore water to migrate as it would in-situ.

2.2.4 Crumb Structure and Cyclic Moisture Fluctuations

The upper portion of clay deposits, several processes work together to aggregate the individual clay particles (Popescu 1980). Cyclic moisture fluctuations, freezing and thawing, leaching, oxidation or reduction can all play a role in developing a crumb structure within a clay deposit. Crumbs refer to small clusters of clay minerals that become bound together with a binding agent such as calcium carbonate, iron oxide or colloidal silica. Crumbs are most volatile near the surface where the voids between crumbs may be open and permeable; inter-crumbs voids are generally closed at greater depths, but may be opened by stress relief.

Well-developed crumb structures result in an overall secondary structure of the clay soil. The secondary structure undergoes changes as the individual crumbs are slaked and aggregated during cycles of wetting and drying. Shrinking generally encourages the soil to group into larger, denser crumbs. Subsequent wetting can break the larger crumbs apart, exposing additional surface areas of active clay minerals. After multiple cycles of wetting and drying, the crumbs tend to cluster and slake in a more stable, repeatable fashion.

3 Properties of Taylor Clay at the Lymon C. Reese Research Wall

3.1 Geology

The Taylor Group comprises several clay strata that were deposited in east-central Texas during the late Cretaceous period. Deposition of the Taylor and overlying Navarro Groups took place under a slowly receding shallow sea. The deposition began near the end of the Austin Chalk deposition. The dominant clay mineral in the Taylor group is montmorillonite (Beall, 1964). A number of studies throughout the twentieth century contributed to a more detailed understanding of the Taylor group.

Walcott (1901) described the Taylor formation as calcareous clay marls, locally known as “joint clays”. The local terminology likely refers to Walcott’s observation that the clay is jointed, laminated and friable throughout, having a crackled appearance when dry. Also noted was the presence of lime, in a chalky condition, as an accessory constituent. Fossils of *Exogyra ponderosa* (Figure 7) were reported to be frequent, but only in the lower portion of the formation. Finally, Walcott noted some difficulty in delineating the boundary between the Taylor and overlying Navarro formations.

Burford (1928) continued investigating the Taylor Group, and again encountered difficulty mapping the Taylor-Navarro contact. One contact was found 0.25 miles west of Kimbro, and was delineated as a straight line that intersected Old US Highway 20 approximately 2.5 miles east of Manor, TX, Figure 8. Burford described the contact as a 6-inch stratum of chalky, sandy clay.



Figure 7. Example of Exogyra Ponderosa Fossil, Walcott (1901)

The upper portion of the Taylor Group is described as pure bentonite clay with common occurrences of *Exogyra ponderosa*. The lower portion of the Navarro Group was characterized by a lack of *Exogyra ponderosa* and a 10-ft stratum of greenish-yellow clay. Faulting with an Eastern throw was present at and around the contact. West of the fault, fossils indicate the clay is of the Taylor Group; east of the fault, fossils and sediments were typical of the middle Navarro. The throw of the fault was approximated as at least 200 feet.

Beall (1964) summarized the historical efforts to classify strata within and surrounding the Taylor Group, Figure 9. Ambiguous contacts had led to a general confusion regarding the Taylor-Navarro contact. Beall suggested combining the

contact's two adjacent members – the Upper Taylor Marl Member and the Neylandville Marl – to a single, mappable member of the Taylor Group.

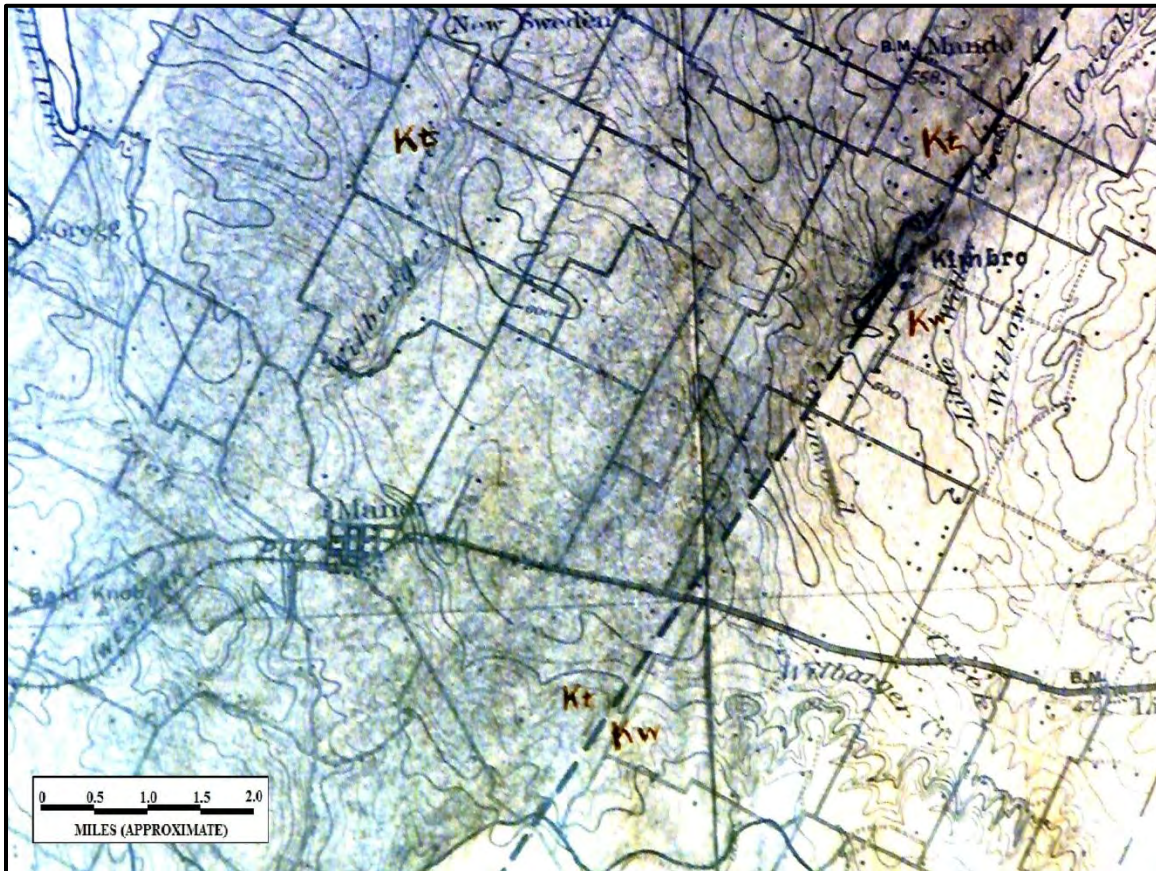


Figure 8. Delineation of Taylor-Navarro Contact, Burford (1928)

In addition, Beall presented the measured chemical contents of 46 samples from the Taylor Formation, Figure 10. Chemical contents were obtained by X-ray diffraction. The results confirm that montmorillonite is the formation's primary clay mineral. Sodium, calcium and magnesium were the montmorillonite's primary cations.

Young (1965) later proposed renaming the Upper Taylor member to the Bergstrom Formation, Figure 11. In doing so, he presented a summary of what would come to be called the Bergstrom Formation. It was described as a greenish-gray to brownish-gray, unctuous, montmorillonitic claystone, more calcareous toward the base. The Taylor-Navarro contact was described as a 6-inch thick calcareous siltstone bed.

Tipple (1975) conducted a series of tests on samples from a well that was dug through the Taylor Group in the vicinity of Manor, TX. Figure 12 shows a geologic map of the region. The results from his tests are presented in Figure 13. The well encountered the Bergstrom Formation from the surface to a depth of approximately 85 feet, followed by approximately 20 feet of Pecan Gap and 70 feet of Sprinkle. Montmorillonite was the dominant clay mineral throughout the profile.

Tipple used the method of Jonas and Brown (1959) to identify the interlayer ion population for all of the samples obtained from the Manor Well. The results indicate that calcium is nearly the exclusive interlayer ion for the montmorillonite at the well. This is compatible with Tipple's calcium carbonate measurements. Throughout the Taylor Group, calcium carbonate contents are typically around 40 percent.

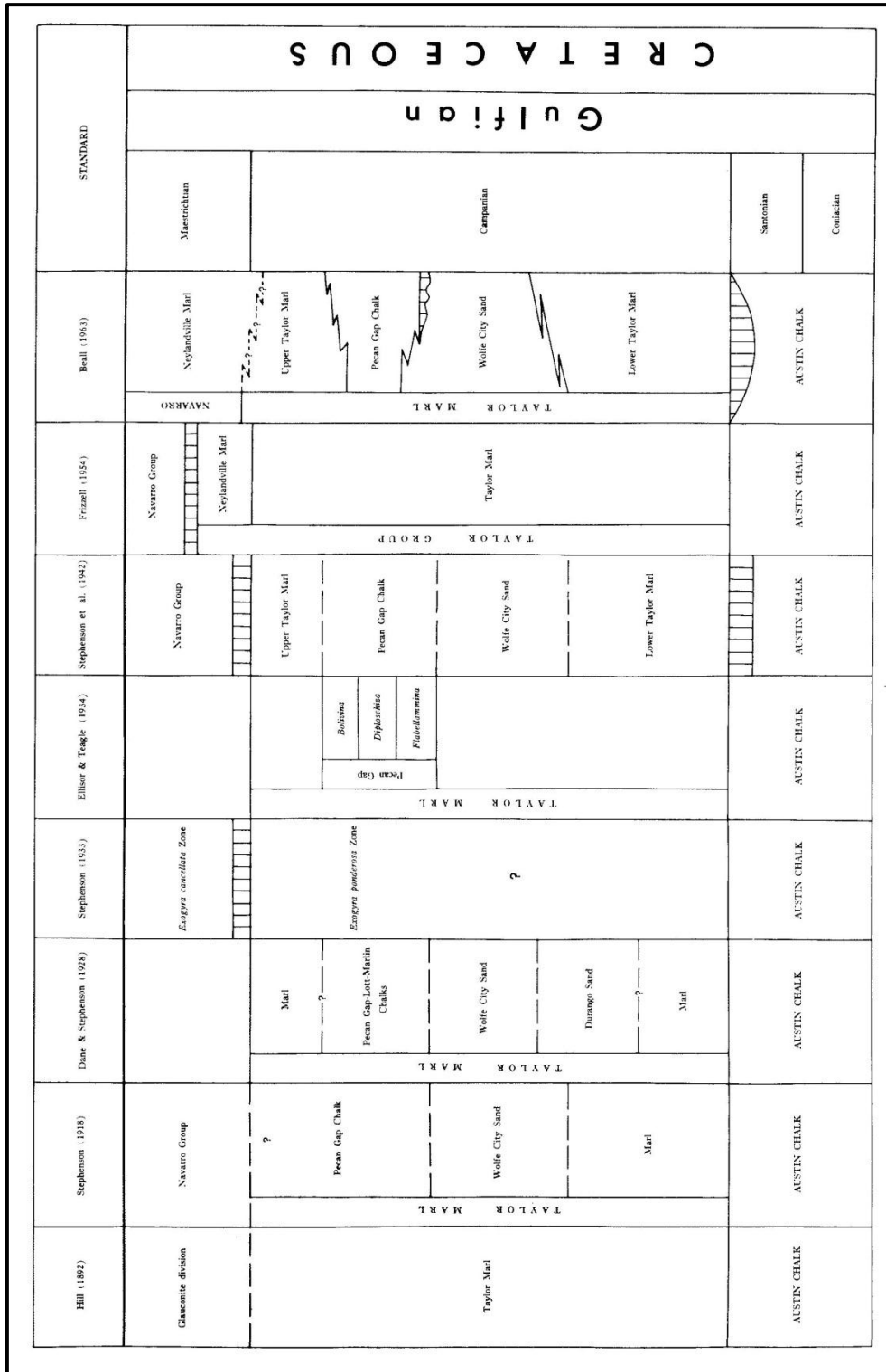


Figure 9. Historical Classifications of Strata within the Taylor Group, Beall (1964)

2/Sample No.	Locality No.	Montmorillonite Na:CaMg	Montmorillonite %	Kaolinite %	Illite %	Quartz %	Calcite %	Diffraction Peak: Montmorillonite (001)
1	172	100:0	55	10	3—	20+	10—	broad
2	172	95:5	55	10	3—	20	10	broad
3	146	20:80	65	—	3—	10	20+	broad
4	109	30:70	60	5	5	20+	10	broad
5	137	50:50	50	10	tr.	20	20+	broad
6	161	40:60	60	—	tr.	20	20+	broad
7	111	40:60	60	8	tr.	20+	10	
8	171	40:60	60	10	—	20+	10	
9	157	50:50	55	15	—	20+	10	sharp
10	112	50:50	55	15	—	20	10	
11	136	50:50	50	8	8	20	10	broad
12	125	50:50	60	—	3—	30+	5	sharp
13	142	100:0	40	15	5	30	10—	broad
14	176	45:55	70	—	—	20+	10	sharp
15	176	45:55	70	—	tr.	20+	10	
18	158	60:40	65	3—	—	20	10	sharp
19	163	50:50	60	3—	3—	20	10+	
20	155	60:40	50	10	3—	30	5—	
21	113	50:50	60	5	5	20—	10	

2/Sample No.	Locality No.	Montmorillonite Na:CaMg	Montmorillonite %	Kaolinite %	Illite %	Quartz %	Calcite %	Diffraction Peak: Montmorillonite (001)
22	3/99	100:0	60	5	5	20+	10	sharp
23	99	100:0	55	5—	3—	30	5+	sharp
24	165	50:50	60	3—	—	5—	30+	diffuse
25	159	10:90	60	3—	—	5	30+	broad
26	159	50:50	55	3—	?	5—	35+	broad
27	159	50:50	55	—	—	5—	35+	broad
29	108	35:65	60	5	5	20+	10—	sharp
30	108	40:60	90	—	—	3—	3—	very sharp
31	104	50:50	90	—	—	3—	3—	very sharp
32	168	20:80	45	3—	10	5—	35+	broad
37	168	10:90	55	—	—	—	45+	diffuse
39	114	40:60	65	10	tr.	15	10	sharp
40	114	50:50	60	10	tr.	20	10—	sharp
41	170	5:95	60	—	—	?	40	diffuse
42	99	95:5	65	3—	3—	20	5—	broad
43	99	95:5	65	5	5	20+	5—	broad
44	99	50:50	60	10	5	20	5	
45	99	95:5	60	5	5	20+	10—	broad
46	99	95:5	60	5	10	20	5—	broad

¹These clay data are estimates based on comparison of diffraction intensities of Taylor Formation samples with mixtures of pure minerals (weight percentages). The ratio of sodium (Na) montmorillonite to calcium-magnesium (CaMg) montmorillonite is given in parts per hundred. All percentages are based on the total sample and are correct within approximately 5 percent. Note the following symbols: slightly less than (—); slightly greater than (+).

²Refer to Figure 12 for position of sample in facies of Taylor Formation.

³Lytle, Holloway and Phillips, No. 1 Atlantic Refining Company, located north and slightly east of area.

Figure 10. Chemical Analysis of Samples from Taylor Group, Beall (1964)

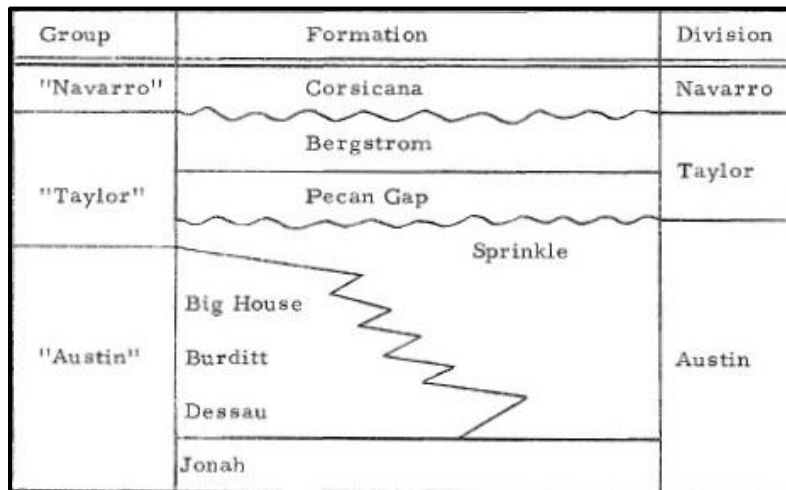


Figure 11. Revised Nomenclature for Upper Taylor Member, Young (1965)

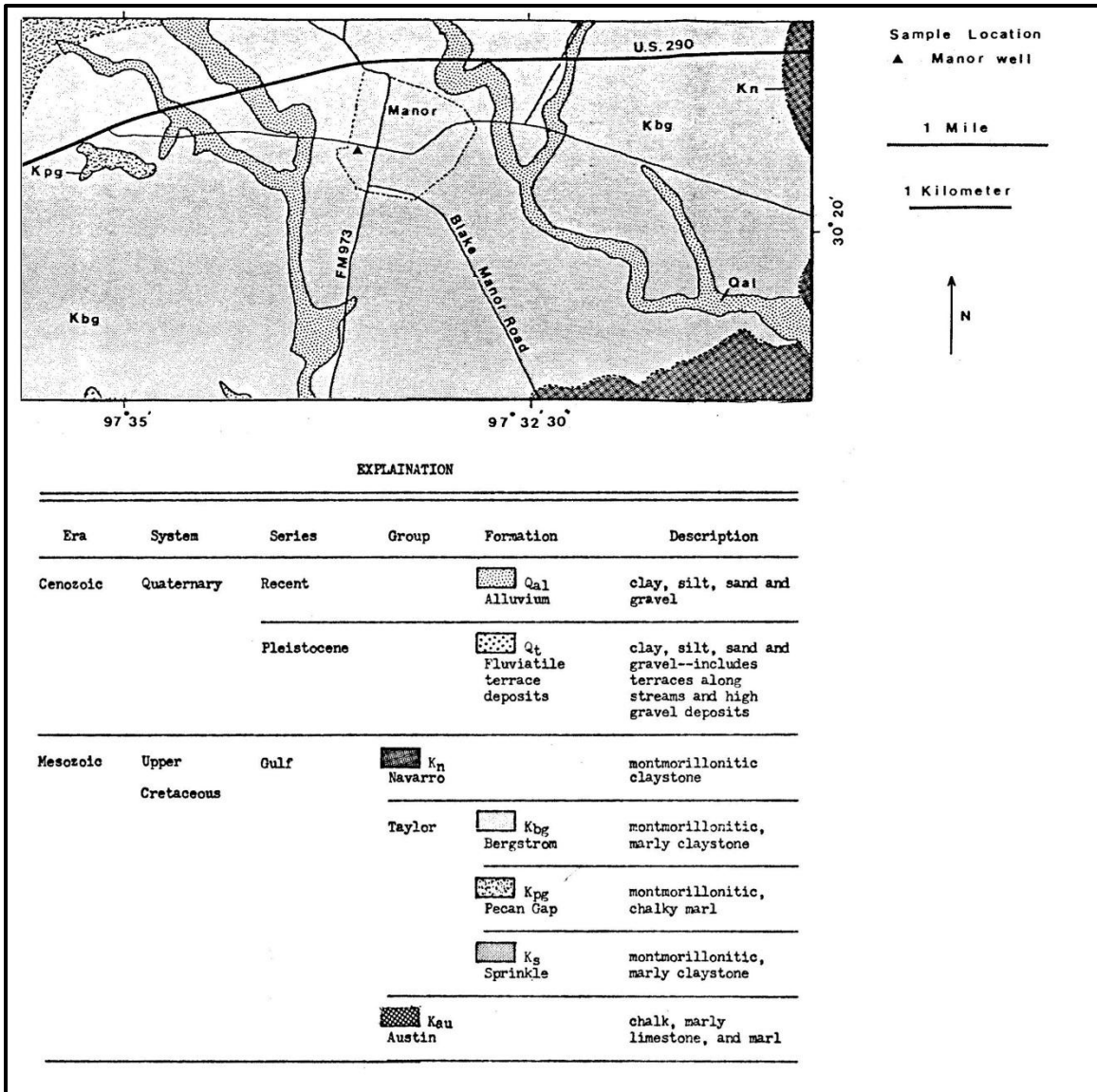


Figure 12. Geologic Map of the Vicinity of Manor, TX, Tipple (1975)

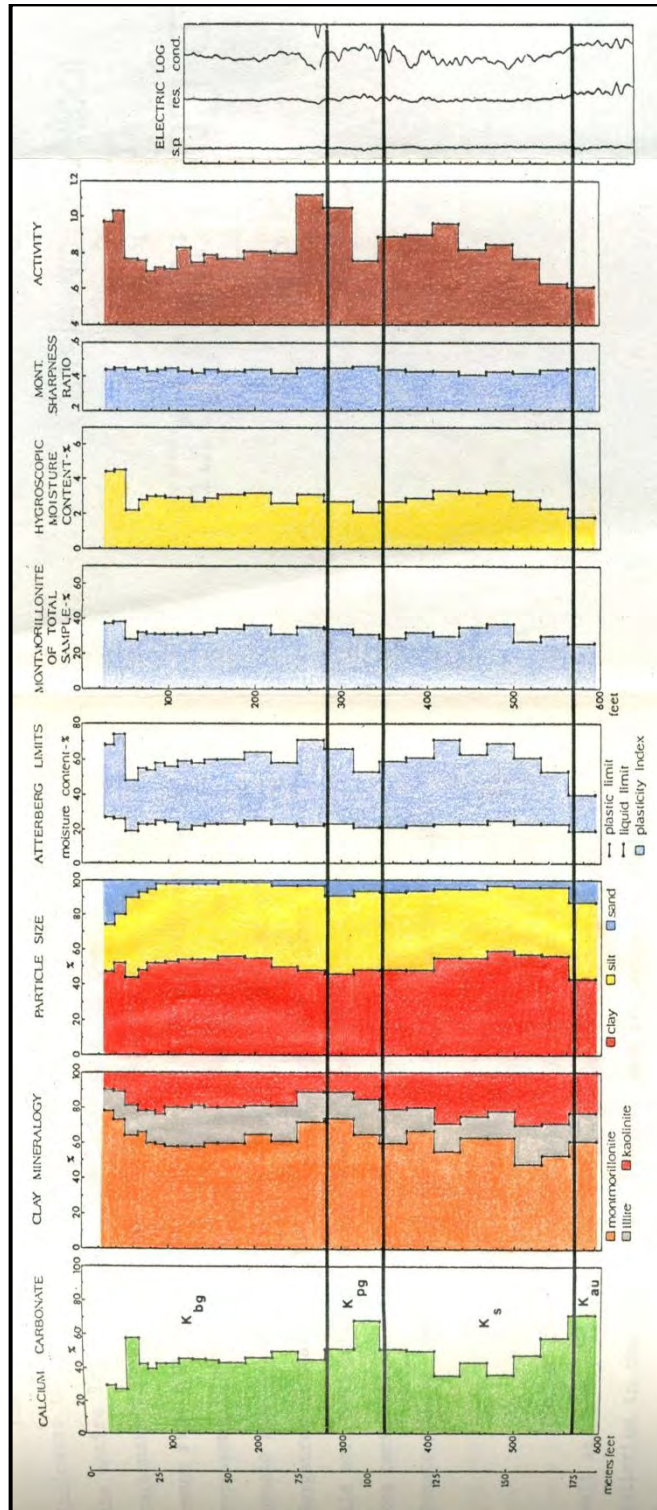


Figure 13. Test Results from Samples Retrieved from Manor Well, Tipple (1975)

3.2 Laboratory and Field Investigations

The engineering characteristics of clays from the Taylor Group have been repeatedly studied and reported in the literature. The clay is known to be quite stiff and overconsolidated with a pronounced secondary structure (Long, 1983). Garner and Young (1976) presented a profile of the engineering properties that are typical within the Taylor Group, Figure 14. Most notable in their summary is the interplay between calcium carbonate content and liquid limits. Just as Tipple (1975) observed, the liquid limits are inversely proportional to the calcium carbonate contents.

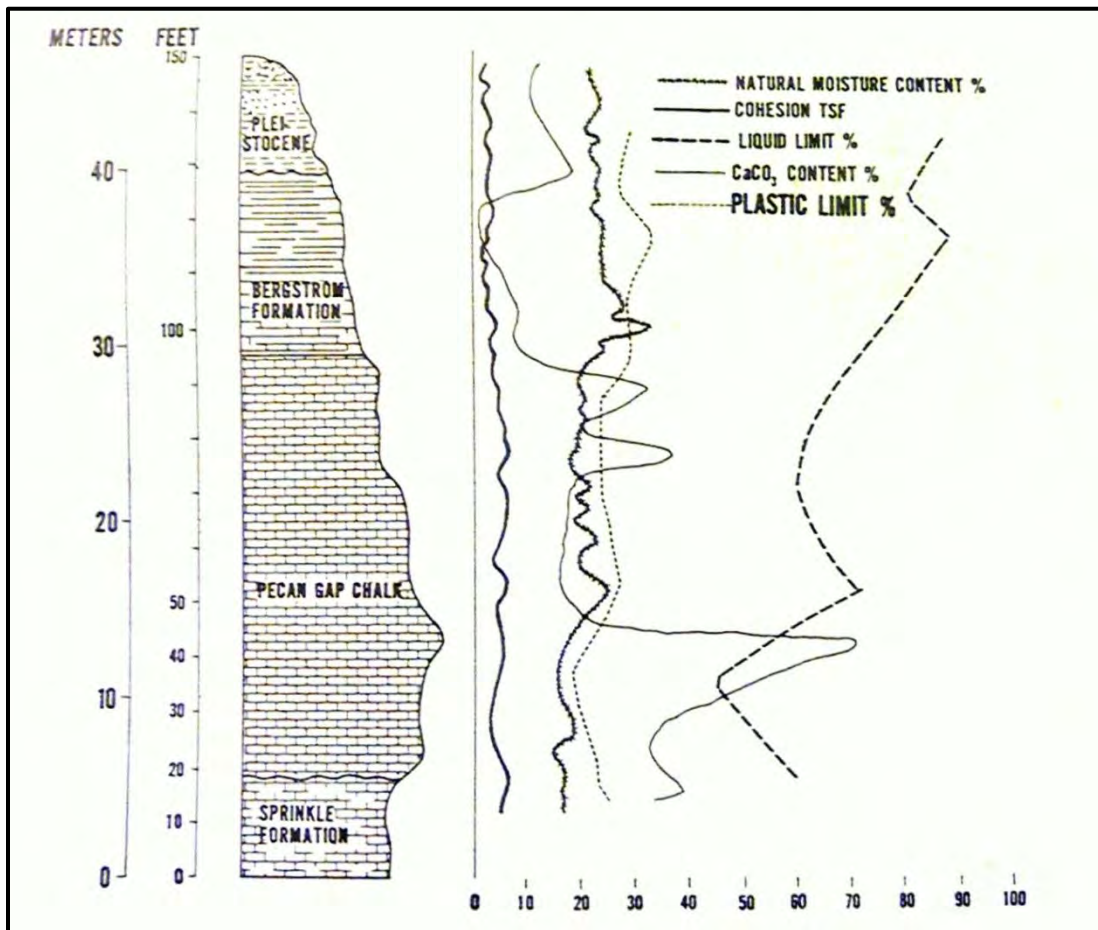


Figure 14. Typical Properties of the Taylor Group, Garner and Young (1976)

Long (1983) reported the engineering properties of soils from the Taylor Group at the site of his lateral load tests in Manor, TX. The test site was located along US Highway 290 at Station 319.5. The site was originally investigated in 1966 after a 6-foot deep rectangular test pit was excavated. Figure 15 summarizes the measured soil profile and shear strengths, which were measured by unconfined compression, unconsolidated undrained triaxial and pocket penetrometer tests. Note that the vertical scale represents depth below the base of the test pit, which was six feet below the ground surface.

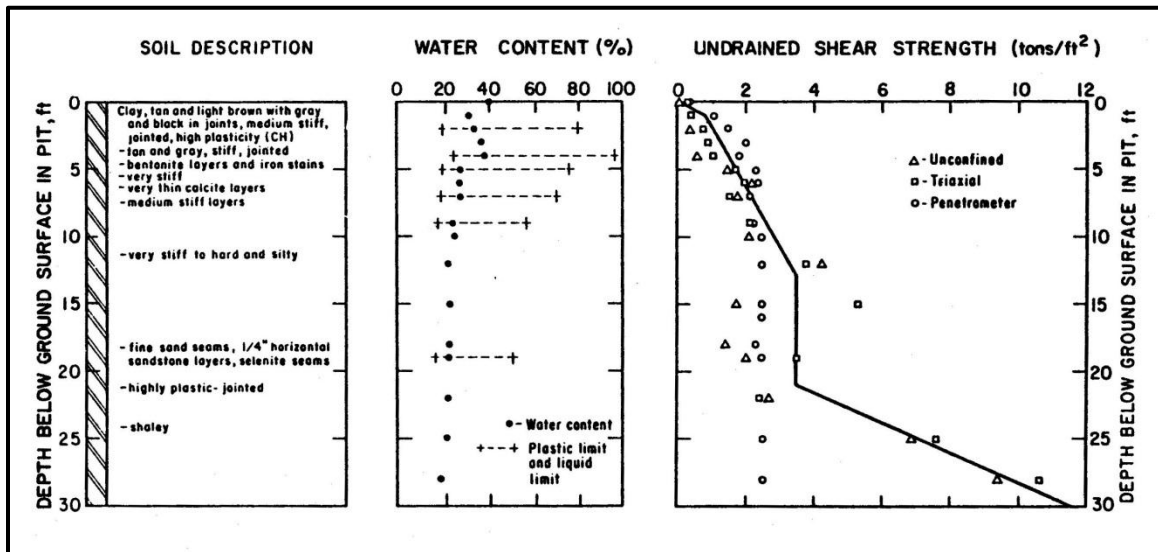


Figure 15. Soil Profile and Shear Strengths from 1966 Manor Tests, Long (1983)

The same test site was revisited in 1981 for additional research activities. Additional borings were drilled to obtain undisturbed samples for testing. While logging the soil, depths were correlated to the original 1966 investigation based on the depths of easily distinguishable layering.

One-dimensional consolidation tests were conducted on 2.5-inch diameter, 0.5-inch thick specimens. During testing, the specimens were initially loaded with 125 psf. If swelling occurred, additional pressure was applied until no swelling was apparent. From that point on, the tests used load increment ratios of one for loading, and one-half for unloading. A summary plot of vertical strain versus log of effective vertical pressure is shown in Figure 16. Long described the curves as typical of heavily overconsolidated clay. Namely, there is no clear indication of any point which might represent the transition from over- to normally-consolidated behavior. The recompression indices (R_r) were not included in the original report. They were calculated by the present author for this thesis.

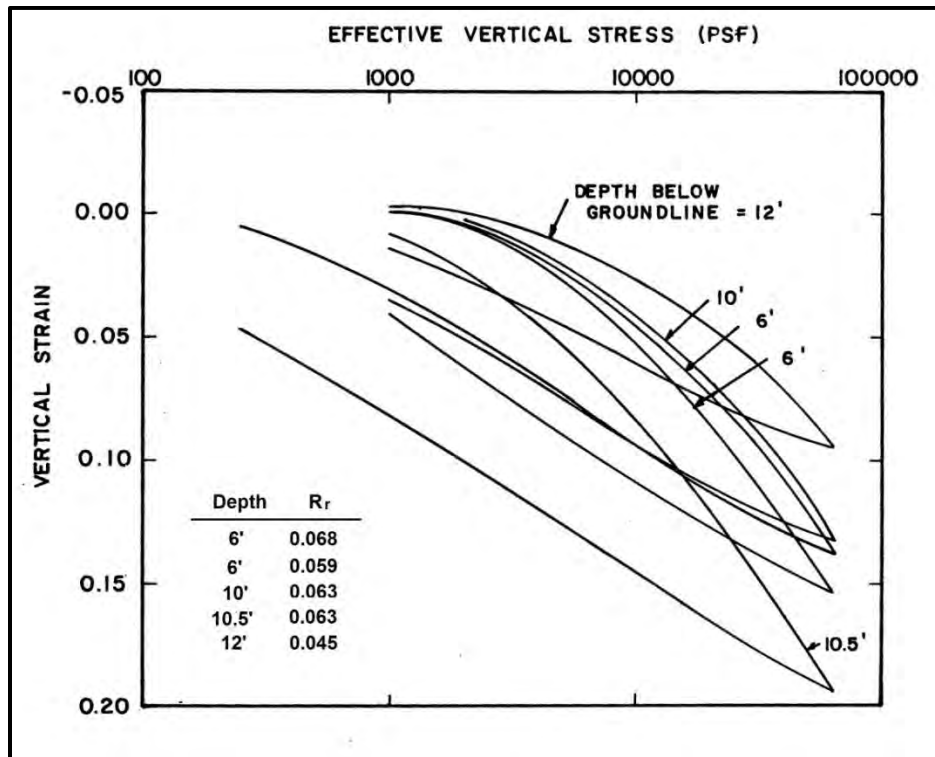


Figure 16. Consolidation Test Results from 1981 Manor Tests, Long (1983)

Long (1983) also reported the results from a series of isotropically consolidated, undrained triaxial compression tests with pore water pressure measurements. He presented the data as a collection of effective stress paths in P'-q space, Figure 17. Tests were conducted on specimens from depths between 8 and 17 feet. The linear trend, effective friction angle and effective cohesion intercept were not included in the original report. They were added separately by the present author for this thesis.

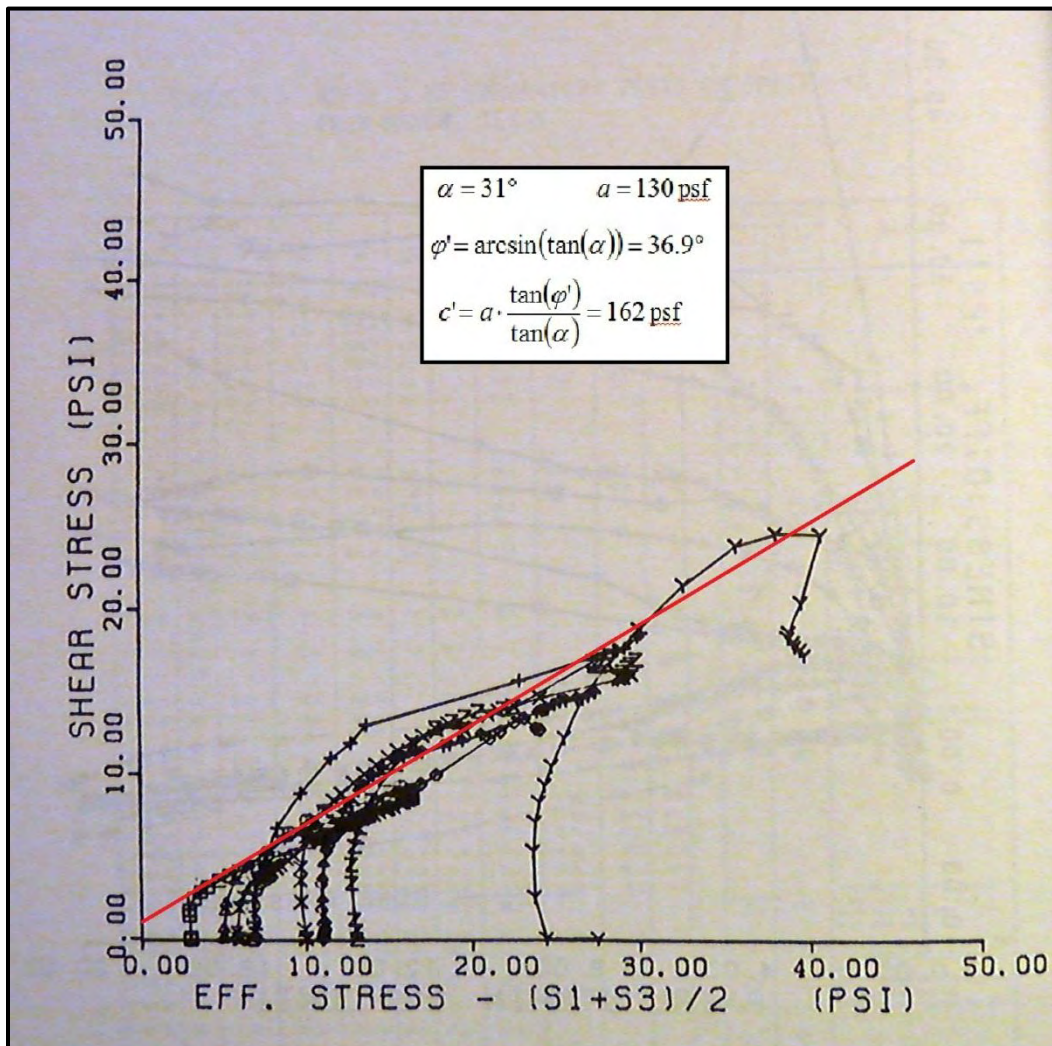


Figure 17. Effective Stress Paths from 1981 Manor Tests, Long (1983)

Compression tests from soils at the Manor site exhibited several different types of failure. The soil's secondary structure caused the behavior to vary based on the arrangement of joints and fissures within the test specimens. Figure 18 summarizes the types of shear failure that were observed.

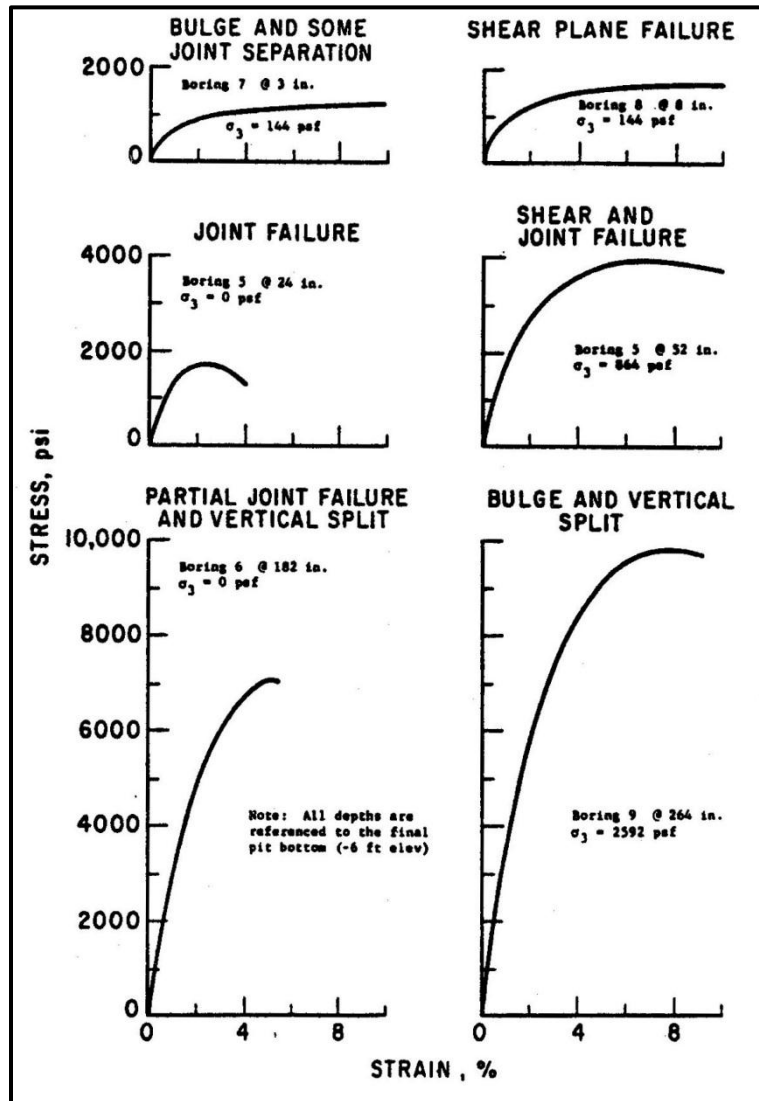


Figure 18. Typical Stress-Strain Curves from 1981 Manor Tests, Long (1983)

Funk (1975) and Tipple (1975) conducted extensive tests on Taylor soils from around the vicinity of Austin and Manor. Their focus was aimed at correlating the clay chemical contents with Atterberg limits. On average, they found soils in the Taylor Group to have relatively constant plastic limits, ranging mostly between 20 and 30. The various changes in chemical contents had much greater effects on the liquid limits. Liquid limits tended to increase with higher montmorillonite – and particularly sodium montmorillonite – contents and decrease with higher calcium carbonate contents. Liquid limits varied mostly between 55 and 80, but reached values as high as 100.

Tipple drew several additional conclusions about the soils' behavior around the contact between oxidized and unoxidized zones. In general, the Atterberg limits and colloidal activity increased just above the contact going up into the weathered zone. Simultaneously, the calcium carbonate content and clay fraction tended to decrease. These observations are generally consistent with the laboratory results presented by both Tipple and Funk. Figure 19 shows the observed relationship between montmorillonite content and plasticity, Tipple (1975). The effect of carbonate content on the plasticity index is illustrated in Figure 20, Tipple (1975).

The only major difference in the two studies was sodium montmorillonite content of the samples. Tipple suggested a testing error that probably caused Funk to measure erroneously high sodium contents. Nevertheless, there exists a large variation in Atterberg limits throughout the Taylor Group. Geotechnical researchers in the Austin area have reported liquid limits for the Taylor clays ranging from 50 (Van-Hue, 1966) to 110 (Kayyal, 1986).

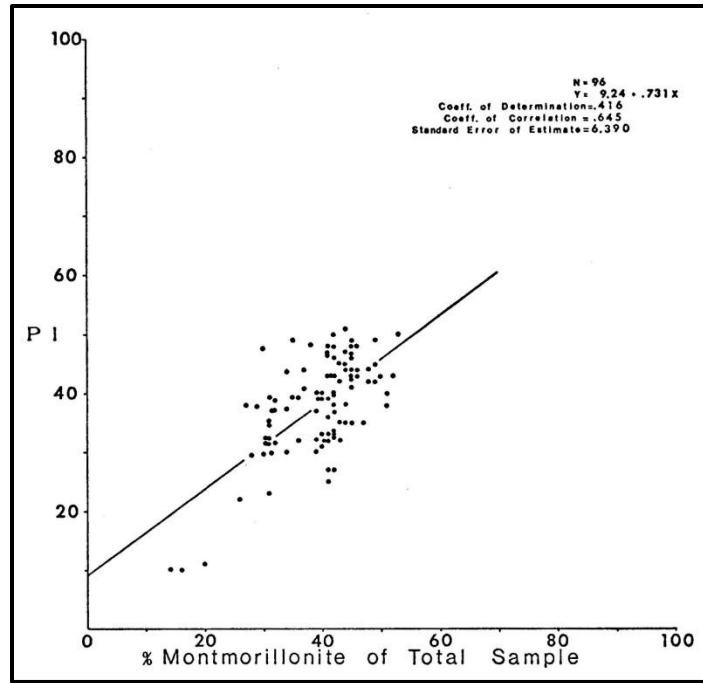


Figure 19. Montmorillonite Content vs. PI for Taylor Clays, Tipple (1975)

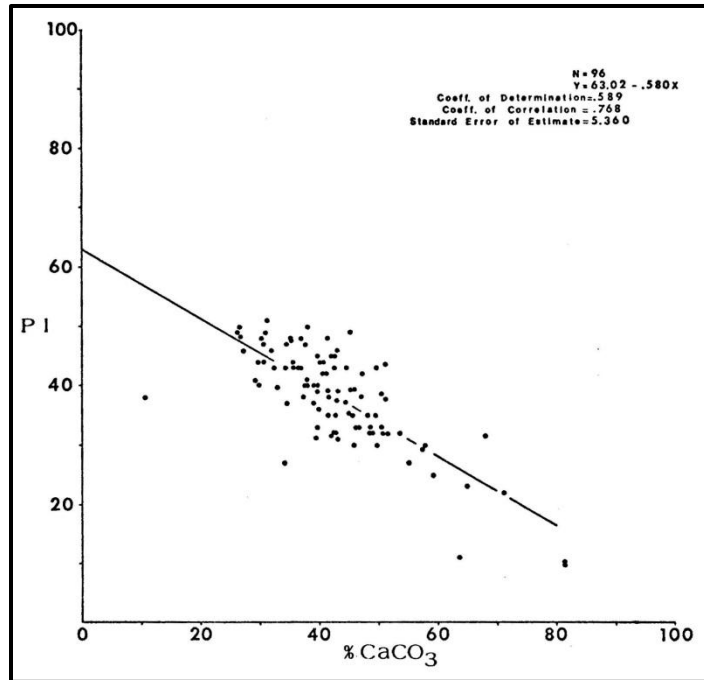


Figure 20. Calcium Carbonate Content vs. PI for Taylor Clays, Tipple (1975)

Marr (2003) ran a number of tests on clay from the Taylor group while developing the cyclic swell test described in Section 2.1.4. The soil was sampled in Austin, TX near the intersection of US Highway 183 and 51st Street. The sampled depths were between 10 and 20 ft. The soil's plastic and liquid limits ranged from 24 – 27 and 77 – 85, respectively. The soil's swell pressure was determined to be approximately 4200 psf during a one-dimensional consolidation test. The e-log-P' curve was too rounded to distinguish between over- and normally-consolidated stress ranges, Figure 21. The results of Marr's cyclic swell tests indicate that for a given change in moisture content, smaller vertical swelling strains occur under higher total stresses.

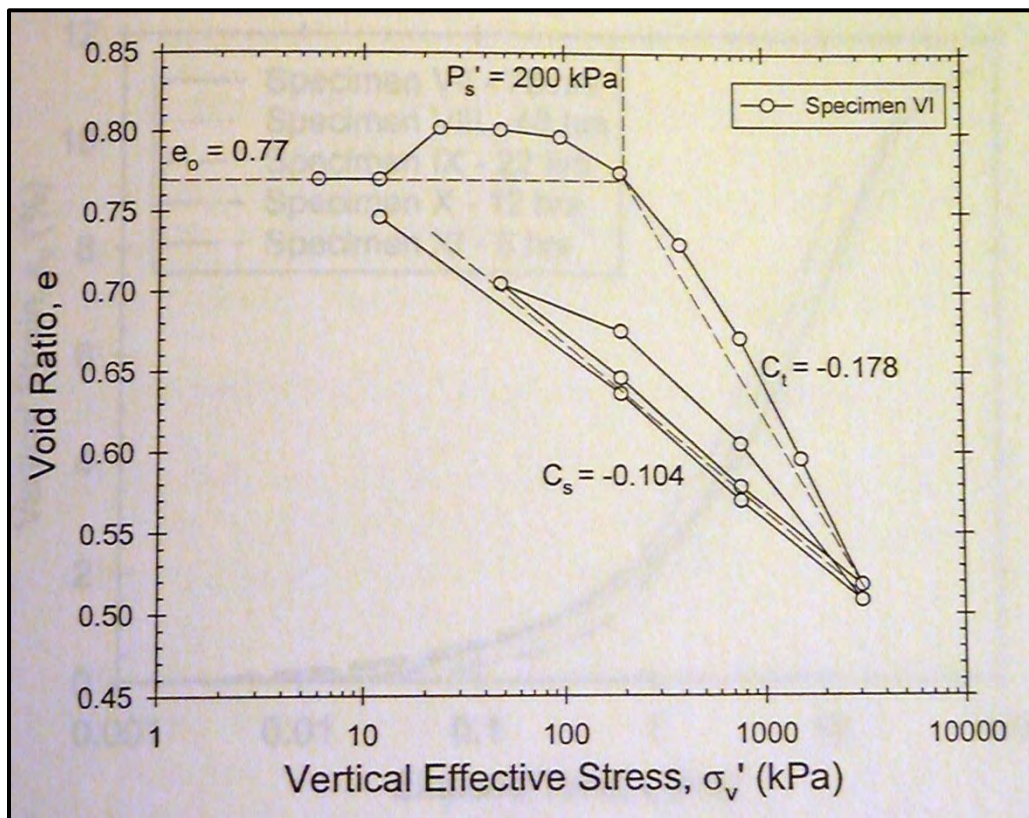


Figure 21. Consolidation Results from Taylor Clay from Austin, TX, Marr (2003)

4 Field Investigation at the Lymon C. Reese Research Wall

4.1 Overview

4.1.1 Site Location and Subsurface Investigation

The field and laboratory tests described in Chapters 3 and 4 were conducted on soils from the Lymon C. Reese Research Wall test site. The address is 13806 Old Highway 20, Manor, Texas 78653, Figure 22. Fugro Consultants, Inc. drilled three exploratory borings at the site on January 12 and 13, 2010. A piezometer was installed in boring B-1 to monitor groundwater. McKinney Drilling Company installed a drilled shaft retaining wall at the site during the spring of 2010. The cut side of the wall was excavated by the owner during August and September of 2010. Locations of the borings, drilled shafts and excavation are shown schematically in Figure 23. Boring logs from the exploratory borings are provided in Appendix A.



Figure 22. Location of Lymon C. Reese Research Wall in Manor, TX

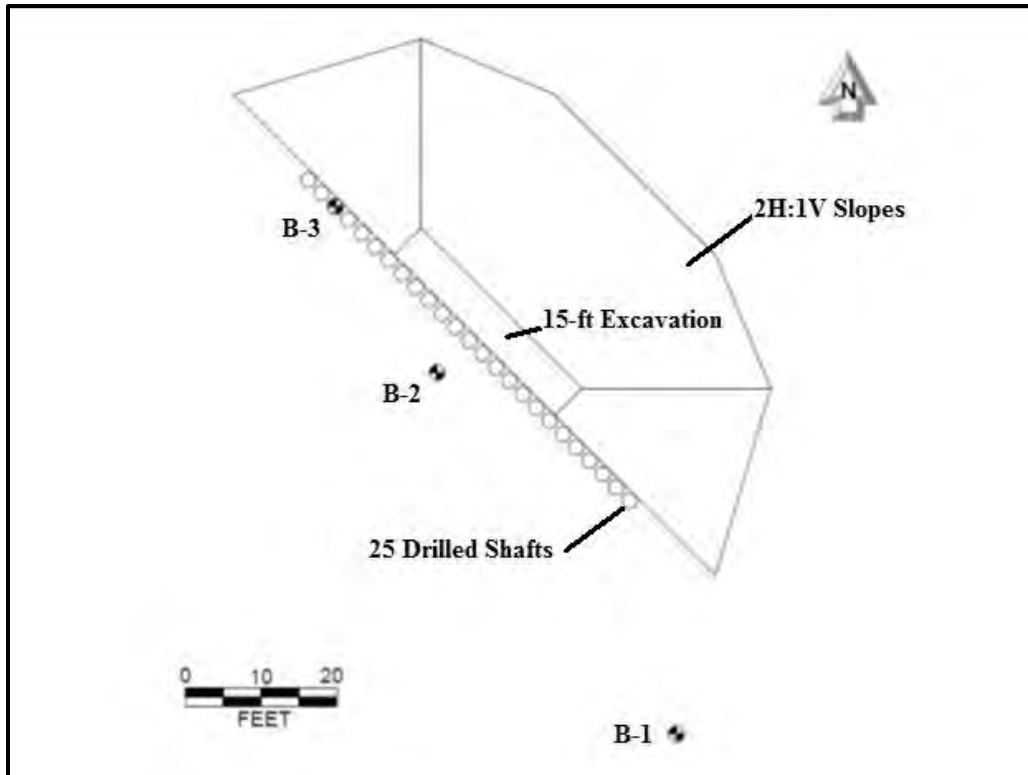


Figure 23. Site Schematic with Boring Locations

4.1.2 Geologic Setting

Exploratory borings revealed a shallow layer of dark, weathered clay that became a dull yellowish brown color and much stiffer with depth. The weathered zone extends from the surface to a depth of approximately 8 feet. The soil was closely fissured and blocky throughout the profile, but particularly so below the weathered zone. None of the borings detected sandy strata, but selenite seams were observed. Figure 24 shows the thickest band of selenite that was encountered, approximately 0.2 inches thick. This seam was intersected in boring B-2 at a depth of 38 feet.



Figure 24. Large Selenite Seam Intersected by B-2 at a Depth of 38 ft

Excavation of the cut side of the wall provided a clearer picture of the subsurface. Figure 25 illustrates the transition from dark brownish gray to dull yellow clay that was observed during excavation at depths of approximately 8 – 10 feet. Figure 26 is a close-up picture that provides better detail on the colors and transition. Numerous *Exogyra ponderosa* fossils were discovered in the excavated soil, Figure 27. The exact depths the fossils were discovered could not be recorded, but the depths of most frequent occurrence seem to have been between 5 and 10 feet.



Figure 25. Transition from Dark Gray to Dull Yellow Clay



Figure 26. Close-Up View of Transition from Dark Gray to Dull Yellow Clay



Figure 27. Exogyra Ponderosa Fossils Unearthed during Excavation

4.1.3 Climactic Setting

The site investigation and was conducted after several months of frequent precipitation. That precipitation, however, was only a temporary break from an ongoing drought in central Texas. Figure 28 illustrates when important sampling and construction activities occurred during this weather event.

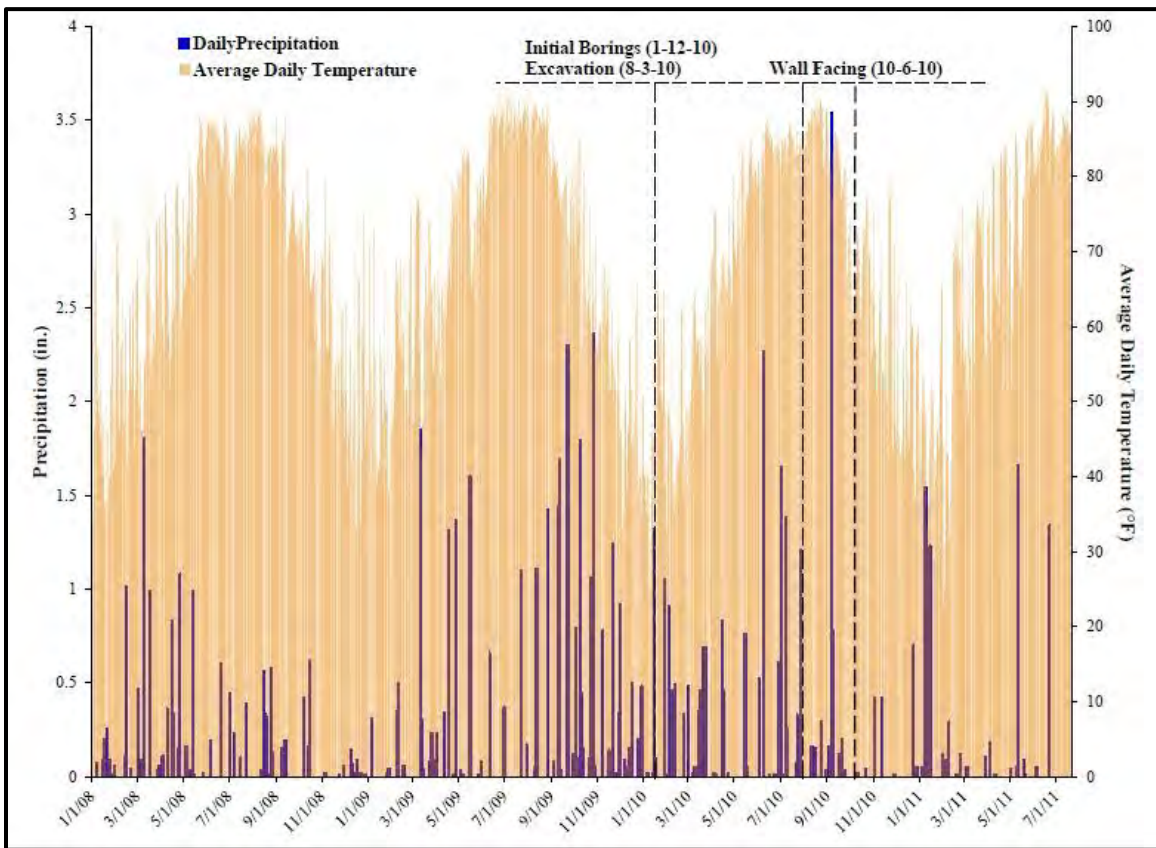


Figure 28. Weather Records During Central Texas Drought

4.2 In-Situ Tests

4.2.1 Pocket Penetrometer

Pocket penetrometer measurements were recorded throughout sampling. After extruding a sample from the seamless push tube and cutting one end squarely with a knife, the pocket penetrometer was pushed into the cut surface, Figure 29. Although this technique produces only the most approximate of measurements, Figure 30 illustrates that the predicted soil strengths are consistently high. Nearly half of the pocket penetrometer tests met refusal and are plotted as the maximum possible reading, 9000 psf.



Figure 29. Pocket Penetrometer Testing

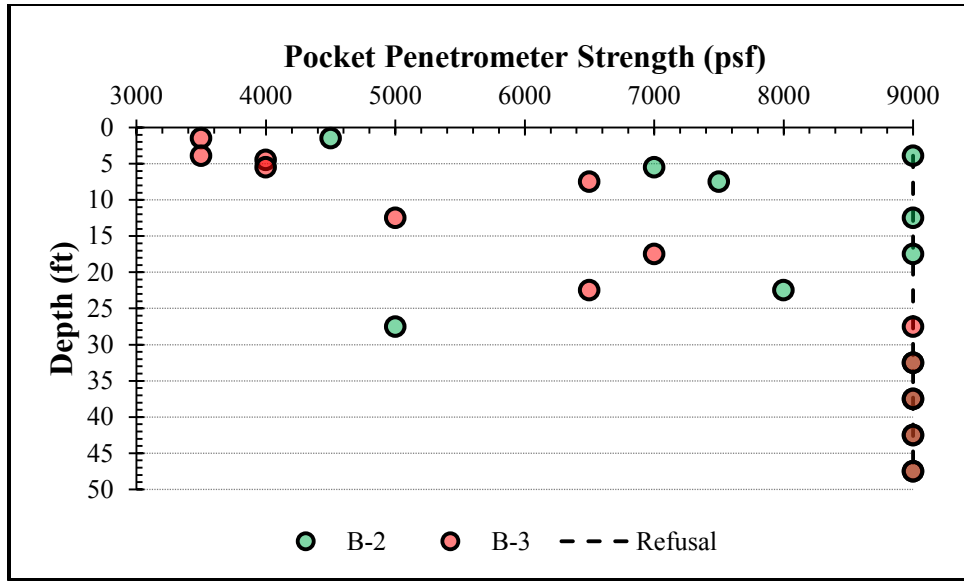


Figure 30. Results from Pocket Penetrometer Tests

4.2.2 Standard Penetration Test (SPT)

Standard penetration tests (SPT) were conducted in boring B-1 at 5-ft intervals while retrieving split-spoon samples for index tests. These tests were conducted in accordance with ASTM D1586 with the exceptions of hammer weight and drop height. The standard test calls for a hammer weight of 140-lb and drop height of 30 inches. These tests were conducted with a 170-lb hammer and 24-inch drop height. A simple energy correction was used to standardize the blow count, Equation 2. The energy-corrected blow counts (N') are plotted in Figure 31. SPT blow counts are not typically correlated to undrained strengths or other properties for clays (Reese et al. 2006).

$$N' = N \cdot \frac{W_{hammer} \cdot H_{drop}}{140lb \cdot 30in.} \dots\dots\dots Eq. 2$$

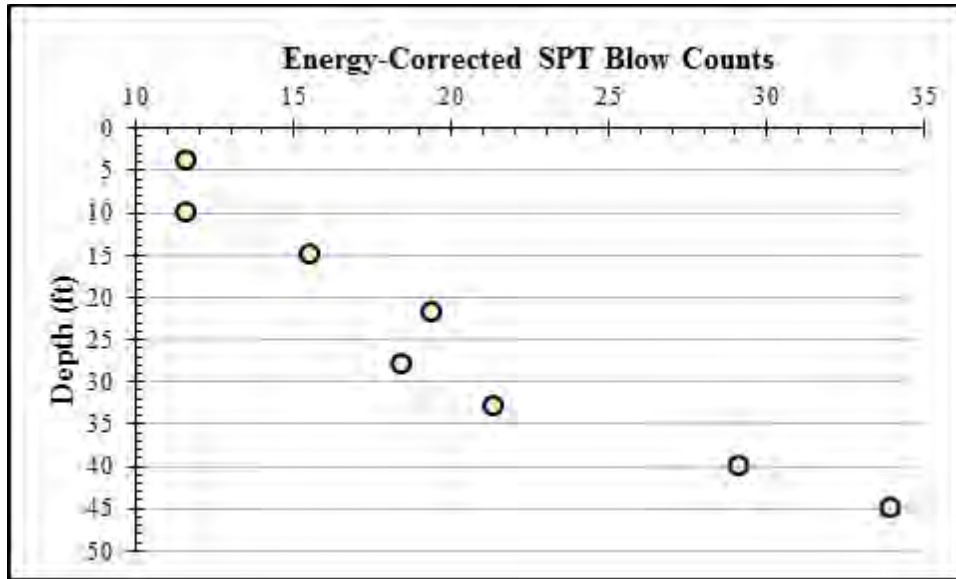


Figure 31. Energy-Corrected SPT Blow Counts

4.2.3 Texas Cone Penetration Test

Texas cone penetration (TCP) tests were conducted at 5-ft intervals in boreholes B-1 and B-3 in accordance with TxDOT test procedure Tex-132-E. The number of blows required to drive the cone twelve inches (N_{TCP}) was converted to undrained shear strength (S_u) using Equation 3 (2000 TxDOT Geotechnical Manual). Note that Equation 3 returns S_u in units of tons/ft². The resulting S_u profiles are plotted in Figure 32. The final four tests in B-3 met refusal and are signified by a vertical dashed line at the maximum TCP-generated undrained shear strength, 8000 psf.

$$S_u = \frac{N_{TCP}}{25} \dots\dots\dots \text{Eq. 3}$$

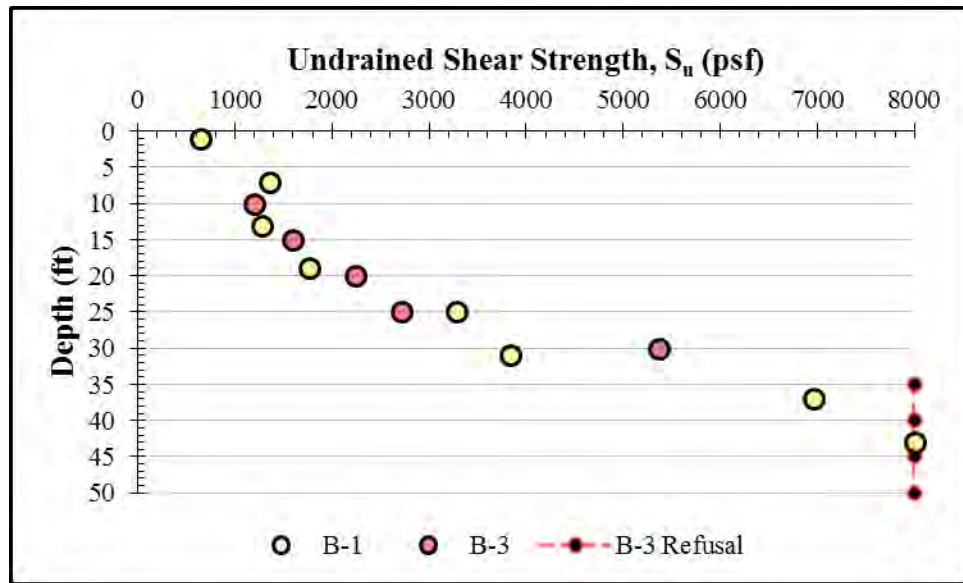


Figure 32. Undrained Strength Profile from TCP Correlations

4.2.4 Spectral Analysis of Surface Waves (SASW)

The spectral analysis of surface waves (SASW) test method was performed at the test site on June 15 and July 26, 2010. As a reference, the retaining wall's drilled shafts were installed on the week of March 30, 2010 and excavation of the cut side of the retaining wall began July 29, 2010. Each test was conducted with two different sensor arrays as illustrated in Figure 33. Sensory array #3 is also pictured in Figure 34.

The tests from each date are summarized in Tables 4 and 5. Equation 4 was used to convert shear wave velocities (v_s) to shear moduli (G). The soil's unit weight was idealized as constant with depth at a value of 125 lb/ft^3 . P-wave velocities identified the groundwater table at a depth of 7.5 ft.

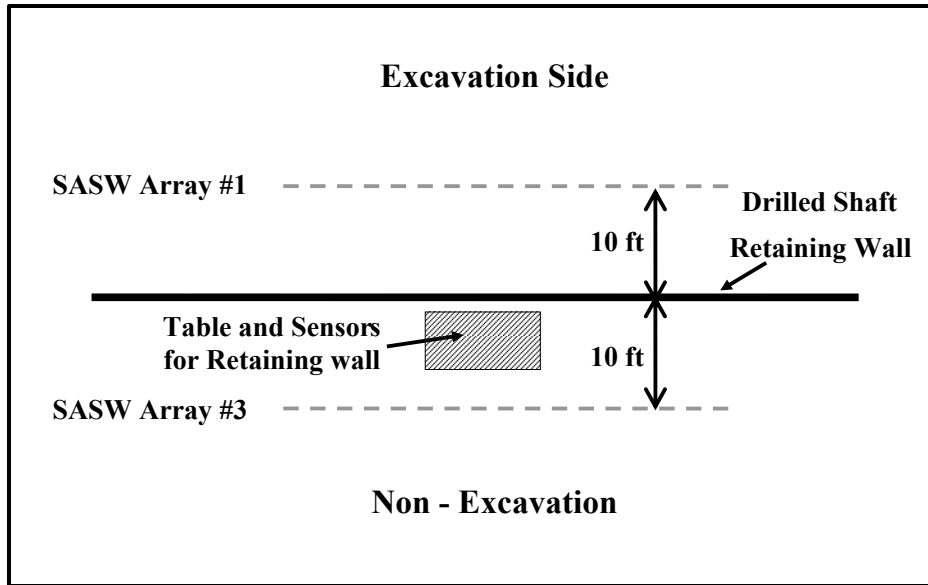


Figure 33. Sensor Arrays for SASW Tests Two Days Before Excavation



Figure 34. SASW Sensor Array #3

Table 4. SASW Results from 6-15-2011

	Depth (ft)	Shear Wave Velocity, v_s (ft/s)	Shear Modulus, G (k/ft ²)
Sensor Array #1	0 – 0.1	200	149
	0.1 – 1.0	250	233
	1.0 – 2.9	359	480
	2.9 – 7.5	379	535
	7.5 – 22.5	421	688
	22.5 – 32.5	550	1174
	32.5 – 40	950	3503
Sensor Array #3	0 – 0.6	109	44
	0.6 – 1.4	181	122
	1.4 – 2.9	250	233
	2.9 – 7.4	319	379
	7.4 – 19.6	382	566
	19.6 – 29.4	550	1174
	29.4 – 37	950	3503

$$G = v_s^2 \cdot \frac{\gamma}{g} \dots\dots\dots \text{Eq. 4}$$

Table 5. SASW Results from 7-26-2011

	Depth (ft)	Shear Wave Velocity, v_s (ft/s)	Shear Modulus, G (k/ft ²)
Sensor Array #1	0 – 3.0	310	358
	3 – 7.5	360	483
	7.5 – 22.5	420	685
	22.5 – 32.5	550	1174
	32.5 - 144	850	2805
Sensor Array #3	0 – 2.9	320	382
	2.9 – 7.5	320	382
	7.5 – 20.5	410	653
	20.5 – 30.5	570	1261
	30.5 - 77	820	2610

Shear modulus profiles for the excavation and non-excavation sides of the retaining wall are shown in Figures 35 and 36, respectively. Only slight differences were observed between the two array positions and testing dates, Figure 37.

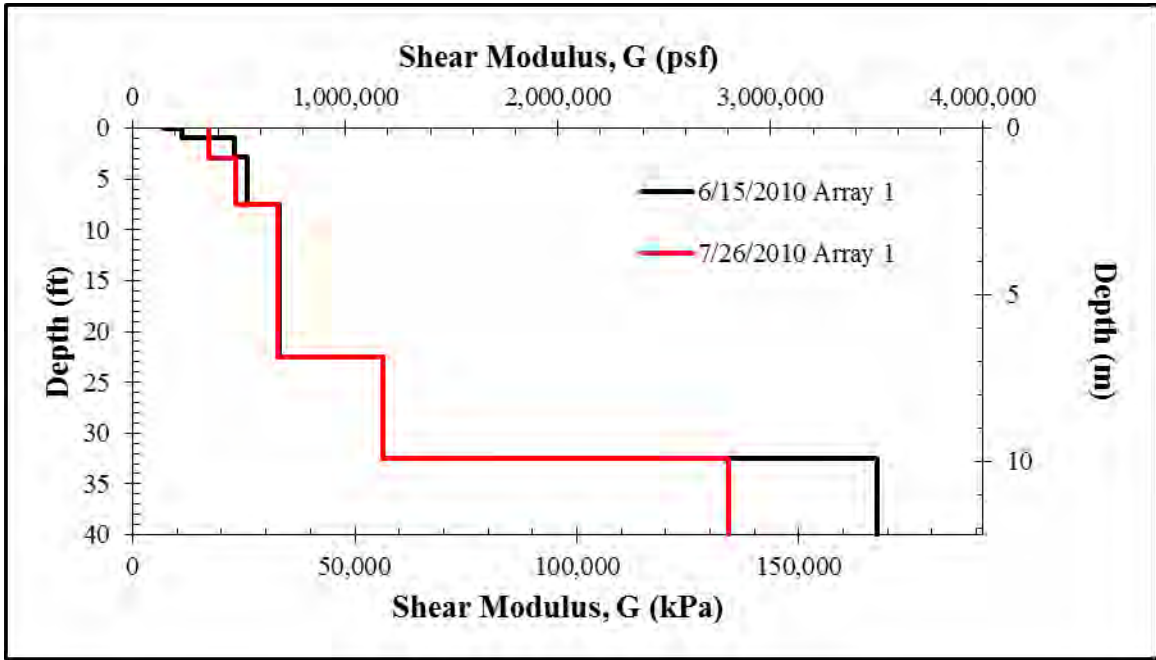


Figure 35. Shear Modulus Profiles from Excavation Side of Wall

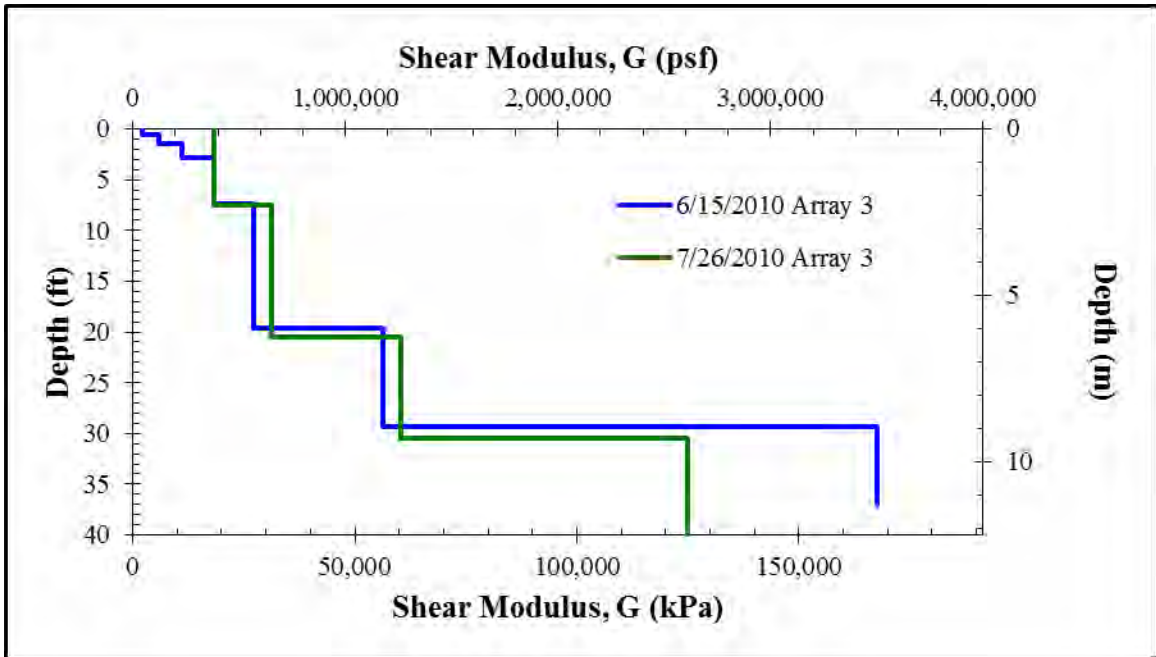


Figure 36. Shear Modulus Profiles from Non-Excavation Side of Wall

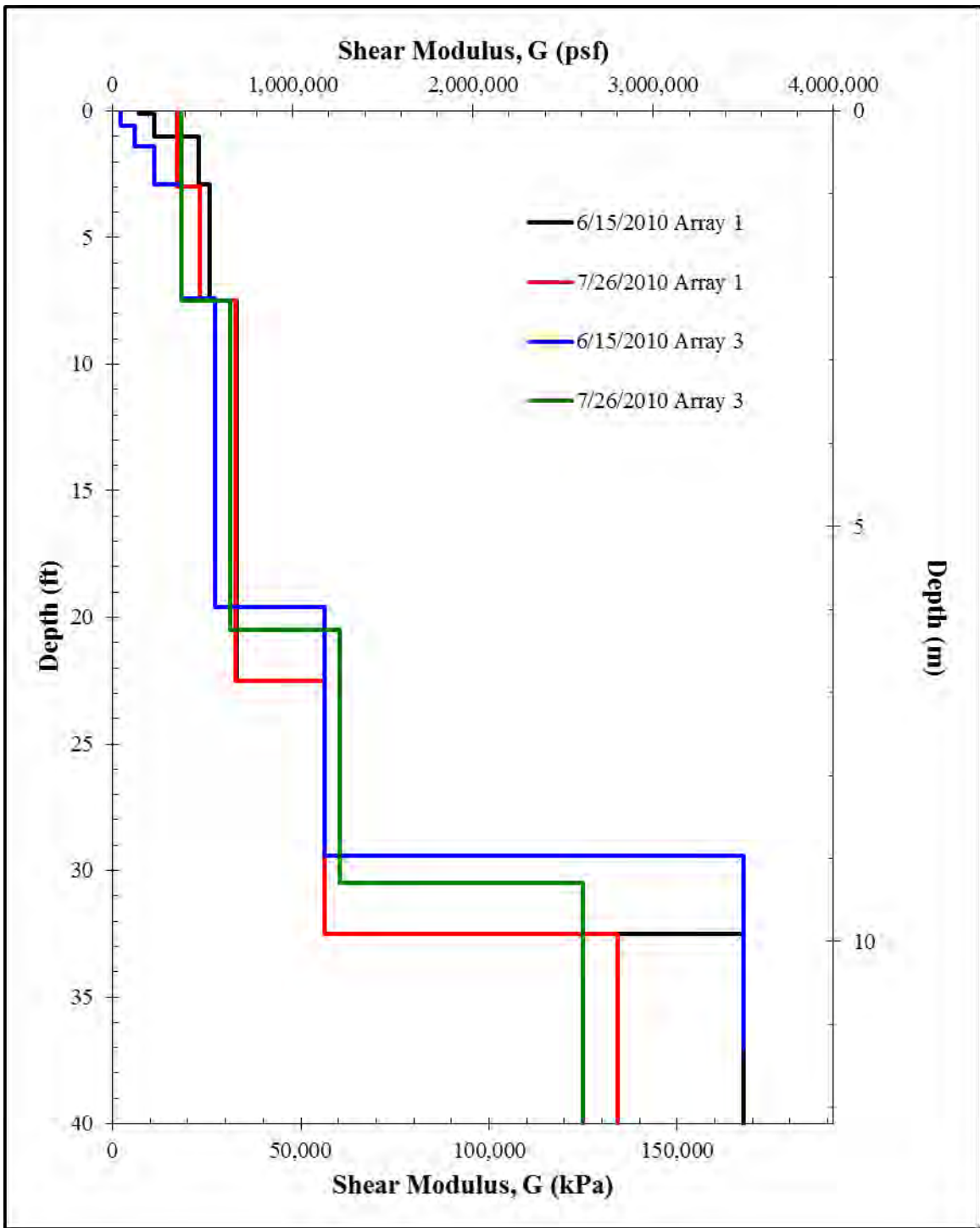


Figure 37. Summary of Measured Shear Modulus Profiles

5 Laboratory Investigation

5.1 Index Properties

5.1.1 Moisture Content

Moisture contents were directly measured in accordance with ASTM D2216. The moisture profile was first determined on samples retrieved during the initial subsurface investigation. Samples also were retrieved and tested when the soil was exposed during subsequent construction activities. Additional samples – none deeper than 5 feet – were sampled using a 1.5-inch hand auger. All of the samples were taken from within 50 feet of the Lymon C. Reese Research Wall and within two years of the initial subsurface investigation. The groundwater table was monitored with a piezometer that was installed in borehole B-1 (Dellinger, 2011).

The results, shown in Figure 38, reflect the extreme drought that plagued central Texas both before and during the course of this research. The top several feet of soil often dried to moisture contents between 18 and 23 percent. Periodic precipitation wetted the same depths to moisture contents near 30 percent, and sustained ponding raised moisture contents above 30 percent. The observed fluctuations tapered to a smaller magnitude with depth, but insufficient samples were obtained at depths below 5 ft to determine the depth at which moisture fluctuations ceased to occur. The depth to water increased steadily with time as the region's drought continued. Construction activities, mainly excavation, may have had significant effects on the measured groundwater level.

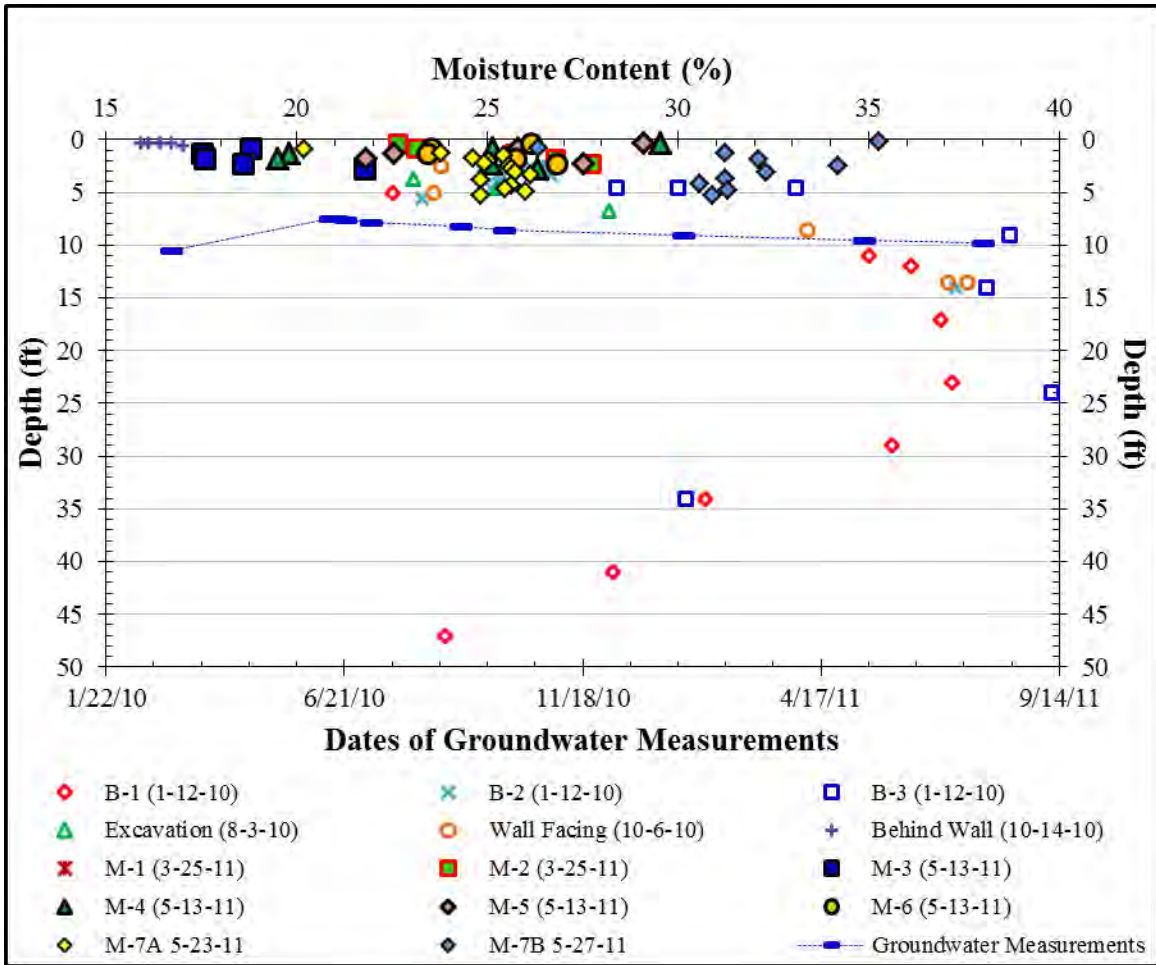


Figure 38. Summary of Moisture Content Measurements

5.1.2 Atterberg Limits

The liquid and plastic limits were measured on samples obtained from the initial subsurface investigation. The plasticity indices are in excess of 50 – and as high as 79 – throughout the soil profile.

Several testing parameters were varied to ensure that these large values were not relics of poor soil preparation or user error. The first round of tests was conducted at the

University of Texas soil mechanics laboratory. The soil was broken down and soaked in distilled water until it softened, and then it was blended in a high-speed shear mixer. Coffee filters were used to contain the soil while the moisture content dropped to a level near the liquid limit. The same drying process was used to prepare the soil for the plastic limit tests. The procedural aspects of each test were conducted in accordance with ASTM D4318.

A second round of Atterberg Limit tests at the University of Texas used a similar procedure. The soil was again soaked in distilled water, but the curing time was allowed to extend between two and three weeks. After the extended curing period, small portions of the wet soil were mixed with an equal portion of additional distilled water and blended in the high-speed shear mixer. Tiny clumps of clay that could not be broken down in the mixer were removed from the sample prior to testing. Only liquid limit tests were conducted on these samples.

A second party (Fugro Consultants Inc.) ran a third set of Atterberg Limits tests. This round was prepared in accordance with the TxDOT dry preparation method TEX-101-E. Although this method of preparation is significantly different than the wet preparation method that was used during the first two rounds of tests, and despite the fact that the tests were conducted in a different lab and by a different technician, all three rounds of tests showed close agreement.

Figure 39 summarizes the three rounds of tests. The highest plasticity indices occur between 15 and 20 feet. The Atterberg limit and moisture profiles are combined in

Figure 40. Moisture contents are slightly higher than the plastic limits throughout the profile.

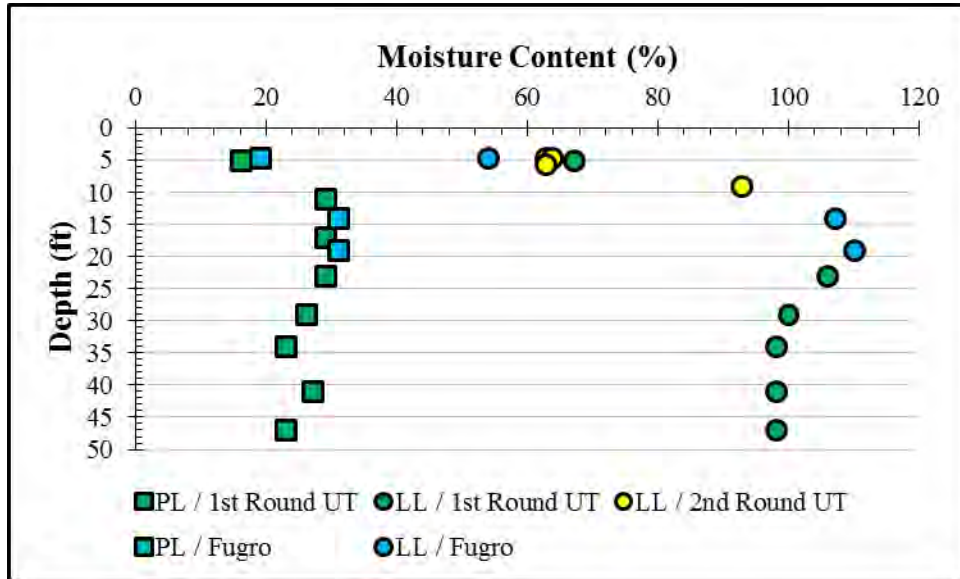


Figure 39. Summary of Atterberg Limit Measurements

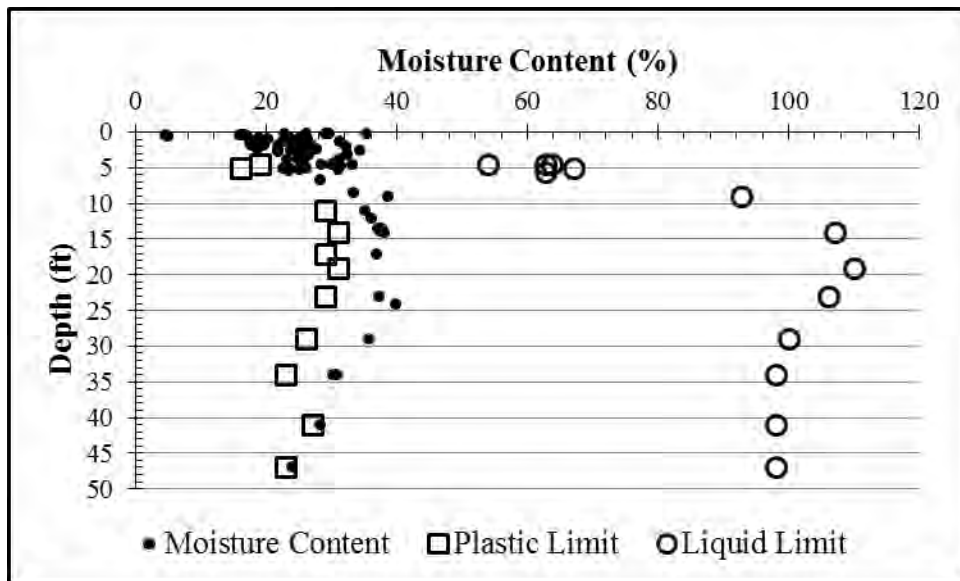


Figure 40. Summary of Atterberg Limits and In-Situ Moisture Contents

5.1.3 Unit Weight

Unit weights were measured from undisturbed samples that were trimmed to specific dimensions for laboratory testing. Trimming was a tedious procedure that usually required two to three hours per specimen. The soil's stiff and blocky structure necessitated sharp, rigid cutting tools to remove very thin slices of soil without disengaging larger blocks from the secondary mosaic structure. Figure 41 shows the tools that proved most useful for trimming: wire saw, Hyde safety knife, razor blades, open-type miter box and trimming guide.

The first step in trimming a specimen was cutting an appropriate length of soil off of the 8-inch long undisturbed sample that had previously been extruded from the seamless push-tube, Figure 42. This involved laying the undisturbed sample in the miter box and using a wire saw to cut the sample to length. The wire saw commonly encountered a small stone or pre-sheared surface, either of which resulted in a very rough cut. In these cases, the rough surface was carefully trimmed flush using a razor blade. Finally, a Hyde safety knife or other rigid metal straightedge would be used with the miter box to ensure a perfectly square and flush trim.

Next, the specimen would be loaded into the trimming guide. The specimen was seated on the surface that was already trimmed to ensure a square seating during trimming. Once the specimen was properly positioned, the trimming ring was pressed firmly down onto the top of the specimen, enough to penetrate roughly 0.1 inches. A razor blade was then used to remove very thin slices of soil in the close vicinity of the trimming ring, uniformly around the circumference of the specimen. Once the soil was



Figure 41. Trimming Tools



Figure 42. Rough Cutting Surface Associated with Wire Saw

trimmed nearly flush with the diameter of the ring, the ring was pushed further down and trimming was continued. This process was repeated until the specimen had been trimmed completely into the ring.

Isolating trimming to the vicinity of the ring was beneficial for preserving the in-situ moisture content, but it was also favorable to taper the trim downward (Figure 43) to avoid stress concentrations that tended to cause a blocky disintegration of the specimen. Whenever small pieces of rock were encountered, they were removed and replaced with fresh cuttings.

Once the soil was trimmed into the ring, the two ends were trimmed flush with the top and bottom edges of the ring. In some cases, a spacer was used for trimmed to a height slightly less than that of the ring. After removing the ring and soil from the trimming guide, a razor blade was used to trim the soil very close to the edges of the ring. Finally, a Hyde safety knife or other stiffer metal straightedge was used to ensure that the soil was flush with the ring's edge. If any rock material was encountered at the edge, it was removed and replaced with soil cuttings, Figure 44.

Because all of the density specimens were 2.5-inch diameter cylinders with thicknesses no larger than 1 inch, even small trimming imperfections could have caused a considerable underestimation of density. Specifically, the removal and replacement of small stones and the presence of chalky regions seemed to cause an underestimation of unit weights. These problems occurred at all depths, but proved most common below the weathered zone.



Figure 43. Tapered Trimming Surface



Figure 44. Rock Particle Requiring Removal and Replacement

The higher quality measurements from the weathered zone reveal an average total unit weight of approximately 123 lb/ft³, Figure 45. Other measurements, including several that were taken by a second party, suggest that the unit weight decreases with depth. It seems more likely that these measurements are the relic of trimming problems. A more realistic profile of total unit weights has been interpreted from the more reasonable data, Table 6.

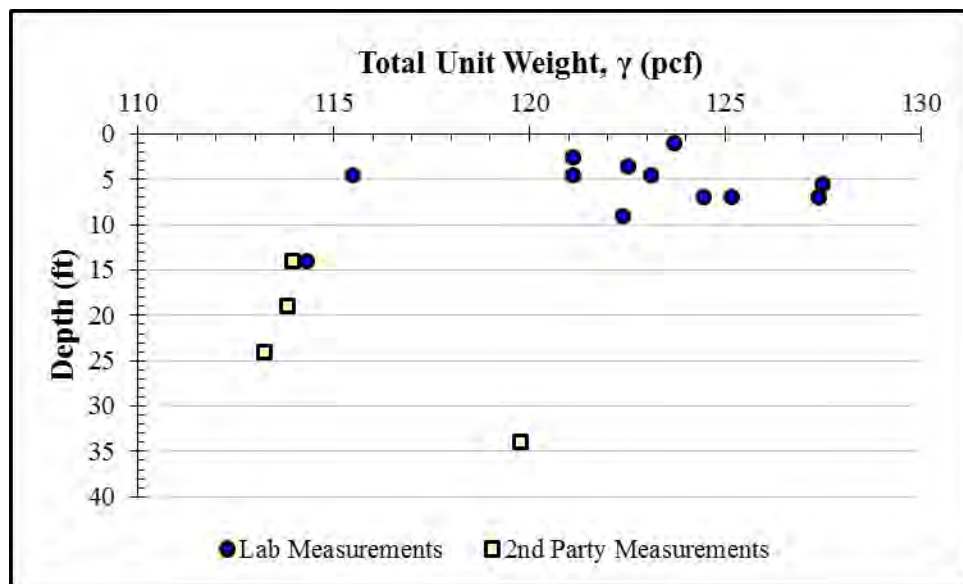


Figure 45. Profile of Total Unit Weights

Table 6. Interpreted Profile of Total Unit Weight

Depth (ft)	Total Unit Weight, γ (lb/ft ³)
0 – 5	120
5 – 10	123
Below 10	126

5.1.4 Grain-Size Analysis

The grain size distribution was determined by running hydrometer tests in accordance with ASTM D422. The soil was prepared by soaking in distilled water treated with sodium hexametaphosphate. After several days of particle dispersement and softening, a high-speed shear mixer was used to further mix the soil-water solution. The results are presented in Figure 46. The clay fractions – the percent finer than 0.002 mm – are summarized in Table 7. The variability may be explained by isolated patches of chalky material.

Table 7. Summary of Clay Fractions

Borehole	Depth (ft)	Clay Fraction, CF (%)
B-3	6 - 8	51.5
B-1	10.5 - 12	80
B-1	16.5 - 18	65
B-1	28.5 - 30	72

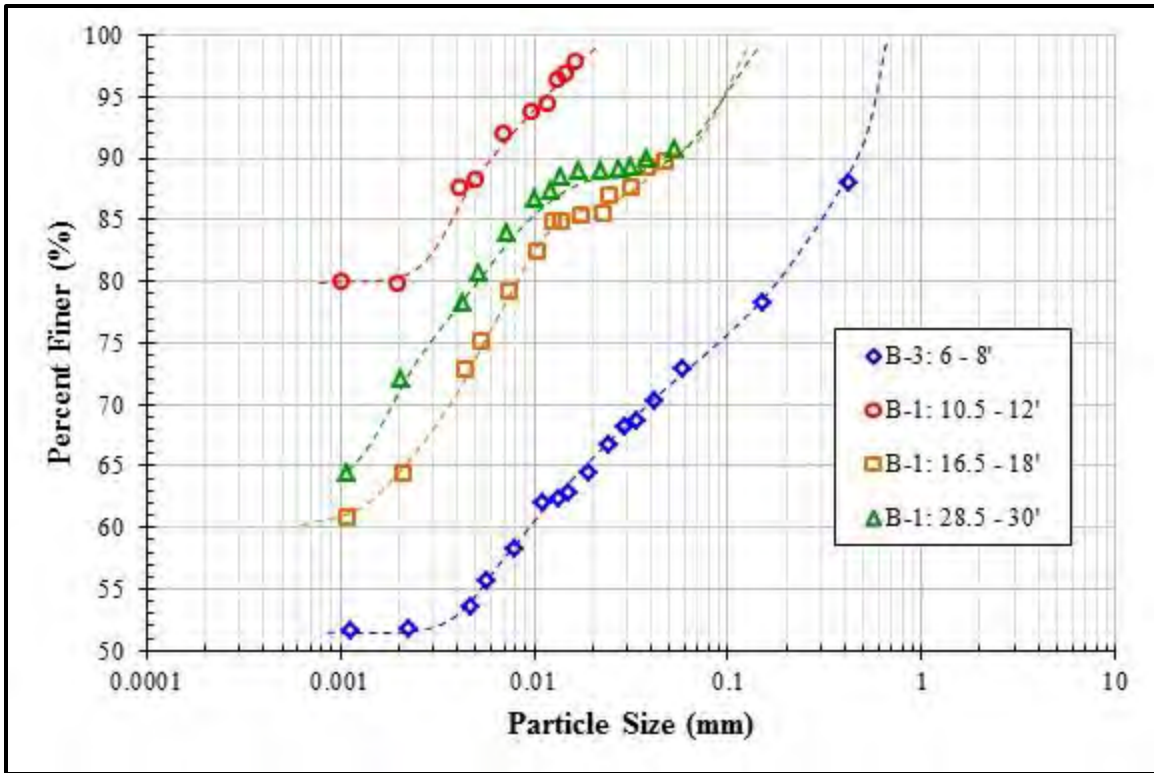


Figure 46. Summary of Grain Size Distributions

5.2 Consolidation

5.2.1 Test Procedures

Five one-dimensional consolidation tests were conducted to assess the soil's compressibility and stress history. The test specimens were all carefully trimmed from seamless push-tube samples and subject to at least two load-rebound cycles. The specific loading and wetting sequences had a significant effect on the measurements. The magnitude and duration of the initial dry seating load were particularly controlling factors.

The time-settlement data was very scattered and sometimes downright chaotic for each of the five consolidation tests. It was often difficult to define a load increment's settlement, making it impossible to differentiate between primary and secondary strains. The heterogeneity and anisotropy of this type of soil is significantly different than the idealized material upon which Terzaghi's theory of consolidation is derived. Nevertheless, Terzaghi's theory provides a useful framework for characterization in terms of total observed settlement, Olson (2009).

Theoretical time-settlement curves were fitted to the raw data using a forward modeling approach that involved fitting a theoretical time-settlement curve to match the raw data. The formulation for the theoretical curve is simply Terzaghi's theory of consolidation. The forward model allows the user to adjust several input values until the theoretical data matches the raw data.

The user-defined values of S_0 , S_{100} , H_{dr} and c_v generate a theoretical consolidation curve spanning degrees of consolidation from zero through 99. The theoretical curve stretches through excessive time values for degrees of consolidation larger than 99. The drainage distance (H_{dr}) was calculated separately for each load increment as half of the specimen's height at the beginning of that increment. Initial values of S_0 and S_{100} are then entered to match the raw data. Next, the coefficient of consolidation (c_v) is adjusted within reasonable bounds until the theoretical curve begins to match the raw data. Finally, S_0 , S_{100} and c_v are finely tuned to achieve the best fit.

The forward model was set up as an array in a spreadsheet so that it would automatically plot on the same graph as the raw data. The first column of the array

contains degrees of consolidation (U) ranging from zero to 99. This column essentially provides the model's independent variable. The next column calculates the time factor (T) using Equation 5. The next column calculates elapsed time (t) using Equation 6. The theoretical settlement is then calculated as a function of U, S₀ and S₁₀₀, Equation 7.

$$T = \begin{cases} \frac{\pi}{4} \cdot \left(\frac{U}{100}\right)^2 & U < 60\% \\ \sqrt[3]{\frac{\left(\frac{U}{100}\right)^6}{2 \cdot \left[1 - \left(\frac{U}{100}\right)^6\right]}} & U \geq 60\% \end{cases} \dots\dots\dots \text{Eq. 5}$$

$$t = \frac{T \cdot H_{dr}^2}{c_v} \dots\dots\dots \text{Eq. 6}$$

$$S = S_0 - \left(\frac{U}{100}\right)(S_0 - S_{100}) \dots\dots\dots \text{Eq. 7}$$

Every load increment's raw time-settlement data is fitted with theoretical curves in Appendices B – F. Both square-root of time and log of time graphs are presented for each load increment. The square-root of time plots also contain horizontal dashed lines corresponding to S₆₀. This simply delineates the zone between S₀ and S₆₀ through which S-√t should be linear. Non-Terzaghiian effects often result in distorted time-settlement measurements in the first minute or so of a load increment. It was often beneficial to use the first 60% of settlement to define S₀ instead of the first 30 seconds. In every case, an effort was made to fit both plots. Many times it was impossible to fit a theoretical curve

on either time scale. In these cases judgment was used to achieve the best fit possible using reasonable input parameters.

Still using the theoretical consolidation framework, the soil's hydraulic conductivity was back-calculated for each load increment. The coefficient of compressibility was calculated using Equation 8. Again, S_0 and S_{100} refer to total observed settlement. The change in effective stress is equal to the increase or decrease in effective stress from the previous to the current load increment. The hydraulic conductivity (k) is then calculated using Equation 9.

$$a_v = -\frac{S_{100} - S_0}{H_s \Delta\sigma'} \dots\dots\dots \text{Eq. 8}$$

$$k = \frac{c_v a_v \gamma_w}{1 + e_{50}} \dots\dots\dots \text{Eq. 9}$$

Each test was run in accordance with ASTM D2435, but the individual loading and wetting sequences were not identical. Each load sequence used a load increment ratio of 1 and an unloading ratio of ½. Tests 1 and 2 were initially loaded with 125 psf and then inundated after a waiting period of several minutes. The data acquisition system failed during several load increments of Test 1. Tests 3 – 5 were initially loaded with weights approximating their in-situ vertical effective stresses, and they were loaded in the dry condition for precisely 30 minutes before inundation. Test 3 was allowed to swell under its in-situ vertical stress after inundation. Additional weights were applied to maintain constant volume after inundation for Tests 4 and 5.

5.2.2 Summary of Results

Figures 47 – 51 present the hydraulic conductivities, coefficients of consolidation and void ratios from the five tests. The back-calculated hydraulic conductivities are small, generally ranging from 2×10^{-7} down to 2×10^{-9} ft/day through the load cycles. Based on these results, the hydraulic conductivities at in-situ effective stresses are summarized in Table 8.

The e-log-P' plots verify that the soil is heavily overconsolidated. The virgin compression curves for Tests 1 and 2 are too rounded to define a compression index or a clear transition to normally consolidated compression. The higher dry seating loads for Tests 3 – 5 resulted in a clearer transition to normally consolidated compression and discernible compression indices. Overconsolidation ratios ranged from 9 – 14. The results from all five tests are summarized in Table 9. Figures 52 and 53 compare the initial load and rebound curves for each test in terms of strain and void ratio, respectively.

Table 8. Back-Calculated Hydraulic Conductivities (k) at In-Situ Stresses

Test ID	Depth (ft)	Hydraulic Conductivity, k (ft/day)	k (cm/sec)
1	6 – 8	3×10^{-9}	1×10^{-12}
2	8 – 10	8×10^{-9}	3×10^{-12}
3	4 – 5	4×10^{-9}	1×10^{-12}
4	4 – 5	4×10^{-9}	1×10^{-12}
5	13 - 15	4×10^{-9}	1×10^{-12}

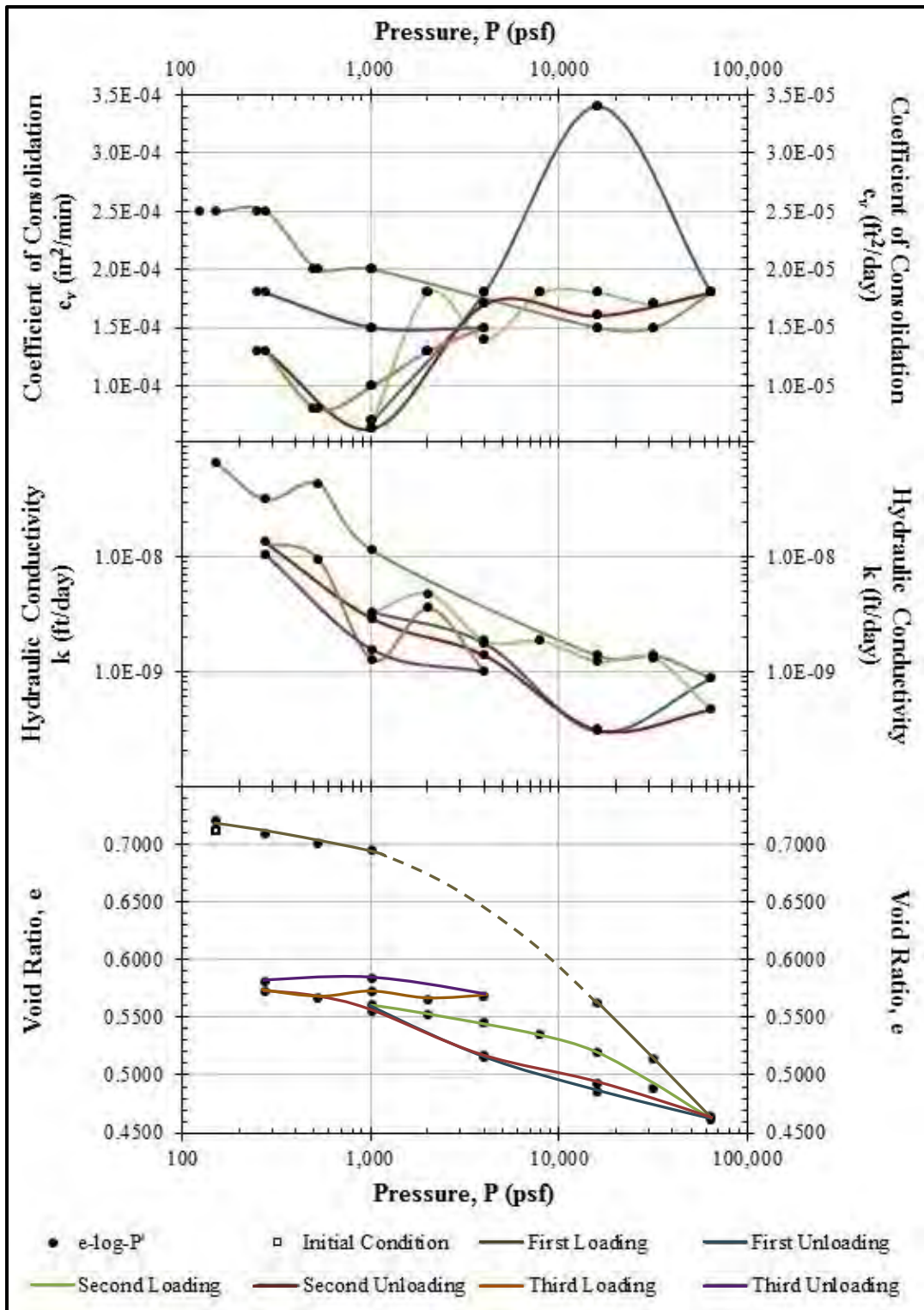


Figure 47. Consolidation Test #1: B-3, 6 – 8 ft

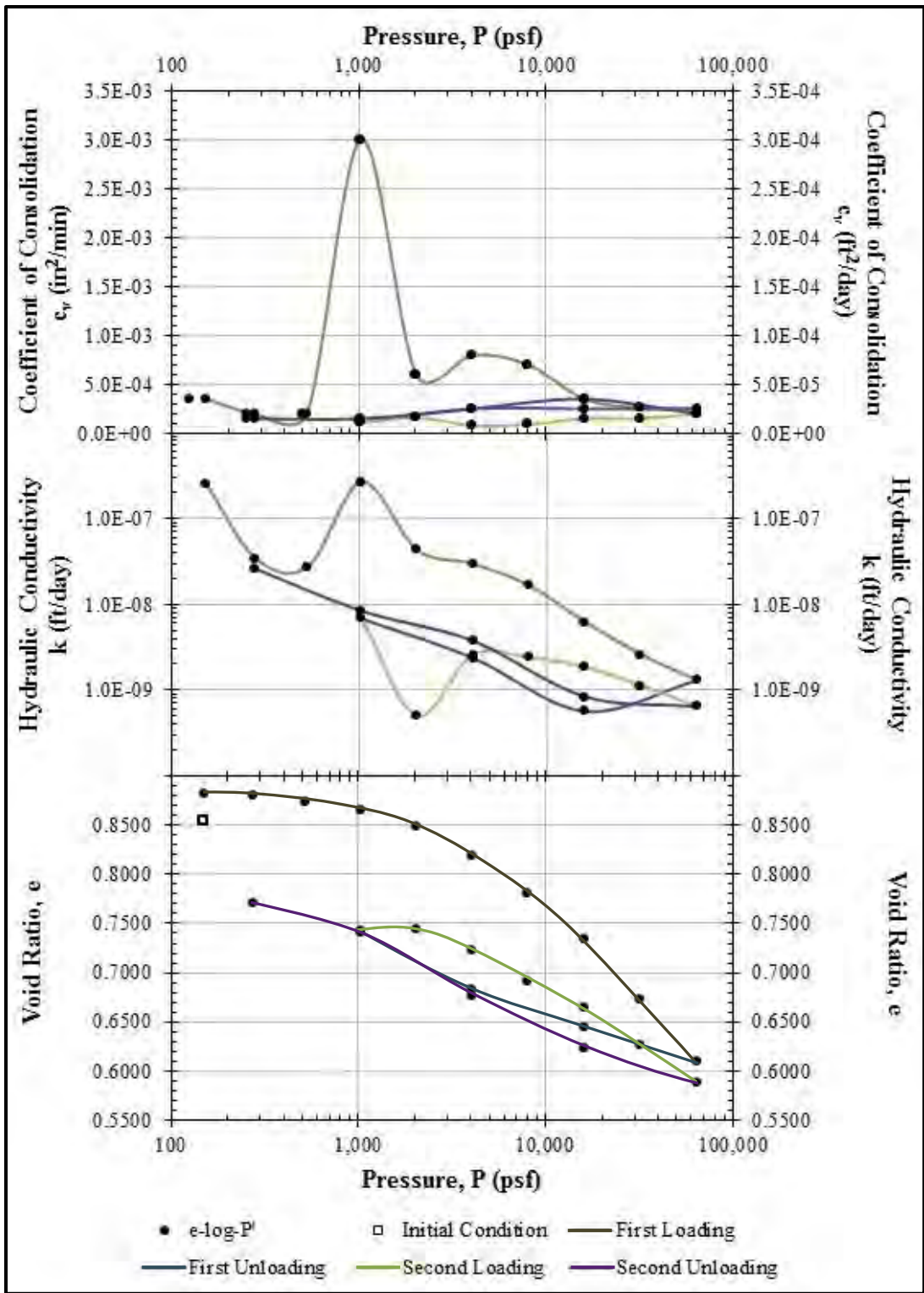


Figure 48. Consolidation Test #2: B-3, 8 – 10 ft

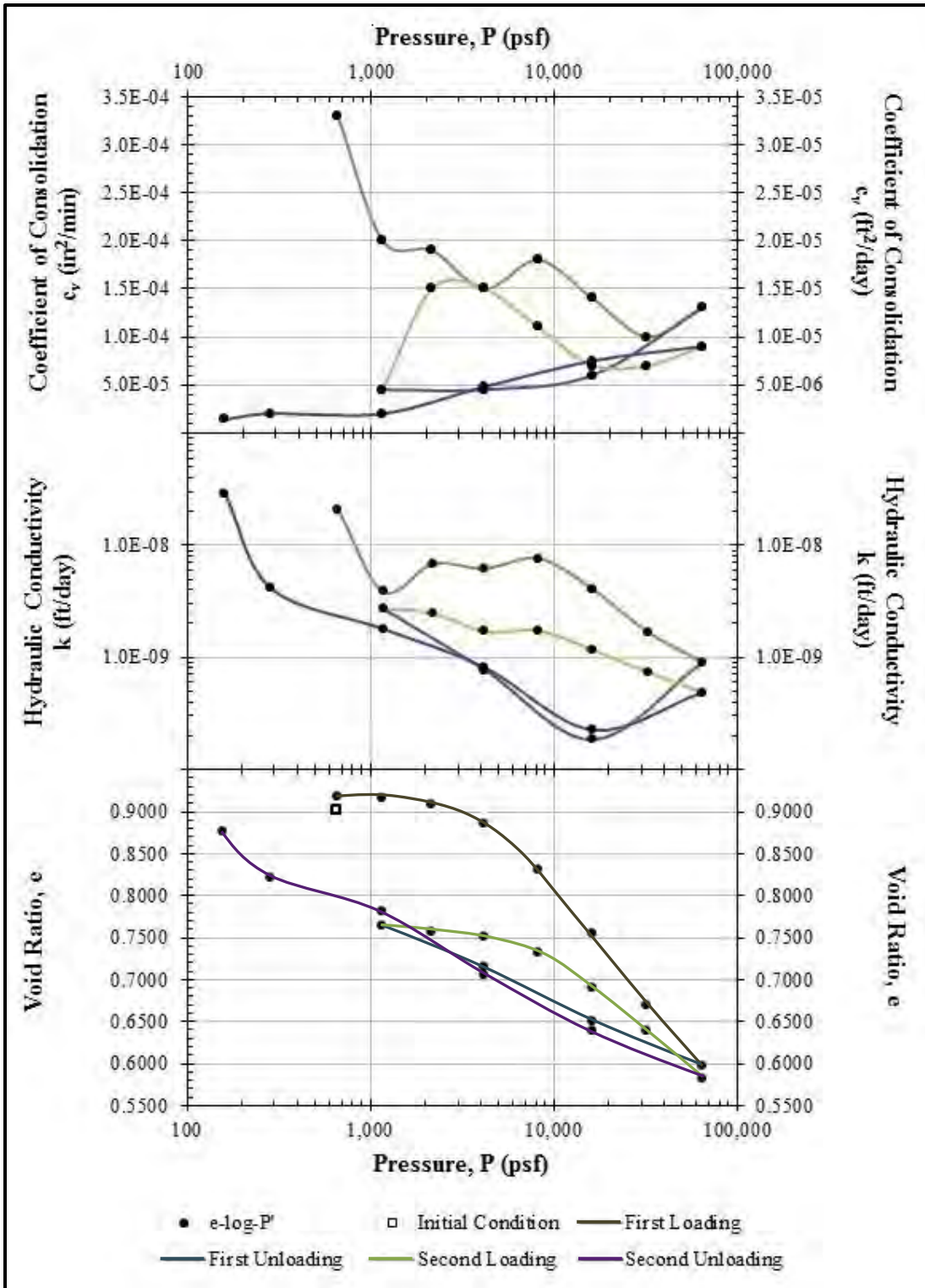


Figure 49. Consolidation Test #3: B-3, 4 – 5 ft

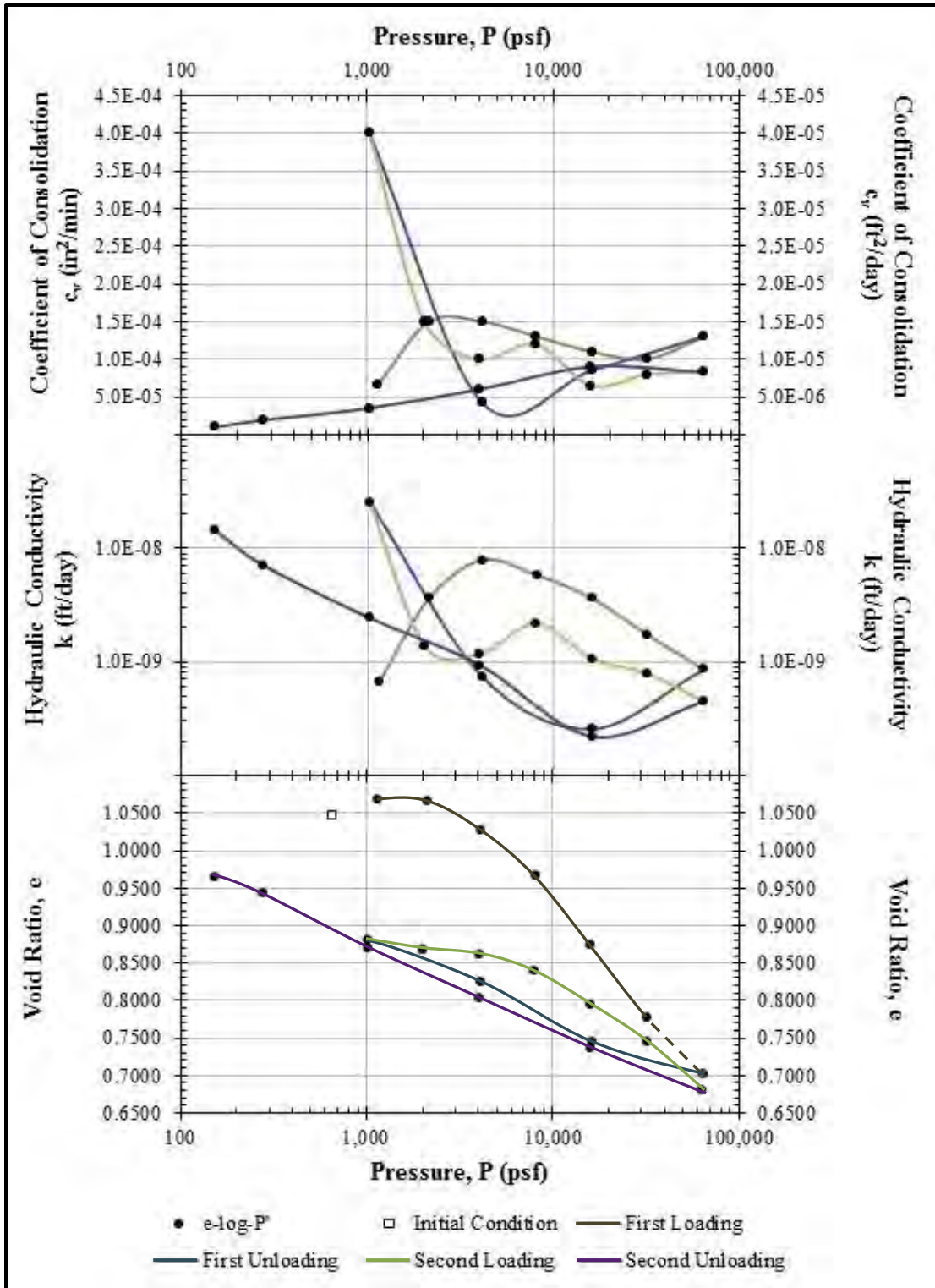


Figure 50. Consolidation Test #4: B-3, 4 – 5 ft

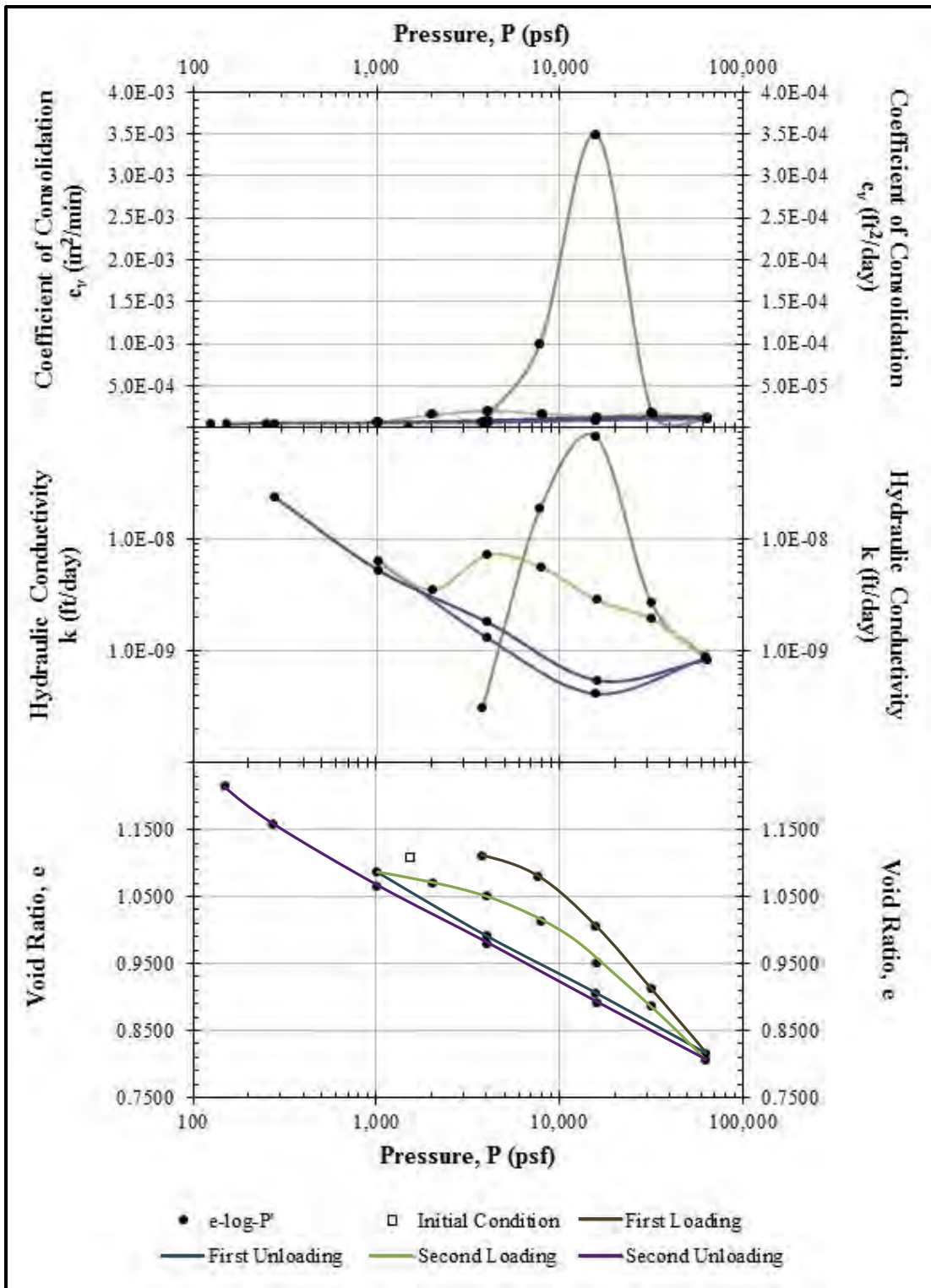


Figure 51. Consolidation Test #5: B-3, 13 – 15 ft

Table 9. Summary of Consolidation Tests

Test #	Boring	Depth (ft)	c_r	c_c	σ'_v (pcf)	OCR	PL	PI	e_0
1	B-3	6 - 8	0.033	-	750	-	23	55	0.7117
2	B-3	8 - 10	-	-	900	-	26	67	0.8541
3	B-3	4 - 5	0.103	0.288	500	14	19	44	0.9019
4	B-3	4 - 5	0.112	0.319	500	12	19	44	1.0454
5	B-2	13 - 15	0.150	0.313	1150	9	31	76	1.1076

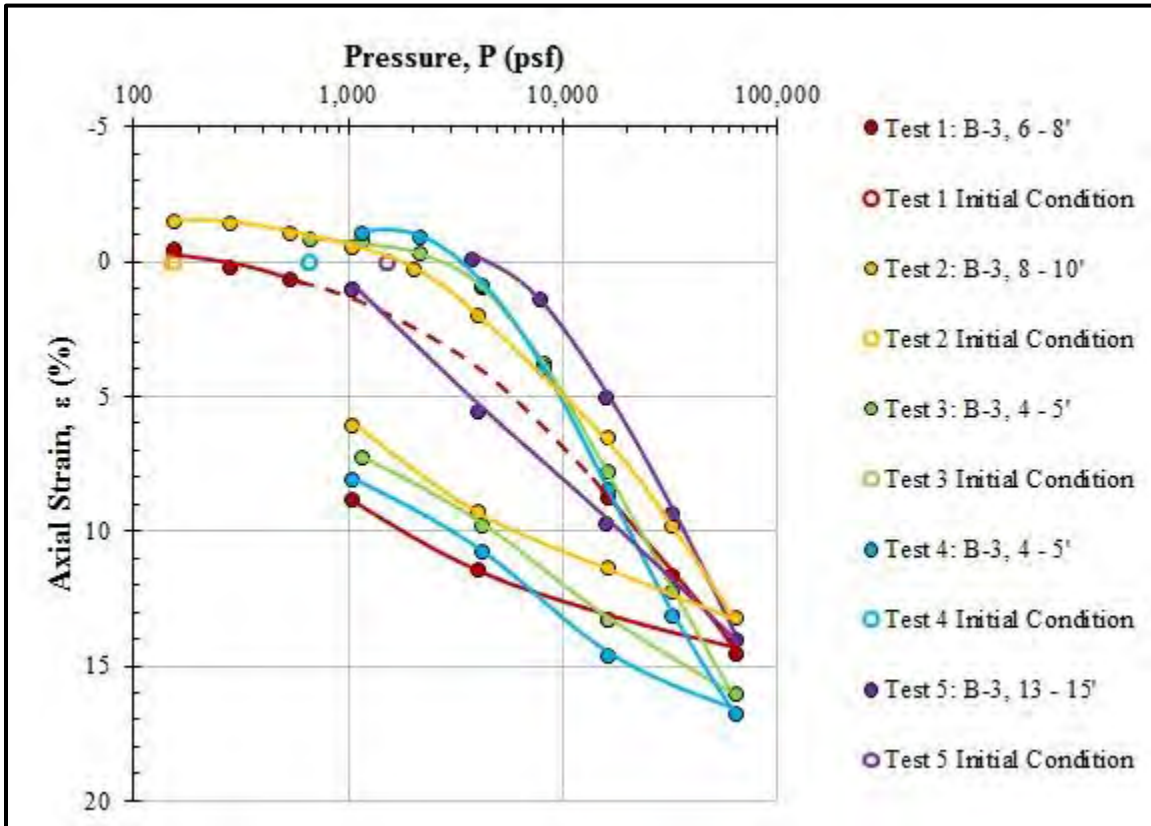


Figure 52. Summary of Load-Rebound ϵ -log-P Curves

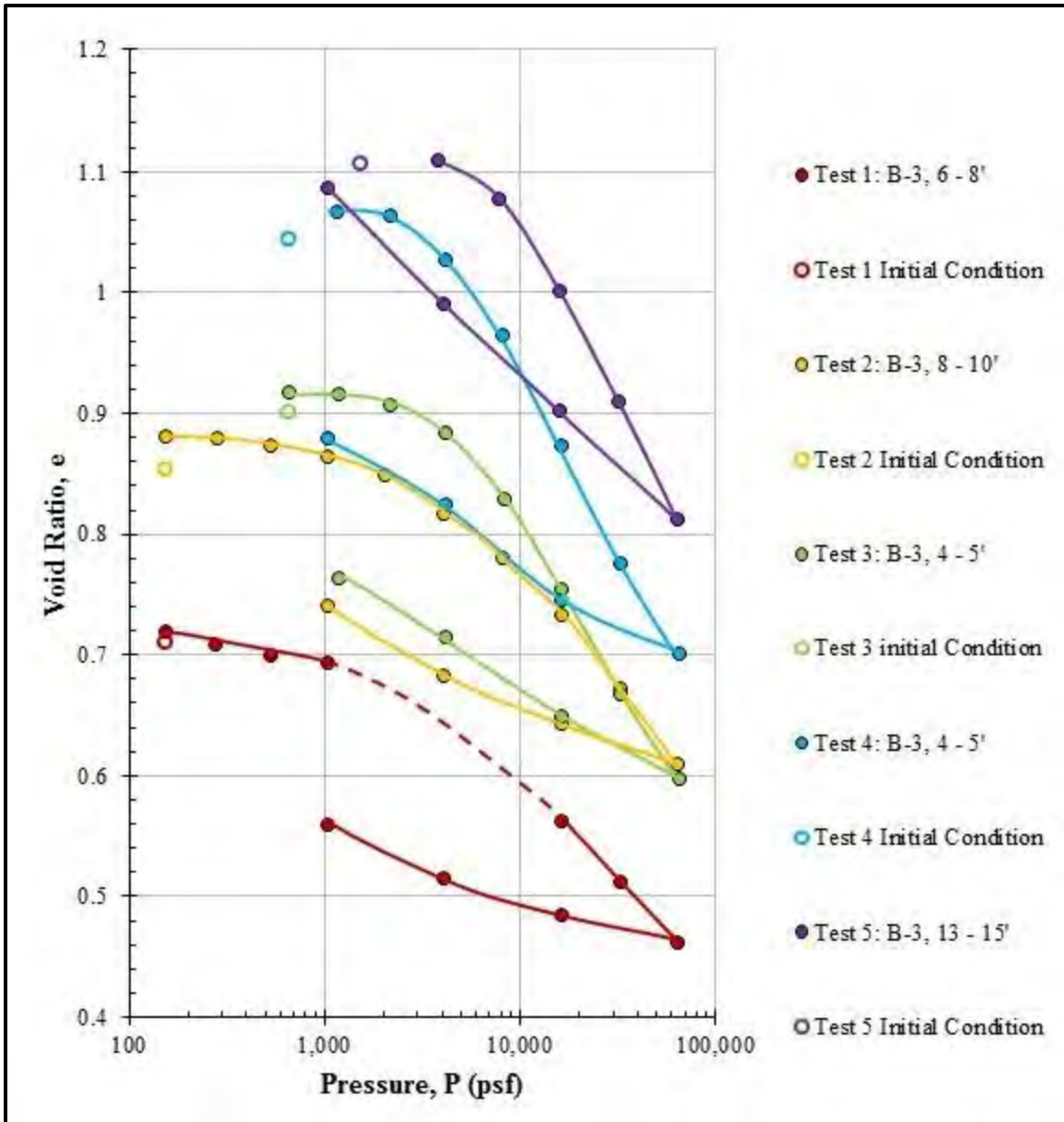


Figure 53. Summary of Load-Rebound e -log- P Curves

5.3 Cyclic Lateral Shrink and Swell

5.3.1 *Overview of Test Method*

A series of cyclic shrink-swell tests were conducted on horizontally trimmed specimens to estimate the soil's response to cyclic changes in moisture content. In these tests, the axial strain and moisture content are measured while the sample is repeatedly wetted and force-ventilated under a constant total normal stress. Because the samples were trimmed horizontally, the normal stress is analogous to the lateral restraint provided by a retaining wall. The test method was adapted from a similar test developed by Marr (2003) and Allen (2005).

5.3.2 *Trimming Procedure*

Specimens were trimmed from vertically sampled undisturbed seamless push tube samples. The specimens were trimmed transversely through the samples so that the specimens' longitudinal axes corresponded to a horizontal plane in the field. The first step in specimen preparation was cutting a 3-inch length of soil from the undisturbed sample. Because these tests were only conducted on the relatively soft weathered clay from the active zone, a wire saw was adequate for cutting through the undisturbed sample. A Hyde safety knife or other rigid metal straightedge was then used along with an open type miter box to square and flush one of the specimen's edges, Figure 54a.

The specimen would then be seated on its squared end inside the miter box. Holding the soil firmly against one of the miter box walls, a wire saw could be used to cut a roughly 1/2-inch secant through the specimen's diameter. This cut was continued across the specimen to form a plane parallel to the sample's original longitudinal axis.

Next, the specimen was rotated 180 degrees in the miter box and a second ½-inch secant plane was trimmed parallel to the first, Figure 54b.

Once both secant planes were trimmed square and flush, one was used to seat the specimen on a plastic trimming surface. The cutting edge of a lightly greased 2.5-inch diameter, 1-inch tall ring was then carefully centered and seated on specimen's exposed secant plane. Because of geometric limitations, this was a nontrivial step that required careful attention. After a light seating, a level was used to ensure the ring was plumb. At this point, it was convenient to trim away the specimen's four corners for high quality moisture samples, Figure 54c.

Finally, a razor blade was used to slowly trim soil away from the area just outside the cutting surface of the ring. Once the soil was nearly flush with the ring, the ring was pushed down further into the sample. This was done very slowly, and the level was constantly checked to ensure that the ring remained plumb as it was pushed down around the soil specimen, Figure 54d.

Once the maximum thickness of soil was trimmed into the ring, the specimen was trimmed squarely at the top and bottom of the ring. A spacer was then used to push and trim enough soil away from the top – cutting edge – of the ring to make room for a filter paper and porous stone. Whenever small pieces of rock material were encountered, they were removed and filled with compacted soil trimmings.

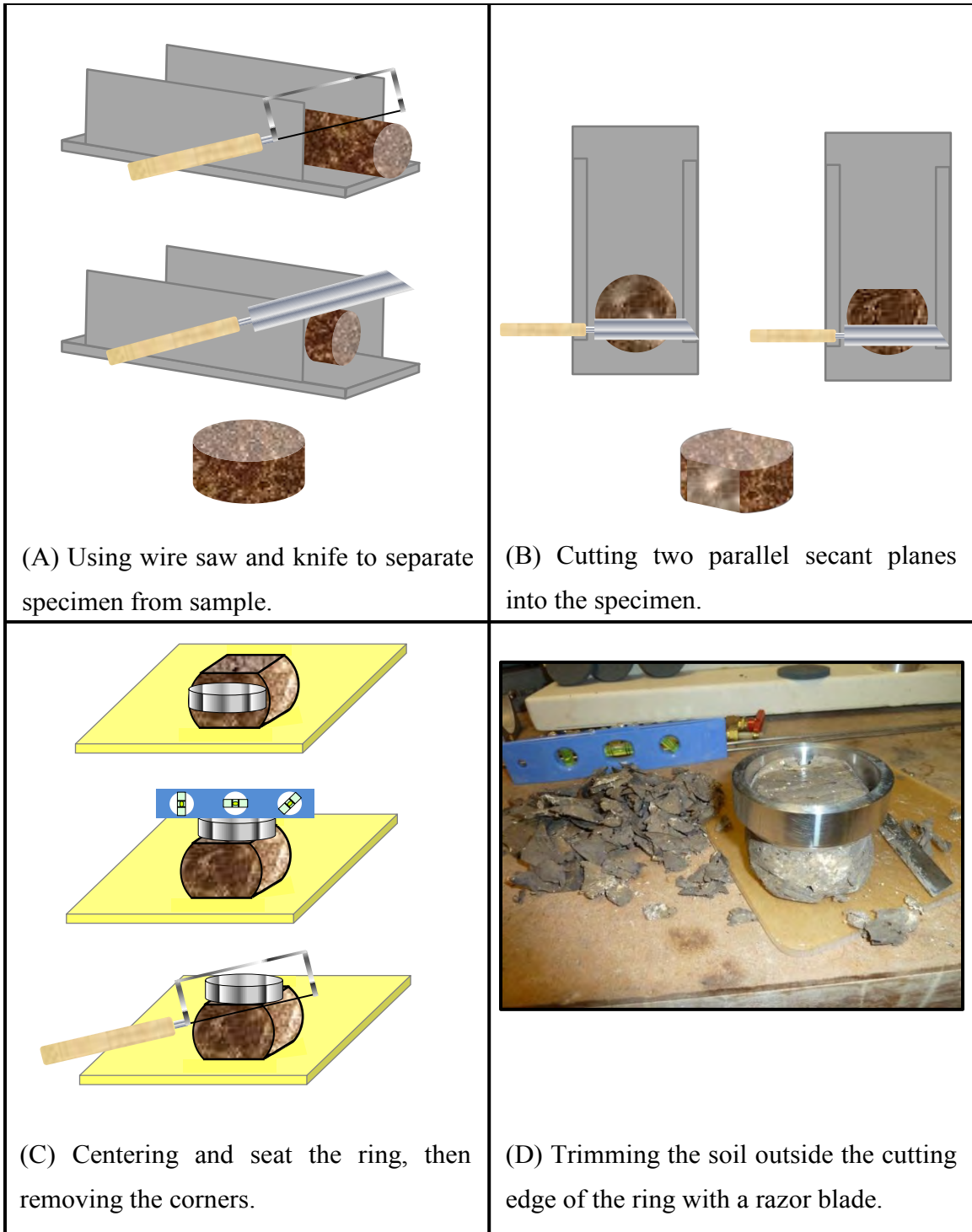


Figure 54. Trimming Procedure for Lateral Cyclic Swell Tests

5.3.3 Equipment Setup

The cyclic swell tests were conducted using standard constant rate of strain (CRS) consolidation equipment. This includes a floating ring CRS consolidation cell, two columns of a pressure panel and a GeoJAC load frame from GEOTAC. GeoJAC software was used to control the load frame from a computer, and an integrated data acquisition system (DAS) was used to collect measurements of displacement, load and pressure. A schematic of the setup is shown in Figure 55.

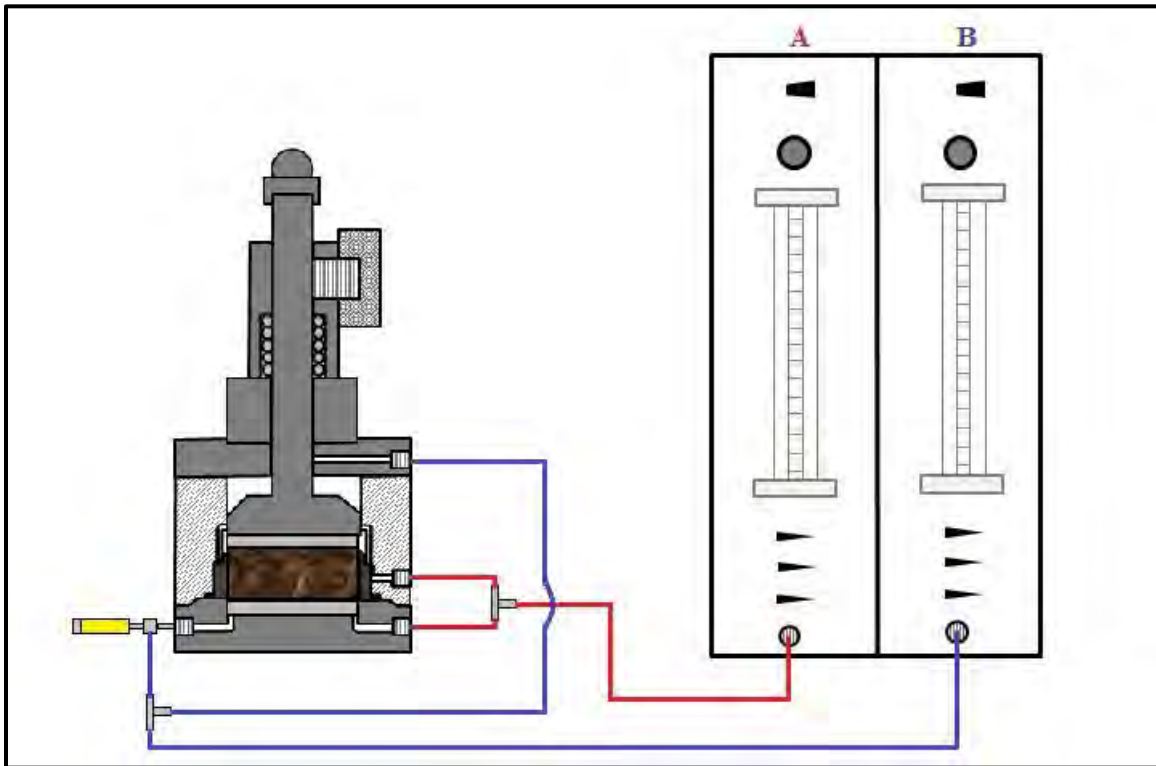


Figure 55. Equipment Setup for Cyclic Swell Tests

The top and bottom halves of the consolidation cell are isolated from one another, and each half has two available ports. Two columns of a pressure panel were utilized for each test. Each column was connected to both a top and bottom port of the consolidation cell, with one line being connected to the bottom half of the cell through a pressure transducer. Note that the column labels – “A” and “B” – from Figure 55 will be referenced in the discussion of test procedures in Section 5.3.4. An LVDT and a load cell were mounted on the GeoJAC. The top and bottom halves of the CRS cell were connected with three mounting screws and sealed water tight using a greased O-ring.

5.3.4 Test Method

The CRS cell and DAS are both readied prior to trimming the soil specimens. With their bottom valves closed, the burette and annulus of column A are filled with water and those of column B are drained. Masses are recorded for the ring, porous stones – both wet and dry – and filter papers. Throughout the test, these masses are occasionally required as tare weights to calculate intermediate specimen weights. The specimen diameter, height and mass are all measured immediately after trimming.

After recording the initial specimen measurements, the specimens are loaded into the CRS cell. One porous stone is laid into its recessed position and covered with a damp filter paper. The soil and ring are placed on top of the filter paper. Another filter paper and porous stone are placed on top of the soil, within the ring. The O-ring is then placed around the base of the ring. The top half of the CRS cell is clamped to the bottom half

and all of the fluid lines are connected to the CRS cell ports. The load piston is then firmly seated against the soil and locked into place.

Once assembled, the cell is loaded onto the GeoJAC load frame and the load cell is zeroed. Using the computer to control the GeoJAC in Displacement Control mode, the load ram is slowly lowered until it makes slight contact with the CRS load cap. The LVDT is then zeroed. Next, the software is changed to Load Control mode and the predetermined normal load for the test is applied. Immediately thereafter, the load cap piston is unlocked. The specimen should be loaded in this dry condition for a period of time between 10 and 30 minutes. Dry seating periods for the tests reported herein were typically between 5 and 10 minutes.

After the dry seating period, the CRS cell is filled with water while the normal load is held constant. The cell is filled by making the following adjustments to pressure panel columns A and B: turn the top valve to the vent position, enable both the pipette and annulus and open the bottom valve. Depending on the test setup, a pressure of 2 or 3 psi may need to be applied to the top of column A to force water through the CRS cell. At some point while filling the CRS cell, the pressure transducer should be flushed and zeroed. Note that column A will have to be closed and refilled with water at least once to finish filling the CRS with water. The CRS cell is sufficiently full when the water level in column A recedes at the same rate that water level in column B rises.

When the cell is filled, temporarily close the bottom valves of columns A and B and adjust the water levels. The annulus levels should be at a maximum so that the tick marks on the pipette are amplified. The water level in each pipette should be equal, at the

pipettes' middle reading. The enabling valves on each column should then be set to the pipette position. Finally, note the time and zero-readings for each pipette, and open the bottom valves. The soil is then allowed to swell until significant changes in height no longer occur.

After the first swell stage, the cell is drained and the specimen is removed and weighed. The first step in draining the cell is locking the load cap into place and closing the bottom valves of columns A and B. The annulus and pipette of each column are then drained. Leaving column A in the drain position, a pressure of 3 – 5 psi is applied to column B and each column's bottom valve is opened. When the cell is essentially dry, column B is turned back to the vent position and close the bottom valves of columns A and B.

At this point the specimen may be removed and weighed. The GeoJAC's load piston is raised by switching the software back to Displacement Mode and entering the command. The three clamping screws are then removed, and – depending on the length of the fluid lines – some of the fluid lines will have disconnected from cell ports so that the top half of the cell can be lifted off of the base. The weight of the specimen is quickly recorded, along with details of any tare weights. If possible, both filter papers are replaced with fresh, dry papers and the assembly is returned to the CRS cell for the first shrink stage.

The CRS cell is again assembled as it was for the swell stage, except that each column's pipette and annulus are drained and the inside of the CRS cell is wiped dry. Once the clamping screws and fluid lines are reconnected, the CRS cell is positioned on

the GeoJAC just as it was for the swell stage and the same predetermined total normal load is applied. A new zero for the LVDT is noted while the GeoJAC's load piston is seated, and a new DAS task is initiated to record the shrink stage measurements.

Air is now force ventilated through the CRS cell to accelerate the natural process of shrinkage. For this process, the top of column A is set to the vent position and pressure is applied to the top of column B. The bottom valves of both columns are opened, and the pressure is increased until the pressure transducer attached to the CRS cell reads approximately 5 psi.

Periodically during the shrink stage, the specimen is removed and weighed to obtain a measurement of moisture content. The forced ventilation pressure is removed prior to removing the specimen, and then the CRS cell is removed from the GeoJAC and opened. The specimen is removed and weighed, then returned to the CRS cell. As more time elapses during the shrink stage and the specimen develops large cracks (Figure 56), it becomes more difficult to remove and handle the specimen. Special care must be taken during these measurements to ensure that there is no loss of solid soil particles during weighing. The cracked specimens provide a valuable representation of desiccation that occurs near the surface in the field, Figure 57.

After each weighing, the specimen is returned to the CRS for continued forced ventilation. The shrink stage is continued until significant changes in height cease to occur. At the end of the shrink stage, the specimen is again removed and weighed. The test is concluded at the end of the final shrink stage. At that time, the specimen is removed, weighed and then oven dried. Unless significant solids are lost during the test,

the oven dry weight reveals the true weight of solids and should be used to backcalculate moisture contents from throughout the test.



Figure 56. Examples of Extreme Cracking from Shrink Stage of Cyclic Swell Test



Figure 57. Examples of In-Situ Desiccation Cracking

The relationship between height or strain and moisture content is nearly linear. By assuming the relationship is linear, each swell-shrink cycle may be summarized by a single best-fit line with slope k_s . The steady state value of k_s , hereafter termed the cyclic swell coefficient, can either be taken from the final swell-shrink cycle or the average of several similar cycles. It is a dimensionless value, technically percent per percent. If multiple tests are run at different normal stresses, a constitutive surface can be constructed in terms of total stress, moisture content and height or strain, Figure 58. This constitutive surface can also be simplified by plotting values of k_s versus the log of total stress, Figure 59.

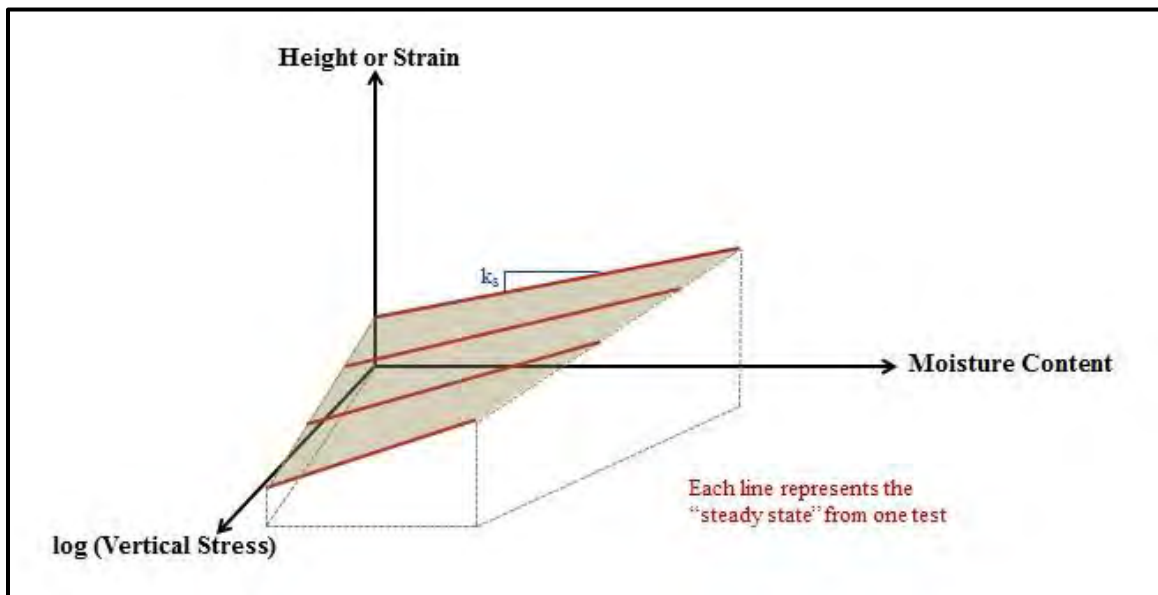


Figure 58. Constitutive Surface for Cyclic Swell Tests

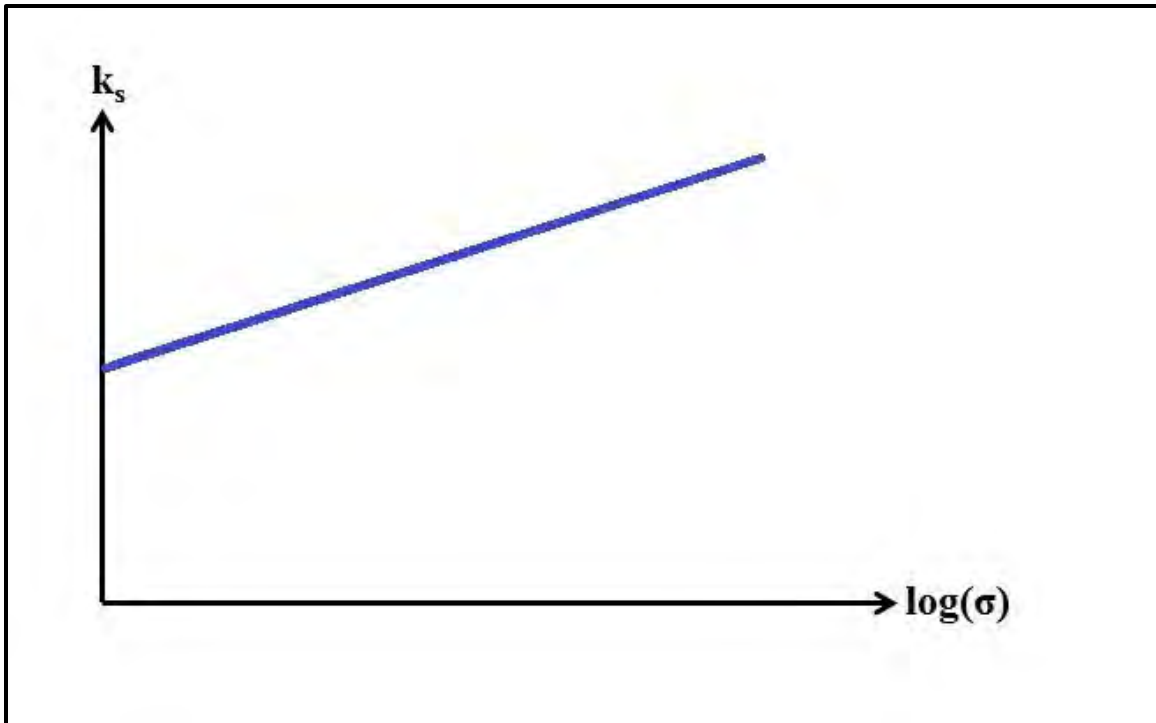


Figure 59. Practical Presentation of Constitutive Surface

5.3.5 Summary of Results

Four cyclic swell tests were conducted. The specimens were trimmed from dark, weathered clay sampled from depths ranging from 2 – 6 feet. The four tests' parameters are summarized below in Table 10. The total stress for each test was chosen to replicate lateral stresses in the field. Test 1 was loaded at less than in-situ conditions, while tests 3 – 4 were loaded at stresses that either approximated or overestimated in-situ pressures.

Table 10. Summary of Accelerated Swell-Shrink Tests

Test ID	Boring	Depth (ft)	σ_t (psf)	γ_t (pcf)	$w_{c,ini}$ (%)	$w_{c,min}$ (%)	$w_{c,max}$ (%)
1	B-2	3 – 4	150	122.4	25.4	4.3	31.3
2	B-2	2 – 3	500	121.1	26.6	3.3	28.7
3	B-2	4 – 5	1000	123.1	26.7	4.3	28.4
4	B-2	5 - 6	4050	127.5	23.3	3.3	24.6

The cumulative time-strain measurements from Test 1 are presented in Figure 60. The specimen achieved successively larger swelling strains after the first three shrink cycles and then reached its steady state. The moisture-strain measurements are shown in Figure 61. Least squares linear regressions were fitted to each cycle's data set to determine k_s values. The coefficients of consolidation from swell stages and the cyclic ranges of moisture content are illustrated in Figure 62. The k_s and c_v values are summarized in Table 11.

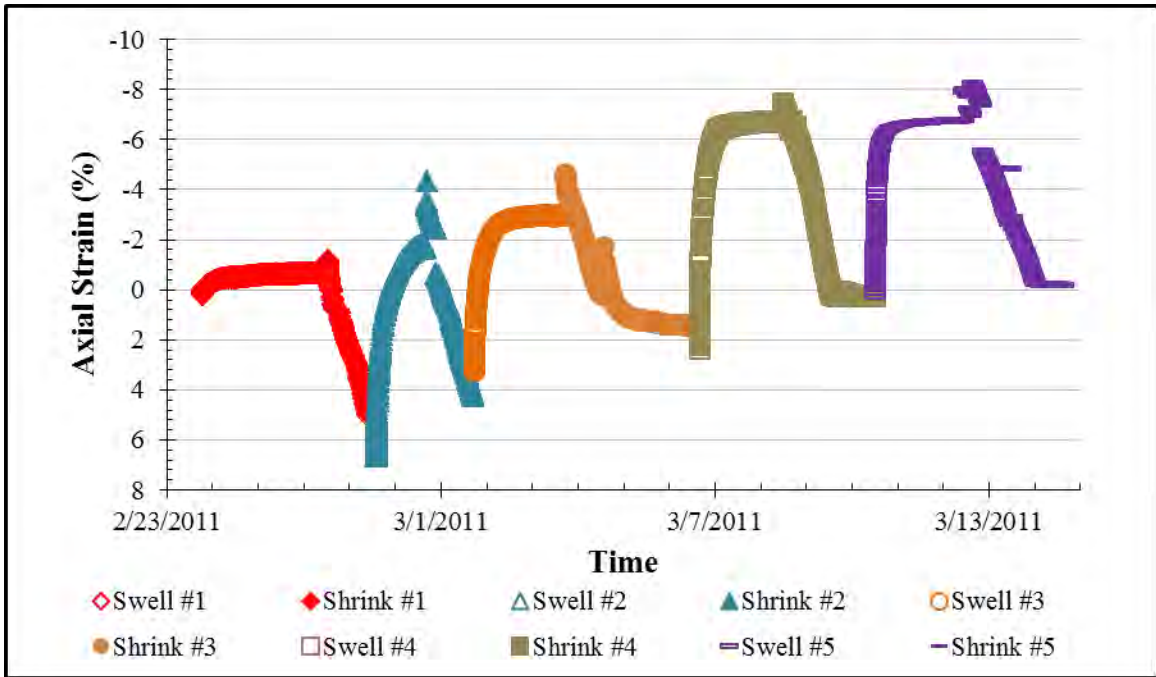


Figure 60. Cyclic Swell Test 1: Cumulative Time-Strain Measurements

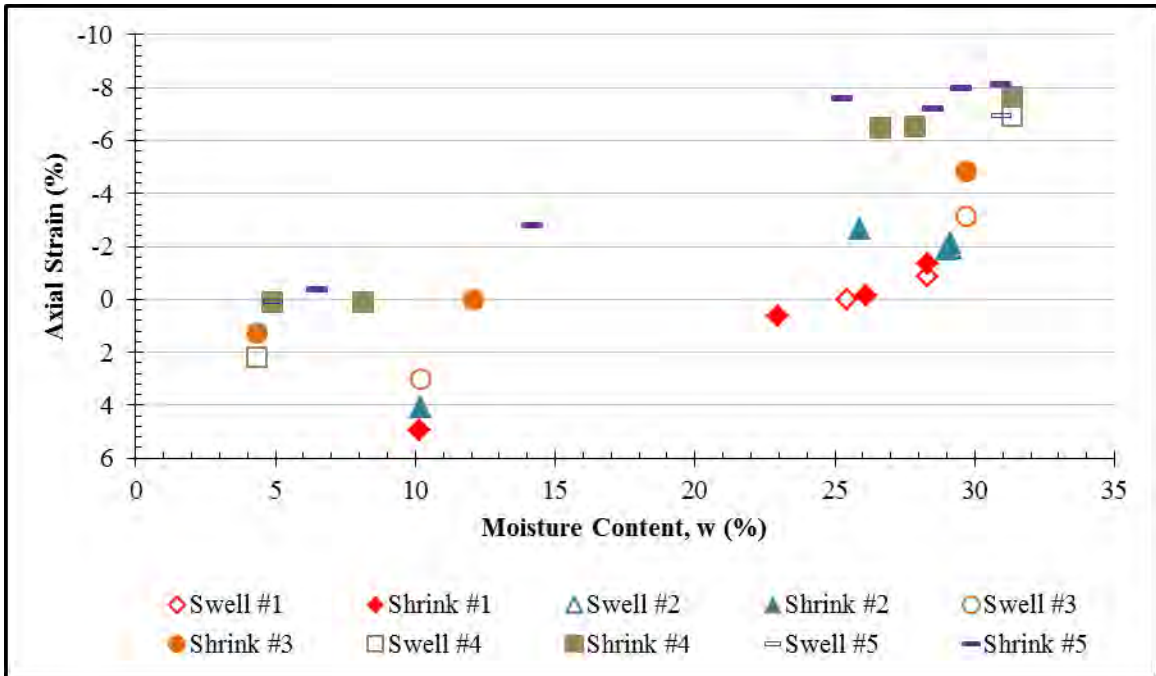


Figure 61. Cyclic Swell Test 1: Strain vs. Moisture Content

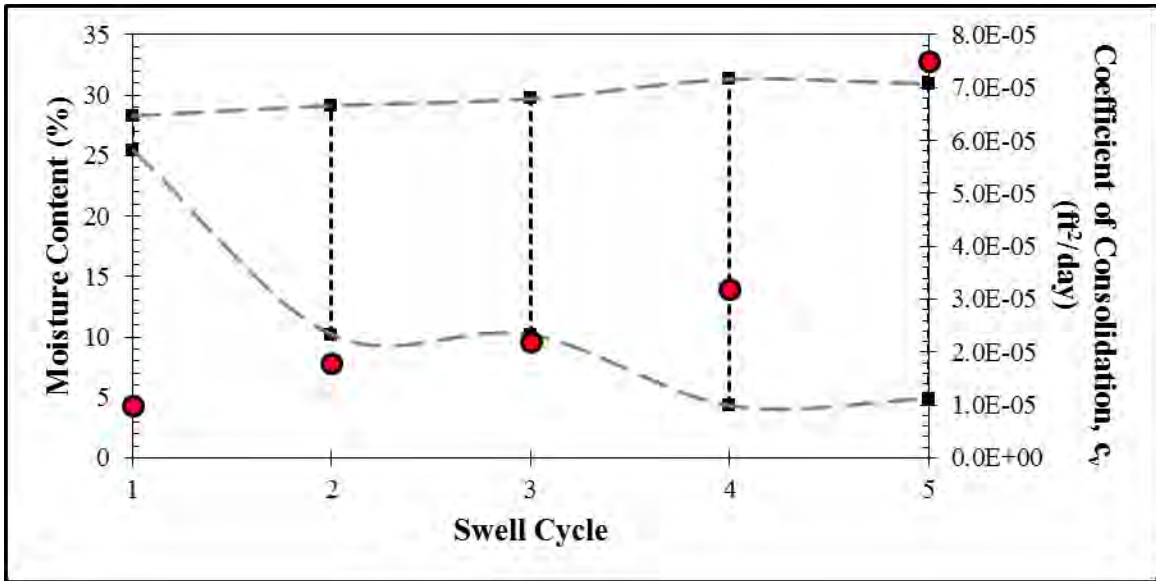


Figure 62. Cyclic Swell Test 1: Cyclic Moisture Variations

Table 11. Cyclic Swell Test 1: Summary of k_s and c_v Values

Cycle	1	2	3	4	5
c_v (ft ² /day)	1.0×10^{-5}	1.8×10^{-5}	2.2×10^{-5}	3.2×10^{-5}	7.5×10^{-5}
k_s	0.329	0.400	0.248	0.325	0.311

The cumulative time-strain measurements from Test 2 are presented in Figure 63. The specimen achieved successively larger swelling strains after the first three shrink cycles and then reached its steady state. The swelling strains appeared to reach a steady state by the end of the fifth cycle, but the cycle-to-cycle variations were somewhat chaotic. In addition, the specimen's height appears to have been altered during its removal for a moisture measurement during the third cycle. The moisture-strain measurements are shown in Figure 64. Least squares linear regressions were fitted to each cycle's data set to determine k_s values. The coefficients of consolidation from swell stages and the cyclic ranges of moisture content are illustrated in Figure 65. The k_s and c_v values are summarized in Table 12.

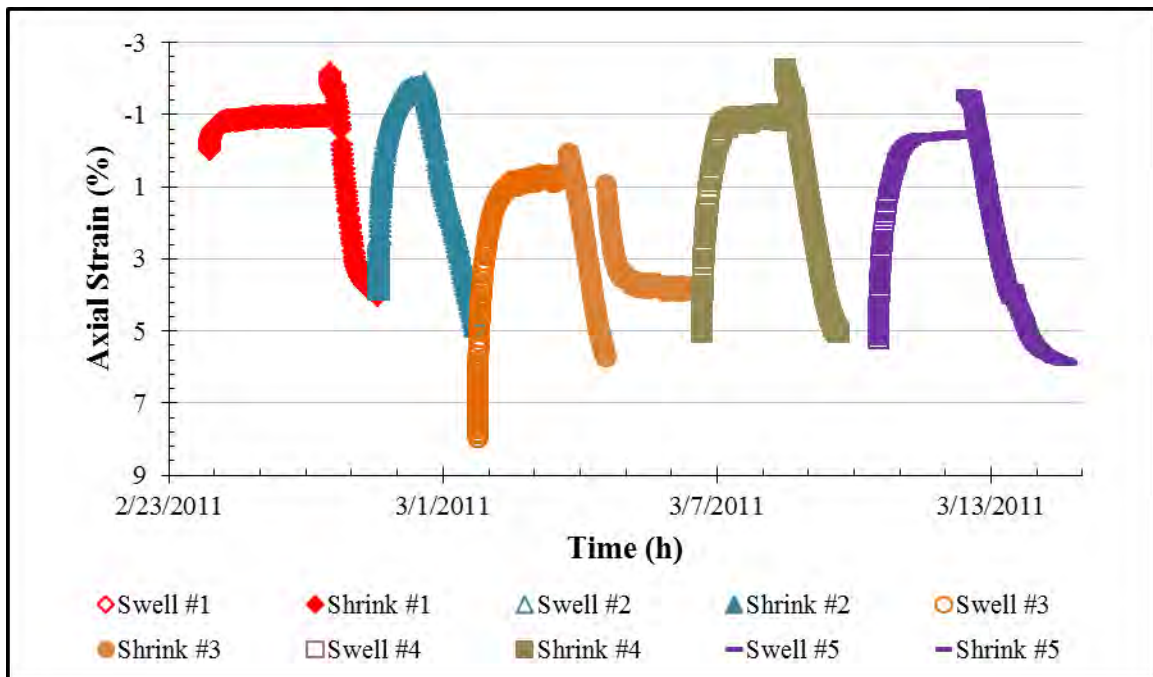


Figure 63. Cyclic Swell Test 2: Cumulative Time-Strain Measurements

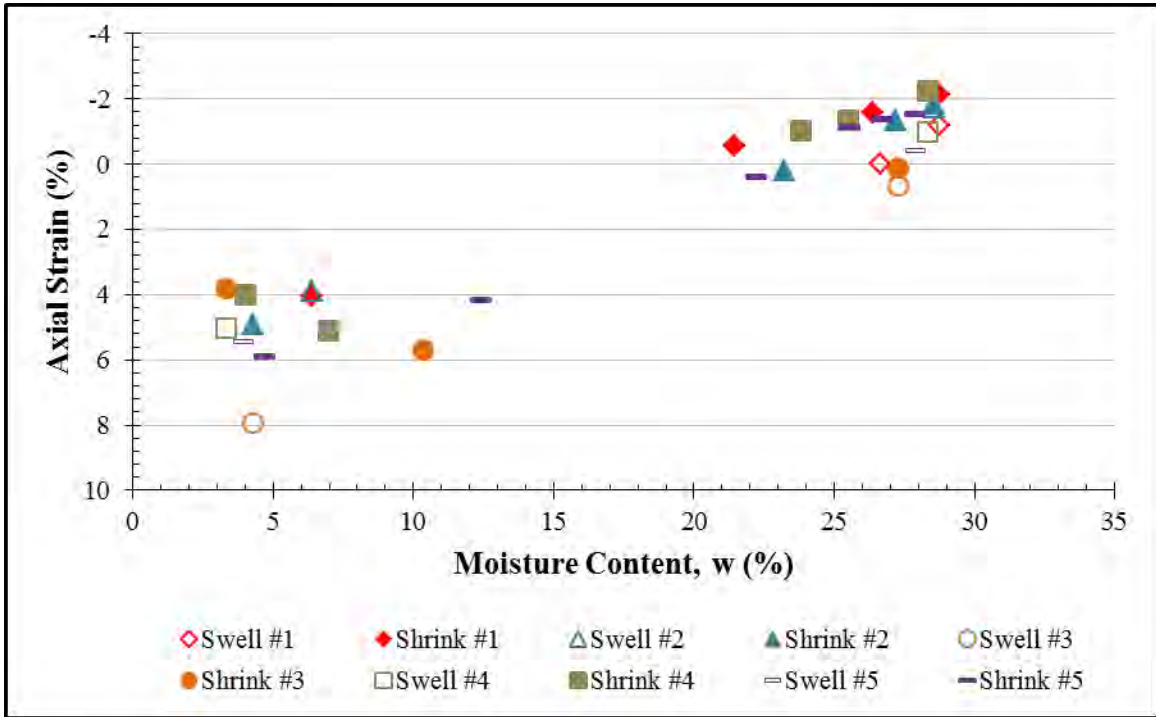


Figure 64. Cyclic Swell Test 2: Strain vs. Moisture Content

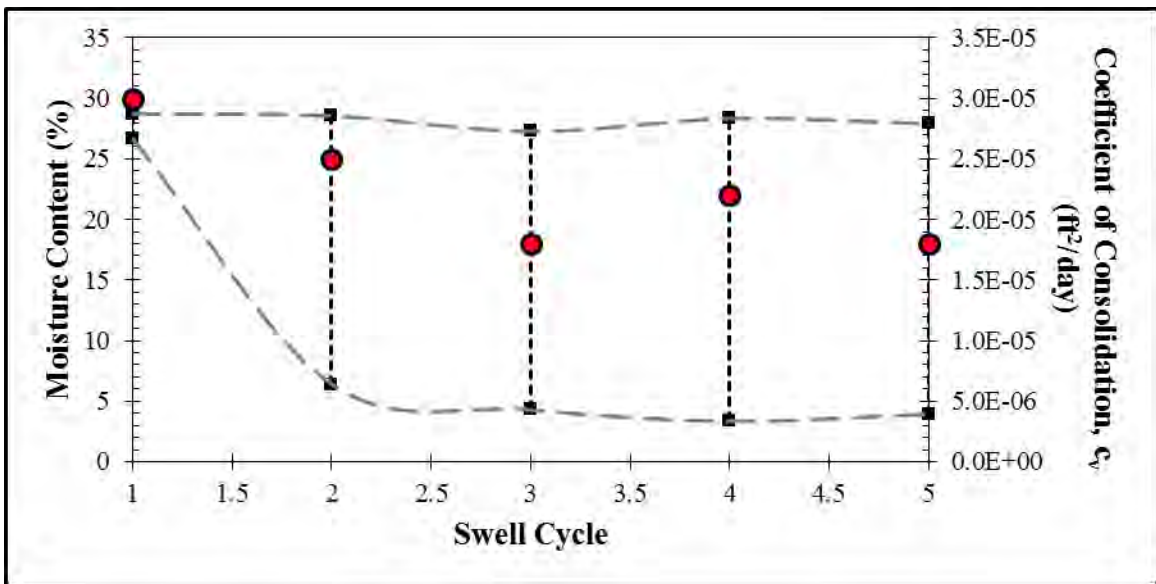


Figure 65. Cyclic Swell Test 2: Cyclic Moisture Variations

Table 12. Cyclic Swell Test 2: Summary of k_s and c_v Values

Cycle	1	2	3	4	5
c_v (ft²/day)	3.0×10^{-5}	2.5×10^{-5}	1.8×10^{-5}	2.2×10^{-5}	1.8×10^{-5}
k_s	0.246	0.263	0.240	0.276	0.304

The cumulative time-strain measurements from Test 3 are presented in Figure 66. The specimen achieved successively smaller swelling strains after the first two shrink cycles and then began to level off toward its steady state. The moisture-strain measurements are shown in Figure 67. Least squares linear regressions were fitted to each cycle's data set to determine k_s values. The coefficients of consolidation from swell stages and the cyclic ranges of moisture content are illustrated in Figure 68. The k_s and c_v values are summarized in Table 13.

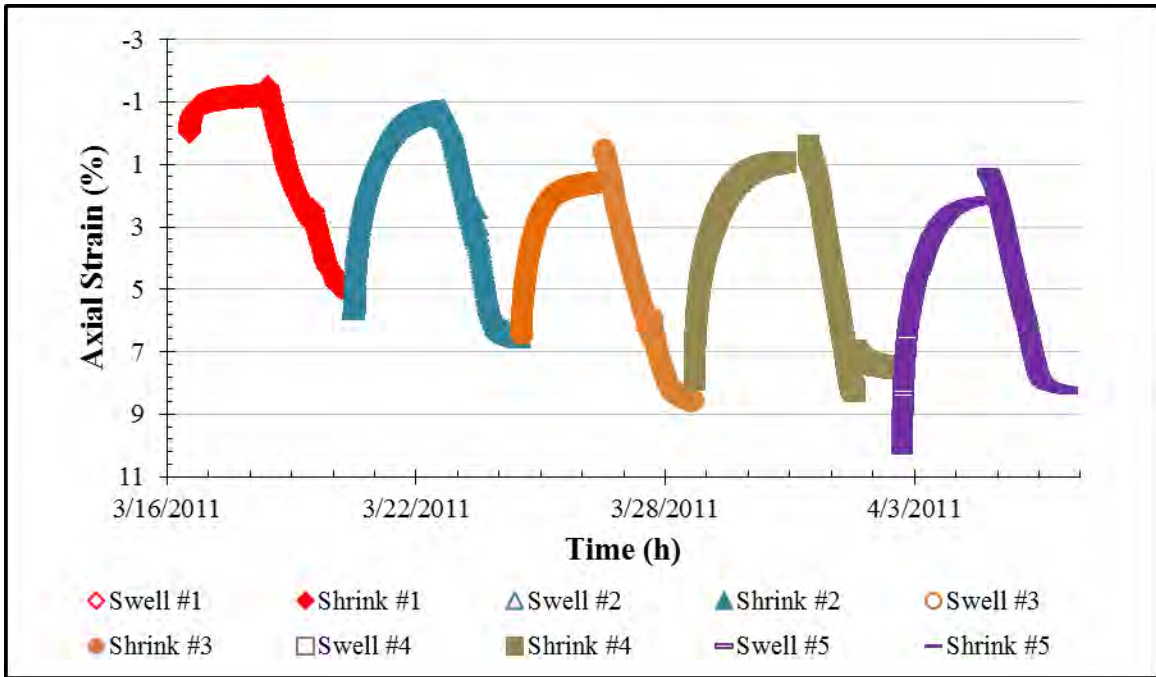


Figure 66. Cyclic Swell Test 3: Cumulative Time-Strain Measurements

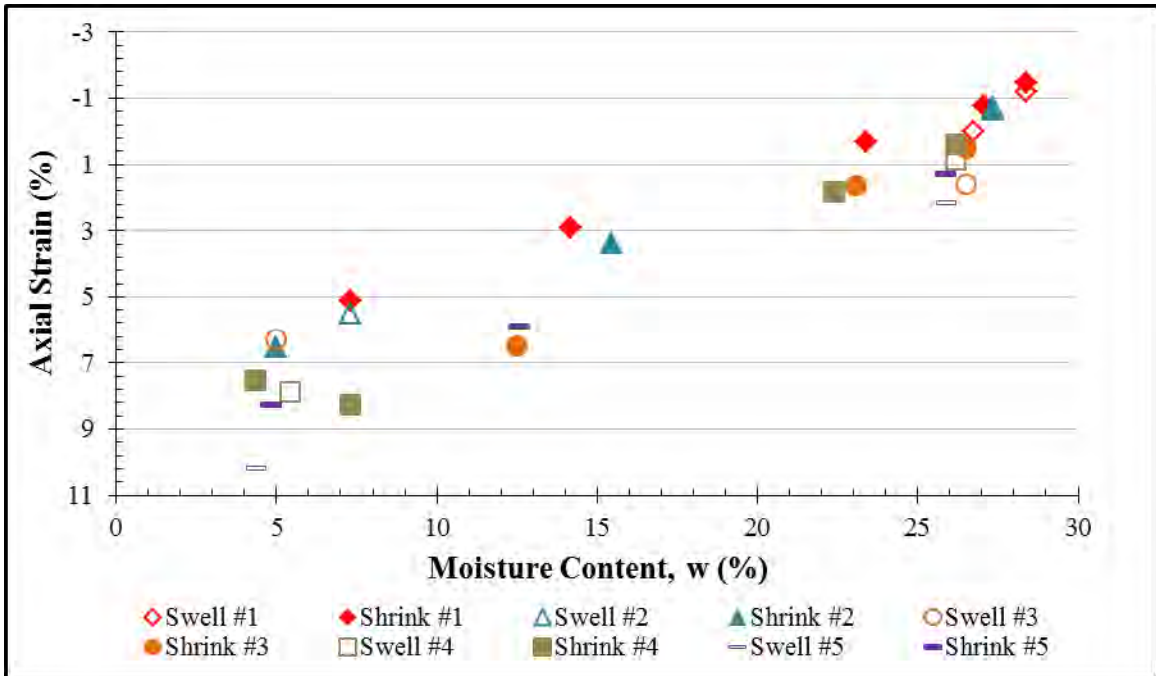


Figure 67. Cyclic Swell Test 3: Strain vs. Moisture Content

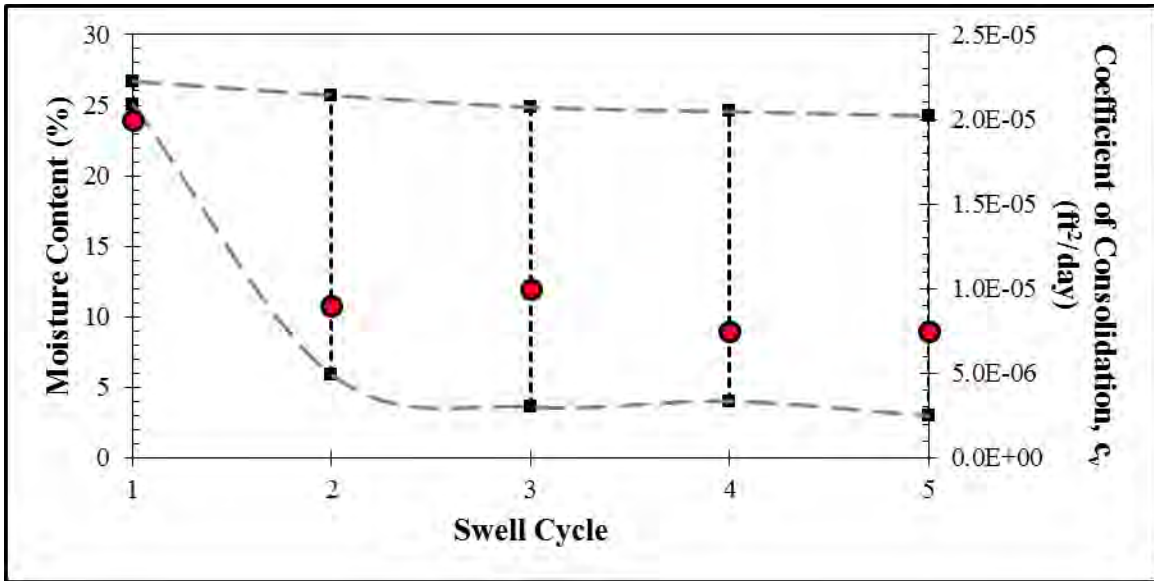


Figure 68. Cyclic Swell Test 3: Cyclic Moisture Variations

Table 13. Cyclic Swell Test 3: Summary of k_s and c_v Values

Cycle	1	2	3	4	5
c_v (ft ² /day)	2.0×10^{-5}	9.0×10^{-6}	1.0×10^{-5}	7.5×10^{-6}	7.5×10^{-6}
k_s	0.293	0.318	0.314	0.351	0.351

The cumulative time-strain measurements from Test 4 are presented in Figure 69. The specimen compressed through the successive cycles and began to reach its steady state by the fifth cycle. The moisture-strain measurements are shown in Figure 70. Least squares linear regressions were fitted to each cycle's data set to determine k_s values. The coefficients of consolidation from swell stages and the cyclic ranges of moisture content are illustrated in Figure 71. The k_s and c_v values are summarized in Table 14.

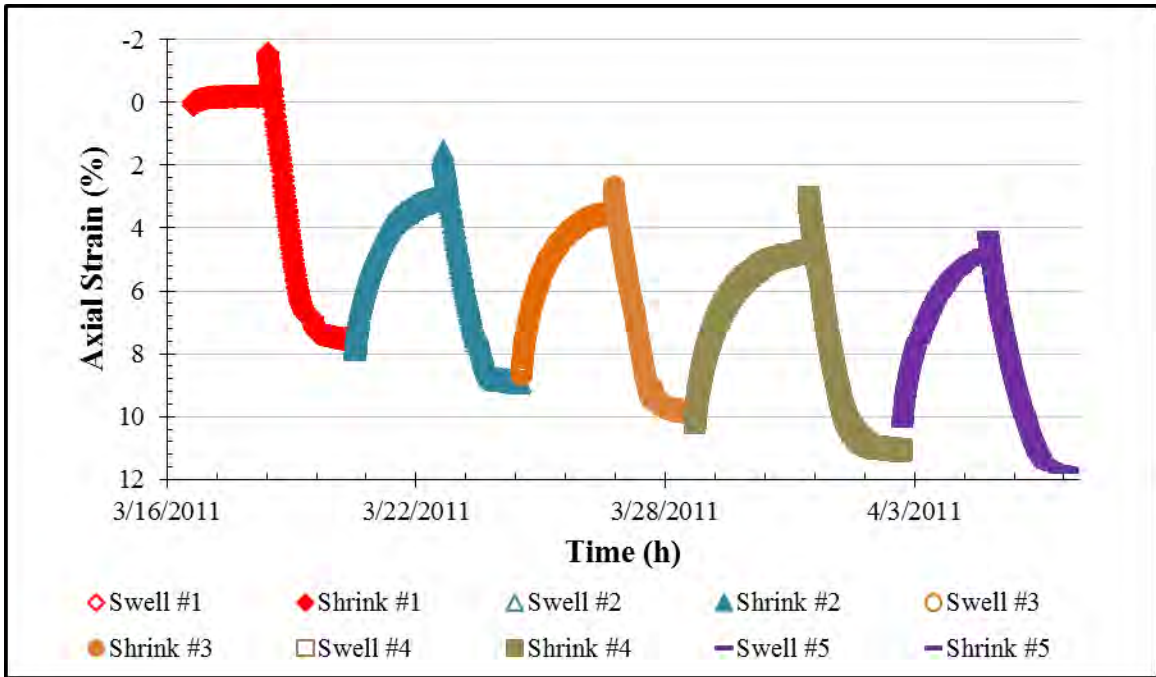


Figure 69. Cyclic Swell Test 4: Cumulative Time-Strain Measurements

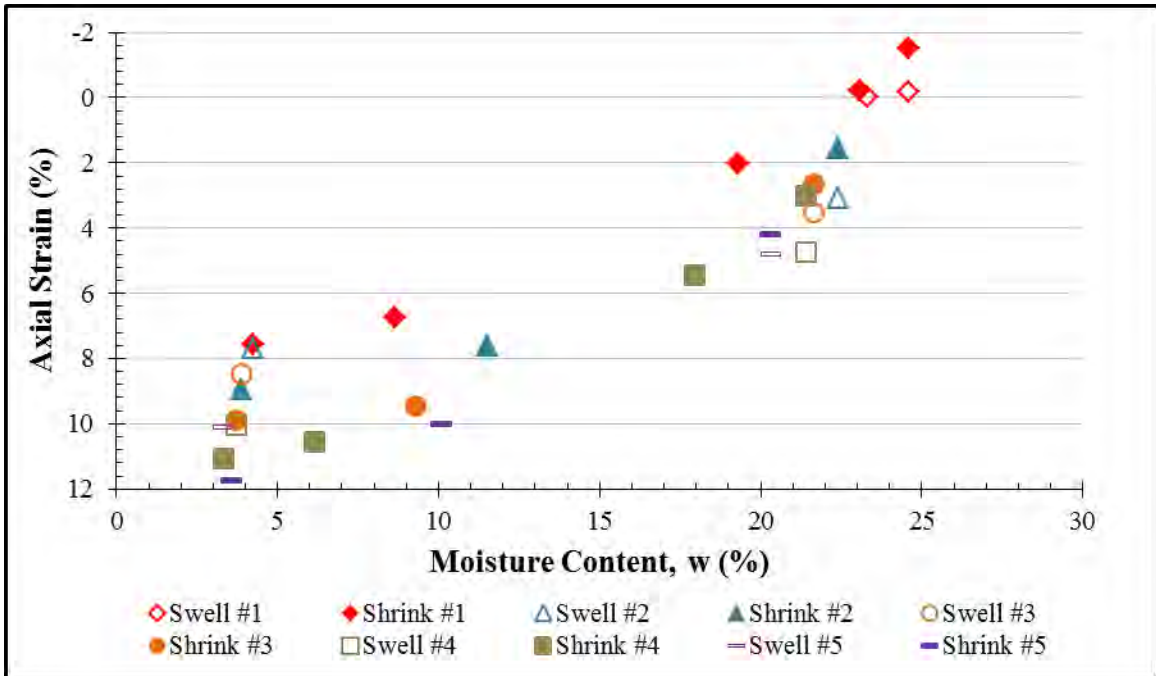


Figure 70. Cyclic Swell Test 4: Strain vs. Moisture Content

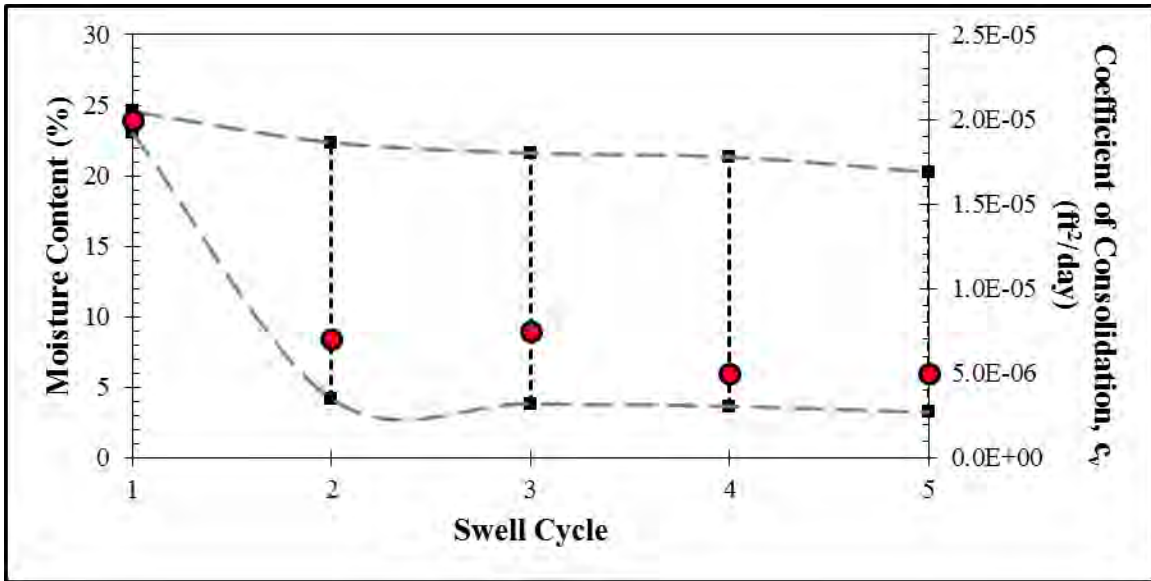


Figure 71. Cyclic Swell Test 4: Cyclic Moisture Variations

Table 14. Cyclic Swell Test 4: Summary of k_s and c_v Values

Cycle	1	2	3	4	5
c_v (ft ² /day)	2.0×10^{-5}	7.0×10^{-6}	7.5×10^{-6}	5.0×10^{-6}	5.0×10^{-6}
k_s	0.430	0.335	0.359	0.385	0.388

Each test's steady state cyclic swell coefficient was calculated as an average of the fourth and fifth cycle k_s values. The steady state values are given in Table 15. Figure 72 shows the steady state line from each test plotted over the range of moisture contents that were observed throughout each test. The constitutive surface is summarized by the plot of k_s versus total stress, Figure 73.

Table 15. Steady State Cyclic Swell Coefficients

Test	1	2	3	4
k_s	-0.319	-0.290	-0.351	-0.386

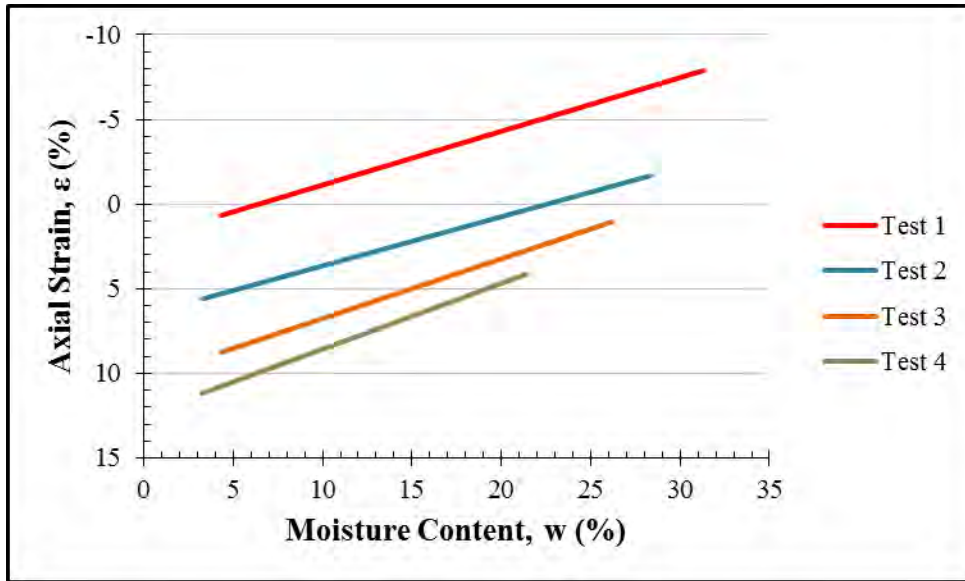


Figure 72. Summary of Steady State Shrink-Swell Behavior

Several observations were made from the results. First, the tedious trimming procedure may inflict varying degrees of disturbance on different samples. Figure 74 summarizes the first swell stage curves from each test. Although each specimen was trimmed from similar samples from the same borehole, there is no clear relationship between the initial swell and total normal stress. It must be noted, however, that the test site's profile of Atterberg limits – and thereby swell potential – is not constant, or even linear. Finally, any interpretation of Figure 74 must recognize that the normal stress applied for Test 1 was considerably lower than any likely in-situ condition.

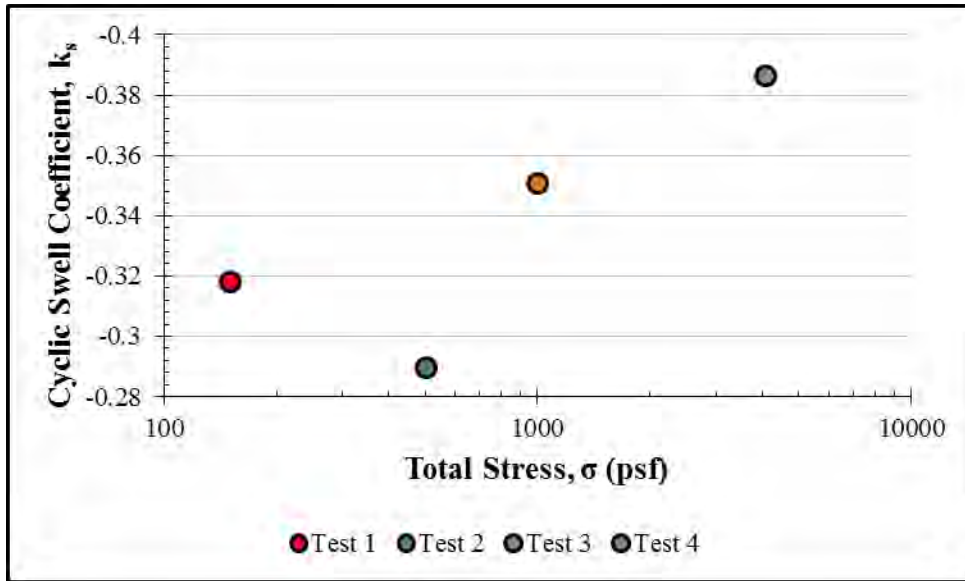


Figure 73. Simplified Constitutive Surface

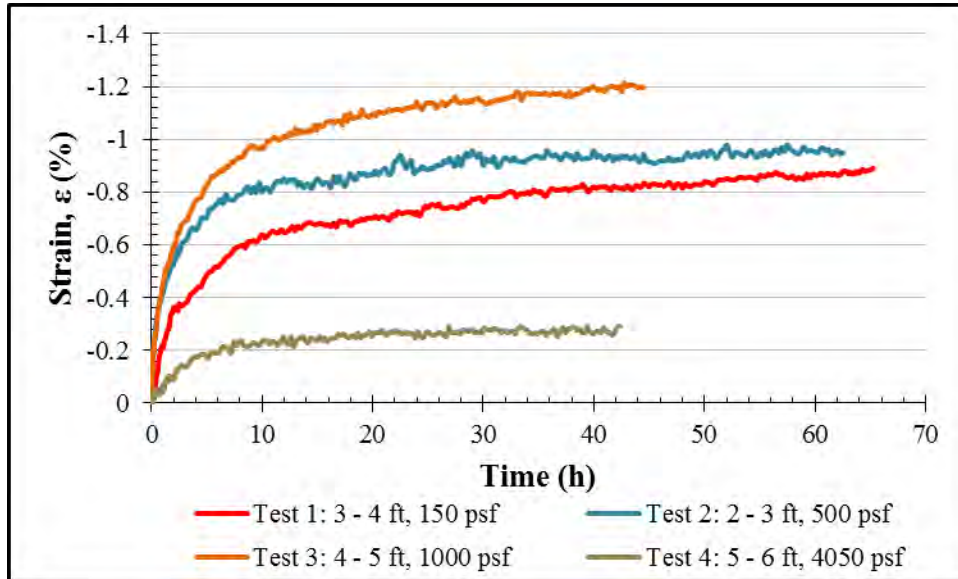


Figure 74. Summary of Initial Swell Stage Curves

The results generally became more reasonable after the first cycle, once the specimens had been remolded by drying and rewetting. In general, the specimens swelled to progressively higher magnitude strains through successive cycles. This seems to indicate that cycles of drying and rewetting break down the soil's crumb structure, unlocking more and more swell potential.

Each test's total normal stress also had a noticeable effect on the results. As the total stress is increased, the soil reaches a smaller range of moisture contents. The lower bound, analogous to the shrinkage limit, remained fairly constant through the different stress levels. The upper bound for moisture content was more strongly affected, with the relatively lightly loaded specimens reaching significantly higher moisture contents.

Although the range of moisture contents was lower for higher total stresses, the cyclic swell coefficient (k_s) was higher. That is, for a given change in moisture content at the steady state, larger swelling strains occurred under higher total stress conditions. The caveat to this observation is that the steady state coefficients of consolidation decrease with increasing total stress, Figure 75.

Ultimately, the total stress level did affect the maximum magnitude of steady state strains. Lightly loaded specimens achieved larger swelling strains through successive swell cycles, while the more heavily loaded specimens contracted from cycle to cycle. These cycle-to-cycle changes in strain appeared to have the most significant effect on steady state behavior.

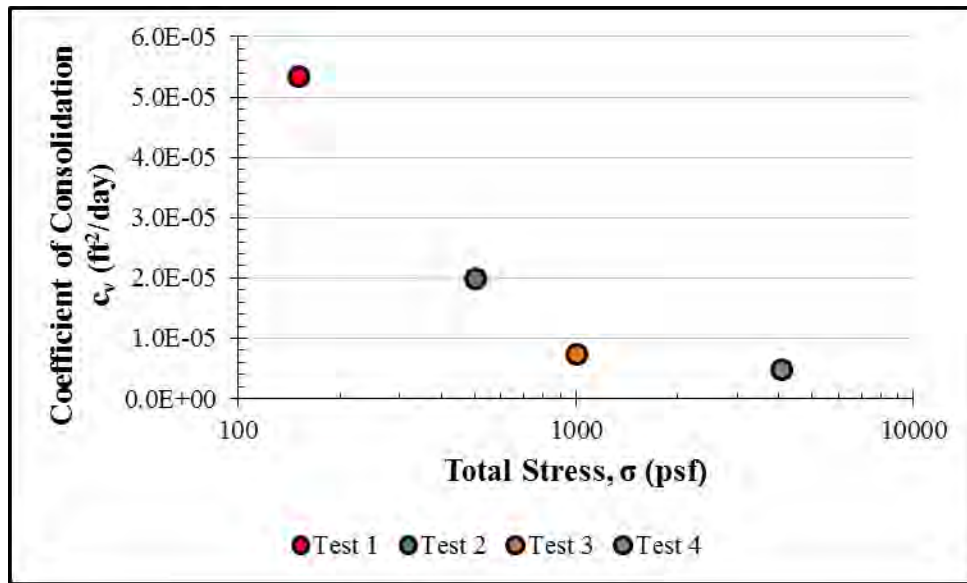


Figure 75. Cyclic Swell Steady State Coefficients of Consolidation

5.4 Undrained Shear Strength

The undrained shear strength was evaluated in the laboratory with unconsolidated undrained (UU) triaxial compression tests that were run in accordance with ASTM D2850. The UU triaxial tests were run in the University of Texas and the Fugro Consultants, Inc. laboratories. The tests indicate that the undrained shear strength increases with depth, but also that the soil's secondary structure facilitates the development of shear displacements before shear planes have developed in the intact soil. This characteristic manifested as abrupt decreases in the deviator stress during testing which caused the software to terminate the test.

The first two tests – illustrated with dashed lines in Figures 76 and 77 – were conducted on specimens trimmed to diameters of 1.4 inches at the University of Texas. The trimming was intended to remove soil that was disturbed during sampling, but instead appeared to cause visible structural damage to the final soil specimen. The other five tests were conducted on 2.8-inch diameter specimens at the Fugro Consultants, Inc. laboratory in Austin. The samples' ends were trimmed square and flush for this round of tests, but the diameters were not trimmed. Further details of each test are included in Appendix G.

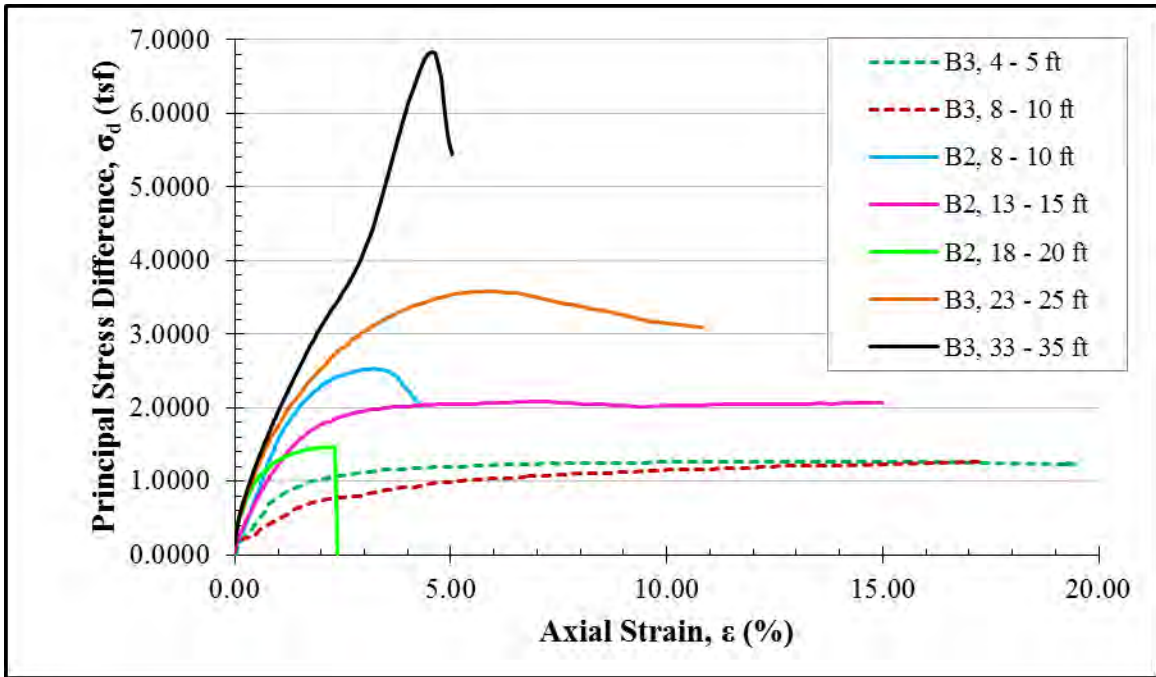


Figure 76. Summary of UU Triaxial Stress-Strain Measurements

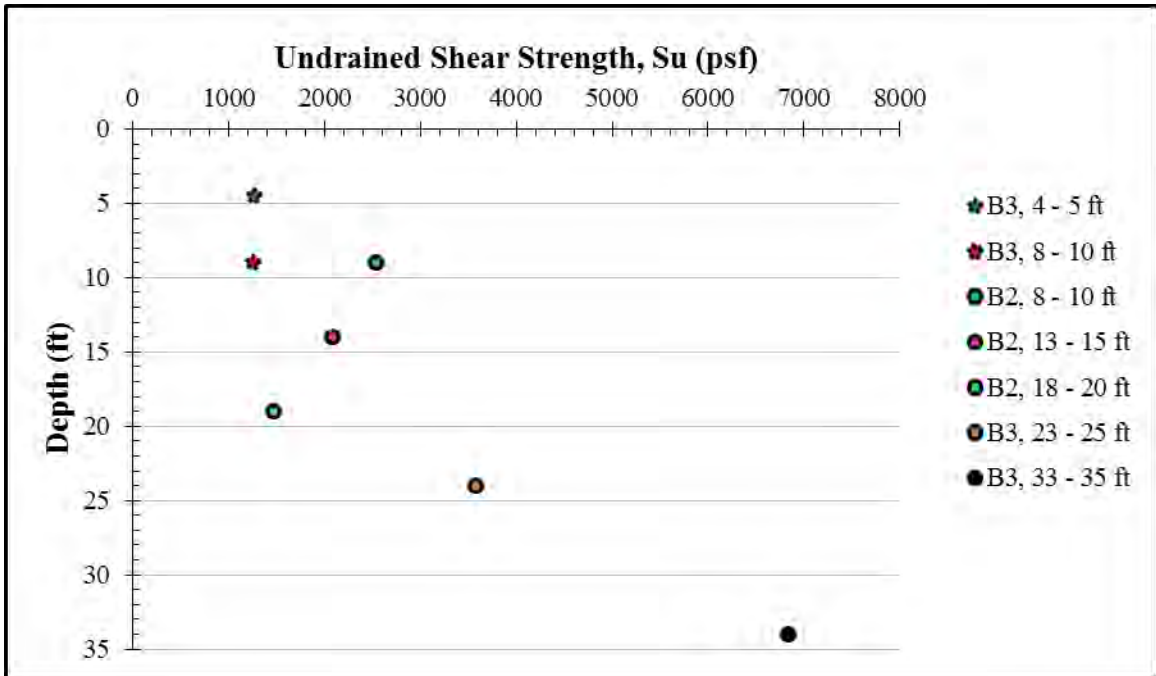


Figure 77. UU Triaxial Strength Profile

5.5 Drained Shear Strength

5.5.1 Testing Procedure

A series of consolidated drained direct shear tests were conducted to evaluate the peak and residual drained failure envelopes. The tests were performed in accordance with ASTM D 3080 at normal stresses equal to one, two and four times the estimated in-situ vertical effective stress. It was difficult to predict an appropriate shear rate due to the soil's ambiguous time-settlement characteristics. In an effort to both shear the soil slowly enough for pore pressures to dissipate and to conduct the tests over a practical and repeatable period of time, each test was set up to shear through a distance of 0.5 inches over a period of 4 days. The corresponding shear rate is 0.000087 in/min.

All three specimens were trimmed from a single undisturbed seamless push-tube sample. The specimens were trimmed into a 2.5-inch ring and then extruded directly into the top half of the shear box. The ends were then trimmed to flush 90-degree angles using the top half of the shear box as a guide. Once trimmed, the two halves of the shear box were connected with clamping screws, and the specimen was seated against the bottom porous stone.

Each test consisted of one peak shear stage and a series of residual shear stages. The soil was consolidated to the appropriate normal stress prior to each shear stage. Each consolidation stage comprised roughly 10 minutes of dry consolidation to close fissures and microcracks followed by one to two days of inundated consolidation under the same normal load. Clamping screws were always used to align the shear box during

consolidation and removed immediately prior to recording zero values for the subsequent shearing stage.

Each specimen's residual drained strength was measured under at least two different normal stresses. Two residual shear stages were performed at the same normal stress that was used for the initial peak shear, then additional residual shear stages were performed at two and/or four times that load. The weight of the specimen was measured immediately following each shear stage and after smoothing the shear surface. After the final shear stage, the specimens were removed from the shear box and oven dried.

The shear surface was smoothed with a putty knife prior to each residual strength measurement. If large lumps or other discontinuities formed during the peak shear stage, they were preserved when smoothing the shear surface for the first residual shear stage, Figure 78. Then, for all subsequent shear stages, the shear surface was both flattened and smoothed, Figure 79. Note that only Test 1 developed a pronounced lump during the peak shear stage.

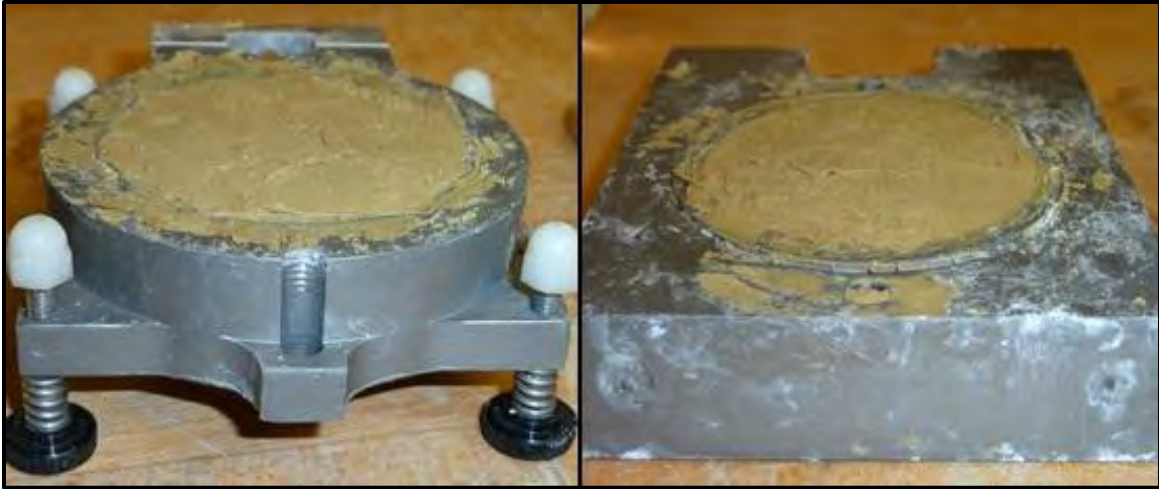


Figure 78. Lumped Shear Surface Smoothed for Residual Shear



Figure 79. Flattened Shear Surface Smoothed for Residual Shear

5.5.2 Summary of Results

Peak and residual drained strength envelopes were defined from the test data and are presented in Figure 80. The envelope for drained peak strength is curved, but at least one additional data point would be needed at a lower normal stress to define the curve with confidence. The friction angle and cohesion intercept values for both envelopes are reported in Table 16.

The parameters for peak strength are only applicable to the normal stresses – one, two and four times the in-situ vertical effective stress – that were tested. The residual envelope, though it contains some scatter, is more linear and may be more readily extrapolated. The stress-displacement curves for each test are presented in Figures 81 - 83. Photographs and moisture contents from each shear stage are given in Appendix H.

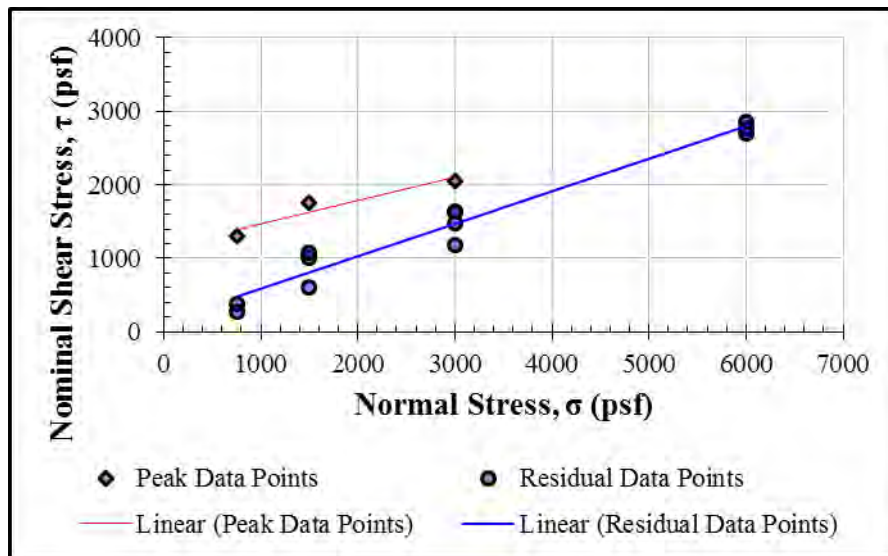


Figure 80. Drained Failure Envelopes from Direct Shear Tests

Table 16. Summary of Drained Failure Envelope Parameters

Envelope	Friction Angle, Φ' (°)	Cohesion Intercept, c' (psf)	Stress Range (psf)
Peak	17.7	1150	750 - 3000
Residual	24.0	135	750 - 6000

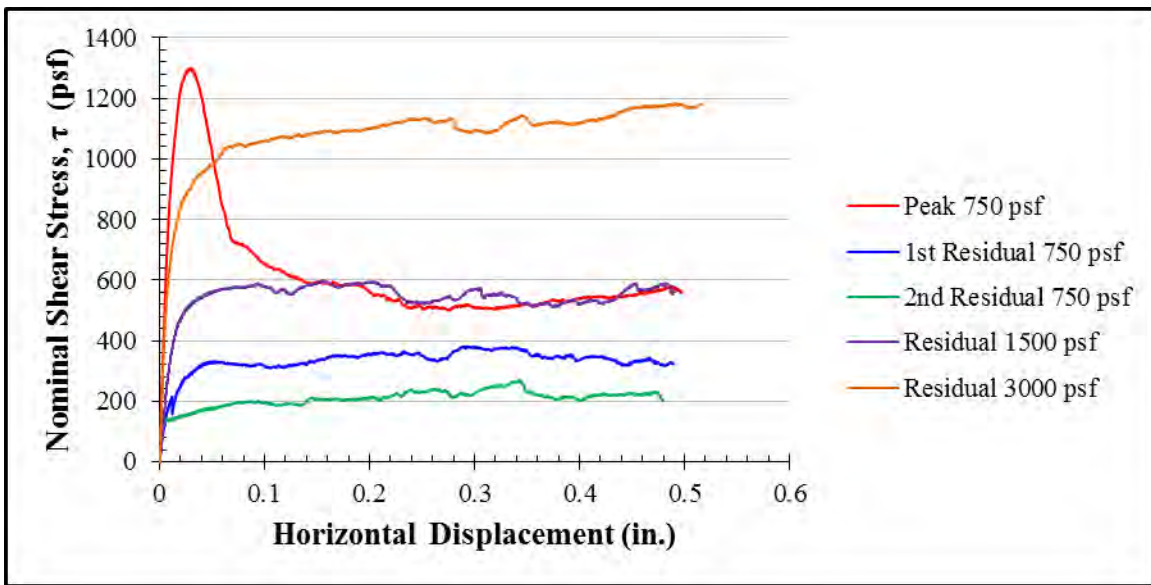


Figure 81. Stress-Displacement Curves from Direct Shear Test #1

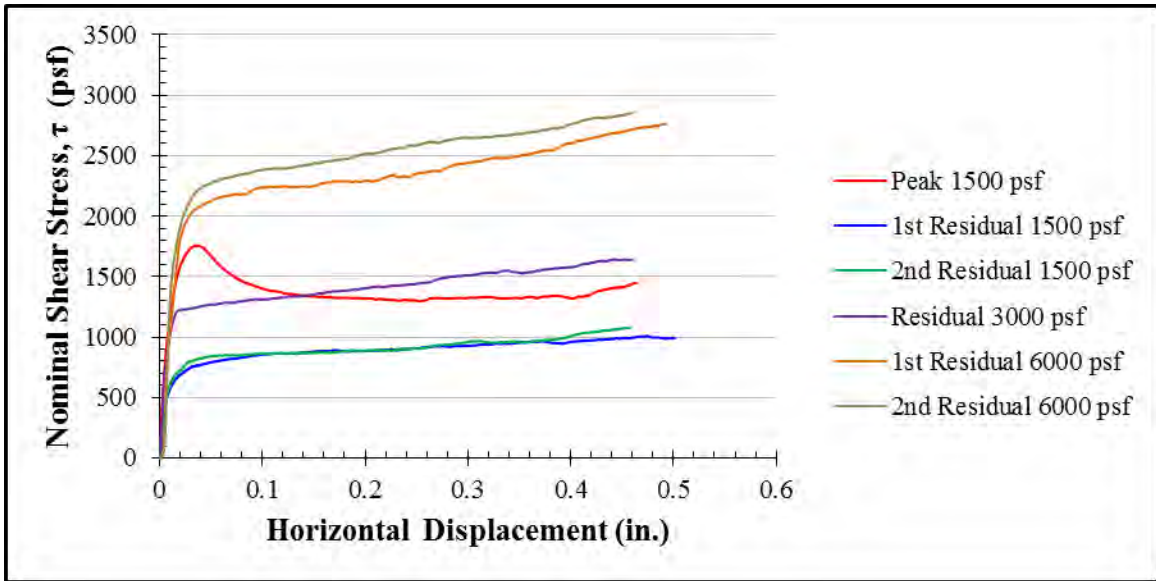


Figure 82. Stress-Displacement Curves from Direct Shear Test #2

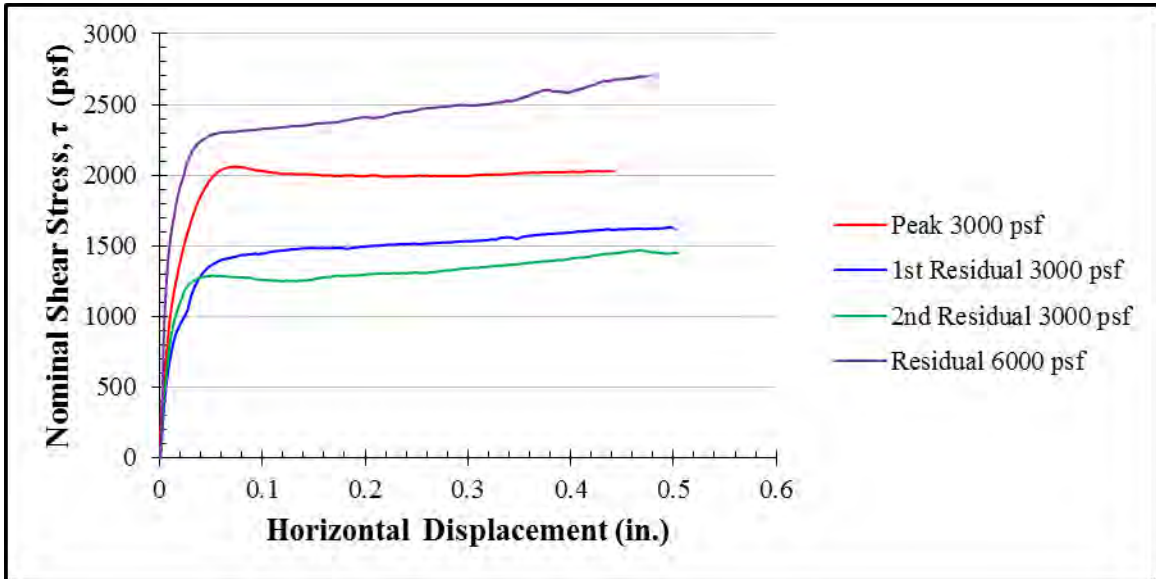


Figure 83. Stress-Displacement Curves from Direct Shear Test #3

6 Comprehensive Analysis of the Taylor Clay

6.1 Soil Classification

The soil is classified in the United Soil Classification System (USCS) in accordance with ASTM D 2487. Figure 84 shows that the Atterberg limits plot well above the A-line, indicating substantial plasticity. For every depth that clay fractions were measured, the soil classifies as fat clay (CH).

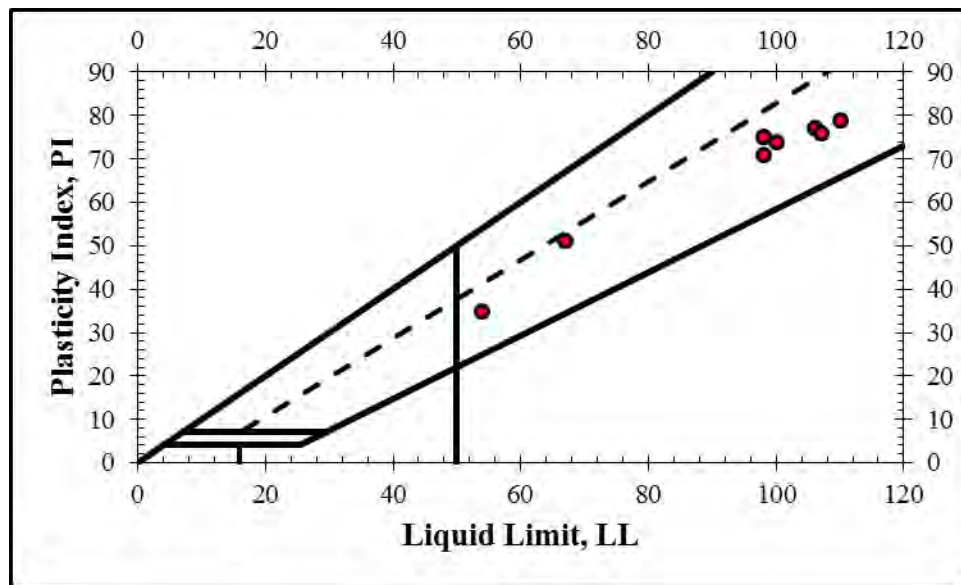


Figure 84. USCS Plasticity Chart

Geologic maps from Burford (1928) and Tipple (1975) suggest that the site is very near the Taylor-Navarro contact. The presence of *Exogyra ponderosa* at shallow depths suggests that the site is on the Taylor side of the contact. The lack of an observed

contact – one that, according to Young (1965), would be conspicuous – confirms that the soils for this study are indeed from the Taylor group. More specifically, they are from the top of the Bergstrom Formation. Burford described this specific zone of soil as highly bentonitic, indicating very high montmorillonite content.

6.2 Identifying the Active Zone

The active zone is the depth through which seasonal moisture fluctuations are observed (Nelson and Miller, 1992). Multiple measurements confirmed substantial changes in moisture content through the first five feet, but very limited samples were available for deeper moisture measurements. The moisture contents from two sets of samples that were retrieved 9 months apart from each other appear to converge between depths of 8.5 and 13.5 feet. Based on the observation, the active zone may only be cautiously estimated as approximately 10 feet deep.

6.3 Delineation of Strata

The subsurface conditions are best described as two dominant strata separated by a thin transitional zone. The top stratum is an 8-foot thick layer of dark brownish gray, highly weathered clay. This top layer proved sticky and unworkable when wet, but quickly dried upon exposure to become a dusty rock-like material.

At a depth of roughly 8 feet, the top layer begins to lighten to a tannish yellow color. Specimens trimmed from this depth contained small pockets of a white chalky material. As the color became more yellow, the soil structure also became stiffer and

more rock-like. The secondary structure became more pronounced around this depth. This transition stratum is difficult to delineate, but is approximately two feet thick. This zone more than likely marks the historical range of groundwater level. The yellow color still indicates that iron within the clay has been oxidized.

Below a depth of 10 feet, the soil becomes very stiff and the color remains tannish, eventually transitioning to a darker brown. Chalky deposits become less frequent with depth. Upon exposure and drying, the soil from this layer breaks down into small gravel-size crumbs. The primary structure of this layer is very strong and resistant to shear. In handling the soil, it was clear that shear displacements could only be achieved along existing fissures and micro-cracks.

6.4 Compressibility

This particular soil's compressibility is a relatively elusive parameter to characterize. The results from one-dimensional consolidation tests, which were presented in Section 5.2, did not always indicate a clear transition from over- to normally-consolidated behavior. More often, as Long (1983) reported, the e -log- P curves are too rounded to identify a maximum previous vertical effective stress. Even with load increments applied up to 64,000 psf, some of the e -log- P' curves only appear to approach linear virgin compression. The application of large, approximately in-situ, dry seating loads resulted in a clearer transition to normally consolidated compression in Tests 3 – 5.

Although the e -log- P' curves for tests 3 – 5 appear to reveal a transition to normally consolidated behavior, the resulting compressibility parameters are not

consistent with historical trends. Terzaghi and Peck (1948) reported that liquid limits correlate well with compression indices (c_c) with a relationship defined by Equation 10. The results from Tests 3 – 5 are plotted against this relationship in Figure 85, showing no agreement at all. Although the correlation was developed for normally consolidated soils, some general agreement would have been expected. Furthermore, the ratio of compression to recompression indices (c_c/c_r) usually falls between 5 and 10. The measured ratios vary outside of this range, rather consistently, between 2 and 3. It is worth noting that the measured recompression indices from Tests 3 – 5 are in agreement with those reported by Long (1983).

$$c_c = 0.009 \cdot (LL - 10) \dots\dots\dots \text{Eq. 10}$$

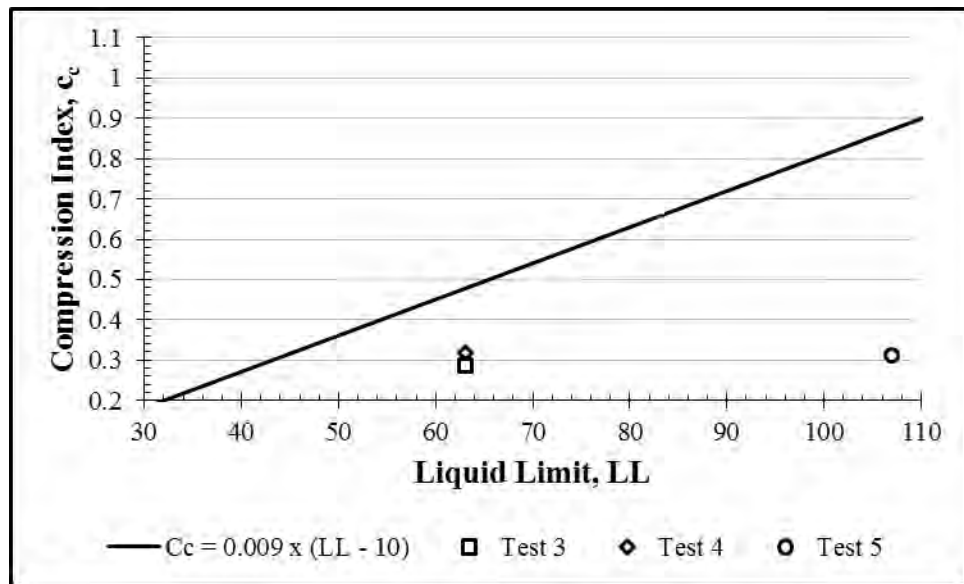


Figure 85. Measured vs. Expected c_c vs. LL Values

The disparity between measured and expected compression characteristics may be explained by several factors. The soil could be so heavily overconsolidated that higher loads would be required to actually observe normally consolidated behavior. Carbonates are known to be present throughout the Taylor clays, and some degree of cementation could have taken place within the clay. Finally, although the specimens were carefully trimmed for each test, sampling by seamless push tube could have caused a significant amount of disturbance. Any or all of these factors could explain the erratic compressibilities that were observed in the laboratory.

6.5 Shear Strength

The soil's undrained shear strength was evaluated in the lab and the field. Results from the different tests agree well, but the undrained shear strength does not exhibit a typical linear increase with depth. Instead, the increase is nearly bilinear, as illustrated by the heavy dashed curve in Figure 86. The undrained shear strength at the surface is approximately 1200 psf. The c/P' ratios for the shallow (ψ_{shallow}) and deep (ψ_{deep}) linear segments are 0.23 and 4.34, respectively. Oddly enough, the values for ψ_{shallow} and ψ_{deep} are exact inverses of one another. The bilinear undrained shear strength profile is very similar to that reported by Long (1983).

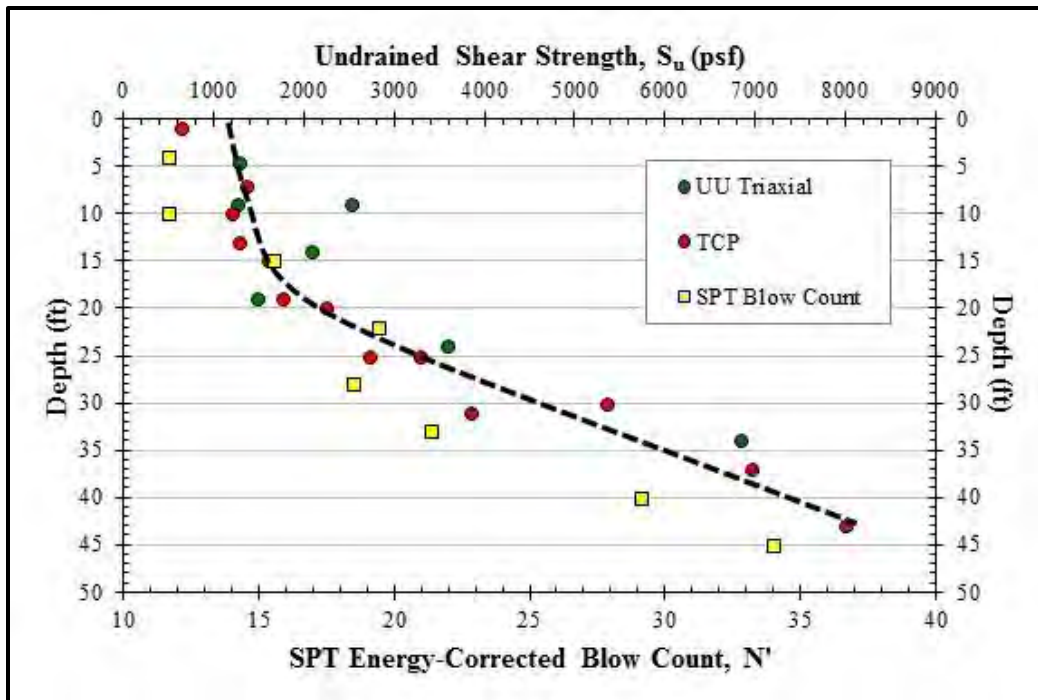


Figure 86. Combined Test Results for Undrained Shear Strength

Both peak and residual drained failure envelopes were constructed from the results of direct shear tests. The soil's peak envelope is curved concave downwards, and its cohesion intercept is not readily discernible from the limited number of measured data points. The secant friction angles for each data point on the peak envelope are shown in Figure 87. The secant friction angles are also illustrated for the stress levels that were tested for residual shear in Figure 88, although there is much less variation for the secant friction angles for the residual envelope. Figure 88 shows the range of secant friction angles corresponding to the range in residual strength data points at each normal stress. In each case, the secant friction angles are much higher than usual.

Stark and Eid (1994, 1997) presented design charts to help characterize the curved failure envelopes that are common for drained conditions with stiff fissured clays. The authors essentially provided a set of curves that relate liquid limit and clay fraction to a soil's secant friction angle at various normal stresses. By interpolating between curves that pertain to specific normal stresses, a soil's curved failure envelope can be predicted in terms of its liquid limit and clay fraction. One chart was developed for fully softened peak envelopes (Figure 89) and another for residual envelopes (Figure 90).

The measured secant angles do not fit the expected range for either peak or residual data points. It is not immediately clear why the data deviates so much from the trend, but there are several possibilities. Stark's range was generated with normally consolidated specimens. The soil being tested in this study is heavily overconsolidated. In addition, it could be cemented. The individual test results – that is, stress-displacement curves – are reasonable, but the soil itself appears stronger than typical clays.

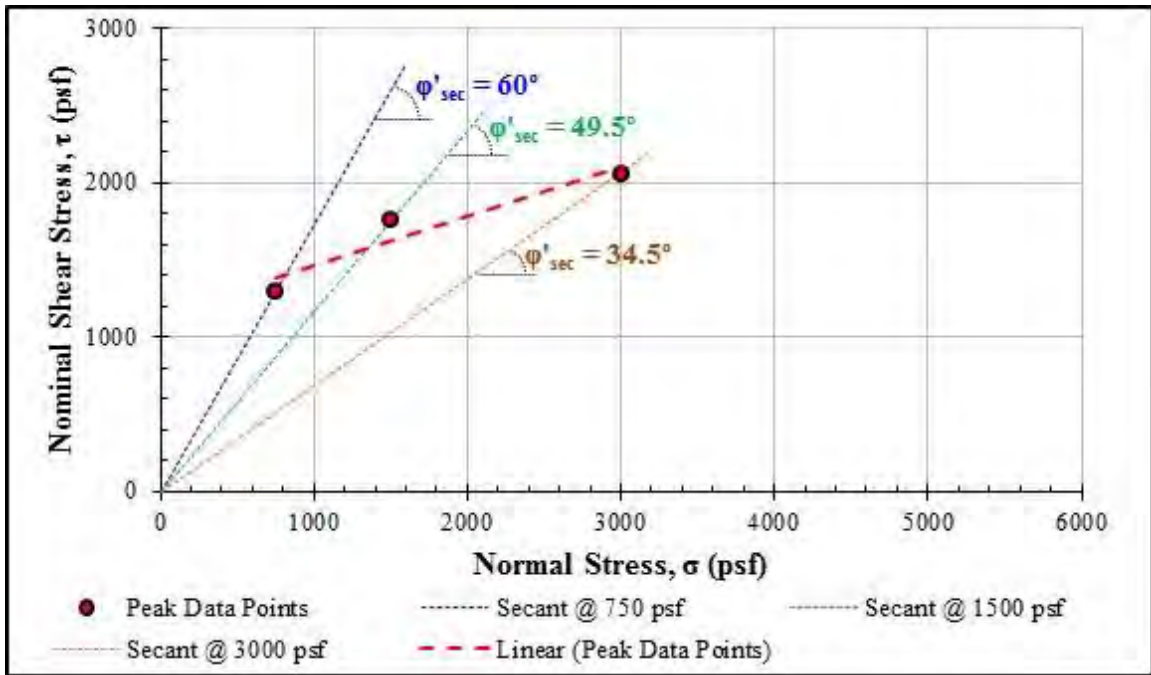


Figure 87. Secant Friction Angles for Peak Drained Strengths

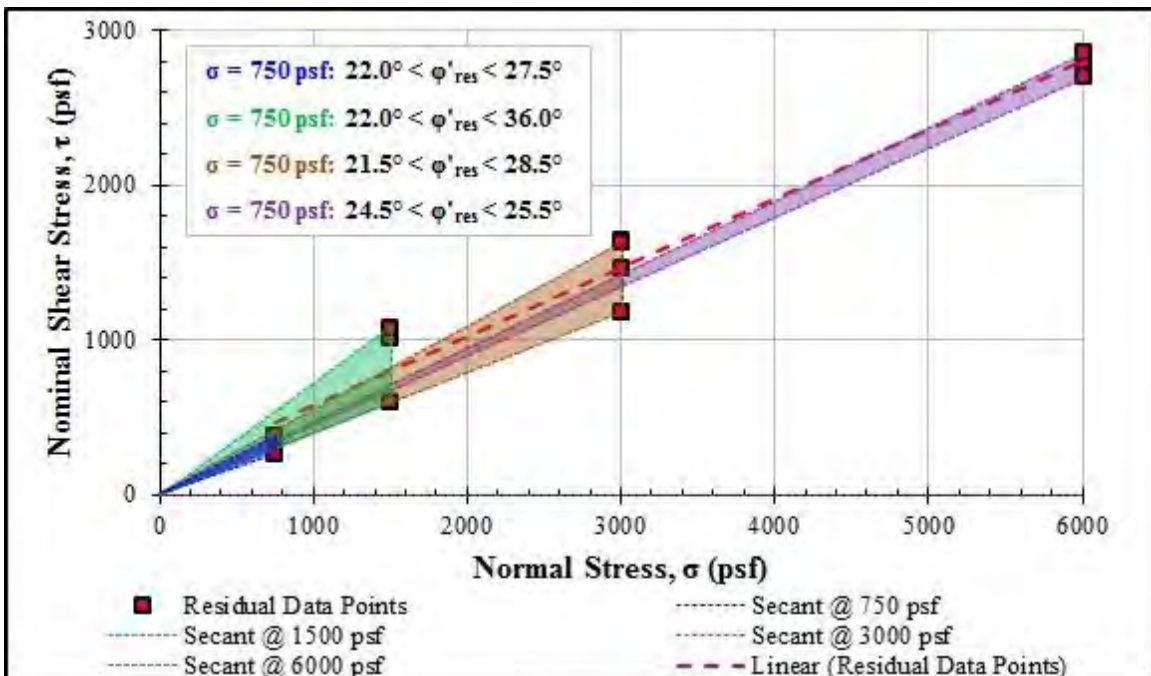


Figure 88. Secant Friction Angles for Residual Drained Strengths

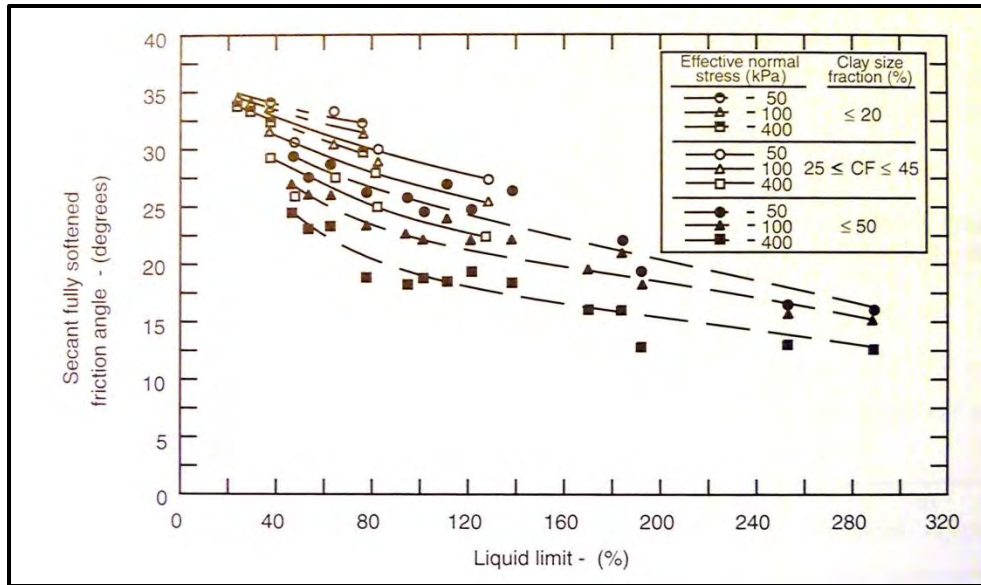


Figure 89. Correlation between Liquid Limit, Clay Fraction and Secant Peak Friction Angle, Stark & Eid (1997)

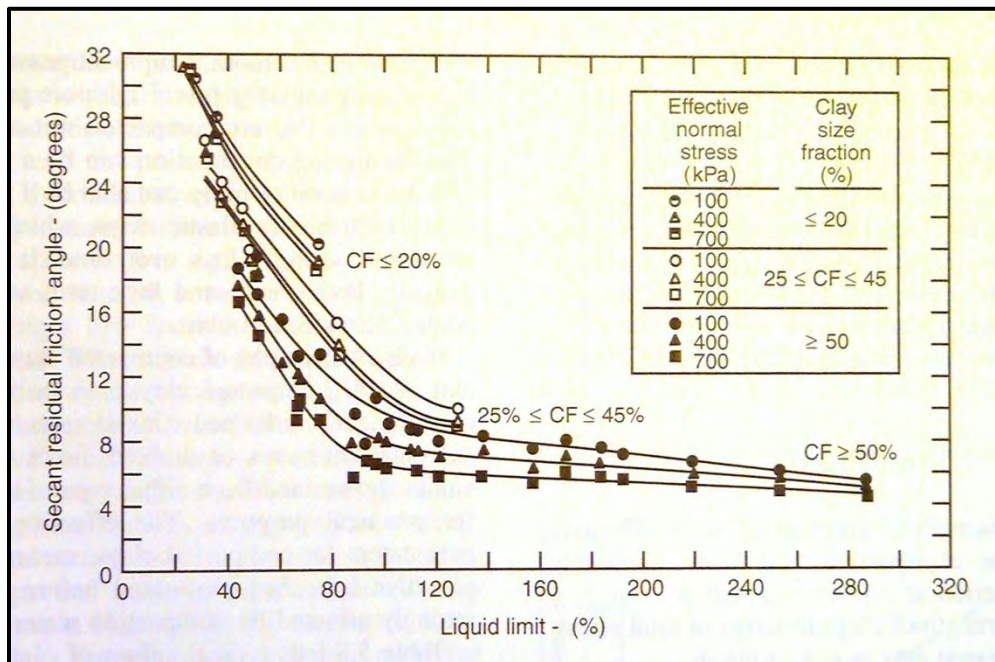


Figure 90. Correlation between Liquid Limit, Clay Fraction and Secant Residual Friction Angle, Stark & Eid (1994)

6.6 Hydraulic Conductivity

Time-settlement curves from consolidation and swell tests provided a means to back out the soil's hydraulic conductivity using a modified application of the theory of consolidation in which total settlements were considered. The method is described in Section 5.2.1. Results from all tests indicate the soil's hydraulic conductivity is approximately 5×10^{-9} ft/day. These results are indicative of the soil's primary, dense clay structure.

The soil contains a complicated network of fissures and microcracks that may act as preferential moisture pathways. In addition, wide desiccation cracks form when the soil dries. These cracks play a significant role in the transport of water, as shown in Figure 91. The figure shows five moisture profiles that were measured in the same area. M-2 was measured after a long period of dry weather, and the other four profiles were measured 24 hours after the first major precipitation that interrupted that dry period. The inflections of the four profiles that were measured after the rainfall estimate the points of the water's downward progress after 24 hours, and thereby estimate the hydraulic conductivity.

The two sets of measurements are drastically different. The observational tests suggest hydraulic conductivities between 1 and 2 ft/day. The two estimates of hydraulic conductivity vary by 10 orders of magnitude. The two different types of tests may represent bounding parameters for the soil's actual hydraulic conductivity. The lab tests failed to model the presence of preferential moisture pathways, while the observational field tests exploited such pathways.

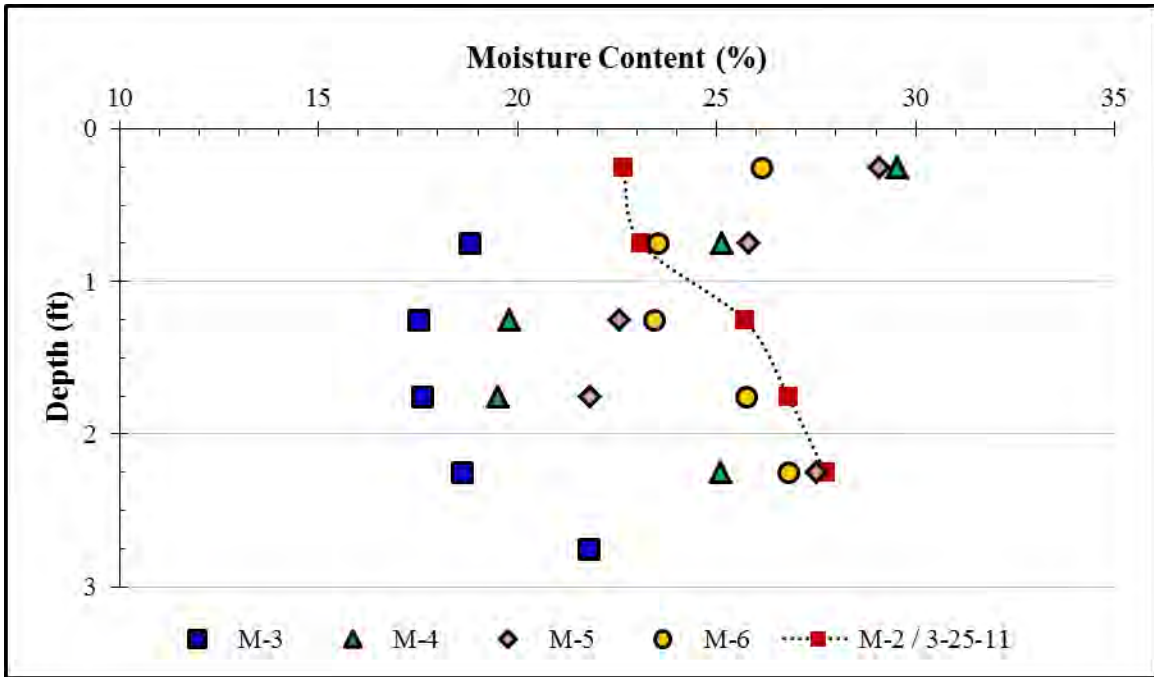


Figure 91. Observational Field Measurements for Hydraulic Conductivity

6.7 Swell Potential

According to index properties, the soil's swell potential is "very high". Table 17 summarizes a profile of representative soil properties for the empirical swell guidelines. The plasticity indices are much larger than necessary for a very high swelling potential classification. The soil's colloidal activity (A_c) values average around 1.1, which is considered normal and indicative of calcium montmorillonite. According to Seed's chart that relates swell potential to activity and clay content, the soil exhibits very high swell potential, Figure 92. The chart by Daksanamurthy and Raman, relating swell potential to LL and PI, gives the same designation, Figure 93. Overall, the soil's characteristics meet or exceed the empirical guidelines for a "very high swell potential" classification.

Table 17. Representative Index Properties

Depth	Liquid Limit, LL	Plasticity Index, PI	Clay Fraction, CF (%)	Activity, A_c
7	78	55	51.5	1.1
11	96	80	80	1.0
17	108	79	65	1.2
29	100	72	72	1.0

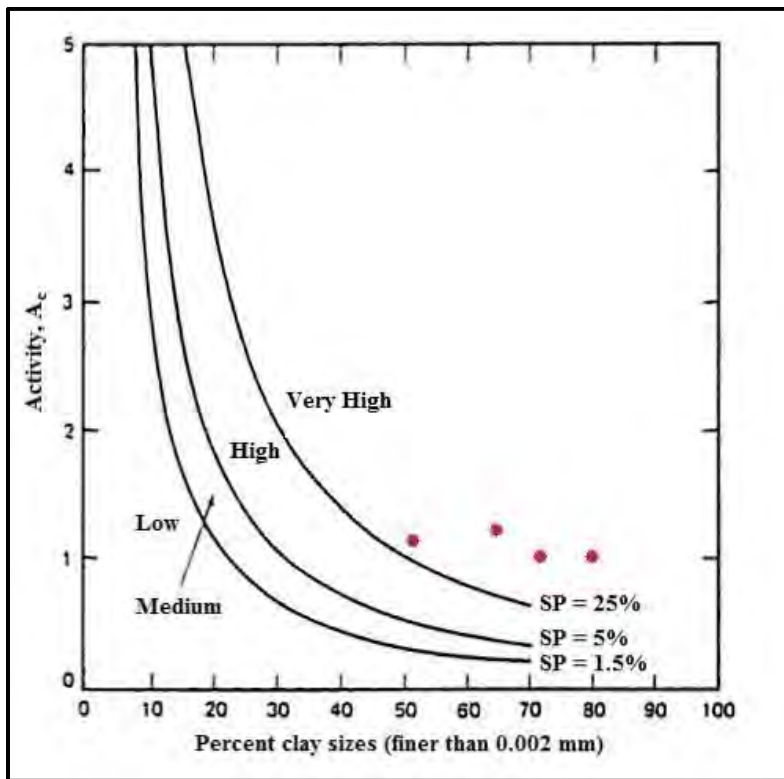


Figure 92. Qualitative Swell Potential, Seed (1962)

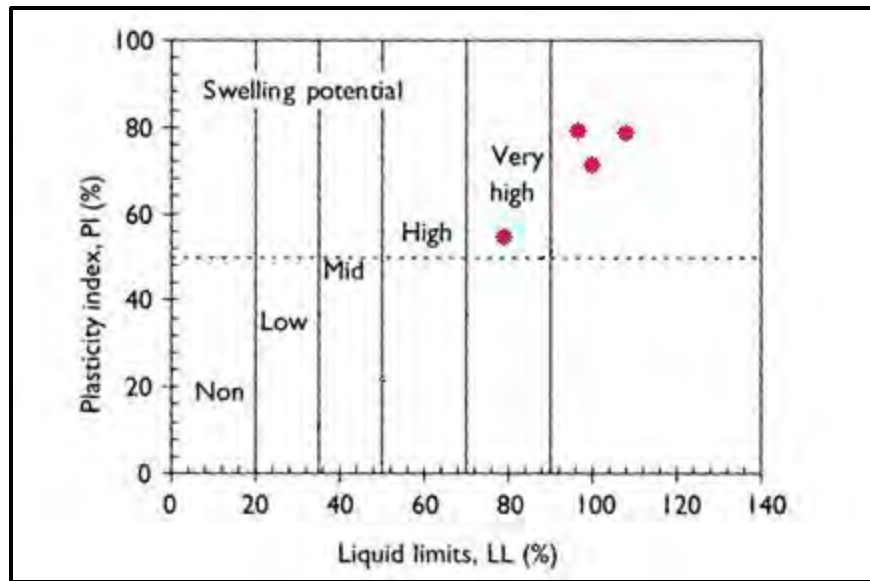


Figure 93. Qualitative Swell Potential, Daksanamurthy and Raman, 1973

Laboratory tests focused on measuring the cyclic swell potential in the lateral direction. Initial swelling from in-situ moisture under a constant total stress generally resulted in approximately 1% axial swelling strains. Under the same total stresses, but through the soil's full range of potential moisture contents, the swelling strains increased to the range of 6 – 8%. It seems that the cycles of wetting and drying progressively unlocked additional surface area from within relatively active crumbs of the soil structure. The magnitudes of swelling strains are similar to those measured by Marr (2003), but the overall behavior is different. The current study found that k_s increased with increasing total stress. That is, for a given change in moisture content, larger strains occurred under larger total stresses. Marr's study showed the opposite trend; that, for a given change in moisture content, higher total stresses resulted in smaller vertical strains.

Vertical swell potential was also inferred from some of the consolidation results. In particular, Tests 4 and 5 were inundated under constant volume conditions to measure the swell pressure. The tests revealed swell pressures of approximately 1200 and 3800 psf at depths of 5 and 15 feet, respectively. This is in agreement with Marr's (2003) measurement of 4200 psf at approximately the same depth in a similar deposit.

7 Conclusions and Recommendations

The Lymon C. Reese Research Wall was installed in the very top portion of the Bergstrom Formation, the upper member of the Taylor Group. The soil profile consists chiefly of three dominant zones:

- The top stratum is approximately 8 feet thick. The soil is dark brownish gray and highly weathered. The primary clay mineral is montmorillonite, and the swell potential is very high. The soil is stiff, fissured and very sticky when wet.
- A transitional zone occurs between depths of approximately 8 and 10 feet. The soil lightens to a dull yellow color, and small patches of chalk are present. The soil's secondary structure becomes more pronounced.
- Below 10 feet, the dull yellow color begins to turn a darker brown with depth. The soil becomes very stiff, much like claystone. The secondary structure becomes a dominant feature.

All soils tested in the study were heavily overconsolidated, with overconsolidation ratios no smaller than 9. In some cases it was impossible to distinguish a transition between over- and normally-consolidated stress ranges. The more discernible test results still didn't conform to typical behavior. The soil's undrained strength increases with depth in a typical manner until a depth of approximately 15 feet. Beyond this depth, the strength increases much faster than would be expected for typical soils.

Trimming the soil for laboratory tests was a tedious procedure, and sampling with seamless push tubes may have disturbed the soil to an extent that trimming could not erase. The most repeatable and reasonable test results were obtained from specimens that were subjected to repeated loading or wetting/drying. That is, the residual drained strengths from direct shear tests and the steady state swell condition. It seems that the repeated loading conditions acclimate the soil to its trimmed condition and restore some sense of in-situ conditions.

The cyclic swell tests provided an indication of the upper stratum's lateral swell potential. Swelling from in-situ moisture contents and approximately in-situ stresses resulted in swelling strains in the range of 0.8 – 1.0 percent. A stress smaller than in-situ resulted in 1.2% strain; larger than in-situ resulted in 0.2%. After reaching steady state and swelling from their driest to wettest conditions, the swelling strains for all tests increased to the range of 7 – 8%.

The standard CRS consolidation equipment proved very useful for the cyclic swell tests. The computer-operated load frame may provide an opportunity to automate the test to some degree. One major challenge remains the unloading and reloading of the specimen throughout the test to obtain intermediate moisture contents. Great care is required to keep the soil intact and maintain a continuous set of measurements.

The hydraulic conductivity varied drastically between back-calculated lab measurements and field observations, which corresponded to two very different flow paths. The in-situ hydraulic conductivity probably varies within those bounds, its value depending on depth or confinement and moisture content.

Appendix A: Boring Logs

TERMS AND SYMBOLS USED ON TxDOT BORING LOGS



SOIL TYPES

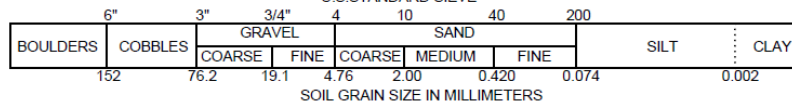
	CH, Fat Clay		Sand
	CL, Lean Clay		Gravel
	ML, Silt		Fill/Other

ROCK TYPES

	Limestone
	Shale

SOIL GRAIN SIZE

U.S. STANDARD SIEVE



STRENGTH OF GRANULAR SOILS ⁽¹⁾		STRENGTH OF COHESIVE SOILS ⁽¹⁾		BEDROCK HARDNESS ⁽¹⁾	
CONSISTENCY	THD Penetrometer (blows/ft or blows/300mm)	DENSITY	THD Penetrometer (blows/ft or blows/300mm)	HARDNESS	THD Penetrometer (blows/ft or blows/300mm)
Very Loose	0 to 8	Very Soft	0 to 8	Very Hard	0" - 2"/100 (0 - 50mm/100)
Loose	8 to 20	Soft	8 to 20	Hard	1" - 5"/100 (25 - 125mm/100)
Slightly Compact	20 to 40	Stiff	20 to 40	Soft	4" - 6"/100 (100 - 150mm/100)
Compact	40 to 80	Very Stiff	40 to 80		
Dense	80 to 5"/100 (125mm/100)	Hard	80 to 5"/100 (125mm/100)		
Very Dense	5"/100 to 0"/100 (125mm/100 to 0mm/100)	Very Hard	5"/100 to 0"/100 (125mm/100 to 0mm/100)		

1) TxDOT Geotechnical Manual, Chapter 3 - Soil and Bedrock Classification & Logging (3-15)

ASTM D 2488 TABLE 7 Criteria for Describing Structure

Description	Criteria
Stratified	Alternating layers of varying material or color with layers at least 6 mm thick; note thickness
Laminated	Alternating layers of varying material or color with the layers less than 6mm thick; note thickness
Fissured	Breaks along definite planes of fracture with little resistance to fracturing
Slickensided	Fracture planes appear polished or glossy, sometimes striated
Blocky	Cohesive soil that can be broken down into small angular lumps which resist further breakdown
Lensed	Inclusion of small pockets of different soils, such as small lenses of sand scattered through a mass of clay; note thickness
Homogeneous	Same color and appearance throughout

Criteria for Describing Inclusions

Description	Criteria
Parting	Inclusion <1/8" thick extending through sample
Seam	Inclusion 1/8" to 3" thick extending through sample
Layer	Inclusion >3" thick extending through sample

Terms used in Additional Remarks on Wincore Logs

Description	Criteria
PP	Pocket Penetration Test (tsf)
SPT	Modified Standard Penetration Test (bpf)
REC	Rock Core Recovery (%)
RQD	Rock Quality Designation, ASTM (D 6032)
Q	Unconsolidated Undrained Triaxial Test (tsf)
U	Unconfined Compression Test (tsf)



WinCore
Version 3.1

DRILLING LOG

1 of 1

County	Travis	Hole	B-1	District	
Highway		Structure	Retaining Wall	Date	1/12/10
CSJ	UT Manor Wall Project	Station		Grnd. Elev.	0.00 ft
		Offset		GW Elev.	-45.70 ft

Elev. (ft)	LOG	Texas Cone Penetrometer	Strata Description	Triaxial Test		Properties				Additional Remarks	
				Lateral Press. (psi)	Deviator Stress (psi)	MC	LL	PI	Wet Den. (pcf)		
		4 (6) 4 (6)	CLAY, soft, dark brown, w/scattered sand and fine gravel. (Residual Soil) (CH)							SPT = 12	
-5.5		9 (6) 8 (6)		CLAY, soft to hard, tan and light gray, blocky, calcareous, w/ferrous staining and selenite seams. (Taylor) (CH)							SPT = 12
10		8 (6) 8 (6)									SPT = 16
15		10 (6) 12 (6)									w/increasing selenite seams
20		19 (6) 22 (6)									SPT = 20
25		24 (6) 24 (6)									SPT = 19
30		37 (6) 50 (6)	CLAYSHALE, low to moderate hardness, dark gray, slightly fissile, w/occasional pyritic seams and nodules. (Taylor)							SPT = 22	
35		50 (6) 50 (6)								w/occasional tan seams	
-39										SPT = 30	
40										SPT = 35	
45											
-47											
50											
55											
60											

Remarks: Boring was drilled to the 47.0-ft depth using dry drilling techniques. Upon completion of the bore hole, groundwater recorded at 45.7 ft after a 1.5 hour waiting period. A 2-inch diameter piezometer was set in the borehole with a screened interval of 5.0 to 20.0 ft below ground surface. Standard Penetration Test (SPT) blowcounts were performed using a 170-lb hammer with a 24-inch hammer drop.

Any ground water elevation information provided on this boring log is representative of conditions existing on the day and for the specific location where this information was collected. The actual groundwater elevation may fluctuate due to time, climatic conditions, and/or construction activity.

Driller: Fugro Consultants, Inc.

Logger: Fugro Consultants, Inc.

Organization: Fugro Consultants, Inc.

M:\GEOIREPORTS\2009\04.3009\1079 UT Manor Wall Project\UT Manor Wall logs 1-28-10.clg



WinCore
Version 3.1

DRILLING LOG

1 of 1

County	Travis	Hole	B-2	District	
Highway		Structure	Retaining Wall	Date	1/12/10
CSJ	UT Manor Wall Project	Station		Grnd. Elev.	0.00 ft
		Offset		GW Elev.	-29.10 ft

Elev. (ft)	LOG	Texas Cone Penetrometer	Strata Description	Triaxial Test		Properties				Additional Remarks
				Lateral Press. (psi)	Deviator Stress (psi)	MC	LL	PI	Wet Den. (pcf)	
-6.0			CLAY, very stiff to hard, dark gray, w/scattered shell fragments, roots, and fine rounded gravel. (Residual Soil) (CH)							PP = 2.25 PP = 4.5+
-10.0			CLAY, very stiff to hard, tan and light gray, blocky, calcareous, w/ferrous staining and selenite seams. (Taylor) (CH)							PP = 3.5 PP = 3.75 PP = 4.5+
-15.0										PP = 4.5+
-20.0										PP = 4.0
-25.0										PP = 2.5 w/increasing selenite seams
-30.0										PP = 4.5+
-35.0										PP = 4.5+ w/selenite-coated joints at 38 ft
-39.5			CLAY SHALE, low to moderate hardness, dark gray, slightly fissile, w/occasional pyritic seams and nodules. (Taylor)							PP = 4.5+ w/occasional tan seams
-45.0										PP = 4.5+
-50.0										
-55.0										
-60.0										

Remarks: Boring was drilled to the 50.0-ft depth using dry drilling techniques and groundwater was recorded at 29.1 ft after a 15 minute waiting period. Upon completion of the borehole, groundwater was recorded at 41.0 ft. A slope inclinometer casing was set in the borehole.

Any ground water elevation information provided on this boring log is representative of conditions existing on the day and for the specific location where this information was collected. The actual groundwater elevation may fluctuate due to time, climatic conditions, and/or construction activity.

Driller: Fugro Consultants, Inc.

Logger: Fugro Consultants, Inc.

Organization: Fugro Consultants, Inc.

M:\GEO\REPORTS\2009\04.30091079 UT Manor Wall Project\UT Manor Wall logs 1-28-10.clg



WinCore
Version 3.1

DRILLING LOG

1 of 1

County	Travis	Hole	B-3	District	
Highway		Structure	Retaining Wall	Date	1/13/10
CSJ	UT Manor Wall Project	Station		Grnd. Elev.	0.00 ft
		Offset		GW Elev.	-42.50 ft

Elev. (ft)	LOG	Texas Cone Penetrometer	Strata Description	Triaxial Test		Properties				Additional Remarks
				Lateral Press. (psi)	Deviator Stress (psi)	MC	LL	PI	Wet Den. (pcf)	
-6			CLAY, stiff to very stiff, dark gray, w/scattered shell fragments, roots, and fine rounded gravel. (Residual Soil) (CH)							PP = 1.75 PP = 1.75 PP = 2.0 PP = 2.0
10		7 (6) 8 (6)	CLAY, very stiff to hard, tan and light gray, blocky, calcareous, w/ferrous staining and selenite seams. (Taylor) (CH)							PP = 3.25
15		9 (6) 11 (6)								PP = 2.5
20		13 (6) 15 (6)								PP = 3.5
25		14 (6) 20 (6)								PP = 3.25 w/increasing selenite seams
30		34 (6) 33 (6)								PP = 4.5+
35		50 (6) 50 (4)								PP = 4.5+
40		30 (6) 50 (4.25)								PP = 4.5+
-43.3		50 (2.25) 50 (1.25)	CLAY SHALE, low to moderate hardness, dark gray, slightly fissile, w/occasional pyritic seams and nodules. (Taylor)							PP = 4.5+ w/occasional tan seams
-50.3		50 (0.75) 50 (3)								PP = 4.5+

Remarks: Boring was drilled to the 50.3-ft depth using dry drilling techniques and groundwater was recorded at 42.5 ft after a 15 minute waiting period. Upon completion of the borehole, the boring was backfilled with soil cuttings.

Any ground water elevation information provided on this boring log is representative of conditions existing on the day and for the specific location where this information was collected. The actual groundwater elevation may fluctuate due to time, climatic conditions, and/or construction activity.

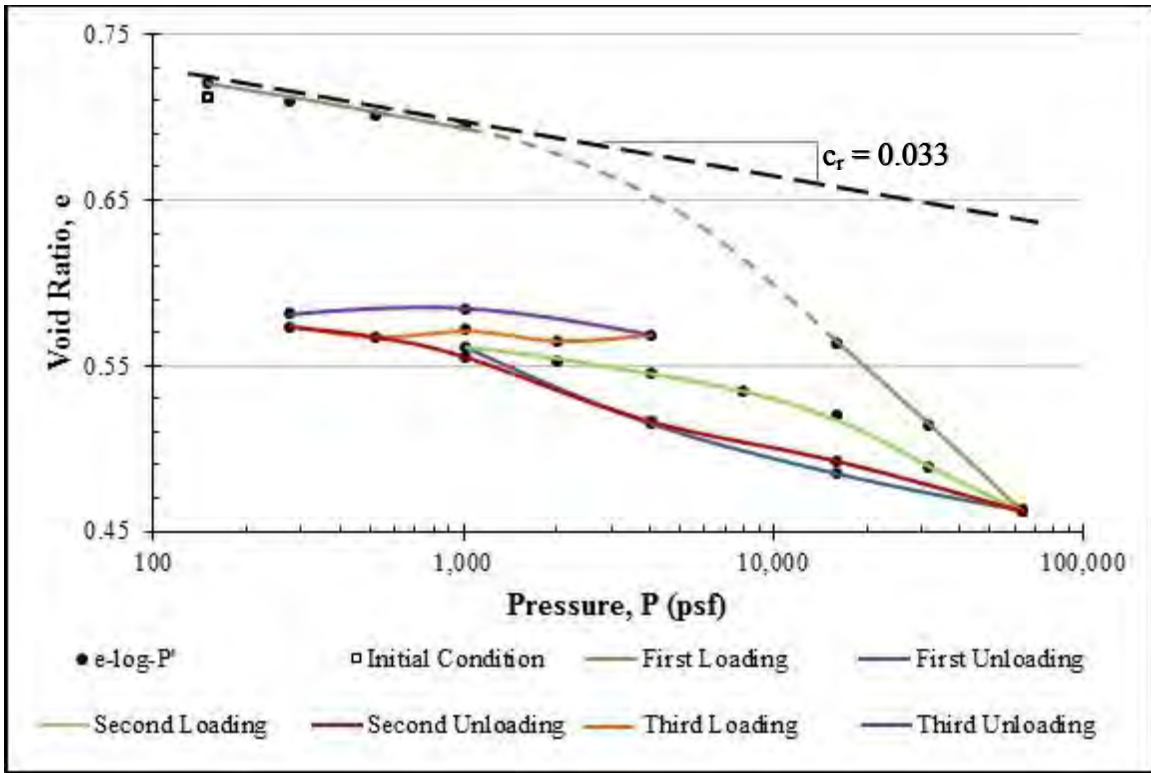
Driller: Fugro Consultants, Inc.

Logger: Fugro Consultants, Inc.

Organization: Fugro Consultants, Inc.

M:\GEO\REPORTS\2009\04.30091079 UT Manor Wall Project\UT Manor Wall logs 1-28-10.clg

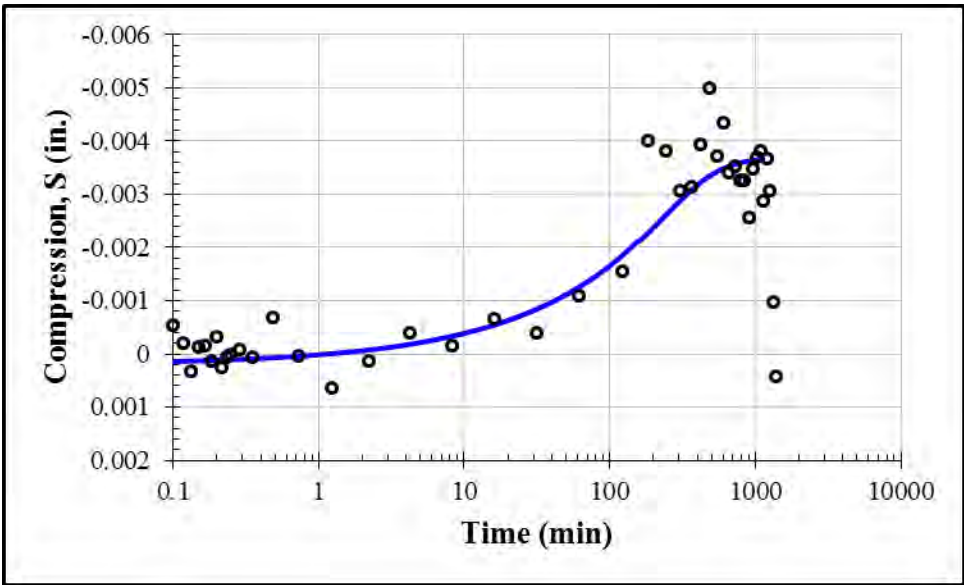
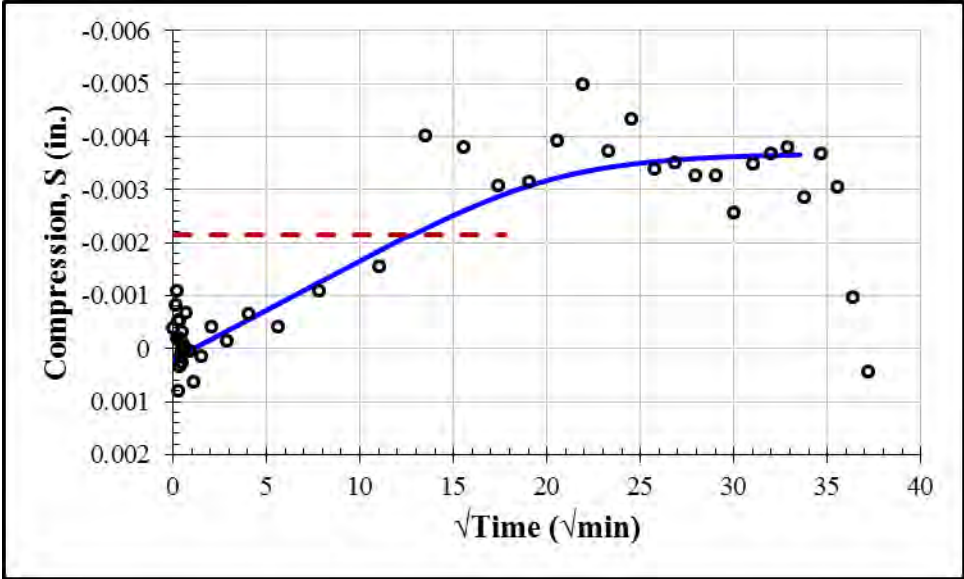
Appendix B: Consolidation Test 1



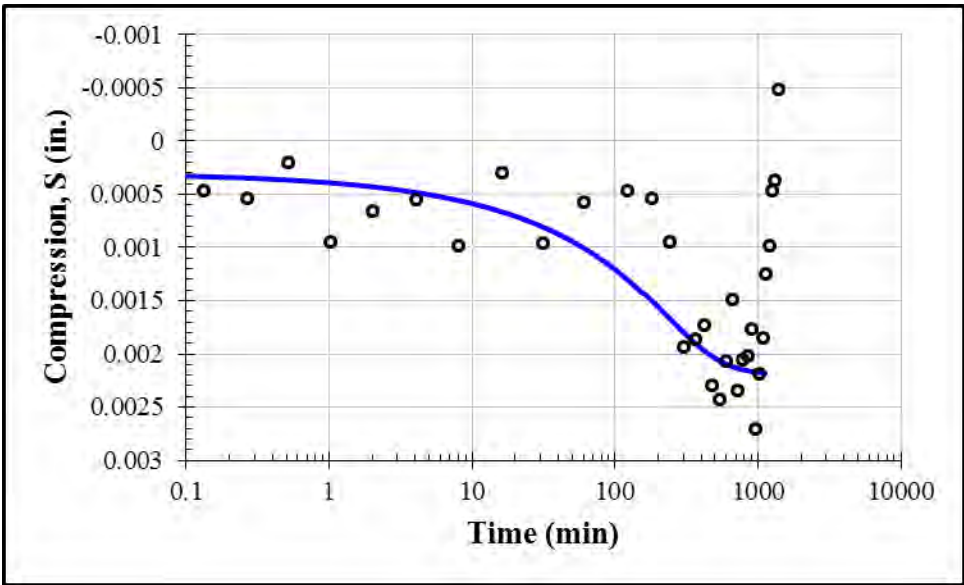
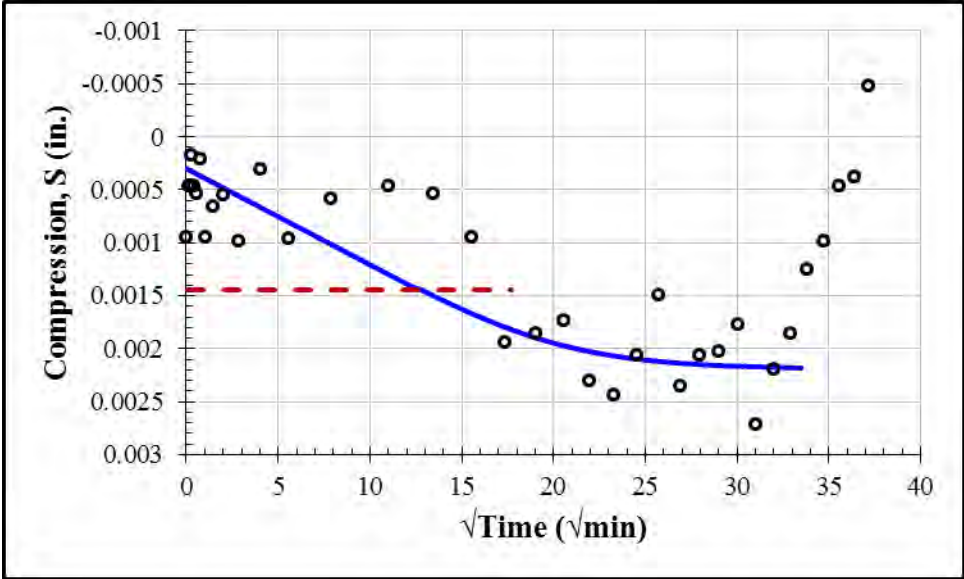
$$c_r = -\frac{e_2 - e_1}{\log(\sigma_2 / \sigma_1)} = -\frac{0.645 - 0.720}{\log(40000 / 200)} = 0.033$$

$$R_r = \frac{c_r}{1 + e_0} = \frac{0.033}{1 + 0.7117} = 0.019$$

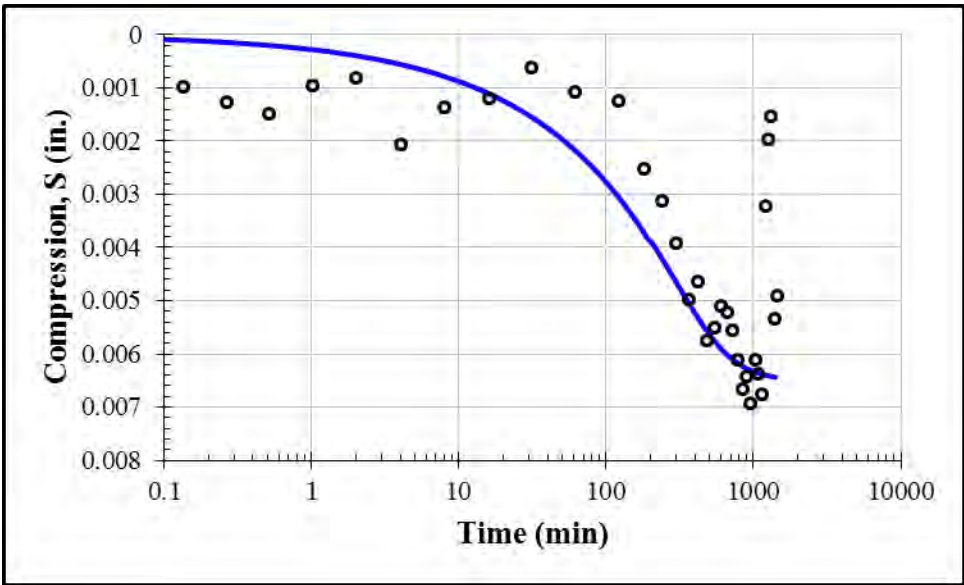
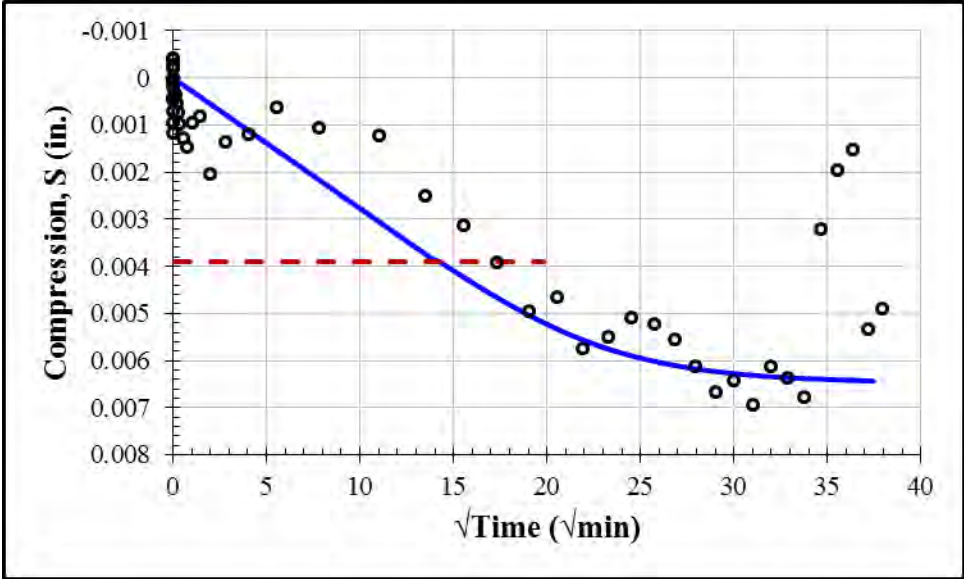
Inundation: 125 psf				
S_0 (in.)	S_{100} (in.)	c_v (in ² /min)	k (ft/day)	t_{50} (min)
0.0002	-0.0037	0.00025	6.5×10^{-8}	110



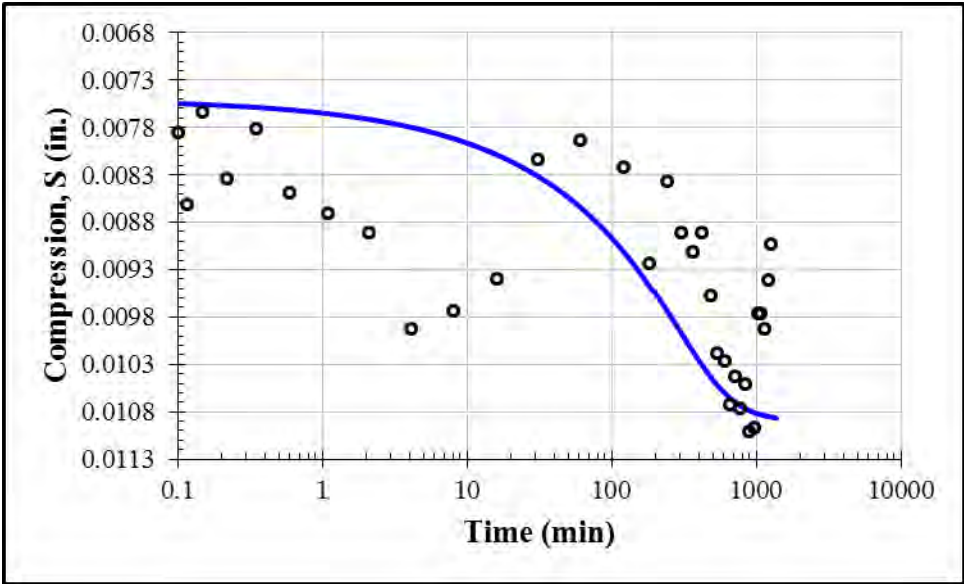
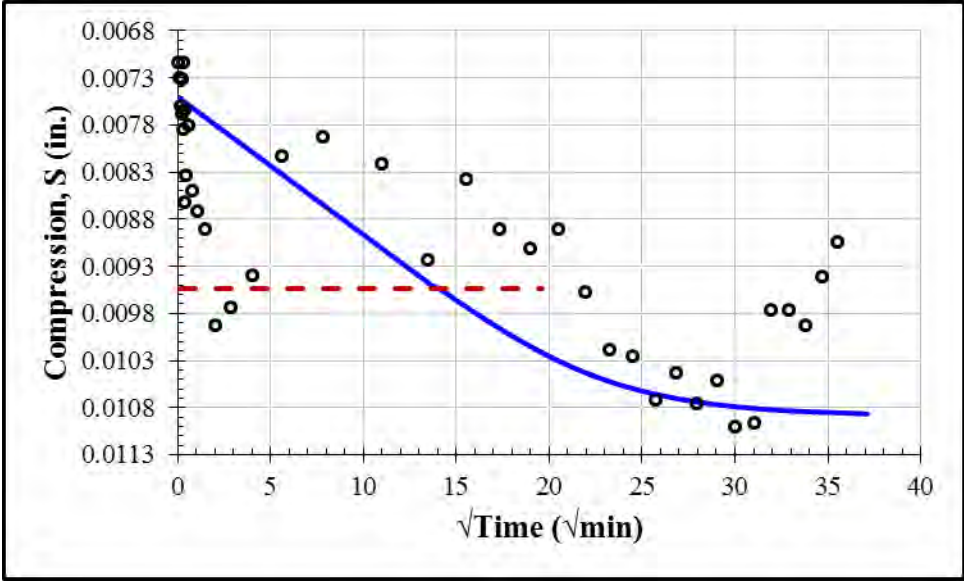
First Loading: 250 psf				
S_0 (in.)	S_{100} (in.)	c_v (in ² /min)	k (ft/day)	t_{50} (min)
0.0003	0.0022	0.00025	3.2×10^{-8}	110



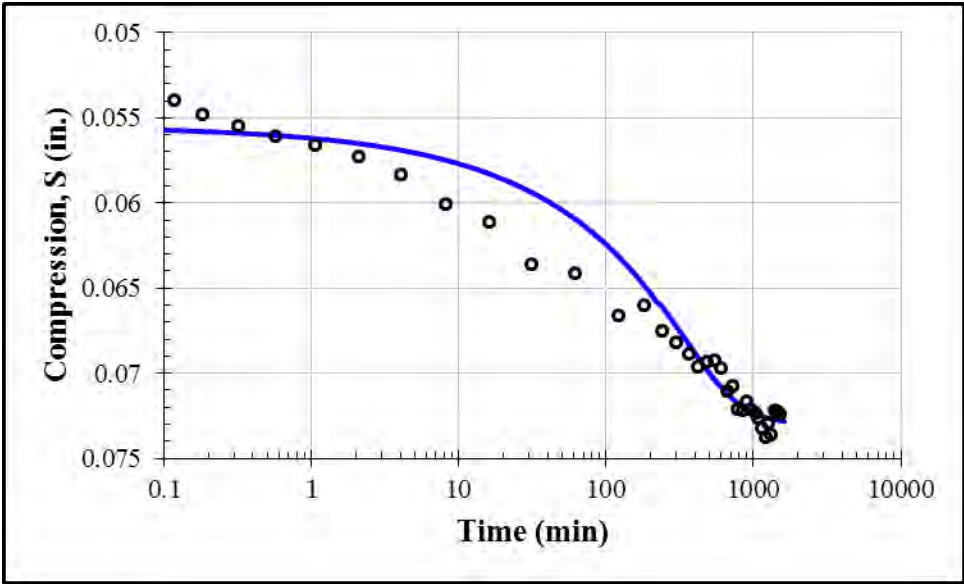
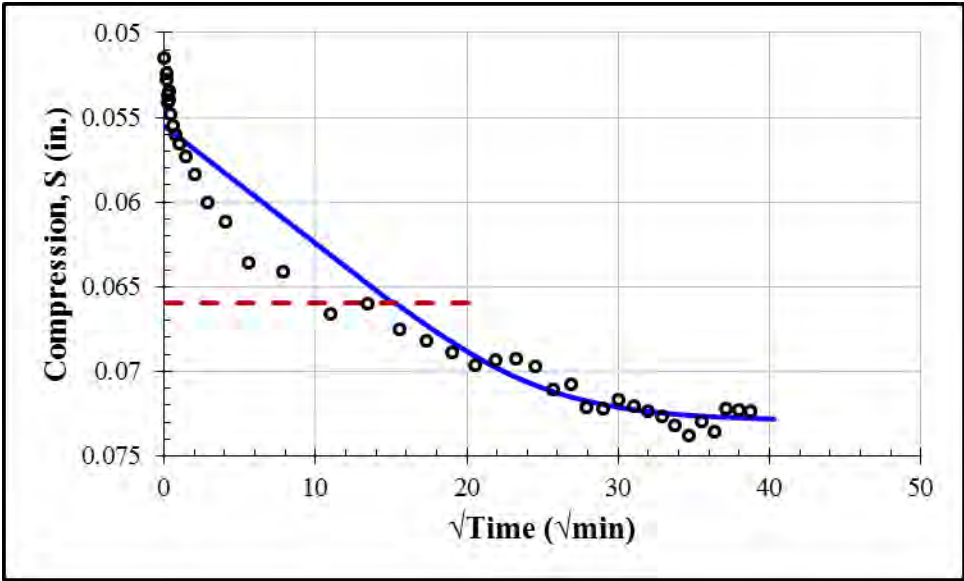
First Loading: 500 psf				
S_0 (in.)	S_{100} (in.)	c_v (in ² /min)	k (ft/day)	t_{50} (min)
0.0000	0.0065	0.0002	4.3×10^{-8}	138



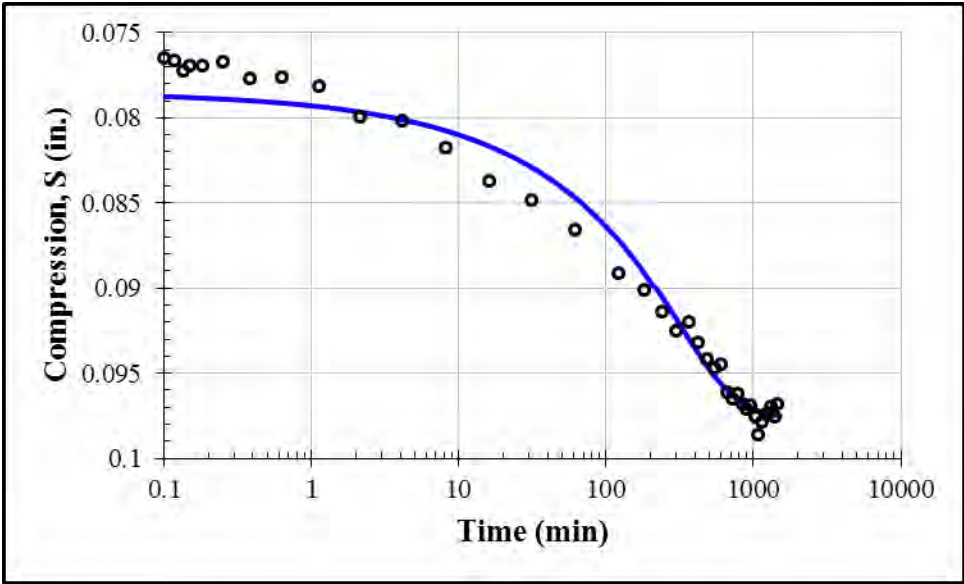
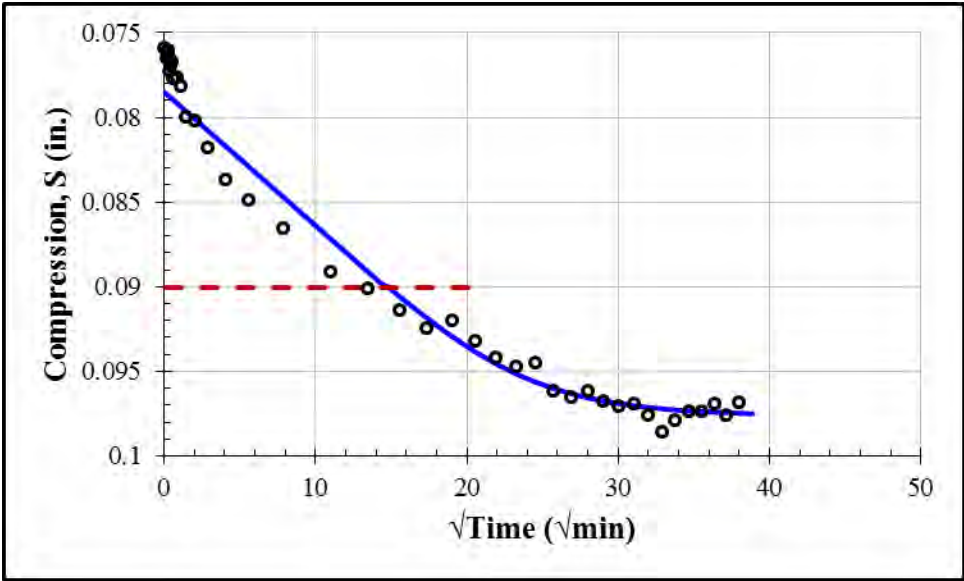
First Loading: 1000 psf				
S_0 (in.)	S_{100} (in.)	c_v (in ² /min)	k (ft/day)	t_{50} (min)
0.0075	0.0109	0.0002	1.1×10^{-8}	135



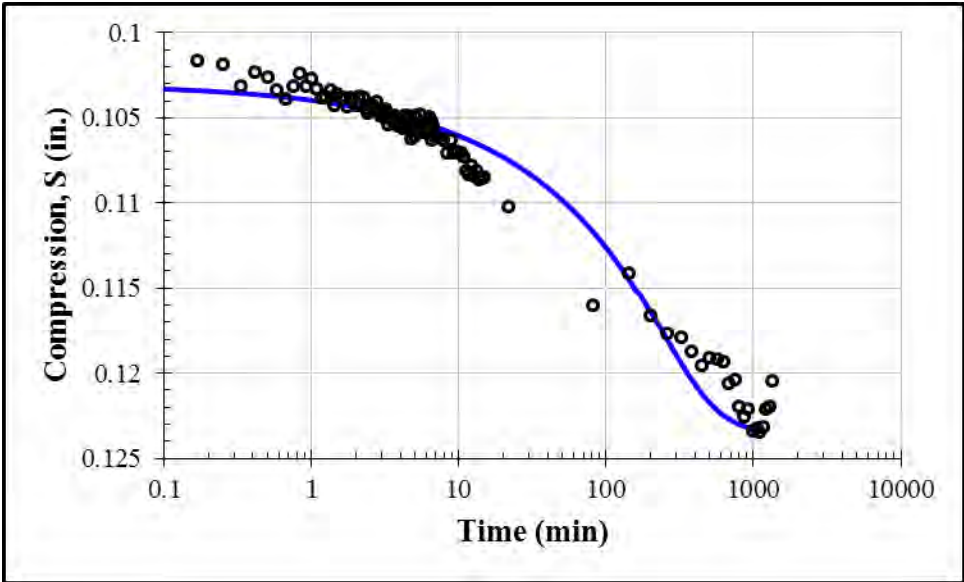
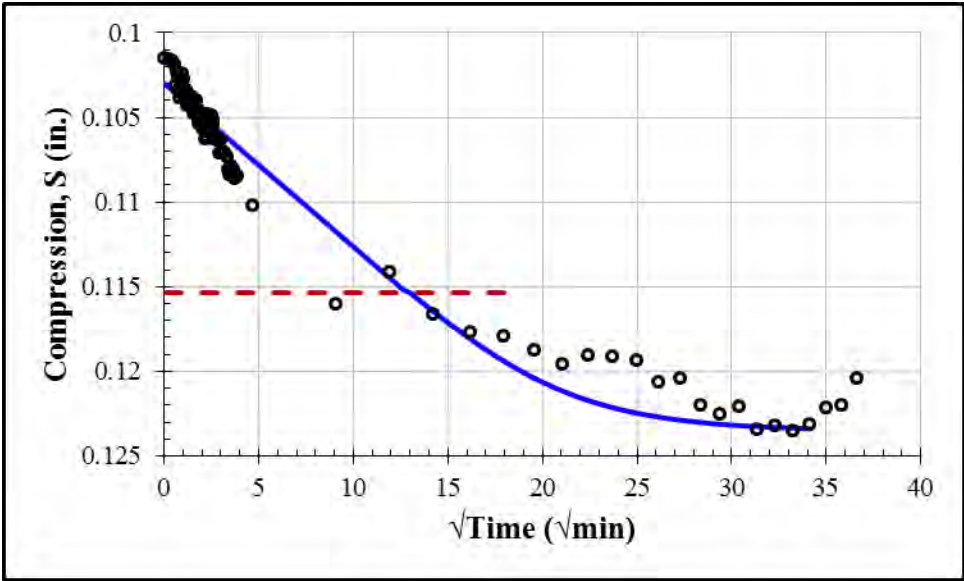
First Loading: 16000 psf				
S_0 (in.)	S_{100} (in.)	c_v (in ² /min)	k (ft/day)	t_{50} (min)
0.0555	0.0730	0.00015	1.4×10^{-9}	159



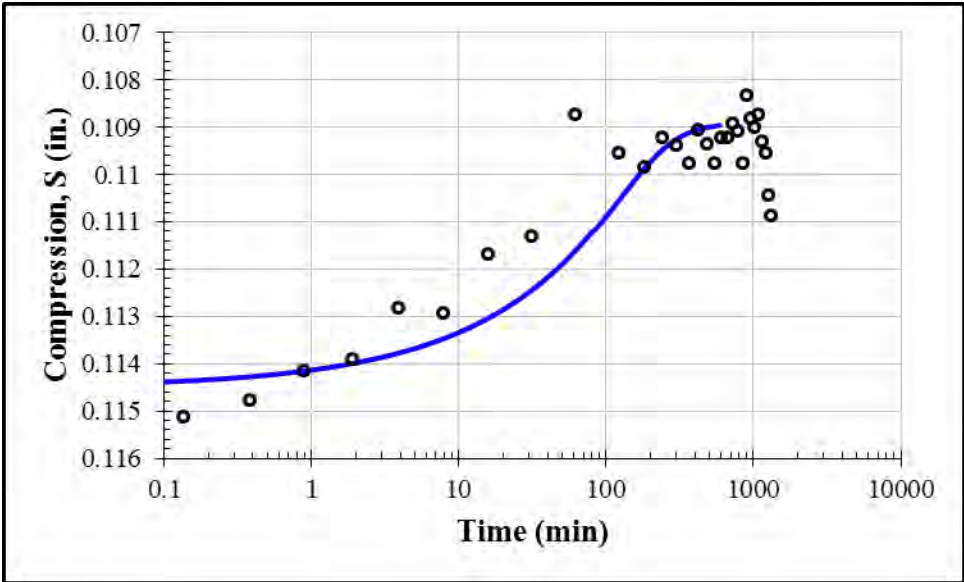
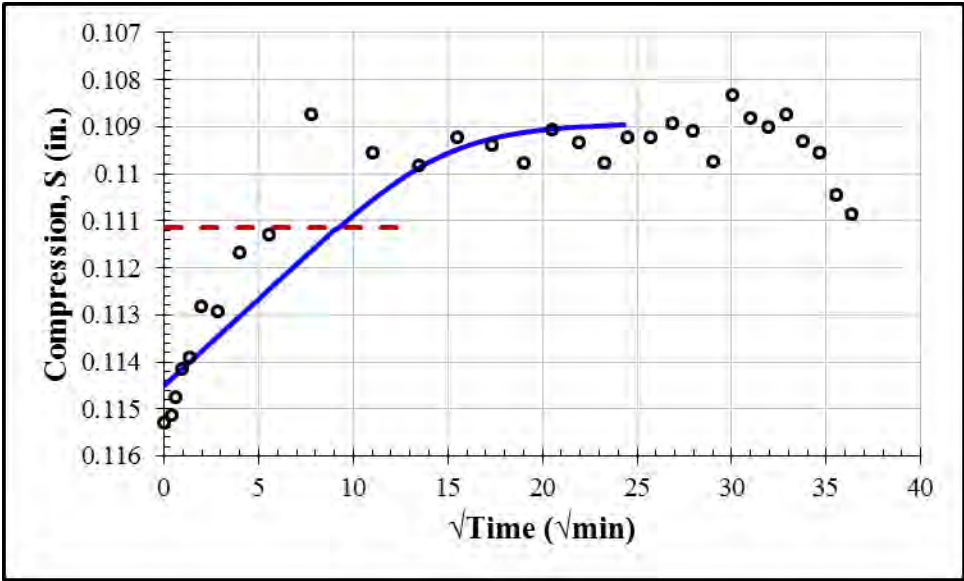
First Loading: 32000 psf				
S_0 (in.)	S_{100} (in.)	c_v (in ² /min)	k (ft/day)	t_{50} (min)
0.0785	0.0977	0.00015	1.4×10^{-9}	148



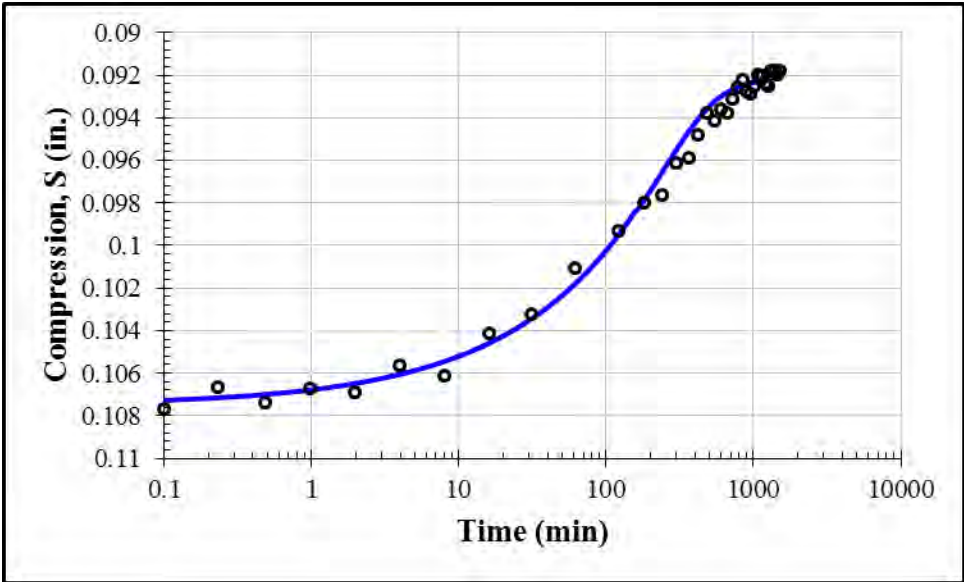
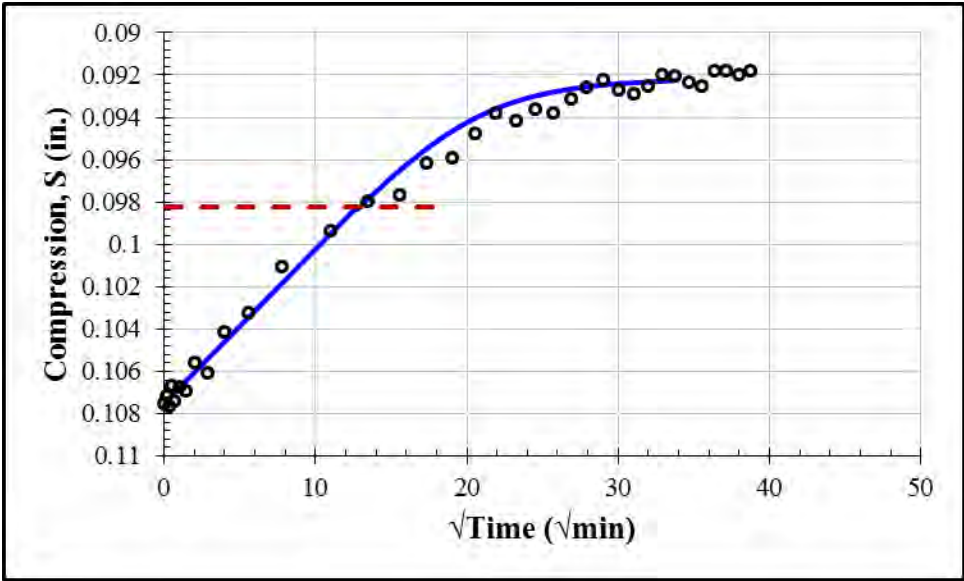
First Loading: 64000 psf				
S_0 (in.)	S_{100} (in.)	c_v (in ² /min)	k (ft/day)	t_{50} (min)
0.1030	0.1236	0.00018	8.7×10^{-10}	114



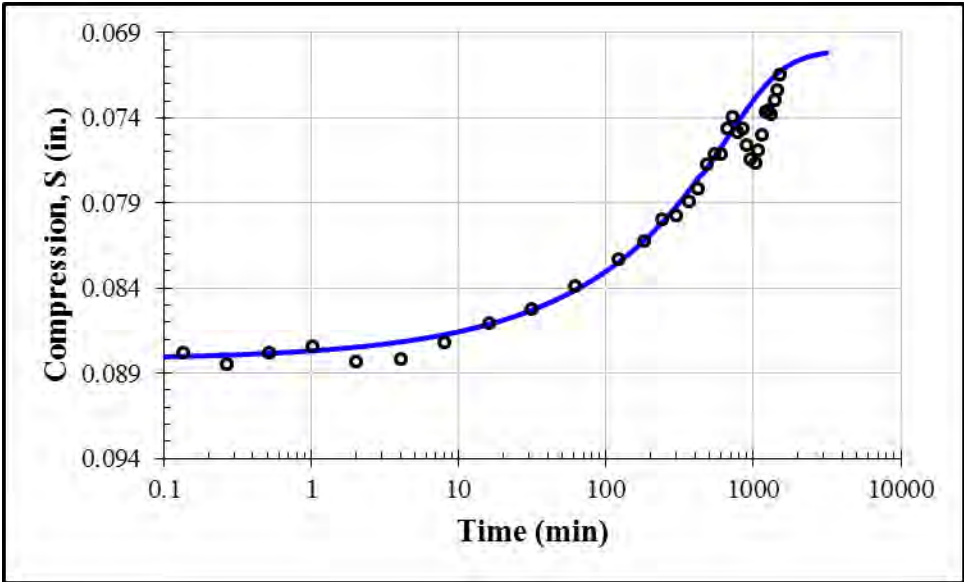
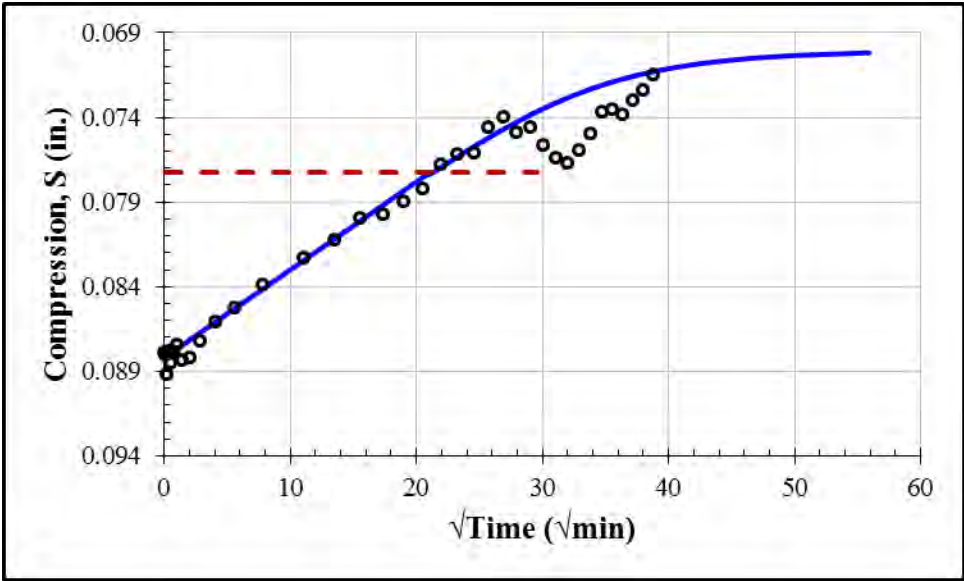
First Unloading: 16000 psf				
S_0 (in.)	S_{100} (in.)	c_v (in ² /min)	k (ft/day)	t_{50} (min)
0.1145	0.1089	0.00034	3.0×10^{-10}	58



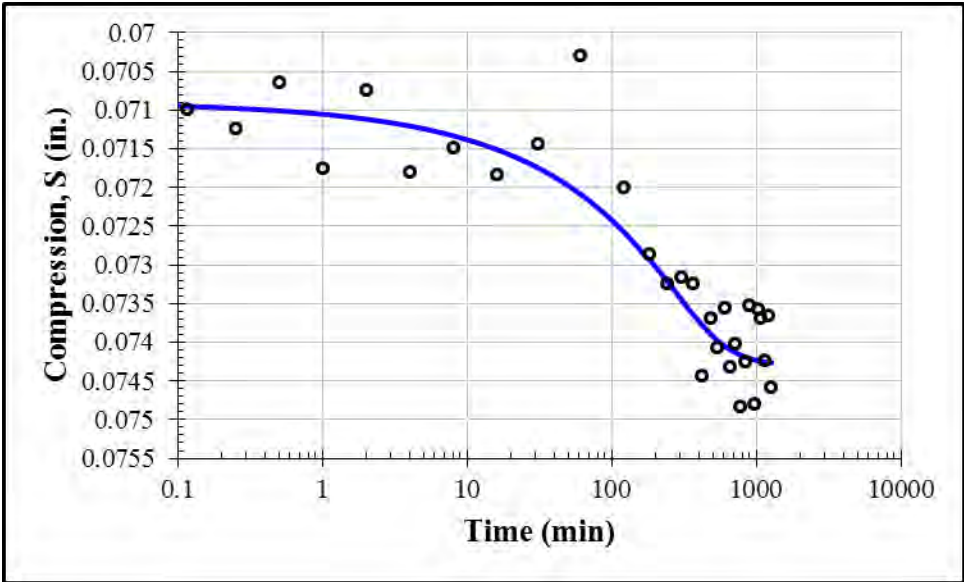
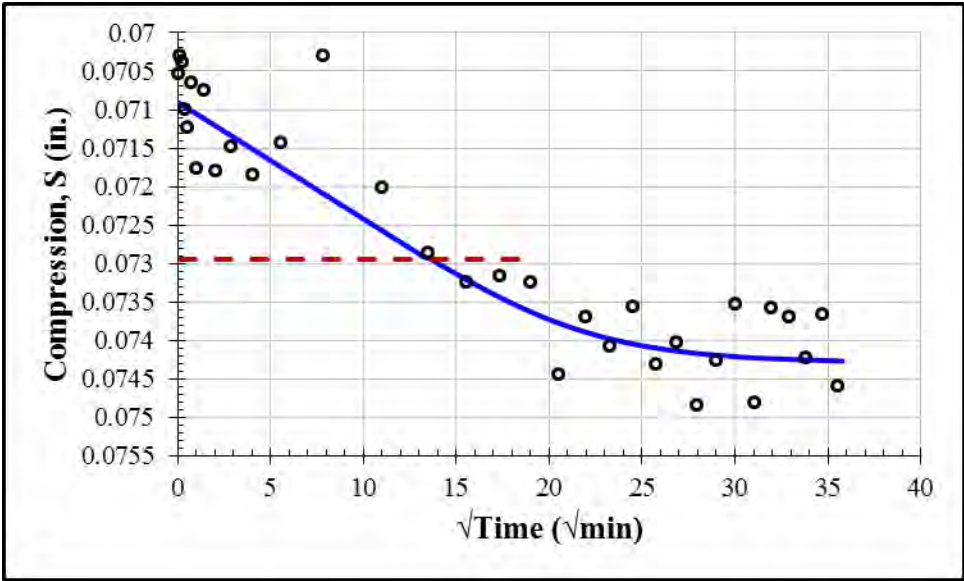
First Unloading: 4000 psf				
S_0 (in.)	S_{100} (in.)	c_v (in ² /min)	k (ft/day)	t_{50} (min)
0.1075	0.0921	0.00018	1.8×10^{-9}	112



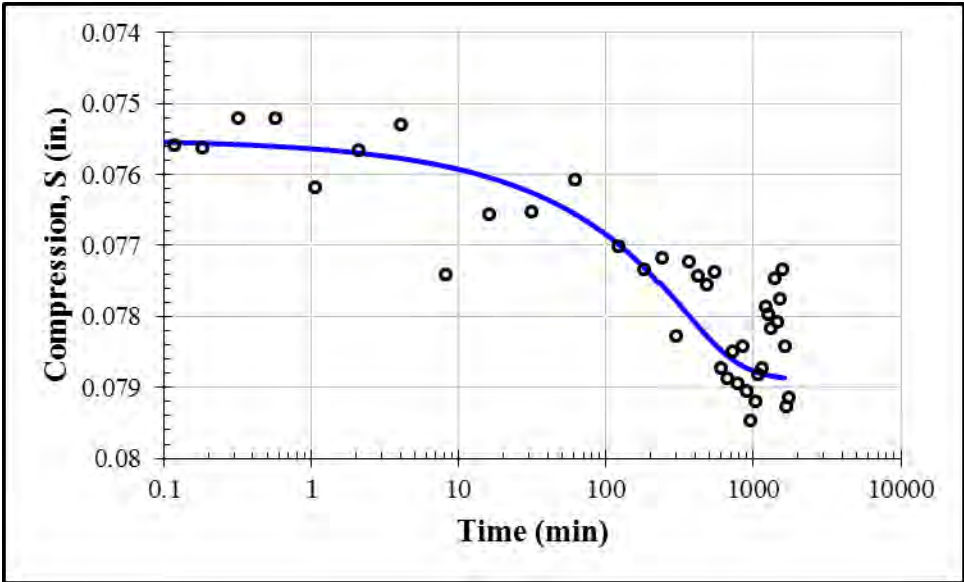
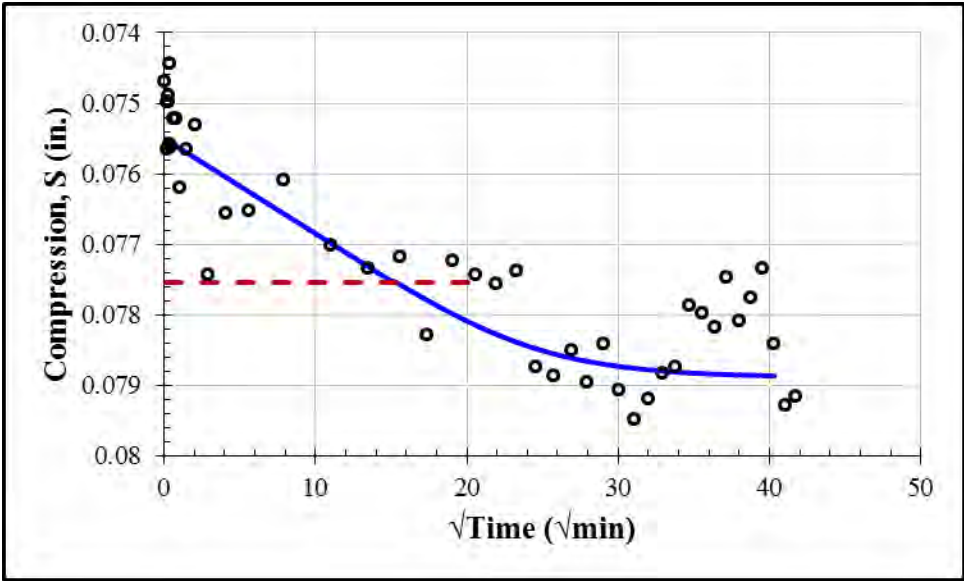
First Unloading: 1000 psf				
S_0 (in.)	S_{100} (in.)	c_v (in ² /min)	k (ft/day)	t_{50} (min)
0.0882	0.0700	0.00007	3.3×10^{-9}	306



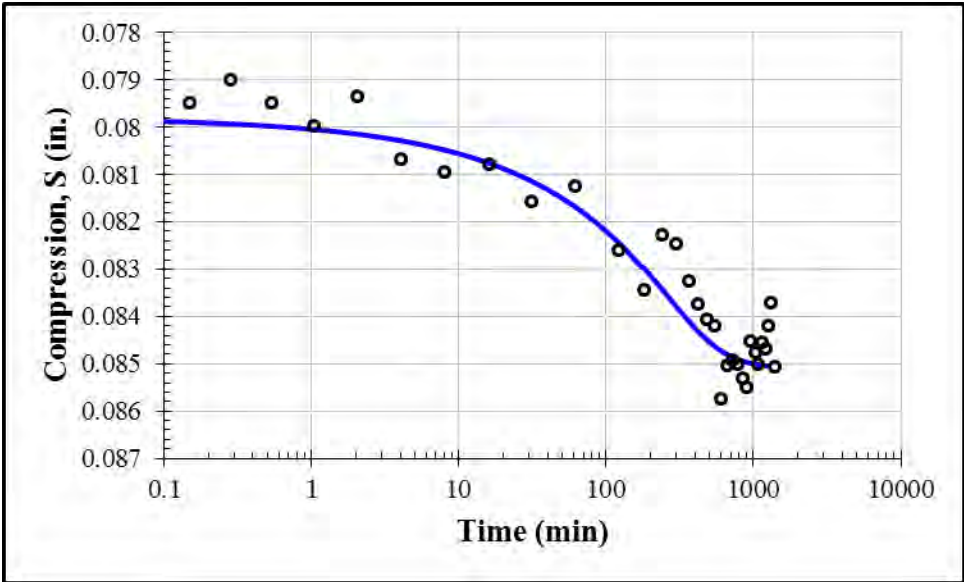
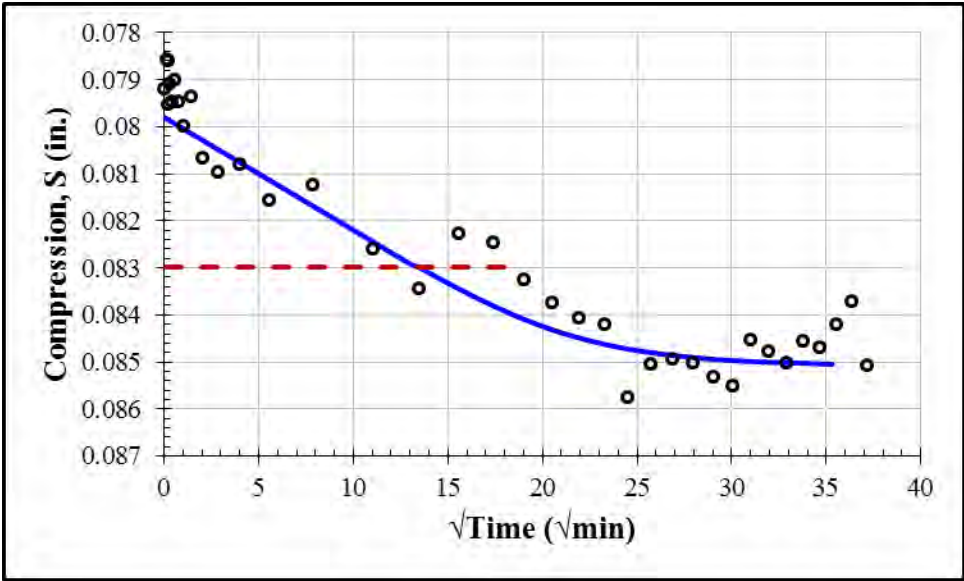
Second Loading: 2000 psf				
S_0 (in.)	S_{100} (in.)	c_v (in ² /min)	k (ft/day)	t_{50} (min)
0.0709	0.0743	0.00018	4.6×10^{-9}	125



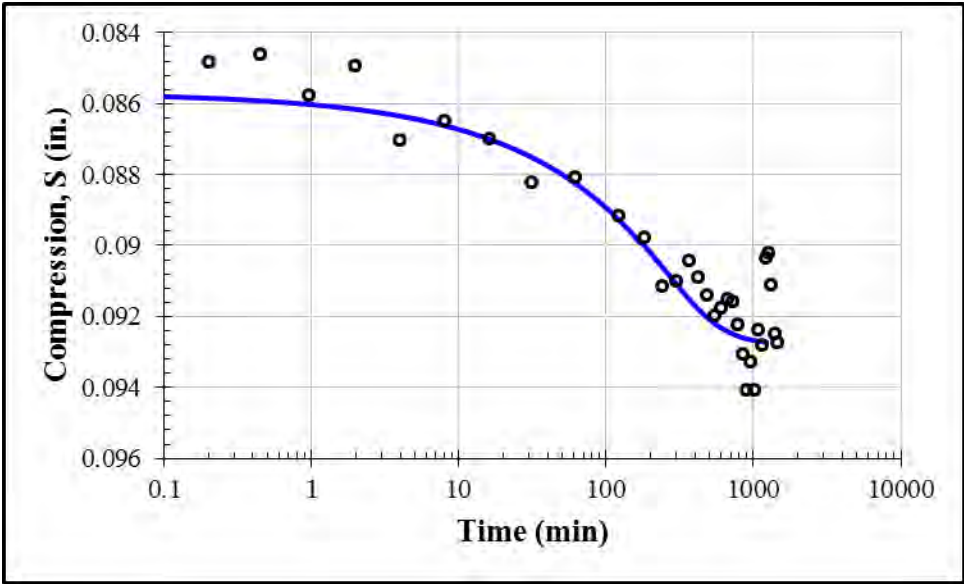
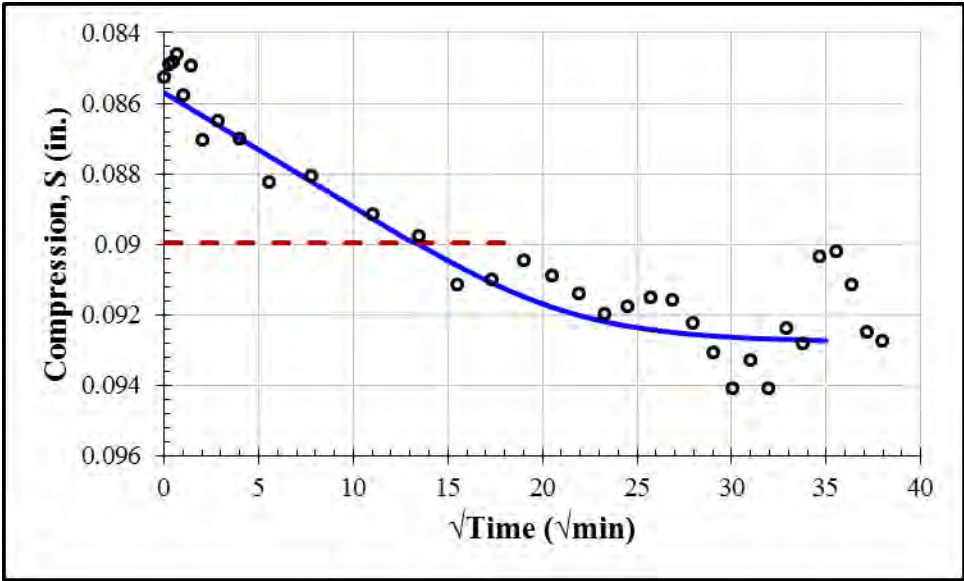
Second Loading: 4000 psf				
S_0 (in.)	S_{100} (in.)	c_v (in ² /min)	k (ft/day)	t_{50} (min)
0.0755	0.0789	0.00014	1.8×10^{-9}	159



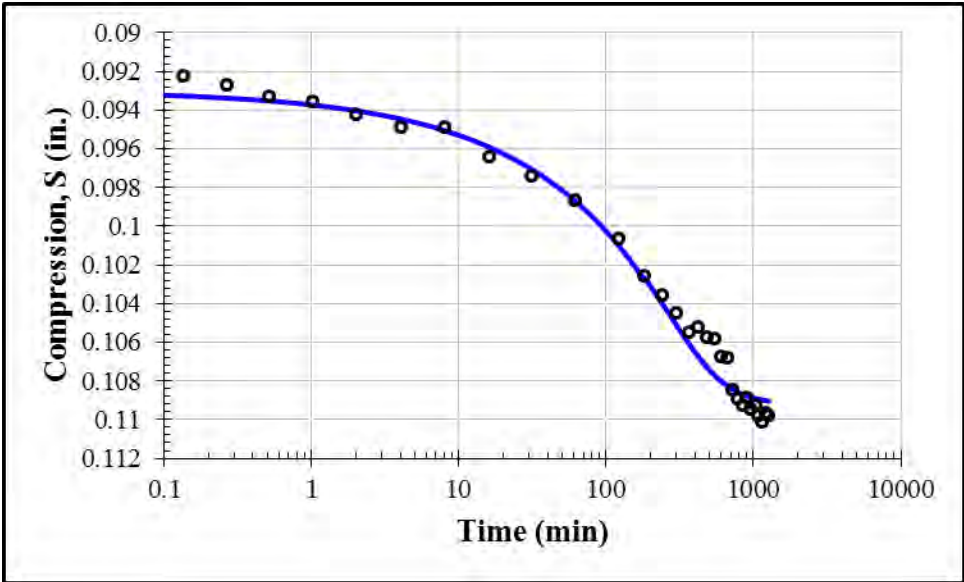
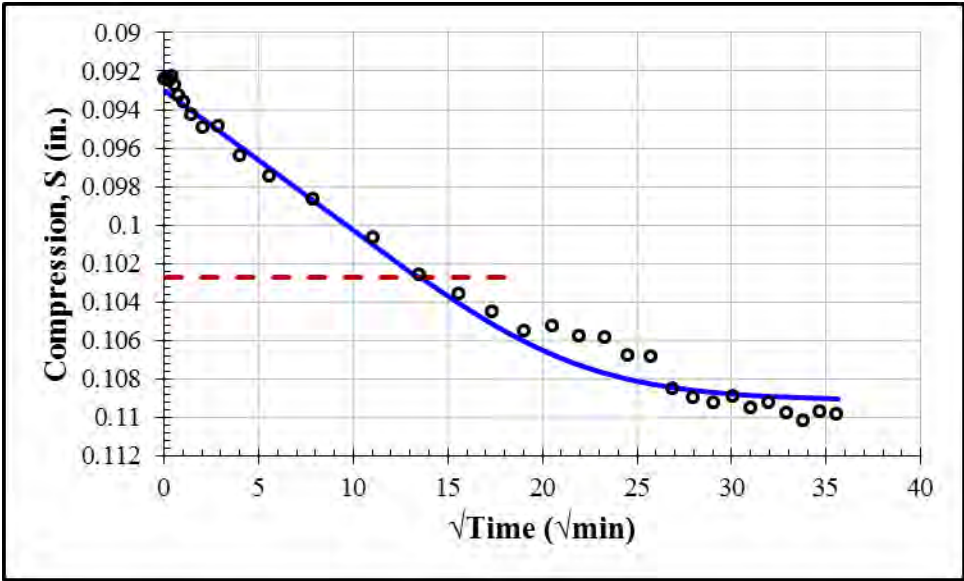
Second Loading: 8000 psf				
S_0 (in.)	S_{100} (in.)	c_v (in ² /min)	k (ft/day)	t_{50} (min)
0.0798	0.0851	0.00018	1.8×10^{-9}	122



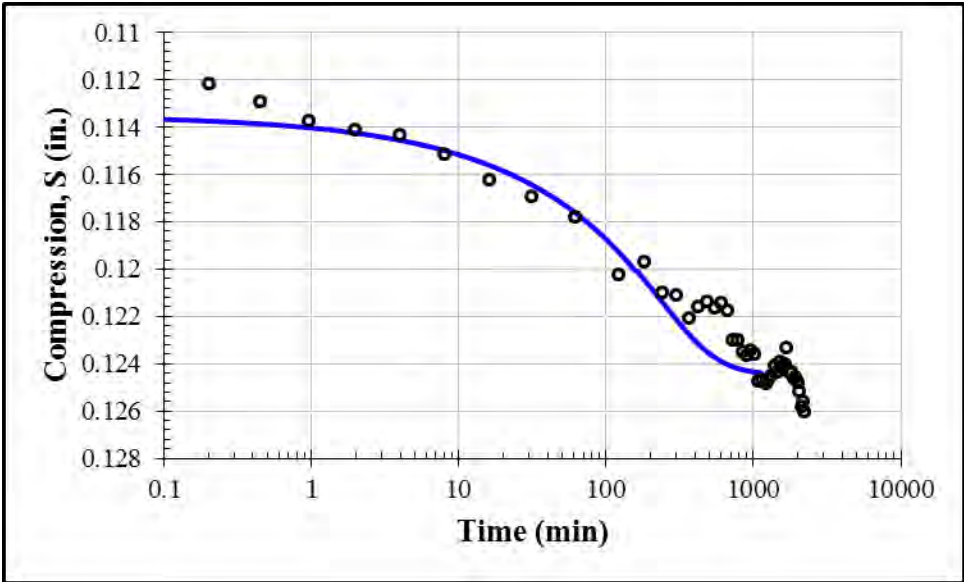
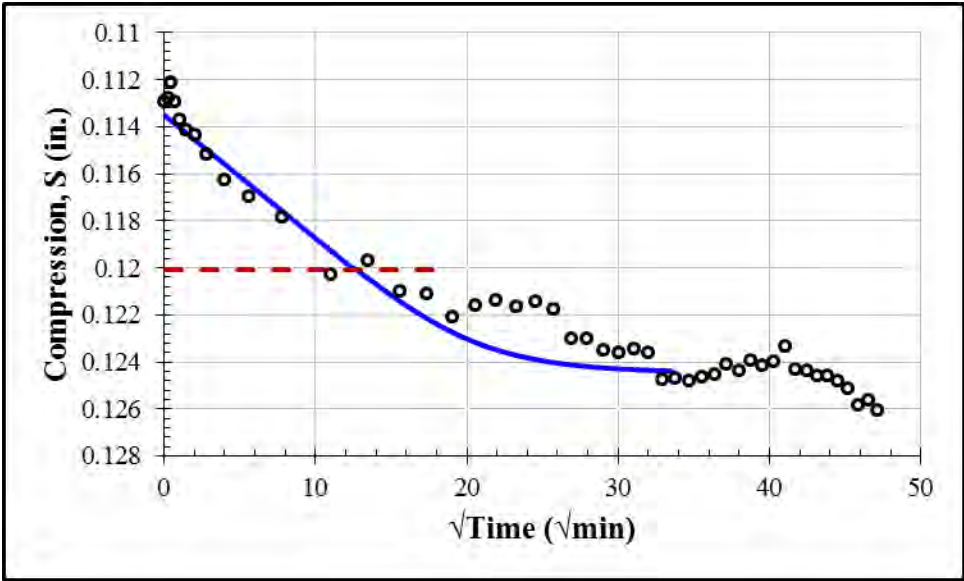
Second Loading: 16000 psf				
S_0 (in.)	S_{100} (in.)	c_v (in ² /min)	k (ft/day)	t_{50} (min)
0.0857	0.0928	0.00018	1.2×10^{-9}	120



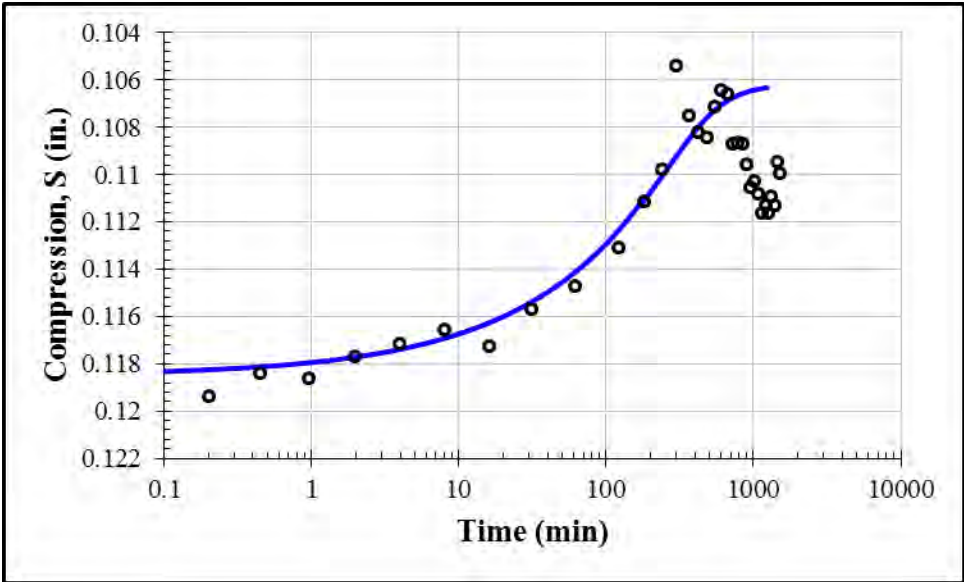
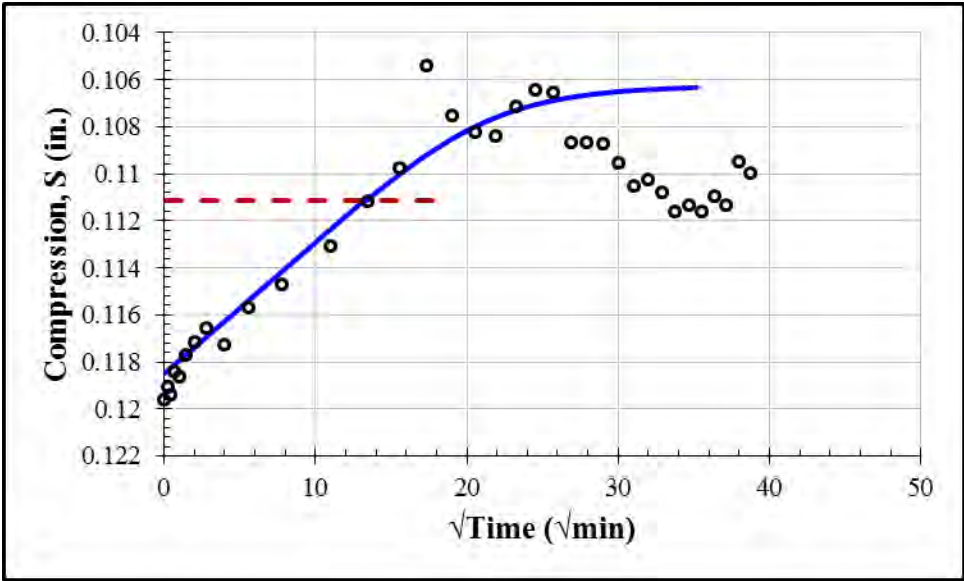
Second Loading: 32000 psf				
S_0 (in.)	S_{100} (in.)	c_v (in ² /min)	k (ft/day)	t_{50} (min)
0.0930	0.1092	0.00017	1.3×10^{-9}	124



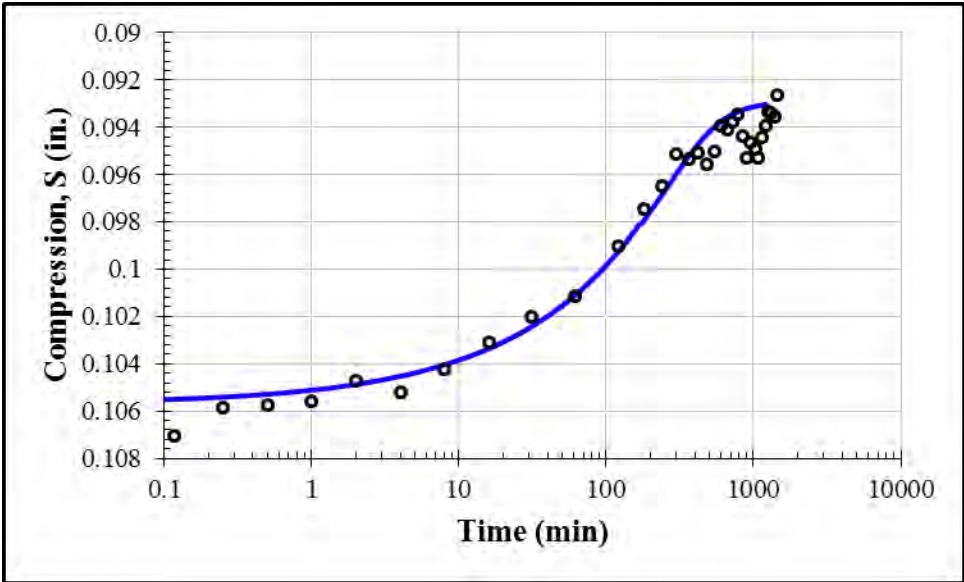
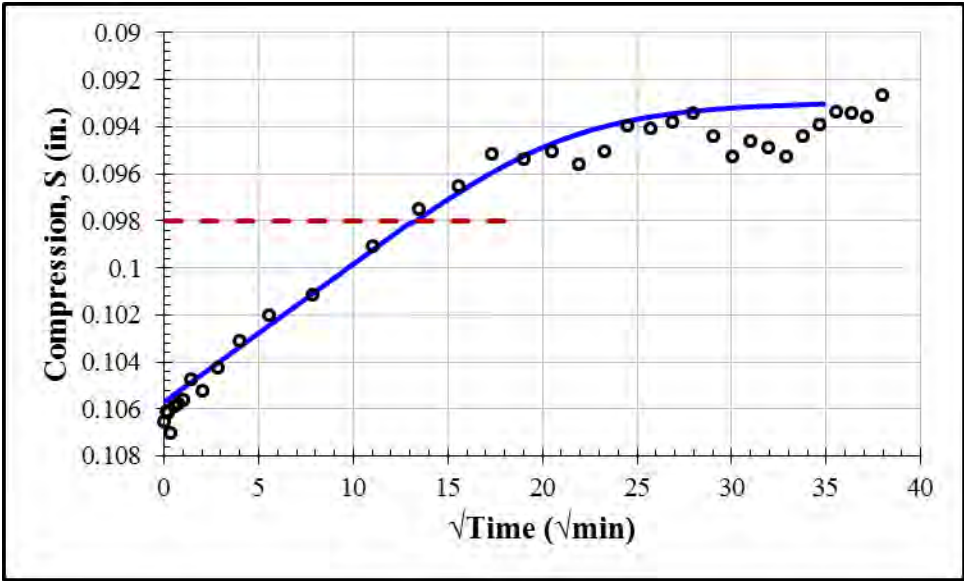
Second Loading: 64000 psf				
S_0 (in.)	S_{100} (in.)	c_v (in ² /min)	k (ft/day)	t_{50} (min)
0.1135	0.1245	0.00018	4.6×10^{-10}	110



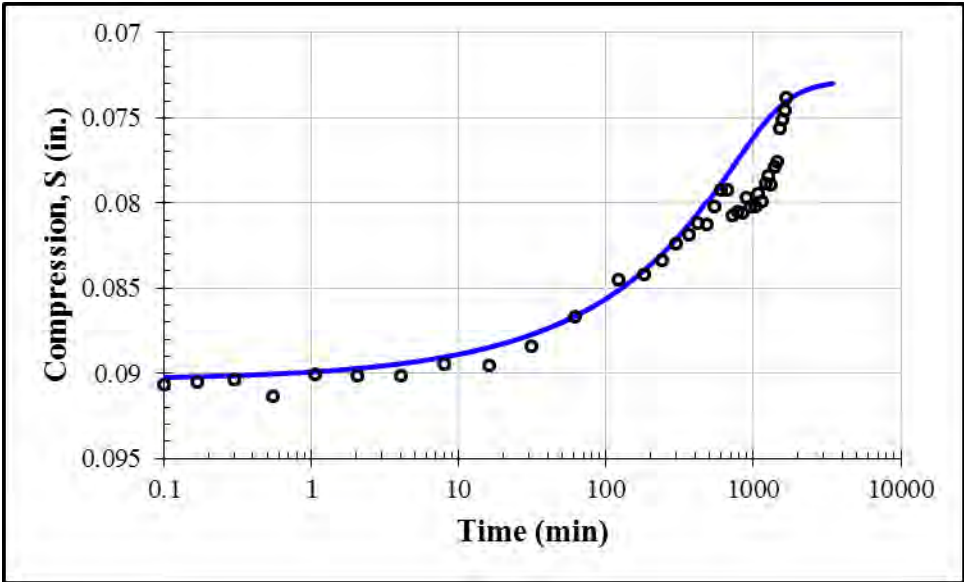
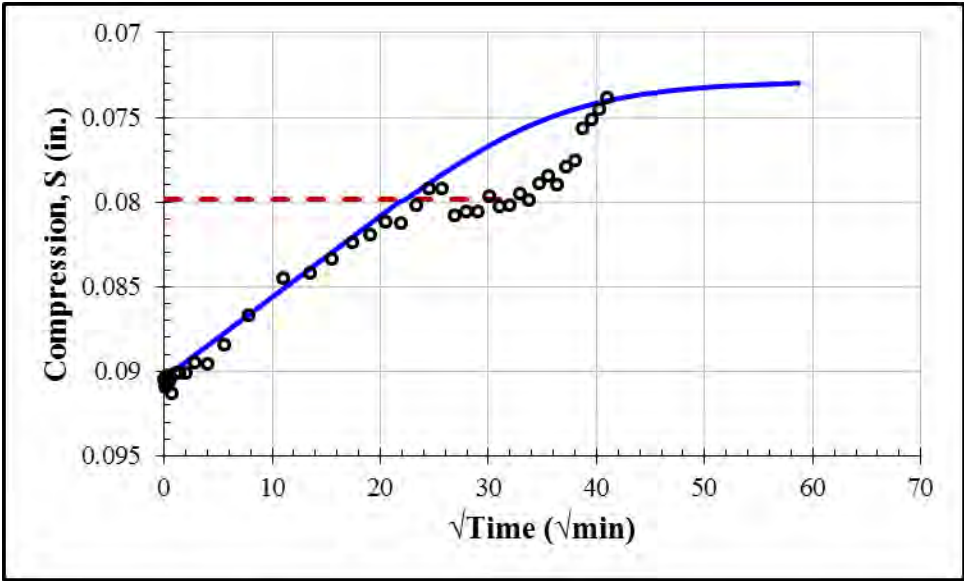
Second Unloading: 16000 psf				
S_0 (in.)	S_{100} (in.)	c_v (in ² /min)	k (ft/day)	t_{50} (min)
0.1185	0.1062	0.00016	3.1×10^{-10}	121



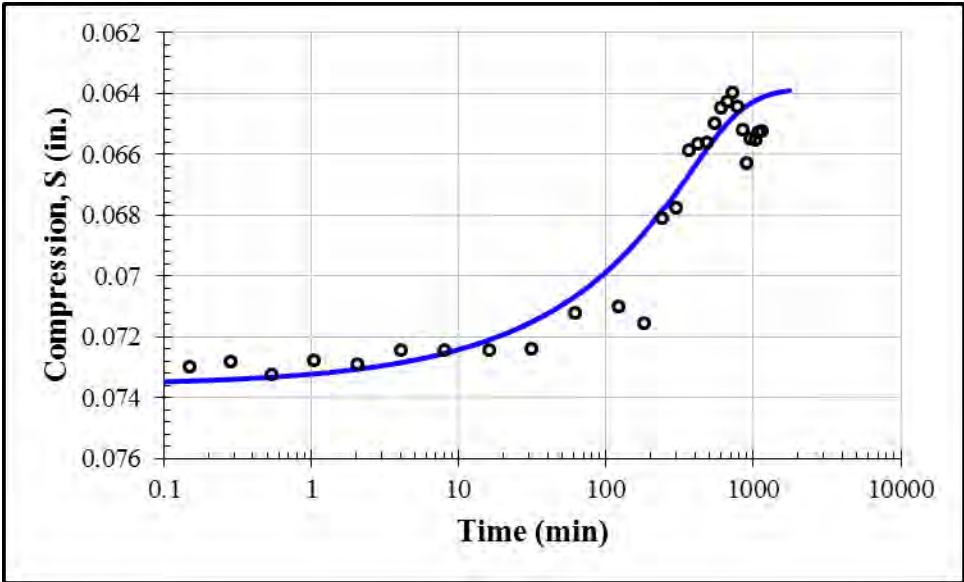
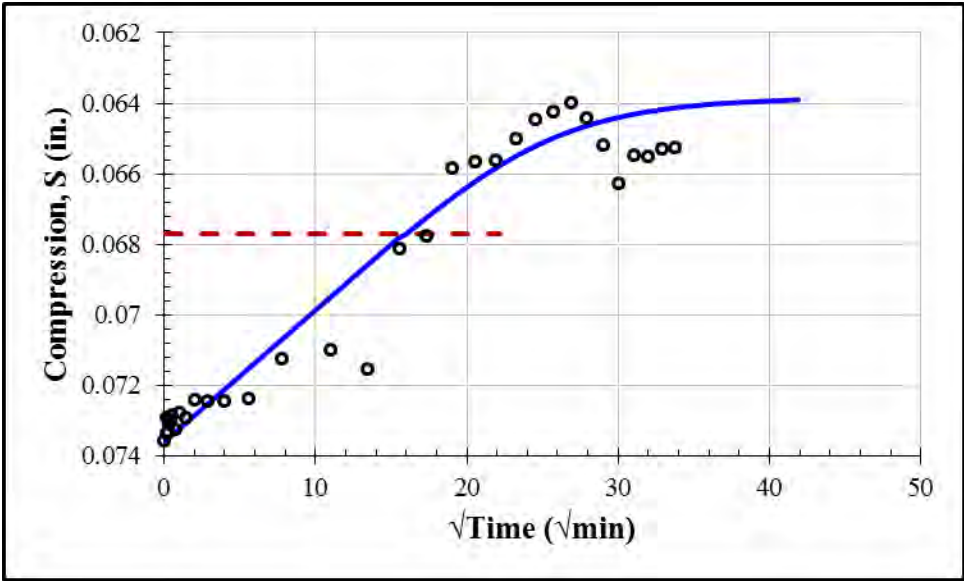
Second Unloading: 4000 psf				
S_0 (in.)	S_{100} (in.)	c_v (in ² /min)	k (ft/day)	t_{50} (min)
0.1057	0.0929	000017	1.4×10^{-9}	119



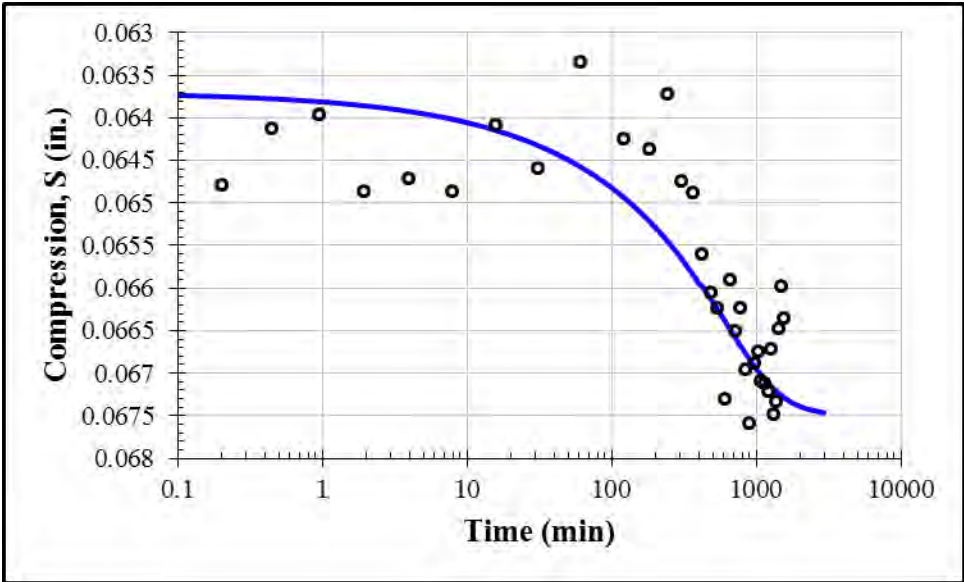
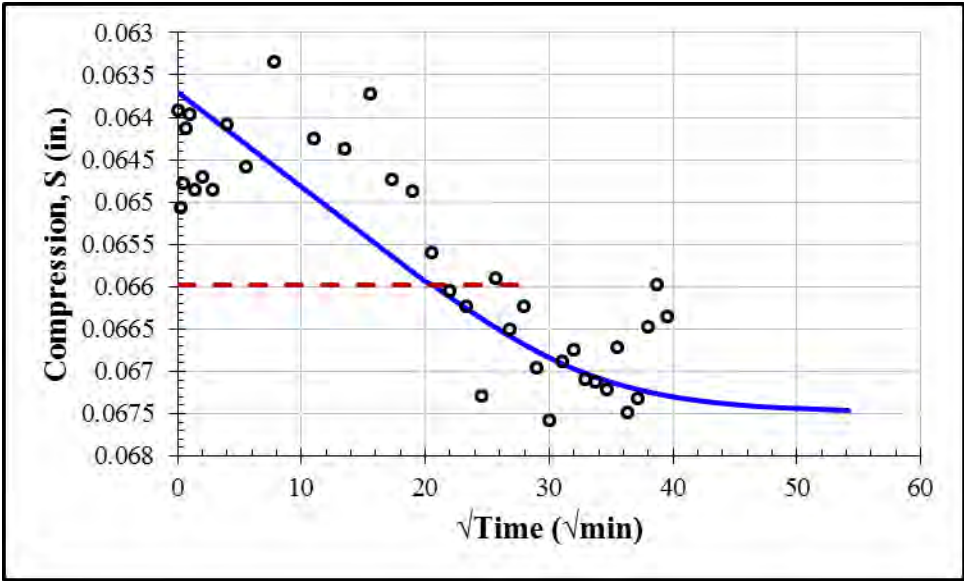
Second Unloading: 1000 psf				
S_0 (in.)	S_{100} (in.)	c_v (in ² /min)	k (ft/day)	t_{50} (min)
0.0904	0.0728	0.000063	2.8×10^{-9}	338



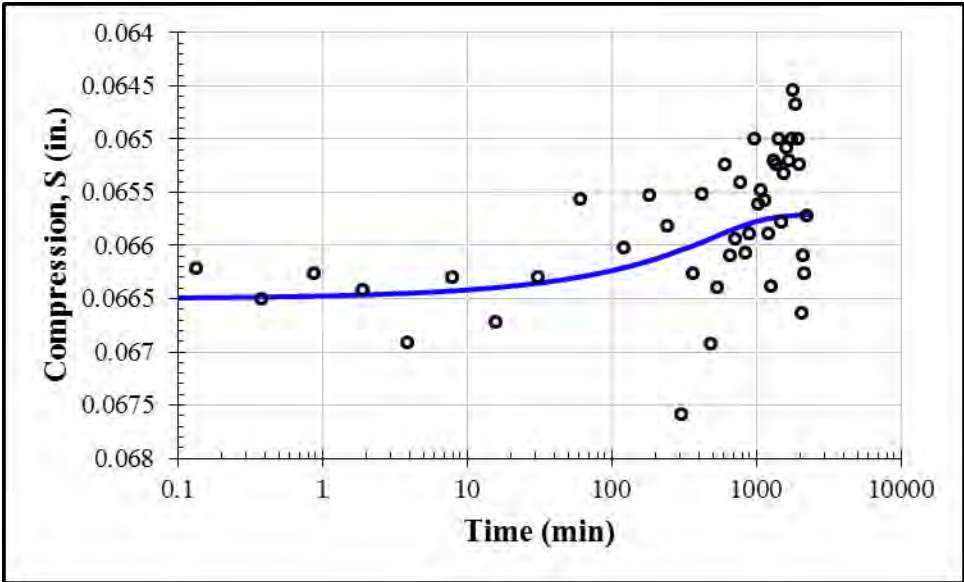
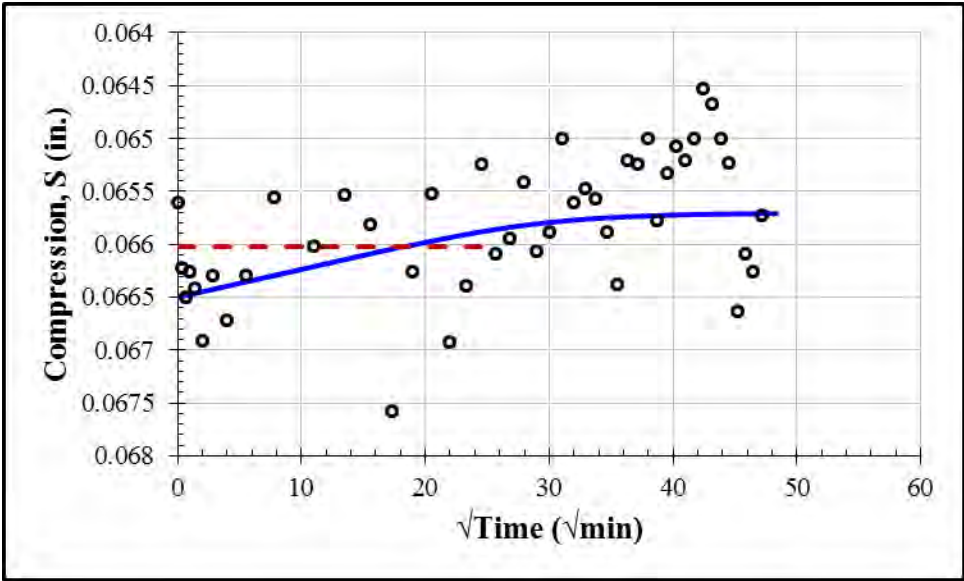
Second Unloading: 250 psf				
S_0 (in.)	S_{100} (in.)	c_v (in ² /min)	k (ft/day)	t_{50} (min)
0.0736	0.0638	0.00013	1.3×10^{-8}	172



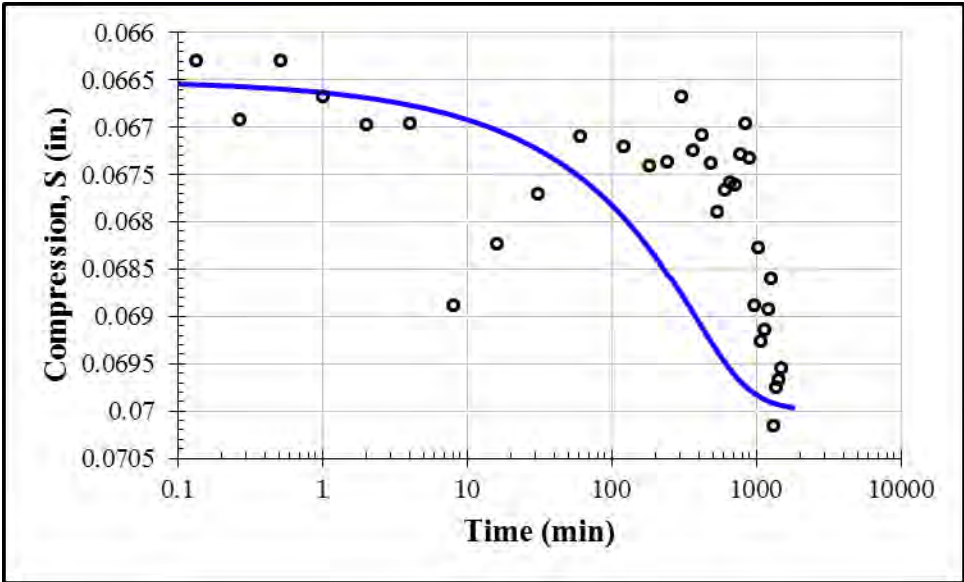
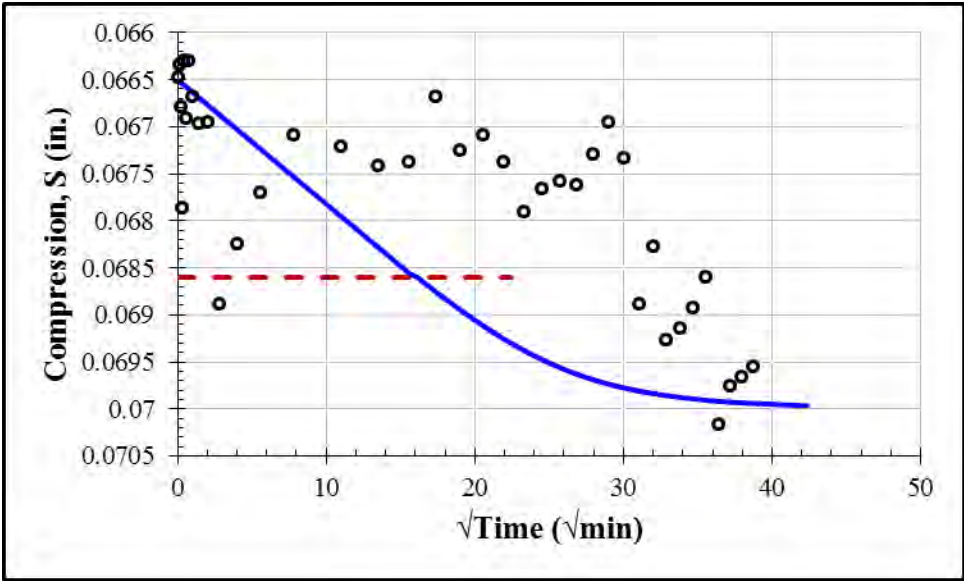
Third Loading: 500 psf				
S_0 (in.)	S_{100} (in.)	c_v (in ² /min)	k (ft/day)	t_{50} (min)
0.0637	0.0675	0.00008	9.5×10^{-9}	288



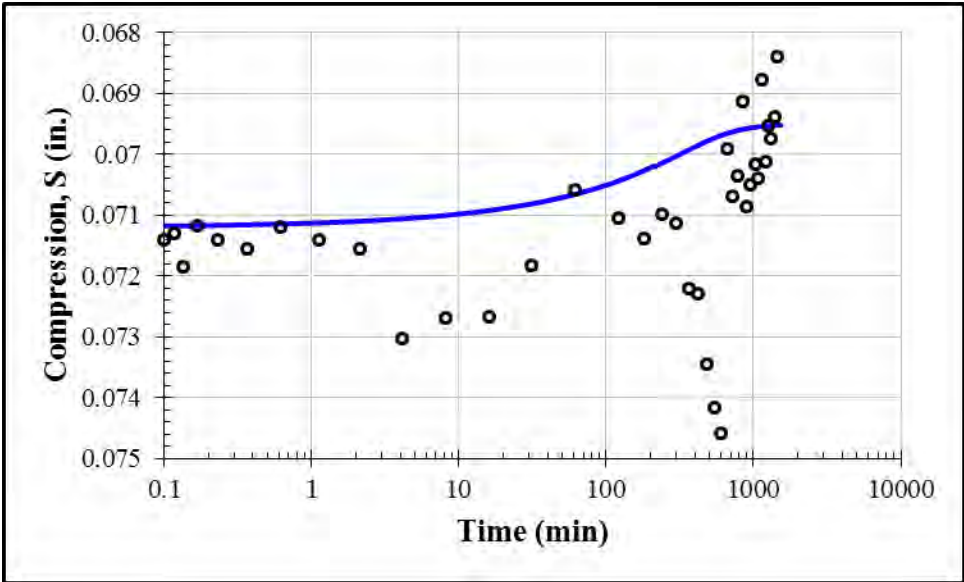
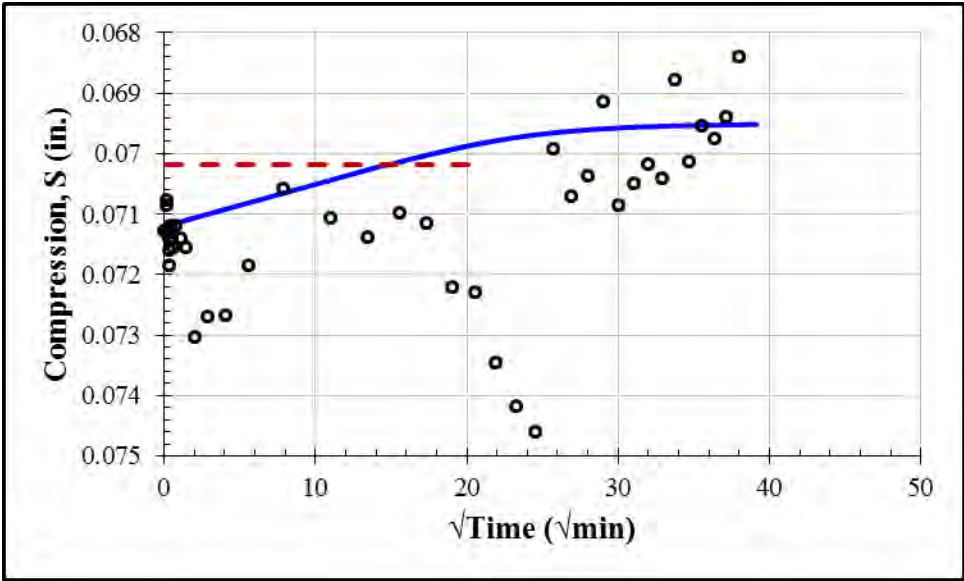
Third Loading: 1000 psf				
S_0 (in.)	S_{100} (in.)	c_v (in ² /min)	k (ft/day)	t_{50} (min)
0.0665	0.0657	0.0001	1.3×10^{-9}	229



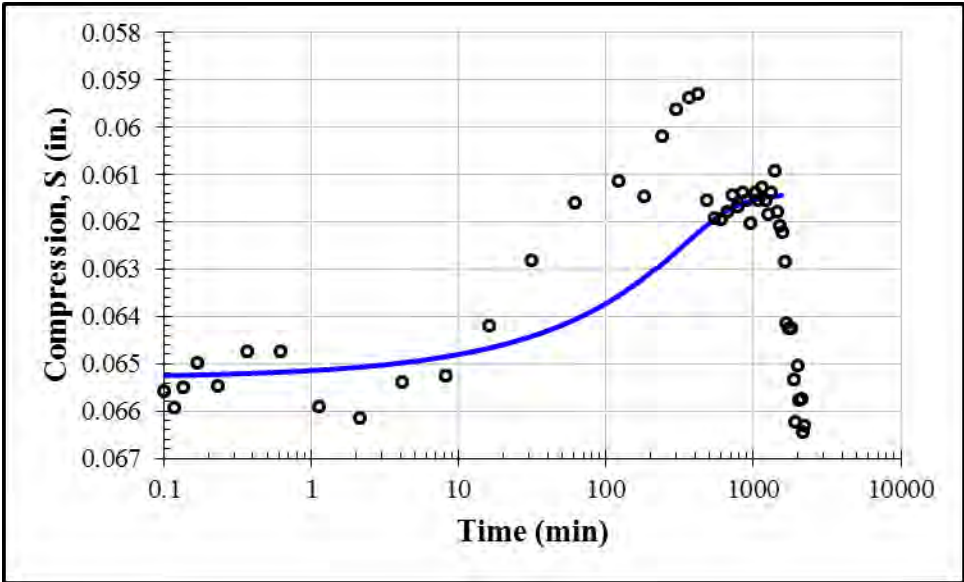
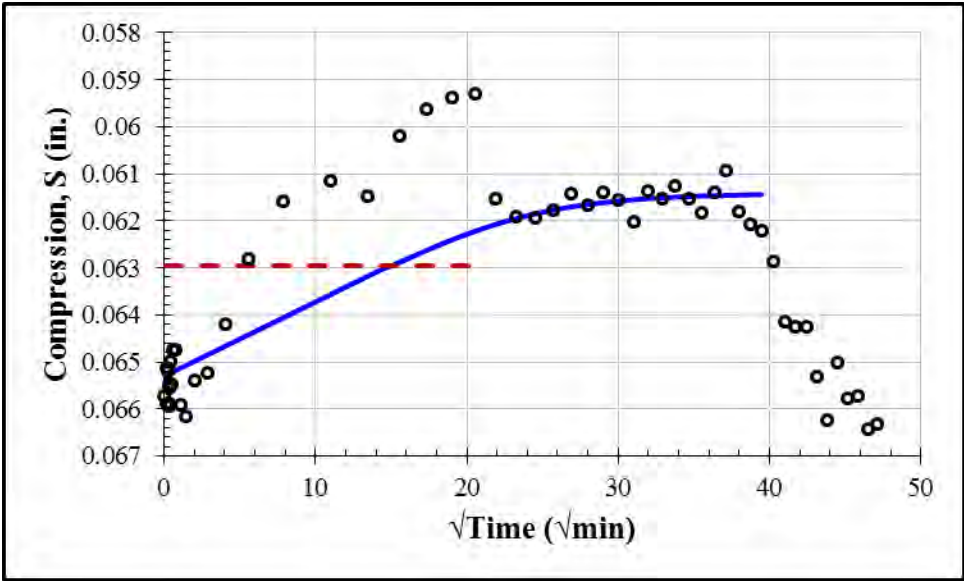
Third Loading: 2000 psf				
S_0 (in.)	S_{100} (in.)	c_v (in ² /min)	k (ft/day)	t_{50} (min)
0.0665	0.0700	0.00013	3.6×10^{-9}	176



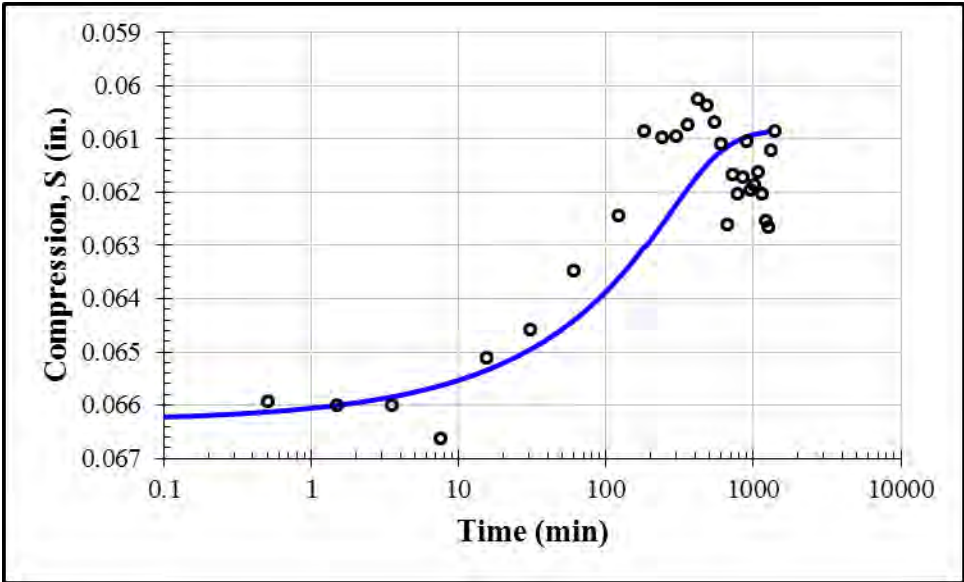
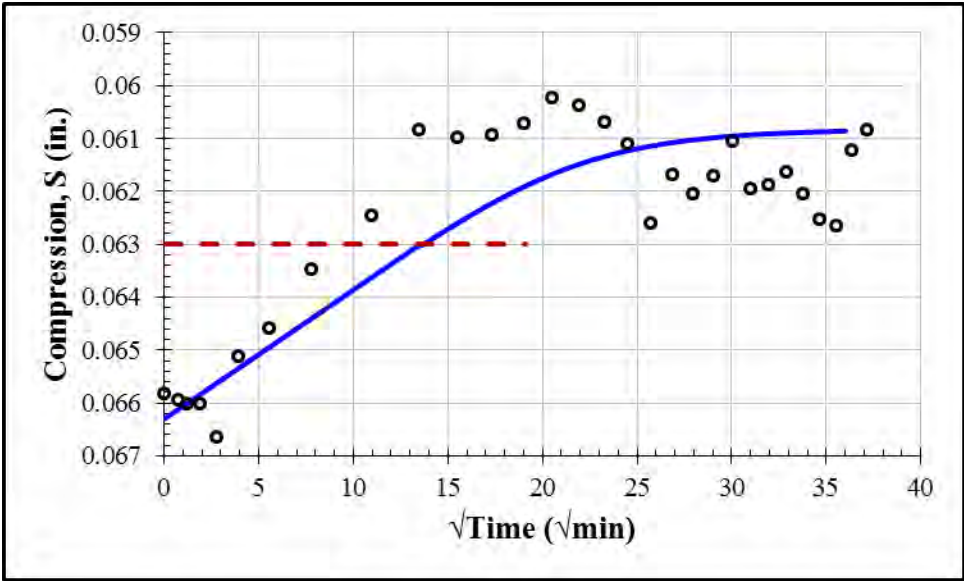
Third Loading: 4000 psf				
S_0 (in.)	S_{100} (in.)	c_v (in ² /min)	k (ft/day)	t_{50} (min)
0.0712	0.0695	0.00015	9.9×10^{-10}	150



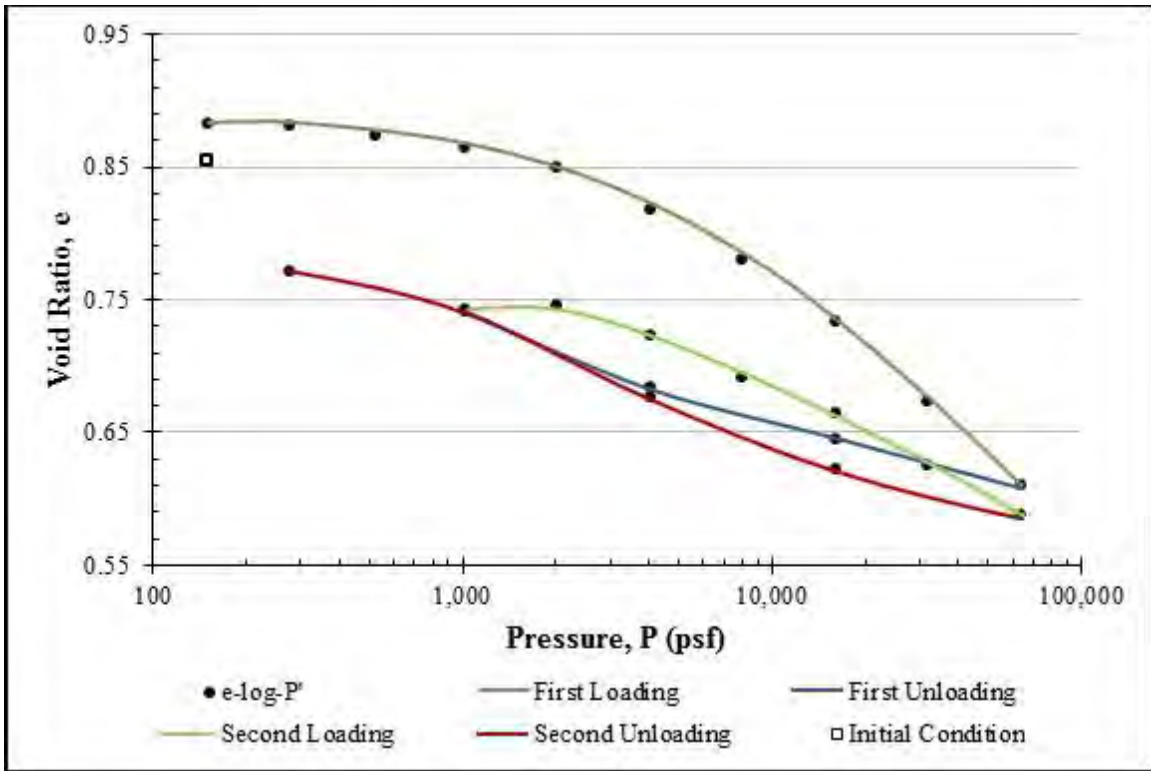
Third Unloading: 1000 psf				
S_0 (in.)	S_{100} (in.)	c_v (in ² /min)	k (ft/day)	t_{50} (min)
0.0653	0.0614	0.00015	1.5×10^{-9}	153



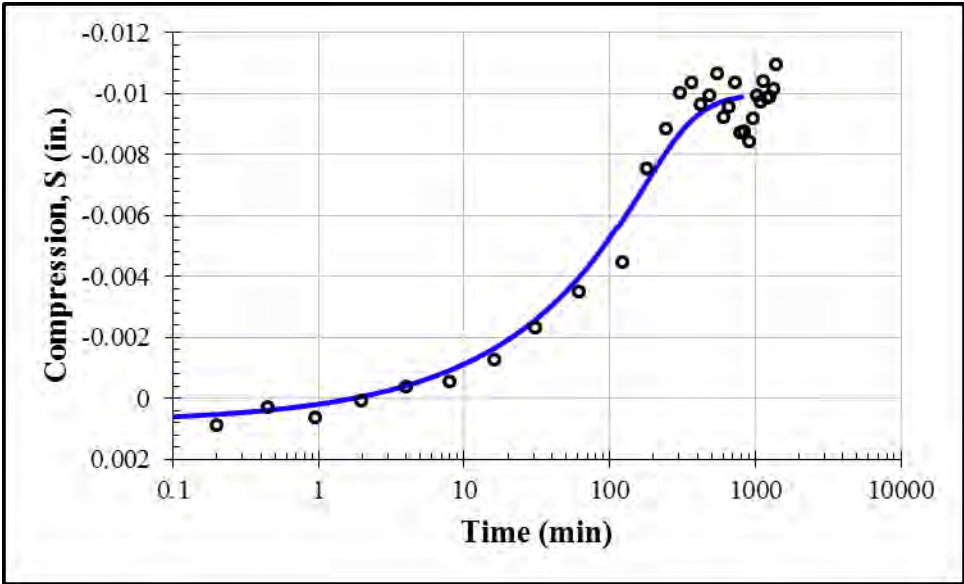
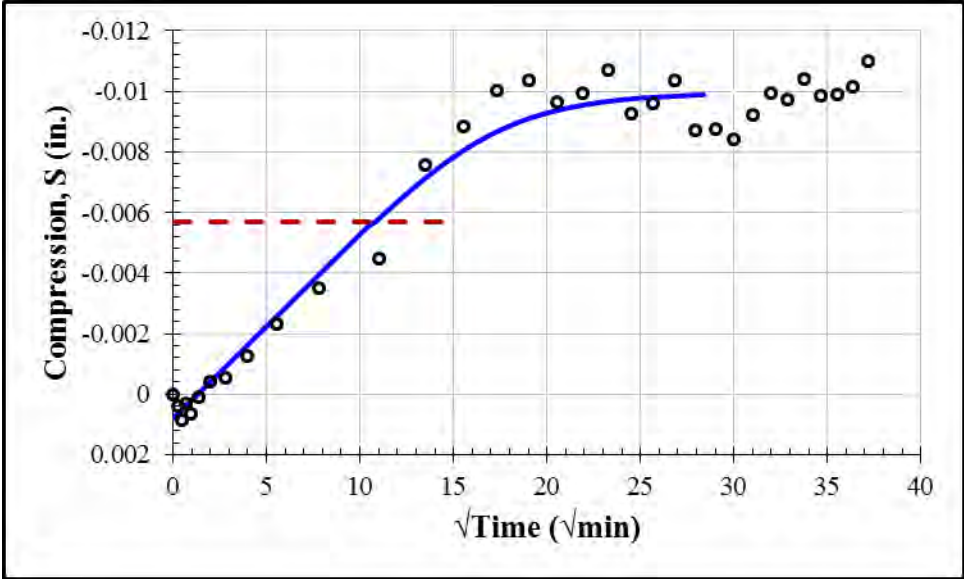
Third Unloading: 250 psf				
S_0 (in.)	S_{100} (in.)	c_v (in ² /min)	k (ft/day)	t_{50} (min)
0.0663	0.0608	0.00018	1.0×10^{-8}	127



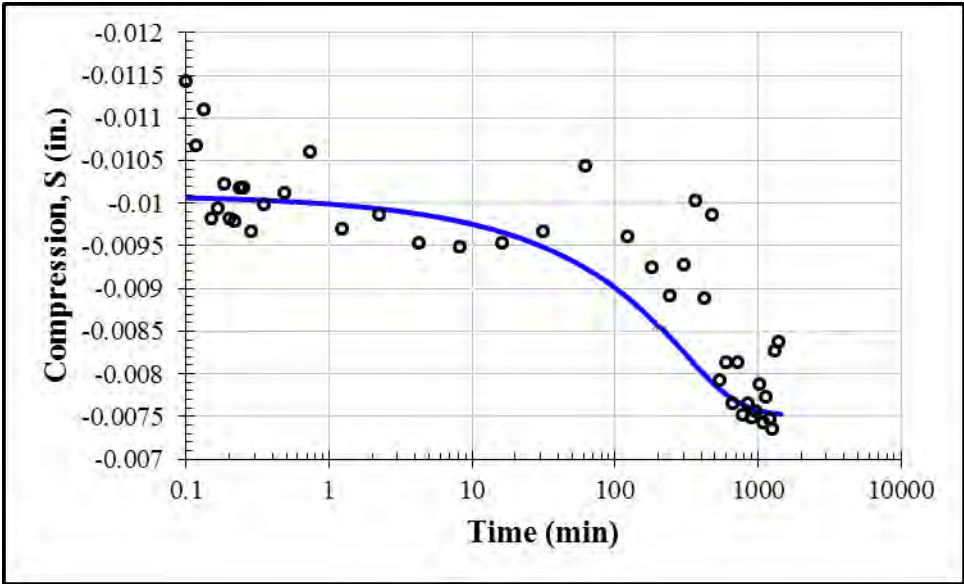
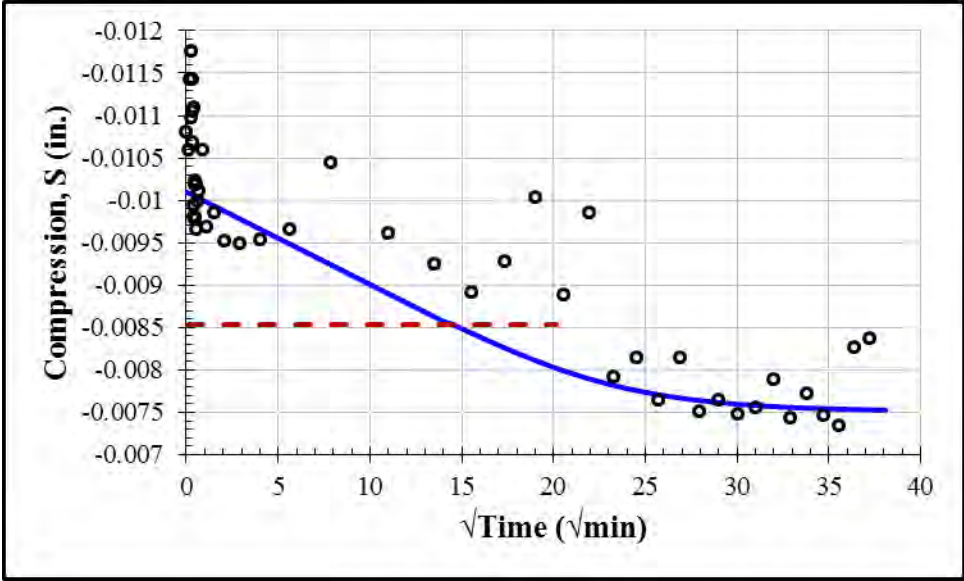
Appendix C: Consolidation Test 2



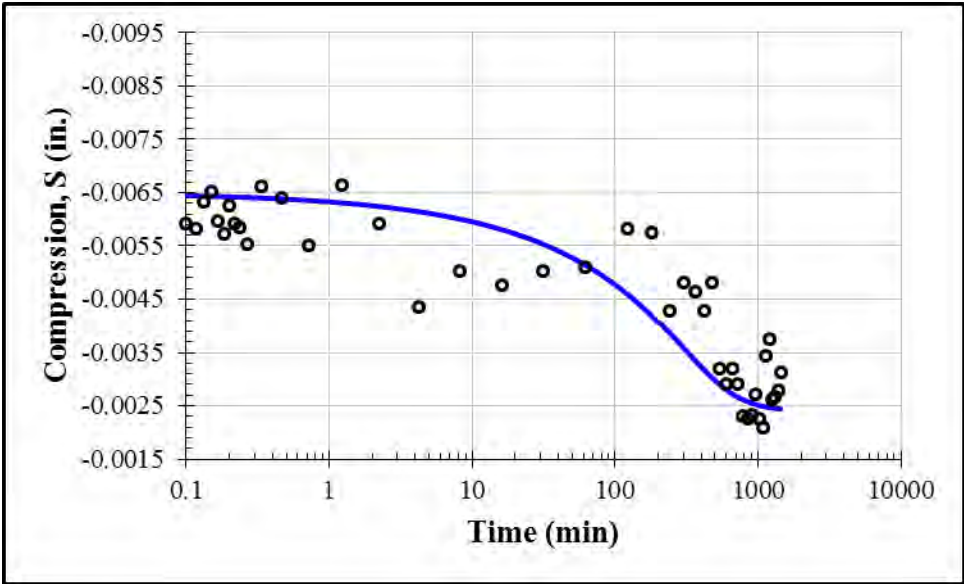
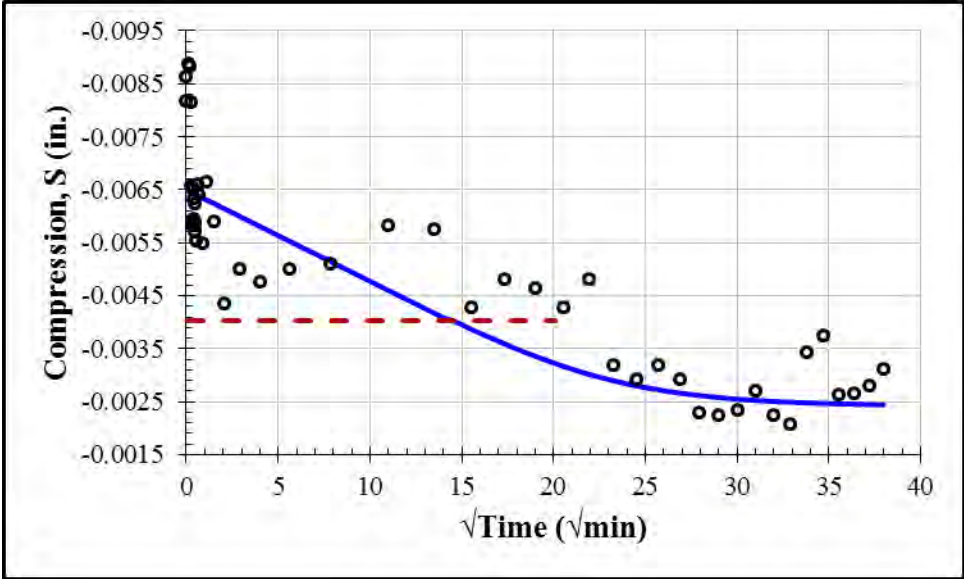
Inundation: 125 psf				
S_0 (in.)	S_{100} (in.)	c_v (in ² /min)	k (ft/day)	t_{50} (min)
0.0008	-0.0100	0.00035	2.5×10^{-7}	79



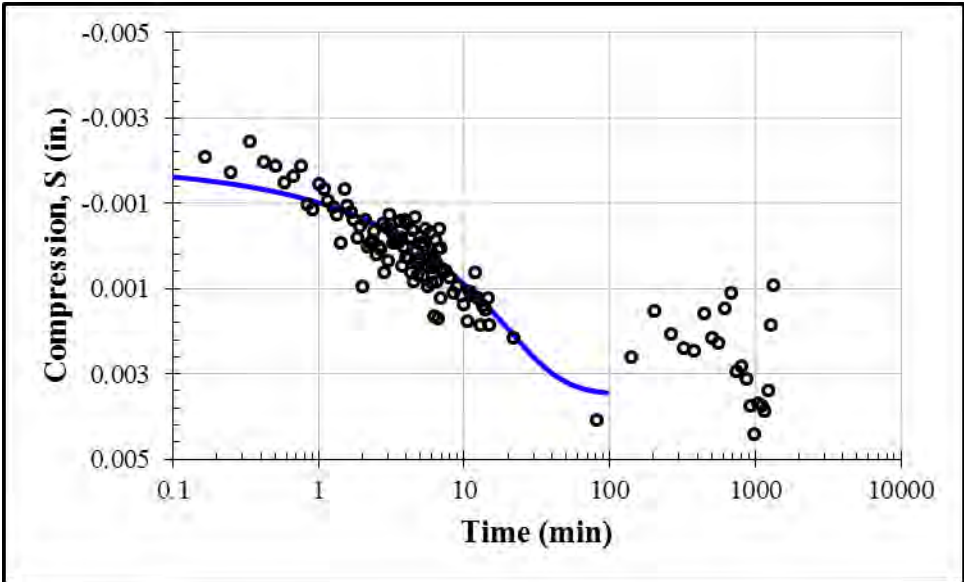
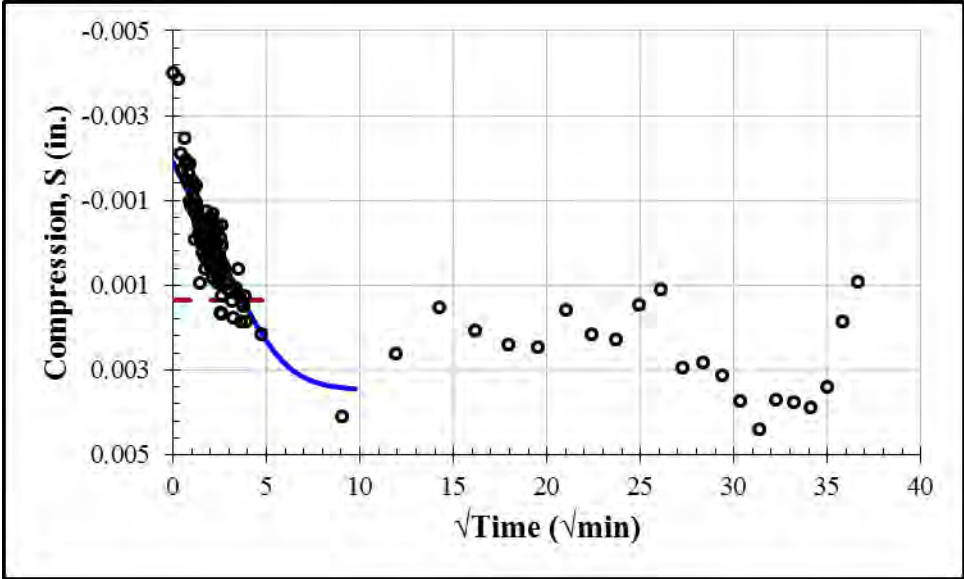
First Loading: 250 psf				
S_0 (in.)	S_{100} (in.)	c_v (in ² /min)	k (ft/day)	t_{50} (min)
-0.0101	-0.0075	0.0002	3.5×10^{-8}	142



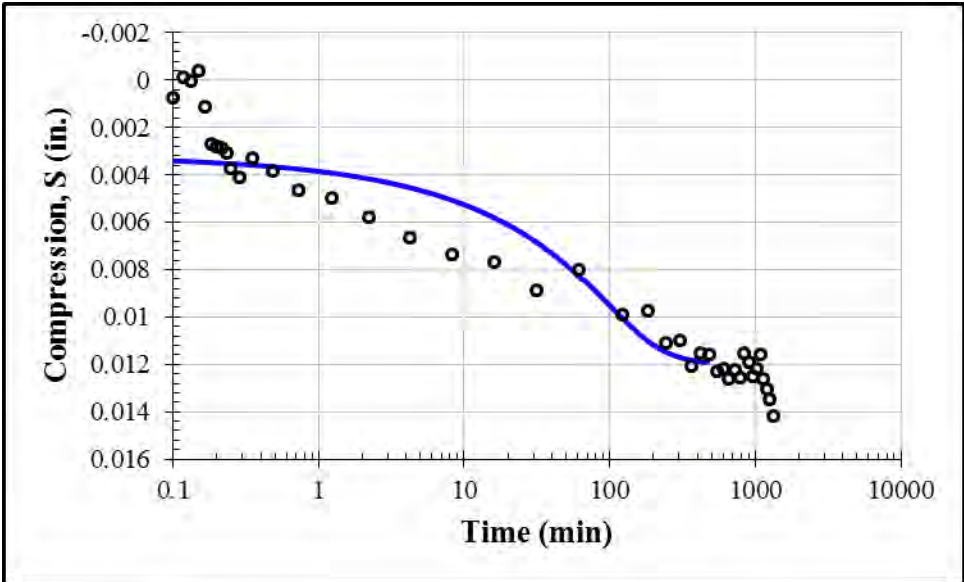
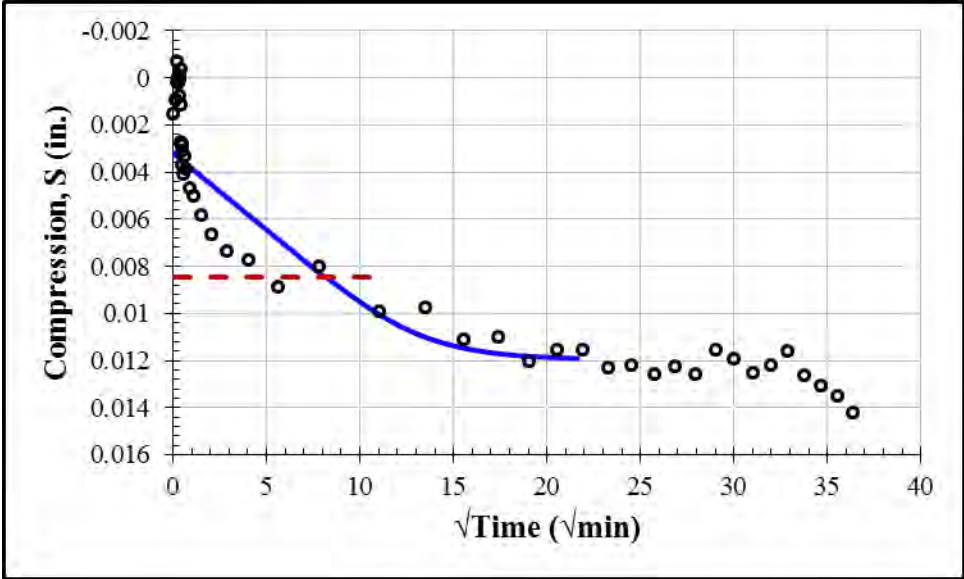
First Loading: 500 psf				
S_0 (in.)	S_{100} (in.)	c_v (in ² /min)	k (ft/day)	t_{50} (min)
-0.0065	-0.0024	0.0002	2.7×10^{-8}	141



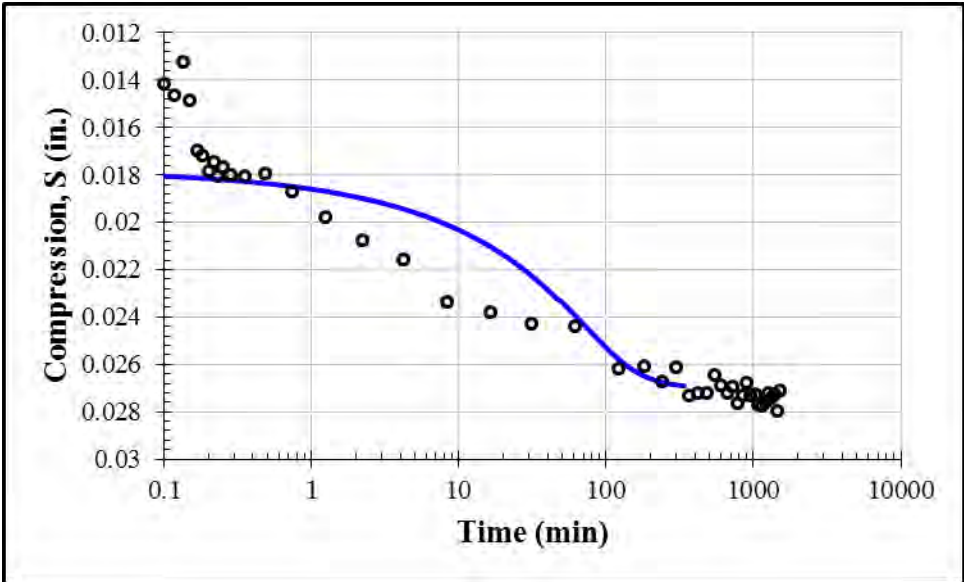
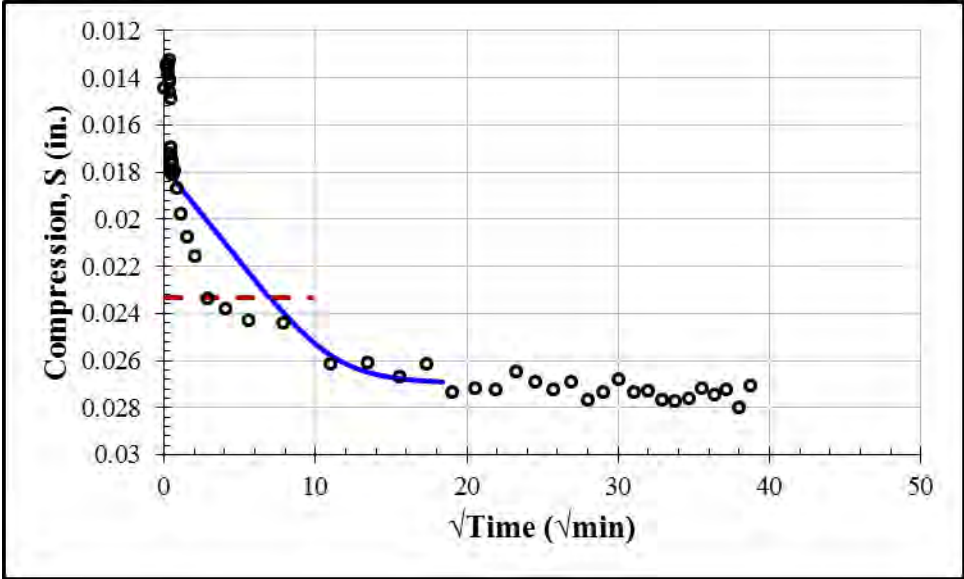
First Loading: 1000 psf				
S_0 (in.)	S_{100} (in.)	c_v (in ² /min)	k (ft/day)	t_{50} (min)
-0.0019	0.0035	0.003	2.7×10^{-7}	9.3



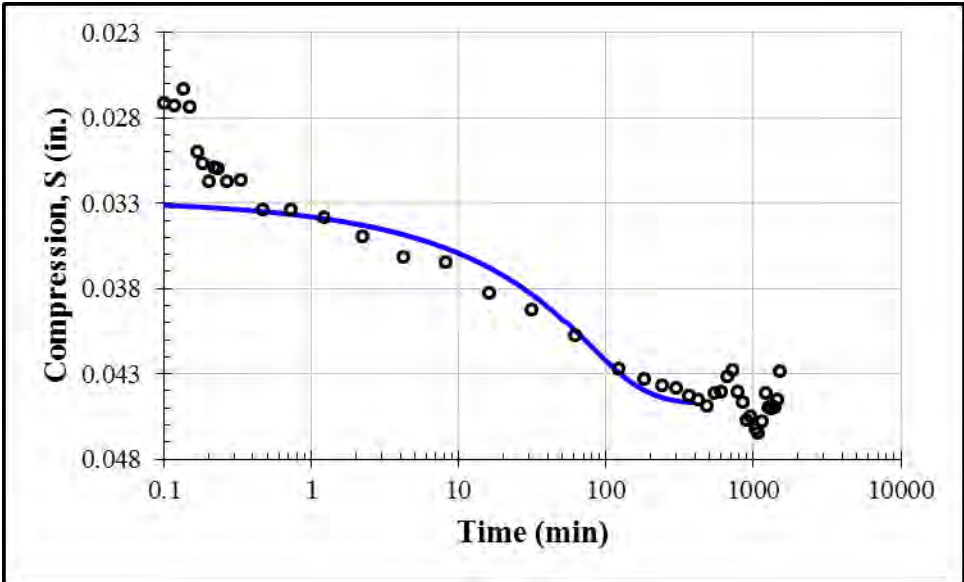
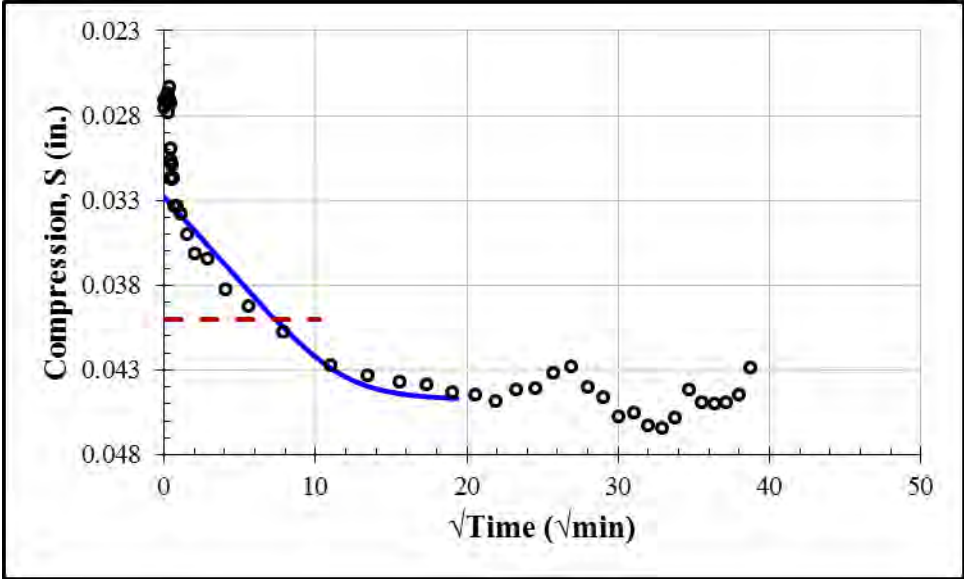
First Loading: 2000 psf				
S_0 (in.)	S_{100} (in.)	c_v (in ² /min)	k (ft/day)	t_{50} (min)
0.0032	0.0120	0.0006	4.4×10^{-8}	46



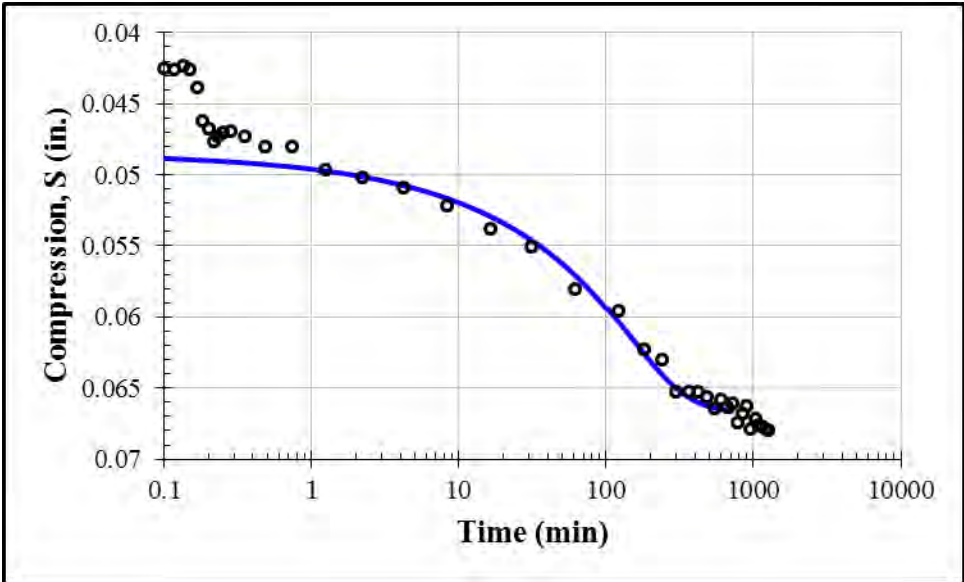
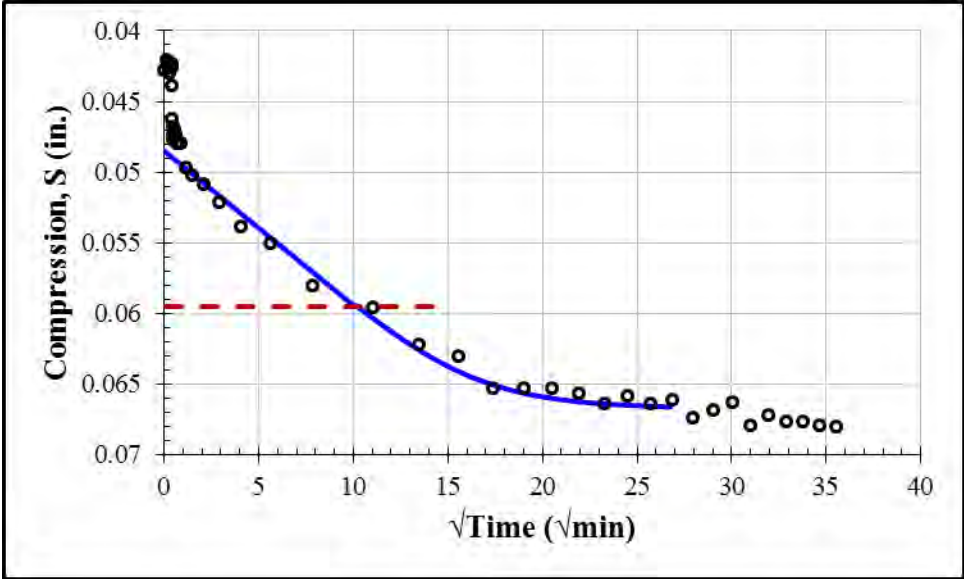
First Loading: 4000 psf				
S_0 (in.)	S_{100} (in.)	c_v (in ² /min)	k (ft/day)	t_{50} (min)
0.0178	0.0270	0.0008	3.0×10^{-8}	33



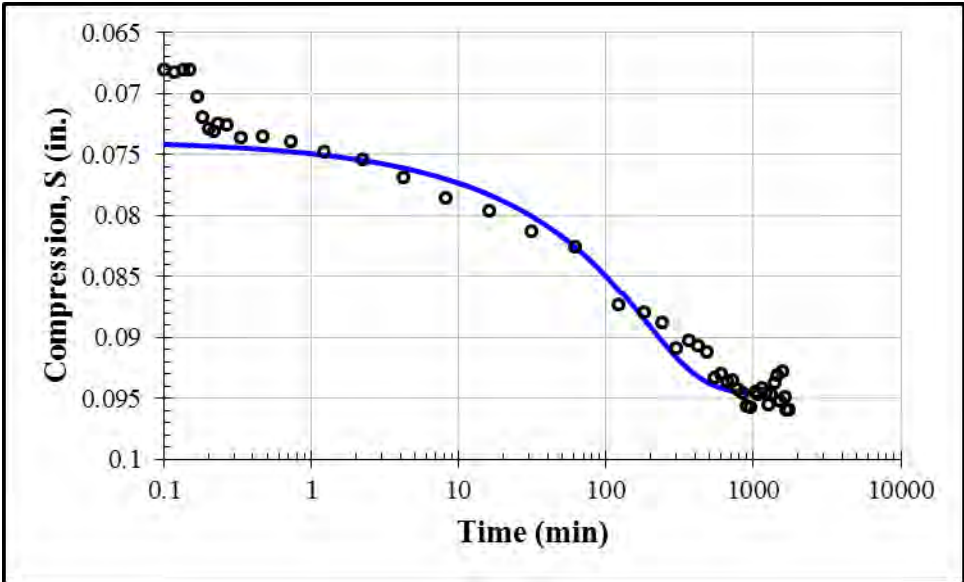
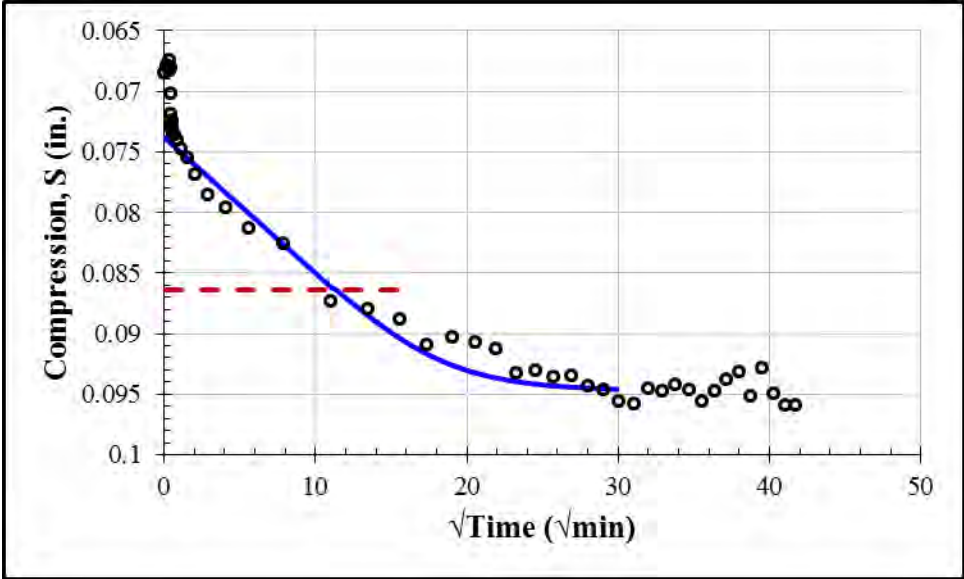
First Loading: 8000 psf				
S_0 (in.)	S_{100} (in.)	c_v (in ² /min)	k (ft/day)	t_{50} (min)
0.0328	0.0448	0.0007	1.7×10^{-8}	37



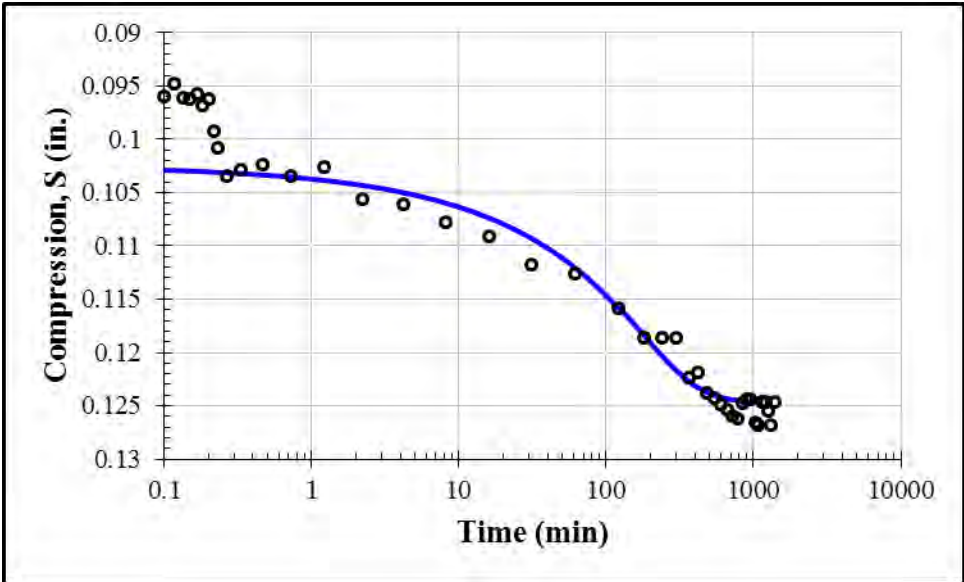
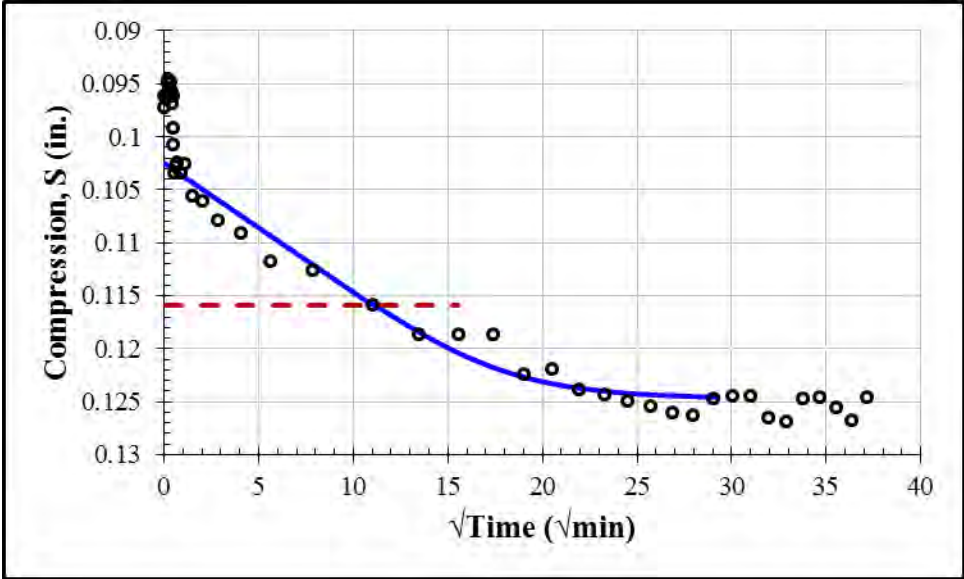
First Loading: 16000 psf				
S_0 (in.)	S_{100} (in.)	c_v (in ² /min)	k (ft/day)	t_{50} (min)
0.0485	0.0668	0.00035	6.3×10^{-9}	70



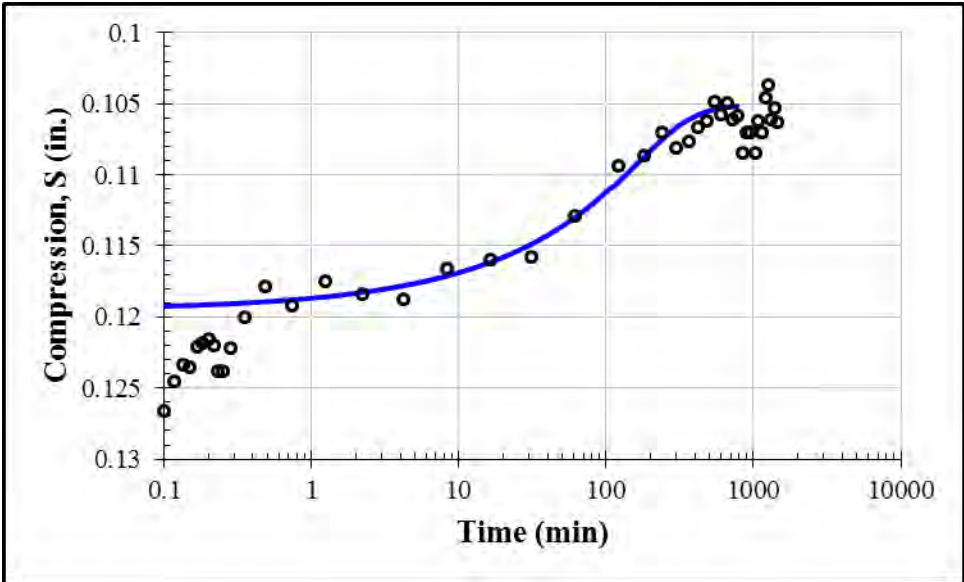
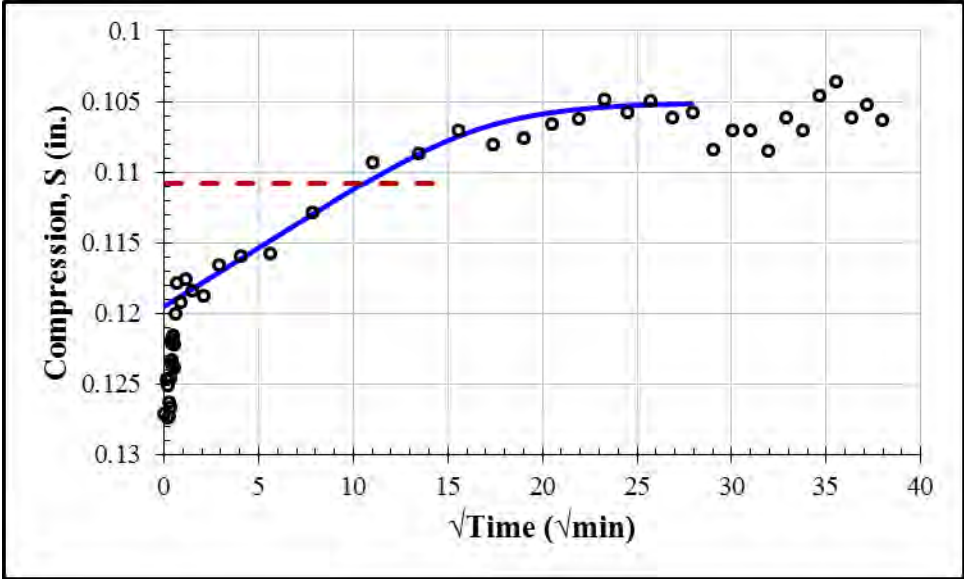
First Loading: 32000 psf				
S_0 (in.)	S_{100} (in.)	c_v (in ² /min)	k (ft/day)	t_{50} (min)
0.0738	0.0948	0.00026	2.6×10^{-9}	88



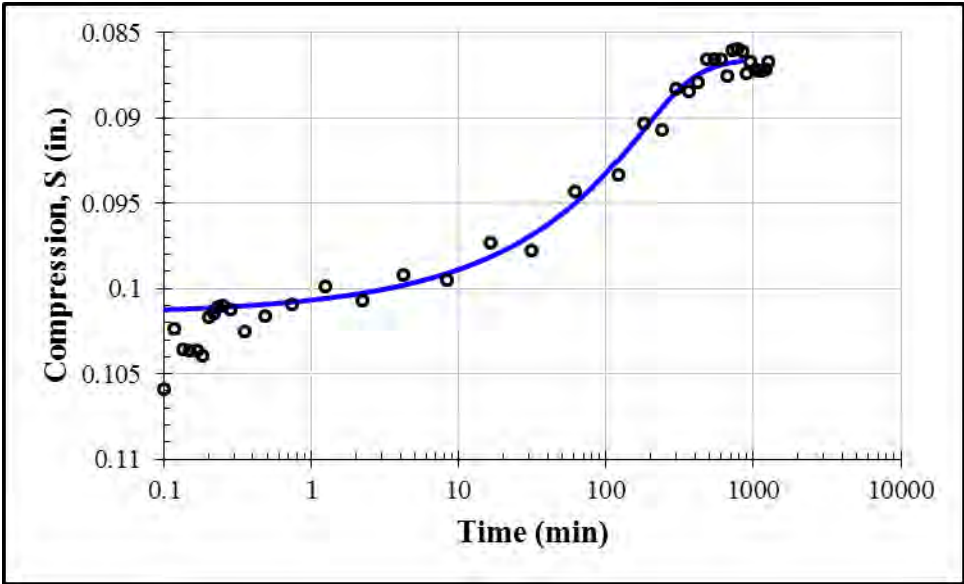
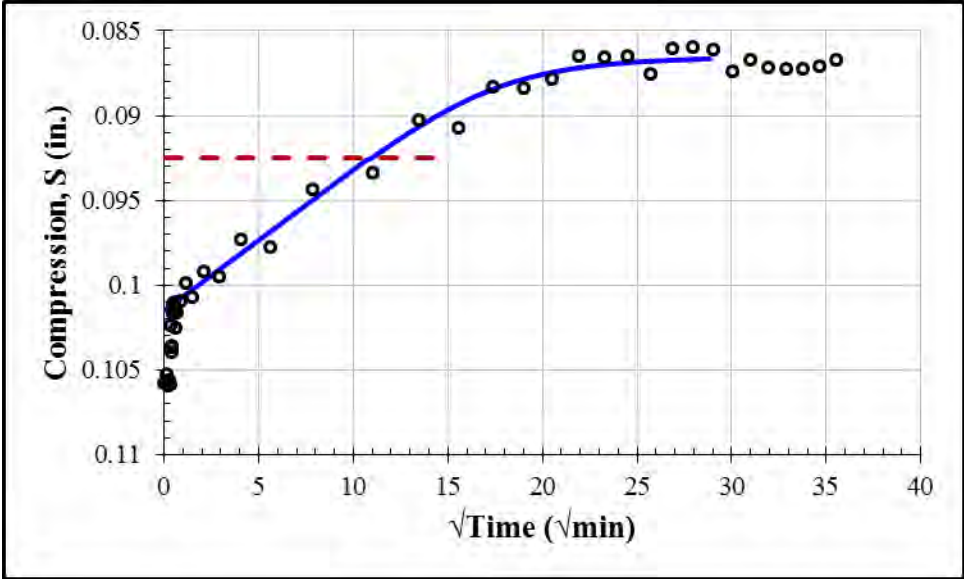
First Loading: 64000 psf				
S_0 (in.)	S_{100} (in.)	c_v (in ² /min)	k (ft/day)	t_{50} (min)
0.1025	0.1248	0.00025	1.3×10^{-9}	84



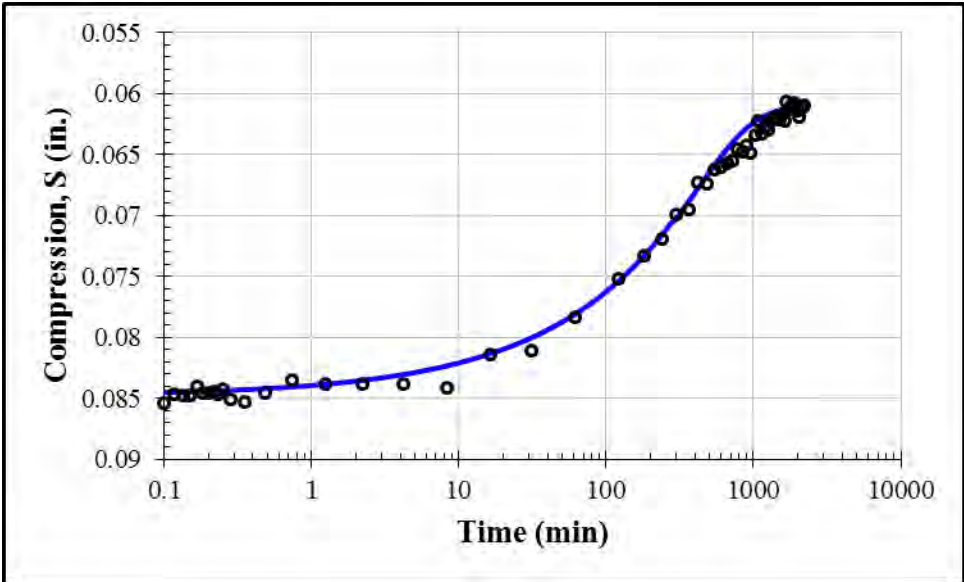
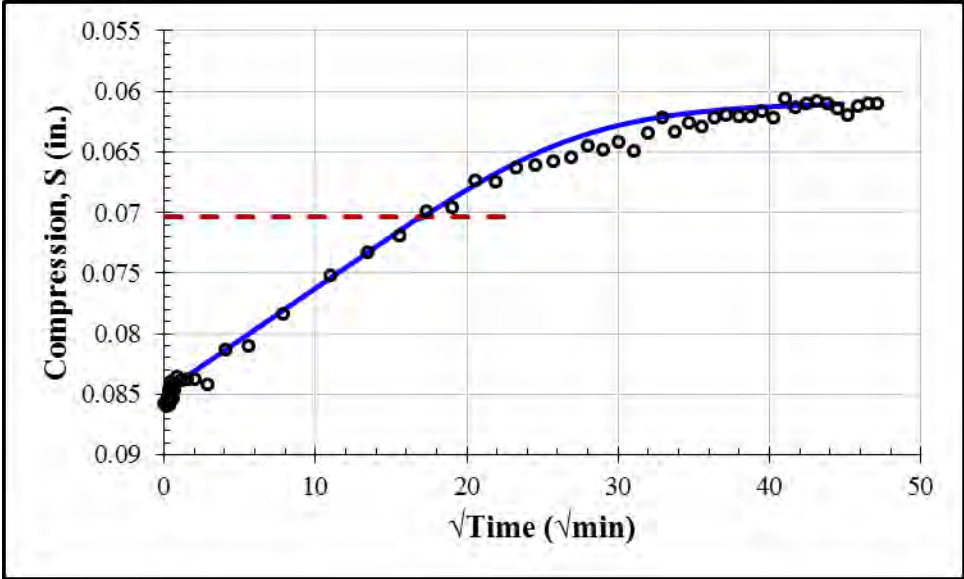
First Unloading: 16000 psf				
S_0 (in.)	S_{100} (in.)	c_v (in ² /min)	k (ft/day)	t_{50} (min)
0.1195	0.1050	0.00025	5.6×10^{-10}	76



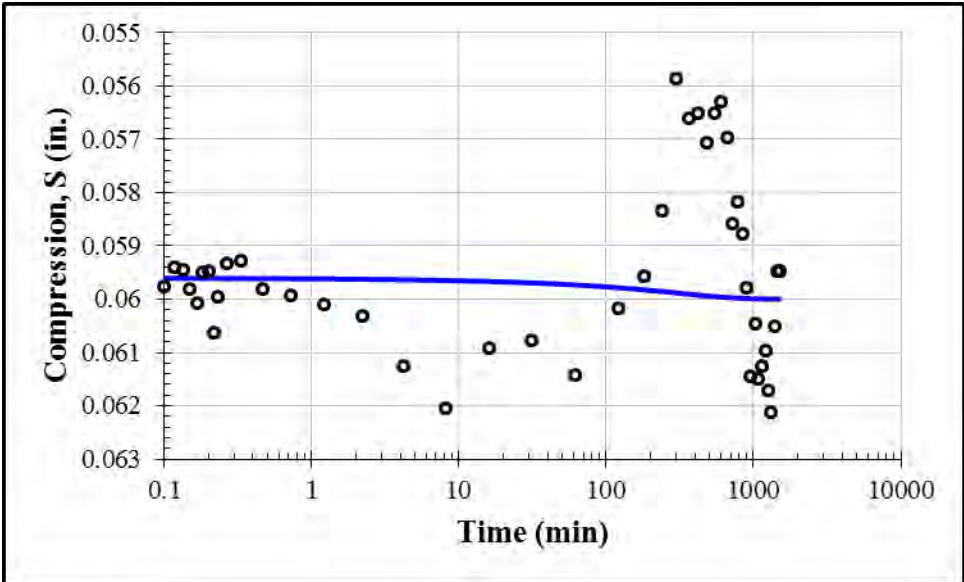
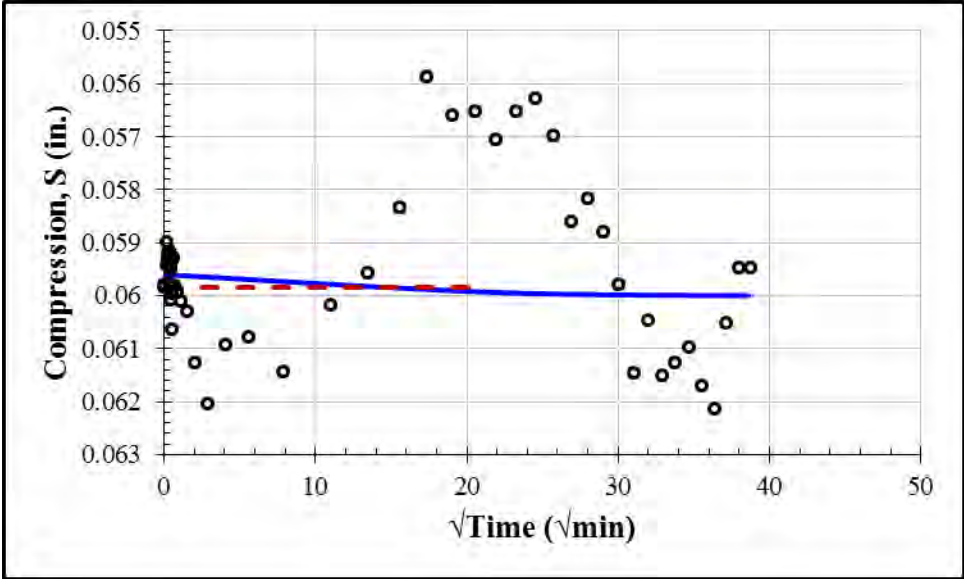
First Unloading: 4000 psf				
S_0 (in.)	S_{100} (in.)	c_v (in ² /min)	k (ft/day)	t_{50} (min)
0.1015	0.0865	0.00025	2.4×10^{-9}	81



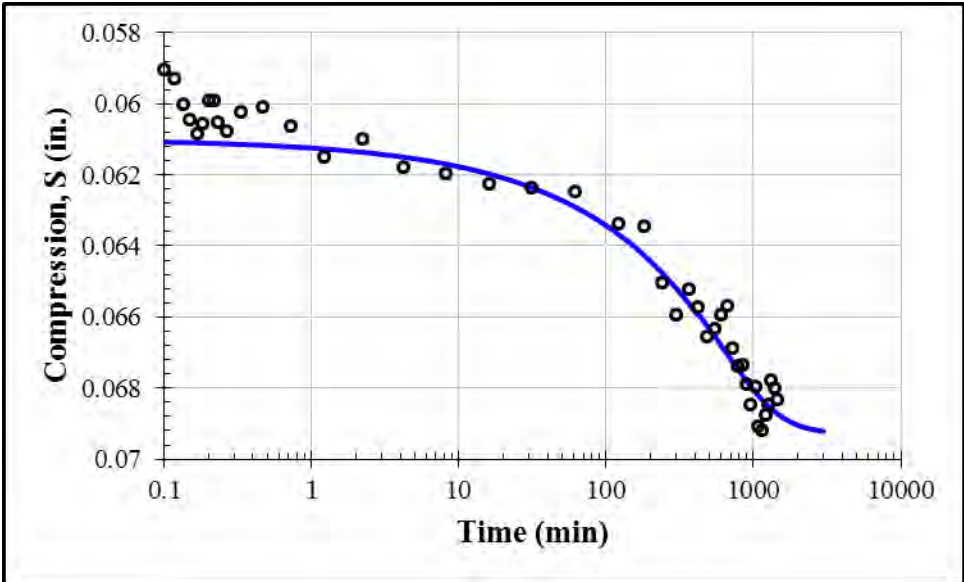
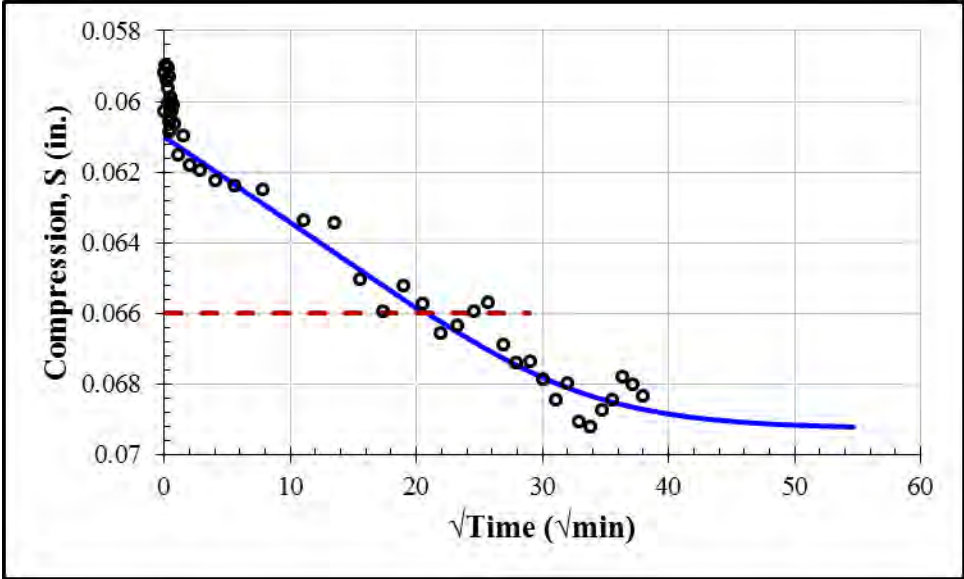
First Unloading: 1000 psf				
S_0 (in.)	S_{100} (in.)	c_v (in ² /min)	k (ft/day)	t_{50} (min)
0.0848	0.0608	0.00011	6.8×10^{-9}	197



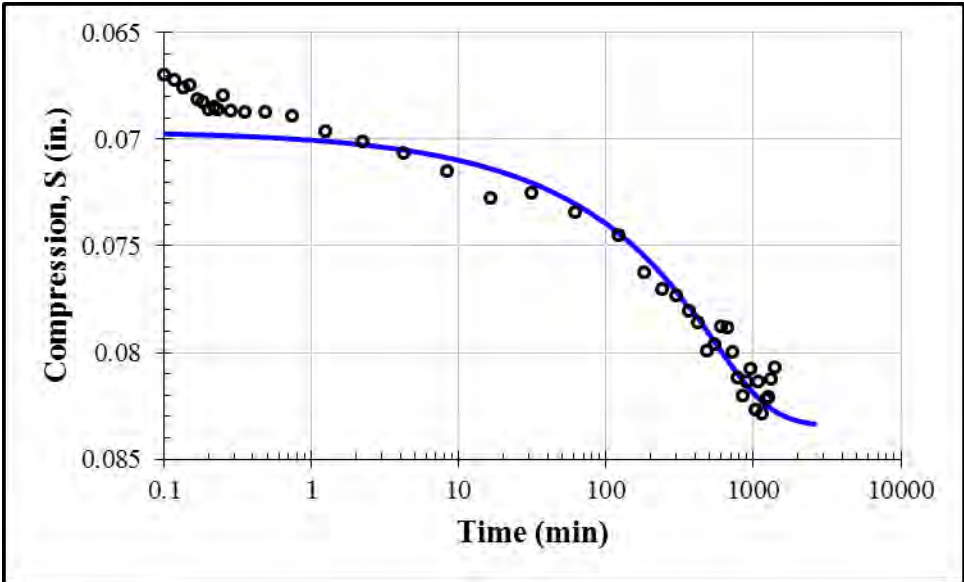
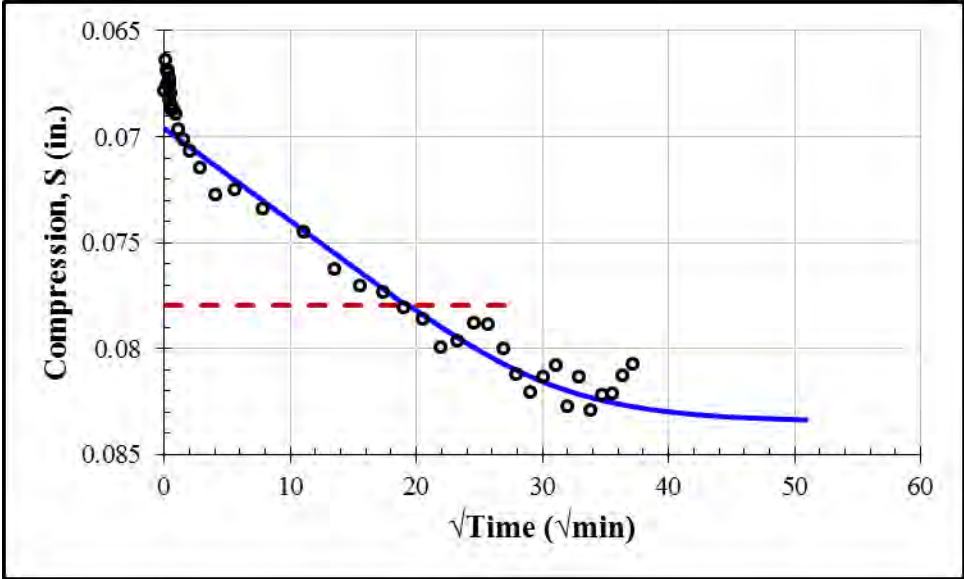
Second Loading: 2000 psf				
S_0 (in.)	S_{100} (in.)	c_v (in ² /min)	k (ft/day)	t_{50} (min)
0.0596	0.0600	0.00016	5.0×10^{-10}	146



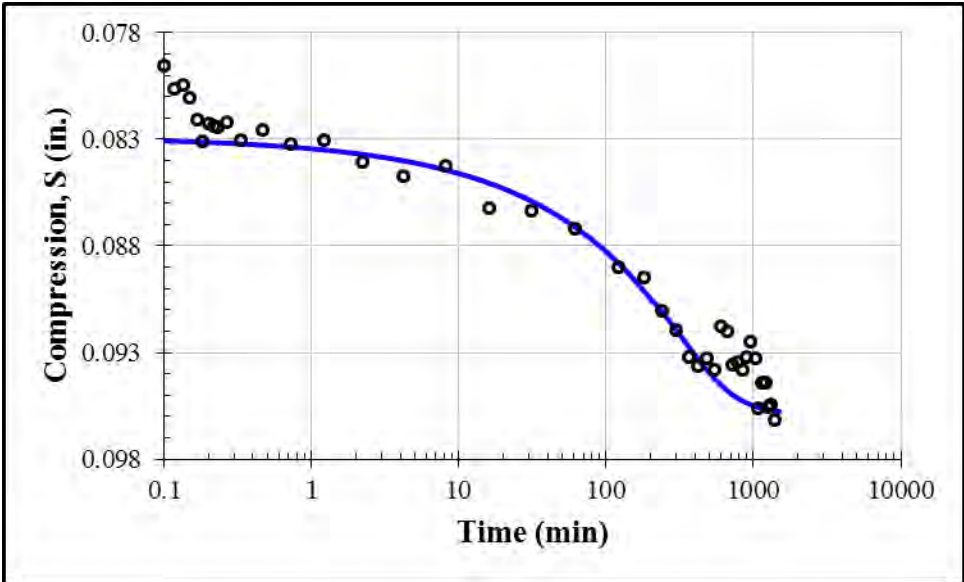
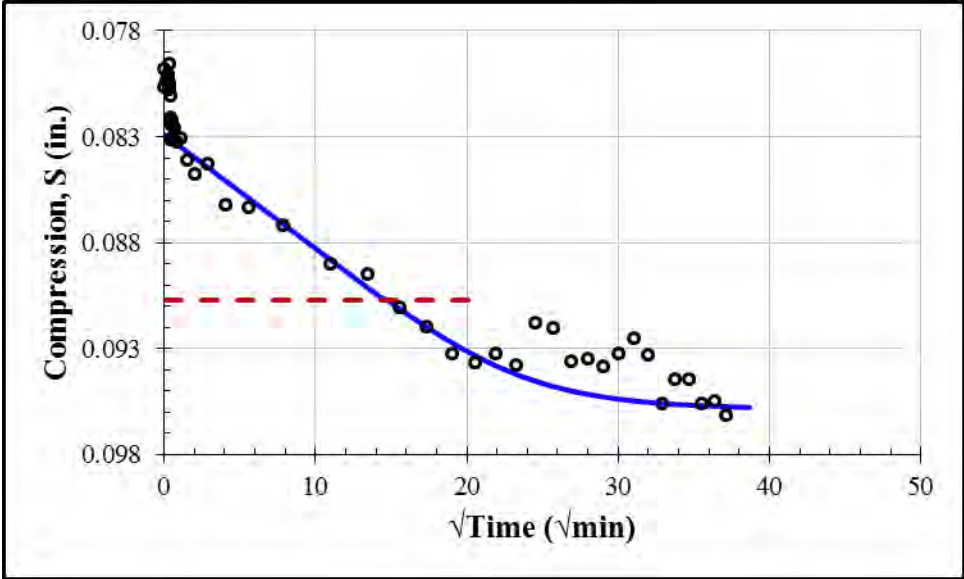
Second Loading: 4000 psf				
S_0 (in.)	S_{100} (in.)	c_v (in ² /min)	k (ft/day)	t_{50} (min)
0.0610	0.0693	0.00008	2.6×10^{-9}	293



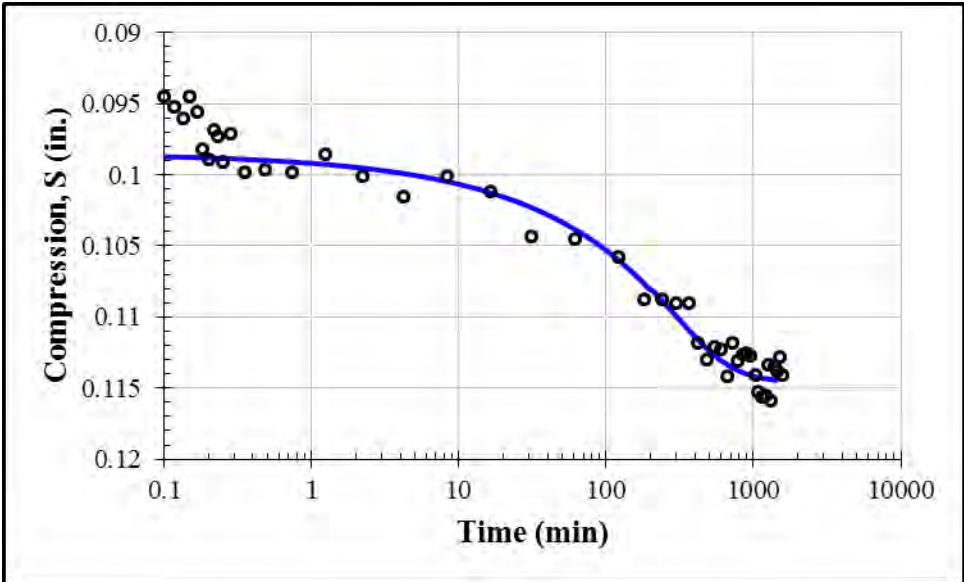
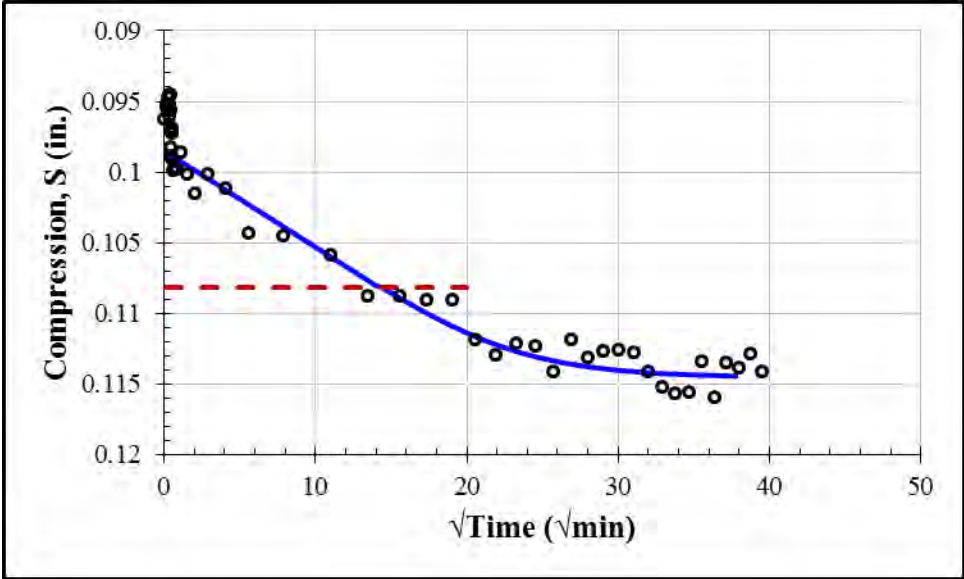
Second Loading: 8000 psf				
S_0 (in.)	S_{100} (in.)	c_v (in ² /min)	k (ft/day)	t_{50} (min)
0.0696	0.0835	0.00009	2.4×10^{-9}	254



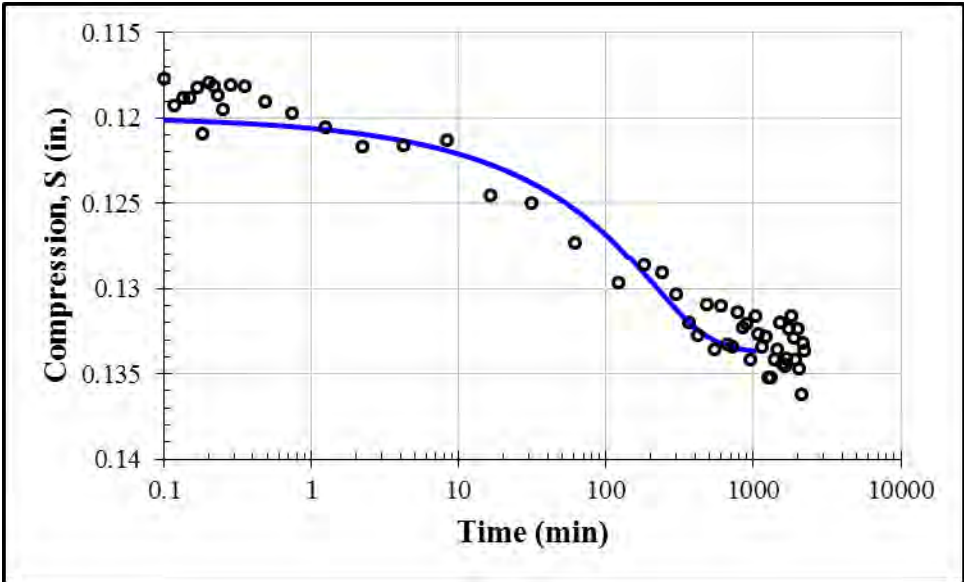
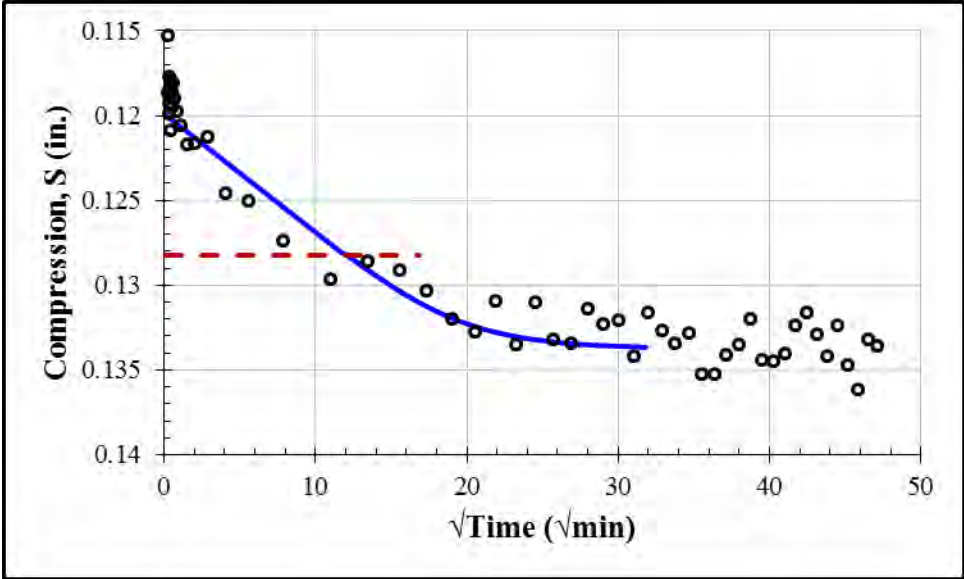
Second Loading: 16000 psf				
S_0 (in.)	S_{100} (in.)	c_v (in ² /min)	k (ft/day)	t_{50} (min)
0.0829	0.0959	0.00015	1.9×10^{-9}	147



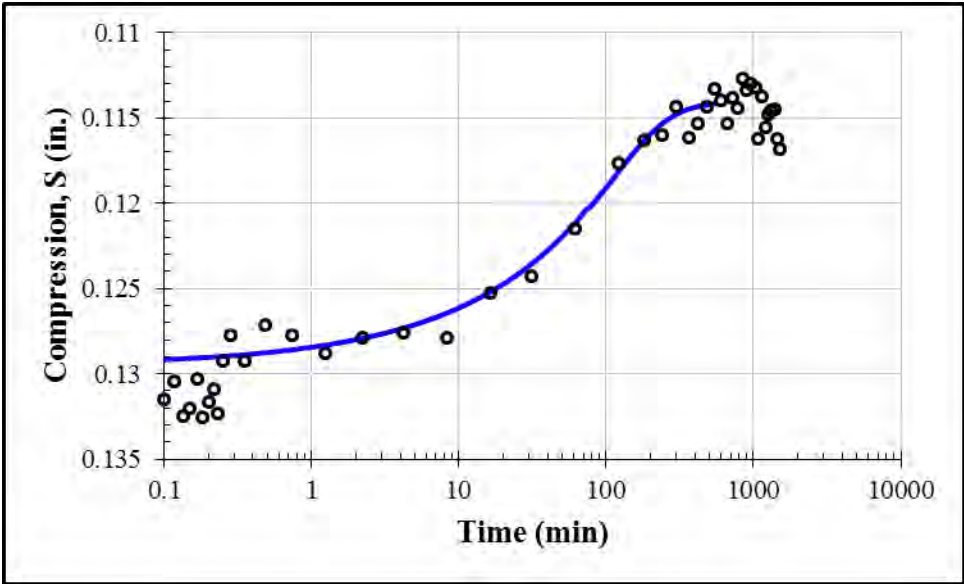
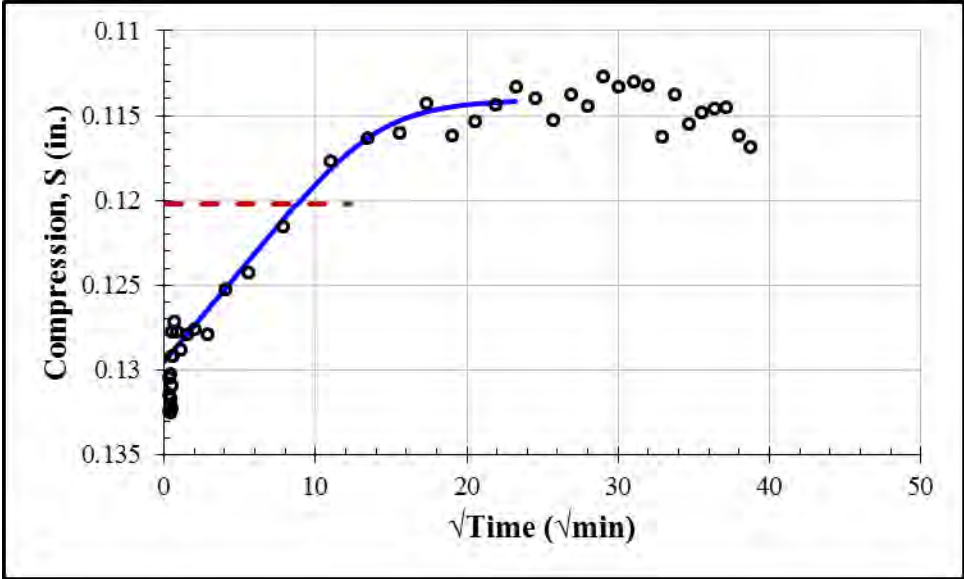
Second Loading: 32000 psf				
S_0 (in.)	S_{100} (in.)	c_v (in ² /min)	k (ft/day)	t_{50} (min)
0.0985	0.1146	0.00015	1.1×10^{-9}	140



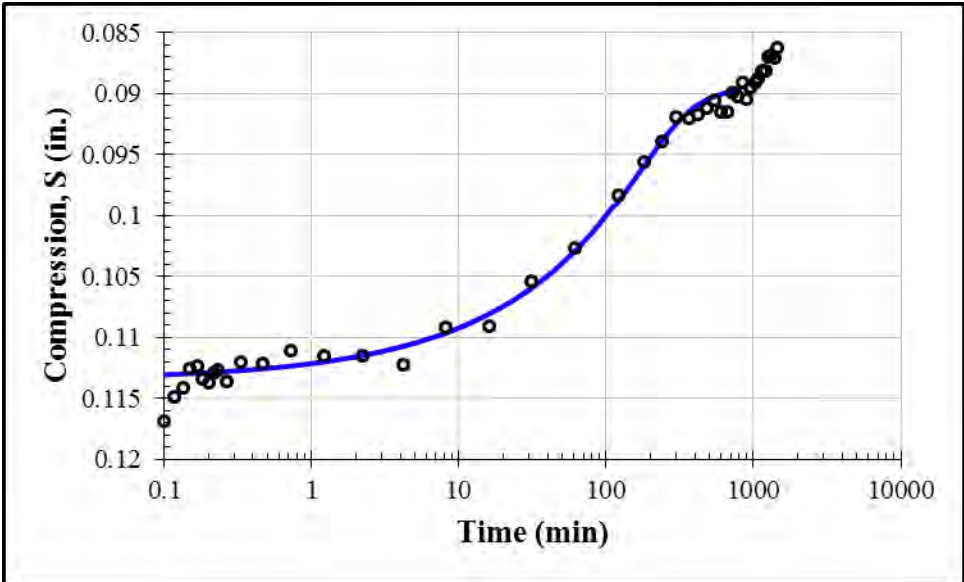
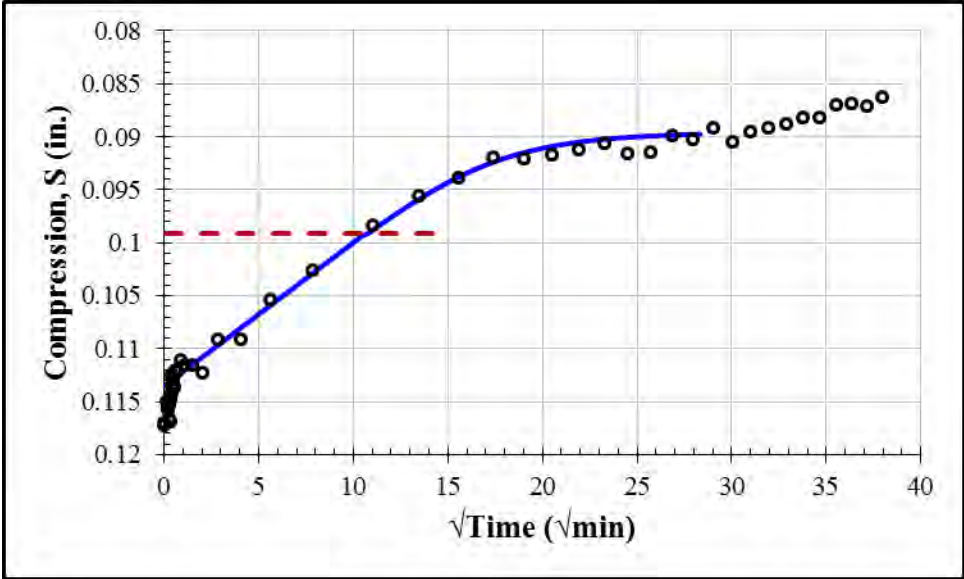
Second Loading: 64000 psf				
S_0 (in.)	S_{100} (in.)	c_v (in ² /min)	k (ft/day)	t_{50} (min)
0.1199	0.1338	0.0002	6.4×10^{-10}	99



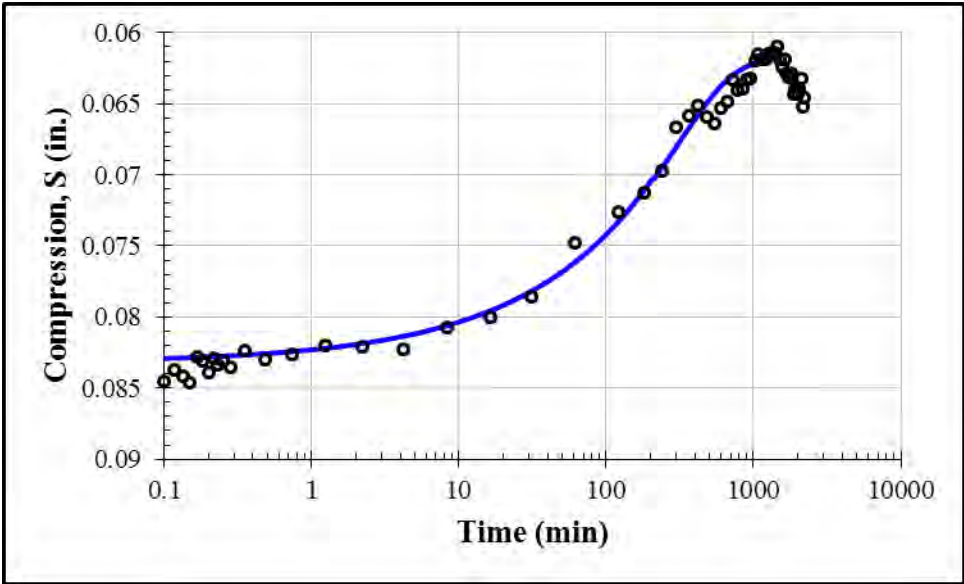
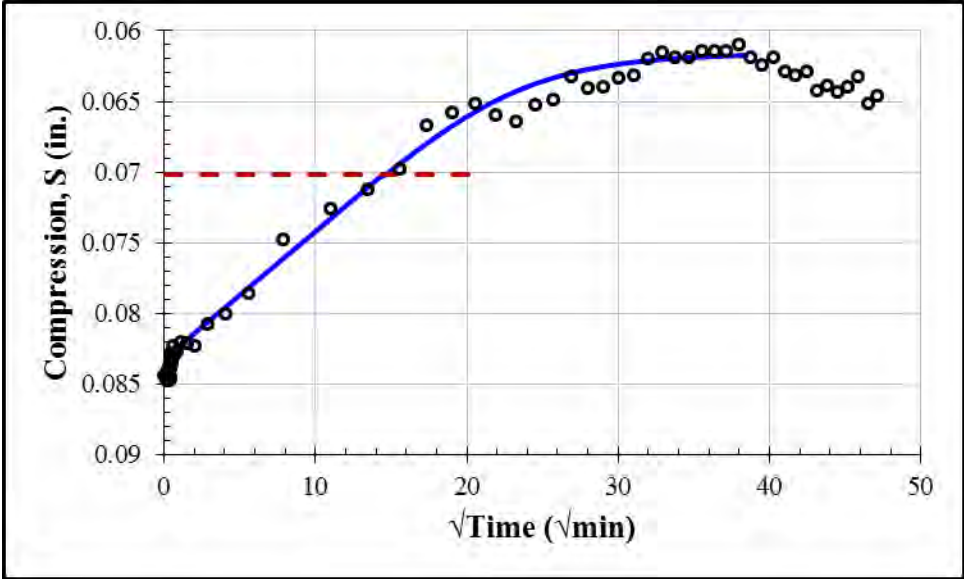
Second Unloading: 16000 psf				
S_0 (in.)	S_{100} (in.)	c_v (in ² /min)	k (ft/day)	t_{50} (min)
0.1295	0.1140	0.00035	8.4×10^{-10}	53



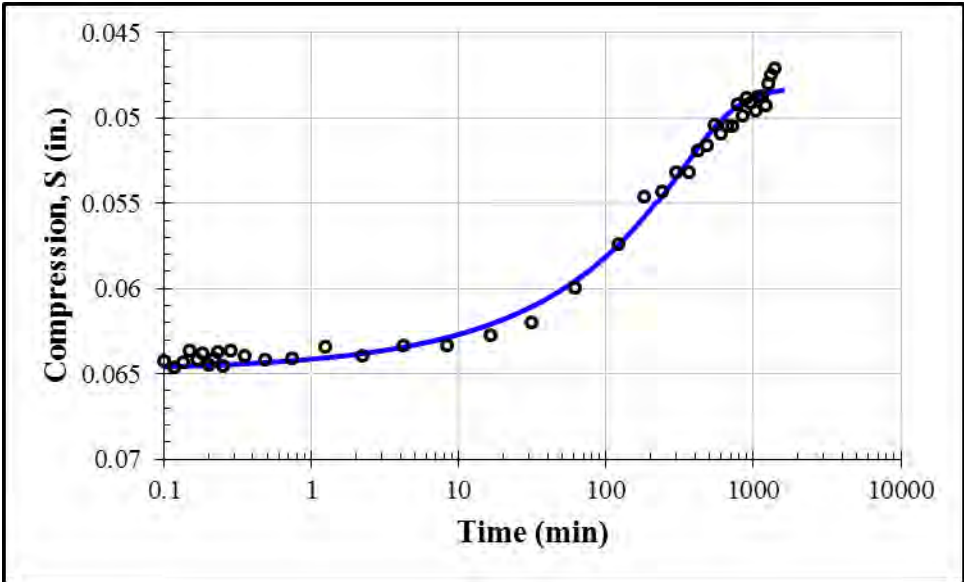
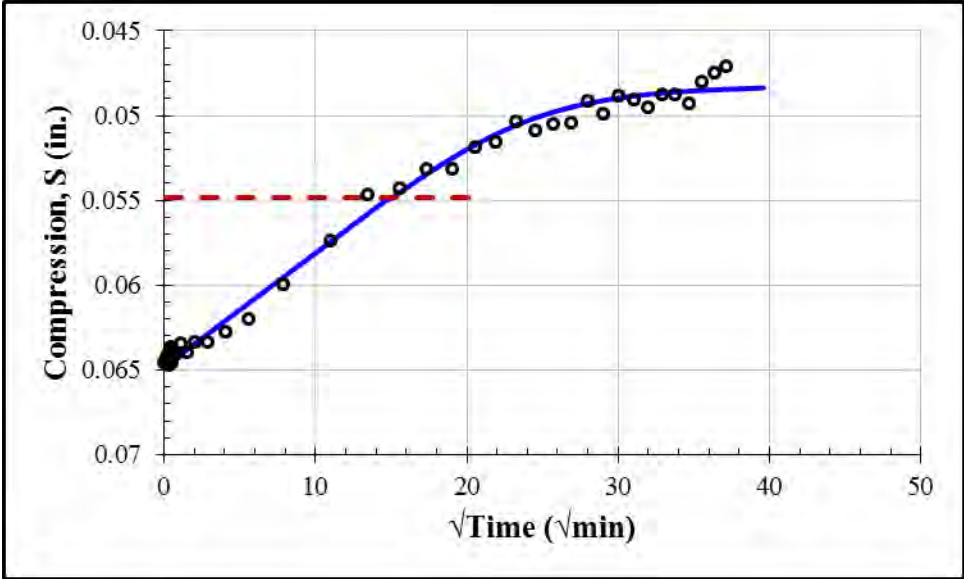
Second Unloading: 4000 psf				
S_0 (in.)	S_{100} (in.)	c_v (in ² /min)	k (ft/day)	t_{50} (min)
0.1135	0.0895	0.00025	3.8×10^{-9}	79



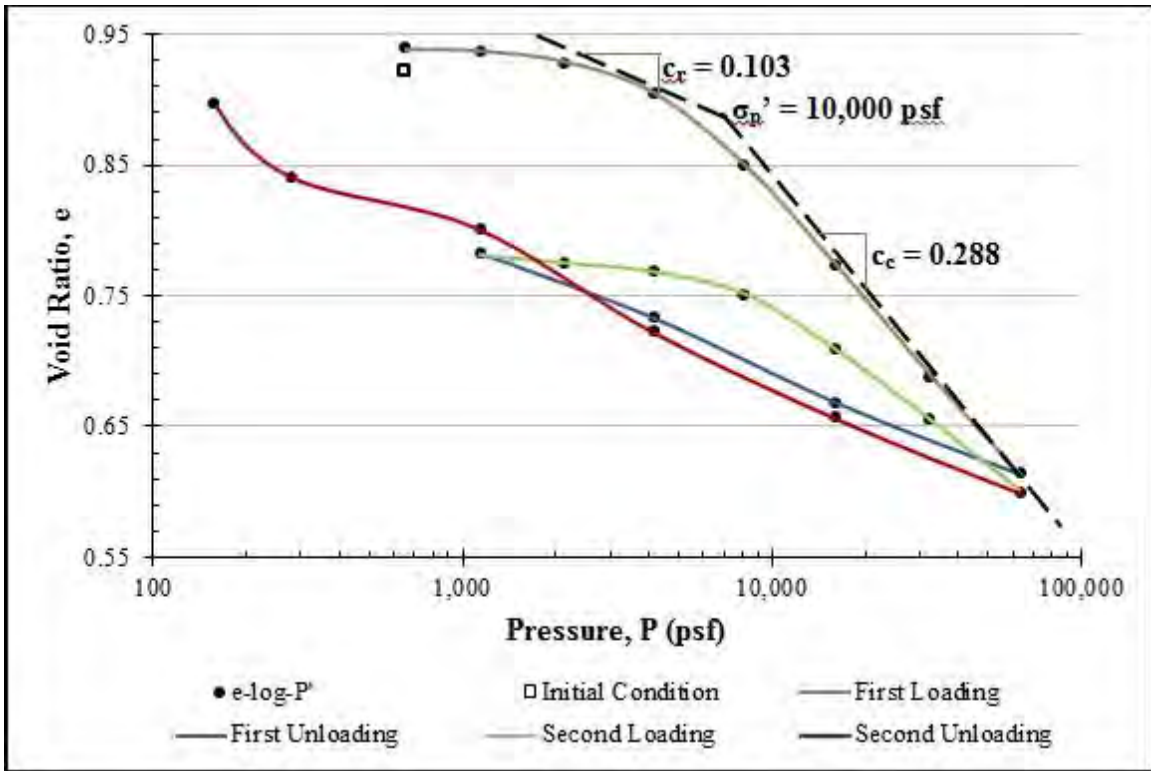
Second Unloading: 1000 psf				
S_0 (in.)	S_{100} (in.)	c_v (in ² /min)	k (ft/day)	t_{50} (min)
0.0832	0.0615	0.00015	8.4×10^{-9}	145



Second Unloading: 250 psf				
S_0 (in.)	S_{100} (in.)	c_v (in ² /min)	k (ft/day)	t_{50} (min)
0.0648	0.0482	0.00015	2.6×10^{-8}	154



Appendix D: Consolidation Test 3



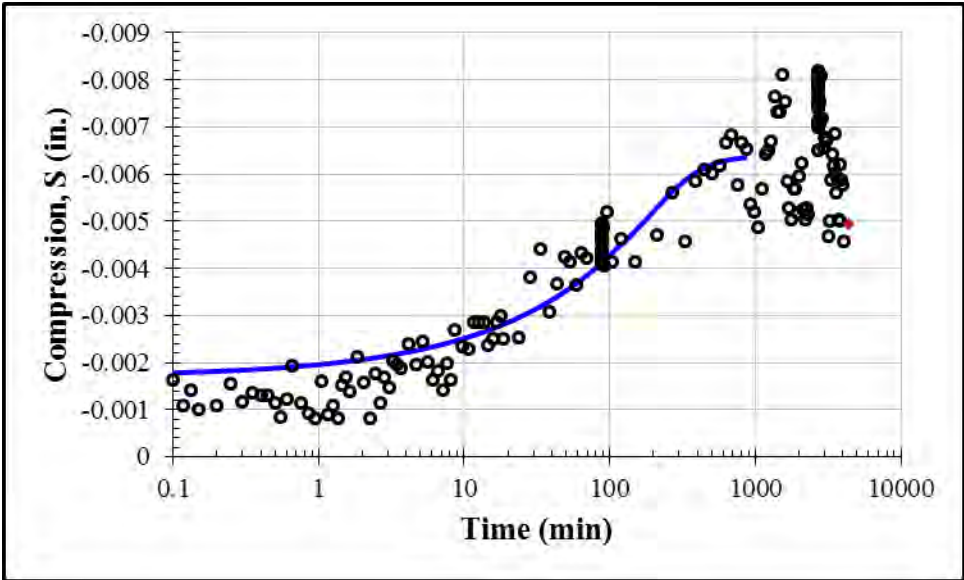
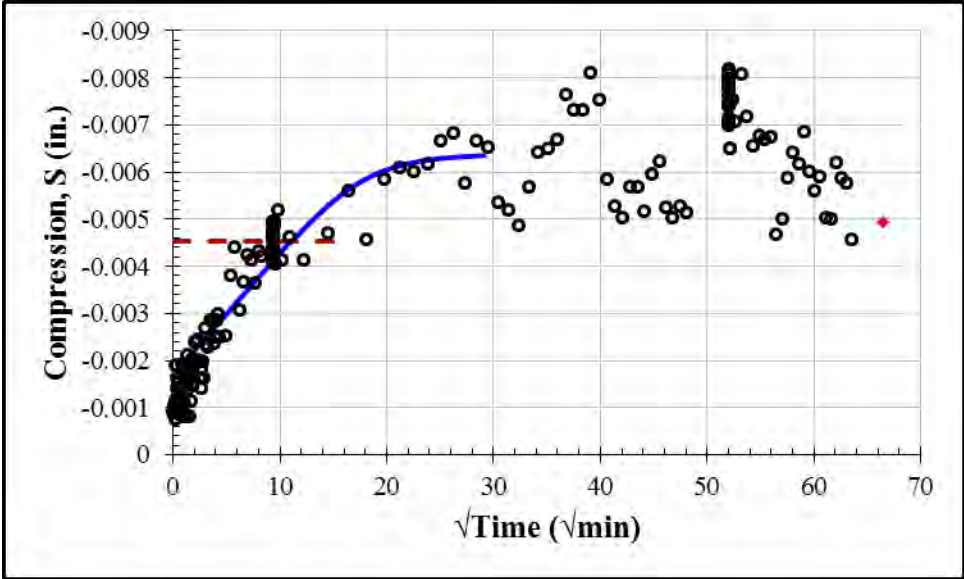
$$c_c = -\frac{e_2 - e_1}{\log(\sigma_2 / \sigma_1)} = -\frac{0.641 - 0.842}{\log(50000 / 10000)} = 0.288$$

$$c_r = -\frac{e_2 - e_1}{\log(\sigma_2 / \sigma_1)} = -\frac{0.901 - 0.942}{\log(5000 / 2000)} = 0.103$$

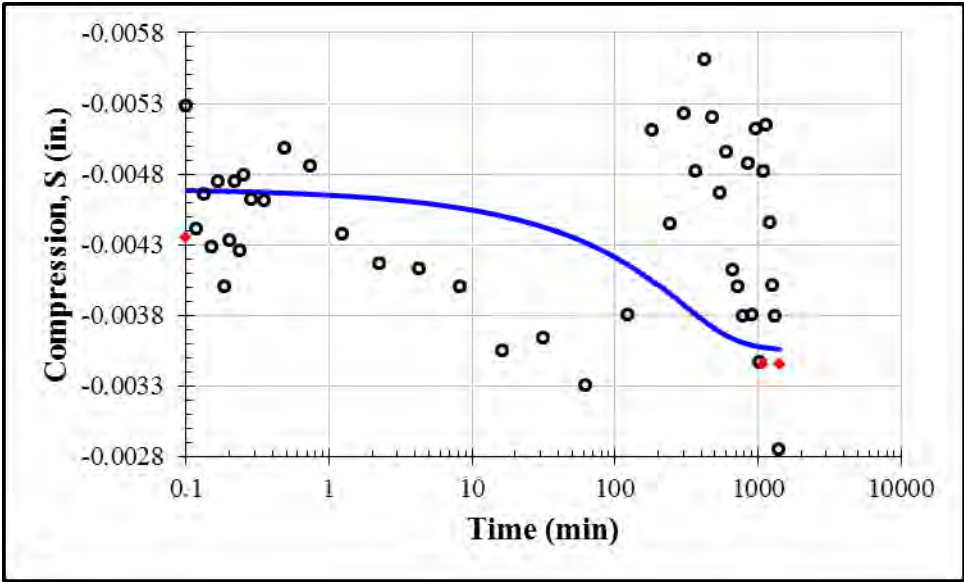
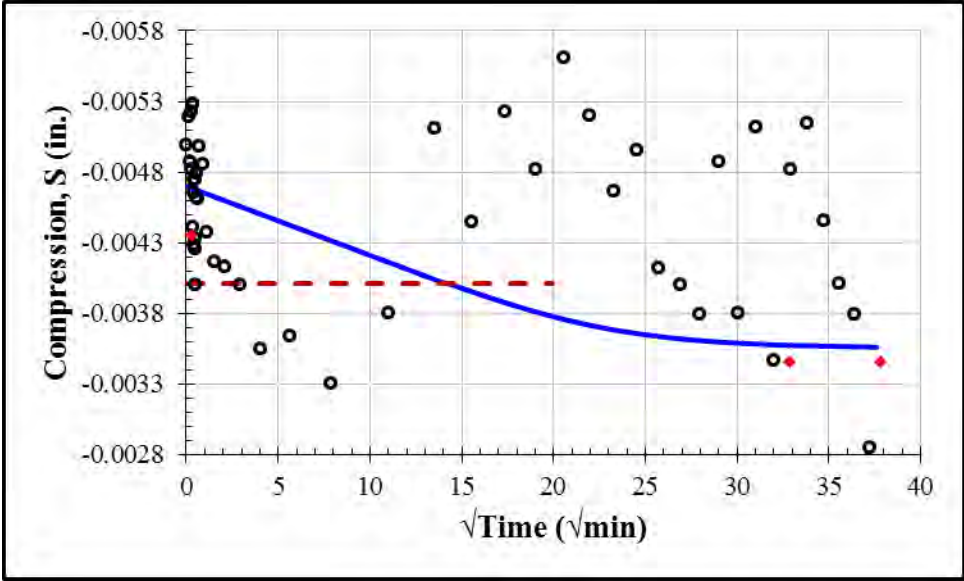
$$R_c = \frac{c_c}{1 + e_0} = \frac{0.288}{1 + 0.9019} = 0.151$$

$$R_r = \frac{c_r}{1 + e_0} = \frac{0.103}{1 + 0.9019} = 0.054$$

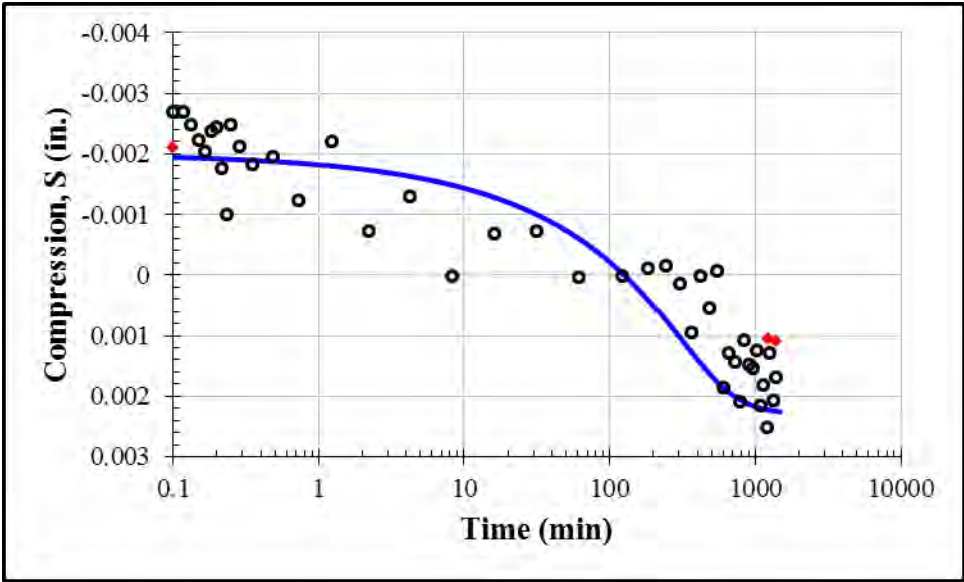
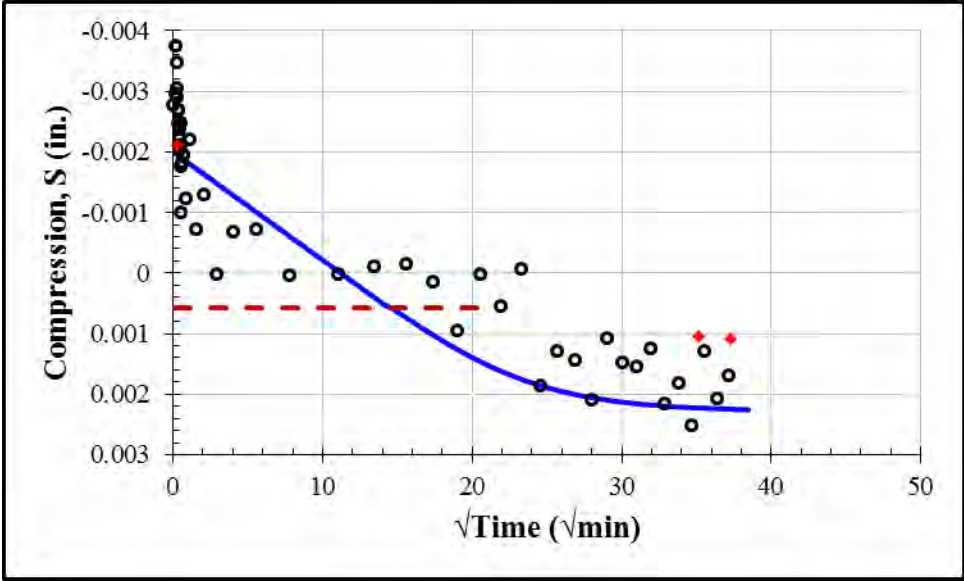
Inundation: 625 psf				
S_0 (in.)	S_{100} (in.)	c_v (in ² /min)	k (ft/day)	t_{50} (min)
-0.0017	-0.0064	0.00033	2.1×10^{-5}	83



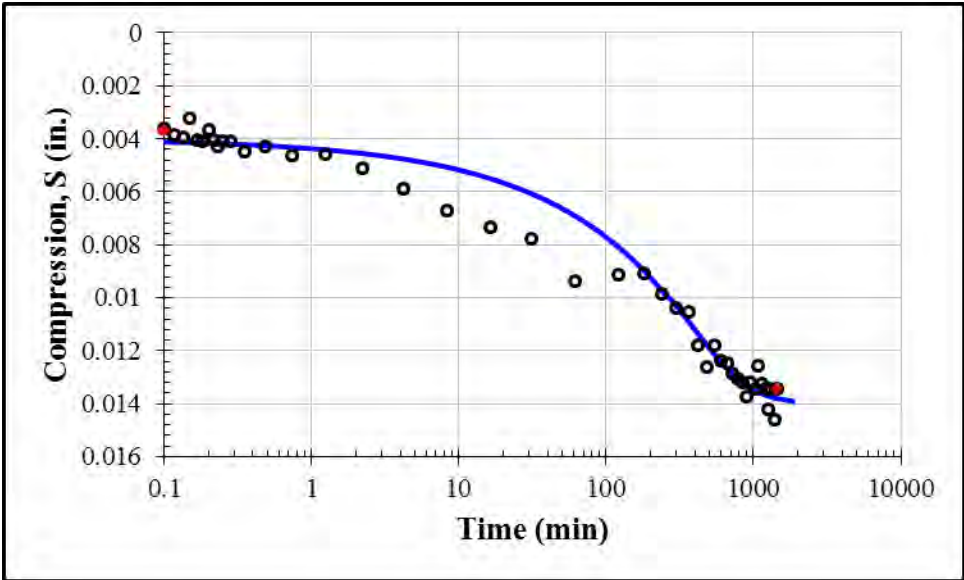
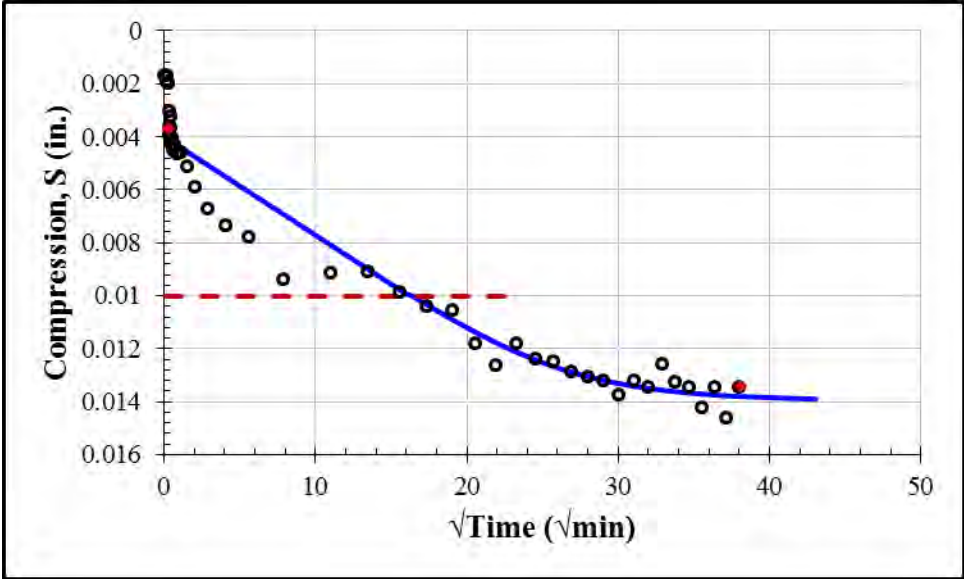
First Loading: 1125 psf				
S_0 (in.)	S_{100} (in.)	c_v (in ² /min)	k (ft/day)	t_{50} (min)
-0.0047	-0.00355	0.0002	3.9×10^{-9}	139



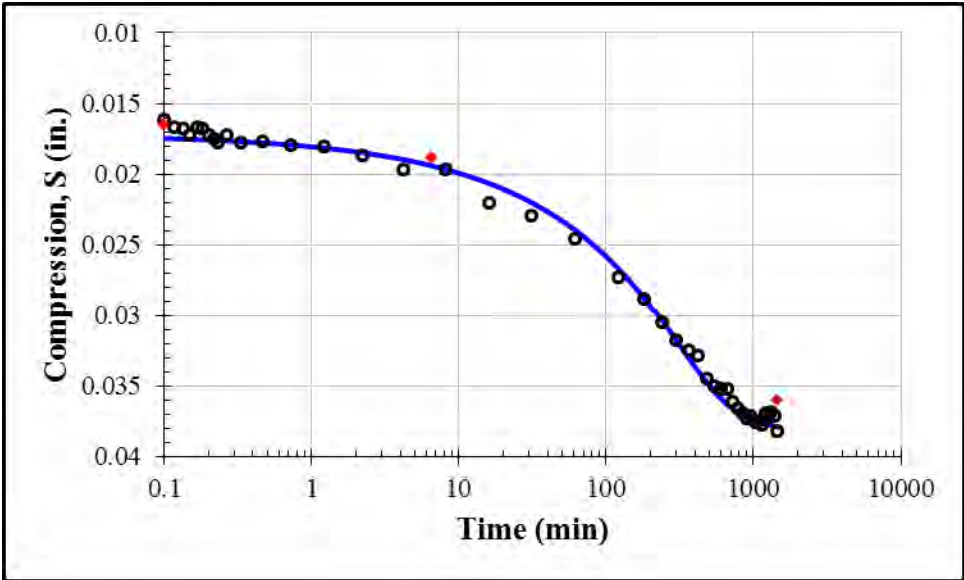
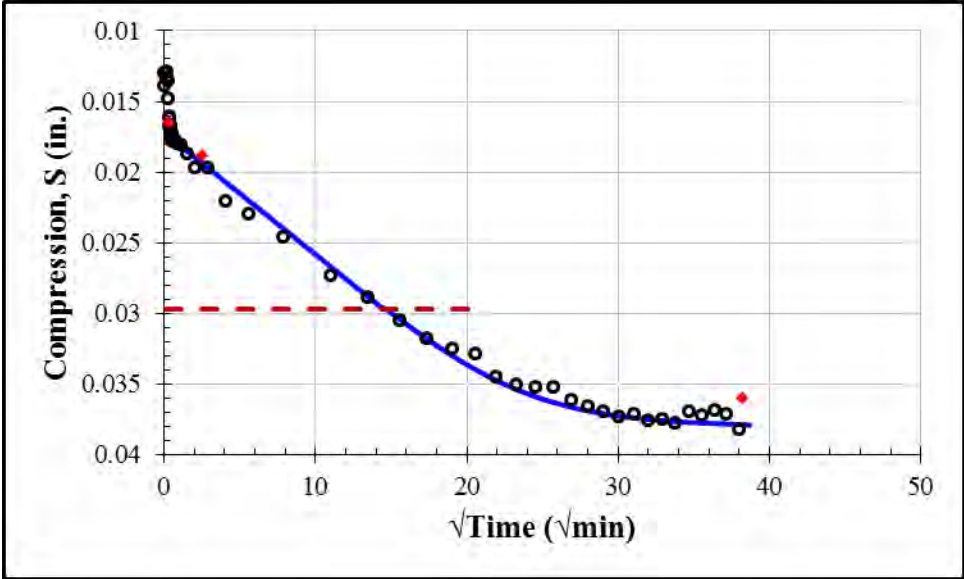
First Loading: 2125 psf				
S_0 (in.)	S_{100} (in.)	c_v (in ² /min)	k (ft/day)	t_{50} (min)
-0.0220	0.0023	0.00019	6.8×10^{-9}	145



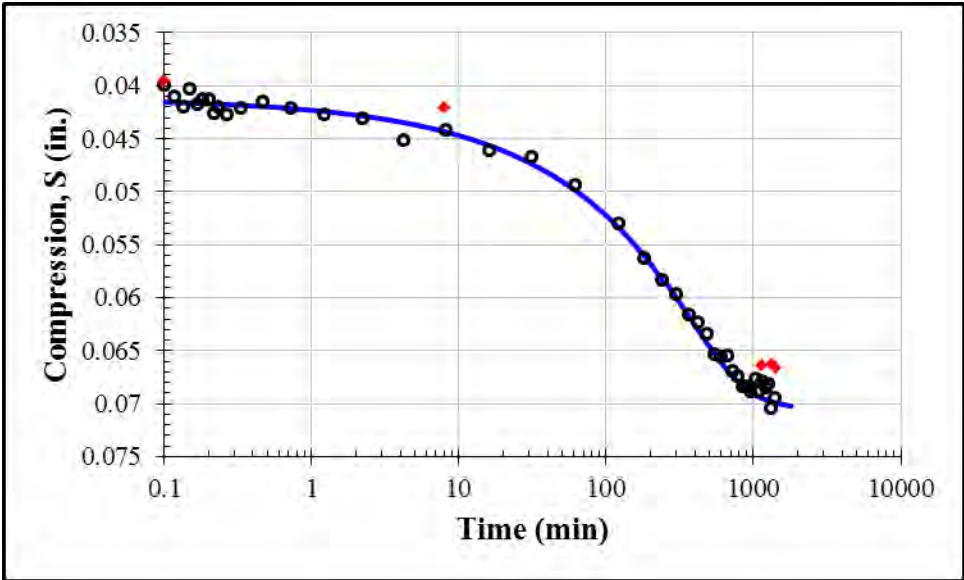
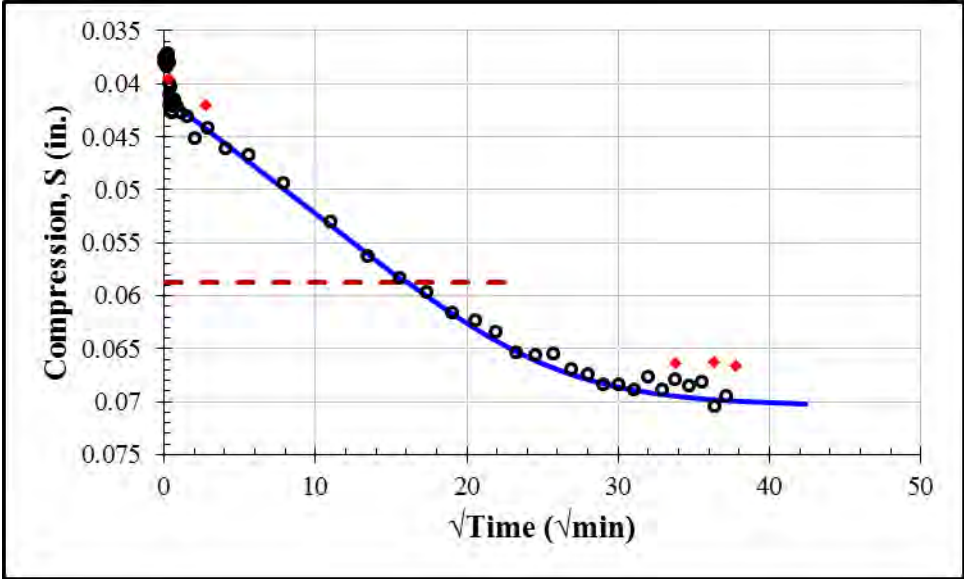
First Loading: 4125 psf				
S_0 (in.)	S_{100} (in.)	c_v (in ² /min)	k (ft/day)	t_{50} (min)
0.0040	0.0140	0.00015	6.2×10^{-9}	182



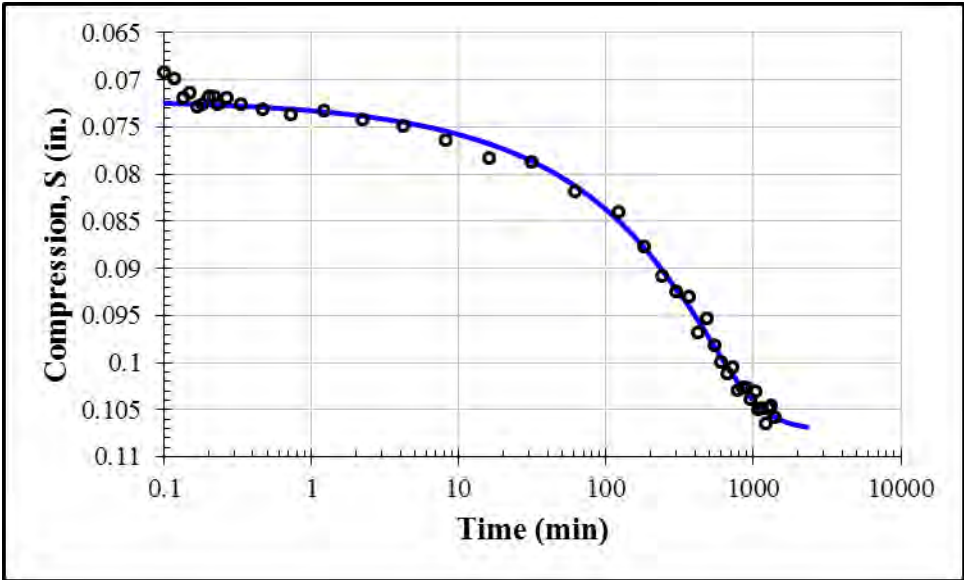
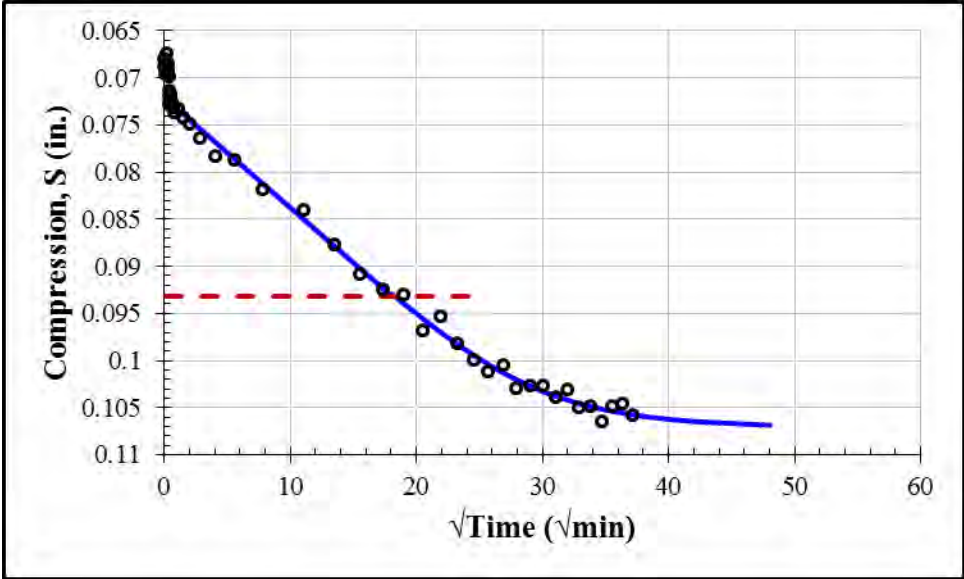
First Loading: 8125 psf				
S_0 (in.)	S_{100} (in.)	c_v (in ² /min)	k (ft/day)	t_{50} (min)
0.0172	0.0381	0.00018	7.7×10^{-9}	147



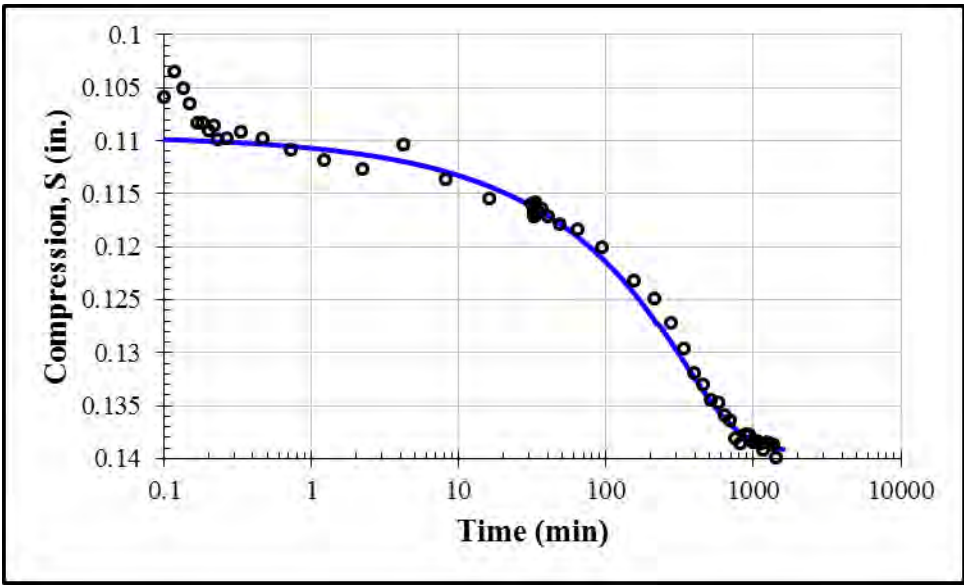
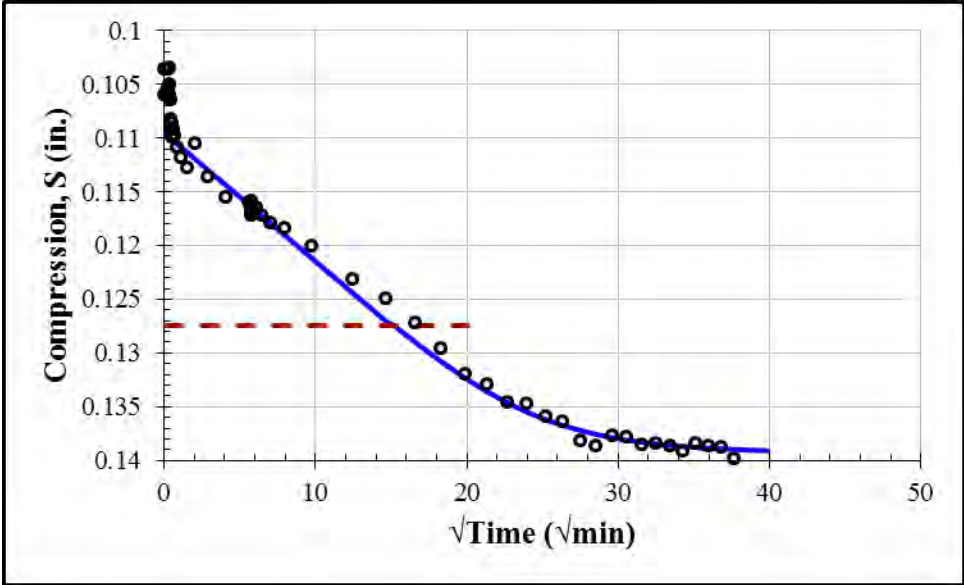
First Loading: 16125 psf				
S_0 (in.)	S_{100} (in.)	c_v (in ² /min)	k (ft/day)	t_{50} (min)
0.0412	0.0705	0.00014	4.1×10^{-9}	176



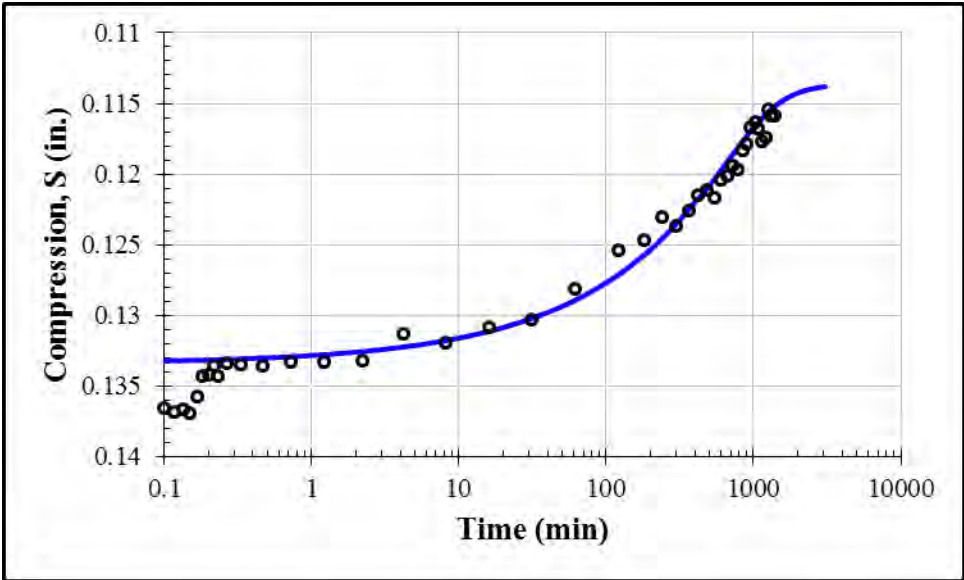
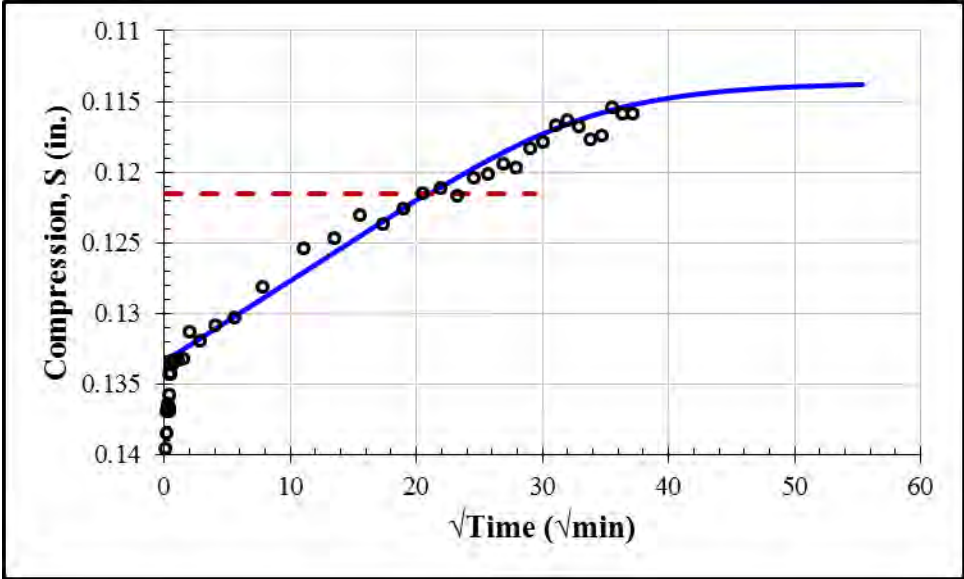
First Loading: 32125 psf				
S_0 (in.)	S_{100} (in.)	c_v (in ² /min)	k (ft/day)	t_{50} (min)
0.0721	0.1072	0.0001	1.7×10^{-9}	226



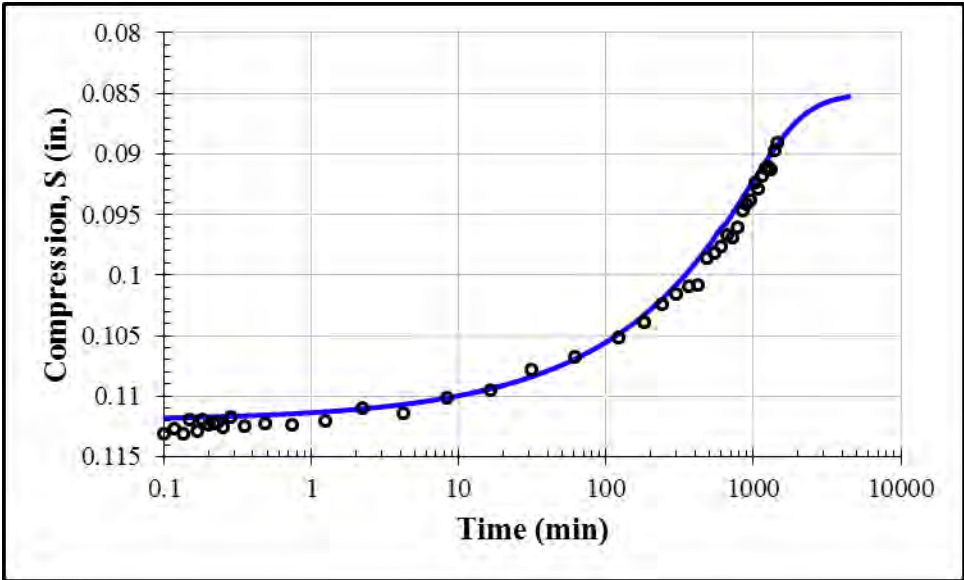
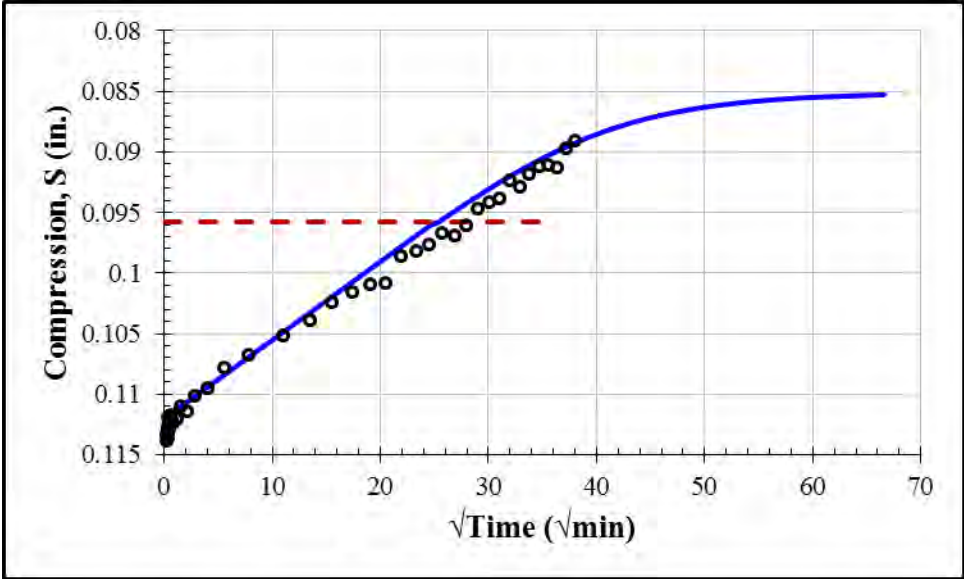
First Loading: 64125 psf				
S_0 (in.)	S_{100} (in.)	c_v (in ² /min)	k (ft/day)	t_{50} (min)
0.1095	0.1394	0.00013	9.0×10^{-10}	156



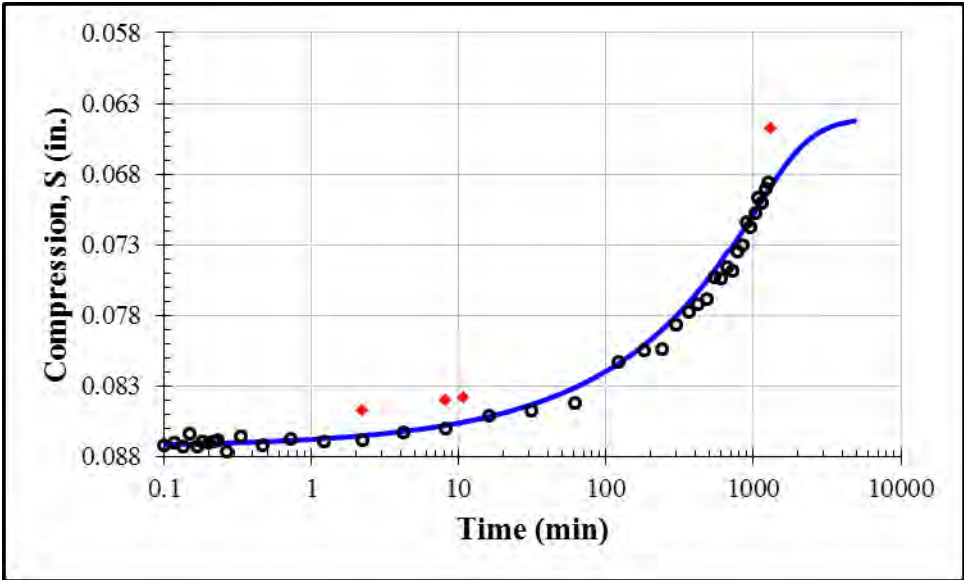
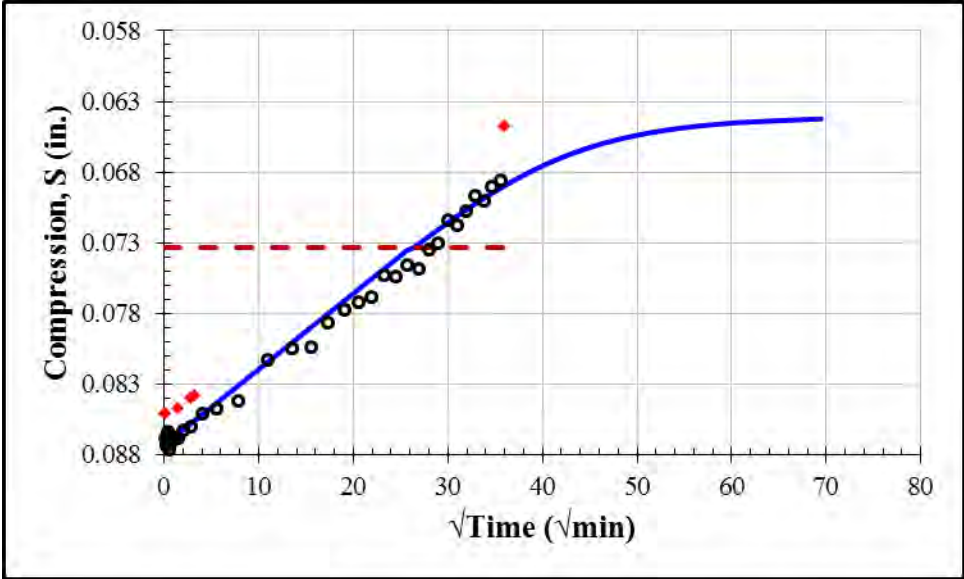
First Unloading: 16125 psf				
S_0 (in.)	S_{100} (in.)	c_v (in ² /min)	k (ft/day)	t_{50} (min)
0.1334	0.1136	0.00006	1.8×10^{-10}	300



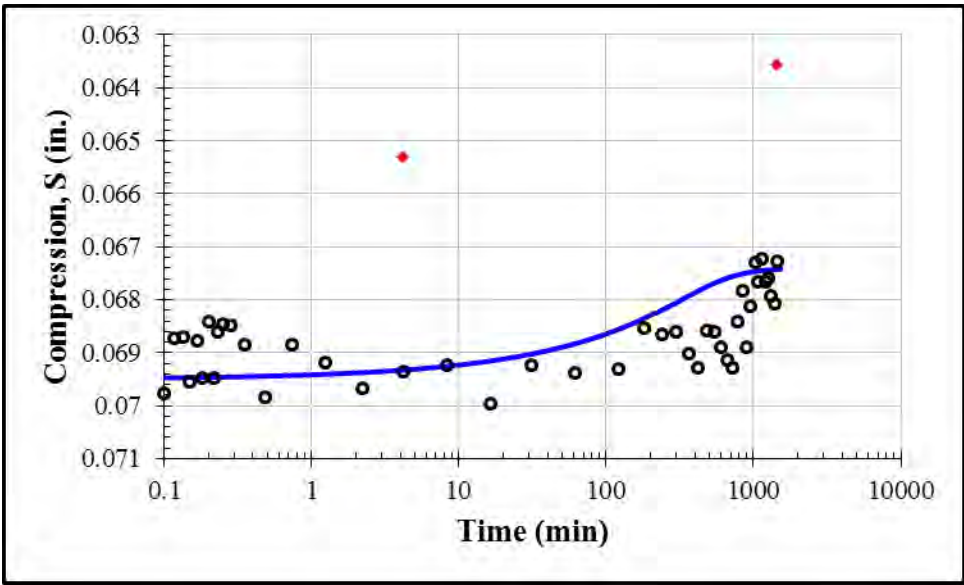
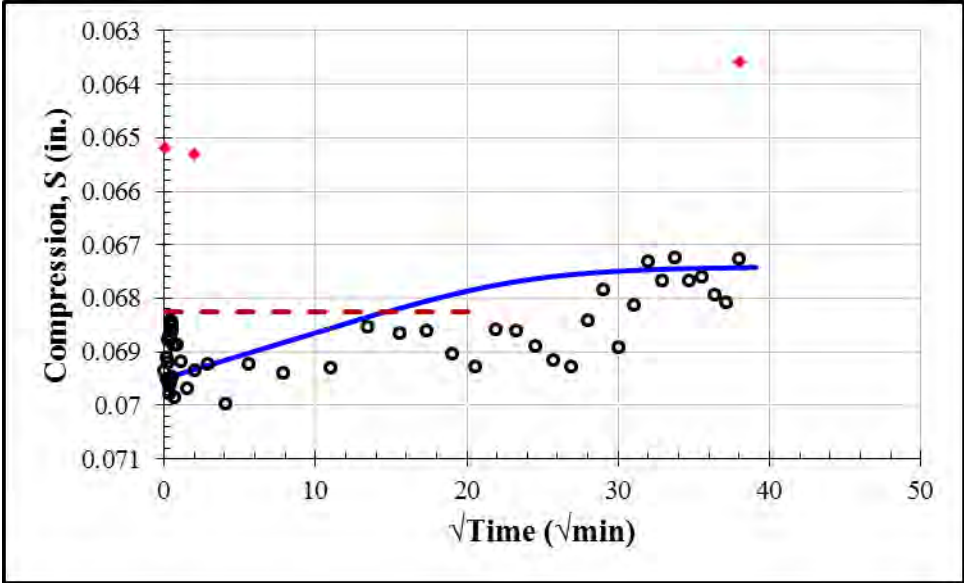
First Unloading: 4125 psf				
S_0 (in.)	S_{100} (in.)	c_v (in ² /min)	k (ft/day)	t_{50} (min)
0.1120	0.0850	0.000045	7.7×10^{-10}	435



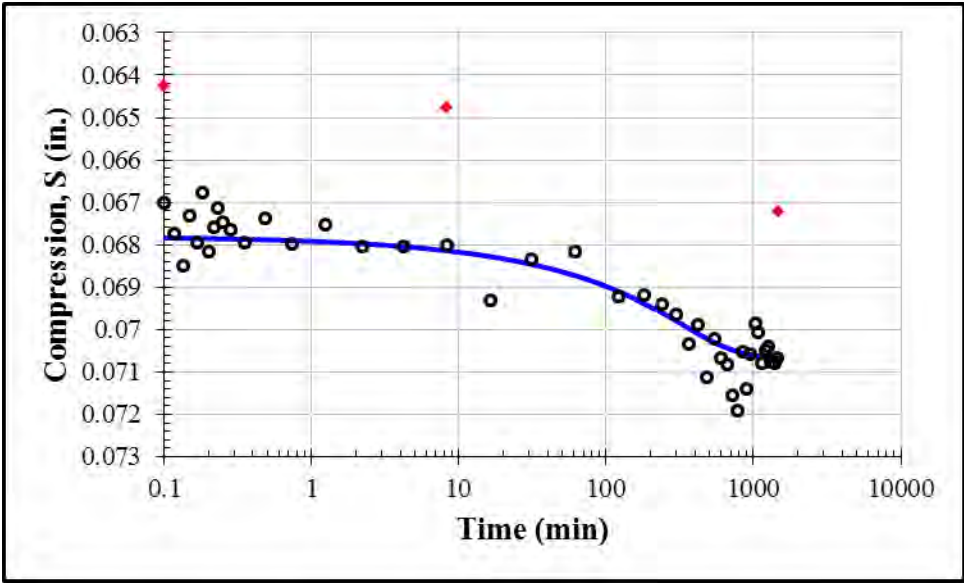
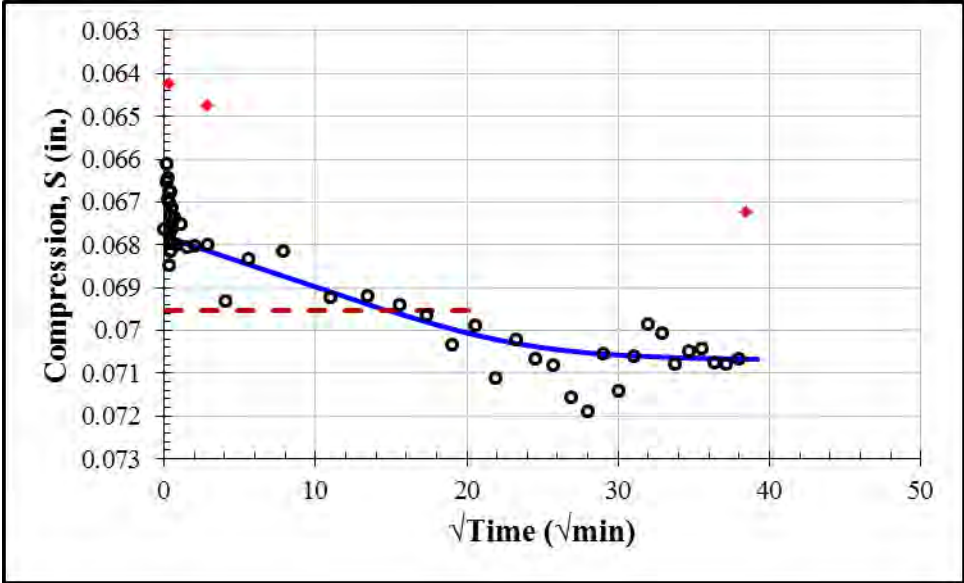
First Unloading: 1125 psf				
S_0 (in.)	S_{100} (in.)	c_v (in ² /min)	k (ft/day)	t_{50} (min)
0.0873	0.0640	0.000045	2.7×10^{-9}	472



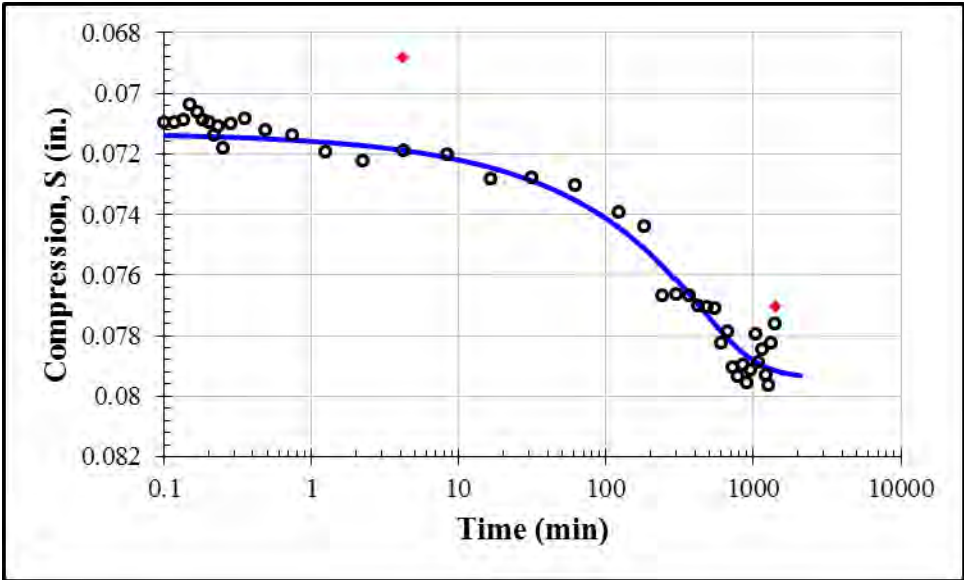
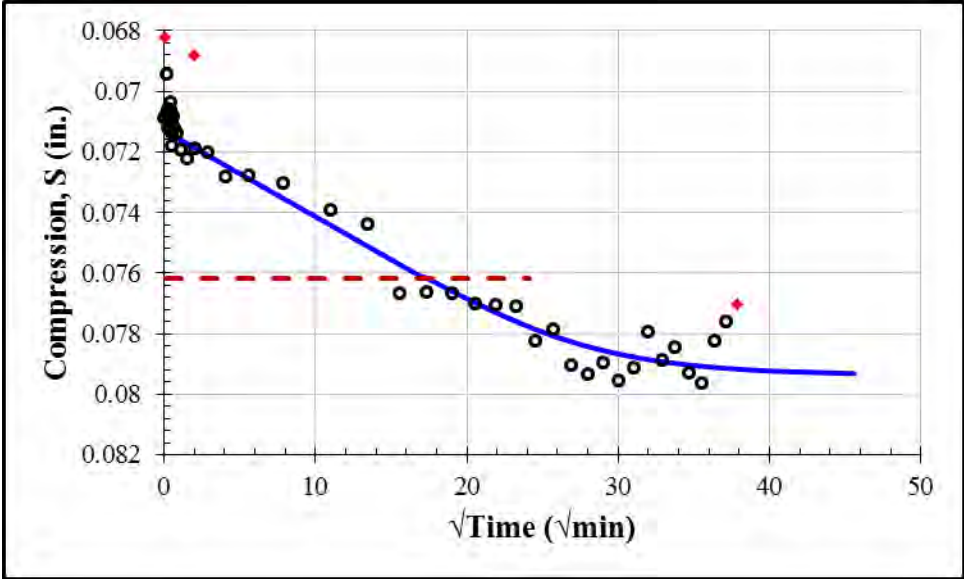
Second Loading: 2125 psf				
S_0 (in.)	S_{100} (in.)	c_v (in ² /min)	k (ft/day)	t_{50} (min)
0.0695	0.0674	0.00015	2.5×10^{-9}	150



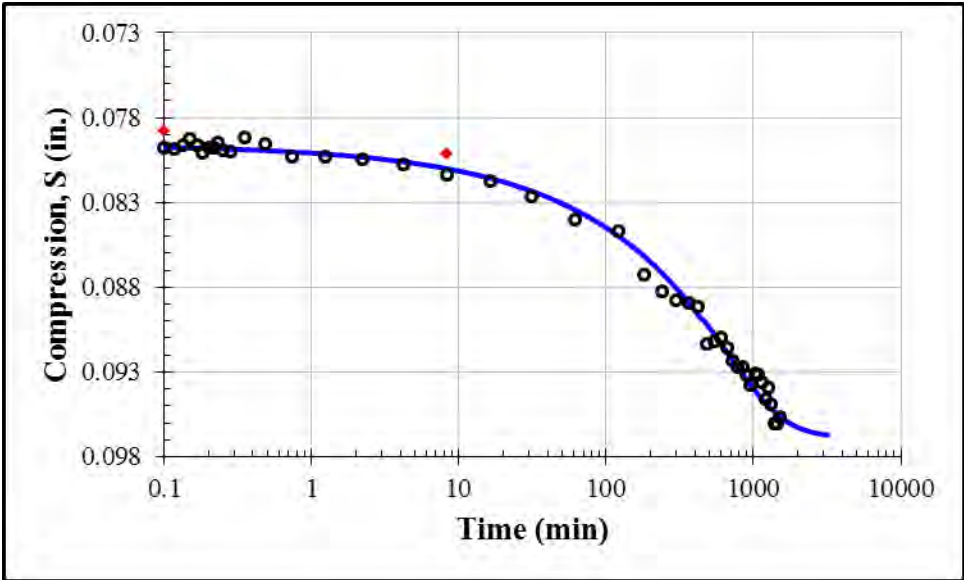
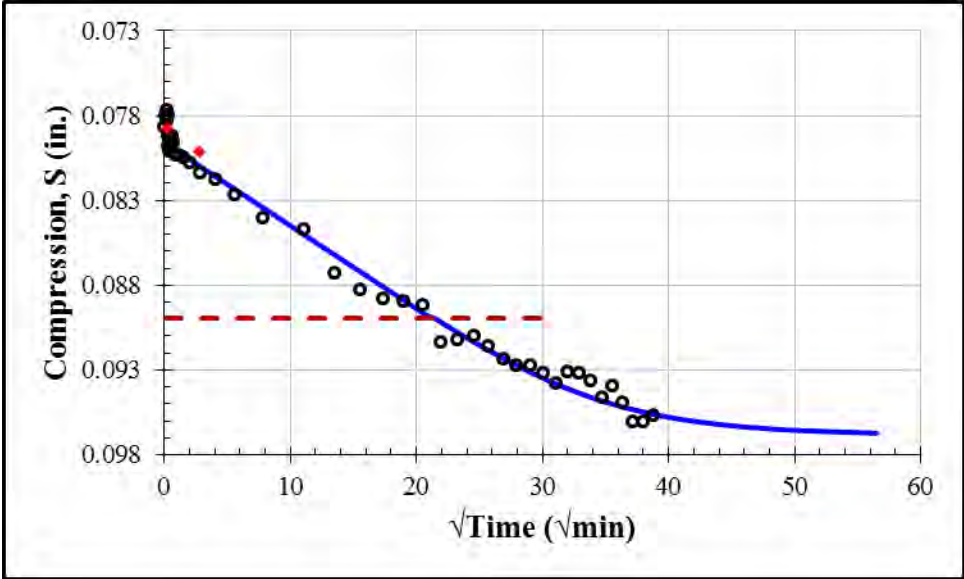
Second Loading: 4125 psf				
S_0 (in.)	S_{100} (in.)	c_v (in ² /min)	k (ft/day)	t_{50} (min)
0.0678	0.0707	0.00015	1.7×10^{-9}	151



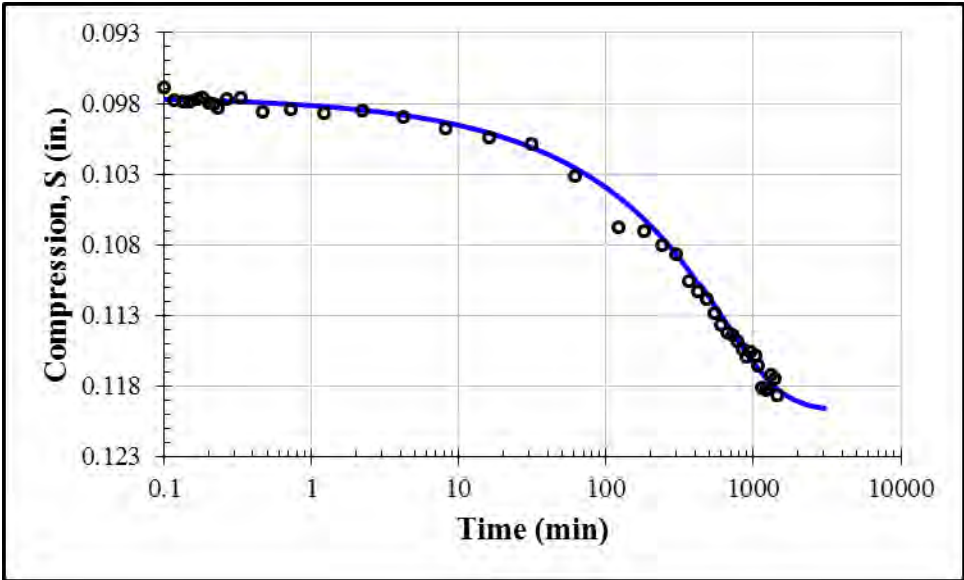
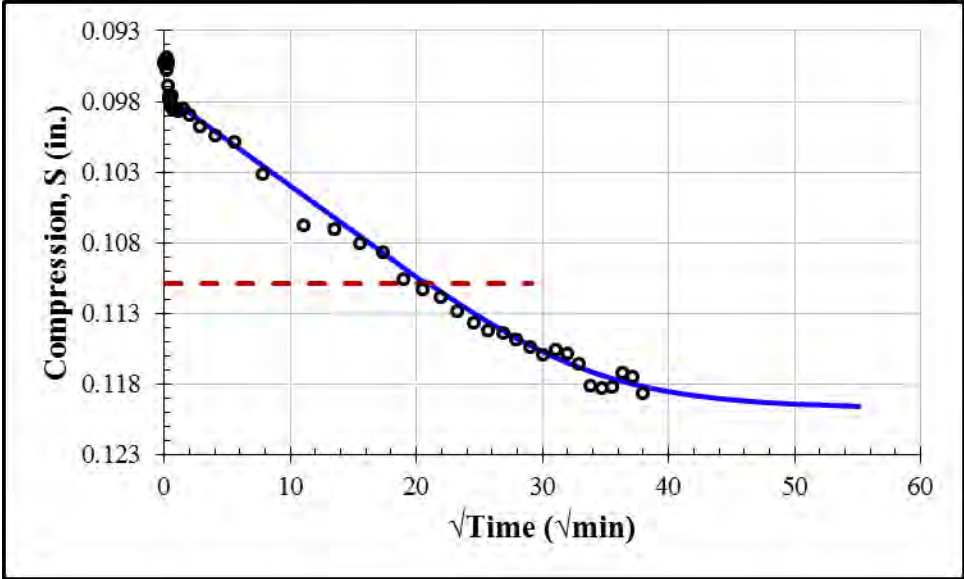
Second Loading: 8125 psf				
S_0 (in.)	S_{100} (in.)	c_v (in ² /min)	k (ft/day)	t_{50} (min)
0.0713	0.0794	0.00011	1.7×10^{-9}	204



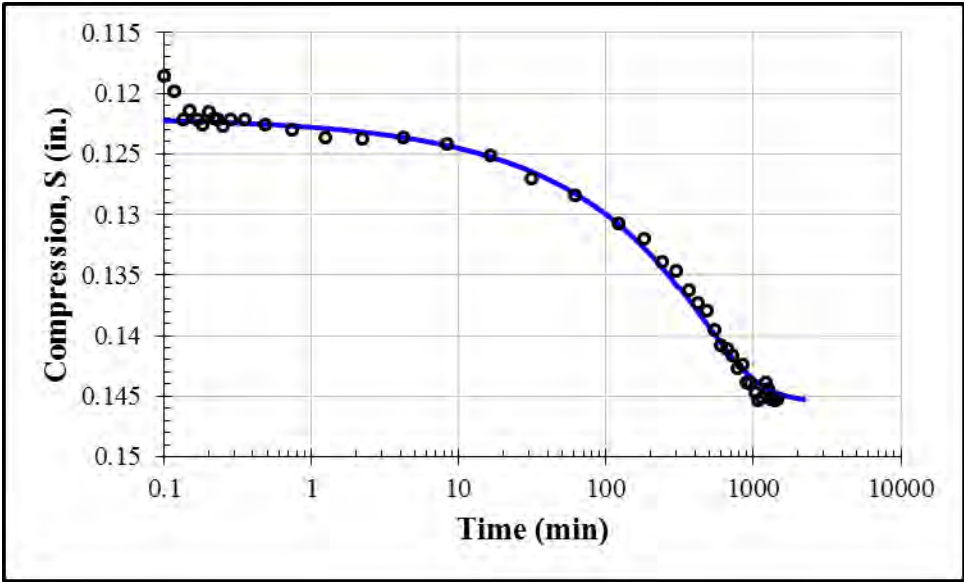
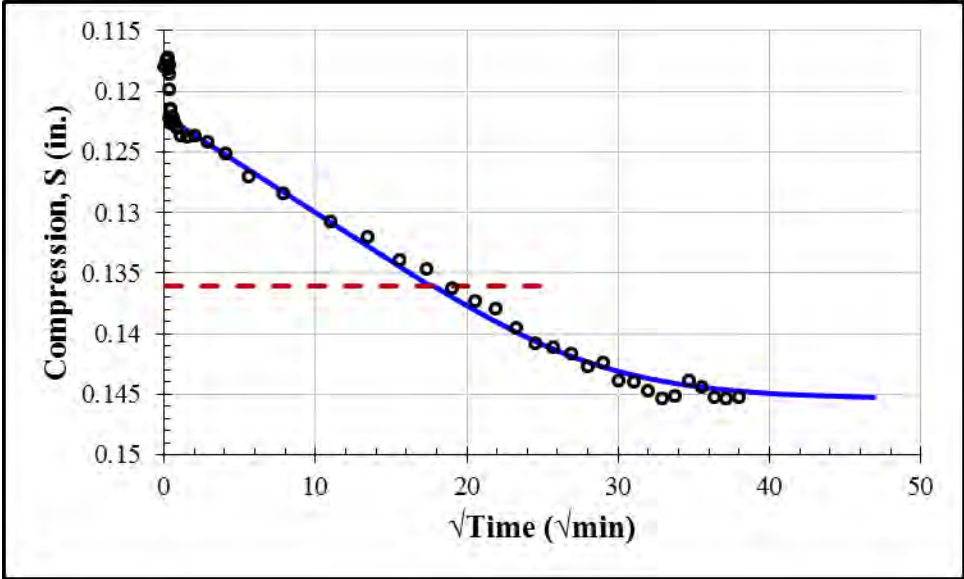
Second Loading: 16125 psf				
S_0 (in.)	S_{100} (in.)	c_v (in ² /min)	k (ft/day)	t_{50} (min)
0.0796	0.0969	0.00007	1.2×10^{-9}	313



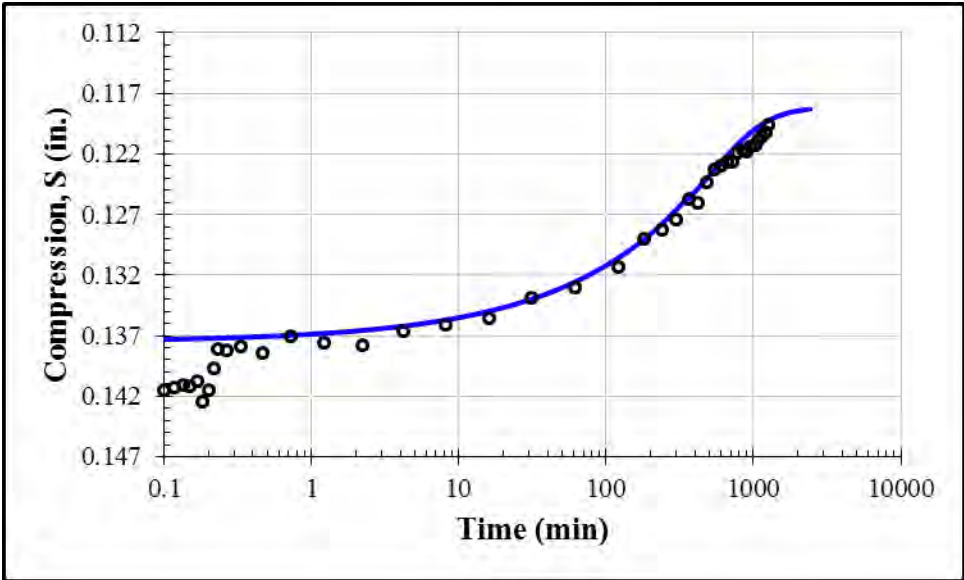
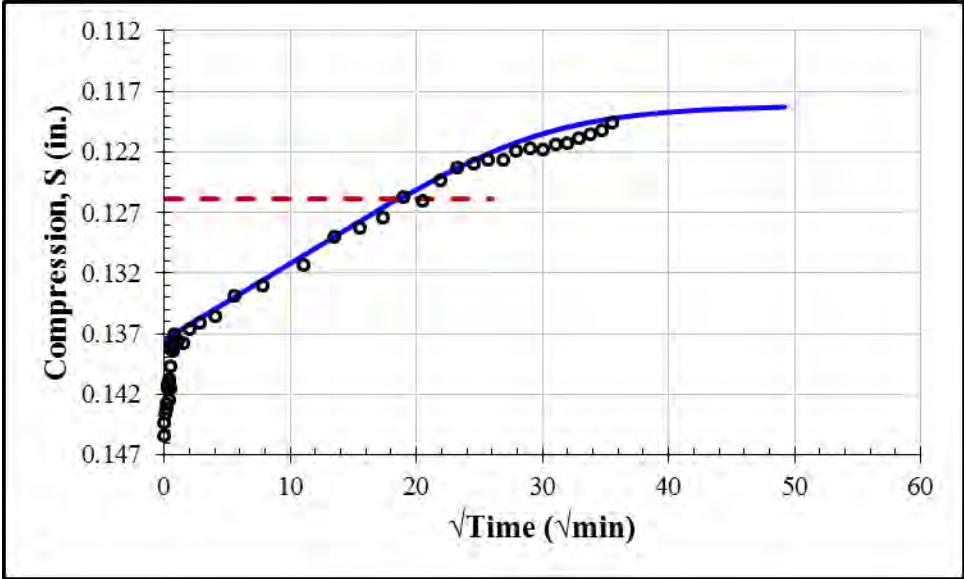
Second Loading: 32125 psf				
S_0 (in.)	S_{100} (in.)	c_v (in ² /min)	k (ft/day)	t_{50} (min)
0.0975	0.1198	0.00007	7.4×10^{-10}	297



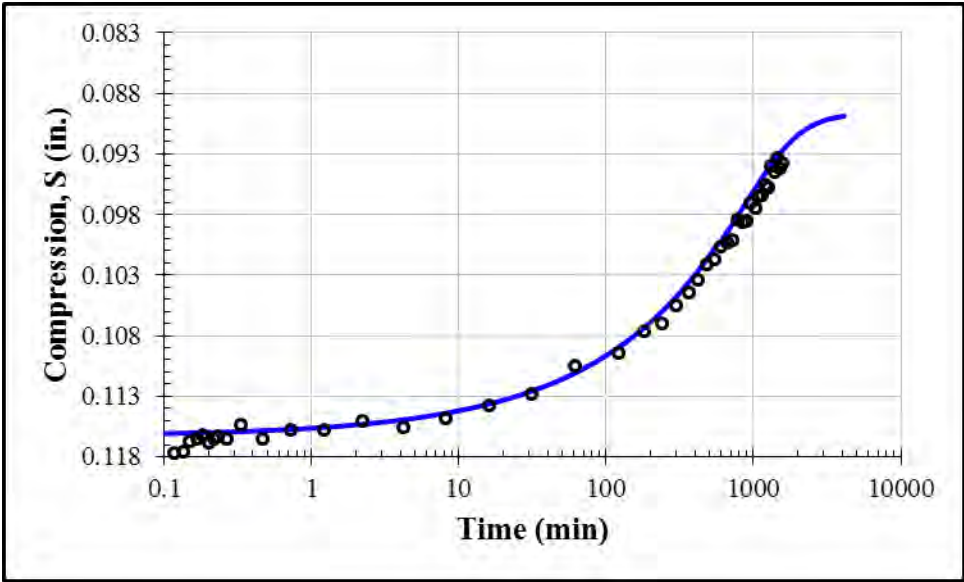
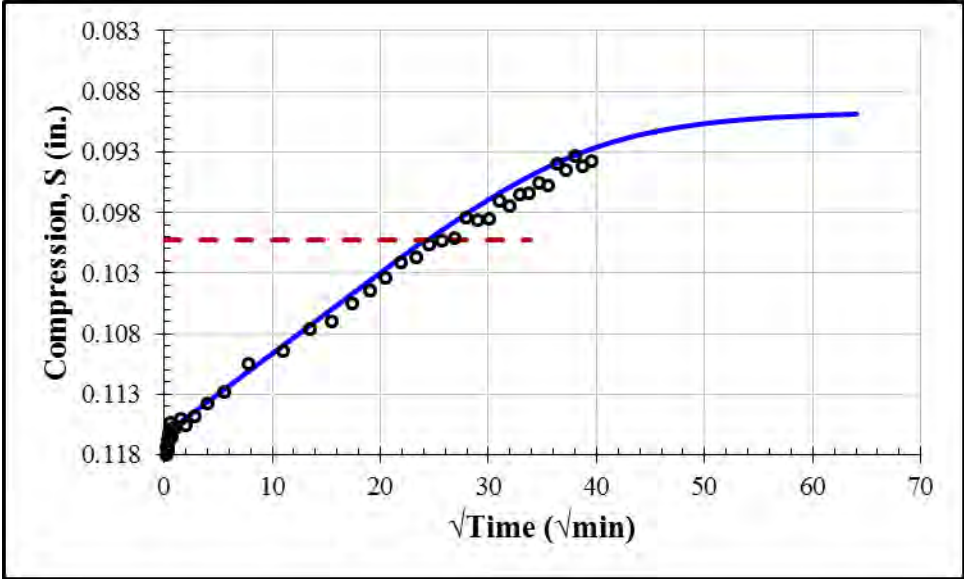
Second Loading: 64125 psf				
S_0 (in.)	S_{100} (in.)	c_v (in ² /min)	k (ft/day)	t_{50} (min)
0.1220	0.1455	0.00009	4.9×10^{-10}	215



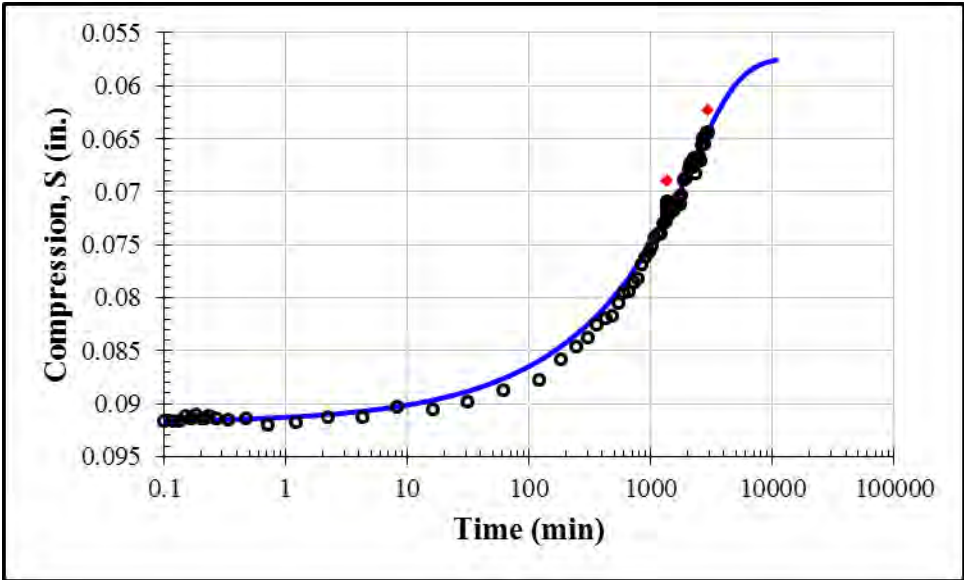
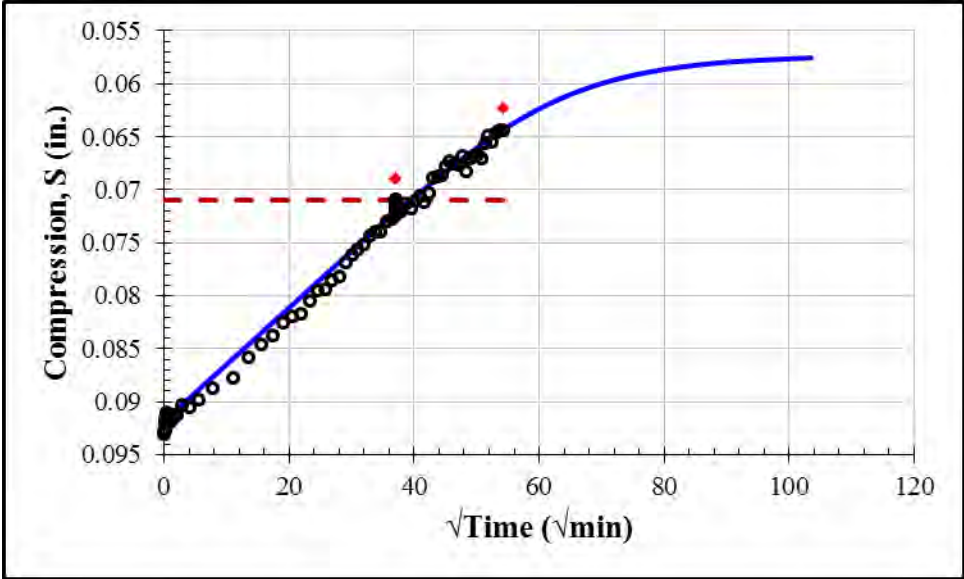
Second Unloading: 16125 psf				
S_0 (in.)	S_{100} (in.)	c_v (in ² /min)	k (ft/day)	t_{50} (min)
0.1375	0.1181	0.000075	2.2×10^{-10}	237



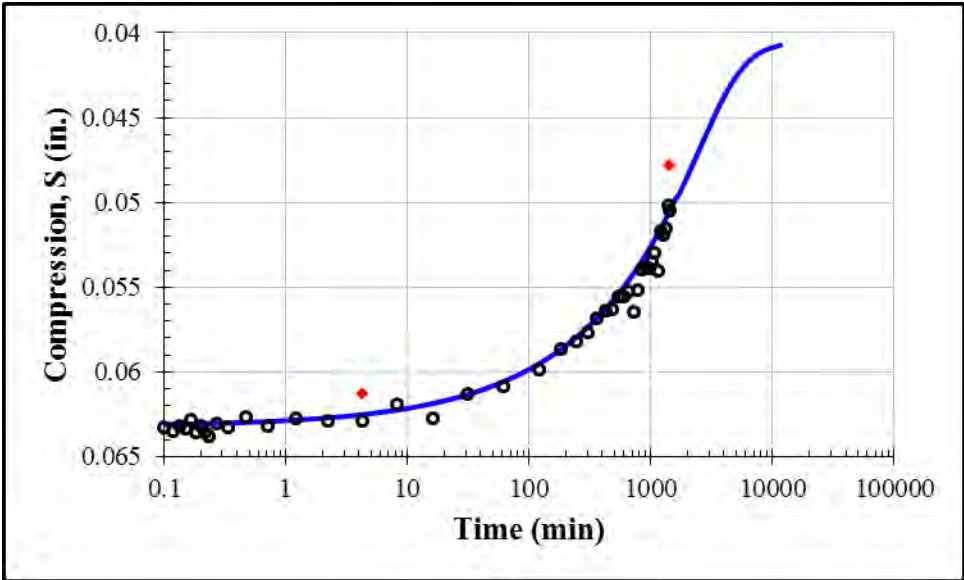
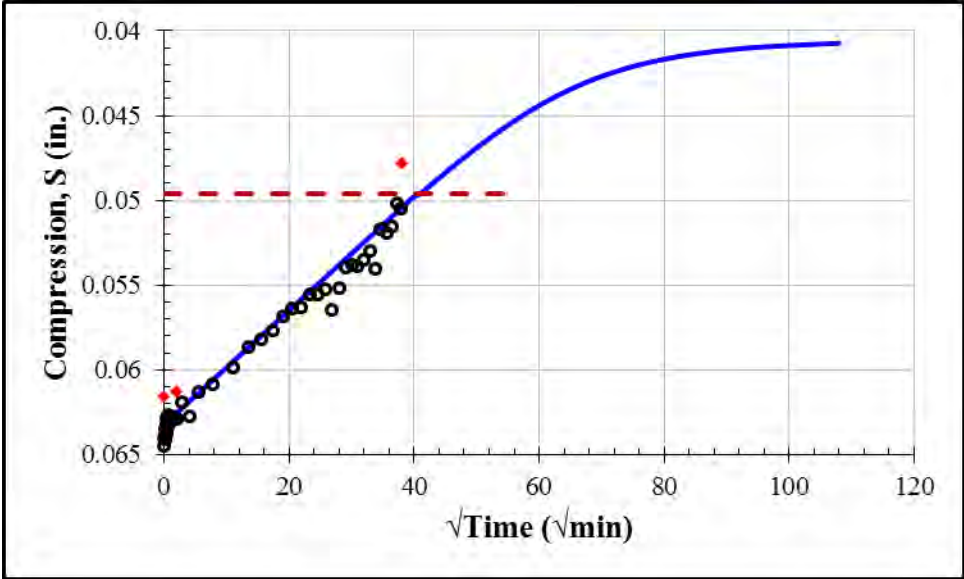
Second Unloading: 4125 psf				
S_0 (in.)	S_{100} (in.)	c_v (in ² /min)	k (ft/day)	t_{50} (min)
0.1163	0.0896	0.000048	8.1×10^{-10}	402



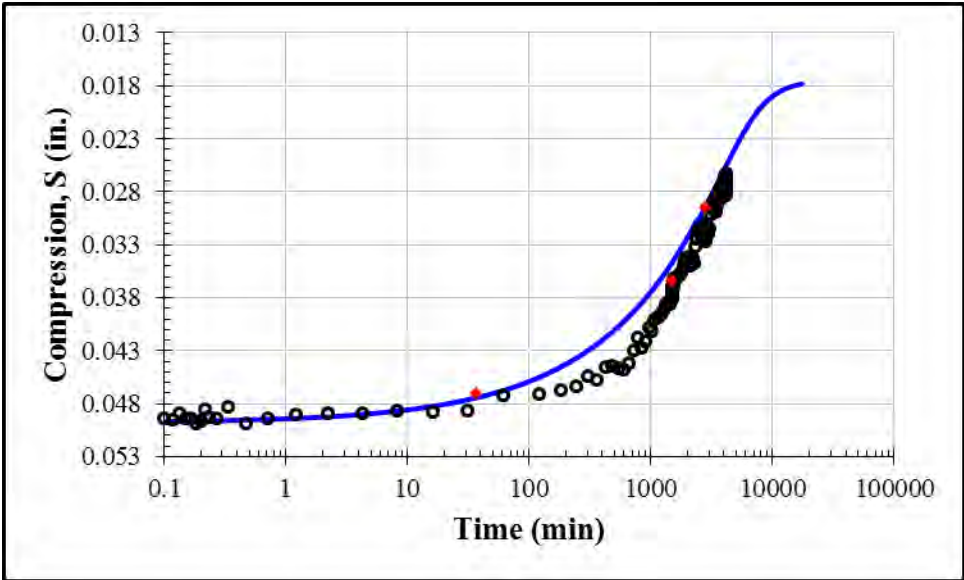
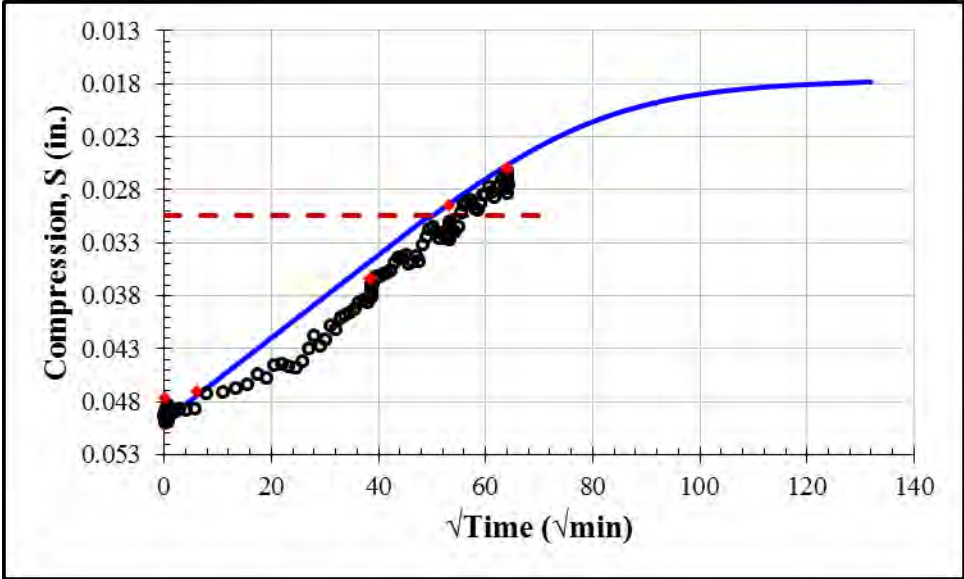
Second Unloading: 1125 psf				
S_0 (in.)	S_{100} (in.)	c_v (in ² /min)	k (ft/day)	t_{50} (min)
0.0918	0.0572	0.00002	1.8×10^{-9}	1049



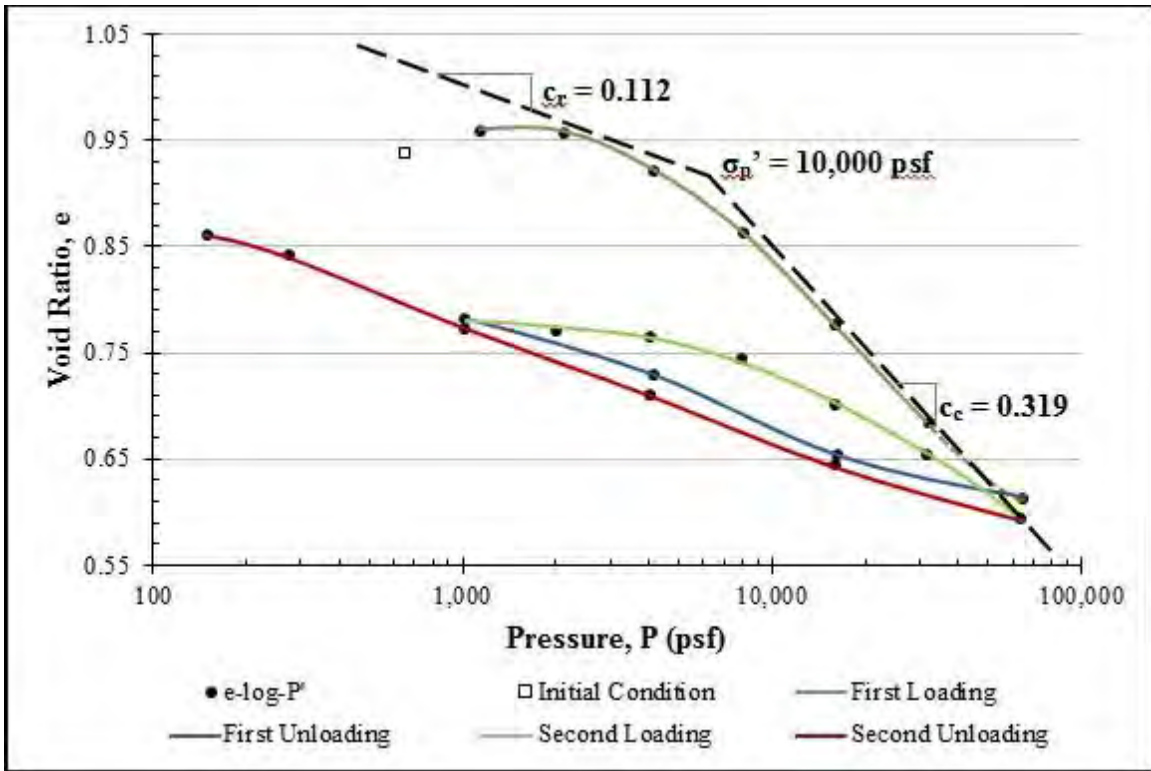
Second Unloading: 250 psf				
S_0 (in.)	S_{100} (in.)	c_v (in ² /min)	k (ft/day)	t_{50} (min)
0.0632	0.0405	0.00002	4.1×10^{-9}	1141



Second Unloading: 125 psf				
S_0 (in.)	S_{100} (in.)	c_v (in ² /min)	k (ft/day)	t_{50} (min)
0.0498	0.0175	0.000014	2.9×10^{-8}	1704



Appendix E: Consolidation Test 4



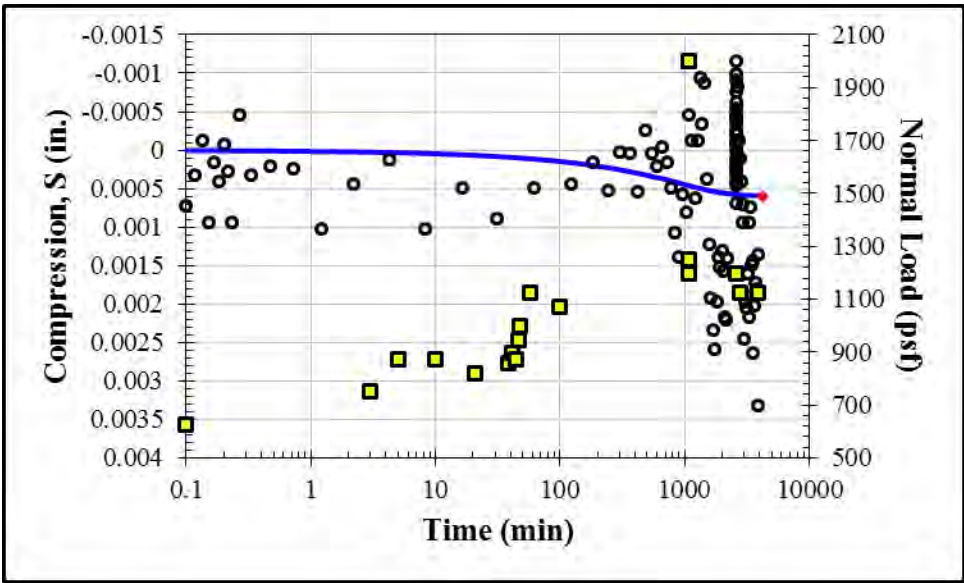
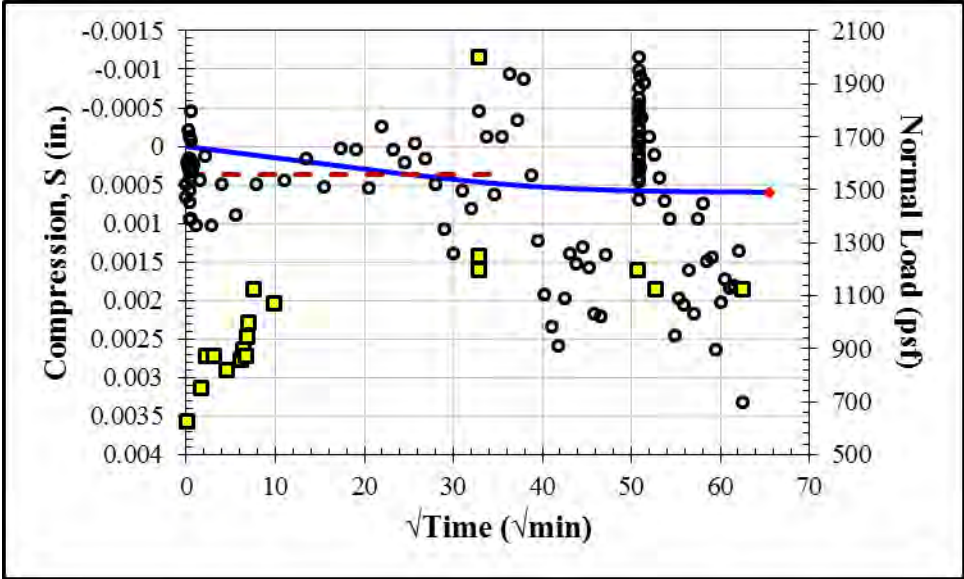
$$c_c = -\frac{e_2 - e_1}{\log(\sigma_2 / \sigma_1)} = -\frac{0.628 - 0.851}{\log(50000 / 10000)} = 0.319$$

$$c_r = -\frac{e_2 - e_1}{\log(\sigma_2 / \sigma_1)} = -\frac{0.950 - 1.028}{\log(3000 / 600)} = 0.112$$

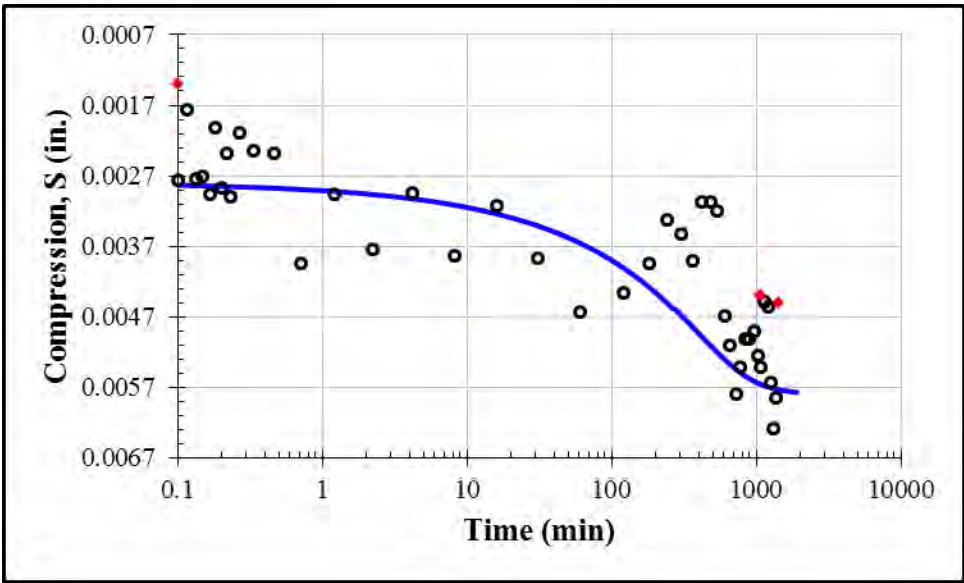
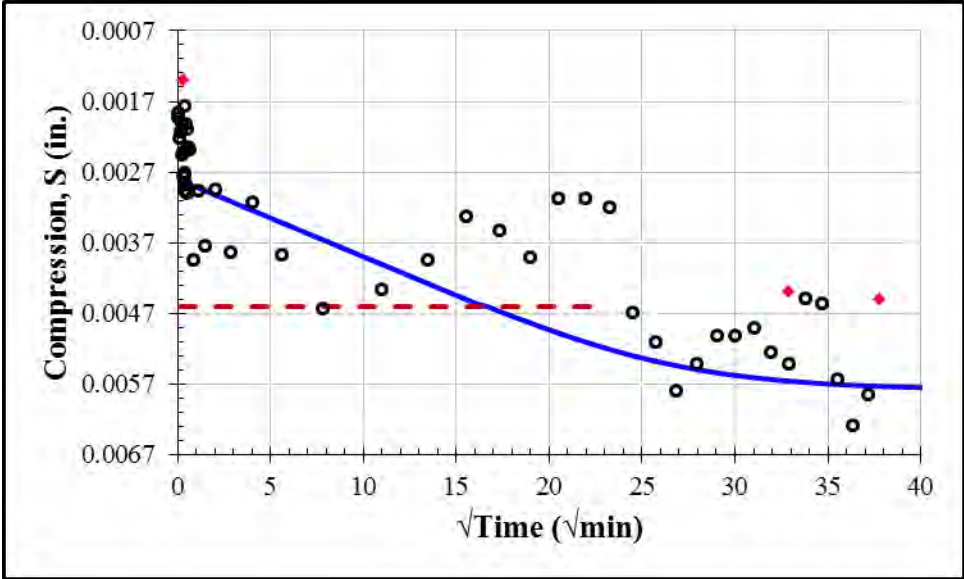
$$R_c = \frac{c_c}{1 + e_0} = \frac{0.319}{1 + 1.0454} = 0.156$$

$$R_r = \frac{c_r}{1 + e_0} = \frac{0.112}{1 + 1.0454} = 0.055$$

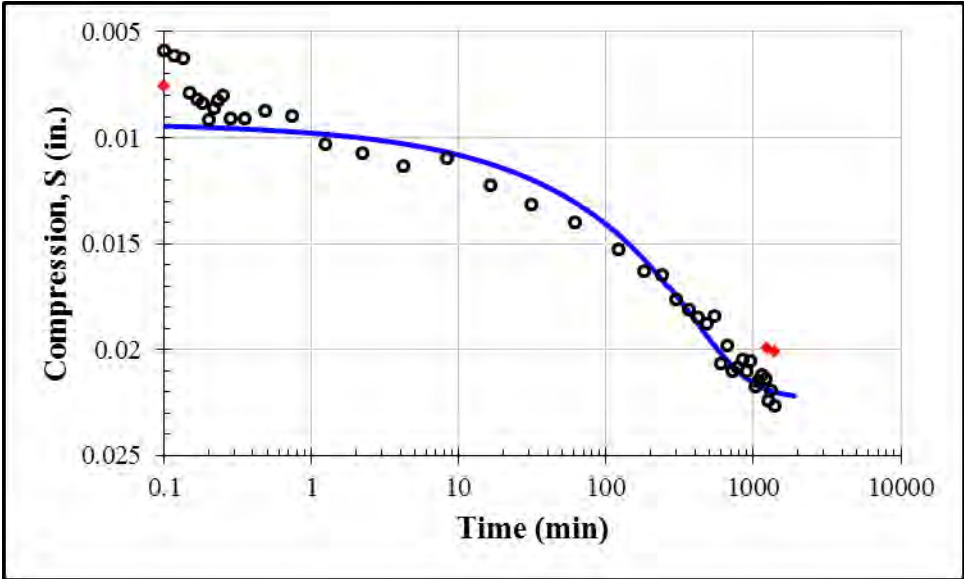
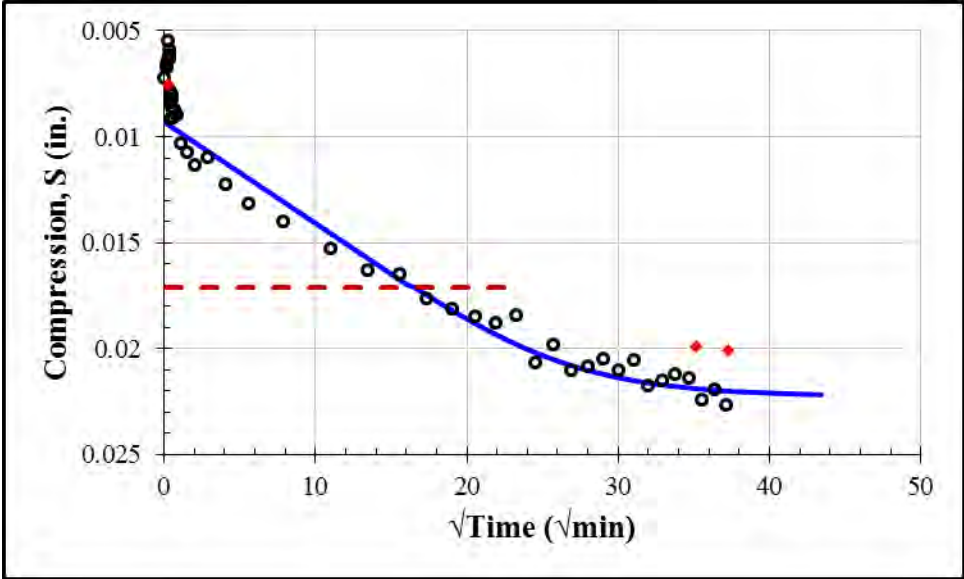
Soaking at Constant Volume Starting at 625 psf				
S_0 (in.)	S_{100} (in.)	c_v (in ² /min)	k (ft/day)	t_{50} (min)
0.0000	0.0006	0.000067	6.6×10^{-10}	421



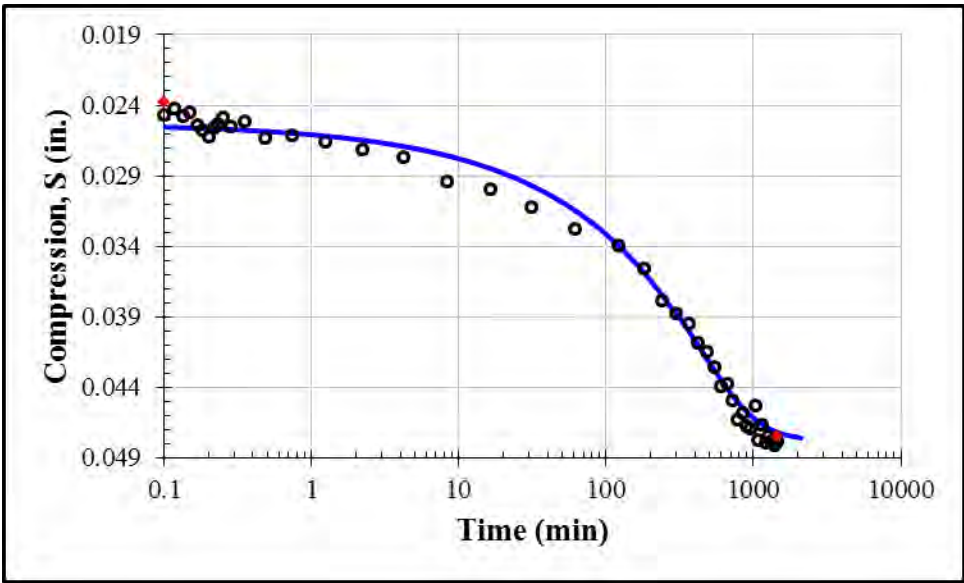
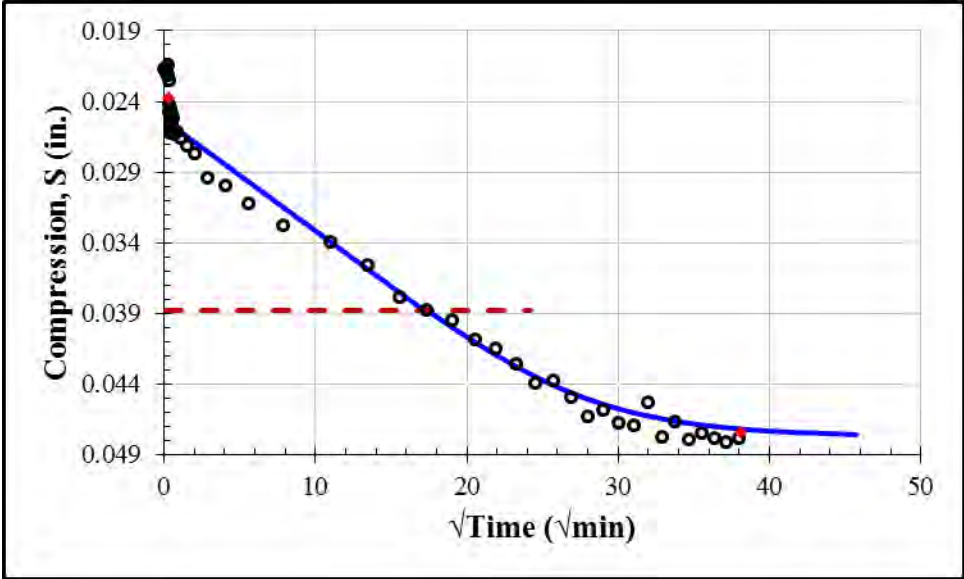
First Loading: 2125 psf				
S_0 (in.)	S_{100} (in.)	c_v (in ² /min)	k (ft/day)	t_{50} (min)
0.0028	0.0058	0.00015	3.7×10^{-9}	187



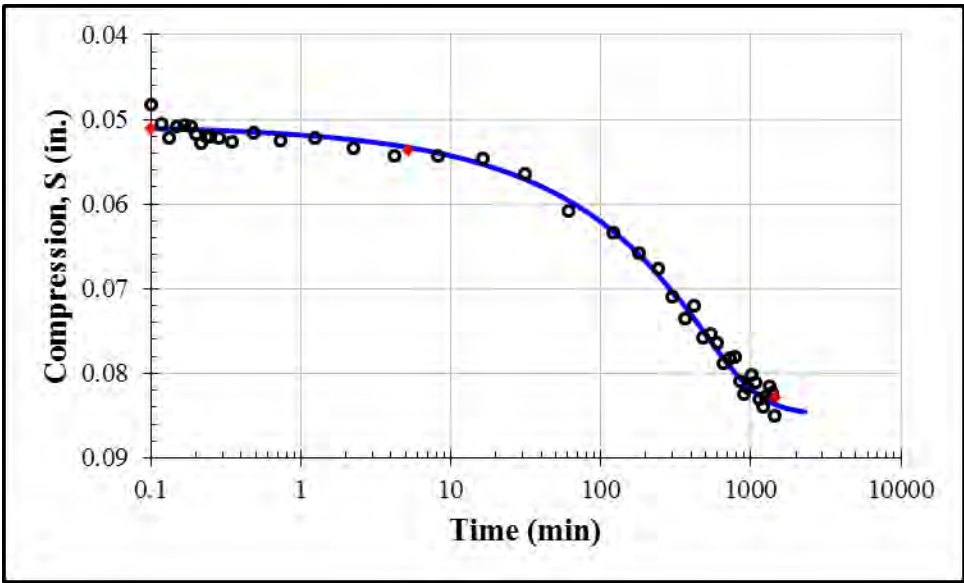
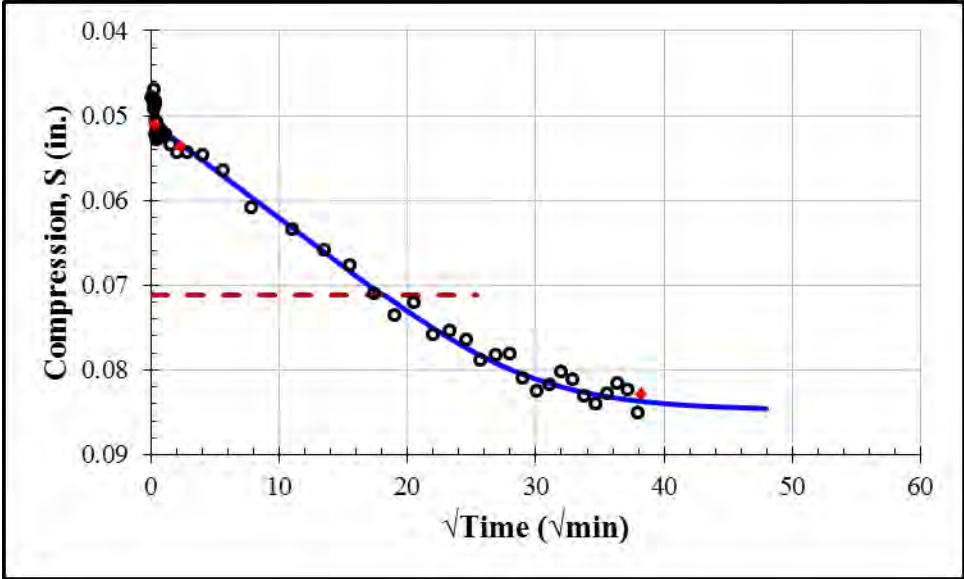
First Loading: 4125 psf				
S_0 (in.)	S_{100} (in.)	c_v (in ² /min)	k (ft/day)	t_{50} (min)
0.0093	0.0223	0.00015	7.9×10^{-9}	185



First Loading: 8125 psf				
S_0 (in.)	S_{100} (in.)	c_v (in ² /min)	k (ft/day)	t_{50} (min)
0.0253	0.0478	0.00013	5.8×10^{-9}	205

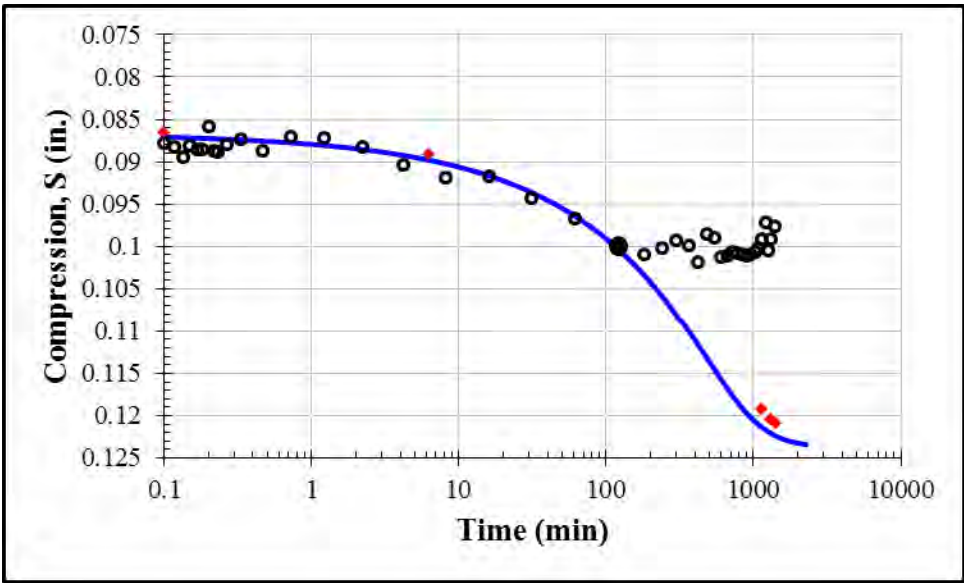
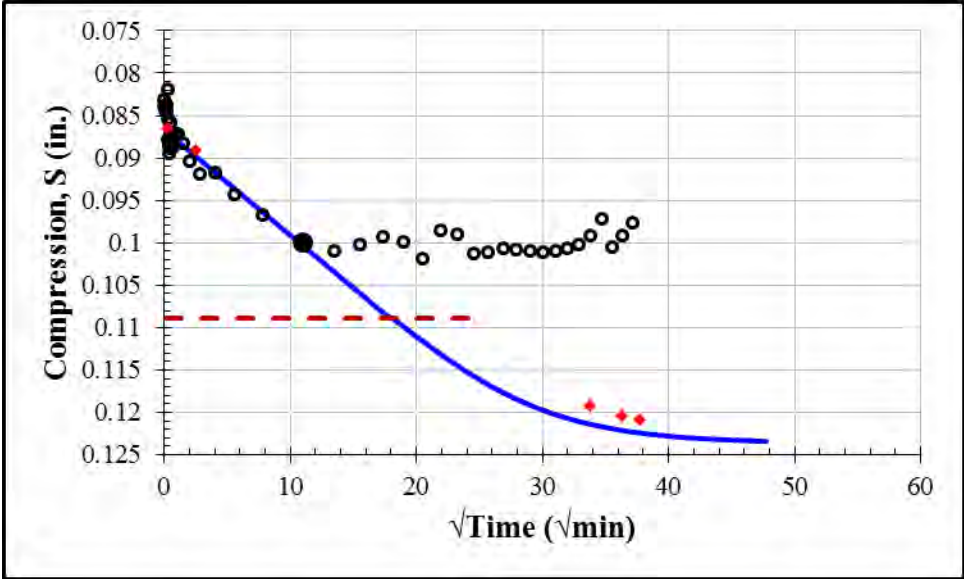


First Loading: 16125 psf				
S_0 (in.)	S_{100} (in.)	c_v (in ² /min)	k (ft/day)	t_{50} (min)
0.0507	0.0849	0.00011	3.6×10^{-9}	225



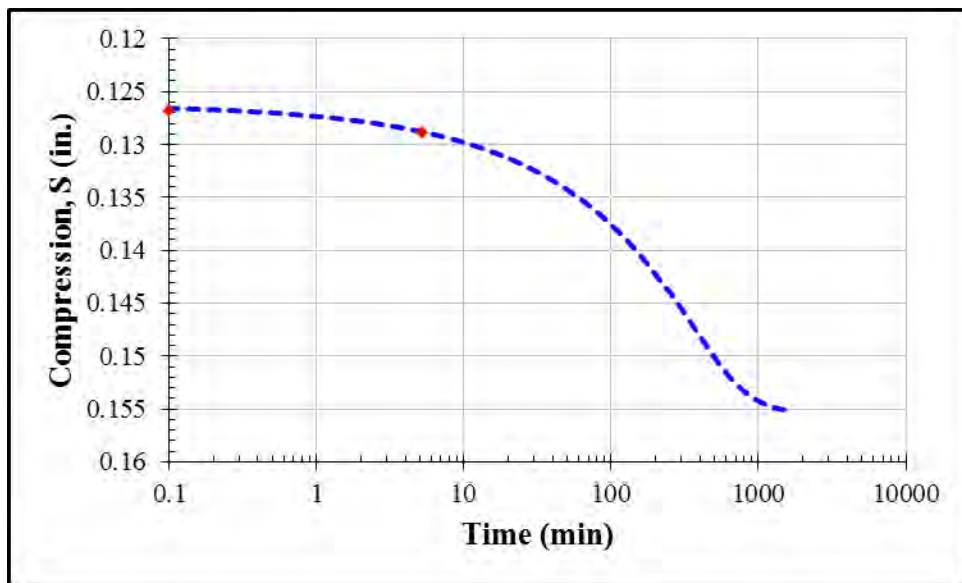
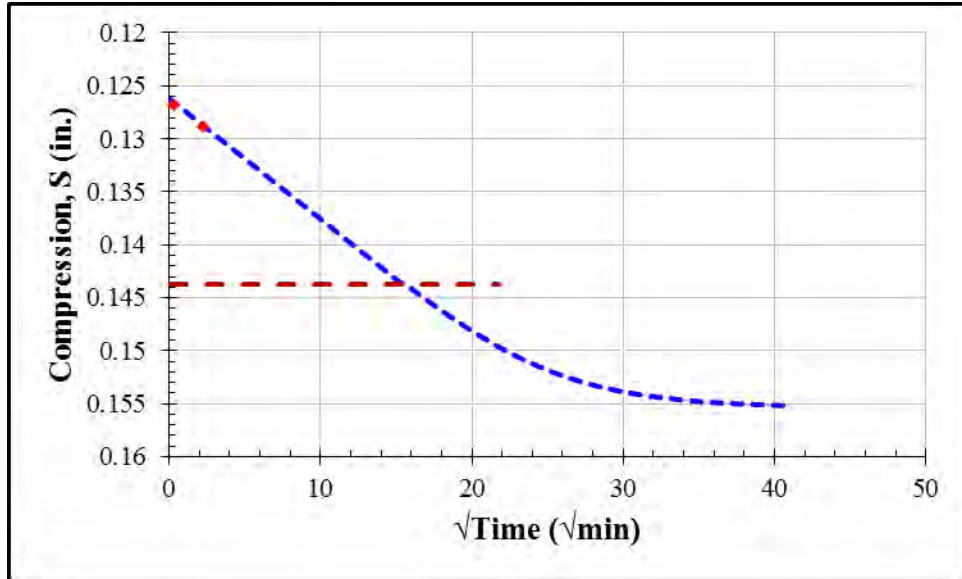
First Loading: 32125 psf				
S_0 (in.)	S_{100} (in.)	c_v (in ² /min)	k (ft/day)	t_{50} (min)
0.0867	0.1238	0.0001	1.7×10^{-9}	223

Note: LVDT lost contact during this increment. Dial gage readings were used instead.

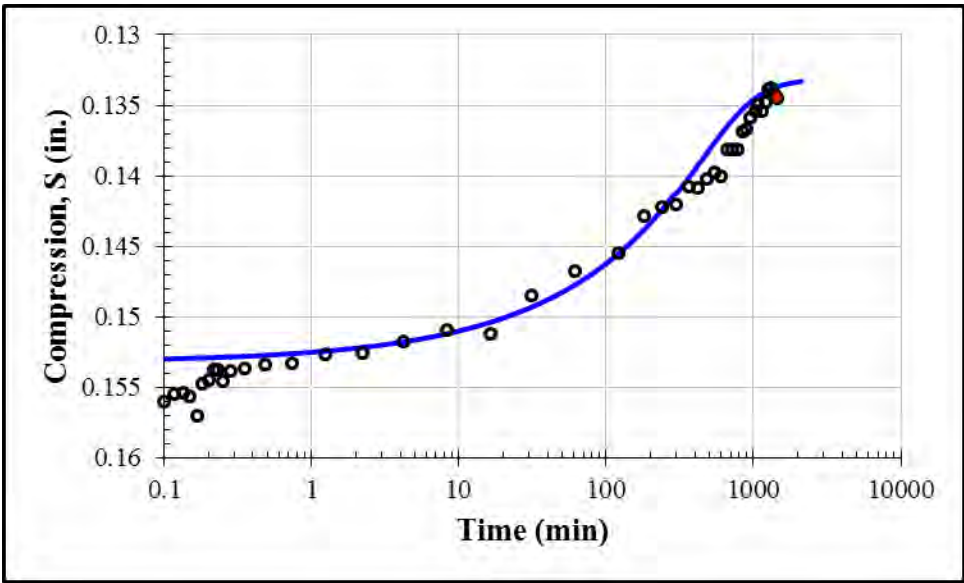
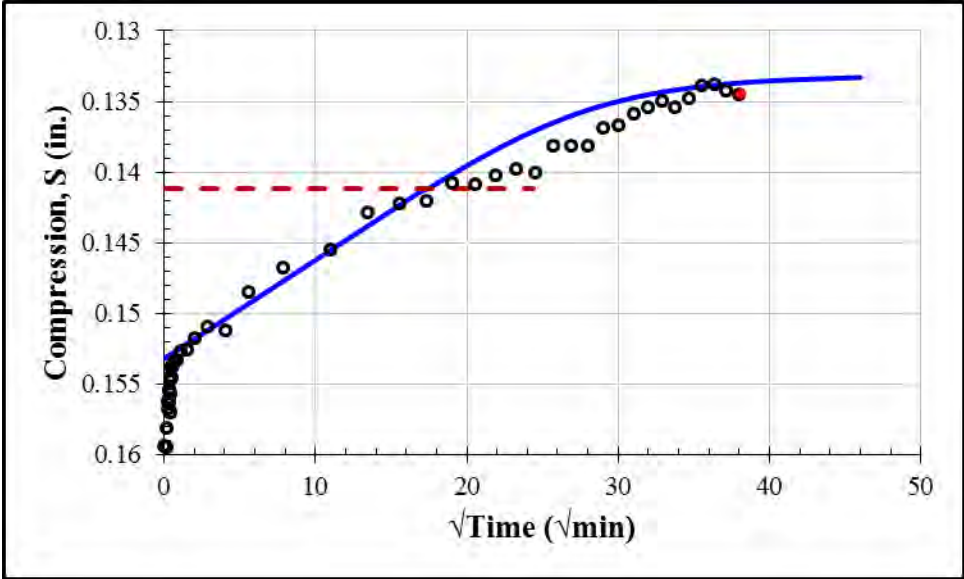


First Loading: 64125 psf				
S ₀ (in.)	S ₁₀₀ (in.)	c _v (in ² /min)	k (ft/day)	t ₅₀ (min)
0.1262	0.1555	0.00013	8.6 x 10 ⁻¹⁰	166

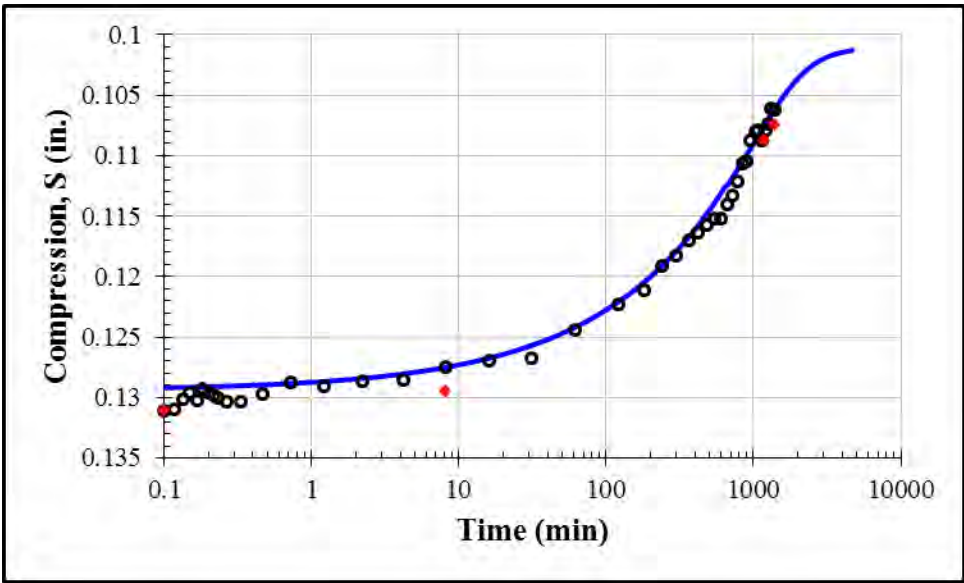
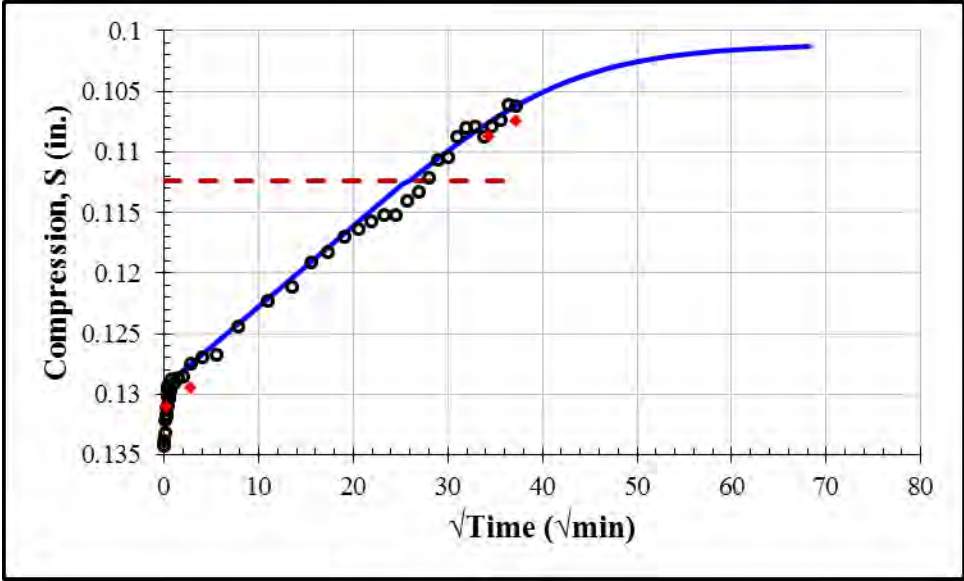
Note: LVDT and dial gage lost contact. Curve was predicted based on past experience.



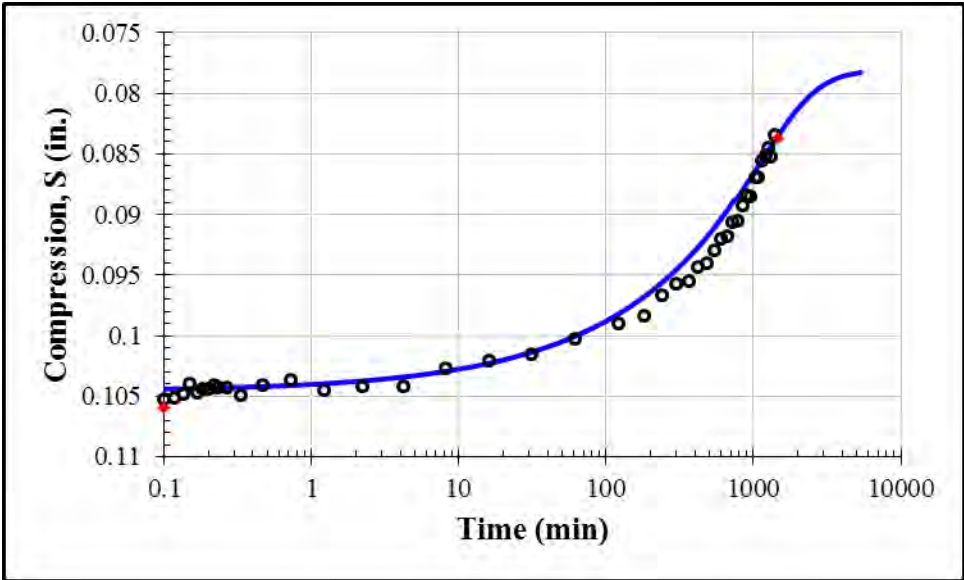
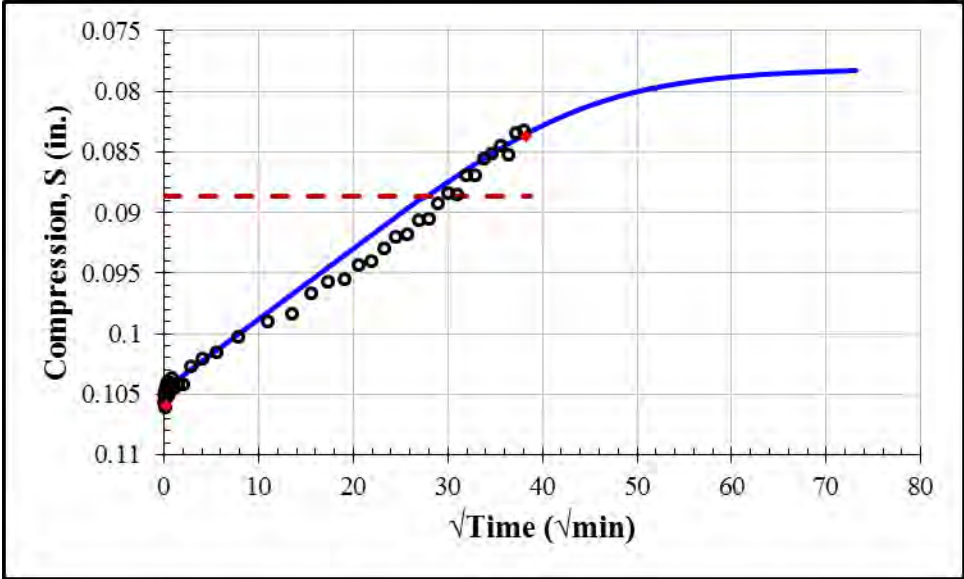
First Unloading: 16125 psf				
S_0 (in.)	S_{100} (in.)	c_v (in ² /min)	k (ft/day)	t_{50} (min)
0.1532	0.1331	0.000085	2.6×10^{-10}	207



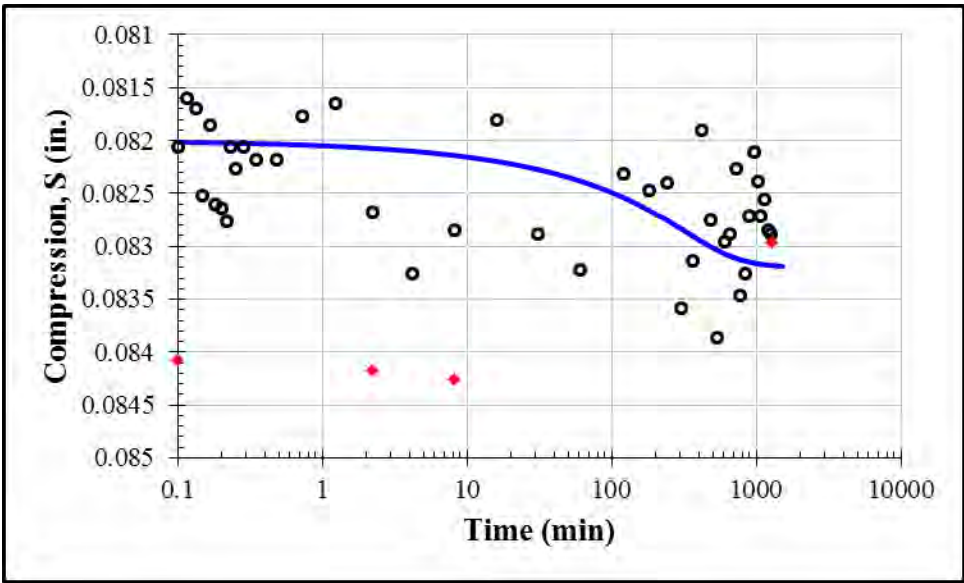
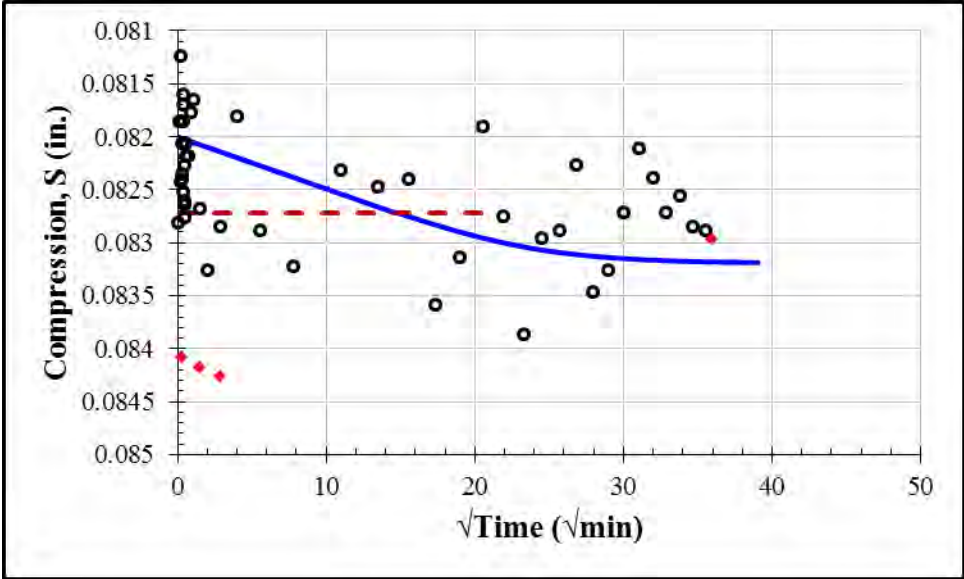
First Unloading: 4125 psf				
S_0 (in.)	S_{100} (in.)	c_v (in ² /min)	k (ft/day)	t_{50} (min)
0.1294	0.1010	0.000042	7.3×10^{-10}	456



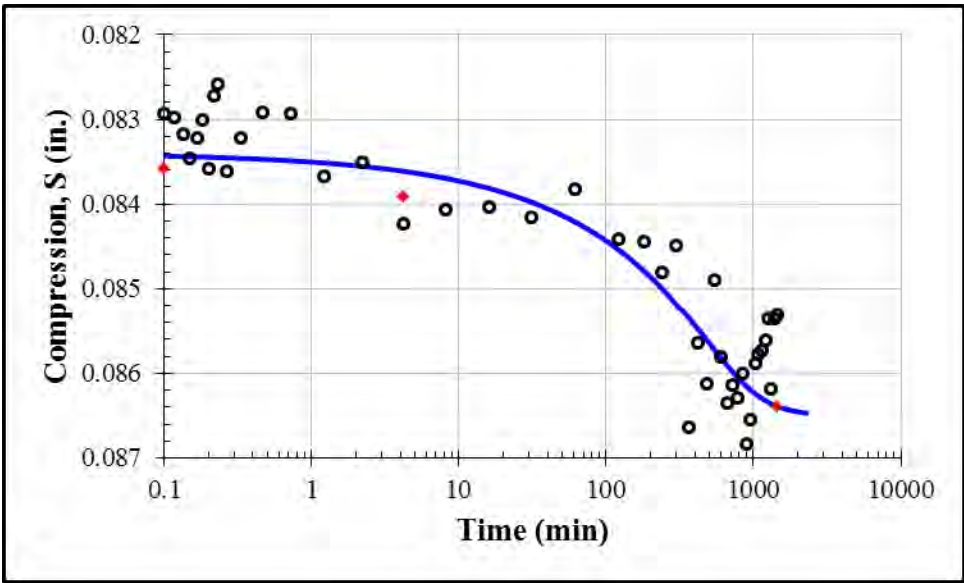
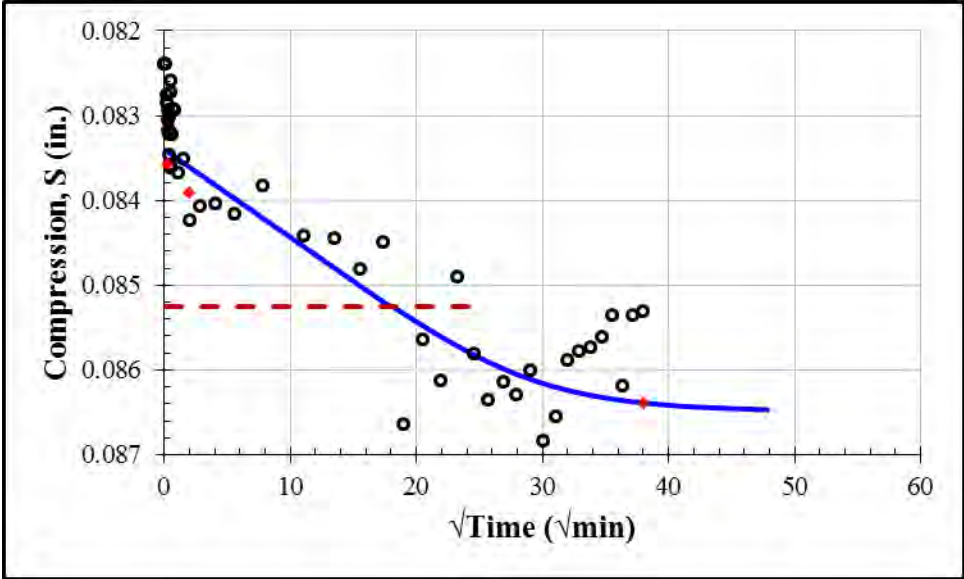
First Unloading: 1000 psf				
S_0 (in.)	S_{100} (in.)	c_v (in ² /min)	k (ft/day)	t_{50} (min)
0.1046	0.0780	0.00004	2.6×10^{-10}	524



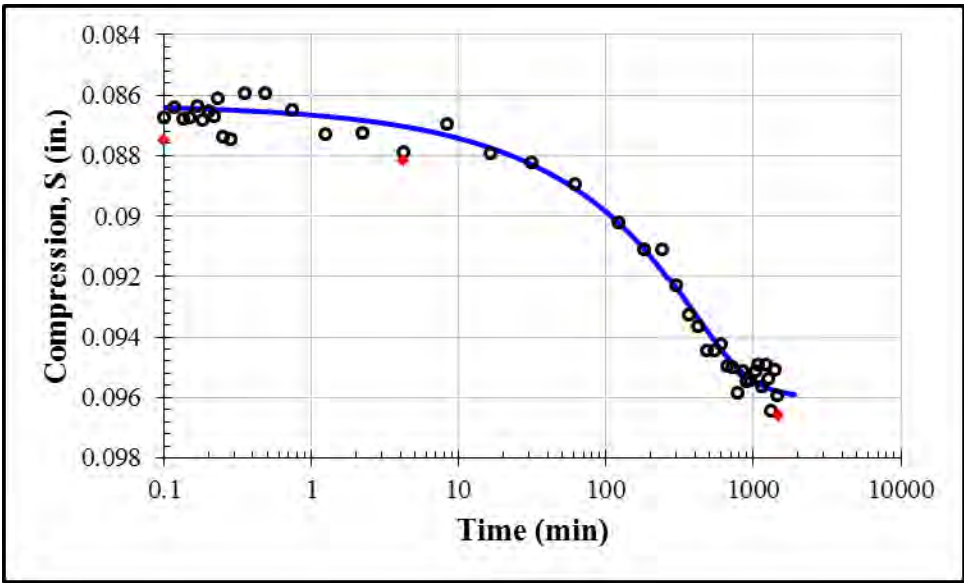
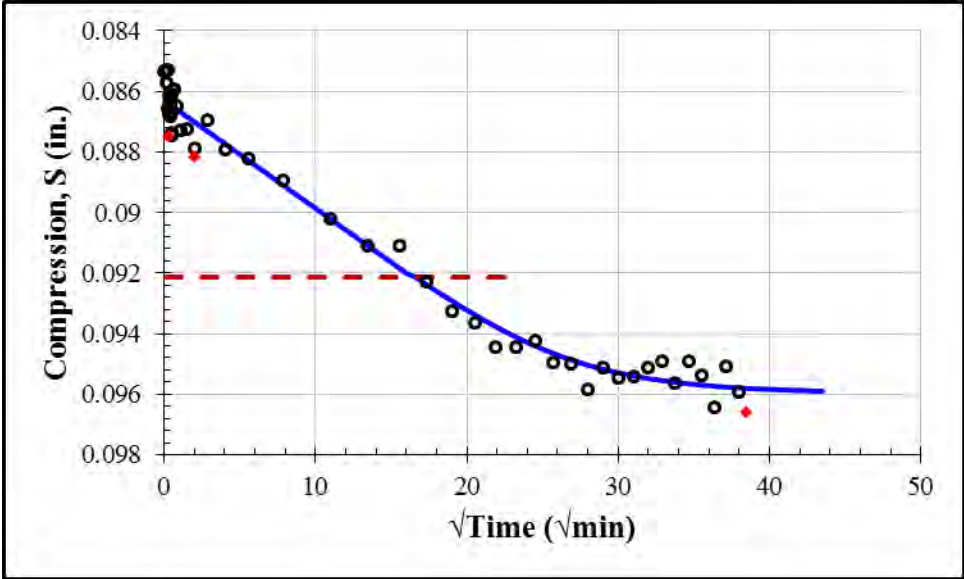
Second Loading: 2000 psf				
S_0 (in.)	S_{100} (in.)	c_v (in ² /min)	k (ft/day)	t_{50} (min)
0.0820	0.0832	0.00015	1.4×10^{-9}	149



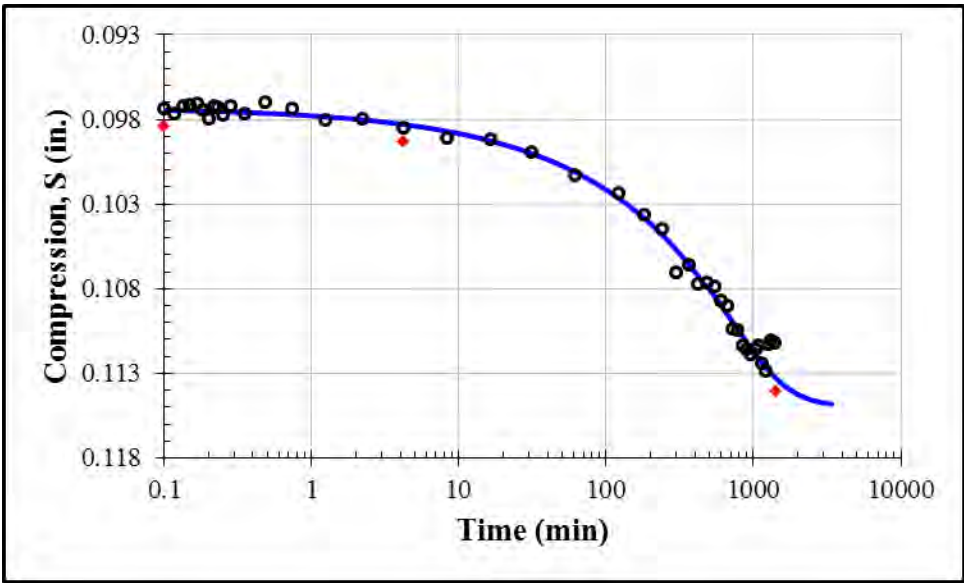
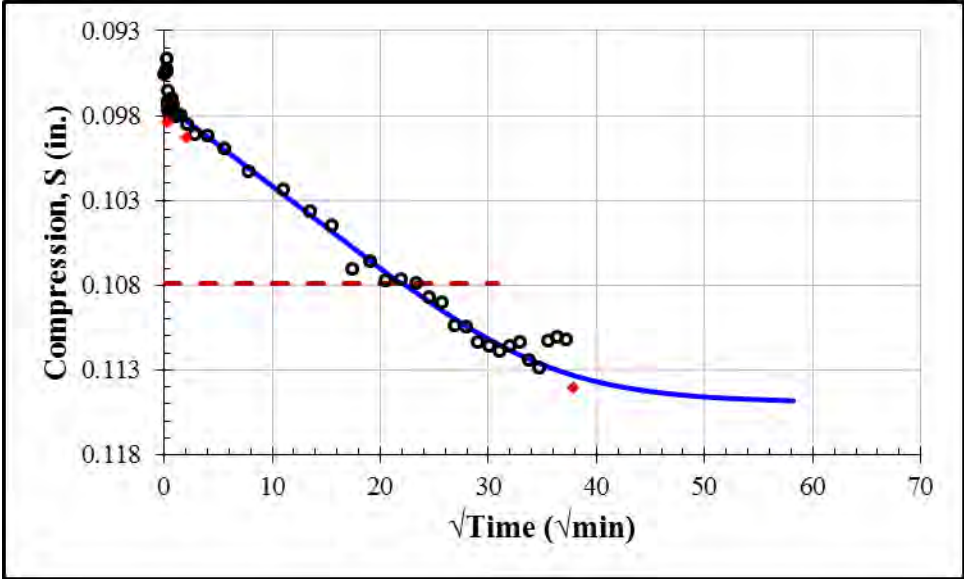
Second Loading: 4000 psf				
S_0 (in.)	S_{100} (in.)	c_v (in ² /min)	k (ft/day)	t_{50} (min)
0.0834	0.0865	0.0001	1.2×10^{-9}	224



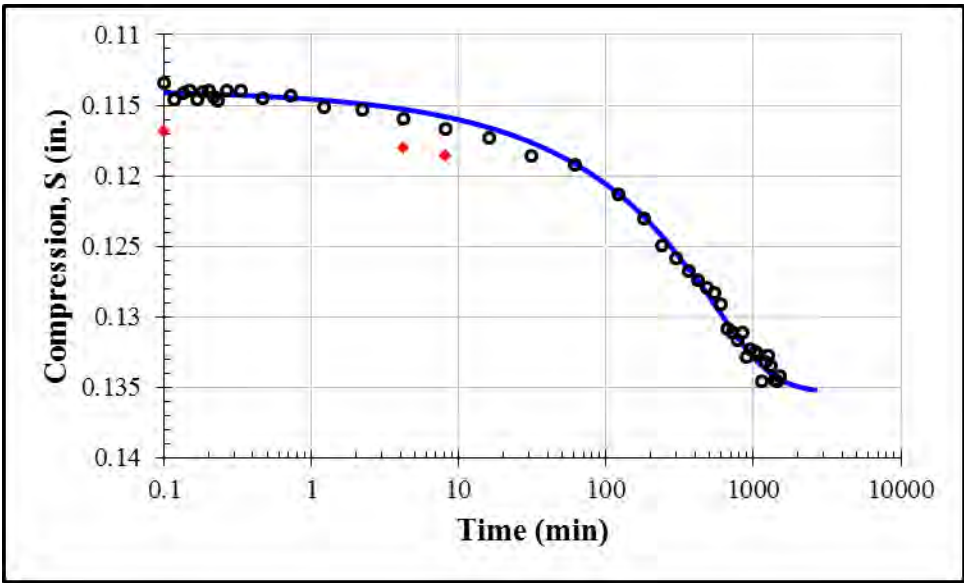
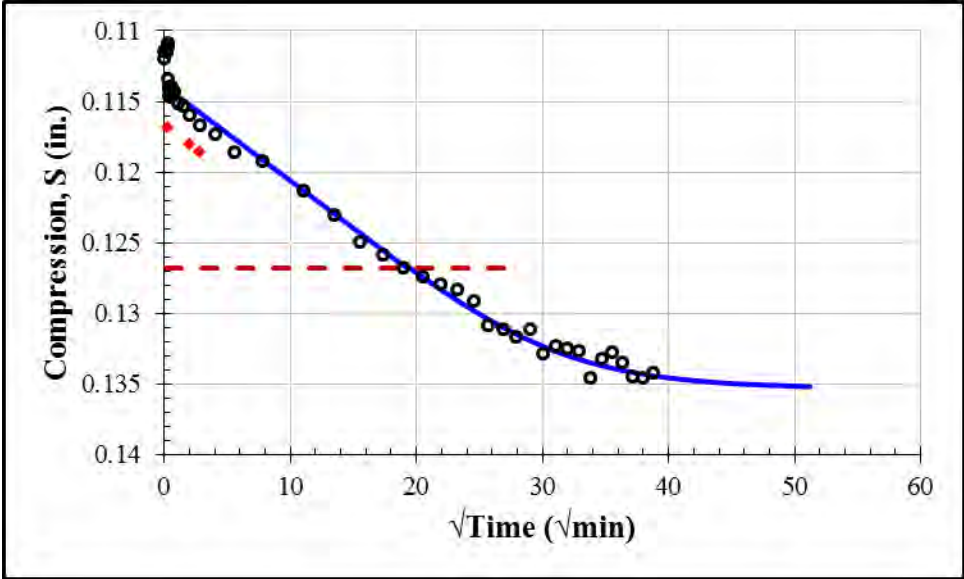
Second Loading: 8000 psf				
S_0 (in.)	S_{100} (in.)	c_v (in ² /min)	k (ft/day)	t_{50} (min)
0.0863	0.0960	0.00012	2.2×10^{-9}	185



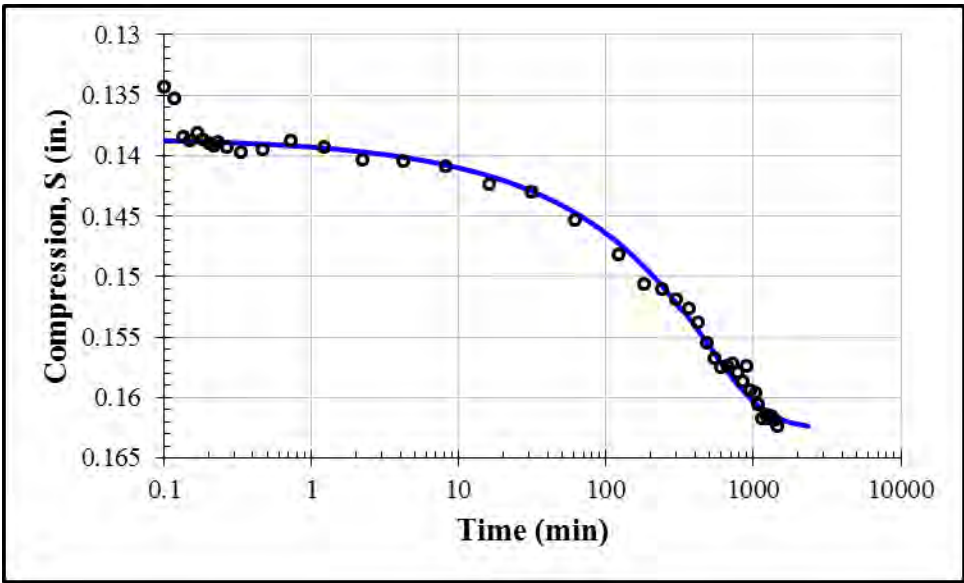
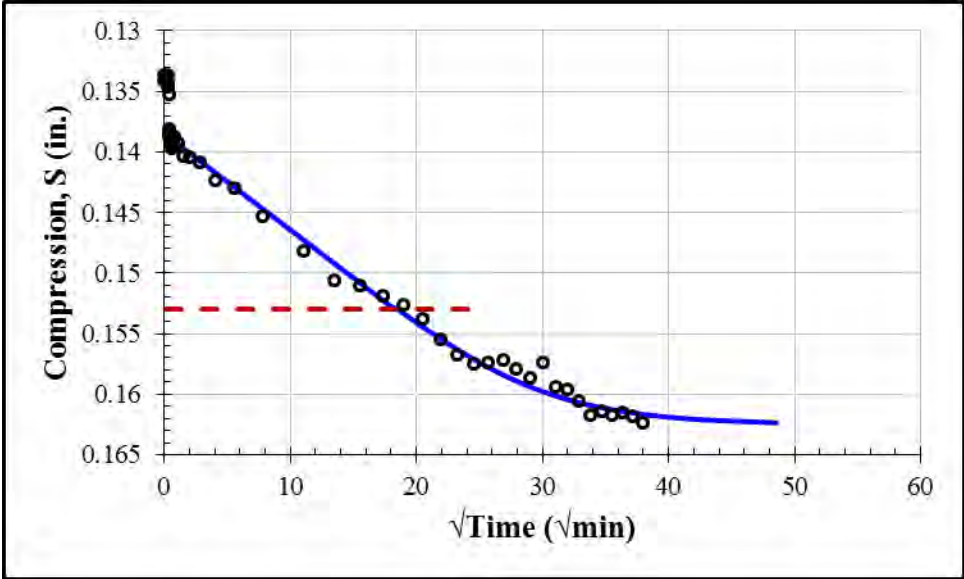
Second Loading: 16000 psf				
S_0 (in.)	S_{100} (in.)	c_v (in ² /min)	k (ft/day)	t_{50} (min)
0.0973	0.1150	0.000065	1.1×10^{-9}	332



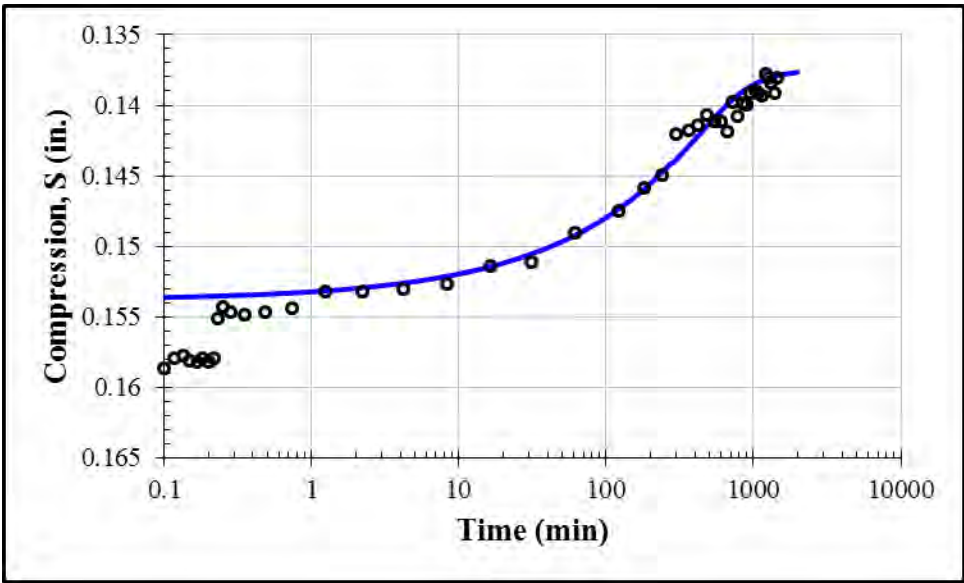
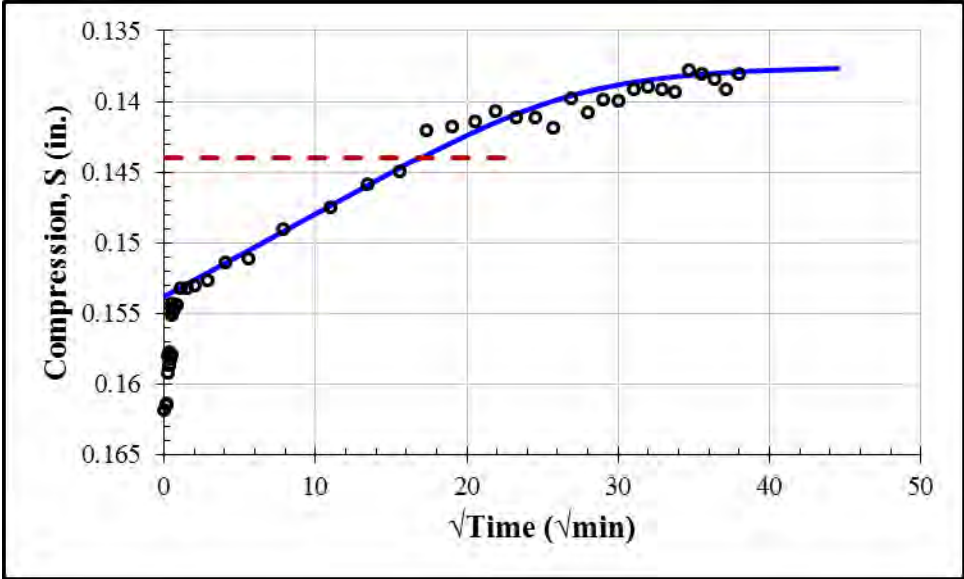
Second Loading: 32000 psf				
S_0 (in.)	S_{100} (in.)	c_v (in ² /min)	k (ft/day)	t_{50} (min)
0.1139	0.1354	0.00008	7.9×10^{-10}	257



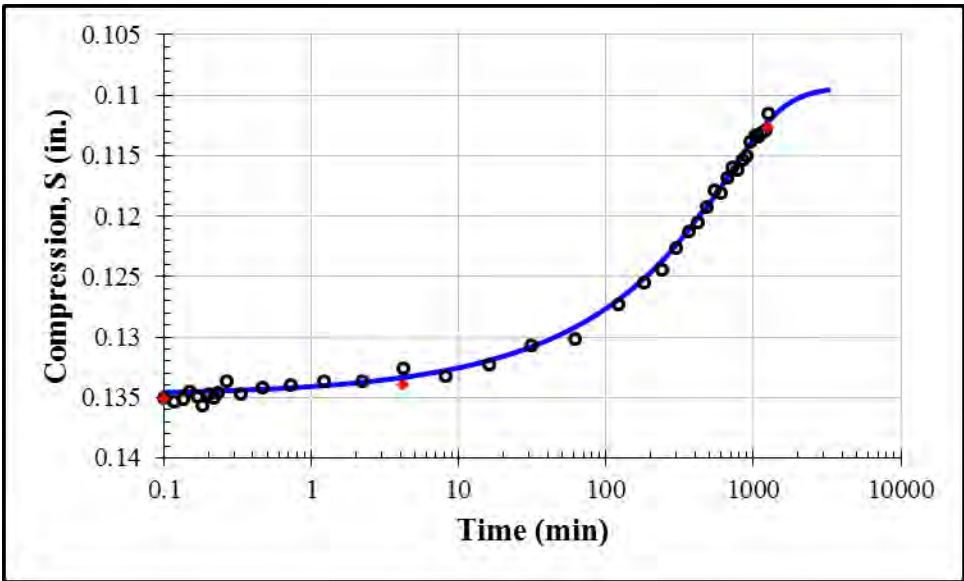
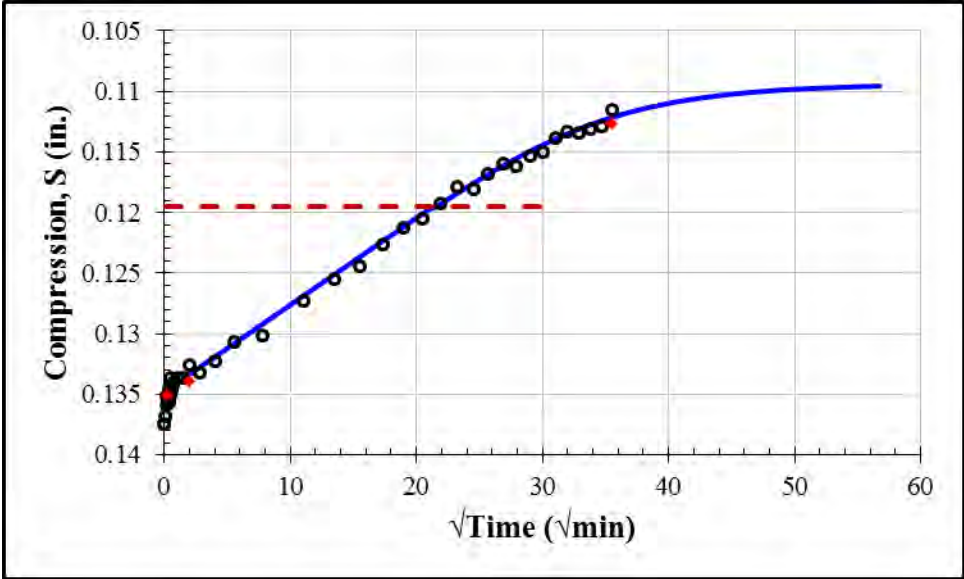
Second Loading: 64000 psf				
S_0 (in.)	S_{100} (in.)	c_v (in ² /min)	k (ft/day)	t_{50} (min)
0.1385	0.1626	0.000083	4.5×10^{-10}	231



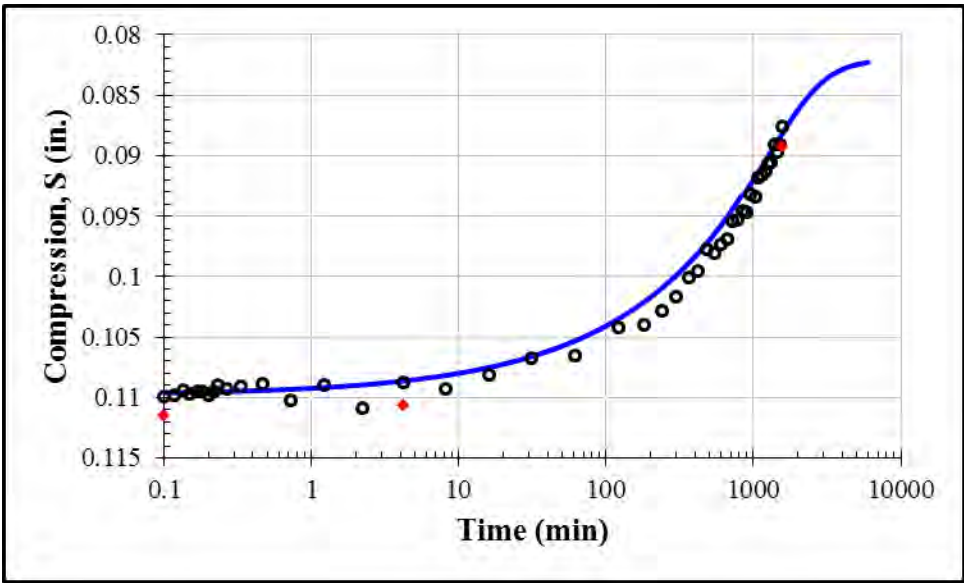
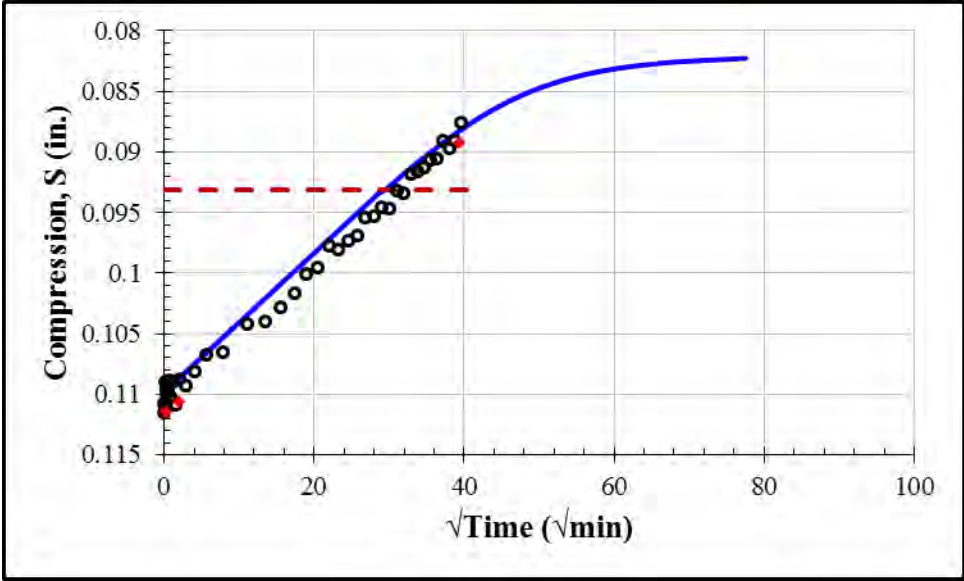
Second Unloading: 16000 psf				
S_0 (in.)	S_{100} (in.)	c_v (in ² /min)	k (ft/day)	t_{50} (min)
0.1538	0.1375	0.00009	2.2×10^{-10}	194



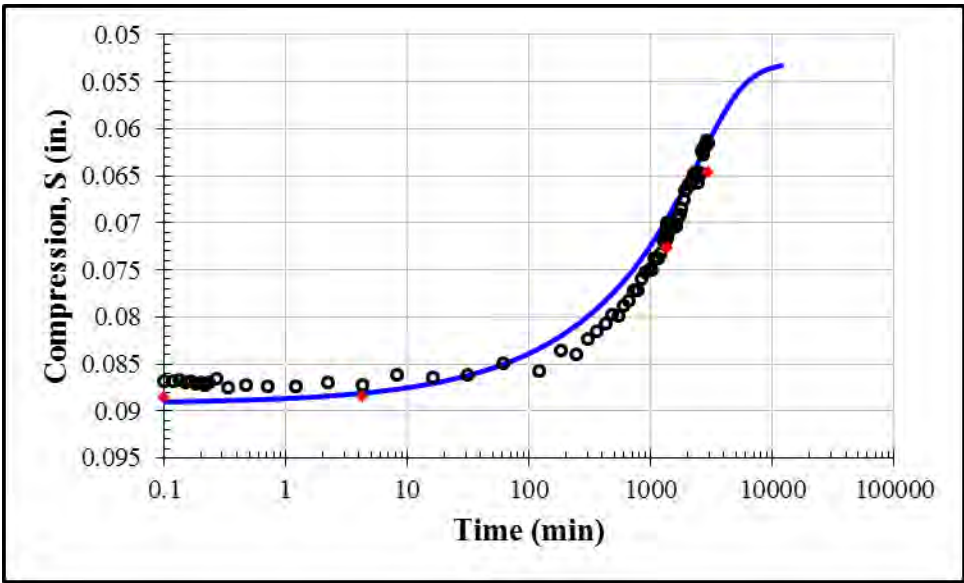
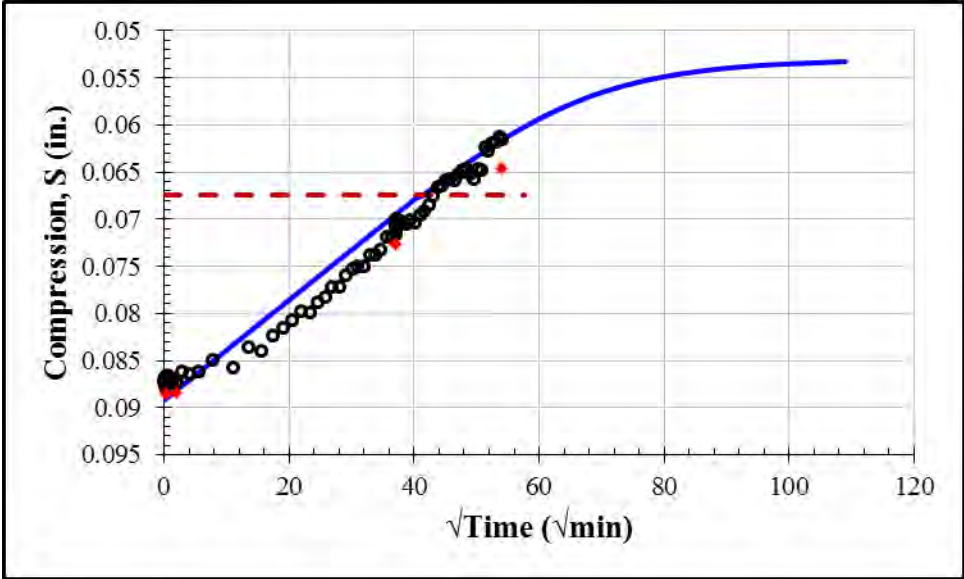
Second Unloading: 4000 psf				
S_0 (in.)	S_{100} (in.)	c_v (in ² /min)	k (ft/day)	t_{50} (min)
0.1348	0.1093	0.00006	9.4×10^{-10}	315



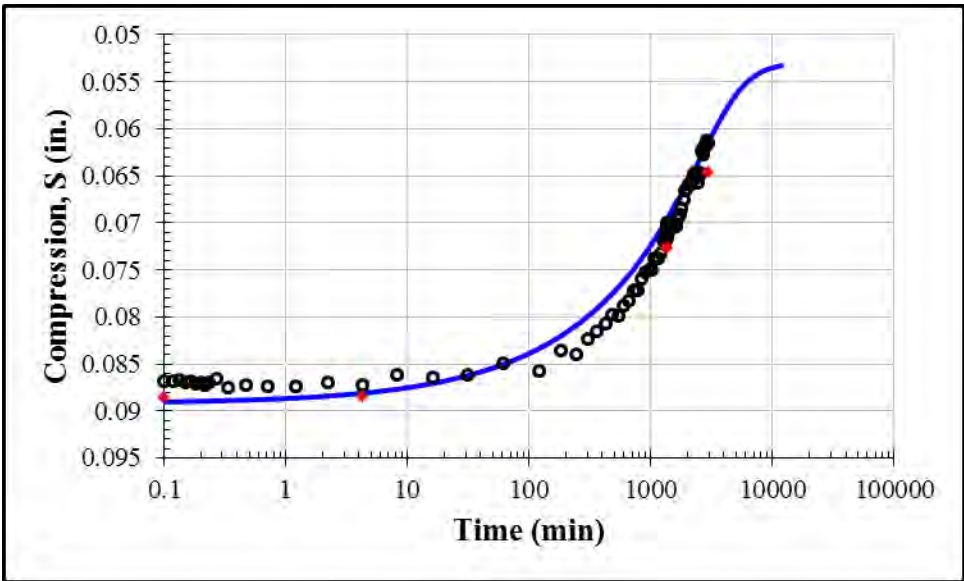
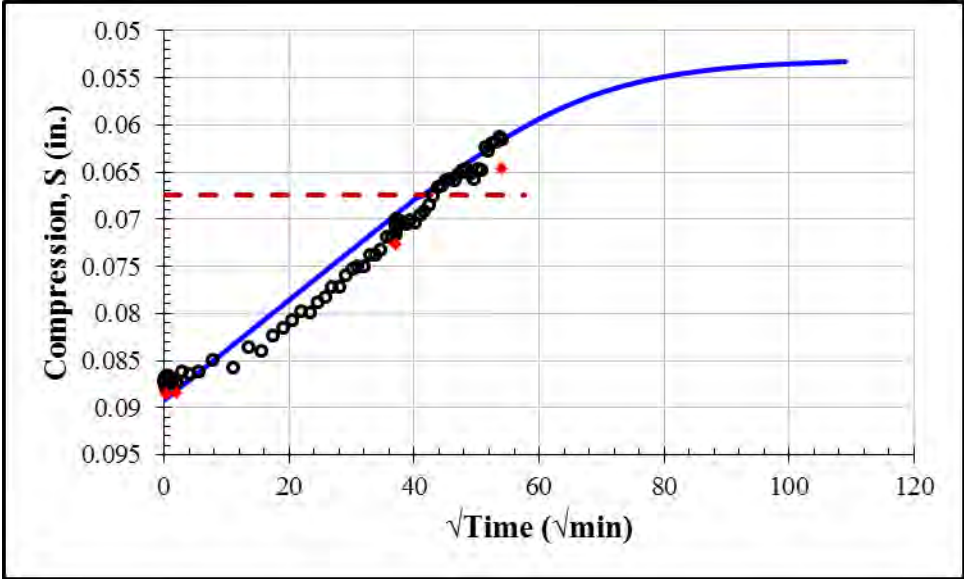
Second Unloading: 1000 psf				
S_0 (in.)	S_{100} (in.)	c_v (in ² /min)	k (ft/day)	t_{50} (min)
0.1098	0.0820	0.000035	2.4×10^{-9}	588



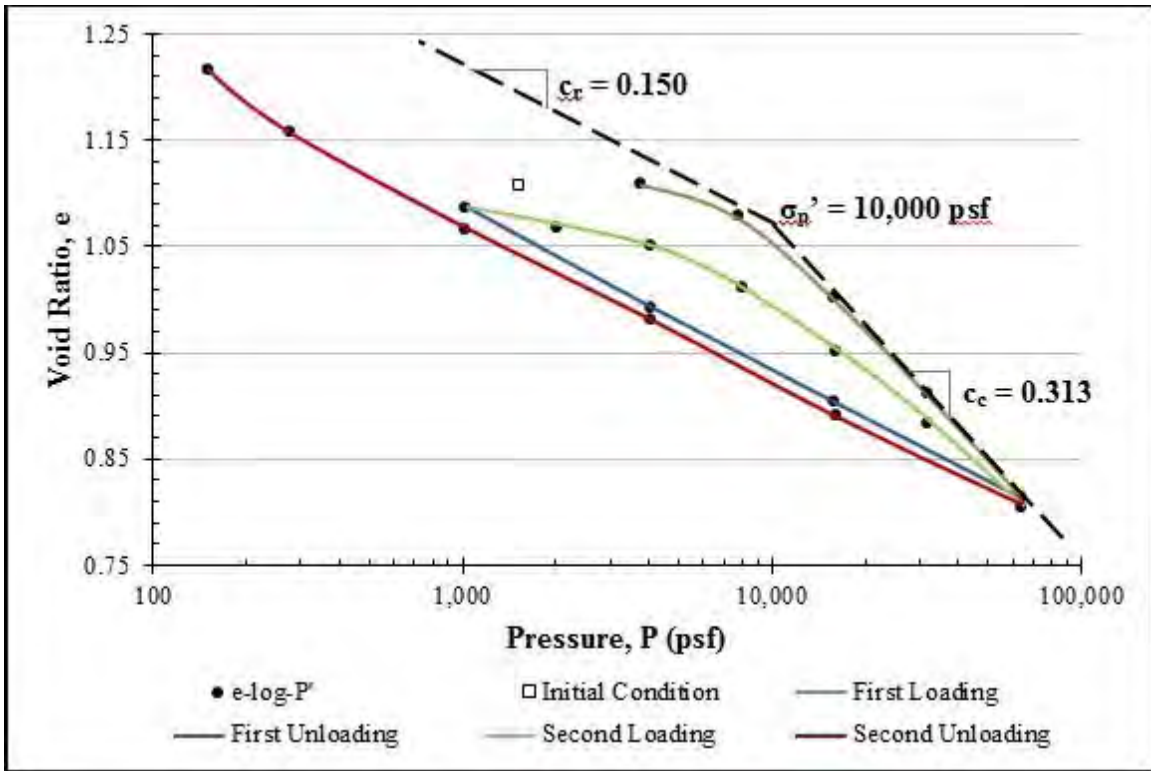
Second Unloading: 250 psf				
S_0 (in.)	S_{100} (in.)	c_v (in ² /min)	k (ft/day)	t_{50} (min)
0.0892	0.0529	0.000019	7.1×10^{-9}	1164



Second Unloading: 125 psf				
S_0 (in.)	S_{100} (in.)	c_v (in ² /min)	k (ft/day)	t_{50} (min)
0.0892	0.0529	0.000019	1.4×10^{-8}	1164



Appendix F: Consolidation Test 5



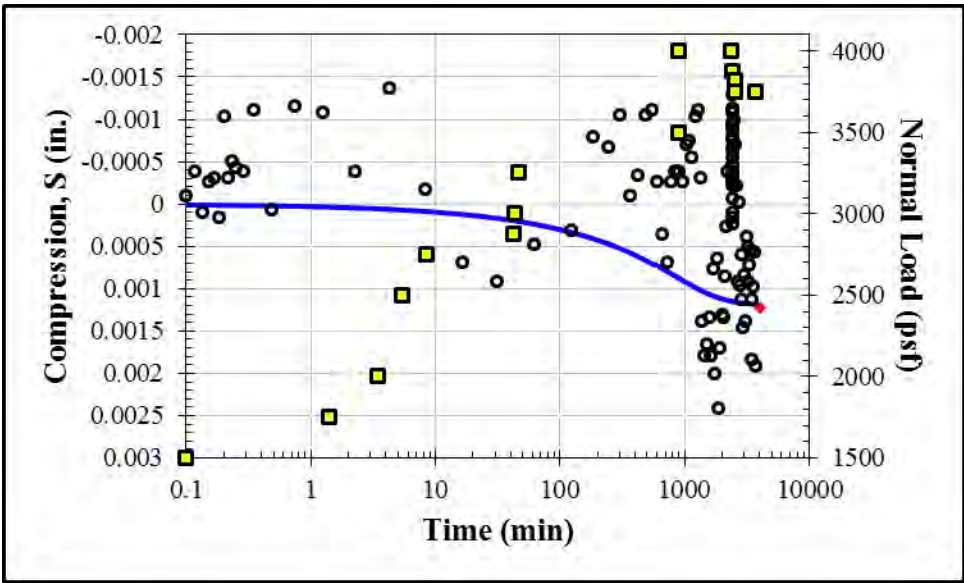
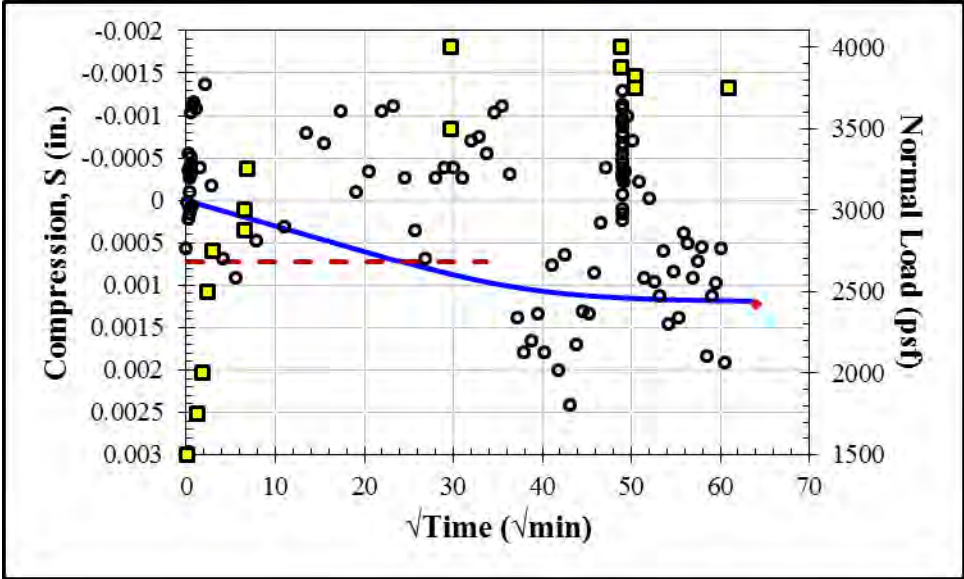
$$c_c = -\frac{e_2 - e_1}{\log(\sigma_2 / \sigma_1)} = -\frac{0.788 - 1.071}{\log(80000 / 10000)} = 0.313$$

$$c_r = -\frac{e_2 - e_1}{\log(\sigma_2 / \sigma_1)} = -\frac{1.071 - 1.235}{\log(10000 / 800)} = 0.150$$

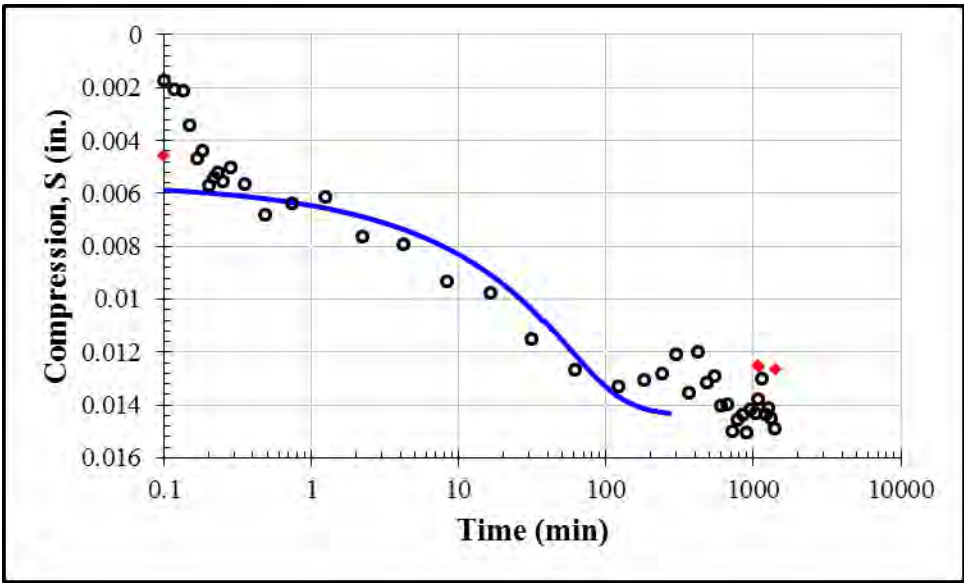
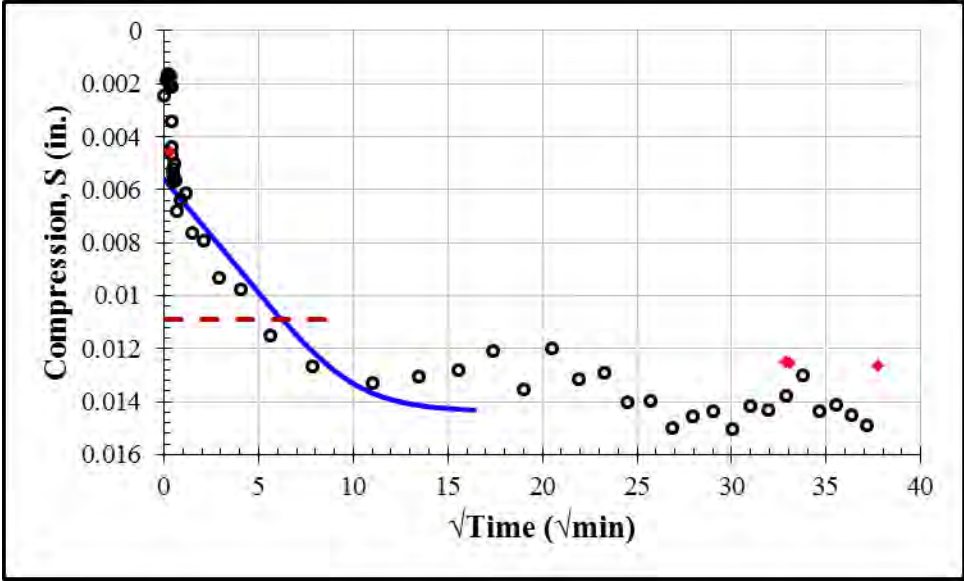
$$R_c = \frac{c_c}{1 + e_0} = \frac{0.313}{1 + 1.1076} = 0.149$$

$$R_r = \frac{c_r}{1 + e_0} = \frac{0.150}{1 + 1.1076} = 0.071$$

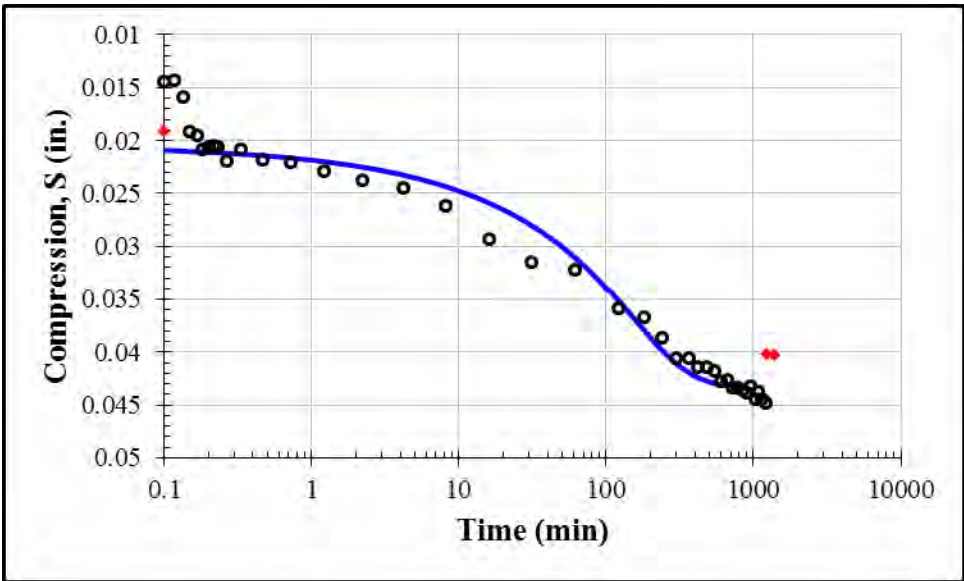
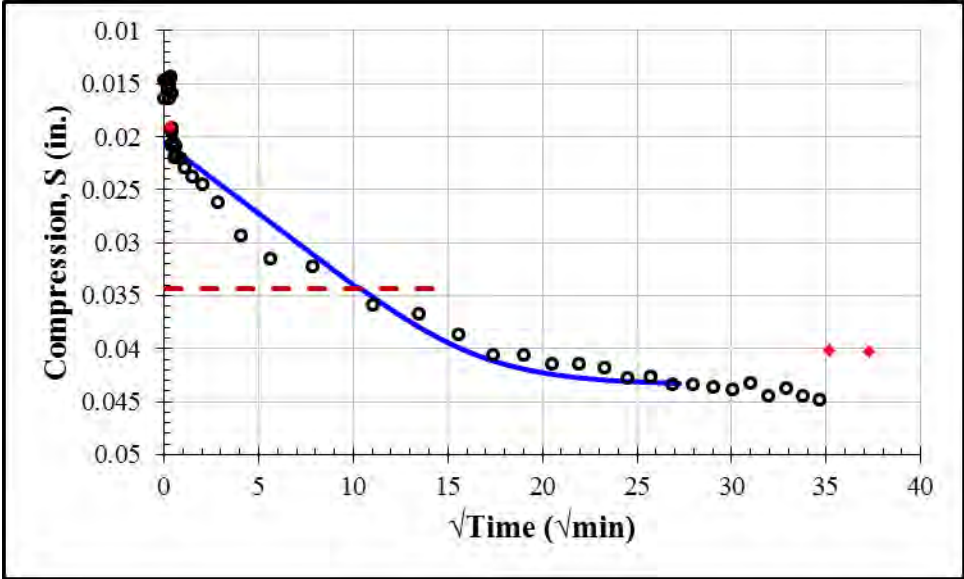
Soaking at Constant Volume Starting at 1500 psf				
S_0 (in.)	S_{100} (in.)	c_v (in ² /min)	k (ft/day)	t_{50} (min)
0.0000	0.0012	0.000067	3.0×10^{-10}	395



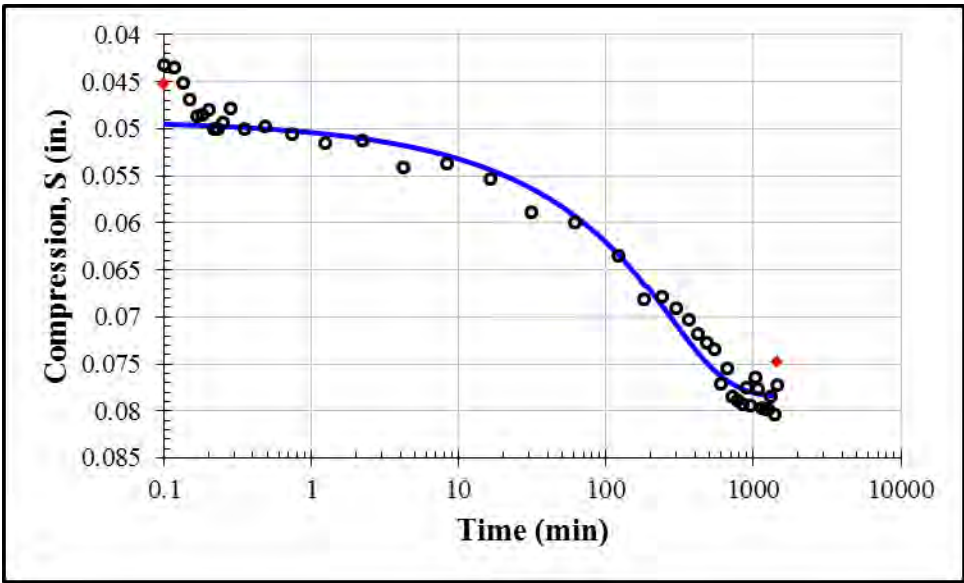
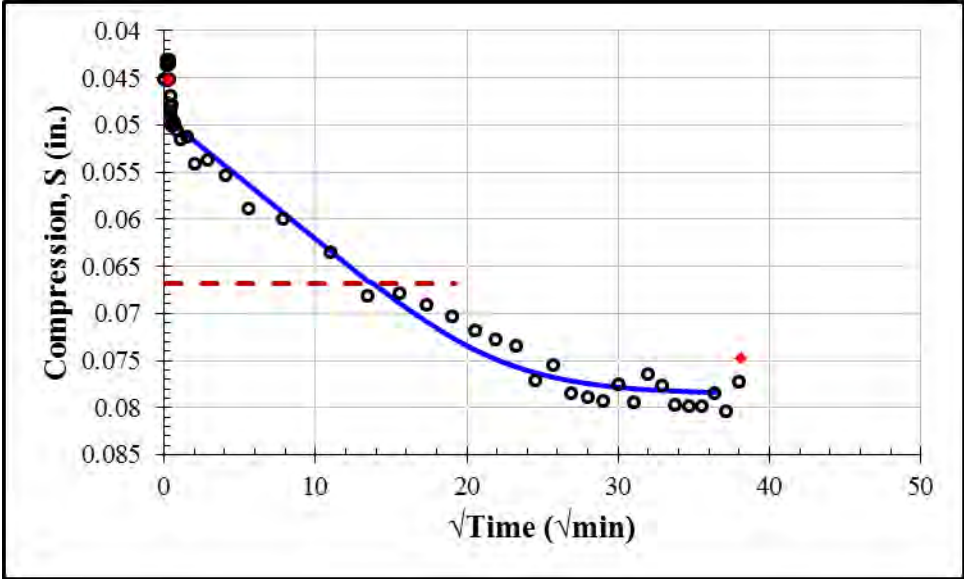
First Loading: 7750 psf				
S_0 (in.)	S_{100} (in.)	c_v (in ² /min)	k (ft/day)	t_{50} (min)
0.0056	0.0144	0.001	1.9×10^{-8}	26



First Loading: 15750 psf				
S_0 (in.)	S_{100} (in.)	c_v (in ² /min)	k (ft/day)	t_{50} (min)
0.0205	0.0435	0.00035	8.3×10^{-8}	73

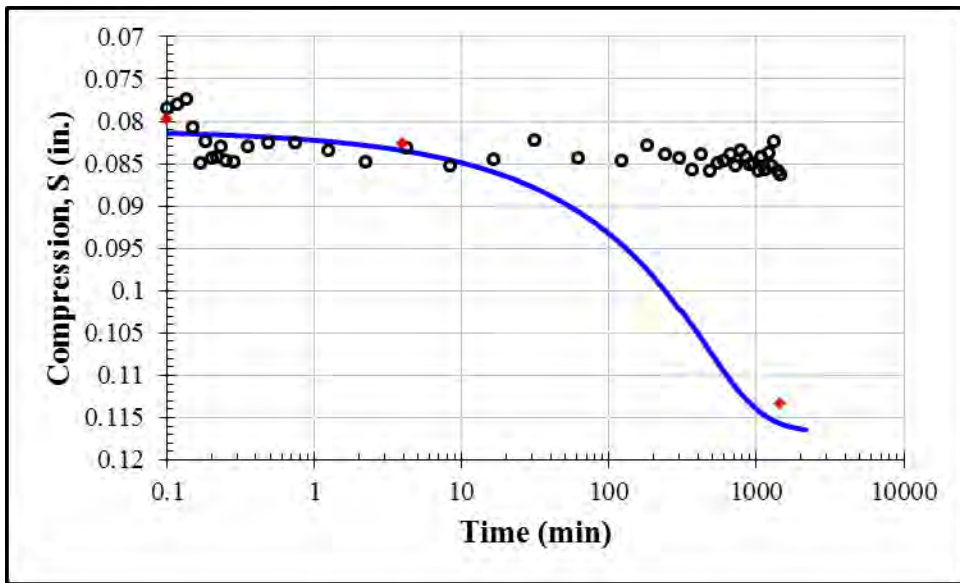
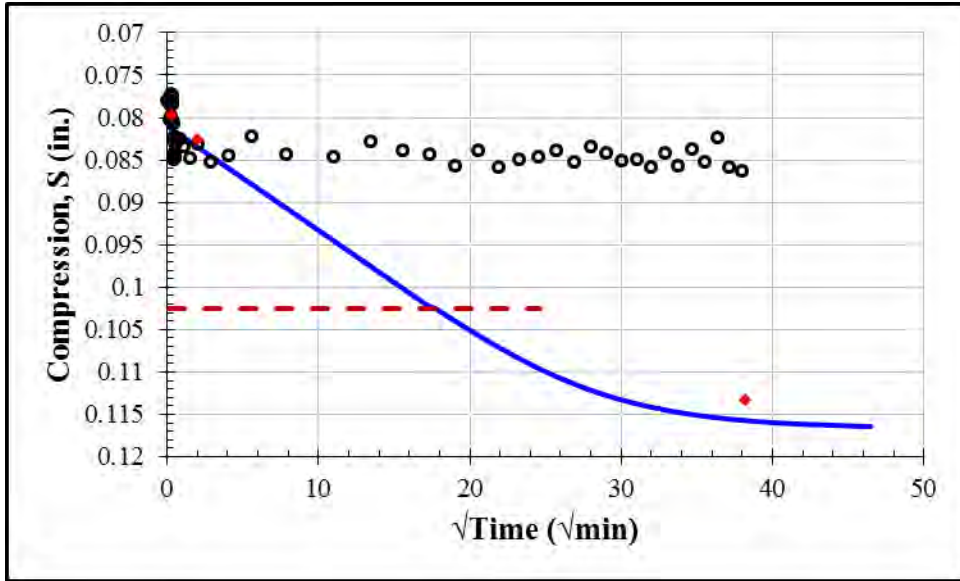


First Loading: 31750 psf				
S_0 (in.)	S_{100} (in.)	c_v (in ² /min)	k (ft/day)	t_{50} (min)
0.0491	0.0787	0.00018	2.7×10^{-9}	130

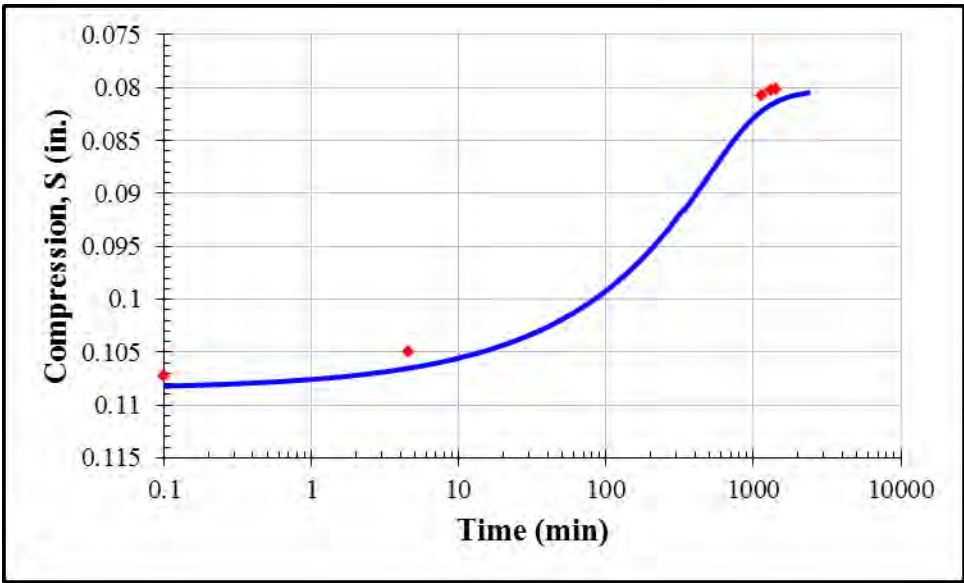
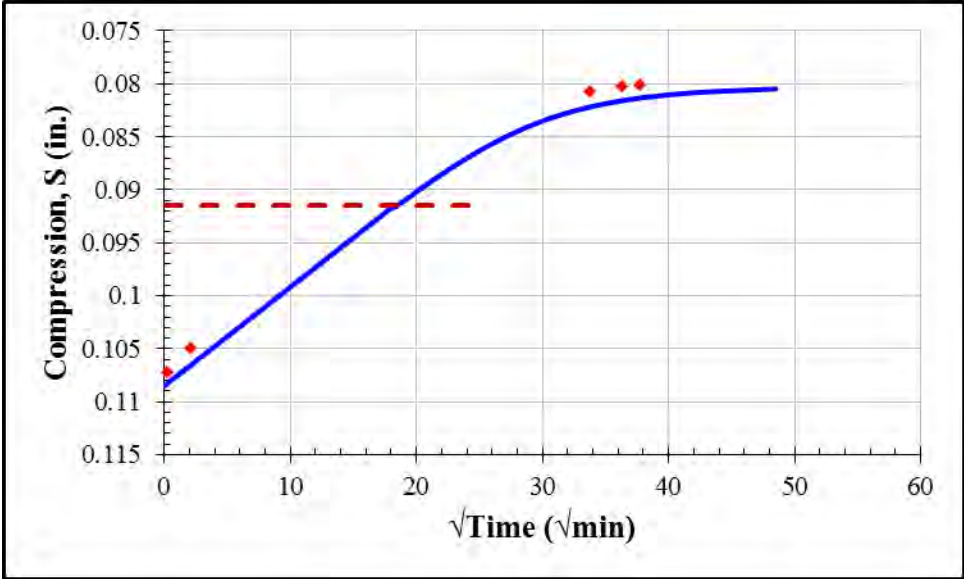


First Loading: 63750 psf				
S_0 (in.)	S_{100} (in.)	c_v (in ² /min)	k (ft/day)	t_{50} (min)
0.0810	0.1168	0.0001	8.6×10^{-10}	212

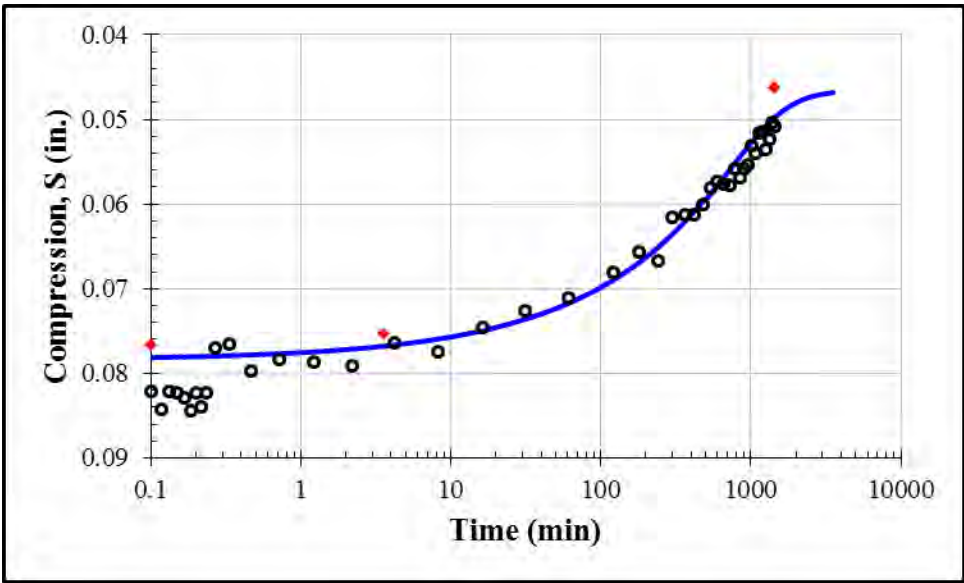
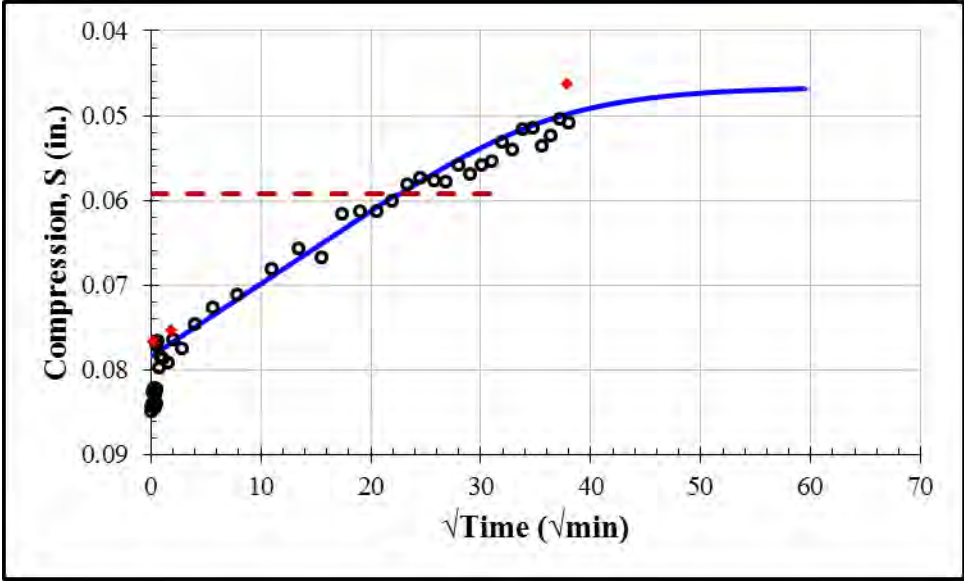
Note: The LVDT lost contact during this load increment. The dial gage was used instead.



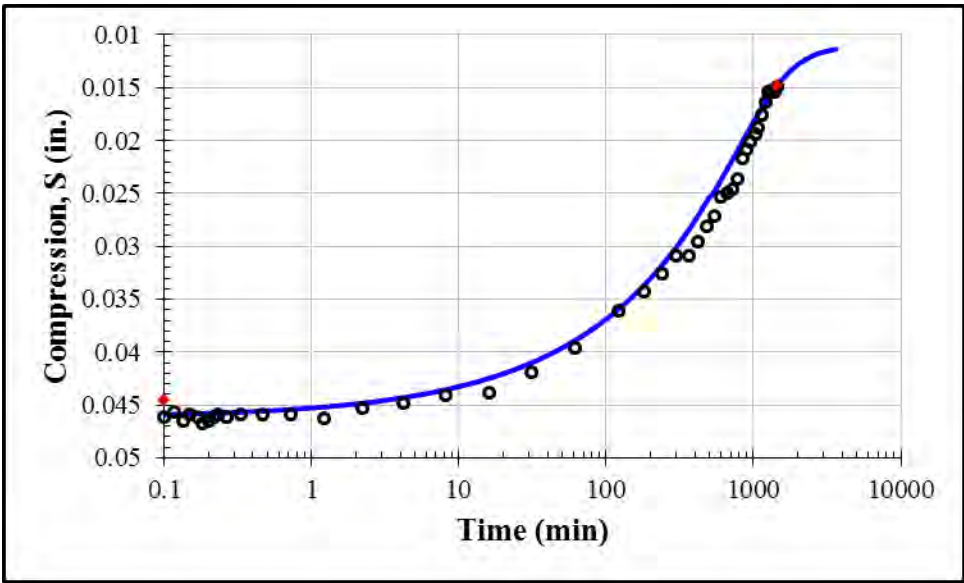
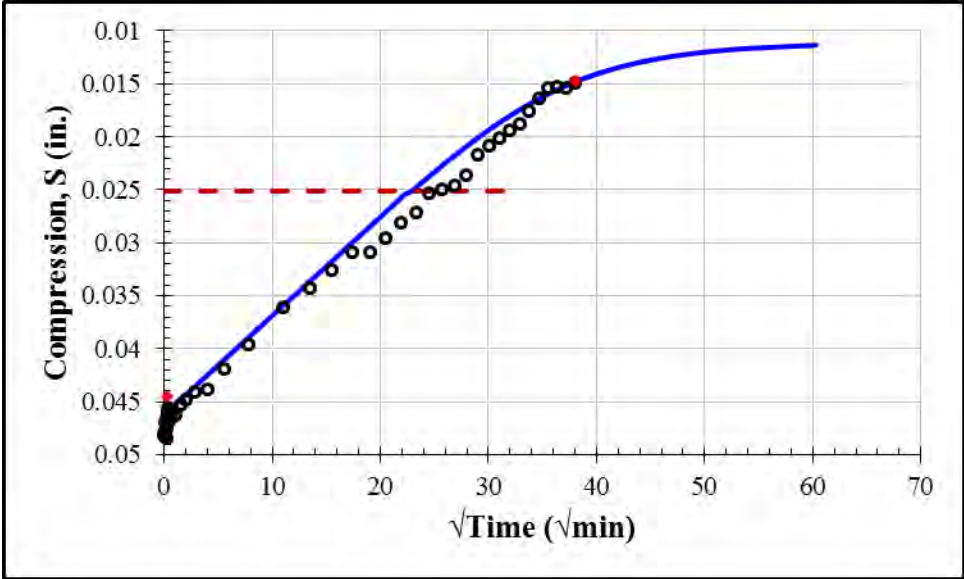
First Unloading: 15750 psf				
S_0 (in.)	S_{100} (in.)	c_v (in ² /min)	k (ft/day)	t_{50} (min)
0.1085	0.0802	0.00009	4.1×10^{-10}	230



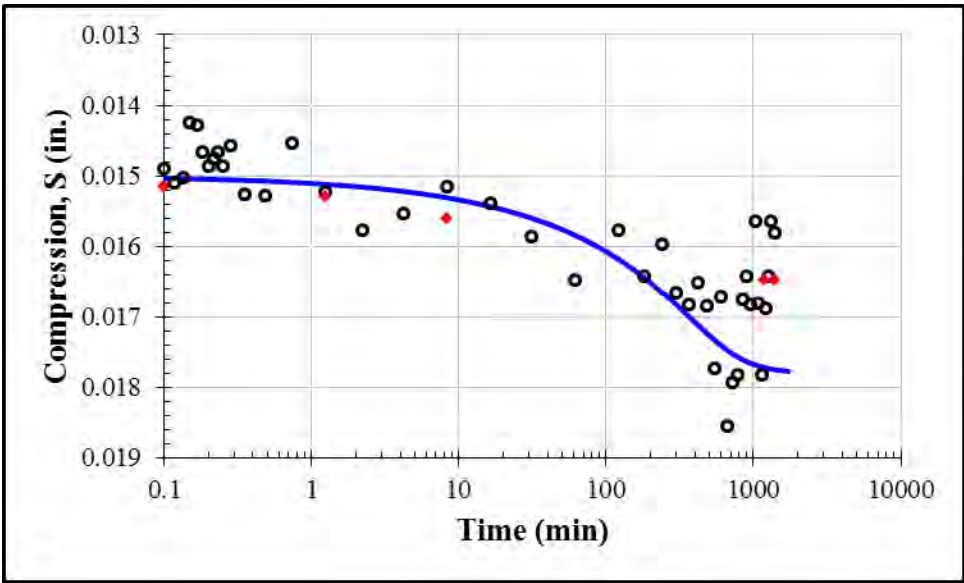
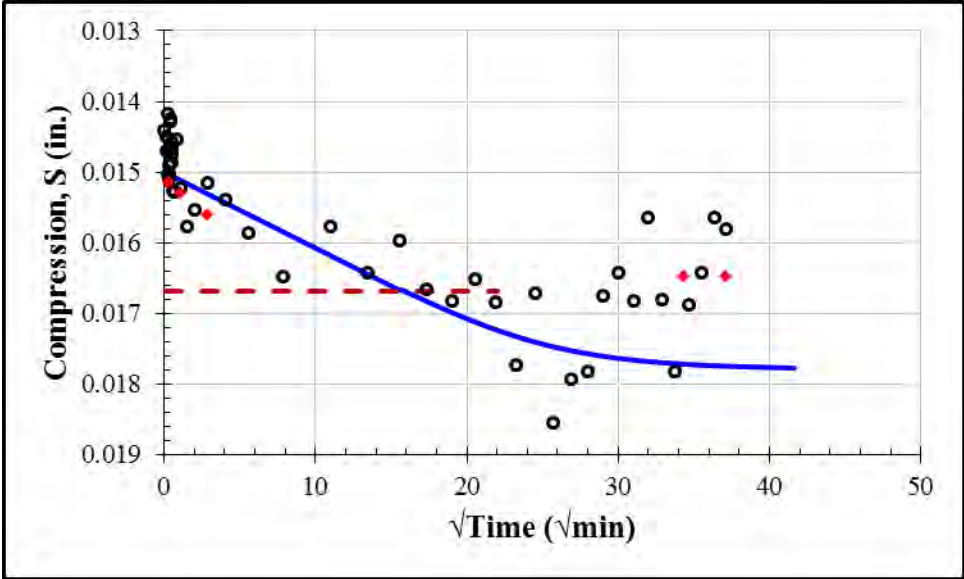
Second Unloading: 4000 psf				
S_0 (in.)	S_{100} (in.)	c_v (in ² /min)	k (ft/day)	t_{50} (min)
0.0784	0.0465	0.00006	1.3×10^{-9}	346



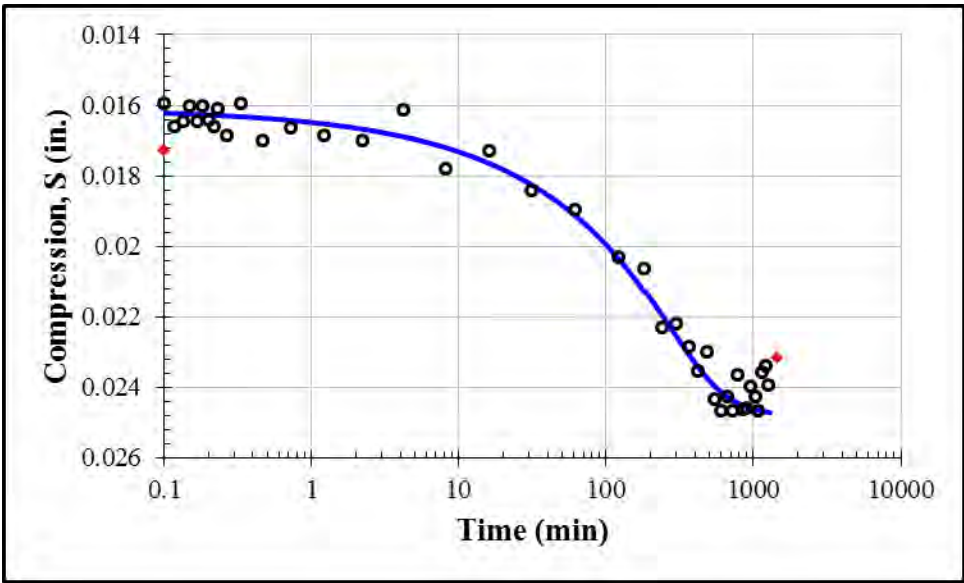
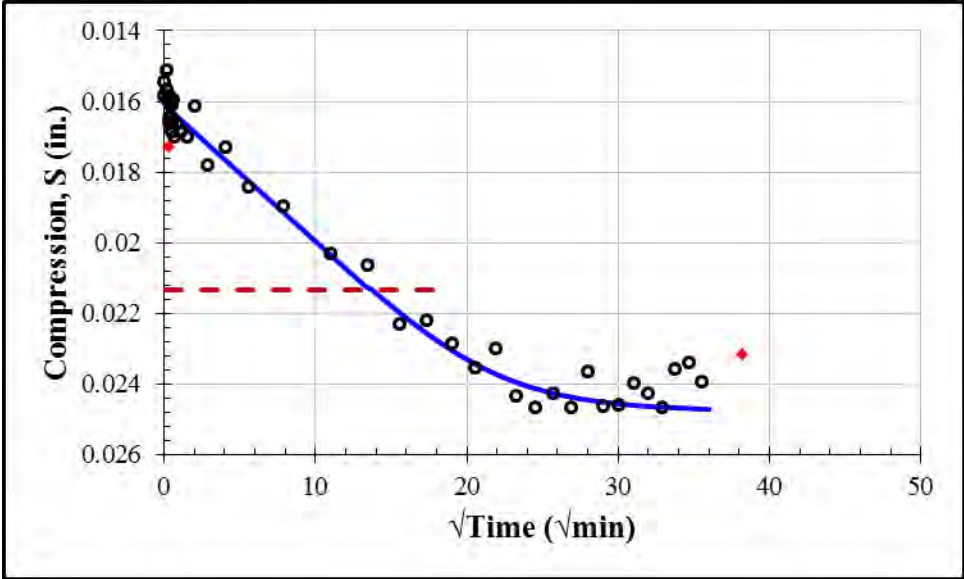
First Unloading: 1000 psf				
S_0 (in.)	S_{100} (in.)	c_v (in ² /min)	k (ft/day)	t_{50} (min)
0.0462	0.0110	0.000065	6.3×10^{-9}	356



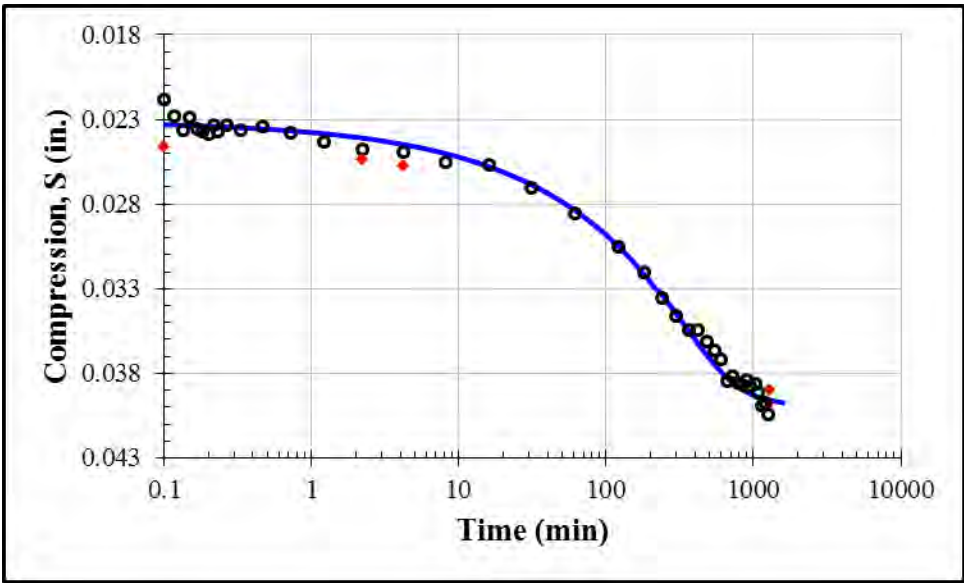
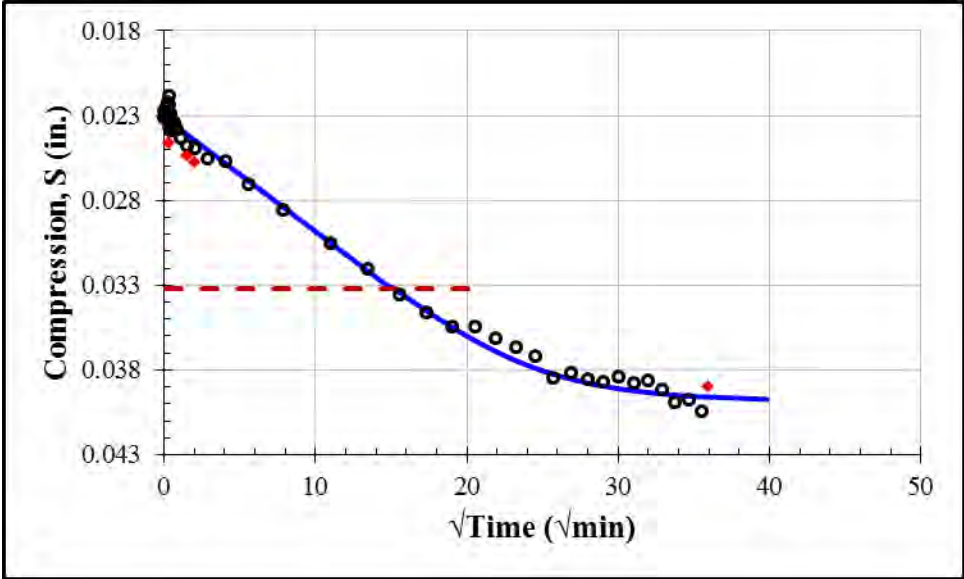
Second Loading: 2000 psf				
S_0 (in.)	S_{100} (in.)	c_v (in ² /min)	k (ft/day)	t_{50} (min)
0.0150	0.0178	0.00015	3.5×10^{-9}	170



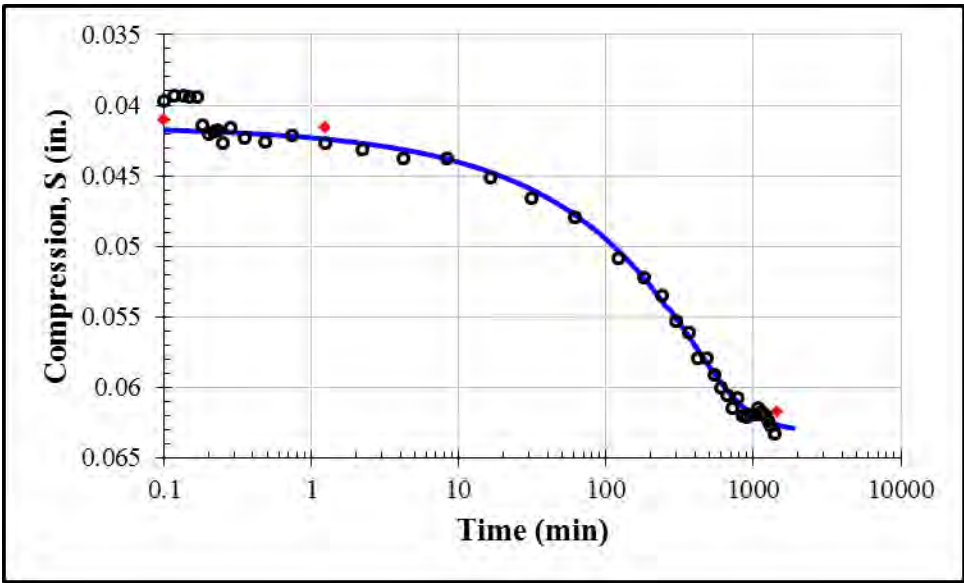
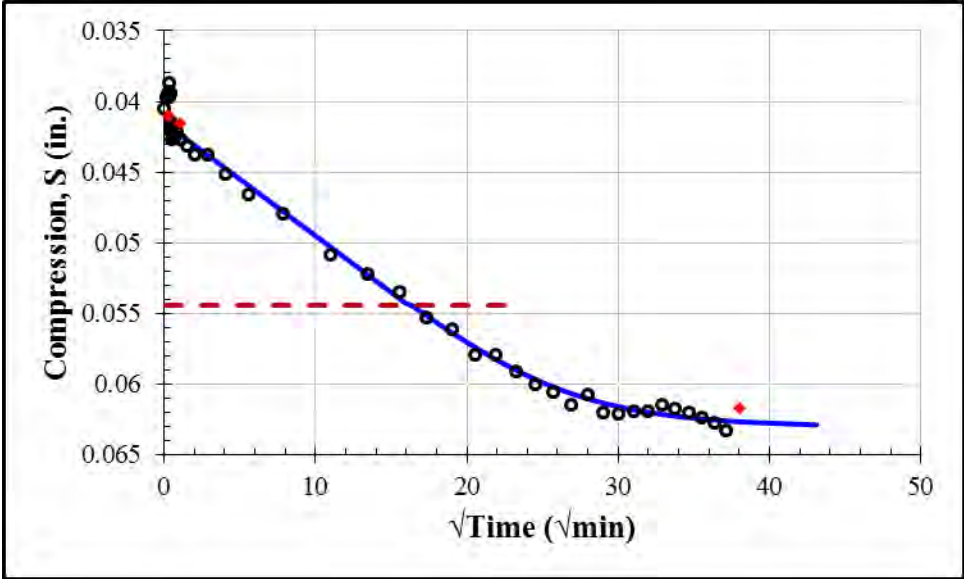
Second Loading: 4000 psf				
S_0 (in.)	S_{100} (in.)	c_v (in ² /min)	k (ft/day)	t_{50} (min)
0.0161	0.0248	0.0002	7.2×10^{-9}	127



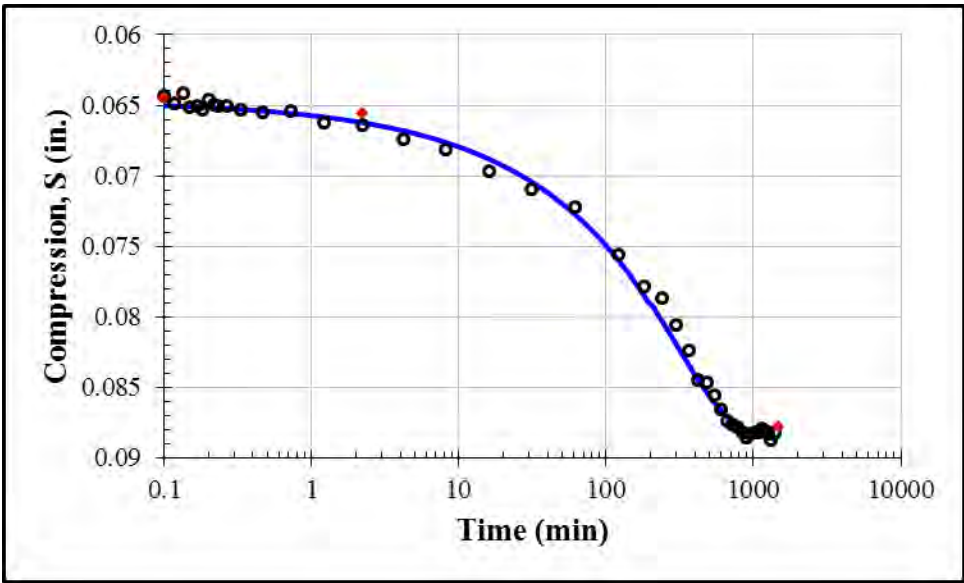
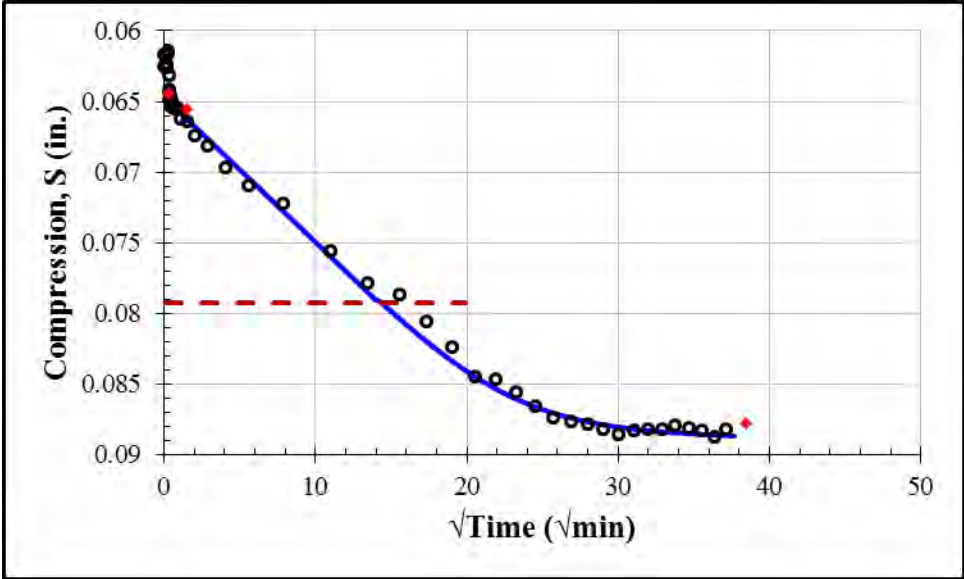
Second Loading: 8000 psf				
S_0 (in.)	S_{100} (in.)	c_v (in ² /min)	k (ft/day)	t_{50} (min)
0.0231	0.0399	0.00016	5.5×10^{-9}	156



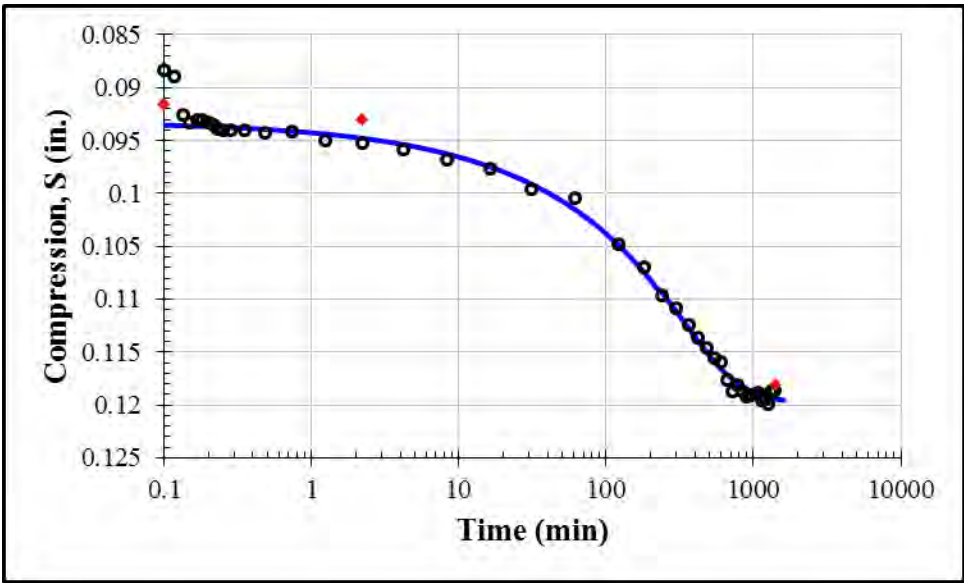
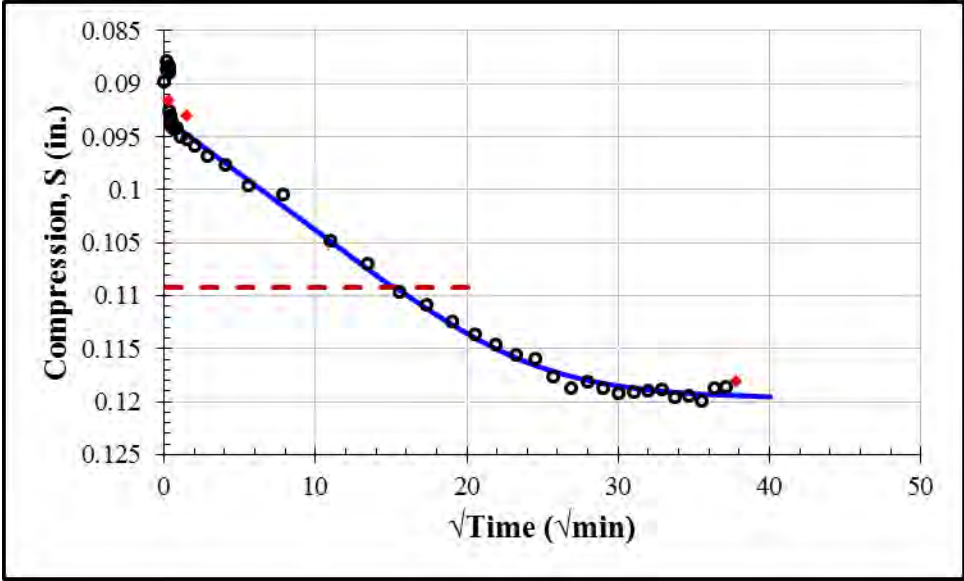
Second Loading: 16000 psf				
S_0 (in.)	S_{100} (in.)	c_v (in ² /min)	k (ft/day)	t_{50} (min)
0.0415	0.0631	0.00013	2.8×10^{-9}	182



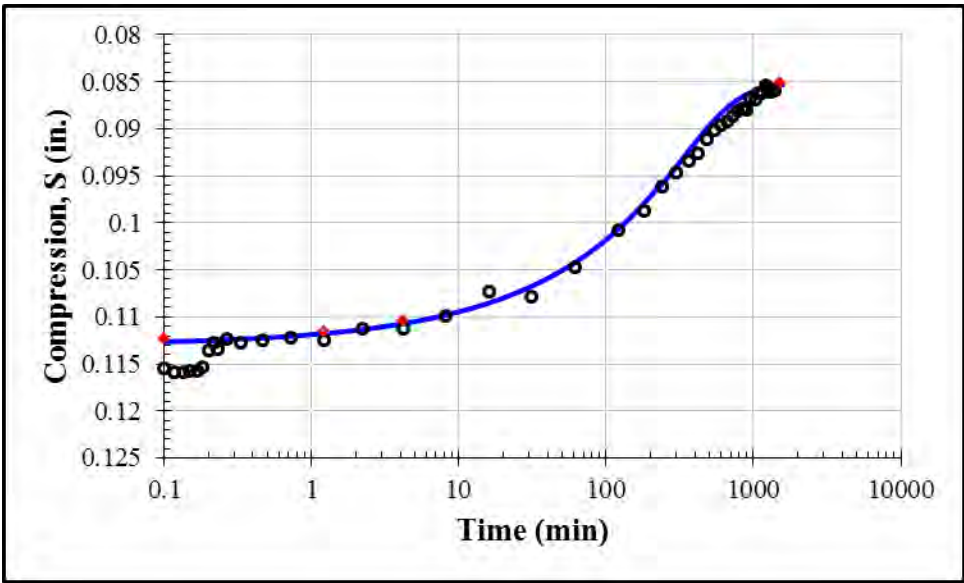
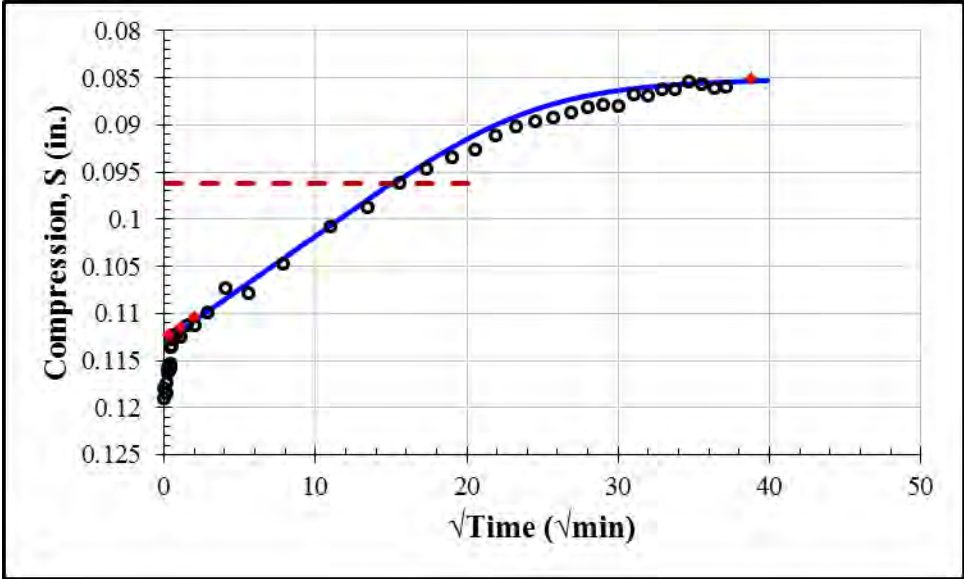
Second Loading: 32000 psf				
S_0 (in.)	S_{100} (in.)	c_v (in ² /min)	k (ft/day)	t_{50} (min)
0.0647	0.0889	0.00016	1.9×10^{-9}	139



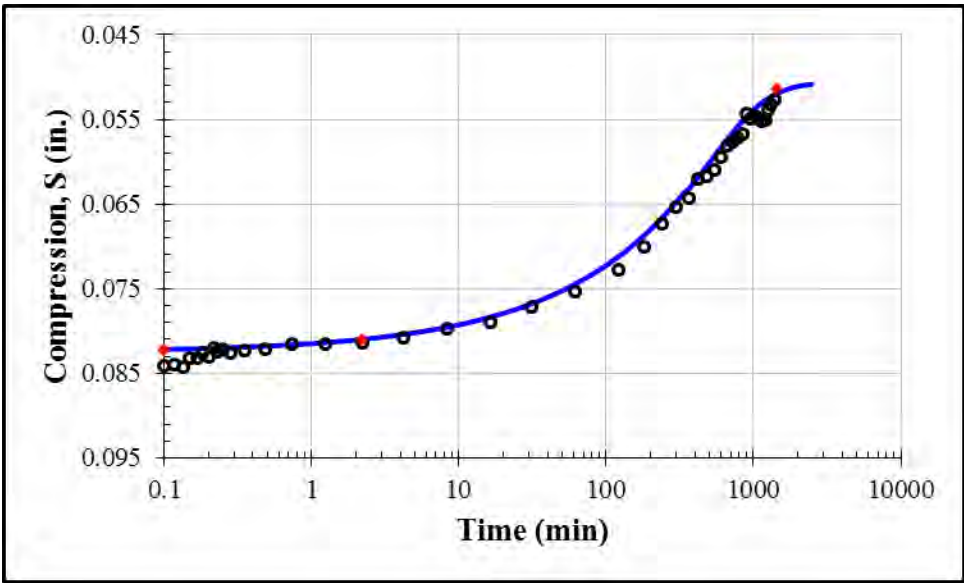
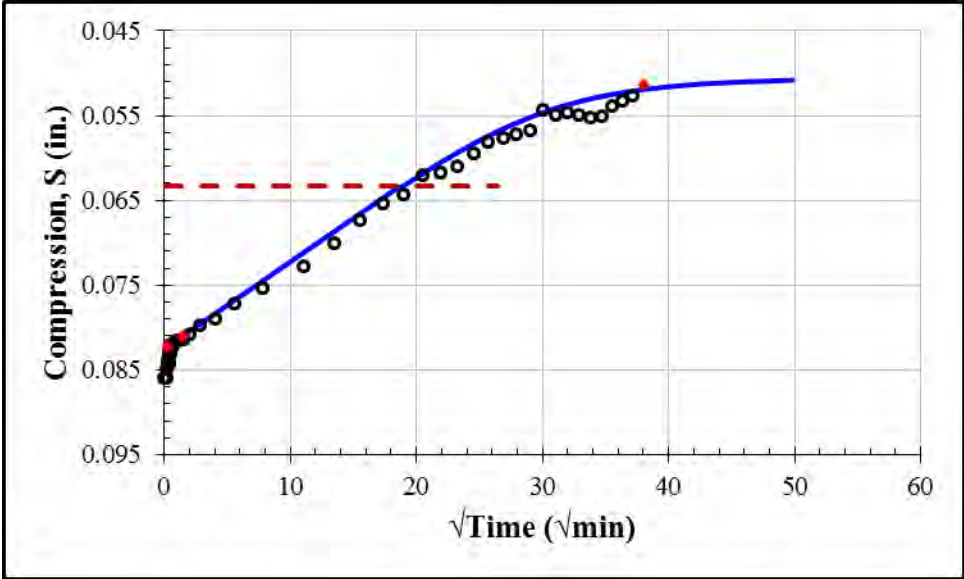
Second Loading: 64000 psf				
S_0 (in.)	S_{100} (in.)	c_v (in ² /min)	k (ft/day)	t_{50} (min)
0.0932	0.1198	0.00013	8.3×10^{-10}	157



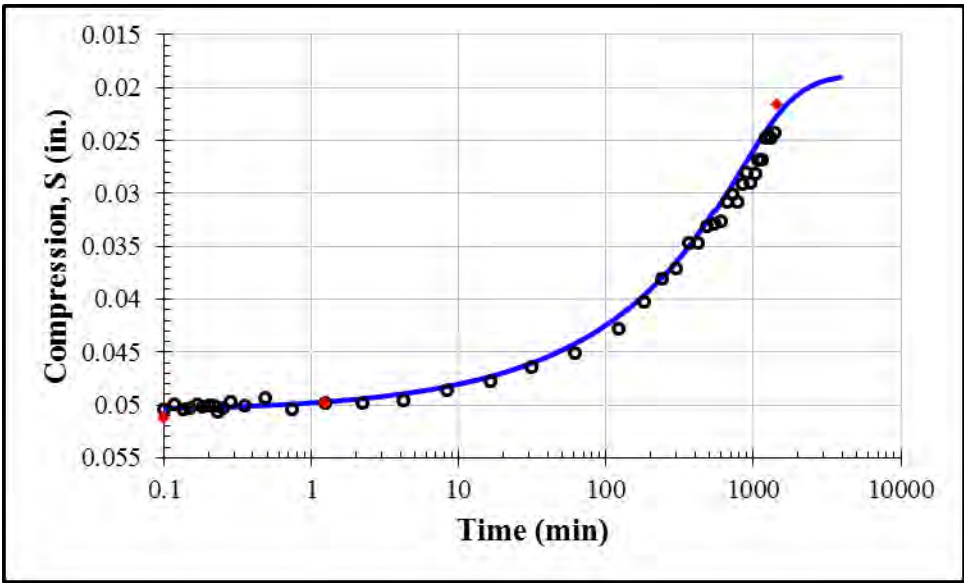
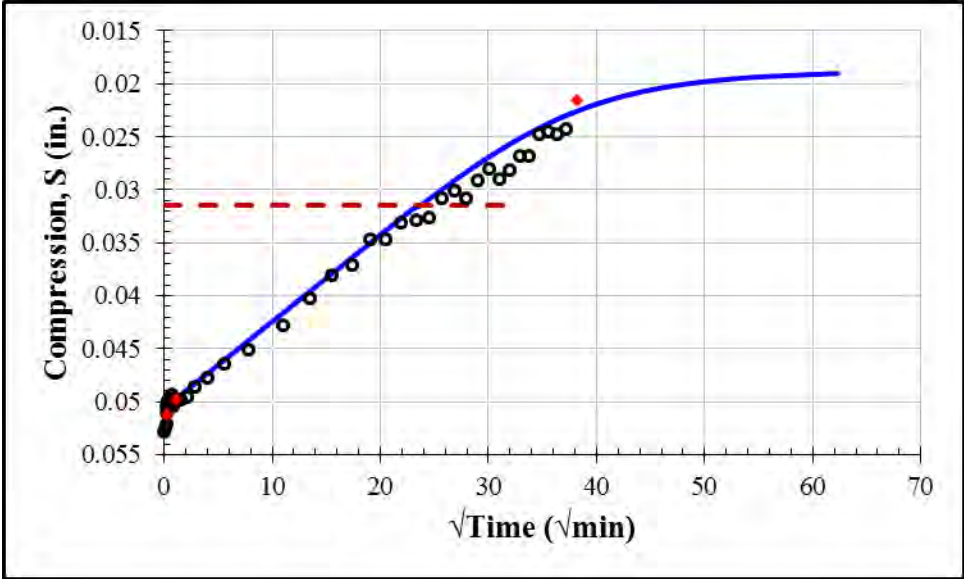
Second Unloading: 16000 psf				
S_0 (in.)	S_{100} (in.)	c_v (in ² /min)	k (ft/day)	t_{50} (min)
0.1130	0.0850	0.00012	5.4×10^{-10}	156



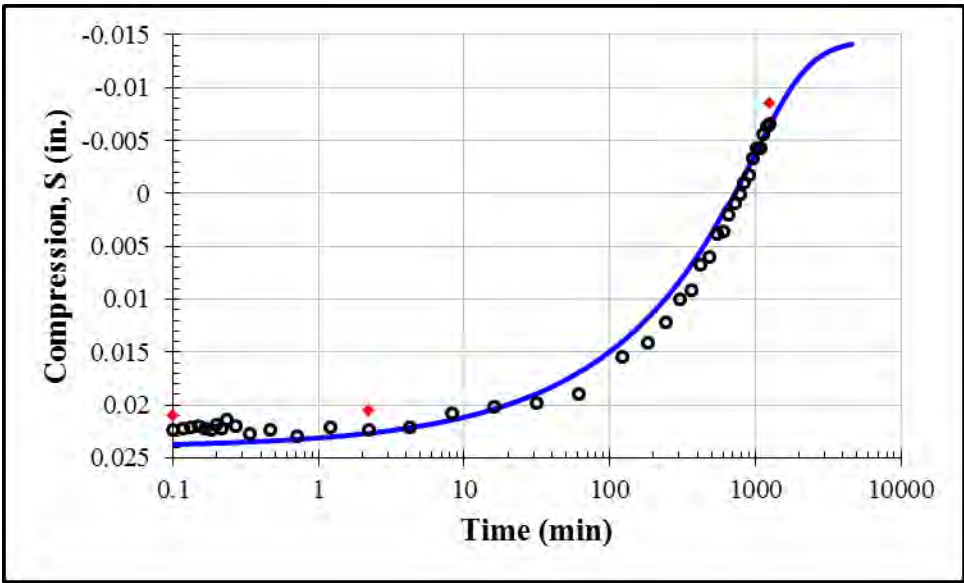
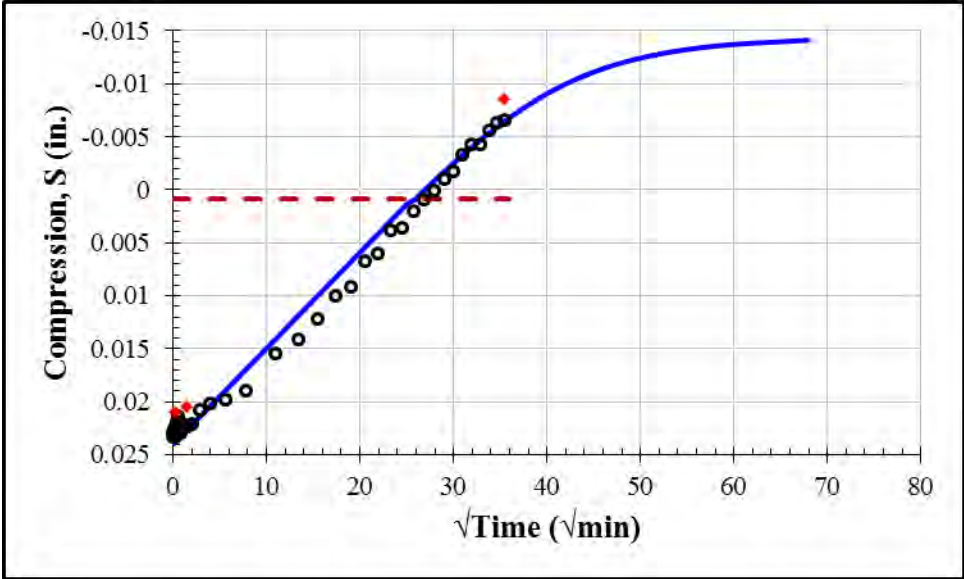
Second Unloading: 4000 psf				
S_0 (in.)	S_{100} (in.)	c_v (in ² /min)	k (ft/day)	t_{50} (min)
0.0825	0.0505	0.000085	1.8×10^{-9}	243



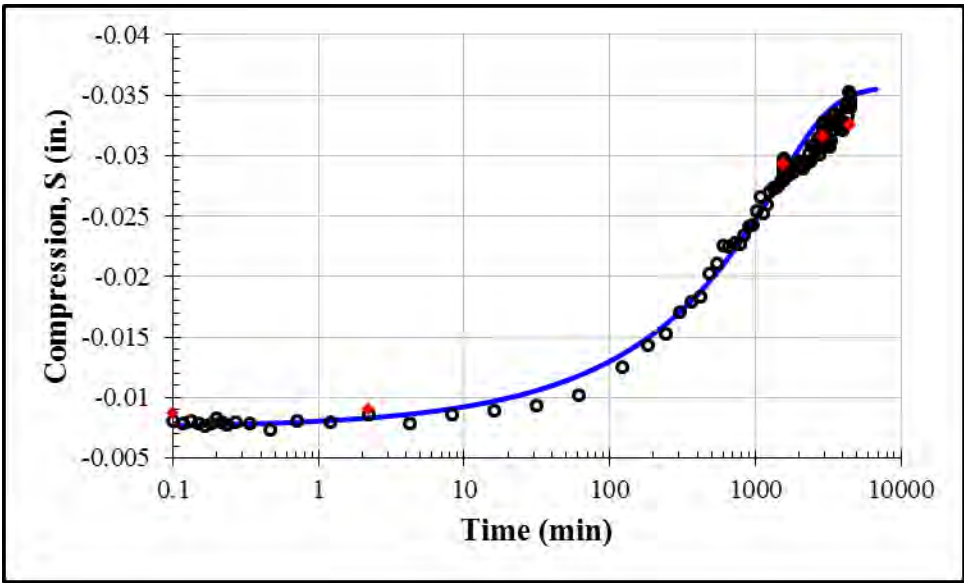
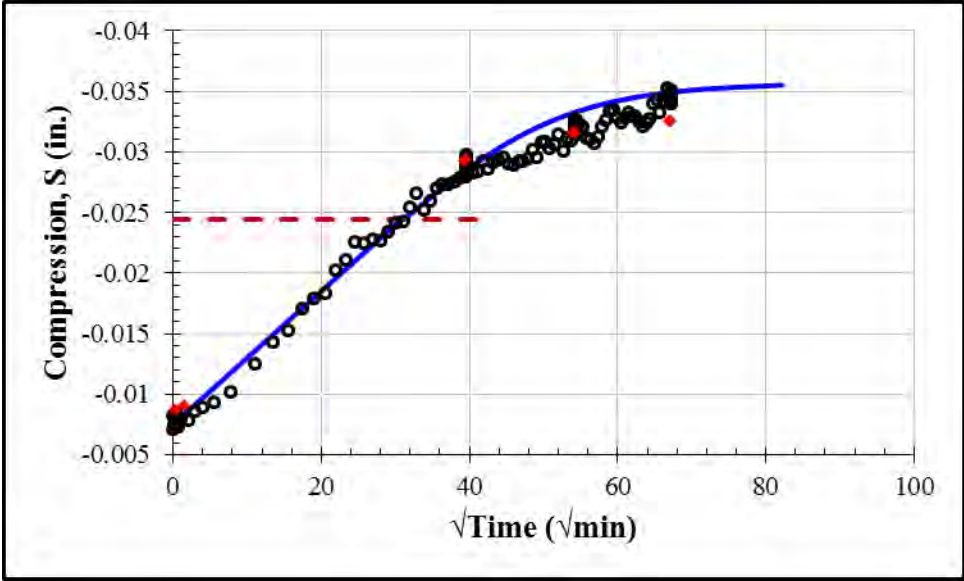
Second Unloading: 1000 psf				
S_0 (in.)	S_{100} (in.)	c_v (in ² /min)	k (ft/day)	t_{50} (min)
0.0506	0.0187	0.00006	5.2×10^{-9}	381



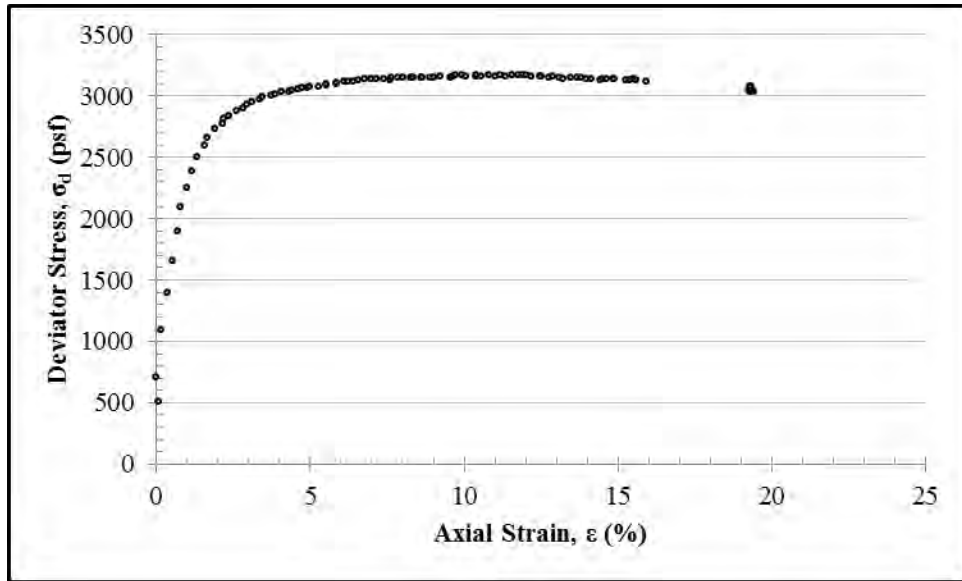
Second Unloading: 250 psf				
S_0 (in.)	S_{100} (in.)	c_v (in ² /min)	k (ft/day)	t_{50} (min)
0.0240	-0.0145	0.000055	2.4×10^{-8}	452



Second Unloading: 125 psf				
S_0 (in.)	S_{100} (in.)	c_v (in ² /min)	k (ft/day)	t_{50} (min)
-0.0075	-0.0358	0.000041	8.1×10^{-8}	661

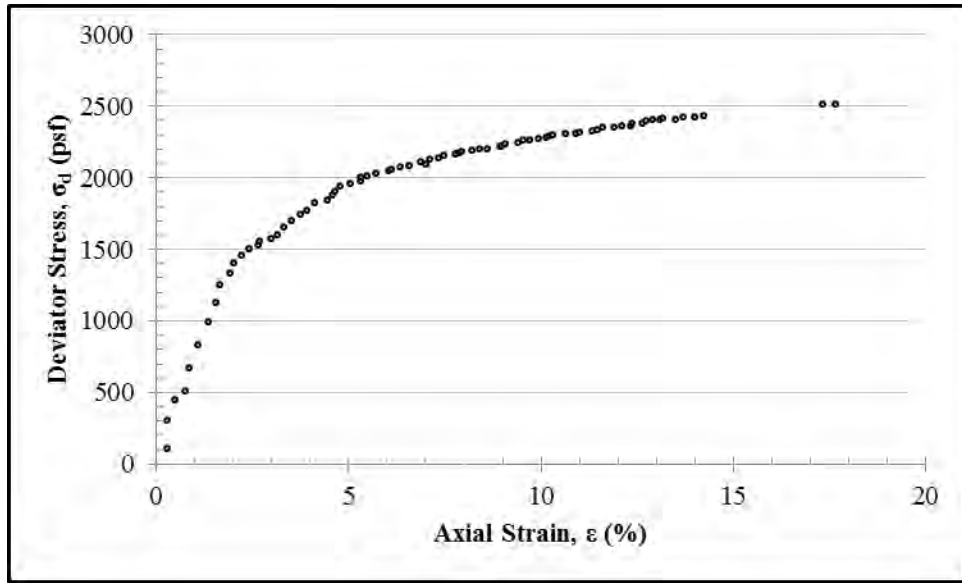


Appendix G: Unconsolidated Undrained Triaxial Test Results



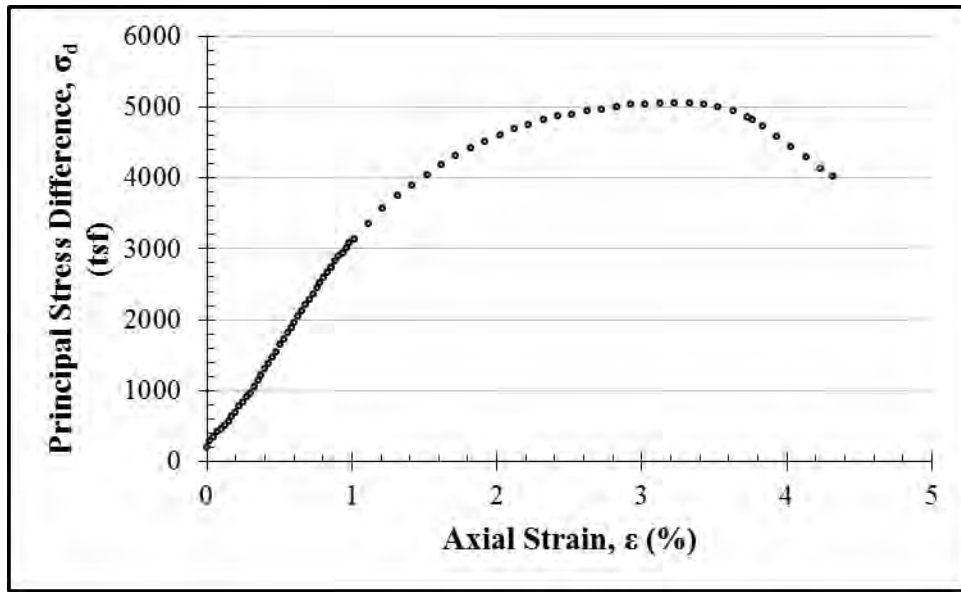
S_u (psf)	1587 psf
-------------	----------

Boring ID	B-3
Depth (ft)	4 – 5
Description	dk brown
Confining Pressure (psi)	5
Strain Rate (%/min)	0.7
Average Sample Diameter (in.)	1.43
Average Sample Height (in.)	2.93
Moisture Content (%)	28.4
Unit Dry Weight (pcf)	-
Failure Type	-
Peak Deviator Stress (psf)	3174
Axial Strain at Peak (%)	10.8



S_u (psf)	1257 psf
-------------	----------

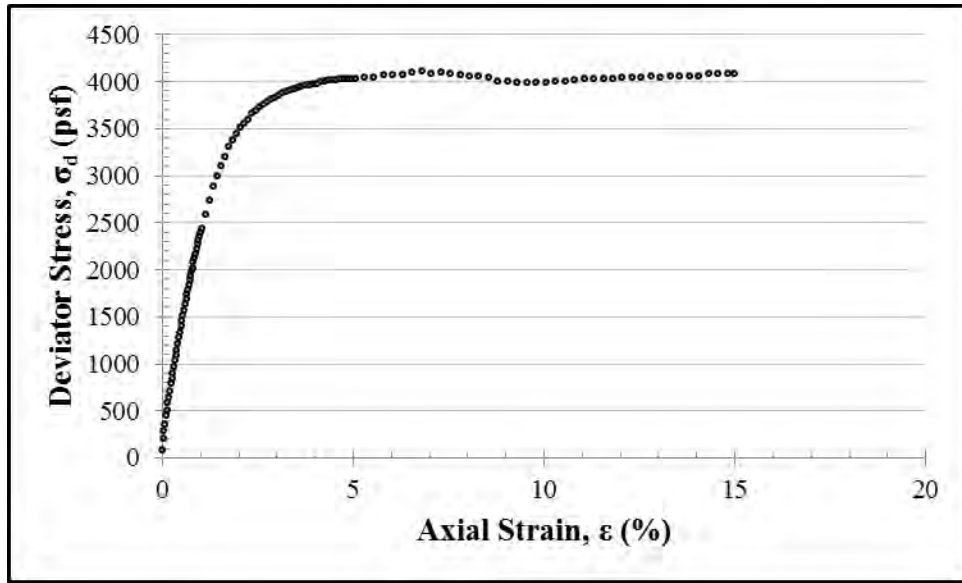
Boring ID	B-3
Depth (ft)	8 – 10
Description	tan
Confining Pressure (psi)	9
Strain Rate (%/min)	0.75
Average Sample Diameter (in.)	1.48
Average Sample Height (in.)	2.74
Moisture Content (%)	38.7
Unit Dry Weight (pcf)	-
Failure Type	-
Peak Deviator Stress (psf)	2514
Axial Strain at Peak (%)	17.3



S_u (psf)	2350
-------------	------

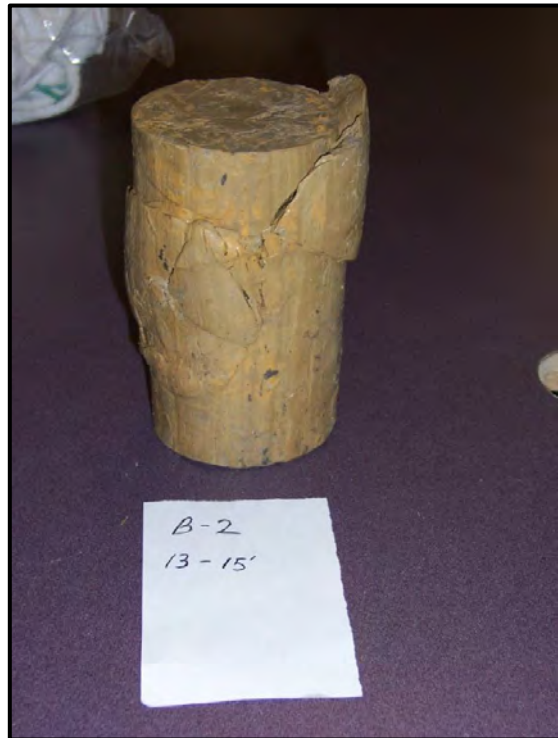
Boring ID	B-2
Depth (ft)	8 – 10
Description	tan
Confining Pressure (psi)	10
Strain Rate (%/min)	0.5
Average Sample Diameter (in.)	2.74
Average Sample Height (in.)	5.74
Moisture Content (%)	23.2
Unit Dry Weight (pcf)	80
Failure Type	Multi
Peak Deviator Stress (psf)	12.0
Axial Strain at Peak (%)	4.5

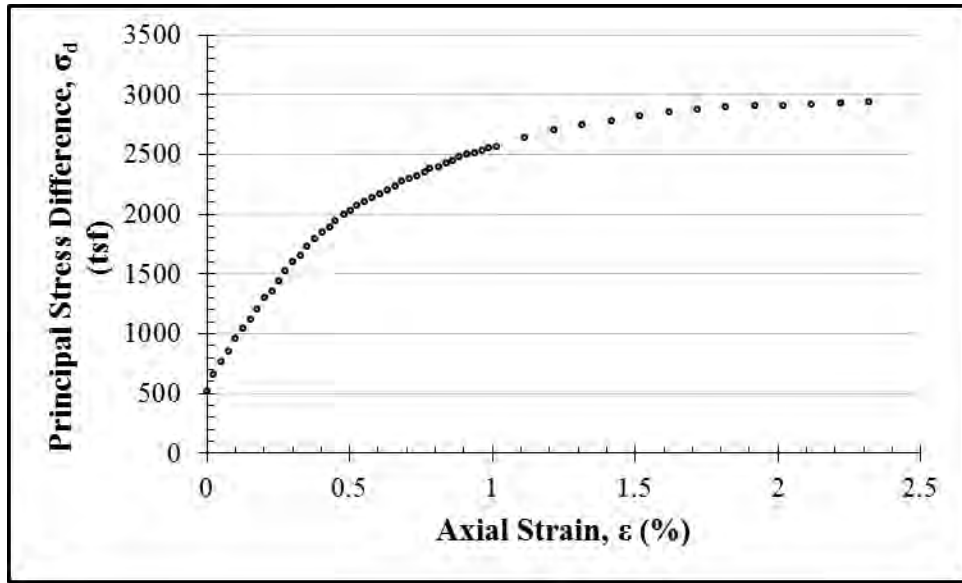




S_u (psf)	2055 psf
-------------	----------

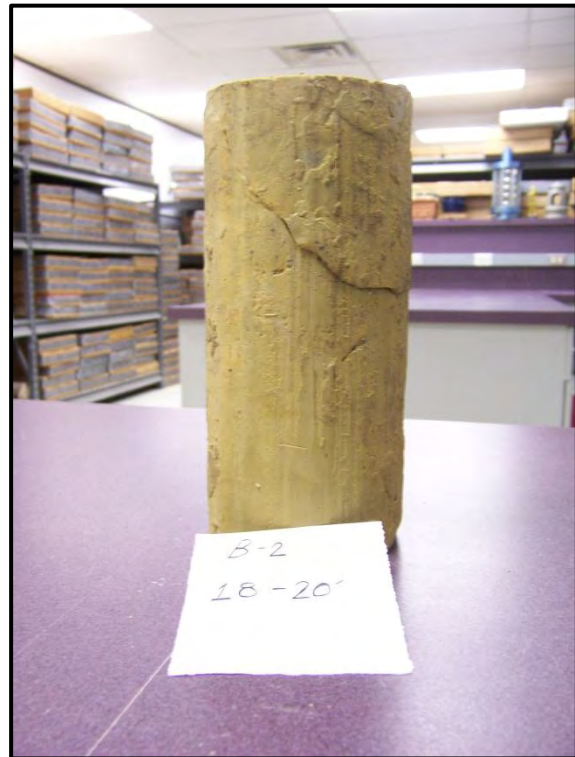
Boring ID	B-2
Depth (ft)	13 – 15
Description	tan
Confining Pressure (psi)	14
Strain Rate (%/min)	0.5
Average Sample Diameter (in.)	2.73
Average Sample Height (in.)	5.54
Moisture Content (%)	37.3
Unit Dry Weight (pcf)	83
Failure Type	Multi
Peak Deviator Stress (psf)	4111
Axial Strain at Peak (%)	6.8

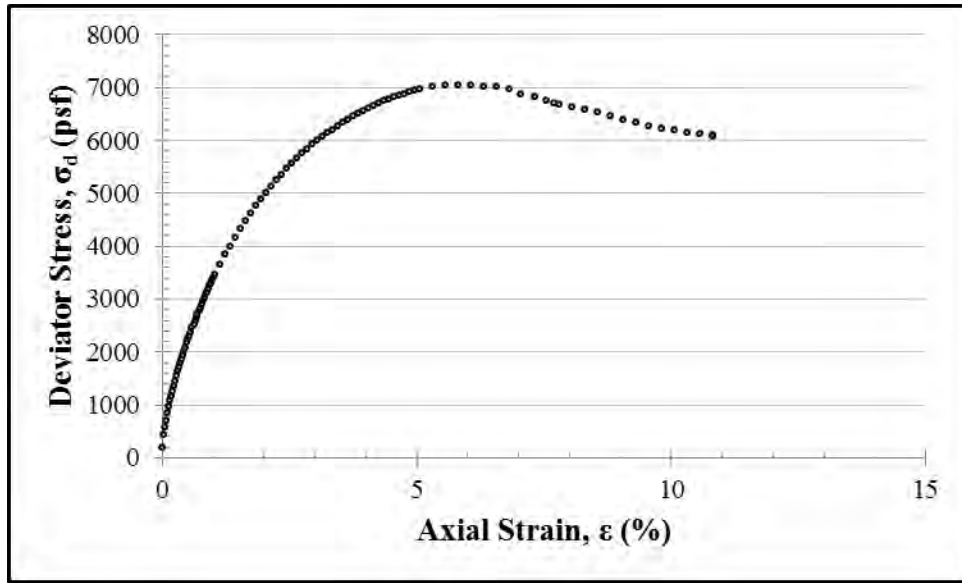




S_u (psf)	1470
-------------	------

Boring ID	B-2
Depth (ft)	18 – 20
Description	dk brown
Confining Pressure (psi)	19
Strain Rate (%/min)	0.5
Average Sample Diameter (in.)	2.73
Average Sample Height (in.)	6.01
Moisture Content (%)	38.8
Unit Dry Weight (pcf)	82
Failure Type	Shear
Peak Deviator Stress (psf)	2934
Axial Strain at Peak (%)	2.32

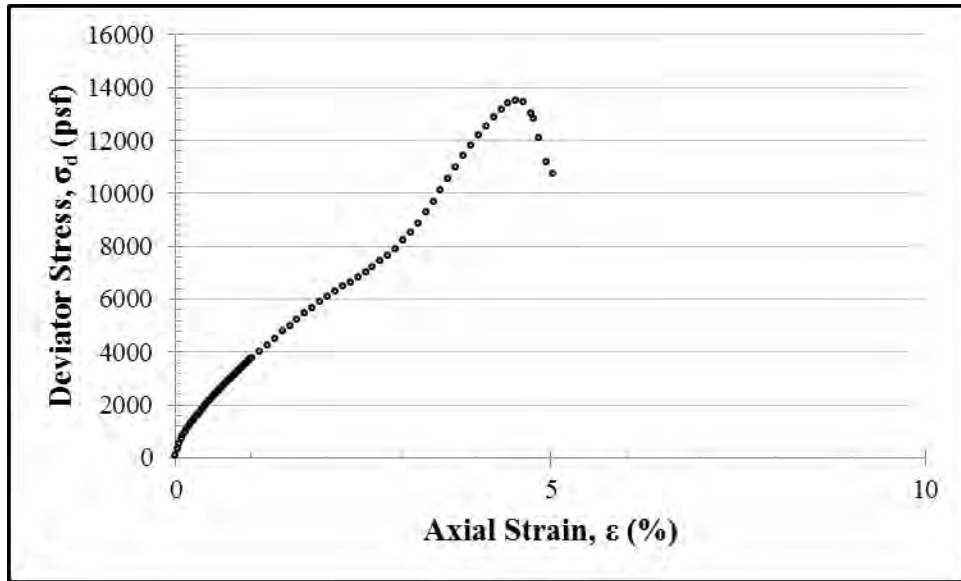




S_u (psf)	3527
-------------	------

Boring ID	B-3
Depth (ft)	23 – 25
Description	tan
Confining Pressure (psi)	24
Strain Rate (%/min)	0.5
Average Sample Diameter (in.)	2.77
Average Sample Height (in.)	5.33
Moisture Content (%)	39.8
Unit Dry Weight (pcf)	81
Failure Type	Multi
Peak Deviator Stress (psf)	7054
Axial Strain at Peak (%)	5.8





S_u (psf)	6753
-------------	------

Boring ID	B-3
Depth (ft)	33 – 35
Description	stiff
Confining Pressure (psi)	34
Strain Rate (%/min)	0.5
Average Sample Diameter (in.)	2.76
Average Sample Height (in.)	5.79
Moisture Content (%)	30.2
Unit Dry Weight (pcf)	92
Failure Type	Shear
Peak Deviator Stress (psf)	13507
Axial Strain at Peak (%)	4.54



Note: The horizontal crack shown above occurred during trimming. The actual shear surface was not as obvious.

Appendix H: Direct Shear Test Results

Test 1: Peak Shear at 750 psf		
Initial Moisture Content $w_{c,i}$ (%)	Failure Moisture Content $w_{c,f}$ (%)	Nominal Shear Stress at Failure, τ_f (psf)
23.4	25.6	1300



Test 1: 1 st Residual Shear at 750 psf		
Initial Moisture Content $w_{c,i}$ (%)	Failure Moisture Content $w_{c,f}$ (%)	Nominal Shear Stress at Failure, τ_f (psf)
25.6	27.6	382



Test 1: 2 nd Residual Shear at 750 psf		
Initial Moisture Content $w_{c,i}$ (%)	Failure Moisture Content $w_{c,f}$ (%)	Nominal Shear Stress at Failure, τ_f (psf)
27.6	27.8	270



Test 1: Residual Shear at 1500 psf		
Initial Moisture Content $w_{c,i}$ (%)	Failure Moisture Content $w_{c,f}$ (%)	Nominal Shear Stress at Failure, τ_f (psf)
27.8	27.1	600



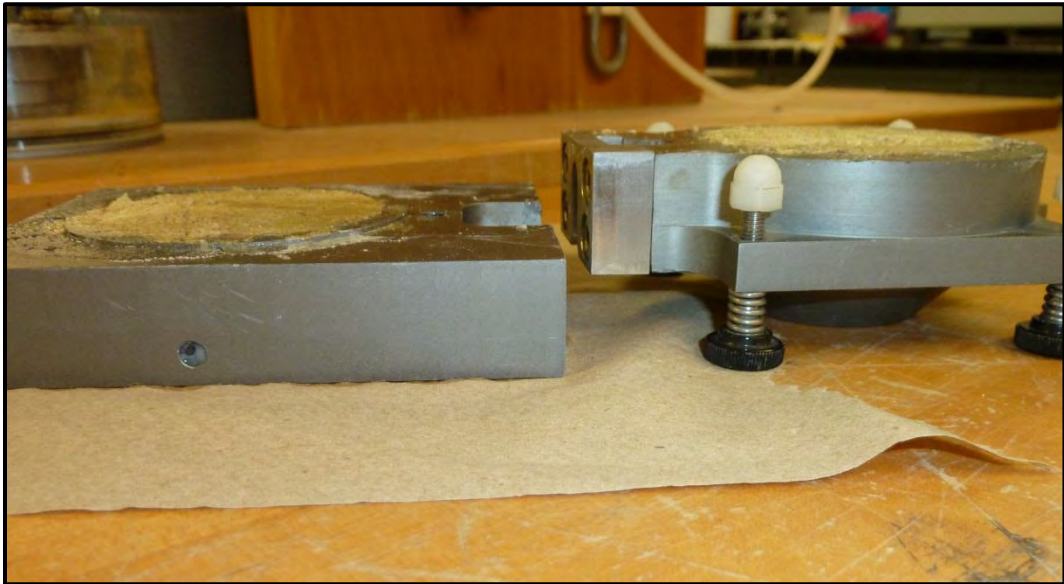
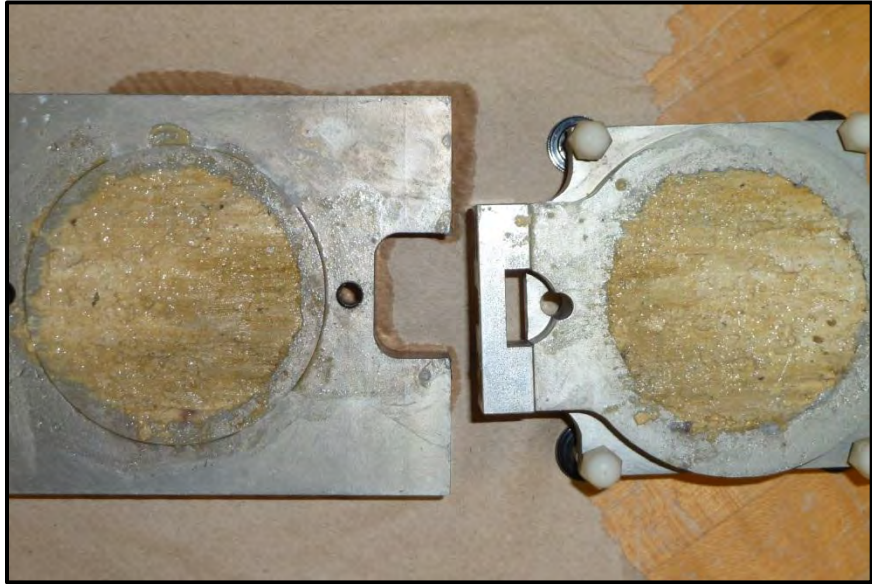
Test 1: Peak Shear at 3000 psf		
Initial Moisture Content $w_{c,i}$ (%)	Failure Moisture Content $w_{c,f}$ (%)	Nominal Shear Stress at Failure, τ_f (psf)
27.1	26.1	1185



Test 2: Peak Shear at 1500 psf		
Initial Moisture Content $w_{c,i}$ (%)	Failure Moisture Content $w_{c,f}$ (%)	Nominal Shear Stress at Failure, τ_f (psf)
24.8	23.8	1758



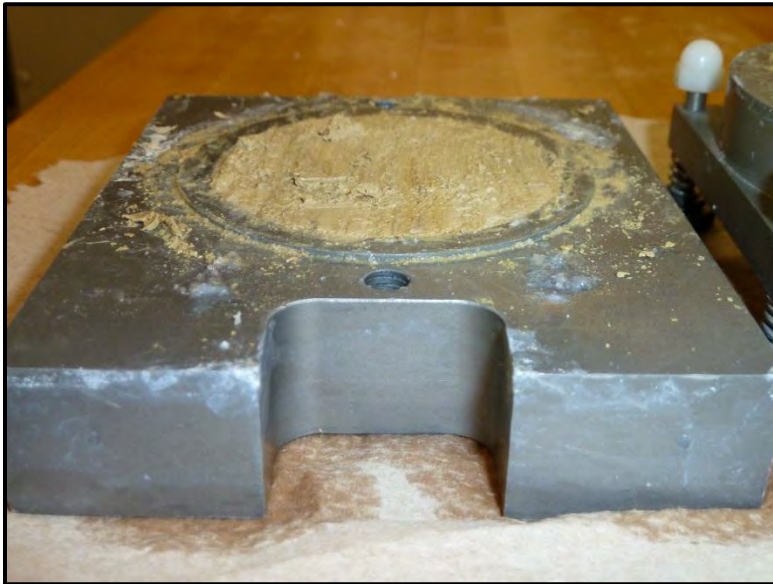
Test 2: 1 st Residual Shear at 1500 psf		
Initial Moisture Content $w_{c,i}$ (%)	Failure Moisture Content $w_{c,f}$ (%)	Nominal Shear Stress at Failure, τ_f (psf)
23.8	26.0	1011



Test 2: 2 nd Residual Shear at 1500 psf		
Initial Moisture Content $w_{c,i}$ (%)	Failure Moisture Content $w_{c,f}$ (%)	Nominal Shear Stress at Failure, τ_f (psf)
26.0	26.4	1082



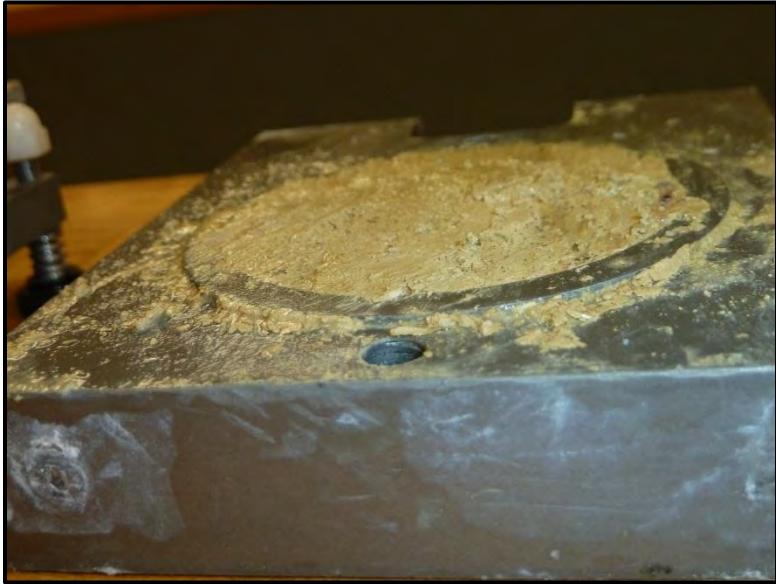
Test 2: Residual Shear at 3000 psf		
Initial Moisture Content $w_{c,i}$ (%)	Failure Moisture Content $w_{c,f}$ (%)	Nominal Shear Stress at Failure, τ_f (psf)
26.4	28.2	1644



Test 2: 1 st Residual Shear at 6000 psf		
Initial Moisture Content $w_{c,i}$ (%)	Failure Moisture Content $w_{c,f}$ (%)	Nominal Shear Stress at Failure, τ_f (psf)
28.2	24.8	2766

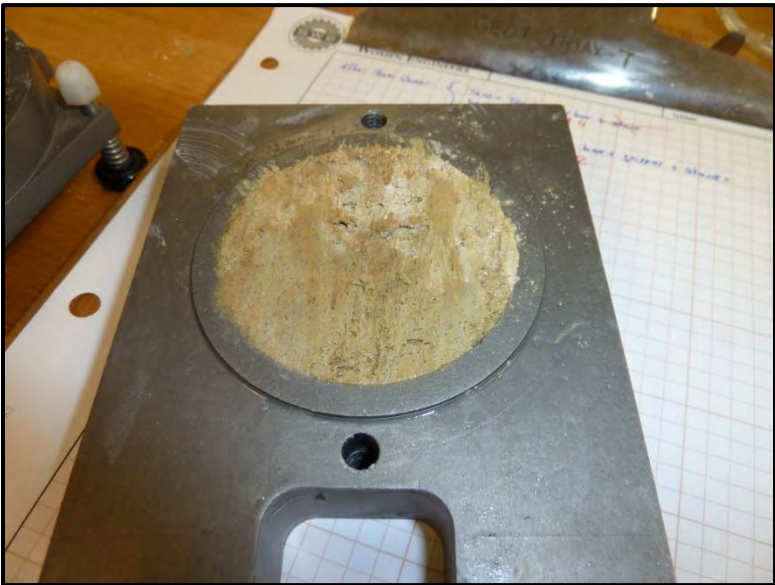


Test 2: 2 nd Residual Shear at 6000 psf		
Initial Moisture Content $w_{c,i}$ (%)	Failure Moisture Content $w_{c,f}$ (%)	Nominal Shear Stress at Failure, τ_f (psf)
24.8	28.4	2860

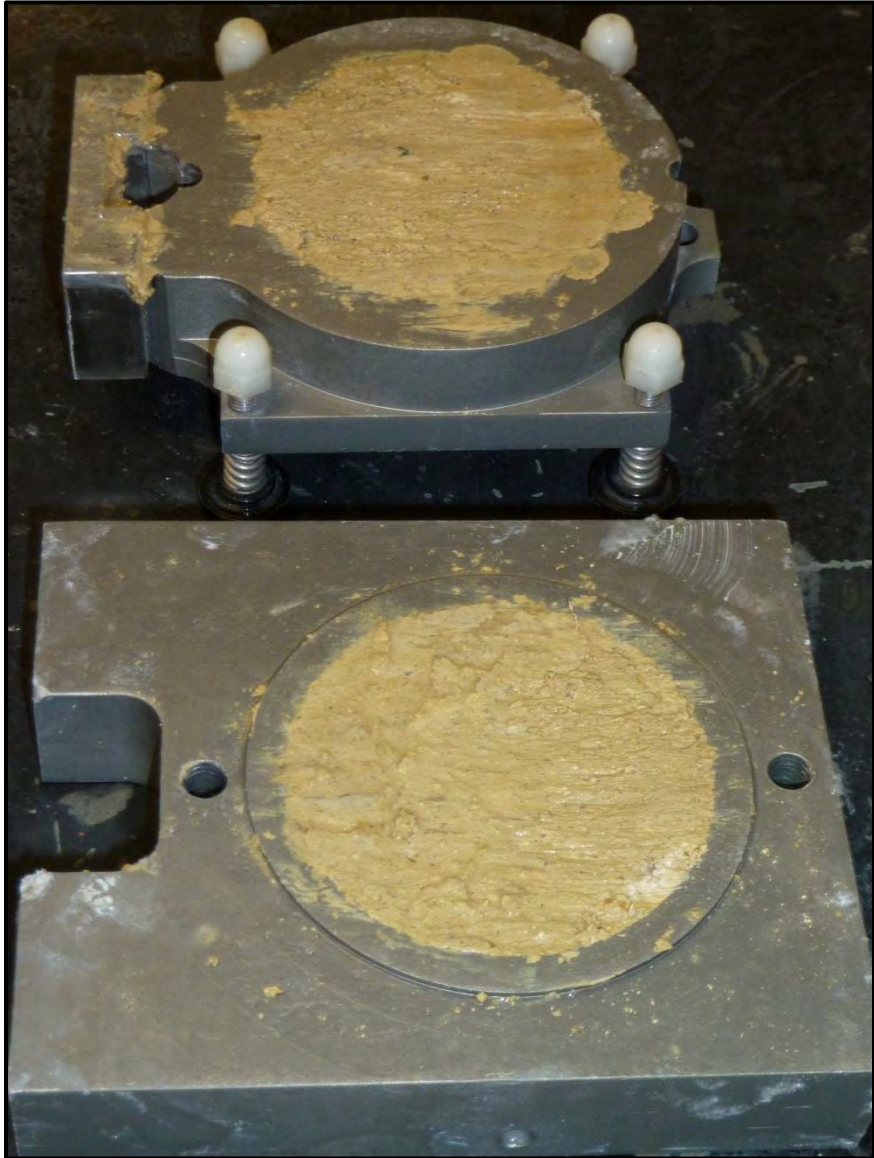


Test 3: Peak Shear at 3000 psf		
Initial Moisture Content $w_{c,i}$ (%)	Failure Moisture Content $w_{c,f}$ (%)	Nominal Shear Stress at Failure, τ_f (psf)
21.8	26.1	2061

Note: Top half of specimen was ejected from shear box while separating halves after peak shear.



Test 3: 1 st Residual Shear at 3000 psf		
Initial Moisture Content $w_{c,i}$ (%)	Failure Moisture Content $w_{c,f}$ (%)	Nominal Shear Stress at Failure, τ_f (psf)
26.1	28.9	1634



Test 3: 2 nd Residual Shear at 3000 psf		
Initial Moisture Content $w_{c,i}$ (%)	Failure Moisture Content $w_{c,f}$ (%)	Nominal Shear Stress at Failure, τ_f (psf)
28.9	28.7	1471



Test 3: Residual Shear at 6000 psf		
Initial Moisture Content $w_{c,i}$ (%)	Failure Moisture Content $w_{c,f}$ (%)	Nominal Shear Stress at Failure, τ_f (psf)
28.7	29.1	2705



References

- Allen, J. A. 2005. Forced Ventilated Swell-Shrink Test for Potential Vertical Expansive Soil Movement. M.S. Thesis, The University of Texas at Austin.
- ASTM D1586 “Standard Test Method for Standard Penetration Test (SPT) and Split-Barrel Sampling of Soils”
- ASTM D2216 “Standard Test Methods for Laboratory Determination of Water (Moisture) Content of Soil and Rock by Mass”
- ASTM D2435 “Standard Test Methods for One-Dimensional Consolidation Properties of Soils Using Incremental Loading”
- ASTM D2487 “Standard Practice for Classification of Soils for Engineering Purposes (Unified Soil Classification System)”
- ASTM D2850 “Standard Test Method for Unconsolidated-Undrained Triaxial Compression Test on Cohesive Soils”
- ASTM D3080 “Standard Test Method for Direct Shear Test of Soils Under Consolidated Drained Conditions”
- ASTM D422 “Standard Test Method for Particle-Size Analysis of Soils”
- ASTM D4318 “Standard Test Methods for Liquid Limit, Plastic Limit, and Plasticity Index of Soils”
- ASTM D4546 “Standard Test Methods for One-Dimensional Swell or Settlement Potential of Cohesive Soils”
- Beal, A. O. 1964. Stratigraphy of the Taylor Formation (Upper Cretaceous), East-Central Texas. Baylor Geological Studies Bulletin No. 6, Baylor University.
- Burford, S. O. 1928, Characteristics of the Taylor Marl of Travis County, Texas. M.A. Thesis, The University of Texas at Austin.
- Chen, F. H. 1988. Foundations on Expansive Soils. American Elsevier Science Publication, New York.
- Daksanamurthy, V. and Raman, V. 1973. A Simple Method of Identifying an Expansive Soil, Soil and Foundations. Japanese Society of Soil Mechanic and Foundation Engineering. 13(1): 97 – 104.

- Dellinger, G. 2011. The Use of Time Domain Reflectometry Probes for Moisture Monitoring of a Drilled Shaft Retaining Wall in Expansive Clay. M.S. Thesis, The University of Texas at Austin.
- Fredlund, D. G., Hasan, J. U. and Filson, H. L. 1980. The Prediction of Total Heave. 4th International Conference on Expansive Soils. American Society of Civil Engineers.
- Funk, A. C. 1975. The Relationships of Engineering Properties to Geochemistry in the Taylor Group, Travis County, Texas. M.A. Thesis, The University of Texas at Austin.
- Garner, L. E. and Young, K. P. 1976. Environmental Geology of the Austin Area: An Aid to Urban Planning. Austin: Bureau of Economic Geology, University of Texas at Austin.
- Jonas, E. C. and Brown, T. E. 1959. Analysis of Interlayer Mixtures of Three Clay Mineral Types by X-ray Diffraction. Jour. Sed. Petrology, v. 29: 77 – 86.
- Joshi, R. P. and Katti, R. K. 1980. Lateral Pressure Development Under Surcharges. 4th International Conference on Expansive Soils. American Society of Civil Engineers.
- Katti, R. K. and Katti, A. R. 1994. Behaviour of Saturated Expansive Soil and Control Methods. New Delhi Central Board of Irrigation and Power. A. A. Balkema, Rotterdam, pp 33 – 42.
- Kayyal, M. K. 1986. Effects of Wetting and Drying on Long-Term Strength of Compacted Taylor Marl Clay. M.S. Thesis, The University of Texas at Austin.
- Kodikara, J., Barbour, S. L. and Fredlund, D. G. 1999. Changes in Clay Structure and Behaviour Due to Wetting and Drying. Proceedings of the 8th Annual Australian-New Zealand Conference on Geomechanics, Hobart. pp 179 – 186.
- Marr, S. A. 2003. A Practical Method for Modeling Expansive Soil Behavior. M.S. Thesis, The University of Texas at Austin.
- Mitchell, J. K. and Kenichi, S. 2005. Fundamentals of Soil Behavior, Third Edition. John Wiley & Sons, Inc.
- Nelson, J. D. and Miller, D. J. 1992. Expansive Soils: Problems and Practice in Foundation and Pavement Engineering. John Wiley & Sons, Inc.
- Olson, R. E. 2009. Incremental Vertical-Flow Consolidation Test. Class Notes, The University of Texas at Austin.

- Popescu, M. 1980. Behavior of Expansive Soils with a Crumb Structure. 4th International Conference on Expansive Soils. American Society of Civil Engineers.
- Long, J. H. and Reese, L. C. 1983. An Investigation of the Behavior of Vertical Piles in Cohesive Soils Subjected to Repetitive lateral Loads. Geotechnical Engineering Report GR83-7. Geotechnical Engineering Center, the University of Texas at Austin.
- Reese, L. C., Isenhower, W. M. and Wang, S. T. 2006. Analysis and Design of Shallow and Deep Foundations. John Wiley & Sons, Inc.
- Seed, H. B., Woodward, R. J., Jur. and Lundgren, R. 1962. Prediction of Swelling Potential for Compacted Clays. Journal of Soil Mech. Found. Div., American Society of Civil Engineers, 88 (SM3):53-87.
- Skempton, A. W. 1953. The Colloidal Activity of Clays. Proceedings of the 3rd International Conference on Soil Mechanics and Foundation Engineering, Switzerland. V.1:57 -61.
- Skempton, A.W. and LaRochelle, P. 1965. The Bradwell Slip: A Short-Term Failure in London Clay. Geotechnique, 15:3, pp 221-242.
- Stark, T. D. and Eid, H. T. 1994. Drained Residual Strength of Cohesive Soils. ASCE, Journal of Geotechnical Engineering, 120, 856-871.
- Stark, T. D. and Eid, H. T. 1997. Slope Stability Analyses in Stiff Fissured Clay. ASCE, Journal of Geotechnical and Geoenvironmental Engineering, 123(4), 335-343.
- Tawfiq, S. and Nalbantoglu, Z. 2009. Swell-Shrink Behavior of Expansive Clays. 2nd International Conference on New Developments in Soil Mechanics and Geotechnical Engineering, Nicosia, North Cyprus, 28 – 30 May, 2009.
- Tex-101-E “Test Procedure for Preparing Soil and Flexible Base Materials for Testing”
- Tex-132-E “Test Procedure for Texas Cone Penetration”
- Terzaghi, K. and Peck, R. 1943. Soil Mechanics in Engineering Practice. New York, John Wiley & Sons, Inc.
- Tipple, G. L. 1975. Clay Minerology and Atterberg Limits of the Taylor Group in the Vicinity of Austin, Texas. M.A. Thesis, The University of Texas at Austin.
- TxDOT Geotechnical Manual. 2000. Texas Department of Transportation, Bridge Division, Austin, Texas.

Van-Hue, N. 1966. The Effects of Repeated Loading on the Strength and Deformation of Taylor Marl Clay Stabilized with Lime. M.S. Thesis, The University of Texas at Austin.

Walcott, C. D. 1901. Twenty-First Annual Report of the United States Geological Survey to the Secretary of the Interior, 1899-1900. Part VII – Texas. pp. 336-338.

Young, K. 1965. A Revision of Taylor Nomenclature, Upper Cretaceous, Central Texas. Bureau of Economic Geology, Geology Circular 65-3.

Copyright

by

Gregory Fred Dellinger

2011

**The Thesis Committee for Gregory Fred Dellinger
Certifies that this is the approved version of the following thesis:**

**The Use of Time Domain Reflectometry Probes for the Moisture
Monitoring of a Drilled Shaft Retaining Wall in Expansive Clay**

**APPROVED BY
SUPERVISING COMMITTEE:**

Supervisor:

Robert B. Gilbert

Jorge G. Zornberg

**The Use of Time Domain Reflectometry Probes for the Moisture
Monitoring of a Drilled Shaft Retaining Wall in Expansive Clay**

by

Gregory Fred Dellinger, B.S.

Thesis

Presented to the Faculty of the Graduate School of

The University of Texas at Austin

in Partial Fulfillment

of the Requirements

for the Degree of

Master of Science in Engineering

The University of Texas at Austin

August 2011

Dedication

To everyone who reads this.

Acknowledgements

I would like to thank my advisor, Dr. Robert B. Gilbert, for his support and guidance. Also, I would like to thank Dr. Jorge G. Zornberg for taking the time to review this and his assistance and I would like to thank Dr. Chadi El Mohtar for his assistance. I would like to thank Andrew Brown and Trent Ellis for their invaluable work and contributions to this project. The support and encouragement of my family is also greatly appreciated.

I would also like to extend my gratitude and thank Fugro Consultants, Inc. for their financial support.

Abstract

The Use of Time Domain Reflectometry Probes for the Moisture Monitoring of a Drilled Shaft Retaining Wall in Expansive Clay

Gregory Fred Dellinger, M.S.E.

The University of Texas at Austin, 2011

Supervisor: Robert B. Gilbert

Currently there is no consensus on how to account for the lateral earth pressures when designing drilled shaft retaining walls in expansive clay soils. Typically an equivalent fluid pressure is assumed which can range from 40 psf/ft to over 100 psf/ft. The range of assumptions currently in use can cause more than a factor of two difference in the maximum bending moment in the shaft. This range could cause the walls to be over-designed or under-designed.

A full-scale test drilled shaft retaining wall was constructed on a site underlain by approximately 50 feet of the expansive Taylor Clay. Analysis of the wall is intended to provide information to be considered in design about the effects of the moisture cycles which cause shrinking and swelling.

In order to monitor the moisture changes within the clay, 20 Time Domain Reflectometry (TDR) probes were installed behind the wall. This thesis discusses the monitoring plan, calibration, installation, and initial results from these probes. The objectives of this thesis is to provide information regarding the site conditions and

reasons for using TDR probes for this project and to describe the monitoring plan, calibration, installation, and the field performance of the TDR probes and the moisture values that have been seen on the site to date.

Previous studies show that difficulties can be expected when using TDR probes in highly plastic clays. Results from this study are typical of these results seen previously. The initial results show that 4 of the 20 probes are recording reasonable waveforms. However, the waveforms cannot be analyzed using conventional methods. This result was because the waveform reflection that indicates the end of the probe cannot be defined due to attenuation of the signal, which is typical of highly conductive soils. Also, the large amount of scatter in the electrical conductivity values does not allow for the moisture content to be correlated to the electrical conductivity.

In order to use the TDR probes to measure moisture content at the project site, an alternative method needs to be employed to analyze available waveforms. If another method can be successfully employed for the functional probes, the subsequent step would involve recovering the probes that are not functioning properly in order to get a moisture profile along the full cantilevered height of the wall. Direct moisture measurements should also be taken periodically to provide a moisture profile.

Table of Contents

List of Tables	x
List of Figures	xi
CHAPTER 1: INTRODUCTION	1
1.1: Motivation.....	1
1.2: TxDOT Research Project.....	2
1.3: Objectives for Thesis	3
1.4: Organization of Thesis.....	3
CHAPTER 2: BACKGROUND	5
2.1: Theory for Time Domain Reflectometry (TDR) Probes	5
2.2: Studies Using TDR Probes	9
2.2.1: TDR Rod Alignment.....	13
CHAPTER 3: SITE CONDITIONS AND TEST WALL	14
3.1: Site Conditions.....	15
3.1.1: Moisture Contents and Atterberg Limits	16
3.1.2: Undrained Shear Strengths	16
3.2: Test Wall.....	18
3.2.1: Instrumentation for Displacement and Stress	21
CHAPTER 4: MOISTURE MONITORING PLAN AND CALIBRATION	23
4.1: Moisture Monitoring Plan.....	23
4.1.1: Water Table Measurements	25
4.1.2: TDR System Enclosure.....	26

4.2: Set-up	27
4.3: Probe Constant Calibration	28
4.3.1: Probe Constant Calibration	28
4.3.2: Probe Offset Calibration	31
4.3.3: Soil Specific Calibration	31
CHAPTER 5: TDR PROBE INSTALLATION	33
5.1: Installation of Sensors through the Wall Facing	34
5.2: Installation of Sensors from the Ground Surface	39
5.3: Installation Problems	40
CHAPTER 6: FIELD PERFORMANCE	43
6.1: Moisture Measurements	43
6.2: Performance	45
6.2.1: Functional Probe	46
6.2.2: Semi-Functional Probes	52
6.2.3: Non-Functional Probes	54
6.2.4: Rainfall Events	57
6.3: Troubleshooting	58
6.3.1: Possible Solutions for Functioning Probes	58
6.3.2: Possible Solutions for Non-Functioning Probes	59
CHAPTER 7: CONCLUSIONS	60
7.1: Recommendations	61
Appendix A	63
Appendix B	74
References	85

List of Tables

Table 4.1: Location of the TDR probes installed in the soil.....	24
Table 5.1: Location of the probes installed through the facing of the wall	34
Table 5.2: Location of the probes installed through the ground surface	39

List of Figures

Figure 2.1: A sample TDR probe used in this study (rod length: 7.5 cm; rod diameter: 0.159 cm)	6
Figure 2.2: A typical waveform showing the key points (Campbell Scientific, Inc., 2010)	7
Figure 2.3: Comparison of the Topp et al. (1980) equation and the actual volumetric water content in Eagle Ford Clay (Kuhn 2005)	11
Figure 3.1: A view of the test wall after excavation and installation of the shotcrete facing	14
Figure 3.2: A sample of the Taylor Clay at the project site	15
Figure 3.3: The Atterberg Limits of the Taylor Clay and the water content on January 12, 2010	17
Figure 3.4: Undrained shear strength profile from UU testing	18
Figure 3.5: Plan view of the wall and excavation	19
Figure 3.6: Layout of the drilled shafts	20
Figure 3.7: Cross-section of wall and excavation	21
Figure 3.8: Instrumented cage before concrete placement	22
Figure 4.1: Location of the 20 TDR probes installed behind the wall	25
Figure 4.2: TDR system within the NEMA 4 steel enclosure	27
Figure 4.3: PCTDR-Version 2.07 calibration screen	30
Figure 5.1: Location of the 20 TDR probes installed behind the wall	33
Figure 5.2: Layout of TDR probes installed through the facing of the wall	35
Figure 5.3: A sample installation of a probe installed through the facing of the wall	36
Figure 5.4: A hole being drilled by Craig Olden, Inc	37
Figure 5.5: The PVC pipe protection for the TDR probe cables to minimize damage from the shotcrete	38
Figure 5.6: A sample probe installation through the ground surface	40

Figure 5.7: A sample probe installation where the probe could not be pushed completely into the soil.....	42
Figure 6.1: Moisture Measurements taken from January 2010 to May 2011 (Ellis 2011).....	44
Figure 6.2: Daily precipitation measurements from January 2008 to July 2011 (Ellis 2011).....	45
Figure 6.3: Location of the 20 TDR probes installed behind the wall.....	46
Figure 6.4: Electrical conductivity measurements for Probe 4.....	47
Figure 6.5: Electrical conductivity measurements over a 24 hour period on March 3, 2011.....	48
Figure 6.6: La/L data for Probe 4 inferred by the Campbell Scientific, Inc. algorithm ...	49
Figure 6.7: Waveform data for the functioning probe	50
Figure 6.8: Waveforms for differing cable length in a sandy loam (Campbell Scientific, Inc., 2010).....	51
Figure 6.9: TDR waveforms in a sandy loam with a high electrical conductivity of 10.2 dS/m (Campbell Scientific, Inc., 2010)	51
Figure 6.10: Electrical conductivity measurements for Probe 9.....	52
Figure 6.11: La/L data for Probe 9.....	53
Figure 6.12: Sample waveforms from Probe 9	54
Figure 6.13: Electrical conductivity data from Probe 15.....	55
Figure 6.14: La/L data from Probe 15	56
Figure 6.15: A sample waveform from Probe 15	56
Figure 6.16: Electrical conductivity measurements for Probe 16.....	57

CHAPTER 1: INTRODUCTION

1.1: Motivation

Expansive clay soils are common throughout Texas and the United States. These expansive soils have been reported to cause billions of dollars in structural damage a year in the United States (Jones and Holtz, 1973). In Texas, retaining walls are often used in areas with expansive clay soils. An understanding of the behavior of the interaction between expansive clay and retaining walls is important in being able to design and construct these walls properly and cost efficiently.

Drilled shaft retaining walls are commonly used throughout Texas, especially by the Texas Department of Transportation (TxDOT). Recently in the state of Texas, there have been questions regarding the performance of these drilled shaft walls in the expansive clay soils.

When expansive clay soils experience moisture changes, the clay will shrink and swell. When estimating the lateral earth pressures acting on a wall, an important challenge is to predict swell pressures from moisture changes. The uncertainties that are associated with designing a drilled shaft retaining wall in expansive clay are what the distributions of lateral earth pressures versus depth below the ground surface should be and how the moisture cycles of the clay should be considered. It is currently not clear how to account for the shrinking and swelling of the expansive clay soils and the earth pressures applied on a wall during these processes. It is common practice to assume an equivalent fluid pressure for design. Typical fluid pressures used range from 40 to 80 psf/ft with some engineers using more than 100 psf/ft. A range of 55 to 80 psf/ft is recommended for expansive clay soils by the Foundations Engineering Handbook (1991).

The range of assumptions currently in practice can cause more than a factor of two difference in the maximum bending moment in the shaft (Brown et al., 2011). This uncertainty could cause walls to be over-designed or under-designed, depending on the assumptions made.

1.2: TxDOT Research Project

While TxDOT has not seen widespread failures of their drilled shaft retaining walls in expansive clay, they would benefit from a better understanding of the pressures that can realistically be exerted on drilled shaft walls. TxDOT has provided funding to the University of Texas at Austin in order to determine the performance of their current drilled shaft retaining walls in expansive clays and to provide guidance in the design of these walls by instrumenting and monitoring a full-scale test wall. The goal of the test wall is to assess the effects of seasonal moisture changes on the lateral earth pressures acting on the wall and use the information to provide TxDOT guidelines for the design of drilled shaft retaining walls in expansive clay soils.

The TxDOT 0-6603 research project involves instrumenting and monitoring a full-scale drilled shaft retaining wall constructed in the expansive Taylor Clay. This retaining wall is to be monitored for three years after construction. The wall has been instrumented with optical strain gauges to measure the bending strains within the shafts as they deflect and inclinometers are installed to measure the deflected shape of the wall over time. Thermocouples within the instrumented shafts are used to measure the temperature within the concrete. A linear potentiometer is connected to the wall to compare the deflection at ground level with the inclinometer data. Time Domain Reflectometry (TDR) probes are installed in the soil behind the wall to measure moisture

fluctuations. A rain gauge on site is used to measure the amount of rainfall in the area of the wall. Also, a piezometer is located near the wall to measure the location of the water table. Currently the wall has been monitored for approximately 16 months.

1.3: Objectives for Thesis

This thesis deals with aspects of the initial construction and monitoring of the drilled shaft retaining wall. This study includes the calibration, installation, and initial performance of the TDR probes. The objectives of this thesis are the following:

1. Present background regarding TDR probes
2. Describe the site conditions and reason for using TDR probes
3. Discuss the monitoring plan to measure the moisture on the site
4. Describe the calibration and installation procedure
5. Discuss the field performance
6. Present the conclusions and recommendations for further study

1.4: Organization of Thesis

This thesis is divided into seven chapters. Chapter 1 consists of the introduction material and is followed by the background of previous research in Chapter 2. The background includes reviews of Taylor Clay, TDR probes and their use in expansive clay soils. Chapter 3 discusses the site conditions and test wall for the TxDOT 0-6603 project. The moisture monitoring plan and calibration are discussed in Chapter 4. Chapter 5 discusses the installation of the TDR probes into the soil. The field performance of the

probes and a discussion of the results are provided in Chapter 6. Chapter 7 presents a short summary of the findings and the conclusions drawn from this study.

CHAPTER 2: BACKGROUND

The background gathered from past studies is presented in this chapter. Specifically, how Time Domain Reflectometry (TDR) probes work, and previous studies using TDR probes.

2.1: Theory for Time Domain Reflectometry (TDR) Probes

Originally, TDR technology was developed for to find small breaks in transmission lines (Antle, 1997, Siddiqui et al., 2000). The technology was adapted into a method for determining the dielectric constant of soil. Water has a high dielectric constant compared to the soil solids or air, which makes the soil dielectric constant highly dependent upon the volume of water in the soil (Siddiqui et al., 2000). An empirical relationship between volumetric water content and the dielectric constant of the soil was discovered by Topp et al. (1980).

A TDR system works by sending an electromagnetic waveform through the system to the TDR probes. The dielectric constant of the soil causes a change in the velocity of the waveform that is reflected and recorded. By using the reflected waveform, the dielectric constant can be estimated. The volumetric water content can then be estimated by using the empirical relationship such as that established by Topp et al. (1980).

A sample TDR probe used for this study is shown in Figure 2.1. The probes can vary in size, metal rod spacing and lengths. The electromagnetic pulse is sent through the center rod and the outer two rods act as a shield. These probe designs make it so an average volumetric water content is being measured of a small volume of soil. The time for the reflected waveform is measured during a period of time of nanoseconds.

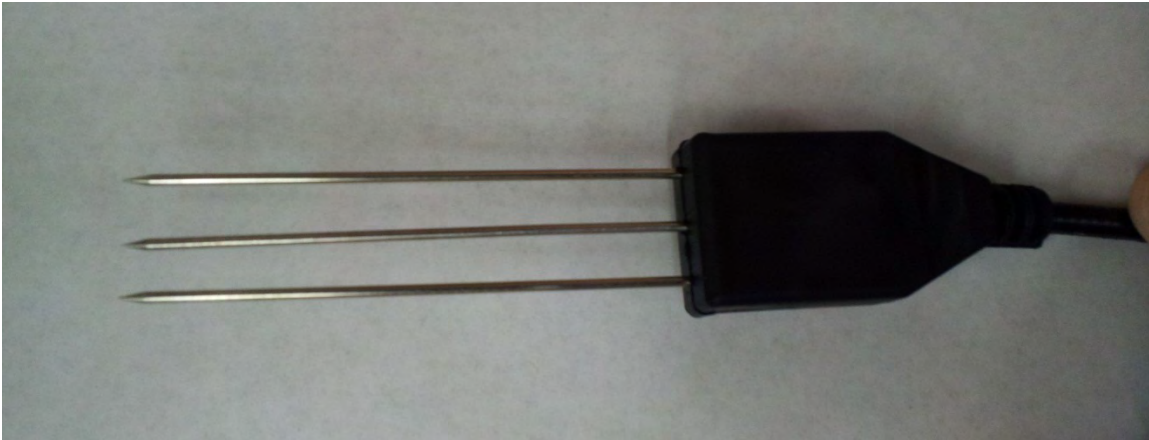


Figure 2.1: A sample TDR probe used in this study (rod length: 7.5 cm; rod diameter: 0.159 cm)

The reflected waveform that is measured consists of three reflection points. These points are shown as points 1-3 in Figure 2.2. Point 1 is the reflection point between the cable and the probe rods that are surrounded by the probe head. This portion of the probe is still not in contact with the soil. The second reflection point (point 2) is the transition point from the rods surrounded by the probe head and the rods in contact with the soil. The third reflection point (point 3) is the point where the signal reaches the end of the metal rod. Using the distance between the second and third point, the dielectric constant of the soil can be estimated.

Figure 2.2 shows a typical waveform taken from a TDR probe (Campbell Scientific, Inc., 2010). The y-axis consist of reflection coefficient and the x-axis can be presented as time, distance, or waveform data point; depending on the preference of the operator and the method used to analyze the waveform. The data points recorded to generate the waveform are taken on the order of nanoseconds.

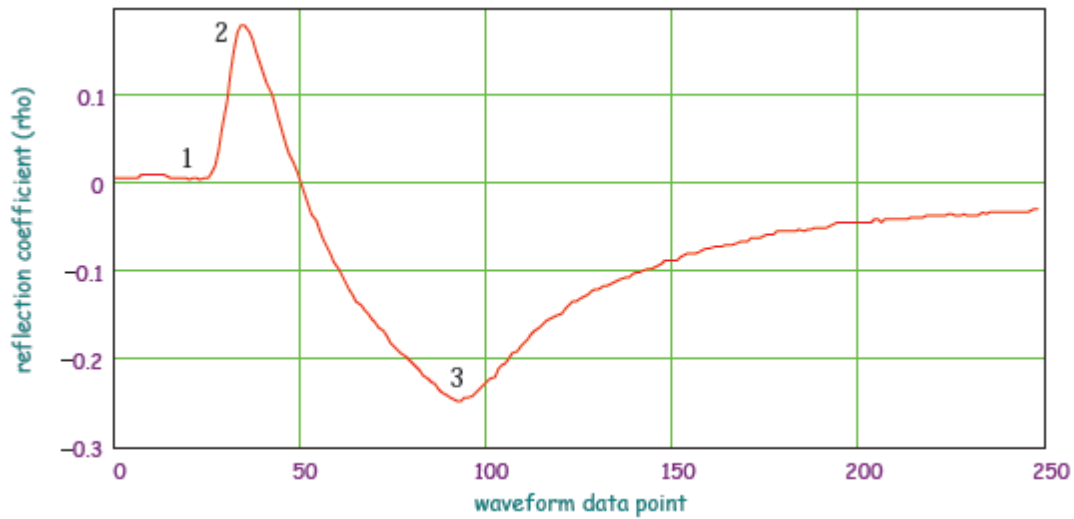


Figure 2.2: A typical waveform showing the key points (Campbell Scientific, Inc., 2010)

Siddiqui et al. (2000) described the relationship between the dielectric constant and the time between points 2 and 3. The velocity (v) of the electromagnetic wave through the probe is equal to the distance travelled ($2L$) divided by the time between points 2 and 3 (Equation 2.1), where $2L$ is twice the length of the probe and t is the time between points 2 and 3.

$$v = \frac{2L}{t} \quad \text{(Equation 2.1)}$$

Siddiqui et al. (2000) also shows the velocity of the electromagnetic wave is equal to the speed of light through a vacuum (c) divided by the square root of the apparent dielectric constant of the soil (K_a).

$$v = \frac{c}{\sqrt{K_a}} \quad \text{(Equation 2.2)}$$

The combination of Equation 2.1 and Equation 2.2 results in Equation 2.3 to determine the apparent dielectric constant for the soil (Siddiqui et al., 2000). Only the time between points 2 and 3 is needed to determine the apparent dielectric constant of the soil as the speed of light and the length of the probes are constants.

$$K_a = \left(\frac{ct}{2L}\right)^2 \quad (\text{Equation 2.3})$$

Campbell Scientific, Inc. uses an algorithm in their programming that determines the electrical apparent dielectric constant by using an apparent probe length (L_a) between point 2 and point 3. When determining the dielectric constant using lengths, the apparent length is the length that the probe appears to be when viewing the waveform. The theory of the algorithm is the same as presented by Siddiqui et al. (2000), but it uses an apparent probe length that is equal to the speed of light in a vacuum multiplied by the time and divided by 2 (Campbell Scientific, Inc., 2010).

$$t = \frac{2L\sqrt{K_a}}{c} \quad (\text{Equation 2.4})$$

Combining Equation 2.4 and Equation 2.3 produces the equation used by Campbell Scientific, Inc. in their algorithm (Campbell Scientific, Inc., 2010).

$$\frac{L_a}{L} = \sqrt{K_a} \quad (\text{Equation 2.5})$$

With the apparent dielectric constant, an empirical relationship developed by Topp et al. (1980) can be used to estimate the volumetric water content of the soil (θ_v) (Equation 2.6).

$$\theta_v = 5.3 * 10^{-2} + 2.92 * 10^{-2}K_a - 5.5 * 10^{-4}K_a^2 + 4.3 * 10^{-6}K_a^3 \quad (\text{Equation 2.6})$$

The TDR probes also record the bulk electrical conductivity of the soil (σ). This is done by measuring the reflection coefficient (ρ). The reflection coefficient ranges between plus and minus one and is the ratio of the reflected voltage to the applied voltage (Campbell Scientific, Inc., 2010). Equation 2.7 is used to calculate the bulk electrical conductivity using the reflection coefficient (Giese and Tiemann, 1975).

$$\sigma = \frac{K_p}{Z_c} \frac{1-\rho}{1+\rho} \quad (\text{Equation 2.7})$$

where K_p is a probe constant determined by a calibration and Z_c is the cable impedance. The probe constant is determined by doing a calibration and is the ratio of the electrical conductivity to the electrical conductance.

2.2: Studies Using TDR Probes

Topp et al. (1980) introduced an empirical method of using TDR probes to determine water content of soil. A wide range of soil specimens, from sandy loam to clay, were used to establish the empirical equation (Equation 2.6). Topp et al. (1980) concluded that electrical losses from the TDR system were negligible, the dielectric constant is not frequency dependent from the range of 1 MHz to 1 GHz, there was no

significant temperature dependence, and the equation was almost independent of soil density, texture, and salt content. However, the specific surface area of the soil particles is important when correlating the dielectric constant of the soil to the moisture content. Lower moisture contents have a lower dielectric constant that is closer to what would typically be for water in ice structures, and higher moisture contents had higher dielectric constant values.

Empirical relationships for determining the volumetric water content from TDR probe measurements have been reported to be inaccurate for high plasticity clays (Reedy and Scanlon, 2002, and Kuhn, 2005). Kuhn (2005) noticed a significant difference between the volumetric water content obtained using the Topp et al. (1980) equation and the actual value in the Eagle Ford Clay. The Eagle Ford formation used had a Plasticity Index of 49 percent. Both the Eagle Ford Clay and the Taylor Clay used for this study are highly plastic clays that can be found in the Austin area. Kuhn (2005) conducted laboratory experiments using the TDR probes to compare the volumetric water content at a measured dielectric constant compared to the results of using the Topp et al. (1980) equation. Figure 2.3 shows the results where the volumetric water content is plotted versus the square root of the dielectric constant.

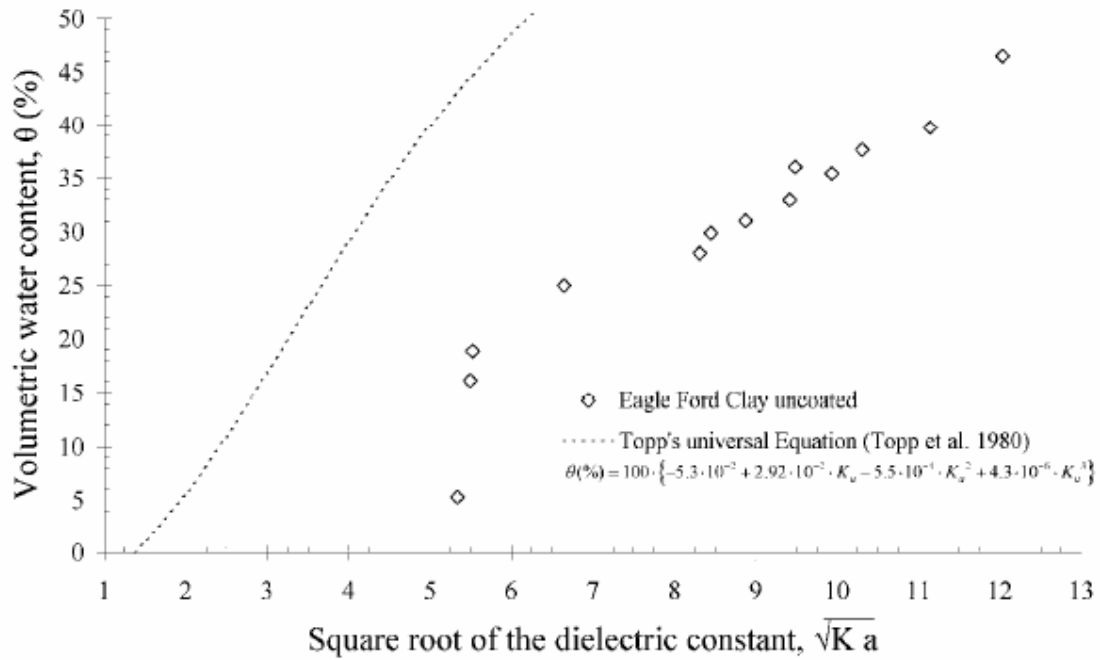


Figure 2.3: Comparison of the Topp et al. (1980) equation and the actual volumetric water content in Eagle Ford Clay (Kuhn 2005)

When TDR probes are used in highly plastic clays, the waveforms often show poor signal reflections. This result is due to the high electrical conductivity of the highly plastic clays, which cause attenuation of the signal (Jones and Or, 2004). Typically when the electrical conductivity increases, the water content is overestimated (Campbell Scientific, Inc., 2010). Several studies have reported results that show a reflected waveform that does not show the reflection that defines the end of the probe (Point 3 in Figure 2.2) (Reedy and Scanlon, 2002, Chen et al., 2007, Jones and Or, 2004).

In order to use TDR probes in highly conductive soils, different methods have been utilized. Kuhn (2005) and Moret-Fernandez et al. (2009) used coating on the probes to help reduce the interference of the electrical conductivity of the soil. Moret-Fernandez et al. (2009) used probes partially coated with a different percentage of the probe being

covered. It was noticed that almost completely coated the probe allowed for the inflection that indicates the end of the probe to be seen in the waveform. An issue with the coating is that the coating has the potential to wear over time which would affect the calibration of the probe.

Chen et al. (2007) developed a model-based method that analyzes the reflection of the waveform at the surface of the soil instead of at the end of the probes to determine the dielectric constant. The approach showed a reasonable accuracy in estimating the dielectric constant of the soil. To use the procedure a calibration needs to be performed first.

Jones and Or (2004) presented a method to transform the waveform data so it could be analyzed in the frequency domain. An artificially generated step function in the time domain is used to provide the necessary input signal. Smaller probes (on the order of 2 cm) are needed for this analysis in the frequency domain in order to reduce the signal attenuation compared to the optimal 10 to 15 cm probe lengths for conventional time domain methods. This method also needs a precise calibration in order to work properly.

The benefits of using a TDR system instead of the FDR system were reported to be less affected by soil type and temperature (Seyfried and Murdock, 2004). TDR probes perform well in soils with higher electrical conductivities as long as they are below a limit of 5.0 dS/m, according to the TDR100 Manual (Campbell Scientific, Inc., 2010). Based on their studies, Seyfried and Murdock (2004) expect that the FDR probes used in their studies would be more sensitive to soil conditions than the TDR probes used. The TDR system also does not typically need to have a soil specific calibration performed to produce reliable results.

2.2.1: TDR ROD ALIGNMENT

Campbell Scientific Inc. performed a test in air and water to determine the effects of the TDR rods not being in the correct alignment (Brown 2011). CS 640 probes, which have a 7.5 centimeter probe length, were used with 20 feet of cable. Tests were performed with the rod alignment being correct and with three different rod alignment scenarios. The first two scenarios consisted of deflecting the outside rods outward and inward four millimeters. In the third scenario, the center rod was deflected out of alignment by four millimeters and the outer rods were deflected outward four millimeters. The tests show that the measured results were not affected by more than 0.03 percent. Campbell Scientific Inc. also noted that the results may not be typical when applied to soils due to the problem of causing compaction of the soil or causing air voids to be developed.

CHAPTER 3: SITE CONDITIONS AND TEST WALL

The drilled shaft retaining test wall is explained in this chapter. Specifically, the design of the wall and the instrumentation within the wall and on site are described. Also, the site location and conditions are discussed. A picture of the retaining wall is shown in Figure 3.1. The pouring of the concrete shafts was done from March 30, 2010 to April 6, 2010. Excavation was gradually done during the month of August 2010 and the shotcrete facing was added on the wall on October 1, 2010.



Figure 3.1: A view of the test wall after excavation and installation of the shotcrete facing

3.1: Site Conditions

The project site is located in Manor, TX underlain by approximately 50 feet of the highly expansive Taylor Clay. The clay is blocky, highly fissured and heavily overconsolidated. A picture of a sample taken from the Taylor Clay on site is shown in Figure 3.2.



Figure 3.2: A sample of the Taylor Clay at the project site

On January 12 and 13, 2010, three borings were drilled to a depth of 50 feet by Fugro Consultants, Inc. During the borings, Texas Cone Penetration (TCP) tests and Standard Penetration Tests (SPT) were performed and split-spoon samples were taken in order to provide information consistent with the standard of practice in Texas. An inclinometer and a piezometer were installed in two of the borings. The third boring was backfilled with cuttings.

3.1.1: MOISTURE CONTENTS AND ATTERBERG LIMITS

Atterberg Limits were performed according to the standard of practice. Liquid Limits reached ranged from approximately 50 percent to over 100 percent over the length of the profile. The Liquid Limits measured below approximately 5 feet were all above 80 percent. Plastic Limits were between approximately 20 and 30 percent. The water contents on January 12, 2010 were between 20 and 40 percent. Figure 3.3 shows the Atterberg Limits and the moisture contents from January 12, 2010.

3.1.2: UNDRAINED SHEAR STRENGTHS

Several Unconsolidated Undrained (UU) triaxial tests were performed on the split-spoon samples taken from the field investigation. Two tests were done by trimming the samples to a 1.5 inch diameter. Due to the highly fissured nature of the clay, the trimming process was difficult. The remaining tests were done at the Fugro laboratory in Austin, Texas, using test specimens with the split-spoon diameter of 2.7 inches. The strengths ranged from 1500 psf to over 6000 psf. The undrained strength profile is shown in Figure 3.4.

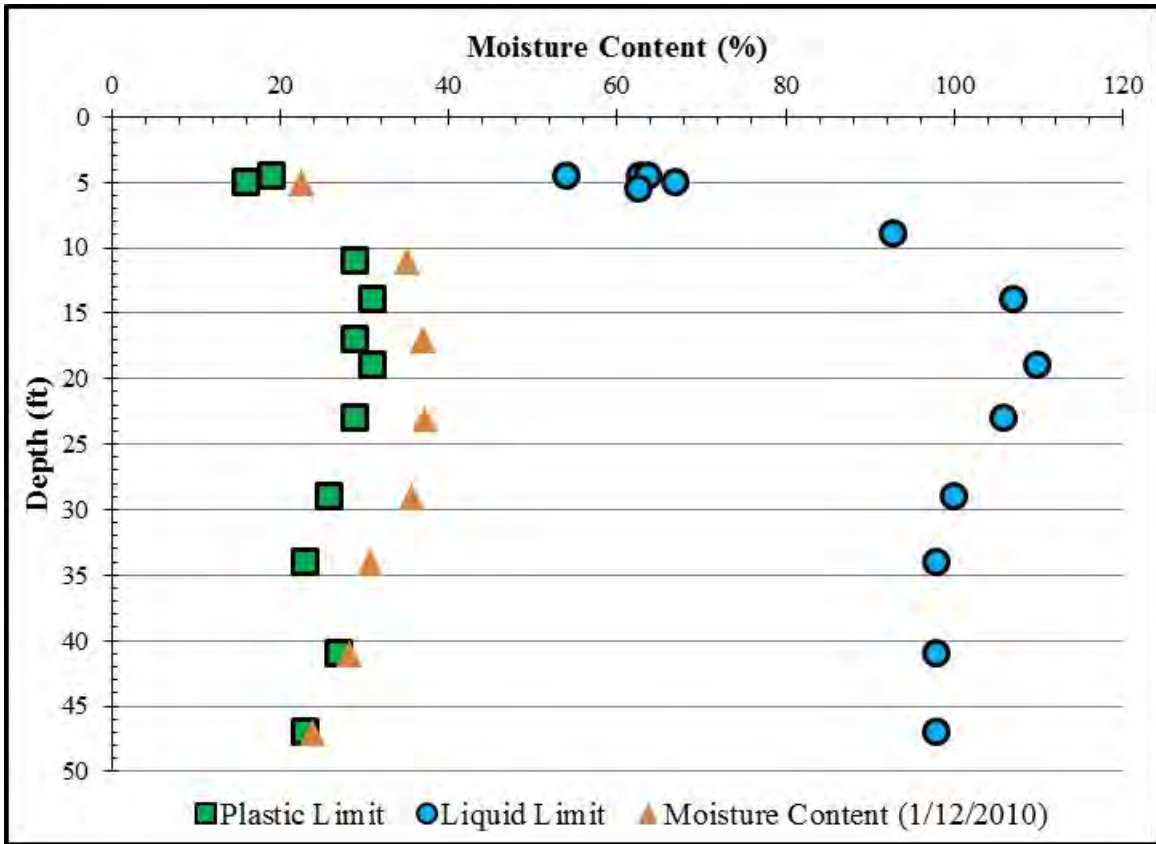


Figure 3.3: The Atterberg Limits of the Taylor Clay and the water content on January 12, 2010

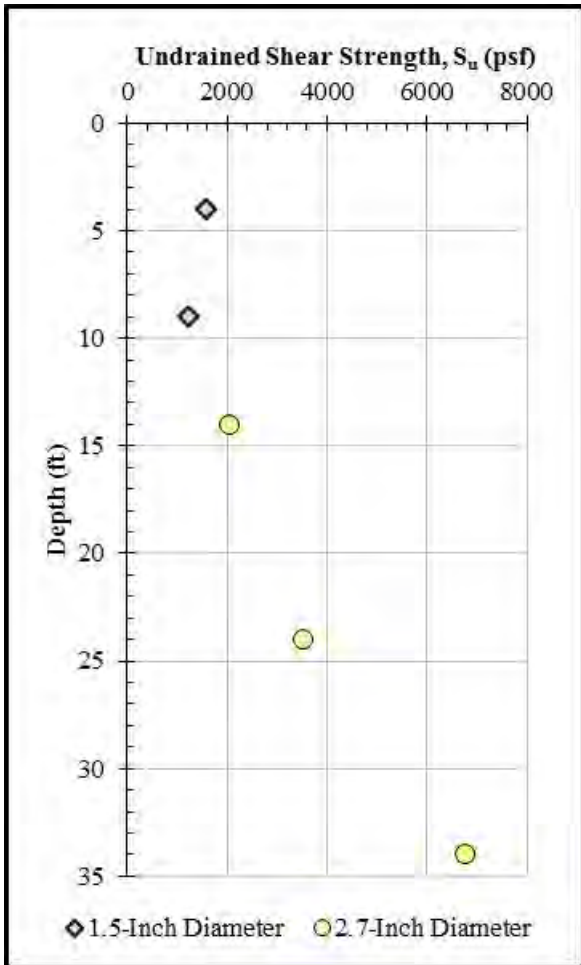


Figure 3.4: Undrained shear strength profile from UU testing

3.2: Test Wall

The test wall was designed to be in accordance with typical TxDOT design procedures, but flexible enough to see movements from the wall in order to estimate the earth pressures exerted on the wall. This wall consists of 25 drilled shafts with a 24 inch diameter spaced six inches edge to edge (Figure 3.5). The shafts are embedded to depths from 18 to 35 feet below the ground surface with the deepest shafts being in the center

(Figure 3.6). At the center of the wall, the cantilever height is 15 feet, the penetration depth is 20 feet, and top of the shafts is four feet above the ground surface (Figure 3.7). The four foot stickup allows for the possibility of doing a lateral load test at the end of the project. The rebar reinforcing cage contains 12 #7 bars.

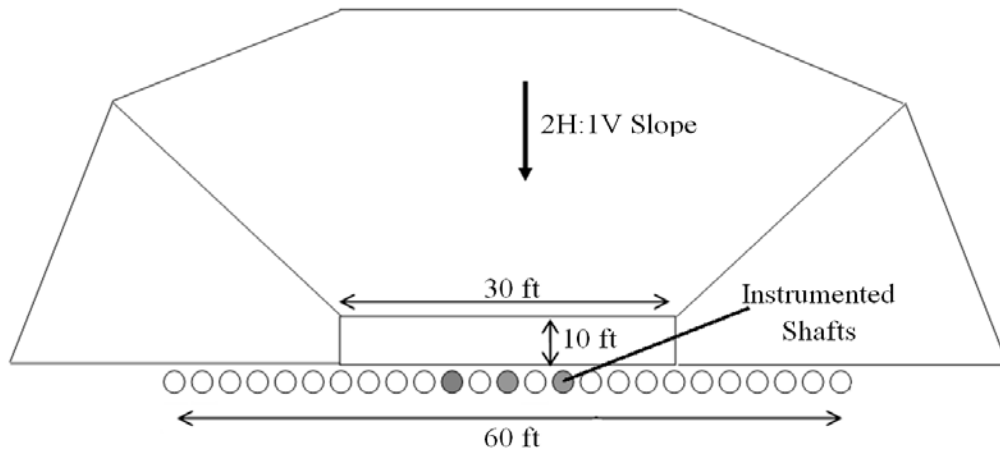


Figure 3.5: Plan view of the wall and excavation

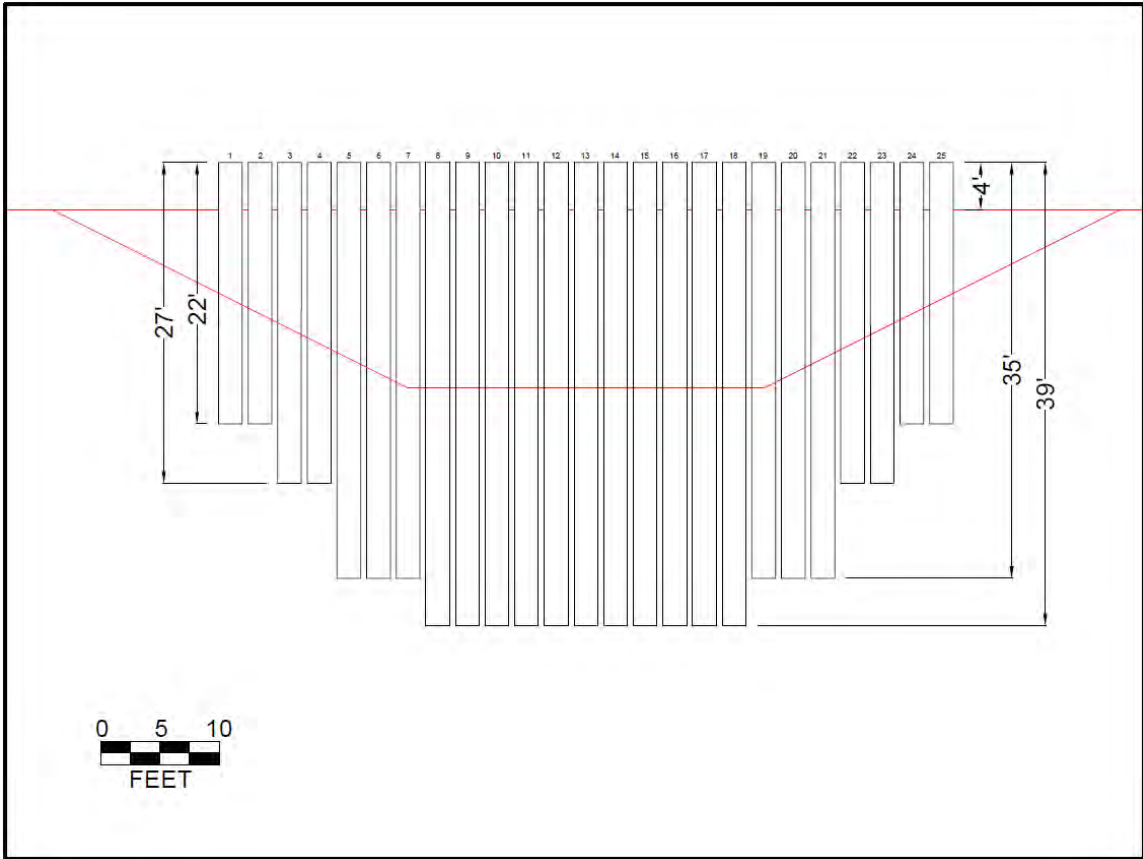


Figure 3.6: Layout of the drilled shafts

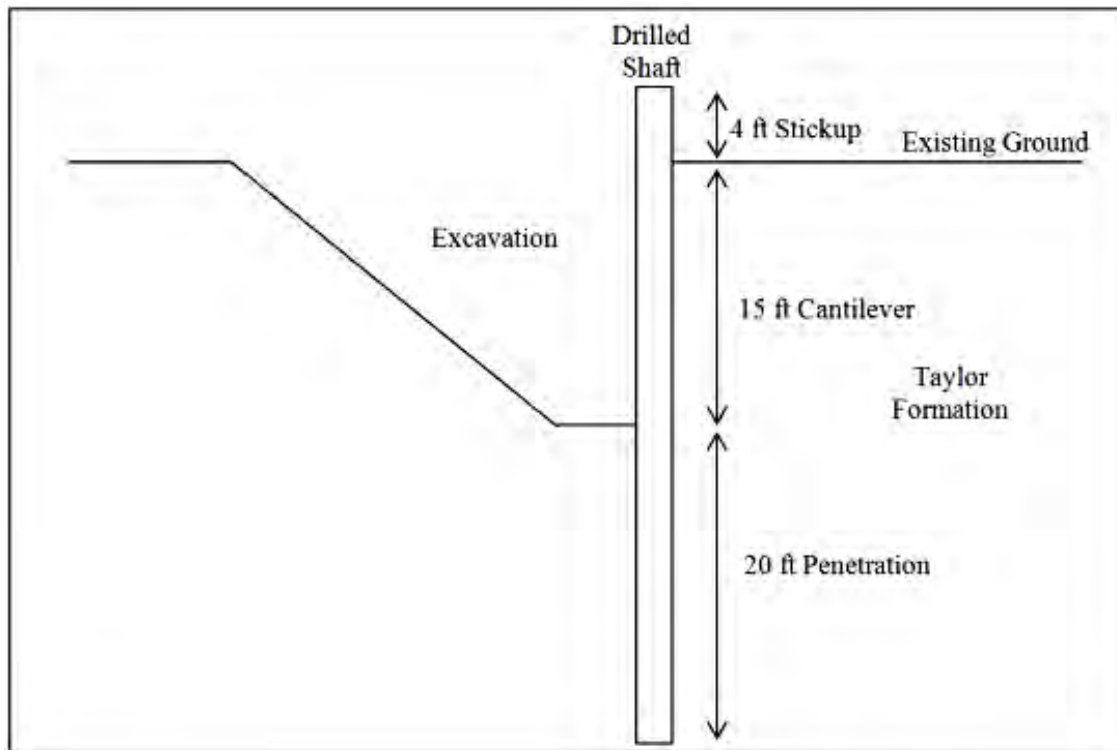


Figure 3.7: Cross-section of wall and excavation

3.2.1: INSTRUMENTATION FOR DISPLACEMENT AND STRESS

There are three shafts instrumented for this project (Figure 3.5). Within each instrumented shaft is an inclinometer casing and 30 optical strain gauges; 15 on the tension side and 15 on the compression side, spaced two feet center to center. The optical strain gauge wires are protected in a slotted PVC pipe. One inclinometer is also installed 5.5 feet behind the wall. There are three thermocouples within the center shaft at depths of three, 15, and 29 feet below the ground surface and seven thermocouples in a non-instrumented shaft spaced every two feet from depths of one to 13 feet below the ground surface. Figure 3.8 shows an instrumented shaft placed in the ground before concrete

placement. Additionally, there is a linear potentiometer attached to the top of one of the shafts to measure the lateral deformation of the wall at the ground surface.

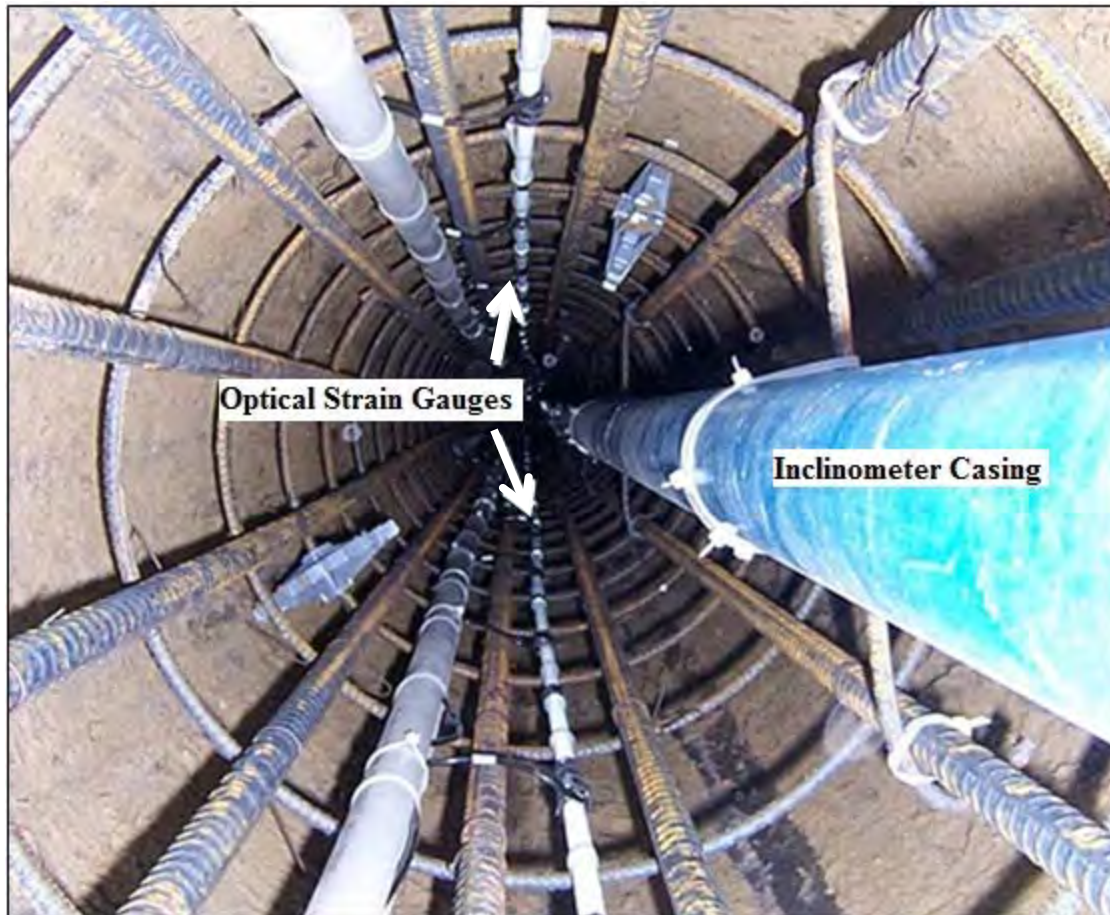


Figure 3.8: Instrumented cage before concrete placement

CHAPTER 4: MOISTURE MONITORING PLAN AND CALIBRATION

The description of the moisture monitoring plan and the system schematic of the moisture monitoring plan are presented in this chapter. Also, the description of the calibration performed on the TDR system is presented.

4.1: Moisture Monitoring Plan

TDR probes were used to monitor the volumetric water content of the soil on site. The system consists of 20 Campbell Scientific, Inc. CS645-L probes with 70 feet of LMR-200 low loss cable length, a Campbell Scientific, Inc. TDR100, three Campbell Scientific, Inc. SDX50 multiplexers, and a Campbell Scientific, Inc. CR1000. The TDR100 generates the signals that are sent to the probes and the CR1000 logs the data. CS645-L probes are manufactured with rod lengths of 7.5 centimeters (2.95 inches) and rod diameters of 0.159 centimeters (0.06 inches).

The TDR probes were to be installed at various depths behind the wall along the 15 feet cantilevered height of the wall. Table 4.1 and Figure 4.1 show the location of the 20 TDR probes in the ground. Physical moisture samples, taken periodically using a hand auger, will supplement the measurements obtained by the TDR probes.

Table 4.1: Location of the TDR probes installed in the soil

Probe #	Depth below Ground Surface (feet)	Distance Behind the Wall (feet)
1	1	20
2	1.75	1
3	13.5	1.6
4	1.5	1
5	0.9	1
6	0.5	10
7	3.7	5.2
8	13.6	1.7
9	6	3.5
10	2.5	1.7
11	9.2	1.8
12	1.8	1.9
13	1.5	4.9
14	5.8	5.3
15	5.1	0.9
16	0.9	10
17	1.75	1
18	0.5	1
19	0.5	1
20	0.5	20

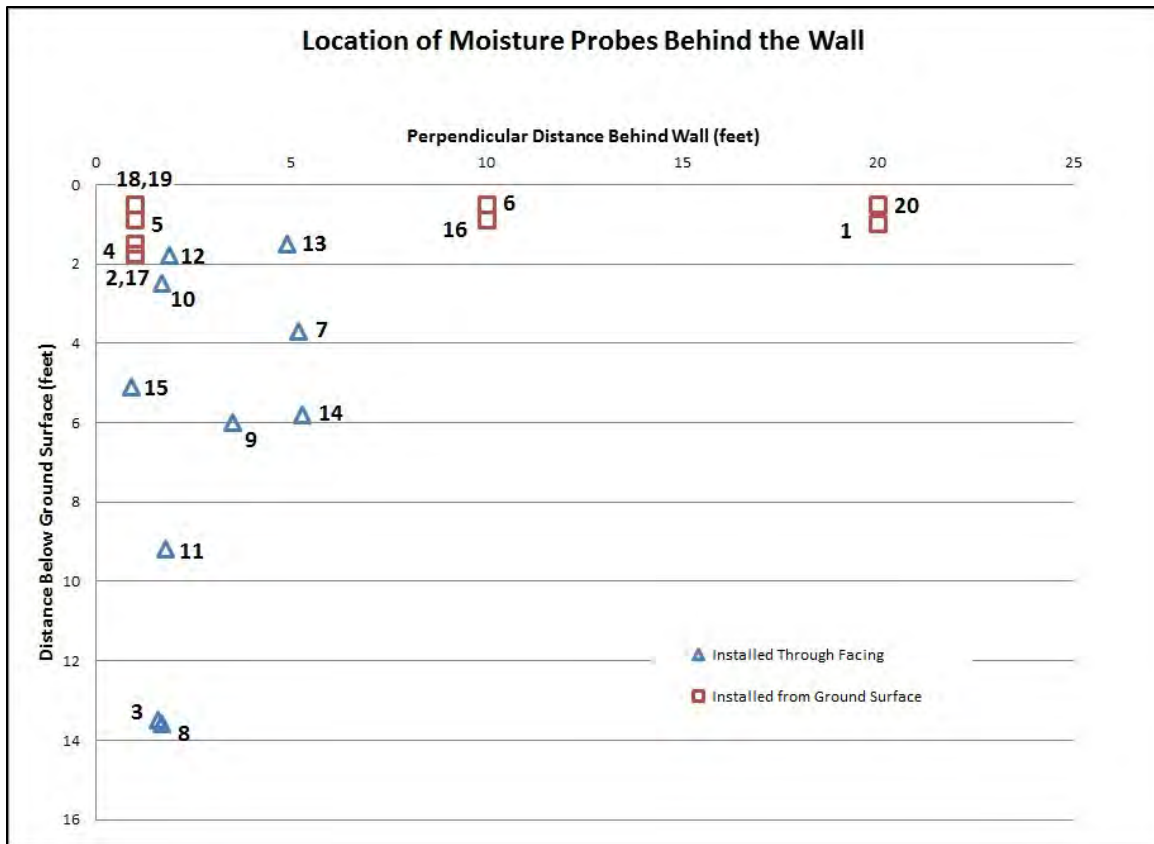


Figure 4.1: Location of the 20 TDR probes installed behind the wall

4.1.1: WATER TABLE MEASUREMENTS

The piezometer has been used to take records of the approximate location of the water table near the wall. This 1.25 inch diameter piezometer is grouted at the base of the borehole. The screen is located between five and 20 feet and the water level was determined using an electronic water level meter. Analysis of an initial rising head test that was performed over a period of weeks produced a saturated hydraulic conductivity of approximately 10^{-8} cm/sec. Since the piezometer has been installed, the depth to water has ranged from 7.5 feet below the ground surface (April 2010) to approximately 9.5 feet

below the ground surface (June 2011). While the water table in the area is most likely not at the same depth as the piezometer, the piezometer should give a good indication of what the water level is near the wall. The excavation of the wall has caused the water level to be affected. Small amounts of water can consistently be seen at the bottom of the excavation near the wall. Elevations taken from a pond on the owner's site show an elevation difference of approximately two feet.

4.1.2: TDR SYSTEM ENCLOSURE

The instruments needed to be enclosed on site in a box that can withstand the weather conditions. Historical temperature data has shown that yearly highs and yearly lows can vary up to 100 degrees Fahrenheit, with typical temperature above 100 degrees Fahrenheit in the summer and below freezing in the winter. Thunderstorms and large rainfall events are common, which means lightning protection is necessary. The site is limited to one AC power cord to run the instruments on site which consists of the TDR system and the optical strain gauge system.

In order to meet the onsite needs, the TDR operating system was placed in a NEMA 4 steel enclosure. The AC power cord runs from the on site power source to the box containing the optical strain gauge equipment. In this box, a surge protector is used to power both the optical strain gauges and a TDR system by a power cord leading to the TDR enclosure. From the optical strain gauge enclosure, the power cord then goes to a trickle charger in the TDR enclosure connected to a 12 Volt battery to keep the battery charged. The battery is connected to the TDR100 which powers the TDR system. In case the power goes out, the battery will be able to keep the system working until the power is back on. A lightning module is connected within the system to protect the system if struck by lightning and the system is grounded to one of the rebar cages in an

non-instrumented shaft. The cables entering and leaving the box were waterproofed by using cable glands and heavy duty tape. Figure 4.2 shows the system within the NEMA 4 steel enclosure.

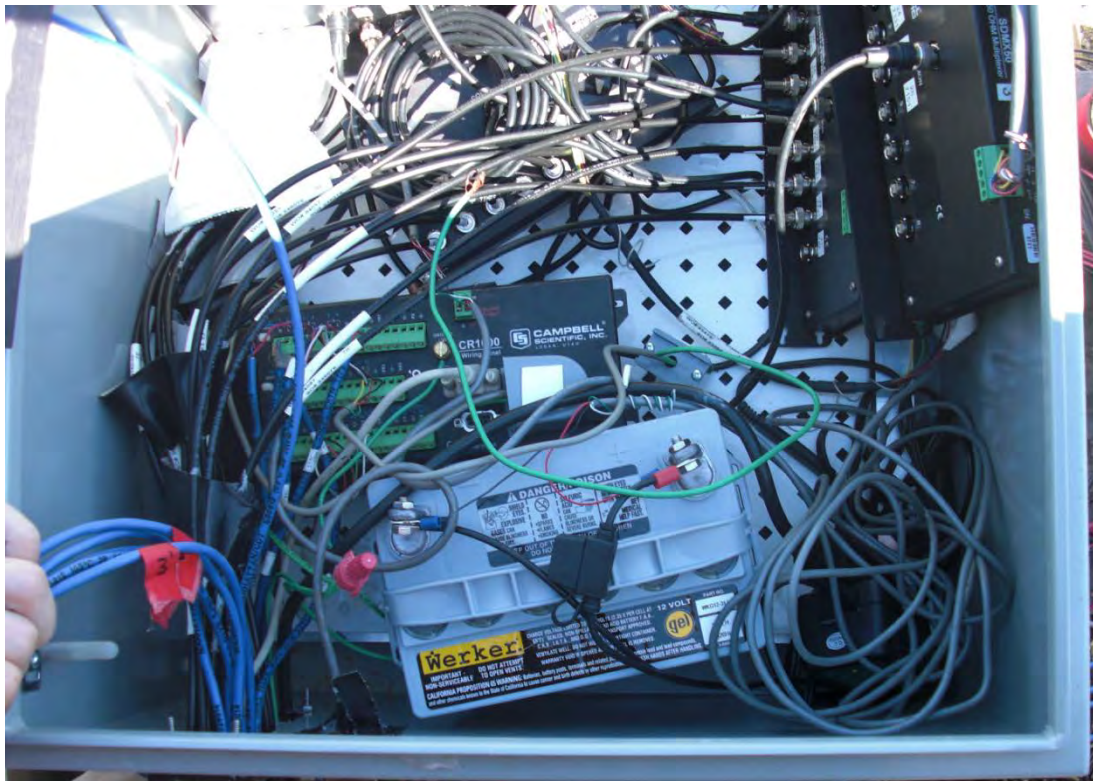


Figure 4.2: TDR system within the NEMA 4 steel enclosure

4.2: Set-up

The TDR probes were set up to record data on the Campbell CR1000 datalogger. The program on the CR1000 stores the probe constants and probe offsets in order to provide partially reduced data as an output. The measurement plan consists of recording electrical conductivity measurements and L_a/L measurements every 15 minutes and

recording full waveforms for each probe every two hours. The capacity of the CR1000 requires these data to be downloaded every two to three weeks.

As mentioned in Chapter 2, the L_a/L values are taken from the waveform using an algorithm from the TDR100. The L_a/L is calculated from the waveform, stored on the CR1000, and the waveform is discarded. Having L_a/L allows for the dielectric constant (K_a) to be calculated. The equation (Equation 2.6) from Topp et al. (1980) allows for the moisture content to be determined empirically.

The full waveforms are only taken every two hours due to the amount of memory space waveforms fill. Each waveform consists of 251 points that need to be stored for each probe. Having full waveforms allow for the L_a/L values to be checked or calculated if there is a issue with the algorithm reading the correct points on the waveform.

4.3: Probe Constant Calibration

The calibration of the TDR system was performed at Ensoft, Inc. in Austin, Texas. These calibrations were performed in accordance with the TDR 100 Manual (Campbell Scientific, Inc., 2010). The calibration process was done using PCTDR-Version 2.07 from Campbell Scientific, Inc.

4.3.1: PROBE CONSTANT CALIBRATION

The probe constant (K_p) is required for the measurement of electrical conductivity. The calibration procedure and equations used were obtained from TDR100 Manual (Campbell Scientific, Inc., 2010). Electrical conductivity is calculated using Equation 4.1.

$$\sigma = K_p * G \quad \text{(Equation 4.1)}$$

Where σ is electrical conductivity and G is the electrical conductance. The probe constant is the ratio of the electrical conductivity to the electrical conductance. By immersing the TDR probes in a solution of known electrical conductivity and measuring the electrical conductance, the probe constants can be determine. Distilled water mixed with a specified amount of Potassium Chloride (KCl) was used as the solution with known electrical conductivity. The electrical conductance is determined by Equation 4.2 (Campbell Scientific, Inc., 2010).

$$G = \left(\frac{1}{Z_u}\right) \left(\frac{1-\rho_{corrected}}{1+\rho_{corrected}}\right) \quad (\text{Equation 4.2})$$

where Z_u is the system impedance (50 ohms) and $\rho_{corrected}$ is the corrected reflection coefficient. The corrected reflection coefficient is calculated using Equation 4.3 (Campbell Scientific, Inc., 2010).

$$\rho_{corrected} = 2 \left(\frac{\rho_{uncorrected}-\rho_{open}}{\rho_{open}+\rho_{shorted}}\right) \quad (\text{Equation 4.3})$$

where $\rho_{uncorrected}$ is the uncorrected reflection coefficient measurement, ρ_{open} is the reflection coefficient measured when the probes are left in air, and $\rho_{shorted}$ is the reflection coefficient measured when the probe rods are shorted. The probes were shorted by firmly covering the probe rods with a hand (Campbell Scientific, Inc., 2010).

Using Equations 4.1-4.3 and following the directions provided by the TDR100 Manual (Campbell Scientific, Inc., 2010), the probe constants were found for each probe.

The process was performed using the program, PCTDR-Version 2.07 from Campbell Scientific, Inc.

During this calibration of the probe constants, the waveform settings are determined for each probe. Figure 4.3 shows the screen that is used when calibrating with the PCTDR-Version 2.07 from Campbell Scientific Inc. The number of points used to define the waveform is entered into the program. The standard number of points used to define the waveforms by Campbell Scientific, Inc. is 251. The window that shows the waveform has to be adjusted for each probe. This window is determined by the cable lengths from the TDR100 to the probe.

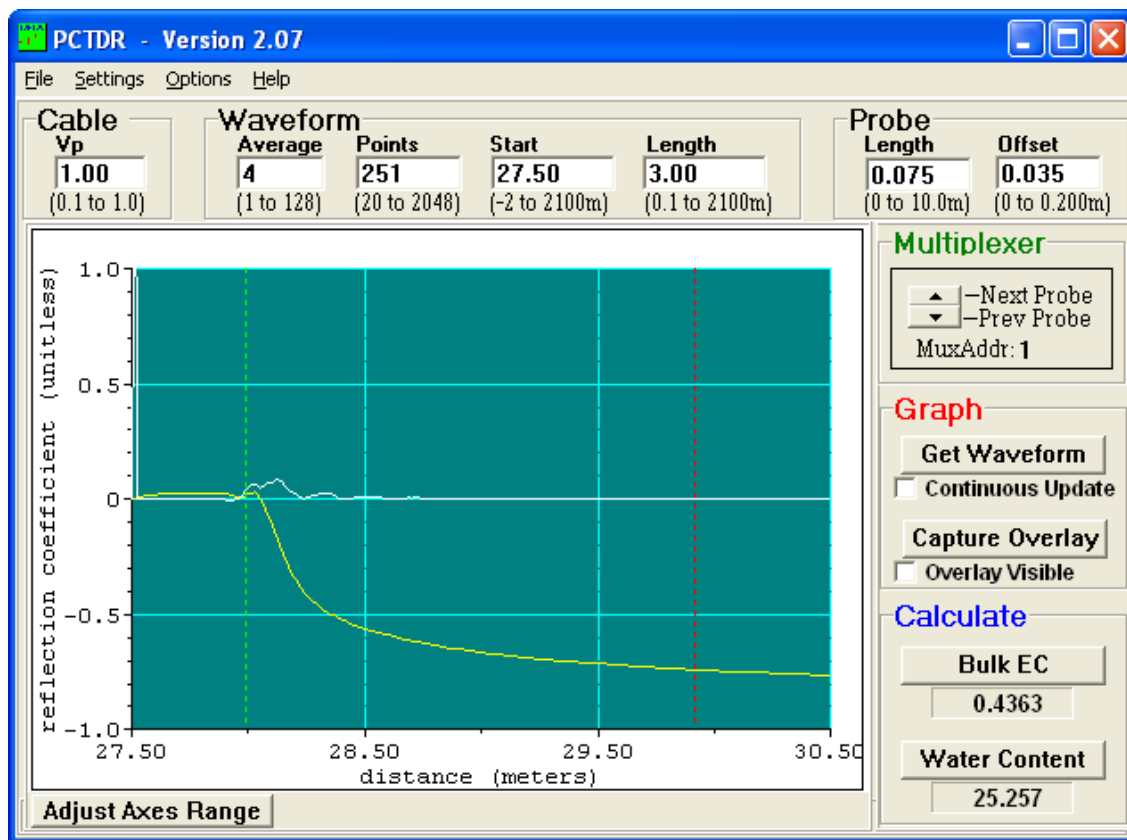


Figure 4.3: PCTDR-Version 2.07 calibration screen

4.3.2: PROBE OFFSET CALIBRATION

Part of the TDR rods of the probe are enclosed by the head material and thereby not exposed to the soil when installed in the ground. In order to account for this in the calculations, a probe offset is needed. A procedure for calibrating each probe's offset is described in the TDR100 Manual (Campbell Scientific, Inc., 2010).

This calibration was not done for the probes in this project, however. This decision was made after a phone conversation with Glenn Jarell from Campbell Scientific Inc. (2010). The reason for not calibrating the offset is that Campbell manufacturing tolerances are tight enough that there is more uncertainty associated with the calibration process than just using the specification values provided by Campbell Scientific, Inc. (Jarell 2010). The specification offset value for the Campbell Scientific Inc. CS645-L probes is 0.035 meters.

4.3.3: SOIL SPECIFIC CALIBRATION

The reason to do a soil specific calibration is to define the sensor behavior for the specific soil that the instrument is being used in. In many cases TDR probes do not need a soil specific calibration for accurate data to be produced. However, Topp et al. (1980), Jones and Or (2004), Reedy and Scanlon (2002) and several others found that the TDR probes become inaccurate in soils with a high electrical conductivity.

The issues with performing a soil specific calibration at the project site are that the soil is highly overconsolidated and has a high occurrence of fissures and dense soil blocks. Reproducing the in situ soil conditions is very difficult in the lab. The Taylor Clay also has a high Plasticity Index which presents a problem when performing a soil specific calibration. Reedy and Scanlon (2002) had difficulty performing a soil specific calibration for a clay with a high Plasticity Index.

Campbell Scientific, Inc. Tech Support, (2010) suggested that performing a soil specific calibration for the TDR probes on the project was probably not necessary. The reason for not doing soil specific calibration was because, in their experience, it was more likely that a mistake made during calibration would cause more inaccuracies than just using the Topp et al. (1980) equation. If there was a problem, electrical conductivity and the waveforms could be used to determine the water content of the soil. Due to the difficulty of performing a soil specific calibration, construction time constraints, and conversations with Campbell Scientific Inc. Tech Support (2010), a soil specific calibration was not done for the TDR probes on this project.

CHAPTER 5: TDR PROBE INSTALLATION

The installation of the TDR probes into the soil on site is described in this chapter. Installation of the probes occurred in two stages. On September 30 and October 1, 2010, 10 probes were installed through the facing of the wall. On October 14, 2010, the remaining 10 probes were installed from the ground surface. Monitoring of the probes started immediately after they were installed. The layout of the 20 probes is shown in Figure 5.1.

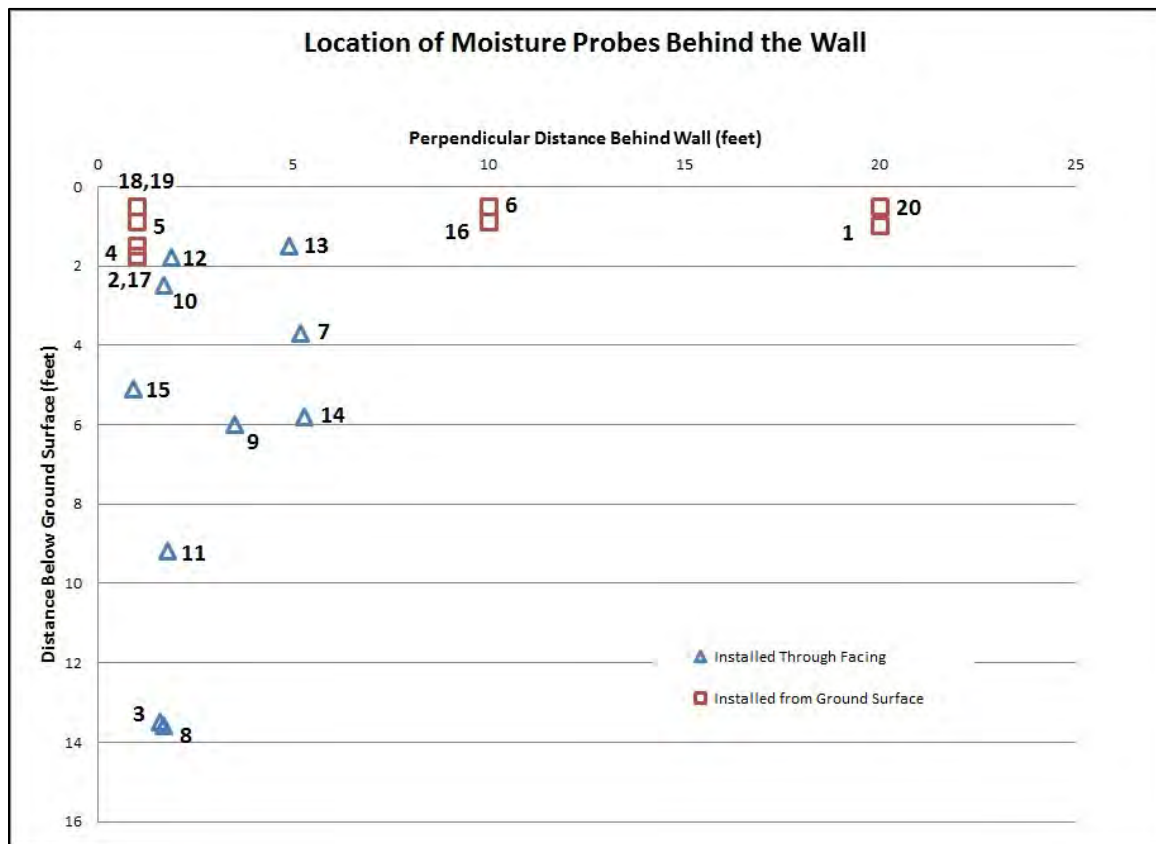


Figure 5.1: Location of the 20 TDR probes installed behind the wall

5.1: Installation of Sensors through the Wall Facing

The sensors installed through the facing of the wall were placed on September 30 and October 1, 2010. This was done before the shotcrete facing on the wall was placed in the afternoon of October 1, 2010. The facing of the wall was put on by Craig Olden, Inc.

Figures 5.1 and 5.2 show the layout of the probes placed through the facing of the wall. Probes were placed at a depth of 1.5 feet to 13.5 feet below the ground surface and at a distance of 0.9 feet to 5.3 feet behind the wall. Table 5.1 shows the depth below the ground surface and the distance behind the wall of each of the probes installed through the facing of the wall. Figure 5.3 shows one of the probes installed through the facing of the wall.

Table 5.1: Location of the probes installed through the facing of the wall

Probe #	Depth below Ground Surface (feet)	Distance Behind the Wall (feet)
3	13.5	1.6
7	3.7	5.2
8	13.6	1.7
9	6	3.5
10	2.5	1.7
11	9.2	1.8
12	1.8	1.9
13	1.5	4.9
14	5.8	5.3
15	5.1	0.9

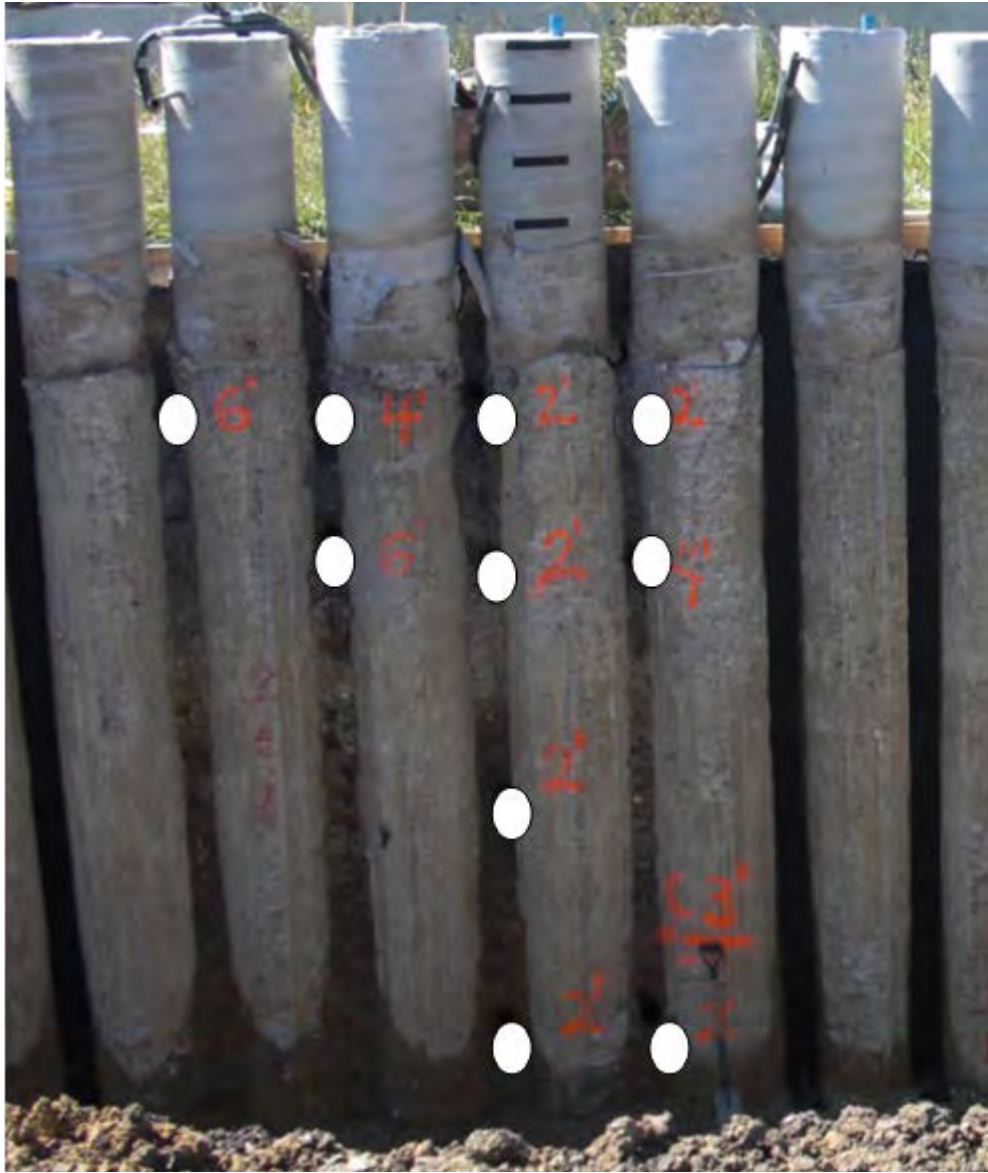


Figure 5.2: Layout of TDR probes installed through the facing of the wall



Figure 5.3: A sample installation of a probe installed through the facing of the wall



Figure 5.4: A hole being drilled by Craig Olden, Inc

The ten holes to place the probes in the soil were drilled by Craig Olden, Inc. using a soil nail rig. Each hole was drilled with an angle of approximately 15 degrees from horizontal. Figure 5.4 shows Craig Olden, Inc. drilling one of the holes for the probes.

In the locations the probes could not be installed by hand, the probes were pushed into the soil using a slotted PVC pipe. Once the probe was in place, the hole was backfilled with dry native clay from the site. The holes were backfilled with native dry clay so the soil would swell and fill the voids when the water reached the dry soil. The dry clay fill was tamped into place and sealed with a wet clay to hold the fill until the shotcrete was placed.

The cables from the TDR probes were protected from damage from the shotcrete impact by placing the cables in slotted PVC pipes. Tape and cable ties were used to keep the cables within the PVC pipe and the slotted side was faced towards the inside of the wall to prevent the shotcrete from directly hitting the cables. Figure 5.5 shows the cables being protected by the PVC pipe.



Figure 5.5: The PVC pipe protection for the TDR probe cables to minimize damage from the shotcrete

5.2: Installation of Sensors from the Ground Surface

The sensors that were installed through the ground surface behind the wall were placed on October 14, 2010. Ten probes were installed at depths from 0.5 feet to 1.75 feet and at a distance of one foot to 20 feet behind the wall. Table 5.2 shows the depth below the ground surface and the distance behind the wall of each of the probes installed through the ground surface.

Table 5.2: Location of the probes installed from the ground surface

Probe #	Depth below Ground Surface (feet)	Distance Behind the Wall (feet)
1	1	20
2	1.75	1
4	1.5	1
5	0.9	1
6	0.5	10
16	0.9	10
17	1.75	1
18	0.5	1
19	0.5	1
20	0.5	20

The holes for these probes were dug for the first foot by using a pick axe since there is an initial layer of base course on site that was stiff and difficult to excavate. For the probes that were deeper than one foot, a drill with a custom drill bit, made by owner of site, was used to reach the desired depths. Once the probes were placed in the soil, the holes were backfilled with the dried native clay soil so the fill would swell and fill the voids when wetted. Figure 5.6 shows one of the probes installed in the ground before the dried native clay fill was placed.



Figure 5.6: A sample probe installation from the ground surface.

5.3: Installation Problems

Site conditions made installation of the probes difficult. A large amount of force was required to push the probe rods completely into the soil because of the high shear strength of the highly overconsolidated Taylor Clay. Since the force required was large, it was more likely for air gaps to be created by accidental movement of the probe when trying to gain the necessary force to completely push in the probe rods. The use of the PVC pipe to install the probes in longer holes through the facing of the wall made it difficult to uniformly push the probe in the soil.

In some cases it was not possible to put enough force on the probes to push the probes completely into the clay. Figure 5.7 shows an example of a probe that could not be pushed completely into the clay. In these cases, the dried native clay fill was backfilled around the end of the probe and it was hoped that any air caps would close when the clay fill swelled.

The soil on site has many rocks and fossilized shells within it which could damage the probes when installed. Several probes were bent during installation. The rods were straightened when noticed but it was not possible to detect if the rods of the probes had deviated by hitting a rock or shell in the clay once pushed into the soil. Also, when installing the probes into deep holes, there was no way to verify if the probe was installed with the rods in the correct orientation.

Tests by Campbell Scientific Inc. showed only 0.03 percent change in the results when the probes were deflected four millimeters (Brown 2011). However, it was noted that the tests were performed in air and water so the results could differ in soils due to the causing of air gaps or the soil compacting. It is possible that the rods deviated by more than four millimeters when installed into the soil. Some of the rods that were bent during installation and fixed had deviated by more than four millimeters.



Figure 5.7: A sample probe installation where the probe could not be pushed completely into the soil

CHAPTER 6: FIELD PERFORMANCE

The moisture measurements taken and performance of the TDR probes are described in this chapter. Also, the possible problems and potential solutions are discussed.

6.1: Moisture Measurements

Since the site investigation, moisture samples have been taken in the upper six feet of the Taylor Clay near the wall. The moisture contents in the upper six feet have ranged from approximately 35 percent to approximately 17 percent. Figure 6.1 shows the moisture contents taken since the site investigation in January 2011. The moisture contents that are labeled M-7B are moisture contents taken after an eight hour inundation test was performed in an area away from the wall. This inundation test was done by ponding water at a head between two and six inches.

Also in Figure 6.1 are the ground water measurements taken from the piezometer near the wall. On February 16, 2010, the piezometer was bailed out to a depth below ground surface of 19 feet for a rising head test to be performed. By June 2010, the water level had risen to a depth of 7.5 feet below the ground surface. Since June 2010, the water level has gradually fallen to a depth of 9.5 feet below the ground surface in June 2011. This decrease in the water level since June 2010 correlates with the lack of rainfall that the area has experienced. Figure 6.2 shows the daily precipitation data from January 2008 to July 2011.

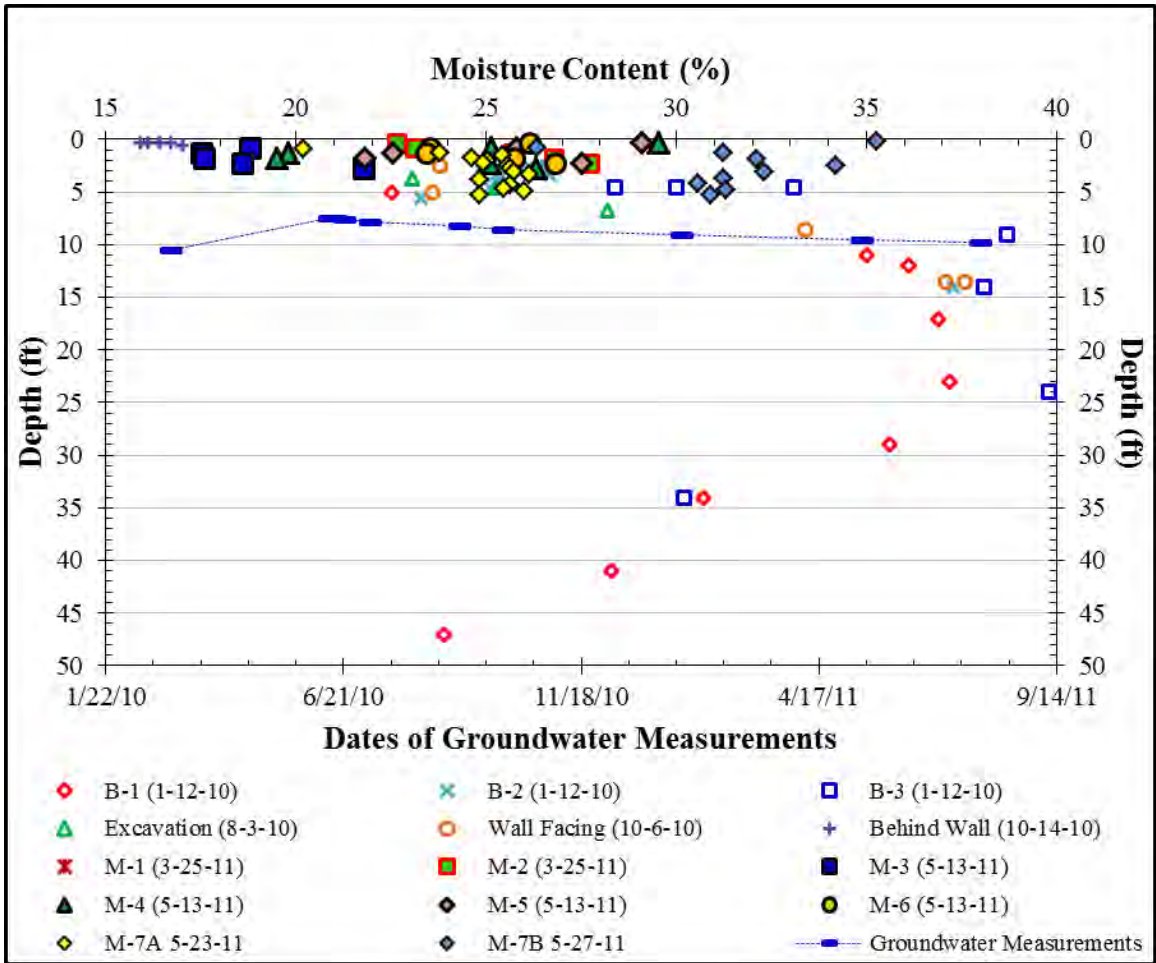


Figure 6.1: Moisture Measurements taken from January 2010 to May 2011 (Ellis 2011)

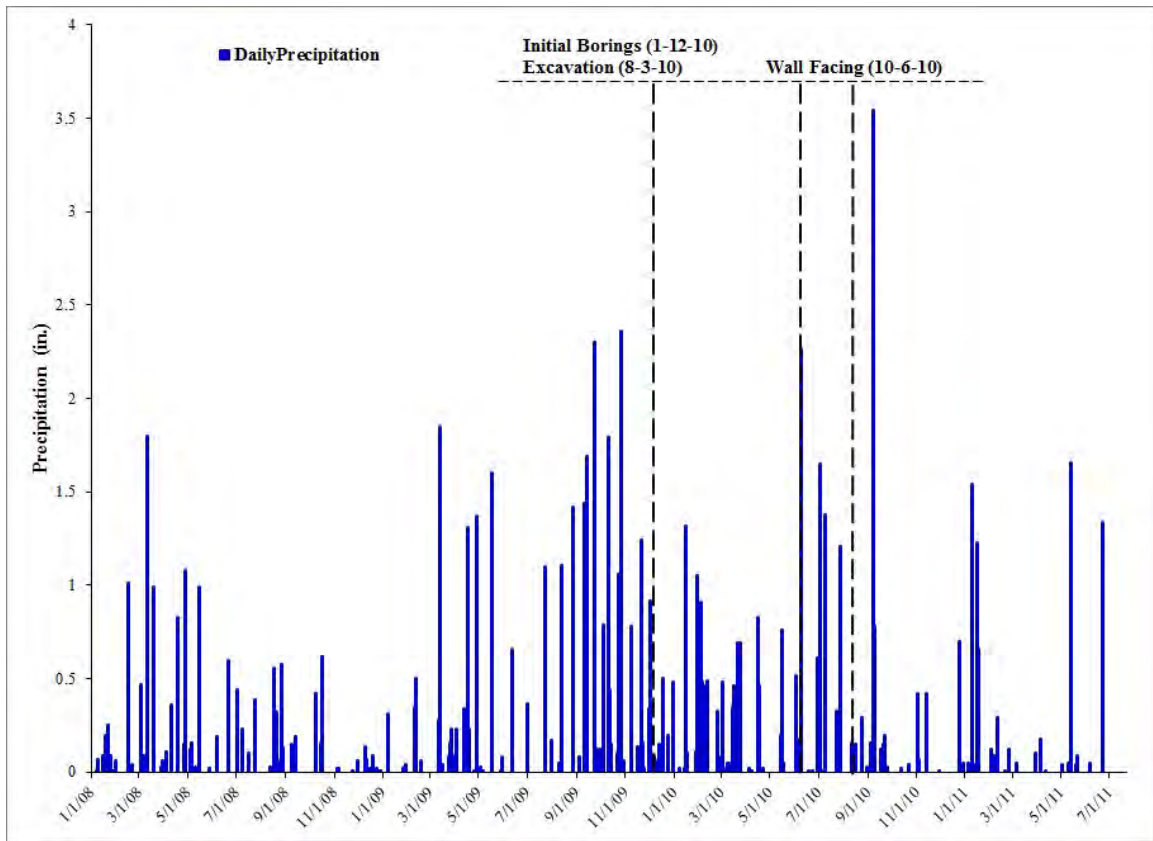


Figure 6.2: Daily precipitation measurements from January 2008 to July 2011 (Ellis 2011)

6.2: Performance

Initially, 15 probes were non-functional, four probes were semi-functional, and one probe was functional. For this study, non-functional means the probes were not giving data that indicate the probes are measuring the dielectric constant of the soil. Semi-functional probes are probes that are giving waveforms that are reasonable but with a large amount of noise. A probe that gives reasonable waveforms is classified as a functional probe for this study. Campbell Scientific, Inc. uses a computer algorithm to determine the L_a/L values from the waveforms. The use of L_a/L data to analyze the

waveform was not possible due to an inability of the computer algorithm to read the correct points of the waveforms. A large amount of scatter was seen in the electrical conductivity measurements.

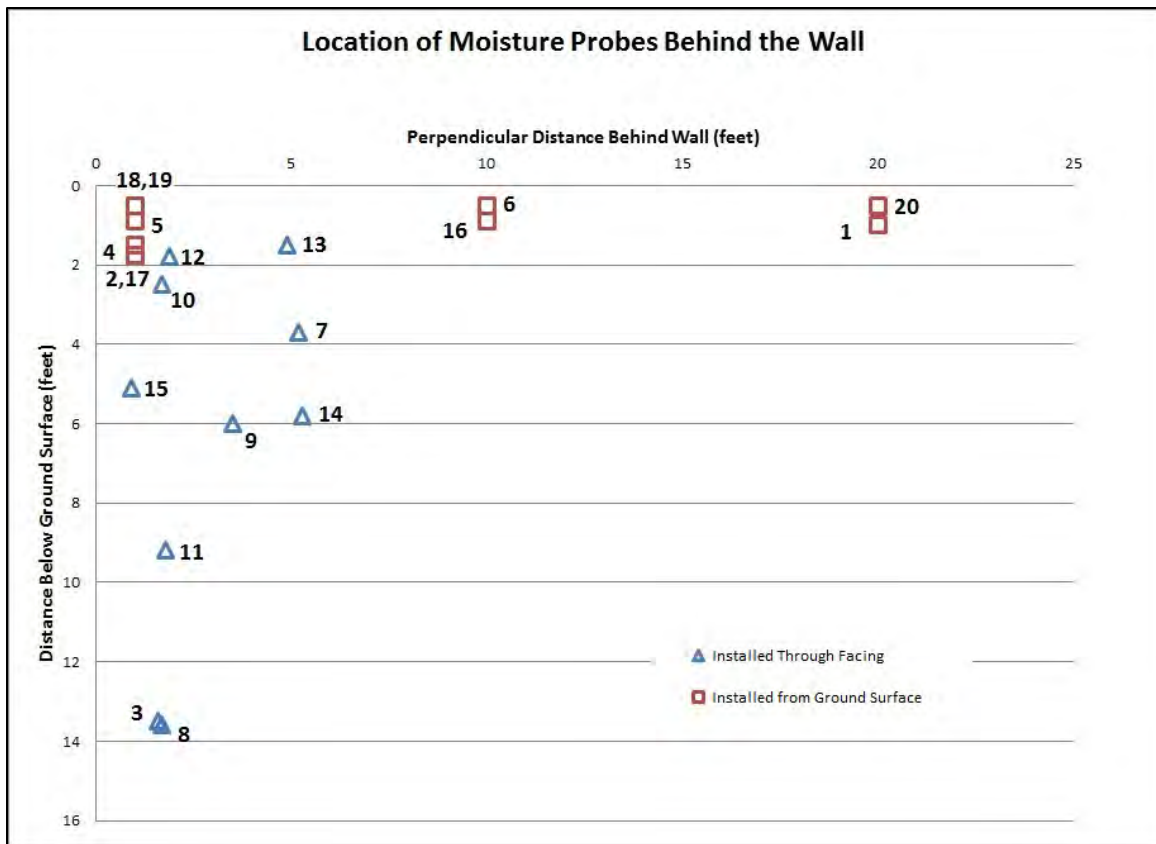


Figure 6.3: Location of the 20 TDR probes installed behind the wall

6.2.1: FUNCTIONAL PROBE

Probe 4 (Figure 6.3) was the only probe that was fully functional and is located at a depth of 1.5 feet below the ground surface and one foot behind the wall. Electrical conductivity measurements from Probe 4 are shown in Figure 6.4. Initial electrical conductivity data show a wide band of values ranging between 13 and 26 Siemens/meter.

Based on a conversation with Robert Reedy (2010) of the University of Texas at Austin Bureau of Economic Geology, electrical conductivity measurements are more robust than L_a/L measurements for soils of this type, and can be correlated with moisture content. However, the data here varies too much to usefully correlate the electrical conductivity to the moisture content of the soil. Also, the TDR probes for this study have a manufacturing specification of a maximum electrical conductivity of 0.5 Siemens/meter, which could be a reason for the large amount of scatter (Campbell Scientific, Inc., 2010). Patterson and Smith (1985), Campbell Scientific, Inc. (2010), Reedy (2010), and several others also indicated that better measurements would come from a combination of shorter cable lengths and longer probe lengths, which is not the situation for this project (70 feet cables and 2.95 in probes).

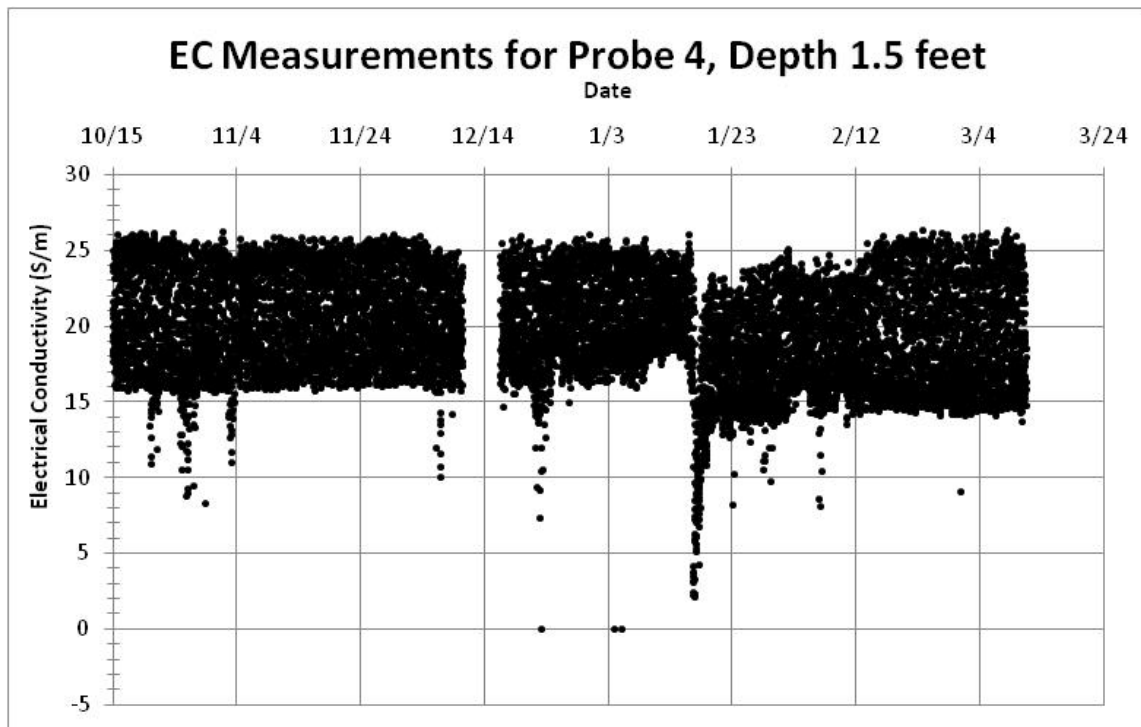


Figure 6.4: Electrical conductivity measurements for Probe 4

Daily temperature cycles of the electrical conductivity are expected since the electrical conductivity is temperature dependent. The electrical conductivity increases with increasing temperature. However, closer analysis of the electrical conductivity does not show any daily variation with temperature. Closer analysis of data over a 24 hour period on March 3, 2011 shows a large amount of scatter and no clear temperature dependence (Figure 6.5)

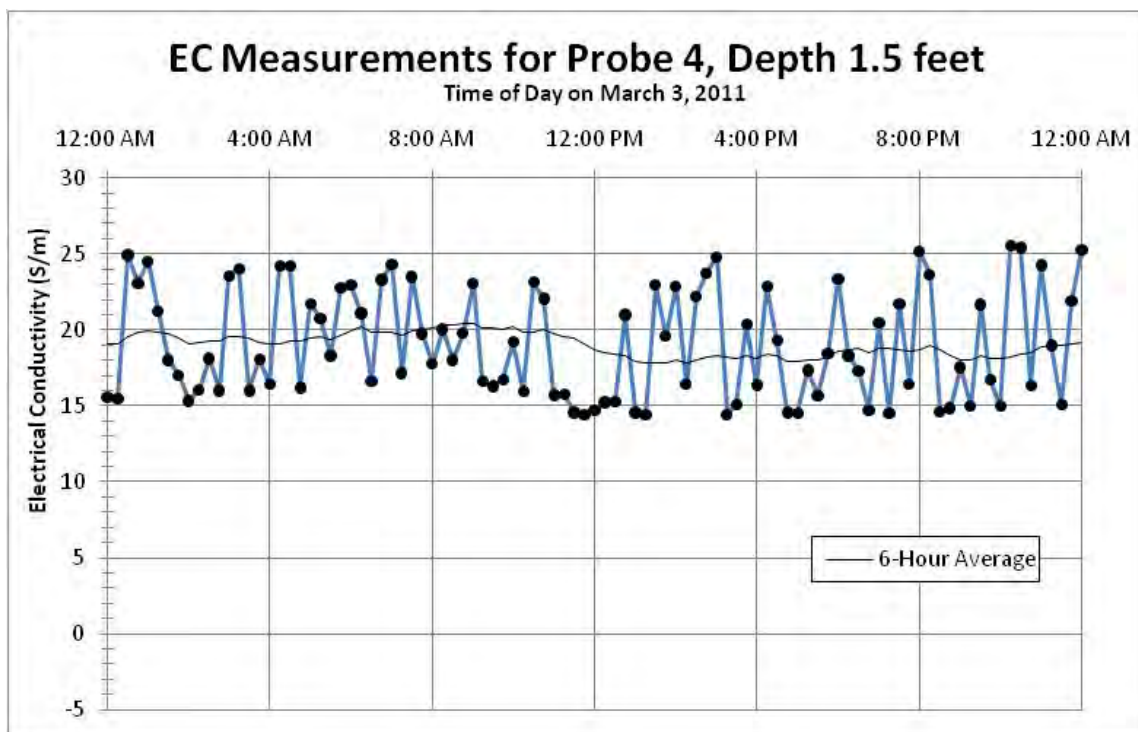


Figure 6.5: Electrical conductivity measurements over a 24 hour period on March 3, 2011.

The L_a/L data for this functional probe has not been giving good measurements. Data show up as separate bands of measurements (Figure 6.6). This result was due to the inability of the computer algorithm to find the points at the beginning and end of the

probe. Since the computer algorithm could not find the necessary points on the waveform, it is necessary to manually inspect the waveform.

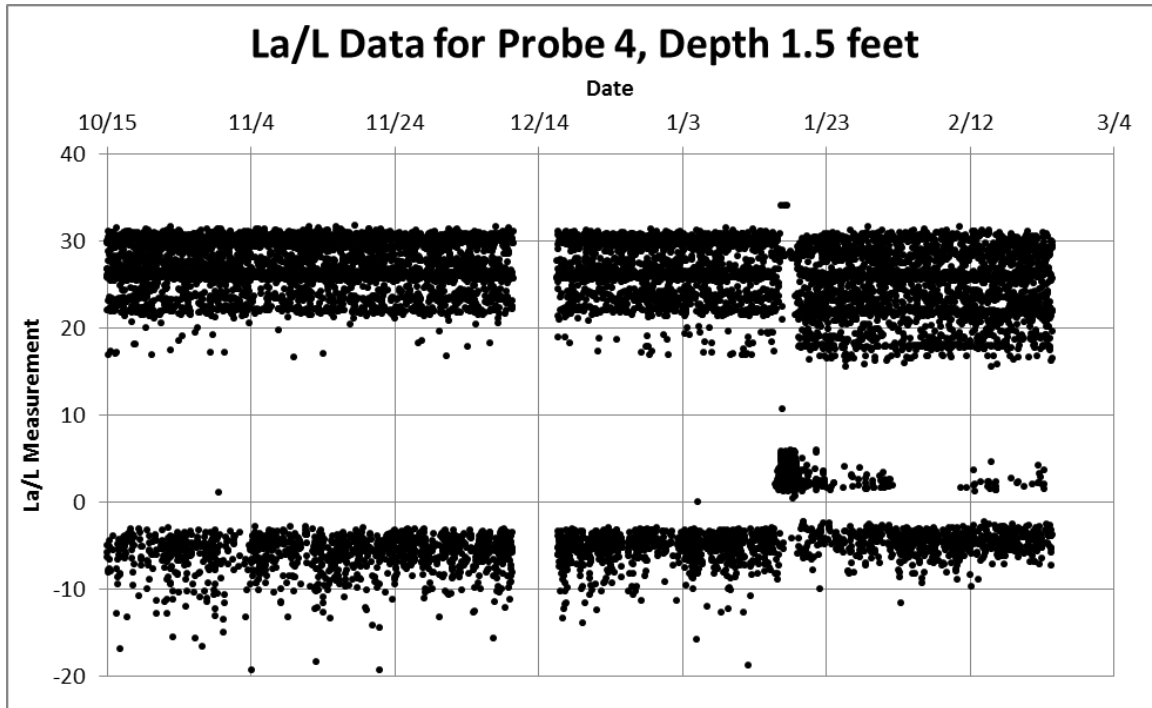


Figure 6.6: La/L data for Probe 4 inferred by the Campbell Scientific, Inc. algorithm

The waveform data for the functional probe is the most useful data that has been received from any of the waveforms. Figure 6.7 shows waveforms from the functioning probe. The waveforms for this probe show some AC noise but the shape is clearly visible.

These waveforms show the probe is measuring the soil but due to attenuation of the signal, the waveform does not show the reflection point indicating the end of the probe. This is most likely due to the high electrical conductivity of the soil and the long cable lengths. Figure 6.8 and 6.9 show an example the effects of differing cable lengths

and high electrical conductivity in a sandy loam. The waveforms look like the waveforms in soils with high electrical conductivity described in the TDR100 Manual Campbell Scientific, Inc. (2010). Reedy and Scanlon (2002) also observed these types of waveforms in soils with a high electrical conductivity without the second peak (point 3). They were unable to use the waveforms so Reedy and Scanlon (2003) correlated the moisture measurements to electrical conductivity values.

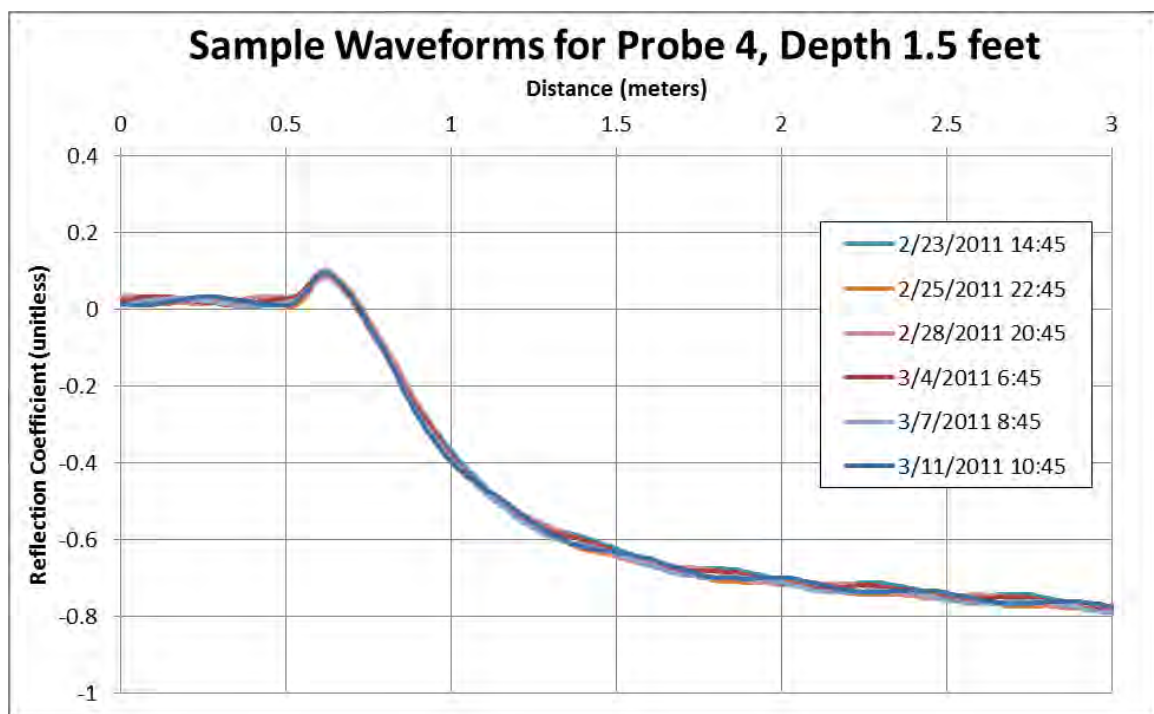


Figure 6.7: Waveform data for the functioning probe

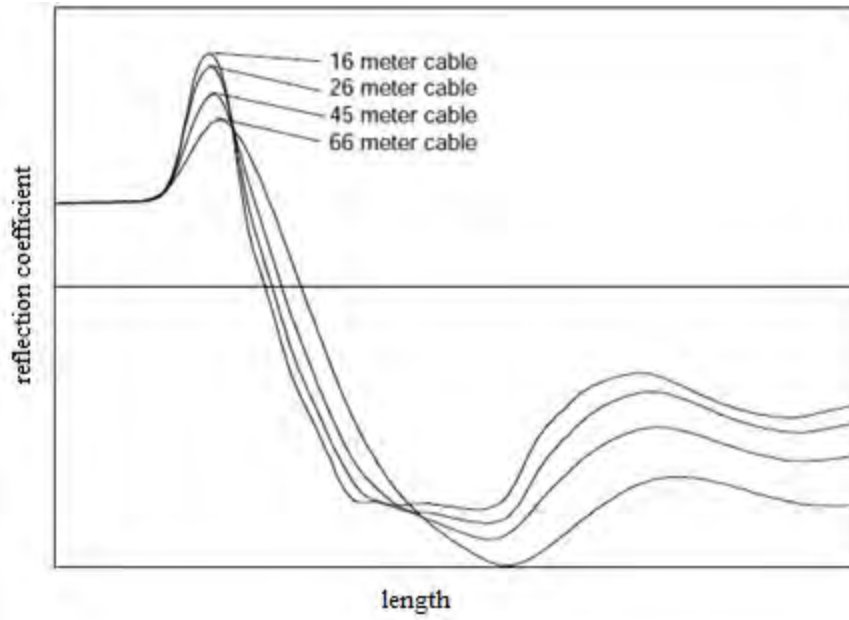


Figure 6.8: Waveforms for differing cable length in a sandy loam (Campell Scientific, Inc., 2010)

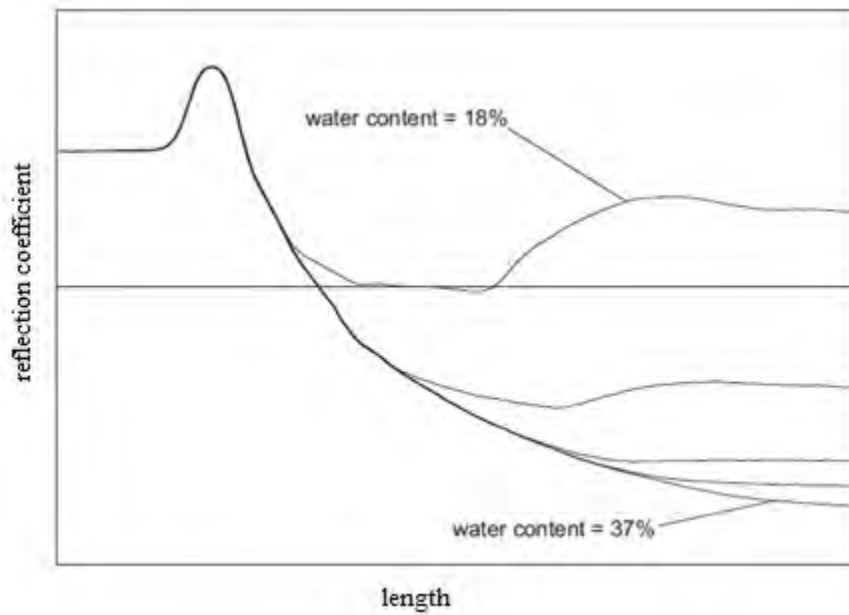


Figure 6.9: TDR waveforms in a sandy loam with a high electrical conductivity of 10.2 dS/m (Campell Scientific, Inc., 2010)

6.2.2: SEMI-FUNCTIONAL PROBES

Probes 7, 9, and 10 (Figure 6.3) have been semi-functional and Probe 16 was initially semi-functional but became non-functional in January 2011. The electrical conductivity data for these semi-functional probes show as a wide localized band of data typically between 10 and 30 Siemens/meter which is similar to Probe 4 which has values ranging from 13 to 26. This data follows the same pattern as the functional probe and shows no daily temperature cycles. Figure 6.10 shows the electrical conductivity data for Probe 9.

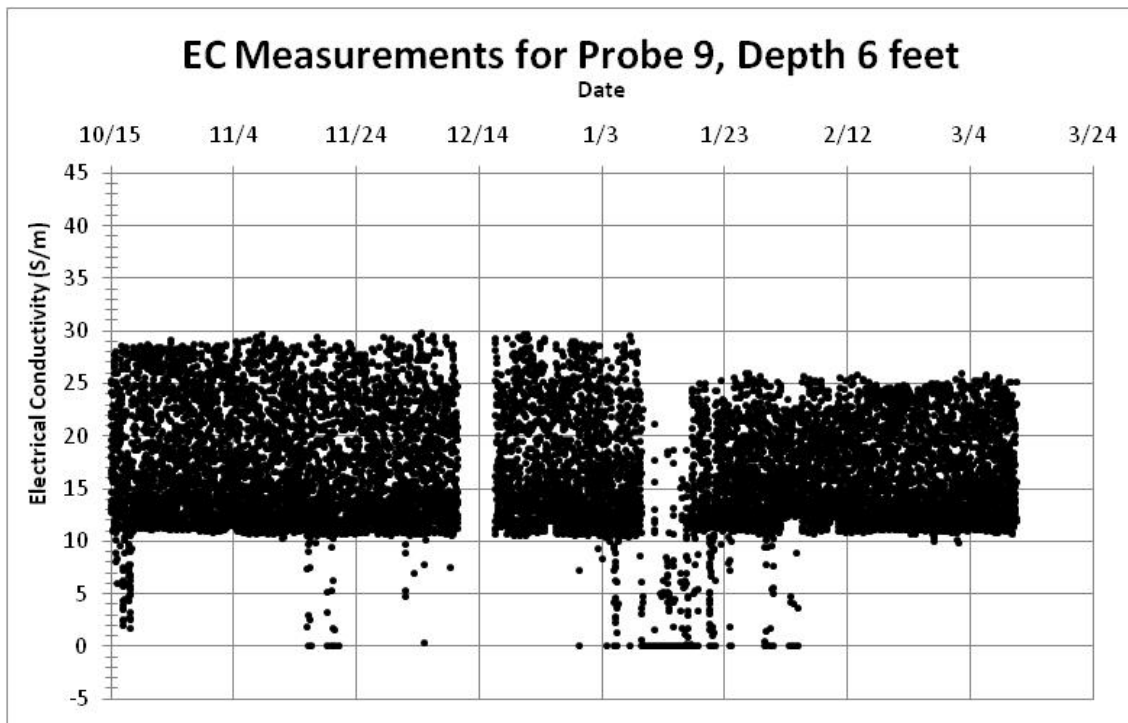


Figure 6.10: Electrical conductivity measurements for Probe 9

The automated inference of L_a/L for these probes provides no useful measurements. The data shows as distinct separate bands of measurements (Figure 6.11).

This result is due to the computer algorithm picking incorrect points from the waveforms that are showing a large amount of what appears to be AC noise.

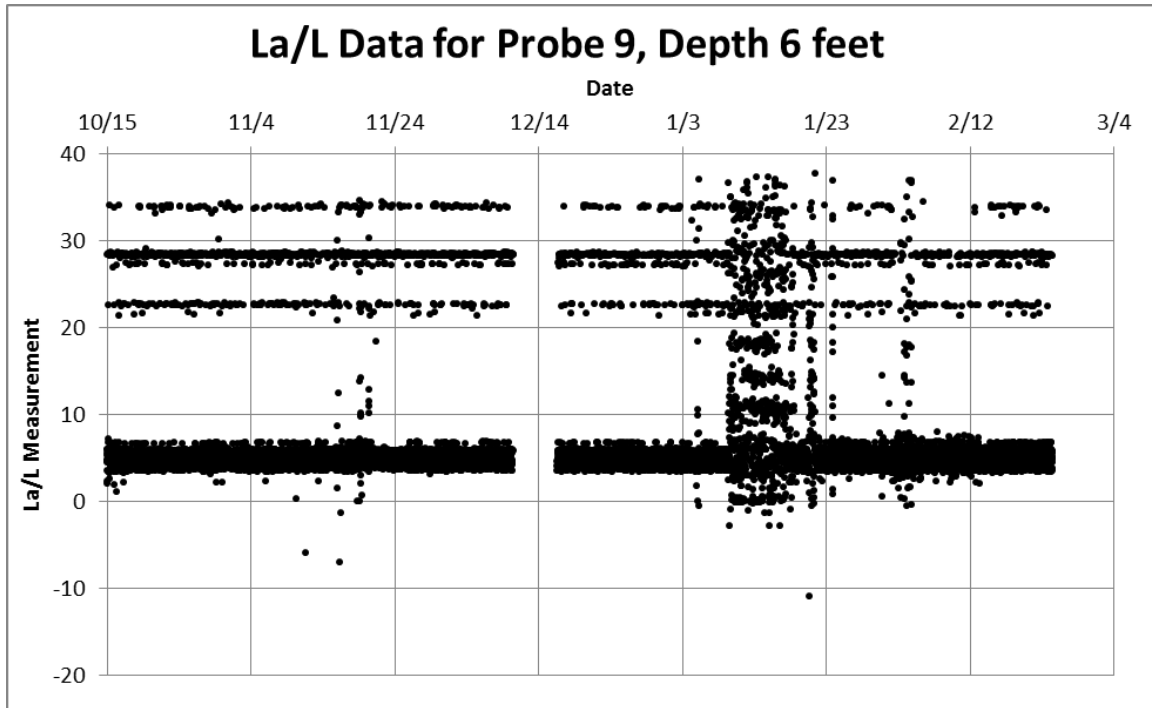


Figure 6.11: La/L data for Probe 9

The waveform data for the semi-functional probes is similar to the waveforms for the functional probe except there is a large amount of AC noise being seen in the waveform. Filtering the AC noise by using median waveform values over the period of one day was needed in order to get waveforms that do not show as much AC noise. Figure 6.12 shows a sample waveform from Probe 9. The AC noise likely comes from the power cords that are used to run the monitoring system on site.

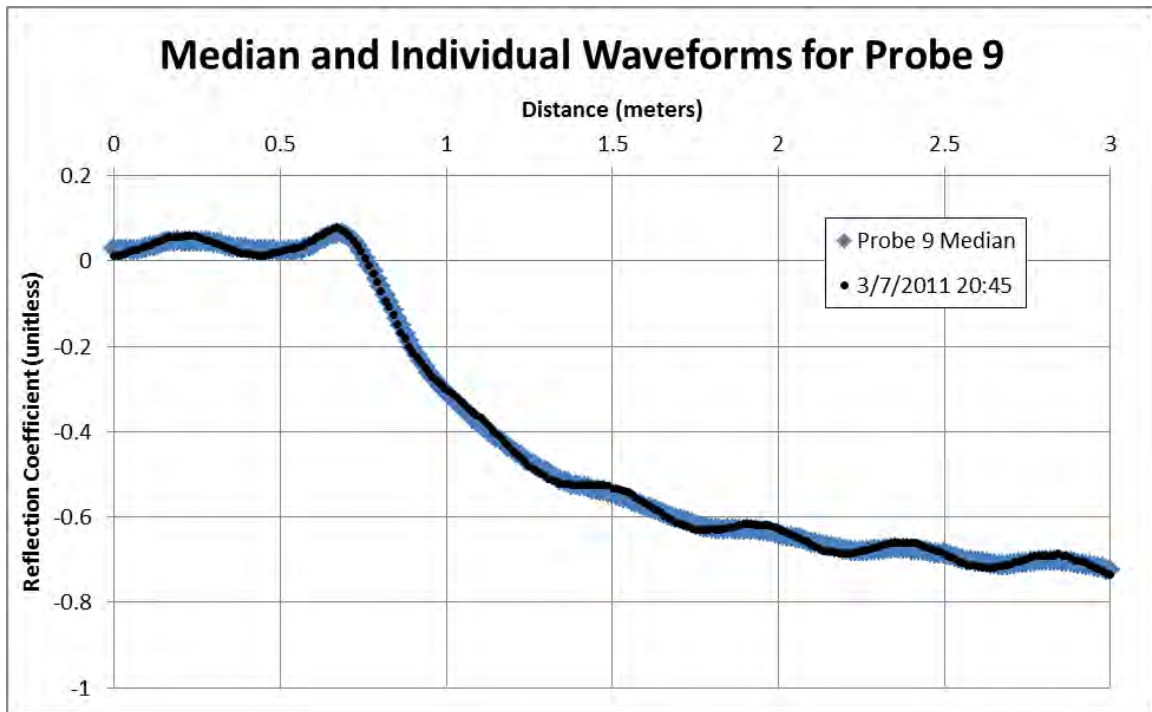


Figure 6.12: Sample waveforms from Probe 9

6.2.3: NON-FUNCTIONAL PROBES

Probes 1-3, 5-6, and 11-15, and 17-20 (Figure 6.3) have been non-functional since installation. As mention in the previous section, Probe 16 also became non-functional in January 2011. The data did not show values that would indicate the probes were measuring the properties of the soil. Data from the electrical conductivity measurements would often show that the TDR probe was not able to record a measurement for the soil. When the TDR probes did provide an electrical conductivity values, the values would range from -2 to 2 S/m. Electrical conductivity data ranged from -1.5 to 2. Other values that are seen are scattered values that are not reasonable. A possible reason for this result is that the probe rods do not have good contact with the soil. Electrical conductivity data from probe 15 is shown in Figure 6.13.

The inferred values of L_a/L show as distinct bands that have no apparent meaning since the waveform data is also not good (Figure 6.14). The waveform data also suggest that the probe rods could not have good contact with the soil as one of the best waveforms from these probes is shown in Figure 6.15. These data appears to show AC noise that could possibly come from the power cords on site.

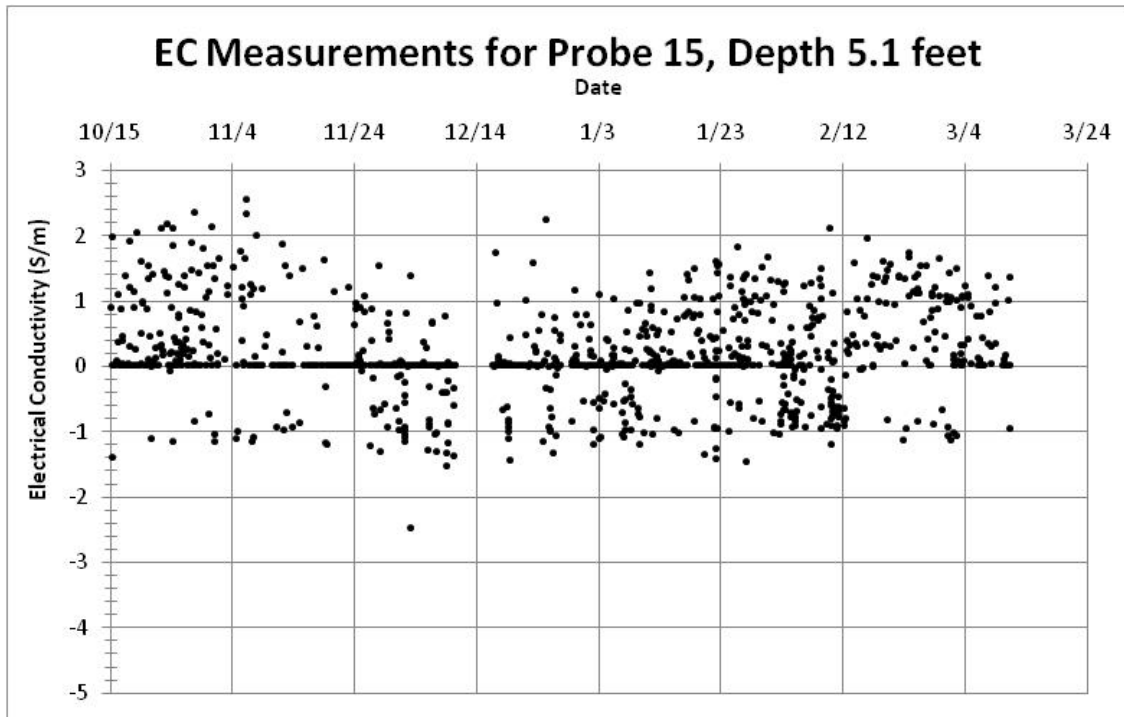


Figure 6.13: Electrical conductivity data from Probe 15

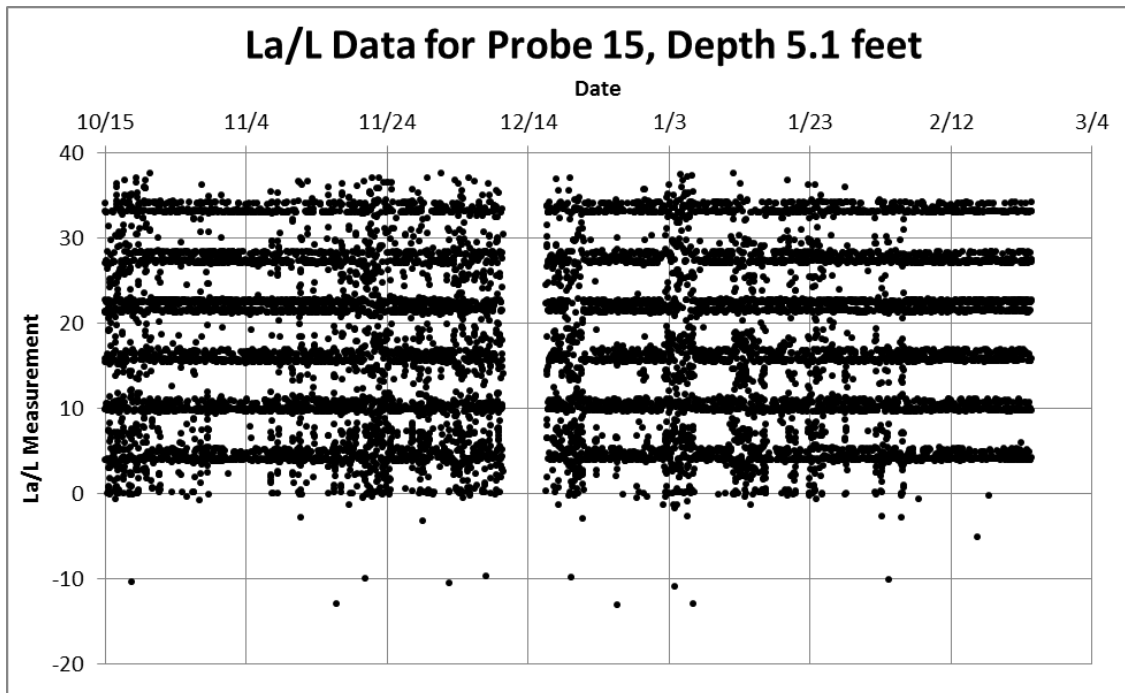


Figure 6.14: La/L data from Probe 15

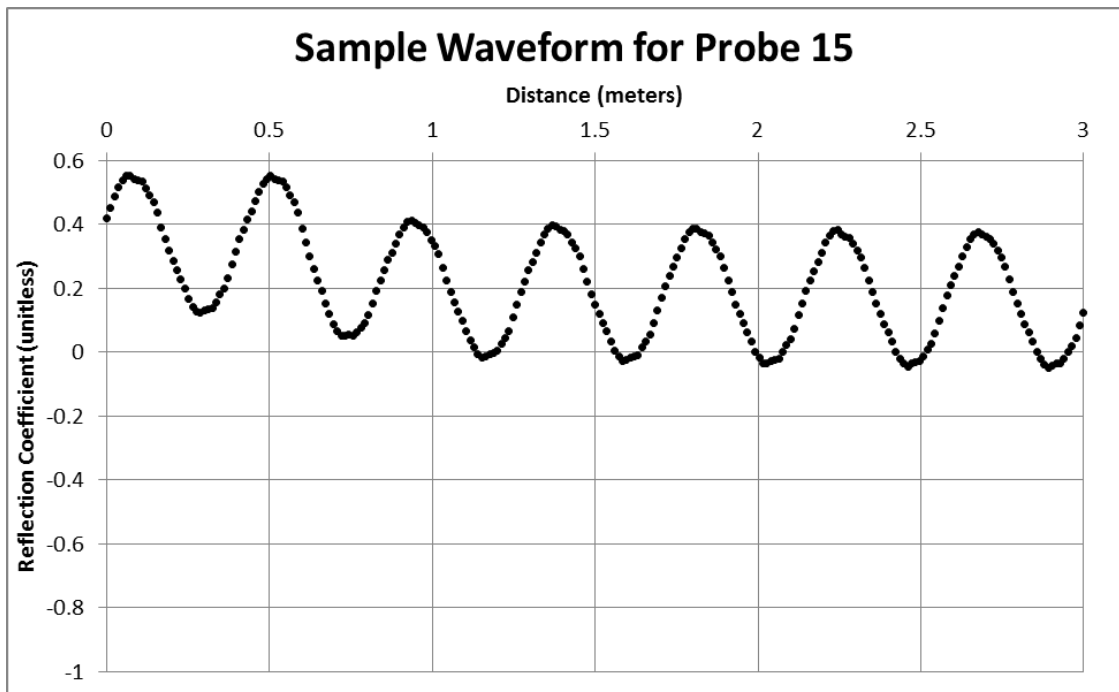


Figure 6.15: A sample waveform from Probe 15

6.2.4: RAINFALL EVENTS

From installation of the probes in October 2010 to January 2011, there was no significant rainfall. Approximately three total inches of rain fell in two events on January 9 and January 16, 2011. On these dates, many of the sensors show a change in data and in some cases the change stayed constant. Each of the semi-functional probes and the functional probe showed a change in the electrical conductivity data. Those changes can be seen in Figures 6.4, 6.10 and 6.16.

It was during these events that the semi-functional Probe 16 became nonfunctional. Based on email correspondence with Glenn Jarrell and Jason Ritter of Campbell (Jarrell and Ritter 2011), the most likely reason for the change is an increase of electrical conductance of the soil due to a change in the moisture content. The electrical conductivity data for Probe 16 is shown in Figure 6.16.

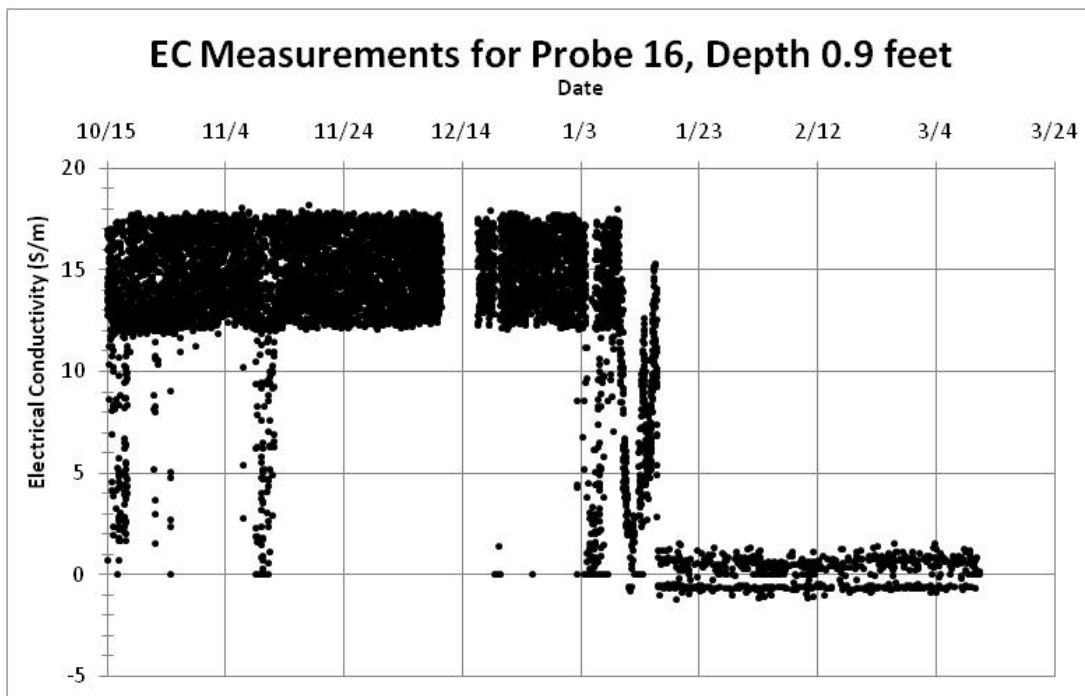


Figure 6.16: Electrical conductivity measurements for Probe 16

6.3: Troubleshooting

The main issue with the data from the TDR probes is the high electrical conductivity of the soil. High electrical conductivity of the soil causes attenuation of the signal which caused the end of the probe rods to not be seen in the waveform data. Without the end of the probes seen in the waveform data, the apparent probe length cannot be established. The moisture content of the soil is determined by the comparison of the apparent probe length compared to the actual probe length (L_a/L). The effects of the long cable lengths also exacerbate the problem of being able to identify the end of the probes in the high electrical conductivity soil.

6.3.1: POSSIBLE SOLUTIONS FOR FUNCTIONING PROBES

Reedy and Scanlon (2002) correlated the moisture measurements to electrical conductivity since the waveform data also could not find the end of the probes. This method is not a likely solution for this study as there is too large of a scatter for filtering of the data.

A Fast Fourier Transform could be used on the waveform data to perform an analysis in the frequency domain (Jones and Or, 2004). Jones and Or (2004) found that the data could be recovered by using the Fast Fourier Transform in soils with electrical conductivity values five times greater than the upper limit in the time domain. The issue with using this method for this study is that Fast Fourier Transform method works better with very short probes lengths (on the order of two centimeters) while the probes for this study are 7.5 centimeters. Having shorter probes reduce the energy attenuation of the signal needed to perform analysis in the frequency domain.

Chen et al. (2007) discussed a method of using the TDR signal from the reflection at the surface of the soil instead of using the reflection from the end of the probe in soils

with a high electrical conductivity. This method could possibly be applied to this project. The model proposed by Chen et al. (2007) inverts the dielectric constant from the reflected signals at the soil surface. This model would require the TDR system currently in use to be recalibrated. Using this model could possibly be applicable for this project and could be further explored.

If the waveforms are not able to give values for the moisture content within the soil, the changes in the waveforms could be assessed to observe trends. Seeing a moisture front could be possible by observing changes to the waveforms. The amount of change or the exact moisture content could not be determined by conventional methods but a change in the waveform could indicate that the moisture front has reached the probes.

6.3.2: POSSIBLE SOLUTIONS FOR NON-FUNCTIONING PROBES

The issue with the non-functioning probes is that they are not giving reasonable waveforms. A possible method for determining the problems is to inspect the probes near the surface by removing them. It is possible that fissures or voids are causing some of the probes to not work properly. If fissures or voids are an issue then it is possible that the clay could swell with an increase in moisture content and fill the fissures or voids. Inundating the volume of soil surrounding a probe would provide useful information regarding this issue. If the issue with the non-functioning probes can be determined then the probes could be reinstalled to try to minimize the problems.

CHAPTER 7: CONCLUSIONS

TDR probes were installed at a test wall in the highly expansive Taylor Clay in Manor, Texas. Monitoring of the moisture on site is important as the amount of lateral earth pressure exerted on the wall by the clay is related to the amount of moisture within the clay. Twenty TDR probes were installed in September and October 2010. The process of installing the probes and the initial results have been described in this thesis. The following conclusions can be drawn from this study.

- Currently, four of the 20 probes are recording waveforms that are functioning as expected. However, these waveforms cannot be analyzed by typical methods due to the waveforms not showing the reflection that indicates the end of the probe. The most likely reason for this is due to attenuation of the signal from the high electrical conductivity of the Taylor Clay. These waveforms are commonly seen in other studies with highly conductive soils (Campbell Scientific, Inc., 2010, Chen et al., 2007, Jones and Or, 2004, Reedy and Scanlon, 2002).
- The Campbell algorithm that finds the L_a/L values does not work with the waveforms received from the probes. The algorithm is unable to find the correct points on the waveforms due to noise within the waveforms and the waveforms not showing the reflection indicating the end of the probe.
- There is a large scatter of the electrical conductivity values for all the probes. Daily temperature effects are not apparent and the scatter is too large to reliably correlate to moisture content.

Problems with the TDR probes were exacerbated by the long cable lengths, short probe lengths, and the difficulty of installing the TDR probes in the soil. It is not possible to know if the probes were installed correctly at larger distances behind the wall. The Taylor Clay is filled with rocks and fossils that could have damaged the probes during installation. Also, it is not possible to know if the probes went through one of the many fissures that exist within the Taylor Clay.

7.1: Recommendations

More probes working properly would be needed to thoroughly monitor the moisture content behind the test wall. A possible method for determining the issues with the probes is to dig up some probes near the surface that are not working correctly and inspect them for possible issues. If fissures or voids caused by installation are causing some probes to not work properly then it is possible that when the moisture content increases, the clay could swell and fill the voids. Performing a test where the volume of soil around a probe near the surface is inundated with water could also provide useful information to this problem.

Even if the reason for the 16 probes not giving good waveforms is determined and fixed, they still could not be analyzed by the typical methods. Another method needs to be used to analyze the waveforms without the reflection point that indicates the end of the probe. Chen et al. (2007) developed a method which could be used for this study that does not need the reflection point that indicates the end of the probe.

Taking periodic physical measurements using a hand auger should be done to measure the moisture content of the soil. The physical measurements could supplement

the TDR measurements if the TDR data can be used. If the TDR measurements cannot be used then the physical measurements taken more often could provide the required moisture profile over time.

Appendix A

The following consists of the electrical conductivity figures for each of the 20 TDR probes.

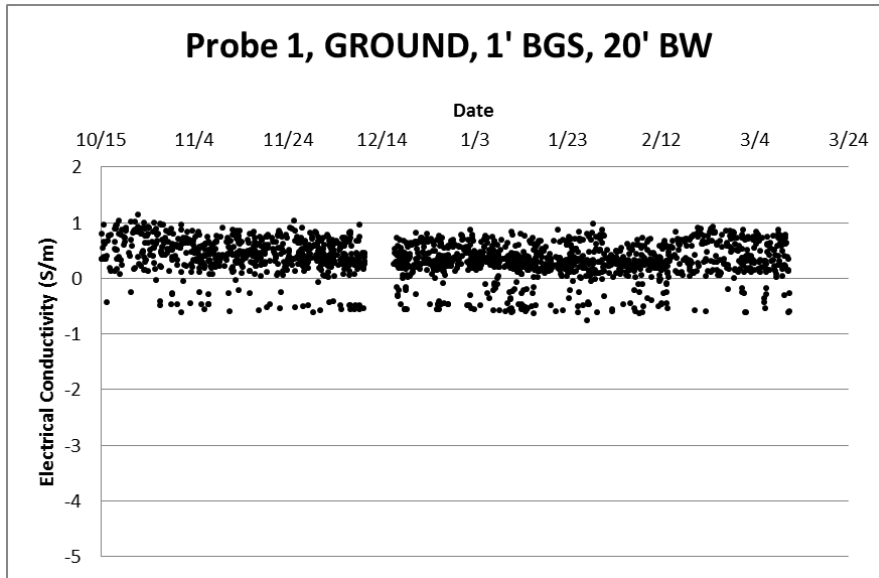


Figure A.1: Electrical conductivity for Probe 1 located 1 foot below the ground surface and 20 feet behind the wall

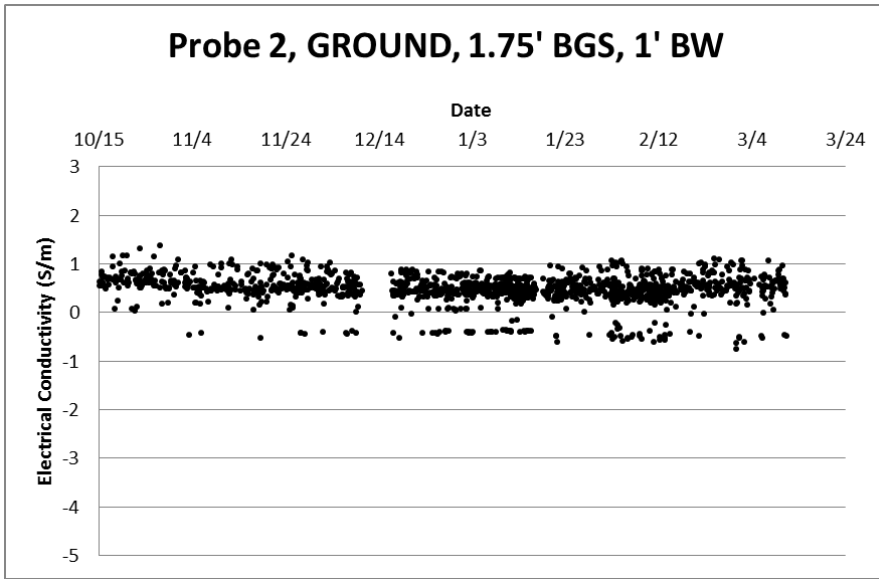


Figure A.2: Electrical conductivity for Probe 2 located 1.75 feet below the ground surface and 1 foot behind the wall

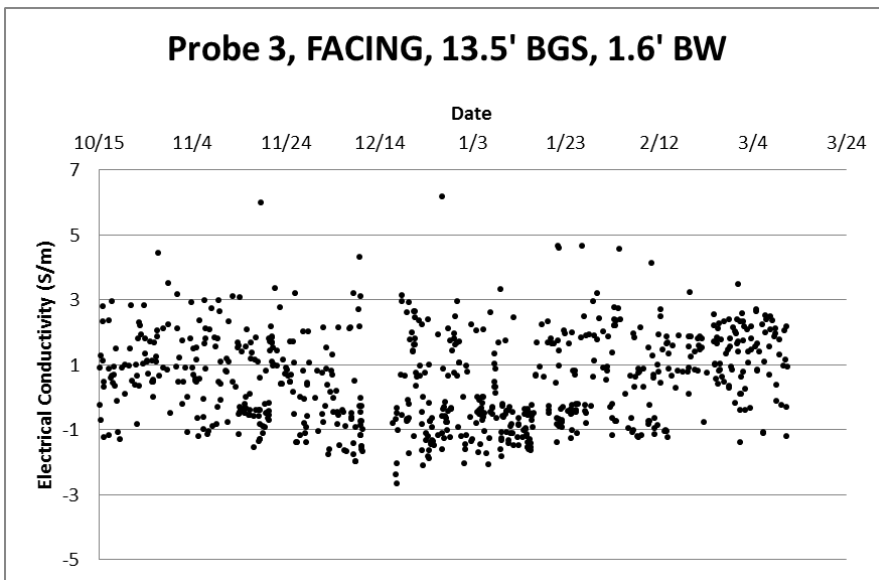


Figure A.3: Electrical conductivity for Probe 3 located 13.5 feet below the ground surface and 1.6 feet behind the wall

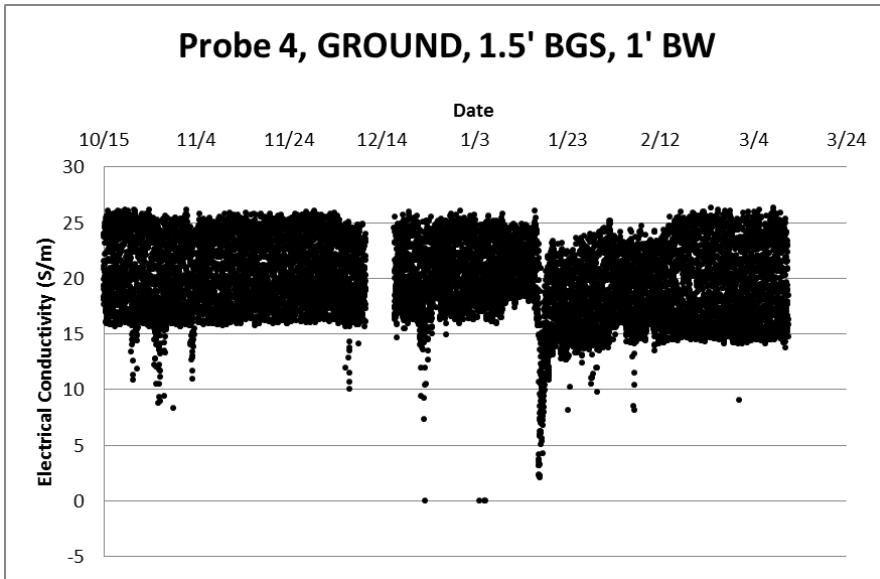


Figure A.4: Electrical conductivity for Probe 4 located 1.5 feet below the ground surface and 1 foot behind the wall

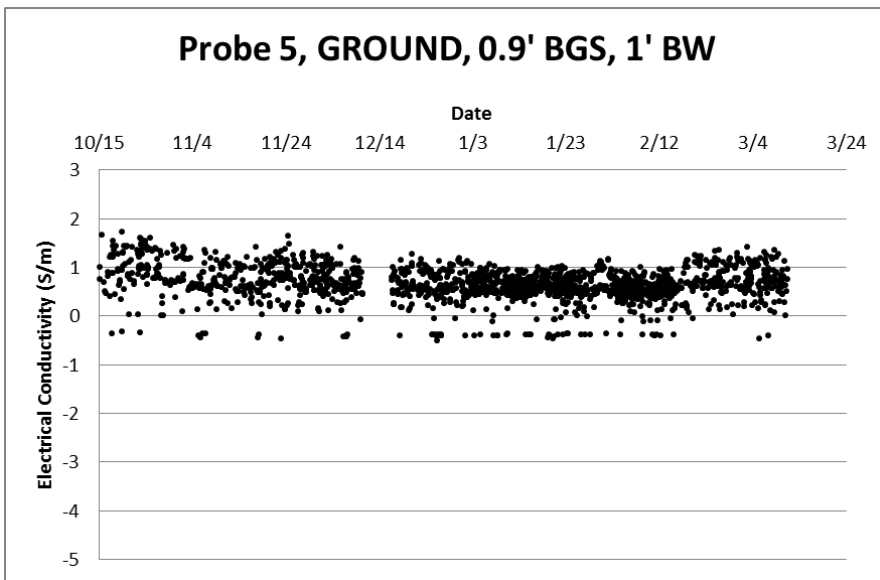


Figure A.5: Electrical conductivity for Probe 5 located 0.9 feet below the ground surface and 1 foot behind the wall

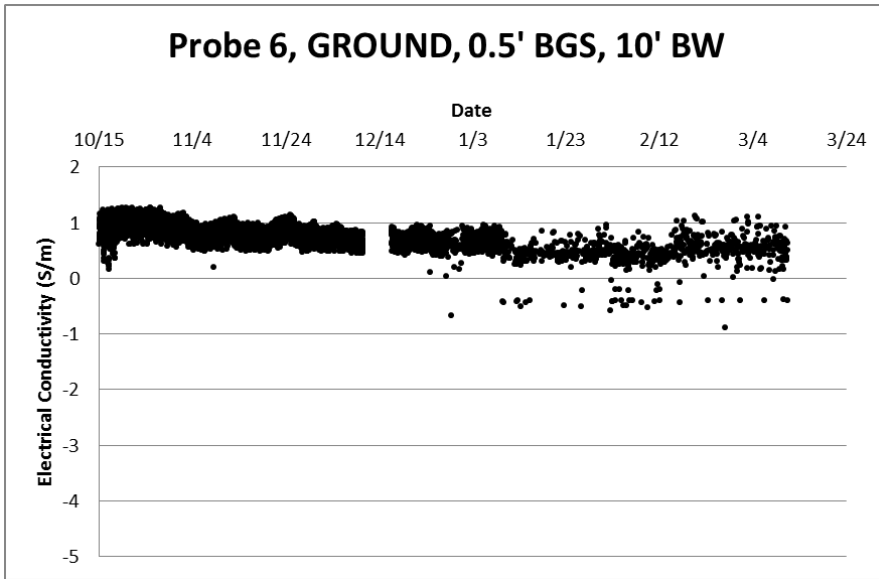


Figure A.6: Electrical conductivity for Probe 6 located 0.5 feet below the ground surface and 10 feet behind the wall

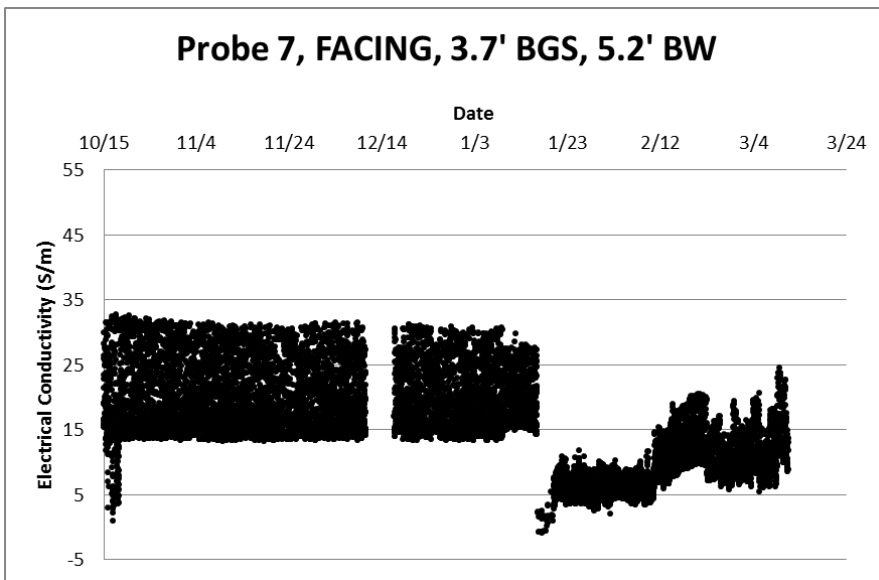


Figure A.7: Electrical conductivity for Probe 7 located 3.7 feet below the ground surface and 5.2 feet behind the wall

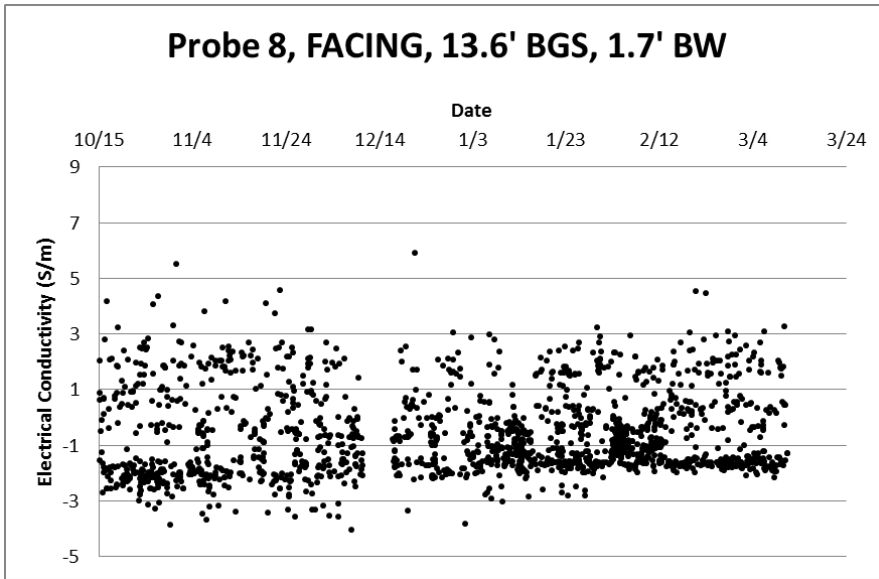


Figure A.8: Electrical conductivity for Probe 8 located 13.6 feet below the ground surface and 1.7 feet behind the wall

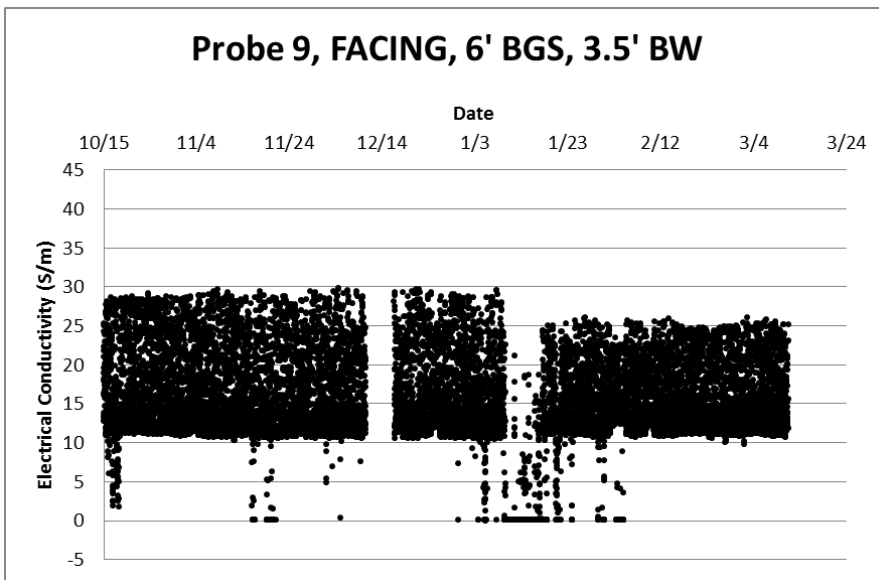


Figure A.9: Electrical conductivity for Probe 9 located 6 feet below the ground surface and 3.5 feet behind the wall

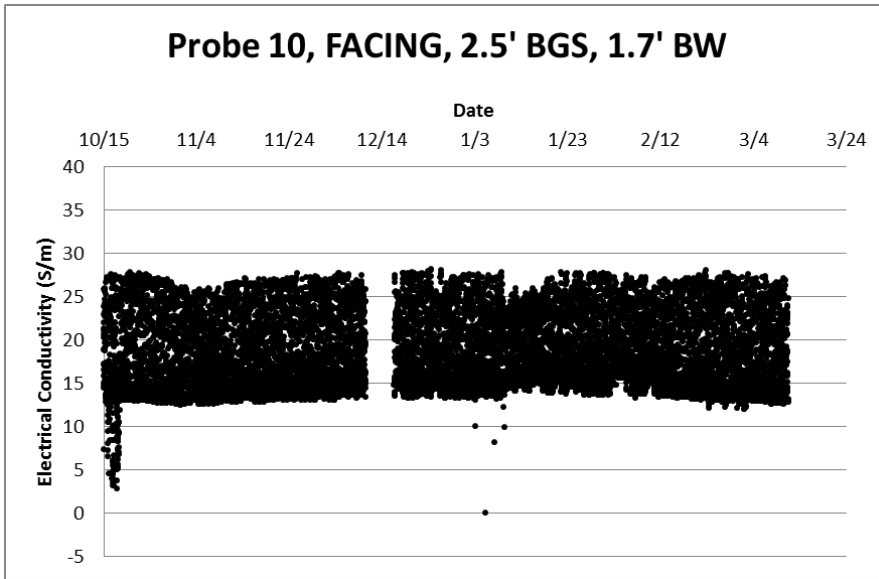


Figure A.10: Electrical conductivity for Probe 10 located 2.5 feet below the ground surface and 1.7 feet behind the wall

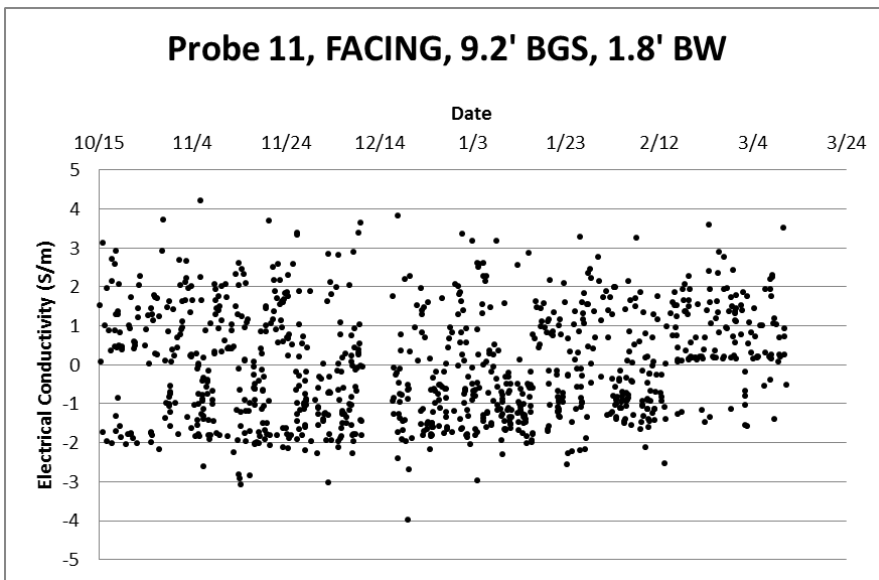


Figure A.11: Electrical conductivity for Probe 11 located 9.2 feet below the ground surface and 1.8 feet behind the wall

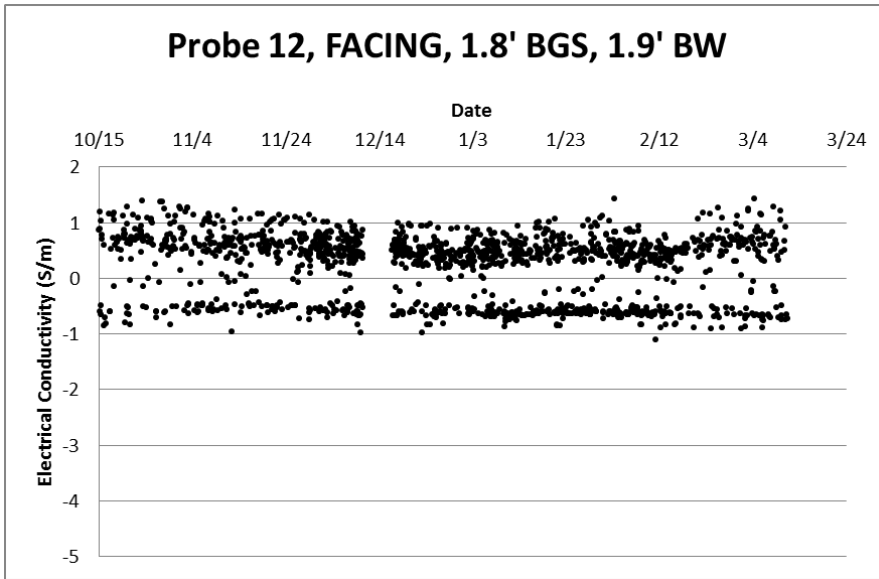


Figure A.12: Electrical conductivity for Probe 12 located 1.8 feet below the ground surface and 1.9 feet behind the wall

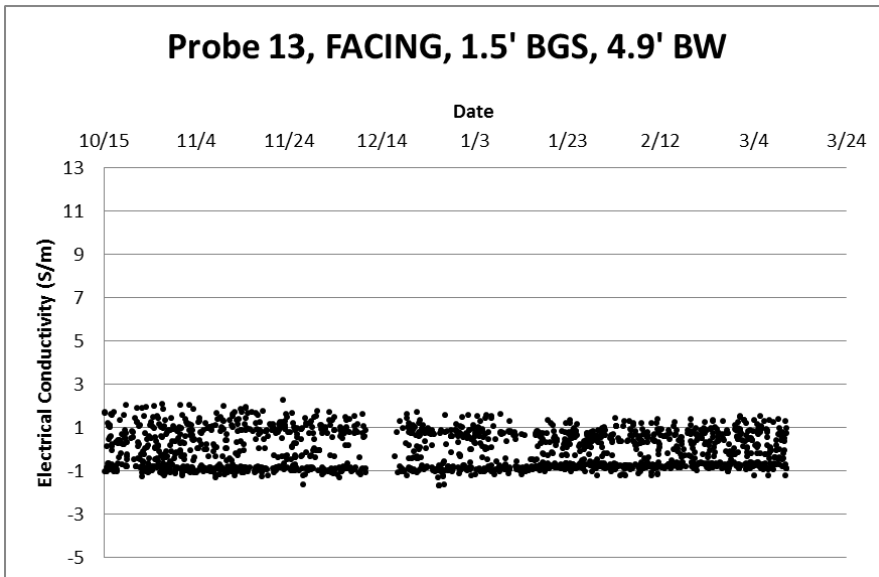


Figure A.13: Electrical conductivity for Probe 13 located 1.5 feet below the ground surface and 4.9 feet behind the wall

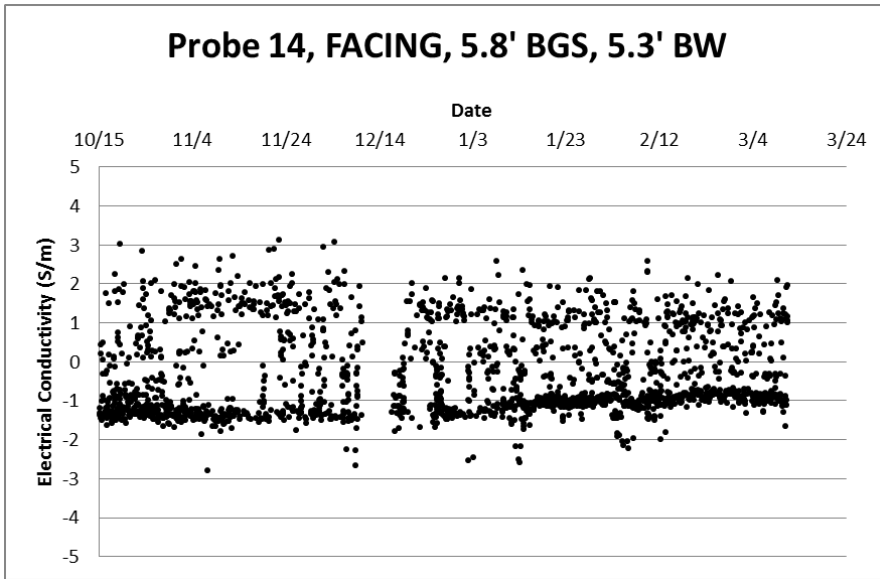


Figure A.14: Electrical conductivity for Probe 14 located 5.8 feet below the ground surface and 5.3 feet behind the wall

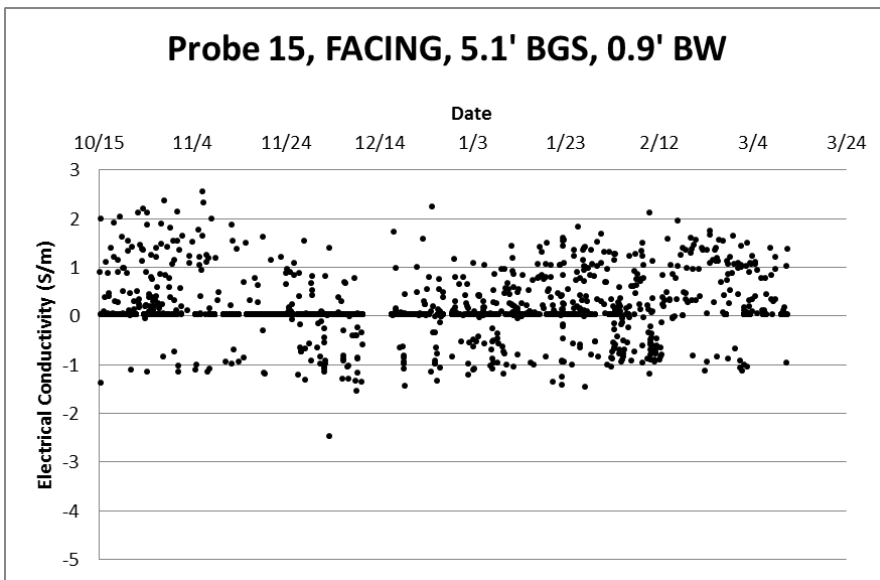


Figure A.15: Electrical conductivity for Probe 15 located 5.1 feet below the ground surface and 0.9 feet behind the wall

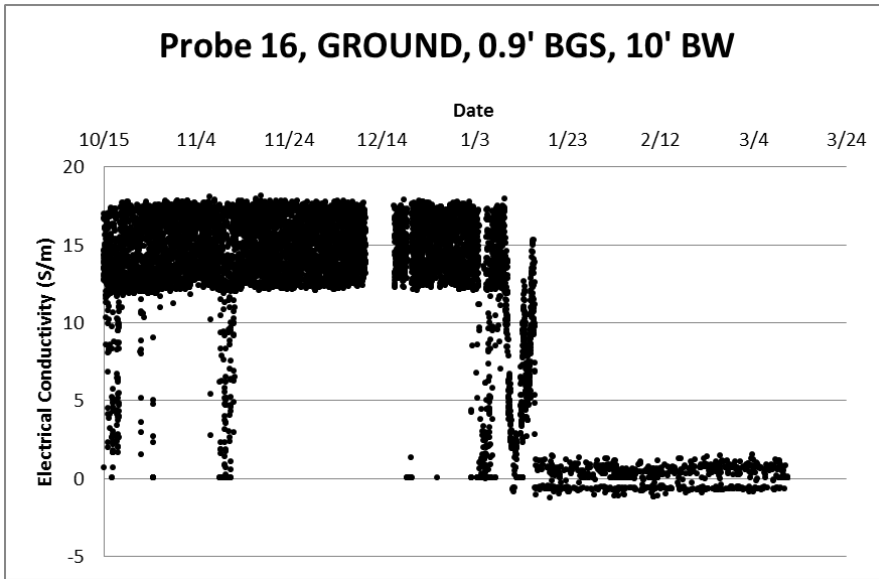


Figure A.16: Electrical conductivity for Probe 16 located 0.9 feet below the ground surface and 10 feet behind the wall

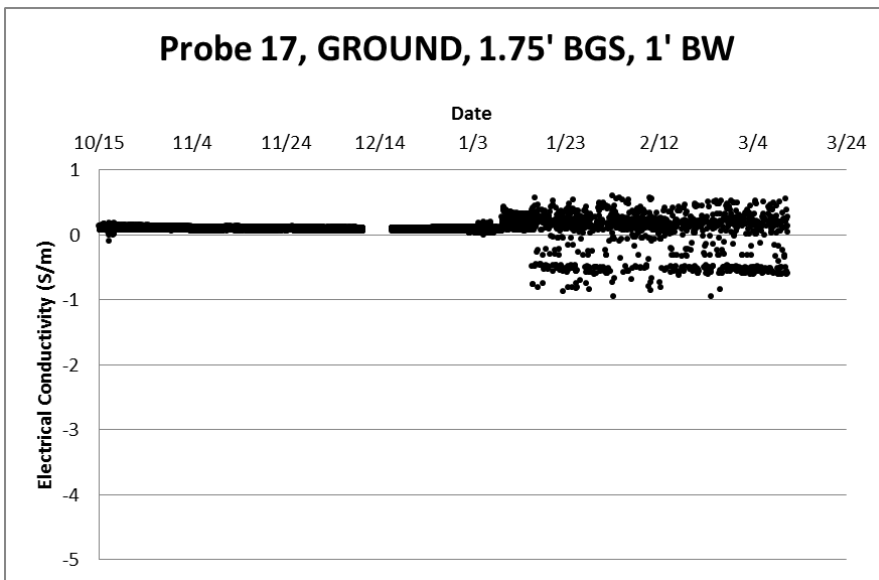


Figure A.17: Electrical conductivity for Probe 17 located 1.75 feet below the ground surface and 1 foot behind the wall

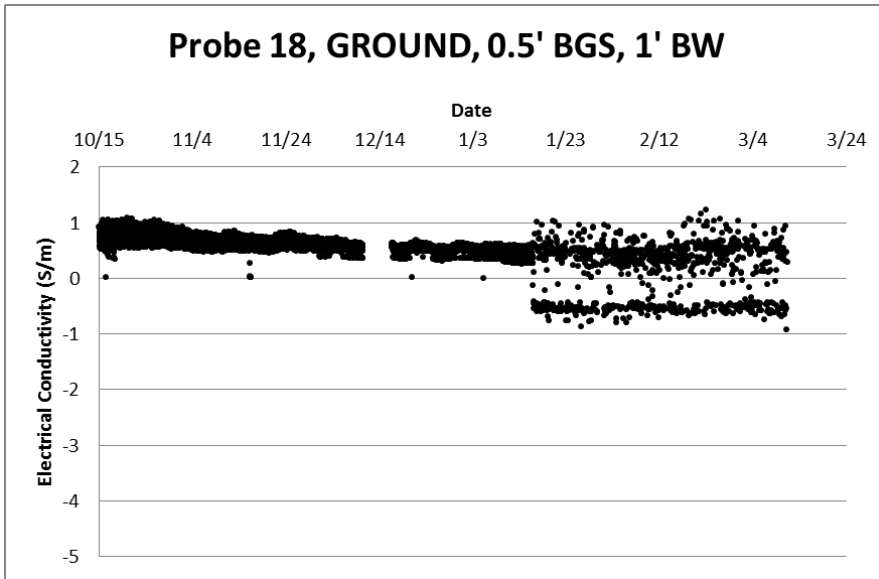


Figure A.18: Electrical conductivity for Probe 18 located 0.5 feet below the ground surface and 1 foot behind the wall

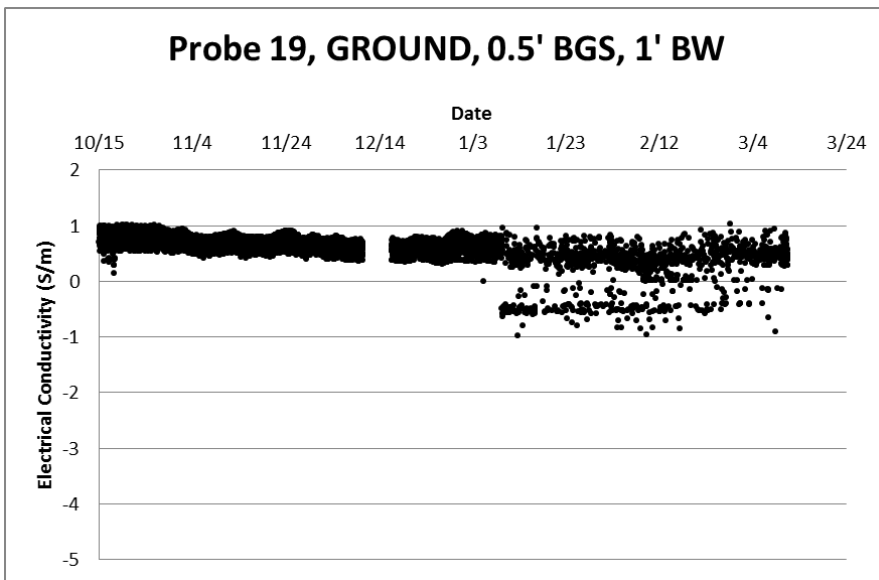


Figure A.19: Electrical conductivity for Probe 19 located 0.5 feet below the ground surface and 1 foot behind the wall

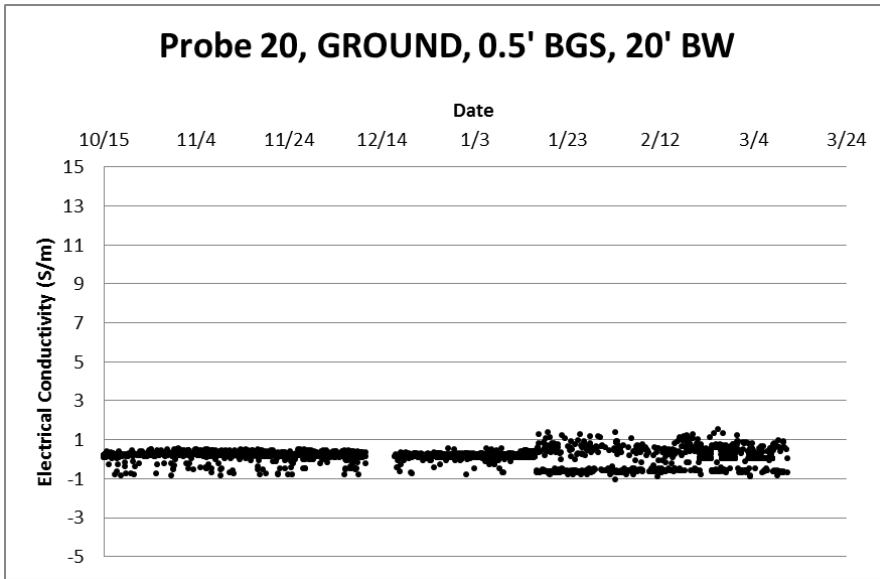


Figure A.20: Electrical conductivity for Probe 20 located 0.5 feet below the ground surface and 20 feet behind the wall

Appendix B

The following consists of the L_a/L versus time figures for each of the 20 TDR probes.

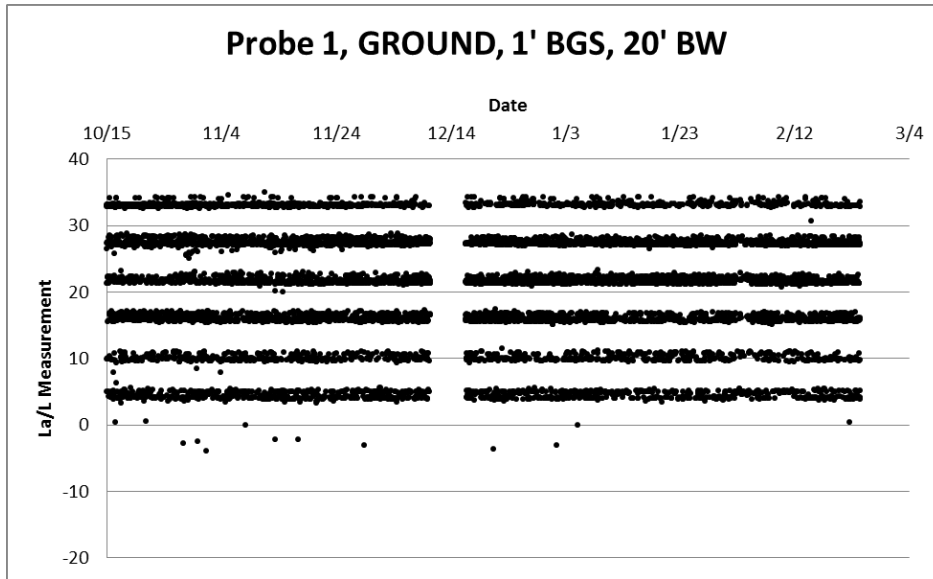


Figure B.1: L_a/L values for Probe 1 located 1 foot below the ground surface and 20 feet behind the wall

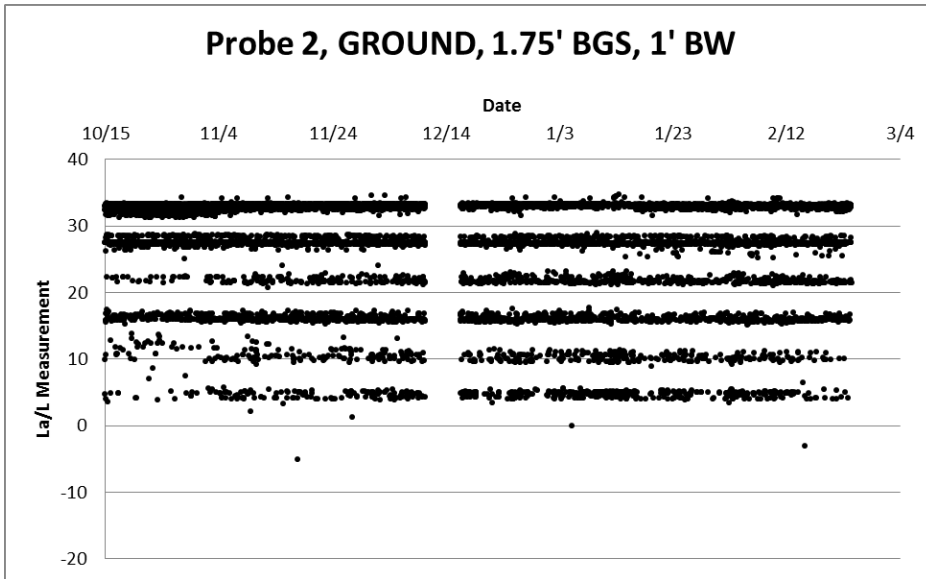


Figure B.2: L_a/L values for Probe 2 located 1.75 feet below the ground surface and 1 foot behind the wall

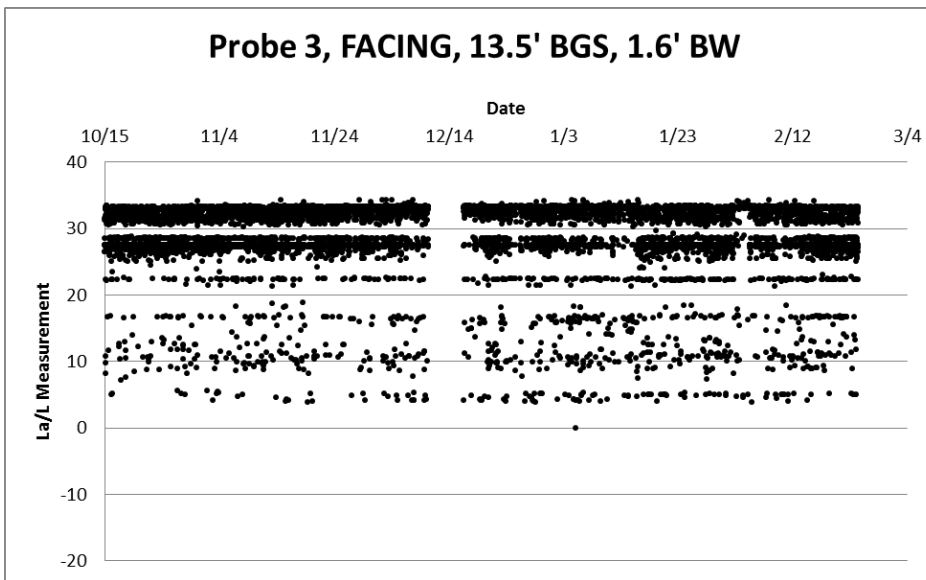


Figure B.3: L_a/L values for Probe 3 located 13.5 feet below the ground surface and 1.6 feet behind the wall

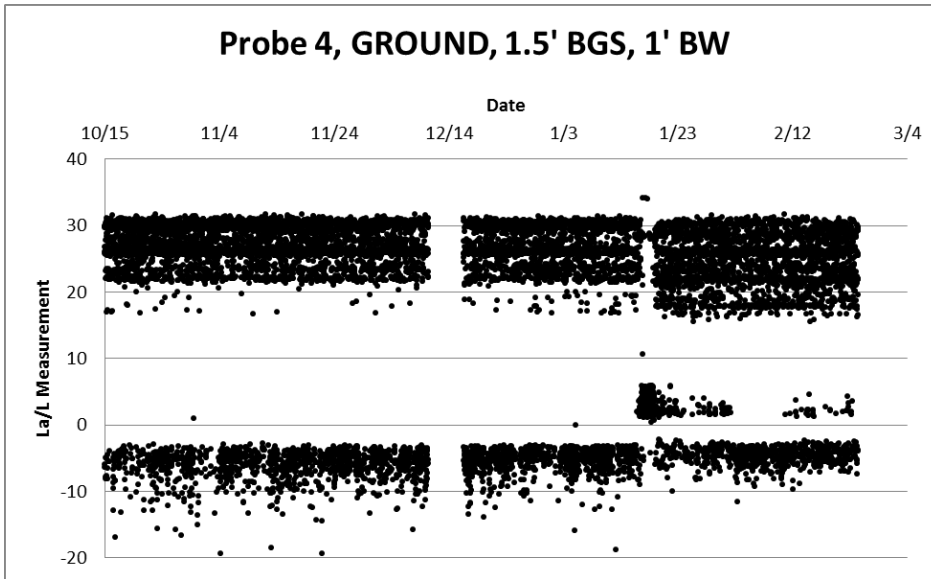


Figure B.4: L_a/L values for Probe 4 located 1.5 feet below the ground surface and 1 foot behind the wall

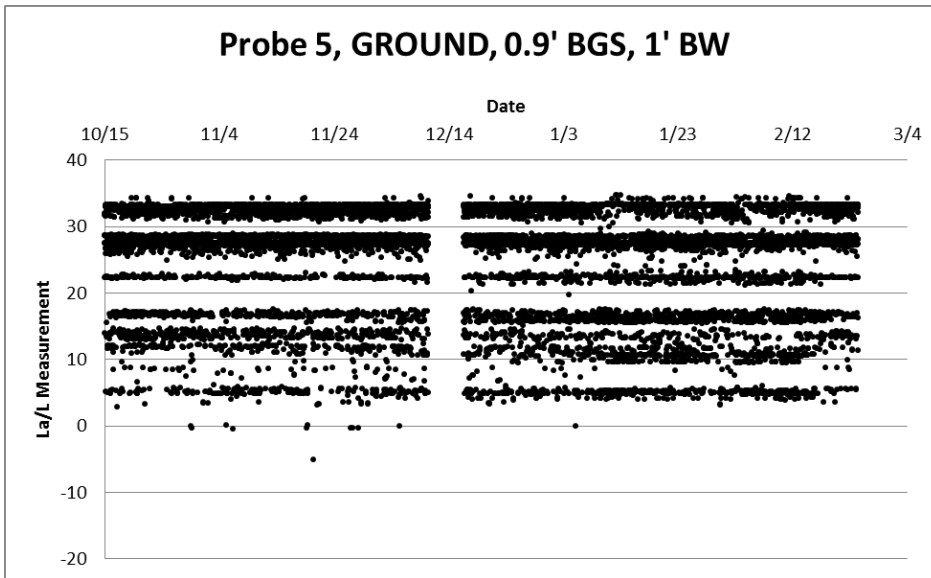


Figure B.5: L_a/L values for Probe 5 located 0.9 feet below the ground surface and 1 foot behind the wall

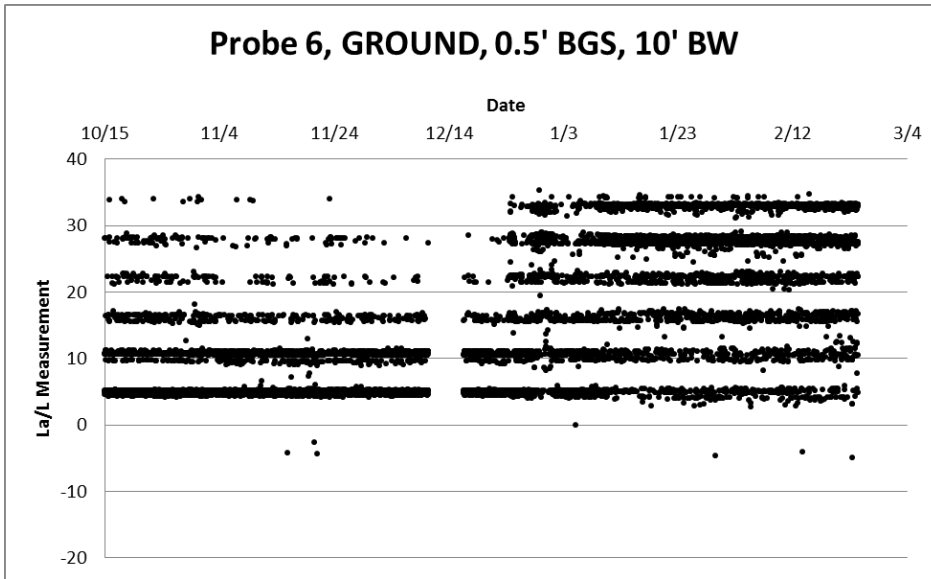


Figure B.6: L_a/L values for Probe 6 located 0.5 feet below the ground surface and 10 feet behind the wall

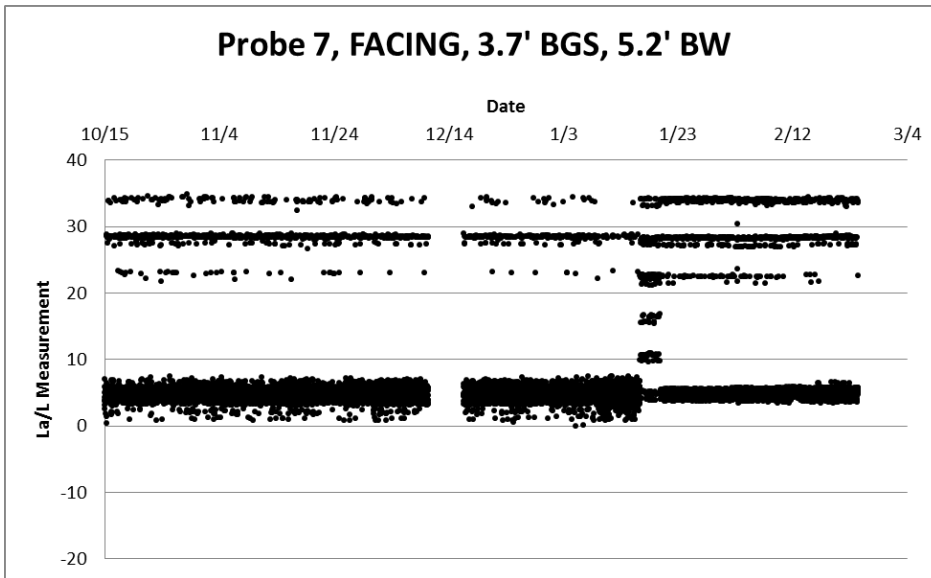


Figure B.7: L_a/L values for Probe 7 located 3.7 feet below the ground surface and 5.2 feet behind the wall

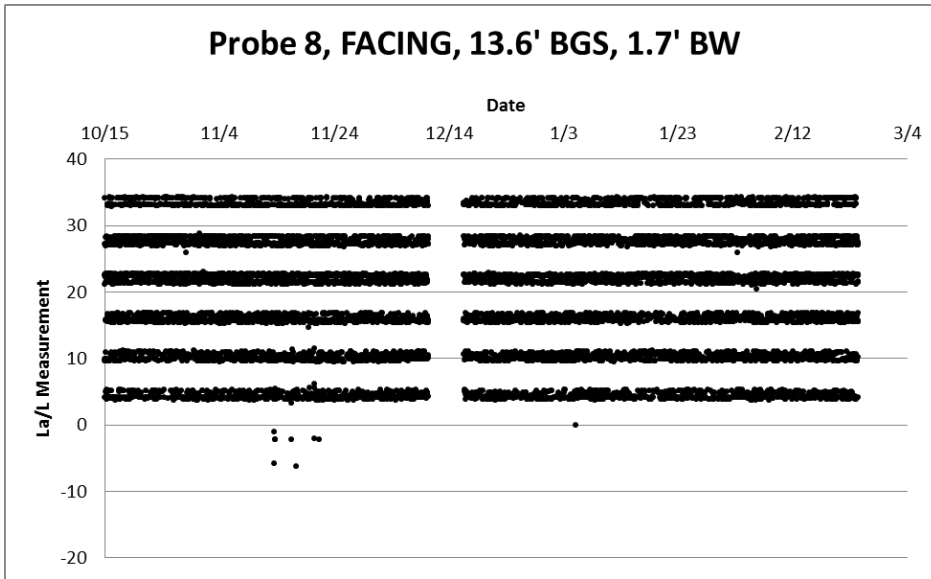


Figure B.8: L_a/L values for Probe 8 located 13.6 feet below the ground surface and 1.7 feet behind the wall

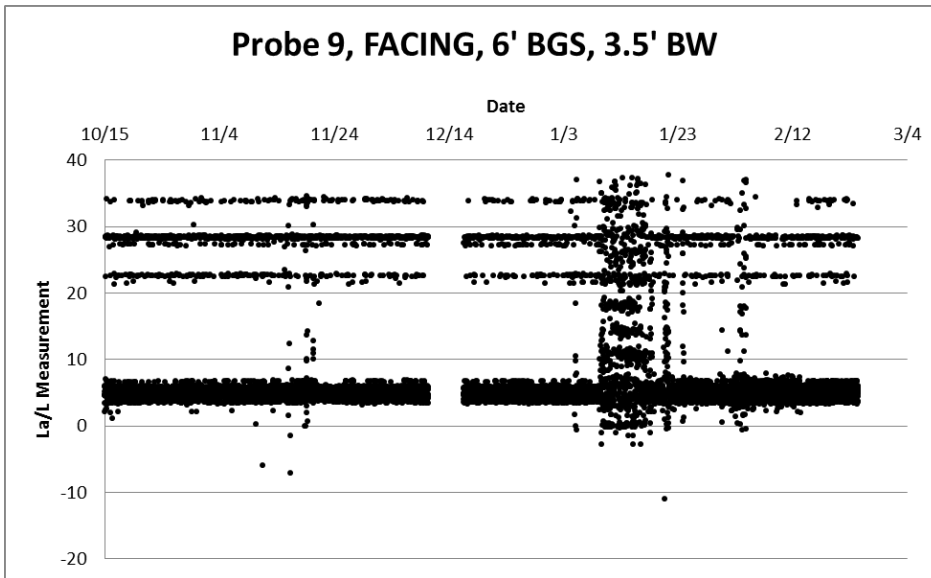


Figure B.9: L_a/L values for Probe 9 located 6 feet below the ground surface and 3.5 feet behind the wall

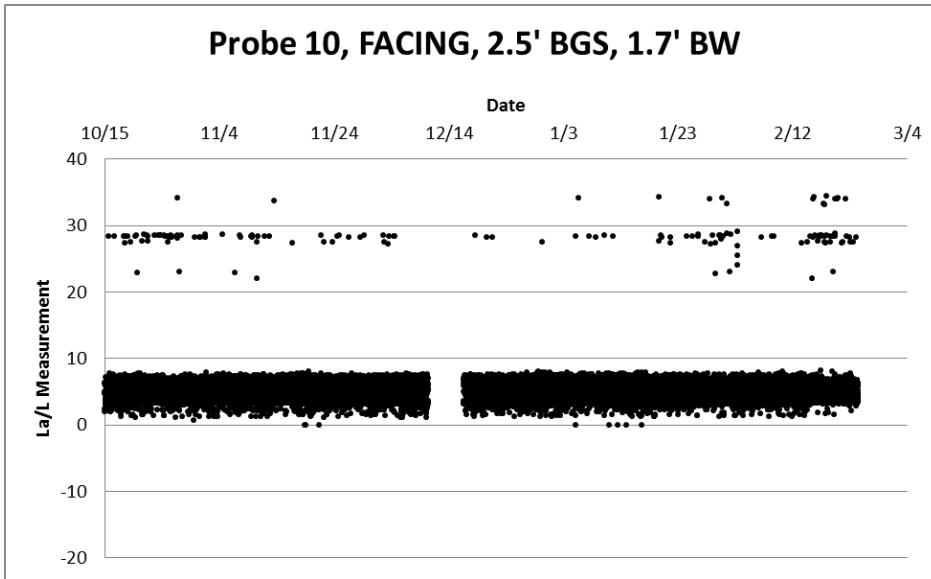


Figure B.10: L_a/L values for Probe 10 located 2.5 feet below the ground surface and 1.7 feet behind the wall

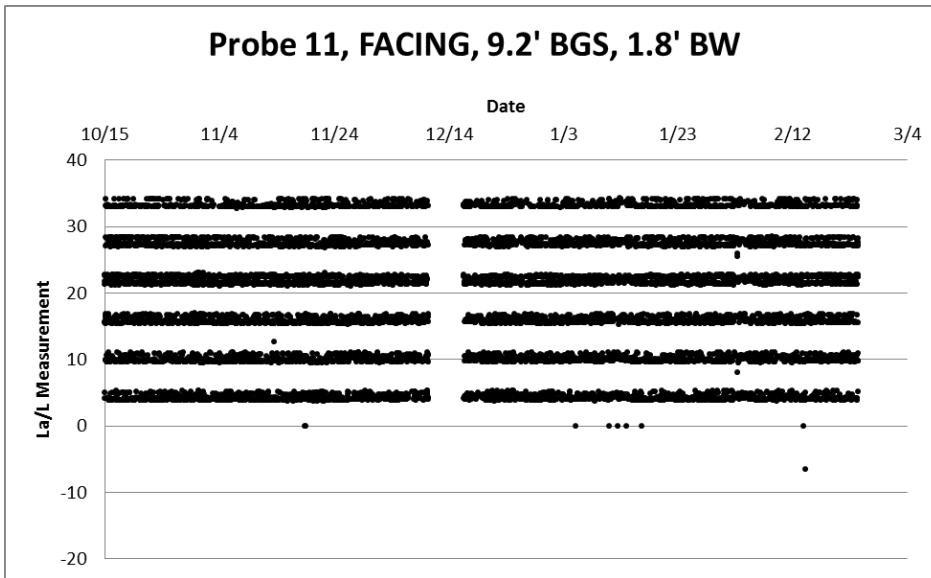


Figure B.11: L_a/L values for Probe 11 located 9.2 feet below the ground surface and 1.8 feet behind the wall

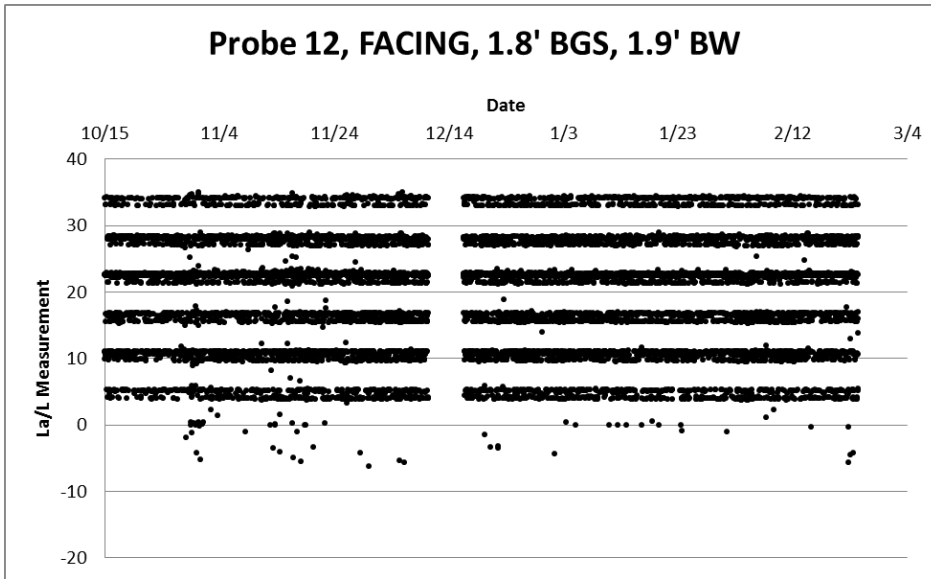


Figure B.12: L_a/L values for Probe 12 located 1.8 feet below the ground surface and 1.9 feet behind the wall

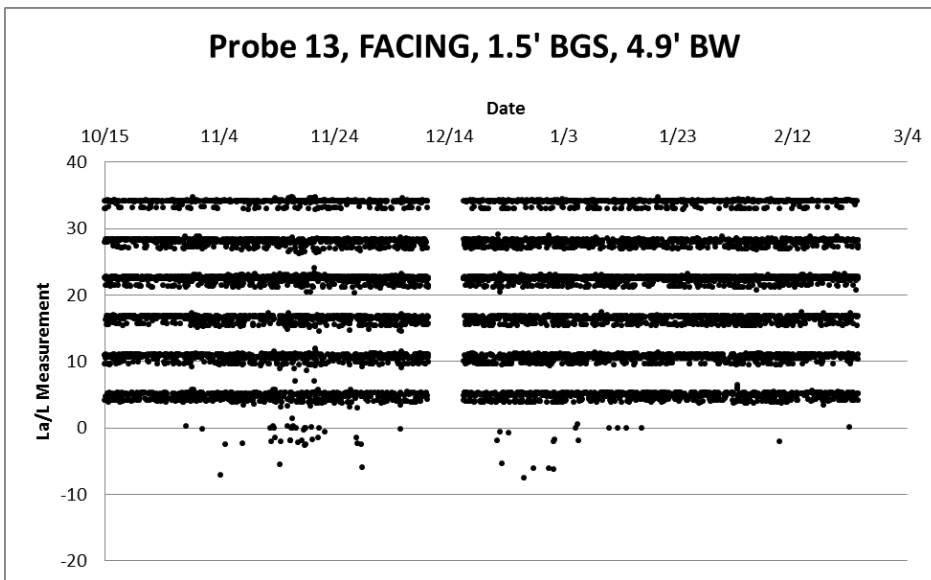


Figure B.13: L_a/L values for Probe 13 located 1.5 feet below the ground surface and 4.9 feet behind the wall

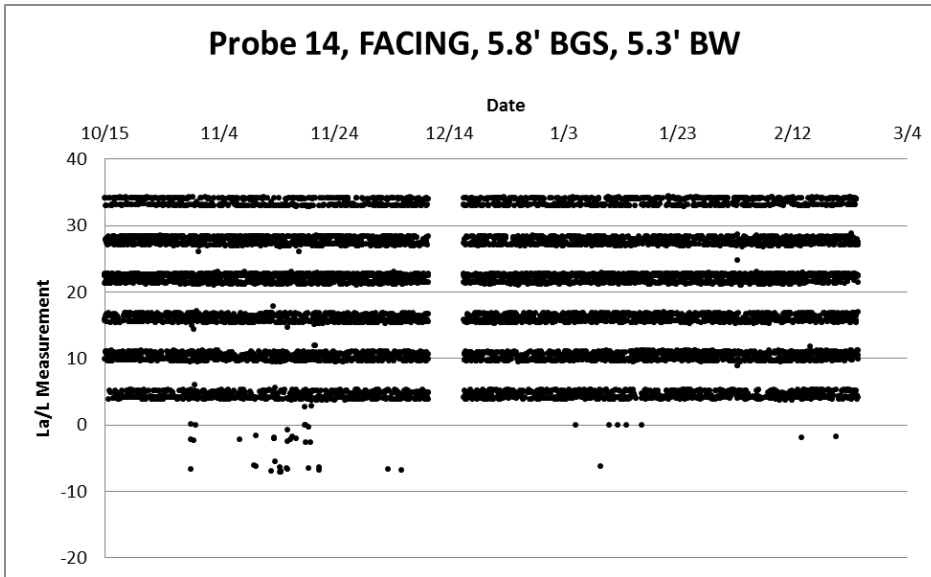


Figure B.14: L_a/L values for Probe 14 located 5.8 feet below the ground surface and 5.3 feet behind the wall

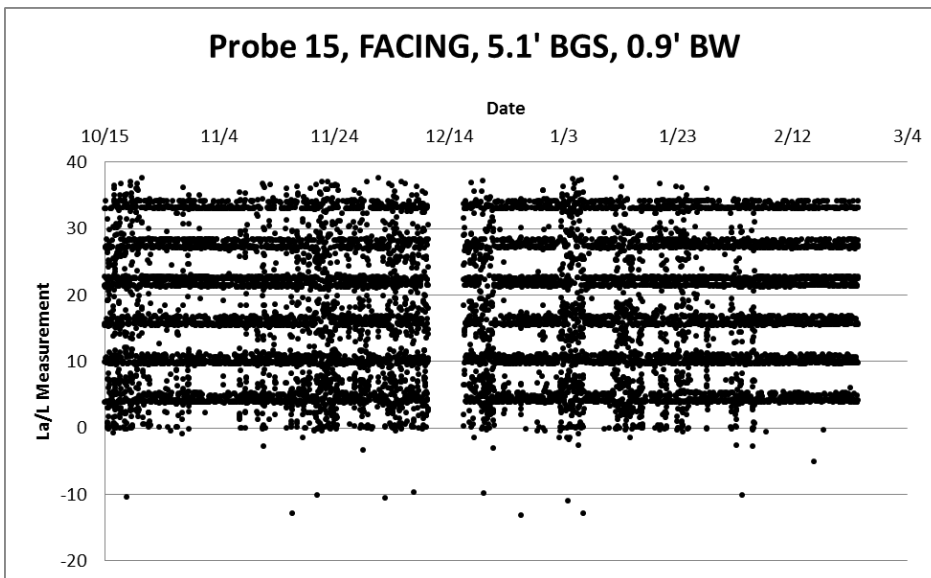


Figure B.15: L_a/L values for Probe 15 located 5.1 feet below the ground surface and 0.9 feet behind the wall

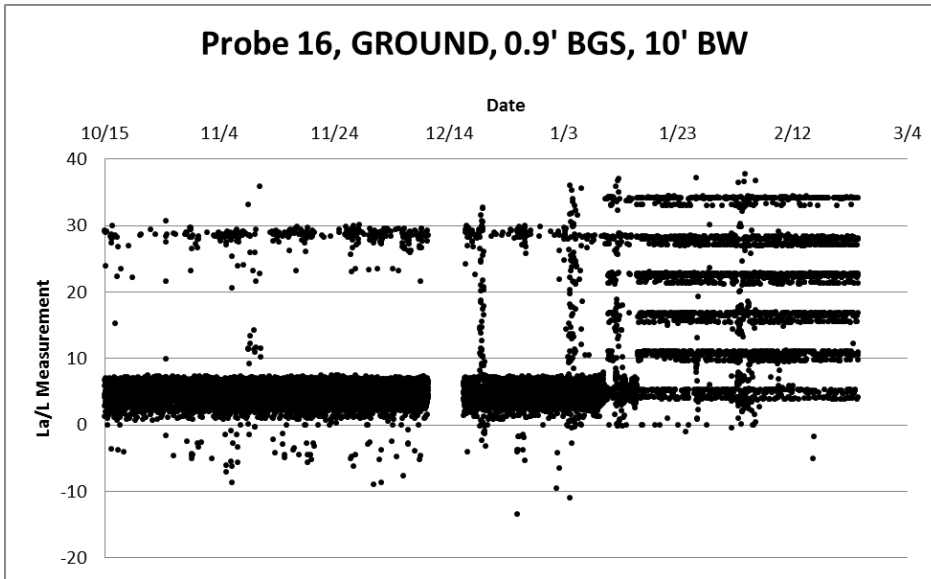


Figure B.16: L_a/L values for Probe 16 located 0.9 feet below the ground surface and 10 feet behind the wall

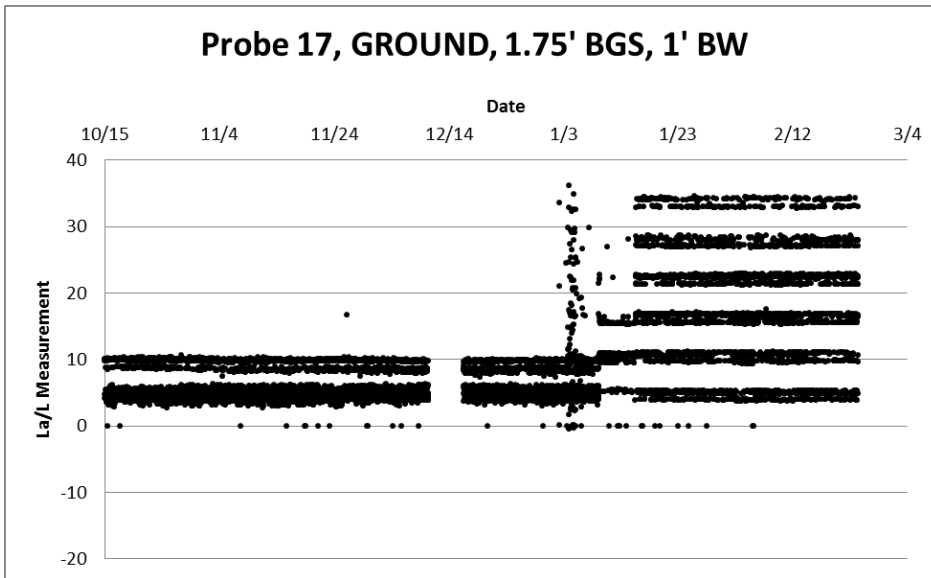


Figure B.17: L_a/L values for Probe 17 located 1.75 feet below the ground surface and 1 foot behind the wall

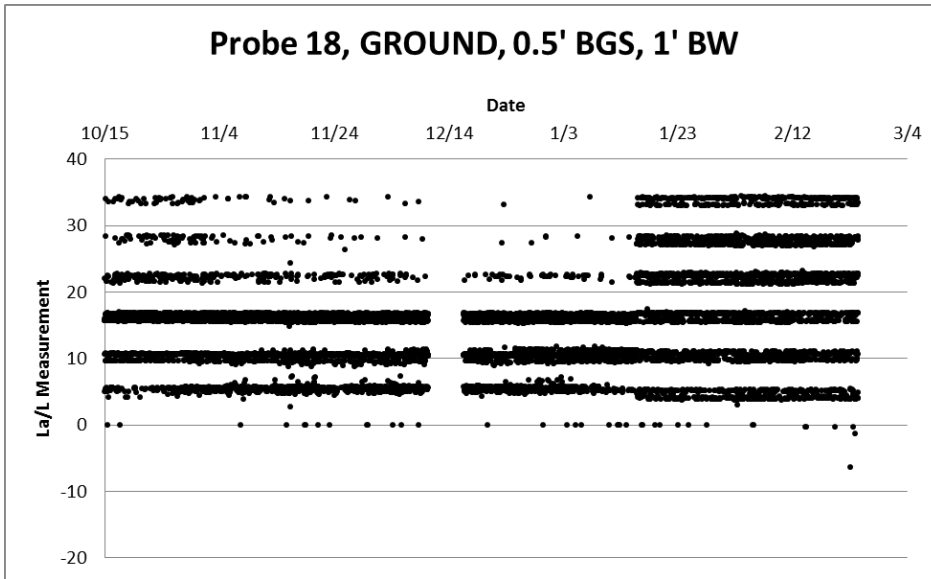


Figure B.18: L_a/L values for Probe 18 located 0.5 feet below the ground surface and 1 foot behind the wall

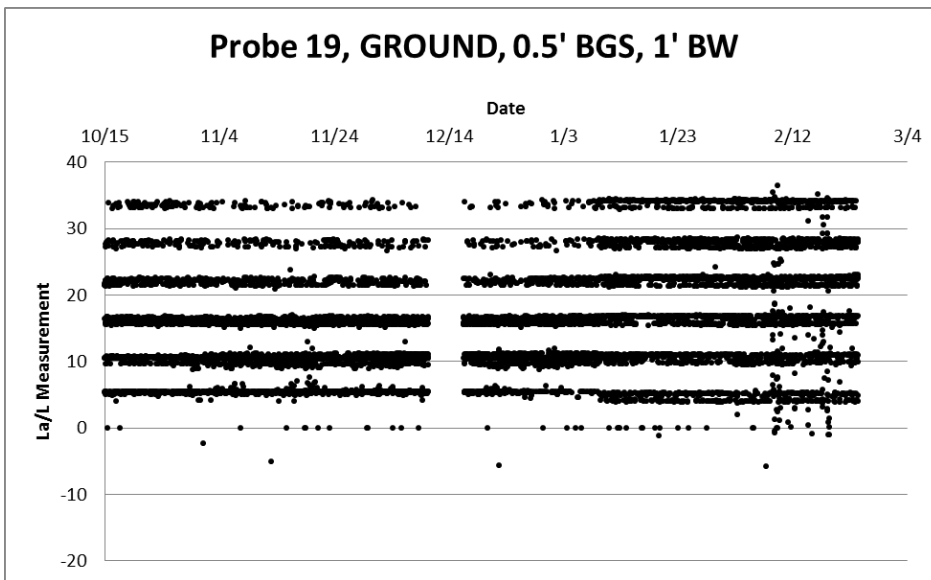


Figure B.19: L_a/L values for Probe 19 located 0.5 feet below the ground surface and 1 foot behind the wall

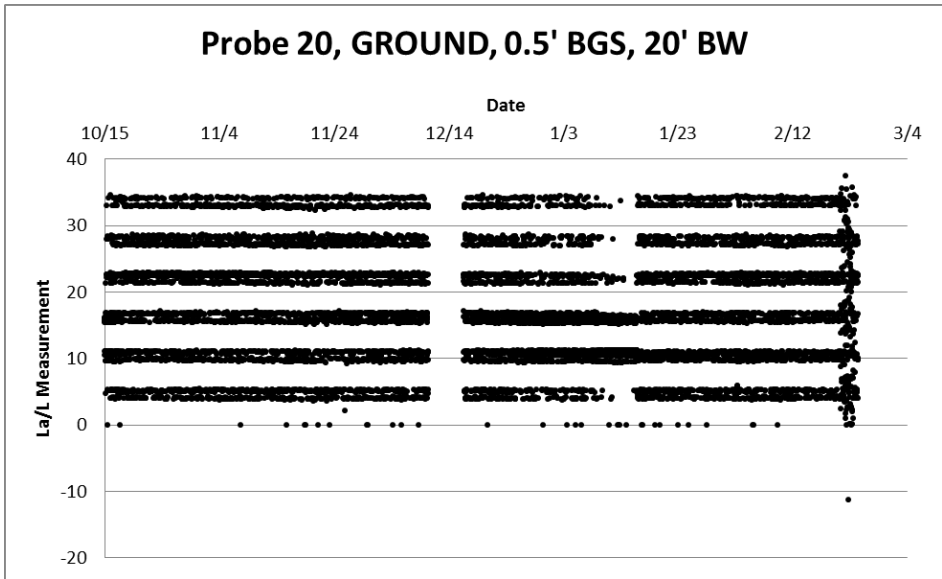


Figure B.20: L_a/L values for Probe 20 located 0.5 feet below the ground surface and 20 feet behind the wall

References

- Antle, Chad L. Soil Moisture Determination by Frequency and Time Domain Techniques. Master's Thesis, Ohio University, 1997
- Brown, A. C., Ellis, T., Dellinger, G., El-Mohtar, C., Zornberg, J., & Robert, G. B. (2011). Long-term monitoring of a drilled shaft retaining wall in expansive clay: Behavior before and during excavation. *Geo-Frontiers 2011: Advances in Geotechnical Engineering* , 3516-3525.
- Brown, J. "TDR Probe Rod Deflection" Email to Andy Brown. August 2011
- Campbell Scientific, Inc. (2010). TDR100 Instruction Manual.
- Campbell Scientific, Inc. Tech Support (2010). Personal Communication. Campbell Scientific, Inc., Logan, Utah.
- Chen, R., Drnevich, V. P., Yu, X., Nowack, R. L., & Chen, Y. (2007). Time Domain Reflectometry Surface Reflections for Dielectric Constant in Highly Conductive Soils. *Journal of Geotechnical and Geoenvironmental Engineering* , 133, 1597-1608.
- Dean, T. J., Bell, J. P., & Baty, A. J. (1987). Soil Moisture Measurement by an Improved Capacitance Technique, Part 1. Sensor Design and Performance. *Journal of Hydrology* , 93, 67-78.
- Foundation Engineering Handbook (1991), Second Edition, Edited by H-Y. Fang, Van Nostrand Reinhold, New York.
- Ellis, Trent. A Subsurface Investigation in Taylor Clay. Master's Thesis, The University of Texas at Austin, 2011
- Gaskin, G. J., & Miller, J. D. (1996). Measurement of Soil Water Content Using a Simplified Impedance Measuring Technique. *Journal of Agricultural Engineering Research* , 63, 153-160.
- Giese, K., & Tiemann, R. (1975). Determination of the complex permittivity from thin-sample time domain reflectometry, Improved analysis of the step response waveform. *Advances in Molecular Relaction Processes* , 7 (1), 45-59.
- Jarell, Glenn, 2010, Personal Communication. Campbell Scientific, Inc., Logan, Utah.

- Jarell, G., Ritter, J. "GJ & Jason/csi review c/o Andy Brown interpreting erratic TDR100 La/L & EC measurement Ref: UT Manor Wall" Email to Andy Brown. April 2011
- Jones, D. J., & Holtz, W. (1973). Expansive Soils - The Hidden Disaster. *Civil Engineering* , 43, 49-51.
- Jones, S. B., & Or, D. (2004). Frequency Domain Analysis for Extending Time Domain Reflectometry Water Content Measurement in Highly Saline Soils. *Soil Science Society of America Journal* , 68, 1568-1577.
- Kuhn, Jeffrey. Effect of Cracking on the Hydraulic Properties of Unsaturated Highly Plastic Clays. Master's Thesis, The University of Texas at Austin, 2005
- Moret-Fernandez, D., Lera, F., Arrue, J. L., & Lopez, M. V. (2009). Measurement of Soil Bulk Electrical Conductivity Using Partially Coated TDR Probes. *Valdosa Zone Journal* , 8 (3), 594-600.
- Patterson, D. E., & Smith, M. W. (1985). Unfrozen water content in saline soils: results using time-domain reflectometry. *Canadian Geotechnical Journal* , 22, 95-101.
- Reedy, R. C., and Scanlon, B. R., 2002, Long-term water balance monitoring of engineered covers for waste containment, in 2001 International Containment and Remediation Technology Conference, Orlando, Florida, Institute for International Cooperative Environmental Research, Florida State University, Paper ID. No. 073, <http://www.iicer.fsu.edu>, 3 p
- Reedy, Robert, 2010, Personal Communication. Bureau of Economic Geology, Austin, Texas.
- Roth, K., Schulin, R., Fluhler, H., & Attinger, W. (1990). Calibration of Time Domain Reflectometry for Water Content Measurement Using a Composite Dielectric Approach. *Water Resources Research* , 26 (10), 2267-2273.
- Seyfried, M. S., & Murdock, M. D. (2004). Measurement of Soil Water Content with a 50-MHz Soil Dielectric Sensor. *Soil Science Society of America Journal* , 68, 394-403.
- Siddiqui, S. I., Drnevich, V. P., & Deschamps, R. J. (2000). Time Domain Reflectometry Development for Use in Geotechnical Engineering. *Geotechnical Testing Journal* , 23, 9-20.
- Topp, G. C., Davis, J. L., & Annan, A. P. (1980). Electromagnetic Determination of Soil Water Content Measurements in Coaxial Transmission Lines. *Water Resources Research*, 16 (3), 574-582.

Copyright
by
Iraklis Koutrouvelis
2012

**The Thesis Committee for Iraklis Koutrouvelis
Certifies that this is the approved version of the following thesis:**

**Earth Pressures Applied on Drilled Shaft Retaining Walls in Expansive
Clay during Cycles of Moisture Fluctuation**

**APPROVED BY
SUPERVISING COMMITTEE:**

Supervisor:

Robert B. Gilbert

Richard E. Klingner

**Earth Pressures Applied on Drilled Shaft Retaining Walls in Expansive
Clay during Cycles of Moisture Fluctuation**

by

Iraklis Koutrouvelis, Diploma C.E.

Thesis

Presented to the Faculty of the Graduate School of

The University of Texas at Austin

in Partial Fulfillment

of the Requirements

for the Degree of

Master of Science in Engineering

The University of Texas at Austin

May 2012

Dedication

Dedicated to my parents Dimitri Koutrouveli and Lefainio Morfakidou

Acknowledgements

I would like to express my sincere gratitude to Dr. Robert Gilbert for the opportunity that he gave me to work under his supervision and his guidance towards the completion of my thesis. It was without doubt one of the most valuable experiences in my life while his attitude, passion and profound knowledge in geotechnical engineering will always be an inspiration for my career and life.

I would also like to thank Dr. Richard Klingner for reviewing this thesis and for his invaluable advices. His remarkable knowledge in structural engineering and his kindness will always follow me.

In addition, I acknowledge the assistance of all the people involved in this project including Dr. Jorge Zornberg, Dr. Chadi el Mohtar, Andy Brown and Greg Delinger. Without their contribution, this thesis would have never been completed.

Moreover, I would also like to express my appreciation for having the opportunity to meet and create lifetime bonds with such amazing people during the two years that I spent in Austin. George Zalachoris, Giannis Tsiapas, Chris Guy and Todd Sheridan will always be in my heart while our amazing experiences and unforgettable memories will follow me for the rest of my life.

Finally, I would like to pay my respect to my parents Dimitri Koutrouveli and Lefainio Morfakidou, my brother Stergio Koutrouveli and to the most amazing woman I have met in my life Dimitra Tsiaousi. Without their help and support I would never have the chance to fulfill my dream and study in the United States.

Abstract

Earth Pressures Applied on Drilled Shaft Retaining Walls in Expansive Clay during Cycles of Moisture Fluctuation

Iraklis Koutrouvelis M.S.E.

The University of Texas at Austin, 2012

Supervisor: Robert B. Gilbert

Estimating the earth pressures applied on drilled shaft retaining walls in expansive clays is challenging due to the soil's tendency to shrink and swell under cycles of moisture fluctuation. While empirical suggestions do exist, significant uncertainty exists regarding the effect of volumetric changes of the soil on the earth pressures.

In order to investigate this uncertainty, a fully instrumented drilled shaft retaining wall named in the honor of Lymon C. Reese, was constructed in the highly expansive clay of the Taylor formation. Inclined meters and optical fiber strain gauges were installed in three instrumented shafts and time domain reflectometry sensors were placed within the soil to measure changes in the moisture content. Nearly two years of monitoring data have been obtained which are used to estimate the earth pressure distribution at different moisture conditions.

Processing of the raw strain data was required to eliminate the effects of tension cracks and other microscale factors that caused significant variation in the results. Good

agreement was obtained between the processed strain and inclinometer data as the deflected shapes predicted from both monitoring elements were similar. Finally, the earth pressure distribution for six dates that represent different moisture conditions of the Taylor clay were plotted and the results of the strain gauge and inclinometer analysis were consistent.

A p-y analysis was also conducted to estimate the range of earth pressures applied on the wall. A triangular earth pressure diagram was used as external load above the excavation level and the equivalent fluid pressure was evaluated by matching the deflected shapes generated from the inclinometer data to those predicted by the p-y model. The results were compared to the empirical values that TxDOT uses for design of similar type of walls in expansive clay.

Finally, the side shear and temperature effects on the lateral response of the wall were quantified. A differential linear thermal model was used to evaluate the temperature effects and a t-z analysis was conducted to account for the side shear applied on the wall due to volumetric changes of the soil. It is recommended that their combined effect be considered in the design.

Table of Contents

List of Tables	xii
List of Figures	xiii
Chapter 1: Introduction	1
1.1: Motivation.....	1
1.2: TxDOT project - Lymon C. Reese research wall	2
1.3: Objectives of the Thesis.....	3
1.4: Organization of the Thesis	4
Chapter 2: Literature Review	6
2.1: Drilled shaft retaining walls.....	6
2.2: Analytical methods of analyzing laterally loaded drilled shafts.....	7
2.3: Derivation of the differential equation.....	9
2.4: Winkler approach - Elastic soil behavior.....	12
2.5: Analytical methods using p-y curves - Non-linear soil behavior	13
2.6: Developing p-y curves for cohesive soils under undrained conditions.....	17
2.7: Recommended p-y curve for stiff fissured clays from field load tests.....	22
2.8: Numerical modeling of laterally loaded piles.....	25
2.8.1: Computer programs based on finite difference methods	25
2.8.2: Computer programs based on finite element methods.....	28

2.9: Effect of axial loads on laterally loaded piles.....	29
2.9.1: Differential equation describing an axially loaded pile.....	30
2.9.2: Load transfer curves for cohesionless soils	32
Chapter 3: Site Conditions and Test Wall.....	34
3.1: Introduction.....	34
3.2: Site location and geologic conditions	35
3.3: Geometry of the research wall	39
3.4: Instrumentation program for predicting the earth pressures.....	42
3.5: Hydrogeology	52
3.6: Summary.....	52
Chapter 4: Methods of Analysis Used and Data Prior to Excavation.....	53
4.1: Methods of analysis used to predict the earth pressures.....	53
4.2: Residual stresses and strains before excavation	55
4.3: Predicting the moment-curvature diagram	64
Chapter 5: Analyzing the Results of the Instrumentation Program	70
5.1: Analyzing the results of the inclinometers	70
5.2: Analyzing the results of the strain gauges	79
5.2.1: Processing the raw strain gauge data	79
5.2.2: Predicting the deflected shape from the strain gauge data.....	86

5.2.3: Analyzing the results of the strain gauges	95
5.3: Conclusions on the results of the instrumentation program	102
Chapter 6: Simulating the Lateral Response of the Wall Using a p-y Model.....	104
6.1: Introduction to p-y analysis	104
6.2: Input data used in the p-y analysis.....	106
6.3: Sensitivity analysis on the p-y model	110
6.4: Introducing the theory of the initial global displacements	118
6.5: Predicting the deflected shape for different moisture conditions	120
6.6: Predicting the active earth pressures using the p-y curve.....	127
6.7: Comparing the results of the p-y model to the instrumentation data.....	135
Chapter 7: Side Shear and Thermal Effects on the Lateral Deflections of the Wall	137
7.1: Introduction.....	137
7.2: Evaluating the axial strains from the strain gauge data	139
7.3: Details on the t-z analysis	142
7.4: Generating the t-z and Q-z curves for stiff fissured clays	144
7.5: Induced strains and curvature due to side shear	146
7.6: Induced strains and curvature due to temperature effects.....	156
7.7: Conclusions and final remarks.....	163

Chapter 8: Conclusions and Future Work.....	166
8.1: Conclusions and comments on the results	166
8.2: Recommendations for future work	169
Appendix A.....	170
A.1: Residual processed strains along the "global" shaft.....	170
A.2: Residual stresses along the "global" shaft	176
Appendix B.....	182
B.1: Strains throughout the monitoring period along the instrumented shafts.....	182
B.2: Processed strains throughout the monitoring period along the "global" shaft.....	206
Bibliography	212
Vita	215

List of Tables

Table 2.1: Representative values of the initial clay stiffness on laterally loaded piles.....	17
Table 3.1: Construction schedule of the research wall	42
Table 4.1: Concrete Strengths for various curing times.....	58
Table 4.2: Estimates of the composite Young's modulus for different curing times	60
Table 4.3: Geometric properties of the shafts used in the evaluation of the M- ϕ curve...66	
Table 5.1: Values of initial prescribed rotation developed at the tip of the shafts.....	91
Table 6.1: Recommended values of ϵ_{50} for different soil types	112
Table 6.2: Analysis for estimating the shear strength after full consolidation	115
Table 6.3: Equivalent fluid pressures assuming 0% and 20% shear strength reduction.....	127
Table 6.4: Comparison on the active thrusts from the results of the various analysis....	135
Table 7.1: Mean daily temperatures at the selected dates and during excavation	158

List of Figures

Figure 2.1: Infinitesimal element from the "beam column on a foundation" theory (Hetenyi, 1946)	9
Figure 2.2: Typical results from the solution of the differential equation for a laterally loaded pile with zero axial load (Reese et al., 2006)	11
Figure 2.3: Winkler assumption for a beam lying on elastic soil (Winkler, 1867)	12
Figure 2.4: Distribution of the unit stresses on a random cross-section of the pile before and after lateral deflection occurs (Reese et al., 2006)	14
Figure 2.5: Soil response under combined loading conditions of the pile (Reese et al., 2006)	15
Figure 2.6: Mechanisms of soil resistance on a laterally loaded pile (Smith and Slyh, 1986)	15
Figure 2.7: Typical shape of the p-y curve showing the soil resistance to lateral pile deflections (Reese et al., 2006)	18
Figure 2.8: Wedge failure of the soil near the ground surface for clays (Reese, 1962) ..	19
Figure 2.9: Mode of failure of lateral flow around a pile in clay (Reese, 1962)	19
Figure 2.10: Effect of different loading conditions on the p-y curves: (a) short-term monotonic loading; (b) effect of cyclic loading; (c) possible effect of sustained loading (Reese et al., 2006)	23
Figure 2.11: Characteristic shape of the p-y curve for stiff overconsolidated clay (Welch and Reese, 1972)	25
Figure 2.12: Computer representation of a deflected pile using finite difference methods (Reese et al., 2006)	26
Figure 2.13: Analysis of a drilled shaft retaining wall using LPILE	27

Figure 2.14: Simulation of the drilled shaft retaining wall using ABACUS (Brown et al., 2011)	29
Figure 2.15: Numerical model of a pile subjected to axial load using finite difference techniques (Reese et al., 2006)	31
Figure 2.16: Load displacement curves for side resistance and end bearing (Reese et al., 2006)	31
Figure 2.17: Load transfer curve in side resistance for piles in clay (Reese et al., 2006)	33
Figure 2.18: Load transfer in end bearing for piles in clay (Reese et al., 2006).....	33
Figure 3.1: Current view of the research wall in Manor, Texas	34
Figure 3.2: Location of the research wall in Manor, Texas	35
Figure 3.3: Taylor clay sample taken from the project site (Brown et al., 2011).....	36
Figure 3.4: Distinct transition from the weathered dark gray to the stiffer dull yellow clay.....	37
Figure 3.5: Combined test results for the undrained shear strength profile (Ellis, 2010).	38
Figure 3.6: Drained peak and residual failure envelope from the direct shear tests (Ellis, 2010)	38
Figure 3.7: Moisture Content profiles for different dates	39
Figure 3.8: Cross-Section of the research wall and embedment depths for the various shafts	40
Figure 3.9: Plan view of the wall and location of the instrumented shafts	41
Figure 3.10: Cross-section and dimensions of the center shaft	41
Figure 3.11: Schematic representation of the instrumentation program applied on the research wall	43
Figure 3.12: Basic elements of an optical fiber sensing system (Micron Optics, 2011)..	44
Figure 3.13: Layout of a Fabry-Perot Interferometer (Micron Optics, 2011)	45

Figure 3.14: Fiber optic strain gauge before installation within the instrumented shaft ..	46
Figure 3.15: Strain gauges attached to the sister bar before installation within the shafts.....	47
Figure 3.16: Inclinomter probe and casing showing the wheels and guide grooves used to measure the rotation between two successive points (Deep Excavation LLC, 2012).....	48
Figure 3.17: Inclinomter casing and strain gauges attached to the reinforcing bar cage	49
Figure 3.18: Time Domain Reflectometry (TDR) moisture content probe before installation within the soil (Delinger, 2010)	50
Figure 3.19: Linear potentiometer attached in a fixed location.....	51
Figure 4.1: Flow chart showing the methods used to generate the earth pressure diagrams.....	54
Figure 4.2: Residual strains developed at a depth of 9ft on the compression side of the center shaft.....	56
Figure 4.3: Residual strains for various depths along the center shaft	57
Figure 4.4: Concrete strength (f'_c) and incremental increase of E_c and E_{com} for various curing times.....	59
Figure 4.5: Residual stresses over time at a depth of 9 ft on the compression side of the center shaft.....	61
Figure 4.6: Residual stresses for different depths along the center shaft	62
Figure 4.7: Residual strain profile versus depth for different curing times of the center shaft.....	63
Figure 4.8: Residual stress profile versus depth for different curing times of the center shaft.....	63

Figure 4.9: Characteristic stress-strain curves used in the evaluation of the M- ϕ curve (FHWA manual)	63
Figure 4.10: Characteristic stress-strain curves used in the evaluation of the M- ϕ curve (FHWA manual)	63
Figure 4.11: Linear strain change along the diameter of the drilled shaft is assumed to derive the M- ϕ curve using the method of slices.....	67
Figure 4.12: Predicted M- ϕ curves using different methods that assume cracked section and no concrete cracking	68
Figure 5.1: Rotation profiles and smoothing spline curve fitting for different dates	71
Figure 5.2: Deflected shape of the center shaft for different times throughout the two year monitoring period.....	72
Figure 5.3: Deflections at the top of the shaft and at a depth of 14 ft during the two year monitoring period	72
Figure 5.4: Piecewise quadratic curve fitting process to predict the curvature profile from the inclinometer data (Ooi and Ramsey, 2003)	75
Figure 5.5: Rotation profile for different dates throughout the two year monitoring period	76
Figure 5.6: Bending curvature profile for different dates throughout the two year monitoring period	76
Figure 5.7: Bending moment profile for different dates throughout the two year monitoring period (using M- ϕ curve from the method of slices)	77
Figure 5.8: Shear force profile for different dates throughout the two year monitoring period	77
Figure 5.9: Net earth pressure diagram for different dates throughout the two year monitoring period	78

Figure 5.10: Unexpected constant increase in tension for the gauge at the compression side of the center shaft	79
Figure 5.11: Tension cracks for both gauges at the same depth during concrete curing.....	80
Figure 5.12: Malfunction of the gauge at the tension side a year upon its installation	80
Figure 5.13: Sharp unexpected increase in tension for the tension gauge followed by a gradual decrease in compression	81
Figure 5.14: Good set of data at a depth of 23 ft of the center shaft	81
Figure 5.15: Processed plot of strain over time at a depth of 1 ft.....	84
Figure 5.16: Processed plot of strain over time at a depth of 3 ft.....	85
Figure 5.17: Processed plot of strain over time at a depth of 7 ft.....	85
Figure 5.18: Processed plot of strain over time at a depth of 15 ft.....	86
Figure 5.19: Bending curvature profiles for different dates throughout the two year monitoring period	88
Figure 5.20: Sixth order polynomial curve fitting for the processed strains at the selected dates	89
Figure 5.21: Deflected Shapes generated using processed and initial strain data at the selected dates	90
Figure 5.22: Incremental polynomial curve fitting on the curvature profile at the selected dates	92
Figure 5.23: Initial and adjusted rotation profiles to account for the prescribed rotation at the tip of the shaft at the selected dates	93
Figure 5.24: Initial and adjusted deflected shapes to account for the prescribed rotation at the tip of the shaft at the selected dates	94

Figure 5.25: Bending curvature profile for different dates throughout the two year monitoring period	96
Figure 5.26: Bending moment profile for different dates throughout the two year monitoring period (using M- ϕ curve from the method of slices)	97
Figure 5.27: Shear force profile for different dates throughout the two year monitoring period	97
Figure 5.28: Net earth pressure diagrams for different dates throughout the two year monitoring period	98
Figure 5.29: Comparison of the net earth pressure distribution evaluated using the results of the strain gauges and inclinometers - 8/19/2010	98
Figure 5.30: Comparison of the net earth pressure distribution evaluated using the results of the strain gauges and inclinometers - 12/10/2010	99
Figure 5.31: Comparison of the net earth pressure distribution evaluated using the results of the strain gauges and inclinometers - 3/11/2011	99
Figure 5.32: Comparison of the net earth pressure distribution evaluated using the results of the strain gauges and inclinometers - 7/28/2011	100
Figure 5.33: Comparison of the net earth pressure distribution evaluated using the results of the strain gauges and inclinometers - 10/27/2011	100
Figure 5.34: Comparison of the net earth pressure distribution evaluated using the results of the strain gauges and inclinometers - 1/10/2012	101
Figure 6.1: Schematic representation of the p-y model used to predict the magnitude of the earth pressure distribution	105
Figure 6.2: Shear strength profile along the shafts for the Taylor Clay	107
Figure 6.3: Ultimate soil resistance profile for the Taylor Clay from the original ground surface	108

Figure 6.4: Normalized p-y curve for the Taylor Clay	109
Figure 6.5: Comparison between the deflected shapes from the inclinometer and the initial p-y analysis	111
Figure 6.6: Sensitivity analysis on the stiffness of the soil assuming an equivalent fluid pressure of 40 psf/ft	112
Figure 6.7: Overconsolidation ratio for different depths along the shafts	114
Figure 6.8: Different scenarios for the reduction of the shear strength on the passive zone.....	115
Figure 6.9: Sensitivity analysis on the shear strength reduction at the passive zone assuming an equivalent fluid pressure of 40 psf/ft	116
Figure 6.10: Sensitivity analysis on the non-dimensional coefficient (J) related to the soil type assuming an equivalent fluid pressure of 40 psf/ft	117
Figure 6.11: Matching the deflected shape between the p-y analysis and the inclinometer data assuming an equivalent fluid pressure of 23.4 psf/ft.....	118
Figure 6.12: Profile of initial "global" displacements generated from the results of the p-y analysis immediately after excavation	119
Figure 6.13: Deflected shapes from the initial and final p-y analysis compared to the inclinometer data.....	121
Figure 6.14: Bending moment profiles for different dates throughout the two year monitoring period (using M- ϕ curve from the method of slices)	122
Figure 6.15: Shear force profiles for different dates throughout the two year monitoring period	122
Figure 6.16: Soil resistance profiles for different dates throughout the two year monitoring period	123

Figure 6.17: Deflected shapes from the initial and final p-y analysis compared to the inclinometer data.....	124
Figure 6.18: Bending moment profiles for different dates throughout the two year monitoring period (using M- ϕ curve from the method of slices)	125
Figure 6.19: Shear force profiles for different dates throughout the two year monitoring period	125
Figure 6.20: Soil resistance profiles for different dates throughout the two year monitoring period	126
Figure 6.21: Gradient of the triangular earth pressure distribution assuming 0% and 20% shear strength reduction on the passive zone.....	127
Figure 6.22: Earth pressure distributions - 8/19/2010	129
Figure 6.23: Earth pressure distributions - 12/10/2010	129
Figure 6.24: Earth pressure distributions - 3/11/2011	130
Figure 6.25: Earth pressure distributions - 7/28/2011	130
Figure 6.26: Earth pressure distributions - 10/27/2011	131
Figure 6.27: Earth pressure distributions - 1/10/2012	131
Figure 6.28: Earth pressure distributions - 8/19/2010	132
Figure 6.29: Earth pressure distributions - 12/10/2010	132
Figure 6.30: Earth pressure distributions - 3/11/2011	133
Figure 6.31: Earth pressure distributions - 7/28/2011	133
Figure 6.32: Earth pressure distributions - 10/27/2011	134
Figure 6.33: Earth pressure distributions - 1/10/2012	134
Figure 7.1: Curvature induced due to side shear and thermal effects when the water content of the soil is high and the air temperature is low	138

Figure 7.2: Curvature induced due to side shear and thermal effects when the water content of the soil is low and the air temperature is high	138
Figure 7.3: Axial strains induced in the shafts due to temperature effects and volumetric changes of the soil under cycles of moisture fluctuations	139
Figure 7.4: Net axial strain profiles for the selected dates after eliminating the residual strains and the strains due to the weight of the concrete mass	141
Figure 7.5: Schematic representation of the t-z model	143
Figure 7.6: Bending moment generated on the wall due to the side shear applied only on one side of the shafts.....	144
Figure 7.7: Normalized load transfer curve for side resistance of the Taylor clay.....	145
Figure 7.8: Normalized load transfer curve for end bearing of the Taylor clay	145
Figure 7.9: Annual precipitation at the project site during the two year monitoring period.	147
Figure 7.10: Maximum side shear applied on the shafts based on the results of the geotechnical investigation.....	147
Figure 7.11: Forces due to side shear applied at each increment under extreme moisture conditions.....	149
Figure 7.12: Bending moment profiles due to volumetric changes of the soil under extreme moisture conditions.....	150
Figure 7.13: Bending curvature profiles due to volumetric changes of the soil under extreme moisture conditions.....	150
Figure 7.14: Lateral deflections due to volumetric changes of the soil under extreme moisture conditions.....	151
Figure 7.15: Incremental displacements for the selected dates throughout the two year monitoring period	152

Figure 7.16: Cumulative displacements for the selected dates throughout the two year monitoring period	153
Figure 7.17: Side shear applied on the wall due to volumetric changes of the soil.....	154
Figure 7.18: Forces due to side shear applied on the wall due to volumetric changes of the soil.....	154
Figure 7.19: Bending curvature applied on the shaft due to volumetric changes of the soil.....	155
Figure 7.20: Bending curvature applied on the shaft due to volumetric changes of the soil.....	155
Figure 7.21: Lateral deflections imposed by volumetric changes of the soil at different dates	156
Figure 7.22: Recorded mean daily temperatures at the project site throughout the two year monitoring period.....	158
Figure 7.23: Temperature induced axial strains along the shafts assuming linear thermal expansion	159
Figure 7.24: Simple model assumed to account for the differential thermal effects	161
Figure 7.25: Thermal strains on the tension and compression side	162
Figure 7.26: Temperature induced curvature for the selected dates	162
Figure 7.27: Temperature induced lateral deflections for the selected dates.....	163
Figure A.1: Residual strains at a depth of 1ft	170
Figure A.2: Residual strains at a depth of 3ft	170
Figure A.3: Residual strains at a depth of 7ft	171
Figure A.4: Residual strains at a depth of 9ft	171
Figure A.5: Residual strains at a depth of 11ft	172
Figure A.6: Residual strains at a depth of 13ft	172

Figure A.7: Residual strains at a depth of 15ft	173
Figure A.8: Residual strains at a depth of 17ft	173
Figure A.9: Residual strains at a depth of 21ft	174
Figure A.10: Residual strains at a depth of 23ft	174
Figure A.11: Residual strains at a depth of 27ft	175
Figure A.12: Residual strains at a depth of 29ft	175
Figure A.13: Residual stresses at a depth of 1ft	176
Figure A.14: Residual stresses at a depth of 3ft	176
Figure A.15: Residual stresses at a depth of 7ft	177
Figure A.16: Residual stresses at a depth of 9ft	177
Figure A.17: Residual stresses at a depth of 11ft	178
Figure A.18: Residual stresses at a depth of 13ft	178
Figure A.19: Residual stresses at a depth of 15ft	179
Figure A.20: Residual stresses at a depth of 17ft	179
Figure A.21: Residual stresses at a depth of 21ft	180
Figure A.22: Residual stresses at a depth of 23ft	180
Figure A.23: Residual stresses at a depth of 27ft	181
Figure A.24: Residual stresses at a depth of 29ft	181
Figure B.1: Strains throughout the monitoring period for the west shaft at a depth of 1ft.....	182
Figure B.2: Strains throughout the monitoring period for the west shaft at a depth of 3ft.....	182
Figure B.3: Strains throughout the monitoring period for the west shaft at a depth of 5ft.....	183

Figure B.4: Strains throughout the monitoring period for the west shaft at a depth of 7ft.....	183
Figure B.5: Strains throughout the monitoring period for the west shaft at a depth of 9ft.....	184
Figure B.6: Strains throughout the monitoring period for the west shaft at a depth of 11ft.....	184
Figure B.7: Strains throughout the monitoring period for the west shaft at a depth of 13ft.....	185
Figure B.8: Strains throughout the monitoring period for the west shaft at a depth of 15ft.....	185
Figure B.9: Strains throughout the monitoring period for the west shaft at a depth of 17ft.....	186
Figure B.10: Strains throughout the monitoring period for the west shaft at a depth of 19ft.....	186
Figure B.11: Strains throughout the monitoring period for the west shaft at a depth of 21ft.....	187
Figure B.12: Strains throughout the monitoring period for the west shaft at a depth of 23ft.....	187
Figure B.13: Strains throughout the monitoring period for the west shaft at a depth of 25ft.....	188
Figure B.14: Strains throughout the monitoring period for the west shaft at a depth of 27ft.....	188
Figure B.15: Strains throughout the monitoring period for the west shaft at a depth of 29ft.....	189

Figure B.16: Strains throughout the monitoring period for the center shaft at a depth of 1ft.....	190
Figure B.17: Strains throughout the monitoring period for the center shaft at a depth of 3ft.....	190
Figure B.18: Strains throughout the monitoring period for the center shaft at a depth of 5ft.....	191
Figure B.19: Strains throughout the monitoring period for the center shaft at a depth of 7ft.....	191
Figure B.20: Strains throughout the monitoring period for the center shaft at a depth of 9ft.....	192
Figure B.21: Strains throughout the monitoring period for the center shaft at a depth of 11ft.....	192
Figure B.22: Strains throughout the monitoring period for the center shaft at a depth of 13ft.....	193
Figure B.23: Strains throughout the monitoring period for the center shaft at a depth of 15ft.....	193
Figure B.24: Strains throughout the monitoring period for the center shaft at a depth of 17ft.....	194
Figure B.25: Strains throughout the monitoring period for the center shaft at a depth of 19ft.....	194
Figure B.27: Strains throughout the monitoring period for the center shaft at a depth of 21ft.....	195
Figure B.29: Strains throughout the monitoring period for the center shaft at a depth of 23ft.....	195

Figure B.30: Strains throughout the monitoring period for the center shaft at a depth of 25ft.....	196
Figure B.31: Strains throughout the monitoring period for the center shaft at a depth of 27ft.....	196
Figure B.32: Strains throughout the monitoring period for the center shaft at a depth of 29ft.....	197
Figure B.33: Strains throughout the monitoring period for the east shaft at a depth of 1ft.....	198
Figure B.34: Strains throughout the monitoring period for the east shaft at a depth of 3ft.....	198
Figure B.35: Strains throughout the monitoring period for the east shaft at a depth of 5ft.....	199
Figure B.36: Strains throughout the monitoring period for the east shaft at a depth of 7ft.....	199
Figure B.37: Strains throughout the monitoring period for the east shaft at a depth of 9ft.....	200
Figure B.38: Strains throughout the monitoring period for the east shaft at a depth of 11ft.....	200
Figure B.39: Strains throughout the monitoring period for the east shaft at a depth of 13ft.....	201
Figure B.40: Strains throughout the monitoring period for the east shaft at a depth of 15ft.....	201
Figure B.41: Strains throughout the monitoring period for the east shaft at a depth of 17ft.....	202

Figure B.42: Strains throughout the monitoring period for the east shaft at a depth of 19ft.....	202
Figure B.43: Strains throughout the monitoring period for the east shaft at a depth of 21ft.....	203
Figure B.44: Strains throughout the monitoring period for the east shaft at a depth of 23ft.....	203
Figure B.45: Strains throughout the monitoring period for the east shaft at a depth of 25ft.....	204
Figure B.46: Strains throughout the monitoring period for the east shaft at a depth of 27ft.....	204
Figure B.47: Strains throughout the monitoring period for the east shaft at a depth of 29ft.....	205
Figure B.48: Processed strains throughout the monitoring period at a depth of 1ft.....	206
Figure B.49: Processed strains throughout the monitoring period at a depth of 3ft.....	206
Figure B.50: Processed strains throughout the monitoring period at a depth of 7ft.....	207
Figure B.51: Processed strains throughout the monitoring period at a depth of 9ft.....	207
Figure B.52: Processed strains throughout the monitoring period at a depth of 11ft.....	208
Figure B.53: Processed strains throughout the monitoring period at a depth of 13ft.....	208
Figure B.54: Processed strains throughout the monitoring period at a depth of 15ft.....	209
Figure B.55: Processed strains throughout the monitoring period at a depth of 17ft.....	209
Figure B.56: Processed strains throughout the monitoring period at a depth of 21ft.....	210
Figure B.57: Processed strains throughout the monitoring period at a depth of 23ft.....	210
Figure B.58: Processed strains throughout the monitoring period at a depth of 27ft.....	211
Figure B.59: Processed strains throughout the monitoring period at a depth of 29ft.....	211

Chapter 1: Introduction

1.1: Motivation

Drilled shaft retaining walls are common types of earth retaining structures widely used around the state of Texas especially by the Texas Department of Transportation (TxDOT). They are durable and resilient under different environmental conditions and they can be constructed in a variety of soil deposits. Extensive research has been conducted and theories including those by Coulomb and Rankine have been developed to predict the earth pressures applied on these walls for normally consolidated or overconsolidated clays of low plasticity. Nevertheless considerable uncertainty still exists for the case of expansive clays.

Expansive clays are very challenging materials for geotechnical engineers. Due to their high plasticity index, they are subjected to shrinking and swelling during cycles of moisture fluctuation. This dynamic behavior over time is responsible for billions of dollars per year in structural damages at various constructions within the United States (Jones and Holtz, 1973). Studies have been and are being conducted to better understand the basis of this behavior and to establish design procedures that account for extensive soil movements. Also, over geologic times such soils experienced excessive stresses due to desiccation and became highly overconsolidated. They are characterized by a secondary structure of slickensided fissures, mineral-filled bands and micro-cracks that significantly affect their shear strength and permeability in a macro scale consideration.

The reliable estimation of the lateral earth pressures applied on drilled shaft retaining walls in expansive clay is important during design. While empirical approaches

exist, there is uncertainty on how the cycles of shrinking and swelling of the soil affect the earth pressures. Current design procedures for the Texas Department of Transportation (TxDOT) use an equivalent fluid pressure of 40 psf/ft while practicing engineers are in some cases more conservative using an equivalent fluid pressures of 80 to more than 100 psf/ft.

The above considerations can lead to substantial variations in estimating the maximum shaft bending moments and required shaft diameters. Hence, more insight would be valuable to accurately predict the earth pressures that generate the bending moments developed in the shafts.

1.2: TxDOT project - Lymon C. Reese research wall

Texas Department of Transportation (TxDOT) has provided funding to the University of Texas at Austin in order to investigate the effect on shrinking and swelling of the highly plastic clays on drilled shaft retaining walls and to develop recommendations on the earth pressure diagrams to be used in design.

A research wall named in the honor of Lymon C. Reese was constructed for this purpose in the highly expansive clay of the Taylor formation in Manor. This wall consists of 25 drilled shafts and has a 15 ft cantilever section. A full scale instrumentation program was established in order to monitor the wall for several years. Inclined meters and optical fiber strain gauges were installed in three of the shafts while an additional inclinometer was placed a few feet behind the wall. The instrumentation program also includes time domain reflectometry (TDR) sensors that measure changes in the moisture content, piezometers to monitor the ground water level, a linear potentiometer to measure lateral deflections at the top of the center shaft and thermocouples embedded in the shafts

to measure temperature within the concrete. A rain gauge was also installed to record precipitation at the project site.

In the future and due to limited rainfall events at the project site during the first two years of monitoring, an inundation berm will be constructed behind the wall. The berm will be filled with water which will cause extensive swelling of the Taylor clay. In such case, an upper bound of the earth pressure distribution will be predicted for design purposes.

1.3: Objectives of the Thesis

The objectives of this thesis are summarized below:

- Estimation of the residual stresses and strains developed in the drilled shafts during and after concrete curing up until the time the soil was excavated.
- Prediction of the magnitude and shape of the earth pressure distribution at different times using the results of the instrumentation program.
- Prediction of the range of lateral earth pressures applied on the wall using a p-y model.
- Estimation of the effect of axial side shear due to volumetric changes of the soil on the lateral response of the drilled shafts.
- Estimation of thermal effects on the lateral response of the drilled shafts.

In addition to the above, the quality of the instrumentation data is evaluated by comparing the deflected shapes generated from the strain gauges and inclinometers for the same moisture conditions of the soil. Bending moment and curvature profiles are developed from both monitoring elements and the maximum moments experienced by the drilled shafts are estimated for design purposes.

With respect to the p-y model, a triangular earth pressure distribution above the excavation level is assumed as external load. This assumption is in accordance to the current design procedures followed by TxDOT for drilled shaft retaining walls in expansive clay. The equivalent fluid pressures derived from the results of the p-y analysis for different moisture conditions are compared to the empirical suggestions by TxDOT.

Finally, using a linear thermal model, the temperature effects (T) on the lateral response of the wall are quantified and compared to the curvature induced by side shear (t) which is predicted using a t-z model. Design recommendations are given to incorporate the combined effect of temperature and side shear.

1.4: Organization of the Thesis

This thesis is divided into seven chapters. The first chapter includes introductory information about the description and objectives of this project. The second chapter is a literature review of the different ways to solve the differential equation that describes a laterally loaded pile and the different methods used to interpret the instrumentation data. The basis of the p-y and t-z analysis is also presented. Chapter three includes background information about the geometrical characteristics of the research wall and the layout of the instrumentation program. Useful data from the results of the geotechnical investigation of the Taylor clay are also included in this chapter.

Chapter four is related to analyzing the results of the instrumentation program. The performance of the monitoring elements is evaluated by comparing the deflected shapes and moment profiles derived using the inclinometer and strain gauge data. Residual stresses and strains are evaluated and their significance in the behavior of the wall is discussed. Chapter five deals with the prediction of the earth pressures applied on

the shafts using a p-y model. In chapter six, a t-z analysis is conducted to evaluate the significance of the side shear generated by volumetric changes of the soil on the lateral response of the drilled shafts. The importance of the temperature fluctuations on the excavated side is also studied. Finally in chapter seven, conclusions from the various types of analysis are summarized and recommendations are given for future work.

Chapter 2: Literature Review

2.1: Drilled shaft retaining walls

Drilled shaft retaining walls consist of a number of drilled shafts that are either tangent, secant or separated from each other to a specified distance. Drilled shafts are reinforced concrete elements cast in previously excavated drilled holes. Their dimensions and reinforcement layout are determined based on the project requirements and the expected earth pressures. The construction sequence includes drilling the hole, placing the reinforcing bar cage and pouring the concrete. The excavation is usually scheduled after sufficient time is allowed for the concrete to cure and to reach its specified strength.

Drilled shaft retaining walls belong to the category of externally stabilized cut walls, because the drilled shafts apply external forces on the soil mass to retain it. Moreover, since the excavation starts from the ground surface the construction sequence follows a "top-down" method. An estimated construction cost according to FHWA is \$430 - \$810 per square meter of wall face which includes the cost of concrete, reinforcing elements, facing panels (which are prefabricated or CIP), anchors, labor, equipment and wall construction.

Drilled shaft retaining walls have many potential advantages and disadvantages that determine their suitability for a specific project. First of all, the expected displacements are limited and thus they are highly recommended for urban environments where the existence of nearby structures imposes strict requirements on the expected deflections. In the case of secant pile walls, adequate water tightness is achieved which is a significant factor depending on the depth of the ground water table. Moreover,

significant horizontal curvatures can be followed in contrast to other type of retaining structures such as semi-gravity cantilever walls.

However, several limitations may prevent the contractor from selecting drilled shaft retaining walls for a specific project. Such walls consist] of concrete elements, which may require significant time to cure. In addition, heavy equipment must be mobilized to pour the concrete and place the reinforcing bar cages in the shafts. Hence, apart from the increased construction cost, drilled shaft retaining walls are generally used only for permanent applications.

2.2: Analytical methods of analyzing laterally loaded drilled shafts

Drilled shaft retaining walls consist of several drilled shafts that retain the soil while their resistance to lateral deflections is defined by their bending stiffness. The structural behavior of a drilled shaft in such walls is similar to those used as deep foundation elements with the only difference being the absence of the soil at the excavated side. The problem is based on soil structure interaction theory and a solution is obtained by solving a differential equation describing the deflected shape of a beam subjected to a distributed load from the soil. Due to the non-linear behavior of the soil and the drilled shafts, iterations are required to obtain a solution for a particular loading case.

In common soil deposits, the axial forces applied on the shafts are close to zero as they are generated only by the concrete weight. If such structures are constructed on expansive clays, axial loads may also be induced by side shear developed at the interface between the soil and the shafts. This side shear is caused by volumetric changes of the

soil during cycles of moisture fluctuations and is expected to interact with the lateral movement of the wall.

From the results of full scale, centrifuge and model tests researchers have recommended several methods for analyzing the behavior of laterally loaded drilled shafts. Among them, the most widely known are the following:

1. To relate the load-displacement response of a transversely loaded beam, Winkler (1867) correlated the subgrade resistance to the linear characteristics of a number of springs that simulate the soil stiffness. The response of the beam is similar to piles subjected to lateral loading.
2. The most popular and widely used method for analyzing laterally loaded piles includes the use of p-y curves to simulate the resistance of the soil to lateral movements. In this method, Matlock (1970) and Reese (1974) modified the Winkler approach by representing the soil as a non-linear characteristic material. In addition, the non-linear response of the drilled shafts is simulated in the analysis.
3. Finite element and finite difference methods where the soil-structure interaction problem is numerically modeled can also provide reliable solutions and save computational time. Several computer programs were developed and are available in the market. They can take into account the non-linearity and non-homogeneity of the soil, along with soil-pile interaction effects.

As indicated above, the method that uses p-y curves to simulate the non-linear behavior of the soil is the most popular in practice and is described in detail in the following sections.

2.3: Derivation of the differential equation

The governing differential equation is derived in the basis of the "beam on a foundation" theory (Hetenyi, 1946). In this theory, we assume that we have a bar on an elastic foundation subjected to a distributed horizontal load (w) and a pair of compressive forces (P_x) acting on the edges of the bar as indicated in figure 2.1.

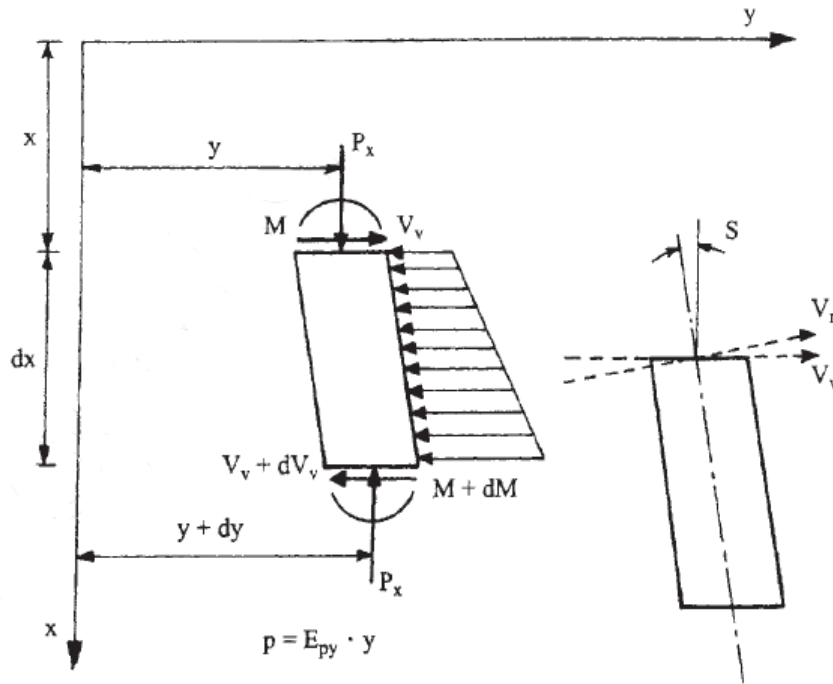


Figure 2.1: Infinitesimal element from the "beam column on a foundation" theory (Hetenyi, 1946)

By taking the moment equilibrium of an infinitesimally small element and by differentiating both sides of the equation with respect to x , we get the following differential equation:

$$E_p I_p \frac{d^4 y}{dx^4} + P_x \frac{d^2 y}{dx^2} - p + w = 0 \dots\dots\dots(2.1)$$

where:

- E_p = modulus of elasticity of the pile (lbs/in.²)
- I_p = moment of inertia of the pile (in.⁴)
- y = lateral deflection of the pile perpendicular to its longitudinal axis (in.)
- x = distance along the longitudinal axis of the pile (in.)
- P_x = axial load of the pile (lbs)
- p = reaction of the soil against the pile (lbs/in.)
- w = distributed load along the longitudinal axis of the pile (lbs/in.)
- E_{ps} = modulus of soil reaction (lbs/in.²)

In the above equation we should note the following:

$$\theta = \frac{dy}{dx} \dots\dots\dots(2.2)$$

$$\varphi = \frac{d^2y}{dx^2} = \frac{M}{E_p I_p} \dots\dots\dots(2.3)$$

$$M = E_p I_p \frac{d\theta}{dx} = E_p I_p \frac{d^2y}{dx^2} \dots\dots\dots(2.4)$$

$$V = \frac{dM}{dx} \dots\dots\dots(2.5)$$

$$p = \frac{d^2M}{dx^2} = E_{ps} y \dots\dots\dots(2.6)$$

In order to solve the above differential equation we need to apply boundary conditions. The boundary conditions used in this project are the known deflection at the top of the wall and the zero deflection at the tip of the shafts. Several assumption that are used to make the solution feasible are the following:

1. The pile has a uniform cross-section and is initially straight.

2. The pile has a longitudinal symmetry plane and the various loads are applied in that plane.
3. The material of the pile (concrete and steel reinforcing bar cage) is homogeneous and isotropic.
4. The modulus of elasticity of the pile material is the same in tension and compression.
5. Transverse deflections of the pile are small.

A complete solution of the differential equation would yield values of lateral deflection, slope, moment, shear and soil reaction along the shaft such as those depicted in figure 2.2. The mathematic relationships for the various curves are given in the shape figure for the case where no axial loads are applied on the pile.

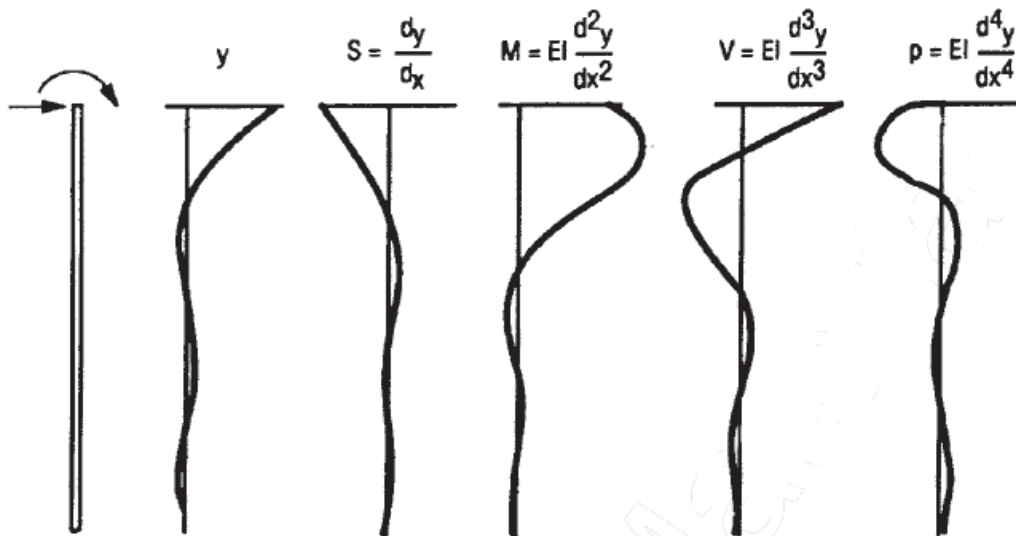


Figure 2.2: Typical results from the solution of the differential equation for a laterally loaded pile with zero axial load (Reese et al., 2006)

2.4: Winkler approach - Elastic soil behavior

A very simple method of analyzing the behavior of a foundation element under lateral loading is the Winkler Approach, based on the "beam on a foundation" theory. The assumptions that Winkler used in this method are the following:

1. The soil acts as a series of closely spaced, discrete and linear elastic springs
2. There is no coupling between the adjacent soil elements.
3. The soil deforms only under the loaded area.

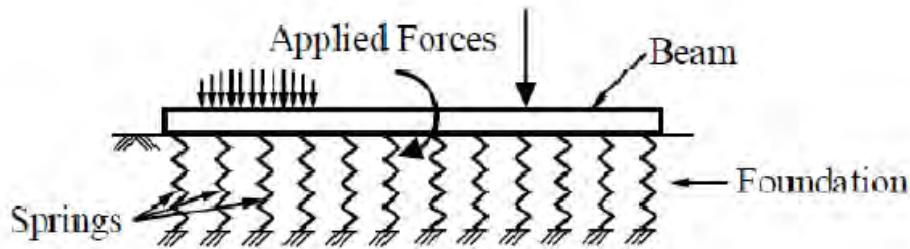


Figure 2.3: Winkler assumption for a beam lying on elastic soil (Winkler, 1867)

Winkler (1867) suggested that the resistance of the subgrade against lateral external forces is proportional to the ground deflection given that the soil is modeled as a set of linear elastic springs. In such case, the elastic deflection of each spring represents the displacement of the beam under the applied load. The spring coefficient depicts the material properties of the soil and is known as the coefficient of subgrade reaction (k).

As indicated in the above figure, the force on each spring is given by Hooke's law as illustrated in the following equation:

$$F = ky \dots\dots\dots(2.7)$$

where:

- F = force on each spring (lbs)
- k = spring stiffness coefficient (lbs/in.)
- y = spring or ground displacement (in.)

According to Hetenyi (1946), Winkler's assumption is often more representative of the actual conditions in the field than more complicated analytical methods. Other researchers such as Davisson (1970) and Mattlock and Reese (1956), applied Winkler's approach on laterally loaded piles by considering the pile as a laterally loaded beam against lateral loading. A limitation of Winkler's model is that the soil is assumed to behave elastically. In reality this is true only for very small strains. Subsequently, several models were developed that account for the non-linear behavior of different soil types.

2.5: Analytical methods using p-y curves - Non-linear soil behavior

The accuracy of the solution of the differential equation derived previously depends on estimating the soil resistance on lateral deflections of the pile. Hence, the modulus of soil reaction (E_{py}) that represents the stiffness of the soil is a very important parameter that should be evaluated with caution. This modulus of soil reaction to lateral pile movements decreases with increasing displacements, and by plotting the soil reaction (p) for different pile deflections (y) the p-y curves are generated. These curves, which are the most significant tool in analyzing laterally loaded piles, depend on the soil properties and can be affected by the overburden pressure and depth below the ground surface.

To better understand the nature of the p-y curves, the state of stress around a cross-section of the pile is examined. As indicated in figure 2.4, as long as the pile remains vertical with zero lateral deflection, the distribution of unit stresses around it

remains uniform. Once lateral deflections (y_1) are induced, the stress distribution is no longer uniform and the bulb of stresses is displaced towards the direction of movement. By integrating the unit stresses, the values of the soil resistance are evaluated.

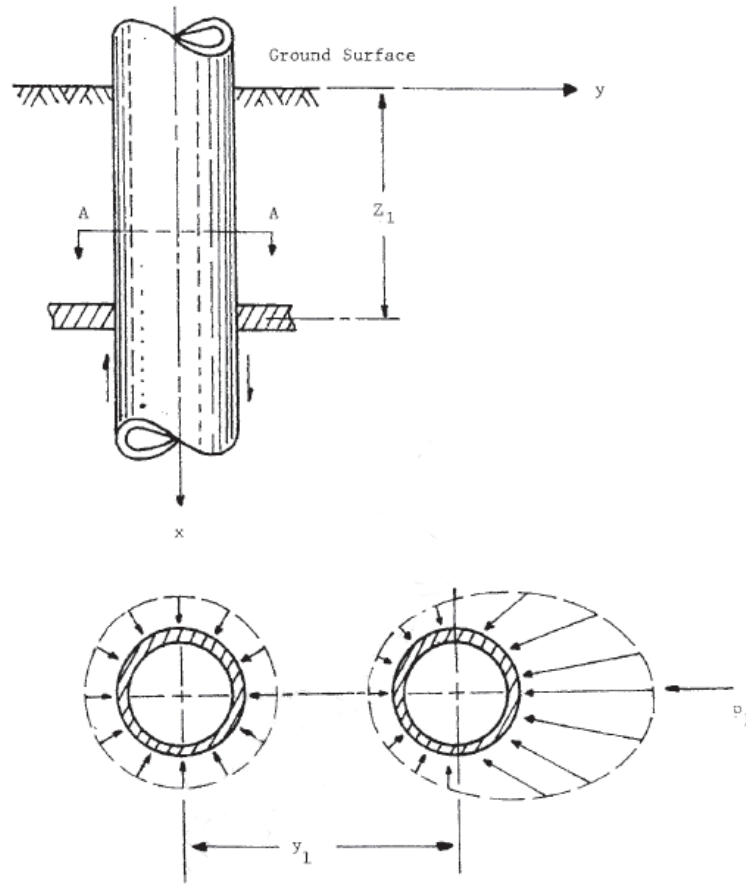


Figure 2.4: Distribution of the unit stresses on a random cross-section of the pile before and after lateral deflection occurs (Reese et al., 2006)

The soil resistance varies significantly along the pile, because it is a function of its lateral displacements. In more general cases where the pile is subjected to lateral loads, axial loads and bending moments, the solution of the differential equation becomes more complicated. A possible deflected shape derived from the solution of the differential

equation and an estimation of the soil resistance depicted on various p-y curves along the pile are presented in figure 2.5.

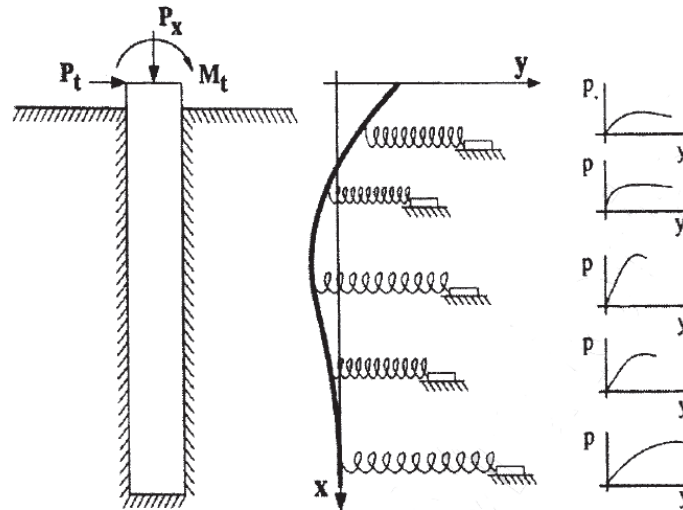


Figure 2.5: Soil response under combined loading conditions of the pile (Reese et al., 2006)

Numerous methods were developed for deriving p-y curves from the results of field load or laboratory tests. According to Smith and Slyh (1986), when lateral loads are applied on the pile, the soil resistance is a function of the following components:

1. Frictional resistance developed by tangential interface stresses; this is also called side shear (F).
2. Soil resistance at the front side of the pile in the form of passive earth pressures (Q).

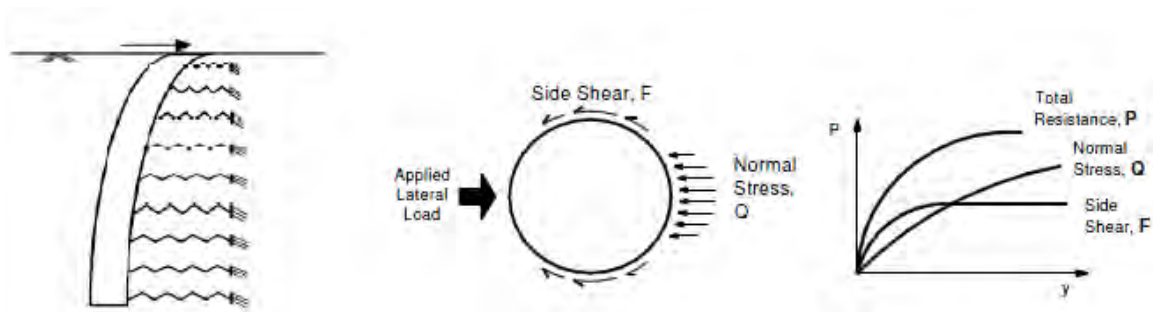


Figure 2.6: Mechanisms of soil resistance on a laterally loaded pile (Smith and Slyh, 1986)

McClelland and Focht (1958) correlated the p-y curves to the stress strain relationships obtained from triaxial laboratory tests. According to their theory, the ultimate lateral soil resistance which is a very important parameter in the p-y relationship, is given by the following equation:

$$P_u = 5.5B\sigma_{\Delta} \dots\dots\dots(2.8)$$

where:

- P_u = ultimate soil resistance (lbs)
- B = diameter of the pile (in.)
- σ_{Δ} = deviatoric stress from the triaxial test results at a displacement (y) equal to $B \cdot \varepsilon / 2$ and a confining pressure equal to the overburden stress (psi)

Reese and Matlock (1960), incorporated the non-linear behavior of the soil in Winkler's model, by simulating the pile as a flexible beam and the soil as a set of independent non-linear springs. The characteristics of these springs represent the non-linear resistance of the soil to lateral deflections of the pile. They used finite differences to solve the problem by dividing the pile into equidimensional elements and assuming that the pile stiffness and the modulus of soil reaction vary arbitrarily with depth. In addition, the stiffness of the drilled shafts vary as well. Their solution requires iterations with incremental application of the elastic theory by adjusting the modulus of soil reaction (E_{py}) until the soil reaction (p) and the lateral deflection (y) of the pile are compatible with the actual properties of the soil. To date, this method is the most commonly used as it provides a reliable estimate of the response of a pile subjected to lateral loading.

2.6 Developing p-y curves for cohesive soils under undrained conditions

Different mathematical functions can be used to describe the non-linear p-y relationship for different types of clay under undrained conditions. Power, exponential and hyperbolic functions are most commonly used for this purpose. They consist of an initial straight portion that indicates the initial elastic response, followed by a parabola that reflects the non-linearity of the soil. While the elastic response can easily be evaluated through the respective portion of the stress-strain curves from typical laboratory tests, for the second part there is no analytical solution that could predict its exact shape. Hence, the above mathematical functions are used to represent this non-linear portion of the p-y curves. Another straight line at the end indicates that when the soil resistance reaches its ultimate value, at which the behavior of the soil is perfectly plastic as it experiences no loss of shear strength with increasing strains. A typical shape of a p-y curve along with estimates of the elastic clay stiffness on laterally loaded piles are presented below.

Table 2.1: Representative values of the initial clay stiffness on laterally loaded piles

<i>Representative Values of K_{py} for Clays</i>			
Average Undrained Shear Strength (Kpa)	50 - 100	200 - 300	300 - 400
K_{py} (static) - MN/m ³	135	270	540
K_{py} (static) - lbs/in ³	500	1000	2000
K_{py} (cyclic) - MN/m ³	55	110	540
K_{py} (static) - lbs/in ³	200	400	2000

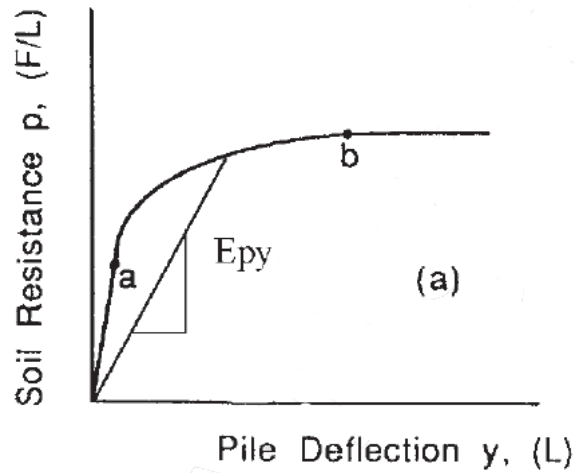


Figure 2.7: Typical shape of the p-y curve showing the soil resistance to lateral pile deflections (Reese et al., 2006)

The p-y relationship is unique for each clay type and depends on several parameters such as the shear strength, the moisture conditions, the effective stresses and the stress history. Moreover, it is different for short-term static, sustained, cyclic and dynamic loading. Since the p-y curves depend on the properties of the in situ soil, using a single curve for various depths is not representative to the actual field conditions. To deal with this problem we can either use a model in which different p-y curves are simulated at various depths or account for a normalized p-y curve to the ultimate soil resistance.

To evaluate the ultimate soil resistance, the modes of failure are hypothesized. Near the surface, the failure mechanism is described by a passive wedge of soil moving upwards and outwards of the pile, while at bigger depths the soil fails by flowing around it. The effective unit weight and the shear strength of the soil along with the width of the pile determine the depth of transition between the two failure mechanisms.

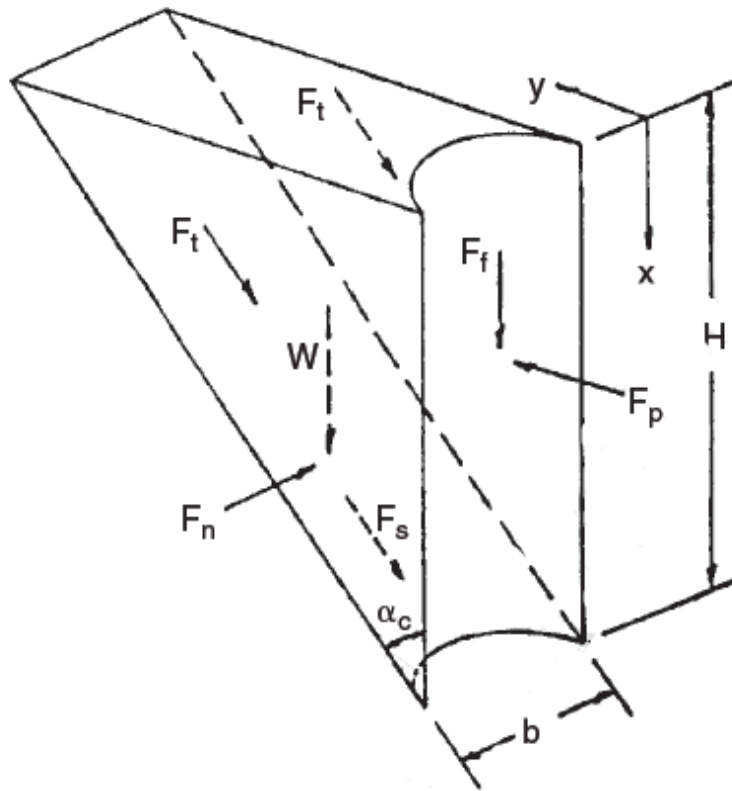


Figure 2.8: Wedge failure of the soil near the ground surface for clays (Reese, 1962)

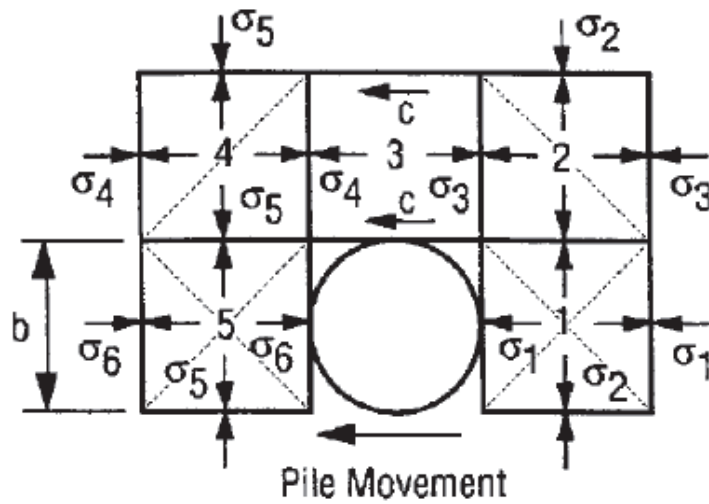


Figure 2.9: Mode of failure of lateral flow around a pile in clay (Reese, 1962)

According to Matlock (1970), the ultimate soil resistance of a clay profile under undrained loading is only reached at a very small area near the ground surface and thus the structural capacity of the pile defines failure at larger depths. However, it should be evaluated in order to define the soil deformability characteristics. For a confined soft clay, plastic flow is restricted to occur horizontally and the following equation is used to predict the ultimate resistance of the soil:

$$P_u = N_p cd \dots\dots\dots(2.9)$$

where:

- P_u = ultimate soil resistance (lbs)
- N_p = non-dimensional bearing capacity factor
- d = diameter of the pile (ft)
- c = undrained shear strength (psf)

With respect to the non-dimensional ultimate resistance coefficient, a value of $N_p = 9$ is recommended for soft clays when the soil flows horizontally around a cylindrical pile. In contrast, very near the surface where the failure mode is similar to a wedge type of failure, this coefficient is reduced to $N_p = 3$. Therefore, the value of the ultimate clay resistance increases with depth until it reaches its maximum value at a depth x_r where $N_p = 9$. This is called the depth of reduced resistance. Until this depth the resistance of the soil to vertical movement is mainly due to the overburden pressure and the deformations of the surrounding soil mass. For this upper soil layer, the non-dimensional ultimate resistance coefficient is given by the following equation:

$$N_p = 3 + \frac{\sigma_x}{c} + J \frac{x}{d} \dots\dots\dots(2.10)$$

where:

- σ_x = overburden pressure (psf)
- J = non-dimensional coefficient related to the soil type
- x = depth below the ground surface (ft)

In the above equation, the first term is the part of soil resistance near the ground surface, the second term indicates the increase in soil resistance due to the overburden pressure and the third term is related to geometrical constraints on the upward soil movement which are not affected by the soil weight. This equation is similar to the one used by Reese (1960) to describe the soil resistance to a wedge mode of failure as indicated in the following relationship:

$$P_u = N_p cd = \left(3 + \frac{\sigma_x}{c} + 2.83 \frac{x}{d} \right) cd \dots\dots\dots(2.11)$$

The only difference between the two equations, is that in the above relationship the coefficient J equals to 2.83 which is not in accordance to the experimental results by Mattlock (1960), based on which he suggested values of $J = 0.5$ for normally consolidated clays and $J = 0.25$ for stiff fissured clays. Finally, given that the shear strength and the effective unit weight are constant, the depth of reduced resistance x_r , is evaluate using the following equation:

$$x_r = \frac{6d}{\frac{\gamma d}{c} + J} \dots\dots\dots(2.12)$$

We should keep in mind that the above relationship is not suitable for cases where the undrained shear strength vary considerably with depth. In such cases, a system of thin layers is used and the value of x_r is evaluated separately for each layer.

2.7 Recommended p-y curve for stiff fissured clays from field load tests

While significant information about the initial stiffness and the ultimate soil resistance are obtained by analyzing the failure mechanisms of the soil around a laterally loaded pile, the development of p-y curves is mainly based on empirical fits from full scale lateral load tests on instrumented piles. The instrumentation program most commonly includes an inclinometer and pairs of strain gauges at close intervals along the pile that are used to directly generate the curvature and bending stresses. From these results, the lateral deflections and the associated soil resistances along the pile are obtained. By repeating the same process for different loading scenarios and by plotting the soil resistance (p) versus lateral deflections (y), a family of p-y curves is generated.

There are four different loading conditions that affect the response of the soil around a laterally loaded pile which are presented below. For each of those, a unique normalized p-y curve is generated from the results of the respective full scale lateral load tests.

1. Short-term static loading
2. Dynamic loading
3. Sustained loading
4. Repeated loading

The above loading conditions are an important design consideration. For example seismic events and vibrations from machines impose dynamic loading conditions. An additional discrimination refers to the presence of free water. For the purpose of this thesis, only the case of short-term monotonic loading or "static loading" in the absence of free water is used. Examples of the various shapes of the p-y curves for different loading conditions are presented in figure 2.10.

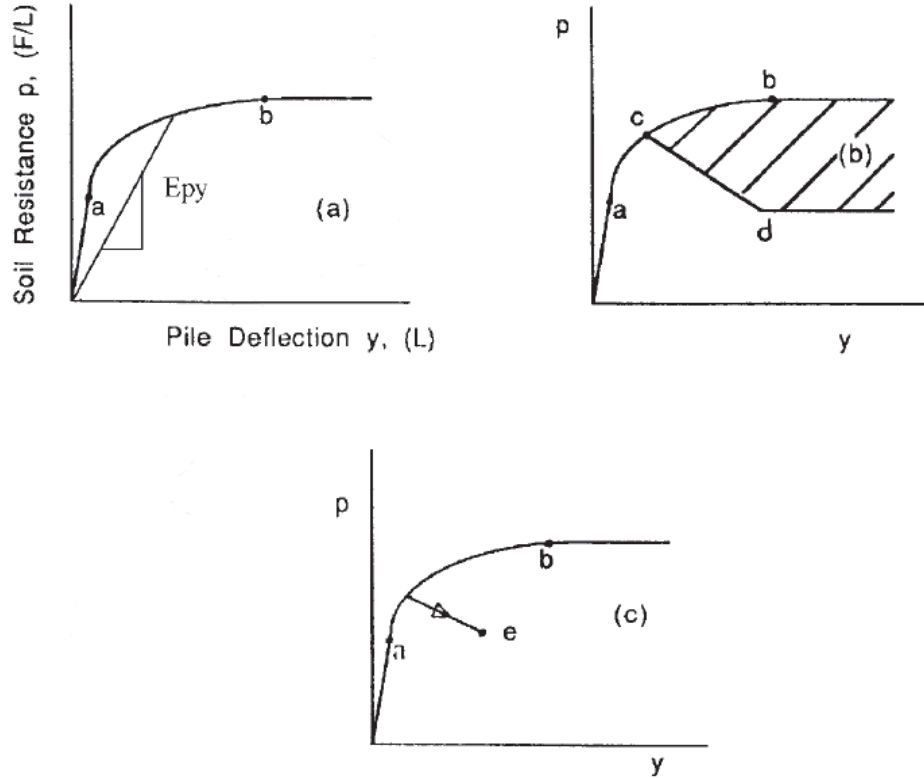


Figure 2.10: Effect of different loading conditions on the p-y curves: (a) short-term monotonic loading; (b) effect of cyclic loading; (c) possible effect of sustained loading (Reese et al., 2006)

Expansive clays belong to the family of highly overconsolidated, stiff fissured clays. Based on the results of full scale field tests on this type of soil, recommended p-y curves have been developed to model the response of laterally loaded piles. According to Welch and Reese (1972), the following procedure is used to estimate the p-y relationship of stiff clays:

1. Use field or laboratory tests to obtain the profile of undrained shear strength. From the stress strain curves, obtain the value of ϵ_{50} which refers to the strain at 50% of the maximum principal stress difference ($\sigma_{d,max}$).

2. Evaluate the ultimate soil resistance per unit length of the pile using the following relationship:

$$p_u = \min \left[\left(3 + \frac{\gamma'}{c} + J \frac{z}{b} \right) cb, 9cb \right] \dots\dots\dots(2.16)$$

where:

- γ' = submerged unit weight (psf)
- J = non-dimensional coefficient related to the soil type
- z = depth below the ground surface (ft)
- b = pile diameter (ft)
- c = undrained shear strength of the soft clay (psf)

For stiff clays we assume that $J=0.25$.

3. Evaluate the deflection at 50% of the ultimate soil resistance using the following equation:

$$y_{50} = 2.5 \varepsilon_{50} b \dots\dots\dots(2.14)$$

where:

- ε_{50} = strain at 50% of the maximum principal stress difference

4. The p-y curve up the point where the soil reaches its ultimate resistance is expressed by the following equation:

$$\frac{p}{p_u} = 0.5 \left(\frac{y}{y_{50}} \right)^{0.25} \dots\dots\dots(2.15)$$

1. The soil resistance (p) remains constant for the last part of the curve where the soil behaves plastically. Such conditions occur for big lateral displacements beyond a value of $y = 18y_{50}$.

The above procedure is depicted in figure 2.11.

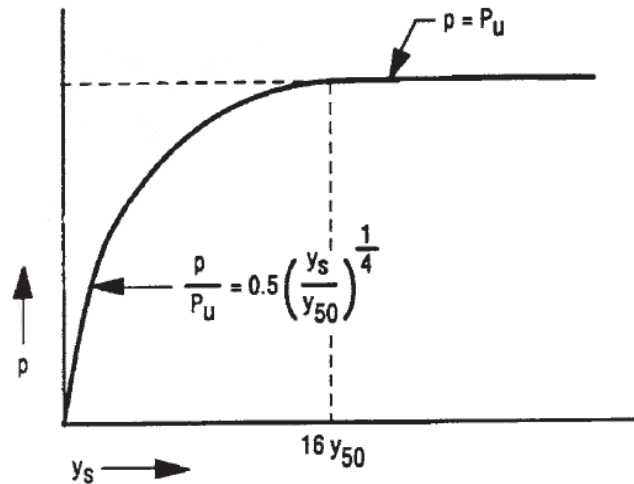


Figure 2.11: Characteristic shape of the p-y curve for stiff overconsolidated clay (Welch and Reese, 1972)

2.8: Numerical modeling of laterally loaded piles

Several computer programs are available in the market for simulating piles subjected to lateral loading. Such programs use finite element or finite difference techniques and are able to simulate the non-linear characteristics of the soil and pile. Examples of such programs include LPILE (Reese et al., 1997), FLPIER (McVay et al., 1996) and ABACUS which are described in the following paragraphs.

2.8.1: Computer programs based on finite difference methods

Finite difference methods are used to overcome several limitations on solving the differential equation due to the complexity of the model. The main advantages of using such methods to solve the problem of laterally loaded piles are presented below:

1. A unique p-y curve is used at every element along the pile.

2. Non-linear behavior of the pile is assumed using the respective bending moment - bending stiffness diagram.
3. Distributed loads from either lateral earth pressures or flowing water can be taken into account.
4. The effect of axial loading can be considered in the analysis.
5. The boundary conditions can vary to account for different cases at various practical applications.
6. Rapid solutions are obtained that allow the investigator to conduct sensitivity analysis and estimate the effect of different parameters on the final response of the pile.
7. Incremental loading allows the investigation of plastic hinge development on the pile at the point of the maximum bending moment.

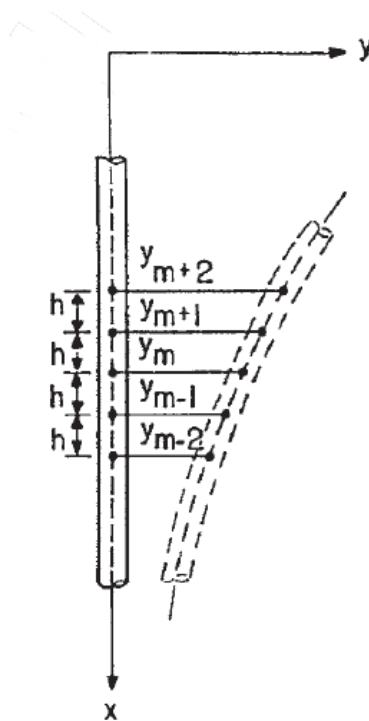


Figure 2.12: Computer representation of a deflected pile using finite difference methods (Reese et al., 2006)

A widely known computer program that uses finite difference techniques to solve the problem of laterally loaded piles is LPILE. This program simulates the pile as a beam which lateral stiffness is based on its modulus of elasticity and moment of inertia. The soil is model with a series of non-linear springs, one for each element. The stiffness of the pile is assumed to be non-linear using the appropriate bending moment - bending stiffness diagram.

The required input information refer to the structural properties of the pile and the geotechnical properties of the soil layers. Recommended p-y curves are including in the program for different soil types, while the user have also the option of inputting them manually. The output file includes the displacement, shear and moment profiles along the laterally loaded pile.

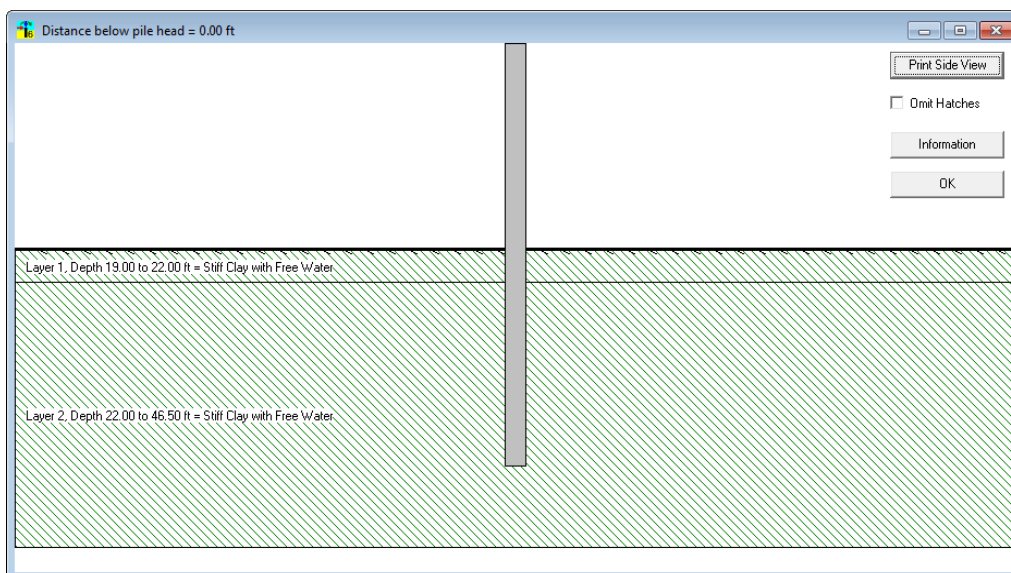


Figure 2.13: Analysis of a drilled shaft retaining wall using LPILE

In the case of drilled shaft retaining walls, the earth pressures are simulated as an external lateral load distributed along the cantilever section. Most commonly this distributed load is assumed to be triangular.

2.8.2: Computer programs based on finite element methods

Finite element techniques are also used to simulate the response of laterally loaded piles. The finite element programs simulate the pile and the soil mass with a number of triangular or rectangular finite elements with predefined degrees of freedom. In addition, the ability to use three dimensional elements is provided in some cases which allows the investigation of more complex geometries.

The finite element grid is generated automatically in most programs while a variety of constitutive models is available to describe the particular non-linear response of the different soil types. The yield function of each model indicates failure in terms of plastic behavior while the flow rule defines the deformability of the soil subjected to the various external or internal loads.

Finite element programs can also take into account soil structure interaction effects between the soil and the pile by using the appropriate p-y relationship. Interface forces due to swelling of the expansive clay can be simulated. Finally, reliable solutions are obtained including the deformed mesh and the final response of the pile in terms of deflections, shear forces and bending moments.

For the purpose of this project, ABACUS was used to simulate the response of the drilled shaft retaining wall. The soil properties along with the stiffness of the pile are used as input parameters and numerous results are obtained. The earth pressures applied on the wall are estimated by matching the deflected shape of the shafts to the inclinometer data. Another non-linear finite element program that could be used in this project is FLPIER that was developed at the University of Florida for analyzing bridge pier structures. This program is flexible as it can model different pile and pier configurations.

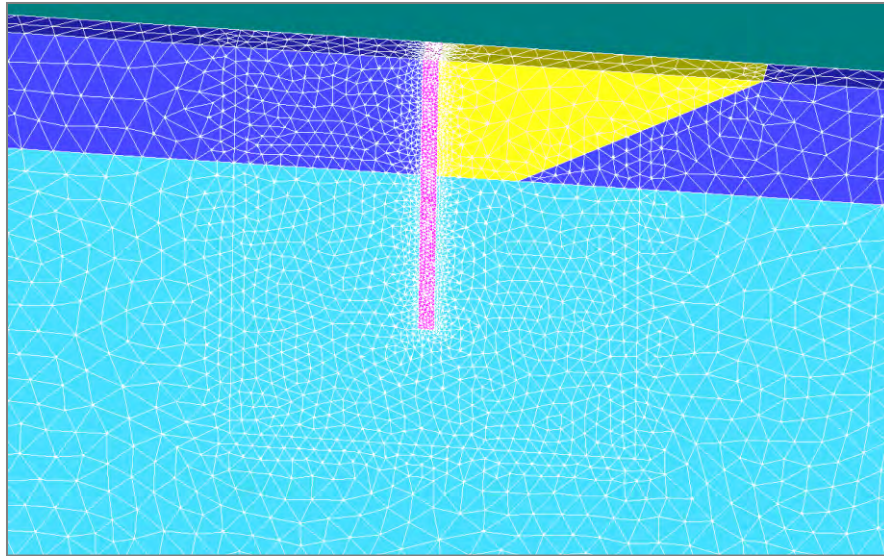


Figure 2.14: Simulation of the drilled shaft retaining wall using ABACUS (Brown et al., 2011)

2.9: Effect of axial loads on laterally loaded piles

When piles are constructed in clays of low plasticity the axial loads induced by the soil are negligible. However, in expansive soils significant axial loads are generated due to volumetric changes of the clay. These axial loads can either be compressive (downdrag) or tensile (uplift) depending on whether the soil shrinks or swells.

The structural capacity of piles in expansive clay may be affected by this side shear as the axial loads are different than those expected to be developed from the overlying structure. Especially in the case of drilled shaft retaining walls, where the axial loads are close to zero, the shaft could be in tension during swelling of the clay and thus jeopardize its structural integrity. This phenomenon will be examined later in this thesis.

The most common method to analyze the displacement characteristics of axially loaded piles is the "load-transfer" or "t-z" method (Seed and Reese, 1957). This method accounts for the load transfer mechanisms in side resistance along the length of the pile and in end bearing at its tip. Finite difference techniques are used and iterative procedures

are required to achieve compatibility between pile displacements and load transfer along the pile and between displacements and end bearing resistance at its tip.

According to the t-z method, the load transfer mechanism at a certain point along the pile is independent to the pile displacement at any other point. In addition, at each element distinct load transfer curves for side resistance are simulated. At the tip of the pile, a load transfer curve for end bearing is generated that represents the stiffness of the soil at this depth.

2.9.1: Differential equation describing an axially loaded pile

Consider an element dx subjected to an axial load (P). The axial strains in that element are given by the following equation:

$$P = -EA \frac{dz}{dx} \dots\dots\dots(2.22)$$

where:

- P = axial force in the element (lbs)
- E = Young's modulus of the pile (psi)
- A = Cross-sectional area of the pile (in²)

Using the modulus μ from the load transfer curve as indicated in figure 19, the total load transfer through the element dx is evaluated from the following relationship:

$$\frac{dP}{dx} = -\mu z l \dots\dots\dots(2.23)$$

where:

- l = circumference of a cylindrical pile (in)
- μ = modulus in the load transfer curve

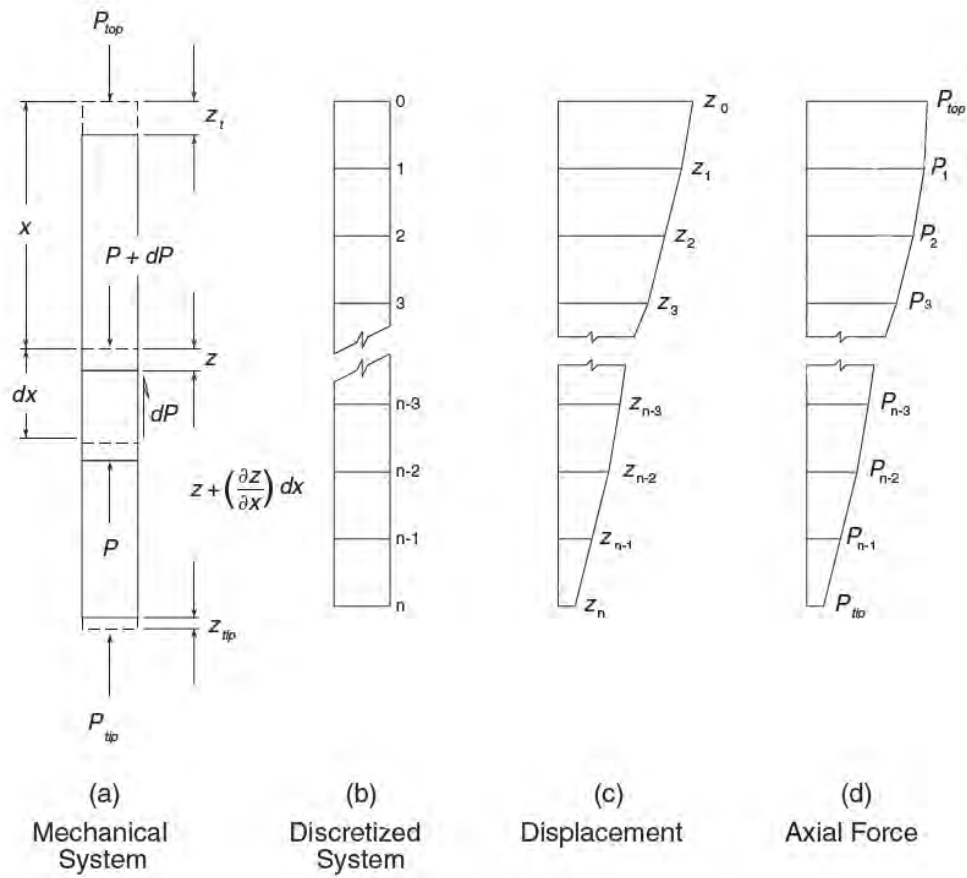


Figure 2.15: Numerical model of a pile subjected to axial load using finite difference techniques (Reese et al., 2006)

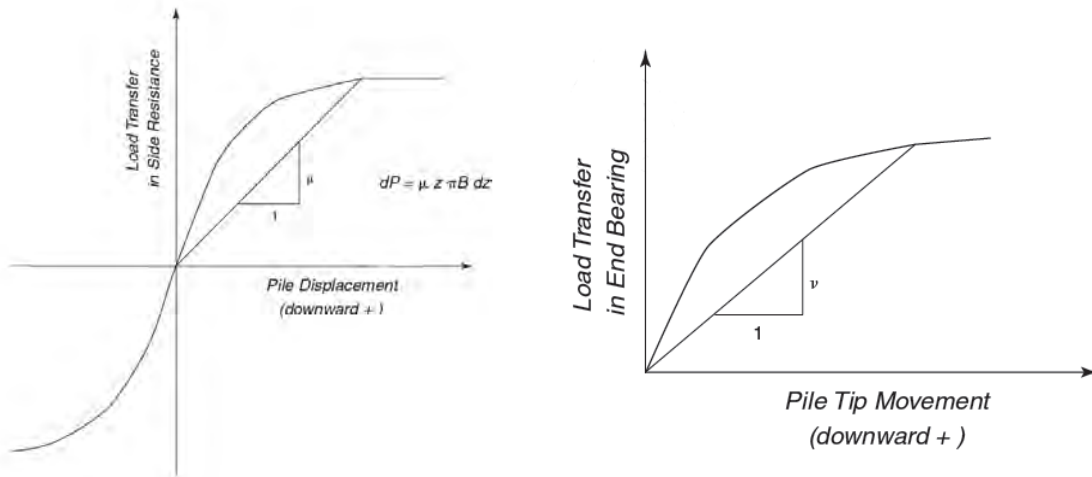


Figure 2.16: Load displacement curves for side resistance and end bearing (Reese et al., 2006)

The differential equation that describes this problem is derived using the previous relationships and is presented below:

$$\frac{d}{dx} EA \frac{dz}{dx} = \mu z l \dots\dots\dots(2.24)$$

Finally, the pile-tip resistance is related to the secant modulus (ν) from the load transfer curve in end bearing and the pile-tip movement z_{tip} as indicate in the following equation:

$$P_{tip} = \nu z_{tip} \dots\dots\dots(2.25)$$

In order to solve the differential equation for this problem, the boundary conditions should be determined. At the pile tip equation (2.25) can be used to evaluate the axial movement while at its top either the known force or the measured displacement can be used as boundary conditions.

2.9.2: Load transfer curves for cohesive soils

In order to generate load-transfer curves, full scale load tests are conducted on instrumented piles as significant effort is required to obtain analytical expressions. Reese and O'Neill (1988) used the results from several field tests on instrumented bored piles in clay and developed the recommended load transfer curves for side resistance presented in figure 20. From these curves, the maximum load transfer occurs at approximately 0.6% of the pile diameter. Since the piles used in these tests had diameters equal to 24 - 36 inches, the displacement at full load transfer is estimated to be approximately 0.2 inches.

Reese and O'Neill (1988) also recommended load transfer curves for end bearing resistance. As indicated in figure 21, a displacement of 1.2 inches is required for the

development of ultimate bearing stress, which is greater than the displacement required for the development of ultimate skin friction. This is easily demonstrated by considering the soil elements that are strained in end bearing compared to those strained in side shear.

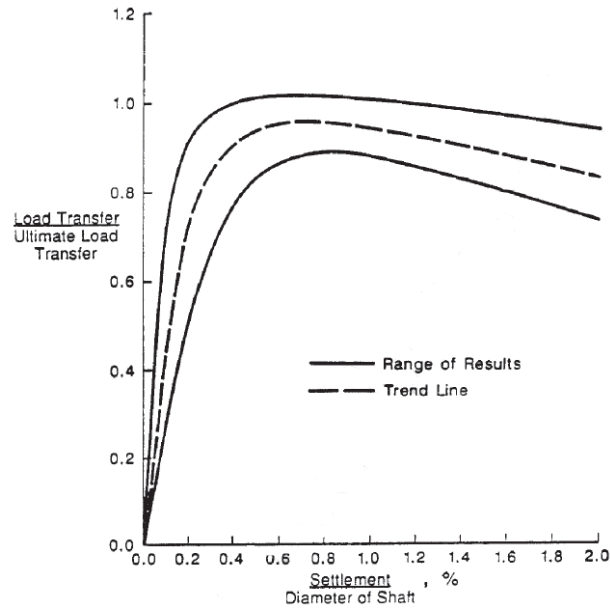


Figure 2.17: Load transfer curve in side resistance for piles in clay (Reese et al., 2006)

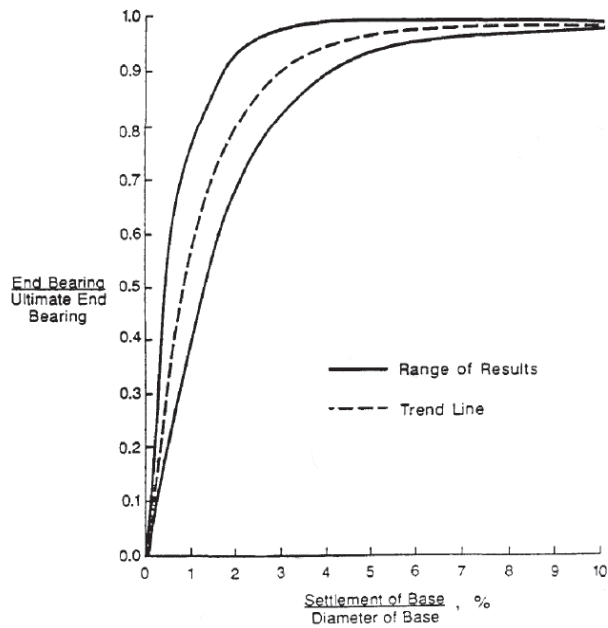


Figure 2.18: Load transfer in end bearing for piles in clay (Reese et al., 2006)

Chapter 3: Site Conditions and Test Wall

3.1: Introduction

In order to investigate the behavior of drilled shaft retaining walls on expansive clay, a fully instrumented wall, named in honor of Lymon C. Reese, was constructed in the highly expansive clay of the Taylor formation. Inclometers and Fabry-Perot optical fiber strain gauges were installed in three of the shafts and time domain reflectrometry sensors were placed within the soil to measure changes in the moisture content. Thermocouples were also installed within the instrumented shafts adjacent to the strain gauges to measure temperature fluctuations of the concrete. A picture of the current condition of the research wall is presented in figure 3.1.



Figure 3.1: Current view of the research wall in Manor, Texas

In this chapter, useful information about the geometry and specifications of the drilled shaft retaining wall is presented, along with details of the instrumentation program. The properties of the Taylor clay that will be used in the subsequent p-y and t-z analysis are also given along with details of the site location.

3.2: Site location and geologic conditions

The research wall is located in Manor, Texas at a site underlain by approximately 50 ft of Taylor clay. The address is 13806 Old Highway 20, Manor, Texas 78653 and a map of the area is presented in figure 3.2.



Figure 3.2: Location of the research wall in Manor, Texas

Taylor clay is an overconsolidated, highly plastic, stiff, fissured clay. Its secondary structure significantly affects its strength and hydraulic conductivity. To define the properties of this type of soil, large samples should be taken from the field in order to account for the presence of fissures in the behavior of the clay. In addition, due to the high plasticity index, fluctuations on the moisture content cause significant volumetric

strains. Increasing water content causes the expansive clay to swell, while decreasing water content causes it to shrink. This behavior has a very significant impact on the earth pressures that act on structures that are used to retain the soil.

Finally, despite the fact that an intact piece of expansive clay is almost impermeable, its hydraulic conductivity is significantly increased by the presence of fissures, which work as water conduits. Hence, notable changes in the water content occur above the ground water table for depths shallower than 8 ft.

After a thorough geotechnical investigation conducted in January 2010 and before the wall's construction, the properties of the Taylor clay were evaluated. Exploratory boring revealed a shallow layer of dark weathered clay underlain by a much stiffer layer of dull yellow-colored clay. The weathered layer extends to a depth of approximately 8 ft, and is clearly distinguished from the underlying layer by the change in color, as indicated in figure 3.4.



Figure 3.3: Taylor clay sample taken from the project site (Brown et al., 2011)



Figure 3.4: Distinct transition from the weathered dark gray to the stiffer dull yellow clay

To investigate the properties of the Taylor clay, three borings were drilled to a depth of 50 ft. Pocket Penetrometer (PP), Texas Cone Penetration (CPT) and Standard Penetration Tests (SPT) were used to define the properties of the in situ soil while split spoon samples were taken for laboratory tests. Subsequently, a piezometer was installed in one of the borings.

The geotechnical investigation included several laboratory tests. The moisture content and unit weight of the soil were defined, along with Atterberg limits and grain size distribution curves. The expansivity of the Taylor clay is indicated by the plasticity index (PI), which was found to be about 50%. Cyclic lateral shrinking and swelling tests were also conducted for this purpose.

In this thesis, the undrained shear strengths were used as input to the p-y and t-z analysis. Unconsolidated Undrained (UU) triaxial and Consolidated Drained Direct Shear tests were conducted to determine the drained and undrained shear strength of the soil. The results of the laboratory tests agree well with those of the field tests. Final recommendations for the shear strength profile are given below.

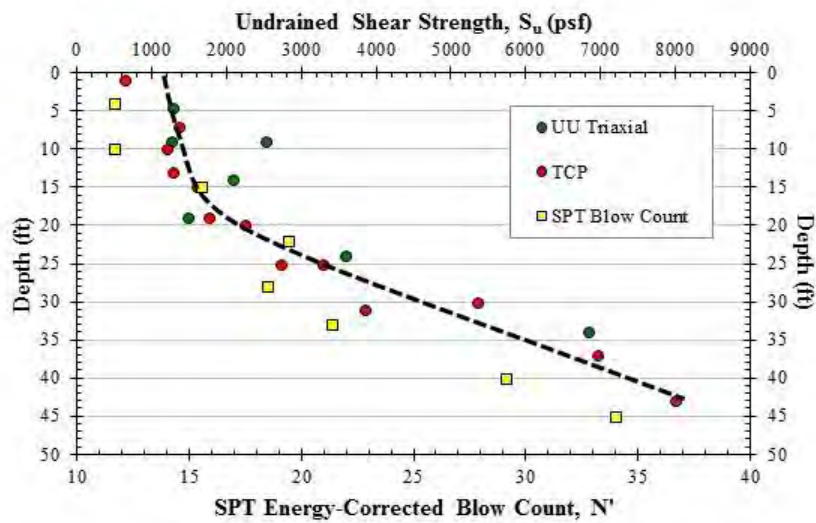


Figure 3.5: Combined test results for the undrained shear strength profile (Ellis, 2010)

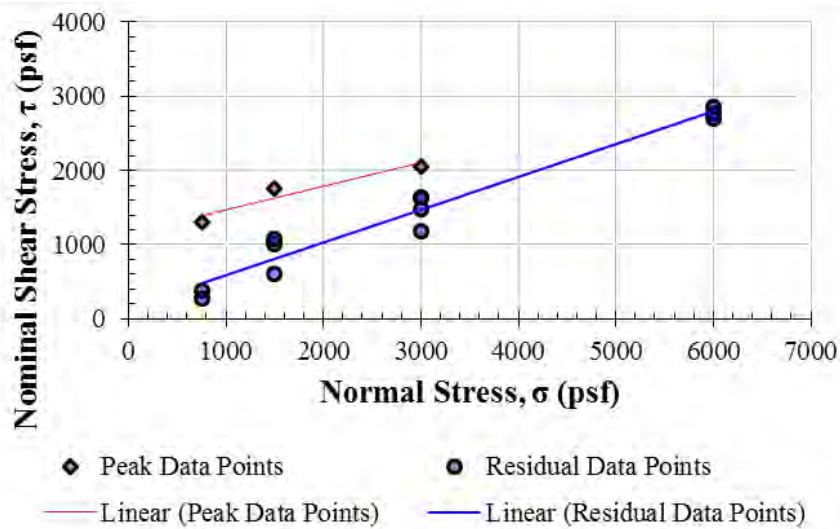


Figure 3.6: Drained peak and residual failure envelope from the direct shear tests (Ellis, 2010)

Several methods were used to measure the moisture content profile of the soil, including direct measurements from soil samples taken from the field at various depths and the results from the TDR moisture content probes installed behind the wall after the soil was excavated. Limited data exist for depths larger than 8 ft; for shallower depths, at which moisture content fluctuates significantly, values are between 16% and 30%.

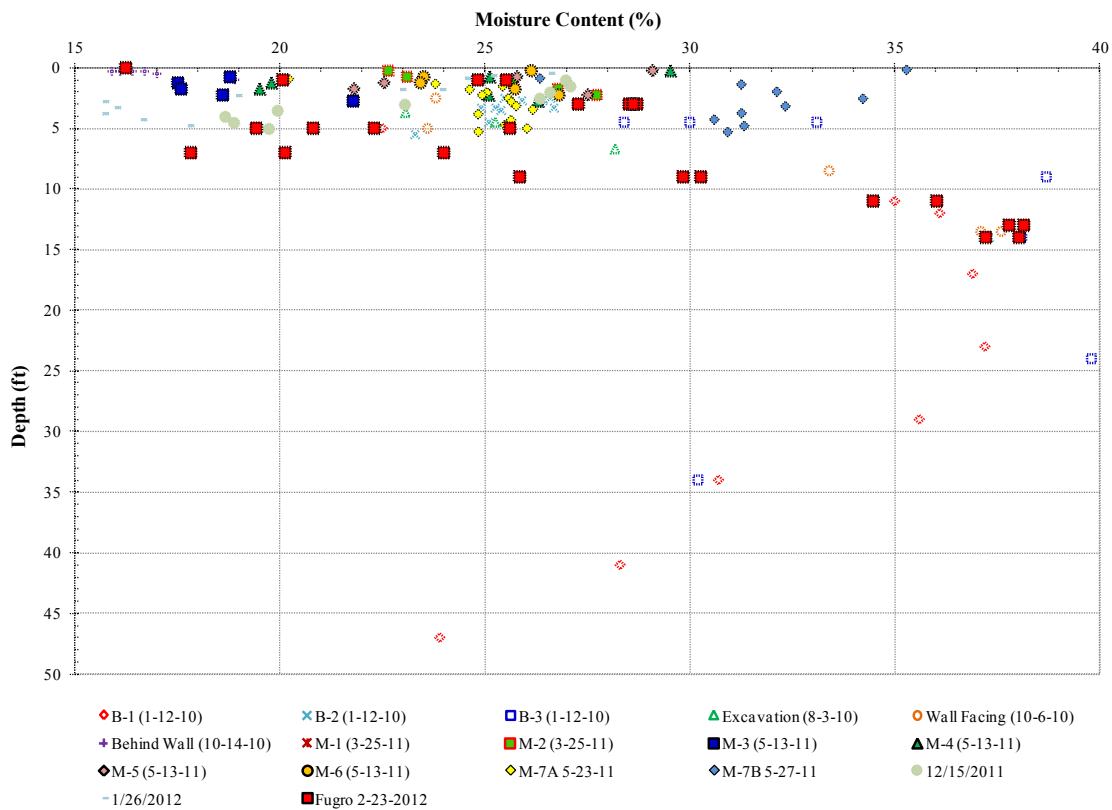


Figure 3.7: Moisture Content profiles for different dates

3.3: Geometry of the research wall

The research wall was constructed according to TxDOT design specifications while its flexibility was selected to be consistent with the purpose of this project. In that

sense, enough deformations are allowed to extrapolate the earth pressures applied on the wall from the results of the instrumentation program.

The wall consists of 25 drilled shafts embedded to depths of 18 to 35 ft below the ground surface. The are 24 inches in diameter, and spaced at 30 inches center to center. The concrete used has a specified 28-day compressive strength of 4000 psi, and the reinforcing bar cage consists of 12 #7 bars (1.6% of the area of the shaft) conforming to Grade 60 of ASTM A615. The cantilever height is 15 ft in the center area of the wall and the penetration depth is 20 ft. A 4 ft stickup (extension of the wall above the existing grade) will allow the project team to run lateral load tests on the drilled shafts and the owner to use the wall as a loading dock upon completion of the project. The final wall geometry is presented in the following figures.

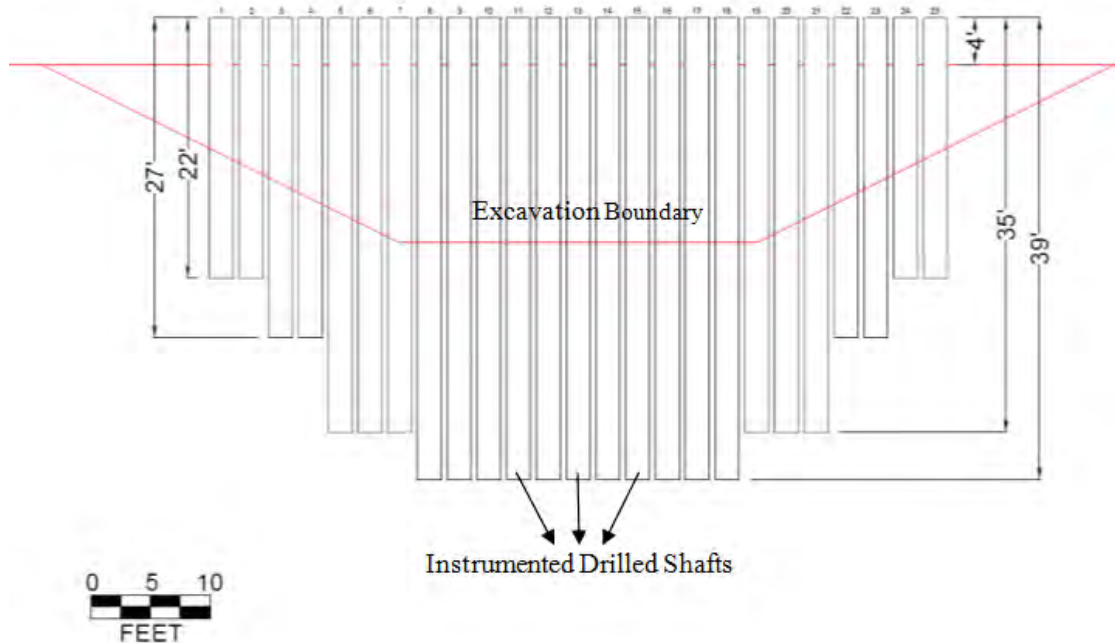


Figure 3.8: Cross-Section of the research wall and embedment depths for the various shafts

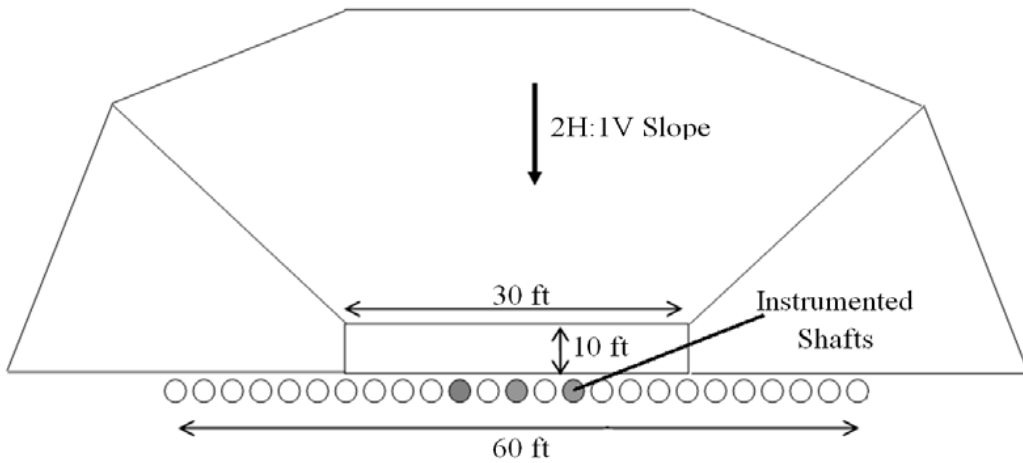


Figure 3.9: Plan view of the wall and location of the instrumented shafts

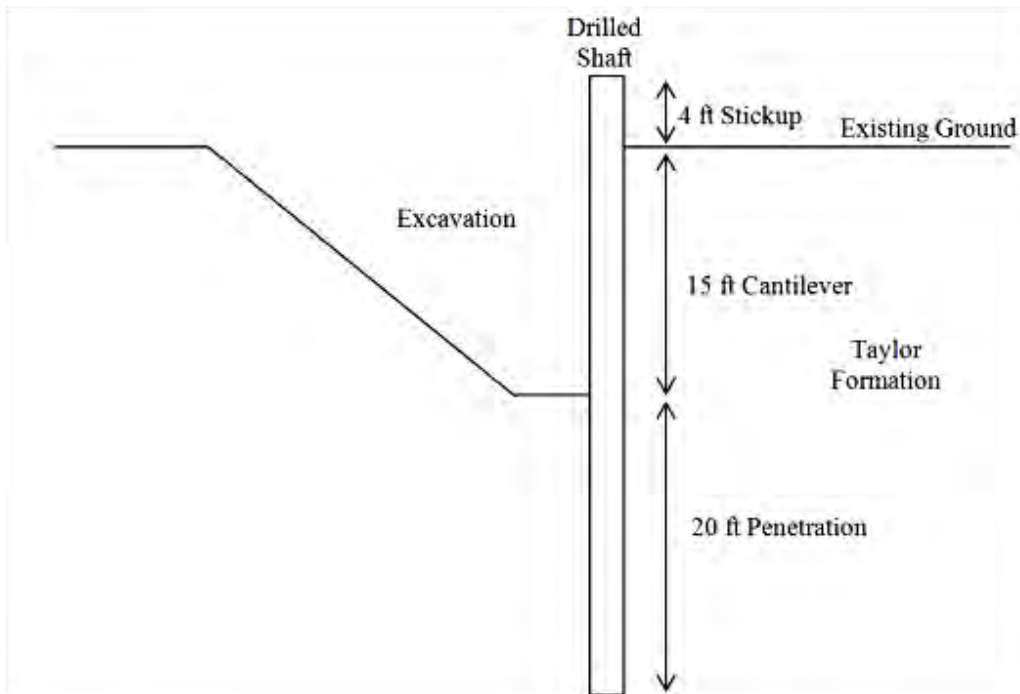


Figure 3.10: Cross-section and dimensions of the center shaft

At the beginning of April 2010, the shafts were constructed; almost four months later excavation of the soil in front of the wall began. In October 2010 a shotcrete facing was installed to protect the soil between the shafts from eroding. The shotcrete has a

minimum thickness of 3 inches, and it is reinforced with a wire mesh, anchored to the drilled shafts. Finally, an erosion control blanket was placed in the excavated side of the wall to prevent the erosion of the soil due to rainfall and runoff of surface water. A construction schedule that includes all the above mentioned operations is presented in table 3.1.

Table 3.1: Construction schedule of the research wall

<i>Construction Schedule</i>		
<i>Stage</i>	<i>Operation</i>	<i>Date</i>
A	Pouring of the Concrete	March 30th - April 6th, 2010
B	Curing of the Concrete	April 6th - May 4th, 2010
C	Excavation	July 29th - August 5th, 2010
D	TDR Moisture Content Probes	September 30th, 2010
E	Shotcrete Facing	October 1st, 2010
F	Erosion Control Blanket	October 18th, 2011

3.4: Instrumentation program for predicting the earth pressures

To estimate the earth pressures applied on the drilled shafts during cycles of moisture fluctuation, an instrumentation schedule was implemented. The main objective of this schedule is to monitor the deflections and strains on the drilled shafts along with the moisture content changes on the expansive clay. Three drilled shafts were instrumented and a layout of the instrumentation plan is presented in the following figure. The instrumentation plan includes the following monitoring elements:

- a. Fabry-Perot optical fiber strain gauges (30 per instrumented shaft)
- b. Probe Inclinerometers (1 per instrumented shaft, 1 in the soil behind wall)
- c. Time Domain Reflectometry (TDR) moisture probes distributed within the soil
- d. Thermocouples distributed across the project site and within the shafts
- e. One linear potentiometer attached on top of the center shaft

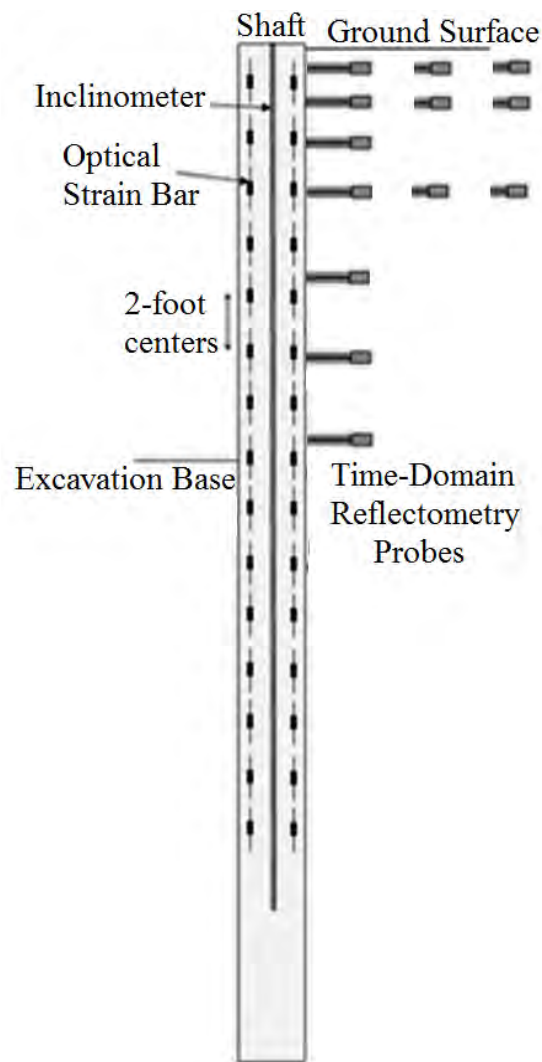


Figure 3.11: Schematic representation of the instrumentation program applied on the research wall

a. Fabry-Perot optical fiber strain gauges

Optical fiber sensors provide an alternative to traditional electrical resistance or vibrating wire strain gauges for several types of applications, particularly those that require long-term reliable measurements and operation in harsh environments. An optical fiber sensing system consists of an optical fiber cable, a light source, a sensing element or

transducer and a detector. The principle of operation is that the transducer modulates some parameters of the optical system (intensity, wavelength, polarization, phase, etc.) which changes the characteristics of the signal received by the detector. The fiber sensor can be either intrinsic if the modulation occurs directly in the fiber, or extrinsic if the modulation is performed by an external transducer.

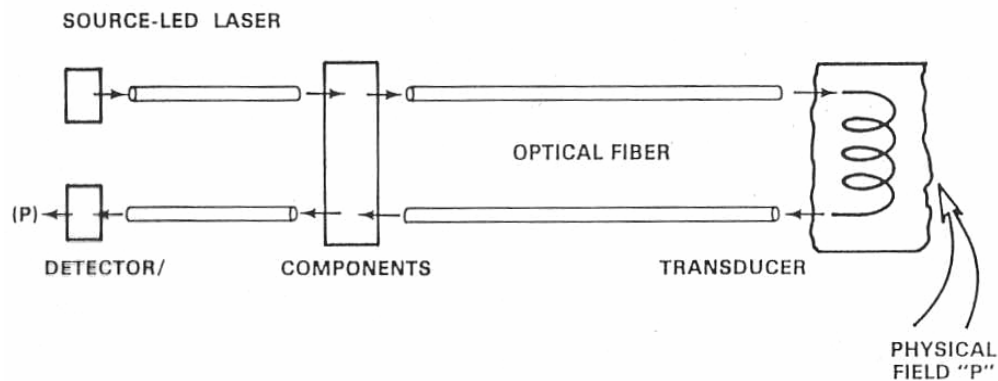


Figure 3.12: Basic elements of an optical fiber sensing system (Micron Optics, 2011)

The most common type of fiber optic strain gauges are made of Fabry-Perot sensors. These sensors measure strains using the phase difference or “shift” between reference and reflected white light. They consist of a multimode optical fiber cable that transmits white light, with a sensing element at its tip. This sensing element is defined by a micro capillary tube that holds the end of the fiber close to another small piece of the same fiber, leaving a small cavity in between. The fiber-ends that define the cavity are deposited with a reflective coating, so that the white light entering the cavity is reflected and hence frequency-modulated. A schematic configuration of a typical Fabry-Perot interferometer sensor is shown in figure 3.13.

Approximately 4% of the incident light is reflected at the output end face of the fiber, and returns directly back down. When the sensor is bonded to a surface, the length

of the cavity expands or contracts by exactly the same amount of strain experienced by this surface. The change in length of the cavity determines the frequencies of the reflected light which are measured and used to evaluate the strains.

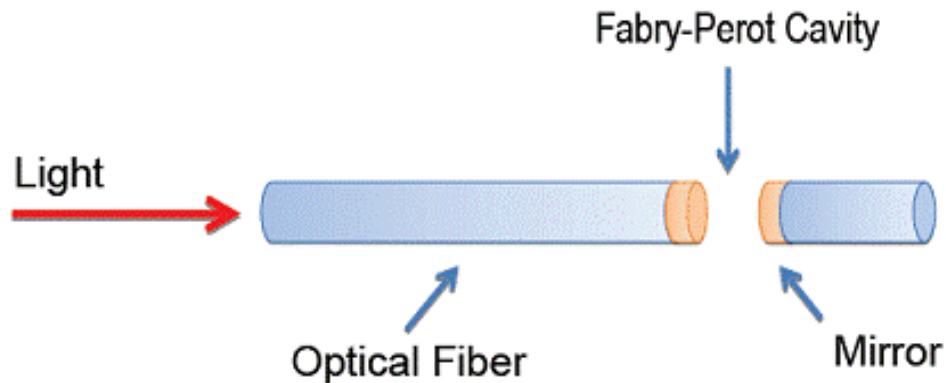


Figure 3.13: Layout of a Fabry-Perot Interferometer (Micron Optics, 2011)

The Fabry-Perot optical fiber has many advantages over electrical-resistance and vibrating-wire strain gauges:

- Immunity to electromagnetic interference and excellent resolution
- Increased water and corrosion resistance and insensitivity to changes in moisture and temperature
- Durability and fatigue resistance
- Absoluteness of readings (the sensor can be disconnected and reconnected and still give the same reading without any adjustment)
- Small size, enabling sensors to be embedded within composite materials such as concrete elements
- Ability to multiplex sensor signals, allowing many sensors to be connected in series

For the purposes of this project, 90 Fabry-Perot optical fiber strain gauges were purchased from OPSSENS. Each gauge was calibrated in the laboratory prior to installation to ensure linearity within their operating range of 1,000 $\mu\epsilon$ and to establish response curves. During installation, the gauges were attached using epoxy to sister bars that were put in the shafts prior to pouring of the concrete. A membrane cover was used to protect the gauges during installation as depicted in the figure 3.14. Readings are taken as the output signal is sent through the fiber optic cable to a signal conditioner. A multi-channel signal conditioner is used to record continuous strain measurements for the center shaft using a notebook computer, while a single-channel handheld signal conditioner is used to record strains on the west and east shafts.



Figure 3.14: Fiber optic strain gauge before installation within the instrumented shaft

The strain gauges are embedded in pairs within the instrumented shafts (one on the compression and the other on the tension side) at intervals of 2 ft. This configuration allows direct estimation of the location of the neutral axis and the curvature profiles of

the shafts. Details of data interpretation are presented on the next chapter. The fact that three drilled shafts were instrumented allows strain measurements to be compared and the performance of the strain gauges to be evaluated.



Figure 3.15: Strain gauges attached to the sister bar before installation within the shafts

b. Probe Inclinometers

Slope inclinometers are widely used in civil engineering applications to measure lateral soil and wall movements in slurry walls and deep excavations. They generally fall into two categories, probe inclinometers and fixed-in-place inclinometers (Laplante, 1998). In probe inclinometers, a casing with four axial grooves (spaced circumferentially at equal intervals) is installed in a borehole or within a retaining wall. The grooves are designed to fit the wheels of the inclinometer probe. The angle of the probe from the vertical axis is measured in both directions using a sensitive gravity pendulum, tilt meter, or servo accelerometer. The deflections are calculated automatically from the rotation profile given the distance between the wheels. For more accuracy, measurements are

taken every two feet while the inclinometer casing extends to a firm stratum or sufficient depth so that the inclinometer base does not move. The limitation of inclinometers is that they measure only horizontal deformations and thus they do not account for vertical movements.

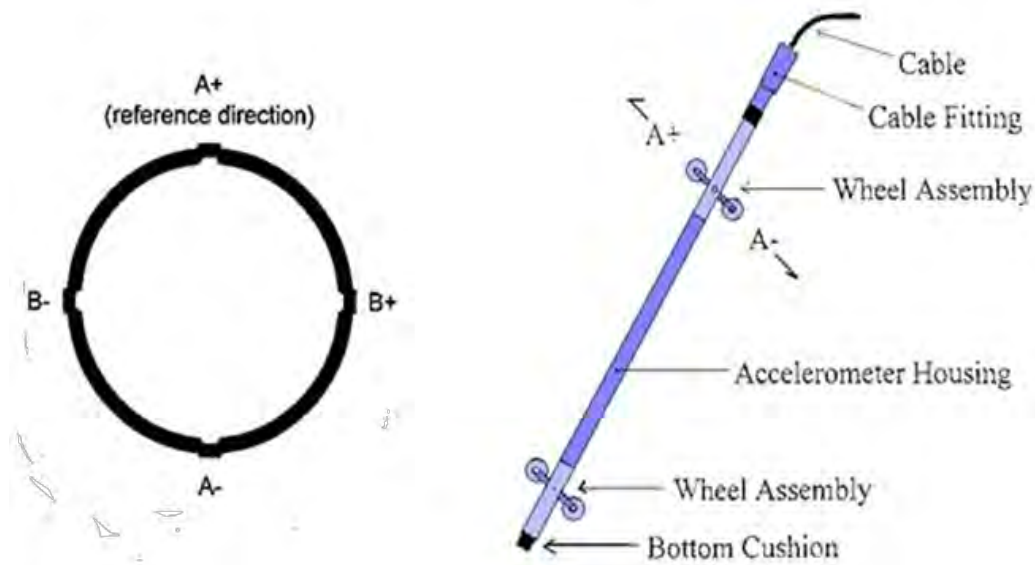


Figure 3.16: Inclinometer probe and casing showing the wheels and guide grooves used to measure the rotation between two successive points (Deep Excavation LLC, 2012)

In this project, probe inclinometers are embedded in the instrumented shafts to directly measure the deflected shape. The inclinometer casing was attached to the reinforcing bar cage before pouring of the concrete. To measure the rotation profile, an external probe is inserted into the casing and lowered to the bottom of the shaft. Readings are taken every two feet and the angles between the two points are used to evaluate the lateral deflections. The inclinometer casing and strain gauges within an instrumented shaft before pouring of the concrete are shown in figure 3.17.

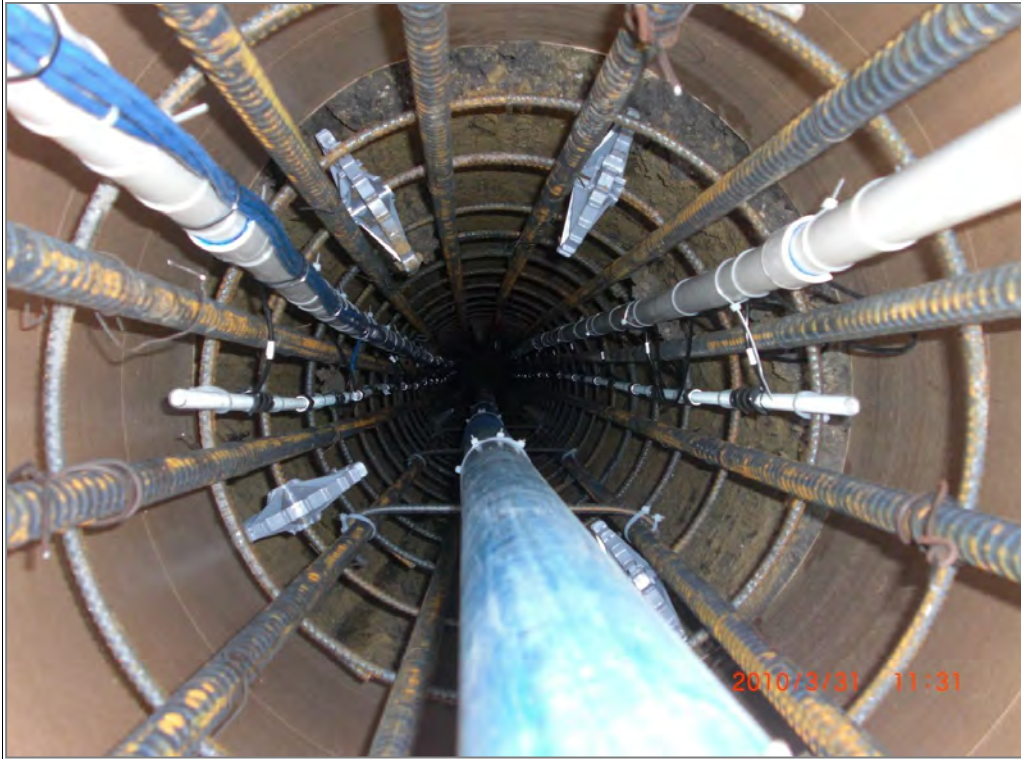


Figure 3.17: Inclinometer casing and strain gauges attached to the reinforcing bar cage

c. Time Domain Reflectometry (TDR) moisture content probes

Time Domain Reflectometry (TDR) moisture content probes are used to measure moisture content. Their operating principle is based on determining the dielectric constant of the soil. Because water has a much higher dielectric constant than air and solids, the dielectric constant of the soil profile depends highly on the volume of water. By placing TDR moisture content probes at various depths within the soil, the water content profile can be estimated and changes on the water content throughout the monitoring period can be recorded.

In this project, 29 Time Domain Reflectometry (TDR) moisture content probes were installed at various depths behind the wall to monitor moisture fluctuations of the Taylor clay. They operate by sending an electromagnetic wavefront through the system to

the TDR probes. The velocity of the reflected wavefront is recorded and used to estimate the dielectric constant of the soil. Using empirical relationships such as that of Topp et al. (1980), the volumetric water content of the soil is estimated.

The moisture content probes did not operate as expected, and only four out of twenty showed reasonable results. Reasons for this include the high electrical conductivity of the Taylor Clay (which causes scatter in the recorded wavefronts); installation errors; and the presence of small rocks and fossils within the soil mass (Delinger, 2011).

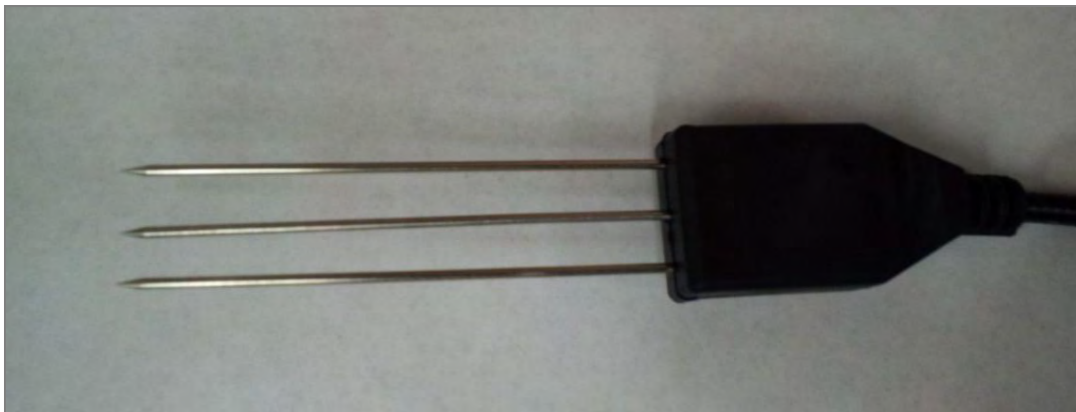


Figure 3.18: Time Domain Reflectometry (TDR) moisture content probe before installation within the soil (Delinger, 2010)

d. Thermocouples

Thermocouples were placed at various locations within the instrumented shafts, mainly adjacent to the strain gauges and the soil to measure temperature fluctuations. The significance of temperature effects on the behavior of drilled shafts is evident from previous published data. Because the shafts are exposed to temperature fluctuations only at the excavated side, curvature is generated apart from the axial strains due to swelling or shrinking of the concrete. Hence, strain-gage readings should be corrected for these

temperature-induced so that the final readings represent only the strains generated by earth pressures.

e. Linear Potentiometer

A linear potentiometer is a transducer used to detect and measure linear position and velocity using a spring-loaded variable resistor, of spiral configuration, attached to a flexible but axially stiff wire. In the research wall, a linear potentiometer was attached on top of the center instrumented shaft to measure absolute displacements. The potentiometer was installed at a fixed reference location; its steel wire, protected within a PVC pipe, was connected to the shaft. Deflections of the shaft with respect to the fixed reference caused the wire to rotate (unwind) the spiral, creating a change in measured resistance. The main advantage of a linear potentiometer is that it can measure global displacements, which the inclinometer cannot.

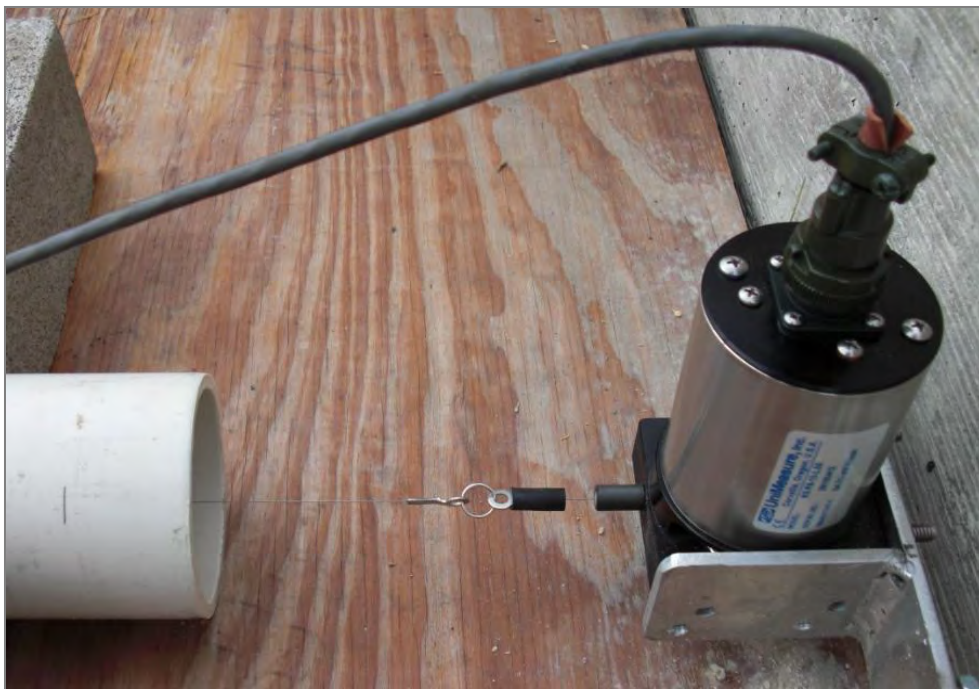


Figure 3.19: Linear potentiometer attached in a fixed location

3.5: Hydrogeology

A rain gauge was also used for the purposes of this project to record rainfall events and relate them to observed moisture fluctuations within the soil. In addition, a piezometer was installed in one of the boreholes from the geotechnical investigation that was conducted before the wall construction, to monitor fluctuations in the ground water level.

3.6 Summary

The instrumentation program is expected to provide us with all the required information to accomplish the purposes of this project. However, the nature of the in-situ soil and the fact that the strain gauges are embedded in concrete elements is expected to cause significant complexity in the results of the instrumentation program. All the different parameters that may affect the results need to be quantified. Finally, instrumentation elements that are malfunctioning need to be identified. The procedure of interpreting the results from the instrumentation program to predict the earth pressures applied on the wall during cycles of moisture fluctuations is presented in the following chapter.

Chapter 4: Methods of Analysis Used and Data Prior to Excavation

4.1: Methods of analysis used to predict the earth pressures

There are two ways to predict the earth pressures applied on drilled shaft retaining walls on expansive clay during cycles of moisture fluctuation. The first is to interpret the results of the instrumentation program (specifically, the inclinometers and strain gauges); and the second is to simulate the lateral response of the wall using a p-y model. For the purposes of this thesis, both methods are used and the results are compared to the empirical approaches that TxDOT uses for design.

Analyzing the results from the instrumentation program includes multiple differentiation and integration, combined with curve-fitting to eliminate the effects of local spikes and discontinuities in the results. To evaluate the accuracy of the strain measurements from the strain gauges, the deflected shapes of the instrumented shafts are predicted and compared to those generated from the inclinometer data. Given that sound measurements are taken from both instrumentation elements, the deflected shapes should be similar.

To predicting earth pressures, the net earth pressure diagrams that represent the lateral forces applied on the free body diagram of the respective instrumented shaft are generated by double differentiation of the bending moment profile. Finally, given the soil resistance, the active and passive earth pressures are evaluated for different moisture conditions of the Taylor clay. The distributions of shear forces and earth pressures predicted from the strain gauges and inclinometers are compared to each other. Both the magnitude and the range of the earth pressure distributions are important and final

recommendations are given for the design of drilled shaft retaining walls in expansive clay.

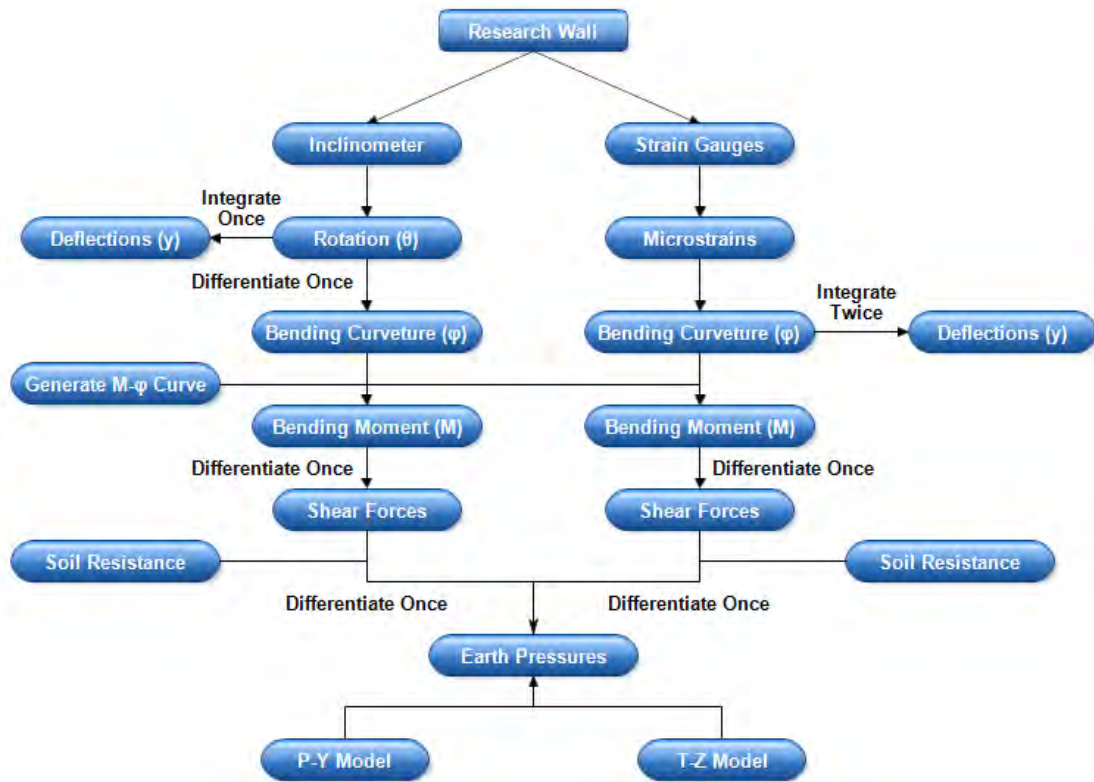


Figure 4.1: Flow chart showing the methods used to generate the earth pressure diagrams

In the above flow chart, the various procedures followed to generate the deflected shapes and to predict the earth pressures applied on the instrumented shafts are presented. Several types of software, including Microsoft Excel® and Matlab®, are used in the analysis to make all the required calculations. Apart from analyzing the results of the instrumentation program, p-y and t-z models are simulated in Excel®. In the following chapters, the procedures used to do this are described. In the appendix, the results of the instrumentation program are presented for future use.

4.2: Residual stresses and strains before excavation

Fellenius (2002) and Falconio and Mandolini (2003) recognized that residual loads developed in drilled shafts during concrete curing are significant and should be taken into account during the design stage. These residual loads are influenced by the expansion/contraction of the concrete and the stratigraphy of the project site. Especially when drilled shafts are constructed on expansive clays, the volumetric changes of the soil due to cycles of moisture fluctuations induce significant residual loads due to side shear developed at the interface of the shafts. If such loads are neglected, the structural response and capacity may be over or under predicted depending on the particular case.

In the research wall, strain measurements are first taken before pouring of the concrete that occurred in April 2010. Hence, the strain profiles during concrete curing are generated directly from the strain measurements and the residual stresses when the soil was excavated can be evaluated. As indicated in figure 4.2, the strains in the instrumented center shaft changed significantly during the four month period between concrete pouring and excavation of the soil. More specifically, for three days after the concrete was poured in the shafts, the strain gauges indicated a rapid increase in tension followed by a gradual decrease towards compression. These plots of strains during concrete curing are in good agreement with other published data from Fellenius et al. (2009) and Nam S. Moon (2010).

In the following diagram the trend of an initial sharp increase in tension due to concrete shrinkage followed by a gradual decrease towards compression as the concrete cools is evident. Compressive strains are developed mainly within the 28-day period of concrete curing. However, after concrete curing has stopped there are additional changes in strain. These long-term changes are attributed to volumetric changes of the soil

imposing compressive strains on the shafts. Given the fact that concrete pouring took place in April 2010 and the soil was excavated in August 2010 when the climate is much drier, the water content of the soil decreased. This decrease caused shrinking of the soil and thus the side shear applied on the interface between the soil and the shafts induced compressive stresses along the concrete elements.

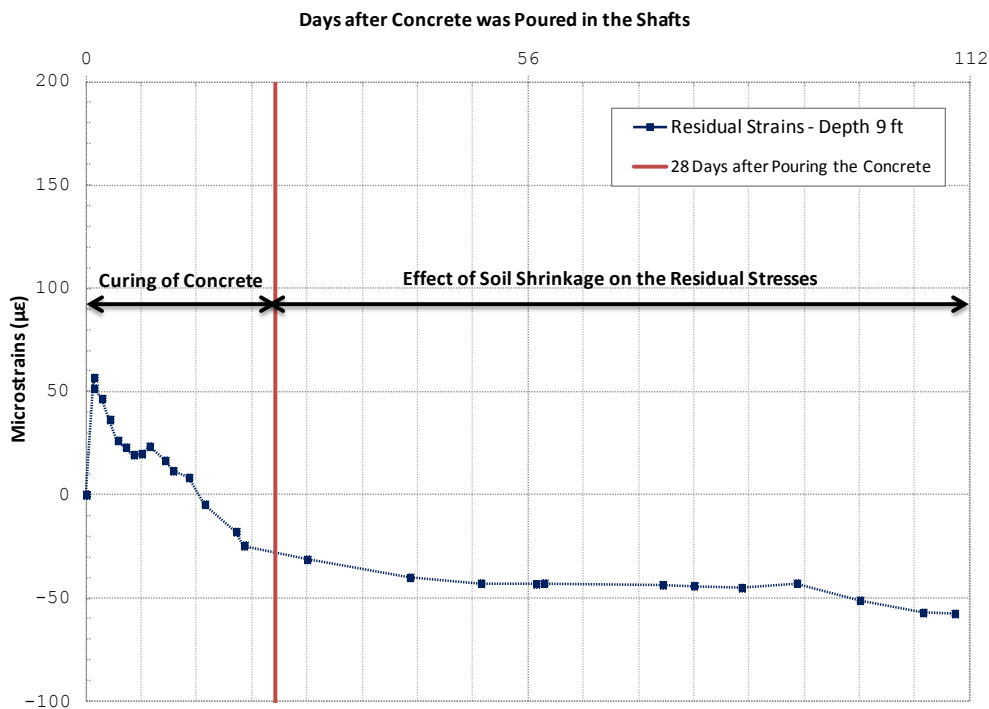


Figure 4.2: Residual strains developed at a depth of 9ft on the compression side of the center shaft

Site conditions and soil stratigraphy affect the range of residual stresses and strains and they are more evident near the surface where the volumetric changes of the soil are more prominent. In addition, since the water content varies throughout the year between the summer and the winter, the time that the retaining wall is constructed is important in estimating the range of residual stresses applied in the drilled shafts.

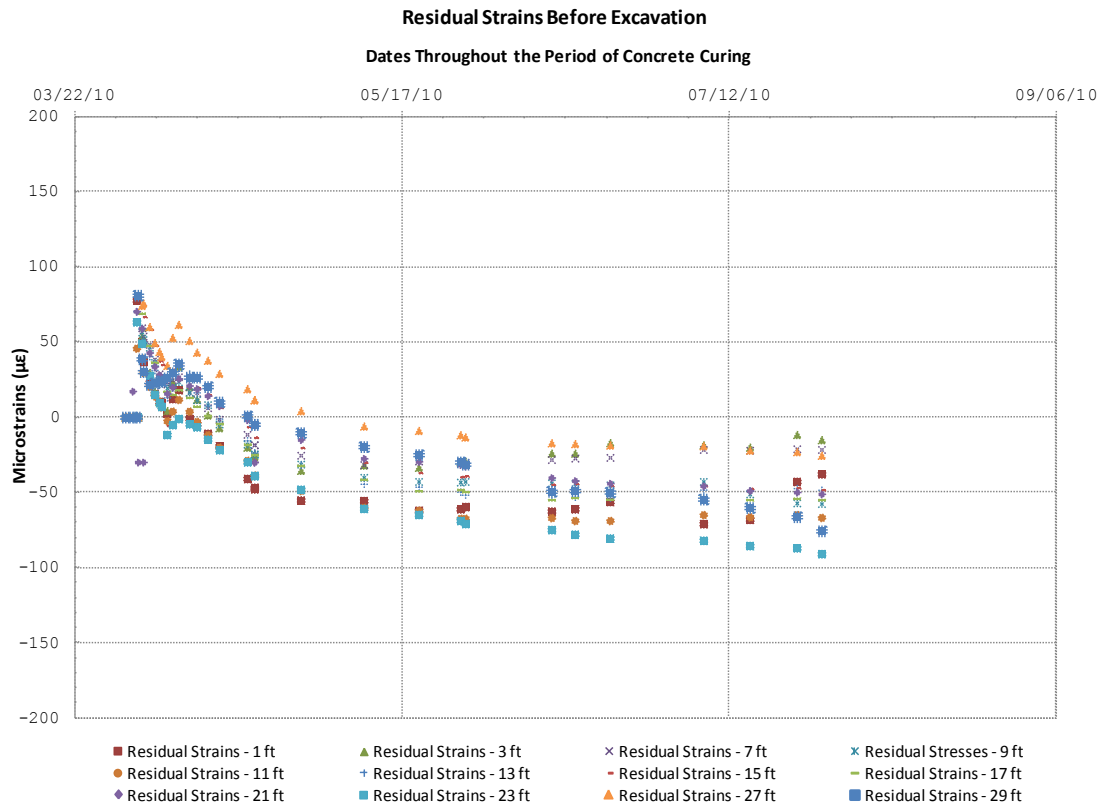


Figure 4.3: Residual strains for various depths along the center shaft

In figure 4.3, the residual strains are plotted with respect to time for various depths. Microscale effects such as tension cracks cause discrepancy on the results but generally higher compressive stresses are developed for bigger depths where the shafts support the weight of the overlying concrete mass. In addition, it is notable that the effect of soil shrinkage that occurs mainly at shallow depths causes additional compressive stresses beyond the 28-day period of concrete curing. Temperature effects within the concrete mass are also significant.

In order to estimate the residual stresses, the procedure described by Nam Moon (2010) is followed. Concrete specimens are taken from the field and tested in compression by HVJ to estimate the strength (f'_c) and stiffness of the concrete (E_c) at

various curing times. In table 4.1, the 7-day and 28-day concrete strengths are presented for the different drilled shafts. As indicated in this table, significant discrepancy is observed on the concrete strengths while in most cases it is greater than the expected value of 4000 psi according to the specifications of the respective concrete type.

Table 4.1: Concrete Strengths for various curing times

Date	Notes (* = Instrumented Shaft)	Concrete 7-Day Strength (psi)	Concrete 28-Day Strength (psi)
March 30, 2010	Mobilized Equipment, Assembled Instrumented Cages, Constructed Shafts 1 and 4	6055	7955
March 31, 2010	Constructed Shafts 7, 10, 13*, 22, and 25	4970	7000
April 1, 2010	Constructed Shafts 2, 5, 8, 11*, 15*, and 17	4480	6065
April 2, 2010	Constructed Shafts 3, 6, 9, 16, 19, and 23	4410	5875
Apr. 3 - 4, 2010	Weekend	N/A	N/A
April 5, 2010	Constructed Shafts 18, 21, and 24	4000	5950
April 6, 2010	Constructed Shafts 12, 16, and 14	4400	6800
April 7, 2010	Demobilize Equipment	N/A	N/A

From the compressive tests on the concrete specimens, the Young's modulus (E_c) at the end of the curing process is evaluated. Assuming that the ratio of E_c/f'_c is nearly constant during the concrete curing, the intermediate values of E_c are evaluated. Since the stiffness of the shafts depends on the type of concrete and the layout of the reinforcement, the composite Young's modulus (E_{com}) according to the following:

$$E_{com} = \frac{A_c E_c + A_s E_s}{A_c + A_s} \dots\dots\dots(4.1)$$

where:

- A_c = Area of the concrete = 444.78 in²
- A_s = Area of steel = 7.61 in²
- E_s = Young's modulus of steel = 29,000,000 in²
- E_c = Young's modulus of concrete (depends on the concrete age)

The results of the composite Young's modulus (E_{com}) for different times during the concrete curing are presented in the following figures. The concrete becomes stiffer with time, up to and after the age of 28 days at which the strength is commonly specified.

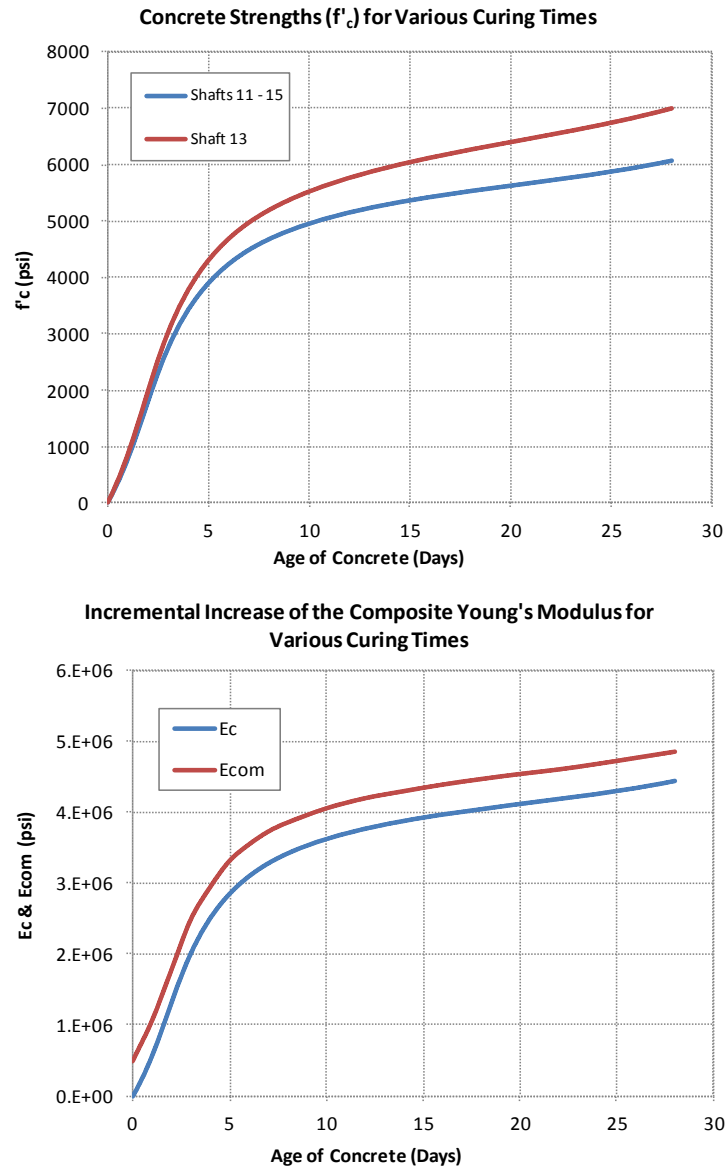


Figure 4.4: Concrete strength (f'_c) and incremental increase of E_c and E_{com} for various curing times

Table 4.2: Estimates of the composite Young's modulus for different curing times

Days	Ec (psi)	E _{com} (psi)	Ec/f'c
0	0	487739	732
1	580151	1058132	732
2	1305340	1771124	732
3	2030528	2484116	732
4	2494649	2940431	732
5	2871747	3311187	732
6	3106708	3542197	732
7	3292357	3724723	732
8	3422891	3853061	732
10	3625943	4052699	732
12	3770981	4195297	732
14	3872508	4295116	732
16	3966782	4387805	732
18	4046553	4466234	732
20	4119072	4537534	732
22	4184339	4601703	732
24	4264109	4680132	732
26	4351132	4765691	732
28	4439052	4852132	732

The values of E_{com} for different curing times are used to evaluate the residual stresses from the results of the strain gauges. In addition, to account for the effect of relaxation, we use the creep coefficient (CI 209R-92):

$$c_t = \frac{t^{0.6}}{10 + t^{0.6}} v_t \dots\dots\dots(4.2)$$

where:

- c_t = non-dimensional creep coefficient
- t = time after load application (days)
- v_t = ultimate creep coefficient = 2.35 for typical concrete

Therefore, assuming strain increments between successive strain measurements and using the respective values of E_{com} and creep coefficient for each increment, the

following equation can be used to derive the residual stresses at a particular depth along the shaft, during concrete curing:

$$\sigma = \sum_{t=0}^{t=t_{\max}} \frac{(\varepsilon_t - \varepsilon_{t-1}) \left(\frac{E_{com,t-1} + E_{com,t}}{2} \right)}{(1 + c_{t,t-1})} \dots\dots\dots(4.3)$$

This method of estimating the residual stresses is based on assuming strain increments and applying the respective value of E_{com} for each increment. The main advantage is that it can capture the load transfer from the steel reinforcement to the concrete as the concrete gains its strength during the curing process. The plots of calculated residual stresses over time for various depths along the center shaft are presented in figures 4.5 and 4.6.

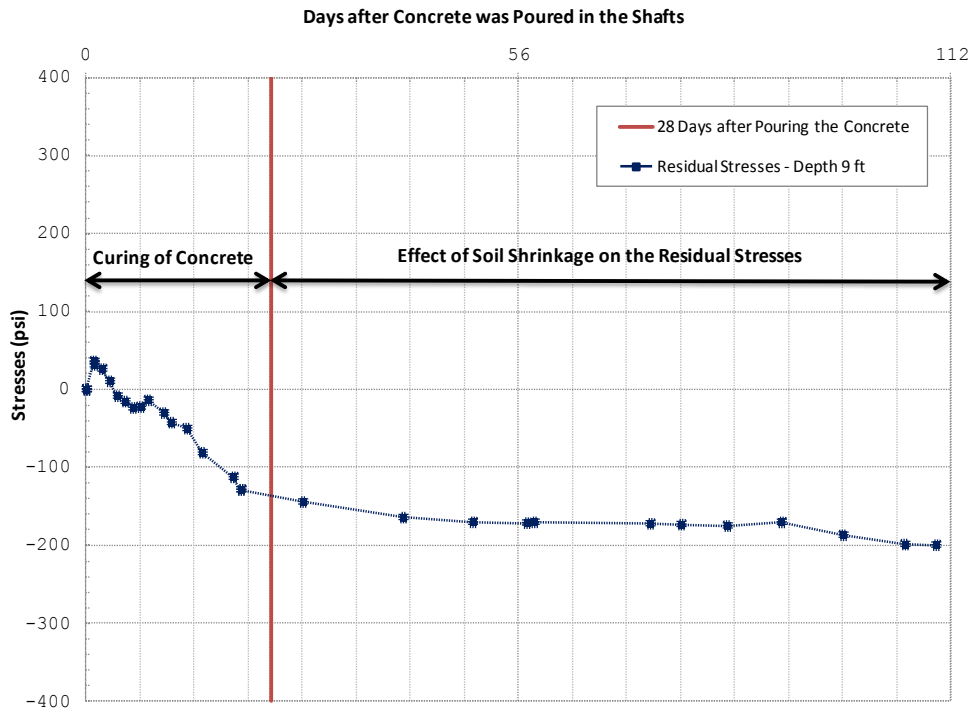


Figure 4.5: Residual stresses over time at a depth of 9 ft on the compression side of the center shaft

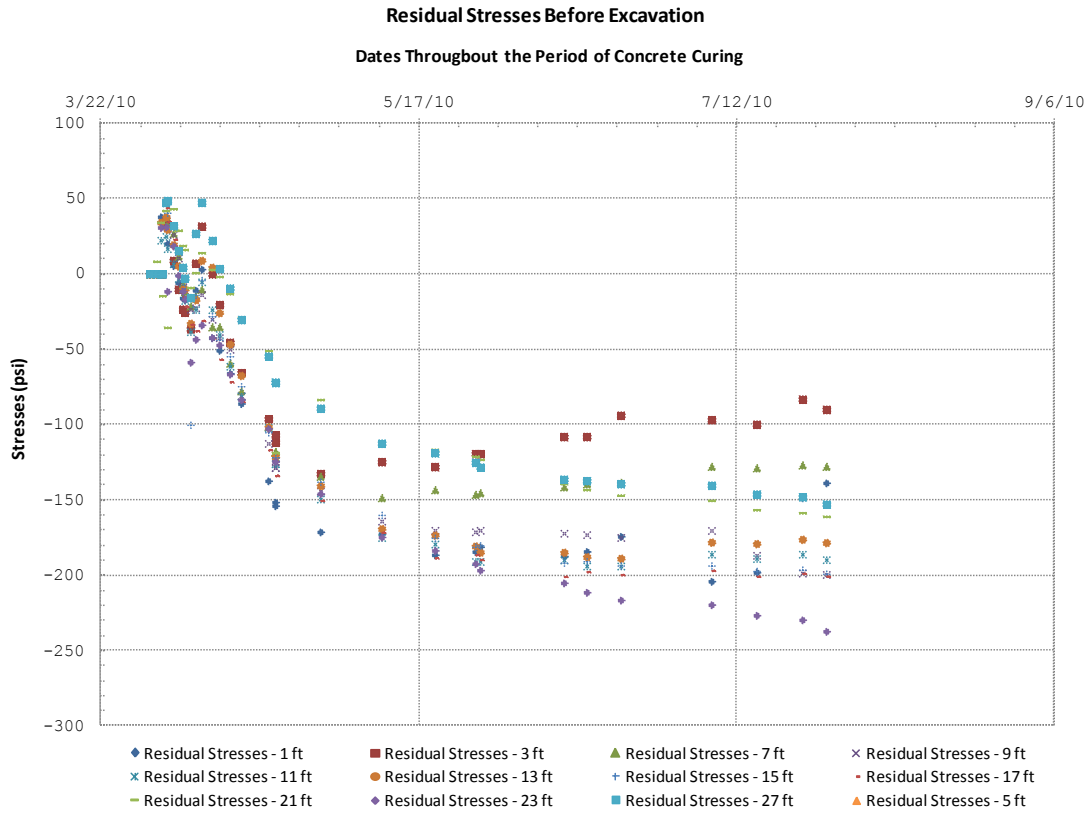


Figure 4.6: Residual stresses for different depths along the center shaft

The same trend observed for residual strains over time applies to residual stresses as well. A sharp initial increase in tension is followed by a gradual decrease towards compression as the concrete cures. The fact that the shafts were initially in tension and a few days after pouring of the concrete went into compression is illustrated in the profiles of residual stresses and strains at different dates during concrete curing as illustrated in figures 4.7 and 4.8.

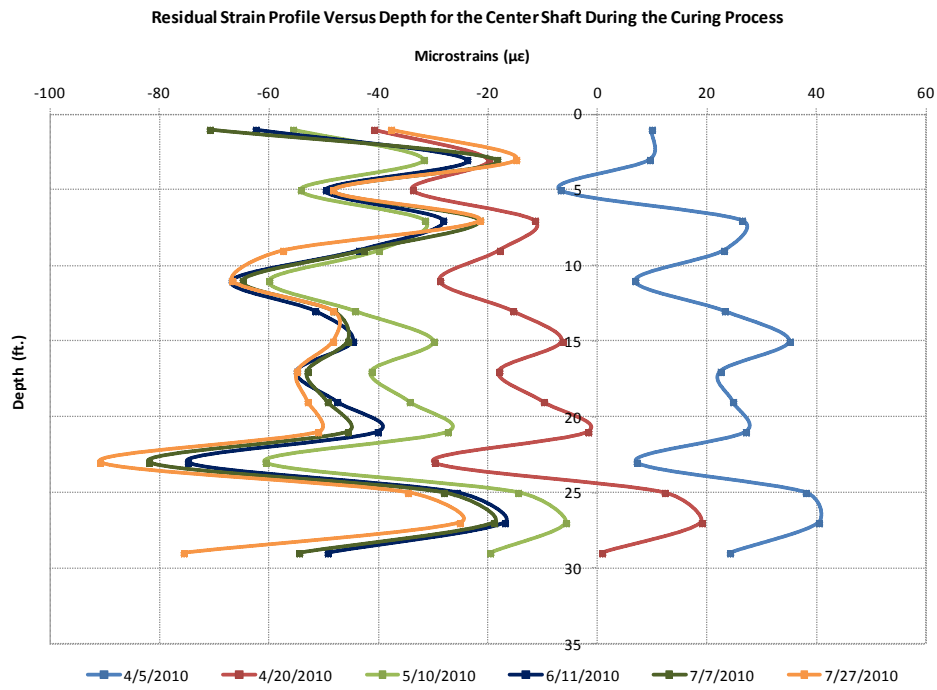


Figure 4.7: Residual strain profile versus depth for different curing times of the center shaft

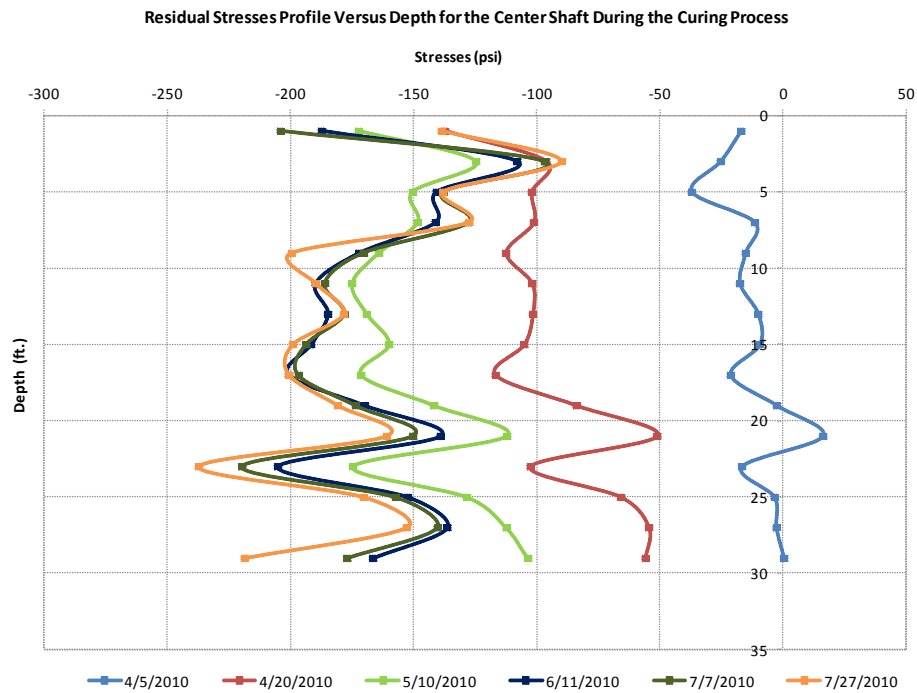


Figure 4.8: Residual stress profile versus depth for different curing times of the center shaft

Significant residual stresses were present in the shafts at the time the soil was excavated. Especially in this particular case where the geologic conditions are characterized by an expansive clay material, the following conclusions are drawn:

- Concrete curing and site conditions both affect the magnitude of the residual stresses and strains. While the stresses due to concrete curing follow a specific pattern, the effect of site conditions depends on the type of soil and its potential to undergo significant volumetric changes during cycles of moisture fluctuation.
- When the shafts are constructed is important in estimating the magnitude of the residual stresses. Since the water content of the soil varies significantly throughout the year, the effect of soil shrinking and swelling will be different if the wall is constructed during the summer or during the winter.
- In this project, apart from the weight of the concrete, additional compressive stresses were developed due to shrinkage of the soil which occurred between April and August 2010.
- The magnitudes of the residual stresses developed in the shafts at the time the soil was excavated were significant and thus in similar projects they should be taken into account during the design stage.

4.3: Predicting the moment-curvature diagram

From the results of the inclinometer and strain gauges the bending curvature profiles of the drilled shafts at different moisture conditions are evaluated. More specifically, the strains at the tension and compression side are directly related to the curvature while the inclinometer results require a single differentiation. To correlate the moments to the curvature profiles, the corresponding curve of bending moment (M)

versus bending curvature (ϕ) curve is generated. The shape of this curve depends on the properties and the layout of the concrete and the reinforcing bar cage within the shafts, and can be plotted using several different methods.

The drilled shafts in this project were made of specified 4000-psi concrete and the reinforcing cage consist of 12 #7 bars, Grade 60. The characteristic stress strain curves for the respective concrete and steel types that were used in the subsequent analysis are presented in figures 4.9 and 4.10. In addition, the geometric properties along with all the input parameters used in the subsequent calculations of the M- ϕ diagrams are included in table 4.3.

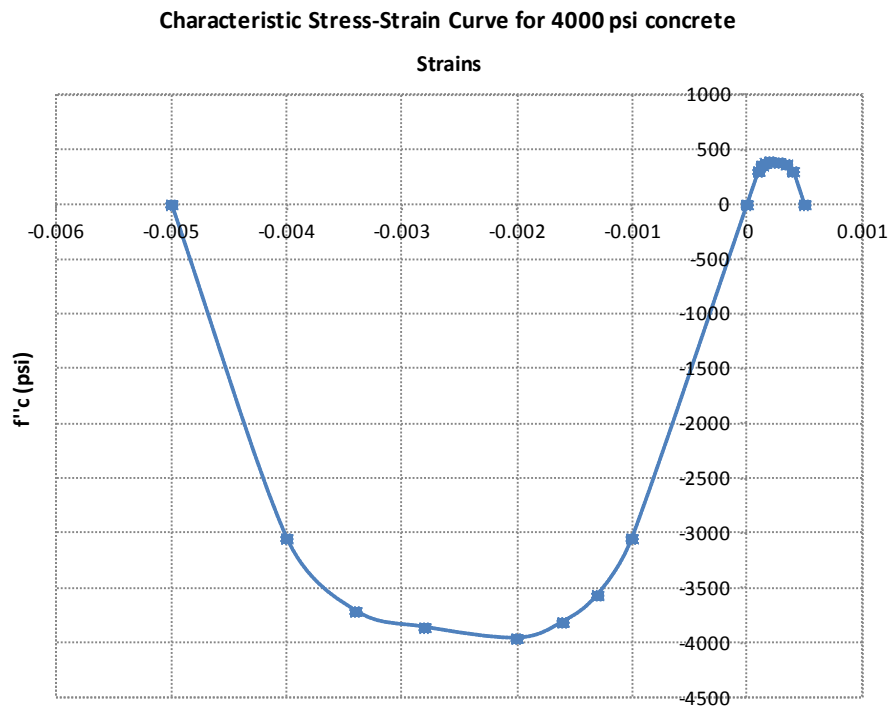


Figure 4.9: Characteristic stress-strain curves used in the evaluation of the M- ϕ curve (FHWA manual)

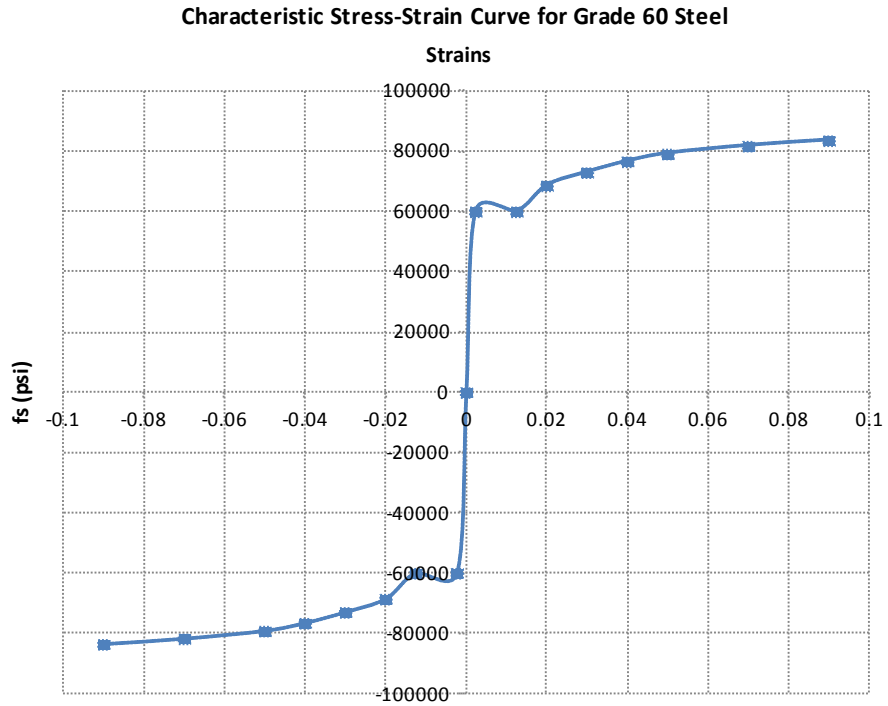


Figure 4.10: Characteristic stress-strain curves used in the evaluation of the M- ϕ curve (FHWA manual)

Table 4.3: Geometric properties of the shafts used in the evaluation of the M- ϕ curve

Center Instrumented Shaft (No. 13)	
Shaft Embedment (ft)	20
Shaft Diameter (in.)	24
Unembedded Height (ft)	15
Stickup Height (ft)	4
Total Height (ft)	39
Gap Between Shafts (ft)	6
Steel Properties	
Number and Type of Steel Bars	12#7
Steel Diameter (in)	0.875
Number of Steel	12
Area of Steel (in ²)	7.22
Clearance (in)	3
E (ksi)	29000
G (ksi)	11200

To predict the M- ϕ diagram the method of slices developed by Reese and O'Neill (1999) was followed initially. This various steps of this method are described below:

1. Divide the cross-section of the shaft into slices of finite width.
2. For the various slices, evaluate the distance (y) from the edge of the shaft, the centroid and the area (A) of each slice. In addition, based on the location of each steel rebar, evaluate their distance (y) from the edge of the shaft as well.
3. Assume a linear strain diagram along the diameter of the shaft.
4. For various edge strains, evaluate the forces applied on each concrete slice and the moments with respect to the edge point.
5. Based on the assumed linear strain diagram along the diameter of the shaft and for various edge strains, evaluate the forces applied at each rebar and the moments with respect to the edge point.
6. Determine the location of the neutral axis.
7. Evaluate the bending curvature (ϕ) for the different edge strains.
8. The bending moment (M) that generates the respective curvature (ϕ) is evaluated by adding the edge moments from the different concrete slices and steel rebars.

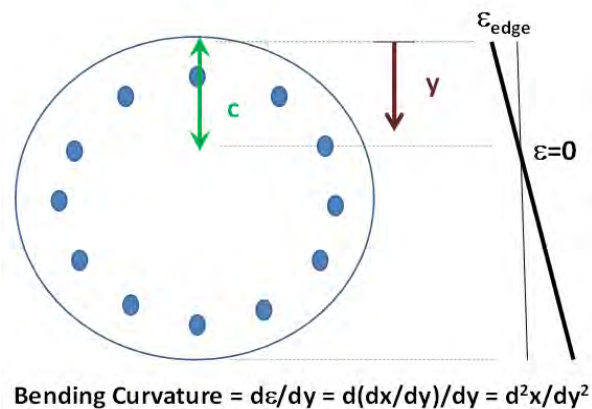


Figure 4.11: Linear strain change along the diameter of the drilled shaft is assumed to derive the M- ϕ curve using the method of slices

In order to check the developed M- ϕ curve that was derived using the method of slices, the "RECONASANCE" program (Alaoui 2004) was also used and the results compared. In this case three different stress-strain curves were assumed including the idealized concrete stress-strain curves by Park and Kent (1971), Scott Park and Priestley (1988) and the parabolic curve suggested by Hognestad (1980). The main difference between the two methods is that "RECONASANCE" uses a cracked concrete section while in the method of slices, no concrete cracking is assumed at the initial part of the M- ϕ curve. The results were in good agreement and the curve developed using the method of slices was used in subsequent analyses.

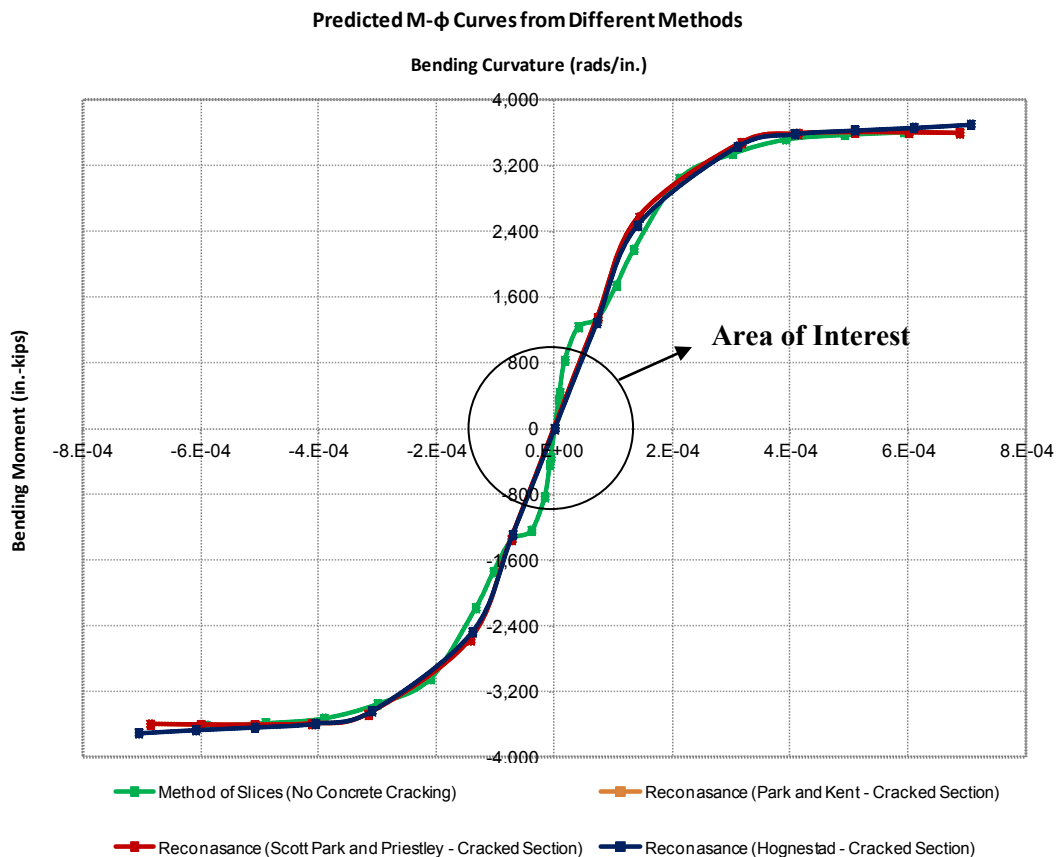


Figure 4.12: Predicted M- ϕ curves using different methods that assume cracked section and no concrete cracking

In figure 4.12, the M- ϕ curves from the various methods are presented. A very important issue in these diagrams is the fact that the results of the instrumentation program indicate that the developed curvatures on the instrumented shafts are limited in the area of interest as presented in figure 4.12 which includes the curvatures that concrete cracking occurs. Hence, despite their similar shape, the curves differ significantly in the area of interest. This is because "RECONASANCE" uses a cracked concrete section to generate the M- ϕ curves, while the method of slices uses the uncracked, transformed section for the initial part of the M- ϕ curve.

Chapter 5: Analyzing the Results of the Instrumentation Program

5.1: Analyzing the results of the inclinometers

Four inclinometers were installed on the project site. Three of them were embedded in the instrumented shafts and one was installed behind the wall. As mentioned in a previous chapter, the inclinometers directly measure the rotation between two points at various depths along the drilled shafts. Hence, the rotation profiles (θ) for different dates throughout the two year monitoring period are generated from the raw inclinometer data. Integrating the rotation profiles, the deflected shapes are plotted.

Inclinometers, are less affected than strain gauges by environmental conditions (temperature, moisture) and provide an easy and accurate way to measure the deflected shapes of the drilled shafts. Their main limitation is that three differentiations are needed to derive the earth pressure distributions and thus the accuracy is decreased during the process.

In order to better understand the behavior of the wall, six dates throughout the two year monitoring period are selected that represent different moisture conditions of the soil. To get smoother lines for the deflected shapes, smoothing spline curve fitting was used on the rotation profiles of these dates. Both the raw data and the smoothing splines are presented in figure 5.1. The deflected shapes of the center shaft are generated by integrating the rotation profile as illustrated in figure 5.2. In addition, the deflections at the top of the wall and at a depth of 14 ft below the ground surface throughout the two year monitoring period are also presented in figure 5.3.

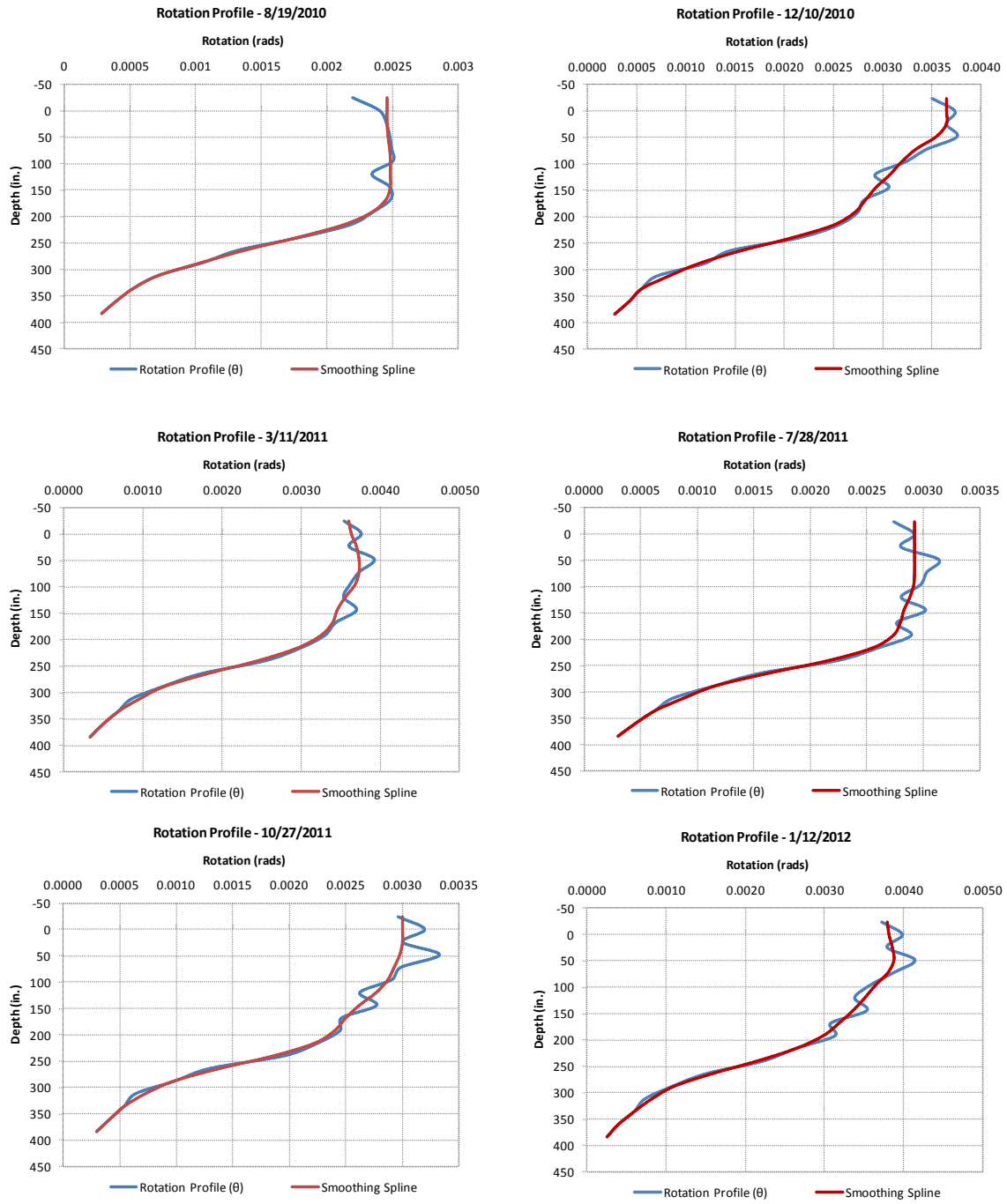


Figure 5.1: Rotation profiles and smoothing spline curve fitting for different dates

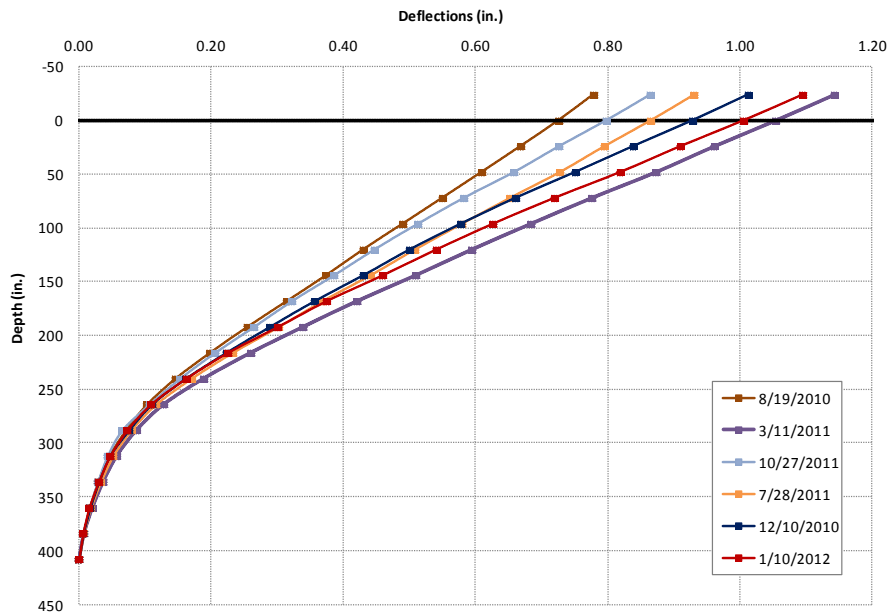


Figure 5.2: Deflected shape of the center shaft for different times throughout the two year monitoring period

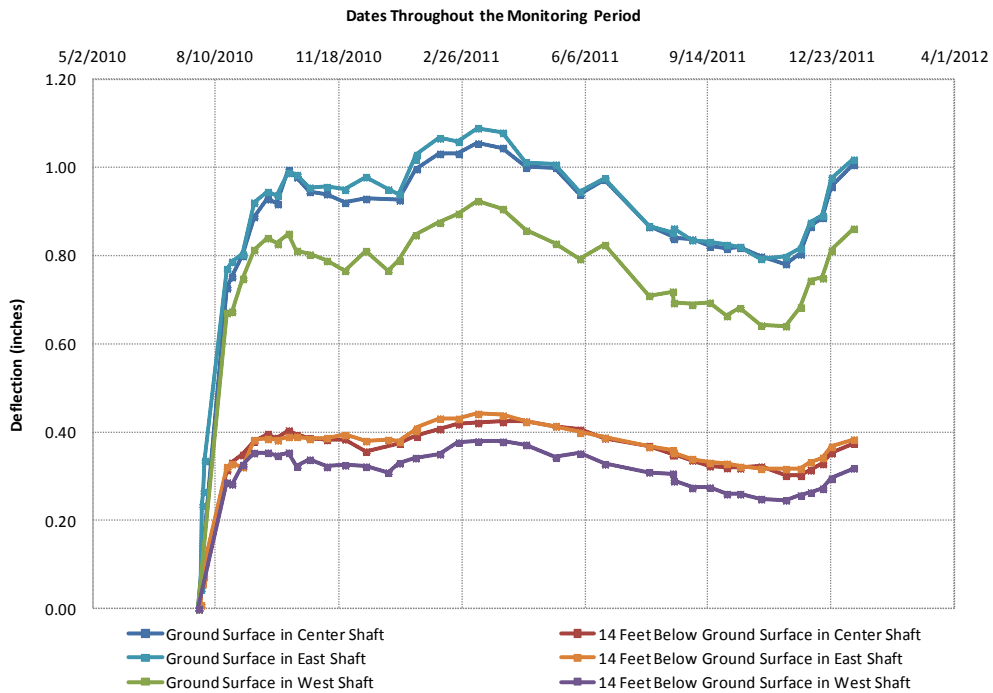


Figure 5.3: Deflections at the top of the shaft and at a depth of 14 ft during the two year monitoring period

The main conclusions from the analysis of the inclinometer results are the following:

- The effect of moisture or temperature fluctuations on the deflected shapes is evident. Maximum deflections are observed between December and March when the moisture content of the soil is high; and the wall bounces back during the summer when the water content decreases due to water evaporation.
- The shafts are not fixed and a non-zero initial rotation developed at the tip of the wall due to excavation. This is a very important issue as the shafts were expected to be fixed during the design stage.

Apart from the deflected shapes of the drilled shafts at various moisture conditions, the earth pressures are also evaluated using the inclinometer results. The rotation profile (θ) is differentiated once to generate the curvature (ϕ) profile. Using the M- ϕ curve the bending moment profile (M) is evaluated, and is differentiated twice to produce a diagram of net earth pressure diagram (w). Although this procedure is theoretically valid, the probable accuracy of the earth pressure distribution is low due to the multiple differentiations that are required during the process.

In order to generate the bending curvature profile (ϕ) from the inclinometer data, the piecewise quadratic curve fitting process is followed (Ooi and Ramsey 2003). The curvature is evaluated based on the following equation:

$$\phi = \frac{d^2 y}{dz^2} / \left[1 + \left(\frac{dy}{dz} \right)^2 \right]^{-3/2} \dots\dots\dots(5.1)$$

Since the first derivative of the displacements with respect to depth (dy/dz) is very close to zero, the above relationship is approximated as:

$$\varphi = \frac{d^2 y}{dz^2} \dots\dots\dots(5.2)$$

According to the piecewise quadratic curve fitting process and using the central difference approximation for a second order differential equation, the above relationship equals to:

$$\varphi = \frac{d^2 y}{dz^2} = \frac{y_A - 2y_B + y_C}{L^2} \dots\dots\dots(5.3)$$

The above equation can be used in the drilled shaft retaining wall of this project since the data points from the inclinometer measurements are evenly spaced. In the case where the data points are unevenly spaced the following relationship is used:

$$\varphi = \frac{d^2 y}{dz^2} = \frac{2}{L_{AB} + L_{BC}} \left[\left(\frac{y_C - y_B}{L_{BC}} \right) - \left(\frac{y_B - y_A}{L_{AB}} \right) \right] \dots\dots\dots(5.4)$$

The method of Ooi and Ramsey (2003) is based on fitting a quadratic curve into two consecutive displacement intervals (through three adjacent data points). Repeating this process at various points results in unrealistic local spikes at the bending curvature profile. A smoothing process is applied which includes averaging the curvature between three or five consecutive points as indicated in the following relationships:

$$\overline{\varphi}_B = \frac{\varphi_A + \varphi_B + \varphi_C}{3} \dots\dots\dots(5.5)$$

$$\overline{\varphi}_C = \frac{\varphi_A + \varphi_B + \varphi_C + \varphi_D + \varphi_E}{5} \dots\dots\dots(5.6)$$

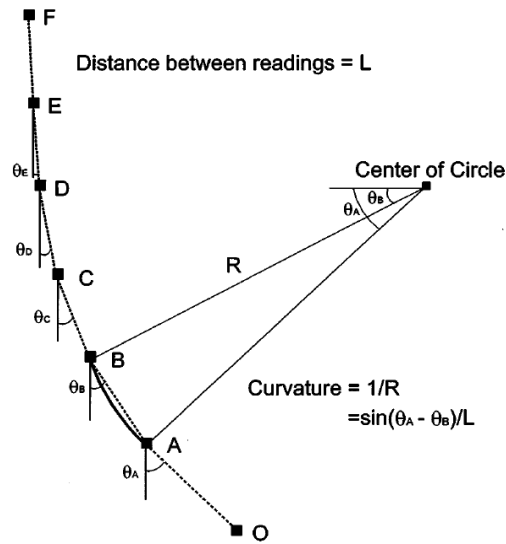


Figure 5.4: Piecewise quadratic curve fitting process to predict the curvature profile from the inclinometer data (Ooi and Ramsey, 2003)

Following the above procedure, the bending curvature profiles are generated. The equation that relates the deflection (y) to the rotation (θ) and the curvature (ϕ) is the following:

$$\phi = \frac{d\theta}{dz} = \frac{d^2y}{dz^2} \dots\dots\dots(5.7)$$

Using the $M-\phi$ diagram that was generated in the previous chapter by following the method of slices, the bending moment profile is generated (M). The shear forces (S) and the net earth pressures (w) which represent the pressures applied on a free body diagram of each instrumented shaft, are given by the following equation:

$$w = \frac{dS}{dz} = \frac{d^2M}{dz^2} \dots\dots\dots(5.8)$$

Since the above procedure includes several differentiations, the results are very sensitive to local spikes. In order to eliminate this limitation, smoothing splines were used to smooth the various curves. The results for the center shaft are presented below.

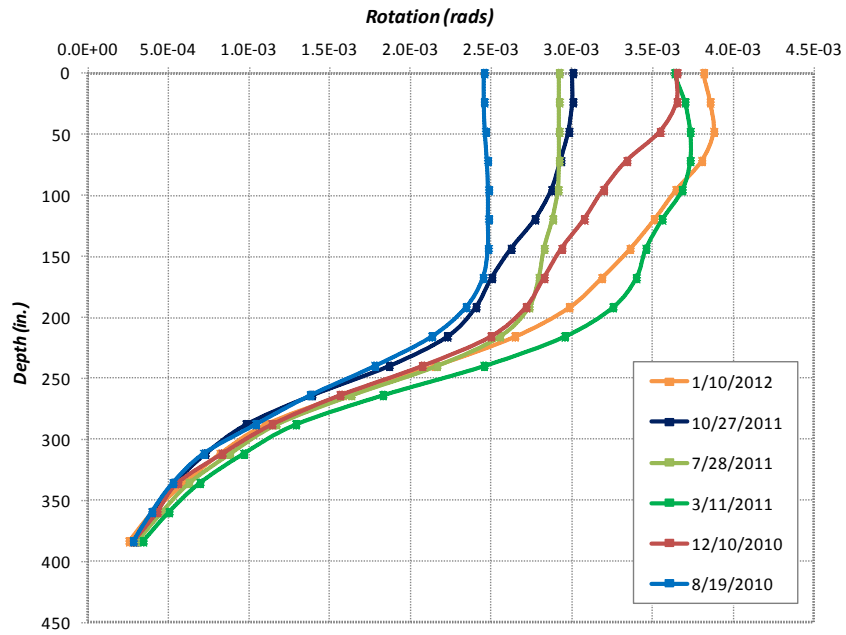


Figure 5.5: Rotation profiles for different dates throughout the two year monitoring period

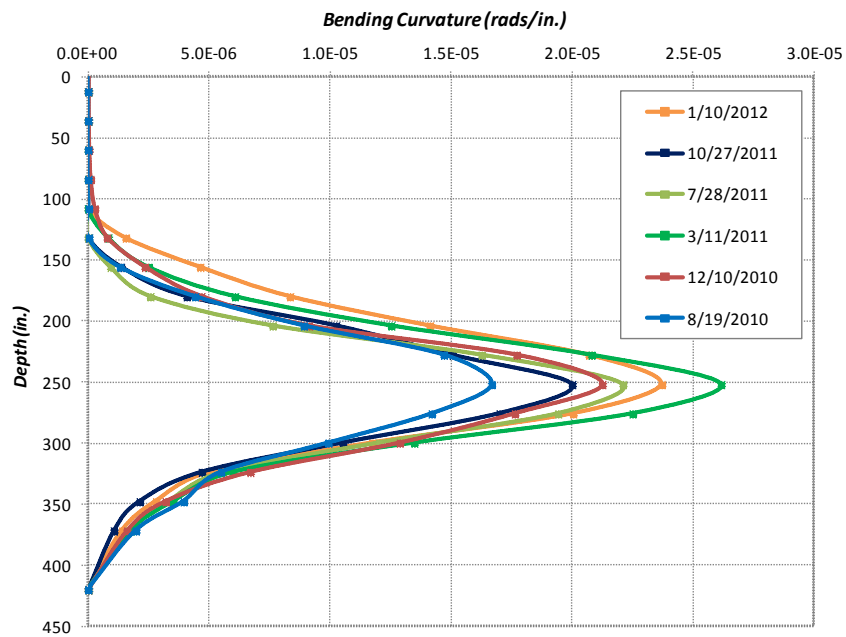


Figure 5.6: Bending curvature profiles for different dates throughout the two year monitoring period

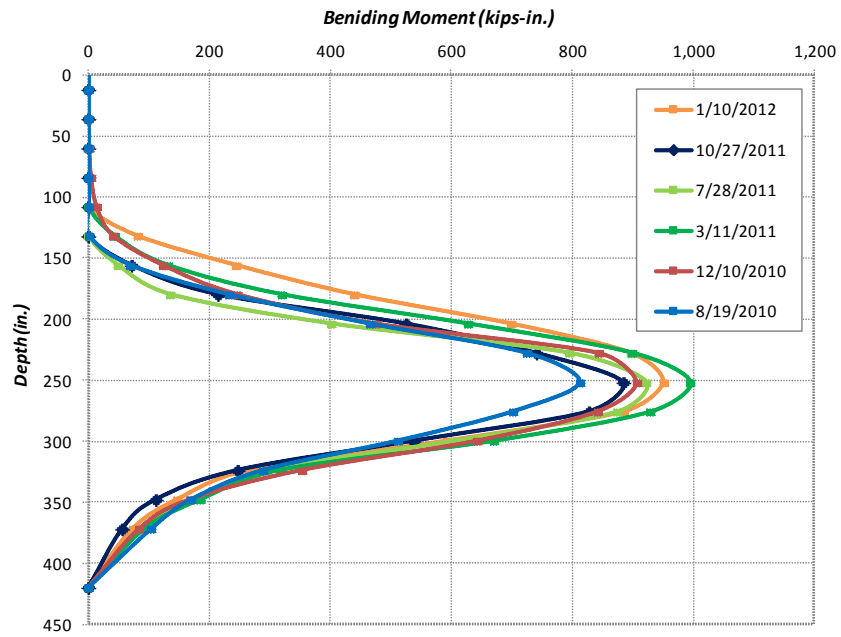


Figure 5.7: Bending moment profiles for different dates throughout the two year monitoring period (using M- ϕ curve from the method of slices)

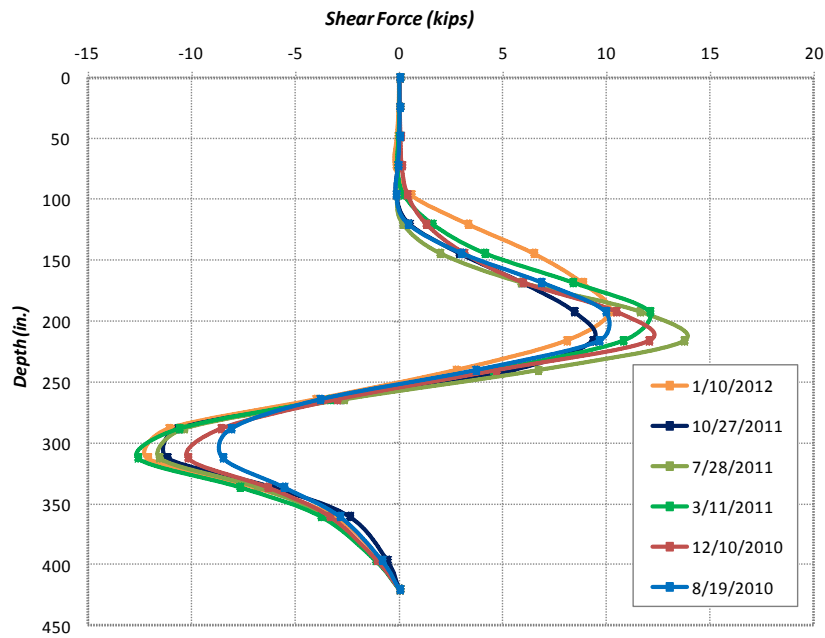


Figure 5.8: Shear force profiles for different dates throughout the two year monitoring period

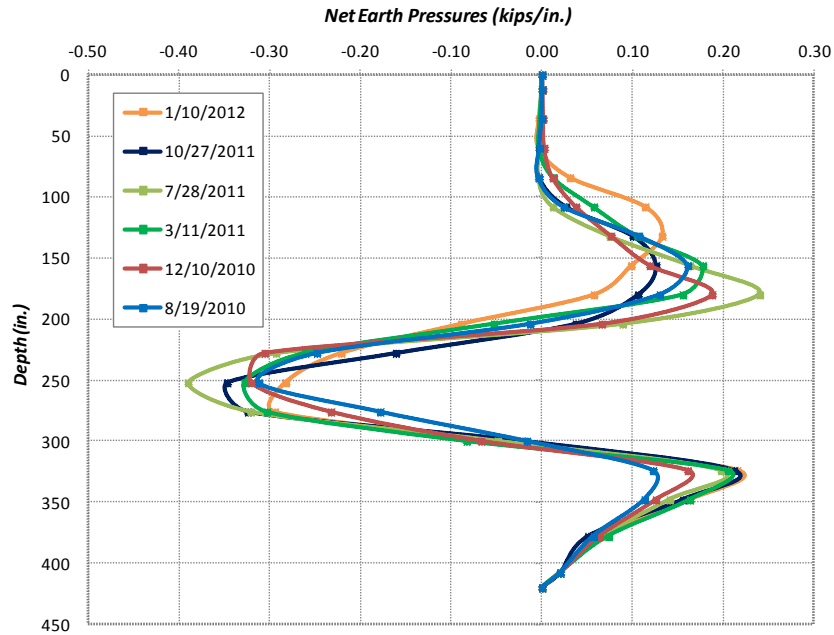


Figure 5.9: Net earth pressure diagrams for different dates throughout the two year monitoring period

Many useful conclusions can be drawn from the results of the above analysis:

- In order to evaluate the earth pressures from the rotation profile, three differentiations are required. Hence, local spikes and discrepancy on the results require use of curve fitting techniques.
- The effect of moisture fluctuation on the magnitude of earth pressures and the response of the wall is evident. The higher bending moments and active thrusts are developed during the winter when the moisture content of the soil is high and the temperature is low.
- The depth of the tension crack is significantly larger when the water content of the soil is low and the soil shrinks.
- In some cases, mainly during periods of increased water content, a negative curvature is generated. This does not significant affect on the overall response of the wall. It is

attributed to temperature effects and to the side shear developed due to volumetric changes of the soil.

5.2: Analyzing the results of the strain gauges

5.2.1: Processing the raw strain gauge data

Because the strain gauges are embedded in concrete, they are severely affected by microscale effects such as tension cracks and other environmental factors (temperature and moisture). Significant internal discrepancies were observed on the raw data from the strain gauges and an effort was made to identify, in the raw strain data, those strains developed by earth pressures due to bending of the shafts. The following plots of strain over time for the two year monitoring period time indicate the nature of the internal discrepancies in the raw strain gauge data.

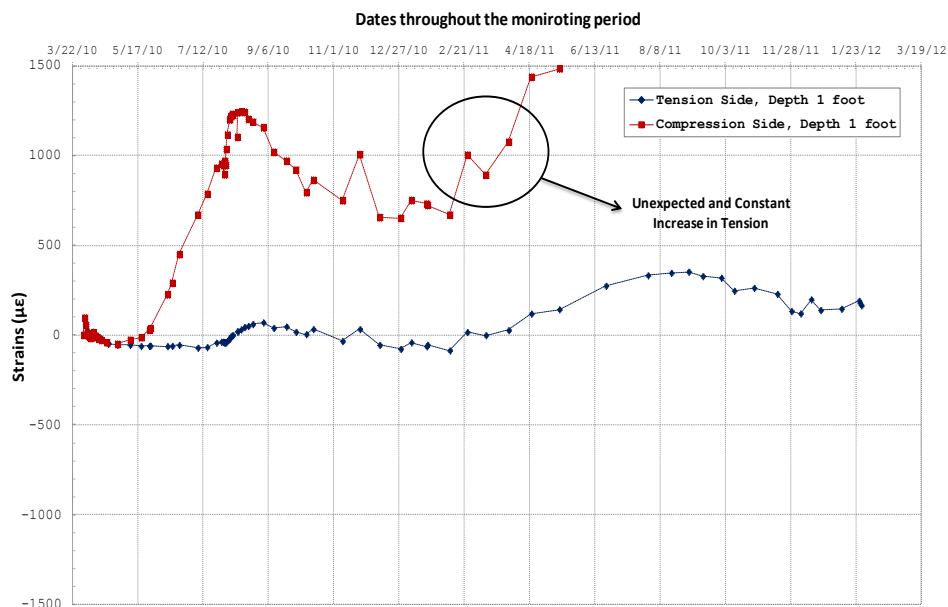


Figure 5.10: Unexpected constant increase in tension for the gauge at the compression side of the center shaft

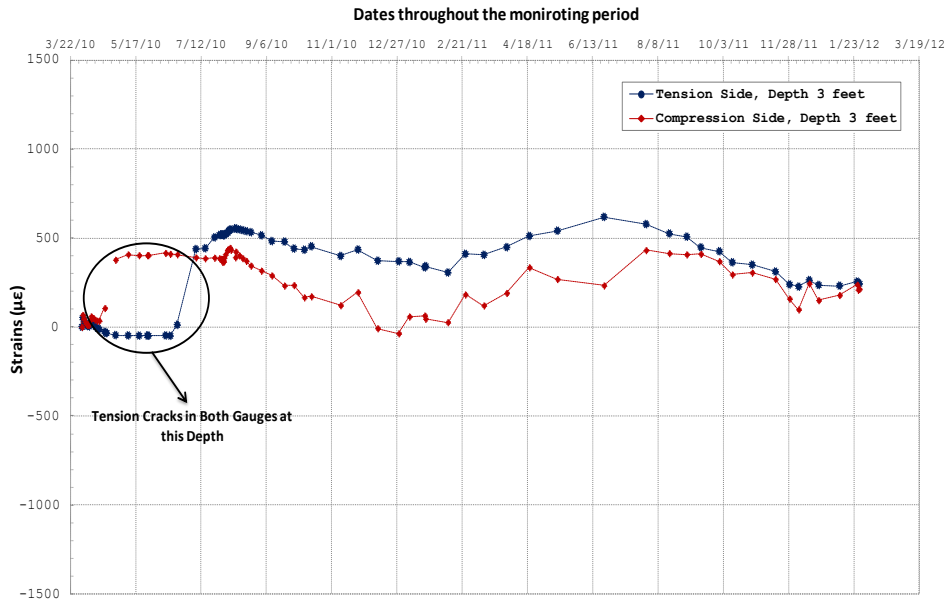


Figure 5.11: Tension cracks for both gauges at the same depth during concrete curing

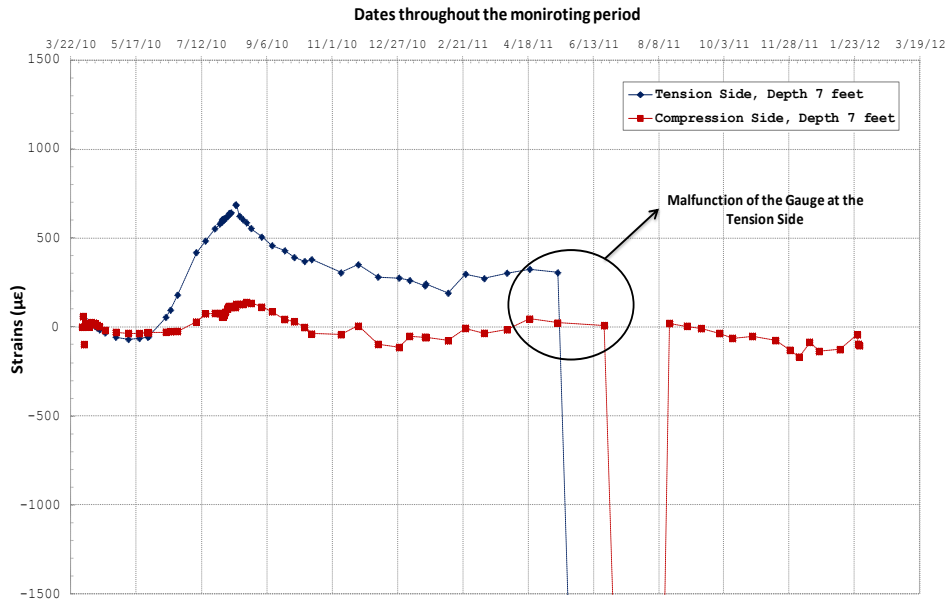


Figure 5.12: Malfunction of the gauge at the tension side a year upon its installation

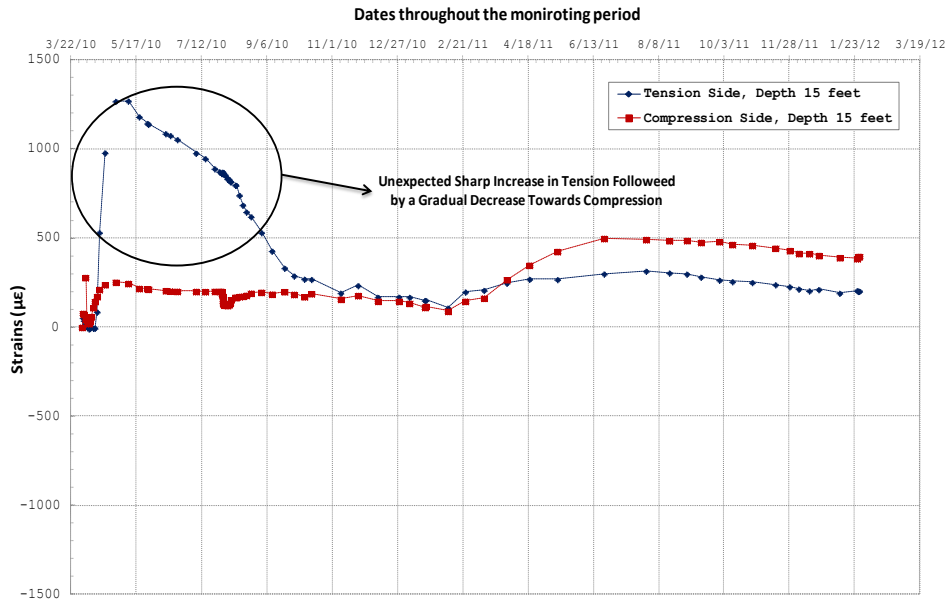


Figure 5.13: Sharp unexpected increase in tension for the tension gauge followed by a gradual decrease in compression

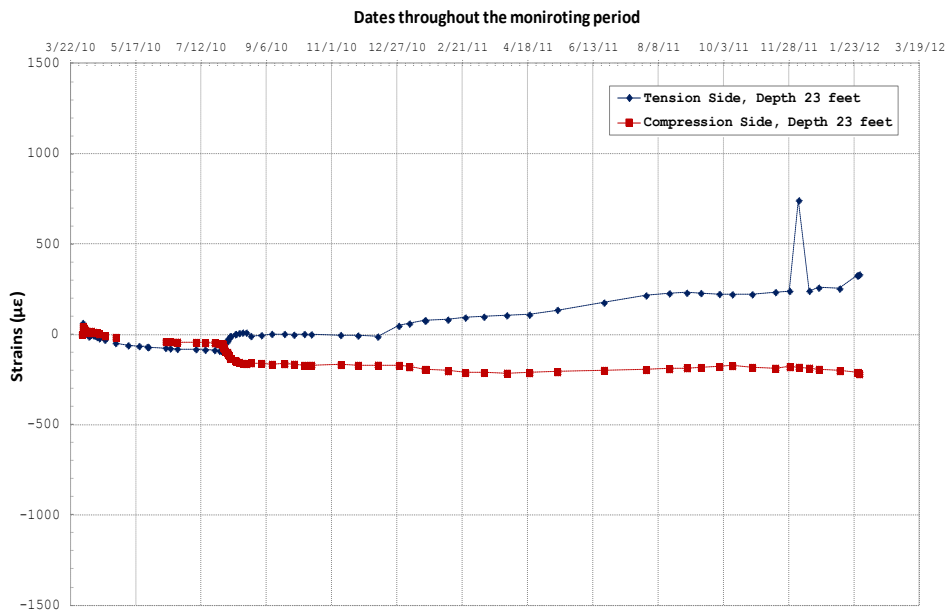


Figure 5.14: Good set of data at a depth of 23 ft of the center shaft

From the above diagrams, the sensitivity of the strain gauge results to the various factors mentioned before is evident. Specific patterns of unexpected behavior, observed in the results from the three instrumented shafts, include the following:

1. Tension Cracks: Approximately 30% of the strain gauges showed that tension cracks developed. The tension cracks are expected to have a range of 300 $\mu\epsilon$ and are developed mainly during the concrete curing. However, several tension cracks were in the order of 400 $\mu\epsilon$. Despite their microscale dimensions they are very important in the subsequent prediction of the earth pressures, because they generate an apparent local increase bending curvature which is due not to a corresponding increase in bending moment from earth pressure, but rather to a crack within the length measured by the gage. Because the gauges were attached to sister bars using epoxy and then protected with a membrane over a length of 4 inches, the chances of a tension crack are increased given the size of this effective length.
2. Unexpected increase in tension: Unexpected increases in tension were evident in a number of gauges. In some of those cases, there was a recovery trend towards more reasonable values while in others the gauges show increased tension even to date. Although the reason for this peculiar behavior is not clear, many hypothesis are available. Locked-in stresses due to heating of the epoxy could have caused a sudden release of energy towards the tension side which was higher than the energy released by the formation of a tension crack. Alternatively, temperature fluctuations could have caused differential strains within the white-light cables and the gauges, which could have affected the recorded results. Finally, in some cases the reflective quality of the coating within the reflecting cavity of the gauge could have degraded.

3. Spikes: Several cases of transient “spikes” were observed in the plots of strains over time. These spikes could be due to bad measurements taken in the field or to temporary malfunction of the instrumentation equipment. They do not indicate concrete cracking, because they are transient only, and real tension cracks do not heal themselves.
4. Malfunction of the gauges: Approximately 25% of the gauges have stopped responding two years after their installation. This behavior could be due to degradation of the epoxy used to attach the strain gauges on the sister bars or due to deterioration of the connecting cables or damage to the data acquisition equipment.

To date, about 20% of the gauges have not recorded a tension crack and are still functioning properly. Given that in order to use the results from the strain gauges, reasonable measurements should be taken by both gauges at the same depth, a systematic process is needed to analyze the raw data and predict the earth pressure distribution along the shafts. This process is based on the following principles:

1. Combine the results of the strain gauges from the instrumented shafts: From the deflected shapes measured by the inclinometers, the center and the east shafts exhibit similar deflections, while the west shaft deflects slightly less. Since the environmental conditions are the same for all three instrumented shafts, the results from the strain gauges at the same depth and side can be combined to generate a set of data for a "global" shaft, for use in subsequent analyses.
2. Eliminate the effect of tension cracks: As mentioned previously, tension cracks generate an increased bending curvature that does not represent the overall behavior of the shaft. In order to use the results from the strain gauges that include a tension crack, the offset that is generated in the plots of strain over time should be eliminated.

3. Do not use the gauges that show a constant increase in tension: Some gauges showed an abrupt increase in tension followed either by a constant tension or by a trend towards compression. These gauges should not be used in the analysis, because the reasons for this behavior are not clear and thus any possible anomalies cannot be quantified and eliminated from the results.
4. Eliminate the effect of spikes: Spikes, which could be due to bad readings or temporary gauge malfunction, should be eliminated from the plots of strain over time, because they do not represent the actual behavior of the instrumented shafts.

Following a process based on the above principles, a set of data is generated for a "global" shaft that includes strain results from all three instrumented shafts. Reasonable results were obtained for most depths. In the following figures the processed strains over time after are presented for various depths. In all these plots, the times when soil was excavated is evident as a significant change in bending moment, represented as the summation of changes in strains on the tension and compression sides.

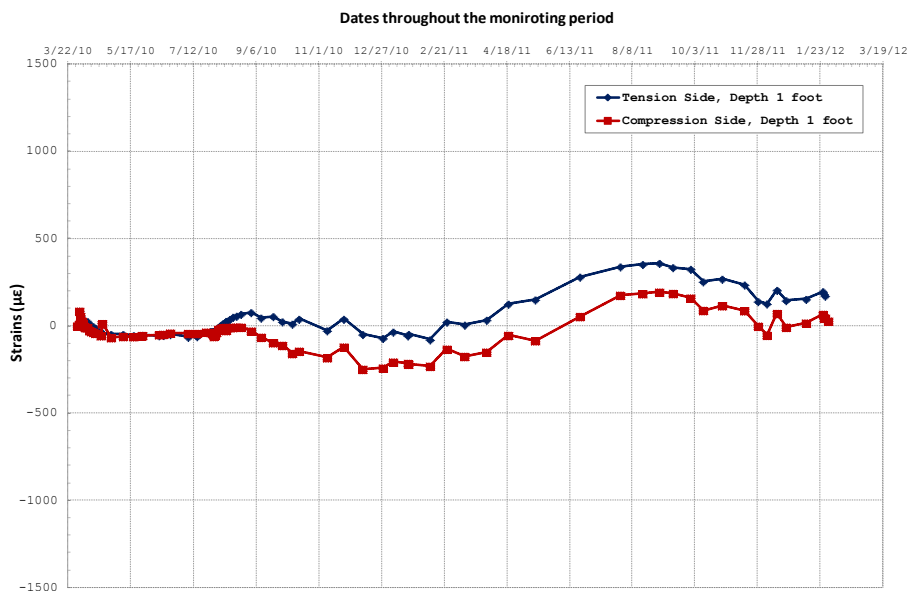


Figure 5.15: Processed plot of strain over time at a depth of 1 ft

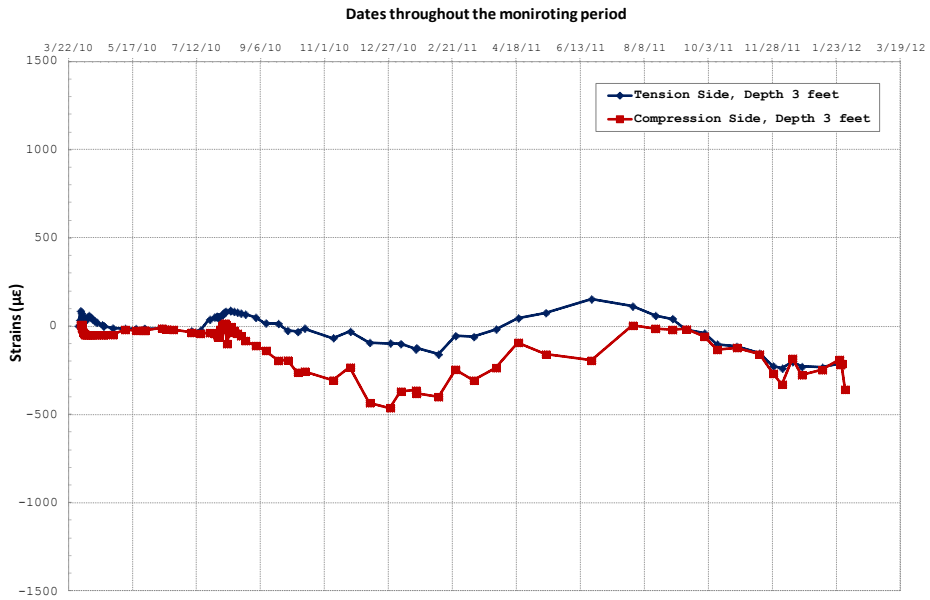


Figure 5.16: Processed plot of strain over time at a depth of 3 ft

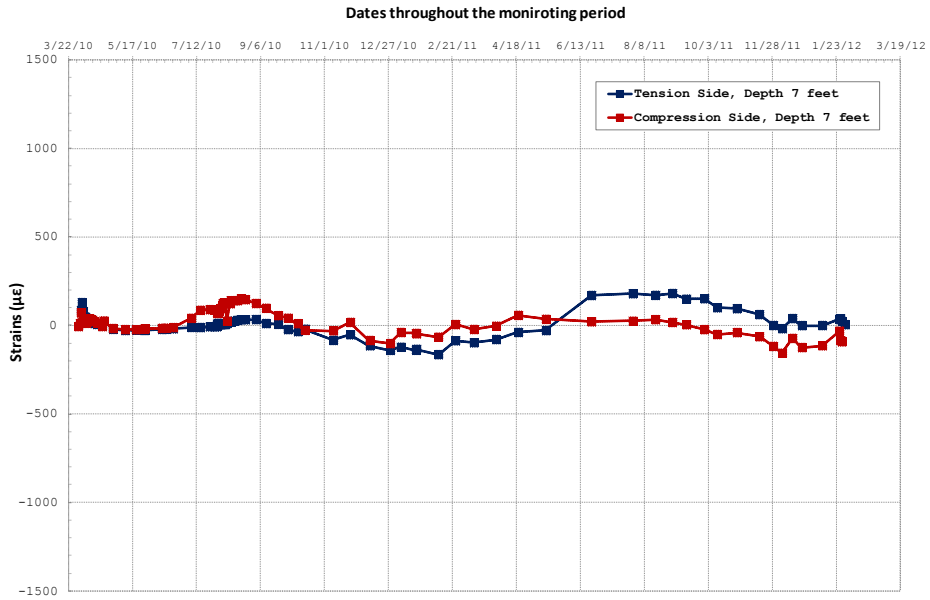


Figure 5.17: Processed plot of strain over time at a depth of 7 ft

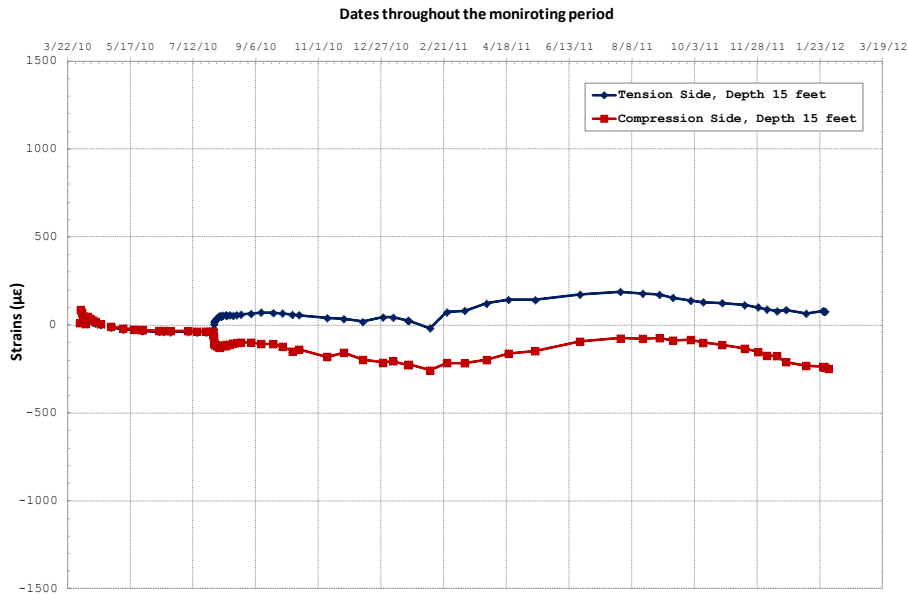


Figure 5.18: Processed plot of strain over time at a depth of 15 ft

5.2.2: Predicting the deflected shape from the strain gauge data

To evaluate the effectiveness of the procedure described above in processing the results of the strain gauges, the deflected shapes of the shafts are generated and compared to those derived from the inclinometer data. To evaluate the deflections along the shaft from the results of the strain gauges, the curvature profile is generated directly from the strain measurements using the following equation:

$$\varphi = \frac{\varepsilon_t - \varepsilon_c}{d} \dots\dots\dots(5.9)$$

where:

- φ = bending curvature
- ε_t = strain at the tension side of the shaft
- ε_c = strain at the compression side of the shaft
- d = horizontal distance between the strain gauges at the same depth

Given that the diameter of the shaft is 24 inches and the clearance on each side is 3 inches the horizontal distance between the strain gauges is constant at 18 inches. The processed strains at the tension and compression side of the "global" shaft are considered in the subsequent analysis and the bending curvature profiles for the selected dates are generated.

The derived curvature profiles are presented in figure 5.19. Due to the variability in the results, smoothing techniques are used in the subsequent analysis. Nevertheless, the effect of moisture fluctuations on the lateral response of the wall is evident. Another important issue is that curvature has developed below the excavation level down to the tip of the pile. This could be an effect of plastic behavior in the passive zone or heave of the soil at the excavation side caused by stress relief due to excavation of the soil. Also, negative pore pressures would have generated immediately after the soil was excavated; thus, as they dissipate, the strength of the soil would be reduced as it takes in water over time.

The curvature profiles are used to generate the deflected shapes of the "global" shaft at the selected dates. Sixth-order polynomial curve fitting was selected to smooth the curvature profiles. Matlab was used for this purpose and the polynomial equation was integrated twice to give the deflected shape. Due to the double integration process, two boundary conditions are needed, as follow:

- An assumed zero deflection at the tip of the shaft
- The measured deflections at the top of the shaft from the inclinometer data

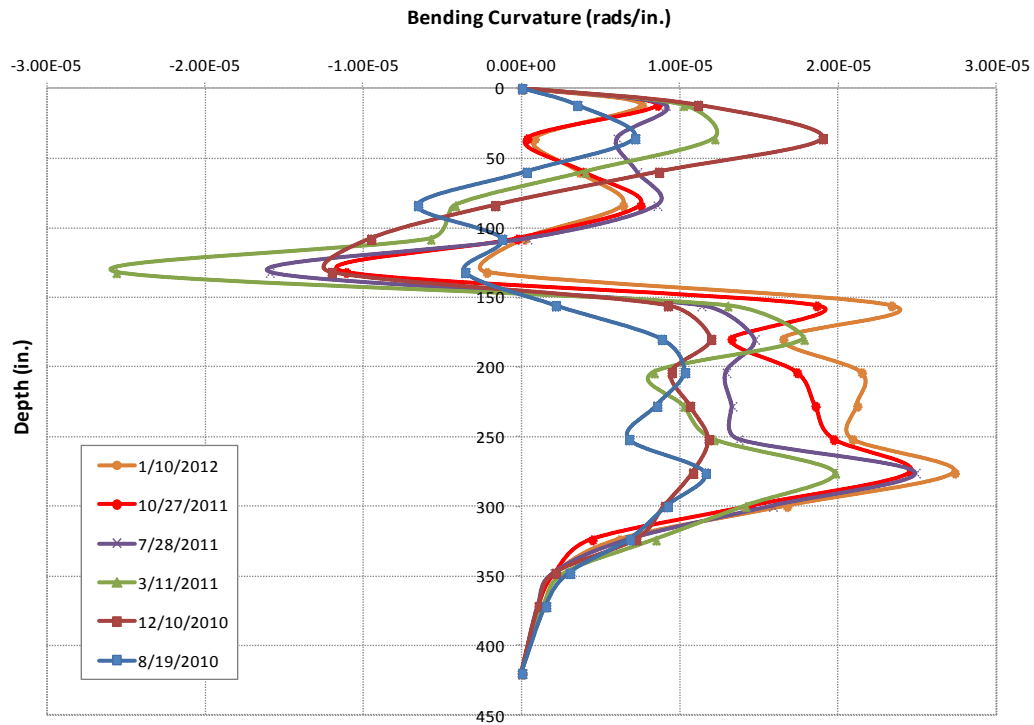


Figure 5.19: Bending curvature profiles for different dates throughout the two year monitoring period

In the following figures, the fitted sixth-order polynomial curves are presented, along with the deflected shapes predicted from the raw and the processed strain measurements for the selected dates. Processing of the raw strain measurements results in a more consistent and reasonable set of data for use in predicting earth pressures. The primary limitation of this procedure is that deflections at the top and bottom of the shaft are forced to be equal to the inclinometer data, because those data were used as boundary conditions.

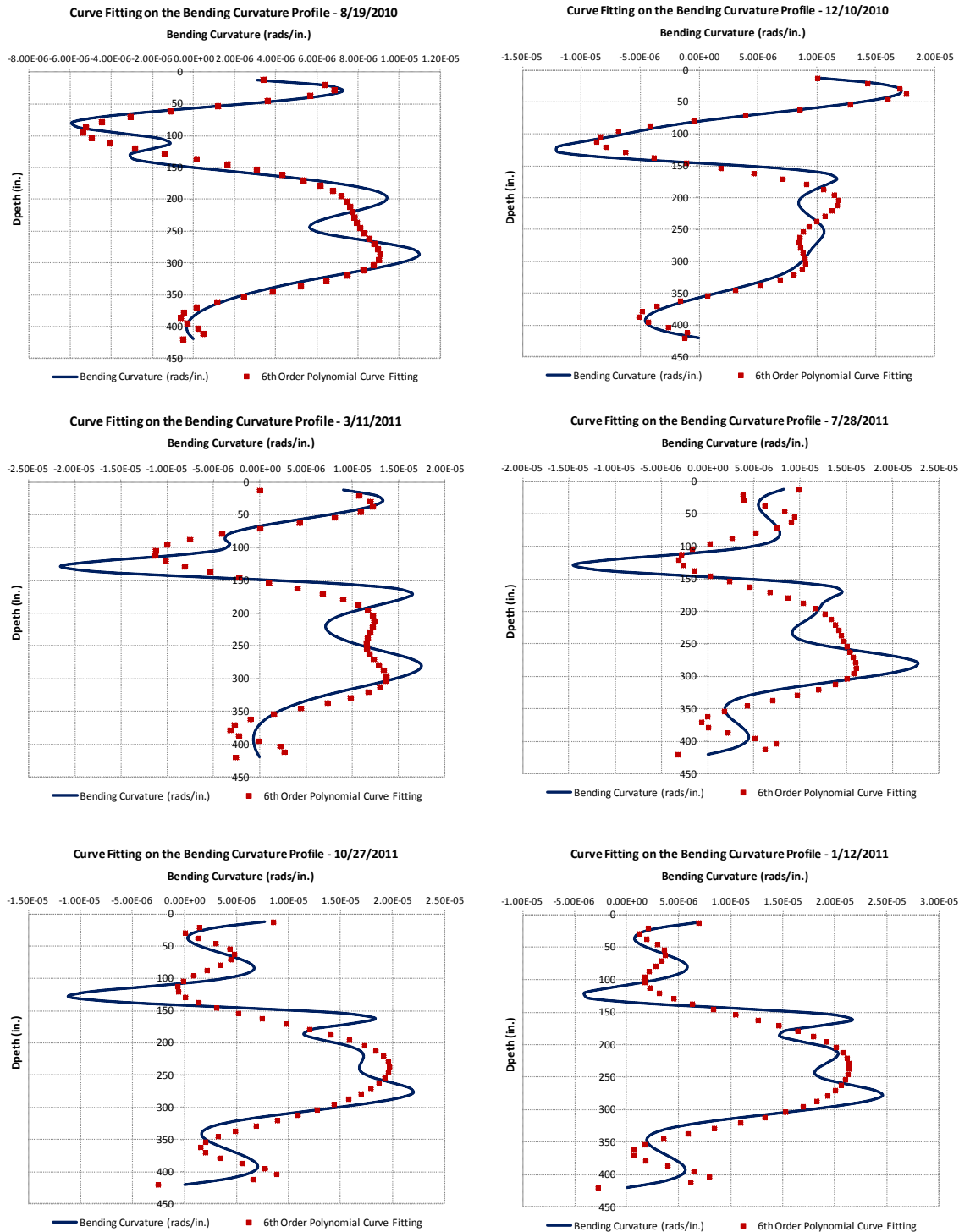


Figure 5.20: Sixth order polynomial curve fitting for the processed strains at the selected dates

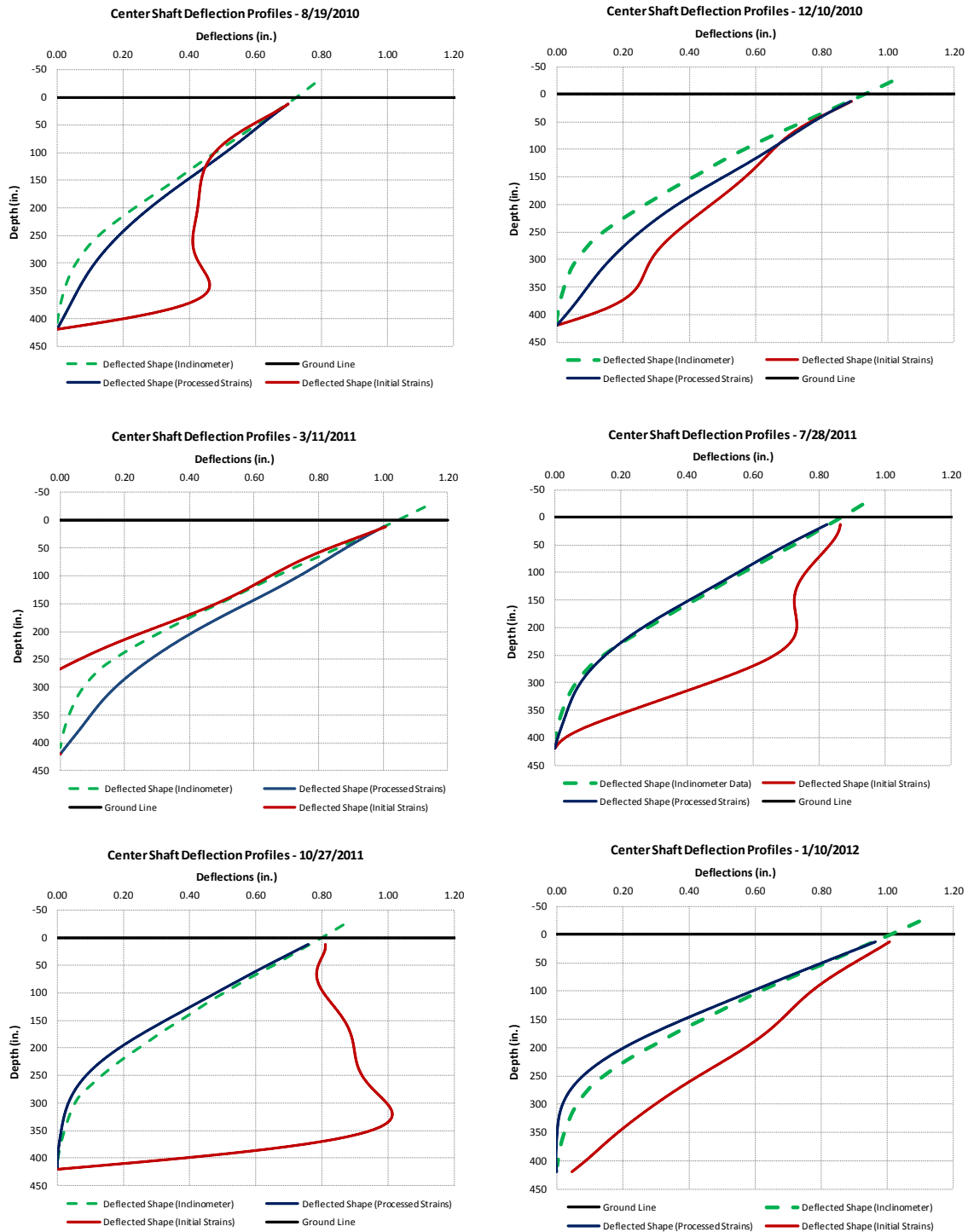


Figure 5.21: Deflected Shapes generated using processed and initial strain data at the selected dates

Another way to evaluate the effectiveness of processing the results from the strain gauges is to use numerical integration. With numerical integration, no boundary conditions are required to predict the rotation (θ) profiles and the deflected shapes (y). Simpson's rule is used for this purpose as described in the following equation:

$$\int_a^b f(x)dx = \frac{b-a}{6} \left[f(a) + 4f\left(\frac{a+b}{2}\right) + f(b) \right] \dots\dots\dots(5.10)$$

Incremental polynomial curve fitting is applied on the raw curvature profiles due to the internal discrepancies in the processed strain data above the excavation level. These profile are double-integrated using Simpson's rule, and the deflected shapes are generated and compared to those derived using the inclinometer data.

In the initial time period after construction, the deflections obtained from the strain gauges were lower than those derived from the inclinometer results. The strain gauges measure only relative deflections with respect to the tip of the shaft, assuming that that point has zero rotation. However, from the inclinometer data it is clear that a non zero initial rotation develops at the tip of the shafts which is not depicted on the strain measurements. This initial rotation, which is evaluated from the raw inclinometer data, was imposed as boundary condition., Those prescribed rotations were applied at the tip of the shaft for the selected dates as indicated in table 5.1.

Table 5.1: Values of initial prescribed rotation developed at the tip of the shafts

Date	Prescribed Rotation at the Tip (rads)
8/19/2010	0.000279
12/10/2010	0.000282
3/11/2011	0.000328
7/28/2011	0.000302
10/27/2011	0.000261
1/10/2012	0.000251

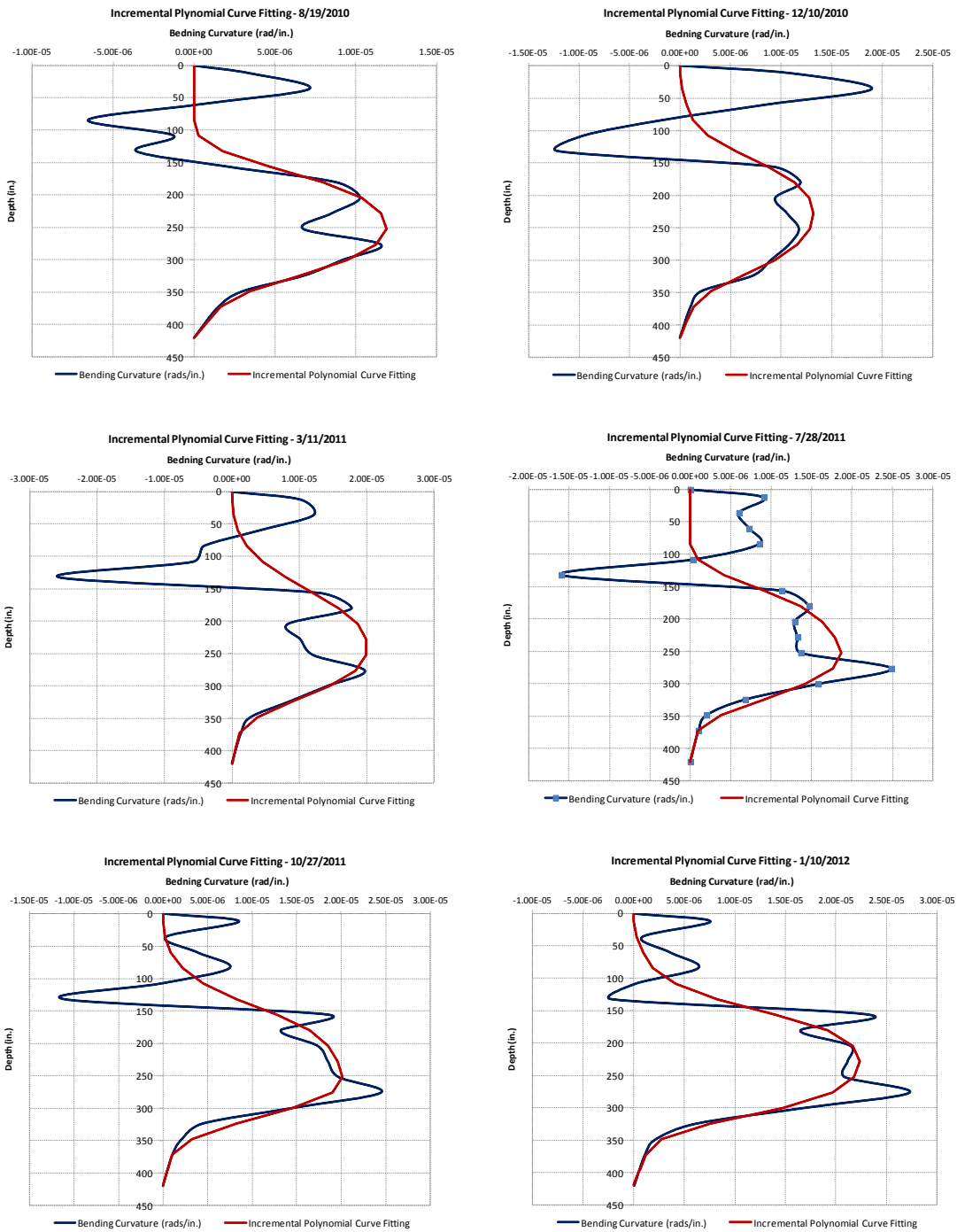


Figure 5.22: Incremental polynomial curve fitting on the curvature profile at the selected dates

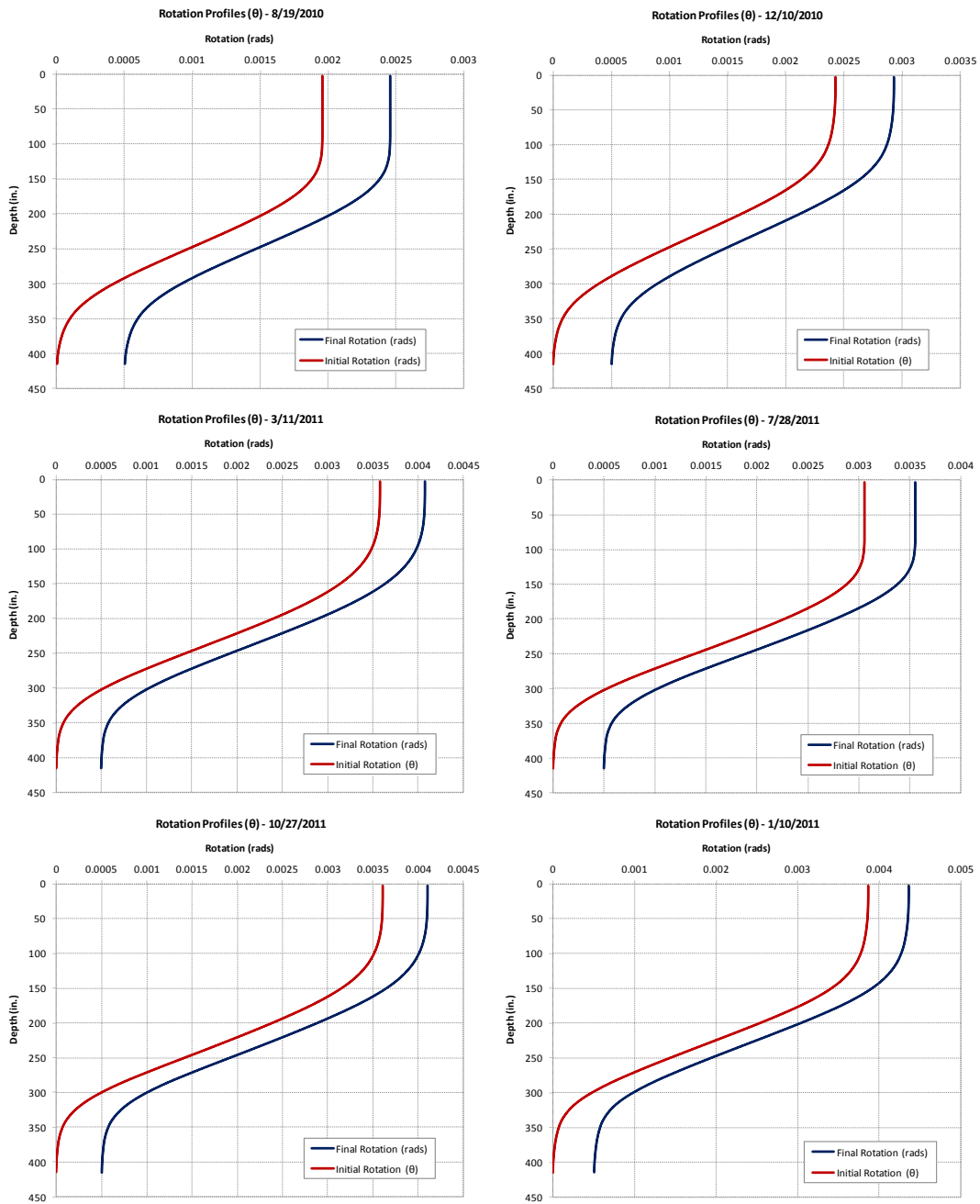


Figure 5.23: Initial and adjusted rotation profiles to account for the prescribed rotation at the tip of the shaft at the selected dates

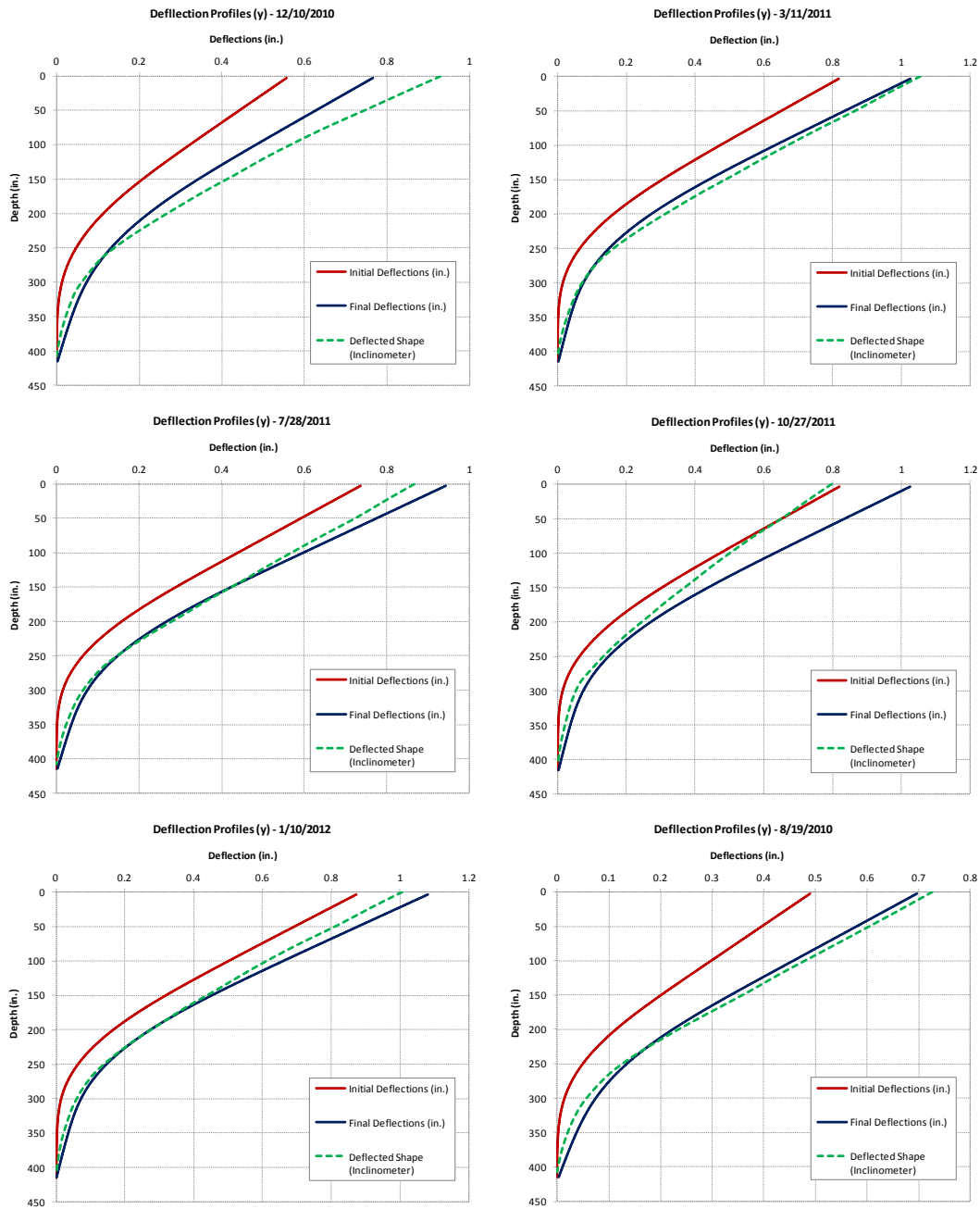


Figure 5.24: Initial and adjusted deflected shapes to account for the prescribed rotation at the tip of the shaft at the selected dates

Several useful conclusions can be drawn from the above analysis with respect to the results of the instrumentation program and more specifically the strain gauges and the inclinometers:

- Raw strain-gage results varied significantly due to tension cracking and temperature effects.
- Raw strain-gage should be processed by eliminating the spurious local effects of tension cracking and to combine the strain gauges from the three instrumented shafts at the same depth and side, for increased reliability.
- The effectiveness of the above procedure was evaluated by predicting the deflected shapes from the processed strains and comparing it to the inclinometer data. Initially, sixth-order polynomial curve-fitting was used for the curvature profiles, and the polynomials were integrated twice to generate the deflection profiles. Good agreement was observed between the deflected shapes from the inclinometer data and the strain data.
- Incremental polynomial curve fitting and numerical integration using Simpson's rule was also used on the curvature profiles. A prescribed initial rotation at the tip of the shafts was added on the rotation profiles, and good agreement was obtained for the deflected shapes from the inclinometer data and the strain data.

5.2.3: Analyzing the results of the strain gauges

A significant limitation on using the inclinometer data to predict the lateral earth pressures applied on drilled shafts is the fact that three differentiations are required to generate the net earth pressure distributions from the measured slopes. In that sense, the data from strain gauge are much more reliable as the curvature profiles are evaluated directly from the strain measurements using equation (5.9).

The processed strains are used in the subsequent analysis and incremental polynomial curve fitting is applied to smooth the curvature profiles. The moment profiles for the selected dates that represent different moisture conditions of the Taylor clay are generated using the $M-\phi$ plot obtained by the method of slices. The shear force (S) profiles and net earth pressure diagrams (w) are generated from the moments along the shafts according to the following equation:

$$w = \frac{dS}{dz} = \frac{d^2M}{d^2z} \dots\dots\dots(5.12)$$

The above procedure is similar to that followed previously to analyze the inclinometer data. The bending moment, shear force and net earth pressure profiles for the selected dates are presented in the following figures. The effect of moisture fluctuations of the Taylor clay on the lateral response of the drilled shaft retaining wall is evident.

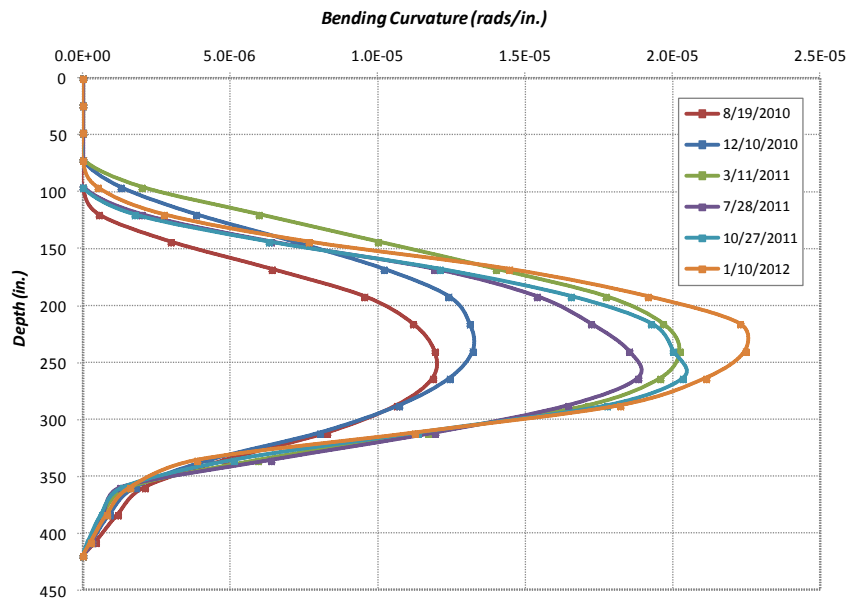


Figure 5.25: Bending curvature profiles for different dates throughout the two year monitoring period

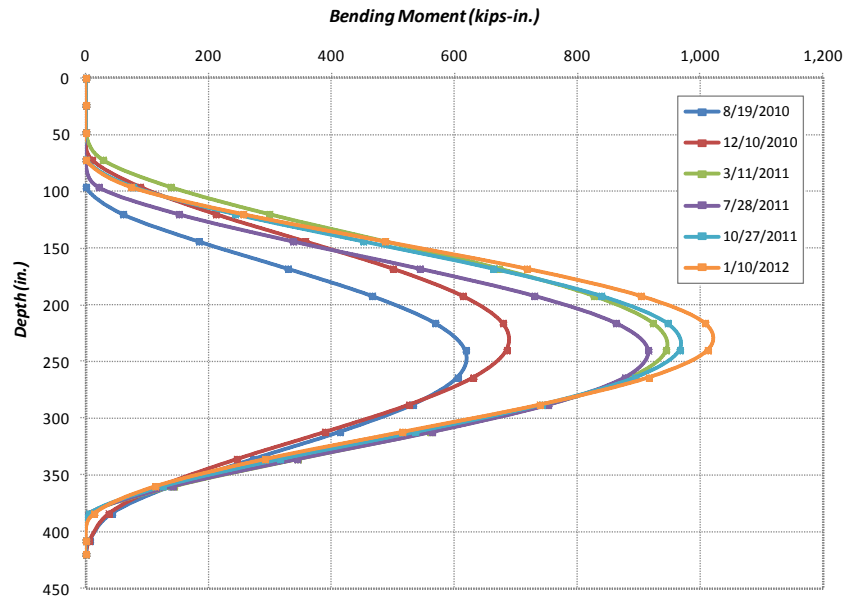


Figure 5.26: Bending moment profiles for different dates throughout the two year monitoring period (using M- ϕ curve from the method of slices)

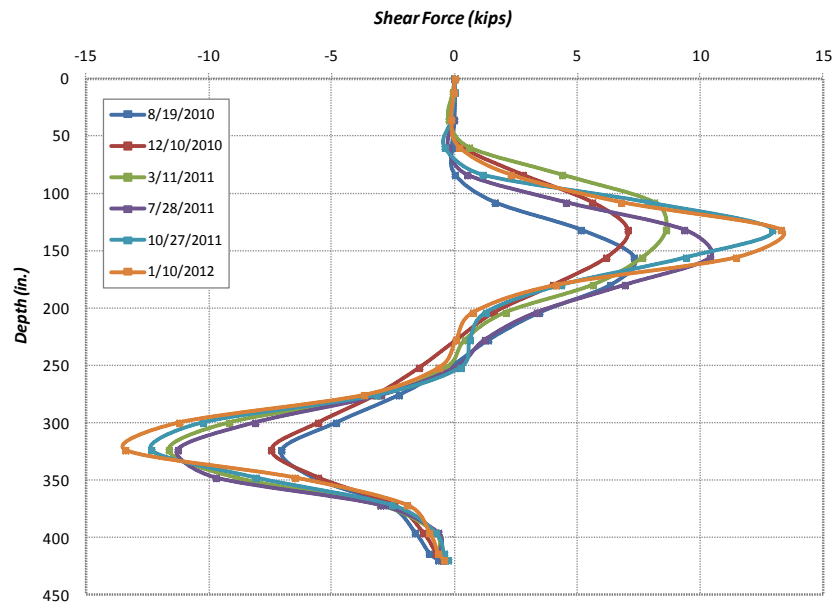


Figure 5.27: Shear force profiles for different dates throughout the two year monitoring period

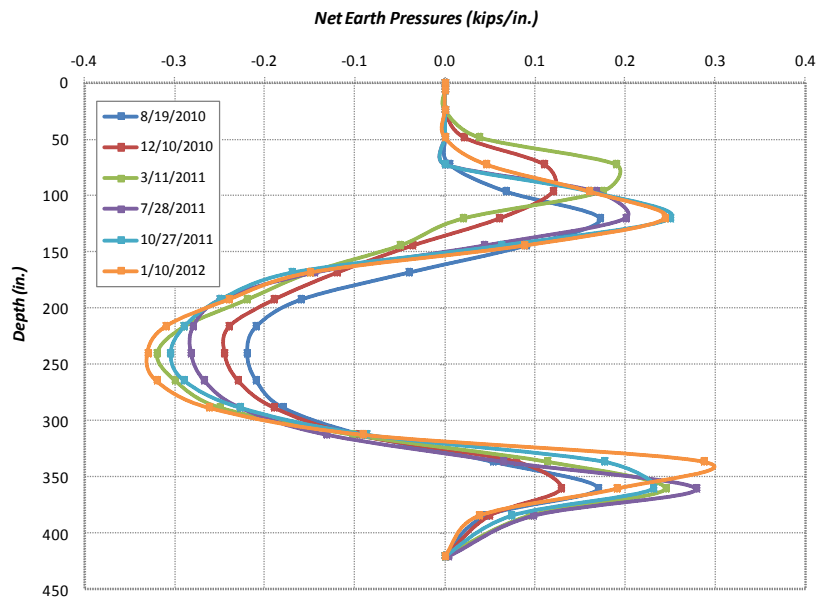


Figure 5.28: Net earth pressure diagrams for different dates throughout the two year monitoring period

The net earth pressure distributions predicted by the inclinometer and the strain gauge data are compared in the following figures.

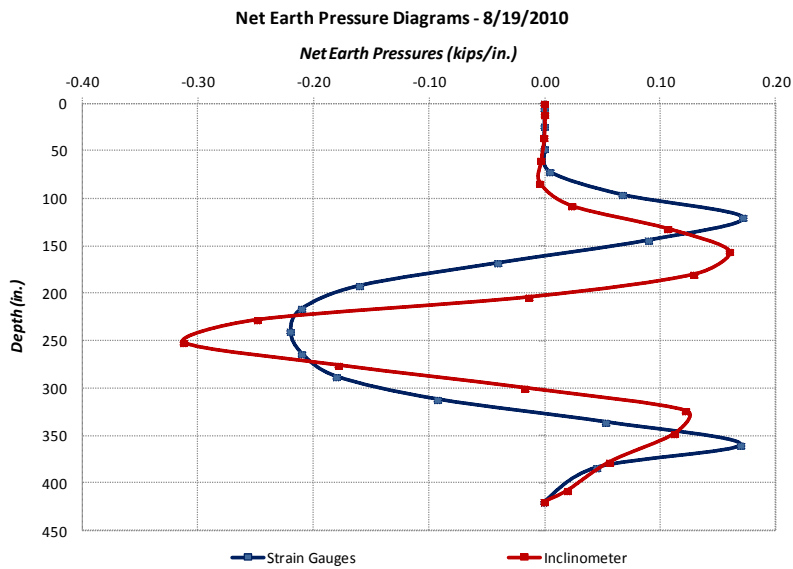


Figure 5.29: Comparison of the net earth pressure distribution evaluated using the results of the strain gauges and inclinometers - 8/19/2010

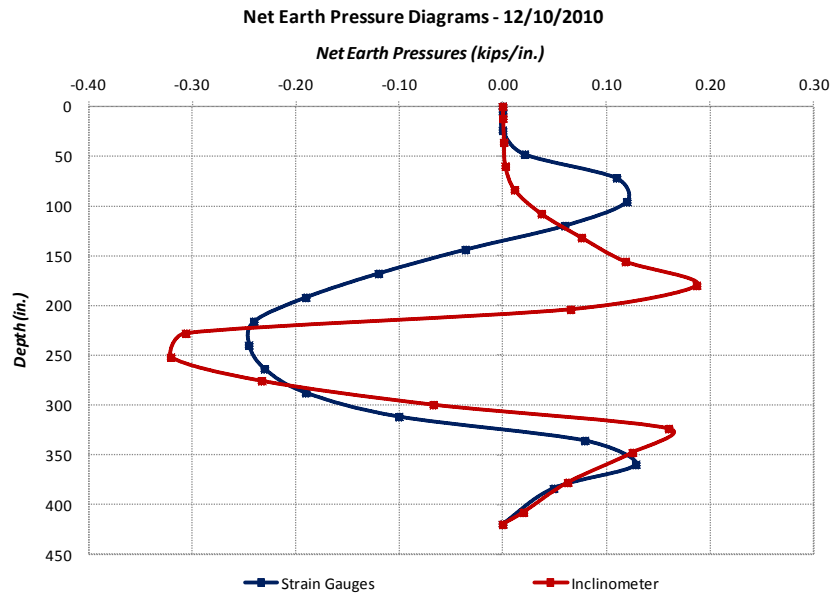


Figure 5.30: Comparison of the net earth pressure distribution evaluated using the results of the strain gauges and inclinometers - 12/10/2010

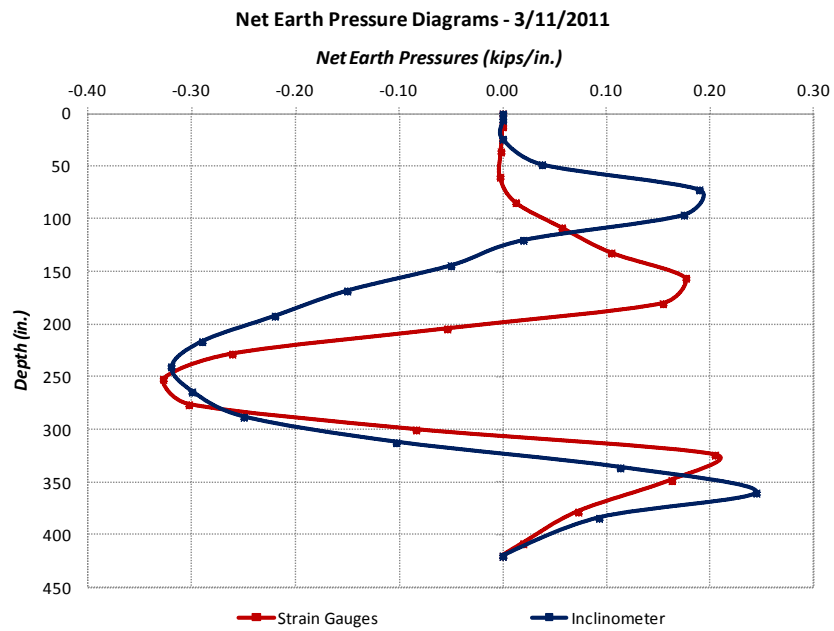


Figure 5.31: Comparison of the net earth pressure distribution evaluated using the results of the strain gauges and inclinometers - 3/11/2011

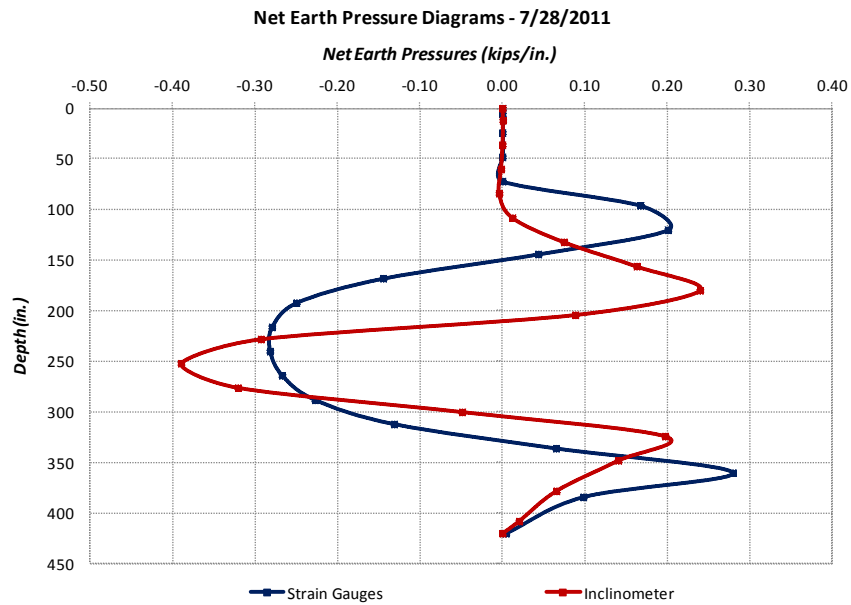


Figure 5.32: Comparison of the net earth pressure distribution evaluated using the results of the strain gauges and inclinometers - 7/28/2011

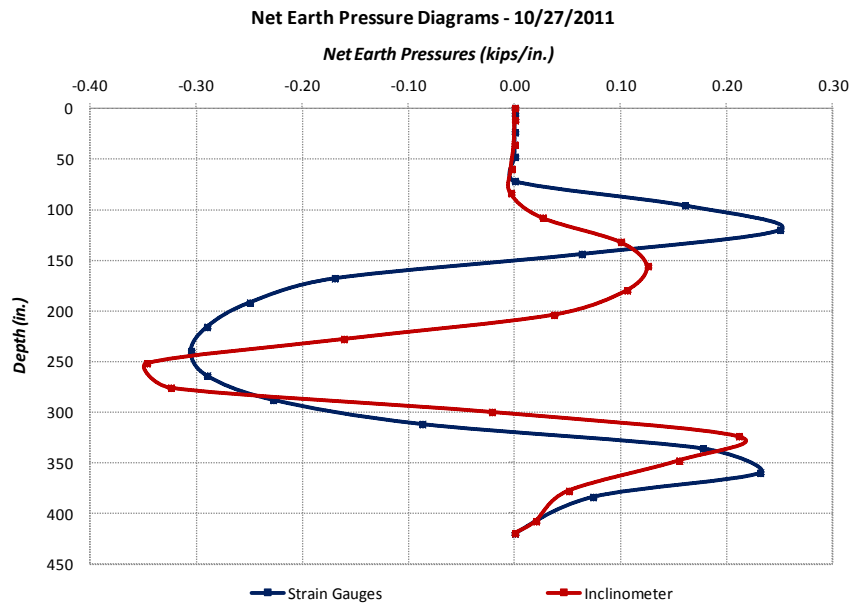


Figure 5.33: Comparison of the net earth pressure distribution evaluated using the results of the strain gauges and inclinometers - 10/27/2011

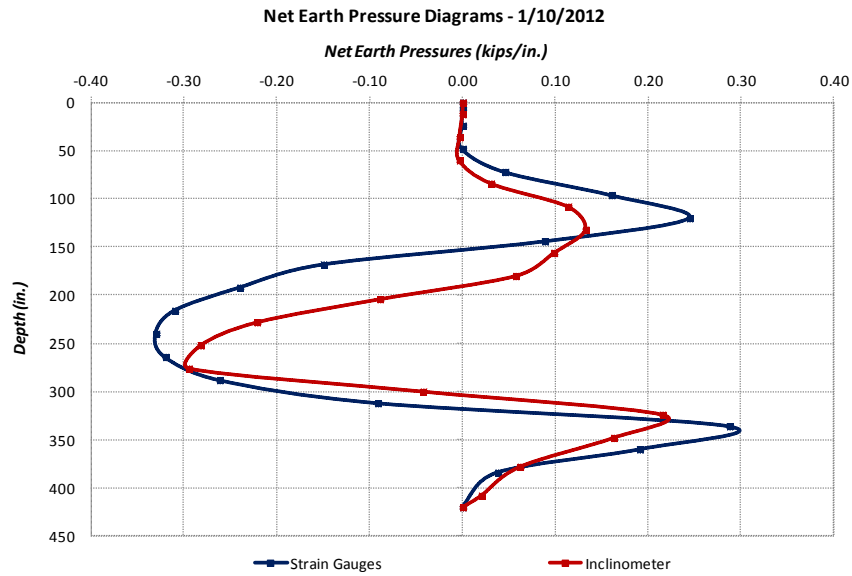


Figure 5.34: Comparison of the net earth pressure distribution evaluated using the results of the strain gauges and inclinometers - 1/10/2012

Many useful conclusions are drawn from the analysis of the strain gauges:

- Because the strain gauges are embedded in concrete, they are sensitive to micro-scale effects such as tension cracks or environmental factors such as temperature and moisture. For that reason, incremental polynomial curve-fitting was used to generate the curvature profiles. While theoretically correct, such curve-fitting is always somewhat subjective, and the results should be evaluated with understanding of this. Below the excavation level, where the effects of temperature and moisture are significantly smaller, local spikes on the curvature profile are minimized. However, similar distributions and magnitudes of curvature profiles are evaluated using the strain gauge data and the inclinometer data.
- The net earth pressure distributions predicted from the strain gauge and inclinometer data are similar. Although different curve-fitting methods were used, the shapes and

magnitudes of these profiles are similar, and correspond well to those expected for such shaft deflections.

- The curvature and moment profiles are smaller for the first two selected dates (8/19/2010 and 12/10/2010). As indicated from the deflected shapes for these two days, the deflections predicted using the strain data are smaller than those predicted using the inclinometer results. As a result, the curvature and moment profiles are smaller as well.
- Negative curvature develops above the excavation level. While this could be related to the sensitivity of the strain gauges to temperature fluctuations, it could also be an effect of negative side shear applied on the walls of the shafts due to the volumetric changes of the surrounding soil. Because the magnitude of the negative curvature is in most cases unrealistic, it was not taken into account in the analysis. It is discussed later in this thesis.
- The widths of tension cracks calculated based on the net earth-pressure diagrams from strain gauge data are highly sensitive to the curve-fitting method used to develop the curvature profile. As significant discrepancy was observed on the curvature profiles above the excavation level the point where the curvature is generated that depicts the size of the tension crack, depends on the curve fitting method.

5.3: Conclusions on the results of the instrumentation program

Although not apparent from the raw data, quite good agreement was obtained between processed strain-gauge data and inclinometer data. Raw strain-gage data had to be processed to eliminate the effects of tension cracks. Processed strain-gauge data were

evaluated by comparing the corresponding deflected shapes to those derived from inclinometer data.

Deflection profiles were predicted from strain-gage data using numerical and classical integration of a sixth-order polynomial. For the numerical integration, incremental polynomial curve fitting was used and an initial rotation at the tip of the shafts evaluated from the inclinometer data was added to the rotation profiles. Good agreement was observed on the deflected shapes, and the processed strain gauge results were used in predicting the earth pressures.

To generate the net earth pressure distributions using the inclinometer data, three differentiations are required. Using the strain gauges, in contrast, the curvature profile is generated directly from the strain measurements and only two differentiations are required in the subsequent evaluation of the earth pressures. However, significant discrepancies were found in the results from the strain gauges, and subjective curve-fitting was applied to the curvature profiles. For this reason, the inclinometer data are much more reliable in predicting the earth pressure distributions than the strain-gage data, especially above the excavation level. To use the results from the strain gauges, in addition to processing the results as described previously, corrections should be made to account for temperature and moisture effects.

Bending moments, shear force, net earth pressure profiles were plotted using both the inclinometer data and the strain data for different dates, corresponding to different moisture conditions of the Taylor clay. The effect of shrinking and swelling of the soil is evident, as higher earth pressures are applied on the wall during the winter months when the moisture content of the soil is high. Good agreement was observed between strain data and inclinometer data.

Chapter 6: Simulating the Lateral Response of the Wall Using a p-y Model

6.1: Introduction to p-y analysis

The so-called p-y analysis uses finite differences to analyze laterally loaded piles. Its solution includes the deflected shape, shear force, bending moment, and soil-pressure profiles along the pile. Several available programs (such as LPILE) simulate the p-y response of various types of piles or drilled shafts. However, due the nature of this project and given the unusual geometric characteristics and the soil type, a spreadsheet was developed for this purpose. This spreadsheet allows for several input parameters to be adjusted and provides better insight than commercial software into the numerous factors that affect the p-y response of a drilled shaft subjected to lateral loading.

Because soil is excavated on one side only of drilled shaft retaining walls, the non-linear springs that simulate the soil stiffness only exist below the excavation level. Because the soil cannot sustain tension under drained conditions, the springs act in compression only. The earth pressures applied on the wall above the excavation level are simulated using a triangular pressure distribution. This distribution was selected because it is consistent with empirical suggestions by TxDOT for similar walls and soil type, permitting direct comparison with the results of our analysis. As future work, other pressure distributions should be considered, as well as the fact that the loads are a function of the lateral displacements of the wall.

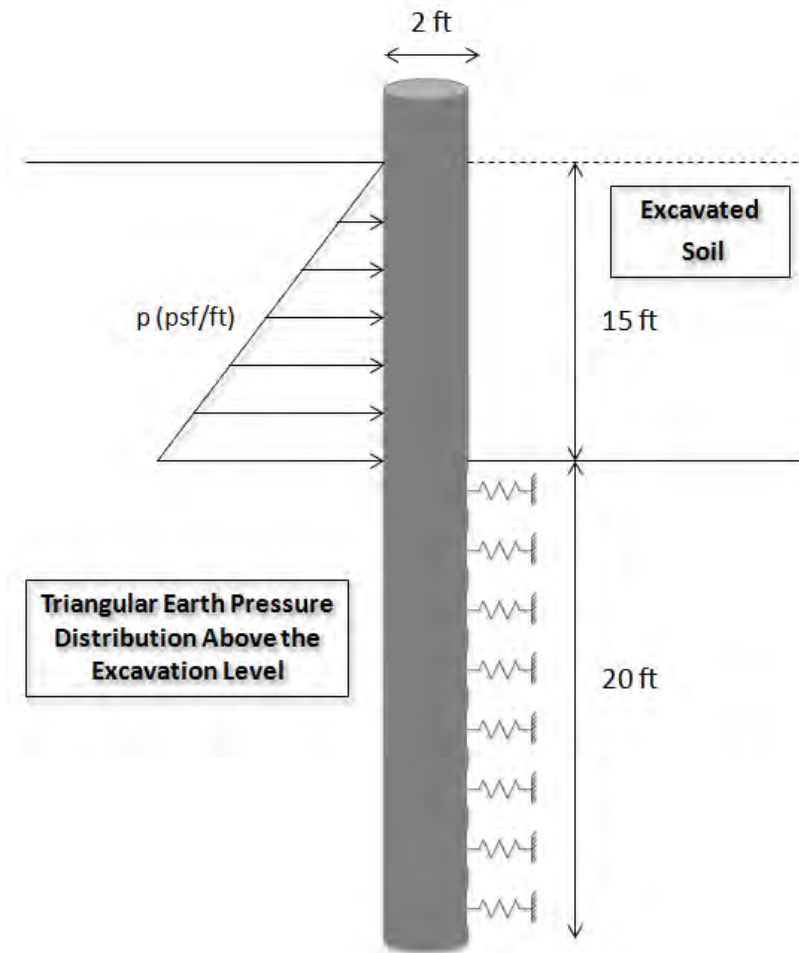


Figure 6.1: Schematic representation of the p-y model used to predict the magnitude of the earth pressure distribution

Given the small deflections measured in the first two years of monitoring, the soil could be assumed to behave linearly. However, a non-linear p-y curve is suggested to better capture the actual behavior of the Taylor clay. This curve can be generated from the results of the instrumentation program or developed from empirical recommendations in the literature for similar soil types. Finally, due to the non-linearity of the soil and the drilled shafts as described by the $M-\phi$ curve, iterations are required to obtain the final solution.

6.2: Input data used in the p-y analysis

P-y curves for different soil types are developed mainly from the results of full scale lateral loading tests on piles or drilled shafts. This thesis uses the p-y curves for stiff fissured clays under undrained conditions recommended by Reese et al. (YYYY), based on the results of lateral load tests at a similar site in Houston. Although the response of the wall is currently characterized by drained conditions, there are no empirical p-y curves for stiff clays under drained loading. More importantly this type of analysis was selected in order to be consistent with the current design procedures followed by TxDOT for drilled shaft retaining walls in expansive clays.

To generate the p-y curve for use in the p-y analysis, several input parameters are required related to the ultimate soil resistance profile of the Taylor clay. For this purpose, the shear strength profile from the geotechnical investigation that preceded the wall construction is used. As indicated in the following figure there are two zones of linear shear strength increase along the shafts. The average unit weight of the soil is 126 pcf.

Another significant parameter required to generate the p-y curve is the stiffness of the soil, described by the value of ϵ_{50} from triaxial stress-strain curves. From empirical correlations, recommended values for very stiff fissured clays are $\epsilon_{50} = 0.005$ to 0.006 . From the results of the triaxial UU tests, however, an average value of $\epsilon_{50} = 0.01$ was obtained for the Taylor clay, which is typical for medium clays. A sensitivity analysis is made in this chapter to investigate the significance of this parameter on the final response of the wall.

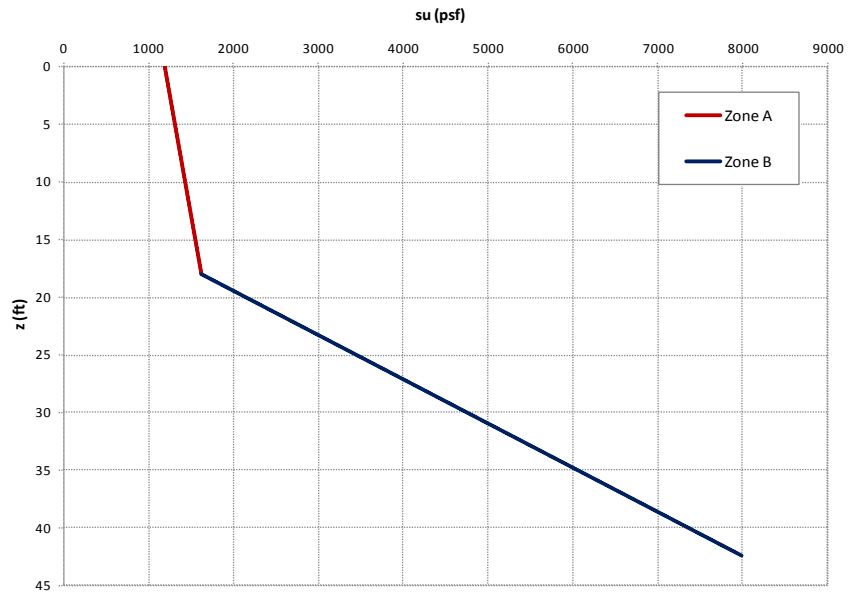


Figure 6.2: Shear strength profile along the shafts for the Taylor Clay

The ultimate soil resistance is evaluated based on the following equation:

$$p_u = \min \left[\left(3 + \frac{\gamma'}{c} + J \frac{z}{b} \right) cb, 9cb \right] \dots\dots\dots(6.1)$$

where:

- γ' = submerged unit weight = 126 pcf
- J = non-dimensional coefficient related to the soil type = 0.25
- z = depth below the ground surface (ft)
- b = pile diameter (ft)
- c = undrained shear strength for the stiff clay (psf)

Given the properties of the Taylor clay, the soil resistance profile is generated as indicated in the following figure. As in the case of the shear strength profile, two zones of linear increase are observed along the shafts.

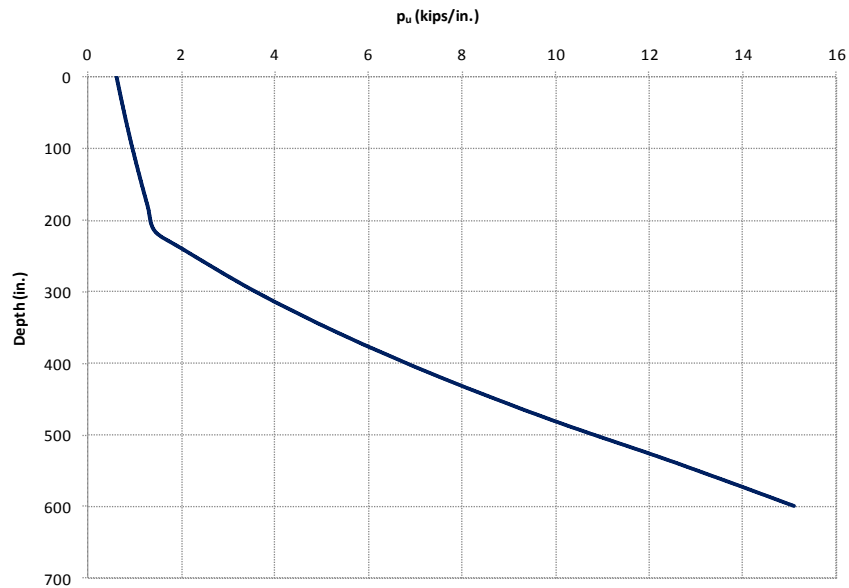


Figure 6.3: Ultimate soil resistance profile for the Taylor Clay from the original ground surface

The deflection y_{50} at one half of the ultimate soil resistance is evaluated from the following equation:

$$y_{50} = 2.5\varepsilon_{50}b \dots\dots\dots(6.2)$$

Assuming that $\varepsilon_{50} = 0.005$ we get that $y_{50} = 0.3$ inches. Ultimately, the p-y curve is described by the following equation:

$$\frac{P}{P_u} = 0.5 \left(\frac{y}{y_{50}} \right)^{0.25} \dots\dots\dots(6.3)$$

The straight portion of the p-y curve equals the ultimate soil resistance and is reached for displacements higher than $16y_{50}$. the wall. Since the ultimate soil resistance varies along the shafts, a unique p-y curve is developed for each depth. Therefore, a normalized p-y curve should be developed with respect to p_u and y_{50} , respectively.

Following the above procedure, which applies to static loading, the normalized p-y curve for the Taylor clay is generated and presented in figure 6.4.

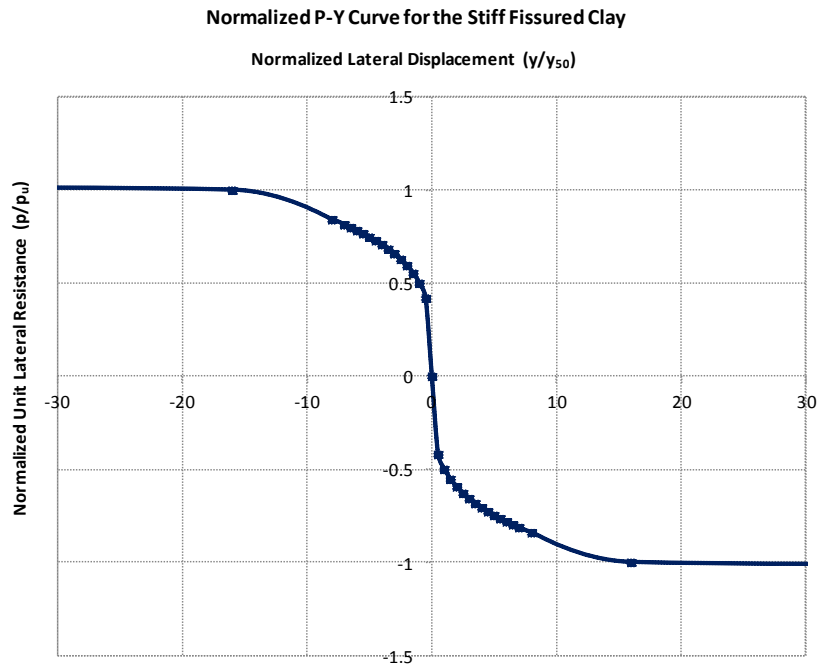


Figure 6.4: Normalized p-y curve for the Taylor Clay

Apart from the p-y curve, the stiffness of the shafts described by the M- ϕ curve is important. Different methods were used to develop this curve as described in a previous chapter. The curve generated using the method of slices and not assuming a cracked section, is used in the subsequent analysis.

Finally, the earth pressure distribution above the excavation level is used as an external load on the p-y model and an effort is made to predict the range of earth pressures by matching the deflected shape to the inclinometer data. Although subjective, a triangular earth pressure diagram is used in accordance with recommendations by TxDOT for this particular soil type.

6.3: Sensitivity analysis on the p-y model

An initial attempt is made to use the p-y model to match the deflected shape from the inclinometer data, using the shear strengths derived from the geotechnical investigation without accounting for any changes in the properties of the soil on the passive zone due to the excavation. In this analysis, the M- ϕ curve from the method of slices is used to describe the non-linearity of the drilled shafts. The stiffness of the soil is described using a value of $\epsilon_{50} = 0.005$, which is an average value for stiff fissured clays. A value of 40 psf/ft is used for the triangular earth pressure distribution, and the deflected shape of the shaft from the p-y analysis is compared to the inclinometer data for similar top deflections.

As indicated in figure 6.5, the top deflection of the shaft based on the p-y model equals 0.72 inches. However, the deflected shapes from the p-y analysis and the inclinometer data are significantly different. More specifically, in the case of the p-y results, the tip of the shaft is fixed with zero rotation (θ) below a depth of 270 inches. The inclinometer data, in contrast, shows a non-zero initial rotation.

To better understand the reason for this difference, a sensitivity analysis is made of the various parameters that could affect the deflected shape generated from the p-y model. These are the following:

- The stiffness of the soil depicted in the value of ϵ_{50} .
- The ultimate soil resistance (p_{ult}) related to the shear strength on the passive zone.
- The non-dimensional coefficient related to the soil type (J)

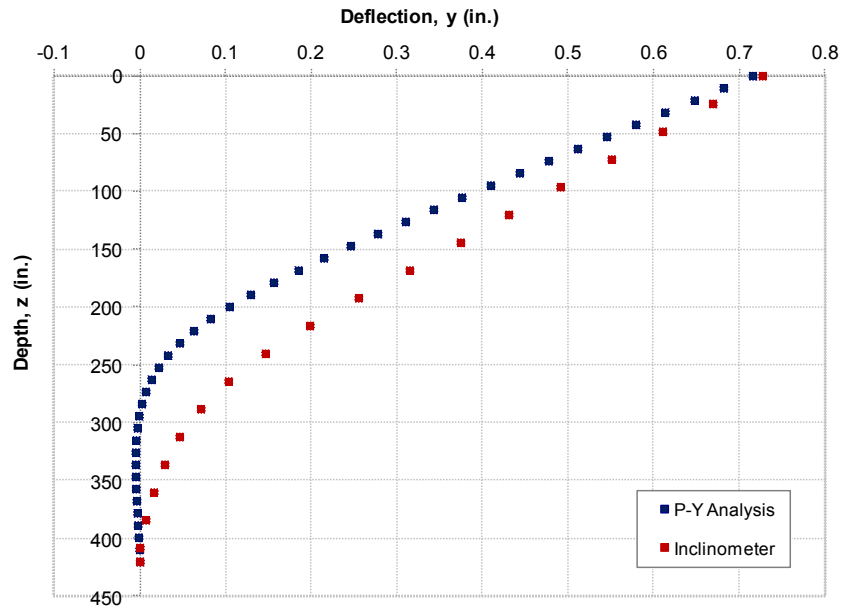


Figure 6.5: Comparison between the deflected shapes from the inclinometer and the initial p-y analysis

The initial p-y model assumes that the shear strength and stiffness of the soil on the passive zone are not affected by the stress relief due to the excavation. However, because the stiff clay is highly overconsolidated, negative pore pressures were generated immediately after the excavation and then started to dissipate over time. Therefore, the effective stresses and the shear strength of the soil decrease as consolidation occurs. Moreover, because the excavation level is lower than the average ground water table at the project site, changes on the hydrostatic conditions could also result in a softer and weaker soil. Because water is occasionally pumped out of the excavation, upward seepage occurs, leading to smaller effective stresses and shear strengths in the passive zone. Heave of the soil on the excavated side also significantly reduces the stiffness of the soil in the passive zone. The results of the sensitivity analysis are as follows.

1. Sensitivity analysis on the stiffness of the soil (ϵ_{50}):

Typical values for ϵ_{50} for stiff clays are from 0.005 to 0.006. However, the soil on the passive zone is affected by the stress relief after the excavation and thus it may have become softer. Hence a sensitivity analysis is valuable, as it indicates the importance of the parameter ϵ_{50} on the final response of the wall. According to Reese (2006), ϵ_{50} varies from 0.005 to 0.02 for different clay types. The results of the sensitivity analysis are presented in figure 6.6.

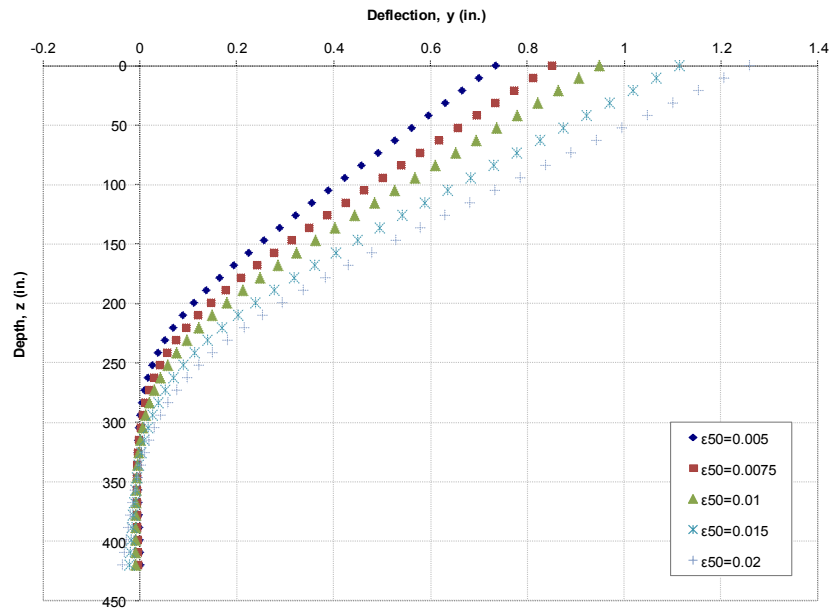


Figure 6.6: Sensitivity analysis on the stiffness of the soil assuming an equivalent fluid pressure of 40 psf/ft

Table 6.1: Recommended values of ϵ_{50} for different soil types

Consistency of clay (psf)	Undrained Shear Strength (psf)	Undrained Shear Strength (Kpa)	ϵ_{50}
Very Soft	>250	>12	0.02
Soft	250-500	12-24	0.02
Medium	500-1000	24-48	0.01
Stiff	1000-2000	48-96	0.006
Very stiff	2000-4000	96-192	0.005
Hard	<2000	<192	0.004

As expected, the deflections are bigger for higher values of ϵ_{50} representing softer soils. The differences on the deflected shapes are significant as a notable non-zero rotation is generated at the tip of the shafts assuming that the soil is soft in the passive zone.

2. Sensitivity analysis on the shear strength of the soil at the passive zone:

The shear strength on the passive zone is also expected to decrease due to the stress relief and the potential heave of the soil at the excavation level. An upper bound refers to the values indicated by the geotechnical investigation before the soil was excavated. A lower bound can be obtained by translating the shear strength profile from the original ground surface to the excavation level.

An intermediate analysis is made assuming that partial consolidation occurs within the soil mass in the passive zone. In such case, as the negative pore pressures generated immediately after the excavation dissipate, the effective stresses and thus the shear strength decrease. To estimate the reduction in undrained strength for different degrees of consolidation, the following empirical relationship is used:

$$(c/p)_{OC} = (c/p)_{NC} \cdot OCR^m = 0.25 \cdot OCR^{0.8} \dots\dots\dots(6.4)$$

In the above equation, a typical value of 0.25 is used for the c/p ratio of the normally consolidated state of the Taylor clay, and a typical value of 0.8 is used for the coefficient m. Hence, the only unknown is the overconsolidation ratio profile (OCR), generated using the results of the consolidation tests from the geotechnical investigation.

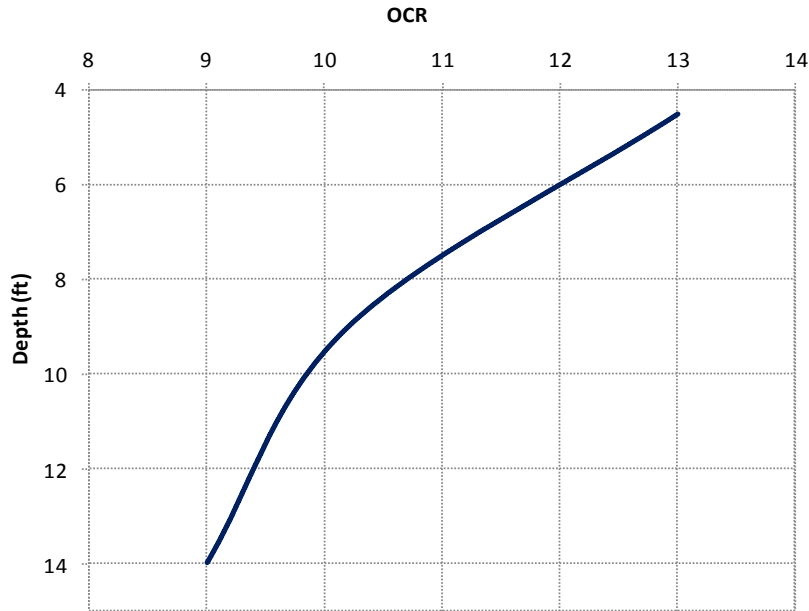


Figure 6.7: Overconsolidation ratio for different depths along the shafts

The largest depth at which the OCR was measured from the consolidation test results equals to 14 ft. This is due to the fact that to approach the virgin compression line in a consolidation test for such highly overconsolidated clays, extremely high loads are required that cannot be simulated in the lab. Hence, extrapolations are made to estimate the values of OCR for depths beyond 14 ft.

Assuming that the ground water table is at the excavation level and using the OCR profile and equation (6.4), the effective stresses after full consolidation (σ'_v) and the preconsolidation stresses (σ'_p) for different depths are evaluated. The shear strength profile after full consolidation represents the worst case scenario. Given that moisture content changes are observed in the ground profile, drained conditions should be considered in the design. This issue should be further investigated.

Other factors that could contribute to the strength reduction on the excavation side are heave or degradation of the soil imposed by temperature and moisture fluctuations

near the surface. To account for these factors, the sensitivity analysis on the p-y model includes percentages of shear strength reduction ranging from 10 to 70%. The results are presented in the following figures.

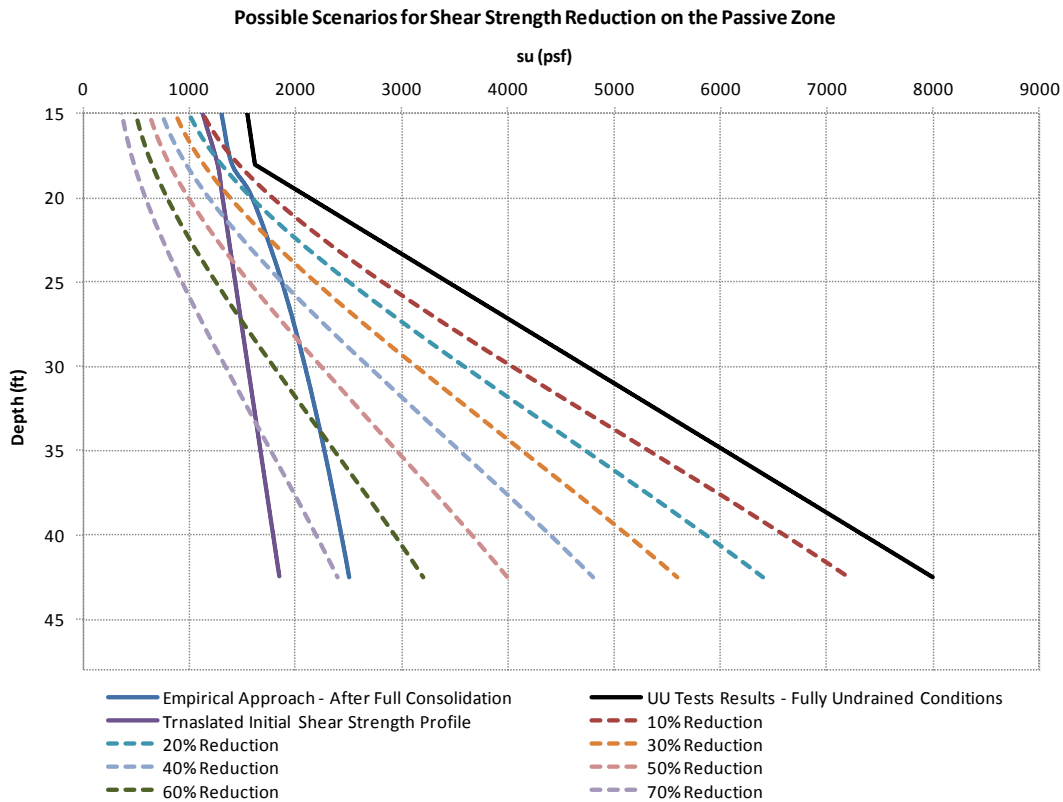


Figure 6.8: Different scenarios for the reduction of the shear strength on the passive zone

Table 6.2: Analysis for estimating the shear strength after full consolidation

<i>Shear Strength Reduction on the Passive Zone</i>									
Time	Depth	su (psf)	σ'_p (psf)	σ'_v (psf)	OCR	c/p'	$(c/p')_{\text{empirical}}$	$su_{\text{empirical}}$ (psf)	$su_{\text{translated}}$ (psf)
Before Consolidation - Initial Ground Surface	0	1200	-	0	-	-	-	-	-
	18	1625	-	1644	-	-	-	-	-
	42.5	8000	-	3202.2	-	-	-	-	-
After Consolidation - Excavated Ground Surface	0	-	-	-	-	-	-	-	-
	15	-	10718.6	0.0	-	-	-	1300.0	1130.0
	18	5887.0	11344.7	329.8	34.4	17.8	4.2	1397.8	1269.4
	20	3660.6	11706.5	552.6	21.2	6.6	2.9	1589.2	1316.6
	25	2338.1	12472.9	966.4	12.9	2.4	1.9	1869.6	1434.5
	30	1810.9	13099.0	1378.4	9.5	1.3	1.5	2087.4	1552.5
	35	1526.0	13628.4	1791.7	7.6	0.9	1.3	2270.6	1670.4
	40	1351.0	14086.9	2204.9	6.4	0.6	1.1	2430.4	1788.3
42.5	1288.5	14295.1	2411.5	5.9	0.5	1.0	2503.5	1847.3	

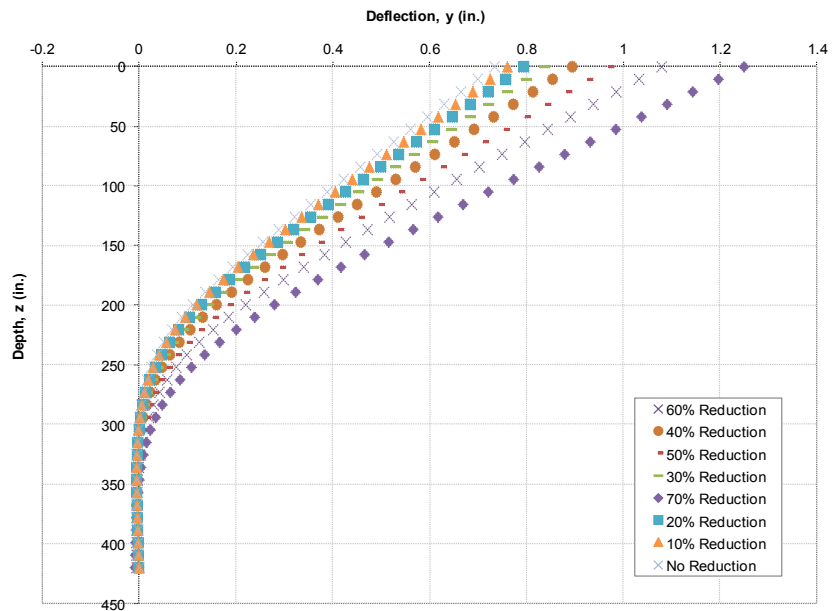


Figure 6.9: Sensitivity analysis on the shear strength reduction at the passive zone assuming an equivalent fluid pressure of 40 psf/ft

According to the p-y analysis, reducing the shear strength in the passive zone significantly affects the response of the drilled shafts. The weaker the soil, the higher the deflections that are generated. However, the degree of fixity at the tip of the shaft is not affected significantly by the shear strength reduction.

3. Sensitivity analysis on the non-dimension coefficient J:

A sensitivity analysis was made on the range of the non-dimensional coefficient J. Two values were selected: 0.25 (typical for stiff clays) and 0.5 (typical for soft clays). According to figure 6.10, the parameter J has little effect on the final response of the wall.

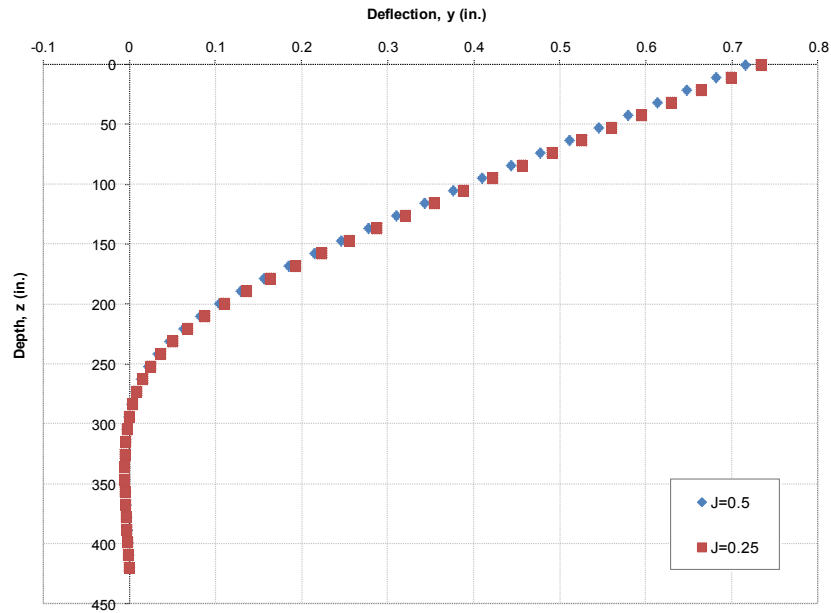


Figure 6.10: Sensitivity analysis on the non-dimensional coefficient (J) related to the soil type assuming an equivalent fluid pressure of 40 psf/ft

Given that the shear strength and stiffness on the passive zone are related, the results of the sensitivity analysis are combined to obtain a better solution for the final response of the drilled shaft. Assuming that the shear strength of the soil was reduced by 50%, that the value of ϵ_{50} is 0.01 and using an equivalent fluid pressure of 23.4 psf/ft, good agreement is observed between the results of the p-y analysis and the inclinometer data. Especially shortly after the excavation, undrained conditions dictate a negligible reduction in shear strength. The inclinometer results, however, indicate that the non-zero rotation at the tip of the drilled shafts developed during excavation.

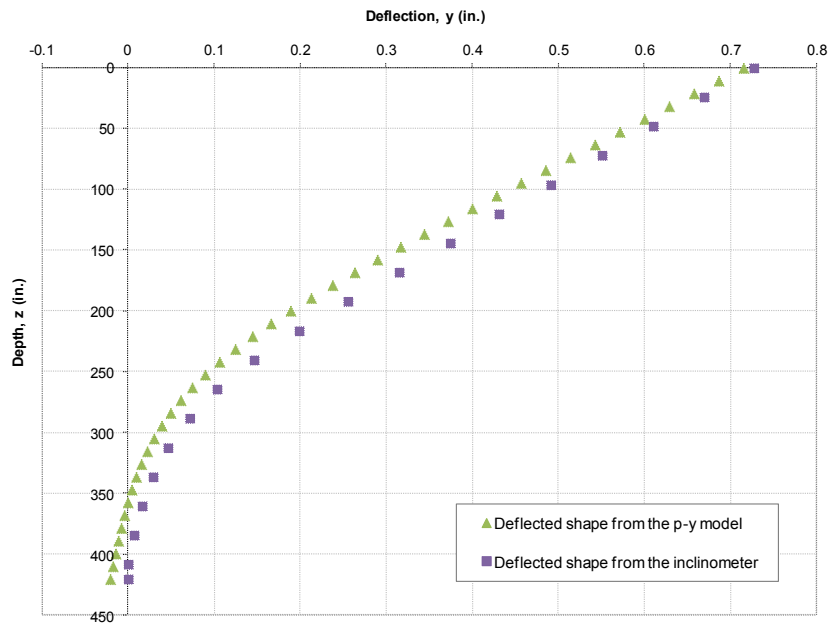


Figure 6.11: Matching the deflected shape between the p-y analysis and the inclinometer data assuming an equivalent fluid pressure of 23.4 psf/ft

6.4: Introducing the theory of the initial global displacements

From the results of the sensitivity analysis it becomes clear that the differences observed on the deflected shapes from the p-y analysis and the inclinometer data cannot be explained merely by assuming weakening of the soil in the passive zone. Especially under undrained conditions, the shear strength is not expected to decrease significantly, and thus another hypothesis is needed to explain the deflections measured by the inclinometer.

Based on the finite element analysis that simulated the wall response, initial "global" displacements occurred immediately after the excavation. During this initial global movement both the soil and the shafts moved together. Because the non-linear springs that represent the soil resistance to lateral movements in the p-y model can

account only for relative deflections between the soil and the shafts, such displacements are not captured on the final results.

To quantify the profile of the initial global displacements, the results of the finite element model are used. In addition, assuming that the shear strength on the passive zone is not affected by the excavation (a reasonable assumption for undrained conditions), this initial displacement profile is indicated by the difference between the deflected shape from the p-y model, and the inclinometer data.

Two types of analysis were made to predict the range of earth pressures applied on the wall during cycles of moisture fluctuation. In the first type, no shear strength reduction was assumed; in the second, the shear strength of the soil was taken as 20% smaller than the results of the geotechnical investigation. Different initial "global" displacement profiles were assumed for both types of analysis as indicated in figure 6.12.

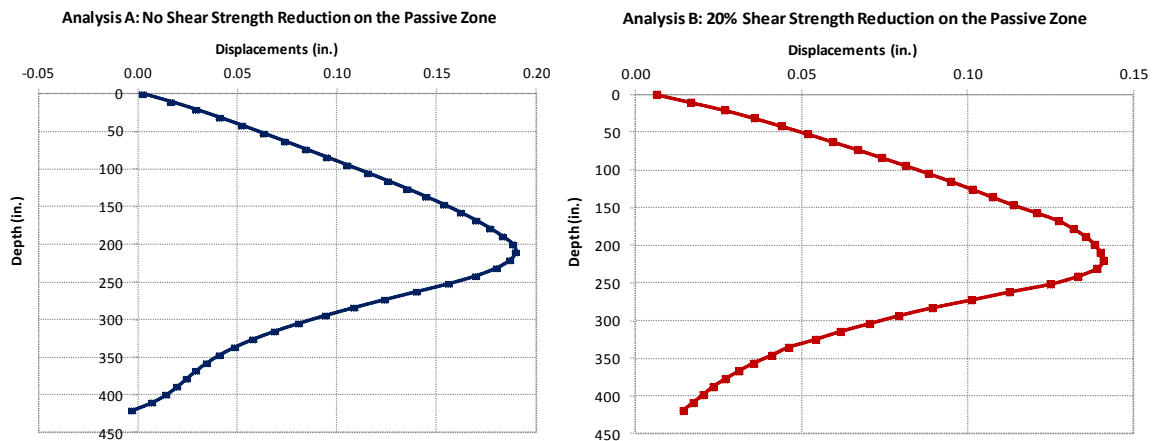


Figure 6.12: Profile of initial "global" displacements generated from the results of the p-y analysis immediately after excavation

Measuring the shear strength of the soil in the passive zone will provide insight to the input variables of the p-y model and the profile of the initial displacements.

6.5: Predicting the deflected shape for different moisture conditions

The p-y model is used to predict the range of earth pressures applied on the wall at different dates throughout the two-year monitoring period. The same dates selected while analyzing the results of the instrumentation program are used in order to be able to make direct comparisons. The first analysis assumes no strength reduction on the passive zone and is characterized by the following input parameters:

- The value of ϵ_{50} is taken as 0.005, an average value for stiff fissured clays.
- The shear strength in the passive zone is obtained from the geotechnical investigation assuming no reduction in the passive zone.
- The non-dimensional coefficient J is taken as 0.25, typical for stiff fissured clays.

Because the response of drilled shafts to lateral loading is a soil structure interaction problem, the earth pressures (w) are a function of lateral displacements (y). In addition, the shape of the earth pressure distribution is not triangular, and different scenarios should be examined in the future. Results of the instrumentation program should be used for that purpose.

Using the above parameters, an effort has been made to match the deflected shape from the p-y analysis to the inclinometer data. Good agreement is obtained as the non-zero rotation at the tip of the shafts is generated from the p-y results. In the following figures, the results obtained for the selected dates are presented. The final p-y analysis refers to the case where the initial "global" displacements are taken into account (in contrast to the initial p-y model).

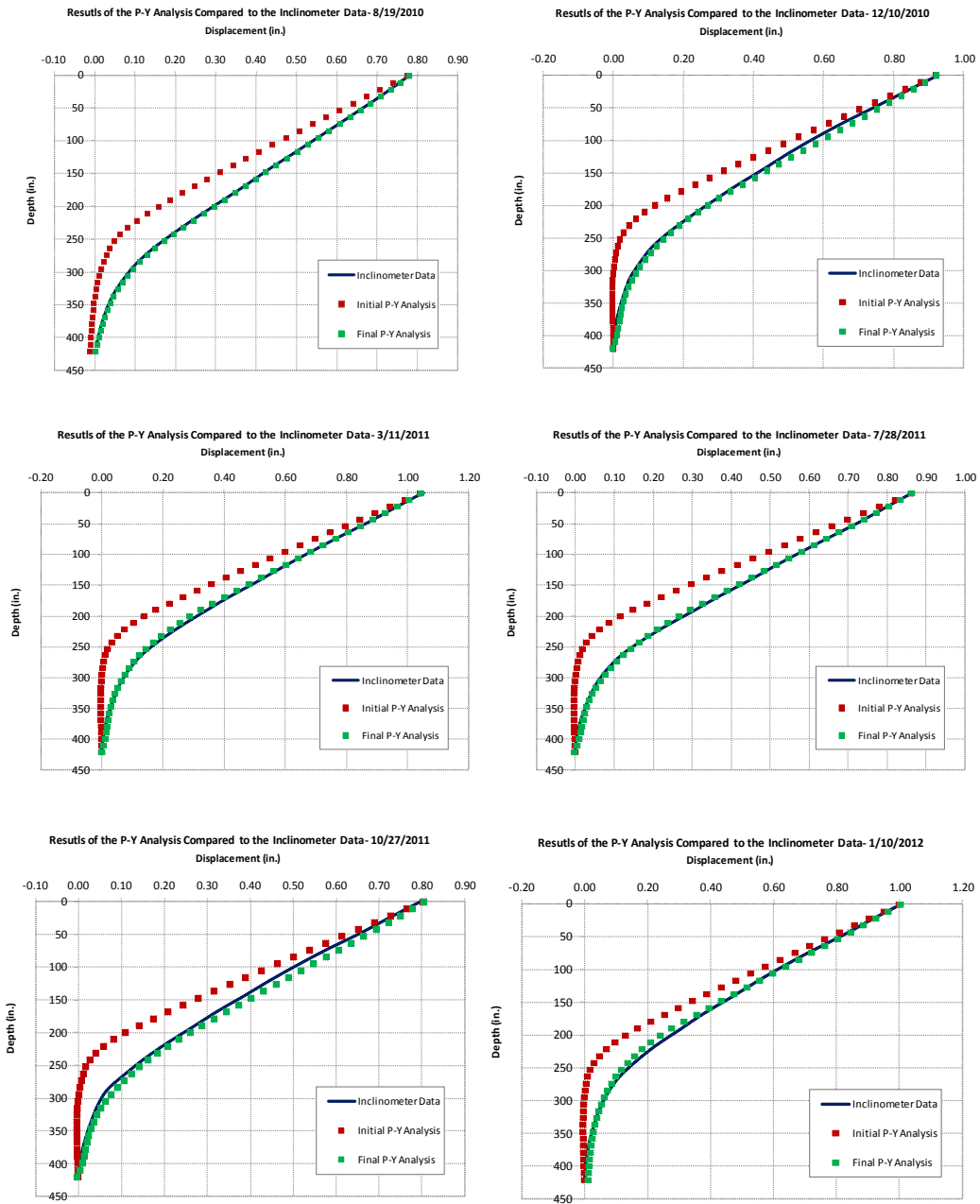


Figure 6.13: Deflected shapes from the initial and final p-y analysis compared to the inclinometer data

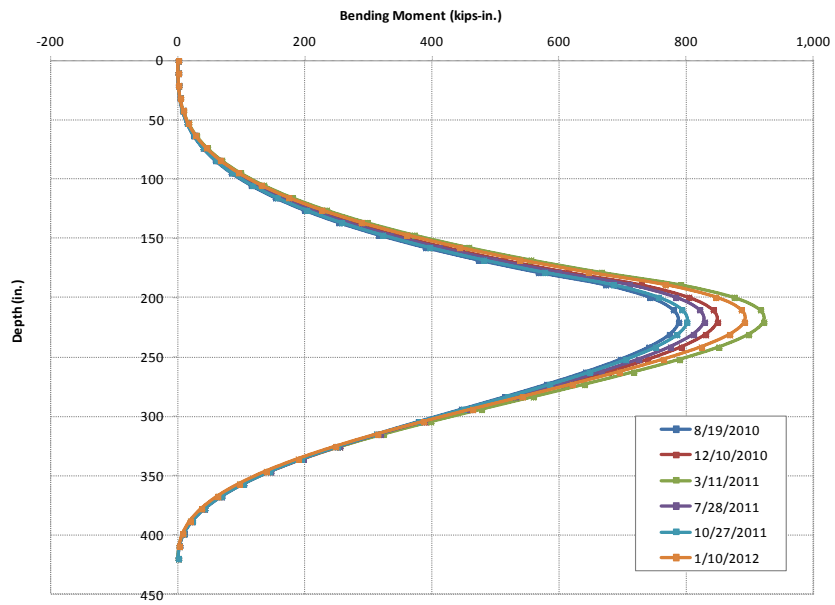


Figure 6.14: Bending moment profiles for different dates throughout the two year monitoring period (using M- ϕ curve from the method of slices)

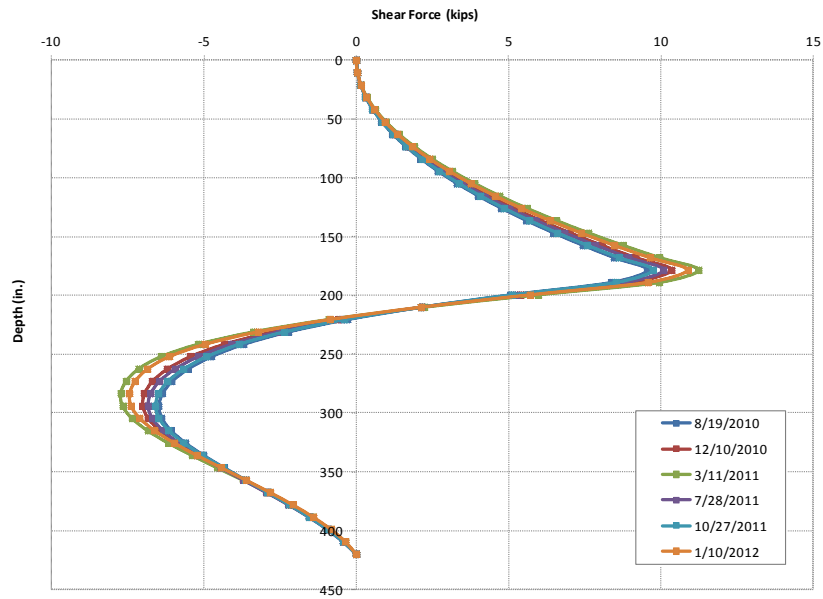


Figure 6.15: Shear force profiles for different dates throughout the two year monitoring period

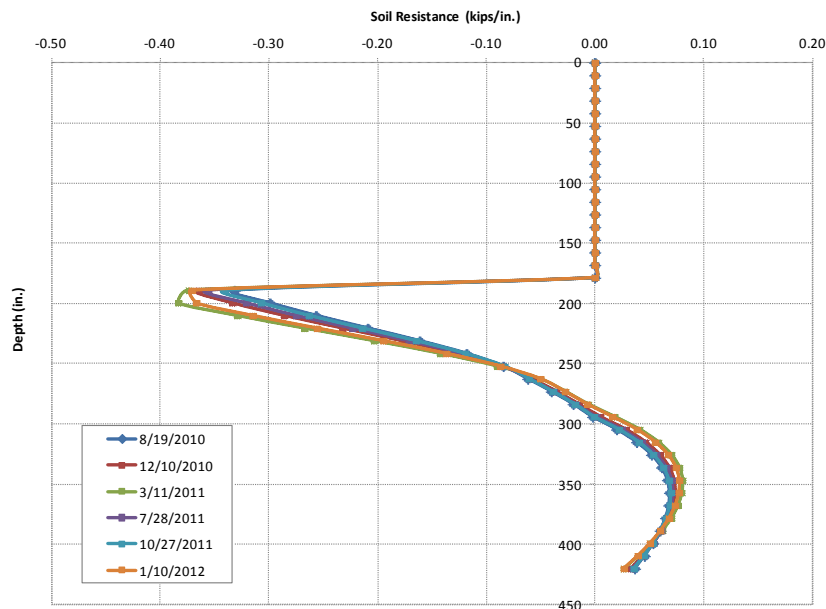


Figure 6.16: Soil resistance profiles for different dates throughout the two year monitoring period

To evaluate the effect of shear strength and stiffness reduction on the lateral response of the drilled shafts, a second p-y analysis is made assuming the following parameters:

- The value of ϵ_{50} is taken as 0.01, typical for medium clays.
- The shear strength in the passive zone is assumed to be reduced by 20% due to the stress relief imposed by the excavation.
- As in the previous case, the non-dimensional coefficient J is taken as 0.25, typical for stiff fissured clays.

As in the previous analysis, accounting for the initial "global" displacements, good agreement is obtained between the deflected shapes from the p-y analysis and the inclinometer data. The results are presented below.

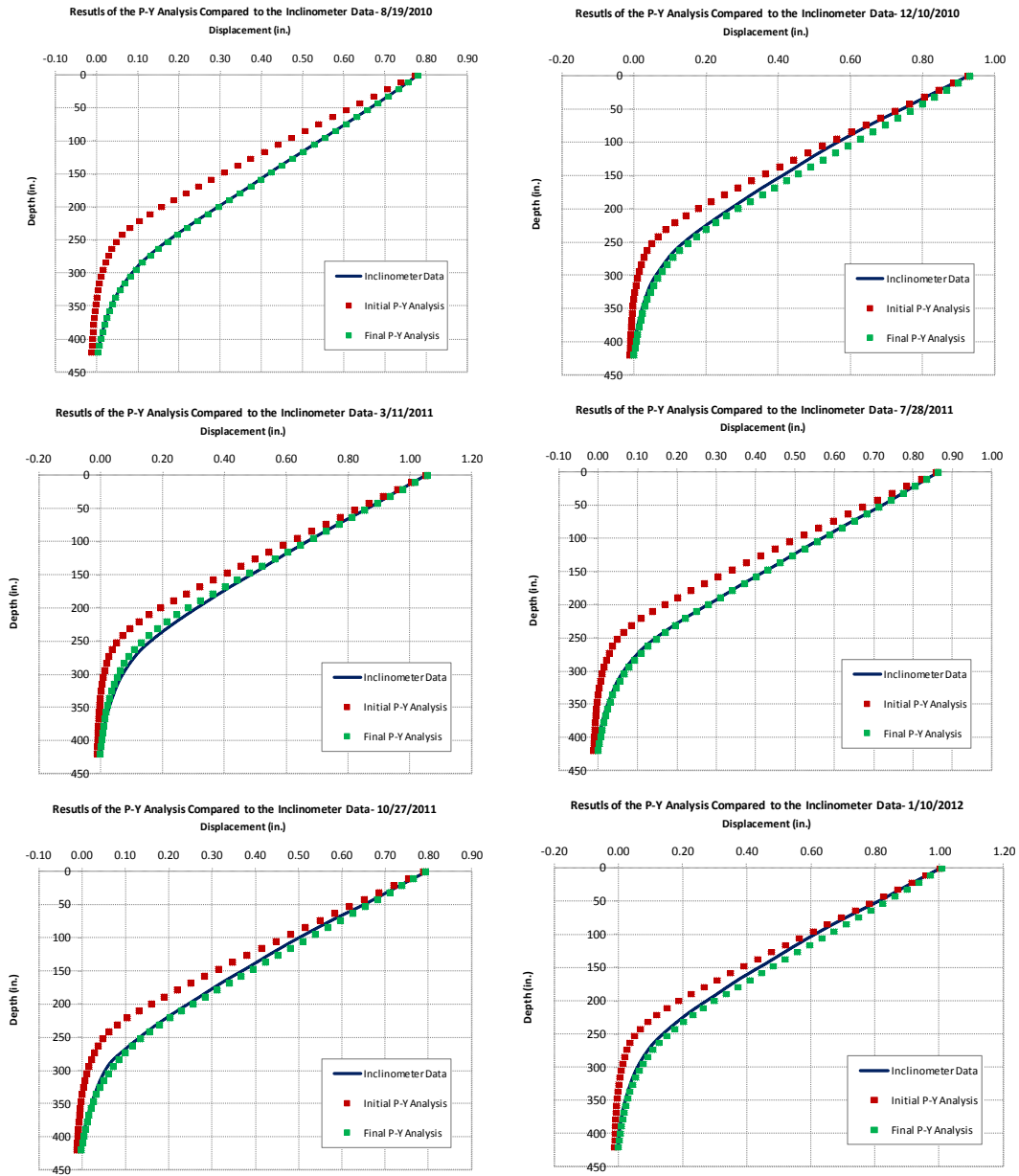


Figure 6.17: Deflected shapes from the initial and final p-y analysis compared to the inclinometer data

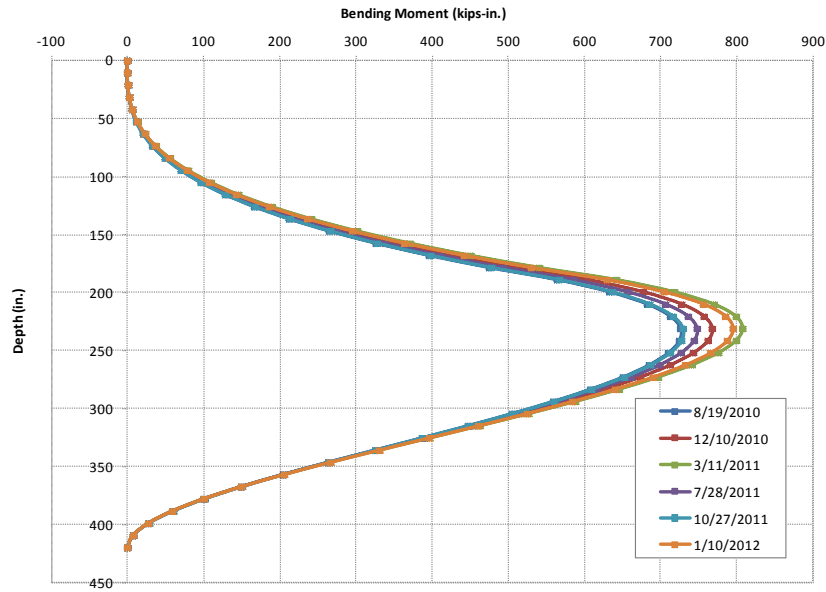


Figure 6.18: Bending moment profiles for different dates throughout the two year monitoring period (using M- ϕ curve from the method of slices)

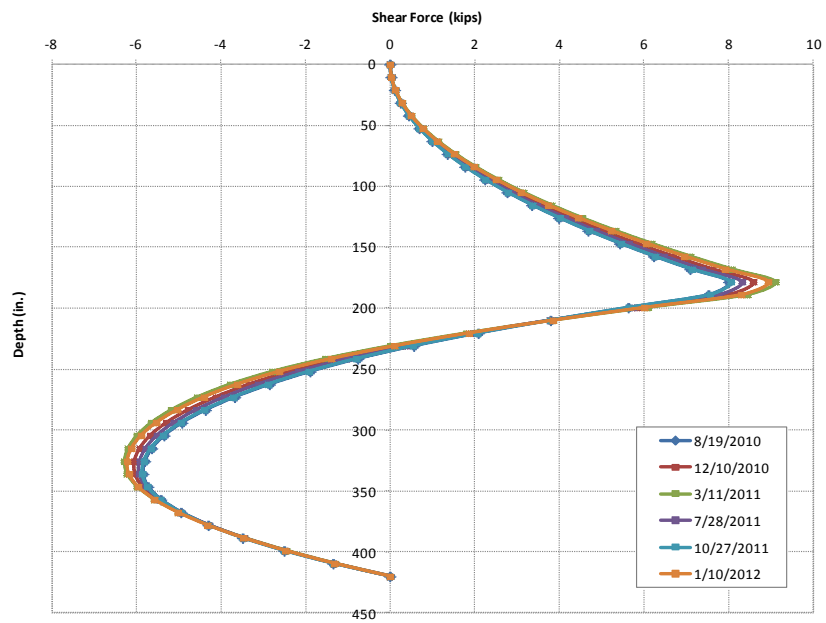


Figure 6.19: Shear force profiles for different dates throughout the two year monitoring period

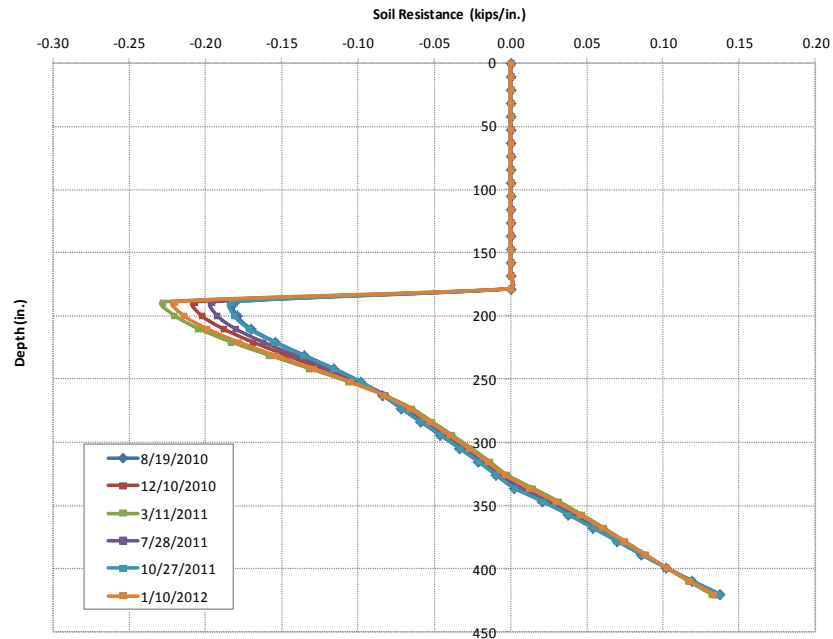


Figure 6.20: Soil resistance profiles for different dates throughout the two year monitoring period

The range of earth pressures derived from the results of the p-y analysis can be compared directly with the empirical recommendations of TxDOT. As indicated in figure 6.21, the gradients of the earth pressure diagram derived from the p-y model are near the lower limit of what TxDOT uses for similar retaining walls in expansive clay. Given that a typical drilled shaft retaining wall has a design life of at least 70 years, and that higher earth pressure are expected to be developed in the future during extreme cases of increased rainfall, the results of the p-y analysis should be applied with caution.

Another key point in the above analysis is the fact that the undrained shear strength of the soil was considered. Although assuming undrained conditions is consistent with current TxDOT design procedures, an additional p-y analysis should be conducted in the future assuming drained shear strength parameters. Empirical p-y curves for sands (Reese 2006) or for stiff fissured clays under sustained loading can be used.

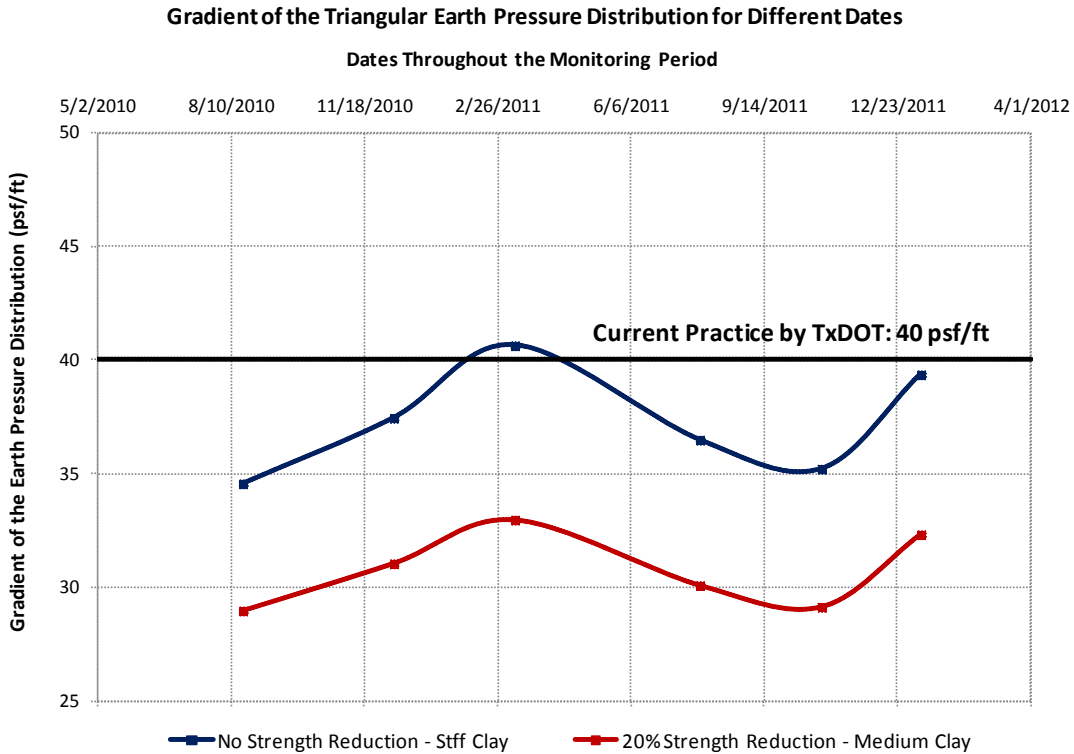


Figure 6.21: Gradient of the triangular earth pressure distribution assuming 0% and 20% shear strength reduction on the passive zone

Table 6.3: Equivalent fluid pressures assuming 0% and 20% shear strength reduction

Gradient of the Triangular Earth Pressure Distributions Used in the P-Y Analysis		
Date	No Shear Strength Reduction - w (psf/ft)	20% Shear Strength Reduction - w (psf/ft)
8/19/2010	34.56	28.96
12/10/2010	37.44	31.04
3/11/2011	40.64	32.96
7/28/2011	36.48	30.08
10/27/2011	35.2	29.12
1/10/2012	39.36	32.32

6.6: Predicting the active earth pressures using the p-y curve

To design a drilled shaft retaining wall on expansive clay, the active earth pressures are needed. To predict those pressures, the net earth pressure diagrams derived

from the results of the instrumentation program are used along with the soil resistance profiles evaluated using the p-y curve. Above the excavation level, because the soil resistance is zero, the net earth pressure distribution equals the active earth pressures. Below the excavation level, in contrast, the soil resistance (p) should be deducted from the net earth pressure diagram according to the following equation:

$$w(z) = p(z, y) - \frac{d^2 M(z)}{dz^2} = p(z, y) - \frac{1}{\Delta z} \left(\frac{M(z + \Delta z) + M(z - \Delta z)}{\Delta z} \right) \dots\dots\dots(5.5)$$

In the above equation, the soil resistance (p) is a function of the horizontal displacements, and varies along the shafts. The soil resistance profiles for the selected dates are evaluated based on the p-y curve developed for stiff clays, and on the corresponding lateral displacements measured by the inclinometers. The net earth pressures and the soil resistance are functions of lateral and horizontal displacements. In addition, the rigidity of the shafts precludes abrupt changes in the earth pressure diagrams. Finally, in the very shallow zone below the excavation level, the soil resistance is reduced by 25% to account for factors such as presence of water at the excavated side or heave of the soil, both of which significantly reduce the stiffness of the Taylor clay.

In most cases, active earth pressures increase linearly with depth, and their gradients are largest when the water content of the soil is high. Accordingly the equivalent fluid densities of the soil can be evaluated and design recommendations could be given based on the following results. In addition, evaluating the active thrusts applied on the wall above the excavation level is of great importance. These active thrusts can directly be compared with the area of the triangular earth pressure distributions assumed in the p-y model for the same dates. The respective results are presented in the following paragraphs.

A. Results from the inclinometers:

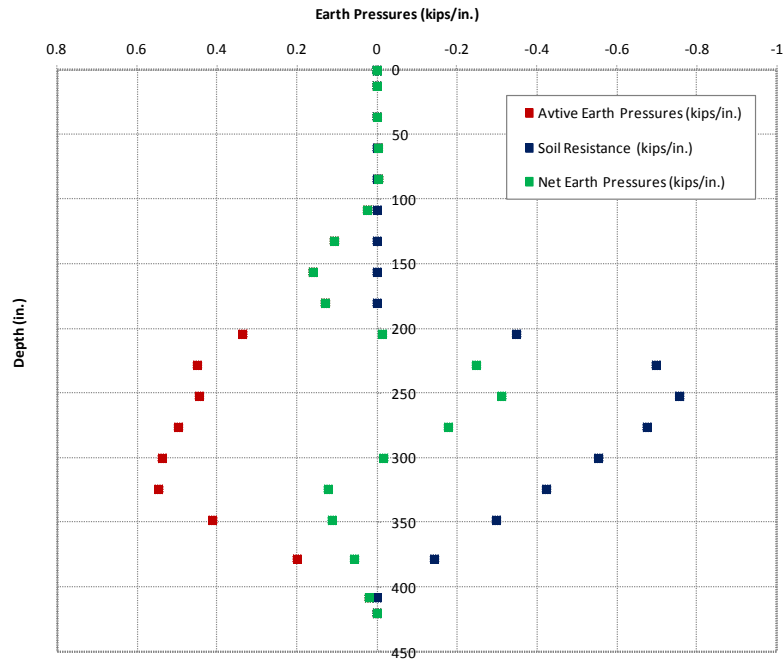


Figure 6.22: Earth pressure distributions - 8/19/2010

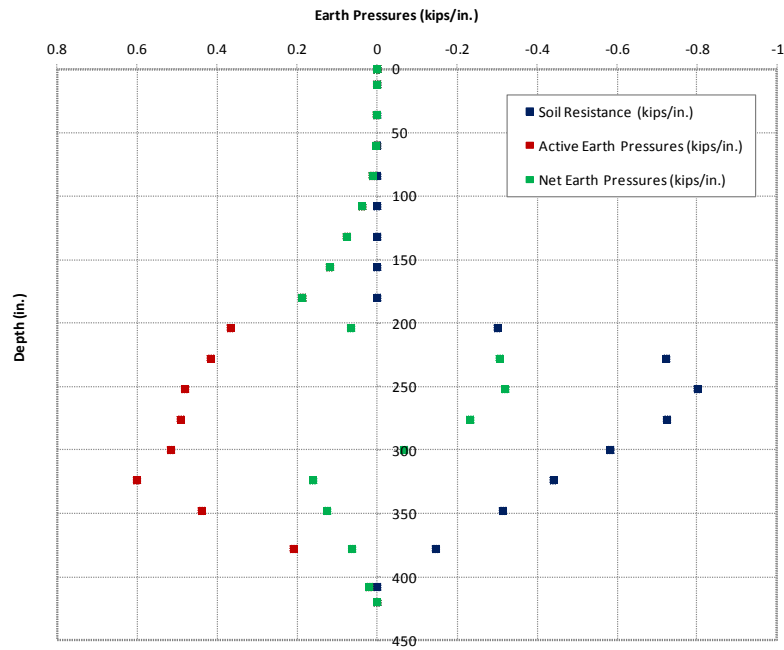


Figure 6.23: Earth pressure distributions - 12/10/2010

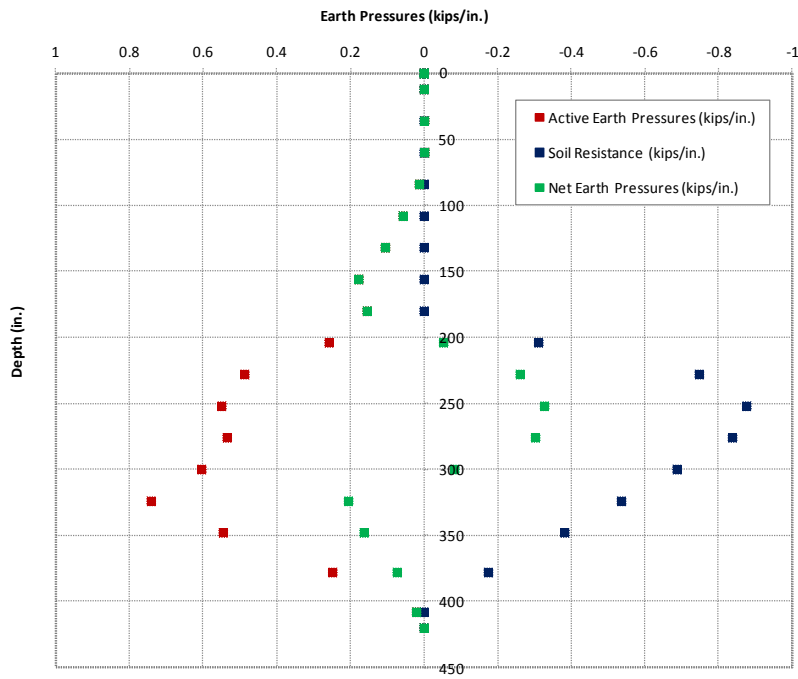


Figure 6.24: Earth pressure distributions - 3/11/2011

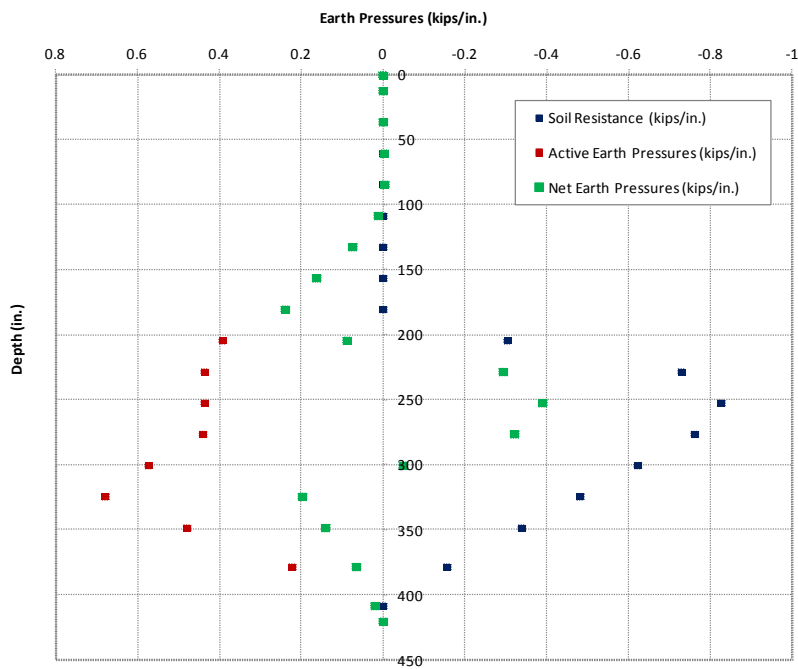


Figure 6.25: Earth pressure distributions - 7/28/2011

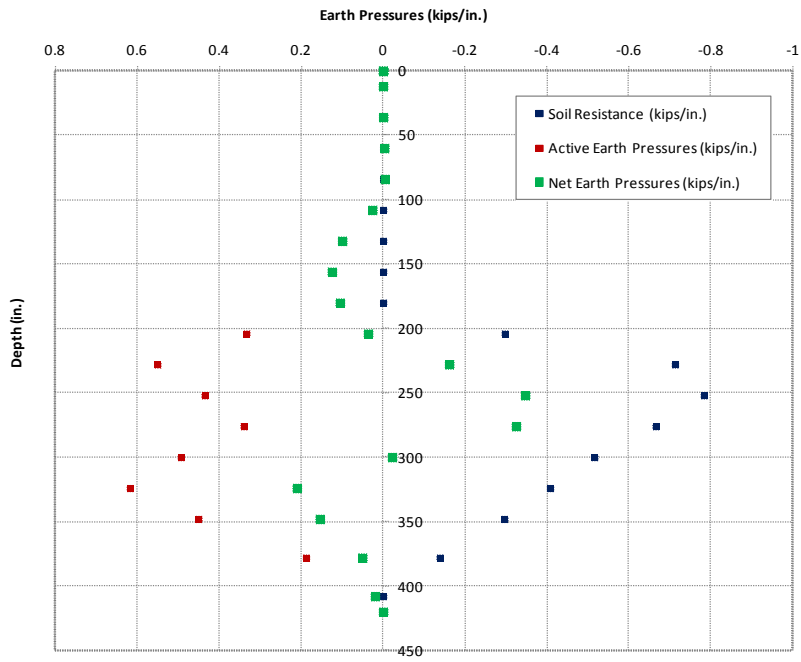


Figure 6.26: Earth pressure distributions - 10/27/2011

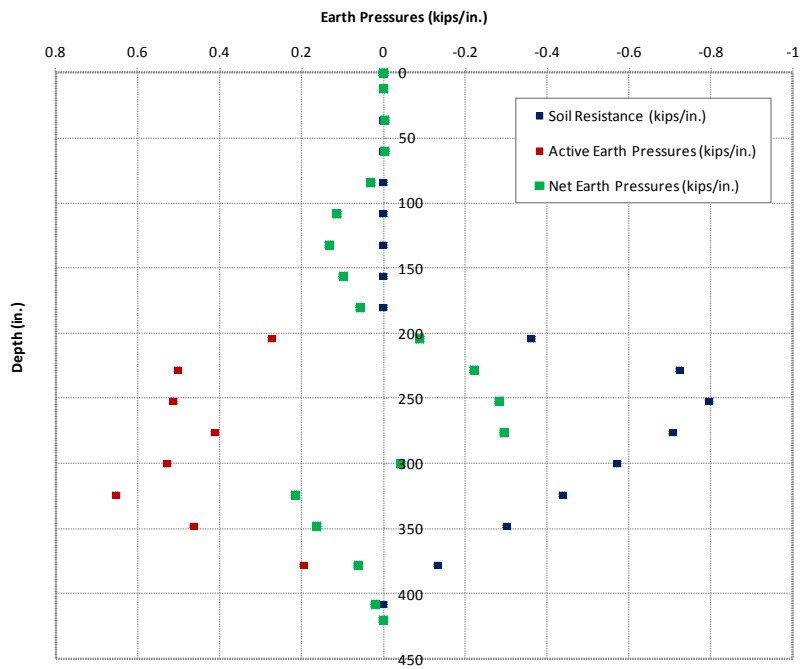


Figure 6.27: Earth pressure distributions - 1/10/2012

B. Results from the strain gauges:

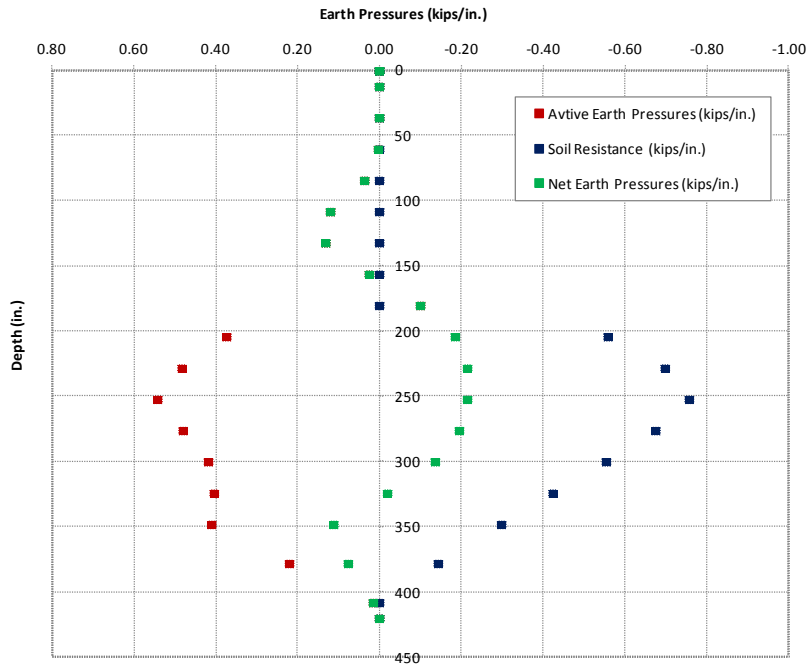


Figure 6.28: Earth pressure distributions - 8/19/2010

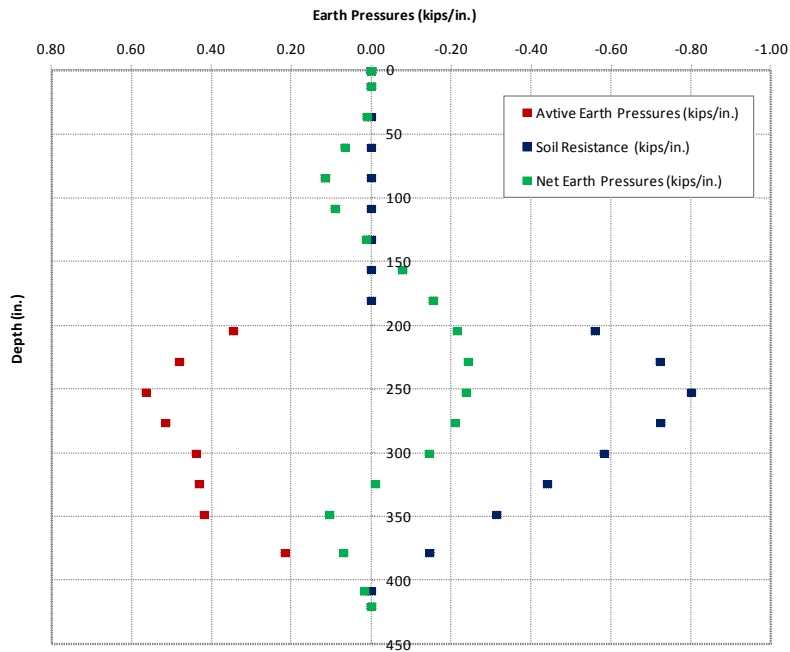


Figure 6.29: Earth pressure distributions - 12/10/2010

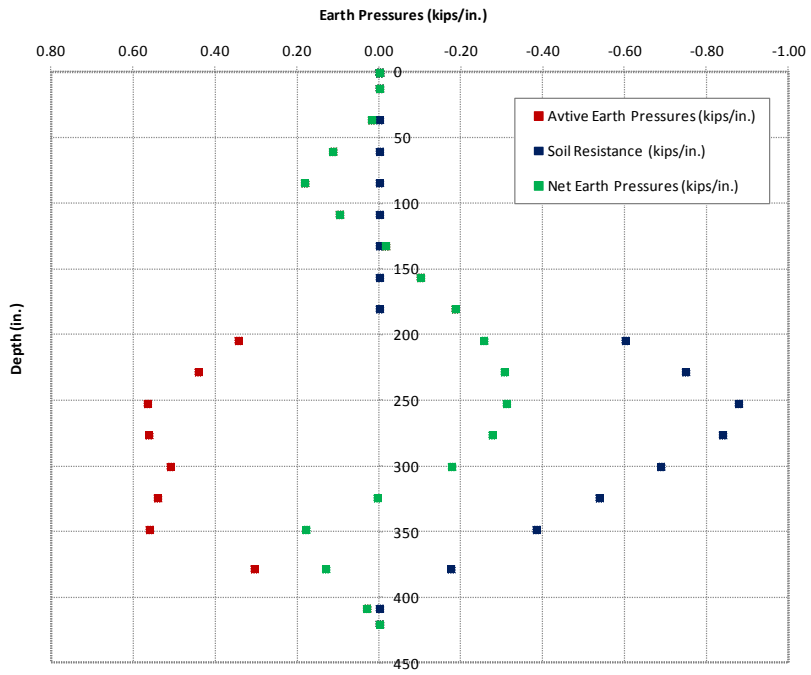


Figure 6.30: Earth pressure distributions - 3/11/2011

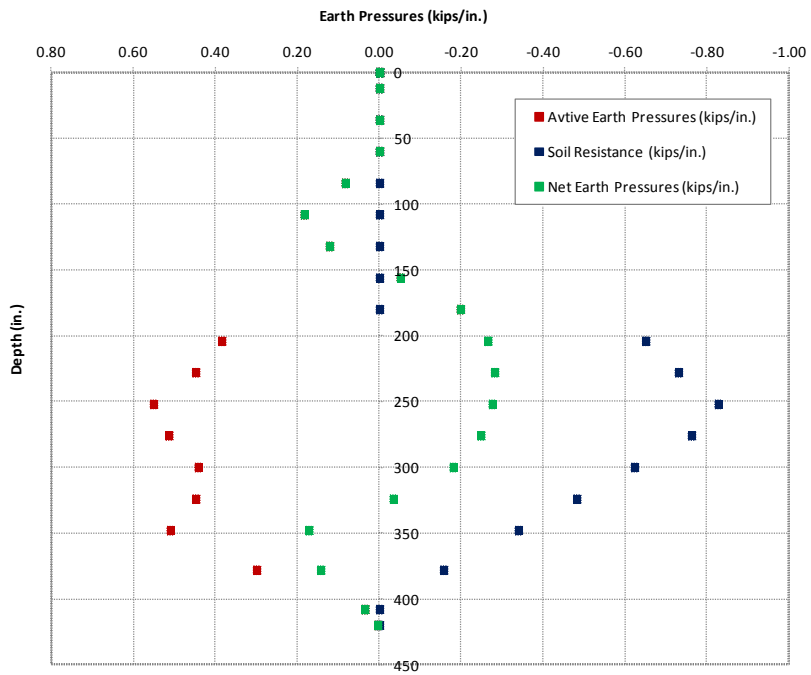


Figure 6.31: Earth pressure distributions - 7/28/2011

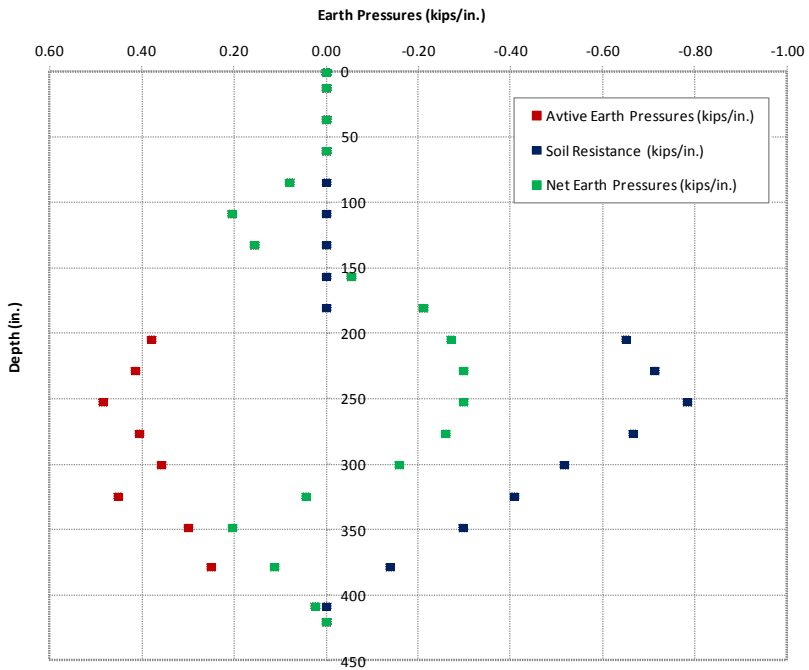


Figure 6.32: Earth pressure distributions - 10/27/2011

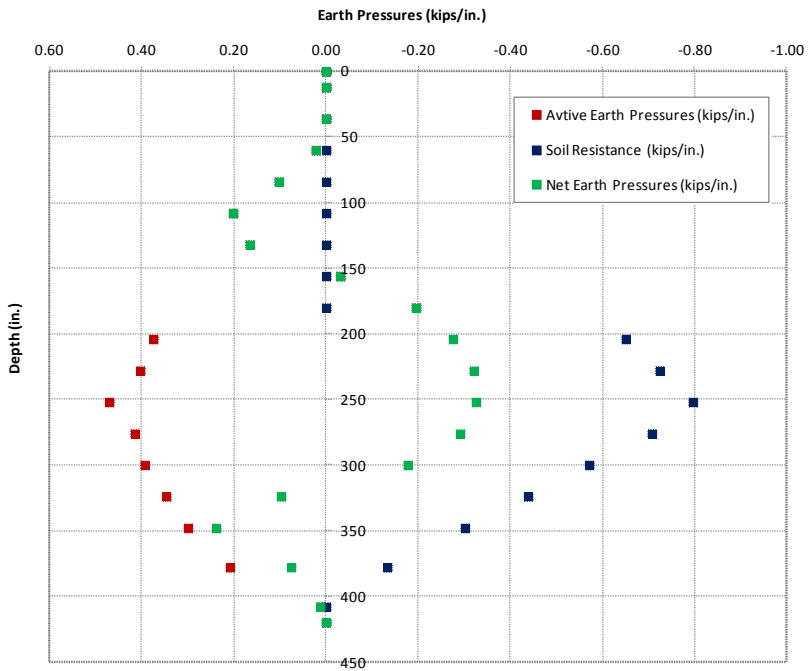


Figure 6.33: Earth pressure distributions - 1/10/2012

6.7: Comparing the results of the p-y model to the instrumentation data

The bending moment, shear force and soil resistance profiles generated from the results of the instrumentation program and the p-y analysis are compared to each other. Agreement is generally good, and differences in the shapes of those profiles are attributed to the different assumptions made on the analysis. Because there is no soil above the excavation level, the soil resistance is zero for this part of the drilled shafts.

To directly compare the results from the p-y model and the instrumentation data, the active thrusts (the area of the active earth pressure diagrams above the excavation level) are evaluated using the trapezoidal rule to compute the area of the earth pressure diagrams derived from the instrumentation data. The results are presented in table 6.4:

Table 6.4: Comparison on the active thrusts from the results of the various analysis

Comparison of the Active Thrusts from the P-Y and Model and the Instrumentation Program			
Date	P-Y Analysis (kips)	Strain Gauge Analysis (kips)	Inclinometer Analysis (kips)
8/19/2010	9.72	8.03	8.39
12/10/2010	10.53	8.12	8.68
3/11/2011	11.43	10.15	10.19
7/28/2011	10.26	9.87	9.03
10/27/2011	9.9	9.85	7.2
1/10/2012	11.07	10.8	9.5

According to the above table, good agreement is observed among different methods for predicting earth pressure distributions. Given the assumptions made in the p-y analysis (including the assumption of a triangular earth pressure distribution), the results from the instrumentation program are more reliable because they are based on direct field measurements. In addition, subjectivity was induced in the analysis of the strain gauge data mainly due to the different curve fitting methods used and the internal discrepancies observed in the raw strain data (especially above the excavation level).

Therefore, although three differentiations are required when using inclinometer data to predict earth pressures, this method is the most reliable and consistent.

Chapter 7: Side Shear and Thermal Effects on the Lateral Deflections of the Wall

7.1: Introduction

The lateral response of a drilled-shaft wall is affected by thermal effects and side shear applied on the wall due to volumetric changes of the soil under cycles of moisture fluctuations. The soil shrinks when the water content decreases and swells when it increases, inducing axial strains and curvatures in the shafts. In addition, as the wall is exposed to temperature fluctuations on one side only, thermal effects in the concrete also induce axial strains and curvatures. The significance of those effects is investigated in this chapter using a t-z analysis and a linear thermal analysis.

Because side shear and thermal effects occur simultaneously, their combined contribution to the lateral response of the wall should be considered in design. During the winter, In addition, tensile stresses are induced in the concrete elements by side shear applied in the wall during the winter while the decrease in temperature at the same time causes contraction of the concrete and thus compressive strains are generated. During the winter, the air temperature is low and the soil swells, generating a positive curvature towards the excavated side. During the summer, when the soil shrinks and the air temperature reaches its highest values, the opposite occurs. The curvatures and axial strains that develop under different conditions of moisture and air temperature are presented in figures 7.1 and 7.2. In the subsequent analysis, the curvature and lateral deflections induced by side shear and temperature fluctuations are quantified at the selected dates that represent different moisture conditions of the Taylor clay.

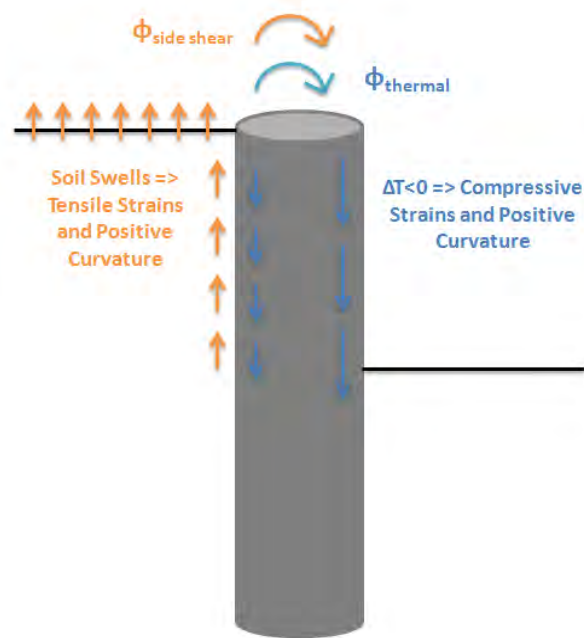


Figure 7.1: Curvature induced due to side shear and thermal effects when the water content of the soil is high and the air temperature is low

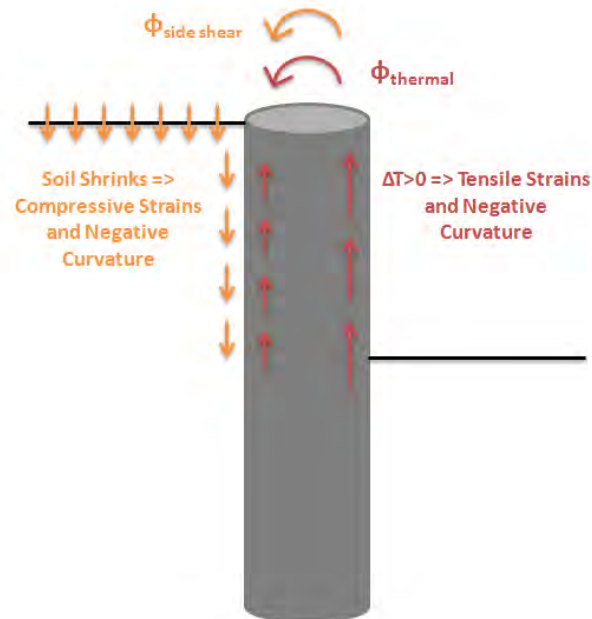


Figure 7.2: Curvature induced due to side shear and thermal effects when the water content of the soil is low and the air temperature is high

7.2: Evaluation of the axial strains from the strain gauge data

To quantify the effect of side shear and temperature fluctuations on the lateral response of the wall, the axial strains developed in the middle of the instrumented shafts are required. To evaluate them, the strain gauge data on the compression and tension side are required according to the following equation:

$$\varepsilon_a = \frac{\varepsilon_t + \varepsilon_c}{2} \dots\dots\dots(7.1)$$

The strain gauge data from the center shaft are used in the subsequent analysis and the following profiles of axial strains are obtained for the selected dates.

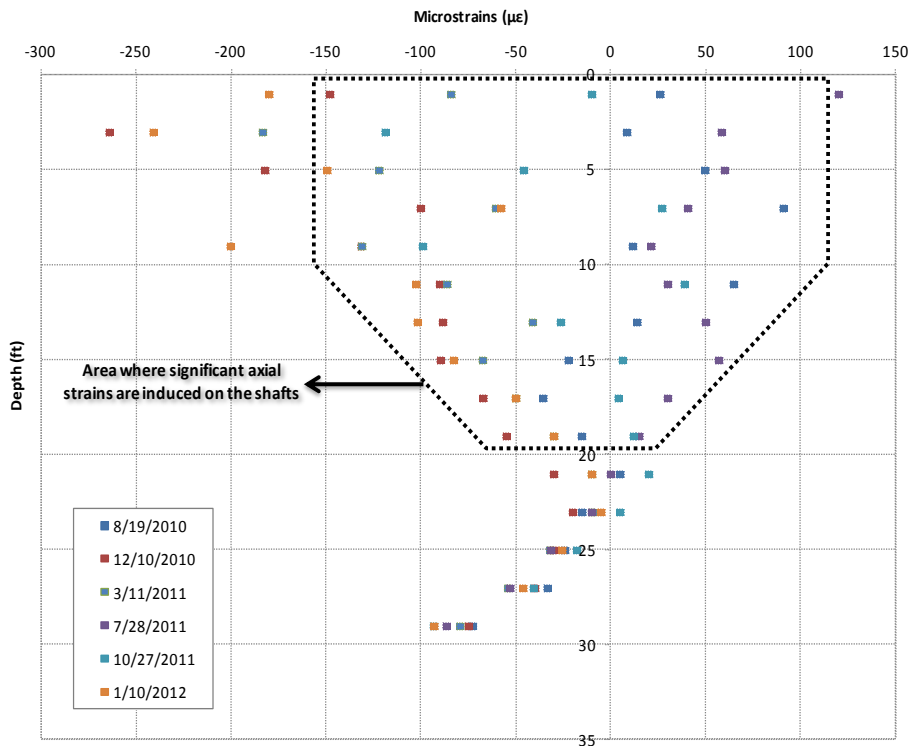


Figure 7.3: Axial strains induced in the shafts due to temperature effects and volumetric changes of the soil under cycles of moisture fluctuations

Based on the above figure, several useful conclusion are drawn:

- Temperature effects and the volumetric changes of the soil behind the wall induce significant axial strains and thus axial stresses in the shafts.
- The soil undergoes volumetric changes due to moisture fluctuations at depths shallower than the elevation of the ground water table. In addition, significant axial strains in the cantilever section of the wall are induced by temperature fluctuations above the excavation level.
- During the winter, compressive strains are induced in the shafts when the air temperature is low and the concrete contracts. During the summer, when very high temperatures are recorded at the site, the opposite occurs.
- The maximum axial strains occur near the surface where the pile head is free to move. At the tip of the pile where temperature and moisture effect are negligible, compressive stresses are developed mainly due to the weight of the overlying concrete shaft.
- Significant discrepancies is observed on the final results due to the fact that the strain gauges are severely affected by microscale effects as explained in a previous chapter.

To isolate the effects of side shear and temperature, the residual strains and the strains induced by the weight of the concrete mass are eliminated from the raw strain data. Assuming the residual strain profile derived in a previous chapter and using a unit weight of reinforced concrete mass equal to 150 pcf, the net axial strain diagrams are generated as illustrated in figure 7.4. A smoothing spline is used to smooth these diagrams in order to be used in the subsequent analysis.

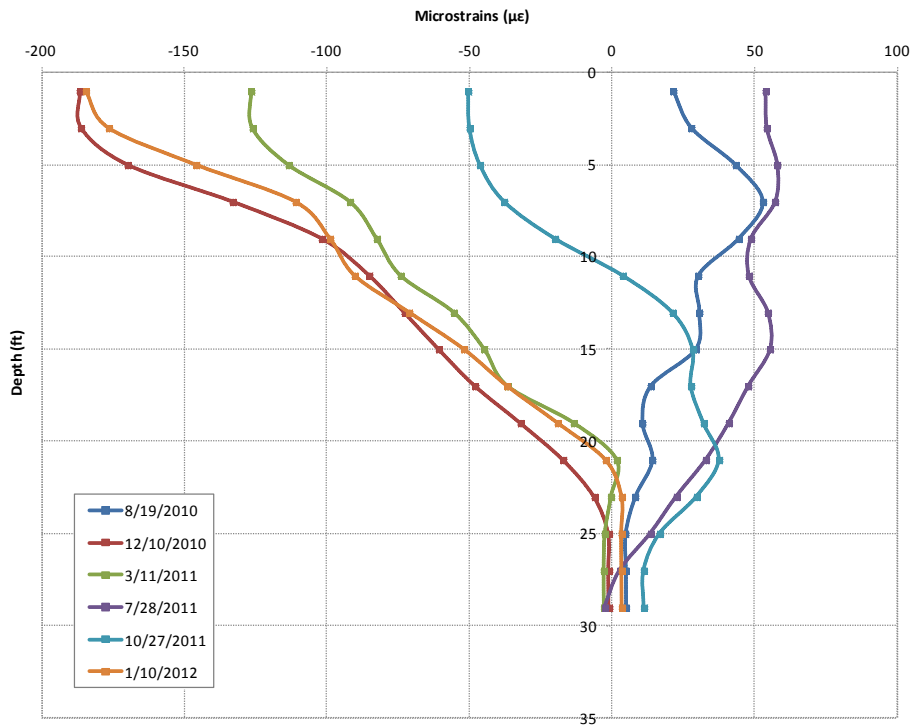


Figure 7.4: Net axial strain profiles for the selected dates after eliminating the residual strains and the strains due to the weight of the concrete mass

A very useful conclusion is that temperature effects dominate the axial response of the wall. On the above figures we derived that during the winter the shafts are in compression. However, if we assume that temperature effects are negligible, the exact opposite would happen and the shafts would be in tension. However, the measured axial strains are in accordance to the expected behavior under temperature fluctuations as the concrete contracts during the winter when the temperature is low thus inducing compressive strains in the shafts. A quantitative analysis is made in the following paragraphs.

7.3: Details on the t-z analysis

The t-z analysis is a method of estimating the response of drilled shafts subjected to axial loading. It is based on soil structure interaction theory and is similar to the p-y analysis in that the stiffness of the soil is simulated using non-linear curves called "t-z curves".

The respective differential equation derived in the literature review is solved using finite differences and therefore the shaft is divided into a finite number of increments. The t-z curve representing side shear and the Q-z curve representing end bearing simulate the response of the soil to axial loading of the drilled shafts, and are unique for the particular soil type. For this project, empirical t-z and Q-z curves (Reese 2006) are used. The drilled shafts are assumed to behave linearly under axial loading due to the low axial strains measured by the strain gauges. The assumed boundary conditions are the axial displacement at the tip of the shaft and the axial load applied at its head. The iterative procedure followed in the t-z analysis is summarized below:

1. Assume a force at the top of an element (P_t).
2. Calculate the displacement at the top (ρ_s) and the relative displacement (Δ) at each increment.
3. Calculate the value of the force due to side shear (F_s) using the t-z curve and the relative displacement (Δ) at each increment.
4. Evaluate the new value of the force at the top of the element (P_t) and repeat until the assumed and the final values are similar.

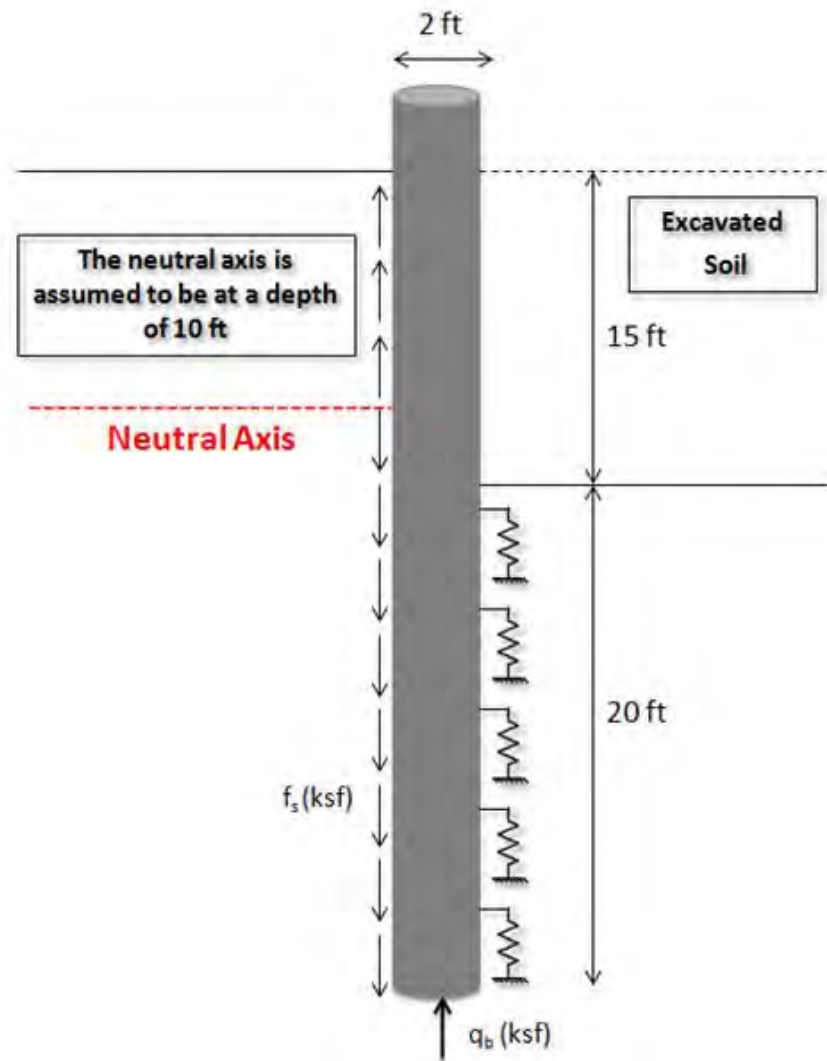


Figure 7.5: Schematic representation of the t-z model

The results of the t-z model include the axial forces, the forces due to side shear and the displacements along the shaft. However, the effect of side shear in a drilled shaft retaining wall is significantly different than in the case of axially loaded piles. Therefore, since the lateral response of the wall due to side shear is the key point in this analysis, the original model is adjusted to account for the particular nature of this problem.

The ultimate goal is to estimate the effect of side shear applied on the wall and the bending moments and lateral displacements that it generates. This side shear is applied above the ground water table where volumetric changes of the soil occur. Because it is applied on one side of the wall only, bending moments are generated that are either positive or negative depending on whether the soil swells or shrinks. This is indicated in figure 7.6.

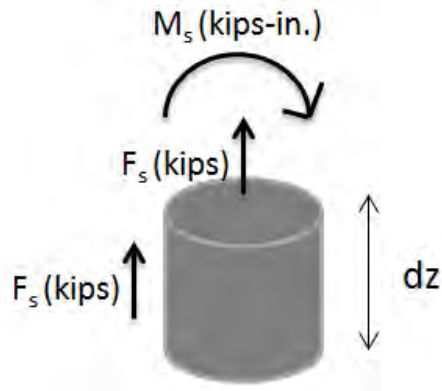


Figure 7.6: Bending moment generated on the wall due to the side shear applied only on one side of the shafts

7.4: Generating the t-z and Q-z curves for stiff fissured clays

The t-z and Q-z curves used in the subsequent analysis were generated based on empirical recommendations for cohesive soils. With respect to the t-z response of the shafts, the empirical curve by Coyle and Reese (1966) was used which was developed by analyzing the results of three instrumented full scale field tests. In this curve, the side shear (f_s) is normalized to the maximum side shear ($f_{s,max}$) which increases for larger depths. The movement required for the full load transfer to be developed is quite small, about 0.05 inches.

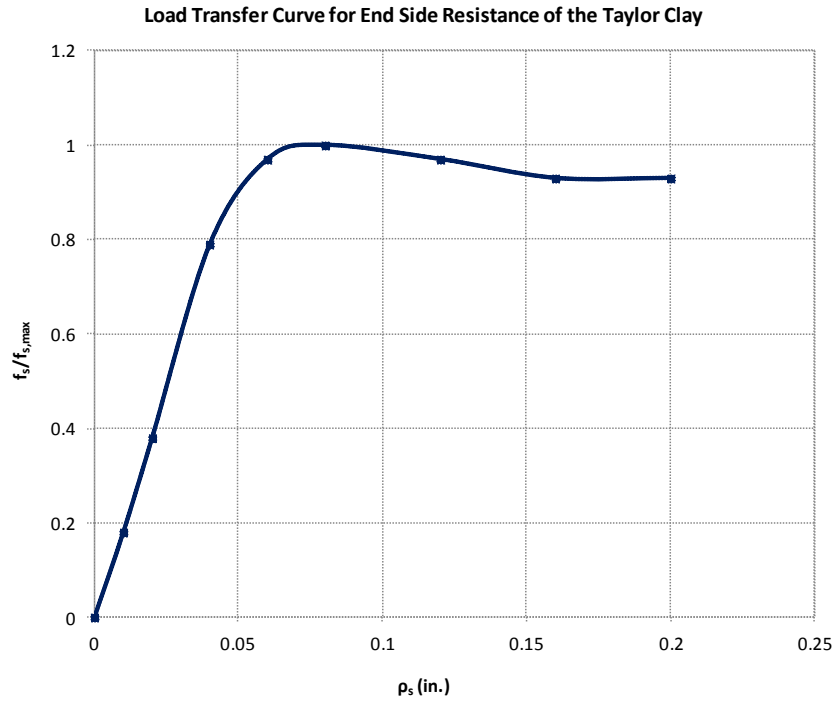


Figure 7.7: Normalized load transfer curve for side resistance of the Taylor clay

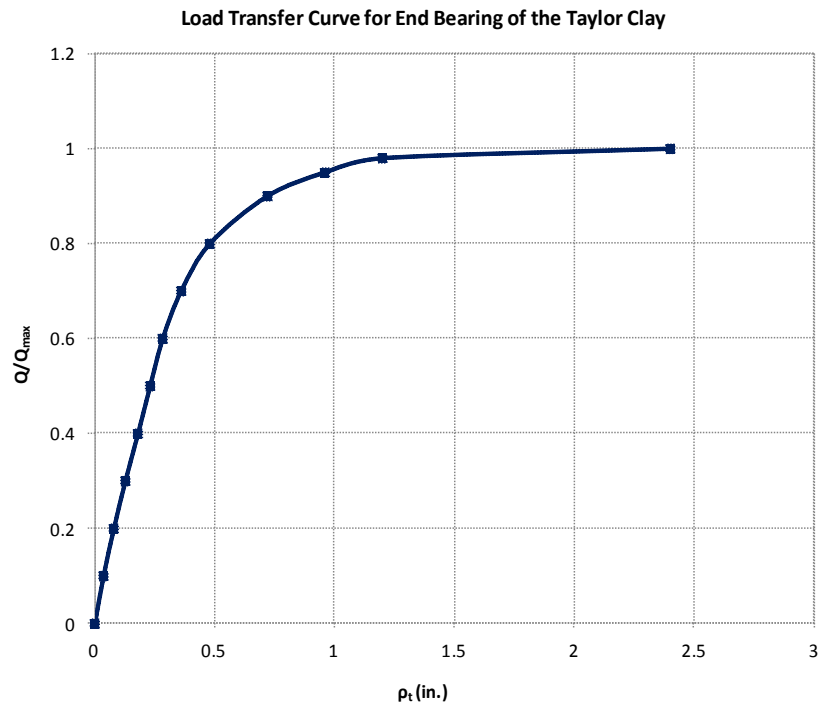


Figure 7.8: Normalized load transfer curve for end bearing of the Taylor clay

Skempton (1951), developed a method for predicting the load at the end bearing of drilled shafts as a function of the axial displacements at their tip. This method uses the values of ϵ_{50} measured from laboratory tests or estimated based on recommendations for similar soil types. In this project, assuming a value of ϵ_{50} equal to 0.005 and applying the theory of elasticity, the Q-z curve for the Taylor clay is generated as indicated in figure 7.8.

7.5: Induced axial strains and curvature due to side shear

The highly plastic Taylor clay experiences significant volumetric strains during cycles of moisture fluctuation, applying side shear to the shafts. Because this side shear is developed only on one side of the wall only, bending moments are generated that vary depending on the moisture content of the soil. Given that the soil swells during periods of increased rainfall, the daily precipitation at the project site measured during the two year monitoring period is illustrated in figure 7.9.

To estimate the curvature induced by volumetric changes of the soil, the empirical t-z curve derived in this chapter is used. Initially, the upper and lower bound values of side shear applied on the wall are evaluated given that enough axial displacements are developed to generate the ultimate shear resistance along the shafts. This assumption is reasonable due to the very limited displacements required for the side shear to reach its ultimate value which are about 0.05 inches.

To evaluate the maximum side shear applied on the wall, the recommendations by O'Neill and Reese are followed which indicate that a common value of the skin friction factor (α) for drilled shafts is 0.5. In addition, the side friction is neglected up to a depth of 3 ft because zero normal forces are applied in the upper part of the wall and thus no

side shear is developed. The profile of the maximum side shear is presented in figure 7.10.

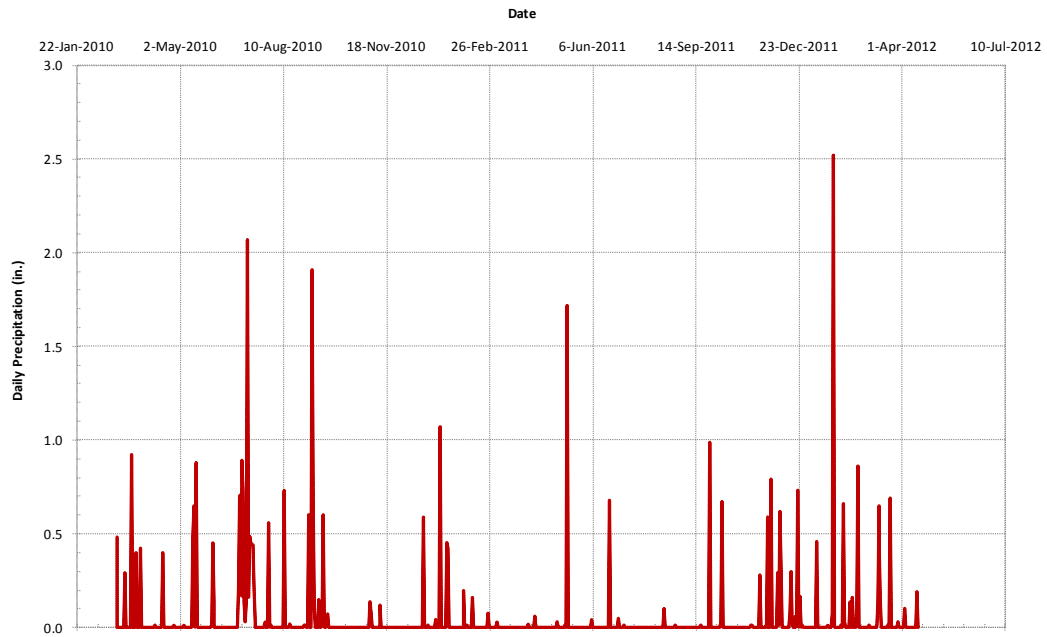


Figure 7.9: Annual precipitation at the project site during the two year monitoring period

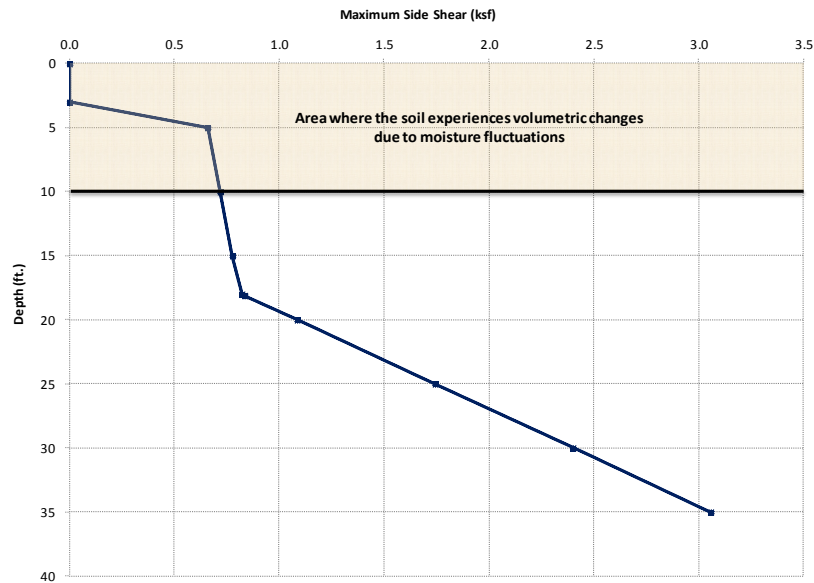


Figure 7.10: Maximum side shear applied on the shafts based on the results of the geotechnical investigation

Undrained conditions are assumed to generate the t-z curve. However, given that drained conditions govern the axial and lateral response of the wall, the results should be evaluated with caution and a subsequent drained analysis should be conducted in the future.

Volumetric changes are expected to occur up to a depth of 8 ft because for larger depths the soil is not affected by seasonal fluctuations of moisture content. Therefore, the neutral axis of the axial forces due to side shear is approximately 10 ft below the ground surface. To evaluate the curvature and moment profiles that would be developed at the wall if the maximum side shear was generated, the shafts are divided into 2 ft equally spaced increments. The axial forces applied on the wall due to volumetric changes of the soil are estimated by multiplying the respective side shear by half the area of each increment, because on the excavated side, the shafts are not in contact to the soil. Therefore, the forces due to side shear at each increment (F_s) are given by the following equation:

$$F_s = f_s \cdot \pi \cdot R \cdot 2 \dots\dots\dots(6.3)$$

To estimate the moments developed at the wall due to these forces, the cumulative force profiles are evaluated. Finally, the moment arm is the centroid of the semicircular half-area of the shafts, as indicated by the following equation:

$$c = \frac{4R}{3\pi} \dots\dots\dots(6.4)$$

Therefore, the bending moment profiles applied on the wall due to volumetric changes of the soil are given by the following equation:

$$M_s = \sum_{i=1}^n F_s c \dots\dots\dots(6.5)$$

The bending curvature profiles are evaluated using the $M-\phi$ curve, developed using the method of slices. From the curvature profiles, the upper and lower bound lateral deflections generated due to side shear are evaluated. The curvature profiles are integrated twice numerically, using the trapezoidal rule, to evaluate the lateral deflections along the shafts. The results of this initial effort to estimate the upper and lower bound lateral response of the wall under moisture fluctuations are presented in the following figures.

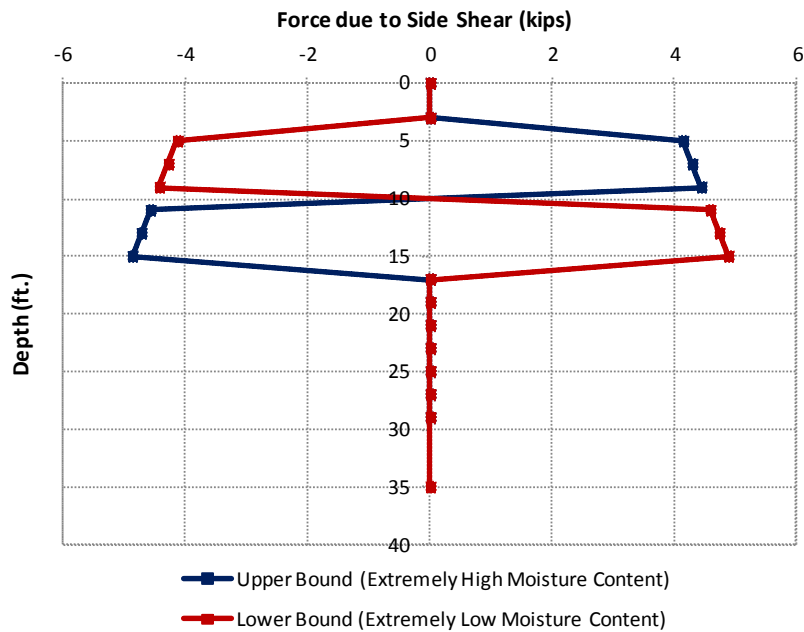


Figure 7.11: Forces due to side shear applied at each increment under extreme moisture conditions

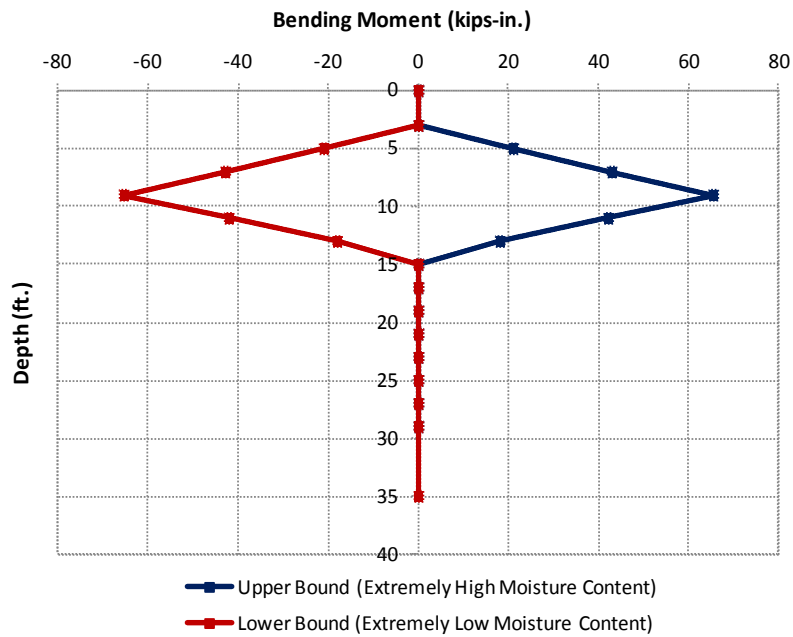


Figure 7.12: Bending moment profiles due to volumetric changes of the soil under extreme moisture conditions

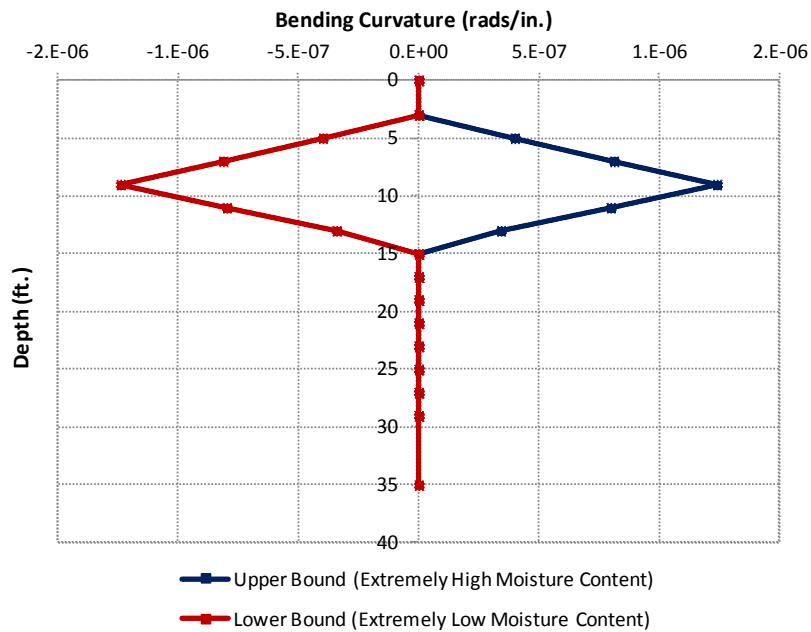


Figure 7.13: Bending curvature profiles due to volumetric changes of the soil under extreme moisture conditions

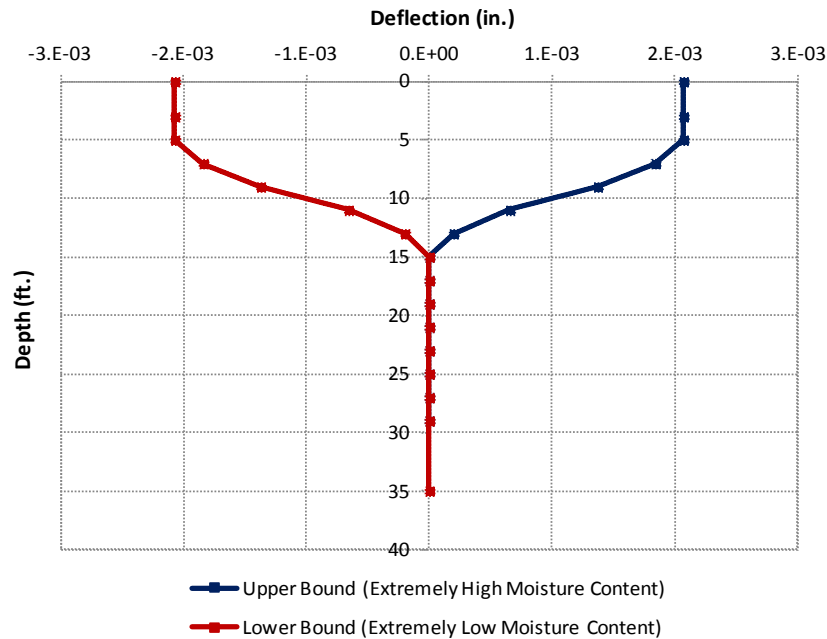


Figure 7.14: Lateral deflections due to volumetric changes of the soil under extreme moisture conditions

To evaluate the side shear applied to the wall at the selected dates that represent different moisture conditions of the Taylor clay, the net axial strain profiles derived previously are used. Given those profiles, the axial displacements (Δ) at each increment are evaluated to permit their use in the adjusted t-z model. There are two ways to evaluate these axial displacements along the shafts:

1. Using the composite Young's modulus of the shafts (E_{com}), the axial stress profiles are evaluated directly from the strain measurements. Multiplying the axial stresses by the cross-sectional area of the shafts (A_c), the axial forces (P_{avg}) applied at each increment are estimated. In addition, assuming that along each increment the axial stresses are constant and using the stiffness of the pile (K_i), the relative displacements (Δ) are determined. Finally, the cumulative displacements (ρ_s) along the shafts are estimated and used in the subsequent analysis to evaluate the side shear (f_s) applied on the wall.

2. The optical fiber strain gauges during installation were attached to sister bars using epoxy and then protected with a rubber membrane to prevent direct contact to the concrete. The effective length where strain measurements are made is considered to be equal to 4 inches which is the length of this membrane. Assuming that the strains are constant along the 2 ft intervals, the displacements (Δ) of each increment are evaluated by multiplying the strains by the length of these increments. Finally, the cumulative displacements (ρ_s) are estimated and used in the subsequent analysis to evaluate the side shear (f_s) applied on the wall.

Both methods were used to derive the axial displacement profiles for the selected dates and the results were similar. The first method is used ultimately in the subsequent analysis and the results of the incremental and cumulative displacements are presented in figures 7.15 and 7.16.

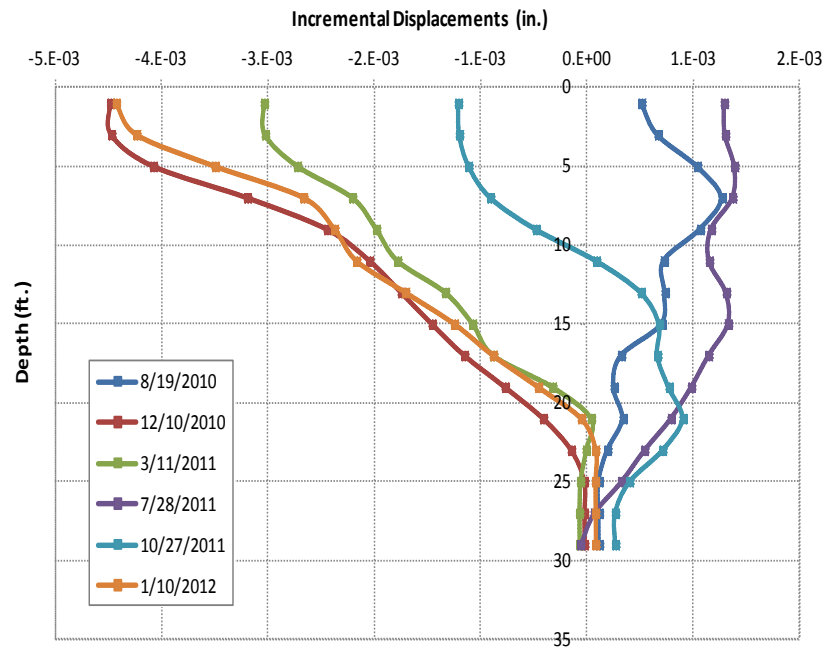


Figure 7.15: Incremental displacements for the selected dates throughout the two year monitoring period

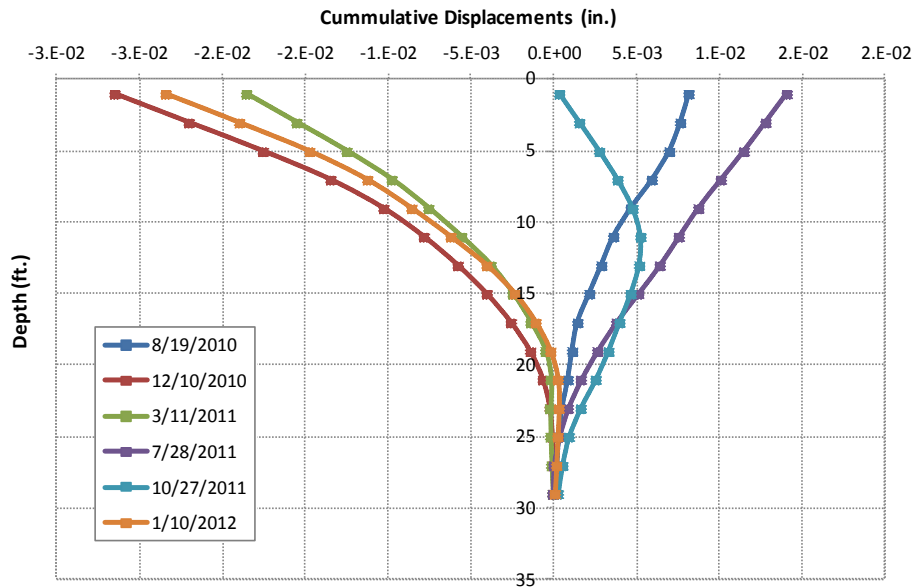


Figure 7.16: Cumulative displacements for the selected dates throughout the two year monitoring period

The next step is to use the t-z curve and evaluate the side shear (f_s) profile which is assumed to be uniform along each increment. Because the values of side shear in the t-z curve are normalized to the ultimate shear resistance, the maximum side shear profile derived previously is used. In addition, given the side shear profiles for the selected dates and following the procedure described in the previous paragraphs the curvature and moment profiles due to side shear imposed by volumetric changes of the soil are generated for the selected dates. Forces due to side shear at each increment are evaluated, and the cumulative force profiles along the shafts are used to estimate the bending moments. Moreover, using the M- ϕ curve for the drilled shafts, the curvature profiles are plotted. Finally, using the curvature profiles, the lateral deflections due to side shear applied on the wall are evaluated. The curvature profiles along the shafts are integrated twice numerically, using the trapezoidal rule, to determine the lateral displacements along the shafts. The results are presented in the following figures.

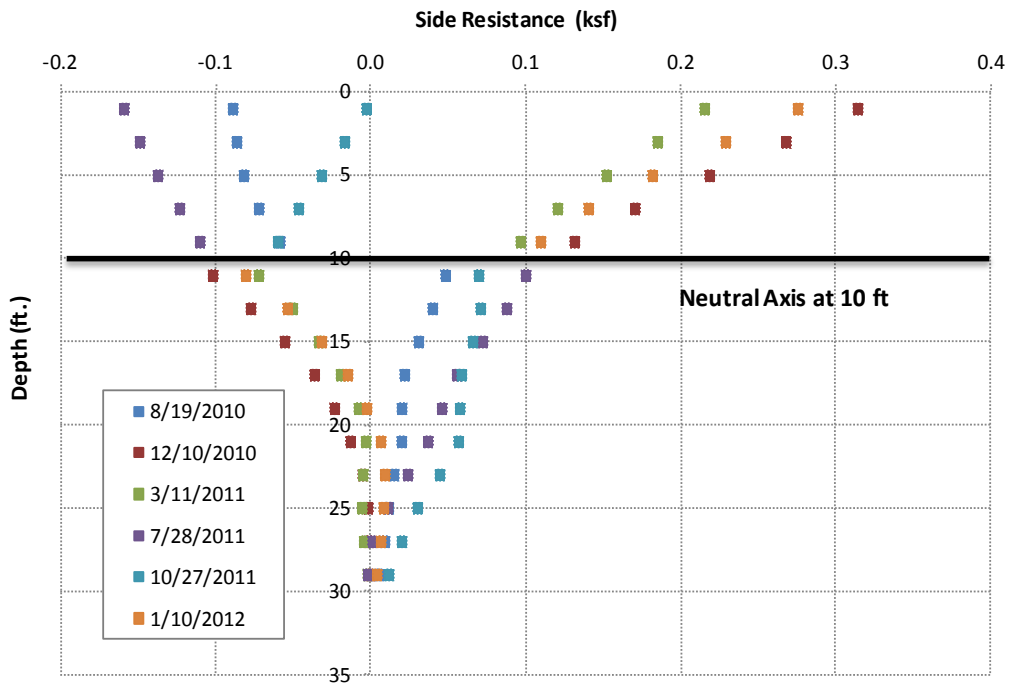


Figure 7.17: Side shear applied on the wall due to volumetric changes of the soil

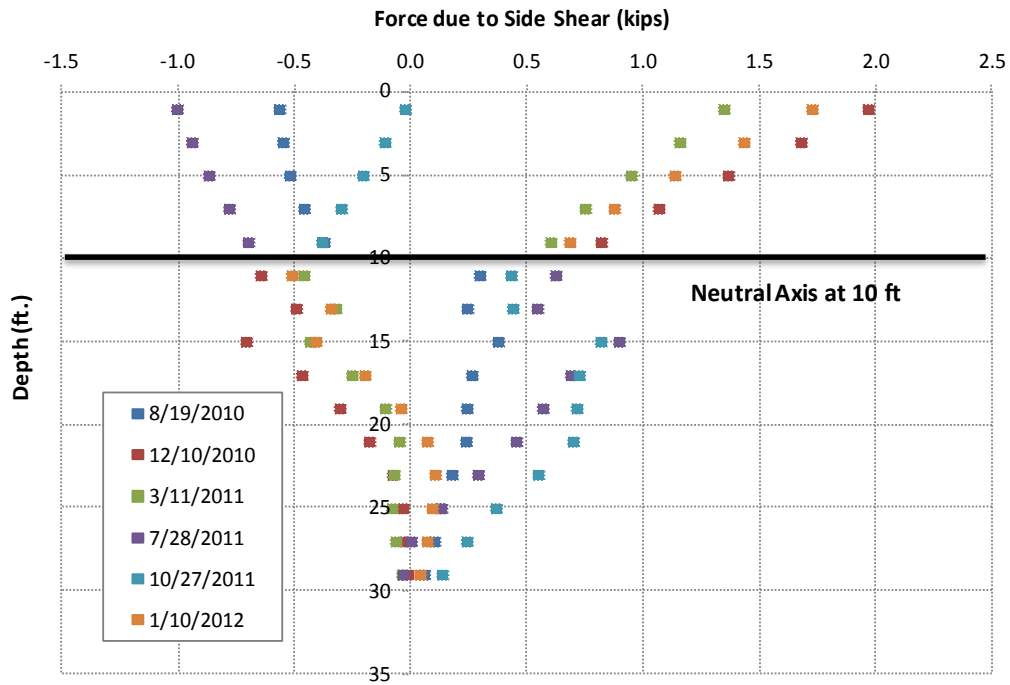


Figure 7.18: Forces due to side shear applied on the wall due to volumetric changes of the soil

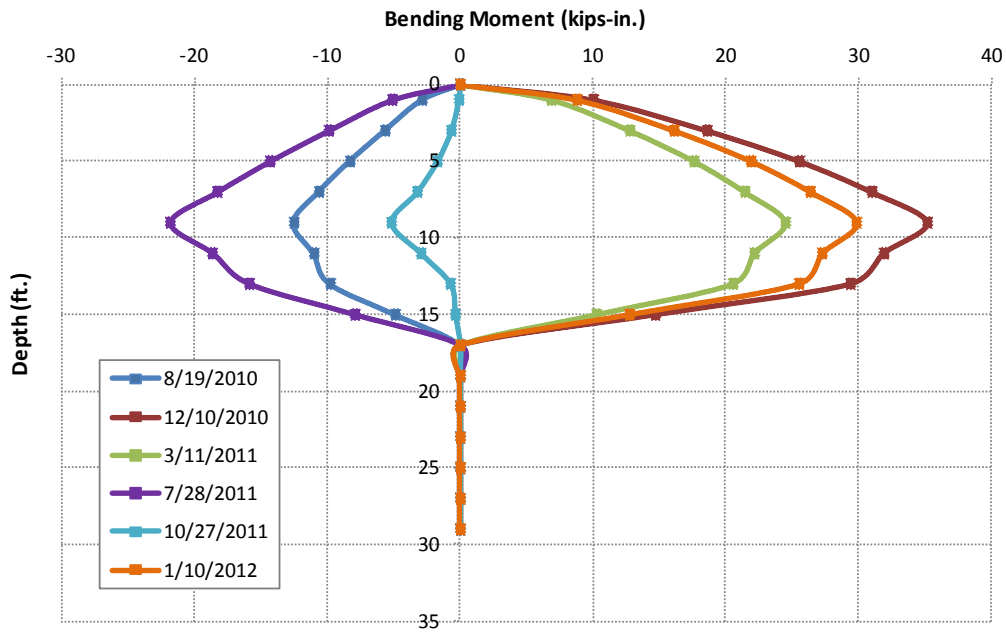


Figure 7.19: Bending curvature applied on the shaft due to volumetric changes of the soil

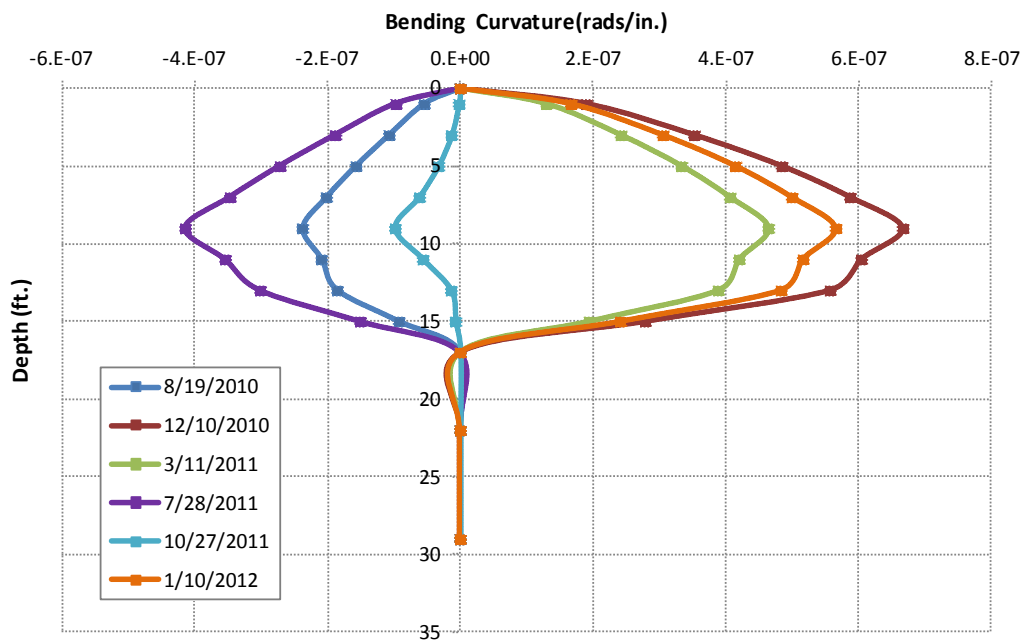


Figure 7.20: Bending curvature applied on the shaft due to volumetric changes of the soil

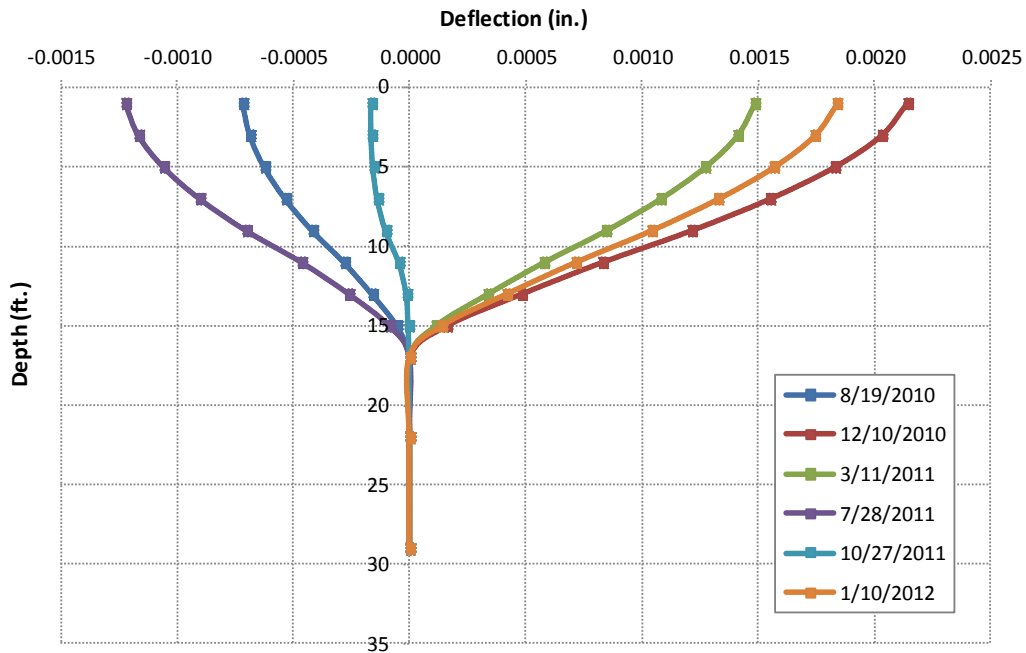


Figure 7.21: Lateral deflections imposed by volumetric changes of the soil at different dates

As indicated in the results of the t-z model, the effect of side shear on the lateral response is not significant as the estimated displacements are very small compared to those measured by the inclinometers in the field. However, the combined response of the wall due to side shear and temperature effects should be investigated.

7.6: Induced strains and curvature due to temperature effects

A very important factor on the lateral response of the wall is related to temperature effects on the concrete mass. As the shafts are influenced by air temperature fluctuations on one side only, significant curvature is introduced in the wall which is either positive or negative depending on the prevailing atmospheric conditions. In fact, given the size of the drilled shafts and the fact that volumetric changes of the soil are limited to the upper 8 feet and are significantly reduced by the small normal forces

applied on the upper 5 feet, temperature effects dominate. A simple linear thermal model is used to account for thermal expansion or contraction of the wall. This model represents the actual behavior of the shafts due to their elongated shape.

According to the linear thermal model, a uniform strain profile is generated which is proportional to the change in temperature. Changes in a material's linear dimensions are related to changes in temperature through a linear thermal expansion coefficient as indicated in the following equation:

$$\varepsilon_{thermal} = \alpha_{concrete} \cdot \Delta T \dots\dots\dots(6.2)$$

where:

- $\varepsilon_{thermal}$ = axial strains induced due to thermal deformation of the concrete
- $\alpha_{concrete}$ = coefficient of thermal expansion for concrete elements = $5.5 \cdot 10^{-6} / F^{\circ}$
- ΔT = temperature change over a specified time interval

To use the above equation, the recorded temperatures at the project site throughout the two year monitoring period are required. The mean daily temperatures are used in this analysis as the daily fluctuations do not affect significantly the behavior of the drilled shafts. These mean daily temperatures as recorded by the nearest meteorological station in Manor are presented in figure 7.22.

Temperature fluctuations affect the shafts only on the excavated side, because the temperature within the soil is not affected significantly by seasonal changes especially below a certain depth very near the surface. Temperature differences between the two sides of the shafts are not considered in this initial analysis and the estimated axial strains refer to the simple case of linear thermal expansion. The mean temperature at the date

that the soil was excavated in front of the wall is selected as the reference date and the strain profiles are presented in figure 7.23.

Table 7.1: Mean daily temperatures at the selected dates and during excavation

Date	Mean Temperature (F°)
Soil Excavation	82
08/19/10	87
12/10/10	48
03/11/11	60
07/28/11	91
10/27/11	74
01/10/12	49

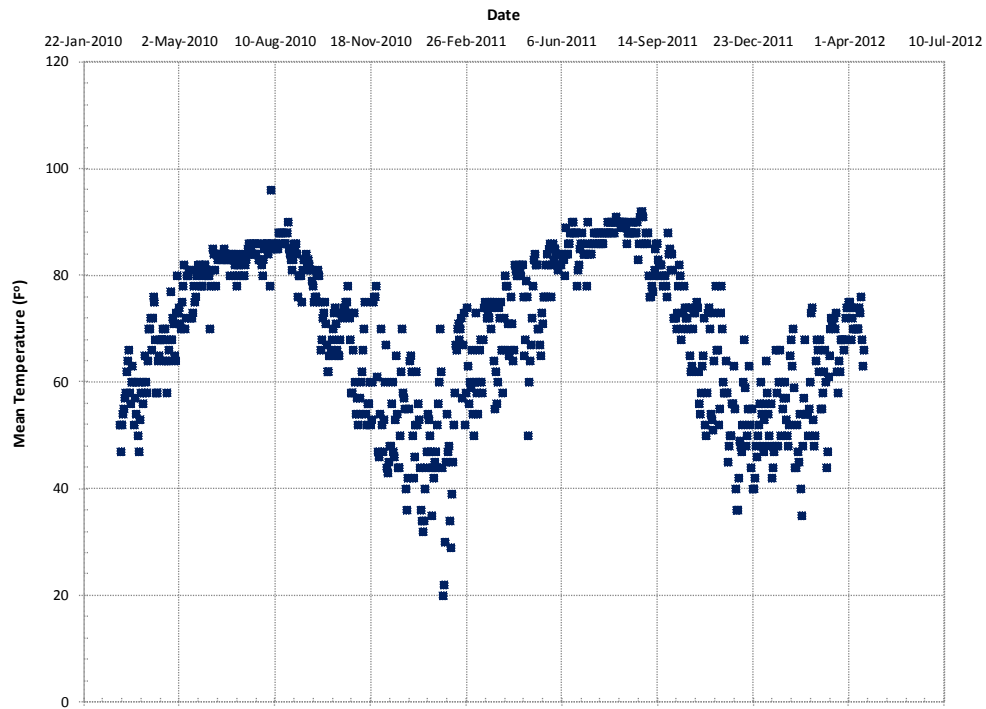


Figure 7.22: Recorded mean daily temperatures at the project site throughout the two year monitoring period

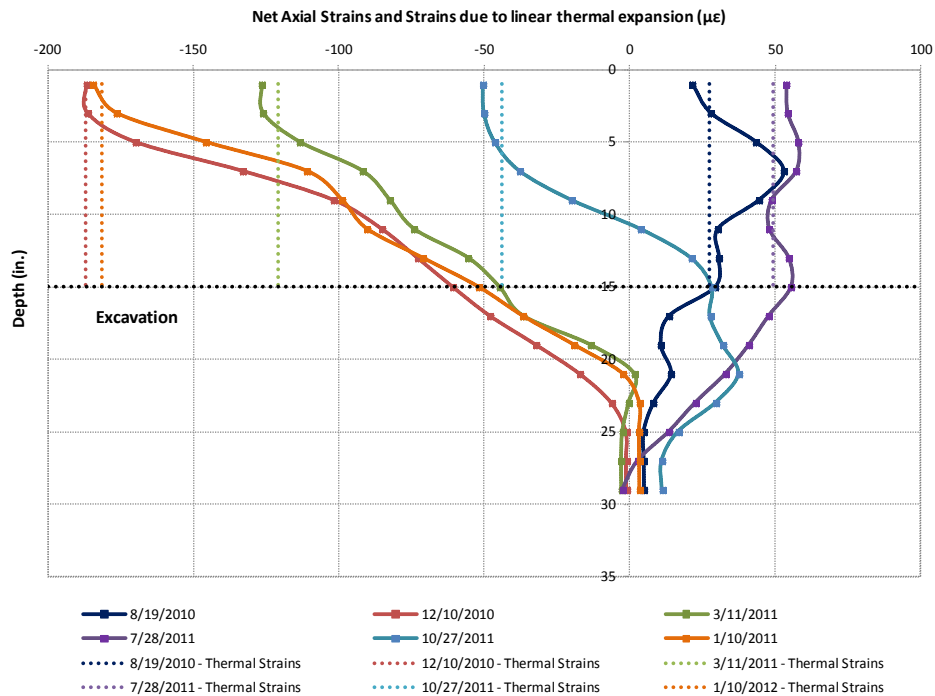


Figure 7.23: Temperature induced axial strains along the shafts assuming linear thermal expansion

The following useful conclusions are drawn by comparing the results of the linear thermal model to the axial strains measured by the strain gauges along the shaft:

- The thermal strains in the linear thermal model are uniform for the cantilever section of the shafts.
- The results of the linear thermal model are consistent to the axial strains measured by the strain gauges very near the surface up to a depth of 3 ft. This surface layer of soil is affected by seasonal changes of temperature in both sides and therefore the linear thermal model is accurate enough to predict the axial strains.
- Given that no side shear is applied on the shafts near the surface, the temperature effects determine the axial response of this upper part of the wall. This is in

accordance to the above results because the strains measured by the strain gauges are equal to the thermal strains predicted by the linear thermal model.

- Below this surface layer, the axial strains measured in the field are smaller than those predicted by the linear thermal model. This is because the soil below a depth of approximately 3 feet does not experience significant changes in temperature. In contrast, the linear model assumes that both sides of the shafts are affected by temperature fluctuations. In addition, side shear is applied in this part of the wall due to volumetric changes of the soil that significantly affects the recorded strains as any axial movement imposed by thermal effects is resisted.

As indicated previously, temperature fluctuations affect only the excavated side of the shafts and therefore curvature is generated on the cantilever section of the wall. This curvature could be quantified and eliminated from the results of the instrumentation program in order to account only for the effect of lateral earth pressures on the final response of the wall. To do that, a simple approximation is made assuming that the temperature of the soil is constant and equal to 70F° two feet behind the wall. This assumption is reasonable given the low thermal conductivity of concrete.

Assuming linear change in temperature between the point within the soil where the temperature is constant and the point where the wall is in contact to the atmospheric air, the temperatures at the tension and compression gauges are evaluated. Therefore, using the linear thermal model on the two sides of the wall, the induced curvature is estimated.

According to the linear thermal model, uniform strain profiles are generated for the tension and compression sides of the shafts for the selected dates. Because differential

strains are induced, curvature is developed in the wall which is evaluated based on the procedure described while analyzing the results of the instrumentation program.

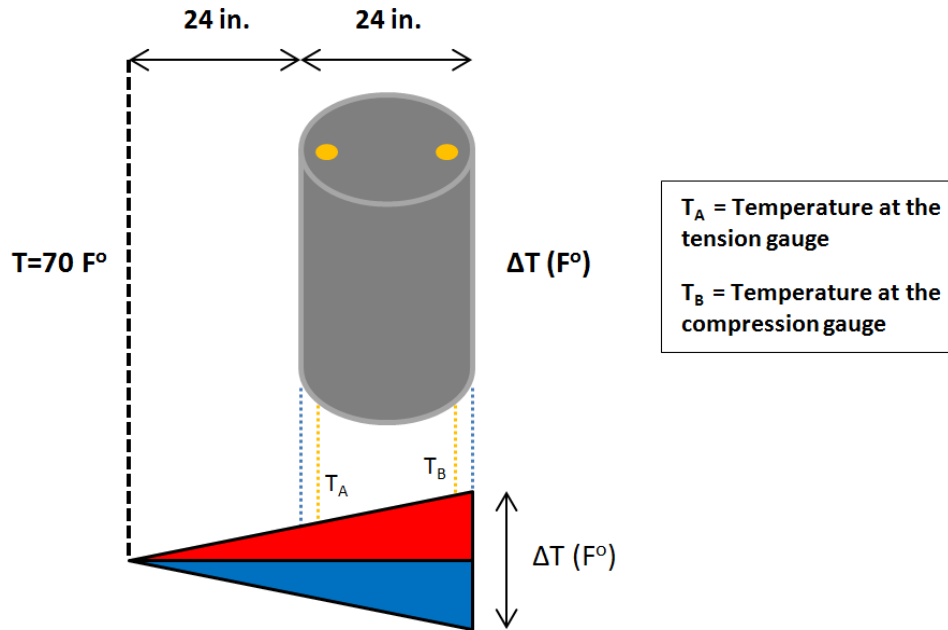


Figure 7.24: Simple model assumed to account for the differential thermal effects

The results of this analysis indicate the significance of the temperature effects on the lateral response of the wall. The bending curvature due to differential thermal movements constitute approximately 15% of the curvatures measured in the wall as presented in a previous chapter. In addition, the strains predicted on the tension and compression sides of the shafts are about $100\ \mu\epsilon$, much bigger than the strains measured in the field by the monitoring elements.

The effect of side shear is less significant than the thermal effects on the lateral response of the wall. The curvatures generated in extreme cases of moisture fluctuations are approximately 30% of those predicted by the linear thermal model. However, both thermal and side shear effects occur concurrently and the net curvature profile should be accounted for design purposes that includes both thermal and side shear effects.

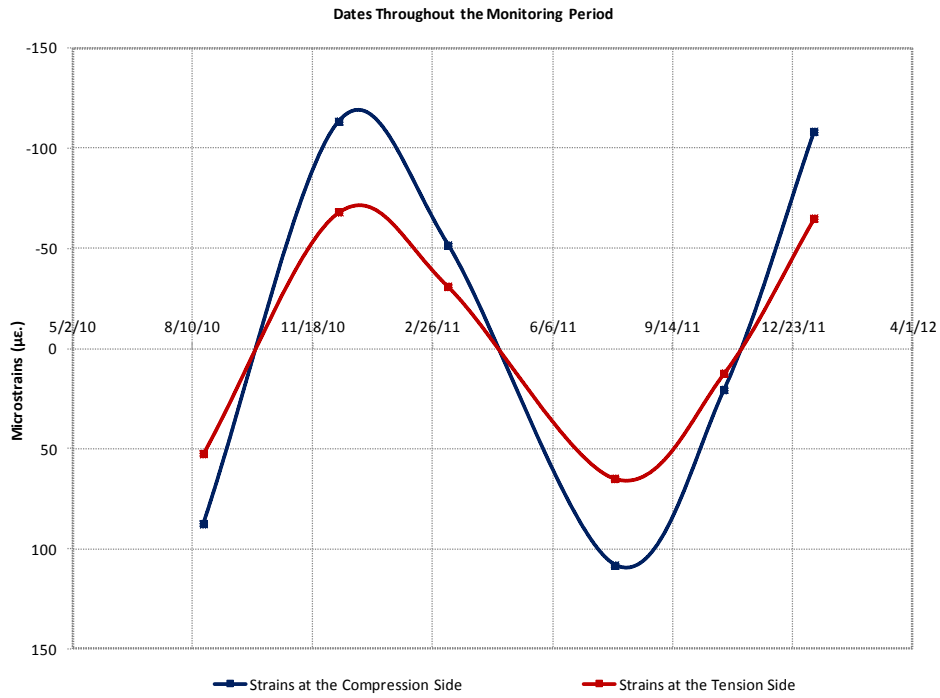


Figure 7.25: Thermal strains on the tension and compression side

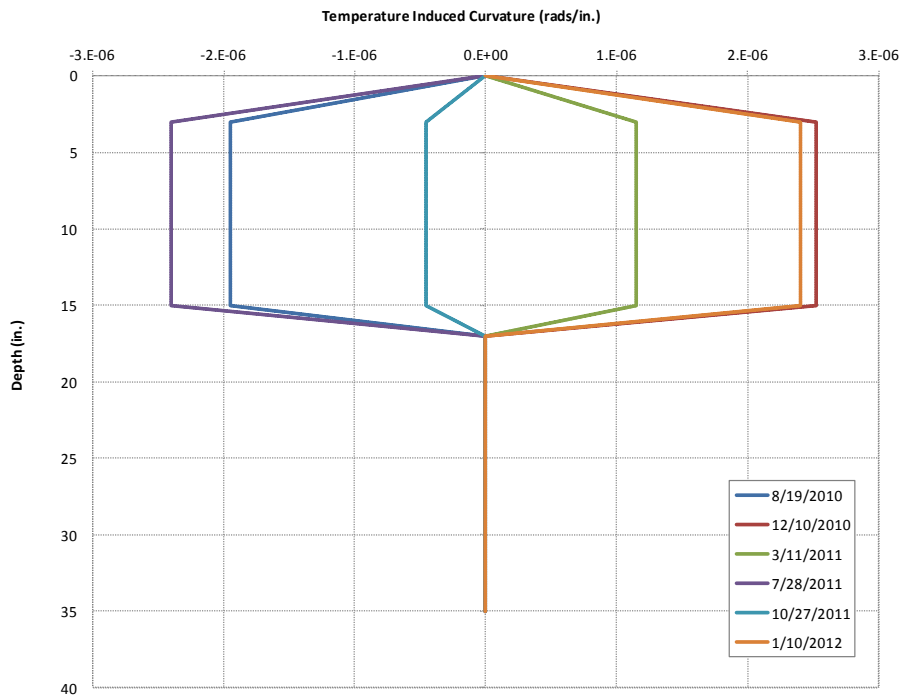


Figure 7.26: Temperature induced curvature for the selected dates

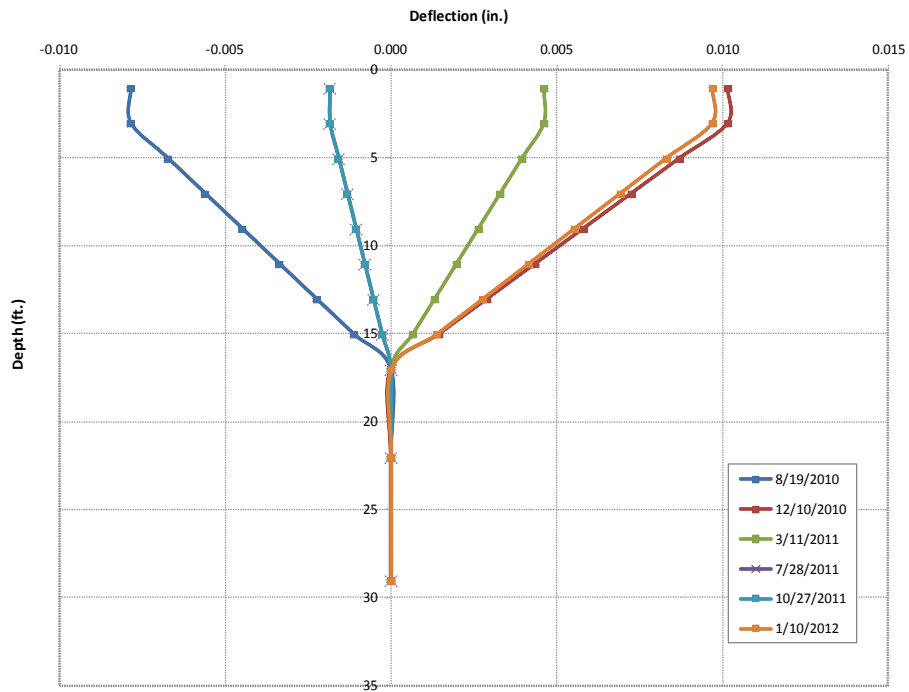


Figure 7.27: Temperature induced lateral deflections for the selected dates

7.7: Conclusions and final remarks

Several useful conclusions are derived from the t-z and the linear thermal model. It becomes evident that the temperature effects are more significant on the lateral response of the wall while the combined effect of side shear and temperature fluctuations on the concrete elements should be taken into account for design purposes. Generally, the following issues are important:

- From the net axial strain profiles at the selected different dates, the maximum axial strains are developed near the surface. The boundary conditions at the tip and the head of the shafts are the main reason for this behavior, because there is no resistance to axial movement at the top of the wall. In addition, thermal effects are much more

significant in this part of the wall, because both sides of the shafts are affected by temperature fluctuations.

- The thermal axial strains and the curvatures generated due to the differential thermal effects are significant. Raw data containing them should be processed to exclude them, retaining only the response of the wall due to earth pressures. The results of the differential thermal model are a starting point for later design recommendations.
- Side shear applied on the wall does not have a large effect on the lateral response of the shafts. In the case of drilled shaft retaining walls, shear forces are applied only on one side of the wall and are significantly reduced by the lateral movements of the shafts. In contrast to the case of drilled shafts used as foundation elements, uplift or down-drag phenomena are limited in the field.
- The bending moments generated by side shear are positive when the moisture content of the soil is high, and negative when it is low. This is consistent with the expected behavior of the wall under volumetric changes of the soil. However, part of this side shear is generated by the friction induced at the interface of the wall due to thermal straining on the tension side. The behavior of the wall under different moisture and temperature conditions is presented in the following figures.
- The date that the soil is excavated is not important for the thermal effects, but is very important on the side shear applied on the wall. Temperatures in the shafts reach equilibrium a few days after excavation, while the moisture content of the soil takes several months to change.
- The lateral deflections due to the curvature generated by thermal effects and side shear are small compared to those measured in the field. However, the moments are significant and should be taken into account for design purposes.

The above analysis is important to better understand the lateral response of the wall and to isolate the effect of lateral earth pressures applied on the shafts. Corrections should be made to account for the combined thermal and side shear effect. Due to the several assumptions made in the above procedures, the results should be evaluated with caution.

Chapter 8: Conclusions and Future Work

8.1: Conclusions and comments on the results

Several useful conclusions have been drawn from the results of the instrumentation program, and the different types of analysis including the p-y, the t-z and the linear thermal model. These conclusions are summarized below:

A. Residual stresses and strains:

- The magnitudes of the residual stresses developed in the shafts at the time the soil was excavated were significant and thus in similar projects they should be taken into account during the design stage.
- Both concrete curing and site conditions affect the magnitude of the residual stresses and strains. While the stresses due to concrete curing follow a specific pattern, the effect of site conditions depends on the type of soil and its potential to undergo significant volumetric changes during cycles of moisture fluctuation.
- The time of year that the shafts are constructed is important in estimating the magnitude of the residual stresses. Since the water content of the soil varies significantly throughout the year, the effect of soil shrinking and swelling will be different if the wall is constructed during the summer or during the winter.

B. Inclinometer data:

- The shafts are not fixed and a non-zero initial rotation was developed at the tip of the wall due to excavation. This is a very important issue as the shafts were expected to be fixed during the design stage.

- The effect of moisture or temperature fluctuations on the deflected shapes is evident as the maximum deflections are observed between December and March when the moisture content of the soil is high while the wall bounces back during the summer when the water content decreases due to evaporation.
- The depth of the tension crack is significantly larger when the water content of the soil is low and the soil shrinks.

C. **Strain gauge data:**

- Significant variability was observed in the raw results of the strain gauges due to various microscale and environmental factors (tension cracks and temperature effects).
- Processing of the raw strain data is required to eliminate the effect of tension cracks and combine the strain gauges from the three instrumented shafts at the same depth and side.
- The shear forces and the net earth pressure distributions predicted from the strain gauge and inclinometer data are similar. Although, different curve fitting methods were used, the shapes and magnitudes of these profiles are similar and correspond well to those expected for such shaft deflections.
- The size of the tension cracks evaluated based on the net earth pressure diagrams from the strain gauge data is highly sensitive to the curve fitting method used on the curvature profile. Significant variability was observed on the curvature profiles above the excavation level. Therefore, the point where the curvature is generated that depicts the size of the tension crack, depends on the curve fitting method.

D. P-y analysis:

- The various input parameters are very important on the results of the p-y model. The sensitivity analysis indicated that the stiffness of the soil as described by the values of ϵ_{50} greatly affects the lateral response of the wall.
- Initial "global" displacements were developed during excavation and a non-zero rotation at the tip of the shafts was generated.
- The ranges of earth pressures predicted from the p-y analysis at the selected dates during the two year monitoring period are similar to those estimated from the instrumentation program.

E. T-z analysis and thermal effects:

- The axial strains and curvatures generated due to differential thermal effects are significant and should be eliminated from the raw data so that the processed data represent only the response of the wall due to earth pressures. The results of the differential thermal model are a starting point for the subsequent design recommendations.
- Side shear applied on the wall does not greatly affect the lateral response of the shafts. Shear forces are applied on one side only of drilled shaft retaining walls, and are significantly reduced by the lateral movements of the shafts.
- The bending moments generated by side shear are positive when the moisture content of the soil is high and negative when it is low. This is in accordance to the expected behavior of the wall under volumetric changes of the soil. However, part of this side shear is generated by the friction induced at the interface of the wall due to thermal straining on the tension side.

- The lateral deflections due to the curvature generated by thermal effects and side shear are small compared to those measured in the field. However, the moments are significant and should be taken into account for design purposes.

8.2: Recommendations for future work

The above conclusions constitute the basis for future design recommendations for drilled shaft retaining walls on expansive clay. However, many factors that affect the wall behavior have not yet been quantified, and include the following:

- In the various types of analysis conducted for the purposes of this thesis, undrained conditions were assumed for consistency with current TxDOT design procedures for similar walls in expansive clay. However, the current response of the wall is governed by drained conditions and an additional drained analysis is suggested in the future.
- With respect to the p-y analysis, the shear strength on the passive zone should be measured in the field in order to evaluate the initial "global" displacements developed during excavation with sufficient accuracy. In addition, various shapes of the earth pressure distribution should be used and the fact that the active thrust is a function of the lateral displacements should be incorporated in the final p-y model.
- Different thermal models should be used to simulate the effect of temperature fluctuations on the lateral response of the wall. The results from the thermocouples should be used to estimate the effect of thermal fluctuations on the tension side.

Appendix A

A.1: Residual processed strains along the "global" shaft

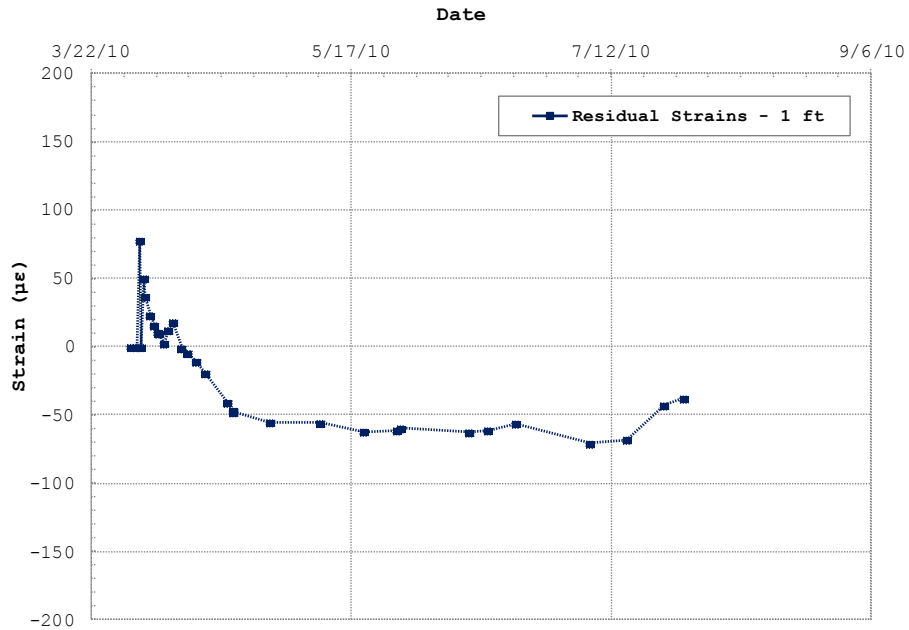


Figure A.1: Residual strains at a depth of 1ft

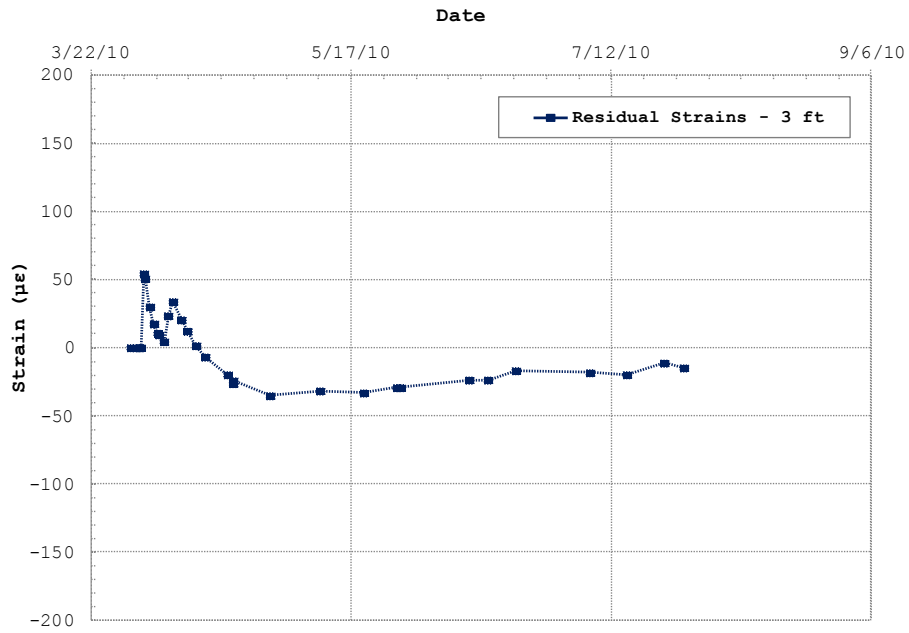


Figure A.2: Residual strains at a depth of 3ft

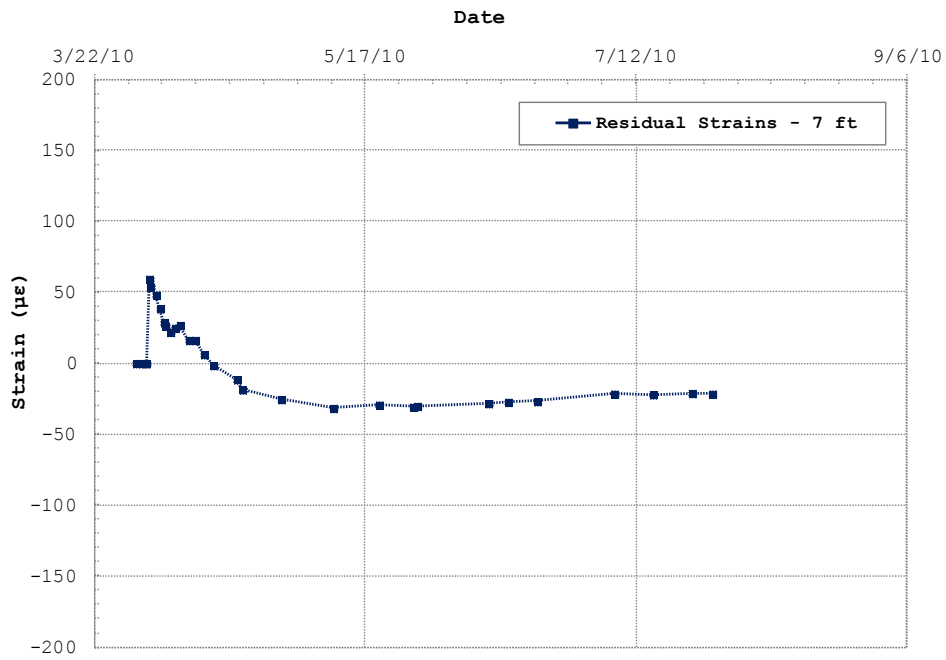


Figure A.3: Residual strains at a depth of 7ft

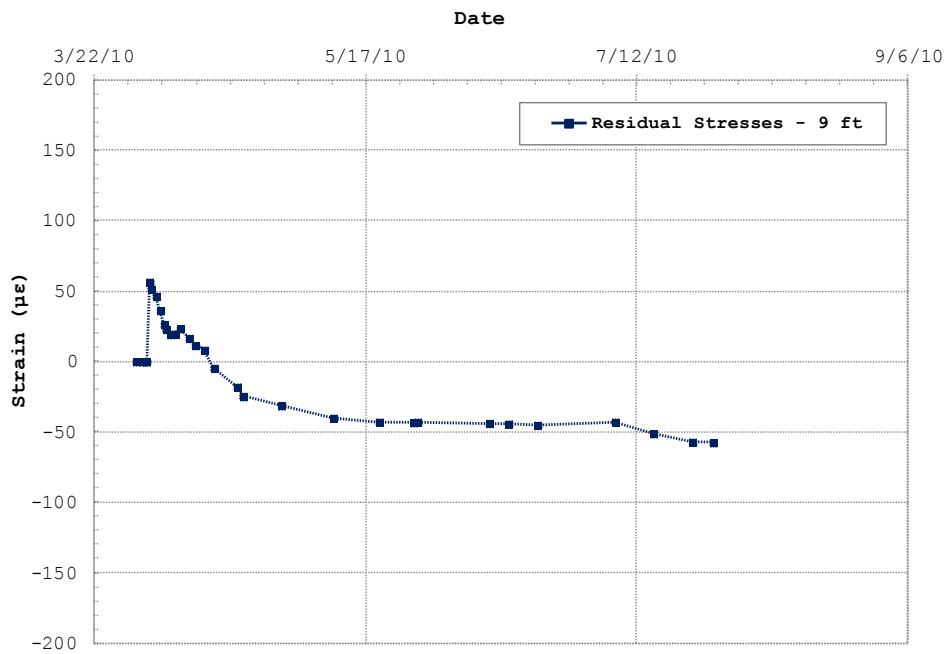


Figure A.4: Residual strains at a depth of 9ft

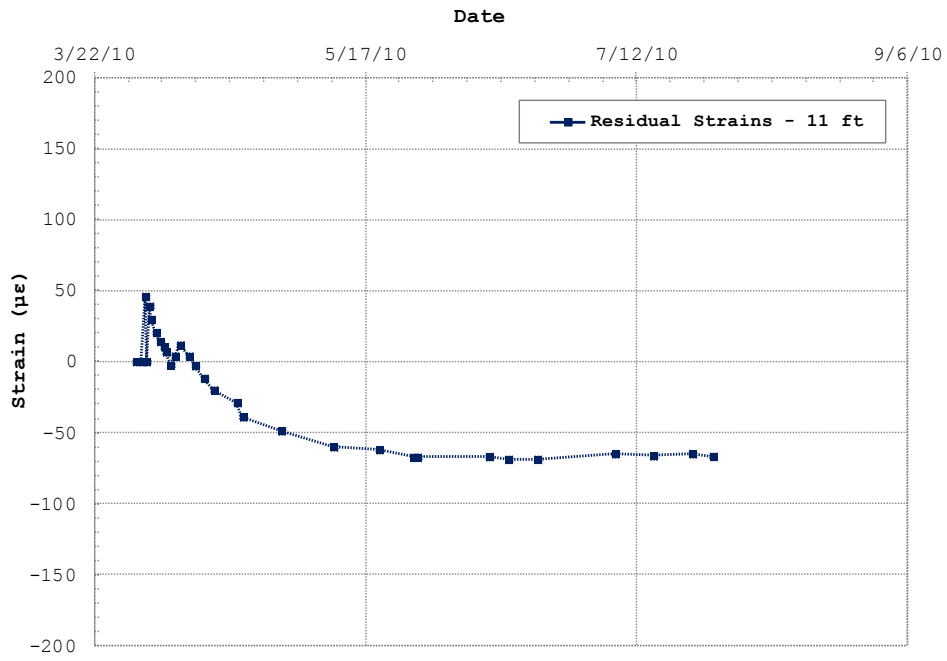


Figure A.5: Residual strains at a depth of 11ft

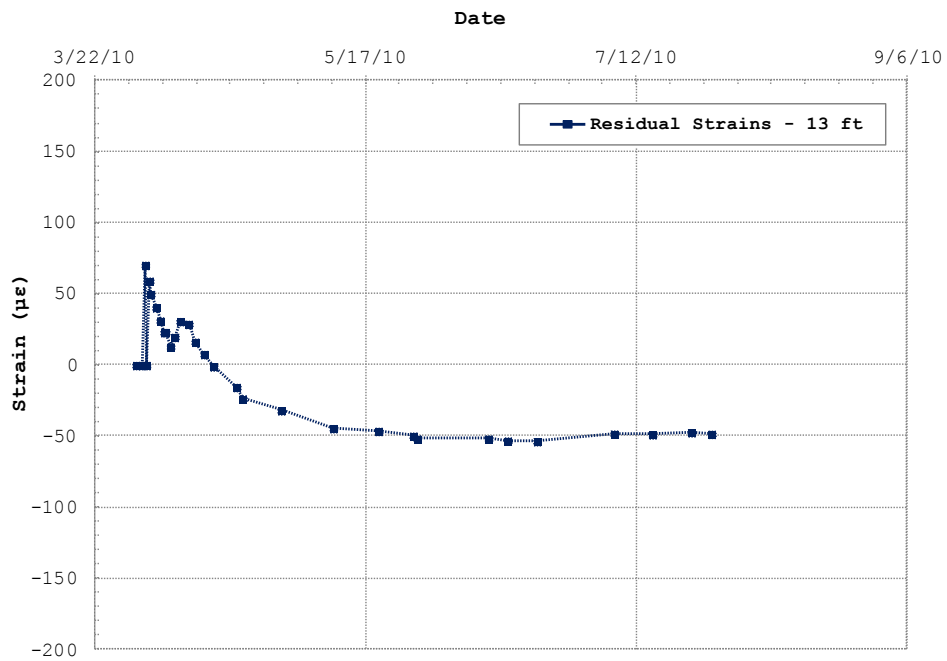


Figure A.6:Residual strains at a depth of 13ft

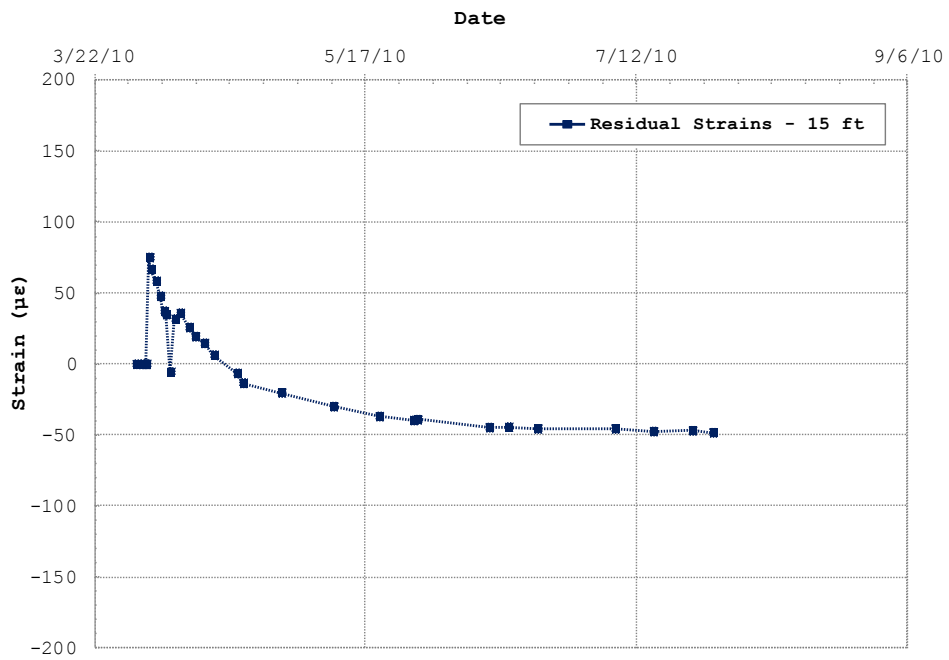


Figure A.7: Residual strains at a depth of 15ft

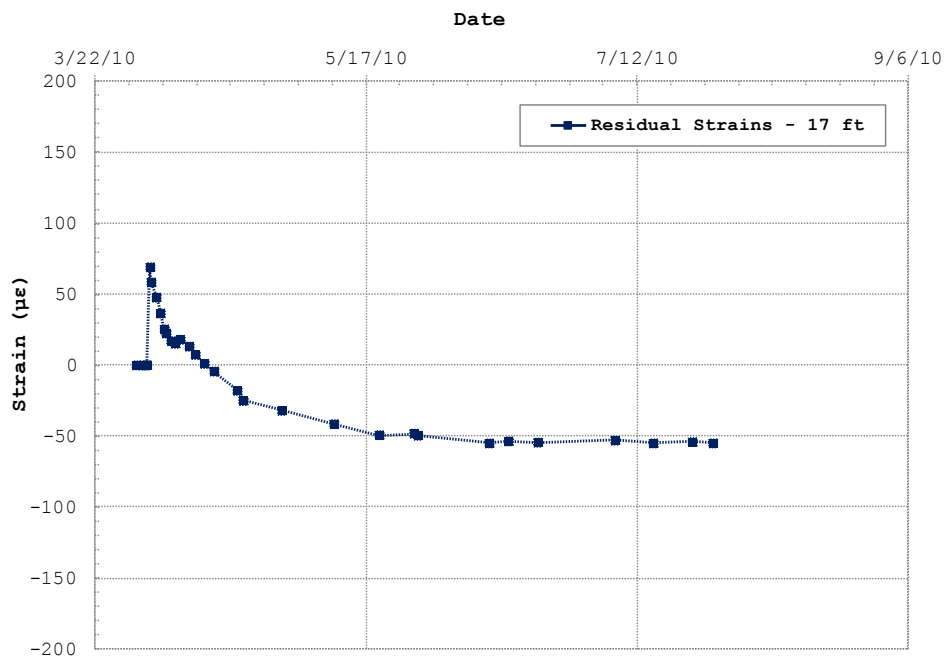


Figure A.8: Residual strains at a depth of 17ft

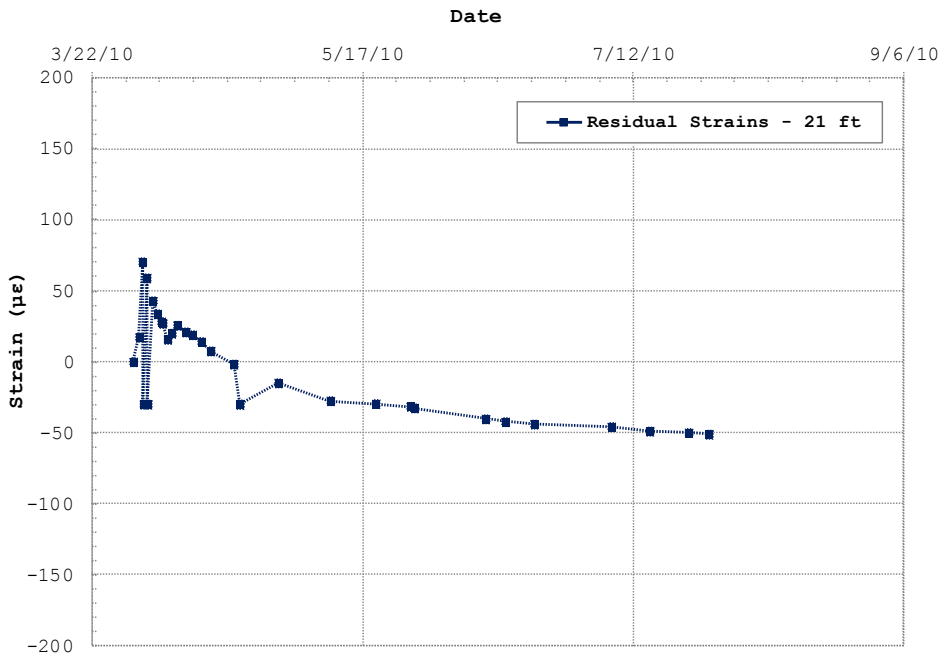


Figure A.9: Residual strains at a depth of 21ft

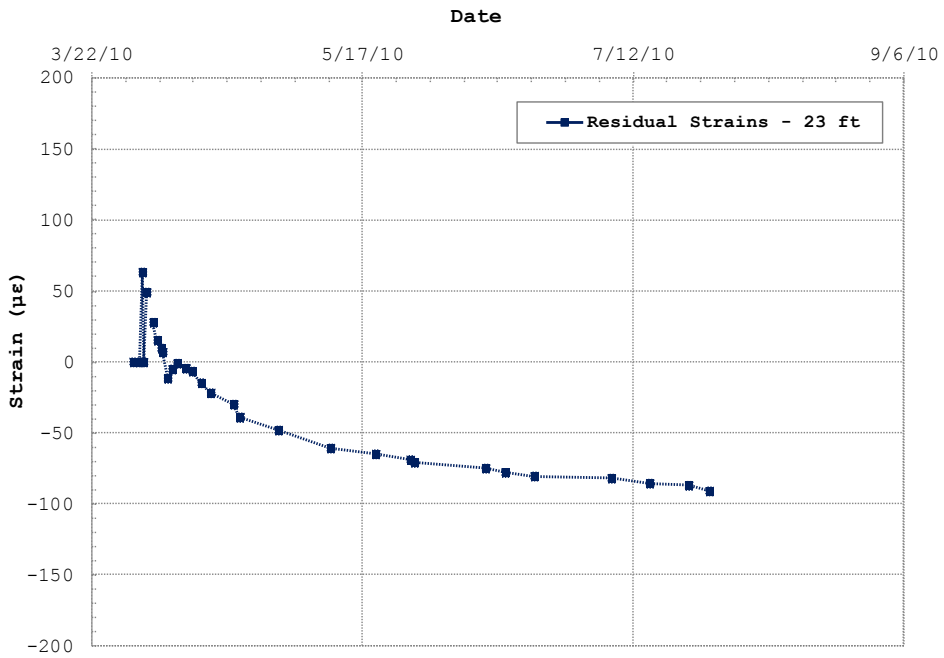


Figure A.10: Residual strains at a depth of 23ft

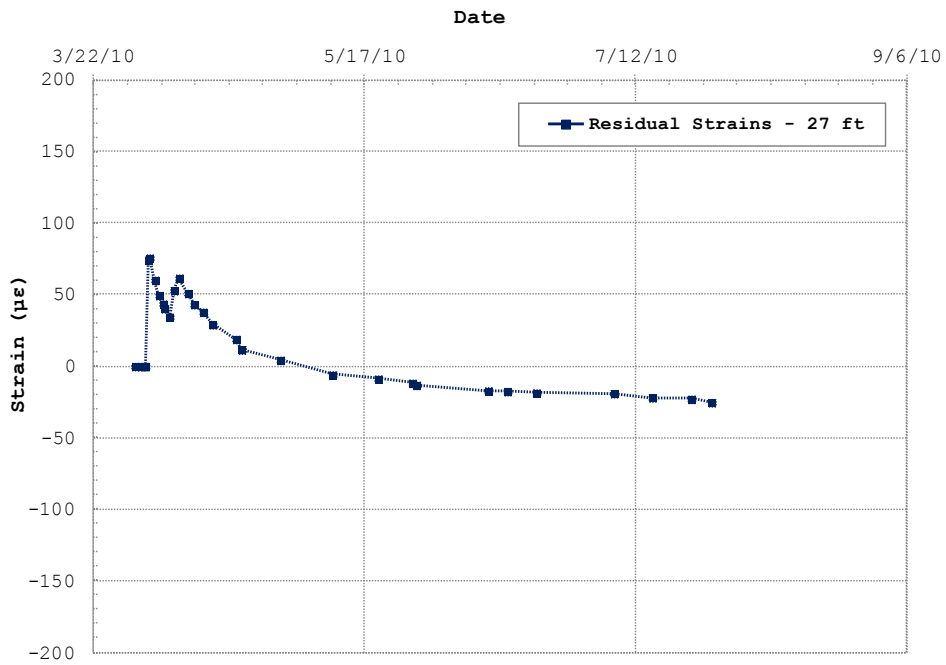


Figure A.11: Residual strains at a depth of 27ft

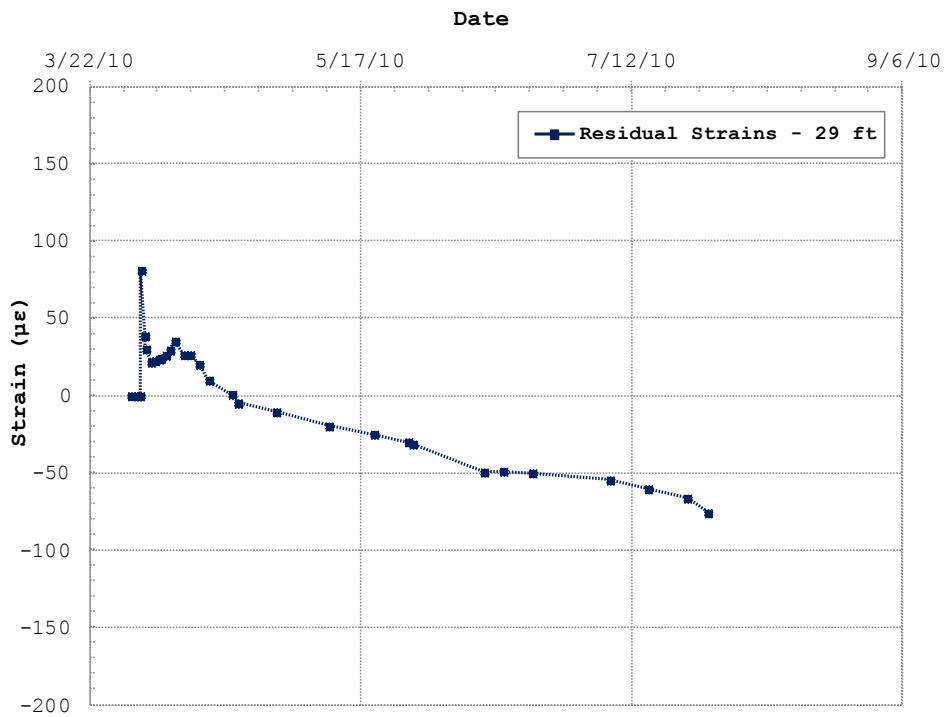


Figure A.12: Residual strains at a depth of 29ft

A.2: Residual stresses along the "global" shaft

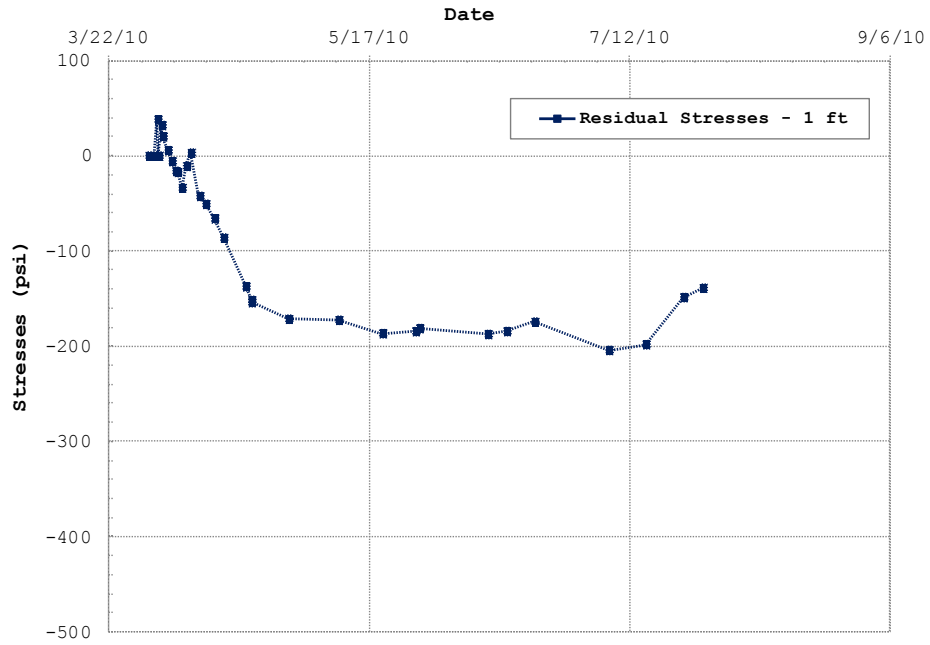


Figure A.13: Residual stresses at a depth of 1ft

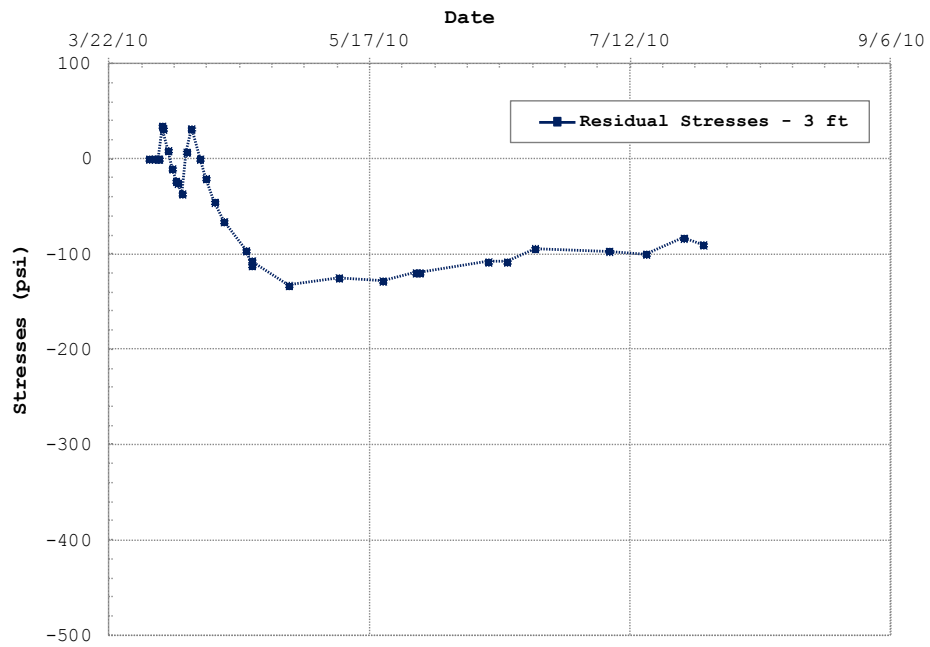


Figure A.14: Residual stresses at a depth of 3ft

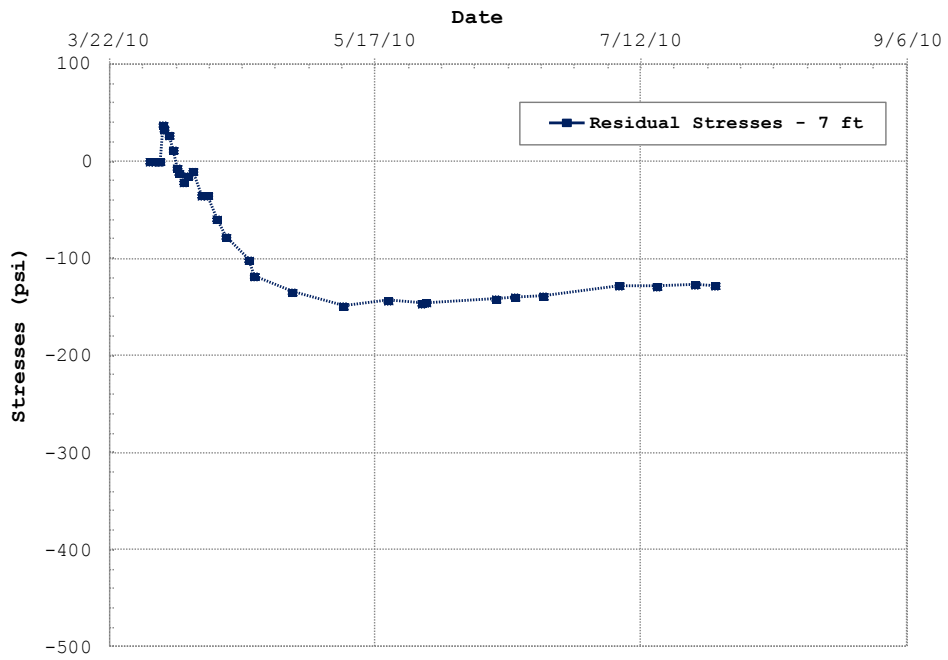


Figure A.15: Residual stresses at a depth of 7ft

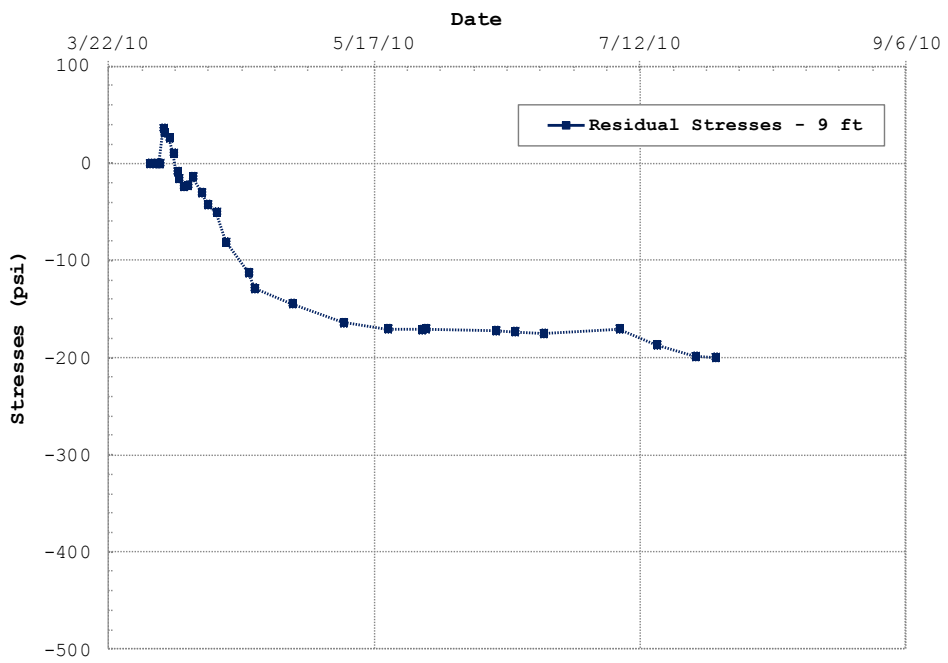


Figure A.16: Residual stresses at a depth of 9ft

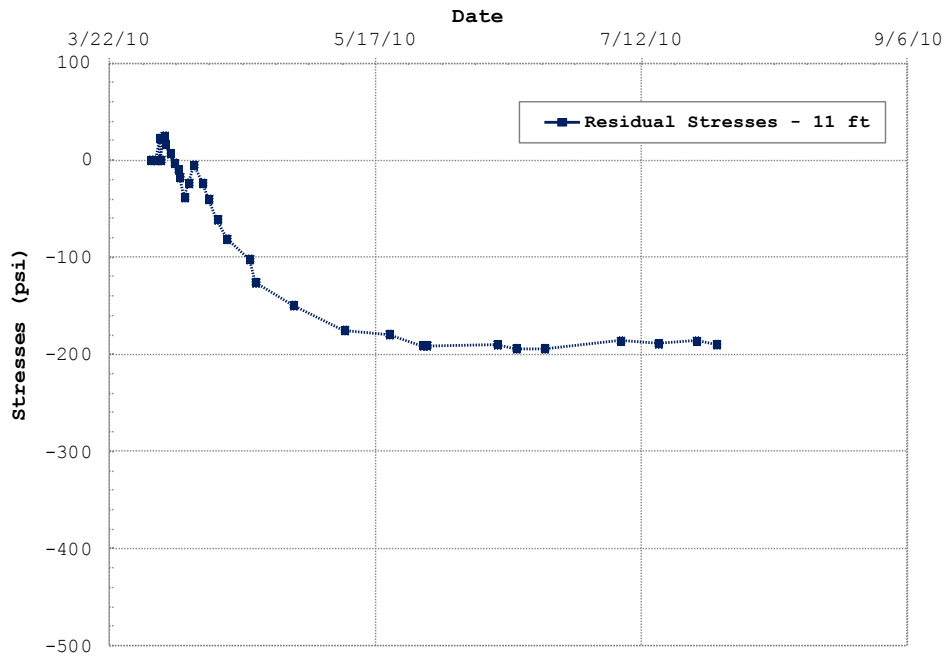


Figure A.17: Residual stresses at a depth of 11ft

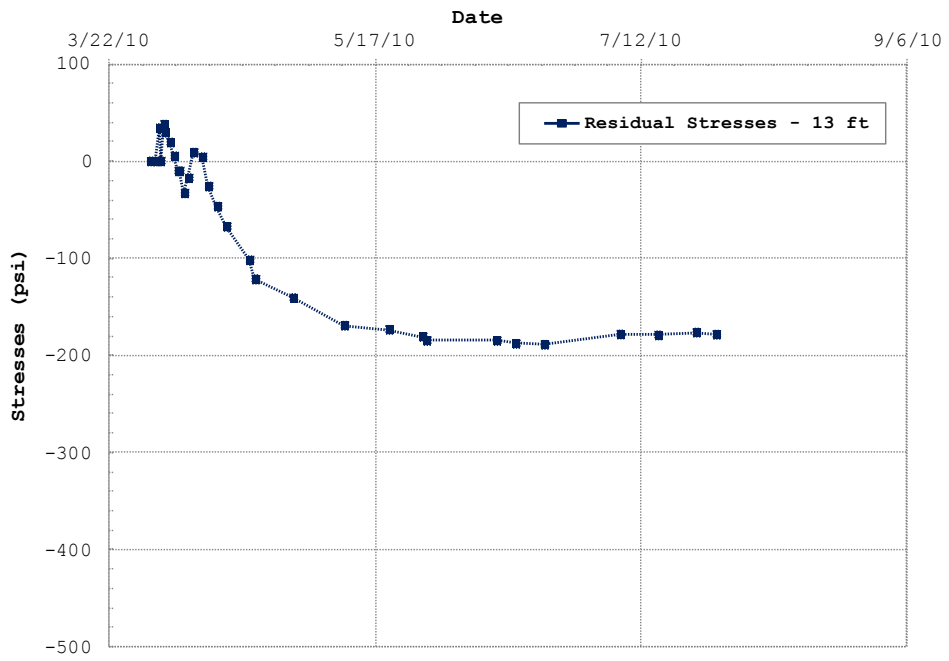


Figure A.18: Residual stresses at a depth of 13ft

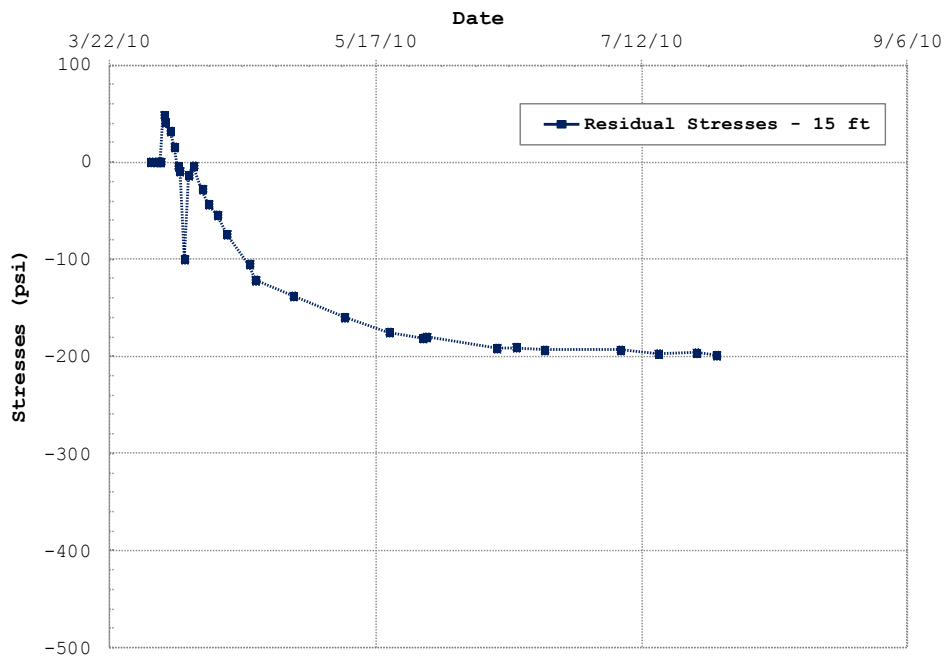


Figure A.19: Residual stresses at a depth of 15ft

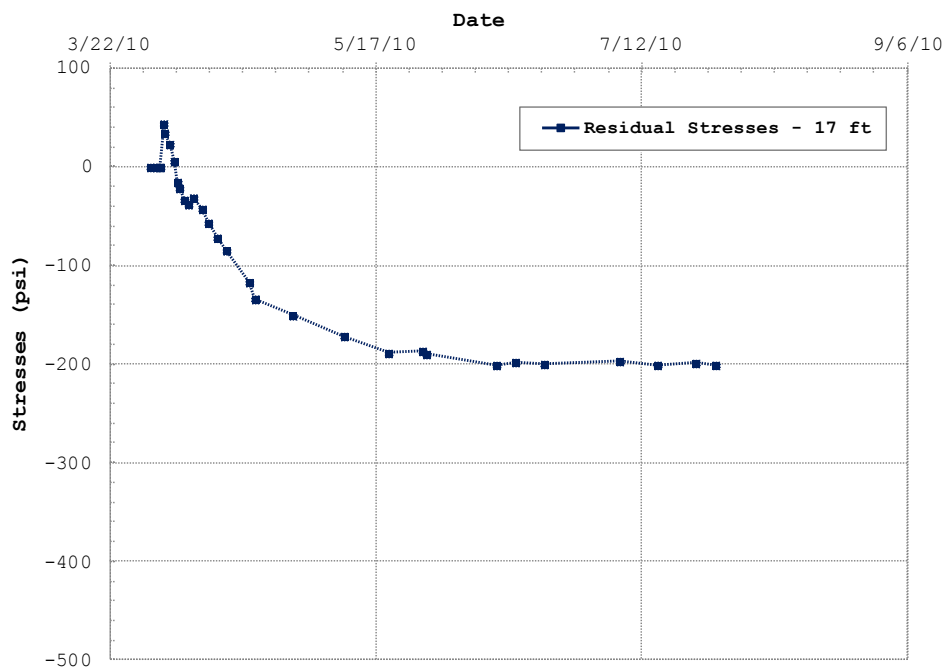


Figure A.20: Residual stresses at a depth of 17ft

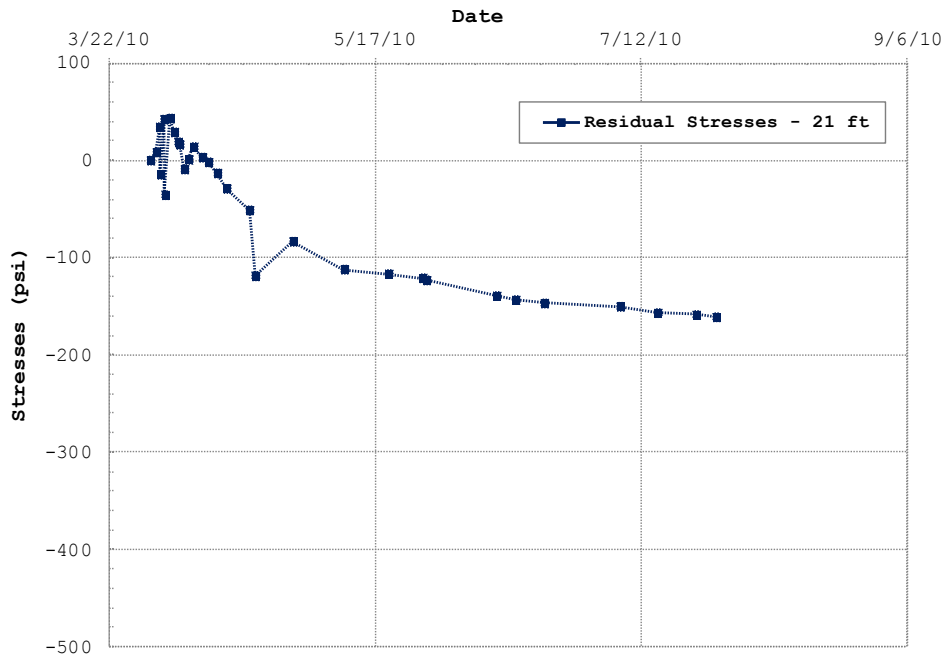


Figure A.21: Residual stresses at a depth of 21ft

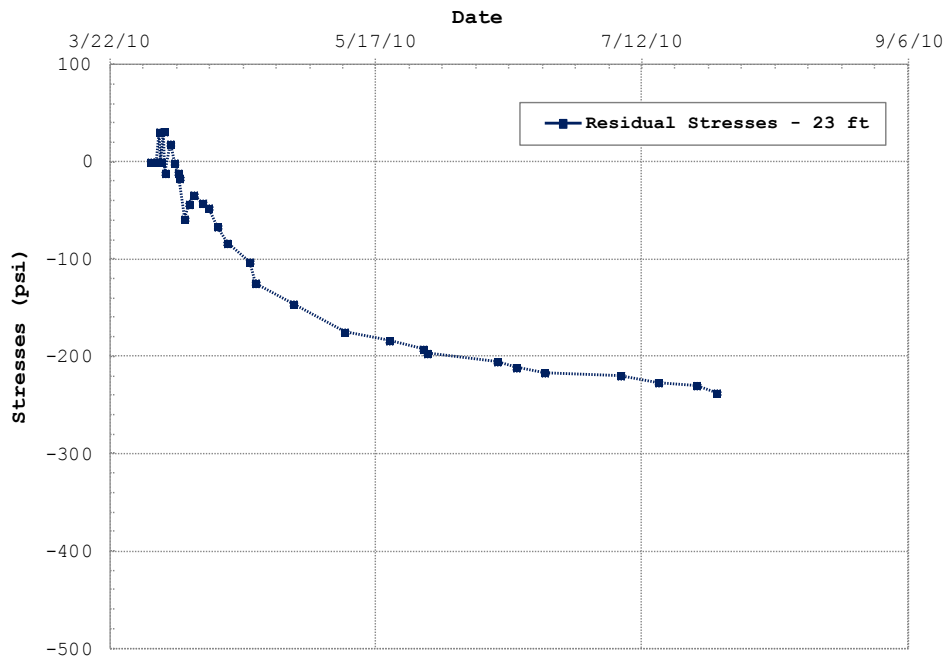


Figure A.22: Residual stresses at a depth of 23ft

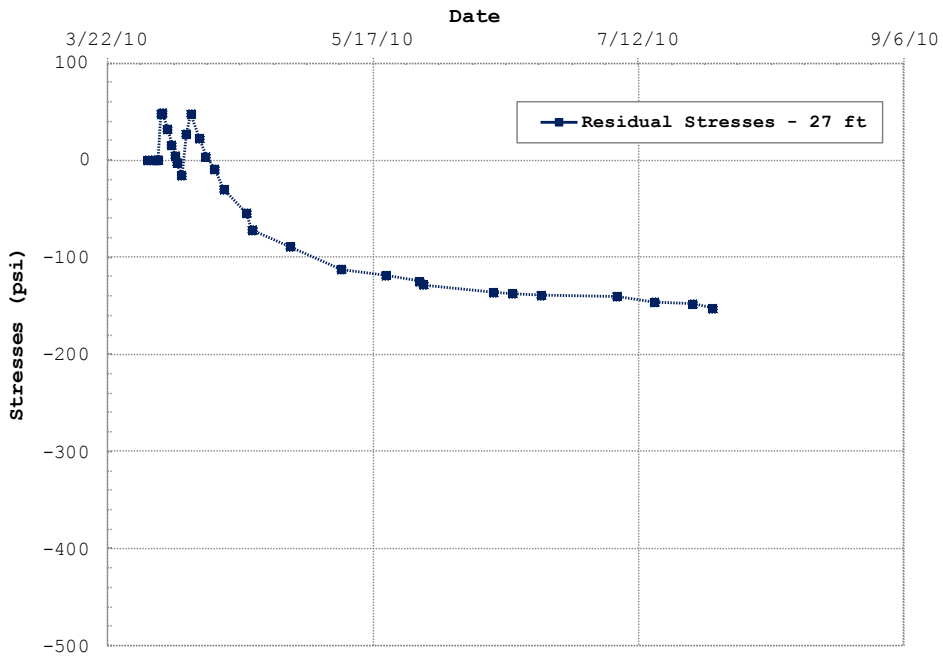


Figure A.23: Residual stresses at a depth of 27ft

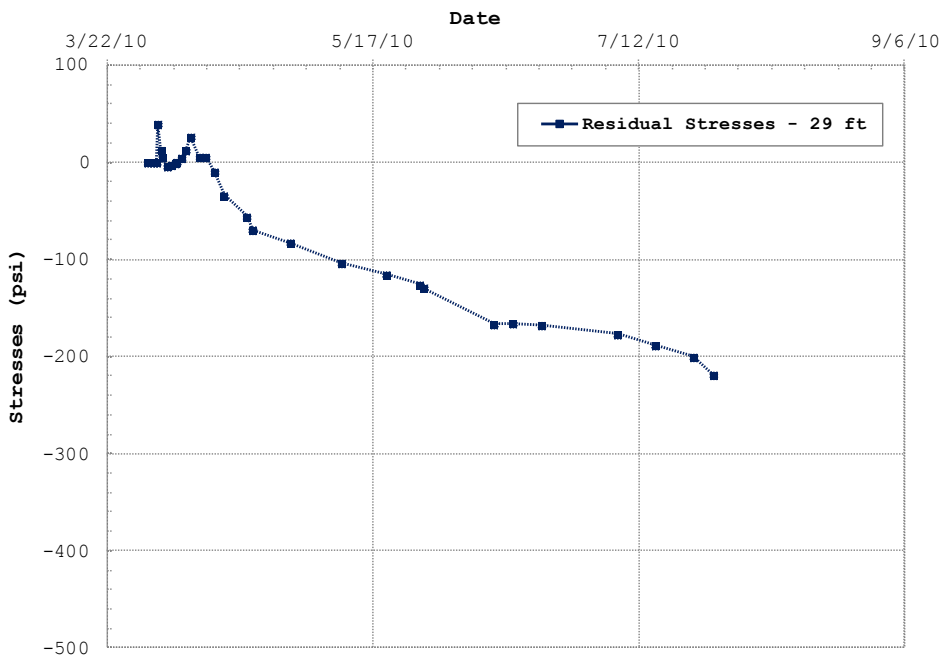


Figure A.24: Residual stresses at a depth of 29ft

Appendix B

B.1: Strains throughout the monitoring period along the instrumented shafts

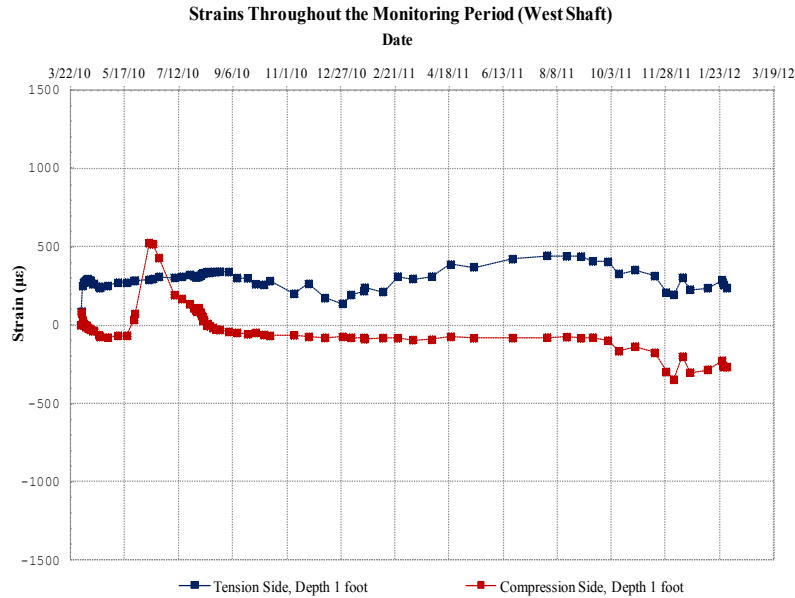


Figure B.1: Strains throughout the monitoring period for the west shaft at a depth of 1ft

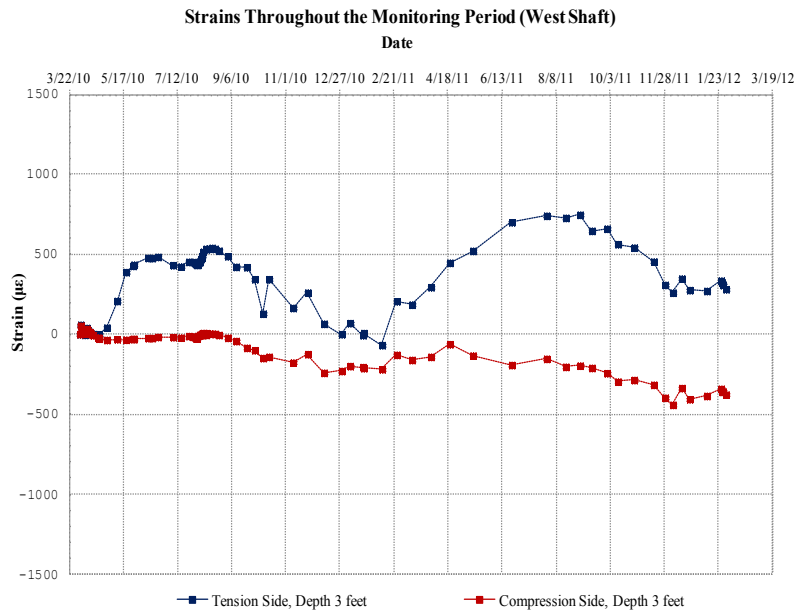


Figure B.2: Strains throughout the monitoring period for the west shaft at a depth of 3ft

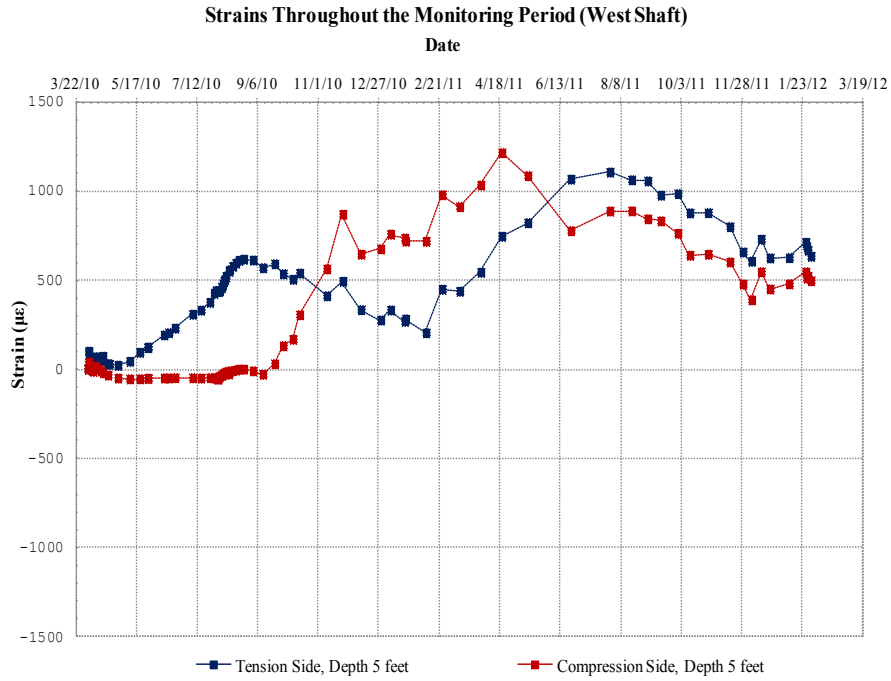


Figure B.3: Strains throughout the monitoring period for the west shaft at a depth of 5ft

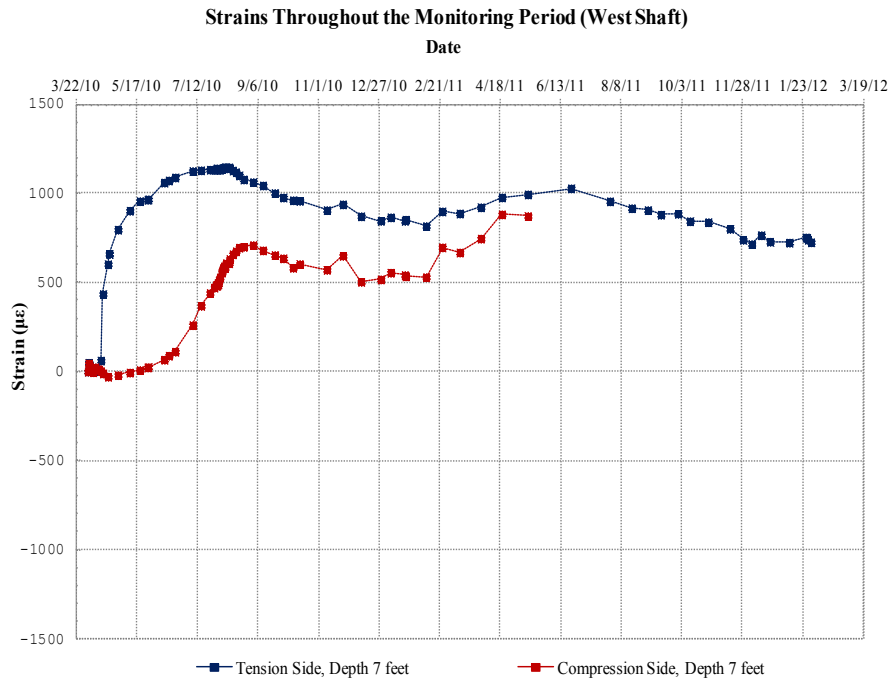


Figure B.4: Strains throughout the monitoring period for the west shaft at a depth of 7ft

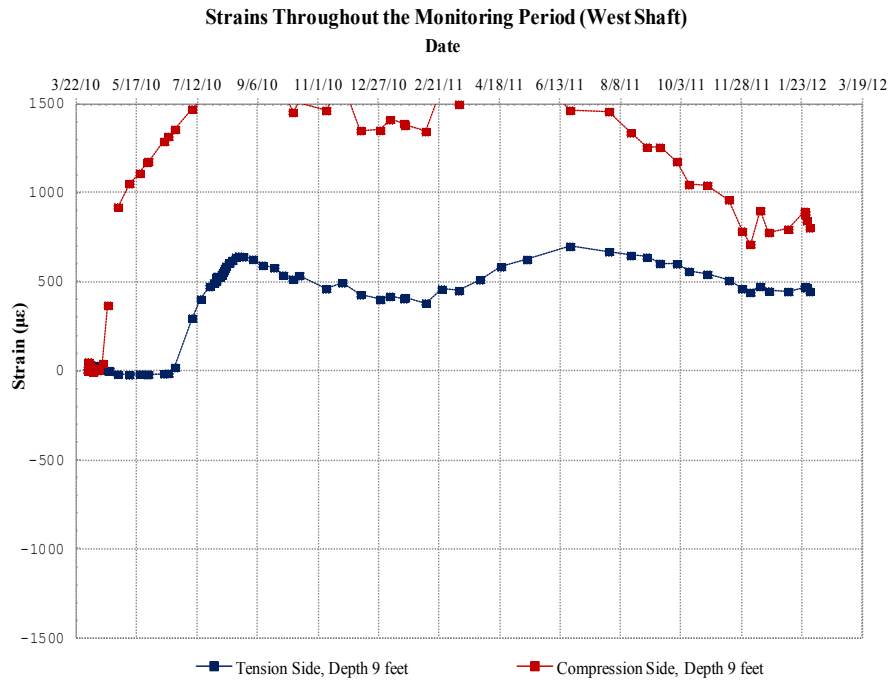


Figure B.5: Strains throughout the monitoring period for the west shaft at a depth of 9ft

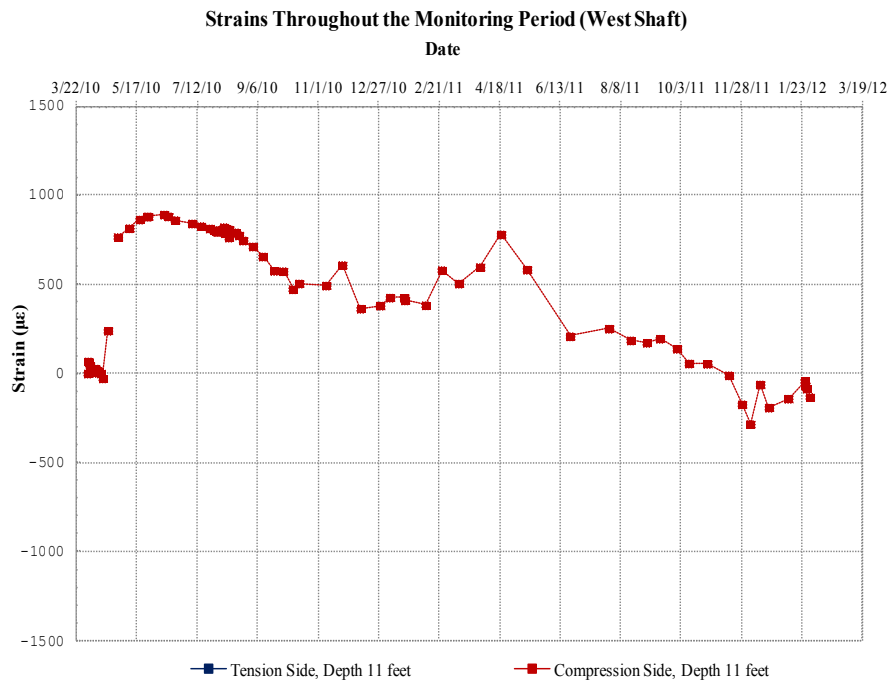


Figure B.6: Strains throughout the monitoring period for the west shaft at a depth of 11ft

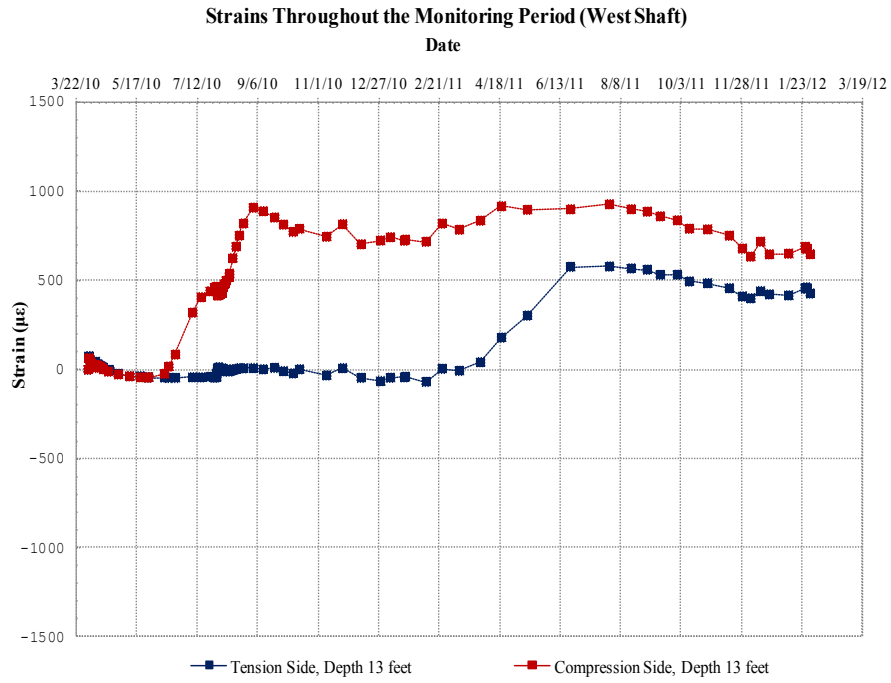


Figure B.7: Strains throughout the monitoring period for the west shaft at a depth of 13ft

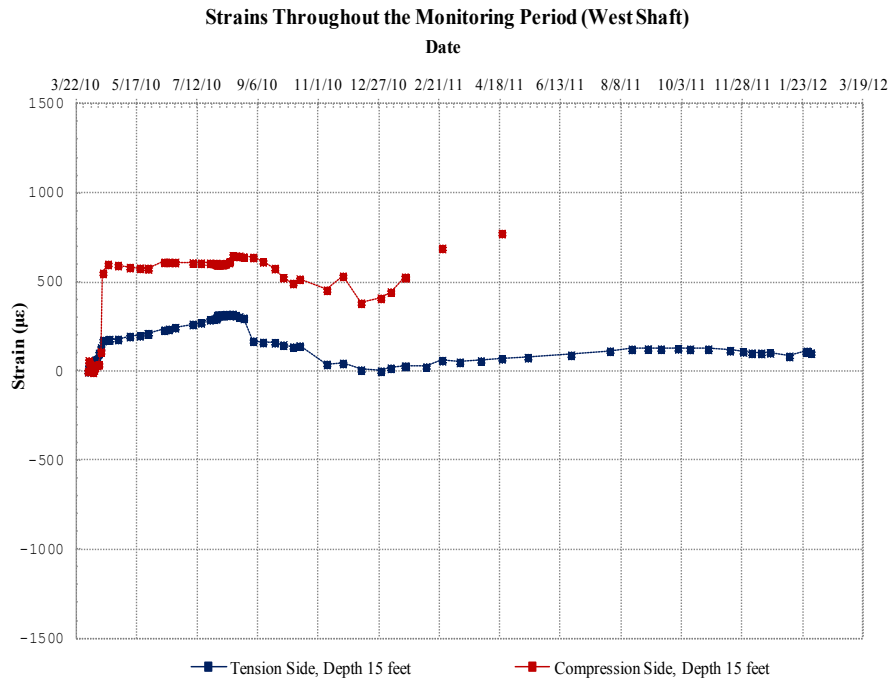


Figure B.8: Strains throughout the monitoring period for the west shaft at a depth of 15ft

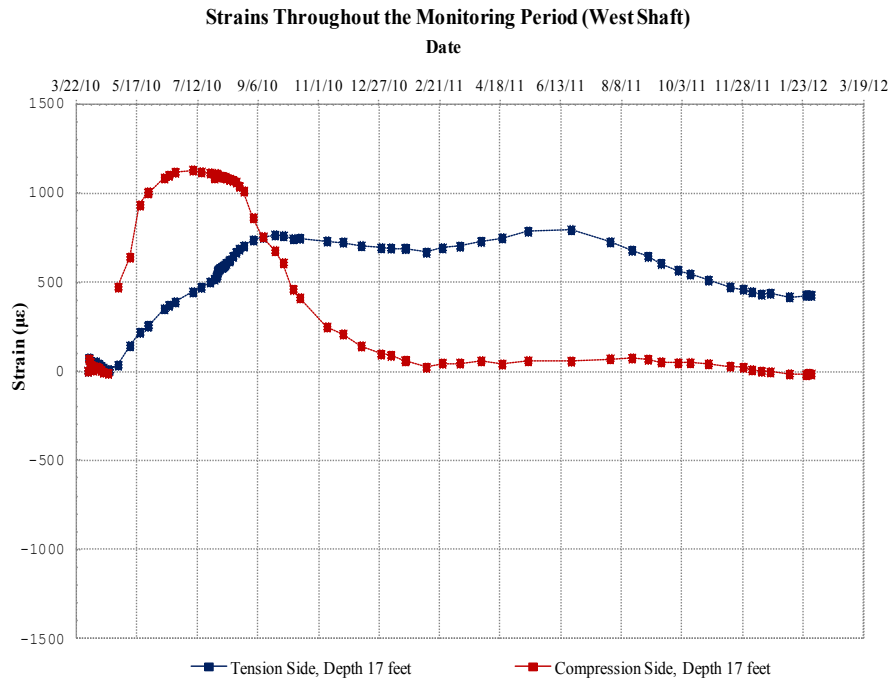


Figure B.9: Strains throughout the monitoring period for the west shaft at a depth of 17ft

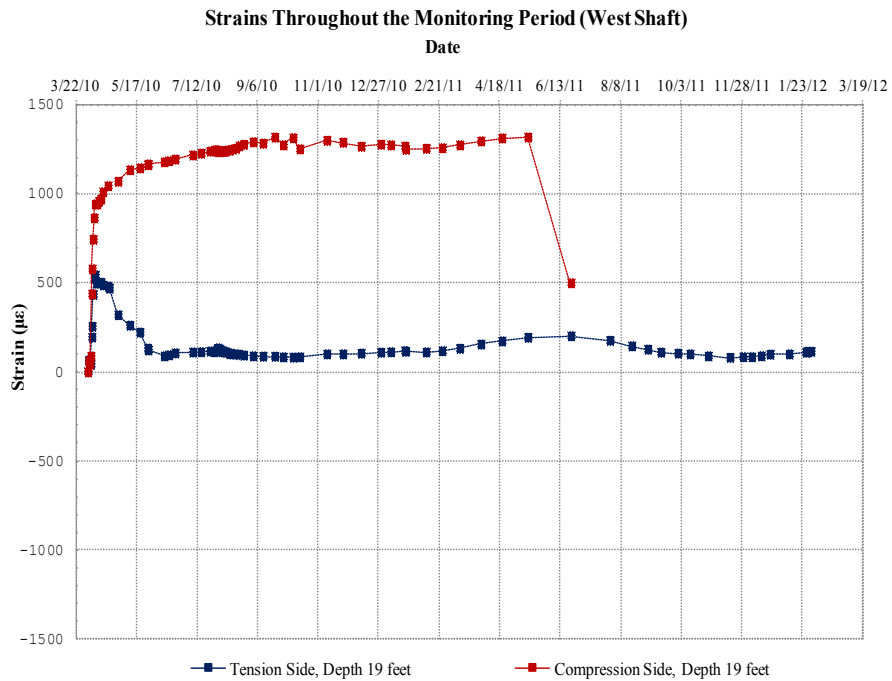


Figure B.10: Strains throughout the monitoring period for the west shaft at a depth of 19ft

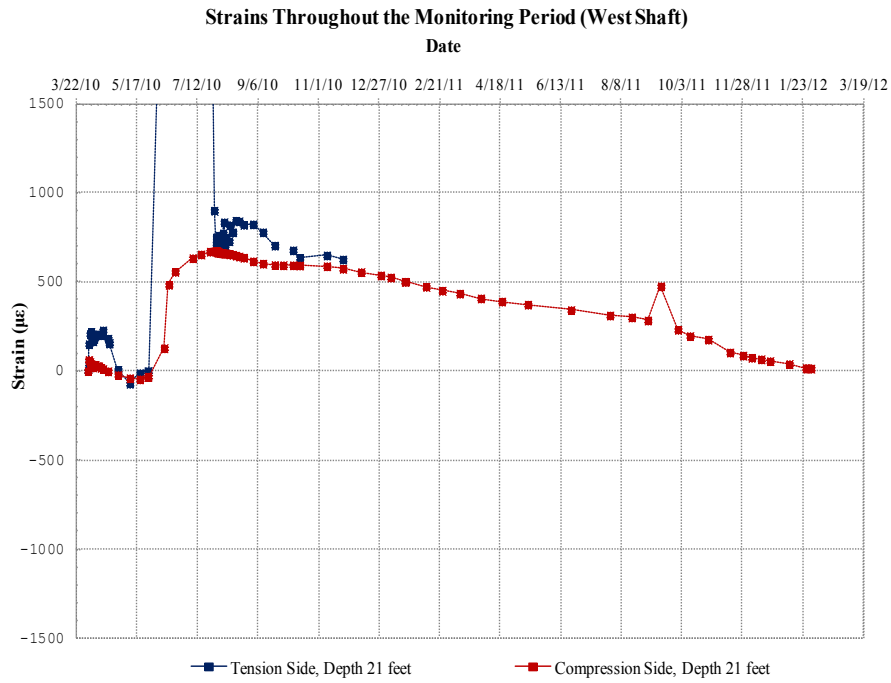


Figure B.11: Strains throughout the monitoring period for the west shaft at a depth of 21ft

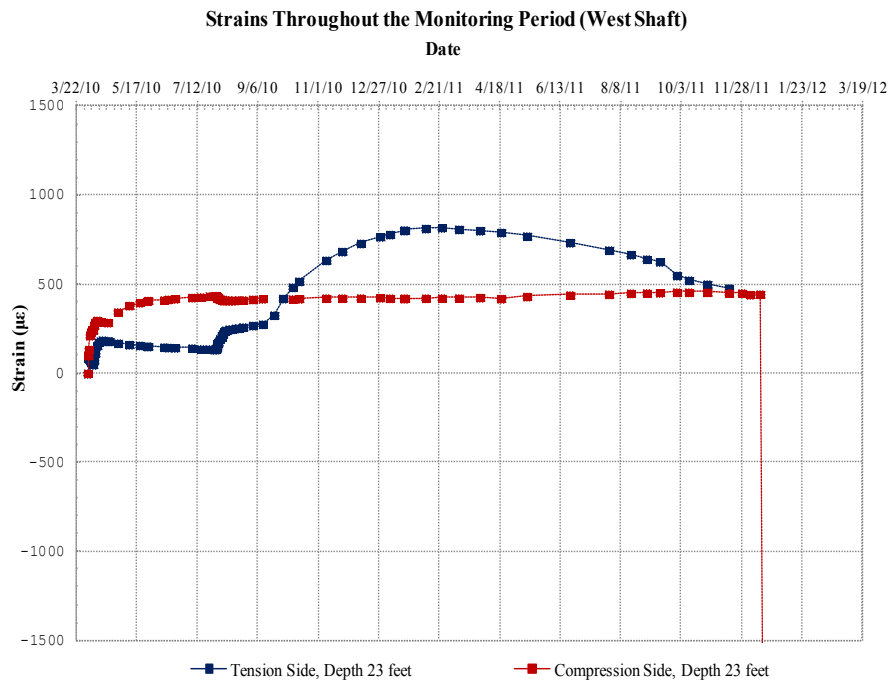


Figure B.12: Strains throughout the monitoring period for the west shaft at a depth of 23ft

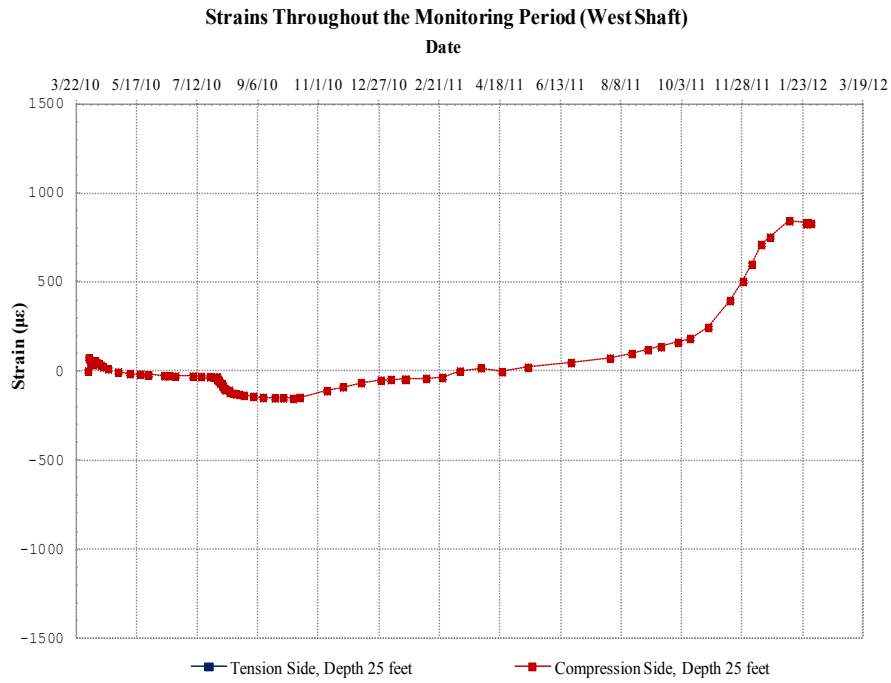


Figure B.13: Strains throughout the monitoring period for the west shaft at a depth of 25ft

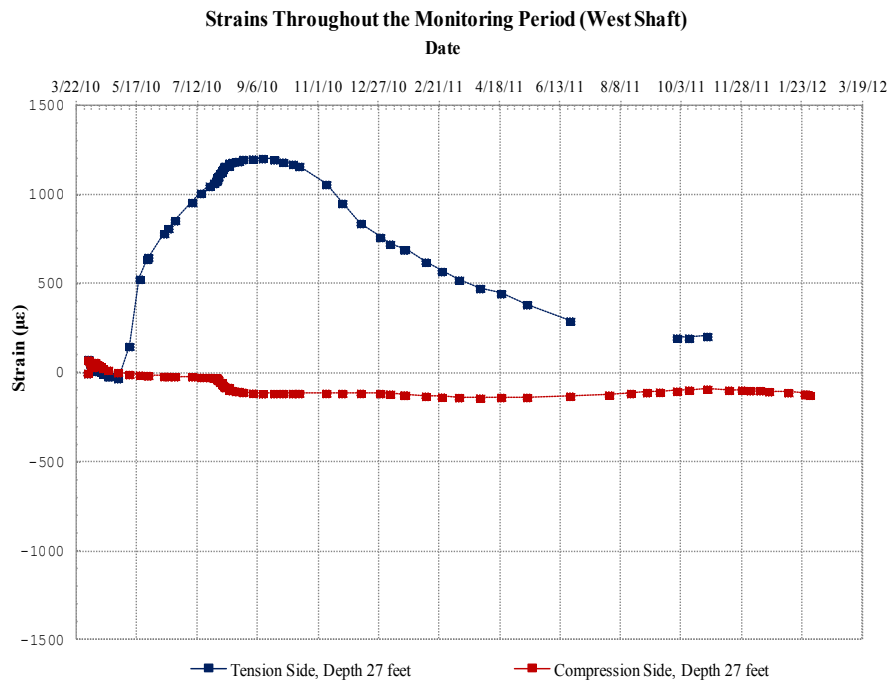


Figure B.14: Strains throughout the monitoring period for the west shaft at a depth of 27ft

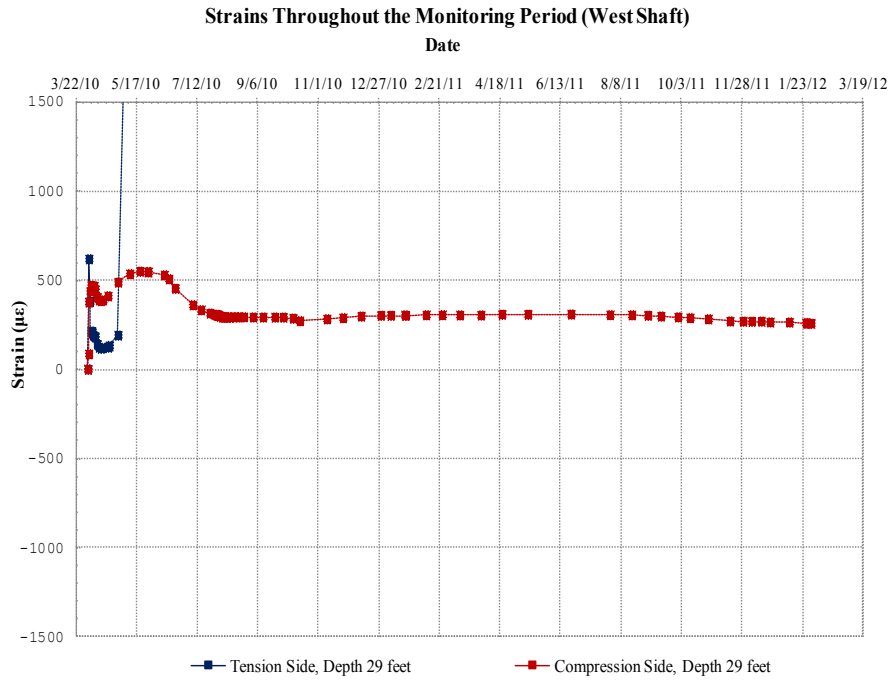


Figure B.15: Strains throughout the monitoring period for the west shaft at a depth of 29ft

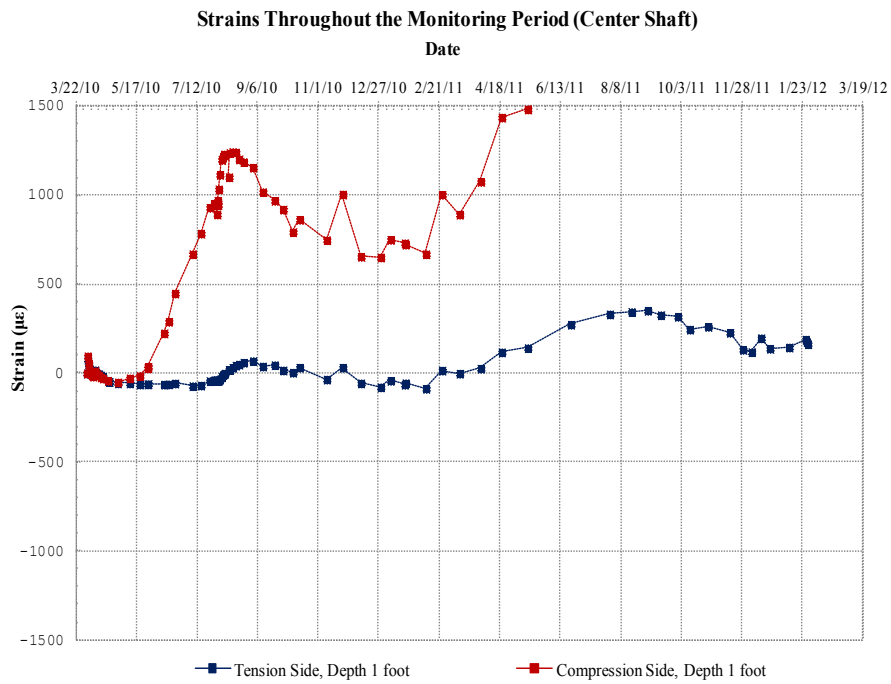


Figure B.16: Strains throughout the monitoring period for the center shaft at a depth of 1ft

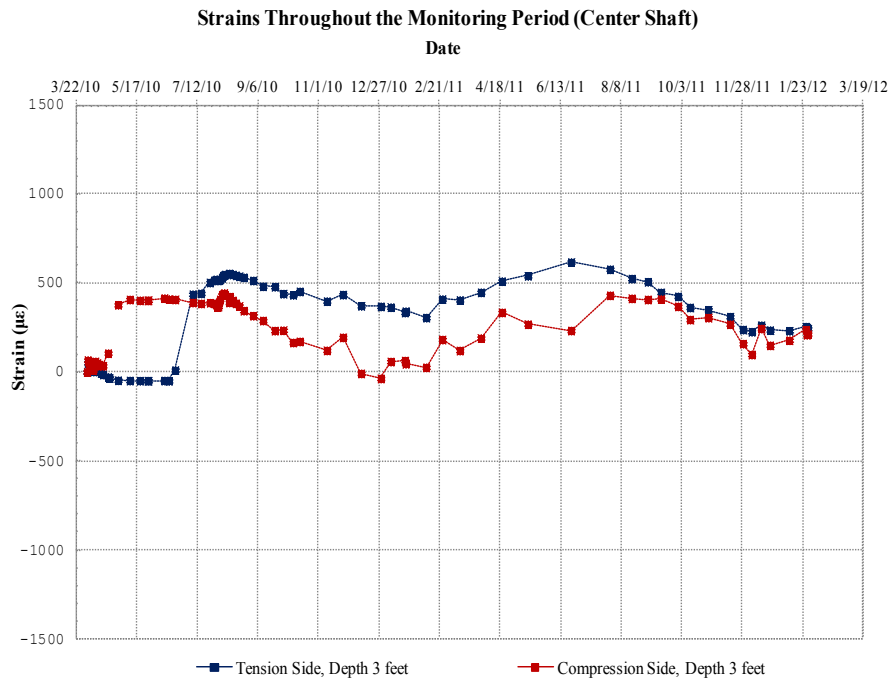


Figure B.17: Strains throughout the monitoring period for the center shaft at a depth of 3ft

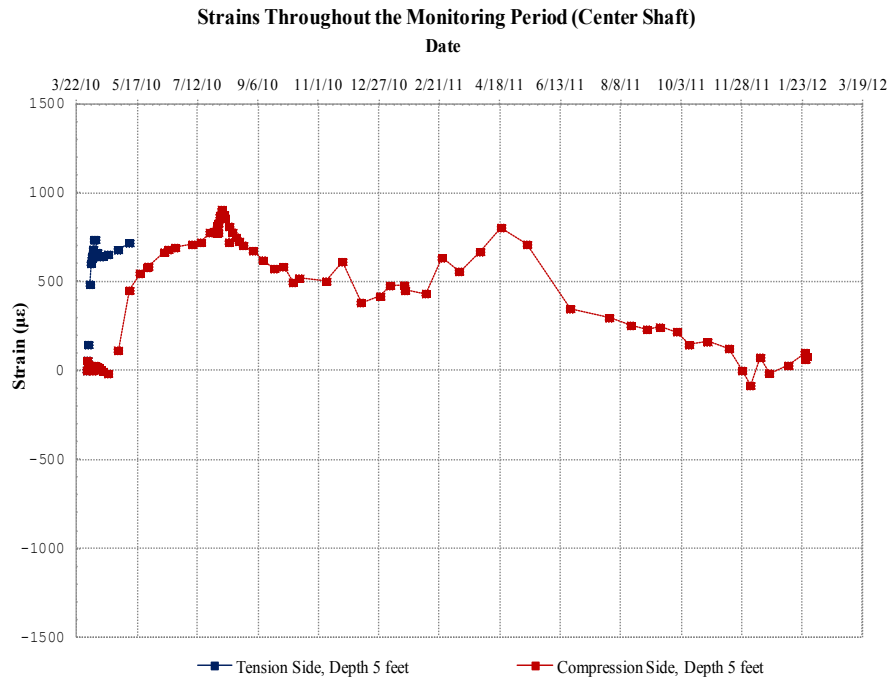


Figure B.18: Strains throughout the monitoring period for the center shaft at a depth of 5ft

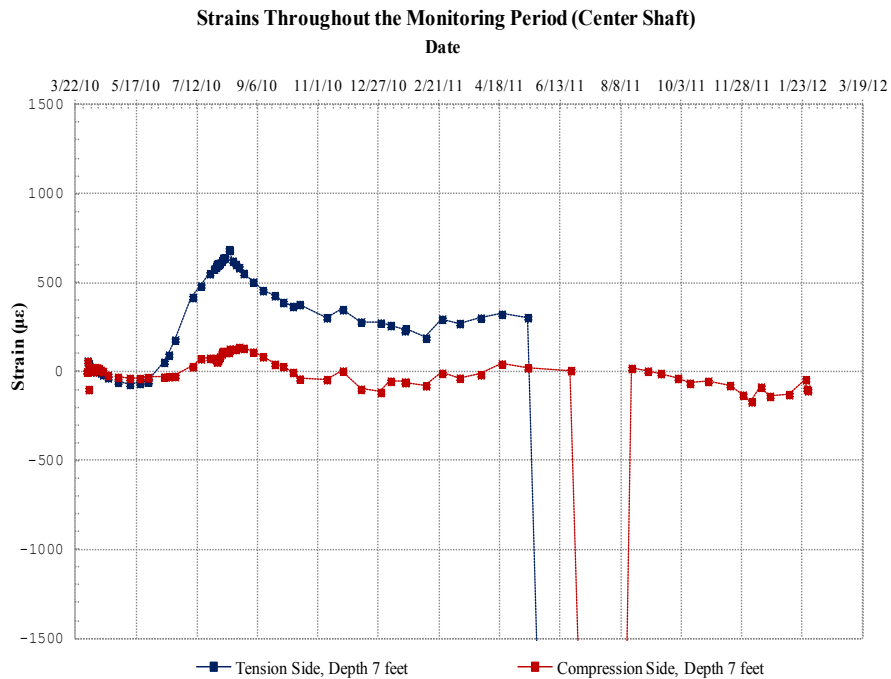


Figure B.19: Strains throughout the monitoring period for the center shaft at a depth of 7ft

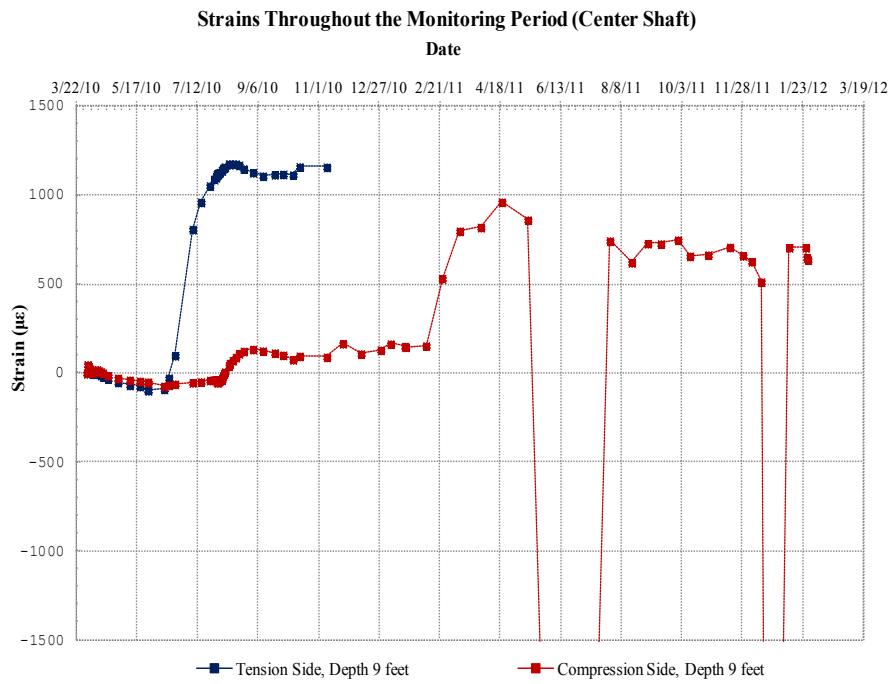


Figure B.20: Strains throughout the monitoring period for the center shaft at a depth of 9ft

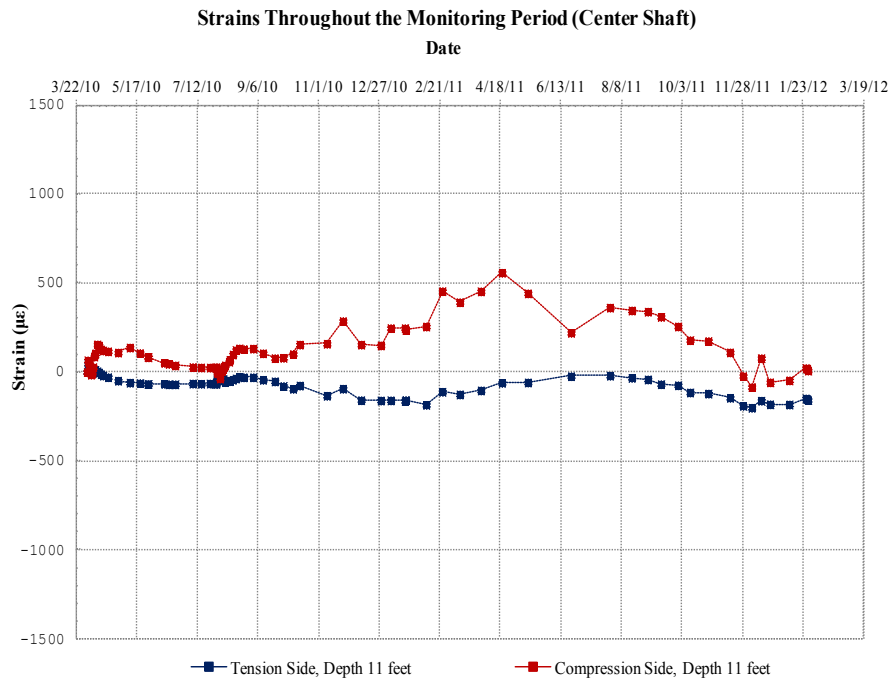


Figure B.21: Strains throughout the monitoring period for the center shaft at a depth of 11ft

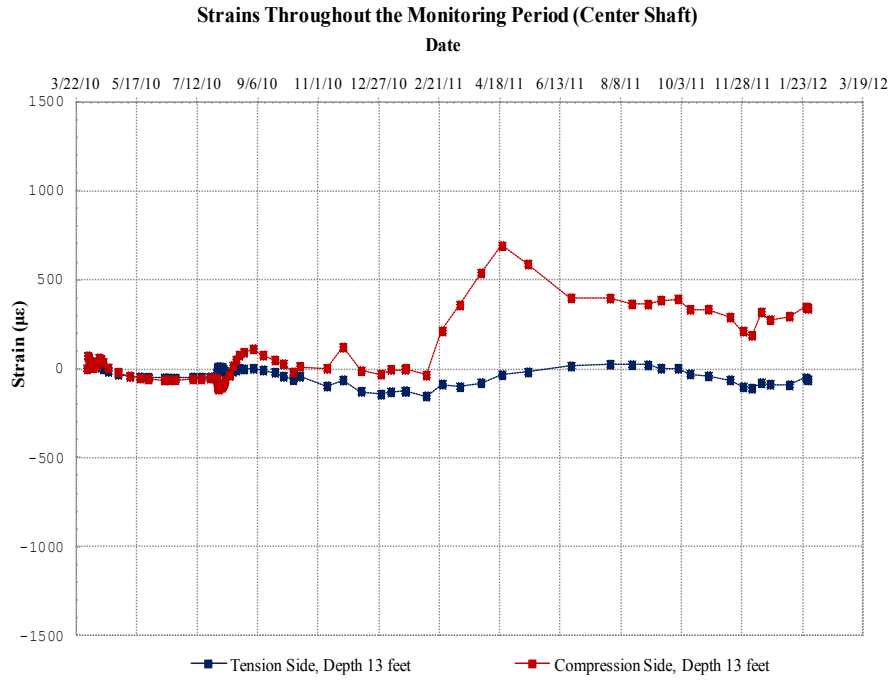


Figure B.22: Strains throughout the monitoring period for the center shaft at a depth of 13ft

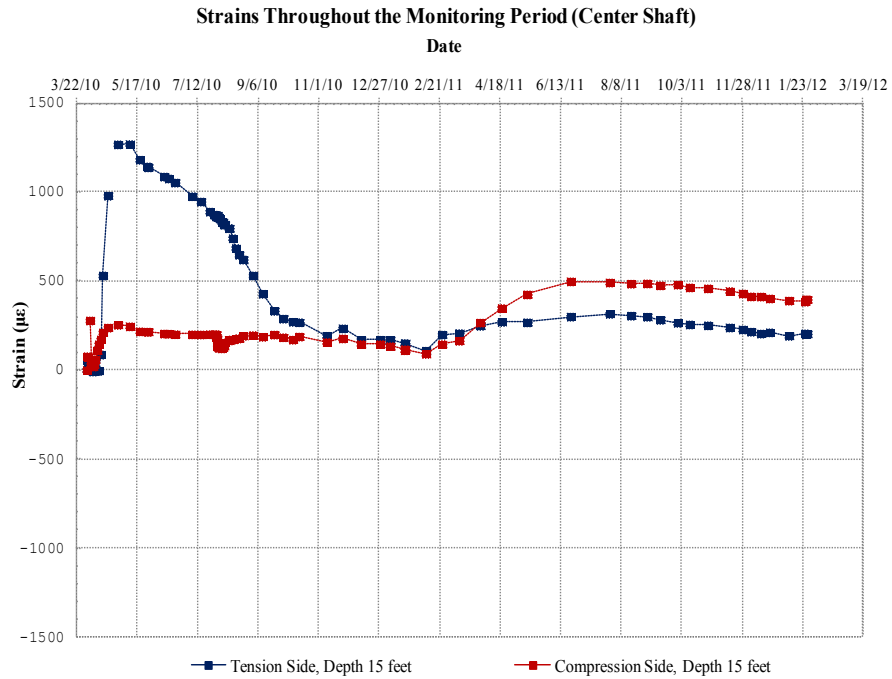


Figure B.23: Strains throughout the monitoring period for the center shaft at a depth of 15ft

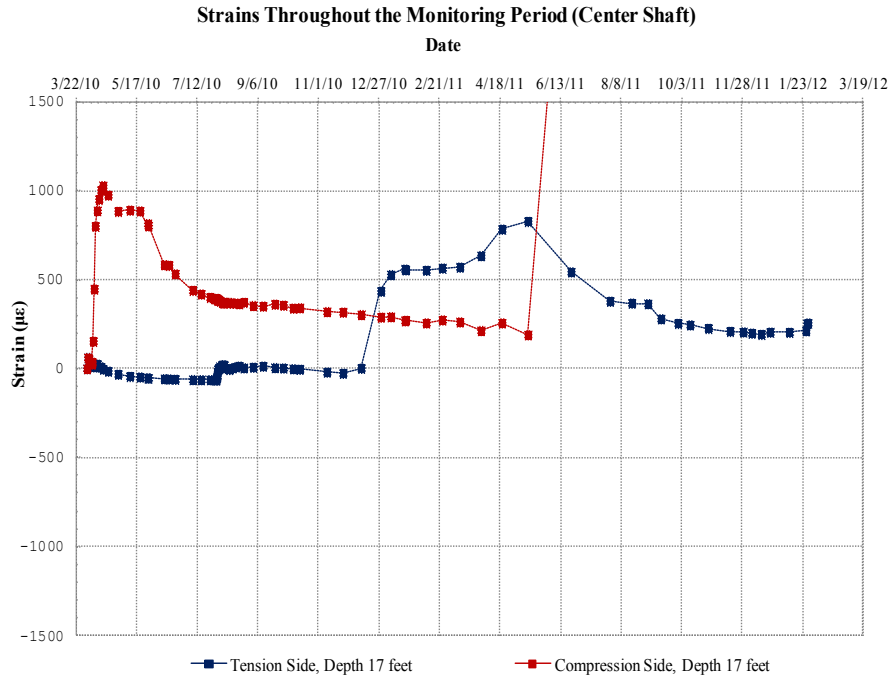


Figure B.24: Strains throughout the monitoring period for the center shaft at a depth of 17ft

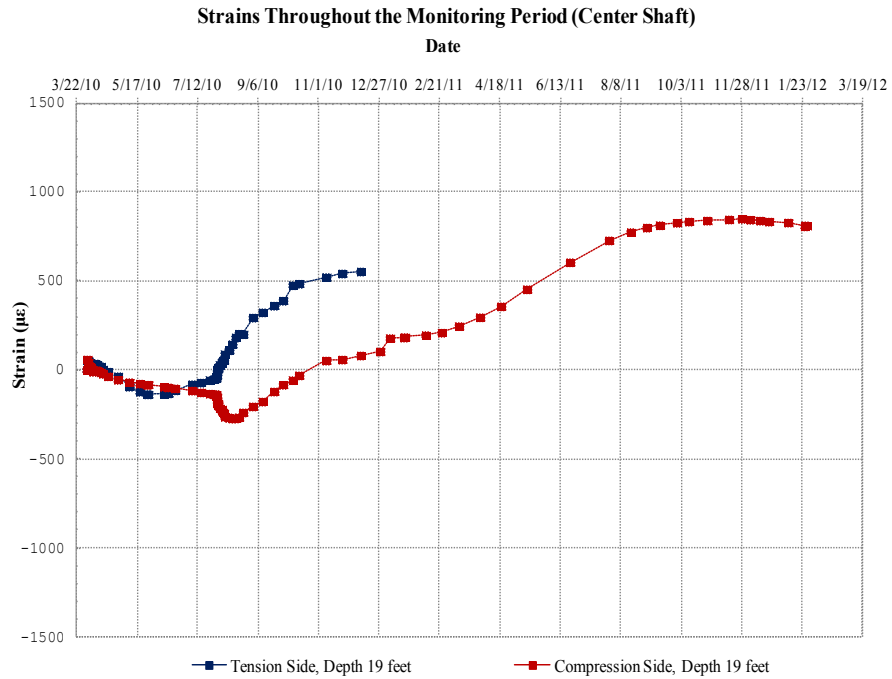


Figure B.25: Strains throughout the monitoring period for the center shaft at a depth of 19ft

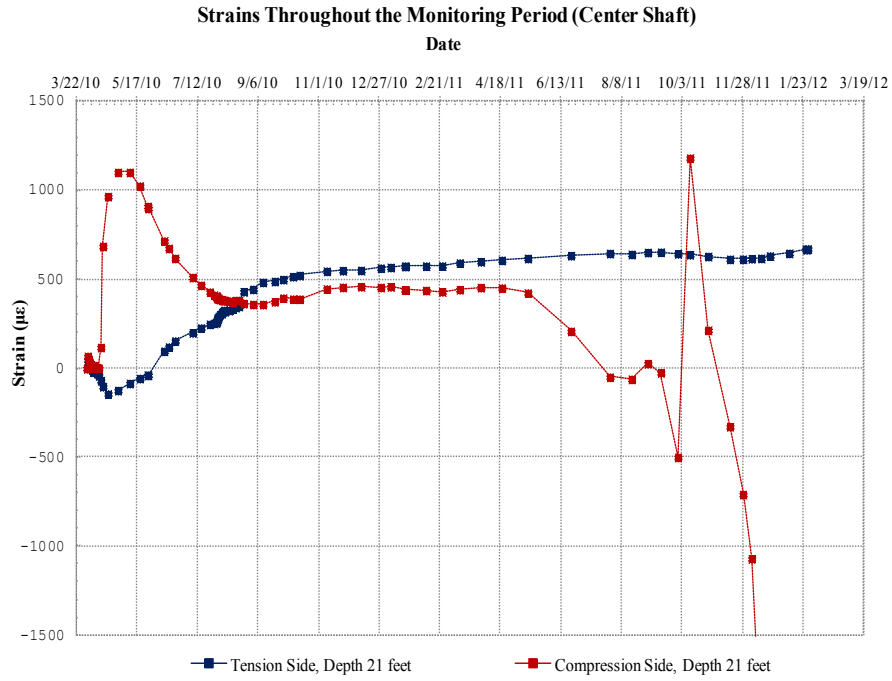


Figure B.27: Strains throughout the monitoring period for the center shaft at a depth of 21ft

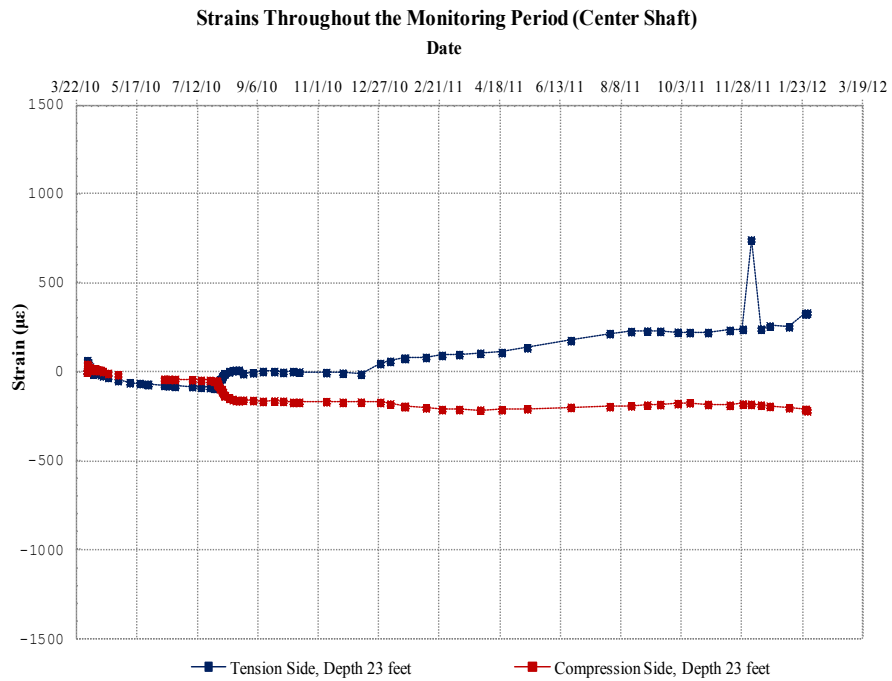


Figure B.29: Strains throughout the monitoring period for the center shaft at a depth of 23ft

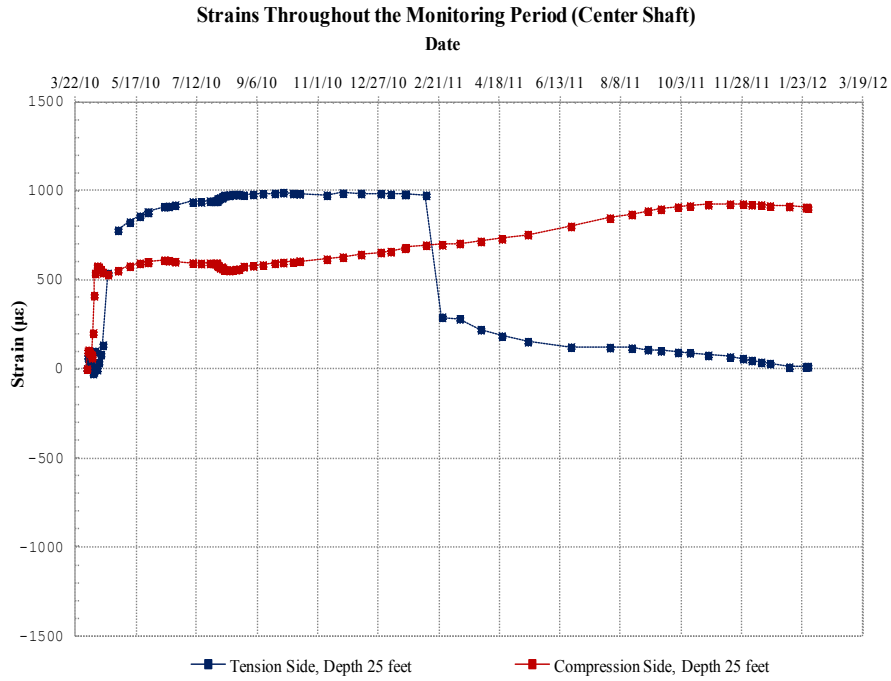


Figure B.30: Strains throughout the monitoring period for the center shaft at a depth of 25ft

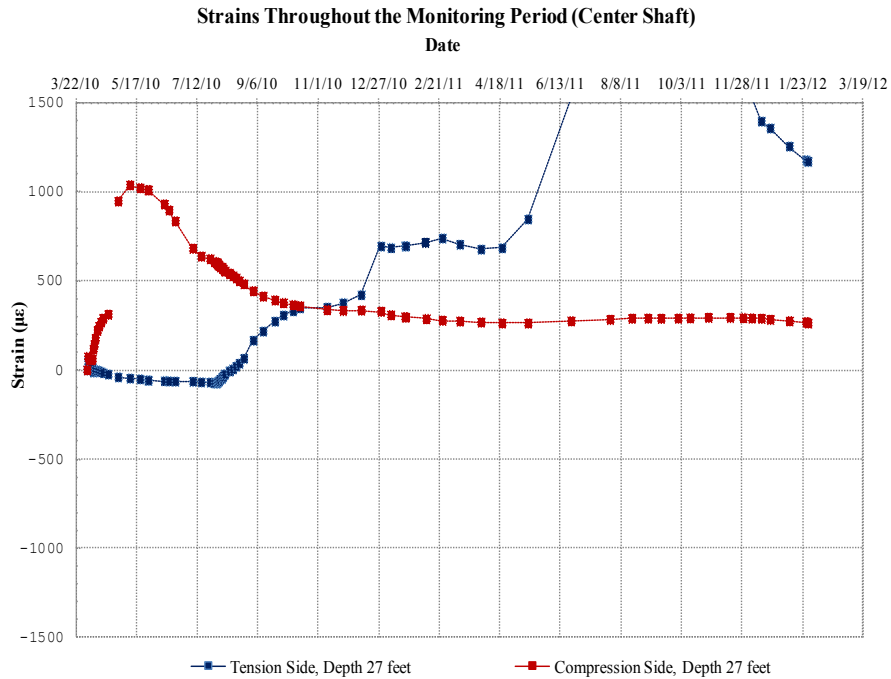


Figure B.31: Strains throughout the monitoring period for the center shaft at a depth of 27ft

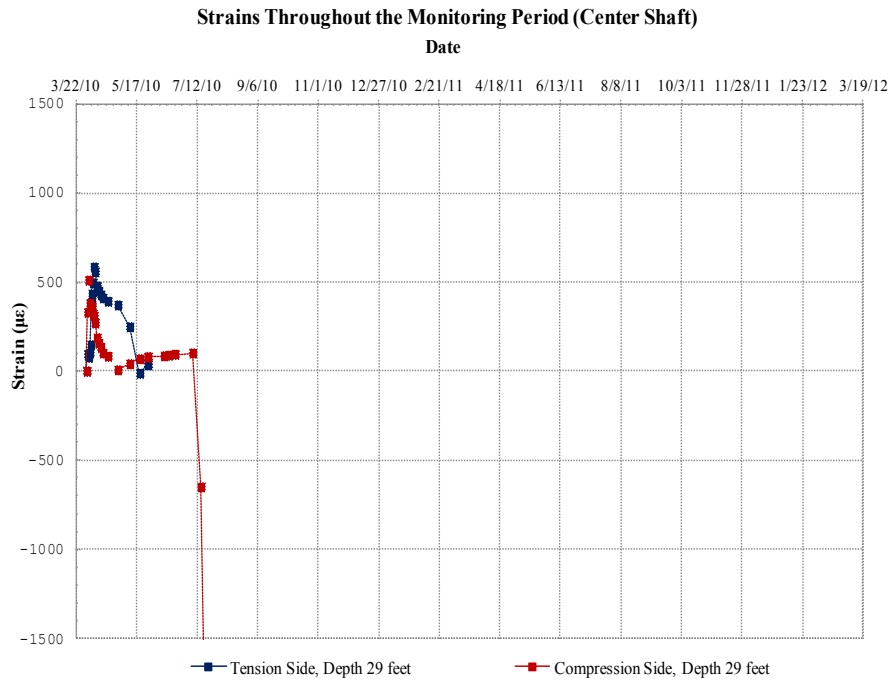


Figure B.32: Strains throughout the monitoring period for the center shaft at a depth of 29ft

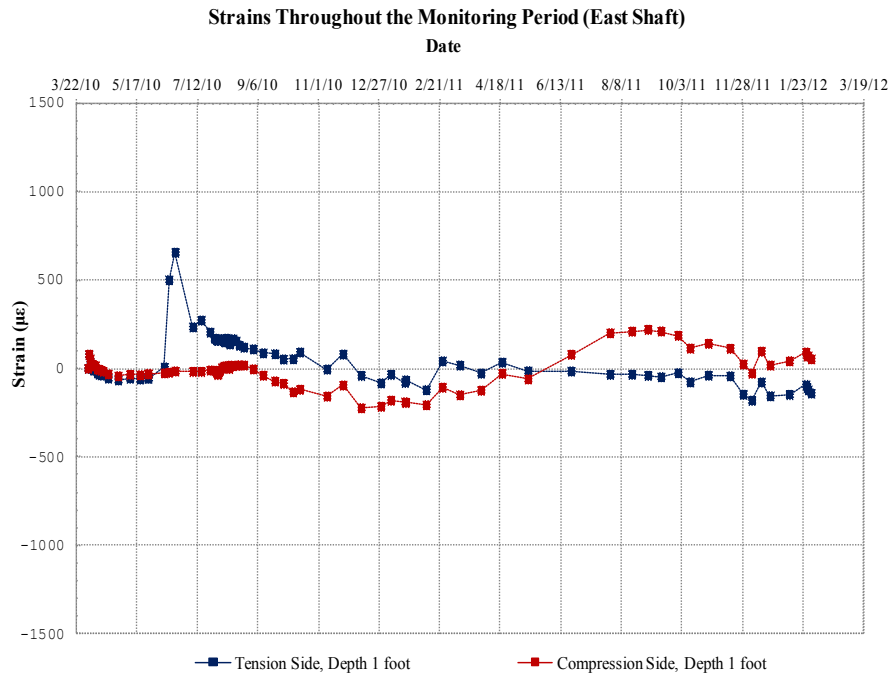


Figure B.33: Strains throughout the monitoring period for the east shaft at a depth of 1ft

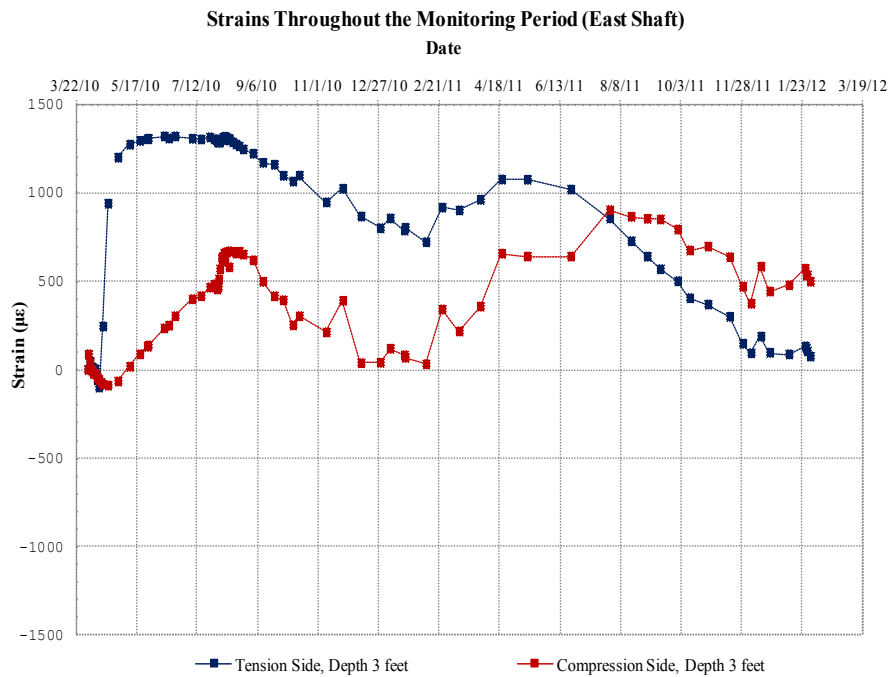


Figure B.34: Strains throughout the monitoring period for the east shaft at a depth of 3ft

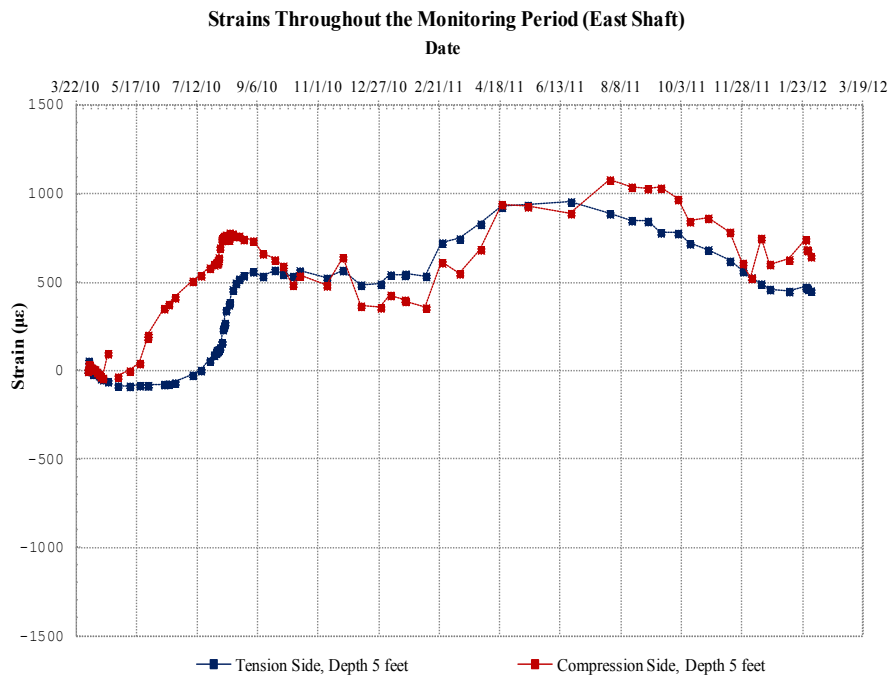


Figure B.35: Strains throughout the monitoring period for the east shaft at a depth of 5ft

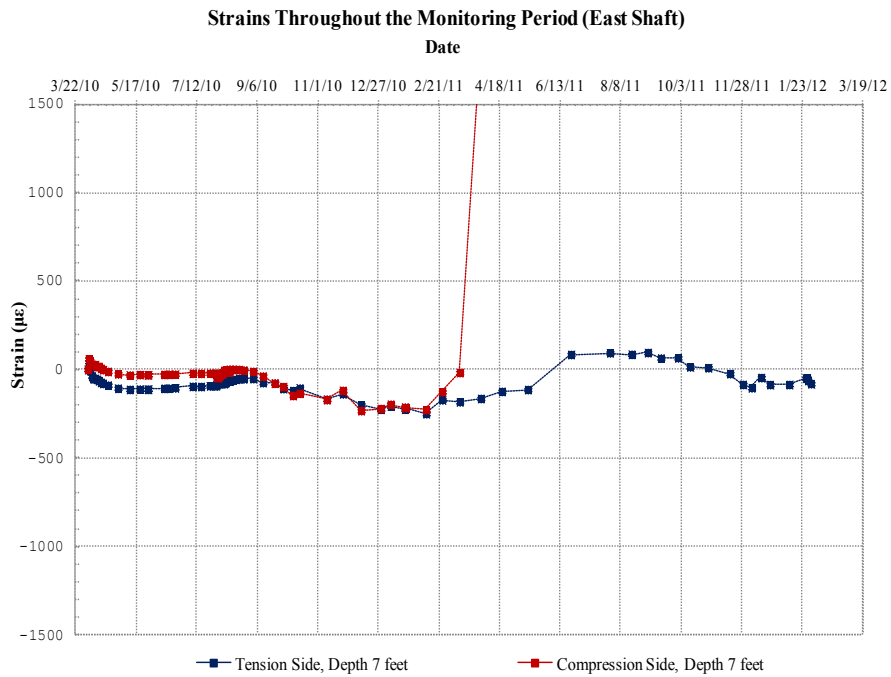


Figure B.36: Strains throughout the monitoring period for the east shaft at a depth of 7ft

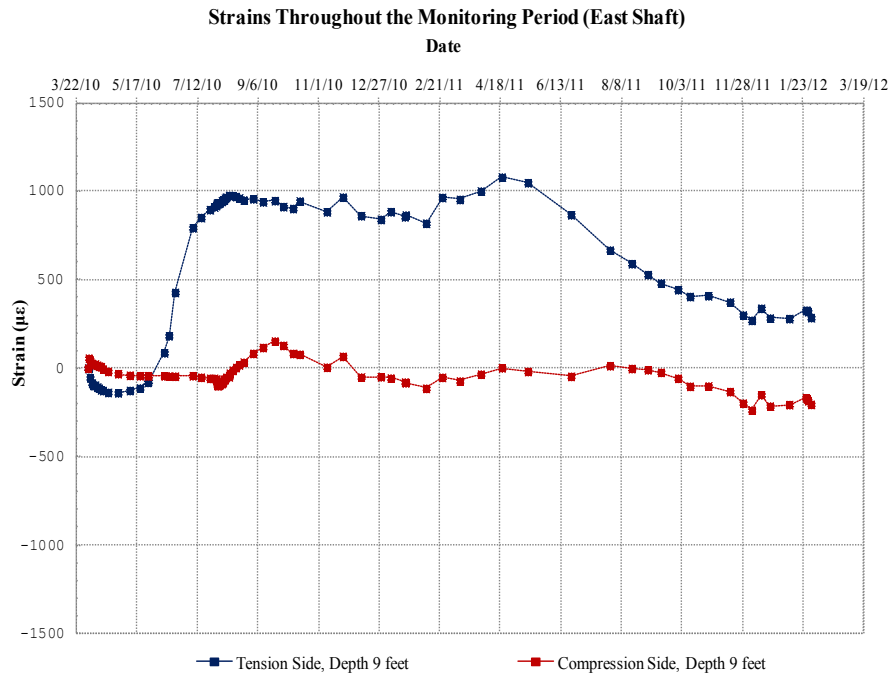


Figure B.37: Strains throughout the monitoring period for the east shaft at a depth of 9ft

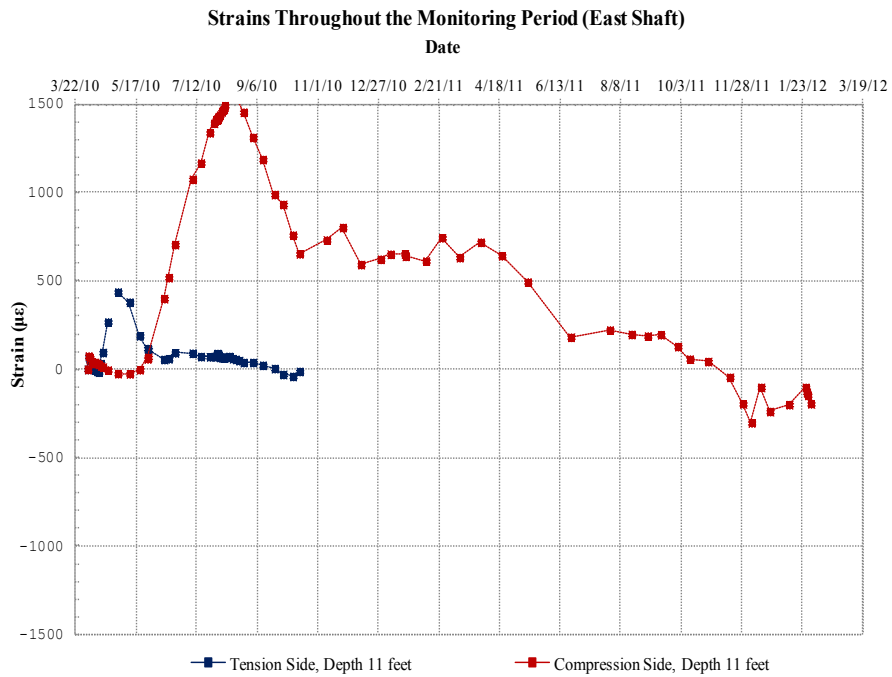


Figure B.38: Strains throughout the monitoring period for the east shaft at a depth of 11ft

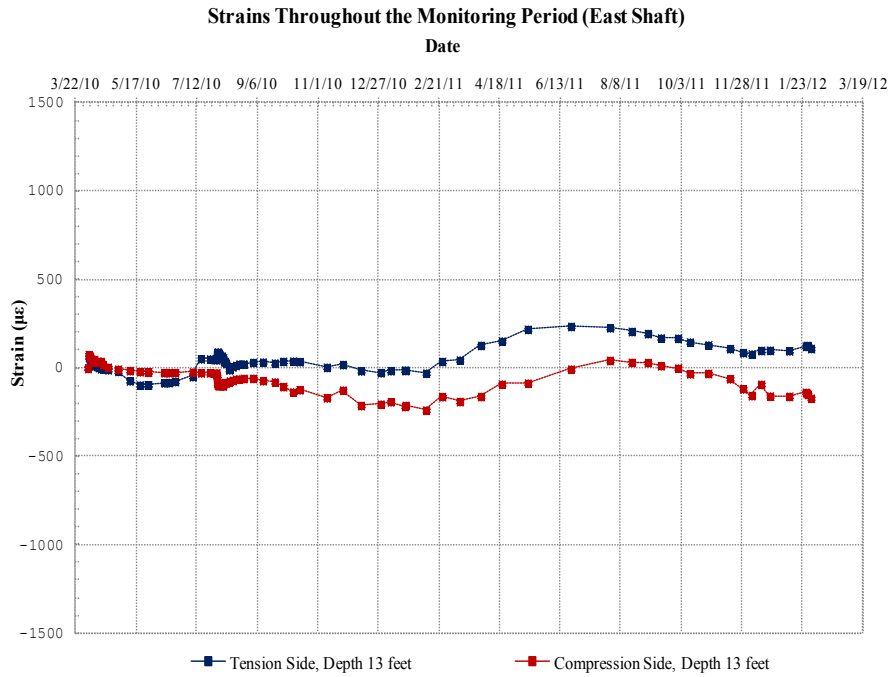


Figure B.39: Strains throughout the monitoring period for the east shaft at a depth of 13ft

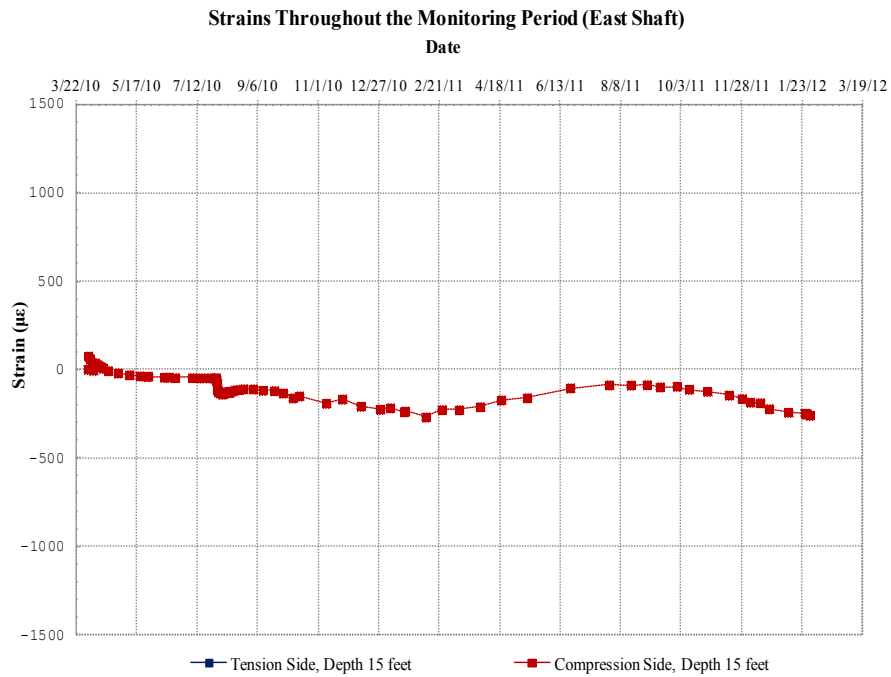


Figure B.40: Strains throughout the monitoring period for the east shaft at a depth of 15ft

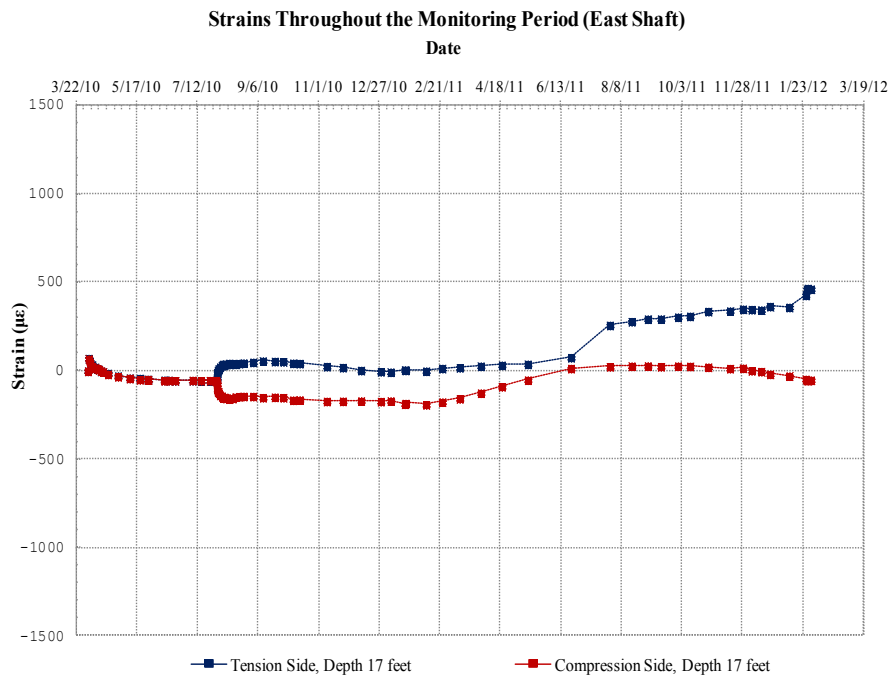


Figure B.41: Strains throughout the monitoring period for the east shaft at a depth of 17ft

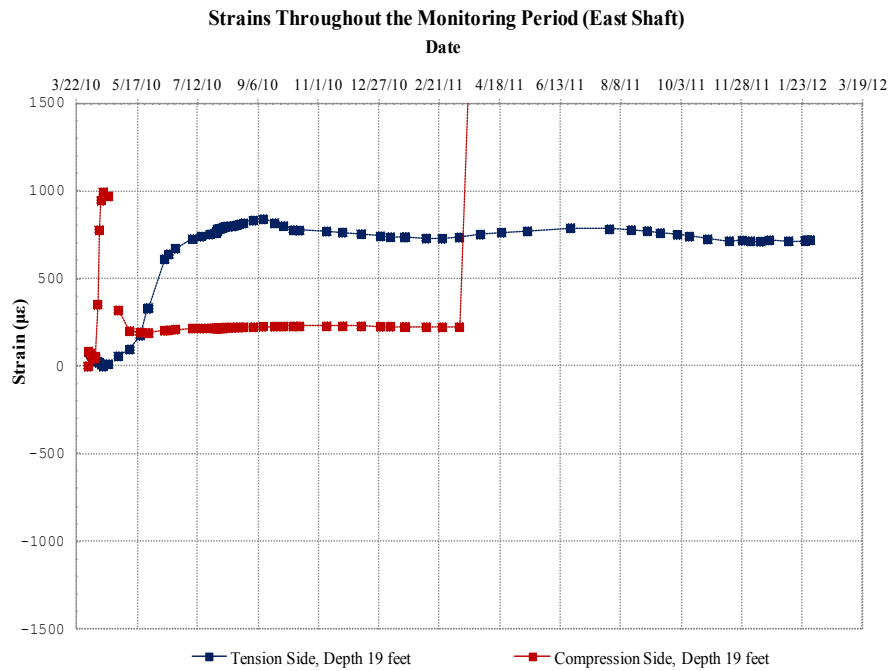


Figure B.42: Strains throughout the monitoring period for the east shaft at a depth of 19ft

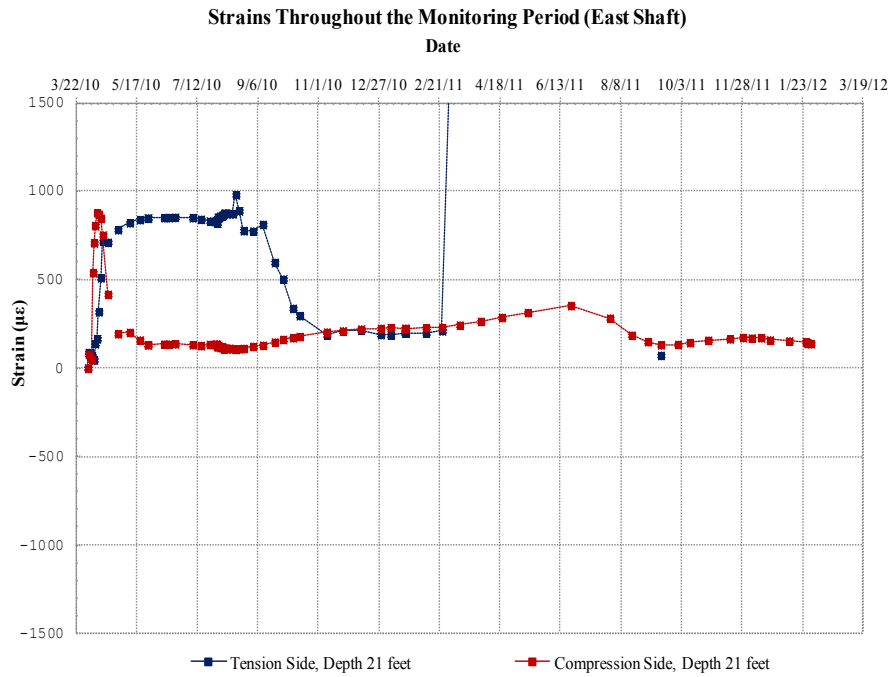


Figure B.43: Strains throughout the monitoring period for the east shaft at a depth of 21ft

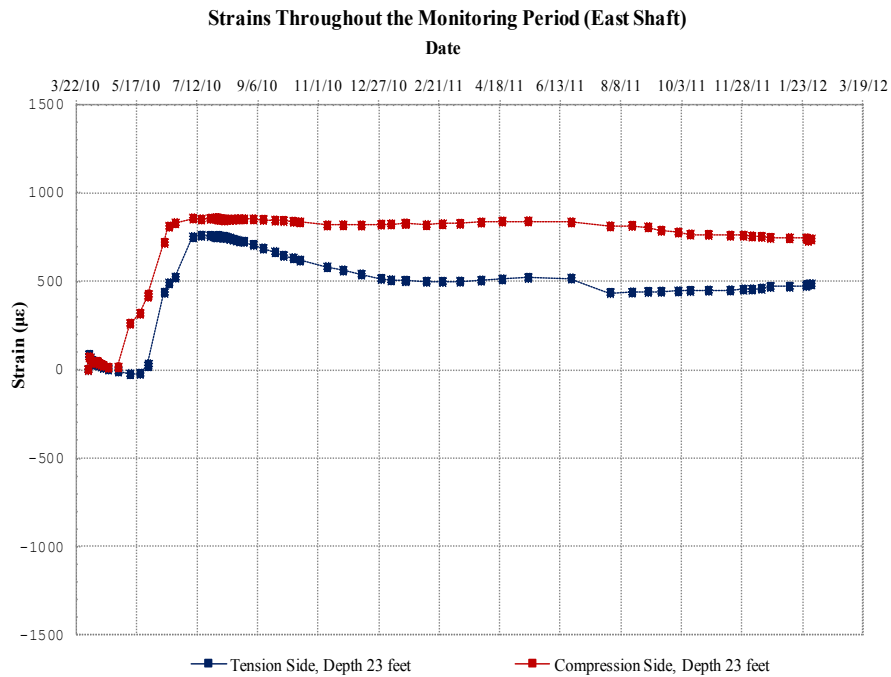


Figure B.44: Strains throughout the monitoring period for the east shaft at a depth of 23ft

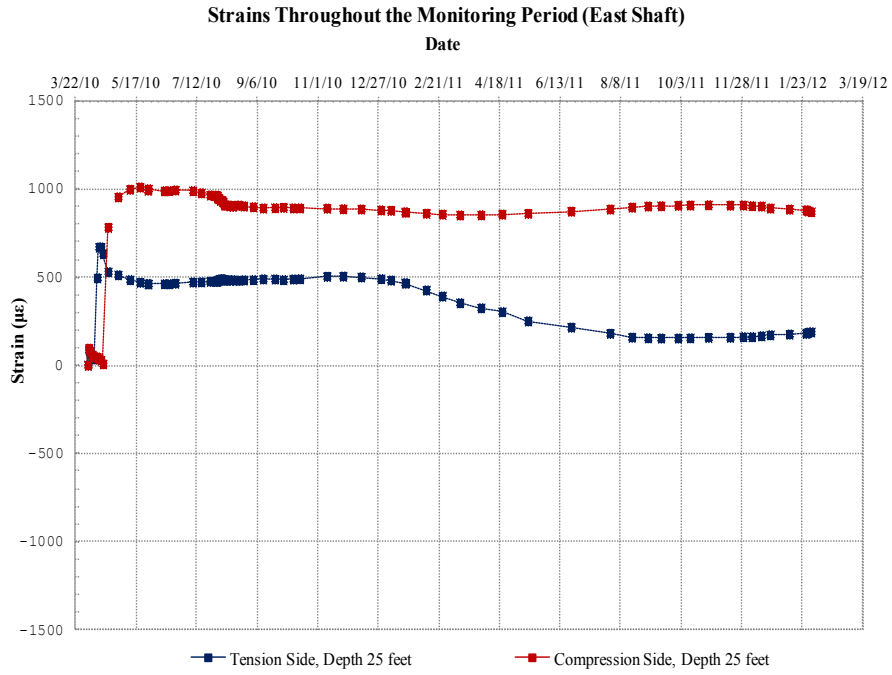


Figure B.45: Strains throughout the monitoring period for the east shaft at a depth of 25ft

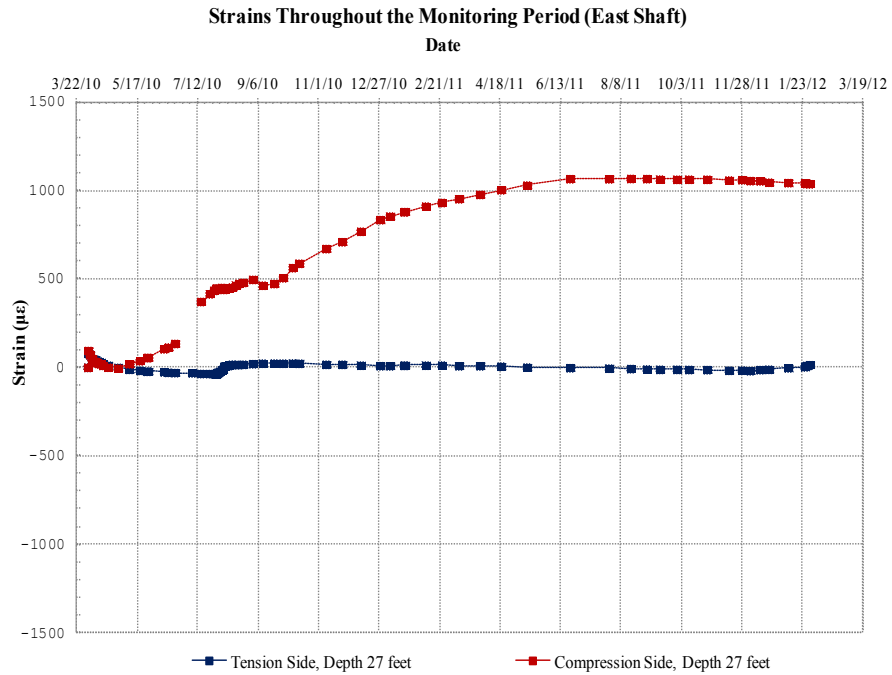


Figure B.46: Strains throughout the monitoring period for the east shaft at a depth of 27ft

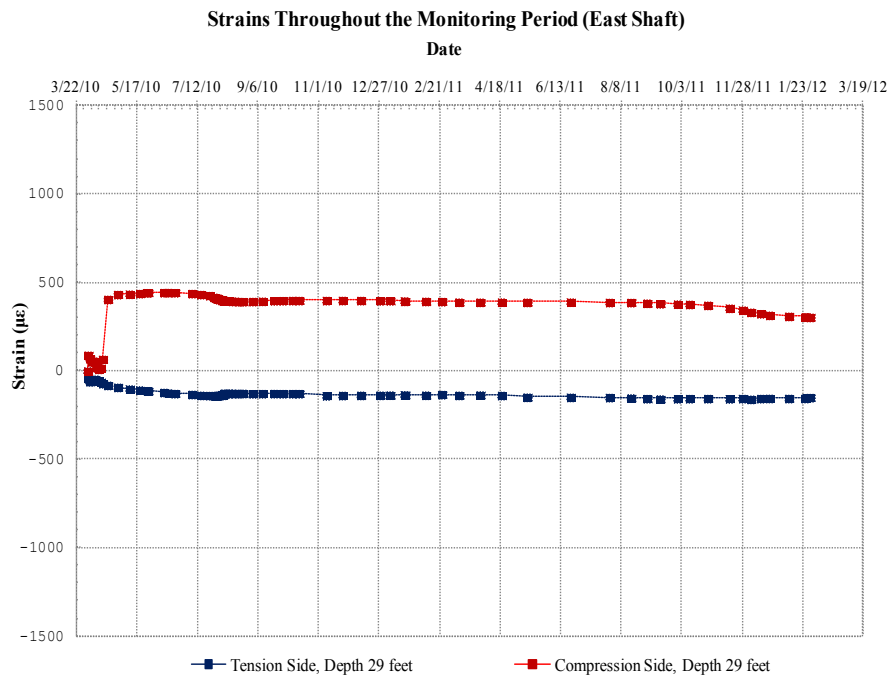


Figure B.47: Strains throughout the monitoring period for the east shaft at a depth of 29ft

B.2: Processed strains throughout the monitoring period along the "global" shaft

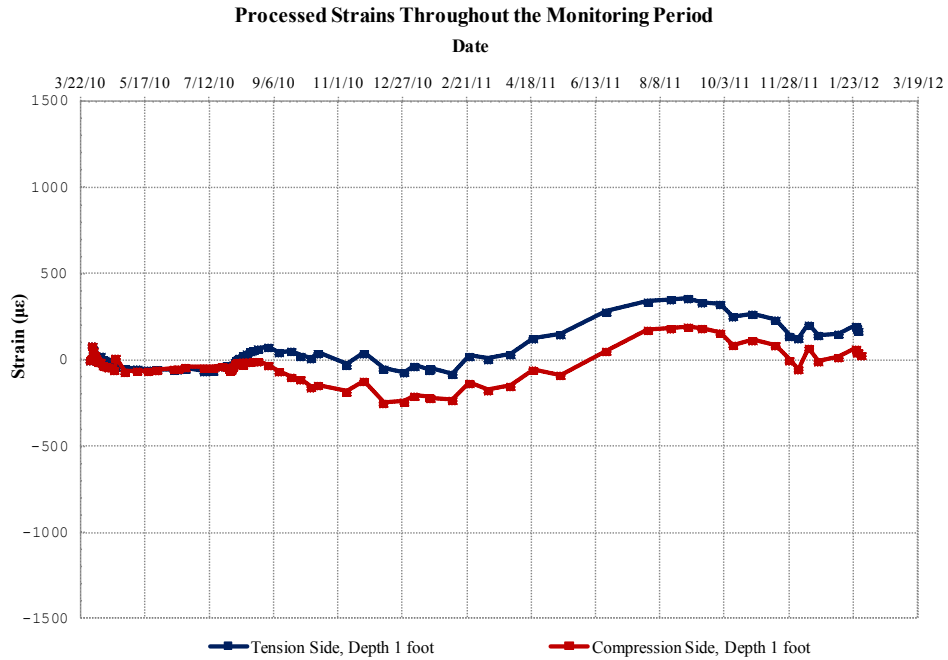


Figure B.48: Processed strains throughout the monitoring period at a depth of 1ft

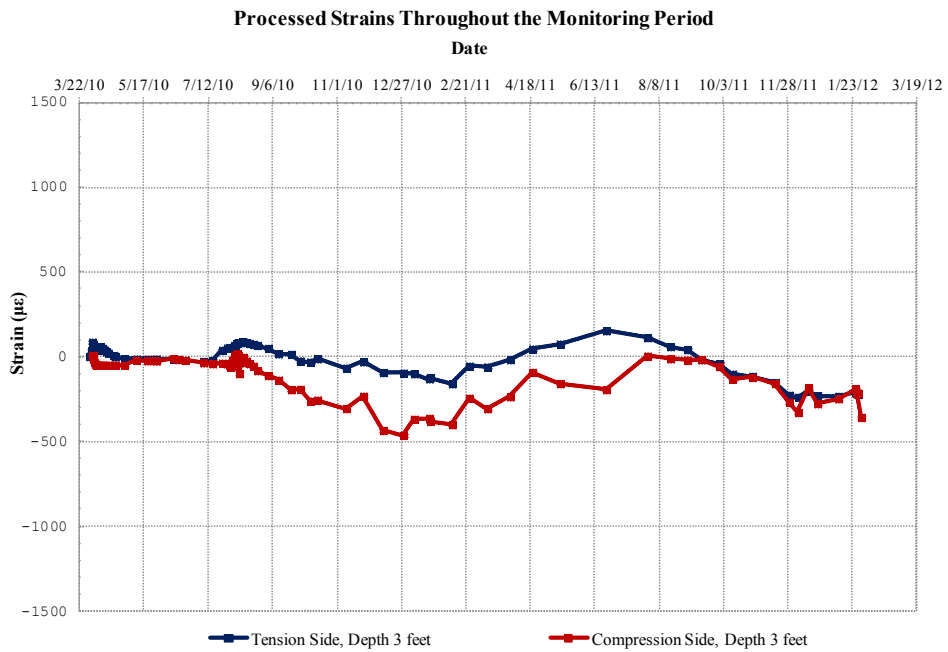


Figure B.49: Processed strains throughout the monitoring period at a depth of 3ft

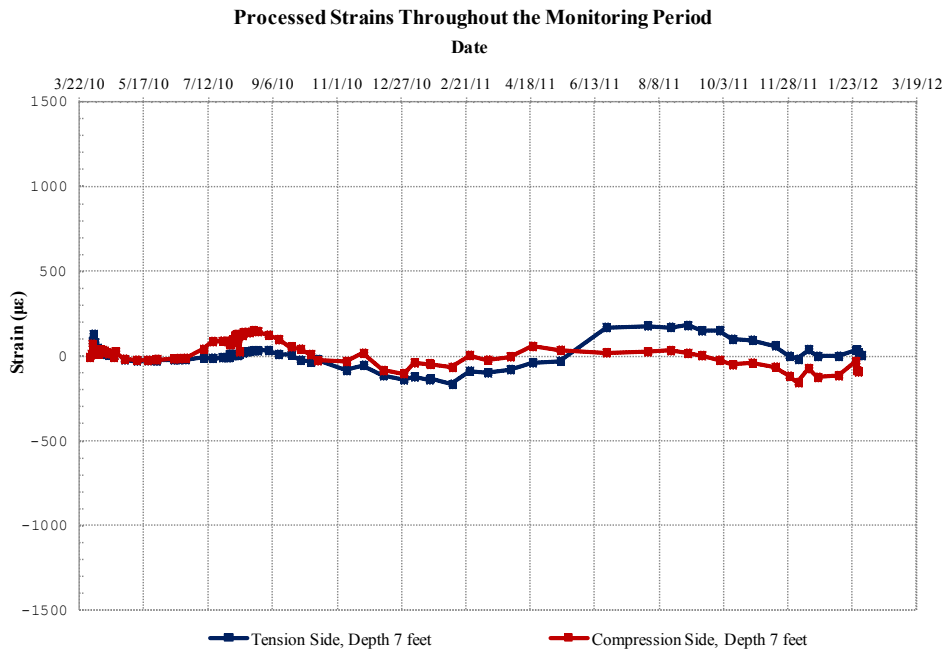


Figure B.50: Processed strains throughout the monitoring period at a depth of 7ft

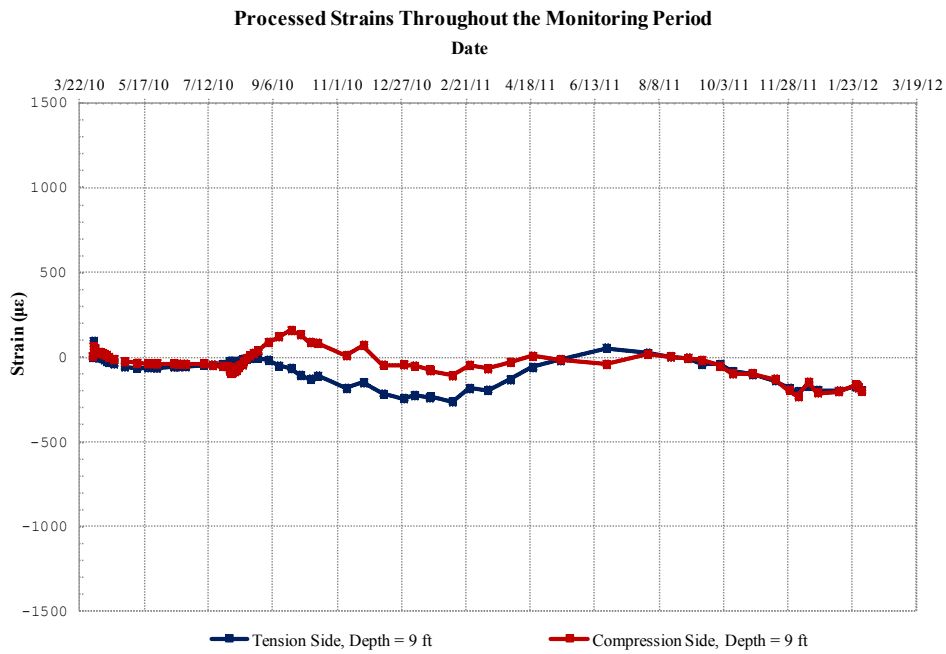


Figure B.51: Processed strains throughout the monitoring period at a depth of 9ft

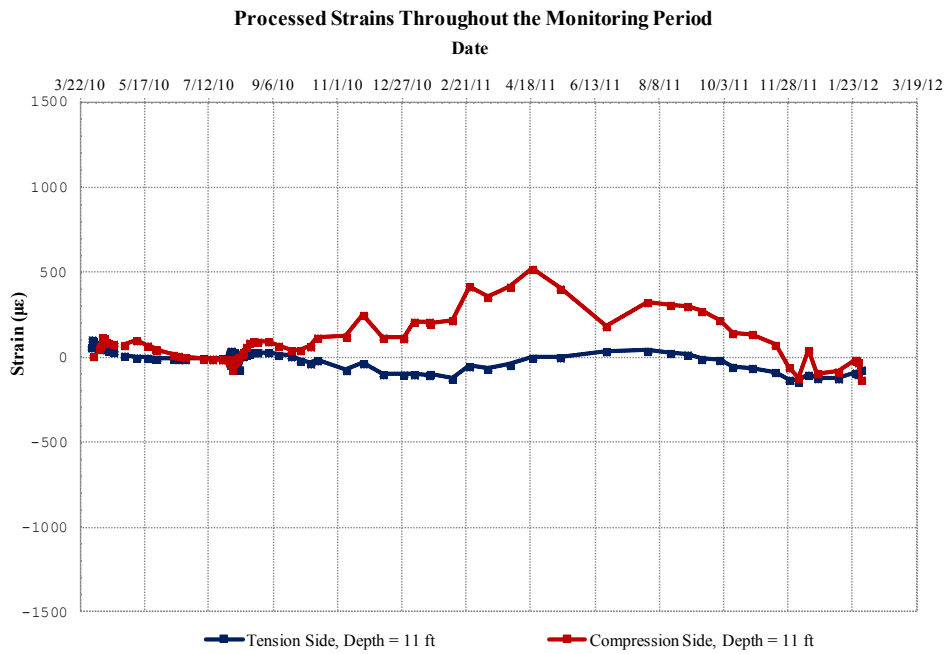


Figure B.52: Processed strains throughout the monitoring period at a depth of 11 ft

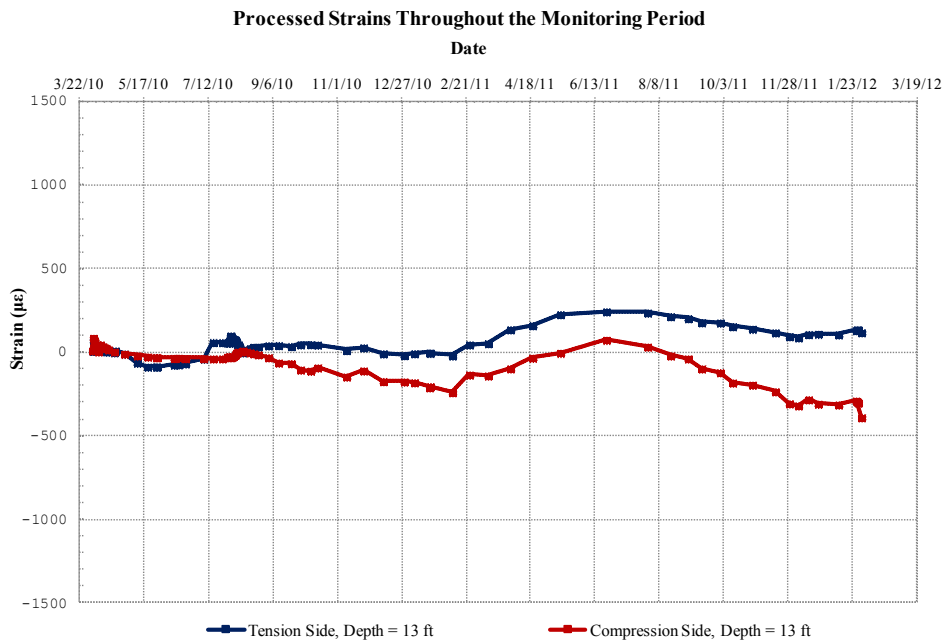


Figure B.53: Processed strains throughout the monitoring period at a depth of 13 ft

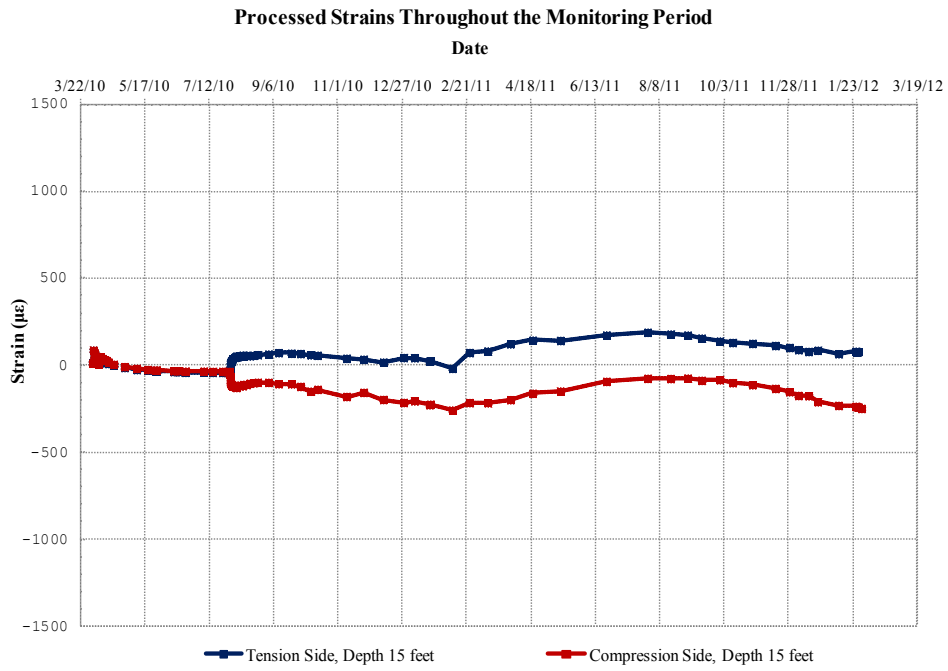


Figure B.54: Processed strains throughout the monitoring period at a depth of 15ft

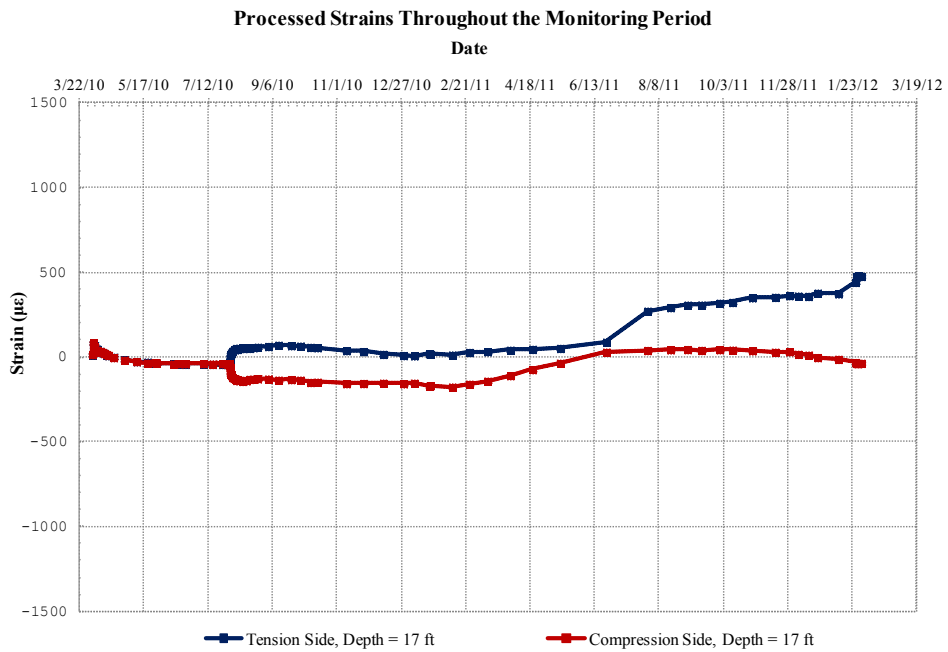


Figure B.55: Processed strains throughout the monitoring period at a depth of 17ft

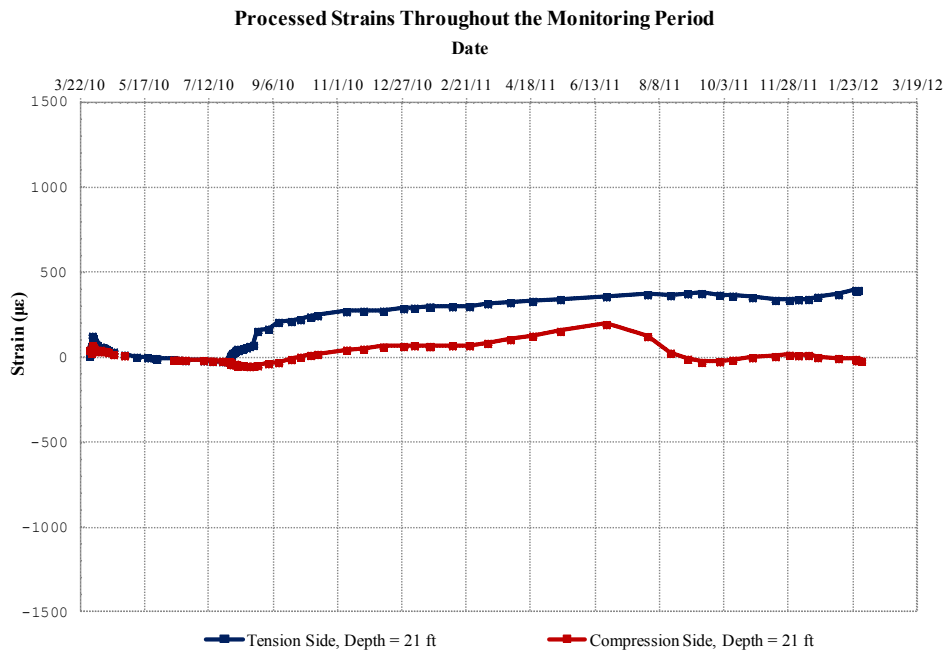


Figure B.56: Processed strains throughout the monitoring period at a depth of 21ft

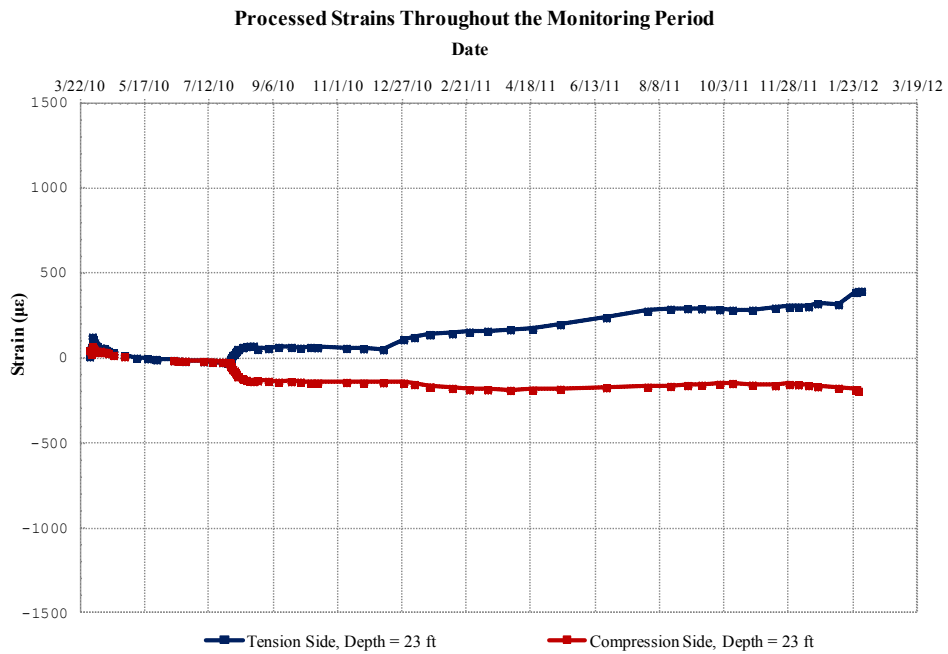


Figure B.57: Processed strains throughout the monitoring period at a depth of 23ft

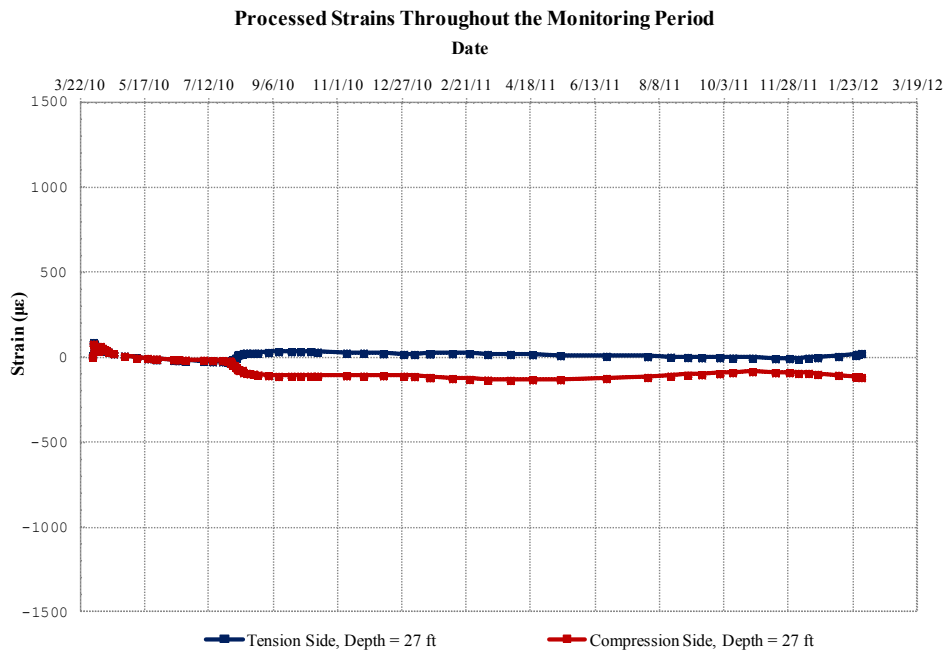


Figure B.58: Processed strains throughout the monitoring period at a depth of 27ft

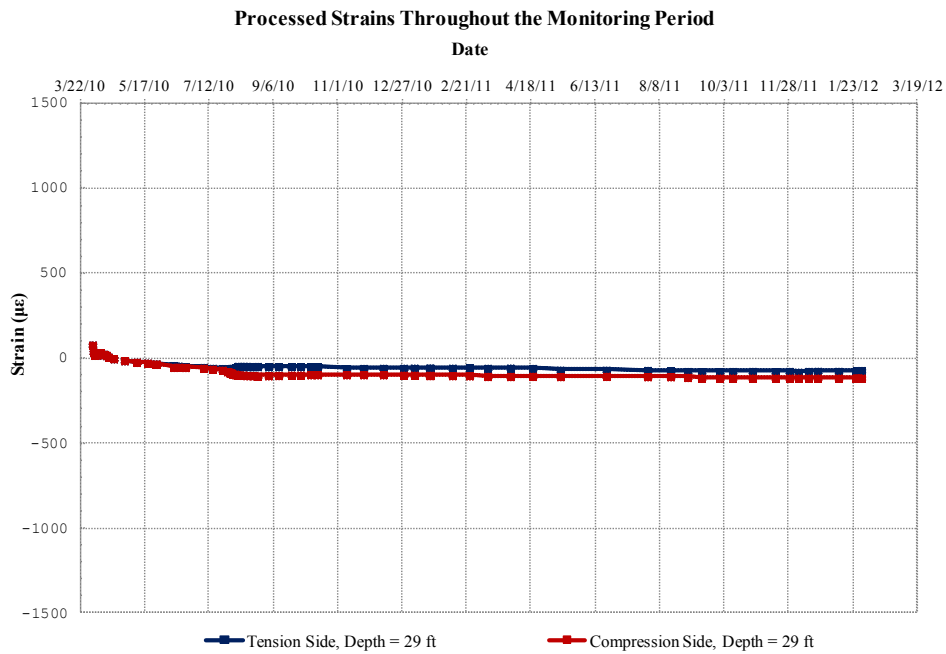


Figure B.59: Processed strains throughout the monitoring period at a depth of 29ft

Bibliography

- Brown, A. C., Ellis, T., Dellinger, G., El-Mohtar, C., Zornberg, J., & Robert, G. B. (2011). "Long-term monitoring of a drilled shaft retaining wall in expansive clay: Behavior before and during excavation". Geo-Frontiers 2011, ASCE
- Delinger, Gregory (2011). "The Use of Time Domain Reflectometry Probes for the Moisture Monitoring of a Drilled Shaft Retaining Wall in Expansive Clay". Master's Thesis, The University of Texas at Austin
- Ellis, Trent (2011). "A Subsurface Investigation in Taylor Clay". Master's Thesis, The University of Texas at Austin
- Holtz, W. G., and Gibbs, H. J. (1954). "Engineering Properties of Expansive Clays". Journal of the Soil Mechanics and Foundations Division, ASCE, Vol. 80
- Matlock, H. (1970). "Correlations for Design of laterally loaded piles in soft clay". 2nd Offshore Technology Conference, Houston Texas
- Matlock, H., and Reese, L.C. (1961). "Generalized solution for laterally loaded piles". Journal of Soil Mechanics and Foundation, ASCE
- Matlock, H., and Ripperger, E. A. (1956). "Procedures and Instrumentation for Tests on a Laterally Loaded Pile". Proceedings, Eighth Texas Conference on Soil Mechanics and Foundation Engineering, Special Publication 29, Bureau of Engineering Research, University of Texas at Austin
- O' Neill M. W., and Reese, L. C. (1999). "Drilled Shafts: Construction Procedures and Design Methods". Report No. FHWA-IF-99-025, prepared for the U.S. Department of Transportation, Federal Highway Administration, Office of Implementation, McLean, VA

- Reese, L.C. (1958). "Discussion of Soil modulus for laterally loaded pile analysis".
Proceeding, third International Conference on Numerical Methods in offshore
Piling, Editions Technip, Paris, France
- Reese, L.C. and Welch, R.C. (1975). "Lateral Loadings of Deep Foundations in Stiff
Clay". Journal of Geotechnical Engineering, ASCE
- Reese, L. C., and Wang, S.-T. (1983). "Evaluation of Method of Analysis of Piles Under
Lateral Loading". Preprint, Shanghai Symposium on Marine Geotechnology and
Nearshore/Offshore Structures, Shanghai
- Reese, L. C., and O'Neill, M. W. (1988). "Drilled Shafts: Construction Procedures and
Design Methods". U.S. Department of Transportation, Federal Highway
Administration, Office of Implementation, McLean, VA
- Reese, L. C., Cox, W. R., and Koch, F. D. (1975). "Field Testing and Analysis of
Laterally Loaded Piles in Stiff Clay". Proceedings, VII Annual Offshore
Technology Conference, Houston, TX
- Reese, L.C. (1968). "Interpretation of Data from Load Test of a Drilled Shaft, Ship
Channel Crossing, State Highway 146, Harris County Texas". Letter Report to
McClelland Engineers, Houston, TX
- Tomlinson M. J. (1980). "Foundation Design and Construction". 4th Edition, Pitman
Advanced Publishing Program
- P. K. Ooi and T. L. Ramsey (2003). "Curvature and Bending Moments from Inclinator
Data". International Journal of Geomechanics, ASCE
- Jiun-Yih Chen et al. (2010). "Development of Project-specific p-y Curves for Drilled
Shaft Retaining Wall Design". Earth Retention Conference, ASCE

- Hisham Mohamad (2011). "Performance monitoring of a secant pile wall using distributed fiber optic strain sensing". Journal of Geotechnical and Geoenvironmental Engineering, ASCE
- Barbara Bonfiglioli and Giovanni Pascale (2003). "Internal Strain Measurements in Concrete Elements by Fiber Optic Sensors". Journal of Materials in Civil Engineering, ASCE
- Osborne N.H et al. (2007). "Factors Influencing the Performance of Strain Gauges: A Singapore Perspective". Field Measurements in Geomechanics, ASCE
- Xiaobin Lin¹ and Robin M. Lim (2011). "Field Measurements and Predictions of Concrete Temperatures in Large Diameter Drilled Shafts in Hawaii". Geofrontiers 2011, ASCE
- Fellenius, B.H. (2001). "From strain measurements to load in an instrumented pile". Geotechnical News Magazine
- Marco Quirion and Gerard Ballivy (2000). "Concrete Strain Monitoring With Fabry-Perot Fiber-Optic Sensor". Journal of Materials in Civil Engineering, ASCE
- H-Y. Fang and Van Nostrand Reinhold (1991). " Foundation Engineering Handbook". Second Edition, New York

Vita

Iraklis Koutrouvelis was born in Serres, Greece on January 10th, 1986 and is the second child of Dimitrios Koutrouvelis and Lefainio Morfakidou. After completing his studies at Mantoulides Educators high school in Thessaloniki, Greece he entered the Aristotle University of Thessaloniki (Auth) in 2003. He received his Diploma in Civil Engineering in April 2009. In August 2010, he entered the Graduate Program at the Cockrell College of Engineering at The University of Texas at Austin.

E-mail: akis_koutrouvelis@utexas.edu

This thesis was typed by Iraklis Koutrouvelis

Copyright

by

Andrew Charles Brown

2013

The Dissertation Committee for Andrew Charles Brown Certifies that this is the approved version of the following dissertation:

The Behavior of Drilled Shaft Retaining Walls in Expansive Clay Soils

Committee:

Robert B. Gilbert, Supervisor

Jorge G. Zornberg

Chadi S. El Mohtar

Sharon L. Wood

Bridget R. Scanlon

The Behavior of Drilled Shaft Retaining Walls in Expansive Clay Soils

by

Andrew Charles Brown, B.S.C.E., M.S.C.E.E.

Dissertation

Presented to the Faculty of the Graduate School of

The University of Texas at Austin

in Partial Fulfillment

of the Requirements

for the Degree of

Doctor of Philosophy

The University of Texas at Austin

August 2013

Dedication

For my wife and family.

Acknowledgements

The author would like to thank his supervisor, Dr. Robert B. Gilbert, for his assistance throughout his undergraduate and graduate education. Many thanks are extended to the Texas Department of Transportation, whose funding made this research possible. The author would also like to thank Drs. Jorge G. Zornberg, Chadi S. El Mohtar, Sharon L. Wood, Bridget R. Scanlon, and Richard E. Klingner for their contributions to the development and review of this research. The author is indebted to Roy Lee, for donating the use of his property to this research, and the staff at Lymon C. Reese and Associates, Fugro Consultants, Inc., McKinney Drilling Company, and HVJ and Associates for their assistance at the testing site. In particular, the author would like to thank Dr. Shin-Tower Wang, Jose Arrellaga, Dr. Gonzalo Vasquez, Dr. Bill Isenhower, Rebecca Russo, and Russell Sieg for their personal assistance with research and testing activities. The author thanks his colleagues Greg Dellinger, Trent Ellis, Iraklis Koutrouvelis, and Ali Helwa, who provided tremendous assistance during the research process and whose presence made the many hours of field work much more entertaining. Finally, the author wishes to thank his friends, family, and especially his wife Jennifer, for their support during his doctoral studies.

The Behavior of Drilled Shaft Retaining Walls in Expansive Clay Soils

Andrew Charles Brown, Ph.D.

The University of Texas at Austin, 2013

Supervisor: Robert B. Gilbert

Drilled shaft retaining walls are common earth retaining structures, well suited to urban environments where noise, space, and damage to adjacent structures are major considerations. The design of drilled shaft retaining walls in non-expansive soils is well established. In expansive soils, however, there is no consensus on the correct way to account for the influence of soil expansion on wall behavior. Based on the range of design assumptions currently in practice, existing walls could be substantially over- or under-designed.

The goal of this research is to advance the understanding of the effects of expansive clay on drilled shaft retaining walls. The main objectives of this study are to identify the processes responsible for wall loading and deformation in expansive clay, to evaluate how these processes change with time, and to provide guidance for design practice to account for these processes and ensure adequate wall performance.

The primary source of information for this research is performance data from a four-year monitoring program at the Lymon C. Reese research wall, a full-scale instrumented drilled shaft retaining wall constructed through expansive clay in Manor, Texas. The test wall was instrumented with inclinometers and fiber optic strain gauges, and performance data was recorded during construction, excavation, during natural moisture fluctuations, and during controlled inundation tests that provided the retained soil

with unlimited access to water. In addition to the test wall study, a field assessment of existing TxDOT drilled shaft retaining walls was conducted.

The main process influencing short-term wall deformation was found to be global response to stress relief during excavation, which causes the wall and soil to move together without the development of large earth pressures or bending stresses. Long-term wall deformations were governed by the development of drained conditions in both the retained soil and the foundation soil after approximately eight months of controlled inundation testing. To ensure adequate wall performance, the deformations and structural loads associated with short- and long-term conditions should be combined and checked against allowable values.

Table of Contents

List of Tables	xv
List of Figures	xvi
CHAPTER 1: OVERVIEW OF RESEARCH STUDY	1
1.1: Introduction.....	1
1.2: Objectives	1
1.3: Methodology.....	2
1.4: Organization.....	2
CHAPTER 2: BACKGROUND INFORMATION AND SIGNIFICANCE OF WORK	4
2.1: Overview.....	4
2.2: The Design and Use of Drilled Shaft Retaining Walls in Texas	4
2.2.1: Drilled Shaft Walls in Texas.....	4
2.2.2: Estimation of Lateral Earth Pressures.....	4
2.2.3: Summary of Current TxDOT Design Procedure for Stiff Clays (after TxDOT, 2009).....	5
2.3: The Effects of Expansive Clay on Retaining Structures.....	9
2.3.1: Swell Pressures, Overconsolidation, and Other Concerns.....	9
2.3.2: Recent Failures in Overconsolidated, Expansive Clay	10
2.4: Field Performance of Existing TxDOT Walls	11
2.4.1: Expansive Clay Concerns versus Real-World Mitigating Factors	11
2.4.2: Assessment of Existing TxDOT Walls.....	12
2.5: Proposed Models for Lateral Earth Pressure and Foundation Soil Response.....	13
2.5.1: Proposed Models of Long-Term Earth Pressure Loading	13
2.5.2: Proposed p-y Models of Foundation Soil Response	14
2.5.2.a: Stiff Clay Without Free Water	15
2.5.2.b: Stiff Clay With Free Water	15

2.5.2.c: Drained p-y Curves for Cohesionless Soil.....	15
2.5.2.d: Summary of Proposed p-y Curves for Comparison.....	19
2.6: Previous Reports on Lymon C. Reese Research Wall.....	20
2.6.1: Ellis (2011): A Subsurface Investigation in Taylor Clay	20
2.6.2: Dellinger (2011): The Use of Time Domain Reflectometry Probes for the Moisture Monitoring of a Drilled Shaft Retaining Wall in Expansive Clay	21
2.6.3: Koutrouvelis (2012): Earth Pressures Applied on Drilled Shaft Retaining Walls in Expansive Clay during Natural Cycles of Moisture Fluctuation	22
CHAPTER 3: DESIGN AND CONSTRUCTION OF FULL-SCALE INSTRUMENTED TEST WALL.....	24
3.1: Location of Test Wall	24
3.2: Site Conditions.....	25
3.2.1: Overview.....	25
3.2.2: Preliminary Geotechnical Investigation (January 2010)	26
3.3: Design of Test Wall.....	27
3.4: Design of Instrumentation Program.....	30
3.4.1: Overview.....	30
3.4.2: Strain Gauges.....	31
3.4.3: Inclinometers	32
3.4.4: Additional Instrumentation	32
3.5: Construction of Full-Scale Instrumented Test Wall	34
3.6: Monitoring Plan.....	36
3.7: Data Reduction and Analysis.....	36
3.7.2: Strain Gauge Data Reduction	37
3.7.3: Inclinometer Data Reduction.....	39
3.7.3.a: Rotation Profiles Recorded in the Field.....	39
3.7.3.b: Combining and Smoothing Rotation Profiles.....	40

3.7.3.c: Obtaining Bending Moment Profiles from Rotation Data	48
3.7.3.d: Obtaining Net Earth Pressures from Bending Moment Profiles	52
3.7.3.e: Generating p-y Curves from Inclinometer Data	55
3.7.3.e.1: Discussion of “Net” Soil Resistance	55
3.7.3.e.2: Correcting Soil Resistance for Excavation Location ..	55
3.7.3.e.3: Correcting Horizontal Deflections for Center of Rotation	56
3.7.3.e.4: Example p-y Curves Developed from Inclinometer Data	58
3.8: Summary and Conclusions	59
CHAPTER 4: TEST WALL PERFORMANCE BEFORE EXCAVATION (APRIL 2010 – AUGUST 2010)	61
4.1: Overview	61
4.2: Climatic Information.....	61
4.3: Summary of Field Instrumentation Data	62
4.3.1: Strain Gauge Data	62
4.3.2: Stand Pipe Piezometer	71
4.4: Data Interpretation	71
4.4.1: Concrete Curing.....	71
4.4.2: Shrinkage Cracking in Concrete	72
4.4.3: Expansive Soil Movement	74
4.4.4: Development of Residual Stresses and Strains.....	75
4.5: Summary and Conclusions	77
CHAPTER 5: TEST WALL PERFORMANCE DURING EXCAVATION (AUGUST 2010 – SEPTEMBER 2010)	78
5.1: Overview	78
5.1.1: Summary of Excavation Progress.....	78
5.1.2: Climatic Information.....	79

6.3.3: Strain Gauge Data.....	129
6.4: Data Interpretation.....	138
6.4.1: Phases of Wall Motion.....	138
6.4.1.a: Drying Cycle 1: October 8, 2010 – January 6, 2011 (3 months)	138
6.4.1.b: Wetting Cycle 1: January 6, 2011 – March 11, 2011 (2 months)	139
6.4.1.c: Drying Cycle 2: March 11, 2011 – November 16, 2011 (8 months).....	140
6.4.1.d: Wetting Cycle 2: November 16, 2011 – April 10, 2012 (5 months).....	142
6.4.2: Deflected Shapes at Key Dates.....	143
6.4.3: Earth Pressure Reductions from Soil Shrinkage.....	146
6.4.4: Thermal Strains and Bending Curvatures.....	149
6.4.4.b: Daily Variation in Temperature and Bending Strains.....	151
6.4.4.c: Analysis of Thermal Deformations on March 11, 2011 and November 16, 2011.....	154
6.4.5: Earth Pressure Increases from Soil Expansion.....	158
6.5: Summary and Conclusions.....	158
CHAPTER 7: TEST WALL BEHAVIOR DURING CONTROLLED INUNDATION TESTING (MAY 2012 – JULY 2013).....	161
7.1: Overview.....	161
7.2: Summary of Key Events.....	161
7.2.1: Site Investigation and Installation of Inundation Berm and Piezometers	161
7.2.2: Summary of Inundation Cycles.....	164
7.2.2.a: First Inundation Cycle (May 2012 – July 2012).....	164
7.2.2.b: First Drying Cycle (July 2012 – February 2013).....	164
7.2.2.c: Second Inundation Cycle (February 2013 – June 2013).....	164
7.2.2.d: Second Drying Cycle (June 2013 – July 2013).....	165
7.2.3: Climatic Information.....	166

7.3: Summary of Field Instrumentation Data	168
7.3.1: Inclinometer Data	168
7.3.2: Soil Moisture Content Data	171
7.3.3: Stand Pipe Piezometer Data.....	172
7.3.4: Time Domain Reflectometry (TDR) Probe Data.....	176
7.3.5: Strain Gauge Data.....	179
7.4: Data Interpretation	188
7.4.1: Immediate Response to Water	188
7.4.2: Development and Characterization of Drained, Fully Softened Strengths	193
7.4.3: LPILE Analysis.....	194
7.5: Summary and Conclusions	203
CHAPTER 8: DEVELOPMENT OF DESIGN GUIDELINES.....	205
8.1: Long-Term Design Guidelines	205
8.1.1: Summary of Long-Term Guidelines.....	205
8.1.2: Design Predictions vs. Observed Behavior.....	210
8.1.3: Hypothetical Test Wall Redesign Using Fully Softened Strengths and Hydrostatic Pressures from Natural Water Table	215
8.2: Short-Term Design Guidelines	218
8.3: Summary and Conclusions	220
CHAPTER 9: CONCLUSIONS AND RECOMMENDATIONS.....	223
9.1: Overview.....	223
9.2: Summary of Research Study.....	223
9.2.1: Instrumentation Program	223
9.2.1.a: Structural Performance of Drilled Shafts.....	223
9.2.1.b: Soil Moisture Monitoring	224
9.2.2: Behavior Before Excavation.....	224
9.2.3: Behavior During Excavation	225

9.2.4: Behavior During Natural Moisture Cycles	225
9.2.4.a: Response to Moisture Fluctuations	225
9.2.4.b: Thermal Strains and Bending Curvatures	226
9.2.5: Behavior During Controlled Inundation Testing	226
9.2.6: Development of Design Guidelines	227
9.2.6.a: Long Term Behavior After Cycles of Wetting and Drying ..	227
9.2.6.b: Short-Term Behavior During Excavation	228
9.3: Conclusions of Research Study	228
9.4: Recommendations for Future Work	230
References	232
Vita	235

List of Tables

Table 3.1: Baseline assumptions and design parameters for test wall.	28
Table 3.2: Summary of wall construction activities and measured concrete strengths.	35
Table 5.1: Baseline assumptions and design parameters for short-term LPILE analysis.....	98
Table 5.2: Baseline assumptions and design parameters for modified LPILE analysis.	113
Table 6.1: Baseline assumptions and design parameters for initial soil shrinkage LPILE analysis.....	147
Table 7.1: Baseline assumptions and design parameters for long-term LPILE analysis of inundation conditions.	201
Table 8.1: Baseline assumptions and design parameters for LPILE analysis using proposed long-term design guidelines.	210

List of Figures

Figure 2.1: Initial estimation of maximum moment using TxDOT design procedure.	7
Figure 2.2: Ultimate load ratio vs. clear spacing / drilled shaft diameter (after TxDOT, 2012).....	8
Figure 2.3: Examples of proposed long-term earth pressure envelopes for expansive clay (pressures are acting on a 2.5-foot shaft width).	14
Figure 2.4: Typical k_{py} values for clays (after Dodds and Martin, 2007).....	17
Figure 2.5: Typical k_{py} values for sands (after Dodds and Martin, 2007).	18
Figure 2.6: Illustration of strength reductions due to passive failure wedge interaction of closely spaced piles in sand (after Wang and Reese, 1986).	19
Figure 2.7: Summary of proposed p-y curves, calculated for the test wall at a depth of 16 feet below the original ground surface (1 foot below excavation line).	20
Figure 3.1: Location of full-scale test wall (Google, Inc.).....	24
Figure 3.2: Detailed site plan with location of test wall.	25
Figure 3.3: Taylor Clay from the project site in Manor, Texas.	26
Figure 3.4: Results of Atterberg Limit and UU testing from January, 2010 (three months before shaft construction; seven months before excavation).27	
Figure 3.5: Cross-section of wall and excavation at center shaft, facing east (not to scale).	29
Figure 3.6: Plan view of wall and excavation.....	29
Figure 3.7: Plan view of instrumented rebar cage before concrete placement.	30
Figure 3.8: Distribution of sensors within an instrumented shaft.....	31

Figure 3.9: Instrumentation on the project site. Clockwise from top left: temperature resistant datalogger and enclosure for continuous strain readings; signal conditioner for individual strain readings; linear potentiometer; TDR probe installed through facing.	33
Figure 3.10: Construction of test wall, April 2010.	34
Figure 3.11: Lifting an instrumented cage with two cranes.	35
Figure 3.12: Mathematical relationship between deflection (y), slope (S), bending moment (M), shear force (V), and soil reaction force (p) for a laterally loaded pile (after Reese and Van Impe, 2001).	37
Figure 3.13: Strain gauge data reduction (after Koutrouvelis 2012).	38
Figure 3.14: Sample rotation data from May 28, 2013. Reference survey is July 27, 2010, immediately before excavation.	40
Figure 3.15: Tukey's method of end value smoothing (after Tukey 1977).	44
Figure 3.16: Illustration of the 3RH smooth with re-roughing applied to the center shaft rotation data between 0 and 14 feet.	45
Figure 3.17: Comparison of original and smoothed rotation data from the center shaft on 5/28/2013.	46
Figure 3.18: Comparison of raw rotation data from the three instrumented shafts with the final smoothed rotation profile for differentiation.	47
Figure 3.19: Illustration of piecewise third-order polynomial fitting to a moving window of five points at a depth of 14 feet. First derivative at 14 feet is estimated numerically using a central difference approximation between polynomial values at 13.5 and 14.5 feet.	49
Figure 3.20: Relationship between bending curvature and bending moment (M- Φ relationship) used for LPILE and field instrumentation data analysis.	51

Figure 3.21: Bending moment profile generated from piecewise polynomial fitting of smoothed rotation profile and M- Φ relationship from LPILE.....	52
Figure 3.22: Soil resistance profiles generated using piecewise polynomial differentiation of averaged rotation profiles (with and without data smoothing applied during the differentiation process).	54
Figure 3.23: Using a third-order polynomial to adjust values of net soil resistance for p-y curves.....	56
Figure 3.25: Example p-y curves generated from inclinometer data at the test wall. Reference survey is October 8, 2010.	59
Figure 4.1: Monthly rainfall totals for Austin, Texas (Jan. 2009 - Jul. 2010; data from www.wunderground.com). Drilled shafts were installed in early April, 2010.....	62
Figure 4.2: Pre-Excavation Strain Data for Gauges 1 Foot Below Ground Surface.	63
Figure 4.3: Pre-Excavation Strain Data for Gauges 3 Feet Below Ground Surface.	64
Figure 4.4: Pre-Excavation Strain Data for Gauges 5 Feet Below Ground Surface.	64
Figure 4.5: Pre-Excavation Strain Data for Gauges 7 Feet Below Ground Surface.	65
Figure 4.6: Pre-Excavation Strain Data for Gauges 9 Feet Below Ground Surface.	65
Figure 4.7: Pre-Excavation Strain Data for Gauges 11 Feet Below Ground Surface.	66
Figure 4.8: Pre-Excavation Strain Data for Gauges 13 Feet Below Ground Surface.	66
Figure 4.9: Pre-Excavation Strain Data for Gauges 15 Feet Below Ground Surface.	67

Figure 4.10: Pre-Excavation Strain Data for Gauges 17 Feet Below Ground Surface.	67
Figure 4.11: Pre-Excavation Strain Data for Gauges 19 Feet Below Ground Surface.	68
Figure 4.12: Pre-Excavation Strain Data for Gauges 21 Feet Below Ground Surface.	68
Figure 4.13: Pre-Excavation Strain Data for Gauges 23 Feet Below Ground Surface.	69
Figure 4.14: Pre-Excavation Strain Data for Gauges 25 Feet Below Ground Surface.	69
Figure 4.15: Pre-Excavation Strain Data for Gauges 27 Feet Below Ground Surface.	70
Figure 4.16: Pre-Excavation Strain Data for Gauges 29 Feet Below Ground Surface.	70
Figure 4.17: Three weeks of strain measurements during concrete curing. Concrete placed on April 1; concrete in adjacent shafts placed on April 6. Positive strain indicates tension.	72
Figure 4.18: Illustration of tension crack formation in concrete near gauge.	73
Figure 4.19: Strains occurring between concrete curing and excavation. The gauge at a depth of 7 feet may be experiencing changes in side shear due to moisture fluctuations in the active zone (e.g., Kim & O'Neill, 1998).	75
Figure 4.20: Development of residual strains at a depth of 9 feet between shaft construction and excavation (after Koutrouvelis, 2012).	76
Figure 5.1: Photos of initial excavation progress (7/29/2010 – 8/5/2010).	78
Figure 5.2: Photos of later excavation progress (8/23/2010 - 10/1/2010).	79

Figure 5.3: Monthly rainfall totals for Austin, Texas (Jul. 2010 – Oct. 2010; data from www.wunderground.com).....	80
Figure 5.4: Daily precipitation for Manor, Texas (Jul. 2010 – Oct. 2010; data from www.wunderground.com).	80
Figure 5.5: Daily temperature data for Manor, Texas (Jul. 2010 – Oct. 2010; data from www.wunderground.com).....	81
Figure 5.6: Progression of lateral deflections and key events during excavation.	82
Figure 5.7: Deflected shape of east instrumented shaft at various dates during excavation.	83
Figure 5.8: Cumulative deflections recorded in inclinometer installed through the soil 5.5 feet behind the center instrumented shaft.	84
Figure 5.9: Deflection measured at top of wall during excavation. Excavation began on July 29 and continued through August 27.	85
Figure 5.10: Strain Data 1 Foot Below Ground Surface During Excavation.	86
Figure 5.11: Strain Data 3 Feet Below Ground Surface During Excavation.	86
Figure 5.12: Strain Data 5 Feet Below Ground Surface During Excavation.	87
Figure 5.13: Strain Data 7 Feet Below Ground Surface During Excavation.	87
Figure 5.14: Strain Data 9 Feet Below Ground Surface During Excavation.	88
Figure 5.15: Strain Data 11 Feet Below Ground Surface During Excavation.	88
Figure 5.16: Strain Data 13 Feet Below Ground Surface During Excavation.	89
Figure 5.17: Strain Data 15 Feet Below Ground Surface During Excavation.	89
Figure 5.18: Strain Data 17 Feet Below Ground Surface During Excavation.	90
Figure 5.19: Strain Data 19 Feet Below Ground Surface During Excavation.	90
Figure 5.20: Strain Data 21 Feet Below Ground Surface During Excavation.	91
Figure 5.21: Strain Data 23 Feet Below Ground Surface During Excavation.	91

Figure 5.22: Strain Data 25 Feet Below Ground Surface During Excavation.....	92
Figure 5.23: Strain Data 27 Feet Below Ground Surface During Excavation.....	92
Figure 5.24: Strain Data 29 Feet Below Ground Surface During Excavation.....	93
Figure 5.25: Progression of excavation depth along wall face.	94
Figure 5.26: Contour plot of final surveyed excavation dimensions (all units in feet).	94
Figure 5.27: Development of bending strains in a pair of strain gauges located 23 feet below ground surface in the center shaft.	95
Figure 5.28: Strains related to temperature changes in exposed concrete. Gauge located 1 foot below ground surface on exposed side of wall. Soil at gauge location was excavated on July 29-31.....	96
Figure 5.29: Comparison of p-y prediction with measured field data. P-y analysis used a triangular earth pressure distribution of 40 psf/ft.	99
Figure 5.30: Comparison of predicted and measured shaft rotation profiles induced by removal of soil during excavation.....	100
Figure 5.31: Comparison of predicted and measured bending moment profiles induced by removal of soil during excavation.	101
Figure 5.32: Global response to removal of soil in linear elastic FEM.	103
Figure 5.33: Global shear strains in response to removal of soil in linear elastic FEM.	103
Figure 5.34: Comparison of linear elastic finite element model predictions with measured field data.	104
Figure 5.35: SASW testing at the test wall prior to excavation, June 2010.	105
Figure 5.36: Comparison of measured shear modulus profiles from SASW testing with finite element model prediction (after Ellis, 2011).....	106

Figure 5.37: Calculated values of bending moment and net soil resistance during excavation, based on measured rotation profiles from inclinometer data.	108
Figure 5.38: Comparison of calculated p-y curves during excavation with proposed p-y curves at a depth of 16 feet below original ground surface.	109
Figure 5.39: Comparison of calculated p-y curves during excavation with proposed p-y curves at a depth of 18 feet below original ground surface.	110
Figure 5.40: Comparison of calculated p-y curves during excavation with proposed p-y curves at a depth of 20 feet below original ground surface.	111
Figure 5.41: Comparison of calculated p-y curves during excavation with proposed p-y curves at a depth of 22 feet below original ground surface.	112
Figure 5.42: Comparison of measured and calculated profiles of deflection and bending moment in advanced LPILE analysis.....	115
Figure 5.43: Comparison of measured and calculated profiles of soil resistance in advanced LPILE analysis.....	116
Figure 5.44: Estimated horizontal deflection due to global movements of the soil-shaft system during excavation.....	117
Figure 6.1: Installation of Shotcrete Facing on October 1, 2010.....	120
Figure 6.2: Installation of TDR Moisture Probes Behind Wall Facing.	121
Figure 6.3: Installation of TDR Moisture Probes Through Ground Surface.	121
Figure 6.4: Approximate Locations of TDR Moisture Probes.	122
Figure 6.5: Excavation slopes are reshaped on August 17, 2011.	123
Figure 6.6: Erosion control material is installed on October 18, 2011.	123
Figure 6.7: Monthly Rainfall Totals for Austin, Texas (Oct. 2010 – Apr. 2012; data from www.wunderground.com).....	124

Figure 6.8: Daily Temperature Data for Manor, Texas (Oct. 2010 – Apr. 2012; data from www.wunderground.com).....	125
Figure 6.9: Variation of top-of-wall deflection with natural moisture cycles. Deflections are referenced to installation of facing on October 8, 2010.	126
Figure 6.10: Electrical conductivity data from a TDR probe located 1.5 feet below ground surface (Oct. 2010 – Apr. 2012).	128
Figure 6.11 Electrical conductivity data from a TDR probe located 1.5 feet below ground surface, presented on a logarithmic scale (Oct. 2010 – Apr. 2012).	128
Figure 6.12: Strain Data 1 Foot Below Ground Surface (Oct. 2010 – Apr. 2012).	130
Figure 6.13: Strain Data 3 Feet Below Ground Surface (Oct. 2010 – Apr. 2012).	131
Figure 6.14: Strain Data 5 Feet Below Ground Surface (Oct. 2010 – Apr. 2012).	131
Figure 6.15: Strain Data 7 Feet Below Ground Surface (Oct. 2010 – Apr. 2012).	132
Figure 6.16: Strain Data 9 Feet Below Ground Surface (Oct. 2010 – Apr. 2012).	132
Figure 6.17: Strain Data 11 Feet Below Ground Surface (Oct. 2010 – Apr. 2012).	133
Figure 6.18: Strain Data 13 Feet Below Ground Surface (Oct. 2010 – Apr. 2012).	133
Figure 6.19: Strain Data 15 Feet Below Ground Surface (Oct. 2010 – Apr. 2012).	134
Figure 6.20: Strain Data 17 Feet Below Ground Surface (Oct. 2010 – Apr. 2012).	134
Figure 6.21: Strain Data 19 Feet Below Ground Surface (Oct. 2010 – Apr. 2012).	135
Figure 6.22: Strain Data 21 Feet Below Ground Surface (Oct. 2010 – Apr. 2012).	135
Figure 6.23: Strain Data 23 Feet Below Ground Surface (Oct. 2010 – Apr. 2012).	136
Figure 6.24: Strain Data 25 Feet Below Ground Surface (Oct. 2010 – Apr. 2012).	136
Figure 6.25: Strain Data 27 Feet Below Ground Surface (Oct. 2010 – Apr. 2012).	137
Figure 6.26: Strain Data 29 Feet Below Ground Surface (Oct. 2010 – Apr. 2012).	137

Figure 6.27: Inclinator Data from January 6, 2011.....	139
Figure 6.28: Inclinator Data from March 11, 2011.....	140
Figure 6.29: The use of a deep inclinometer casing and concrete pad as a qualitative indicator of soil shrinkage near the test wall (not to scale).....	141
Figure 6.30: Inclinator Data from November 16, 2011.	142
Figure 6.31: Inclinator Data from April 10, 2012.....	143
Figure 6.32: Deflected shapes of test wall at key dates, referenced to the installation of facing on October 8, 2010, compared with the initial p-y design analysis.....	145
Figure 6.33: Profiles of shaft rotation and estimated reduction in net earth pressures in response to soil shrinkage between March 11 and November 16, 2011.	148
Figure 6.34: Comparison of LPILE prediction with horizontal deflections and bending moments between March 11 and November 16, 2011.....	149
Figure 6.35: Air temperature in Manor, Texas on March 11 and November 16, 2011 (data from www.wunderground.com).....	151
Figure 6.36: Comparison of air temperature in Manor, Texas and strain data at a depth of 3 feet in the center instrumented shaft (October 22 – October 27, 2011; weather data from www.wunderground.com).	152
Figure 6.37: Comparison of air temperature in Manor, Texas and measured bending curvature in the test wall at various depths in the center shaft (temperature data from www.wunderground.com).	153

Figure 6.38: Comparison of LPILE prediction with horizontal deflections and bending moments between March 11 and November 16, 2011. A bending moment of 150 in-kip was applied at the top of the shaft to simulate thermal effects.	156
Figure 6.39: Comparison of measured and calculated soil reaction forces due to expansive soil shrinkage.	157
Figure 7.1: Location of inundation zone and stand pipe piezometers. Piezometers A and C are screened from 5 to 15 feet; piezometer B is screened between 3.4 and 4.6 feet; piezometer D is screened between 3.6 and 4.8 feet.	162
Figure 7.2: Schematic of inundation berm.	163
Figure 7.3: Inundation berm and stand pipe piezometers (April 26, 2012).	163
Figure 7.4: Flooding in response to a large storm before the May 6, 2013 data surveys. Water level in the excavation reached ground surface.	165
Figure 7.5: Inundation zone on June 17, 2013, two weeks into second drying cycle. Stand pipe piezometer casing is 4" across.	166
Figure 7.6: Monthly rainfall totals for Austin, Texas (May 2012 - Jun. 2013; data from www.wunderground.com).	167
Figure 7.7: Daily average temperature data for Manor, Texas (May 2012 - Jul. 2013; data from www.wunderground.com).	168
Figure 7.8: Average deflected shapes at key dates during inundation testing. Data is referenced to installation of facing in October, 2010.	169
Figure 7.9: Top-of-wall deflections during inundation testing (key dates indicated by vertical dashed lines). Reference survey is facing installation in October, 2010.	170

Figure 7.10: Rate of deflection at ground surface during inundation testing (key dates indicated by vertical dashed lines).....	170
Figure 7.11: Summary of measured soil moisture contents during controlled inundation testing.....	172
Figure 7.12: Water level in Piezometer B-3 (outside inundation zone) during inundation testing.....	174
Figure 7.13: Data from shallow-screened stand pipe piezometers during second inundation cycle.....	175
Figure 7.14: Data from deeper-screened stand pipe piezometers during second inundation cycle.....	175
Figure 7.15: Electrical conductivity data from a TDR probe located 1.5 feet below ground surface (May 2012 – Jul. 2013).....	177
Figure 7.16: Electrical conductivity data from a TDR probe located 1.5 feet below ground surface during first inundation cycle (May – Jul. 2012).....	177
Figure 7.17: Electrical conductivity data from a TDR probe located 1.5 feet below ground surface during first drying cycle (Jul. 2012 – Feb. 2013)....	178
Figure 7.18: Electrical conductivity data from a TDR probe located 1.5 feet below ground surface during second inundation cycle (Feb. – Jun. 2013).	178
Figure 7.19: Electrical conductivity data from a TDR probe located 1.5 feet below ground surface during second drying cycle (Jun. – Jul. 2013).	179
Figure 7.20: Strain Data 1 Foot Below Ground Surface (May 2012 – July 2013).	181
Figure 7.21: Strain Data 3 Feet Below Ground Surface (May 2012 – July 2013).	181
Figure 7.22: Strain Data 5 Feet Below Ground Surface (May 2012 – July 2013).	182
Figure 7.23: Strain Data 7 Feet Below Ground Surface (May 2012 – July 2013).	182
Figure 7.24: Strain Data 9 Feet Below Ground Surface (May 2012 – July 2013).	183

Figure 7.25: Strain Data 11 Feet Below Ground Surface (May 2012 – July 2013).	183
Figure 7.26: Strain Data 13 Feet Below Ground Surface (May 2012 – July 2013).	184
Figure 7.27: Strain Data 15 Feet Below Ground Surface (May 2012 – July 2013).	184
Figure 7.28: Strain Data 17 Feet Below Ground Surface (May 2012 – July 2013).	185
Figure 7.29: Strain Data 19 Feet Below Ground Surface (May 2012 – July 2013).	185
Figure 7.30: Strain Data 21 Feet Below Ground Surface (May 2012 – July 2013).	186
Figure 7.31: Strain Data 23 Feet Below Ground Surface (May 2012 – July 2013).	186
Figure 7.32: Strain Data 25 Feet Below Ground Surface (May 2012 – July 2013).	187
Figure 7.33: Strain Data 27 Feet Below Ground Surface (May 2012 – July 2013).	187
Figure 7.34: Strain Data 29 Feet Below Ground Surface (May 2012 – July 2013).	188
Figure 7.35: The inundation zone is filled on May 3, 2012.....	189
Figure 7.36: Electrical conductivity data from one TDR probe shows a response within minutes of beginning the inundation test. Probe is located 1.5 feet below ground surface.....	190
Figure 7.37: Water infiltration into the excavation was first observed 90 minutes from the start of inundation.....	190
Figure 7.38: Moisture content profiles immediately before and after first inundation cycle. Natural water table is located at a depth of approximately 8 feet.	192
Figure 7.39: Comparison of measured fully softened strength test data from the project site with data from Ellis (2011) and established correlations.	194
Figure 7.40: Comparison of calculated long-term p-y curves during inundation testing with proposed p-y curves at a depth of 16 feet below original ground surface.....	196

Figure 7.41: Comparison of calculated long-term p-y curves during inundation testing with proposed p-y curves at a depth of 18 feet below original ground surface.....	197
Figure 7.42: Comparison of calculated long-term p-y curves during inundation testing with proposed p-y curves at a depth of 20 feet below original ground surface.....	198
Figure 7.43: Comparison of calculated long-term p-y curves during inundation testing with proposed p-y curves at a depth of 22 feet below original ground surface.....	199
Figure 7.44: Comparison of calculated long-term p-y curves during inundation testing with proposed p-y curves at a depth of 24 feet below original ground surface.....	200
Figure 7.45: Comparison of long-term LPILE Prediction and calculated soil reaction forces.....	202
Figure 8.1: Summary of long-term design guidelines.	206
Figure 8.2: Typical k_{py} values for clays (after Dodds and Martin 2007).....	208
Figure 8.3: Typical k_{py} values for sands (after Dodds and Martin 2007).	209
Figure 8.4: Summary of measured and predicted values of deflected shapes using long-term design guidelines.....	212
Figure 8.5: Summary of measured and predicted bending moments using long-term design guidelines.....	213
Figure 8.6: Comparison of Long-Term Modified LPILE Prediction and Calculated Soil Reaction Forces.	214

Figure 8.7: Comparison of long-term p-y curves predicted by modified LPILE analysis with p-y curves estimated from field data (reference survey is after installation of shotcrete facing on October 8, 2010).215

Figure 8.8: Input earth pressure envelope for wettest test wall conditions prior to inundation testing (natural groundwater table at 8 feet below ground surface).....217

Figure 8.9: Comparison of deflected shapes and bending moments for hypothetical test wall redesign using proposed long-term conditions.....218

Figure 8.10: Comparison of measured data with predictions from linear elastic finite element model including anisotropy and stiffness reductions.220

CHAPTER 1: OVERVIEW OF RESEARCH STUDY

1.1: Introduction

The design of drilled shaft retaining walls in non-expansive soils is well established. In expansive soils, however, there is no consensus on the correct way to model the effects of soil expansion on wall behavior during cycles of wetting and drying. Based on the range of design assumptions currently in practice, existing walls could be substantially over- or under-designed. The purpose of this research is to advance the understanding of the behavior of drilled shaft retaining walls installed through expansive clay. The primary source of information for this study will be data from a full-scale instrumented test wall, which was installed through highly overconsolidated, expansive clay in Manor, Texas, and monitored for a period of four years. This study includes a summary of existing research, technical information on the design and construction of the instrumented test wall, an examination of the relationship between soil behavior and wall deformation during the three year monitoring period, and recommendations on how to account for the effects of expansive soil in design. The analysis of test wall response includes summaries of behavior before excavation, during excavation, during long-term moisture fluctuations which included an extreme drought, and during controlled inundation testing which provided the retained soil unlimited access to water until the wall deflections reached equilibrium.

1.2: Objectives

The goal of this research is to advance our understanding of the long-term behavior of retaining structures in expansive clays. The observed performance and instrumentation data from our test wall will be used to address the following objectives:

1. Identify and analyze the processes responsible for wall loading and deformation.

2. Evaluate how these processes change with time and moisture cycles.
3. Provide guidance for design practice to account for these processes and ensure adequate wall performance.

1.3: Methodology

The objectives of this research study will be accomplished according to the following methodology:

1. Design and construct a full-scale instrumented test wall through expansive clay.
2. Monitor the performance of the test wall during construction, excavation, natural seasonal moisture fluctuations, and controlled inundation testing which provides the expansive clay with unlimited access to water.
3. Analyze test wall performance data using standard of practice design methods.
4. Develop guidance for design practice based on results of analyses.

This study is primarily based on data from the Lymon C. Reese research wall in Manor, Texas. While the Taylor clay at the research site is typical of an overconsolidated, high plasticity, stiff-fissured clay in Texas, the behavior of other expansive soil deposits may deviate from the behavior presented in this dissertation. Unless otherwise noted, the conclusions presented in this study are not intended to be applied to walls or sites beyond the Lymon C. Reese research wall.

1.4: Organization

Because data from the Lymon C. Reese research wall provides the primary basis for this research, this dissertation will address the design, construction, performance monitoring, and data analysis for the test wall. A background on the design and use of

drilled shaft retaining walls in expansive clays, along with a summary of existing research on the Lymon C. Reese research wall, is presented in Chapter 2. The design, construction, and data reduction procedures for the test wall and instrumentation program are covered in Chapter 3. Analyses of test wall behavior before excavation, during excavation, during long-term moisture fluctuations which included an extreme drought, and during controlled inundation testing which provided the retained soil unlimited access to water are respectively presented in Chapters 4 - 7. The development of design guidelines, including a discussion of how to represent earth pressures in the retained soil and p-y curves in the foundation soil, is covered in Chapter 8. The conclusions of the research study are presented in Chapter 9.

CHAPTER 2: BACKGROUND INFORMATION AND SIGNIFICANCE OF WORK

Note: Portions of this section have been previously submitted by the author in Report No. FHWA/TX-11/0-6603-1 (Brown et al., CTR 2011).

2.1: Overview

This section presents background information on the topic of drilled shaft retaining walls in expansive clay soils and a summary of published research on the Lymon C. Reese research wall. Additional discussion of existing research, where applicable, is included in subsequent chapters.

2.2: The Design and Use of Drilled Shaft Retaining Walls in Texas

2.2.1: DRILLED SHAFT WALLS IN TEXAS

Cantilever drilled shaft retaining walls are common earth-retaining structures in Texas. They are well suited to use in urban environments where noise, space, and damage to adjacent structures are major considerations (Wang and Reese 1986). Additionally, because of the prevalence of drilled shaft foundations in Texas, experienced contractors are readily available. The design of drilled shaft retaining walls has changed over time. While initial design methods were based on limit equilibrium calculations, more refined p-y analyses based on soil-structure interaction have been developed and are currently in use by TxDOT (Wang and Reese 1986; TxDOT 2009).

2.2.2: ESTIMATION OF LATERAL EARTH PRESSURES

There is uncertainty in how to account for lateral earth pressures acting on drilled shaft walls installed through expansive clay. In Texas, some of the most problematic expansive clay deposits are also highly overconsolidated. For this reason, an examination

of retaining wall design procedures for stiff, overconsolidated clay can provide a reference point for the design of walls in expansive clay deposits.

Commonly, the earth pressure on walls in stiff, overconsolidated clay is estimated using Coulomb active earth pressures with drained properties (Wang and Reese 1986). The TxDOT Design Procedure for Cantilever Drilled Shaft Walls employs this method with a recommended friction angle of 30 degrees for “medium to stiff clays” (TxDOT 2009). For clays common in Texas, this approach results in earth pressures that correspond to an equivalent fluid unit weight of approximately 35 to 40 pounds per cubic foot (pcf).

2.2.3: SUMMARY OF CURRENT TxDOT DESIGN PROCEDURE FOR STIFF CLAYS (AFTER TxDOT, 2009)

In the current TxDOT design procedure, drilled shaft size and spacing is based on moment capacity. The following section presents a shortened version of the procedure that appears in TxDOT (2009). More detailed design information can be found in TxDOT (2012).

1. Determine earth pressures to be applied as loads using a Coulomb analysis with cohesion equal to zero.
 - a. For stiff clays, use a friction angle of 30 degrees. Assume angle of wall friction is equal to two-thirds the soil friction angle.
 - b. Assume no water behind the wall.
 - c. Include soil or traffic surcharge loads where appropriate.
2. Estimate maximum moment in shaft.
 - a. Compute groundline moment from earth pressure distribution.
 - b. Increase groundline moment by 50% to estimate the maximum earth pressure below the excavation line, i.e. $M_{\max} = 1.5 \cdot M_{GL}$ (Figure 2.1).
3. Choose trial drilled shaft size and spacing based on moment capacity.

- a. Use load factor of 1.7 for earth pressure to compute ultimate moment (M_u)
- b. Use nominal moment (M_n) from shaft properties, then check that the factored moment capacity ($\phi \cdot M_n$) exceeds M_u with $\phi = 0.9$.
4. Determine properties of the soil below the finished groundline.
 - a. Use ultimate soil strengths for p-y curves.
 - b. Reduce soil strengths from 0 to 5 feet below the excavation line by 50% to account for loss of strength after excavation.
5. Run p-y analysis using COM624 or LPILE.
 - a. Reduce soil strengths to account for close shaft spacing based on Figure 2.2.
 - b. Use uncracked section properties for the shaft.
 - c. Ensure bending moments and deflections are within allowable values.
Limit deflections to 1% of the cantilever height.
6. Determine depth of shaft fixity based on several embedment values.
 - a. Determine depth of fixity where top-of-wall deflection is no longer affected by embedment depth.
 - b. Determine final embedment depth by multiplying depth of fixity by 1.33.

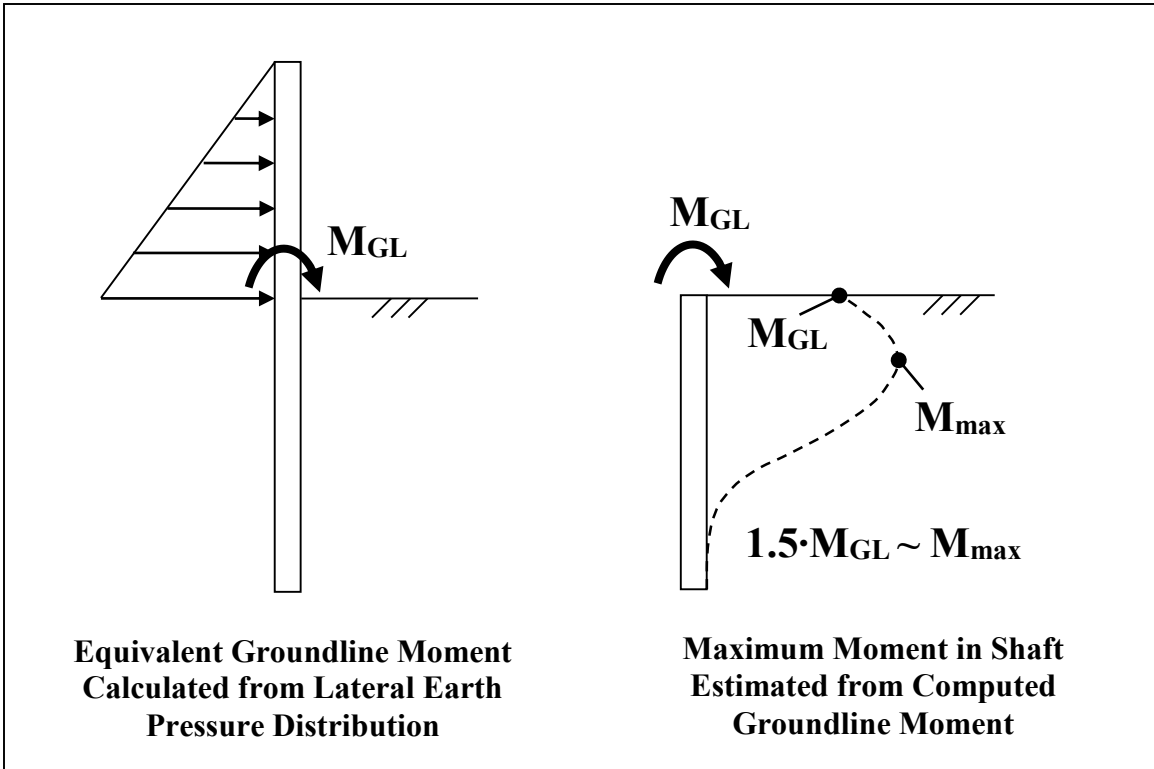


Figure 2.1: Initial estimation of maximum moment using TxDOT design procedure.

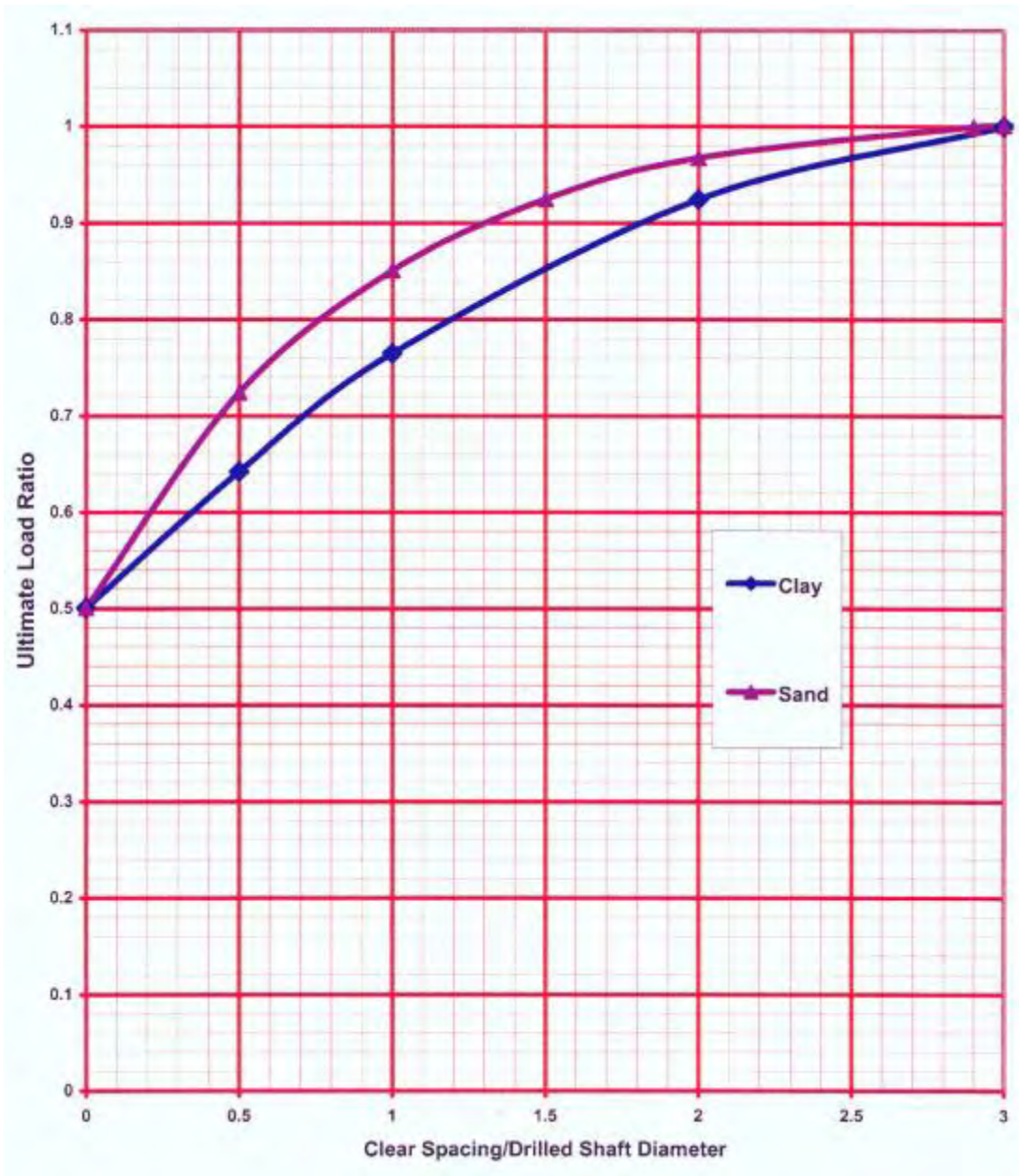


Figure 2.2: Ultimate load ratio vs. clear spacing / drilled shaft diameter (after TxDOT, 2012).

2.3: The Effects of Expansive Clay on Retaining Structures

2.3.1: SWELL PRESSURES, OVERCONSOLIDATION, AND OTHER CONCERNS

There have been concerns raised over the potential effects of expansive soils on retaining structures. The most common of these concerns is the magnitude of horizontal swelling pressures exerted on the wall by the expansive soil. Lytton (2007) summarizes some relevant studies that seek to quantify this effect. Various, the potential lateral pressures acting on a wall in expansive clay have been estimated to be four times the overburden pressure, 6000 psf at three feet of depth in a lab study, 8000 psf at three feet of depth in another lab study, and 1700 psf at three feet of depth in a field study – any of these scenarios are significantly higher than the currently accepted values used for retaining wall design. These studies are described in more detail in Lytton (2007). In general, the expansive soil pressure exerted on a wall is considered to be limited by the passive resistance of the retained soil (Pufahl et al. 1983 and Hong 2008).

In addition to the potential for high lateral pressures, other potential concerns have been identified for retaining walls in expansive clay. Pufahl et al. (1983) describe a hypothetical structure “ratcheting” out with wetting and drying cycles. During dry seasons, the soil could pull back from the wall, incompressible debris could fill the gap, and soil expansion could push the wall and debris further out with each new rewetting cycle. Puppala et al. (2011) describe that cracks near drilled shafts could create zones for moisture infiltration, increasing the depth of the active zone near the shafts.

In Texas, many expansive soil deposits are also heavily overconsolidated. In overconsolidated clay, in-situ horizontal stresses can be very large. When the unloading associated with retaining wall excavation takes place, these large horizontal stresses can impact wall performance. Furthermore, the residual strength of overconsolidated clay can be very low – residual friction angles of 18 degrees or less have been widely reported. The

transition from peak-drained strength to residual-drained strength could influence the increase in lateral earth pressures with time (Wang and Reese 1986). The lateral swell pressures from moisture changes in overconsolidated clay have been reported to be higher than those in normally consolidated clay (Ellis 2011).

2.3.2: RECENT FAILURES IN OVERCONSOLIDATED, EXPANSIVE CLAY

Because the potential for expansion and a high degree of overconsolidation coexist in expansive clays in Texas, it is difficult to separate the effects of swelling from the effects of overconsolidation when considering wall failures. Smith et al. (2009) examine the failure of a bridge deck completed using top down construction in the overconsolidated, expansive Eagle Ford shale near Dallas, TX. In this case, the bridge deck was installed before complete excavation of the underpass and installation of tiebacks. Ultimately, an estimated four inches of inward movement caused the failure of the bridge deck. The authors concluded that the major issue was the use of a design at-rest earth pressure coefficient (K_o) value of approximately 0.7; actual values of K_o for the Eagle Ford shale and other overconsolidated clays are often reported to be between 2 and 3. Expansive soil movement was cited as a “likely” contributing factor (Smith et al. 2009).

Another wall failure in the Eagle Ford shale, this time of a Vertically Earth Reinforced Technology (VERT) wall system, is detailed by Adil Haque and Bryant (2011). This paper indicates that the high K_o values and low residual strengths of overconsolidated clay, as well as expansion from moisture changes, should have been considered in design. The paper also states that “the swell pressure due to unloading could also exert a significant pressure on the wall, much greater than the swell pressure on the walls from moisture changes” (Adil Haque and Bryant 2011).

2.4: Field Performance of Existing TxDOT Walls

2.4.1: EXPANSIVE CLAY CONCERNS VERSUS REAL-WORLD MITIGATING FACTORS

Despite the numerous problems potentially associated with the expansive soils in Texas, relatively few failures of drilled shaft retaining walls have been observed. There are several possible explanations for the general lack of problems associated with drilled shaft retaining walls in expansive clays in Texas.

First, the load factors and deflection requirements used by the TxDOT design procedure will result in drilled shafts that can withstand higher pressures than the nominal values used in design. After calculating the maximum moment in the shaft, a load factor of 1.7 is applied to estimate the design moment. If the differences in active Coulomb earth pressures induced by residual soil strength and/or soil swell are within the range encompassed by this load factor, it is possible that the potential increases in soil pressures are not causing visible distress on walls (for reference, a Coulomb analysis using a residual friction angle of 18 degrees results in an equivalent fluid pressure of approximately 60 psf/ft, about 50% higher than the nominal value of 40 psf/ft). While the top-of-shaft deflections might exceed one percent of the wall height, the structural integrity of the shafts may be preserved. Furthermore, the final as-built drilled shafts may have greater capacity than the minimum allowed by design due to other factors such as constructability (although the risk for lower-than-design capacities due to poor construction exists as well).

Additionally, pavement and drainage systems behind drilled shaft walls may limit the severity of moisture changes causing shrinking and swelling. In pavements with expansive subgrades, moisture contents tend to increase from their natural moisture content to a “steady state” value after the installation of pavement (Snethen et al. 1975, Wise et al. 1971). While the subgrade is still subject to moisture changes, the magnitude of these changes may be smaller than those of exposed soil. The presence of pavement near the

shaft can also prevent the problems associated with water and/or debris entering the gap between the shaft and the soil (Puppala et al. 2011).

Finally, despite the potential to generate very large swell pressures under confinement, swell pressures can be reduced by allowing relatively small wall deformations to take place (Thomas et al. 2009). For projects as large as the typical TxDOT drilled shaft retaining wall, it is possible that expansive soil pressures are being accommodated by small wall deformations that would not be noticed without careful instrumentation.

2.4.2: ASSESSMENT OF EXISTING TxDOT WALLS

In 2011, our research team completed an assessment of existing TxDOT walls. The report provides assessment information and analysis for three drilled shaft walls constructed through expansive clay in Houston, Texas. The walls assessed in this study are generally representative of typical drilled shaft walls in Texas. The three walls have cantilevered heights ranging from 5 to 23 feet, and at the time of the study, the walls had been in service for 14, 9, and 2 years. Over this time period, Houston experienced a range of climate related soil moisture fluctuations that could potentially lead to expansive soil movement. A field inspection of each wall revealed no obvious signs of distress. Based on LPILE analyses of these walls, earth pressures greater than a linear increase of 80 psf/ft would likely be required to produce significant distress that could be readily observed (Brown et. al. 2011).

2.5: Proposed Models for Lateral Earth Pressure and Foundation Soil Response

2.5.1: PROPOSED MODELS OF LONG-TERM EARTH PRESSURE LOADING

Long-term conditions generally govern retaining wall design in high plasticity clays. Often, for embankments and retaining walls, the development of drained, fully softened strengths is a suitable ultimate condition for design (Wright 2005). A variety of models have been proposed for representing the long-term earth pressures induced by expansive soil. For clays in the Taylor formation, where the Lymon C. Reese research wall is constructed, peak drained friction angles are approximately 37 degrees (Long 1983 and Ellis 2011), and average fully softened friction angles in the upper 15 feet are estimated to be approximately 24 degrees based on liquid limit relationships (e.g. Wright 2007) and laboratory test data discussed in Chapter 7. The resulting earth pressure envelopes using the fully softened strengths of the Taylor clay, assuming both no water behind the wall and hydrostatic conditions behind the wall, are pictured in Figure 2.3, along with TxDOT's typical design earth pressure envelope and a hypothetical model of expansive soil swelling pressures similar to that presented in Hong (2008).

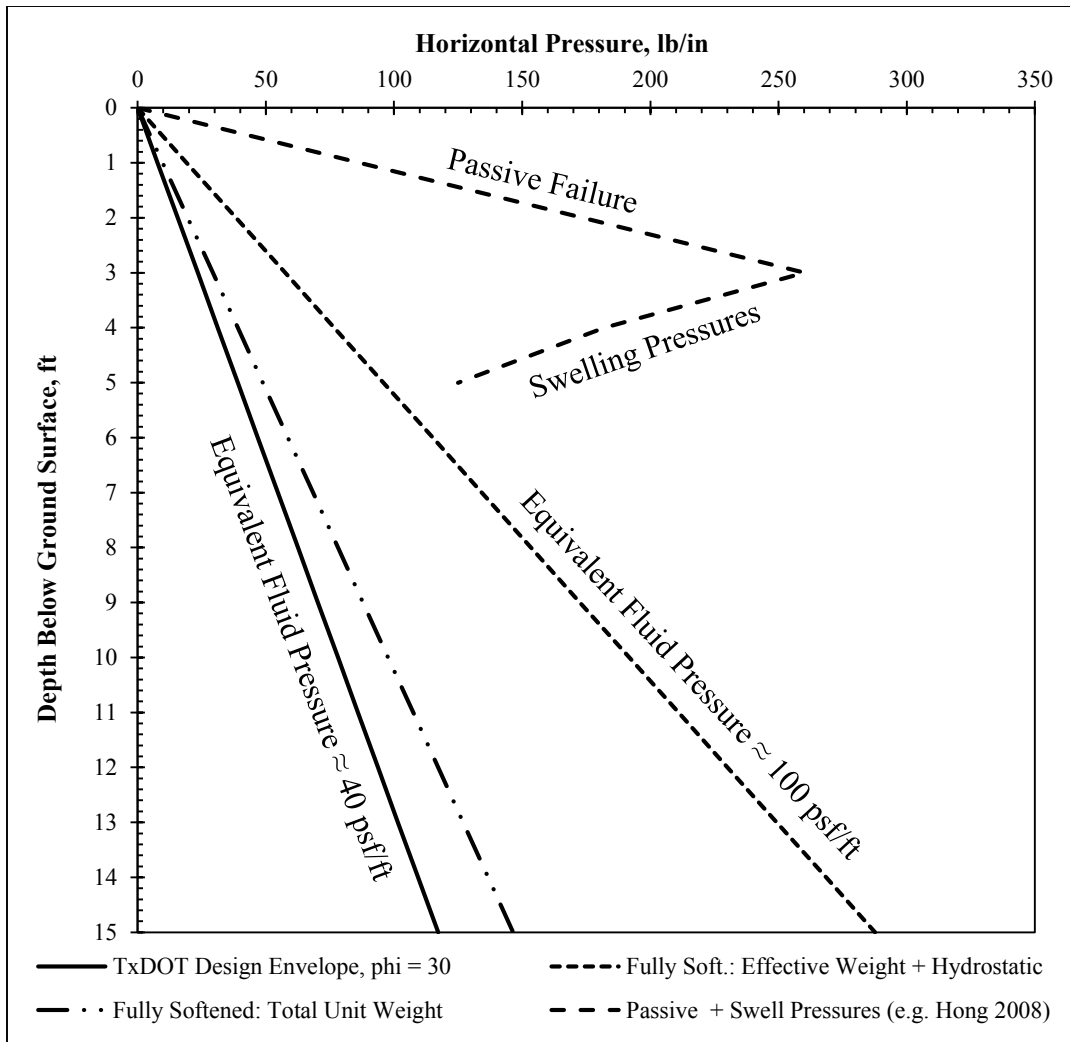


Figure 2.3: Examples of proposed long-term earth pressure envelopes for expansive clay (pressures are acting on a 2.5-foot shaft width).

2.5.2: PROPOSED P-Y MODELS OF FOUNDATION SOIL RESPONSE

In addition to the uncertainty associated with the behavior of the retained soil, several p-y models have been proposed to model the response of the foundation soil in expansive clay. Some of these curves are briefly explained below; illustrations of the calculated curves at a depth of 16 feet below the original ground surface (1 foot below the

design excavation base) for the Lymon C. Reese research wall are provided for comparison in Figure 2.7.

2.5.2.a: Stiff Clay Without Free Water

Typically, the TxDOT design procedure for stiff clays uses p-y curves for “stiff clay without free water,” developed from tests in Houston, Texas (TxDOT 2009, Reese et. al. 2006, Reese and Welch 1972). To account for strength reductions due to the removal of overburden pressures during excavation, a common procedure for excavations in stiff-fissured clay is to translate the profile of undrained strengths from the original ground surface down to the excavation line. Additionally, soil strengths are reduced to account for the effect of close pile spacing as shown in Figure 2.2 (TxDOT 2012; Wang and Reese 1986). For the Lymon C. Reese wall, average undrained strengths used for the development of representative p-y curves shown in Figure 2.7 were approximately 1600 to 2000 psf (before strength reductions). Total soil unit weights are used for these curves.

2.5.2.b: Stiff Clay With Free Water

It is possible that if water stays in the excavation base, the use of curves developed for “stiff clay in the presence of free water” may be appropriate. These curves were developed from load tests in the Taylor formation in Manor, Texas (Reese et. al. 1975). Strength reductions to account for the removal of overburden pressures and close pile spacing are applied before calculating the curves as shown in Reese et. al. 2006. Curves developed for clays in the presence of free water use effective unit weights.

2.5.2.c: Drained p-y Curves for Cohesionless Soil

If the long-term conditions of drilled shaft walls in expansive clays are governed by the development of drained conditions, the use of drained p-y curves developed for cohesionless soils may be appropriate. Because the initial stiffness of the clay in response

to loading at small strains is governed by undrained behavior, the initial stiffness value k_{py} for the p-y curves is selected according to the undrained properties of the clay as shown in Figure 2.4. The use of default k_{py} values for modeling curves at low friction angles associated with expansive clay soils results in unrealistically low values of initial stiffness (Figure 2.5). The selection of unit weight is based on the expected hydrostatic conditions on the project site.

The selection of drained friction angle and appropriate strength reductions due to pile spacing is less straightforward for long-term, drained conditions in clay. Drained friction angles for the Taylor clay can range from 37 degrees at peak, to approximately 24 degrees under fully softened conditions, to as low as 15 – 18 degrees under residual conditions. For short-term drained loading in sand, at low values of clear spacing, the passive soil resistance wedges from each shaft interact with each other, and a “shadowing” effect is present as shown in Figure 2.6. For short-term drained loading in sands, ultimate soil loads are reduced in accordance with Figure 2.2. For long-term loading in clay, however, the mechanism of pile interaction at close spacing is less clear. For the curves shown in Figure 2.7, no reductions are applied for close pile spacing (test wall data will be compared with the proposed curves to evaluate this condition).

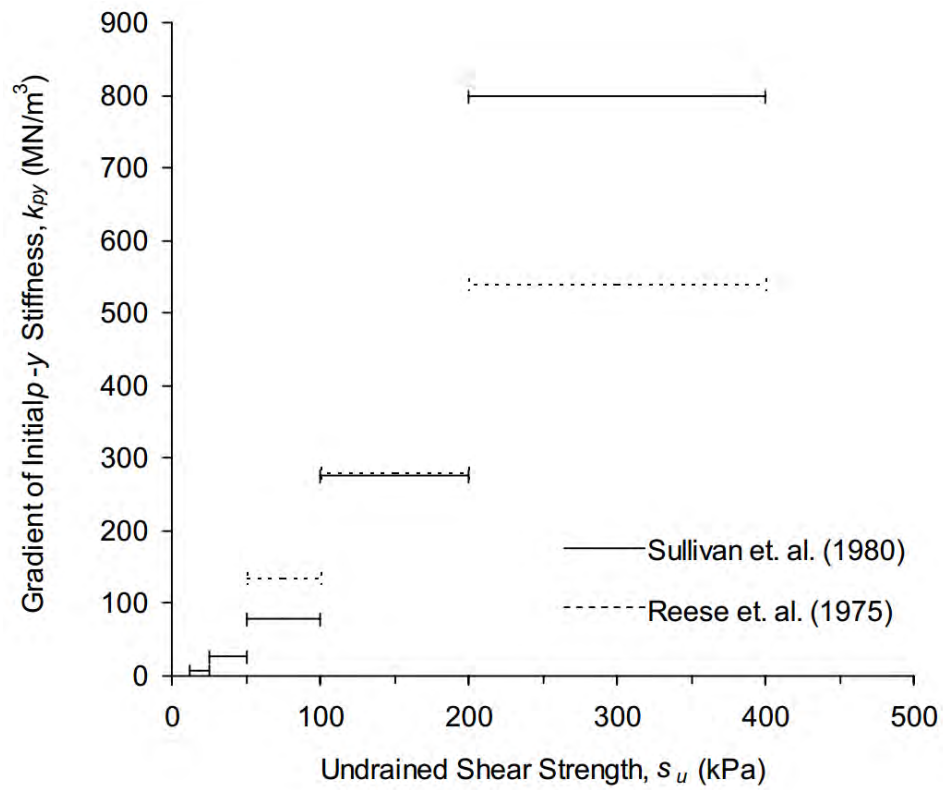


Figure 2.4: Typical k_{py} values for clays (after Dodds and Martin 2007).

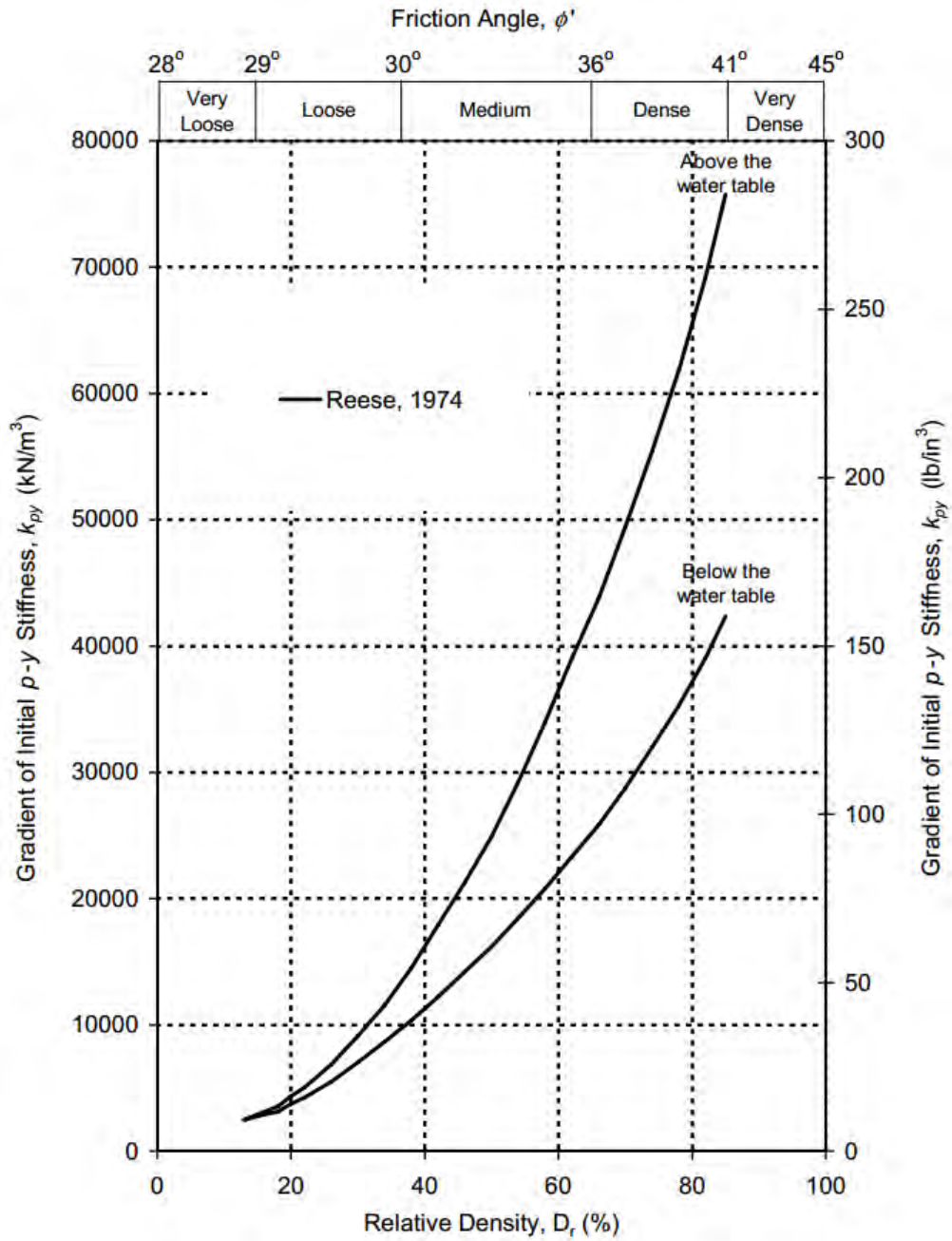


Figure 2.5: Typical k_{py} values for sands (after Dodds and Martin 2007).

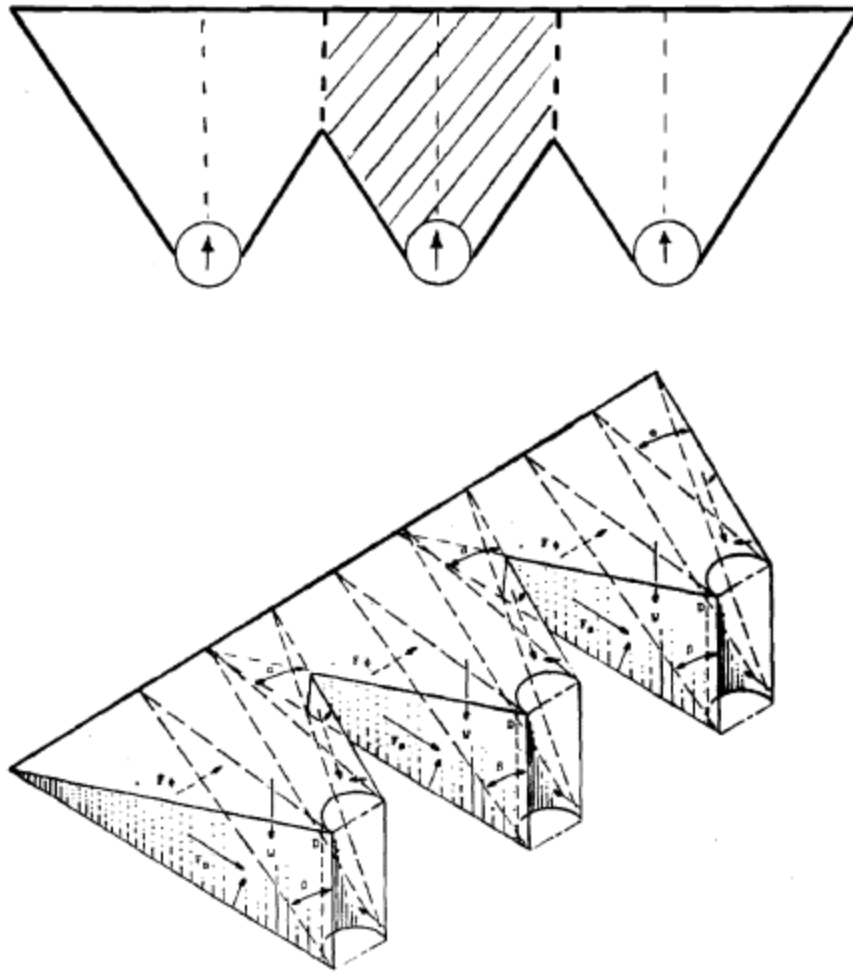


Figure 2.6: Illustration of strength reductions due to passive failure wedge interaction of closely spaced piles in sand (after Wang and Reese 1986).

2.5.2.d: Summary of Proposed p-y Curves for Comparison

A summary of the proposed p-y curves discussed in the previous sections, calculated for the test wall at a depth of 16 feet below the original ground surface (1 foot below the excavation line) is shown in Figure 2.7 for comparison. For this research study, p-y curves estimated from test wall data will be compared with the family of curves discussed in this section.

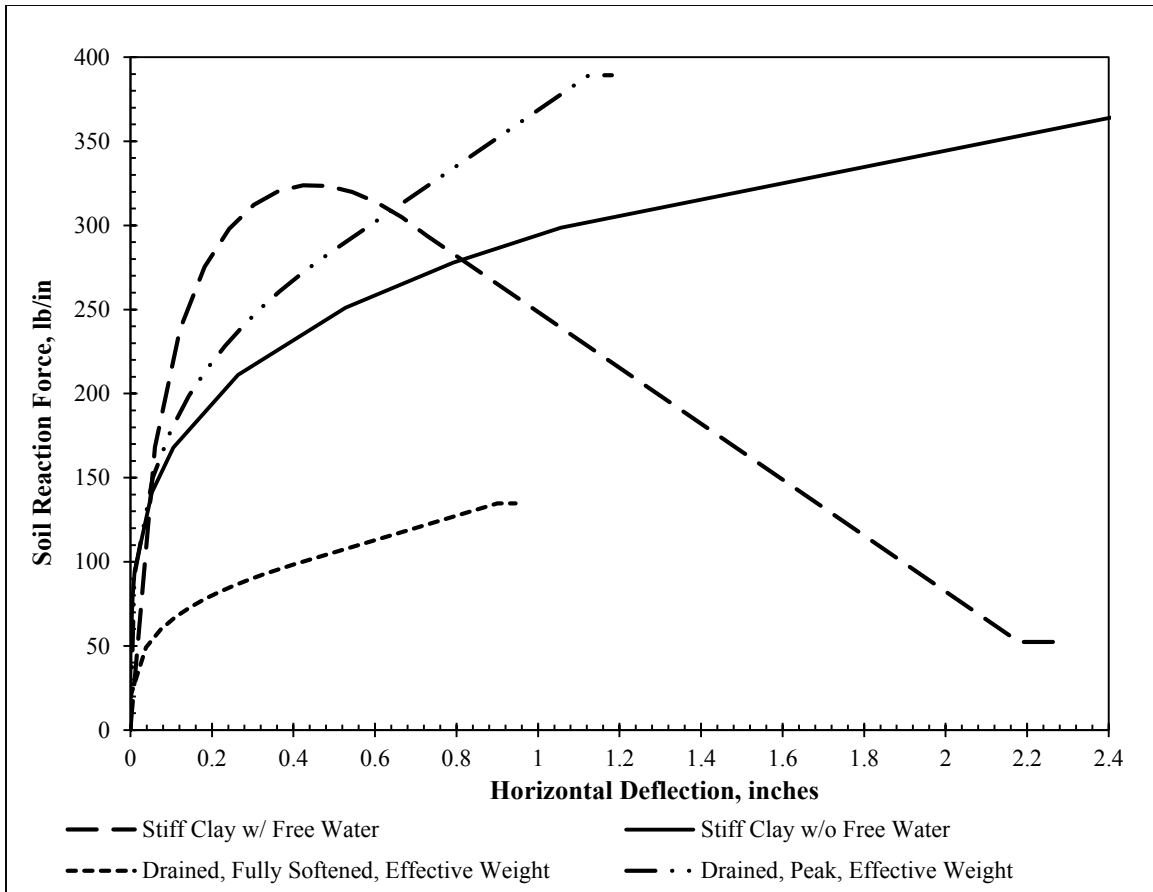


Figure 2.7: Summary of proposed p-y curves, calculated for the test wall at a depth of 16 feet below the original ground surface (1 foot below excavation line).

2.6: Previous Reports on Lymon C. Reese Research Wall

Three graduate research assistants at the University of Texas at Austin have used the Lymon C. Reese research wall as the subject of their Master’s thesis. Their findings are summarized in this section.

2.6.1: ELLIS (2011): A SUBSURFACE INVESTIGATION IN TAYLOR CLAY

Ellis (2011) presents “a comprehensive field and laboratory investigation at the location of the Lymon C. Reese Research Wall.” Geological information for the project

site is presented, along with the measured properties of the Taylor clay from field and laboratory investigations. In addition to standard tests for index properties, consolidation parameters, and undrained shear strength, several advanced tests were performed, including cyclic lateral shrink-swell testing.

Relatively high undrained shear strengths were measured on the project site, and a secondary structure in the soil often resulted in sample disturbance that made precise laboratory testing difficult. The soil's swelling strain from in-situ moisture conditions was estimated to be approximately 0.8 – 1.0 percent; repeated cycles of wetting and drying with large changes in moisture content resulted in a higher swell potential. The active zone was estimated to extend to a depth of approximately 10 feet. Estimates of laboratory and field values of hydraulic conductivity were “drastically different,” with field estimates being up to 10 orders of magnitude higher than laboratory estimates due to the presence of preferential moisture pathways created by fissures in the secondary soil structure. These results are generally consistent with the behavior of heavily overconsolidated, stiff-fissured clays (Ellis 2011).

2.6.2: DELLINGER (2011): THE USE OF TIME DOMAIN REFLECTOMETRY PROBES FOR THE MOISTURE MONITORING OF A DRILLED SHAFT RETAINING WALL IN EXPANSIVE CLAY

Dellinger (2011) summarizes the use of Time Domain Reflectometry (TDR) probes for moisture monitoring at the Lymon C. Reese research wall. The theory governing the application of TDR probes is presented, along with a summary of previous research using TDR probes in expansive clay. The calibration and installation of TDR probes at the research site is presented, along with a summary of field performance data.

In general, TDR probes installed at the project site were unable to produce reliable measurements of moisture content due to signal attenuation from the high electrical

conductivity of the soil. These results are consistent with other studies in highly conductive soils. Additionally, because TDR probes require a consistent contact surface with the soil, loss of probe rod contact during drying cycles is an inherent problem for expansive soils which shrink and swell with moisture changes.

While moisture contents could not be directly measured with TDR probes in the highly conductive, expansive soil on the project site, the use of electrical conductivity data from the probes to qualitatively describe moisture conditions is possible. Electrical conductivity measurements, combined with periodic physical sampling using a hand auger, can provide reasonable insight on moisture conditions at the project site (Dellinger 2011).

2.6.3: KOUTROUVELIS (2012): EARTH PRESSURES APPLIED ON DRILLED SHAFT RETAINING WALLS IN EXPANSIVE CLAY DURING NATURAL CYCLES OF MOISTURE FLUCTUATION

Koutrouvelis (2012) summarizes the behavior of the Lymon C. Reese research wall during natural cycles of moisture fluctuation. A summary of the different types of analysis used for drilled shaft retaining walls is presented, including methods for estimating the p-y relationship for stiff-fissured clays. Data reduction and analysis procedures for the test wall instrumentation are summarized, along with an analysis of the various microscale effects that can introduce errors into the strain gauge data, including the development of residual stresses and strains prior to excavation. Various methods of obtaining moment-curvature relationships for the test wall are explored. Profiles of deflection, bending moment, and earth pressures are presented for various dates, and the influence of side shear and thermal effects on wall behavior is estimated.

The research concluded that residual stresses and strains developed prior to excavation were “significant” and caused by a combination of concrete curing and local site conditions, including the soil moisture content at the time of construction. Based on

analysis of the inclinometer data, the base of the wall was not fixed and experienced rotation during the excavation process. Moisture fluctuations in the soil influenced the deflected shapes, along with (to a much lesser degree) temperature fluctuations in the concrete. Additionally, the presence of a tension crack behind the wall was exacerbated by low moisture contents causing soil shrinkage.

The results of the strain gauges were highly variable due to a combination of “various microscale and environmental factors (tension cracks and temperature effects).” In order to directly use the strain data for calculations of bending moments and curvatures, data processing to eliminate these effects was deemed to be necessary. After data processing, results generated from strain gauge data were comparable to those generated from inclinometer data. A p-y analysis of the research wall indicated that the lateral response of the wall is strongly affected by the selection of the value of ϵ_{50} , which is developed from the stress-strain response of the soil and influences the shape of the p-y curves. The use of an initial “global” displacement profile was introduced to provide consistency between field inclinometer measurements and p-y predictions. The influence of thermal effects and side shear on lateral wall movements was found to be small; however, the potential influence of thermal effects and side shear on bending moments is more significant and may need to be accounted for. When natural soil moisture content is high, the predicted bending moments due to side shear were positive (Koutrouvelis 2012).

CHAPTER 3: DESIGN AND CONSTRUCTION OF FULL-SCALE INSTRUMENTED TEST WALL

Note: Portions of this section have been previously published by the author (Brown et al., Geo-Frontiers 2011).

3.1: Location of Test Wall

To allow for complete control of project scheduling and access to the test site, a full-scale test wall was constructed specifically for this project. The Lyman C. Reese research wall is located in Manor, Texas on the property of R&L Transfer & Storage Co., Inc. (Figure 3.1). A site plan, showing the location of the test wall, is shown in Figure 3.2.

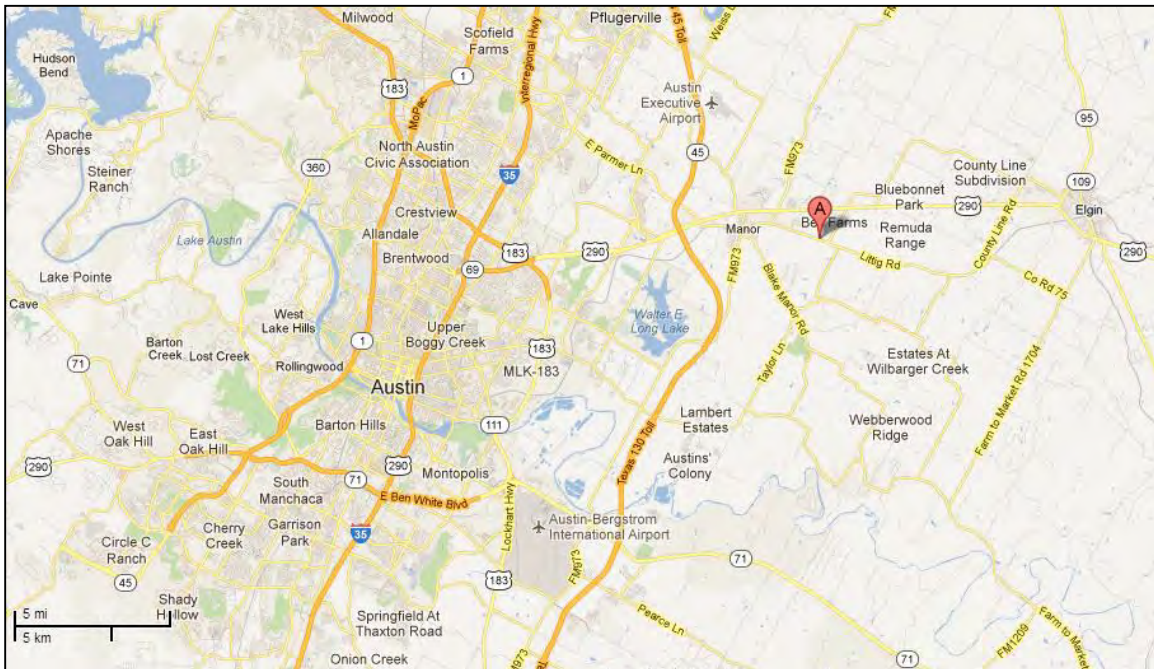


Figure 3.1: Location of full-scale test wall (Google, Inc.).

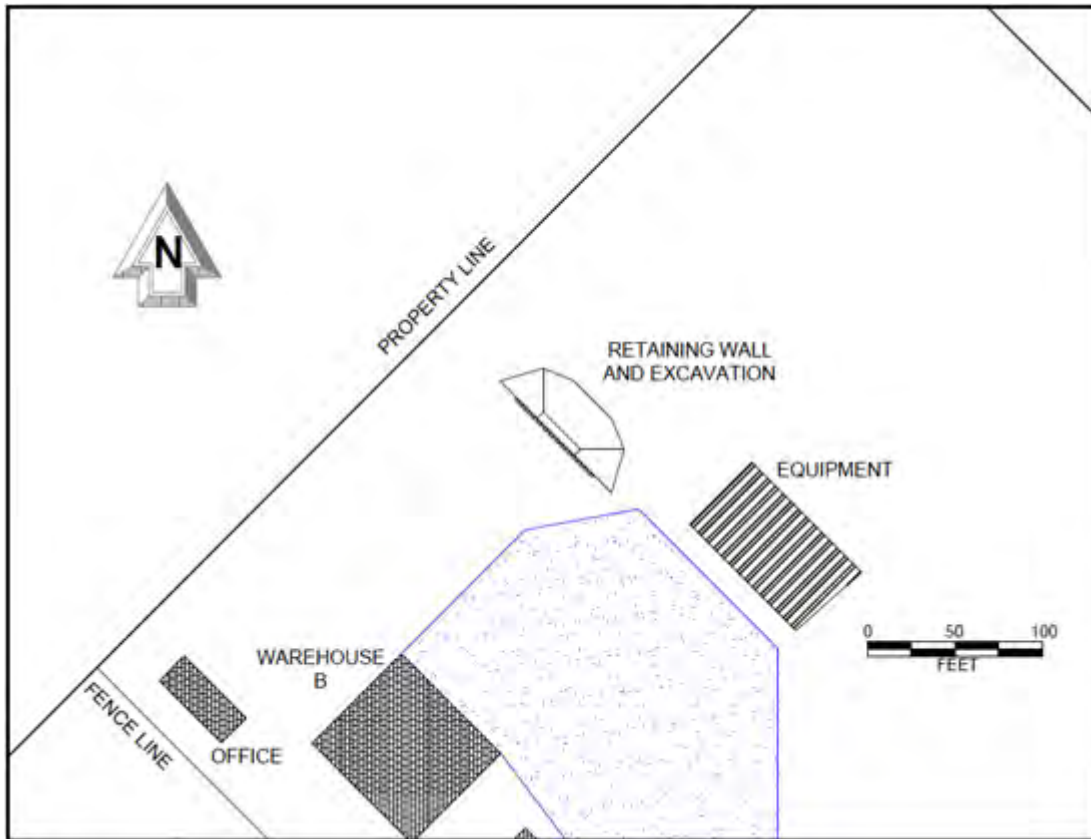


Figure 3.2: Detailed site plan with location of test wall.

3.2: Site Conditions

3.2.1: OVERVIEW

The test wall is underlain by approximately 50 feet of the Taylor Formation, a highly expansive and problematic clay. A sample of the Taylor Formation from the project site is pictured in Figure 3.3.



Figure 3.3: Taylor Clay from the project site in Manor, Texas.

3.2.2: PRELIMINARY GEOTECHNICAL INVESTIGATION (JANUARY 2010)

Three 50-foot deep soil borings were drilled in January 2010, a relatively wet season. Both Texas Cone Penetrometer (TCP) testing and Standard Penetration Testing (SPT) were performed to provide information consistent with the standard of practice in Texas. An inclinometer was installed in one boring and a piezometer in another. The liquid limit ranges from about 80 to 100 percent and the plastic limit ranges from about 20 to 30 percent. Natural water contents at the time of investigation averaged 38 percent. The profiles of natural water content and undrained shear strength from UU testing are shown in Figure 3.4. The water table has remained about 8 feet below the ground surface during construction and excavation.

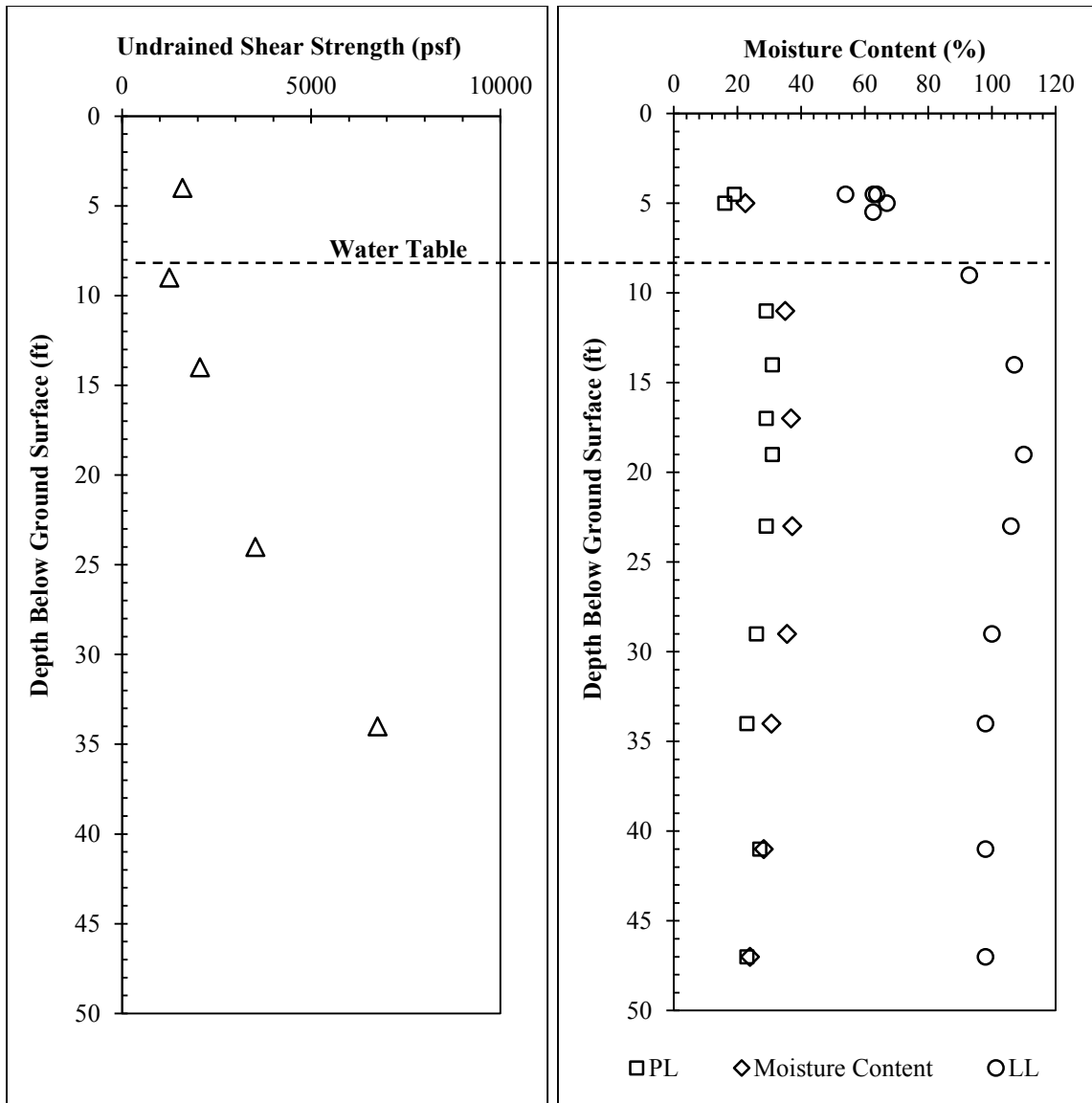


Figure 3.4: Results of Atterberg Limit and UU testing from January, 2010 (three months before shaft construction; seven months before excavation).

3.3: Design of Test Wall

The design for the test wall was developed using a procedure similar to the existing TxDOT design procedure for cantilever drilled shaft walls (TxDOT 2009). The goal was to create a structure which would be structurally sound and consistent with typical TxDOT

walls, but would produce enough deformations to infer the earth pressures acting on the wall. A summary of design assumptions and shaft geometry for the test wall is provided in Table 3.1. The test wall consists of 25 drilled shafts embedded to depths from 18 to 35 feet below ground surface (Figure 3.5). The shafts have a diameter of 24 inches and a center to center spacing of 30 inches. The reinforcing bar cage consists of 12 #7 bars. The cantilevered height is 15 feet, the penetration depth is 20 feet, and the shafts end four feet above ground surface. The shaft stickup allows the project team to run a lateral load test if desired; it also allows the site owner to use the wall as a loading dock upon completion of the project. The final wall design is pictured in Figure 3.5 and Figure 3.6.

Table 3.1: Baseline assumptions and design parameters for test wall.

Parameter	Value
Total Unit Weight of Soil, γ_t	130 pcf
Equivalent Fluid Pressure Loading, γ_{EF}	40 psf/ft
Coefficient of Active Earth Pressure, k_a	0.31 (from γ_{EF} / γ_t)
Undrained Shear Strength, S_U	4,000 psf
Foundation Soil p-y Curves	Stiff Clay Without Free Water
Cracking Moment, M_{Cr}	680 k-in.
Yielding Moment, M_y	3,200 k-in.
Uncracked Bending Stiffness, EI_{uc}	67×10^6 k-in.
Cracked Bending Stiffness, EI_{cr}	18×10^6 k-in.
c-c Spacing Between Shafts, B	30 in.
Shaft Diameter	24 in.
Height of Retained Soil, H	180 in.
Reinforcement	12 #7 bars (1.6% of gross area)

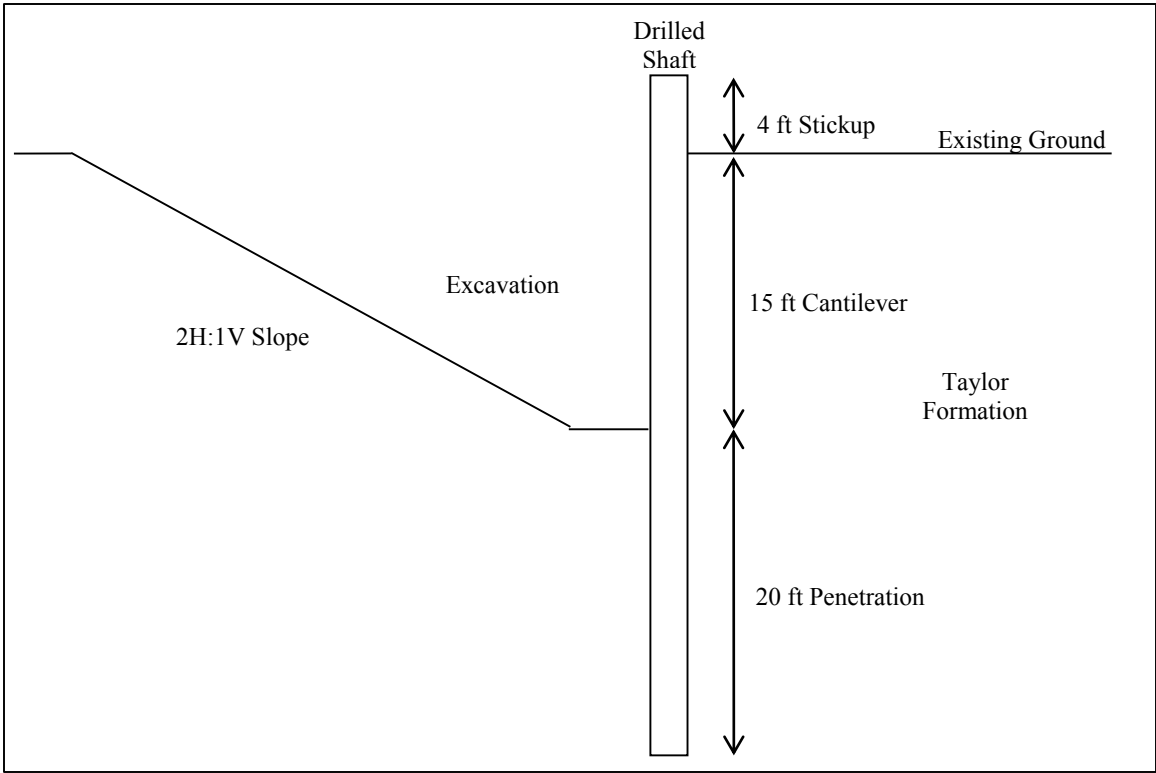


Figure 3.5: Cross-section of wall and excavation at center shaft, facing east (not to scale).

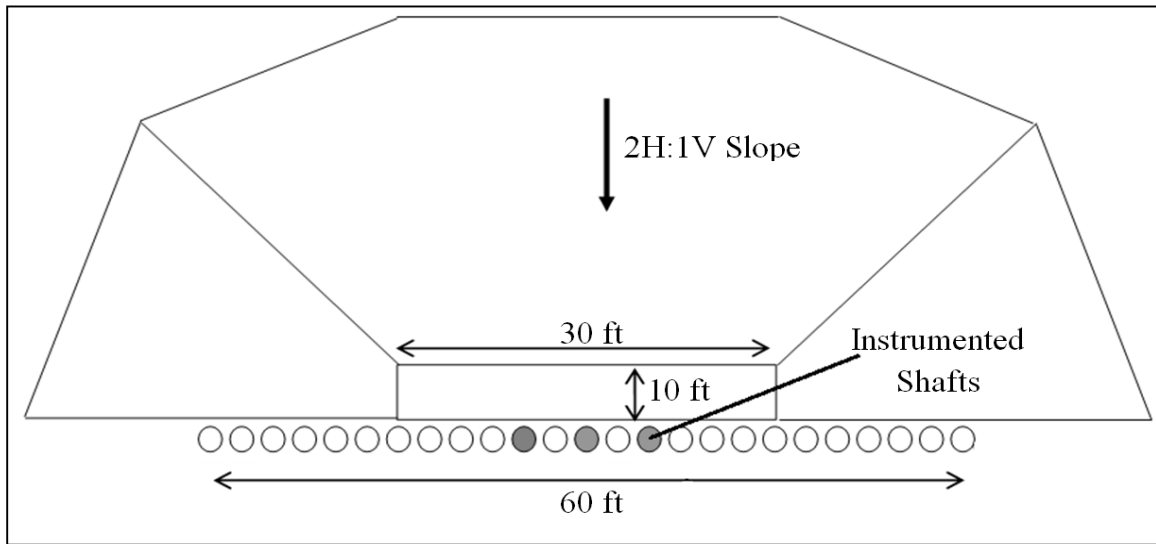


Figure 3.6: Plan view of wall and excavation.

3.4: Design of Instrumentation Program

3.4.1: OVERVIEW

The primary objectives of the instrumentation program are to accurately monitor deformations in the test wall, and to estimate the lateral earth pressures applied to the shaft over a period of three years. Three shafts in the test wall are instrumented (shaded in Figure 3.6). In each of these shafts, there are 30 fiber optic strain gauges and one inclinometer casing. Additionally, one inclinometer casing was installed 5.5 feet behind the wall, and thermocouples were installed in the center shaft at depths of 3, 15, and 29 feet below ground surface for temperature monitoring. In the soil surrounding the wall, 20 Time Domain Reflectometry (TDR) moisture sensors were installed after excavation. Figure 3.7 shows an instrumented cage as it is lowered into the ground, and Figure 3.8 shows the distribution of sensors within each instrumented shaft.

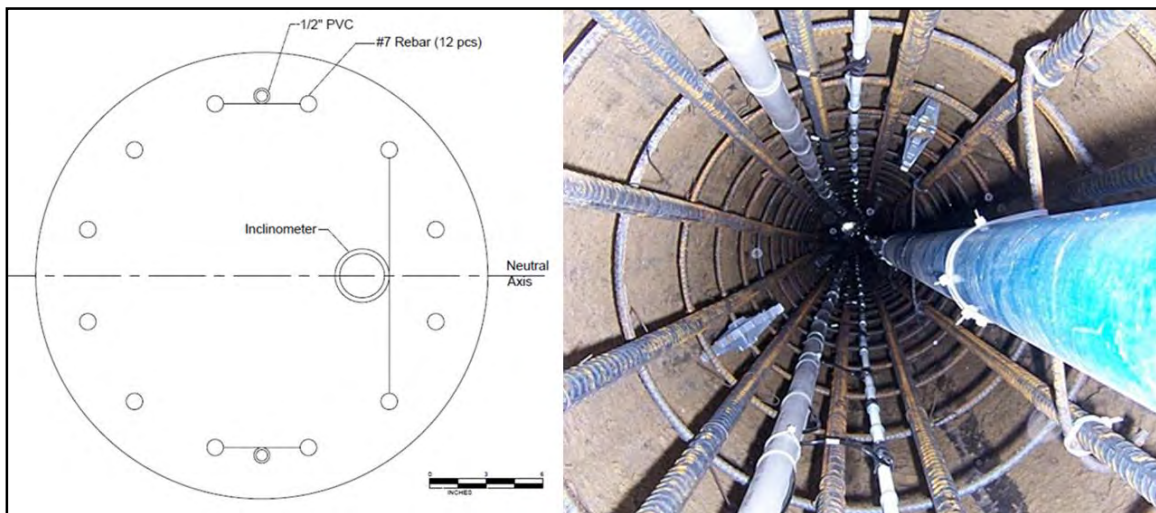


Figure 3.7: Plan view of instrumented rebar cage before concrete placement.

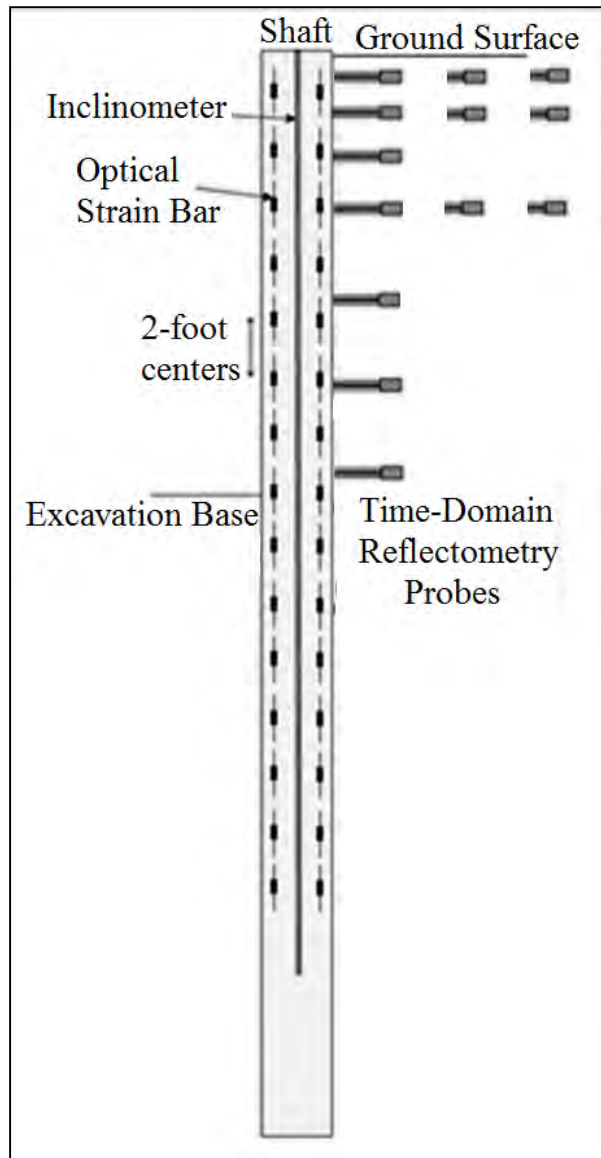


Figure 3.8: Distribution of sensors within an instrumented shaft.

3.4.2: STRAIN GAUGES

Because of their reputation for stability with time and relative insensitivity to moisture and temperature changes, optical strain gauges (Fabry-Perot type) were selected for strain monitoring. Optical gauges provide higher resolution than conventional electrical resistance or vibrating wire gauges, and are less susceptible to zero-drift over

time. Additionally, because their strain measurements are generated using a light source, optical strain gauges are less affected by moisture and temperature changes than conventional gauges. The optical strain gauges were purchased from OPSSENS in Canada, and the sister bars were fabricated by Lymon C. Reese and Associates of Austin, Texas. Prior to installation, each sister bar was calibrated to ensure linearity in the readings within the operating strain range of 1,000 microstrains and to establish a response curve. There are a total of 90 optical strain gauges installed in the test wall; in each instrumented shaft, there are 15 gauges on either side of the neutral axis (Figure 3.8).

Large temperature fluctuations occurred at the project site, and thermal expansion of the shafts produced significant strains. Additionally, the potential for errors in measurements due to rapid changes in temperature of the optical light source and datalogger was a design consideration. To minimize these errors, temperature resistant dataloggers were designed and installed in enclosures that limit rapid temperature change (Figure 3.9).

3.4.3: INCLINOMETERS

The rotation profile along the length of the drilled shaft is measured directly with an inclinometer, and integrated to yield a profile of deflected shape. Three inclinometer casings were attached to the reinforcing bar cage and cast into the shaft during construction. Readings are taken every 2 feet over the length of the shaft using a readout unit manufactured by Slope Indicator.

3.4.4: ADDITIONAL INSTRUMENTATION

To provide redundancy in top-of-wall deflections measured by the inclinometers, a linear potentiometer was installed on the project site prior to excavation and anchored to the wall near the ground surface. It was attached to shaft #16, adjacent to the west

instrumented shaft (shaft #15). The linear potentiometer provides continuous data on top-of-wall deflection and redundancy with the inclinometer data. To provide information on the moisture conditions in the retained soil, a total of 20 Time Domain Reflectometry (TDR) moisture probes were installed in behind the wall. Because of the high spatial variability of rainfall across the region, an electronic tipping bucket rain gauge was installed at the test wall to augment measurements from nearby weather stations. The linear potentiometer, TDR moisture probes, and rain gauge are monitored continuously. Figure 3.9 shows some of the instrumentation installed on the project site.



Figure 3.9: Instrumentation on the project site. Clockwise from top left: temperature resistant datalogger and enclosure for continuous strain readings; signal conditioner for individual strain readings; linear potentiometer; TDR probe installed through facing.

3.5: Construction of Full-Scale Instrumented Test Wall

The drilled shafts and instrumentation were installed in early April, 2010 by McKinney Drilling Company (Figure 3.10). In order to prevent excessive bending of the rebar cage and damage to the instrumentation, the instrumented cages were lifted with two cranes (Figure 3.11). To prevent sensor damage during concrete placement, cables were protected within slotted PVC pipes and concrete was directed down the center of the rebar cage with shovels. Initial sensor survivability was excellent, with 88 of 90 strain gauges and all inclinometer casings functional after rebar cage placement and concrete installation. A summary of wall construction activities and concrete strength data is provided in Table 3.2.



Figure 3.10: Construction of test wall, April 2010.



Figure 3.11: Lifting an instrumented cage with two cranes.

Table 3.2: Summary of wall construction activities and measured concrete strengths.

Date	Notes (* = Instrumented Shaft)	7-Day Concrete Strength (psi)	28-Day Concrete Strength (psi)
March 30, 2010	Mobilize Equipment, Assembled Instrument Cages, Constructed Shafts 1 and 4	6055	7955
March 31, 2010	Constructed Shafts 7, 10, 13*, 22, and 25	4970	7000
April 1, 2010	Constructed Shafts 2, 5, 8, 11*, 15*, and 17	4480	6065
April 2, 2010	Constructed Shafts 3, 6, 9, 16, 19, and 23	4410	5875
Apr. 3 - 4, 2010	Weekend	N/A	N/A
April 5, 2010	Constructed Shafts 18, 21, and 24	4000	5950
April 6, 2010	Constructed Shafts 12, 16, and 14	4400	6800
April 7, 2010	Demobilize Equipment	N/A	N/A

3.6: Monitoring Plan

Since installation of instrumentation, the activity of the test wall has been closely monitored. An automated datalogger records strain readings from the center shaft at 6-minute intervals. The linear potentiometer, rain gauge, thermocouples, and TDR moisture probes are measured by another datalogger at 15-minute intervals. Inclinator profiles, piezometer water levels, and strain readings from the east and west shafts are recorded, on average, once per week. The frequency of these measurements has changed according to the amount of activity at the wall site, ranging from several readings per day to once per month. Additionally, meteorological data from nearby weather stations and observational information from the test wall supplement our instrumentation data.

3.7: Data Reduction and Analysis

Because the magnitude and distribution of earth pressures acting on the test wall is a primary goal of this research, methods of using strain gauge and inclinometer data from the test wall to estimate earth pressures must be developed. A summary of the mathematical relationship between deflection, slope, bending moment, shear, and earth pressures for a typical pile is shown in Figure 3.12. The methods described in the following section are applicable to data from the Manor, Texas test wall only, and should not be used for other projects or data sets without careful validation.

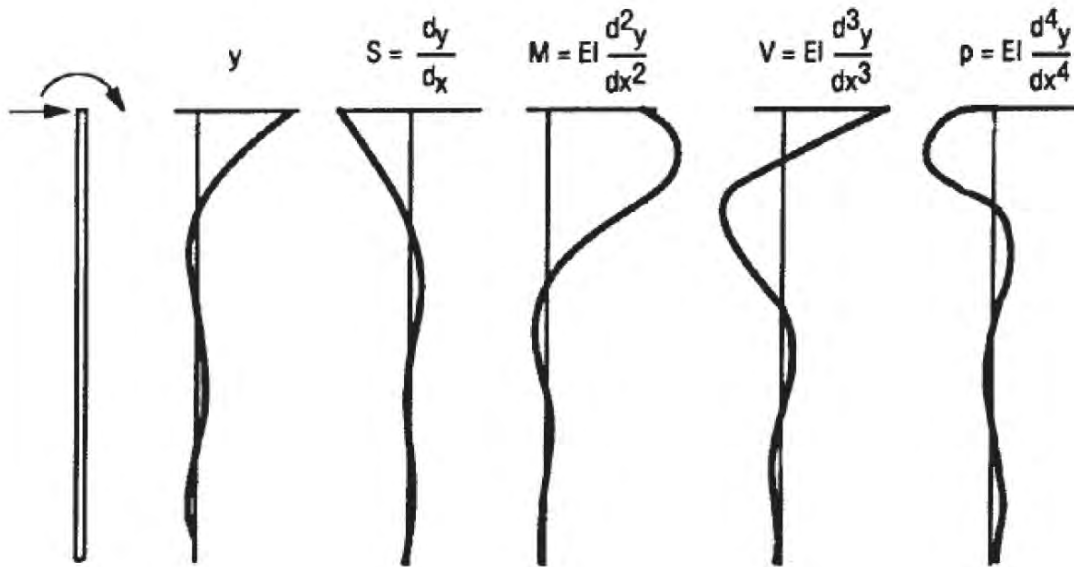


Figure 3.12: Mathematical relationship between deflection (y), slope (S), bending moment (M), shear force (V), and soil reaction force (p) for a laterally loaded pile (after Reese and Van Impe, 2001).

3.7.2: STRAIN GAUGE DATA REDUCTION

The strain gauges placed on either side of the shaft's neutral axis measure axial strains in the tensile and compressive direction (ϵ_t and ϵ_c , respectively). The difference in tensile and compressive strains on either side of the neutral axis is divided by the horizontal distance between the gauges to obtain a value of bending curvature at a given depth. The calculated value of bending curvature is converted to a value of bending moment according to the moment-curvature relationship defined by the structural properties of the shaft. Following this procedure at each depth where strain gauges are installed yields a profile of bending moment in the shaft versus depth, which can be differentiated once to obtain a profile of shear force versus depth, or differentiated twice to obtain a profile of soil resistance versus depth. This process is summarized in Figure 3.13. A more detailed

explanation of strain gauge data reduction for the Lymon C. Reese research wall can be found in Koutrouvelis (2012).

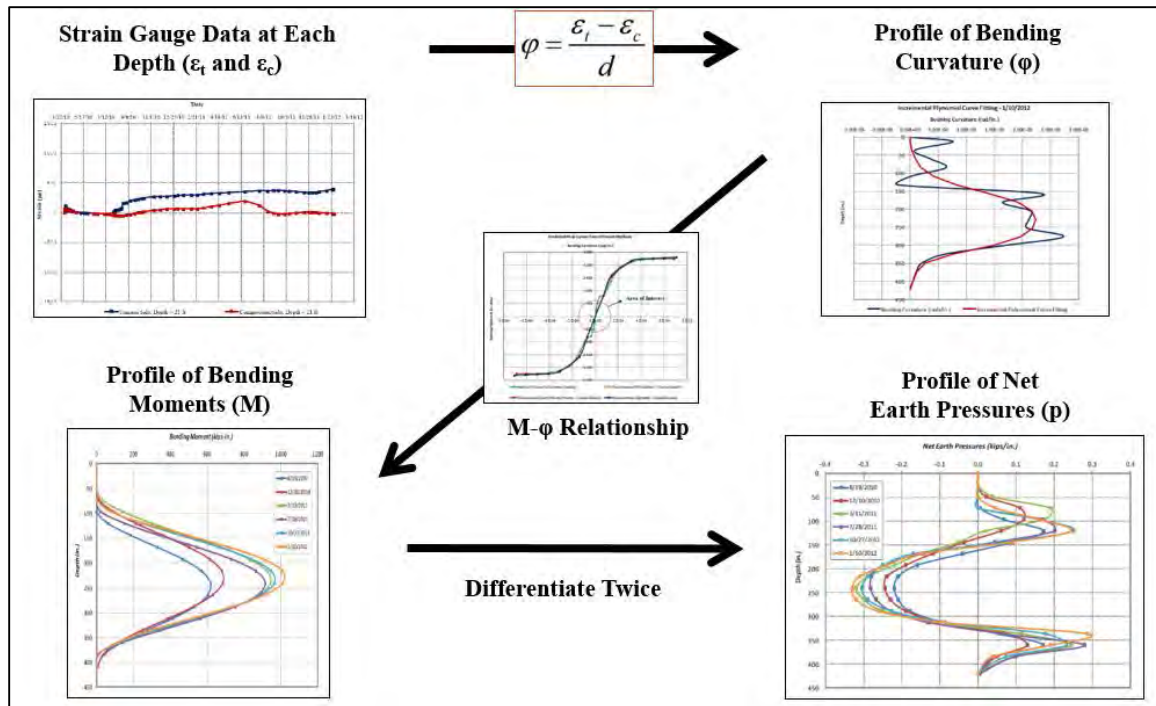


Figure 3.13: Strain gauge data reduction (after Koutrouvelis 2012).

For this research study, strain gauge nomenclature indicates which instrumented shaft the gauge is installed in (East, Center, or West), the depth of the strain gauge below original ground surface (1 – 29 feet), and which side of the neutral axis the gauge is installed on (Tension or Compression; tensile strains are positive). Using this nomenclature, gauge E.17.T is located in the east instrumented shaft, 17 feet below ground surface, on the tensile side of the neutral axis.

3.7.3: INCLINOMETER DATA REDUCTION

3.7.3.a: Rotation Profiles Recorded in the Field

While inclinometer data is most commonly presented as a displacement profile, the instrument itself records rotation data; these data are then integrated to calculate displacement. By extracting the raw rotation data from the instrument, a profile of bending curvature can be obtained with just one derivative. Sample rotation data from the three instrumented shafts on May 28, 2013, when the wall was near its maximum deflection, is presented in Figure 3.14. It is important to note that the last data point is at a depth of 32 feet for the center and west shafts, and 30 feet for the east shaft (shaft base is at 35 feet).

The inclinometer probe measures the shaft rotation in two directions; the A-axis (in the direction of the wheels) and the B-axis (in the direction perpendicular to the wheels). This allows for the lateral deflection to be determined in any direction. For the purposes of this analysis, all deflections are assumed to be perpendicular to the wall, and the cumulative deflection is calculated by combining the rotation profiles from the A-axis and B-axis using the distance formula:

$$y_{total} = \sqrt{y_A^2 + y_B^2}$$

This method of estimating deflections can slightly overestimate deflections in the case of very noisy data set, since it interprets any small amount of instrument error to be a positive deflection perpendicular to the wall. However, the method is reliable, slightly conservative, and is much more straightforward to apply to the data set than more advanced correction methods.

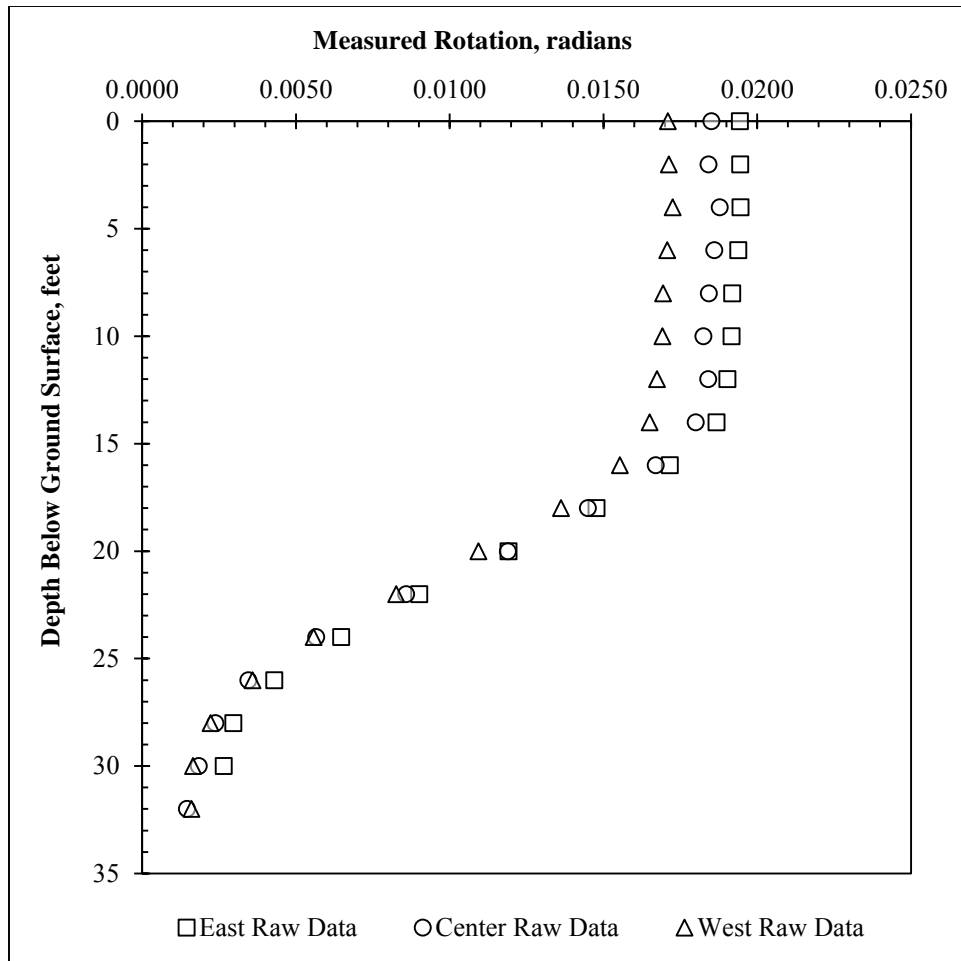


Figure 3.14: Sample rotation data from May 28, 2013. Reference survey is July 27, 2010, immediately before excavation.

3.7.3.b: Combining and Smoothing Rotation Profiles

While there are small differences in the behavior of the instrumented shafts, combining the three slope profiles into an average slope profile results in values that are similar to those obtained from the center instrumented shaft, and provides a much smoother curve for differentiation. To account for the presence of base rotation, the final rotation measurement is extended vertically down from the last measurement to the shaft base. In a typical analysis, the shaft base is assumed to be a fixed point – zero deflection, zero

rotation. However, based on the instrumentation data from the test wall, it is clear that some base rotation occurred (rotation measurements near the shaft base were consistently above zero throughout the life of the test wall; unrealistic loads would need to be present to return the shaft base rotation to zero in the remaining few feet). Mathematically, extending the final slope measurement to the shaft base indicates that the shaft base has rotated, but is not experiencing a bending moment.

A smoothing algorithm was applied to the data from each shaft before averaging the three profiles. The final averaged profile was smoothed again, although after averaging, the effects of smoothing are minimal. The smoothing algorithms are summarized in Tukey (1977), and are adapted for use in Excel by Quantdec (2004). To smooth each shaft's rotation profile, a "3RH" smooth with re-roughing is applied to the original data set. The process is summarized below; more detailed explanations of the individual smoothing processes are explained in the subsequent paragraphs, Figure 3.15 to Figure 3.18, and in Tukey (1977).

1. Apply a repeated medians-of-three smooth (3R) to each rotation profile.
 - a. Each point in the data set is replaced by the median of the original point and the two adjacent data points:

$$\theta_{i,3 \text{ smoothed}} = \text{median}(\theta_{i-1}, \theta_i, \theta_{i+1})$$

- b. Repeat the process until there are no further changes in the data:

$$\theta_{i,3R \text{ smoothed}} = \theta_{i,3 \text{ smoothed}} = \text{median}(\theta_{i-1}, \theta_i, \theta_{i+1})$$

2. Hann the 3R smoothed data to create a 3RH smooth (end values are not Hanned):

$$\theta_{i,hann \text{ smoothed}} = 0.25\theta_{i-1} + 0.50\theta_i + 0.25\theta_{i+1}$$

3. "Re-rough" the smooth.
 - a. Calculate a profile of residuals:

$$\theta_{i,residual} = \theta_{i,original} - \theta_{i,smoothed}$$

- b. Smooth the profile of residuals using a 3RH smooth as described above.
- c. Add the profile of smoothed residuals to the original smoothed data set:

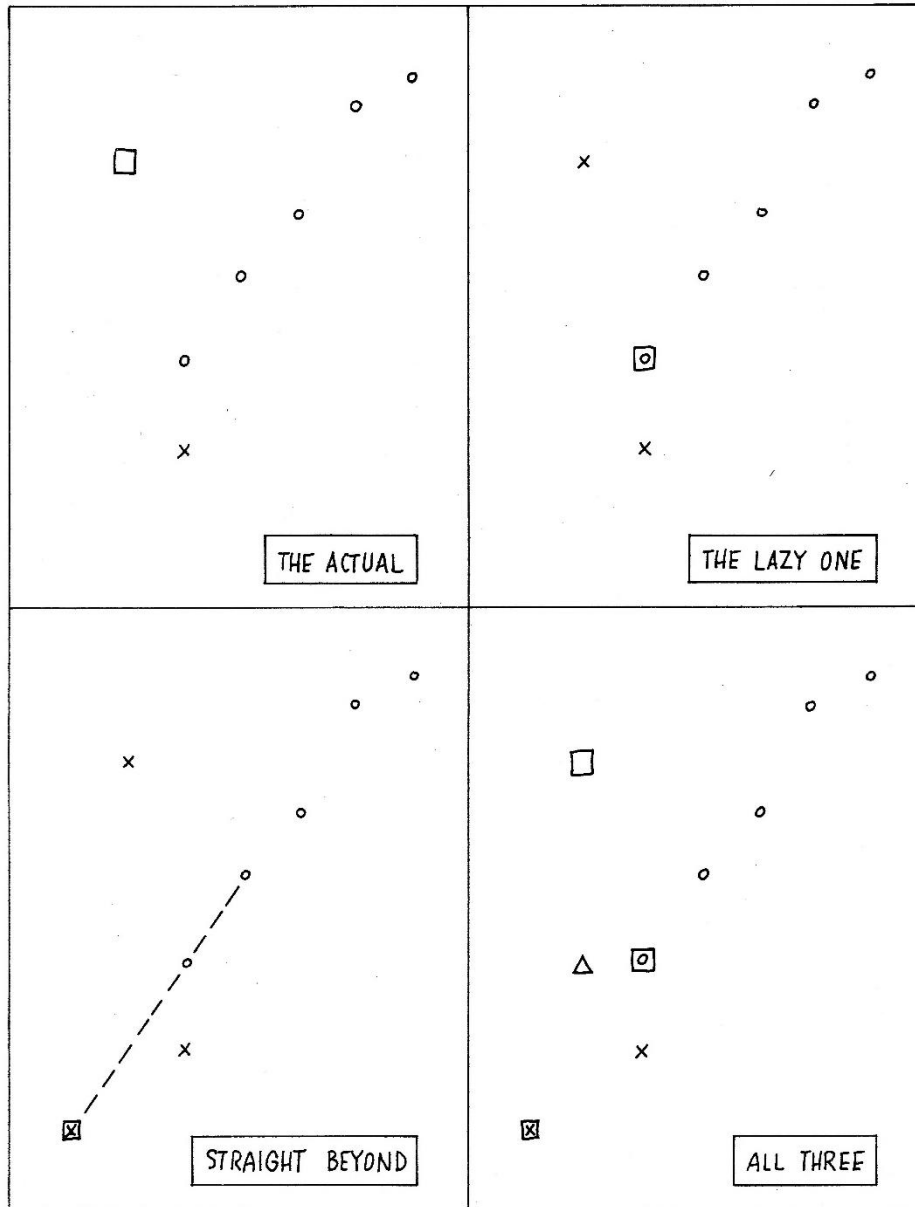
$$\theta_{i,smoothed,re-roughed} = \theta_{i,smoothed} + \theta_{i,residual}$$

End values are smoothed after the application of the 3R smooth (before Hanning) by calculating the median of the previous two points on the smoothed curve and a point extrapolated one unit beyond the end of the smoothed curve (e.g. (θ_{32}') is the median of (θ_{28}') , (θ_{30}') , and $(3 \cdot \theta_{28}' - 2 \cdot \theta_{30}')$, after Quantdec (2004)). In the author's opinion, while the method developed by Quantdec (2004) is simple and easy to apply to a large data set, it is less accurate than the original method described by Tukey (1977), which also incorporates the original raw data into the final end value (Figure 3.15). For this research study, however, because the most important conclusions are drawn from the middle portions of the data set, the method of end value smoothing does not greatly affect the final results and the simple method developed by Quantdec (2004) is adequate.

To “re-rough” the smooth, a profile of residuals is calculated as the difference between the original raw data and the smoothed data. A 3RH smooth is then applied to the profile of residuals, and the smoothed residuals are added to the original smoothed data set. An illustration of the 3RH smooth with re-roughing is provided in Figure 3.16 for depths of 0 to 14 feet in the center shaft, with the entire profile shown in Figure 3.17. Re-roughing ensures that the smoothed data points remain reasonably close to the original values. This smoothing method kept the maximum bending moments and top-of-wall deflections consistent with the original raw data values, but provided a curve more suitable for piecewise differentiation. Other combinations of smoothing methods (e.g. medians-of-three smoothing only, 3RH smoothing without re-roughing, etc.) provide similar results when applied to the measured rotation data, but change the final data points slightly more

than the re-roughed 3RH smooth which was selected for subsequent analysis. A comparison of the original raw data from the three instrumented shafts with the final smoothed slope profile for differentiation is provided in Figure 3.18.

End-value smoothing: parts and result



x = end input values □ = the actual Δ = the smooth end value
 o = medians of 3 ⊠ = the lazy one = the median of ⊞, ⊠,
 ⊞ = straight beyond and □

Figure 3.15: Tukey's method of end value smoothing (after Tukey 1977).

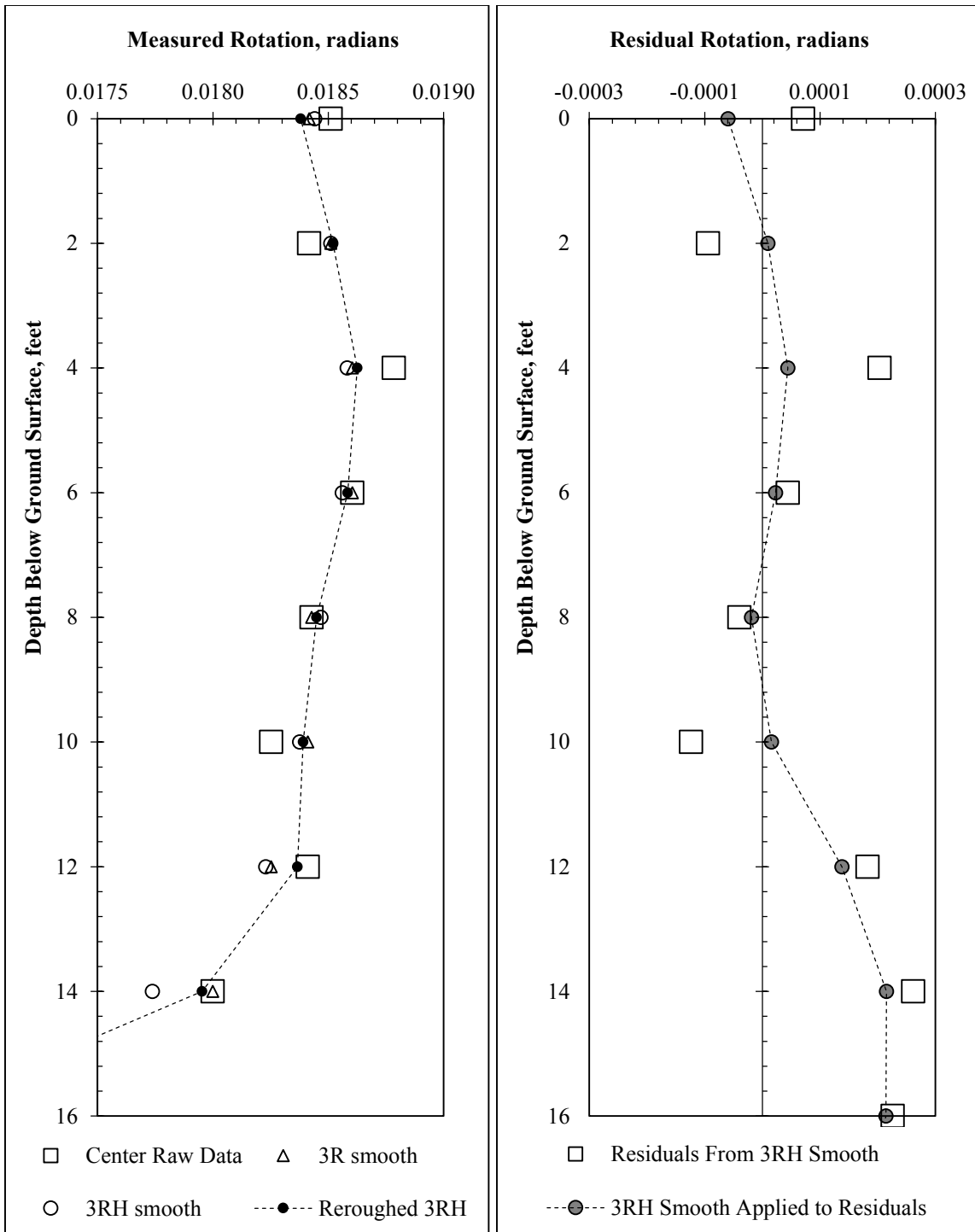


Figure 3.16: Illustration of the 3RH smooth with re-roughing applied to the center shaft rotation data between 0 and 14 feet.

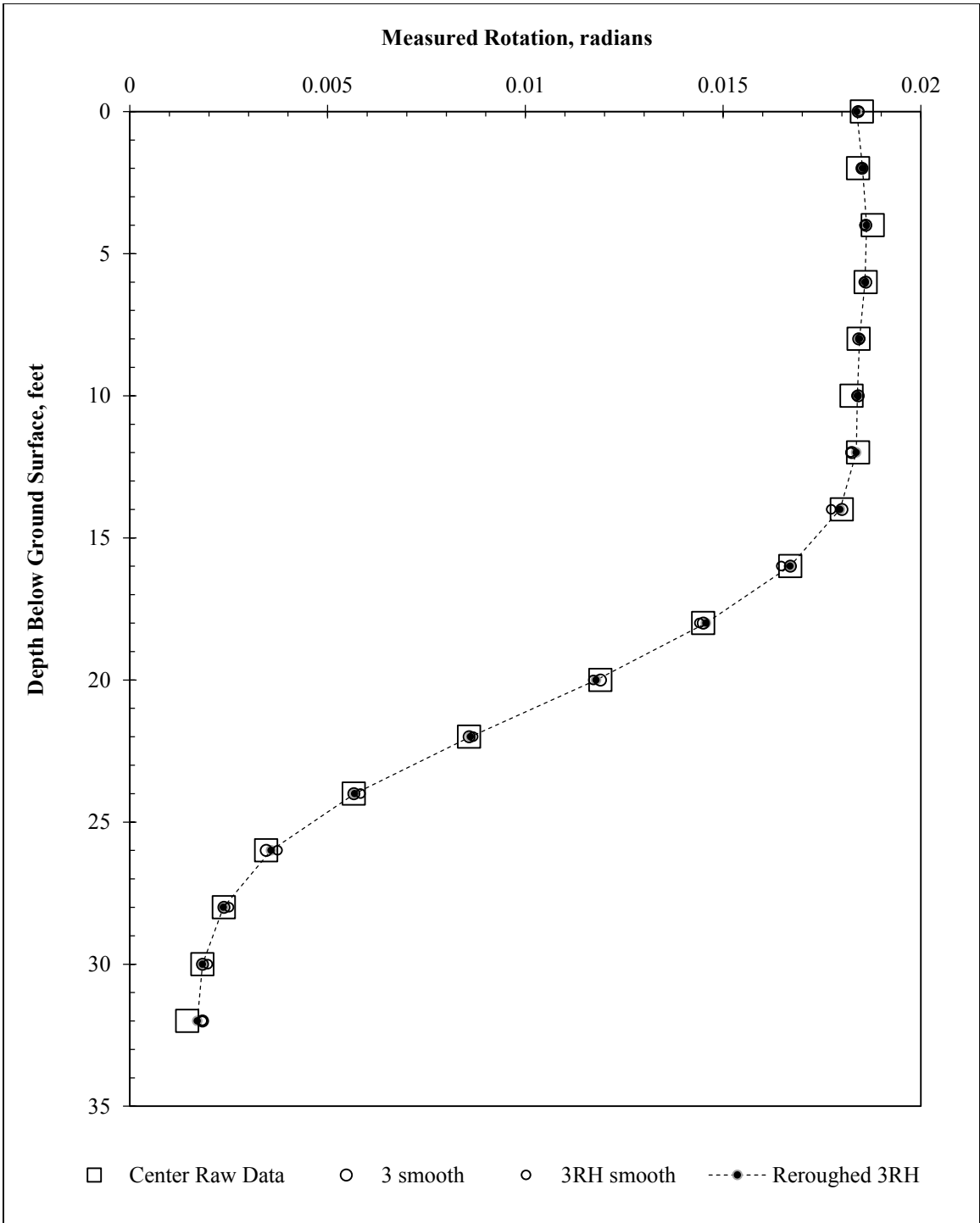


Figure 3.17: Comparison of original and smoothed rotation data from the center shaft on 5/28/2013.

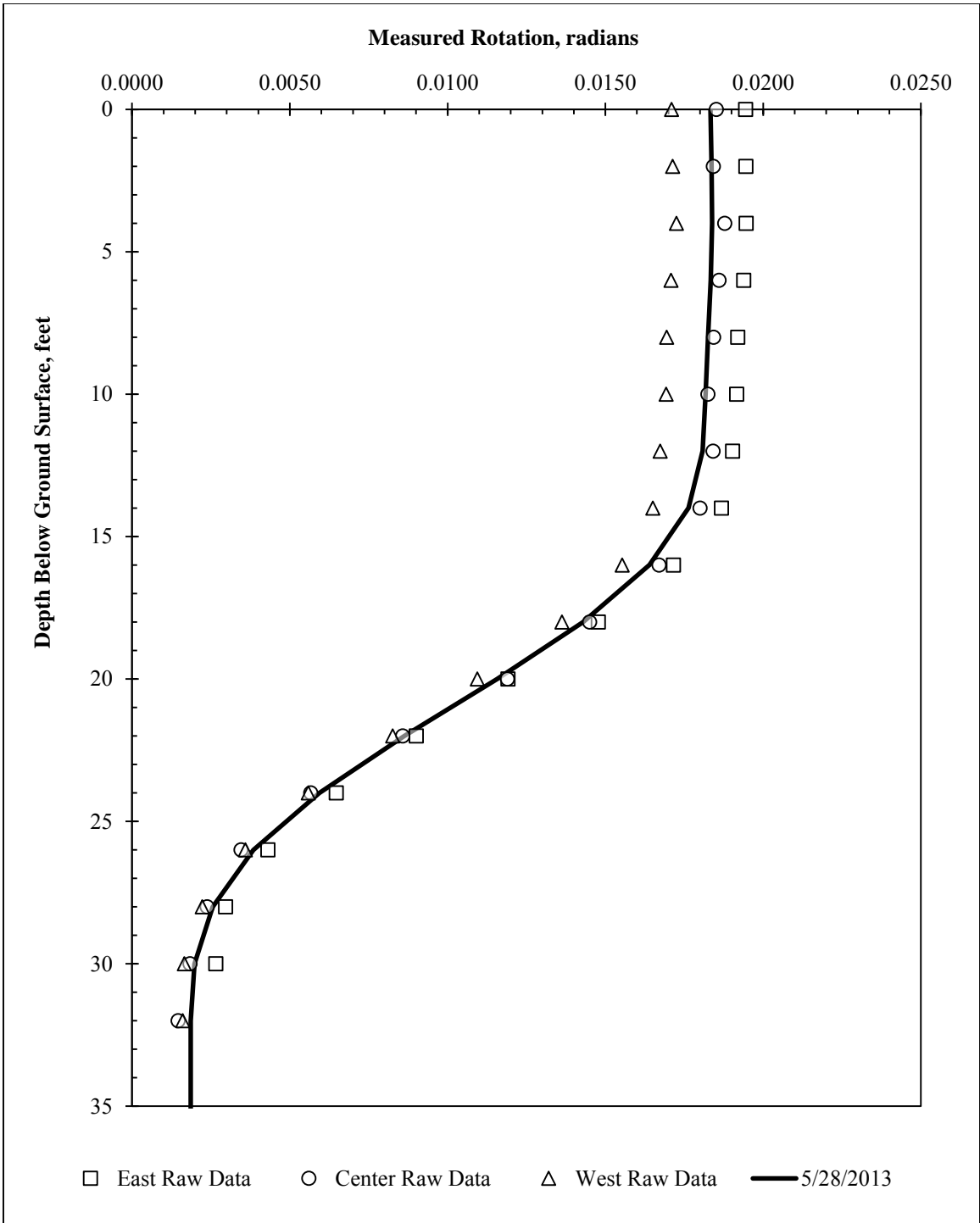


Figure 3.18: Comparison of raw rotation data from the three instrumented shafts with the final smoothed rotation profile for differentiation.

3.7.3.c: Obtaining Bending Moment Profiles from Rotation Data

Ooi and Ramsey (2003) detail a variety of methods for obtaining bending moments and curvatures from inclinometer data. Of the methods surveyed, the most favorable was found to be fitting a third-order polynomial to a moving window of five points along the deflection profile, then analytically taking the second derivative of this curve to obtain a profile of bending curvature. For inclinometer data recorded at the test wall, a third-order polynomial was fit to a moving window of five points along the smoothed rotation profile, and the first derivative was taken numerically at the center point (using a central difference approximation at depths ± 0.5 feet from the center point). This process is illustrated in Figure 3.19 at a depth of 14 feet.

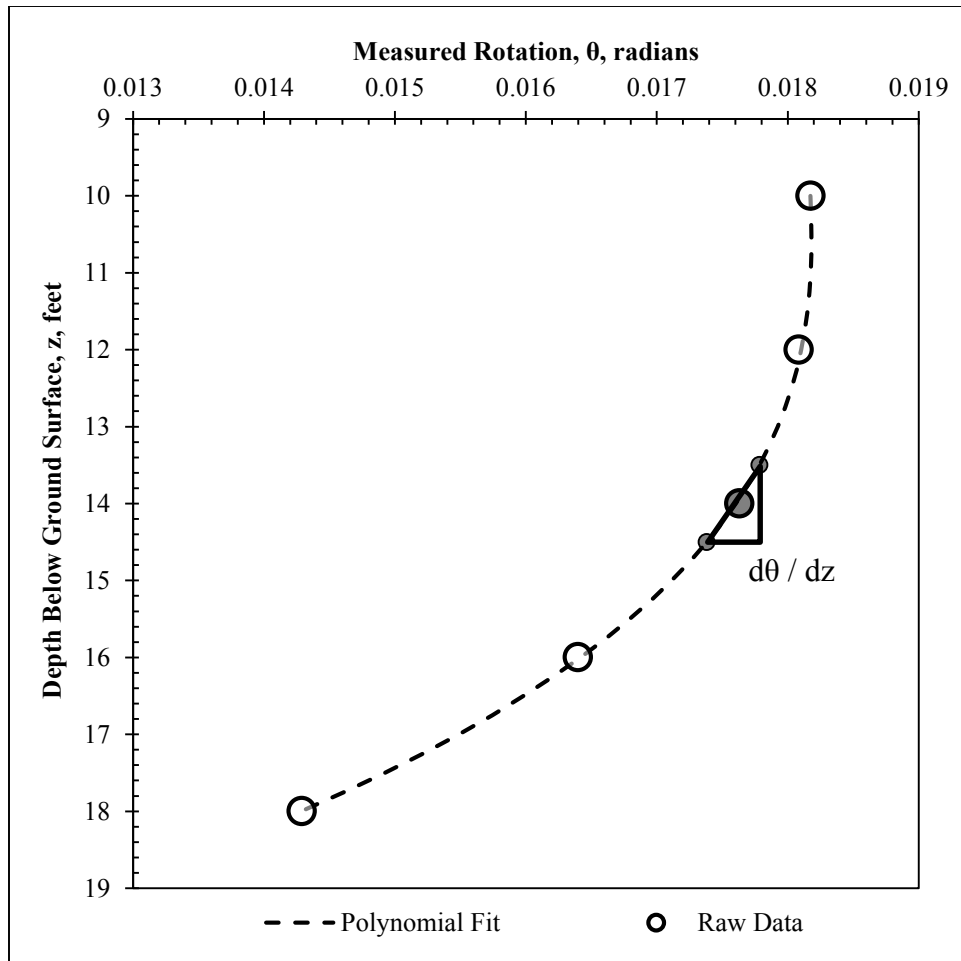


Figure 3.19: Illustration of piecewise third-order polynomial fitting to a moving window of five points at a depth of 14 feet. First derivative at 14 feet is estimated numerically using a central difference approximation between polynomial values at 13.5 and 14.5 feet.

Repeating the piecewise polynomial fitting process for each depth yields a profile of bending curvature. The profile of bending curvature is smoothed using a 3RH smooth with reroughing. To provide consistency with standard of practice methods, the values of bending curvature are converted into bending moments using the $M-\Phi$ relationship generated by the computer program LPILE (Figure 3.20). The resulting bending moment profile, calculated by converting values of bending curvature to the corresponding values

of bending moment as shown in Figure 3.20, is shown in Figure 3.21. Using cracked section properties in the $M-\Phi$ relationship generates a smoother profile of bending moment versus depth (there is no “hitch” near the cracking moment), but analysis of the test wall data for this project indicates that the earth pressures estimated at locations with small bending curvatures are unrealistically small when using cracked section properties. This may be a function of the heterogeneous nature of the concrete itself, which inherently produces variations in local stress-strain behavior at different locations within the shaft. If structural stresses are concentrated in the stiff (i.e. uncracked) sections of the shaft, and deformations are primarily located in the more flexible (i.e. cracked) sections, some difficulty in data interpretation can be encountered in the range of small strains. Despite this difficulty, because bending moments in the range of interest are larger than the cracking moment, the interpretation of maximum bending moment in the shaft is relatively unaffected by the choice of cracked or uncracked properties. The influence of concrete cracking on data interpretation is discussed in more detail in subsequent chapters.

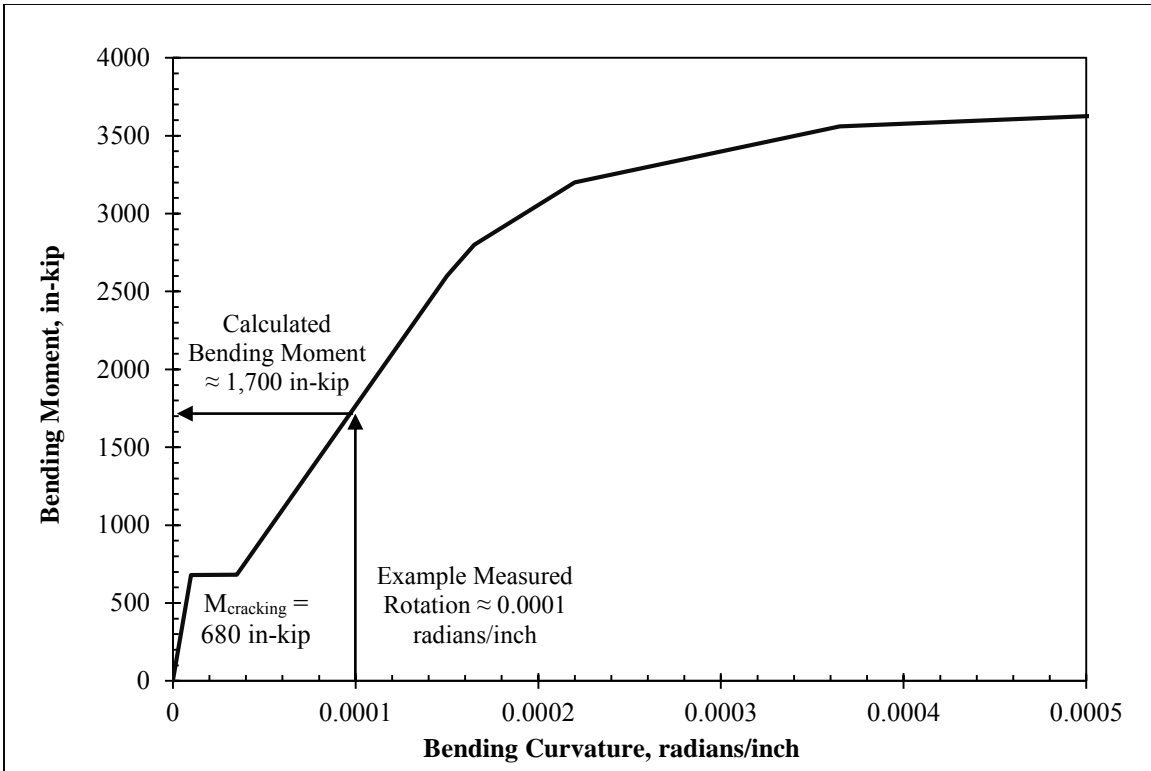


Figure 3.20: Relationship between bending curvature and bending moment (M- Φ relationship) used for LPILE and field instrumentation data analysis.

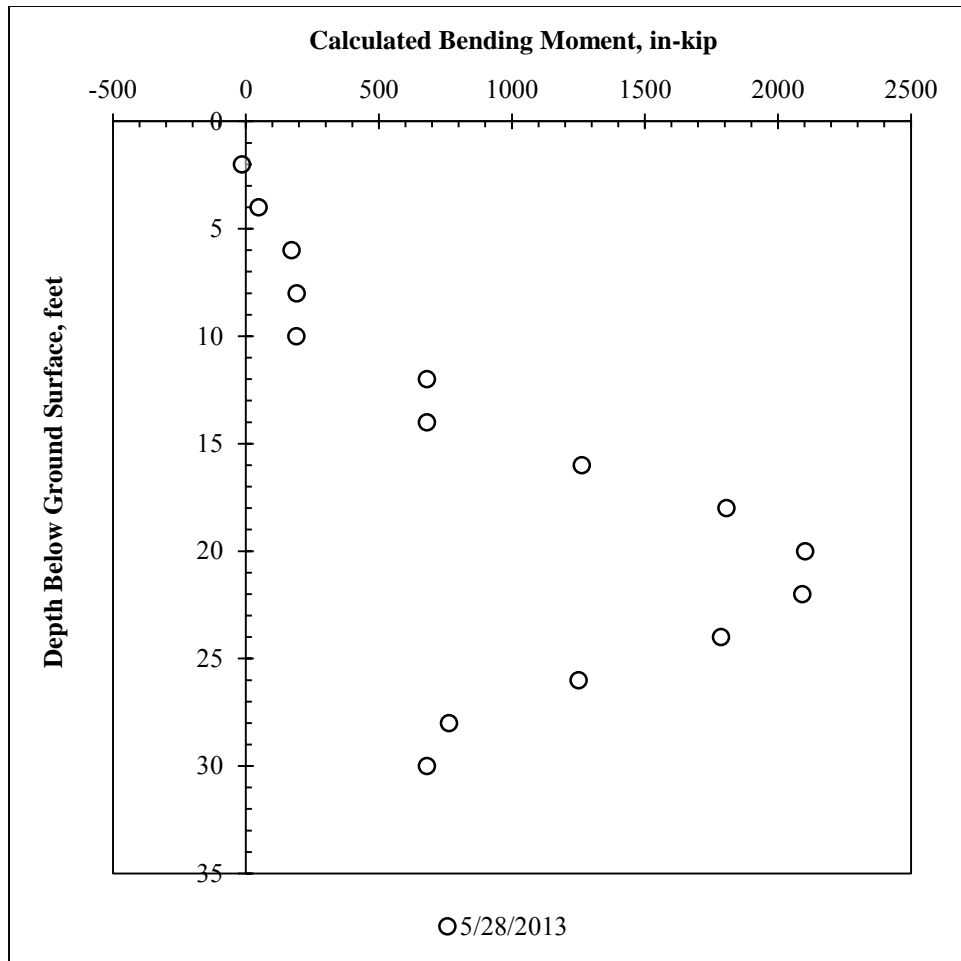


Figure 3.21: Bending moment profile generated from piecewise polynomial fitting of smoothed rotation profile and M- Φ relationship from LPILE.

3.7.3.d: Obtaining Net Earth Pressures from Bending Moment Profiles

To generate profiles of shear forces in the shaft, the same procedure used to differentiate the smoothed rotation profile is applied to the bending moment profile. Because the bending moment profile was generated from a smoothed profile of bending curvature, and to preserve the nonlinear moment-curvature behavior displayed in Figure 3.20, no smoothing is applied to the bending moment profile. To differentiate the profile of bending moment, piecewise third-order polynomials are fit to a window of five points

along the depth of the shaft. The resulting shear force profile is smoothed using a 3RH smooth with re-roughing, then differentiated using piecewise polynomials to obtain a profile of soil resistance, which is smoothed again with a re-roughed 3RH smooth. The resulting soil resistance values for the 5/28/13 profile are shown in Figure 3.22, along with comparison values calculated using only the averaged rotation profile with piecewise polynomial differentiation (no smoothing used). In Figure 3.22, the large values of soil resistance in the non-smoothed data above the excavation line are the result of small errors in the original raw rotation data. Small jumps in the original data set become larger with each successive differentiation; after three differentiations, small errors can become large, unrealistic spikes. The judicious use of data smoothing during differentiation can minimize the effects of random errors on the final result.

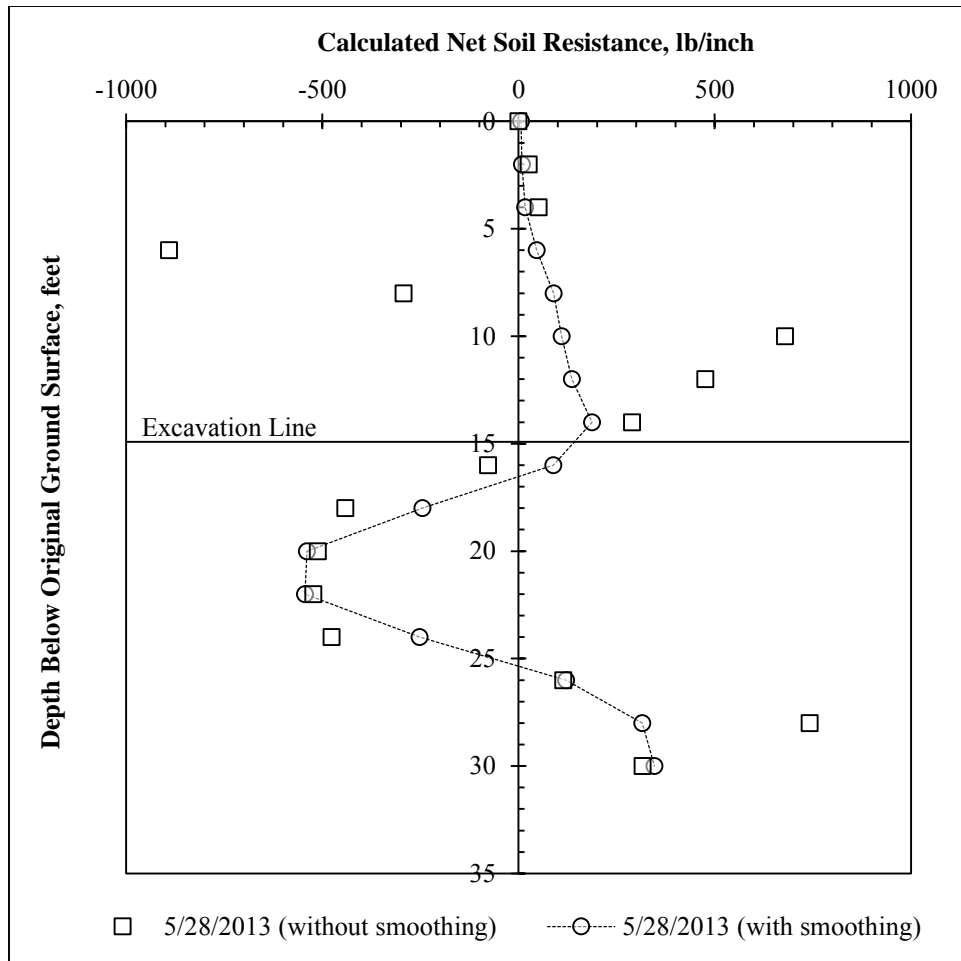


Figure 3.22: Soil resistance profiles generated using piecewise polynomial differentiation of averaged rotation profiles (with and without data smoothing applied during the differentiation process).

On inspection, the differentiation process produces reasonable results when the data smoothing algorithm is used throughout the differentiation process. The profile of net soil resistance reaches zero value close to the excavation depth of 15 feet, and reaches zero again near the shaft's center of rotation at approximately 27 feet. While the soil pressures between 30 and 35 feet must be inferred due to the lack of inclinometer data at those depths, the earth pressures above 30 feet are consistent with those obtained from LPILE results.

3.7.3.e: Generating p-y Curves from Inclinometer Data

With the procedure described above, values of soil resistance (p) and horizontal deflection (y) are obtained for each depth. With readings for a variety of dates, corresponding to a variety of deflections, p and y can be plotted against each other at each depth to create a family of p - y curves.

3.7.3.e.1: Discussion of “Net” Soil Resistance

In the following sections, it should be noted that the driving earth pressures acting toward the excavation are defined as (w), and the earth pressures resisting this motion are defined as (p). The profile of net soil resistance generated using the differentiation process is actually a profile of ($w - p$). Above the excavation line, p is zero and $(w - p) = w$. At large depths below the excavation line, w is generally assumed to be negligible relative to p , and $(w - p) = p$. However, near the excavation line, both w and p are acting on the shaft, and their effects can be difficult to separate from one another. For the purposes of this analysis, w is assumed to reach zero at the excavation line.

3.7.3.e.2: Correcting Soil Resistance for Excavation Location

Because the soil resistance values near the excavation line are influenced by points above the excavation line, and the influence of driving earth pressures extending slightly beyond the shaft base, the soil resistance at the excavation line obtained from point-by-point differentiation is often a negative value. Because this is not physically possible with a positive deflection, polynomial curve fitting is applied to ensure net soil resistance values are not negative at the excavation line. To provide consistency with design practice, which often assumes a value of zero soil resistance at the excavation line, a third-order polynomial fit using least-squares regression was used to represent the profile of soil resistance versus

depth. This maintains the general magnitude and shape of the soil resistance profile, but allows every profile to reach zero at the excavation line (Figure 3.23).

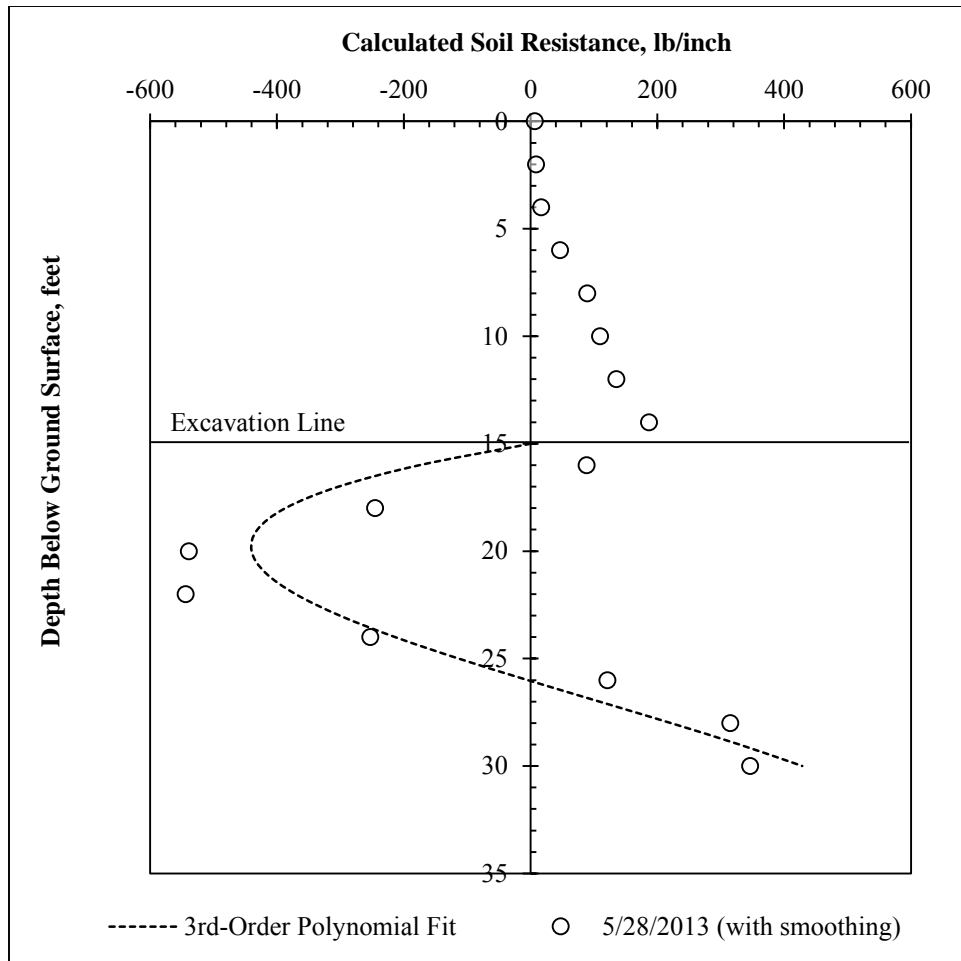


Figure 3.23: Using a third-order polynomial to adjust values of net soil resistance for p-y curves.

3.7.3.e.3: Correcting Horizontal Deflections for Center of Rotation

In limit equilibrium and numerical models such as LPILE, the shaft rotates about a center of rotation (at approximately 26 feet in Figure 3.1). Above the center of rotation, deflections are positive, and below, the deflections are negative. In a standard deflected

shape generated from inclinometer data, however, the shaft base is assumed to be fixed, and all deflections appear to be positive. This can provide misleading results for p-y curves; if the raw inclinometer deflections are used, at the center of rotation, the shaft appears to have moved without any corresponding increase in earth pressure. Similarly, without corrections to deflection data, at the shaft base, nonzero soil forces appear to be present without any shaft deflections. To prevent unrealistic results such as these in data interpretation, and to allow for pile conditions closer to force equilibrium, the inclinometer data is adjusted to allow the shaft to rotate about the center of rotation (defined for the purposes of this analysis as the depth at which the soil resistance below the excavation is equal to zero) as shown in Figure 3.24.

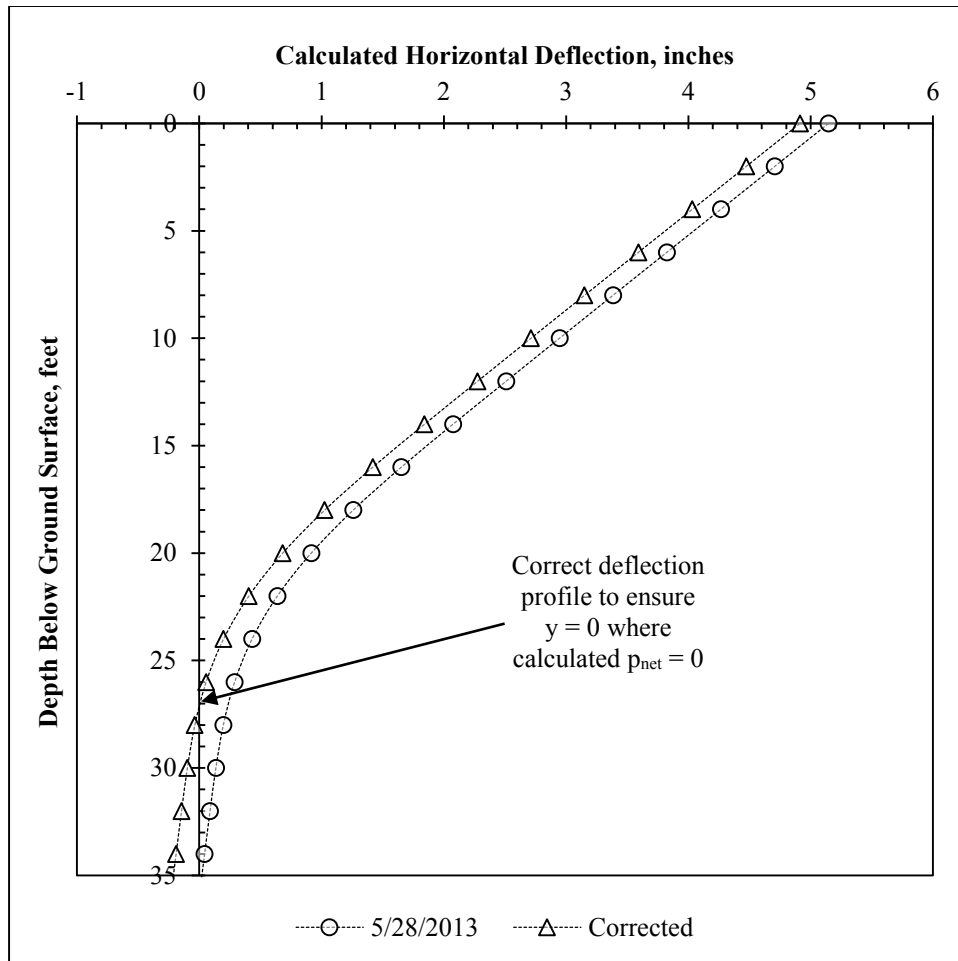


Figure 3.24: Correction of deflected shape about center of rotation for p-y curves

3.7.3.e.4: Example p-y Curves Developed from Inclinometer Data

By plotting corrected values of soil resistance (p) against corrected values of deflection (y), p-y curves comparable to those used for analysis in programs such as LPILE can be generated. An example family of curves for depths between 16 and 24 feet below the original ground surface, zeroed on October 8, 2010, and consisting of all measurements through May 28, 2013, is shown in Figure 3.25.

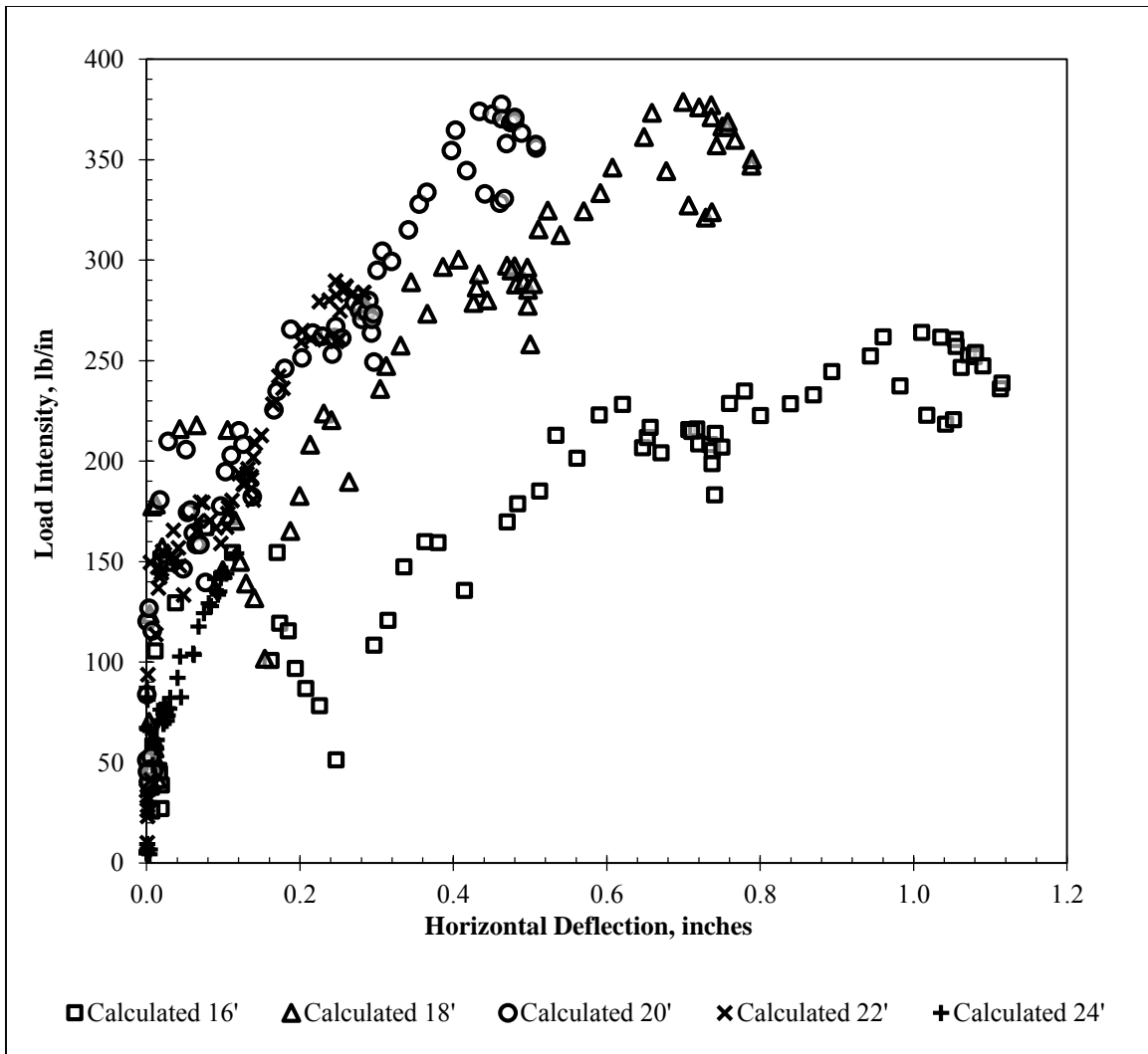


Figure 3.25: Example p-y curves generated from inclinometer data at the test wall. Reference survey is October 8, 2010.

3.8: Summary and Conclusions

The Lymon C. Reese research wall is constructed through expansive clay in Manor, Texas. The wall was designed according to standard of practice methods, and is instrumented with inclinometers, strain gauges, and Time Domain Reflectometry (TDR) moisture probes. Conclusions include:

- The drilled shafts and instrumentation were installed during early April, 2010. The design goal was to provide a wall which was structurally sound and consistent with design practice, but would produce enough deformations to infer the earth pressures acting on the wall.
- Strain gauges record values of axial strain on either side of the shaft's neutral axis. By dividing the difference in axial strain at a given depth by the horizontal distance between gauges, axial strains can be converted to values of bending curvature. Values of bending curvature can be converted to values of bending moment using standard nonlinear moment-curvature relationships for reinforced concrete.
- Inclinerometers record values of rotation along the length of the shaft. The rotation profile can be integrated to calculate a profile of lateral deflections, or differentiated to calculate a profile of bending curvature.
- A method of developing p-y curves from inclinometer data is presented. Rotation profiles from the three instrumented shafts are combined and differentiated using a combination of piecewise polynomial differentiation and numerical smoothing techniques. To achieve force equilibrium conditions consistent with existing design practice, corrections are applied to the calculated values of soil resistance to ensure soil resistance reaches zero at the excavation line, and to ensure the shaft deflection is zero where the net soil resistance reaches zero at depth. The resulting values of net soil resistance (p_{net}) are compared with calculated horizontal deflections (y) to develop a model of nonlinear soil response at each depth below the excavation line.

CHAPTER 4: TEST WALL PERFORMANCE BEFORE EXCAVATION (APRIL 2010 – AUGUST 2010)

Note: Portions of this section have been previously published by the author (Brown et. al., Geo-Frontiers 2011).

4.1: Overview

Between installation of the drilled shafts and instrumentation in early April, 2010, and test wall excavation in August, 2010, strain measurements shed light on the processes that take place within the concrete of a drilled shaft retaining wall prior to excavation. In order to fully understand these measurements, excavation was delayed until early August 2010. This section explains the deformations observed in the wall prior to excavation.

4.2: Climatic Information

Monthly rainfall totals for Austin, Texas between January, 2009 and July, 2010 are presented in Figure 4.1. For approximately eight months prior to shaft construction in early April, 2010, the test wall site experienced average to above average rainfall. Rainfall totals were significant enough that surface water was frequently present at the test wall site beginning in November, 2009, softening the surface soils and delaying initial site investigation until January, 2010. After shaft construction, the wall site experienced two months of below average rainfall in April and May, followed by two months of above average rainfall in June and July.

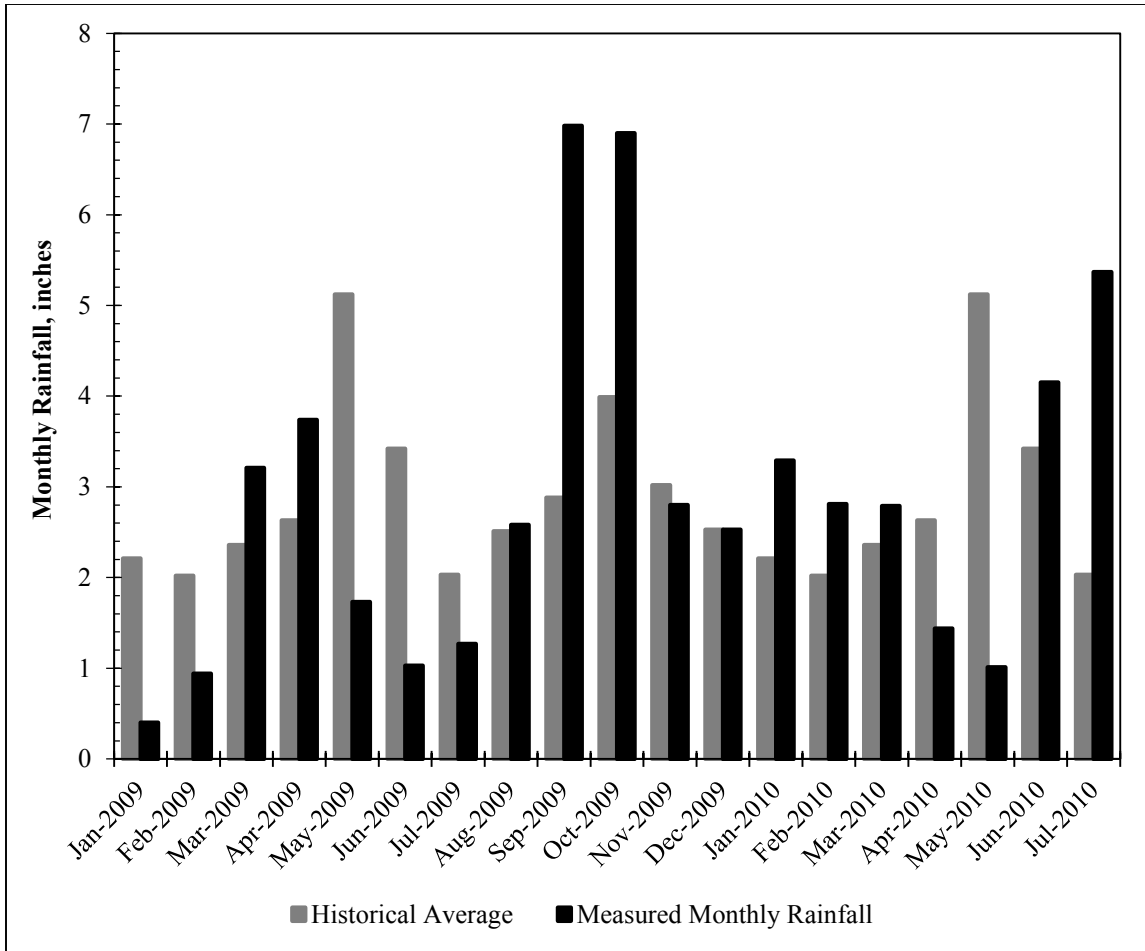


Figure 4.1: Monthly rainfall totals for Austin, Texas (Jan. 2009 - Jul. 2010; data from www.wunderground.com). Drilled shafts were installed in early April, 2010.

4.3: Summary of Field Instrumentation Data

4.3.1: STRAIN GAUGE DATA

After test wall construction was completed, strain gauge data were recorded at least once per week until excavation occurred. Early in the concrete curing process, the measurement interval was approximately once per day; as the concrete curing activity slowed down, the frequency of measurements decreased to approximately once per week

until excavation began. The pre-excavation strain data is presented in Figure 4.2 - Figure 4.16.

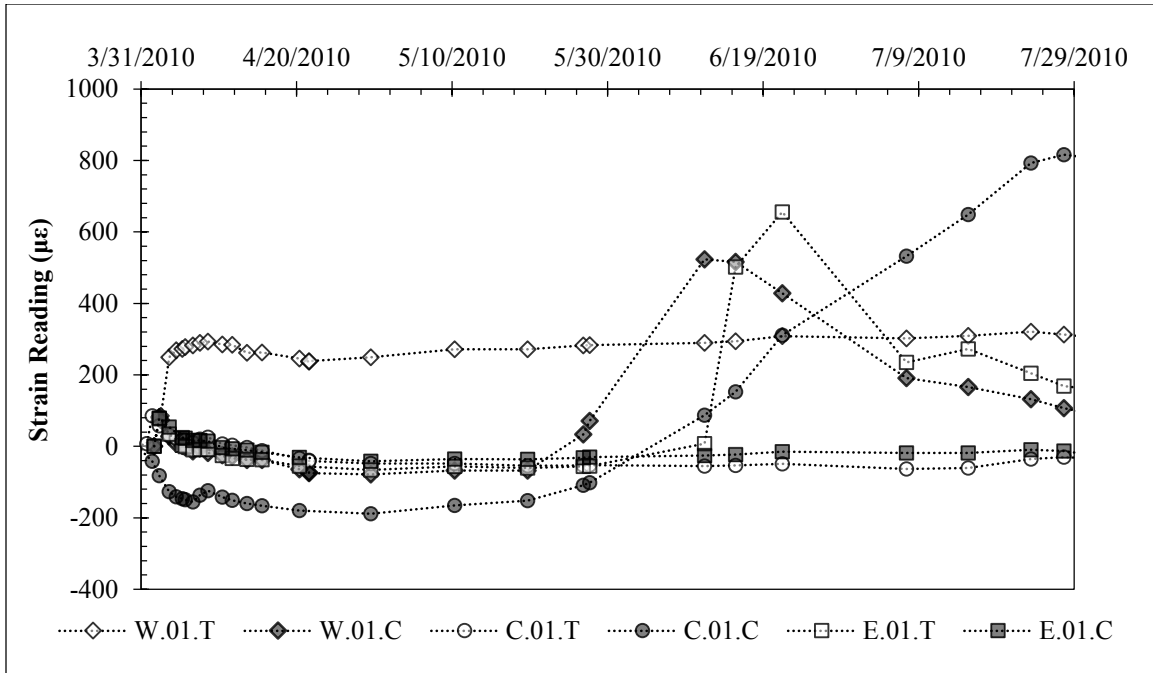


Figure 4.2: Pre-Excavation Strain Data for Gauges 1 Foot Below Ground Surface.

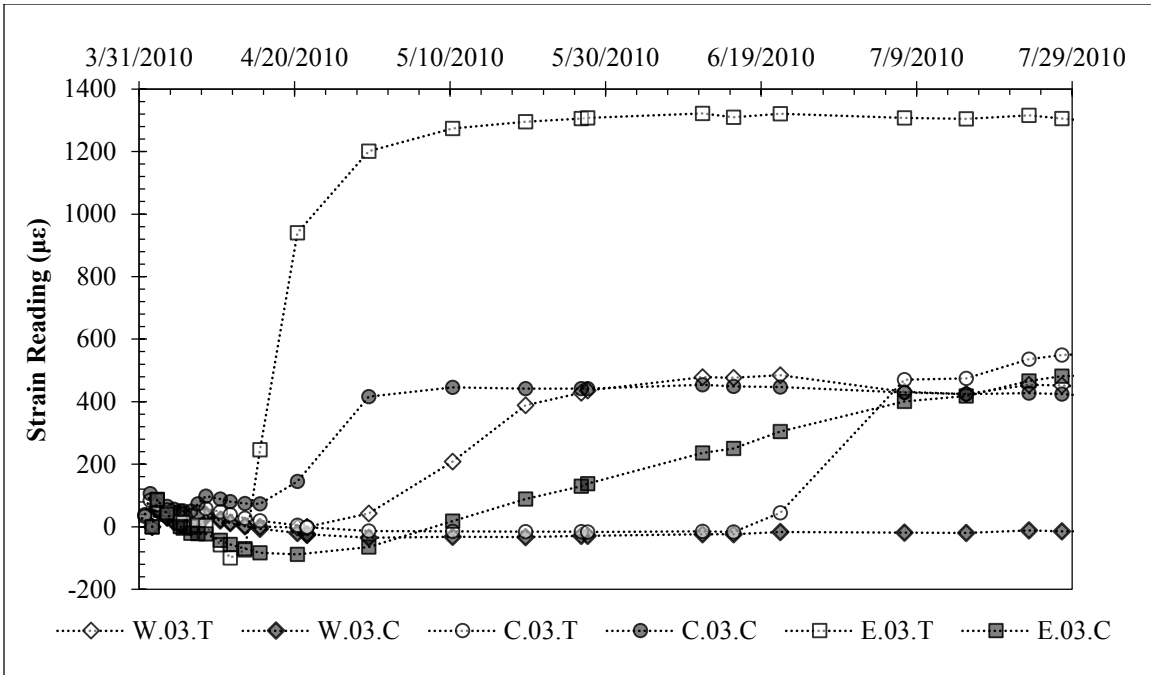


Figure 4.3: Pre-Excavation Strain Data for Gauges 3 Feet Below Ground Surface.

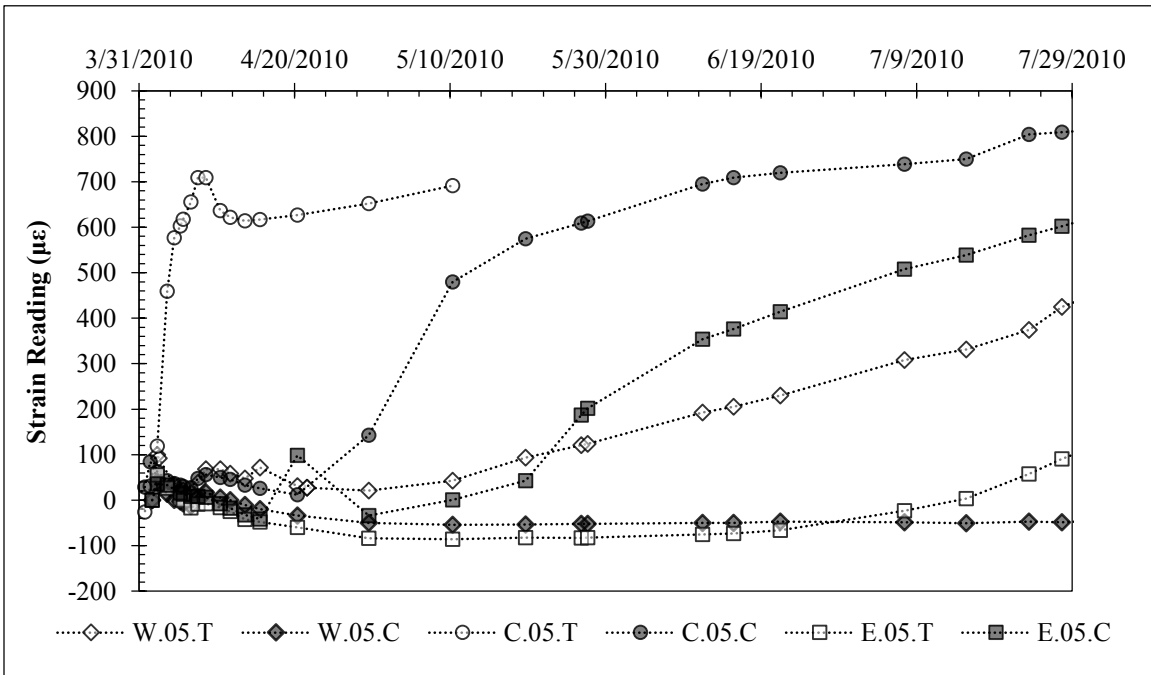


Figure 4.4: Pre-Excavation Strain Data for Gauges 5 Feet Below Ground Surface.

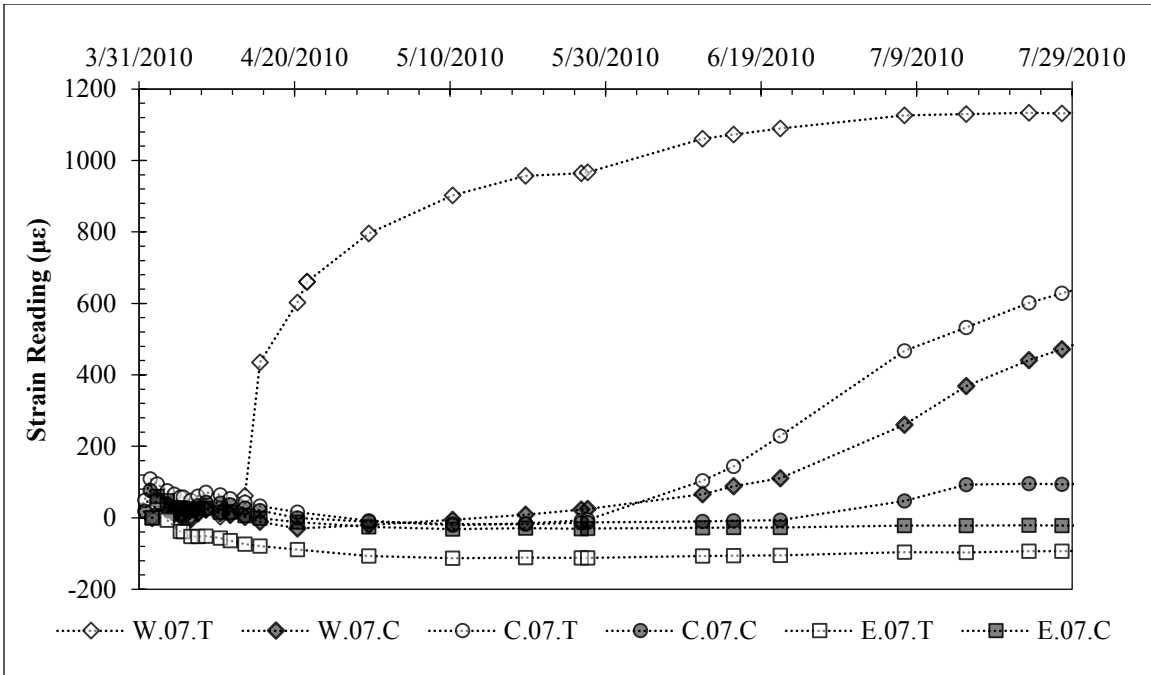


Figure 4.5: Pre-Excavation Strain Data for Gauges 7 Feet Below Ground Surface.

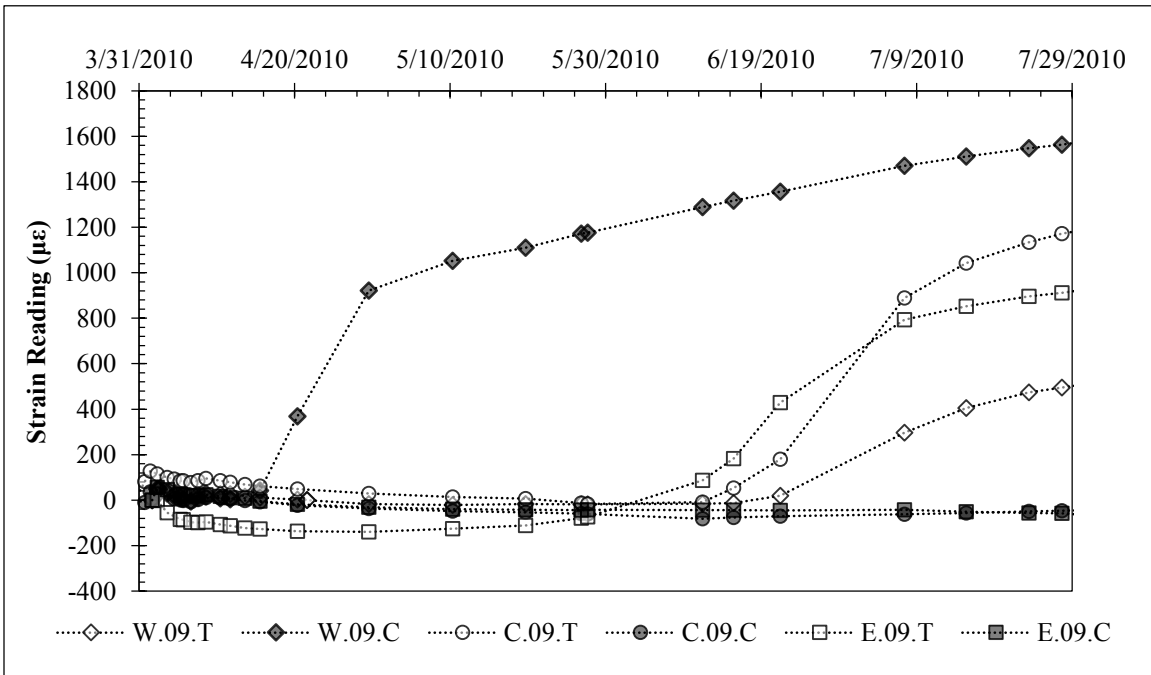


Figure 4.6: Pre-Excavation Strain Data for Gauges 9 Feet Below Ground Surface.

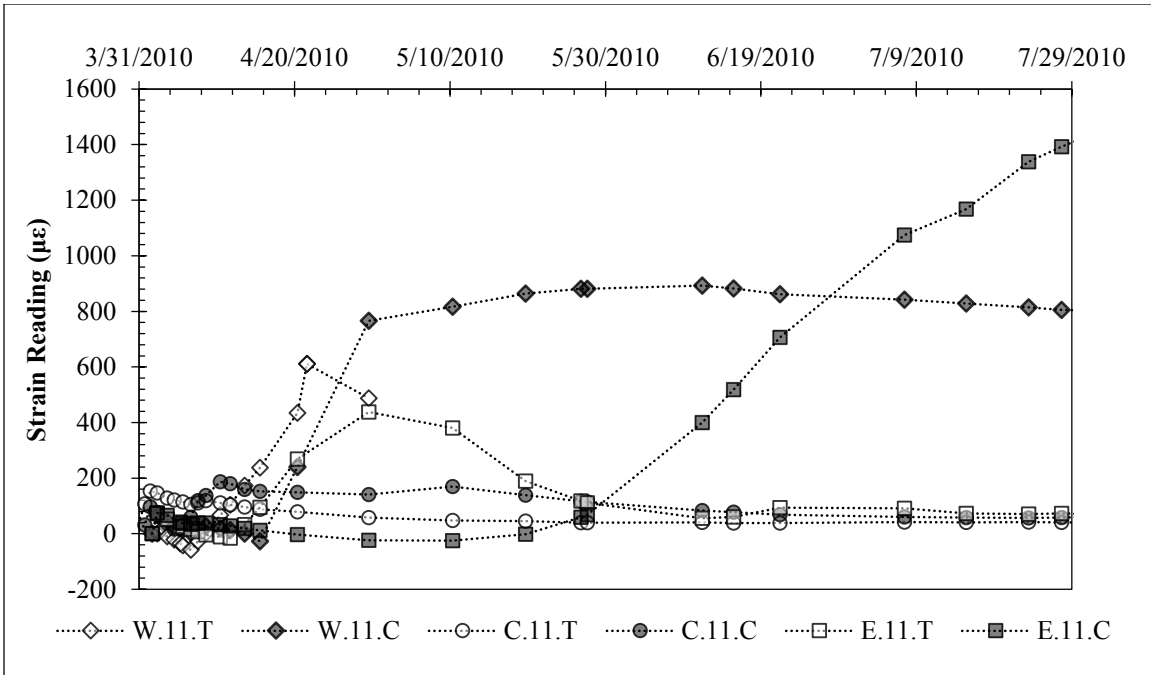


Figure 4.7: Pre-Excavation Strain Data for Gauges 11 Feet Below Ground Surface.

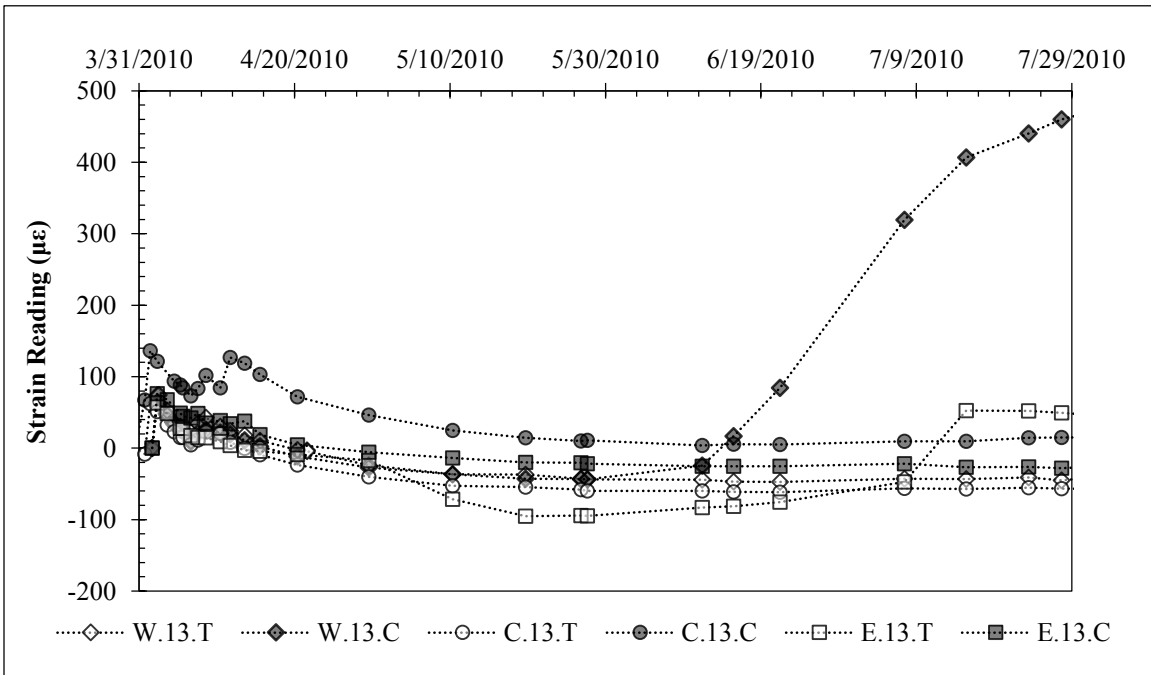


Figure 4.8: Pre-Excavation Strain Data for Gauges 13 Feet Below Ground Surface.

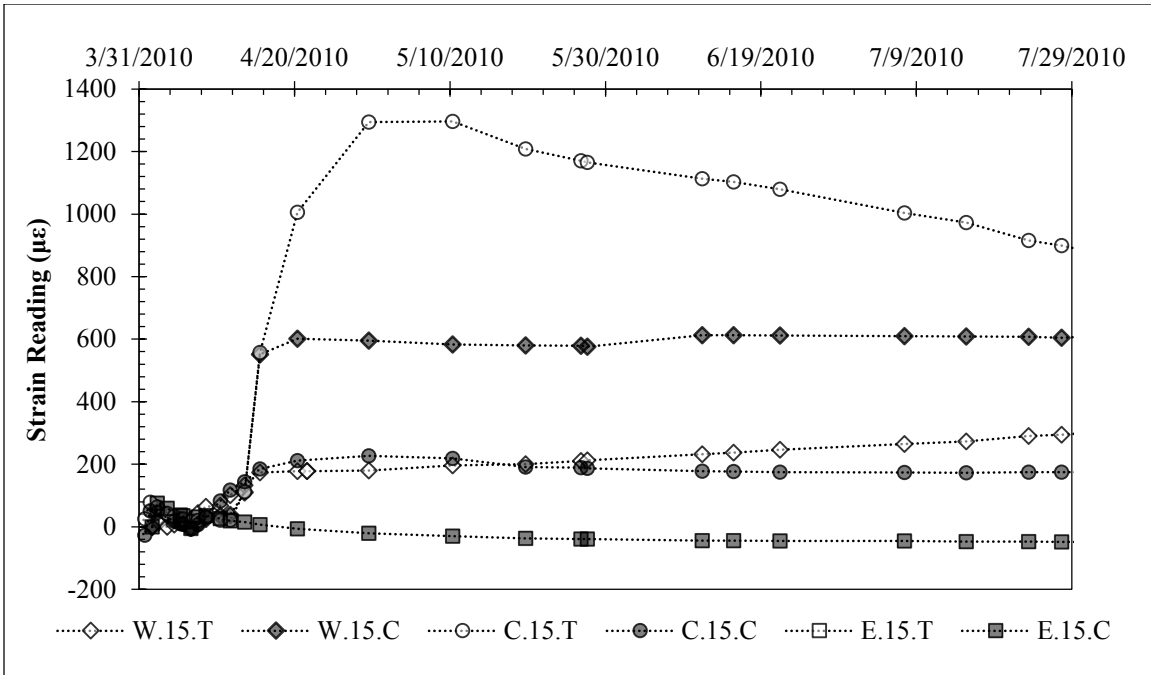


Figure 4.9: Pre-Excavation Strain Data for Gauges 15 Feet Below Ground Surface.

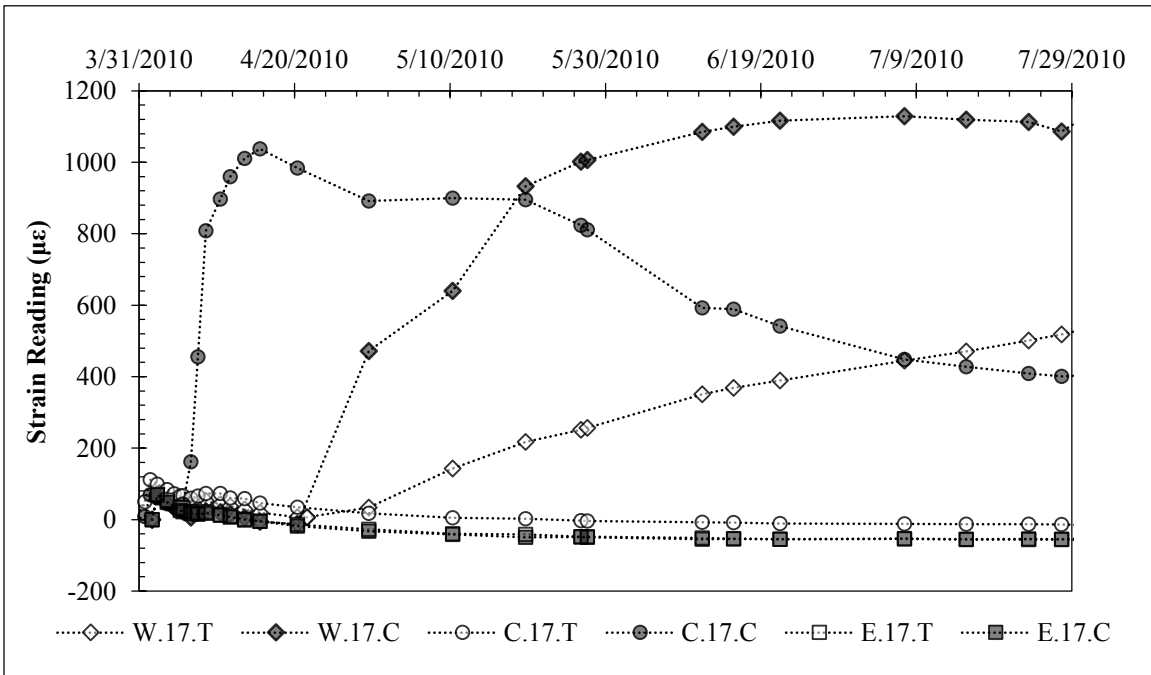


Figure 4.10: Pre-Excavation Strain Data for Gauges 17 Feet Below Ground Surface.

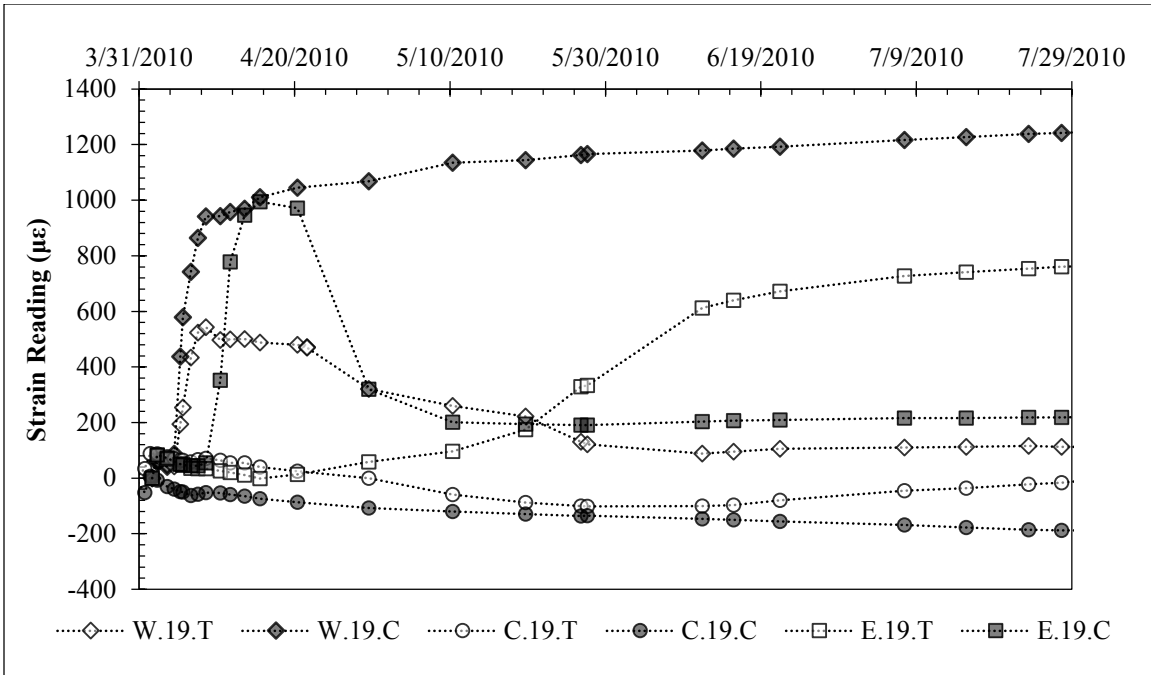


Figure 4.11: Pre-Excavation Strain Data for Gauges 19 Feet Below Ground Surface.

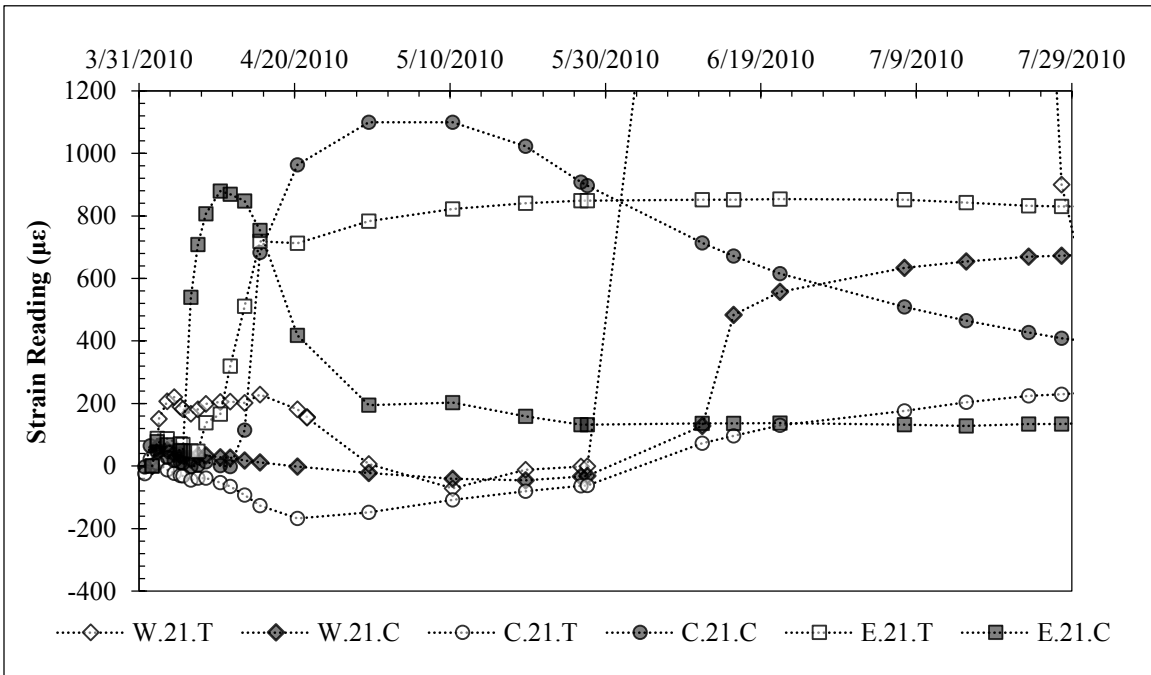


Figure 4.12: Pre-Excavation Strain Data for Gauges 21 Feet Below Ground Surface.

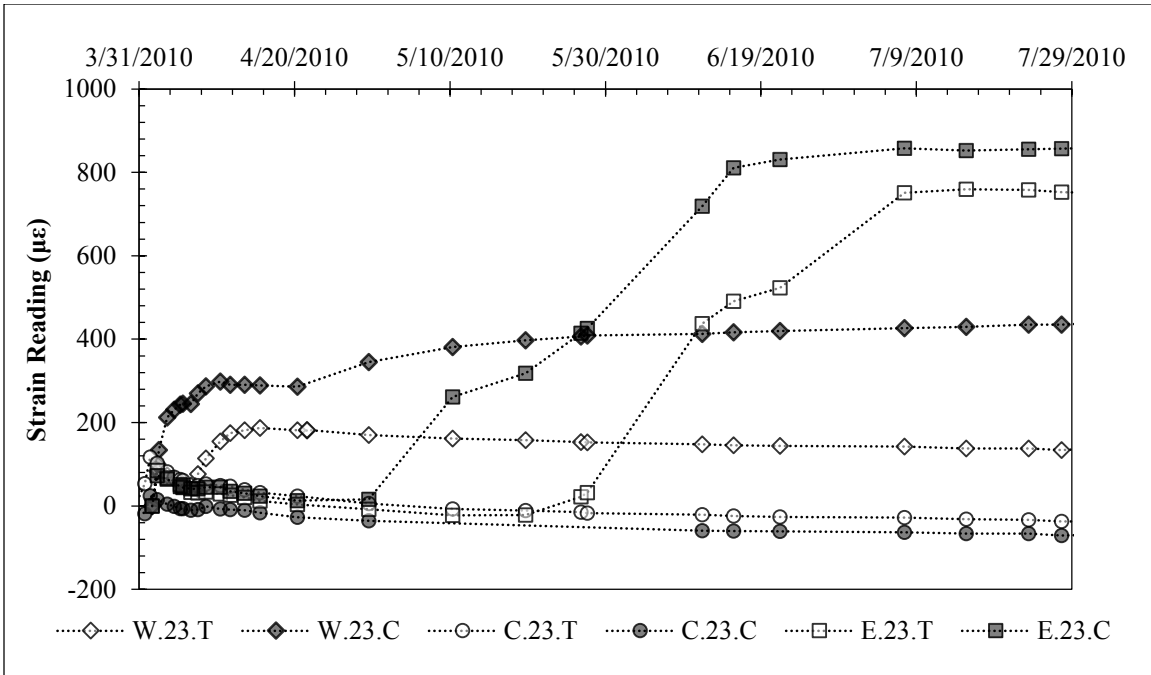


Figure 4.13: Pre-Excavation Strain Data for Gauges 23 Feet Below Ground Surface.

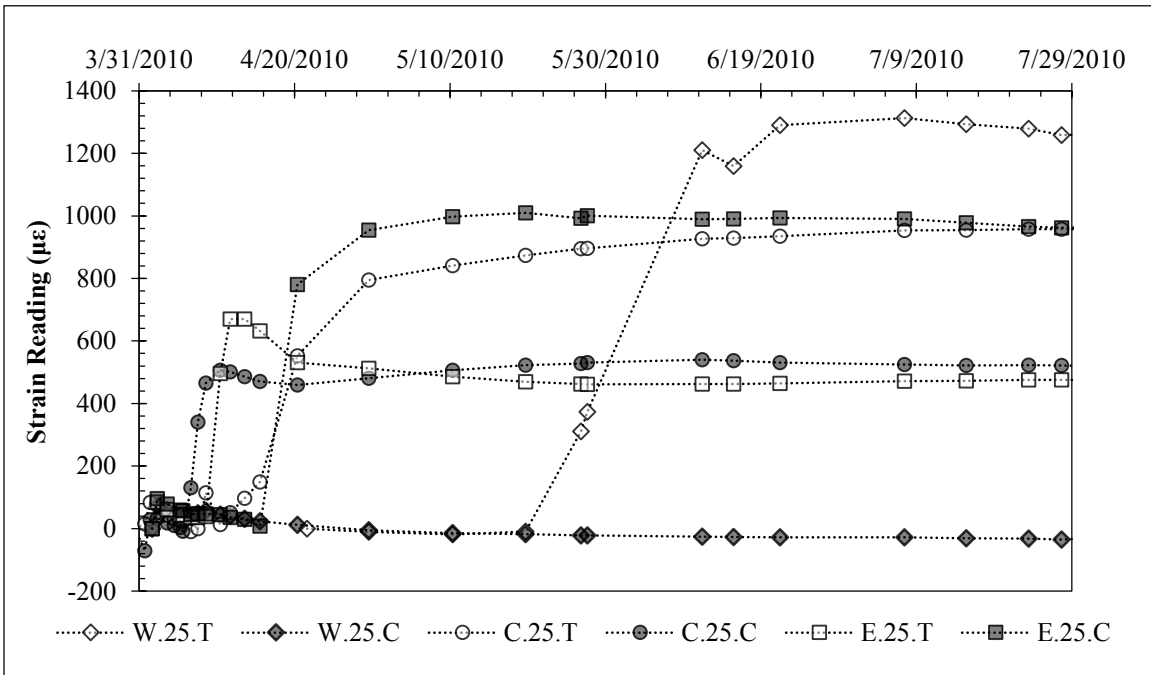


Figure 4.14: Pre-Excavation Strain Data for Gauges 25 Feet Below Ground Surface.

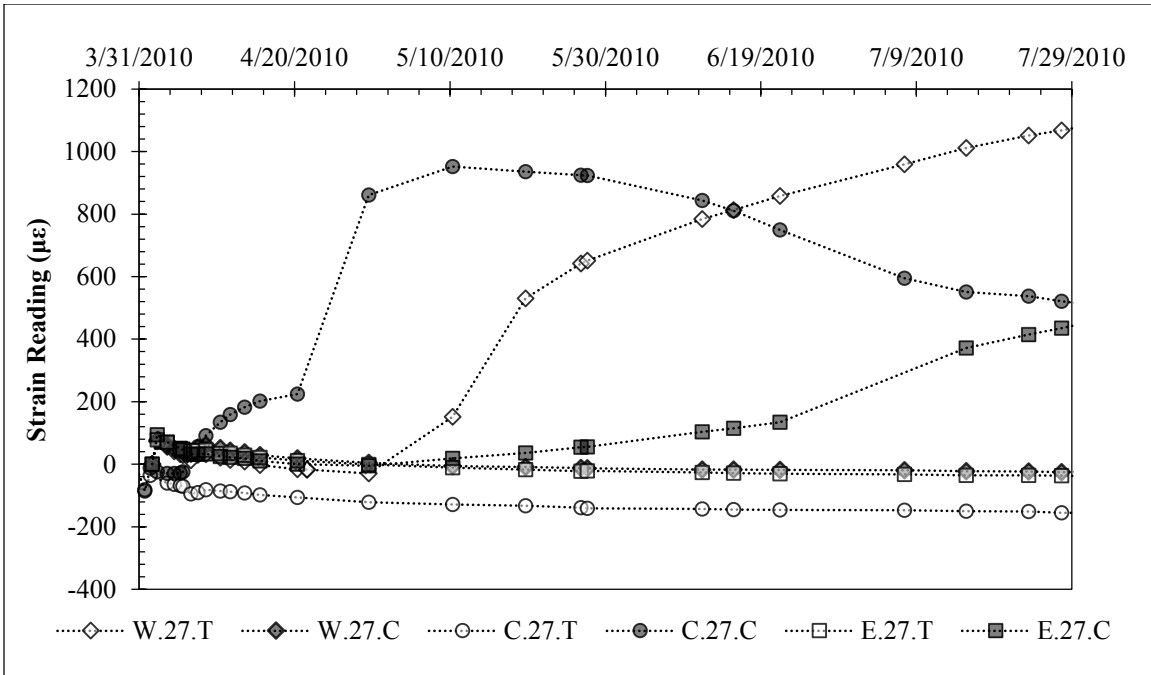


Figure 4.15: Pre-Excavation Strain Data for Gauges 27 Feet Below Ground Surface.

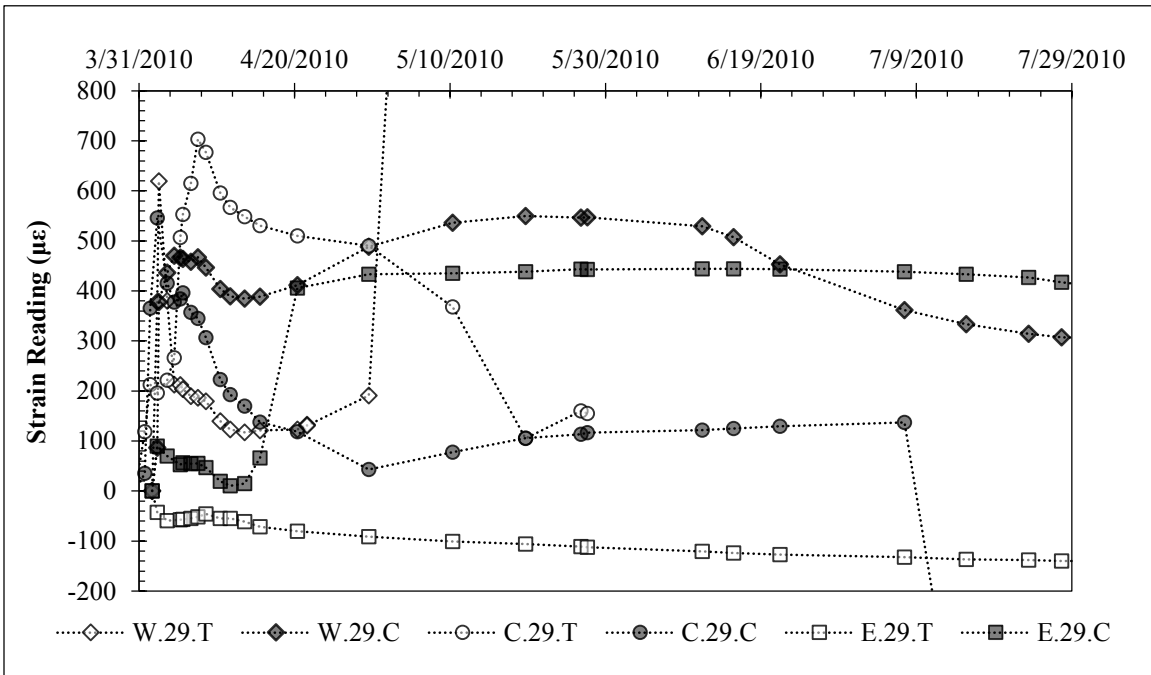


Figure 4.16: Pre-Excavation Strain Data for Gauges 29 Feet Below Ground Surface.

4.3.2: STAND PIPE PIEZOMETER

The groundwater level was measured prior to excavation, and the piezometer was developed by removing water from the piezometer casing with a hand bailer and allowing the water level to return to its natural value over time. If the resulting values of water level versus time are analyzed as a rising head test, the hydraulic conductivity is approximately 3×10^{-5} ft/day (approximately 10^{-8} cm/s) below the water table. While this was far from a formal test, the results are consistent with other published data for the Taylor formation (e.g. Ellis, 2011) and with general values for high plasticity, fine-grained clays. Final groundwater level at excavation was approximately 8 feet below ground surface.

4.4: Data Interpretation

4.4.1: CONCRETE CURING

After successful installation of the strain gauges and field enclosure, strain measurements were taken at least once per day for several weeks. Initial strain measurements behaved similarly as other published data from concrete curing (e.g., Fellenius et al 2009). As the concrete heated after placement, tensile strains tended to rise sharply and then decrease gradually as the concrete cooled (Figure 4.17). Heating from adjacent shafts also caused less pronounced spikes in tension (Figure 4.17). Because the gauges were zeroed in the lab to a value of zero force and no drift has been observed, nonzero initial strains are assumed to represent forces picked up during installation and concrete placement prior to the first reading.

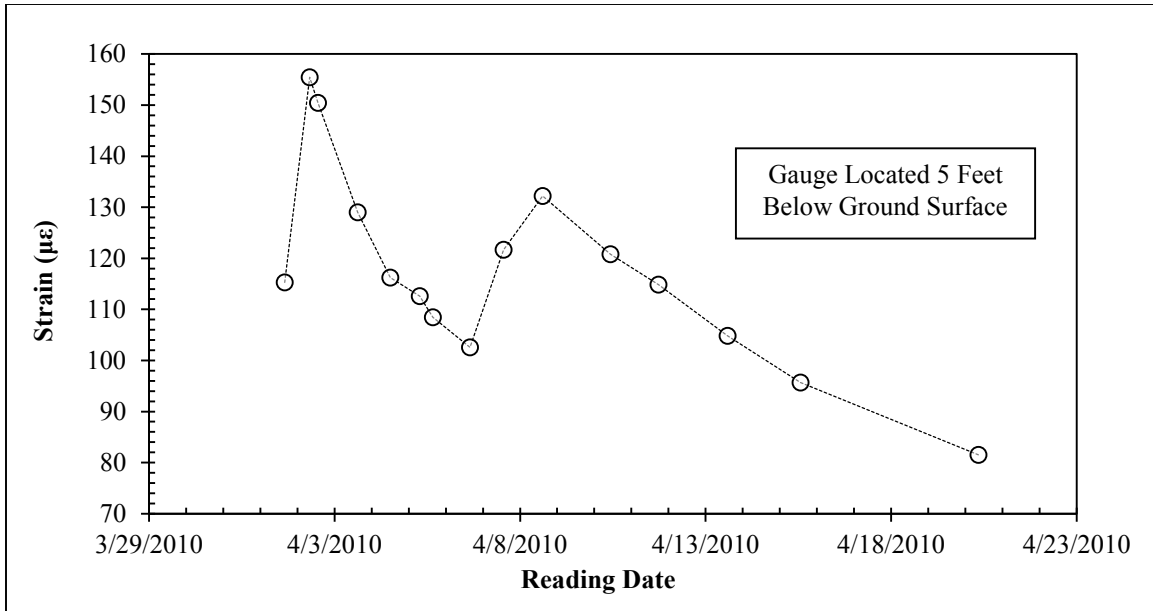


Figure 4.17: Three weeks of strain measurements during concrete curing. Concrete placed on April 1; concrete in adjacent shafts placed on April 6. Positive strain indicates tension.

4.4.2: SHRINKAGE CRACKING IN CONCRETE

Beginning approximately one week after concrete placement, and continuing over the next several weeks, about 20 percent of the strain gauges exhibited large and sudden jumps into tension. These jumps occurred between one and four weeks after concrete placement, were most frequent in the second and third weeks, and have no clear relationship with depth. Figure 4.18 shows measurements recorded for one gauge as an example.

These jumps are likely the result of small tension cracks forming in the concrete due to shrinkage. For example, at seven days, the concrete compressive strength was approximately 4 kips/in², giving an average tensile strength of about 0.4 kips/in². Distributed throughout the shaft, this represents a tensile load of about 180 kips. If this tensile load is released as a crack extends across the shaft, the load will be redistributed to

the 12 #7 bars. A tensile force of 180 kips corresponds to a strain of about 900 microstrains in the bars, which is consistent with the magnitude of tensile strains associated with these jumps (Figure 4.18).

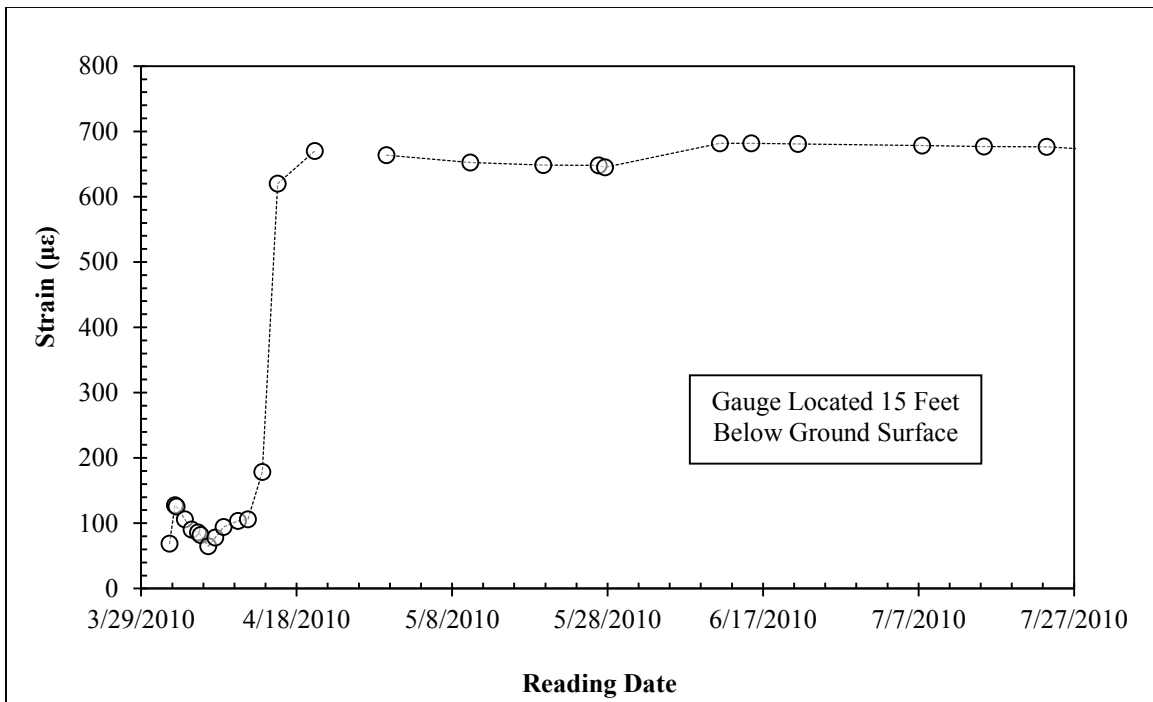


Figure 4.18: Illustration of tension crack formation in concrete near gauge.

Another issue with concrete cracking is the risk of breaking the strain gauge. If a tension crack forms very close to the exposed optical fiber, the fiber can be damaged and the gauge can be lost (Fuhr et al., 1993). Soon after cracking in the concrete began, two gauges jumped to over 3,000 microstrains, which was outside their range of measurement and likely indicated damage to the gauge. Over the course of the project, gauges which suddenly register measurements in this range have usually malfunctioned shortly thereafter.

4.4.3: EXPANSIVE SOIL MOVEMENT

After the influence of concrete curing and tension cracks diminished, approximately 10 percent of gauges showed steady increases in tension over the remaining three months between concrete placement and excavation. The increases in tension occurred most commonly in gauges located between 0 and 10 feet below the ground surface. Figure 4.19 shows a gauge, located seven feet below ground surface, exhibiting this behavior. A gauge at 23 feet showed similar strain behavior early on, but did not exhibit the same increase in tension with time. Qualitatively, the increase in tension begins at a similar time as the transition from below average rainfall in April and May to above average rainfall in June and July. A pre-excavation strain value of approximately 700 microstrains also suggests that a tension crack may also be present near the gauge. The shaft may be experiencing changes in side shear stresses due to moisture content changes in high plasticity clay (e.g., Kim and O'Neill, 1998), along with the effects of tension cracking in the concrete. This behavior is most pronounced in gauges located between 5 and 9 feet below ground surface, above the water table where the natural moisture content fluctuates in response to weather patterns.

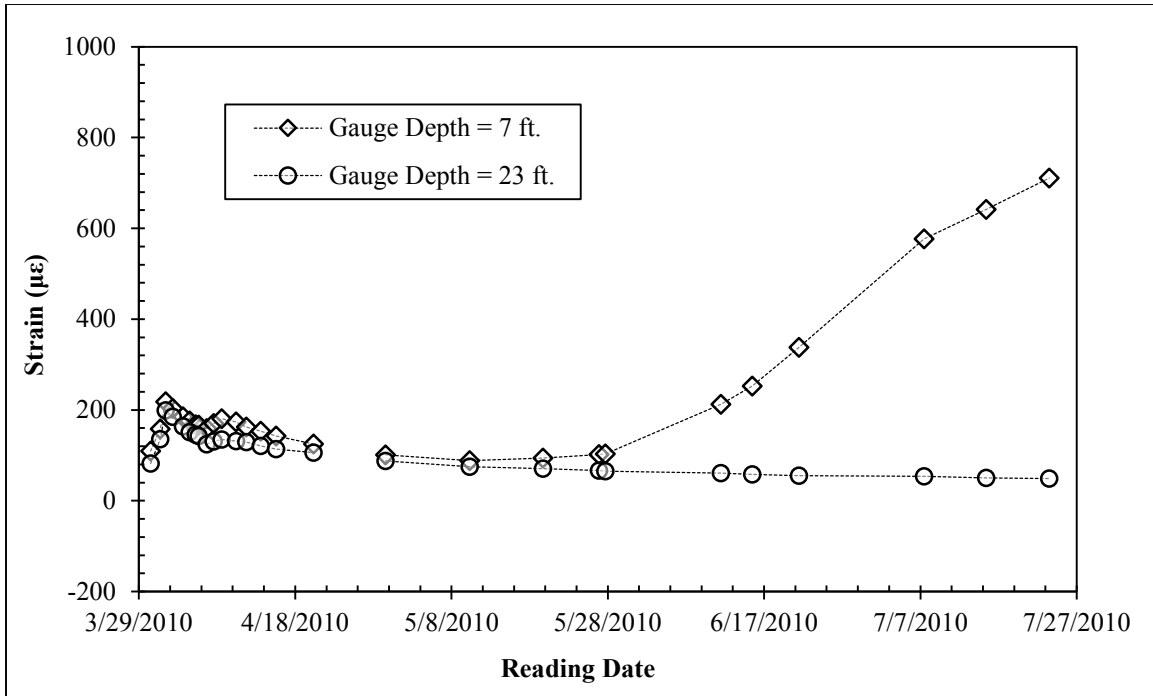


Figure 4.19: Strains occurring between concrete curing and excavation. The gauge at a depth of 7 feet may be experiencing changes in side shear due to moisture fluctuations in the active zone (e.g., Kim & O'Neill, 1998).

4.4.4: DEVELOPMENT OF RESIDUAL STRESSES AND STRAINS

Koutrovelis (2012) attempted to idealize the residual stresses that existed in the concrete of the Manor test wall prior to excavation by interpreting data from the optical strain gauges. The analysis suggested that, on average, our test wall experienced an initial increase in tension followed by a period of compression (Figure 4.20).

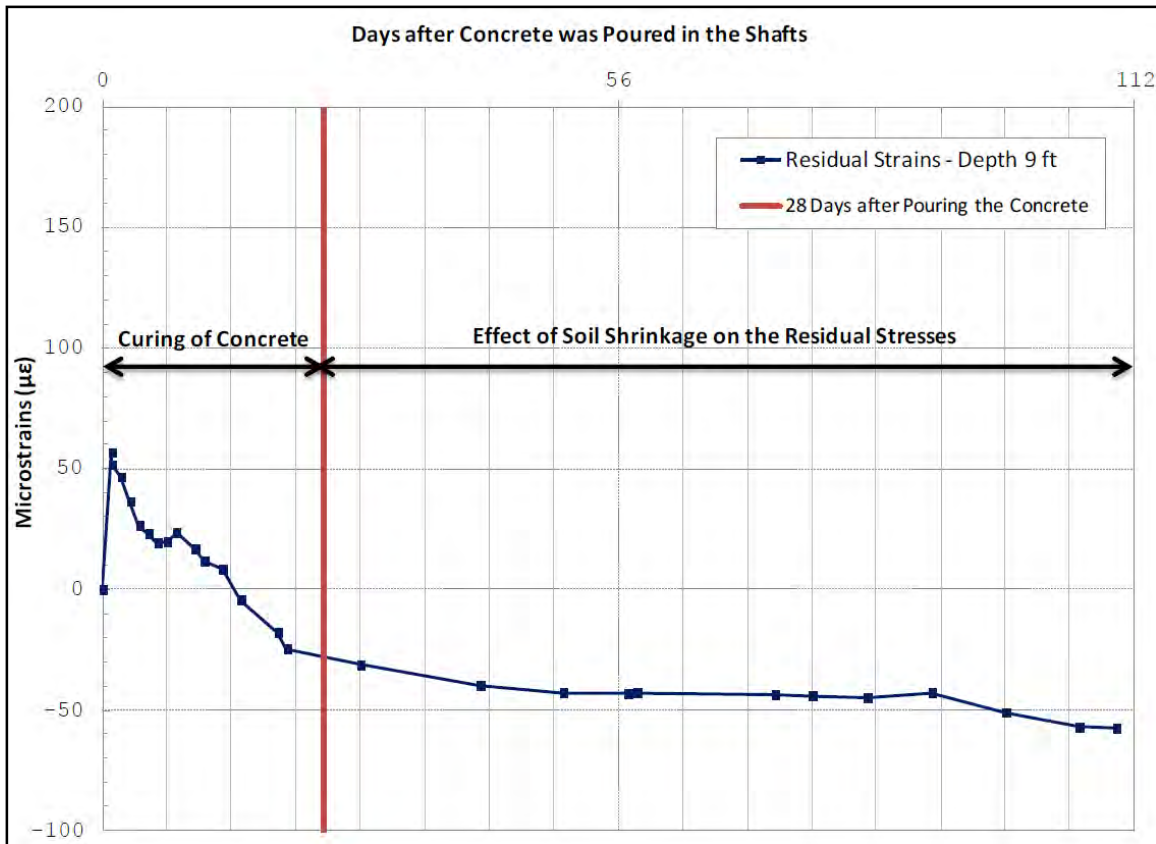


Figure 4.20: Development of residual strains at a depth of 9 feet between shaft construction and excavation (after Koutrouvelis, 2012).

During the first three to four weeks after concrete placement, the development of residual strains is governed by the concrete curing. After most of the activity associated with concrete curing subsided, moisture changes in the expansive clay may have contributed to the development of residual compressive strains in the shaft before excavation (Koutrouvelis, 2012). The existence of residual stresses and strains can lead to difficulties in data interpretation, and may influence the shafts' response to loading. While stresses and strains in the shaft are generally assumed to be negligible prior to excavation, in some cases, it may be necessary to consider the effects of residual stresses and strains on the shafts when interpreting wall performance data.

4.5: Summary and Conclusions

An examination of test wall behavior between shaft construction and excavation has shed light on the processes which occur in drilled shaft retaining walls prior to excavation. Key findings include:

- Prior to shaft construction, the test site experienced approximately eight months of above average rainfall. Between shaft construction and excavation, the wall experienced two months of below average rainfall, followed by two months of above average rainfall.
- Axial strains developed in the shafts prior to construction due to a combination of concrete curing and expansive soil movement. In many cases, the development of axial strains suggests that tension cracks developed throughout the shaft.
- Residual stresses and strains are present in the shafts prior to excavation. The distribution of residual stresses and strains is highly variable within each shaft.

CHAPTER 5: TEST WALL PERFORMANCE DURING EXCAVATION (AUGUST 2010 – SEPTEMBER 2010)

Note: Portions of this section have been previously published by the author (Brown et. al., Geo-Frontiers 2011).

5.1: Overview

5.1.1: SUMMARY OF EXCAVATION PROGRESS

Excavation of the test wall began on July 29, 2010 and took place over a period of approximately four weeks. The full cantilever height of 14 to 15 feet was reached on August 13, 2010, and the preliminary slopes were completed on August 19, 2010. The slopes were improved on September 30, 2010, and facing was installed on October 8, 2010. Photos of the excavation progress are provided in Figure 5.1 - Figure 5.2.



Figure 5.1: Photos of initial excavation progress (7/29/2010 – 8/5/2010).



Figure 5.2: Photos of later excavation progress (8/23/2010 - 10/1/2010).

5.1.2: CLIMATIC INFORMATION

Prior to the start of excavation, the project site had experienced a relatively dry spring, followed by a summer with above average rainfall. During excavation, hot, dry weather during August was followed by above average rainfall during the month of September (Figure 5.3), punctuated by approximately 1.9 inches of rain on September 7 (Figure 5.4). Average daily temperatures decreased from about 85 degrees Fahrenheit at the start of excavation to about 65 degrees at the installation of facing, a decrease of approximately 20 degrees (Figure 5.5).

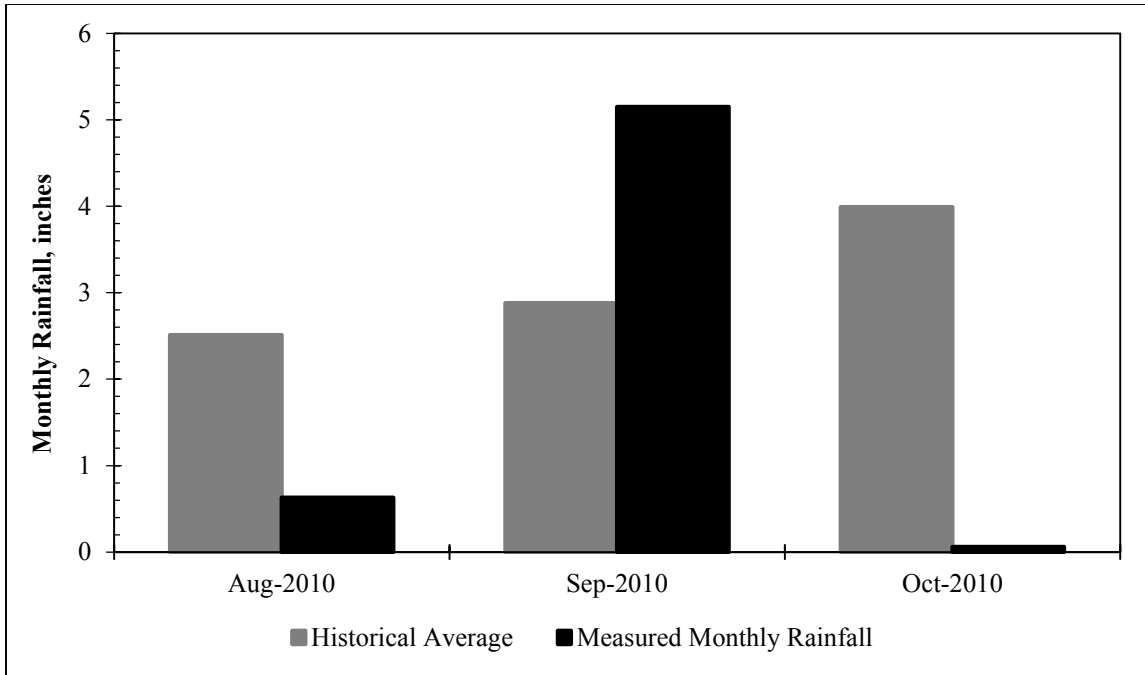


Figure 5.3: Monthly rainfall totals for Austin, Texas (Jul. 2010 – Oct. 2010; data from www.wunderground.com).

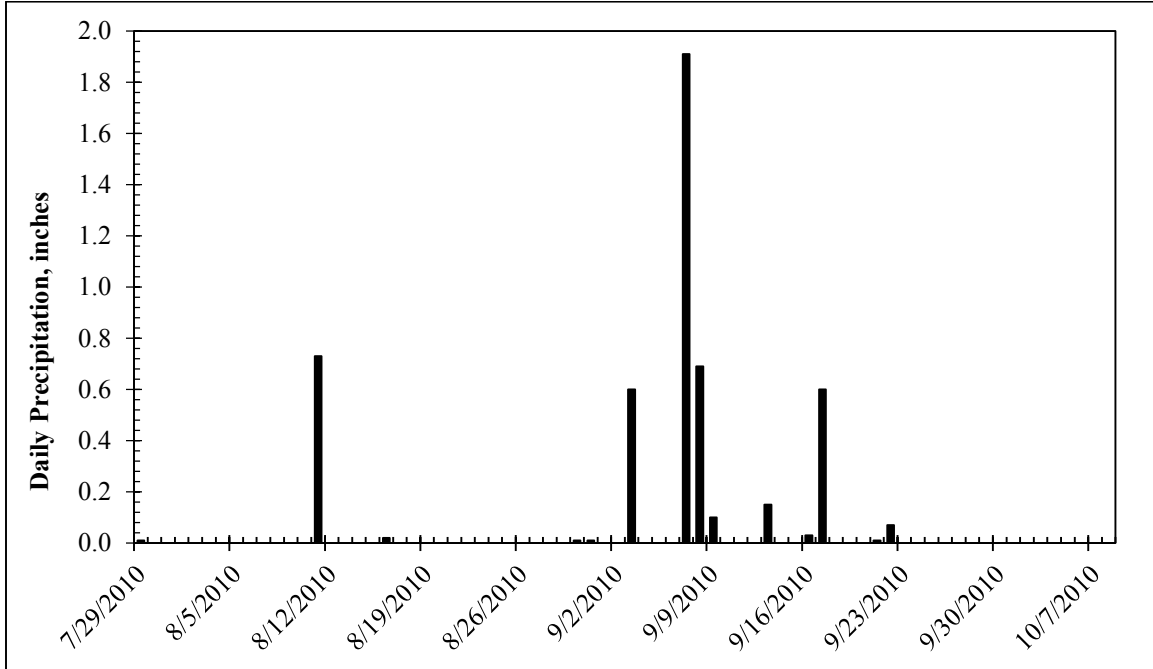


Figure 5.4: Daily precipitation for Manor, Texas (Jul. 2010 – Oct. 2010; data from www.wunderground.com).

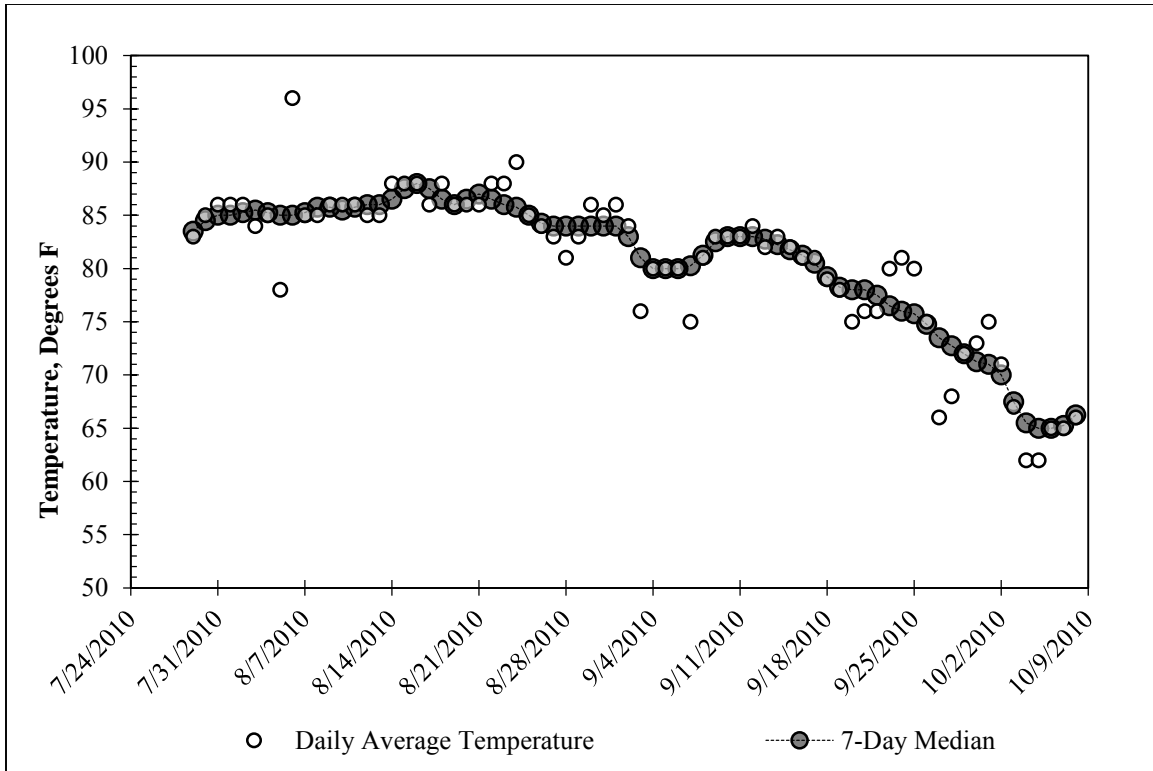


Figure 5.5: Daily temperature data for Manor, Texas (Jul. 2010 – Oct. 2010; data from www.wunderground.com).

5.2: Summary of Field Instrumentation Data

5.2.1: INCLINOMETER DATA

Beginning on July 27, 2010, inclinometer data from the east instrumented shaft was recorded at regular intervals throughout the excavation process. Lateral deflections at ground surface and a depth of 14 feet, along with a summary of key excavation events, are shown in Figure 5.6. Deflected shapes at various points during excavation are provided in Figure 5.7, and cumulative deflections in the soil 5.5 feet behind the centerline of the wall are provided in Figure 5.8.

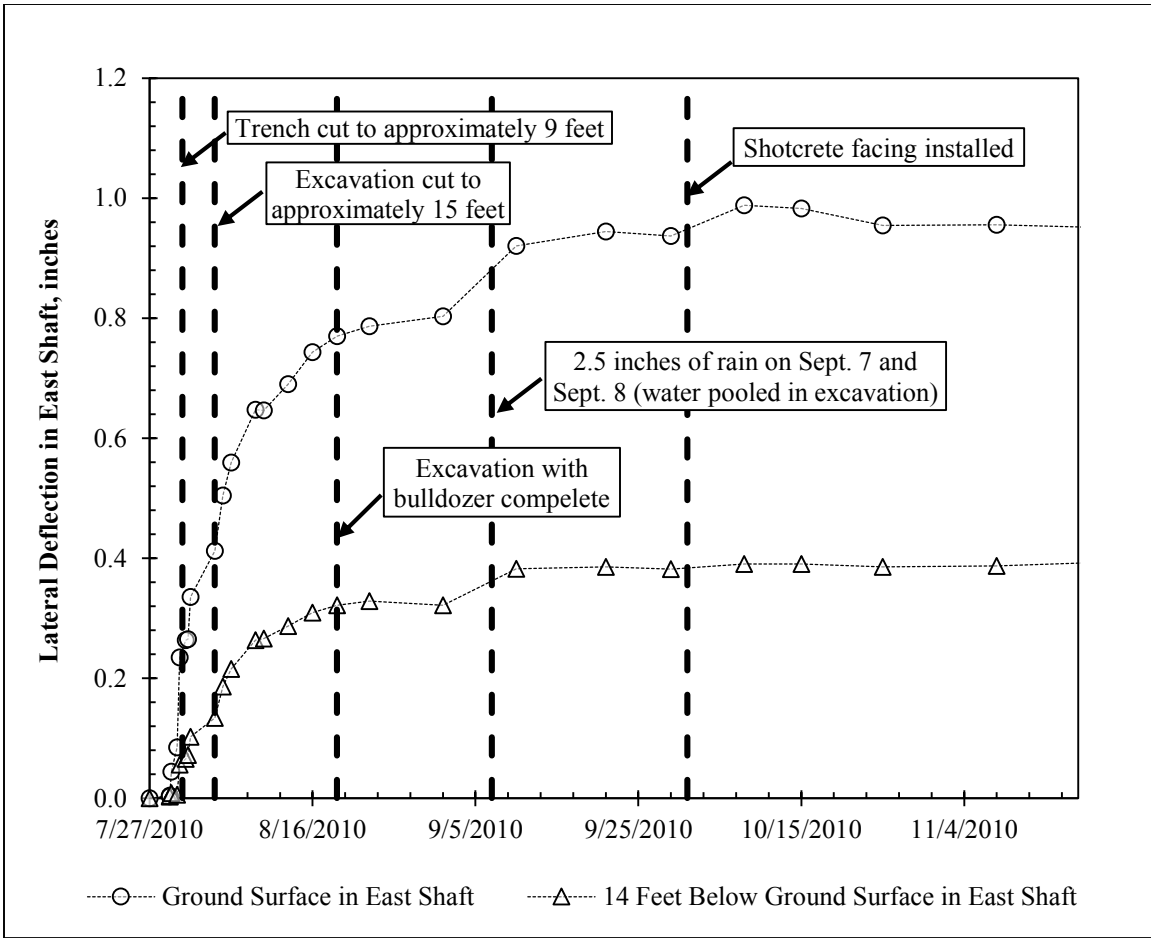


Figure 5.6: Progression of lateral deflections and key events during excavation.

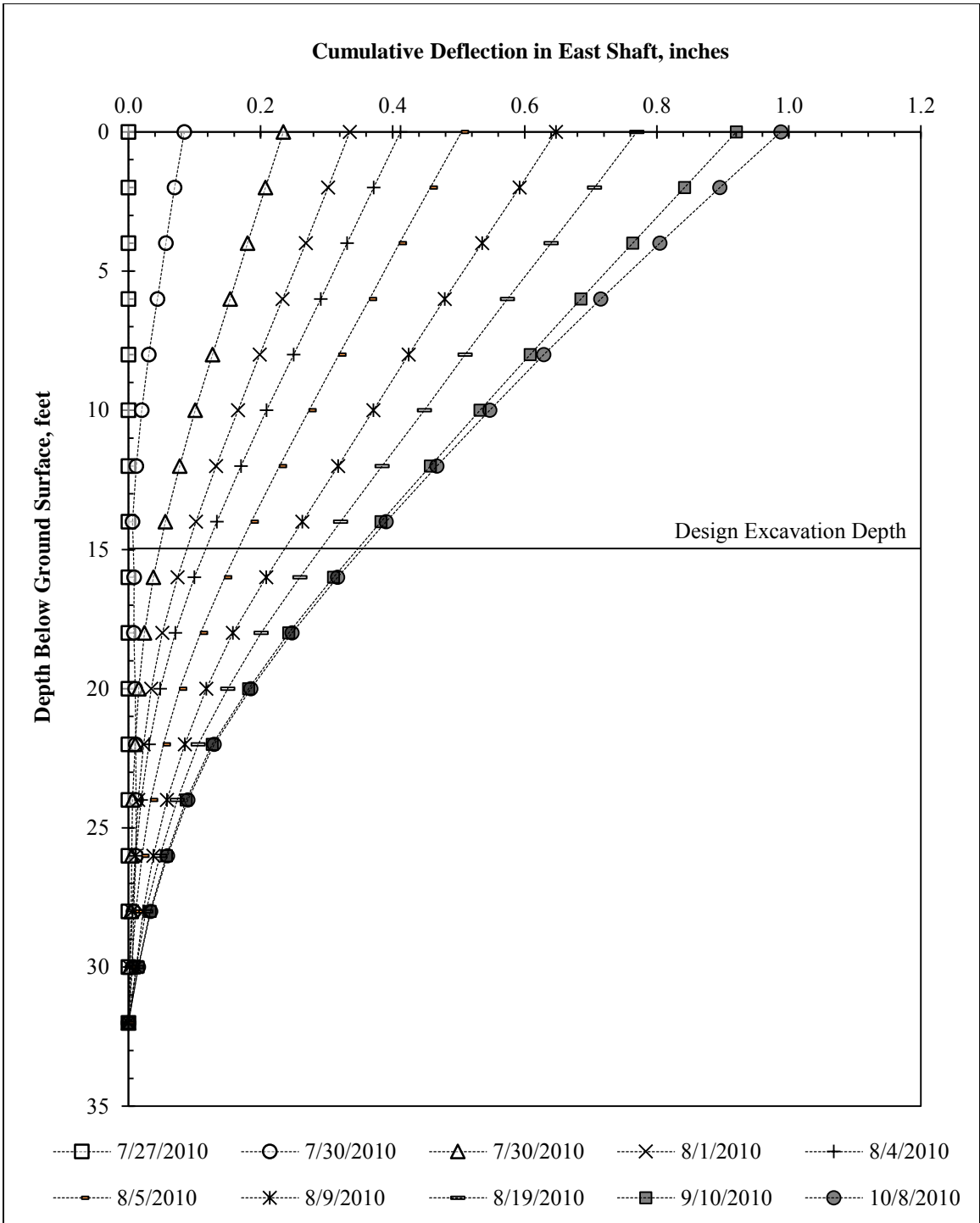


Figure 5.7: Deflected shape of east instrumented shaft at various dates during excavation.

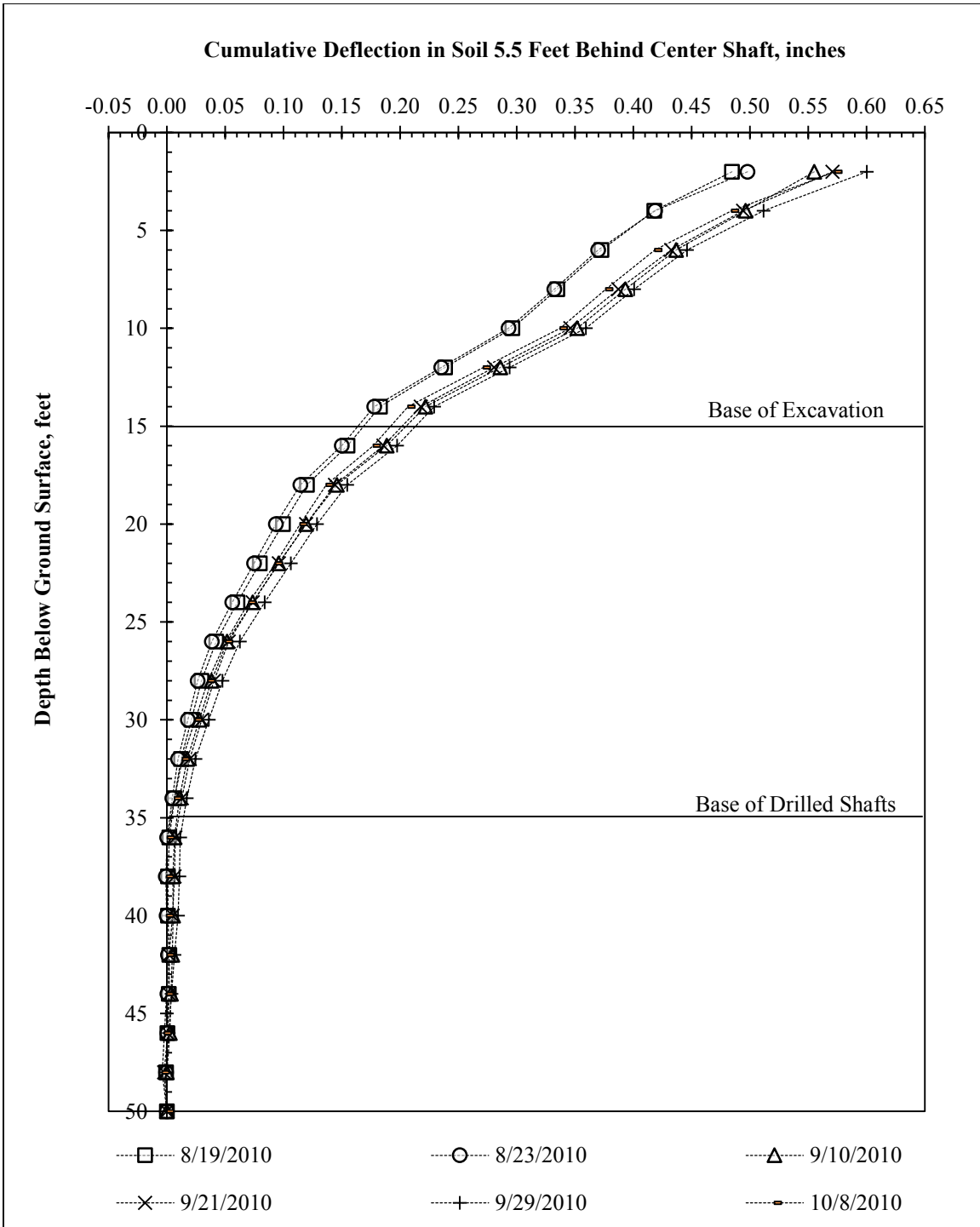


Figure 5.8: Cumulative deflections recorded in inclinometer installed through the soil 5.5 feet behind the center instrumented shaft.

5.2.2: LINEAR POTENTIOMETER DATA

A linear potentiometer was installed prior to excavation. It was attached to shaft #16, adjacent to the west instrumented shaft (shaft #15). It provides continuous data on top-of-wall deflection and redundancy with the inclinometer data. Linear potentiometer data during the first month of excavation, along with top-of-wall deflections for the three instrumented shafts, is provided in Figure 5.9.

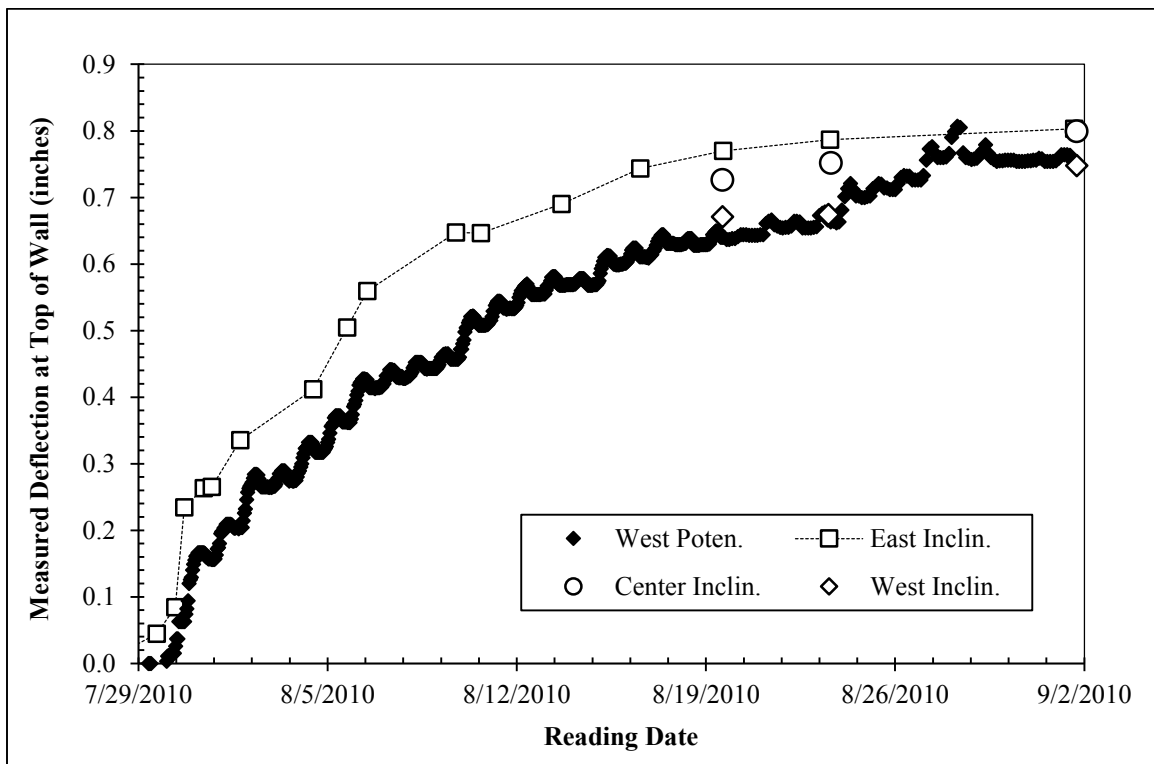


Figure 5.9: Deflection measured at top of wall during excavation. Excavation began on July 29 and continued through August 27.

5.2.3: STRAIN GAUGE DATA

Throughout the excavation progress, strain gauges were monitored in the three instrumented shafts. Strain data is presented in Figure 5.10 - Figure 5.24. In the following figures, strain data is zeroed on July 27, 2010.

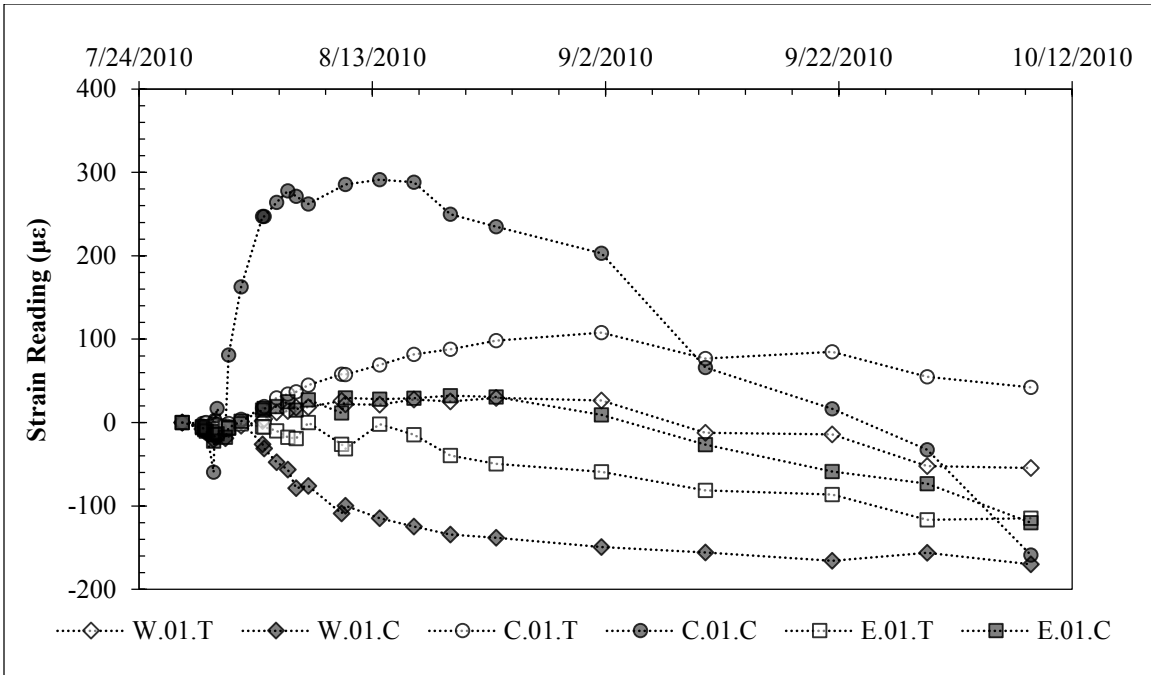


Figure 5.10: Strain Data 1 Foot Below Ground Surface During Excavation.

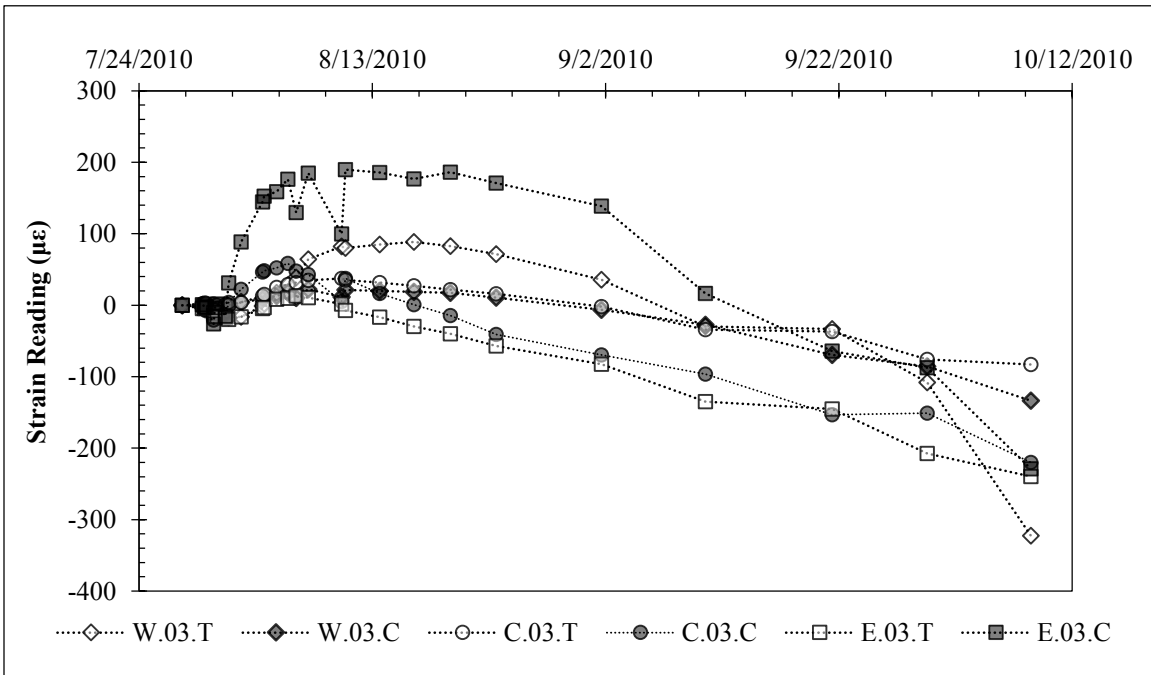


Figure 5.11: Strain Data 3 Feet Below Ground Surface During Excavation.

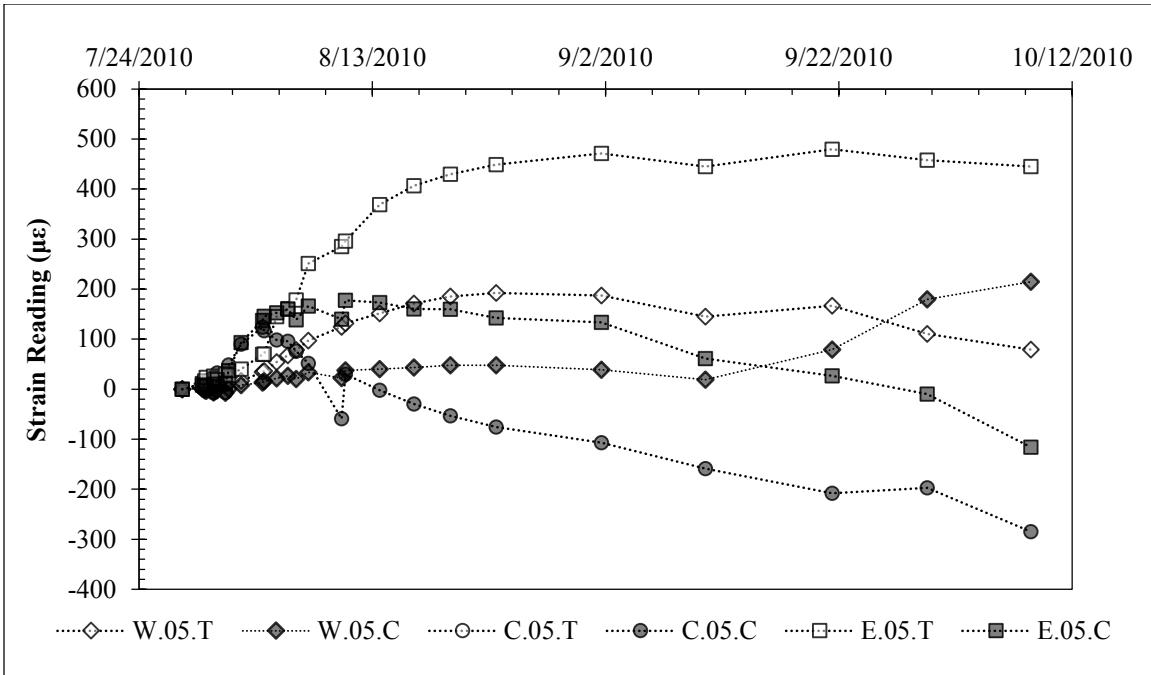


Figure 5.12: Strain Data 5 Feet Below Ground Surface During Excavation.

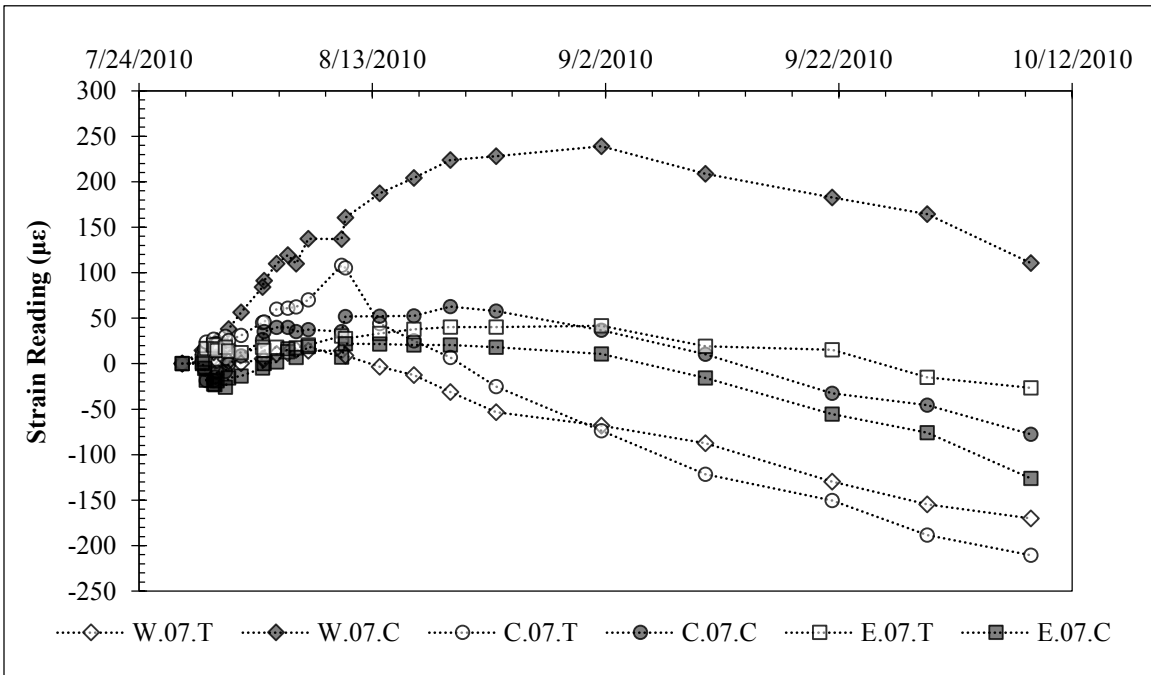


Figure 5.13: Strain Data 7 Feet Below Ground Surface During Excavation.

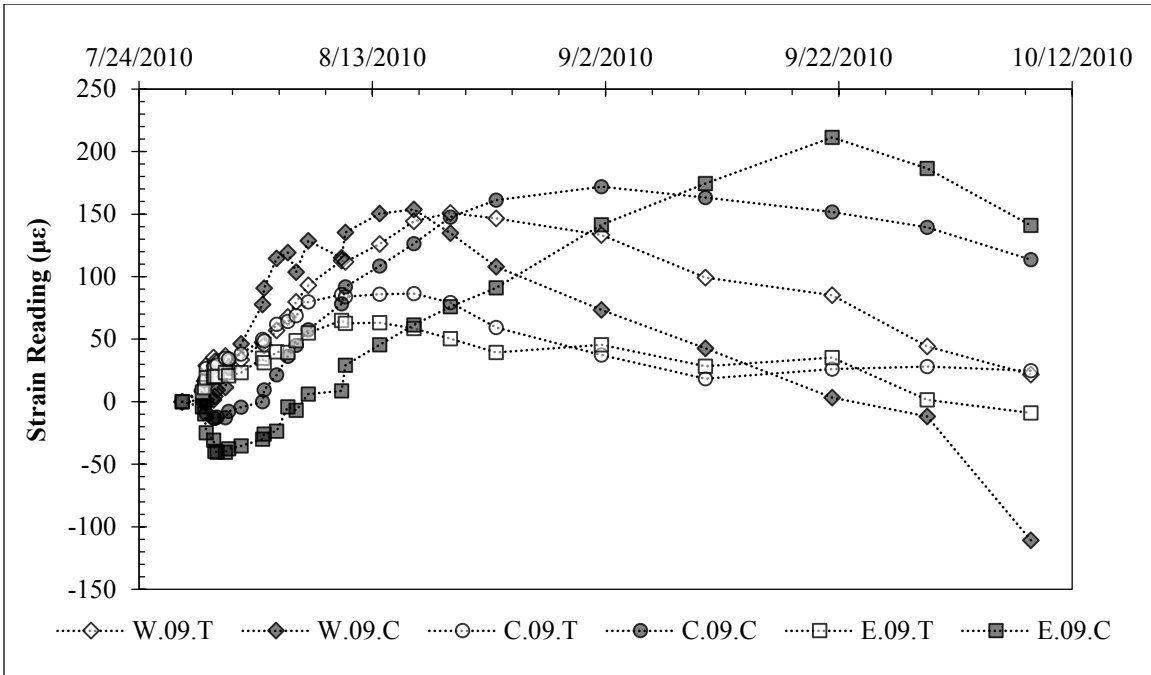


Figure 5.14: Strain Data 9 Feet Below Ground Surface During Excavation.

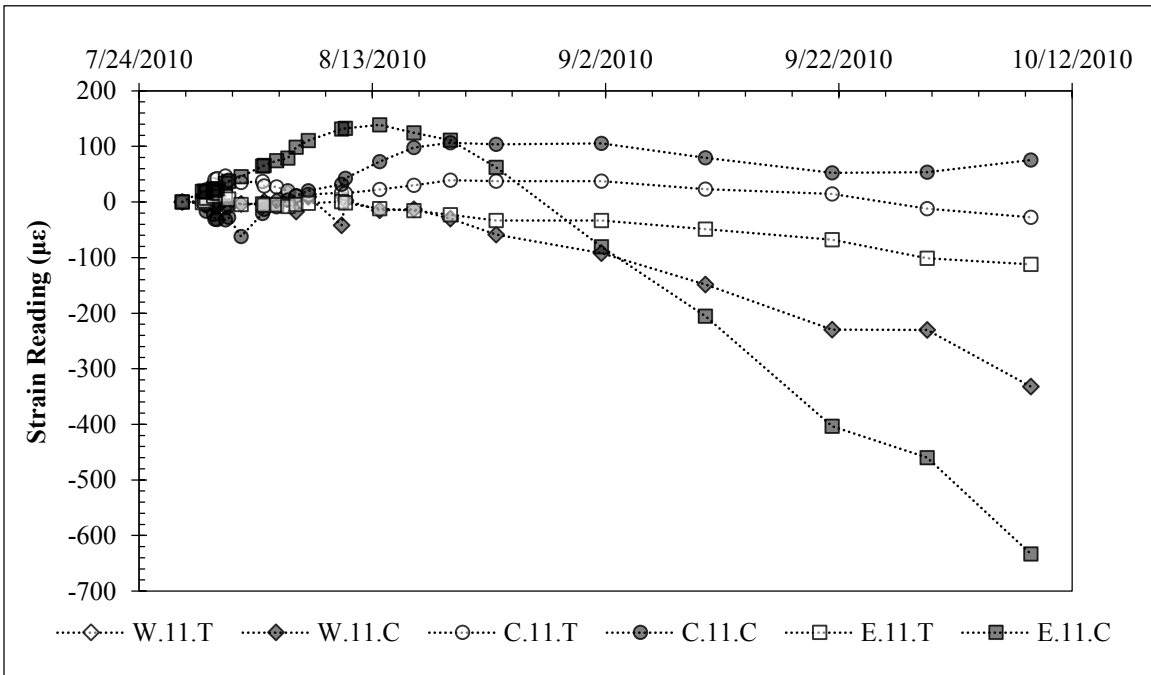


Figure 5.15: Strain Data 11 Feet Below Ground Surface During Excavation.

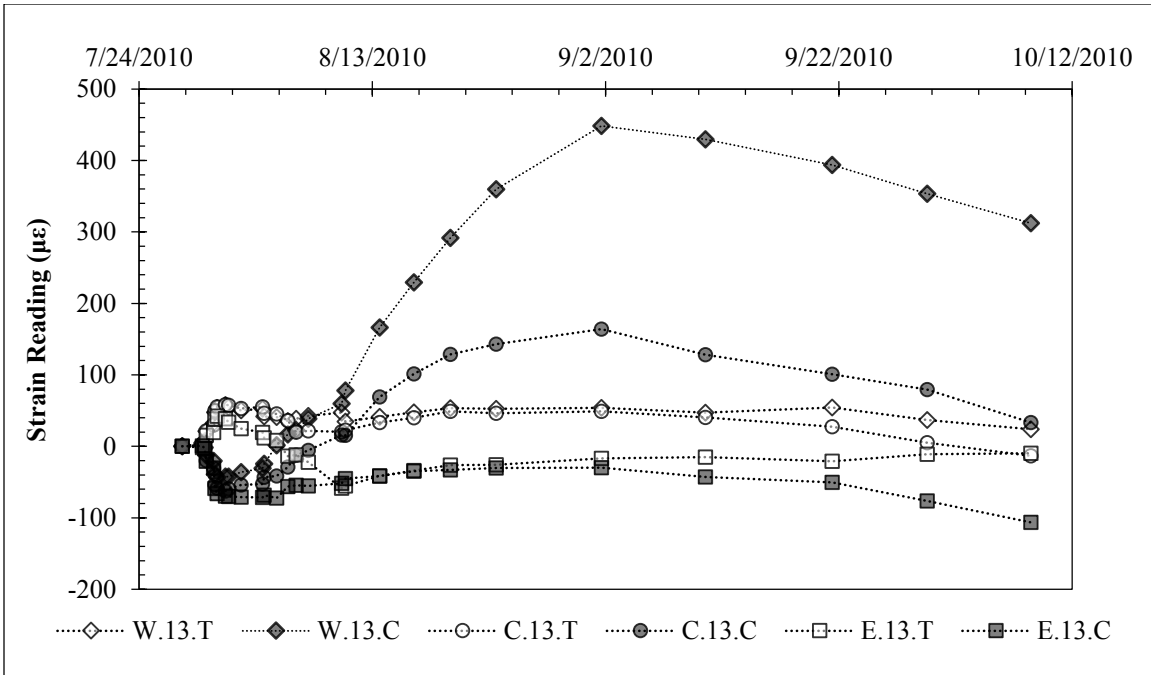


Figure 5.16: Strain Data 13 Feet Below Ground Surface During Excavation.

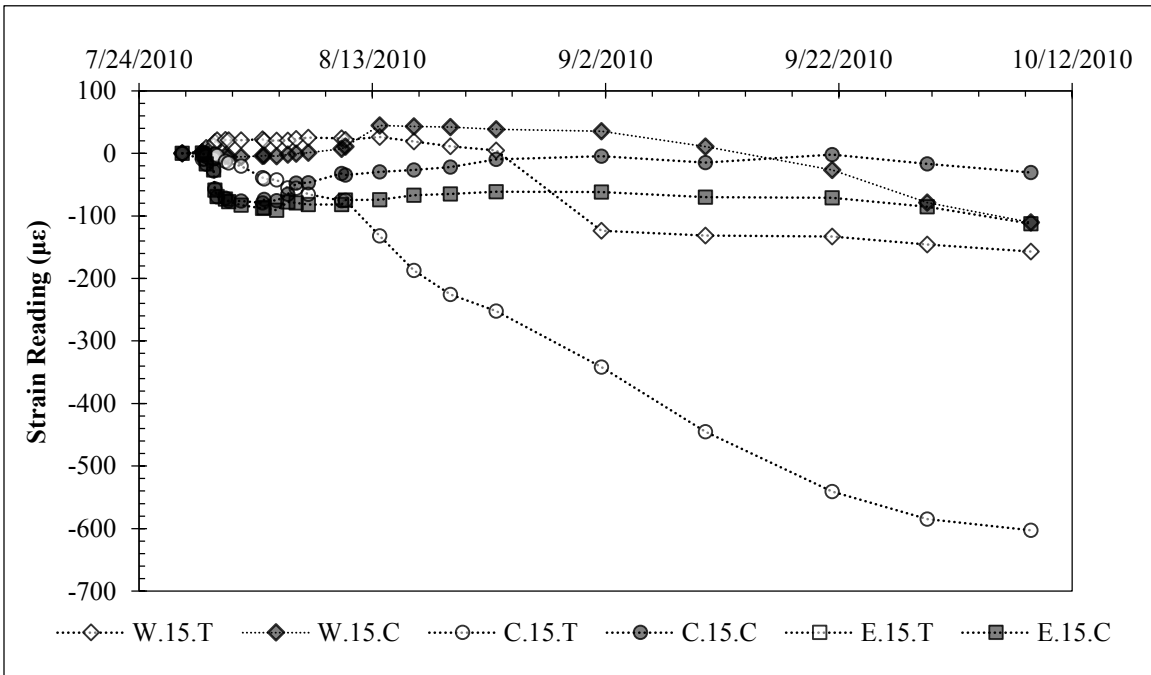


Figure 5.17: Strain Data 15 Feet Below Ground Surface During Excavation.

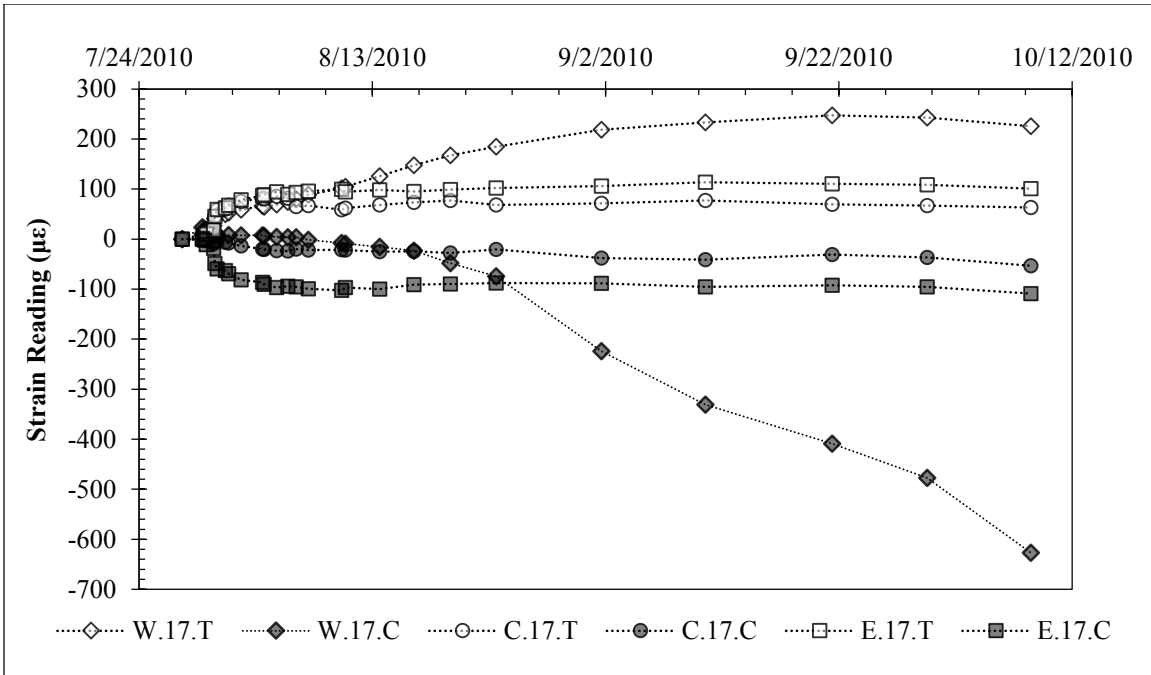


Figure 5.18: Strain Data 17 Feet Below Ground Surface During Excavation.

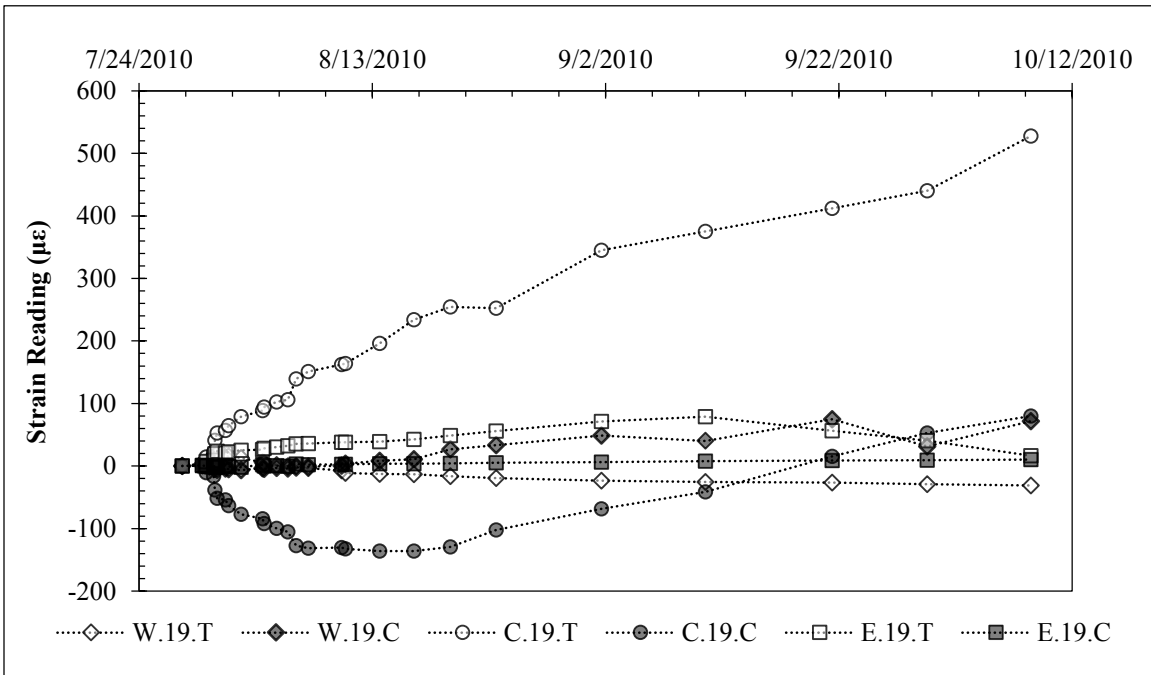


Figure 5.19: Strain Data 19 Feet Below Ground Surface During Excavation.

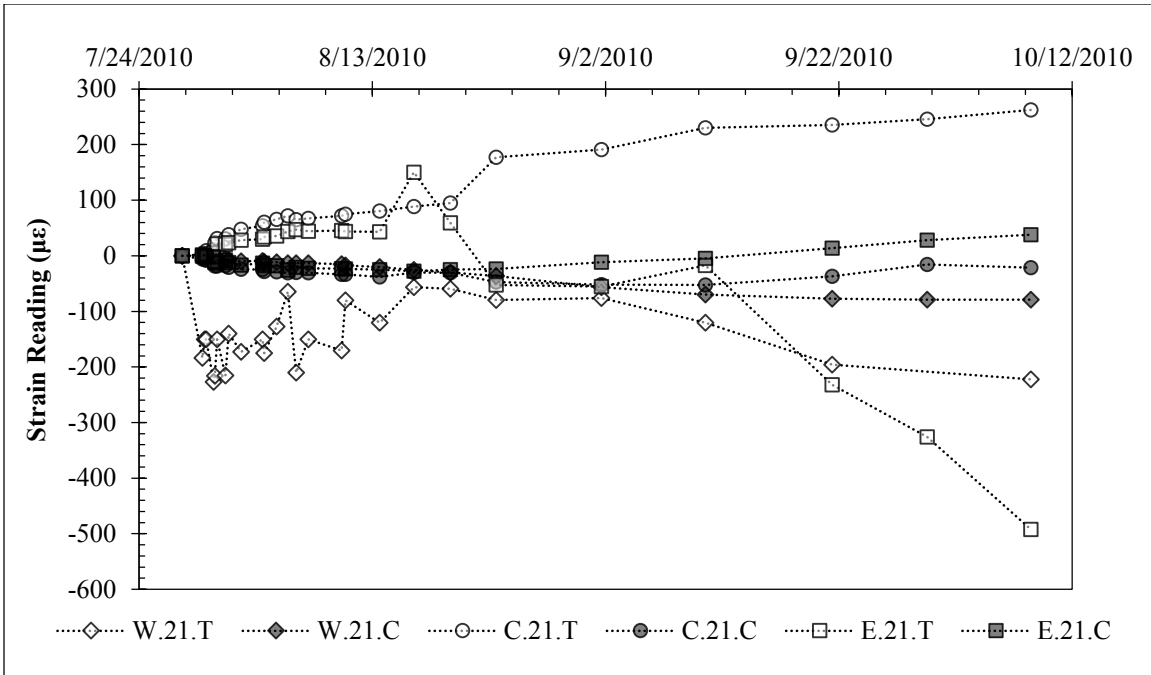


Figure 5.20: Strain Data 21 Feet Below Ground Surface During Excavation.

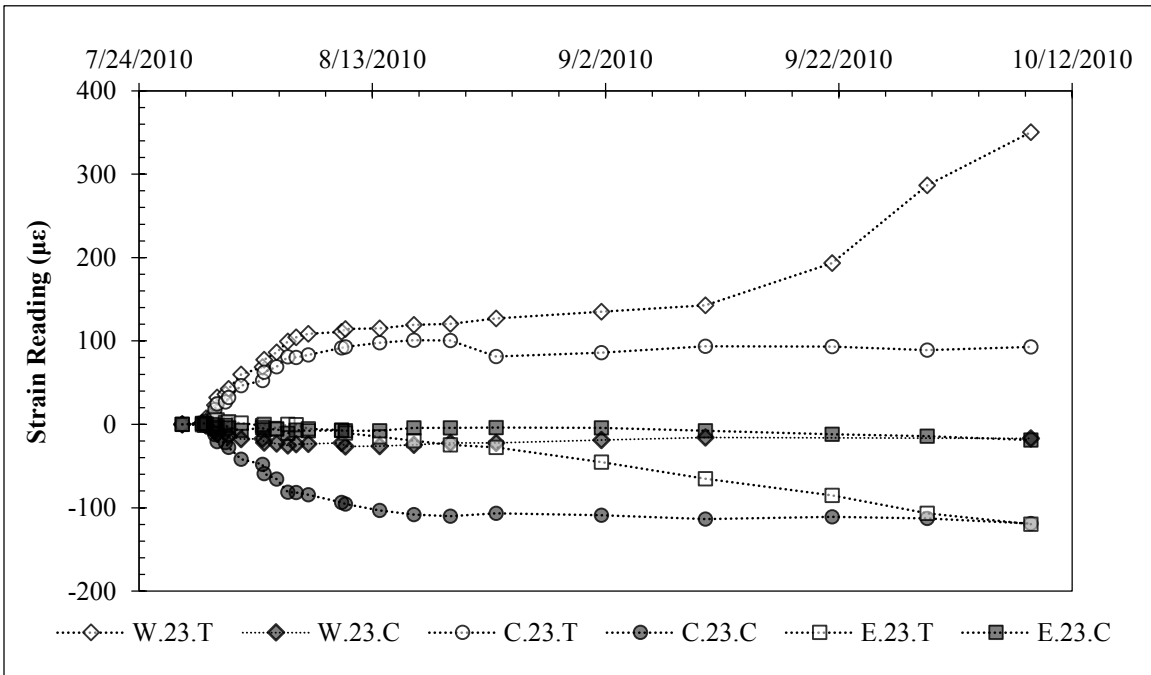


Figure 5.21: Strain Data 23 Feet Below Ground Surface During Excavation.

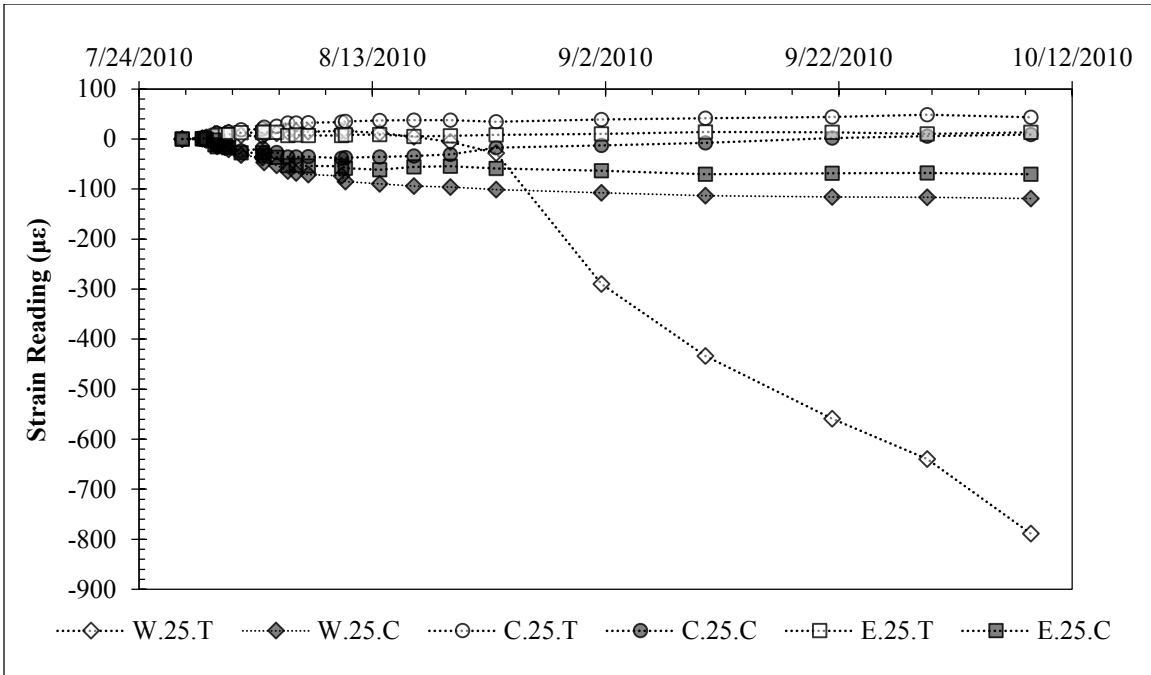


Figure 5.22: Strain Data 25 Feet Below Ground Surface During Excavation.

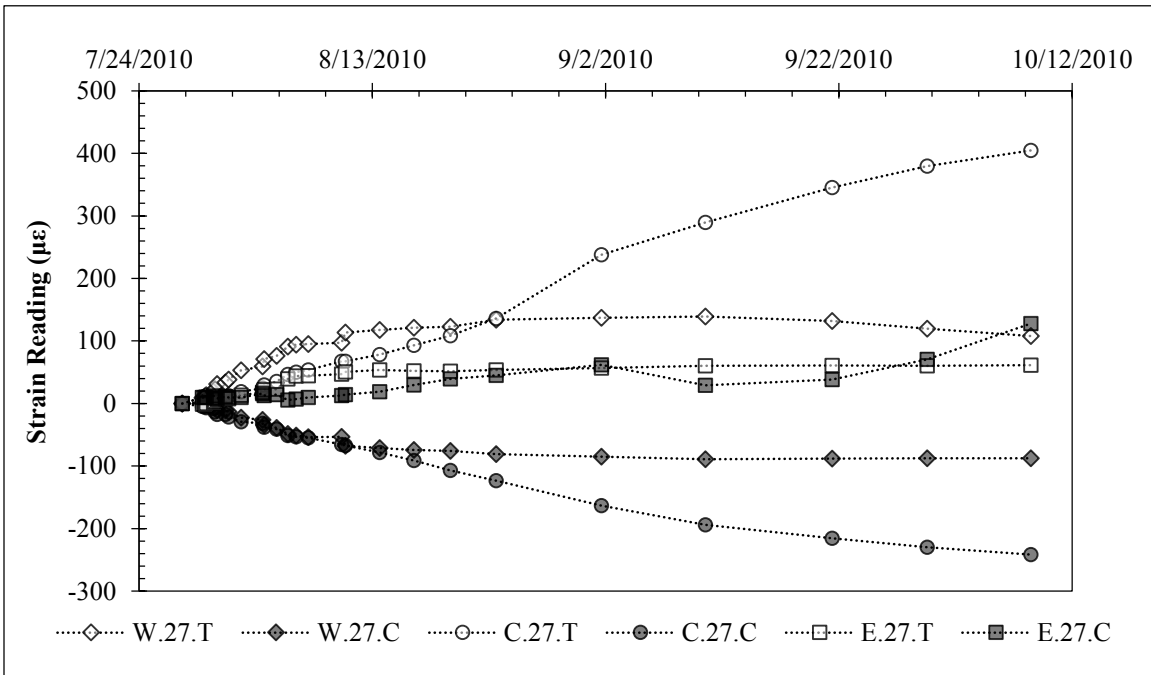


Figure 5.23: Strain Data 27 Feet Below Ground Surface During Excavation.

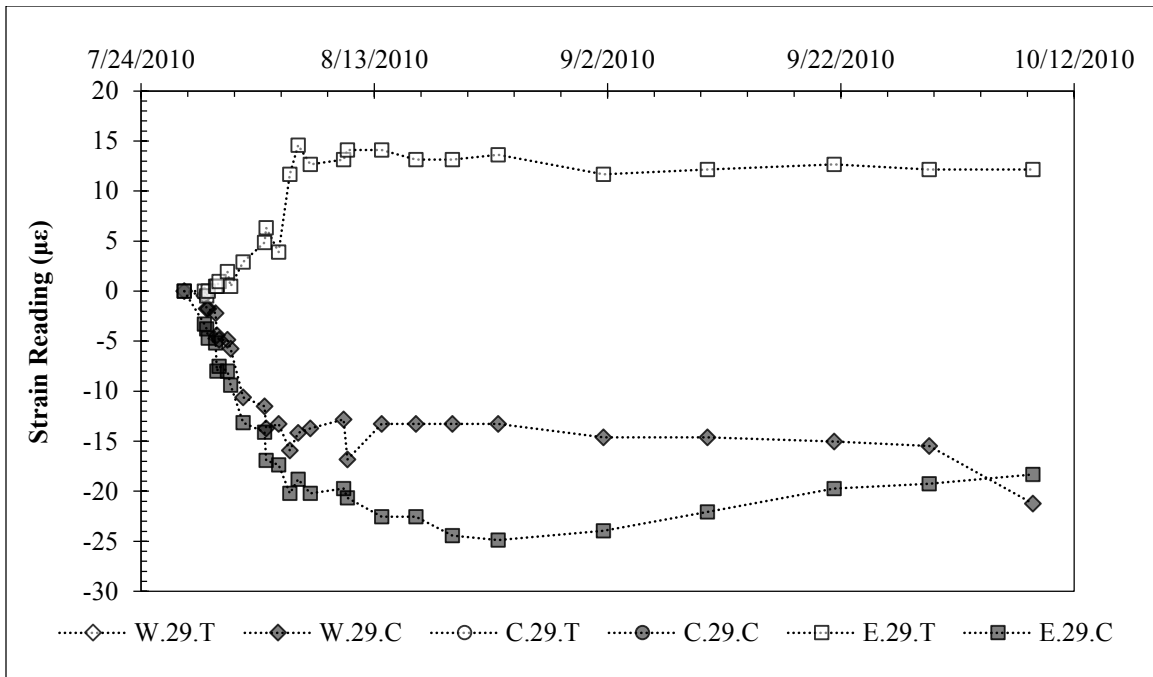


Figure 5.24: Strain Data 29 Feet Below Ground Surface During Excavation.

5.3: Data Interpretation

5.3.1: IMMEDIATE RESPONSE TO STRESS RELIEF

During excavation, the wall responded almost immediately to the relief of stress. The deflection at the top of the wall, measured directly with a linear potentiometer and in three inclinometers, is shown on Figure 5.9. The top-of-wall deflections developed more quickly on the east versus the west side because a larger volume of soil was initially removed from the east side (Figure 5.25). The final excavation dimensions at the centerline of the wall were, on average, reasonably close to the design values (Figure 5.26). The final deflections immediately after the excavation was completed were similar between the three shafts (Figure 5.9).

Between depths of 20 and 30 feet below the original ground surface (5 to 15 feet below the cantilever), the shafts developed a bending moment. Figure 5.27 shows axial

strains from a pair of strain gauges on either side of the shaft's neutral axis at the approximate location of the maximum bending moment. The strains are nearly equal and opposite, and their development is qualitatively similar to the increase in deflection with time at the top of the wall (Figure 5.9).

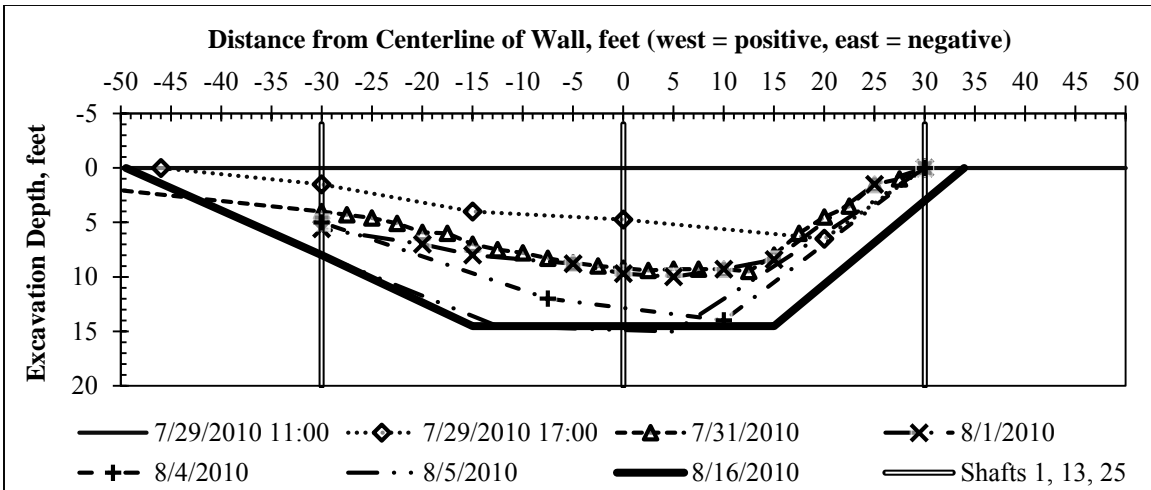


Figure 5.25: Progression of excavation depth along wall face.

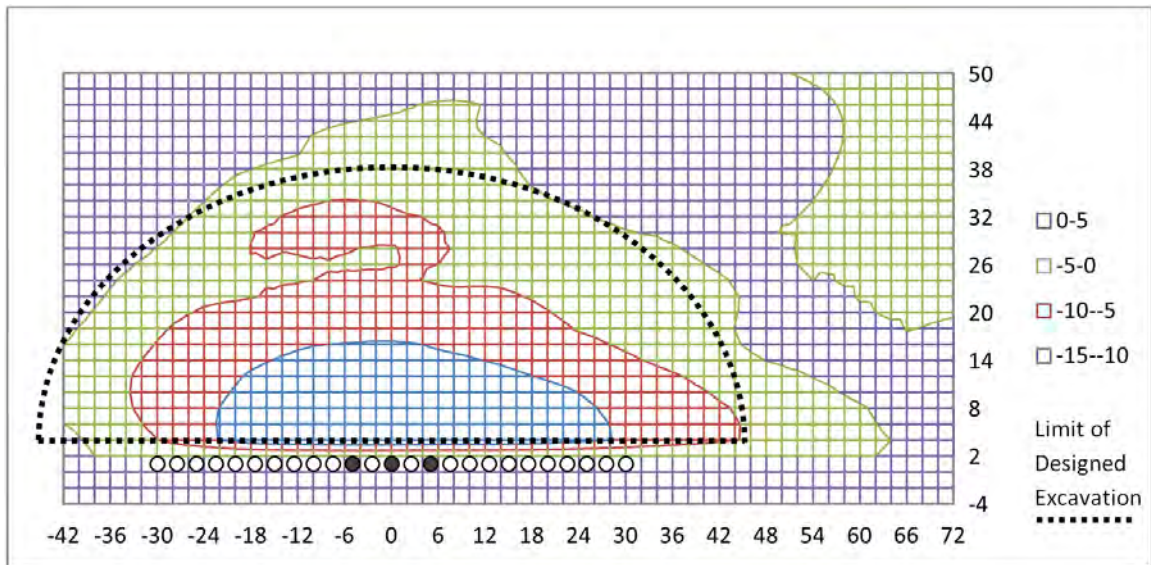


Figure 5.26: Contour plot of final surveyed excavation dimensions (all units in feet).

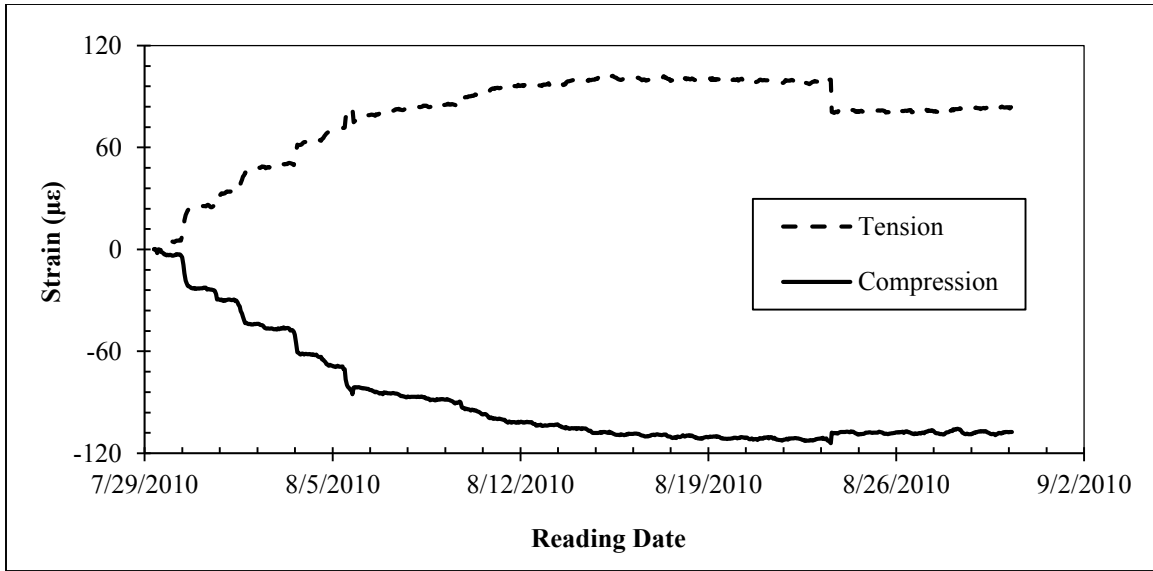


Figure 5.27: Development of bending strains in a pair of strain gauges located 23 feet below ground surface in the center shaft.

5.3.2: STRAIN GAUGE BEHAVIOR

5.3.2.a: Thermal Strains

As concrete was exposed to temperature changes during excavation, gauges on the exposed side of the wall began to register strains consistent with daily temperature fluctuations (Figure 5.28). Additionally, the average daily strain value increased as the shafts were exposed to the high ambient temperatures encountered during excavation. At a depth of 1 foot below ground surface, predicted bending moments are relatively small; the majority of the measured strains at shallow depths appear to be related to temperature increases, rather than increases in bending curvature caused by earth pressure loading. When strain gauge data are compared with daily temperature data, the strain gauges on the exposed side of the test wall register approximately 7 to 8 microstrains per degree Fahrenheit. Thermal strains will be analyzed in more detail in subsequent chapters.

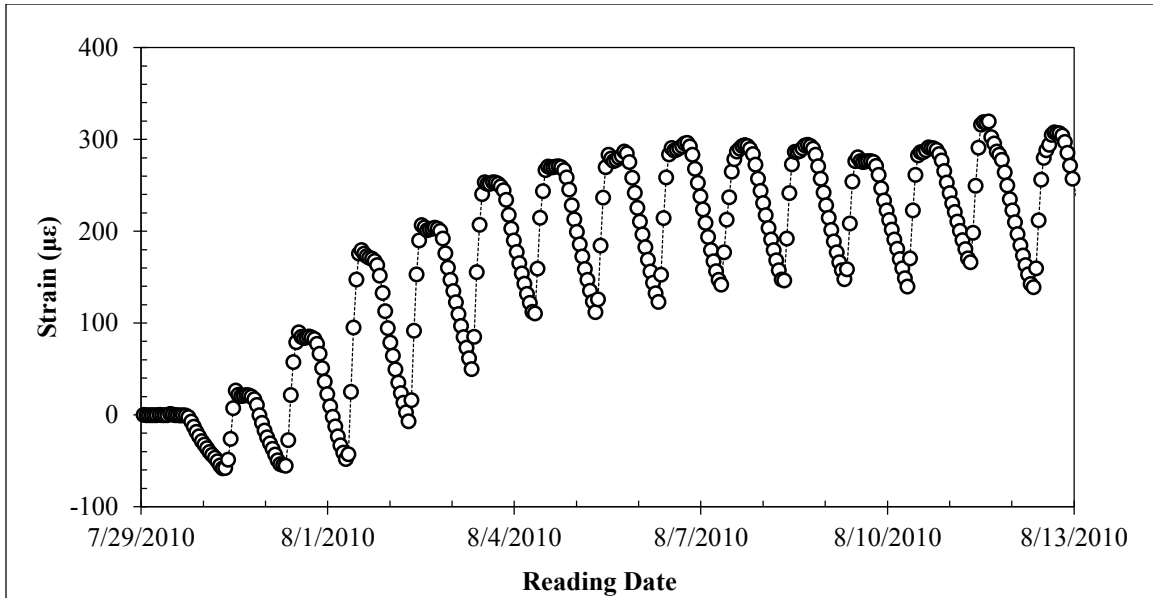


Figure 5.28: Strains related to temperature changes in exposed concrete. Gauge located 1 foot below ground surface on exposed side of wall. Soil at gauge location was excavated on July 29-31.

5.3.2.b: Gauges Above Excavation Line (1-13 feet below ground surface)

As a group, the strain gauges above the excavation line exhibited a response consistent with other data. Every functional gauge showed a response within days of the start of excavation. In general, this response was marked by a combination of bending curvature (tension gauge shows positive strain; compressive gauge shows a similar negative strain) and thermal strains. Some gauges (e.g. C.01.C, W.07.C) exhibited signs of tension cracking, despite being under primarily compressive loads. Additionally, some other pairs of gauges (e.g. C.03.T / C.03.C and E.07.T / E.07.C) exhibited signs of axial strains while maintaining a constant bending curvature. Effects such as these could be an indication of residual stresses developed prior to excavation influencing gauge response during excavation.

5.3.2.c: Gauges Below Excavation Line (15-29 feet below ground surface)

Below the excavation line, where predicted bending moments were higher and the concrete was not exposed by removal of soil, gauges showed more pronounced bending strains and minimal thermal effects. Some pairs of gauges (e.g. E.17.T / E.17.C and C.23.T / C.23.C) showed bending strains which are very close to ideal behavior for the observed deflection profile; these ideal gauges can be used to monitor relatively small changes in bending moment at those depths over time. Other pairs of gauges (e.g. C.19.T / C.19.C) maintained a consistent bending strain, but display axial strains that steadily increased in a tensile direction. Similar to the shallow gauges, some peculiar gauge behavior was observed, such as gauges steadily moving toward unusually large compressive strains (e.g. C.15.T, W.17.C, W.25.T), or large tensile strains in gauges that should be under compression (e.g. W.13.C). It is likely that unusual gauge behavior such as this was a result of residual stresses, tension cracking, or simply damage to the gauge. The deepest pair of functional gauges (E.29.T / E.29.C) displayed a small but measurable bending curvature which is consistent with estimates from inclinometer data.

5.3.3: DESIGN PREDICTIONS VERSUS OBSERVED BEHAVIOR

At the conclusion of excavation, the measured top-of-wall deflections were consistent with the initial design analysis predicted by a p-y analysis using a triangular earth pressure distribution of 40 psf per foot of depth (the current standard of practice in Texas). The input parameters for this analysis are summarized in Table 5.1: Baseline assumptions and design parameters for short-term LPILE analysis.. However, while the predicted and measured top-of-wall deflections are similar, the deflected shapes show significant differences (Figure 5.29).

Table 5.1: Baseline assumptions and design parameters for short-term LPILE analysis.

Parameter	Value
Total Unit Weight of Soil, γ_t	125 pcf
Equivalent Fluid Pressure Loading, γ_{EF}	40 psf/ft
Coefficient of Active Earth Pressure, k_a	0.31 (from γ_{EF} / γ_t)
Undrained Shear Strength, S_U	3,200 psf
Foundation Soil p-y Curves	Stiff Clay Without Free Water
Cracking Moment, M_{Cr}	680 k-in.
Yielding Moment, M_y	3,200 k-in.
Uncracked Bending Stiffness, EI_{uc}	67×10^6 k-in.
Cracked Bending Stiffness, EI_{cr}	18×10^6 k-in.
Soil Strength Reduction Due to Clear Spacing	0.5
Shaft Diameter	24 in.
Height of Retained Soil, H	180 in.
Reinforcement	12 #7 bars (1.6% of gross area)

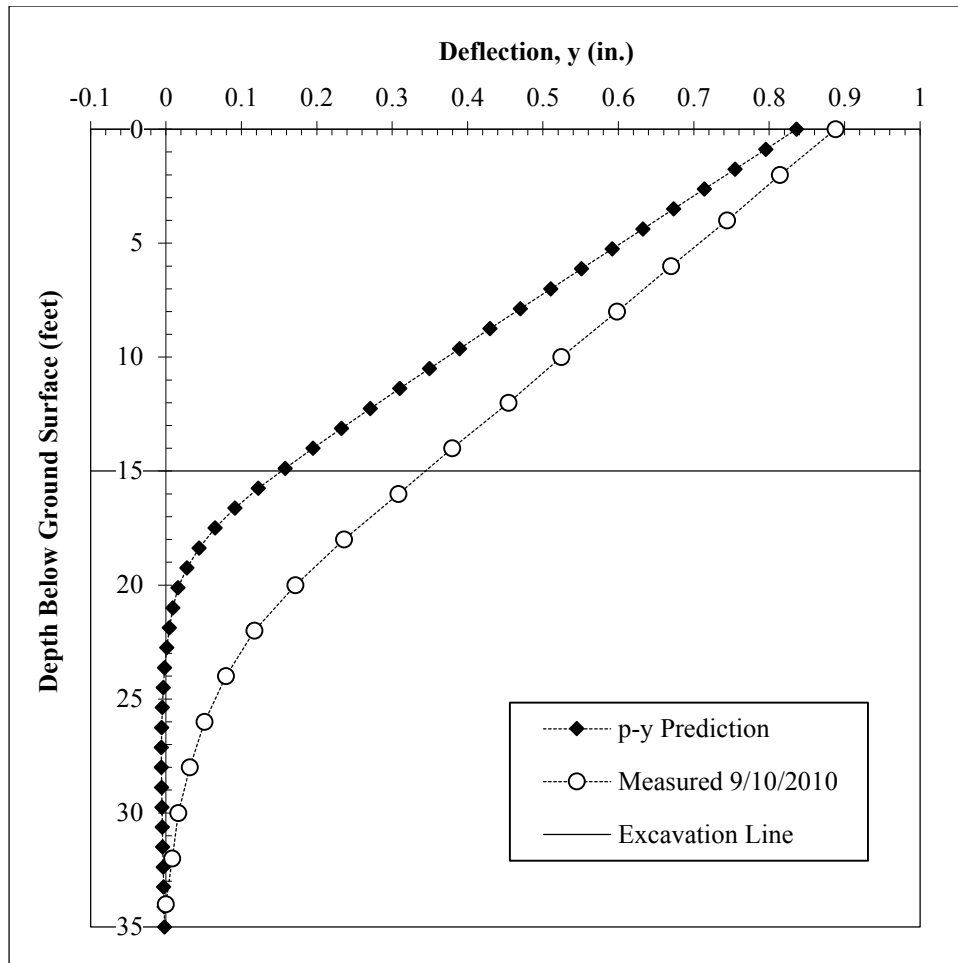


Figure 5.29: Comparison of p-y prediction with measured field data. P-y analysis used a triangular earth pressure distribution of 40 psf/ft.

Further examination of the field inclinometer data indicates that a significant amount of shaft base rotation occurred during excavation (Figure 5.30). This contrasts with the typical p-y formulation, in which the shaft base remains fixed and the shaft behavior is governed by an external load.

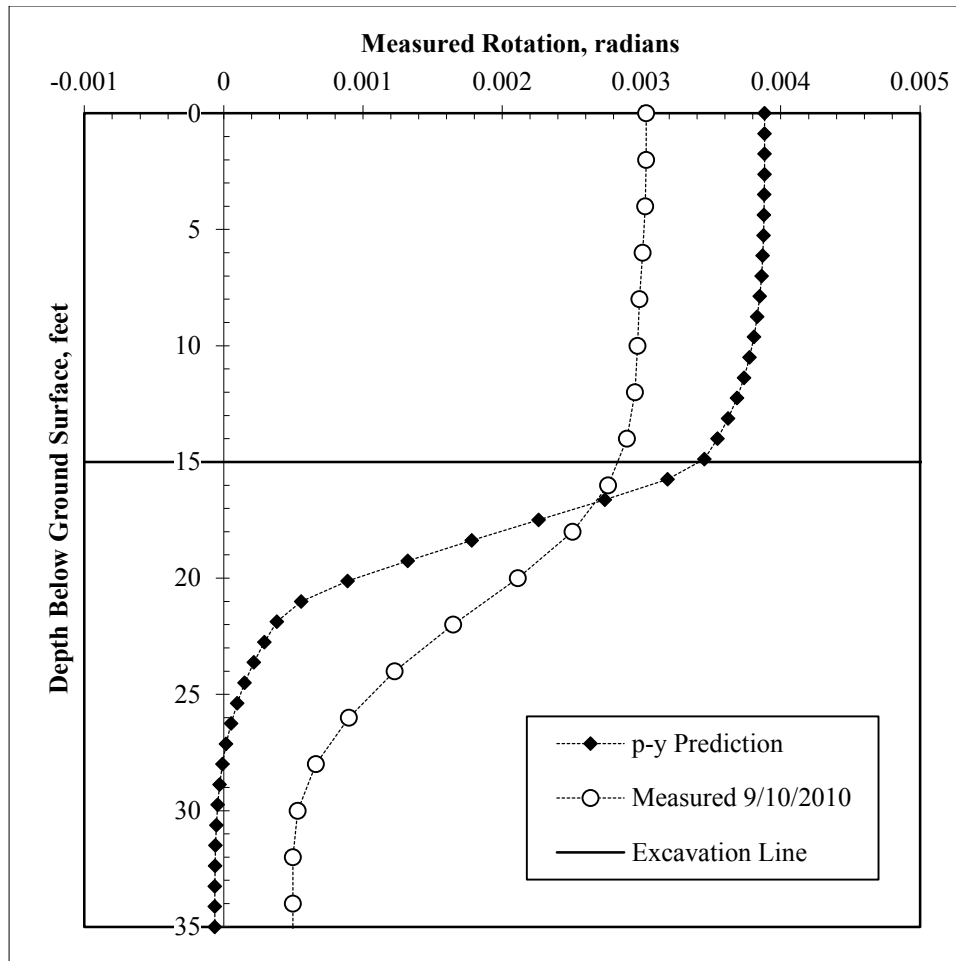


Figure 5.30: Comparison of predicted and measured shaft rotation profiles induced by removal of soil during excavation.

Because a significant amount of the measured top-of-wall deflection is the result of global soil/shaft movement and shaft base rotation, neither of which directly stress the shaft, the observed bending moments in the test wall are lower than those predicted by the p-y formulation (Figure 5.31). In a typical p-y formulation, where the deflection and rotation at the shaft base are taken to be zero, every increase in shaft deflection is accompanied by a corresponding increase in stress within the shaft. In the test wall, however, the presence of base rotation and global soil/shaft movement allows the shaft to

accommodate movements in other ways besides an increase in bending moment. As a result, our measured maximum bending moments are approximately 50% of the predicted value at a top-of-wall deflection of 0.9 inches (Figure 5.31). While deflection requirements often govern design and performance considerations, it is important to note that for a given top-of-wall deflection in our test wall, there may be more remaining bending moment capacity than a traditional p-y analysis would suggest.

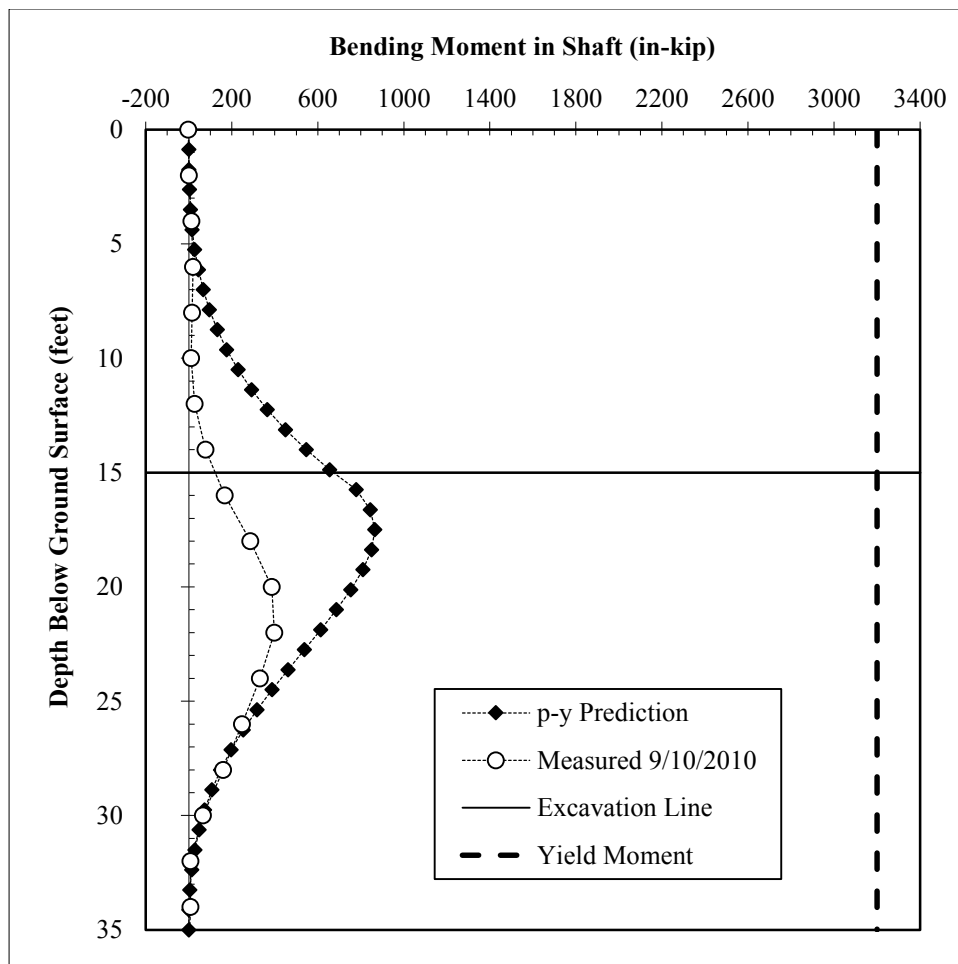


Figure 5.31: Comparison of predicted and measured bending moment profiles induced by removal of soil during excavation.

5.3.4: FINITE ELEMENT MODEL

It is possible that the differences between measured and predicted data are primarily due to global movements of the shaft/soil system in response to stress relief during excavation. To illustrate this concept, a simple linear elastic finite element model was used to represent the process of soil removal during excavation. In this model, the removal of excavated soil initiated a global response that extended well beyond the shaft base (Figure 5.32 - Figure 5.33). The quality of these global motions is consistent with the observed data, and with some adjustment of model soil parameters, the finite element model is consistent with the measured field inclinometer data (Figure 5.34).

The finite element model, although it is tremendously oversimplified, may provide some insight into the nature of soil response during excavation. In a sensitivity analysis, using commonly reported values of K_o for overconsolidated clays in Texas ($K_o = 2$ to 3), to achieve a deflected shape similar to the field measurement, average values of E/S_u were between 100 and 500 (Figure 5.34). The soil stiffness suggested by the finite element model is softer than our measured stiffness data from Spectral Analysis of Surface Waves (SASW) testing on the project site (Figure 5.35 – Figure 5.36) and the commonly used E/S_u value of 1000 for stiff clays, but is consistent with our stiffness data from UU testing and the general observation that stiff-fissured clays experience significant stiffness reductions during and after unloading (e.g. Cripps and Taylor, 1981).

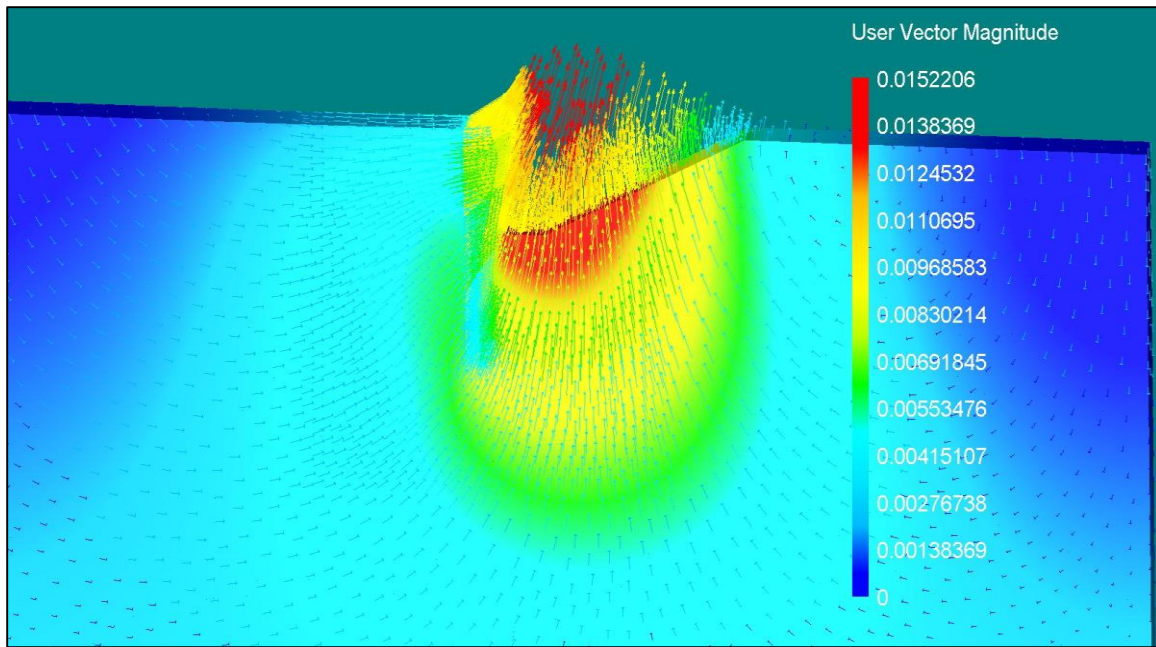


Figure 5.32: Global response to removal of soil in linear elastic FEM.

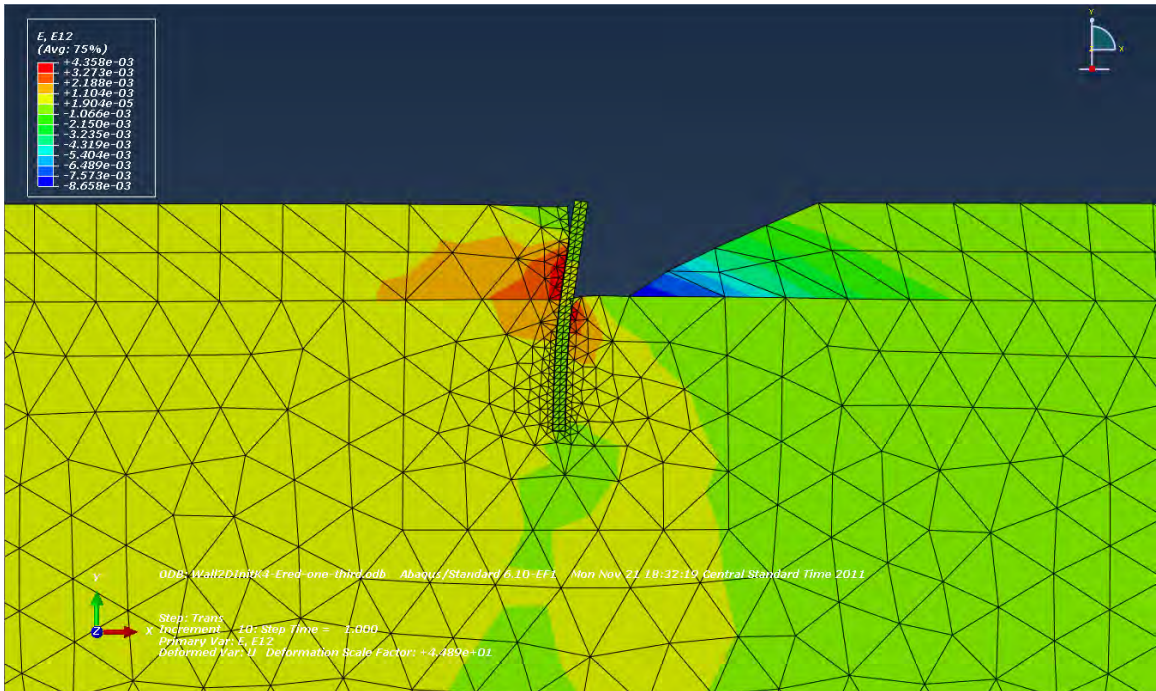


Figure 5.33: Global shear strains in response to removal of soil in linear elastic FEM.

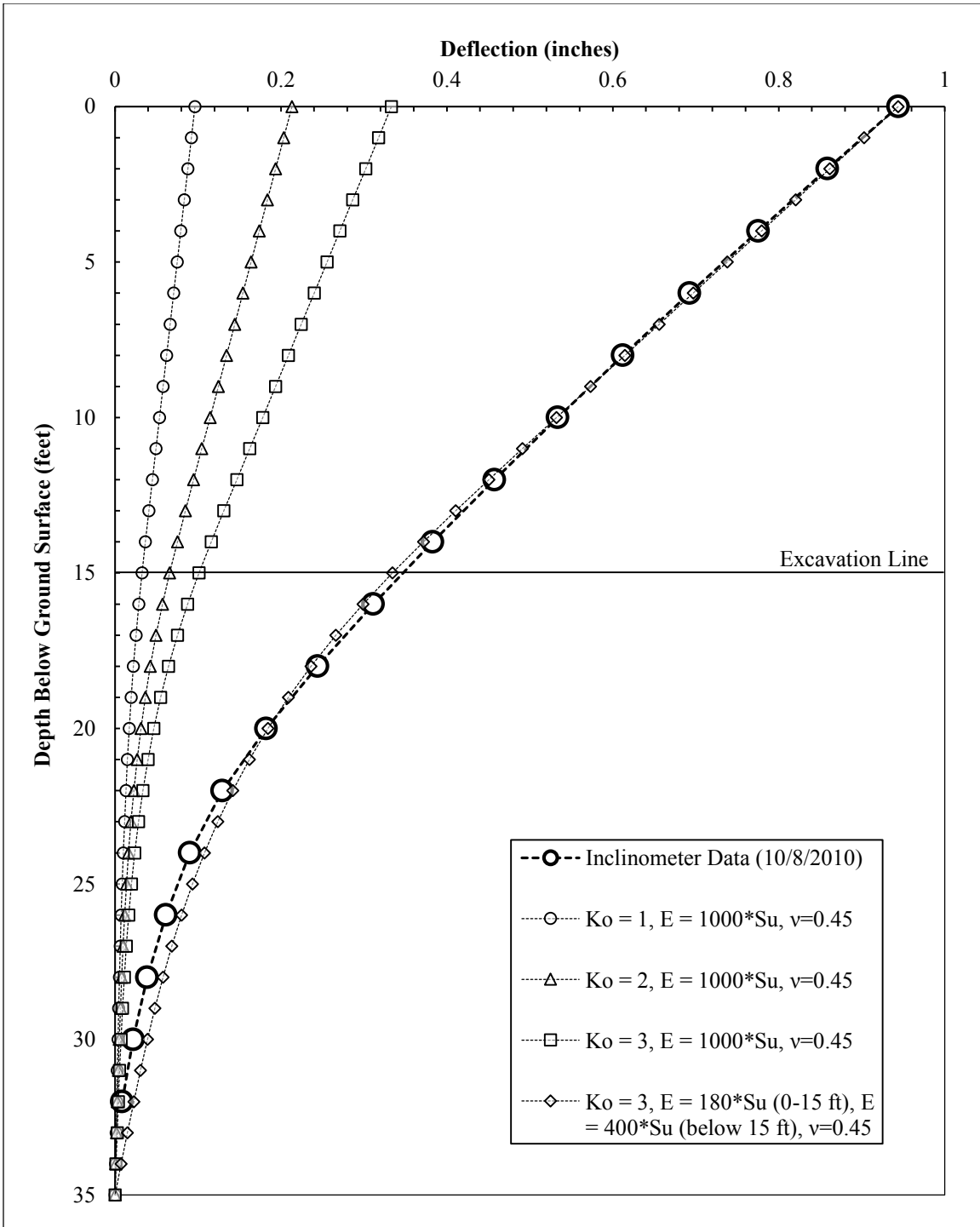


Figure 5.34: Comparison of linear elastic finite element model predictions with measured field data.



Figure 5.35: SASW testing at the test wall prior to excavation, June 2010.

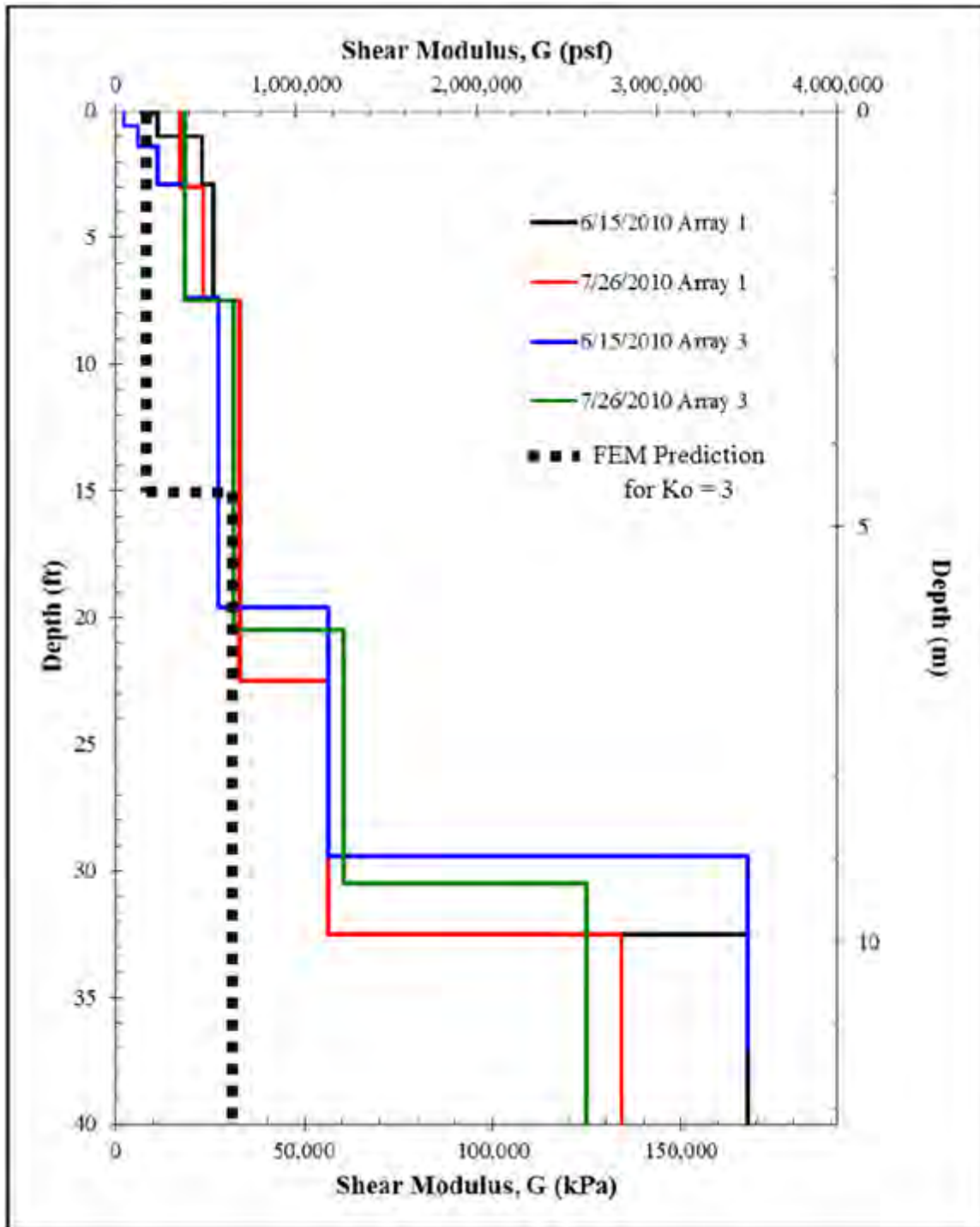


Figure 5.36: Comparison of measured shear modulus profiles from SASW testing with finite element model prediction (after Ellis, 2011).

5.3.5: MODIFIED LPILE ANALYSIS

5.3.5.a: Selection of Loading Conditions and p-y Curves

Based on the results of the finite element model and differentiation of the bending moment curves estimated from field data, a modified LPILE analysis was conducted. To minimize the effects of thermal deformations on data interpretation, the survey taken on September 10, 2010 is used for analysis. Additional discussion of thermal deformations is provided in the next chapter. Estimated values of bending moment and soil resistance are presented in Figure 5.37. The input earth pressure envelope for the LPILE analysis was defined using the calculated earth pressures from Figure 5.37 at depths of 0 to 14 feet. To simulate the effects of small thermal bending curvatures on wall movement, a bending moment of 40 in-kip was applied at the top of the shaft to provide consistency with the measured bending moment diagram above the excavation line (the development of this process is discussed in Chapter 6). A “thermal moment” of 40 in-kip is consistent with a small positive bending curvature due to the front of the wall being cooler than the back of the wall (it is important to note, however, that thermal curvatures do not directly stress the wall). The excavation depth was set at 14 feet for consistency with the as-built measurements of the excavation.

The p-y curves calculated from the field inclinometer data are compared with representative curves at depths between 16 and 22 feet below the original ground surface in Figure 5.38 to Figure 5.43. Of the proposed curves surveyed, the curves based on drained, fully softened strength parameters ($\phi = 24$) with effective weights and non-default values of initial stiffness ($k_{py} = 375 \text{ lb/in}^3$) provide a reasonable approximation of the foundation soil response. Based on the heavily fissured structure of the soil, the presence of stress relief due to unloading, and the softer-than-expected soil response, it is possible that the stiff-fissured clay in the base of the excavation has already reached drained

conditions. In the subsequent LPILE analysis during excavation, drained, fully softened curves with non-default initial stiffness values are used to model the foundation soil behavior. A summary of input parameters for the modified LPILE analysis is provided in Table 5.2.

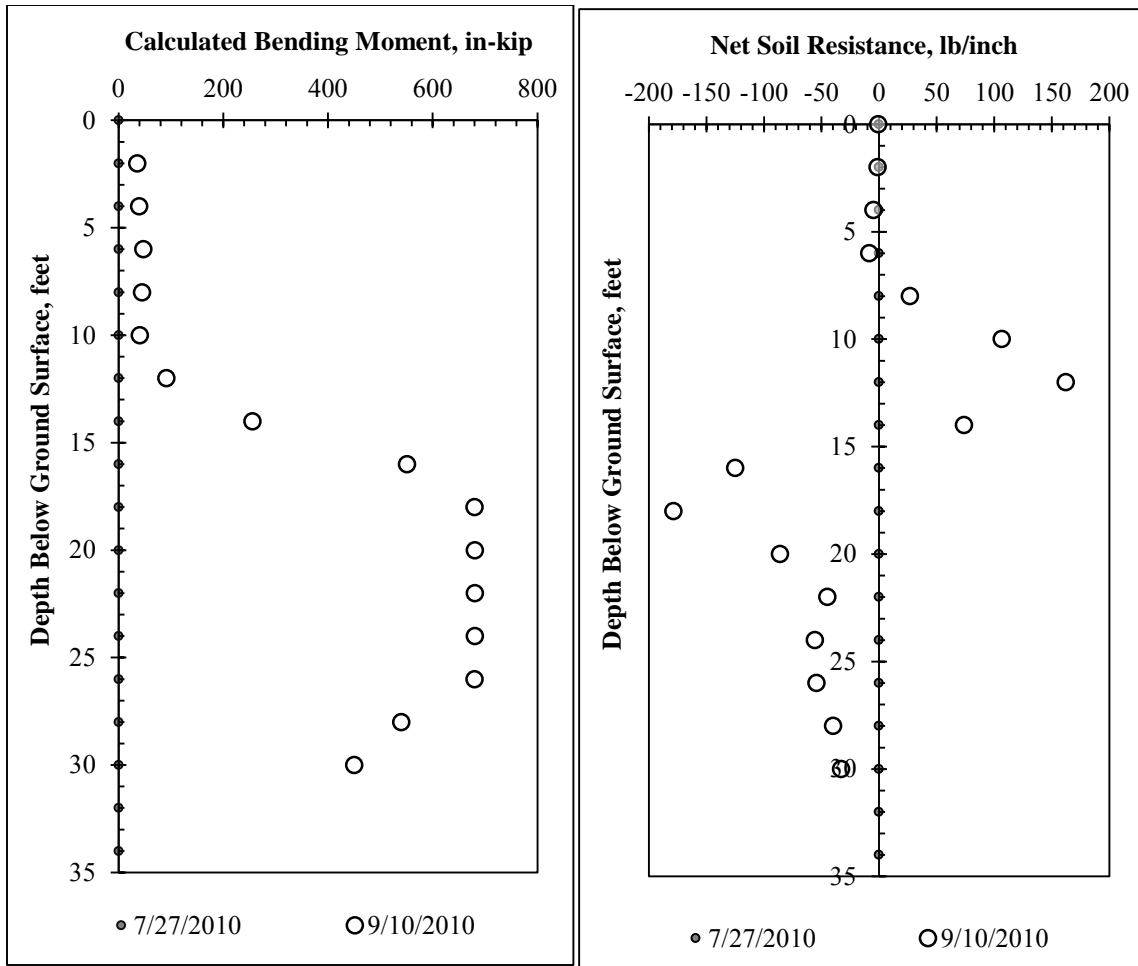


Figure 5.37: Calculated values of bending moment and net soil resistance during excavation, based on measured rotation profiles from inclinometer data.

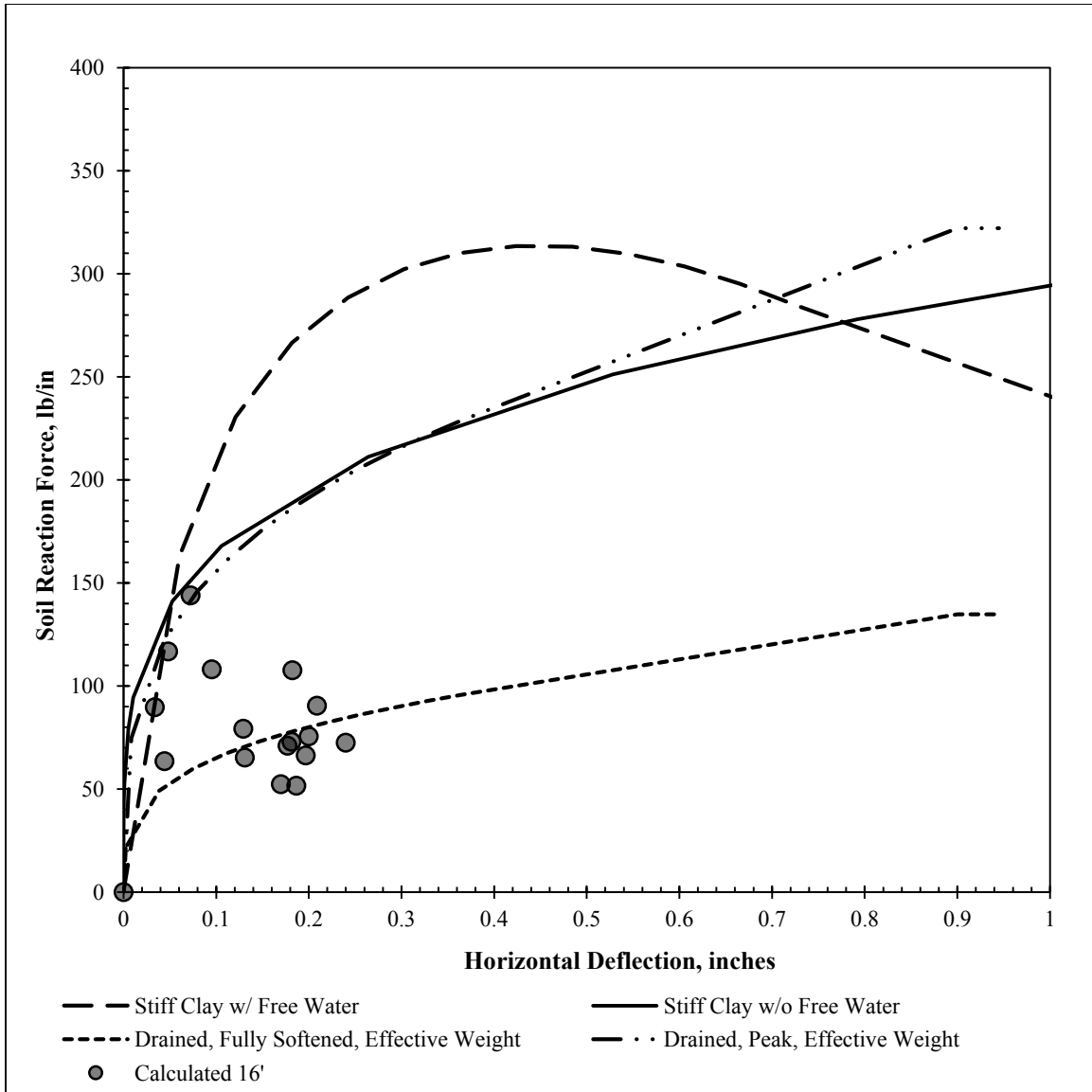


Figure 5.38: Comparison of calculated p-y curves during excavation with proposed p-y curves at a depth of 16 feet below original ground surface.

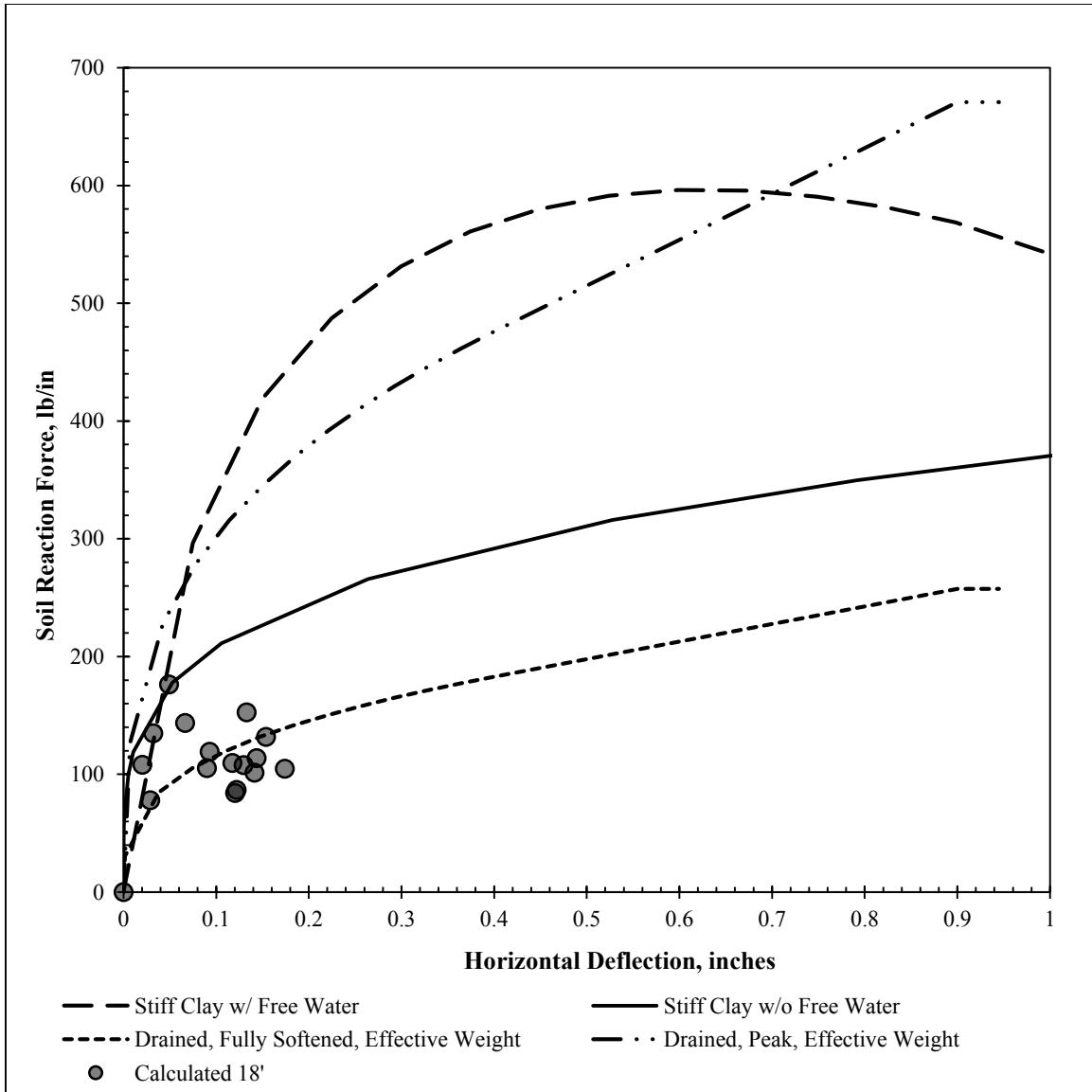


Figure 5.39: Comparison of calculated p-y curves during excavation with proposed p-y curves at a depth of 18 feet below original ground surface.

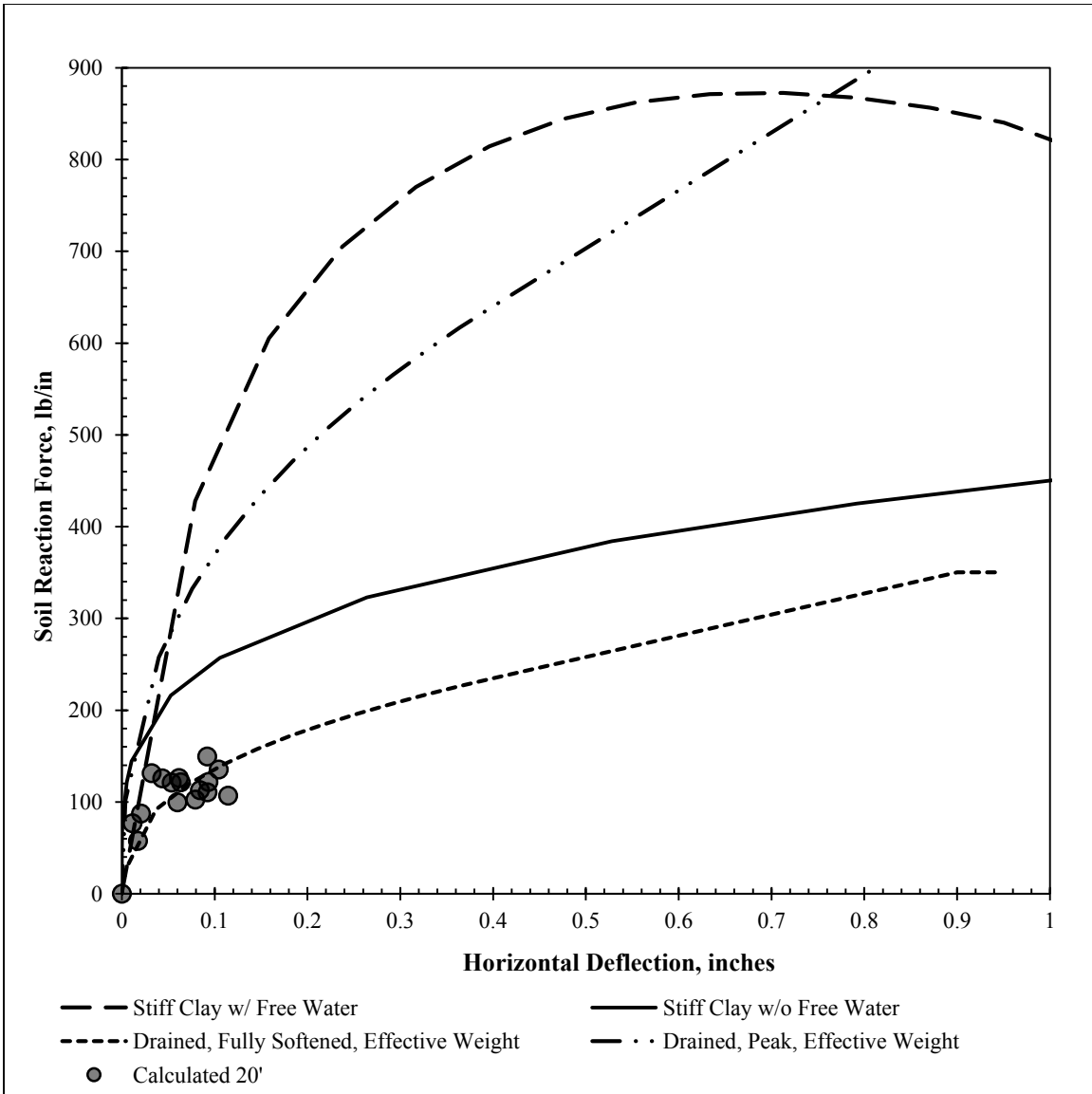


Figure 5.40: Comparison of calculated p-y curves during excavation with proposed p-y curves at a depth of 20 feet below original ground surface.

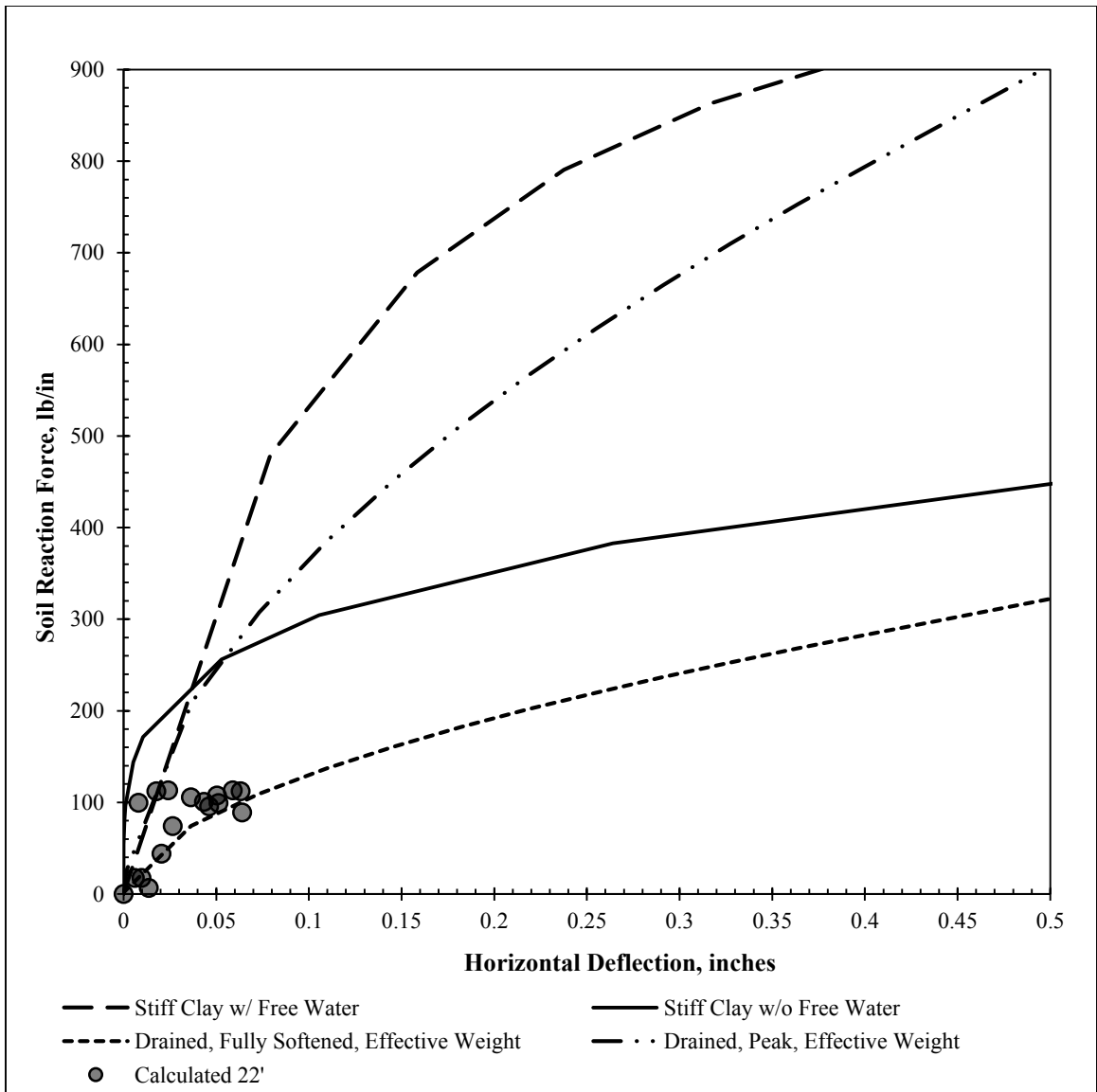


Figure 5.41: Comparison of calculated p-y curves during excavation with proposed p-y curves at a depth of 22 feet below original ground surface.

Table 5.2: Baseline assumptions and design parameters for modified LPILE analysis.

Parameter	Value
Effective Unit Weight of Soil, γ	62.6 pcf
Earth Pressure Loading	Input Envelope from Calculated p_{net}
Additional Moment Applied at Top for Thermal Effects	40 k-in
Friction Angle of Foundation Soil	24 degrees
Foundation Soil p-y Curves	Sand (Reese)
Non-Default Initial Stiffness, k_{py}	375 lb/in ³
Cracking Moment, M_{Cr}	680 k-in.
Yielding Moment, M_y	3,200 k-in.
Uncracked Bending Stiffness, EI_{uc}	67×10^6 k-in.
Cracked Bending Stiffness, EI_{cr}	18×10^6 k-in.
Shaft Diameter	24 in.
Height of Retained Soil, H	168 in.
Reinforcement	12 #7 bars (1.6% of gross area)

5.3.5.b: Results of Modified LPILE Analysis

Based on the results of the modified LPILE analysis, measured values of bending moments (Figure 5.42) and soil reaction forces (Figure 5.43) are slightly larger than those predicted by LPILE. The use of fully softened strengths for p-y curves may influence this discrepancy, as the field behavior of the soil has likely not degraded to fully softened conditions over the entire shaft depth. The consistency in bending moments, earth pressures, and soil reaction forces between the measured values and the LPILE analysis suggests that the loading conditions on the pile have been modeled reasonably well; despite this, the measured and predicted deflection profiles show considerable differences (Figure

5.42). This is likely due to global movements of the soil-shaft system similar to those predicted by the FEM.

By subtracting the measured deflection profile from the profile predicted by LPILE under similar loading conditions, a profile of global soil movements can be estimated. The results of this analysis are presented in Figure 5.44. The profile of global horizontal soil movement with depth can be nearly bounded between two straight lines corresponding to top-of-wall deflections of 0.10 and 0.15 percent of the wall height, extending to zero at the shaft base (Figure 5.44). The influence of horizontal deflection becomes slightly less pronounced near the shaft base, further from the stress relief of the excavation. Based on the results of this analysis, global movements of the soil-shaft system may account for approximately 30% of the measured top-of-wall deflection.

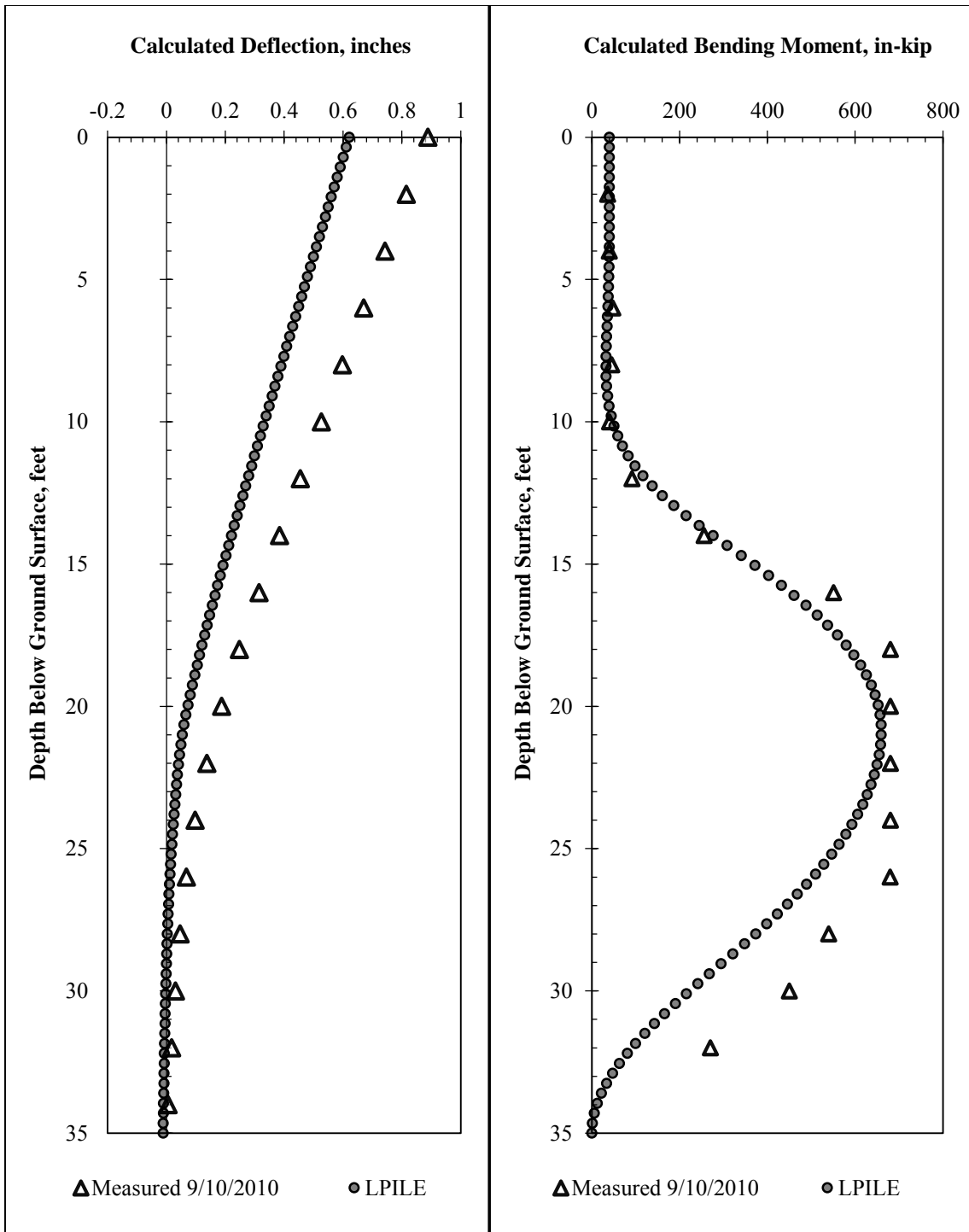


Figure 5.42: Comparison of measured and calculated profiles of deflection and bending moment in advanced LPILE analysis.

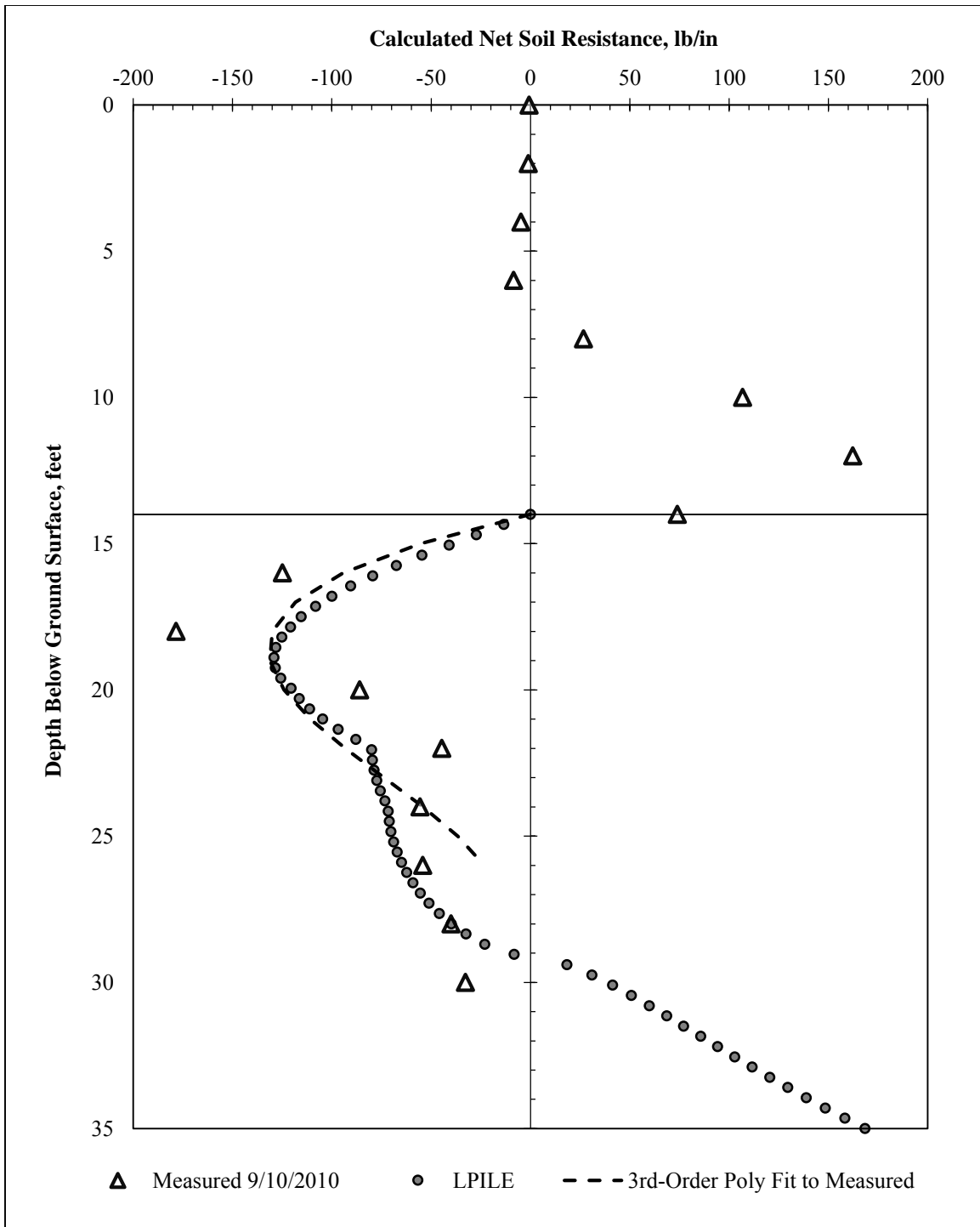


Figure 5.43: Comparison of measured and calculated profiles of soil resistance in advanced LPILE analysis.

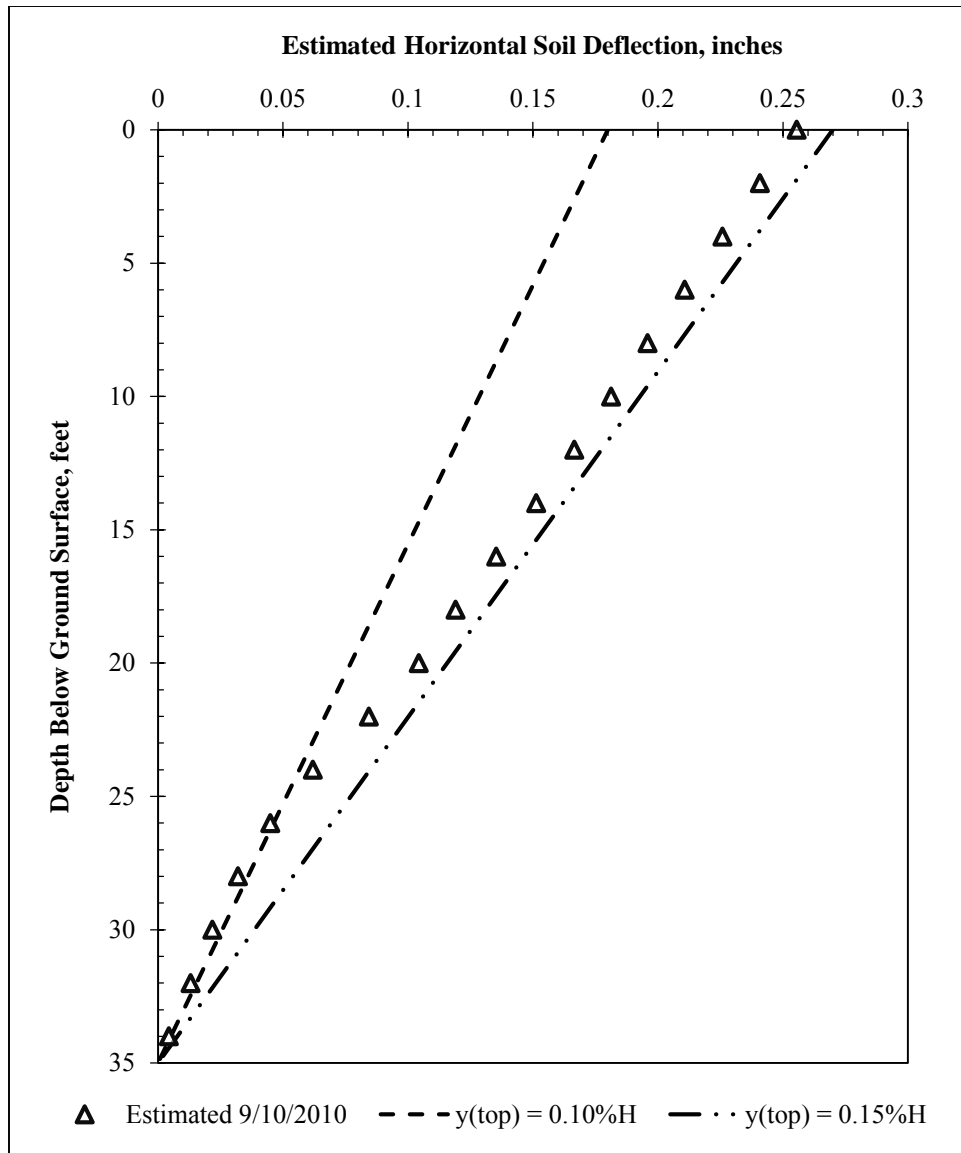


Figure 5.44: Estimated horizontal deflection due to global movements of the soil-shaft system during excavation.

5.4: Summary and Conclusions

The behavior of the Lymon C. Reese wall suggests that standard of practice design methods may not accurately account for what occurs during excavation. Based on the results of the instrumentation and data analysis program, several conclusions can be drawn:

- The standard design procedure for stiff clay predicts top-of-wall deflections fairly well for the test wall. However, it does not accurately predict the deflected shape at depth, and significantly overestimates the bending stresses in the shaft.
- The response of the foundation soil is much softer than the design prediction. Additionally, calculated values of earth pressure above the excavation line are smaller than the typically assumed design values.
- Within the time frame of excavation for the test wall (approximately 6 weeks), foundation soil response can be approximated with p-y curves using drained strength parameters, with initial curve stiffness (k_{py}) defined by the measured profile of undrained shear strength with depth. In a heavily overconsolidated, fissured clay such as the Taylor formation, stress relief during excavation may lead to relaxation of stresses along the fissures, dramatically shortening both drainage path lengths and drainage times.
- A significant amount of the measured test wall deflection was due to a combination of global movement of the soil-shaft system and shaft base rotation, neither of which directly stress the wall. These motions are not accounted for in the design analysis, and because they are visually obscured by the application of facing material, they may not be noticed without careful monitoring. While estimates of global movements for the test wall are provided, additional data from other drilled shaft walls in expansive soils are required to formulate reliable recommendations for design.
- Deformations prior to the application of facing accounted for approximately 50% of the test wall's allowable top-of-wall deflections. As pore pressures dissipate and earth pressures above the excavation line increase, top-of-wall deflections are expected to increase further. Because deflection requirements often govern design

in practice, an understanding of the soil and shaft deformations during excavation may be important in some cases to ensure adequate wall performance.

CHAPTER 6: TEST WALL BEHAVIOR DURING NATURAL MOISTURE CYCLES (OCTOBER 2010 – APRIL 2012)

6.1: Overview

After the completion of excavation in September 2010, shotcrete facing material was installed on October 1, 2010. Between October 2010 and April 2012, the wall experienced a range of climatic conditions, which were reflected in the observed wall movements. Because the application of facing represents a practical “zero” value for field measurements, subsequent test wall measurements are referenced to the October 8, 2010 survey (the most recent survey after facing installation).

6.2: Important Events and Qualitative Observations

6.2.1: INSTALLATION OF SHOTCRETE FACING

To prevent soil erosion from between the shafts and provide consistency with design practice, shotcrete facing material was installed on October 1, 2010 (Figure 6.1).



Figure 6.1: Installation of Shotcrete Facing on October 1, 2010.

6.2.2: INSTALLATION OF TIME-DOMAIN REFLECTOMETRY PROBES

Prior to the application of shotcrete facing, time-domain reflectometry probes were installed. A total of 10 probes were installed through the wall facing on September 30 – October 1, 2010 (as shown in Figure 6.2), and 10 were installed through the ground surface on October 14 (as shown in Figure 6.3). The approximate locations of all installed TDR probes are shown in Figure 6.4. Additional discussion of TDR probe installation, calibration, and data analysis can be found in Dellinger (2011).



Figure 6.2: Installation of TDR Moisture Probes Behind Wall Facing.



Figure 6.3: Installation of TDR Moisture Probes Through Ground Surface.

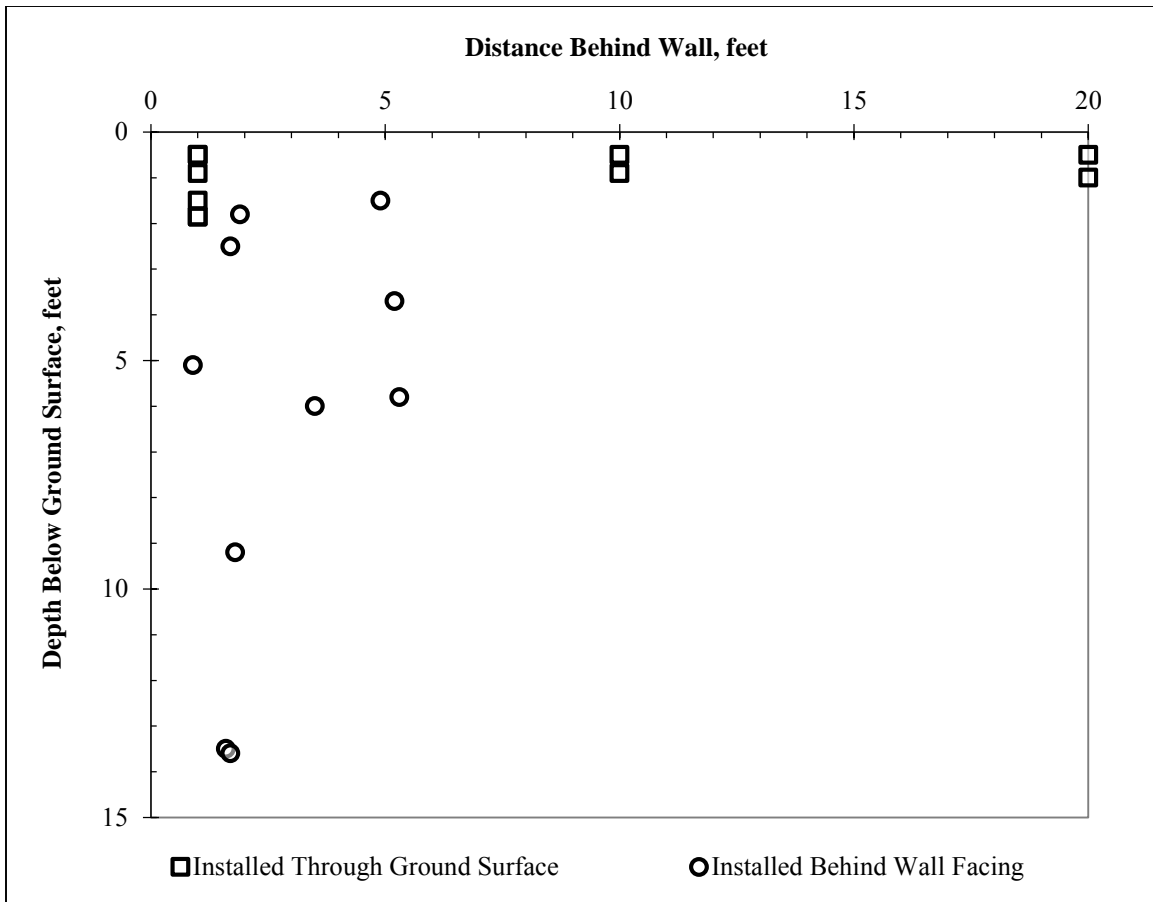


Figure 6.4: Approximate Locations of TDR Moisture Probes.

6.2.3: EXCAVATION SLOPE REPAIR AND EROSION CONTROL

On August 17, 2011, the slopes were reshaped to reduce erosion and prevent surface water from draining into the excavation (Figure 6.5). On October 8, 2011, erosion control material was installed (Figure 6.6).



Figure 6.5: Excavation slopes are reshaped on August 17, 2011.

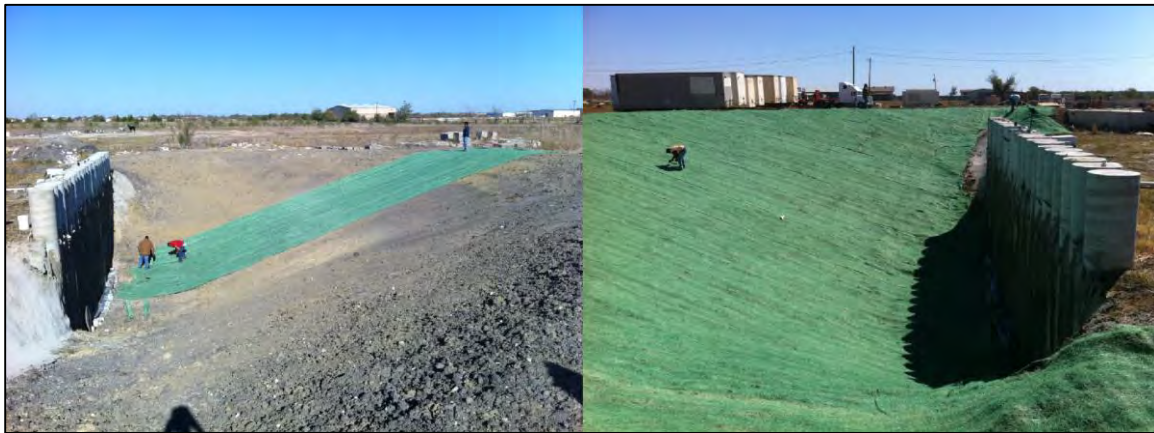


Figure 6.6: Erosion control material is installed on October 18, 2011.

6.2.4: CLIMATIC INFORMATION

After facing installation was completed in October 2010, the test wall experienced approximately three months of below average rainfall, followed by a series of storms in January 2011. During the spring and summer of 2011, the test wall experienced an extended period of below average rainfall, widely reported to be the most severe drought Austin, Texas had experienced since record keeping had begun over 100 years before. During the fall and winter of 2011 and early 2012, rainfall totals were above average, and the project site was frequently flooded by heavy rains. By the time controlled inundation

testing had begun in early May, 2012, the project site had seen several weeks with high temperatures and minimal rainfall. Rainfall patterns are summarized in Figure 6.7; daily temperature data is presented in Figure 6.8.

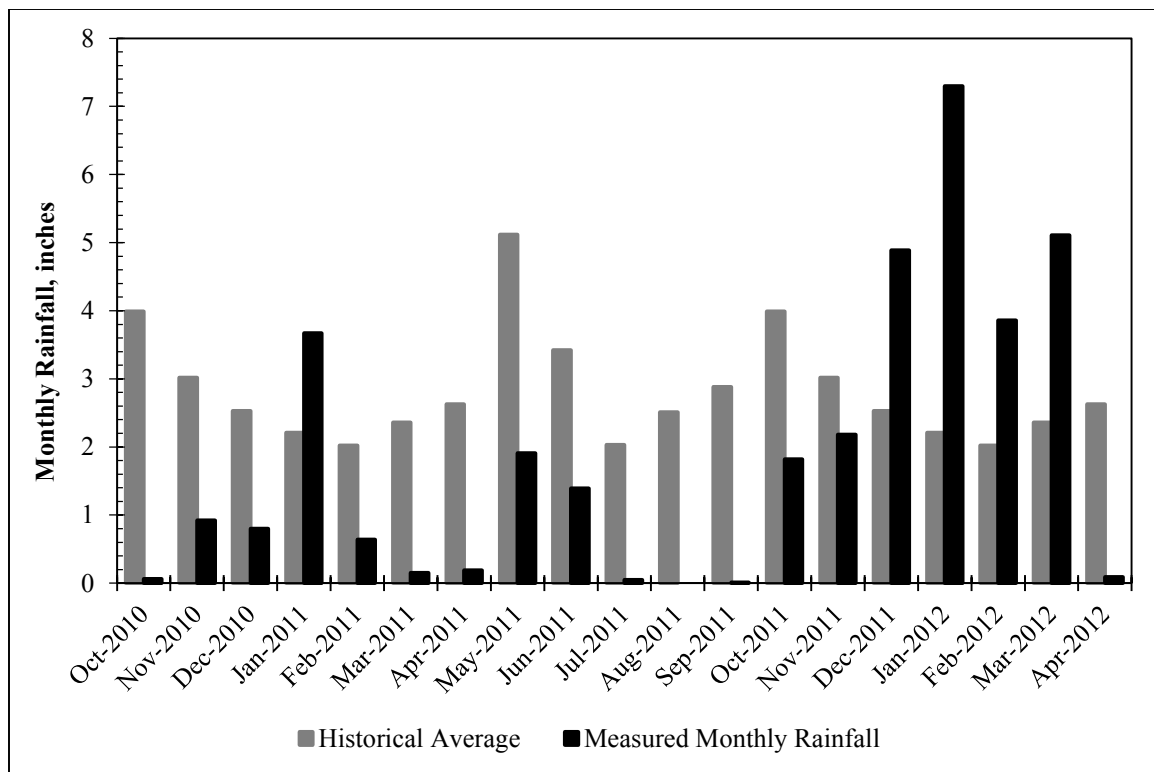


Figure 6.7: Monthly Rainfall Totals for Austin, Texas (Oct. 2010 – Apr. 2012; data from www.wunderground.com).

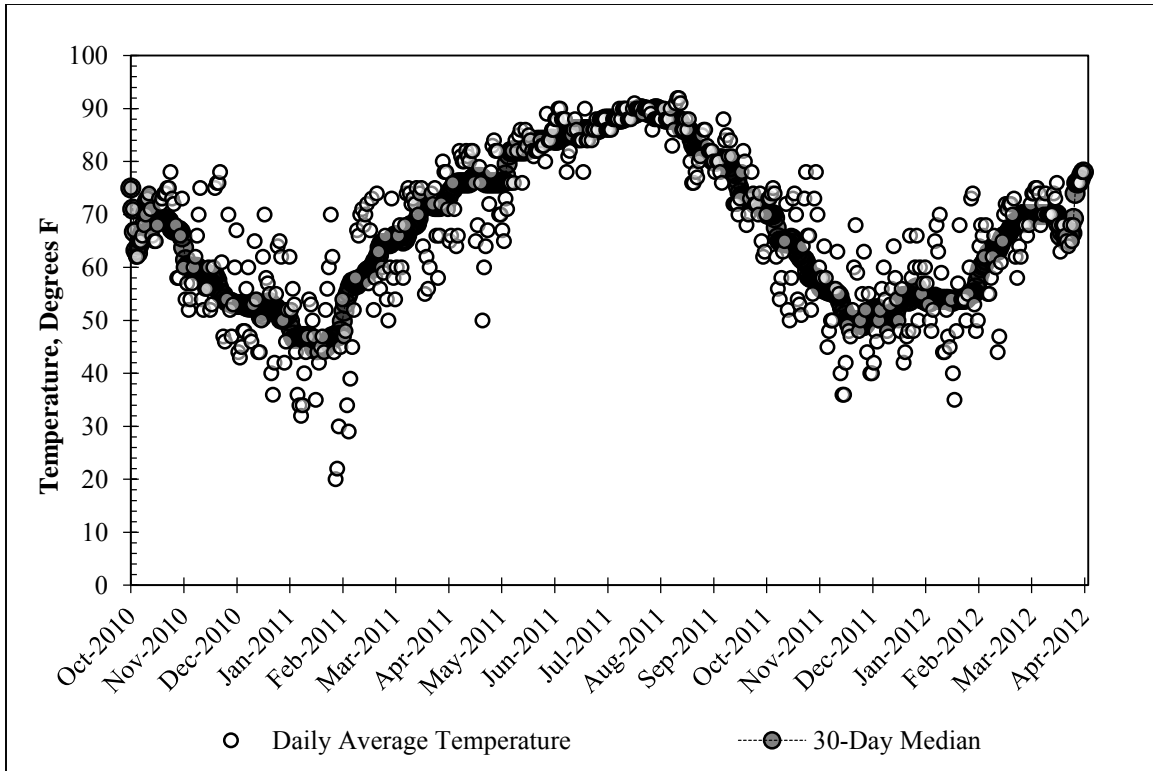


Figure 6.8: Daily Temperature Data for Manor, Texas (Oct. 2010 – Apr. 2012; data from www.wunderground.com).

6.3: Summary of Field Instrumentation Data

6.3.1: INCLINOMETER DATA

At the time of facing installation, the total top-of-wall deflection was approximately 0.97 inches relative to the beginning of excavation. In practice, the application of facing often represents the de facto “zero” date for a wall in service, because any deformations that have occurred during excavation will be visually obscured by the facing material. Without any internal instrumentation, subsequent wall assessments will rely largely on observed deformations and distress in the facing. For this reason, test wall deformations in response to natural soil moisture fluctuations are referenced to our facing installation date of October 8, 2010. The influence of natural moisture cycles on our measured top-of-

wall deflection is illustrated in Figure 6.9. In general, top-of-wall deflections tend to increase with increased rainfall, and stabilize or decrease during periods of drought (rainfall data is presented in Figure 6.7).

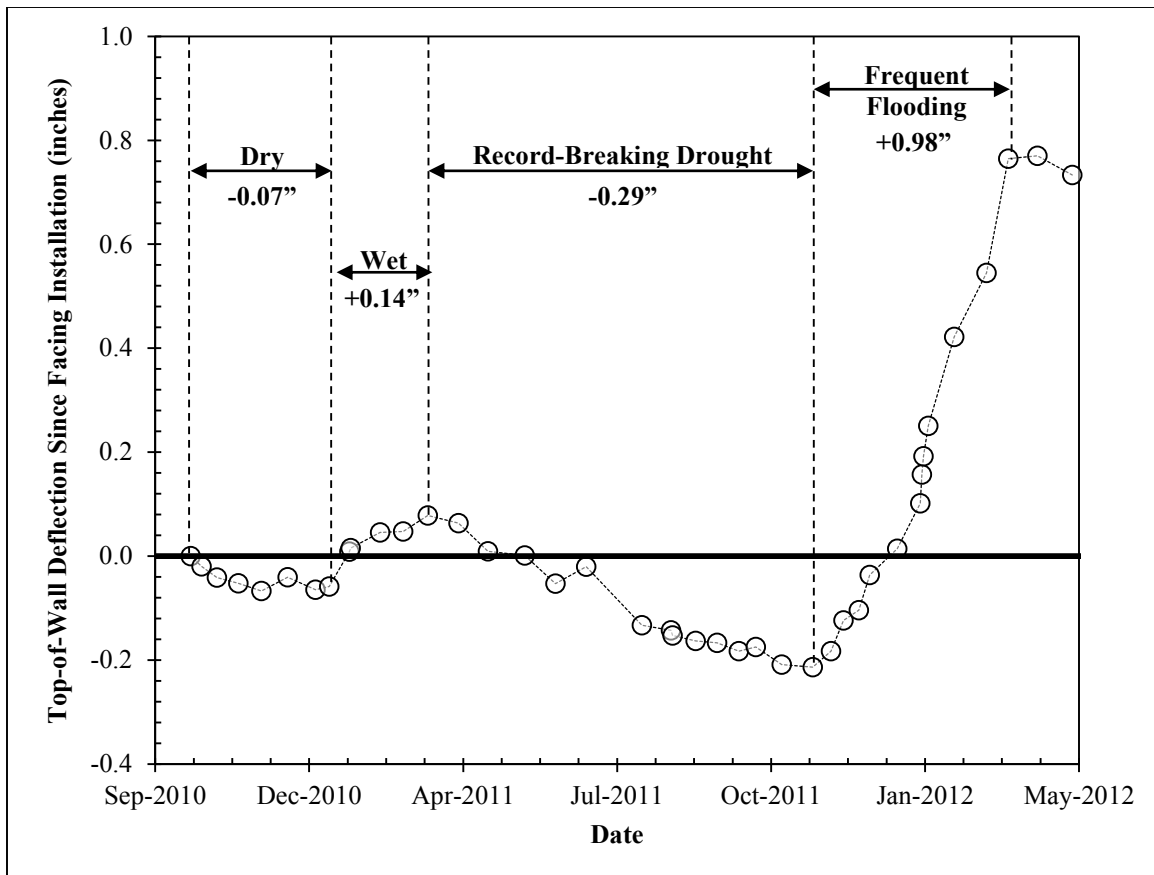


Figure 6.9: Variation of top-of-wall deflection with natural moisture cycles. Deflections are referenced to installation of facing on October 8, 2010.

6.3.2: TIME DOMAIN REFLECTOMETRY (TDR) PROBE DATA

Data from the most functional TDR probe, which was installed 1 foot behind the wall through the ground surface to a depth of 1.5 feet, is presented in Figure 6.10. Because large variations in electrical conductivity readings were observed during natural moisture cycles, the same data set is presented on a logarithmic scale in Figure 6.11. After

installation in October, 2010, values remained generally consistent before decreasing dramatically in April, 2011. The sudden decrease in electrical conductivity values occurred approximately one month into a severe drought, and most likely represent the loss of soil contact with the TDR probe rods as the soil decreases in volume and shrinks away from the probe (Figure 6.11). The decrease in electrical conductivity values also occurred at the same time the top-of-wall deflections began to decrease significantly (Figure 6.9), which suggests that soil shrinkage during drying cycles is responsible for both events. After the dramatic drop in April, 2011, electrical conductivity values continued to decrease until November, 2011, when rainfall returned to the project site and the electrical conductivity values increased in response (Figure 6.11). The increase in electrical conductivity values occurred at approximately the same time top-of-wall deflections began to increase in response to rainfall (Figure 6.9), and values remained fairly consistent until the commencement of controlled inundation testing in May, 2012. In late May and April, 2012, a small decrease in top-of-wall deflections was accompanied by a slight, but qualitatively similar, decrease in electrical conductivity values during the same time period (Figure 6.9, Figure 6.11).

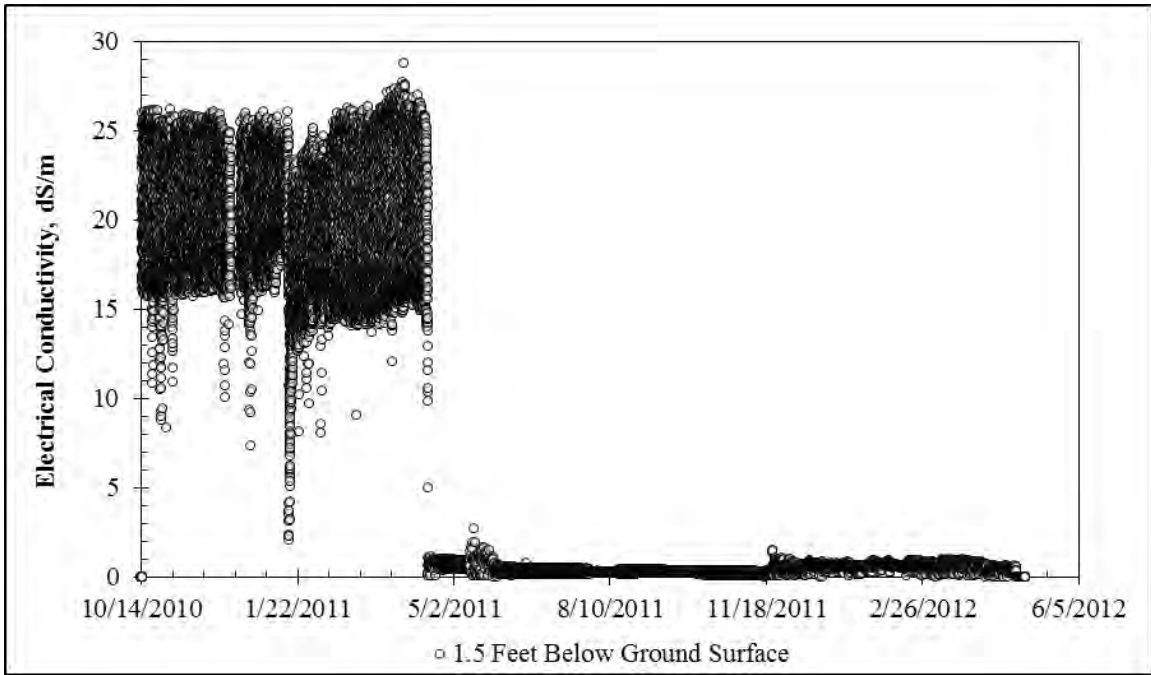


Figure 6.10: Electrical conductivity data from a TDR probe located 1.5 feet below ground surface (Oct. 2010 – Apr. 2012).

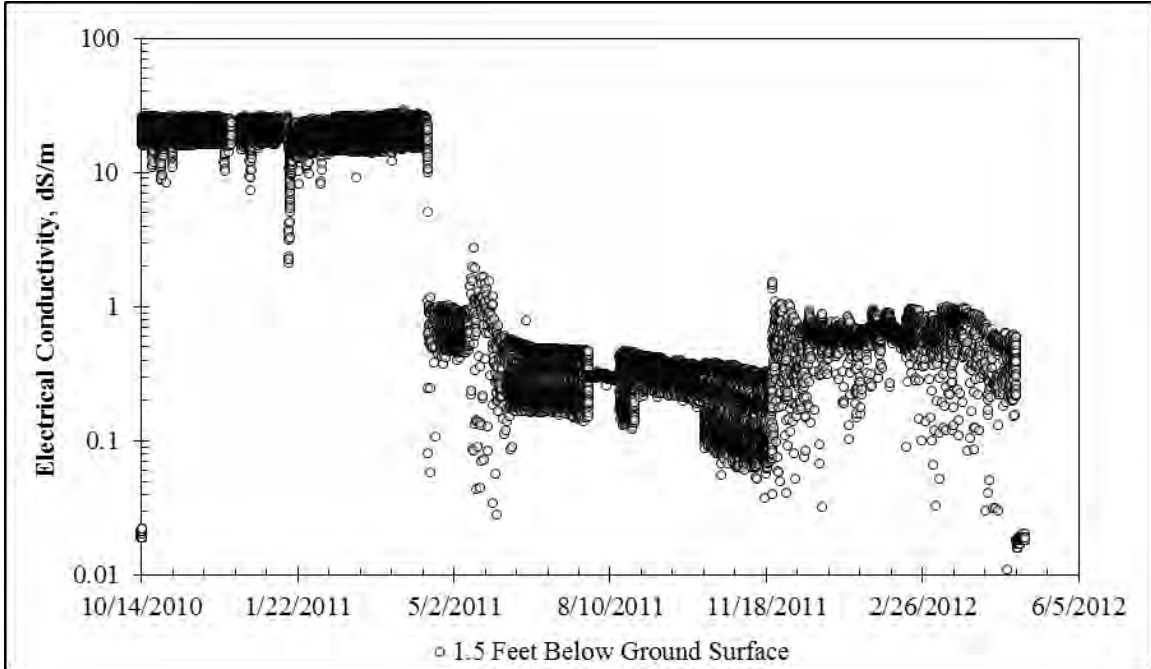


Figure 6.11 Electrical conductivity data from a TDR probe located 1.5 feet below ground surface, presented on a logarithmic scale (Oct. 2010 – Apr. 2012).

6.3.3: STRAIN GAUGE DATA

Strain data is presented in Figure 6.12 - Figure 6.26. In the following figures, strain data is zeroed at the first measurement after installation of facing (October 8, 2010). Strain gauge nomenclature indicates which instrumented shaft the gauge is installed in (East, Center, or West), the depth of the strain gauge below original ground surface (1 – 29 feet), and which side of the neutral axis the gauge is installed on (Tension or Compression; tensile strains are positive). Using this nomenclature, gauge E.17.T is located in the east instrumented shaft, 17 feet below ground surface, on the tensile side of the neutral axis.

In shallow gauges from 0 to 13 feet below the original ground surface, small bending strains consistent with the observed inclinometer data exist in many of the gauges. However, the influence of tension cracking seems to increase as more tension cracks appear to develop during this time (e.g. C.09.C). Axial strains consistent with seasonal temperature fluctuations are seen in the majority of shallow gauges, but relative values of bending curvature between pairs of gauges seem to be generally unaffected by seasonal temperature fluctuations (e.g. E.01.T / E.01.C). Some evidence of the development of negative bending curvatures during cycles of soil shrinkage can be seen (e.g. E.01.T / E.01.C, E.03.T / E.03.C). Some gauges display erratic behavior or strain readings outside their range of measurement, which likely indicates the gauge has been damaged and can no longer be used for data interpretation (e.g. C.01.C).

Data from gauges below the excavation line, from 15 – 29 feet below the original ground surface, shows gauge behavior which is generally similar to data from the shallow gauges. The influence of thermal strains is less pronounced due to the insulating presence of the overburden soil. Several of the gauges below the excavation line show evidence of tension cracking. The appearance of cracks is consistent with the measured bending curvatures from inclinometer data; the measured bending curvatures correspond to bending

moments close to the shaft's cracking moment of approximately 680 in-kip. Some gauges continue to show behavior that is very similar to the theoretical expectations (e.g. C.23.T / C.23.C, W.25.T, E.29.C). In addition to the development of cracks in the concrete, several gauges failures were observed. Gauge failures were generally preceded by erratic behavior, and failure was usually indicated by a sharp dive in a tensile or compressive direction before losing the gauge signal (e.g. C.21.C).

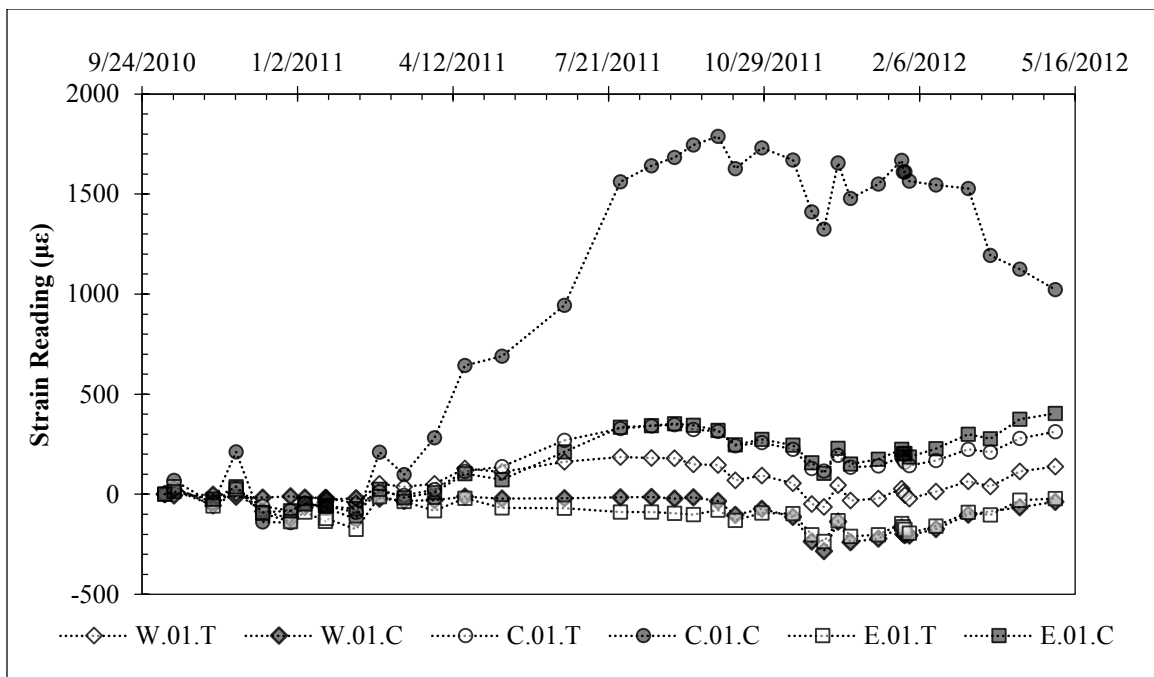


Figure 6.12: Strain Data 1 Foot Below Ground Surface (Oct. 2010 – Apr. 2012).

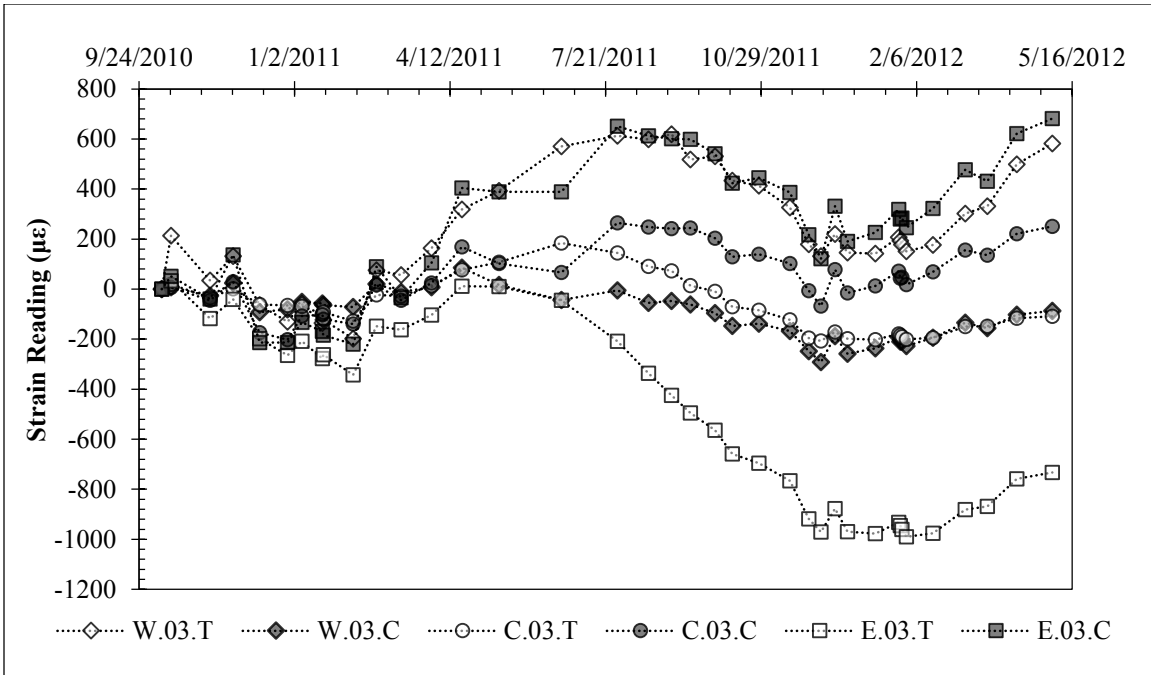


Figure 6.13: Strain Data 3 Feet Below Ground Surface (Oct. 2010 – Apr. 2012).

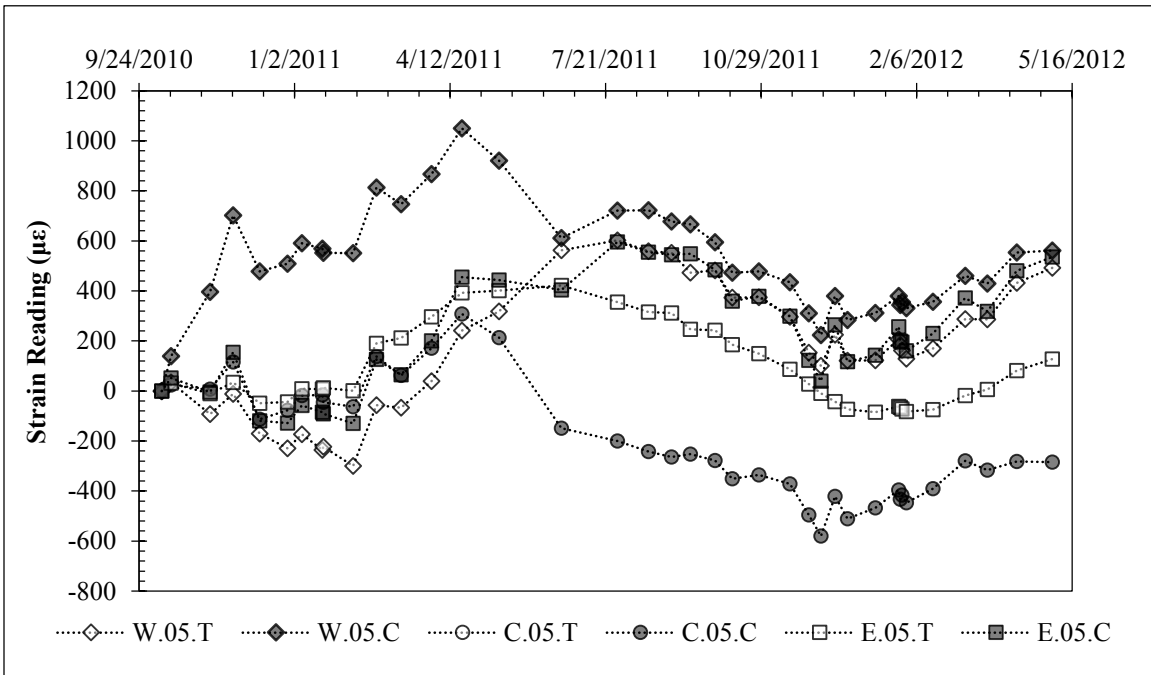


Figure 6.14: Strain Data 5 Feet Below Ground Surface (Oct. 2010 – Apr. 2012).

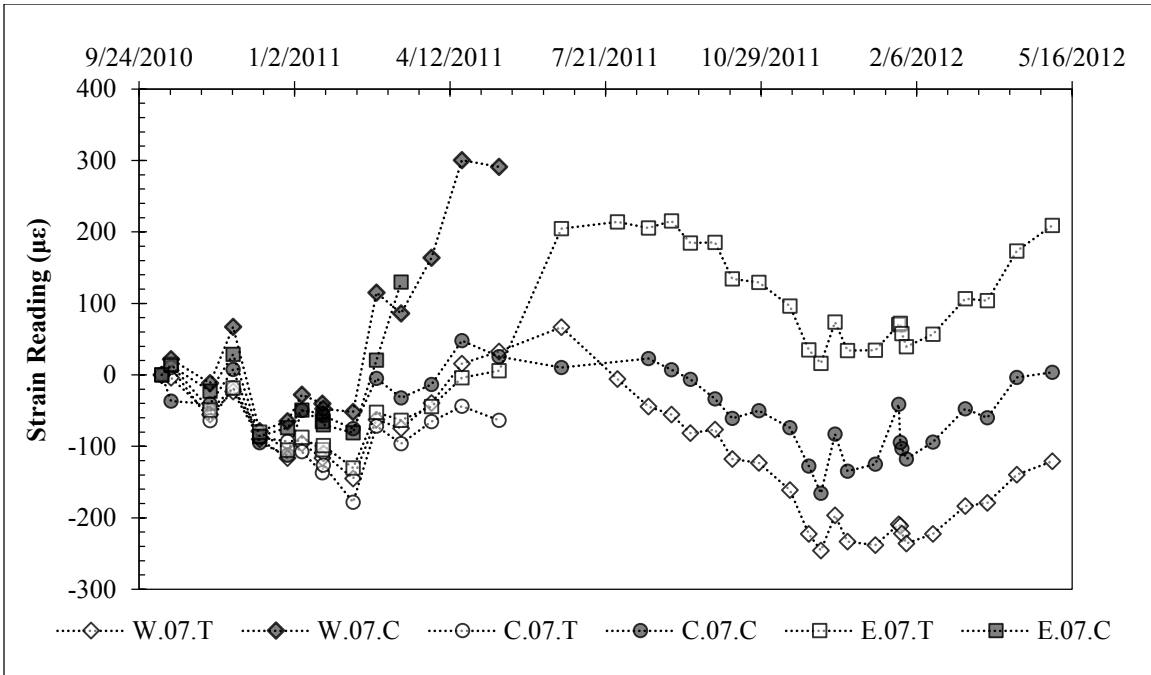


Figure 6.15: Strain Data 7 Feet Below Ground Surface (Oct. 2010 – Apr. 2012).

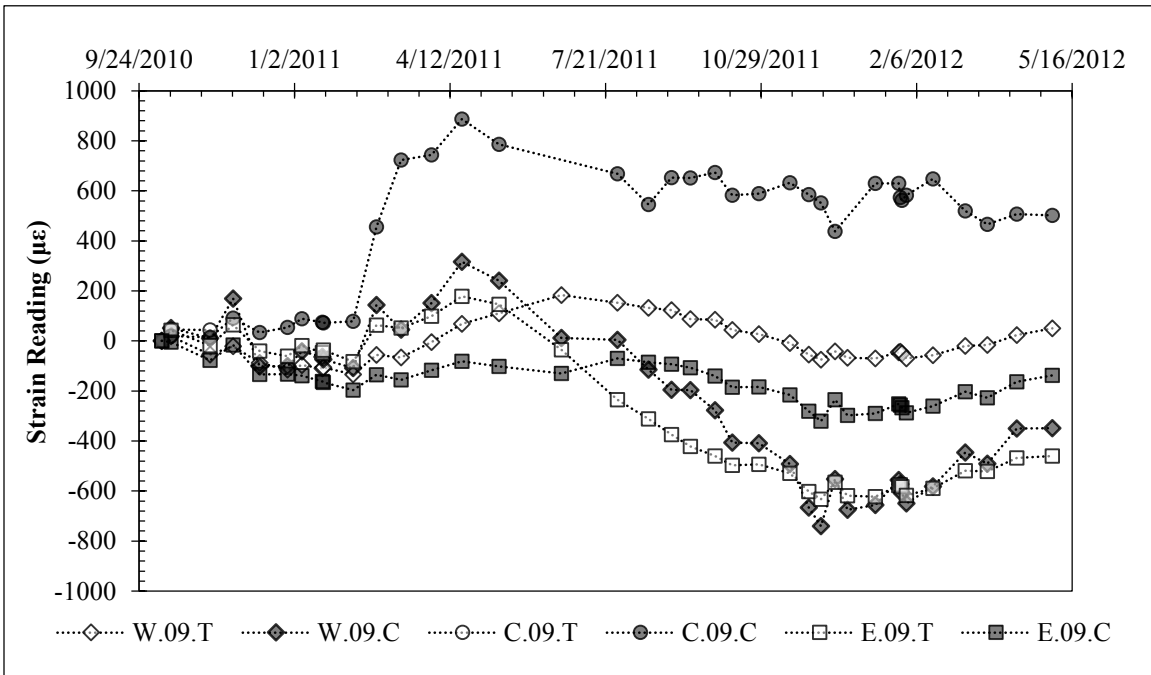


Figure 6.16: Strain Data 9 Feet Below Ground Surface (Oct. 2010 – Apr. 2012).

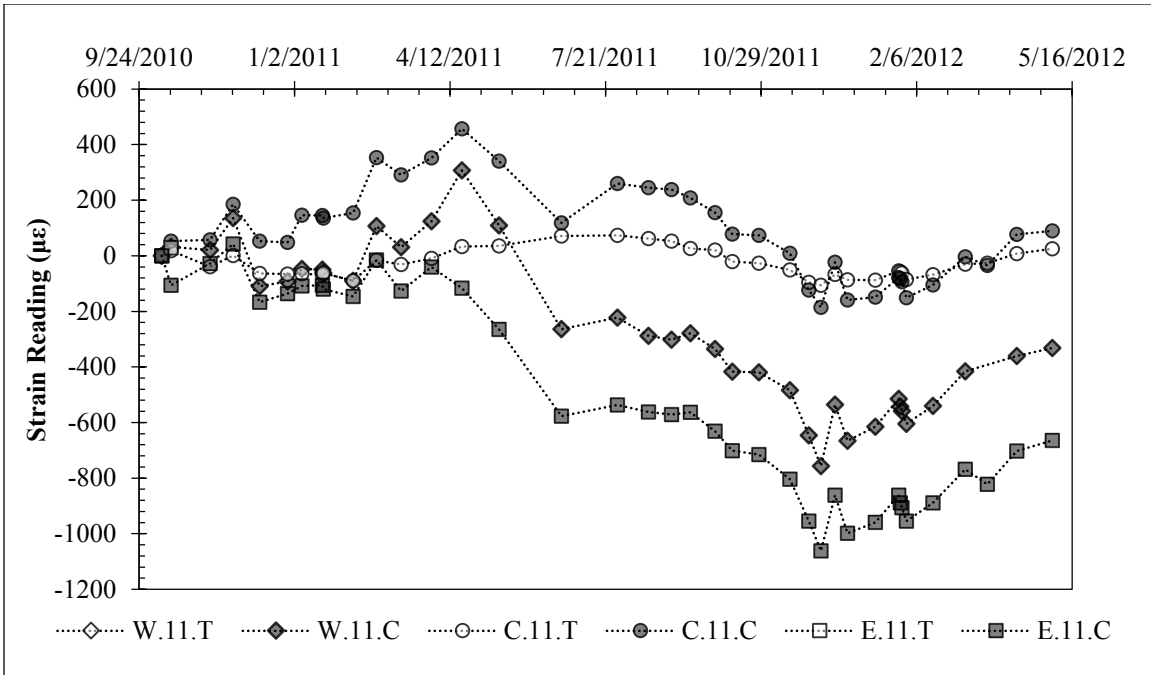


Figure 6.17: Strain Data 11 Feet Below Ground Surface (Oct. 2010 – Apr. 2012).

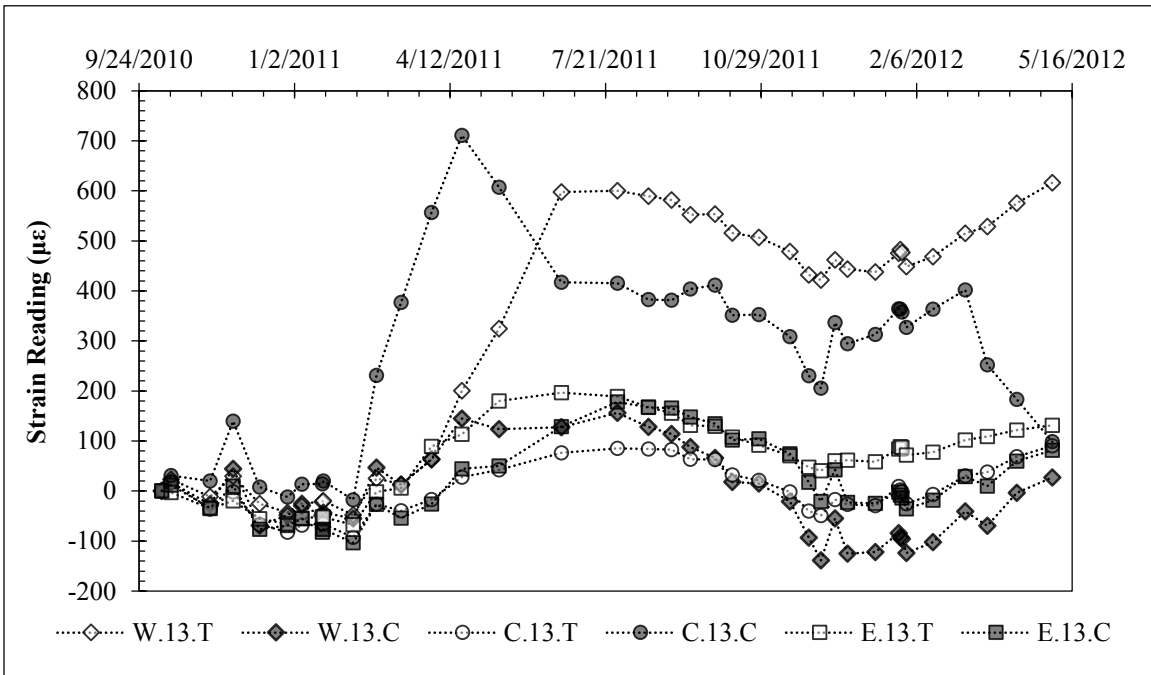


Figure 6.18: Strain Data 13 Feet Below Ground Surface (Oct. 2010 – Apr. 2012).

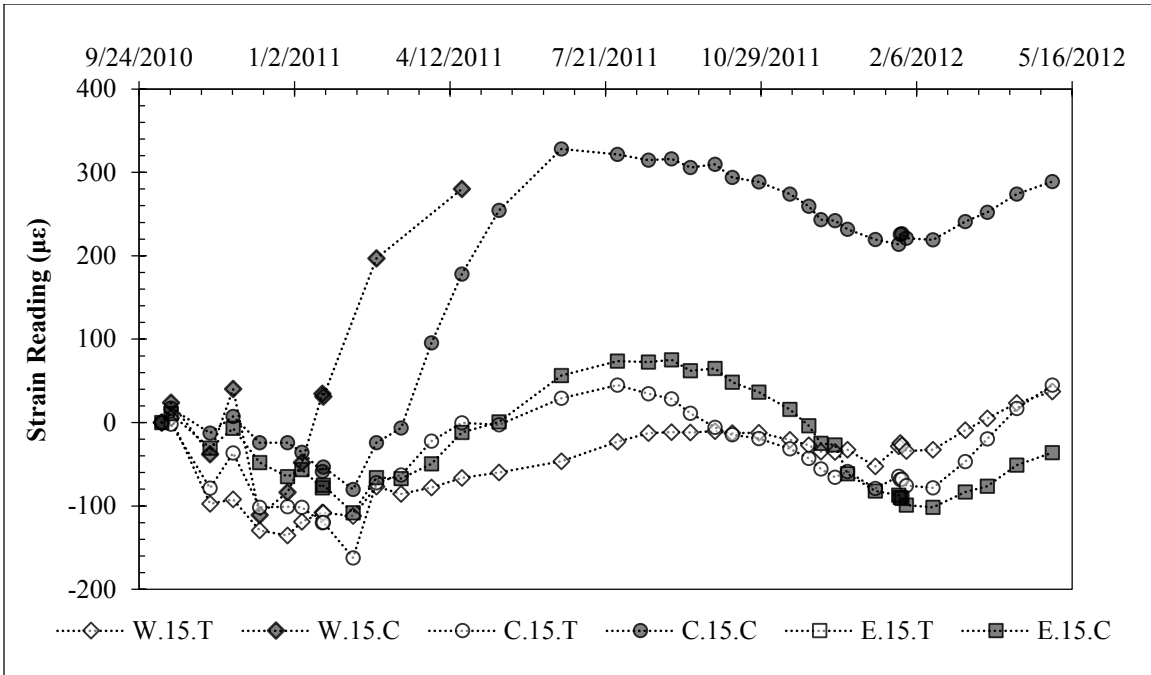


Figure 6.19: Strain Data 15 Feet Below Ground Surface (Oct. 2010 – Apr. 2012).

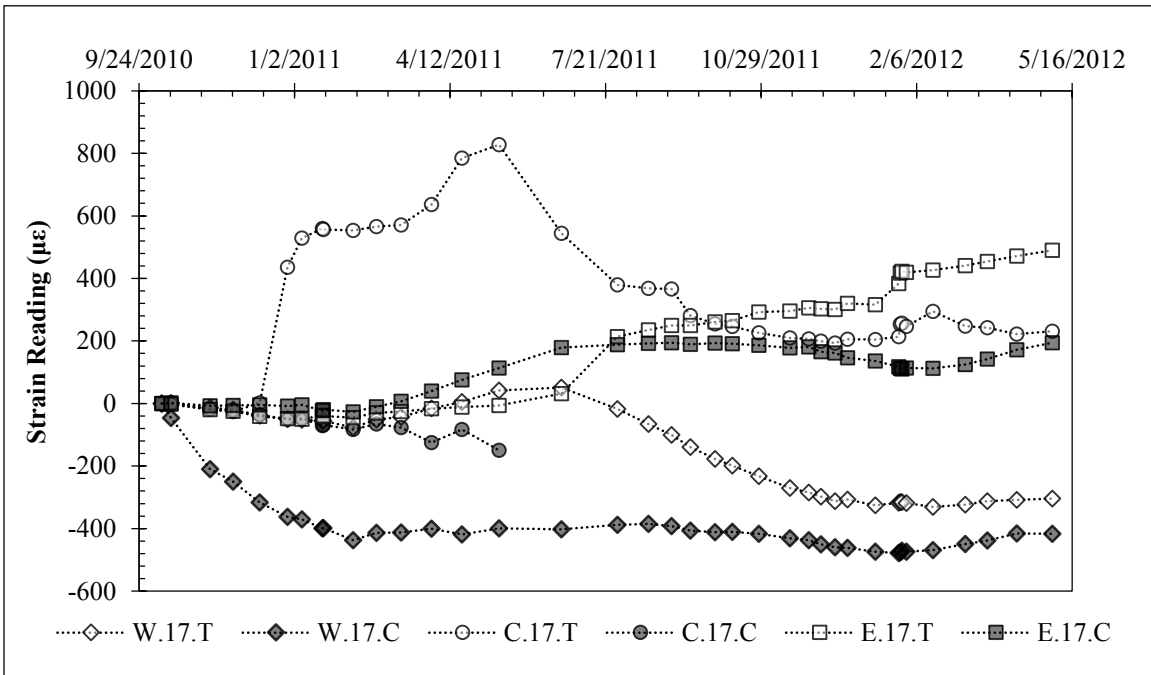


Figure 6.20: Strain Data 17 Feet Below Ground Surface (Oct. 2010 – Apr. 2012).

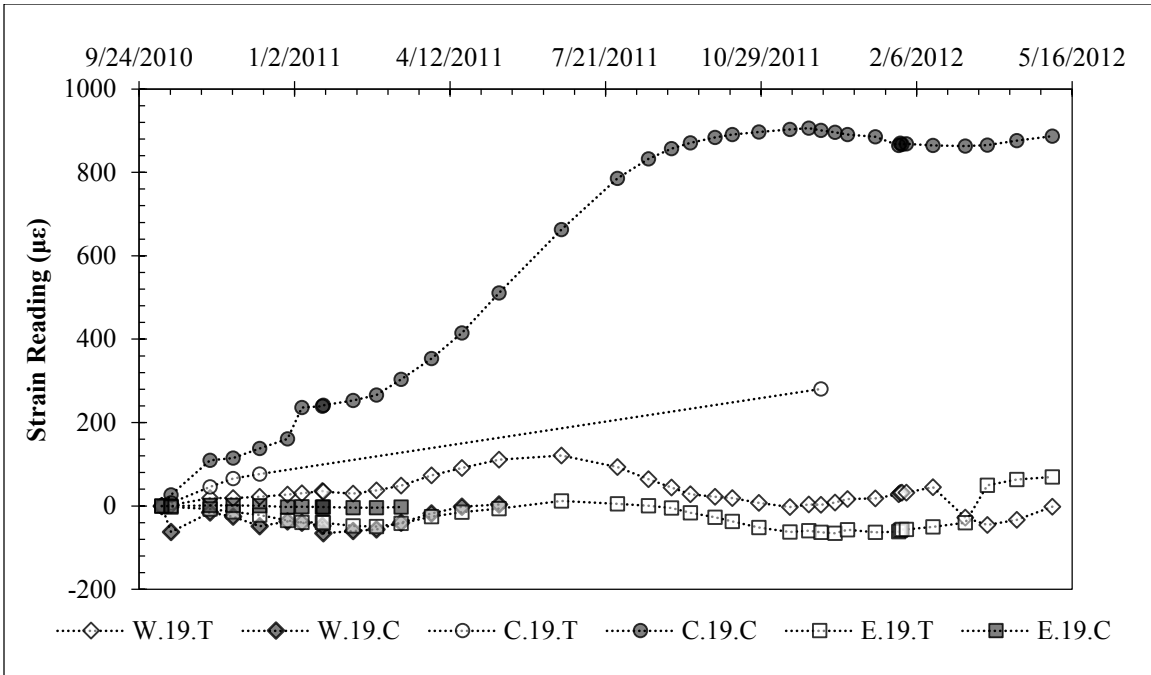


Figure 6.21: Strain Data 19 Feet Below Ground Surface (Oct. 2010 – Apr. 2012).

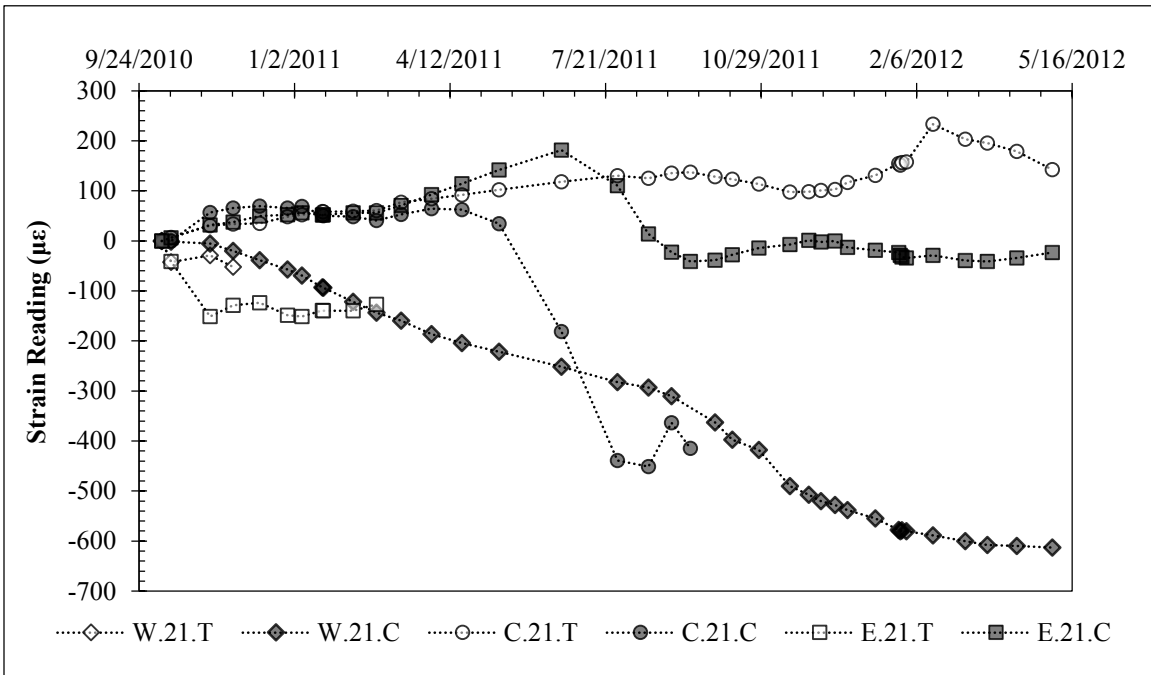


Figure 6.22: Strain Data 21 Feet Below Ground Surface (Oct. 2010 – Apr. 2012).

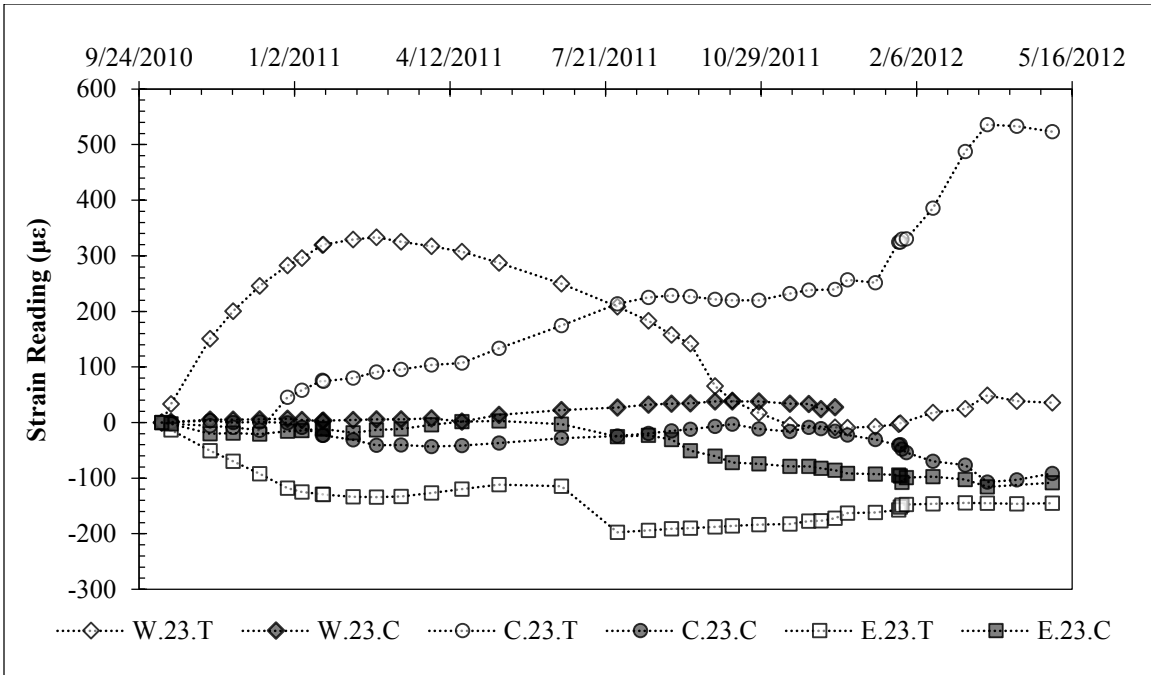


Figure 6.23: Strain Data 23 Feet Below Ground Surface (Oct. 2010 – Apr. 2012).

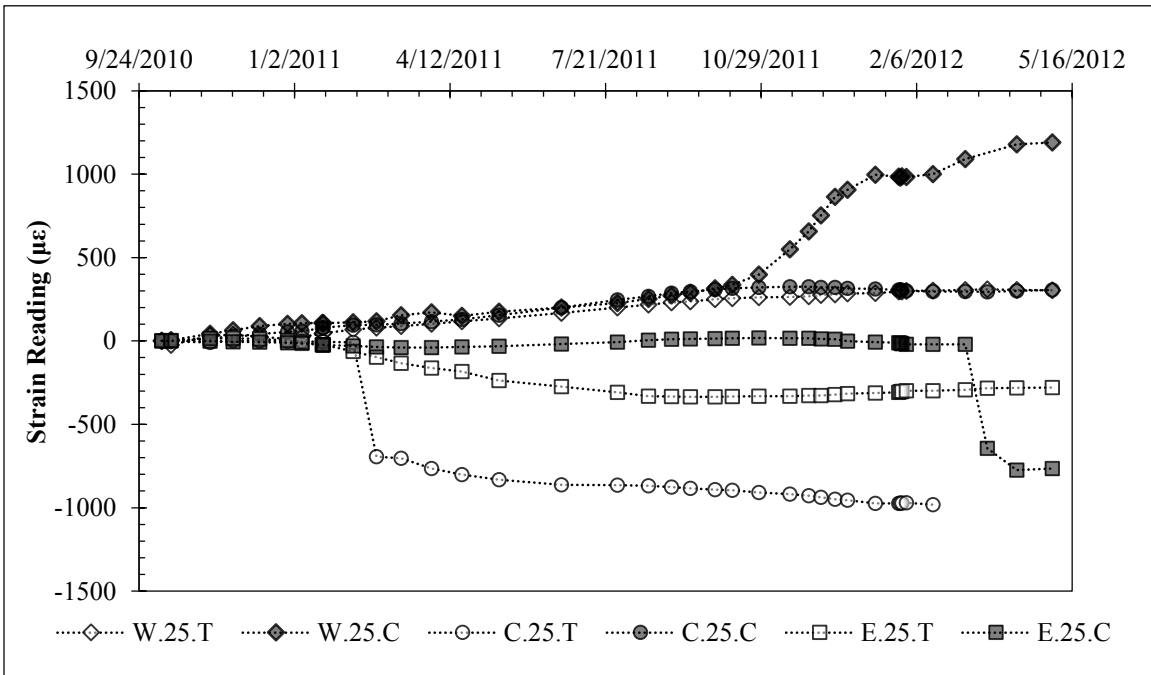


Figure 6.24: Strain Data 25 Feet Below Ground Surface (Oct. 2010 – Apr. 2012).

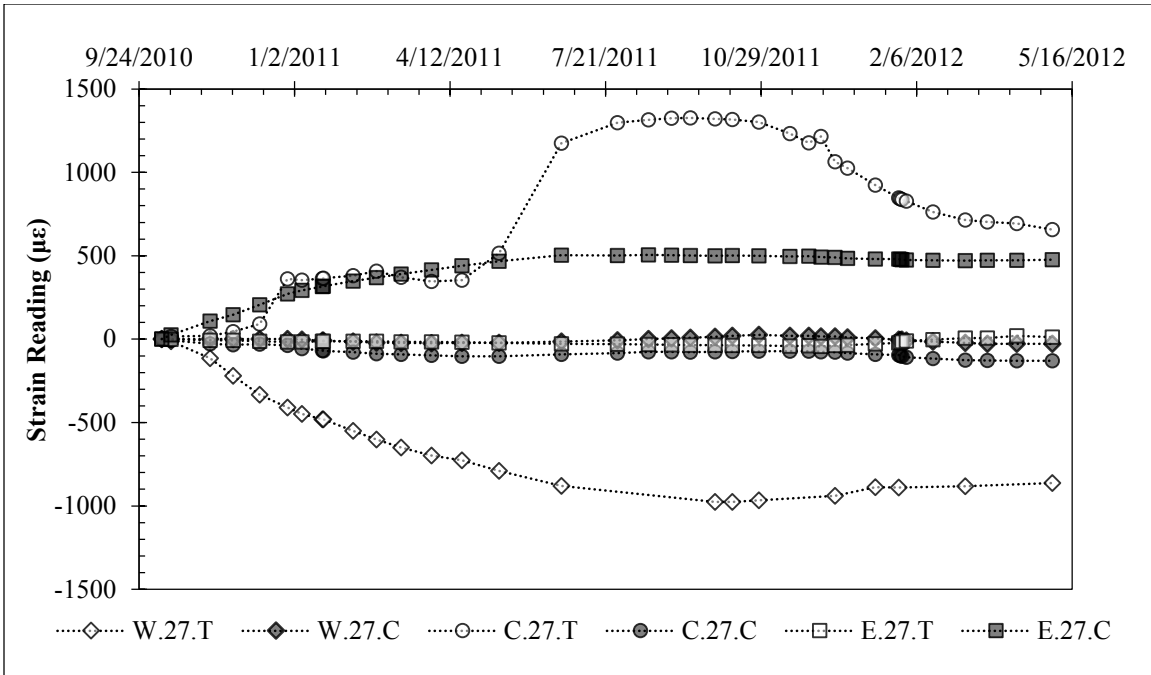


Figure 6.25: Strain Data 27 Feet Below Ground Surface (Oct. 2010 – Apr. 2012).

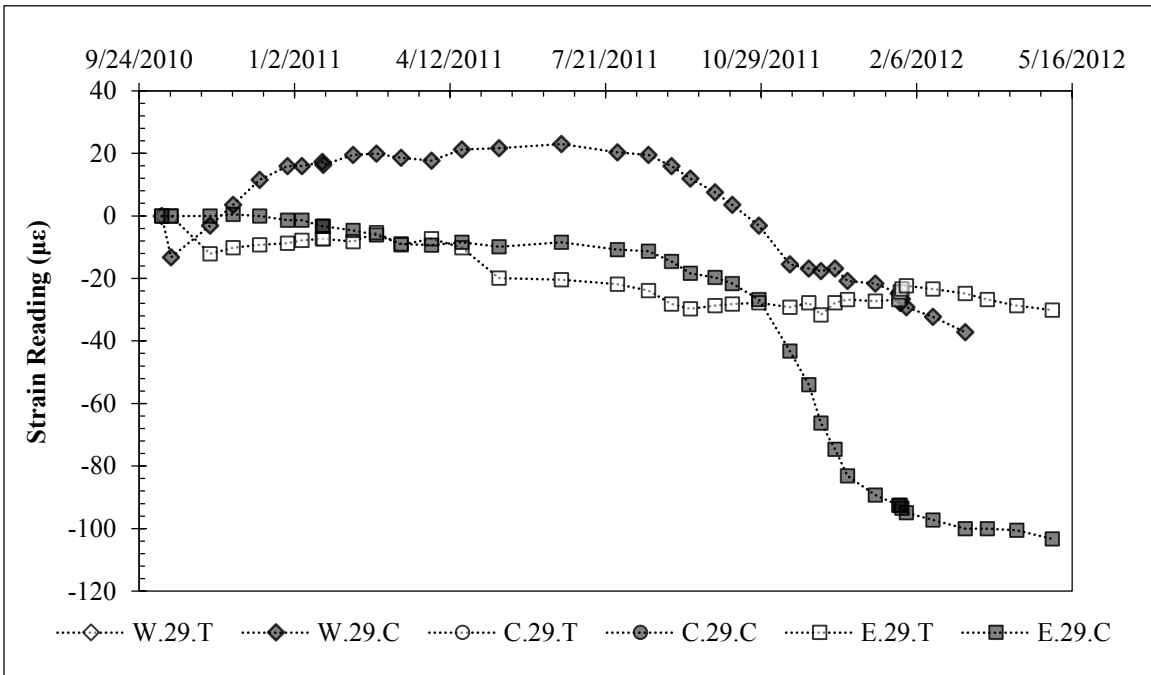


Figure 6.26: Strain Data 29 Feet Below Ground Surface (Oct. 2010 – Apr. 2012).

6.4: Data Interpretation

6.4.1: PHASES OF WALL MOTION

Over the 22 months in which wall deflection was monitored, the test wall experienced a range of climatic conditions and corresponding deflections. These can be simplified into four basic phases of wall motion, using the variation in top-of-wall deflections as the parameter of interest. In the following sections, inclinometer data is presented as a profile of cumulative deflections versus depth; beneath the deflection profile, a plan view of the A- and B-axis of the inclinometer probe is shown. While wall motion can generally be assumed to be one-dimensional and perpendicular to the wall, inspection of plan view data can provide some insights on the nature of wall movement. It is important to note that in each instrumented shaft, the as-built inclinometer casing alignments are slightly different; this is normal and does not indicate the shafts are moving in different directions.

6.4.1.a: Drying Cycle 1: October 8, 2010 – January 6, 2011 (3 months)

After the installation of the wall facing on October 8, the top-of-wall deflections decreased by a small amount, around 0.07 inches in three months. In this phase, the first possible effects of soil shrinkage are observed.

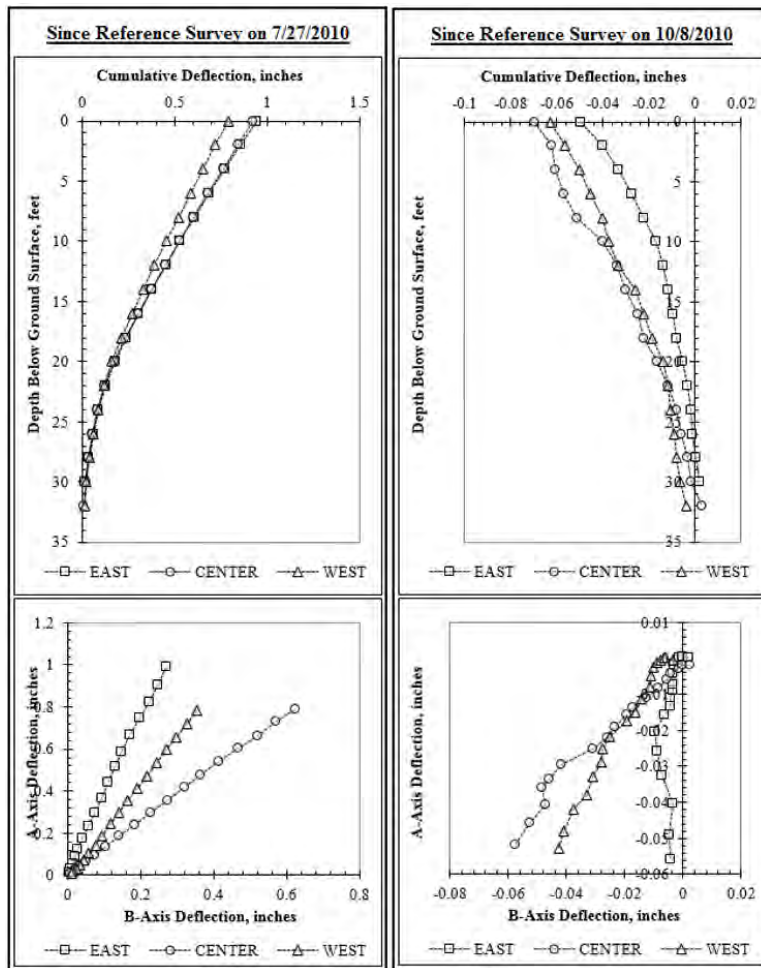


Figure 6.27: Inclinometer Data from January 6, 2011.

6.4.1.b: Wetting Cycle 1: January 6, 2011 – March 11, 2011 (2 months)

After a dry fall with below average rainfall, two large rainfall events in January led to flooding in the excavation and access to moisture for the retained and foundation soil. In response to these events, the average top-of-wall deflections increased by approximately 0.14 inches over two months.

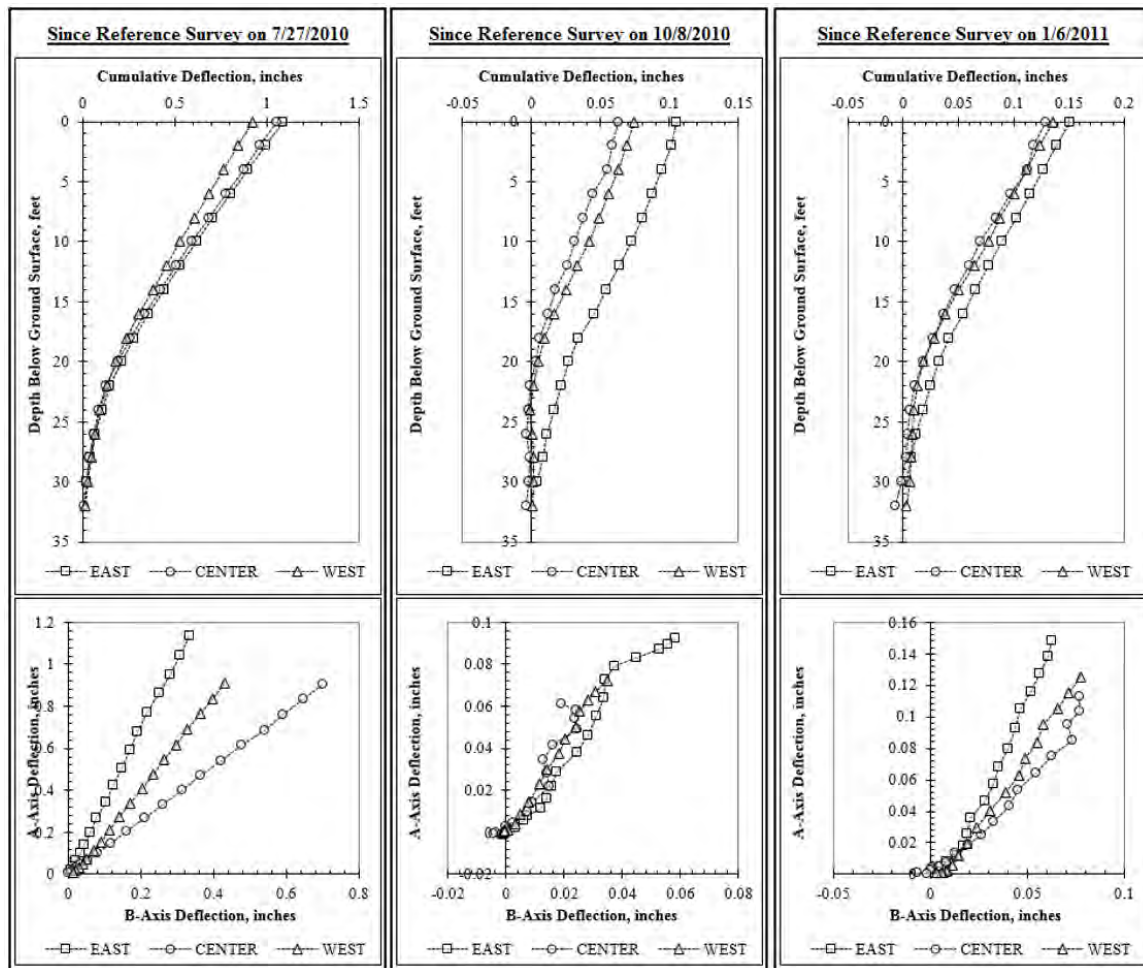


Figure 6.28: Inclinometer Data from March 11, 2011.

6.4.1.c: Drying Cycle 2: March 11, 2011 – November 16, 2011 (8 months)

During this phase, a record-breaking drought caused the soil on the project to dry and shrink significantly. In response, the top-of-wall deflections decreased by approximately 0.29 inches over eight months. As an indication of drying-related soil shrinkage on the project site, noticeable differential settlement between the inclinometer casing (installed to a depth of 50 feet) and its surrounding concrete pad (connected to the ground surface independently of the casing) was observed. While this is far from a perfect

measurement, it does indicate significant shrinkage of the retained soil occurred (Figure 6.29). The top-of-wall deflections reach a minimum during this phase.

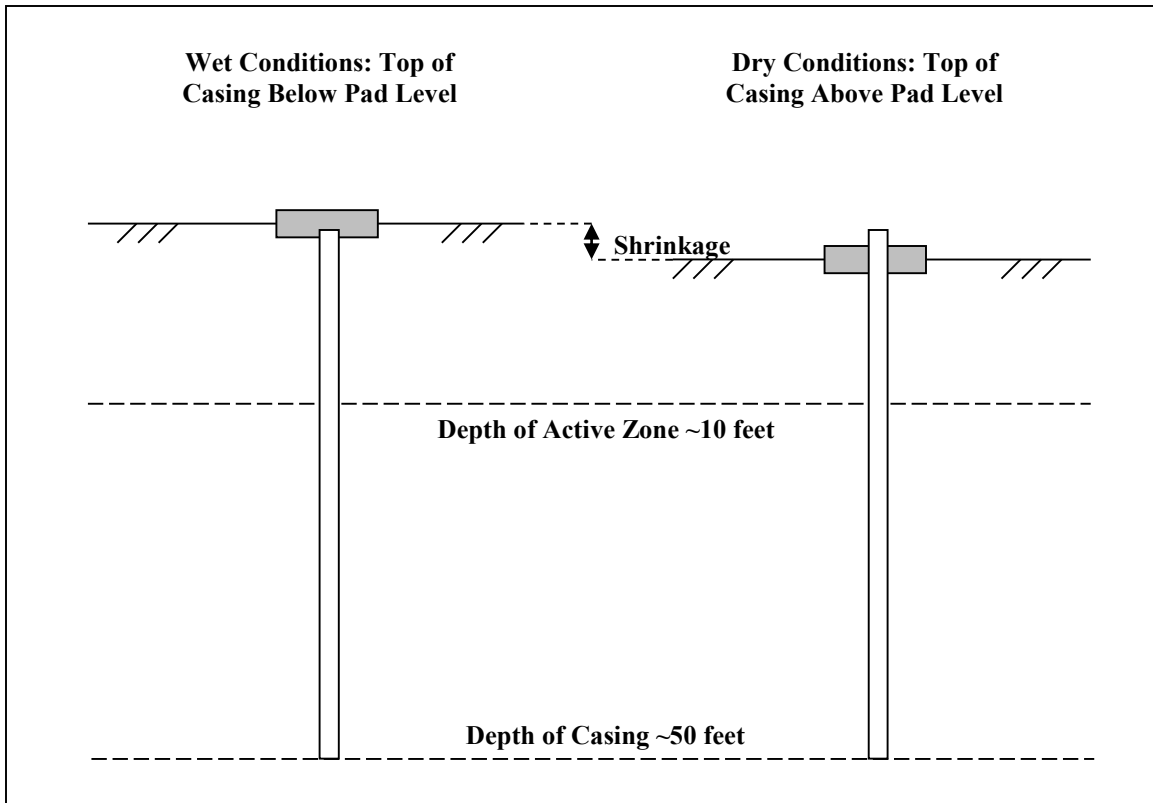


Figure 6.29: The use of a deep inclinometer casing and concrete pad as a qualitative indicator of soil shrinkage near the test wall (not to scale).

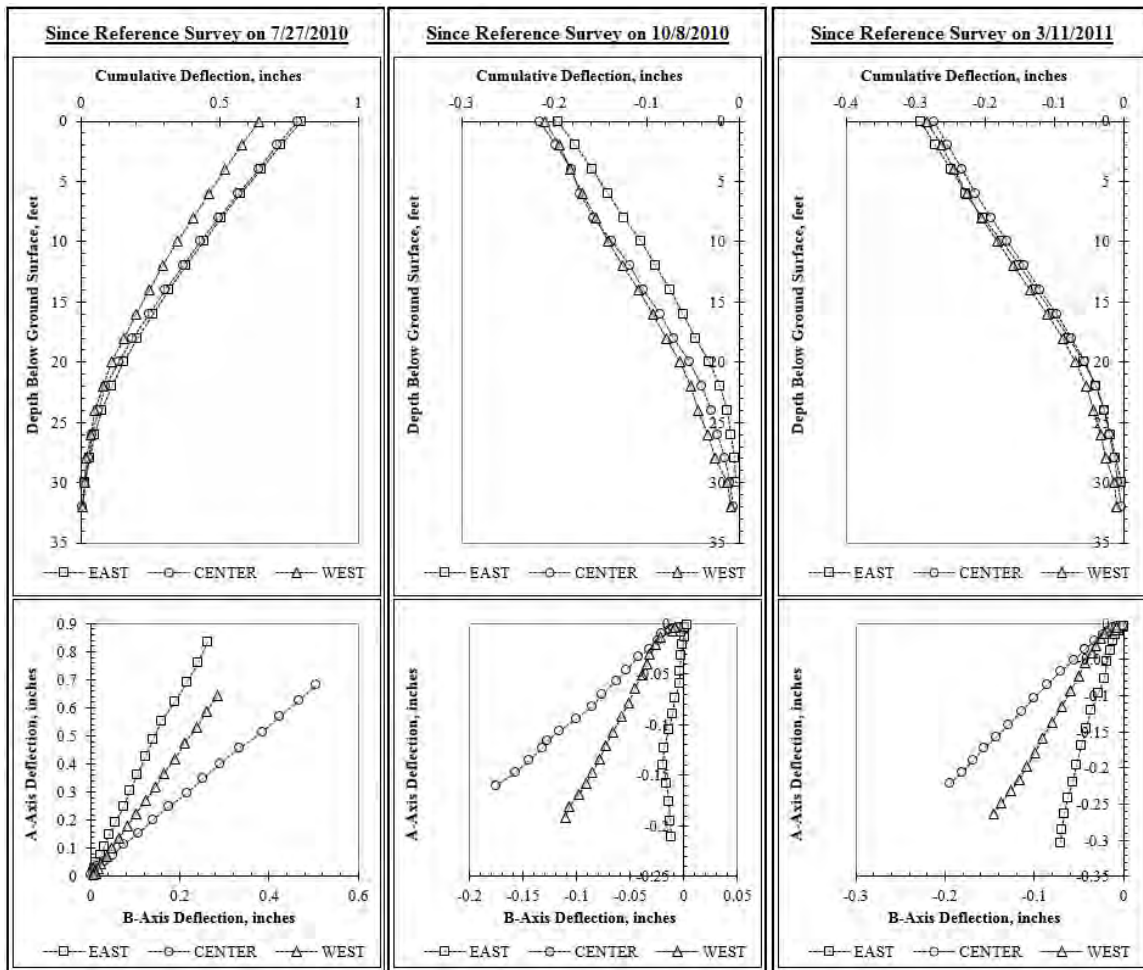


Figure 6.30: Inclinometer Data from November 16, 2011.

6.4.1.d: Wetting Cycle 2: November 16, 2011 – April 10, 2012 (5 months)

During this phase, a very wet winter with two exceptionally large rainfall events caused top-of-wall deflections to increase to their maximum values. In response to the continued presence of water in the excavation and frequent access to moisture for the retained soil during rainfall events, the top-of-wall deflections increased by approximately 0.98 inches over five months. Between April 10, 2012 and the start of the artificial inundation test on May 2, 2012, the top-of-wall deflections stabilized and began to decrease after a short period of hot, dry weather.

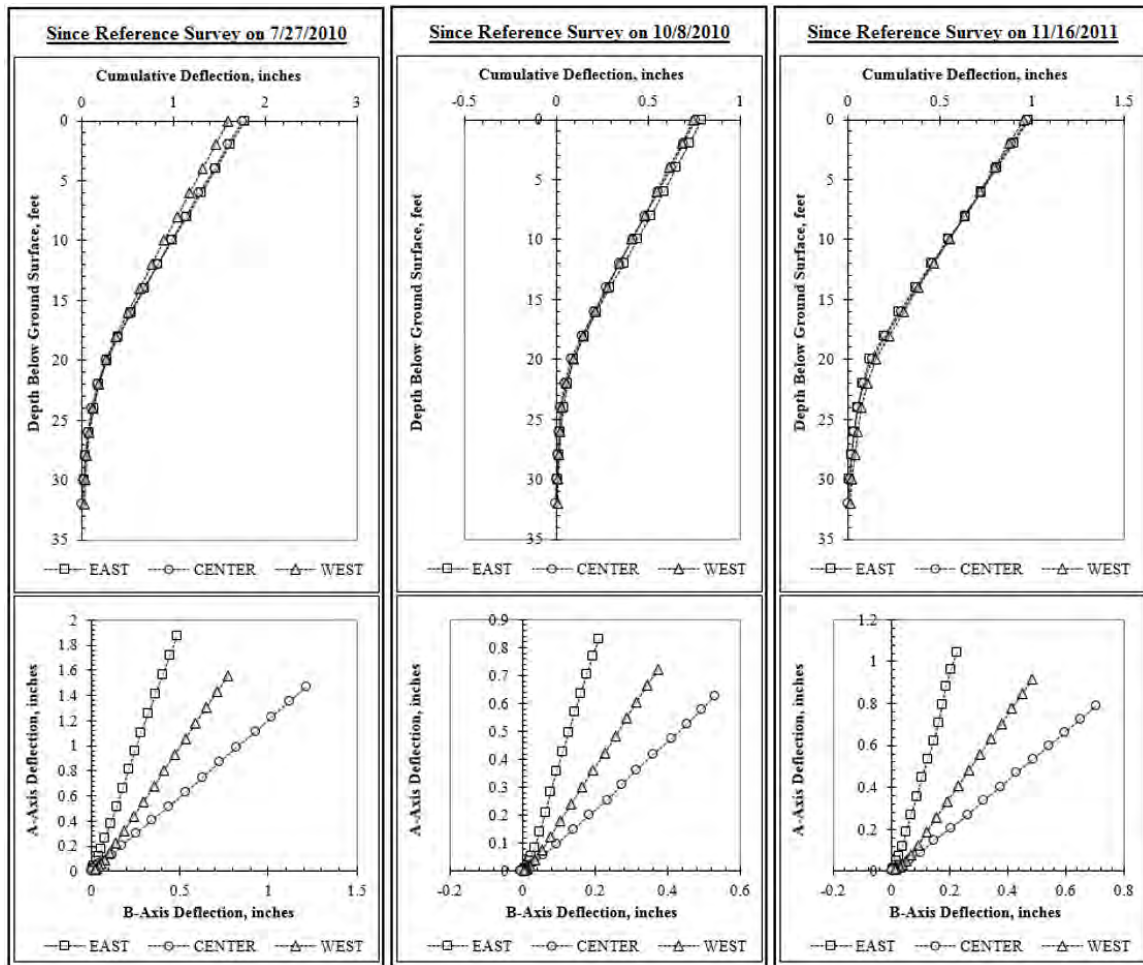


Figure 6.31: Inclinometer Data from April 10, 2012.

6.4.2: DEFLECTED SHAPES AT KEY DATES

During each of the phases of wall motion described above, the deflected shape of the shaft varied in ways that cannot be easily modeled using a typical p-y analysis. In Figure 6.32, the deflected shape of the shaft at the conclusion of each phase of motion is plotted. When these are compared with the deflected shape predicted by the original design p-y analysis using a commonly assumed earth pressure of 40 psf/ft and stiff clay curves for the foundation soil, the qualitative differences in the predicted and measured values are similar to the differences observed during excavation. Throughout both wetting and drying

cycles, the observed foundation soil response is softer than the response predicted by the stiff clay curves. More complex loading mechanisms, the influence of shaft base rotation, weakening of the soil in the base of the excavation, and various other factors may all influence these discrepancies.

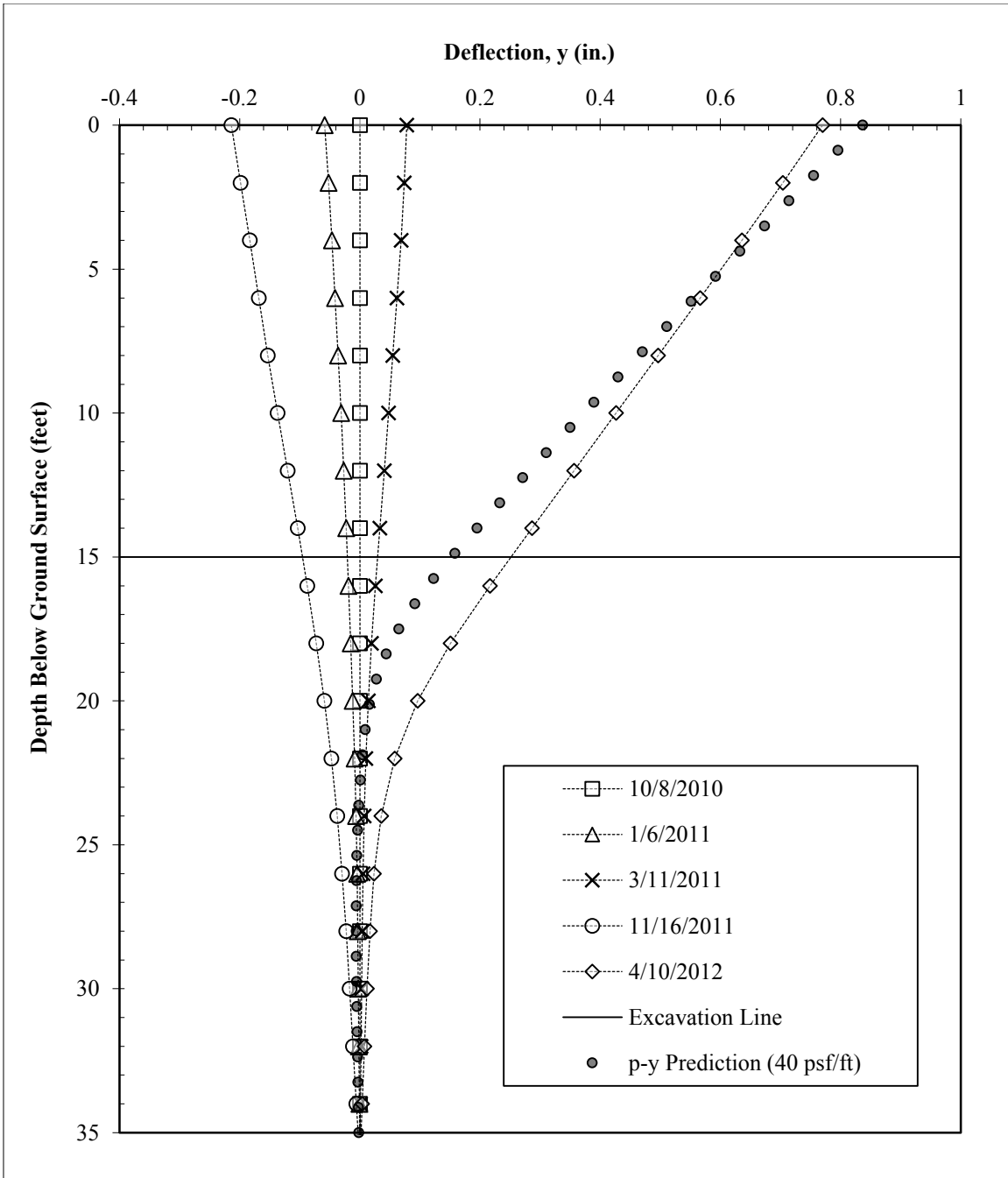


Figure 6.32: Deflected shapes of test wall at key dates, referenced to the installation of facing on October 8, 2010, compared with the initial p-y design analysis.

6.4.3: EARTH PRESSURE REDUCTIONS FROM SOIL SHRINKAGE

The maximum negative wall movement was observed between March 11, 2011 and November 16, 2011, in which top-of-wall deflections decreased by approximately 0.3 inches. Rotation profiles for the three instrumented shafts were differentiated to obtain an envelope of bending moments and equivalent soil reactions in response to soil shrinkage (Figure 6.33). The change in earth pressures corresponds to a reduction in equivalent fluid pressure of approximately 20 psf/ft (defined as the triangular distribution which will produce a profile of bending moments and deflections similar to the results of the calculated earth pressure distribution). The results of an LPILE analysis using the input parameters from Table 6.1 is presented in Figure 6.34. While top-of-wall deflections are fairly well predicted, wall behavior at depth is somewhat stiffer in the LPILE prediction. Additionally, the bending moment diagram appears to be shifted in a positive direction by approximately 120 in-kip at ground surface, and an average of 150 in-kip over the depth of the shaft (Figure 6.34).

Table 6.1: Baseline assumptions and design parameters for initial soil shrinkage LPILE analysis.

Parameter	Value
Effective Unit Weight of Soil, γ	62.6 pcf
Earth Pressure Loading	Input Envelope from Calculated p_{net}
Additional Moment Applied at Top for Thermal Effects	N/A
Friction Angle of Foundation Soil	24 degrees
Foundation Soil p-y Curves	Sand (Reese)
Non-Default Initial Stiffness, k_{py}	375 lb/in ³
Cracking Moment, M_{Cr}	680 k-in.
Yielding Moment, M_y	3,200 k-in.
Uncracked Bending Stiffness, EI_{uc}	67×10^6 k-in.
Cracked Bending Stiffness, EI_{cr}	18×10^6 k-in.
Shaft Diameter	24 in.
Height of Retained Soil, H	168 in.
Reinforcement	12 #7 bars (1.6% of gross area)

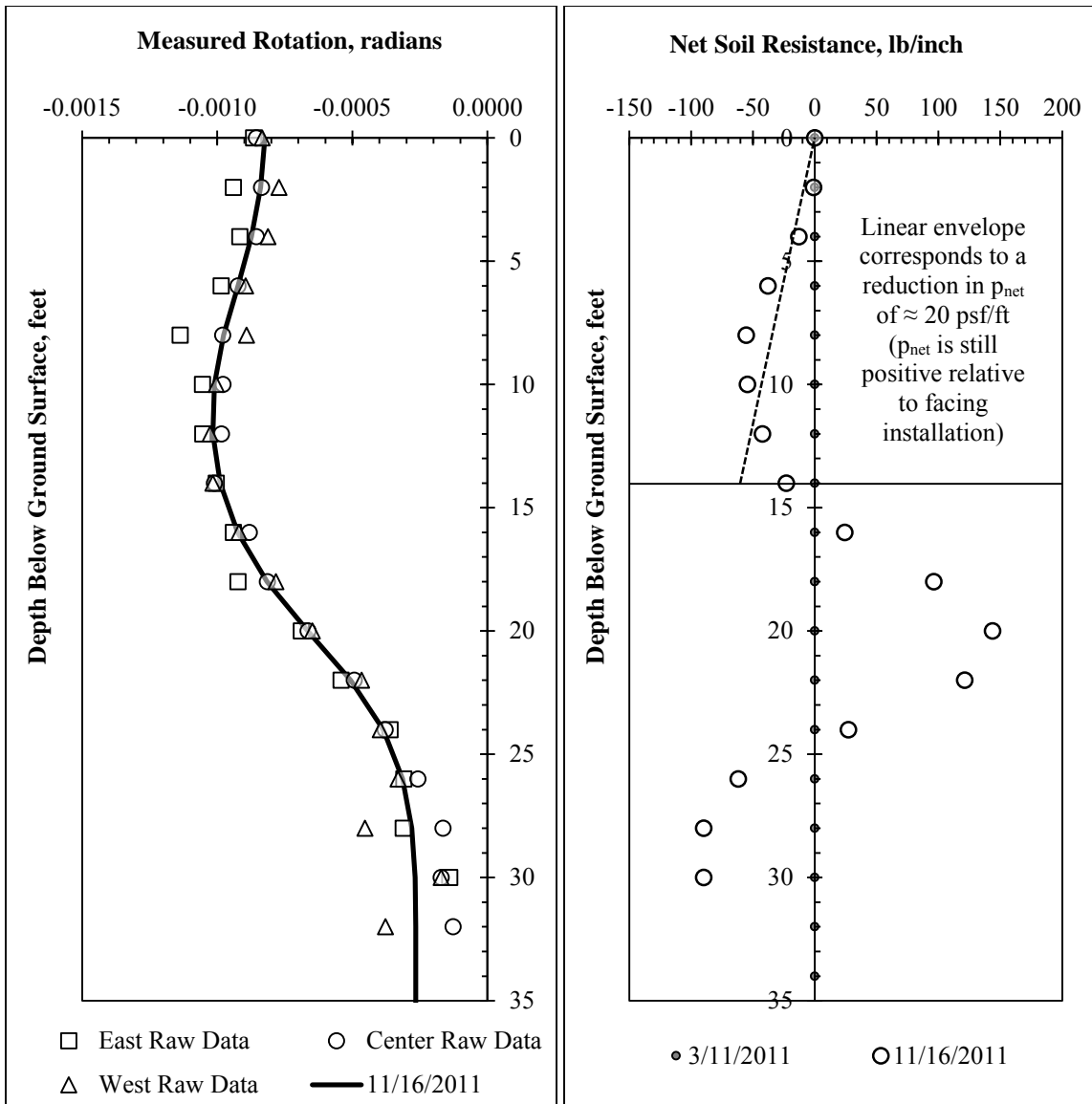


Figure 6.33: Profiles of shaft rotation and estimated reduction in net earth pressures in response to soil shrinkage between March 11 and November 16, 2011.

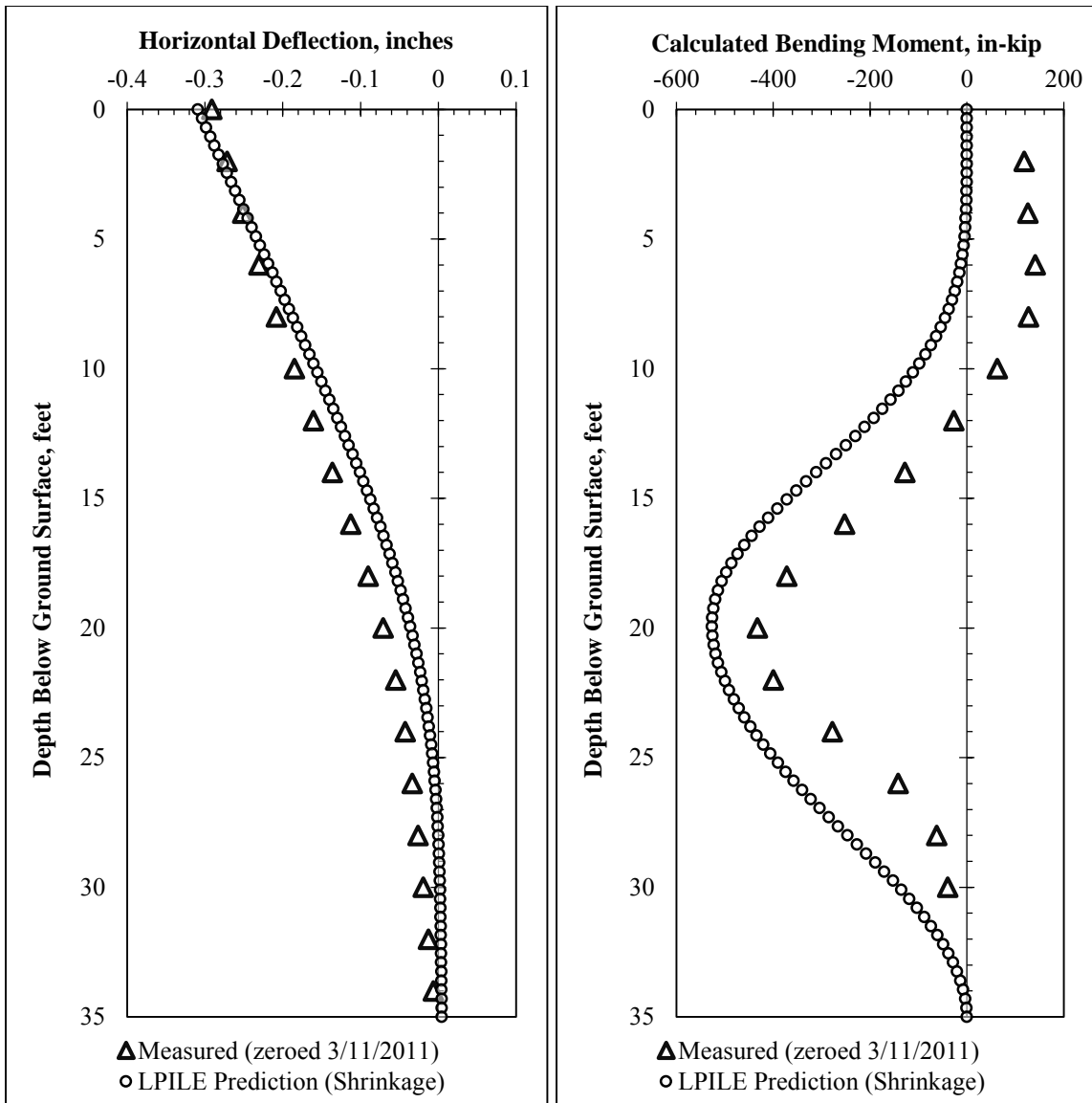


Figure 6.34: Comparison of LPILE prediction with horizontal deflections and bending moments between March 11 and November 16, 2011.

6.4.4: THERMAL STRAINS AND BENDING CURVATURES

The discrepancy in measured and predicted bending moments in Figure 6.34 can be partially explained by thermal strains. Temperature differentials between the front and back side of the shaft can lead to the appearance of bending curvatures. As the exposed

side of the shaft heats up and expands, the back of the shaft moves less because of the insulating presence of the retained soil. The difference in thermal strains on the front and back sides of the shaft results in the development of a bending curvature. Although thermal deformations do not directly stress the shaft, the influence of thermal strains on recorded values of bending curvature can be mistaken for an applied bending moment in the loading analysis.

While the ambient air temperatures at the time of data recording were the same on March 11 and November 16, the temperature conditions preceding each reading were different. At the reference survey on March 11, a temperature increase of approximately 30 degrees Fahrenheit occurred in the four hours prior to the inclinometer survey. On November 16, the temperature increase during the same time period was approximately 13 degrees. Air temperature readings from a weather station near the test wall site are presented in Figure 6.35.

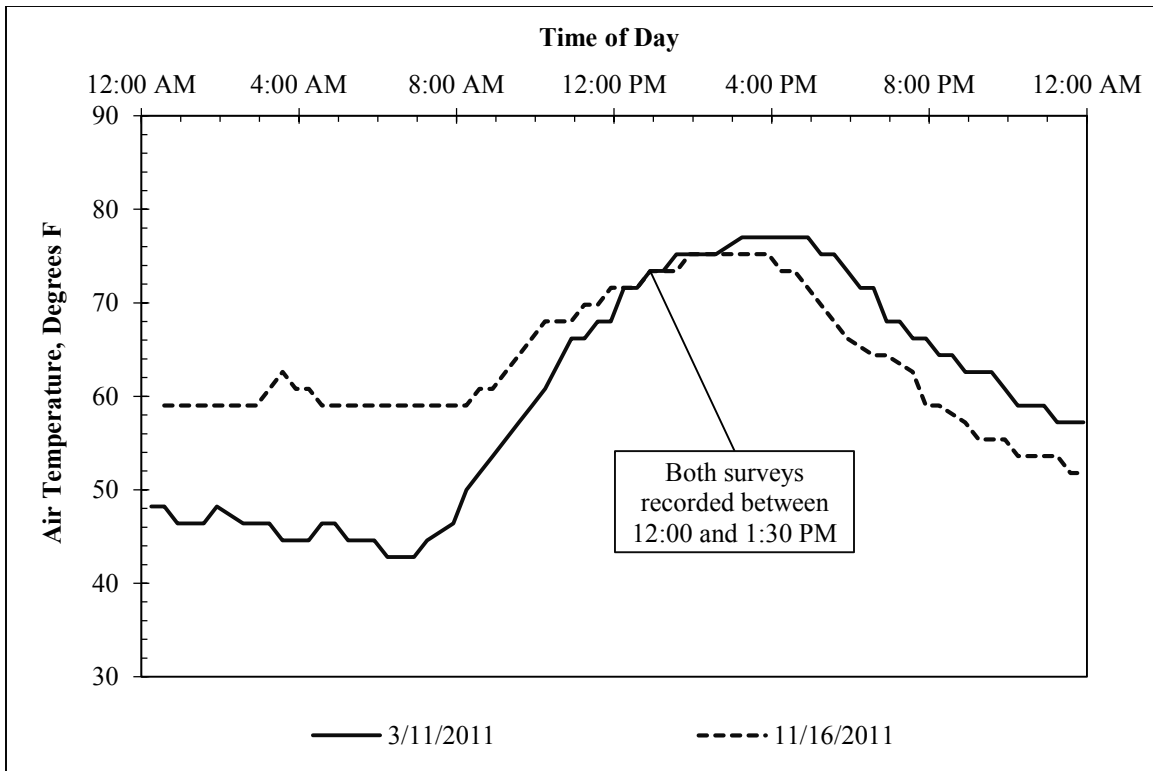


Figure 6.35: Air temperature in Manor, Texas on March 11 and November 16, 2011 (data from www.wunderground.com).

6.4.4.b: Daily Variation in Temperature and Bending Strains

To illustrate the daily effects of temperature fluctuation on the test wall, strain data from the center shaft can be compared with temperature data from a nearby weather station. To minimize the effects of wall deformation and seasonal temperature changes on data interpretation, five days of data from October 22 to October 27, 2011 are presented. During this time, the wall experienced minimal changes in deflection, and the daily values of maximum, minimum, and average temperature were similar. Results are presented in Figure 6.36.

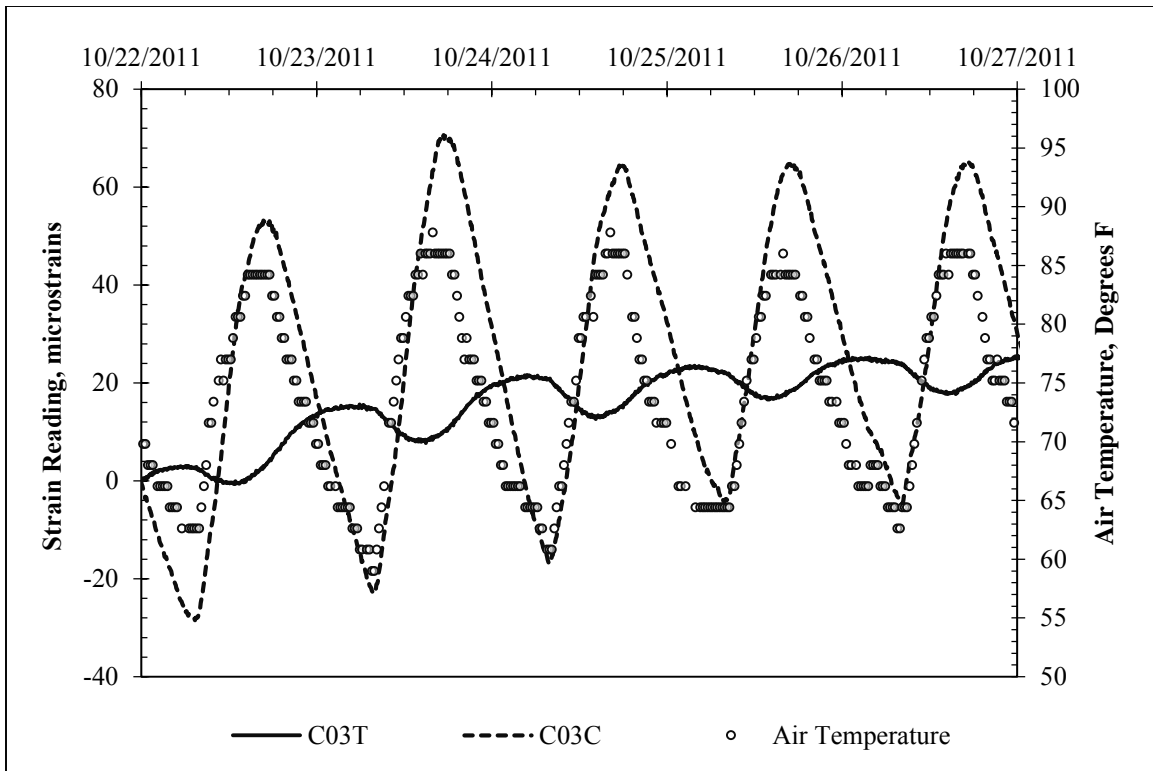


Figure 6.36: Comparison of air temperature in Manor, Texas and strain data at a depth of 3 feet in the center instrumented shaft (October 22 – October 27, 2011; weather data from www.wunderground.com).

The wall responds relatively quickly to daily temperature fluctuations. The gauges on the compression side of the wall (3 inches from the exposed surface) reach their maximum strain within 3 to 4 hours after the air temperature reaches its maximum. The gauges on the tension side (21 inches from the exposed surface), however, do not reach their maximum until around 9 to 10 hours after the maximum air temperature. By this point, the air temperature has begun to decrease and reaches a minimum value soon after the tension side of the shaft reaches its maximum. Because bending curvatures in the shaft are related to the difference in strains between the front and back sides of the shaft, bending curvatures are affected by this hysteresis. Comparisons of bending curvature fluctuations in the test wall at depths of 3, 11, and 13 feet are presented in Figure 6.37.

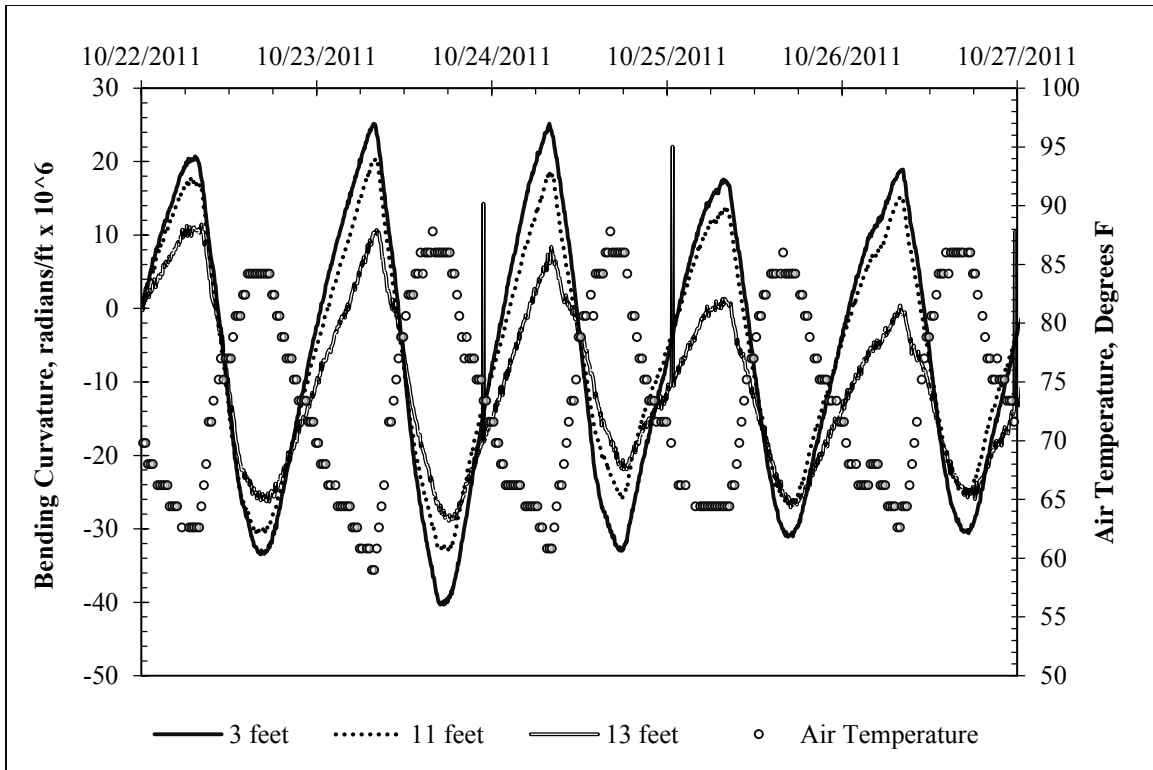


Figure 6.37: Comparison of air temperature in Manor, Texas and measured bending curvature in the test wall at various depths in the center shaft (temperature data from www.wunderground.com).

From October 22 – 27, 2011, the daily temperature fluctuation ranged from 22 to 28 degrees Fahrenheit. During the same time, the average measured bending curvatures in the shaft above the excavation line were approximately 40×10^{-6} to 50×10^{-6} radians per foot. Although all gauges are the same distance from the exposed side of the shaft, the bending curvature induced by a given temperature change appears to decrease with depth below original ground surface (Figure 6.37). The maximum and minimum values of thermal bending curvature occur, respectively, at approximately the same time as the minimum and maximum values of air temperature (e.g. if temperatures are at their maximum at 5:00 PM, bending curvatures and wall deflections are at their minimum).

Based on the moment-curvature relationship for the test wall, the range of measured thermal bending curvatures are equivalent to applied “moment” fluctuations of approximately 250 to 300 in-kip.

If the measured bending curvatures are applied above the excavation line only (from 0 to 15 feet) and integrated twice, they correspond to a daily variation in top-of-wall deflection of approximately 0.05 to 0.10 inches (0.03 to 0.06% of the wall height). Over the entire monitoring period of three years, the test wall experienced an average daily temperature fluctuation of 22 degrees Fahrenheit, with a maximum recorded daily fluctuation of 48 degrees.

6.4.4.c: Analysis of Thermal Deformations on March 11, 2011 and November 16, 2011

On March 11, 2011, the bending curvatures induced by temperature change were relatively high, corresponding to a short-term increase of approximately 30 degrees Fahrenheit. On November 16, the temperature increase was much smaller, approximately 13 degrees, and the thermal bending curvatures were accordingly smaller. When March 16, 2011 is used as the reference survey, the reduced thermal bending curvatures on November 16 appear in the analysis as additional bending moments of between 100 and 150 in-kip. Based on the data from Figure 6.37, an air temperature difference of approximately 18 degrees is consistent with a bending curvature corresponding to a bending moment of about 150 in-kip.

To simulate the effects of thermal bending curvatures in the LPILE analysis, a bending moment of 150 in-kip (equivalent to the average difference between measured and predicted moment curves) was applied to the top of the shaft. Input parameters for the LPILE analysis are summarized in Table 6.2. Results of the LPILE analysis are provided in Figure 6.38 and Figure 6.39.

Table 6.2: Baseline assumptions and design parameters for soil shrinkage LPILE analysis, accounting for thermal bending curvatures.

Parameter	Value
Effective Unit Weight of Soil, γ	62.6 pcf
Earth Pressure Loading	Input Envelope from Calculated p_{net}
Additional Moment Applied at Top for Thermal Effects	150 k-in
Friction Angle of Foundation Soil	24 degrees
Foundation Soil p-y Curves	Sand (Reese)
Non-Default Initial Stiffness, k_{py}	375 lb/in ³
Cracking Moment, M_{Cr}	680 k-in.
Yielding Moment, M_y	3,200 k-in.
Uncracked Bending Stiffness, EI_{uc}	67 x 10 ⁶ k-in.
Cracked Bending Stiffness, EI_{cr}	18 x 10 ⁶ k-in.
Shaft Diameter	24 in.
Height of Retained Soil, H	168 in.
Reinforcement	12 #7 bars (1.6% of gross area)

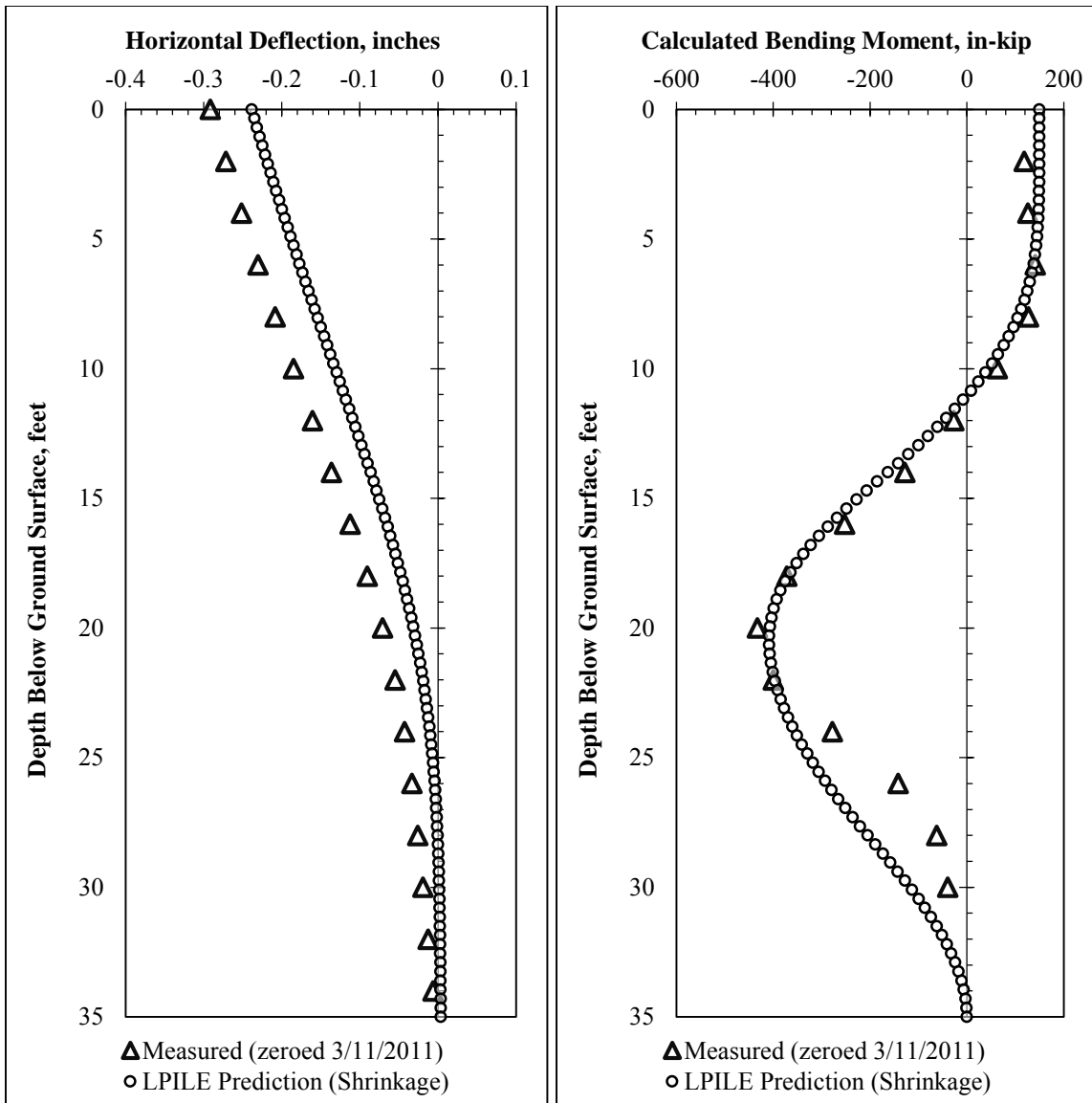


Figure 6.38: Comparison of LPILE prediction with horizontal deflections and bending moments between March 11 and November 16, 2011. A bending moment of 150 in-kip was applied at the top of the shaft to simulate thermal effects.

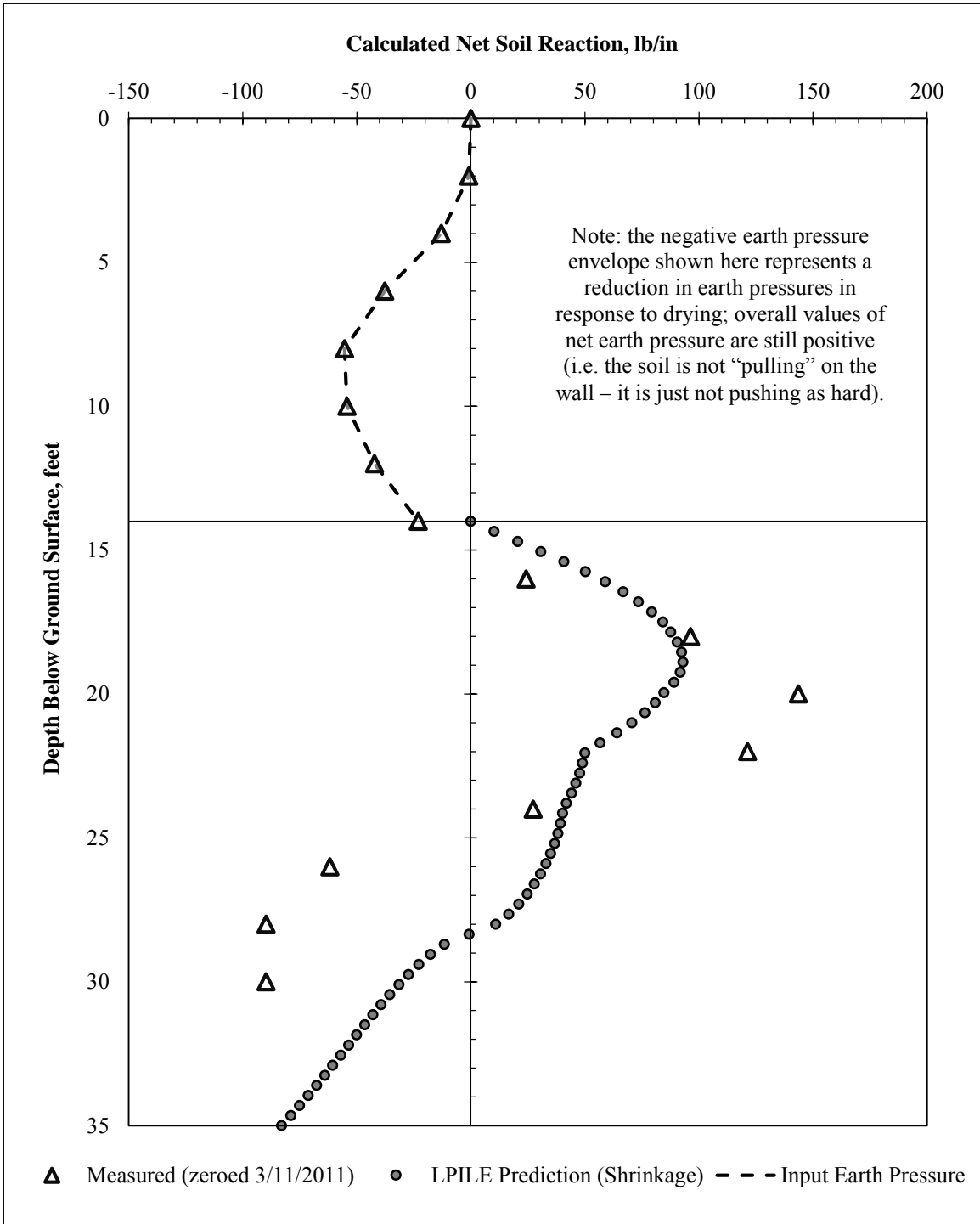


Figure 6.39: Comparison of measured and calculated soil reaction forces due to expansive soil shrinkage.

6.4.5: EARTH PRESSURE INCREASES FROM SOIL EXPANSION

The analysis of earth pressures induced by soil wetting during inundation testing (discussed in Chapter 7) suggests that the increases in wall deflections due to wetting are due to the presence of water causing softening of the retained soil and loss of resistance in the foundation soil. The increase in deflections with increased moisture content is gradual and takes place over a period of months. There is limited evidence to suggest that extremely high earth pressures due to soil expansion exist at the test wall (in the upper three to five feet of soil, where the theoretical potential for large swell pressures exists, calculated earth pressures are consistently low). Because the response of the test wall to natural wetting cycles is similar to the response during controlled inundation testing, earth pressure increases due to soil expansion are covered in the following chapter.

6.5: Summary and Conclusions

Data recorded at the Lymon C. Reese research wall during natural moisture cycles has provided some insight into the behavior of drilled shaft retaining walls during cycles of wetting and drying. Conclusions include:

- During cycles of drying, wall deflections decreased. This is primarily due to volumetric shrinkage of the soil, which leads to an equivalent reduction in earth pressures. After 8 months of extreme drought, deflections at the test wall decreased by approximately 0.3 inches, and the earth pressure reduction corresponds to a decrease in equivalent fluid pressure of approximately 20 psf/ft. The effects of soil shrinkage can be approximated with the use of an equivalent “negative earth pressure” envelope with p-y curves using fully softened, drained strength parameters with initial stiffness k_{py} defined by the original profile of undrained

shear strength. This method provides approximations close to the measured values, but does not account for the increase in soil stiffness with drying.

- During cycles of wetting, wall deflections increased. This is primarily due to a combination of soil swelling and the dissipation of negative pore pressures. The presence of water contributes to both increased earth pressures (softening of the retained soil) and decreased resistance (softening of the foundation soil). There is little evidence at the test wall to suggest that high lateral earth pressures due to soil expansion are imposed.
- The use of Time Domain Reflectometry (TDR) probes to measure moisture content in expansive clay is problematic because of the soil's high electrical conductivity and tendency to pull back from the probe rods during drying cycles. However, electrical conductivity measurements from one TDR probe appear to correlate with moisture contents and top-of-wall deflections. While the electrical conductivity data cannot be directly related to moisture content, it can provide a qualitative indicator of the moisture conditions on the project site.
- The direct use of strain gauge data for the determination of bending curvature generally requires more advanced data interpretation than simply taking the first derivative of rotation profiles measured from inclinometer data. This difficulty is primarily due to the heterogeneous behavior of the concrete with depth, the appearance of tension cracks at bending moments close to the cracking moment, and the tendency of strain gauges to measure a variety of processes in addition to wall deformations resulting from lateral loads. While individual strain gauges measure localized, variable processes within the shaft, the inclinometer casing measures global behavior that can be more easily used directly without subjective data analysis.

- Daily cycles of thermal strains can influence data interpretation. If the climatic conditions on survey dates are substantially different, bending curvatures induced by daily temperature differences can be mistaken for bending moments caused by changes in earth pressure. The test wall experiences an average daily temperature fluctuation of approximately 22 degrees Fahrenheit, which corresponds to a daily variation in top-of-wall deflection of approximately 0.05 to 0.1 inches. Daily temperature fluctuations as high as 48 degrees have been recorded at the test site.
- Because thermal deformations are tedious to model without detailed weather data, and their effect on wall behavior is relatively small, large-scale corrections to the data set for temperature effects are generally not practical. However, if isolated surveys with unusual deflection, rotation, or bending curvatures are observed in the data, consideration of thermal effects is needed.

CHAPTER 7: TEST WALL BEHAVIOR DURING CONTROLLED INUNDATION TESTING (MAY 2012 – JULY 2013)

7.1: Overview

During the extremely dry summer of 2011, the research plan was modified to include cycles of artificial inundation of the retained soil. Based on climatic history and the available long-term weather forecasting, it was deemed unlikely that the soil on the project site would ever sustain the high moisture contents necessary to investigate the effects of soil expansion on wall behavior. By increasing soil moisture content behind the wall to an upper-bound condition, the influence of soil wetting and expansion on the earth pressures can be more readily estimated. Beginning in May 2012, the retained soil was provided unlimited access to water for two months, followed by a seven month drying cycle. In February 2013, the retained soil was inundated until the top-of-wall deflections reached equilibrium, a period of approximately four additional months.

7.2: Summary of Key Events

7.2.1: SITE INVESTIGATION AND INSTALLATION OF INUNDATION BERM AND PIEZOMETERS

On February 23, 2012, a site investigation was conducted and four stand pipe piezometers were installed as shown in Figure 7.1. On April 26, 2012, the inundation berm was constructed as shown in Figure 7.2 – Figure 7.3.

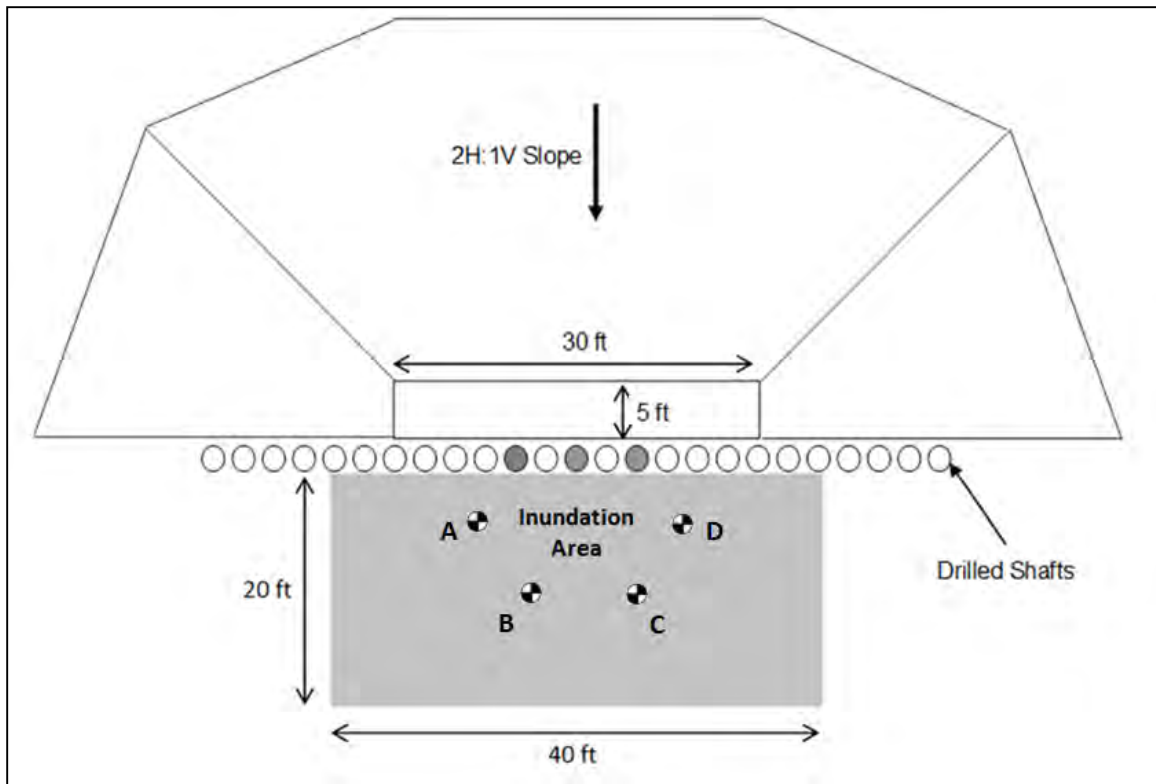


Figure 7.1: Location of inundation zone and stand pipe piezometers. Piezometers A and C are screened from 5 to 15 feet; piezometer B is screened between 3.4 and 4.6 feet; piezometer D is screened between 3.6 and 4.8 feet.

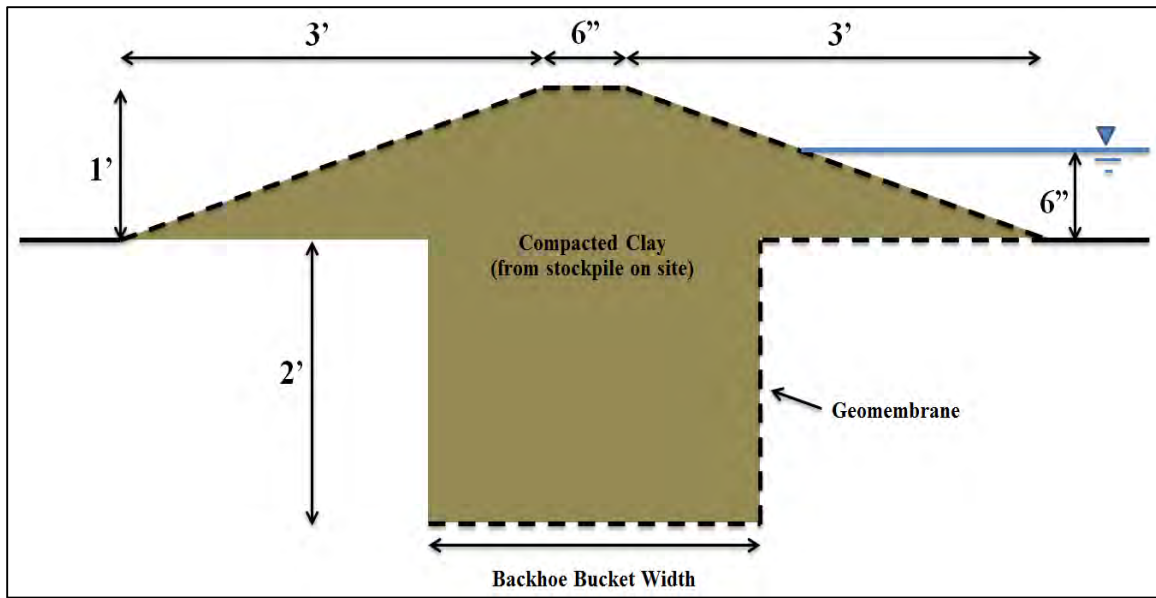


Figure 7.2: Schematic of inundation berm.

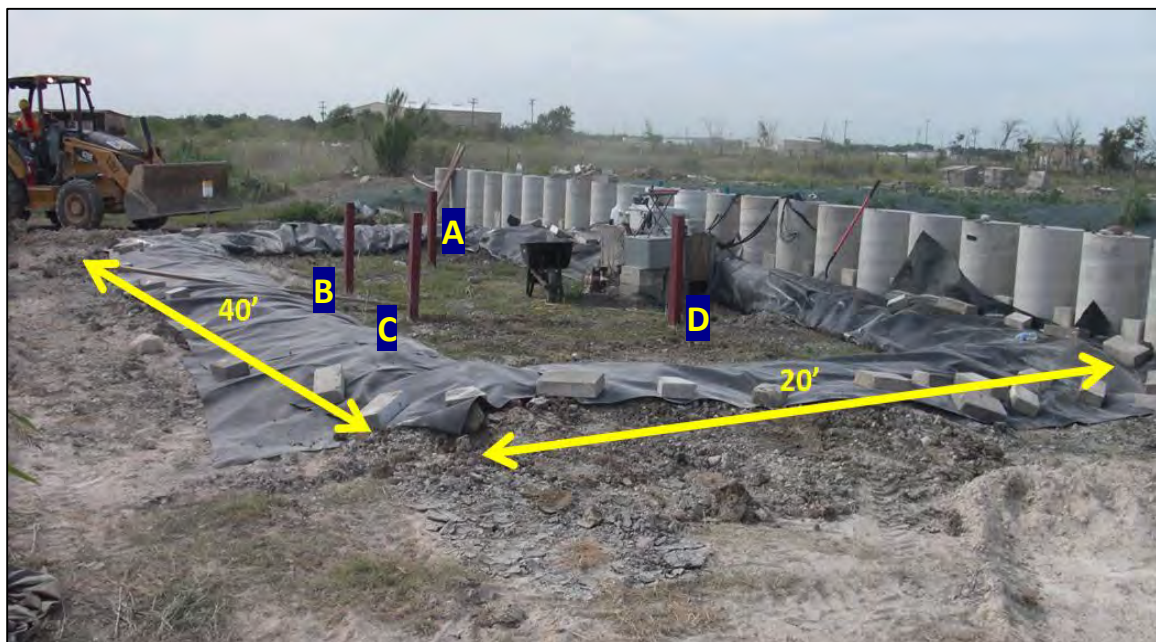


Figure 7.3: Inundation berm and stand pipe piezometers (April 26, 2012).

7.2.2: SUMMARY OF INUNDATION CYCLES

7.2.2.a: First Inundation Cycle (May 2012 – July 2012)

Beginning on May 3, 2012, the inundation zone was filled. Wall deflections increased steadily for approximately two months until July 2, 2012, when the water supply to the pond was stopped and the wall was allowed to return to its natural state.

7.2.2.b: First Drying Cycle (July 2012 – February 2013)

From July 2012 to February 2013, the wall was not provided access to moisture beyond naturally occurring rainfall on the project site. Over this time period, deflections fluctuated slightly, but did not increase or decrease to a degree consistent with a significant change in loading conditions.

7.2.2.c: Second Inundation Cycle (February 2013 – June 2013)

Beginning on February 5, 2013, the inundation zone was filled a second time. After approximately four months of inundation, the wall deflections and piezometer water levels stabilized. In response to a large storm event, a major flood occurred in which the water level in the excavation reached the ground surface prior to the inclinometer and strain gauge data surveys recorded on May 6, 2013 (Figure 7.4). During this flood event, significant erosion of the excavation slopes occurred; due to additional soil transported to the excavation base, the excavation depth had decreased to approximately 13.5 feet below ground surface.



Figure 7.4: Flooding in response to a large storm before the May 6, 2013 data surveys. Water level in the excavation reached ground surface.

7.2.2.d: Second Drying Cycle (June 2013 – July 2013)

On June 3, 2013, a second drying cycle began. Water moved out of the soil quickly, and shrinkage cracks appeared in the surface soil (Figure 7.5). As water moved out of the soil, top-of-wall deflections began to decrease fairly quickly. At the time of this writing, the wall deflections had been monitored during drying for a period of approximately two months. At the conclusion of data recording in July 2013, top-of-wall deflections and stand pipe piezometer levels had nearly stabilized, but had not completely reached equilibrium. Based on previous observations, it is likely that when water levels return to their natural values of approximately 8 feet below ground surface, the top-of-wall deflections will stabilize.



Figure 7.5: Inundation zone on June 17, 2013, two weeks into second drying cycle. Stand pipe piezometer casing is 4" across.

7.2.3: CLIMATIC INFORMATION

Monthly rainfall totals for Austin, Texas during controlled inundation testing are presented in Figure 7.6. Daily temperature measurements for Manor, Texas are presented in Figure 7.7. While rainfall data during periods of wall inundation is useful to get a sense of the soil conditions outside the influence of the inundation zone, rainfall data during the drying cycle from July 2012 to February 2013 is of most interest. For the first three months of the drying cycle during July through September 2012, rainfall totals were above average, followed by four months of below average rainfall between October and December, 2012. During January 2013, rainfall totals began to increase before the beginning of the second inundation cycle in February 2013.

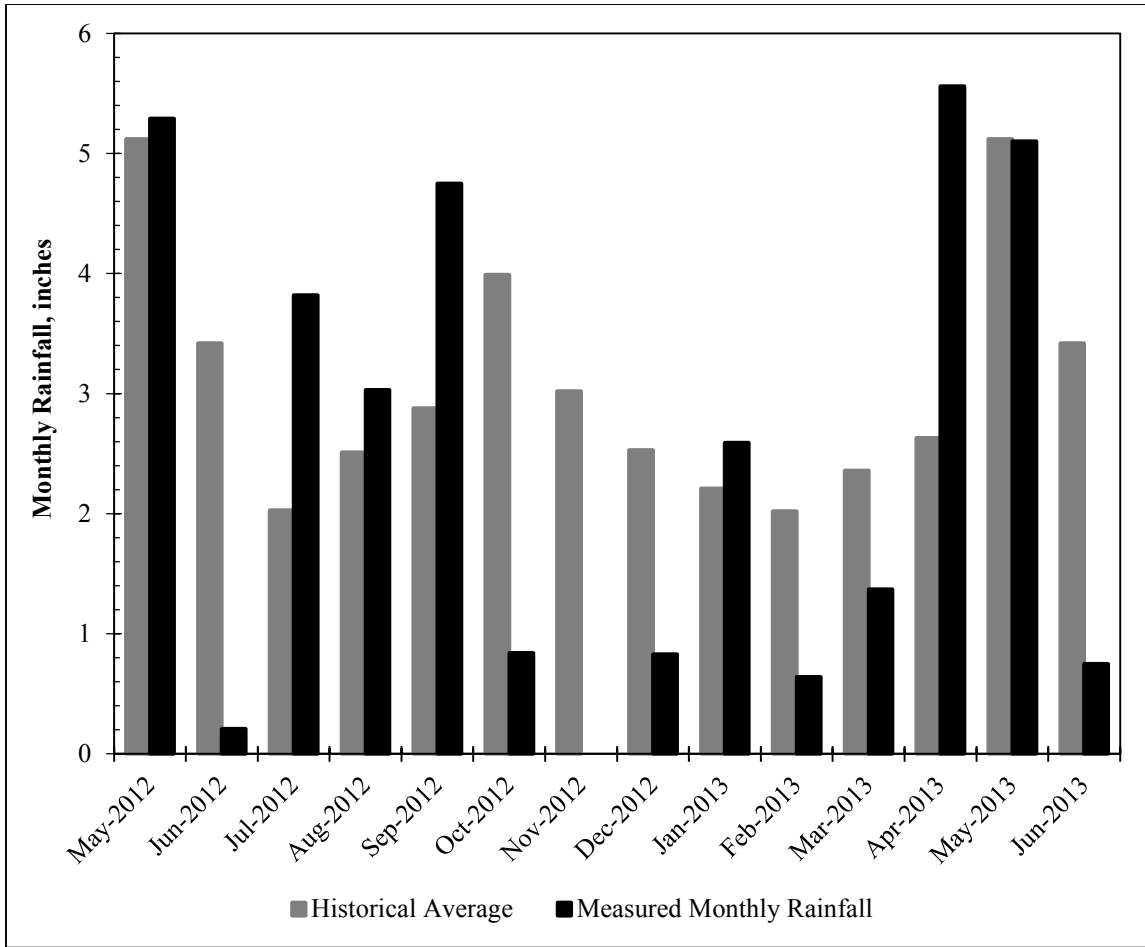


Figure 7.6: Monthly rainfall totals for Austin, Texas (May 2012 - Jun. 2013; data from www.wunderground.com).

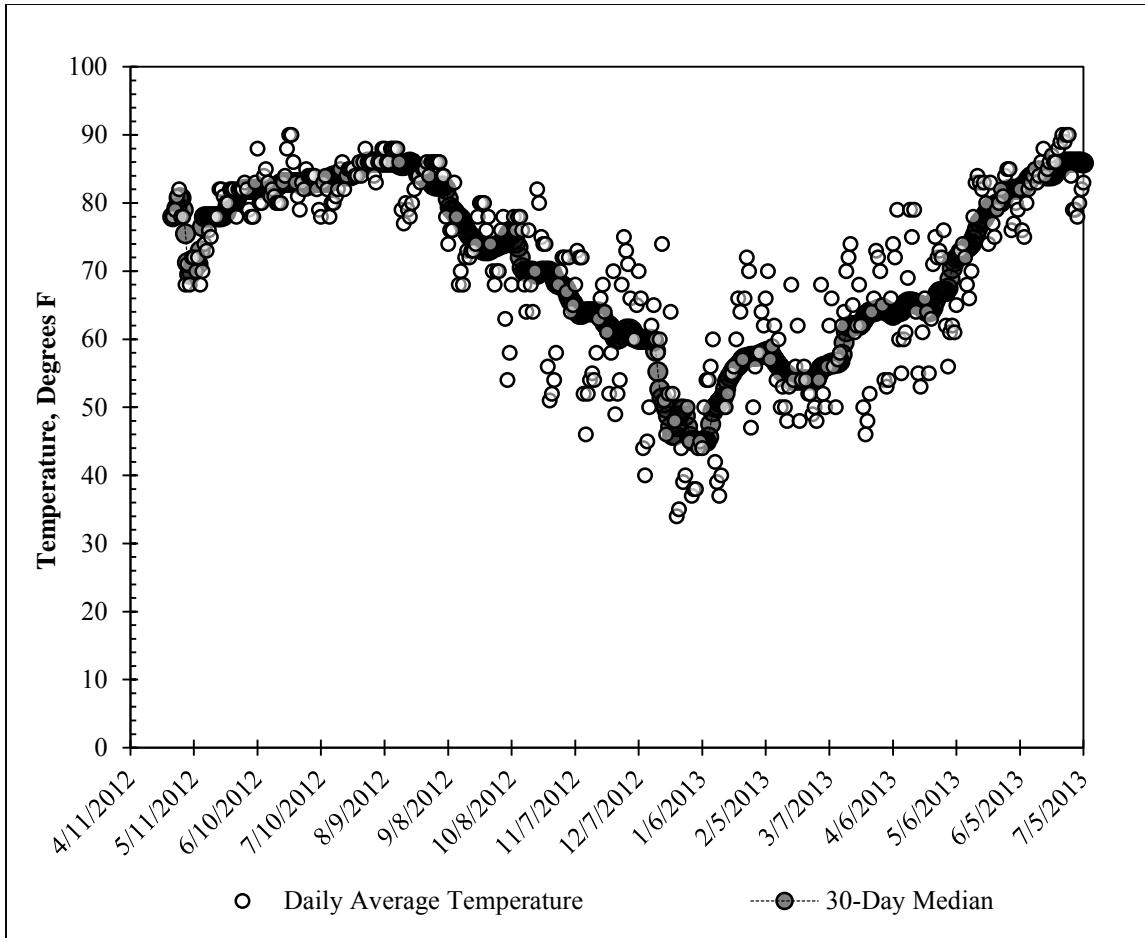


Figure 7.7: Daily average temperature data for Manor, Texas (May 2012 - Jul. 2013; data from www.wunderground.com).

7.3: Summary of Field Instrumentation Data

7.3.1: INCLINOMETER DATA

Inclinometer data is referenced to the installation of facing in October, 2010. Average deflected shapes are presented in Figure 7.8, top-of-wall deflections are presented in Figure 7.9, and the rate of deflection at ground surface is presented in Figure 7.10.

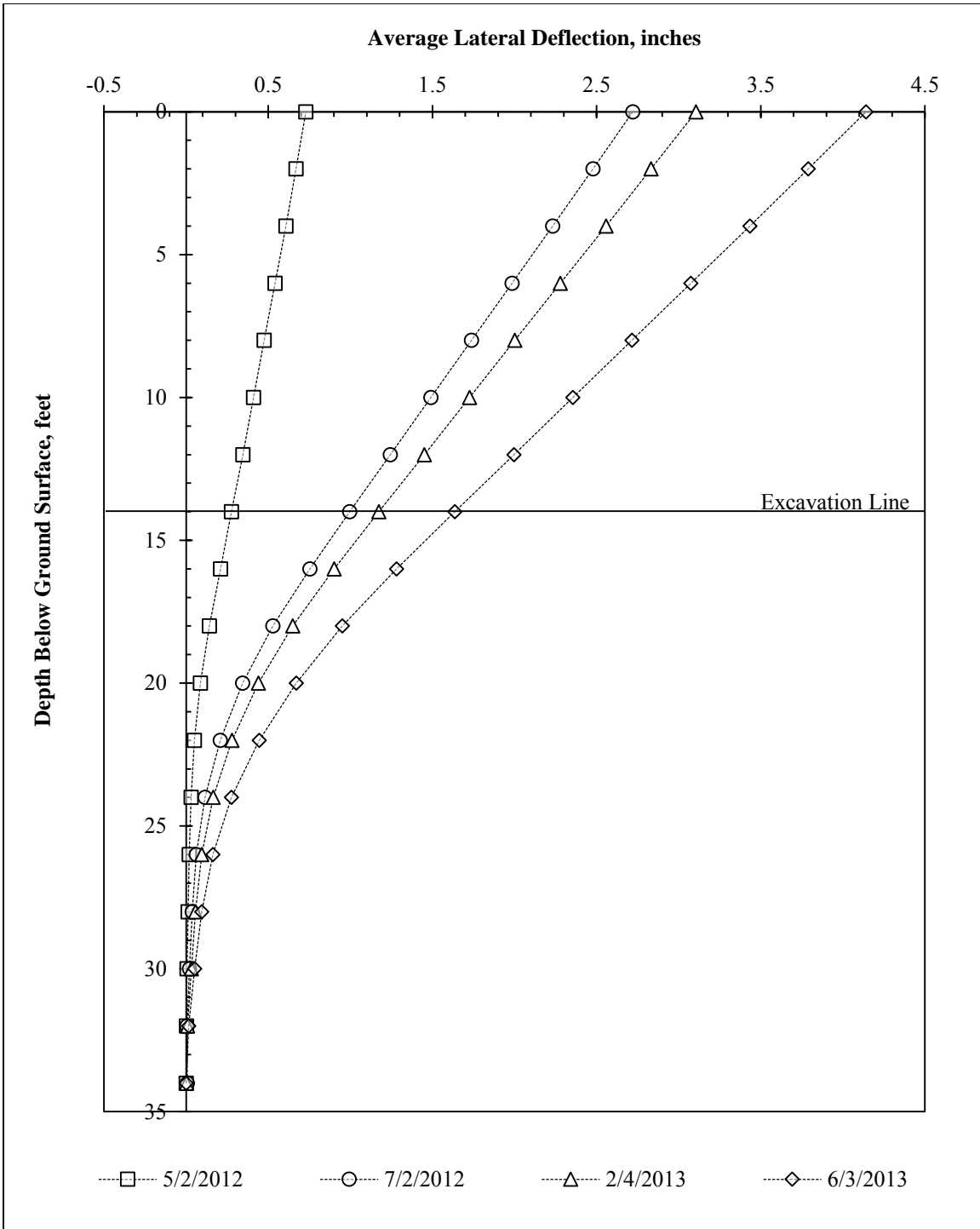


Figure 7.8: Average deflected shapes at key dates during inundation testing. Data is referenced to installation of facing in October, 2010.

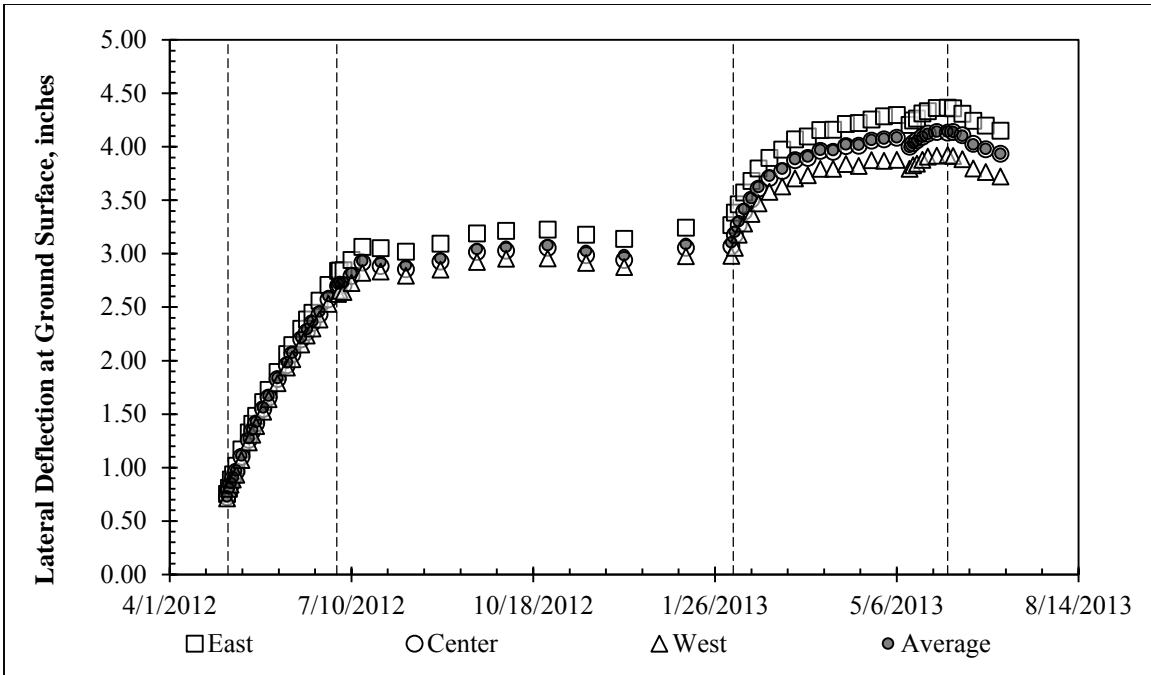


Figure 7.9: Top-of-wall deflections during inundation testing (key dates indicated by vertical dashed lines). Reference survey is facing installation in October, 2010.

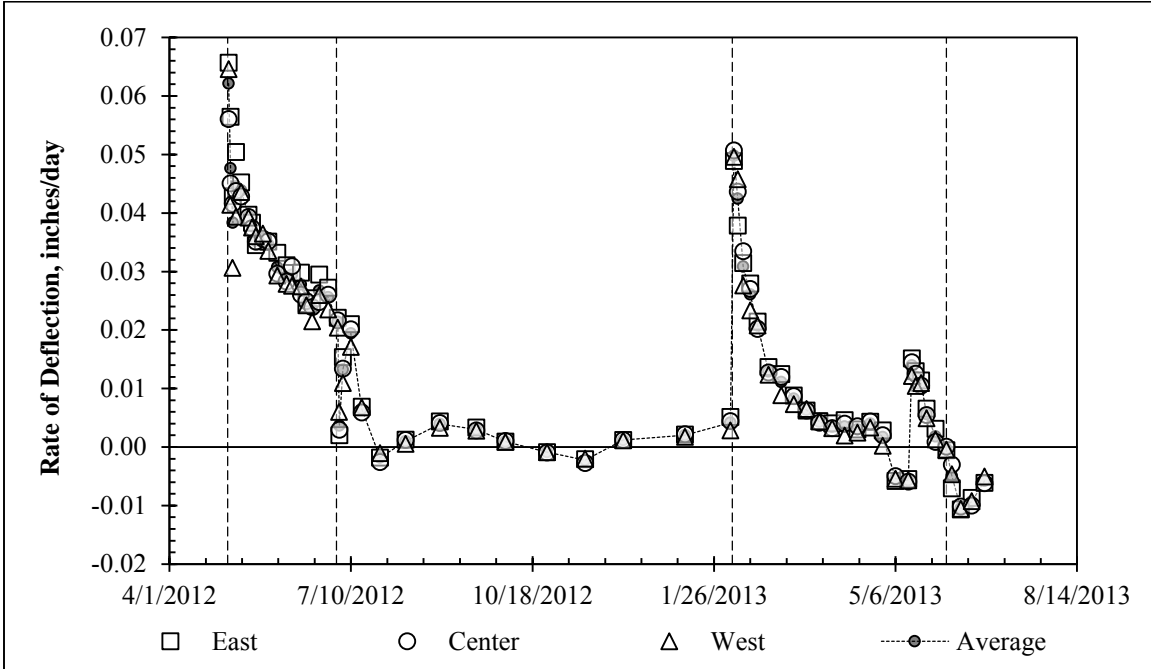


Figure 7.10: Rate of deflection at ground surface during inundation testing (key dates indicated by vertical dashed lines).

7.3.2: SOIL MOISTURE CONTENT DATA

A summary of measured soil moisture contents during controlled inundation testing is provided in Figure 7.11. Data from samples using a hand auger, as well as data from geotechnical investigations conducted by Fugro Consultants, Inc., is provided. While a wide range of moisture contents were measured throughout the testing, in general, measured moisture contents ranged from approximately 15 to 35 percent in the zone above the natural groundwater table. At the conclusion of the second inundation cycle, moisture contents had increased to approximately 30 percent over the entire depth of the active zone (above the natural groundwater table at 8 feet below ground surface). While the final values of moisture content were similar at the conclusion of the first and second inundation cycles between 0 and 4 feet below ground surface, the second inundation cycle resulted in additional wetting of the soil between 4 and 8 feet below ground surface. Below the groundwater table at a depth of 8 feet, the soil transitions from dark brown Taylor clay to tan Taylor clay, and the natural moisture contents increase to between approximately 34 and 40 percent.

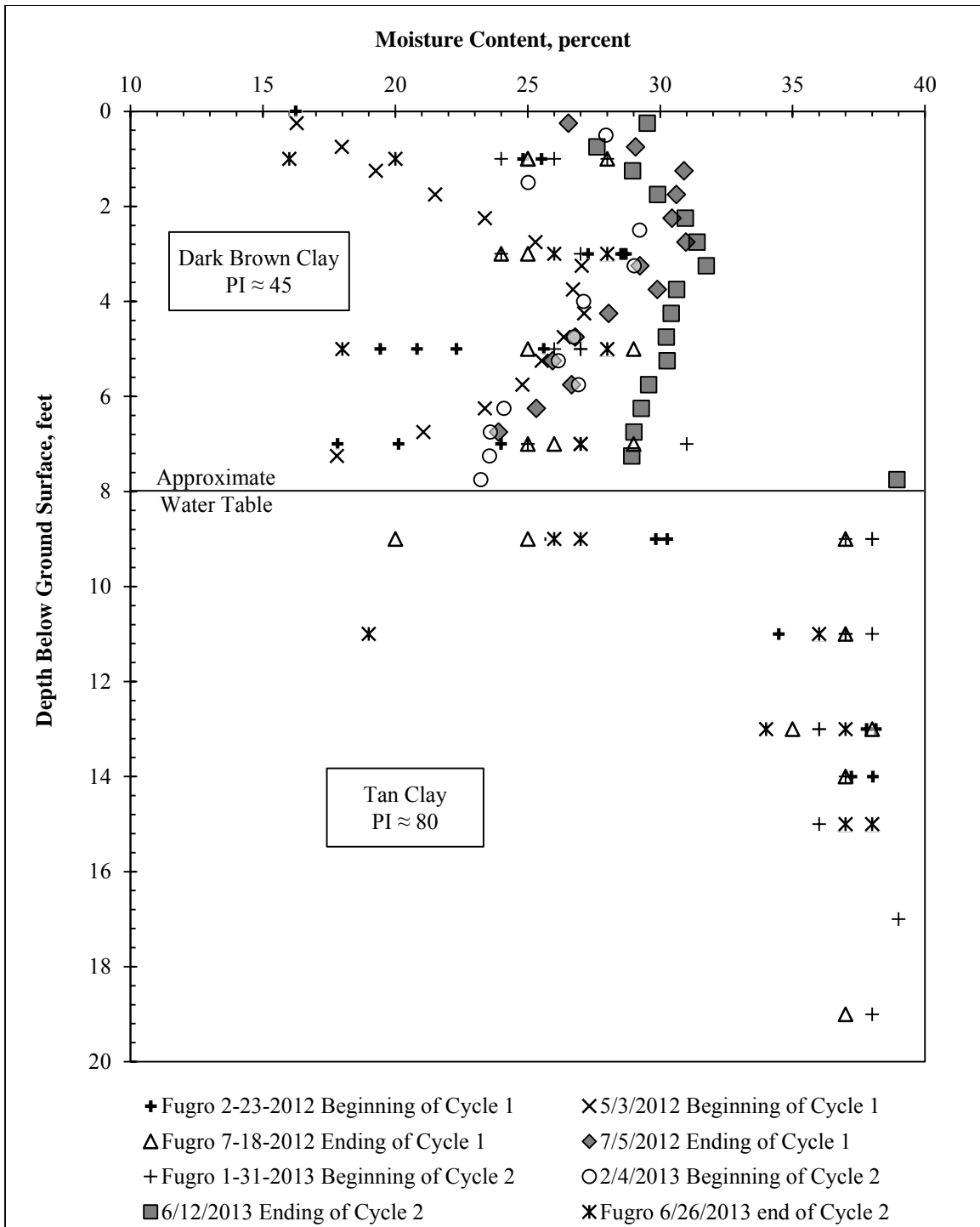


Figure 7.11: Summary of measured soil moisture contents during controlled inundation testing.

7.3.3: STAND PIPE PIEZOMETER DATA

Data from the stand pipe piezometers were recorded at regular intervals for the duration of inundation testing. Piezometer B-3 was installed and developed in 2010; consequently, water levels can be plotted for all inundation cycles (Figure 7.12). Piezometers A, B, C, and D were not properly developed after installation and did not show reliable data until the second inundation cycle. Data from the second cycle is presented in Figure 7.13 (piezometers with shallow screen intervals) and Figure 7.14 (piezometers with deeper screen intervals).

The water level in Piezometer B-3 was relatively unaffected by the presence of water in the inundation zone. The increased values in May, 2012 were associated with flooding on the project site that infiltrated the piezometer casing, and most likely do not represent the actual groundwater conditions. At the conclusion of inundation testing in July, 2013, the water level had stabilized at approximately 8.5 to 9 feet below ground surface.

The water levels in the piezometers with shallow screen intervals stabilized at approximately 0.5 and 1.3 feet below ground surface during the second inundation cycle, before increasing during a large flood in May, 2013 by approximately 0.3 feet. After the flood, water levels returned to values slightly higher than their original equilibrium values. The discrepancy in equilibrium water heights may be due to the development of steady-state seepage conditions, in which a cone of depression near the wall face leads to lowered water levels in stand pipe piezometers close to the wall (Figure 7.13). In piezometers with deeper screen intervals, water levels showed a similar trend, with equilibrium water levels increasing slightly after flooding in May, 2013. Water levels were similarly lowered in the piezometer closer to the wall face. At the conclusion of inundation testing, despite the small cone of depression near the wall facing drains, conditions close to hydrostatic pressures had likely developed in much of the retained soil. After the water supply was

stopped in June, 2013, water levels in all piezometers immediately began to decrease toward their pre-inundation values.

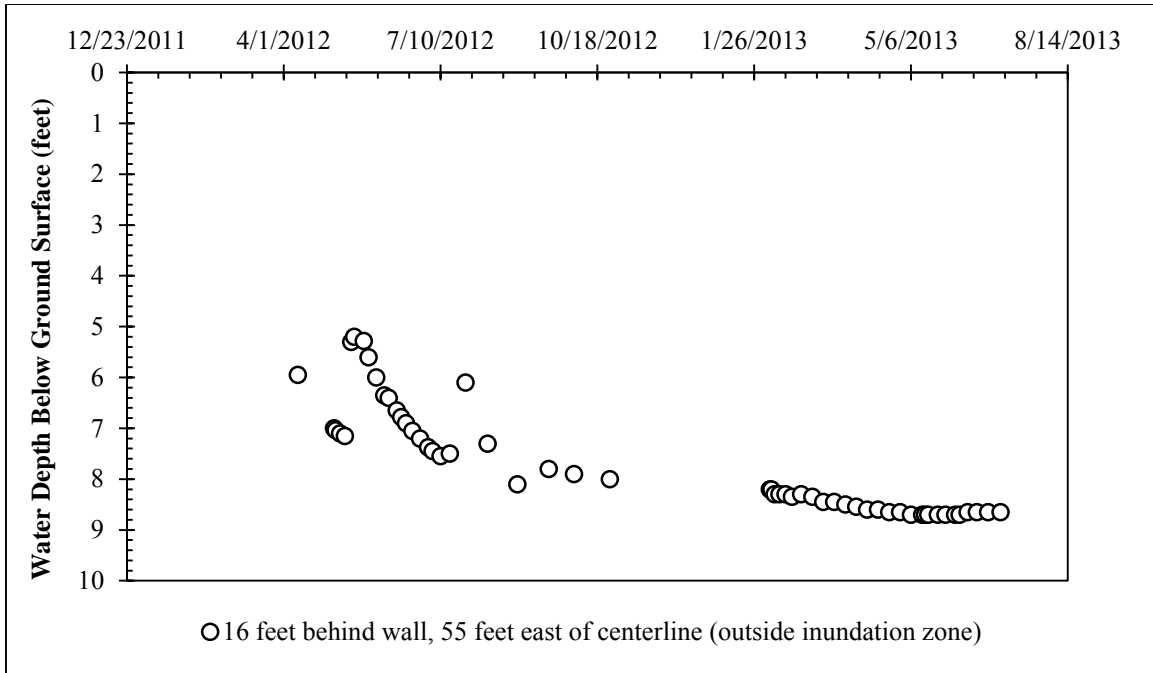


Figure 7.12: Water level in Piezometer B-3 (outside inundation zone) during inundation testing.

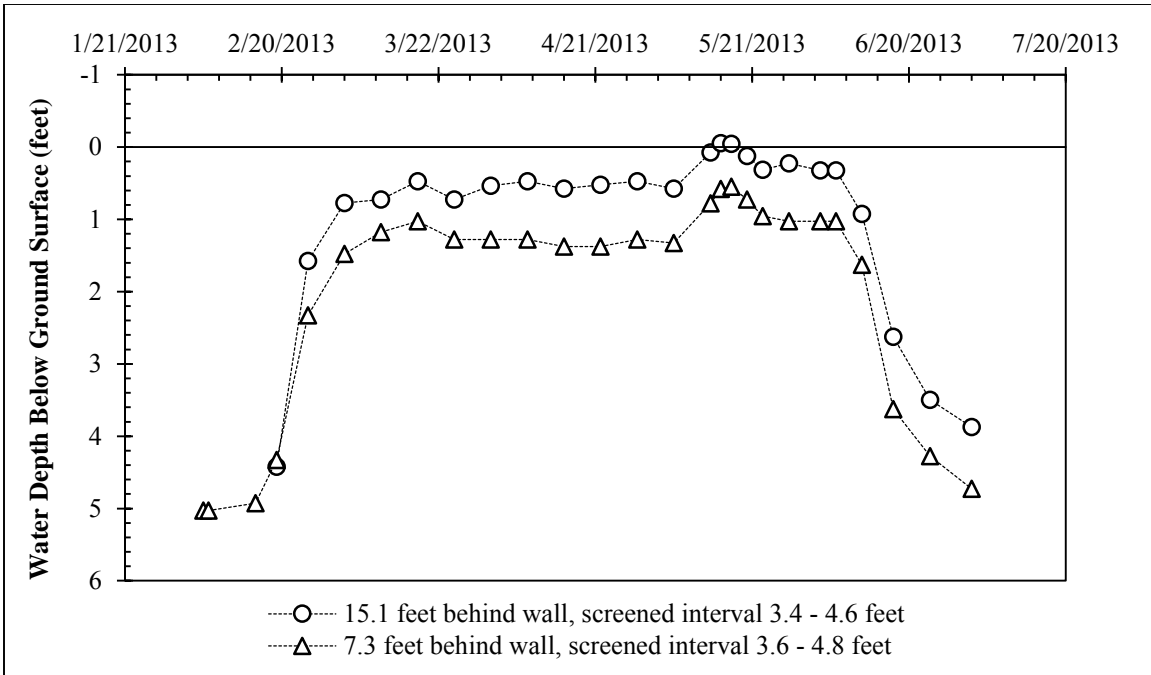


Figure 7.13: Data from shallow-screened stand pipe piezometers during second inundation cycle.

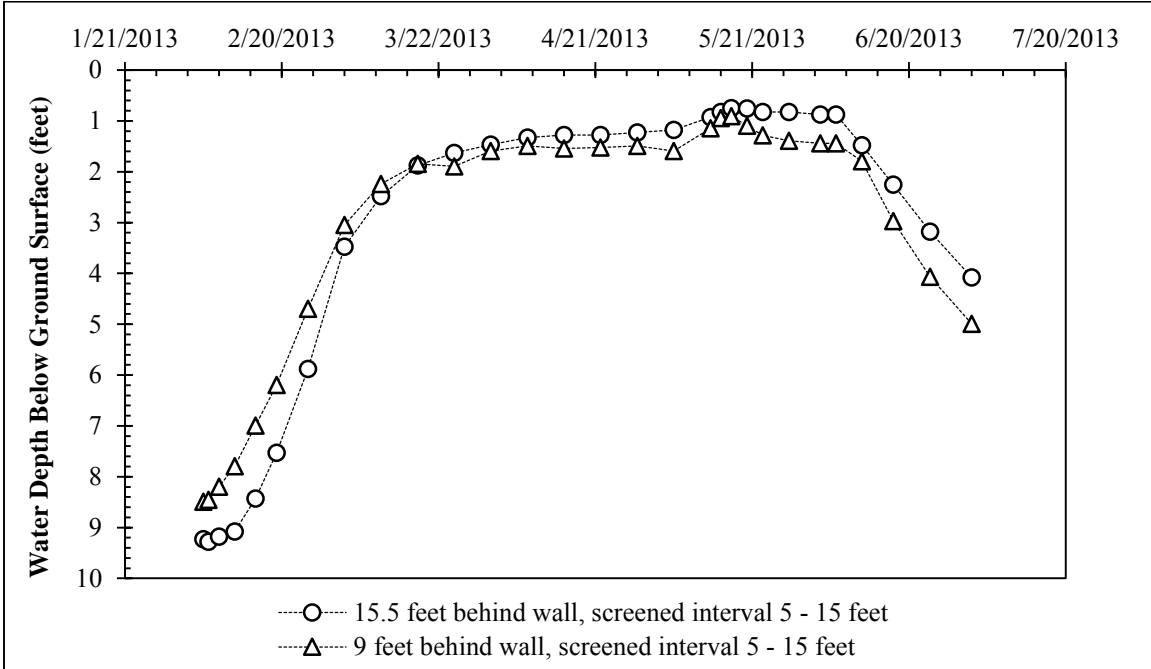


Figure 7.14: Data from deeper-screened stand pipe piezometers during second inundation cycle.

7.3.4: TIME DOMAIN REFLECTOMETRY (TDR) PROBE DATA

Data from the most functional TDR probe, which was installed 1.5 feet below ground surface, is presented in Figure 7.15 to Figure 7.19. Over the course of inundation testing, measured electrical conductivity values ranged from approximately 1.5 dS/m during the first inundation cycle, to zero during periods of drying (Figure 7.15).

During the first inundation cycle, electrical conductivity values increased immediately in response to the presence of water. Within one month, values had stabilized and had begun to steadily increase at the conclusion of the first inundation cycle (Figure 7.16). During the first drying cycle, values began to decrease quickly after the water supply to the inundation zone was removed, and had reached a zero value within six weeks (potentially indicating soil shrinkage leading to loss of probe rod contact). Rainfall events in August and September, 2012 led to short increases in electrical conductivity, followed immediately by gradual returns to zero during drying (Figure 7.17). The second drying cycle concluded with a period of above average rainfall in January, 2013, in which electrical conductivity values remained above zero for several weeks.

During the second inundation cycle, the probe again showed immediate response to the presence of water. Measured values of electrical conductivity continued to increase throughout the second inundation cycle, though not to values as high as those recorded during the first inundation cycle (Figure 7.18). After wall deflections and water levels stabilized, the second inundation cycle was stopped. Within one week after stopping the water supply to the inundation zone, a sudden decrease in electrical conductivity values occurred (perhaps indicating the local water level dropping below the probe), and within three weeks, values had returned to zero (Figure 7.19).

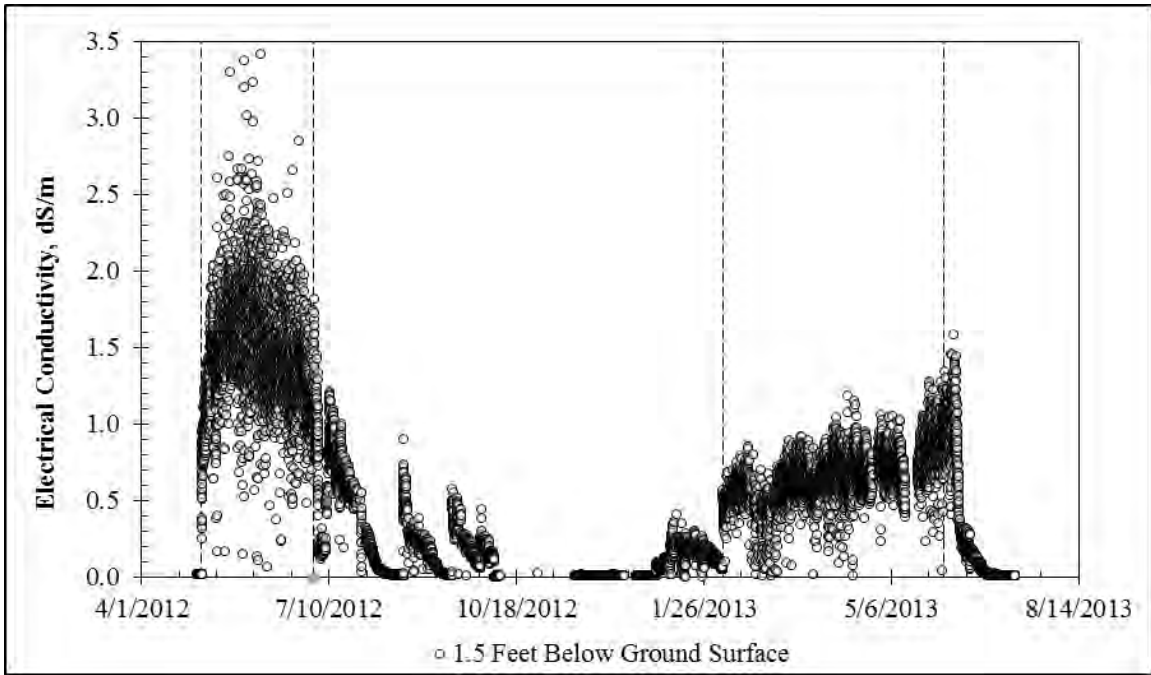


Figure 7.15: Electrical conductivity data from a TDR probe located 1.5 feet below ground surface (May 2012 – Jul. 2013).

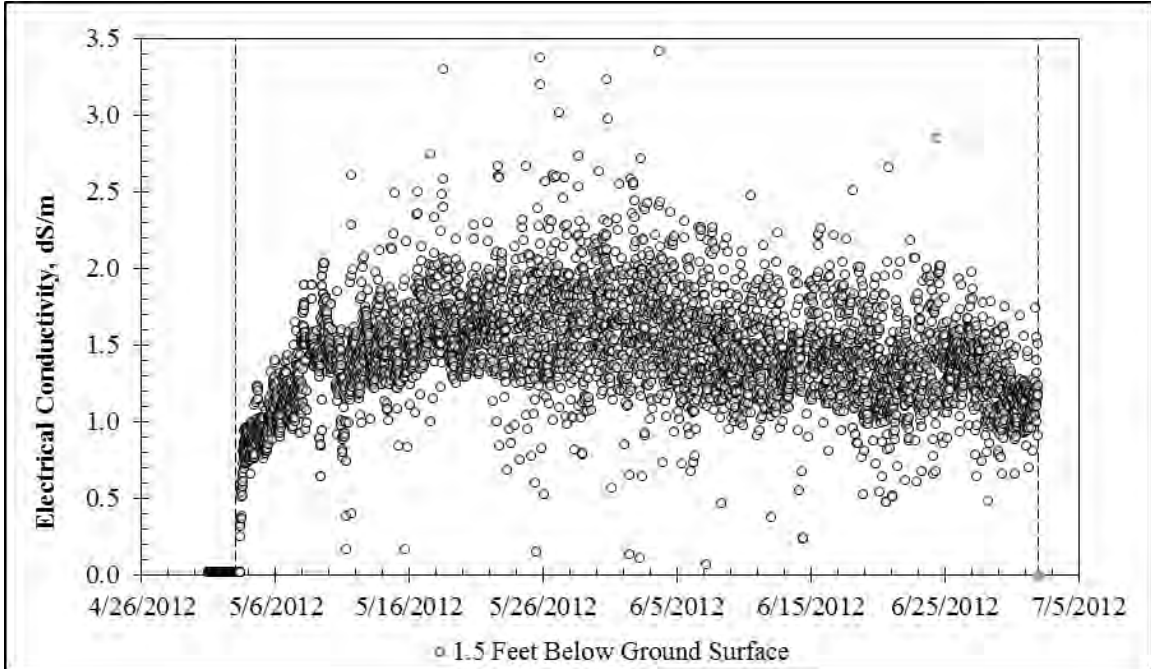


Figure 7.16: Electrical conductivity data from a TDR probe located 1.5 feet below ground surface during first inundation cycle (May – Jul. 2012).

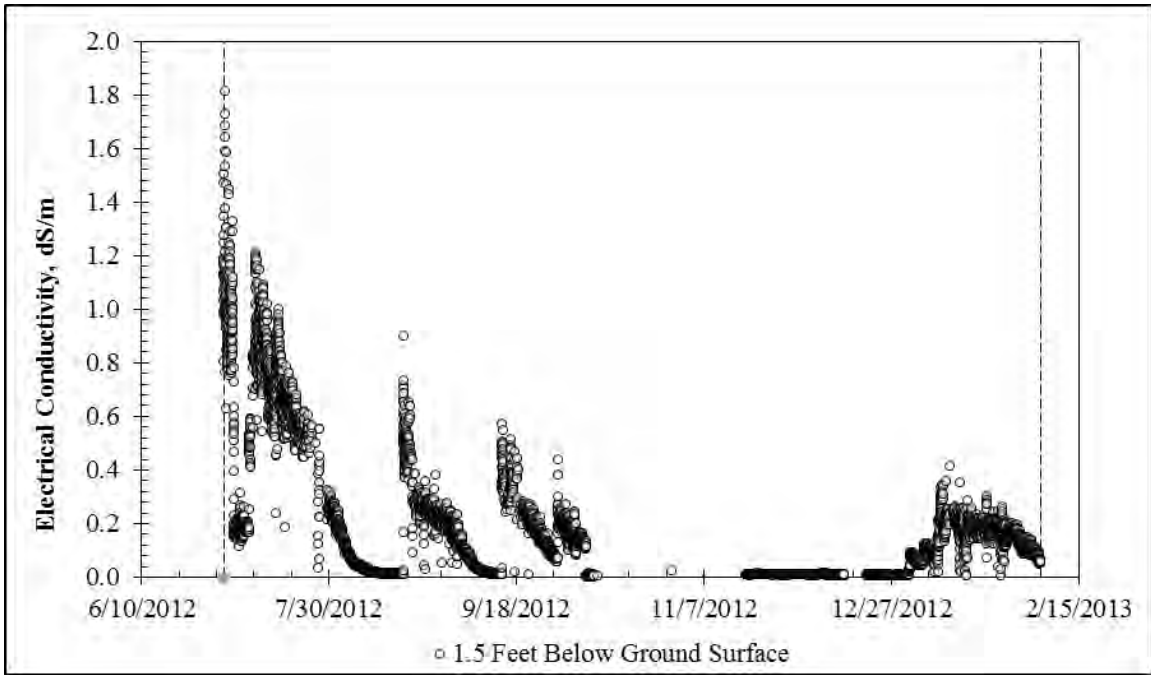


Figure 7.17: Electrical conductivity data from a TDR probe located 1.5 feet below ground surface during first drying cycle (Jul. 2012 – Feb. 2013).

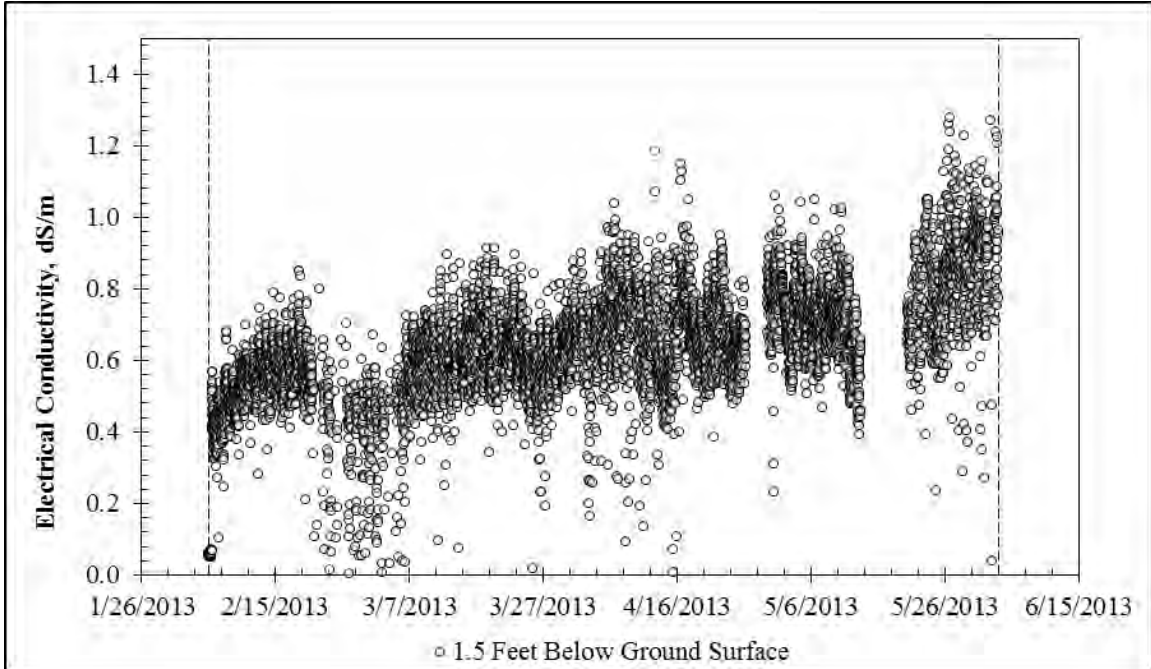


Figure 7.18: Electrical conductivity data from a TDR probe located 1.5 feet below ground surface during second inundation cycle (Feb. – Jun. 2013).

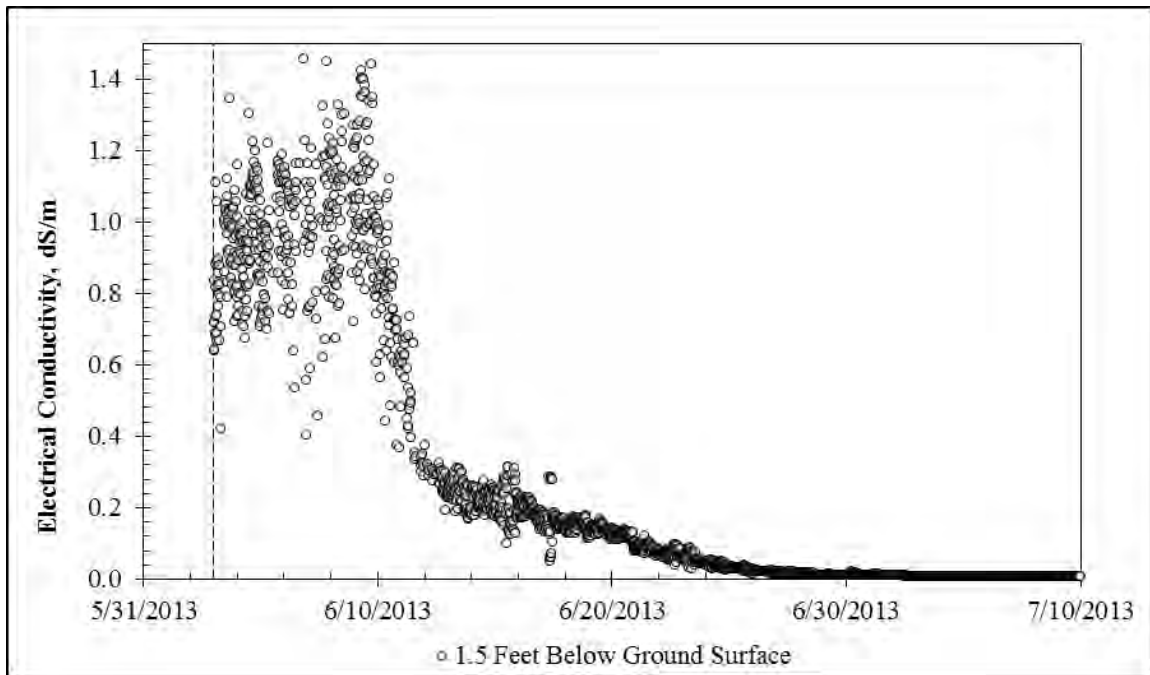


Figure 7.19: Electrical conductivity data from a TDR probe located 1.5 feet below ground surface during second drying cycle (Jun. – Jul. 2013).

7.3.5: STRAIN GAUGE DATA

Strain data is presented in Figure 7.20 to Figure 7.34. In the following figures, strain data is zeroed at the beginning of the first inundation cycle on May 3, 2013. Strain gauge nomenclature indicates which instrumented shaft the gauge is installed in (East, Center, or West), the depth of the strain gauge below original ground surface (1 – 29 feet), and which side of the neutral axis the gauge is installed on (Tension or Compression; tensile strains are positive). Using this nomenclature, gauge E.17.T is located in the east instrumented shaft, 17 feet below ground surface, on the tensile side of the neutral axis.

In shallow gauges above the excavation line (from 1 to 13 feet below ground surface), several gauge failures occurred. These failures were similar to those recorded during natural moisture cycles. Thermal effects due to both seasonal and daily temperature fluctuations are observed in gauges near ground surface with minimal bending strains

(Figure 7.20). As gauge depth and bending curvatures due to loading increase, the importance of thermal effects is generally limited to axial strains, with bending curvatures remaining fairly consistent (e.g. C.13.C and C.13.T). During the first and second inundation cycles, most gauges responded quickly to the presence of water; this response was generally more pronounced during the second inundation cycle. The increased magnitude of response during the second inundation cycle may be due to the development of tension cracks during the increasing deflections of the first cycle, which leads to a softer moment-curvature response consistent with cracked section properties (e.g. W.13.T).

In deeper gauges below the excavation line (15 to 29 feet below ground surface), the influence of thermal effects decreases. Several gauges (e.g. E.17.T, E.19.T, W.25.T, etc.) show immediate response during the first inundation cycle, limited activity during the first drying cycle, and immediate response during the second inundation cycle. Some evidence of tension cracking, both before and during the inundation testing, is indicated by larger than average responses to bending (e.g. C.21.T). The development of bending strains in many gauges is qualitatively similar to the development of top-of-wall deflection during inundation.

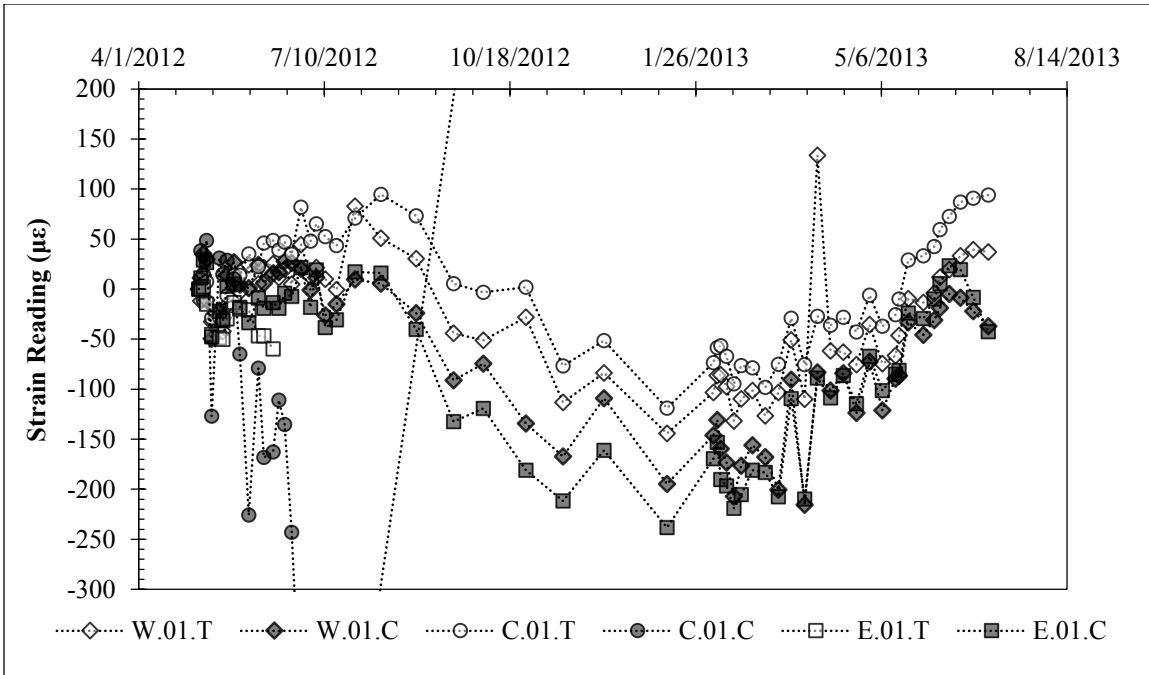


Figure 7.20: Strain Data 1 Foot Below Ground Surface (May 2012 – July 2013).

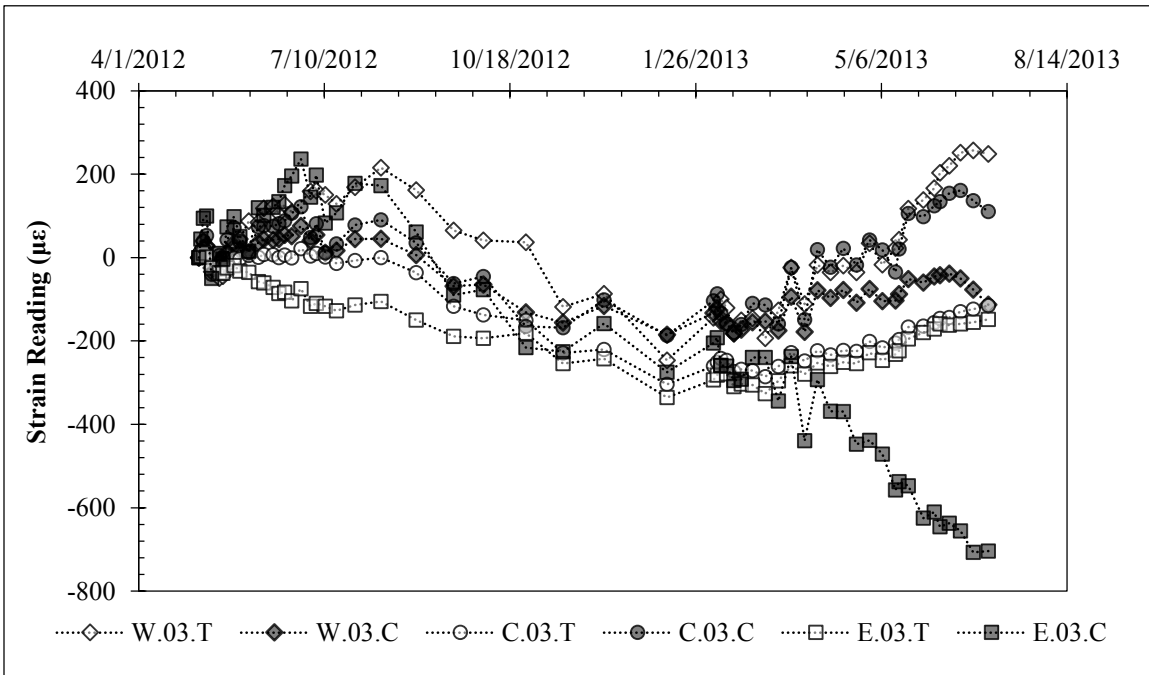


Figure 7.21: Strain Data 3 Feet Below Ground Surface (May 2012 – July 2013).

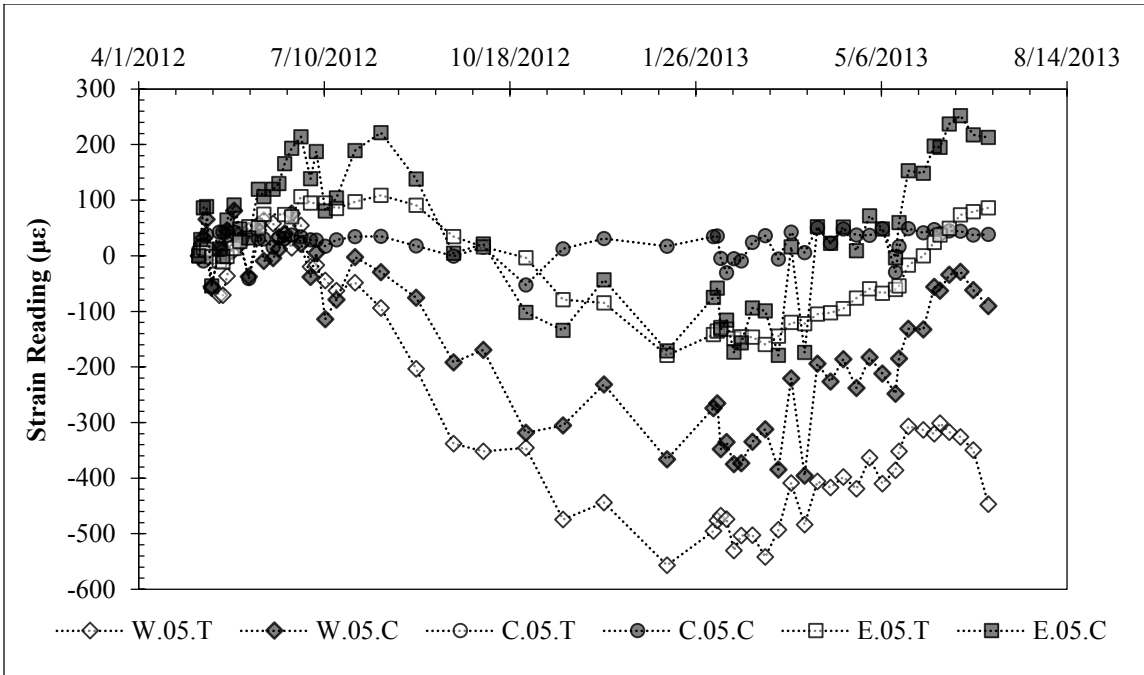


Figure 7.22: Strain Data 5 Feet Below Ground Surface (May 2012 – July 2013).

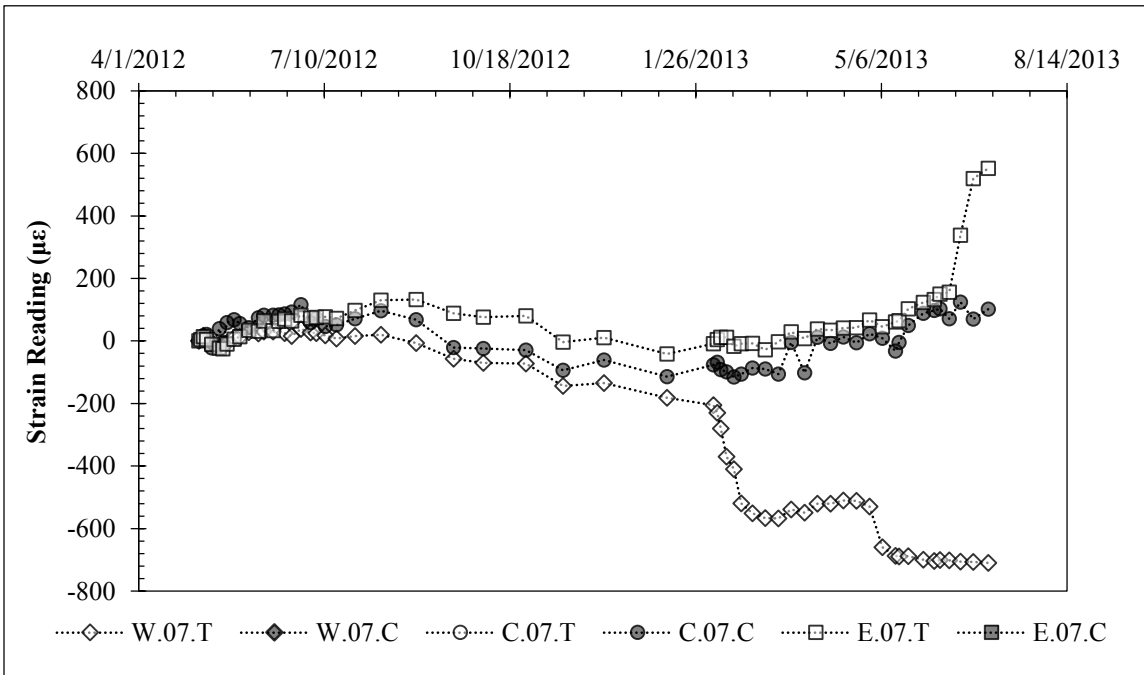


Figure 7.23: Strain Data 7 Feet Below Ground Surface (May 2012 – July 2013).

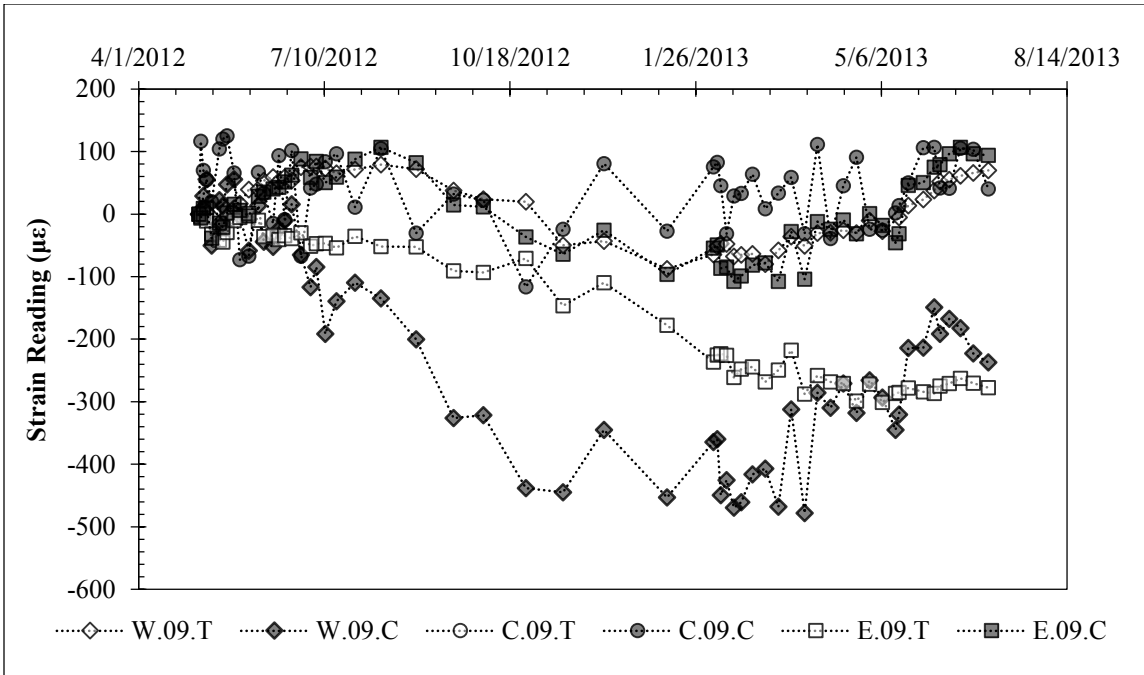


Figure 7.24: Strain Data 9 Feet Below Ground Surface (May 2012 – July 2013).

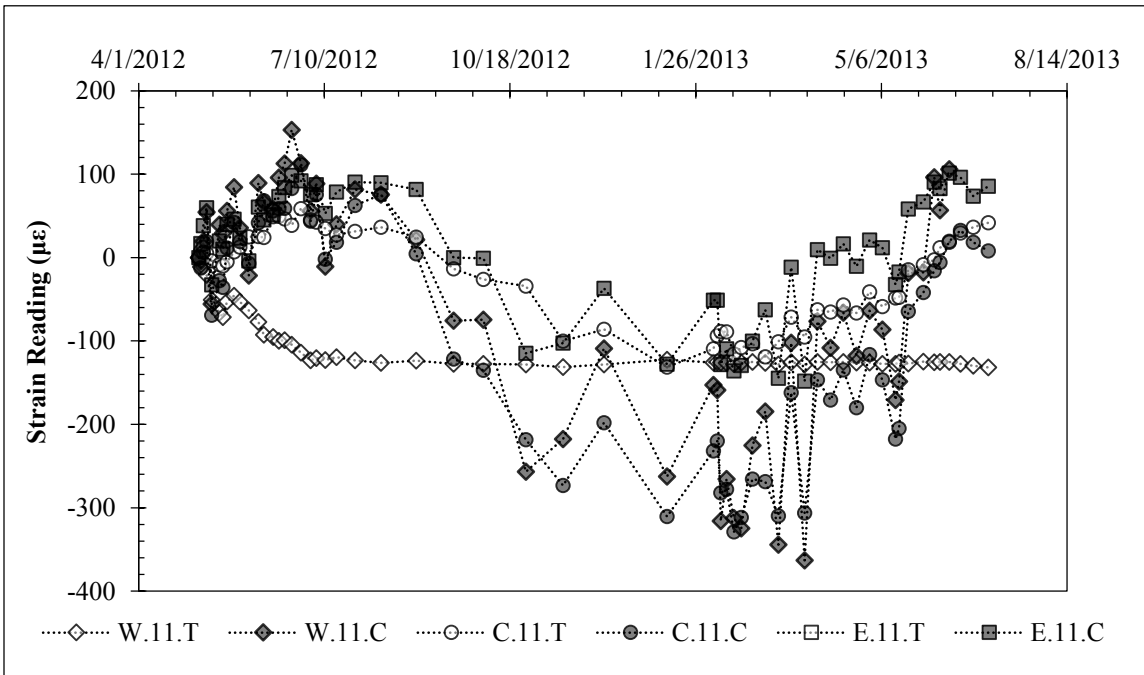


Figure 7.25: Strain Data 11 Feet Below Ground Surface (May 2012 – July 2013).

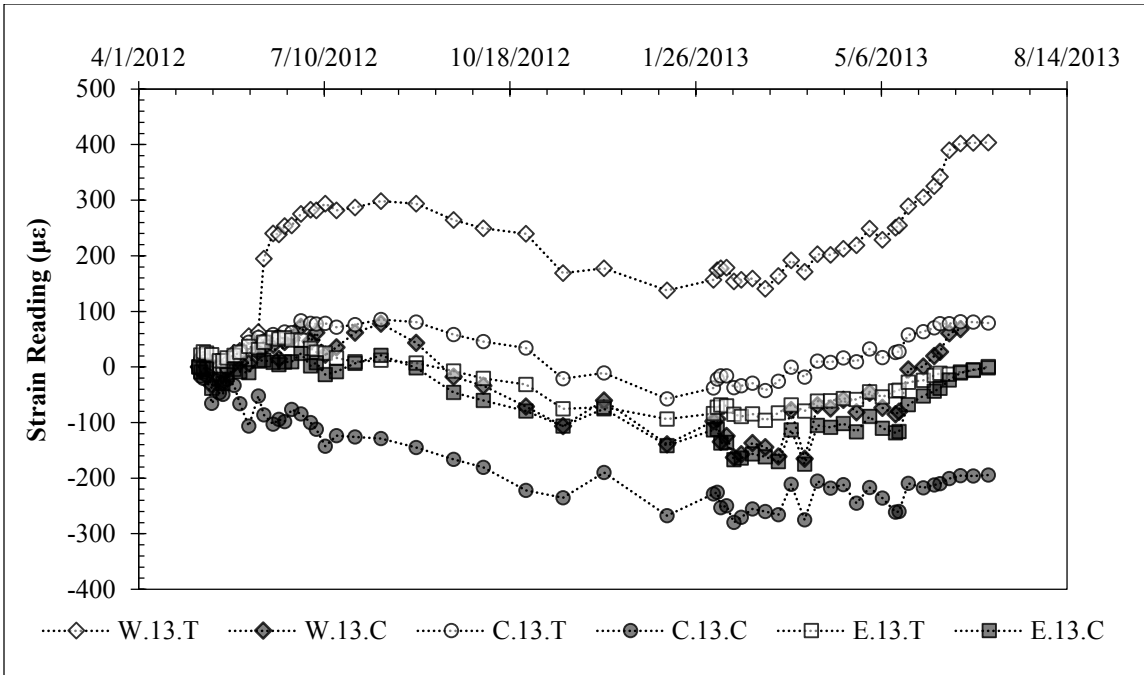


Figure 7.26: Strain Data 13 Feet Below Ground Surface (May 2012 – July 2013).

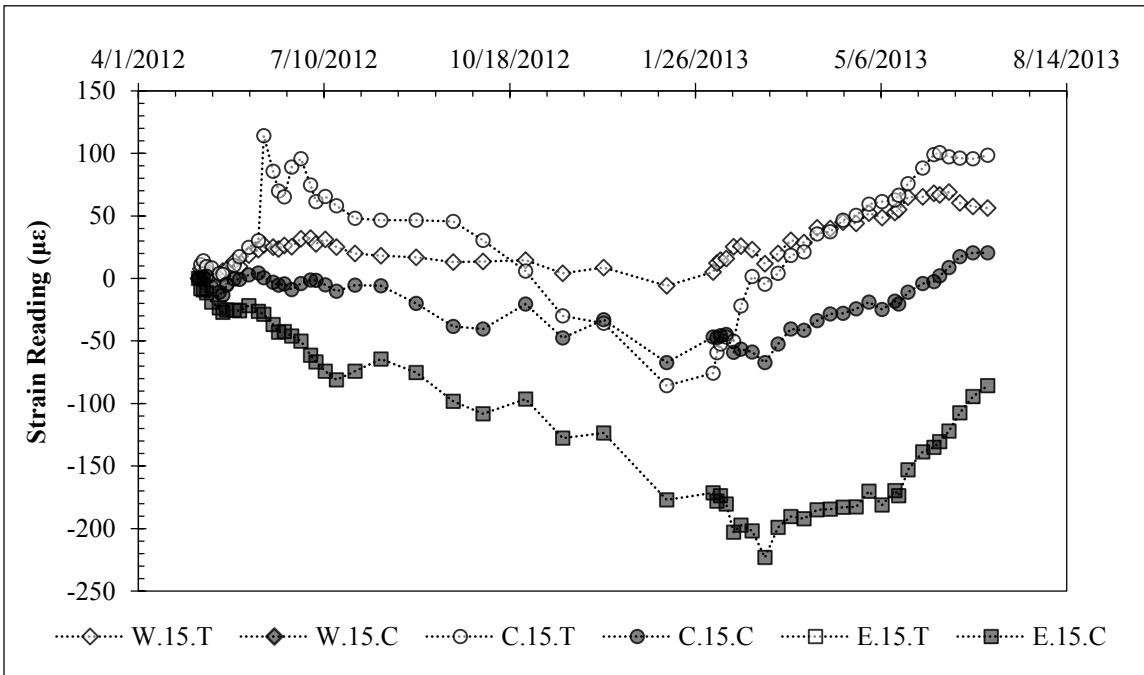


Figure 7.27: Strain Data 15 Feet Below Ground Surface (May 2012 – July 2013).

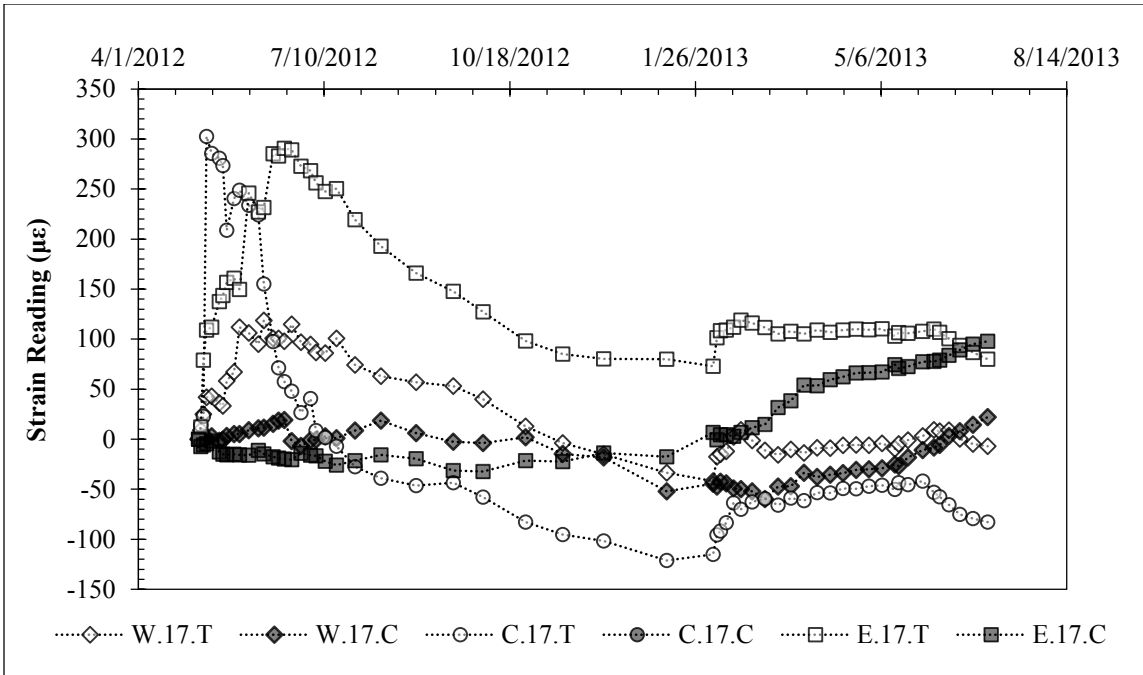


Figure 7.28: Strain Data 17 Feet Below Ground Surface (May 2012 – July 2013).

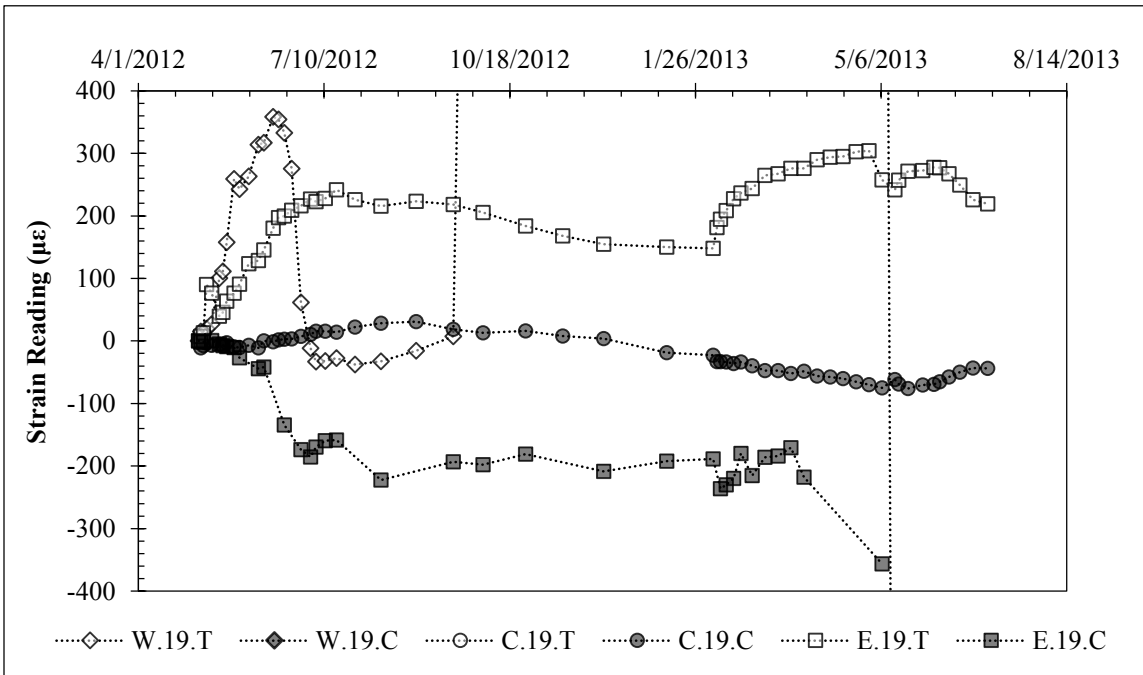


Figure 7.29: Strain Data 19 Feet Below Ground Surface (May 2012 – July 2013).

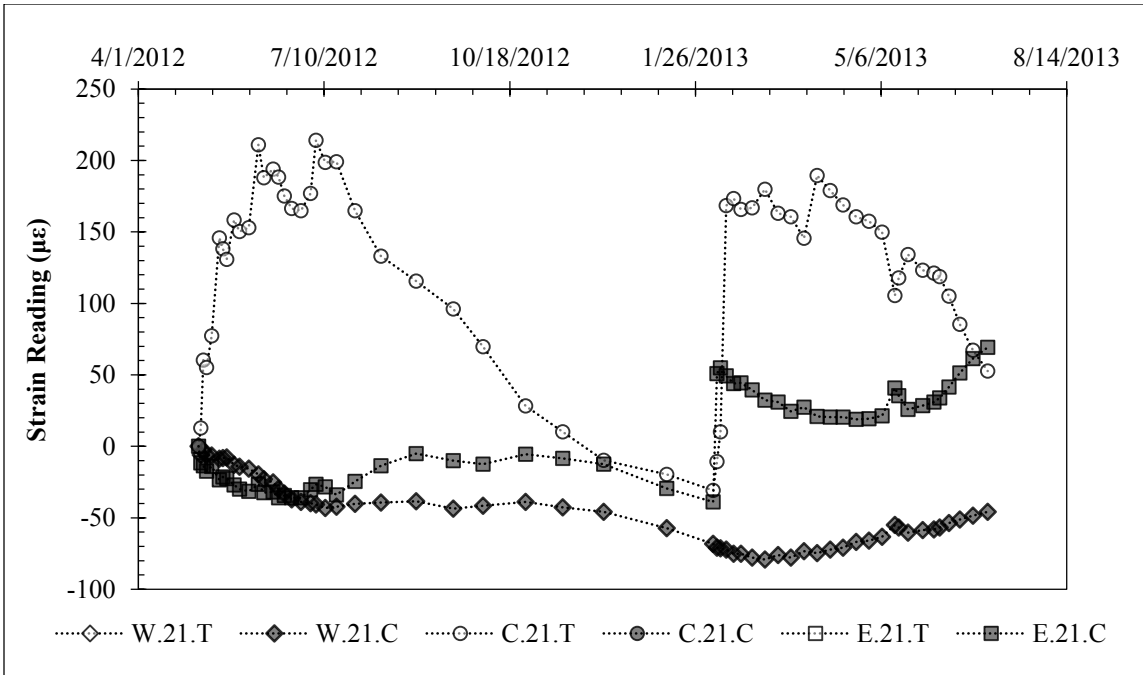


Figure 7.30: Strain Data 21 Feet Below Ground Surface (May 2012 – July 2013).

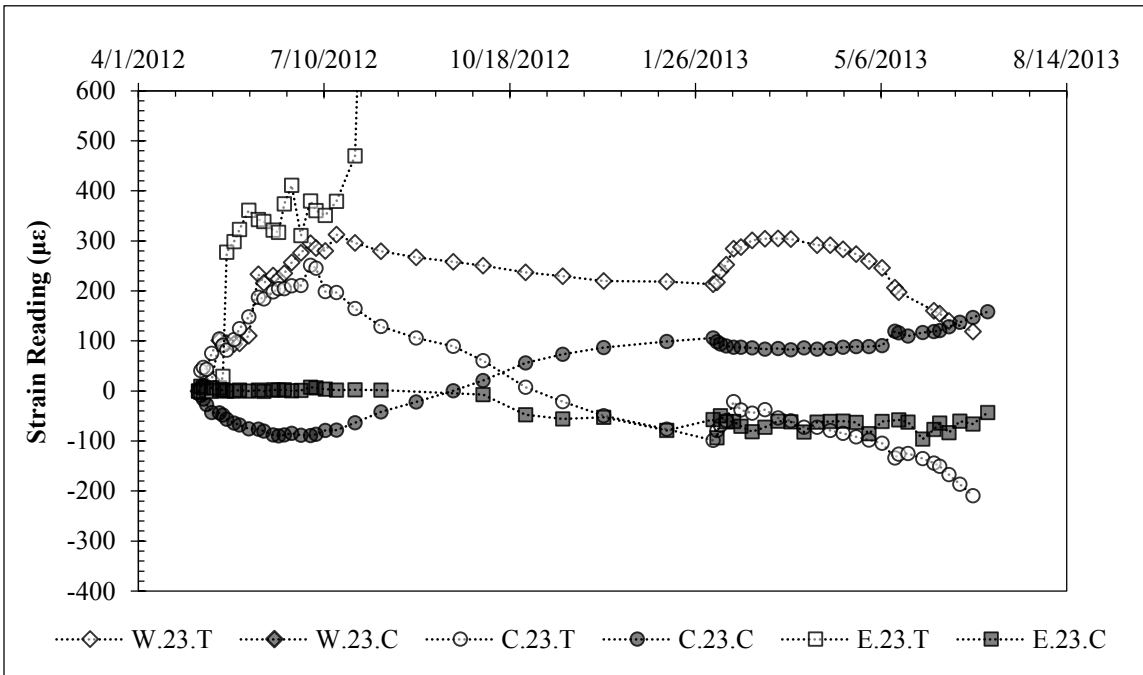


Figure 7.31: Strain Data 23 Feet Below Ground Surface (May 2012 – July 2013).

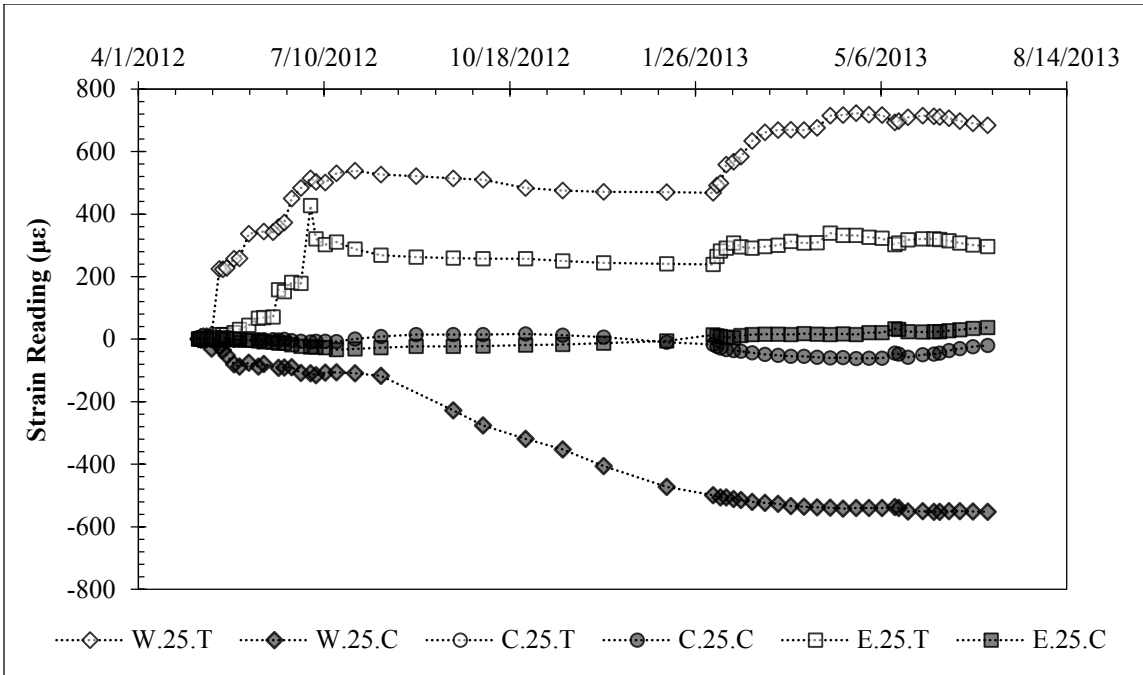


Figure 7.32: Strain Data 25 Feet Below Ground Surface (May 2012 – July 2013).

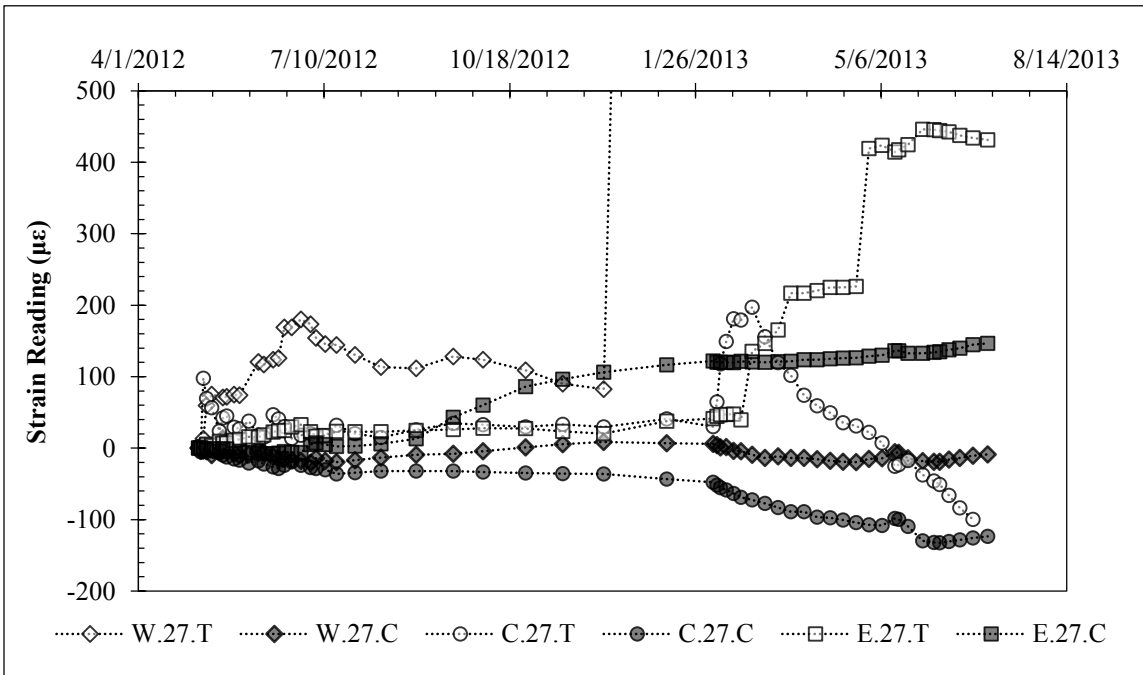


Figure 7.33: Strain Data 27 Feet Below Ground Surface (May 2012 – July 2013).

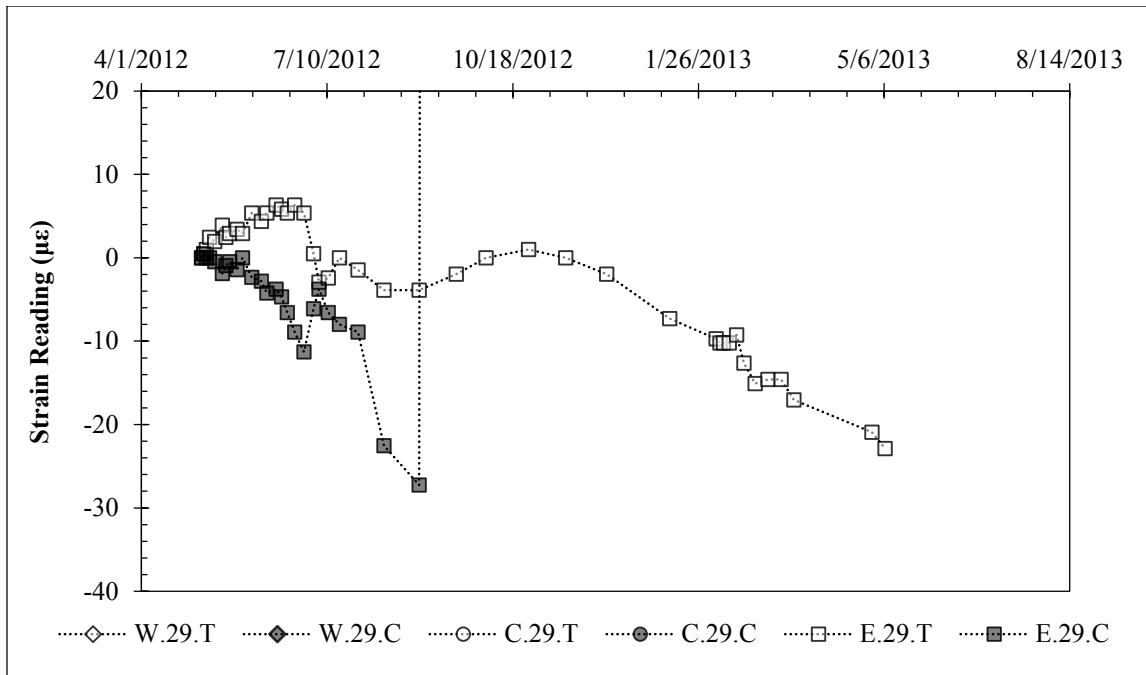


Figure 7.34: Strain Data 29 Feet Below Ground Surface (May 2012 – July 2013).

7.4: Data Interpretation

7.4.1: IMMEDIATE RESPONSE TO WATER

The inundation test began on May 3, 2012, and the wall and soil responded nearly immediately to the presence of water (Figure 7.35). Within minutes, the TDR probes installed throughout the retained soil registered the presence of free water (Figure 7.36), and within hours, water had begun to infiltrate through the wall drainage system into the excavation (Figure 7.37). This immediate response is consistent with the response observed at the test wall during large rainfall events, and suggests that the fissures present in the expansive clay provide preferential pathways for moisture flow.



Figure 7.35: The inundation zone is filled on May 3, 2012.

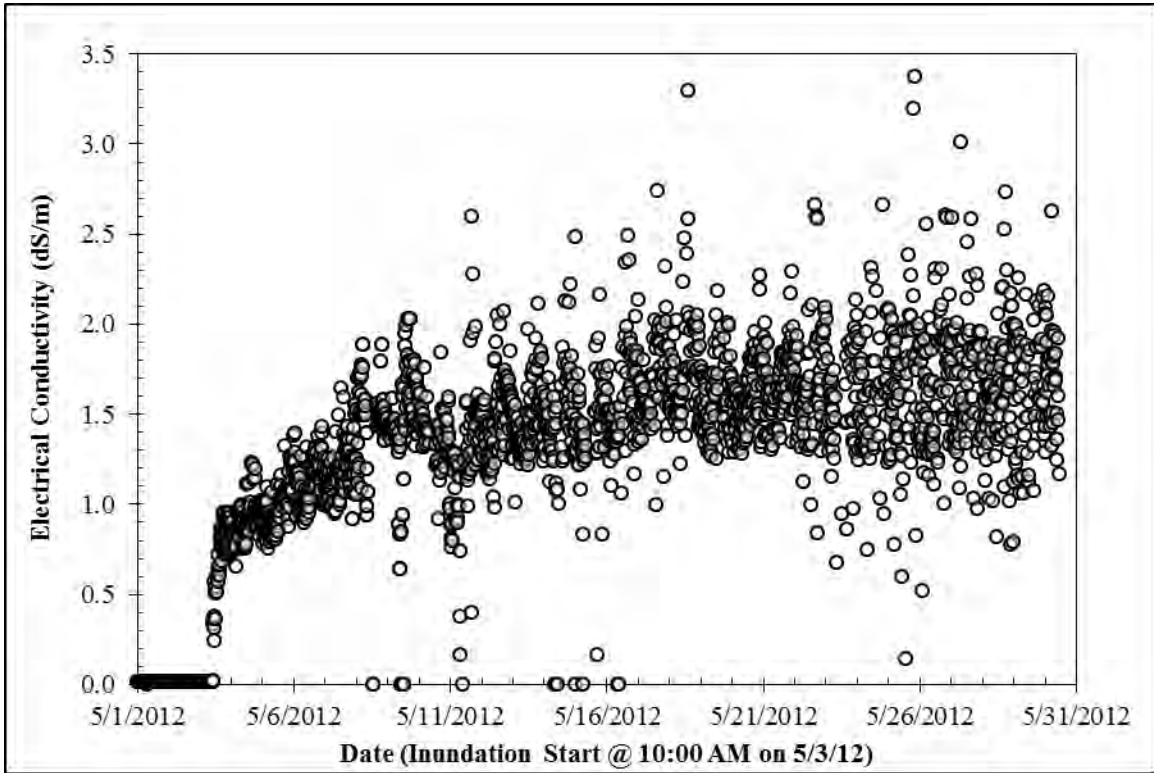


Figure 7.36: Electrical conductivity data from one TDR probe shows a response within minutes of beginning the inundation test. Probe is located 1.5 feet below ground surface.



Figure 7.37: Water infiltration into the excavation was first observed 90 minutes from the start of inundation.

The top-of-wall deflection began to increase almost immediately in response to inundation, and continued at a slightly decreasing rate for the duration of the test (Figure 7.9). Based on the daily rate of deflection, it was inferred that the inundation test would likely need to continue for several additional months before an equilibrium condition was reached (Figure 7.10). Because of this, and in order to allow the soil time to dry out before the next scheduled inundation cycle in January 2013, the first inundation cycle was stopped on July 2, 2012. After the water supply to the inundation area was cut off, the wall deflection stabilized within one day, again suggesting that fissures in the soil mass provide fairly direct access to moisture. Over the two month inundation cycle, the top-of-wall deflections had increased by approximately 2 inches. Had the test not been stopped, it is likely that deflections would have increased beyond this point. After two months of inundation, in the soil above the groundwater table, moisture contents had increased by approximately 5 to 10 percentage points in the active zone above the natural groundwater table (Figure 7.38).

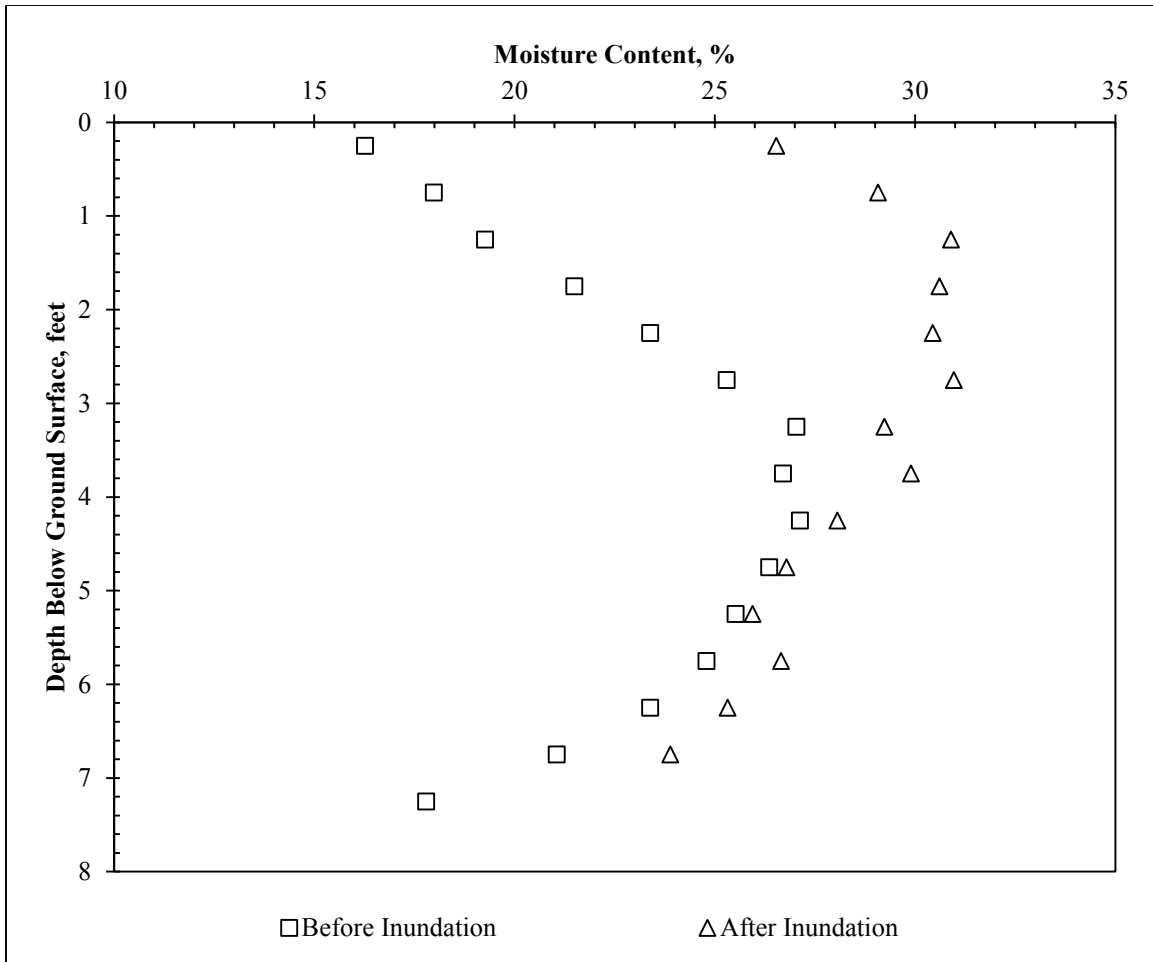


Figure 7.38: Moisture content profiles immediately before and after first inundation cycle. Natural water table is located at a depth of approximately 8 feet.

During the first drying cycle, despite a decrease in soil moisture content, top-of-wall deflections remained relatively stable. During the second inundation cycle, wall deflections began to increase immediately after the re-introduction of water and reached their maximum value as piezometer water levels stabilized near ground surface (Figure 7.9). As the second inundation cycle ended and the second drying cycle began, top-of-wall deflections, TDR electrical conductivity values, and water levels in the stand pipe

piezometers began to decrease (Figure 7.9 to Figure 7.14), suggesting the presence of water plays a key factor in the development of top-of-wall deflections.

7.4.2: DEVELOPMENT AND CHARACTERIZATION OF DRAINED, FULLY SOFTENED STRENGTHS

After being provided with unlimited access to water, and going through multiple cycles of wetting and drying, it is likely that the retained soil reached drained conditions. In high plasticity clays, this often corresponds to the development of fully softened strengths. To develop potential strength envelopes for the retained soil, the use of fully softened strength correlations were plotted as described in Skempton (1977) and Wright (2005). Additionally, fully softened strength tests were conducted on samples of clay from the test site in accordance with the procedures described in Wright et. al. (2007). Because the fully softened strength is very close to a normally consolidated strength, the native soil is mixed into a slurry at values of moisture content near the liquid limit, then consolidated to the in-situ confining pressure. A drained direct shear test then provides an estimate of the soil's fully softened strength at a given confining pressure. A series of tests at different confining pressures can be used to develop an envelope of fully softened strength. Results from the testing program, along with correlations presented in literature, and data from Ellis (2011) are presented in Figure 7.39. For the Taylor clay on the project site, a nominal fully softened friction angle of 24 degrees was selected as a starting point for analysis (the predicted strength envelope is curved, but average measured values are approximately 24 degrees over the depth of interest).

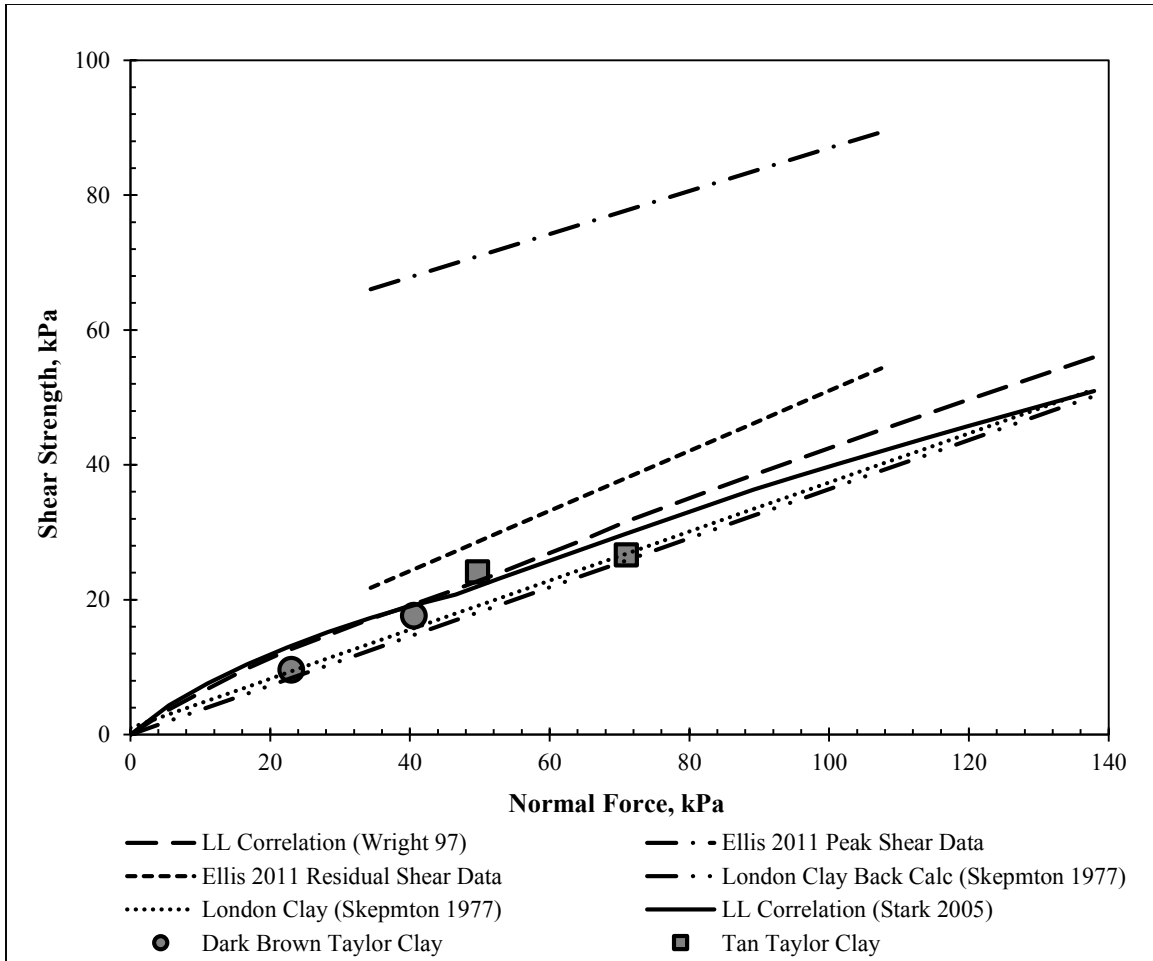


Figure 7.39: Comparison of measured fully softened strength test data from the project site with data from Ellis (2011) and established correlations.

7.4.3: LPILE ANALYSIS

To aid in selection of p-y curves for the foundation soil, the calculated p-y curves were compared against the proposed curves from Chapter 2 in Figure 7.40 to Figure 7.44. While the “stiff clay without free water” curves appear to be reasonable at shallow depths, at depths below 22 feet, their predicted response is much stiffer than the observed soil response. To model the behavior of the foundation soil, drained p-y curves based on the fully softened soil strengths with non-default values of initial stiffness were used. For the

conditions imposed on the test wall during the inundation test, the earth pressures were modeled using the combined force of the drained, fully softened strength with $\phi = 24$ and hydrostatic pressures with the water table at ground surface. The input parameters for the LPILE analysis are provided in Table 7.1, and the earth pressures used to estimate the wall's response using p-y analysis are shown in Figure 7.45. For our test wall data, a reference survey date of October 8, 2010 (installation of facing) was considered to be the most consistent with the assumptions used in p-y analysis, which does not account for immediate global deformations in response to excavation. A p-y analysis using the conditions presented in Table 7.1 predicted a final top-of-wall deflection of approximately 5.4 inches at equilibrium. A summary of the results of the long-term LPILE analysis is provided in Figure 7.45. The selection of p-y curves and input earth pressures for long-term analysis is discussed at length in the following chapter.

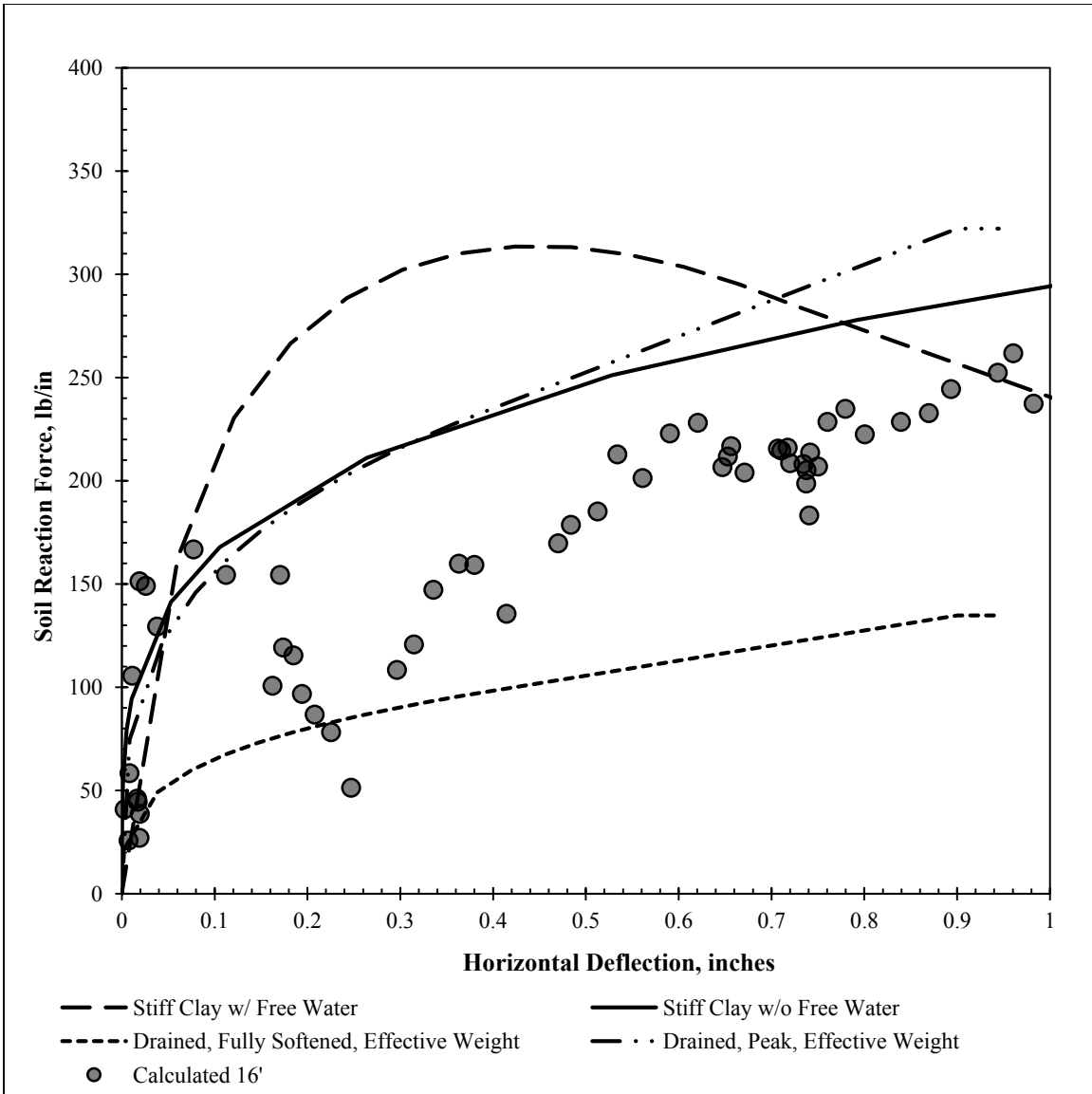


Figure 7.40: Comparison of calculated long-term p-y curves during inundation testing with proposed p-y curves at a depth of 16 feet below original ground surface.

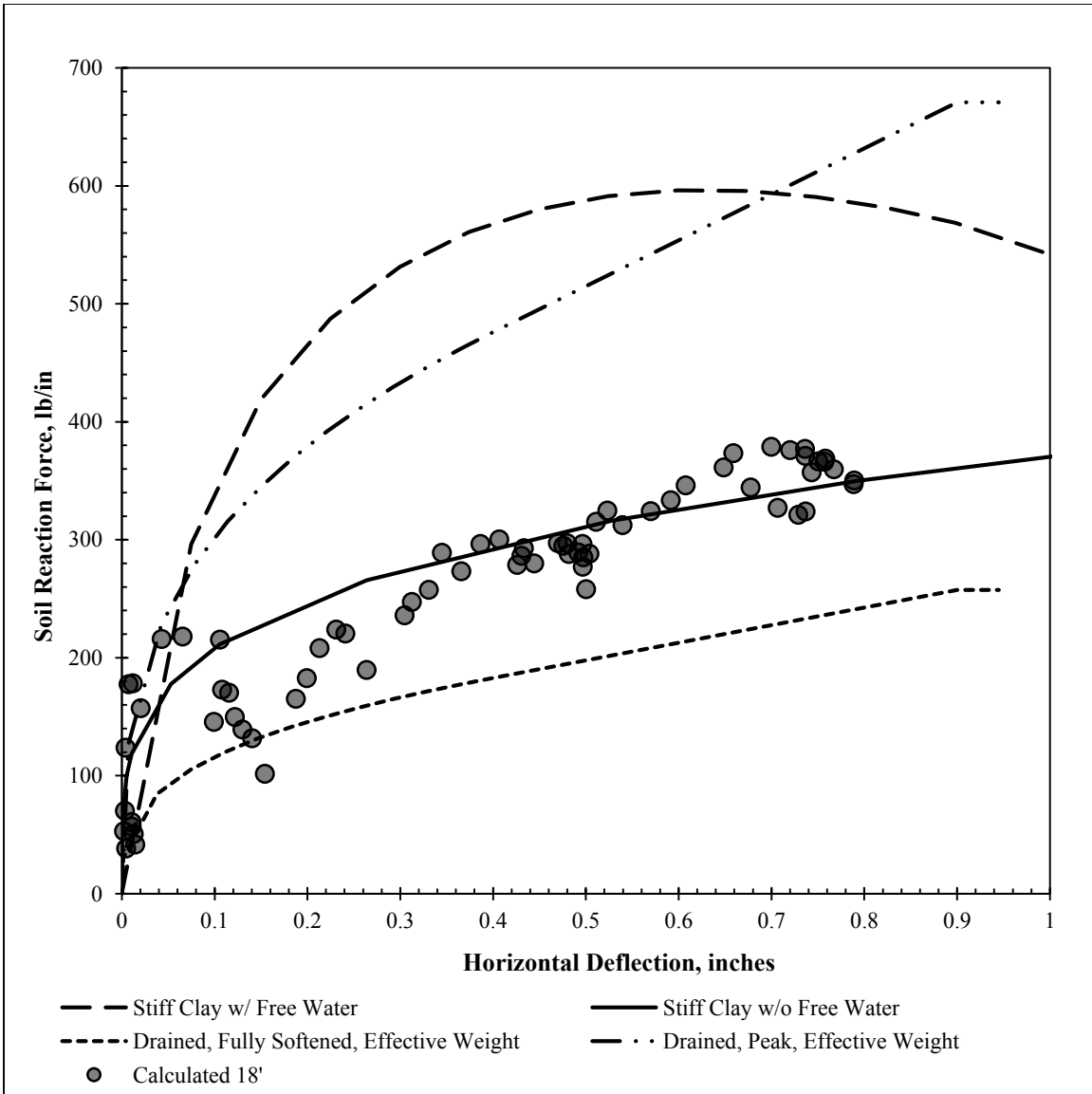


Figure 7.41: Comparison of calculated long-term p-y curves during inundation testing with proposed p-y curves at a depth of 18 feet below original ground surface.

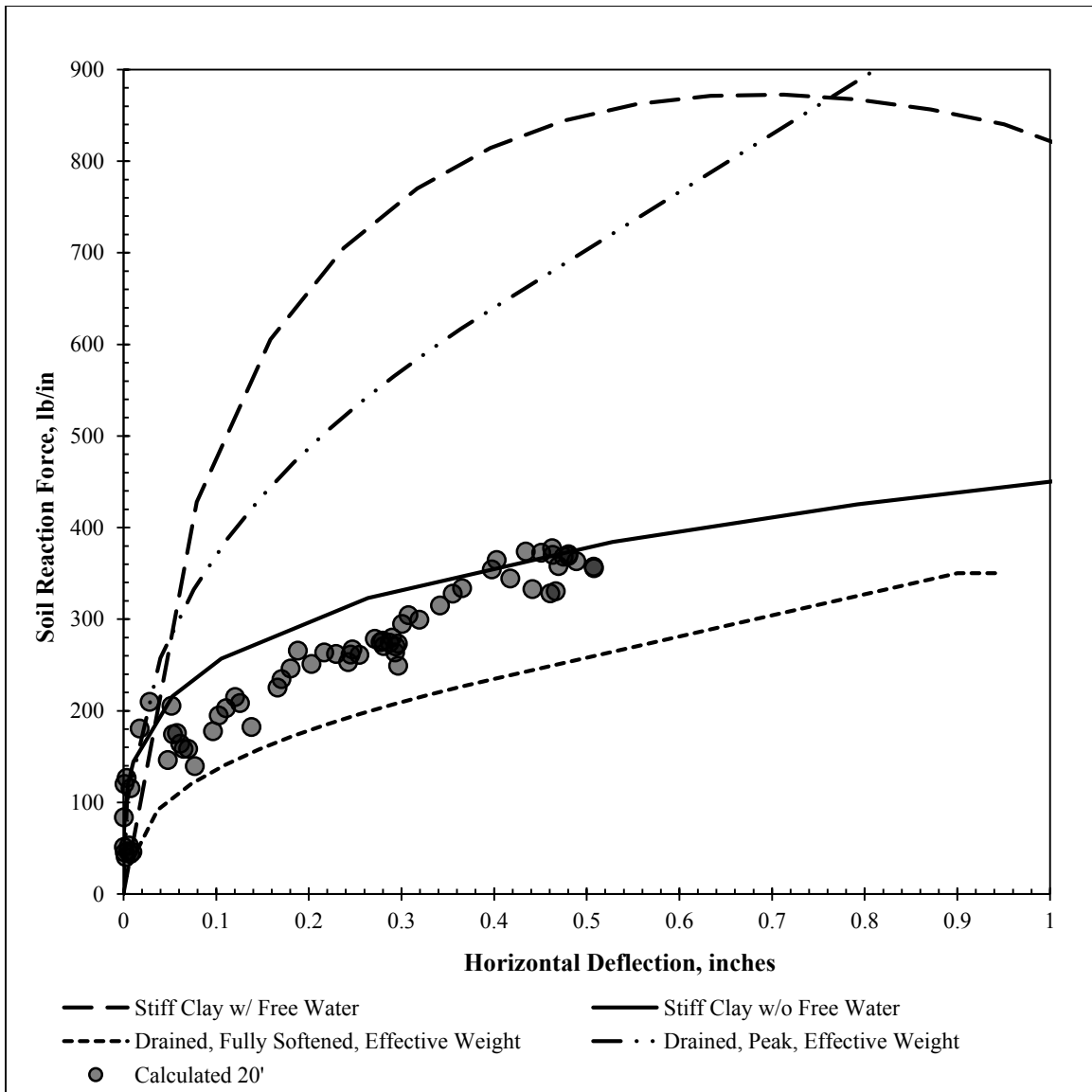


Figure 7.42: Comparison of calculated long-term p-y curves during inundation testing with proposed p-y curves at a depth of 20 feet below original ground surface.

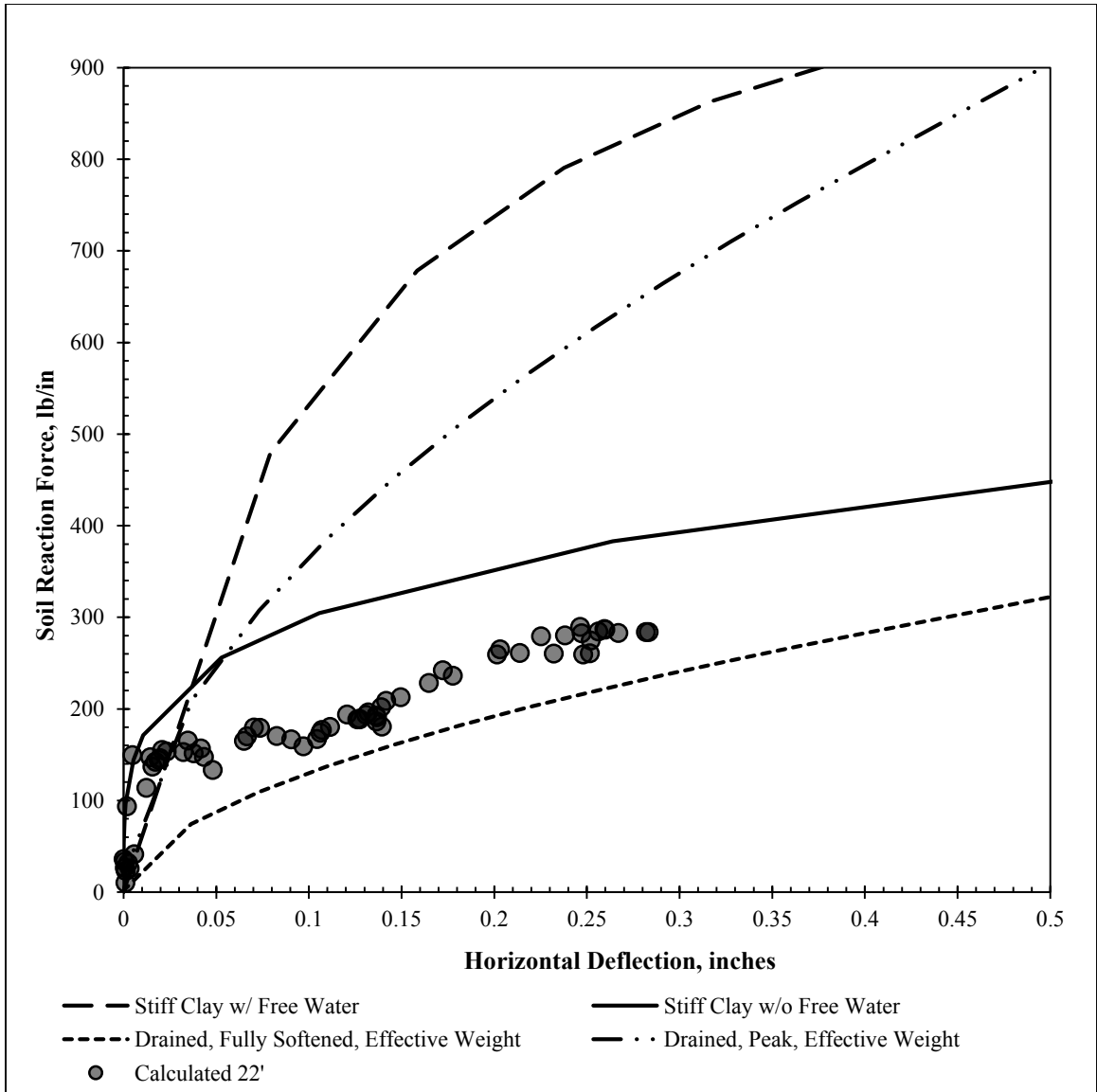


Figure 7.43: Comparison of calculated long-term p-y curves during inundation testing with proposed p-y curves at a depth of 22 feet below original ground surface.

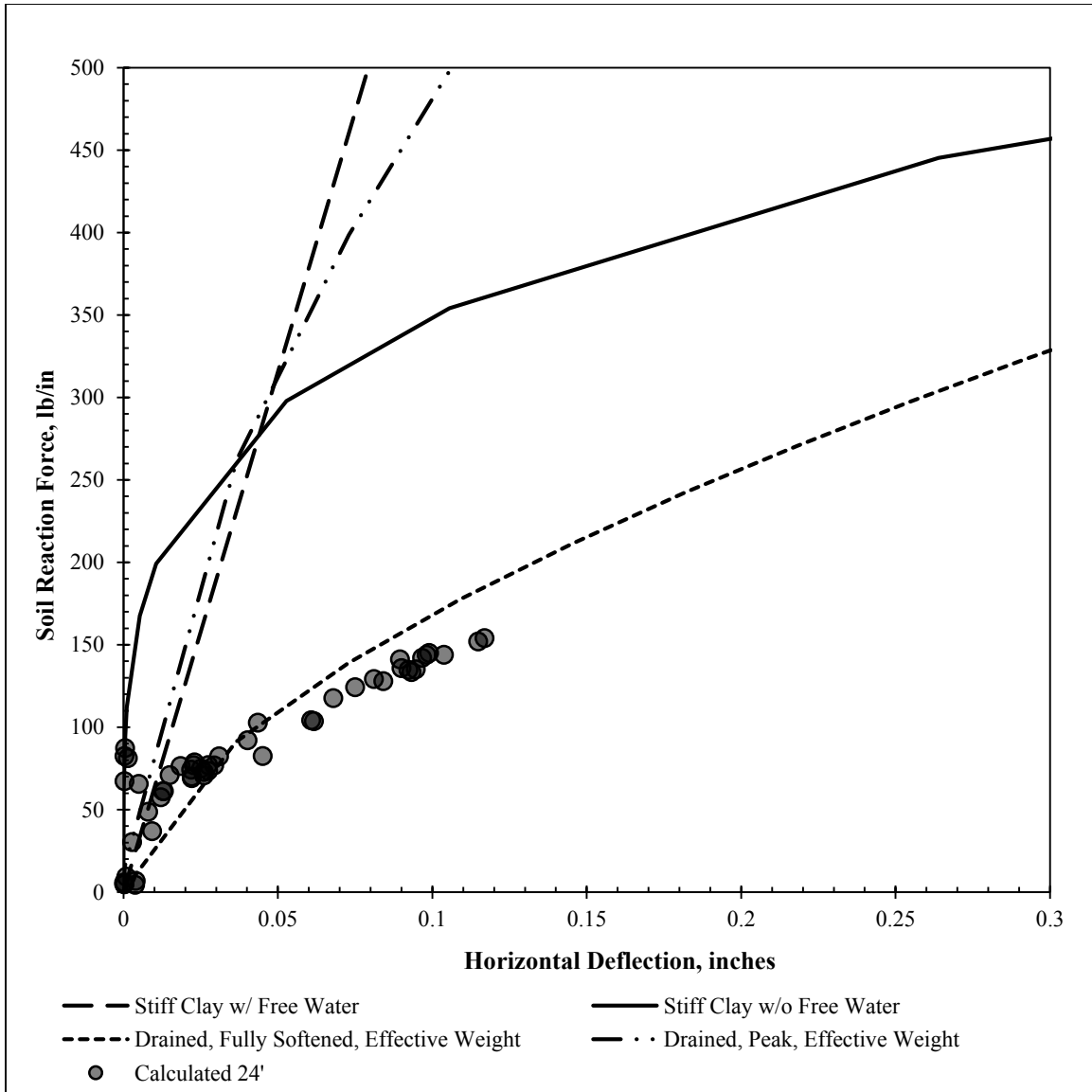


Figure 7.44: Comparison of calculated long-term p-y curves during inundation testing with proposed p-y curves at a depth of 24 feet below original ground surface.

Table 7.1: Baseline assumptions and design parameters for long-term LPILE analysis of inundation conditions.

Parameter	Value
Effective Unit Weight of Soil, γ'	62.6 pcf
Earth Pressure Loading	Fully Softened ($\phi = 24$) + Hydrostatic (approx.. 90 psf/ft)
Friction Angle of Foundation Soil	24 degrees
Foundation Soil p-y Curves	Sand (Reese)
Non-Default Initial Stiffness, k_{py}	375 lb/in ³
Cracking Moment, M_{Cr}	680 k-in.
Yielding Moment, M_y	3,200 k-in.
Uncracked Bending Stiffness, EI_{uc}	67 x 10 ⁶ k-in.
Cracked Bending Stiffness, EI_{cr}	18 x 10 ⁶ k-in.
Shaft Diameter	24 in.
Height of Retained Soil, H	162 in.
Reinforcement	12 #7 bars (1.6% of gross area)

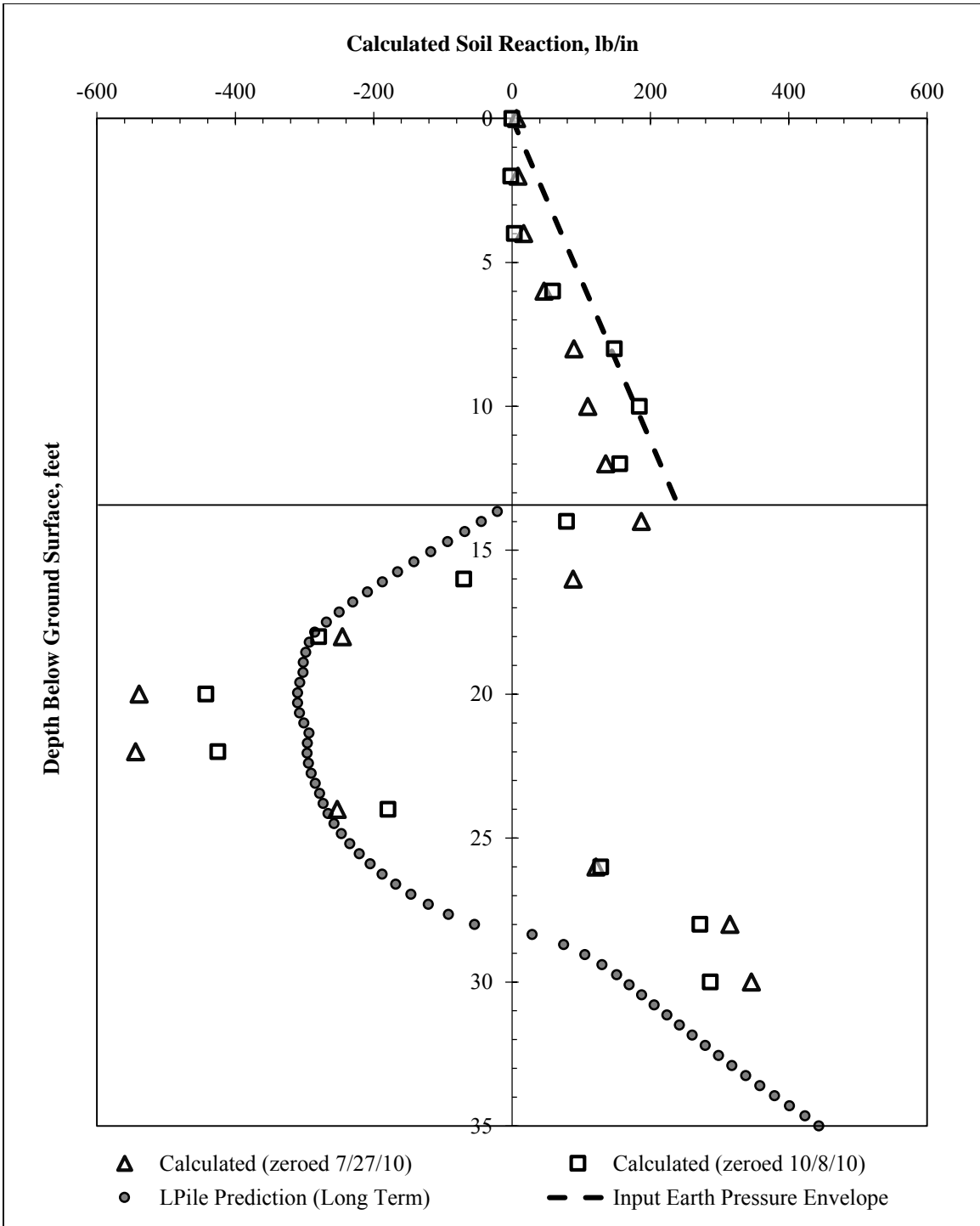


Figure 7.45: Comparison of long-term LPILE Prediction and calculated soil reaction forces.

7.5: Summary and Conclusions

The data recorded at the Lymon C. Reese research wall during cycles of controlled inundation testing has provided insights into the behavior of drilled shaft walls in expansive clay. Some of these insights include:

- Fissures in the clay provide preferential pathways for drainage and moisture flow. Drainage through these fissures occurs very quickly, within minutes, when surface water is present. This is supported by first-hand observations and data from TDR moisture probes and stand pipe piezometers.
- In the six total months of controlled inundation, and eight total months of drying cycles, top-of-wall deflections stabilized at 5.2 inches since shaft installation, and 4.2 inches since the installation of facing. Maximum bending moments in the shaft since installation were approximately 2,100 in-kip, approximately two-thirds of the yield moment.
- Wall deflections stabilized at the same time the water levels in stand pipe piezometers stabilized. As water levels decreased after the conclusion of inundation, top-of-wall deflections decreased accordingly. This result suggests the presence of water behind the wall contributes to the development of deflections.
- Based on the author's field observations, the presence of water in the excavation tends to increase wall deflections to a greater degree than the presence of water in the retained soil. Because of the fissured secondary structure of the soil, water behind the wall invariably results in water in the base of the excavation. Deflections tend to increase as water in the retained soil increases.
- The behavior of the foundation soil can be approximated using p-y curves developed for fully softened, drained strengths, with initial stiffness k_{py} defined by

the original profile of undrained shear strength. Assuming the eventual development of hydrostatic conditions behind the wall during inundation, the upper bound earth pressure envelope for the retained soil can be defined using the drained, fully softened properties of the soil, then adding hydrostatic pressures.

- Even with continued access to water, there is limited evidence to suggest that large earth pressures due to soil expansion are sustained at the test wall. No evidence of earth pressures exceeding the pressure envelope defined by drained, fully softened strengths with additional hydrostatic pressures was observed.

CHAPTER 8: DEVELOPMENT OF DESIGN GUIDELINES

The following chapter presents a summary of the proposed design guidelines for drilled shaft retaining walls in high plasticity clays. The principal source of data for these recommendations is the Lymon C. Reese research wall, a full-scale test wall constructed through high plasticity clay in Manor, Texas. Both long-term and short-term design guidelines are presented, along with comparison data from the test wall.

8.1: Long-Term Design Guidelines

8.1.1: SUMMARY OF LONG-TERM GUIDELINES

Long-term conditions often govern design in high plasticity clays. To check the long-term response of the wall after cycles of wetting and drying, a drained analysis using fully softened shear strengths is recommended. A summary of the proposed long-term design guidelines is provided in Figure 8.1.

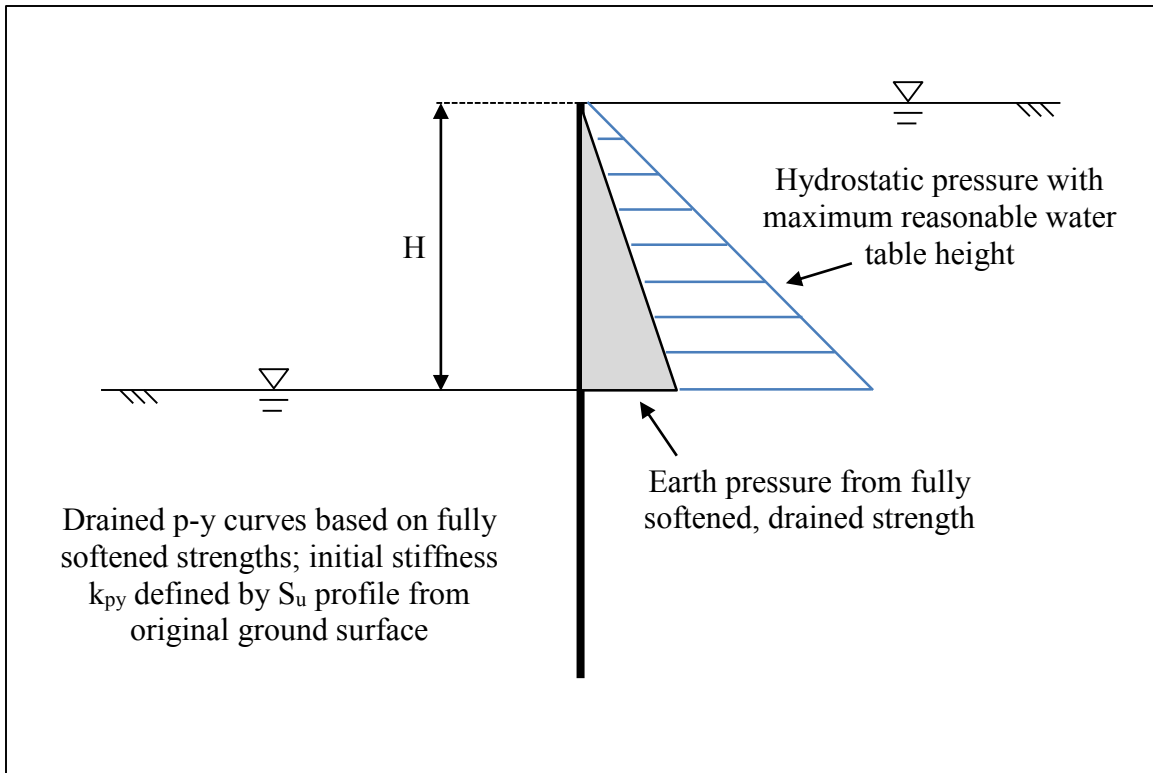


Figure 8.1: Summary of long-term design guidelines.

In the proposed long-term guidelines, the active earth pressure envelope is calculated using the fully softened, drained shear strength of the retained soil (e.g. Wright 2005, Stark et. al. 2005, Wright et. al. 2007). Hydrostatic pressures are calculated with the water table at a reasonable “maximum” level in the retained soil (e.g. during controlled inundation testing, the water table reached the original ground surface), and at the ground level on the excavation side. The long-term presence of hydrostatic pressures acting on a field wall is an unlikely scenario; however, it represents a reasonable “upper bound” value to check allowable deflections and bending moments.

To model the behavior of the foundation soil, drained p-y curves are recommended, based on a friction angle equal to the fully-softened drained shear strength of the soil. The use of non-default initial stiffness values (k_{py}) is recommended, with k_{py} defined by the

original profile of undrained shear strength with depth (Figure 8.2). Because the default initial stiffness for p-y curves in cohesionless soils is defined by friction angle (Figure 8.3), and drained, fully softened friction angles for high plasticity clays are relatively low, the default values of initial stiffness tend to be lower than those observed in the field. To account for the transition from stiff, undrained behavior to soft, drained behavior, an initial stiffness profile defined by the original S_u profile from the original ground surface is recommended (the relationship between S_u and k_{py} for clays is shown in Figure 8.2). While soil strength reductions to account for close pile spacing are recommended for short-term loading in both sand and clay, the test wall data indicates that the use of a friction angle corresponding to the fully softened shear strength of the soil with no reduction factor works reasonably well to model the foundation soil behavior. Further investigation into the long-term loading behavior in expansive clays may be warranted to more clearly define the relationship between ultimate load reductions due to close pile spacing and ultimate load reductions due to the development of fully softened conditions under sustained loading.

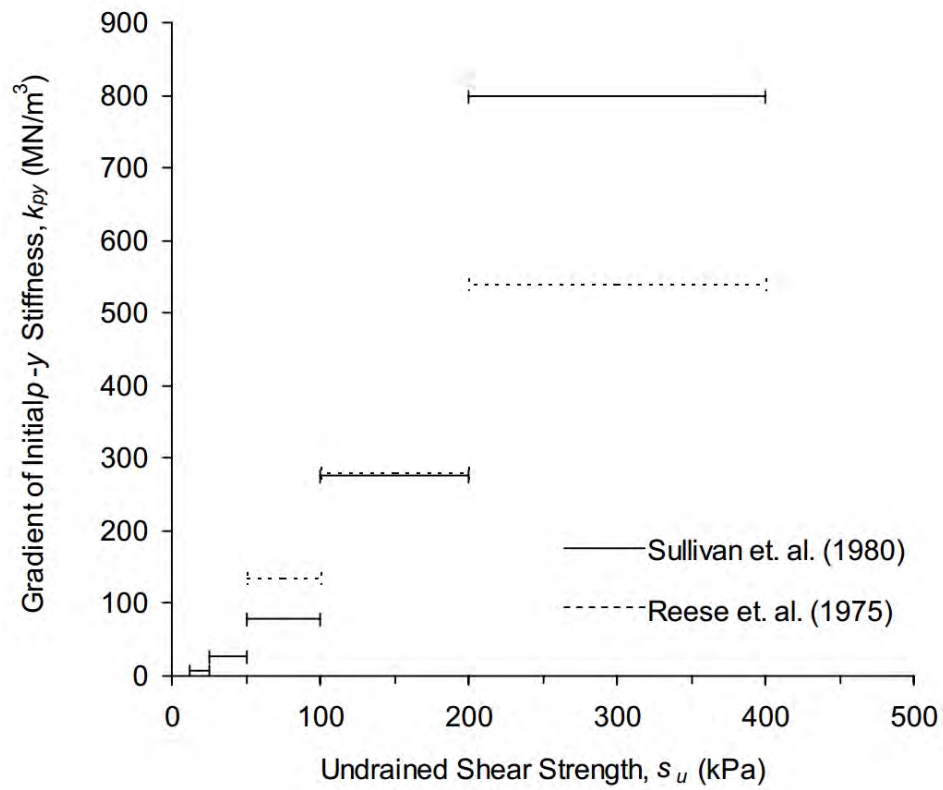


Figure 8.2: Typical k_{py} values for clays (after Dodds and Martin 2007).

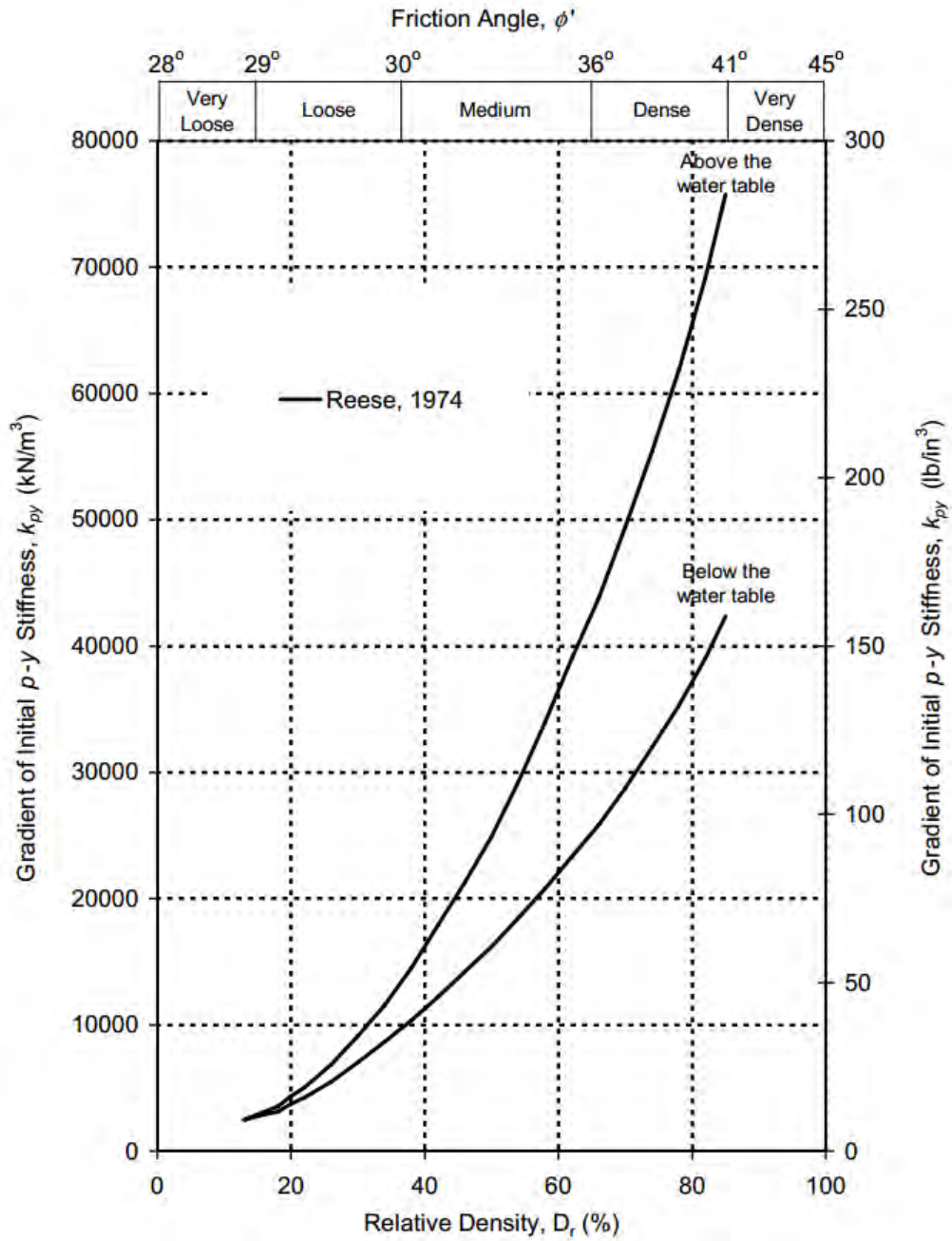


Figure 8.3: Typical k_{py} values for sands (after Dodds and Martin 2007).

8.1.2: DESIGN PREDICTIONS VS. OBSERVED BEHAVIOR

An LPILE analysis was conducted using the proposed long-term guidelines for the Lymon C. Reese research wall in Manor, Texas. Although the test wall had a design height of 15 feet, and an as-built height of 14 feet at the end of excavation, soil erosion into the base of the excavation during large storm events resulted in a final excavation depth of approximately 13.5 feet below ground surface. The small reduction in excavation depth corresponds to a reduction in earth pressure (lower cantilever height) and slightly stiffer response in the foundation soil (additional overburden pressure). Input parameters for the design LPILE analysis are provided in Table 8.1.

Table 8.1: Baseline assumptions and design parameters for LPILE analysis using proposed long-term design guidelines.

Parameter	Value
Effective Unit Weight of Soil, γ	62.6 pcf
Earth Pressure Loading Above Excavation	Fully Softened ($\phi = 24$) + Hydrostatic
Friction Angle of Foundation Soil	24 degrees
Foundation Soil p-y Curves	Sand (Reese)
Non-Default Initial Stiffness, k_{py}	375 lb/in ³
Cracking Moment, M_{Cr}	680 k-in.
Yielding Moment, M_y	3,200 k-in.
Uncracked Bending Stiffness, EI_{uc}	67 x 10 ⁶ k-in.
Cracked Bending Stiffness, EI_{cr}	18 x 10 ⁶ k-in.
Shaft Diameter	24 in.
Height of Retained Soil, H	162 in.
Reinforcement	12 #7 bars (1.6% of gross area)

Using the proposed guidelines, the predicted maximum top-of-wall deflection is approximately 5.5 inches, and the predicted maximum bending moment is approximately 2,200 in-kips (Figure 8.5). After a total of two controlled inundation cycles over a period of approximately 1.5 years, the test wall reached equilibrium at a top-of-wall deflection of approximately 4.2 inches since the installation of shotcrete facing (5.2 inches total since shaft installation). The measured maximum bending moment was approximately 1,800 in-kips since facing installation (2,100 in-kips total). Comparisons of measured and predicted values of deflection and bending moment are provided in Figure 8.4 and Figure 8.5. Comparisons of measured and predicted soil reaction forces and p-y curves using the proposed long-term design guidelines are presented in Figure 8.6 and Figure 8.7.

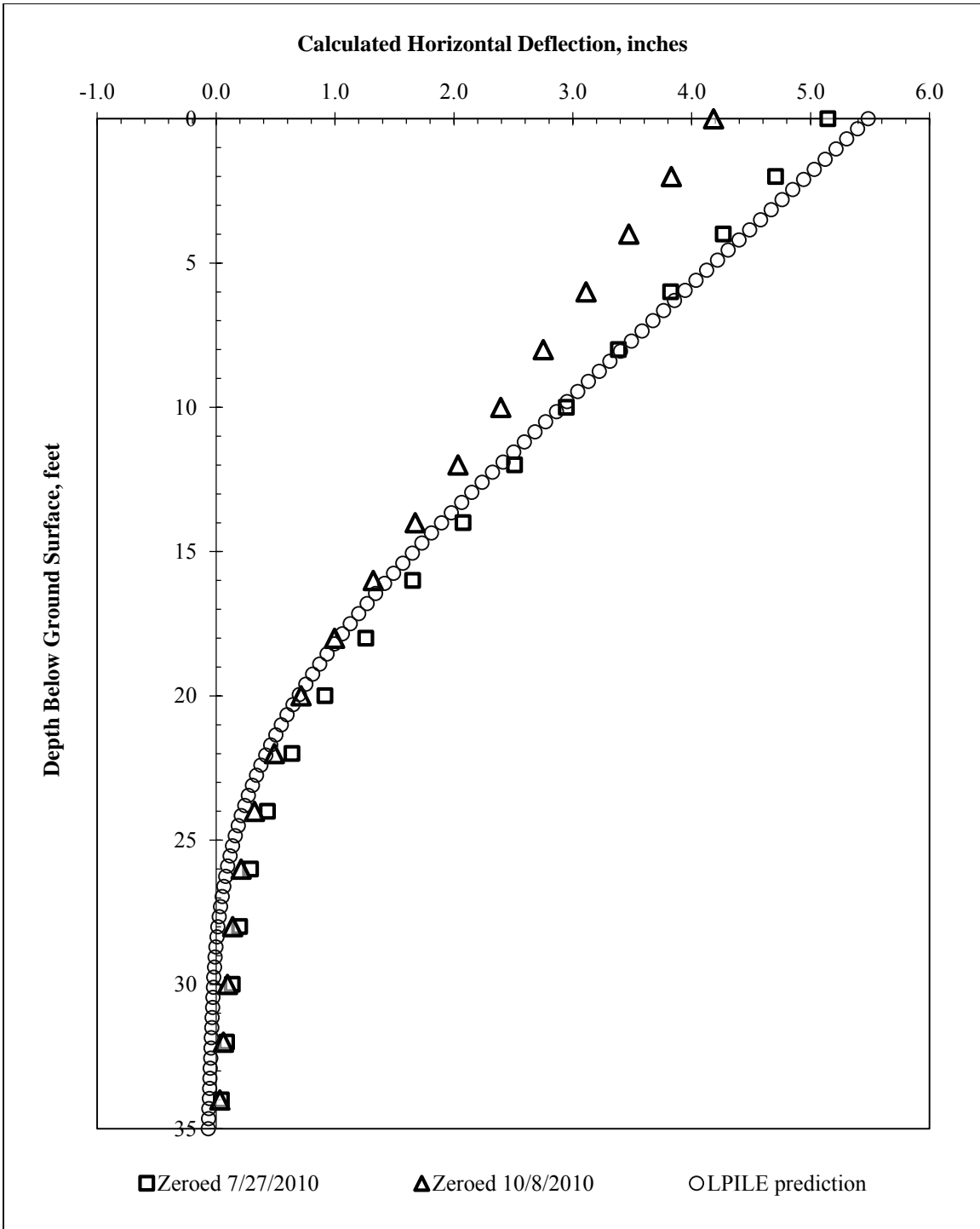


Figure 8.4: Summary of measured and predicted values of deflected shapes using long-term design guidelines.

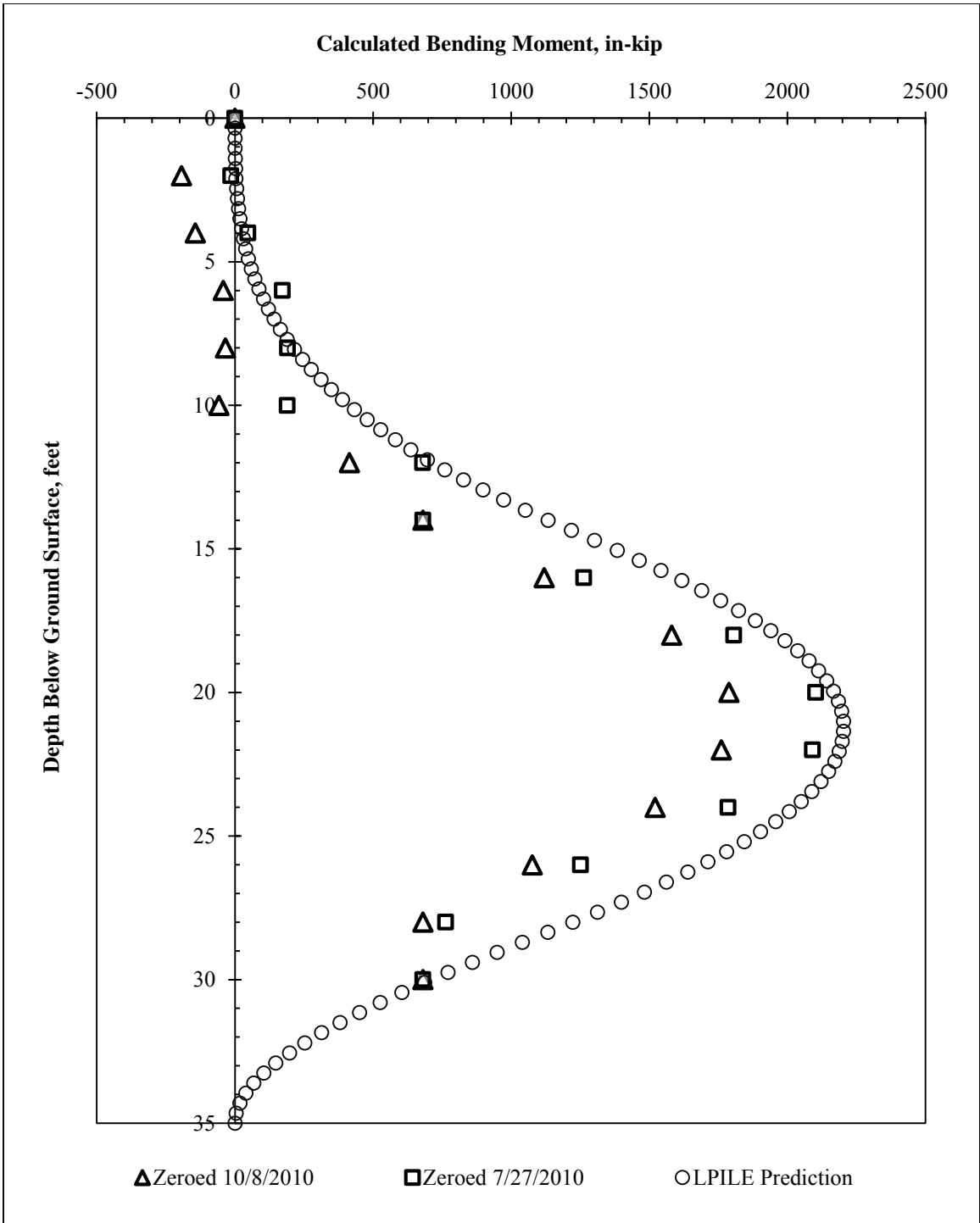


Figure 8.5: Summary of measured and predicted bending moments using long-term design guidelines.

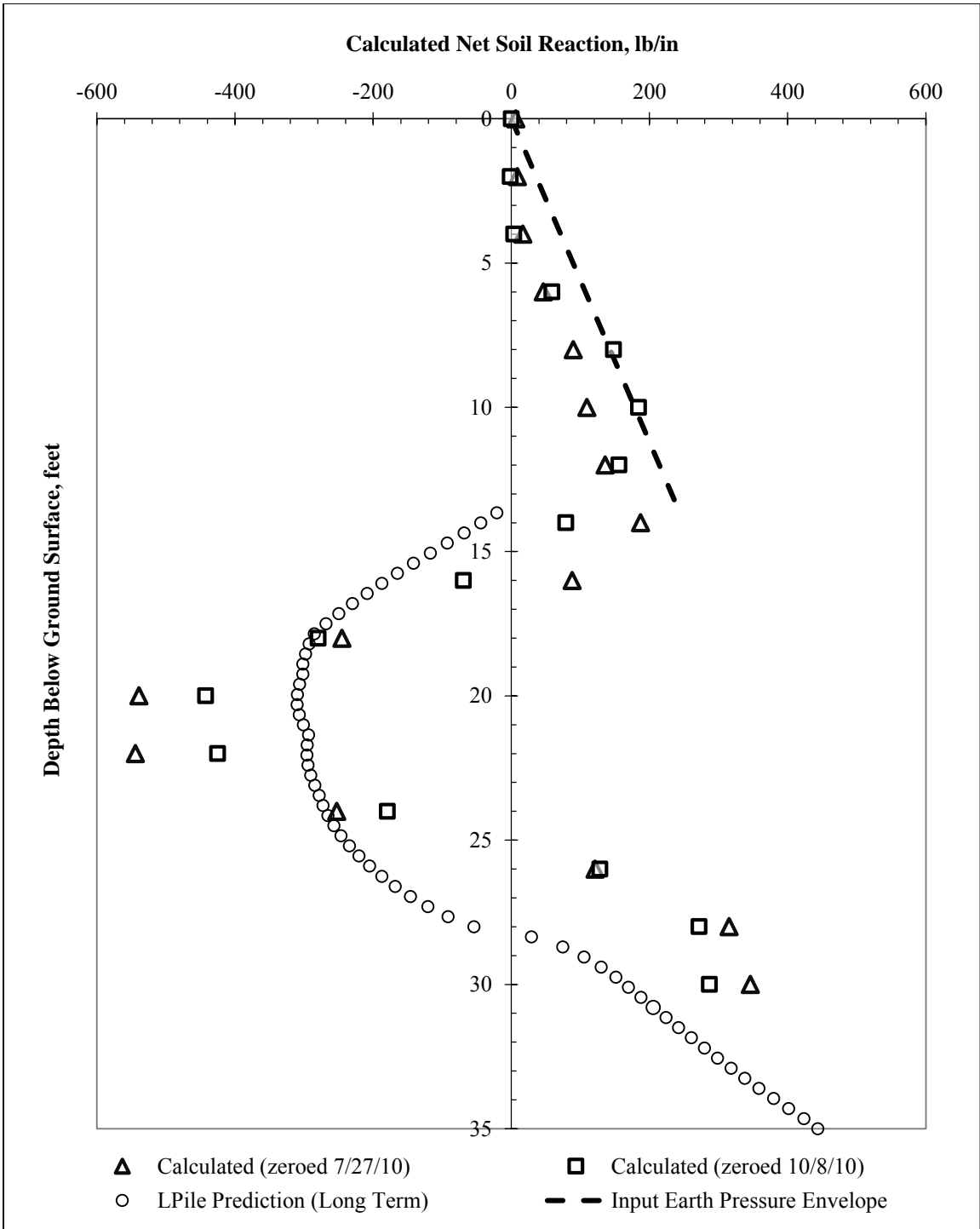


Figure 8.6: Comparison of Long-Term Modified LPILE Prediction and Calculated Soil Reaction Forces.

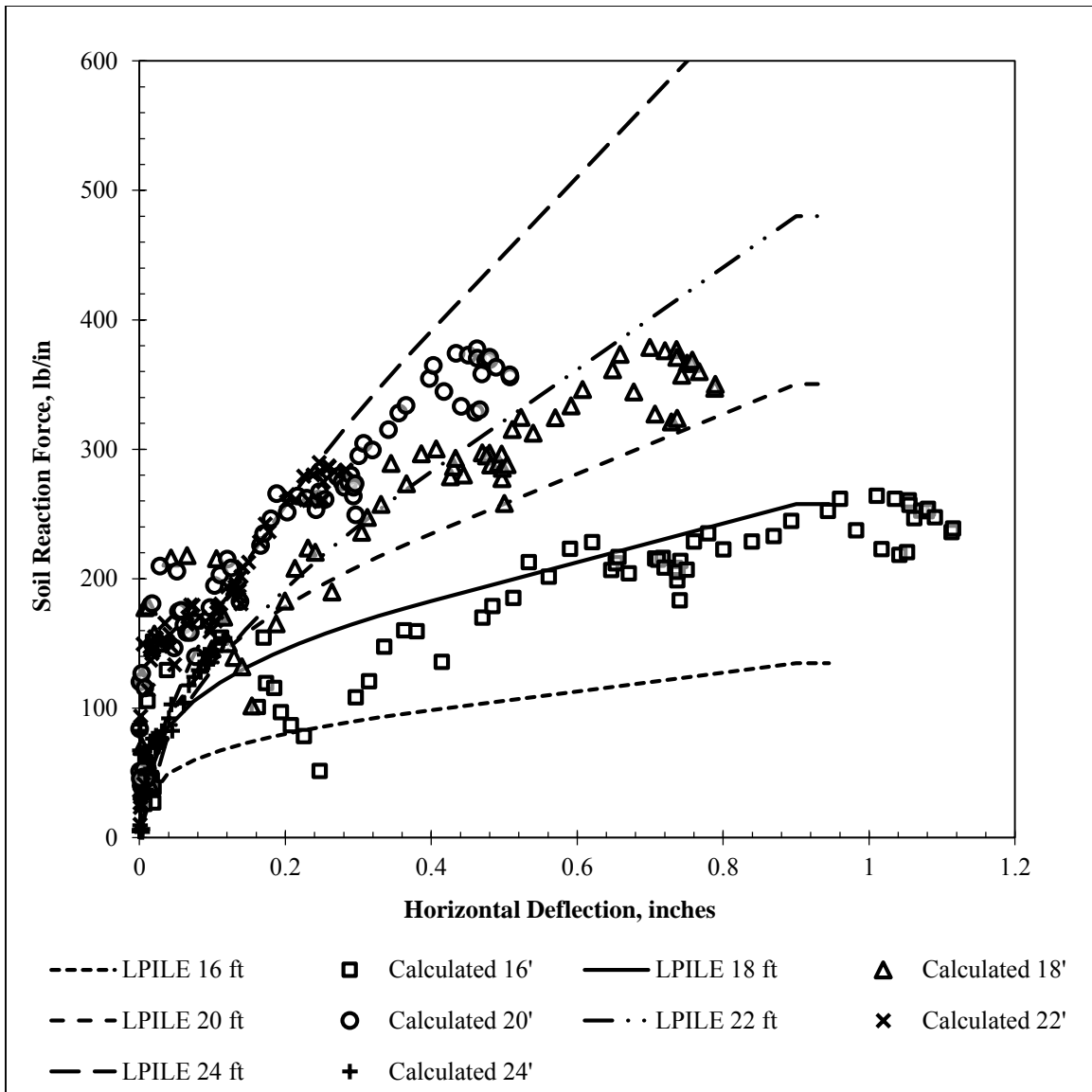


Figure 8.7: Comparison of long-term p-y curves predicted by modified LPILE analysis with p-y curves estimated from field data (reference survey is after installation of shotcrete facing on October 8, 2010).

8.1.3: HYPOTHETICAL TEST WALL REDESIGN USING FULLY SOFTENED STRENGTHS AND HYDROSTATIC PRESSURES FROM NATURAL WATER TABLE

To illustrate the impact of the proposed design guidelines on potential wall design, a simple LPILE design analysis was constructed for the test wall in its wettest state prior

to inundation, with the excavation height at the design value of 15 feet. The input earth pressure envelope was defined by the development of fully softened strengths above and below the water table, with hydrostatic pressures acting on the wall below the natural water table location of 8 feet below ground surface. The purpose of this analysis was to illustrate what design changes would need to be made to ensure the test wall met TxDOT's base fixity and top-of-wall deflection requirements. The input earth pressures for this analysis are summarized in Figure 8.8. Under these conditions, the as-built test wall design deflected approximately 4.2 inches (Figure 8.9). In order to achieve TxDOT's fixity and deflection requirements, the shaft embedment had to be increased from 20 feet to 30 feet, the shaft diameter increased from 24 inches to 30 inches, and the reinforcement upgraded from 12 #7 rebar to 12 #8 rebar to maintain an appropriate steel percentage in the shaft (center-to-center spacing remained 30"). The increase in shaft dimensions led to a reduction in top-of-wall deflections from approximately 4.2 inches using the test wall design to approximately 1.6 inches using the hypothetical increased shaft dimensions, which is within allowable values for TxDOT. Despite the significantly different values of top-of-wall deflection, maximum bending moments were similar between the two shafts. This brief example illustrates one potential implication of the proposed design guidelines. Because the proposed p-y relationships for the foundation soil are softer than the commonly accepted relationships used in design, shaft diameter and/or embedment depths may need to increase to ensure that base fixity is achieved and top-of-wall deflections remain within allowable values.

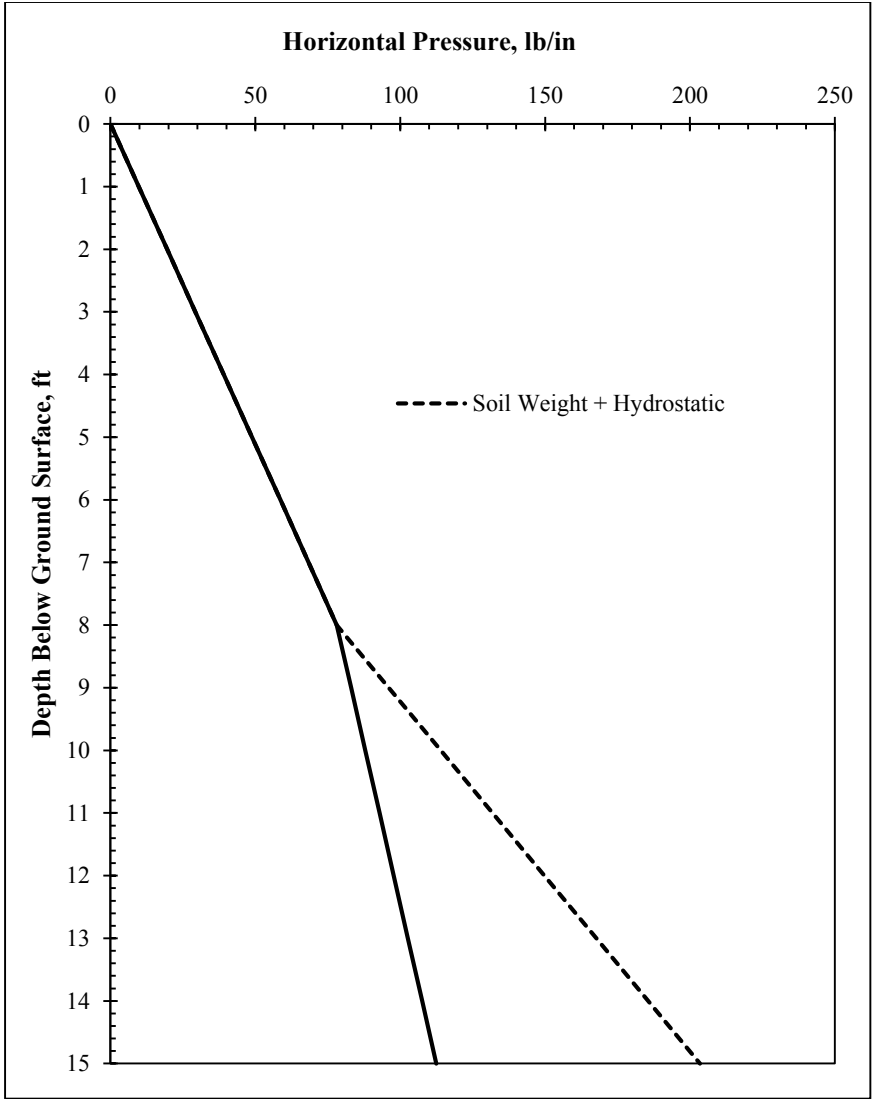


Figure 8.8: Input earth pressure envelope for wettest test wall conditions prior to inundation testing (natural groundwater table at 8 feet below ground surface).

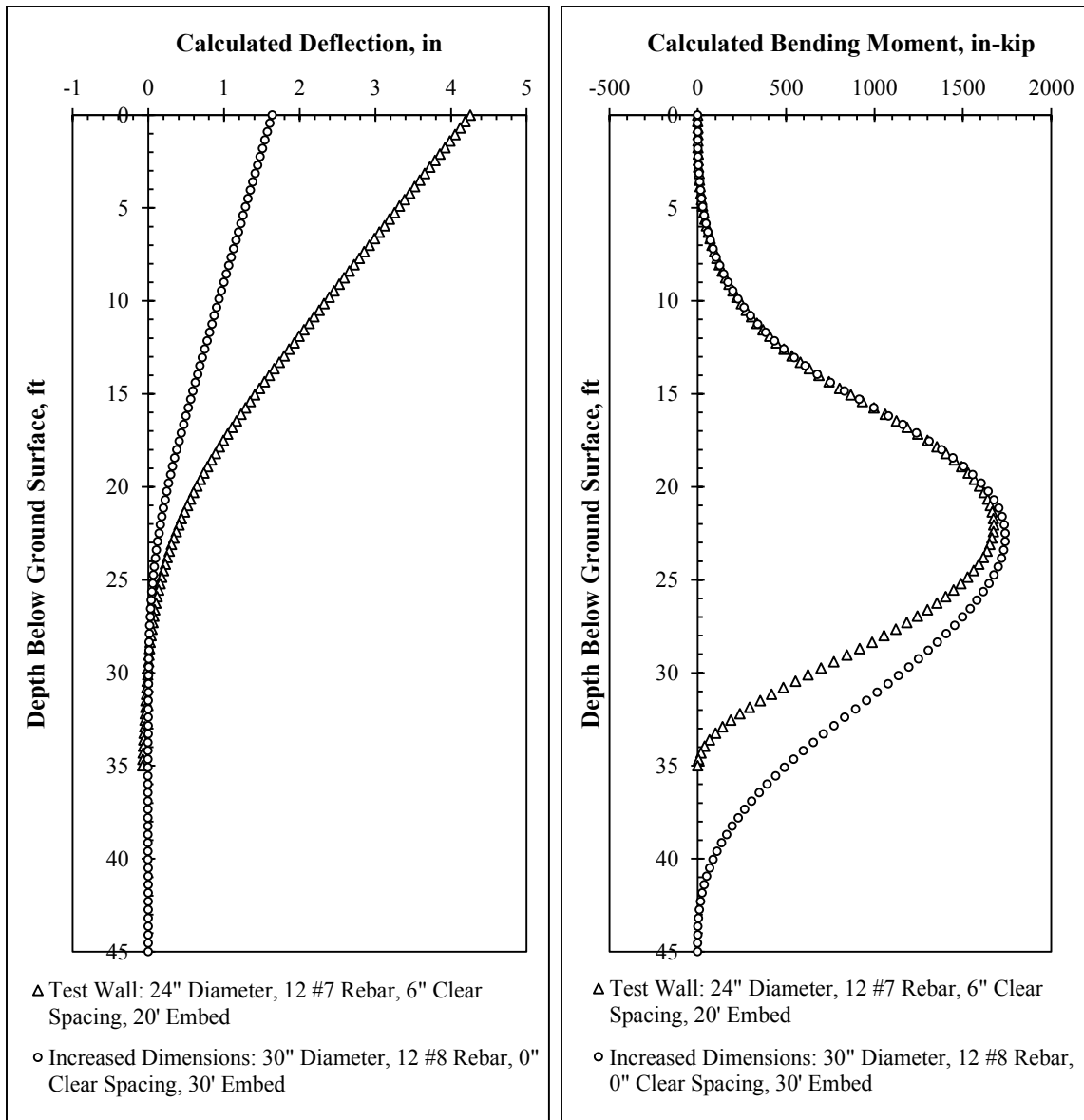


Figure 8.9: Comparison of deflected shapes and bending moments for hypothetical test wall redesign using proposed long-term conditions.

8.2: Short-Term Design Guidelines

The short-term behavior of the wall in response to excavation is dominated by global deformations of the soil-shaft system in response to stress relief. These global deformations cannot be easily represented with a p-y analysis. To check short-term

response when the soil is excavated, the use of two-dimensional finite element modeling is recommended. At small strains, the use of simple linear elastic constitutive models is sufficient to gain an understanding of the nature of the expected global deformations.

The choice of finite element model parameters is highly dependent on local soil conditions and experience, but it is recommended that anisotropy due to high in-situ lateral stresses and stiffness reductions due to unloading are incorporated. In highly overconsolidated, stiff-fissured clays, values of K_o between 2 and 3 are commonly reported (e.g. Cripps and Taylor 1981, Smith et. al. 2009). To account for the high ratio of horizontal to vertical stress, it is recommended that finite element models incorporate anisotropic conditions consistent with the expected field values of K_o . During excavation, significant stiffness reductions due to unloading were observed. While in-situ values of Young's Modulus (E) are commonly estimated to be 1000 times the measured undrained shear strength, stiffness reductions of 60 to 90 percent, corresponding to E/S_u ratios of between 100 and 400, were required to approximate the behavior of the test wall. The reduced values of Young's modulus for the test wall are consistent with the general observation that stiff-fissured clays experience significant stiffness reductions during and after unloading (e.g. Cripps and Taylor 1981). Results of finite element model for the Lymon C. Reese research wall are presented in Figure 8.10.

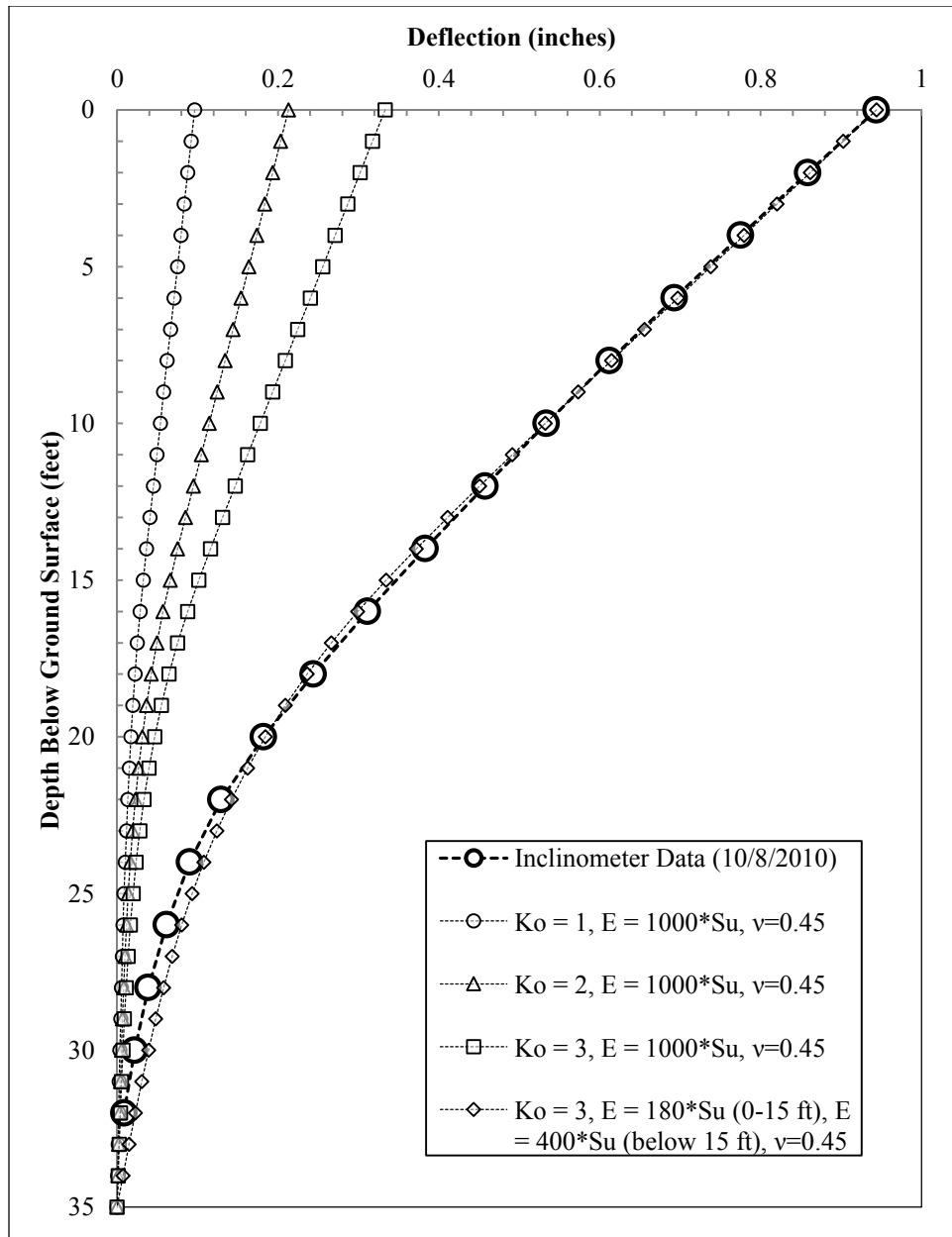


Figure 8.10: Comparison of measured data with predictions from linear elastic finite element model including anisotropy and stiffness reductions.

8.3: Summary and Conclusions

Based on design analysis of the proposed guidelines, some conclusions can be drawn:

- Wall behavior is dominated by the long-term development of fully softened, drained conditions in both the retained soil and the foundation soil, which can be modeled with a p-y analysis.
- Short-term deformations during excavation are primarily due to global deformations of the soil-shaft system in response to stress relief. Prediction of short-term deformations is difficult, but the use of two-dimensional finite element modeling with anisotropic in-situ stresses and stiffness reductions can provide some insight.
- The use of drained p-y curves based on the fully softened, drained friction angle of the clay are recommended for long-term p-y analysis. Non-default values of initial stiffness (k_{py}), based on the original measured profile of undrained shear strength, are recommended to account for the initial transition from undrained to drained behavior.
- The proposed design guidelines slightly over-predict both bending moment and top-of-wall deflections induced by excavation and controlled inundation of our full-scale test wall. Based on the results of our monitoring program, walls designed for structural stability using the proposed guidelines will be adequate for use in expansive clay soils.
- Because of the influence of pavement and drainage systems, the proposed long-term design guidelines represent a worst-case scenario that is unlikely to exist for an extended time in the field. As a result, it may not be necessary for all walls to design for hydrostatic pressures. Should such a condition develop and remain for a long period of time, wall deflections could potentially exceed tolerable values as the soil approaches fully softened conditions with hydrostatic pressures, but structural loads would remain within acceptable limits.

- Beyond the typical formulation of lateral earth pressures, global movements of the soil-shaft system have been recorded in our test wall (e.g. global elastic response to stress relief during excavation, expansive soil volume change). Because the wall is not as severely stressed by these global movements (the soil and wall move together), top-of-wall deflections can fluctuate without a corresponding increase in bending moment or calculated earth pressures.
- Because the fully softened response of the foundation soil is relatively weak, the top-of-wall deflections predicted by the proposed design guidelines are sensitive to small changes in unit weight, wall geometry, and input earth pressure loading. The predicted values of bending moment are much less sensitive to changes in input values. For this reason, it is recommended that moment capacity, rather than top-of-wall deflection, be emphasized in design.

CHAPTER 9: CONCLUSIONS AND RECOMMENDATIONS

9.1: Overview

This chapter presents brief summaries of the key findings from each chapter of this research study. The original objectives of the research study are revisited, along with summaries of the research findings for each item. Finally, brief recommendations for future research and similar projects are provided.

9.2: Summary of Research Study

9.2.1: INSTRUMENTATION PROGRAM

9.2.1.a: Structural Performance of Drilled Shafts

In general, for monitoring the long-term effects of soil moisture on the test wall, inclinometer data was a more consistent indicator of wall behavior than strain gauge data. The direct use of strain gauge data for the determination of bending curvature generally requires more advanced data interpretation than simply taking the first derivative of rotation profiles measured from inclinometer data. Although the precision and resolution of strain gauges is vastly superior to that of an inclinometer, the strain gauges represent the behavior of individual, discrete locations in the shaft. While extrapolating the behavior of individual strain gauges to the entire pile is relatively simple for a short-term lateral load test, for long-term monitoring, inclinometer data provides a more consistent and reliable picture of what is going on in the shaft without the need for subjective data interpretation. After combining rotation profiles from the three instrumented shafts, piecewise polynomial differentiation was used with numerical smoothing methods to approximate p-y curves from inclinometer data at the test wall.

For future studies, or larger scale studies involving several walls, inclinometer data provides a relatively inexpensive, effective, and robust method of performance monitoring. In the test wall, strain gauge data was affected by a number of factors beyond simple lateral loading of the structure, making data interpretation a complex and subjective task. While strain gauges are useful for short-term monitoring, they may not have the long-term stability and consistency of inclinometer data.

9.2.1.b: Soil Moisture Monitoring

For the Lymon C. Reese research wall, the most reliable moisture data came from physical measurements of samples obtained with a hand auger. The use of Time Domain Reflectometry (TDR) probes to measure moisture content in expansive clay is problematic because of the soil's high electrical conductivity and tendency to pull back from the probe rods during drying cycles. However, electrical conductivity measurements from one TDR probe appear to correlate with moisture contents and top-of-wall deflections. While the electrical conductivity data cannot be directly related to moisture content, it can provide a qualitative indicator of the moisture conditions on the project site. If accurate measurements of moisture content in expansive clay are of high importance, laboratory measurement of soil moisture content is recommended.

9.2.2: BEHAVIOR BEFORE EXCAVATION

Between shaft construction and excavation, a combination of concrete curing and expansive soil movement led to the development of residual stresses and strains, and evidence of tension cracks developed throughout the shafts. While there are no lateral loads placed on the shafts prior to excavation, the residual stresses and strains developed during this time affect strain gauge data interpretation and the shafts' response to excavation.

9.2.3: BEHAVIOR DURING EXCAVATION

During excavation of the Lymon C. Reese research wall, the soil and wall responded immediately to the relief of stress, leading to wall deformations without the development of large earth pressures. This immediate response is a global movement of the soil-shaft system that extends beyond the shaft base. In the test wall, these global movements resulted in a top-of-wall deflection of approximately 0.5 percent of the cantilever height. Because these movements represent large-scale strains in response to stress relief, they cannot be easily modeled with a traditional lateral earth pressure envelope. The use of more advanced prediction methods, such as finite element modeling, can provide estimates of the quality of these deformations.

9.2.4: BEHAVIOR DURING NATURAL MOISTURE CYCLES

9.2.4.a: Response to Moisture Fluctuations

Deformations and structural loads in the test wall were affected by moisture conditions on the project site. The test wall's deflection and structural loads were clearly affected by moisture conditions on the project site. During wetting, water infiltrated quickly through the clay fissures; as the retained soil and excavation base had access to moisture, top-of-wall deflections increased. Similarly, during prolonged periods of drying, top-of-wall deflections decreased. While this suggests volume change in expansive soil does play a part in wall deformations, no evidence of extremely high earth pressures or excessive structural loads on the shaft was observed. More importantly, access to moisture allowed negative pore pressures in the soil to dissipate, and volume change allowed the soil to approach a fully softened condition. At the conclusion of approximately 22 months of natural moisture cycles, total top-of-wall deflections since shaft construction had

increased to approximately 0.09 percent of the wall height (approximately 0.04 percent since the installation of shotcrete facing in October 2010).

9.2.4.b: Thermal Strains and Bending Curvatures

Daily and seasonal cycles of temperature fluctuation lead to the development of thermal strains which can influence data interpretation. If the climatic conditions on survey dates are substantially different, bending curvatures induced by daily temperature differences can be mistaken for bending moments caused by changes in earth pressure. The test wall experiences an average daily temperature fluctuation of approximately 22 degrees Fahrenheit, which corresponds to a daily variation in top-of-wall deflection of approximately 0.05 to 0.1 inches (0.03% to 0.06% of the cantilever height). Daily temperature fluctuations as high as 48 degrees have been recorded at the test site.

Because thermal deformations in the wall are generally consistent from day to day, difficult to model without detailed weather data, and their effect on wall behavior is relatively small, large-scale corrections to the data set for temperature effects are generally not practical. However, if isolated surveys with unusual deflection, rotation, or bending curvatures are observed in the data, an investigation into thermal effects is recommended.

9.2.5: BEHAVIOR DURING CONTROLLED INUNDATION TESTING

During controlled inundation testing of the test wall, wall behavior was governed by the development of fully softened, drained conditions in both the retained soil and foundation soil. As inundation testing began, water infiltrated quickly into the soil fissures, first appearing in the excavation 30 minutes after the test began. As inundation testing continued over a period of approximately 14 months (6 months with water impounded, 8 months without), total top-of-wall deflections increased to a maximum of approximately 2.9 percent of the wall height. As wall deflections reached their maximum value, water

levels in stand pipe piezometers throughout the inundation zone had stabilized near the ground surface. Moisture contents had increased by an average of 5 to 10 percentage points in the active zone above the groundwater table. Despite continued access to moisture, no evidence of expansive soil damage or earth pressures greater than the envelope defined by the soil's fully softened strength with hydrostatic pressures were observed.

The soil conditions at the conclusion of the inundation test can be approximated with a simple p-y analysis. The earth pressure envelope is defined using fully softened, drained strength parameters for the retained soil, and hydrostatic conditions with the water table at ground surface. For the foundation soil, p-y curves are defined using drained, fully softened strength parameters, with initial stiffness defined by the original measured profile of undrained strength (this implicitly accounts for the transition from undrained to drained behavior with time and moisture cycles). The long-term behavior of the Manor test wall can be reasonably approximated in LPILE using these parameters with the final as-built dimensions of the wall and excavation. Predicted values of deflections, bending moments, and p-y curves are consistent with those measured in the field.

9.2.6: DEVELOPMENT OF DESIGN GUIDELINES

The behavior of the Manor, Texas test wall can be defined by two distinct stages of wall movement: short-term deformations during excavation and long-term deformations after cycles of wetting and drying. Short- and long-term effects should be combined to check final design deflections and bending moments.

9.2.6.a: Long Term Behavior After Cycles of Wetting and Drying

Long term behavior can be represented in p-y analysis programs such as LPILE using drained, fully softened strength parameters for the retained and foundation soil. Hydrostatic pressures with the water table at a reasonable maximum level is added to the

input earth pressure envelope. In the foundation soil, the initial stiffness of the p-y curves is defined using the original profile of undrained shear strength and established relationships between S_u and k_{py} (e.g. Reese et. al. 1975, Sullivan et. al. 1980). This implicitly accounts for the transition from undrained to drained behavior in the foundation soils.

9.2.6.b: Short-Term Behavior During Excavation

During excavation, the motion of the wall is governed by global response to stress relief. For the Manor test wall, a linear elastic finite element analysis using K_o values between 2 and 3, and E/S_u ratios between 100 and 400, provides a reasonable approximation of the observed behavior during excavation. Values of E/S_u are significantly lower than those measured during SASW testing on the project site, which may be attributable to the presence of fissures and the effects of stress relief. While further study is required to generalize design guidelines, for highly overconsolidated, expansive soils, an analysis using a two-dimensional linear elastic finite element model with anisotropic in situ stresses and stiffness reductions due to unloading is recommended.

9.3: Conclusions of Research Study

The goal of this research study is to advance our understanding of the long-term behavior of retaining structures in expansive clays. The observed performance and instrumentation data from our test wall are used to address the following objectives:

1. Identify and analyze the processes responsible for wall loading and deformation.
2. Evaluate how these processes change with time and moisture cycles.
3. Provide guidance for design practice to account for these processes and ensure adequate wall performance.

Based on the test wall monitoring and analysis program, conclusions of this research study include:

1. During excavation, wall behavior is governed by global deformations in response to stress relief. During seasonal cycles of wetting and drying, wall behavior was governed by volume change of the retained soil (during wetting and drying) and softening of both the retained soil and the foundation soil (during wetting). During controlled inundation testing, wall behavior is primarily influenced by the development of fully softened, drained conditions in both the retained soil and foundation soil.
2. During excavation, short-term deformations occur almost immediately in response to stress relief. During seasonal moisture cycles, lateral earth pressure and wall deflections decrease slowly in response to drying, and relatively quickly during wetting. During controlled inundation testing, fissures in the retained soil provide preferential pathways for moisture flow, and surface water moves through the soil within minutes. Wall deflections, bending moments, and water levels in stand pipe piezometers stabilized after surface water was present for a total of approximately six months.
3. The behavior of retaining walls in expansive clay can be represented by a combination of short- and long-term deformations in design. The long-term development of drained, fully softened conditions leads to the majority of deformations and structural loads.
 - a. To estimate long-term response, a p-y analysis using drained, fully softened strength parameters for both the retained soil and foundation soil is recommended. Above the excavation line, hydrostatic pressures with the water table at a maximum reasonable level behind the wall are included.

The use of non-default values of initial stiffness (k_{py}) defined by the original measured profile of undrained shear strength is recommended to account for the transition from stiff, undrained conditions to fully softened, drained conditions.

- b. To estimate short-term response, a simple two-dimensional finite element analysis to model the effects of stress relief during excavation is recommended. Selection of finite element model parameters is highly dependent on experience and the soil conditions on the project site, but incorporating anisotropy due to high in-situ lateral stresses and stiffness reductions due to unloading is recommended.

9.4: Recommendations for Future Work

The Lymon C. Reese research wall has provided insight on the behavior of a single drilled shaft retaining wall constructed through expansive clay. While some generalizations can be made, more thorough study of real-world walls is necessary to develop a complete understanding and framework for design. Inclinator casings installed in future walls, with deflection profiles recorded at key dates or automated readings from an in-place unit, would provide an inexpensive and effective way to both verify the performance of existing walls and enhance the theoretical understanding of wall behavior. Additionally, a study of the behavior of a wall constructed during an extremely dry period would be of interest, to assess if initial soil moisture content at construction has any impact on wall behavior.

To minimize the local effects of concrete heterogeneity and tension cracking, future instrumented walls using strain gauges could consider further isolating the gauges from direct contact with the concrete. An early suggestion for the Manor test wall, which

ultimately proved too expensive to implement, was attaching all the strain gauges to the interior of a steel pipe running the length of a drilled shaft. The pipe would then be surrounded by concrete to cast it into place, creating a system with similar moment-curvature behavior to a typical drilled shaft, but without the micro-scale effects of concrete behavior causing difficulty in strain data interpretation. This method would completely isolate the gauges from contacting the concrete, which was a major source of error in the test wall's strain data. While this method may provide some improvement in strain data quality, it could substantially increase expense over the sister bars used for the Manor test wall.

References

- Adil Haque, M. and Bryant, J. T. (2011). Failure of VERT Wall System: Forensic Evaluation and Lesson Learned. *Geo-Frontiers 2011: Advances in Geotechnical Engineering* , 3487-3496.
- Brown, A. C., Ellis, T., Dellinger, G., El-Mohtar, C., Zornberg, J., & Gilbert, R. B. (2011). "Long-term monitoring of a drilled shaft retaining wall in expansive clay: Behavior before and during excavation". *Geo-Frontiers 2011*, ASCE.
- Brown, A. C., Dellinger, G. F., & Gilbert, R. B. (2011). Long-Term Performance of Drilled Shaft Retaining Walls: Assessment of Existing Walls. Research Report FHWA/TX-11/0-6603-1. Center for Transportation Research. University of Texas at Austin.
- Cripps, J. C., and Taylor, R K. (1981). The Engineering Properties of Mudrocks. *Quarterly Journal of Engineering Geology*, Vol. 14, 325–346.
- Dellinger, G. (2011). The Use of Time Domain Reflectometry Probes for Moisture Monitoring of a Drilled Shaft Retaining Wall in Expansive Clay. M.S. Thesis, The University of Texas at Austin.
- Dodds, Andrew M. and Martin, Geoffrey R. (2007). Modeling Pile Behavior in Large Pile Groups under Lateral Loading. Technical Report MCEER-07-0004. Multidisciplinary Center for Earthquake Engineering Research
- Ellis, Trent. (2011). A Subsurface Investigation in Taylor Clay. Master's Thesis, The University of Texas at Austin.
- Fellenius, Bengt H., Sung-Ryul Kim, Sung-Gyo Chung (2009). "Long-Term Monitoring of Strain in Instrumented Piles." *Journal of Geotechnical and Geoenvironmental Engineering*, Vol. 135, No. 11, November 2009, pp. 1583-1595.
- Fuhr, Peter L., Dryver R. Huston, Timothy P. Ambrose, and Darrell M. Snyder. (1993). "Stress Monitoring of Concrete Using Embedded Optical Fiber Sensors." *J. Struct. Engrg.* 119, 2263.
- Google Inc. (2011). Google Earth (Version 6.0.3.2197) [Software]. Available from <http://www.google.com/earth/download/ge/agree.html>.
- Hong, Gyeong Taek. (2008). Earth Pressures and Deformations in Civil Infrastructure in Expansive Soils. Ph.D. dissertation, Texas A&M University.
- Kim, Myung Hak and Michael W. O'Neill. (1998). Side Shear Induced in Drilled Shaft by Suction Change." *J. Geotech. and Geoenviron. Engrg.* 124, 771.
- Koutrouvelis, Iraklis. (2012). Earth Pressures Applied on Drilled Shaft Retaining Walls in Expansive Clay during Cycles of Moisture Fluctuation. Master's Thesis, The University of Texas at Austin.

- Lytton, R. (2007, December 12). Design of Structures to Resist the Pressures and Movements of Expansive Soils. Texas A&M University.
- P. K. Ooi and T. L. Ramsey. (2003). "Curvature and Bending Moments from Inclinator Data". International Journal of Geomechanics, ASCE.
- Pufahl, D., Fredlund, D., and Rahardjo, H. (1983). Lateral earth pressures in expansive clay soils. Canadian Geotechnical Journal, 20, 228-241.
- Puppala, A. J., Wejrungsikul, T., Willammee, R. S., Witherspoon, T. and Hoyos, L. (2011). Design of Inclined Loaded Drilled Shaft in High-Plasticity Clay Environment. Technical Report 0-6146-1. Department of Civing Engineering. University of Texas at Arlington.
- Quantdec (2004). "Smoothing." Quantitative Decisions, Inc. Online resource, available from <http://www.quantdec.com/Excel/smoothing.htm>.
- Reese, L. C., Cox, W. R., and Koop, F. D. (1974). Analysis of laterally loaded piles in sand. Sixth Annual Offshore Technology Conference, Paper No. 2080, OTC, Houston, Texas, 473-483.
- Reese, L. C., Cox, W. R., and Koop, F. D. (1975). Field testing and analysis of laterally loaded piles in stiff clay. Seventh Annual Offshore Technology Conference, Paper No. 2312, OTC, Houston, Texas, 671-690.
- Reese, L. C., Isenhower, W. M. & Wang, S.-T. (2006). Analysis and design of shallow and deep foundations. John Wiley & Sons, Inc.
- Reese, L. C. & Van Impe, W. F. (2001). Single piles and pile groups under lateral loadings. A. A. Balkema, Rotterdam.
- Skempton, A. W. (1977). "Slope stability of cuttings in brown London clay." Proceedings, Ninth International Conference on Soil Mechanics and Foundation Engineering, Tokyo, Vol. 3, pp. 261-270.
- Smith, R. E., Smith, D. L., Griffin, J. A. (2009). Top-Down Construction of a Bridge in Clay Shale. American Society of Civil Engineers Conference Proceedings. 337, 76, 598-605.
- Snethen, D. R., Townsend, F. C., Johnson, L. D., Patrick, D. M., Vedros, P. J. (1975). A review of Engineering Experiences with Expansive Soils in Highway Subgrades. Soil Mechanics Division, Soils and Pavements Laboratory. U.S. Engineering Waterways Experiment Station.
- Sullivan, W. R., Reese, L. C., and Fenske, C. W. (1980). "Unified method for analysis of laterally loaded piles in clay." Numerical Methods in Offshore Piling Conference, May 1979. Institution of Civil Engineers, London, 135-146.

- Stark, T. D., Choi, H., and McCone, S. (2005). "Drained shear strength parameters for Analysis of landslides." *Journal of Geotechnical and Geoenvironmental Engineering*, ASCE, Vol. 131, No. 5, May, 2005, pp. 575–588.
- Thomas, M. G., Puppala, A. J., Hoyos, L. R. (2009). Influence of Swell Pressure From Expansive Fill on Retaining Wall Stability. *American Society of Civil Engineers Conference Proceedings*. 337, 75, 590-597.
- Tukey, J. W. (1977). *Exploratory Data Analysis*. Addison-Wesley, Reading, MA.
- TxDOT (2009). *Cantilver Drilled Shaft Wall Design*.
- TxDOT Geotechnical Manual. (2012). Texas Department of Transportation, Bridge Division, Austin, Texas.
- Vipulanandan, C., Josph, D. (2011). Seasonal Moisture Fluctuation in the Active Zone in a Humid-Subtropical Climate. *Geo-Frontiers 2011: Advances in Geotechnical Engineering*, 2759-2767.
- Wang, Shintower and Reese, Lymon C. (1986). Study of design method for vertical drilled shaft retaining walls. Research Report 415-2F. Center for Transportation Research, Bureau of Engineering Research. University of Texas at Austin.
- Weather Underground (2013). <http://www.wunderground.com/>.
- Welch, R. C., and Reese, L. C. (1972). Laterally loaded behavior of drilled shafts. Research Report 3-5-65-89. Center for Highway Research, University of Texas at Austin.
- Wise, J. R. and Hudson, W. R.. (1971). An Examination of Expansive Clay Problems in Texas. Research Report 118-5. Center for Highway Research, University of Texas at Austin.
- Wright, S. G.. (2005). "Evaluation of Soil Shear Strengths for Slope and Retaining Wall Stability Analyses with Emphasis on High Plasticity Clays." Project No. 5-1874-01. Center for Transportation Research, The University of Texas at Austin.
- Wright, S. G., Zornberg, J. G., and Aguetant, J. E.. (2007). "The Fully Softened Shear Strength of High Plasticity Clays." Report No. FHWA/TX-07/0-5202-3. Center for Transportation Research, The University of Texas at Austin.

Vita

Andrew Charles Brown graduated from Dripping Springs High School in Dripping Springs, Texas in May, 2004. He received his Bachelor of Science in Civil Engineering with Honors from the University of Texas at Austin in May, 2008. In August, 2008, he began his graduate studies at the University of California, Berkeley, and received his Master of Science in Civil and Environmental Engineering in May, 2009. He began his doctoral studies at the University of Texas at Austin in August, 2009.

Permanent address: 19301 FM 150 W
Driftwood, TX 78619

This dissertation was typed by the author.